Geotechnical Engineering for the Preservation of Monuments and Historic Sites III

Edited by
Renato Lancellotta, Carlo Viggiani,
Alessandro Flora, Filomena de Silva,
and Lucia Mele

CRC Press
Taylor & Francis Group

GEOTECHNICAL ENGINEERING FOR THE PRESERVATION OF MONUMENTS AND HISTORIC SITES III

The conservation of monuments and historic sites is one of the most challenging problems facing modern civilization. It involves, in inextricable patterns, factors belonging to different fields (cultural, humanistic, social, technical, economical, administrative) and the requirements of safety and use appear to be (or often are) in conflict with the respect of the integrity of the monuments. The complexity of the subject is such that a shared frame of reference is still lacking among art historians, architects, architectural and geotechnical engineers. And while there are exemplary cases of an integral approach to each building element with its static and architectural function, as a material witness to the culture and construction techniques of the original historical period, there are still examples of uncritical reliance on modern technology leading to the substitution from earlier structures to new ones, preserving only the iconic look of the original monument. Geotechnical Engineering for the Preservation of Monuments and Historic Sites III collects the contributions to the eponymous 3rd International ISSMGE TC301 Symposium (Naples, Italy, 22–24 June 2022). The papers cover a wide range of topics, which include:

- Principles of conservation, maintenance strategies, case histories
- The knowledge: investigation, monitoring and performance
- Seismic risk, site effects, soil structure interaction
- Effects of urban development and tunnelling on built heritage
- Preservation of diffuse heritage: soil instability, subsidence, environmental damages

The present volume aims at geotechnical engineers and academics involved in the preservation of monuments and historic sites worldwide.

Taylor & Francis
Taylor & Francis Group
http://taylorandfrancis.com

PROCEEDINGS OF THE THIRD INTERNATIONAL ISSMGE TC301 SYMPOSIUM, NAPOLI, ITALY, 22–24 JUNE 2022

Geotechnical Engineering for the Preservation of Monuments and Historic Sites III

Edited by

Renato Lancellotta
Department of Structural, Geotechnical and Building Engineering
Politecnico di Torino, Turin, Italy

Carlo Viggiani, Alessandro Flora, Filomena de Silva & Lucia Mele
Department of Civil, Architectural and Environmental Engineering
University of Naples Federico II, Naples, Italy

CRC Press
Taylor & Francis Group
Boca Raton London New York Leiden

CRC Press is an imprint of the
Taylor & Francis Group, an **informa** business
A BALKEMA BOOK

CRC Press/Balkema is an imprint of the Taylor & Francis Group, an informa business

Typeset in Times New Roman by MPS Limited, Chennai, India

Library of Congress Cataloging-in-Publication Data

A catalog record has been requested for this book

First published 2022

Published by: CRC Press/Balkema
Schipholweg 107C, 2316 XC Leiden, The Netherlands
e-mail: enquiries@taylorandfrancis.com
www.routledge.com – www.taylorandfrancis.com

ISBN: 978-1-032-31262-0 (Hbk)
ISBN: 978-1-032-31265-1 (Pbk)
ISBN: 978-1-003-30886-7 (ebk)
DOI: 10.1201/9781003308867

Geotechnical Engineering for the Preservation of Monuments and Historic Sites III – Lancellotta, Viggiani, Flora, de Silva & Mele (Eds)

Table of contents

SESSION 1: Principles of conservation, maintenance strategies, case histories

SESSION 2: The knowledge: Investigation, monitoring and performance

SESSION 3: Seismic risk, site effects, soil structure interaction

SESSION 5: Preservation of diffused heritage

Taylor & Francis
Taylor & Francis Group
http://taylorandfrancis.com

Geotechnical Engineering for the Preservation of Monuments and Historic Sites III – Lancellotta, Viggiani, Flora, de Silva & Mele (Eds)

Preface

The International Symposium on the Preservation of Monuments and Historic Sites of 22-24 June 2022 in Napoli (IS NAPOLI 2022) is the third of a series, the first one having been held in 1996 and the second in 2013.

Drawing from the Preface of the latter, we underline that 'TC301 is intended to provide a forum for interchanges of ideas and discussion, to collect case histories and to promote and diffuse the culture of conservation within the geotechnical community. More specifically, it focuses on geotechnical factors affecting historic sites, monuments, cities. TC301 searches for design criteria and construction methods of our ancestors and reports on specific techniques adopted to preserve ancient sites and constructions'.

TC301 is currently supported by AGI, the Italian member society of ISSMGE, that also organized this Symposium in cooperation with the University of Napoli Federico II, and is therefore acknowledged. Special thanks are extended to the AGI Secretary, Mrs. Susanna Antonielli, for her continuous and patient assistance. We would also like to express our appreciation to the Sponsors that helped us in making this conference sustainable.

But the true success of a Symposium is determined by the quality of the scientific contributions. After a process of peer reviewing, 80 papers have been accepted to be presented to the Symposium, written by more than 300 authors coming from all over the world. In addition, an opening address, the third Kerisel Lecture, four keynote lectures and eleven panel lectures will be presented at the Conference. All the papers – including the invited ones - are freely available in open access on the publisher website. The authors are therefore deeply acknowledged for having shared their experience, ideas, proposals, to try and set forth a reference picture of the current state of practice in the engineering approach to heritage preservation. We are confident that the discussion at the Symposium will be fruitful and stimulating and will contribute to the advancement of the discipline.

The Nobel prize poetess Wyslava Syimborska, looking at the Milkmaid, the famous painting by Vermeer, wrote: 'So long as that woman from the Rijksmuseum, in painted quiet and concentration, keeps pouring milk day after day from the pitcher to the bowl, the World hasn't earned the world's end'. In a period of serious difficulties for people everywhere in the world, due to the Covid pandemic and to the fires of war, we believe that it is very important that there are people who do care about our past and its preservation.

Renato Lancellotta
Carlo Viggiani
Alessandro Flora
Filomena de Silva
Lucia Mele

Taylor & Francis
Taylor & Francis Group
http://taylorandfrancis.com

Geotechnical Engineering for the Preservation of Monuments and Historic Sites III – Lancellotta, Viggiani, Flora, de Silva & Mele (Eds)

Symposium Organizers

AGI Associazione Geotecnica Italiana

Università degli Studi di Napoli Federico II

Under the auspices of ISSMGE TC301 "Historic Sites"

SIMSG ISSMGE

Ordine degli Ingegneri della provincia di Napoli

Ordine degli Architetti della provincia di Napoli

Taylor & Francis
Taylor & Francis Group
http://taylorandfrancis.com

Geotechnical Engineering for the Preservation of Monuments and Historic Sites III – Lancellotta, Viggiani, Flora, de Silva & Mele (Eds)

Committees

ORGANIZING COMMITTEE

Stefania Lirer – Chair (Guglielmo Marconi University)
Susanna Antonielli (Associazione Geotecnica Italiana, AGI)
Stefano Aversa (University of Napoli Parthenope)
Riccardo Berardi (University of Genova)
Emilio Bilotta (University of Napoli Federico II)
Luca de Sanctis (University of Napoli Parthenope)
Filomena de Silva (University of Napoli Federico II)
Guido Gottardi (University of Bologna)
Carlo Lai (University of Pavia)
Giuseppe Lanzo (Sapienza University of Roma)
Claudia Madiai (University of Firenze)
Lucia Mele (University of Napoli Federico II)
Sebastiano Rampello (Sapienza University of Roma)
Gianpiero Russo (University of Napoli Federico II)
Francesco Silvestri (University of Napoli Federico II)
Paolo Simonini (University of Padova)
Daniele Spizzichino (Institute for Environmental Protection and Research, ISPRA)
Claudio Soccodato (Associazione Geotecnica Italiana, AGI)
Fausto Somma (University of Napoli Federico II)

SCIENTIFIC COMMITTEE

Renato Lancellotta – Chair (Politecnico di Torino, Italy)
Alessandro Flora (University of Napoli Federico II, Italy)
Jitesh T. Chavda (National Institute of Technology Surat, India)
Carlo Viggiani (University of Napoli Federico II, Italy)
Giovanni Calabresi (Sapienza University of Roma, Italy)
John Burland (Imperial College London, UK)
Efraìn Ovando Shelley (Universidad Nacional Autonoma de Mexico, Mexico)
Jamie Standing (Imperial College London, UK)
Ivo Herle (Technische Universität Dresden, Germany)
Kari Avellan (University of Oulu, Finland)
Merita Guri (POLIS University Albania, Albania)
V. Ulitsky (Saint Petersburg State Transport University, Russia)
Lysandros Pantelidis (Cyprus University of Technology, Cyprus)
Panicos Papadopoulos (Frederick University, Cyprus)
Michael Bardanis (Neapolis University Pafos, Cyprus)
Christos Tsatsanifos (International Society for Soil Mechanics and Geotechnical Engineering, UK)
Rui Tomásio (JETsj Geotecnia, Lisbon, Portugal)
Guilherme Pisco (Tetraplano, Portugal)
Antonio Jaramillo (Universidad de Sevilla, Spain)
Pilar Rodríguez Monteverde (Universidad Politécnica de Madrid, Spain)
Jean Launay (Comité français de mécanique des sols et de géotechnique, CFMS, France)
Jean-David Vernhes (UniLaSalle, France)
Guido Gottardi (University of Bologna, Italy)
Stefano Aversa (University of Napoli Parthenope, Italy)

Masoud Makarchian (Buali Sina University, Iran)
I.V. Anirudhan (Geotechnical Solutions, Chennai, India)
K. Muthukkumaran (National Institute of Technology, India)
Patrick Yong (Arcadis D&E)
Hongwei Sun (Northeastern University College of Engineering, USA)
Mamoru Mimura (Kyoto University, Japan)
Chikaosa Tanimoto (Osaka University, Japan)
Stephan Jefferis (University of Surrey, UK)
Charles Augarde (Durham University, UK)
Daniele Spizzichino (Institute for Environmental Protection and Research, ISPRA)
Michele Jamiolkowski (Politecnico di Torino, Italy)
John Lambert (AECOM, UK)
Harry Saroglou (National Technical University of Athens, Greece)
Orhan Inanir (Istanbul Technical University, Turkey)
Yoshinori Iwasaki (Geo Research Institute, Osaka, Japan)
Heon-Joon Park (Seoul National University of Science and Technology, South Corea)

Geotechnical Engineering for the Preservation of Monuments and Historic Sites III – Lancellotta, Viggiani, Flora, de Silva & Mele (Eds)

Sponsors


ITASCA™
Consultants, s.a.s.


CATA
COM
BE DI
NA
POLI

Opening Address

Taylor & Francis
Taylor & Francis Group
http://taylorandfrancis.com

Geotechnical Engineering for the Preservation of Monuments and Historic Sites III – Lancellotta, Viggiani, Flora, de Silva & Mele (Eds)

Welcome address

C. Viggiani
Emeritus Professor, University of Napoli Federico II

Dear friends, welcome to Napoli. This is the third International Symposium on Geotechnical Engineering for the Preservation of Monuments and Historic Sites organized by TC301 of ISSMGE; Napoli is an ideal location since it is itself an outstanding cultural heritage. It has a long history: it has been founded almost 3 millennia ago. Someone says that it is the only oriental city without a European district; it is indeed the only large European city whose historical center is still inhabited by people and not only by banks, offices, shopping malls. It is rich of thousands of cultural assets ranging from remains of many centuries ago to contemporary art works; many of them have geotechnical interest and/or are affected by geotechnical risks; many of them are very fascinating and will contribute making enjoyable your stay in Napoli.

A review of the history of Napoli through three millennia, as seen through the lenses of geotechnical engineering, has been presented by Aversa et al. (2013). Evangelista and Viggiani (2013) reviewed the geotechnical risks affecting the city. Borrowing from them, a bird eye view is here reported.

Greeks founded Parthenopes (also named Palaepolis, the old city) in IX century b.C. on the Pizzofalcone hill, just behind this building where we are and in front of the small Megaride island (Figure 1), where some centuries later the Castel dell'Ovo (the Castle of the Egg) was built (Figure 2). After the victory against Etruscan in 474 b.C. the city was extended in the plain area East of Palaepolis, founding Neapolis, the new city.

Neapolis was organized following a regular pattern of mutually orthogonal streets (Figure 3): three long main streets called *decumans*, oriented West to East, and many orthogonal *cardines.* The scheme is known as *Ippodameus*, from the name of the Greek architect Ippodamo of Mileto, and is found in many Greek cities of that period. It largely survives in the modern city (Figures 4, 5).

Figure 5 shows one of the old cardines, now via S. Gregorio Armeno, famous for its workshops of figures (*Pastori, i.e. shepherds)* for the Nativity scenes (*presepio*). The street is very crowded with tourists, but also Neapolitans, particularly around Christmas.

The pottery or wooden shepherds of XVIII and XIX century are authentic works of art: some instances are reported in Figures 6 and 7.

But what about geotechnical engineering? Actually, some of the most famous historical nativity scenes (presepi) are exhibited in the museum that now occupies the old S. Martino monastery. The monastery had been founded by the Angevins in 1325, at the top of a steep hill. The tavola Strozzi (Figure 8), the oldest depiction of the medieval city, shows the monastery in a dominant position with a huge retaining wall already clearly distinguishable below.

DOI 10.1201/9781003308867-1

Figure 1. The site of the Hellenic settlement of Palaepolis (the old city) (IX – V century b.C.).

Figure 2. Castel dell'Ovo on the ancient Megaride island, in a painting of A. Pitloo, 1830.

Figure 3. The network of cardines and decumans of Neapolis, superimposed to the present city.

Figure 4. Spaccanapoli (Split Naples): one of the old decumans surviving in the modern city.

Figure 5. (left) Via S. Gregorio Armeno; (right) workshops of nativity figures.

Figure 6. (left). The “Presepe Cuciniello”, S. Martino Museum, Napoli; (right) The Crib.

Figure 7. Some figures of the Presepe Cuciniello. Old mandolon player (G. De Luca, XVIII Century); Angel of the Announcement (G.B. Polidoro, XVIII Century); Black woman giving a baby the breast (XVIII Century); Rustic carrying a barrel (F. Celano, 1729 – 1814).

Figure 8. The Tavola Strozzi, view of the city of Napoli from the sea. Oil on wood, 1470.

Figure 9. Bird's eye view of the S. Martino hill today.

The vineyard contains more than 7 Km of retaining walls with a height over 3 m. The system of retaining walls shows evident signs of degradation because of lack of any maintenance and uncontrolled runoff of water; the densely inhabited underlying built environment is exposed to a high landslide risk. Geotechnical engineering has thus a central role in preserving the underlying city, the S. Martino monastery and the Presepi!

Within the urban perimeter there are so many cultural assets of geotechnical interest, that we can only list some of them; for instance, underground chambers excavated in different periods for different purposes (Figures 10, 11, 12, 13) and still being excavated (Figures 14, 15, 16)

Figure 10. Subterranean tumb in ellenistic style: tomba C, ipogei dei Cristallini.

Figure 11. The S. Gennaro catacombs.

Figure 12. A Roman street beneath S. Lorenzo Maggiore.

Figure 13. The Fontanelle cemetery.

Figure 14. Excavation for a Metro station in Town Hall Square.

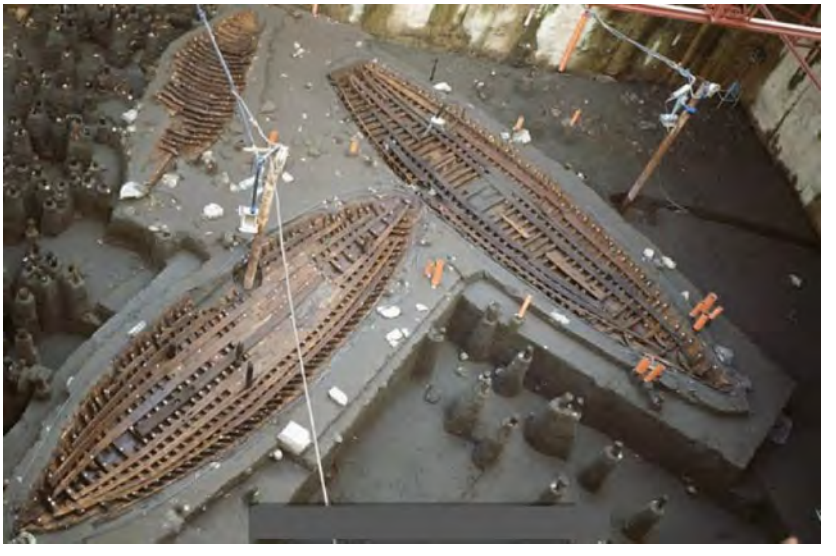

Figure 15. The old Roman harbour in Town Hall Square.

If we go slightly out of the urban perimeter, another world of treasures may be found. For instance, the area of the Phlegrean Fields, east of Napoli, is unique for the beauty of the landscape keeping the traces of its volcanic origin (Figures 17, 18), for the abundance of Roman remains (Figures 19, 20), for legendary events (the entrance to the underworld through the Averno Lake, Figure 21) and mythical figures like the hero Aeneas, founder of Rome, or the Cuman Sybil. The Phlegrean Fields host also the three fantastic tunnels by Lucius Cocceius Aucto (Table 1, Figures 21, 22).

If we move a little further Northwards, we find a small church in a small village, the Benedictine Basilica of S. Angelo in Formis (Figure 23), that was founded in the XI century over the ruin of a Roman temple dating back to the V century b.C. It contains an outstanding cycle of frescoes with stories of Old and New Testament (Figure 24). After the destruction of Montecassino Abbey during the World War II, the S. Angelo frescos are probably the most important document of the medieval painting in Southern Italy.

Starting in 1969 some fissures appeared in the central nave and gradually opened and extended to other parts of the Basilica. Following repeated alarms on the safety of the Basilica, geological survey of the area, subsoil investigations and geodetic monitoring of several points both inside the Basilica and outside have been carried out till present.

The subsoil of the church, as resulted from the site investigations, is schematically shown in Figure 25; it includes three horizons. The upper one is composed by made ground, for a thickness ranging from a few decimeters to some meters. Below the made ground, a layer of fractured rock (dolomite, dolomitic limestone, cemented calcareous debris) is found, with a thickness variable between 15 and 30 m. Finally, the base formation of sandstones and variegated clay shales is found-

The Basilica is located across a stratigraphic discontinuity, with the apses and the backward part of the naves founded on rock, and the front on the debris cover or even on the made ground.

It is known that some repair works have been carried out in XVIII century; in 1930 an earthquake produced the collapse of the roof, reconstructed soon after. Starting in 1969 some fissures appeared in the central nave and gradually opened and extended to other parts of the Basilica (Figure 26).

Cammarota *et al*. (2013) published the data available on settlement of the Basilica in 1980 and 2013; prof. G. Russo kindly made available further measurements in 2021.

Figure 16. Some of the stations of the new Napoli Underground lines. Someone says it is the finest underground system of the world.

Figure 17. The Phlegrean Fields.

Figure 18. The volcanic origin of the Phlegrean Fields.

Figure 19. Left: the “Piscina mirabilis, an underground water reservoir for the Roman imperial fleet. Above. The remains of the Portus Julius, harbour of the imperial fleet, submerged by the sea because of a 16 m volcanic subsidence.

Figure 20. The Flavian amphitheater in Pozzuoli.

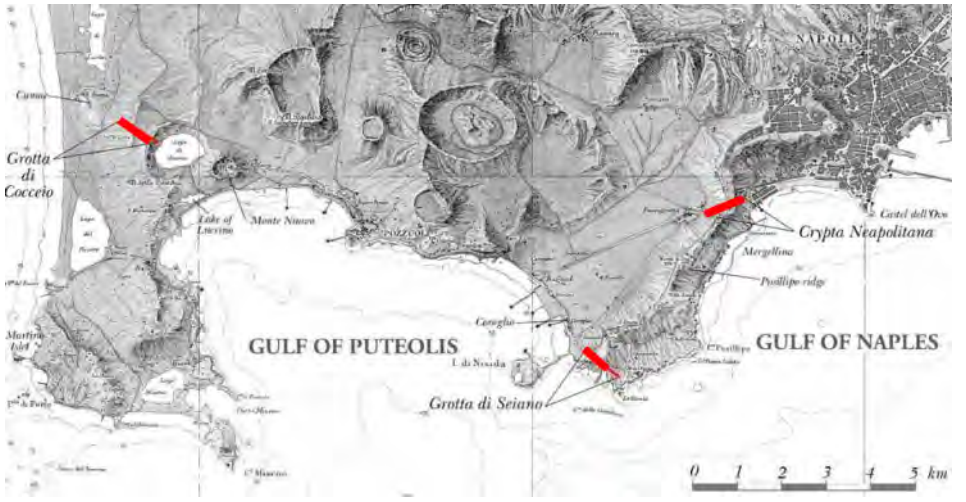

Figure 21. Map of the Phlegrean Fields showing the location of the Roman tunnels.

Table 1. Characteristics of the Roman Tunnels in the Phlegrean Fields.

Name	Length (m)	Width (m)	Height (m)	Notes
Crypta Neapolitana	711	4.5	4.6 ÷ 5.2	2 inclined ventilation shafts
Seianus Grotto	780	4.0 ÷ 6.5	5.0 ÷ 8.0	3 lateral ventilation tunnels
Cocceius Grotto	970	4.5	4.5 ÷ 8.0	5 inclined or vertical vent. shafts

Figure 22. The western intake of the Crypta Neapolitana in a painting by L. Ducros, 1793.

Figure 23. The Benedictine Basilica of S. Angelo in Formis.

Figure 24. The interior of the Basilica.

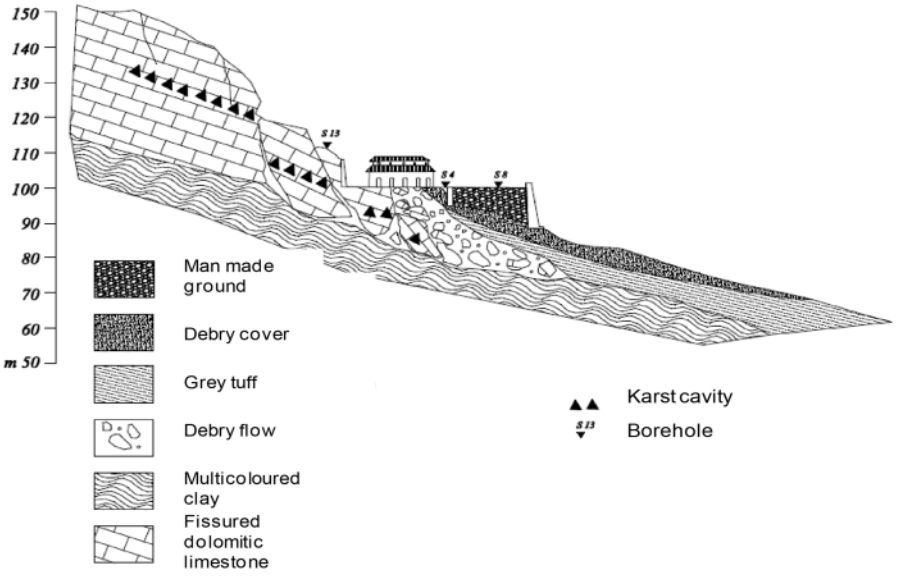

Figure 25. Schematic geological section of the area around the Basilica.

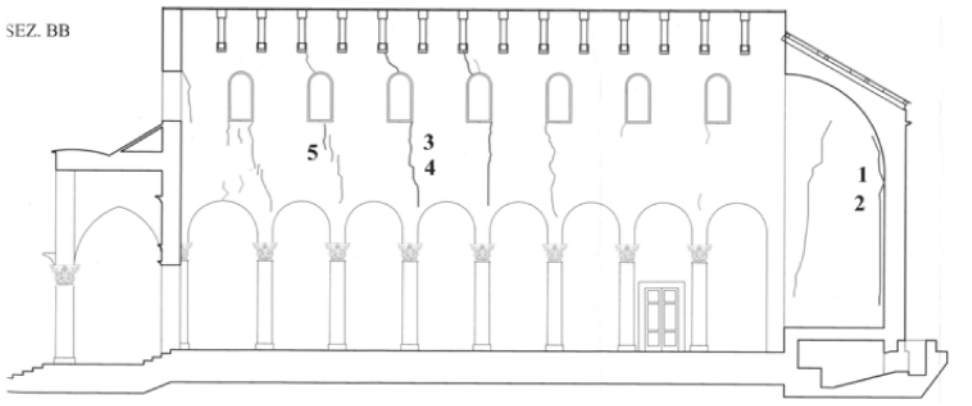

Figure 26. Main fissures of the superstructure.

The trend of differential settlement of the basilica is reported in Figures 27 and 28. The reason of the movements has not yet been understood. At present, the church is monitored and only some structural repairs have been carried out.

In a note published on a magazine some years ago (Montanari 2018) an art historian refers to the church as "…a Benedictine Basilica of clamorous beauty …, one of the most important and fascinating Italian monuments". He regrets "…the unbelievable inability of our generation to repair the structural damages threatening it" and claims that we will succeed in saving S. Angelo in Formis only if we will go deep into ourselves to really understand the problem.

This is a challenge for geotechnical engineers!

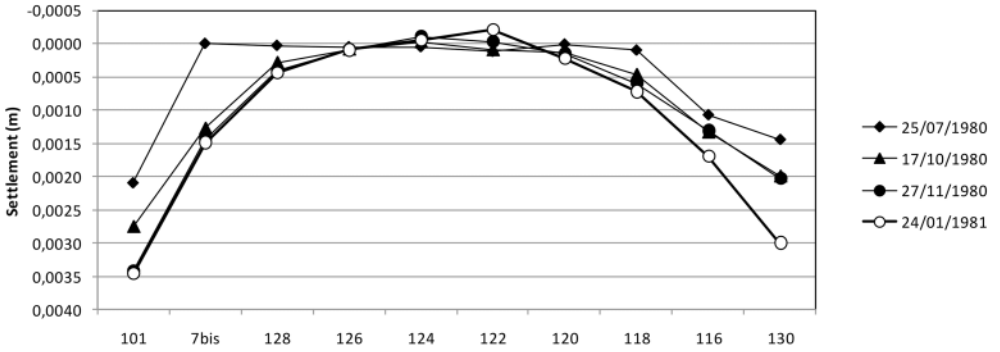

Figure 27. Survey on the internal measuring points: period February 1980-March 1981.

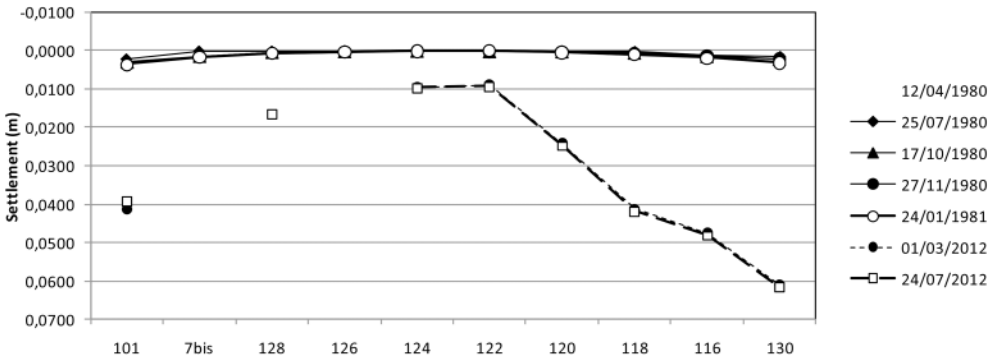

Figure 28. Survey on the internal measuring points: period February 1980-November 2012.

Finally, let me remind another aspect of Napoli: its open-minded character, its multicultural aptitude. A famous Neapolitan song says that Napoli has thousand colors; we have seen these colors in the Presepe Cuciniello. This will find, I hope, correspondence in the discussions of our Symposium, with contributions of different disciplines as structural engineering, architecture and restauration.

REFERENCES

Amato L., Evangelista A., Nicotera M.V., Viggiani C. 2000. The Crypta Neapolitana; a Roman tunnel of the early imperial age. *More than two thousand years in the history of Architecture. UNESCO-ICOMOS Internationl Congress,* Bethlehem.

Amato L., Evangelista A., Nicotera M.V., Viggiani C (2001) The tunnels of Cocceius in Napoli: an example of roman engineering of the early imperial age. *AITES/ITA World Tunnel Congress*.

Aversa S., Evangelista A., Scotto di Santolo A. (2013) Influence of the Subsoil on the urban development of Napoli. *Proc. Intern. Symp. on Geotechnical Engineering for the Preservation of Monuments and Historic Sites, 15 – 44. Bilotta et al. eds.* CRC Press/Balkema.

Cammarota A., Russo G., Viggiani C., Candela M. (2013) The Benedictine Basilica of S. Angelo in Formis (Southern Italy): a therapy without diagnosis? *Proc. Intern. Symp. on Geotechnical Engineering for the Preservation of Monuments and Historic Sites, 225 – 232. Bilotta et al. eds.* CRC Press/Balkema.

Evangelista A., Viggiani C. (2013) A paradise inhabited by devils? The geotechnical risks in the city of Napoli and their mitigation. *Geotechnics and Heritage, 75 - 96 Bilotta et al. eds.* Taylor & Francis London.

Russo G., Viggiani G.M.B., Viggiani C. (2012) Geotechnical design and construction issues for Lines 1 and 6 of Naples underground. *Geomechanics and Tunnelling*, vol. 5, n.3, 300–311.

Montanari T. (2018). Salviamo la Basilica; salveremo noi stessi. *Il Venerdì di Repubblica*, February 22, 2018.
Viggiani C. (2006) Un ingegnere romano di epoca tardo repubblicana: Lucio Cocceio Aucto. *Atti del I Convegno Nazionale di Storia dell'Ingegneria,* Napoli, vol. 2, 785–796.
Viggiani C. (2013) Portus Julius: a complex of Roman infrastructures of the late Republican age. In: E. Bilotta et al. ed., *Geotechnics and Heritage,* CRC Press/Balkema, 243–260.
Viggiani C. Le gallerie romane dei Campi Flegrei. SIG: *"1 anno dal WTC 2019: via per montes excisa, le opere in sotterraneo incontrano architettura, archeologia e arte.* Napoli.

Kerisel Lecture

Taylor & Francis
Taylor & Francis Group
http://taylorandfrancis.com

Geotechnical Engineering for the Preservation of Monuments and Historic Sites III – Lancellotta, Viggiani, Flora, de Silva & Mele (Eds)

Taking care of heritage, a challenge for geotechnical engineers

Alessandro Flora
University of Napoli Federico II, Italy

ABSTRACT: When dealing with monuments or historic sites, engineers may find themselves out of the comfort zone bounded by balance and congruence, being necessary to have an approach guided not only by technical convenience and cost effectiveness, but above all from the need to preserve at the best whatever is the heritage carried by the specific structure under analysis. Such a lack of comfort has to be the guiding light in sharing the solution with experts from other fields, as clearly suggested by Article 2 of the Venice Charter. This paper reports on three case histories taken from the author's personal experience, related to the heritage of completely different cultural environments (respectively Maya, Greek-Roman and Byzantine-Ottoman), in which these constraints had to be faced from the point of view of a geotechnical engineer. The role played by geotechnical engineering differs from case to case, but the examples presented herein demonstrate that, far from being sufficient, our discipline is most times necessary. It is argued that, even though the best technical solution is always the least invasive one, geotechnical engineers should not be scared *a priori* by the possibility of interacting with historic structures, as long as their intervention is informed, necessary, respectful and above all aimed to contribute in preserving the true essence of heritage, which is not the structure in itself but the role it has in its physical and social environment.

1 THE LEGACY

What is the best possible engineering approach in the protection of monuments? This theme has been debated for a long time, and has seen a significant transformation over time. The current ruling paradigm is the result of the substantial change in the cultural approach introduced in Europe between the end of the nineteenth century and the beginning of the twentieth. Until then, in fact, the predominant tendency was to approach failure or damage of historic structures by reconstruction – total or partial – to (presumedly) make them appear as they once were. Eugène Viollet-le-Duc (1814–1879) is typically taken as an example of this old approach, summarised by the statement: '*To restore a building is not to repair or rebuild it but to re-establish it in a state of entirety which might never have existed at any given moment*'.

The new way to look at built heritage that saw the light at the beginning of the twentieth century stems from the original work of many intellectuals, like for instance John Ruskin (1819-1900) and Georg Gottfried Julius Dehio (1850–1932), whose motto '*preserve, and do not restore*' is still often quoted. A decisive contribution to the development of a new culture of preservation in Europe was given by Italian scholars (Brandi, 1963), because of the unique environment in which they were raised and educated. The peculiar and pervasive presence of archaeological sites, historic cities and villages on the Italian territory – whose long-lasting, continuous presence was guaranteed by preservation rules introduced centuries ago – has made local sensibility to the theme always extremely high (D'Agostino, 2022).

Therefore, in the twentieth century in Europe the idea that the legacy carried by a monument did not depend only on its presumed original appearance became largely dominant. Appearance did not necessarily have to be re-proposed, the wounds of time being part of the monument life and contributing to its intangible value. This cultural context explains the highly restrictive position of the Athens Charter (1933) first and of the Venice Charter (1964) subsequently.

DOI 10.1201/9781003308867-2

The Nara Document (1994), the Krakow Charter (2000) and more recent documents have added complementary information and principles to these original references, recognising that the concept of preservation and even the definition of authenticity and heritage must be referred to considering the different cultural contexts existing around the world.

Is all of this relevant for geotechnical engineering? We have learned that it is. In promoting the Technical Committee on Historic Sites of ISSMGE in 1981, Jean Kerisel and Arrigo Croce made an effort to bring to the attention of the geotechnical community the need to face all the existing cultural constraints, when dealing with cultural heritage. Since then, it has been clearly stated that the principles contained in the fundamental reference documents previously mentioned apply not only to the visible part of the structure but to the whole Ground-Monument System (Jappelli 1991). The relevance of geotechnical engineering in preservation has been highlighted many times (e.g. Jappelli & Marconi, 1997) and nicely summarised in the two previous Kerisel lectures through exemplary case histories (Calabresi, 2013, Viggiani, 2017). Clear definitions of material, iconic and historical integrity have been given (e.g. Viggiani, 2013). Historical integrity, in particular, has been dealt with in terms of authenticity from different points of view (e.g. Iwaski et al. 2013), confirming the variety of approaches related to local cultural environments, consistently with the indications of the Nara document.

Figure 1 schematically summarizes the author's personal view of what we could call the conventional relationship between the different kinds of integrity and some possible engineering actions to be carried out for preservation goals. An insight into the meaning of each action, from conservation to reconstruction, can be found in Petzet (2004). This scheme is a conceptual framework posing constraints that cannot be overlooked, even when dealing with the least visible, underground part of built heritage, and with the subsoil directly interacting with it.

Figure 1. Conventional relationship between iconic, material and historical integrity as a function of different kinds of engineering actions.

Indeed, the scheme reported in Figure 1 may not be fully satisfactory, because historical integrity and authenticity are somehow elusive concepts, as already mentioned. An enlightening example of such elusiveness can be taken with reference to the conservation of some shrines in Japan (Flora, 2013): up to the mid of the 19th century, several wooden Shinto shrines periodically underwent complete reconstruction ever since the inception of this custom in the 7th century. Such a practice had the character of an important religious ritual, but was probably set forth to answer to the need of substituting spoiled or damaged parts. Later on, in the 19th century, all the Shinto shrines but one (Ise shrine, Figure 2) stopped the periodic reconstruction because of political changes and economic crisis. Nowadays, while the Ise shrine still keeps its ritual reconstruction every 20 years, all the other shrines are protected by law as architectural heritage, assuming as an indicator of their relevance and integrity the material value, in accordance with Figure 1.

Actually, the interruption of the periodic rebuilding process was an accident and not the norm, the Iso shrine being the only one to follow its originally conceived life cycle. So, the question is: what is authentic in this case? The frozen material situation of the 19th century or the immaterial heritage preserved by the ritual reconstruction of the Ise shrine? The answer is not easy,

Figure 2. Ise shrine (Japan), which still undergoes ritual reconstruction every 20 years ever since the 7th century.

because such problems often face the lack of unicity of the solution (Viggiani, 2017), which is certainly an uncomfortable situation for engineers.

An attempt to answer may be done complementing the list of material and immaterial values of built heritage, or better overcoming the simple distinction between tangible and intangible values, referring to the role the structure has in its social and physical environment. So, the preservation of the role – intending with it the coherence with the original scope of the construction (considered through what we may call its functional integrity, Figure 3) along with the importance it has in the perception of the local historic, physical and spatial environment – leads to the need of looking at preservation in a broader sense. Probably, the supreme value to be preserved is the message coming from the past, and therefore *continuity* may be even more important than *authenticity* (Petzet, 2004).

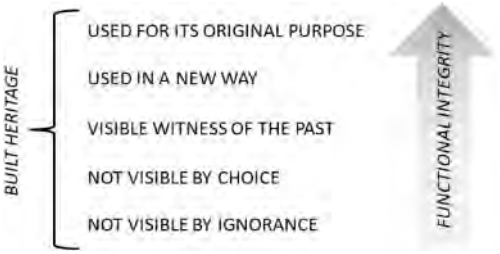

Figure 3. Schematic representation of functional integrity of the built heritage, as one of the elements defining the role it has in its environment.

Far from encouraging arbitrary reconstruction, the concept of functional integrity may certainly be a way to check if the monument or site of interest is in a good shape, alive with wounds, or just dead. In a way, these possible states have to do with the nuanced difference some scholars make between archaeology and architecture, which may seem a semantic dispute but underlays relevant differences in the preservation approach, that could be accepted to be more invasive in the latter case.

A paradigmatic example of built heritage not visible by ignorance is a part of Ercolano, a Greek-Roman town buried by the eruption of Mount Vesuvius in AD 79. Clearly, part of the town (how large? How relevant?) is still buried under modern buildings (Figure 4), built with no respect – ignorance, in its literal meaning – of the underground heritage constraints.

Figures 5 to 8 complement the information summarized in Figure 3 in terms of built heritage functional integrity.

Figure 4. The Greek-Roman town of Ercolano (Italy), still partly buried under low quality modern buildings.

Figure 5. The Samnitic-Roman town of Pompei (Italy), unique witnesses of the past.

Figure 6. Bookstore inside a 13th century Dominican church in Maastricht (Holland). Built heritage used in a new way, with respect of its original conception.

Figure 7. The Roman port of Ventotene (one of the Pontine islands, Italy), still in use (thus at the highest possible level of functional integrity), was entirely excavated in the rock bank, removing some 60.000 m^3 of material, to support emperor Augustus' (63 BC – AD 14) summer residence, as there was no natural harbour on the island.

Figure 8. The Basilica of Saint Peter in Vatican (Rome, Italy), still playing its role of church and centre of the Catholic world (thus being at the highest possible level of functional integrity).

In the framework so far depicted, the case of Ise shrine can be seen as fully respectful of its role and functional value, because able to carry the immaterial, social heritage of the ritual reconstruction.

The consideration of the social role played by the built cultural heritage – well beyond its physical features –indicate that a merely binding preservation culture, as emerging from the strongly conservative constraints posed by the different charts of the twentieth century, may be inappropriate to preserve heritage in its broader sense. Quoting Settis (2018): '*Cities are not museums: they're meant to be lived in, and that's the reason why conservation supervision should not be perceived as a way of leaving everything in a state of hibernation. I don't wish heritage protection to mean hibernation*'.

This is a crucial issue when looking at preservation from the geotechnical engineering point of view. As a matter of fact, our discipline is most often involved in preservation actions when critical mechanisms may affect the Ground-Monument System, with the structure or the site often on the verge of failure. In such cases, geotechnical contribution is typically required to solve critical static problems or to tackle a high seismic risk, often without enough time to explore in depth all the range of technical alternatives. Decisions are easier to take when the geotechnical intervention can be concentrated within the subsoil, i.e. when the action has the goal to remove the cause and not to mitigate the effects on the structure. Soft solutions can overtake on invasive ones in these cases by considering the effect of boundary geotechnical conditions and eventually acting on them, as nicely described for instance by Calabresi (2011) with reference to the Roman Milvius bridge in Rome. In other cases, taking into account the effect of dynamic soil-structure interaction may prevent from useless invasive underpinning interventions (Lancellotta, 2013) or help in better understanding the structural behaviour of monuments (e.g. de Silva et al. 2018, de Silva 2020, Flora *et al*., 2021). The well-known case of Orvieto (Italy) (Pane & Martini, 1997) is also worth mentioning as representative of the quite frequent situations of relevant structures or sites above unstable rock cliffs, where the stabilization of the cliff is an effective, fully respectful solution.

The worldwide famous leaning tower of Pisa is another paradigmatic example of good geotechnical practice, as the preservation was successfully obtained by careful under-excavation (Burland *et al*., 2013), i.e. just carefully removing some soil in specific zones underneath the tower, without even touching it, thus keeping the solution in the uppermost part of the conventional integrity scheme of Figure 1. However, the tower of Pisa may be also seen as a misleading example, in the sense that the successful and fully respectful solution was obtained after almost one century of careful and detailed studies, investigations and monitoring, with no economic constraints, with the support of politics and public opinion, involving in the multidisciplinary study world leading experts. Such an exceptional circumstance is rarely reproducible and cannot be considered as a routine situation, even in the case of extremely valuable historic buildings or sites. In the everyday life of geotechnical engineers, therefore, we know that a compromise is often unavoidable.

If foundation reinforcement with new technologies (to be considered as *modern renovation* only after exploring the possibility of *restoration*, Figure 1) is the only feasible solution and may solve the problem, for instance, it should not be excluded *a priori*, especially if it contributes to keep the built heritage alive (i.e. with the highest functional integrity, Figure 3). In fact, often historically

valuable structures that still have a good degree of functional integrity are the result of continuous transformations that have taken place in a long time span. Therefore, modifications based on sound cultural and mechanical bases (and thus to be considered necessary) should not scare geotechnical engineers, being possible to consider them as part of the lifecycle of the structure, which should not be necessarily frozen to the present, intrinsically assumed as a reference time out of a still evolving historical pattern. Of course, the first attempt should be to use technological solutions consistent with the original structure, whose characteristics should be known (Roca et al., 2019). Apart from the formal distinction between architecture and archaeology that the concept recalls, the solution should be considered case by case, obviously taking into account all possible alternatives and privileging the least invasive ones. Hard interventions in the subsoil (for instance, underpinning) should be taken possibly avoided, considering that still undiscovered heritage may exist underneath the visible structure to protect.

The lack of a general theory, and therefore of a univocal indication of the best engineering solution to preserve built heritage, imposes the need to be extremely more cautious than with new constructions, and technical convenience or cost effectiveness must not be the guiding light in this case. Engineers have to cope with values usually out of their skills, stepping outside of their comfort zone, and have to agree on the technical solutions with archaeologists, architects, art historians and officials in charge of monuments preservation. Indeed, '*a satisfactory equilibrium between safety and conservation, between engineers and restorers, may be found only in the development of a shared culture*' (Viggiani 2013). Unfortunately, this is still to come in common geotechnical preservation practice, and extremely invasive actions on foundations are often felt acceptable just because they are not visible, with no deeper insight. Then, an effort is needed to go beyond purely academic discussion, if we want to avoid being as '*that people who give good advice if they cannot set a bad example*' (De Andrè, 1967). This is, or at least should be, the role of TC301 of ISSMGE.

The considerations reported in this introductory section clearly warn on the unusually complex task of dealing with the preservation of historic sites and buildings. Before planning any intervention, therefore, this complexity should make engineers aware of the heritage value, no other way being possible to truly perceive it than taking a humble bath into the history of the specific structure of interest, quietly listening to the silent voices of those who have imagined, designed, built, used and eventually modified it during history. Only after this empowering bath (Figure 9), balance and congruence can take the lead.

The examples reported in the next sections are taken from the author's personal experience, and have been chosen because they show situations in which the lack of unicity of the solution is clear, and the considerations reported may seem questionable and therefore worth discussing. Covid pandemic has dramatically modified the possibility to carry out site investigations in the last two years. The reported case histories have suffered this limitation, and not all the planned activities were performed. Because of this, some of the results must be considered preliminary.

Figure 9. Inner side of the Tomb of the diver's lid (Greek painting, 480/70 BC, Paestum, Italy).

2 INTERFERE WITH THE PAST HELPING TO DISCOVER

2.1 *Copan*

Copan (UNESCO site since 1980) is an ancient Maya settlement located in the extreme western highlands of Honduras, close to the Copan river (Figure 10). This city-state flourished from the 5th to the 9th century AD – a time-span known as the Classic Maya period – during which it became one of the most important sites of Maya civilization, in that period spread in contemporary southern Mexico, Guatemala, Belize, Honduras and El Salvador. Copan was the intellectual centre of the Classic Maya civilization, where important advances in astronomy and mathematics were achieved (Thompson, 1958). The site was brought to the attention of Europeans in 1576, when Diego Pedro de Palacio visited it and reported on the magnificence of its architecture and sculptures.

Copan is most famous for the so-called Main Group (Figure 10), an architectural compound exquisitely decorated with stone sculptures, comprised of a massive elevated royal complex located south, known as the Acropolis, and a series of connecting plazas and smaller structures located north. One of the most famous pieces of stonework is the superb Hieroglyphic Stairway (Figure 11), the longest known Maya hieroglyphic text, and it's incredibly high relief sculpture, some of the finest ever carved in antiquity (Sharer and Traxler, 2006). Centuries of abandonment left heavy

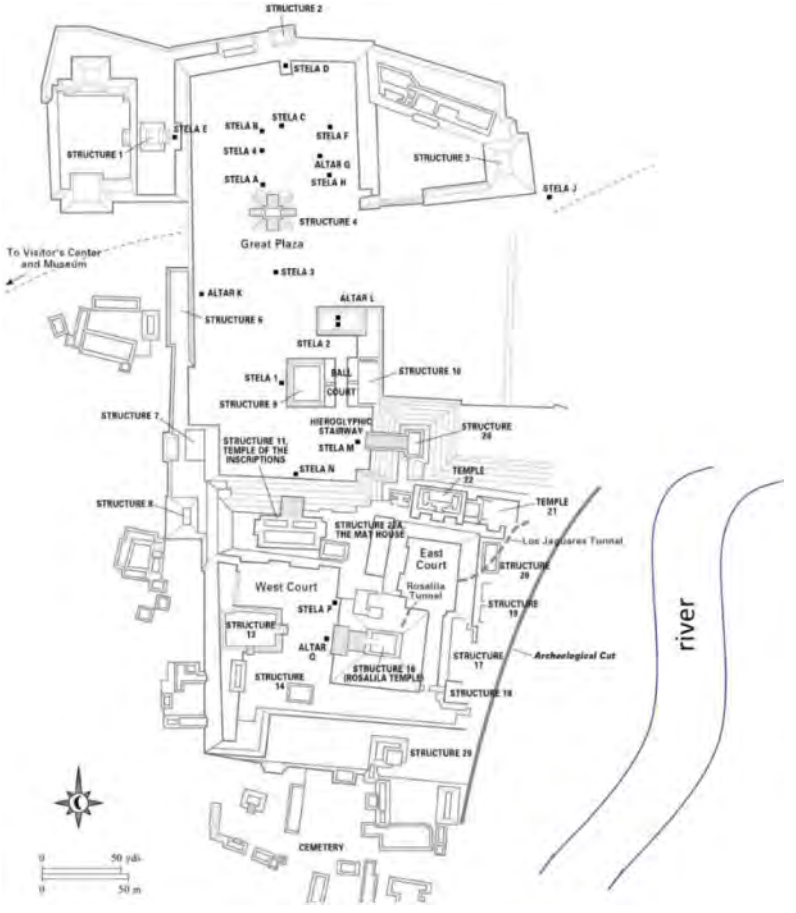

Figure 10. Plan view of the Copan archaeological area, with (sketched, non on scale) the nearby Copan river (modified after Pires, 2020).

signs on the structures, that were mostly ruined at their rediscovery in the 19th century. In 1830's, Juan Galindo was the first to systematically explore the site, bringing attention from the world to the ruins of Copan and inspiring the first official excavations to begin in the late 1880's.

When these first consistent explorations took place, the eastern side of the Acropolis had already been partially destroyed because of a large slope failure that involved part of the pyramids (Figure 12a). Such large collapse was certainly related to the action of the close by Copan river, and the cut - nowadays known as *corte* – is the result of hundreds of years of water action. In fact, at some point of the Classic Period, the Maya artificially diverted the river course. The artificial control of the river path was stopped after the city decline, letting the river meander again. Its widening floodplain eventually became responsible for the undercutting and destruction of the eastern portion of the Acropolis (Bell et al., 2004). Added to centuries of erosion, an earthquake in the 1930's threw the top of three East Court buildings into the river, partially destroying some of the structures recorded by the first archaeologists of Copan (von Schwerin, 2011).

To prevent further catastrophic collapses, in the 1930's the river was diverted again. The large slope failure partially exposed ancient layers of buildings, once hidden in the undergrounds (Figure 12b). This obviously suggested to archaeologists the existence of important buried structures. In fact, the monuments visible in the Acropolis and the enclosed upraised courtyards are just the latest components of a series of additions made by the 400-year dynasty that ruled over Copan, accumulated over the centuries as a result of built layers added by ensuing kings (Fash, 1991). As the relevance of Copan grew, so did the need for Maya rulers of higher and more impressive monuments testifying it and leaving a lasting mark of their reign. The Maya approach to this need was to use the existing pyramids and structures as a core of the new enlarged ones. Therefore, when excavated, the pyramids reveal a series of complete but smaller pyramids, often still with their original coloured stucco decoration. In some cases, individual shrines could be amalgamated into a single bigger complex over time.

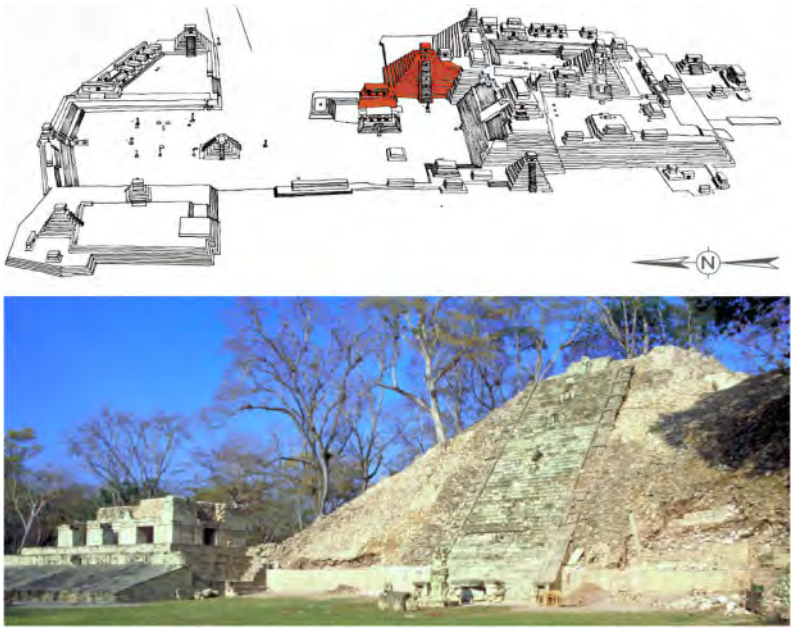

Figure 11. Top: Sketch of the Main Group of Copan with its northern part marked by the low-level plazas, and its southern part constituted by the Acropolis, with emphasis in the Hieroglyphic Stairway Temple (in red) – sketch adapted from Linda Schele's drawing (Schele, 1998); Bottom: Picture of the Hieroglyphic Stairway Court, with the temple at right and part of the Ball Court at left – photo by Linda Schele (modified after Pires *et al*., 2021).

Figure 12. Left (a): looking north at the river cut (*corte*) into the 120-meter-long masonry eastern wall of the Copan Acropolis, photo by Marshall Saville 1891/92 (Peabody Museum 2004.24.66) – Right (b): a view of different entrances to tunnels in the Acropolis archaeological cut in 1989 – left (modified after Sharer *et al.*, 1992).

Once a new and bigger structure had to be built on top of an existing one, the typical erection sequence was the following: first, the ancient superstructure (i.e. the usable building) was dismantled and its construction materials kept for posterior reuse (Abrams, 1994); then, a new and usually larger superstructure and substructure (i.e. the support of the buildings) were built over and around the ancient one. In more dramatic interventions, large platforms (i.e. levelling surfaces) were built. Superstructures were generally made with three-leaf masonry walls, with external leaves composed by dressed tuff stones and an infill core with a sort of "concrete" (Loten and Pendergast, 1984). Substructures were generally composed by a mix of wet-laid earth and stone fill materials, retained peripherally by stone masonry walls.

2.2 *The archaeological tunnels*

To allow for the archaeological investigation of the buried structures under the Acropolis, the first tunnels were excavated in the 1930's. By the 1980's, a new strategy was established and more complex tunnelling started from the *corte* using the exposed layers as references (Figure 12b). In time, an incredible 4 km long and complex tunnel system developed within the monumental compound. Figure 13a reports a sketch of the tunnels network underneath the Hieroglyphic Stairway Temple, in the northern part of the Acropolis. Thanks to this underground investigation approach, extraordinary archaeological discoveries were made. A large number of decorative plasterwork reliefs provided one of the most comprehensive set of information on the origins and development of a Classic Maya complex (Lacombe et al., 2020). At the end of the 1980's, the Copan Acropolis Archaeological Project (PAAC) was established, merging past and new projects under the same direction, and allowing access to part of the tunnels by tourists.

Although most of the tunnels are apparently stable, local collapses required actions to ensure the safety conditions for researchers and visitors, and also to preserve the material cultural heritage still uncovered by the archaeologists. Moreover, in some cases the change in the environmental conditions of the buried heritage in the tunnels is also leading to the deterioration of valuable decorative materials. Since a comprehensive investigation of the conditions of the tunnels network within the site of Copan had never been carried out, a strategic plan was started by the Copan Acropolis Tunnel Conservation Program from Harvard University (Lacombe *et al*., 2020), defining investigations, analyses and interventions to be carried out in subsequent steps. At this stage, structural and geotechnical engineers were invited to join the research group. In this framework, in fact, an important task was to obtain an insight into the stability conditions of the tunnels, starting from the available information, which in terms of the geometrical shape and position of the tunnels was well detailed. On the contrary, very little was known on the mechanical properties of the infill material. In this section, the first considerations done on the stability of the tunnels under the

Hieroglyphic Stairway Temple (Figure 13a) and on the preservation actions to be carried out are reported. Here the tunnels were excavated through Esmeralda (Figure 13b), a large embankment built around 700 AD, that would later become the supporting platform for the Hieroglyphic Stairway Temple (Sharer *et al*., 1999).

The tunnels of Copan can be described as narrow underground passageways excavated by the archaeologists into the man-made earth fill constituting the core of the pyramids, with the goal of seeking buried structures. Because of this, they have an extremely irregular pattern (Figure 14), with sharp changes in direction and depth. When buried structures were found, tunnels usually ran aside substructures and superstructures walls (Sharer et al., 1999). From time to time, some of the tunnels have been excavated to go deeper in the embankment (and consequently to an older period of time in the development of the monumental compound). The earth fills within the pyramids have been created in a long time span, to allow subsequent enlargements of the structures. Because of this, they are not made with a homogeneous material, in terms of grain size distribution, density and even of compaction energy. However, for a certain volume related to a specific enlargement of the structure and at a certain depth, the material can be considered homogeneous, consistently with the fact that the workers were taking each time the fill material from the same pit, and were compacting it with the same tools.

Three main filling soils can be found under the Acropolis. The lowermost layers of the earth fills consist of a dark, clayey river mud (*barro*), which was mixed into a slurry to fill the earlier temples when it was time to build a new one on top (Lacombe *et al*., 2020). The barro is a well compacted fine-grained material, and no instability problems are reported in the tunnel stretches excavated into it.

The tunnels' network was mostly excavated immediately above the barro layer, into a layer of dark reddish-brown earth (*tierra café oscuro*) mixed with construction debris, river cobbles and broken lime plaster (Lacombe *et al*., 2020). This is a clayey silty sand with gravel. However, assuming that the larger gravel or boulder inclusions are floating in the finer matrix, the mechanical behavior of this layer corresponds to that of a sand with fines. The uppermost and outer part of the earth fills, the most recent one to be put in place, is made of a fine yellow sand (*girún*), which is the coarsest soil used for the whole earth fill. This sand was used to refine the oldest temples and to complete the latest structures such as Esmeralda. Most tunnel stretches excavated inside the *girún* layer needed to be supported at a later stage with a stone masonry lining, or suffered diffused collapses that required them to be back-filled.

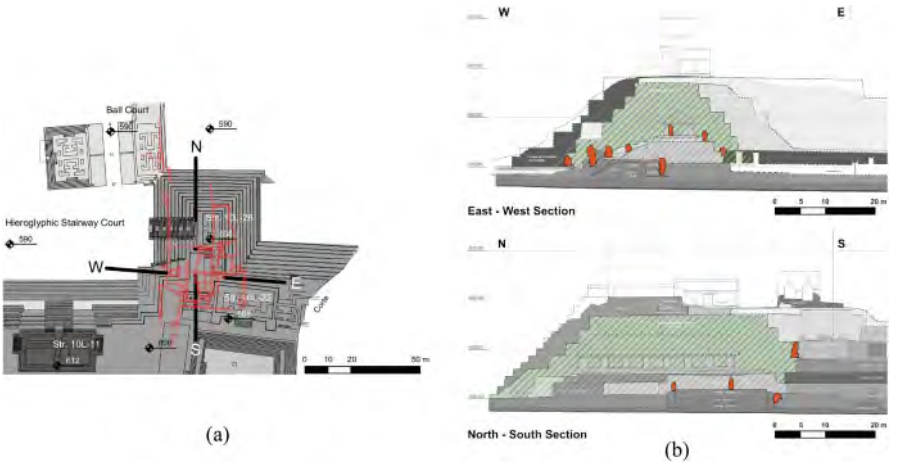

Figure 13. (a) Detail of the Acropolis plan showing the extension of currently open tunnels under the Hieroglyphic Stairway Temple (in red) – adapted from PAAC drawings; (b) Sections of the Hieroglyphic Stairway Temple showing the approximate positions of tunnels (in red) and the green hatch of the Esmeralda volume – adapted from C. Rudy Larios' PAAC drawings (modified after Pires *et al*., 2021).

Data about tunnels position under the Hieroglyphic Stairway Temple, their internal shape, and the presence of lining, sometimes being parts of original Maya structures, were gathered by a recent 3D dimensional survey. Hence, four typical transverse sections were identified to carry out a parametric numerical analysis of their stability conditions (Figure 15) (Pires *et al*., 2021). T1 and T2 identify the 'as excavated' tunnel sections, where no lining was applied to the walls; T3 and T4 those structurally retrofitted, that were supported by thick masonry walls as lining at a later stage. Sections T1 and T3 are fully inside the fill material, while T2 and T4 are sections of tunnel excavated adjacent to buried structures, that therefore play a role in their mechanical behavior.

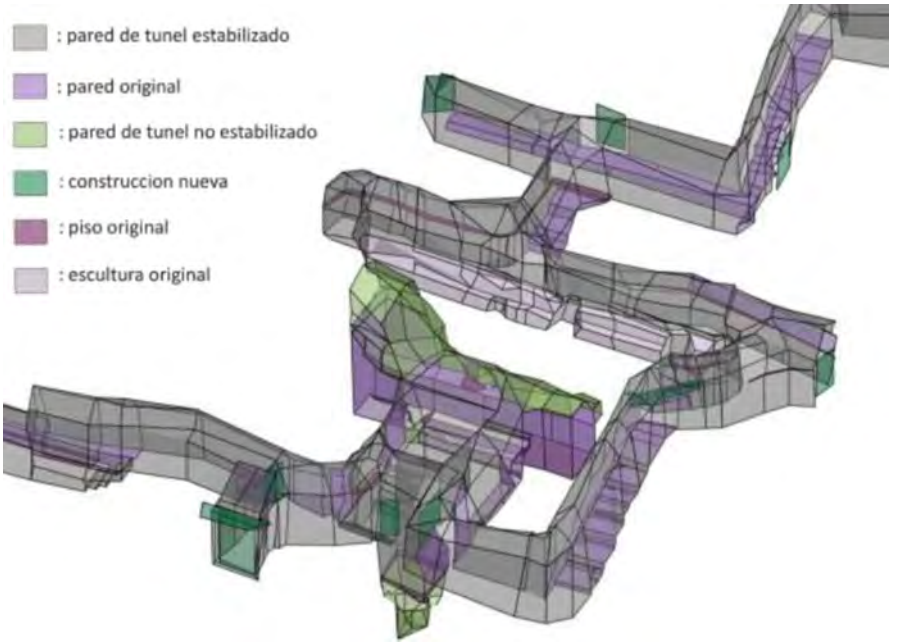

Figure 14. 3D model of part of one of the tunnels in the Acropolis (modified after Lacombe et al., 2020).

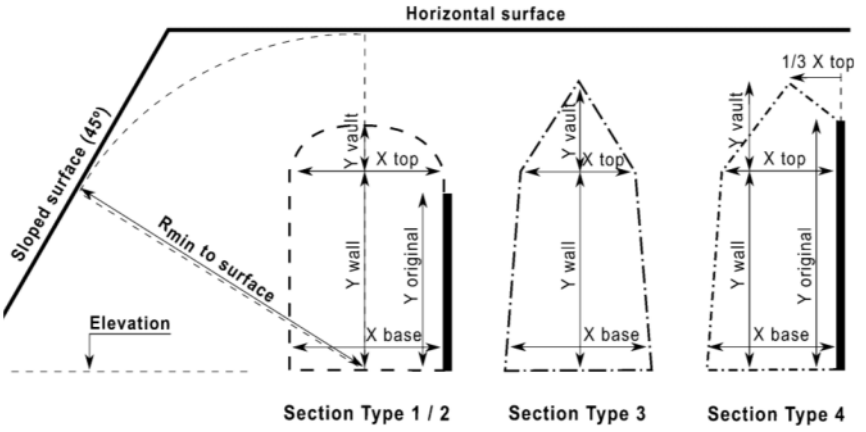

Figure 15. Shapes of typical tunnel sections: Types 1 and 2 (left), Type 3 (center) and Type 4 (right). The difference between type 1 and Type 2 is the presence of a buried Maya structure on one side for Type 2 (indicated as a thick black line) (modified after Pires et al., 2021).

The unlined tunnels in the *tierra café oscuro* layer have a typically stable arched vault (Figure 16), while the lined ones are vaulted on the top with a triangular corbelled arch. In most lined tunnels the lower walls are slanted. Section T4 is rather irregular and the final shape identified in the figure is just a rough approximation. The dimensions vary within each type but, in general, tunnels are small, serving as pathways for the archeologists, with an average width of about 1.0 m and a height ranging from 2.0 m to 3.0 m. Table 1 provides the statistical information obtained from the 3D survey. The distance between tunnels and external surfaces is represented in Figure 15 by the minimum distance R_{min}. This is measured from the axis at the base of the tunnel to the nearest ground surface.

Figure 16. Unlined stretch of a tunnel excavated in the *tierra café oscuro* (modified afterLacombe *et al*., 2020).

Table 1. Dimensions of the four typical tunnel sections (for the definition of $Y_{original}$, Y_{wall} and Y_{vault} see Figure 15; μ = average, s = standard deviation) (Pires *et al*., 2021).

Section	Base width (m)		Top width (m)		$Y_{original}$ (m)		Y_{wall} (m)			Y_{vault} (m)	
type	μ	*s*	μ	*s*	μ	*s*	median	μ	*s*	μ	*s*
T1	1.3	0.2	1.2	0.1	0.0	0.0	1.1	1.3	0.3	0.6	0.2
T2	1.2	0.3	1.2	0.2	2.0	1.1	1.3	2.0	1.1	0.4	0.3
T3	1.0	0.2	0.9	0.2	0.0	0.0	1.6	1.7	0.3	0.6	0.2
T4	1.1	0.2	0.9	0.3	2.6	1.7	1.9	2.5	1.4	0.7	0.2

The full length of the tunnels and the range of distance to the outside surface are summarized in Table 2. Here the surface is classified as sloped or horizontal. The slope of the stepped external surfaces of the pyramid-like structures is about 45º. In total, 360 m of tunnels can be found under the Hieroglyphic Stairway Temple. About 50% of these tunnels have a T3 section, while the other three types of section are equally distributed, as shown in Table 2. Most times, collapses occurred at the interface between lined and unlined tunnels or in unlined tunnels, as shown in the photos of Figure 17.

In 1942, only few years after the excavation of the first tunnels in Copan, stabilization works began by widening the tunnels (except where there were original architectural elements) and putting in place a masonry lining. The masonry walls mimic original structures from Classic Copan, and were made using mortars with Portland cement. The same cement was used also to repoint the ancient walls, making it sometimes hard to discern between additions and the original parts, even

though the modern stones are usually smaller and more regularly sized. The preservation methods from the 1990's changed, keeping stabilization works but also backfilling some stretches. This time, the new masonry walls and arches did not directly touch the original walls, with the installation of plastic tarps between the new masonry and the original when necessary. With time, different local and diffused stabilization works were carried out, unfortunately without a precise strategy (Figure 18). In many sections, the stabilizing masonry structures are affected by crack patterns indicating a critical stress state.

Table 2. Total length of the four type of tunnel sections, and distance to the external surface (μ=average, s=standard deviation) (Pires *et al*., 2021).

		R_{min} to external surface (m)					
Section	Total Length			sloped surface		horizontal surface	
Type	(m)	μ	s	min	max	min	max
T1	51.0	15.0	7.8	4.0	4.0	15.0	20.0
T2	56.0	17.0	4.4	-	-	8.5	20.0
T3	183.5	10.6	3.8	3.0	10.0	9.5	17.0
T4	66.5	7.7	4.3	2.0	11.0	9.0	12.5

Figure 17. Examples of local collapses: (left) at the interface between lined and unlined stretches; (right) in an unlined tunnel excavated in fine yellow sand (*girún*) (modified after Lacombe et al., 2020).

Figure 18. Different kinds of local stabilisation interventions (modified after Lacombe *et al*., 2020).

2.3 *The contribution of geotechnical engineering: rational maintenance of tunnels*

Figure 19 shows in red the tunnel stretches where local collapse was observed from 2017 to 2020, and in blue the ones where the main problem was massive water intrusion during the storms of 2017. Clearly, the extension of damage is such to make the use of the tunnels network critical and dangerous. When looking jointly to the history of collapses and heavy rain or storms, a correlation is observed. Furthermore, the critical sections where collapse concentrates are in the unlined part, but close to the lined ones.

Figure 19. Map of local tunnel collapse and of water intrusion observed from 2017 to 2020 (modified after Pires, 2020).

Since the soil was originally compacted in unsaturated conditions, it has to be expected that a change in the degree of saturation has a mechanical effect, obviously more critical in the unlined sections. A main instance, happened after the installation of an impermeable geomembrane over the East Court (Patio Este) in 1998, confirms this observation: shortly after the installation (which was done without proper collection and disposal of rain water accumulated on top of the geomembrane), an hurricane (hurricane *Mitch*) struck the region, bringing intense rainfalls. Three areas along the East Court perimeter suffered tunnel collapse at the time of the hurricane, and three more the year after (Figure 20).

Figure 20. Aerial photo of the Copan Acropolis (east at top) showing approximate positions of tunnel collapses after hurricane Mitch (1998 in blue, and 1999 in yellow), with the position of the East Court membrane marked in red (modified after Lacombe et al., 2020).

In fact, the tunnel sections adjacent to the perimeter of the East Court suffered major infiltration in the earth fill from the edges of the improperly installed geomembrane because of the water build-up at ground level.

To check water effect on the mechanical behavior of tunnels, 2D FEM analyses were carried out with PLAXIS 2D on both lined and unlined sections. The earth fills in which tunnels have been excavated in the considered area is unsaturated *girún*. In this work, the shear strength of this unsaturated granular soil has been simply considered as:

$$\tau = (\sigma - u_a) \cdot tan(\varphi) + (u_a - u_w) \cdot S_r \cdot tan(\varphi) \quad (1)$$

where $(\sigma - u_a)$ is the net normal stress, $(u_a - u_w)$ is the matric suction (s), S_r is the degree of saturation of the soil and φ is the effective shear strength angle. The second term of the second member of eq. (1) is often designated as 'apparent cohesion':

$$C_{unsat} = (u_a - u_w) \cdot S_r \cdot tan(\varphi) \quad (2)$$

Since the apparent cohesion reduces as the degree of saturation increases, water infiltration caused by the frequent heavy rains locally reduces the available shear strength of the unsaturated soil. Therefore, the numerical analyses were carried out considering the cohesive term of the Mohr-Coulomb strength criterion as a state parameter (eq. (2)) (Figure 21), depending on the relevant soil-water characteristic curve.

The safety factor for the unlined section with an ancient wall on one side (T2) is 10% to 30% higher than for the section with no wall (T1) for low to medium degrees of saturation (Figure 22). However, approaching saturation the values converge, resulting into failure for $S_r > 80\%$.

Clearly, FS increases passing from unlined to lined sections. As long as drainage is ensured (i.e. there is no or little water pressure on the lining), the lining provides high safety margins to the tunnel, whatever the soil saturation degree, and ensures stability with high margins even in fully saturated conditions. But drainage has to be granted, which is not always the case on site. Real safety conditions can therefore be significantly lower, and have to be analyzed case by case.

The numerical results obtained (including those not reported here for the sake of brevity, see Pires et al. 2021) confirm how relevant the role of the degree of saturation in the compacted earth fill is for the stability of the unlined parts of the tunnels excavated in the Acropolis. Clearly, in the lined sections, the degree of saturation is locally higher than in the unlined ones because of the reduced exposure to draining surfaces. This explains why most collapses have taken place at the interface between the two kinds of section, where the gradient of saturation degree caused by the different boundary conditions triggers a water flow towards the closest outcome, which is the first unlined section. Eventually, this will locally result into a degree of saturation higher than in other unlined sections, further from the lined stretch, and thus in lower safety factors that may trigger the collapse of blocks.

To confirm these preliminary results, more extensive survey of the complex 3D tunnels geometrical layout is however needed, along with an adequate experimental characterization of the earth fill and of the tunnels lining masonry materials.

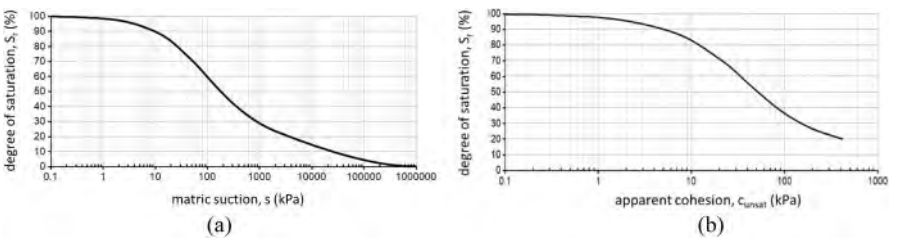

Figure 21. (a) Soil-water characteristic curve and (b) apparent cohesion versus saturation, for the silty sand infill (*'girùn'*).

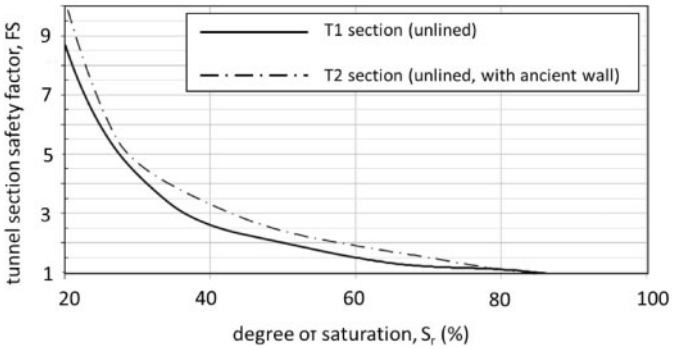

Figure 22. Safety factors for the unlined tunnel sections T1 and T2 at a depth of 20 m as a function of soil degree of saturation of soil (modified after Pires *et al*., 2021).

These activities were planned in 2020 but never carried out because of the Covid pandemic, that dramatically reduced the possibility to operate on site and, for the author, to travel to Copan.

Based on the preliminary results herein summarized, the following recommendations have been made for the short term: correctly collect and dispose rain water at ground level, minimizing infiltration; carry out a constant monitoring of the water content in the soil around tunnels, especially at the transition between lined and unlined sections, to anticipate safety issues (instrumentation still to be put in place); ensure drainage in the lined tunnel sections to minimize water pressure on the lining; avoid the addition of new tunnels too close to the existing ones, continuously updating the 3D map of the tunnels system.

From a strategic point of view, the preservation of the invaluable heritage existing deep inside the Copan Acropolis (Figure 23) would ask for a massive application of these preservation actions.

In the medium to long term, new lining should be installed where necessary, respectful of the critical chemical conditions of the buried Maya stuccos, and possibly new tunnel stretches connecting to the outside or to other tunnels should be added as escape paths for safety reasons, to avoid extremely long blind parts. A complete lack of interaction (either mechanical or chemical) between the Maya buried structures and the new lining should be also ensured.

However, because of the length of the tunnels network and of the critical lack of funding, this whole program is unfeasible, at least in the short period. Therefore, backfilling of some parts in critical safety conditions will be required, after a more detailed analysis of the different parts of the network, sharing the decision among archaeologists, art historians and engineers (geotechnical, structural and chemical). Backfilling will in fact make not accessible sites of possible interest, and will not allow further investigations along those directions.

Figure 23. Examples of parts of the buried Maya structures discovered in Copan through archaeological tunnelling (modified after Lacombe et al., 2020).

3 INTERFERE WITH THE PAST OUT OF NECESSITY

3.1 *The Crypta Neapolitana*

This tunnel has a long-lasting story, that goes along with the development of the town of Napoli (Italy), and has been already dealt with from a geotechnical point of view in the recent past (Amato *et al*., 2001, Viggiani, 2017). Its conception is attributed to Lucio Cocceio Aucto, a Roman architect (in a broad sense, being him a fine engineer as well) of the first century AD, highly appreciated by the emperor Octavianus Augustus and designer of the Temple of Augustus (later turned into the catholic church of San Procolo) in Pozzuoli and of the other two long Roman tunnels (Seiano Grotto and Cocceio Grotto) in the area around Naples. The Crypta Neapolitana runs close to the east-west direction, and crosses the Posillipo hill, that separates the Gulf of Pozzuoli from that of Naples (Figure 24).

According to some recent studies of the Roman tunnels in the Neapolitan area (Escalona, 2022), the hypothesis that a smaller tunnel along its longitudinal axis already existed before Cocceio's work is also considered. Well before the Romans took the area, information reported in the Odyssey of Homer (11.14) and interpreted by historians indicate that the mysterious population of Cimmerians lived in the area around the Lake Avernus (close to the later Cocceio Grotto, see Figure 26 on the left) during Ulysses peregrination on the Italian coasts. The Cimmerians were an old nomadic Indo-European people coming from the Caspian steppes, on the northern shores of the Black Sea, who probably settled in the Campania Region (as also referred by Strabo and Plinius the Old) between 1000 BC and 800 BC. During their migration, they had previously settled in Cappadocia, where they learned to excavate and live in underground spaces. Ever since they have been known as the people of darkness, living in underground houses, connected among them with tunnels. In the Phlegrean Fields, they had an oracle (a Sibyl, a sorority sister) that was venerated by the pre-Hellenic native populations. Those who lived about the oracle had an ancestral custom, that no one should see the sun, but should go outside the caverns only during the night.

Escalona (2022) claims that the existence of a small chapel within the Crypta Neapolitana may indicate a deeply seated room, originally conceived for burial (Cimmerians used to bury their Kings or leaders in the deepest heart of mountains) or religious reasons, to be reached through a small tunnel coming from the western side of the hill. Even though this is still a matter of scientific

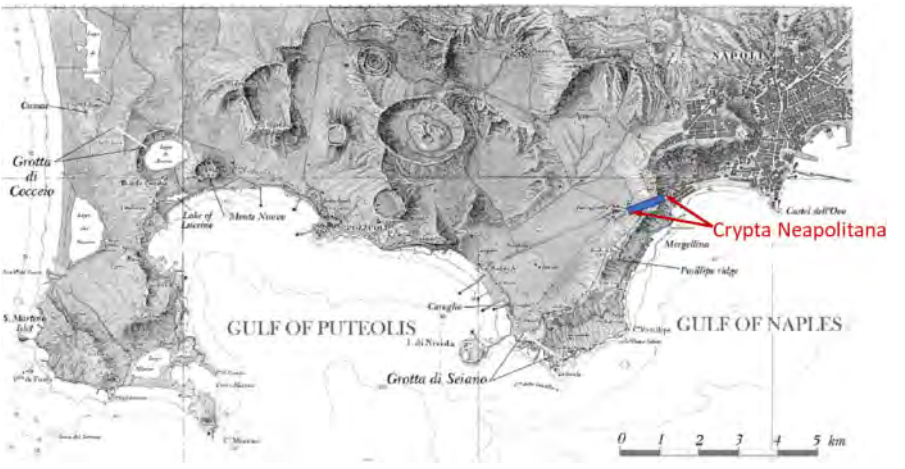

Figure 24. Map of the coastal region called *Phlegrean Fields* with in evidence the location of the Crypta Neapolitana through the Posillipo hill (The old town of Naples is on the East side). The topography refers to the second half of the XIX century, while nowadays the whole area on both sides of the tunnel is densely urbanized, the two towns of Napoli and Pozzuoli merging into a unique built environment.

discussion, it would somehow justify the mediaeval legend claiming that the tunnel was excavated by the poet Virgil in a single night: in fact, this myth could reflect a rather fast construction of the tunnel, corresponding to a possible renovation or enlargement of an originally existing one, and not to a completely new excavation. Just an hypothesis, certainly fascinating.

In any case, the Roman tunnel excavated (or enlarged) in the first century AD had the clear goal to enhance and simplify the communication between the very active town of Puteolis (nowadays Pozzuoli), where the largest commercial harbour of western Mediterranean sea was located, and the growing town of Neapolis (Napoli), and was part of a large number of public works constructed in the area under the coordination of Marcus Vipsanius Agrippa, who was a close friend and son-in-law of the emperor Augustus (Ferrari & Lamagna, 2015). The Aqua Augusta (Serino) aqueduct was built later, crossing the Posillipo hill in parallel to the Crypta Neapolitana and far only a few meters from it, letting the water flow from the far Serino springs to Puteolis. The original Roman cross section of the tunnel was between 4 and 5 m large, and likely no more than 4 m high (may be even less), with a curved vault and vertical side walls. Its shape is mostly lost, because of subsequent reshaping carried out for centuries. The tunnel is 711 m long, with two inclined ventilation shafts on the two sides of the hill. A longitudinal section with the recent shape of the tunnel is reported in Figure 25.

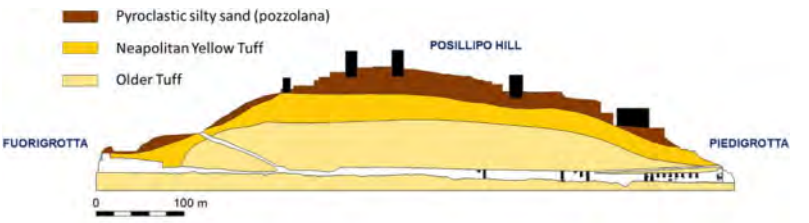

Figure 25. Cross section of the Posillipo hill along the *Crypta* longitudinal axis, with indication of the geological units.

As schematically sketched in the figure, the tunnel crosses different pyroclastic formations. The deeper one is a weakly cemented old tuff, with poor mechanical properties, that can be considered a transition material between an uncemented pyroclastic silty sand (*pozzolana*) and a tuff, with some specific sections in which cohesion is close to zero. Because of the uncomplete cementation process, this formation is not affected by the typical syngenetic cooling fractures observed elsewhere in town in well cemented tuff. Neapolitan Yellow Tuff covers the old tuff in the hill of Posillipo. As well known, it is a soft, light rock with a good degree of cementation, with a number of subvertical and sub-horizontal cooling fractures. The Crypta Neapolitana crosses the Neapolitan Yellow tuff formation only in the first 100 m on the western side, and only for few meters on the eastern one. So, most of the tunnel is excavated in the old tuff. Because of this, the eastern and western parts of the tunnel were unlined, while the central part was lined with masonry, with only few parts of *opus reticulatum* still visible.

The first documented intervention into the tunnel was carried out in 1445 by the king Alphonse of Aragòn to lower the eastern entrance. A century later, the Spanish viceroy Pedro de Toledo further lowered this part of the tunnel, paving the roadway. Other retrofitting works were done under Pedro Antonio d'Aragona (XVII century), Charles III Bourbon (1748), the Municipality of Naples (1893, with the insertion of a number of strengthening masonry arches in the eastern part of the tunnel), till 1917 when, because of ongoing local collapses and of the diffused risk of collapse of blocks, the Crypta Neapolitana was closed, its crucial connecting role between the two sides of the hill being taken from the newly built and close by rail and car tunnels.

In 1930, the eastern part of the Crypta was partly filled, and the floor raised back as much as 9 m, to accommodate the entrance to an outside green area where the supposed tombs of Virgil and of the Italian poet Leopardi are placed. Figure 26 show a reconstruction of the changes in time of floor elevation (Amato *et al*., 2001).

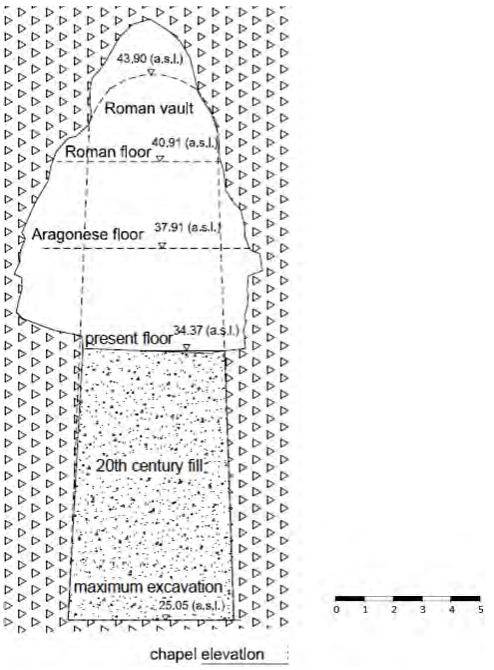

Figure 26. Cross section of the Crypta Neapolitana at 20 m from the eastern entrance in its current state, along with the reconstruction of the different elevations of the floor in time (modified after Amato *et al*., 2001).

Figures 27 and 28 show the two entrances of the tunnel. Recently, bolted steel arches were placed to support the vault in the first 30–40 m on the western side (Figure 27).

The tunnel is actually in very bad static conditions, with diffused collapse of large blocks along its axis, especially in the central part, where site survey is now almost impossible for safety reasons. The Roman masonry lining has collapsed along the whole lined stretch, with only few parts, with no static role, still standing. A large part of the masonry supporting structures placed in the 19th century collapsed. Figures 29 and 30 show some photos of a recent survey (January 2022) from both entrances of the tunnel, giving a clear idea of the widespread state of instability.

Figure 27. Western entrance of the Crypta Neapolitana in a recent photo. On the vault, the recently placed bolted steel arches.

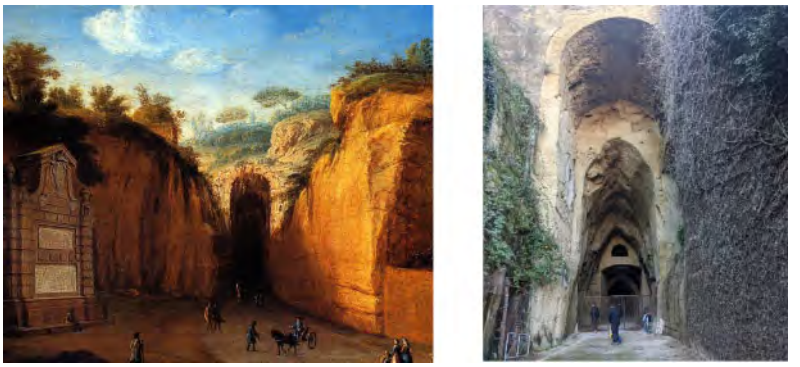

Figure 28. Eastern entrance of the Crypta Neapolitana in a painting (van Wittel, XVIII century, oil on copper) and in a recent photo.

Figure 29. From top left: pictures from the western entrance till ca. progressive 350 m. Collapse of blocks, tension cracks and collapse of masonry lining are clearly visible.

Figure 30. From top left: pictures from the eastern entrance till ca. progressive 150 m. Masonry arches well preserved in the first part, with complete collapse of side walls in the final part. Large subvertical rectangular blocks sometimes on the verge of instability failure.

3.2 *The contribution of geotechnical engineering: tunnels reinforcement and reuse*

To check the static conditions of the tunnel, an in situ investigation was carried out about 20 years ago. Boreholes from the ground surface and core drills from within the tunnel were executed. Samples retrieved during coring were tested to get the uniaxial compressive strength σ_c, while flat jack tests were carried out in some sections of the tunnel to quantify the in situ vertical stress (Figure 32). In the old tuff, i.e. for most of the tunnel length but the parts close to the two entrances, the compressive strength values are in the range 0,5 MPa $< \sigma_c <$ 2 MPa, while in the Neapolitan Yellow Tuff σ_c is as high as 6 MPa. The comparison between σ_c and the vertical stress estimated with flat jack indicates that, for distances from the western entrance between 100 m and 200 m, the rock around the tunnel is locally on the verge of failure, consistently with the evidence of diffused collapse.

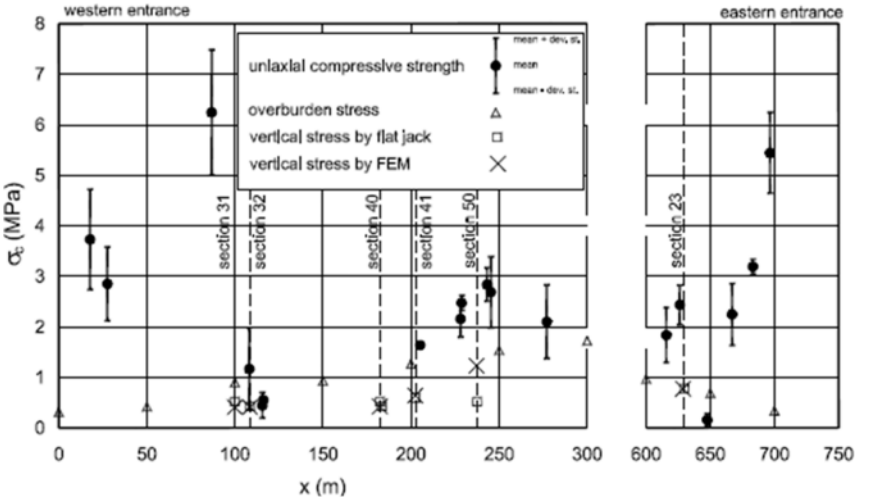

Figure 31. Values of the uniaxial compressive strength of tuff and in situ stress along the axis of the Crypta. Distances taken from the western entrance (modified after Amato *et al*., 2001).

A detailed geometrical survey of the tunnel was also carried out with a laser scanner (Figure 32). The characterization of the rock mass was done using the Hoek & Brown failure criterion (Bilotta, 2022), then converting the parameters into the ones (c, φ) of the Mohr-Coulomb failure criterion, to be used in elastic-perfectly plastic 2D analyses carried out with Plaxis. Figure 33 briefly summarises the results in terms of plastic stress points (red and white points corresponding respectively to shear and tension failure), reporting also the values of the safety factor corresponding to a mechanism of local collapse (blocks failure). As expected, the most critical situation is in section C (see Figure 33) (FS < 1), in the part of the tunnel with the worst mechanical properties, while the other sections are globally stable, with the exception of section F (FS ≈ 1).

Assuming that yielded volumes progressively collapse, the numerical analyses indicate that most times the critical mechanism is the creation of tension cracks on the sides and the subsequent collapse of blocks, consistently with the experimental evidences. Since this mechanism could be perverse (i.e. local collapses, and subsequent reshaping of the sections, may trigger further collapses and reshaping, and so on), the overall indication is that the preservation of this Roman tunnel asks for a diffused reinforcement.

This brings the discussion to the constraints posed by the relevance of the historic site. The wounds of time are in this case clearly visible, and there is no reason to try and replicate the original Roman cross section, whose traces are mostly lost. The largest part of the tunnel has been naturally reshaped as a result of a stress redistribution within the rock mass or later human interventions. Then, the question arises about what should be preserved. In this case, it seems that

the strongest legacy is linked to the role of the Crypta Neapolitana, which is the connection of two neighbourhoods separated by the hill, as demonstrated by their names: *Fuorigrotta* (literally, *out of the grotto*) the one on the west side, and *Piedigrotta* (literally, *at the entrance of the grotto*) the one on the east side, the grotto obviously being the Crypta Neapolitana. This path has been a living part of the city for at least two thousand years, and still keeps traces of this long lasting life (Figure 34).

Therefore, according to the author's opinion a hard interference with the iconic integrity may be justified in this case to let the Crypta Neapolitana return to its role of a connecting path. In particular, it should become a pedestrian tunnel that would correspond to the best possible preservation of its functional integrity. This is actually a matter of discussion with local authorities. Interventions should include: a new lining in the central part of the tunnel, with new materials and local openings to show details of the old masonry lining or of local connections with the close-by Aqua Augusta aqueduct; a retrofitting and underpinning of the masonry arches on the eastern side; bolting of potentially instable blocks, and bolted nets in the unlined western part of the tunnel excavated in the Neapolitan Yellow Tuff.

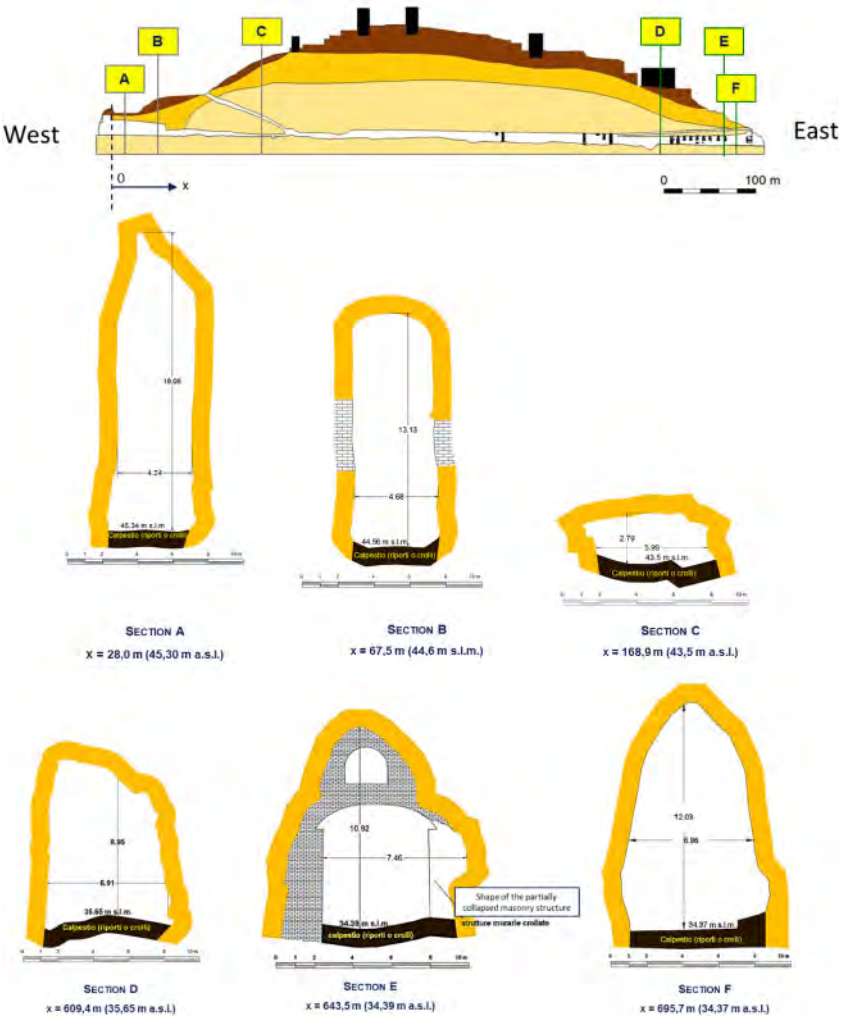

Figure 32. Cross sections (obtained by laser scanning) of the Crypta Neapolitana considered in the numerical analyses, with indication of their position (distance from western entrance) along the tunnel axis.

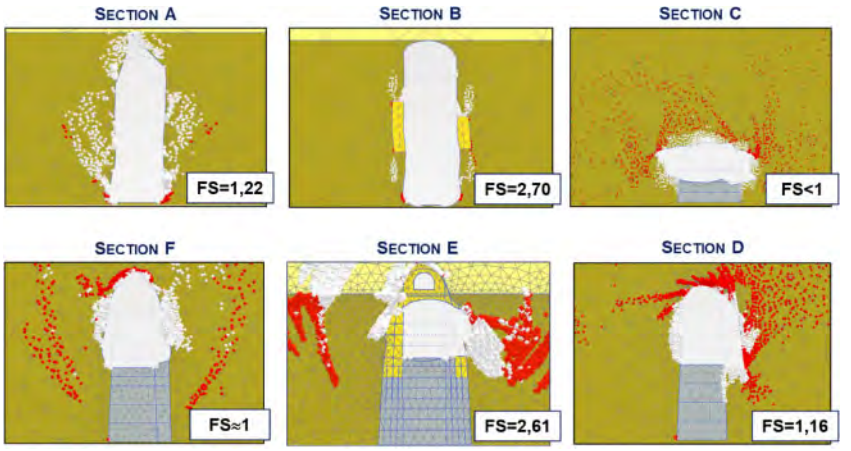

Figure 33. Results of the numerical analyses in terms of plastic stress points (red and white points corresponding respectively to shear and tension failure). FS is the safety factor corresponding to a mechanism of local collapse (blocks failure) (Bilotta, 2022).

Figure 34. Painting of the Persian God Mithra, depicted as the sun, within the Crypta Neapolitana (courtesy of L. Amato). In Napoli, Mithraism dates back to the Hellenistic period, and spread during the 5th century A.C. through prisoners and slaves coming from Cilicia. In some basements in the old town, bas-reliefs depicting the Persian God while sacrificing a bull can be still admired.

4 INTERFERE WITH THE PAST LEARNING FROM IT

4.1 *The Theodosian walls of Constantinople*

The city of Byzantium was relatively unimportant during the early Roman period, but when the Roman influence in the east grew, its strategic position was recognized, and the need to defend it became a priority. Such a need became even more urgent when the Roman emperor Constantine the Great (AD 272-337) gave a sharp impulse to its development, building a new imperial residence in the city and renaming the city Constantinople after himself. In AD 328, the city eventually became the capital of the empire, keeping this role for more than a thousand years. This move, and in general the age of Constantine, conventionally marks the transition from classical antiquity to the Middle Ages.

Since the city was initially located on the European side, it was naturally protected by the sea on the north, east and south, the major problem being to protect it from possible attacks from the inland, on the west side. Constantine arranged a wall to be built (Figure 35) from the Golden Horn to the

Sea of Marmara. As the city grew, however, this confine had to be overcome to accommodate all the people attracted from the new status of the city. An impressive double line of walls was then built on the land side during the reign of Emperor Theodosius II (408–450 AD), after whom they were named, about 2 km to the west of the old Constantinian Wall. The protective system, completed in AD 423, is the result of the skills and dedicated work of Anthemius, a Praetorian Prefect of the East, who did not see his work completed as he died in 414. In their final configuration, the Theodosian walls had a length of about 7 km, completely surrounding the city (Figure 35), thus creating a barrier not only on the west side but also along the whole coastal perimeter.

On the land side the system consisted of two closely spaced defensive lines (Figure 36): an inner wall, with a maximum height of 12 m, and an outer wall, with a lower height, each one fortified by towers placed at some tens of meters apart. The inner towers are as high as 24 m, while the outer ones are ca. 10 m high. The ground level on the terrace (*peribolos*) between the two walls is some meters (ca. 5 m) higher than that (*parateichion*) outside the outer wall, thus giving a dominant

Figure 35. Map of Constantinople at the beginning of the Ottoman Period, with the location of the first defensive wall of Constantine and the location of the outer, much longer Theodosian walls (http://romeartlover.tripod.com/Murter.html). Tower T19, dealt with in this section, is indicated in the south reach of the latter wall.

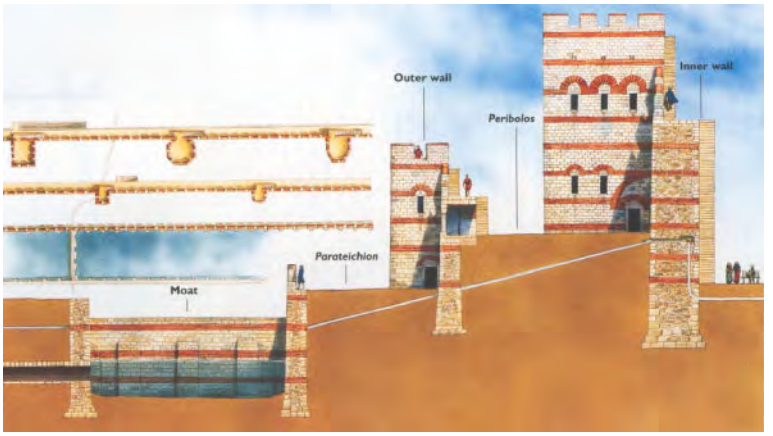

Figure 36. Typical cross section and plan of the Theodosian walls and towers. On the top left of the plan, the different shapes of the towers (modified after Turnbull, 2004).

position to the defenders in case of attack. The *parateichion* is confined on the outside by a moat, originally filled with water supplied by a sophisticated system, as a first defensive means.

Each tower had a battlemented terrace on the top. Its interior was usually divided by a floor into two chambers, not communicating with each other. The lower chamber, opened through the main wall to the city, was used for storage, while the upper one could be entered from the wall's walkway, and had windows for viewing and battling. Access to the wall was provided by large ramps along their side (Turnbull, 2004). The lower floor could also be accessed from the *peribolos* by small posterns.

This defensive system became legendary in the Middle Ages, deemed invincible and considered impregnable for any medieval besieger. The only exception was the sack of 1203-1204 during the fourth Crusade, that was a turning point in medieval history because of the decision of the Crusaders to attack the world largest Christian city. Before and after it, the Theodosian walls saved Constantinople – and the Byzantine Empire with it – during many sieges, even though with the sack of 1203 the city decadence began, and large parts of the empire were lost. The Ottomans unsuccessfully attempted to take the city in 1396 and 1422, eventually succeeding on 29 May 1453 under the guidance of sultan Mehmed the Conqueror, after a six-week siege in which a crucial role was played by the 8 m span cannons used by the besiegers. Part of the walls were largely damaged by the gunpower, and then restored by the Ottomans.

The walls were largely maintained intact during most of the long Ottoman period (1453-1922). Sections began to be dismantled only in the 19th century, as the modern city outgrew its medieval boundaries. Despite the subsequent decadence and lack of maintenance (Figure 37), many parts of the walls and towers survived and are still standing today.

Despite all the sieges they had to face throughout their history, the Theodosian walls were damaged much more by earthquakes and floods than by enemies' attacks. Earthquakes, in particular, were a major source of damage. Figure 38 reports the epicentres and years of the main historical earthquakes around the Marmara region, showing the extremely high seismicity of the area. The strong Kocaeli-Adapazari earthquake of AD 447 (only 24 years after walls completion), for instance, resulted in the partial collapse of 57 towers and large sections of the walls, and also subsequent

Figure 37. State of decadence of the Theodosian walls in the early 20th century, with clear evidence of unrepaired seismic damages to the towers (German Archaeological Institution, 1939).

major earthquakes (1509, 1719, 1754, 1766 and 1894) caused significant damages to the walls and towers (Ispir et al., 2014). Repairs were therefore undertaken on numerous occasions, as testified by the inscriptions commemorating the emperors or their servants who undertook the restoration works, and most of the surviving towers of the main wall have been rebuilt either in Byzantine or in Ottoman times.

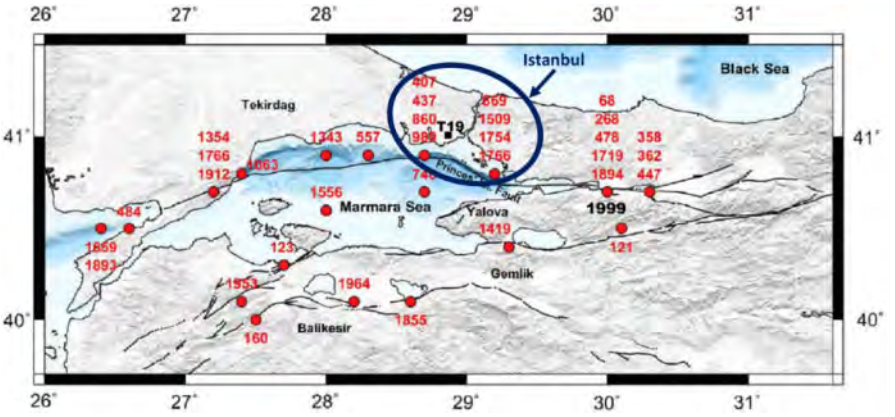

Figure 38. Historical earthquakes in the Marmara region (modified after Ambraseys, 2002), indicated with epicentral position and date. The degrees on the frame indicate North parallels (on the vertical sides) and meridians (on the horizontal sides). The area of modern Istanbul is highlighted, with the position of tower T19.

The inner wall, which is connected to the taller towers, has a thickness of ca. 5.00 m and is made of a rubble core confined between two shells built of nicely shaped squared blocks, having a thickness of 30-50 cm (Ahunbay and Ahunbay, 2000). The original, 5th century Byzantine masonry is of a fine quality, with brick bands – approximately 0.40 m high – laid at regular intervals of dressed stones. These bands run through the entire thickness of the wall, binding the structure firmly at different levels. The blocks used for the inner towers and wall in the original fifth-century construction are made of sandstone, quarried close by. The original mortar was a mixture of lime, crushed bricks and bricks powder. In subsequent restoration works, lime-based mortars were used as well.

While until the end of the 12th century the reconstructions largely replicated the original model, later modifications introduced a clear change, from both the formal and the construction point of view, and the strengthening brick bands were not used any more. Since the nearby quarries run out in the Byzantine period, after the 12th century the blocks used to restore walls and towers had different origin and had a much more irregular shape. Because of all these reasons, the resulting masonry structure was less refined and certainly less stiff.

UNESCO's designation of this defensive system as a World Heritage site in 1985 resulted into an extensive, large-scale restoration and conservation program, still under way. On the towers, the restoration works consisted in cleaning them from the vegetation and rebuilding the masonry structure, trying to replicate wherever possible the original Byzantine style. Most times, the walls and towers were over-restored and refaced rather than being repaired, possibly destroying many historical evidences.

The strong 1999 Kocaeli earthquake, whose epicentre was located about 80 km south-east of Istanbul, caused major damages to parts of the walls and to some towers. Interestingly, in some cases the damages were larger on the towers that had already undergone restoration works. As quoted by Turnbull (2004), prof. Zeynep Ahundbay (chair of Historic Preservation at Istanbul Technical University) said after the 1999 earthquake: '*The restoration campaign of the 1980s has been criticised due to its resort to the reconstruction of ruined towers and gates instead of stabilising*

*and consolidating dangerous structures. The performance of the 20*th *century repairs during the recent (1999) earthquake …omissis…constitutes a good lesson for future restoration*'.

Indeed, words to be reminded. Because of the symbolic heritage carried by this impressive, iconic defensive system, a contribution to interpret the dynamic behaviour of the walls and towers was recently attempted (Flora et al., 2021, Somma *et al*., 2022) with the precise goal to plan better preservation actions for the future, cooling down what seems to be an endless game between men and nature. The attention was initially focused on one rectangular tower (tower T19), located on the south side of the land walls, close to the Marmara Sea and between the Belgrade and Golden Gates (Figure 35). It is one of the tallest towers connected to the inner walls, restored in the early 1990's, thus before the 1999 Kocaeli earthquake struck Istanbul. Different construction and restoration techniques are now superimposed on it (Figures 39 and 40) (Sarimese, 2018): the lower part is still made of original Byzantine masonry, while the upper part is only partially (in the centre of the west side) made of the Ottoman one. The recent restoration works completed the tower in the original Byzantine style. As a consequence, the brick bands do not completely bound the structure. The earthquake largely damaged the tower, causing the opening of cracks at the connection between the reconstructed and the Ottoman masonry (Figure 39b) on the west side, typical diagonal cracks on the windows on the south side and the collapse of the whole east side and of upper corners wedges.

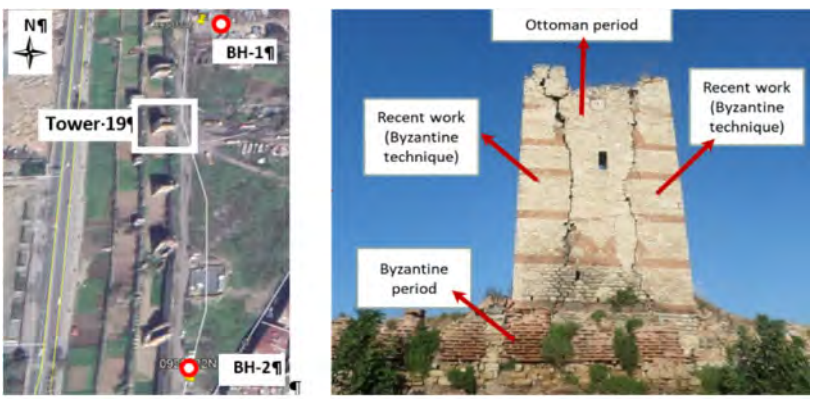

Figure 39. (a) Position of tower 19 with indication of nearby bore holes (BH-1 and BH-2) and (b) recent picture of the west side of the tower. The different, superimposed construction techniques can be clearly seen: the original Byzantine one (before 12th century) in the lower part, the later Ottoman one in the central part, without brick bands, and on the sides the restoration works carried out with the Byzantine technique, using the brick bands (Sarimese, 2018). The damages caused by 1999 Kocaeli earthquake are clearly visible.

Figure 40. Recent views of all sides of tower 19. The damages caused by 1999 Kocaeli earthquake are clearly visible.

4.2 *The contribution of geotechnical engineering: avoid preservation mistakes*

Clearly, all the restoration work was lost in what cannot be considered an unexpected natural event. To carry out a simulation of what has happened in 1999, detailed laboratory and in situ investigation was carried out (Figures 41 and 42), and the closest recorded outcrop motion (Fatih station, 4.8 km away) was deconvolved at the bedrock, using the soil profile and properties at the Fatih station site (Ince, 2008), and then considered as the seismic input at the bedrock of the tower T19 site (Flora *et al*., 2021).

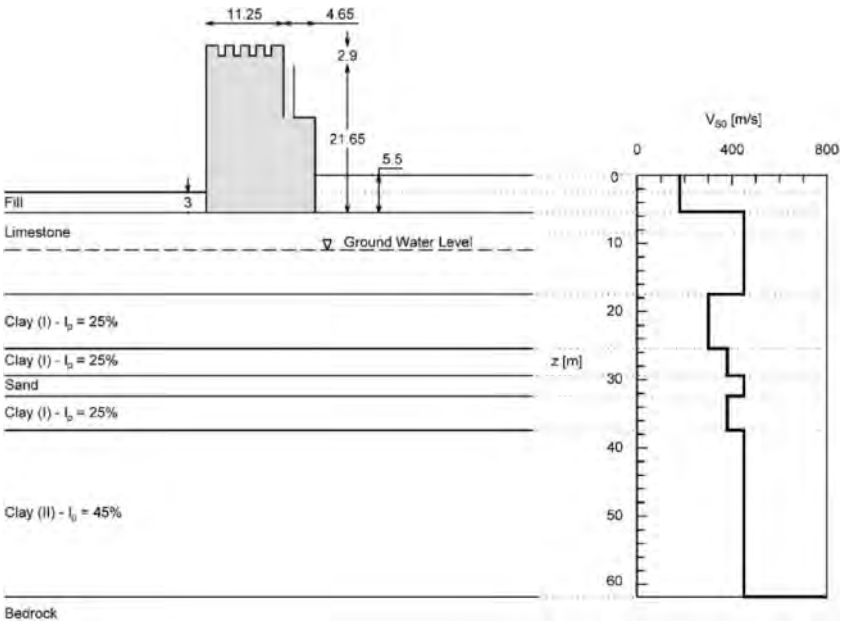

Figure 41. Soil and V_S profiles at the site of tower 19 (modified after Somma *et al*., 2022).

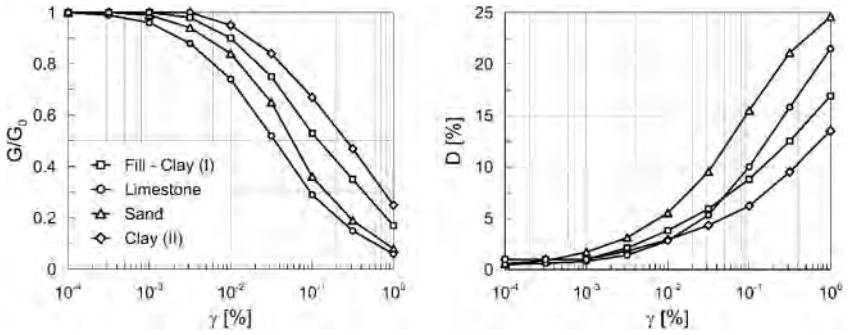

Figure 42. Shear modulus and damping ratio curves for the different soil layers (modified afterFlora *et al*., 2021).

Seismic site response analysis shows a relevant amplification effect, with a fundamental frequency of the subsoil of 1.55 Hz (Figure 43a), close to the predominant frequency of the Kocaeli signal (1,85 Hz, Figure 43b), indicating the occurrence of resonance. Thus, the remarkable amplitude of the Fourier spectrum close to this frequency is not a startling result, with a value of the calculated PGA as high as 0.34 g.

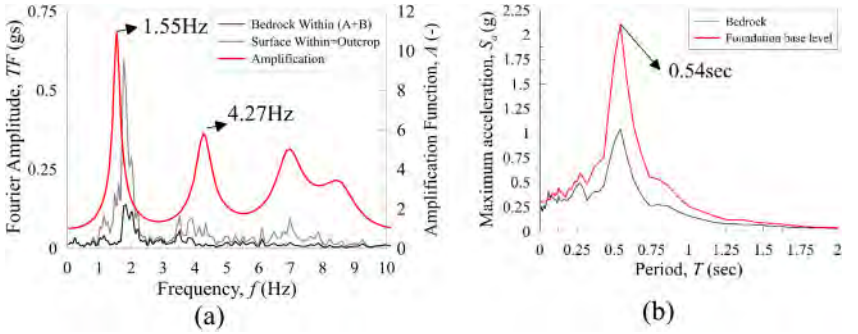

Figure 43. Fourier (a) and acceleration (b) response spectra compared with the input motion applied at the base (bedrock) of the soil profile (Somma *et al*., 2022).

3D dynamic numerical analyses were carried out to interpret tower T19 behaviour during the 1999 earthquake (Figures 44 and 45), considering soil-structure interaction (SSI) or a fixed base, an equivalent linear elastic or a non-linear elastic-plastic behaviour for the subsoil and the tower. The tower was modelled considering two extreme scenarios, i.e. a less stiff Ottoman style masonry (M1) and a stiffer Byzantine style masonry (M2), being the real structure composed of both. The seismic input was separately applied in the x or y directions, defined respectively as the longitudinal and transversal axes of the wall (Figure 44).

The details of the analyses are reported in Somma *et al*. (2022). Figure 46 indicates that the existence of a relatively stiff layer of limestone underneath the foundation reduces the effect of dynamic soil-structure interaction; therefore, the natural period T of the tower shows relatively small increments considering the more realistic, compliant scenario (i.e. with SSI). However, being on the raising part of the response spectrum, even a small increase of T may correspond to a relevant increase of the seismic demand, as extremely evident in the × (less stiff) direction for the Ottoman (M1) masonry (top left of Figure 46), for which the seismic demand is the highest possible (peak of the spectrum). Therefore, this is a typical case in which neglecting SSI would not be conservative and would lead to an underestimate of the seismic action on the tower even if the tower is founded on a relatively stiff material.

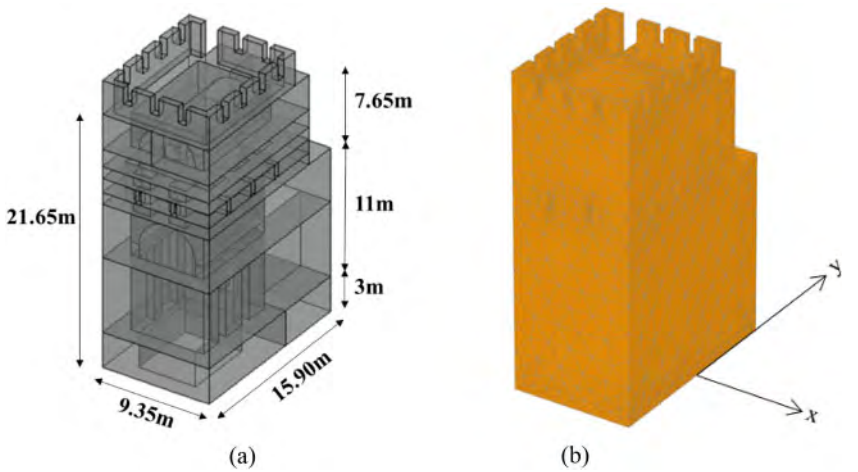

Figure 44. Tower 19: (a) geometric model and (b) Plaxis3D mesh (x=wall's longitudinal axis; y=wall's transversal axis).

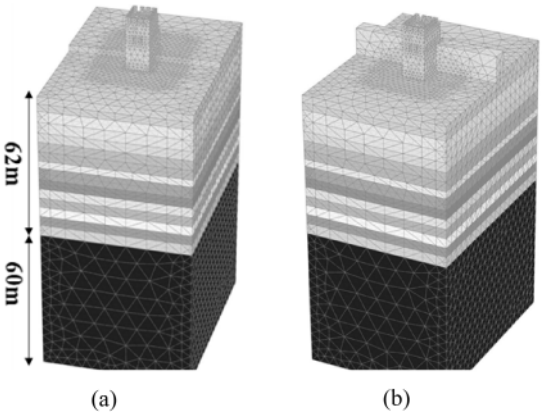

Figure 45. Plaxis3D model of the subsoil with Tower 19 considering (a) or neglecting (b) the inner wall.

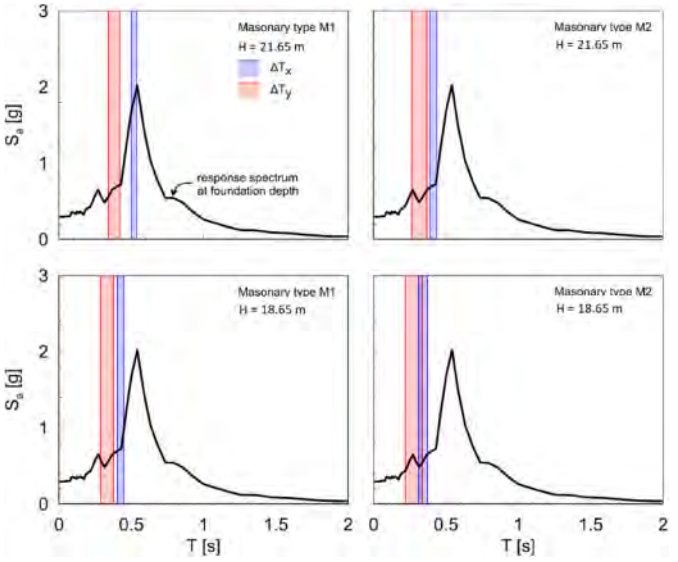

Figure 46. Equivalent elastic analyses: tower 19 seismic demand considering or neglecting dynamic soil-structure interaction in the two directions x and y, for both types of masonries (M1 and M2) and for different ways to consider the height of the mass centroid: at the foundation level (H = 21.65 m) or at ground level (H = 18,65). Period elongation indicated by the coloured bands (see legend on top left) (modified after Somma et al., 2022).

However, Figure 46 also shows that the seismic demand of tower T19 is for the Kocaeli earthquake always very high, whatever the considered scenario and earthquake direction.

The effect of seismic shaking is also shown for the non-linear analyses in terms of maximum principal tensile stress shadings in Figure 47, indicating that tensile strength (200 kPa) is reached in large areas, the red shading suggesting possible critical failure mechanisms, mostly concentrated below the first floor and at the first floor itself. These mechanisms are certainly consistent with the ones that took place in 1999 and largely damaged the freshly restored tower (Figure 40). Despite unavoidable uncertainties and simplifications (taken into account considering different scenarios), all the results demonstrate that the partial collapse of tower T19 during the Kocaeli earthquake is

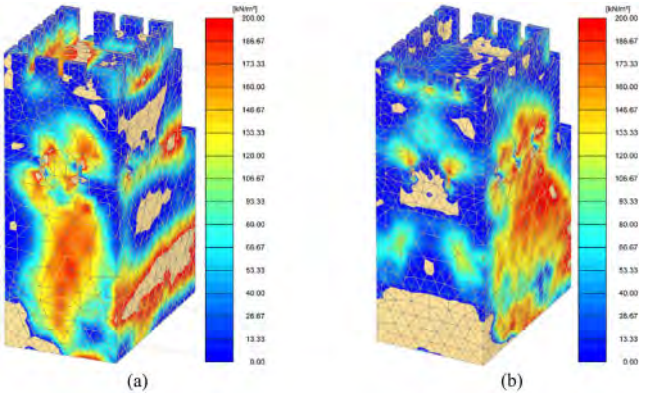

Figure 47. (a) Contours of principal maximum tensile stresses for tower 19 (compliant base, masonry M1): (a) seismic action in the x direction; (b) seismic action in the y direction.

not a surprise, being just the repetition of an event happened several times since Theodosian walls construction in the fifth century. Similar considerations could be done on the other towers damaged during the same earthquake, with differences among them linked to different site amplification effects on the seismic demand.

Then, the question to ask is what to do to step out of this reconstruction and destruction game between man and nature. From the geotechnical engineering point of view, the idea of using a Geotechnical Seismic Isolation (GSI) solution is intriguing, because it is the best way to avoid touching the structure to be protected, thus limiting to a minimum the interference with the heritage carried out by it. GSI technologies may aim to either reduce or increase soil rotational and translational stiffnesses, to increase damping or to add some soil mass to the system. All these actions modify soil-structure interaction, either reducing or increasing the natural period of the structure (the choice therefore depending on the response spectrum of interest and on the original structural period T), and can be achieved with a number of technologies (e.g. Flora et al. 2018). However, because of the high seismicity of the Istanbul area and of the poor structural qualities of tower T19 (and of the others as well), GSI by itself would not be sufficient.

This is confirmed by the results of the analyses carried out considering two simple and opposite GSI interventions: (i) lateral disconnection of the structure from the soil to the foundation base; (ii) stiffening of the soil around the tower, to be obtained with partially overlapped jet grouted columns. The previous approach is extremely simple and respectful, and has the goal to reduce the rotational stiffness of the soil-foundation system (with the trade-off of reducing also radiation damping);

Table 3. Results of the visco-elastic analyses considering the effect of 2 GSI interventions. The variation of spectral pseudo-acceleration Δa is referred to the fixed base scheme (Somma *et al*., 2022).

		masonry M1			masonry M1		
model SSI conditions	earthquake direction	T (s)	a(T) (g)	Δa (g)	T (s)	a(T) (g)	Δa (g)
fixed base	x	0.49	1.60	–	0.39	0.69	–
compliant base		0.50	1.75	+0.15	0.41	0.72	+0.03
foundation lateral disconnection		0.56	1.86	+0.26	0.46	1.19	+0.50
lateral soil stiffening		0.40	0.70	−0.90	0.31	0.50	−0.19
fixed base	y	0.33	1.58	–	0.26	0.54	–
compliant base		0.36	1.63	+0.05	0.31	0.55	+0.01
foundation lateral disconnection		0.38	0.68	+0.10	0.33	0.56	+0.02
lateral soil stiffening		0.29	0.54	−0.04	0.24	0.50	−0.04

the latter has the opposite goal of increasing the rotational stiffness. Table 3 reports the results of the visco-elastic analyses, clearly indicating that for the Kocaely earthquake only a stiffening GSI intervention would have been of some help for the structure, because in this case (very shallow foundation, stiff layer underneath) the lateral disconnection is not sufficient to increase the period T in such a way to pass over the peak of the response spectrum, reducing the seismic action.

Similar considerations can be done looking at the results of the non-linear analyses in terms of the maximum principal tensile stress shadings on the tower, considering the two possible GSI solutions (Figures 48 and 49). Soil stiffening is beneficial, but not sufficient.

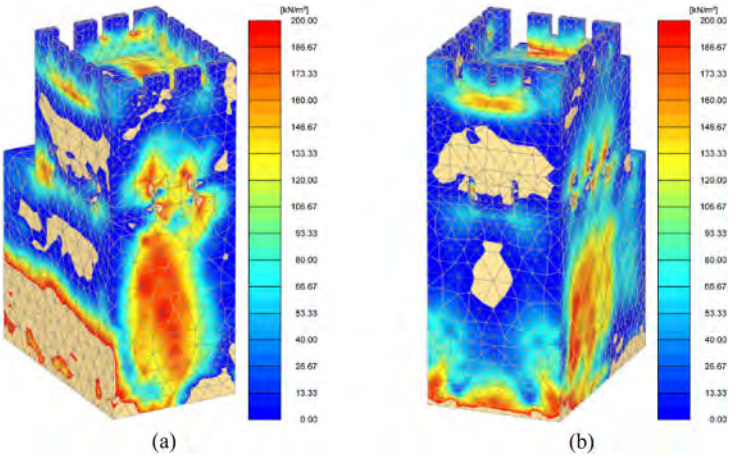

Figure 48. (a) Contours of the principal minimal tensile stresses in the laterally disconnected tower in x-direction at 5.60 s; (b) Contours of the principal minimal tensile stresses in the laterally disconnected tower in y-direction at 7.05 s.

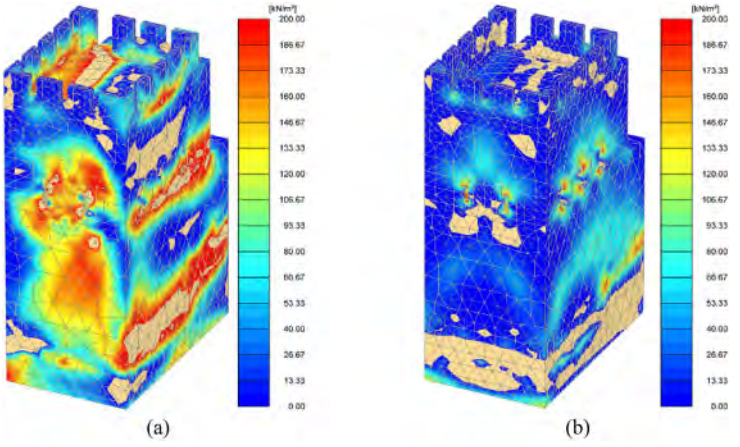

Figure 49. (a) Contours of the principal minimal tensile stresses in the laterally stiffened tower in x-direction at 7.92 s; (b) Contours of the principal minimal tensile stresses in the laterally stiffened tower in y-direction at 6.72 s.

Then, in this case there is no alternative to some strengthening of the structure. From a methodological point of view, after investigating less invasive possibilities, this is certainly consistent with preservation principles, as also explicitly suggested by Brandi himself (1963) with reference to the mitigation of seismic risk for built heritage. There are many literature indications on the best way

to do so (e.g. Cosenza & Iervolino, 2007), and possible alternatives will be taken into account in the future (mitigation of the pushing effect of the vaults, improved interaction between orthogonal walls, improved connection of wall portions built in different periods, strengthening of the weaker portions), discussing about them with structural engineers but also with experts from other disciplines. Obviously, when passing from the back analysis of a single event to the design of future preservation interventions, a probabilistic approach will have to take the place of the deterministic calculations herein reported to back-analyse the effects of the 1999 Kocaeli earthquake.

5 FINAL CONSIDERATIONS (FAR FROM BEING CONCLUSIONS)

The tumultuous development in the last decades of the investigation and monitoring instruments, as well as of the theoretical and numerical tools, has certainly widened the range of options in the hands of engineers when dealing with the preservation of built heritage. When the structure shows wounds of geotechnical origin, these arrows in the quiver should inform the approach, that should concentrate as a first step on the subsoil itself, to understand the causes and possibly to restore equilibrium conditions in the soil or rock mass, lost for a number of possible changes of the boundary conditions. Only if such solutions are not available should the engineer touch the structure to protect. No action should be undertaken without thorough understanding, and the principle of necessity should always be the guiding light. This is possible only if monitoring and surveying, that should be considered as mandatory prevention measures, keep feeding information and alert against critical events.

New technologies should not be considered as enemies of cultural heritage, but their implementation should be taken into account only after a hierarchic analysis of all possible alternatives, that should start by considering the adoption of the original technological choices, consistently with the indications given in Figure 1. In any case, dogmatism should be avoided, being important to save what can be saved in the range of our possibilities, with the highest possible attention to regional traditions of preservation (Petzet, 2004).

In the examples reported in this paper, different geotechnical solutions could be found with the goal of preserving heritage. Partially or highly invasive interventions were also taken into account, when considered necessary. While the reductionistic approach in which civil engineers have been raised is a powerful tool in the solution of most practical problems, the examples show that it may not be suited to face built heritage, for which more sophisticated investigations and analyses are necessary to better catch details that may inform the solution. If it is certainly true that there is no specific geotechnical engineering of monuments and historic sites, we may conclude that there should be a specific need of consistent complexity in the approach to their preservation, for which cost effectiveness should not be the main concern.

Engineers should always face the preservation of built heritage with reference to a principle of responsibility – or rather to an imperative of responsibility, according to Hans Jonas (1984) -, which represents an updated version of Kant's categorical imperative '*act so that the consequences of your actions are compatible with the permanence of an authentic human life on earth*'. Paraphrasing this categorical imperative, we could say to the civil engineer: act in such a way that the consequences of your actions are compatible with the permanence of an authentic life of the historic structure or site on which you operate. When in doubt, we may add, do nothing; and if you have to exceed, exceed in caution, intended not as safety but as preservation.

ACKNOWLEDGEMENTS

Most of the information reported in this paper are the outcomes of team works, with the contribution of many people with different expertise and from different areas of the world, all acknowledged. During the preparation of the manuscript, ideas stemmed from fruitful discussions with (in alphabetic order) Lucio Amato, Giovanni Calabresi, Salvatore D'Agostino, Francesco Escalona, Renato

Lancellotta and Luigi Stendardo, whose contribution is highly appreciated. Emilio Bilotta and Fausto Somma are acknowledged for their valuable help in carrying out the numerical analyses. Above all, the author is indebted with his mentor and friend Carlo Viggiani, who introduced him into the magic world of ageless structures.

REFERENCES

Abrams, E. M. 1994. How the Maya built their world: energetics and ancient architecture. *Austin/University of Texas Press*.

Ahunbay, M., Ahunbay Z. 2000. Recent Work on the Land Walls of Istanbul: Tower 2 to Tower 5. *Dumbarton Oaks Papers*. 54: 227–239.

Amato L. 2022. Personal communication.

Amato L., Evangelista A., Nicotera M.V., Viggiani C. 2001. The tunnels of Cocceius in Napoli: an example of Roman engineering of the early imperial age. *Proc. of AITES/ITA World Tunnel Congress 2001, Progress in Tunneling after 2000*, *Milan 10 –13 June 2001*, vol.1:.15–26, Bologna: Pàtron.

Ambraseys N.N. 2002. The seismic activity of the Marmara Sea region over the last 2000 Years. *Bulletin of the Seismological Society of America*. 92:1–18.

Bell E.E., Canuto M.A., Sharer R.J. 2004. Understanding early classic Copan. *Philadelphia: University Of Pennsylvania Museum of Archaeology And Anthropology.*

Bilotta E. 2022. Personal communication.

Brandi C. 1963. Teoria del restauro. *Edizioni di Storia e Letteratura*. Einaudi.

Burland J., Jamiolkowski M., Squeglia N., Viggiani C. 2013. The Leaning Tower of Pisa. *In Geotechnichs and Heritage, Bilotta, Flora, Lirer & Viggiani Ed.* London: Taylor & Francis Group.

Calabresi G. 2011. The soft approach to saving Monuments and Historic Sites. *Proc. Of the 15th European Conf. of ISSMGE*. Athens.

Calabresi G. 2013. 1st Kerisel Lecture: The role of Geotechnical Engineering in saving monuments and historic sites. *Proc. 18th Int. Conf. of ISSMGE*. Paris: Presse des Pontes.

Cosenza E., Iervolino I. 2007. Case study: Seismic retrofitting of a medieval bell tower with FRP. *Journal of Composites for Construction.* DOI: 10.1061/(ASCE)1090-0268(2007)11:3(319).

Escalona F. 2022. Personal communication.

de Silva F., Ceroni F., Sica S., Silvestri F. 2018. Non-linear analysis of the Carmine bell tower under seismic actions accounting for soil–foundation–structure interaction. Bulletin of Earthquake Engineering, 16(7):2775–2808. DOI: 10.1007/s10518-017-0298-0.

de Silva F. 2020. Influence of soil-structure interaction on the site-specific seismic demand to masonry towers. *Soil Dynamics and Earthquake Engineering 131*. DOI: 10.1016/j.soildyn.2019.106023

D'Agostino S. 2022. Conservation and Restoration of Built Heritage. A history of conservation culture and its more recent developments. *Built Heritage and Geotechnics Series, Lancellotta R. Ed*. London: CRC Press.

De Andrè F. 1967. Bocca di rosa. *Bluebell Records*.

Fash W.L. 1991. Scribes, Warriors and Kings: The City of Copán and the Ancient Maya. *London: Thames and Hudson*.

Ferrari G.W., Lamagna R. 2015. Crypta Neapolitana: non solo un tunnel. *Trasporti e Cultura, Rivista di architettura delle infrastrutture nel paesaggio*, 40, 88–93.

Flora A. 2013. General Report TC301: Monuments, Historic Sites and case histories. *Proc. 18th Int. Conf. of ISSMGE*. Paris: Presse des Pontes.

Flora A., Lombardi D., Nappa V., Bilotta E. 2018. Numerical Analyses of the Effectiveness of Soft Barriers into the Soil for the Mitigation of Seismic Risk. *Journal of Earthquake Engineering, 22(1)*. DOI:10.1080/13632469.2016.1217802.

Flora A., Chiaradonna A., de Sanctis L., Lignola G.P., Nappa V., Oztoprak S., Ramaglia G., Sargin S. 2021. Understanding the Damages Caused by the 1999 Kocaeli Earthquake on One of the Towers of the Theodosian Walls of Constantinople. *Int. Journal of Architectural Heritage*, Taylor & Francis. DOI: 10.1080/15583058.2020.1864512

Ince G. C., Yildirim M., Ozaydin K., Ozner P.T. 2008. Seismic microzonation of the historic peninsula of Istanbul. *Bulletin of Engineering Geology and the Environment.* 67:41–51. DOI 10.1007/s10064-007-0099-9.

Ispir M., Demir C., Alper I., Kumbasar N. 2014. An outline of the seismic damages of several monumental structures in Istanbul after historical earthquakes. *Workshop on Seismicity of Historical Structures*. Istanbul, November.

Iwasaki Y., Zhussupbekov A., Issina A. 2013. Authenticity of Foundations for Heritage Structures. *Proc. 18th Int. Conf. of ISSMGE*. Paris: Presse des Pontes.

Jappelli R. 1991. Contribution to a systematic approach. *in The Contribution of Geotechnical Engineering to the preservation of Italian historic sites.* AGI Associazione Geotecnica Italiana Ed.

Jappelli R., Marconi N. 1997. Recommendations and prejudices in the realm of foundation engineering in Italy: A historical review. *In Carlo Viggiani (ed.), Geotechnical engineering for the preservation of monuments and historical sites*; *Proc. Intern. Symp., Napoli, 3-4 October 1996*. Rotterdam: Balkema.

Jonas H. 1984. The Imperative of Responsibility – In Search of an Ethics for the Technological Age. *The University of Chicago Press*.

Lacombe L., Fash W.L., Fash B. 2020. Plan for the long-term Conservation of the Copan Acropolis Tunnels. *Report presented to the Instituto Hondureno de Antropologia e Historia, October.* University of Harvard.

Lancellotta R. 2013. 11th Croce Lecture: La Torre Ghirlandina: una storia di interazione struttura-terreno. *Rivista Italiana di Geotecnica, 47(2)*. Bologna: Patròn.

Loten S.H. and Pendergast D.M. 1984. A Lexicon for Maya Architecture. *Archaeology Mongraph 8*.

Pane V., Martini E. 1997. The preservation of historical towns of Umbria: the Orvieto case and its observatory. *Proc. of the 1st Int. Conf. on Geotechnical Engineering for the Preservation of Monuments and Historic Sites, Viggiani C. Ed.* Rotterdam: Balkema.

Petzet M. 2004. Principles of preservation. *ICOMOS Open Archive.*

Pires F., Bilotta E., Flora A., Lourenço P.B. 2021. Assessment of Excavated Tunnels Stability in the Maya Archeological Area of Copán, Honduras. *Int. Journal of Architectural Heritage*, Taylor & Francis. DOI: 10.1080/15583058.2021.1931730.

Pires F. 2020. Safety Assessment of the Archaeological Tunnels in Copán – Honduras. *SAHC Masters Course Thesis, Advanced Master in Structural analysis of Monuments and historical Constructions*. University of Minho.

Roca P., Lourenço P.B., Gaetani A. 2019. Historic Construction and Conservation. London: Routledge.

Sarimese F. 2018. Restoration and renovation of 18th and 19th Century Istanbul Land Walls. *Master of Science (MSc) Thesis, Turkish Research Institute of Marmara University* (in Turkish).

Schele L. 1998. Aerial View of Copan. *http://ancientamericas.org/collection/aa010001*.

Settis S. 2018. About the future: the Besieged City. *Interview by Antonio Guerriero*. Electra Vol. 2, 2018.

Sharer R. J., Miller J. C., Traxler L. P. 1992. Evolution of classic period architecture in the eastern acropolis, Copan: A progress report. *Ancient Mesoamerica*, 3(1). DOI: 10.1017/S0956536100002364.

Sharer R. J., Traxler L.P., Sedat D.W., Bell E.E., Canuto M.A., Powel C. 1999. Early Classic Architecture Beneath the Copan Acropolis. *Ancient Mesoamerica, 10(1).* DOI: 10.1017/s0956536199101056.

Sharer R. J., Traxler L.P. 2006. The Ancient Maya. *6th Ed., Stanford University Press*.

Somma F., Bilotta E., Flora A., Viggiani G. 2021. Centrifuge Modelling of Shallow Foundation Lateral Disconnection to Reduce Seismic Vulnerability. *Journal of Geotechnical and Geoenvironmental Engineering*. ASCE 148(2).

Somma F., Lignola G., Ramaglia G., de Sanctis L., Iovino M., Oztoprak S., Flora A. 2022. Earthquake damages to an historic tower: back analysis and possible mitigation measures. *Bullettin of Earthquake Engineering*. Submitted.

Thompson J. E. S. 1958. The Civilization of the Mayas. *Chicago Natural History Museum*.

Turnbull S. 2004. The walls of Constantinople AD 324-1453. *Osprey Publishing*.

Viggiani C. 2013. Cultural Heritage and Geotechnical Engineering: an introduction. *In Geotechnichs and Heritage, Bilotta, Flora, Lirer & Viggiani Ed.* London: Taylor & Francis Group.

Viggiani C. 2017. 2nd Kerisel Lecture: Geotechnics and Heritage. *Proc. Of the 19*th *Int. Conf. of ISSMGE*. Seoul.

von Schwerin, J. 2011. The sacred mountain in social context. Symbolism and history in maya architecture: Temple 22 at Copan, Honduras. *Ancient Mesoamerica, 22(2)*. DOI: 10.1017/S0956536111000319.

Keynote lectures

Taylor & Francis
Taylor & Francis Group
http://taylorandfrancis.com

Geotechnical Engineering for the Preservation of Monuments and Historic Sites III – Lancellotta, Viggiani, Flora, de Silva & Mele (Eds)

The historical underpinning of Winchester Cathedral – Heroic or horrific?

J.B. Burland & J. Standing
Imperial College London, London, UK

J. Yu
Buro Happold, London, UK

ABSTRACT: Winchester Cathedral is not only famous for its size and magnificent Gothic architecture but also for the underpinning work that was carried out between 1905 and 1912. This work ran into a number of serious problems due to a high-water table and poor ground conditions. The former meant that the underpinning work had to be carried out by a diver, William Walker, who has become a legend for his heroic work. The need for the underpinning work has seldom been questioned and the purpose of this paper is to examine the evidence on which this key decision was taken. The lessons learned are important for civil engineers and architects called in to advise on the need for the stabilisation of historic buildings and monuments.

1 INTRODUCTION

Winchester Cathedral is one of the largest Gothic cathedrals in Northern Europe and the longest in overall length. The present building was begun in 1079 and was completed in 1532. It has a cruciform plan, with a long nave, transepts, central crossing tower, choir, presbytery, and lady chapel. The Cathedral is 170 m long, and the vaulting has a height of 24 metres. The central tower is 46 m high. Figure 1 is an aerial view of the Cathedral and Figure 2 is an isometric drawing from the same viewpoint. The various locations within the cathedral are labelled for ease of reference. Figure 3 is a plan view of the present Cathedral. As well as being famous for the magnificence of its architecture, the Cathedral is perhaps equally well known for the heroic efforts of a diver, William Walker, in underpinning virtually the whole Cathedral in the early 20th Century. The need for this underpinning appears to be seldom if ever questioned, yet it was a major undertaking fraught with problems and dangers. The purpose of this paper is to revisit the way in which the decision to underpin was made and the information on which this decision was based.

2 A BRIEF HISTORY OF CONSTRUCTION

2.1 *The Saxon Minster*

Winchester is built on an old Roman settlement with evidence of roads and buildings beneath the present city. The original Saxon church was located just north of the present Cathedral and had its origins in the 7th Century when England's pagan monarchy first became Christian. The church (later known as the Old Minster) was constructed around 648AD. Within a quarter of a century, it had achieved cathedral status. In the early 10th Century, the church was greatly enlarged, going through at least four stages of change and additions within that century. The outlines of the original church and its later extensions have been marked on the ground of the cathedral precincts and

DOI 10.1201/9781003308867-3

Figure 1. Aerial view of Winchester Cathedral looking south.

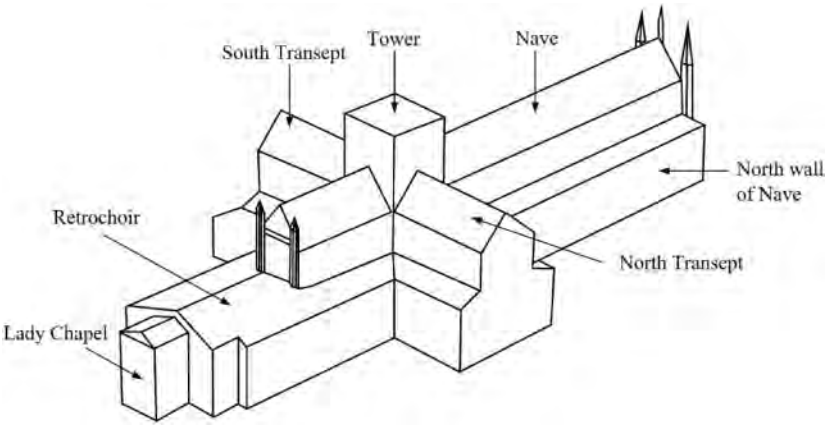

Figure 2. Isometric drawing of Winchester Cathedral looking south.

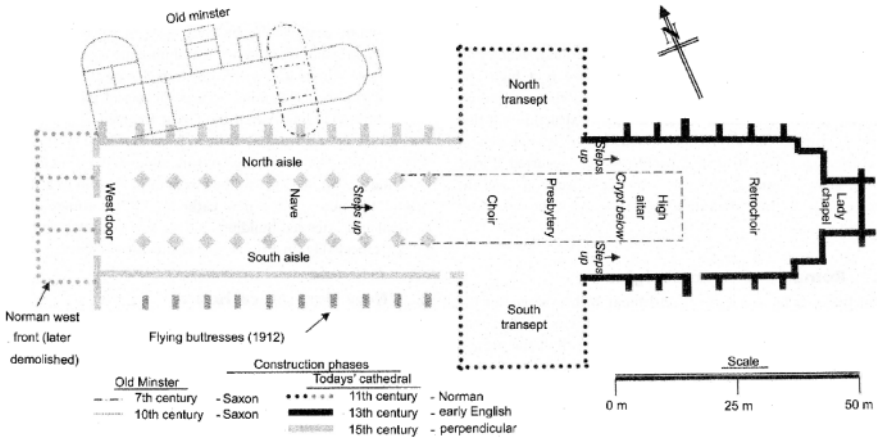

Figure 3. Plan of Winchester Cathedral (Roberts 2013).

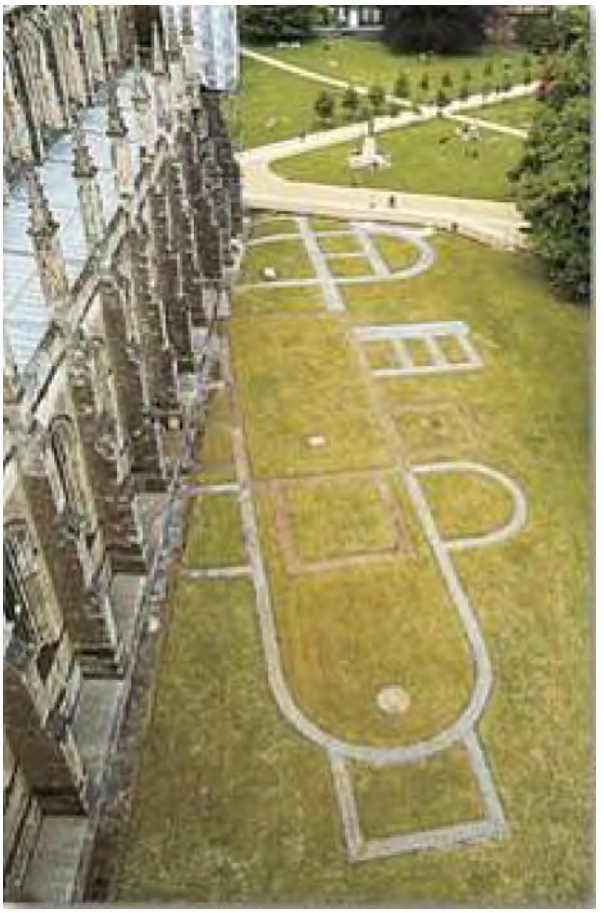

Figure 4. Location of Old and New Minster on the north side of Winchester Cathedral.

can be seen just north of the west end of the present Cathedral as shown in Figure 4. Its location may well have been chosen because it is sited in an area where the foundation conditions are more favourable than elsewhere in the area.

2.2 *The New Norman Cathedral (1079–1120)*

Following the invasion of England by William the Conqueror in 1066, the Saxon bishop of Winchester was replaced by the Norman royal chaplain Walkelin. In 1079 he began the construction of a large new cathedral in the Norman Romanesque style, a plan of which is shown by the broken lines in Figure 5, and probably took 40 years to complete (Henderson and Crook, 1984). As mentioned above, the location of the new Cathedral was south of and immediately alongside the Saxon Minster as shown in Figure 4 and was probably chosen for several reasons. First, the site of the Old Minster was prestigious and important, being directly opposite King William's royal palace. Also, it was an important pilgrimage centre containing the shrine of St Swithun, the patron saint of Winchester Cathedral. Moreover, this arrangement meant that demolition of the Old Minster could be delayed until after the completion of the east end of new Cathedral. Therefore the site of the new cathedral was almost certainly dictated by issues other than ground conditions.

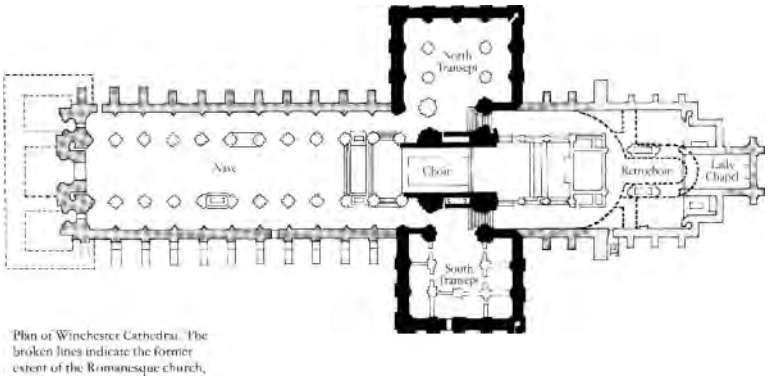

Figure 5. Plan of Winchester Cathedral with the original Norman Romanesque church shown as broken lines (Henderson & Crook 2004).

The design of the new Cathedral was based on that of contemporary Norman churches, with a cruciform shape in plan and a semi-circular aisle behind the Choir and High Altar as shown in Figure 5. Below the Choir, and accessed from the North Transept, is the Crypt which would have been constructed first. Unlike most other crypts, it is only partially below the ground – almost certainly because of the high-water table at the time of construction. Indeed, it now gets flooded most winters with up to 30 cm of ground water implying that the water table may have risen over the centuries.

The 12th Century Cathedral was completed around 1120 but not before some construction problems had been overcome. The ground profile consists of fill, overlying successively, chalky marl, a layer of peat, and dense gravel resting on chalk. The ground water level was about 2m above the top of the peat layer. In general, the bases of the Norman foundations invariably stop at the ground water level of that time, about 2.7m above the top of the gravel and are hence underlain by the peat layer. In places the foundations rest on a mat of timber logs and oak piles some of which were driven through the peat to the top of the underlying gravel layer. Figure 6 gives a typical section through the wall of the Presbytery.

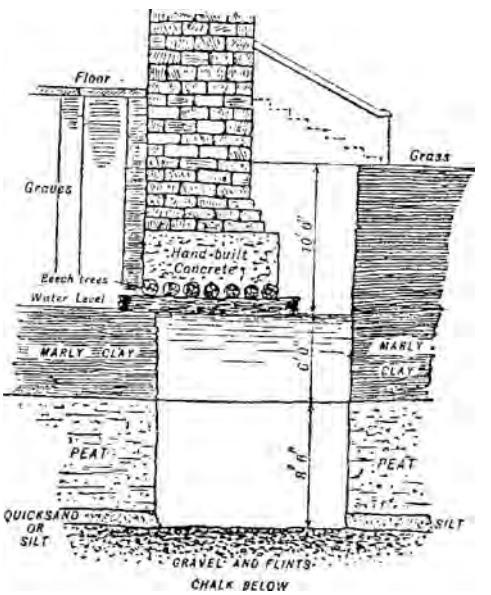

Figure 6. Section through wall of Presbytery, showing underlying soil profile (Henderson & Crook 2004).

Work quickly progressed to the transepts and central tower and was completed by about 1100. In 1107 the central Tower collapsed while work on the Nave was going on. The reason for the collapse is not known but Henderson and Crook (1984) postulate that it may have been due to unstable foundations. They note that the re-built Tower is on exaggeratedly massive piers at the four corners of the central Crossing. They also note the contrast between the exceptionally fine jointing of the replacement Tower and the thick jointing of the earlier masonry. It is therefore also possible that the failure of the original Tower may have been due to poor workmanship.

2.3 *Gothic expansions and refashioning of the Cathedral*

The first alterations to the Norman Cathedral were in 1202 when Bishop Godfrey de Luci started construction of a new Retrochoir at the east end of the Cathedral – see Figure 3. Work continued to progress westwards and ended with the creation of the new Choir and Presbytery in the first half of the 14th Century. Between 1500 and 1528, the Choir clearstory was remodelled, and the Choirisles were rebuilt. Henderson and Crook (1984) note that the architectural history of the entire eastern limb of the Cathedral is complex and remains a matter of controversy amongst architectural historians.

Also, in the 14th Century the west end of the Nave was demolished, shortening the Cathedral by 12.2m. Under Bishop Edington and later Bishop Wykeham, the Nave of the Cathedral was refashioned to the Perpendicular style. This they achieved by encasing the Norman stone in new masonry, recutting the piers with Gothic mouldings and pointed arches and reorganising the three-tier Nave into two tiers. Figure 7 is a photograph of the present refashioned Nave which is truly breath-taking.

Figure 7. The Nave of Winchester Cathedral looking East (courtesy of Michael Beckwith).

2.4 *Continued decay and the decision to underpin the Cathedral*

Henderson and Crook (1984) conclude that, from the early 16th Century to the twentieth, the story of the Cathedral is one of structural neglect and decay with occasional attempts at repair. In 1775 James Essex noted the defective vaulting of the Retrochoir aisles and attributed that to settlement during and immediately after construction. However, he doubted that subsidence was still taking place.

In 1809 a programme of inspection and repair was initiated following the appointment of the Cathedral's first architect, William Garbett. He appears to have shared James Essex's view that subsidence was complete. He did however note the inclinations of the south walls of the Retrochoir and of the South Transept. He also noted 'alarming fissures' in the South Transept walls and recommended filling them so that an eye could be kept on possible movement. At the turn of the 20th Century the structural state of the Cathedral was exceedingly worrying. There were huge cracks in the walls, some of the walls were bulging and leaning and occasional falls of stone took place from the vaults. In 1905 the Cathedral Architect, J. B. Colson, submitted a report to the Dean and Chapter describing these serious structural problems and recommending timber propping of the leaning walls. The Diocesan Architect, Thomas Jackson, then undertook a detailed inspection of the Cathedral in early March 1905. A trial excavation was made on the south side of the east end of the Cathedral and revealed dense gravel at a depth of about 7.5m underlying a thick layer of peat. Jackson in turn decided that he needed specialist advice and recommended the consulting engineer Francis Fox to the Dean and Chapter who agreed to call him in. It is important to note that much of Fox's previous experience had been concerned with bridges, tunnelling and railways. His involvement with historic buildings was minimal. He did have some very limited involvement with St Paul's Cathedral, but it seems to have been controversial.

On 27th June 1905 Fox, Jackson and Colson closely examined a second trial hole, which confirmed the ground profile revealed in the first trial hole, and they agreed unanimously that the south wall of the Retrochoir should be underpinned on to the underlying gravel. On 5th July 1905 Fox presented his recommendations to the Dean and Chapter. In his book "Sixty-three Years of Engineering", Fox (1924) summarised the recommended sequence of remedial measures for the south wall of the Retrochoir as follows.

(1) Shoring up the leaning south wall at the east-end of the Cathedral and the façade of the South Transept
(2) Centring the arched vaulting of the Retrochoir to prevent collapse.
(3) Inserting steel tie-rods between the north and south walls of the Retrochoir.
(4) Grouting with liquid cement under compressed air every portion of the relevant walls commencing at the base.
(5) Lastly, underpinning the walls down to the bed of gravel.

It is very important to note that these recommendations were made very quickly, within a few days of Fox's first visit. Moreover, nothing was included in the recommendations about the need to monitor settlement or structural movement prior to, and during, grouting and underpinning.

3 UNDERPINNING OPERATIONS

3.1 *Preliminary operations*

As described by Roberts (2013), the first operation was to timber up and strut the Retrochoir and South Transept walls followed by the centring of the roof and the installation of the tie-rods. These can still be seen in the Retrochoir tying the north and south walls together. The next stage was

the cement pressure grouting, which at that time was a relatively unknown technique. A pressure grouting machine had been invented in the 1870s by James Greathead, who had specified it for use in the construction of London's Northern and Central line tube railways with which Fox was familiar. The first step of the grouting process was to force in compressed air to blow out the accumulated dust of ages. Water was then injected to wash out the cracks. The grouting was begun at the bottom and, running horizontally, filled in the interstices and cavities. This was continued progressively upwards to the top levels of the walls and tower.

3.2 *Underpinning work encounters problems*

On completion of the grouting, the underpinning operation commenced. It was proposed that the underpinning would be carried out progressively by excavating one-metre-wide trenches (known as drifts) at right angles to the wall to be underpinned. Once the base of the existing foundations was reached, the drift would be extended under the existing foundation and excavation would continue down to the gravel. A bed of concrete would then be placed on the gravel and a solid masonry wall would then be constructed up to the underside of the existing wall. Fox recognised that this would involve excavating beneath the water table, but he believed that the water level within each trench could be controlled by pumping. Work commenced in December 1905 at the southeast corner of the Retrochoir.

The underpinning work soon ran into trouble. It was discovered that the layer of peat overlying the gravel had become so compressed by the foundation pressure that it became very impermeable and difficult to excavate. As excavation of a drift progressed downwards below the water table, initially little water entered the trench. However, as the excavation progressed through the peat, the water under pressure burst through from the underlying very permeable gravel, flooding the trench with black opaque water.

A powerful pump was required to keep the trench dry enough to carry out the work. Serious doubts began to be expressed about the advisability of continuing the work with extensive pumping. These doubts were reinforced by the discovery of a thin layer of silt between the peat and the underlying gravel which could be eroded by the flow of water into the drift thereby risking damaging subsidence.

3.3 *Underpinning commences using a diver*

Fox concluded that the best way forward was to use a diver to carry out the excavation beneath the water table. In April 1906 a trial excavation was undertaken using a diver named William Walker. When the excavation was complete Fox, who was himself an accomplished diver, examined the base of the drift. He reported that the base *"proved to be a hard flinty gravel, quite excellent and, as this overlies the chalk, no better foundation could be either secured or desired"* (Fox, 1924). It was therefore decided to continue with this method of working. Little did William Walker know that he would be engaged until September 1911 in underpinning most of the Cathedral.

A detailed description of the method of working is given by Roberts (2013) and reference is made to Figure 8. Work on a drift began by labourers excavating a short 1m wide trench at right angles to the Cathedral wall and taken down to below the level of the existing footings. Excavation continued down into the peat layer leaving a thickness of peat above the gravel of about 0.6m. A drift or small tunnel up to 7m long was then excavated beneath the existing wall footing. The peat was found to be so compressed by the foundation bearing pressure that a pick was needed to excavate it. It was also necessary to remove beech logs that had been placed there when the walls had been built some seven centuries earlier – often having to resort to sawing them into short lengths. The wall footings were then shored up before the remaining peat layer was excavated, whereupon black opaque peaty groundwater poured into the excavation filling it to a depth of some 4m.

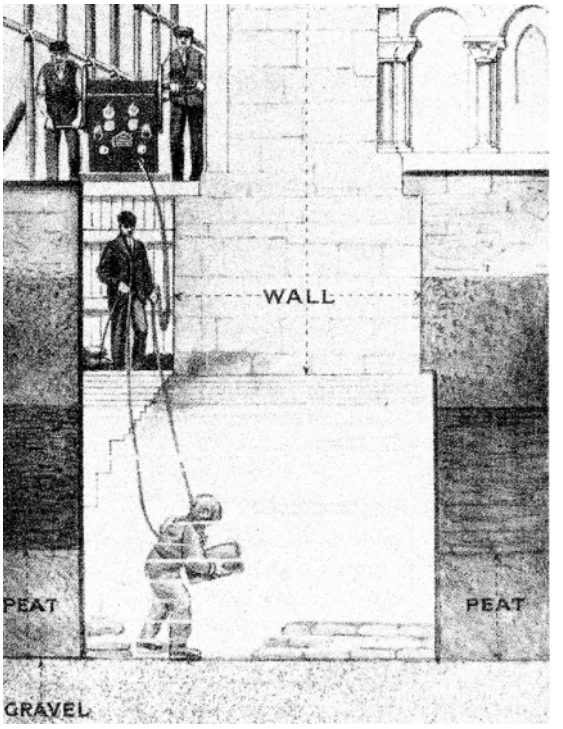

Figure 8. The diver at work (Roberts 2013).

The diver then took over and, working by touch in the opaque black water, completed the excavation down to the gravel. A layer of sacks filled with concrete was then placed on the gravel, packed tightly, trodden into place, and then slit open before being covered by the next layer. Three further layers of concrete filled bags were then similarly laid on top of the first layer. Finally, the bags were grouted to ensure they became a solid mass of concrete. All this had to be done by feel due to the black opaqueness of the water. The grouted bags of concrete made an effective seal that stemmed the flow of water from the gravel, thus enabling the trench to be pumped dry and allowing workmen to complete the underpinning of that section of the wall by means of mass concrete or engineering brick.

Originally it had been anticipated that only the Retrochoir and South Transept would need underpinning, but in July 1906 there was a small collapse of some vaulting of the Nave's south aisle. The opinion was offered that this was due to the historic subsidence of the foundations of the wall causing it to lean outwards thereby distorting the vaulting. This led to the recommendation that the wall of the Nave's south aisle would have to be underpinned. Ultimately this wall was stabilised by means of new flying buttresses and the foundations for these were constructed underwater by William Walker using the same method as was used for the underpinning work. A few months later it was reported that on the north side "every tell-tale has moved, and the whole North Transept will have to be underpinned". This underpinning work was completed in February 1910. In June 1907, Jackson surveyed the South Transept which had clearly undergone significant settlement. It was concluded that underpinning was also required, and this work was completed in April 1911. In his survey of ongoing and completed works in January 1909, Jackson identified problems with the north wall of the Nave. The buttresses which had been added during the 14th Century to support the wall had increased the danger of collapse because the buttress foundations were at a higher level than the Norman foundations. Therefore, the buttresses along the north aisle wall had to be underpinned. This work was completed in November 1910.

By the end of August 1911 virtually the whole of the Cathedral had been underpinned and a total of 235 drifts (trenches) were dug. It was estimated that William Walker had handled 25,800 bags of concrete. The original estimate of total costs was £3250 compared with the actual cost which turned out to be £113,000 which is equivalent to a sum approaching £14 million today. There can be no doubt that the work of the diver was heroic and it is universally recognised as such. But we are faced with the question "was this huge underpinning operation really necessary at that time"?

4 RECENT STUDIES

4.1 *The ground conditions beneath the Cathedral*

In 2006 and 2007 a team from Imperial College London carried out some detailed studies of the Cathedral with a view to ascertaining the following.

1. The ground conditions underlying the Cathedral precincts.
2. The total and differential settlements experienced by the Cathedral.
3. Whether subsidence was still occurring.
4. What surveys were put in place to monitor the foundation and wall movements during underpinning operations.
5. What modern technology would be used now to stabilise the foundations.

Much of the work of the Imperial College Team was carried out as MSc projects (Galdos-Ispizua (2007); Wilkinson (2006); Yu (2006)). The subsurface of the soil profile around the perimeter of the Cathedral was painstakingly pieced together using the records of the underpinning works during 1905 to 1912. These records are kept at the Winchester Cathedral Library Archives as well as the Library Archives at the Institution of Civil Engineers, London. The diver, William Walker, recorded the depths to the top of the gravel for all the drifts. Figure 9 shows the absolute levels of the top of the gravel along the north and south side of the Cathedral. On the north side the Reduced Levels (RL) of the top of the gravel varies from RL 31.4m to RL 30.0m, while the south sideshows a greater range varying from RL 31.6m to RL 29.3m. The diver's records also show that the peat thicknesses and levels vary significantly across the site. Thus, the ground conditions at Winchester Cathedral are highly variable, with appreciable changes in levels and thicknesses over short distances, which is a reflection of its fluvial and alluvial depositional environment.

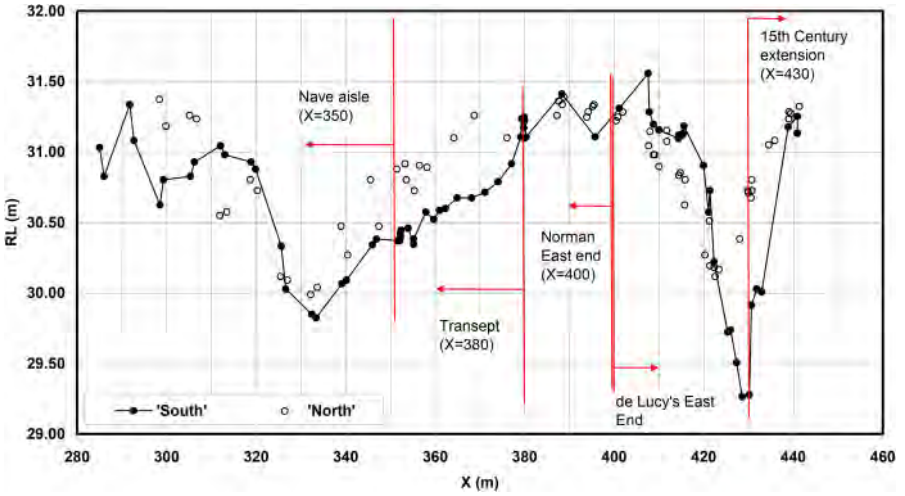

Figure 9. Levels of the top of the gravel layer along the north and south sides of Winchester Cathedral (Yu 2006).

4.2 *Settlement profiles around the Cathedral*

It is reasonable to assume that in laying down the base course or plinth of a medieval building every effort would be made to keep it horizontal. Therefore, it was considered that surveying the Norman plinth course would provide reliable information about the differential settlements of the Cathedral that had taken place during and subsequent to construction. In some locations the plinth course was not obvious and either a ledge course or string course was surveyed. Figure 10 shows

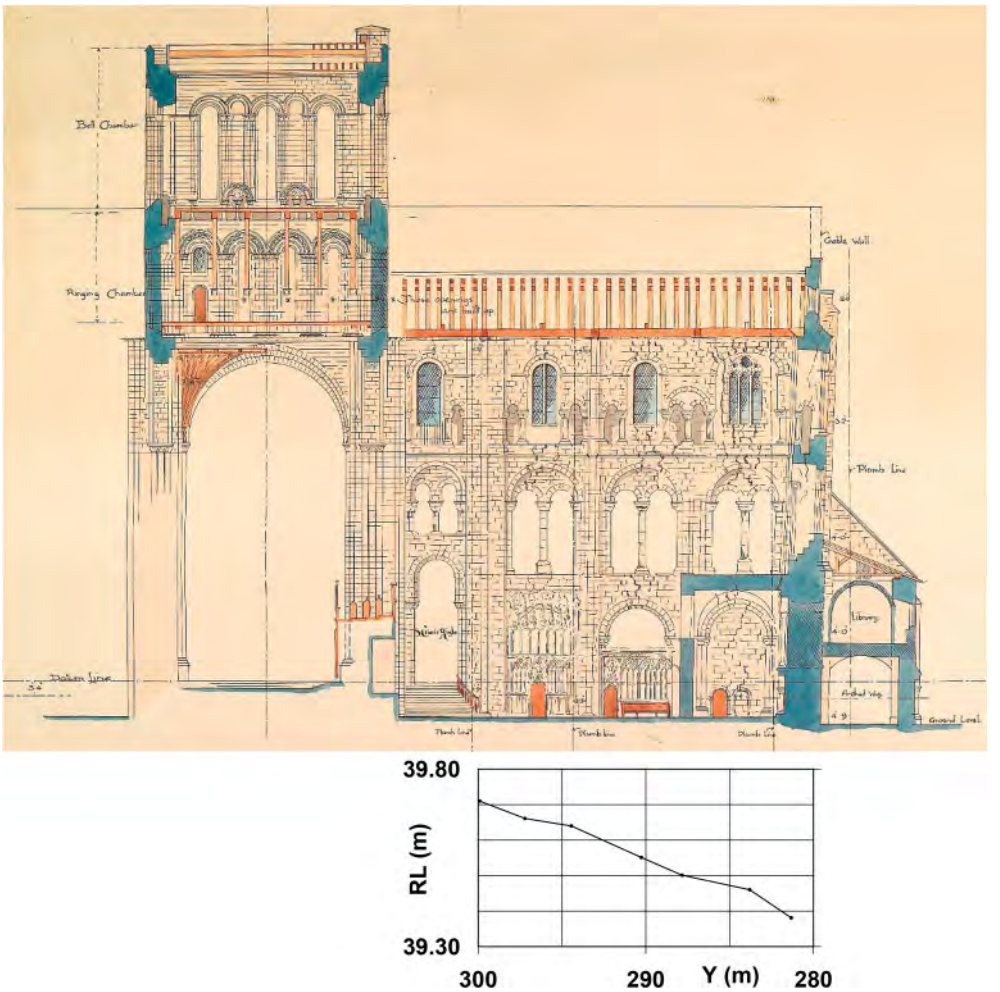

Figure 10. South Transept section through Tower and inside elevation looking East (Yu 2006).

a section through the Tower and inside elevation of the South Transept looking East and beneath it is plotted the levelling profile along the plinth. It is evident that a differential settlement of about 0.3m towards the south has taken place over a length of 18m. Figure 11 shows the elevation of the west wall of the South Transept looking East. It can be seen that the Slype at the southern end of the Transept has settled by about 0.15m and a hogging profile of settlement has taken place giving rise to significant cracking near the top of the west wall. The settlement profiles shown in Figures 10 and 11 also explain the outward tilt of the south façade wall. The value of such levelling surveys is all too apparent, and they do not require sophisticated equipment.

Henderson and Crook (1984) drew a most important conclusion from a study of the tapered masonry courses in the east facing wall of the South Transept that significant subsidence must have taken place during construction and that settlement was complete by the middle of the 14th Century.

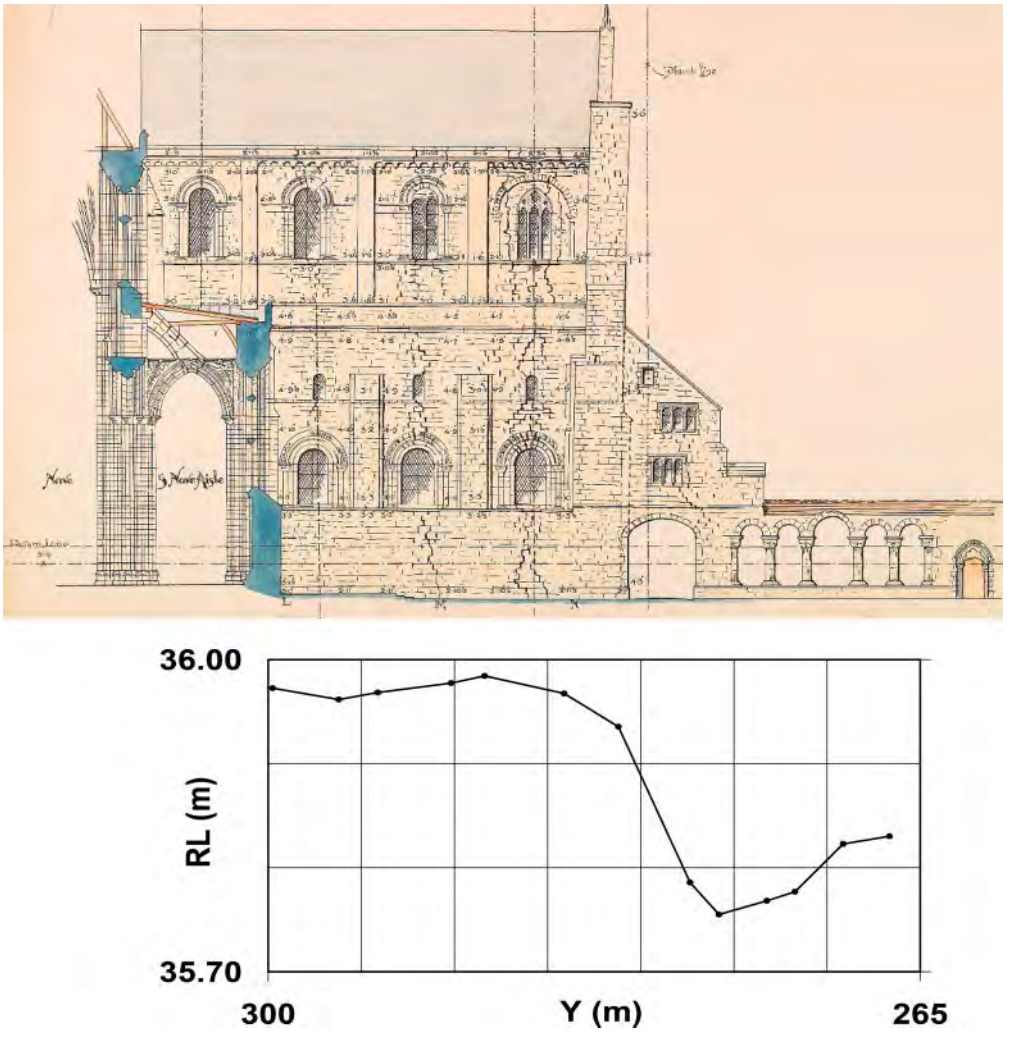

Figure 11. South Transept west elevation showing section through the south aisle of the Nave (Yu 2006).

4.3 *Settlements from precision levelling surveys*

In 1988 Ove Arup and Partners were commissioned to initiate a precision levelling survey of the whole Cathedral. A total of 42 BRE levelling points (Cheney 1973) were installed throughout the Cathedral and on 11th May 1988 initial readings were taken on most of them and referenced to a datum point installed on The Wessex Hotel some distance north of the Cathedral. The Imperial College team carried out a second survey on 24th July 2007 some 19 years after the initial survey. The results showed that over this period, the vertical movements were everywhere extremely small. The average settlement of the Tower, which was not underpinned, was less than 2mm. Elsewhere

towards the western and of the Cathedral and the Transepts the settlements were generally less than about 1mm. At the eastern end small upward movements of generally less than about 1mm were recorded. For all practical purposes it can be concluded that over a period of 19 years no progressive vertical movements had taken place both for those parts of the Cathedral that had been underpinned and for those that had not.

5 DISCUSSION AND CONCLUSIONS

It was mentioned in Section 2.4 that the decision to underpin was made very quickly within a few days of Fox's first visit. It is easy to be critical and wise after the event, but it is most instructive to consider what information was needed and could have been obtained at that time, before making such a momentous, far-reaching and costly decision. It is appropriate to quote from Fox's own account of when and how the decision was taken:

> *"I was requested by Dr Furneaux, the Dean [of the Cathedral] to accompany Thomas Jackson [the consultant architect] on June 27, 1905, to Winchester. The architects had found very serious subsidence in various parts of the Cathedral, that in the Presbytery amounting to nearly 2ft 6in [0.75m]. The outer walls and buttresses had gone seriously out of the perpendicular, while the beautiful, groined arches were distorted in form, and disintegrated in character, and alarm had been caused by the fall of some stone from the roof. Thomas Jackson had sunk a trial pit some few yards distant, and had discovered a bed of peat 8ft [2.4m] below the clay and resting upon a fine solid bed of flints and gravel, into which he had bored to some depth to prove its solidity…. The problem of strengthening the foundations was, therefore, a very formidable one."*

The decision to underpin the Cathedral was evidently based purely on the following information: (1) the current visible structural distortions within the 800-year-old Cathedral; (2) that in the past considerable settlement had taken place; and (3) the knowledge that the foundations were underlain by a layer of peat.

However, the trial pits that were sunk showed that the peat beneath the foundations had been compressed into a very dense and stiff material, but no account seems to have been taken of this. Moreover, the chalk marl revealed in the trial pit overlying the peat would not have given rise to long-term progressive settlement. No attempt was made to measure what, if any, settlement was still taking place. Yet high quality surveying equipment was in wide use at that time. Indeed, it is interesting to note that precision surveying of the Leaning Tower of Pisa was commenced in 1911 (Burland et al. 2021). It seems very probable that the inclination of some of the walls had been caused by the lateral thrust of the internal arches. In which case underpinning would have had little beneficial effect. Indeed, these problems were dealt with by the installation of tie rods and the construction of new buttresses.

There can be no doubt that the structural stabilisation and grouting of the masonry walls and arches that was undertaken by Fox were essential. In this regard it is worth noting that work carried out by Professor Jacques Heyman on the stability of masonry structures has demonstrated how robust masonry arches are, even when significantly distorted. Reference can be made to a fascinating article by Heyman (2021) entitled "Why ancient cathedrals stand up".

Perhaps the most important lesson to be learned from the study described here is that before any work on the foundations of an historic building is carried out, it is essential to establish (1) what foundation distortions have actually occurred, by levelling around plinths or string lines and (2) whether on-going movements are taking place in the foundations or structure. Because of the lack of such information in the case of Winchester Cathedral it is not possible to be definitive about how necessary the underpinning works were. However there is evidence given in this paper to suggest that any progressive settlement must have been very small. There can be no doubt that the work of the diver, William Walker, was indeed heroic and his name is forever linked with Winchester Cathedral.

ACKNOWLEDGEMENTS

The authors are most grateful for the assistance received from The Revd Canon Dr Roland Riem, Vice-Dean of Winchester Cathedral. Dr John Crook, Cathedral Archaeologist, gave us freely of his intimate knowledge of Winchester Cathedral and its history. We are grateful too for the assistance given to us by Mr Carlton Bath, Cathedral Clerk of Works and the Cathedral Archivist.

REFERENCES

Burland, J.B., Jamiolkowski, M.B., Squelia, N. & Viggiani, C. 2021. *The Tower of Pisa – History, Construction and Geotechnical Stabilization.* Taylor and Francis, London, UK.

Cheney, J.E. 1973. Techniques and equipment using the surveyor's level for accurate measurements of building movement. *Proc. Symp. on Field Instrumentation*: 85-89. BGS, London, UK.

Fox, F. 1924. *Sixty-Three Years of Engineering*. John Murray, London, UK.

Galdos-Ispizua, A. 2007. *Winchester Cathedral Foundation Engineering Past and Present Approach.* MSc dissertation, Dept. of Civil and Environmental Engineering, Imperial College London, UK.

Henderson, I.T. & Crook, J. 2004. *The Winchester Diver: The Saving of a Great Cathedral. Henderson & Stirk Publishers*, Crawley, Winchester, UK.

Heyman, J. 2021. Why ancient cathedrals stand up: *Ingenia, Magazine of the Royal Academy of Engineering.* 10:19–23.

Roberts, G. 2013. How a diver saved Winchester Cathedral, UK: and today's solution? *Proc. ICE, Engineering and Heritage,* 166 (EH3): 164-176.

Wilkinson, S. 2006. *A review of the Ground Conditions below Winchester Cathedral and their Effects on the Cathedral's Structure.* MSc dissertation, Dept. of Civil and Environmental Engineering, Imperial College London, UK.

Yu, J. 2006. *Winchester Cathedral – an Engineering Look into the Past.* MSc dissertation, Dept. of Civil and Environmental Engineering, Imperial College London, UK.

Geotechnical Engineering for the Preservation of Monuments and Historic Sites III – Lancellotta, Viggiani, Flora, de Silva & Mele (Eds)

Rethinking preventive conservation: Recent examples

P.B. Lourenço, A. Barontini & D.V. Oliveira
University of Minho, ISISE, Department of Civil Engineering, Guimarães, Portugal

J. Ortega
Instituto de Tecnologías Físicas y de la Información "Leonardo Torres Quevedo" (ITEFI), CSIC, Madrid, Spain

ABSTRACT: The past few decades have seen an increasing awareness of the potential socio-economical and environmental impact of investment in Cultural Heritage (CH). Preserving CH is not only an obligation to sustain and transmit it to the future generation but is also a driver of sustainable growth. Here, recently concluded projects are taken in consideration for a reflective thinking on preventive conservation, as the only viable strategy towards a sustainable and cost-effective management of CH, to face unprecedented challenges posed by increasing natural and man-made threats. Here, the main open issues for a widespread implementation of preventive conservation are identified, moreover, standardised, integrated good practices, validated over significant case studies, are presented within a multi-level replicable framework.

1 INTRODUCTION

Over the past few decades, the awareness of Cultural Heritage (CH) potential and of the benefits brought by it to society as a whole is significantly grown, leading to a strong development of national and international policies. Several examples demonstrated the significant socio-economical and environmental impact of investing in CH. CH has been recognised not only as an irreplaceable asset, but also as a driver of sustainable development and a strategic resource to promote peace, diversity, inclusiveness and participation (Jagodzińska et al. 2015). In order to preserve CH, its intrinsic fragility and the growing threats that is facing are particularly worrying and are calling for the development and enforcement of good and validated practices. To this end, preventive conservation is likely to be the most cost-effective strategy, strongly recommended by international institutions involved in preservation, as the International Council on Monuments and Sites (ICOMOS). The 2003 charter (ICOMOS 2003), for instance, while setting an ensemble of principles for conservation, recognises preventive maintenance as the best therapy for built heritage.

According to preventive conservation philosophy, damage and decay are unavoidable, however they can be tolerated as long as the affected system is fit-for-purpose, namely it meets a set of requirements related, for instance, to structural capacity, aesthetic, comfort and safety of the user, economic and market values and, in the case of historic buildings, authenticity and heritage value. The probability of failing to meet one or more of such requirements is, therefore, reduced by scheduling maintenance and interventions according to prescribed criteria based on performance and/or parameter monitoring and the consequent analysis and prognosis (CEN 2010). This approach allows timely detection of anomalies, optimized long-term allocation of the resources and prioritisation of the required measures.

A preventive conservation framework is the effective integration of condition survey and monitoring with risk assessment (Taylor 2005), where condition survey and monitoring repeat over time

 DOI 10.1201/9781003308867-4

the estimation of the building performance through qualitative and quantitative methods, whereas risk assessment forecasts the potential loss of performance due to specific hazardous events. Their integration allows the identification of the probable causes from the detected damage and the prediction of the remaining service life, based on the expected evolution of the degradation under given scenarios (Taylor 2005). This integration is boosted by the development of a reliable digital twin namely a duplicate of the asset, generated by a fusion of models and data and able to evolve replicating the physical twin evolution in time (Wagg et al. 2020). Documenting the CH asset condition and understanding its need in connection with its environment and its operation become fundamental pillars of conservation. Nonetheless, this asset investigation is complicated by several factors, as further described in the following sections. Such shortcomings should be tackled by validated, replicable and cost-effective strategies able to adapt to the specificity of each asset, without losing objectivity in the interpretation of the evidence.

Two recently concluded European projects led by the University of Minho, with an active involvement of the authors, have been an incredible opportunity to reflect further on CH preventive conservation, formulating a multi-level comprehensive methodology, built on standardised protocols and aimed at addressing the aforementioned shortcomings. These protocols were validated and tested on a large set of assets located in different context and geographical area. The main outcomes of the projects are described in the last part of this paper.

2 PREVENTIVE CONSERVATION: A MEDICAL ANALOGY

The similarities between the diagnostic process for human and building pathologies have led to a medical analogy, embraced by international recommendations and scientific literature. This analogy supports the identification of a standardised framework for conservation, drawing inspiration from a field that has theorised that prevention is better than cure, for a long time. Following this analogy, in (Della Torre 2010) and (Balen 2015), three levels of prevention were defined: (i) a primary level aimed at avoiding the causes; (ii) a second level aimed at an early detection of the symptoms; (iii) a third level aimed at preventing a further spread of the pathology and its side effects. First level encompasses mitigation strategies, ranging from simple measures (e.g. proper use of the asset and constant maintenance) to more systematic modifications of the level of hazard, exposure and/or vulnerability. Second level relies on a systematic screening. Third level consists in an urgent cure. It is clear the change of perspective: the remedial treatment (level 3) should not be the standard way, it is rather an ultimate solution when prevention (level 1 and 2) fails, namely it is a defeat of the conservation system (Balen 2015). Extending the medical analogy, preventive conservation can be, thus, seen as a process of early diagnosis and treatment, repeated across the asset lifespan, in which damage and defects are seen as symptoms of a pathology.

The diagnosis aims at defining with sufficient degree of certainty the most probable causes for these symptoms, following a differential diagnostic procedure, namely comparing multiple alternatives. These alternatives are reduced to the most likely based on the data collected by anamnesis (interview and search for medical history, presenting complaint and relevant data), examination (mainly qualitative and supported by simple tools) and testing (experimental quantitative evaluations). The causes are then tackled through a proper therapy, whose effects are object of control in time. Shifting from cure to prevention requires a change of mindset and the acquisition of a new awareness of its advantages that are often visible only in the long-term and, nowadays, are not always quantifiable yet. Moreover, such positive consequences are only achieved upon an initial investment in screening that may demand considerable economic and societal costs, especially when a proper planning and knowledge is lacking (Balen 2015). In this regard, the implementation of a preventive conservation strategy should be driven by a case-specific cost-benefit analysis, based on factors as time and resources required for a repeated assessment, costs of timely and delayed measures, significance of the asset and level of risk.

3 PREVENTIVE CONSERVATION: CONDITIONS FOR IMPLEMENTATION AND OPEN ISSUES

A wide-spread implementation of preventive conservation rests on (Balen 2015): (i) scientific knowledge; (ii) clear codes and guidelines; (iii) supportive policies; (iv) trained professionals; (v) a society aware of the importance of its heritage and the advantages of prevention. Nowadays, relevant examples for each of these factors exist in many countries, nonetheless, it is argued that there is no system with the compresence of all of them (Balen 2015).

Promoting education of society, making it aware of the benefit of regular control and maintenance and of the significance of heritage, is a paramount strategy to avoid neglection and vandalism and spread the responsibility of prevention among local communities (Balen 2015, Della Torre 2010). Increasing awareness requires consistent regulations and policies including financial supports but also the evidence of the preventive conservation benefit. This evidence consists of good examples that, in turn, requires trained professionals. The legal framework can rely on obligations and recommendations. The former are intended to enforce preventive measures, by indicating, for instance, when the assessment is mandatory or the periodicity of inspection and maintenance. The latter are indications of the steps to take and instructions, aiming at spreading good practices. In different countries, protection, conservation and actuation criteria are commonly defined at completely different scales (e.g. both national and local, only national or only local), with different levels of coordination between the involved entities. Intervention and management strategies may exist, although disperse, or lack completely (Masciotta et al. 2019). Such sparse and vague instructions induce a dangerous state of uncertainty regarding conservation policies and may result in a non-compliance.

The legal framework is also relevant in the field of testing. Lack of accreditations, regulations and guidelines jeopardise the reliability of the tests that are affected by the personal experience and judgment of the operator. Together with laws and regulations, supportive policies and financial investment through grants and incentives may play an essential role in promoting proactive conservation strategies. Indeed, most of the CH buildings and sites are financially non-self-sufficient and rely on public subsidies to invest in conservation, but recent financial crises have led to deep cuts to heritage sector funding (Marjanović 2014). Moreover, funding is mostly addressed to listed assets, neglecting a large number of historic buildings. Preventive habits may optimise resources allocation and management of the limited budget available, but many assets are already in a severe state of decay to a point where financial institutions are unwilling or unable to invest in urgent remedial measures that are preparatory to a preventive management (Marjanović 2014).

Finally, as already mentioned, the evidence of the preventive conservation benefit is essential to spread its practice. All the stages of conservation, including technical and practical activities, require expert professionals. Lack of training and education of the parties involved in conservation is likely the principal cause of inappropriate decision making. It results in interventions that do not address the causes, but just the symptoms, leading to negative consequences like a recurrence of the pathologies, a diffusion of the damage or an acceleration of the decay. Inadequate interventions, including use of incompatible materials or incompatible structural systems, is commonly driven by non-systematic documentation, limited testing, misinterpretation of the collected data and, in general, an excessive appeal to subjective judgment in the absence of conclusive evidence. Even good decision making may be hindered by the lack of skilled craftsmen to carry out the required activities (Balen 2015).

On the other hand, sometimes, the practitioners voluntarily avoid a detailed investigation claiming that it is expensive and time-consuming, reporting the dispersion of information and the inconsequential existing procedures (Gonçalves et al. 2017). This is likely due to the nature of the sought information, cumulative and dependent on the availability of time and sources. Significant data can be non-existent, unreliable or outdated. Documentation, thus, requires iterative and flexible procedures and adequate platforms to store and retrieve it. In this regard, digital technology may offer an unvaluable support to inspection and documentation. Recent advancement in software

and hardware allows to collect, store, retrieve and process an unprecedented large amount of data. Potentially, advanced surveying techniques and structural health monitoring strategies are likely to reduce the time requirement to produce updated and precise information.

Nonetheless, purchasing and maintaining the required software and hardware components, including instrumentation, licences, storage platforms and processing systems, require a significant investment that should be considered in the cost-benefit analysis. More importantly, the information that is generated by such advanced tools, is indiscriminate and growing in size and complexity, is demanding in terms of data management and interrogation and requires a time-consuming processing to become significant and meaningful to the stakeholders. This not only increases the costs but also requires new expertise from fields that were not directly involved in conservation before. On the other hand, saving on the sources or on the post-processing of the data is likely leading to an insufficient level of knowledge. In both the cases, excess or lack of data, confusing and meaningless information is produced, contributing to the scepticism of the stakeholders regarding the diagnostic process.

A final issue, to be mentioned, is the multidisciplinary nature of heritage analysis and preservation that encompasses different approaches, each one with its own terms, methods and sources. A synergistic framework needs a coordination and unification that start from the terminology. Indeed, different disciplines currently use the same words with subtly different meanings or address similar concepts by means of completely different words.

4 RETHINKING PREVENTIVE CONSERVATION: HERITAGECARE METHODOLOGY

Addressing all the aforementioned open issues is not an easy task as they are strongly connected. A non-harmonised, sparse and vague legal framework, without uniform terminology and standardised methodologies for data collection and interpretation, leaves room to subjectivity, prevents interdisciplinary collaboration and hinders successful preventive conservation instances, leading, in some cases, to poor decision making that enhances decay and loss. The lack of good examples contributes to a diffuse scepticism regarding preventive strategies and building diagnosis considered inconclusive, expensive and time-consuming, therefore unworthy.

Unaware owners do not demand preventive conservation, since codes do not enforce it and policies do not provide financial support for it, moreover, they do not resort to expert professionals in case of need that, therefore, are not encouraged to invest in training and perform accurate diagnosis while assessing existing structures. Tackling such issues requires rethinking preventive conservation and the role of academia in disseminating good practices and boosting advancement in scientific knowledge. This process should lead to the development of a consistent and cost-effective preventive conservation framework, defined according to the following steps: (i) review of existing methodologies, documentation and management systems, standards and codes relevant to assessment and conservation; (ii) standardisation of terminology, protocols, recommendations and criteria, integrating the existing ones into a consistent unitary approach harmonised with the current regulations; (iii) identification of flaws or gaps in the overall process flow or in its tasks (e.g. outdated methodologies or conservation needs that are not properly addressed); (iv) development and validation of novel strategies, including testing techniques and diagnostic tools, to fill such gaps; (v) validation of the overall methodology in real scenarios.

A systematic literature review is of paramount importance. Indeed, beside policy-makers, other institutions and scholars have produced a large number of protocols, recommendations and testing strategies, often focused on specific goals within the field of documentation, inspection, diagnosis and conservation (Gonçalves et al. 2018, Kioussi et al. 2011, Pereira et al. 2021). A comparative analysis of these methods aimed at an integration and a harmonisation also with the existing codes is unavoidable. Moreover, the consistency of the framework should be improved by addressing built heritage conservation as a specific case of a wider existing building conservation discipline rather than a separated instance, allowing good practices to be generalised, irrespective of the original field of application. This beneficial integration of the methodologies should follow a

holistic approach that includes in the assessment all the needs of the asset as a whole, thus related, not only to structural safety and material conservation, but also to user comfort, energy efficiency and sustainability among others. This requires a comprehensive and multidisciplinary process of harmonising the good practices towards a cost-effective management, in which any activity or intervention carried out on the building aims at fulfilling more of its needs at the same time or, at least, at minimising the negative impact in case of conflicting needs.

Upon this preliminary analysis, a set of basic requirements for a preventive conservation framework are defined as follows:

- The framework must use a clear and unified terminology. Glossaries of damages, activities, principles, concepts, assets typologies and components have been collected in national and international standards and guidelines, e.g. (EN 15898 2019, ICOMOS 2003). A standardised glossary should be built by harmonising such sources and it should be furnished with clear textual and graphical information for a univocal identification of each item.
- Informed decision-making must be supported by a set of relationship databases connecting at least: (i) symptoms and causes, defining also the most effective diagnostic tools to formulate a correct diagnosis; (ii) causes and remedial measures, based on the urgency of the intervention and the extent reached by the pathology. Such databases are built on scientific knowledge and previous experiences and should be updated upon advancement of research. Their correct use prevents the influence of subjective judgment and experience on the diagnostic process and the implementation of unnecessary or incorrect treatments. Moreover, they can help the stakeholders select the most appropriate equipment for their specific predictive conservation needs, based on ongoing and expected damage scenarios (Pereira et al. 2021).
- For each asset a database must be created to collect all the documentation produced. The database should allow a dynamic updating across the entire lifespan of the asset, adapting to the cumulative nature of information (Kioussi et al. 2011). The preventive conservation framework should aim at a comprehensive documentation of the whole investigated system, including the building envelope, the interior, the technical installations, the equipment and the integrated movable assets, as they all contribute to the value and the performance of the system.
- Documentation and data collection must be as free as possible of biases. In case of qualitative methods, especially visual inspection, subjectivity can be prevented by defining a standardised mean of recording the information, presenting clear requests through fields to be filled and unambiguous options for pre-set multiple choices, to be used according to a protocol for each method. In case of quantitative methods (e.g. on-site or lab tests) errors and uncertainties should be minimised by defining clear protocols including information as the equipment, the data storage and retrieval strategy and the tasks to be performed in preparation, during the execution and afterwards, namely, to plan the activities, apply the method and interpret its outcomes.
- Expert and trained professionals are the main actors of the diagnostic process. The protocol of each task of the framework should clearly specify the needed expertise and the accreditation when relevant. Owners and users, irrespective of their background and education, should contribute by correctly using the asset and its components and by monitoring the application of the technical recommendations. Moreover, they should participate in documentation, not only through interviews, but actively, carrying out non-expert regular inspections, aided by simple checklists or questionnaires, to report in a standardised way malfunctioning, damage and decay in the very early stage. This ensures an adequate level of maintenance and a timely identification of the anomalies, optimising the subsequent expert activity.
- To guarantee a flawless exchange of information, for each party involved (e.g. professionals, owners and managers, stakeholders, policy-makers, etc.), databases access and editing rights must be clear, defining type, amount and format of information that each category can query, produce and/or edit. This ensures the quality control and that each party interacts only with information that is meaningful for its purposes. A standard minimum quality and amount of information needed for each task of the framework should be defined, aiming at a good trade-off between costs and benefits of documentation.

– The framework must be flexible and multi-level, in order to be replicable and scalable, adapting to the expected variability and peculiarity of diverse geographical areas and target assets, with various complexity, level of performance, conservation needs, protection status, local environmental, social, economic and financial conditions. Such factors affect the extent of the information that can be collected and generated. Therefore, the granularity of information should be defined upon agreement among the parties involved, based on the pre-defined level needed for each task. A hierarchic and nested organisation of the levels, where the specific tasks of a lower level are included in the upper levels and complemented by additional activities, allows a dynamic adaptation of the service, over time, to new conditions, resources or needs. At least two levels for the assessment can be identified, in agreement with ISO 13822 standard (ISO 2010), namely a preliminary and a detailed assessment. An harmonisation of standard procedures can be attempted by integrating the preliminary inspection with the condition survey detailed in EN 16096 standard (EN 2012).
– The diagnosis should produce an indication of the recommended measures and their urgency for the asset as a whole, based on the condition grading, the risk and the recommended measures for its components (EN 2012). The criteria and the relevant features used to issue the grade should be clearly expressed as well as the aggregation formulas to estimate the overall score based on the component's values. Standardised criteria should be also defined to link condition and risk to the urgency and type of intervention needed. A colour-coded rating supports the interpretation by making reporting more user-friendly to non-technical users (Abbott et al. 2007).
– The preventive conservation framework should present a high level of digitisation. All the aforementioned relationship databases, glossary, protocols and previously generated documentation on the asset should allow online, real-time exploitation, especially to support on-site activities. This reduces the time invested by the operators in learning the methodology and performing the tasks, reduces the gap in technical knowledge between different operators and increases the accuracy of the inspection (Gonçalves et al. 2018). Moreover, a digital platform supports the definition of clear access and editing rights, automatically filtering the information and providing ad-hoc authorisations and restrictions to each category of user. The digitisation of the information is also essential to establish an effective interoperability between all the parties involved in the management and preservation of the assets. To this end, specific protocols should be defined to guarantee that the documentation is made available for other purposes, as analysing energy efficiency, managing activities within the spaces, estimating quantity take-off, allowing interactive and virtual engagement with the asset, etc.
– The databases created for each instance allow data collection and exploitation at the individual building level. However, a centralised management of the information allows the statistical analysis of an increasing group of assets, offering an invaluable tool for policy-makers to learn from experience and establishing good practices. This higher level analysis, indeed, provides a paramount insight into pathologies occurrence, reliability of the diagnostic techniques and effectiveness of remedial measures.

The recently concluded HeritageCare project (SOE1/P5/P0258) has significantly contributed to this ongoing process of rethinking preventive conservation. This multidisciplinary high-technological effort, involving eight beneficiary partners and eleven associated partners from three countries (Portugal, Spain and Southwestern France), coordinated by the University of Minho, has led to the development of a new validated methodology for heritage preventive conservation, according to the aforementioned requirements.

For a thorough description of the project and its outcomes refer to (Barontini et al. 2021; Masciotta et al. 2019, 2021). HeritageCare multi-level methodology encompasses a set of tasks organised according to a systematic workflow in three following stages, namely prior to, during and after inspection, each one with specific data categories to be collected and generated and activities to be carried out. The granularity of the documentation and information searched, stored and produced varies according to three Service Levels, SLs (Table 1).

Table 1. HeritageCare service level definition.

Service Level	Designation	Functionality
SL1	StandardCare	Provision of what is essential for the primary health and ordinary maintenance of the heritage building.
SL2	PlusCare	Provision of what is necessary for the primary health, ordinary maintenance and thorough screening of the heritage building along with its integrated and movable assets, including monitoring data to support decision making.
SL2	TotalCare	Provision of what is necessary for the primary health, ordinary maintenance, thorough screening and enhanced management of the heritage building along with its integrated and movable assets.

SL1 provides a low-cost and rapid, although complete, assessment of the historic building, harmonised with the methodology described by EN 16096 Standard (EN 2012). Prior to inspection, the off-site documentation is carried out, through historical survey and bibliographic search. The reliability of all the textual and graphical sources is assessed and all the relevant data is extrapolated and collected within the Building ID and management information, namely a series of descriptors, updated over time. These include univocal code, name, category, protection status, property, time of construction, original and current functions, localization, important historical information, architectural features, construction system, principal building materials, previous interventions, inspections, maintenance actions, test reports, number of integrated and movable assets of cultural interest with a description of their significance, age and main geometrical and material features. This documentation is furnished with bibliographic references, sketches and drawings of the main components and spaces. The inspection at SL1 is mainly qualitative and is performed by at least two experienced professionals, with complementary expertise, capable of grading the condition state of the building and its components. The main support on-site is the inspection app (Figure 1), with an e-form to be filled online, with a standardised checklist of items and sub-items to survey. During on-site activities, the surveyors have access to informative materials as the standardised glossary, the damage atlas with definitions and examples and a collection of most common damages and deterioration processes for each sub-item. Each damage affecting the sub-item is graded through a condition index and a risk index, according to a 4-point scale, from 0 to 3 (Figure 2). These indexes are then used to assess the sub-items, the items and the asset as a whole, in a bottom to top cascade. More details on the assessment criteria are provided in (Masciotta et al. 2019).

Upon completion of the inspection process the report for the asset managers and owners is automatically produced and stored on an online platform. The report encompasses an informative section on the overall condition of the building and its main components and a set of clear and schematic recommendations regarding remedial or preventive actions to undertake in the short/medium/long term based on the identified damages, their most likely causes and consequences (Figure 3). The asset managers or the owners are then invited to provide feedbacks, in order to document any following measure undertaken on the building. Building ID, management info and subsequent condition reports constitute a simple but informative attribute-based digital twin. Movable assets hosted within the building may deserve specific attention during the inspection. To this end an ad-hoc documentation protocol is defined, aimed at producing an Asset ID, namely a set of relevant data, similar to the Building ID, used to unambiguously identify any specific heritage object and allow its standardised inspection. This inspection is carried out by means of a dedicated form where damage, alteration and operational and environmental conditions that are likely to affect the asset conservation (e.g. temperature, relative humidity, illumination, etc.) are recorded.

SL2 complements and increases the level of information on the building and the integrated and movable assets, producing a virtual restitution and collecting quantitative information, through testing, monitoring and surveying techniques. Typology, location and number of tests are defined

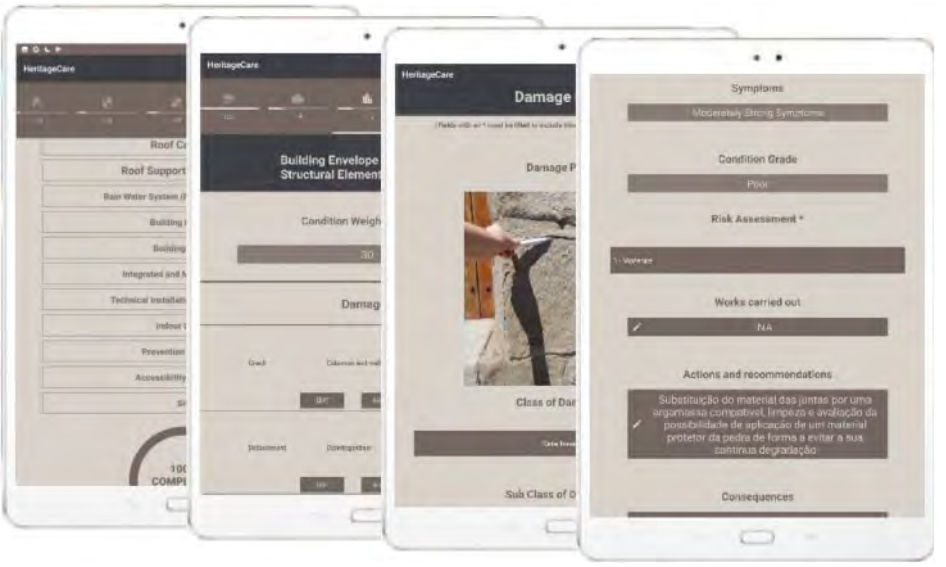

Figure 1. HeritageCare mobile inspection app.

Class N.	Condition index
0	Good – No symptoms
1	Fair – Minor symptoms
2	Poor – Moderately strong symptoms
3	Bad – Major symptoms
NA	Not (safely) accessible

Class N.	Risk index
0	Long term No actions | preventive monitoring
1	Medium term Non-urgent actions | Monitoring
2	Short term Timely repair or additional inspection and diagnosis
3	Urgent and immediate Urgent repair or additional inspection and diagnosis
NA	Not inspected Not safely accessible or not visible

Figure 2. Condition and risk rating indexes.

Figure 3. Excerpt from the Guimarães ducal palace inspection report.

prior to inspection, based on the condition assessment and upon agreement among the involved parties. Each test has a pre-set protocol defining the expertise requested to the operators, the equipment and the procedures for a correct execution. Testing and monitoring is intended to identify and track physical, mechanical and environmental parameters for a detailed assessment of the asset condition and the evolution of its performance. All the required techniques are summed up to build a service that is tailored to the specific asset needs and resources. This flexibility fosters an application of the methodology to any context, without requiring extra costs or specific expertise of the operators.

For instance, the methodology is independent of the surveying strategy, allowing the managers to decide whether to request a traditional metrical survey or a more advanced one, image-based (e.g. terrestrial or aerial photogrammetry) or range-based (e.g. static or dynamic laser scanning). For photogrammetry three protocols exist depending on the goal, namely reconstruction of planar objects, 360° reconstruction of movable assets or detailed reconstructions. The protocol determines the rules and the parameters of the acquisition (e.g. number of captured images, the shot overlap and path, the lens system, the focal length, the exposure triangle), based on the characteristics of the object to capture and the required level of detail. For laser scanners, protocols are more flexible. Nonetheless, essential practical rules are defined and strictly followed to optimize the outcome of the data acquisition. On-site, beside surveying and testing, the operators collect an ensemble of 360° panoramic photos of the whole buildings, recording all its main components and integrated movable assets.

The resulting digital twin integrates the alphanumerical information of SL1 with graphical information obtained by interlinking these 360° panoramic views. This simple, although clear 3D reconstruction allows a virtual tour inside and around the building and is enriched by the identification of hotspots (e.g. damage hotspot, asset hotspot, sensor hotspot, etc.), clearly recognisable through a predefined visual code. Each hotspot is a link to stored information, as SL1 condition reports, specific documents and images concerning the assets, alteration or damage detected during on-site inspections, real-time reading from the monitoring systems installed. When a point cloud is generated, this is also navigable for the stakeholders on the platform, contributing to the information content of the digital twin. Moreover, the platform allows important operations directly on the point cloud, such as slicing to produce 2D drawings (plans, sections and elevations) and segmentation to identify functional parts of the building (e.g. roof, façades and rooms).

Finally, SL3 produces a highly informative 3D model in a BIM environment. A protocol with a standardized workflow to develop and update the BIM model is further discussed in (Barontini et al. 2021). The protocol is based on a clear separation of roles and expertise, a standardisation of the documentation process and the interoperability with the e-form and other professional software. This ensures the exchange of information and its use for other preservation purposes, as for instance organising and performing an inspection, analysing the structural safety or the energy efficiency, designing interventions, managing activities within the spaces, etc., without requiring modelling expertise and holding software licence to any of the parties involved, except for the BIM modeller.

The protocol defines the extent and granularity of the information for each element of the BIM model according to the purpose of the model, to be defined in agreement by all the parties, and in compliance with EN 17412-1 standard (BS EN 2020), as a combination of geometrical data, alphanumerical data and documentation. Indeed, the model consists in an assembly of parametric objects representing the real components of the building with an acceptable level of geometrical detail. These objects are placed in their correct location in the three-dimensional space, as resulting from the existing documentation and the surveys. Accurate measurements and point clouds produced in service level 2 are a fundamental source for the model. The information related to each object is enriched by means of non-graphical attributes and linked documents as, for instance, the outcomes of the historical survey, the bibliographic research and the condition survey. Localised damage can be easily represented by patch-type objects. Similarly, in case of monitoring, the exact location of the sensors can be shown within the 3D model, enabling the real-time reading of their records.

The main purpose of the BIM model is to support on-site activities. Operators can navigate and interrogate it online by using mobile devices or even with the aid of augmented reality technology through mixed reality smart glasses. The availability on-site of an informative model that collects all the previous documentation on the assets is paramount, providing a continuous and timely interaction between virtual objects and physical counterparts. This approach allows a fast comparison of actual damages or alteration phenomena with a previously recorded condition, for a fast decision making regarding urgent measures or an optimisation of the inspection process towards the causes of the phenomena. Augmented reality is a further improvement, permitting a visualisation of the information collected in the BIM model directly on top of the real inspected objects. Smart devices allow also an efficient and rapid data collection by taking pictures or measuring distances. Beside purchasing the smart devices, the surveyors do not need to invest in licences, since navigation and query of the model can be done on free of licence model viewer software or directly on the online platform. No expertise in BIM modelling is demanded to the surveyors, since the manipulation of the model is carried out as back-office activity by an expert BIM modeller upon receiving the inspection forms and reports.

Increasing service level, from SL1 to SL3, implies an increment of the quantity and complexity of the information, requiring more advanced surveying and testing techniques, thus more sophisticated equipment, costs, time and expertise of the operators. It also demands advanced strategy to store, manage and visualise the produced documentation. The flexibility of a multi-level approach allows to provide a service tailored to the specific requirements and financial availability of the owners and the conservation needs and complexity of the specific asset. The adaptability and effectiveness of the methodology were tested over several typologies of heritage buildings (e.g. churches, chapels, palaces, castles, etc.) equally distributed over the three countries. In particular, sixty case-study buildings (twenty per country) were inspected and assessed according to the first service level. Fifteen out of these sixty (five per country) were selected for the implementation of the second service level. Finally, one case study per country was included in the third service level. Two selected case studies, namely São Torcato church and the Guimarães ducal palace, are discussed hereafter to show a complete SL2 and SL3 application, respectively.

4.1 *São Torcato church*

Located in the homonymous village, close to Guimarães, in the north of Portugal, São Torcato church's construction started in 1871, based on the original conception proposed in 1825, featuring a Neo-Manuelino, revival style, and continued in phases for more than 130 years (Ramos et al. 2013). Photos taken during the construction allow documenting the evolution of the work (Figure 4). In its actual configuration, the church has a Latin-cross plan, with a gallery entrance, a single nave (57.5 m long, 17.5 m wide and 26.5 m high) with side chapels and an apse at the north end. The transept is 37 m long and 11.5 m wide. Nave and transept are covered with barrel vaults and a dome with octagonal tambour stands at their crossing. Two towers are placed on the sides of the façade featuring a rectangular plan (7.5×6.5 m^2) and a height of 50 m. Wall thickness varies in the façade, from 2.5 m to 1.7 m. The thickness is 1.3 m in the lateral walls and 1.45 m in the towers (Ramos et al. 2013).

The succession of building phases determined the use of different materials, in particular three-leaf granite masonry for towers, nave and transept, and reinforced concrete for the dome and apse. The gabled roof is supported by timber trusses. Since 1970s the church has been subjected to inspections and regular control, due to a severe cracking in the front area of the church, especially the façade (Figure 5a), likely associated to their differential settlement and tilting, due to the poor mechanical characteristics of the soil. Between 2014 and 2015, the church underwent a structural intervention aimed at eliminating the differential settlement and restoring material continuity, by means of micro-piles, post-stressed tie rods and crack injection (Masciotta et al. 2017). To assess the impact of the construction activities on the church and validate the intervention, a monitoring system was installed and was active before, during and after the works (Masciotta et al. 2017).

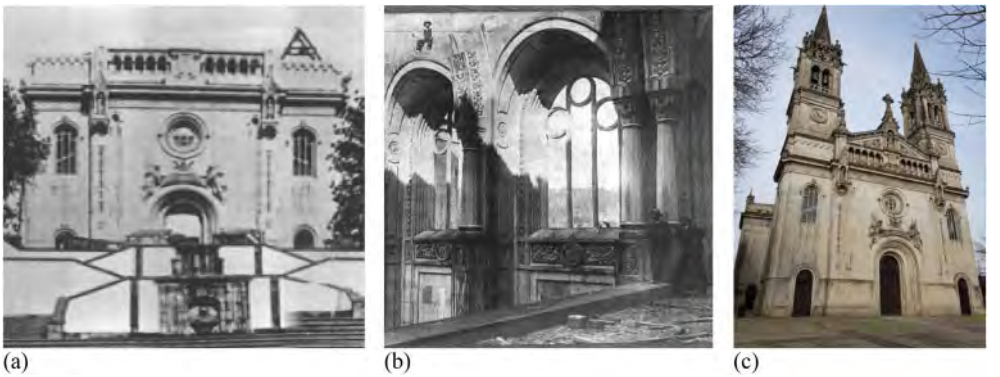

Figure 4. São Torcato church, building phases: (a) exterior view; (b) interior view; (c) actual aspect.

After few years, HeritageCare SL2 protocol was applied to the church. The large number of existing documents was collected and used to constitute the Building ID and management information. In this case, dealing with a quite recent asset that underwent several investigations and a significant intervention, the material available encompasses previous surveys, photos taken during the construction and interventions and test reports. The inspection carried out by the HeritageCare team identified several forms of degradation and damage, such as discolouration, efflorescence, biological growth and bird infestation (Masciotta et al. 2021). Most of the problems were related to water infiltration through roof, walls and openings. After the intervention, a permanent deformation was still evident in the choir, whereas new cracks appeared on the triumphal arch and along the lateral walls of the nave.

3D documentation consisted in a laser scanner survey, by means of a Leica ScanStation P20 (Figure 5). A 3D point cloud with about 3 billion of points, then reduced by processing and filtering to 17 million, was generated over 174 scan stations. The generation of the model required 3 weeks of work to two technicians. Contextually, a photographic survey was carried out in 110 minutes by means of a 360° camera Ricoh theta V at 42 locations, capturing inside and outside. The enriched virtual tour model was generated through the proprietary software Pano2VR®and ad-hoc developed plugins. A more detailed report on this case study can be found in (Masciotta et al. 2021).

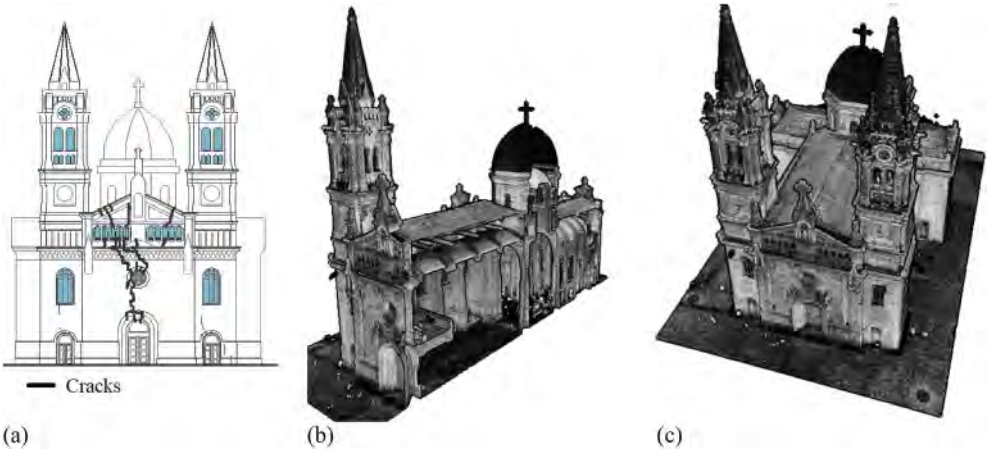

Figure 5. São Torcato church: (a) crack survey before intervention; (b) point cloud of the interior; (c) point cloud of the exterior.

4.2 *Guimãraes ducal palace*

The construction of the ducal palace of Bragança, located in Guimarães, Portugal, was more articulated than the previous case study and was affected by several vicissitudes. The construction, begun in 1420, under the first Duke of Bragança, suffered a first stop after his death. In 1478, the construction continued under the third Duke. In this period, the actual organisation of the spaces was defined. However, the palace remained incomplete, abandoned and subjected to dismantling and reuse of the materials, since the beginning of the 16th century, once the court was moved to another town. The alteration of the building continued during the 19th century, when it was turned into a military barrack. Finally, after the acknowledgment of its importance and the inclusion in the national monument list in 1910, the palace underwent a series of strong interventions, with demolition of the changes occurred in the previous century and addition and reconstruction of several of its parts, aiming at the supposed original aspect of the building. During the repair, an extensive use of reinforced concrete beams was made in the floors and roof. The actual building features a rectangular plan around a central courtyard, surrounded by a colonnade at the two lower storeys. Thirty-nine brick chimneys, among which only four are original, constitute a landmark of the city, as well as the timber trusses of the main rooms are one of the most precious features of the building. These elements are also a major concern for preservation, significantly contributing to the overall vulnerability of the palace.

The diagnosis was based on a detailed inspection that involved more than two professionals to reduce the time-requirement. The staff was interviewed providing a series of relevant information to complement the main findings of the inspection. Degradation and alteration likely due to moisture and water penetration, fostered by the inadequate and poorly maintained drainage system, were identified. Loss of material in the walls is also present, likely due to the incompatibility between the granite blocks and the mortar used in recent repointing works. Finally, superficial cracks are found at the ground floor in load bearing walls. The building features several integrated movable assets, including hundreds of art pieces dating back to the 17th and 18th centuries. The inventory and condition survey of the most significant ones were carried out. Few pieces showing an unsatisfactory conservation state were closely inspected by the HeritageCare team.

Based on the criticalities emerged from this condition survey and according to SL2 protocols, an ad-hoc monitoring system was installed in October 2018 to track structural and environmental parameters. The goals and demands of the monitoring system were defined upon agreement with the directions of the DRCN (Northern Regional Directorate of Culture), aiming at a trade-off between costs, visual impact of the sensors and quality of the collected information for the conservation purpose. The network, still operating, is composed of: (i) 12 temperature and relative humidity sensors (7 surface and 5 ambient sensors) and 5 combined sensors measuring surface temperature, relative humidity and luminosity; (ii) 3 xylophagous sensors at the timber roofing of main room and chapel; (iii) 1 carbon dioxide sensor; (iv) 2 biaxial clinometers on the outer wall; (v) 1 external meteo station recording air temperature, humidity, barometric pressure, wind direction and velocity, precipitations, rain duration, hail, solar radiation and carbon dioxide.

SL2 protocols adopted included a laser scanner survey, carried out, using a Leica ScanStation P20 (Figure 6). Four full working days on-site were necessary for the survey. 360° panoramic views ware taken, concurrently. All these sources of information contributed to the generation of the digital twin of the palace hosted on the HeritageCare platform. This is composed, at SL2, of the 360° panoramic views based virtual tour, enriched by a set of hotspots. Asset hotspots identify the significant movable assets inspected and assessed with more detail, providing the results of the on-site survey (Figure 7).

Damage hotspots locate the anomalies found during previous inspection on-site. Sensor hotspots allow reading the most recent instrumental acquisitions (Figure 8). Here, samples are updated hourly. Based on pre-set threshold values, the acquisition presents a colour-based warning so that the manager can easily identify parameters that are deviating from the acceptable condition. The results of the laser scanner survey are also navigable on the platform.

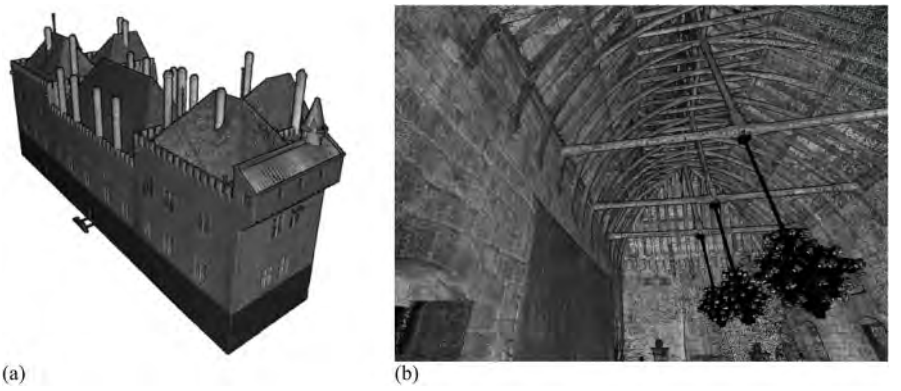

Figure 6. Guimãraes ducal palace point cloud: (a) external view; (b) detail of the interior.

Figure 7. Virtual tour enriched with asset hotspots, linked to condition survey report.

Figure 8. Virtual tour enriched with sensors and damage hotspots, linked to recent acquisition and damage report, respectively.

Finally, SL3 protocol was applied, by building a BIM model of the palace, enriched with all the aforementioned data (Figure 9). The model was generated first resorting to traditional survey techniques and existing documentation, then it was validated through the laser scanner acquisition. The purpose of the model, namely supporting an effective exchange of information between asset manager and surveyors regarding assets condition and ongoing or emerging anomalies is fulfilled by a wise trade-off between graphical and non-graphical information. This allows a reduction in time and costs to generate the model, ensuring a sufficient level of geometrical detail to correctly localise, within the building and its components, damage, movable assets or sensors. An augmented reality aided inspection was carried out by means of a pair of HoloLens and a smart glass inspection app. More information on this case study are provided in (Masciotta et al. 2019).

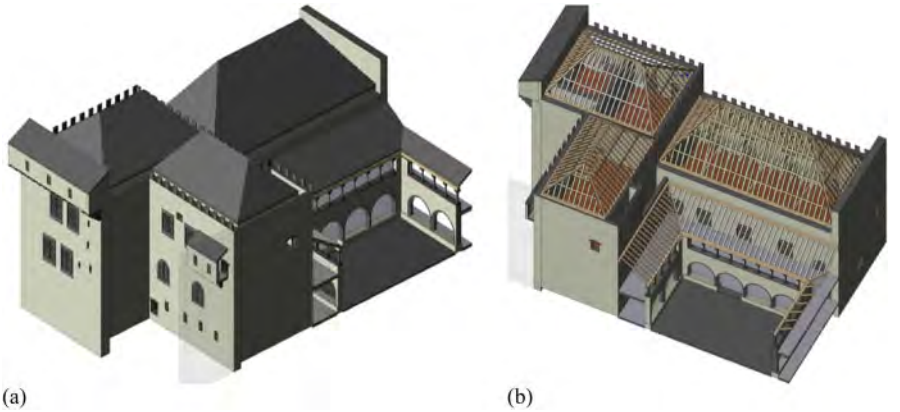

Figure 9. Guimãraes ducal palace BIM model: (a) global view; (b) detail of the roofing system.

5 NEW TECHNIQUES FOR THE INSPECTION AND PRESENTATION OF THE NON-VISIBLE PARTS OF THE BUILT HERITAGE: HWITHIN METHOLODOGY

The Heritage Within (HWITHN) European Research Project (Ortega Heras et al. 2021) aimed to develop new technologies to produce an innovative visualization of the cultural heritage by showing nonvisible features of buildings and archaeological assets. 3D surveying and modelling techniques (e.g. photogrammetry and laser scanning) have greatly evolved in the recent years but they can only reconstruct the exterior surfaces of the elements.

The project aimed to go beyond this barrier to image also relevant information of the interior of its constructive elements and other non-visible data. To this end, the project not only resorted to existing techniques (Ground Penetrating Radar) but also developed new ones, namely a system to perform on-site ultrasonic acoustic tomography of complex architectural elements in an automatized way. As a result, the inner hidden morphology of several columns could be reconstructed, on an almost stone-by-stone basis, and the inner damage and state of conservation of the material could be evaluated.

The final 3D model and associated information was implemented into a Virtual Reality (VR) application to offer an interactive visualization of our heritage, on-site and remotely. The approach proposes to relate the visible with the invisible, looking beyond the surface of the object, which facilitates the identification of inner morphology, cavities, hidden objects or damage. The action proposed as a pilot case study the Archaeological Museum of Carmo, in Lisbon (Portugal), which occupies the ruins of the old church of the Carmo Convent, destroyed during the 1755 Lisbon earthquake.

The Carmo Convent was commissioned in 1389. After two attempts, failed due to local subsoil conditions, the construction works started in the last decade of 14th century and continued until

1423, with alternate vicissitudes, including structural problems still related to subsoil capacity. In the following centuries, further addition and works embellished the church that was also populated with various pieces of art, until 1755 when a catastrophic earthquake caused the collapse of most of the structure. Although in ruin, the building was preserved due to its emblematic value and today is a museum.

All the activities of the Heritage Within project relied on the synergistic contribution of a multidisciplinary team of architects, civil engineers, telecommunication engineers, archaeologists, art historians, and geophysicists, driven by a collaborative definition of goals and demands. The project took advantage of the wide expertise of this team and generated layers of specialized information of the case study (e.g. virtual reconstruction of the original aspect of the church, structural analysis results, thermography studies or location of old art pieces), inserted within the VR platform with two main objectives: (i) make the public more aware of the essential role of professionals in the field of conservation (from art historians to engineers and architects), showing the importance of surveying, diagnostic and analysis activities for the conservation of built heritage; (ii) help specialists in the interpretation of their own results related to other specialists outcomes, by means of novel visualization tools and integration of the results of diagnostic investigations from different sources into a single VR platform.

The use of virtual reality for the dissemination and storytelling of complex results is expected to enhance accessibility to cultural heritage and enrich the visitor's experience. Moreover, it is likely to support technical activities, allowing an easy and informative visualisation on-site instead of at their desks on their computer.

Knowledge of the monument is a key aspect of conservation activities. The HWITHIN project essentially explores the use of VR as a work environment to read and visualize multiparametric information, facilitating the interpretation of technical inspection and analysis results (obtained from non-invasive inspections or structural analysis). The use of such platforms to interrelate heterogeneous data can help to understand cause-effect mechanisms between constructive characteristics, damage and structural behaviour. Nevertheless, beside the primary preservation purpose, the project set as primary objective an enhancement of the visitors' engagement with the building, for example, through the virtual reconstruction of the original aspect of the church. To this end, the multi-layered digital twin created was enriched with technical information, but also made suitable for the implementation of a virtual reality visit of the church in the actual condition and in the reconstructed aspect before its collapse. Based on the goal and the intended user, the complexity of the model can range from a virtual tour based on interlinked 360° panoramas to an advanced 3D photorealistic restitution (Figure 10).

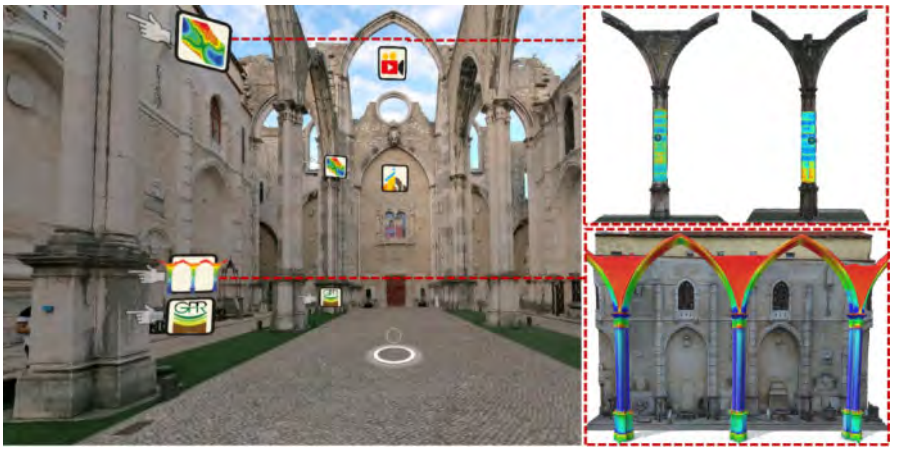

Figure 10. Virtual tour and linked layers: photorealistic 3D restitution, ultrasonic acoustic tomography (above) and structural analysis results (below).

The proposed approach constitutes an effective system for storing and analysing heterogeneous data. The future challenging goal is to integrate the virtual scenarios proposed with an Internet of Things (IoT) system to be used with a digital twin perspective. The Carmo Convent can be equipped with sensors measuring in real time environmental and structural health monitoring parameters. Results can be evaluated on the digital twin and possible interventions can be assessed and managed remotely. The association between physical object and virtual reality makes it possible to activate data analysis and monitoring of the monuments in such a way that it is possible to operate in predictive mode, identifying problems even before they occur. A digital model continuously connected with its physical counterpart and capable to be managed in an interactive form can highly optimize conservation activities.

6 CONCLUSIONS

Although preventive conservation is recognised as the potentially most cost-effective strategy for cultural heritage preservation, its widespread application is complicated by several factors, as its multidisciplinary nature, the sparsity and case-specificity of the available information, the lack of effective guidelines or standards, the limited expertise of the professionals and the lack of awareness of users, owners and managers. Here, a list of essential requirements in the field of preventive conservation is presented, within an ongoing process of rethinking this discipline towards the definition of a comprehensive and cost-effective framework. Moreover, innovative practices developed and validated, with an active involvement of the authors within two European Projects, are presented.

ACKNOWLEDGEMENTS

This work was financed by ERDF funds through the V Interreg Sudoe program within the framework of the project “HeritageCare - Monitoring and preventive conservation of historic and cultural heritage” (Ref. SOE1/P5/P0258). The Heritage Within research project was co-funded by the Creative Europe Programme of the European Union, under the Cross-sectorial subprogramme, Bridging culture and audiovisual content through digital action (Project 614719-CREA-1-2019-1-PT-CROSS-SECT-INNOVLAB). Moreover, this work was partly financed by FCT/MCTES through national funds (PIDDAC) under the R&D Unit Institute for Sustainability and Innovation in Structural Engineering (ISISE), under reference UIDB/04029/2020.

REFERENCES

Abbott, G.R., McDuling, J.J., Parsons, S.A., Schoeman, J.C., 2007. Building condition assessment: a performance evaluation tool towards sustainable asset management.

Balen, K.V., 2015. Preventive Conservation of Historic Buildings. Restoration of Buildings and Monuments 21, 99–104. https://doi.org/10.1515/rbm-2015-0008

Barontini, A., Alarcon, C., Sousa, H.S., Oliveira, D.V., Masciotta, M.G., Azenha, M., 2021. Development and Demonstration of an HBIM Framework for the Preventive Conservation of Cultural Heritage. International Journal of Architectural Heritage 0, 1–23. https://doi.org/10.1080/15583058.2021.1894502

BS EN, 2020. 17412-1: Building Information Modelling. Level of Information Need. Concepts and principles.

CEN, 2010. Maintenance — Maintenance terminology.

Della Torre, S., 2010. Critical reflection document on the draft European standard CEN/TC 346 WI 346013 conservation of cultural property-condition survey of immovable heritage (unpublished discussion document), in: Proceedings of the Seminar on Condition Reporting Systems for the Built Cultural Heritage, Monumentenwacht, Vlaanderen. pp. 22–24.

EN, 2012. 16096: Conservation of cultural property - Condition survey and report of built cultural heritage.

EN 15898, 2019. Conservation of cultural heritage - Main general terms and definitions.

Giovanna Masciotta, M., Sánchez Aparicio, L.J., Bushara, S., V. Oliveira, D., González Aguilera, D., García Alvarez, J., 2021. Digitization of cultural heritage buildings for preventive conservation purposes, in: 12th international conference on structural analysis of historical construction | 29-Septiembre a 1 Octubre 2021 | Barcelona, pp. 1559–1570.

Gonçalves, J., Mateus, R., Silvestre, J.D., 2018. Comparative Analysis of Inspection and Diagnosis Tools for Ancient Buildings, in: Ioannides, M., Fink, E., Brumana, R., Patias, P., Doulamis, A., Martins, J., Wallace, M. (Eds.), Digital Heritage. Progress in Cultural Heritage. Springer International Publishing, Cham, pp. 289–298. https://doi.org/10.1007/978-3-030-01765-1_32

Gonçalves, J., Mateus, R., Silvestre, J.D., Vasconcelos, G., 2017. Survey to architects: challenges to inspection and diagnosis in historical residential buildings. Green Lines Institute for Sustainable Development.

ICOMOS, 2003. ICOMOS Charter – Principles fora the Analysis, Conservation and Structural Restoration of Architectural Heritage.

ISO, 2010. 13822: Bases for design of structures — Assessment of existing structures.

Jagodzińska, K., Sanetra-Szeliga, J., Purchla, J., Van Balen, K., Thys, C., Vandesande, A., Van der Auwera, S., 2015. Cultural Heritage Counts for Europe: full report.

Kioussi, A., Labropoulos, K., Karoglou, M., Moropoulou, A., Zarnic, R., 2011. Recommendations and Strategies for the Establishment of a Guideline for Monument Documentation Harmonized with the Existing European Standards and Codes. Geoinformatics FCE CTU 6, 178–184. https://doi.org/10.14311/gi.6.23

Marjanović , V., 2014. Europe's endangered heritage (No. Doc. 13428). Report, , to Committee on Culture, Science, Education and Media.

Masciotta, M.G., Morais, M.J., Ramos, L.F., Oliveira, D.V., Sánchez-Aparicio, L.J., González-Aguilera, D., 2019. A Digital-based Integrated Methodology for the Preventive Conservation of Cultural Heritage: The Experience of HeritageCare Project. International Journal of Architectural Heritage 1–20. https://doi.org/10.1080/15583058.2019.1668985

Masciotta, M.-G., Ramos, L.F., Lourenço, P.B., 2017. The importance of structural monitoring as a diagnosis and control tool in the restoration process of heritage structures: A case study in Portugal. Journal of Cultural Heritage 27, 36–47. https://doi.org/10.1016/j.culher.2017.04.003

Ortega Heras, J., Gonzalez, M., Izquierdo, M., Masini, N., Vasconcelos, G., Pereira, C., Navarro, R., Gabellone, F., Vitale, V., Abate, N., Liébana, J., Anaya, G., Secanellas, S., Anaya, J., Leucci, G., Sileo, M., Borghardt, J., Ferreira, T., 2021. Heritage Within. European Research Project.

Pereira, C., de Brito, J., Silvestre, J.D., 2021. Harmonized Classification of Repair Techniques in a Global Inspection System: Proposed Methodology and Analysis of Fieldwork Data. Journal of Performance of Constructed Facilities 35, 04020122. https://doi.org/10.1061/(ASCE)CF.1943-5509.0001529

Ramos, L.F., Aguilar, R., Lourenço, P.B., Moreira, S., 2013. Dynamic structural health monitoring of Saint Torcato church. Mechanical Systems and Signal Processing 35, 1–15. https://doi.org/10.1016/j.ymssp.2012.09.007

Taylor, J., 2005. An Integrated Approach to Risk Assessments and Condition Surveys. Journal of the American Institute for Conservation 44, 127–141. https://doi.org/10.1179/019713605806082365

Wagg, D.J., Worden, K., Barthorpe, R.J., Gardner, P., 2020. Digital Twins: State-of-the-Art and Future Directions for Modeling and Simulation in Engineering Dynamics Applications. ASCE-ASME J Risk and Uncert in Engrg Sys Part B Mech Engrg 6. https://doi.org/10.1115/1.4046739

Geotechnical Engineering for the Preservation of Monuments and Historic Sites III – Lancellotta, Viggiani, Flora, de Silva & Mele (Eds)

Protecting the Sagrada Familia temple from railway tunnel construction

E.E. Alonso & A. Ledesma
Department of Civil and Environmental Engineering, Barcelona School of Civil Engineering, UPC, Barcelona, Spain

ABSTRACT: The high-speed railway line crossing downtown Barcelona was immediate to the main façade of Gaudi's modernist temple of Sagrada Familia. The paper describes the precautions adopted to avoid any damage to the church. The façade was protected by a large diameter pile wall. The performance of this wall against volume losses induced by the Earth Pressure Balance Shield construction procedure is analysed by two computational methods which rely on some fundamental solutions for the elastic half-space. The first 2D plane strain method allows a dimensionless formulation which facilitates a sensitivity analysis and helps to adopt main design decisions. The more general 3D approach described may reproduce the spatial distribution of volume loss, it solves the interaction between general pile foundations and tunnel-induced deformations and it is useful to follow the effect of advancing tunnel excavation on pile foundations (pile walls in particular). The very small settlements observed at the street level (less than 2 mm) are compatible with an overall volume loss of 0.1%. The paper describes also the organization and precautions taken to ensure a very small volume loss. Of particular interest is the procedure followed to maintain in perfect conditions the machine cutting head. It required the construction of deep shafts and auxiliary enclosures to permit the maintenance works under atmospheric conditions.

1 THE SAGRADA FAMILIA TEMPLE

The temple, an "expiatory" church to be financed by public donations, was initially designed (not by Gaudí) as a neo-gothic structure and the construction started in 1882. It was designed as a classic, Latin Christian basilica, having a central nave, two aisles, a transept, a circular apse and a tower, 85 m high, above the nave-transept crossing. Gaudí (1852–1926), at the time a 32-year-old architect, was appointed director of construction works in 1883. He started soon to introduce changes in the original design. By 1891 he had already re-designed one of the façades of the church (the Nativity façade) in a modernist (art nouveau) style. The construction of this facade, that became later an iconic landmark of Gaudí's modernist style (Figure 1), began in 1892 when the gothic apse of the church was already well advanced. Gaudí faced successfully the challenge of integrating the apse into the modernist style that he had in mind. The Nativity facade, at one end of the transept, with its four slender and very characteristic geometry and texture was a reference for the two additional portals of the temple: The Passion portal, at the other extreme of the transept, and the main Glory facade, at the entrance of the church.

The towers of the Nativity had a height of 98–107 m and a diameter of no more than 7.2 m. In 1902, when Modernism was widely adopted in Barcelona, Gaudí fully redefined the architecture and dimensions of the temple. In addition to the 12 towers defining the three portals of the church, Gaudí designed six more towers of increasing height located at the nave transept intersection: four named after the four evangelists, one for the Virgin Mary and the tallest one (170 m) to honor Jesus Christ. Gaudí paid special attention to building plaster models of parts of the structure. He was

DOI 10.1201/9781003308867-5

Figure 1. The Nativity façade (darker colour), the first to be built, in a recent photograph, showing the iconic modernist towers designed by Gaudí.

also aware of the increasing loads of the new design, but was confident that new developments in construction materials and procedures would be available in the future to complete the works. He was right. Portland cement and reinforced concrete was used in the pinnacle of the first tower completed of the Nativity portal before the date of Gaudí's death.

Modernism received strong criticisms as an anarchic, decadent and "romantic" style during the first decades of the 20th century and it was replaced in the history of architecture by a rational, ordered, "modern" style. Gaudí designed columns for the nave, inspired in nature, of great beauty. He was an accomplished geometer and his favorite shapes for vaults, column-vault connections and walls were quadric surfaces (hyperboloids, paraboloids, ellipsoids). He integrated often sculptures into his design, but he never forgot the fundamental resisting concepts of his structures. His style is unique and the Sagrada Familia temple is his masterpiece.

After Gaudí's death, his close collaborators continued the construction of the temple. In 1936, the beginning of Spanish civil war, a deliberate fire destroyed many architectural plans and drawings. The plaster models survived and they perpetuated Gaudí's original design. The construction advanced slowly because its financing depended on public donations.

Natural stone (sandstone, granite, basalt and porfyr, in order of increasing strength) was used by Gaudí to build the pillars. Later, as the temple grew in size, reinforced concrete was necessary to guarantee stability. The stone covered the inner concrete structure in a sort of "lost formwork".

Construction advanced slowly until 1980's. Then, tourist revenues allowed a much faster construction pace. Today, the nave and aisles, transept, transept facades and apse are completed. The central high towers are under construction. The main Glory facade will complete the temple. A tentative date for its completion is 2026. Figure 2 is a view of the arborescent columns, vaults and stained-glass windows of the nave. Figure 3 is a recreation of the temple, once finished. The facade in the first place is the Glory façade; on the right, the original modernist Nativity facade completed in 1930.

The Sagrada Familia is currently the second most visited European church after St. Peter's in the Vatican. The initial modernist Nativity facade and the crypt are protected UNESCO's world heritage sites, as well as six additional sites built by Gaudí in or near Barcelona.

Figure 2. A view of the columns and vaults of Sagrada Familia's nave.

Figure 3. Recreation of the finalized temple. Courtesy of Sagrada Familia Foundation.

2 THE TUNNEL PROJECT

Crossing Barcelona, a densely populated city with relatively narrow streets and a well-developed underground metro network, was a real challenge for the designers of a new high-speed railway line. The alternative selected involved the construction of a deep tunnel under Mallorca street (Figure 4), which is at the southeast limit of the Sagrada Familia temple. In fact, the access to the Gloria portal of the church will probably "fly" over Mallorca street. The Foundation in charge of building the temple and other citizen associations expressed their deep concern for the perceived risks of damaging the temple. UNESCO shared these concerns, based on the special care which required any intervention menacing this world heritage site. Therefore, the protection of the temple was a major concern for the Spanish Administration of Railway Infrastructures (ADIF).

The soil profile in the area is given in Figure 5. The substratum is a stiff tertiary (Pliocene) irregular sequence of sandy clays and clays, rather stiff and overconsolidated. The tunnel, whose centerline is 30 m below the street, remains in this Pliocene level. Overlying the Pliocene soils is a quaternary deposit of alluvial fans of clayey gravels and, on top of them, yellow silts, lightly cemented and calcareous crusts. These quaternary deposits are unsaturated and they offer also a good support for shallow foundations of moderate loading. The phreatic level is 15 m below the street level.

The type of foundations of the temple evolved during the long construction period. Figure 6 is a plan view of the different foundation typologies, which correspond to the historic construction phases of the church. The Nativity façade (Figure 1), including its four towers, was founded on a thick slab of "cyclopean concrete" (large pieces of rock in a concrete mass) resting on the ancient quaternary stiff soil layer. The Passion facade, at the other end of the transept, is supported by a 2.50 m thick reinforced concrete slab, lying over the quaternary soil. The main nave and aisles, whose construction began in 1983, the central towers and the towers of the Glory facade, that faces Mallorca street, are supported by large diameter excavated piles, 20 m long, in several configurations, capped by stiff slabs. The original slab foundation of the crypt under the transept

Figure 4. Work in progress and Mallorca street at the time of the construction of the tunnel.

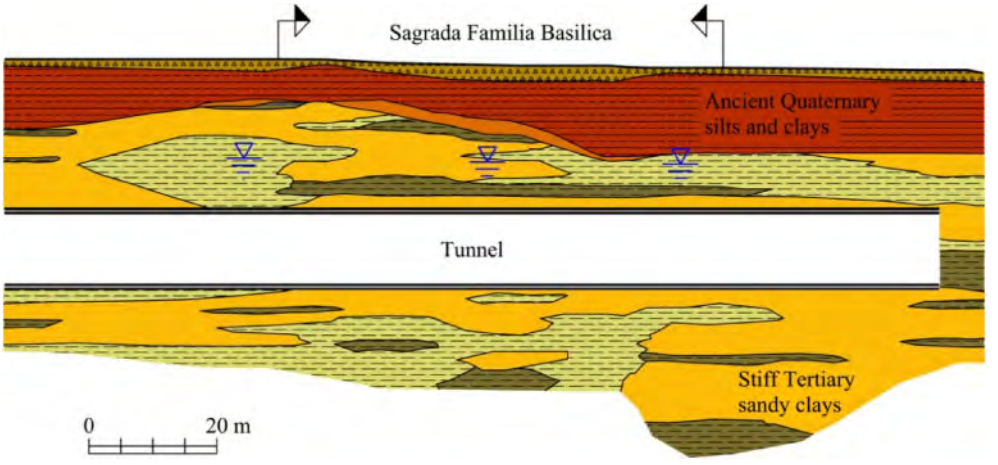

Figure 5. Soil profile along the railway tunnel.

and apse dating back to the beginning of construction in the late 19th century, was reinforced by micropiles to provide an adequate support of the central towers currently under construction. No pathologies associated with foundations have been noticed.

The initial proposal to protect the temple from displacements induced by tunnel construction was to improve the tertiary sands and clays by means of a jet grouting massive treatment shown in Figure 7. The idea was to create a massive arch of stiff treated soil around the tunnel, which would be excavated later on. This solution was discarded, among other foreseen difficulties, because of the risk of deforming the piled foundations of the Gloria facade by the high-pressure jet injection.

The accepted solution was to build a pile wall, represented in Figure 8. The 1.50-meter diameter bored piles are 41 m long and their tips are 5 m deeper than the invert of the tunnel. Pile centers

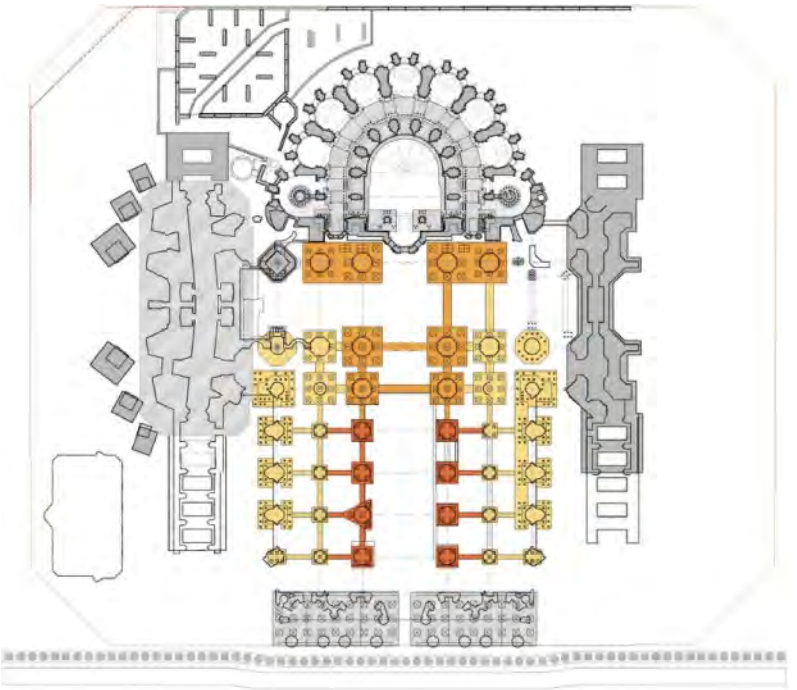

Figure 6. Plan view of Sagrada Familia foundations. Courtesy of Sagrada Familia Foundation.

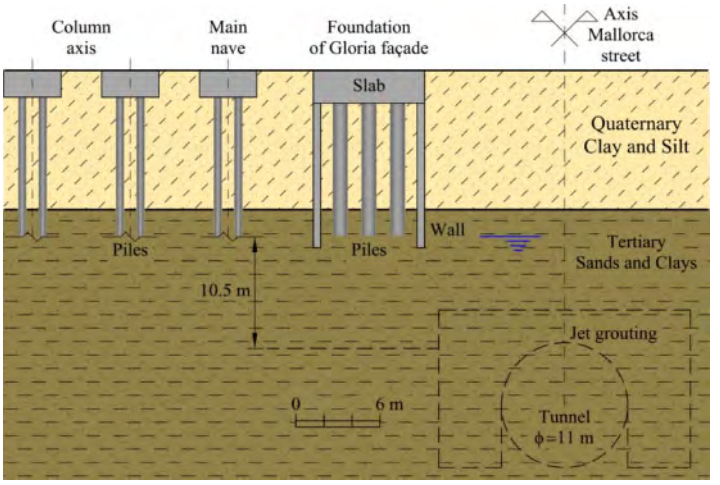

Figure 7. Pile foundations of the Glory façade and nave. Also indicated is a preliminary proposal to protect the church foundations by means of a jet grouting thick shield around the tunnel.

are 2 m apart to allow for the natural seepage flow in the area that goes in SE direction towards the sea.

Figure 6, in its lower part, shows the position and length of the pile wall built to protect the Glory portal and its four towers.

Pile walls are a well-known procedure to protect buildings against tunnelling-induced damage. Figure 9 shows an early example (Peck, 1969). The construction of the high-speed railway tunnel profited from accumulated experience in metro lines in Barcelona and, in particular in the most recent long metro line 9, which provided useful information of virtually all the geotechnical environments of Barcelona and neighboring municipalities: delta areas, Palaeozoic rocks, ancient quaternary soils, tertiary substratum and the transitions among them. Also, the layout of the metro line and the topography of the city required deep tunneling excavations.

Figure 10 (Di Mariano, 2017) shows the relationship between maximum measured surface settlements and the cover ratio H/D (H: depth of the center line; D: tunnel diameter). Two classes of excavated soils are shown: "soft soil" (typically deltaic deposits) and stiff soils (substratum). Note that maximum settlements for alluvial soils in Besós delta are quite significant (20–100 mm).

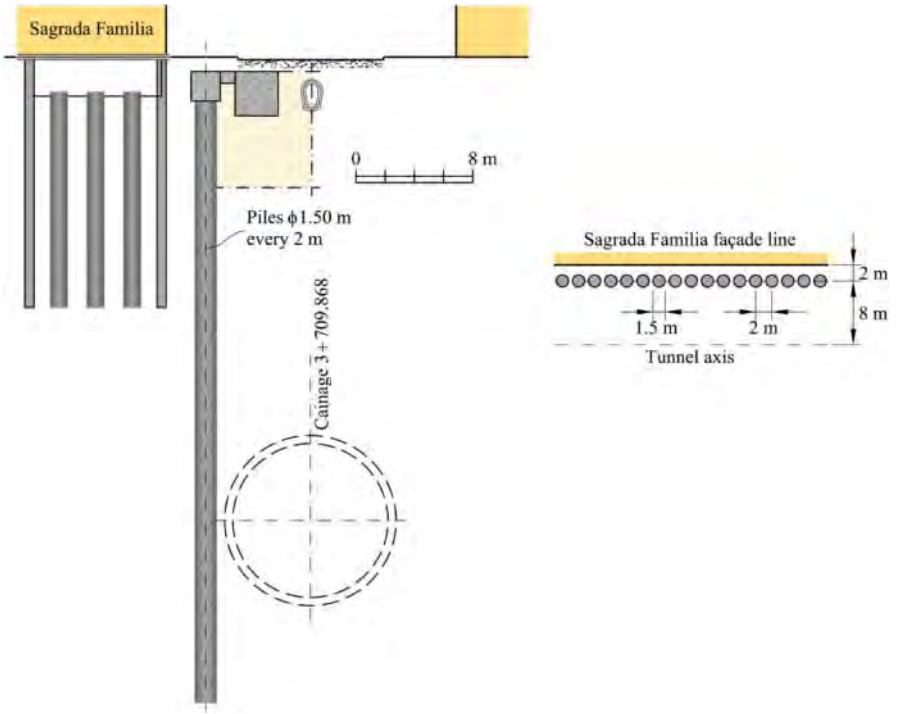

Figure 8. Protection pile wall.

The range of cover ratios of the Mallorca AVE tunnel is also given in the left part of the figure. For $H/D = 3$, which is the cover ratio in the vicinity of the Glory portal, expected settlements are in the range of 3 to 12 mm and an average value close to a settlement of 5 mm.

Figure 11 (Di Mariano et al., 2007) shows a pile wall protection of a building close to metro line 9. The tunnel was excavated in saturated alluvial sand and gravel. Figure 12 shows the measured surface settlements and the results of some FE calculations. The presence of the wall drastically reduced the settlements in the protected part of the wall.

Shown in the figure are two numerical analyses (Plaxis 2D) under greenfield conditions (no wall) and in the presence of the wall, which follows the actual measurements. The figure also suggests that the volume loss was not affected by the presence of the wall. Therefore, the protection of the wall is made "at the expense" of increasing the settlements of the non-protected side (if compared with greenfield conditions).

Walls are also efficient to reduce horizontal displacements, which also contribute to induce damage (Figure 13). The condition of conservation of volume loss may be used to "predict" the

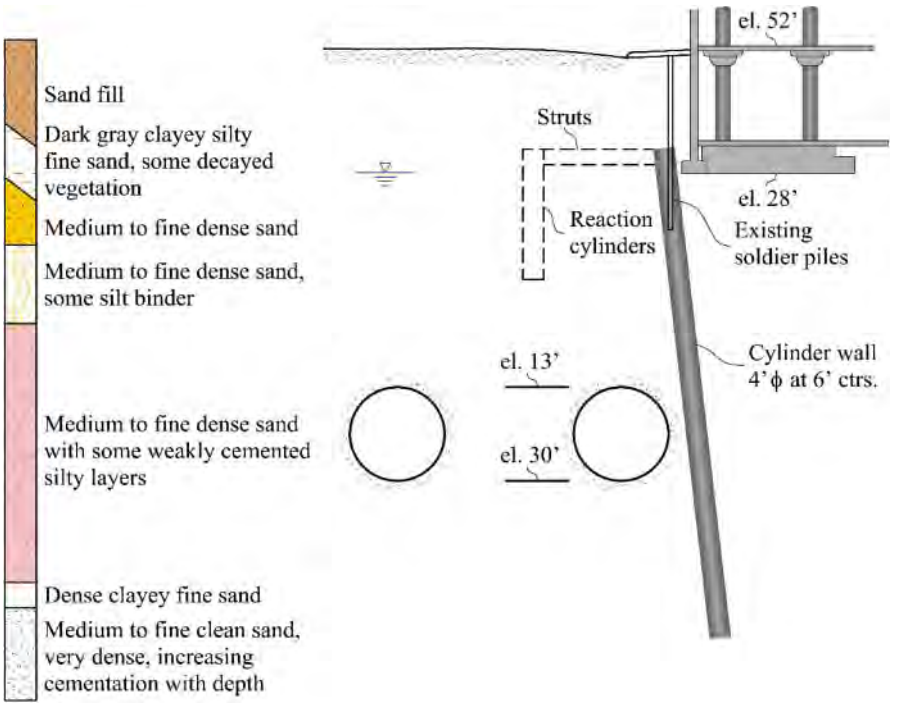

Figure 9. An early example of pile wall to protect buildings against tunnelling induced deformations (Peck, 1969).

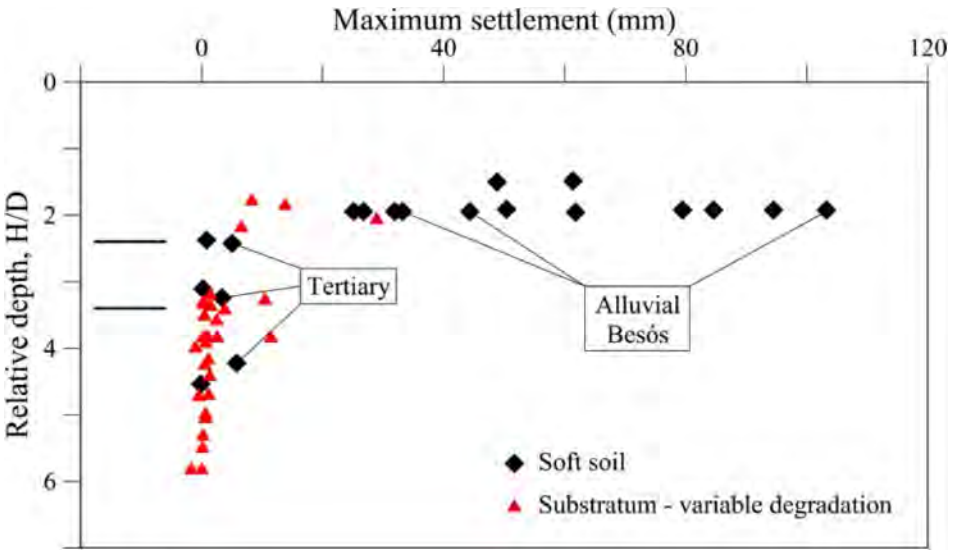

Figure 10. Maximum surface settlement measured in Metro Line 9 of Barcelona plotted against relative depth of tunnels for Alluvial and Tertiary soils of Barcelona. The range of depth ratios of AVE railway crossing of the city are shown on the left of the plot (Di Mariano, 2017).

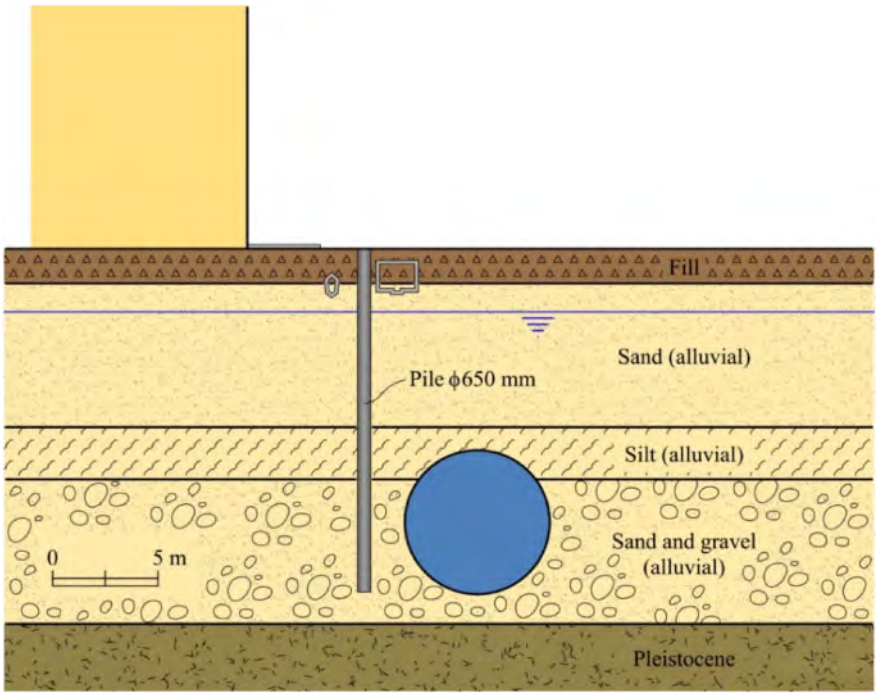

Figure 11. Pile wall protection against a metro tunnel in alluvial saturated soils in Barcelona. Di Mariano et al, (2007).

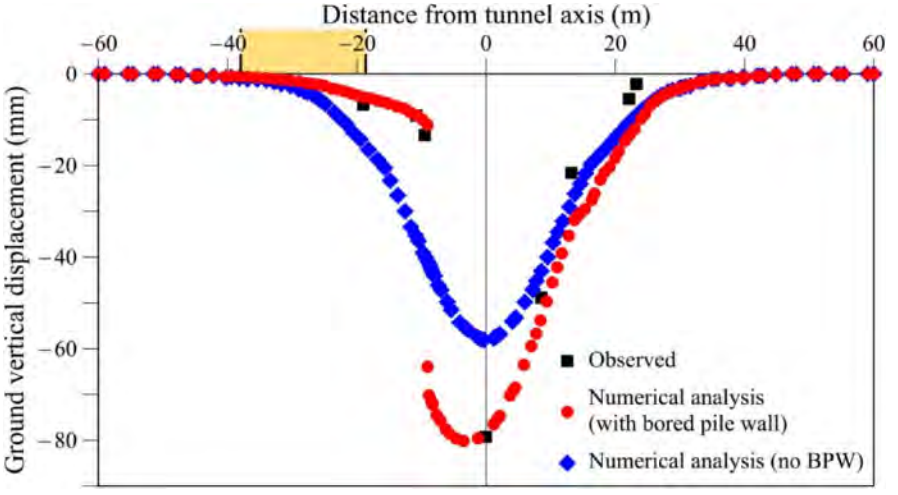

Figure 12. Measured and calculated settlement trough for the case represented in Figure 11. Di Mariano et al, (2007).

effect of a protecting wall without resorting to finite element calculations in view of previous considerations. Figure 14 presents a preliminary exercise of "predicting" the maximum settlement response at street level for an assumed volume loss of 0.5%. The greenfield settlement trough was approximated by the Loganathan & Poulos (1998) semi-analytical formula and the effect of the

proposed pile wall relied on the condition of constant volume loss, irrespective of the presence of the wall.

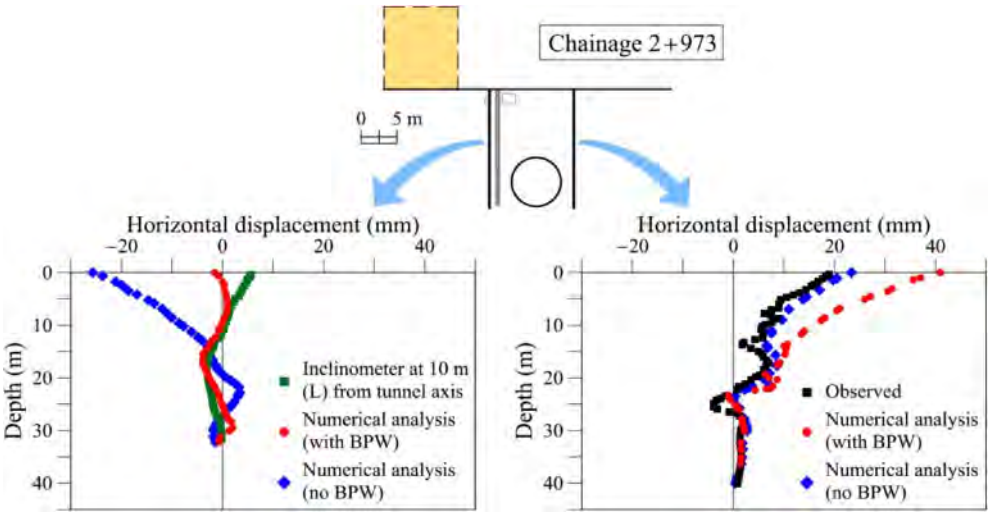

Figure 13. Horizontal displacements measured and calculated, in two vertical profiles on both sides of the tunnel. Di Mariano et al., (2007).

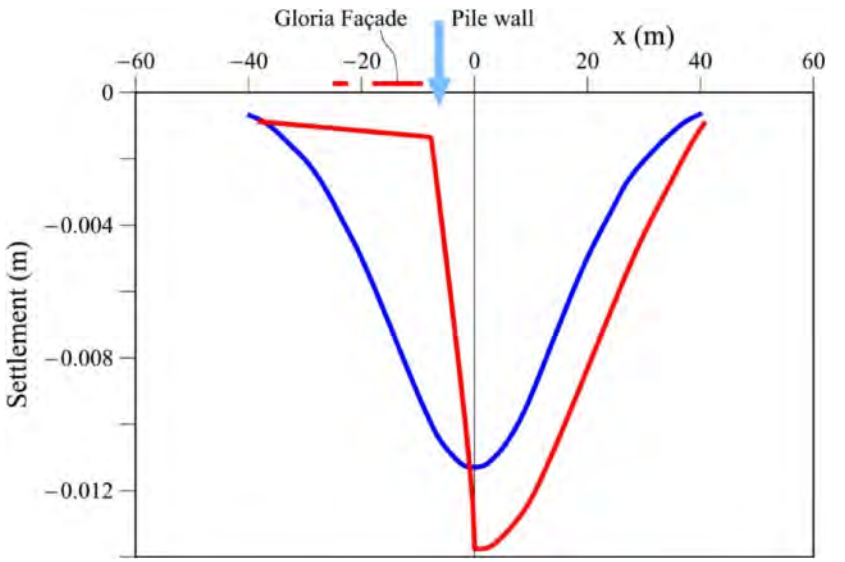

Figure 14. A sketch showing the effect of a protecting wall on settlement trough.

The protection wall designed for the Sagrada Familia maximizes the internal forces developed in the piles subjected to the tunnel-induced displacements by fixing the pile cap, attaching it to a stiff reaction beam (cross section 3×3 m), shown in Figure 8.

3 ANALYTIC SOLUTIONS

Finite element analyses are often performed to quantify the interaction between tunnel construction and building foundations. However, reproducing the set of operations involved in an Earth Pressure Balance Shield (EPBS) construction sequence is a difficult task. In practice, the success of a EPBS construction is the result of a careful planning, past experience, real time interpretation of machine performance and monitoring data, etc. A successful construction minimizes soil volume lost, a critical information difficult to estimate a priori and very difficult to reproduce by a numerical representation of machine operations.

It turns out that volume loss and soil stiffness provide the most significant information to analyze tunnel-foundation interaction. This simplicity opens the possibility of building predictive models by incorporating analytical solutions into relatively simple calculation procedures. One of the advantages of analytical solutions is the possibility of building dimensionless formulations, which offer a powerful and simple procedure to perform sensitivity analyses of controlling variables, a useful tool at the design stage.

Two approaches are described below: A 2D formulation for the tunnel-wall interaction and a more general 3D analysis of tunnel and piled foundations, which can be used also to analyze a piled wall as a particular case of a pile group.

3.1 *A 2D plane strain analysis of protection wall*

Consider in Figure 15a the geometry of the problem. The purpose of the analysis is to calculate the surface settlement induced by a tunnel construction in presence of a wall, as indicated (Ledesma & Alonso, 2018). Displacements are the result of the tunnel construction and the influence of forces developing along the wall shaft. The tunnel effect will be approximated by the solution given by Loganathan & Poulos (1998). Their analysis starts in the previous publication by Verruijt & Booker (1996), which was modified by the authors to better approximate some field data of surface settlements. They argue that the actual volume loss in EPBS tunneling reaches a maximum on the tunnel crown and a minimum at the invert (Figure 16). This is a consequence of the settlement of the tunnel lining where it abandons the protection of the shield. The vertical displacement for $\nu = 0.5$ (no volume change of elastic soil) is given by

$$u_z(x,z) = R^2 \left(-\frac{Z-H}{x^2+(Z-H)^2} + \frac{Z+H}{x^2+(Z+H)^2} - \frac{Z\left[x^2-(Z+H)^2\right]}{\left[x^2+(Z+H)^2\right]^2} \right) \varepsilon \qquad (1)$$

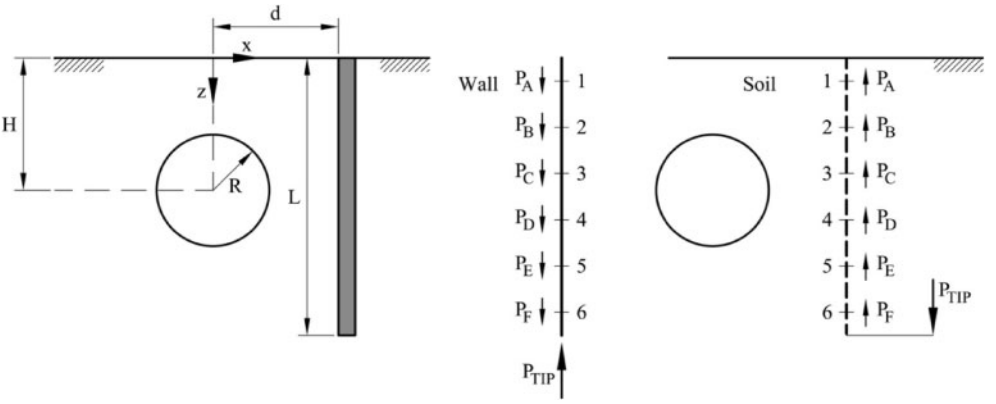

Figure 15. Geometry of the problem and interaction forces (Ledesma & Alonso, 2018).

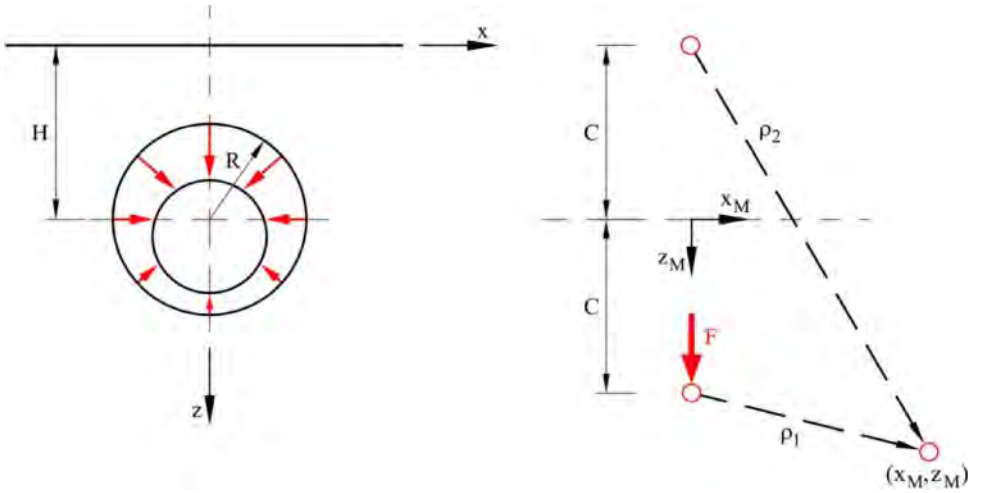

Figure 16. Sketch of volume loss simulated in Loganathan & Poulos (1998) solution and geometry of the 2D Melan' theoretical line loading problem.

where ε is a modified ground loss (illustrated in Figure 16):

$$\varepsilon = \varepsilon_o \exp\left[-\left(\frac{1.38x^2}{(H+R)^2} + \frac{0.69Z^2}{H^2}\right)\right]\varepsilon \tag{2}$$

where H is the depth of the tunnel axis and ε_o is the normalized ground loss: area of the surface settlement trough divided by the tunnel cross sectional area. Note that displacements do not depend on the elastic soil modulus in these expressions.

An additional fundamental solution required, concerns the line load, F, per unit length, applied inside an elastic half-space (Melan, 1932). We use here Sneddon (1951) and Verruijt & Booker (2000) formulae for displacements. The vertical displacements on the wall axis ($x_M = 0$) are

$$u_Z = \frac{3F}{2\pi E_s}\left[\ln\frac{\sqrt{c^2+w^2}}{c+Z_M} - \frac{1}{2}ln\frac{|Z_M - c|}{Z_M + c} + 1 - \frac{c^2}{c^2+w^2} + cZ_M\left(\frac{1}{(c+Z_M)^2}\right)\right] \tag{3}$$

(see Figure 16) where E_s is the soil modulus, w is a horizontal distance from the wall on the ground surface ($z_M = 0$) where the displacement is negligible.

The calculation procedure for the wall-tunnel interaction is formulated by expressing the compatibility between vertical displacements of the wall, at a set of points (1, 2, etc., see Figure 15, where the interface soil-wall loads are applied) and the soil displacements on the same points, under the combined action of tunnel-induced displacements and a set of forces equal but in opposite direction to the forces applied to the wall.

The wall displacements due to forces P_A, P_B, etc. and a tip force, result from an elementary calculation in terms of unit cross sectional area, A_W, and modulus, E_w, of the wall. The fundamental solutions mentioned allow the calculation of soil displacements. Making them equal and ensuring vertical equilibrium, lead to a set of algebraic equations that allow the calculation of interaction forces and displacements at any point. Note that the validity of a superposition principle is applied.

The problem may be formulated in terms of four dimensionless coefficients which are helpful to perform sensitivity analysis: $\Pi_1 = H/R$ (tunnel cover ratio: 2 to 5); $\Pi_2 = d/R$ (wall distance to tunnel: 1 to 3); $\Pi_3 = L/R$ (wall length: 1 to 10) and$\Pi_4 = E_sR/E_wA_w$ (stiffness ratio: 2.5 E–5 to 2.5 E–1). Usual ranges in practice are indicated.

It is of interest to examine some results for a reasonable case ("base case" in the following, characterized by the following data $\Pi_1 = H/R = 3$; $\Pi_2 = d/R = 2$; $\Pi_4 = 0.0025$and a volume loss

of 1%. Figure 17 shows the effect of the length of the protection wall on the expected surface settlement. The greenfield case is a symmetric gaussian-type curve. A useful way of describing the protection of a given wall design is to define an efficiency coefficient (Bilotta & Russo, 2011) as follows:

$$\eta = \frac{S_{greenfield} - S_{behindthewall}}{S_{greenfield}} \tag{4}$$

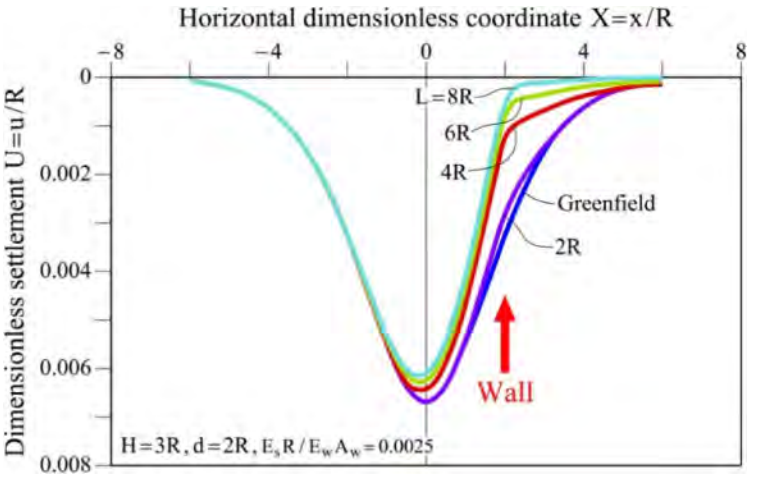

Figure 17. Base case. Effect of length of protection wall on the settlement trough.

where settlements are computed in a point immediate to the wall position, on the protected side. η varies between 0 (no effect) and 1 (full effect).

Figure 18 (curve A) provides a plot of η in terms of the wall length (L/R) for the base case just defined. Also plotted (curve B) is the result of a Finite Element analysis (2D, elastic, plane strain) which reproduces the base case. The calculated efficiency is lower in this case and the

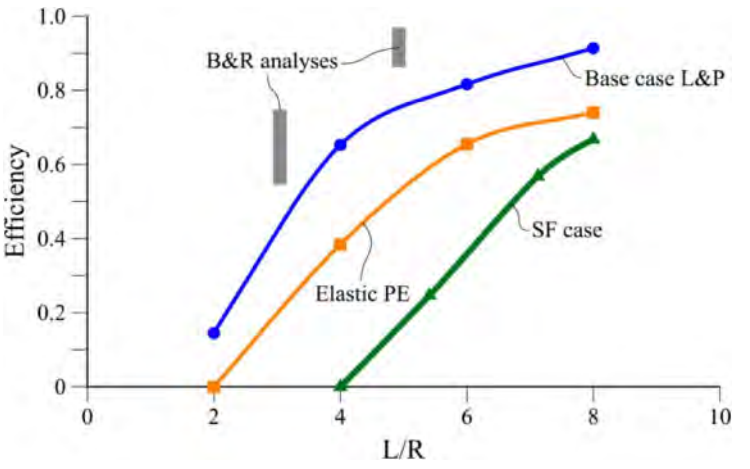

Figure 18. Efficiency of the protection wall in terms of dimensionless wall lengths. The different cases represented are explained in the text.

reason is that the Loganathan & Poulos expression for tunnel-induced displacements provides a surface settlement through narrower than a "standard" elastic solution. Loganathan & Poulos (1998) expression is expected to be closer to displacements associated with EPBS operation. There are also two estimations of efficiency (letters D, E), which were taken from Bilotta & Russo (2011) (B&R) for volume losses ranging from 0.5% to 2.5%, $L/R = 3$ (curve D) and $L/R = 5$ (curve E). Curve A (this paper) and the finite element results (D, E) are quite consistent despite the widely different calculation procedures (Bilotta & Russo introduced also a soil stiffness increasing with depth).

A third efficiency curve (C) corresponds to the Sagrada Familia protection wall discussed below. In all cases, increasing the wall length looks like an efficient procedure to increase the wall efficiency.

Figure 19a shows the effect of stiffness ratio $\Pi_4$on wall efficiency. For a given soil modulus, if$\Pi_4$decreases the efficiency increases. This is shown also in Figure 19b. However, below a given ratio ($\Pi_4 \cong 0.02$) reducing $\Pi_4$does not help to increase efficiency.

The pile wall dimensions for the Sagrada Familia (Figure 8) lead to the following dimensionless coefficients defining the wall: $\Pi_1 = H/R = 5.4; \Pi_2 = d/R = 1.4$ and $\Pi_3 = L/R = 7.1$.

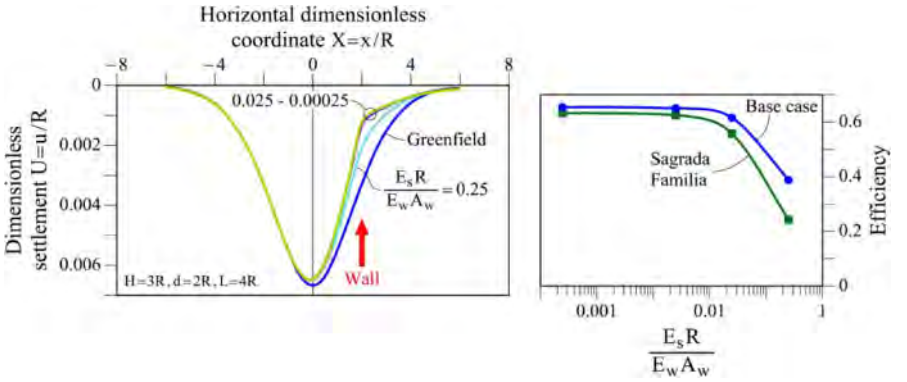

Figure 19. Effect of stiffness ratio on surface settlement (left) and variation of wall efficiency with stiffness ratio.

For $E_s \cong 30$ MPa, $E_w = 30000$ MPa and $A_w = 1$ m^2/m, $\Pi_4 \cong 0.006$. Also, a volume loss $\varepsilon_o = 1\%$ was selected to compare the new analysis with the base case. The calculated efficiency, in terms of pile length was also included in Figure 18. The adopted length to diameter ratio ($L/R = 8$) leads to $\eta = 0.65$ (curve C). For the actual stiffness ratio, Figure 19 shows that increasing wall stiffness does not result in improvement of efficiency. It can be concluded that the designed barrier was an appropriate decision.

The wall design was validated by finite element analysis and elastoplastic models, featuring small strain capabilities for the quaternary and tertiary soils. Identifying a relatively long list of parameters of a complex constitutive model is an involved and uncertain task. However, the critical parameter in these cases is the volume loss, a parameter linked with a different class of information: experience in EPBS handling, workmanship, control in real time of machine performance and interpretation of monitoring data. Figure 20 indicates the FE calculated settlements in a section perpendicular to Mallorca street axis for a conservative value of volume loss (0.5%). The maximum settlement under the street was 6 mm. The wall reduces settlements to less than 3 mm. Two calculations are represented, in terms of introducing or not, building loads. Differences are small. The figure also shows the actual settlement measured: No settlements in the protected zone and a maximum settlement of 2 mm at the street side of the wall. Measured settlements along Mallorca street, at locations away from the Sagrada Familia block, remained also very low.

The next section presents a more advanced 3D calculation procedure, using fundamental solutions for loading and local volume change in an elastic half space.

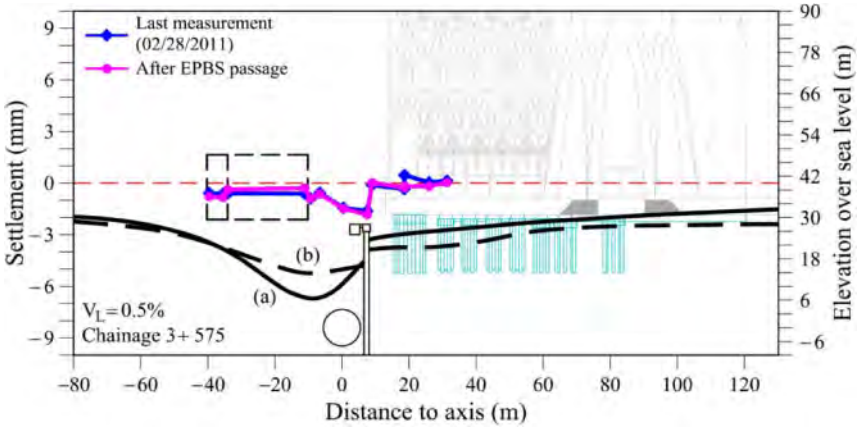

Figure 20. Settlement results of a FE analysis for a volume loss of 0.5% and actual measurements.

3.2 *A 3D analysis of interaction between piled foundations and TBM tunneling*

Volume loss of TBM tunnelling distributes around the tunnel in a non-homogeneous pattern, as mentioned before. This is sketched in Figure 21. If the objective is to reproduce the effect of the advancing tunnel in an underground structure, such as a piled foundation, the actual geometry of volume losses may be "discretized" by adopting a length interval (ΔL) to account for the advancement of the tunnel construction and a suitable subdivision of the ground loss in the cross section. Then, the volume loss can be represented by a set of elementary volumes. Sagaseta (1987) found an analytical solution for the distribution of undrained deformations of a half-space when a spherical volume is lost in an arbitrary position. This solution is useful to analyze the effect of tunnel-induced volume loss in foundations.

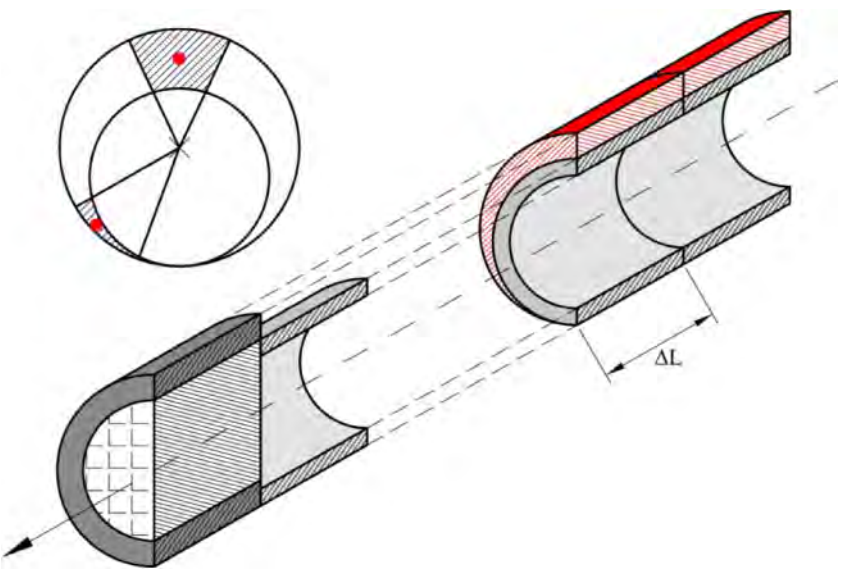

Figure 21. Definition of volume loss and sketch showing the advancement of tunnel construction.

Consider (Figure 22) a piled foundation in the vicinity of the tunnel. The figure represents (left) the capped pile structure subjected to external, as well as "internal", forces and stresses. On the right, the soil is represented. The soil will deform because of the interaction stresses received from the structure and the volume loss associated with tunnelling. Under two hypotheses: superposition of loads applies and there is a compatibility of displacements (vertical and horizontal) of structure and soil, a procedure can be devised to solve the interaction problem. If the analysis is performed in a homogeneous, isotropic and elastic half-space, the well-known fundamental solutions of Boussinesq (1885) for a point load on the surface, Mindlin (1936) for the point load in the half-space and Sagaseta (1987) for the volume loss, compatibility and equilibrium conditions lead to a system of algebraic equations that provide a solution.

This approach was followed to build a computer program, fairly general, which is useful to analyze the effect of an advancing tunnel on an existing piled foundation. Consider one example in Figure 23. A 3×3 capped group of nine 25m long, 1 m diameter piled foundation will experience

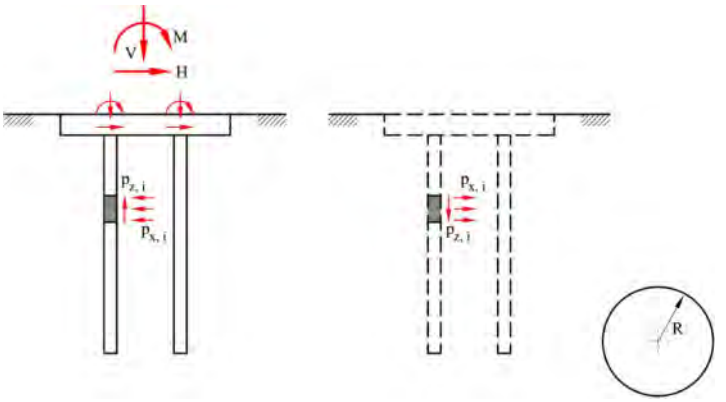

Figure 22. The analysis of a pile foundation in presence of a tunnel construction. Left: the capped pile structure. Right: Soil half space and tunnel.

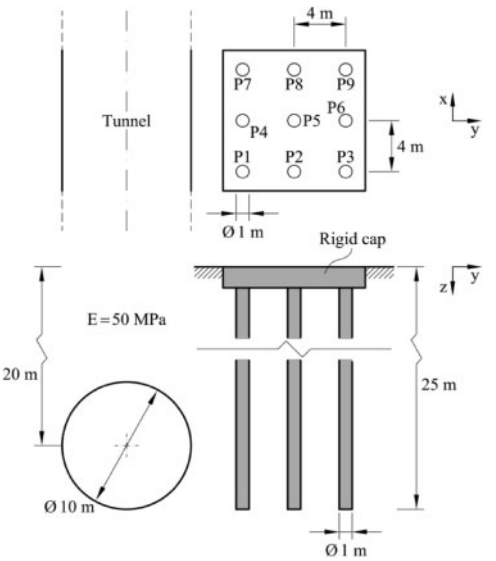

Figure 23. Geometry of a solved example: Interaction between a tunnel construction and a 3x3 capped pile foundation.

the effect of a 10 m diameter tunnel construction in the vicinity. Table 1 summarizes the main parameters of the case.

Table 1. Parameters for the tunnel-piled foundation interaction

Piles (rigid cap; 3×3)	Soil	Tunnel			
Length	25 m	E	50 MPa	Volume loss	1%
Diameter	1 m	ν	0.5	Diameter	10 m
E_C	30,000 MPa			Centerline depth	20 m
ν_C	0.3				

Figure 24 provides a 3D view of the example solved and the length of tunnel excavation, which was divided in 100 steps, 2 m long each.

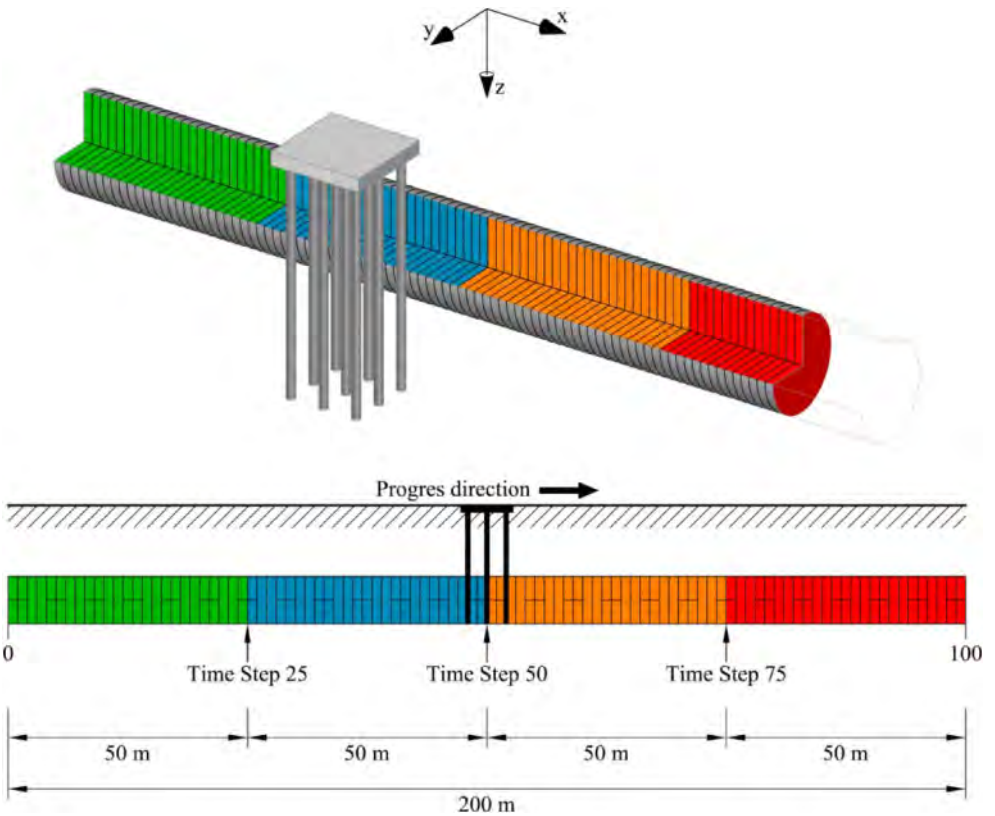

Figure 24. 3D view of the pile foundation and the excavated tunnel. The construction of a 200 m long tunnel is divided in 100 increments 2 m long each one of them.

One pile (number 4, in Figure 25) is selected to provide some calculated results to illustrate the capabilities of the analysis. The solution is general and provides forces, bending moments and displacements of the structure. Soil stresses and displacements are also known.

Figure 25 shows the horizontal x displacements of pile 4. The x direction is the tunnel axis. Displacements are zero when the tunnel front starts operating 100 m apart from the center of the pile group and accumulate progressively as the tunnel head crosses the center position of the pile

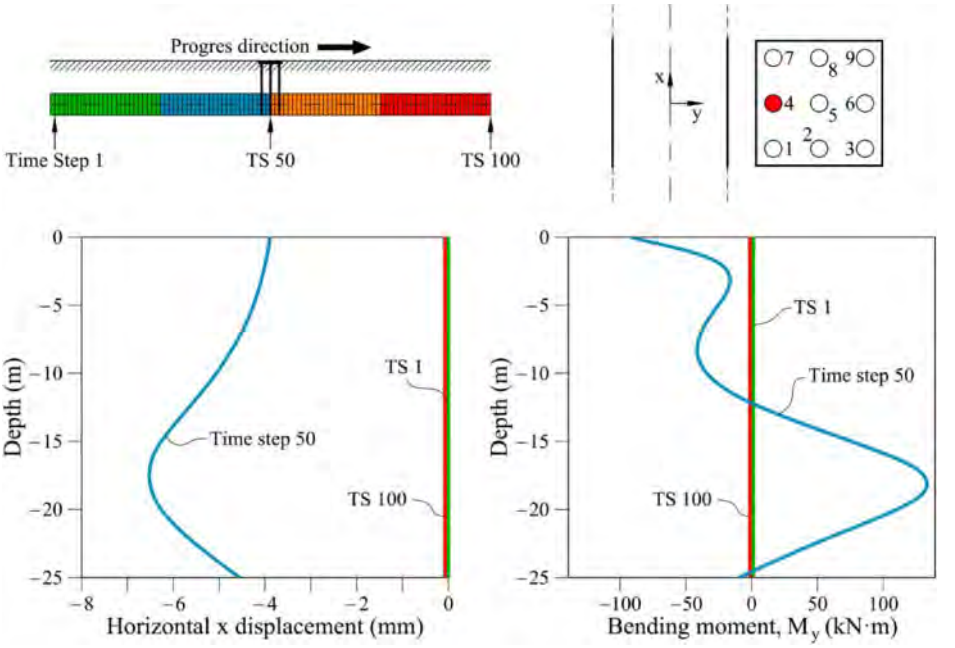

Figure 25. Calculated horizontal x displacements and associated bending moments developing along the shaft of pile 4 during tunnel construction.

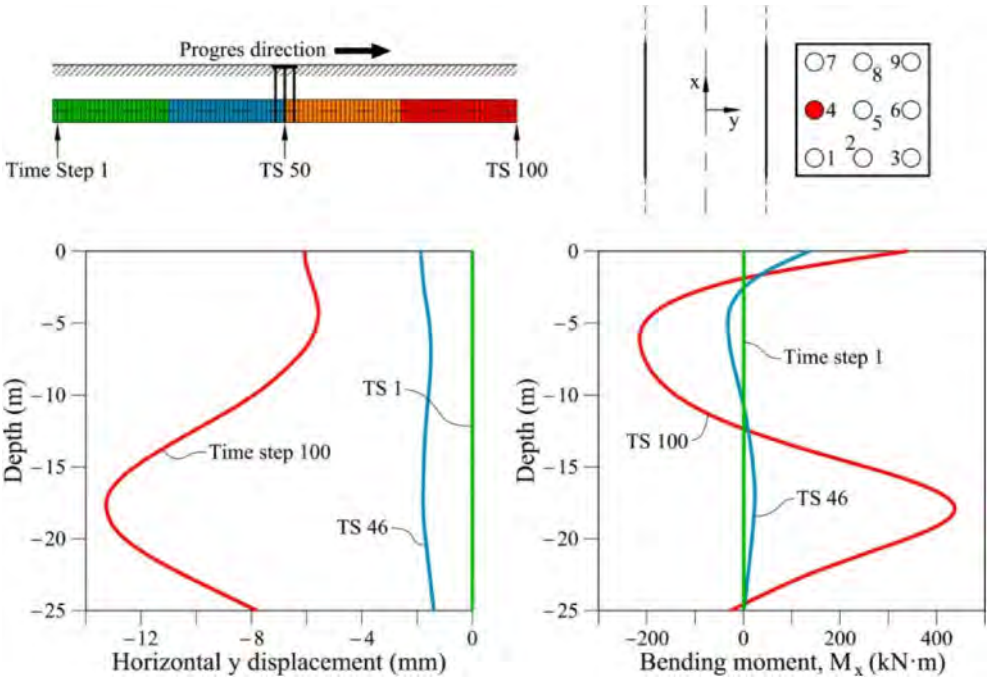

Figure 26. Calculated horizontal y displacements and associated bending moments developing along the shaft of pile 4 during tunnel construction.

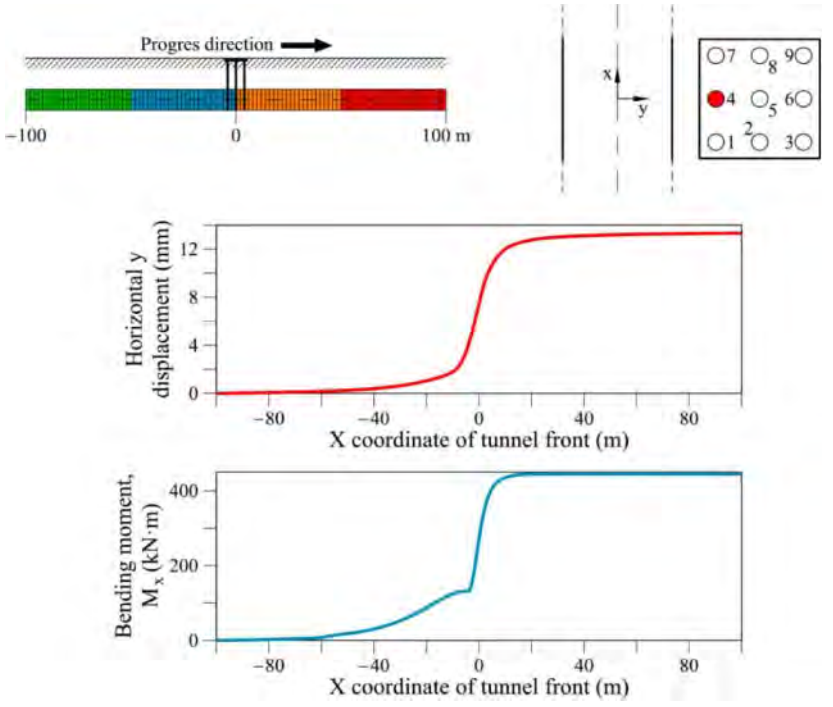

Figure 27. Accumulation of maximum horizontal y displacements and maximum M_x moments in pile 4 during tunnel construction

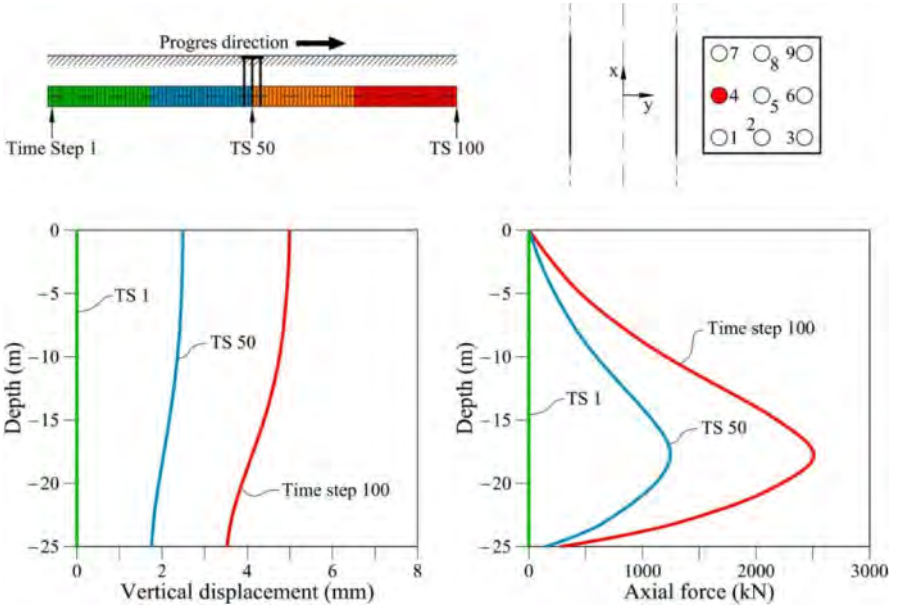

Figure 28. Calculated vertical displacements and axial forces developing along the shaft of pile 4 during tunnel construction.

group (time step 50). These are displacements towards the tunnel front. Further tunnel excavation induces x displacements equal but of opposite sign to the previous excavation stage. At the end of the simulated length of construction (step 100) the x displacements of pile 4 vanish. Note also that the position of the tunnel and the distribution of the volume loss leads to a maximum x displacement of the pile at a depth of 17 m, which is 3 m above the position of the tunnel centerline.

The M_y bending moments follow the distribution of x displacements along the pile and the fixity condition of the cap. They also vanish when the tunnel is already built and the front is 100 m away (step 100) of the pile group centerline.

In contrast, y-displacements accumulated constantly during tunnel passage. This is shown for pile 4 in Figure 26. Maximum y-displacements double the maximum x-displacements and maximum M_x bending moments multiply by 3 the maximum M_y ones.

The development of maximum displacements towards the tunnel, in terms of the position of the tunnel front, indicate that the tunnel effect on the foundations mobilizes when a 20 m long stretch of the tunnel, centred on the location of pile 4 is built (Figure 27). Maximum bending moments follows a similar pattern. It is also interesting to realize that tunnel excavation, because of the particular distribution of volume losses, leads to vertical settlements of the pile and may compress them as shown in Figure 28. This is also a case of continuous accumulation of vertical deformations and loads during the tunnel construction.

A protection pile wall is a particular case of a pile group. Consider in Figure 29 the pile wall protecting the Glory facade of the temple. Given the length of the wall and the large number of piles, let us pay attention to a single representative pile (P7) centred on a short pile group (9 piles

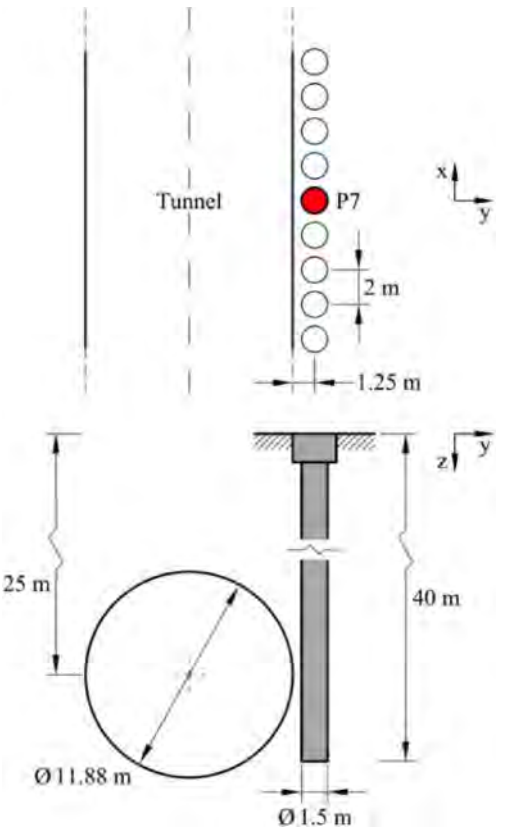

Figure 29. Geometry of the analysed protection pile wall of the Glory façade of Sagrada Familia.

and a rigid cap) at a sufficient distance of the end of the barrier. The excavation length of the wall was also divided into 100 steps. Adopted soil and pile stiffness are $E_s = 30$ MPa; $\nu_s = 0.5$; $E_w =$ 30,000 MPa; $\nu_w = 0.3$. A volume loss of 0.10% reproduces the measured settlements. It was found by fitting measured surface settlements with the model.

Y-displacements of the pile accumulate during the passage of the tunnel and reach a calculated maximum horizontal displacement of 2.6 mm at a depth of 23 m, seven meters above the level of the tunnel centerline. The calculated maximum bending moment (375 kN m) is a very small value for the reinforced 1.50 m diameter pile (Figure 30). Maximum calculated pile settlements are also very small (0.33 mm) (Figure 31). An axial compressive force develops and reaches a maximum (670 kN) when the tunnel front is away from the location of the pile wall. The maximum vertical stress in piles is also a very small value for a reinforced concrete (380 kN/m^2).

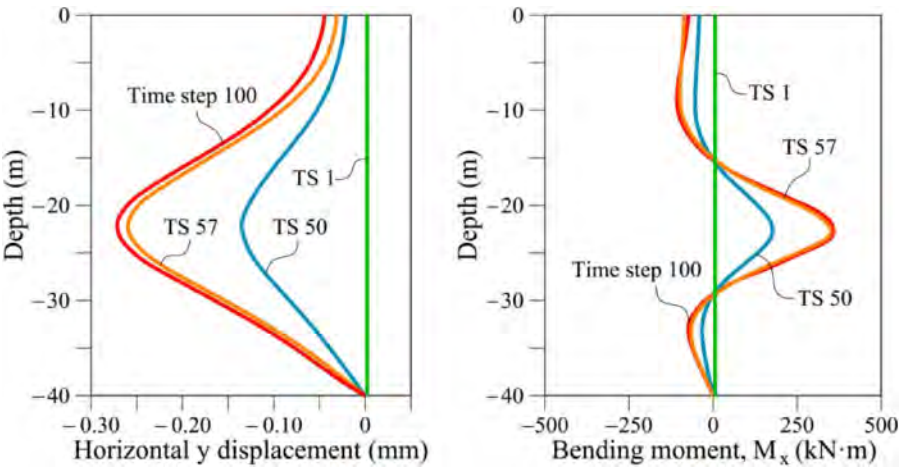

Figure 30. Sagrada Familia protection pile barrier. Calculated y displacements and M_x bending moments of a single pile of the group during tunnel construction.

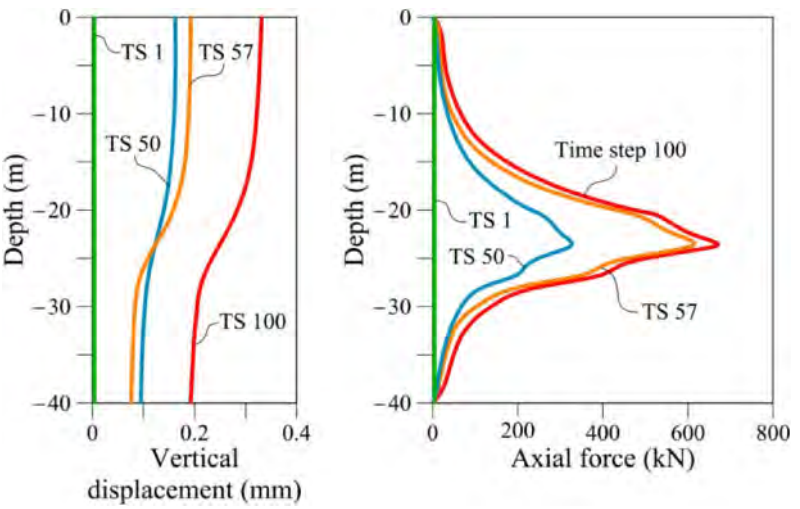

Figure 31. Sagrada Familia protection pile barrier. Calculated vertical displacements and axial forces of a single pile of the group during tunnel construction.

The comparison of measured and calculated settlements in the reference cross section is shown in Figure 32. The agreement is good for a volume loss of 0.1%.

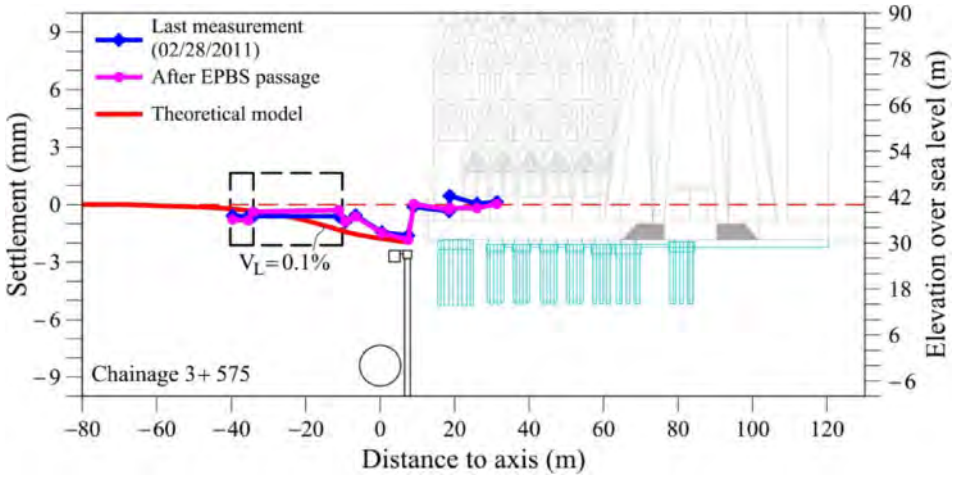

Figure 32. Sagrada Familia. Calculated and measured surface settlement for a volume loss of 0.1%.

4 TUNNELING CHALLENGES

4.1 *General aspects*

The magnitude of the tunnel induced settlements depends on the volume loss of the EPBS machine. Furthermore, there is a general consensus on the relationship between volume loss, soil properties and machine operation. Therefore, settlements are related to the adequate control of the pressurized excavation chamber, the conditioning of the excavated spoil, the screw conveyor operation and both the annulus and tail void grouting (Mair, 2008). Keeping this in mind, the construction of the tunnel was based on the following principles:

- Intense geotechnical site investigation of the whole area, with a total length of geotechnical boreholes equivalent to the tunnel length and performing laboratory and field tests to fully characterize soil mechanical and hydraulic properties.
- Intense monitoring of the main variables that may be affected by tunneling, including ground displacements, soil pore water pressures, building movements and temperature. When possible, measurements were obtained from robotized automatic devices, active 24 hours a day. An independent team was in charge of the monitoring analysis.
- Intense control of the machine operations, with an independent team devoted to that task, in order to have a double check of any EPBS operational decision.
- Design of vertical shafts for machine inspection under atmospheric conditions before each tunnel section including sensitive buildings or involving difficult conditions.

This section presents the main aspects of the EPBS operations that could have impact on soil and building displacements, with emphasis on the last two principles abovementioned. Some hydrogeological issues are also described.

4.2 *Control of EPBS operations*

An independent contract was set up by the Spanish Railway Administration (ADIF) to control all tunnels under construction during that period, including the tunnel next to the Sagrada Familia

Temple. An independent technical team reporting to the Administration was organized, having a replica of the pilot cabin monitors presenting all the control parameters of the EPBS machine and the online measurements from field instrumentation. Any decision considered by the pilot out of the programmed operations had a double check by that team. This was a key factor in the reduction of any risk, allowing a consensual action in case of unexpected warnings. The control was based on several numerical indicators evaluated every 200 mm of advance for which preventive thresholds were defined. In this way, any discrepancy with respect to the theoretical values could be analyzed in an almost continuous manner. The indicators involved:

- Face pressure measured through the sensors in the EPB chamber. Warning is issued if more than a 10% variation was measured and an alarm sign if a 20% variation was detected. An average value of 2 bars was used in the vicinity of Sagrada Familia Temple.
- Apparent density of the material in the chamber. A minimum value of 1.4 g/cm^3 was defined. Lower values could indicate the formation of an air bubble at the top of the chamber. This should be analyzed considering the pressures measured in the chamber as well.
- Weight of excavated material, based on estimations from site investigation. Warning when more than 10% variation was observed.
- Volume of bentonite injected around the shield and values of the injection pressure.
- Volume of mortar injected in the gaps between ground and concrete segments and injection pressure used. Generally, warning was activated if actual mortar volume was less than 90% or more than 120% of the theoretical one. An alarm was turned on when the actual value was below 70% or above 150% of the expected value.
- Measured displacements of specific targets on buildings and on extensometers located just above and close to the tunnel crown. Warning of settlements in buildings in the Sagrada Familia area was fixed in 5 mm, tilting limit was defined as 1/3000 and the warning limit for the ground vertical displacement close to the tunnel crown was 20 mm. Separating displacements due to temperature from movements caused by tunneling was not obvious and became an important task.
- Additional EPBS variables as total thrust, applied torque and velocity.

All these indicators were controlled in a continuous manner, so that any potential incident could be anticipated at early stages. A conventional color code was adopted: green for normal operation, orange for warning and red for alarm. The tunnel length was divided into sectors and for each one a plan with the expected values for the indicators was carried out. Using that code, a protocol to follow, depending on the colour of the indicators, was prepared in advance.

In general, warning situations were very limited and corrected quickly: settlements were below 2 mm not only in buildings, but also in the soil, just above the tunnel crown.

This type of control was fundamental to keep all indicators within limits, avoiding fluctuations of pressure or volume that have been reported to be the source of volume loss increments, particularly in shallow tunnels (Wonsaroj et al., 2006, Mair, 2008).

4.3 *Hydrogeological issues*

An environmental concern was expressed by the Catalan Water Agency before the tunnel construction: any global change in the average water table in the city should be below 1 m. The tunnel runs parallel to the seashore and there is a regular groundwater flow from the hills to the sea that could be interrupted by the tunnel. This is called the barrier effect (Pujades et al., 2014, 2015). Some tunnels that were built in the past in the city became a barrier for the natural groundwater flow, raising the water table in the upstream side of the tunnel and wetting basements in nearby buildings. A particular attention was devoted to the pile wall designed to separate the Sagrada Familia basilica from the tunnel. A barrier effect could raise the water table below the Temple, affecting eventually its foundation or the crypt. To avoid that, a 50 cm gap between consecutive piles was designed. Both upper and lower aquifers became connected due to the construction of the piles and that effect was more important than the barrier effect of the pile wall on the upper

aquifer. Nevertheless, variations of water table in the area were always below 1 m as required by the environmental Agency (Pujades et al., 2015). In fact, the variations of the water table were due to other effect: the construction of the piles connected the upper unconfined aquifer and the lower confined aquifer. The deep aquifer had a piezometric head about 4 m greater than the upper one. Overall, the barrier effect was negligible. The piezometric head of the lower aquifer had, however, some impact on the face pressure to be considered during tunnel excavation.

4.4 *Vertical shafts*

Vertical shafts were designed, intersecting the tunnel, with the aim of allowing the inspection and maintenance of the cutting head of the EPB under atmospheric conditions. After tunnel construction, the shafts were adapted as emergency exits.

Before approaching the Sagrada Familia Temple, a vertical shaft was excavated at Padilla Street (300 m away from the Glory façade), so the excavating tools could be replaced if damaged. A complete revision of the EPBS was carried out before approaching that sensitive area (Figure 33). The construction of the shaft itself was carefully planned to avoid any impact on nearby buildings, also concerned about the works. In fact, the outer diaphragm wall was excavated by means of hydromills, to guarantee a perfect contact joint between vertical panels and to reduce noise during construction in this urban environment. Dewatering was also limited to the excavation of the vertical shafts in order to minimize the potential impact on soil settlements. Thanks to the overconsolidated nature of the soil due to low water tables in the past, changes in effective stresses were always in the elastic range and displacements due to dewatering were small. The unsaturated nature of the upper geotechnical profile implying high soil stiffness had a positive influence on settlements as

Figure 33. Photograph of the Padilla shaft and the head of the EPB Shield, before approaching the Sagrada Familia Temple.

well. Note that water table was about 10 m above tunnel crown and it was reduced inside the shaft to a position below the shaft bottom slab, that is, a reduction of more than 24 m of piezometric head.

The design of the vertical shaft had to consider the risk of bottom uplift. A theoretically closed excavation was possible if the outer walls were deep enough, reaching low permeability layers (tertiary clays below the tunnel). However, there was a need to reduce water pressures at depth, to guarantee stability. The solution was to build relatively deep walls and a parallel control of water pressure under the shaft by permanent pumping from wells (Pujades et al., 2014). That is, the main design criterion for the circular diaphragm wall was not the dewatering condition, but the mechanical containment of the enclosure before and during tunnel crossing of the EPBS. An inner wall was required additionally to reinforce the lower part of the outer wall when the machine was crossing the shaft. Regarding materials, glass fiber reinforced concrete was used in the areas crossed by the shield.

An important issue with respect to vertical shafts is the operations required to enter and leave the enclosure, considering that a face pressure is used by the EPBS and there is a risk of a water inlet to the shaft from the surrounding soil. To cope with that, two additional enclosures were designed, as shown in Figure 34a. These enclosures were not excavated, but diaphragm walls were built to isolate the ground in a particular area. In those additional enclosures, a progressive dewatering was possible when reducing face pressure from 2 bars to atmospheric pressure when entering the shaft, or, when leaving the shaft, a progressive increase of face pressure and ground water pressure was adopted. In this manner, the dewatering operations were concentrated on enclosures, thus limiting the impact of potential settlements on nearby buildings (including the Sagrada Familia Temple). Moreover, when reducing EPB face pressure to atmospheric conditions, or increasing from atmospheric to 2 bars, ground should have enough strength to avoid any local collapse due to insufficient face pressure. For this reason, mortar piles where built inside the enclosures to increase ground shear strength. Figure 34 shows the basic steps followed during the operations of entering and leaving the shaft, defined with the aim of minimizing the ground disturbance:

– EPBS cutting head approaching the first enclosure (Figure 34a).
– EPBS cutting head inside the first enclosure (Figure 34b). Pumping well active. Two pumping wells were installed just in case tail grouting may clog one. Progressive reduction of face pressure.

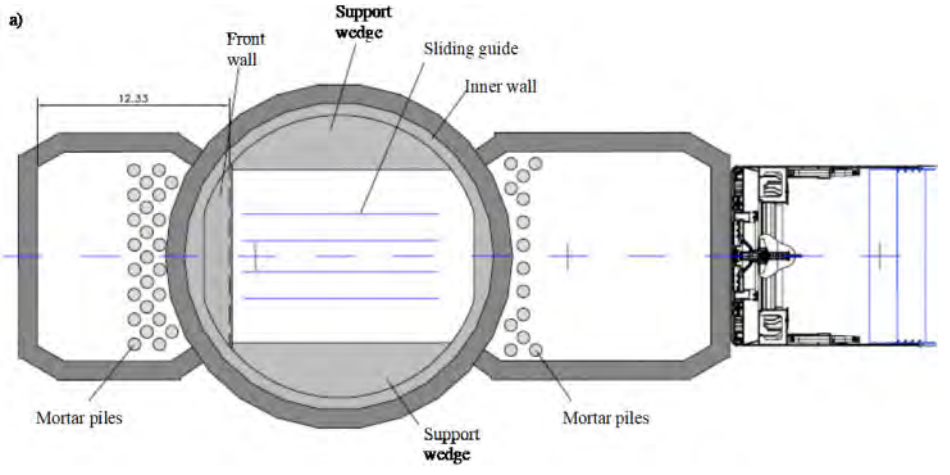

Figure 34. Operation steps when crossing the vertical shaft by the EPBS, a) before entering the enclosure, b) EPBS head in the first enclosure, pumping well active, c) EPBS head in the shaft, d) EPB head in the second enclosure, pumping well active, e) EPBS head leaving the second enclosure.

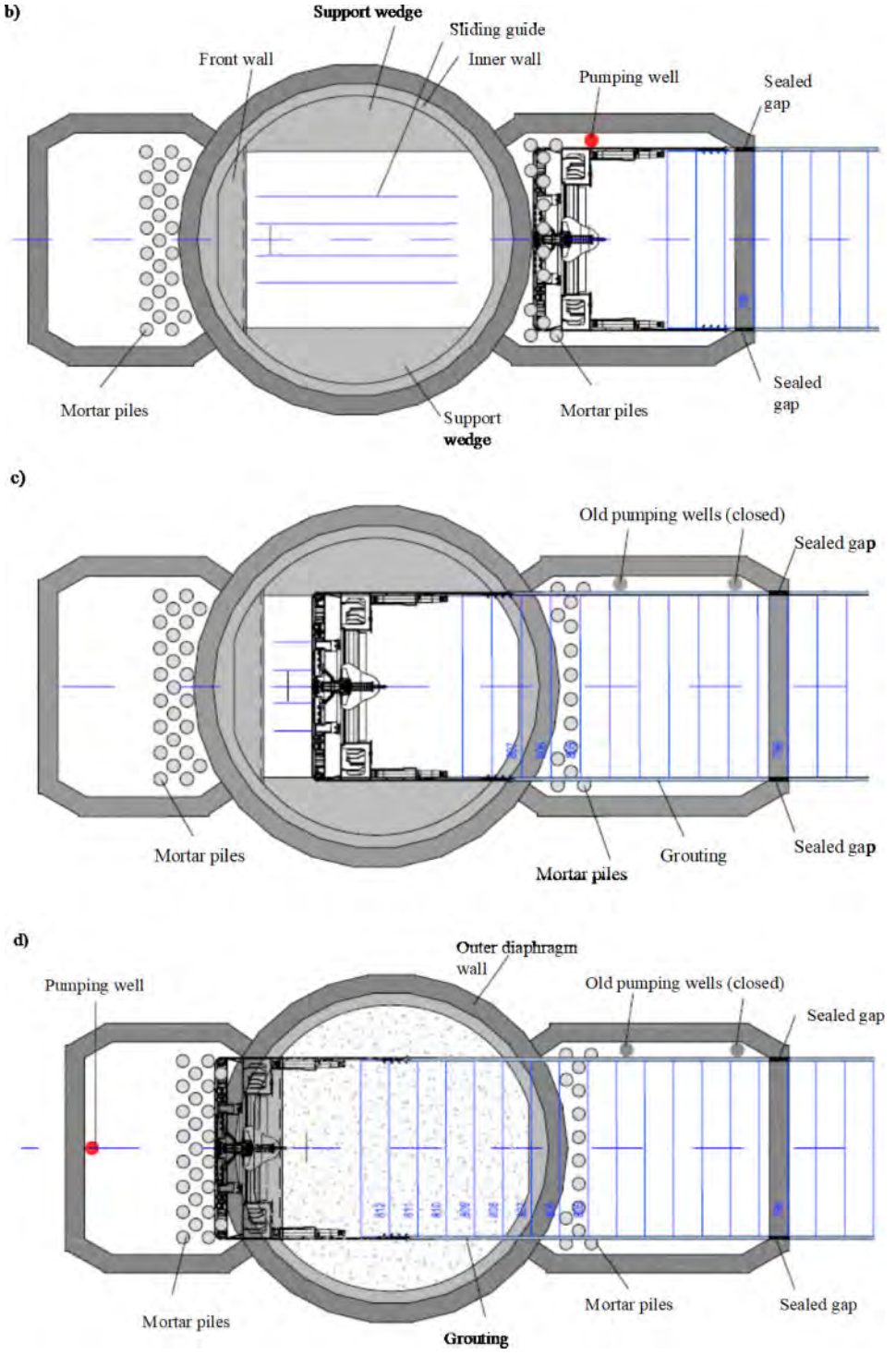

Figure 34. Continued.

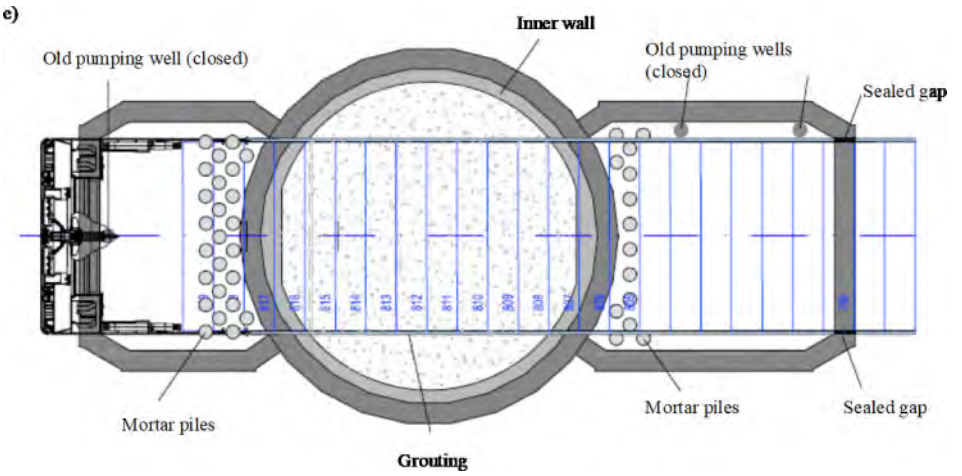

Figure 34. Continued.

– EPBS cutting head inside the vertical shaft at atmospheric pressure. Inspection of the machine and repair of damaged tools (Figure 34c).
– EPBS cutting head leaving the shaft and entering the second enclosure. Filling the lower part of the shaft with low quality mortar, using a geomembrane to protect the tunnel segments. This is to confine the tunnel to gradually increase face pressure and tail grouting. (Figure 34d). Initially a pumping well is active, but pumping is reduced and eventually stopped as face pressure increases.
– EPBS cutting head leaving the second enclosure (Figure 34e).

These operations were carried out smoothly before approaching the Temple and definitely, they had a positive influence on the success of the works and on the negligible impact on the buildings, including the Sagrada Familia Temple.

5 CONCLUSIONS

The Sagrada Familia Temple is a modernist architectural landmark of Barcelona designed by Antonio Gaudi at the transition between the 19th and 20th centuries. It is included in the list of UNESCOs protected monuments. Plans to build a railway tunnel immediate to the main façade of the temple raised a public concern about the risks involved in tunnelling operations. The paper describes briefly the Gaudi's masterpiece, which is expected to be concluded in 2026.

The chosen design by the tunnel was a deep, 11 m diameter segmented structure, having a cover of 25 m and built by an EPBS machine. The stiff Barcelona soils in the area (a surficial quaternary deposit of clay, silt and sand, cemented in some layers, partially saturated, overlying a stiffer tertiary clayey sands) was a positive geotechnical environment. However, the tunnel had to be built under a moderate water pressure (15 m of head over the crown). A deep (41 m) and stiff pile wall (1.5 diameter piles at 2 m intervals) was an added protection for the temple structure, which was founded on piles.

In addition to numerical calculations performed at the design stage, the paper highlights the value of predictive analytical solutions to analyse the behaviour of protection walls under the displacements induced by EPBS tunnelling. They are particularly useful because displacements induced by tunnelling operations have a strong kinematic nature and they are mainly explained by the total amount and distribution of volume losses. Volume losses are much dependent on a few aspects (experience of EPBS machine operators, control of a significant number of machine

variables, integrated evaluation of monitoring surface structures and others) which are difficult to reproduce in numerical models.

The paper describes two analytical approaches: a 2D, plane strain analysis of the tunnel-wall interaction and a more general 3D approach. They require different fundamental solutions for the elastic half space. The 2D case shows the advantage of defining the solution in dimensionless terms, which provide a rapid sensitivity analysis. This is a nice feature to help designers to define the key variables of the project, in particular the position, length and stiffness of the protection barrier. The 3D analysis developed may account for a precise definition of the geometry of the volume loss and it can handle arbitrary pile groups. Displacements, forces and bending moments of piles as well as soil displacements and stresses are found in a rapid manner. The evolving geometry implied by tunnel construction and its accumulated effects on pile foundation behaviour is also a feature of the procedure. The protection pile wall of the Sagrada Familia main portal is a long pile group which was also analysed. It was found that the measured settlement trough at street level (maximum of 2 mm at the unprotected side of the wall and essentially no settlement at the protected side) could be found for a total volume loss of 01%.

The paper concludes by a description of the organization and precautions adopted to ensure a successful operation of the shield machine. The sequence of control operations and warning limits are given in some detail. The permeable pile protection barrier did not create any significant alteration of the natural ground flow towards the coast line. An important precaution to ensure the correct performance of the excavation machine is to guarantee a perfect state of the cutting head. The solution adopted was to inspect and repair, if necessary, the cutting wheel, under atmospheric conditions, before coming close to the temple. This was achieved by excavating a deep shaft at a street intersection 300m away from the Glory façade. The design of this shaft and auxiliary enclosures to allow the machine to enter the shaft to be repaired are described. This operation, which was repeated a few times in other points of the 5.6 km long tunnel crossing downtown Barcelona was an important feature of the tunnel construction aimed at eliminating risks.

ACKNOWLEDGEMENTS

The authors contributed as geotechnical advisors to the design and construction of the project. This important and challenging project is the result of the effort and dedication of many engineers. A special mention is made to the engineers from the Spanish Railway Administration (ADIF), the Contractor (Sacyr – Cavosa – Scrinser), the technical assistance and design team (Intecsa – Inarsa – Censa) and the online external control unit provided by Sener. Our appreciation goes also to Genis Mayoral and Anna Ramon for their important role to develop the 3D analysis described, to Cristian de Santos and Andrés Pinto for their collaboration to some of the FE analyses, all of them from the Universitat Politècnica de Catalunya. Thanks are extended to Architect Director of Sagrada Familia construction, Jordi Faulí, for his help to describe some aspects of the Temple structure.

REFERENCES

Bilotta, E. & Russo, G. 2011. Use of a Line of Piles to Prevent Damages Induced by Tunnel Excavation. *J. Geotech. Geoenviron. Eng.*, 137: 254–262.

Boussinesq, M.J. 1885. *Application des potentiels a l'eìtude de l'eìquilibre et du mouvement des solides eìlastiques, avec des notes eìtendues sur divers points de physique matheìmatique et d'analyse*. Paris: Gauthier-Villard imprimeur libraire.

Di Mariano, A., Gesto, J.M., Gens, A. & Schwarz, H. 2007. Ground deformation and mitigating measures associated with the excavation of a new Metro line. In V. Cuéllar et al. (ed.), *Geotechnical Engineering in Urban Environments; Proc. 14th Eur. Conf. Soil Mech. & Geotech. Engng., Madrid, 24-27 September, 2007,* Rotterdam: Millpress Science, Vol. 4: 1901–1906.

Di Mariano A. (2017). “Large Diameter Tunnels in Urban Environments – The Barcelona L9 Case”. Invited Lecture at the Workshop for the Singapore Building Control Authority (BCA) and Land Transport Authority (LTA) organized by Infraestructures.cat, Barcelona, May 31st.

Ledesma, A. & Alonso, E. E. (2017) Protecting sensitive constructions from tunnelling: the case of world heritage buildings in Barcelona. *Géotechnique*, 67(10): 914–925

Loganathan, N. & Poulos, H.G. 1998. Analytical prediction for tunnelling-induced ground movements in clays. *J. Geotech. Geoenviron. Eng.*, 124(9): 846–856.

Mair, R.J. 2008. Tunnelling and geotechnics: new horizons. *Géotechnique,* 58(9): 695–736.

Melan, E. 1932. Der Spannungszustand der durch eine Einzelkraft in Innern beanspruchteten Halbscheibe. *Z. Angew. Math. Mech.*, 12: 343–346.

Mindlin, R.D. 1936. Force at a point in the interior of a semi-infinite solid. Journal of Applied Physics, 7: 195–202.

Peck, R.B. (1969). “Advantages and Limitations of the Observational Method in Applied Soil Mechanics”, 9th Rankine Lecture, *Géotechnique* 19, No. 2, 171–187.

Pujades, E., Vázquez-Suñé, E., Carrera, J., Vilarrasa, V., De Simone, S., Jurado, A., Ledesma, A., Ramos, G., Lloret, A. 2014. Deep enclosures versus pumping to reduce settlements during shaft excavations. *Engineering Geology*, 169: 100–111.

Pujades, E., Vázquez-Suñé, E., Culí, L., Carrera, J., Ledesma, A., Jurado, A. 2015. Hydrogeological impact assessment by tunnelling at sites of high sensitivity. *Engineering Geology*, 193: 421–434.

Sagaseta, C. 1987. Analysis of undrained soil deformation due to ground loss. *Géotechnique,* 37(3): 301–320.

Sneddon, I. 1951. The Mathematical Theory of Huygens’ Principle. By B. B. Baker and E. T. Copson. Second edition. Pp. vi, 192. 21s. 1950. (Geoffrey Cumberlege, Oxford University Press). *The Mathematical Gazette*, 35(311): 67–67.

Verruijt, A. & Booker, J.R. 1996. Surface settlements due to deformation of a tunnel in an elastic half plane. *Géotechnique*, 46(4): 753–756.

Verruijt, A. & Booker, J.R., 2000. Complex variable analysis of Mindlin’s tunnel problem. *Dev. Theor. Geomech.*: 1–20.

Wonsaroj, J., Borghi, F.X., Soga, K., Mair, R.J., Sugiyama, T., Hagiwara, T. & Bowers, K.H. 2006. Effect of TBM driving parameters on ground surface movements: Channel Tunnel Rail Link Contract 220. In Bakker et al. (ed.) *Geotechnical Aspects of Underground Construction in Soft Ground*. London: Taylor and Francis Group, 335–341.

Geotechnical Engineering for the Preservation of Monuments and Historic Sites III – Lancellotta, Viggiani, Flora, de Silva & Mele (Eds)

Tunnelling under the San Francisco church in Guadalajara, Mexico

E. Ovando-Shelley, E. Botero & M. A. Díaz
Instituto de Ingeniería, Universidad Nacional Autónoma de México

ABSTRACT: The San Francisco de Asis church is a masonry building whose construction began in 1554 was finalised in 1611. A new 51 km line to expand the massive transport system in Guadalajara was built between, 2015 and 2019, includes a 5.1 km underground stretch that required a tunnel 10.6 m in diameter that was excavated with a Tunnel Boring Machine (TBM), at an average depth of 25 m.

The tunnel passes directly under the north east corner of the church. Soil strata beneath the church comprise a complex array of sandy silts and pumitic materials underlain by basalts. To reduce the risk of damage to the church related to induced settlements during the excavation process, the designers (SENERMEX) decided to use jet grouting to improve the mechanical properties of the soils directly under the church to avoid of mitigate damage induced by the excavation of the tunnel. The San Francisco church was profusely instrumented with an automatic monitoring system. Measurements showed that jet grouting induced the larger detrimental settlements, mainly along the east wall whereas settlements induced by the excavation of the tunnel and the passage of the TBM under the church were not as large. These settlements re-activated existing cracks and produced some additional cracking without compromising in anyway the security of the church. Nevertheless, a comprehensive retrofitting program was implemented to restore the structural integrity of the church.

A numerical model was used to study the dynamic response of the church with a three dimensional finite difference computer code. Despite its simplifying assumptions, the model was able to provide fairly close approximations to the overall dynamic properties of the church. The numerical analyses confirmed that jet grouting did not increase the vulnerability of the church to earthquake shaking but, on the contrary, it decreased slightly.

1 INTRODUCTION

Guadalajara, the second largest city in Mexico, is located in the western portion of the Trans-Mexican volcanic range, some 460 km north-west of Mexico City, as indicated in Figure 1.. The range traverses diagonally (NW to SE) the Mexican Republic from its westernmost portion near Guadalajara, close to the Pacific Ocean, to the Gulf of Mexico. The largest and most active volcanoes in Mexico are situated along it. The vicinity of Guadalajara to active volcanoes has had a major influence on the formation of soils and on their stratigraphical sequences.

The city lies on a paleo-valley in which ignimbrites are the uppermost rocks followed by volcanic tuffs that are then underlain by basalts. Guadalajara is notorious for the presence of pumitic silty sands known locally as jales that comprise the uppermost strata. These materials are generally saturated and in terms of compacity, they are medium-dense to dense. Jales originated from pyroclastic flows which, in turn, provide them with various degrees of cementation that can easily be obliterated by water and humidity.

Seismicity in the city is determined by the interaction of the Rivera and Pacific Plates with the North America Plate, as seen in Figure 2. Several large earthquakes have hit the city in the past

 DOI 10.1201/9781003308867-6

Figure 1. Location of the city of Guadalajara.

and seismicity must necessarily be taken into consideration in the design of urban infrastructure of any type.

Figure 2. Tectonic environment around Guadalajara.

A new 51 km line to expand the massive transport system in Guadalajara was built between, 2015 and 2019. It includes a 5.1 km underground stretch that required a tunnel 10.6 m in diameter that was excavated with a Tunnel Boring Machine (TBM), at an average depth of 25 m. In most of the underground segment of the line, the tunnel traverses the uppermost silty sands (jales) which appear in irregular layers and with the water table at shallow depth, which makes it particularly sensitive to be compacted by vibrations.

Ever since the onset of the project it was recognised that a major challenge during the excavation process was the protection of the historical buildings located near the tunnel which runs along one of the main streets in the city and it passes only a few metres away from 20 of its most iconic buildings,

a situation that prompted initially an assessment of their structural condition before the excavation of the tunnel and then their potential vulnerability to suffer damage due to the construction of the underground stretch.

In order to closely follow the structural behaviour of the buildings during the protection works and tunnel excavation, a monitoring system was installed, consisting of a set of high-precision sensors, as well as of automatic surveying equipment, with which the vertical and horizontal displacements of more than one hundred reference points on each structure could be recorded. This allowed real-time monitoring of temple behaviour, so that any signals of displacements exceeding danger thresholds could be detected in a timely manner.

The Institute of Engineering of the National Autonomous University of Mexico, (II UNAM), was called to review the project in regard to the integrity of the historical buildings that could be affected by the excavation of the tunnel and of the underground stations. The preventive and corrective actions to protect structures along the line were also evaluated in terms of settlements and tilts induced by tunnelling and of their consequences with respect to structural damage. In this paper we review, from the perspective of Geotechnical Engineering, the main aspects of the response and behaviour of one of the most important heritage buildings in Guadalajara to the excavation of the tunnel, the temple of Saint Francis (San Francisco). In doing so, we describe and provide evaluations of the protective measures devised by the designers (SENERMEX), jet grouting around and under the San Francisco temple.

2 THE TEMPLE OF SAN FRANCISCO

The San Francisco de Asis church is a masonry building whose construction began in 1554 was finalized in 1611. This structure in addition to the Aranzazu church are the remains of the former San Francisco monastery that was demolished when it was relocated elsewhere in the city. The photographs in Figure 3 show a view of the main façade and of a reconstructed archery of the former cloister.

Figure 3. Left hand side: view of the main façade; right hand side: view of the reconstructed archway of the former cloister along the East side of the church.

The church base dimensions are approximately 63 × 26.5 m, and the structure can be divided into three different sections. The sketches in Figures 4 and 5 illustrate the geometrical features of

the church. Its roof vaults rest on half-point arches supported by pilasters, whose position does not match with the axis of the external abutments. In the past, the two lateral façades experienced significant differential settlements with a general rotation from north to south. Maximum differential settlements was 70 mm on the west axis of the main nave which, additionally, is leaning outwards, probably because it lost part of its counterbalance when the attached convent was demolished. These rotations have caused a large number of vertical cracks in the longitudinal wall, along with a transverse crack in the southern part of the vault.

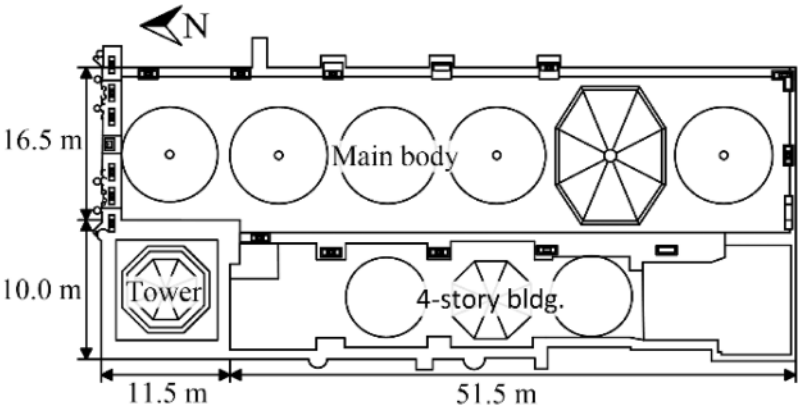

Figure 4. Plan of the San Francisco Church.

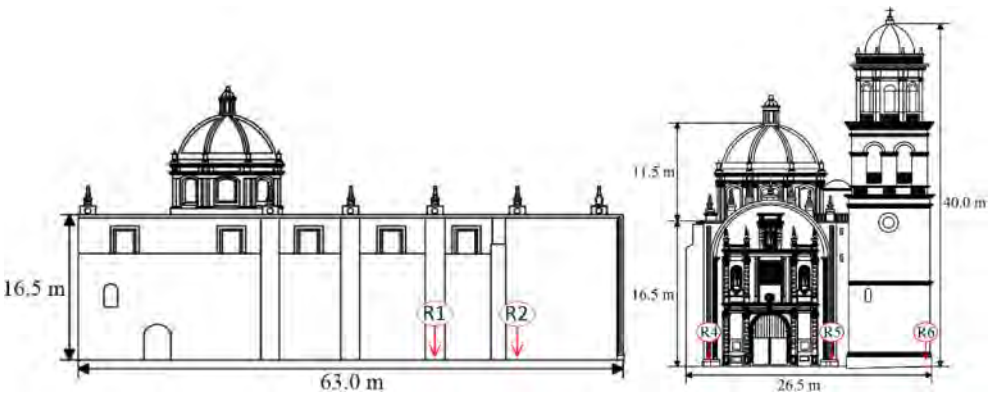

Figure 5. Architectonic details along the west wall and the façade.

Soil strata beneath the church were characterized based on the information of standard penetration tests (SPT tests) and laboratory tests executed by a geotechnical consultant during the design phase of the project. SPT tests were performed every 100 m along the entire length of the project. Laboratory testing included index tests for soil classification (particle-size analyses, plasticity index, moisture content, and mass density). Strength parameters were obtained from UU test and a limited amount of CU tests with pore water pressure measurements were used to derive effective

stress strength parameters. A geotechnical profile along the tunnel axis, on the east side of the church shows a complex array of sandy silts and pumitic materials underlain by basalts and, as seen in Figure 6, there is a geologic fault that produces a discontinuity in the main soil strata.

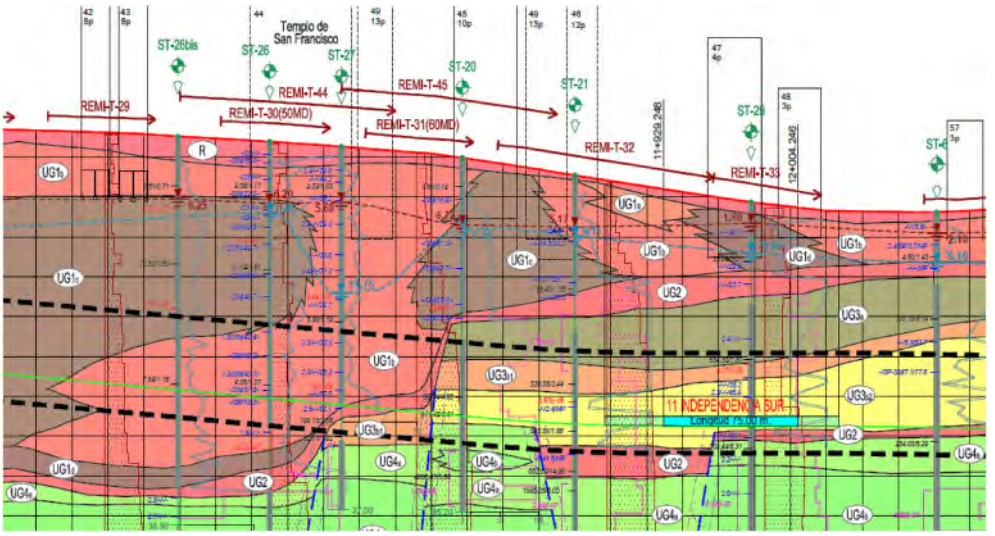

Figure 6. Geotechnical profile along the tunnel axis, on the west side of the church.

Stratigraphical conditions directly under the church are less erratic, as depicted in Figure 7. Artificial fills (rubble and construction debris) form the uppermost layer which is then underlain by layers of nearly horizontal silty sand and smaller portions of non-plastic fine particles with increasing compacity with depth, occasionally interspersed with lenses of pumitic gravels. Silty sands reach a depth of 34 m and are then underlain by basalts. On-site groundwater was located at an average of 5.6 m below the ground level. Data given in Table 1 summarise the mechanical properties of the sequence of sandy silts.

Table 1. Summary of relevant properties for the sandy silts under the San Francisco Temple

Soil layer Id	Layer thickness t m	Unit weight γ kN/m^3	friction angle ϕ' –	Cohesion c' kPa
1	2.0	17.0	29.0	5.0
2	4.0	17.5	31.0	15.0
3	10.0	18.0	33.0	20.0
4	14.0	18.0	31.0	15.0
5	2.0	18.5	36.0	25.0
6	2.0	18.5	35.0	30.0

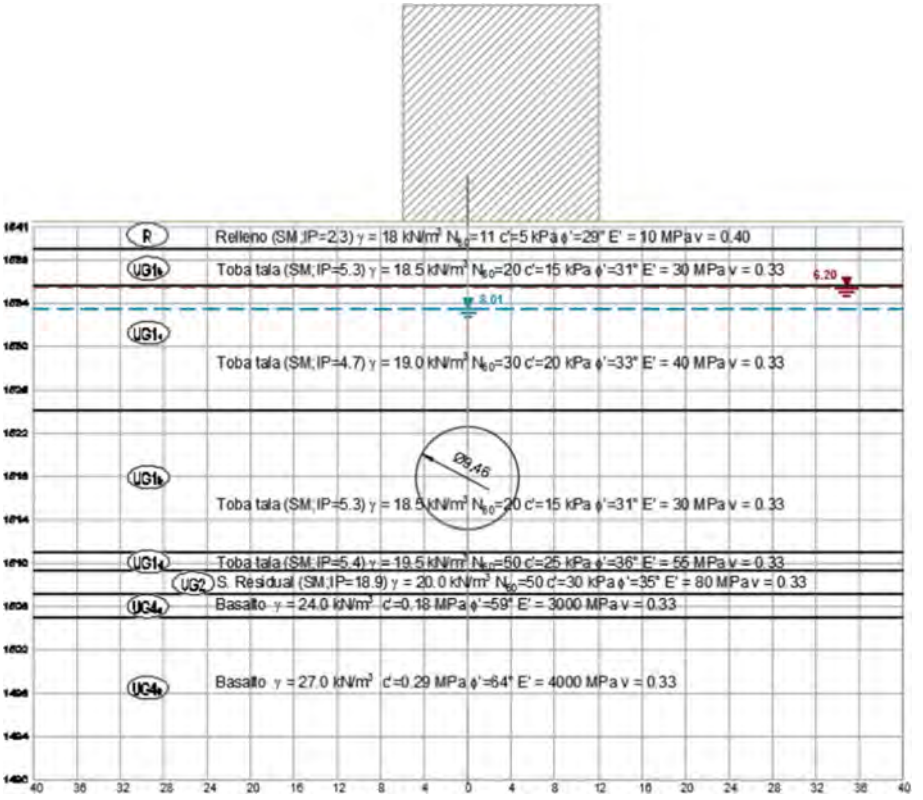

Figure 7. Simplified stratigrahical profile underneath the San Francisco church.

3 JET GROUTING

The tunnel of Line 3 passes directly underneath the north-east corner of the temple of San Francisco and that is why guaranteeing its stability during the passage of the tunnel boring machine and after it, became a source of major concern. To reduce the risk of damage to the church related to induced settlements during the excavation process, the designers (SENERMEX) decided to improve the mechanical properties of the soils directly under the church to avoid of mitigate damage induced by the excavation of the tunnel. SENERMEX chose jet grouting as the soil improvement treatment to be used. The sketch in Figure 8 shows a plan view of the location of the tunnel with respect to the church as well as the distribution of wells for grout injection. Details of the distribution of injection wells are illustrated in Figure 8.

Jet grouting was applied at a depth of 12 m and there on, the grout columns were extended 6.5 m and 18 m deeper, down to the excavation bottom mark. Vertical and inclined arrangements were used for the grouting operations. Inclined wells (as much as 32°) were used to grout areas under the church. Illustrative sketches of the grouting operations are presented in Figure 9. Examples of the mechanical properties of the grouts obtained from compression tests on control specimens are given in Table 2.

3.1 *Instrumental observations during jet grouting*

Jet grouting produces vibrations and it may eventually induce mechanical disturbance in the soils surrounding the injection wells. Consequently, it was the necessary to monitor closely the effects of

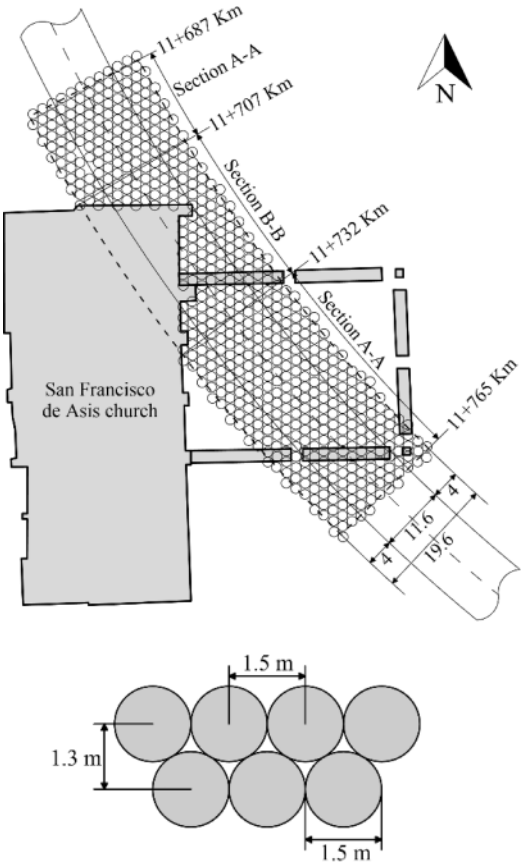

Figure 8. Array of injection wells for jet grouting along the tunnel axis near the San Francisco church.

Table 2. Mechanical properties of the grouts

Sample Id	Sample depth m	Unit weight γ kN/m^3	Compressive strength σ_c MPa	Young Modulus E_{50} MPa
1	22.03–22.35	17.2	24.43	11,647
2	22.68–29.00	17.2	24.83	10,667
3	14.70–15.05	16.3	12.76	9,071
4	18.35–18.70	16.1	15.83	7,208
5	14.25–14.75	16.1	10.44	5,373
6	17.55–18.00	16.1	11.62	3,882

the grouting operations. Topographical levellings were performed daily while grouting was under progress. An example of the results obtained with these levellings is given in Figure 10, showing that induced settlements by grouting from nine wells reached about 5 mm. Vibrations induced during grouting were measured with seismometers along the base of the west wall in terms of particle velocities. As seen in Figure 11, particle velocities fall way below the permissible values for the safe guard of historical buildings (DIN 4150-3 standard). Additional observational data will be presented later.

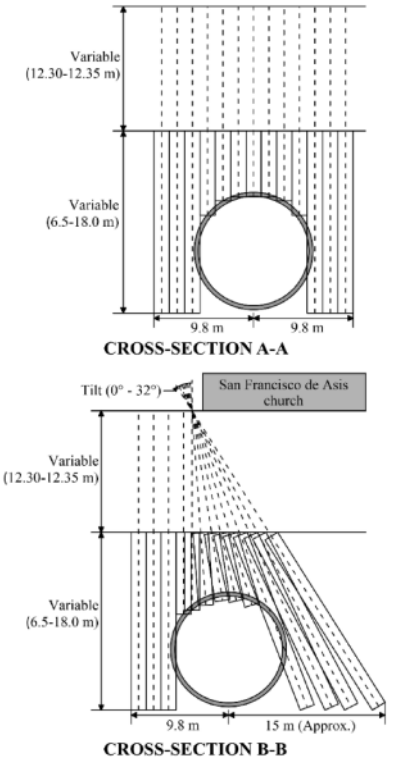

Figure 9. Vertical and inclined grouting wells used along the boundaries of the church. Cross sections are identified in Figure 8.

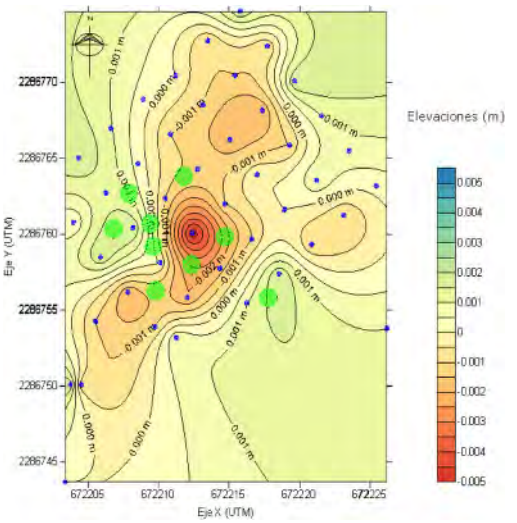

Figure 10. Differential settlements obtained from levellings performed before and after grouting in nine points (indicated by green circles). Blue circles indicate levelling points.

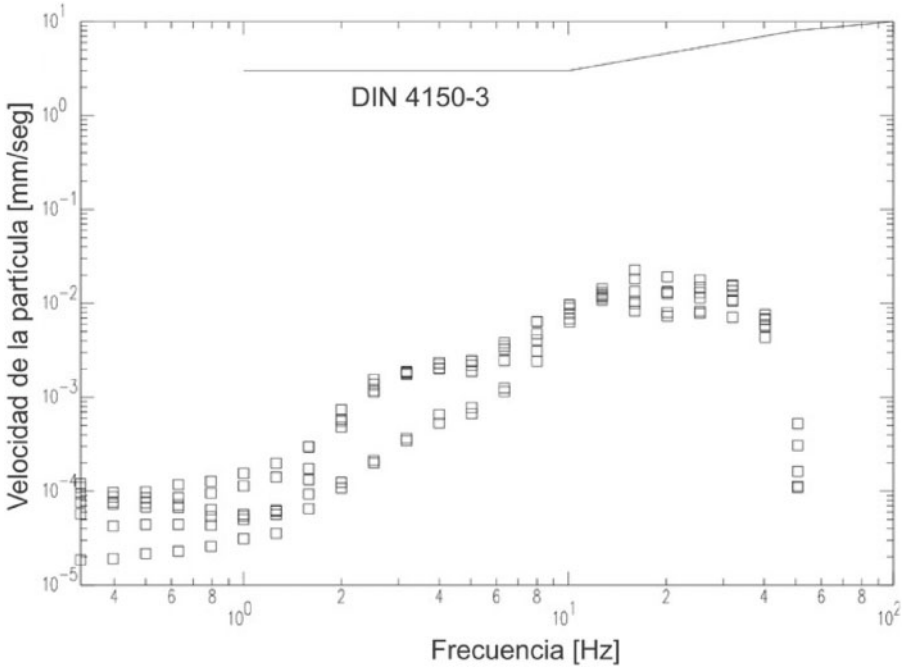

Figure 11. Values in the y axis indicate particle velocities in mm/s as a function of frequency. Measurements performed along the base of the East wall during grouting operations. Allowable values according to accepted standards are also shown.

3.2 *Additional Instrumentation and observations*

The San Francisco church as well as two other important heritage buildings were instrumented profusely with an automatic continuous monitoring system provided by SOLDATA-SIXENSE. For the San Francisco church the system comprised 36 levelling points located along the lateral walls and the main façade, 5 inclinometers were installed around the church as well as 7 vibrating wire piezometers and also 2 accelerometers; 6 tilt meters were also placed inside the church. The system operated before jet grouting, during the injection of grouts and also before and after the passage of the TBM machine along the church. It kept on working until March 2020, some four months after Line 3 was inaugurated.

Records of vertical displacements measured at several points on the west wall are presented in Figure 12. As seen there, the automatic monitoring system began operating towards the end of 2017. Jet grouting took place between 9 January and 20 April that year. Seven of the levelling points responded quite rapidly to the injection of grouts; five of them settled 1 to 2 mm and the other two, located at the base of the wall, displaced vertically almost 7 mm. The effects of jet grouting ceased in April 2017 and the passage of the TBM induced another 2 mm, also as recorded at the base of the west wall. At the beginning of May, the TBM was detained on account of uncontrolled water flowing into the face of the excavation. Additional grouting was carried out until the TBM was able to advance towards the end of August. This induced an additional settlement of about 6 mm at the base of the west wall but in the upper levelling points it only reached about half that amount. Settlement rates reduced thereafter and by the end of September, no significant additional settlements were observed after that date and when the operation of the monitoring system stopped in March 2020, settlement rates were nil.

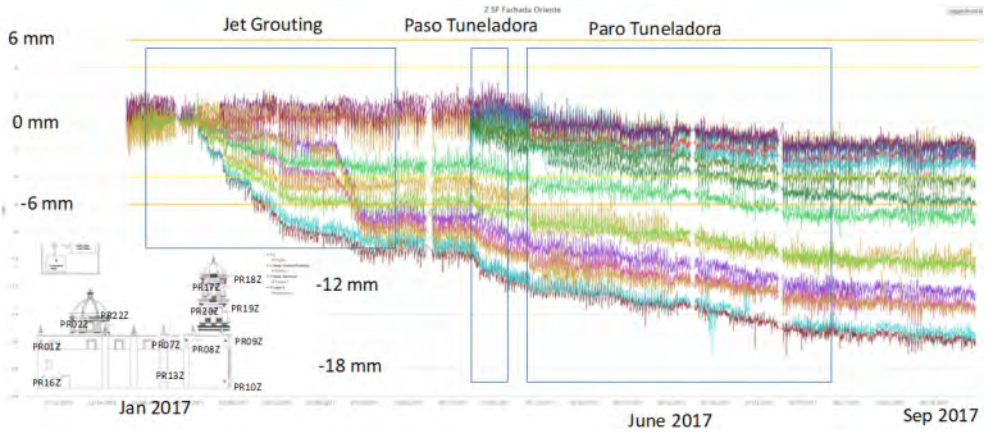

Figure 12. Evolution of vertical displacements along the west wall. Positive values indicate heave. Settlements are associated to negative values.

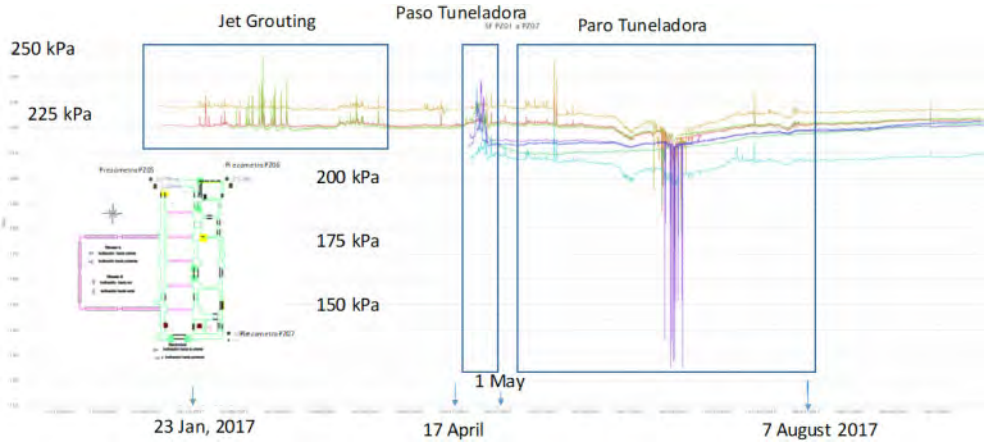

Figure 13. Pore pressure response during jet grouting, passage of the TBM and stoppage of tunnel excavation.

Jet grouting induced pore pressure increments in peaks of about 5 to 20 kPa and exceptionally of nearly 40 kPa all of which dissipated rapidly as soon as injections ceased. The passage of the TBM under the church also induced pore pressure peaks that were not larger than those recorded near the church. Pore pressure transducers placed near the tunnel axis recorded larger peaks as expected (see Figure 13). Excess pore pressure was also observed during the passage of the TBM but it rarely exceeded 20 kPa and it also dissipated in just a few days.

Shortly after the TBM passed under the church, the TBM was detained under the archway (see Figures 12 and 13) between 10 May and 7 August. As seen in the geotechnical profile of Figure 6, a geological fault passes across the axis of the tunnel. The materials before the fault (south side) are the sandy silts that have already been described but much harder volcanic tuffs and basalts were found north of the fault. Necessary adjustments to the TBM were delayed because uncontrolled seepage occurred and it was then necessary to perform additional injections of mortar. As seen in Figure 13 pore pressures decreased sharply indicating that water was flowing without control into the tunnel for a few days, at the beginning of June 2017. Pore pressures went back to normal

almost immediately after the tunnel was sealed again and after adjustments to the TBM were over.

Changes in pore water pressure, i.e. in effective stress within the soil mass in the vicinity of the temple due to jet grouting, to the passage of the TBM under it and to the stoppage near it, induced settlements, mainly along the west wall, as indicated previously. Note however, that settlements and cracks occurred mainly during jet grouting, while the effects of the excavation of the tunnel were smaller and of the stoppage of the TBM were smaller. According to structural experts involved in the project, in no case was the security of the temple compromised (Meli et al. 2018).

4 EFFECTS OF JET GROUTING ON SOIL PROPERTIES

The presence of the tunnel under the temple as well as jet grouting changed soil conditions and, given the seismicity of the zone, it was necessary to assess its seismic response taking into consideration how jet grouting modified soil properties. Ambient vibration measurements (accelerations) were performed at several sites close to the temple before and after jet grouting. Spectral ratios between horizontal (H)and vertical (V) ambient vibration measurements show, as seen in Figure 14, that the dominant frequency in front of temple's main façade was 2.35 Hz before jet grouting and increased slightly to 2.4 Hz after it. In comparing ambient vibration measurements before and after jet grouting over a thickness of about 10 t0 12 m, it became evident that grouting produced a very slight stiffening of the whole soil column. Shear wave velocity profiles obtained with the combining the SPAC and MASW techniques indicate that grouting affected surficial strata (10 m or less) and it also had a slight to moderate stiffening effect over the projected grouting thickness. It should also be noted that the shape of the spectra changed and that after grouting, larger amplifications are to be expected at higher frequencies.

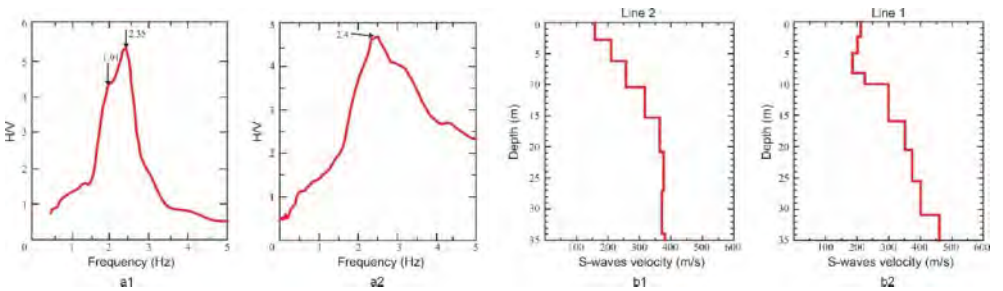

Figure 14. a) Spectral ratio between horizontal and vertical vibration of the soil in the northeastern corner of the San Francisco temple, before (a1) and after (a2), the soil treatment with jet grouting; b) Profile of S-wave velocity in the ground at different depths, measured in front of the main façade (a1) and behind the temple (a2).

Additional geophysical surveys were required to assess the effects of jet grouting. A 3-D seismic tomography was carried out, based on analyses of ambient noise vibrations recorded simultaneously in station-pairs, cross-correlating and stacking data (Bensen, et al, 2007). As an example, the graph in Figure 15 shows the distribution of shear wave velocities under and around the temple, along an E-W cross section near the main façade (CFE, GEIC, 2017). As seen there, shear wave velocities were clearly larger in the zones that were jet-grouted and, it is evident that there is a clear contrast between the surface silty sands that were not grouted.

A plan view of the shear wave distribution at a depth of 25 m, roughly at the tunnel's crown, is given in Figure 16. This graph shows that stiffening by grouting was not uniform and that it concentrated mainly near the façade, N-E corner and, also, outside the church in the N-E atrium.

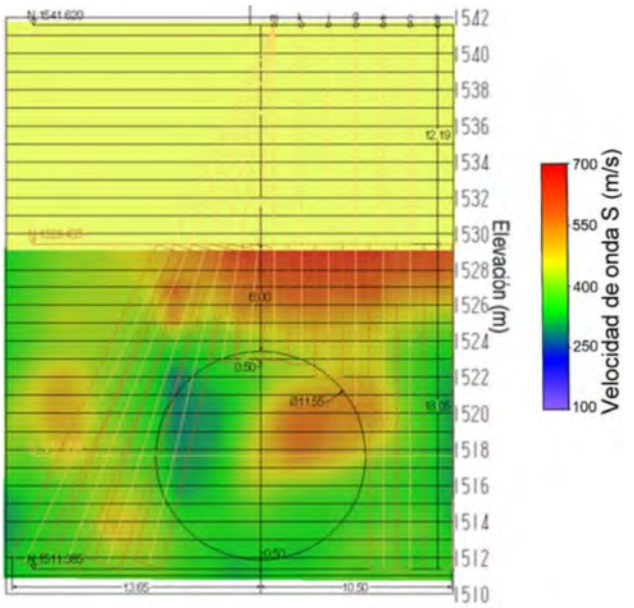

Figure 15. Distribution of shear wave velocities along an E-W cross section near the main façade.

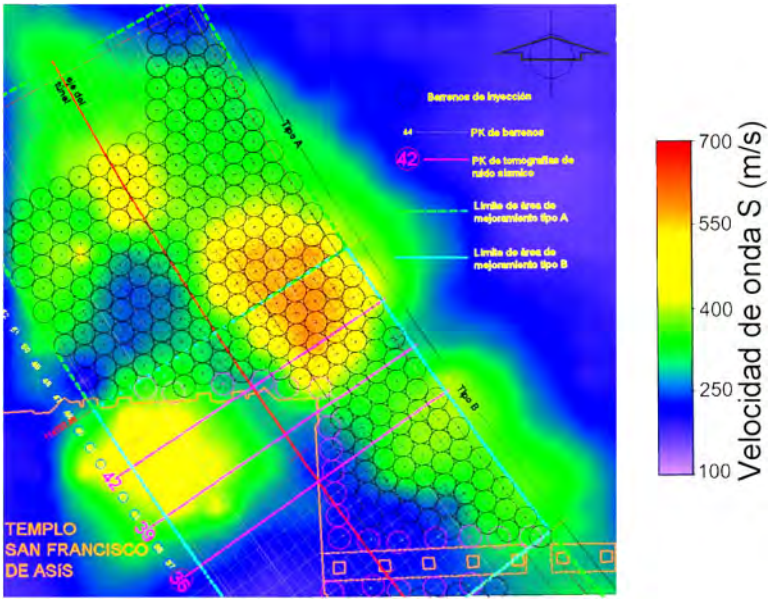

Figure 16. Distribution of shear wave velocities at a depth of 25 m.

5 CONSIDERATIONS FOR SEISMIC RESPONSE

As explained previously, the dominant frequency at the N-E corner was not greatly affected by jet grouting (see Figure 14). However, given the non-uniform distribution of shear wave velocities and also, given the seismicity of the zone, it was only natural that concerns were raised in regard to the

capacity of temple to resist strong earthquake motions. Consequently, a numerical model was used to perform an analysis of dynamic soil-structure interaction.

Acceleration histories applied at the base were obtained by using the time histories recorded during the 9 October, 1995, earthquake (Mb=6.5, Ms=7.3 and Mc=7.5) at a site having similar geotechnical some 1500 m north of the church. This earthquake originated off the Pacific Coast, 260 km from Guadalajara and it is the largest recorded event recorded in the city. In applying this procedure, the recorded acceleration history was adjusted so that it would comply with the design spectrum specified for the city by local recommendations for seismic design (Abramson 1993 & Lilhanand & Tseng, 1988). Recorded movements were then transported to the site and were then deconvolved using a one dimensional wave propagation program to obtain incoming accelerations at the base of the relevant strata at the church (Schnabel et al., 1972). Finally, uniform hazard spectra for different return periods, shown in Figure 17, were created using PRODISIS, a procedure specified by Mexican regulatory agencies (CFE, 2015). Note that the peak spectral ordinates occur at periods that closely resemble dominant periods at the site. Our analyses were made for a return period of 250 years using the component that displayed the largest energy.

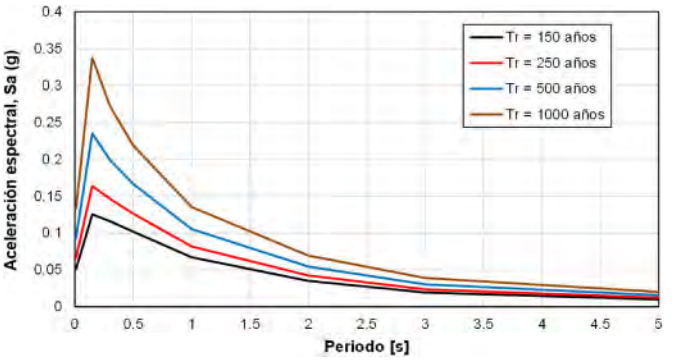

Figure 17. Uniform hazard spectra for different return periods.

5.1 *Analysis of dynamic soil-structure interaction*

The soil structure interaction analysis was performed with a three-dimensional finite difference program in the time domain (Itasca Consulting Group 2003). Soils were modelled as free draining viscous-elastic materials with degrading strain-dependent dynamic stiffnesses and damping ratios obtained from a calibration of the model made with respect to a site response analysis performed with the aforementioned one dimensional wave propagation computer code (Shake, Schnabel et al.,

Table 3. Soil properties for initial soil-structure interaction analysis.

Depth m From to	Geotechnical unit	E kPa	Reference G kPa	Reference internal damping %	Shear train %
0.0–2.00	Fill (rubble)	2044	730	8.2	0.058
2.0–5.40	1b (SM)	6414	2411	8.4	0.065
5.40–16.90	1c (SM)	8275	3111	8.9	0.113
16.90–30.20	1b (SM)	6082	2287	9.3	0.180
30.20–32.00	1d (SM)	11404	4287	8.9	0.109
32.00–34.10	2 (SM)	16963	6377	8.5	0.075
34.10–36.30	4 (Basalt)				

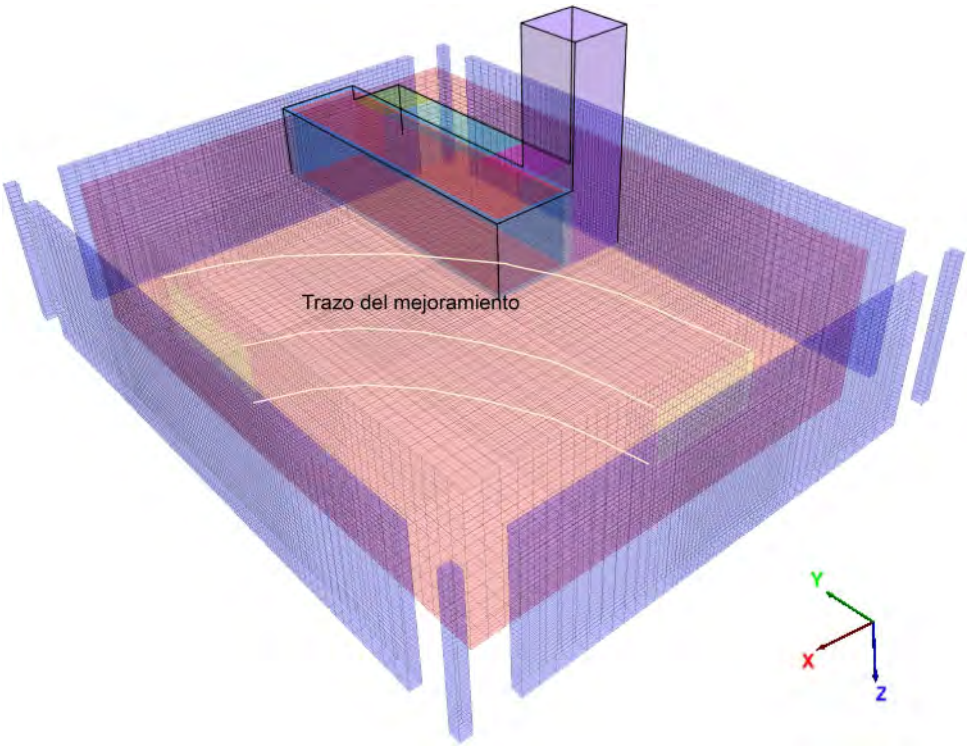

Figure 18. Three-dimensional finite difference model for dynamic soil-structure interaction analyses.

Table 4. Properties of the structural elements used in the dynamic soil-structure interaction analyses.

Structural element	Density kN/m^3	G MPa
Foundation	22.0	4082.5
Walls	22.0	3689.2
Ceiling	18.0	3102.5
Attached building	22.0	2467.5
Tower	22.0	3102.5
Grout columns	16.0	400.0

Note: The value of Poisson's ratio for all elements was 0.3 and 0.4 for the grout columns.

1972). Table 3 shows the soil parameters used in the initial calculations, before taking into account the effects of jet grouting. Properties for the structural elements are summarised in Table 4.

In the analysis the structure was modelled with linearly elastic solid elements with a base raft, perimeter walls and a flat cover, all of which resemble a hollow box. Despite its simplicity, the model still retains the prototype's main dynamic characteristics. The three-dimensional model is depicted in Figure 18. Lateral and base boundaries dissipate incoming shear waves. The seismic excitation was applied at the base of the model at contact of the soil-basalt interface in a direction parallel to the temple's shortest plan dimension.

Analyses were made using the soil properties estimated before considering the effects of jet grouting and after it, modifying shear wave velocities and stiffnesses, as a result of it. The results of the seismic tomograhies were used to this end albeit in a simplified manner. An example of the modified shear wave velocities along a cross section perpendicular to the tunnel axis in the numerical model is shown in Figure 19.

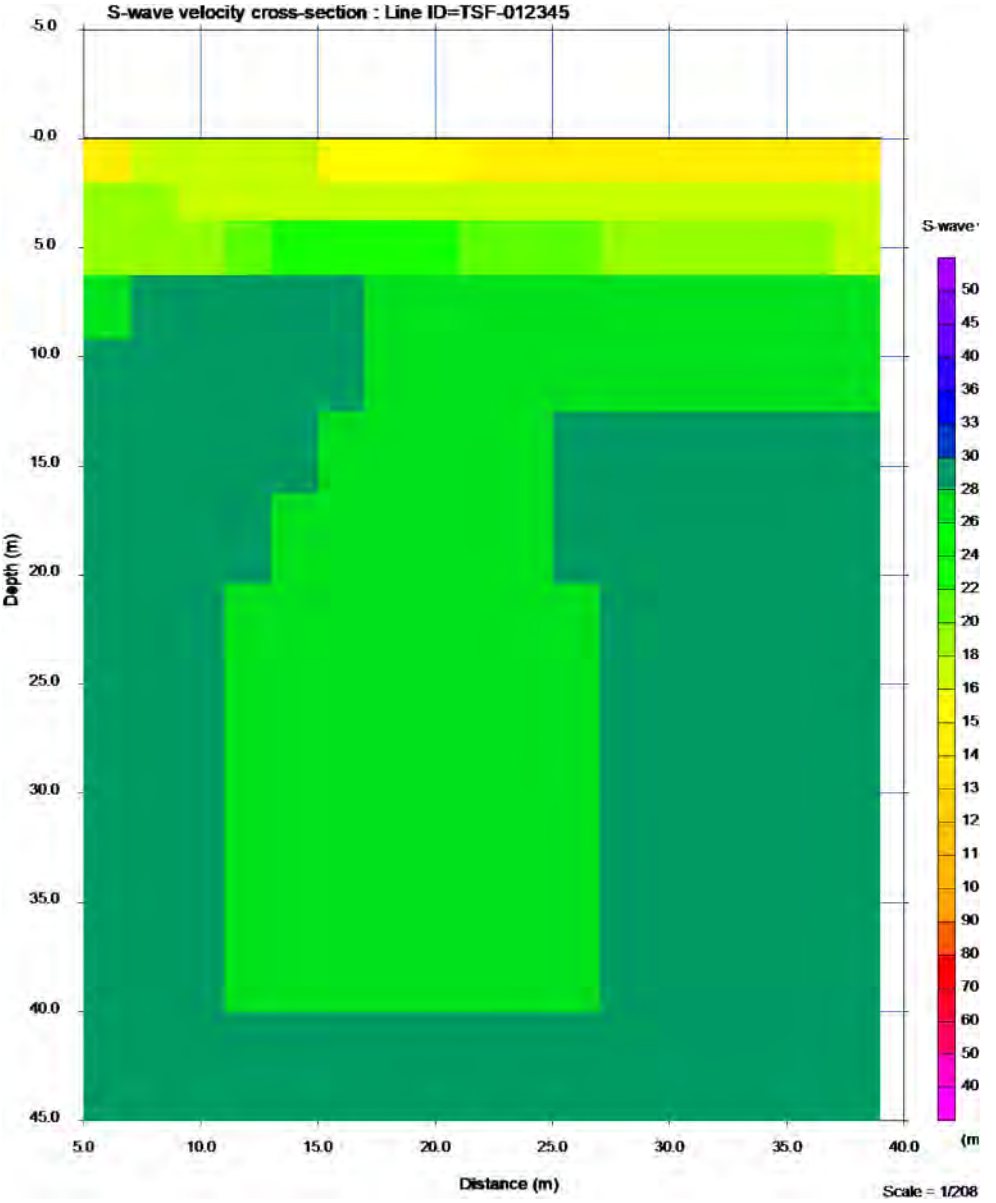

Figure 19. Example of shear wave velocity distribution along a cross section of the numerical model. In the case shown, shear wave velocities were modified to account for the stiffening effect induced by jet grouting.

5.2 *Results of the dynamic soil-structure interaction analysis*

These results are presented by means of pseudo-acceleration response spectra obtained from acceleration time histories calculated during the analyses. Six control points located in different location along different points in the ceiling as well as another one outside the church, in the free field, were used to analyse the results (see Figure 20).

Response spectra from acceleration time histories calculated at the ceiling and located in Figure 20 are shown in Figure 21. These spectra were calculated without considering modified soil properties by jet grouting. A summary of these results is given in Table 5, including data from spectra obtained with modified soil parameters after jet grouting. In Figure 20, peaks that appear at short periods (about 0.28 s, 3.5 Hz) have been associated to the lateral fundamental vibration mode and their amplitude is also influenced by energy concentrating around those shorter periods in the input excitation (see Figure 17). Peaks for the FI and FD points (that appear in periods close to 0.58 s, 1.72 Hz) in the northern portion of the church are also influenced by the vibration of the tower which was estimated to be around that same value and varies about 15% from values estimated from ambient vibration measurements (1.5 Hz). Other researchers have argued that this mode is related to the vibration of the bell tower, and is also detected in the longitudinal direction, thus showing that the vibration is symmetrical in both directions (Meli and Sánchez, 2018). Ambient vibration measurements were made at points FI CD and PI and the frequencies at which peak vibration amplitudes were obtained were, respectively, 1.6, 2.0 and 2.0 Hz; the frequencies for maximum pseudo acceleration from the calculated response spectra of Figure 21 at these same points were 1.72, 2.17 and 2.17, which overestimate the measured values in about 8 %.

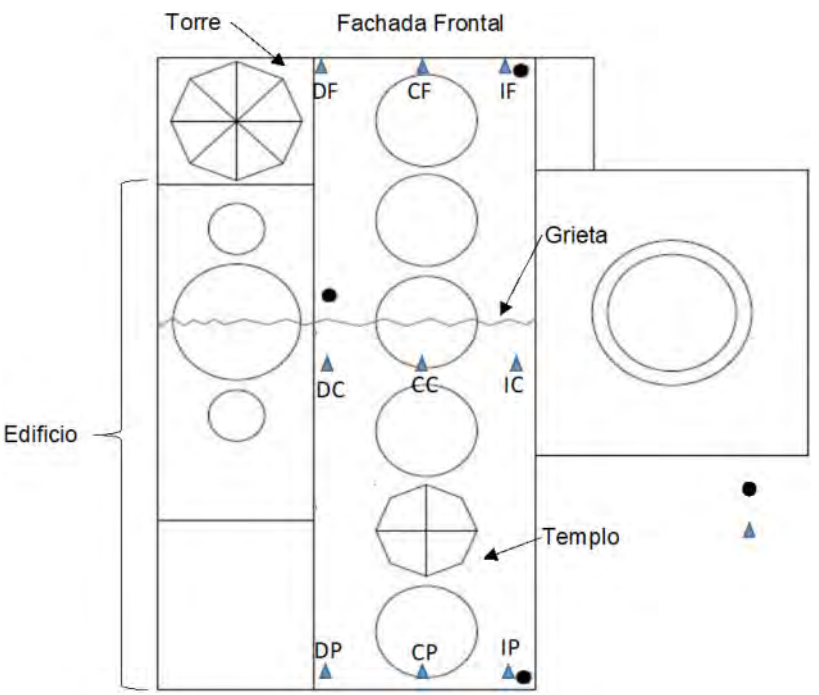

Figure 20. Control points to study the results of the dynamic soil-structure interaction analysis. Dots indicate sites where ambient vibration measurements were made; triangles indicate points where time histories were calculated with the numerical model.

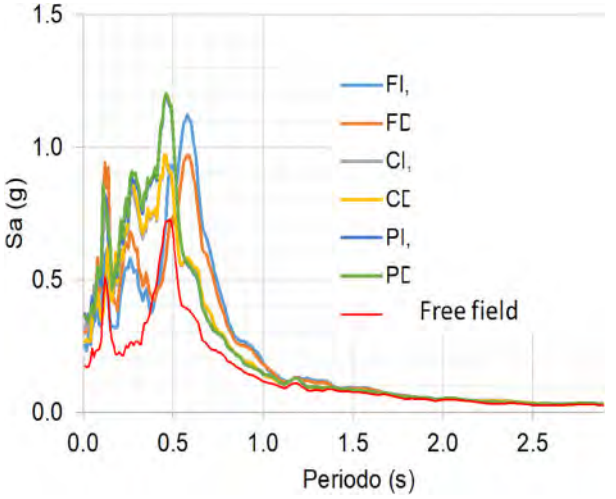

Figure 21. Response spectra obtained at the control points in the ceiling without modifying soil properties due to jet grouting.

Table 5. Ceiling: Peak spectral pseudo accelerations and associated periods and frequencies obtained from the numerical analysis.

Control point	Sa peak g	No grouting Period, s	Frequency, Hz	Sa peak g	With grouting Period, s	Frequency, Hz
FI, front left	1.21	0.580	1.72	1.086	0.590	1.69
FD, front right	0.971	0.580	1.72	0.939	0.590	1.69
CI, centre left	0.961	0.460	2.17	0.957	0.460	2.17
CI, centre right	0.972	0.460	2.17	0.964	0.460	2.17
PD, Back left	1.192	0.460	2.17	1.198	0.460	2.17
PD, Back right	1.201	0.460	2.17	1.208	0.460	2.17

Regarding the response of the bell tower, pseudo acceleration response spectra calculated at different elevations along its north east corner are given in Figure 21, without considering the effects of jet grouting. As seen there, the spectra show that the maximum spectral amplitude lie at a period of 0.49 (2.04 Hz), for points located at heights higher than about 20 m. These frequencies correspond to the bell tower's fundamental mode along the transversal direction. Smaller spectral amplitudes are seen at another peak located at 0.58 s (1.72 Hz) that corresponds to the tower's longitudinal mode and is 23 % larger than the estimated frequency from ambient vibration records. Spectral data are summarised in Table 6, including data obtained from spectra calculated with soil parameters modified by jet grouting.

Response spectra obtained at several control points in the ceiling and the bell tower displayed peaks at frequencies that approximate fairly well the temple's and the tower's fundamental modes identified from the analysis of ambient vibration records. Data given in Tables 5 and 6 confirm that jet grouting had a minor effect on the temple's fundamental frequencies and, also, that the spectral amplitudes did not change significantly. These findings clearly indicate that jet grouting did not increase the vulnerability of the church to earthquake shaking. On the contrary, maximum peak pseudo accelerations turned out to be slightly lower.

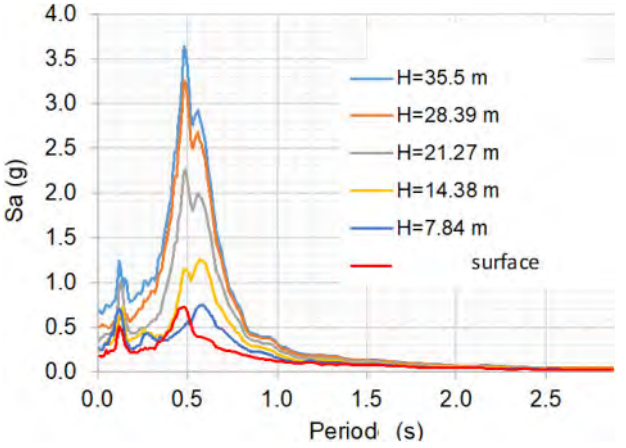

Figure 22. Response spectra obtained at the bell tower's north east corner, at different elevations from the surface.

Table 6. Bell tower: Peak spectral pseudo accelerations and associated periods and frequencies obtained from the numerical analysis.

Height along tower's front right corner m	No grouting			With grouting		
	Sa peak g	Period s	Frequency Hz	Sa peak g	Period, s	Frequency, Hz
35.5	3.641	0.480	2.08	3.532	0.490	2.04
28.39	3.254	0.480	2.08	3.171	0.490	2.04
21.27	2.264	0.490	2.04	2.209	0.490	2.04
14.38	1.251	0.570	1.75	1.214	0.570	1.75
7.84	0.753	0.590	1.69	0.732	0.580	1.72
Surface	0.729	0.480	2.08	0.738	0.490	2.04

6 CONCLUSIONS

Geotechnical studies carried out before the excavation of the tunnel suggested that preventive measures were needed to avoid or mitigate damage induced by tunnelling on the San Francisco church, given the nature and characteristics of the silty sands under it. The authors of this paper formed part of the technical staff called to analyse and assess the effects of jet grouting, the preventive measure adopted by the designers, of the excavation of the tunnel directly under the north east corner of the church, of the stoppage of the TBM right in front of the temple and, also, of its behaviour during the initial months of the operation of Line 3 of the Guadalajara Metro system.

The San Francisco church was profusely instrumented with an automatic monitoring system with which its response to the execution of the preventive works and the excavation of the tunnel were followed closely in terms of induced settlements, tilts, and pore pressure. In the San Francisco church, as well as in other historical constructions of the area, settlements occurred mainly during preventive protection works. Measurements indicate that jet grouting induced the larger detrimental settlements, mainly along the east wall and that settlements induced by the excavation of the tunnel and the passage of the TBM under the church were not as large; further settlements were induced during the stoppage of the TBM in front of the east wall. After that, settlement rates reduced continually and for all practical purposes, settlement rates were practically nil by mid 2020 when

the automatic monitoring system ceased to operate. These settlements re-activated pre-existing cracks and also induced some additional cracking. Nevertheless, according to structural experts the security of the temple was not compromised (Meli & Sánchez 2018). In any case a retrofitting project was initiated towards the end of 2017.

Religious and civil authorities were concerned about the seismic vulnerability of the church since it was thought that jet grouting could have had a detrimental effect on its capacity to resist strong earthquake motions. Ambient vibration measurements as well as seismic tomographies were performed in and around the temple to obtain the dynamic properties of the underlying silty sands. These studies showed that soils were not stiffened uniformly by jet grouting. A numerical model was used to study the dynamic response of the church with a three dimensional finite difference computer code. Despite its simplifying assumptions, the model was able to provide fairly close approximations to the overall dynamic properties of the church. The numerical analyses confirmed that jet grouting did not increase the vulnerability of the church to earthquake shaking but that it decreased slightly.

The automatic monitoring system was a fundamental tool to understand the effects of the protection works, the excavation of the tunnel, and of any other non-accounted for events. It is the opinion of the authors of this paper that these systems should be considered as essential in cases as the one described here, i.e. tunnels excavated in densely urbanized areas

REFERENCES

Abrahamson N. (1993). "Non-Stationary spectral matching program RSPMATCH". Obtenidode: http://www.civil.utah.edu/∼bartlett/NEUP/Rspmatch/RSPmatchdocument.pdf

Bensen, G.D., Ritzwoller, M.H., Barmin, M.P., Levshin, A.L., Lin, F., Moschetti, M.P., Shapiro, N.M., Yang, Y., (2007). Processing seismic ambient noise data to obtain reliable broad-band surface wave dispersion measurements. Geophys J. Int., 169, 3, 1239-1260.

CFE (2015). PRODISIS, A Programme for seismic design. In: Manual de Obras Civiles, Mexico, Comisión Federal de Electricidad (Mexican Electricity Board).

Itasca Consulting Group Inc. (2017) "FLAC 3D: Fast lagrangian analysis of continua in 3 dimensions, User's Guide". Minneapolis, Minnesota, USA.

Lilhanand K. y Tseng W. S. (1988). "Development and application of realistic earthquake time histories compatible with multiple damping response spectra", Proceedings of the 9th World Conference on Earthquake Engineering, Tokyo, Japan, Vol. II, pp 819-824

R. Meli and A. R. Sánchez Ramírez (2018). Protection and monitoring of three temples close to the excavation of a tunnel in Guadalajara, Mexico. Paper 42, Proceedings 11th Int Conference on structural analysis of historical constructions, Cusco, Perú, 11-13 Sept.2018

SHAKE Schnabel, P.B., Lysmer, J., and Seed, H.B. 1972. SHAKE – A computer program for earthquake response analysis of horizontally layered soils. Report No. EERC-72/12, University of California, Berkeley.

Panel Lectures

Taylor & Francis
Taylor & Francis Group
http://taylorandfrancis.com

Geotechnical Engineering for the Preservation of Monuments and Historic Sites III – Lancellotta, Viggiani, Flora, de Silva & Mele (Eds)

Under the skin

P. Smars
National Yunlin University of Science & Technology, Douliu, Taiwan

ABSTRACT: Should we care about what lies behind the surface of the cultural objects we value? If a feature is invisible to our senses, does its existence really deserves our attention and concern? Engineers like doctors obviously needs to know about anatomy, materials... bones and skin diseases. Their job is to preserve what society cherish and their mean of action requires this knowledge. But should said society be concerned only by failures of plastic surgery and façade cleaning, overlook the viscera and leaving their cure to the experts? And should these last understand their duty as not only caring for what people see but also caring for what they, themselves, have the privilege to see?

These are the questions that the paper tries to develop and discuss.

1 HERITAGE

How do we conceive time?

> "Architecture is to be made historical and preserved as such" Ruskin 1849, "The Lamp of Memory", aphorism 27

In matters of heritage, what is the target of society, professionals, deciders? (Figure 1). And how does it relate to their conception of time?

In English — since Ruskin (1849), Morris and the SPAB — *restoration* became a bad word, describing an impossible and destructive operation. "Restoration (*Restaurationwesen*), the illegitimate son of the historicism of the 19th c." was writing Dehio (1905). The emergence of an awareness of the value of our built heritage was sadly also creating new threats.

This is a recurrent observation: not only nature and vandals threaten what we cherish, good intentions too, often lead to unexpected consequences and, later, repentance. The ambivalence of the UNESCO label is an example (Choay 2009; Settis 2017). Engineers too have their share in the history of what can be seen as "good" or "bad" decisions.

Terms like *conservation* and *preservation* are milder but also somehow presumptuous and, to pragmatists — looking at heritage as a useful mean (and not simply as helpful guide like Ruskin did) to create a better society — they may be delusive and backward-looking: the past is out of reach but, hopefully, the future can be shaped.

It is likely to be a personal bias or misunderstanding but *revitalisation* brings to my mind not *life* but *money* and, often, *denaturation*. *Reconstruction*, common after the two World Wars and in archaeological sites is also gaining new supporters, surprisingly or not (Stanley-Price 2009; Houbart 2020).

The "zorg" in Dutch or "Pflege" in German (*monumentenzorg, Denkmalpflege*) are more neutral, they do not inform about the mean, just about an intention: caring.

Leaving for a second what can be seen as questionable, it can be said that each term denotes a historical, cultural, and professional context and aspirations which, if they cannot be perfectly fulfilled, do serve as beacons: "Thy Word is a lamp unto my feet." (Ruskin 1849, – citing Psalm 119:105).

But who is *Thy* and what does he actually desires?

DOI 10.1201/9781003308867-7

Figure 1. Kids in Bamiyan, Afghanistan. Ph.: P. Smars, 2003.

Turning attention to the object of interest may help identifying convergences and divergences between intentions. *Monument* has acquired a connotation of institutional, aristocratic, but its Latin origin is interesting (Choay 1996; Riegl 1903). *Monere* means *to remind*, *to warn*. The term has a foot in the past (remembrance), another in the present (consider), and one in the future (warn). And that is maybe what everyone expects: a future for our past. Visions about cultural heritage are clearly related to visions about time. Saint Augustine (1991, 11–18), while admitting he cannot really understand time — as soon as he tries to explain it — writes about the presence or image of its three moments "wherever they are, they are not there as future or past, but as present": past as "memory", present as "awareness" and future as "expectation" (1991, 11–20).

Each attitude outlined above seems to weight differently the images of the three loci of time drawn by Augustine. And where the balance settled is reflected in how ideas are implemented.

But words in themselves can be manipulated. How they are translated in actions, revealing their nature, is a partly unrelated matter. Riegl (1903) dissected the reasons impeding an agreement about actions. It is a society matter and society is made of individuals which see and value differently. Decisions is then the result of a game of power and persuasion.

Assuming that individuals desire to act *well*, the question remains of what is the meaning of *well*. It is clearly a problem of ethics, carrying along all its attached complications. Moreover, if "all practical laws are the exponents of moral ones" (Ruskin 1849), "morality represents the way we would like the world to work, and economics represents how it actually does work" (Levitt and Dubner, cited by Sandel 2012, p. 88).

Let us dream for a while! The term *monument* itself also leads to ethics: we are reminded and warned! In what follows, the position advocated is that, to fare well, we need memories, attention and expectations…and too act accordingly: "Being, knowing, willing" (Saint Augustine 1991, 13–11).

As someone interested in the material and technical dimension of *monuments*, observing that this position — for a long time shared by many — is not anymore predominant, while recognising the reasons behind this evolution — in part first hand as Figures below will illustrate — I nevertheless sense a danger.

Section 2 describes it; section 3 indicates an escape route: *seeing*; section 4 advocates engineers to follow the route; section 5 discusses one of the practical complication: *uncertainty*; section 6 looks at the decision process and outlines some recommendations.

The main goal of the paper is to shed a bit of light in a dark area: the inside of the fabric.

2 SUPERFICIALITY

What is the context?

> "Le divorce accablant de la connaissance et de la mythologie" Barthes 1957, "Bichon chez les nègres"
> (The overwhelming divorce between knowledge and mythology)

To the dismay of some, movies are now full of super heroes! And for countries and patriots, World Heritage sites (*property* is the official denomination, UNESCO 2021) are also super heroes…thankfully, often in better oufit! Writing about music, Adorno (1991, p. 36) refers to the construction of a "pantheon of bestsellers", there to entertain us. "To like it (music) is almost the same as to recognise it." (Adorno 1991, p. 30), "high" and "voluminous" voices are favoured, and old instruments or conductors are becoming fetishes (Adorno 1991, p. 37). For him, the same can be said of sport and films. Built heritage is not immune to the trend: it has to transmit a clear and simple message. Architecture is particularly vulnerable because it "(…) has always represented the prototype of a work of art the reception of which is consummated by a collectivity in a state of distraction." (Benjamin 1980). People are interested by painting, music, sculpture and literature but not by architecture (Zevi 1948).

Is this a remain of bourgeois thinking? For Benjamin (1980), the advent of means of mechanical reproduction was a way to democratise access to Art. This is certainly a noble intention: another *light beacon*. He saw in particular cinema as a revolutionary and promising medium, liberated of the fetishist *hic and nunc* of the original and unique object. Aura may be lost but reproductions allow access to a greater number (Mozart brought to your home), letting them perceive details or perspectives otherwise left in the dark (approach to closest detail of the Arnolfini Portrait). Translated in the context of built heritage, loosing material authenticity sometimes let visitors see what otherwise would have disappeared. But Benjamin seems to always assume that copies are perfect reproduction of an original. But is it the case? Liberated from the aura, its cult or later merchant value, both residing in the mind of the observer, said observer can access a message. But is it possible to reproduce perfectly the fabric, to preserve the material support, the data for future interpretation and not one which is imposed, pre-digested, ("purified" Stanley-Price 2009)? "Auf der einen Seite die vielleicht verkürzte, verblaßte Wirklichkeit, aber immer Wirklichkeit — auf der andern die Fiktion." (On the one hand, the perhaps diminished, faded reality, but always reality — on the other, fiction) (Dehio 1905). Is following Benjamin ideas in the realm of visual arts, not transforming them in arts of representation, in some form of theater? And does that lead to a long-sighted look on heritage? To the production of a synthetic food, leaving no place to our invention, forcing us to think (Barthes 1957, "Photos chocs").

This is not easy to settle but one cannot help observing that history also followed a path of money, propaganda and delusion. Cinema was rarely used by *communists* and *capitalists* alike with citizen empowerment in mind. Adorno saw Walt Disney as the most dangerous man in America. And the evolution does not only concern only cinema. The "pervasive" and "mundane" role of markets in todays life described by Sandel (2012, p. 15) is steadily growing and influencing the evolution of built heritage management (Montanari 2015). In particular, the influence of tourism on the interest for reconstructions is not new (Giovannoni 1931b). Cities, architecture, archaeology are all concerned. Houbart (2020) cites Roberto Pane who already complained about the excessive

Figure 2. View from the Big Wild Goose Pagoda. Xī'ān, Shā'n-xī province, China. Ph.: P. Smars, 2005.

reconstruction to satisfy the appetite of the tourists. Stanley-Price (2009) lists it among the reasons behind reconstructions in archaeological sites. Money is a universal value and cultural heritage is there to be exploited like petrol (Choay 2009, quoting a communication othe ministry of culture in 2012: "gérable et exploitable", p. XL) (Montanari 2015, quoting Napolitano in 2012: "sfruttare fino in fondo", p. 7). Choay (2009) describes the "great void" created by this evolution: the disappearance of the *memorial* dimension and of the *historical monument* as such. The case of Xī'ān in China (Figure 2) is particularly emblematic (Dunne 2018) and also an opportunity to make a transition to the theme of *identity*. "Historic cities have often been redesigned or undergo a process of renewal in order to promote their ancient historic credentials." (Zhu 2017). Stanley Price also mentioned these political reasons, giving the example of the Parthenon after the independence of Greece or Babylon during the Iran-Irak war. In some cases, it may even lead to real crisis when significance of an heritage is not interpreted and simplified in the same way by various groups (Yang 2018) (Figure 3. Similarly, in Taiwan, after WWII, the Japanese heritage was preserved only if it was of practical utility. Most Shinto shrines were destroyed, abandoned or converted. But nowadays, any trace of Japanese presence become an opportunity to justify and reinforce the country's identity. The way a society deal with its cultural heritage betrays its intentions and values.

Returning to Walter Benjamin and the *aura*, did the infinite reproductions of Mona Lisa, Manneken Pis, the Eiffel tower or the tower of Pisa actually eliminated their aura? Or did their meaning just shifted? Do the modified anatomy of a monument, liberated from the aura of having being built by someone from another time, who left minute traces only seen by a few, change anything about its accessibility, in particular if it is a reproduction? Giovanonni was describing the difference of expectations between the scholar ("érudit"), the architect and the simple citizen (Giovannoni 1931a). Who benefits from the evolution described above? The complexity and richness of signification is displaced, deformed, impoverished by what becomes a myth (Barthes 1957). At least, as long as the material object hiding behind the myth is still there, to paraphrase Barthes, there is a possibility

Figure 3. Hashima Island (Battleship Island), Japan. Ph.: P. Smars, 2016.

to look through the window and see the landscape. They coexist. But what happens when it is not there anymore? We are left with the myth!

In this context which is unlikely to change much, the growing virtualisation of the society — whose negative impact is discussed by Choay (2009) and others — also presents an opportunity (which should be taken) to fight if not defeat superficiality, an opportunity for those acting in the material world: architects, engineers and others, to *virtue-alyse* interventions on the substance. And, doing so, to engage in the positive and democratic process advocated by Benjamin (1980) and some French Revolutionaries (Choay 2009, pp. 84–101: "Félix de Vick d'Azyr"): pass a message, give access and visibility to hidden areas and features; but also clarify the limit between data (keeping it *actual*) and interpretation (using the power of the *virtual*), in a word dispel what would be otherwise deception, in our world of fake news and endangered environment.

But, how does that translate in actions that we, individuals, in the limit of our power and responsibility, can take? First step: to see.

3 SEEING

What is the challenge?

> "far scaturire colori e forme dall'allineamento di caratteri alfabetici neri su una pagina bianca."
> Calvino 1988, "Visibilità"
> (reveal colors and shapes from lines of black alphabetic characters on a white page)

Common sense tell us that what cannot be seen does not matter. But alterity is disliked by common sense (Barthes 1957, "Martiens"). And otherness is what makes the "language" of cultural heritage not a tautology. If one does see, he learns about the other and about himself (Settis 2004, p. 3). If one does not see, it may be because one does not look.

In the countryside of Taiwan, many adobe and wattle and daub farmhouses can still be seen. Few are still in good condition (Figure 4), some are still occupied but most of them are slowly

Figure 4. Adobe house in Jiŭ -a̍n, Yún-lín county, Taiwan. Ph.: P. Smars, 2019.

disappearing, weathered down (Smars 2018; Smars 2022). Asking where such building can be found, their existence is often denied. They are not perceived, they are invisible. Asking to the – usually old – owners why they are left in such a bad condition, reveal how little weight is given to their memorial value. As soon as money permits, or money incentives leads to land sales, new constructions replace them, in the complete indifference of the planning authorities. Maybe it will result in an improvement of the global seismic resilience? But soon they all will be gone.

The Scheepsdalebrug, a 1934 swing bridge designed by Arthur Vierendeel, notwithstanding its unique features, was not deemed worthy of preservation: it was destroyed in 2009: Maybe it did not fit the medieval image of the World Heritage city of Brugge? Maybe it was his condition of *industrial* object? Various specialised associations tried to save it: The Flemish Association for Industrial Archaeology (VVIA), and the International Scientific Committee on the Analysis and Restoration of Structures of Architectural Heritage (ISCARSAH). But without success, most people and the deciders did not *see* its value. This is an example, among many, of the divorce between the smooth aspiration of popular culture and the breaking aspiration of scientific culture (Settis 2004, p. 17).

Long before, in the staircase of a tower of Notre-Dame de Paris, Hugo (1832) saw, and later lamented the disappearance, of a Greek inscription ‘Αναγχη. “Ainsi, hormi le fragile souvenir que lui consacre l’auteur de ce livre, il ne reste plus rien aujourd’hui du mot mistérieux gravé dans la sombre tour de Notre-Dame (…)” (“Thus, with the exception of the fragile memory which the author of this book here consecrates to it, there remains to-day nothing whatever of the mysterious word engraved within the gloomy tower of Notre-Dame” Translation by I.F. Hapgood). He saw something that the restorer, the priest or whoever decided to whitewash the wall did not see. Writing about it, somehow, well-aware Victor Hugo preserved its memory.

This is actually a good example to follow: if because of professional or personal inclination something destined to disappear is identified, if it is deemed important or just interesting, writing about it may — or may not — help but it should be a duty to, at least, document it. Even recognising that Victor Hugo himself was only partially successful in his enterprise.

It is from feeling our misery that proceeds our compassion for indigence (Saint Augustine 1991, 13). So it is likely that, initially at least, some dissatisfaction triggered the work, exhibitions

Figure 5. Temple of Baachus, Lebanon. Ph.: P. Smars, 2015.

and books of Bernd and Hilla Becher on water towers, gas tanks, and other industrial relics (Becher & Becher 1967), and the exhibition and book "architecture without architects" of Bernard Rudofsky (1964). These two examples were emphasising the formal and aesthetic dimension of something broader and richer but they are efficient means to attract the attention of the inattentive citizen (exhibitions are effective), to open eyes, to inspire further enquiries. They also betray motivations which, without any doubt, go deeper than formalism; they document objects, periods and lives (only through their material imprint) which, often, have now disappeared.

In general terms, discussions around the preservation of some built artefact often result in fights, fights between the one who see and the one who don't. If there is progress in the field, it is about raising awareness to a level at which society starts to care.

It is not an easy task. We all speak different languages and each trace of our built heritage, shaped by centuries, speaks its own. There lies its richness. Progress is greatly related to the growing understanding of what we see and then communicate. For John Scotus Erigenia, cited by Borges, the holy scriptures contains an infinite number of meanings (Borges 1980, "Poesía"). And for the Argentinian poet and essayist, it is the case of any book worthy of relecture (Borges 1939; Borges 1980). So are our monuments: our seeing and reading is source of knowledge and imagination. Often, help is needed to perceive, indicate new angles, and then promote the care for the preservation of what is the source of it all; to keep images raining (Calvino 1988, disgressing on Dante in "Visibilità"). That is the challenge: how can knowledge, emotions, about foundations, structures, materials be communicated.

Languages are also often misunderstood. Each profession uses its own, specific, which does not translates well in the language spoken by others (Barthes 1957, "Dominici ou le triomphe de la littérature"). In particular, the language spoken in the theatre where decisions are taken has its peculiarity.

4 WHAT LIES BEHIND?

What do engineers see?

> "Tandis que les grands hommes, portés au fommet de l'édifice, tracent & élèvent les étages fupérieurs, les artiftes ordinaires répandus dans les étages inférieurs, ou cachés dans l'obfcurité des fondemens, doivent feulement chercher à perfectionner ce que des mains plus habiles ont créé." Coulomb 1776

(While great men, on the top of the edifice, trace and raise the upper floors, ordinary artists, on the lower floors, or hidden in the obscurity of the foundations, must only seek to perfect what more skilled hands have created)

Only broad directions are suggested below. This is actually the part that everyone of us has to write for himself, for the benefice of all.

There is a difficulty, related to the conceptions of time discussed in section 1. Engineers are naturally encouraged to look towards the future and to see the solutions of today as better that the ones of yesterday. This is obviously a simplification; the state of the world in the 21th c. challenges everyone's conception of progress. And in the context of the present conference, it is even more likely to be the case.

That is also confirmed by documents written by engineers for engineers. The ISCARSAH charter of 2003 (ICOMOS 2003) emphasises that "the value of architectural heritage is not only in its appearance, but also in the integrity of all its components as a unique product of the specific building technology of its time", that "the distinguishing qualities of the structure and its environment, in their original or earlier states, should not be destroyed" and that "each intervention should, as far as possible, respect the concept, techniques and historical value of the original or earlier states of the structure and leaves evidence that can be recognised in the future". The charter uses the term *distinguishing qualities*, while another document, the annex on heritage structures of the ISO standard on the assessment of existing structures (ISO 13822:2010) uses *character-defining elements*.

This is not by accident that engineers working on historical structures came out with these ideas. As I understand it, they formed first as purely technical problems of compatibility kept appearing; among which one can list:

- The disasters related to the use of steel and concrete in archaeological sites introduced the idea that modern materials are not always better;
- The damages induced in original materials by too rigid, water- or vapour-proof joints introduced the idea that stronger is not necessarily better;
- The observation, after the occurrence of earthquakes, that what modern codes were recommending was not as effective as expected and that traditional mitigation measures sometimes behaved better introduced the idea that a modern frame of thought does not always fit other context (Figure 6);
- The inadequacy of some European-born concepts or measures to other contexts (material, economic) introduced the idea of a relation between engineering and culture and its value.

All these observations required retrospection. They lead to a better appreciation of the value of the *otherness*, of the specificity of the engineering of the past, as a reminder of the traditions and a warning against the dangers of over-confidence.

This story is not smooth. At the conference of Athens of 1931, Paquet (1931) confidently encourages engineers to use of hidden reinforced concrete elements (which proved to be a dangerous recommendation) but he also expressed his concern for the respect of the construction system (which is still seen as important). At the same conference, Giovannoni (1931a) was expressing a great confidence in modern materials and techniques, while also urging caution in relation to monuments far away from our habits and civilisation. To this day, arguments are colliding.

- New materials vs old materials
- Visible interventions vs invisible interventions
- Respect of the original structural system vs innovative reinforcements

In the broader context of cultural heritage protection, even if, as discussed above, the importance of the authenticity of the substance is challenged. it is still officially listed as an important criterion in international documents. Among the 10 criteria used by UNESCO to assess whether a property has an Outstanding Universal Value, criteria 1 to 4 may benefit from contributions related to technique, construction and engineering (Figure 7). In the Operational guidelines (UNESCO 2021, point 82),

Figure 6. After the 1997 Umbria and Marche earthquake. Sellano, province of Perugia, Italy. Ph.: P. Smars, 1998.

Figure 7. Extrados of the vaults of King's College Chapel. Cambridge, UK. Ph.: P. Smars, 2002.

the authenticity, necessary to achieve an Outstanding Universal Value depends among other criteria of the truthfulness and credibility of "material and substance", and "traditions, techniques and management systems".

The critical question of *credibility* is discussed below, in section 6.1.

But the first stage is identification. In the course of preliminary studies and during the works on the fabric, elements and features of technical interest are uncovered by the specialist operators. This material substance has also a cultural meaning (ISO 13822:2010). And so have the technical achievements. They are historical evidences and have a spiritual nature hiding behind and complementing what only appears as mineral to the uninitiated. "Das herrschende Recht berücksichtigt sie nur als körperliche Wesen und doch ist es die allgemeine Überzeugung, daß ihr wahres Wesen ein geistiges sei." (The prevailing law only considers them as physical beings and yet it is the general conviction that their true nature is a spiritual one) (Dehio 1905). They are potentially the *character-defining elements* of Annex I of ISO13822:2010, the *traditions* and *techniques* of the operational guidelines. They may not be perceived by people outside the trade but that does not mean that they are not present and valuable. They are constitutive of the otherness making our built heritage rare and precious.

In the framework of geotechnical engineering, the contribution of the field to the conservation of cultural heritage is clear, at least to fellow engineers (Egglezos et al. 2013; Kérisel 1975). The existence of TC301, the past and present conferences, are witnessing its importance and vitality. But it seems to me that the historical and cultural dimension is less explored. It may be because, being more of a structural engineer, not aware of the existing literature. That is certainly not by lack of interest or need: my first experiences all involved problems related to settlements, my interest for masonry often oriented me towards soil and rock mechanics. And the challenges of structural and geotechnical engineering are strongly linked (Lambe 1973). Historical information about foundations (García Gamallo 2003; Kérisel 1985; Przewłócki et al. 2005) or soil mechanics (Skempton) is still relatively rare. And discussions about the cultural value and the authenticity of foundations are to my knowledge relatively recent, on a cultural heritage time-scale (Calabresi 2003; Iwasaki 2013; Iwasaki et al. 2013; Iwasaki et al. 2021). The members of committee TC301 are on the front-line of this work of raising awareness about the *invisible*. The book collection that they started publishing about case studies are a great initiative!

That is a difficult challenge, especially for foundations. All interventions are deemed to become invisible and what hides behind the skin, as long as it does not bring back to the surface one of the technical compatibility problem mentioned above, seems also to be of little concern to many engineers. The hidden parts of a structure are like the time described by Augustine: they only exist in the memory of their construction and transformation, in the attention given to their existence when they can be seen and touched and in the expectations that we formulate for their future. Documentation is critical. It can transmit what would not be otherwise accessible, bringing art (in the medieval sense of the word), closer to the people (Benjamin 1980).

5 UNCERTAINTY

How can the concept of uncertainty be conveyed to a society in search of certitudes?

> "One would hope that in predicting the performance of constructed facilities, precise data could be combined with scientifically derived methods to obtain precise predictions. The soil engineer knows that this hope remains an unrealistic dream." Lambe 1973

Predictions are at the "very heart" of the practice of civil engineering (Lambe 1973). Engineers are constantly devising and improving techniques to predict and reduce the risk of failures. In the course of history, they encountered many, often with catastrophic consequences. Their occurrence is often the motor of progress and the techniques designed to eliminate them are slowly taming uncertainty (recurrent cost overruns indicate that it is a work in progress). The whole process, from

design to construction and management, is shaped by this intention of control. Without trying to be exhaustive, this involves:

- To produce and use materials of known properties;
- To use structural elements which can be reliably modelled: 1D (beams, columns…) and 2D (walls, slabs…);
- To join them using standard and tested procedures;
- To assemble them to form structures which can be reliably modelled: statically determinate or with sufficient provision of ductility;
- To design structures according to proven scheme (even if, as pointed out by Addis (1994), progress results from creative new designs);
- At each stage, to employ trained and qualified personnel following the rule of their art;
- To have each stage controlled by independent bodies.

The challenges posed by geotechnical problems and historical fabrics offer some resistance to this smooth process. Engineers have to deal with fundamentally 3D, heterogeneous, anisotropic, non-linear, time-dependant problems, only partially understood and depending of parameters often not known, difficult to measure, often indirectly, presenting a great variability, and forming an incomplete set. "Geotechnical engineering is especially damned and blessed by the importance of predictions and the difficulty of making accurate predictions." (Lambe 1973). Kérisel (1975) stresses in particular the importance of time and slow settlements. This is also a frequent concern with superstructures; creep was found responsible of non few collapses (Binda, Anzani, & Mirabella Roberti 2000; Verstrynge & Van Gemert 2018).

In a fuzzy context, formulas are often fuzzy too. They are born from observation and are working in the corresponding situation. They are often semi-empirical. Huerta Fernández (1990) has shown that this is certainly not new and that this does not preclude their effectiveness in said context. Lambe (1973) also points out how methods, parameters and problem to solve "uniquely linked together".

And indeed context is important. The 14th c. expert discussions concerning the cathedral of Milan (Ackerman 1949) or for the cathedral of Gerona, exemplify the difficulty of communication between masters with expertises alien to each other, the use of arguments making no or little or some sense to the next generation, the boldness of the trust that one has in his rules and, surprisingly or not, the effectiveness of the final result. Facing a lack of knowledge about an historical structure, it is a temptation to believe in assumptions or apply methods not fitting the situation, devised for new constructions, or to transform the historical fabric into something which better fits the current assumptions. As Dehio (1905) puts it in relations to the attitudes of the 15th-18th c., destructions can be the result of the boundless trust in the creative power of the present "(. . .) die Folge überströmender Schaffenslust einer sich selbstvertrauenden Gegenwart sein" (Dehio 1905). This attitude is not dead.

Humility is necessary. As mathematical models alone cannot provide sufficient confidence, observation becomes even more necessary. Monitoring is an effective tool (incidentally, "monitoring" and "monument" have the same etymological root). The "observational method" of Terzaghi and Peck (1969), a "learn-as-you-go" approach, is a modern systematic adaptation of what was used by master builders in the past. It also founds its use in structural engineering (ISO 13822:2010). Lambe (1973) also states that sophisticate methods do not always lead to more accurate predictions. These approaches may even be as or more appropriate today, when dealing with structures belonging to another time and place. This idea may be more difficult to accept by structural engineers, educated with a higher confidence in determinism and in the power of science, than by geotechnical engineers. But Torroja Miret (2000) stresses the importance of intuition and Nervi (1997) too refers to it, and to observation and experimentation.

In search of rigour, in the presence of risk and uncertainty, it is natural to consider a probabilistic approach, in an attempt to evaluate the risk quantitatively. PEER, the Pacific Earthquake

Engineering Research Center has for instance developed a very complete framework for a scientific evaluation of seismic performance of buildings: performance-based earthquake engineering (Porter 2003, 6,7). A requirement of this approach is to be able to characterise precisely hazard, vulnerability and losses (which in the framework discussed here require to consider the potential loss of cultural value). This is an interesting direction to follow but of limited applicability for historical structures (Smars et al. 2010). Quantitative evaluations are difficult: both for random uncertainties (which can be dealt by probability methods and PBEE) and for epistemic uncertainties (related to insufficient knowledge on the process involved, to the choice of models…). In many cases, data is too scarce to characterise random uncertainties, especially to estimate vulnerability and losses (precisely enough to lead to useful estimates). And there are numerous epistemic uncertainties (models used to evaluate the vulnerability; methodology to assess the values).

In an attempt to draw a conceptual framework of general applicability, Klinke & Rena (2002) categorise risks, assigning them to six specific classes characterised by the (a) the expected extend of damage, (b) the probability of occurrence and (c) the level of knowledge (the uncertainties on a and b). For each class, they recommend a specific strategy. They argue for instance that a *risk-based* approach (as the PBEE) is not the most suitable when the level of knowledge is low. A decision tree is given to assist risk managers in making their choices.

And for many historical constructions, because of their complex structure, because of their *otherness*, important constituent of their value but requiring flexibility and ingenuity, because of the numerous stakeholders with values difficult to conciliate, the level of knowledge is indeed low. In such cases, the importance of an extensive program of preliminary studies is recognised. It can provide better estimates of the random uncertainties. Research on the construction techniques, on the anatomy of the structures can reduce epistemic uncertainties and provide elements completing the set of values to protect. Some debate is then necessary to eliminate ambiguities on the level of knowledge and on the expectations of the stakeholders.

6 ETHICS AND DECISIONS

6.1 *Ethics*

How hard should we fight?

> "Wir konservieren ein Denkmal nicht, weil wir es für schön halten, sonderrn weil es ein Stück unseres nationalen Daseins ist. Denkmäler schützen heißt nicht Genuß suchen, sondern Pietät üben." Dehio 1905
>
> (We do not conserve a monument because we think it is beautiful but, rather, because it is part of our national existence. Protecting monuments does not mean seeking pleasure, but exercising piety)

Architects, engineers, conservators have a key role in the definition of interventions on cultural heritage. They are the one which define the technical and material aspect of the intervention. As such they have large responsibilities in front of the population (Settis 2017).

They are firstly contracted to do a job with technical duties, according to a professional ethic. This is not what is discussed here. They have in particular to satisfy the requirements fixed by their sponsors and other deciders which, hopefully, reflects what society judge as *good*. The problem arise from the fact that good as an adjective is not the same as red: its meaning depends of the noun to which it is attached (MacIntyre 1998) and of who makes the statement.

As discussed above, in the course of their work, engineers are uncovering features of technico-historico-cultural interest, features which are not always seen or perceived as important by others. The argument defended in the present paper is that they should care about them and act accordingly. This is (or should be seen as) a responsibility in front of the society and of their pairs, past, present and future. They see them through their professional eye, but also because they have the privilege to look behind the skin! They access places normally inaccessible, they use instruments offering them

glimpses of the anatomy of the fabric: materials, construction systems, revealing the ingenuity, the mistakes and the resources of their predecessors.

In many circumstances, this does not lead to difficulties. The chance of most technical endeavours is that, as their implications and the means of their implementation are not clearly understood, if they do not interfere with what matters to others, technicians can decide how to proceed and, if they do care about certain material features, try to preserve them to the best of their ability.

In other circumstances, these material evidences are threatened of alteration or elimination. It may be because of some technical reason (internal) or because of difference of opinions (external). The process of decision is discussed in section 6.2.

The first way to deal with such a situation is passivity: either by being satisfied to be the hand providing what the majority wants, either by seeing it as a lost battle and concentrate strictly on the terms of a contract, either by internalising the discourse which section 2 tried to expose and denounce. The alternative way to deal with the situation is pro-activity:

- Actively search and identify features of technico-historico-cultural interest, the structural *character-defining elements* of the fabric;
- If their protection seems impossible for technical reasons, check whether a change of the terms of the equation would help. Are some non-structural mitigation measures possible (change of program, restriction of access…)? Would more detailed studies, budget modifications or a clarification of the objectives of the whole operation improve the chance of preservation?
- Inform stakeholders and deciders about values, options and consequences.
- Plead for their protection. This is a natural and automatic step if what is mentionned in the first point is done.
- Document and share what will disappear, either because it will be again hidden behind the surface of the fabric, either because it cannot be preserved.
- Ensure that the intervention and the way it is presented is not deceptive. For Ruskin (1849), the ethical dimension of our approach to monuments is fundamental. He thinks that a distinction must be made between malicious deceits and the works of imagination which require, as we could phrase it today, “suspension of disbelieve”. He gives the example of gilding which is a deceit in jewellery but not in architecture. Stanley-Price (2009), proposing some criteria for reconstructions in archaeological sites (which are happening whether or not one believes it is a good idea), relates most of them to the ethical principle of not lying.
- Because, these features are often difficult to apprehend by non-specialists, it is also important to disseminate a translated version of the documentation work to the non-specialist. This is laying a stone which will contribute to the education role of heritage (which at the time of the French revolution was one of the most important value) and which eventually will facilitate de defense of such features.
- Consider that this work of vulgarisation also contributes to the credibility of the interventions on our built environment.

Settis (2017, p. 6) argues that the ethics of the architect should not only be to offer services to a client but also to the community of citizens. This is the idea that is extended above to include the engineer. There is a complication: the community of citizens is not homogeneous and neither are its expectations. Saying that “conservation means the greatest good to the greatest number for the longest time” (Settis 2017, citing Gifford Pinchot, p. 33), is a noble target. It is also the pursuit of democracy, but the recent evolution shows that it does not proceed as smoothly and harmoniously as expected.

How can minority opinions be heard? When you care about something and you don’t have the leverage to convince, a strategy has to be devised. Since its origin, monument conservation as always required fights. Awareness does not come easily.

6.2 *Decisions*

What belongs to science and what belongs to politics?

Figure 8. Wall repair. Bamiyan, Afghanistan. Ph.: P. Smars, 2003.

Decisions are often difficult, conflictual processes. It is not possible to accommodate everyone. The expectations of the various groups in the population, the requirements of the stakeholders, the opinion of the experts, rarely align perfectly. To decide basically comes down to weight values (Smars & Patrício 2016). The current COVID-19 pandemic exemplify the problem in a topical manner: economists emphasise the importance of not hindering business activities; epidemiologists urge to confine the population; prophets prophesy; and finally, politicians weight factors and decide. Who is right? In a democracy one can just expect that:

- Decisions are taken by people which represent the population;
- Stakeholders and experts can voice and defend their opinions and advices;
- Deciders are accountable;
- The press inform.

Sadly, the process is often more opaque (Settis 2004). Even when the object whose fate is discussed is recognised as cultural heritage, it does not mean that it is the only, decisive, factor. It is not always about protecting what is in danger of disappearance. It can be also about affirming an identity, helping a community, insure a re-election…or most of the time a mixture of noble and less noble motives. Development, safety, well-being of the locals are legitimate aspirations. The transmission of a message to the future generation is only one variable of the equation.

Engineers (acting as experts or designers) are advising, proposing and for the most technical matters, they are trusted and decide.

But, in difficult and/or conflictual circumstances, if there is a fear that something may go wrong, everyone gets ready to transfer responsibility to others. This is a natural tendency. Deciders justify taking decisions based on technical ground and expert advises. And they impute hard decisions to the technicians; who themselves minimise their role: they are just operators following orders. And some press castigates the impotence of experts to form a coherent response.

The trial made to the scientists who met the population of L'Aquila the week before the earthquake of 2009 accusing them of unreasonable reassurance was a shock for the community. It illustrates the problem of vocabulary discussed in section 3. Conveying uncertainty is challenging (Scolobig et al. 2014). The danger will be that anyone possibly at risk of being misjudged will too carefully choose his/her words, make them unintelligible, open to multiple interpretations. Judges and lawyers are better prepared. They are not trialled when someone wrongly accused is found innocent.

But, hopefully, misadventures can help clarifying tasks. That was one of the outcome of the introspection of various scientific associations after the misadventure of L'Aquila. Experts and technicians study, honestly inform, propose and implement in the realm of their specific knowledge. They may also decide on matters which do not interfere with other considerations. But for conflicting situations, they are not the main deciders, the one who have to weight all the variables, all the values, in terms of resources and timing and following their conviction and/or policy. In that world, there is no best solution. At the highest level, this is the job of the politicians, elected by the population for this high and heavy responsibility: represent them. Others chose to bear this responsibility too and face the consequences of misjudgments.

How these considerations fit with the responsibility of the technicians discussed in section 6.1? The main answer is information, the duty to inform about the consequences of choices. And, ultimately, the refusal to participate to operations irreconcilable with professional ethics.

6.3 *Priorities*

As in many circumstances related to conservation, it is impossible to generalise and state principles which, because they are inapplicable or just not going to be followed, are deemed to have only a paper life. This is the difficulty or inadequacy of applying European ideas about conservation, born in a context of stone architecture, with a big A, not "bicycle sheds" (Pevsner 1943), to vernacular architecture, wooden or earth buildings, Shinto temples and other foreign traditions, which lead to recognising that there are other values besides *material authenticity* of the fabric. But that does not mean that this was just a mistake, a fetishist and morbid attachment to old flesh which can be forgotten. It seems sometimes just convenient to use it as a pretext to achieve goals which are better left hidden. Invoking the importance of skills, perpetuation of traditions but use modern materials and tools, or apply it to context where tradition has disappeared borders on hypocrisy.

Presumptively, archaeological sites should be the place where most respect is given to the material dimension, to the authenticity of the evidence. Even Lassus & Viollet-le Duc (1843) were pleading for this cause! But this is not the case, far from it. Archaeological sites are not the place where *authenticity* can be expected. This was observed at multiple occasion by the author and noted with equal bewilderment by Houbart (2020). The observer sometimes doubt about the reality of what he sees. Cinema prepared us to enter this world of suspended disbelief. But up to a point: some elements instill suspicion of dishonesty. Sometimes, the law of mechanics seem to have vanished. Sometimes, it is the absence of the traces of age which is suspicious. Sometimes, no clear evidence of corruption is perceived but it is too late, the doubt is there.

The same kind of reasoning can be made for architecture: the feeling of being told a biased story.

Fixing priorities is important. But the infinite variability of situations is rebel to generalisations. A most important point can nevertheless be put in the first position: *transparency*: it attests an intention of honesty and opens the door of accountability (it is also likely to be among the less respected principles in practice). The main point discussed in the paper is then the identification a *character-defining elements*. Not accepting the cultural value of the fabric would make the whole process insignificant for engineers. Beyond these two points, an ordered list of priorities should be drawn on a case by case basis (Figure 8). Possible other points: compatibility, reversibility, retreatability, distinguishability, preservation of the principle of construction, of the material type, of the original material, documentation, dissemination, identification, vulgarisation…

7 CONCLUSION

Engineers have first and foremost the task to understand the structural condition of the structure, evaluate the consequences in terms of risk and, if necessary, to propose action(s) to mitigate the risks. As discussed above, this usually requires a cautious approach, studies, experience.

In the last one hundred years or so, for various reasons: geographical (eurocentric), material (the first buildings for which a cultural importance were often built in stone), sociological (conservation

was mostly in the hands of specialists), historical (reaction against the *restorations* of the 19th c.), great importance was given to material authenticity.

The progressive expansion of the concept of heritage, lead to the observation that this vision, outside of the context in which it formed and evolved, was difficult to apply.

For Michael Petzet (Larsen 1995, Michael Petzet ("In the full richness of their authenticity"), former president of ICOMOS,

> "It was certainly a necessary process for us to take heed not only of beautiful outer surfaces or of the appearance of a monument, but rather than to become concerned with material and structure, with the inner fabric that perhaps only the scientist or the civil engineer can explain to us (…). However, we should still be interested in the front as well, although certain exercises in our modern preservation cult seem to have forgotten this."

In many ways, this is a progress; and a logical development of the idea that in matters of care of monuments, it is not possible to have rules of general applicability. Accepting that contexts have their specificity which has to be respected is recognising that each case has its specificity and requires a tailored approach.

But shifting the problem from a geographical to a professional level, it has to be reminded that differences are not only a matter of country, religion, traditions but that various groups in the population have also their own particular relation with heritage. They see and value different features. Architects, engineers, conservators and other *modifiers* of our built environment do not apprehend in the same way. And for many of them and for various reasons, *material authenticity* has still some meaning and value.

That does not mean that all decisions have to be left in their hands and that, only their values should be protected (even if it was possible, groups are not homogeneous). But, conversely, that does not mean that they just have to be silent implementers. They are also stakeholders. Heritage also matters to them, in a very direct and acute way, and not only because it happens to feed them and their family.

Following this line of reasoning, besides the technical duties to which they are contractually binded and besides the ethical duty of designing and implementing solutions coherent with what the democracy decides, they should also consider the duty of transmitting the message of their predecessors in the full richness of its authenticity.

REFERENCES

Ackerman, J. S. (1949). "Ars Sine Scientia Nihil Est" Gothic Theory of Architecture at the Cathedral of Milan. *The Art Bulletin 31*(2), 84–111.

Addis, B. (1994). *The art of the structural engineer*. London: Artemis.

Adorno, T. W. (1991). *The culture industry*. London & New York: Routledge.

Barthes, R. (1957). *Mythologies*. Paris: Seuil.

Becher, B. & H. Becher (1967). *Industriebauten 1830 - 1930. Eine fotografische Dokumentation*. München: Die neue Sammlung.

Benjamin, W. (1980). Das Kunstwerk im Zeitalter seiner technischen Reproduzierbarkeit. In R. Tiedemann and H. Schweppenhäuser (Eds.), *Walter Benjamin – Gesammelte Schriften Band I, Teil 2*. Frankfurt am Main: Suhrkamp. (Translation: Harry Zohn (1968). "The Work of Art in the Age of Mechanical Reproduction". New York:Schocken/Random House).

Binda, L., A. Anzani, & G. Mirabella Roberti (2000). Tall and massive ancient masonry buildings: Long term effects of loading. In *G. Penelis Int. Symp. On Concrete and Masonry Structures*, pp. 273–284.

Borges, J. L. (1939). Pierre menard, author del quijote. *Sur 56*, 7–16.

Borges, J. L. (1980). *Siete Noches (Seven nights)*. Argentina: Fondo de Cultura Económica.

Calabresi, G. (2003). Problemi geotecnici nel consolidamento delle costruzioni di interesse storico. *Quaderni di scienza della conservazione* (3), 19–34.

Calvino, I. (1988). *Lezioni americane. Sei proposte per il prossimo millennio*. Sagi blu. Milano: Garzanti.

Choay, F. (1996). *L'allégorie du patrimoine*. Paris: Editions du seuil.

Choay, F. (2009). *Le patrimoine en questions - Anthologie pour un combat*. Paris: Editions du seuil.

Coulomb (1776). Essai sur une application des règles de maximis & minimis à quelques problèmes de statique, relatifs à l'architecture. *Mémoires de mathématque et de physique, présentés à l'académie royale des sciences, par divers savans, & lÃ»s dans fes Affemblées 7*, 343–382.

Dehio, G. (1905). *Denkmalschutz und Denkmalpflege im neunzehnten Jahrhundert: Rede zur Feier des Geburtstages Sr. Majestät des Kaisers gehalten in der Aula der Kaiser-Wilhelms-Universität Strassburg am 27. Januar 1905*. Strassburg: J.H. ED. Heitz.

Dunne, E. (2018). How Xi'an's past became a blueprint for its future. Public memory as a tool of development in Xi'an. *The Diplomat*.

Egglezos, D., D. Moullou, & M. Ioannidou (2013). The role of the geotechnical engineer in archaeological work: The greek experience. In Bilotta, Flora, Lirer, and Viggiani (Eds.), *Geotechnical Engineering for the Preservation of Monuments and Historic Sites*, pp. 359–365.

García Gamallo, A. M. (2003). The evolution of traditional types of building foundation prior to the first industrial revolution. In S. Huerta (Ed.), *Proceedings of the First International Congress on Construction History*, Madrid, pp. 943–956.

Giovannoni, G. (1931a). La restauration des monuments en Italie. In *Conférence d'Athènes sur la conservation artistique et historique des monuments*.

Giovannoni, G. (1931b). Les moyens modernes de construction appliqués à la restauration des monuments. In *Conférence d'Athènes sur la conservation artistique et historique des monuments*.

Houbart, C. (2020). "Reconstruction as a creative act": on anastylosis and restoration around the Venice Congress. *Conversaciones 9*, 39–58.

Huerta Fernández, S. (1990). *Diseño estructural de arcos, bóvedas y cúpolas en España ca. 1500, ca.1800*. Ph. D. thesis, ETSAM, Madrid.

Hugo, V. (1832). *Notre-Dame de Paris. 1482* (2d, definitive ed.). Paris: Eugène Renduel.

ICOMOS (2003). Principles for the analysis, conservation and structural restoration of architectural heritage.

ISO 13822:2010. *Bases for design of structures – Assessment of existing structures*. ISO, Geneva, Switzerland.

Iwasaki, Y. (2013). Characteristic elements of authenticity of heritage structures and conservation for integrity in geotechnical engineering. In *ATC19 Workshop Part II, UNESCO*, Paris.

Iwasaki, Y., M. Fukuda, M. Iizuka, R. McCarty, T. Nakagawa, & V. Ly (2021). The authenticity and integrity of soil and foundation of bayon temple in angkor, cambodia. In *IOP Conf. Ser.: Earth Environ. Sci. 856. Second International Conference on Geotechnical Engineering*.

Iwasaki, Y., A. Zhussupbekov, & A. Issina (2013). Authenticity of foundations for heritage structures. In *Proceedings of the 18 International Conference on Soil Mechanics and Geotechnical Engineering*, Paris, pp. 3111–3114.

Klinke, A. & O. Rena (2002). A new approach to risk evaluation and management: Risk-based, precaution-based, and discourse-based strategies. *Risk Analysis (Society for Risk Analysis) 22*(6), 1071–1094.

Kérisel, J. (1975). Old structures in relation to soild conditions. *Géotechnique 25*(3), 433–483.

Kérisel, J. (1985). The history of geotechnical engineering up until 1700. In *11th International Conference on Soil Mechanics and Foundation Engineering (San Francisco)*, pp. 3–93. Balkema. Golden Jubilee Volume.

Lambe, T. W. (1973). Predictions in soil engineering. *Géotechnique 23*(2), 149–202.

Larsen, K. E. (Ed.) (1995). *Nara conference on authenticity in relation to the World Heritage Conservation*. UNESCO, ICCROM, ICOMOS.

Lassus, J.-B. & E.-E. Viollet-le Duc (1843). *Notre-Dame de Paris. Projet de restauration. Rapport*. Paris: Imprimerie de Mme de Lacombe.

MacIntyre, A. (1998). *A short history of ethics. A history of moral philosophy from the Homeric Age to the twentieth century*. London & New York: Routledge.

Montanari, T. (2015). *Privati de Patrimonio*. Torino: Giulio Einaudi editore.

Nervi, P. L. (1997). *Savoir construire (original: Costruire corretamente. Milano:Hoepli, 1995. Translated from the Italian by M. Gallot)*. Paris: Ëdition du Linteau.

Paquet, P. (1931). Le ciment armé dans la restauration. In *Conférence d'Athènes sur la conservation artistique et historique des monuments*.

Peck, R. (1969). Advantages and limitations of the observational method in applied mechanics. *Géotechnique 19*(2), 171–187.

Pevsner, N. (1943). *An Outline of Western Architecture*. Pelican.

Porter, K. A. (2003). An overview of peer's performance-based earthquake engineering methodology. In *Ninth International Conference on Applications of Statistics and Probability in Civil Engineering (ICASP9) July 6–9, 2003, San Francisco*.

Przewłócki, J., I. Dardzińska, & J. Świniański (2005). Review of historical buildings' foundations. *Géotechnique 55*(5), 363–372.

Riegl, A. (1903). *Der moderne Denkmalkultus, sein Wesen, seine Entstehung*. (Translation: K.W. Forster and D. Ghirardo, 1982. The modern cult of monuments: its character and origin. Oppositions 25, 20–51). Wien und Leipzig: W. Braumüller.

Rudofsky, B. (1964). *Architecture Without Architects: A Short Introduction to Non-Pedigreed Architecture*. Garden City, New-York: Doubleday & Company.

Ruskin, J. (1849). *The Seven Lamps of Architecture*. London: Smith, Elder, and co.

Saint Augustine (1991). *Confessions*. Oxford: Oxford University Press. (translated by Henry Chadwick).

Sandel, M. (2012). *What money can't buy. The moral limits of markets*. Allen Lane.

Scolobig, A., R. Mechler, N. Komendantova, W. Liu, S. Dagmar, & A. Patt (2014). The co-production of scientific advice and decision making under uncertainty: Lessons from the 2009 L'Aquila earthquake, Italy. *GRF Davos Planet@Risk 2*(2), 71–76.

Settis, S. (2004). *Futuro del "Classico"*. Torino: Giulio Einaudi editore.

Settis, S. (2017). *Architettura e Democrazia. Paesaggio, città, diritti civili*. Torino: Giulio Einaudi editore.

Skempton, A. A history of soil properties, 1717–1927. In *11th International Conference on Soil Mechanics and Foundation Engineerin (San Francisco)*, pp. 95–121. Balkema. Golden Jubilee Volume.

Smars, P. (2018). Adobe constructions in Yún-Lín county, Taiwan. In I. Wouters, S. Van de Voorde, I. Bertels, B. Espion, K. De Jonge, and D. Zastavni (Eds.), *6th International Congress on Construction History 2018, July 9–13 2018, Brussels (Belgium)*, pp. 1237–1244.

Smars, P. (2022). Documenting traditional architecture in Yún-Lín county. In K.-C. Yang and P. Smars (Eds.), *Challenges of traditional architecture protection. Belgium, Bulgaria, India, Taiwan, UK. (provisional title)*. (to be published).

Smars, P. & T. Patrício (2016). Ethical questions around structural interventions in archaeological sites. In K. Van Balen and E. Verstrynge (Eds.), *10th International Conference on Structural analysis of historical constructions (SAHC 2016), Sept. 13–15, Leuven, Belgium*, pp. 986–993.

Smars, P., T. Patrício, M. Santana, & A. Seif (2010). Archaeological site of Baalbek, Structural Risk Management Strategy. In *International Conference on Disaster Management and Cultural Heritage, 12–14 December, Thimphu (Bhutan)*.

Stanley-Price, N. (2009). The reconstruction of ruins: Principles and practice. In A. Richmond and A. Bracker (Eds.), *Conservation: Principles, Dilemmas and Uncomfortable Truths*, pp. 32–46. London: Elsevier/Butterworth Heinemann.

Torroja Miret, E. (2000). *Razon y Ser de los Typos Estructurales* (10° ed.). Textos Universitarios. Madrid: Consejo Superior de Investigaciones Cientificas.

UNESCO (2021). *Operational Guidelines for the Implementation of the World Heritage Convention*. Paris: UNESCO.

Verstrynge, E. & D. Van Gemert (2018). Creep failure of two historical masonry towers: analysis from material to structure. *Int. J. Masonry Research and Innovation 3*(1), 50–71.

Yang, K.-C. (2018). World heritage in the middle of political conflict: A discourse analysis of mixed reactions in response to the nomination of sites of Japan's Meiji industrial revolution. In N. Prothi Khanna and S. Burke (Eds.), *ICOMOS 19th General Assembly and Scientific Symposium "Heritage and Democracy"*.

Zevi, B. (1948). *Saper vedere l'architettura. Saggio sull'interpretazione spaziale dell'architettura*. Torino: Einaudi.

Zhu, Y. (2017). Use of the past: negotiating heritage in Xi'an. *International Journal of Heritage Studies*. DOI: 10.1080/13527258.2017.1347886.

Geotechnical Engineering for the Preservation of Monuments and Historic Sites III – Lancellotta, Viggiani, Flora, de Silva & Mele (Eds)

Form and construction. The domes of the Baptistery and Santa Maria del Fiore in Florence

P. Matracchi
Department of Architecture, University of Florence

ABSTRACT: Each building requires specific surveys and appropriate instrumental investigations which are often indicated during the course of the analyses. The activities that form part of the architectural and structural diagnostics must aim to identify the actual construction site activities, in operational terms, that over time have generated and altered the architectural structure.

In this regard, the dome of the Baptistery of Florence is particularly significant. It has been the subject of countless studies that have provided different interpretations of the structure. The initial highly idealised approach provided schematic constructive structures. The gradual refinement of the inspections defined a completely different construction concept of the dome from that established up until recently.

This new information also had a significant impact on the interpretation of Brunelleschi's dome, which showed in an even more compelling way characteristics similar to that of the Baptistery.

1 INTRODUCTION

A feature common to some octagonal segmented domes is a curved intrados profile. A curvature whose radius is almost equal to 4/5 of the diameter of the base was identified in the corners of the dome of Florence Baptistery (Aminti 1996). A pointed profile was also used for the dome of Orcagna's Tabernacle (1359), constructed inside the church of Orsanmichele in Florence (Pisetta & Vitali 1996).

Giovanni di Gherardo da Prato, supervisor of the dome of Santa Maria del Fiore, in 1426 traced on a parchment a drawing with comments criticising the use of the 4/5 radius of the diameter of the base that Brunelleschi was creating in the dome. The precision surveys of the intrados revealed deviations from this curvature (Fondelli 2004). However, for long stretches of the intrados profile, there are strong similarities between the dome of the Baptistery and that of Santa Maria del Fiore (Giorgi 2004, pp. 161–163).

The fact that the curve drawn through 4/5 radius of the diameter was a well-known and widespread device was confirmed by Francesco di Giorgio Martini who mentions it in his Treatise (1479–1486) (Trattati di architettura 1967). The same curvature is also found in the dome of the church of Santa Maria delle Grazie al Calcinaio in Cortona, again designed by Francesco di Giorgio; but the dome was executed by the Florentine architect Pietro di Norbo between 1509 and 1514 (Matracchi 1992).

The two larger domes were built with the initial part in stone and the rest in brick; the other two are entirely made of brick, and stone slabs were added to extrados of that of the tabernacle.

But a mere geometric comparison, also taking into account the building materials, is clearly paradoxical (Figure 1). The different scale of magnitude makes it necessary to acquire more information on the specific construction solutions adopted, which always characterize each building. The construction choices were not only affected by the size of the buildings, but also by local traditions, solutions that could have been brought by builders who grew up elsewhere. The construction phase experimentation that went on above all in buildings of great importance is no less important, and

DOI 10.1201/9781003308867-8

there was no shortage of accidental factors that could influence the choices, especially in long-term construction sites.

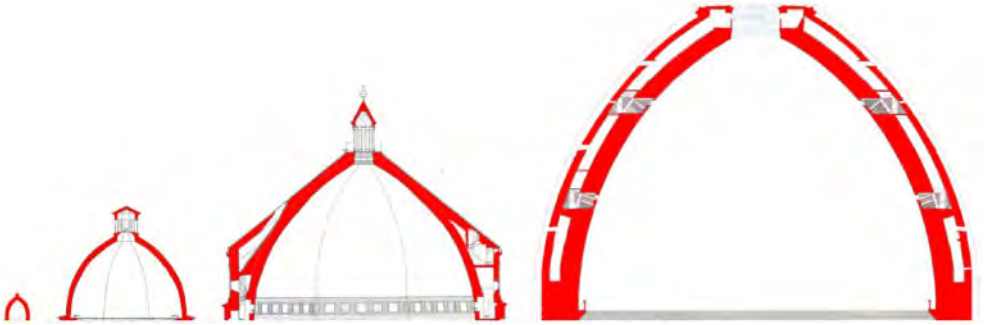

Figure 1. Comparison (from left) at the same scale between the domes of Orcagna's tabernacle, the church of Santa Maria delle Grazie al Calcinaio, the Baptistery and Brunelleschi's dome.

In this regard, a particularly interesting case is Florence Baptistery which, despite having been studied by scholars from the mid-19th century, continues to be analysed in order to obtain important information, to the extent that the constructive structure is evaluated with a profoundly renewed concept.

2 THE BAPTISTERY DOME

Knowledge and in-depth analysis of complex and large dome structures, like that of the Baptistery of Florence, is necessarily a long process linked to the available investigative tools, the conceptual approach guiding the study and the aims to be achieved. If the channel of interest pursued is that of conservation, some construction choices that link the parts to the whole in a holistic vision attentive to the actual act of construction that takes place at the construction site and results in the architectural structure must be explored in-depth. The actions that architecture undergoes over time, which can lead to alterations that are sometimes even substantial, but difficult to identify, are just as important.

The studies of the structure of the Baptistery can be divided into two different seasons. The first is marked by an intuitive approach, which represented the constructional device according to schematic and idealised drawings, which were at times even partial; these representations might have been accurate in graphic terms, but in general they were based on few measurements. They represented what they thought they had understood.

In the drawing by Heinrich Hübsch (1862) the ribs of the dome are envisaged extending until they join the diagonal ribs and the corners of the octagon are solid, but both hypothesis are wrong; the intuition of the box structure at the base of the dome is interesting, with dashed arches indicating the vaulted roofs of each compartment, but there are clear approximations in the dimensions of the masonry (Degl'Innocenti 2017).

The portion of the baptistery dome, depicted by Josef Durm (1887), shows some of the main construction elements, even focusing attention on less striking details. The wall offsets of the extrados at the base of the dome, the transversal walls that divide the various spaces of the garrets, the perimeter wooden tie of the dome, and the vaulted structures supporting the pyramidal roof of the dome are shown. The detail of the internal wall offset was also added to the attic wall.

Auguste Choisy (1899) depicted the dome in a more schematic way in an axonometric drawing, but it has the advantage of showing the entire building highlighting the difference between the section on the sides and on the corner of the octagon; the first shows a considerably hollow structure below the dome due to the presence of columns on the ground floor and the matronea on

the level above; the second highlights the massive section of the corners of the octagonal plan, but does not show the hollowing of the wall mass in the area adjacent to the haunches of the dome.

Walter Horn (1943) effectively combines a half section with an axonometric section of one side of the octagon; he thereby highlights the partition walls that flank the dome, the partition walls of the matroneum and, further below, the columns of the internal perimeter (Degl'Innocenti 2017, p. 96).

The drawings prepared by Hübsch, Drum and Choisy are examples, others have also been prepared, of an approach that includes real elements, intuition and interpretations, according to a vision still limited to the arrangement of presumed key construction features, which depict a structural scheme of the building with a high degree of abstraction.

The 1970s marked the start of a new season of studies conducted with increasingly extensive and accurate survey campaigns, more attentive to the analysis of the architectural structure as a whole, the materials and phenomena resulting in the alteration of the latter and the structures. Over time increasing attention was paid to understanding the relationship between the parts and the whole of the architectural device and assessing the construction features, which can vary even in situations of apparent symmetry. The wealth of information collected over time was gradually refined until a cognitive and interpretative synthesis was found based on architectural diagnostics.

So the drawings indicate the portion of the dome, starting from the springer, built with stone in rows that were initially horizontal and that incline from a certain height (Pietramellara 1973). The brick section of the dome is indicated from the wooden tie. In one plan, executed just below the roofs, the partition walls that stand on the extrados of the dome are clearly represented, with the extension of the rampant vaults that support part of the conical roof. Observations on the continuity of the rows of masonry in the garrets, which place the dome, the transversal walls and the external perimeter wall in a close constructive relationship, are particularly important. This structure is considered a "double dome", or a "cellular structure", highly significant concepts, the implications of which have not been explored in-depth, and to which we shall return later on.

Further investigations highlighted the uniqueness of the vertical connections between the monolithic columns, two on each side of the octagon, except for the one where the scarsella is present, and the partition walls of the matronea above, which continue into the garret until becoming the ribs of the dome. In the corners the ribs form a Y-shaped fork that creates the hollowing of the angular buttress at the level of the dome; at the level below, the corner buttress is crossed by a narrow passage necessary to pass through the matroneum, on the ground floor it is solid (Rocchi Coopmans de Yoldy 1996a). The corner buttresses of the east side where the spiral staircases are located are a case of their own. Therefore a system of orthogonal ribs abuts the extrados of the dome at the sides of the octagon, which stand on the intermediate partition walls of the matronea and, further below, on the monolithic columns placed alongside the perimeter walls. The columns had independent foundations with respect to the wall perimeter, with which they slightly overlap. It should be added that the transition between the parallel bearing walls of the matronea and the columns is borrowed from transversal stone lintels, whose modest span between the column and external wall prevented them from being damaged. The Y-shaped ribbing corresponds to the corner pillars.

The construction organisation of the partition walls, in terms of their arrangement and dimensions, nevertheless shows considerable originality linked to the architectural structure of the Baptistery. The three entrance doors imposed a greater intercolumniation than the intervals between the columns themselves and the corner pillars. Indeed, in each of the remaining sides the spaces between the piers are essentially the same. On the sides of the matroneum above the entrances the central mullion windows are considerably wider than those beside them. The accentuation of the central mullion window was repeated on the sides without entrances, moving the parallel transversal walls to the outer edge or the wider lintels below resting on columns; this was achieved by the lintels being wider than the partition walls. Whereas, on the sides of the matroneum above the entrances the gap between the central space and the side spaces reduces, moving the partition walls towards the centre of the side (Figure 2). As a result, the pillars corresponding to the partition wall of the matroneum are not in axis with the columns below (Rocchi Coopmans de Yoldy 1996a, p. 45).

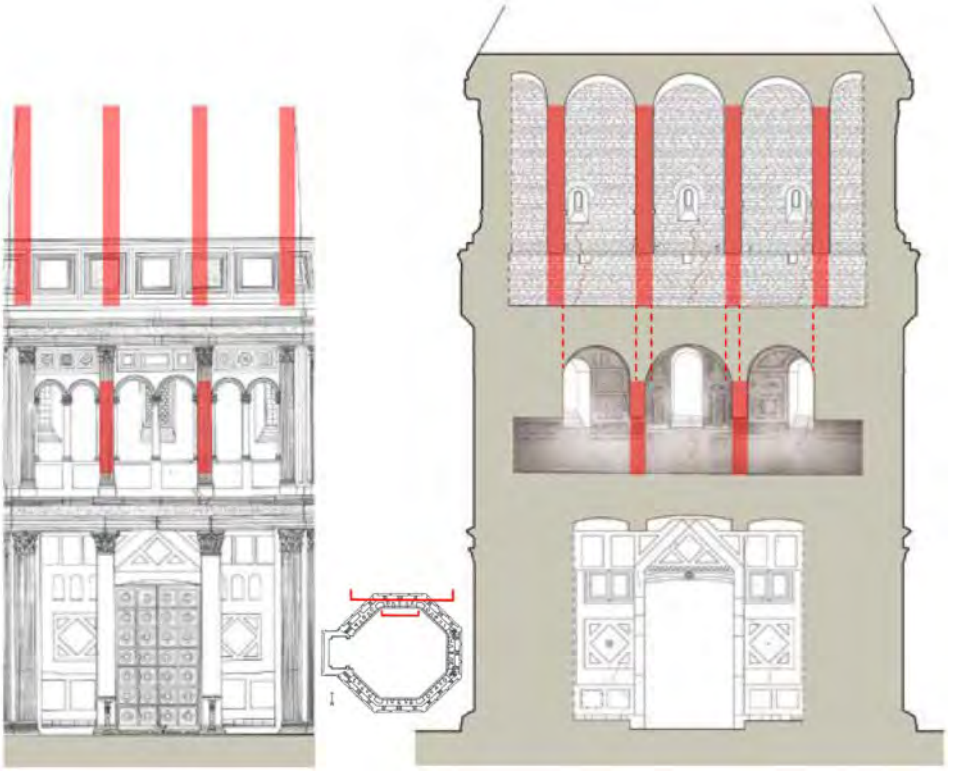

Figure 2. Elevation of the interior north side (left) indicating (in red) the position of the parallel bearing walls; longitudinal section of the north side (right) executed in the intermediate space highlighting the partition walls (in red); the section intercepts the ground floor, the matroneum and the garret.

But these changes in position between structures at different levels are more accentuated in the garret where three compartments of more or less the same width are created on each side (except for the north-west side where the central compartment, with respect to the side ones, is wider by around 30 cm).

Taking the north side into consideration, the two parallel bearing walls of the garrets have an accentuated inward shift, and are positioned outside of the partition walls of the matronea by almost 1/2. The misalignment of the partition walls is borrowed from a sort of wall base which is around 120 cm thick, placed between the transversal barrel vaults of the matronea and the bearing surface of the dome. The difference in the positioning of the structures in this case cannot be visually perceived as it is disguised by the dome, but it is clearly highlighted by the overlapping of the plans and the longitudinal section of the north side. The strong vertical misalignment between the columns and the partition walls is the result of the choice to create three compartments with a similar width close to each side of the dome.

The scarsella side also required specific adaptations, where the continuity of the perimeter wall structure is interrupted. At the base of the dome there are three open windows on each side of the octagon; but on the side above the scarsella it was decided during the works not to complete the two side openings and to infill them (Giorgi & Matracchi 2017). The intention was at least to reinforce the base of the dome, which however exceeded the thickness of the frontal arch of the scarsella. The transverse partition walls and the external perimeter wall completely extended beyond this arch (Giorgi 2004, p. 158). Such impressive structures must not have been placed directly on the vault of the scarsella, but more likely on the relieving arches which rest on the massive adjacent corner pillars of the octagonal perimeter (Figure 3).

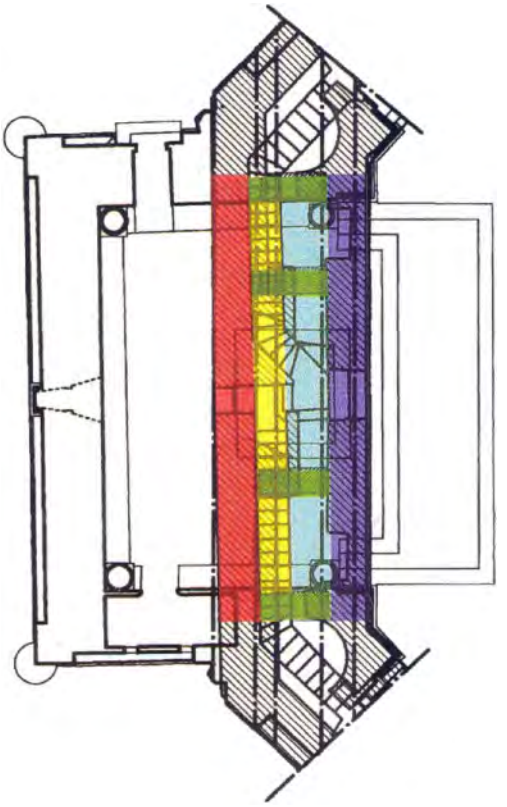

Figure 3. Detail of the plan of the Baptistery with the position of the walls weighing on the vault of the scarsella: the dome (blue), the parallel bearing walls (green), the external wall of the octagonal perimeter (red), (by Giorgi 2004).

Calculation simulations have shown that if the dome had been placed directly on the original vault it would not have been stable due to the small section of this vault (Miceli & Papi 2004). Despite the probable use of reliving arches, the scarsella must have been a vulnerable area from a construction perspective; so the groin vault on columns placed in the corners of the scarsella was added (Figure 4). The geophysical investigations corroborated the existence of two vaults, confirming the use of bricks for the added vault, while the earlier one is made of stone (Morelli 2004).

The further study campaign recently promoted by the Opera di Santa Maria del Fiore produced additional significant cognitive and diagnostic results on different aspects, including some regarding the structures.

The first section of the dome was made with stone ashlars placed in horizontal rows, which with progressive overhangs create the pointed curve of the intrados, while the extrados is vertical (Figure 5). This creates a characteristic reduction of the thickness at the base of the dome: at the springer it is 107 cm, at the summit of the vertical wall it is 130 cm. This level marked the start of a section with offsets on the extrados, until the dome achieves the constant thickness of approximately 103 cm. In the transition zone with wall offsets, the rows of stone start to incline; above, in the north web of the dome, there are small recesses on the extrados which evidence the use of wooden elements used to position the inclination of the rows. The curvature of the intrados established by the centring also generates the inclination of the rows where it is decided to align the rows with the centre, or centres, of curvature of the intrados. This is not the case of the Baptistery dome, where the line of the intrados curve can be distinguished from inclination of the rows.

Figure 4. Transversal partition wall above the scarsella; the crack (in yellow) sealed by vertical plates is visible; the extrados of the dome can be seen on the left.

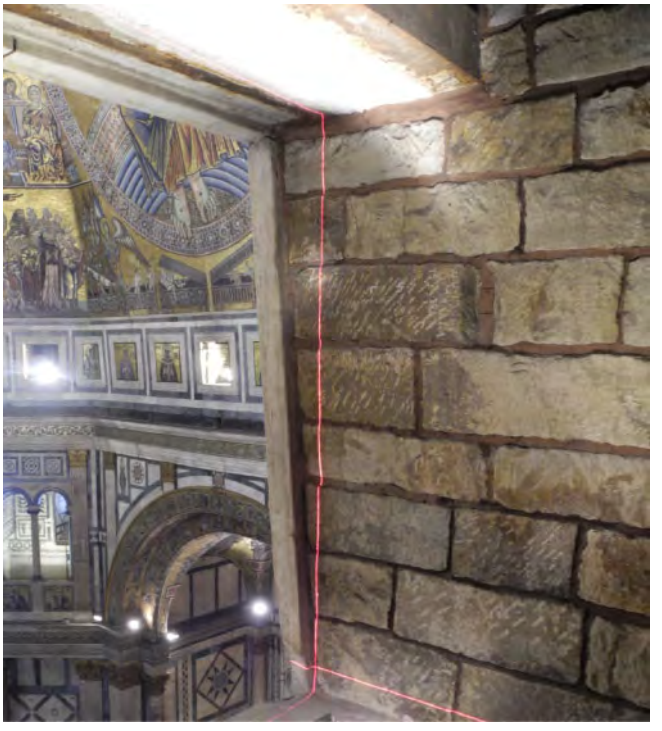

Figure 5. Detail of the dome at the level of the springer. The photo shows the horizontal rows of the masonry positioned with a progressive overhang on the intrados, as shown by the vertical line of the laser.

These latter, in correspondence to the recesses, incline less than the radius of curvature of the intrados of the dome.

The inspection of the top part of the garrets showed that the transversal bearing walls are not adjacent to each other, but are connected with the dome in continuous rows. This results in unique feature: to obtain a better connection between the inclined rows of the dome and the partition

walls, for a stretch the rows of the latter are also arranged on an inclined plane (Figure 6), and then become horizontal again, creating masonry in continuous rows with the external wall of the Baptistery (Giorgi & Matracchi 2017, p. 198).

Figure 6. Detail of a partition wall (right) and the extrados of the dome (left) of the Baptistery; the intersection between the vertical and horizontal red lines of the laser highlight the part of the partition wall with masonry in inclined rows perfectly connected with those of the dome.

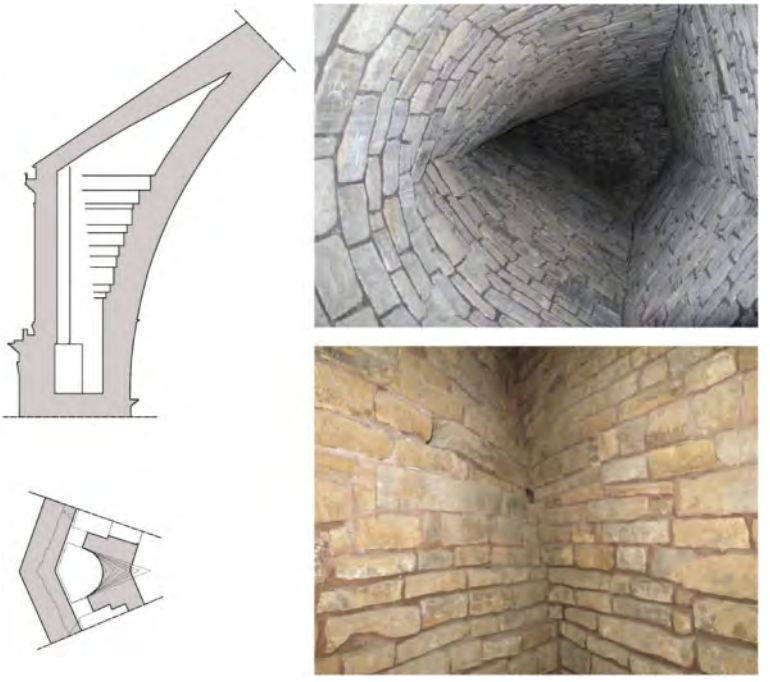

Figure 7. Detail of a corner space at garret level; plan and section with images showing the changes in shape and the continuity of the masonry rows.

The internal wall of the corners of the octagon is shaped as the arc of a circle, a form that follows that of the corners accommodating spiral staircases alongside the east door. In correspondence to the circle arcs of the corners, the thickness of the dome reduces with respect to the sides of the octagon; the dimensions, starting with the south-east side and proceeding in a clockwise direction up to the north-east one, are as follows: 91/90/75/100/89/88 cm. Continuing upwards, the semicircular part becomes triangular, assuming an even more acute angle until creating the Y-shaped fork of the corner ribs. These modifications of the corner spaces are created by maintaining the continuity of the rows for the entire perimeter, except clearly for the base area with the garret crossing points (Figure 7).

The dome, partition walls and external wall therefore create a box structure with continuous rows including the three spaces on each side and the corner compartments. The intention to create a box structure is further confirmed by the fact that this device was extended as far up as possible by means of a constructive expedient created in the corners between the rampant vaults, transversal partition walls and the external wall. The partition walls are covered by stone rampant barrel vaults, on which part of the conical roof of the Baptistery rests, which abut the perimeter wall of the attic. The aim was to prevent the box structure from being interrupted between the partition walls and the external walls at the springer of the barrel vault, in that the radial ashlars of the latter could not have been placed in continuity with the horizontal masonry rows of the lunette of the external wall. Thereby, also exploiting the fact that the vault is rampant, skewed horizontal rows with a progressive overhang were created, which connect to the transversal partition wall and a good part of the edge of the lunette, raising the box structure almost up to the top of the external wall (Figure 8).

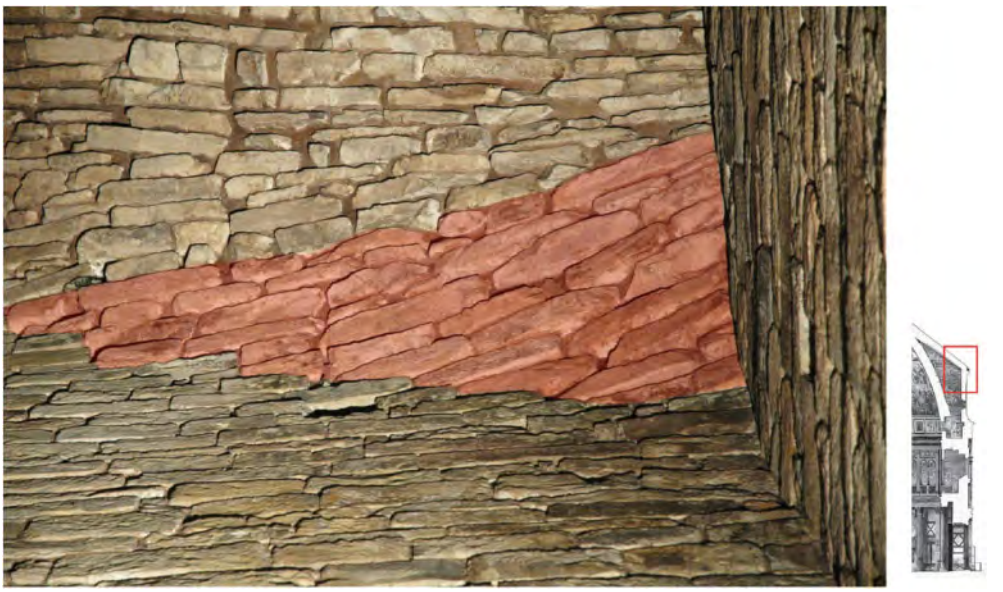

Figure 8. Garret of the Baptistery; detail of the top of the transversal partition wall with the skewed masonry (red) connecting to the edges of the lunette of the outer wall of the attic.

Another distinctive solution linked to the box structure can be found in the external wall: it was reduced to a thickness similar to that of the transversal partition walls (it is just below) and was moved inward creating an overhanging wall offset ending at the bottom with a quarter-circle cornice. The layout with a box structure with symmetrical compartments on each side of the pavilion was pursued with clear intention by the builders, who in order to obtain it had to accept the consequent lack of continuity with the partition walls of the matronea below (Figures 9,10).

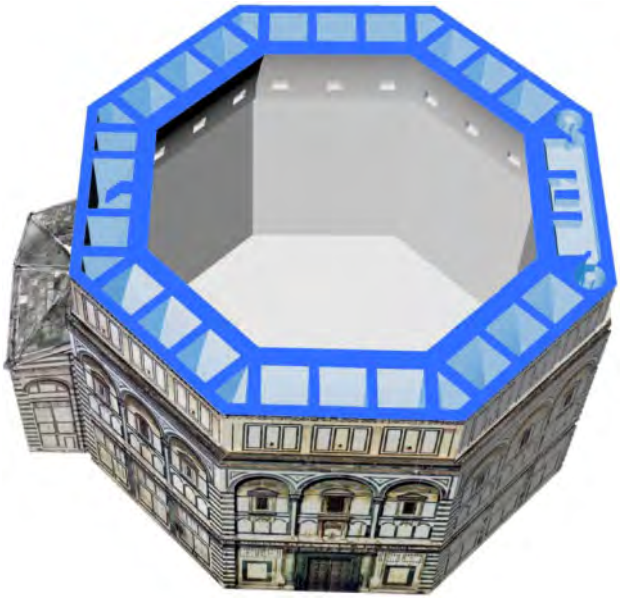

Figure 9. The box structure of the dome at attic level (by Giorgi & Matracchi 2017).

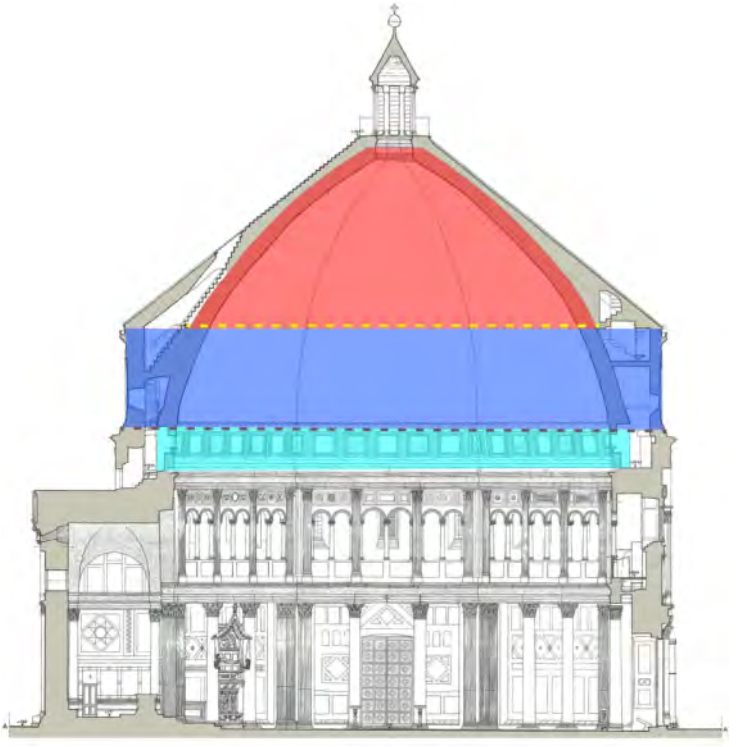

Figure 10. In the dome section the following are highlighted: the first section with horizontal rows (cyan), the box structure part, the final section in brick (red); the wooden tie (yellow dotted line) and the metal tie added in 1514 (brown dotted line) are also indicated (basic drawing Giovannini 1996).

Where the box structure ends, the dome continues with the use of bricks, for the most part salvaged material most likely obtained from the dismantling of the Roman walls of Florence (Giorgi & Matracchi 2017, p. 205). In the transition from the box structure to the single shell structure, a wooden tie is placed along the extrados of the pavilion crossing the transversal partition walls (Figure 11). The original connections visible between the wooden elements show tooth connections with the use of wooden nails. The tests of the state of tension of the wooden tie revealed a modest amount of tensile strength (Negri et al. 2017); the brick dome, with its springer on the inclined row of the stone one, transmits the thrust mainly to the box structure of the stone dome.

Figure 11. The wooden ties intersect at the corners of the octagonal plan of the Baptistery; the image shows the change in material of the dome at the level of the tie: below the masonry is stone, and above brick.

The construction device of the dome is therefore particularly complex. Considering the vertical rise, the stone part and the brick part are almost the same, but if we take into account the surface of the intrados the former would be clearly larger. In the stone part, there are two highly important aspects. The first is the box structure, which extends for 35% of the vertical rise of the dome; the second is the masonry below the box part, which includes an initial section of the dome constructed entirely of horizontal rows and interrupted both by the openings facing onto the inside of the baptistery, and the passages between the compartments of the garret. In view of this construction aspect, the position of the wooden tie at the base of the brick dome formed of a single shell appears justified.

The identification of the box structure profoundly changes how we consider the construction concept of the dome of the Baptistery, which until recently was considered to be a pavilion reinforced by transversal bearing walls, and allows us to understand more fully the position and extent of the system of cracks that has formed.

The dome has limited and essentially stable cracks; this is also due to the metal tie added in 1514 in the wall offset at the base of the attic level (Blasi et al. 2017, pp. 124–125). This tie is highly effective given that it is positioned at the base of the box structure. Moderate traces of cracks have been found in the corners of the intrados of the dome, up to 1-2 cm wide, which are barely visible

in the mosaics where they are hidden by plaster, and more evident in the band of the medallions of the saints close to the springer of the dome, where deviations can be observed between the slabs of the stone cladding (Blasi et al. 2017, p. 120).

The masonry masses of the structure below the dome reduce a great deal on the inner sides of the Baptistery, where there are columns on the ground floor and mullion windows on the matroneum level. It should be noted that the partition walls of the garret are at times strongly misaligned with those of the matroneum, as on the north side. It is no surprise that these construction features together have resulted in the largest cracks in the matroneum area (Figure 12).

More extensive cracks have been observed in particular in the sides of the entrance door (up to 4–5 cm wide). On the inner side of north wall of the matroneum there is a highly visible vertical crack, which has been repaired with brick fragments and extends to the barrel vault above and the wall abutting the mullion window. The small column of the mullion window itself in turn generates a crack in the lintel below supported by columns (Giovannini 1996). On the outer sides clad in marble the cracks have been repaired by inserting marble plugs which restore the continuity of the horizontal cornices (Blasi et al. 2017, pp. 121–122).

The first pioneering modelling of the dome of the baptistery with the calculation of the elements dates back to the mid 1990s (Blasi & Papi, 1996). The topic was addressed there after several times with increasingly refined numerical mode salso thanks to the recentavailability of an accurate laser scanner survey (Bartoli et al. 2017). It would be very interesting and appropriate to further characterise the behaviour of the dome with modelling that takes into account the box structure of the dome. It would be just as useful to check the possible effects caused by the vertical misalignment of the partition walls, considering in particular the displacements between the transversal bearing walls of the box part of the dome and those below of the matroneum.

Figure 12. Detail of the outer wall of the north side of the attic; the obvious repaired crack is shown (in red) (by Giovannini 1996).

3 SHARED CHARACTERISTICS OF THE BAPTISTERY DOME AND BRUNELLESCHI'S DOME

For Brunelleschi, the Baptistery dome was an object to study and consider in order to develop construction solutions for the much larger dome of Santa Maria del Fiore. Several construction

solutions shared by the two buildings have been observed, such as the use of stone in the lower part and then continuing with brick; the wooden tie revived with anchoring in the ribs; the use of two intermediate ribs in each web of the pavilion. Moreover, the roof partly resting on the rampant vaults of the baptistery could have suggested the creation of a double shell dome (Rocchi Coopmans de Yoldy 1996b).

Leaving aside the many and complex aspects linked to the brick masonry structure of Brunelleschi's dome, the strengthening of the connection between corner ribs and intermediate ribs by means of sub-horizontal arches is a significant innovation (Figures 13,14). The corresponding portion of the external ribbed dome is also strengthened by these sub-horizontal arches. To make the cohesion between such elements more effective, the sub-horizontal arches are made up of a segmental arch in vertical bricks to support the bricks arranged in a homogeneous position to that of the bricks of the ribs and of the external dome (Giorgi & Matracchi 2018). It still needs to be ascertained whether the solution of the sub-horizontal arches with variable sections (larger on the corner ribs side) also arises from the need to conceal the metal ties positioned in the external area of the ribs; indeed, a 24-sided polygonal tie could have had sections transversal to the corner ribs arranged partly inside the sub-horizontal arches (Figure 15). In any case, the corner areas of the pavilion of the dome of Santa Maria del Fiore are a clear construction innovation which creates a unitary system consisting of corner ribs, intermediate ribs and sub-horizontal arches (Rocchi Coopmans de Yoldy 2006).

However, perhaps the most significant constructive aspect that Brunelleschi could have taken from the dome of the Baptistery lies behind all of this. Reference is made to the box structure of the stone part, which Brunelleschi reworked with a double dome, intermediate ribs and stiffening arches close to the corners that reinforce the connection between adjacent ribs and at the same time innervate the external dome (0.80 m thick) which is much thinner than the internal one (about 2 meters thick) (Figure 16).

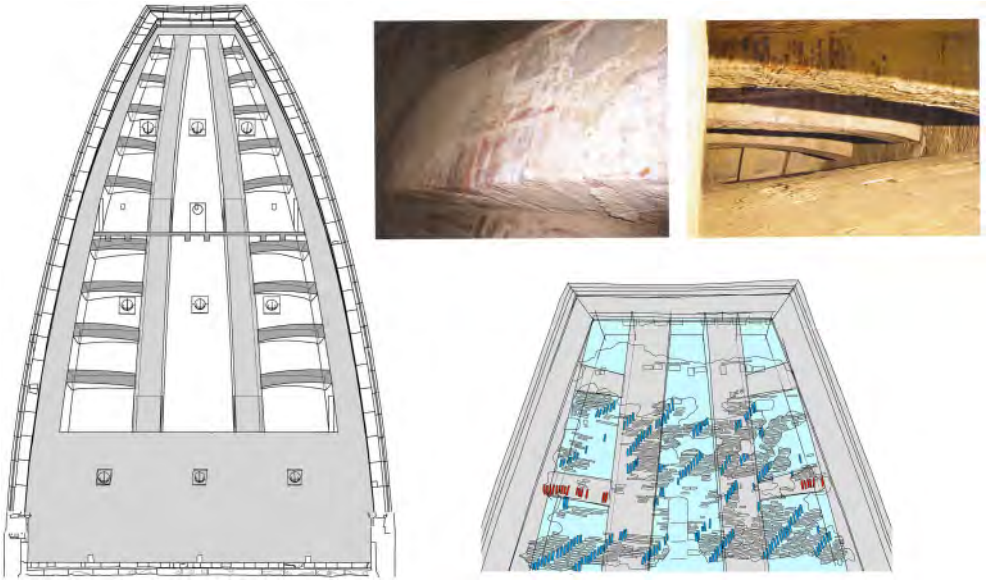

Figure 13. N-NE web of the dome of Santa Maria del Fiore highlighting the ribs and corbel-arches; (left), survey of the masonry structure of the NE outer dome highlighting the bricks (in red) of the corbel-arches placed vertically; (top right) details of corbel-arches with vertical bricks visible in the lower part (by Giorgi & Matracchi 2006).

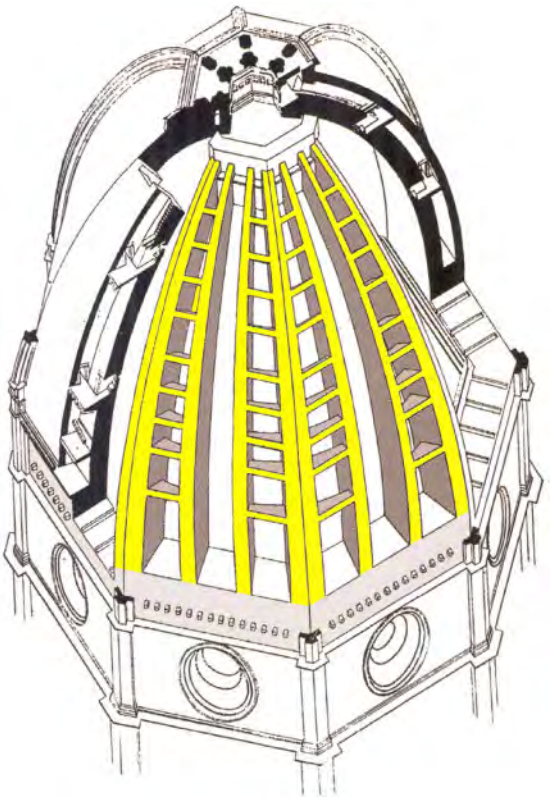

Figure 14. Axonometric diagram of the dome of Santa Maria del Fiore highlighting the connections between the corbel-arches and ribs (by Coompans de Yoldi 2006).

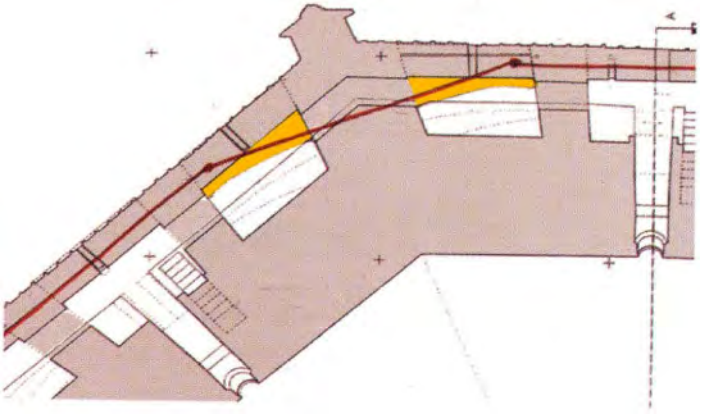

Figure 15. Excerpt of a plan of the dome with the corner ribs, intermediate ribs and corbel-arches (in yellow); hypothesis of a tie (in red) placed transversely to the corner ribs and corbel-arches.

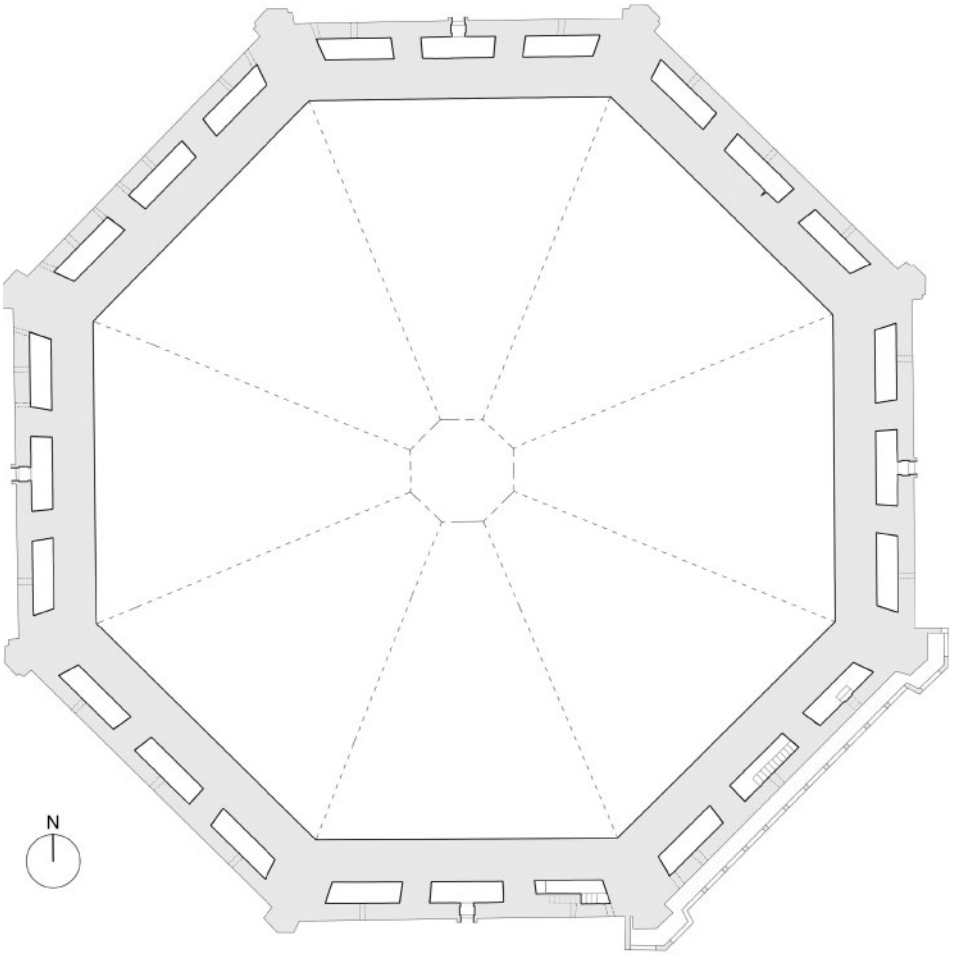

Figure 16. The plan of the Brunelleschi's dome shows the box structure formed by the inner dome, ribs and the outer dome.

4 CONCLUSIONS

The cognitive approach to the buildings should seek to understand their specific features, which are almost never self-evident, without making generalisations, simplifications, or assuming pre-conceived ideas that could place our vision of the construction device far from reality, in a (perhaps refined) metaphysical dimension.

The mere geometric form, even if based on highly detailed surveys, should be considered an indispensable but not exhaustive tool. In order to understand the actual construction elements it is necessary to identify and interpret the construction activities in the context of the construction site practices, or the construction sites that followed one another over time, considering the consequent specific operating methods and the choices made in the production and installation of the materials used. The construction site is a place par excellence of architectural experimentation, where the countless possible options reach executive synthesis. And this is not exempt from rethinking, adaptations and sometimes contradictory choices.

In the case of the Baptistery of Florence, there was no shortage of adaptations on the scarsella side, where the continuity of the octagonal perimeter wall is interrupted. A further vault was therefore added to the scarsella space and, on this same side, a decision was made during the works to close some openings which at the base of the dome would have alternated with mosaics depicting saints. The vertical misalignments between the transversal partition walls on different levels are no less significant, in particular between the mezzanine level and the garret, due to determining architectural choices and the decision to create compartments of a similar width on each side at the base of the dome.

It is customary for an ancient building to be made up of a complex system of construction layouts, which reflect the complexity of the construction history, with conditions of possible local vulnerability. This is made even more complex by the long timeframe of ancient architecture, which introduces further variables as a result of successive transformations, sudden external factors such as earthquakes, or the degradation of the materials themselves.

Knowledge of complex ancient buildings is almost always recognised as a process. This is well exemplified by the identification of the box structure in the stone part of the dome of the Baptistery of Florence, which today provides us with a profoundly different construction concept than the one considered until recently. This finding also has obvious repercussions in the interpretation of Brunelleschi's dome, which in turn is entirely recognised as a box structure with an outer dome innervated by sub-horizontal arches close to the corners of the octagonal pavilion. The recurring interpretation difficulties posed by the construction layouts of the architecture therefore require due caution in making diagnostic interpretations and in the consequent conservation projects, which could be based on reductive or even misleading information.

REFERENCES

Aminti, P. 1996. Rilievo e determinazione della curvature della cupola, analisi sui rapporti dimensionali tra principali elementi strutturali interni, in Giuseppe Rocchi Coopmans de Yoldy (ed.), *S. Maria del Fiore. Piazza*, *Battistero*, *Campanile*, Firenze, Il Torchio, p. 104.

Bartoli et al. 2017. Bartoli G., Betti M., Monchetti S., Modellazione numerica ed analisi strutturale del Battistero di San Giovanni a Firenze, in Francesco Gurrieri (ed.) *Il Battistero di San Giovanni*. *Conoscenza*, *Diagnostica*, *Conservazione*, Firenze, Mandragora, pp. 135–157.

Blasi C. & Papi R. 2004. Geometria e struttura, in Giuseppe Rocchi Coopmans de Yoldy (ed.) *S. Maria del Fiore*. *Piazza*, *Battistero*, *Campanile*, Firenze, Il Torchio, pp., 125–127.

Blasi et al. 2017. Blasi C., Ottoni F., Coïsson E., Tedeschi C., Battistero di San Giovanni in Firenze. Note su dissesti, lesioni e catene, in Francesco Gurrieri (ed.) *Il Battistero di San Giovanni*. *Conoscenza*, *Diagnostica*, *Conservazione*, Firenze, Mandragora.

Choisy A. 1899. Histoire de l'architecture, Paris, Gauthier-Villars, T. II, p. 602.

Degl'Innocenti P. 2017. Misurare, disegnare, conoscere: dai rilievi del San Giovanni alle ipotesi storico costruttive, in Francesco Gurrieri (ed.), *Il Battistero di San Giovanni*. *Conoscenza*, *Diagnostica*, *Conservazione*, Firenze, Mandragora, pp. 90, 96.

Durm J. 1887. *Die Domkuppel in Florenz und die Kuppel der Peterskirche in Rom*: *zwei Grossconstructionen der italienischen Renaissance*, Berlin, Ernst & Korn, plate II.

Fondelli, M. 2004. La Cupola di Santa Maria del Fiore. Antiche testimonianze e nuove ricerche sperimentali, in Giuseppe Rocchi Coopmans de Yoldy (ed.), *S*. *Maria del Fiore e le chiese fiorentine del Duecento e del Trecento nella città delle fabbriche arnolfiane*, Firenze, Alinea Editrice, pp. 343–358.

Giorgi, L. 2004. Il sistema voltato del Battistero, in Giuseppe Rocchi Coopmans de Yoldy (ed.), *S*. *Maria del Fiore* e *le chiesefiorentine del Duecento e del Trecento nella città delle fabbriche arnolfiane*, Firenze, Alinea Editrice.

Giorgi L. & Matracchi P. 2006. Santa Maria del Fiore, facciata, corpo basilicale, cupola, in Giuseppe Rocchi Coopmans de Yoldi, *S*. *Maria del Fiore*. *Teorie e storie dell'archeologia e del restauro nella città delle fabbriche arnolfiane*, Firenze, Alinea Editrice, pp. 316–317.

Giorgi & Matracchi 2017. Le murature a cassone alla base della cupola del battistero e altri aspetti costruttivi, in Francesco Gurrieri (ed.) *Il Battistero di San Giovanni*. *Conoscenza*, *Diagnostica*, *Conservazione*, Firenze, Mandragora.

Giorgi L, & Matracchi P. 2018. I mattoni del Brunelleschi. Osservazioni sulla Cupola di Santa Maria del Fiore, in *Costruire in laterizio*, 2018, 176, pp. 53–61.

Giovannini, P. 1996. L'apparecchio murario e il rivestimento interno del piano terra e del matroneo. Materiali, tecniche di lavorazione e caratteristiche di messa in opera, in Giuseppe Rocchi Coopmans de Yoldy (ed.) *S. Maria del Fiore*. *Piazza*, *Battistero*, *Campanile*, Firenze, Il Torchio, pp. 87–89.

Matracchi, P. 1992. *La chiesa di Santa Maria delleGrazie al Calcinaiopresso Cortona e l'opera di Francesco di Giorgio,*Cortona, Calosci, pp. 18–19.

Miceli E. & Riccardo Papi R. 2004. Sulla statica del battistero alla luce delle nuove indagini e delle interpretazioni dei dati sperimentali, in Giuseppe Rocchi Coopmans de Yoldi (ed.) *S. Maria del Fiore e le chiese fiorentine del Duecento e del Trecento nella città delle fabbriche arnolfiane*, Alinea Editrice, Firenze, pp. 177.

Morelli A. 2004. Indagini geofisiche non invasive sulla volta della scarsella del Battistero, in Giuseppe Rocchi Coopmans de Yoldi (ed.) *S. Maria del Fiore e le chiese fiorentine del Duecento e del Trecento nella città delle fabbriche arnolfiane*, Alinea Editrice, Firenze, pp. 167.

Negri et al. 2017. Negri M., Fellin M., Ceccotti A., I legni della cupola del Battistero, in Francesco Gurrieri (ed.) *Il Battistero di San Giovanni*. *Conoscenza*, *Diagnostica*, *Conservazione*, Firenze, Mandragora, pp. 170–173.

Pietramellara C. 1973.*Battistero di S. Giovanni a Firenze*, Firenze, Polistampa, pp. 20–21, 33.

Pisetta, C. & Vitali G. M. 1996. Nuove acquisizioni sul tabernacolo di Andrea Orcagnaattraverso il rilievo interpretativo, in Diane Finiello Zervas (ed.), *Orsanmichele a Firenze*, Modena, Franco Cosimo Panini, p. 382.

Rocchi Coopmans de Yoldy, G. 1996a. Il Battistero di San Giovanni. Lo svolgimento della fabbrica, in Giuseppe Rocchi Coopmans de Yoldy (ed.) *S. Maria del Fiore*. *Piazza*, *Battistero*, *Campanile*, Firenze, Il Torchio, pp. 43, 47–48.

Rocchi Coopmans de Yoldy G. 1996b. Brunelleschi e il Battistero, in Giuseppe Rocchi Coopmans de Yoldy (ed.) *S. Maria del Fiore*. *Piazza*, *Battistero*, *Campanile*, Firenze, Il Torchio, pp. 64–65.

Rocchi Coopmans de Yoldy G. 2006. Il cantiere del complesso di Santa Maria del Fiore dall'epoca arnolfiano-giottesca a quella brunelleschiana, in Giuseppe Rocchi Coopmans de Yoldi (ed.)*S. Maria del Fiore e le chiese fiorentine del Duecento e del Trecento nella città delle fabbriche arnolfiane*, Alinea Editrice, Firenze, p. 265.

Trattati di architettura 1967. *Trattati di architettura, ingegneria e arte militare*/Francesco di Giorgio Martini, Corrado Maltese (ed.), Livia Maltese Degrassi (tr.), Milano, Edizioni il Polifilo, T. I, p. 92.

Geotechnical Engineering for the Preservation of Monuments and Historic Sites III – Lancellotta, Viggiani, Flora, de Silva & Mele (Eds)

Understanding the mechanical history of the burial monument of the Kasta tumulus at Amphipolis, Greece: A tool for documentation and design of restoration strategy

D. Egglezos
Geoper S.A. Heraklion, Crete, Greece

ABSTRACT: This paper provides an interpretation of the historical pathology of the Kasta burial monument in Amphipolis, Greece. The main goal is the documentation of its mechanical history, i.e. the recognition and interpretation of mechanical events which have left an imprint (damage) on the structure of the monument, via appropriate geostatic analyses at historical stages linking the damage to a sequence of specific mechanical causes (correlation with cause and time sequence of mechanical events). Mechanical historical analyses require data on changes in the geometry of the monument (building phases), changes in the strength of building materials (e.g. ageing), and significant mechanical stresses from the external environment (earthquakes, landslides, etc.) deriving from a variety of scientific fields. This type of analysis highlights the vulnerabilities of a monument's design and allows a reliable estimate of its response to future charges, constituting a powerful tool for taking appropriate protection and restoration measures.

1 INTRODUCTION

From the engineer's point of view, standing monuments are a very interesting case. The cumulative effect of the physical and mechanical events that have affected them during their long history is reflected in their current form and state of preservation. Their image is a "mechanical" historical chronicle, in symbolic "mechanical" script, with "ideograms" in the form of structural damage (fractures, cracks, loss of mass, permanent displacements, etc). For the engineer who undertakes the design of the protective measures and the planning of the restoration of the monument, the above data set as a basic scientific challenge the reading (decryption) of the monument's mechanical history with a double aim: on the one hand the documentation of the history of the monument and on the other the substantial understanding of its mechanical function as a basic condition a) for highlighting of any vulnerabilities and b) designing appropriate measures for its protection and/or restoration.

More specifically, in the context of the present paper, the identification and the interpretation of the mechanical stress (historical pathology) of the burial monument of the Kasta tomb of Amphipolis, Serres, is attempted. The main goal is the documentation of its mechanical history, ie the recognition and interpretation of mechanical events with an imprint (damage) on the structure of the monument. Through this process, an attempt is made to highlight the vulnerabilities in the ancient design of the monument and the (new) design of its long-term protection through effective restoration proposals.

The burial monument of the Kasta tomb is a very interesting case of a complete standing monument. Until its discovery it was completely unknown both archaeologically and historically.

At the present stage, the monument is in the process of documentation, implementation of protection measures and planning of restoration interventions for its presentation to the public. In

DOI 10.1201/9781003308867-9

light of the above, reading its mechanical history is the cornerstone of the development of a rational restoration policy.

2 THE BURIAL MONUMENT

2.1 *The discovery*

The burial monument in the Kasta tumulus in Amphipolis is part of a monumental complex that consists of the tumulus itself, a significant geotechnical work of antiquity, discovered by archaeologist D. Lazarides (1964), its imposing retaining wall almost 500m in circumference (Lazarides 1965; Lefantzis 2014), the burial monument and the surviving part of the foundation of a structure on the top of the tumulus which is interpreted as a burial marker or *sema,* (Lazarides 1972; Lefantzis 2013), located approximately 30 meters above the base of the tumulus (Figure 1). The burial monument extends along a chord of the circular plan of the tumulus. The original terrain in which the monumental complex was built consisted of two hills divided by a col. The ancient construction work made use of these two hills to create the extensive circular tumulus with the minimum fill (Syrides et al. 2016, 2017).

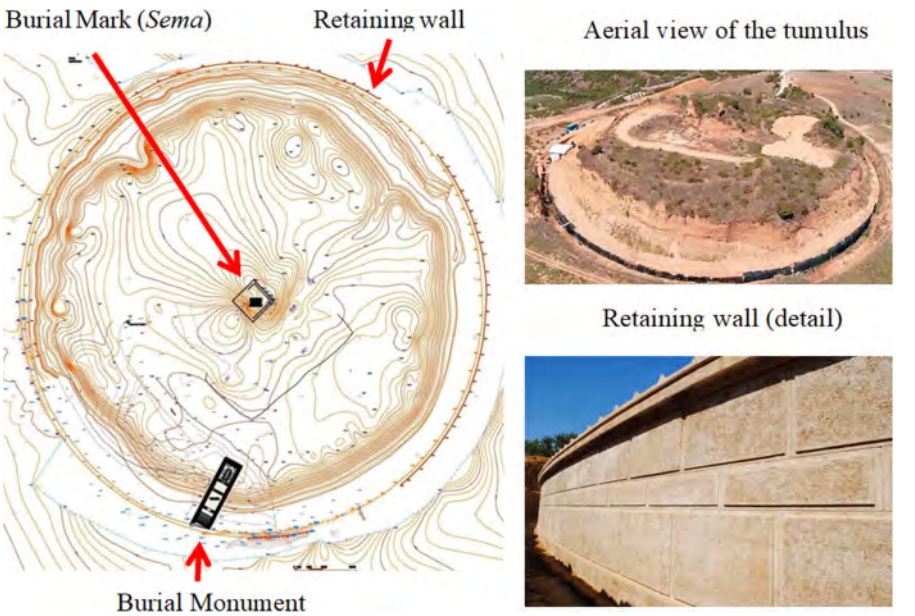

Figure 1. The Kasta tumulus monumental complex.

The monument (Figure 2) came to light during relatively recent archaeological excavations in the area of the Kasta tomb, as part of the excavation activities of the Ephorate of Antiquities of Serres in August 2014, under the supervision of archaeologist Katerina Peristeri. The process of uncovering all the areas of the burial monument was a complex technical work which was assigned to the author by the competent Ephorate of Antiquities and implemented during the period September – November 2014. The uncovering required the archaeological excavation of the exterior and particularly the interior of the monument, which lasted until mid-November 2014. Alongside the excavation, the temporary internal consolidation of the monument was carried out; this was completed in late December 2014.

During the course of the excavation, there were continuous on-site updates of the mechanical documentation of the monument (geometry, structure, materials and properties). An instrumental

monitoring system set up for this purpose also produced useful data. It should be noted that a temporary shelter was erected to protect the burial monument during its excavation.

Figure 2. The entrance of the burial monument during the excavation (2014).

2.2 *Description of the monument*

The monument, of the barrel-vaulted Macedonian tomb type, consists of four distinct spaces (X1-X4) delimited by four partition walls (D1-D4) (Figures 3 and 4):

1. First space (X1): This is the antechamber of the monument, with vertical parallel walls and a staircase (which also functions as an internal support) descending to the level of the floor of the vaulted structure. The antechamber of the monument starts from the crown of the retaining wall.
2. Wall of the Sphinxes (D1): This separates the antechamber from the first chamber of the vaulted monument (X2). It consists of an opening flanked by pillars with an entablature. The pillars support a horizontal beam that forms the horizontal base of the statues of two sphinxes facing each other. Recent investigations into the structure of the pillars of Wall D1 show that they are fake walls hiding the supports inside (Lefantzis 2019).
3. Second space (X2): This is the first chamber of the monument, approximately 6.0m long. It extends from the Wall of the Sphinxes to the Wall of the Maidens.
4. Wall of the Maidens (D2): This separates the first chamber of the monument from the second (X3). It consists of an opening framed by two marble pedestals supporting two statues of maidens (korai), a pillar and an entablature. Above the entablature, a transverse wall (tympanum) of poros stones has been erected, in contact with the vaulted roof. On the west side of the transverse wall is an opening, resulting from the deliberate removal of stone blocks in antiquity.
5. Third space (X3): This is the second chamber of the monument, approximately 3.0m long, which has a smaller internal opening (approximately 4.30m). It extends from the Wall of the Maidens to the Wall of the Marble Door. It has a mosaic floor depicting the abduction of Persephone by Pluto, god of the underworld.
6. Wall of the Marble Door (D3): This separates the second chamber (X3) from the third (X4). It consists of an opening for the marble door between two pilasters, each formed of two adjoining

rectangular pieces of marble, with an entablature. Above the entablature is a tympanum of poros stone blocks, in contact with the vaulted roof. On the west side of the tympanum is a small rectangular hole, resulting from the deliberate removal of stone blocks in antiquity.

7. Fourth space (X4): This is the third chamber of the monument, approximately 6.0m long, with an internal opening measuring approximately 4.50m. The floor of the monument consists of poros stone blocks, while in its central part there is a deeper artificial trench, measuring approximately 4.0 X 2.10m and about 3.0m deep. The trench contains a cist grave. The geostatic investigation by the author has shown that the trench for the cist grave predated the construction of the monument and largely determined its longitudinal axis (Egglezos 2016).
8. End wall of the monument (D4): This is the north external transverse wall, which separates the fourth chamber from the external transitional embankment. Thorough architectural documentation of the structure and construction phases of the burial monument is presented in the corresponding architectural study.

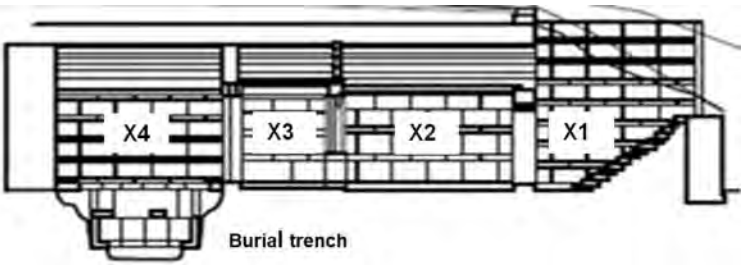

Figure 3. Longitudinal view of the burial monument and the burial trench (Drawing M. Lefantzis).

2.3 *Static function of the monument*

The construction of the monument is intended to support the external (vertical and lateral) geostatic loads from the soils of the transitional lateral embankment and the natural soil on the one hand, and from the overlying fill forming the tumulus on the other. To this end, the side walls act as gravity walls of suitable thickness to bear horizontal earth pressure, supported in places by partition walls and further stabilized by the oblique load transferred to their crown by the arch. The arch is a typical archway of voussoirs (which are in compression due to the pressure each exerts on the other), transferring the mainly vertical geostatic load and the self-weight to the crown of the side walls. As a structure, it is stabilized by the external load of the earth, provided of course that the size of the geostatic load does not exceed the limit of the compressive strength of the vault material, and that support on the vertical side walls is ensured.

The foundation of the monument can be considered as a continuous foundation, of insufficiently documented thickness, set on well-compacted fill which lies on the highly stiff natural soil (dense silty sand) and can safely bear high vertical pressures and reduce settlement to acceptable limits. The floor of the monument (Chambers X2 and X3) also functions, to some extent, in a stabilizing way as a continuous slab, since it consists of hard foundation mortar and gravel, which helps to prevent the internal convergence of the side walls. An exception is the floor of Chamber X4, which is differentiated due to the cist grave.

3 IMPORTANT CONSTRUCTION AND MECHANICAL DATA

For an in-depth understanding of the mechanics of the burial monument, its structural features should be taken into account: these relate to the bonding of its individual parts, the use of the monument in ancient times, the sealing and the internal anthropogenic fill in a later historical

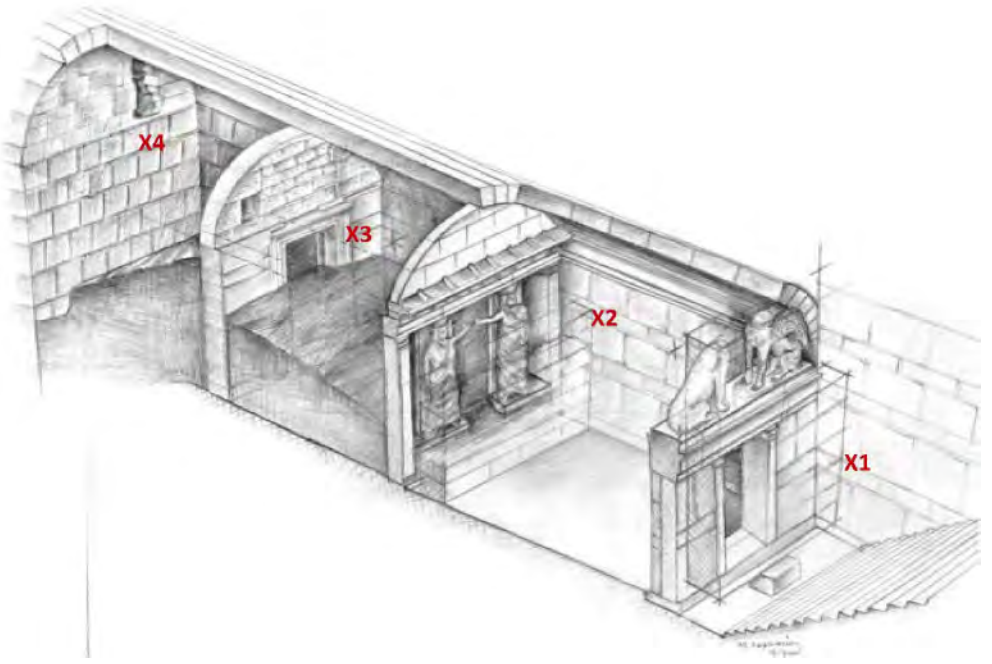

Figure 4. Perspective view of the burial monument. Drawing made during the excavation by M. Lefantzis.

period, and the discovery of metal joints in the marble blocks of the walls and in the vault of the arch. These issues are examined below:

3.1 *Bonding*

The following observations can be made regarding the bonding of the transverse walls with the main structural parts of the monument (walls and arch):

- The possible bonding of partition wall D1 with the longitudinal walls and the vault of Chamber X2 is unclear (Lefantzis 2019).
- Partition wall D2 is bonded with the longitudinal walls through the architrave, and with the arch through the tympanum. The bonding of the wall with the vaulted roof, according to M. Lefantzis, took place at a later construction phase.
- The front of partition wall D3 (marble door pillars) is bonded with the marble revetment of Chamber X3 and connected to the entablature of wall D2 through the surviving slab roof. The rear of the wall (initial phase) is engaged with the longitudinal walls of Chamber X4.

3.2 *Metal joining elements*

Metal joining elements are widely used both in the side walls and in the vault. This reinforcement may reflect the early period of construction of the burial monument (which is dated by the excavator to the last quarter of the 4th century BC, Peristeri 2016) and the concern of the ancient engineer for the stability of the structure.

A further fact worth noting is the great length of the vault (approx. 20m), with a relatively large internal opening (4.50m) between the side walls, and the strong geostatic shear load from the fill of the particularly extensive mound.

The voussoirs are longitudinally connected by lead-coated cast-iron dowels of rectangular cross-section (indicative dimensions, according to Lefantzis 2019: width x height x length = 2.5x7.5x14cm). The marble structural parts of the walls of the monument are also connected horizontally with metal joints. The use of metal joining elements is documented in other vaulted Macedonian monuments (Zambas 2016).

3.3 *Internal fill*

During its excavation, the monument was found to be full of anthropogenic fill in well-formed layers, consisting of relatively loose silty sand. The level of the fill varied along the length of the monument:

- Spaces X1 and X2 are/were completely filled
- Chamber X3 is/was largely filled
- X4 contained a moderate amount of fill (sloping surface from the crown of transverse wall D3 to the middle of Wall D4)

In addition to the fill, the monument was sealed by two sealing walls of poros stone, one at the entrance of Chamber X2 (in front of Wall D1 with the Sphinxes) and the other at the entrance of Chamber X3 (in front of Wall D2 with the Maidens). The sealing walls were dismantled during the work of uncovering the interior of the monument.

3.4 *Use of the monument:*

Systematic construction phases, structural damage and ancient repairs are observed, indicating systematic use before its final filling.

3.5 *Documented construction phases*

The burial monument in the Kasta tomb, according to architect M. Lefantzis (2019), includes characteristic historical building phases, associated with the mechanical history of the monument. A detailed analysis of the construction phases is presented in the architectural documentation study. The main building phases from its construction until its recent archaeological discovery can be summarized as follows:

3.5.1 *Pre-existing phase of the burial monument*

Construction of the cist grave in Chamber X4 (the cist grave predates the burial monument, into which it was then incorporated, Egglezos 2016). The time interval between the construction of the cist grave and the construction of the vaulted monument has not been clarified at present (whether it is a question, for example, of months or a century).

3.5.2 *Main construction phase*

3.5.2.1 Initial construction

i. Construction of the burial monument with the four spaces (X1-X4) using the cut and cover system: Space X1 is covered by a porch or portico, while Chambers X2-X4 are roofed with a continuous vault. The monument seems to have remained open (unfilled) to human presence, as indicated by ancient repairs in various places inside.
ii. Wall D1 consists of the entablature with the sculptures of the sphinxes which stand on a (currently undocumented) form of support.
iii. The tympanum of Wall D2 has probably not yet been constructed (Lefantzis 2019).
iv. In Chamber X3 the marble revetment of the side walls has not yet been constructed.
v. In Wall D3 the marble door has not been constructed for the sealing of Chamber X4.

3.5.2.2 Significant internal building modifications after the initial construction. It is not yet clear when these were implemented.

vi. The fake walls (pillars) are created to cover the columns in Wall D1.
vii. The tympanum of Wall D2 is constructed.
viii. Marble revetment is applied to the side walls of Chamber X3.
ix. Wall D3 is modified for the installation of the marble door.
x. An internal roof covering of Chamber X3 is constructed, using four parallel rectangular marble slabs supported on the entablature of Walls D3 and D2.

3.5.2.3 Significant internal anthropogenic damage. It is not yet clear when this occurred.

xi. the marble door and the floor around the perimeter of the burial case are destroyed
xii. the burial case is excavated/looted in antiquity before the inner filling.

3.5.2.4 Filling – sealing of the burial monument (Figure 6) The time at which it occurred has not yet been documented.

xiii. Holes are pierced in the west parts of the tympana in Walls D2 and D3
xiv. The roof slabs in Chamber X3 are destroyed (except the west one, which bridges the gap between the holes in the entablatures of D2 and D3)
xv. The spaces of the burial monument are filled with an increasing surface level of fill from the interior of the monument to its entrance.
xvi. Two internal sealing walls (partitions transverse to the longitudinal axis of the monument) are constructed in front of Walls D2 and D1 (Figure 5a).
xvii. The area outside the entrance is filled. The monument and (locally at least) the retaining enclosure are concealed

Figure 5. a. The Wall of the Maidens, as found, before the dismantling of the sealing wall, b. detail showing the vertical fracture in the west Maiden.

3.6 *Preservation status – structural damage to the burial monument*

The structural damage to the monument falls under two headings: a) changes to the original geometry of the monument, and b) damage due to the exceedance of the characteristic strength (compressive, tensile, shear and/or a combination of the above).

The damage is connected to the actions that caused it using a computational methodology including geostatic soil - structure interaction analyses in different stages of mechanical history. The main damage to the burial monument can be summarized as follows:

3.6.1 *Fractures – Cracks:*

- Fractures with loss of mass in voussoirs of the vault in Chambers X4 and X3, in characteristic longitudinal zones: western and eastern axis of the burial monument (Figure 6).
- Cracks, with virtually no mass loss, in voussoirs in Chamber X2.
- Fractures in the marble of the side walls of Chambers X3 and X4 and Wall D4, and cracks in the walls (especially the west wall) and the vault of Chamber X2. The phenomenon appears with increasing intensity and frequency from Chamber X2 to Chamber X4 (Figure 6).
- Vertical fractures in the central part of the horizontal beams of the entablature of Walls D1, D2 and D3 of the burial monument (architraves, lintels, etc.) (e.g. Figure 5a).
- Vertical fractures in the heads of the Maidens of Wall D2 (which support the overlying architrave). In particular, the front part of the head of the east Maiden has been completely cut off from the face, while the west head has extensive fractures in vertical planes and is preserved thanks to the binding applied during its uncovering (Figure 5b).
- Fractures in the lower part of the external pilasters and the walls of the front part of Wall D3.
- Systematic vertical cracks of the strong plaster mortar of entrance area X1, located symmetrically on the walls of this space. These fractures extend from the surviving crest to the point where the vault begins.
- Presumed fractures and detachment of the plaster mortar of the intrados of the arch, as a result of geometric deformations of the vault.

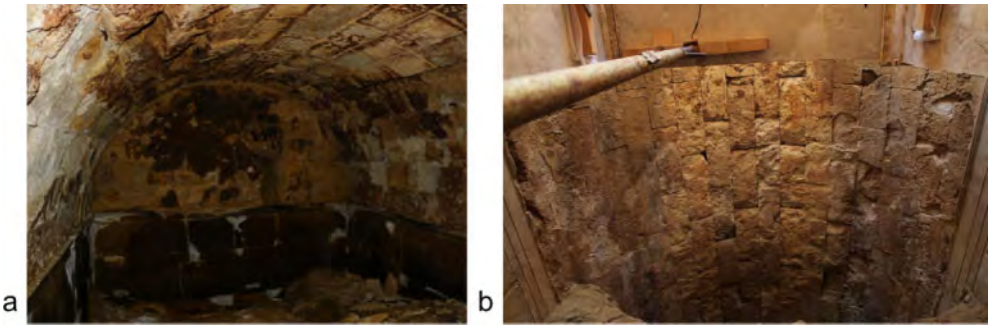

Figure 6. Structural damages to the voussoirs and walls of chamber a. X4, b. X2.

3.6.2 *Geometrical changes – permanent displacements:*

- Convergences and wall distortions: all the vertical side walls show a curvature in both the horizontal and in the vertical plane, towards the inside of the burial monument (plate function). The phenomenon occurs with increasing intensity from Chamber X2 to Chamber X4.
- Rotation of the partition walls: there is a strong rotation of D2 and the front (south) part of D3 (towards the entrance), which dates to a later construction phase (Lefantzis 2019). Wall D3 is in contact with D2 through the surviving roof slab (the roof is assumed to have initially consisted of four slabs, Lefantzis 2019). The rear (north) side of D3, which belongs to the initial construction phase, shows a small rotation. Wall D4 also shows a rotation towards the inside of the monument. In contrast to Walls D2, D3 (front) and D4, Wall D1 (with the Sphinxes) does not appear to show any rotation (at least noteworthy).
- The vault has longitudinal subsidence along its central part, gradually increasing from Chamber X3 (indicative reported subsidence 1.5cm in the middle of the chamber (Lefantzis 2019), to Chamber X4 (indicative reported subsidence 4.5cm in the middle of the chamber).
- The crown of the arch at the entrance of Chamber X2 has a displacement in the longitudinal axis greater than 1.0cm. with respect to Wall D1.

- Between the west and east axis of the longitudinal walls of the monument there is a differential settlement (historical settlement of the west axis with respect to the east) gradually increasing towards Wall D4.

The structural damage is presented in the plans of the documentation study of the burial monument (Lefantzis 2019). The side sections in Figure 7 provide a collective overview of the main structural damage to the monument.

3.7 *Undocumented areas of the burial monument*

Despite the systematic investigation into the structural documentation of the monument, there are still issues that need further clarification. These include, for example, the preservation status of the external surface of the monument, the geotechnical data of the transitional embankment, the bearing conditions of the entablature and sphinxes in Wall D1, and the systematic recording of the metal joints. To overcome these uncertainties, reasonable assumptions have been made for the monument simulations during the mechanical history analyses.

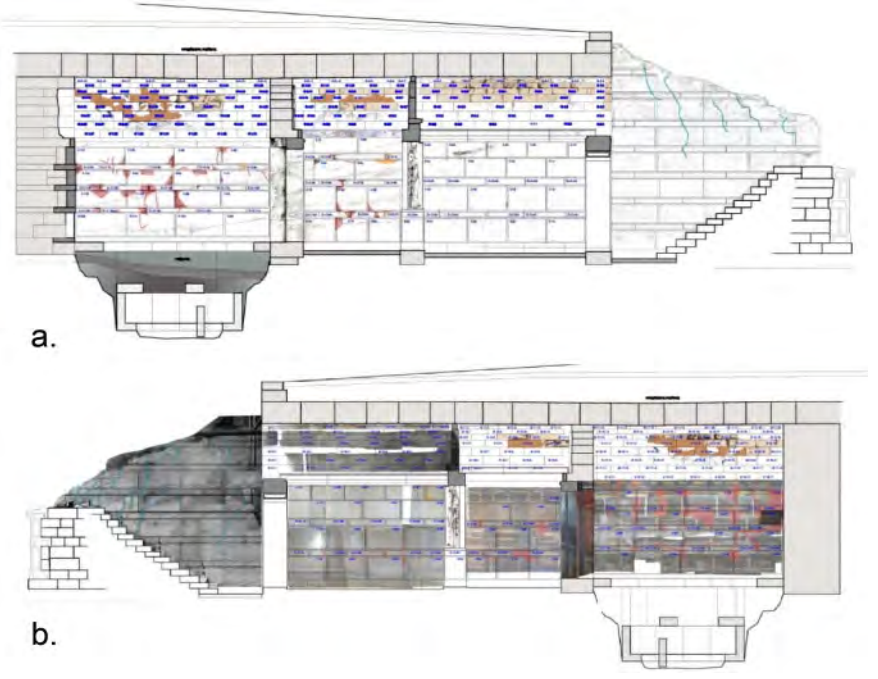

Figure 7. Longitudinal section views with the main structural damage to the burial monument a. west side b. east side (Lefantzis 2019).

3.8 *Actions after the unveiling and temporary fixing of the burial monument*

From the excavation of the monument to the present date (late 2021), a series of documentation and protection actions have been carried out. These include, briefly, studies for upgrading its protection, earthworks and rain protection works, as well increased instrumental monitoring. The monument has already been included in a financial program, the main goal being its systematic documentation, protection and (partial) restoration (Egglezos 2019c; Lefantzis 2019; Sotiropoulos et al. 2020b; Papadopoulos 2020).

4 ANALYSES OF THE BURIAL MONUMENT IN STAGES OF MECHANICAL HISTORY

During the elaboration of the study investigating the structural pathology of the burial monument, analyses were carried out in stages of mechanical history in order to sufficiently correlate and document the observed structural damage with the actions that caused it. These analyses also made it possible to reach important conclusions on the response of the monument under complex loading conditions. The organization, implementation and utilization of these analyses are presented in detail as follows:

4.1 *Methodology*

The methodology for interpreting the mechanical stress of the monument includes appropriate geostatic analyses of the interaction of the soil environment and the monument at different historical stages, in order to adequately document the structural damage to the monument (correlation with cause and time sequence of mechanical events).

These analyses require data on changes in the geometry of the monument (construction phases), changes in the strength of building materials (ageing, reduction of strength due to mechanical stress, etc.) and documentation of significant mechanical actions from the external environment (earthquakes, earth pressures, etc.).

Data from various scientific fields were used for the elaboration of the historical mechanical stages: archaeology, history, architecture, topography, geology, geotechnics, geophysics, seismology, strength of building materials, instrumental monitoring, etc.

4.2 *Available data*

The discovery of the burial monument in the Kasta tumulus is a happy coincidence, with the available data allowing, with the proper utilization, the more or less successful reconstruction of the mechanical history of the monument. The main sources for the mechanical historical data are listed below:

- Architectural documentation study of the burial monument, recording its structural pathology and main construction phases (Lefantzis 2019)
- Geotechnical survey to determine the geotechnical conditions in the immediate vicinity of the burial monument (Sotiropoulos et al. 2020a)
- Topographical survey of the Kasta Tomb provided by the Directorate of Restoration of Ancient Monuments (DAAM) of the Hellenic Ministry of Culture and Sports
- 3-D scan of the burial monument displaying its current geometry (Prof. V. Pagounis)
- Geophysical investigation of the Kasta mound with detection of soil layers of variable stiffness according to depth from the surface (Tsokas et al. 2016, Tsokas et al. 2018)
- Structural investigation with laboratory tests to determine natural and mechanical properties of the building materials of the monument (Directorate of Research and Technical Support for Restoration Projects - DETYMEA 2019)
- Archaeological data for the assessment of the sequence of the mechanical phases of the monument, e.g. construction, internal filling, etc. (Peristeri 2016)
- Data from instrumental monitoring measurements, confirming assumptions about the mechanical properties of the individual structural parts of the monument (Egglezos 2015)
- Collection of historical seismicity data from the available literature, identifying events with an estimated impact on the monument (Egglezos 2019c)
- Study for the interpretation of the structural pathology of the burial monument with computational documentation of the damage to it, linking each type of damage with a cause (Egglezos 2019c). This essentially formed the basis of the present work.

The successful selection and synthesis of data from the above reports is the framework within which the analyses are developed in mechanical history stages: the data allow the most accurate simulation of the monument and its environment, the selection of appropriate (possibly time-varying) values for the natural and mechanical properties of the monument's materials, the assessment of relatively realistic historical actions, and the description of the evolution of the structure over time (building phases, etc.).

4.3 *Important historical mechanical stages of the burial monument*

The following historical mechanical phases emerge from the management of the available data for the burial monument:

- Digging of the burial trench in the natural hill
- Construction of the burial trench and the cist grave (in X4)
- Construction of the main vaulted monument with parallel construction of the transitional embankment
- External artificial filling of the monument
- Building changes inside the monument
- Internal filling and sealing of the monument
- Gradual degradation of building material properties (ageing)
- Stress from a strong earthquake (620 AD, with an estimated magnitude of 6.8 on the Richter scale and epicenter distance about 15 km) (Papazachos and Papazachou 2003, Pavlidis et al. 2016)
- Loading of the monument with additional external anthropogenic fill (loose soil accumulation) in the decades before the discovery of the monument
- Earthworks during the excavation phase (August 2014) (resulting to OC effects on the soil surrounding the monument)
- Use of construction machinery near the arch of the monument (2014)
- Removal of internal fill in phases (2014)
- Construction of temporary consolidation devices (struts-pillars) in phases (2014)
- Accidental events (loading of Chamber X4 by surface slip upstream) (2014)
- Earthworks for earth pressure relief (Chamber X4) (2014)
- Strong precipitation action (2015)
- Construction of a medium-term (conforming to normative requirements) redesigned fastening device (2019)

4.4 *Geostatic analyses for the documentation of the structural damages of the monuments of the Kasta tumulus*

The geostatic calculations include 2-D analyses with finite and distinct elements in four characteristic cross-sections of the monument. These cross-sections correspond to the central cross-section of the Chambers X2, X3 and X4 and a simplified indicative simulation of its longitudinal central cross-section. The use of 2-D analyses is acceptable (certainly for the cross-sections of the chambers), as conditions of plane strain prevail (taking into account the width-to-length ratio of the burial monument). Regarding the longitudinal section, a case in which conditions of plane strain clearly do not strictly apply (3-D problem), the following measures are adopted in order to make the simulation realistic:

1. Vertical and horizontal springs are inserted, corresponding to the contribution of the vault (as an arch) and the side walls as a bearing element of the vault (compression only vertical elastic springs and friction horizontal springs).
2. The stiffness of the partition walls is proportionally reduced in order to effectively represent the real 3-D geometry, which includes large openings.

The simulation of the geometry of the burial monument is based on the architectural data (Lefantzis 2019). The soil simulation is based on the geotechnical data produced by the geotechnical investigation in the environs of the monument (Sotiropoulos et al. 2020a). All geomaterials, building materials as well as interfaces (joints between structural elements and interfaces with the surrounding soil) are simulated elastoplastically based on the Mohr-Coulomb and Hoek-Brown failure criteria.

It should be noted that the quality geological strength index (GSI) on the micro-scale of the stone is used for the quantitative assessment of the effects of ageing on the strength of stone blocks and their interface. The GSI values applied to account for the ageing of materials and interfaces at different historical stages of the monument are shown in Table 1. The properties of the geomaterials, the structural materials and their interfaces are presented in Tables 2, 3 and 4 respectively.

The values for the initial (reflecting the construction stage of the monument) normal and shear stiffness of the interfaces are selected based on the relevant (staged) values of the elastic modulus of the materials in contact. The degradation of interface stiffness values, in the following historical stages, is based on Barton's formula for estimating joint stiffness in rockmass (Barton, 1972).

Table 1. Quantification of Ageing effect on structural materials (GSI application in microscale).

Main historical stage	GSI values porous stone		GSI values marble	
	Initial	Residual	Initial	Residual
4th century B.C.	95	85	95	90
Before the internal filling	90	80	90	95
2nd half of 20th c. (extra soil)	80	75	85	90
Before the excavation 2014	75	70	80	85

The corresponding GSI value from Table 1 is used for the application of Barton's formula at each stage of the analysis. The elements of the temporary support structure (struts and columns) were simulated using appropriate linear structural elements.

Table 2. Structural material properties in relation to historical stages of the monument.

	Dolomite POROUS Stones*				MARBLE Stones*			
	σ_{cm}**= 13 MPa				σ_{cm}**= 39 MPa			
GSI_{ini}	95	90	80	75	95	90	85	80
GSI_{res}	85	80	75	70	90	85	80	75
$\sigma_{cm,ini}$ (MPa)	10,66	8,38	5,58	4,71	30,45	24,10	19,55	16,25
$\sigma_{cm,res}$ (MPa)	6,75	5,58	4,71	4,05	24,0974	19,5521	16,2541	13,81
m_i	9	9	9	9	9	9	9	9
E_i (MPa)	7500	7500	7500	7500	57375	57375	57375	57375
$E_{RM,inI}$ (MPa)	7351	7190	6603	6123	56236	55001	53163	50510
$E_{RM,res}$ (MPa)	6949	6603	6123	5496	55001	53163	50510	46838
γ (kN/m^3)	23	23	23	23	26	26	26	26

* Intact Rock Stone properties: GSI=100, E_i, ** Compression Strength

Moreover, in order to examine the possible effect of the metal joints on the vault of the arch and the marble members of the side walls, analyses were performed both with and without the metal joints.

Based on the above, eight analyses were performed in total, attempting to represent the mechanical history of the monument as realistically as possible.

Table 3. Interface properties in relation to historical stages of the monument.

	Interfaces*					
	P-P	M-M	P-M	P-GC	M-SM	P-SM_
Normal stiffness, kn, ini (kPa/m)	$75x10^6$	$550x10^6$	$75x10^6$	200000	150000	150000
Shear stiffness, ks, ini (kPa/m)	$7.5x10^6$	$55x10^6$	$7.5x10^6$	40000	30000	30000
c (kPa)	0	0	0	0	0	0
ϕ,ini (o)	32	35	32	25	22	22
ϕ,res (o)	32	35	32	25	22	22

* P = POROUS FACE, M= MARBLE FACE, GC = Transitional Backfilling FACE, SM = SOIL FACE

Table 4. Kasta Tumulus: geo-material properties.

	I1	II2	III3	IV4	V5_
AUSCS	GM/GC	SM/SC	SM/SC	SM-SC	SM
γ (kN/m^3)	21 1	9-21[2]	19	19	20-21
c (kN/m^2)	3	0	0	1	5-25*
ϕ (°)	35	30-32	30	30	32-35
ϕ_{res}(°)	32	30	30	30	30-32
c_u(kN/m^2)	-	-	-	-	-
v	0,30	0,30	0,30	0,30	0,25
E_i (MPa)	0,30	0,30	0,30	0,30	0,25
DR(%)	60 - 80	50-70	30-40	40-50	65-90*
OCR	44652	1-5	1	1	1-3

* Depending on the depth
(1) Transitional artificial Embankment - GC
(2) External ancient undisturbed soil filling for the tumulus formation: SM/SC, γ=21 for fully saturated soil
(3) External disturbed loose cover soil deposition on the tumulus: SM/SC, γ=21 for fully saturated soil
(4) Internal anthropogenic loose filling of the burial monument: SM/SC
(5) Natural soil deposit -Silty SAND: SM

4.5 *Results of analyses in mechanical history stages:*

The results of the 2-D analyses include (among others):

- the permanent deformation of the geometry of the burial monument (horizontal – vertical displacements)
- the settlement of the foundations of the monument
- the stress state of the structural elements of the monument (zones of plastic condition/cracking)
- the earth pressures from the surrounding soil on the monument

The results of the analyses show a good matching of the computational results with the observed structural condition of the monument. An indicative overview of results of the above analyses in mechanical loading history stages is presented in the following figures (Figures 8–12), in which the computational estimate is contrasted with the observed structural condition of the chambers of the monument.

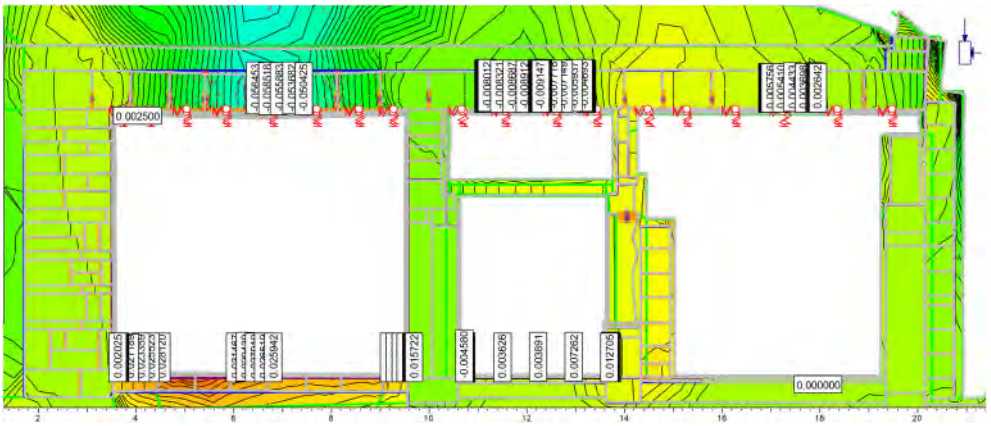

Figure 8. Calculated subsidence of the vault keystone. X4. 5.5cm calculated subsidence vs 6cm measured, X3: 0.9cm calculated subsidence vs 1.5cm measured, X2: 0.2-0.5cm calculated subsidence vs <0.5 cm measured.

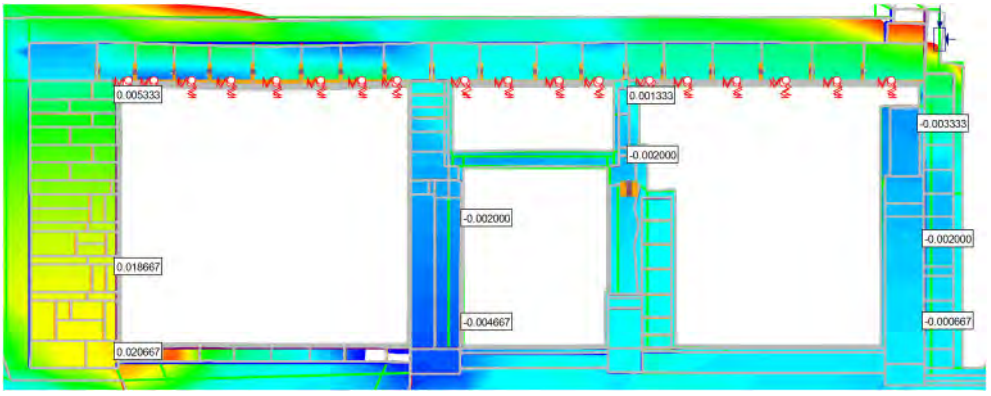

Figure 9. Permanent horizontal deformations of the partition walls (Di-D4). The measured rotations from 3D scanning are in good agreement with the calculations.

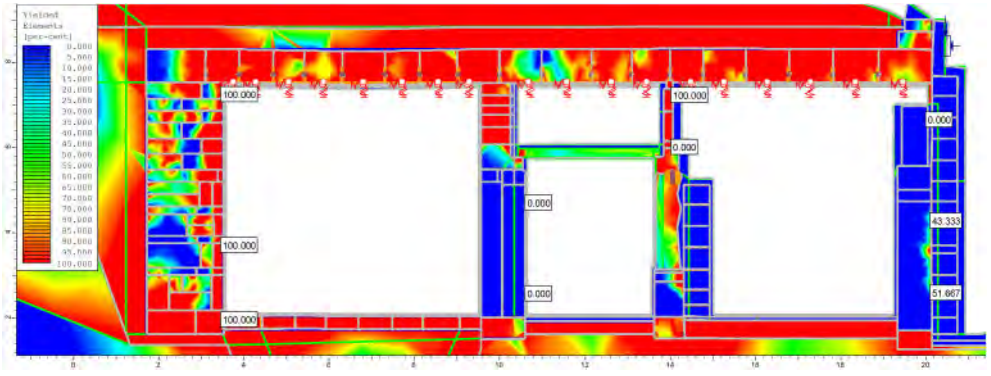

Figure 10. Longitudinal section views showing the main structural damage to the burial monument. For comparison see Figures 6 and 7.

5 EVALUATION OF RESULTS

The geostatic analyses in stages of mechanical history have produced conclusions regarding the ancient design of the monument, the interpretation of its structural pathology, the calibration of the simulation of the burial monument, and the guidelines for the design of the restoration program. These conclusions can be summarized as follows:

- The ancient design (based on the estimated geometry of the tumulus around the monument) is considered absolutely satisfactory. In particular, there is computational stability of the monument and low stress of the structural elements. The foundation of the monument is also considered sufficient, despite the (calculated and observed) differential settlement (approx. 1-1.5cm) on the west side of the monument in relation to the east. This settlement occurred on completion of the construction of the monument and the tomb. The settlement is considered acceptable even by modern regulatory standards.
- The presence of metal joining elements, as the analyses show, does not differentiate the resulting structural damage (permanent geometric deformations and main zones of cracking of building materials) on the macro scale. On a micro scale, it seems to affect the concentration of damage to the stone blocks and vault in the vicinity of the joints, due to the imposed constraint on the deformation. Similar observations may have led ancient engineers to abandon the use of joints in structures of this type (vaulted roofs).
- The strong historical earthquakes which struck the site of the monument (Figure 11) do not seem (computationally) to have substantially burdened its structural elements, as is to be expected with buried structures, (in this case with internal fill, which offers additional resistance). Of course, had the monument not been filled, it would have suffered greater shear strain due to the seismic action of the external fill.
- The main stressing factors on the monument are due to recent mechanical events: the accumulation of high soil deposition coming mainly from the top of the mound (during the 20th century) and the asymmetric earthworks during the 2014 archaeological excavation of the monument (Figures 10–11).

The analysis in stages of mechanical history is used for the evaluation of the attempted simulation of the burial monument. The result shows a good correlation of computational predictions with the observed structural image of the monument. This makes the simulation reliable for the realistic assessment of the response of the monument to adverse future stresses and the design of protection - restoration measures (adoption and location of appropriate measures based on real needs).

5.1 *Proposal for interpretation of the structural damage of a burial monument:*

The results of the geostatic calculations in mechanical history stages show the following connections between damage type and cause:

- The fractures of structural members and the permanent deformations of the monument walls in Chamber X4 arise computationally from the high loose fill, which accumulated anthropogenically over the burial monument in the last decades of the 20th century. The observed fractures of the voussoirs in Chambers X4 and X3 are due to the same cause. The damage to the walls in Chambers X2 and X3 is computationally attributed to the external asymmetric earthmoving configuration during the uncovering of the burial monument (Aug. 2014). It should be noted that the observed damage to the vault (from the vertical component of the external soil pressure) matches the general qualitative interpretation scheme in relevant works on Macedonian tombs (Athanasiou et al. 2012; Zambas 2016).
- The differential subsidence of the west walls of the monument with respect to the east walls is due to a historical differential settlement, which results computationally from the very beginning of the construction of the monument and its overlap with the earthworks of the tumulus. This subsidence is attributed to the fact that the west side is filled to a slightly greater height than the

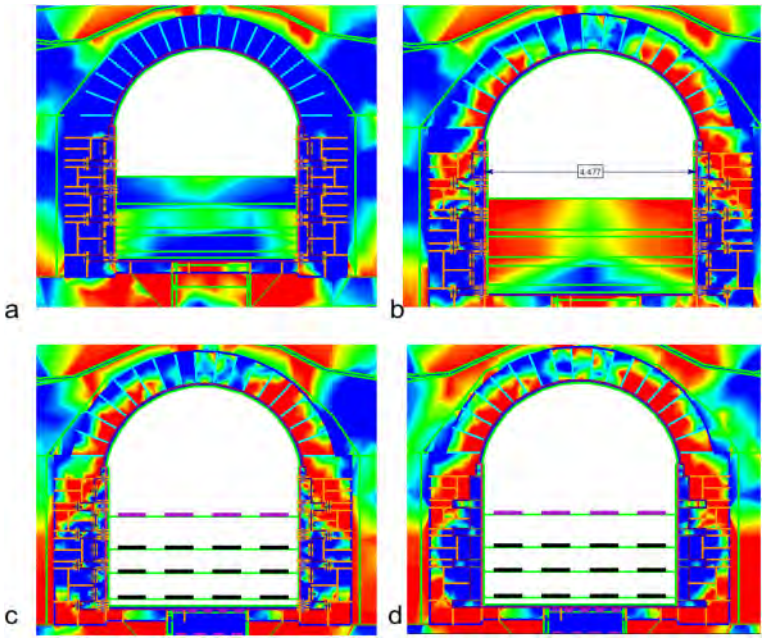

Figure 11. Computational evolution of the stress state of the voussoirs and the side walls of Chamber X4, from the analyses in historical stages (metal joining elements are included) a) post 7th century earthquake b) soil accumulation of the 2nd half of the 20th century on top of the monument c) current state, d) current state from a staged analysis without metal joining elements.

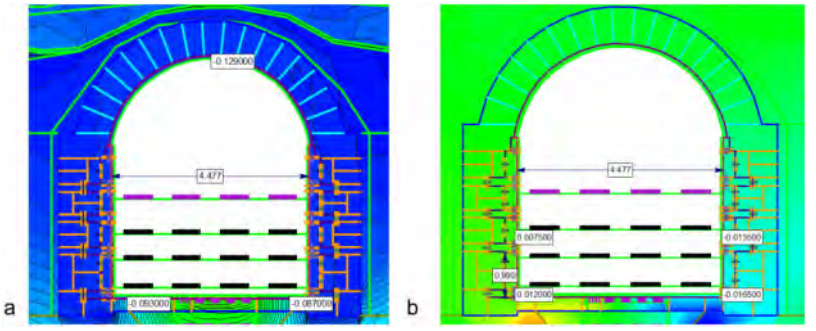

Figure 12. Permanent deformations in the mid-section of Chamber X4 a) subsidence of the vault b) convergence of the side walls. The measured rotations from 3D scanning are in good agreement with the calculations.

east side, as a result of the original topography at the site of the monument. The fracture of the (poros stone?) architrave in Wall D1 must also be attributed to this settlement. It should be noted that this subsidence has been exacerbated by the loading of high loose fill from the excavations on the top of the mound in recent decades.

– The rotation of Wall D2 towards the entrance of the monument occurs computationally as a result of the shear action of the slope on the arch and the bonding of the tympanum of D2 with the arch. Since, according to the architectural study, the tympanum is placed in a construction phase following the completion of the construction of the slopes of the tumulus, it appears computationally that the mechanical events which affected the rotation of Wall D2 are the strong

earthquakes (late 6th - early 7th c. AD) focused with epicentres on Mt. Paggaion, and the high loose fill which has accumulated anthropogenically over the burial monument in recent decades.
- The rotation of the front of Wall D3 is logically and computationally related to the rotation of D2, since the two partition walls are connected to the roof slab through which the imposed stresses are transferred by friction from one to the other (mainly from D2 to D3). The absence of rotation from the rear of D3 (towards X4) should be attributed to the bonding of that part with the longitudinal walls.
- Wall D1 does not present rotation, because there is no bonding with the vault of the monument.
- The extensive vertical cracks in the coating in Space X1 must be attributed firstly to the out-of-plane bending of the walls of Space X1 (quasi-triangular plate function), and secondly to their compression between the main vaulted monument and the circular retaining perimetric wall of the tumulus (most probably as a result of the strong seismic events of the 6th and 7th centuries AD). The contribution of the differential settlement between the west and east wall during the initial construction phase should also be taken into account.
- The rupture of the architrave and the heads of the Maidens is computationally attributed to the settlement of the tympanum and the flexural stress of the architrave, combined with the asymmetric loading as a result of from the west hole in the tympanum. The fractures of the heads / supports of the Maidens are due to indirect tension, resulting from the compressive stress imposed by the entablature. The observed breakage of the marble head of the east Maiden, with the loss of its anterior half, is probably due to an event dating back a very long time. This is also indicated by the state of preservation of the preserved surface of the marble. Based on the above, it is possible that the initial rupture was due either to a strong historical (unknown) earthquake or to anthropogenic action, but in any case it occurred before the internal filling and sealing of the monument. This supposition is based on the fact that during the excavation of the monument in 2014, the broken part of the head of the east Maiden was not found.
- The rupture of the coating of the vault is attributed to its deformation (mainly transversal). The discovery of a large volume of coating fragments on the surface of the fill of Chambers X2 and X4 indicates that the event occurred predominantly after the internal filling of the monument. Since the basic deformation of the vault is due to the strong earthquakes of the 6th and 7th centuries AD and the high external fill of recent decades, the coating failure should be associated with these mechanical events.
- The observed longitudinal shear deformation and/or displacement of the arch towards the entrance of the monument is the cumulative effect of the shear action of the slopes of the mound on the arch under static and seismic conditions (initial displacement on the completion of the slopes of the mound, next established displacement with the strong earthquakes of the 6th and 7th centuries AD, and finally additional longitudinal displacement due to the high fill of recent decades).
- Based on the geostatic calculations, there is no structural damage to the monument from the use of earthmoving equipment on the mound during the uncovering of the monument.

The structural damage to the monument in correlation with its causes is presented in Table 5.

5.2 *Key vulnerabilities of the burial monument:*

The evaluation of the results of the analyses in stages of mechanical history led to the following conclusions on the vulnerabilities of the burial monument (and of corresponding structures in general):

- The height of the external artificial fill (according to the typical ancient design of the tumulus) determines the external lateral and vertical pressures on the vaulted structure, the two basic actions for the stability of the monument. It is also responsible for the longitudinal action on the monument (through frictional forces). Exceedance of the geostatic intensity of the ancient design can lead to significant permanent structural damage.

– The mechanical and natural properties of the external artificial fill (achieved density, compressibility, water permeability) are directly related to the magnitude of the pressures on the monument (geo- and hydrostatic) and to the action of physicochemical factors responsible for the degradation of structural material strength (water and/or moisture action).
– The asymmetry of the external fill: in the case of asymmetry along the transverse axis of the monument, strong stress is expected in case of seismic action.
– The bonding of the partition walls with the main structure (vault and side walls) creates conditions for their intense out of plane stress. The bonding of the partition walls D3 and D2 with a marble slab, thus forming a frame structure, is an effort to improve their out-of-level stability.
– The presence of metal joining elements, without being decisive for the imposed stress state on the structural members, locates the main fractures around the joining area. This conclusion mainly concerns the marble blocks of the side walls and to a lesser extent the voussoirs of the vault. Finally, the trench of the cist grave is crucial to the stability of Chamber X4 (it corresponds to a deep excavation at the edge of a structure with surface foundations).

Table 5. Correlation of structural damages with causative agent.

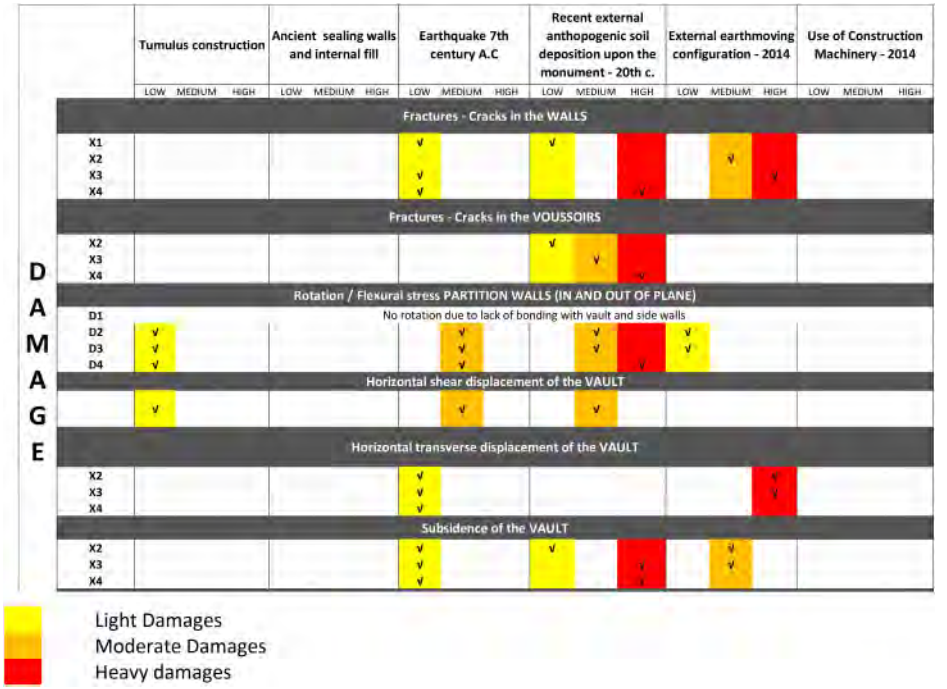

5.3 *Utilization of the results from the analyses in mechanical historical stages for the design of protection-restoration measures of the monument:*

Understanding the mechanical behavior of the burial monument and highlighting its vulnerabilities determined the main directions of intervention for the internal and external protection of the monument. In particular, the studies for the external protection of the monument (Sotiropoulos et al. 2020b), propose the removal of the asymmetric earth fill on the west side of the burial monument. The favorable effect of this intervention is confirmed by the calibrated simulation of the monument (based on the analyses in historical stages). It is also planned to restore the external fill with lightweight geomaterials with reduced inertial characteristics, to deal with the regulatory seismic

action, while provisions have been made to prevent water flow to the interior of the burial monument by creating a geotechnical sealing layer. The structural restoration study of the monument (Papadopoulos 2020) also proposes that the dense fixing support of Chamber X4 should be preserved until the arch has been fully restored, based on macroscopic observations and computational predictions of the existence of extensive zones (largely invisible) of cracked/fragmented voussoirs. Finally, it is worth mentioning the usefulness of the analyses in mechanical historical stages, in determining the optimal time sequence of the external protection and structural restoration work, in order to ensure minimal impact on the burial monument.

6 CONCLUSIONS

This paper presents the general methodology for the comprehensive qualitative and computational treatment of the mechanical history of monuments. The application of the above methodology in the case of the burial monument of the Kasta Tomb allows a convincing interpretation of its preservation status. In particular, the investigation of its mechanical stress provided basic conclusions on the historical development of its structural pathology: it proved possible to connect damage with a sequence of specific mechanical causes. The vulnerabilities of the design of the monument were also highlighted. This, in combination with the calibrated - through the observed damage - simulation of the burial monument, allows a reliable assessment of its response to future actions. Therefore the successful reading of the mechanical history of the burial monument (and indeed of every monument) is a powerful tool in the toolbox of the researcher / restorer, allowing the appropriate measures to be taken for its effective protection and promotion.

REFERENCES

Athanasiou F., Malama V., Miza M., Sarantidou M., Papasotiriou A., 2012 The restoration of the Macedonian tomb of Makridis Bey in Derveni, Thessaloniki, *Proceedings of the 3rd Panhellenic Congress of Restoration ETEPAM*, 2012 (in Greek).

Barton N. R., 1972, A model study of rock-joint deformation, *Int.J. Rock. Mech. Min. Sci*. 9. 579-602

GEOPER 2015, *Study for the redesign of the temporary fixing device for the support of the Kasta Tomb burial complex*, Unpubl. Study. Archive of Ephorate of Antiquities of Serres (in Greek).

DETYMEA, 2019, *Examination of stone and marble samples from the surrounding area of the Kastas mound in Amphipolis*, Serres, Unpubl. Study, Athens. Archive of the Directorate of Research and Technical Support for Restoration Projects of the Hellenic Ministry of Culture and Sports-DETYMEA Archive (in Greek).

Egglezos D., 2015a, *Construction and Computational support of KH EPKA for the uncovering of the monument of the Kasta Tomb and ensuring its stability by designing temporary measures: Contractual submission of a Technical Consultant for the period 1-9-2014 to 31-10- 2014*, Unpubl. Study. Archive of Ephorate of Antiquities of Serres (in Greek).

Egglezos D. 2015b, *Geostatic stability study of the Kasta burial complex*, Unpubl. Study. Archive of the Directorate for the Restoration of Ancient Monuments of the Hellenic Ministry of Culture and Sports-DAAM Archive (in Greek).

Egglezos D. 2016, The Burial Complex of the hill-tomb Casta from the side of a Civil Engineer, *Proceedings of the 29th Meeting of the Archaeological Project of Macedonia-Thrace (AEMTH)*, Thessaloniki (in Greek).

Egglezos D. 2019a, The effect of the excavation process on monumental structures interacting with the surrounding soil, *Proceedings of the 5th Panhellenic Restoration Conference (ETEPAM)*, Athens (in Greek).

Egglezos D. 2019b, Preliminary Geostatic analyses in stages of "mechanical history" for the interpretation of the structural condition of standing monumental structures: the example of the monuments at the Kasta mound in Amphipolis, *8th Panhellenic Congress of Geotechnical Engineering*, Athens (in Greek).

Egglezos D. 2019c, *Issues of structural pathology of the monumental complex of the Casta mound*, Unpubl.Study. Archive of the Directorate for the Restoration of Ancient Monuments of the Hellenic Ministry of Culture and Sports -DAAM Archive (in Greek).

Lazaridis D. 1964, Excavations and research in Amphipolis, *Proceedings of the Archaeological Society (PAE)*, 35-40 (in Greek)

Lazaridis D. 1965, Excavations and research in Amphipolis, *Proceedings of the Archaeological Society (PAE)*, 47-52 (in Greek)

Lazaridis D. 1972, Excavations and research in Amphipolis, *Proceedings of the Archaeological Society (PAE)*, 63-72 (in Greek)

Lefantzis M. 2013, New research on the base of the Lion of Amphipolis, *Proceedings of the 26th conference of the Archaeological Project of Macedonia-Thrace (AEMTH)*, Thessaloniki (in Greek).

Lefantzis M. 2014, The architecture of the Casta Tomb, *Proceedings of the 27th conference of the Archaeological Project of Macedonia-Thrace (AEMTH),* Thessaloniki (in Greek).

Lefantzis M. 2019, *Architectural study of the tomb of Kasta of Amfipolis, Part B: The burial monument,* Unpubl. Study. Archive of the Directorate for the Restoration of Ancient Monuments of the Hellenic Ministry of Culture and Sports- DAAM Archive (in Greek).

Papadopoulos Ch. 2020, *Static Study of Structural Restoration - Restoration of the Tomb Monument of Kasta Tomb*, Unpubl. Study. Archive of the Directorate for the Restoration of Ancient Monuments of the Hellenic Ministry of Culture and Sports (DAAM Archive)

Papazachos B. and Papazachou K. 2003, *The earthquakes of Greece*, Thessaloniki, Ziti Publications (in Greek).

Pavlides S., Chatzipetros A., Syrides G., Lefantzis M. 2016, Tectonic structure and paleoseismology of Kastas Hill and the wider region of eastern Macedonia, *Proceedings of the 29th Meeting of the Archaeological Project of Macedonia-Thrace (AEMTH)*, Thessaloniki (in Greek).

Peristeri K. 2016, Excavation of the Kasta tomb of Amfipolis 2014, *Proceedings of the 29th Meeting of the Archaeological Project of Macedonia-Thrace (AEMTH)*, Thessaloniki (in Greek).

Peristeri K., Lefantzis M., Corso A. 2016, Study of scattered marble reliefs from the wider area of the tomb of Kasta Amfipolis, *Proceedings of the 29th Meeting of the Archaeological Project of Macedonia-Thrace (AEMTH)*, Thessaloniki (in Greek).

Sotiropoulos and Associates ATE, 2020a, *Presentation of geotechnical research and geotechnical evaluation*, Unpubl. Study. Archive of the Directorate for the Restoration of Ancient Monuments of the Hellenic Ministry of Culture and Sports -DAAM Archive (in Greek).

Sotiropoulos and Associates ATE, 2020b, *Soil Technical - Geostatic Study for the protection of the Burial Monument from the surrounding soils*, Unpubl. Study. Archive of Directorate for the Restoration of Ancient Monuments of the Hellenic Ministry of Culture and Sports (DAAM Archive)

Syrides G., Pavlides S., Chatzipetros A., Tsokas G., Lefantzis M. 2016, The geological structure of Kastas (Amphipolis), *Proceedings of the 29th Meeting of the Archaeological Project of Macedonia-Thrace (AEMTH),* Thessaloniki (in Greek).

Syrides G., Pavlides S., Chatzipetros A. 2017, The geological structure of Kastas hill archaeological site, Amphipolis, Eastern Macedonia, Greece. *Bulletin of the Geological Society of Greece*, 51, 39–51.

Tsokas G., Tsourlos P., Vargemezis G., Fikos I., 2016, Course of geophysical surveys on the Kasta hill, *Proceedings of the 29th Meeting of the Archaeological Project of Macedonia-Thrace (AEMTH)*, Thessaloniki (in Greek).

Tsokas G. N., Tsourlos P. I., Kim J. H, et al., 2018, ERT imaging of the interior of the huge tumulus of Kastas in Amphipolis (northern Greece), *Archaeological Prospection*, 1–15.

Zambas K. 2016, Remarks on the Design and Construction of Macedonian Tombs, *Honorary Volume for Professor Manolis Korres*, Athens: Melissa Publishing House (in Greek).

Geotechnical Engineering for the Preservation of Monuments and Historic Sites III – Lancellotta, Viggiani, Flora, de Silva & Mele (Eds)

Structural health monitoring of historic masonry towers: The Case of the Ghirlandina Tower, Modena

Donato Sabia
Politecnico di Torino, Department of Structural, Geotechnical and Building Engineering, Torino, Italy

Giacomo Vincenzo Demarie
Structural Engineer, Torino, Italy

Antonino Quattrone
Politecnico di Torino, Department of Structural, Geotechnical and Building Engineering, Torino, Italy

ABSTRACT: Masonry towers are an important architectural heritage, whose conservation and maintenance requires a deep understanding of their structural behaviour. To this end, monitoring the dynamic response to ambient and service loads is a fundamental source of information. By repeating the data acquisition over the time, it is moreover possible to check for variations in the structure's response, whose entity may be correlated to the appearance or growth of a damage (e.g. following some exceptional event as an earthquake or as a consequence of materials and components ageing). The complexity of some existing structures and their interaction with the environment claim for a detailed monitoring plan, to support an evidence-based decision process. If the sensor network acquires data continuously over time, the evolution of the structural behaviour may be tracked continuously as well. This process needs the proper methods and algorithms to manage the large amount of available data and extract actionable information from it. This paper presents a methodology for the automatic structural long-term monitoring, which relies on existing methods from the Machine Learning and Data Mining fields. The results of its application to the real-world case of an ancient masonry bell tower, the Ghirlandina Tower (Modena, Italy) are also discussed.

1 INTRODUCTION

The main goal of the Structural Health Monitoring is to transform the experimental data into information for the assessment of the structural conditions (Farrar CR & Worden K 2007). To this extent, two general approaches can be applied: physics-based and data-driven.

The physics-based approach involves building a model of the for analysis and prediction, starting from the "first principles" of Physics. In this case, the model formulation must be appropriate enough to characterize the actual structure.

In the data-driven approach no assumptions are made about the system generating the data, the model from the data only and has not any specific physical meaning. Such models are very general in their nature and well suited when large amount of data is available or the structural behaviour is too complex to be described from basing on physical principles (Ying EJ et al. 2013).

The purpose of long-term monitoring systems is generally to track over time the status of a structure and to answer questions about the safety and the serviceability after specific events, or as a consequence of the materials and components ageing (Cross EJ et al. 2013). In areas with

DOI 10.1201/9781003308867-10

high levels of seismicity, for example, the assessment of the structural integrity can be paramount during the post-event activities.

The long-term monitoring produces a large amount of data and proper methods and algorithms are required to extract valuable and reliable information. In this context the methods and algorithms rooted in the Machine Learning and Data Mining fields have proven to be extremely effective (Farrar CR & Worden K 2013; Worden K & Manson G 2007).

The objective of this research is to define a method for the automatic identification of the vibration modes of a structure, so that they can be tracked continuously over a long period of time. The proposed approach unfolds into four steps: the model selection and validation, the system identification, the clustering and the classification steps. The natural frequencies, damping factors and mode shapes are automatically identified from the measured data and monitored over time to detect possible changes in the health state of a structure. Moreover, the observation of the environment parameters, such as the temperature, helps in classifying the stream of data and recognizing structural novelties.

The long-term monitoring of an ancient masonry bell tower, the Ghirlandina Tower (Modena, Italy), has been selected as a real-world case application for the proposed method. The structural characterization is performed by identifying the first modes of vibration, whose evolution over time has been tracked.

2 MACHINE LEARNING APPROACH

The methodology presented in this work aims to characterize the structural response, assuming the starting point in time as the normal condition with no damage and following its evolution over time. The time tracking is performed by detecting deviations from the normal condition (Demarie G & Sabia D 2019).

The proposed method is implemented as a four-step process: Model selection and validation, System Identification, Clustering and Automatic Monitoring.

2.1 *Model Selection and Validation*

A linear model is used to describe the relationship among the signals at different time instants. For the case of a single channel available, this assumption translates in the following equation:

$$y_t = w_0 + w_1 y_{t-1} + \cdots + w_p y_{t-p} \tag{1}$$

For N different instants leads to the following system of linear equations:

$$\begin{cases} y_{t_1} = w_0 + w_1 y_{t_1-1} + \cdots + w_p y_{t_1-p} \\ y_{t_2} = w_0 + w_1 y_{t_2-1} + \cdots + w_p y_{t_2-p} \\ \cdots \\ y_{t_N} = w_0 + w_1 y_{t_N-1} + \cdots + w_p y_{t_N-p} \end{cases} \tag{2}$$

The system of equations 2 can be written in matrix form:

$$\{y\} = [Y]\{w\} \tag{3}$$

For the case where n_{ch} signals are acquired an expression similar to equation (1) holds. Specifically, the $i-$th signal at a certain time instant can be obtained as a linear function of itself and all the remaining signals at p previous instants.

$$\begin{aligned} y_{i,t} \;=\; & w_{i,0} + w_{i,1}^{(1)} y_{1,t-1} + \ldots + w_{i,n_{ch}}^{(1)} y_{n_{ch},t-1} + w_{i,1}^{(2)} y_{1,t-2} + \ldots + w_{i,n_{ch}}^{(2)} y_{n_{ch},t-2} + \ldots \\ & + w_{i,1}^{(p)} y_{1,t-p} + \ldots + w_{i,n_{ch}}^{(p)} y_{n_{ch},t-p} \end{aligned} \tag{4}$$

For N different instants of time we can write the following linear system:

$$[Y_{current}] = [Y_{past}][W] \tag{5}$$

The proper model order "p" and the signal length in samples "N" are estimated from a subset of the measured data.

2.2 *System Identification*

The linear model coefficients are repeatedly estimated from the measured signals by solving a sequence of linear regression problems.

The data produced by the monitoring system can be thought of as a continuous succession of blocks of data, each consisting of n_{ch} signals made of $N + p$ samples.

For each block of data the linear system of equations 5 can be set up and the matrix $[W]$ estimated from it. The process can be performed by applying it each time a new block of data is acquired. It results in a succession of matrices $[W]_1$,$[W]_2$, ... $[W]_i$, ... which constitutes the basis for the long-term monitoring of the structure. The coefficients of the matrix $[W]$ can be re-organized in a way that allows for the eigenmodes of the structure to be evaluated. To this aim, Equation 4 can be re-stated in the following way:

$$\{y_t\}^T = \{w_0\} + \left[W^{(1)}\right]\{y_{t-1}\}^T + \left[W^{(2)}\right]\{y_{t-2}\}^T + \ldots + \left[W^{(p)}\right]\left\{y_{t-p}\right\}^T \tag{6}$$

The system of equations 6 can be written in matrix form:

$$\{z_t\} = \{w_0\} + [A]\{z_{t-1}\} \tag{7}$$

The system is characterized by $n_{ch} \cdot p$ modes of vibration.

2.3 *Clustering*

The modes of vibration identified over a limited period are clustered based on the natural frequencies, damping values and the mode shapes. A decision is made on each cluster if it must be considered important and worth to be monitored. Such a decision is taken on top of a domain-specific knowledge and engineering judgement and it is intended to limit the monitoring only to the modes that are deemed as relevant for the practical case at hand.

2.4 *Automatic Monitoring*

A classifier is built on top of the clusters found as the outcome of the previous phase. Each new identified mode of vibration is automatically classified and, by repeating the process over time, the monitoring of the relevant modes is accomplished.

The first and third phases are performed at least once, but in general very few times, to properly define the model order and the clusters (that are the class types or relevant modes). The second and fourth steps, instead, are executed on every acquisition as soon as it is recorded or, alternatively, off-line.

The proposed method has been applied to the data provided by the monitoring system installed on the Ghirlandina Tower (Modena, Italy). The results obtained are discussed in detail in the Section 3.

3 LONG-TERM MONITORING OF THE GHIRLANDINA TOWER

The Ghirlandina is the bell tower of the Cathedral of Modena, Italy (Figure 1). The construction was started around the year 1160 and completed on 1184, following the initial five floors project.

An additional sixth floor was built on 1261 and the gothic octagonal cusp closed the construction phase on 1319, reaching a final height of 89.3 m (Cadignani R & Lugli S 2010; Cadignani R et al. 2017).

During the first half of 2012 an experimental modal analysis was carried out so to characterize the dynamics of the tower by measuring its response to the ambient excitation. The results obtained showed the interaction with the cathedral and the important contribution of the soil-structure interaction on the tower's modes of vibration (Lancellotta R & Sabia D 2013; Lancellotta R & Sabia D 2014; Sabia D et al. 2015; Cosentini R et al. 2015).

Figure 1. The Cathedral of Modena and the Ghirlandina Tower.

During the same year a sensor network made of 12 capacitive accelerometers and 3 thermocouples was permanently installed on the tower, in order to implement a monitoring system acquiring data continuously over a long period of time (Figure 2). Since the end 2012 the network has been measuring the accelerations at the rate of 100 Hz.

The whole database of acquisitions from August 2012 to August 2013 has been considered and each phase of the 4-step process is addressed and detailed.

3.1 *Model Selection and Validation*

The correlation structure between the signals at the current instant and their past values is expressed through the linear system in Equation 4, whose dimensions depend from the system order p and the length in samples N.

A set of 50 couples of 1 hour long acquisitions have been randomly chosen from the entire August 2012 – August 2013 database. The selected signals have been used for the estimating the linear regression coefficients "w". The parameters p and N has been determined by averaging across the values obtained from each couple of signals in the set considered for the model selection and validation.

The optimal value of the system order "p", as defined above, turned out to be equal to 9 and the minimum signal length to be considered for the identification step has been found equal to 24 minutes.

Figure 2 compares the experimental signal acquired by the channels 10 and 12 respectively with the corresponding linear regression model fit. The good level of approximation given by the model fit prove that the dynamics of the Ghirlandina Tower has been well captured.

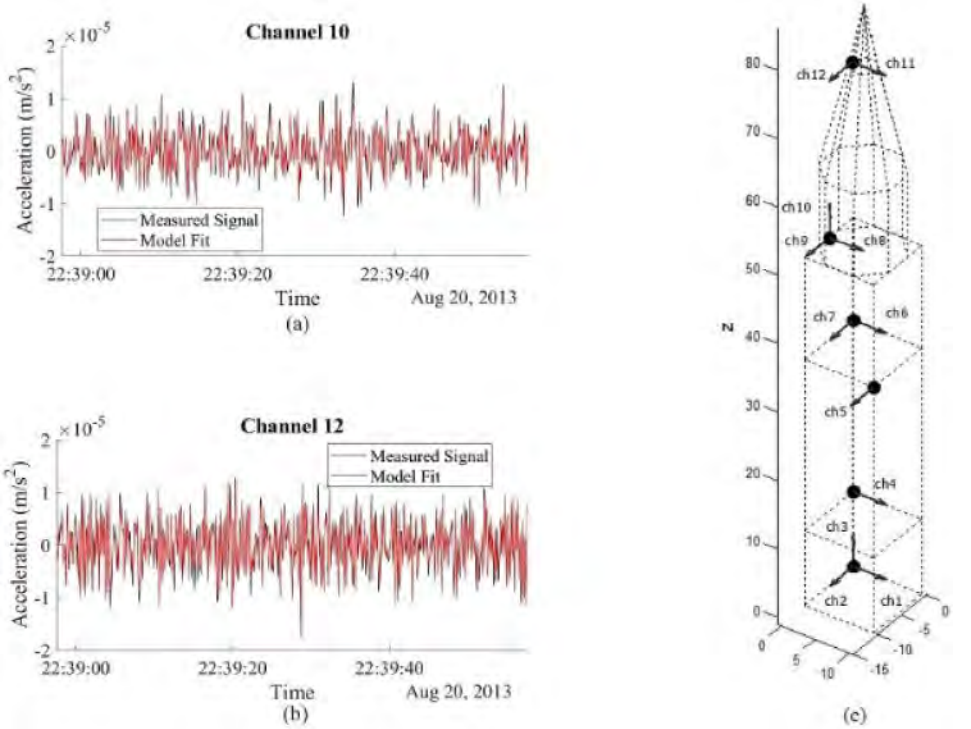

Figure 2. (a) Linear regression accuracy channel 10, (b) Linear regression accuracy channel 12, (c) Sensor positions and channel names (Modified, source: Demarie G & Sabia D 2019).

3.2 *System Identification and Clustering*

The database of signals acquired by the sensor network from August 1st 2012 to August 28th 2013 has been processed and the matrix $[W]$ of the linear regression coefficients has been repeatedly estimated according to the values of p and N determined in the previous section, for a total of 16944 times. Each time the matrix $[A]$ of the first order difference representation has been formed from $[W]$ and the eigenmodes of the systems evaluated. Provided that $p = 9$ and the number of channels is 12, a database of 1829952 identified modes has been built.

Before clustering the data, a significant portion of the modes have been excluded based on the engineering criteria. A correlation coefficient higher than 0.975 has been assumed as the threshold for considering a modal shape as "almost" real. Furthermore, a threshold in the damping factor equal to 25% has been adopted, this leading to the exclusion of all the modes characterized by higher damping. At the end of the preliminary selection based on the engineering criteria 56537 modes of vibration have been retained.

The clustering process is essential to detect the modes that are worth to be tracked over time. To this end, the complete set of modes identified in the interval August – September 2012 has been clustered. Figure 3 summarizes some of the outcomes obtained from the identification of the signals in the August – September 2012 interval. The charts (a) and (b) also suggest the existence of six clusters. The figures 4 show some of the principal mode shapes identified.

The type of the mode along with the frequency and damping values are summarized in Table 1.

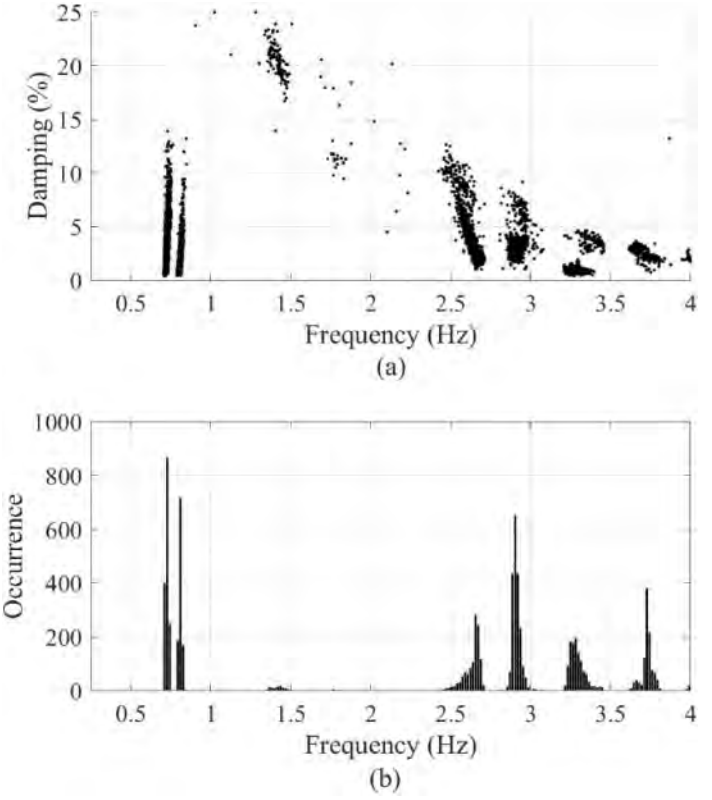

Figure 3. Identified mode (August – September 2012) (Modified, source: Demarie G & Sabia D 2019).

Table 1. Correspondence between clusters and mode types (Modified, source: Demarie G & Sabia D 2019).

Cluster #	Frequency (Hz)	Damping (%)	Type
1	0.73	3.6	1st bending (*y*-direction)
2	0.81	2.4	1st bending (*x*-direction)
3	2.65	2.7	2nd bending (*y*-direction)
4	2.91	2.9	2nd bending (*x*-direction)
5	3.28	0.8	1st torsional

3.3 *Monitoring*

The last step of the process implements the continuous time monitoring by making automatic the classification of the identified modes. To this end, a rule is needed so that each time a mode is identified it is possible to decide which mode it is, that is, which is the class it belongs to. This is implemented through a classification algorithm drawn from the Machine Learning literature, which for the case at hand is the *k*-nearest neighbor (*k*NN) classification (Gareth J et al. 2013).

The time evolution of the modal frequencies for four structural modes over the entire monitoring period is represented in Figures 5.

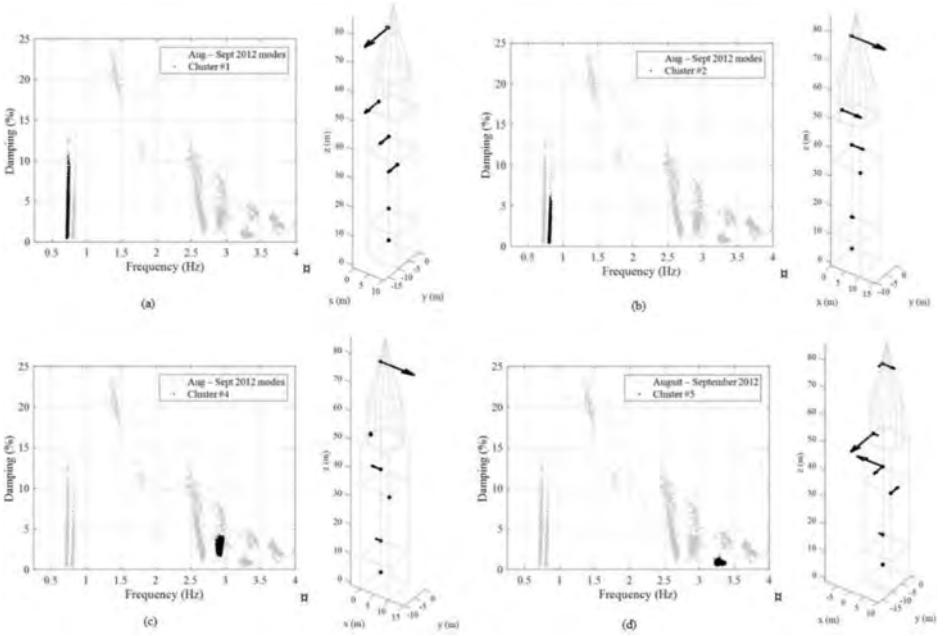

Figure 4. Clusters and mode shapes identified: (a) 1st bending mode (y-direction), (b) 1st bending mode (x-direction), (c) 2st bending mode (x-direction), (d) 1st torsional mode (Modified, source: Demarie G and Sabia D, 2019).

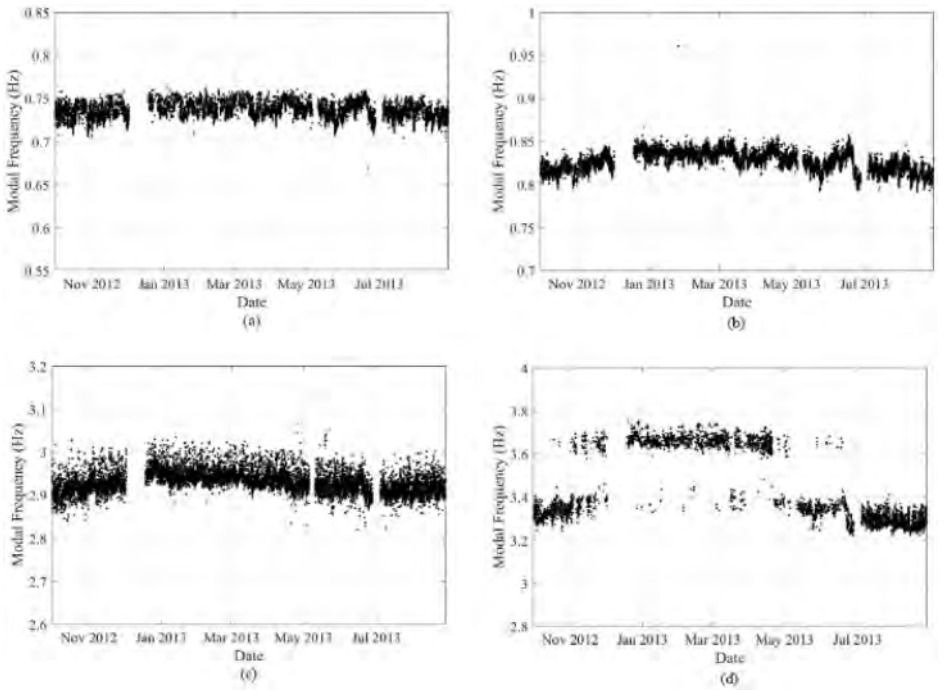

Figure 5. Modal frequency evolution: (a) 1st bending mode (y-direction), (b) 1st bending mode (x-direction), (c) 2st bending mode (x-direction), (d) 1st torsional mode (Modified, source: Demarie G & Sabia D 2019).

The modal frequencies, particularly those related to the bending modes along the x-direction and the torsional mode, clearly show a trend. The frequency values tend to increase from October to December 2012, remain stable on the average until April 2013 and then reduce to the initial values from July 2013 on. Such a variation is smooth for the bending modes, while it shows up abrupt for the torsional mode. The Figure 6 proposes once again the torsional modal frequency along with the time evolution of the temperature overlapped, showing the correlation between the quantities: the lower the temperature is, the higher the modal frequency are. Figure 7 shows the seasonal movements of the tower detected by a pendulum, and the trend of the temperature over the years (Lancellotta R & Sabia D 2013). The cause of such trends is likely to be found in the movement of tower towards the Cathedral when the temperature decreases, which is likely to affect the interaction between the two structures.

During the period considered for the monitoring a few relevant earthquakes happened, but no evidence of causing a change in the structural behaviour has been found in the identified modes.

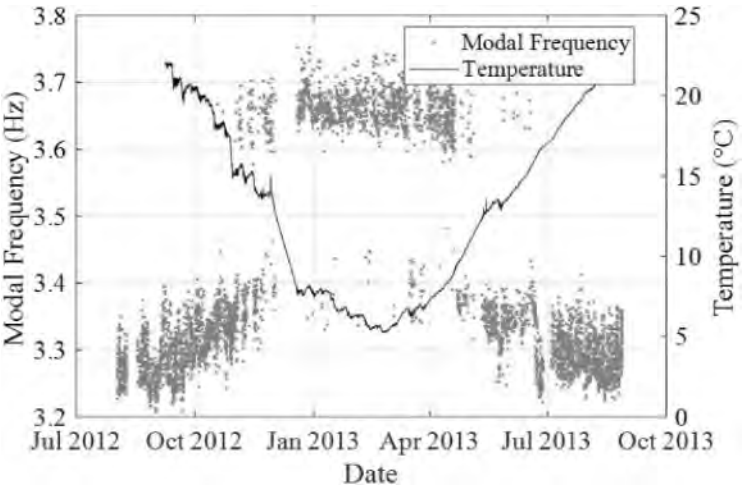

Figure 6. 1st torsional modal frequency and temperature time evolution (Modified, source: Demarie G & Sabia D 2019).

3.3.1 *The impact of temperature*

The hypothesis of correlation between the frequency variation of the tower, its seasonal movements recorded by the pendulum and the trend of the temperature over the year has been verified implementing a novelty detection algorithm able to recognize the deviations from a "normal" condition of data, i.e. the modal parameters.

The robustness of the procedure has been tested processing the data recorded in 2016. The evolution of the modal frequencies in this period resembles that observed in 2013. The algorithm classifies as an anomaly the variation of the 5th mode from 3.7 Hz to 3.35 Hz with respect of a training period of two month of data streaming. The Figure 8a shows the trend of the torsional mode in 2016, highlighting in red the detected novelties. Two distinct distributions of the variable frequency are clearly observable in Figure 8b.

Under the hypothesis of a correlation between the frequency variations and the temperature, the novelty detection algorithm has been finally trained using a one-year series of frequencies and temperature data, adopting a bivariate normal distribution and a 95% confidence interval as a rejection criterion. Introducing the temperature variable, the novelties are only detected when a mode shows a high frequency at warmer temperature and vice versa (Figure 9, red dots). The results confirm the interaction between the Ghirlandina tower and the Cathedral is highly influenced by the seasonal variation of temperature.

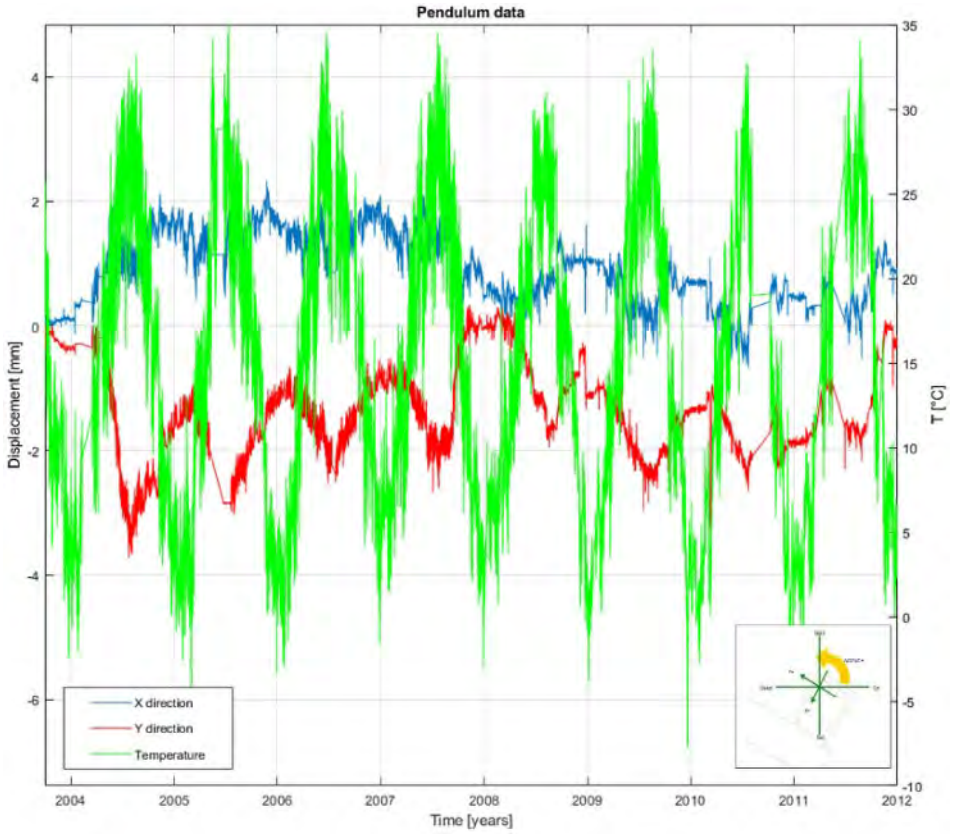

Figure 7. Seasonal movements of Ghirlandina tower and the trend of temperature.

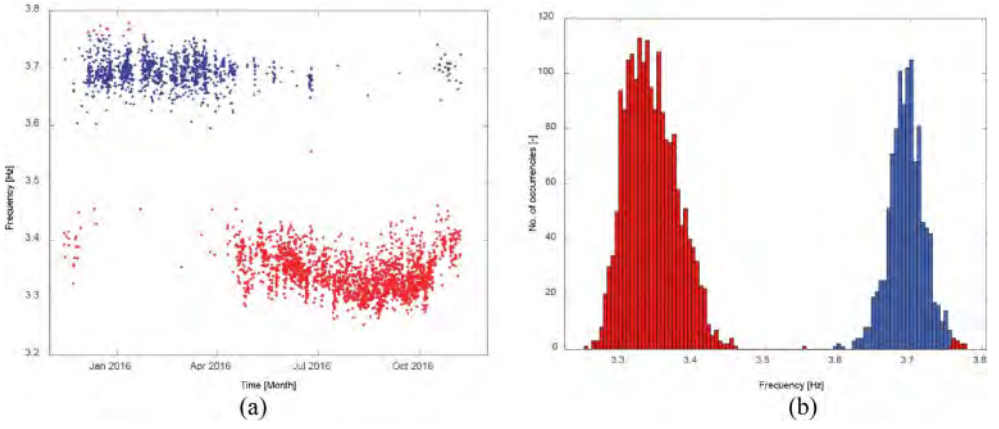

Figure 8. (a) 1st torsional modal frequency time evolution during the year 2016 and (b) statistical distribution.

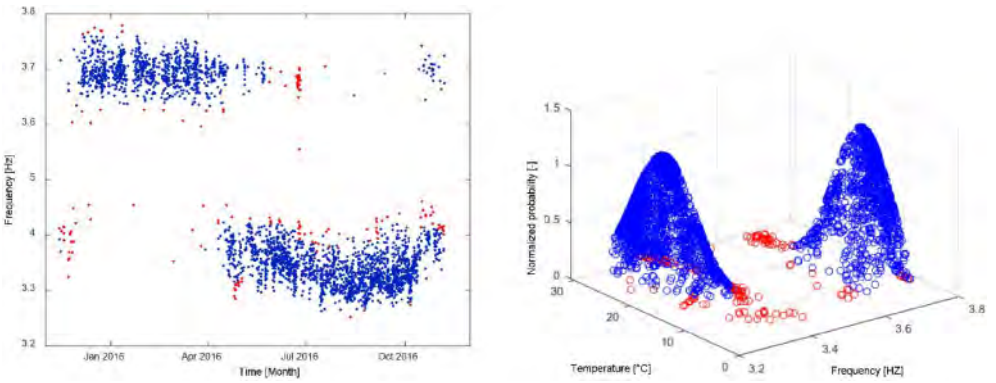

Figure 9. 1st torsional modal frequency evolution during the year 2016 with temperature correlation.

4 CONCLUSIONS

This paper introduces a novel method for the automatic identification of the vibration modes of a structure and implements a concrete approach for the long-term continuous structural health monitoring. The method belongs to the data-driven framework, it relies on some existing algorithms in the Machine Learning and Data Mining fields.

The long-term monitoring of an ancient masonry bell tower, the Ghirlandina Tower (Modena, Italy), has been selected as a real-world case application.

The obtained results prove the capability of the method not only to automatically identify the relevant structural modes with a very limited classification error, but also to highlight some long-term trends which have shown up during the August 2012 – August 2013 and January – December 2016 periods. In particular, the consistency between the seasonal trends of the modal frequencies, the movements of the tower and the temperature suggests the latter as affecting the structural interaction between the Tower and the Cathedral.

A novelty detection algorithm, based on a bivariate distribution which integrates the modal data and the temperature, has been implemented. The algorithm correctly classified the seasonal trends, recognizing the variation in frequencies correlated to the temperature.

As a final remark, even if the method has been applied off-line to a large database of measurement, it naturally allows for the extension to the on-line monitoring and classification of stream of data.

REFERENCES

Cadignani R, Lugli S. La torre Ghirlandina. Storia e restauro. Italy: Luca Sossella Editore, 2010.

Cadignani, R., Lancellotta, R. & Sabia, D. 2019. *The restoration of Ghirlandina Tower in Modena and the assessment of soil-structure interaction by means of dynamic identification techniques.* CRC Press, Taylor&Francis Group, London.

Cosentini RM, Foti S, Lancellotta R and Sabia D. Dynamic behaviour of shallow founded historic towers: validation of simplified approaches for seismic analyses. International Journal of Geotechnical Engineering, 2015; 9(1): 13–29.

Cross EJ, Koo KY, Brownjohn JMW and Worden K. Long-term monitoring and data analysis of the Tamar Bridge. Mechanical Systems and Signal Processing 2012; 35: 16–34

Demarie G, Sabia D. A machine learning approach for the automatic long-term structural health monitoring. Structural Health Monitoring, 2019(3): 819–837.

Farrar CR and Worden K. An introduction to structural health monitoring. Philos. Trans. Soc. A: Math. Phys. Eng. Sci. 2007; 365: 303–315.

Farrar CR and Worden K. Structural Health Monitoring: A Machine Learning Perspective. John Wiley & Sons Inc., 2013.

Gareth J, Witten D, Hastie T and Tibshirani R. An Introduction to Statistical Learning with Applications. Springer Text in Statistics, 2013.
Lancellotta R and Sabia D. The role of monitoring and identification techniques on the preservation of historic towers. Keynote Lecture in: 2nd Int. Symposium on Geotechnical engineering for the preservation of monuments and historic sites. London: CRC Press/Taylor and Francis Group, 2013.
Lancellotta R and Sabia D. Identification technique for soil structure analysis of the Ghirlandina tower. International Journal of Architectural Heritage, 2014; 9: 391–407.
Sabia D, Aoki T, Cosentini RM and Lancellotta R. Model Updating to Forecast the Dynamic Behavior of the Ghirlandina Tower in Modena, Italy. Journal of Earthquake Engineering, 2015; 19: 1–21.
Worden K and Manson G. The application of machine learning to structural health monitoring. Philos. Trans. Soc. A: Math. Phys. Eng. Sci. 2007; 365: 515–537.
Ying Y, Garrett JH Jr, et al. Toward Data-Driven Structural Health Monitoring: Application of Machine Learning and Signal Processing to Damage Detection. Journal of Computing in Civil Engineering. 2013; 27(6): 667–680.

Geotechnical Engineering for the Preservation of Monuments and Historic Sites III – Lancellotta, Viggiani, Flora, de Silva & Mele (Eds)

Shake table testing of pillared historical stone constructions (mandapam) of South India

Arun Menon, Tamali Bhowmik, Shibu Samson & Jofin George
National Centre for Safety of Heritage Structures (NCSHS), Department of Civil Engineering
Indian Institute of Technology Madras (IITM), Chennai, India

ABSTRACT: The earthquake vulnerability of historical pillared dry-stack constructions in granite, of a typology which is widespread in south India, is studied through dynamic uniaxial shake table tests on a full-scale model prepared as per ancient traditional rules for proportioning, dimensioning and construction. The non-linear kinematic method based on the upper bound rigid body limit analysis provide collapse factor and maximum deformation for the governing overturning mechanism, which agree with the results of the dynamic shake table tests. Though these constructions do not have joints articulated between posts, plinths, and lintels, and rely on frictional resistance against seismic action, the capacity of these constructions appear to be adequate for the level of acceleration and displacement demands due to seismic ground shaking in south India.

1 INTRODUCTION

A *mandapam* is a multi-purpose trabeated hypostyle hall, a common archetypal feature of the ancient Dravidian temple architecture of south India (see Figure 1). *Mandapas* typically originated as a single storied entrance hall with multifunctional use near the sanctum sanctorum of the presiding deity in a temple (Manohar et al., 2020, 2021; Ronald et al., 2018). In larger temple complexes, the *mandapam* serves as a spatial linkage between various hierarchical spaces of a Hindu temple, with a series of intricately carved stone pillars (e.g., thousand-pillared hall of Madurai Meenakshi Temple in south India). The primary structural members of a *mandapam* are the monolithic stone pillars and corbels, stone beams, and slabs, all typically in granite, which is found in abundance in peninsular India.

Figure 1. Typical Dravidian style four-pillared and sixteen-pillared symmetrical granite mandapa.

 DOI 10.1201/9781003308867-11

Extreme damage and loss of historical constructions of such architectural typology have been encountered in the past significant seismic events in the active regions in India such as Bhuj earthquake in 2001 (Mathews et al. 2003) and Barpak and Kodari earthquakes in Nepal in 2015 (Menon et al. 2017). A total collapse of pillared halls in sandstone triggered by the mass of the heavy domical roof in Rao Lakha Chattri in Bhuj (see Figure 2a-b) and complete overturning of the stone pillared construction in Nepal, despite the interlocking provided by the tenon and mortise joint (see Figure 2c-d) are common. Historical constructions in these seismically active regions do show evidence of seismic-resistant features such as positive interconnections between pillars and beams using iron dowels or articulated joints in stone. However, they prove to be inadequate in the presence of significant acceleration and displacement demands.

Although peninsular and south India is seismically less active than the northern and western regions, the complete absence of any seismic-resistant features such as interconnections at the post-lintel joints, and the reliance only on joint frictional resistance imply that these heritage structures may be highly vulnerable to even moderate earthquakes.

Figure 2. (a)-(b) Observed collapse in historical mandapa Rao Lakha Chattri in Gujarat (Bhuj. 2001) and (c)-(d) Collapse in a stone mandapa in Nepal (2015) with significant tenon-mortise joints.

Past investigation by the research team on historical constructions of the region aimed at the implementing a multidisciplinary methodology integrating seismic hazard, local site response, vulnerability, and exposure of historical building stock for seismic risk reduction in architectural heritage in India and Italy (Lai et al. 2009; Magenes et al. 2006; Palmieri et al. 2012). Limit analysis based seismic assessment of the mandapam revealed that their vulnerability is mainly due to the lack of proper interconnection between structural members (Ronald et al. 2018). The research work presented in the current paper is a culmination of the past research in dynamic shake table testing of a full-scale model of a mandapa conducted at the biaxial shake table facility at the structural engineering laboratory of IIT Madras. The earthquake ground shaking was simulated on a physical model designed and constructed by a traditional architect as per ancient Indian treatises on construction of temple structures.

2 SELECTION AND CONSTRUCTION OF EXPERIMENTAL MODEL

2.1 *Description of structural geometry*

In its simplest form, a mandapam is a free-standing unit constructed with in the post and lintel (or trabeated) technique in stone. The structural members are the monolithic pillars with pedestal,

shaft and stone capital, corbels, and beams, typically in granite. In Dravidian architecture, these members are merely juxtaposed over each other with dry joints, and lime mortar at the interface is used only for purposes of levelling, implying a total absence of interlocking at the joints and a total reliance on frictional resistance and precompression for lateral resistance. The typical spacing of pillars vary between 2-3 m. Wide stone sunshades rest on the beams, which are held in place, by the weight of overlying stone slabs of the roof spanning between beams, lime concrete overlay as a weathering course and short parapet walls.

2.2 *Expected behaviour under seismic action*

Past research based on limit analysis revealed that the collapse of such structures under lateral action is due to instability governed by the overturning mechanism, and not sliding despite the absence of interlocking at joints. Significant resistance to sliding is generally present and readers can see detailed research on characterization of joint parameters in such constructions elsewhere (Naik et al. 2021). Overturning resistance on the other hand depends on the geometry of the structure. Shorter mandapam are more vulnerable than taller ones due to their high fundamental frequency (3.6 Hz and 2.5 Hz were the fundamental frequencies of the 4-pillared and 16-pillared short mandapas, respectively). This is evident from the graph showing factors of safety against the governing overturning mechanism, for four different geometries of *mandapas* all symmetrical in plan, to peak ground accelerations corresponding to return periods: 95. 475, 975 and 2475 years for the south Indian town of Kancheepuram in Figure 3 (Ronald et al. 2018).

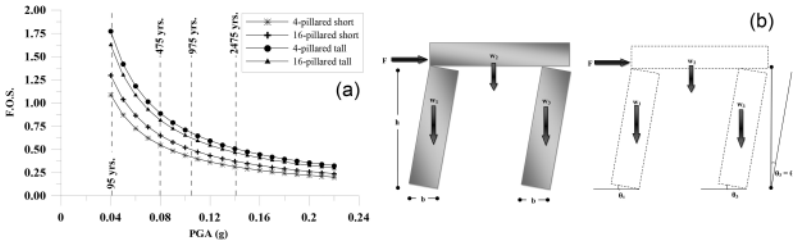

Figure 3. (a) Comparison of factors of safety against the governing overturning mechanism for the 4 mandapams to PGA corresponding to return periods: 95. 475, 975 and 2475 years for the south India town of Kancheepuram; (b) Idealisation of loads and geometry and kinematic action for overturning mechanism (Ronald et al. 2018).

2.3 *Description of Prototype and Model*

To experimentally study the structural typology using dynamic testing in the current research, a four-pillared granite *mandapa* was designed and constructed by a traditional architect (referred to as *Stapathy*) as per the traditional rules encoded in the ancient Indian treatises on temple architecture. To overcome the limitations imposed by the dimension of the shake table (i.e., 3.0 × 3.0 m: see section 3.1 for further details) and its payload of ten tons, necessitating a scaled model and consequent scaling of mass and time as per similitude requirements, a different approach was adopted based on the traditional rules for proportioning and dimensioning of structures. A real mandapa that could be accommodated within the table area, and within the maximum payload of the table was designed by the traditional architect (as the prototype) and its full-scale model was built on the shake table.

The plan dimension of the four-pillared mandapa worked out to 1.509×1.509 m and the total height of the structure worked out to 2.282m. The sectional elevation and plan of the mandapa are provided in Figure 4 showing the different components (plinth, stone pillars, corbels, beams, stone slabs, sunshade and lime concrete roof: respective traditional names are also provided in the figure) and the isometric view of the stone structure can be seen in Figure 5. The monolithic granite

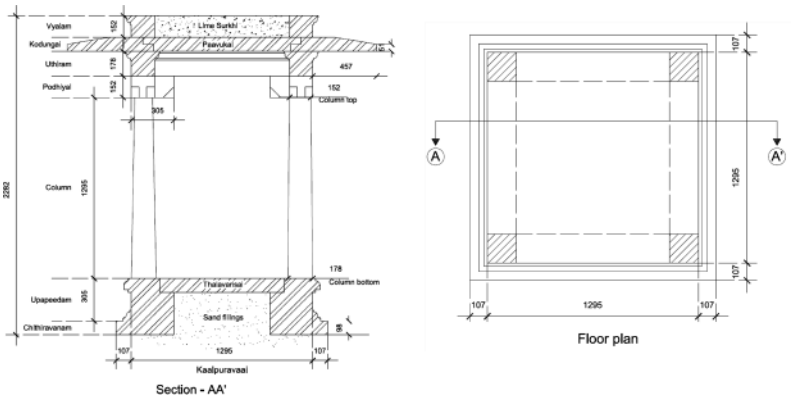

Figure 4. Cross-sectional elevation and plan of the full-scale model of the four-pillared mandapa.

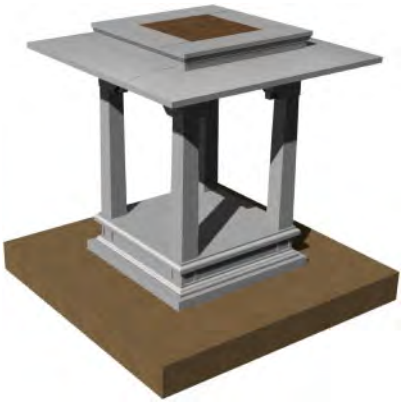

Figure 5. Isometric view of the mandapa.

columns are of height 1.295 m and have a base square cross section with side dimension of 178 mm, tapering to 152 mm at their top. The central volume of the plinth is filled with graded sand.

The different structural components in granite (i.e., monolithic pillars, beams, corbels and stone blocks for the plinth and sunshades) were sculpted at the traditional architect's sculpting yard, transported to the laboratory, and assembled on the table, predominantly as a dry stack construction with minimal use of joint mortar (traditional lime) only to serve for purposes of levelling and not as a bonding agent. The different stages of construction of the mandapa can be seen in the sequence of photographs in Figure 6.

The stone blocks of the plinth are assembled over a saturated graded sand bed 150 mm deep confined using steel channels around its edge. The purpose of the sand bed is to allow for levelling of the different blocks of stone so that verticality of the construction is maintained as the construction progresses. The depth of the sand bed is not significant enough to alter the table motion characteristics before being transmitted to the specimen. The monolithic pillars, corbels are assembled on the completed plinth, and the monolithic beams and multiple stone blocks composing the sunshades are assembled thereafter. The stone slabs spanning between the beams lock the cantilevered sunshades in place (see cross-sectional elevation in Figure 4). A weathering course in brick jelly lime concrete is provided over the stone roof slabs, and together with the parapet wall constructed finally, act as the counterweight for the cantilevered sunshades.

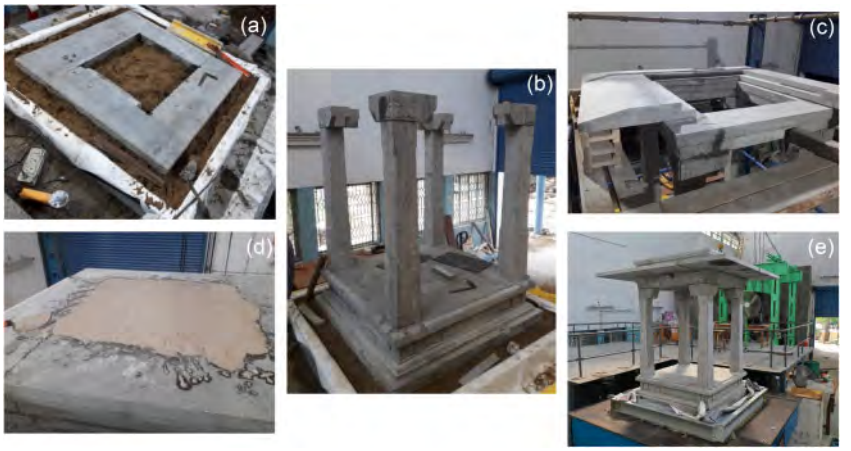

Figure 6. Construction sequence of the mandapa on the shake table: (a) assembly of stone blocks of the plinth over a graded sand bed; (b) placement of pillars and corbels on the completed plinth; (c) assembly of sunshades over the beams; (d) provision of lime concrete weathering course over the stone roof slabs; (e) completed model with parapet wall as counterweight for the cantilevered sunshades.

3 EXPERIMENTAL TEST SET UP AND SELECTION OF GROUND MOTION

3.1 *Description of shake table facility*

The biaxial seismic test simulator (see Figure 7) is a shake table of dimension 3.0 m x 3.0 m in plan, operated by two 25-tonne servo-hydraulic actuators in two horizontal directions. The table has a maximum payload of 10 tons and can generate a maximum velocity of 1.0 m/s, a maximum stroke (displacement) of +/- 250 mm, and a maximum acceleration of 1.1 g (110% of g), all with maximum payload. The bare table can generate a maximum velocity of 1.4 m/s, and a maximum acceleration of 2.17 g (217% of g). Scaled or full-scale specimens of structural components and systems can be mounted on the table and subjected to real earthquake acceleration records or sine sweeps within a frequency range: 0-50 Hz. The table is supported on a reaction mass of 750 T created by in-situ concreting, going down to a depth of 4.5 m from the finished floor. The actuators are protected by a raised steel structural floor from falling debris of the test specimen. In the current testing program, only one actuator was active, while the second was kept locked.

Figure 7. Biaxial 3.0×3.0m shake table test facility at structural dynamics laboratory at IIT Madras.

3.2 *Instrumentation Plan*

Ambient vibration test (AVT) was carried out on the mandapa model prior to the seismic test to establish global dynamic modes and frequencies through Dynamic Identification (DI). The modal information from AVT has been estimated by using the Operational Modal Analysis (OMA) which is also referred to as output only modal analysis. AVT was performed using 8 numbers of PCB®piezo-electric accelerometers with sensitivity equal to 1.0 V/g and with a dynamic range of ± 5.0g and a Quantum X 840B 24 bit 8-channel analogue-to-digital converter system. The graphical user interface (GUI) for data visualization and real time control was achieved by CATMAN®– a commercial software. The identified natural frequencies of the model were 7.86 Hz (first translational mode) and 10.01 Hz (second translational mode) and 13.43 Hz (torsional mode).

A total of uniaxial 16 PCB®piezoelectric accelerometers with sensitivity equal to 1.0 V/g and with a dynamic range of ± 5.0g were mounted at different levels of the model, namely at the plinth, on the columns, on the beams and at the parapet level, to measure the response of the model during the seismic testing. In-built sensors of the shake table provide the table acceleration and displacement response. The positions of the uniaxial accelerometers along the loading direction are shown in Figure 8 below.

In addition, linear variable differential transducers (LVDTs) were placed to measure the model displacements, and five digital video cameras were positioned around the model to capture the response of the model.

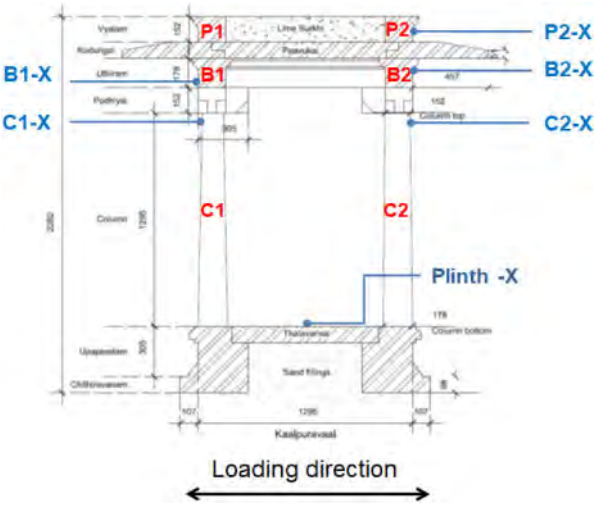

Figure 8. Positions of uniaxial accelerometers mounted on the specimen.

3.3 *Selected ground motion record*

Based on an estimate of the fundamental frequency of the model, the ground motion record was so chosen to ensure significant seismic energy around the structural frequencies of interest. In addition, a ground motion record with multiple significant oscillations is preferred to take the model through enough inelastic cycles.

In the absence of instrumented significant earthquakes from south India, the acceleration record pertaining to the Montenegro (ex-Yugoslavia) earthquake of 15th April 1979, registered at Bar-Skupstina Opstine station for a total length of 47.84 seconds, was adopted for the seismic test on the mandapa. The acceleration, velocity and displacement time histories of the record are reported in Figure 9. The PGA of the record was 0.35g.

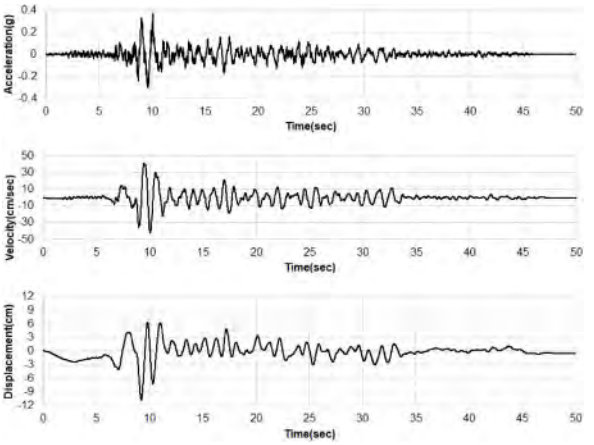

Figure 9. Input acceleration, velocity, and displacement time history (Montenegro, 1979 at Bar-Skupstina Opstine station).

4 DYNAMIC TESTING AND OUTCOME

A sufficient number of tests within the elastic range of the structural response was selected before acceleration levels capable of inducing mechanism formation and potential collapse. The necessary scale factors were selected based on analytical estimates of model response discussed in section 5 of the paper.

Table 1 reports the seven runs that were performed before the collapse of the model in the final run. The target peak table acceleration and the recorded peak table acceleration are reported showing significant disparity between the targeted and achieved peak accelerations, which is typically expected at low levels of input acceleration. Satisfactory convergence between target and achieved table accelerations are seen in the runs 5 and above. The peak table displacements provide an indication of the increasing displacement demands that the model has been subjected to in the seven runs.

The test was prematurely terminated after the loss of the specimen in Run-7 at a table peak acceleration of 0.146 g with a maximum displacement demand of 46 mm. The first instance of formation of overturning mechanism was observed in Run-7, while even in Run-6 when the table PGA reached 0.12g with the peak displacement demand at 30.5 mm, overturning was apparently not triggered.

Table 1. Shake table runs.

Test	Target peak table acceleration		Peak table acceleration (g)	Peak table displacement (mm)
	% Montenegro EQ	PGA (g)		
Run 1	2%	0.008	0.14	16.8
Run 2	5%	0.018	0.10	17.4
Run 3	10%	0.0326	0.15	16.5
Run 4	15%	0.055	0.13	12.0
Run 5	20%	0.06	0.086	20.23
Run 6	30%	0.11	0.12	30.5
Run 7	50%	0.175	0.146	46

The recorded response accelerations in the direction of seismic excitation are reported in Figure 10 at three of the instrumented locations, namely the top of the plinth, at the level of the beams

(B4-X) and at the level of the parapet (P3-X). Graphs in Figure 10 a, b & c report the response in Run-6, while Figure 10 d, e & f report the response in Run-7. The model showed overturning mechanism formation with hinges at the base of the pillars and on top of the corbels at the first significant oscillation of Run-7.

The peak response of the model at none of the levels exceeds 0.2g in Run-6 (table peak acceleration was at 0.12g), whereas in Run-7 with a table peak acceleration of 0.146g, the accelerations recorded at the plinth, beam and parapet levels are 0.6g, 0.6g and 1.0g, respectively, just before the collapse of the specimen.

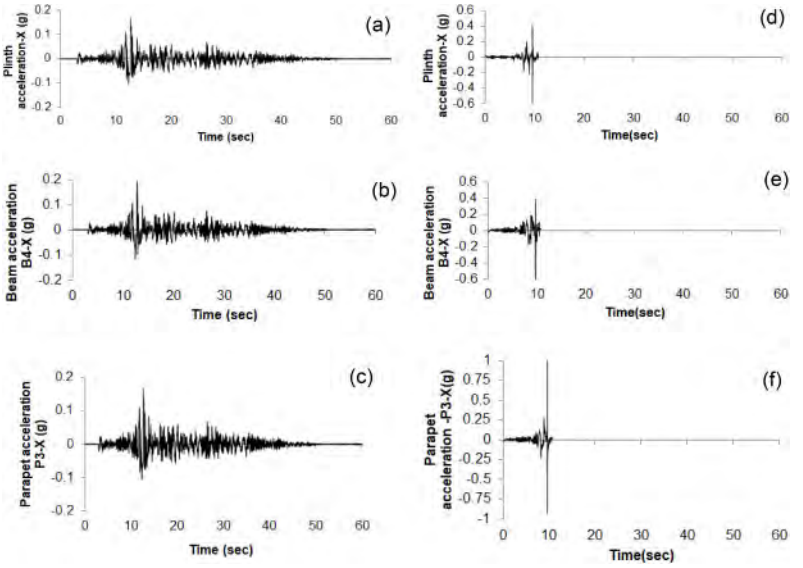

Figure 10. Run-6 (a, b, c) and Run-7 (d, e, f) response accelerations at top of the plinth, at the level of the beams (B4-X) and at the level of the parapet (P3-X) in the direction of the applied seismic excitation.

The series of images in Figure 11a-f are video captures of the model response in Run-7 from the different cameras positioned around the model. It is interesting to note how the monolithic pillar and the superimposed corbel acted as one integral unit with hinges at their base and top in the overturning mechanism at the rear end of the model, whereas the hinges have formed at the top and base of the monolithic pillar at the lead end. The reason for this lack of symmetry needs further investigation but might not be due to bonding from the mortar in the joint used for levelling purposes. The analytical model discussed in section 5 does not consider the difference in location of hinges.

Images in Figure 11e-f show the top view of the model confirming almost total response in the fundamental lateral mode. No slippage of the cantilevered sunshades or stone blocks of the parapet were observed during the tests, implying monolithic response of the construction. Disintegration was observed only at collapse of the model and upon impact of parts of the model with the protective steel scaffolding positioned around the model.

After the collapse of the model, examination of the structural members, particularly the stone pillars, revealed no crushing of the edges of the pillars implying rigid rocking response with no softening whatsoever. This is to be expected given the compressive strength of the granite, which is above 150 MPa. Softening can be expected in weaker varieties of stone such as sandstone and limestones, as observed in the Chattris of Bhuj in 2001.

No disintegration of the plinth was observed, nor was any sliding of the model. It must be mentioned here that the model was not restrained at the base of the plinth. The frictional resistance

of the granite-graded sand interface at the base of the model was greater than the lateral force demand at that level in all the seven runs.

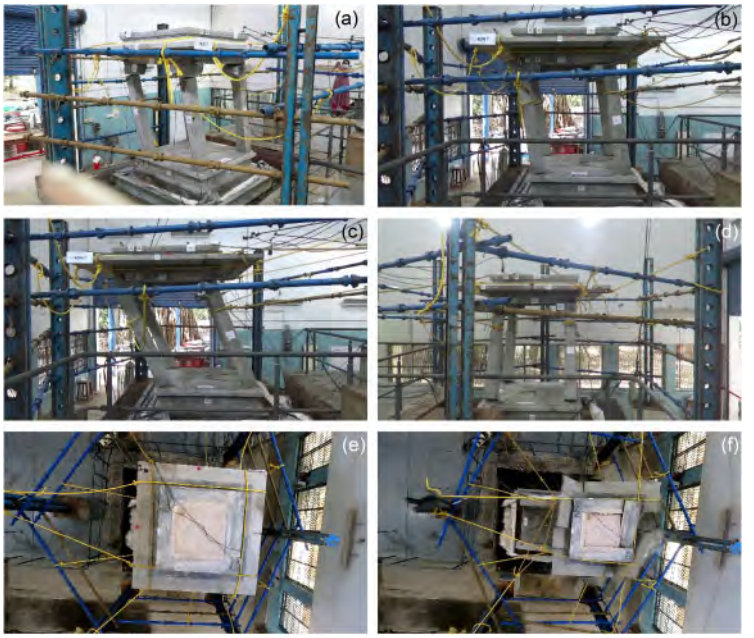

Figure 11. Images from video capture during Run-7 (a)-(b) Overturning mechanism with hinges at the bottom and top of the corbels in the lead pillars versus the rear pillars, respectively; (c)-(d) side views of the model at the verge of collapse; (e) top view of the model at initiation of mechanism; (f) top view at collapse showing disintegration of the stone slabs of the sunshades.

5 ANALYTICAL MODEL PREDICTIONS

As demonstrated from the experimental tests, the portion of the Mandapa above the plinth (i.e., *upapeedam*) is involved in the collapse mechanism. The system behaves like a chain of rigid bodies connected at the hinges at the onset of the collapse mechanism. Further, as mentioned earlier, there was no evidence of crushing of the stone observed at the hinges. Since the system deformations are restricted to the plane of loading, kinematic limit analysis can be used to validate the experimental behaviour.

The theory of limit analysis assumes that the developed kinematic chain formed by rigid bodies linked by hinges is on the verge of collapse if the equilibrium of external and internal forces is maintained and sufficient number of hinges form to turn the structure into a mechanism. This essentially means that the failure is by the formation of a collapse mechanism rather than exceedance of material strength (Clemente et al. 2010; Fanning et al. 2001; da Porto et al. 2007). The structure in this condition is now statically determinate. The theory of limit state analysis is based on the following fundamental assumptions.

- Equilibrium condition: As per the equilibrium condition, the external and internal loads should be balanced.
- Mechanism condition: Required number of hinges need to be generated to change the system to a mechanism.
- Yield condition: Material stresses should not be greater than the compressive strength (Block et al. 2006; Ochsendorf 2006).

The virtual work method is adopted, which proceeds by the identification of virtual displacements of each rigid block calculated at their center of gravity. The side view in Figure 12 shows the collapse configuration of mandapa geometry. The collapse configuration consists of a total of eight hinges, of which four symmetric hinges (HA, HB, HC, and HD) visible in the side view are shown in Figure 12. Hinges HA and HD allows rotation alone (θ) while the horizontal members of the kinematic chain such as beams, and the slab undergo translation without rotation.

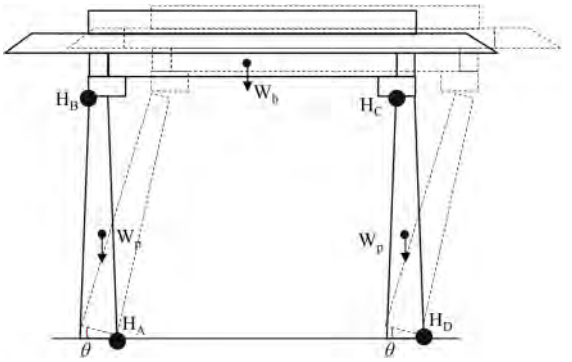

Figure 12. Collapse configuration of the mandapa.

The virtual displacements in each rigid block are calculated as follows. For the four pillars, the virtual displacements can be calculated as,

$$\begin{aligned} \delta x_{ij} &= (y_{ij} - y_i)\delta\theta \\ \delta y_{ij} &= (x_{ij} - x_i)\delta\theta \end{aligned} \tag{1}$$

Where x_i and y_i are the position coordinates of the rotating hinge, δx_{ij} and δy_{ij} are the virtual displacements of the pillar in the horizontal and vertical directions, respectively, and y_{ij} and x_{ij} are the centroidal coordinates of the pillars. For the four beams (i.e., *uthiram*), the virtual displacements remain identical as the member is subjected to translation alone, with no rotation. The virtual displacements can be written as:

$$\begin{aligned} \delta x_{jk} &= (y_j - y_i)\delta\theta \\ \delta y_{jk} &= (x_j - x_i)\delta\theta \end{aligned} \tag{2}$$

δx_{jk} and δy_{jk} are the virtual displacements of the beam in the horizontal and vertical directions, respectively. The self-weight of the slab contributed by stone slabs (i.e., *paavukkal*) and the sun-shades (i.e., *kodungai*) is equally distributed on to the four beams considering their tributary areas. The self-weight of the members in the kinematic chain is assumed to act at their center of gravity. The equilibrium equation of the Mandapam can now be written as:

$$\alpha = -\frac{4W_p\delta y_{ij} + 4W_b * \delta y_{ij} + W_{\frac{sl}{4}} * \delta y_{ij}}{4W_p\delta x_{ij} + 4W_b * \delta x_{ij} + W_{\frac{sl}{4}} * \delta x_{ij}} \tag{3}$$

Where W_p and W_b are the self-weights of the pillars, and beam (i.e., *pothiyal*) respectively, $W_{sl/4}$ is the self-weight contribution of the slab acting on a beam, δx_{ij} and δy_{ij} are the horizontal and vertical virtual displacement caused by the member of the kinematic chain in the horizontal and vertical direction, respectively. Unit weight of granite and the lime concrete are assumed as 2700kg/m^3 and 1300kg/m^3, respectively. The members above the plinth are only involved in the kinematic chain, as observed in the experimental campaign. Solving Eq.3 using linear kinematic

analysis gives the value of horizontal collapse multiplier, α, which triggers the collapse mechanism as 0.246.

Formulation of the capacity curve for the collapse geometry essentially requires the elaboration of a nonlinear kinematic analysis procedure. The support rotation at HA is incremented by $\delta\theta$, and the corresponding rotations and displacements in the other members of the kinematic chains are identified using equations 1 and 2. The equilibrium equation can now be written as:

$$\alpha(\theta) = -\frac{4W_p\delta y_{ij} + 4W_b * \delta y_{ij} + W_{\frac{sl}{4}} * \delta y_{ij}}{4W_p\delta x_{ij} + 4W_b * \delta x_{ij} + W_{\frac{sl}{4}} * \delta x_{ij}} \tag{4}$$

Eq.4 is applied to the deformed geometry of the *mandapa* corresponding to the increment in rotation, $\delta\theta$. The developed capacity curve for the *mandapa* is shown in Figure 13 using linear and nonlinear kinematics. The ultimate displacement capacity (d_o), where the horizontal seismic resistance drops to zero, is obtained as 71mm. A performance limit is imposed on the capacity curve which is termed as a near collapse limit state (DL), which is the displacement threshold a little before overturning (Lagomarsino, 2015), adopted as $0.4d_o$. The seismic collapse multiplier corresponding to d_{DL} is obtained as 0.15, which agrees with the experimental results. The results from rigid body limit analysis are normally an upper bound.

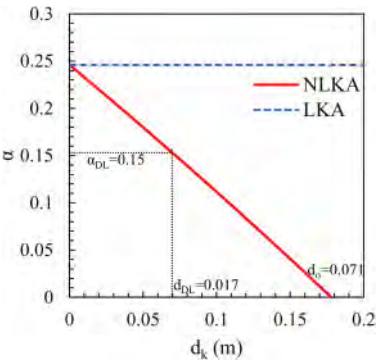

Figure 13. Capacity curve of the *mandapa* developed from non-linear kinematic analysis.

6 CONCLUSIONS

The seismic vulnerability of historical stone pillared constructions abundantly present in religious structures in India referred to as *mandapas* has been studied experimentally. Previous field-based investigations and analytical studies showed the vulnerability of the typology of dry stack stone pillared post and lintel constructions devoid of any positive interconnections between the monolithic posts and the plinth, and posts and lintels (or beams).

Dynamic shake table tests on a full-scale model in granite with a fundamental natural frequency of 7.86 Hz (natural period: 0.127 s) established from AVT, were conducted using scaled earthquake excitation from the Montenegro earthquake of 1979 with significant energy content between 0.1 and 1.0 Hz. The collapse of the structure is governed by the overturning mechanism with hinge formation at the base and top of the pillar or base of the pillar and top of the corbel, with the monolithic pillar and the corbel acting as one unit in the latter.

Mechanism formation was not observed even at a peak table acceleration of 0.12g and peak displacement demand of about 30.5 mm, which was the penultimate run of the dynamic test. The mechanism was triggered at a peak table acceleration of 0.146g and a peak displacement demand of 46 mm. These results are in agreement with those based the upper bound non-linear kinematic analysis from limit theory considering rigid rocking, which indicates that failure should be expected by overturning at a collapse factor of 0.15g and a displacement demand exceeding 28.4 mm.

These results show that the historical structural typology (mandapas) can be expected to have adequate safety against collapse for the level of seismic demand in south India but can be vulnerable in the active seismic zones of the country, where the resistance will depend on the strength and deformation capacity of the interlocking at the locations of hinge formation.

ACKNOWLEDGEMENTS

Research work presented in the paper was carried out with financial support from Dept. of Science & Technology (DST Grant No. SR/WOS-A/ET-103/2017), Govt. of India. The authors acknowledge infrastructural support from National Centre for Safety of Heritage Structures (NCSHS), Civil Engineering Dept., IIT Madras (Ministry of Human Resource Development, GoI D.O. No. 5-62013-TS-1). This work would not have been feasible without the assistance for design and construction of the *mandapa* from traditional architects (*Stapathy*) Mr. S. Kumaragurubaran and Mr. K. Gowri Sankar from Panrutti, Tamil Nadu.

REFERENCES

Block, P., Dejong, M., and Ochsendorf, J. 2006. *As hangs the flexible line: Equilibrium of masonry arches*. Nexus Network Journal, 8(2), 13–24.

Clemente, P., Buffarini, G., and Rinaldis, D. 2010. Application of limit analysis to stone arch bridges. *ARCH'10 – Proc. of 6th International Conference on Arch Bridges. Fuzhou, China, October 11–13, 2010.*

Da Porto, F., Franchetti, P., Grendene, M., Ranzato, L., Valluzzi, M., and Modena, C. 2007. Structural capacity of masonry arch bridges to horizontal loads. *Proc. of 5th International Conference on Arch Bridges (ARCH'07). Madeira, Portugal, 12–14 September 2007.*

Fanning, P. J., Boothby, T. E., and Roberts, B. J. (2001). *Longitudinal and transverse effects in masonry arch assessment*. Construction and Building Materials, 15(1), 51–60.

Jetson Ronald A., Menon, A., Prasad, A.M., Menon, D., & Magenes, G. 2018. *Modelling and analysis of a South Indian temple structures under earthquake loading*, Sādhanā, 43(74), 1–20.

Lagomarsino, S. (2015). *Seismic assessment of rocking masonry structures*. Bulletin of Earthquake Engineering, 13(1), 97–128.

Lai, C.G., Menon, A., Corigliano, M., Ornthamarrath, T., Sanchez, H.L. Dodagoudar, G.R. 2009. *Probabilistic seismic hazard assessment and stochastic site response analysis at the archaeological site of Kancheepuram in Southern India*, Research Report EUCENTRE 2009/01, IUSS Press, Pavia, pp. 250.

Magenes, G., Prasad, A.M., Dodagoudar, G.R., Lai, C.G., Macchi, G., Mathews, M.S., Menon, D., Menon, A., Pavese, A. and Penna, A. 2006. Indo-Italian joint research programme on seismic vulnerability of historical centres in south India, In P.B. Lourenco, P. Roca, C. Modena, S. Agrawal (ed.), *Proc. of the V International Conference on Structural Analysis of Historical Constructions, New Delhi, India, 2006,* pp. 1667-1674.

Manohar, S., Balamurugan, K., Shukla, S., Haneefa, M., Santhanam, M., Menon, A. 2021. *Multiscale fire damage assessment stone trabeated hypostyle halls*, International Journal of Architectural Heritage, Published online: 27 October 2021. DOI: 10.1080/15583058.2021.1992535.

Mathews, M.S., Menon, A., Chandran, S. 2003. Rehabilitation and retrofit of earthquake damaged monuments in Gujarat, in V. Jeyaraj (ed.) *Special volume on conservation of stone objects, The Commissioner of Museums, Chennai.*

Menon, A., Shukla, S., Samson, S., Aravaind, N., X. Romão, E. Paupério, A. 2017. Field Observations on the Performance of Heritage Structures in the Nepal 2015 Earthquake: Invited Lecture, *Proc. 16th World Conference on Earthquake Engineering, Santiago, Chile, January 9-13, 2017*.

Naik, P.M., Bhowmik, T. and Menon, A. [2021] *Estimating joint stiffness and friction parameters for dry stone masonry constructions*, Int. J. Masonry Research and Innovation, Vol. 6, No. 2, pp.232–254.

Ochsendorf, J. A. 2006. *The masonry arch on spreading supports*. Structural Engineer, 84(2), 29–35.

Palmieri M., Magenes G., Lai C.G., Penna A., Bozzoni F., Rota M., Macchi G., Auricchio F., Mangriotis M.D., Menon A., Meher Prasad A. & Murty C.V.R. 2012. Reduction of seismic risk of Roman and Hindu temples. In P.B. Lourenco, P. Roca, C. Modena, (ed.), *Proc. of VIII International Conference on Structural Analysis of Historical Constructions, 15–17 October, Wroclaw, Poland, 2012*.

Geotechnical Engineering for the Preservation of Monuments and Historic Sites III – Lancellotta, Viggiani, Flora, de Silva & Mele (Eds)

Site effects and intervention criteria for seismic risk mitigation in the ancient city of Pompeii: The case of the *Insula dei Casti Amanti*

L. de Sanctis, M. Iovino, R.M.S Maiorano & S. Aversa
University of Naples Parthenope, Naples, Italy

ABSTRACT: This paper deals with site amplification effects and possible strategies for seismic risk mitigations in the ancient Roman city of Pompeii, the well–known archaeological site near Naples, Italy, buried under 4–6 m of volcanic ashes and pumices during the eruption of Mount Vesuvius in 79 AD. The attention is focused on the restoration works of the *Insula dei Casti Amanti*, a block of masonry buildings in the city centre partly excavated in recent years, which included the stabilization of the excavation fronts, the preservation of the archaeological ruins and the replacement of the actual roofing system realised some decades ago. Two dimensional site amplification analyses carried out to quantify the seismic demand in the excavation fronts allowed to recognize the occurrence of remarkable aggravation phenomena at the crest of the slopes owing to the strong interference between morphology and topography. It is shown that a Newmark–type approach is adequate in this case to define the profile of the artificial slopes in a sustainable way. The focus is then set on the foundations of the new covering system of the *Insula*, a single span steel truss. A proper consideration of the load path followed until failure and the concept of interaction diagrams are fundamental ingredients to reduce as much as possible the impact of the new foundation system. As a final remark, the attention is placed on the likelihood occurrence of a double resonant mechanism between the subsoil and the archaeological ruins and on actions that have to be taken for the protection of the ancient city from future earthquakes.

1 INTRODUCTION

The ancient Roman city of Pompeii, near Naples, is among the most famous UNESCO World heritage sites. It was buried under 4 to 6 m of ashes and pumices after the eruption of Mount Vesuvius in 79 AD. This catastrophic event destroyed the city, killing about two thousand inhabitants but, at the same time, it paradoxically preserved its buildings, with their contents, for many centuries, until the breakthrough of its ruins, during the Reign of Bourbon King Carlo III, in 1748.

After the major earthquake of 62 AD, which caused widespread destruction in the bay of Naples, especially in Pompeii and surroundings, Mount Vesuvius erupted violently on 79 AD spewing forth a cloud of hot ashes and super–heated gases 14–32 km high as proved by Carey & Sigurdsson (1987). The eruption lasted 19 h from 1 pm of August, 24th to 8 am of August, 25th. On the first day, pumices and ashes began to fall down at an accumulation rate of 15 cm/h blanketing the city up to 2.8 m (Sigurdsson et al. 1985) and forming what is known as *Fall Units* (FU) or *Pyroclastic Fall*. Under the weight of the accumulated material, the roofs of many *Domus* collapsed, causing approximately 38% of the total casualties in Pompeii (Luongo et al. 2003). Yet rescues and escapes were still possible at that time. But the eruptive column collapsed and a rapid–moving, dense and very hot flow of molten rock, ashes and gas, referred to as *Pyroclastic density current* (PDC) or *Surge* of the Plinian event, began to slide downhill, knocking down every structure along its path

 DOI 10.1201/9781003308867-12

and, what is more, burning and/or asphyxiating any living being. Unfortunately, many inhabitants had just come back in the city after fleeing from the pyroclastic flow to rescue their stuff, thus going to meet a dreadful death. On the morning of August 25th, the large part of the Pompeii buildings resulted almost completely destroyed and only some buildings were still standing. It goes noting saying that this was a tragedy. From a different perspective, the circulation of air in the deposit of *Fall Units* allowed to keep the buried remnants almost dry, while the overlying *Surge* acted as a waterproof layer against rain infiltration. This was a lucky condition that made it possible to protect the ancient city for many centuries. Nowadays, two third of the urban agglomerate within the city walls have already been excavated. The ruins brought to light are like 'story–tellers', since they tell us – with an extraordinary narrative intensity – the last hours of life in Pompeii and, above all, the dynamic of the catastrophic event. Such preliminary discussion has great relevance to plan and implement actions for the preservation of the archaeological site.

In this paper, the focus is set on the case study of the *Insula dei Casti Amanti*, a block of masonry buildings in the city centre brought to light by recent archaeological excavations. This choice comes from the fact that the area surrounding this block has the utmost density of in situ investigations within the city walls. This is a very lucky circumstance, as the chance to carry out boreholes and other in–situ investigations is strongly limited because of the very severe restrictions of the *Archaeological Park of Pompeii*. However, the geotechnical issues related to the restoration works in the *Insula* are widespread in the ancient city of Pompeii, so that this case study can be hold as a paradigm for future actions in the archaeological site. An attempt is finally made to fathom the main findings of this local study into general conclusions so as to stimulate the debate about the most appropriate actions to be taken in the future for the seismic protection of the site.

2 SUBSOIL PROFILE IN THE ANCIENT CITY

Figure 1 shows the plan view of the ancient city of Pompeii, with the position of the boreholes carried out for a major project granted by the *Italian Government,* aimed at the preservation, conservation and public utilization of the archaeological resources of the ancient city and referred to as *Grande Progetto Pompei*. Most of the available investigations is from the ground surface of *Regiones* I–III–IV–V–IX – that have been only partly excavated – and just outside the city walls, while ample areas are devoid of boreholes, where the archaeological excavations have already been completed (*Regiones* VI–VII–VIII).

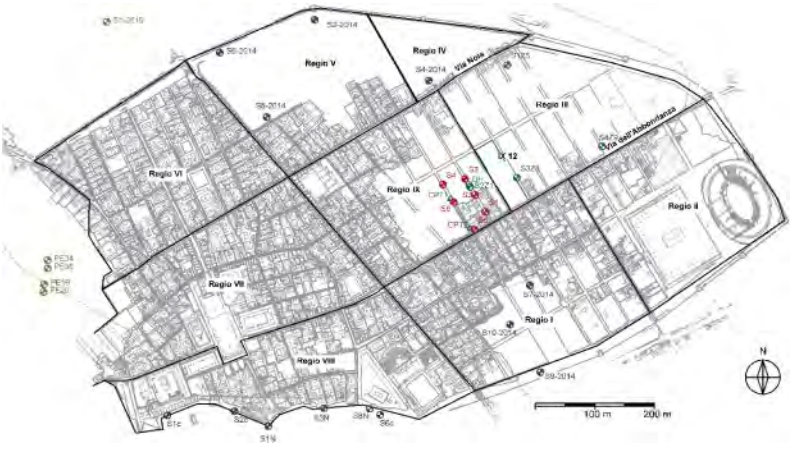

Figure 1. Plan view of the ancient city of Pompeii with the boreholes within the city walls.

The soil profile has been reconstructed in some of the *Regiones*. The typical subsoil conditions are shown in Figures 2–3. From ground surface, after a tiny layer of made ground, we first encounter the column of the Plinian eruption, consisting of the volcanic ashes of the so–called *Surge* underlain by the pumices deposit of the first phase of this eruption, until a depth of 4.7–6.8 m, which is the thickness of the materials blanketing the city. The level below the pumices consists of a paleosoil with varying thickness, interbedded with pyroclastic gravelly sand originated from the explosion of previous eruptive cycles, so that the separation between the paleosoil and the pyroclastic gravelly sand cannot be clearly distinguished. This layer was found until a depth varying between 8.0 and 9.7 m from ground level and, below it, a transition zone consisting of lava slags and dense sandy gravel can be considered the alteration of the underlying lava layer. The transition zone has often an erratic profile, as shown in Figures 2 and 3. Particularly, the morphological depression detected along the east alley of *Insula* XI–12 is worthy of note, as it will be explained in the ensuing.

In some boreholes (for example S10 in Figure 2), a chaotic level of building materials, including fragments of masonry, brick strips and travertine, mixed with pyroclastic sand and pumices, was found below the ancient paved road. In all likelihood, such levels are heaps of building ruins coming from the collapses caused by the major earthquake in 62 AD.

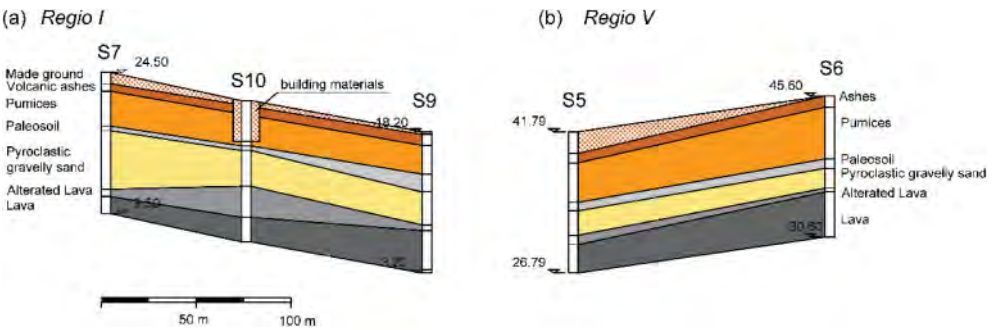

Figure 2. Soil stratigraphy in the area of *Regio V* (a) and *Regio V* (b). Ratio of elevation over distance is 1/5.

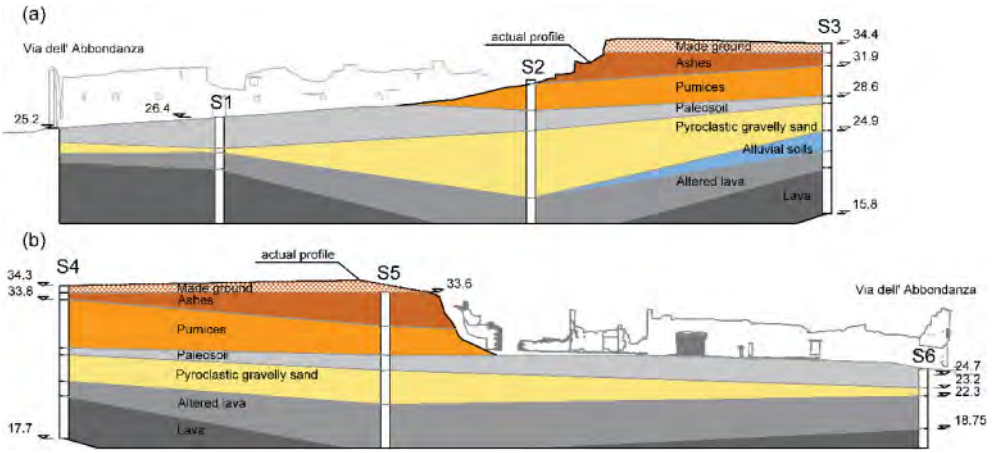

Figure 3. Soil stratigraphy in the area of *Insula* IX–12. Ratio of elevation over distance is 1/1.

3 THE CASE STUDY OF INSULA DEI CASTI AMANTI

3.1 *The Insula dei Casti Amanti: a magnificent story–teller*

The *Insula dei Casti Amanti* takes its name from a fresco on a wall in one of the houses located in this block, in which two lovers are kissing in a chaste way, in comparison with the subjects of other frescos in Pompeii (Figure 4). It is also referred to as IX–12, where the Latin number indicates the *Regio* in which the block is located. As shown in Figure 1, *Insula* IX–12 is delimited by the east–west paths of *Via Nola* and *Via dell'Abbondanza*, two of the main roads called *decumani*, and it is crossed by two alleys, which have been partly brought to light because of some recent archaeological excavations.

Figure 4. The fresco of the Chaste Lovers.

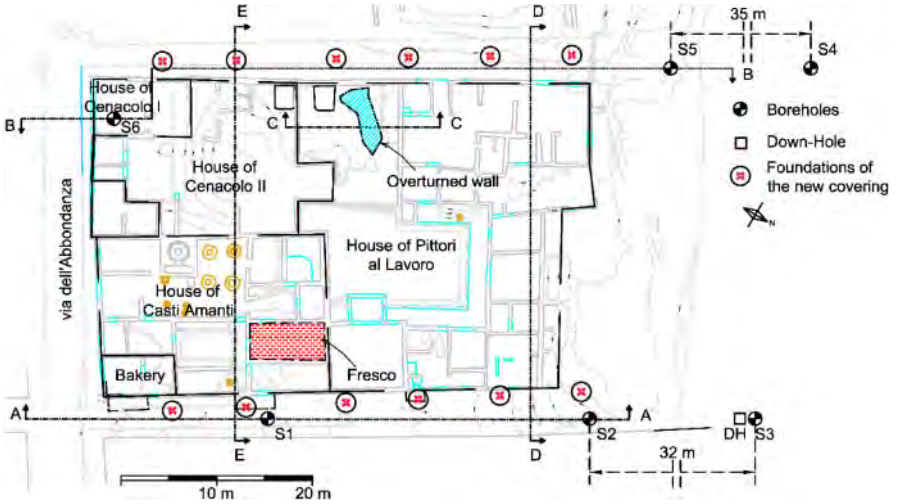

Figure 5. Plan view of the *Insula dei Casti Amanti*.

The archaeologist Vittorio Spinazzola began the excavations, which brought to light the *Insula* in 1911, starting from *Via dell'Abbondanza*. The basic idea of Spinazzola's project was to proceed along the main streets, in order to avoid problems generated by previous excavations strategies, such as the collapse of the *domus* upper floors, whose presence was proved by wall paintings recovered up until then. The idea of Spinazzola revealed as correct and, during the excavations in

Via dell'Abbondanza, the fronts of two– and three–storey buildings were recovered and, for the first time, the productive and commercial fabric of Pompeii, until then completely unknown, came to light. In 1924, the archaeologist Amedeo Maiuri followed the work of Spinazzola, continuing with the excavations in *Via dell'Abbondanza* and completely recovering all the *Insulae* of *Regiones I and II*. The *Insula dei Casti Amanti* was partly recovered in the period 1928–1934. It includes the following buildings: the *Casa del Cenacolo I and II*, the *Casa dei Casti Amanti*, partly devoted to bakery, the *Casa dei Pittori al Lavoro* (Figure 5). In all likelihood, at the time of the eruption in 79 AD, the *Casa dei Casti Amanti* was undergoing repair works after the damage produced by the 62 AD earthquake, while the *Casa dei Pittori a Lavoro* was distinguished by some preparatory works for wall paintings. Unfortunately, the *Casa del Cenacolo II* was seriously and irremediably damaged by a bombing raid in 1943, during World War II.

The soil profile near the faces of the artificial slopes was directly obtained from the visual examination of the outcropping soil. Along the western alley, the local stratigraphy clearly shows the transition between the pumices and the overlying volcanic ashes. There is also a perfect correspondence between the soil layering and the profile of the slope in that the front is steeper on the ashes layer and flatter on the pumices deposit, as shown in Figure 6a. As a noteworthy point, the ancient masonry walls on the boundary of adjacent *Insula* IX–11 improperly act as retaining walls, because of the excavation of west alley. Not surprisingly, these walls suffered severe damages, such as the partial collapse which brought to light the colonnade of *Insula* IX–11 and the pronounced tilting at the beginning of this alley, as shown in Figure 6b. A startling tale comes from a portion of wall still lying on a bed of pumices in a partially submerged room (Figure 7). This block collapsed by overturning under the impact of the pyroclastic flow and is a clear witness of the dynamic of the eruptive event. As highlighted by Luongo et al. (2003), the pyroclastic flow moved downslope along the direction perpendicular to *via dell'Abbondanza*.

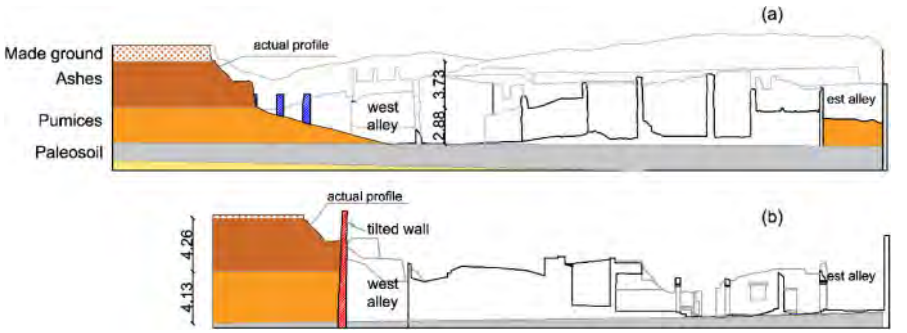

Figure 6. Soil stratigraphy in cross section DD (a) and EE (b). Ratio of elevation over distance is 1/1.

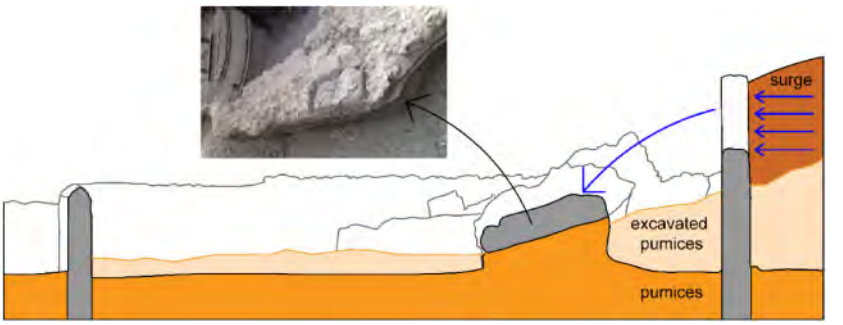

Figure 7. Cross section CC: overturned wall laying on the bed of pumices.

3.2 *Subsoil conditions in the area of the Insula*

The subsoil conditions in the area of the *Insula* have been already shown in Figure 3. They are in line with the general description of the subsoil layering supplied for the whole city in Section 2. The stratigraphy in this area may be summarized as follows: made ground from the soil surface until a depth of 1.3 m; volcanic ashes of the *Surge* up to a depth between 1.6 and 3.7 m; pumices deposit until a depth of 4.7–6.8 m; paleosoil with varying thickness up to a depth varying from 8 and 9.7 m, interbedded with pyroclastic gravelly sand originated from the explosion of the previous eruptive cycle; a transition zone consisting of lava slags and sand gravel; the bedrock of lava.

Figure 8 shows a schematic subsoil profile together with the results of the Down–Hole test, the Standard Penetration Test blow counts (N_{SPT}) and the geotechnical parameters obtained from all the available in situ and laboratory investigations carried out within the city walls (de Sanctis et al. 2019). It is worth mentioning that the cohesion of the volcanic ashes in Figure 8 is partly an 'apparent' term, due to the partial saturation of the soil. This quantity was back–figured by limit equilibrium analysis of a very steep front located in *Regio I* in which the safety factory was taken equal to 1.

From the roof of the altered lava downward, the average value of the shear velocity exceeds 800 m/s, so that this lava layer can be idealized as the reference bedrock. Figure 9 shows the decay of normalized shear modulus, G/G_0, and the variation of damping ratio, D, with the level of shear strain, γ, as obtained from soil samples retrieved from the volcanic ashes (S7C2) and the paleosoil (S7C5). For the purpose of the ground response analyses, the curves for the pumices and the pyroclastic gravelly sand are taken coincident with that of the paleosoil.

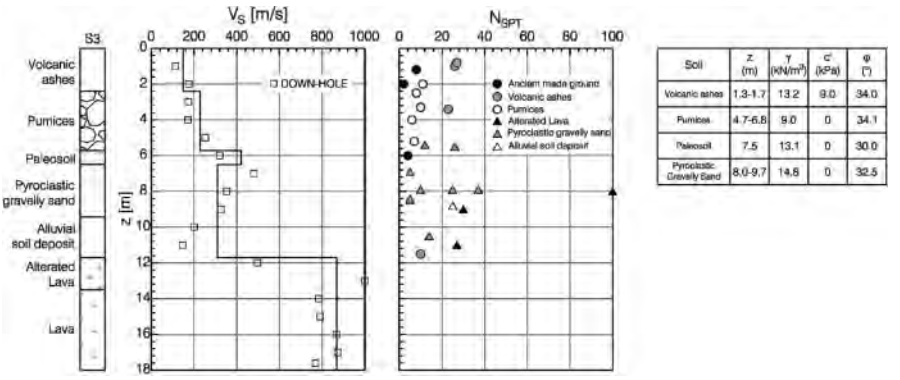

Soil	z (m)	γ (kN/m³)	c' (kPa)	φ (°)
Volcanic ashes	1.3-1.7	13.2	9.0	34.0
Pumices	4.7-6.8	9.0	0	34.1
Paleosoil	7.5	13.1	0	30.0
Pyroclastic Gravelly Sand	8.0-9.7	14.8	0	32.5

Figure 8. Subsoil properties.

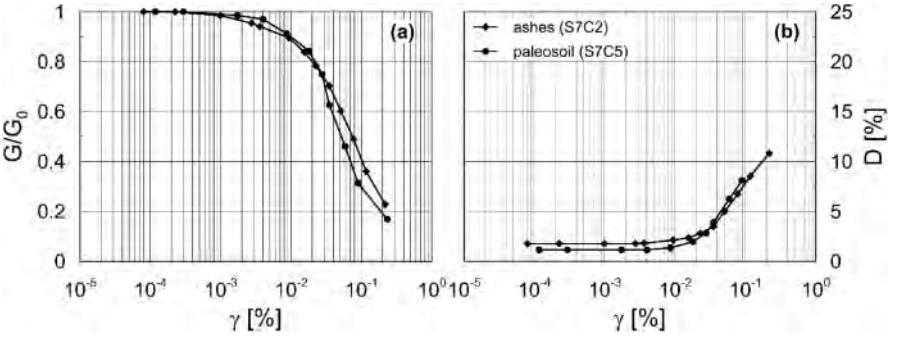

Figure 9. Results of the Resonant Column tests.

3.3 *Restoration works*

The restoration interventions of *Insula* IX–12, planned in the *Grande Progetto Pompei*, include the conservative restoration of masonry and paintings, safety measures for the excavation fronts and the design of the new *Insula* roof. The existing slopes surrounding the *Insula dei Casti Amanti* originated from previous archaeological excavations. Many small sliding events occurred in the past, indicating that these artificial slopes need to be stabilized. The excavation of the inner part of the *Insula*, not yet completed, was carried out in different phases. For this reason, the *Insula* was protected against rain and other meteorological events by a system of provisional roofs, each of them designed and built during the related excavation. Now this cover system is no longer adequate and it must be replaced with a single–span roof, which will permit the ground level of the whole *insula* to be left free of pillars. The third important purpose is the protection of the archaeological ruins from degradation owing to ageing effects and future earthquakes.

The geotechnical aspects considered in this projects are: (a) site amplification phenomena; (b) the stability of excavation fronts and elevator walls against the action of gravity and earthquakes; (c) seismic demand in the new covering and the limit state analysis of the pertinent foundations; (d) the seismic protection of the archaeological ruins. The geotechnical design was carried out taking into account the very relevant archaeological and historical value of the site, and taking advantage of what was defined by the ISSMGE – TC301 – *Preservation of Historic sites* (Aversa 2007, Burland & Standing 1997, Calabresi & D'Agostino 1997, Croce 1985, Flora 2013, Jappelli 1997, Viggiani 2013). Specifically, the following principles were adopted for the selection of the most appropriate solutions: (a) preservation of still–buried archaeological ruins; (b) minimum invasiveness of the excavations needed to re–profile the artificial slopes; (c) reduction of the impact of the new roof foundations; (d) reversibility and removability of the interventions; (e) reduction of the earth pressure on the walls of adjacent *Insula* IX–11; (f) full access to the archaeological site.

4 GROUND MOTION AMPLIFICATION

4.1 *Background seismicity and selection of natural recordings*

The seismic hazard is affected by far–field tectonic earthquakes originating from the Appennine chain, and by the activity of the two volcanic districts surrounding the city of Naples, the *Phlaegreas Fields* and the Somma–Vesuvius. The 6.9 moment magnitude (M_w) Irpinia earthquake in 1980 originated from the tectonic faults along of the Appennines (Meletti et al. 2008). A detailed representation of the main seismogenic sources in Campania Region has been recently reported by Ebrahimian et al. (2019). From data collected in the Parametric Catalogue of Italian Earthquake (Rovida et al. 2016), it is argued that the background area has been struck by 10 events with M_w in the range 6.1–7.2 over the period 1349–1980. Further details can be found in Licata et al. (2019) and Ebrahimian et al. (2019).

According to the recommendation of the Italian Ministry for Cultural Heritage, a life span of 50 years and a class of use IV were adopted for the excavation fronts. This is a reasonable choice, because the boundary of the excavated area will certainly expand in the near future. The return period of the life–safety limit state (ULS) is therefore 949 years. Since the depth of the Lava's roof is lower than 30 m, according to the Italian code (NTC 2018), adopting a similar soil classification criterion as Eurocode 8 EN–1998–1 (CEN 250 2003), the subsoil is classifiable as type E. Thus the maximum acceleration expected at the crest of the slope, a_{max1}, is:

$$a_{max1} = S_r \cdot a_r = 1.539 \times 0.168 = 0.259g \tag{1}$$

where S_r is the soil amplification factor and a_r the peak acceleration on outcropping rock. On the other hand, the life span of the new covering systems is taken equal to 100 years. With the same class of use as per the excavation fronts, the maximum acceleration at ground surface, a_{max2}, is

$$a_{max2} = S_r \cdot a_r = 1.415 \times 0.205 = 0.290g \tag{2}$$

On the other hand, the life span of the new covering system is taken equal to 100 years with the same class of use. The return periods of the life–safety limit states are therefore 949 and 1898 years, respectively. The same set of outcropping recordings defined by de Sanctis et al. (2020) is adopted for seismic site response analyses for both the excavation fronts and the new steel truss covering. In particular, the design earthquakes (M_w = 5.5–7 and epicentral distance, R = 25–70 km) were defined by a preliminary de–aggregation (partitioning) of the seismic hazard into selected magnitude and distance, so as to identify the modal contributions to the overall site hazard. Table 1 summarizes the main characteristics of the input signals (EQ) selected to define the response spectrum of the horizontal acceleration and the scaling factors (scal) corresponding to Equations (1) and (2).

Table 1. Input signals and scaling factors.

EQ	Code	Event	Date	M_w	R [km]	a_{max} [g]	scal (1)	scal (2)
1	290xa	Campano–Lucano	23/11/1980	6.9	32	0.216	0.777	0.950
2	290ya	Campano–Lucano	23/11/1980	6.9	32	0.323	0.521	0.636
3	292xa	Campano–Lucano	23/11/1980	6.9	25	0.060	2.804	3.428
4	292ya	Campano–Lucano	23/11/1980	6.9	25	0.060	2.805	3.429
5	949xa	Sicilia–Orientale	13/12/1990	5.6	29	0.061	2.754	3.367
6	4678ya	South Iceland	17/06/2000	6.5	32	0.053	3.146	3.846
7	5271ya	Mt. Vatnafjoll	25/05/1987	6.0	42	0.053	12.595	15.397

Figures 10a,b show the response spectra at a damping ratio ξ equal to 5% of the selected accelerograms scaled to 0.168g and 0.205g, respectively. Also shown for comparison is the mean spectral function and the spectrum specified by the Italian code for the life–safety limit state (SLV). In both situations, the mean spectral function compares well with the reference spectrum prescribed by the Italian code.

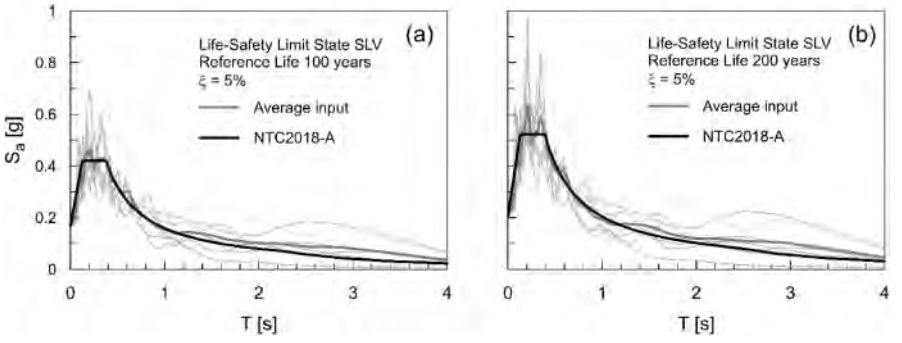

Figure 10. Response spectra of selected earthquake for excavation fronts (a) and the new covering (b).

4.2 *Excavation fronts: one– and two–dimensional wave propagation analyses*

Site amplification effects are evaluated by two dimensional (2D) analyses of wave propagation using the equivalent linear (EL) approach. The code LSR–2D (Local Seismic Response 2D rel. 4.3.1, Stacec) based on the finite element (FE) approach developed by Hudson et al. (1993) is adopted. Figures 11–12 illustrate the FE element domain for cross sections AA and BB, respectively. The natural recordings scaled to 0.168 g for seismic analysis of the excavation fronts are considered. They are applied to all nodes belonging to the lower boundary of the mesh, taking into account the change due to wave propagation from the outcropping rock to the lower bound of the model.

The energy dissipation due to radiation through the base of the model is accomplished by means of horizontal (c_x) and vertical (c_y) viscous dampers with properties:

$$c_x = \rho_b \cdot V_{sb}$$
$$c_y = \rho_b \cdot V_{pb} \tag{3}$$

where ρ_b, V_{sb} and V_{pb} are density, shear (s) and compression–dilation (p) wave velocity of the underlying lava layer. Theoretically, the displacement of the lateral boundary of the FE mesh should be equal to those in free–field. However, in case of low soil damping, the lateral boundaries should be far distant from the slopes to match the above conditions so that they are coupled with an isolated soil column with the same soil stratigraphy through a series of viscous dashpots, thus avoiding the re–introduction into the model of reflected waves.

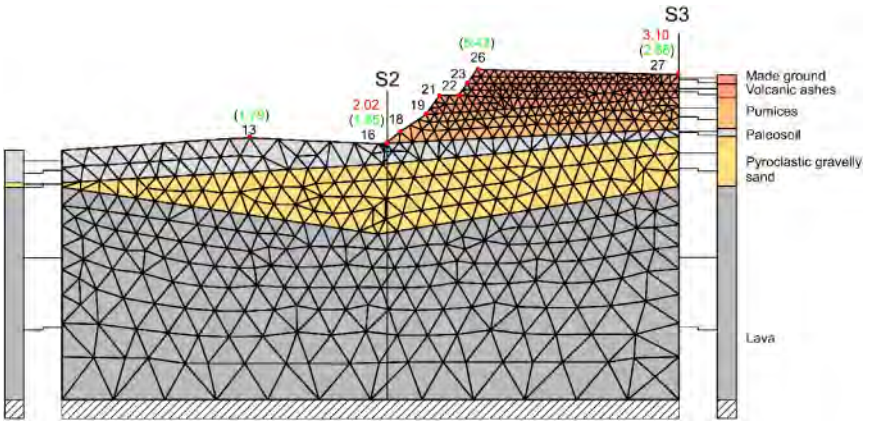

Figure 11. Section A, amplification function in 1D (out of brackets) and 2D analyses (in brackets).

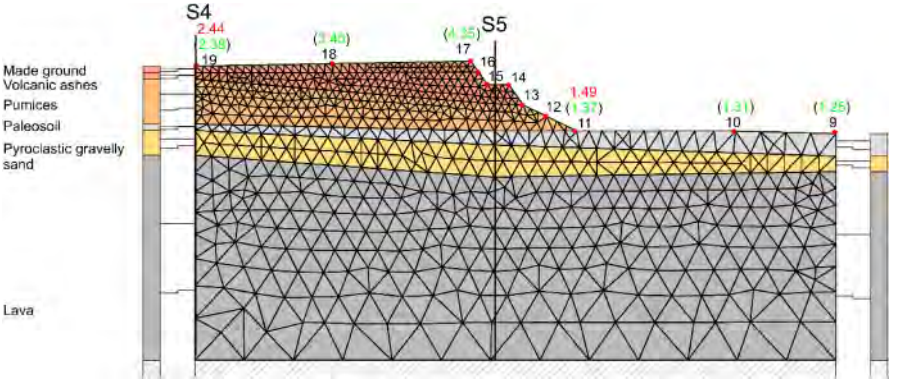

Figure 12. Section B, amplification function in 1D (out of brackets) and 2D analyses (in brackets).

The amount of amplification at some locations are shown in both the Figures 11 and 12 as well. The peak acceleration has to be intended as the mean value of the maximum ground acceleration for the selected earthquakes. The outcome of one dimensional (1D) ground response analysis is also shown for comparison at the toe and behind the crest of the slope. Such data have been gathered with the soil stratigraphy of the vertical line containing the selected point, so as to decouple soil (1D) effects from surface (topography) and morphology (valley) amplification. For cross section AA, the amplification factor is 5.42 at the crest (point 26), 1.85 at the toe (point 16) and 2.68 on the

boundary (point 27). The effect at the crest is worthy of note and, what is more, far greater than the amplification factor based on conventional subsoil classification (1.539). The situation for cross section BB is similar; in this case the amplification factor is 4.32 at the crest (point 17), 1.37 at the toe (point 11) and 2.38 on the boundary (point 19). This outcome indicates that the method based on conventional subsoil classification fails completely the prediction of amplification effects behind the slope. The overall effect in cross section AA is even greater than that expected for cross section BB because of the additional amplification owing to the local morphological depression of the lava layer. Following Ashford et al. (1997) and Bouckovals & Papadimitriou (2005), topography and valley effects may be expressed through the 'aggravation' factors, A_{crest} and A_{toe}, defined as:

$$\begin{aligned} A_{crest} &= \frac{a_{max}}{a_{crest}} \\ A_{toe} &= \frac{a_{max}}{a_{toe}} \end{aligned} \tag{4}$$

where a_{max} is the maximum acceleration of the reference point at ground surface from 2D analysis, a_{toe} the maximum acceleration at the base of the slope and a_{crest} the one occurring at the crest with the last two quantities evaluated in free–field. The aggravation factor A_{crest} is 1.75 for cross section AA and 1.78 for cross section BB. According to Bouckovalas & Papadimitriou (2005), who provided a deep insight into the phenomenon of aggravation in proximity of a slope in homogeneous soil conditions, this factor lies in between 1.15 and 1.45. They also suggest to take a unit aggravation factor at the toe. This recommendation is fully consistent with the value of 0.92 coming from 2D analysis. The very pronounced peak of ground acceleration at the crest gathered from FE analysis is due not only to surface (topography) and morphology (valley) effects, but also to the intense interaction between topographic amplification and soil effects originating from the very shallow compliant rock. As a final comment, a proper modelling of local soil condition and geomorphological properties is mandatory for a reliable estimation of the seismic demand in the excavation fronts.

Figure 13 illustrates the profile of maximum acceleration at ground surface from the selected earthquakes scaled to 0.168 g. The leap of this function on the crest is certainly remarkable. Yet the profile is almost constant on the side of the covering, suggesting that a 1D response analysis may be acceptable to evaluate the seismic demand in this structure.

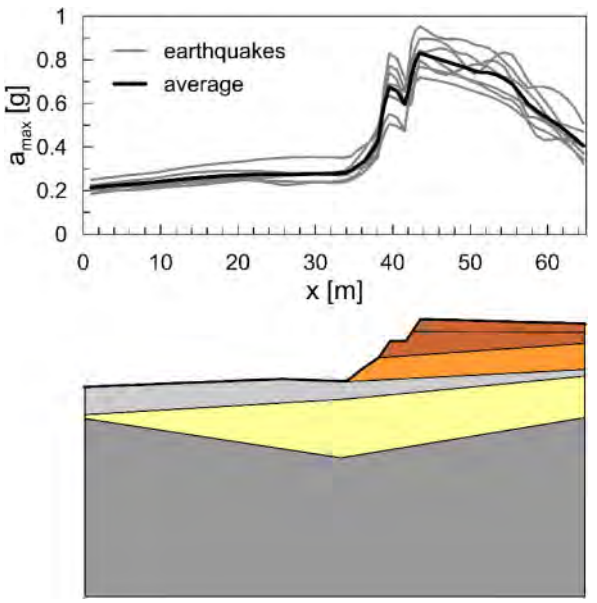

Figure 13. Profile of maximum acceleration at ground surface.

4.3 *New covering system: one-dimensional wave propagation analysis*

The local stratigraphy corresponding to the position of borehole S2 is first adopted for 1D ground response analysis. Figure 14a shows the response spectra of the selected earthquake at ground surface, the mean spectrum and the reference one based on conventional subsoil classification. Compared to this last function, the reduction of spectral acceleration at the very large period of the isolated structure is worthy of note. By contrast, at the very low structural periods, the mean function outstrips the code–spectrum, but this does not matter for the new covering. The change of mean spectra occurring from one alley to another is also investigated. Figure 14b shows the mean function corresponding to point 11 in Figure 12, on the opposite alley. It is argued from the comparison between these two figures that the local stratigraphy has a very little influence on the seismic demand for the covering system.

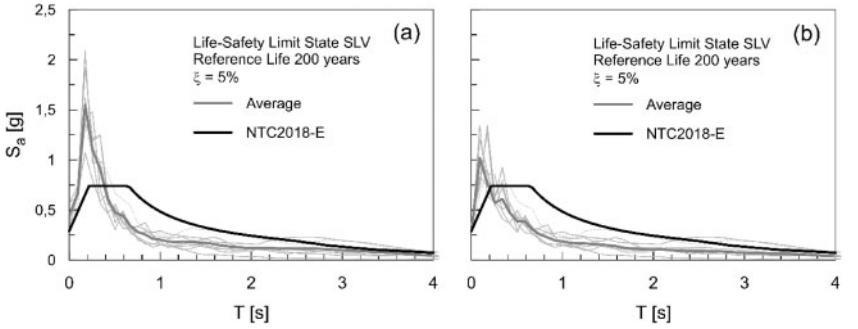

Figure 14. Response spectra from 1D analyses for cross sections AA (a) and BB (b).

5 EXCAVATION FRONTS

5.1 *General*

The most widespread approach in geotechnical engineering for slope stability analysis is the limit equilibrium method. It allows to identify the factor of safety (SF) of any potential failure surface. Many works in the literature deal with this approach. In all these methods, the earthquake action is idealized by a seismic coefficient (k_h) constant in space and time (pseudo–static analysis). The critical slip surface is defined as the slip line associated with the minimum safety factor. It may be defined under both static and pseudo–static assumptions, with the two critical surfaces not necessarily equal to one another. The value of the seismic coefficient bringing the soil mass above the critical sliding line to a status of incipient failure (SF = 1) is also referred to as 'critical' (k_{hc}) (and corresponding acceleration as critical acceleration a_c).

According to the Italian building code the seismic coefficient can be evaluated as:

$$k_h = \alpha \frac{a_{max}}{g} \tag{5}$$

where a_{max} is the maximum acceleration within the potentially unstable soil mass and α is a reduction factor accounting for the amount of tolerable displacement of the slope. In case of excavation fronts, for the earthquake action of the life–safety limit state the above reduction factor is equal to 0.38. Therefore, evaluating the maximum acceleration at the soil surface through the conventional subsoil classification would lead to $k_h = 0.10$. According to EN–1998–5 (CEN 250 2019), the equivalent seismic coefficient shall be taken as:

$$k_h = \frac{\beta}{\chi} \frac{a_{max}}{g} \tag{6}$$

where β is a reduction coefficient reflecting the ground motion asynchrony and χ a reduction coefficient accounting for the amplitude of the acceptable residual displacement for the considered limit state. As a matter of fact, χ is equivalent to the inverse of reduction factor α in Equation (5). For the life–safety limit state this coefficient shall be taken equal to 2. The reduction factor reflecting the spatial variability of ground motion may be evaluated as:

$$\begin{aligned} &\beta = 1 \lambda \leq 0.05 \\ &\beta = 1 - \tfrac{0.65}{0.35}(\lambda - 0.05) \;\; 0.05 < \lambda \leq 0.4 \\ &\beta = 0.35 \lambda > 0.4 \\ &\lambda = \tfrac{H}{T_m V_s} \end{aligned} \tag{7}$$

where H is the height of the slope, T_m the average period of the seismic action (Rathje et al. 1998) and V_s the mobilized shear wave velocity over the height of the slope. This simplified approach yields $\beta = 0.85$ for cross section AA and $\beta = 0.83$ for cross section BB, indicating about an additional 16% reduction due to the asynchrony of the motion as an average. Therefore, according to the above draft, the equivalent seismic coefficient would be about 0.11 for both the examined cross sections.

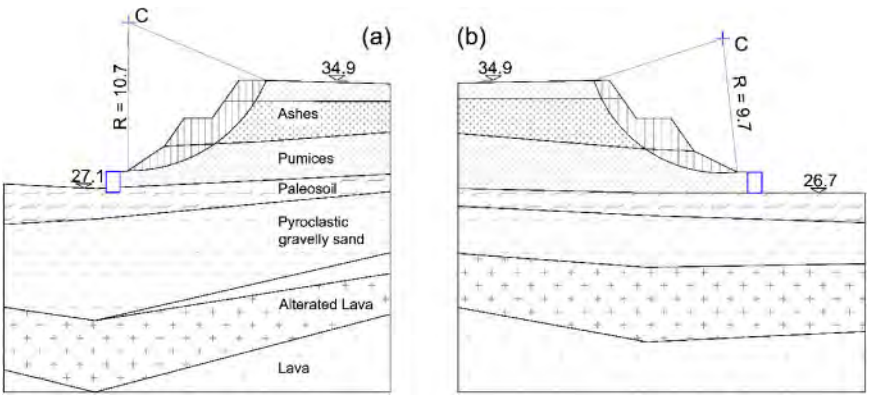

Figure 15. Critical surfaces for cross sections AA (a) and BB (b). Distances and elevation above sea level are in m.

The stability analyses are preliminary carried out by the pseudo–static approach following the method of Sarma (1975), which allows to evaluate the seismic coefficient corresponding to any prescribed value of the safety factor and vice versa. The selected method of analysis can be also applied under static conditions, by setting the seismic coefficient equal to zero. In this case, the critical slip lines (chosen as circular) represented in Figure 15 are obtained. The corresponding factor of safety are 1.342 and 1.463 for cross sections AA and BB, respectively. According to NTC (2018), under static conditions the partial safety factor for soil parameters (γ_M) is equal to 1.25, while the partial factor for resistance (γ_R) is 1.1. Since the slopes under examination are not subjected to variable load, the minimum allowable safety factor is $SF_{min} = \gamma_R \cdot \gamma_M = 1.375$. Although the SF of cross section AA is slightly smaller than SF_{min}, the excavation fronts can be considered stable enough under static conditions.

5.2 *Pseudo–static analysis*

A problem arises from the definition of the seismic coefficient equivalent to the earthquake induced lateral forces, variable both in space and time. Notably, while there is – at any instant of time – a remarkable variation of the calculated acceleration within the soil domain along the vertical

direction, the variation in the horizontal direction is almost negligible. Based on this outcome, the asynchronism of ground motion is taken into account in a simplified manner. First, reference is only made to points at ground surface from the toe to the crest of the slope. Second, for each input signal, the evolution by time of the acceleration profile corresponding to points at ground surface on the slope is evaluated and the instant of time at which the integral of this profile is maximum (or minimum) is identified. The critical profiles of the selected earthquakes obtained by projecting horizontally target points at the ground surface on the y–axis are plotted in Figure 16. The resulting mean profile is also shown for both sections. This procedure leads to an average acceleration of 0.4 g for section A and 0.37 g for section B. The corresponding seismic coefficients (k_h), evaluated by taking the above equivalent accelerations in conjunction with a reduction factor α = 0.38, are 0.152 and 0.140. They include soil surface (topography), morphology and ground motion asynchrony effects. As a noteworthy point, they are much greater than that gathered through the simplified approach by either the Italian code ($k_h = 0.10$) or EN–1998–8 revision ($k_h = 0.11$). The effect of the spatial variability of the ground motion may be roughly estimated by relating the average acceleration within the height of the slope to that expected at the crest. The ratio of these two quantities, which is equivalent to reduction factor β in Equation (5), is equal to 0.44 for Section A and 0.51 for Section B. Therefore, the simplified approach recommended by draft of EN–1998–5 revision underestimates the effect of ground motion asynchrony in a remarkable way.

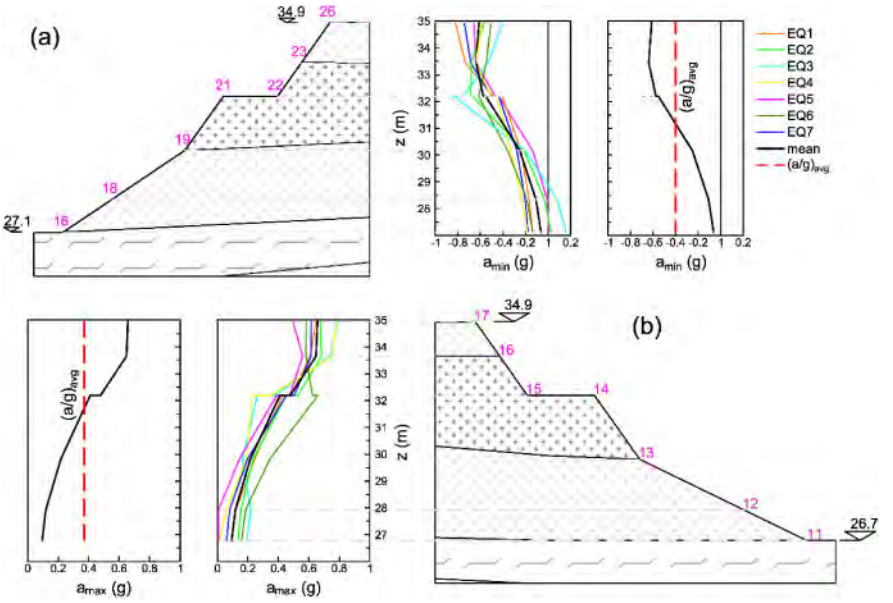

Figure 16. Acceleration profiles for cross section AA (a) and cross section BB (b).

The critical slip lines under pseudo–static assumption are identical to those identified in static conditions (Figure 15). The safety factors obtained by this approach for cross sections AA and BB are 1.05 and 1.17, respectively. Both are below the lowest allowable value prescribed by the Italian code for excavation fronts under earthquake actions ($SF_{min} = 1.2$). The distance from this value is particularly relevant for cross section AA, characterized by the morphological depression of the lava layer. As a final outcome, the slopes would be not stable enough according to the pseudo–static approach. Yet they could be re–profiled as shown in Figure 17. However, this expanded excavation would invade the archaeological remnants still buried. Furthermore, a flatter slope akin that in Figure 17 would imply far greater rainfall infiltration, a reduction of water suction and, consequently, a decrease of the 'apparent' cohesion. This design option is therefore in contrast with the need of preserving the archaeological ruins.

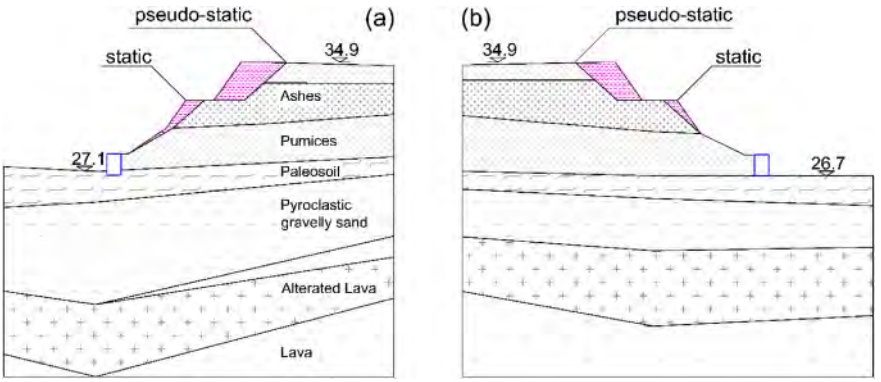

Figure 17. Slope profiles after conventional pseudo-static analysis for cross sections AA (a) and BB (b).

5.3 *Dynamic analysis by rigid block theory*

The stability of engineered earth slopes may be evaluated in several ways. The pseudo–static approach can only check whether or not slope instability will occur by judging the safety factor. An alternative, more elegant, option is the dynamic analysis by the rigid block theory (Newmark 1965), in which the landslide is modelled as a rigid–plastic friction block having a known critical acceleration. This method permits to evaluate the permanent displacements of the block subjected to an earthquake; the significance of the accumulated displacement is then judged. Compared to more sophisticated finite element calculations, the Newmark's model is a workable means, yielding much more useful information than the conventional pseudo–static approach (Jibson 1993). Permanent displacement analysis begins exactly when pseudo–static analysis ends, at the point where the critical acceleration, a_c, is exceeded. The block continues to move until the relative velocity between the soil mass and the base reaches zero and will slip again if the acceleration exceeds one more a_c. The process continues until the relative velocity drops to zero for the last time. While the classical Newmark theory was developed for translational sliding mechanism, the critical surface of the examined slopes has a circular shape. In this case, the damage or failure mechanism is represented by the accumulation of permanent rotations. A modification of the classical Newmark theory was therefore developed in this work to calculate the rotational displacement of the slopes. A similar approach has been proposed for instance by Zeng & He (2013).

The first step is the evaluation of the critical acceleration of the unstable soil mass. For the problem at hand, the pseudo–static analysis yields a critical seismic coefficient of 0.18 and 0.24 for cross sections AA and BB, respectively. The second step is the selection of ground input motion. In this case, an artificial earthquake is generated from each input signal, by averaging at any instant of time the acceleration profile within the height of the slope gathered from 2D analysis. Therefore, an artificial set of recordings is defined which encompasses the asynchronism of ground motion. Unlike the classical Newmark theory, reference is made to the rotation θ of the rigid friction block. When the seismic coefficient exceeds the critical one, the equation of dynamic rotational equilibrium of the sliding mass yields:

$$I_p\ddot{\theta} = (k_h - k_{hc}) \cdot W \cdot y_G \tag{8}$$

where I_p is the polar moment of inertia of the unstable soil mass, W is the weight of the same mass and y_G the lever arm of horizontal inertial action from the centre of rotation. Cumulated rotations are then calculated by double integrating those parts of the artificial ground motion lying above the critical acceleration using the rigorous algorithm of Wilson & Keefer (1983), taking into account explicitly the asymmetrical resistance of downslope and upslope sliding. A specific Matlab code was developed for the purpose of this work in which upslope rotations are prohibited. This is a reasonable assumption in many engineering problems as the critical acceleration in the upslope

direction is usually much greater than the peak ground acceleration. The time histories of rotation evaluated by this approach are plotted in Figure 18. In line with what recommended by Italian code, the mean effect can be chosen to evaluate the seismic performance of the slope. The average permanent rotations yield to the following permanent displacements, *w*:

$$\begin{aligned} w_{pA} &= R_A \cdot \theta_{pA} = 33 \text{ mm} \\ w_{pB} &= R_B \cdot \theta_{pB} = 8 \text{ mm} \end{aligned} \tag{9}$$

where θ_{pA} and θ_{pB} are the average accumulated rotations, while R_A and R_B are the radii of the critical surfaces for cross sections AA and BB, respectively.

The main practical problem related to the application of the sliding block method is how to define tolerable permanent displacements. The limits on calculated values could be related to (Matasovic 1991): (a) functionality of structures on the crest or at the toe of the slope; (b) the post–earthquake stability of the slope. With regard to the last point, the main problem related to excessive slope movements comes from earthquake–triggered macroscopic ground cracking in that water percolation in earthquake opened cracks can significantly reduce the static stability. Ideally, the dilemma about whether displacement can be tolerated or not may be overcome through database in which observed earthquake–triggered slope movements are correlated to measures of damage. The first attempt set for slopes in this direction is the one by the *State of Alaska's Geotechnical Evaluate Criteria Committee* (Idriss 1985). According to this criterion, for earthquake events with a probability of exceedance of 10% in 100 years as those considered in this work, earthquake triggered movement must not exceed 12 inches. Wilson & Keefer (1983) held a value of 100 mm as a conservative estimate corresponding to the occurrence of macroscopic ground failure. Jibson & Keefer (1995) used the (5, 10) cm range as the level of critical displacement leading to ground cracking and general failure of landslides in Mississippi Valley. The *Guidelines for Analyzing and Mitigating Landslide Hazard in California* (Blake et al. 2002) claim that the median displacement should be kept less than 50 mm to avoid damage in buildings that might be potentially affected by the critical line. Finally, the *Guidelines for Evaluating and Mitigating Seismic Hazard in California* (California Geological Survey 2008) recommend that calculated displacements do not exceed 100 mm. Based on this review about tolerable earthquake–triggered slope movements, the calculated displacements for the problem under examination can be considered compatible with the life–safety limit state. Therefore, the profiles labelled 'static' in Figure 17 can be finally adopted for the stabilization of the excavation fronts.

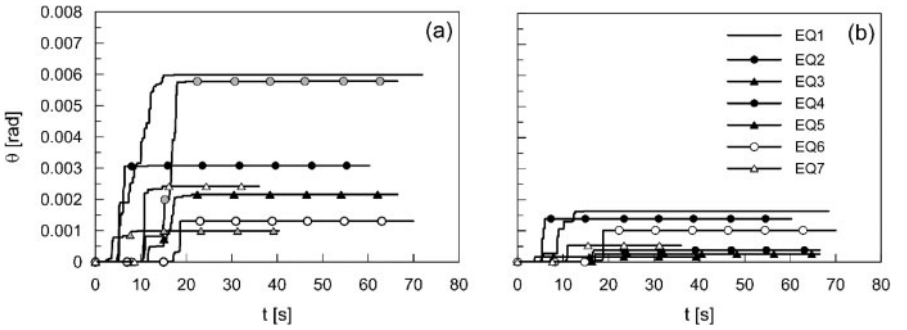

Figure 18. Permanent rotations of unstable soil mass by the sliding block theory.

6 FOUNDATIONS OF THE NEW COVERING SYSTEM

As mentioned before, the archaeological excavation of the *Insula* took place in more phases, simultaneously with the development of a disarticulated and uneven roofing system made up

of corrugated aluminium sheets, steel pipes and joints, which were connected to a number of tubular steel frames protecting the archaeological ruins. The design of restoration interventions included the replacement of this roofing system with a single–span steel truss covering, as shown in Figure 19. The new single–span covering, supported by two alignments of heavy steel columns distributed along the lateral alleys, is equipped with classical double–concave friction–pendulum seismic isolators. Such devices were put at the top of the steel columns, in order to facilitate their maintenance and, what is of the utmost importance, to create a unique isolation plane.

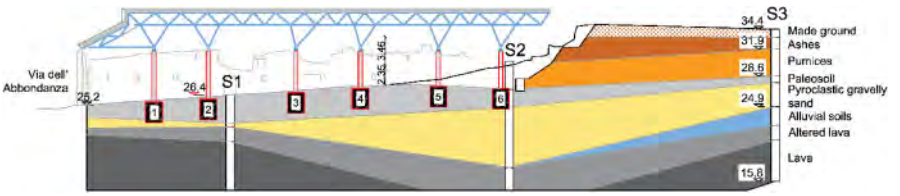

Figure 19. New covering system in place of the actual roof of steel pipes.

Concerning the foundation system, the key question to be answered is: what is the most appropriate choice in such difficult conditions? The large, multi–component loads transmitted by the columns are a critical issue, with the most severe eccentricity coming from the wind action (the effect of earthquake is of little importance due to the isolation devices). The design of the foundation system was inspired by the principles of the Venice Charter (1964) and the Cracovia Charter (2000), which suggest the choice of removable elements and the limitation of any visual impact. A weave of reinforced concrete, isolated caissons 2.1 m in diameter (D), 2.5 m high (h) and an embedment of 2.75 m, as shown in the cross section of Figure 20, has been adopted. It must be considered that this choice is mandatory to avoid the failure in uplift of the foundations under the leeward wind action. Yet it leads to undeniable advantages in comparison with shallow foundations. First of all, the irregular morphology of the lava layer is an inherent source of differential settlements which in turn may cause operational damages, while foundation settlements are minimized with such a choice. Second, the action of fluid concrete during installation on the adjacent ancient walls, if any, is of little importance due to arching effect in the soil. Third, the bearing behaviour of any caisson is independent of the wind direction. An effort is needed so as to minimize the impact of the circular foundations in the archaeological site by reducing their volume as much as possible.

Due to their geometric configuration, caissons are not easily treatable as shallow or deep foundations. From a conceptual point of view, the classical methods dealing with the calculation of bearing capacity of shallow foundations (e.g. Brinch Hansen 1970) may be indeed adapted to foundation caissons. Nevertheless, this method would neglect the tensile resistance and the shaft contribution to the ultimate capacity. An alternative approach is to use failure envelopes or more frequently, with respect to granular materials under drained conditions, yield envelopes, pointing out that the stress dependency of shear strength for granular materials leads to gradual yield and hardening with increased displacement in this case (Randolph & Gouvernec, 2011). Early studies on the yield surface of shallow foundations in sand were based on data collected by single gravity ($1g$) experiments (Butterfield & Ticof 1979, Dean et al. 1992, Georgiadis 1993, Gottardi & Butterfield 1993, Gottardi et al. 1999, Martin 1994, Nova & Montrasio 1991, Tan 1990, Ticof 1978), whose results indicated that the yield surface of such kind of foundation can be described by a rotated parabolic ellipsoid in (Q, H, M) force space, that is a rotated ellipse in the (M, H) plane and a parabola in planes along the Q axis at constant M/H ratio. A number of works has then focused on the response of caissons foundation for offshore wind turbines to combined loads (Achmus et al. 2013, Ahlinhan et al. 2019, Byrne & Houlsby 1999, Byrne & Houlsby 2001, Li et al. 2015, Villalobos 2006, Villalobos et al. 2009, Zafeirakos & Gerolymos 2016). Byrne & Houlby (2001) have extended the failure envelope equation by Gottardi et al. (1999) to include the effect to the foundation embedment ratio. Model tests on skirted foundations carried out in loose

sand have highlighted also the existence of non-zero horizontal and moment capacity in the tensile range of vertical loads (Villalobos 2006). In order to accommodate these experimentally observed behaviours, Villalobos et al. (2009) have proposed the yield surface equation:

$$\left(\frac{M/D}{m_0 Q_0}\right)^2 + \left(\frac{H}{h_0 Q_0}\right)^2 - 2a\frac{HM/D}{m_0 h_0 Q_0^2} - \beta_{12}^2\left(\frac{Q}{Q_0}+t_0\right)^{2\beta_2}\left(1-\frac{Q}{Q_0}\right)^{2\beta_2} = 0$$
$$\beta_{12} = \frac{(\beta_1+\beta_2)^{(\beta_1+\beta_2)}}{\beta_1^{\beta_1}+\beta_2^{\beta_2}} \tag{10}$$

where Q_0 is the uniaxial vertical yield load, a accounts for the rotation of the elliptical cross section in the $(M/D, H)$ plane, β_1 and β_2 are shape parameters influencing where the peak horizontal and moment loads occur under vertical load, the coefficients (m_0, h_0) control the size of the yield surface in the (H, M) load plane, Q_t is the pullout resistance and $t_0 = Q_t/Q_0$. In this study, the Brinch Hansen (1970) equation is first adapted to determine the axial capacity in compression. The tensile capacity, arising only from friction on the sides of the caisson, is then calculated. The values of m_0 in Equation 9 is a function of the caisson aspect ratio h/D and, for the case at hand, it can be assumed equal to 0.1 (Villalobos 2006). In this case, the lateral load transmitted by the column under the wind action is only a few percentage of the axial load, so that, for the purposes of this study, reference can be made to the problem of a caisson foundation under vertical and eccentric load. Figure 20 shows the failure envelope in the (Q, M) plane evaluated through Equation (10) for caisssons No. 2 and 5 (see Figure 19) and the load paths expected under the upward and leeward wind action, referred to as path 1 and 2, respectively. Notably, the latter action yields to a remarkable reduction of the axial load upon the caisson foundation. But, what is more, the current state (C) along with the pertinent load path (ACC') is far closer to the failure envelope. In a radial mapping criterion (Butterfield 2006), the partial resistance factor relies upon the direction of the load path (= AB'/AB or AC'/AC). The minimum value is 2.71 for caisson No. 2 and 2.44 for caisson No. 5. They are both consistent with that prescribed by the Italian building code ($\gamma_R = 2.3$). It is clear from this example that the contribution from the embedded shaft of the caisson to the ultimate moment is crucial for a sustainable design of the foundation layout. A proper consideration of the load path direction is essential as well.

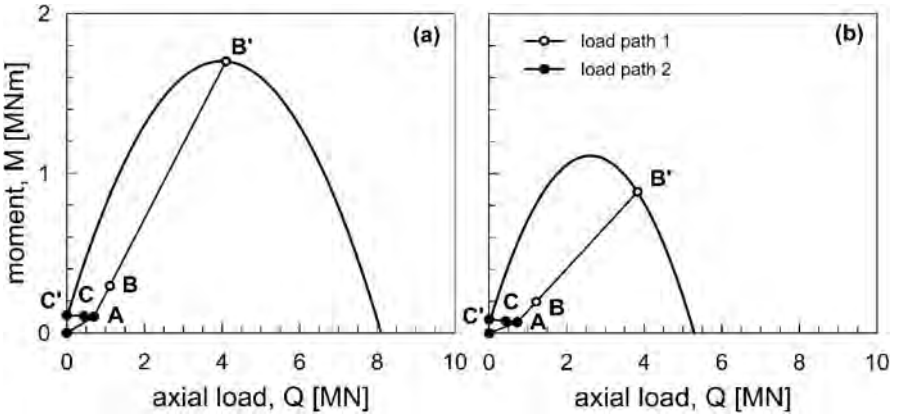

Figure 20. Interaction diagrams and load paths under the wind action for caissons (a) No. 2 and (b) No. 5.

7 DISCUSSION AND CONCLUSIONS

In this work the case study of the *Insula dei Casti Amanti* has been introduced as a ploy to discuss about the main geotechnical issues for the preservation of the ancient city of Pompeii. The restoration works included the re–profiling of the artificial slopes, the replacement of the actual roofing

system with a single–span truss covering and the restoration and protection of the archaeological ruins.

The seismic demand in the artificial slope was evaluated by means of two–dimensional analysis of wave propagation using the equivalent linear approach. A remarkable and unexpected aggravation was identified at the crest of the slope owing to the intense interference between soil effect and the very shallow bedrock. The asynchronism of ground motion was tackled by averaging at any instant of time the spatial distribution over the slope height, turning out a seismic coefficient far greater than that evaluated with the conventional subsoil classification. Thus, a proper modelling of wave propagation is crucial for a safe and reliable prediction of the seismic demand in the artificial slopes. Re–profiling action based on the classical pseudo–static approach would have not been compatible with the need of preserving the archaeological remnants surrounding the *Insula*. By contrast, the alternative, dynamic analysis by the rigid block theory was proved to be a sustainable approach for slope analysis in the archaeological site.

The foundation of the new covering system consisted of fully embedded circular caissons. As the new roof is equipped with seismic isolators, the effect of the earthquake action was of minor concern. By contrast, large and multi–component loads transmitted by the columns under the wind action are a critical issue, with the leeward pressure on the exposed face of the roof being the most severe load combination. In this case, a proper consideration of the load path direction and the use of the interaction diagram concept are fundamental to minimize the impact of the foundation system in the *Insula*.

Notably, the very pronounced peak in the average spectrum for seismic analysis of the covering system corresponds about to the fundamental frequency interval of the subsoil, as it was argued from amplification function calculated with the Equivalent Linear analysis. In all likelihood, the fundamental periods of the ancient masonry textures fall within the same critical interval. Should this be the case, a double–resonance phenomenon could occur, with potential destructive effects for the archaeological site. As a matter of fact, after the Irpinia earthquake in 1980, a number of *domus* in *Pompeii* suffered severe damages, especially those without roofs. The major collapses occurred in *Regio* VII and cracking patterns appeared elsewhere in a very widespread manner, such that repair works of the earthquake damages started in 1982 and lasted about 10 years. It is difficult to establish what really happened then in terms of soil–structure dynamic interaction for the archaeological ruins, and this is beyond of the scope of the present work. This is indeed the aim of a specific research agreement between the Universities of Naples Parthenope and Federico II with the *Archaeological Park of Pompeii* defined at the end of 2021.

As a last comment, the geotechnical issues have been tackled through a strong interaction with a multitude of disciplines, with very different sensibilities, with the common aim of the preservation and enhancement of the archaeological site of Pompeii. The restoration works, in particular those related to geotechnical engineering, were not based on the principles of efficiency, economy, symmetry or uniformity of the behaviour, as it is usual in civil engineering, but rather on the principles of adaptation, removability and reversibility, which, in turn, led to solutions characterized by asymmetry and unevenness of the behaviour.

AKNOWLEDGMENTS

This work has been carried out under a three year research agreement between the Universities of Naples Federico II and Parthenope and the *Archaelogical Park of Pompeii*. The Authors are grateful to Dr. Vincenzo Calvanese from the Archaeological Park for his invaluable support.

REFERENCES

Achmus, M., Akdag, C.T. & Thieken, K. 2013. Load-bearing behavior of suction bucket foundations in sand. *Applied Ocean Research*, 43, 157–165.

Ahlinhan, M.F., Adjovi, E.C., Doko, V. & Tigri, H.N. 2019. Numerical analysis of the behaviour of a large-diameter monopile for offshore wind turbines. *Acta Geotechnica Slovenica* 16(1), 53–69.
Ashford, S., Sitar, N., Lysmer, J. & Deng, N. 1997. Topographic effects on the seismic response of seismic slopes. *Bulletin of the Seismological Society of America* 87(3), 701–709
Aversa, S. 2007. Preserving cities and monuments. *Proc. of Geotechnical Engineering in Urban Environments*. Madrid, 24–27 sept., vol. 5, Millpress, 453–462.
Blake, T.F., D'Antonio, R., Earnest, J., Gharib, F., Hollingsworth, R.A., Horsman, L., Hsu, D., Kupferman, S., Masuda, R., Pradel, D., Real, C., Reeder, W., Sathialingam, N., Simantob, E. & Stewart, J.P. 2002. Guidelines for analyzing and mitigating landslide hazards in California, Recommended procedures for implementation of DMG special publication 117. Southern California Earthquake Center pub., Los Angeles, CA, Blake, Hollingsworth & Stewart eds., 127 pp.
Bouckovals, G.D. & Papadimitriou, A.G. 2005. Numerical evaluation of slope topography effects on seismic ground motion. *Soil Dynamics and Earthquake Engineering* 25(7–10), 47–558.
Hansen, J.B. 1970. A revised and extended formula for bearing capacity.
Burland, J.B. & Standing, J. R. 1997. Geotechnical monitoring of historic monuments. In *Geotechnical engineering for the preservation of monuments and historic sites* (pp. 321–341).
Butterfield, R. & Ticof, J. 1979. Design parameters for granular soils (discussion contribution). In *Proc. 7*th *International Conference Soil Mechanics & Foundation Engineering*, 259–261.
Butterfield, R. 2006. On shallow pad-foundations for four-legged platforms. *Soils and Foundations* 46(5), 427–435.
Byrne, B.W. & Houlsby, G.T. 1999. Drained behaviour of suction caisson foundations on very dense sand. In Offshore Technology Conference. OnePetro.
Byrne, B. W. & Houlsby, G.T. 2001. Observations of footing behaviour on loose carbonate sands. *Géotechnique*, 51(6), 463–466.
Calabresi, G., & D'Agostino, S. 1997. Monuments and historic sites: Intervention techniques. *Proc. Arrigo Croce Memorial Symposium – Geotechnical Engineering for the Preservation of Monuments and Historic Sites*, Napoli, Viggiani ed., Balkema, 409–425.
California Geological Survey. 2008. Guidelines for Evaluating and Mitigating Seismic Hazards in California. *California Geological Survey Special Publication* 117A, 98 pp.
Carey, S. & Sigurdsson, H. 1987. Temporal variations in column height and magma discharge rate during the 79 AD eruption of Vesuvius. *Geological Society of America Bulletin* 99(2), 303–314.
Croce, A. (1985) Old monuments and cities. Research and preservation. Geotechnical Engineering in Italy: An overview, Special volume for ISSMFE – *Golden Jubilee, Associazione Geotecnica Italiana* ed., 361–415.
de Sanctis, L., Iovino, M., Maiorano, R.M.S. & Aversa, S. 2020. Seismic stability of the excavation fronts in the ancient Roman city of Pompeii. *Soils and Foundations* 60(5), 856–870.
de Sanctis, L., Maiorano, R.M.S., Brancaccio, U. & Aversa, S. 2019. Geotechnical aspects in the restoration of Insula dei Casti Amanti in Pompeii. *Proceedings of the Institution of Civil Engineers: Geotechnical Engineering* 172(2), 121–130.
Dean, E.T.R., James, R.G., Schofield, A.N., Tan, F.S.C. & Tsukamoto, Y. 1992. The bearing capacity of conical footings on sand in relation to the behaviour of spudcan footings of jackups. In Predictive soil mechanics: Proceedings of the Wroth Memorial Symposium held at St Catherine's College, Oxford, 27–29 July 1992, 230–253, Thomas Telford Publishing.
Ebrahimian, H., Jalayer, F., Forte, G., Convertito, V., Licata, V., d'Onofrio, A. & Manfredi, G. 2019. Site-specific probabilistic seismic hazard analysis for the western area of Naples, Italy. *Bulletin of earthquake engineering* 17(10), 4743–4796.
EN–1998–5 (CEN 250 2019). (pr)EN–1998–5:2019.2. Eurocode 8: Earthquake resistance design of structures – Part 5: Geotechnical aspects, Foundations, Retaining and Underground structures. European Committee for Standardization TC 250, Brussels, Belgium
Flora, A. 2013. Monuments, historic sites and case histories. General Report. *Proc. 18*th *International Conference on Soil Mechanics and Geotechnical Engineering*, Paris 2013, 3087–3094.
Georgiadis, M. 1993. Settlement and rotation of footings embedded in sand. *Soils and Foundations* 33(1), 169–175.
Gottardi, G. & Butterfield, R. 1993. On the bearing capacity of surface footings on sand under general planar loads. *Soils and Foundations* 33(3), 68–79.
Gottardi, G., Houlsby, G.T. & Butterfield, R. 1999. Plastic response of circular footings on sand under general planar loading. *Géotechnique* 49(5), 453–469.
Hudson, M.B., Idriss, I.M. & Beikae, M. 1993. QUAD4M – A computer program for evaluating the seismic response of soil structures by variable damping finite element procedures. Center for Geotechnical

Modeling, Department of Civil and Environmental Engineering, University of California at Davis, CA, USA.
Idriss, I.M. 1985. Evaluating the seismic risk in Engineering Practice. *Proc. 11*th *International Conference on Soil Mechanics and Foundation Engineering*, San Francisco, August 12–16, vol. 1, 255–320.
Jappelli, R. 1997. An integrated approach to the safeguard of monuments: The contribution of Arrigo Croce. *Proc. Arrigo Croce Memorial Symposium – Geotechnical Engineering for the Preservation of Monuments and Historic Sites*, Viggiani ed., A.A. Balkema, 11–27.
Jibson, R.W. & Keefer, D.K. 1993. Analysis of the Seismic Origin of Landslides: Examples from the New Madrid Seismic Zone. *Geological Society of America Bulletin* 105(5), 521–536.
Jibson, R.W. 1993. Predicting Earthquake–Induced Landslide Displacement Using Newmark's Sliding Block Analysis. *Transportation Research Record* 1411, 9–17.
Li, D., Zhang, Y., Feng, L. & Gao, Y. 2015. Capacity of modified suction caissons in marine sand under static horizontal loading. *Ocean Engineering* 102, 1–16.
Licata, V., Forte, G., d'Onofrio, A., Santo, A. & Silvestri, F. 2019. A multi–level study for the seismic microzonation of the Western area of Naples (Italy). *Bulletin of Earthquake Engineering* 17(10), 4711–4741.
Luongo, G., Perrotta, A., Scarpati, C., De Carolis, E., Patricelli, G. & Ciarallo, A. 2003. Impact of the AD 79 explosive eruption on Pompeii, II. Causes of death of the inhabitants inferred by stratigraphic analysis and areal distribution of the human casualties. *Journal of Volcanology and Geothermal Research* 126(3–4), 169–200.
Martin, C.M. 1994. Physical and numerical modelling of offshore foundations under combined loads. PhD thesis, University of Oxford, UK.
Matasovic, N. 1991. Selection of Method for Seismic Slope Stability Analysis. *Proc. 2nd International Conference on Recent Advances in Geotechnical Earthquake Engineering and Soil*, March 11–15, St. Louis, Missouri, Paper No. 7.20.
Meletti, C., Galadini, F., Valensise, G., Stucchi, M., Basili, R., Barba, S., Vannucci, G. & Boschi, E. 2008. A seismic source zone model for the seismic hazard assessment of the Italian territory. *Tectonophysics* 450, 85–108.
Newmark, N.W. 1965. Effects of earthquakes on dam and embankments. *Géotechnique* 15(2), 139–159.
Nova, R. & Montrasio, L. 1991. Settlements of shallow foundations on sand. *Géotechnique* 41(2), 243–256.
Rathje, E.M., Abrahamson, N.A., & Bray, J.D. 1998. Simplified frequency content estimates of earthquake ground motions. *Journal of Geotechnical and Geoenvironmental Engineering* 124(2), 150–159.
Randolph, M. & Gourvenec, S. 2017. Offshore geotechnical engineering. CRC press.
Rovida, A., Locati, M., Camassi, R., Lolli, B. & Gasperini, P. 2016. CPTI15, the 2015 version of the parametric catalogue of Italian earthquakes. Istituto Nazionale di Geofisica e Vulcanologia, doi: org/10.6092/INGV.IT–CPTI1 5.
Sarma, S.K. 1975. Seismic stability of earth dams and embankments. *Géotechnique* 25(5), 743–761.
Sigurdsson, H., Carey, S., Cornell, W. & Pescatore, T. 1985. The eruption of Vesuvius in A.D. 79. *National Geographic Research* 1(3), 332–387.
Tan, F.S.C. 1990. Centrifuge and theoretical modelling of conical footings on sand. PhD thesis, University of Cambridge, UK.
Ticof, J. 1978. Surface Footings on Sand Under General Planar Loads. PhD thesis, University of Southampton, UK.
Viggiani, C. 2013. Cultural heritage and geotechnical engineering: An introduction. *Proc. 2nd International Symposium on Geotechnical Engineering for the Preservation of Monuments and Historic Sites*, Napoli, Italy, CRC Press/Balkema, 3–12.
Villalobos, F.A. 2006. Model testing of foundations for offshore wind turbines. PhD thesis, University of Oxford, UK.
Villalobos, F.A., Byrne, B.W. & Houlsby, G.T. 2009. An experimental study of the drained capacity of suction caisson foundations under monotonic loading for offshore applications. *Soils and Foundations* 49(3), 477–488.
Wilson, R.C. & Keefer, D.K. 1983. Dynamic analysis of a slope failure from the 6 August 1979 Coyote Lake, California, Earthquake. *Bulletin of the Seismological Society of America* 73(3), 863–877.
Zafeirakos, A. & Gerolymos, N. 2016. Bearing strength surface for bridge caisson foundations in frictional soil under combined loading. *Acta Geotechnica* 11(5), 1189–1208.

Geotechnical Engineering for the Preservation of Monuments and Historic Sites III – Lancellotta, Viggiani, Flora, de Silva & Mele (Eds)

Long term strategies for monuments care: The importance of monitoring and of a proper diagnosis

G. Russo
Department of Civil, Environmental and Geotechnical Engineering, University of Napoli Federico II

ABSTRACT: This paper is dedicated to highlight the importance of monitoring to determine a diagnosis. Two case studies are presented. The former case deals with the Benedictine Basilica of S. Angelo in Formis constructed in the XI century. It contains an outstanding cycle of medieval frescoes. Monitoring was carried out with the combined use of terrestrial survey and of satellite data. The Incurabili complex in Napoli with its Pharmacy (XVI – XVIII century) is the second case presented in the paper. The rooms of the Pharmacy with its paintings, its ceramics and its decorated floor is a marvelous monument located in the historical center of the ancient greek Neapolis. In this case movements were detected too and a monitoring plan was organized and carried out. The diagnosis was easier than in the first case and the remedial works have been fully designed.

1 INTRODUCTION

Italy is one of the countries with the highest concentration of monuments and historical sites in the world. The cities with their historical-architectural environment constitute a treasure of inestimable cultural, historical and artistic value. Most of the italian cities, even the smallest, hides art treasures that have always attracted a large number of visitors since the eighteenth century, when Italy was an obligatory stop on the "grand tour". As well evidenced by the various theories of restoration starting from the well-known Brandi's treatise (1963) the restoration after the damage is occurred is not the only possible one. There is also a preventive restoration well explained by Brandi himself (1963) which is concretely reflected in the prevention of the degradation process through the control of the artistic, historical asset to be protected but also through the control of the environment in which the asset is inserted or of the surrounding territory. On the basis of the knowledge acquired on the asset and on the environment in which the asset is inserted, it is possible to schedule a maintenance program that contributes to preventive restoration. Monitoring (Russo & Viggiani 2000) and analysis (Russo et al. 2009) with appropriate tools are quantitative indispensable steps to define preventive restoration programs. In this report two case studies are presented. They relate to monuments subjected to monitoring (Candela et al. 1997) and diagnostics operations for the subsequent development of hypotheses of intervention in order to stop a current degradation process. As it will be cleared in the present report, the diagnosis is not always simple and the interventions cannot always be said to be decisive. Obviously, in the protection of monuments and historical sites, other concepts such as vulnerability analysis and risk reduction with respect to extreme events (Russo et al. 2017) are becoming increasingly important but they will not be dealt with in this report for space reasons.

2 THE BASILICA OF SANT'ANGELO IN FORMIS

A temple dedicated to Diana Tifatina had been erected in V century BC at the base of the South West side of the Tifata calcareous mountains in Southern Italy (De Franciscis 1956). In AD 595

 DOI 10.1201/9781003308867-13

a Longobard church dedicated to the Archangel Michael was constructed over the ruins of the Roman temple, as reported in the "Regesto" of S. Angelo in Formis", in the library of the great Montecassino Abbey. In 1072 the Norman Richard the 1st, prince of Capua and count of Aversa, presented the church to the Abbott Desiderio, rector of Montecassino (Jacobitti, Abita 1992). At the site of the ancient church Desiderio erected the present Basilica whose façade is reported in the picture on the left of Figure 1.

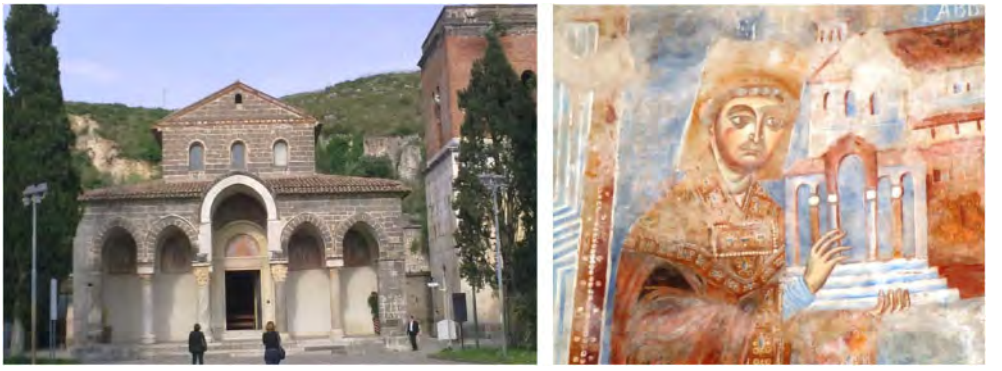

Figure 1. The Benedictine Basilica of S. Angelo in Formis: on the left the present façade and on the right a painting representing an old version of the main façade.

On the right of the same Figure 1 a detail of the internal paintings is reported for comparison and is rather evident the difference between the two porticos: the present portico is characterized by 5 pointed arches while the one depicted in the painting show 5 round arches. This is in agreement with the findings occurred during relatively recent archeological excavations which provides the proof of the collapse of the original portico.

The floor is still lined with the white marble mosaic of the stylobates of the Diana temple, dating back to 150 – 170 BC. Several archeological excavations were carried out to determine the relationship in plan and in elevation between the old temple and the medieval basilica. In Figure 2 the picture on the right represents the old basement walls existing immediately below the current floor with holes excavated in different ages and for different purposes. Capitals, columns and marbles were also reused for the construction. The Basilica, in a simple and appealing Romanesque style, contains an outstanding cycle of frescos over the walls of its three naves.

Figure 2. The blessing Christ. Fresco in the central apse and the old structures of the temple to Diana.

They represent stories of the Old Testament in the lateral naves, and of the New Testament in the central one; a blessing Christ surrounded by the symbols of the four Evangelists is painted on

the central apse (Figure 2 left), while the Final Judgment is painted on the opposite wall of the counterfaçade (Figure 3, right).

The frescoes may be dated back to 1087, i.e. to the time of construction of the Basilica; they are inspired by the iconography of the byzantine art and are believed to have been painted by at least five different artists (Wettstein, 1960). After the destruction of the Montecassino Abbey during the World War II, the S. Angelo frescoes are probably the most important document of the medieval painting in Southern Italy; they have been saved in relatively good conditions, probably because they have been covered by whitewash in XVIII and XIX centuries. The church has a plan divided in three naves, each one ending in semicircular apse (Figure 3, left). The columns that divide the naves are made of different materials (granite, white marble and green marble) and have original Corinthian capitals from the temple of Diana. The façade is graced with a delicate portico or narthex of five arches, upheld by four Corinthian columns (Figure 1 left).

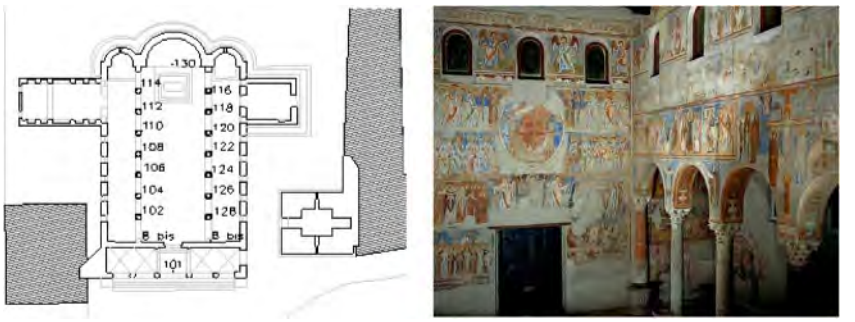

Figure 3. The Benedictine Basilica of S. Angelo in Formis: schematic geometrical plan (left) and the Western internal façade with a portion of the left colonnade (right).

2.1 *The subsoil of the Basilica and its geological setting*

The slope (Figures 4 and 5) is composed by limestone and dolomite belonging to Trias – Cretacic, heavily fractured, somewhere brecciated and even mylonitized, interested by diffuse karst phenomena. The limestone is superimposed to Oligocene – Miocene deposits, composed by sandstones and variegated shaley clays with a chaotic structure. Limestone slipped over the Miocene formation, and such a tectonic superposition generated the fracture system affecting it. The rock formation is crossed by significant fracture lines in the North – South direction and become thinner towards the plain located in front of the basilica.

Later on (30,000 to 35,000 years B.P.) the plain and the slopes have been covered by the grey Campanian tuff erupted by the Phlegrean volcanoes. Since then, the morphological and structural pattern of the area remained unchanged, except for some anthropic actions. Among them the retaining walls and the fill (Figure 6, left) to realize, in different stages, the courtyard of the Basilica, and the opening of stone quarries. At least three of such quarries are located within a few hundred meters from the Basilica; they have been cultivated till the 1980s with extensive use of explosives.

The water table is generally found at the boundary of the limestone, very permeable by fracturation and the Boreholes and geophysical investigations allowed a detailed reconstruction of the subsoil of the zone surrounding the Basilica, which includes three horizons. The upper one is composed by made ground, for a thickness ranging from a few decimeters to some meters. Below the made ground a layer of fractured rock is found with a thickness variable between 15 and 30 m; it includes dolomite, slightly cemented dolomitic limestone and intensely fractured dolomite, besides cemented calcareous debris. Finally, the base formation of sandstones and variegated shaly clays is found. The geological sketch in Figure 6 shows clearly that the Basilica is located across a stratigraphic discontinuity, with the apses and the backward part of the naves founded on rock, and the front on the debris cover or even on the made ground.

Figure 4. The basilica in the calcareous dolomitic slope.

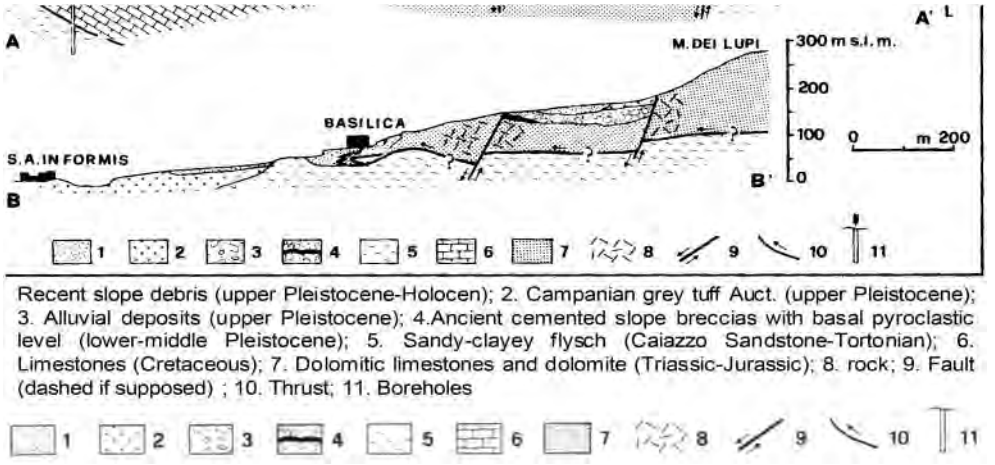

Figure 5. Geological section of the slope; A) North – South; B) East -West (after Corniello & Santo 1995).

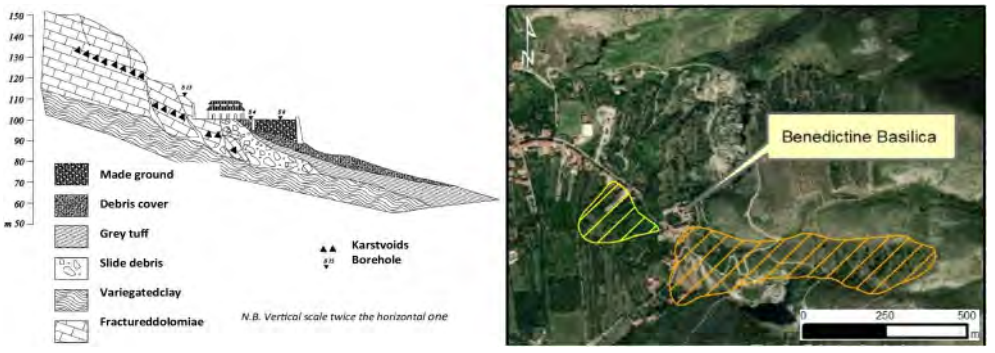

Figure 6. Geological section of the area (left) and landslide inventory map (right) within the area of Basilica (after ISPRA 2008).

As regards the slope instability phenomena, "IFFI" project, dedicated to landslide inventory complex, respectively (ISPRA 2008) (Figure 6 right) while no landslides were detected as involving the site of the Basilica.

2.2 *Previous restoration works and damages*

A stone in the right apse of the Basilica refers to repair works carried out in 1732 under the Cardinal Giuseppe Renato. Little is known about the damage requiring such interventions; it is likely they were consequence of an earthquake occurred in the same year with an MCS intensity equal to X in Irpinia. In 1930 a similar earthquake produced the collapse of the wooden roof. A number of fissures in the walls were repaired and the frescoes restored "with the help of German experts". As far as known however further earthquakes registered in 1962, 1970 and 1980 produced only minor effects.

In 1969 some fissures appeared in the walls above the columns of the central nave; in the following years the fissures gradually opened and extended to other parts of the Basilica, with a concentration in the right side of the façade and in the right nave near the façade. The occurrence of fissures was interpreted as the consequence of distortions caused by differential settlement at the foundation level and monitoring activities started in 1972/73. At the end of the 1970s, following repeated alarms on the safety of the Basilica, a Committee formed by a geotechnical engineer, a structural engineer and a geologist was installed, promoting a geological survey of the area, some further subsoil investigations, a geodetic monitoring of a number of points both inside the Basilica and outside and some further measurements of the fissures opening. Results of investigation and monitoring are discussed in Adriani et al. (1980) and in Pellegrino and Pescatore (1981) documents. The Committee conclusions related the damage mainly to the activity of the nearby quarries, where explosives were systematically used. Accordingly, the quarrying has been completely stopped since 1981. Neverthless, fissures in the Basilica went on increasing, endangering the integrity of the frescoes; as consequence, a new cycle of investigation and monitoring has thus been started in 2012, with the aim of planning remedial and consolidation works. Some of the monitoring data have been reported in a previous paper by Cammarota et al. (2013) together with the description of remedial works. Here new data are presented and discussed. A recent comparison with data obtained via satellite is also reviewed with the aim to fix at least some conclusions on the observed type and rate of movement. In the last decade, a growing interest has been directed towards the exploitation of remote sensing approach as a tool for displacements monitoring of monuments (Di Martire et al., 2016; Tapete & Cigna, 2019; Tomás et al., 2012): in particular, Differential Interferometry Synthetic Aperture Radar (DInSAR), based on processing of multi-temporal repeat-pass SAR images, has demonstrated to be a powerful technique to measure displacement annual rates and evolution of scatterers identified on Earth's surface. The availability of non-operating (ERS, ENVISAT-ASAR) and operating (COSMO-SkyMed, SENTINEL-1) satellite images, acquired with spatial resolution up to 3×3 m and revisiting time up to 6 days, allows to detect spatial and temporal historical movements since 1992, from large to local-site investigations, also at the scale of a single building (Infante et al., 2019; Zhou et al., 2015).

2.3 *Monitoring data: summary of the available experimental evidence*

Apart from some historical information on repair works reported in the previous section the evidence of movements and their records is not so large. The earliest detected and systematically collected data are those coming from the early '70 of the previous century. Two series of measurements of width of cracks in the walls are available: the first one in 1974/75 and the second one in 1980/81. The increase in the width of fissures was up to 0.5 mm, in nearly two years period spanning over 1974/75, and to 0.8 mm in 1980/81. Remarkable was the fact that the trend of the fissures measured in 1974/75 was compatible with a hogging deformation of the church. Furthermore, in January 1980, the offset of the columns, measured with reference to the vertical direction, was accurately determined. The offsets ranged from 10 to 89 mm depending on the columns location. These offsets

were obtained via topographic technique and were indeed more compatible with a sagging mode of deformations. Indeed, the recorded offsets kept constant over a range of 1 year and were judged as small enough to be attributed to possible original construction defects.

As to regards the monitoring of displacements, both geodetic and satellite data are available.

In the periods February 1980-March 1981, May 2012-January 2013 and 2018/2021 vertical displacements of some points inside and outside the Basilica (Figure 7) have been measured. The benchmarks inside the church are better represented in the zoom of Figure 3 while in the Figure 7 the local geomorphology of the site and the outside benchmarks CS1 and CS2 are represented.

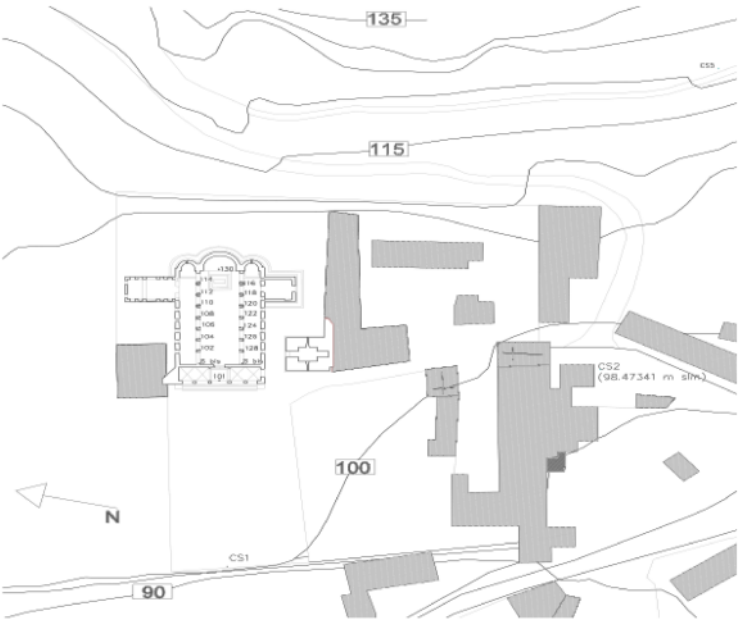

Figure 7. Plan of benchmarks used for topographic survey.

The survey was carried out with optical levels at the beginning and now is going on with electronic level using an invar bar based on the technology of the bar code has a reference system for the electronic level. The benchmarks CS1 and CS2 are substantially stable and relative movements in the monitoring period have been always fluctuating within the range of a couple of mm. Furthermore, since the 2018 the GPS is also used to independently check the possible movements of the references CS1 and CS2.

In Figure 8 it can be appreciated that in the first period (1980-1981) the maximum settlement was about 3.5 mm and occurred near the front façade and in the columns close to the three apses confirming an hogging mode of deformation. Forty years later with a few intermediate surveys carried out in the last decade a maximum value of nearly 80 mm is recorded at the benchmark 130 which is on the floor of the central apse which underwent significant remedial works in the 18th century when also the overall cycles of frescoes were cleaned by white cover applied at the beginning of the same century. The hogging mode of deformation is clearly confirmed, and the average value of the distortions applied to the masonry above the columns in the central nave are respectively 0.8×10^{-3} on the left and 1.5×10^{-3} on the right. In terms of velocity the phenomenon going on, whatever it is, is producing nearly 2mm/year increase in the settlement of the benchmarks close to the central apse. For the front façade the velocity is larger than 1 mm/year and in the central zone of the church the slowest rate of movement is recorded in the range between 0.5 mm/year and 1 mm/year. The above rates are only confirmed by the comparisons between sets of measurements taken at rather long-time interval.

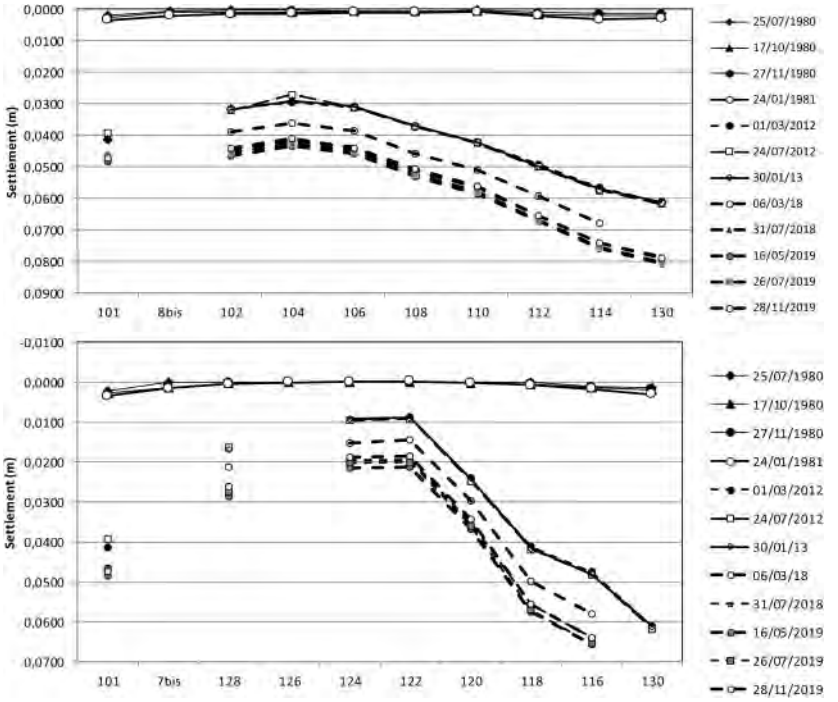

Figure 8. Settlement profile measured with optical survey at the base of the columns.

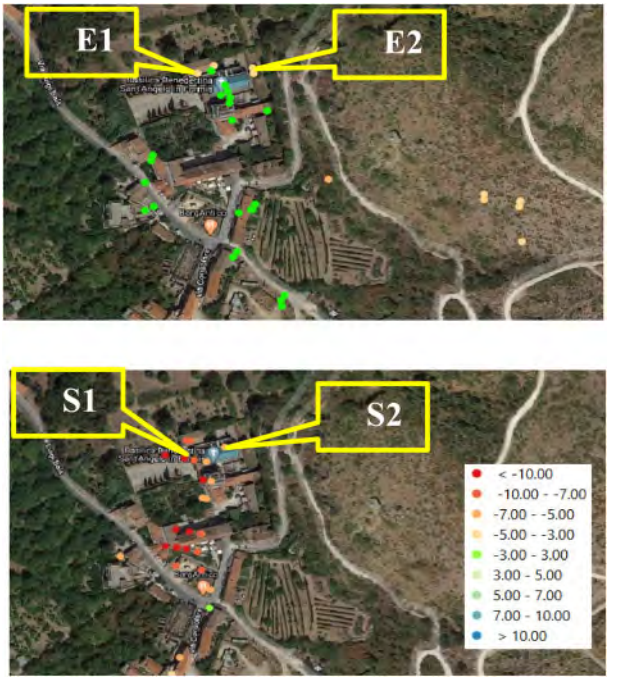

Figure 9. "LoS" displacement velocity map (mm/yr) of targets identified by descending ENVISAT ASAR (a) and SENTINEL-1 (b) interferometric products.

To further check the outlined trend, C-band interferometric data have been used: firstly, ENVISAT ASAR descending products, just available on the Geoportal of the Italian Environmental Ministry in the period June 2003-June 2010, have been analyzed. Subsequently, 91 SENTINEL-1 descending images, acquired in the period January 2017- January 2020 have been processed by means of Coherent Pixels Technique (CPT, Mora et al. 2003). As a result, for each dataset, displacement mean velocity maps of identified targets, measured along Line of Sight (LoS), have been obtained (Figure 9). Moreover, starting from 'LoS' displacement value, vertical component of movement has been evaluated according to Di Martire et al. (2013), as function of satellite incidence angle in descending geometry.

Such analysis allows to obtain settlements time series of some targets identified on the Basilica, as indicator of structure deformations (Figure 10). Maximum value of measured settlement is about 25 mm in the time span June 2003-June 2010 and about 15 mm in the time span January 2017-January 2020. As it can be seen by the proposed simple linear fitting in the period 2003-2010 the selected points E1 and E2 which are located on two opposite sides of the church are showing similar scatter and, above all, similar velocities (i.e. 3.5 mm/year). This rate was already recorded in the early years of optical survey (1980–1981).

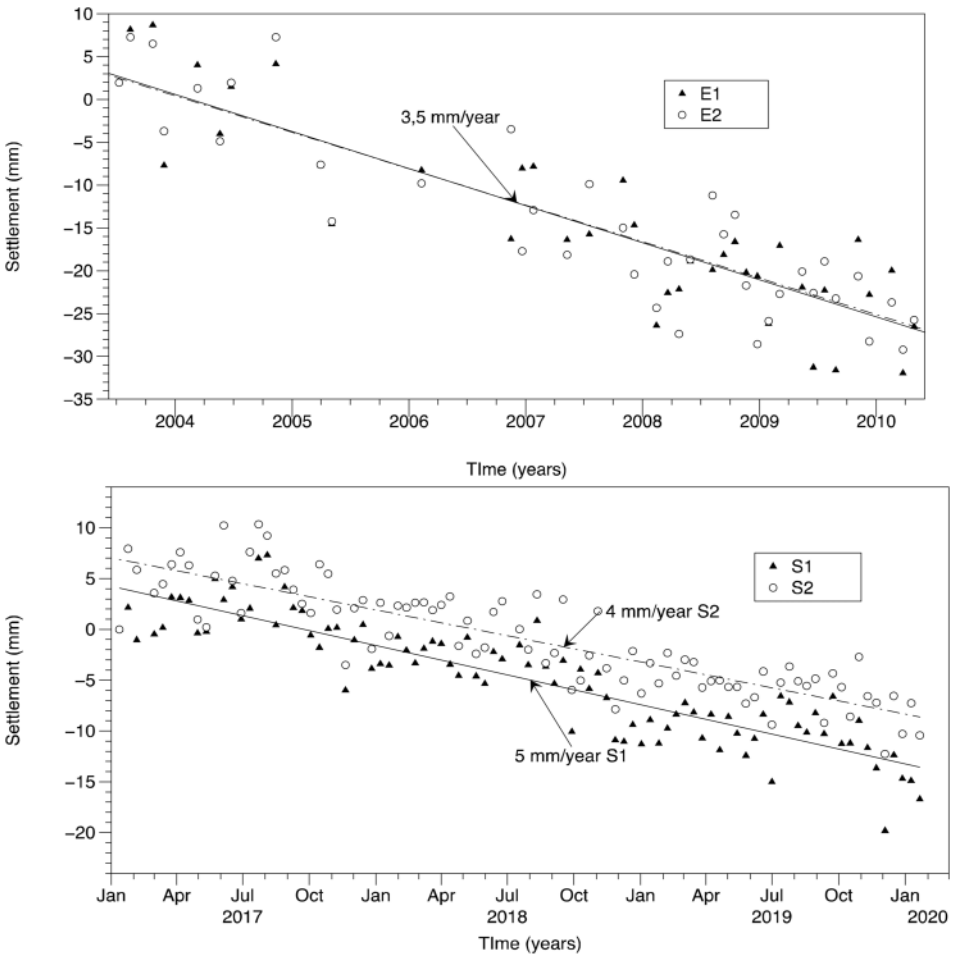

Figure 10. Settlements time series of some targets identified on the Benedictine Basilica by ENVISAT ASAR (a) and SENTINEL-1 (b) interferometric products.

In the lower part of Figure 10 the data from Sentinel Satellite in the three years period 2017–2020 show for the selected points S1 and S2 a slightly faster rate of movement which approaches on the average 4 to 5 mm/years. It is noteworthy that the rate of the point S2, approximately located in the middle of the church, is smaller than the rate of point S1 located on the front façade of the church confirming the hogging mode of deformation deduced by survey via electronic level.

Finally in Figure 11 the available data are plotted all together showing a rather clear trend. The plot has been obtained using as a reference the linear fitting trough the survey data (i.e. benchmark 130). The movement obtained by satellite data have been simply averaged on the two selected points and adapted to the trend provided by the terrestrial survey data.

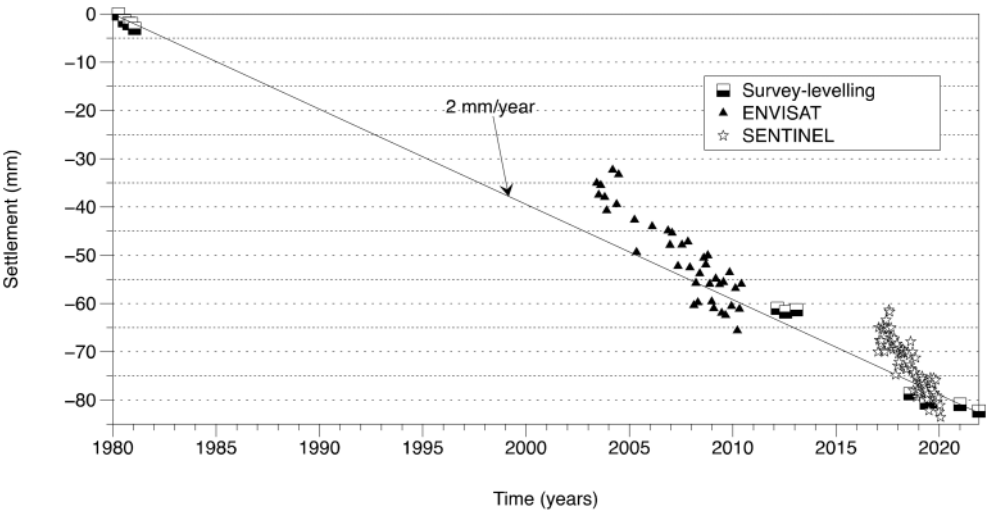

Figure 11. Settlement time series recorded in the last 40 years for the Basilica di Sant'Angelo in Formis.

2.4 *Discussion of the monitoring results and latest repair works*

All the data reported in the previous section show that the basilica is affected by a rather continuing settlement at least since 1980. The average initial rate was of 1.5 mm/year in 1980/81 with the marks moving faster approaching even a rate of 3.5 mm/year. The average rate on the whole observation period (i.e. 40 years) mainly based on terrestrial survey is in the range between 1.2 mm/year, for the right nave, and 1.5 mm/year for the left nave. The satellite data have contributed to throw light on periods where the survey was not available. They confirm the general trends commented before with slightly larger rate of movements obtained by fitting the typical scattered response. What maybe alarming is that the last three years covered by satellite have shown the largest movement rate ever detected in the range between 4 and 5 mm/year.

The deflection ratios calculated separately for the two naves and already introduced in the previous section are compatible with the occurrence of fissuring (Burland & Wroth 1975) which were clearly present in the church in the period 2012–2014. In those years some remedial works were decided, planned and carried out (Figure 12).

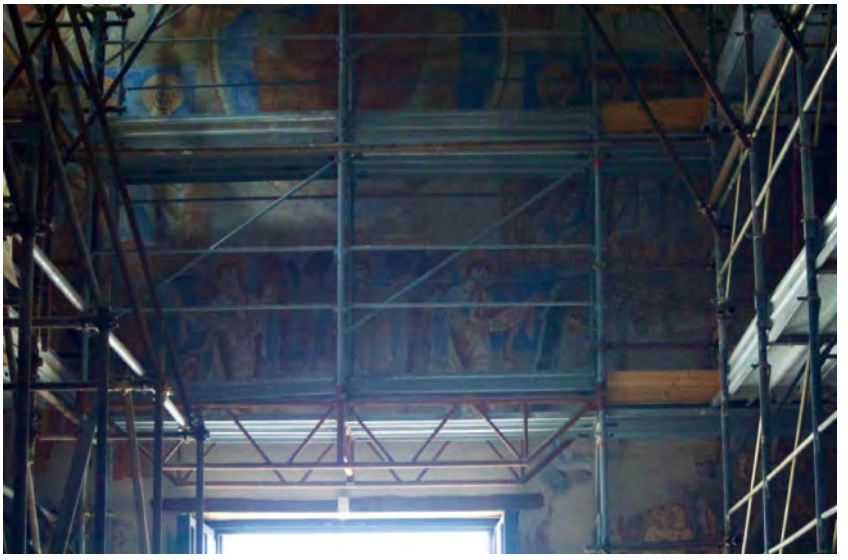

Figure 12. Recently carried out remedial works in the church.

The interventions could only cure the symptoms rather than removing the cause(s).

Interventions at the foundation level were difficult to conceive and to realize without interacting with the underlying structures of the ancient roman temple and with the floor which is still lined with marbles coming from the mosaic of the ancient temple. Without having yet a precise idea of the causes of the movements and considering the limitations described above any intervention at the foundation level was at least delayed.

On the other hand, as already mentioned at the beginning of the paper, the roof of the Basilica was completely rebuilt, after the collapse of the existing wooden roof due to the earthquake occurred in 1930. Large attention has been paid to this relatively new roof which was made by bricks and concrete and covered by wood thus resulting in a heavy load both on the side masonry and on the foundation.

This roof has been dismantled allowing first the construction of peripheral concrete beam at the top of the lateral masonry walls, to strengthen the structural box against seismic events. A new wooden roof, lighter than the existing one, has been finally installed. Further interventions have been dedicated to recover and protect the frescoes after appropriate and careful sealing of the existing cracks.

However, both satellite data and terrestrial survey data confirm that the movements at the foundation level are still going on and as matter of fact some new small cracks in the recently plastered walls are appearing.

On the other hand, it must be outlined that if the recorded rate of settlement had been active since the construction of the basilica, an average settlement between one meter and two meters should have accumulated; such figure is clearly impossible. It is evident that the observed movements initiated relatively recently, for some unknown reason; they have a rather continuous trend at least in the last 40 years with no traces of cycling.

In previous papers possible reasons that have been considered by various Authors are: (i) the extensive use of explosives in the nearby stone quarries; (ii) the effect at the surface of karst phenomena in the limestone; (iii) residual slow tectonic movements of the slope. None of these suggestions seems totally convincing. The quarrying activity which was considered one of the most likely causes has been completely stopped in the early ’80’s when the evidence of movements was first detected but the movements are continuing 40 years later. There are no evident reasons why the karst phenomena should begin at a time of some decades ago. The third hypothesis (Di Nocera

2013) is based on the possibility that a tectonic activity has been triggered either by recent seismic activity or by the explosions in the quarries. At the time being, no definite conclusion can be drawn from the available data; it is believed however that there is a clear need for keeping active a careful, long term and relatively frequent monitoring.

3 THE INCURABILI COMPLEX WITH ITS PHARMACY

The eighteenth-century pharmacy of the INCURABILI COMPLEX is the place where Art meets Science. Here the Rococo Baroque style, designed by Domenico Antonio Vaccaro, is combined with the enlightenment of the masters of Anatomy and Botany (Domenico Cotugno, Domenico Cirillo) in the most important Hospital of the Bourbon Kingdom. The alchemical preparations of the ancient tradition open the passage to medicinal chemistry in the place where skilled craftsmen of wood, gilding and ceramics prepared rooms where the voices of researchers who wrote the history of European thought resounded. In particular, the saplings, the hydras and the "riggiole" (tiles) of the Massa brothers represent an extraordinary unicum for the elegance of the colors, the refinement of the iconographic program aimed at the esoteric-masonic function of the Great Hall, where the uterine matrix operated is proudly displayed.

The Incurabili complex is quite articulated with its history from the beginning to the current situation covering a span of many centuries. In particular as reported also in a recent ph.d thesis (Micillo 2013), the main construction phases can be summarized as follows:

1. The foundation from 1519 to 1585;
2. The extension on the viceregal walls of 1729 operated by Alessandro Manni;
3. The first restoration from 1747 to 1751 directed by Bartolomeo Vecchione;
4. The incorporation of the conterminous monastic structures of the XIX century (1800 Santa Maria delle Grazie, 1836 Santa Maria della Consolazione);
5. Minor construction episodes and modifications of the XX century.

The whole hospital complex is delimited to the North, from East to West, by Maria Longo street, to the West (from North to South) by Madonne delle Grazie square; to the East (from North to South) by Consolazione alley, Domenico Capozzi and Luciano Armanni street, to the South by the monastic complex of Santa Maria delle Grazie and that of Santa Maria Regina Coeli.The investigations in the subsoil show clearly that if we include in the complex and in its monumental part its subsoil as it should always be done in highly stratified areas respecting the concept of the uniqueness of the ground-monument system the history that is covered extends over two thousand five hundred years, reaching the ancient Greek Neapolis with its surrounding walls still in place (Figure 13).

Maria Lorenza Longo founded the Incurabili hospital. Born in Barcelona with the original name of Lorenza Requenses, she arrived in Naples in 1506 with her husband Giovanni Lonc, minister of the king Ferdinand the Catholic of Spain, suffering from a severe form of rheumatoid arthritis. After the death of her husband, she went to the sanctuary of Loreto to ask for a cure, promising to devote herself to the care of others if received. And so it happened and Maria Lorenza Longo began her work in Naples by founding the Hospital of the Incurable in 1519. The history of the oldest part of the city of Naples had begun many centuries earlier. For example, the Greek wall of the fifth century BC arranged in an east-west direction and characterized by a double curtain made of regular large blocks of tuff and filled in Roman times with walls in opus reticulatum is still visible along Constantinopoli street and Foria street. In the picture in Figure 13 a section of the original greek wall (the so-called "second phase wall") of the fourth century BC with a scarp and a stepped foundations for an overall height of 9.20 m is visible. Traces of the greek walls were also found in the boreholes carried out for soil investigations purposes and summarized in the next paragraph. The Incurabili Hospital was from about 1525 until 1813 the only institution destined to the reception of the mentally ill people and only during the "french decade" in compliance with a law by Joachim Murat the sick were transferred to the asylum of Aversa.

Figure 13. Greek walls surrounding the original Greek city of Neapolis.

The hospital keeps substantially its original conformation from the end of the sixteenth century until the intervention of the engineer Alessandro Manni in the 1729 who executed the designs of D. A. Vaccaro. In this phase the hospital is enlarged, and the pharmacy is created with its current configuration. In Figure 14 the façade of the complex on the Consolazione alley is sketched as reconstituted on the basis of many ortophotos. By an historical point of view this is an interesting perspective because the initial period of the hospital started from the existing XVth century houses.

Figure 14. Façade on Consolazione alley with the back windows of the Incurabili Pharmacy.

In Figure 15 the marvelous grocery room of the Pharmacy with the roof frescoes by Pietro Bardellino and the monumental stairs in the courtyard of the Incurabili complex.

3.1 *The subsoil of the INCURABILI COMPLEX and its geological setting*

The foundation levels of the monumental buildings of the INCURABILI COMPLEX are placed at different elevations. The oldest part of the complex visible today and founded at lower levels is certainly the one on the Consolazione alley. The inspections in the existing houses and their maps allowed to determine the main levels of the foundation walls on that side of the complex. These walls are made by continuous masonry similar to the ones that continues in elevation with thicknesses often unchanged for several meters above the foundation level.

The soil layering as deduced by boreholes reported in Figure 16 can be summarized as follows:

Figure 15. The eighteenth-century pharmacy of the INCURABILI COMPLEX: internal picture of the main hall and external picture of the monumental stair.

a) topsoil with a thickness varying from a minimum of a few decimetres in the borehole S4 to less than a metre in soundings S2 and S3 and up to a little less than three metres in the soundings S1 (in the center of the courtyard) and S5, along the Consolazione alley;
b) under the topsoil (manmade), with the exception of survey S4, located near the access from Maria Longo street, which logged for about 10 m walls that are part of the ancient greek walls (Neapolis), in all cases there are alternations of sandy-silt cinerites, layers of volcanic pumices and layers of coarser sand sometimes mixed with lava slags; the alternating layers correspond to a well-known stratigraphic series linked to the activity of nearby volcanic complexes;
c) at the end of the series of alternating pyroclastic uncemented materials, in all the surveys Neapolitan yellow tuff, a well-known soft rock, is found with a top layer locally named “cappellaccio” and characterized by poorer mechanical properties and often lacking a significant degree of cementation.

The yellow Neapolitan tuff found in the final part of all the surveys is at a rather constant level above sea level ranging between +26 m and +30 m asl. The deepest point of the roof of the tuff is just that relative to the borehole S4 that in on the line of the ancient Greek walls (+26 m asl).

Taking into account the distance among the boreholes the variation of the tuff layer elevation is in the ordinary range.

Figure 16. Plan view with locations of boreholes Si and Dpsh tests.

In the area of the Incurabili Hospital during subsoil investigations several deep shafts have been detected. They connect the above buildings with a very deep network of rather small tunnels excavated in the tuff basement. The network is partially related to the famous ancient roman Bolla aqueduct. These vertical wells are 20 meters deep or more and generally end inside the tuff basement where a network of horizontal or sub-horizontal tunnels connects the most of them (Figure 17). The smaller wells were used to draw water inside the hospital complex and in the houses facing on the Consolazione alley. Many of these wells today are filled with debris and waste material. Some larger wells are empty, inspectable and located close to the foundations walls of the Incurabili Pharmacy on the edges of its plan area. In the recent past these shafts have been involved in problems with water infiltration from above produced by huge leaks caused by failures of the pipes of the internal white water drainage system. Some available video inspections carried out with the support of speleologists (Figure 17) show that the upper part of these wells, which is developed in loose and uncemented soils above the the water table, is lined with walls of tuff blocks that are not always in good conditions.

3.2 *Damages, monitoring data and diagnosis*

In its recent history the Incurabili monumental complex has been seriously affected by damages represented by crack openings in the walls, in the floors, sometimes also highlighting detachments between structurally independent bodies. To keep the monumental building under observation, considering both its value and the concerns that inevitably accompanied the sporadic appearance of new cracks, a monitoring system was implemented. At the present time several months (about 10

Figure 17. Shafts, cavities close to the Incurabili Pharmacy foundations.

months) of precision survey carried out by leveling on the benchmarks in the wall and on nails/bolts on the floor referred to fixed points in external areas close to the complex are available.

In this section these data referred to medium-term monitoring are presented and discussed aware that one or more full annual cycles are by far the best option to make a satisfactory interpretation of the phenomena going on and to filter off the thermal influence on the measurements if any. The Figure 18 reports the settlement of the external benchmarks R2 and R3 referred to the main reference R1 versus the temperature. In this case all the movements are very small and whitin +/− 0.5 mm without showing a particular trend with the temperature even in the rather large experienced range from 10°C to 32°C. In the same figure the temperature recorded is plotted vs. the time during the whole monitoring period.

On the other hand, Figure 19 reports plots of movements versus temperature to show how close correlations can be sometimes detected. In this case the correlations can be adversely affected by the fact that the temperature in the plots represent a unique record measured in the entrance area of the complex. Of course, a bad correlation may also simply represent the fact that observed movements are related to causes other than the simple temperature. Keeping this in mind it can be remarked that the marks on the Consolazione alley have movements strictly related to temperature with a R^2 value close to 0.8 and quite small value of the residuals in the whole range of records, while the marks inside the courtyard on the façade of the Pharmacy and on the hospital monumental chairs present much lower value of R^2.

The same can be clearly observed by direct comparison of the trend of the benchmarks movement with the time in Figure 20 and the temperature with the time in Figure 18. This finding can confirm the fact that real movements nonrelated to thermal response of the measuring systems and of the buildings are occurring mainly in the area inside the courtyard of the complex where the largest settlement with a lower correlation with temperature are clearly observed. Some benchmarks inside the courtyard have reached during the period of observation even values close to 5 mm, which although small in less than 1 year represent a significant value. To summarize the above findings in Figure 21 is plotted a 2D contours map of the measured subsidence, obtained filtering out, at the best possible, effects of temperature on the records. The maximum values corresponding to the colors of the central zone of the basin are between 2 and 3 mm. Therefore, net of thermal effects,

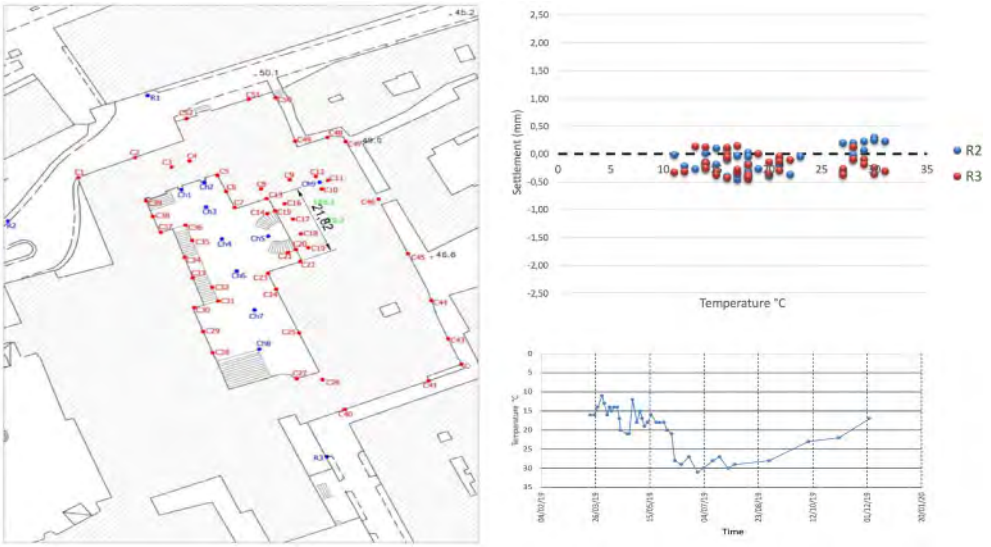

Figure 18. Settlement and temperature: Fixed benchmarks in the area outside the Incurabili Complex.

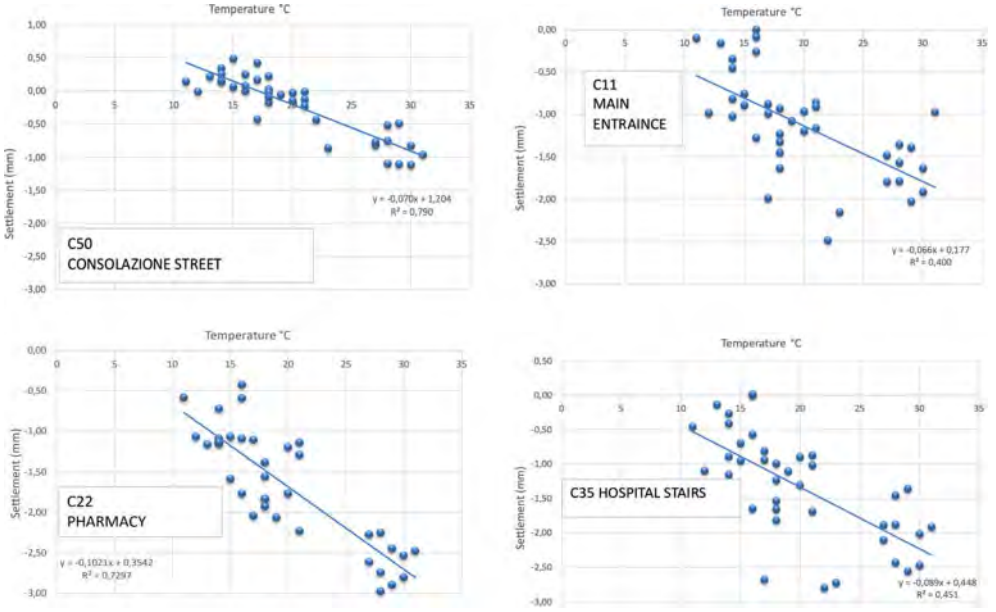

Figure 19. Settlement vs. temperature for different zones of the monument.

the values are rather small and tend to stabilize over time as can be seen from the diagrams in Figure 20. Obviously, the monitoring should continue for time longer than the exposed period and cover, as mentioned before, at least one or two full year cycles, but in this case, at least, the diagnosis was quite simple.

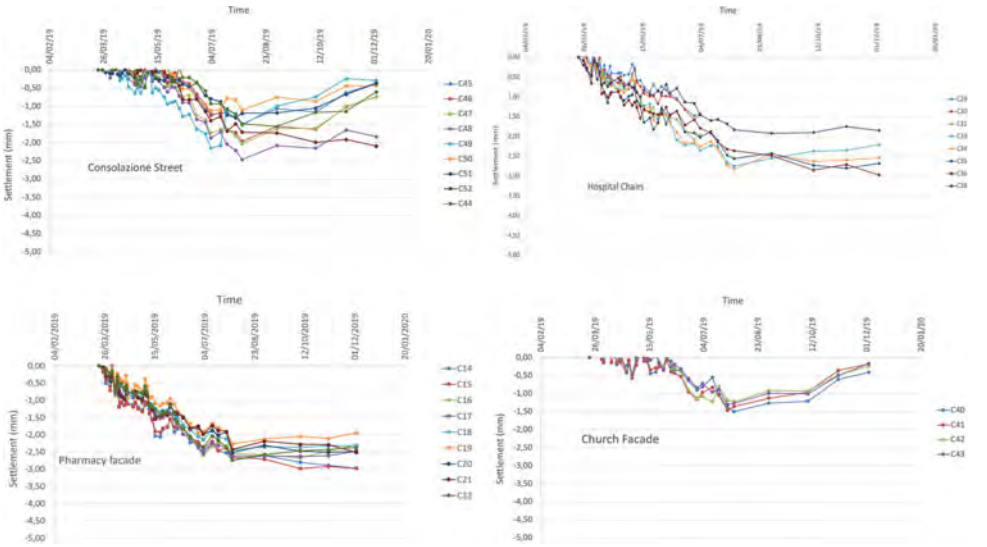

Figure 20. Settlement vs. time for different zones of the monument.

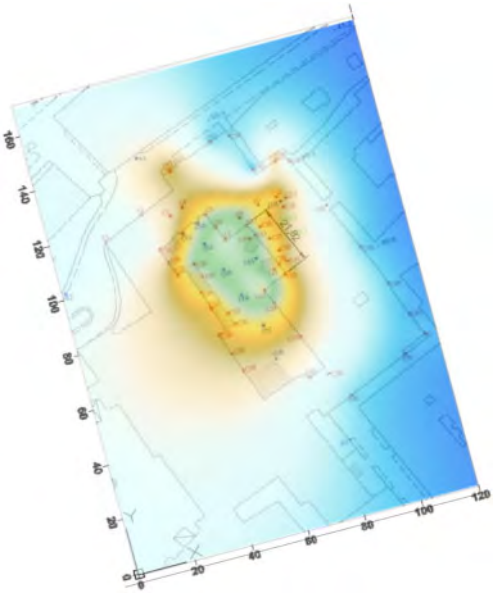

Figure 21. 2D settlement contours after filtering out thermal effects on measurements.

3.3 *Diagnosis and therapy*

The available evidence including the monitoring data reported in the previous paragraph and the survey of the cracks (Figure 22) that are not documented in detail to be brief outlines a fairly clear situation. Based on its history and of the available documents the Incurabili monumental complex has been certainly stable for a few centuries from its foundation. Apart from problems related to the ordinary maintenance of the structures no problems have been discovered looking at the history of the monument. A few years ago, some subsidence problems have appeared involving in different

ways and with different degree of danger several parts of the monumental complex. Some problems which are not documented here for space reason have been clearly related to structural failures of weakened portion of the roofs or of the slabs. In the case of the Pharmacy the problems were clearly related to subsidence problems involving the bearing walls starting from the foundation level.

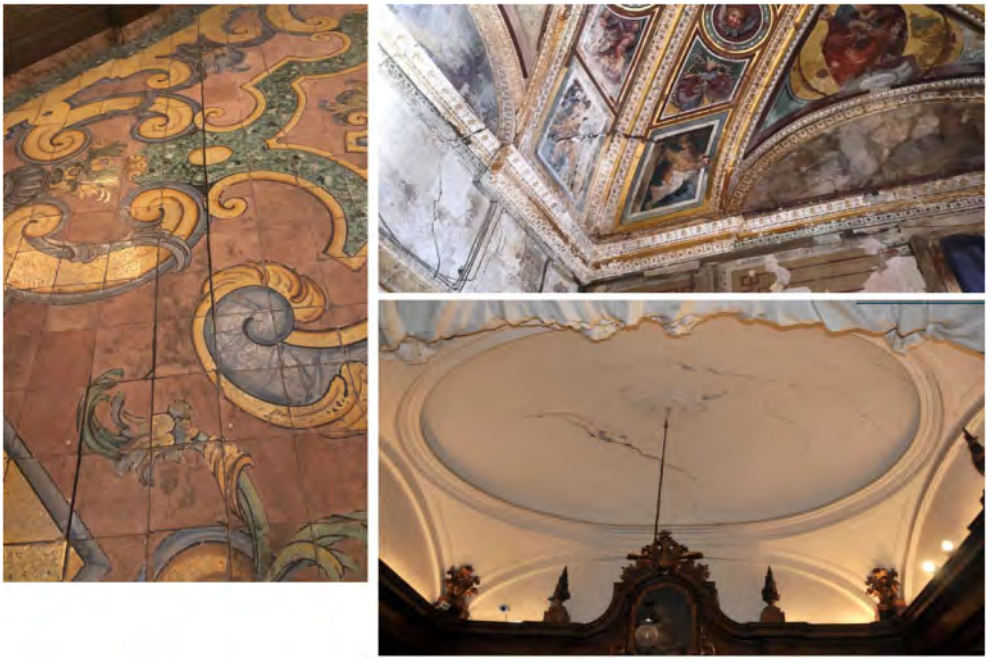

Figure 22. Cracks in the rooms and on the floor of the INCURABILI PHARMACY.

As previously mentioned in the months preceding the start of the monitoring operations and during the previous autumn and winter at the turn of 2018–2019 several reports had been made to the authorities in charge for sudden manifestations of water leaks in pipes present in the subsoil of the courtyard of the complex. Being the ancient monumental complex partially used as an hospital with all the needed sewers and aqueduct pipes it is not hard to guess that problems with the water system could have occurred even before. A careful program of inspection of the whitewater and the blackwater sewer systems was organized. In some cases, given the antiquity of the complex, it was not even possible to reconstruct exactly all the passages of the sewer systems even using video inspections and other modern techniques. However, it is a fact that, as for example reported in the picture of Figure 23, conspicuous water losses occurred at several times with consequent dragging of fine sandy material that sometimes was even delivered inside the deep wells inspected and described previously.

Once established a close relationship between the severe cracks in the monumental complex and the problems with water leakages in the sewer system, the patients of the hospital were quickly cleared out and the drains were quickly interrupted. It is to be underlined that also the inhabitants of the houses on the Consolazione alley immediately below the floor of the Pharmacy were for the first time in the history of the complex cleared out. The white-water network was sectioned at the base of the building and was delivered to the sewer with temporary by-passes. These decisions were promptly taken, and the actions consequently made just at the beginning of the monitoring period. Therefore, as anticipated above, it is extremely likely that the observed settlements or subsidence effects net of the thermal effects are simply the viscous tails of phenomena induced by erosion of

Figure 23. Evidence of damaged pipes of the sewer system of the Incurabili complex.

fine material and micro-collapse by saturation in limited areas of pozzolana above the free surface of the water table.

An overall project of recovery of the prestigious monument is in progress because the degradation induced by the crumbling networks of underground services was coupled with degradation by infiltration of rainwater from above through floors and waterproofing no longer suitable.

4 CONCLUSIONS

In the paper two examples of very valuable monuments in the city of Napoli and in its surroundings are presented to show how vulnerable may be such structures that have however a very long life and many lessons to give us.

In the case of the medieval basilica of Sant'Angelo in Formis even if the overall picture is not one of fear for its future it has to be recognized the substantial difficulty to understand the movements recorded in the last 40 years of its life. The use of satellite data has confirmed the findings obtained via terrestrial survey with more precise but less continuous in time methods. In such a case remedial works have been carried out even recently removing some effects or damages but, probably, non-removing the ultimate cause of the movements that is not yet been certainly identified.

The case of Incurabili Complex on the other hand represents a typical situation of the historical center of the city of Napoli where the monumental buildings are still used and sometimes their use is not at all compatible with the safety and mainly with the preservation of the artistic part. The movements recorded for about 1 year have clearly shown that some viscous effects were still taking place while the causes of the movements had been likely removed simply preventing additional water leakage occurring from an old and widely damaged sewage system.

REFERENCES

Adriani, L., Pellegrino, A., Bescatore, T.S. (1980). La Basilica Benedettina di S. Angelo in Formis: prima relazione. Indagini sui terreni e sulle strutture del monumento per lo studio dei dissesti. Unpublished report, Soprintendenza ai Monumenti della Campania, Napoli.

Brandi, C. (1963) Teoria del restauro, Ed. di Storia e Letteratura, Torino – pp. 1–158

Candela, M., Mandolini, A., Russo, G. (1997). Monitoring Castel dell'Ovo in Napoli – Preliminary results. Proc. *Geotech. Eng. For the Preservation of Monuments and Historical Site*s, Balkema, pp. 343–347.

Corniello, A., Santo, A. (1995). I dissesti della Basilica Benedettina (XI secolo) di Sant'Angelo in Formis (Capua) ed il complesso assetto geologico dell'area. *Geologia Applicata e Idrogeologia*, vol. XXX, I, 125–137

De Franciscis, A. (1956). Templum Dianae Tifatinae. Soc. Di Storia Patria di Terra di Lavoro, Caserta, 60 pp.

Di Martire, D., De Luca, G., Ramondini, M., Calcaterra, D., (2013). Landslide-related PS data interpretation by means of different techniques. In *Landslide science and practice* (pp. 347–355). Springer Berlin Heidelberg

Di Martire, D., Novellino, A., Ramondini, M., Calcaterra, D., (2016). A-Differential Synthetic Aperture Radar Interferometry analysis of a Deep Seated Gravitational Slope Deformation occurring at Bisaccia (Italy). *Science of The Total Environment*, Volume 550, 15 April 2016, Pages 556–573. doi:10.1016/j.scitotenv.2016.01.102

Di Nocera, S. (2013) Personal communication.

Jacobitti, G.M., Abita, S. (1992). La Basilica Benedettina di Sant'Angelo in Formis. ESI, Napoli, 97 pp

Infante, D., Di Martire, D., Confuorto, P., Tessitore, S., Tòmas, R., Calcaterra, D., Ramondini, M. (2019). Assessment of building behavior in slow-moving landslide-affected areas through DInSAR data and structural analysis. *Engineering Structures*, 199, 109638.

Italian National Institute for Environmental Protection and Research, ISPRA, 2008. Landslides in Italy. Special Report 2008. ISPRA, Rapporti, 83/2008.

Micillo, A. (2013). Il Complesso Ospedaliero di Santa Maria del Popolo degli Incurabilidi Napoli: evoluzione storico urbanistica. Ph.d. thesis XXV Ciclo, Dottorato di Ricerca in
Storia e Conservazione dei Beni Architettonici del Paesaggio, Tutor prof. L. Di Mauro

Mora, O., Mallorquí, J.J., Broquetas, A., (2003). Linear and nonlinear terrain deformation maps from a reduced set of interferometric SAR images. *IEEE Trans. Geosci. Remote Sens.* 41, 2243–2253. http://dx.doi.org/10.1109/TGRS.2003.814657.

Pellegrino, A., Pescatore, T.S. (1981). La Basilica di S. Angelo in Formis. Indagini sui terreni di fondazione ed analisi dei dissesti: relazione finale. Unpublished report, Soprintendenza per i Beni Ambientali e Architettonici della Campania, Napoli.

Russo, G., Viggiani C. (2000) The stability of monuments over coastal cliffs in the bay of Napoli. Proc. International Millenium Conference on Safeguarding of our Cultural Heritage Vol. (U) pp.10 held by UNESCO & ICOMOS in Bethlehem (Palestine), Oct. 2000.

Russo, G., D'Agostino, S., Lombardi, S., Viggiani C.(2009) Structural engineering and geology applied to the static problems of the Etruscan "Tomba dell'Orco" (Tarquinia, Central Italy). Journal of Cultural Heritage ISSN 1296-2074, vol. 11(2010), available on line since 2009, pp. 107–113 – doi 10.1016/j.culher.2009.11.001

Russo G., Viggiani C., Cammarota A., Candela M. (2013) The Benedictine Basilica of S. Angelo in Formis (Southern Italy): a therapy without diagnosis?. pp.225–232. In Geotechnical Engineering for the Preservation of Monuments and Historic Site (2013) vol. 1 Int. Conf. TC. 301

Russo G., Alterio, L. Silvestri, F. (2017) Seismic Vulnerability Reduction for Historical Buildings with Non-Invasive Subsoil Treatments: The Case Study of the Mosaics Palace at Herculaneum. International Journal of Architectural Heritage, 11 (3), pp. 382–398. DOI: 10.1080/15583058.2016.1238969

Tapete, D., & Cigna, F. (2019). COSMO-SkyMed SAR for detection and monitoring of archaeological and cultural heritage sites. *Remote Sensing*, 11(11), 1326.

Tomás, R., Garcia-Barba, J., Cano, M., Sanabria, M. P., Ivorra, S., Duro, J., & Herrera, G. (2012). Subsidence damage assessment of a gothic church using Differential Interferometry and field data. Structural Health Monitoring, 11(6), 751–762.

Zhou, W., Chen, F.L., Guo, H.D. (2015). Differential radar interferometry for structural and ground deformation monitoring: A new tool for the conservation and sustainability of cultural heritage sites. *Sustainability*, 7, 1712–1729.

Wettstein J. (1960) Sant'Angelo in Formis et la peinture médiévale en Campanie. Geneve

Geotechnical Engineering for the Preservation of Monuments and Historic Sites III – Lancellotta, Viggiani, Flora, de Silva & Mele (Eds)

The Grand Canal at Versailles: Geotechnical investigation, II

J.-D. Vernhes
UniLaSalle, Beauvais, France

P. Saulet
ESRI, Meudon, France

A. Heitzmann
Etablissement Public du Château, du Musée et du Domaine National de Versailles, Versailles, France

ABSTRACT: The park of the Palace of Versailles required major geotechnical developments whose center-piece is called the Grand Canal, designed by André Le Nôtre and dug in the 1670s on behalf of King Louis XIV. This exceptional work was the subject of an archival study, the main results of which were communicated on the occasion of the ECSMGE in Reykjavik in September 2019. The article proposed for the 3rd TC301 International Symposium reports on the in situ investigations and numerical field models carried out, with UniLaSalle students, over a period of two years, allowing in principle to answer questions that remained unaddressed.

The construction of the current relief map and of the supposed relief map before work makes it possible to estimate a volume of excavated material and embankments of nearly 700,000 m^3 and 500,000 m^3 respectively, realistic orders of magnitude. The apparent unbalance has no justification other than the current uncertainties in topographic models. The question of the canal watertightness and its hydraulic relationship to the surrounding ground, given the available field data, paradoxically appears less clear today than in the conclusions of the previous article. The real nature of the basin deposit, apparently colluvial to significant depths, complicates attempts to interpret both Le Nôtre's project and the current functioning of his work.

1 MAIN ELEMENTS OF THE WORK FROM THE FIRST ARTICLE

For a general presentation of the Grand Canal of Versailles today, we refer the reader to the first article dedicated to its geotechnical analysis (Vernhes & Heitzmann 2019).

The scientific contribution of this article consisted of a detailed analysis of the '*Comptes des bâtiments du roi sous le règne de Louis XIV*' in their simplified form, published in five successive volumes by Jules Guiffrey at the end of the nineteenth century (Guiffrey 1881-1901). These volumes have been reviewed for all that concerns the works related to the Grand Canal of Versailles, for a total of 137 articles explicitly related to this work. The construction of the water body was carried out over a period of nearly 14 years, from 1667 to 1680. Here is the main information resulting from this survey.

1.1 *Phasing of the work*

The irregularity of expenditure over the 14-year period made it possible to identify four phases of work. The first (1668-1669) and the third (1671-1672) are intense periods of activity. They see respectively the construction of most of the East-West and North-South branches of the cruciform canal. It represents 200,000 m^2, nearly 85% of the total surface of the built basin. This area does not include peripheral earthworks, which double the area of natural land likely to have been topographically modified, slightly or strongly – in particular at the western end of the canal (Figure 1).

 DOI 10.1201/9781003308867-14

Figure 1. View to the West of the Grand Canal of the park of the Palace of Versailles taken from the Latona basin (Sept. 2018). Below the Green Carpet and slightly above the canal, the Basin of Apollo and the sculptures of its fountain. At the other end of the water body, the Basin of Gally, that is not very visible on this picture.

An important aspect of these results for further earthworks analysis is that a coherent scenario of land movement should take into account this phasing: the balance of movements at the end of a phase should be in equilibrium.

1.2 *Earthworks volumes*

For a basin area of about 230,000 m^2 and an excavated depth rounded to 2 m, we obtain an earthworks volume of about 460,000 m^3. This first figure makes it possible to fix the order of magnitude of a minimum volume of the lands moved and deposited – because the draught of the canal is two meters and the excavation depth is therefore a little higher – assuming that the Grand Canal would have been built entirely out of excavated material.

1.3 *Draining nature of the Grand Canal in question*

The Grand Canal is, in terms of altimetry, the lower basin of the complex of basins and fountains of the park of the Palace of Versailles, therefore its first outlet, before the waters return to the natural environment in the Gally creek by means of drain plugs.

As we see in *Les Comptes* (‘*The Accounts*’), the canal, navigable and intended for a ceremonial fleet, had been designed during the first phase of work as a water reserve for the upstream of the park thanks to return mills. Furthermore, it is reported that the large and very flat area of the park where the canal is now largely situated, with a historically marshy nature, presented development difficulties during the attempts of sanitation by drainage. This would have led the designer of the project, André Le Nôtre, to suggest and carry out a permanent draining work (Baridon 2013).

2 FIELD SURVEYS IN 2018 AND 2019

During the academic years 2018–19 and 2019–20, field surveys were carried out on the site of the Grand Canal in Versailles, thanks to the work of geological engineering students. The types and quantities of surveys carried out are given in Table 1 below, located on the map in Figure 2 and detailed in the following paragraphs.

Table 1. In situ surveys carried out in 2018 and 2019 (modified according to Cordier et al. 2019).

Type	Quantities
Manual augers, number	122
Manual augers, linear (m)	76.4
Manual penetrometer, number	60
Seismic refraction array, number	7
Seismic refraction array, linear (m)	161
Electrical panels, number	11
Electrical panels, linear (m)	1072
Topographic profiles (levelling X,Z), number	43
Topographic profiles (levelling X,Z), points X,Z	1602
Topographic profiles (leveling X,Z), linear (m)	5072

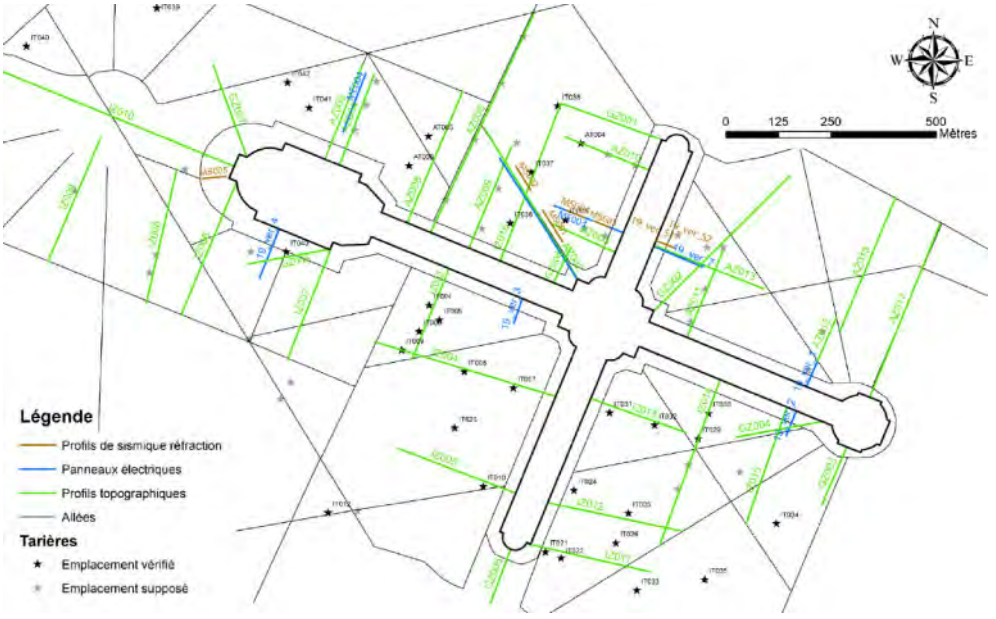

Figure 2. Map schematizing the in situ implementation of the measurements carried out around the Grand Canal in 2018 and 2019 (Cordier et al. 2019, p. 20).

2.1 *Geotechnical measurements*

2.1.1 *Manual auger*

The purpose of manual auger samplings was to highlight lithological variations in the first meter of soil around the Grand Canal. The agreed idea was to associate them with the stratigraphic

changes visible on the geological map (Figure 5) but also with the “lithological anomalies” linked to earthworks.

2.1.2 *Portable dynamic penetrometer*

The purpose of indirect soil compactness measurements using the portable dynamic penetrometer was similar: to detect, at a depth limited to 1 m, a possible global variation in soil response depending on its geotechnical state: in place, excavated or backfilled.

2.1.3 *Assessment of geotechnical measurements*

Even taking into account the presence of a recent surface cover rich in organic matter, which can locally be several decimeters thick, auger and penetrometer survey data showed a wide dispersion of the results. These results proved to be refractory for a direct interpretation according to the criteria initially planned, which were intended to highlight a difference distinguishing between in place and remoulded soil, in other words between natural and excavated material on the one hand, embankment on the other hand.

We thought at some stage that the wide dispersion of the results was related to the natural variability of tertiary rocks at advanced stages of alteration in place. In a geostatistical language, it would then be a “nugget effect” problem, a problem that can be solved by a better distribution and densification of the sampling. The discussion presented in Part 3 sheds significant enlightenment on these difficulties.

2.2 *Geophysical measurements*

2.2.1 *Seismic refraction*

The purpose of the seismic refraction measurements (Figure 3) was comparable to the purpose of penetrometric tests. It has indeed been implemented in order to identify variations in the state of

Figure 3. Installation of a base of seismic refraction measurements (Sept. 2018). The device is installed near the Gally basin. To the east, above the other end of the canal, we can see the Palace.

compactness of the soil by correlation with the seismic velocities of the P wave in the ground. The depth of investigation of the method, with the adopted equipment and parameters, was in the order of 5 to 10 m.

2.2.2 *Electrical panels*

The purpose of electrical panel measurements, through a resistivity imaging, was always to look for signs of variation in the compactness of soil in relation to the effects of earthworks. This approach previously required hypotheses on lithology but also on the water content of soils, to which electrical resistivity measurements are particularly sensitive. The depth of the investigation of the method, with the equipment and settings used, was in the order of 15 m.

2.2.3 *Assessment of geophysical measurements*

As a synthesis of the findings, geophysical measurements have everywhere highlighted a stratified structure of the soils. This is an unsurprising result in seismic tests since the method is firstly adapted to highlight velocities variations of the P wave (v_P) on both sides of interfaces more along horizontal than vertical direction. The observation stated above is less clear with electrical panels and, in fact, this method is not supposed to favor one direction over another in geometric field modelling.

In seismic refraction, a "seismic bedrock" in a range of velocities v_P from 1700 to 2000 m/s is encountered at moderate depths from three to five meters. It is systematically surmounted by a complex of two "slower" horizons, the most superficial from one to two meters thick for $v_P \approx 300$ m/s, the deepest from one to three meters thick for $v_P \approx 1000$ m/s.

In electrical panel, it is more convenient to describe the general situation through the following observation. Soils are characterized by low to moderately low resistivities, from 10 to 50 Ohm.m, except, where appropriate, near the surface. In these cases, the resistivities of the soil layers are typically in the range of 50 to 300 Ohm.m on very variable thicknesses from a few decimeters to a few meters.

Whatever the method, and as in geotechnics, difficulties of interpretation emerged by establishing a link with the indications of the geological map and the categories of remoulded / in place soil. This is discussed in Part 3. However, general reasonings makes it possible to take advantage of the information provided by geophysical prospection. For example, it is very likely that the soil is water saturated at few meters depth. This hypothesis can be supported on two points: the general weakness of the resistivities measured on site below a possible resistant layer, fresh water having a resistivity in the order of 40 Ohm.m and significantly influencing the resistivity of the soils it soaks; on the other hand on the velocities v_P, which overcome in depth the threshold of 1500 m/s, speed of compression-al waves in the water. A persistent problem is that this saturation is not necessarily synonymous with superficial phreatic level since phenomena of capillarity may very well pro-duce the same geophysical results.

2.3 *Topographic measurements*

2.3.1 *Airborne photogrammetry by drone*

As part of the students' work, a drone photogrammetry campaign (with a three-color RGB sensor) took place in December 2018. It aimed to set up a Digital Elevation Model (DEM) for the entire perimeter of the Grand Canal. This campaign gave a result difficult to exploit for the geotechnical survey. We have chosen not to include the data in the final DEM.

Anticipating the problem, we were going to encounter with the canopy of woods arranged around the Grand Canal, we chose the beginning of the winter season to carry out the campaign. The characteristic shaving lighting of this season at the latitude of Versailles, producing ample drop shadows, added to a particularly dense twigs vegetation, disrupted the process that should have allowed the photographic cover to produce reliable and continuous altimetry data. We now consider that only a relatively expensive LIDAR-type sensor would allow to achieve the expected result.

2.3.2 *Levelling (X,Z) with level and target*

More modest means of topographical measurements were implemented by the teams of students, a levelling type according to a profile determined in advance (Figure 4). These profiles consist of points known by their horizontal distance to a point of origin (X) and by their relative altitude to that point (Z) measured with a level and a target. The resulting accuracy is in the order of one centimeter over aiming distances of a few tens of meters, very sufficient for a geotechnical objective. The advantage of these measures in the context of the site is that they have not been prevented, but only complicated, by vegetation. All the gathered data were then linked to a fixed reference, the limestone margin of the canal, established at 109 m NGF (General Levelling of France). The resolution (the measuring step) of the measured profiles is variable, the accuracy obtained is in the order of 1 to 10 cm in altimetry and from 10 cm to 1 m in planimetry.

The obtained result, combined with a public data source from the National Geographical Institute, is presented and discussed in parts 4.2 and the following parts.

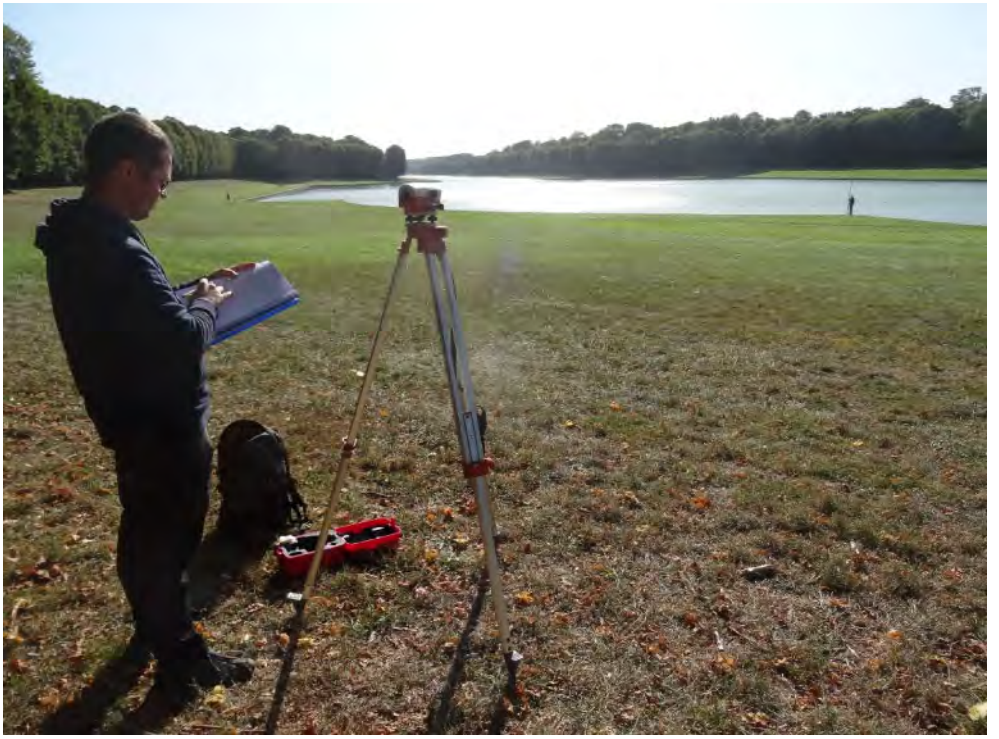

Figure 4. Levelling measures (Sept. 2019). View taken to the East, the visible part of the Grand Canal is the Gally Basin.

3 A SUBSURFACE GEOLOGY PROBLEM

3.1 *Data from the geological map of France*

The geological map of France at 1:50,000, Versailles sheet (n° 182) was published in 1967 under the authority of Jean Goguel (Figure 5). It has not been updated since then. It highlights a system of Tertiary formations frequently encountered in the Paris Basin. These are the sandy, clayey, marly or limestone ensembles, from the Stampian to the Lutetian, aged about 30 to 45 million years. The principle of drawing the cartographic boundaries of these strata is to associate with their

sub-horizontal character the pattern of the relief, with the result of relating approximately these boundaries to the topographical level lines. The Grand Canal was mainly developed in the topographic depression of the ru de Gally, within which the geological map indicates as supragypsous Marls of the Ludien (code e7), level dated on average 35 million years, the most recent of the Eocene in the Paris Basin.

Figure 5. Extract from the geological map of France at 1:50,000, Versailles sheet (GOGUEL, 1967), cen-tered on the Grand Canal. The castle is about 1 km east of the canal.

The 2018 and 2019 field measurements were based on the principle that, apart from a first decimetric layer of "topsoil" covering the entire site, the lithology encountered on site had to correspond to the stratigraphic data of this map or be affected by changes related to earthworks. These modifications were not meant to be purely random but to be unified by simple principles of excavated areas and deposit areas, in connection with the Grand Canal construction project of course.

Initial difficulties in interpreting the survey results presented in Part 2 of this article are now explained.

3.2 *Taking into account the data of surveys carried out in 1997 and consequences*

In the period of exploitation of the field surveys of 2018 and 2019, we have accessed an internal report of the Palace of Versailles issued in December 1997 by the Chief Architect of Historic Monuments at that time (Lablaude 1997), dealing with the restoration project of the banks and margins of the Grand Canal. This project resulted in the installation of four piezometric tubes in boreholes carried out with the helical auger Φ 80, at depths of about 8 meters, positioned around the perimeter of the water body at the cross of the North-South and East-West branches, as well as in the vicinity of its western end.

These four boreholes all show the presence of a high thickness of colluvium from the Fontainebleau sands and quaternary spreading silt (Lablaude 1997, p. 254), up to depths of 5 to 8 m. These materials are described as incoherent fine sand interspersed with clay lenses, very different from the expected plastic and homogeneous marl-clay facies, lithological translation of the supragypsous Marls of the Ludien. At the scale of the seventeenth century earthworks, this means that a large part of the displaced materials do not correspond to the indications of the geological map, which primarily describes the tertiary or anterior geological substratum and commonly excludes surface formations. For topographical reasons, this condition probably does not apply to the North

and especially South end of the North-South arm of the Grand Canal, in areas where the project approached the outcropping sands of Fontainebleau. However, the idea that the earthworks under Le Nôtre's remoulded materials that had been in place for several tens of millions of years, turned out to be false. Colluviums, materials already reworked during the quaternary, cannot present a geotechnical facies as different before and after earthworks as was initially expected.

This evidence explains the difficulties of correlations between the indications of the geological map and the results of the geophysical and geotechnical investigations on all the sectors investigated in 2018 and 2019. Under these conditions and at the stage of the current results, possible criteria for differentiating the soils in place from those remoulded by means of intrusive or indirect investigation are unfortunately too ambiguous to allow for a conclusion. The analysis of the topographic models is the only tool to make advancements in the problem.

4 EARTHWORKS: SEARCH FOR A BALANCE OF MOVEMENTS

4.1 *Status of the issue in 1997*

The map in Figure 6 appears in the report of the late Pierre-André Lablaude presented above. On the occasion of his general diagnosis before the planned works, the architect wonders about what he calls the "anthropogenic topography", resulting from the lands reprofiling by earthworks. His analysis led him to use the level line at 110 m altitude NGF to distinguish two opposite situations: the one, in general case, where the canal is built in a "natural recess", and the one where this situation is in "artificial trench", which according to him corresponds to the particular cases "of the western ends (Gally basin), North (Horseshoe basin) and South (Menagerie basin)" (Lablaude) 1997, p. 241). Its conclusion is mapped by a modification of the route of the 110 m NGF level line at these three ends of the Grand Canal.

Our own analysis of his work is divided in two stages. Firstly, we note the ambiguity of his geotechnical vocabulary. Is it necessary to understand that the canal originally under 110 m was built in an embankment, or in a levelled surface, and excavated above this height? The equidistance of the level lines drawn on his maps being 5 m, he does not seem to seek to give details on this issue, especially in cases where he considers that the canal was developed under the natural altitude 110 NGF. Secondly, by interpolating this level line as he does on his interpretative map, he assumes that the canal axes at the three North, West, and South ends were almost always orthogonal to the

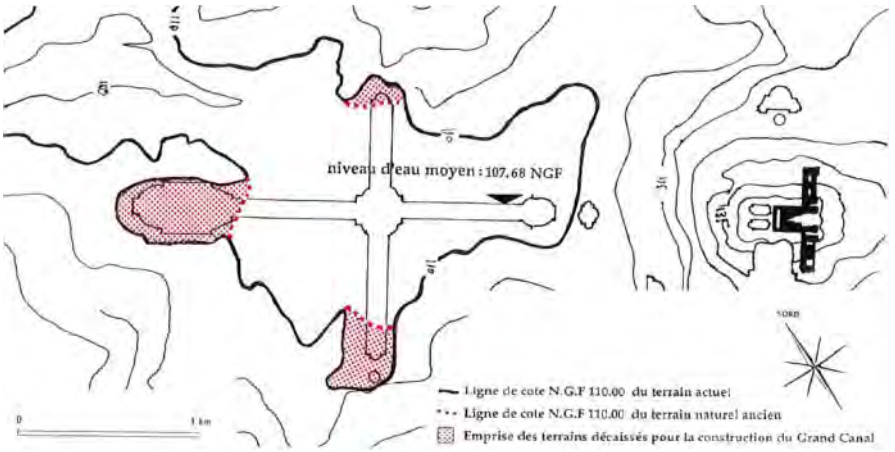

Figure 6. Grounds altimetry plan with location of the NGF 110 m altimetric line, extract from the map p. 242 (Lablaude 1997).

level line. In doing so, he considers that these three ends, and particularly the western end, caused only excavated earthworks. The problem of their deposit does not arouse his attention. These two re-marks about Lablaude's work are extended in the following paragraphs.

4.2 *Current topography*

The map in Figure 7 was developed from two data sources: the synthesis of on-site leveling profiles made by the students in 2018 and 2019 (see section 2.3.2), and the 5 m resolution Digital Elevation Model (DEM) of the National Geographical Institute (IGN). It should be noted that we have accessed the IGN 1 m resolution DEM but to note that, for the park of the Palace of Versailles, it has not a real gain in resolution. All the difficulty of the work then focused on the problem of harmonizing two sources of topographic information with their own characteristics, on the one hand the profiles (X, Z) precise but with a very heterogeneous planimetric arrangement, therefore very artefactual in a DEM, and on the other hand the DEM of the IGN, with a very homogeneous dot pattern, but insufficient resolution/accuracy for the geotechnical survey conducted.

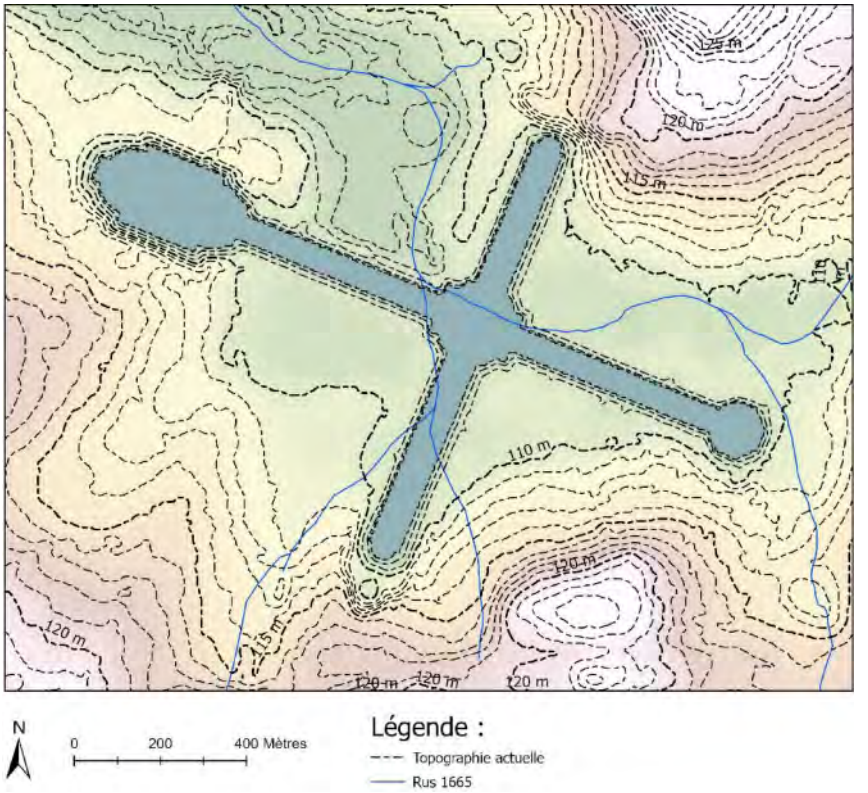

Figure 7. Topographic map of the current terrain centered on the Grand Canal of Versailles (IGN and Uni-LaSalle data). Equidistance of 1 m level lines. Location of the water streams according to the plan attributed to Delapointe 1664/65, Bibliothèque nationale de France, Va 448 f.

The obtained map is the most accurate available at present and therefore makes it possible to lay a basis for the analysis of earthworks by observing the terrain model. However, this map has its limits, with a real resolution that is between 1 and 5 m and not 1 m everywhere, and furthermore, it suffers from visible artifacts, for example the effect of steep slope instead of a vertical at the place where the peripheral edge is located. This situation is taken into account in the analysis

proposed at the stage of this article. This map makes it possible to find the first-order facts already known, for example the role of the level line at 110 m NGF, but it provides everywhere decisive precisions. We georeferenced and then superimposed on this map the system of streams prior to the development of the canal (named “Rus 1665”) in order to use these archival hydrographic data to support morphological reasoning. These arguments are presented in the next chapter.

4.3 *Topography before works (“1665”)*

The map in Figure 8 was constructed on the one hand by means of a naturalistic reasoning, based on the observation of the natural environment, and on the other hand on the integration of the logic of earthworks, including their phasing in four stages. The naturalistic reasoning is based on the fact that the lines of levels distant from the Grand Canal, those which are considered to be unchanged by other sites in the park, are shaped by a principle of hydrographic erosion following lines of weakness in the geological substratum, and those at several scales nested in each other. We therefore analyze the location of high points and thalwegs, considering the gravity trajectory of the flows of water or mate-rial transported by water. According to this principle, it is noted that the streams are logically located in the thalwegs or more generally following the lines of topographical low points.

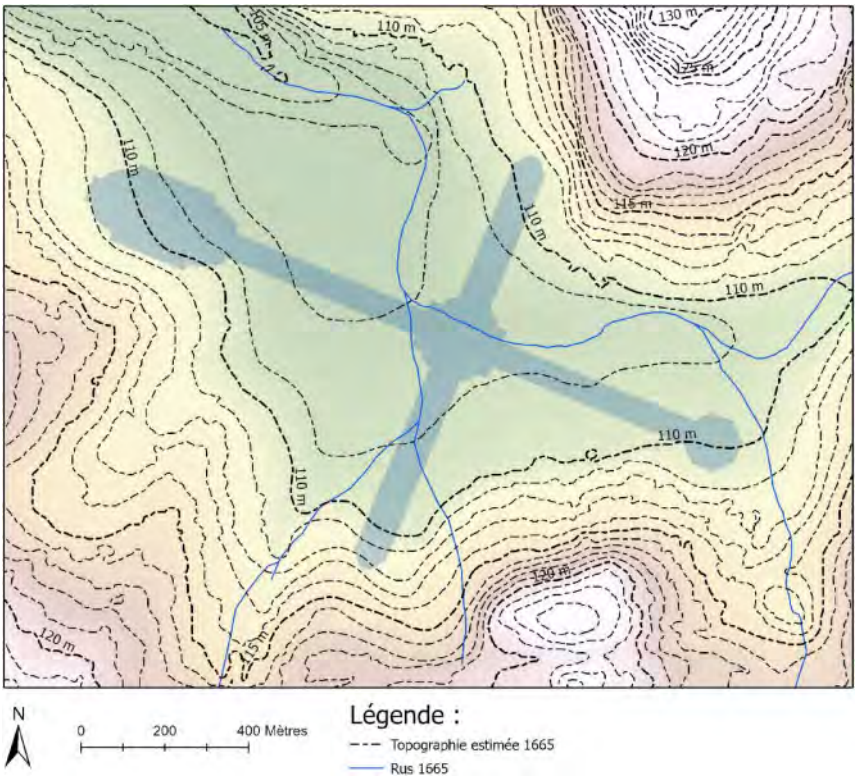

Figure 8. Topographic map of the land before work (symbolic date: 1665) centered on the Grand Canal of Versailles (IGN and UniLaSalle data). Equidistance of 1 m level lines.

Thus, the topography of 1665 (Figure 8) in the large central sector of the canal appears very horizontal, while a light steep difference in altitude is observed in the area of land bounded by the North and West arms of the cross. The level lines have thus been rede-signed with an assumption of greater progressivity of the difference in altitude throughout the area in question. On the other

hand, two sectors were identified since the first article as embankment deposits, delimited by steep embankments in comparison with all the slopes observed elsewhere in the park. They are particularly visible thanks to the leveling profiles measured on the field. This concerns the area west of the north arm of the canal and the area north of the Gally basin. These artificial mounds have therefore been "erased" in the map in Figure 8. According to the morphological principles set out above, the level lines at the northern and southern ends of the Grand Canal, but also on the side of the Apollo Basin to the east, have been smoothed to obtain a more regular relief. Finally, to complete the description of the main changes made to the current level lines, we corrected in the field area between the west and south arms of the canal the concavity reversal of the level line at 110 m NGF. This correction consisted in "erasing" a kind of earth platform with no apparent link to the system of relatively marked thalwegs that go up to the south, and where two arms of one of the streams that existed there before 1665 flowed.

4.4 *Deduction of a cut and fills Map*

The map in Figure 9 was obtained by subtracting the previous two maps. This subtraction had to be delimited by a boundary beyond which we considered the impact of the works – especially the embankment depositing activities – as 'negligible'. This hypothesis was made necessary by the observation that large quantities of embankments can, by calculation, be generated by an infra-decimetric difference in altitude between the map 1665 and the current, therefore by the minimum of uncertainty on the topographic data. On the other hand, in anticipation of future improvements, areas related to the four phases of work have been demarcated on this map, in order to extract detailed cubatures phase by phase – for the moment not exploited. These internal limitations, however, pose other problems because it is likely that the areas thus associated with a single stage of construction may have been affected by several successive phases of work.

These intuitions have remained qualitative until then, and now they are visualized and become accessible to quantification. This is particularly the case of the large deposits West of the northern arm of the canal (height up to 2.5 m) and North of the Gally basin (height up to 4 or even 5 m). With regard to the embankment of the Gally basin, André Le Nôtre's skill is to have used a topography angled to the main axis of the canal to manufacture from scratch, by an earthmoving process, a symmetry of the banks on both sides of the basin, with all the appearance of a natural theater.

4.5 *Resultant from the movement of land: an unbalance in the current state of knowledge*

We recall here the result of part 1.2 where we put forward the initial figure of excavated material produced by the work of the Grand Canal in the order of 460,000 m^3.

From the work on Digital Elevation Model presented above, there are nearly 705,000 m^3 of excavated material for about 515,000 m^3 of embankments. There should not be this considerable difference. First, it is not reported in *Les Comptes* (Guiffrey 1881-1901) to evacuate excavated material at a distance from the park, none of the excavated materials having any real economic value and the principle of the lower energy consumption prevailing at that time as today. Then, the deposition of materials that have been damaged because of phenomena of proliferation and natural recompaction over several centuries, in our opinion should not cause significant variations in the volumes initially occupied, therefore those resulting from our calculations. This means that our map of the current terrain combined with the 1665 map hypothesis and the resulting embankment-excavated volumes, although representing an improvement over the previous state of the issue, is still unsatisfactory. As an indication and subject to all the constraints expressed above, details of the calculations phase by phase are provided in Table 2.

As discussed in Section 2.3.1, significant progress is likely to occur if a more accurate/resolution DEM can be exploited, for example obtained by a LIDAR coverage of the land. It would remove uncertainties that are not definitive, which would justify a more detailed work on the original topography of the site.

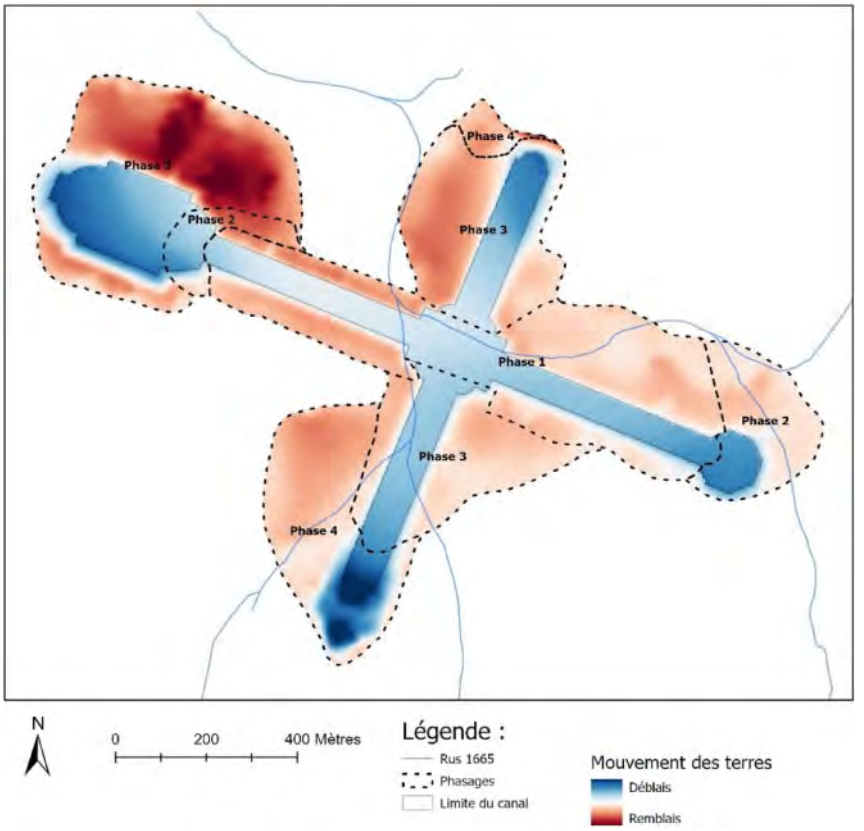

Figure 9. First interpretative cuts and fills map resulting from the digging work of the Grand Canal of Versailles.

Table 2. Results of embankment-excavated volumes by phase in 2021.

Construction phase.	Excavated material (m^3)	Embankment (m^3)
1	165	85
2	75	25
3	350	340
4	115	65
Total 1667–1680	705	515

5 WATERTIGHTNESS OF THE CANAL

5.1 *Two opposing points of view*

In part 1.3 we highlighted an ambiguity about the problem of the watertightness of the Grand Canal. The first functions assigned to it (navigable basin, reservoir for the fountains of the park) suggest that it had to be sealed to guarantee a water level and therefore a minimum available volume at any time of the year. But the analysis of André Le Nôtre reported by Michel Baridon seems on the contrary to indicate that there should have been no perimeter wall or watertight invert between the

basin and its casing so that the canal can fulfill its function of drainage and sanitation of the old swamp, by catchment or permanent drawdown of water levels in the surrounding land.

This ambiguity is not clearly removed by the analysis of the *Comptes*, and on this point, we qualify the opinion expressed in our first article (Vernhes & Heitzmann 2019) where we defend the thesis of generalized watertightness, a thesis translated by a schematic section showing a continuous lateral and bottom processing by application of waterproof clay. It has certainly been noted that resources have been devoted to this processing of the water body under construction, but without knowing precisely where (among the spaces between temporary embankments and peripheral wall, at the bottom of the excavation), under what conditions and how systematically this was done throughout the years of construction.

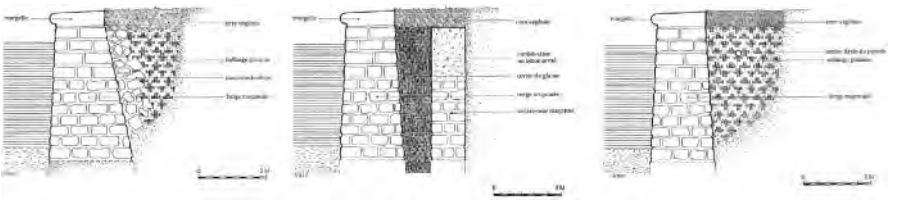

Figure 10. Interpretative diagrams of the results of the three borehole surveys of the peripheral masonry wall of the Grand Canal (June 1997), carried out with a manual shovel, in Lablaude 1997 (pp. 280, 282 and 284). They represent, from left to right, a variety of situations at the northern, southern and eastern branch of the Grand Canal.

5.2 *Observations and analyses in 1997*

The Lablaude 1997 report, already cited, provides interesting hydrogeological information on the Grand Canal site. One of the architect's goals was to restore at least part of the clay core that he assumes he will find behind the entire perimeter retaining wall of the Grand Canal. To justify the reconstruction, he must affirm its importance for the proper maintenance of water levels in the basin.

The report is based on piezometric levels measured in the terrains surrounding the canal in four points. These four points are not precisely identified on the map of the survey performer (Sol Progrès company, Figure 11a) while their altitude is curiously of great precision and stability in the documents of exploitation of the piezometric data provided by the architect, always at 108.24 NGF. This elevation is also given in the document as the nominal altitude of the edge capping the retaining wall. We express a doubt in particular about the real altitude of the head of PZ3 (Figure 11b), which seems to us possibly higher and therefore far from the piezometric surface.

Lablaude notes that the water level in the surrounding soil of the canal is lower or almost equal to the level observed at the same time in the Grand Canal. The height differences are from a few centimeters to one meter in PZ1, PZ2 and PZ4. They are more marked, from one to two meters, in the PZ3, without any explanation of Lablaude. The architect highlights that the phreatic water sits in a formation of sandy-silt colluvium and that the muddy level of the bottom of the basin is on average two meters below the margin. He does not consider the colluvium or the muddy bottom as impermeable.

What is surprising in the rest of his analysis is that he believes that the water in the field feeds the canal as soon as its static level is higher than the level of the bottom of the canal and not that of the water in the canal, which contradicts the principle of communicating vessels. He therefore believes that, except for the PZ3, all levels recorded in the autumn of 1997 attest that the canal is primarily an outlet for the ground waters sur-rounding it, from the bottom. In doing so, Lablaude admits both that the bottom of the canal has no sealing function, that it would therefore not have been wrought, and that work to repair the wrought on the peripheral wall is of interest since it would maintain the operating regime of this wall originally planned.

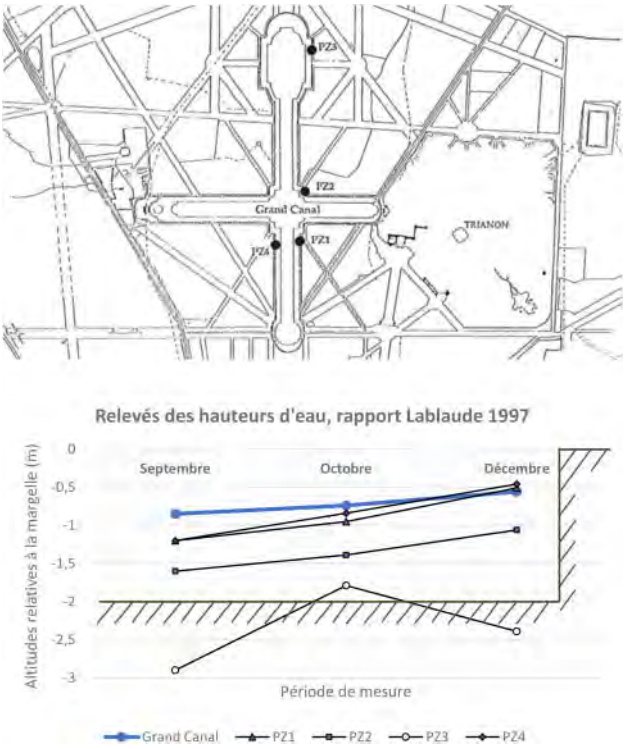

Figure 11. (a) map of the 1997 piezometric boreholes provided in the Sol Progrès report and reproduced on p. 252 of Lablaude 1997. (b) Graphical translation of the point water levels recorded in the autumn of 1997 in the Grand Canal and in the piezometers, with casing showing the level of the edge and the average level of the muddy bottom. Water data, op. cit. cit., pp. 268, 270, 272.

The Lablaude reasoning we tried to understand is therefore ultimately difficult to follow, but it illustrates the difficulty that the question of the sealing of the Grand Canal represents.

5.3 *Current hydraulic analysis: three possible regimes*

Assuming that the decimetric variations in the water level observed in the Grand Canal are naturally stabilized over the long term around an average satisfactory for its functions as a navigable reservoir basin, three possible solutions could concurrently explain such a condition:

a. Effective watertightness everywhere at the basin/terrain interface and therefore independence of water levels in the ground (piezometrics) and in the canal (limnimetrics); this hypothesis is associated with the generalized presence of a wrought several decimeters thick with an effective permeability in the order of 10^{-6} m/s or less. This hypothesis seems to be contradicted by the condition of the foot of the perimeter wall on the landward side on excavation surveys with shovels (Figure 10), according to Lablaude,1997.
b. It is the low permeability of the surrounding soil that actually ensures the watertightness of the Grand Canal. Even when the water level in the basin is higher than the water level in the field, the flows transmitted to the ground are negligible over time, especially compared to other loss phenomena such as evaporation. Under these conditions, the discontinuous nature of the sealing works and a certain heterogeneity of soils at the basin/terrain interface are no longer at the heart of the hydraulic analysis of the Grand Canal and can be relegated to the rank of second-order causes.

c. The phreatic level is stable during the year. In this case, regardless of the permeability of the soil, the water levels between the land and the Grand Canal are slowly or rapidly balanced and no problem arises if the natural water levels in the land are close to those required for the water body.

With the evolution of our own thinking, in the end only solutions b. and c. are retained as possible, and can even complement each other. One way to check the preponderance of one over the other would be to look at the degree of correlation between piezometric levels and water level in the canal by continuous measurements over at least an entire year.

6 CONCLUSIONS

This article draws a picture of the knowledge acquired on the Grand Canal from a geotechnical perspective through archival studies, field investigations conducted in 2018 and 2019, and through the exploitation of a Digital Elevation Model initiated in 2019 and recast in 2021. The main advance is the one obtained by the creation of a DEM leading to a first hypothesis of the volume of the earthworks by excavated material and embankments. The corresponding figures are, respectively, 705 000 m^3 and 515 000 m^3. These figures, which will have to be even better placed, show the order of magnitude of the works carried out, very comparable to those currently assumed in the period 1679-1686 for the earthworks in the park of Marly (Vernhes, 2017), which followed almost immediately the last finishes for the Grand Canal.

ACKNOWLEDGMENTS

I wish to acknowledge the students of UniLaSalle (Beauvais, France) who dedicated their Thesis or Collective Research Project in Geoscience to the Grand Canal in Versailles: Abdel Hussein Cissé, Guillaume Le Motheux du Plessis, Maxime Peron, Corentin Rubio, Ghislain Cordier, Félix Fleuriot, Pauline Lesecq, Yesmine Meslamani, Guillaume Meyfroidt, Matthieu Poulain, Michael Vanhee, Nicolas Dubeau and Elodie Ricard. Our thanks also go to Gilles Bultez, Head of the Fountains Department of the Parc deVersailles, Sandrine Pallandre, Head of the State Resources Department and Daniella Manar, historian of the Fountains Service, for their scientific support.

REFERENCES

Baridon, M. 2013. “Les jardins de Le Nôtre et d’Hardouin-Mansart”, dans Arizzoli-Clementel P. (dir.), Versailles, Paris, Citadelles et Mazenod.

Cordier, G., Fleuriot, F., Lesecq, P., Meslamani, Y., Meyfroidt, G., Poulain, M. & Vanhee, M. 2019. Rapport de Project Collectif Géotechnique 5A sur le Grand Canal de Versailles, 80 p. Non publié.

Guiffrey, J. (éd.) 1881-1901 (5 tomes), *Comptes des bâtiments du roi sous le règne de Louis XIV* (1664-1715). Source gallica.bnf.fr / Bibliothèque nationale de France.

Goguel, J. 1967. Versailles, Carte géologique de la France à 1/50000, n° 182, Orléans, Bureau de recherches géologiques et minières.

Lablaude, P.-A. 1997. Etude préalable à la restauration des berges et margelles du grand canal, rapport destiné à l’Etablissement Public du Musée et du Domaine National de Versailles, 145 p. Non publié.

Le Guillou, J.-C. 2000. Le domaine de Versailles de l’Aube à l’Aurore du Roi Soleil (1643-1663), in Versalia n° 5. Reproduction en p. 65 d’un plan attribué à Delapointe 1664/65, Bibliothèque nationale de France, Va 448 f.

Vernhes, J.-D. 2017. Grands travaux d’aménagement du vallon de Marly. Bulletin du Centre de recherche du château de Versailles. DOI : https://doi.org/10.4000/crcv.14555

Vernhes, J.-D. & Heitzmann, A. 2019. Le Grand Canal à Versailles : enquête géotechnique. XVII European Conference on Soil Mechanics and Geotechnical Engineering. 2019, Reykjavik, Iceland. ISBN 978-9935-9436-1-3

Geotechnical Engineering for the Preservation of Monuments and Historic Sites III – Lancellotta, Viggiani, Flora, de Silva & Mele (Eds)

Geotechnical studies to optimize the protection measures against flooding of St. Mark square (Venice, IT)

P. Simonini & F. Ceccato
Università degli Studi di Padova, Padova, Italy

ABSTRACT: The famous St. Mark square, located on an island characterized by the lowest gap between ground and sea level, is currently flooded during high tide, even though the MOSE barrier system is operative. To design cost-effective interventions to safeguard this historical heritage, a understanding of flooding mechanisms and the relationship between groundwater pressure and tidal oscillations was necessary. This paper presents the results of a recent monitoring campaign carried out at St. Mark square as well as a discussion on the selected interventions to protect the square against flooding.

1 INTRODUCTION

The historic city of Venice, located on several islands in the middle of a lagoon, and the surrounding environment are characterized by a rather precarious equilibrium, with the safety margin reducing at an accelerated rate. The rate of deterioration is due to the increasing flooding frequency of the historic city, that is caused by the natural eustatic rise of the sea level, by the natural subsidence and by the regional man-induced subsidence, which was significant between the ‘40s and ‘70s of the last century.

The city of Venice is located in the middle of the omonimous lagoon, whose origin is traced around 6000 years ago, when the sea water diffused into a preexisting lacustrine basin during the deglaciation period. The tide flows in and out from three lagoon inlets; its normal excursion is around 60–70 cm and lasts approximately 6 hours.

Since the gap between the ground level of Venice islands and the sea (lagoon) water level is small, at tides exceeding +0.8 m above mean sea level (referred to as mean sea level at the *Basilica di Punta della Salute* - s.l.P.S.), a few of island pavements begin to be flooded. At tide levels exceeding 1.1 m., occurring under low atmospheric pressure, strong winds blowing from Adriatic Sea and enduring rain, the flooding of a great part of the city is observed.

To protect the city of Venice against this recurrent flooding, several projects have been undertaken, the most important being the design and construction of movable gates located at the three lagoon inlets, namely the MOSE barriers (MOSE is acronym for *Modulo Sperimentale Elettromeccanico*: Experimental Electromechanical Module). These gates, controlling the tidal flow, temporarily separate the lagoon from the sea at the occurrence of high tides exceeding 1.1 m above s.l.P.S..

Other relevant interventions consisted in erosion mitigation of marshes and wetlands, morphological cost-line restoration, renovation of the existing jetties at the inlets, fishing farms reopening and, as far as the historic city concerns, raising the elevation of banks, pavements and sidewalks in some selected areas to prevent the floods due to tide below +1.1 m.

DOI 10.1201/9781003308867-15

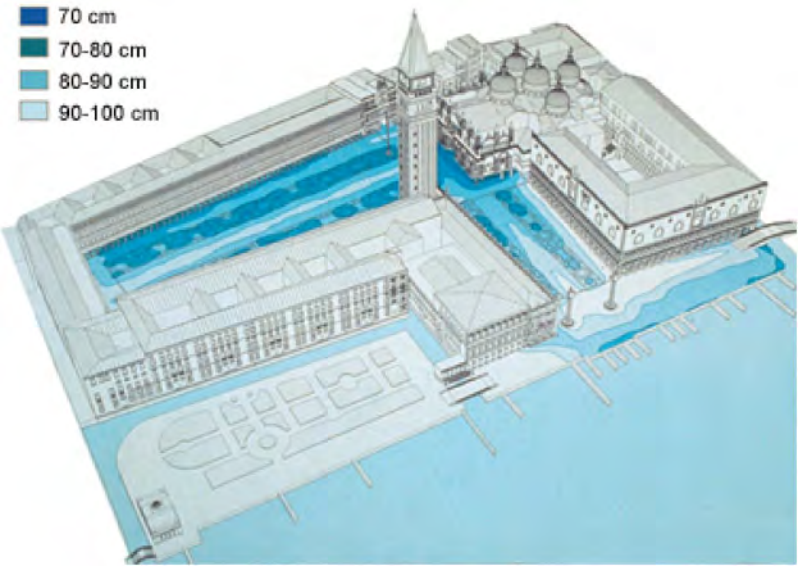

Figure 1. View of St. Mark's island with flooded area at corresponding values of tidal level (cm) (adapted from www.mosevenezia.eu).

The St. Mark's square is the lowest part of the historic center of Venice and is characterized by an elevation between +0.80 m and +0.90 m above s.l.P.S. More particularly the area facing the St. Mark's Cathedral is located at an even lower level, approaching +0.60 m above s.l.P.S.

The increasing frequency of flooding of the St. Mark's square induces considerable deterioration of masonry walls, foundations and decorative architectural elements of very important ancient buildings (Bettiol et al. 2015; Ceccato et al. 2014; Fletcher & Spencer 2005), jeopardizing the historical heritage of city and especially of that facing the St. Mark's inner square. When the water level reaches +0.60 m above s.l.P.S., a small zone in front of the Basilica and its narthex begin to be flooded. At +0.90 m, approximately 65% of the square is covered by water and at 1.15 m it is fully submerged. A tide exceeding +0.90 m is currently recorded at around one per cent of the time on the annual basis, but this percentage will rise considering a small effect of natural subsidence (0.5 mm/year) and sea level rise due to climate change.

The activation of the MOSE gates, when +1.10 m above s.l.P.S. (or higher) is forecasted, does not prevent the historical area of St. Mark's square to be flooded. Specific protection countermeasures are therefore needed, but selecting optimal solutions in this special context was not straightforward as it might be respectful of the historical heritage, compatible with the touristic activities as well as cost-effective.

Figure 2 shows a cross-section of a typical quay-wall facing the surrounding canals or the St. Mark's basin with an indication of different flow paths potentially concurring to flooding:

1 Back-flow through the existing drainage system;
2 Overtopping, from the St. Marks' basin;
3 Heavy rainfalls;
4 Seepage through the soil.

As shown in Figure 2, seepage flow may currently occur through or below the quay-walls, through the ancient and pervious drainage network, the open joints between the stones forming the pavement, which are in hydraulic connection with the water basin through the soil.

To protect the square against flooding a preliminary project was proposed in 1998, in which several countermeasures have been planned, the most important being the construction of vertical

cut-off continuous sheet pile walls around the perimeter of St. Mark's island to avoid water infiltrating through and below the quay walls and the installation of an impermeable membrane below the stone pavement, to prevent seepage flow through the permeable joints between the stone elements of the pavement. Some doubts of the need and effectiveness of such huge interventions arise in the late '10 s and therefore different studies have been undertaken. More particularly, mechanisms 1–3 have been investigated in maritime and hydraulic studies (Ruol et al. 2020; P. Salandin 2020;) while mechanism 4 was investigated by specific geotechnical investigations presented and discussed in the following.

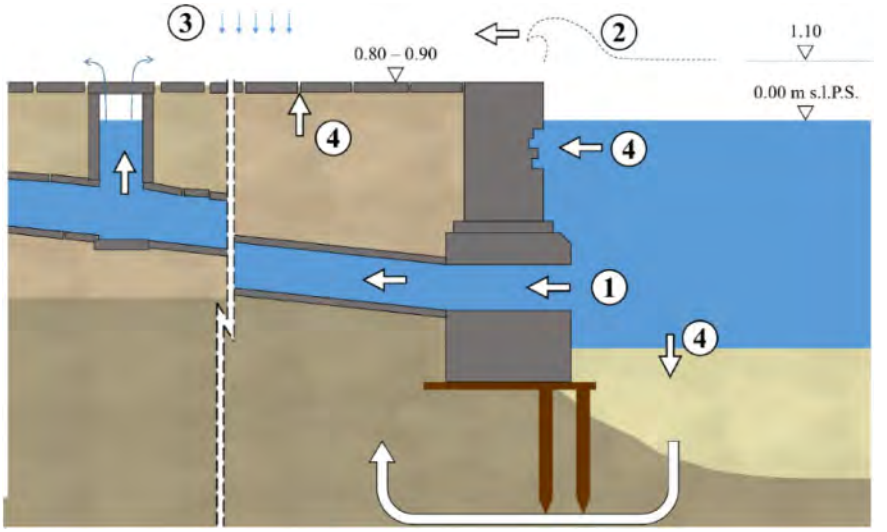

Figure 2. Main flooding mechanisms of St. Mark's Square: 1. Back-flow through the drainage system, 2. Overtopping, 3. Heavy rainfalls, 4. Seepage through the soil.

2 THE OLD DRAINAGE NETWORK

The still active ancient drainage system of the St. Marks' square, formed by a network of masonry tunnels (referred to as *gatoli* in Venetian language) collecting both rainfall and wastewater, was mostly constructed in the 18th century by the Republic of Venice.

The typical sections of these *gatoli* (Figure 3a) are characterized by rectangular sections between 0.4 m and 0.8m wide and between 0.6 and 0.9 m high. The vertical masonry walls are about 0.30 m-thick; the *gatoli* are closed above by a massive calcareous block, called *stelere*. For larger *gatoli*, an arch vault reaching a width of 1.50 m and a height of 2 m is used (Figure 3b). As a consequence of the construction technique, they are relatively pervious and seepage water can flow through the fissures between the *stelere* and the lateral walls, and, for the most deteriorated ones, between the brick elements forming the lateral walls.

Figure …shows an inner view of one conduct in good conditions and one in worst conditions.

The embedded drainage elements are gently sloping toward the canals or the St. Mark's basin. The water discharge rate is therefore very slow, thus fostering sediment deposition, which can reduce over time their cross section to 50–75% or, completely obstructing it in some cases (Volpato 2019). Hydraulic measurements and models (Volpato 2019) showed that the hydraulic head inside the *gatoli* coincides with the lagoon water level, i.e. the system is fully connected to the lagoon such as water can flow in and out according to tide oscillation.

Due to the perviousness of the *gatoli*, the water flowing into drainage system, is in direct connection with the surrounding shallowest soil forming the foundation ground of the entire square.

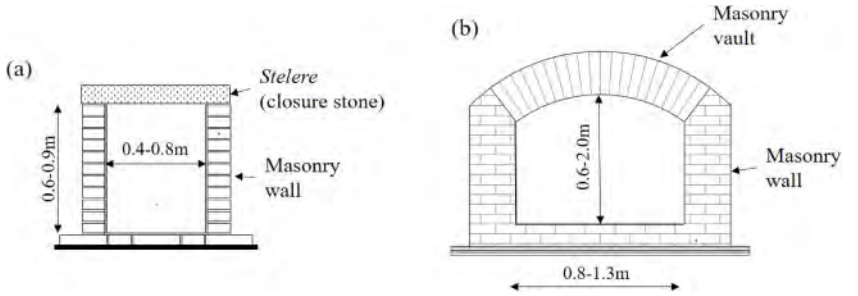

Figure 3. Typical cross section of Venetian *gatoli*.

Figure 4. Inner view of two drainage conducts in S. Mark's square: (a) gatolo in good conditions, (b) gatolo in bad conditions.

3 GEOTECHNICAL SITE INVESTIGATIONS

The heterogeneity of the soils in the Venice lagoon is well known (Biscontin et al. 2007; Cola et al. 2008; Ricceri 2007; Simonini et al. 2007) and the island of St. Mark is no exception. Given the complexity of the system, three main geotechnical campaigns have been carried out in St. Mark square in order to define the geotechnical model of the subsoil. The first set of site investigations was commissioned by CVN in 1993 and included 6 geotechnical boreholes (16 m-deep) with collection of undisturbed samples, 10 standard penetration tests (SPT), 6 Lefranc permeability tests, 3 Piezocone Cone Pentration tests (CPTU) with dissipation tests. In 1997–1998, 6 geotechnical boreholes up to 20 or 32 m depth (with undisturbed sample collection), 9 standard penetration tests (SPT), 8 Piezocone Cone Pentration tests (CPTU), Boutwell in situ permeability tests were conducted. The third campaign was carried out in 2019 and consisted in 10 geotechnical boreholes up to a depth of 20 m, with collection of undisturbed samples; 13 CPTU, 5 seismic piezocone tests (SCPTU), 5 Dilatometer tests (DTM); 5 Seismic Dilatometer tests (SDTM) driven 20m-deep. Geotechnical laboratory tests included classification tests (grain size distribution, specific gravity, water content, Atterberg limits, etc.), permeability tests in triaxial cells, with constant head and variable head permeameters and one-dimensional oedeometric compression tests. The locations of the tests are shown in Figure 4.

The results of these site investigation campaigns allow us to identify a superficial anthropic layer (Unit 1/1A) with a thickness of 3.0 to 4.5 m. This layer is extremely heterogeneous because it experienced several different anthropic actions along the centuries and it hosts the drainage network (Bortoletto 2019). In particular, the permeability varies along 7 order of magnitudes, depending on the type of test, the depth, and the location. Higher values, up to 1.210^{-3} m/s, are measured for Boutwell permeability tests at very shallow depth; lower values, up to 210^{-10} m/s, are obtained from CPTU dissipation tests and oedometric tests.

A low permeability layer (Unit 2/2A) lies below Unit 1 and it has a thickness between 2.0 m and 7.0 m. The material ranges from sandy silt (2) to clayey silt (2A). The permeability varies between 110^{-10} m/s and 110^{-7} m/s. Beneath this layer there is a more permeable sandy formation, characterized by uniform fine sand (Unit 3) and silty sand (Unit 3A). The thickness varies from

0.50 m to approximately 8.0 m. From the depth of −9.80 m below s.l.P.S., up to the maximum sounding depth, there is the typical alternation of prevalently clayey layers (4A) with lenses of moderately silty sand (4). A typical stratigraphy is shown in Figure 6.

Figure 5. Position of in-situ geotechnical tests (CPTU, SCPTU, DMT, SDMT), boreholes, piezometric stations and old drainage pipes (*gatoli*).

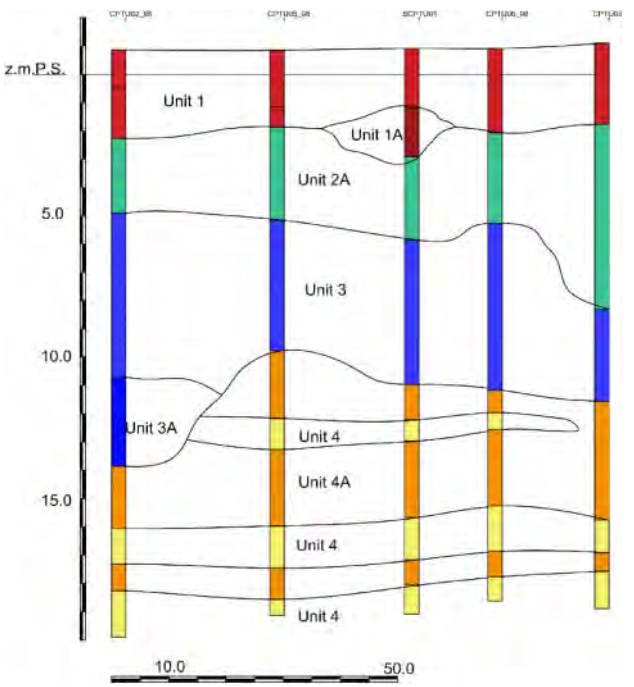

Figure 6. Typical stratigraphic section of St. Mark's Island (Section AA' in Figure 3).

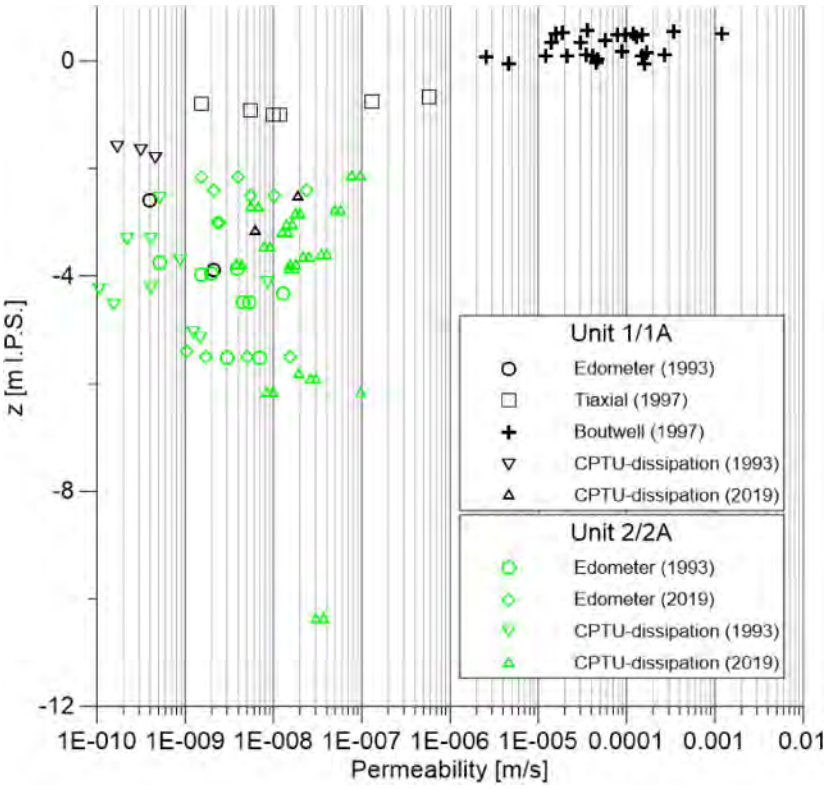

Figure 7. Results of permeability measures along depth.

4 MONITORING OF PORE WATER PRESSURES

4.1 *Pore-water pressure readings*

One of the key aspects for the optimization of the safeguarding measures is understanding of the seepage flows and the pore pressure distribution under St. Mark square in response of tidal oscillations. To achieve this goal, 9 Casagrande piezometers were installed at 2018 in a pilot site at the south of St. Mark's Basilica (piezometric station P in Figure 5). 4 piezometers are located in Unit 1 at a depth between 2.0 m and 2.3 m, 4 piezometers are located in Unit 2 at a depth between 3.2 m and 3.8 m, and 1 piezometer is located in Unit 3 at a depth of 7.6 m. The Casagrande cell was instrumented with a pressure transducer collecting readings every 6 minutes and transferring the data to the server, where they could be easily inspected and downloaded for elaboration.

Figure 8 shows the oscillation of the average piezometric level measured in soil units 1, 2, and 3 and the sea water level from October 16 to November 15th, 2018. In this period, the water level increased above ground level several times and the square was repeatedly flooded for a few hours. Moreover, a 156 cm (above s.l.P.S.) very high tidal level was registered on October 29th due to a storm surge. The amplitude of the pore pressure oscillation is reduced compared to the tidal wave in all layers, but the reduction is minimum for soil Unit 1, which reaches pressure levels closer to sea level when the floor of the square is flooded because water can easily enter from the permeable pavement. During this observation period, the maximum piezometric level measured in Unit 1 is 129 cm, in Unit 2 it is 106 cm and in Unit 3 it is 91 cm.

During high tide, higher water levels are observed in Unit 1 compared to Unit 3, thus the hydraulic gradient is directed downward. This proves that during high tides seepage flow from deeper layers could be excluded. During low tide levels, lower groundwater levels are observed in Unit 1 compared to Unit 3 and, therefore, the hydraulic gradient is directed upwards.

The average piezometric level in Unit 3 is slightly higher than the average level in Unit 1, meaning that these two layers can be considered hydraulically disconnected and Unit 2 can effectively prevent the flooding mechanism 4.

Since local soil heterogeneities, distance from the perimeter quay walls and the *gatoli* network, as well as their geometric features and state of preservation, significantly influence the hydraulic response of the entire subsoil system, 25 new piezometers were installed in 2019 at 10 monitoring sites distributed throughout St. Mark's square. According to the local conditions, it was decided to use 2 or 3 piezometers for each specific site, measuring the absolute pore water pressure in the different soil units (1, 2 or 3).

The main findings of the pilot site highlighted above are confirmed; moreover, new interesting considerations can be drawn. Figure 9 shows the pore pressure response in units 1 and 3 as a function of sea level for piezometer S05. The minimum ground level near this piezometric vertical is +84 cm l.P.S. When the tide increases, water enters the *gatoli* and can infiltrate the soil through their permeable walls; thus, the piezometric level in unit 1 increases. When the paving becomes submerged, the pressure response in the superficial layer is very fast because water can infiltrate from the top boundary. The maximum piezometric level may eventually be higher than the maximum sea level, as a consequence of some other significant contributions, such as rainfall or anthropic sources. After the peak, while the tidal level decreases rapidly, a slower response is observed in Unit 1, and for a certain time the pressure can be higher than the sea level. This can be explained considering that for medium water levels, water drains out mainly from the walls of the *gatoli*, and then, for very low tide level, only from quay walls or very deep ducts, resulting in a slower pressure dissipation rate. In addition, part of the superficial layer may become unsaturated during low tide, thus reducing its permeability. Numerical analyses considering different boundary conditions and unsaturated material properties confirmed this explanation (Ceccato et al. 2021).

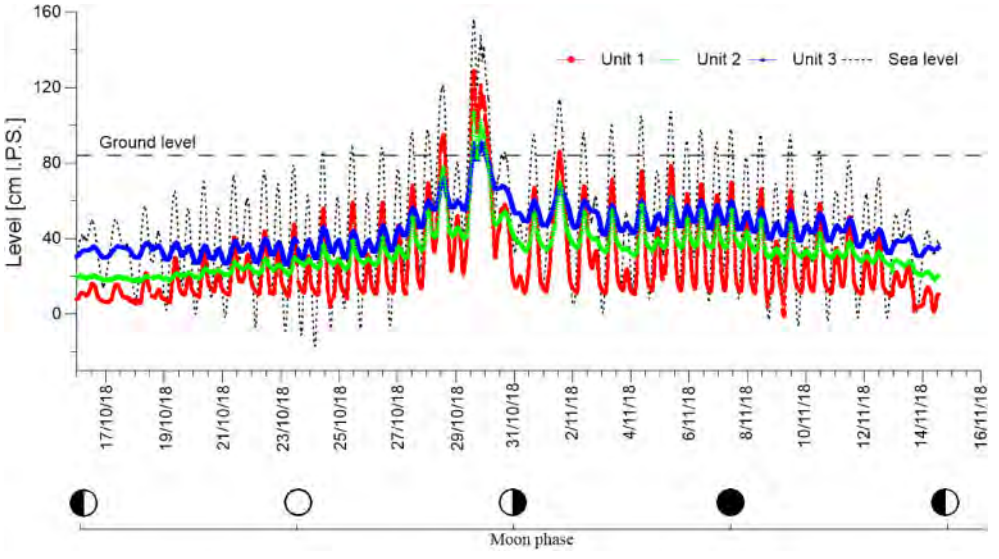

Figure 8. Piezometric level in different formations and sea water level along time.

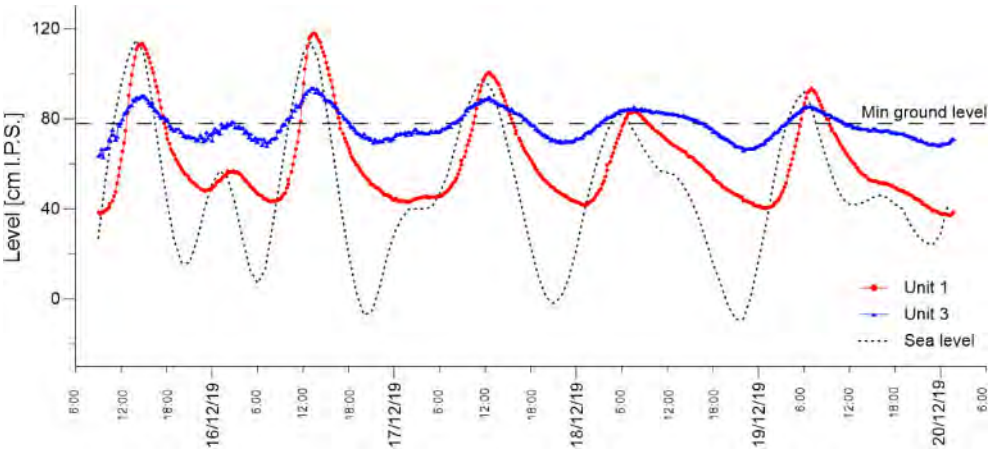

Figure 9. Piezometric level in different formations and sea water level along time in station S05.

5 OPTIMIZATION OF PROTECTION MEASURES OF ST. MARK'S SQUARE

As pointed out in Section 1, to protect the square against tides up to 1.1 m above s.l.P.S. a preliminary project was proposed in 1998, in which several countermeasures were planned such as:

- installation of vertical cut-off continuous sheet piling around the perimeter of St. Mark's island to avoid water infiltrating through and below the quay walls;
- installation of an impermeable membrane just below the stone pavement, to prevent seepage flow through the permeable joints between the stone elements;
- closure of the ancient drainage network by realizing a new one, collecting the rainfall water to be pumped and then discharged into a specific caisson realized close to the quay-wall facing St. Mark's basin.

This type of intervention appeared to be not only highly expensive, but also to impact heavily on the delicate equilibrium of the entire square subsoil. The main questions that arise in the more recent years are concerned with the real need of the sheet pile walls, which is very difficult to realize along with the island perimeter, as well as the effect of the impermeable membrane below the pavement, which could be subjected to uplift water pressure that rises into soil Unit 1 after high tides, as observed and shown in previous sections and in Figures 8 and 9.

For these reasons, a more gentle approach was discussed and selected, taking into account that:

- the seepage rate from the surrounding canals through the quay walls might be not so relevant as hypothesized in the project of 1998;
- the water uplift pressure could affect the long-terms stability of pavements if no free dissipation is allowed;
- the old drainage network system could be restored (as already done in the past) and used in a proper way to discharge the rainfall water.

To examine the effect of this updated approach to the design of the long-term safeguarding protection measures, a pilot test site was set up around the St. Mark's Basilica, whose narthex is the first one to be flooded, being its minimum level located at +0.62 m above s.l.P.S. The outcome of this field trial is discussed in the next section.

6 PROTECTING ST. MARK'S BASILICA

In 2018 specific protection measures for St. Mark's Basilica were realized to reduce the frequency of flooding of its nartex and surrounding areas that are the lowest of the entire island. The intervention consisted in the restoration of the old drainage pipes next to the Basilica with the installation of closing systems (valves) to avoid water backflow during high tides and a pumping station (Figure 10a).

The system is designed to operate for medium-high tides, i.e. between 62 cm above s.l.P.S. (the lowest level of the nartex floor) and 88 cm above s.l.P.S. (maximum ground level around the nartex). For sea levels lower than 62 cm, water can freely flow in and out of the system (Figure 10b). When the tidal level rises above 62 cm, the valves close and eventually the pumping station turns on, preventing the flooding of the nartex (Figure 10c). If the sea level rises above 88 cm, an overflow occurs, nartex flooding cannot be avoided and the pumping system is turned off (Figure 10d).

The MOSE system is currently operating to limit the maximum tidal level at 130 cm s.l.P.S. and in the next future this level will be progressively lowered to 110 cm s.l.P.S. The protection measures of the St. Mark Island is designed with this reference value and will be progressively realized in the coming years. Meanwhile, additional measures to prevent overflow are currently under discussion. The construction of a transparent and impermeable barrier of 1.20 m height around the basilica is being considered, among others.

The piezometric station at the south of St. Mark Basilica, that is, station P in Figure 5, is very close to the pumping system and these measurements offer information on the effects of the operating protection system on the pore water pressures in the subsoil.

Figure 11 shows the average piezometric level in units 1, 2, and 3 during the activation of the system. Only the piezometric level in Unit 1 appears to be influenced. When the sea level reaches 62 cm, the system switches on and the pressure immediately decreases. Afterward, it increases again following the tide, but the maximum piezometric level is lower compared to the case without an operating system. After the peak, when the tide decreases below 62 cm the system is deactivated and the pressure increases slightly, but it reduces rapidly following the descending sea water level.

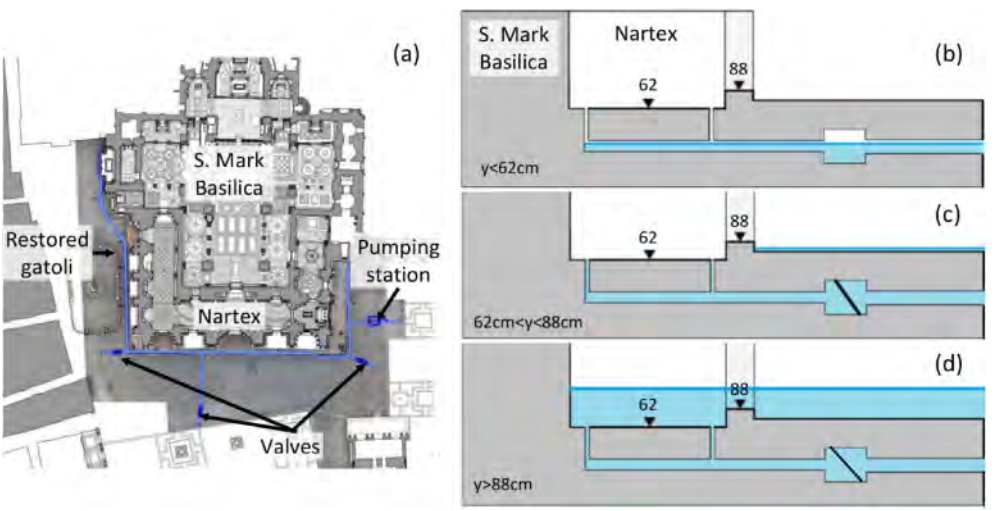

Figure 10. Protection measures of the St. Mark Basilica: (a) plan view of the improved drainage system, (b-d) simplified view of operating phases.

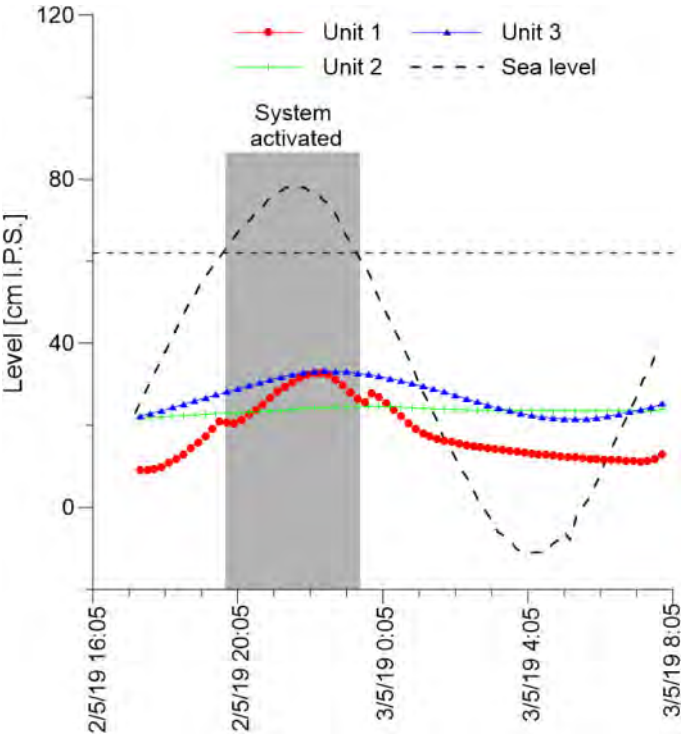

Figure 11. Average piezometric level in the ground measured in station P and sea water level during the activation of the protection measures.

7 CONCLUSIONS

The design of suitable flood mitigation measures to protect St. Mark's square against tide less than 110 cm required a multidisciplinary approach within which the geotechnical study played a fundamental role.

Within this frame, the results of geotechnical testing as well as the measurements of pore pressure oscillations in the soil of St. Mark's Square in Venice provided relevant information to guide the designer to optimize the most effective solutions that must also be respectful of the ancient situation of the entire area.

The local soil profile is characterized by a heterogeneous alternance of layers composed of a mixture of sand, silt, and clay in different proportions, but basically subdivided in three layers, whose intermediate one is composed of a fine-grained soil separating the upper permeable anthropic layer from the lower natural fine sands.

Fluctuation of the tide influences the pore pressure in both formations 1 and 3. The local vertical component of hydraulic gradient between these two layers is directed downward for higher tides and upward for the lower ones. Thus, seepage flow from deeper layer is impossible during high tide peaks. In the shallower layer, maximum water levels are close to lagoon level, whereas minimum ones are higher; moreover, the pore pressure may remain higher than the water level during tide decrease. This is a key phenomenon when carrying uplift analysis for the long term stability of paving especially in the more depressed area of St. Mark's Square.

In addition, it was noted that the seepage in the formation is characterized by very small flow rates, thus the actual infiltration flow to be drained is very low.

From all the observations and interpretation carried out so far, it was clear that the intervention such as the one selected for the area surrounding the Basilica and its narthex, could be extended to the whole square, showing that the previously hypothesized impermeabilization systems could not the proper solution to prevent the flooding due to seepage.

ACKNOWLEDGEMENTS

This work was supported by Consorzio Venezia Nuova [Prot. N. 14224 UGA/VA, 30/11/2018]. The authors thank the companies belonging to the Consortium Kostruttiva, in particular Mate Eng. and Thetis, and the colleagues of ICEA Department for the fruitful discussions regarding the flood protection of St. Mark's Square.

REFERENCES

Bettiol, G., Ceccato, F., Pigouni, A.E., Modena, C., Simonini, P., 2015. Effect on the structure in elevation of wood deterioration on small-pile foundation: Numerical analyses. *Int. J. Archit. Herit.* 3058. https://doi.org/10.1080/15583058.2014.951794.

Biscontin, G., Cola, S., Pestana, J.M., Simonini, P., 2007. Unified compression model for venice lagoon natural silts. *J. Geotech. Geoenvironmental Eng.* 133, 932–942. https://doi.org/10.1061/(ASCE)1090-0241(2007)133:8(932).

Bortoletto, M., 2019. Relazione archeologica - Interventi di salvaguardia dell'Insula di Piazza San Marco a Venezia.

Ceccato, F., Simonini, P., Koppl, C., Schweiger, H.F., Tschuchnigg, F., 2014. FE Analysis of degradation effects on the wooden foundations in Venice. *Riv. Ital. di Geotec.* 2, 27–37.

Ceccato, F., Simonini, P., Zarattini, F., 2021. Monitoring and Modeling Tidally Induced Pore-Pressure Oscillations in the Soil of St . Mark ' s Square in Venice , Italy. *J. Geotech. Geoenvironmental Eng.* 147, 1–14. https://doi.org/10.1061/(ASCE)GT.1943-5606.0002474.

Cola, S., Sanavia, L., Simonini, P., Schrefler, B. a., 2008. Coupled thermohydromechanical analysis of Venice lagoon salt marshes. *Water Resour. Res.* 44, n/a-n/a. https://doi.org/10.1029/2007WR006570.

Fletcher, C.A., Spencer, T. (Eds.), 2005. *Flooding and environmental challenges for Venice and its lagoon: state of knowledge.* Cambridge University Press.

P. Salandin, 2020. Evaluation of flooding of the Sankt Mark's Island in: 'Analysis of possible interventions to safeguard the Sankt Mark's Island from high tides' Part 3 (in italian). Padova.

Ricceri, G., 2007. *Il ruolo della geotecnica nella salvaguardia della città di Venezia e della sua laguna*.

Ruol, P., Favaretto, C., Volpato, M., Martinelli, L., 2020. Flooding of Piazza San Marco (Venice): Physical model tests to evaluate the overtopping discharge. *Water* (Switzerland) 12. https://doi.org/10.3390/w12020427.

Simonini, P., Ricceri, G., Cola, S., 2007. Geotechnical characterization and properties of Venice lagoon heterogeneous silts, in: Leroueil, Hight (Eds.), *Characterisation and Engineering Properties of Natural Soils.* Taylor & Francis Group, London, London, pp. 2289–2327. https://doi.org/10.1201/noe0415426916.ch17.

Volpato, M., 2019. Relazione idrologica e idraulica - Interventi di salvaguardia dell'Insula di Piazza San Marco a Venezia. Venice.

Geotechnical Engineering for the Preservation of Monuments and Historic Sites III – Lancellotta, Viggiani, Flora, de Silva & Mele (Eds)

Observed interaction between Line C of Roma underground and the *Cloaca Maxima*

G.M.B. Viggiani
Cambridge University Engineering Department, UK
Università di Roma Tor Vergata, Italy

N. Losacco
Politecnico di Bari, Italy

E. Romani
Metro C S.c.P.A., Rome, Italy

A. Sonnessa
Politecnico di Bari, Italy

ABSTRACT: Contract T3 of Metro C crosses the archaeological area of the historical centre of the city of Rome. In the final part of the contract, the running tunnels, which were excavated using two Earth Pressure Balance (EPB) shields, pass directly under one of the earliest sewage systems of the world, the *Cloaca Maxima*, functional to the present day. This ancient sewer consists of two arch shaped masonry and conglomerate tunnels, at a relatively close spacing. The monitoring data gathered during the passage of the TBMs underneath the ancient tunnel indicate that the ancient sewers are relatively flexible, substantially conforming to the greenfield displacements.

1 INTRODUCTION

Excavation of underground railway tunnels through the historic centre of big cities is increasingly common, given the growing urban population and the consequent need to reduce traffic and CO_2 emissions, while providing efficient and sustainable mobility systems. Although construction techniques have been developed to address minimisation of tunnelling-induced displacements, particularly with the adoption of state-of-the-art tunnel boring machines, the assessment of the effects induced by tunnel construction on existing structures is mandatory, especially when these are highly vulnerable and highly exposed. In this context, Rome represents an extreme example, as the excavation of the twin running tunnels of Contract T3 of the third line of Roma underground (Line C) was carried out underneath the archaeological area of the historic centre, crowded with both surface and buried archaeological remnants of outstanding documental, historical, monumental, and artistic value.

As shown in Figure 1, Contract T3 of Line C comprises approximately 3 km of running tunnels, two stations and two ventilation shafts. A third station, Piazza Venezia, located at the end of the contract, is currently under design. The tunnels run from San Giovanni station, at the boundary with Contract T4, where there is a connection with the existing Line A, to Piazza Venezia, delimiting the boundary with Contract T2. The tunnels were excavated mainly using two identical Earth Pressure Balance (EPB) shields, with a maximum diameter of 6.71 m at the cutting wheel and a length of approximately 11 m. The precast reinforced concrete segmental lining, consisting of 1.4 m long and 0.3 m thick rings with an internal diameter of 5.8 m, was erected inside the shield. In order to minimise induced ground displacements, pressurised backfill grouting of the tail void was carried out during each advancement stage of the EPB shield, using a bi-component fast-hardening grout.

In the last stretch of Contract T3, approximately halfway between the Basilica of Maxentius and Piazza Venezia, the tunnels were excavated at relatively short vertical distance beneath two

 DOI 10.1201/9781003308867-16

ancient sewer tunnels of Roman age, belonging to the *Cloaca Maxima* sewage system, and a more recent sewer tunnel built in the Renaissance, the *Chiavicone della Suburra* (simply referred to as *Chiavicone* in the following). This paper describes the effects of the construction of the twin tunnels of Line C underneath the ancient sewer tunnels, in terms of measured settlements induced both in the soil – in quasi-greenfield conditions – and on the buried structures.

Figure 1. Aerial view of the historic centre of Rome showing the route of Contract T3 of Line C.

2 THE CLOACA MAXIMA AND THE CHIAVICONE DELLA SUBURRA

The *Cloaca Maxima* represents the most important sewage system of ancient Rome, dating to the end of the 6th century BC. Initially conceived as an open-air canal, supposedly by Tarquinius Priscus, it was subsequently covered and expanded into a sewer tunnel by Tarquinius Superbus. The sewage served as a drainage system for spring and rainfall waters coming from the valley between the Esquiline and Viminal hills, as well as for the frequent floods of the Tiber that made the Roman Forum and the *Argiletum* valleys swampy and unhealthy. During the Flavian Age, the *Cloaca Maxima* was truncated and diverted, first by Vespasian, to build the *Templum Pacis*, and later by Domitian, to construct the new Forum of Nerva (Antognoli & Bianchi 2009). This last intervention was carried out on the stretch of the *Cloaca Maxima* that today crosses via dei Fori Imperiali, beneath which the running tunnels of Line C were excavated, and left a deactivated branch that is the remnant of the western end of the Vespasian's route of the sewage.

Today, the active branch of the *Cloaca Maxima* channels the urban wastewater and storm water run-off coming from the Esquiline, the *Fora* valley, and the buildings located between the Roman Forum and the Velabrum, which then flows into the collector sewer built at the end of the nineteenth century under the Tiber Embankment (Corsetti 1925). In the area where intersection with the Line C running tunnels occurs, shown in plan in Figure 2(a), the active branch of the *Cloaca Maxima* runs approximately North-East to South-West; it bends some 20° northwards while crossing via dei Fori Imperiali, and then it recovers the initial direction, as it leaves the embankment of the main road. The deactivated branch extends approximately 36 m beyond the South-West retaining wall of the main road embankment. As shown in the cross-section in Figure 2(b), the tunnels of both the active and the deactivated branch are arch-shaped, with an average height of 3.5 m, a width of 3.0 to 3.5 m and cross-sectional areas of 10.5 m^2 and 9.2 m^2, for the active and deactivated branch, respectively. In the stretch in which they underpass via dei Fori Imperiali (with a ground level of approximately 22.0 m a.s.l.), the crowns of the two sewers are located at a depth of 8.0 to 8.5 m below the modern ground level.

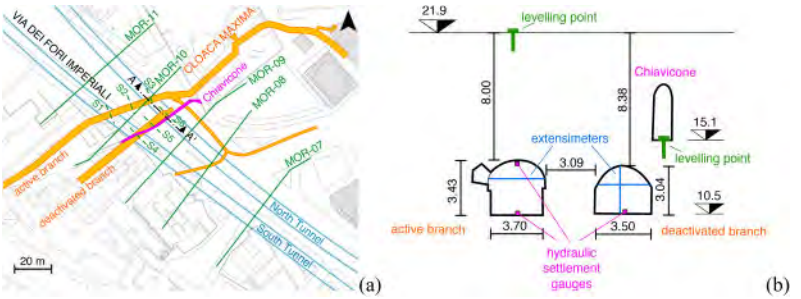

Figure 2. (a) Relative plan position of the ancient sewers and Metro C running tunnels and (b) cross section (AA') through the *Cloaca Maxima* and the *Chiavicone*.

In the context of the site investigation carried out by Metro C S.C.p.A. during the design stage of Contract T3, a detailed exploration of the active branch of the *Cloaca Maxima* was carried out, which included coring of the tunnel lining, digital photogrammetry, laser scanning and topographic surveys (Di Mucci & Miniero 2015). The results of these investigations showed that a variety of construction techniques had been employed for the ancient tunnel lining.

In the first part of the sewer, North-East of the via dei Fori Imperiali, and in the deactivated branch, both belonging to the sewer of Vespasian age, see Figure 3, the sewer tunnel rests on pozzolanic mortar conglomerate foundations (1) and the lining consists entirely of blocks of *Tufo Lionato* (2). The vault is made of 9-11 radial ashlars, while the abutments are made of three rows of superimposed blocks.

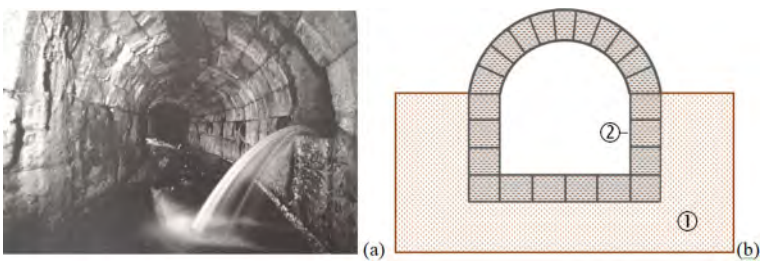

Figure 3. Lining of functional stretch and de-activated branch of Vespasian sewer: (a) photograph (E. Bianchi) (b) schematic drawing.

In the currently active branch, belonging to Domitian sewer, see Figure 4, the floor consists of travertine blocks (1) resting on a pozzolanic mortar conglomerate foundation slab (2). The abutments are made of two or more rarely three courses of large blocks of *Lapis Gabinus* (3), surmounted by *Opus Latericium* (4), *i.e.*, bricks with lime and pozzolana mortar, of varying height up to about 1 m, serving as a levelling layer on which a vault in cement conglomerate (5) is set. Despite the lack of homogeneity of the construction systems, the state of conservation of the sewer appears to be of an extraordinary level.

The *Chiavicone* was built at the end of the 16th century, to expand the existing ancient sewage system, as required by the creation of the Alessandrino district, between the Coliseum and the current location of Piazza Venezia (Antognoli 2015). As shown in Figure 2(a), starting from the Forum of Nerva, the *Chiavicone* follows the route of the deactivated branch of *Cloaca Maxima*, although at a shallower depth, as its floor is located at approximately 6.8 m below ground level, see Figure 2(b). The initial and final stretch of the sewer were demolished in the recent past – in the 1930s and during the archaeological surveys carried out in 1985-1986 and 1995-1997, respectively. The remaining part of the *Chiavicone* crosses via Alessandrina and via dei Fori Imperiali, extending

some mere 4.0 m beyond the South-West retaining wall of the via dei Fori Imperiali. The tunnel is currently used as a pedestrian underpass walkway joining the two unburied parts of the Forum of Nerva. It is narrow and arch-shaped with an average height of 3.6 m and a width of 1.2 m, and the lining is made of reused material from Roman Age houses. The abutments consist of alternating courses of brickwork, tuff blocks, marble, and travertine fragments, grouted with hydraulic mortar. The barrel vault is made in *opus cementicium*; the floor is composed of two rows of stone slabs and is slightly concave at the centreline.

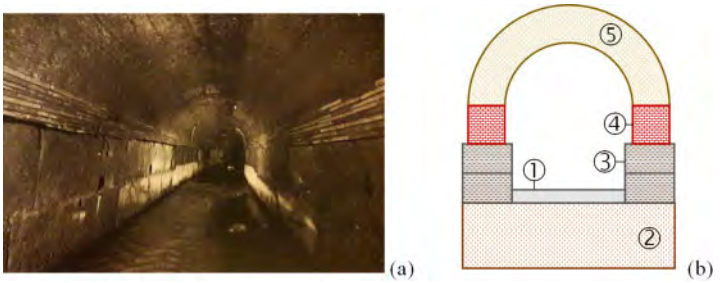

Figure 4. Lining of functional stretch of Domitian sewer: (a) photograph (E. Bianchi) (b) schematic drawing.

3 THE RUNNING TUNNELS OF METRO C UNDER THE CLOACA MAXIMA

3.1 *Layout of tunnels and monitoring sections*

As shown in Figure 2(a), the twin tunnels of Line C run almost parallel to one another under via dei Fori Imperiali and start diverging slightly as they approach Piazza Venezia just before passing under the *Cloaca Maxima*. The average distance between the tunnel axes beneath the ancient sewers is about 20 m. The tunnels cross the *Chiavicone* and the deactivated branch of the *Cloaca Maxima* almost at a right angle, whereas the active branch of the *Cloaca Maxima* forms an angle of about 60° with the axes of the new tunnels. These run at an average depth of 30.3 m below ground level, midway between the two branches of the *Cloaca Maxima*, with a minimal slope, less than 3.5%, and the North Tunnel 1.25 m deeper than the South Tunnel. Excavation of the North Tunnel started in March 2018 and was followed by the excavation of the South Tunnel, about three months later. The North and South Tunnel passed under the *Cloaca Maxima* in September 2019 and two months later, respectively, at advancement rates as high as 20 m/day.

A number of monitoring sections transverse to the tunnel axes, shown in Figure 2(a), were installed along the stretch before the construction of Line C by the general contractor, Metro C S.C.p.A. These were intended to assess the effects induced by the excavation on the existing archaeological and monumental environment and inform implementation of mitigation and protective measures, if required. Five of these sections (MOR-07 to MOR-11), with an average spacing of 25 m, are located in the area where the new tunnels run under the *Cloaca Maxima*, and are considered in this study. They consist mainly of surface levelling points, with the exception of section MOR-09, located 25 m South-West of the ancient sewers, where a number of Trivec extensimeters-inclinometers were installed down to a maximum depth of 34 m below ground level, to measure all components of displacement below ground surface.

3.2 *Soil profile and groundwater regime*

The ground conditions in the area of the *Cloaca Maxima* can be obtained from the geological longitudinal profile of the South Tunnel, shown in Figure 5, resulting from the repeated and extensive campaigns of ground investigation carried out since 1995, when the preliminary design of the line began.

Starting from the ground surface, the following layers can be identified:

- Anthropogenic, made-ground layer (R) with variable thickness that can be as large as about 14 m in the area under examination. This consists mainly of medium-coarse grained materials, with some silt, often embedding heterogeneous rocky inclusions and occasionally some ancient masonry walls remnants.
- Mid-Pleistocene synvolcanic fluvial-lacustrine deposits (Tb1), with significant vertical and horizontal variability. Two different eteropic facies can be distinguished: the first (Tb1a) composed of lenses and discontinuous levels of fine sands in abundant fine-grained matrix, oxidised yellowish/reddish sandy or clays silts; the second (Tb1b) made of medium-fine, slightly gravelly sand including cobbles with 1 – 2 cm maximum diameter.
- Plio-pleistocene Paleotevere deposits, made of heterometric medium-fine gravel in abundant sandy matrix (SG).
- Pliocene stiff silty clays with occasional thin sandy levels (Apl), known as "Argille Vaticane", highly overconsolidated, exhibiting very low permeability, high stiffness and shear strength, also due to their significant marl content.

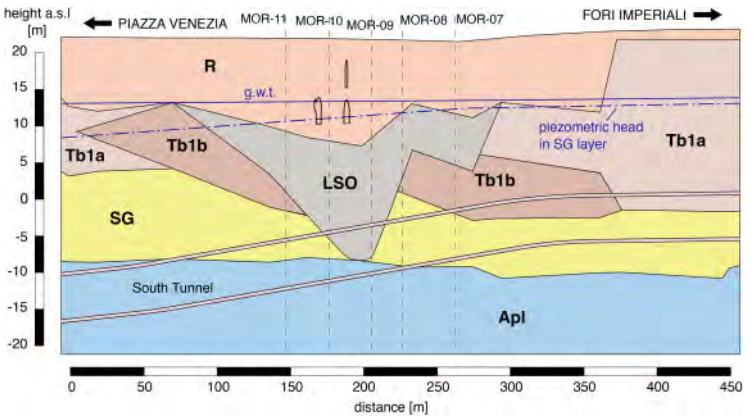

Figure 5. Soil profile and groundwater conditions, along the longitudinal section of South Tunnel.

Occasionally, along the whole of Contract T3, the continuity of the Pleistocene soil layers is broken by channels filled with recent Holocene Tiber alluvial deposits (LSO), consisting of soft heterogeneous silts, either clayey or sandy, with levels of organic matter and isolated tuff inclusions. In particular, in the area of interest, see Figure 5, a thick LSO layer, filling a paleo-valley in the pyroclastic soils, is found below the shallow R layer, from a depth of about 14 m b.g.l.. This extends approximately 100 m ahead and behind the Cloaca Maxima, and has a maximum thickness of about 15 m right under the ancient sewers, where it reaches the top of the Apl base layer.

As shown in Figure 5, in the vicinity of Fori Imperiali station the running tunnels are excavated in mixed face conditions, in the Tb1 and SG layers, and then they plummet into the SG layer, approximately under the monitoring section MOR-07, and finally in the underlying Apl layer towards the end of the stretch, after almost full-face crossing of the LSO layer.

Pore water pressure measurements performed prior to tunnel construction pointed out that the hydraulic head in the Tb1 deposits corresponds to a groundwater table depth of 7.5 – 8.0 m below ground level. An aquifer with a South-East to North-West directed seepage flow, approximately in the same direction as the running tunnels, connected to a hydraulic recharge located far outside the urban centre is confined in the SG layer. In the area under examination, the hydraulic head corresponding to this aquifer is consistently lower than that of the overlying less permeable layers by a few meters. In particular, this difference is larger where there LSO layers are present, showing evidence of a downward groundwater flow in the fine-grained materials, consistently with observations made in other stretches located at the beginning of Contract T3 (Losacco et al. 2020).

Table 1 summarises the indicative geotechnical parameters of all the soil layers described above as obtained from both laboratory and *in-situ* tests carried out for the design of the line.

Table 1. Physical and mechanical parameters of soil layers.

Layer	w (%)	γ (kN/m3)	w_L (%)	I_P (%)	φ' (°)	c' (kPa)	s_u (kPa)	E_{oed} (MPa)	k (m/s)
R	61.5	17.0	–	–	35	–	–	–	5×10^{-5}
LSO	20–32	17.5	35–48	12–29	30	0–16	75	7–9	2.2×10^{-5}
		19.5					200		7.7×10^{-7}
Tb1a	25–27	19.0	25	15	31	7–20	110	17.5	5×10^{-6}
Tb1b		19.4	–	–	34	–	–	–	5×10^{-5}
SG	22–28	20.0	–	–	35	–	–	–	1×10^{-4}
Apl	19–21.5	20–20.4	36–46	18–21.5	26–30	40–60	250–450	21.5–50	5×10^{-7}

4 TUNNELLING-INDUCED SOIL SETTLEMENTS

4.1 *Surface settlements*

Figure 6 shows the transverse surface settlement troughs induced by the construction of each of the running tunnels of Line C. These were obtained from surface precision levelling carried out at monitoring sections MOR-07 to MOR-11 during the advancement of the EPB shields beneath the *Cloaca Maxima*.

In Figure 6, the settlements generated by the second bore – the South Tunnel – are incremental, *i.e.*, they do not include the settlements induced by the excavation of the North Tunnel. The average centreline position of the two tunnels between section MOR-07 (axes spacing $s = 14.7$ m) and MOR-11 ($s = 24.1$ m) is also indicated in the figure. For each monitoring section, the plotted settlement profiles are representative of steady-state conditions, in the sense that they are measured when the excavation face has travelled a sufficient distance beyond the monitoring section (approximately 100 m for the North Tunnel and 120 m for the South Tunnel) and no additional settlements are generated by further excavation.

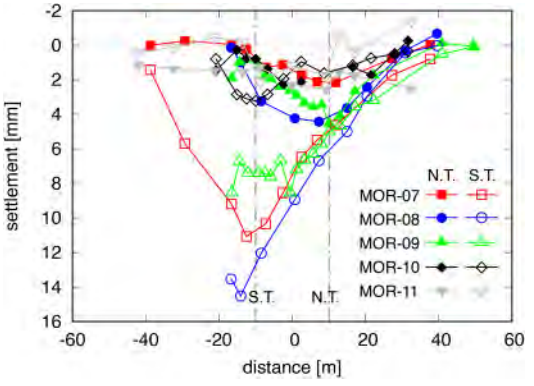

Figure 6. Recorded transverse surface settlement troughs in monitoring sections MOR-07 to MOR-11.

The first notable feature of the measured settlement profiles plotted in Figure 6 is that, consistently with what observed in many case histories (Fargnoli et al. 2015; Wan et al. 2017), the settlement troughs induced by the excavation of twin tunnels are not symmetric, with the second bore inducing significantly larger settlements than the first. Previous research (Losacco & Viggiani 2019) has shown that, when the tunnels are closely spaced, this is related mainly to the disturbance

induced in the soil by the first excavation, even when the operational parameters of the TBM are the same for the two bores.

Figure 6 shows also that excavation of the North Tunnel induces small maximum settlement in section MOR-07, of approximately 2.2 mm, and twice this value in sections MOR-08 and MOR-09. Minimal settlements are recorded also for section MOR-10, located between the two branches of the *Cloaca* Maxima, and in section MOR-11. The settlements recorded in the successive monitoring sections were even smaller than those in section MOR-11 and are not reported in the figure. The volume loss values and the trough width parameters reported in Table 2 were obtained interpolating the measured settlements with Gaussian functions (Peck 1969). The values of volume loss follow the same trend as the maximum settlements, with a value of volume loss $V_L = 0.18\%$ in section MOR-07, $V_L = 0.49\%$ in section MOR-08 and progressively reducing in the following monitoring sections down to negligible values beyond the *Cloaca Maxima*.

Table 2. Trough width parameter and volume loss recorded for passage of North and South Tunnel.

	North Tunnel		South Tunnel			
Monitoring section	K	V_L (%)	K_{South}	$V_{L,South}$ (%)	K_{North}	$V_{L,North}$ (%)
MOR-07	0.41	0.18	0.54	1.13	0.63	1.31
MOR-08	0.53	0.49	–	–	0.63	1.81
MOR-09	0.41	0.31	–	–	0.79	1.23
MOR-10	0.46	0.23	0.25	0.17	0.62	0.42

The difference of tunnelling-induced surface settlements observed in the monitoring sections under examination is even more evident during passage of the South Tunnel. In this case, maximum settlements as high as 11.1 mm, *i.e.*, more than five times the settlement induced by the first excavation, were recorded for section MOR-07, increasing to 14.1 mm in section MOR-08, *i.e.*, more than three times the settlement induced by the first excavation in the same section, and then somewhat reducing to 7.4 mm, or almost twice the settlement recorded after the passage of the first tunnel. Consistently with what observed for the excavation of the North Tunnel, relatively small maximum settlements, as low as 3.2 mm for section MOR-10 and 2.1 mm for section MOR-11 were measured with the progress of the South Tunnel beyond the *Cloaca Maxima*. Given the significant asymmetry of the settlement trough generated by the South Tunnel with respect to the centreline, two different interpolations of the measured settlements with Gaussian functions were attempted for the two sides, the North side yielding larger K and V_L, in general. The corresponding volume loss values vary from $V_L = 1.3\%$ in section MOR-07 to a maximum $V_L = 1.8\%$ in section MOR-08, and then progressively reduce down to negligible values in the following sections. Settlement trough parameters V_L and K for the South Tunnel are also reported in Table 2.

4.2 *Effect of face support pressure*

If compared to other cases reported in the literature (Fargnoli et al. 2015; Losacco & Viggiani 2019b), the observed increase in settlements induced by the excavation of the second tunnel is too large to be attributed solely to the disturbance induced by the excavation of the first tunnel and it is likely to be related to variations in the soil conditions or to significant changes in operational parameters of the EPB shield during tunnel advancement. The different response observed in the various monitoring sections during excavation of the North Tunnel also supports this hypothesis. To give an insight of the likely causes of the observed phenomena, Figure 7 shows the average values of face pressure recorded during the construction of each lining ring, at the six face pressure sensors located in the excavation chamber of the EPB shield.

Inspection of the plots in Figure 7 reveals that, during the excavation of the North Tunnel, most of the pressure sensors experience limited oscillations around a mean value of 350 kPa, with some isolated lower recorded values of 250 kPa or less, such as *e.g.*, while crossing monitoring section MOR-08, which might in part explain the slightly larger settlement recorded in this section after

the first bore. On the contrary, remarkably low face pressure values were measured during the initial phases of excavation of the South Tunnel, between sections MOR-07 and MOR-09, with the topmost sensors, P1 and P6, measuring pressures consistently below 300 kPa until section MOR-09 and recording minimum values as low as 230 kPa between sections MOR-07 and MOR 08, which is very consistent with the observed large settlements displayed in Figure 6 for the second bore.

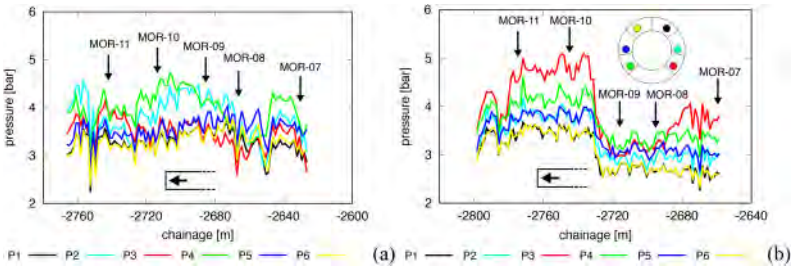

Figure 7. Pressure in the excavation chamber during construction of (a) North and (b) South tunnel.

Between sections MOR-09 and MOR-10, the operational parameters of the EPB shield were changed so that the recorded pressure in the topmost sensors, P1 and P6 was almost constant at approximately 350 kPa, while the recorded pressures at the lowermost sensors were constantly between 400 kPa (P4) and 500 kPa (P3), which justifies the limited settlements measured from section MOR-10 onwards. It is likely that the low face support pressure exerted during the initial phases of excavation are due to the tunnel face approaching the big paleo-valley filled with LSO soil right under the *Cloaca Maxima*. A thorough assessment of the potential role played by the geotechnical conditions and by other operational parameters of the EPB shield (*e.g.*, the tail void grouting pressure) would require further analyses, which are out of the scope of this paper.

4.3 *Subsurface settlements*

Besides surface levelling points, monitoring section MOR-09 was also equipped with five integrated Trivec inclinometers and extensimeters. The measurements of vertical displacements obtained from the Trivec were integrated starting from ground surface, where the values of the settlement obtained from precision levelling could be used as known boundary conditions.

The plots in Figure 8 represent the incremental subsurface settlement troughs obtained at 5 m depth intervals between ground level and a depth of 20 m below, after excavation of each tunnel. The data in Figure 8 show quite clearly that the maximum settlement is almost constant down to a depth of 15 m below ground level, while a sudden increase in maximum settlement, and a simultaneous reduction of the settlement trough width, are recorded at 20 m depth. The relative increase in maximum settlement between ground surface and this depth is +29% for the North Tunnel and +62% for the South Tunnel.

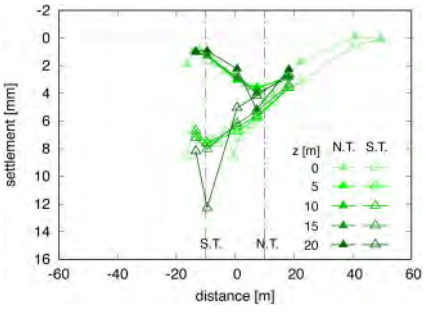

Figure 8. Recorded transverse sub-surface settlement troughs in section MOR-09.

Table 3. Subsurface maximum settlement, trough width parameter and volume loss in section MOR-09.

	North Tunnel			South Tunnel		
Depth (m)	w_{max} (mm)	K	V_L (%)	w_{max} (mm)	K_{North}	$V_{L,North}$ (%)
0	3.4	0.41	0.31	7.4	0.79	1.23
5	3.6	0.53	0.34	7.7	0.93	1.20
10	3.7	0.64	0.34	7.6	1.17	1.18
15	4.0	0.78	0.33	8.0	1.35	1.06
20	5.1	0.71	0.27	12.3	1.09	0.82

Table 3 summarises the values of maximum settlement, trough width parameter K and volume loss obtained at different depths for the two tunnels. Figure 9 shows the variation of the maximum settlement w_{max}, of the relative trough width parameter K, and of the volume loss V_L as a function of the depth normalised by the depth of the tunnel axis, z/z_0, in which $z_0 = 30.1$ m and $z_0 = 28.7$ m for the North and the South Tunnels, respectively. For the South Tunnel, interpolation with a Gaussian function was only attempted for the northern half of the settlement troughs, due to lack of data on the other side.

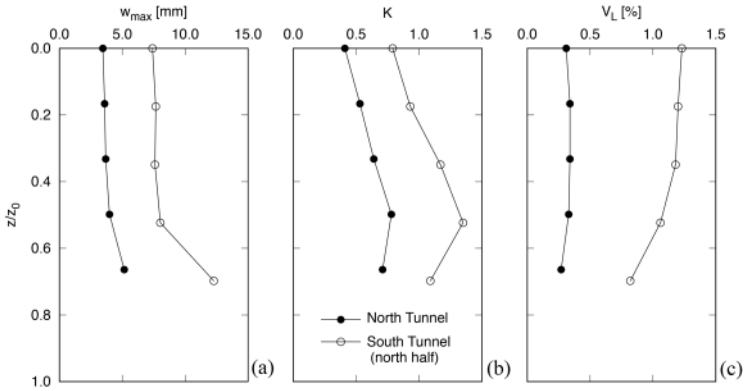

Figure 9. Variation with depth of: (a) maximum settlement, (b) trough width parameter and (c) volume loss.

As mentioned above, the transverse settlement trough induced by the South Tunnel is wider and larger than that induced by the North Tunnel at all depths, and this is reflected in the values of both K and V_L. For both tunnels, the trough width parameter K increases gradually with depth in the made ground layer, to decrease sharply at the transition with the LSO layer. The volume loss does not change significantly over the thickness of the made ground layer, indicating a limited amount of dilation, while it decreases slightly in the LSO layer, even if, due to the significant reduction of K, the settlement above the tunnel crown increases. A qualitatively similar response was observed both in the field, at the beginning of Contract T3 (Losacco et al. 2020), and numerically (Losacco &Viggiani 2019).

5 OBSERVED INTERACTION WITH THE ANCIENT TUNNELS

5.1 *Settlement profiles*

During excavation of the tunnels, the response of the ancient sewers was monitored by means of levelling points installed in the floor of the *Chiavicone* and hydraulic level settlement gauges

installed in the floor of the deactivated branch and on both the floor and the vault of the active branch of the *Cloaca Maxima*. Figures 10(a) and (b) illustrate the incremental settlement profiles obtained from the measurements carried out after the excavation of the North and the South Tunnel, respectively. The surface settlement trough obtained for monitoring section MOR-10 is also shown as a reference. The comparison between surface and deep displacements is justified because, as shown by the data in Figure 9, the vertical displacements are practically constant down to a depth of 15 m, and the floor of the *Cloaca Maxima* is located at a depth of approximately 12 m.

Consistently with the limited surface settlements induced by the excavation of the North Tunnel beyond section MOR-09, possibly related to the fairly high face support pressure applied between sections MOR-09 and MOR-11, with mean values in the range 350 – 400 kPa, the settlement profiles observed for all the buried structures and for MOR-10 are practically superimposed, see Figure 10(a). The deformed configuration induced in the ancient tunnels by the excavation of the South Tunnel has the same shape as the surface settlement trough observed in section MOR-10, although some differences exist in the magnitude of measured settlements, see Figure 10(b).

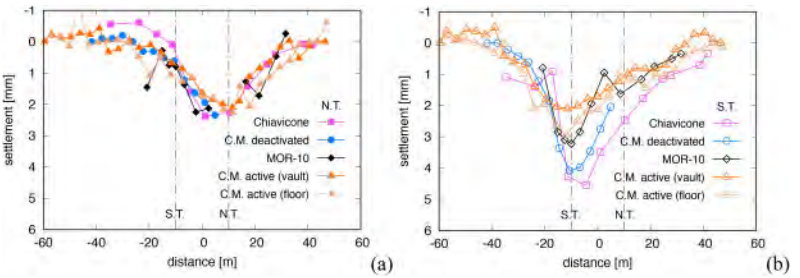

Figure 10. Recorded incremental settlement profiles along the sewers after construction of (a) North Tunnel and (b) South Tunnel.

In particular, the measured maximum settlements progressively reduce moving from the *Chiavicone* ($w_{max} = 4.5$ mm) to the active branch of the *Cloaca Maxima* ($w_{max} = 3.0$ mm at the floor, almost coincident with the maximum surface settlement of MOR-10), which somewhat recalls the reduction of maximum surface settlements observed between monitoring section MOR-09 and monitoring section MOR-11, see Figure 6 and Table 2. A smaller settlement is measured at the crown of the active branch of the Cloaca Maxima ($w_{max} = 2.1$ mm) if compared to the floor, suggesting that the cross-section of the existing tunnel has undergone a slight ovalisation. The observed change in induced settlement is likely to be due to a combination of the changes in applied face pressure – or any other operational conditions of the TBM – and of soil-structure interaction effects due to the finite bending and shear stiffness of the ancient tunnels. The relative importance of these aspects is currently under investigation.

5.2 *Deformed shape of cross-sections of Cloaca Maxima*

As indicated schematically in Figure 2, three cross-sections for each of the two branches of the *Cloaca Maxima* (S1 – S6 in Figure 2(a)) were instrumented with rod extensimeters to measure the convergence induced by excavation of the new tunnels under the ancient sewers. In particular, both vertical and horizontal extensimeters were installed in the deactivated branch (S4 – S6), while horizontal rods only were used in the active one (S1 – S3). Incremental vertical and horizontal strains in the monitoring sections, as induced by the construction of each of the new tunnels, have been calculated by assuming a circular-shaped cross-section, having the same area as the real tunnels of the *Cloaca Maxima*. In the absence of vertical extensimeters, the vertical strains of the cross-section of the active branch of the Cloaca Maxima were inferred from the differential settlements between crown and invert of the tunnel measured by the hydraulic level gauges. The results of these calculations are reported in Figures 11 (a) to (d), in which a qualitative representation of

the incremental deformed configuration of the cross-section is also displayed, assuming a circular shape as said above.

For the deactivated branch of the *Cloaca Maxima*, see Figures 11(a) and (b) for the North and South tunnel respectively, the collected data indicate that excavation of the new tunnels induces significant elongation in the vertical direction and some minor elongation in the horizontal direction, in the cross sections located immediately above the tunnel under construction, while it causes squatting of the farthest cross-section, with vertical shortening and horizontal stretching of comparable magnitude. For the active branch, Figures 9(c) and (d), significant ovalisation is induced by excavation, particularly for the South Tunnel, while squatting of the farthest cross-section is not observed. In all cases, the cross-section located between the new tunnels undergoes slight homothetic expansion.

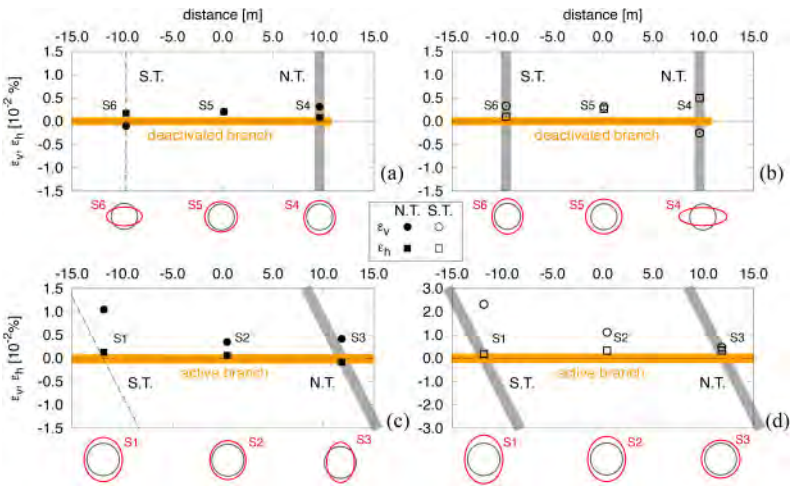

Figure 11. Incremental vertical and horizontal strains in the deactivated, (a) and (b), and active branch, (c) and (d) of the *Cloaca Maxima*, induced by the construction of Line C tunnels.

6 CONCLUDING REMARKS

The *Cloaca Maxima* is one of the earliest sewer systems in the world; its concrete and masonry tunnels channelled Rome refuse beneath the Fora and around the hills, and stood among other extensive drainage networks (Hopkins 2007). The sewer played a key role in the process of urbanization in the area that became the *Forum Romanum*, thus solidifying Rome's economic and military hold on central Italy and was acclaimed in the first century as a work "[…] for which the new magnificence of these days has scarcely been able to produce a match […]" (Livy, I.56.2). Repaired and restored frequently, has been functioning continuously for more than 2500 years.

As it is often the case with large infrastructural projects, construction of Line C represented a unique opportunity to increase our knowledge of the monument. Aimed at the acquisition of the information required to carry out the interaction analyses between the line and the monument, the extensive investigations carried out by Metro C S.C.p.A. at the design stage, which included coring of the tunnel lining, digital photogrammetry, laser scanning and topographic surveys, made it possible to define precisely the internal geometry of the sewer pipe and to identify the techniques used for its construction and the mechanical properties of the materials. This knowledge was used for a preliminary assessment of the risk of damage and for the design of the monitoring system.

The vertical displacements of the sewers, measured by means of precision levelling on the floor of the *Chiavicone* and hydraulic level settlement gauges installed in the floor and the vault of the

Cloaca Maxima, show that the ancient sewers are relative flexible and substantially conform to the greenfield displacements. The most significant factors affecting the magnitude of the vertical displacements of the sewers are the local variations of the geological profile and the operational parameters of the EPB shield. The measurements of horizontal and vertical convergence provided interesting information on the evolution of the deformed shape of the cross-sections of *Cloaca Maxima* as Line C tunnels were driven in the vicinity of the sewer.

The *Cloaca Maxima* is a very peculiar monument because it is a large active sewer and at the same time a monument of great archaeological value, so that the evaluation of the effects of the construction of Line C had to be carried out under this double profile, even if the lack of decorative elements did not create particular problems of conservation from the point of view of the latter. The constructive simplicity of the structures and the good quality of the materials used have shown high durability and, overall, the condition of burial of the monument has favoured its conservation. As far as the hydraulic and static functionality are concerned, the threshold values on the acceptable deformations for sewers reported in the literature are all much larger than those that were measured and, as a matter of fact, construction of the tunnels was completed without significant impact on the monument.

Recent work has been carried out to address rationally the problem of excavation-induced ground movements affecting existing tunnels and pipelines, and quantify the relative role played by bending and shear deformations (Franza & Viggiani 2021). This depends largely on the ratio of the shear and bending stiffness of the tunnel lining, which in turn affects the soil structure interaction induced by ground settlements. Work is currently under way to obtain characteristic values of this ratio for the various types of lining identified in the *Cloaca Maxima* but also other types of historical linings such as, *e.g.*, Victorian brick tunnels or cast iron segmental linings.

REFERENCES

Antognoli L. 2015. Il Chiavicone della Suburra, in Elisabetta Bianchi (ed.) *La* Cloaca Maxima *e i sistemi* fognari *di Roma dall'antichità ad oggi*. Roma: Palombi Editori: 159–166.

Antognoli, L. & Bianchi, E. 2009. La *Cloaca Maxima* dalla suburra al foro romano. *Studi Romani* 12: 89–125.

Corsetti, G. 1925. I collettori bassi delle fogne di Roma, *Annali dei Lavori Pubblici*, Roma: Stabilimento Litografico del Genio Civile.

Di Mucci G. & Miniero N. 2015. Indagini sperimentali su un tratto della Cloaca Maxima nell'ambito degli studi interazione linea-preesistenze della tratta T3 della nuova linea C, in Elisabetta Bianchi (ed.) *La* Cloaca Maxima *e i sistemi fognari di Roma dall'antichità ad oggi*. Roma: Palombi Editori: 207–222.

Fargnoli, V., Boldini, D., & Amorosi, A. 2015. Twin tunnel excavation in coarse grained soils: Observations and numerical back-predictions under free field conditions and in presence of a surface structure. *Tunnelling and Underground Space Technology* 49:454–469.

Franza, A. & Viggiani G.M.B. 2021. Role of shear deformability on the response of tunnels and pipelines to single and twin tunnelling. *J. Geotech. Geoenvironmental Eng. ASCE* 147(12): 04021145.

Hopkins, J.N.N. 2007. The *Cloaca Maxima* and the monumental manipulation of water in archaic Rome. Waters *of Rome Journal* 4:1–15

Losacco, N. & Viggiani, G.M.B. 2019. Class A prediction of mechanised tunnelling in Rome. *Tunnelling and Underground Space Technology* 87:160–173.

Losacco, N. & Viggiani, G.M.B. 2019b. Mechanised tunnel excavation through an instrumented site in Rome, in *National Conference of the Researchers of Geotechnical Engineering*, Springer, Cham: 245–254.

Losacco, N., Romani, E., Viggiani, G.M.B & DiMucci G. 2020. Embedded barriers as a mitigation measure for tunnelling induced settlements: a field trial for the Line C in Rome, in *Tunnels and Underground Cities: Engineering and Innovation Meet Archaeology, Architecture and Art*, Volume 12: Urban Tunnels-Part 2: 5845.

Palombi, D. 2013. Cloaca massima e storia urbana, *Archeologia Classica* 64:133–168

Wan, M.S.P., Standing, J.R., Potts, D.M., & Burland, J.B. 2017. Measured short-term subsurface ground displacements from EPBM tunnelling in London Clay. *Géotechnique*, 67(9):748–779.

Geotechnical Engineering for the Preservation of Monuments and Historic Sites III – Lancellotta, Viggiani, Flora, de Silva & Mele (Eds)

Safeguarding of the *Aurelian Walls* at *Porta Asinaria* from conventional tunnelling

S. Rampello & L. Masini
University of Rome La Sapienza

ABSTRACT: Construction of the line C of Rome underground is being carried out in a complex context due to the presence of archaeological artefacts, historical buildings and monuments of invaluable value. Along the contract T3 of the line, between the shaft 3.3 and *San Giovanni* station, two tunnels have been excavated for a length of about 140 m following a three step procedure: excavation of two small diameter tunnels with a mini TBM; soil improvement via low-pressure cement grouting; and conventional excavation of the two line tunnels in the improved soil. The tunnels, excavated at a depth of about 25 m, reach *San Giovanni* station passing at a short distance from the ancient Aurelian Walls. This paper presents the displacement measured at ground surface during the construction activities, showing the efficiency of a protective barrier made by a line of piles in reducing the movements induced by tunnelling in the Aurelian Walls.

1 INTRODUCTION

The construction of new underground railway lines and the extension of existing ones require deep open excavations and bored tunnels in urban environments, in close vicinity to existing buildings and structures. In these conditions, the main design requirement is to contain ground movements during and after the excavation works to prevent nearby structures from undergoing excessive deformations. This is particularly relevant for existing structures of monumental and historical value for which the limits in allowable movements are very onerous, as it often the case in European cities.

Contract T3 of the new line C of the Rome underground, currently under construction, underpasses the historical centre of the city encountering the historical monuments of Roman age (I to V century): these are the Aurelian Walls at *Porta Asinaria* and *Porta Metronia*, the Church of *Santo Stefano Rotondo*, the *Acquedotto Celimontano*, the *Anfiteatro Flavio* (Coliseum), the *Basilica di Massenzio*, the *Colonnacce* and the *Foro di Cesare*.

Due to the exceptional archaeological and historical value of the structures potentially affected by the construction of the line, the design included a detailed study of the interaction between the construction activities and the monuments. To this aim, the general contractor, Metro C, set-up a multidisciplinary steering technical committee with the assignment of implementing all the necessary procedures to safeguard the monuments and historical buildings.

The main tasks of the steering committee were: (i) to evaluate the influence of the construction of the line C (tunnelling and deep open excavations) on the existing monuments; (ii) to suggest, where necessary, appropriate geotechnical or structural mitigation measures; (iii) to develop a comprehensive and redundant monitoring scheme to follow in real time the response of the monuments to construction; (iv) to assist the general contractor during construction with the evaluation of the monitoring data, to optimise construction sequences and procedures.

The analysis of the interaction between the excavation activities and built environment was carried out following procedures of increasing complexity.

 DOI 10.1201/9781003308867-17

At a first stage, simplified (Level 1) analyses were performed computing surface and near-surface displacements by semi-empirical methods, ignoring the stiffness and weight of the existing monuments (e.g.: Attewell & Woodman 1982; Attewell et al. 1986; Ou & Hsieh 2011); evaluation of the potential damage induced by tunneling and deep excavations was carried out through the interaction diagrams proposed by Burland & Wroth (1974), which relate the deflection ratio and the horizontal tensile strain to given damage categories. Based on the outcome of these evaluations, the study ended if the damage was deemed negligible, or continued to a higher level of complexity (Level 2).

At this second stage, the interaction between the tunnels or the deep excavations and the monuments was studied through 2D or 3D Finite Element (FE) analyses that studied the soil-structure interaction adopting a simplified description of the mechanical behaviour of the monuments. Damage was then re-evaluated using the interaction diagrams. Depending on the computed results, either damage was deemed acceptable, or prospective remedial techniques were suggested (Burghignoli et al. 2013; Rampello et al. 2012).

Structural and geotechnical mitigation interventions have been adopted in the project of the line C, the first being aimed to strengthen the structures, while the second to reduce the ground movements induced by tunnelling or deep excavations.

Definitive structural interventions mainly consisted of reinforcements made by steel wire ropes, or chains made by steel bars (e.g.: Church of *Santo Stefano Rotondo* and *Basilica di Massenzio*), while temporary structural intervention manly consisted of buttresses made of steel tube-joint structures and multiprop towers (e.g.: Aurelian Walls at *Porta Asinaria* and *Porta Metronia*, and *Basilica di Massenzio*).

The geotechnical mitigation interventions were of active or passive type, the first permitting to control the ground settlements during tunnelling, while the second producing a favourable variation of the displacement field induced by tunnelling.

Compensation grouting is an example of active mitigation intervention whose efficiency has been shown by site applications (e.g.: Mair 2008; Mair & Hight 1994) and laboratory tests (e.g.: Masini et al. 2012, 2014). A protective embedded barrier is instead an example of passive mitigation intervention that can be adopted when the structure lies to the side of the tunnel: it is installed before tunnelling, between the tunnel and the structure for which damage must be prevented, providing a restraint to ground movements (e.g.: Bai et al. 2014; Bilotta, 2008; Bilotta & Taylor, 2005; Di Mariano et al. 2007; Fantera et al. 2016; Katzenbach et al. 2013; Masini & Rampello, 2021; Rampello et al. 2019).

During construction of the line C, compensation grouting was adopted to prevent potential damage induced by tunnel excavation under the Aurelian Walls at *Porta Metronia*, while an embedded barrier was preinstalled to protect the Aurelian Walls at *Porta Asinaria*. In both cases, field monitoring was carried out to verify the design assumptions and evaluate the actual performance of the excavation works, having also the opportunity of calibrating the semi-empirical methods.

This paper describes the displacement field monitored during conventional excavation of two tunnels, about 140 m long, connecting the multifunctional shaft 3.3, operating as a launch pit for the TBM/EPB machines which excavated the tunnels in the direction of *Amba Aradam* station, and the existing *San Giovanni* station. Both the shaft 3.3 and the tunnels were excavated close to the Aurelian Walls at *Porta Asinaria* (3rd century A.D.). To prevent any damage eventually induced by tunnelling on the ancient city wall, a protective barrier made by adjacent piles was preinstalled close to the North-bound tunnel, where the walls are closest to the tunnel, at 23 m to 26 m from its axis.

Field monitoring provided the surface ground movements induced by the three-step procedure adopted to construct the tunnels: (i) mechanised excavation of two mini-tunnels; (ii) soil improvement via low-pressure cement grouting; (iii) conventional excavation of the main tunnels in the improved soil.

In this paper, the reduction of the surface settlements obtained behind the barrier, in the portion of soil facing the ancient city wall, is evaluated through the comparison of the monitoring data collected in *green-field* conditions and in the presence of the barrier, demonstrating the efficiency of this kind of mitigation intervention.

2 THE AURELIAN WALLS AT PORTA ASINARIA

The Aurelian Walls are large defensive walls built by Emperor Aurelian between 270 and 275 A.D. with most of their length (12.5 km over 19 km) having survived past centuries in a fair preservation state. Aurelian Walls at *Porta Asinaria* belong to the South-Eastern part of the town wall and are located at a distance of 24 m to 27 m from the diaphragm wall of a 30 m-deep excavation and of 23 m to 34 m from the axis of the North-bound tunnel of the line C of the Rome underground. Figure 1a shows the aerial view of the Aurelian Walls at *Porta Asinaria*, together with the multifunctional pit 3.3. The latter operated as a launch pit for the two TBM/EPB machines that bored the 6.7 m-diameter twin tunnels in the direction of *Amba Aradam* station, while the two conventional tunnels, about 140m long, were excavated towards *San Giovanni* station.

The wall is 4 m thick and about 18 m tall from the foundation plane, with the foundation located at 8–9 m below ground surface. The structure of the Aurelian Walls is made of combined tuff and brick masonry, with an inner core of poorly bonded tuff blocks. Initially, the ground surface was at the same level on both sides of the walls but, over the centuries, material has been accumulated on the side facing the *Basilica di San Giovanni*. Nowadays the city wall retains a backfill of anthropic origin, about 10 m high, cumulated since medieval times without installing any drainage system, which has caused the development of outwards displacements as high as about 0.4 m at the top of the walls and diffused cracks along the masonry surface. The aerial photo of Figure 1b shows the Aurelian Walls and *Porta Asinaria* during the excavation of the multifunctional pit 3.3, together with the temporary safeguarding interventions installed against the wall façade and the back-excavation carried out to reduce the earth trust acting in the wall.

Unlike the wall, *Porta Asinaria* is characterised by the same elevation of the ground surface on both the *extra-* and the *intra-moenia* sides (Figure 1c–d). Its current state largely corresponds to the restorations of the time of the Emperor Honorius. The structure of *Porta Asinaria* is essentially composed of two semi-circular towers connected to each other by two walkways placed on two different levels. The towers today are about 25 m high from the elevation of ground surface on the *extra-moenia* side (+33.9 m asl) with a diameter of about 4.9 m, while the walkway area is about 18 m high.

Thanks to the recent restorations carried out since 1950, *Porta Asinaria* is characterised by a good state of conservation, with extensive portions of the masonry completely rebuilt. However, the restoration mainly concerned the external façade, while the core continues to have rather modest mechanical properties.

According to the FE interaction (Level 2) analyses carried out at the design stage, excavation of the multifunctional pit 3.3, as well as that of the two tunnels, would have induced not negligible effects on the walls, with an increment of wall rotation. Specifically, the numerical simulation of the shaft excavation estimated a wall rotation $\alpha = 0.11°(0.2\%)$ with a maximum settlement of the wall of 27 mm, while the numerical analysis simulating tunnels excavation, with an assumed volume loss $V_L = 2.5\%$, provided a wall rotation $\alpha = 14°$ with a maximum wall settlement of 16 mm.

The above quantities were deemed to be potentially dangerous for an already damaged ancient masonry structure. Therefore, the primary design challenge was that of preventing any damage induced by the excavation activities on the ancient and vulnerable Aurelian Walls, located a short distance away from the pit and the North-bound tunnel.

To this end, in order to attain an estimated reduction of wall rotation of about 36%: (i) about 8 m of the backfill were removed behind the wall prior to the excavation of the pit 3.3, starting from the middle plane of the shaft, located at a distance of 30 m from the Aurelian Walls, thus eliminating the earth thrust acting on it; (ii) a very stiff retaining system was designed for the shaft using 1.2 m-thick diaphragm walls, top-down construction with five levels of props made by cast-in-situ concrete stiff slabs, and a high embedment ratio of the diaphragm walls below the dredge line ($L/H = 1.56$), with the diaphragms extending in the stiff and overconsolidated Pliocene clay, thus preventing any deep-seated movement.

The monitoring data collected during shaft excavation confirmed that the back-excavation carried out to safeguards the ancient structure and the high stiffness of the support system, together with the high embedment ratio of the diaphragm walls below the dredge line, were the key to minimise the

effects induced by the excavation of the multifunctional pit on the Aurelian Wall at *Porta Asinaria* (Masini et al. 2021).

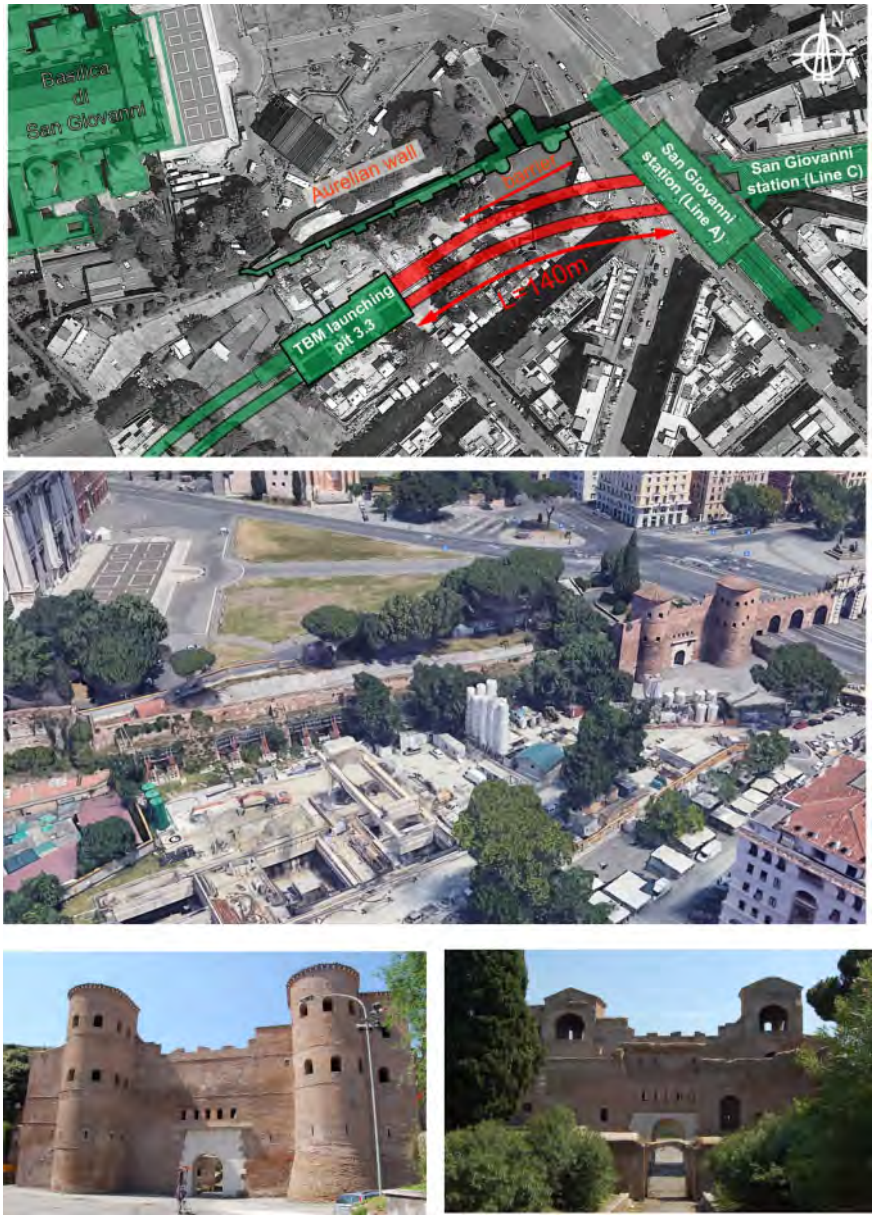

Figure 1. Aerial view of Aurelian Walls at *Porta Asinaria* (a-b); front view of *Porta Asinaria* (*extra moenia*) (c); front view of *Porta Asinaria* (*intra moenia*) (d).

To mitigate tunnelling effects, a protective barrier made by a line of piles was instead pre-installed close to the North-bound tunnel, in order to achieve an estimated reduction of about 54% in the wall rotation (see Figure 2). The efficiency of this kind of intervention, preliminary evaluated through a numerical study (Rampello et al. 2019) and a field test carried out in *green-field* conditions (Losacco et al. 2019; Masini & Rampello 2021), is discussed in this paper.

3 PROJECT DESCRIPTION AND CONSTRUCTION SEQUENCE

Figure 2 shows the two tunnels that were excavated using conventional procedures at a depth of about 25 m and for a length of 140 m, between the lunch pit 3.3 and the existing *San Giovanni* station, with the axis of the North-bound tunnel located at a distance of 23 m to 34 m from the ancient city wall.

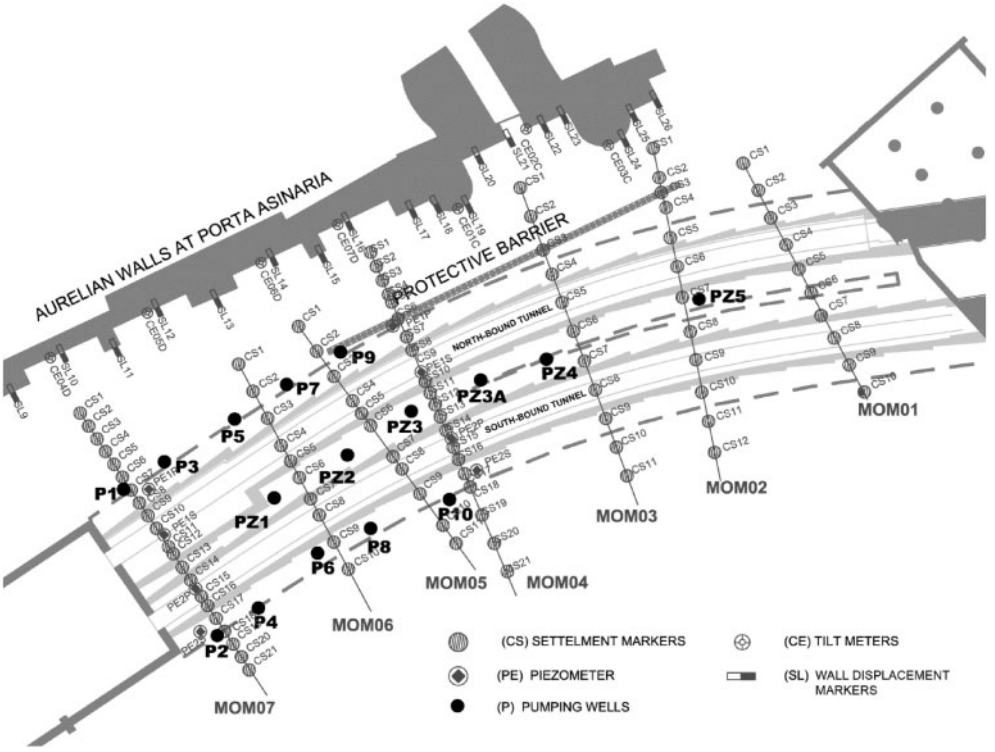

Figure 2. Plan view of the monitoring system.

To mitigate tunnelling-induced effects on the city wall, an embedded barrier made by adjacent piles was installed before tunnelling activities begun. It extends for 63 m in the zone where the North-bound tunnel is closer to the wall: 23 m and 26 m at MOM-02 and MOM-04 alignments, (Figure 2). The piles have a diameter $D = 0.8$ m, a length $L = 28$ m, and are installed at a spacing $s = 1.0$ m. The barrier runs approximately parallel to the wall with a minimum distance of about 8 m from the axis of the North-bound tunnel, about 8 m wide, and 18 m from the ancient city wall. An embedded capping beam (cross-section of $1 \times 1\text{m}^2$) connects the head of the piles. The capping beam and the piles are made of cast-in-place reinforced concrete, with a 28-day compressive strength of 32 MPa and Young's modulus of 31 GPa, while the yield strength of the rebar steel is equal to 235 MPa.

To monitor the ground movements induced by the tunnelling activities, seven arrays of instruments were set up about normal to the tunnels, named sections MOM 01-02-03-04-05-06-07. The instrumentation along the MOM alignments included settlement markers installed at ground surface and vibrating-wire piezometer cells. Arrays MOM-07 and MOM -04 were instrumented with closer displacement markers (spacing 2.5 m) and vibrating-wire piezometer cells, as well as with inclinometer and Trivec casings, the first providing horizontal displacements only, while the second measuring the three orthogonal components Δx, Δy and Δz of the displacement vectors along the

vertical measuring line, with a depth spacing of 0.5 m. The displacement markers installed at the ground surface incorporate sockets into which a removable survey plug can be screwed with good positional repeatability for manual surveying.

In this paper, reference is made to surface ground settlements measured by precision levelling only: this was performed using a digital level which can detect the height of the plane of collimation on a suitable bar-coded staff to a resolution of 0.01 mm.

Monitoring of the wall movements during the excavation activities was performed through precision levelling on displacement markers installed along the wall side facing the tunnels, about 0.5 m above the ground level, and by electric tiltmeters installed at wall mid-height to measure the out-of-plane rotation.

Ground conditions at *Porta Asinaria* are described by Fantera et al. (2016), Masini et al. (2019a–b, 2021a–b), Masini and Rampello (2021) and Rampello et al. (2019), to which reference is made for further details. Table 1 reports the strength parameters and the overconsolidation ratio as obtained from laboratory tests.

A section through the instrumented array MOM-04 is plotted in Figure 3, showing soil layering, the two tunnels, and the protective barrier. A 14 m-thick layer of made ground (MG) is first encountered, from ground surface at about +35 m asl, mainly consisting of coarse grained material, sand and gravel; recent alluvial soils of the Tiber river are found underneath, extending down to a depth of 26 m (+8.7 m asl). The alluvia are variable in grading involving slightly overconsolidated clayey silt and sandy silt (CS-SS); they overly a layer of sand and gravel of Pleistocene age (SG), with a thickness of about 14m, followed by a thick layer of stiff and overconsolidated silty clay (OSC), the blue Vatican clay of Pliocene age.

Table 1. Strength parameters and overconsolidation ratio.

Soil	γ (kN/m^3)	c' (kPa)	ϕ' (°)	OCR (−)	S_u (kPa)
Made Ground (MG)	17	5	34	1	–
Clayey silt and Sandy Silt (CS-SS)	19.5	28	27	1.25	120
Sandy Gravel (SG)	20	0.1	40	1	–
Overconsolidated Stiff Clay (OSC)	20.9	41.3	25.7	2.5	400

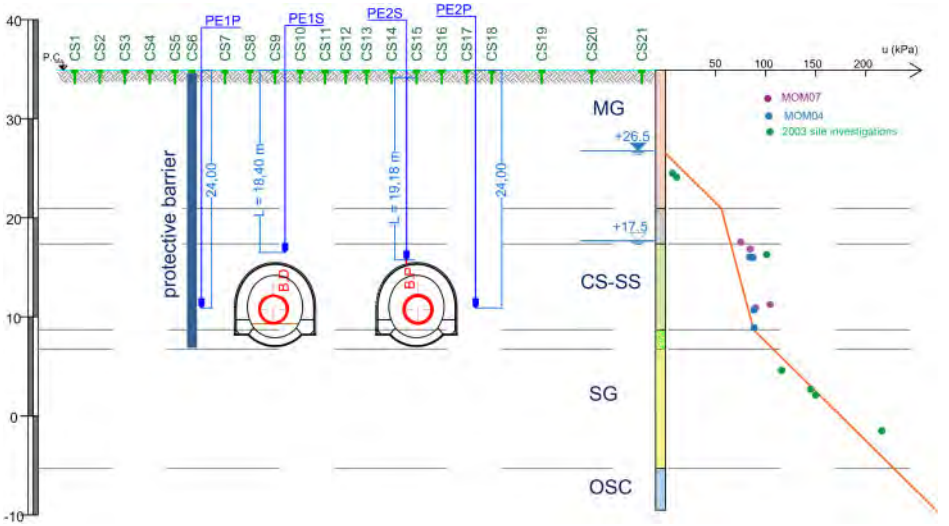

Figure 3. Transversal section through instrumented array MOM-04.

The pore water pressure regime is characterised by downwards seepage in the silty soils from the made ground, where a constant hydraulic head $H = 26.5$ m asl was measured, to the deep layer of sandy gravel, at constant head $H = 17.5$ m asl. This is a typical condition encountered along the line C of Rome underground, induced by pumping from the deep and permeable layer of sandy gravel for anthropic purposes. Tunnels excavation was carried mainly in the alluvia sandy silt whose permeability was preliminary reduced via low-pressure cement grouting.

The two tunnels connecting the multifunctional pit 3.3 to *San Giovanni* station were excavated following a three-step procedure: (i) two small-diameter tunnels ($D = 3$ m) were first excavated using a mini-slurry shield, tunnelling boring machine at a depth of about 25 m (cover to diameter ratio $C/D = 7.8$); (ii) soil improvement via low-pressure cement grouting was then carried out using t*ubes à manchettes* installed in boreholes excavated radially to the bored tunnels; (iii) tunnel construction was finally completed through conventional excavation of the main tunnels in the improved soil. Both the tunnels have a curvilinear cross-section with an average diameter of the equivalent circular cross-section $D_{eq} = 8.03$ m. At the alignment MOM-07, the initial portion of the North-bound tunnel has an enlarged cross-section with an equivalent diameter $D_{eq} = 10.3$ m.

Figure 4 shows the mini-TBM at the launching pit (Figure 4a) and at the intermediate jacking station (Figure 4b), a view from the inside of a mini-tunnel after completion of the radial injections (Figure 4c) and an intermediate stage of tunnel excavation in the improved soil (Figure 4d – primary lining installed).

At stage (ii), the *tubes à manchettes* (4 *manchettes*/m) were installed in 20 boreholes per section, drilled at a longitudinal spacing of 0.6 m: the boreholes had a diameter of 80 mm, a length of 5–7 m and a spacing of 18° in the radial direction. Soil improvement was obtained injecting first a Mistrà-type cement grout with 10–15% of bentonite content and a water-cement ratio of 2.5–3.5, and a chemical mixture of silica components in a second stage, to reduce further the permeability of the improved soil that had to be excavated during tunnelling.

Figure 4. Mini-TBM at the launching pit and at the intermediate jacking station (a-b); mini tunnel at the completion of radial injections (c); conventional tunnelling in the improved soil.

In the conventional excavation procedure, fan-like overlapping pipe umbrellas, made by 114.7 mm-diameter steel pipes, were drilled and grouted at the roof of the tunnel, parallel to the direction of advancement of the excavation face. Each roof shield consisted of 41 steel pipes, 12 m long, covering an excavation span of 8m. Full face excavation was carried out along with the installation of the primary support 1m away from the excavation face, which consists of IPN 160 steel ribs and 0.2 m-thick shotcrete. The final concrete lining, 0.8–1.0 m-thick, was installed 35 m away from the excavation face.

At the early stages of excavation of the invert of the South-bound tunnel, the first to be excavated, a local collapse involved a small portion of soil at the tunnel spring line as a result of basal heave of the improved soil. Therefore, before continuing the tunnelling activities, 16 relief wells were activated (see Figure 2), which induced an average drawdown of the hydraulic head of about 9.5 m in the layer of sandy gravel.

4 FIELD MONITORING

In this section the vertical displacements measured at ground surface by the settlement markers installed along the 6 instrumented arrays, MOM-07 to MOM-02, are discussed for each excavation stage, interpreting the transversal displacement profiles attained in plane strain conditions through the empirical relationships currently adopted in applications (e.g.: Moh et al. 1996; O'Reilly & New 1982; Peck 1969).

For evaluating the effects induced by mini-tunnelling, the reference undeformed ground surface was calculated as the average over the time of the displacement readings taken for distances of the excavation face not lower than 30 m from each instrumented section. The effects induced by radial borehole drilling were instead evaluated assuming as base-line the time average of the readings in the time interval between the end of excavation of the North-bound mini-tunnel and the start of drilling (31/03/17–27/06/17), while the reference of each section for the low-pressure grouting injections was taken considering the displacement measured about two months before the start of the injection activities.

Table 2 reports the start and end dates of each construction phase: excavations of both the small-diameter tunnels using the mini TBM was carried out in about two months (70 days), while soil improvements around the mini-tunnels took about 16 months (7 months for boreholes drilling and 9 months for grout injections). Conventional tunnelling required a much longer time, of about one year and a half for the South-bound tunnel due to some problems occurring during the excavation of the tunnel invert, while North-bound tunnel was excavated in about half year.

Typical time histories of the vertical displacements observed at the instrumented arrays are shown in Figure 5 with reference to section MOM-04 (see Figure 2), while Table 3 reports the volume per unit length described by the settlement profiles, the corresponding volume loss (mini-tunnel diameter $D = 3$ m) and the maximum observed settlements (−)/heaves (+) measured during the construction stages preliminary to excavation of the main tunnels.

Table 2. Construction stages.

construction stage		start	end
mini-tunnelling	South-bound tunnel	20/01/17	16/02/17
	North-bound tunnel	13/03/17	31/03/17
soil improvement	borehole drilling	27/06/17	22/01/18
	grouting injections	23/01/18	19/10/18
activation of relief wells		from 20/11/18	
South-bound running tunnel		18/01/19	07/07/19
North-bound running tunnel		26/04/19	21/10/19

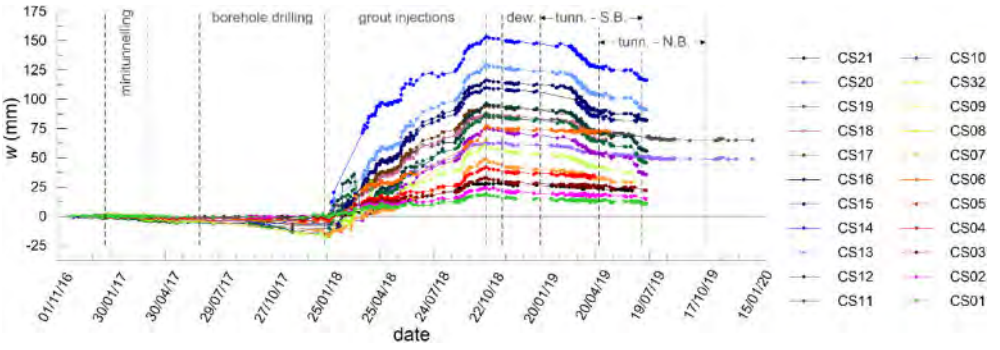

Figure 5. Time histories of the vertical displacements measured at section MOM-04.

Excavation of both the mini-tunnels induced negligible settlements, with average and maximum values $w_{ave} = -3.6$ mm and $w_{max} = -5.6$ mm, respectively, while radial boreholes drilling caused a progressive increase of the settlements as drilling activities approached the instrumented section, with $w_{ave} = -12$ mm and $w_{max} = -20.5$ mm, which are about three times higher than the corresponding values observed at the end of mini-tunnels excavation. The subsequent low-pressure grout injections caused a massive heave, with average and maximum values as high as $w_{ave} = 137.3$ mm and $w_{max} = 165.6$ mm.

Table 3. Effects induced by construction activities preliminary to excavation of main tunnels.

	tunnelling with mini-TBM			drilling of radial boreholes			low-pressure grout injections		
MOM	ΔV (m^3/m)	V_L (%)	w_{max} (mm)	ΔV (m^3/m)	V_L (%)	w_{max} (mm)	ΔV (m^3/m)	V_L (%)	w_{max} (mm)
07	0.110	0.78	–4.01	0.211	1.49	–8.43	–3.035	–21.47	95.75
06	0.202	1.43	–5.61	0.892	6.31	–20.47	–4.032	–28.52	132.7
05	0.095	0.67	–2.98	0.284	2.00	–12.92	–12.29	–86.23	141.5
04	0.099	0.70	–3.26	0.451	3.19	–13.06	–5.65	–39.96	150.0
03	0.084	0.59	–3.41	0.212	1.50	–12.33	–5.89	–41.66	165.6
02	0.062	0.44	–2.61	0.098	0.69	–4.55	–4.59	–32.47	138.4

Part of the measured heave was lost during excavation of the main tunnels, as a result of both the conventional tunnelling activities and the dewatering from the relief wells in the deep layer of sandy gravel.

Measurements provided by precision levelling during mini-tunnelling and borehole drilling are characterised by a significant scatter do not highlighting any clear difference between the volume losses computed in the presence and the absence of the barrier.

Figure 6a–b show the heave profiles induced by the grout injections carried out to improve the soil strength and reduce its permeability. Although the low pressures adopted to inject the grout, the heave measured at ground surface was not negligible in *green-field* conditions (MOM 07-06-05), being equal to about 96 mm to 140 mm, and was even higher in the sections interacting with the barrier (MOM 04-03-02), being in the range of 138 mm to 166 mm. The barrier did not produce any appreciable reduction of the ground uplift behind its location, in the portion of the soil facing the walls.

At the start of construction of the South-bound running tunnel, during the excavation of the tunnel invert, water came into the tunnel due basal heave of the improved soil, so that the excavation was

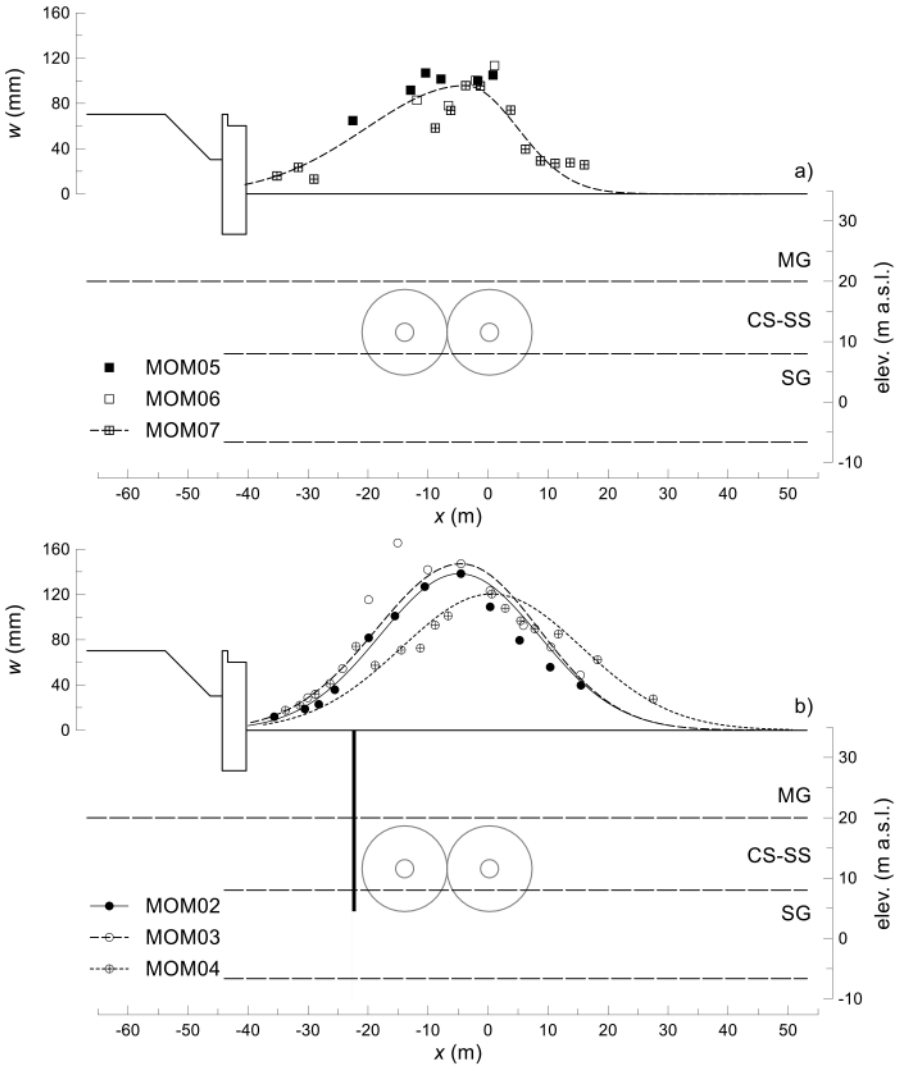

Figure 6. Settlement profiles induced by low-pressure grout injections at the *green-field* monitoring sections MON-05-06-07 (a), and in the presence of the barrier (sections MON-02-03-04) (b).

suspended while activating the pumping wells to reduce the hydraulic head at the base of the improved soil (see Figure 2). The excavation was resumed about two months later.

Pumping from the relief wells lowered the hydraulic head by about 9.5 m in the layer of sandy gravel (SG), with an increase of the effective stresses in the layer of clayey silt and the development of further settlements at ground surface.

To assess the effect of dewatering in the sandy gravel, the time needed to attain the end of consolidation in the layer of clayey silt and sandy silt (CS-SS) was evaluated using Terzaghi's theory of one-dimensional consolidation assuming a consolidation coefficient $c_v = 2 \cdot 10^{-4}$ m^2/s, and a drainage path of 12 m, evaluating an end-of-consolidation time of about 10 days. Therefore, the settlements induced at ground surface by dewatering can be assumed to be nearly fully developed before the start of tunnel excavation.

As an example, Figure 7a shows the time-history of the surface settlement measured by the settlement marker CS14 of the array MOM-07, starting from the beginning of well activation (20/11/2018).

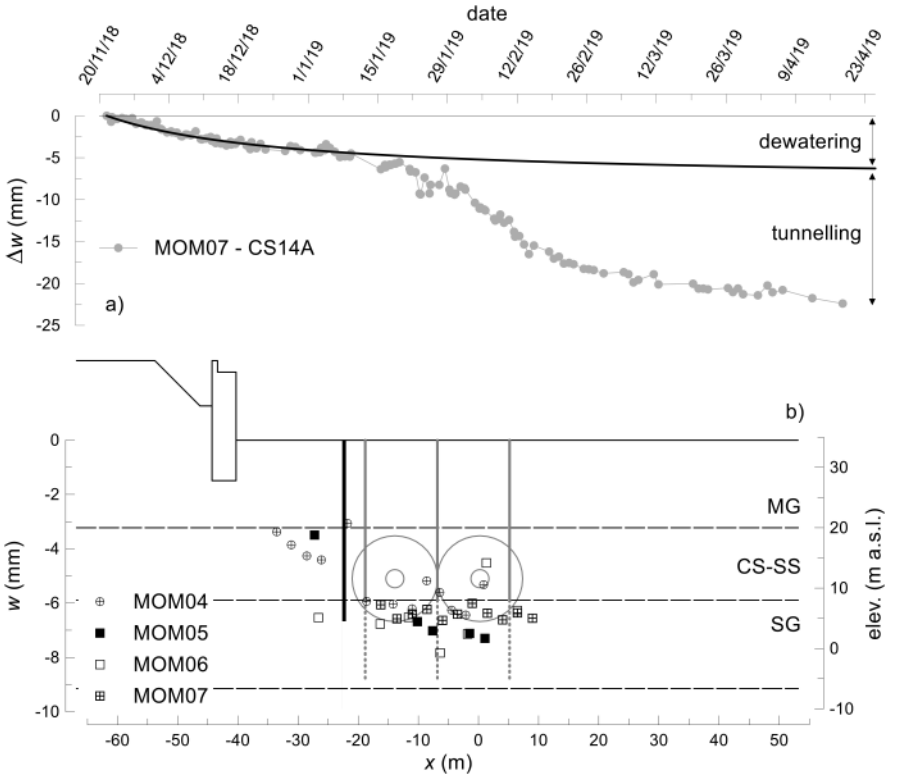

Figure 7. Time-history of the relative settlements observed during dewatering and excavation of the South-bound tunnel (a); settlements induced by the dewatering operations (b).

The first portion of the curve is characterised by a slow increase in the settlements, attributable to the consolidation process induced by dewatering, while the second presents a sharper increase associated to tunnels excavation. The first portion of the curve can be best-fitted using a hyperbole, the origin of which corresponds to the start of the pumping activities, thus estimating the final settlements induced by dewatering.

The ground surface settlements induced by lowering the pore water pressure in the sandy gravel are plotted in Figure 7b in a section transversal to the axes of the mini-tunnels. All the monitoring arrays affected by the dewatering activities exhibit similar behaviour, with a large scatter of the data and maximum settlements of –7 mm to –8 mm between the relief wells, above the two mini-tunnels.

The barrier made of adjacent piles and partially embedded in the layer of sandy gravel had, as expected, no effect in the observed settlement profiles.

Figure 8a–b show the settlement troughs induced by the excavation of both the tunnels in the green-field sections (MOM 07-06-05) and in the sections interacting with the barrier (MOM 04-03-02): the zero abscissa is referred to the axis of the South-bound tunnel.

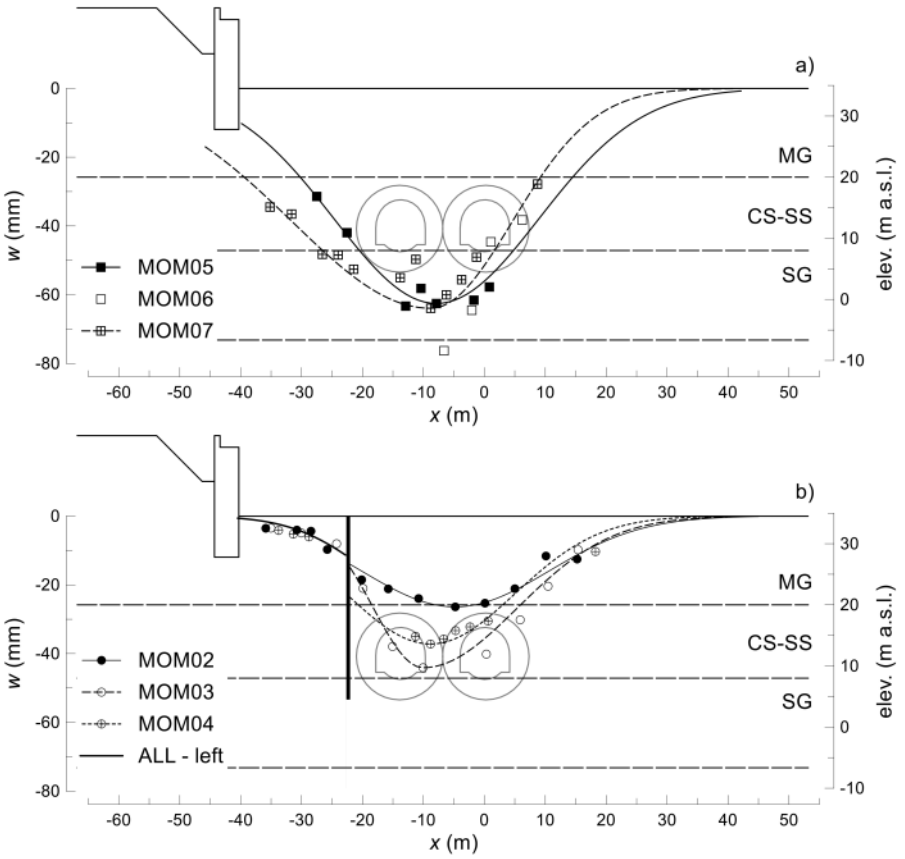

Figure 8. Settlement profiles induced by excavation of South-bound tunnel at the *green-field* monitoring sections MON-06-07 (a), and in the presence of the barrier (sections MON-04-05) (b).

The *green-field* sections show higher settlements, with maximum values of about –65 mm (Table 4), attained at about the mid plane between the tunnels. An asymmetrical settlements trough was also observed at section MOM-07, due to the larger excavated cross-section of the North-bound tunnel, so that separate best-fit Gaussian approximation of the surface settlements was carried out to the wright (+) and the left (−) of the maximum settlement, providing a trough width factor $i^{(-)} = 22.7$ m much higher than $i^{(+)} = 13.4$ m. Surface settlements evaluated at the location of the Aurelian Walls were also higher at section MOM-07, being equal to about −20 mm, if compared with the ones at section MOM-05, that are equal to about −12 mm.

For the sections interacting with the protective barrier (Figure 8b), lower settlements were measured both above the tunnels and close to the Aurelian Walls: maximum settlements above the tunnels were of about –26 mm to –44 mm (Table 4), while at the location of the Aurelian Walls, the surface settlements were not higher than –5 mm. At the wall façade a settlement reduction of 58% was obtained, while at the location of the embedded barrier the measured settlements reduced by about 72% being equal to about –43 mm in *green-field* conditions (sect. MOM-05, Figure 8a) and about –12 mm in the presence of the embedded barrier (MOM 04-03-02, Figure 8b). The efficiency of the adopted mitigation intervention is also appreciable considering the volume loss computed for green-field conditions, $V_L = 2.60\%$ (sect. MOM-05) and in the presence of the protective barrier, $V_L = 0.96\% - 1.31\%$, with an average reduction of about 56%.

It is worth mentioning that the FE interaction analyses predicted slightly lower reductions of the surface settlements at the wall and the barrier locations, equal to 41% and 66%, respectively, that were in a fair agreement with the observed reductions mentioned above, equal to 58% and 72%, respectively.

Table 4. Effects induced by tunnels excavation.

	MOM	$i^{(-)}$	$i^{(+)}$	$\Delta \quad V$ (m^3/m)	V_L (%)	w_{max} (mm)
green-field	07	22.7	13.4	3.643	2.71	–64.0
	05	16.8	16.8	2.635	2.60	–62.6
	04	13.9	13.9	1.163	1.15	–37.2
protective barrier	03	8.2	15.5	1.327	1.31	–44.1
	02	15.4	15.4	0.969	0.96	–26.4

It is worth noting that the maximum settlements induced by dewatering plus conventional excavation of the main running tunnels (≈ -75 mm) were sensibly lower than the maximum heave induced by the grout injections carried out at low pressure from by the radial *tubes à manchettes* ($\approx$ 165 mm).

5 MOVEMENTS OF THE AURELIAN WALLS AT PORTA ASINARIA

The Aurelian Walls at *Porta Asinaria* are about parallel to the tunnels in the portion facing sections MOM-06 to MOM-03. Prior to start with the excavation activities, Metro C implemented temporary safeguarding interventions on the city wall, consisting of buttresses made by steel tube-joint structures (Figure 9) to prevent any damage eventually induced by unexpected events.

Figure 9. Temporary safeguarding interventions installed at the Aurelian Walls.

The portion of the wall facing the multifunctional pit 3.3 and the tunnels were also equipped with 10 electric tiltmeters, installed at wall mid-height to measure out-of-plane rotation, and 24 displacement markers installed at about 0.5 m above the ground surface, for monitoring the vertical

displacements of the wall (see Figure 2). Precision levelling on the displacement markers and monitoring of tiltmeters started before the tunnelling activities, on November 23rd, 2016.

The effects induced by the TBM excavation of the South-bound and North-bound mini-tunnels, as well as those induced by the radial borehole drilling to install the *tubes à manchettes* were negligible, causing displacements ≤ 2 mm, and are not discussed in the following.

To evaluate the effects of the low-pressure grout injections, the displacement measurements were referred to the start of the injections (23/01/2018), evaluating the base-line displacement profile of each section in the time interval ranging from the end of borehole drilling and the start of injections.

The maximum heave produced by the grout injections, equal to $+10.5$ mm, occurred at the displacement marker SL13, located close to the *green-field* section MOM-06, while the displacement markers located behind the protective barrier experienced substantially lower heaves, decreasing from about $+7.5$ mm (SL14–SL19) to $+3$ mm (SL22-SL26).

Tiltmeters CE 04D-05D-06D, located in front of the *green-field* sections MOM 07-06-05, provided small wall rotation towards the *Basilica di San Giovanni*, equal to about $+0.05°$, while the tiltmeters installed in the portion of the wall located behind the protective barrier, as well as those located behind the multifunctional shaft 3.3, were not substantially affected by the injection activities.

The settlements induced by conventional excavation of the South-bound and North-bound tunnels were referred to the end of the grout injections, about one month after the start of dewatering.

Figure 10 shows the isochrones of the wall settlements induced by the excavation of both tunnels. Negative abscissas in the figure refer to the displacement markers installed in the portion of the Aurelian Walls located in front of the multifunctional shaft 3.3 (SL3–SL9). The maximum settlement of the wall, equal to -12.3 mm, was measured at the location of the displacement marker SL12, located in the portion of the wall facing the *green-field* section MOM-06.

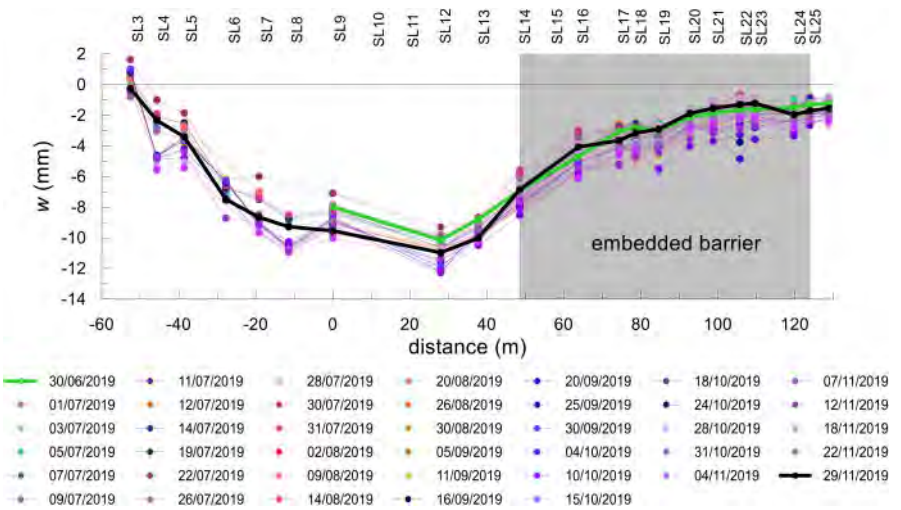

Figure 10. Settlement profiles induced by tunnelling in the Aurelian Walls.

By contrast, the wall settlements are seen to decrease behind the embedded barrier made by adjacent piles (Figure 10): moving from the displacement marker SL14, located behind the left end of the barrier, towards the displacement marker SL25, located behind its right end, the wall settlements reduce from about 7 mm (43%) to about 2 mm (84%), demonstrating the efficiency of this type of mitigation intervention. However, the reduction of wall settlement observed as *Porta Asinaria* is approached is also affected by the slight increasing distance between the North-bound tunnel and the city wall.

The maximum deflection ratios in sagging and hogging were $(\Delta_s/L_s)_{max} = 6.2 \cdot 10^{-5}$ and $(\Delta_h/L_h)_{max} = 2.7 \cdot 10^{-5}$, respectively, both resulting substantially lower than the threshold values proposed by Burland & Wroth (1974): $(\Delta_s/L_s)_{lim} = 8 \cdot 10^{-4}$ and $(\Delta_h/L_h)_{lim} = 4 \cdot 10^{-4}$.

The time histories of the out-of-plane rotations induced in the Aurelian Walls by the tunnels excavation are plotted in Figure 11.

Tiltmeters CE 01D-02D-0D3, installed in the portion of the wall facing the multifunctional shaft 3.3 show nearly constant and negligible rotations towards the excavation, of about $-0.03°$, with similar values also observed for tiltmeters CE-04D and CED-06D, installed in portion of the wall close to the transversal diaphragm wall of the shaft and the left-end of the barrier, respectively. By contrast, a maximum rotation of about $-0.08°$ was measured on the displacement marker CE-05D, installed close to the displacement marker SL12, in the portion of the wall facing the instruments array MOM-06.

Conversely, the tiltmeters installed in the portion of the wall located behind the protective barrier (CE-07D, CE 01C-02C-03C) were observed to undergo nearly zero rotations, showing once again the efficiency of the embedded barrier in reducing tunnelling effects on the ancient Aurelian Walls at *Porta Asinaria*.

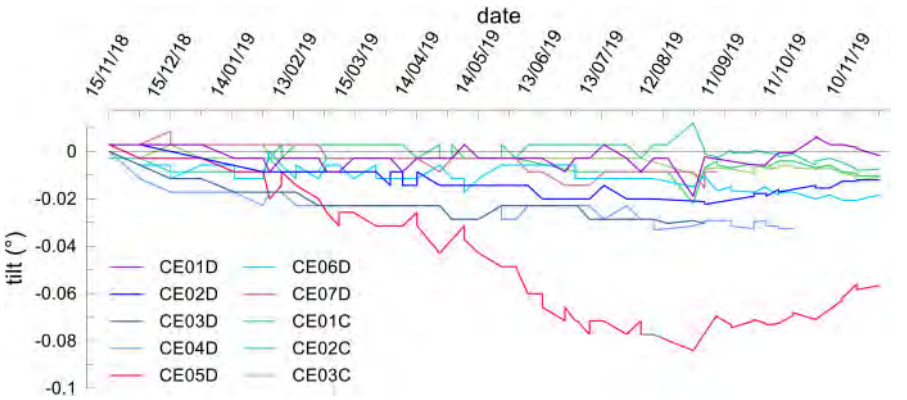

Figure 11. Time histories of the out-of-plane rotation of the Aurelian Walls at *Porta Asinaria*.

The walls were also instrumented with 11 vibrating-wire crack-meters installed over the major cracks observed in the wall façade before starting the excavation activities. Figure 12a shows the opening (−)/closure (+) measured by the crack-meters in a two-years-long time interval from 01/01/2018, before starting soil improvement via low-pressure grout injections. In the considered monitoring period, the crack-meters showed small changes in crack amplitude, with maximum values of about 0.6 mm, largely attributable to changes in the temperature. The periodic changes in crack amplitude may indeed be associated to daily and seasonal changes of temperature.

To highlight the effects of thermal excursion, Figure 12b–c show the time histories of crack opening/closure and of the changes in temperature, respectively: the data refer to a shorter time period (30/05/18–19/07/18), to make clear the strong correlation between the changes in crack-amplitude and temperature in the short (daily) and the long (seasonal) periods. Specifically, the crack-meters show amplitude changes of 0.3–0.6 mm, associated to temperature changes of about 20°C. Correlation between the changes in crack-amplitude and temperature is shown in Figure 12d for the crack-meter MG-06C, in the time period ranging from 1/1/2018 to 27/5/2019: the high computed correlation coefficient $R^2 = 0.989$ demonstrates that the observed variations in crack amplitude are mainly due to changes in the temperature. The slope of the regression line, equal to 0.017 mm/°C, provides an estimate of crack-amplitude variation of about 0.34 mm for a thermal excursion of 20°C, and of about 0.85 mm for the maximum thermal excursion monitored in the

time period 20/02/2018–31/07/2018, equal to 50.2°C: both these evaluations are consistent with the data shown in Figure 12.

It can be then concluded that the crack-meters monitored negligible effects on the main cracks present in the façade of the walls, since the changes in their amplitude are essentially attributable to thermal excursions.

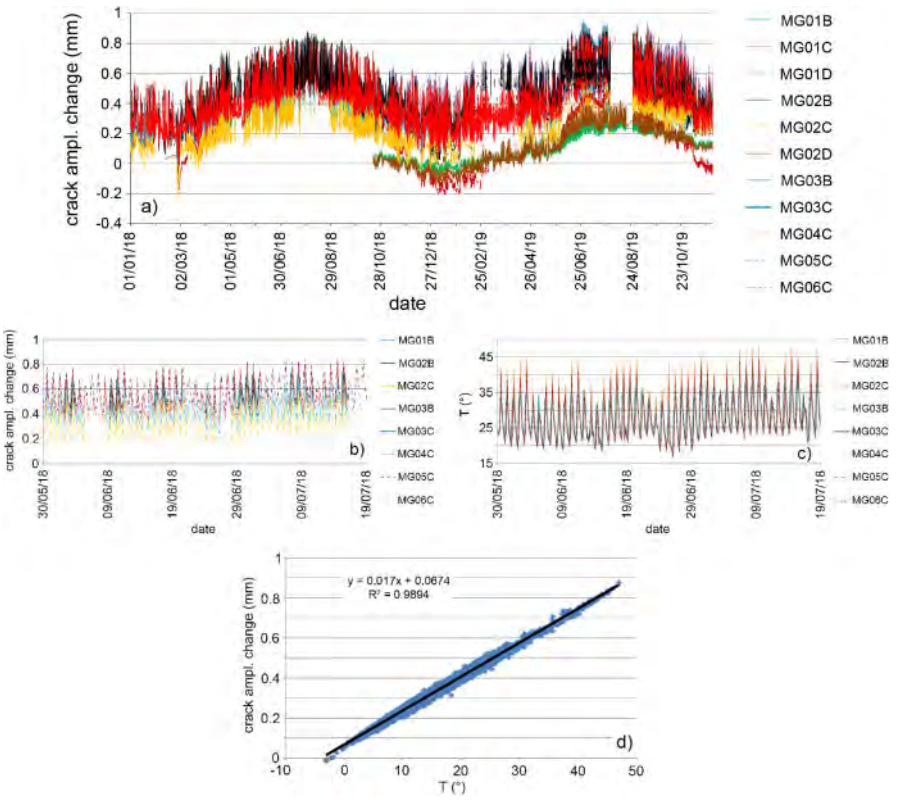

Figure 12. Measured opening (−)/closure (+) of the cracks in the Aurelian Walls.

6 CONCLUSIONS

The analysis of the monitoring data collected in a time period of about 3 years, during the excavation of two tunnels of the Line C of the Rome underground, about 140 m long, permitted to evaluate the effects induced in the Aurelian Walls at *Porta Asinaria* by the construction activities: the low-pressure grout injections preliminary carried out to improve the soil properties of the clayey silt to be excavated during tunnelling and the subsequent excavation of both running tunnels via conventional techniques.

Grout injections, though carried out under low-pressures, induced substantial heave of ground surface above the mini-tunnels, of 80 mm to 150 mm, that were seen to be larger than the maximum settlements induced by subsequent activities: dewatering by the relief wells, which induced maximum settlements of about −10 mm, and tunnels excavation, that produced surface settlement in the range −60 mm to −80 mm.

To prevent any damage in the Aurelian Walls at *Porta Asinaria*, a protective barrier of horizontal extension $L_h = 63$ m, made of adjacent piles 28 m long, partially embedded in the layer of sandy

gravel was installed about parallel to the city wall, at a distance of about 8m from the axis of the North-bound tunnel, and of about 18 m from the wall.

The barrier demonstrated to be effective in reducing the settlements induced by tunnels excavation behind its location. Indeed, at the location of the embedded barrier the measured settlements reduced by about 72%, being equal to about -43 mm in *green-field* conditions and to -12 mm in the presence of the embedded barrier. Presence of the barrier was also effective in reducing by about 56% the volume loss evaluated in the arrays interacting with it: values of $V_L = 0.96\% - 1.31\%$ were computed in the presence of the barrier, against a *green-field* volume losses $V_L = 2.60\%$.

The beneficial effects of the protective barrier were also evident for the Aurelian Walls that experiences maximum settlements of about 12 mm in the portion of the wall facing the *green-field* sections, while substantially lower values, of 3 to 7 mm, were measured in the portion of the wall located behind the barrier.

Despite the differential settlements measured along the wall development, the subsidence profile always provided maximum deflection ratios Δ/L lower than the threshold values suggested in the literature, both in sagging and hogging. Moreover, the barrier was effective in reducing the out-of-plane rotation of the wall towards the tunnels: this was equal to a maximum of about $-0.08°$ in the wall portion facing the *green-field* sections, reducing to about $-0.03°$ for the wall portion protected by the embedded barrier.

It may be concluded that the embedded barrier was effective in preventing any damage potentially induced by conventional tunnelling to the Aurelian Walls at *Porta Asinaria* and that the excavation activities were performed within the design prescriptions, without causing any detrimental effect on the ancient city wall.

ACKNOWLEDGEMENTS

The Authors are indebted to Metro C ScPA, particularly to Mr. Eliano Romani, for making available all the monitoring data.

REFERENCES

Attewell, P.B. & Woodman, J.P. 1982. Predicting the dynamics of ground settlement and its derivatives caused by tunnelling in soil. *Ground Engineering*, **15**(8), 13–22, 36.

Attewell P.B., Yeates, J. & Selby, A.R. 1986. Soil movements induced by tunnelling and their effects on pipelines and structures. Glasgow: Blakie.

Bai, Y., Yang, Z. & Jiang, Z. 2014. Key protection techniques adopted and analysis of influence on adjacent buildings due to the Bund Tunnel construction. *Tunnelling and Underground Space Technology*, **41**, 24–34.

Bilotta, E. & Taylor, R.N. 2005. Centrifuge modelling of tunnelling close to diaphragm wall. *Int. J. Phys. Model. Geotech.* **1**, 25–41.

Bilotta, E. 2008. Use of diaphragm walls to mitigate ground movements induced by tunnelling. *Géotechnique* **58** (2), 143–155.

Burghignoli, A., Callisto, L., Rampello, S., Soccodato, F.M. & Viggiani, G.M.B. 2013. The crossing of the historical centre of Rome by the new underground Line C: a study of soil structure-interaction for historical buildings. In *Geotechnics and Heritage: Case Histories*: 97–136. London: CRC Press.

Burland, J.B. & Wroth, C.P. 1974. Settlements of buildings and associated damage. *Proc. Int. Conf. on Settlements of Structures*, Cambridge, 611–654.

Di Mariano, A., Gens, A., Gesto, J.M. Schwartz, H. 2007. Ground deformation and mitigating measures associated with the excavation of the new Metro line. In *Geotechnical Engineering in Urban Environments*, Proc. of the 14th ECSMGE, Millpress Science Publisher, Rotterdam, The Netherlands, vol. **4**: 1901–1906.

Fantera, L., Rampello, S. & Masini, L. 2016. A Mitigation Technique to Reduce Ground Settlements Induced by Tunnelling Using Diaphragm Walls. *Procedia Engineering* **158**, 254–259.

Katzenbach, R., Leppla, S., Vogler, M., Seip, M. & Kurze, S. 2013. Soil-structure interaction of tunnels and superstructures during construction and service time. In: *Proc. of the 11th Int. Conf. on Modern Building Materials, Structures and Techniques*, MBMST 2013. Procedia Engineering, vol. **57**: 35–44.

Losacco N., Romani E., Viggiani G.M.B., Di Mucci G. 2019. Embedded barriers as a mitigation measure for tunnelling induced settlements: A field trial for the line C in Rome. In: *Proc. of the WTC 2019 ITA-AITES World Tunnel Congress*, Naples, Italy

Mair, R.J. & Hight, D. 1994. Compensation grouting. *World Tunnelling Subsurface Excavation* **7** (8).

Mair, R.J. 2008. 46th Rankine Lecture: Tunnelling and geotechnics: new horizons. *Géotechnique* **58** (9), 695–736.

Masini, L., Rampello, S., Viggiani, G.M.B., & Soga, K. 2012. Experimental and numeri-cal study of grout injections in silty soils. Proc. *7th International Symposium on Geotechnical Aspects of Underground Construction in Soft Ground*, Rome, 495–503.

Masini, L., S. Rampello, & K. Soga. 2014. An approach to evaluate the efficiency of compensation grouting. *J. Geotechnical and Geoenvironmental Engineering* **140** (12): 04014073.

Masini, L., Rampello, S. & Romani, E. 2019a. Performance of a deep excavation for the new Line C of Rome underground. In *Geotechnical Research for Land Protection and Development* – Proc. of CNRIG 2019 Springer Nature Switzerland AG 2020 F. Calvetti et al. (Eds.): CNRIG 2019, Lecture Notes in Civil Engineering (LNCE) **40**: 575–582.

Masini, L., Rampello, S., Carloni, S. & Romani, E. 2019b. Ground response to mini-tunnelling plus ground improvement in the historical city centre of Rome. *In Tunnels and Underground Cities: Engineering and Innovation meet Archaeology, Architecture and Art,* WTC2019, Naples 3–9 May: 5876–5885.

Masini, L., Gaudio, D., Rampello, S. & Romani, E. 2021a. Observed Performance of a Deep Excavation in the Historical Center of Rome. *Journal of Geotech. Geoenviron. Eng*., ASCE, **147**(2): 05020015.

Masini, L., Rampello, S., Fantera, L. & Romani, E. 2021b. Mitigation of tunnelling effects via pre-installed barriers: the case of Line C of Rome underground. In *Challenges and Innovations in Geomechanics*, *Proc. 16th Int. Conf. of IACMAG*, Springer Nature Switzerland AG 2021, M. Barla et al. (Eds.): IACMAG 2021, Lecture Notes in Civil Engineering (LNCE), Torino 2021, **126** (2): 197–205.

Masini, L. & Rampello, S. 2021. Predicted and observed behaviour of pre-installed barriers for the mitigation of tunnelling effects. *Tunnelling and Underground Space Technology*, 118: 104200.

Moh, Z.C., Huang, R.N. & Ju, D.H. 1996. Ground movements around tunnels in soft ground. *Proc. Int. Symp. on Geotechnical Aspects of Underground Construction in Soft Ground*, London, 725–730.

O'Reilly, M.P. & New, B.M. 1982. Settlements above tunnels in the United Kingdom – Their magnitudes and prediction. *Proc. Tunnelling '82 Symposium*, London: 173–181.

Ou C.Y. & Hsieh P.G. 2011. A simplified method for predicting ground settlement profiles induced by excavation in soft clay. *Comput. Geotech*. **38** (8): 987–997.

Peck, R. B. 1969. Deep excavation and tunnelling in soft ground. State-of-the-art-report, Mex-ico City, State of the Art Volume, *Proc. 7th Int. Conf. on Soil Mech and Found. Engng* (ICSMFE): 225–290.

Rampello, S., Callisto, L., Viggiani, G.M.B. & Soccodato, F.M. 2012. Evaluating the effects of tunnelling on historical buildings: the example of a new subway in Rome. *Geomechanics and tunnelling* **5** (3): 275–299.

Rampello, S., Fantera, L. & Masini, L. 2019. Efficiency of embedded barriers to mitigate tunnelling effects. *Tunnelling and Underground Space Technology* **89**: 109–124.

Taylor & Francis
Taylor & Francis Group
http://taylorandfrancis.com

SESSION 1: Principles of conservation, maintenance strategies, case histories

Taylor & Francis
Taylor & Francis Group
http://taylorandfrancis.com

Geotechnical Engineering for the Preservation of Monuments and Historic Sites III – Lancellotta, Viggiani, Flora, de Silva & Mele (Eds)

Principles and practices for conservation of historical buildings: the case history of the Saint John Baptistery at Florence, Italy

M. Coli & A.L. Ciuffreda
Dipartimento di Scienze della Terra, UNIFI, Firenze, Italy

S. Caciagli & B. Agostini
Opera del Duomo di Firenze, Firenze, Italy

ABSTRACT: The Saint John Baptistery at Florence, Italy, dates back to the XI century, it was built by and is property of the People of Florence. The Baptistery was built with deep and well-done foundations, a strong structure made up with a very good masonry, constituted by mortared hard stone pieces, and columns in granite; a marble revetment entirely covers its inner and outer faces, and the roof, too. In this first millennium of its life, it has been surviving to earthquakes, floods, wars, weathering, pollution and daily use by millions of people, being always in use. In this paper, we analyse its history through times in order to outline those principle and practices that has been allowing it to survive to Time and Men. A few milestone principles emerged by that: Intrinsic vulnerability, Induced vulnerability, Integrity, Authenticity, Maintenance, lasting of use and functions. We discuss these principles in the paper. The practices that have been permitting its conservation can be mainly ascribed to Opera del Duomo, a private board established in 1296 by the People of Florence with the mission to manage, maintain and conserve the Baptistery. During this millennium, arts and crafts knowledge and operative techniques has been handing down through traditions and a staff of skilled workers and technicians. Advice and support by external experts for specialist analysis and intervention guidelines complete the framework. In the last years, the Opera launched a conservation project based on these points: Anamnesis, Analysis, Diagnosis, Therapy and Maintenance. These actions and the results are here described and reported. The result is that Saint John Baptistery is in a good health and by ensuring monitoring and maintenance a long time ahead can be expected.

1 PRINCIPLES FOR CONSERVATION

The concept of taking care of heritage was already present in the Roman culture two thousand years ago: *Dis immortalibus, qui me non accipere modo haec a maioribus voluerunt, sed etiam posteris prodere* (To the Immortal Gods, who not only wanted me to receive this from my ancestors, but also that I leave it to posterity – M.T. Cicerone (106–43 B.C., Cato Maior – *De Senectute*, VIII/25)

This principle is applicable to cultural heritage buildings, too, because historical buildings are the tangible heredity of our culture, history and roots. To leave them to posterity is now on our charge.

In the XX century, principles of restoration were fixed in subsequent documents called "Restoration Charters" (Table 1); the main principles fixed are that Integrity and Authenticity must be preserved.

In Italy, the D.Lgs. 42/2004, art, 29, and the MIBAC 2011 "Guidelines rules for conservation of cultural heritage and the reduction of seismic risk for cultural heritage buildings" are in force.

DOI 10.1201/9781003308867-18

Table 1. Restoration charters.

Restoration Charters
Athens Charter, 1931
Italian Charter for Restoration, 1932
Venice Charter, 1964
Italian Charter for Restoration, 1972
Amsterdam Charter, 1975
Washington Chart, 1987
Nara Document of Authenticity, 1994
Krakow Charter, 2000
ISO 13822-2010, 2010
ICOMOS Recommendation 2010

According to these principles and rules, conservation of historical buildings, including foundations, has strong constraints when devising remedial measures and intervention techniques (Coli & Iwasaki 2021) because:

– Integrity and Authenticity of the building and its foundation must be preserved.
– Vulnerability must be reduced.

In particular, for Vulnerability is important to distinguish between Intrinsic Vulnerability and Induced Vulnerability.

– Intrinsic Vulnerability does not matter for the built heritage today we observe, because we lost constructions with intrinsic severe defects.
– Induced Vulnerability is linked to the reduction in time of the quality of the construction, due to the natural decay of properties of the materials constituting the masonry apparatus or to induced decay due to violent external inputs like earthquakes, wars, revolutions and spoliation, pollution.

We can work for avoiding/reducing Induced Vulnerability through Conservation by removing any cause of Added Vulnerability in order to elongate the life of the building. The main tools we have for ensuring this goal are:

– Monitoring: which means daily ordinary visual control plus constant instrumental measurements and planned in situ controls.
– Maintenance: which means daily maintenance plus spot extraordinary interventions of restoration works in event of necessity for conserving the Integrity of the building according to the Authenticity principle.

This virtuous chain asks a constant flux of economic resources, in ancient times incomes from temples or religious complexes real estate and properties were used for supporting and maintain them, or they were under the patronage of a public or private institution or of a notable that had taking care for its maintenance (Figure 1).

Figure 1. The conservation chain, with respect for Authenticity and Integrity.

This and the persistence of use for compatible functions has been ensuring the conservation of the building heritage, the lack of this leads to decadence, ruin and the need for extensive and expensive conservation interventions. Conservation asks for a virtuous chain of well-addressed actions.

2 THE SAINT JOHN BAPTISTERY AT FLORENCE (ITALY)

The Saint John Baptistery at Florence (Figure 2) is one of the most outstanding historical monuments in the city, which historical city centre is under the UNESCO patronage since 1982.

Figure 2. The Saint John Baptistery at Florence (Italy) from SE, after the recent cleaning conservation works.

The Baptistery was consecrated in 1059, its maintenance is in charge of the Opera del Duomo (OPA), a private institution established in 1296 by the People of Florence with the mission to take care of the building; all other centuries the OPA has been providing to manage, maintain and conserve the Baptistery.

The Saint John Baptistery was built as a holy place for the Catholic Christian religion to be used for baptisms and religious functions, these use and function have been active since its consecration, and in the last 30 years is has also become a site for touristic visits, numbering about 3,000 people a day before Covid19 pandemic.

Arts and crafts knowledge and operative techniques has been handling down through traditions and a staff of skilled workers and technicians, and documents by the archive of the OPA.

Advice and support by external experts for specialist analysis, in a continuous connection with scientific research and within the framework of the intervention guidelines have been ensuring high quality of the conservation works.

In 2013, OPA launched a series of integrated multidisciplinary researches for updating historical and scientific knowledges, executing well addressed conservation works and creating a digital archive and a georeferenced system for managing the maintenance of the Baptistery. These knowledge upgrading had been developed according to the conservation chain (Figure 1).

3 ANAMNESIS

3.1 *History*

Archives of the OPA and literature (Cardini 1996; Degl'Innocenti 2017; Morolli 1994; Rocchi 1994) date the end of construction of the Saint John Baptistery to the XI century, it was built by the will of the People of Florence, which through the OPA still is its owner.

The Baptistery was erected onto Roman and Early Medieval ruins; in the early XIII century the apse was changed from circular to squared, in the XV century the roof was renewed.

3.2 *Maintaining works*

From the analysis of the documents in the Archive of the OPA several maintaining works result (Table 2), the largest and better documented being that of 1939–1944 (Bianchini 1996; Nenci 2004).

Table 2. Main conservation works documented for the Saint John Baptistery in the OPA archives.

Year	Work
1150	Closing of the dome with the Lanterna and completion of the external cladding
1202–1225	Change of the apse from circular to square
1225–1300	Making of mosaics if the dome and the apse
1293	Cladding with white and green marble of the eight external corner pillars
1334–1472	Roof renovation, placing on an internal wooden chain (white fir and chestnut, dated to 1268), in the lower segment of the dome
1525	Placing on an iron chain, outside at the base of the dome
1778–1792	Substitution of several cladding slabs
1818	Renovation of the external basement of the curtain walls
1939–1944	Substitution of several cladding slabs; due to WWII constraints the original slabs of Hymettus Marble from Greek to be substituted were replace with Lasa Marble from Northern Italy
1993–1996	External cleaning and substitution of a few pieces of Verde Prato, no more available on the market, with Verde Malenco from Northern Italy
2016–2020	External and internal cleaning, implementation of the data into a GIS

3.3 *Survey*

The survey is the base for any analysis and/or intervention on a building, in the Archives of the OPA many surveys are conserved (Table 3).

Table 3. Survey available for the Baptistery.

Direct surveys	Strumental surveys	Photogrammetric surveys	Laser Scan
Sangallo G., 1490	Padelli, 1938–44	Ippolito, 1996 North façade	Tucci, 2014
Buontalenti B., 1577	Aminti, 1989	Ferri, 1998 inner dome	Area 3D, 2020
Nelli G.B. & Sgrilli S., 1733	Giorgi, 1995		
Isabelle C.E., 1843	Caroti & Fangi, 1999		
Seroux d'Agincout J.B., 1826			
Sabatini, 1938–44			
Pietramellara C., 1973			
Dalzocchio M., Pedini L., 1986			
Giovannini P., 1996			

On the base of the recent laser-scan surveys, the Department of Architecture developed a 3D points' cloud model, Department of Civil Engineer a 3D-CAD model and the Department of Earth Science a 3D-HBIM content, all of the Departments from the University of Florence.

3.4 *Structural setting*

From a structural point of view the Baptistery has eight sides, with eight corner pillars connected at the ground floor by an outer curtain wall and an inner colonnade (Giorgi & Matracchi 2917; Giovannini 2006) (Figure 3).

In the first and second floor there are continuous inner and outer walls with a corridor in between, acting as "*matroneo*", with 16 intermediate ribs with transversal connection curtains and windows opened towards the inner hall.

The three doors (North, South, and East) have a plat-band as architrave, the cover presents an inner dome and an outer pyramidal cover.

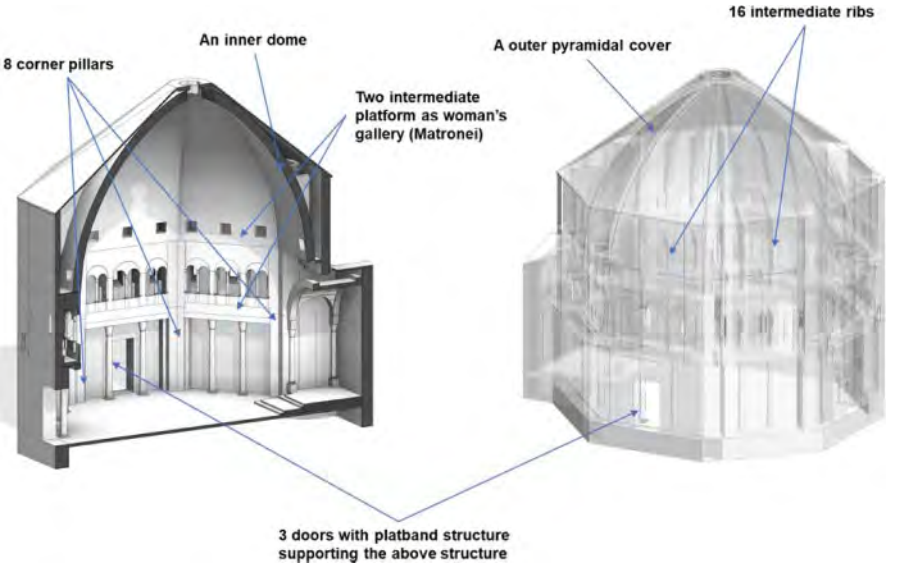

Figure 3. Structural setting of the Baptistery, extracted by the 3D-HBIM content model.

3.5 *Cladding*

Internal and external facades, and the roof too, are totally covered by slabs of marble, corners ribs were cladded in the XIV century (Coli et al. 2021). The inner dome and the apse are covered by a Mosaic of the XIV century (Cresti 2017).

Most of the original slabs, and columns, are thought to be from Roman monuments and edifices, ruined during the Early Medieval time. Columns maybe from the *Capitolium* of *Florentia*, marbles from the spolia of Fiesole, a close Etruscan-Roman town conquered and destroyed by *Florentia* in the XII century (Coli et al. 2021; Garzonio et al. 2017).

4 ANALYSIS

4.1 *Soil and foundation*

Florence is settled in an alluvial plane, which subsoil has been intensely studied in the last twenty years (Briganti et al. 2003; Coli & Rubellini 2013) six drillings are present in the Baptistery area (Figure 4), with technical details available in the public GeoDataBase of the Florence Municipality (http://maps.comune.fi.it/geo/).

These drill-holes reach the bedrock (at about 18 m of depth) and allow defining the subsoil setting, down-hole survey performed in one drill-hole defined the seismic parameters of the site,

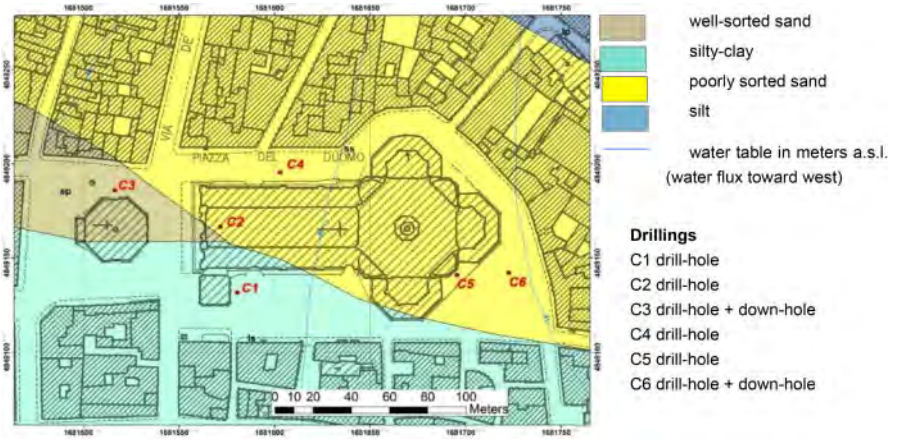

Figure 4. Firenze, Santa Maria del Fiore religious complex: surface lithology according to USCS and location of the drillings made in the area.

the water table is about 6 m below the ground datum, and appears to have been stable during centuries.

Laboratory tests, performed for the definitive design of a tram-way around the Baptistery-Cathedral complex, and available in the public GeoDataBase of the Florence Municipality (http://maps.comune.fi.it/geo/), and Vannucchi et al. (2003) allowed defining soil geotechnical parameters (Table 4).

Table 4. Site geotechnical data for subsoil of the Baptistery.

		unit	Archeo layer	Sandy gravels	Bedrock (shales)
d	depth from the ground datum	m	0.00–3.00	3.00–17.40	>17.40
γ_{nat}	volume weight in natural conditions	kN/m^3	18.50	18.00	26.00
γ_{sat}	volume weight in saturated conditions	kN/m^3	18.63	19.00	27.00
ϕ'	Angle of internal resistance	°	25.9	31.5	17.1
c	Cohesion	kPa	0	0	633.0
s_u	undrained shear strength	kPa	45.6	0	–
Eoed	edometric modulus	MPa	3,150	5,720	6,000
Vs	shear wave velocity	m/s	121	500	800
Vp	compression wave velocity	m/s	600	1,400	2,800

A recent paper by Coli et al. (2022), devoted to the near Giotto's Bell-Tower, envisage the excellent bearing capacity of this type of soil; no settlements or differential settlements are present for Baptistery, Cathedral with the Brunelleschi's Dome and Giotto's Bell-Tower.

Foundation walls are about 3 m thick and are thought to be 6 m deep, rooted into sandy-gravels (GS of the USCS) at top of the water table; as we can see in the crypt they are made by well mortared blocks of hard quartz-calcareous sandstone.

4.2 *Masonry and cladding*

Of course, no any design data is available for the masonry of the Baptistery, its assemblage and setting are to be derived from in situ analysis.

Three different types of approach can be applied for determining the type of material used:

– organoleptic analysis: carried out by experts on the basis of their knowledge and regarding lithology, grain-size, texture and warp,

– technical analysis: petrographic, mineralogical, geochemical and isotopic analysis allowing on the basis of existing date-base to attribute the sample analysed to a lithotype,
– document analysis: carried out on archives and historical texts that report orders, origin and types of the stone materials.

An attribution is reliable if more of these approaches point towards the same attribution.

According to the rules on force (MIBAC 2011 Guidelines), and with the permit by the local Superintendence, a series of NDT had been developed (Table 5).

Table 5. The NDT surveys performed for acquiring knowledge on the Baptistery masonry.

NDT surveys
Direct visual investigations
Georadar survey
Sonic/Ultrasonic survey
Pacometer tests
DAC-Tests
Microcoring
Endoscopy
Lab analysis of small samples
Sclerometer tests on mortar, stones and bricks
Bricks and mortar dating

The results defined that:

– Corner pillars are made by well mortared hard quartz-felspathic sandstone quoins (Pietra Serena).
– Intermediate ribs are in composite structure with at the ground level masonry consisting of an outer wall in mortared hard quartz-calcareous sandstone elemnts (Pietraforte) and an inner gallery with granite columns, at the upper levels masonry is made of mortared hard quartz-calcareous sandstone quoins (Pietraforte).
– Mortar has been dated to XI–XII century and is very well done (Garzonio et al. 2017).
– The inner dome has the lower segment in mortared hard quartz-calcareous sandstone (Pietraforte) thin slabs and the upper one in mortared bricks, which date back to the X–XI century (Garzonio et al. 2017).
– Outer pyramidal cover is in white marble slabs.
– Inner and outer faces are covered by white marble slabs, most of which Greek marble as spolia of roman buildings of Fiesole, others from Carrara, and green-stone-quoins (Verde Prato) (Coli et al. 2021).

4.3 *Mapping*

A systematic organoleptic analysis, made in contradictory by two experts, allowed recognizing for each marble tile of the external cladding (20,112 tiles) the lithology and the historical-commercial name (Coli et al. 2021) (Table 6).

Table 6. Ornamental stone types of the external cladding.

Marble historical name	Tiles	Marble historical name	Tiles
Verde Prato	10,920	Verde Malenco	4
Carrara Marble	6,817	Porfido Verde Antico	2
Hymettus Marble	1,256	Cipollino Rubrio from Eubea	2
Lasa Marble	584	Calcschist	2
Punta Bianca Marble	315	Tassos Marble	1
Pentelicum Marble	147	Breccia Grecia Antica	1
Apuane slate	51	Granito	
Porfido Rosso Antico	9		

From this analysis resulted that only a few slabs had been substituted in the centuries with no original historical materials (Lasa Marble and Verde Malenco).

A few lab analyses (21) confirmed the expert attributions (Garzonio et al. 2017).

Marble types, geometric and decay data had been implemented into informative content models, by a 2D-GIS and a 3D-HBIM (Coli et al. 2019; Iandelli et al. 2021), that allowed the implementation of all the information regarding: Structural setting, Structural attribution, Materials properties, Historical documents, Geological framework, Seismic framework, Analysis results, Images, videos… (Figure 5).

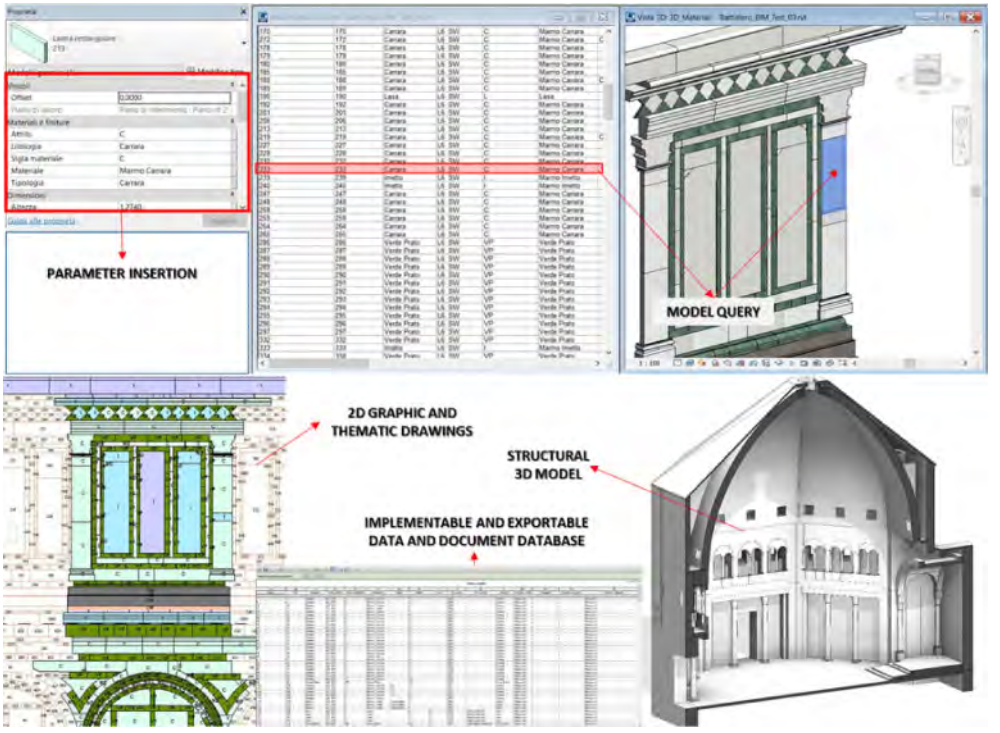

Figure 5. BIM implementation for the Saint John Baptistery.

4.4 *Dynamic survey*

A passive seismic survey campaign had been executed by means of broadband seismometers with μm accuracy, operating in the field of engineering interest (<0.5 s), and positioned at various altitudes and in various positions in the building and operating in synchrony via GPS.

This survey allowed to define, in an elastic regime, the modal shapes of the building and the damping at height with processing in the frequency domain with the EFDD (Enhanced Frequency Domain Decomposition) technique. These data had been used as anchor for the numerical dynamic analysis of its structural behaviour (Lacanna et al. 2016). These analyses (Figure 6) point in favour of a first mode at 2.67 Hz, second mode at 2.88 Hz, third mode at 4.80 Hz, and others mode at 5.88 Hz, 6.34 Hz and 6.93 Hz.

Interferometric radar measures (GbSAR) performed from inside and outside the Baptistery are coherent with this data (Figure 6); numerical dynamic analysis executed by FEM (Bartoli et al. 2017) well fit the above numbers, thus confirming the modes of natural vibration of the Baptistery.

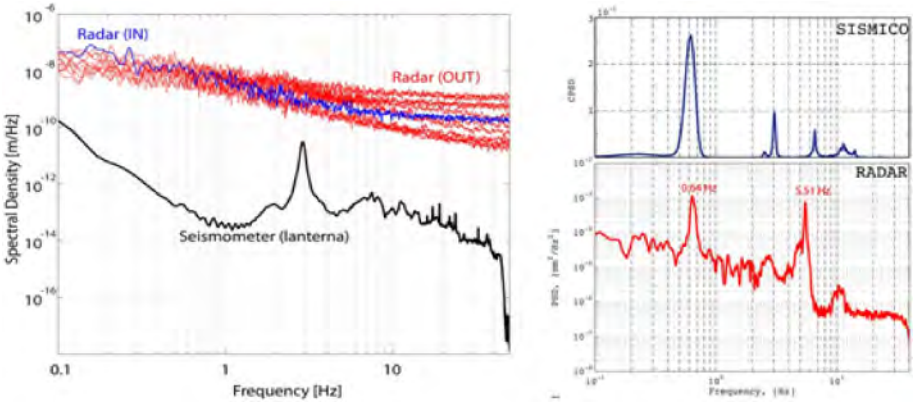

Figure 6. Dynamic measures by seismometers and interferometric radar on the Saint John Baptistery.

4.5 *Structural damages*

– *Intrinsic vulnerability:* The survey pointed out the presence of main fissure cracks (up to 10 cm wide) located above the doors and in the corners, with elongation of the sides, which tend to an outward rotation; the plat-band above the doors has been stretched with rotation of the arch stones (Blasi et al. 2017) (Figure 7).

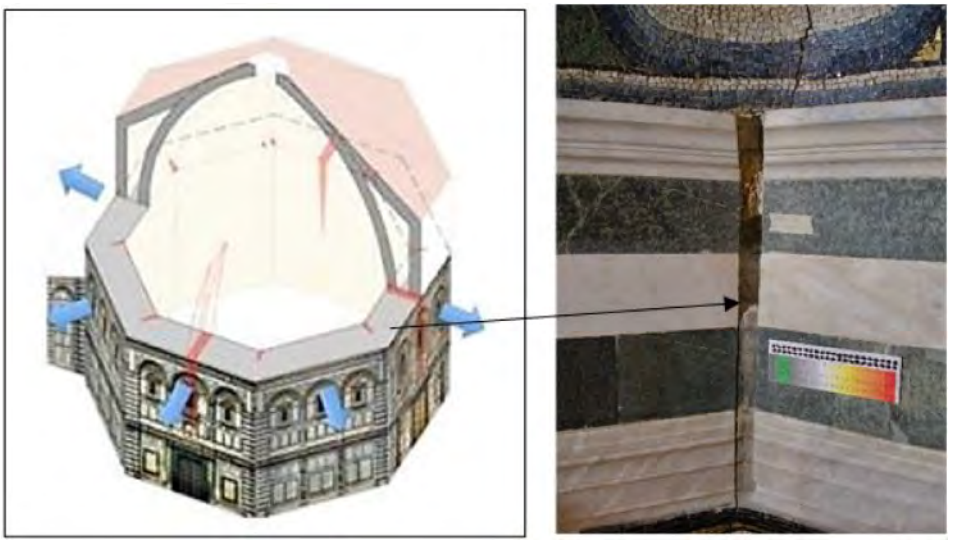

Figure 7. Left: outward thrust force of the dome on the lateral walls; right: angular crack.

– *Induced vulnerability.* Earthquakes, floods and wars have not added structural vulnerability to the Baptistery or induced structural damages, but several degradation processes affect the marble cladding (Garzonio et al. 2017): red stains, biological degradation, black crusts, surficial deposits, abrasions, fouling, integrations, and stains.

5 DIAGNOSIS

5.1 *Intrinsic vulnerability – structural faults*

The thrust of the dome points for the outward opening of the curtain walls. In order to contrast the thrust, a wooden chain was placed during construction at middle height of the dome, and an iron chain (5×5 cm) was put in the year 1514 at the base of the dome; this last slowed the opening rate (Blasi et al. 2017) (Figure 8).

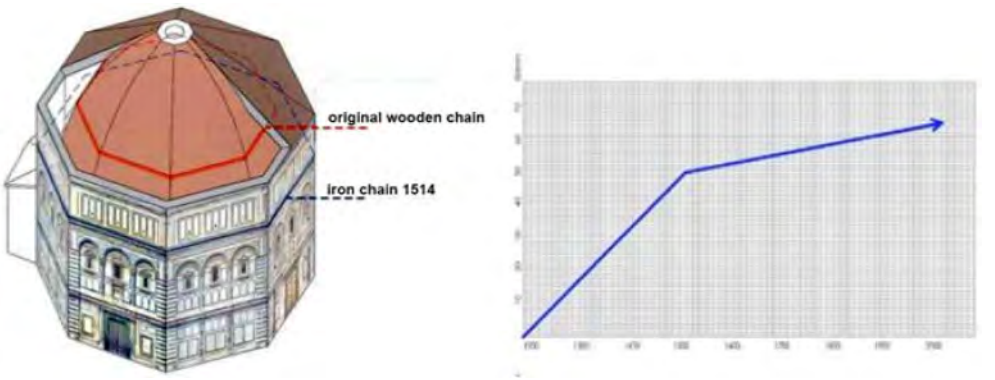

Figure 8. Left: chains position in the structure of the dome; right: outward displacement in the time.

But, in respect to a thrust force of 1,250 kN this chain only acts for 537.50 kN, therefore cracks opening is still active, even if at a slower rate (Blasi et al. 2017).

5.2 *Induced vulnerability – materials decay*

The type of degradation affecting the Marble cladding are mainly ascribing to pollution; the degradation phenomena surveyed (Garzonio et al. 2017) are related to:

- chemical degradation: sulfation
- mechanical degradation: abrasion, disintegration, de-cohesion, exfoliation
- photochemical degradation from smog
- calcium oxalates from alteration of protective agents applied in previous conservation works.

6 THERAPY

6.1 *Intrinsic vulnerability – structural interventions*

The interventions suitable for overcoming the intrinsic structural defects can consists into placing on a further chain by steel bars and/or carbon fibres for a total strength of 1,308 kN and grouting the main fissure cracks by means of two-component epoxy resin o superfluid malt.

That is a very complex subject and is still under discussion, in the event, these interventions need to be approved by the Superintendence.

6.2 *Induced vulnerability – smog reduction*

Recent general interventions on pollution origin (traffic limitation, green energy, green fuel, …) drastically lowered the level of pollution at Florence, it needs to foster this polity, as now expected with the planned green-transition.

Moreover, a systematic planned periodical cleaning of the marble cladding is to schedule.

6.3 *Monitoring*

Monitoring is compulsory for conservation; in the case of the Saint John Baptistery, the surveillance staff secure daily visual monitoring.

Every six months experts operate a direct control of the cladding by means of mobile elevating work platform; on more, instrumental monitoring with extensometers, thermometers, and seismometers are acting h24/7 with real time transmission of the data to a server for archiving.

7 CONCLUSIONS

For a continuous control of the state of health of the Baptistery a monitoring system, based on a network of instruments operating continuously and with real-time web connection, is active, operating with: Extensometers on fissure cracks, Seismometers, Thermometers and Hygrometers

In conclusion, the OPA actions for the conservation of the Saint John Baptistery positively check the main principles for conservation (Table 7).

Table 7. Check for the conformity of the conservation of the Baptistery with the Conservation Principles.

Principles	Checked	Actions
Authenticity	Yes	Only a few slabs substituted with no original historical materials
Integrity	Yes	A few main crack fissures affect the building, with no collapses, or missing of elements or structural substitutions
Monitoring	Yes	A real-time instrumental monitoring is on Twice a year physical direct control of all the slabs with data implementation on GIS

In addition, the OPA does weakly visual inspection and half-yearly direct inspection by means of crane-wagon of the external and internal walls and cladding.

A tailored App, for smartphone, tablet and laptop (Iandelli et al. 2018, 2021) that allows real-time updating of the DataBase, including photo documentation, is in use.

We can conclude stating that the conservation of the Saint John Baptistery at Florence (Italy) is verified.

REFERENCES

Bartoli G., Betti M. & Monchetti S. (2017) *Modellazione numerica ed analisi strutturale del Battistero di San Giovanni a Firenze*. In "Il Battistero di San Giovanni, conoscenza, diagnostica, conservazione", F. Gurrieri Ed., Mandragora, Firenze, 135–157.

Bianchini P. (1996) *I Paramenti esterni. I materiali, i restauri degli anni 1938–1944 e cenni sullo stato di conservazione attuale*. In "Santa Maria del Fiore – Piazza, Battistero, Campanile" Ed. G. Rocchi Coopmans de Yoldi, Università degli Studi di Firenze, Dipartimento di Architettura, Il Torchio, Firenze, 97–98.

Blasi C.,Ottoni F., Coïsson E. & Tedeschi C. (2017) *Battistero di San Giovanni in Firenze. Note su dissesti, lesioni e catene*. In "Il Battistero di San Giovanni, conoscenza, diagnostica, conservazione", F. Gurrieri Ed., Mandragora, Firenze, 119–133.

Briganti R., Ciufegni S., Coli M., Polimeni S. & Pranzini G. (2003) *Underground Florence: Plio-quaternary evolution of the Firenze area.* Boll. Soc. Geol. It.,122, 435–445.

Cardini M. (1996) *L'ipotesi tardo antica del Battistero*. In "Il bel San Giovanni e Santa Maria del Fiore", D. Cardini Ed., Le Lettere, Firenze, 62–93.

Coli M. & Iwasak Y. (2021) Novel Approaches and Technologies for Heritage Buildings Conservation: Editorial. Appl. Sci. 2021, 11, 10597. https://doi.org/10.3390/app112210597

Coli M. & Rubellini P. (2013) *Geological anamnesis of the Florence area, Italy*. Z. Dt. Ges. Geowiss. (German J. Geosci.), Schweizerbart'sche Verlagsbuchhandlung, Stuttgart, Germany, 581–589.

Coli M., Ciuffreda A.L. & Donigaglia T. (2019) *Informative models for the cultural heritage buildings: applications and case histories*. ReUSO Matera, Patrimonio in divenire, A. Conte & A. Guida Eds. Gangemi Ed. Int., 421–432.

Coli M., Ciuffreda A.L., Donigaglia T., Bencaster A., Caciagli S., Agostini B. & Iandelli N. (2021) *Saint John Baptistery at Florence (Italy): studies for conservation of the external marble cladding.* Appl. Sci. 2021, 11, 6329. https://doi.org/10.3390/

Degl'Innocenti P. (2017) *Misurare, disegnare, conoscere: dai rilievi del San Giovanni alle ipotesi styorico-costruttive*. In "Il Battistero di San Giovanni, conoscenza, diagnostica, conservazione", F. Gurrieri Ed., Mandragora, Firenze, 87–103.

Garzonio C.A., Cantisani E., Coli M., Cuzman O., Del Luca D., Lubrito C., Ricci M., Vettori S., & Sibilia E. (2017) *I materiali costitutivi del Battistero*. In "Il Battistero di San Giovanni, conoscenza, diagnostica, conservazione", F. Gurrieri Ed., Mandragora, Firenze, 179–191.

Giorgi L. & Matracchi P. (2017) *Le murature a cassone alla base della Cupola del Battistero e altri aspetti costruttivi.* In "Il Battistero di San Giovanni, conoscenza, diagnostica, conservazione", F. Gurrieri Ed., Mandragora, Firenze, 193–207.

Giovannini P. (1996) *L'apparato murario e il rivestimento interno del piano terra e del matroneo. Materiali, tecniche di lavorazione e caratteristiche di messa in opera*. In "Santa Maria del Fiore – Piazza, Battistero, Campanile" Ed. G. Rocchi Coopmans de Yoldi, Università degli Studi di Firenze, Dipartimento di Architettura, Il Torchio, Firenze 72–96.

Iandelli N., Agostini B. & Coli M. (2018) *Strumenti GIS come aiuto nella gestione, monitoraggio e conservazione dei beni culturali*. Conferenza ESRI Italia 2018, Roma https://www.youtube.com/watch?v=SFZpwJZqZ84&list=PL8TX2bZOHutH-uGDZNa_4cobxpbYGhg6R&index=23&t=0s

Iandelli N., Coli M., Donigaglia T. & Ciuffreda A.L. (2021) *An Unconventional Field Mapping Application: A Complete Opensource Workflow Solution Applied to Lithological Mapping of the Coatings of Cultural Heritage*. ISPRS Int. J., Geo-Inf. 2021, 10, 357. https://doi.org/10.3390/ijgi10060357

Lacanna G., Ripepe M., Marchetti E., Coli M. & Garzonio C.A. (2016) *Dynamic response characterization of the Baptistery of San Giovanni in Firenze, Italy, based on ambient vibration test*. J. Cultural Heritage, 20, 632–640.

Morolli G. (1994) *L'architettura del Battistero e "l'ordine antico*. In "Il Battistero di San Giovanni", Mirabilia Italie, A. Paolucci Ed, Franco Cosimo Panini, Modena, 33–132.

Nenci C. (2004) *I documenti dell'Archivio dell'Opera del Duomo relativi ai restauri eseguiti negli anni 1939–1944*. In "Santa Maria del Fiore – Piazza, Battistero, Campanile" Ed. G. Rocchi Coopmans de Yoldi, Università degli Studi di Firenze, Dipartimento di Architettura, Il Torchio, Firenze, 179–186.

Rocchi G. Coopmans de Yoldi (1996) *Il Battistero di San Giovanni: Lo svolgimento della fabbrica*. In "Santa Maria del Fiore – Piazza, Battistero, Campanile" Ed. G. Rocchi Coopmans de Yoldi, Università degli Studi di Firenze, Dipartimento di Architettura, Il Torchio, Firenze 27–72.

Vannucchi G., Severi M. & Narcisi D. (2003) *Sistema di micrometropolitana per Firenze studio di fattibilità 2ª fase.* Università degli Studi di Firenze, Firenze.

Geotechnical Engineering for the Preservation of Monuments and Historic Sites III – Lancellotta, Viggiani, Flora, de Silva & Mele (Eds)

The authenticity and the integrity of the soil and the foundation of heritage structure in Angkor

Y. Iwasaki
Geo Research Institute, Osaka, Japan

M. Fukuda
Taisei Geotech, Kurume, Japan

M. Ishizuka and R. McCarthy
JASA Office, Siem Reap, Cambodia

Y. Akazawa
Japan Cultural Heritage Consultancy, Tokyo, Japan

T. Nakagawa
Waseda University, Tokyo, Japan

V. Ly
Cambodia National Committee for World Heritage, Phnom Penh, Cambodia

ABSTRACT: Soils and foundation of Bayon temple of Angkor Thom has been studied since 1994 by Japanese Government Team for Safeguarding Angk Japanor (JSA). The character defining elements of the authenticity are identified as 1. trenched foundation system for the temple zone, 2. uniform grain size distribution of silty sand of the manmade fill, 3. simple shallow direct foundation of the main tower of 32 m in height standing upon thick silty sand compacted fill. The compacted filled platform is very hard with SPT N-value of 100–200 in dry condition but collapses in water. Amazing fact is the central tower has been standing without failure for more than 800 years since it had been constructed in late 12th century or early 13th century.

1 AUTHENTICITY OF CULTURAL HERITAGE

1.1 *Authenticity*

Authenticity was defined in the Venice Charter of 1964 as heritage composed from original material, original position, original design as well as original procedure (Venice Charter, 1964). The concept behind the Venice Chapter is called "anastylosis (Greek)," which means "take column back to original position." Anastylosis implies that original stone columns spread over a historical ruin shall be rebuilt at their original positions.

The principle of anastylosis was developed based on conservation of stone structure in Europe and does not give any values of heritage to such repaired materials as often seen in wooden structures in Japan. Later in 1994, the concept of the authenticity was expanded by the Nara Document on Authenticity to cover various methods characterized by the region to which the heritage belongs. Region specific methods that were developed in some areas are also accepted as the characteristic of authenticity (Nara Doc 1994).

DOI 10.1201/9781003308867-19

Character-defining elements are defined as historic materials, forms, locations, spatial configurations, morphology, concept and details, structural design, uses, and cultural associations that contribute to the heritage value of a structure that shall be retained to preserve its heritage value.

1.2 *Authenticity of Soil and Foundation*

In 2005, ISO 13822 (Bases for design of structures – Assessment of existing structures) was reviewed for renewal. ISCARSAH (International Scientific Committee on the Analysis and Restoration of Structures of Architectural Heritage under ICOMOS) had proposed to include heritage structures in the standard and worked together for five years to develop such a standard. The ISO 13822 has been updated in 2010 and added an Annex-I (informative) Heritage Structure, which has expanded the heritage structure to include foundation as a part of the structures. (ISO, 2010) The Annex I clearly state as in paragraph of I.5.3 Authenticity of foundation as follows.

I.*5.3 Authenticity of Foundation* *From the point of view of conservation, foundations are not different from the rest of the structure and should be assessed and rehabilitated taking into consideration their heritage value. This involves the requirement to identify their authenticity and character-defining elements.*

2 BAYON TEMPLE IN ANGKOR THOM

2.1 *Trenched foundation*

Bayon, as shown in Figure 1, is the central temple of Angkor Thom constructed around in late 12th to early 13th century. Figure 2 shows section and plan view of the Bayon temple. UNESCO had

Figure 1. Bayon Temple (from south-eastern side).

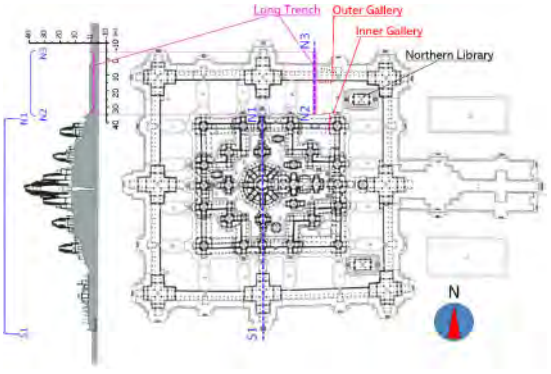

Figure 2. Plan and section.

an international meeting in Tokyo as to how to save Angkor after the civil war (UNESCO, 993). Japanese Government for Safeguarding Angkor Team (JSA) performed an archaeological trench at the north-eastern corner as a “Long trench” as shown in Figure 2.

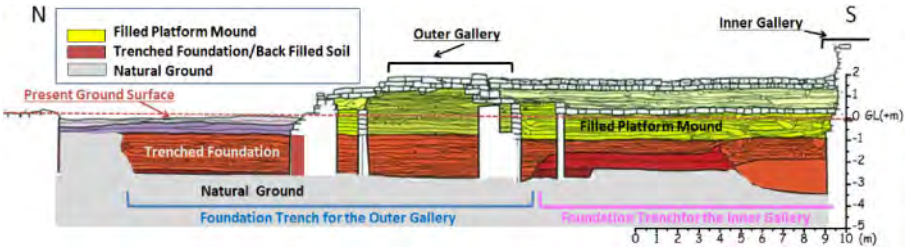

Figure 3. Long trench for archaeological study.

The result of the long rench has revealed the following facts as shown in Figure 3. (Narita 2000)

1. The surface of the first terrace was covered with sandstone and laterite block, beneath which a densely compacted sandy filled layer was identified.
2. Compacted sandy filled layer continued with an additional laterite block layer to the level of the original ground surface.
3. It was identified that the compacted sandy filled layer continues from the original ground level to 2–3 meters in thickness.
4. The compacted sandy filled layer below the original surface was found to continue horizontally to about 10 m outside of the outer gallery plinth.

Based upon the trenched foundation of compacted sandy fill, a platform mound of sand fill with three stepped terrace was constructed. Central tower of about 42 m in height from the ground has been standing over 800 years.

In 1933, French EFEO excavated a vertical shaft at the center of the main tower and found a Buddha statue fragments that were later reconstructed. Laterite block was detected by several borings beneath the pave stone down to the top of the 2nd terrace. The block is 6 m in thickness and seems surrounding the main tower as shown in Figure 4.

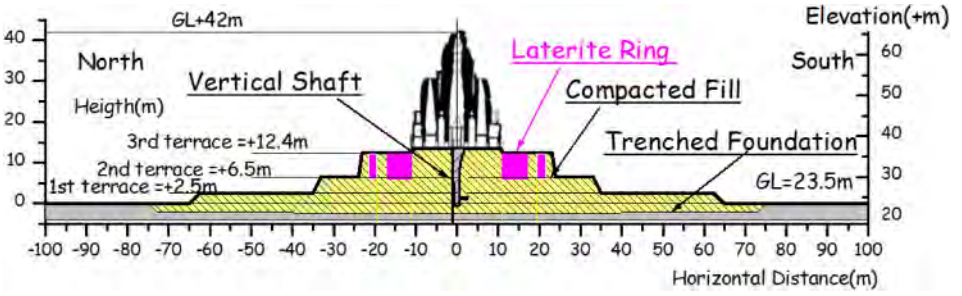

Figure 4. Trenched foundation with filled high mound of Bayon, N-S Section.

2.2 *Direct Shallow foundation*

A base stone is placed beneath the bottom of the central tower as shown in Figure 5. JSA conducted archaeological trench excavation along the inside of the base stone and geotechnical hand auger sounding beneath the stone to determine if any special base structure was installed to support the heavy central tower.

Horizontal hand auger tests were carried out at 5 points as shown in Figure 6 and has resulted in finding no supporting stones, but only very dense sandy fills beneath the base stone support.

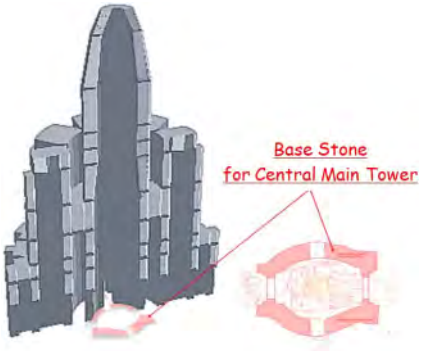

Figure 5. Base stone for central tower Bayon.

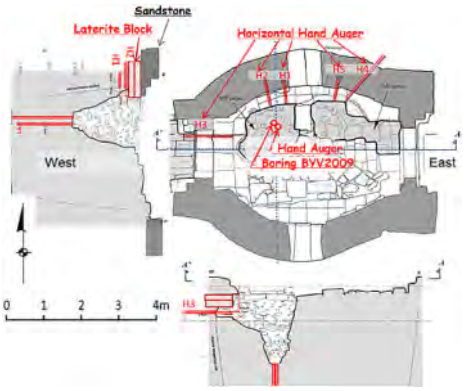

Figure 6. Hand auger sounding beneath the base stone.

2.3 *Foundation mound with vertical shaft at the center*

EFEO, a France sponsored organization, in 1933 dug out the center of the base of the main central tower below the pavement and found a Buddha statue as previously stated. It was recorded that the vertical shaft had been backfilled. Geotechnical boring was performed at the backfilled vertical shaft and at the original manmade filled mound as shown in Figure 7.

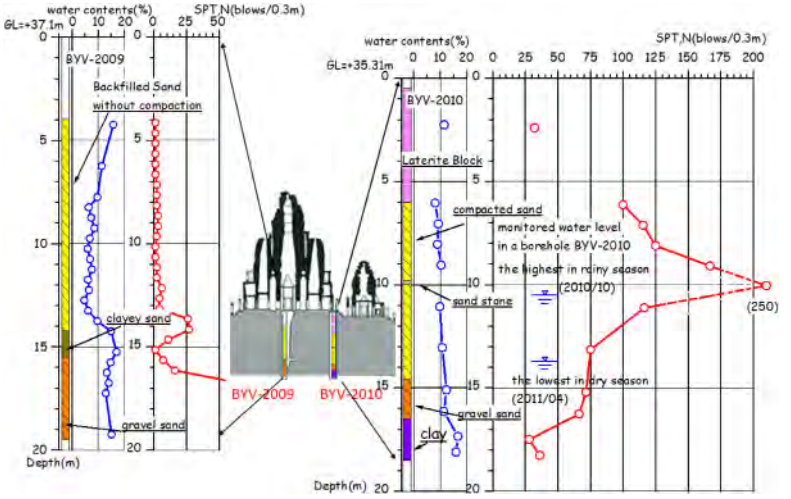

Figure 7. Boring BYV2009 at the backfilled shaft and Boring BYV2010 at the original mound.

The back filled soil for BY09 was found in a very loose state of SPT, N-values $N < 4$ of BYV2009 in Figure 7. Another boring of BYV2010 at the top terrace shows the sandy fill lower than GL-6 m of $N = 100–150$, which is a very large value compared to the expected values of 20–40 for common filled sandy soil.

The grainsize distributions of the sampled soil by the boring of BYV2010 and BYH2010-30 as well as other sites are shown in red and blue color for sand and clay soils respectively in Figure 8. The sandy soil is filled soil and the entire samples of the filled soil show the same distribution, which implies very uniform fill material.

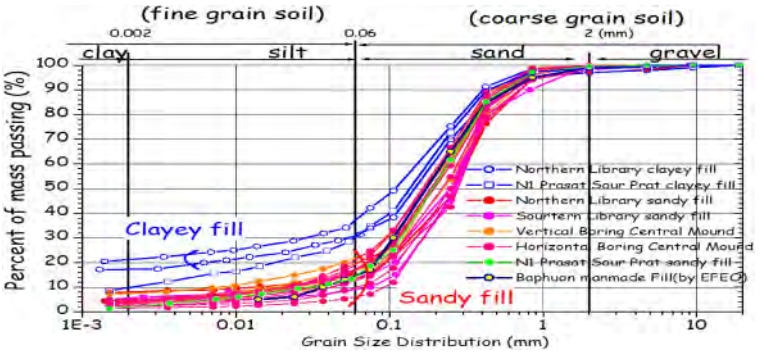

Figure 8. Grain size distribution of BYV2010 and BYH2010-30.

2.4 *Characteristics of strength of silty sand of the foundation mound*

The obtained SPT, N-values in Figure 7 are plotted against water contents of the sampled soils for both borings and shown in Figure 9. No relationship is found for BYV2009 of the backfilled soil. However, the decrease of water is found to result in the increase of the strength for boring BYV2010. Compared to the common SPT, N-value of 40–50 for dense sand, the obtained STP N-value of 100–200 is very large. The mechanism of increased N-value might be caused by not only density but also some additional mechanism.

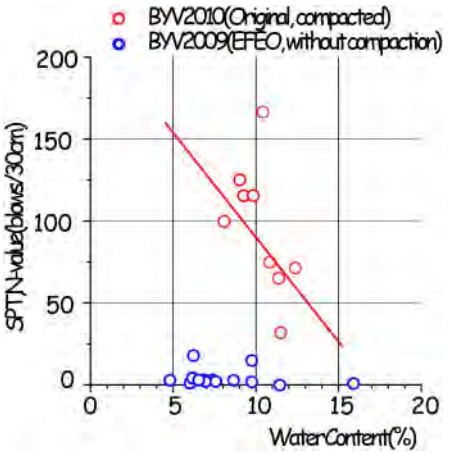

Figure 9. Relationship between SPT, N-values for B09(BY2009) and B10(BY2010).

Figure 11 shows the response of the dense sandy fill when it was submerged in water.

Sampled soil looks like soft sandstone, however, it collapsed when immersed in water within 10 minutes as shown in Figure 10.

Water is being sucked up at 3 second and the water has permeated the top of the sample at 2 minutes followed by the initiation of the collapse at 3 minutes with completely collapse in 10 minutes.

X-ray diffraction analysis was applied to the fine particle of the filled sand shown in Figure 11. In addition to quartz sand, halloysite (kaolinite group) was detected as the clay component.

Micrograph of the section of the sample is shown in Figure 12, where the round shape of quartz is seen filled with clay material.

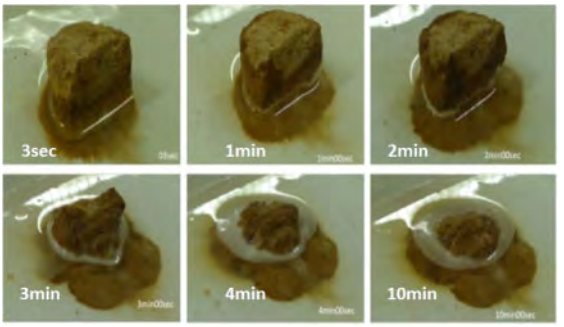

Figure 10. Collapse of stiff sand under water within 10 minutes.

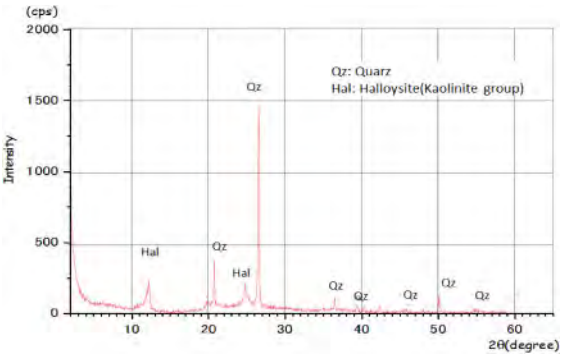

Figure 11. X-ray diffraction for fine particle of the filled soil.

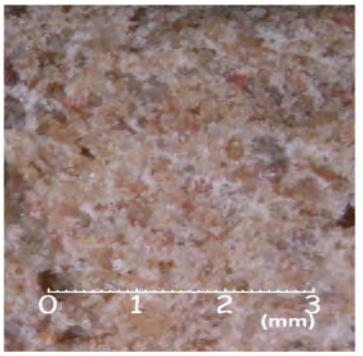

Figure 12. Micrograph of clayey sand of the filled soil.

2.5 *Laboratory test of the relationship between strength and water contents*

A series of laboratory tests were performed to see how much strength changes due to the decrease of the moisture contents. More than 25 samples in containers were prepared with water content of 15%, which almost creates a 100% saturated condition. The samples were placed outdoor, and the water naturally evaporates from the sample and the water content decreases day by day. A Yamanaka cone penetration test mechanism tested these samples as shown in Figure 13, The test results in Figure 14 shows clearly an increase of strength more than 50 times due to the decrease of the water contents.

Figure 13. Yamanaka cone test.

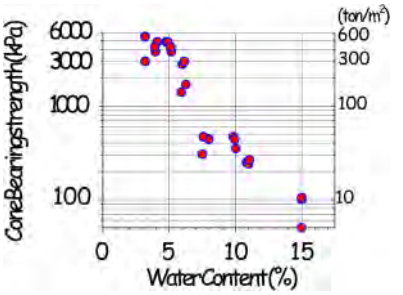

Figure 14. Cone bearing strength and water contents.

2.6 *Characteristic defining elements of the authenticity for foundation*

Character defining elements of the authenticity for the foundation that have been discussed in the Angkor heritage structure for Bayon are as follows,

1. Trenched foundation extended outside the temple domain.
2. Platform foundation consists of densely compacted fill of uniform grain size distribution of silty sand.
3. Thick laterite ring block under the outside of the main tower.
4. Direct foundation upon densely compacted layered fill.
5. The compacted filled soil is very strong in a dry condition but weakened in wet condition.

Angkor belongs to a subtropical zone in southeast Asia with the rainy season from May to October and dry season from November to April. Under heavy rain, some of the soil filled Angkor monuments had suffered from foundation failures as follows,

1. Baphuon temple failed in 1943
2. Retaining wall of west causeway of Angkor Wat collapsed in 1952

3 RESTORATION OF FILLED MOUND AND MASONRY STRUCTURES IN ANGKOR

Restoration of any cultural heritage is required to be followed by the following three basic principles.

1. Minimum intervention
2. Incremental approach
3. Removable measures

The first principle requires identification of the characteristic of authenticity for the original material and special mechanical, chemical other characteristics and to keep the original authenticity as close as possible. The following section discusses the restoration of filled mound and masonry structures that have been taken in the past in relation to authenticity.

3.1 *Baphuon temple*

The Baphuon temple as shown in Figure 15 was built in mid11th century in Angkor Thom and dedicated to the Hindu God Shiva. In the late 15th century, the temple was converted to a Buddhist temple.

Figure 15. Baphuon temple (from Eastern side).

In 1943, the northeastern side of the slope of the Baphuon temple failed as a result to excessive water penetration due to rainfall. The vertical section of the temple in Figure 16 shows a very steep retaining structure.

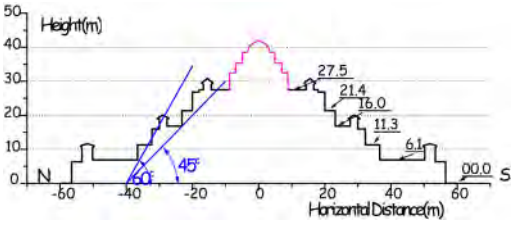

Figure 16. Vertical section of Baphuon temple.

The slope angle is around 45 degrees, and the large high sandy compacted fill was inevitably unstable. The grain size distribution of the fill of the Baphuon is shown in Figure 8 in black color and implies the same large strength character in a dry condition as the platform fill of the Bayon temple.

Fig.17 shows the original structure of the stone masonry retaining wall. Thin layers of crushed laterite chips of 1–2 cm in thickness were embedded in compacted sandy layers for possibly drainage of infiltrated water, they extend some 4 to 5 m behind the masonry stone wall.

French EFEO had started the restoration work in 1958 and tried to reconstruct the original structure but failed when the fill mound reached at 5 m in height. They tried three times to replicate the original structure, but in vain.

The reinforced concrete retaining wall was introduced as an alternative shown in Figure 18 (Launay 1994). The original stones were reused to cover the front face of the retaining concrete. The restoration work was interrupted by the start of civil war in 1970. A second project to restore the temple was launched in 1996 by EFEO and completed in April 2011 after 51 years of work (Royere 2016).

3.2 *West causeway of Angkor Wat*

West causeway of Angkor Wat is the gateway that overpasses the wide moat of 190 m in width as shown in Figure 19. The causeway consists of earthen embankment with a masonry retaining system. The original structure of laterite masonry retaining wall is shown in Figure 20(a). After the

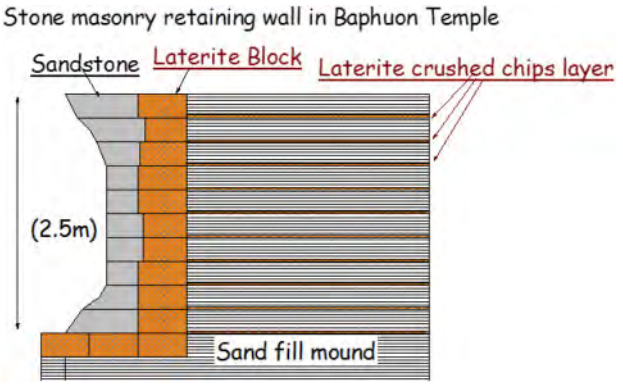

Figure 17. Original masonry retaining wall.

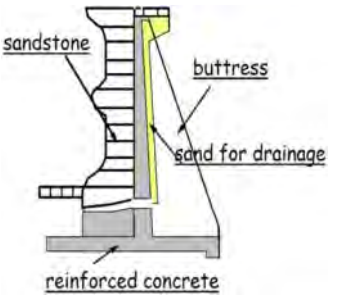

Figure 18. Reinforced concrete.

Figure 19. Retaining wall structure of the west causeway of Angkor Wat (south side).

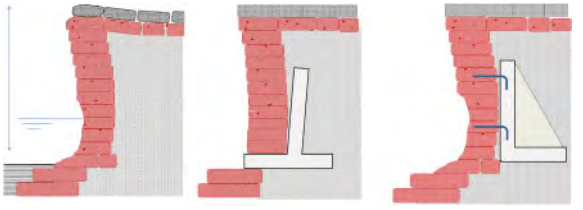

Figure 20. (a) Original structure, (b) RC-retaining wall (EFEO) and (c) RC-retaining wall (Sophia Univ.).

failure of the causeway in 1952 due to the infiltration of water due to heavy rain, EFEO performed restoration work for the southern side of the retaining structure using reinforced concrete as shown in Figure 20(b).

Based upon the excavation study by Sophia University (Katagiri 1999), the restoration work by EFEO was reported as in Figure 20(b) for the southern side of the west causeway.

At present in 2018, the second phase of the restoration work for the northern side of the west causeway of Angkor Wat has been initiated by Sophia University as shown in Figure 20(c).

The restoration of Figure 20(c) is a modified version based upon a concrete retaining structure. The backfilled soil behind the masonry wall is excavated first and the reinforced concrete retaining wall is placed behind the existing laterite block retaining wall. The existing weathered and decayed laterite blocks are to be cramped to the RC wall and maintained as it is.

3.3 *Prasat Suor Prat*

Prasat Suor Prat consists of 12 towers and located on the east side of the Royal Plaza, Angkor Thom. The towers are constructed almost exclusively of laterite with sand-stone accessories and door/window jambs.

Figure 21 shows one of 12 towers and stands near the north pond and designated as N1 tower.

Figure 21. Prasat Suor Prast N1 tower (west side).

N1-tower has inclined 4–5 degrees northward from the vertical and represent the largest inclination in all towers of Prasat Suor Prat.

N1 tower was found not only inclined but also the foundation was spreading outwards in four directions.

It was difficult to identify the reason why the tower was inclined and spread out. Therefore, it was decided to dismantle the upper structure as well as foundation to excavate archaeological trench. The base of the tower is 10 m by 10 m on a filled mound with laterite masonry retaining structure.

Archaeological trench study has revealed the compacted filled of the base mound.

Figure 22 shows N-S section of foundation of the N1 tower. The surrounding retaining wall was inclined to the north by 0.4 m settlement for 10 m width. Unexpectedly, the compacted fill was found not inclined but horizontal as the original state. The weight of the tower was supported by base rock which was further transferred to the retaining masonry laterite block.

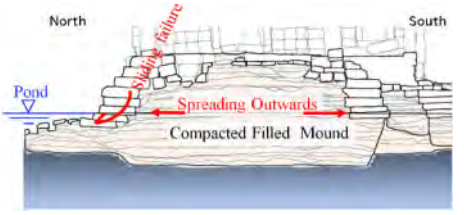

Figure 22. Trenched section of N1 tower.

The basement of the retaining structure at the north side was found to have settled and slid outwards as shown in Figure 22.

The vertical weight had caused compression of the fill as well as spreading outwards.

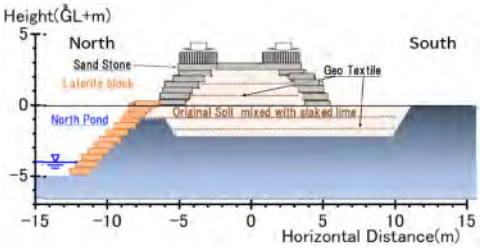

Figure 23. Restoration of foundation of N1 tower.

JSA had introduced a traditional technology of slake lime mixed with the original sand, which improves the strength characteristics with geo-textile to increase the tension strength of the fill. Adding about 10% of the slaked lime to the original soil resulted in increasing strength with durability against water submersion.

The soil improvement of the slake lime mixed with the original soil provides the basic original design style of masonry retaining wall as well as using the original soil, which keeps the authenticity of the original design and increases the safety of the heritage structure.

If ion or steel was used as the reinforcing element in the RC retaining wall, it would be deteriorated within half a century and cause damage to the heritage structure.

3.4 *Integrity of the restored foundation in Angkor*

The general basic meaning of the word 'integrity' refers to material wholeness, completeness, and unimpaired condition. Integrity of heritage structure is the completeness of the original characteristics of the heritage.

3.4.1 *Material of filled soil*

In the past, the special characteristics of the basic material of filled soil which composes the foundation mound has not been recognized and never discussed by conservators in Angkor until 2010 when the boring study had initiated the geotechnical study and revealed the uniqueness of the filled platform mound. "A Charter for Angkor" published in 2014 (APSARA 2014) as guidelines for safeguarding the heritage site of Angkor did not yet include the authenticity of the filled material. Most of the heritage sites in Angkor have not recognize the defining character and sometimes reused the original soil at the site. JSA had introduced a traditional method of slake lime mixing with the original sand to increase durability and strength and applied the methodology at the Northern Library, Bayon in 2000, at the restoration of N1 tower, Prasat Suor Prat in 2005 (JSA 2005), and at the Southern Library, Bayon in 2010 (JASA 2010). Table 1 shows a summary of the state of integrity of the filled mound with countermeasures performed in the past.

Table 1. State of integrity of filled mound of several sites in Angkor.

Site	Originalmaterial/method	Restoration material/method	Integrity
Baphuon temple	sandy soil/compacted	original soil/compaction	preserved
West causeway Angkor Wat	sandy soil/compacted	original soil/compaction	preserved
Northern Library Bayon	sandy soil/compacted	original soil with slake lime/compacted	modified
Southern Library Bayon	sandy soil/compacted	original soil with slake lime/compacted	modified
N1, Prasat Suor Prat	sandy soil/compacted	original soil with slake lime/compacted	modified

3.4.2 *Retaining wall structure*

Original retaining wall for the foundation mound as well as the filled mound of the causeway is masonry stone (sandstone) or laterite block retaining wall. EFEO changed the original design to RC retaining wall, which resulted the change of material as well as structural design. EFEO

constructed the concrete structure and put the original stones in front of the concrete to create a façade of originality. It is a fake structure.

JSA had introduced the slake lime mixed with the original sand as backfill of the masonry retaining wall and for the restoration work of Northern and Southern Libraries of Bayon temple. Table 2 shows a summary of the state of integrity of the retaining wall structure in Angkor.

Table 2. State of integrity of masonry retaining wall structure of several sites in Angkor.

Site	Original design/material	Restoration design/material	Integrity
Baphuon temple	masonry/stone	RC wall/concrete	lost
West causeway Angkor Wat	masonry/laterite	RC wall/concrete	lost
Northern Library Bayon temple	masonry/stone	masonry/stone	preserved
Southern Library Bayon temple	masonry/stone	masonry/stone	preserved
N1 Tower, Prasat Suor Prat	masonry/stone, laterite	masonry/stone, laterite	preserved

4 CONCLUSIONS

Authenticity of soils and foundations of heritage structures have been neglected in the past. But the foundation is now generally recognized as one of the important elements to support the upper structure. In conservation work, the foundation of heritage structure has been easily changed and modified without discussion or concern for authenticity.

In 2010, ISO13852 (ISO 2010) added Annex-I "Heritage Structure", introducing the authenticity of foundation. Geotechnical engineers who work on the conservation of heritage structures must discuss the possibility of any special characters of soils and foundation and try to define the character defining element of authenticity of the foundations to be conserved.

REFERENCES

APSARA, 2014 A Angkor Charter, 2014, http://apsaraauthority.gov.kh/?page=detail&menu1=647&ctype≒document&id=647&ref_id=6&lg=e

EFEO, 1990. Conservation of Angkor 1907–1972, International Round Table on the Preservation of the Angkor Monuments, Bangkok, UNESCO/CC-90/Conf.801/6, 1990.

ISO, 2010, ISO_STANDARD 13822-2010, 2010. Bases for design of structures – Assessment of existing structures, Annex I Heritage Structures.

Iwasaki, Y. and Fukuda, M., 2018. Preservation of the main tower of Bayon temple, Angkor, Cambodia, Geotechnics and heritage – Historic Towers, CRC Press, Balkema 2018, pp. 191–227.

Iwasaki. Y., 2000, 3.5.4 Structural stability of the Northern Library and monitored behavior, Report on the Conservation and Restoration Work of the Northern Library of Bayon, Angkor Thom, kingdom of Cambodia, pp 95–100.

Katagiri. M. 1999, A consideration on the process of restoration work of the west causeway of Angkor Wat, Renaissance Culturelle du Cambodge (16), Sophia Asia Center for Research and Human Development, Tokyo, pp 17–30 (in Japanese).

Launay, J. 1994. A Geotechnical and Structural Engineering Approach, Proc. of XIII International Conference of Soil Mechanics and Foundation Engineering, New Delhi, India, 1994 (in French) pp. 191–194.

Nara Doc, 1994: www.icomos.org/charters/nara-e.pdf

JASA, Japan APSARA Safeguarding Angkor, 2011, "Chapter 3 Report on the Restoration Work of the Southern Library of Bayon", Report on the Conservation Research of the Bayon, pp. 35–193.

JSA, 2005. Report on the Conservation and Restoration Work of the Prasat Suor Prat Tower, pp. 249–324.

Narita. T., Nishimoto. S, Shimizu, M., Akazawa Y. 2000. Outline of excavations and investigation at the outer gallery of Bayon complex, Annual technical report 2000, JASA, Tokyo, pp 3–22.

UNESCO,1993. Safeguarding and Development of Angkor, prepared for The Intergovernmental Conference on the Safeguarding and Development of the Historical Area of Angkor, Tokyo, 12–13 October 1993.

Royere, P. 2016. Le Baphuon, EFEO, 2016 (in French).

Venice Charter, 1964, www.icomos.org/charters/venice_e.pdf

Geotechnical Engineering for the Preservation of Monuments and Historic Sites III – Lancellotta, Viggiani, Flora, de Silva & Mele (Eds)

Digital transformation in the visual inspection of heritage railways tunnels: Technology, artificial intelligence and methodology

F. Foria
ETS Srl, Geology and Hydraulics Department

G. Miceli
ETS Srl

M. Calicchio
ETS Srl, Geology and Hydraulics Department

G.M. Catigbac & G. Loprencipe
Sapienza, University of Rome, Department of Civil, Building and Environmental

ABSTRACT: The knowledge, the preservation and the maintenance of heritage infrastructures is one of the most challenging matters facing modern civilization. It involves, in inextricable patterns, factors belonging to different fields (cultural, humanistic, social, technical, economical, administrative) coupled with the requirements of safety that can be in conflict with the integrity of part of the infrastructure.

For these reasons, it is fundamental to carry out investigations and new planning strategies to know and predict the conditions of very old structures. The paper focused on heritage railway tunnels, one of the most crucial elements of the railway infrastructures in Europe.

ETS Srl introduced a new method for diagnostic of existing tunnels through multi-dimensional mobile mapping systems, and a new approach for the Management and Identification of the Risk for Existing Tunnels. The approach belongs to the digital strategies for infrastructure maintenance that are very fast and minimally invasive. The integrated instrumentation allows to have almost all the information necessary for the diagnostics of a structure with non-destructive tests, preserving the integrity of very old structures in a phase of preliminary assessment. In such a way, the process of visual inspection is automatized and back-officed. The results, in terms of defects on the structures, are digitalized and manipulated in different IT environments. The results can be incorporated in the information modelling and virtual reality inspections. The use of artificial intelligence will be necessary to speed-up the back-office phase and introduce the technologies as a new inspection standard.

A case study for the application is presented through the methodologies, including some preliminary applications of AI algorithms for the detection of water defects.

1 INTRODUCTION

Europe, the cradle of railway development, has seen its infrastructures develop particularly from the second half of the 19th century until the beginning of the 20th century. Thus, the works of art of rail networks see their average age approaching a century touching two centuries over the first lines built. Railway Infrastructure Managers therefore now have an aging park of tunnels to be maintained (Mili et al. 2021). Subject to degradation through time and the permanent interactions with the environment, the tunnel structures can face substantial maintenance and repair, the purpose of which is to mitigate the risk of incidents or even to extend its life-span (Foria et al. 2022).

DOI 10.1201/9781003308867-20

Figure 1. Number of railways tunnels managed by the main European Railway Infrastructure Managers (on the left) and average age of the same tunnels (on the right).

In Italy RFI (Rete Ferroviaria Italiana) manages 1.671 km of railway lines with an average age of 70 years and the oldest Italian tunnel is 150 years old, as shown in Figure 1.

2 VISUAL INSPECTION AND MANAGEMENT OF HERITAGE TUNNELS

2.1 *State of the art*

The planning and the management of existing tunnels and, in particular, of heritage tunnels is a central challenge for industrialized countries. The main challenge is the coexistence and collaboration of environmental sustainability and exponential technology growth. However, careful, and effective management of tunnels that involves all the stakeholders and all the activities, such as inspection, planning, design, construction, and maintenance, is not yet usual.

ETS Srl carries out the diagnostic and the maintenance of existing tunnels through multi-dimensional survey system and digital methodologies for the analysis, the integration and the management of the priorities along the tunnel.

Nowadays, the inspection of tunnels is still performed mainly by operators on the line during a partial disruption of the line (mainly during the night) or total disruption. The operator fills technical sheets following the owner's standards, national code, and practice. Generally, these forms contain general information about the tunnel (e.g., name, line, length, excavation type, lining material) and the outcome of the inspection in terms of defects detection of the tunnel structures and collateral elements. A set of photos is taken to be attached to the report showing the main compliance (Foria et al. 2021).

Even if this methodology might seem outdated with technologies available nowadays, it's still the state of the art considering that a large set of infrastructures worldwide are not checked at all.

More recent technologies allow the survey and inspection of tunnels and infrastructures with mobile mapping. Mobile mapping has the advantage of speed, efficiency, and safety reducing the time of work on the line, but brings the drawbacks of calibration, signal loss, and management of the data. However, these issues can be overcome offering multi-dimensional mobile mapping systems with different equipment in order to have a set of integrated outputs.

The current challenge in the innovation of heritage tunnel diagnostics is to enhance the quality of acquired images, developing massive data collection and processing capabilities, and analyzing the data with high-level technical experience and engineering judgment. Therefore, the automatic elaboration of big datasets is mandatory. The traditional computer vision solutions, widely developed in the industry, are not suitable to process big amounts of data in semi-supervised or weakly supervised ways. On the other hand, the supervision provided by human operators is highly dependent on the operator's skill and experience. Moreover, the operator's experience is so interdisciplinary and complex that it is unlikely to be well described by a traditional computer vision model. Besides, the learning process is an ongoing knowledge process, its transfer and reinforcement dynamics being hardly embeddable in traditional models. In contrast, the progression in machines' computational power allows solutions devised within the artificial intelligence (AI) framework to capitalize on

the full precious operators' experience, efficiently applying the knowledge learnt to the collected data. Such an approach can provide a baseline for the training of new operators, thus helping in the operators' generational change.

2.2 *Methodology and technologies for the digital management*

ETS Srl has started investing in a new approach for the manipulation of the survey-inspection data to get a more objective and dynamic diagnostic, maintenance, and risk assessment to manage existing tunnels. The procedure's final aim is the Management and Identification of the Risk for Existing Tunnels (Foria et al. 2021).

The complete procedure can be defined through the following milestones (Figure 2):

- *Survey & Inspection (S&I)* with multi-dimensional mobile mapping systems to have internal geometry (laser scanner), thicknesses (GPRs), and condition of the structure (thermal and linear cameras, visual inspections, and measures). In the approach, the S&I phase can be repeated to update the data through different time steps, with this instrumentation it is possible to carry out surveys and inspections with non-destructive investigations, preserving the integrity of heritage tunnels;
- *Digitalization (DI)* of the geometric survey to obtain a 3D CAD model or IFC model;
- *Defect Analysis (DA)* from HD linear photo to map and digitalize the defects in a CAD environment. The defects are statistically elaborated and combined to obtain easy and user-friendly indexes;
- *Planning & Design (P&D):* the digital twin and the defects detection are combined in a Common Data Environment (CDE);
- *Work & Maintenance (W&M):* the maintenance and construction works are performed according to the indication of the P&D phase. The completed works are ready for a new S&I phase to determine the new condition of the structure;
- *Monitoring (MO)* is fundamental to have continuous data input through different phases, allowing a dynamic database and assessment of the structures.
- *Facility Management Platform*: an environment in which it is possible to have a complete view of the conditions of the infrastructure (e.g., geometry, geomorphological context, and risk and hazard indices, etc.). Each index value falls within specific ranges which, (e.g., with a value from 1 to 4), indicate the health of the infrastructure. The index value is not defined a priori but varies according to the aspects considered, in fact, it is possible to deconstruct it to adapt the assessment to different situations and to make it more usable by different users. Moreover, it is possible to view monitoring alerts that show the exceeding of critical thresholds.

Figure 2. Puzzle chart of the workflow (Foria et al. 2021).

The methodology is suitable for the management of heritage infrastructure. In fact, it is possible to assess, without compromising the integrity of the infrastructure, the conditions of the heritage tunnels and, consequently, plan interventions in a targeted way on the most critical areas. In addition,

by repeating the process over time, it is possible to have constant monitoring of the work with the advantage of knowing the infrastructure conditions over time and catch predictive behaviors.

2.2.1 *Mobile mapping survey*

A multi-dimensional mobile mapping system adapts well to the digitalization and management of heritage infrastructure. The integrated instrumentation in fact allows to make very precise surveys, avoiding destructive investigations and minimizing the impact on working lines.

In the case of ETS srl, the system developed is ARCHITA, a multi-dimensional mobile mapping system consisting of linked and integrated equipment (Foria et al. 2019). It carries out the survey activity with an average speed of 15-30 km/h, minimizing the impact on existing lines with shortstop of the traffic and without disconnection of the electrical tension (for railway). The system can work in two different configurations (Figure 3): RAIL and ROAD.

Figure 3. ARCHITA: RAIL (on the left) and ROAD (on the right) configuration (Foria et al. 2019).

The system consists of (Figure 4):

- Laser scanner to acquire 3D point cloud;
- Linear cameras to take high-resolution photos of the tunnel lining, detecting the components and the conservation state;
- GPRs to survey the ballast thickness, status and humidity, the lining thickness, and the cavities that lie behind;
- Thermal cameras to detect and double-check defects on the lining.

The different tools are integrated and linked to each other, allowing to acquire multiple information for every single point simplifying the acquisition. Engineering experience and judgment are fundamental when processing and interpreting the huge amount of data back in the office, especially when using multidimensional surveying tools.

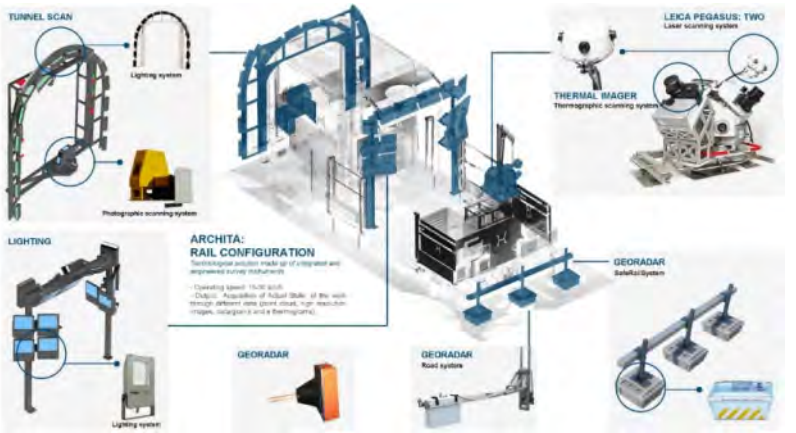

Figure 4. ARCHITA rail configuration: technological solution made up of integrated and engineered survey instruments (Foria et al. 2019).

2.2.2 *Defects analysis*

The use of measurement instruments allows obtaining more clear, objective, and repeatable data compared to traditional methods of inspections. For the defects analysis, both the manual and the automatic method (Artificial Intelligence) have been used even though the last is still under sever research and development.

For manual digitalization, a specific IT environment can process the HD images of the camera installed on the mobile mapping system. The software allows drawing both linear and areal defects thanks to the implementation of a catalog that is adapted to the specificities of the tunnel. It is also possible to associate to each defect information related to extension, intensity, and the instant of time in which the analysis is made.

The extension and intensity information is then processed to obtain indices that can be used in the different analyses (e.g., SMCA, Hazard Analysis).

For automatic digitalization, an artificial intelligence algorithm was used. A partnership between ETS Srl, Sapienza University and RMT Srl is working to obtain an algorithm capable to detect defects (Foria et al. 2021). To date, the development is focused on the use of an algorithm to detect, and segment defects related to the presence of water, cracks, and detachments in mechanized tunnels with prefabricated segment lining.

The development started from the implementation of Crack SegNet (Ren et al. 2020), with a Convolutional Neural Network (CNN) capable of automatically detecting and segmenting cracks starting from image analysis (Figure 5).

The implementation was carried out in Python and C++ using Google's Tensorflow software library. The algorithm training was carried out on a dataset of 100–1,000 images. Validation and tests on images not used in the training phase show a slight overestimation of defects by the AI, 10% more (on average) than manual detection. This overestimation was deliberately calibrated to obtain evaluations that, for the sake of safety, do not underestimate the problems of the tunnel.

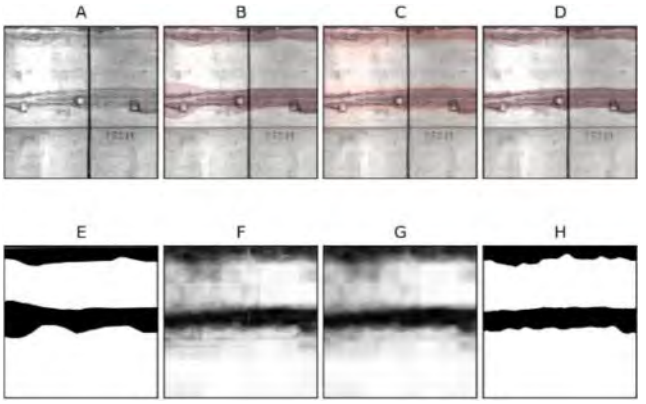

Figure 5. Example of comparison between the reference human-made annotation and the automatic annotation obtained. A – original image; B – image + human-made annotation; C – image + classification probability map; D – image + AI annotation; E – human annotation; F – classification probability map; G – blurred classification probability map; H – binarized and blurred classification probability map (Foria et al. 2021).

The use of AI for tunnels maintenance of the railway line Andora-San Lorenzo won the trust of international expert in innovation and technology who have rewarded its value inserting it among the finalist of the category "Best Use of Technology: Artificial Intelligence" at NCE TechFest 2021 in London.

Figure 6 shows a stretch of tunnel in which there is comparison between manual digitization and automatic digitization (AI) for water defects detection in mechanized tunnel (Foria et al. 2021).

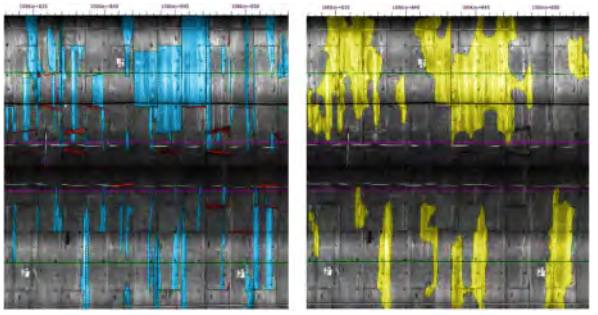

Figure 6. Manual detection (on the left) vs automatic detection (on the right) in mechanized tunnel (Railway Line Andora-San Lorenzo).

2.2.3 *Spatial Multi-Criteria Analysis (SMCA)*

In the proposed methodology, data from defects mapping are statistically processed and combined with additional parameters (e.g., geological context) that provide descriptive and analytical information about the envinronment and boundary conditions of the infrastructure. These parameters are combined through a Space Multicriteria Analysis (SMCA). It is needed when the parameter to be measured is a function of many not-directly-comparable variables, which need to be weighted and normalized (Foria et al. 2021). The use of the SMCA is essential to have a proper overview of the tunnel conditions with a structured and repeatable index (Priority Index) that combines the hazard of the phenomena and the vulnerability of the structures, to make comparisons over time and between different works. The Priority Index defines the level of attention or condition that determines the order for the management of the infrastructure elements according to their relative importance. This assessment aims at managing and identifying the risk for existing tunnels for the strategic management of resources and infrastructural assets.

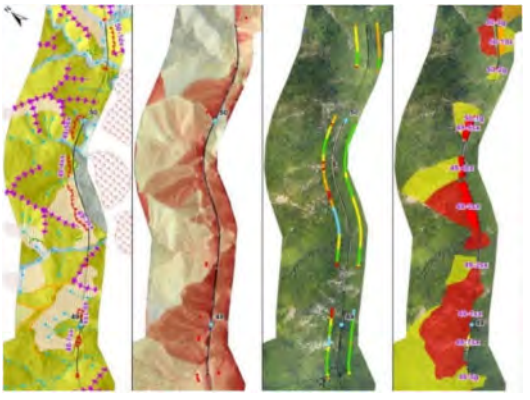

Figure 7. An example of Priority Analysis for the infrastructure management. The figure shows an application to landslide. From left to right: Geomorphological map, Connectivity index map (red dots indicate overcomes of a threshold value), Final index value, calculated every 10m along the line, on both sides, and the Hazard map (Foria et al. 2021).

This process is important to immediately highlight the critical issues and intervene promptly by identifying the causes of damages and to plan maintenance interventions effectively and efficiently (Foria et al. 2021). The priority index obtained fall within four priority classes that allow to establish which sectors have higher priority than others. This is important in the field of Facility Management to manage the budget correctly and intervene proactly. The results of this analysis can be showed in a single environment. An example in Figure 8 show of a platform currently undergoing development.

Figure 8. Priority Index of the Railway Line Andora-San Lorenzo: high priority (red), medium priority (orange), low priority (yellow), no priority (green).

3 CASE STUDY

3.1 *Galleria Sipicciano I*

The Galleria Sipicciano I is located between ch. 7+076 and ch. 7+228 of the Attigliano – Viterbo railway line within the municipal area of Graffignano (VT) (Figures 9 and 10) (Foria et al. 2020).

Figure 9. Galleria Sipicciano I – Regional Technical Cartography (CTR).

The morphological layout of the area is the result of a continuous evolution of the course of the Tiber River and its tributaries which, with various erosive and depositional cycles, has changed the tectonic depression called graben of the Tiber and the surrounding areas.

The entire area is characterized by two distinct morphological zones: the first, adjacent to the stream, mainly sub-horizontal, which extends to the hills; the second, which borders the first on both sides, consists of low-steep hills.

Figure 10. Galleria Sipicciano I: Photo of tunnel entrance ch. 7+228 (on the left) and photo inside the tunnel (on the right).

The surface drainage network has a high density, characteristic of soils with low permeability, which determine lines of impluvium incised, of limited amplitude, with torrential water circulation.

The railway line is located between approximately 115 m a.s.l and 150 m a.s.l. The maximum height of the ground level above the Galleria Sipicciano I has been estimated to be 128 m s.l.m., while the rail level has an altitude of approximately 117 m, the maximum coverage is less than 5 m.

Considering the low coverage above the structures, the poor urbanization of the area, and following the lithologies found during the investigation, it is very likely that the tunnel was built using the Cut and Cover methodology.

3.2 *Visual inspection and diagnostic*

For the survey and inspection of Galleria Sipicciano I, a multi-dimensional mobile mapping survey was performed in 2017. During the survey it was possible to obtain (Figures 11 and 12):

- High-resolution photos of the tunnel lining using linear cameras;
- The ballast thickness, status and humidity, the lining thickness, and the cavities that lie behind using GPRs;
- Thermal images thanks to thermal imaging cameras.

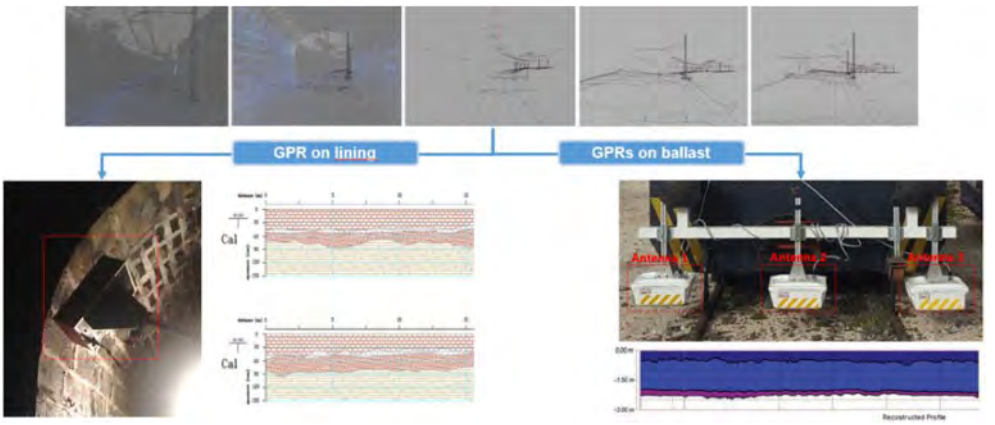

Figure 11. Tunnel digitalization through GPR on lining and ballast (Foria et al. 2019).

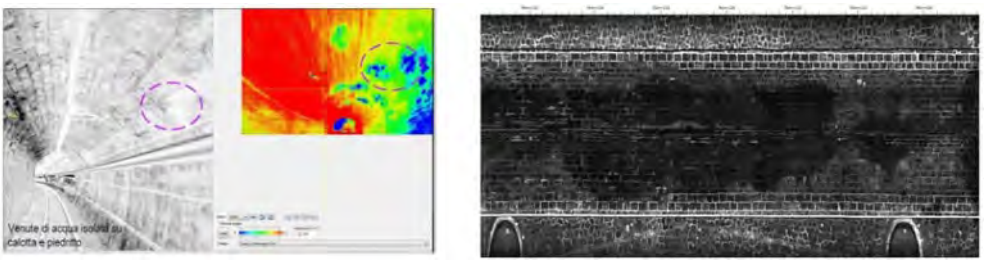

Figure 12. Tunnel diagnostic through thermal images (on the left) and HD images (on the right) (Foria et al. 2019).

For this case study, it was possible to obtain the photogrammetric profile with the use of a software, to characterize the tunnel, to identify and map the presence, extent, and intensity of any defects as described in the next paragraph (Figures 13 and 14).

3.3 *Defect mapping*

The defects mapping has been carried out through two fundamental operating tools: the catalog of defects developed for masonry tunnels and HD photos/thermal images.

This system allows to constantly monitor the conservation status of the work and evaluate the effectiveness of maintenance interventions even after years from the execution. The standardization of the analysis process also allows the comparison between different tunnels at different times (macro-scale analysis).

Moreover, the data obtained from the mapping of defects can be exported to the CAD environment and spreadsheets to be viewed and processed.

For Galleria Sipicciano I it was decided to divide the tunnel into 7 homogeneous sectors of 20 m each as indicated in the Tunnel Inspection Manual 2020 (Ministero delle Infrastrutture e dei Trasporti 2020).

After the defects digitalization, the extension information relating to defects was processed to obtain the extension index for each sector (Figure 15). The extension index is defined according to the extent of the defect with respect to sector area. The sector area corresponds to the lining portion inspected with the photo (referring to 210° of maximum photographable aperture).

These indices were then used in the SMCA analysis (3.5) for the evaluation of the priority index. In Figures 13 and 14, the results of Manual Digitalization on Galleria Sipicciano I are shown.

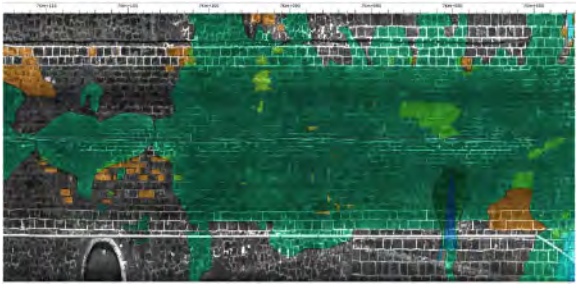

Figure 13. Defects Map (Sector 1).

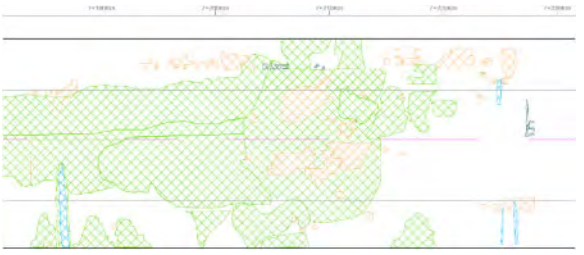

Figure 14. Defects map in CAD environment (Sector 1).

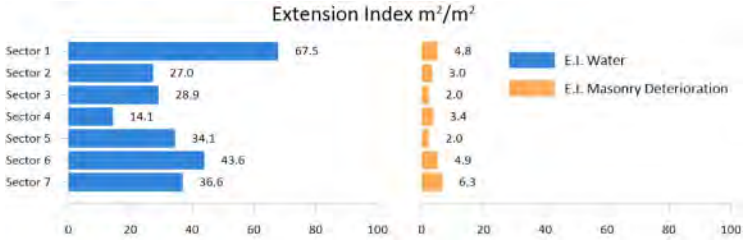

Figure 15. Extension Index: Water (on the left) and Masonry deterioration (on the right).

From the results obtained it can be seen that Sector 1 (ch. 7+076) shows a massive presence of humidity inside it due to the accumulation of water above the sector. The main causes of this phenomenon are due to the increasing slope towards Sector 7 (ch. 7+208) and to the slope discharge.

As regards the deterioration of the masonry, this is homogeneous throughout the tunnel with an increase in the entrances, in particular in Sector 7.

From these considerations we can say that the sectors at the entrances are those that need more attention.

3.3.1 *Artificial Intelligence*

Considering the positive results obtained in the use of AI for defect detection it was chosen to use the algorithm WaterSegnet (Foria et al. 2021) also in this case study.

The total area of defect digitalized manually is 1006.8 m^2 while the total area of defect digitalized with IA is 1100.6 m^2. Even if the results obtained seem good, they are not optimal, as you can see in Figure 16. This is because the algorithm, as mentioned before, has been trained on mechanized tunnels while the Galleria Sipicciano I, is a masonry tunnel. Currently, we are working on the development of an algorithm suitable for defects detection in masonry tunnel that use an appropriate neural network.

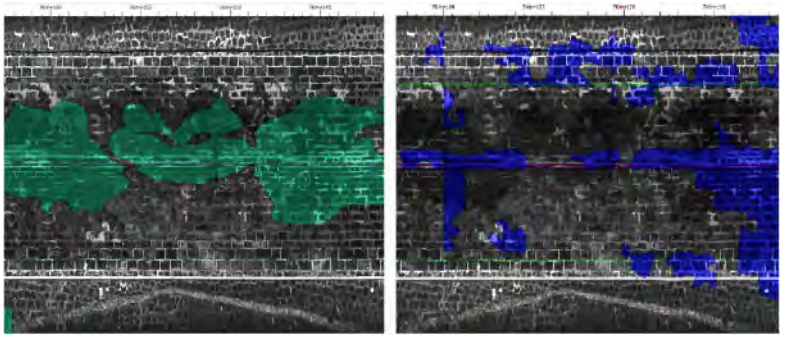

Figure 16. Manual detection (on the left) vs automatic detection (on the right).

3.4 *Digitalization*

The digitalization of the tunnel has been carried out starting from the point cloud of the laser scanner set in relative coordinates.With Autodesk Recap it was possible to process the point and to obtain the 3D model of Galleria Sipicciano (Figure 17) that served as input for the BIM modelling.

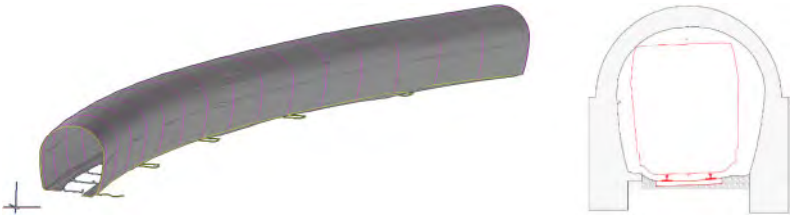

Figure 17. 3D model from geometric survey (on the left) and example of clearance overlapping (on the right): in grey the existing clearance of the tunnel, in red the clearance of the new train (PC80).

On the 3D model obtained it was carried out a dynamic clearance analysis by overlapping the clearance of the new trains (PC80) with the existing clearance of the tunnel (Figure 17) (Foria et al. 2020).

From this analysis it is possible to carry out assessments that can lead to interventions (e.g., milling or lowering of rail level) in case of interferences between clerances.

3.5 *Spatial Multi-Criteria Analysis (SMCA)*

To assess the tunnel conditions, in addition to deterioration of the masonry and water defects detected from the survey, it was decided to consider other categories that take into account the context in which the tunnel is located. A Spatial Multi-Criteria Analysis was used to combine all the categories to obtain the priority index. The SMCA allows to combine specific weights, calibrated on railway literature experience, to different categories.

For Galleria Sipicciano I, six categories were considered: Deterioration of the masonry, Water defects, Seismicity, Hydrology, Superficial Geology, Deep Geology. To have comparable analysis, it was decided to maintain the same sectors used for defect analysis. The results obtained for each sector are shown in Figure 18.

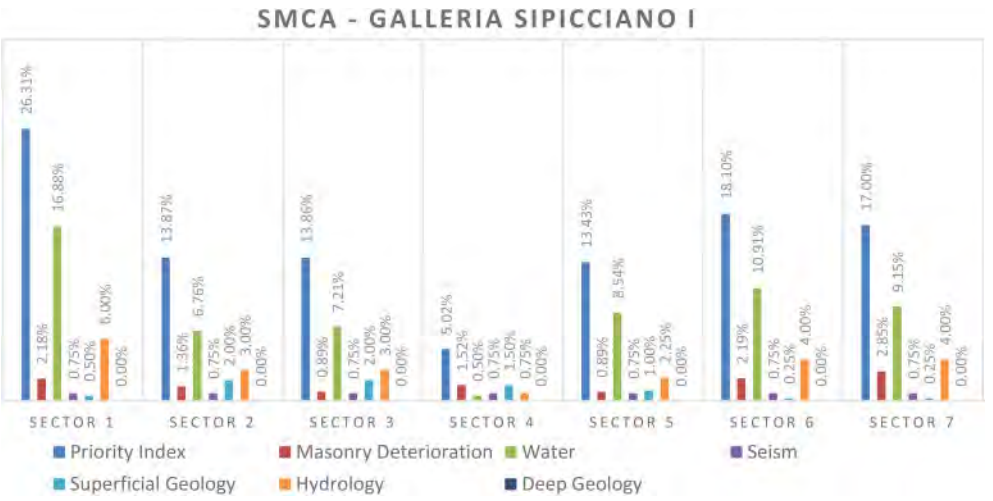

Figure 18. Priority Index.

The results obtained highlight what was shown in defect analysis. The piority index indicates a high component linked to the presence of water and hydrology,\ especially in the sections of the tunnel entrance.

In conclusion, the priority of intervention on this tunnel, barring hydraulic problems near portals and center of the tunnel, is low and the actions to be carried out must be precise and will mainly concern water disposal.

3.6 *Virtual reality for inspection*

Virtual reality is an integral part of the proposed digital methodology involving both design and maintenance of tunnel and infrastructure heritage. With this technology, it is possible to verify in real time the infrastructure conditions, acting in a timely and appropriate manner. VR's use in maintenance reduces processing times and error in diagnostic phases. In addition, the new innovative representations in Virtual Reality create three-dimensional axonometry, 3D rendering, movies and animations of the work. To assess the tunnel conditions, in addition to the analysis already described in 3.2, 3.4, 3.5 it was carried out a Virtual Reality Inspection (Figure 19). The VR inspection is aimed to verify the current state of the tunnel and allows to obtain objective geometric data and visual information available for all the parties infinitely. It is also aimed as an innovative approach for tunnel management by verifying the survey results of the investigation phase and the construction work performed.

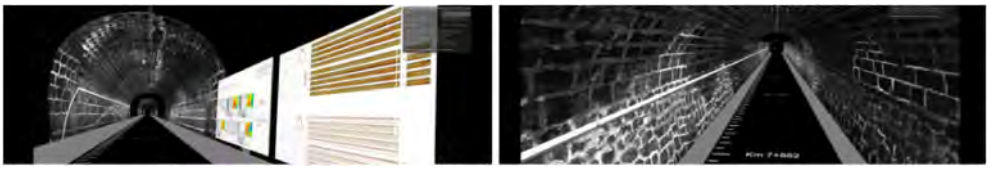

Figure 19. Virtual Reality Inspection.

4 CONCLUSIONS

The knowledge, the preservation, and the maintenance of heritage infrastructures can be carried out with new approaches. The approach belongs to the digital strategies for infrastructure maintenance that are very fast and minimally invasive.

The integration with multi-dimensional mobile mapping systems allows having almost all the information necessary for the geometries and the diagnostics of a structure with non-destructive tests, preserving the integrity of very old structures such as the infrastructural heritage. The results obtained for the case study, give a solid base for preliminary technical assessments in the management of the tunnel structures and the whole infrastructure. Moreover, these analyses are a direct input for later stage of planning, design and construction.

Within the framework of the proposed methodology (MIRET), the authors are investing in the development of Artificial Intelligence (AI) for defects detection and digitalization. The results obtained show that, to date, there are still limitations, but they can be overcome in the future developing a specific algorithm suitable for masonry tunnel.

REFERENCES

Foria, F., Avancini, G., Ferraro, R., Miceli, G. & Peticchia, E. 2019. ARCHITA: an innovative multidimensional mobile mapping system for tunnels and infrastructures. *MATEC Web of Conferences*: 295, p. 01005.

Foria, F., Giordano, R., Cordua, G., Miceli, G. & Chiaino, D. 2020. Analisi transitorie FEM per il dimensionamento di sistemi di smaltimento acque in gallerie esistenti. *IAGIG*.

Foria, F., Giordano, R., Tommasi, D & Miceli, G. 2020. Galleria Olmata, from survey to construction: an integrated design approach for the renewal of railway tunnels. *ITA-AITES World Tunnel Congress: WTC2022 and 46th General Assembly*.

Foria, F., Miceli, G., Tamburini, A., Villa, F., Rech, A. & Epifani, F. 2021. Application of Spatial Multi-Criteria Analysis (SMCA) to assess rockfall hazard and plan mitigation strategies along long infrastructures. *IOP Conference Series: Earth and Environmental Science*: 833(1).

Foria, F., Calicchio, M., Tarquini, A., Miceli, G., Chiaino, D., Cuccato, D., Rinaldo, S., Bomben, G., Rosetti, G. & Allegro, A. 2021. Artificial intelligence and image processing in the MIRET approach for the water detection and integrated geotechnical management of existing mechanized tunnels: methodology, algorithm and case study. *Rocscience International Conference 2021*: pp. 1–7.

Foria, F., Ferraro, R., Peticchia, E., Sannino, F. & Miceli, G. 2021. Modélisation des défauts et maintenance des tunnels existants avec une approche novatrice (MIRET): l ' étude de cas de la ligne de chemin de fer Gênes – Vintimille et du métro de Rome. *AFTES 2021*: pp. 1–10.

Foria, F., miceli, G., Nascetti, A., Loprencipe, G., Crespi, M., Belloni, V., Ravanelli, R. & cordaro, S. 2022. Digitalization and defects analysis for the maintenance of mechanized tunnels. *ITA-AITES World Tunnel Congress: WTC2022 and 47th General Assembly*.

Ministero delle Infrastrutture e dei Trasporti. 2020. *Manuale Ispezione Gallerie*.

Ren, Y., Huang, J., Hong, Z., Lu, W., Zou, L. & Shen, X. 2020. Image-based concrete crack detection in tunnels using deep fully convolutional networks. *Construction and Building Materials*: 234.

Mili, M., Chille, F. & Thuaud, C. 2021. Comparison of international repair works practices in railways tunnels. *AFTES 00261*.

Geotechnical Engineering for the Preservation of Monuments and Historic Sites III – Lancellotta, Viggiani, Flora, de Silva & Mele (Eds)

Sans-Soucis Site, Haiti Republic – A case study for a project of preservation, interpretation and highlighting of a worldwide heritage patrimony

J. Palisse
Egis (Geotechnical Segment), Seyssins, France – Member of the Design Consortium EGIS/AGENCE BORTOLUSSI/VIA ARCHITECTES/HYADES/COMPAC/CCET/TROPISME for the described project

ABSTRACT: Built in the early XIX Century under the reign of King Christophe, just after the freedom of Haiti from slavery, the Sans-Soucis site – mainly a Palace and outbuilding among the National Historic Parc (Site Sans Soucis, Citadelle Laferrière, Ramier) was damaged in 1842 by a major seismic event. In order to preserve the site that remains a pearl in the country, ISPAN (Haiti Government) and UNESCO started many operations of securing and protecting between 1979 and 1990, but the site continues to deteriorate and remains highly vulnerable. In order to preserve the patrimony and to develop tourism, the Haitian Government launched a project to preserve patrimony and help touristic sector (PAST project). For this project, a designated private design consortium has to reinforce, restore, interpret and highlight the historic monuments in the Sans-Soucis site.

This paper discusses the geotechnical issues and complexity of the case and the project that is still in progress. Among the main subjects, the paper will present the geological understanding of the site done from abroad (pandemic situation with no-displacement on site and few monitoring), an important seismic hazard context (masonry wall and huge retaining masonry wall), a mountain site with potential instable slopes and geological anomaly. We will also discuss the priorities of the project modified during the mission because the site continues to be damaged (roof fire of the chapel's site), the solutions that must be face to the material reality of the country…and the specificity of the mission that needs to preserve but also prepare for tourism.

Finally, the paper deals with the approach of this complex project for geotechnical subjects and the need to go out of the comfort zone of well-known design and include other disciplines (history, archeology, local social culture…). The main goals remain to find solutions that fit for the monument and its integrity but also for the local population who needs to appropriate their history and be involved in determining the way it is restored.

1 INTRODUCTION

The interest for the conservation of the site started in 1934 but had to deal within the complex history of the Haitian Republic, one of the poorest countries according to the United Nations and mainly vulnerable to natural disasters, especially seismic activity. In 2019, the Haitian Government launched a tender using a donation from IDA (International Development Agency). The actual consortium was selected among five other consortium, mainly from Canadian, Haitian, French and Italian firms.

The mission really started in 2020 in the beginning of the pandemic situation and the worldwide shutdown. As it was impossible to arrange an on-site visit, the consortium had to rely on visits used for the proposal and on personal visits done before. The first preliminary design begun using

DOI 10.1201/9781003308867-21

dematerialized material and quickly two unfortunate events strike: money from IDA to realize work was given back and the roof of the Royal's Chapel burned in a fire. Nevertheless, work achieve the preliminary studies by the end of 2020 continued.

By the spring 2021 a window seemed to open to enable a visit before the next phase that was quickly closed due to a strong swell made of a combination of a new Covid19 wave and abduction wave in Haiti that clearly discouraged work travel. This setback was closely followed by the assassination of the Haitian President Jovenel Moïse and an earthquake that logically delayed the project due to other emergency priorities for the authorities.

At this point, we must remind the audience that "Sans-Soucis" literally means "no problem".

Nevertheless, one axis of the design mission was to highlight this incredible site and its history in order to make it known and enable, in a possible future, tourism. Despite the interruption of the project, this paper summarizes the preliminary studies following two main goals:

– Communicate about the site itself to make it known and begin to highlight it.
– Gives some thinking about this kind of design mission from the geotechnical point of view.

2 BRIEF HISTORY AND DESCRIPTION OF THE SITE

Jean-Jacques Dessalines, a former slave became an officer in the French army, lieutenant of Toussaint Louverture declared the independence of Haiti from France in 1804 and proclaimed to be the first Emperor of Haiti, Jacques 1st. In 1806, he was assassinated by, among others, Henry Christophe and Alexandre Pétion. A civil war started and Pétion created a Republic in the South as Christophe, former governor of the north under Dessalines, but also a former freed slave that had many profession, created a kingdom in the North in 1811 and became its king, Henry 1st, commonly known as "King Christophe" (Consortium Egis et al. 2020a).

As a state founder, Christophe was a builder king and rapidly, the whole complex (Palais Sans-Soucis and then the Citadel) came out (Hyvert, G. 1979). The beginning of the construction of the Sans-Soucis remains unknown but it was quickly achieved using drudgery of men and women as for the Citadel. King Christophe seemed to use a system of exploitation inspired by the former colonial society to achieve the construction in such a short time. A "code Henry" was put in place instigating a harsh regime and he recreated a kingdom and its royal court inspired by the European countries: Princes, dukes, counts, African bodyguard corps (deliciously named "Royals-bonbons") came with the palace. Seeing the site knowing its legend makes it exciting and enables to appreciate it and imagine the golden age. This history is also at the origin of an important literature that maintains the myth (for examples Carpentier, 1954, Césaire 1963).

Figure 1. Aerial view of the site (top left), view of the back of the palace (bottom left), zenithal view of the site (right).

The Palais Sans-Soucis overhangs the city of Milot, a rural city 25 km South-West from Cap Haitian. In the middle of a valley, on a little hill, surrounded by mountains (Mountain range from Bonnet à l'Evêque), the palace and its complex built as an amphitheater covers 8 hectares. From the palace starts the path to the Citadel Laferrière. The place of the Citadel was clearly chosen for strategical reasons of interior defense, but it seems that King Christophe created from nothing the Sans-Soucis city and his palace, on the actual location of Milot.

The Sans-Soucis site is composed of residential and administrative buildings: the royal chapel, the palace itself, the board of state, ministry, military barracks, prison, maintenance workshop, hospital, etc…and also queen's gardens, bath of the king…the name seemed to come from the "Schloss Sanssoucis" of Frederic II in Potsdam. Indeed, the amazing reliefs of the site leave the feeling of an architectural design in rainforest (Figures 1 and 2).

The end of the golden age of the site came with the suicide of King Christophe in 1820 who didn't want to face the insurrection that was coming to him. His death led to the quick collapse of the kingdom. Just after, the palace was looted then abandoned. The South reunified the North. The earthquake of 1842 severely damaged the site.

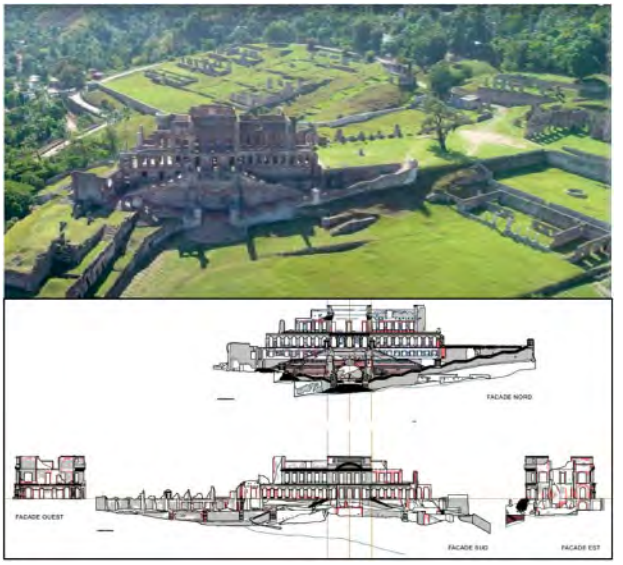

Figure 2. Closer view of the palace (top), projection of the different facade (bottom).

A lot must be said about the architecture of the site, his author and their inspiration (Consortium Egis et al. 2020a). As this article deals finally with geotechnical aspect, we are going to focus on the ground and the place chosen for the palace.

It is pretty obvious, on the first visit or on the picture, that the palace was settled on an outcrop (Figure 2). Is this outcrop natural, and preexisting to the palace? Even if the Sans-Soucis site was not a stronghold place in first intention (unlike the Citadel), we must remind that those buildings were linked, in one way or another, to military engineering and strategy. More than probably, the designers of the Citadel were also in charge of the construction of the Sans-Soucis site (ISPAN 2021): research is ongoing to reveal the name of the architect itself but among the choice, almost all the contenders would have had experience in military engineering. We also have to recall the work of Charles-Augustin Coulomb in 1764 for the Bourbon fort in Martinique that lead in 1772 to his book *Essai sur une application des règles de maximis et de minimis à quelques problèmes de Statique relatifs à l'Architecture* (1773). We can clearly assume that the builders of the Citadel and the Sans-Soucis site, from military engineering too, were part of the same French military genius

that had already good experience in geotechnical engineering. That mainly explains that there is still today subsequent ruins of the site instead of nothing at all.

The choice of a high point seems coherent with a military vision. We can also imagine, like in Versailles, that the choice was purely architectural: the visitor had to ascend to the King. Nevertheless, there was clearly a natural spur, maybe amplified by human work that was used to settle the site. And this consideration is central for the actual geotechnical issue.

3 GEOTECHNIC CONTEXT OF THE SITE

Since 1934, many operations occurred, but really few focused on geotechnical aspects. It must be said that the most important data and work on this topic rely on two major documents that are:

- *Confortement du Palais de Sans-Souci – Analyse géologique et géotechnique* by Chambon & Delétie (1997).
- *PAST études techniques du site de la Citadelle* by BRGM (2018).

Only those documents relate the visit of specialized geologists (former geologists in EDF for Chambon & Delétie, and from Monique Terrier, geologist expert from BRGM).

As already explained, since there was no possibility to realize the visit of the site for the consortium, the geological analysis is mainly based on the review done by M.Terrier in the BRGM report that are already integer the works of Chambon & Delétie. Nevertheless, the mission of the BRGM finished with survey program that has been launched since then (LNBTP 2018). The work of the consortium could be summarize by taken into account the results of the survey and cross the information.

With those two documents, it must also be said that the consortium was able to use the results of imagery mission lead respectively by the society Geoscan and Iconem. The first one created, using photography of the site, an informatic tool enables to have 360° view in different places of the site and the other totally recreates a 3D model of the site using drone.

3.1 *The Palace*

The outcrops bordering the site of the Palace, as well as the general topography of the site (palace on a promontory) suggest that the Palace itself would be based in part on an emergence of the bedrock (or its altered part). The bedrock could be considered as a volcanic substratum (Andesite) (BRGM 2018), although this point is not clearly specified (a characterization of this basement still to be done). The presence of the base seems to be confirmed by the MASW measurements carried out (Figure 3 – LNBTP, 2018), with a Vs30 selected at 660 m/s.

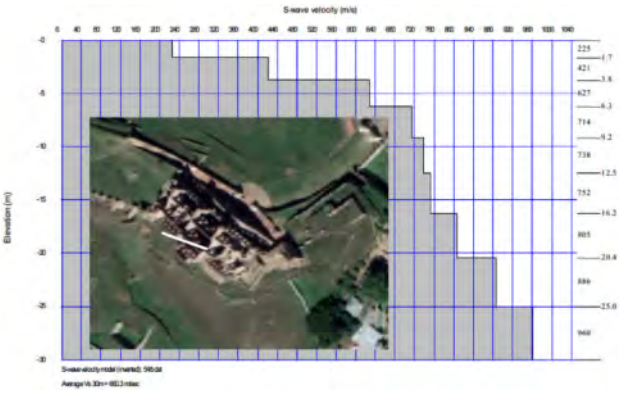

Figure 3. MASW4 next to the palace (white line).

3.2 *The Chapel*

For the Chapel, according to BRGM (2018) "*The Chapel is built on soil or embankment close to 5 m thick. The embankment under the platform of the Chapel and the Sans-Souci Palace have no retaining wall (S51, S52, S55, S56, S57, S43), nor barbicans (S54). In several places, the bare rock corresponds either to soil (greater than 1 m thick), or to slope colluvium, or to volcanic breaches*".

The MASW analysis carried out in LNBTP (2018) clearly reflects this interpretation (Figure 4). Indeed, the different measurements suggest that a significant thickness of the overlap (colluvium) is present from the North Gardens (and the Palace), to Milot. So it would seem that the Chapel is based on an infill of the order of 5 m before reaching a substratum. The MASW profile suggests a value of Vs30 of around 560 m/s confirming this thickness of backfill and / or more altered substratum. It is also noted in fact that if the propagation speed values are much lower than 800 m/s up to more than 20 m, however, they reach the value of 773 m/s.

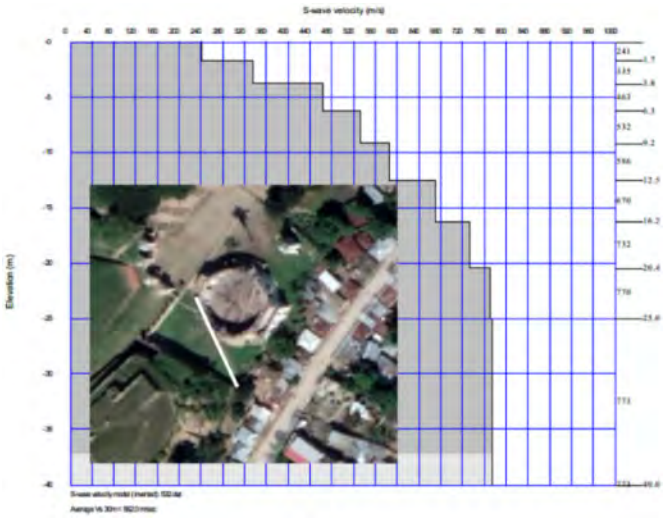

Figure 4. MASW1 next to the Chapel (white line).

Thus, the first visual impression is confirmed by the seismic profile: under the focus building. The site is based on a rocky outcrop. At this point, it is important to take a step back on this information in order to understand what it can induce for the project. Indeed, it appears that whatever work is done on the foundation it is going to be complicated to improve (or change) the acceleration suffered by the building at an economic cost. It is also obvious that the site suffered many seismic events, and what would collapse initially has collapsed and what is able to resist to the acceleration suffered still stands. The main goal is to reinforce the exterior masonry in order to lengthen its durability, what is going to be discuss in §4.

Nevertheless, even if it seems pointless to "do something" from a geotechnical point of view on the site (at an economic cost), a last point about the site must be reported to put together all the information.

3.3 *An anomaly to investigate*

BRGM (2018) indeed specifies a geological anomaly identified as a fault crossing the site on a NNE-SSW axis. This anomaly directly overlaps with the basis of the annex to the Chapel (Figure 5) and extends towards SSW, on the eastern edge of the Council of State and the Palace, intersecting the sliding and instability observed visually downstream of the military camp. However, this fault is not directly related to the instabilities observed in the area. What's more, the review of the local

seismic hazard in BRGM (2018) does not establish any modification of the site effect or topographic due to this anomaly. Note also that no seismic profile across this anomaly has been achieved yet.

Chambon & Delétie (1997) present for this anomaly a fault mirror with an identification soils like Limestone. In particular, concerning this fault it is indicated for the identification massive limestones: "*These outcrops of particularly resistant rock have limited erosion in the area and allowed to the promontory itself to form [….]. On some documents, a fault zone is indicated in the sector. Perhaps these are recrystallized cracks or very broken marl sheets, but from a geotechnical point of view, this sector must be considered as resistant and very compact. Outcrops Limestone can also be seen near the Church, between the village and the site, and in the vicinity of barracks, especially on the edge of the thalweg. These limestones are attributed to the Lower Eocene*"

However, Chambon & Delétie (1997) do not report any instability in the basis of the annex to the Chapel, nor instability on the mentioned fault, but only a superficial slide downstream from the Palace.

In conclusion on the geological review of the eastern instability of the site, we can only note the presence of an anomaly, a priori a fault, but the characterization of which remains vague, even contradictory, by the different site surveys. The very composition of the soils (volcanic substratum, or limestone, or alluvial filling) is unclear. These analyses were not taken any further, as the available investigations are not interested in this area or its development downstream.

As for the foundation of the building, we can conclude by saying that whatever is the impact of this anomaly on the site, it is illusory to consider "stabilize it" at an economic cost. Nevertheless, its nature and characterization are important because the site is located just above and dwellings of Milot just on it or downstream.

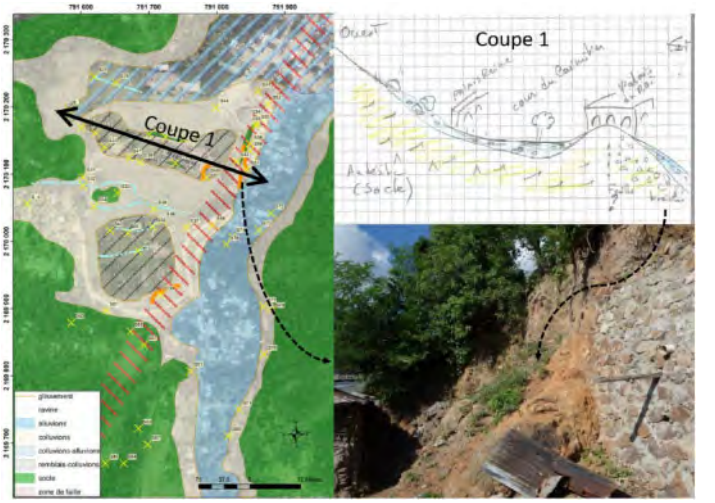

Figure 5. Geological interpretation of the site: plan view (left), cut on the palace (top right) and picture of the breaches (bottom right) – from M.Terrier (BRGM).

In general summary of this review, our geological analysis would be as follows:

The study area is located on a platform limited to the east by a narrow but relatively steep slope compared to the rest of the slope. From a direction parallel to the valley, these slopes inclined between 25 and 30° continue towards the North towards the Chapel where the difference in level between the latter and the houses of the city is locally taken up by a masonry retaining wall about 4 m high.

On this embankment surrounding the study area, signs of instability of the circular sliding type of which the scale in-depth remains to be defined by a field mission and more in-depth reconnaissance. *A priori* given the context, it is likely that these landslides affect the cover lands because the roof of

the bedrock seems to be located at shallow depth according to Chambon & Delétie (1997). BRGM (2018) notes the presence of an NNE-SSW axis fault in the same direction and significantly located to the right of this drop which limits the study area to the east and the village and the Milot valley to the west. The dip and the lateral extension of this fault are not specified but the morphological irregularities of the Eastern limit of the palace domain is very probably the result of this structural heritage. This accident being covered with tectonic breccia and altered terrain, characterization is difficult to demonstrate without an adapted geotechnical and geophysical campaign. Indeed, the available investigations and the surveys topography is largely confined to the west area of this accident.

4 THE DIAGNOSIS OF THE BULDING AND FIRST TRACKS OF REINFORCEMENT

For the preliminary studies, the design consortium was organized in many pole of which was the geotechnical-structure pole which has to determine the natural hazards and the actual damage status of the Palace and the Chapel (Consortium Egis et al. 2020b,c,d,e)). The other pole, regrouping Patrimony-Architect-Archeology-Landscape-Networks has to engage first thought about how using the restoration to highlight the site and enables tourism on it, work that begins with understanding its story (Consortium Egis et al. 2020a).

The work of the geotechnical-structure pole mainly used the actual report done on the site but also all the history work done by the other pole and mainly the history part of it to understand the story of the building. All this work leans on the previous studies already achieved and compiled by ISPAN and the PAST project. According to the geological comprehension of the site, although there was no clear identification of the foundation, it was possible to give first estimation of superficial foundation stiffness (Consortium Egis et al. 2020c) for the structure team which was able to recreate a TreMuri model of both the Palace and the Chapel (Consortium Egis et al. 2020d, e). TreMuri is a software that enables the non-linear modelisation for masonry in 3D under a seismic solicitation (http://www.3muri.com/). The dynamic analysis leads qualitative analysis of the state of damage of the buildings (Figures 6 and 8).

4.1 *The palace*

For the palace, this analysis shows that the structure is vulnerable to the efforts off-plan given the absence of floors and roofs. The structure is mainly composed of walls slender masonry carriers, free at the head presenting a marked risk of overturning and spill. The partial or complete destruction of certain parts of the structure also creates areas fragile, especially the walls which are no longer supported laterally and thus become very vulnerable to stresses out of plan. The problem of the infiltration of rainwater into the basement due to the non-waterproofing of the floor at level 1 must be resolved before any structural reinforcement intervention. Attention should be paid to the possible loss of plumb of load-bearing walls.

Three different approaches to stabilize walls in their out-of-plane direction have been analyzed in this preliminary study (Figure 6):

- Approach 1: create flexible floors made of wooden sleepers or metal serving as transverse support to the walls at different levels and thus preventing their out-of-plane spill
- Approach 2: create a partial redistribution of the forces in the structure to using a system of diaphragms creating a stronger central core, on which come lean on the struts to block out-of-plane movements of the facades
- Approach 3: modify approach 1 by integrating diagonal elements of type pulling locally between facades and longitudinal walls in order to reduce stresses in the lintels while limiting the additional rigidity introduced into the building by the system reinforcement

Before the implementation of these reinforcement solutions, it is however necessary to rule on the geological “anomaly” spotted before.

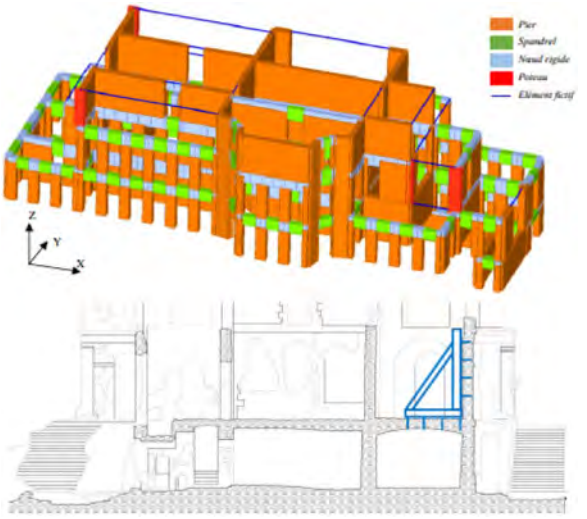

Figure 6. Tremuri model of the palace (top) and one of the reinforcement principle (bottom).

4.2 *The Chapel*

For the Chapel this analysis shows that the vulnerability of the structure is moderate and that the settlement of the eastern part of the extension generated by a settlement is the main risk factor.

The Chapel is currently without its roof following the fire that took place in April 2020, however the fire does not seem to have damaged the masonry elements.

The geotechnical interpretation of the site and the dynamic analysis are confirmed by the statement of a crack in the wall of the annex that it just above a masonry retaining wall (Figure 7).

Figure 7. crack in the annex of the chapel (left), 3D view of the Chapel (center, source Iconem) and retaining wall in masonry (right).

Reinforcement measures are proposed according to two different approaches (Figure 8):

- The first approach consists in separating the extension from the main body of the Chapel in order to remove the eccentricity created by this added mass which is the main point of vulnerability of the structure in the event of an earthquake. This solution is advantageous for the main part of the structure, but requires a level of reinforcement high to ensure the holding of the annex in the event of future earthquakes.
- The second approach, consisting in strengthening the critical areas of the annex and the separation wall by improving the connection between these two structures by tie rods or by an external belt seems easier to implement in the cases where the annex should be retained

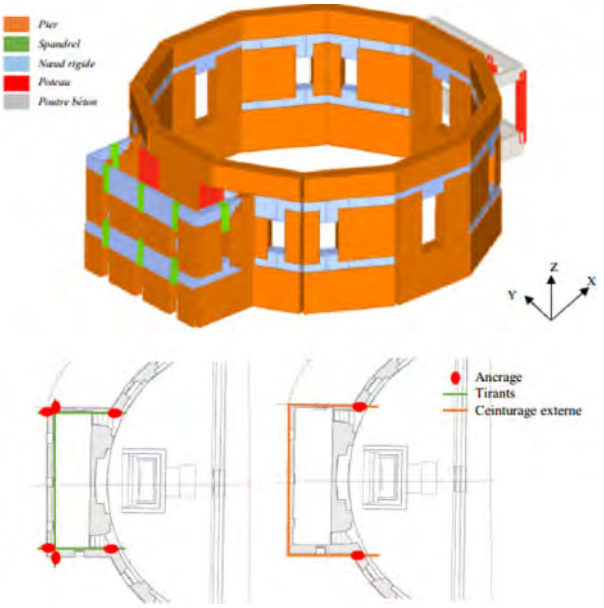

Figure 8. Tremuri model of the chapel (top) and one of the reinforcement principle (bottom).

Before the implementation of these reinforcement solutions it is however necessary to stabilize the failing retaining wall east of the Chapel and to repair the cracked areas to prevent further damage to the structure. The reparation of the masonry wall seems to be the only geotechnical work that can be considered on the site. In first approach, a reinforcement using passive nails could concretize reinforcement, but the lack of information leads to the need to ask for a special investigation on the masonry wall. Indeed, the pictures of the Figure 7 are the only information that the consortium had on the wall.

Those first studies can be related to a diagnosis of the different building: how it behaves and what can be done to stabilize it. However, those studies do not solve the issue of how create among this site a space of tourism that is secure according to actual construction rules and that respects the patrimony and the story of the Haitian population with their site. Indeed the site, and especially the Chapel, was frequently used by the Milot population. The fire was a real tragedy for the local population that leads PAST to ask to the consortium to make rebuilding the roof the first priority.

This necessity to welcome in security a public in those historical buildings (ruins) as the one to preserve their patrimony status introduce a paradox hard to solve for the next step of the design: how to secure the site (to welcome a public in safety, according to building norms) without denaturing the spirit of the site (at an acceptable cost). Compromises must be made that are going to be the main subject of next design phases. Fortunately, there was no discussion at the time to rebuild the Chapel's roof at the identical aspect, but maybe it will be raised (according to the important discussion in France about the reconstruction of the Notre-Dame's nave in Paris that happened at the same period).

5 REFLECTION ABOUT THE MISSION

The context as well as the mission itself were unusual: geotechnical engineers have mainly the habits to follow know how and security principles from rules and norms. From this point of view, French norms and recommendations, especially the Norme NF P 94-500 (2013), were useful to draw an objective for the start of the mission as there are no well-known guidelines for those

special missions. We rely on the reinforcement mission that we already follow for common recent infrastructures: that means we need to get interested in the way the construction was done. For recent construction, we have plans, ancient guidebook, etc…for historical building, we need to get interested by History itself. In the design consortium team we must notice that there are French Chief Architect of Historic Monuments as well as personnel from the French INRAP (National Institute for Preventive Archeological Research): those competences enable a precious information source for the engineers for this type of mission. For a geotechnical engineer, understanding the initial purpose of the people who did the building, as well as the used technology is important for determining the way to preserve it. This is true for recent and modern construction. In this spirit, archeological and geotechnical surveys should be reunited into one.

Continuing with this idea, a whole movement of imagery data was created to keep a picture of worldwide patrimony that can face destruction (see the work of Iconem in war country). The used technology (mainly drone) does not need a lot more to also give precious information about the stability of site from a geotechnical point of view. As a worldwide site, it should be followed in its evolution, not only in the visual aspect, but also for the ground itself for natural hazard (that has no link with a design project of reinforcement but that is an integrant part of the site patrimony). The idea to create a geologic/geotechnic cells in UNESCO to follow the worldwide heritage site is not so far...

The final thought is more about the fact that the mission is led by a private foreign consortium firm. It is possible to understand that design studies could be done from afar or by a foreign private entities from the country: different experiences, expertise, ideas from abroad…but the designer must keep in mind that it deals with the patrimony of a nation, and a patrimony that the people created by freeing themselves from foreign influence. Thus, rather than impose a method, the designer is more here to bring a different point of view, analysis and means to enables the very owner of the patrimony to choose the way they want for their patrimony and bring it to the world. For example, instead of using a foreign firms to realize the survey, why not using the National Laboratory of Haiti (LNBTP) rather than call for a foreign company? They realize the survey campaign conceived by the BRGM in a good way and even if we can imagine that there are more sophisticated survey companies in the world (but not so resourceful), it seems logical that they keep on for this site. Another concrete example is the work of drilling that inevitably will happen for the wall under the Chapel. It is well known that drilling work should be done carefully through an existing retaining wall: a lot of examples can be quote in the old Europe, which lead many firms to develop some creative technology like self-drilling nails or sonic drilling. Instead of bringing a team from abroad to do the job, it seems more attractive to imagine how to develop this technology in Haiti, especially because it is surely not the last masonry retaining wall to reinforce. Those missions must also face the necessity to give the means for the local authorities to manage the site after the work of preservation. It can lead to an increase of capacity for the country in reinforcement of structure: as we have spoken about the fault on the site, we shall not forget that actual dwellings are just under that do not seem to be as solid as the ruins of the Palace.

6 CONCLUSION

Finally, even if complicated and not recommended, it seems possible to do some preliminary geotechnical studies of a site without making a physical displacement on it…but this relies on a quality survey of the site done by geological and geotechnical experts who put their feet on the site.

Also, as a site receives the title of worldwide patrimony, it would seem logical that a worldwide entity would then centralize and compile all the data of the site and also ensure a longtime survey, especially from a geotechnical point of view (stability).

At last, if it is possible to diagnose the state of a worldwide patrimony site, creating a project of highlighting and tourism should rely on the local population that must appropriate the site and the way they want to make it evolves. The Haitian population well understood those issues, with the PAST project, that clearly leads the design consortium in the way the Haitian population want

to live their patrimony and make it known. In this spirit, the role of the design consortium is more about accompanying the local population and decision makers, enabling a knowledge transfer (in both directions) and staying aware that the final works must preferably be done by the Haitians themselves. The Haitians build it, they live it, and it is their patrimony before being Humanity's one: the only way to ensure the site to continue is that the Haitian populace gets involved in all aspects of the project.

It only remains the hope that destiny will enable Haiti to continue this project and also that the paper gave some velleities to decider or curious tourist to be interested in this magnificent site. Hopefully to be continued…

REFERENCES

BRGM. 2018. *PAST Etudes techniques du site de la Citadelle* BRGM.

Carpentier, Alejo. 1954. *Le royaume de ce monde*. Editions Gallimard.

Césaire, Aimé. 1963. *La tragédie du roi Christophe*. Présence africaine.

Chambon, J & Delétie, P. 1997. *Confortement du Palais de Sans-Souci – Analyse géologique et géotechnique*. PNUD – Ministère de la Culture – UNESCO.

Consortium Egis & Agence Bortolussi & Via Architectes & Hyades & Compac & CCET & Tropisme. 2020. *Pôle préservation Patrimoine, Architecture, Archéologie, Paysage, Réseaux. HSS-PRE-T-CPA/ARC/APR/ CPY/IFR-R-101.* République d'Haïti, Ministère de l'Economie et des Finances, Unité Technique d'Exécution.

Consortium Egis & Agence Bortolussi & Via Architectes & Hyades & Compac & CCET & Tropisme. 2020. *Synthèse du contexte géologique et géotechnique, HSS-PRE-T-RPA-R-301*. République d'Haïti, Ministère de l'Economie et des Finances, Unité Technique d'Exécution.

Consortium Egis & Agence Bortolussi & Via Architectes & Hyades & Compac & CCET & Tropisme. 2020. *Définition des raideurs statiques et dynamiques (Palais et Chapelle), HSS-PRE-T-RPA-R-302.*République d'Haïti, Ministère de l'Economie et des Finances, Unité Technique d'Exécution.

Consortium Egis & Agence Bortolussi & Via Architectes & Hyades & Compac & CCET & Tropisme. 2020. *Etude préliminaire – Etats endommagements et propositions de renforcements structurels – Palais du Roi, HSS-PRE-T-RPA-R-303*. République d'Haïti, Ministère de l'Economie et des Finances, Unité Technique d'Exécution.

Consortium Egis & Agence Bortolussi & Via Architectes & Hyades & Compac & CCET & Tropisme. 2020. *Etude préliminaire – Etats endommagements et propositions de renforcements structurels – Chapelle royale, HSS-PRE-T-RPA-R-304.* République d'Haïti, Ministère de l'Economie et des Finances, Unité Technique d'Exécution.

Hyvert, G. 1979. *Conservation et restauration de la citadelle Laferrière, du palais de Sans Souci et du Site des Ramiers*.

ISPAN. 2021. *Qui est l'architecte de la citadelle Henry? Peut-on élucider ce mystère aujourd'hui?* Bulletin ISPAN n° 43.

LNBTP. 2018. *PAST Campagne de reconnaissance géotechnique dans le cadre de l'étude BRGM*.

Norme NF EN 1998. 2005. *Eurocode 8 Calcul des structures pour leur résistance aux séismes*. AFNOR.

Norme NF P 94-500. 2013. *Missions d'ingénierie géotechnique – classification et spécifications.* AFNOR.

Geotechnical Engineering for the Preservation of Monuments and Historic Sites III – Lancellotta, Viggiani, Flora, de Silva & Mele (Eds)

The characteristics of "Artificial Stone Construction" used in civil engineering structure – A case of Doudo lumberyard

K. Takeuchi & Y. Fujii
Department of Civil Engineering, Meijo University, Nagoya, Japan

ABSTRACT: Artificial stone construction is a combination of Tataki and building stones. Tataki is a kind of plaster which is composed of decomposed granite soil, quicklime, and seawater. Many of them had been constructed more than 100 years ago and they have been deteriorated. It's a problem how to repair them for future preservation. However, the specification of the construction method is unknown because few original documents. In this study, the target structure is the Doudo lumberyard. At first, we conducted the metric survey by means of photogrammetry using an UAV. In addition, strength measurement was carried out for the original Tataki in the lumberyard by using needle penetrometer. After that, we conducted laboratory tests to understand the characteristics of Tataki. As the results, Doudo lumberyard has been kept in good condition and the unconfined compression strength is from 1 to 2 N/mm^2 for both original and newly formed Tataki.

1 INTRODUCTION

Artificial stone construction is a civil engineering method developed by HATTORI Choshichi who was born in Aichi Prefecture, Japan. It had been used for civil engineering construction, such as seawalls and embankments around 1900 before the spread of the concrete construction method. Artificial stone construction is mainly composed of Tataki and building stones (many of them are granite). Tataki is composed of decomposed granite soil, quicklime and water or seawater. A mixture of them is compacted tightly. Also, the unconfined compression strength of Tataki is about 1 to 2 N/mm^2 from the previous studies (Amano 2020). However, there are no original documents for the construction of artificial stone construction, and many of their properties are still unknown. So, it is difficult to maintain their cultural and technical value with the original construction method to restore them.

In the case of restoration and preservation of historical structures, it is necessary to clarify the deterioration status of their structures. We conducted the metric survey by means of photogrammetry using an UAV for the Doudo lumberyard. In addition, strength measurement was carried out by using needle penetrometer in the lumberyard. After that, laboratory experiments had been applied to the artificial stone specimens, which were made of new soils, quicklime and so on. For clarifying the basic properties of artificial stone, compaction and unconfined compression tests were conducted in the laboratory.

2 DOCUMENT THE CURRENT STATE OF THE DOUDO LUMBERYARD

2.1 *About Doudo lumberyard*

Doudo lumberyard was a transfer facility, in which woods were stored and sold. This lumberyard is in Toyota City, in the central part of Japan, and was constructed in the middle reaches of the Yahagi River (Figure 1). Main facilities are made of artificial stone, and it's the only underwater

 DOI 10.1201/9781003308867-22

lumberyard construction, which is made of artificial stone and located in the middle reaches of river, in Japan. It has great significance as a civil engineering structure that shows the history of wood transportation. It was registered as a tangible cultural property of Toyota City in 1997 (Aichi Prefecture 2005; Amano et al. 2006).

It was completely built in 1918. However, it has not been used since 1930 due to the construction of the Koshido dam in the upstream area. The lumberyard was left and buried due to the inflow of sediment from the river. In 1998, excavation work was conducted. After that, restoration and conservation activities were carried out by Toyota City about five years after the excavation. It shows the state at the time of construction and keeps its original shape. At present, riverbank, sluice gate, timber pond, slope, and lumber mill site are still in existence (please see Figure 2 for the locations). Some basic or lower parts of them have been composed of artificial stone structures (Figure 3). They are made of Tataki and building stones of granite. Almost all part of Tataki is covered by Menuri, which is cement plaster for the protection of weathering, except of the side parts of the lumber mill site in the lumberyard. We can observe the original Tataki only on the lumber mill site.

Figure 1. Location of Doudo lumberyard (Background is used electronic topographic map (tile) of Geospatial Authority of Japan).

Figure 2. Perspective view of Doudo lumberyard.

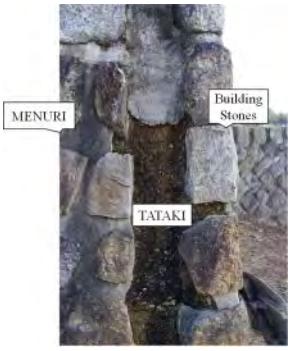

Figure 3. Characteristics of artificial stone structure.

2.2 *Research method*

In this study, we used Phantom 4 Pro^{+}V2.0 (DJI) to take aerial photographs of the site. The onboard camera has a 1-inch CMOS sensor with 20 megapixels, and lens with focal length of 8.8 mm. The field survey was conducted in January 2021 when the vegetation was less comparison to other warmer seasons. Flight was performed manually, and the heights was about 30 meters from the ground. The number of photographs were 266 and they were taken vertically and obliquely downward. Surveying work using a total station was also carried out for metric survey of control points (markers). Twelve markers were set up in the lumberyard.

The photogrammetric software used was Agisoft Metashape, a SfM/MVS (Structure from Motion/Multi View Stereo) software. The procedure is to load the photographs, select the markers, extract the feature points (key points and tie points) that are common to multiple photographs, and then create a dense 3D point cloud with more than tie points. A mesh is created from the dense point cloud. After that, a digital elevation model (DEM) and ortho mosaic image are created. The root mean squared error of the bundle calculation for camera positions and rotations was about 0.015 m.

There are no original blueprints or drawings for the construction of Doudo lumberyard. There is a documentation in which the dimensions were recorded for the design of lumberyard. Therefore, we could compare the photogrammetric survey results with the documentation. The target structures are timber pond, piers, sluice gate, slope, and rail trail (Figure 2).

2.3 *Research results*

The results of comparison between the photogrammetric survey results and the document of design are shown in Tables 1 to 5. There was a little difference in the main structures. About 0.5 m difference could be recognized in the height of the pier. The old documentation is higher than the photogrammetric results. Sedimentation is observed on the floor of the timber pond. Therefore, it is considered that the difference is caused by the inflow of sediment from the river and the depth of sedimentations might be about 0.5 m. Similarly, there are a few decades centimeters difference in the width of the pier. However, each pier almost has constant width, and the result in Figure 2

Table 1. Comparison of timber pond.

	Design document	Survey results
Perimeter length (m)	237	237
Area (m^2)	3,590	3,530

Table 2. Comparison of pier (m).

	Design document			Survey results		
	Length	Width	Height	Length	Width	Height
East side 1	18.2	1.8	2.1	18.1	1.4	1.7
East side 2	7.6	1.8	2.1	7.5	1.4	1.7
West side	18.2	1.8	2.1	18	1.4	1.8
South side	10	1.8	2.1	10	1.6	1.5
North side 1	18.2	1.8	2.1	18	1.5	1.7
North side 2	10.9	1.8	2.1	10.5	1.5	1.8

Table 3. Comparison of sluice gate (m).

	Design document	Survey results
Length	4.6	4.5
Width	4.6	4.5
Height	4.3	4.3

Table 4. Comparison of slope.

	Design document	Survey results
Inclination angle (°)	45	44

Table 5. Comparison of rail trail (m).

	Design document	Survey results
Length	49	49
Width	2.4	2.3

shows average width for each pier. It is considered due to the changes during construction, and the piers have enough widths for the passage of workers in the lumberyard. About other structures, there are no difference or less than a decade centimeter for the gate, slope, and rail trail. From these results, it can be considered that the Doudo lumberyard, which had been constructed more than 100 years ago, has been not deteriorated so much and kept in good condition.

3 STRENGTH MEASUREMENTS BY NEEDLE PENETRATION TESTS

3.1 *Survey method*

It's difficult to apply some destructive in-situ tests to heritages. Non-destructive needle penetration test is one of acceptable methods to evaluate the material strength of the heritages. The tests were conducted based on the method of Japanese Geotechnical Society (JGS 3431; JGS 2018). The outline drawing of a needle penetration tests device is shown in Figure 4. The elastic resistance of spring spindle, P (N), and penetration length of the needle, L (mm), are measured when the needle penetrates the materials from the surface. Unconfined compression strength, q_u (kN/m^2) is converted from the penetration resistance, $N_p = \mathrm{P/N}$ (N/mm), using the following Equation (1),

$$Log\ q_u = \alpha \log N_p + \beta \tag{1}$$

In this study, $\alpha = 0.978$ and $\beta = 2.599$ are applied from the result of MARUTO Testing Machine Company, Japan.

Needle penetration tests were applied to the Tataki on the side parts of the lumber mill site. The measurement points were set up on 0.5 m and 1.0 m from the ground (Figure 5). The survey

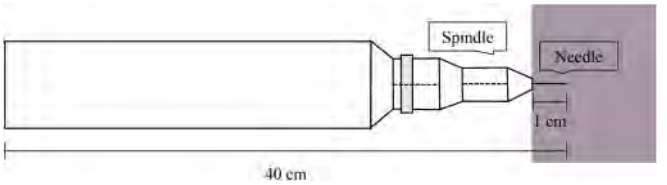

Figure 4. Outline drawing of needle penetration tests.

Figure 5. Measurement location.

was conducted at four locations, so totally eight points are selected. Five times measurements were taken at each point, and the average values were converted into the average unconfined compression strength.

3.2 *Survey results*

The survey results are shown in Table 6. The average values of unconfined compression strength are from 0.38 to 2.41 N/mm^2. The highest point is No. 2 and the lowest point is No. 4. The values of Nos. 1, 2 and 3 are about 1 to 2 N/mm^2. The values are consistent with previous study, which was conducted to similar material in another site (Amano 2020). The value of No. 4 was lower than other points. One of the possible cause is deterioration. Compared to the other locations, point No. 4 is close to the vegetation field and easily supplied with water. In addition, the are is faced to the northside and surface is not easily dried.

Table 6. Unconfined compression strength.

Point No.	Height (m)	$N_p = P/N$ (N/mm)	q_u (N/mm^2)
1	0.5	3.7	1.50
	1.0	4.8	1.94
2	0.5	5.0	2.01
	1.0	6.0	2.41
3	0.5	2.2	0.90
	1.0	2.8	1.14
4	0.5	0.9	0.38
	1.0	2.0	0.82

4 LABORATORY TESTS OF ARTIFICIAL STONE SPECIMENS

4.1 *Experimental methods*

First, artificial granite soil is created instead of natural one. We considered that it would be difficult to conduct experiments under the same conditions with soil collected from outcrop, because of the variation in its properties. Artificial granite soil is created from the combination of some kinds of sieved soil (see section 4.2 in detail). Using this artificial granite soil, compaction test was conducted to clarify the optimum water content and compaction energy. Next, the unconfined compression test was conducted. For the unconfined compression test, the specimens were prepared to match the optimum water content and compaction energy clarified in the compaction test.

4.2 *Selection of artificial decomposed granite soil*

Properties of decomposed granite soil depend on the nature of the original granite and the weathering degree. It is difficult to conduct the experiment under the same condition on the field-collected natural decomposed granite soil. Therefore, artificial granite soil was prepared from available soil materials. Artificial granite soil has the average grain size distribution of the decomposed granite soil throughout Japan (Sueoka 1990). The mixing ratio of artificial granite soil is shown in Table 7 and the grain size accumulation curves are shown in Figure 6.

Mikawa siliceous sand is an artificial high quality siliceous sand made from quartz schist, which is distributed around the eastern part of Okazaki City, Aichi Prefecture, Japan. This sand is crushed and sieved for various applications. It is characterized by its high purity of SiO_2, with content of about 98%. Grain size of Mikawa siliceous sand is divided into 5 classes, from No.4 to No.8, with the smaller number indicating a larger particle size.

Crushed rock is similar to Mikawa siliceous sands; however, it has grain size up to 20 mm. In this case, we used grain size from 4.75 mm to 2 mm in the crushed rock.

Table 7. Mixing ratio for artificial granite soil.

Material	Mixing ratio (%)
Crushed rock	13.1
Mikawa siliceous sand No.4	33.1
Mikawa siliceous sand No.6	27.9
Mikawa siliceous sand No.8	16.7
DL clay	9.2

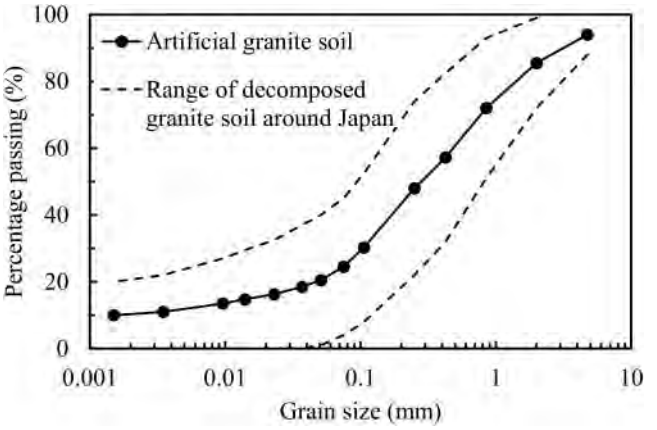

Figure 6. Grain size accumulation curve of decomposed granite soil.

4.3 *Compaction test*

Compaction tests were conducted using artificial granite soil based on Japanese Industrial Standards (JIS 1210 is as same as JGS 0711; JGS, 2015). An air-dried sample of the soil is mixed with water. It compacted in a metal mold of internal diameter 105 mm using 2.5 kg rammer of 50 mm diameter, free falling from 300 mm above the top of the soil. Compaction is done in three layers of approximately equal depth. Each layer is given 25 blows which are distributed evenly over the surface of the soil. Nonrepeating method, in which each sample of the soil is prepared in each water content, was applied. The clarified compaction curve is shown in Figure 7. From the experimental results, the optimum water content ratio to artificial granite soil is about 10%. In addition, the compaction energy was about 550 kJ/m^3. It was calculated from Equation (2),

$$E_C = \frac{W_R \times H \times N_L \times N_B}{V} \tag{2}$$

where W_R = rammer weight (kN); H = falling height of rammer (m); N_L = number of layers; N_B = compaction times per layer; and V = mold volume (m^3).

4.4 *Unconfined compression test*

Artificial stone specimens were prepared to conduct unconfined compression tests. Cylindrical specimens are used, and its size is 50 mm in diameter and 100 mm in length. An air-dried sample of the soil and quicklime is mixed with water. In addition, artificial seawater containing magnesium chloride was also used instead of water. The experimental conditions for quicklime and each material are shown in Table 8. Compaction is done in three layers. To match the compaction energy calculated in the previous section, the first layer with 6 blows, the second layer with 7 blows and

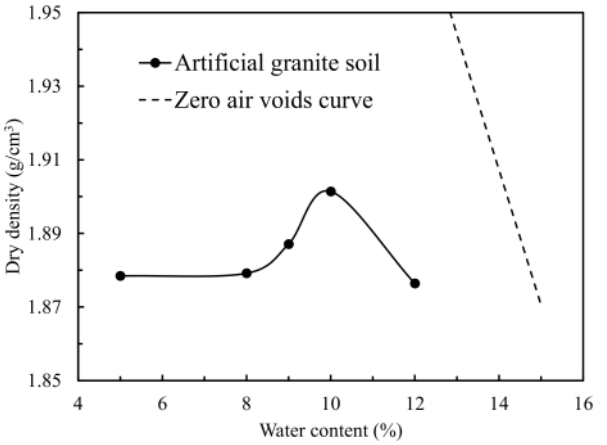

Figure 7. Compaction curve of the artificial granite soil.

the third layer with 9 blows has been compacted. Therefore, the total of 22 blows has been done for each specimen (Figure 8). After 7 days of natural drying, the unconfined compression tests were conducted based on Japanese Industrial Standards (JIS A 1216 is as same as JGS 0511; JGS 2015). The unconfined compression strength was calculated as an average value of three cylindrical specimens for each experimental condition.

Table 8. Experimental conditions.

Artificial seawater (%)	Mixing ratio (Quicklime : Artificial decomposed granite soil)
0, 3, 10%	1 : 8 1 : 10 1 : 15

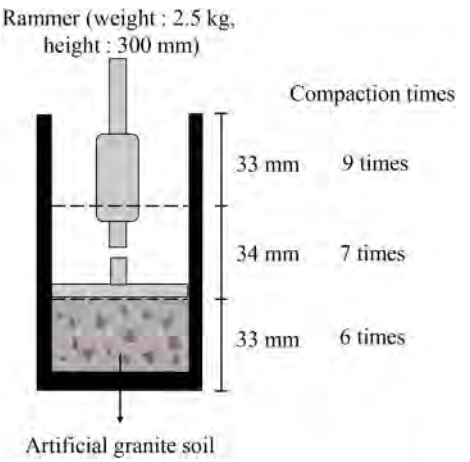

Figure 8. Preparation of artificial granite soil specimens for unconfined compression tests.

4.5 *Experimental results*

Experimental results are shown in Figure 9. The highest strength of about 2.5 N/mm^2 is obtained at the weight ratio of one quicklime to eight artificial granite soil with the concentration of seawater 3%. The lowest strength of about 0.7 N/mm^2 is one quicklime to fifteen artificial granite soil with the seawater 10%. The unconfined compression strength tends to decrease as the increasing ratio of granite soil to quicklime. The average strength is 1 to 2 N/mm^2, and this value is as same as one obtained in Doudo lumberyard by means of needle penetration tests.

The unconfined compression strength tends to decrease as the concentration of seawater increased. A large decrease of unconfined compression strength is observed at the concentration of seawater 10%. Takeshita et al. (2006) revealed that unconfined compression strength of artificial stone specimens decreases with increasing added salt. It might be caused by the slowing down of the electrical aggregation and grouping phenomena of soil particles due to calcium ion exchange reaction, which inhibits the stabilizing of quicklime. This suggests that decreasing strength with increasing added salt of the present case is also caused by the same reaction.

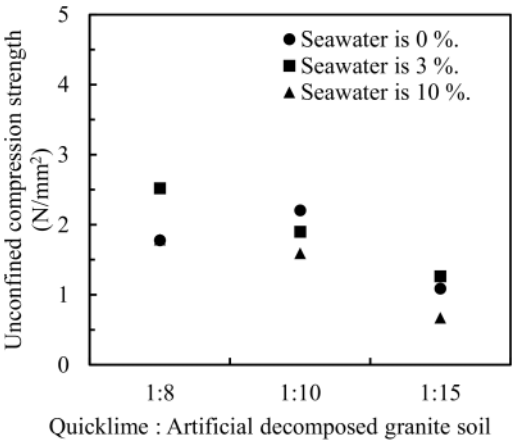

Figure 9. Results of unconfined compression tests.

5 CONCLUSION

In this study, for the purpose of restoration and preservation of artificial stone structures, a metric survey and strength measurement were conducted to document the current state of Doudo lumberyard. In addition, laboratory experiments were done to clarify the characteristics of the artificial stone specimens, Tataki. The results obtained are written as follows.

1) Photogrammetric survey using an UAV was conducted for Doudo lumberyard and its results was compared with the design documentation at the time of construction. As a result, there was almost no difference from the design documentation. The Doudo lumberyard had been constructed more than 100 years ago. However, it has been not deteriorated so much and kept in good condition.
2) The needle penetration tests were applied to Tataki in the Doudo lumberyard, to measure the strength of the original material. As a result, the average values of unconfined compression strength are from 1 to 2 N/mm^2, which is consistent with similar material in another site (Amano 2020).
3) Compaction tests and unconfined compression tests were conducted for artificial stone specimens, Tataki, in the laboratory. Artificial granite soil was prepared from available soil materials

to conduct the experiment under the same condition. The results of compaction tests clarified that the optimum water content ratio is 10%. Unconfined compression tests were conducted with the optimum water content ratio. The average values of unconfined compression strength are from 1 to 2 N/mm^2, which is consistent with the original materials, Tataki, in the lumberyard. In addition, the strength is influenced by the ratio of quicklime to the decomposed granite soil and the salt ratio added to water.

Doudo lumberyard has been kept in good condition under the preservation of Toyota City. However, it might be repaired for weathering and deterioration in the future. We could propose one possibility for repairing it by the original method of artificial stone construction with new artificial stone materials, Tataki.

ANKNOWLEDGEMENT

We sincerely thank Cultural Properties Section of Toyota City for supporting the survey of Doudo lumberyard and much information of the site. We thank Imai Family for the permission of browsing the design documentation of the lumberyard, which was constructed by their ancestor, IMAI Zenroku.

REFERENCES

Amano, T. 2020. On the 100th Anniversary of Hattori Choshichi's Death, Let's Refocus on the Historical Civil Engineering Method "Artificial Stone Construction", 38th Symposium Range and Scope of History of Technology in Japan: 5–28.

Amano, H., Amano, T., Ohashi, K., Sasaki, J., Natsume, K., Hori, K. 2006. Site of an underwater lumberyard in the middle reaches of the river, Doudo lumberyard timber transport on the Yahagi River, Toyotashi Kindai-no Sangyo-to Kurashi Hakken-kan.

Aichi Prefecture. 2005. Modern Heritage in Aichi Prefecture: Report on Comprehensive Survey of Modern Heritage (Buildings, etc.), Board of Education Office for the Protection of Cultural Properties, Lifelong Learning Division: 94–96.

Japanese Geotechnical Society (JGS). 2015. Japanese Geotechnical Society Standards: Laboratory Testing Standards of Geomaterial, Vol.1: p.262.

Japanese Geotechnical Society (JGS). 2018. Japanese Geotechnical Society Standards: Geotechnical and Geo-environmental Investigation Methods, Vol.3: p.400.

Sueoka, T. 1990. Geotechnical Engineering Study on Weathered Residual Soils, Doctoral Dissertation Kyoto University: 101–104.

Takeshita, Y., Tanimoto, K., Oyama, T., Tamura, J. 2006. Considerations in Geotechnical Characteristics of "Tataki" Soil, Chugoku Branch of Japanese Geotechnical Society, Vol.24 No.1: 101–106.

Geotechnical Engineering for the Preservation of Monuments and Historic Sites III – Lancellotta, Viggiani, Flora, de Silva & Mele (Eds)

Subsoil characterization and stability analysis for the Bourbon del Monte Palace in Piancastagnaio (Siena, Italy)

G. Ciardi, G. Bartoli & C. Madiai
Department of Civil and Environmental Engineering, University of Florence, Italy

ABSTRACT: The historical Bourbon del Monte Palace in Piancastagnaio (Siena, Italy) dates to the 17th century and represents an uncommon example of feudal architecture in Tuscany. It was inhabited until the end of the ’80s of the last century when, due to the high degree of instability achieved, it was declared unfit for use by the Public Authorities. The Palace lays on a sloping site, on the edge of fractured trachyte blocks mixed with alluvial deposits. It is characterized by four floors above ground and a basement at the South-East corner, while the North façade has two floors. Severe degradation phenomena of the building consist of multiple cracks diffused along the external and the inner masonry; furthermore, significant water infiltration from the floor has been observed in the South-East basement since the ’80s. Previous investigations have shown that the Palace has undergone two distinct settlements systems: one dates before the ’70s and may have caused the cracks along the South wall of the building; the other, more recent and probably related to the water infiltration on the basement, may have caused the damage to the South-East wall. This paper investigates the source of this second settlements system by modeling and analyzing a 2D soil section close to the South-East corner of the building. Firstly, the collected geotechnical and geological data and the modeling of the analyzed section are presented. Afterwards, the results of the numerical simulations are shown and discussed, analyzing the effects of the estimated settlements on the observed structural damage.

1 INTRODUCTION

Piancastagnaio is a small Italian town located in southern Tuscany. It was established during the late medieval age close to the Amiata Mountain which is a part of a massif of volcanic origin in the Italian Central Apennines. Located close to the center of Piancastagnaio, the *Bourbon del Monte* Palace is a typical example of baroque architecture. It dates to the beginning of the XVII century and consists of a huge masonry building ($\approx$ 31 m width and 34 m length) that was partially founded on ancient town-walls; the external walls thickness is approximately 1.2 m, and the texture of the masonry could be an infilled one; the floor levels are made of different types of masonry vaults (e.g. cross and cloister vaults). The geometrical configuration is quite regular, characterized by almost orthogonal masonry walls (Betti et al. 2010). The Palace rests on a sloping area, on the edge of fractured volcanic rock (trachyte blocks) mixed with silty deposits. It consists of two floors above ground on the North façade and four floors above ground on the South façade, in addition to a lower ground floor (basement) at the South-East corner. Specifically, as discussed in detail in the following sections, the outside East wall is partly built on trachyte (upward from the basement, toward the North wall) and partly on silty deposits (downward to the basement and to the South wall).

Originally belonging to the Bourbon del Monte Family, the Palace was sold in the XIX century. Thereafter it has been used for different purposes (e.g. for commodities recovery) and today it belongs to the Local Administration of Piancastagnaio. The building was inhabited until the end

DOI 10.1201/9781003308867-23

of the ’80s of the last century when it was declared unfit for use by the Public Authorities. Such a drastic decision was motivated by the high degree of instability that characterizes the whole building and that started growing significantly from the ’70–’80’s. Figure 1a shows the outside of the Bourbon del Monte Palace with the South-East corner in the foreground. Figure 1b shows the extreme degradation in the biggest central room inside the building.

Figure 1. The Bourbon del Monte Palace in Piancastagnaio: (a) outside view; (b) inside view.

At date, severe degradation phenomena consist of multiple cracks’ systems diffused along the external and the inner masonry, and of water infiltration from the basement at the South-East corner where the crack pattern is the most critical. Numerous investigations (geotechnical and geophysical surveys, numerical analysis of the building) have been performed in the past 30 years (e.g. Baldi 2008; Bartoli et al. 2008; Bartoli & Betti 2012; Betti et al. 2010; Montini 1990), trying to shed light on the origin of such a diffuse degradation. According to Bartoli & Betti (2012), the Palace has undergone two distinct differential settlements systems in the foundation soil underneath the South-East edge. The first dates before the 70’s and may have caused the crack system along the South wall of the Palace, letting the edge starting to detach, while the second, developed during the second half of the 80’s, may be the cause of the damage observed in the East wall. The latter system could also probably be related to the water infiltration from the basement, a phenomenon that has been observed since the ’80s. The reasons for the two settlements systems have never been univocally clarified, although research results from numerical analysis on the Palace showed that the two mechanisms are distinct (Bartoli & Betti 2012). Figure 2 shows the crack systems along the South and East walls, as reported in Picchioni (2008); Bartoli et al. (2009).

As previously pointed out by researchers (Bartoli et al. 2008, 2009; Bartoli & Betti 2012; Betti et al. 2010; Picchioni 2008), a soil settlement system located in the basement should be responsible for the diffused crack system along the East wall (Figure 2a), while the detachment of a portion of the South wall (Figure 2b) could be ascribed to slope instability. With reference to the former settlement system (Figure 2a), however, the mere difference in the mechanical properties of the foundation soils (trachyte upward the North wall, alluvial deposits toward the South wall, in the basement) can’t be the only responsible for the observed degradation phenomena, because the instability of the East wall dates to the ’80s, not before. It is likely that water infiltration, due to a change in the groundwater flow configuration (Baldi 2008) had modified the soil-structure interaction conditions.

This paper aims to investigate the most recent settlement system, probably related to a change in the mechanical characteristics of the foundation soil under the basement. Because the two settlements systems are distinct (Bartoli & Betti 2012), this paper deals with the geotechnical and numerical modeling of a subsoil section located along the East wall of the Palace, with the aim of clarifying the instability mechanisms observed in the East side of the building. After a brief description of the main geological characteristics of the subsoil in the area of Piancastagnaio, the geological and geotechnical data used to define the geotechnical model are presented. Finally, the numerical model implementation and the analysis results are shown and discussed.

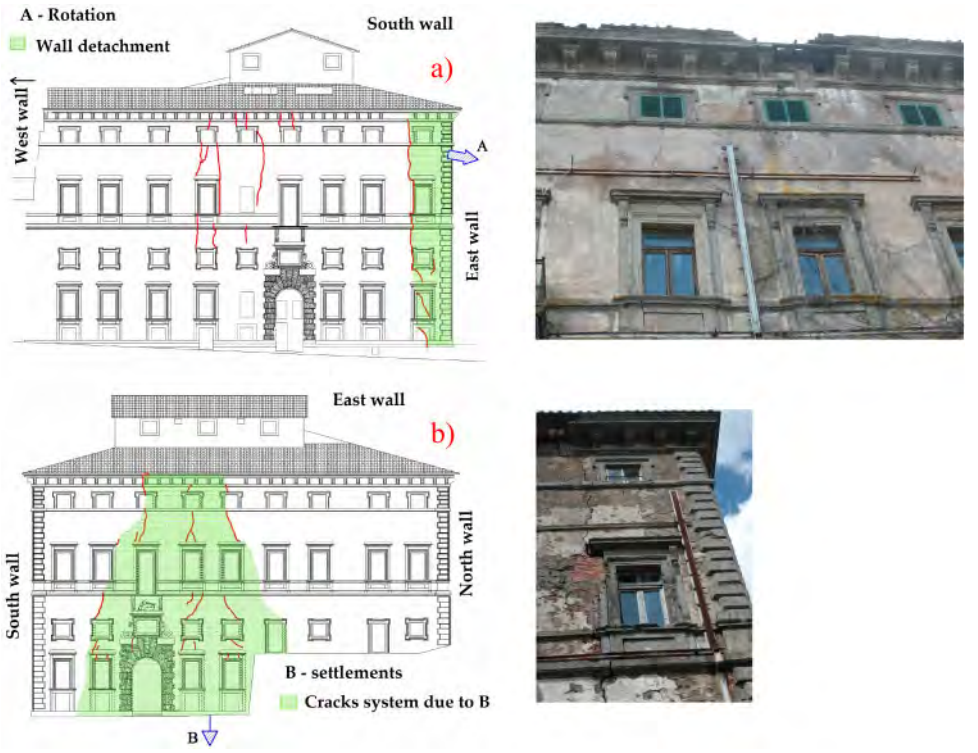

Figure 2. The actual crack systems: (a) East wall; (b) South wall (from Picchioni 2008).

2 GEOLOGICAL FEATURES OF PIANCASTAGNAIO AREA

Piancastagnaio is located at the edge of a limited plateau of volcanic origin (the Amiata Mountain is an effusive extinct volcan), approximately 800 m above the sea level. The geological configuration of the area is related to the volcanic activity of the Amiata Mountain: generally speaking, the actual area configuration is characterized by volcanic rocks overlying marine deposits. The town is on the edge of the Val di Paglia graben; the East slope is mainly composed of pliocenic clays, while the South slope is composed of argillites with intercalated calcareous rocks. Piancastagnaio is at the South-East corner of the Basal Trachydacitic Complex, a formation of volcanic rock dating to 430.000 years ago. Due its evolution, this formation is today characterized by integer blocks in the upper plateau (where the newer village is located), and by fractured blocks under the older village, where the Palace is located (Baldi 2008). The volcanic rock lies on marine deposits characterized by the following stratigraphy (from the bottom to the top) (Baldi 2008): 1) Ligurian Tectonic Unit, a heterogeneous lithotype composed of tectonised grey clay (argillites) alternating with banks of grey calcareous rock; this formation outcrops at the South side of Piancastagnaio. 2) marine Pliocene deposits, outcropping at the East side of Piancastagnaio; 3) sandy, silty deposit with clay (Pleistocene age), interlaying between the pliocenic clays and the surficial volcanic rock.

3 SUBSOIL CHARACTERIZATION FOR NUMERICAL MODELING

3.1 *Data availability and soil types*

Data collected from previous testing surveys were used to get all the parameters needed for the numerical implementation of a 2D-model section. At date, the most recent and comprehensive

results from geological/geotechnical analysis are reported in Baldi (2008) which was therefore taken as the reference in this paper. Other studies (e.g. Losito 2010) have been prevalently used for data integration, when possible.

The geophysical/geotechnical tests described in Baldi (2008) consist of: 1) *in situ* tests, namely: a) 4 boreholes located around the building and equipped with a piezometer (1 borehole) and inclinometers (3 boreholes); b) 8 shallow survey excavations (7 located in the basement, 1 in the ground floor); c) Standard Penetration Tests (SPT) performed within the 4 boreholes; d) seismic refraction and *ReMi* (Refraction Microtremor) tests, with estimation of compressional and shear seismic waves velocities V_p and V_s, respectively; 2) laboratory tests, namely: a) soil classification tests; b) shear strength tests (direct shear and unconfined compression tests) and oedometer tests on undisturbed soil samples collected at various depths in 2 boreholes.

Seven different soil types can be distinguished from the 4 litho-stratigraphic borehole profiles (Baldi 2008): filling soil (R), loose brown sand (Sa), sand with trachyte small clusters (Sa+Tra), fractured trachyte (Tra), grey silty sand (Sl), grey-brown sandy silt (Ls), and silt (L). Figure 3 shows the location of the 4 boreholes described in Baldi (2008) and the cross Section CC' that was used for numerical analysis (see Section 3.2).

Figure 3. Survey Boreholes location (red dots) and Section CC'. The basement is located close to borehole n°4.

From borehole surveys, it follows that the soil profile at the Northern side of the building (borehole n°1) includes trachyte (Tra) blocks (≈26 m thick) overlying silt (L); at borehole n°2, it is characterized by ≈9 m-thick Sa+Tra layer laying above silt (L), while boreholes n°3 and n°4 show the presence of a thin sand (Sa) layer (≈1.5–1 m thick at boreholes n°3 and n°4, respectively) overlying ≈4.5 m constant-thick sandy silt (Ls) layer, placed above a silt (L) layer. Shortly, some important conclusions can be drawn: a) the Palace lies on heterogeneous soil and rock types; b) significantly different subsoil configurations can be found at the Northern and Southern sides of the building. The Northern façade stands on trachyte blocks, while the subsoil under the Southern side is characterized by a sandy silt lens included between a thin Sa+Tra layer and the underlying L. The transition between trachyte and sandy silt at this side of the Palace is somewhere located at the entrance of the basement, where outcropping rock was used in the past as the foundation of the masonry arch that leads downward to the basement (Figure 4a).

According to piezometric measurements within the borehole n°3, the groundwater table is located at a depth of 3 m; a piezometer installed in the Palace basement (thus, at the South-East corner) revealed that the groundwater table is 0.5–1.0 m below the ground level. 2D electrical resistivity tomography performed within the basement (Losito 2010) confirmed that the subsoil was water-saturated. During a more recent visual survey conducted in 2015 by the authors, the groundwater had emerged and filled the survey excavations carried out at the basement (Figure 4b).

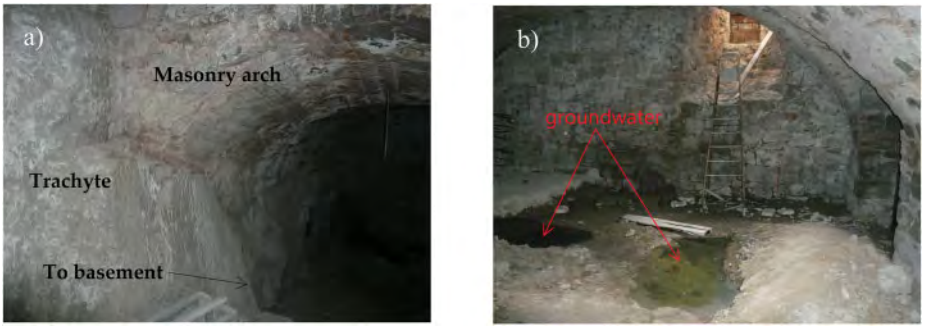

Figure 4. The basement: trachyte outcropping at the entrance (a); groundwater emerging from the floor (b).

3.2 *Section modeling*

3.2.1 *Geotechnical modeling*

The subsoil morphology of the analyzed Section CC' was reconstructed based on the profiles obtained from boreholes n°1 and n°4 located close to the East wall (Figure 3), assuming each litho-stratigraphic profile as a boundary condition for lithotypes identification and location; an additional boundary condition was represented by the lithotype Tra, outcropping at the basement entrance (Figure 4a). The surficial morphology in correspondence of the Palace was easily obtained by architectural surveys and previous analysis (Bartoli & Betti 2012; Betti et al. 2010). The Section CC' layout is shown in Figure 5. As can be seen, the separation between lithotypes Ls and Tra

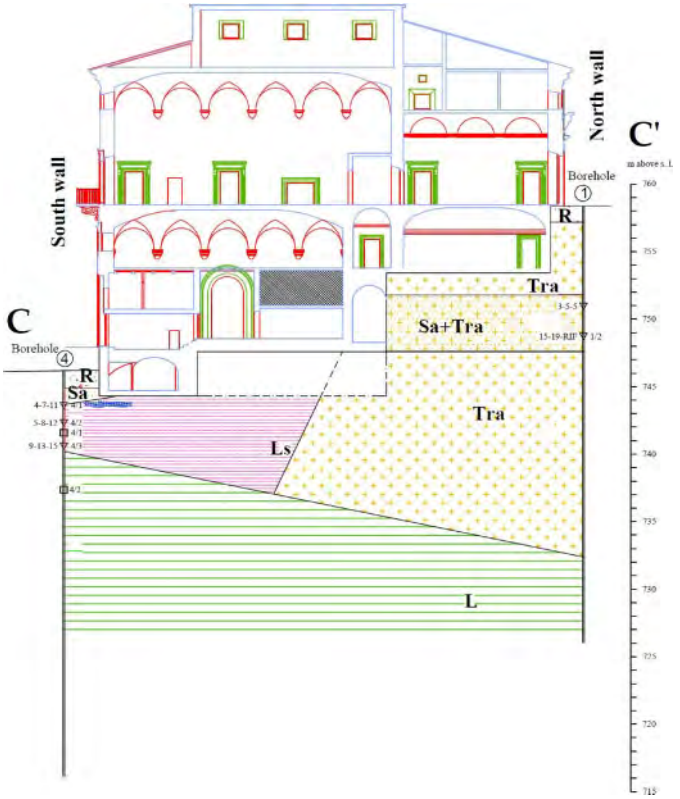

Figure 5. Section CC'.

occurs somewhere below the basement: due to the lack of data, the slope of the separating surface has been initially hypothesized in 45°.

The geotechnical properties and parameters of each soil type were obtained from the results of *in situ* investigations and laboratory tests on specimens collected from the four boreholes. Literature correlations were used to estimate the relative density, D_r, the angle of shearing resistance, φ', and the undrained cohesion, c_u, from the SPT parameter (N_{SPT}) (e. g. Gibbs & Holtz 1957; Hatanaka & Uchida 1996; Meyerhof 1957; Skempton 1986, among others). By way of example, Table 2 shows the *in situ* SPT test results. For the same lithotype, values of parameters obtained from N_{SPT} pertaining to different SPT tests or boreholes were averaged excluding the maximum and minimum values. Data were obtained for soil types Sa+Tra, L, Ls. The shear and compressional wave velocities were determined using the results of seismic refraction tests (Baldi 2008); the Poisson's coefficient, ν, for each soil type was thus calculated. Laboratory tests (direct shear tests, odometer tests, unconfined compression tests) were available for lithotypes L, Ls, and Sa, allowing to quantify the following soil parameters: unit weight, γ, angle of shearing resistance, φ', effective and undrained cohesion, c' and c_u, overconsolidation ratio, OCR, Young modulus, E, shear modulus, G, and bulk modulus, E_b. The obtained values, when pertinent, were averaged (weighted mean) with *in situ* test results, assuming a different weight depending on the level of test accuracy or on the reliability of literature correlations (e.g. a weight $= 0.6 < 1$ was used for c_u estimated from N_{SPT}). Table 1 shows the properties for each lithotype assumed in the numerical analysis; further details on the geotechnical subsoil characterization can be found in Ciardi (2015). Despite the amount of test/site investigations, the obtained mechanical soil properties are rather uncertain; while for some lithotypes results from field and/or laboratory tests could be compared, for others few (or none) data were available. For instance, in the case of lithotype Tra, the parameters were inferred from literature data, in order to simulate a rock-like behavior.

Table 1. SPT test results.

Borehole #	Depth (m)	Lithotype	N_1	N_2	N_3	N_{SPT}
1	7.20	Sa+Tra	3	5	5	10
1	9.40	Sa+Tra	15	19	50	69
2	3.40	Sa+Tra	5	6	13	19
2	7.20	Sa+Tra	12	14	19	33
2	10.00	L	8	11	15	26
2	14.00	L	14	16	19	35
3	8.80	Sl	11	35	34	69
4	2.30	Ls	4	7	11	18
4	3.60	Ls	5	8	12	20
4	5.30	Ls	9	13	15	28

Table 2. Geotechnical properties of soil types in Section CC'.

Lithotype	R	Sa+Tra	Tra	Ls	L
γ (KN/m^3)	17.5	18.5	22	20	21
D_r (%)	/	64	/	75	65
φ' (°)	28	38	40	30	32
c' (kPa)	0	0	200	0	5
c_u (kPa)	0	0	1e+4	182	153
ν (–)	0.44	0.38	0.46	0.40	0.48
E (kPa)	2.05e+5	6.38e+5	1.04e+6	5.16e+5	1.28e+6
G (kPa)	7.14e+4	2.31e+5	3.59e+5	1.83e+5	4.33e+5
E_b (kPa)	5.69e+5	8.86e+5	4.33e+6	8.60e+5	1.07e+7

3.2.2 *Numerical modeling*

The numerical model of Section CC' has been implemented using the finite difference code FLAC 2D (v. 7.0) (Fast Lagrangian Analysis of Continua) (Itasca 2011). The traditional Mohr-Coulomb constitutive model was used in the analysis. The presence of the Palace was simulated by normal distributed stresses applied to the soil surface obtained from the support forces calculated by a numerical model of the Palace (Picchioni 2008). A parametric analysis on the contact sloping surface between Ls and Tra was performed. Five different FLAC models were analyzed, with increasing complexity. Firstly, the presence of the slope at the South-East side of Piancastagnaio was neglected, extending the model surface horizontally, assuming the soil was dry (model 1). In model 2, the groundwater was considered, letting FLAC calculate the saturation contours after imposing the basement was fully saturated, as evident from field observations; in model 3, the mechanical properties of Ls were reduced. This simulates a decay in the mechanical characteristics of Ls due to the presence of water in the basement and it is justified by previous observations: Montini (1990) defined the base soil as a sort of "squished, pudding-like clay". The angle of shearing resistance was therefore decreased of 50% and the moduli (elastic, shear and bulk) of an order of magnitude. This reduction is not related to any observation/test result; however, results of numerical analysis from model 3 were not used for a quantitative estimation of soil settlements, but rather for comparison with outputs from model 2, to appreciate the influence of Ls parameters on the shape/location of settlements basin. Model 4 is equal to model 3 with varying the inclination of the separation surface between Ls and Tra; the variation of the angle of inclination (positive clockwise), α, was assumed between a minimum of 0° (vertical surface) and a maximum 80° (Ls is detected in borehole n°4 profile, thus representing a boundary for the upper α values). At last, model 5 considers the sloping ground at the South-East wall with varying α. Topographic surveys showed that the slope has inclination of $\beta \approx 13°$ (positive counterclockwise). However, no geotechnical data are available for the soil within the slope, that was therefore assumed equal to lithotype L; thus, model 5 essentially represents a change in the boundary conditions. Furthermore, due to the presence of a road, a retaining wall and some buildings along the slope, it would not be possible to build a satisfactory model of the slope.

4 RESULTS AND DISCUSSION

The results of numerical models are described in this section for all models. Figure 6a shows the vertical displacements obtained from model 1; the maximum vertical displacement was ≈8.8 mm, located under the South-East corner of the East wall. Figure 6b shows a detail of the settlement basin under the South-East corner; all results are reported in meters. When groundwater is considered (model 2), the shape and location of the settlements' basin did not essentially change; the maximum vertical displacement was ≈10 mm. It is worth observing that, despite the heavy simplifications of

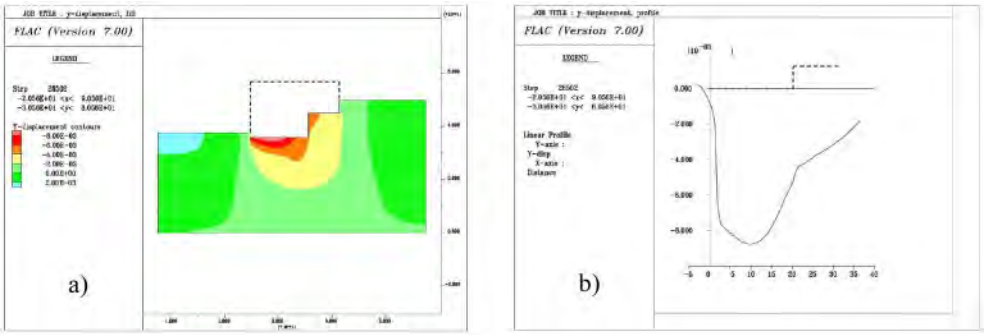

Figure 6. Section CC'. Vertical displacement from model 1 (a); zoom at the South-East corner (b).

the proposed models, the location and shape of the settlements' basin is compatible with the crack systems along the building East wall (Figure 2a).

Model 3 introduces the decay of mechanical properties of Ls lithotype, related to water infiltration. Figure 7 shows a comparison among the settlements' basin obtained from models 1–3: as can be noted, the shape and location are essentially the same. Despite the numerical values obtained from model 3 (as stated in Section 3, the reduction of Ls mechanical characteristics is not test-based), this model confirms that the settlements' basin is strongly influenced by Ls characteristics, as it may be hypothesized considering that the upper side of the East wall is built on rock; thus, a decay of Ls mechanical properties would have essentially increased differential settlements without significantly changing the location of the settlements basin.

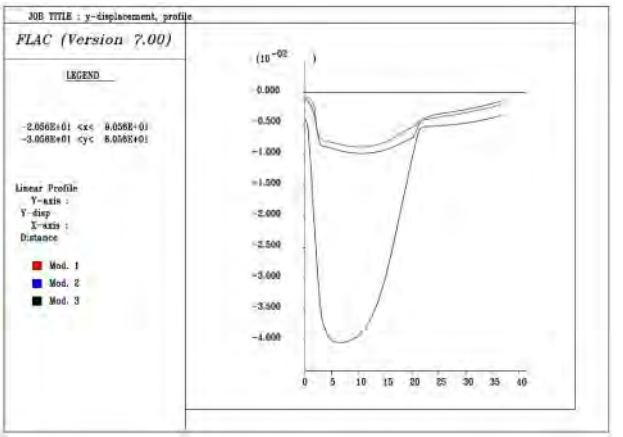

Figure 7. Vertical displacement comparison among Models 1–3.

Figure 8 shows the effects of the slope (α) of the contact surface between the lithotypes Ls and Tra. The maximum vertical displacement, y_d, occurs for $\alpha = 45°$; absolute minimum of y_d occurs for $\alpha = 80°$, which corresponds to a thinner layer of Ls under the basement, while a relative minimum occurs for the (unlikely) condition of $\alpha = 0°$ (vertical separation between Ls and Tra) (Figure 8b). When considering the sloping ground on the South side of the Palace, the maximum vertical displacements are expected to increase because of the change in boundary conditions. Figure 9 shows the displacement vectors resulting from numerical analysis ($\alpha = 45°$). The maximum displacement vector is located at the basement (with maximum vertical component ≈62 mm); the

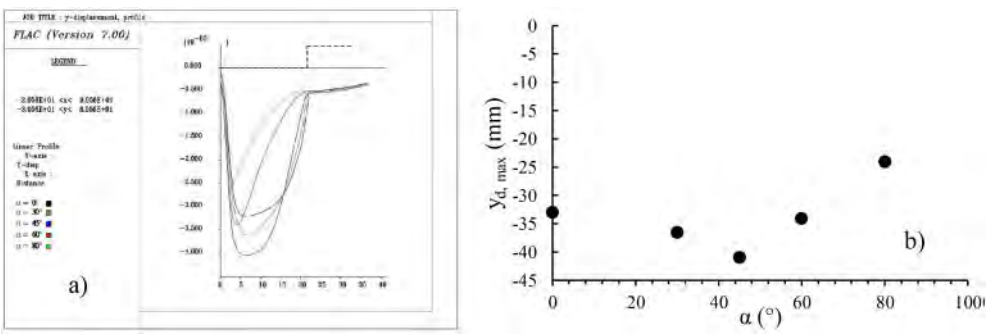

Figure 8. Section CC'. Zoom of vertical displacement from model 4 (a); maximum vertical displacement versus slope of Ls-Tra contact surface (b).

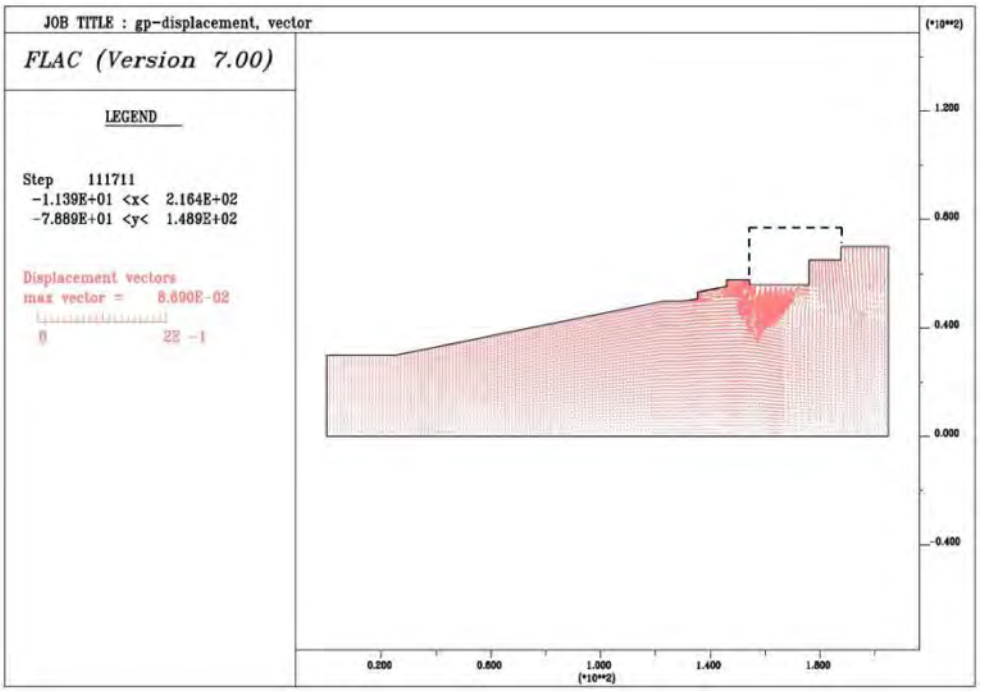

Figure 9. Section CC'. Displacement vectors from model 5.

shape of the settlements basin agrees with the actual crack systems on the East wall. As it was for model 4, the condition associated with maximum y_d was for $\alpha = 45°$.

It should be noted that, in the numerical models, the Palace has been simulated by the normal stresses it applies to the underlying soil (see Section 3.2.2). This assumption, which implies neglecting the stiffness characteristics of the building, is essentially justified by the aim of this study (namely, to verify the relative influence of different soil types on the settlements' basin at a side of the Palace). However, it is essential that a proper soil-structure interaction analysis, which considers the different stiffness of the soil and the structure, is performed in order to point out more realistic conclusions.

5 SUMMARY AND CONCLUSIONS

The Bourbon del Monte Palace in Piancastagnaio (Siena) is a historical building dating to the XVII century, located in southern Tuscany (Italy) in an area where the geological characteristics are related to the volcanic activity of the effusive, extinct Amiata volcan. The Palace is affected by extreme degradation phenomena, like multiple and diffused cracks systems, and water infiltration from the basement. It lies on a sloping ground, partly on fractured volcanic rock (trachyte), partly on sandy silt deposits. Many studies have highlighted that the Palace has experienced two independent settlements systems: the first connected to the crack system along the South wall of the Palace, which dates before the 70's, and a second, more recent, that may have caused the damage observed in the East wall.

Attempting to account for this latter system of settlements, a series of extremely simplified numerical analysis have been performed in this study on a cross section located along the South-East wall. Firstly, the geotechnical characteristics of the subsoil are identified from previous studies;

then, five numerical models, with increasing complexity, are analyzed. As emerged from numerical results, some conclusions can be drawn:

- the shape of the settlements basin obtained in all models is compatible with the observed crack system along the East wall;
- differential settlements may have increased significantly due to a reduction of the mechanical characteristics of sandy silt soil (Ls), above which the South-East edge of the Palace is built on;
- the location of the settlements' basin is related to the different types of foundation soils;
- a change in the model boundary conditions did not lead to a significant change of the settlements' basin location.

The proposed numerical models suffer of a certain degree of uncertainty, especially related to the mechanical characterization of Ls lithotype, and they do not aim to a quantitative estimation of soil settlements. A supplementary in situ and laboratory testing survey, with the purpose of a comprehensive analysis of the subsoil underneath the South-East wall, should have been performed in 2015; however, due to various impediments, no further actions were undertaken. As a result, the Palace is still in a situation of profound crisis, and no solutions are, unfortunately, in sight.

REFERENCES

Baldi, A. M. 2008. Consolidamento del Palazzo Bourbon del Monte di Piancastagnaio – Relazione geologica e geotecnica. Technical report (in Italian)

Bartoli, G., & Betti, M. 2012. Indagini diagnostiche nel Palazzo Bourbon del Monte in Piancastagnaio (SI). Technical report (in Italian)

Bartoli, G., Betti, M., Orlando, M., Picchioni, A., & Spinelli, P. 2009. Analisi ed interpretazione del dissesto statico di Palazzo Bourbon-Del Monte a Piancastagnaio. Bollettino Ingegneri, n° 12 (in Italian)

Bartoli, G., Orlando, M., Betti, M., & Picchioni, A. 2008. Monitoraggio ed indagini diagnostiche nel Palazzo Bourbon del Monte in Piancastagnaio (SI). Technical report (in Italian)

Betti, M., Bartoli, G., & Orlando, M. 2010. Evaluation study on structural fault of a Renaissance Italian palace. *Engineering Structures*, 32(7): 1801–1813

Ciardi, G. 2015. Il Palazzo Bourbon del Monte a Piancastagnaio (SI): analisi e modellazione numerica del terreno di fondazione e proposta d'intervento. Master's degree thesis (in Italian)

Gibbs, H. J., & Holtz, W. G. 1957. Research on Determining the Density of Sands by Spoon Penetration Testing. Proc. 4th Int. Conference on Soil Mechanics and Foundation Engineering, Vol. 1: 35–39

Hatanaka, M., & Uchida, A. 1996. Empirical correlation between penetration resistance and internal friction angle of sandy soils. *Soils and foundations*, 36(4): 1–9

Itasca, 2011. FLAC version 7.0. Itasca Consulting Group Inc

Losito, G. M. S. 2010. Palazzo Bourbon-Del Monte a Piancastagnaio – campagna di prospezione geofisica: ert e profiler. Technical report (in Italian)

Meyerhof, G.G. 1957. Discussion on Research on determining the density of sands by penetration testing. Proc. 4th Int. Conference on Soil Mechanics and Foundation Engineering, Vol. 1: 110

Montini, P. 1990. Intervento di massima urgenza per opere di presidio e salvaguardia del Palazzo Bourbon del Monte e della estremità sud dello abitato di Piancastagnaio – relazione geologica geotecnica. Technical report (in Italian)

Picchioni, A. 2008. Il Palazzo Bourbon-Del Monte in Piancastagnaio (SI): analisi dei dissesti statici e proposta di consolidamento. Master thesis (in Italian)

Skempton, A. W. 1986. Standard penetration test procedures and the effects in sands of overburden pressure, relative density, particle size, ageing and overconsolidation. *Géotechnique*, 36(3): 425–447

Geotechnical Engineering for the Preservation of Monuments and Historic Sites III – Lancellotta, Viggiani, Flora, de Silva & Mele (Eds)

Experimental study on the influencing factors of repairing white marble beam by MICP

Jing Qiao, Jianhong He, Xichen Xu, Hongxian Guo & Xiaohui Cheng
Department of Civil Engineering, Tsinghua University, Beijing, China

ABSTRACT: Due to the natural environment and man-made destruction, many outdoor stone relics have been weathered and damaged. To restore and protect these historical heritages, microbially induced $CaCO_3$ precipitation (MICP), one of the most novel technologies, can be applied in an environmentally friendly way. This study repairs the broken white marble beams ($40 \times 40 \times 160$ mm) with dolomite sand by MICP technique and investigates the effects of different factors on the restoration process. Firstly, the broken beams with different surface roughness are prepared. The prepared broken beams are treated with two different repairing methods (injection grouting and gravity-driven infiltration). During the MICP treatment, different concentrations of the cementation solution are provided to the samples. After completing the MICP process, the three-point bending tests are conducted to obtain the mechanical properties of the repaired white marble beams and evaluate the effects of the restoration. Overall, this paper can help researchers understand the effects of repairing method, surface roughness, and cementation solution concentration in MICP on repairing white marble beams.

1 INTRODUCTION

Stone cultural relics often play a significant role in studying history and ancient structures for humans. There are many outdoor stone relics around the world, such as the Yungang Grottoes in China, the Alhambra Palace in Spain, and the Great Sphinx in Giza. However, due to their *in-situ* large size, most stone relics are difficult to move indoors for protection (Xu et al. 2019). Traditionally, to protect the outdoor cultural relics from the damage of man-made destruction and natural environment, many chemical materials have been used to repair and strengthen the historical heritages (Zhang et al. 2013). Among these materials, the inorganic materials (e.g. cement) may act well at aging resistance yet the compatibility between the inorganic materials and the stone relics is poor, and the organic materials (e.g. epoxy resin) perform well in reinforcement and water resistance, but they still have some disadvantages such as short effective lifetime, low permeability and poor compatibility with relics (Liu et al. 2006; Yang et al. 2015). Therefore, it is necessary to explore new materials and methods to repair stone cultural relics.

To repair the stone relics more environmentally friendly, microbially induced $CaCO_3$ precipitation (MICP), as one of the most novel technologies, has attracted worldwide attention. This MICP technology is a biologically driven $CaCO_3$ precipitation process, which includes two major stages: urea hydrolysis and $CaCO_3$ precipitation (Dejong et al. 2010). The MICP process starts with the urea hydrolysis by urease released from bacteria, then the $CaCO_3$ crystals are formed with the bacterial cells as nucleation sites (Mujah et al. 2017). The precipitated $CaCO_3$ crystal bonds the sand particles together through effective bridges thereby turning natural sand particles into bio-sandstone and improving their mechanical properties (Whiffin et al. 2007).

DOI 10.1201/9781003308867-24

Nowadays, MICP technique, including bio-deposition and bio-cementation has already been investigated for protecting and restoring stone relics. Le Métayer-Levrel et al. (Le Métayer-Levrel et al. 1999) utilized carbonatogenic bacteria and induced $CaCO_3$ precipitation as protecting surficial coatings on limestone buildings. De Muynck et al. (De Muynck et al. 2010) also investigated the protection and consolidation of stones with bacterially induced carbonate precipitation, showing that the sample repaired via bio-deposition can achieve the same performance as that treated with ethylsilicates. Minto et al. (Minto et al. 2010) carried out MICP treatment in a column filled with marble grains and found out that the induced $CaCO_3$ precipitate was strong enough to cement the marble sand together. Tan et al. (Tan 2017) successfully applied MICP to sealing the V-grooves on white marble beams with dolomite sand and conducted four-point bending tests to examine their mechanical behaviors. Moreover, Tan (Tan 2017) also repaired white marble cubes through MICP technique, and after the repaired cubes were exposed to 40 freezing thaw cycles, they remained whole with only several tiny cavities on the surfaces. He et al. (He 2019) restored the white marble beams with V-grooves and cracks by MICP, and their CT scanning results indicated that the quality of the bonding layer played an important role in enhancing the flexural strength. These researches indicate that MICP is a potential approach to not only strengthening stone relics but helping relics resist weathering.

Nevertheless, MICP cementation is a complex biochemical process. To achieve a better bio-cementation effect, this study investigates the factors which may affect the bio-cementing for restoration of stone relics. First, the introduction of bacterial suspension and cementation solution to the specimens can be achieved generally through two main methods including injection grouting and gravity-driven infiltration, therefore both two methods were applied in this experiment. Then, according to previous researches by Tan (Tan 2017) and He et al. (He et al. 2019), the bonding layer seemed to be easily damaged when the fracture surfaces were excessively smooth; thus to study the effect of surface roughness, the fracture surfaces were pretreated with different roughness before the MICP process. Moreover, the concentration of cementation solution is another critical factor in MICP process. The research by Tan (Tan 2017) demonstrated that the unconfined compressive strength (UCS) of bio-cemented dolomite sand column was closely related to the concentration of used $CaCl_2$. Al Qabany et al. (Qabany et al. 2013) treated sand samples with different concentrations of cementation solution and found that a high concentration solution resulted in stronger samples, yet a low concentration would ensure more homogeneity in cementation. Thereby, this study investigates the influence of cementation solution with different concentrations, meanwhile exploring whether the cementation solution with a low concentration can achieve the same effect as the one with a high concentration on stone relics restoration.

Overall, this study aims at examining the influencing factors (treatment method, surface roughness, and cementation solution concentration) on the white marble beams with dolomite sand. After the MICP treatment, the three-point bending tests were conducted for bio-cemented samples to investigate the effects of different factors. Although this study focuses on the restoration of white marble, a kind of metamorphic rock widely used in palaces and royal gardens in China, such as the Forbidden City and the Old Summer Palace, the results of this paper can provide a reference for other stone relics.

2 MATERIALS AND METHODS

2.1 *Materials*

2.1.1 *Sample preparation*

The stone relics repaired in this MICP study are white marble beams (40 × 40 × 160 mm) sampled from Dashiwo Town, Fangshan District, Beijing, China, the major composition of which is dolomite

($CaMg(CO_3)_2$). Meanwhile, the dolomite sand acts as the filling material, and the particles own sizes from 0.1 to 0.2 mm in diameter.

The intact white marble beams were broken off by three-point tests, and their crack widths were held to 2 mm when repairing the beams by MICP technique. Figure 1 (a) and (b) present the beam samples before and after being broken in half respectively. In order to investigate the effect of surface roughness, the repairing surfaces are divided into smooth surfaces and rough surfaces. The fracture surfaces without any additional pretreatment are called "smooth surfaces" yet the fracture surfaces with 7–8 grooves are called "rough surfaces". The depth of the grooves on the rough surface is approximately 2 mm. Moreover, in this paper, the surface roughness of the specimens with two smooth sections is regarded as "smooth", and for the samples where one of the two repairing sections is pretreated as a rough surface, the surface roughness is called "rough".

Figure 1. The experimental beams: (a) the original intact beams and (b) the beams broken in half.

2.1.2 *Bacterial suspension*

The urease active strain of *Sporosarcina pasteurii* (ATCC11859) was selected to induce urease hydrolysis in this study. *Sporosarcina pasteurii* was cultivated in yeast extract based medium (20 g/L yeast extract, 10 g/L $(NH_4)_2SO_4$, 10 μM $NiCl_2$, pH 8.5–9.0). After 14–16 hours of incubation at 30° with a continuous shaking speed of 180 r/min, the bacterial suspension was harvested. The average urease activity and the optical density (OD_{600}) of the harvested culture are 15 mM/min and 3 respectively.

2.1.3 *Fixation solution*

The fixation solution was 0.05 M $CaCl_2$ solution to fix the bacteria on the fracture and dolomite sand surfaces, thereby achieving a more homogeneous $CaCO_3$ precipitation later (Tobler et al., 2012).

Cementation solution. In this study, two different concentrations of the cementation solution are utilized: the higher concentration solution consists of 0.5 M urea and 0.5 M $CaCl_2$, and the lower concentration solution consists of 0.33 M urea and 0.15 M $CaCl_2$.

2.1.4 *Cementation solution*

In this study, two different concentrations of the cementation solution are utilized: the higher concentration solution consists of 0.5 M urea and 0.5 M $CaCl_2$, and the lower concentration solution consists of 0.33 M urea and 0.15 M $CaCl_2$.

2.2 *Experiment*

2.2.1 *Scheme design*

To examine the effects of different influencing factors, this study treats the broken beams with different methods. The detailed scheme of this experiment is presented in Table 1. Each group has five replicates, such as Group A-1, A-2, A-3, A-4, A-5.

Table 1. The scheme of laboratory tests.

Group	Repairing method	Surface roughness	Cementation solution
A	Injection grouting	Smooth	0.5 M urea, 0.5 M $CaCl_2$
B	Gravity-driven infiltration	Smooth	0.5 M urea, 0.5 M $CaCl_2$
C	Injection grouting	Rough	0.5 M urea, 0.5 M $CaCl_2$
D	Gravity-driven infiltration	Rough	0.5 M urea, 0.5 M $CaCl_2$
E	Gravity-driven infiltration	Smooth	0.33 M urea, 0.15 M $CaCl_2$

2.2.2 *Pretreatment*

Before the MICP cementation, the epoxy resin and two semicircular iron hoops were used to fix the broken beam, as presented in Figure 2, and the crack width was held to 2 mm. The broken beams were placed horizontally during the MICP process. The bottom and two sides of the crack were sealed with gauzes. The top of the crack was not only sealed with the epoxy resin but also with a plastic film with three reserved grouting holes, making sure that all the dolomite sand would be retained in the crack instead of being flushed away.

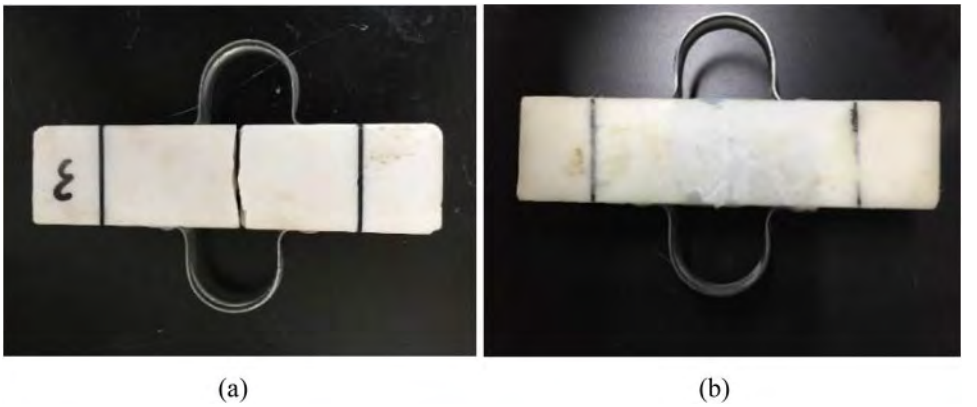

Figure 2. The fixing method for the broken beams: (a) the beam is fixed by two semicircular iron hoops with a 2 mm crack and (b) the beam is sealed by the epoxy resin.

2.2.3 *Restoration treatment*

The MICP treatment process can be divided into two stages, the former stage taking 9 days and the latter one taking 5 days. Three baches of grouting were applied to the broken beam samples each day. For each patch, 1.6 ml bacterial suspension, 0.2 ml fixative solution, and 8 ml cementation solution were provided to the samples with the rate of about 70 μL/min, respectively. For clarity, the experimental setup and procedure are sketched in Figure 3.

During the first stage, the samples were treated by two different methods as shown in Table 1: the broken beams repaired by injection method were added with 10 g dolomite sand at the beginning

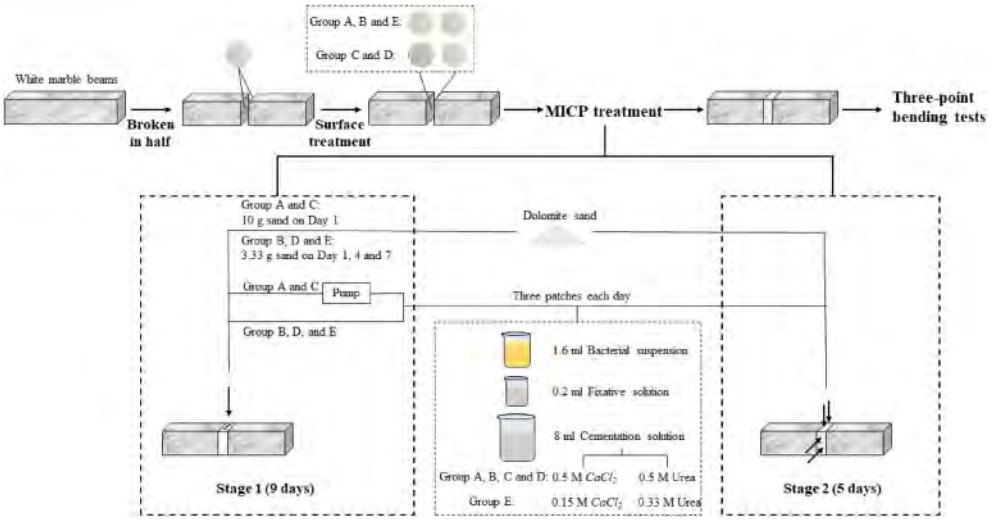

Figure 3. The sketch of the experimental setup and procedure.

of the MICP process and the samples treated by gravity-driven infiltration were added with 3.3 g sand every three days.

2.3 *Measurement*

After completing the MICP treatment, the three-point bending tests were conducted to obtain the strength of the repaired beams through a Material Test System 810 (MTS810) in Building Materials Laboratory of Tsinghua University. During the test, the load was applied at a constant rate of 0.3 mm/min. The distance L of the two symmetrical simple supports was 100 mm, and the concentrated force acted on the middle of the beam.

For each sample, the dimensions including the width b and the height h of the beams were measured, and the failure load F was obtained by the three-point bending tests. Then the bending strength R of the specimen could be calculated as $3FL/(2bh^2)$.

3 RESULTS AND DISCUSSION

3.1 *Bending strength*

Prior to MICP treatment, the three-point bending tests were conducted on the original intact beams, and the results presented that the average bending strength of all the original intact beams is 13.81 MPa with a low standard deviation of 1.24 MPa. After the experiment, the bending test results showed that the average flexural strength of the repaired beams via the MICP technique could reach 3.46 MPa, almost 25.1% of the strength for the intact beams. The detailed bending strength of the intact beams and the repaired beams in each group is shown in Figure 4 respectively, and the percentages in Figure 4 are the ratios of the strength of the intact beams to the corresponding repaired beams. Besides, the repaired bending strength results of Group B-1, B-5 and C-5 were missing because the three specimens were broken accidentally before conducting the three-point bending test.

To study the effect of the repairing method, the samples treated by different methods were compared with the same surface roughness and cementation solution concentration. It is obvious that the average bending strength of the two injection grouted groups could both reach

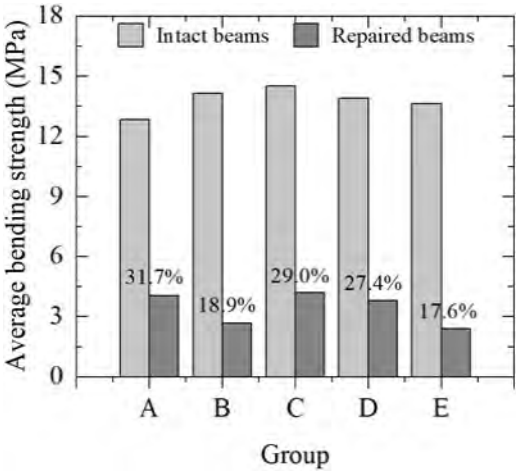

Figure 4. The bending strength results of the intact beams and the repaired beams. The percentages are the ratios of the strength of the intact beams to the corresponding repaired beams.

4 MPa. As can be seen from Figure 5, for the specimens with smooth surfaces, the average bending strength of Group A is 1.5 times that of Group B, yet the standard deviation of Group B is greatly higher than that of Group A. Figure 5 also shows that for the rough surface samples, the average bending strength of Group C is higher with a lower standard deviation. Therefore, it seems that when the beams are repaired with the same surface roughness and cementation solution concentration, the bending strength of the samples grouted by the injection method is higher than that of the samples bio-cemented by the gravity-driven infiltration method, and the performance of the specimens treated by injection grouting method is also more stable.

Additionally, the relationship between the bending strength and surface roughness pretreated to the broken beams can also be obtained from Figure 5. It is worthwhile mentioning that for the specimens treated with both injection grouting and gravity-driven infiltration method, the average bending strength of the samples with rough surfaces is higher than that of the smooth surface samples, and the standard deviation of the rough surface specimens is relatively low, indicating that the pretreated rough surfaces could help to enhance the bending strength of the repaired beams and to stabilize the performance. Moreover, for Group A and C where the beams are repaired by injection method, the bending strength is likely to be the same (4.06 MPa and 4.21 MPa), but the surface roughness is different. However, for Group B and D repaired by gravity-driven infiltration, the strength of the rough surface samples can reach 1.42 times the strength of the smooth surface samples. Hence, the gravity-driven infiltration method is more sensitive to surface roughness.

In terms of the effect of cementation solution concentrations, this study only conducts an experiment on two different concentrations of cementation solution with the smooth surface samples treated by gravity-driven infiltration. As can be seen from Figure 5, the average bending strength of Group B and E is 2.68 MPa and 2.39 MPa respectively. Although the B Group bending strength is a little higher than the E Group strength, the difference between the beams provided with the two different concentrations is small. However, the amount of urea and $CaCl_2$ provided to Group B is significantly higher than that used for Group E. Meanwhile, the standard deviation of Group E is much lower than that of Group B. Therefore, it can be concluded that a low concentration of the cementation solution might help the repaired beams to reach high performance with less cost.

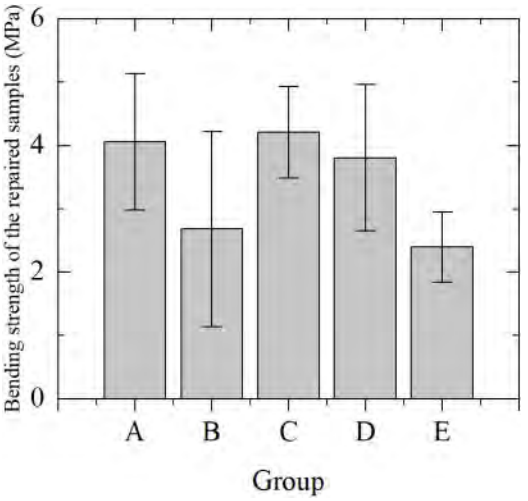

Figure 5. The results of bending strength for repaired samples.

3.2 *Failure mode*

The fracture surfaces of the repaired beams are presented detailedly in Table 2. There are mainly two different failure modes of the specimen in all groups, and Figure 6 presents these two failure modes with different fracture surfaces.

The injection grouted beams, i.e. Group A and C, are all broken with the same failure mode that the original stone beam separates from the bonding layer, as presented in Figure 6 (a). With respect to Group C where the sample has both a rough surface and a smooth surface, the damage always occurs to the smooth side, suggesting that the rough interface may improve the interface strength.

In comparison with the injection grouted beams, there are two different types for the specimens repaired by gravity-driven infiltration (Group B, D, and E): 4 (Group B-1, B-2, B-5, and Group D-5) of the 15 gravity-driven infiltration samples are cracked with the original stone beams separating from the bonding layer as well as the injection grouted beams; the other 11 specimens are cracked with another failure mode that the fracture surface arises from one side of the original beam and propagates through the bonding layer to the opposite side, as shown in Figure 6 (b). It is worth mentioning that Group D-4 is damaged with its fracture surface expanding through the original stone beam, showing that the white marble beam and the dolomite sand grains are bonded together well. The bending strength of Group D-4 is also the highest (5.46 MPa) among the beams repaired by gravity-driven infiltration. For the rest of the 10 samples, only the two original sections and the bonding layer are damaged. The results potentially demonstrate that in this study, for the beams treated by gravity-driven infiltration, the interface strength and the bonding layer strength are closed while the bonding layer strength of the injection grouted samples is clearly higher than the interface strength, meaning that there are some weak cementations in the bonding layer of the gravity-driven infiltration specimens.

Figure 6. The failure mode of the repaired beams: (a) Group C-2, (b) Group D-3.

3.3 *Discussion*

In this study, a series of experiments were carried out to investigate the effects of different factors on the restoration process and find the favorable method of MICP repairment. Based on the experimental results summarized in Table 2, the relationship between the performance of the repaired beams and different influencing factors are discussed as follows.

Table 2. Summary of white marble beams repaired by different MICP treatment.

Group	A	B	C	D	E
Repairing method	Injection grouting	Gravity-driven infiltration	Injection grouting	Injection grouting	Gravity-driven infiltration
Surface roughness	Smooth	Smooth	Rough	Rough	Smooth
Cementation solution	0.5 M urea, 0.5 M $CaCl_2$	0.5 M urea, 0.5 M $CaCl_2$	0.5 M urea, 0.5 M $CaCl_2$	0.5 M urea, 0.5 M $CaCl_2$	0.33 M urea, 0.15 M $CaCl_2$
Bending Strength of the repaired beams (MPa)	4.06 ± 1.08	2.68 ± 1.54	4.21 ± 0.72	3.81 ± 1.15	2.39 ± 0.55
Failure mode*	The first failure mode	Group B-1, B-2, and B-5: the first failure mode Group B-3 and B-4: the second failure mode	The first failure mode (the damage occurs to the smooth side)	The second failure mode (the original stone of Group D-4 is also damaged)	The second failure mode
Fracture surface					

*The first failure mode means that the original stone beam separates from the bonding layer, as presented in Figure 6 (a); the second failure mode means that the fracture surface arises from one side of the original beam and propagates through the bonding layer to the opposite side, as shown in Figure 6 (b).

Previous studies have already attempted to use MICP technique to restore stone relics with different repairing methods. Tan (Tan 2017) repaired the white marble beams by injection grouting method, and the restoration process in He et al. (He et al. 2019) consisted of two stages: injection grouting and gravity-driven infiltration. This study restored the cracked beams with these two methods separately aiming to find the favorable restoration method, and the experimental results demonstrated that both injection grouting and gravity-driven infiltration methods could successfully repair the fracture beams. However, it should be noted that compared with gravity-driven infiltration method, injection grouting is the preferred MICP treatment method in stone relics restoration due to the higher strength of the beams achievement. The reason why the injection method performs well is probably that the bacterial culture and cementation solution could flow through the pores easily under the additional injection pressure so that more $CaCO_3$ crystals can be precipitated in the pore spaces thereby improving the flexural strength of specimens.

As for the influence of the surface roughness, He et al. (He et al. 2019) mentioned that for the specimens with V-grooves, the repaired beams mostly damaged along with the interface between the bio-cemented sand grains and the grooves, suggesting that excessively smooth contact surface is detrimental to the bonding between the cemented dolomite sand and the fracture surface. To investigate the effect of surface roughness further, this study compared the beams with different

interface roughness then confirmed that the rough surface is beneficial to improve the strength of the bonding layer, especially for the samples treated by gravity-driven infiltration. This phenomenon is presumably because the samples with a rough surface have a higher ability to keep the bacteria on the interface, thereby precipitating more $CaCO_3$; besides, the rougher surface might also provide a larger contact area between the cracked surface and the sand grains, thus benefiting to enhance the frictional resistance of the bonding layer. Compared with the injection samples, the improvement is more effective in the samples treated by gravity-driven infiltration.

As Tan (Tan 2017) successfully cemented the dolomite sand column with the cementation solution of 0.15 M $CaCl_2$ and 0.33 M urea and achieved a higher average UCS, this study set up a separate group provided with the cementation solution of 0.15 M $CaCl_2$ and 0.33 M urea to preliminarily analyze the impact of the cementation solution concentration. The bending strength result indicated that the difference in average flexural strength between samples treated by 0.5 M $CaCl_2$ and 0.5 M urea and 0.15 M $CaCl_2$ and 0.33 M urea is not obvious. This suggests that a lower concentration of cementation solution can achieve a similar effect as a higher concentration, which might be attributed to the sizes of precipitated $CaCO_3$ crystals by different concentrations (Al Qabany et al. 2012; Xu et al. 2021). According to Al Qabany et al. (Qabany et al. 2013), the larger precipitated crystals produced by a high concentration solution may clog the pores and result in inhomogeneity along the bio-cemented sand. On the contrary, the usage of low concentration solution would ensure more homogeneity and more consistency during the MICP treatment.

4 CONCLUSIONS

This study treats the broken white marble beams by MICP technique with different grouting methods, surface roughnesses, and concentrations of the cementation solution, aiming at finding a favorable method of repairing white marble beams by MICP.

The experimental results convince that MICP can be successfully applied to repair the stone relics. Compared with the gravity-driven infiltration, the injection grouting method is more effective to cement the dolomite sand particles in the cracks to enhance the strength of the repaired beams.

Additionally, the beams pretreated with a rough surface can reach a higher bending strength no matter which approach is selected to treat the cracked samples. Besides, the performance of the rough surface samples is also more stable than the smooth surface ones.

Furthermore, based on the current experimental results, it seems that the concentration of the cementation solution (urea: 0.33M–0.5M, $CaCl_2$: 0.15M–0.5M) has little influence on the bending strength of the repaired beams. There is no significant difference between the specimens provided with different concentrations of cementation solution, so low concentration might be the more favorable choice.

To summarize, this study gives basic research for the effects of different factors on the restoration of the white marble beams with the MICP technique. This study only focuses on the three-point bending strength of the repaired beams, and considering that real stone relics might damage in different modes, further study on the restored specimens damaged in other modes of deformation (e.g., shear, compression) is still necessary. Moreover, the real size of the stone relics is greatly larger than the experimental beams. Therefore, it is necessary to upscale the size of stone relics in the future.

ACKNOWLEDGEMENTS

The authors would like to acknowledge Beijing Guowenyan Company, especially Rong Zhang, Qi Wang, and Zhuyin Chen, for providing assistance in the experiment. This research is supported by the finding from Beijing Natural Science Foundation (No.8162025).

REFERENCES

Al Qabany, A., Soga, K., Santamarina, C., 2012. Factors Affecting Efficiency of Microbially Induced Calcite Precipitation. Journal of Geotechnical and Geoenvironmental Engineering 138, 992–1001.

Dejong, J.T., Mortensen, B.M., Martinez, B.C., Nelson, D.C., 2010. Bio-mediated soil improvement. Ecological Engineering 36, 197–210.

De Muynck, W., Verbeken, K., De Belie, N., Verstraete, W., 2010. Influence of urea and calcium dosage on the effectiveness of bacterially induced carbonate precipitation on limestone. Ecological Engineering 36, 99–111.

He J, Guo X, Tan Q, et al., 2019. Experiment research on the restoration of white marble beams using microbially – induced carbonate precipitation. Sciences of Conservation and Archaeology 31(6), 331–339.

Le Métayer-Levrel, G., Castanier, S., Orial, G., Loubière, J.-F., Perthuisot, J.-P., 1999. Applications of bacterial carbonatogenesis to the protection and regeneration of limestones in buildings and historic patrimony. Sedimentary Geology 126, 25–34.

Liu, Q., Zhang, B., Shen, Z., Lu, H., 2006. A crude protective film on historic stones and its artificial preparation through biomimetic synthesis. Applied Surface Science 253, 2625–2632.

Minto, J.M., Tan, Q., Lunn, R.J., El Mountassir, G., Guo, H., Cheng, X., 2018. 'Microbial mortar'-restoration of degraded marble structures with microbially induced carbonate precipitation. Construction and Building Materials 180, 44–54.

Mujah, D., Shahin, M.A., Cheng, L., 2017. State-of-the-Art Review of Biocementation by Microbially Induced Calcite Precipitation (MICP) for Soil Stabilization. Geomicrobiology Journal 34, 524–537.

Qabany, A.A., Soga, K., 2013. Effect of chemical treatment used in MICP on engineering properties of cemented soils. Géotechnique 63, 331–339.

Tan Qian, 2017. Research on marble relics repairmen by microbially induced carbonate precipitation technology. Tsinghua university.

Tobler, D.J., Maclachlan, E., Phoenix, V.R., 2012. Microbially mediated plugging of porous media and the impact of differing injection strategies. Ecological Engineering 42, 270–278.

Whiffin, V.S., Van Paassen, L.A., Harkes, M.P., 2007. Microbial Carbonate Precipitation as a Soil Improvement Technique. Geomicrobiology Journal 24, 417–423.

Xu, F., Zeng, W., Li, D., 2019. Recent advance in alkoxysilane-based consolidants for stone. Progress in Organic Coatings 127, 45–54.

Xu X, Guo H, Li M, et al., 2021. Bio-cementation improvement via CaCO3 cementation pattern and crystal polymorph: A review. Construction and Building Materials 297.

Yang Z, Cheng X., 2015. Experimental study of deteriorated historic masonry structures reinforced by microbial grouting method. Industrial Construction 45, 48–53.

Zhang, H., Liu, Q., Liu, T., Zhang, B., 2013. The preservation damage of hydrophobic polymer coating materials in conservation of stone relics. Progress in Organic Coatings 76, 1127–1134.

Geotechnical Engineering for the Preservation of Monuments and Historic Sites III – Lancellotta, Viggiani, Flora, de Silva & Mele (Eds)

Shake-table tests for the dynamic characterisation of an innovative isolator for seismic protection of statues

F. Castelli, V. Lentini, F. Lo Iacono & G. Navarra
Faculty of Engineering and Architecture, "Kore" University of Enna, Italy

ABSTRACT: The seismic protection of the historic heritage artefacts and statues, has become of the utmost importance due to the intrinsic high cultural significance and their poor behaviour observed during past earthquakes. In fact, due to the height of their centres of gravity compared to the width of their bases, statues are generally prone to experience strong non-linear dynamic effects when subjected to large seismic excitations, that may cause also the overturning of the statue itself. In this context, the base isolation has proven to be a very effective tool in seimic protecion of statue-like items. This paper describes the preliminary results from an extensive and accurate experimental campaign carried out at Laboratory of Earthquake engineering and Dynamic Analysis Research Institute at the "Kore" University of Enna. The experimental campaign was devoted to the dynamic characterisation of the seismic performance of a innovative base-isolation system and to the assessment of the seismic protection of statue-like structural systems through full-scale model shaking table tests. The innovative base-isolation system consists of a simple and non-intrusive base that allows the free movements of the statue in both horizontal directions by means of a multiple articulated quadrilateral mechanism patented as Kinematic Steel Joint system. The allowable large stroke of the device and damping charactestics of the pinned joints are adequate to decouple the motion of the protected item from the ground and to dissipate the seismic energy, thus avoiding the occurrence of bumps or overturnings. The Goddess of Morgantina statue has been selected as a case study for its peculiar story. In fact, the statue was provided of an isolated base, designed by Paul Getty Museum's engineers, when exposed in California and in its present placement at Aidone's Archaeological Museum after its return to Italy.

Keywords: Statue, earthquake protection, cultural heritage, base isolation

1 INTRODUCTION

Several recent major seismic events in Mediterranean area, especially in Turkey, Greece and Italy, caused extensive damages to monuments, historic structures but also to the contents of museums, particularly to artefacts and statues (Parisi & Augenti 2013; Oliveira et al. 2012). Beside to the protection of historic buildings and sites, the seismic safeguard of their content deserves the attention of scholars and practitioner engineers due to the high cultural significance and the inestimable value of most of them. Unfortunately, seismic codes do not provide specific provisions for museum artefacts, which are usually considered as non-structural elements (Spyrakos et al. 2017).

The first systematic studies regarding the seismic protection of art objects are related to the research activities carried out at Jean Paul Getty Museum in Malibu (California, USA) where, since 1984, investigations and practical approaches for the protection of the collections from seismic activity have been developed (Agbabian et al. 1991; Podany, 2015).

Usually, museum objects, statues and displays can be modelled as rigid block and analysed in the context of non-linear dynamic. Starting from the early work by Housner (1963), a lot of research work has been devoted to this subject through, in most of cases, analytical studies (Caliò & Marletta 2003; Palmeri & Makris 2008; Shenton & Jones 1991; Spanos & Koh 1984), whereas the experimental works in this area remain limited.

DOI 10.1201/9781003308867-25

Among the other developed approaches, base isolation techniques have proven to be very effective tools for amphoras or statue-like items (Podany 2015). In fact, due to the height of their centres of gravity compared to the width of their bases, these objects are generally prone to experience strong non-linear dynamic effects in case of seismic events, that may cause also their overturning. The characteristics of an isolation system are low lateral stiffness (to decouple the motion of the isolated level from the ground), damping (to dissipate seismic energy and to limit the displacement demand) and self-center capability (to come back at the central rest position when the dynamic excitation ends) (Christopoulos & Filiatrault 2006). In Vestroni and Di Cinto (2000) the response of a statue, modelled ad a single-degree-of-freedom system and protected by an isolator with a hysteretic force-displacement relationship, has been investigated. In Stavridis et al. (2006) the design study of a two-dimensional base isolator to reduce the risk of seismic damage of an ancient Amphora at Getty Museum is presented. The isolator consists of three metal frames and two sets of compression springs able to provide re-centering restoring forces. Indeed, this configuration represents the final design of a revision and modification process started in mid 1980s with the production of other isolation devices.

The research presented in this work is conducted within the Research Project *eWAS – An Early-Warning System for Cultural Heritage*, funded by the MUR (Italian Ministry of University and Research), whose final goal is the implementation of a monitoring system integrated with smart-wireless and ICT technologies to evaluate the natural hazards undergone by the monumental and historical heritage of some areas of the Sicily.

As case-study, the Goddess of Morgantina statue (illustrated in Figure 1) has been selected due to its peculiar story. In fact, this 2.2 meters tall statue, sometimes identified with Aphrodite for its prosperous forms and the beauty of the face, but also with Demeter or Hera (Marconi 2011; Zisa 2018), was carved in the 5th century BC in Sicily and realized with two different materials, i.e. white marble and calcareous tuff, by a direct disciple of Phidias, operating in Magna Graecia.

It was illegally excavated from the archaeological site of Morgantina in late 1970s and dissected into three elements to facilitate the transportation and the illegal exportation. Then, the statue was sold in Switzerland in 1986 by an art dealer of doubtful reputation and acquired and exposed by the Paul Getty Museum in Malibu for several years. The statue was finally returned to Italy on 2011 at the end of a long legal dispute between Italy and the United States. In particular, the Sicilian origin of the Goddess of Morgantina has been conclusively determined by mineralogical-petrographic analyses which confirmed that the material of the statue coincided with the Miocene calcarenite

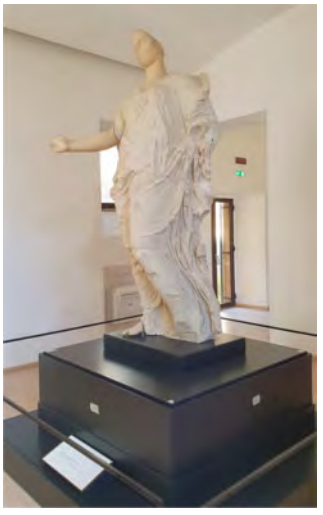

Figure 1. The statue of the Goddess of Morgantina at Aidone's Archaeological Museum.

Figure 2. KSJ bidirectional isolator for seismic protection of statue-like structures.

emerging in the Hyblean area, not far away (about 50 km) from the ancient settlement of Morgantina (Alaimo et al. 2007; Raffiotta 2011).

During its time in California, the statue was equipped with a one-direction base-isolating device, designed by Paul Getty Museum's engineers, which has been retained also in its present placement at Aidone's Archaeological Museum. In the framework of *eWAS* project, an extensive and accurate study has been performed to characterise the dynamic performance of an innovative bidirectional base-isolation device, through full-scale model shaking table tests at L.E.D.A. (*Laboratory of Earthquake engineering and Dynamic Analysis*) Research Institute at the "Kore" University of Enna, Italy. The device consists of a simple and non-intrusive base that allows the free movements of the statue in both horizontal directions in order to decouple the protected item from the ground motion. The allowable stroke of the device and energy dissipation characteristics are adequate to allow for large displacements, avoiding the occurrence of bumps.

The paper is organized as follows: in section 2 the geotechnical characterization of the Aidone area, in which the statue is located, is presented, in Section 3 the description of the device is provided, whereas in section 4 the test facilities and the adopted test sequence are briefly illustrated. Section 5 is devoted to present the main test results and their interpretation and, finally, some conclusions are drawn.

2 SEISMIC RISK AND DESIGN OF PROTECTION SYSTEM

Aidone's Archaeological Museum is not located in a high seismic risk area, nevertheless, the design of protection system must take into consideration the high seismic hazard of the Sicilian region, where urban areas are characterized by significant level of vulnerability. In this context, the prevention and mitigation of the earthquake's effects (Cavallaro et al. 2018; Ciancimino et al. 2020) on the cultural and artistic heritage play an important and strategical role. In the past, strong earthquakes occurred in northeastern Sicily (1908) and in the southeastern Sicily (1169, 1693) and, most recently, the St. Lucia earthquake of 13th December 1990. For the design of a protection system the accelerations expected at the ground surface must be evaluated, considering the possibility of seismic local effects. With this aim, several urban areas in the Mediterranean have already been subjected to seismic micro-zonation studies as, for example, those carried out for the municipalities of the Enna area in the framework of a research project (Castelli et al. 2017). Among these, the municipality of Aidone, where the Goddess of Morgantina is placed at Aidone's Archaeological Museum. The study includes an accurate evaluation of the subsoil geotechnical model based on in situ and laboratory tests, including investigations such as Down-Hole (DH), Multichannel Analysis of Surface Wave (MASW), Horizontal to Vertical Spectral Ratio (HVSR), Refraction Microtremor (REMI) and electrical tomography tests. The results of in situ tests were used to represent thematic map in which are reported the values of the average shear wave velocities in the top 30 m depth ($V_{S,30}$), computed according to the Italian Technical Regulations. Non-linear behaviour of several soil samples retrieved by all the municipalities of the Province of Enna was evaluated by of fixed-free Resonant Column/Torsional Shear (RC-CTS) devices, at the "Soil Dynamics and Geotechnical Engineering Laboratory" of the "Kore" University of Enna. The results, in terms of normalized shear modulus and damping ratio versus shear strain, were used for the purposes of seismic micro-zonation.

3 DESCRIPTION OF THE ISOLATED BASE

The isolators currently available on the market can be roughly defined into two categories: elastomeric bearings and friction pendulum bearings. The cost for these device and their maintenance is an issue that limited the wide diffusion of the base-isolation technology. In order to overcome these difficulties and to extend the applicability of the base-isolation also to the protection of non-structural elements or cultural heritage items, Kyneprox S.r.l. has designed and patented a new

isolator device, exploiting the beneficial effects of a double steel articulated quadrilateral with crossing rods, called *Kinematic Steel Joint* (KSJ).

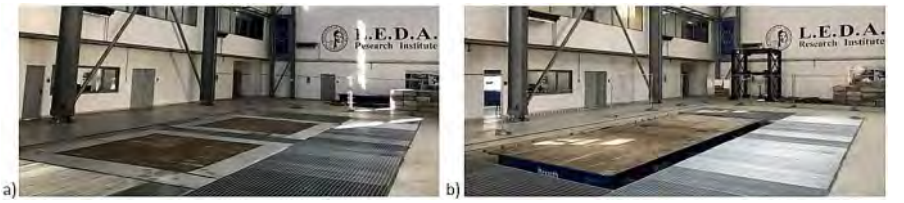

Figure 3. Shaking tables system at L.E.D.A. Research Institute: a) Single tables; b) Connected Tables.

The device behaves as a pendulum-like isolator, giving rise to vertical upward displacements when it moves away from the central rest position, so that the trajectory undergone by an object fixed to the top of the device lies on of a double-curved concave surface, thus realizing a behaviour similar to a friction pendulum. Hence, the self-centring behaviour is assured by the slope of the trajectories and the damping is granted by dry friction in its pinned connections. Moreover, since KSJ is entirely made of cut and folded steel sheets, lower production and maintenance costs than the other available technologies are involved (Guerrini et al. 2019). Several different configurations of KSJ device can be assembled, depending on the size of item to be protected and to the related earthquake hazard. If, for instance, one-direction isolators may be adequate to protect high-value goods storage shelves, the seismic isolation of statue-like objects, as in the present case, requires that KSJ elements are deployed to realize a bidirectional device.

In this paper, the behaviour of the KSJ-based device illustrated in Figure 2 is discussed. The prototype has been designed in order to protect a 900 kg real-scale model of the Goddes of Morgantina statue, which is currently under construction. It consists of a rigid base capable of undergoing horizontal bidirectional relative displacements due to two double-rail stacked systems of KSJ elements. The isolated item may be mounted on the top rigid base. The isolator bottom rails are bolted to U-shaped plates which allowed connecting the device to the shaking table and the horizontal motion of the top rails is perpendicular to the motion of the bottom rails. Thus, the two rails allow displacements in two uncoupled directions. The device resists the overturning moment since sliding bearings prevent uplift as the frame displaces. The vertical component of the ground motion acceleration has a very little effect on the horizontal system response and the device cannot isolate the vertical component of seismic excitation, as occurred in most isolation systems (Christopoulos & Filiatrault 2006).

According to the ideal behaviour of friction pendulum devices, the natural period should be dependent only on the curvature of the surface, but independent of the mass of the object mounted on it. However, due to the deformability of the steel parts under static and dynamic loads or to other unpredictable phenomena, the behaviour of the device could deviate from the ideal one, being non-linearly depending on the mass of the object to be protected and on the frequency and intensity of the ground motion. Therefore, the test campaign described in the next section has been specially designed and implemented for the assessment of the dynamic behaviour of the device.

4 TEST PROGRAM AND SETUP

The experimental campaign has been carried out by using the shaking table system available at the L.E.D.A. Research Institute of the "Kore" University of Enna, which is briefly described in the following. This section also presents the instrumentation of the device in order to achieve a complete description of the dynamic behaviour of the isolated base and the adopted test program.

4.1 *Test facilities*

The L.E.D.A. shaking table system (Lo Iacono et al. 2017) consists of two identical 6-degrees-of-freedom (DOFs) 4 m × 4 m shaking tables. Taking advantage of the control system capabilities,

each table can operate separately and simultaneously, and with asynchronous or synchronous motion (Figure 3-a).

Furthermore, the two tables can be connected by means of a rigid steel link exploiting a 10 m × 4 m 6-DOFs shaking table, to date the largest 6-DOFs shaking table operating in Europe (Figure 3-b). Table 1 summarizes the main characteristics of the two configurations.

Table 1. Features of the shaking tables system at L.E.D.A. Research Institute.

Feature	Single table	Connected Tables
Fixture area:	4 × 4 m	10 × 4 m
Maximum payload:	60 t	100 t
Operative freq. range:	0.01 ÷ 60 Hz	0.01 ÷ 60 Hz
Stroke (horizontal):	±0.40 m	±0.40 m
Stroke (vertical):	±0.25 m	±0.25 m
Velocity (horizontal):	±2.20 m/s	±2.20 m/s
Velocity (vertical):	±1.50 m/s	±0.75 m/s
Acceleration* (horizontal):	±1.50 g	±1.0 g
Acceleration* (vertical):	±1.05 g	±0.70 g

*At maximum payload.

In order to perform multi-axis tests, each shaking table is driven by 8 large hydraulic actuators (2 for each horizontal direction and 4 in vertical) coupled to the table by means of frictionless spherical joints in order to minimize friction. A 1.6 MW hydraulic power unit supplies clean oil at a pressure of 270 bar and up to 3200 l/min continuous flow, whereas flow peaks are covered by a set of nitrogen accumulators. The system of shaking tables is enclosed in a 3000 metric tons concrete reaction mass, isolated from ground by mean of 96 large air springs, which was designed to be dynamically stiff and well damped in the frequency range of interest. The accuracy and repeatability of each test is guaranteed by a three-variable-nested real-time high-performance closed-loop vibration control system which is able to process all signals from the actuators, the manifolds and the hydraulic power unit and to apply the control strategy two thousand times for each second.

4.2 *Test setup and instrumentation*

The isolated base device has been connected to the shaking tables by means of four interface plates, each of them fixed with four M30 12.9 bolts with a torque of 1200 Nm. The device has been mounted in order to have the two orthogonal rails aligned with the principal axes of the shaking table.

In order to capture the dynamical behaviour of the device under test, several sensors have been deployed to acquire the response time-histories in terms of accelerations and displacements at selected critical points of the test setup. In particular, two tri-axial piezoelectric high-sensitivity accelerometers have been used to measure the acceleration at the geometrical centre of the shaking table (sensor called R1, acting as input) and on the upper surface of the device (sensor A1). Moreover, a congruous number of absolute displacement time histories spatial components have been acquired by means of a optical-electronic motion capture system consisting of a set of high-resolution, high frame rate infra-red cameras and several spherical markers having high reflectance in infra-red field.

Figure 4 shows the test setup, the locations of accelerometers and spherical markers and the overlay with the virtual model obtained by the markers themselves. It should be noted that the markers *base4* and *base5*, located on the upper surface of the device, have been removed for those tests in which steel plates are used to simulate mass loads.

4.3 *Test Sequence*

Aiming at the dynamical characterization of the device and at measuring the level of seismic protection, a test campaign has been planned and executed. The performed experimental tests can be

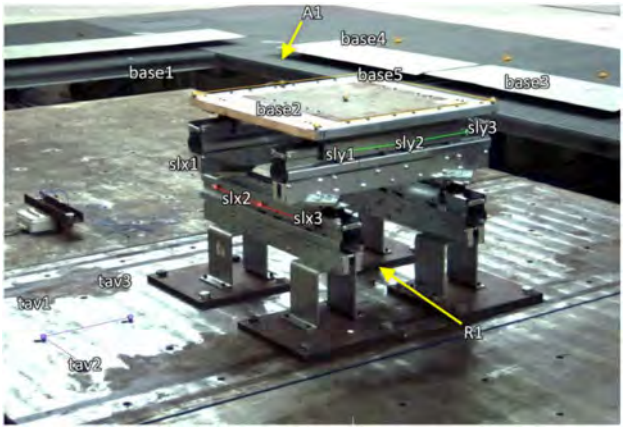

Figure 4. Test setup and location of measure sensors.

classified into the three following typologies: (a) static tests for the geometrical characterization of the double curvature surface enclosing the trajectories of the isolated base; (b) dynamic broadband random noise shaking table tests for the measurement of the frequency response of the device; and (c) shaking table seismic tests with natural historical earthquakes records for the assessment of the seismic protection level of the device.

In particular, the broadband random noise tests have been carried out separately for each horizontal axis, with reference to two increasing amplitudes and for four different load configurations, realized by a subsequent mounting of heavy steel plates to the upper surface of the device. The load level C0 has no added masses, in C1 and C2 levels the added masses are 320 kg and 760 kg, respectively, whereas the highest load level (C3) is correspondent to a mass of 900 kg, approximately the same mass of the real-scale model of the Goddess of Morgantina statue. In total, 16 noise tests have been performed.

In order to assess the device protection level over a wide class of events, the seismic tests have been performed by reproducing the four natural historical ground motion acceleration time-histories described in the following: 1) Kobe (16/01/1995, $M_w = 6.9$, recorded at Takatori, Japan); 2) Irpinia (23/11/1980, $M_w = 6.9$, recorded at Sturno, Italy); 3) Norcia (30/10/2016, $M_w = 6.5$, recorded at Norcia, Italy); and 4) L'Aquila (06/04/2009, $M_w = 6.1$, recorded at L'Aquila V. Aterno, Italy). These signals have been selected to have different characteristics in terms of frequency content, impulsive behaviour, duration and intensity. Each ground motion record has been applied to the test setup at two increasing intensity levels, namely at 50% and at 100% of the actual intensity, and for the same load levels above defined. It is to be remarked that only the two orthogonal horizontal components of the earthquake records have been applied. In Table 2 the seismic tests (Qxx tests in the following) are summarized.

Table 2. Seismic shaking tables tests.

	Load level (added mass)							
	C0 – 0 kg		C1 – 320 kg		C2 – 760 kg		C3 – 900 kg	
Signal Intensity	50%	100%	50%	100%	50%	100%	50%	100%
Kobe	Q01	Q02	Q11	Q12	Q21	Q22	Q31	Q32
Irpinia	Q03	Q04	Q13	Q14	Q23	Q24	Q33	Q34
Norcia	Q05	Q06	Q15	Q16	Q25	Q26	Q35	Q36
L'Aquila	Q07	Q08	Q17	Q18	Q27	Q28	Q37	Q38

5 TEST RESULTS

5.1 *Characterisation of the device kinematic*

The dynamic performances of friction pendulum-like isolators, as well as their capacity to protect from earthquakes, strongly depend on the geometry of the sliding surface. In the present case, there is no an actual curved surface, but the protected item is constrained by the pinned joint system to move on a double-curvature surface, which should be preliminary characterized from the geometrical point of view.

Aiming at this, quasi-static tests have been performed for the load configuration C0 (with no added masses), in which slowly-varying random horizontal displacements have been imposed to the moveable part of the device. Taking advantage of the motion capture system and of the instrumentation of the device trough the spherical markers, the three displacement component time-histories of the upper surface of the device have been acquired and processed. In particular, in Figure 5 these components have been plotted against each other with reference to the *base5* marker (located at the centre of the device moveable part), although similar results can be obtained using other markers, since the upper base behaves as a rigid body.

From these measurements, it appeared that the device allows for horizontal displacements of ± 150 mm for each direction, giving rise to upward vertical displacements up to 15 mm when the device moves away from the central rest position. From Figure 5 is also evident that the trajectories are contained in a double-curved surface which can be accurately approximated by an elliptical paraboloid with vertical axis of symmetry and represented by the following equation:

$$z = a\,x^2 + b\,y^2 \qquad (a > 0,\ b > 0) \tag{1}$$

In eq.(1) the origin of the reference system coincides with the vertex of the elliptical paraboloid, the parameters a an b govern the shape of the quadric surface and they have been obtained by a fitting procedure, minimizing – in a least square sense – the error between the vertical co-ordinate of an ideal surface predicted by eq.(1) for a given set of parameters a an b and the actual measured vertical position. The values obtained by the fitting procedure are $a = 3.391 \cdot 10^{-4}\ \mathrm{mm}^{-1}$ and $b = 3.190 \cdot 10^{-4}\ \mathrm{mm}^{-1}$ and for both parameters the 95% confidence interval is equal to $\pm 0.014 \cdot 10^{-4}\ \mathrm{mm}^{-1}$. The coefficient of determination R^2 is equal to 0.9277 which proves the very good agreement of the selected model to the experimental data. Furthermore, since the values of the parameters a and b are very close each other, the expected dynamic behaviour should be the same for each horizontal direction.

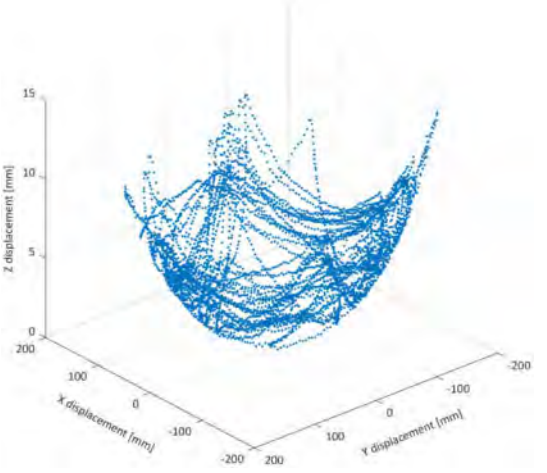

Figure 5. Trajectory of the moveable part of the device.

The elliptical paraboloid results from the composition of two orthogonal motions that occur in the rails. Therefore, at each rail level the trajectories of the protected item can be represented as parabolas depending on only one co-ordinate (x or y) and thus having variable curvatures along the stroke. The analytical expressions of curvatures in X and Y directions, respectively, can be expressed as:

$$\rho_x(x) = \frac{2a}{\left(1+4a^2x^2\right)^{3/2}};\ \rho_y(y) = \frac{2b}{\left(1+4b^2y^2\right)^{3/2}}; \tag{2}$$

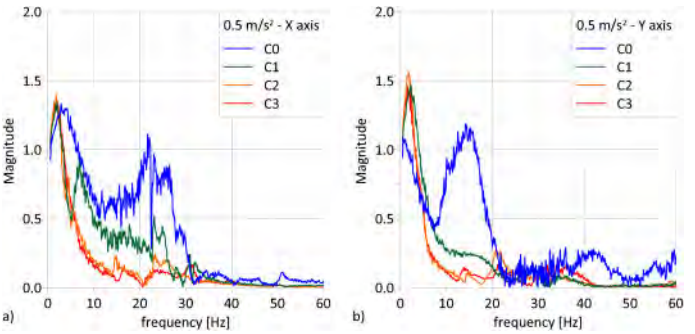

Figure 6. FRFs during random noise test at $0.5 m/s^2$ RMS: a) X direction; b) Y direction.

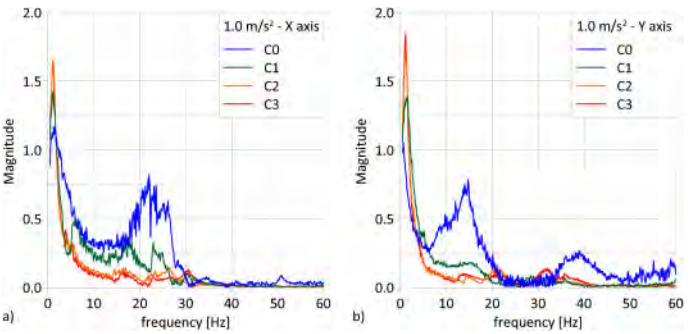

Figure 7. FRFs during random noise test at $1.0 m/s^2$ RMS: a) X direction; b) Y direction.

The equivalent oscillation periods can be determined as (Christopoulos & Filiatrault 2006):

$$T_x(x) = \frac{2\pi}{\sqrt{g\,\rho_x(x)}};\ T_y(y) = \frac{2\pi}{\sqrt{g\,\rho_y(y)}}; \tag{3}$$

Although the equivalent periods depend on the local values of the curvatures, by substituting the values for a and b in eq.(2), it appears that their values are very close in the range of interest of co-ordinates x and y (i.e. ± 150 mm). In fact, the periods at central rest position are $T_x(0) = 2.44$ s and $T_y(0) = 2.51$ s for the rails in X and Y directions, respectively, whereas the periods for maximum displacements of the device are $T_x(\pm 150) = 2.46$ s and $T_y(\pm 150) = 2.53$ s. These period values are close to the expected ones and are typical of base-isolation devices.

5.2 *Results of broadband random noise tests*

For each of the broadband random noise tests the Frequency Response Functions (FRFs) have been computed by adopting the readings from accelerometer R1 as input and the signals from sensor A1 as output. Although it is common practice in system dynamics to plot both amplitude and phase of

FRFs, in the following, for clarity's sake, only the magnitude plots are reported and only FRFs of the output component acting in the same direction of the applied input acceleration are shown. In Figures 6 and 7 the FRFs amplitudes are plotted for each load level, for each direction and for the two selected input intensities.

Experimental results show that the device under test is able to significantly attenuate the horizontal components of vibrations with an high degree of robustness with respect to the variation of the input intensity and of the mass load.

As the mass load increases (load levels from C1 to C3) the behaviour of the device changes, remaining practically unchanged for the last two load conditions. In these cases, the inertial forces prevail and the isolator tends to behave close to the ideal one. The frequency range for which a very marked reduction in the transmission of vibrations is attained extends to frequencies higher than 10 Hz for both directions, with a tendency to a further reduction as the intensity of the input increases. On the other hand, during the tests conducted at the lower intensity level, only a zone of dynamic magnification is observed, with a peak at frequencies between 1.5 Hz and 2.0 Hz. For higher intensity level, the magnification zone tends to be even narrower, with slightly higher peaks at frequencies between 1.0 Hz and 1.15 Hz.

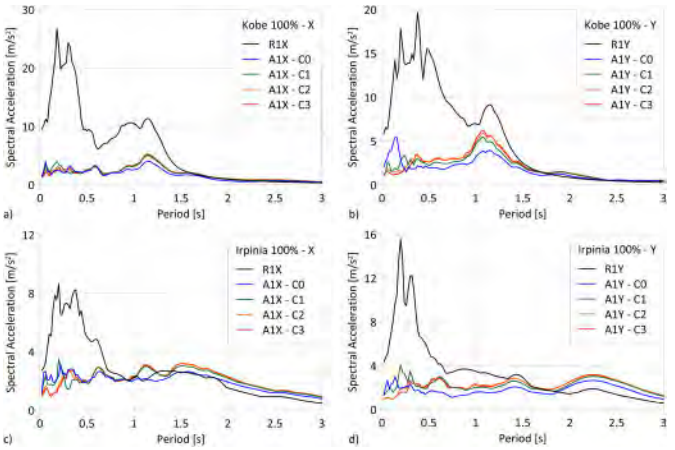

Figure 8. RS during seismic tests: a) and b) Kobe; c) and d) Irpinia signals.

5.3 *Results of seismic tests*

For each seismic test described in Table 2, the acquired data have been processed in terms of acceleration and displacement time-histories and in terms of Response Spectra (RS) of signals from both R1 and A1 sensors. Furthermore, residual displacements and maximum strokes of the device have been annotated.

In the following, for the sake of brevity, only the most relevant results are reported. Figures 8 and 9 illustrate the comparison between the RS of the input (acceleration recorded on the shaking table) and the RS of the accelerations experienced by the item to be protected for all four load levels and for both horizontal directions. RS have been computed with reference to 5% damping level. Only plots for tests at 100% intensity are reported, but similar results have also been obtained for tests at 50% intensity.

The RS illustrated in Figures 6 and 7 prove that the device under test is able to effectively reduce the horizontal accelerations suffered by the protected item. A similar behaviour is observed for each seismic test performed, i.e. in every load condition and for each of the selected natural seismic wave. As expected, spectral accelerations calculated for sensor A1 at very large periods may be greater than the correspondent ones computed for R1 sensor. This occurrence, however, does not affect the protection capacity of the device, since these large periods refer to already isolated structural systems.

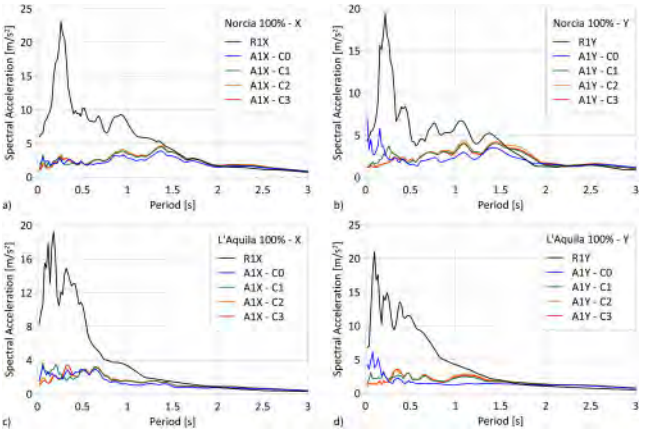

Figure 9. RS during seismic tests: a) and b) Norcia; c) and d) L'Aquila signals.

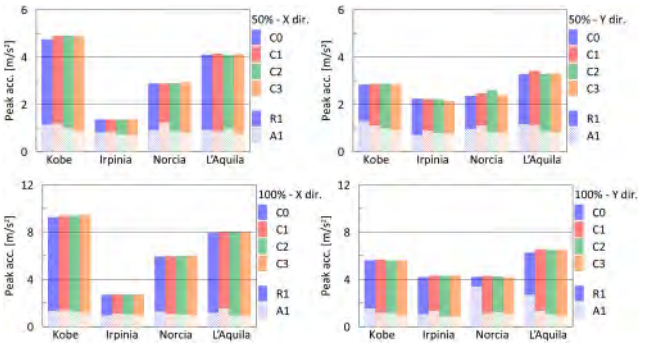

Figure 10. Comparison between peak accelerations.

Looking at the acceleration signals in the time domain, and especially during the strong motion phase of the earthquake, the device appears to be able in reducing transmitted accelerations by means of two concurrent mechanisms. The first one is a sort of *filter effect* that cuts away most of the dangerous harmonic components having frequencies grater than the equivalent period of the device and associated to the highest spectral accelerations. This effect appears to be in agreement with the dynamic characterization of the device, attained by broadband random noise tests.

The second protection mechanism is a sort of *fuse effect* which operates a clipping in the peak accelerations transmitted by the device. Regardless of the intensity level, load configuration and imposed seismic wave, the maximum accelerations experienced by the moveable part of the isolator was found always around the value of about $1\,m/s^2$, as it is shown in Figure 10 in which peak accelerations at shaking table and on the device are compared for all the seismic tests. This effect is probably related to the overcoming of a friction threshold by inertial forces but it deserves to be more in-depth investigated in further studies. The combined effect of these two mechanisms is particularly evident in Figure 11, where the acceleration time-histories for Kobe earthquake at 100% of intensity and load level C3 are depicted.

Comparing the trajectories of the shaking table and of the isolated base in terms of absolute displacements, it is observed that the device always undergoes greater displacements with respect to the shaking table, with only marginal increments due to the increasing loads. However, the trajectories on the moveable part of the device are smoother, since lower accelerations are involved.

During seismic tests, also residual displacements of the device and the peak rail strokes have been annotated. These results show that the kinematic of the isolated base ensures its re-centering at the end of the ground motion. In fact, the maximum values of the residual displacements are

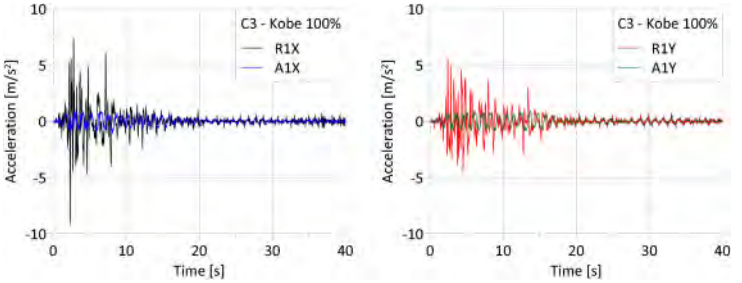

Figure 11. Accelerations during Kobe seismic tests at 100% intensity and at C3 load level.

about 10 mm in X direction and between 15 mm and 20 mm in Y direction. In any case, the relative displacements of the device rails have been found lower than the maximum allowable strokes, which has proven that the rails are adequate for both horizontal directions.

CONCLUSIONS

In this paper, preliminary results of an experimental campaign on the dynamic performances of an innovative bi-axial isolation device, based on the patented *Kinematic Steel Joint* system are reported. Static and dynamic experimental tests have been conducted at the Laboratory of Earthquake engineering and Dynamic Analysis Research Institute at the "Kore" University of Enna by means of a large shaking table system.

The isolation system's kinematic characteristics have been studied by means of pseudo static tests. The analytical characterization of the displacement trajectories of the device top base have been achieved, confirming the construction specifications. Also equivalent vibration periods have been computed. The characterization of the isolation device has been conducted by random noise and seismic shaking table tests on four increasing load configurations. Frequency response functions computed from the random noise experiments show that the device can significantly attenuate the horizontal components of vibrations with a high degree of robustness with respect to the variation of the input intensity and of the mass load. Seismic tests have been conducted by using the horizontal components of four historical earthquakes. Experimental results show that the device can drastically reduce maximum accelerations transmission to the top base for all loading configurations and for different levels of the seismic input. The comparison of the response spectra, computed from both the shaking table and the device base accelerations, shows that for all the frequency range of interest the device can effectively reduce the horizontal accelerations suffered by the protected item. The device maximum displacements need to be correctly designed with respect to expected input excitations in order not to encounter dangerous bumps and shocks on the protected item. Moreover, from the measured residual displacements, the re-centering property of the device is assessed. Therefore, it is possible to ascertain the efficacy of the isolated base in seismically protecting the supported object regardless of its mass and of the characteristics of the seismic input.

Future developments of the present paper will regard both the development of a theoretical model of the isolation device and the completion of the experimental test campaign in presence of a full-scale statue-like payload. As case study, the Goddess of Morgantina statue, whose full-scale reproduction is currently under construction, has been selected for its peculiar story and since it was provided of an isolated base, designed by Paul Getty Museum's engineers, when exposed in California and in its present placement at Aidone's Archaeological Museum.

ACKNOWLEDGEMENTS

This research has been developed within the "eWAS – An Early-Warning System for Cultural Heritage" research project (code PON ARS01_00926) funded by the Italian Ministry of University and Research, whose financial support is gratefully acknowledged.

REFERENCES

Agbabian, M. S., Ginell, W. S., Masri, S. F. and Nigbor, R. L. 1991. Evaluation of-earthquake damage mitigation methods for museum objects. *Studies in Conservation* 36:2, 111–120.

Alaimo, R., Giarrusso, R., Montana, G., Quinn P. 2007. Petrographic and micropalaeontological data in support of a Sicilian origin for the Statue of Aphrodite. *In: Cult Statue of a Goddess, Summary of Proceedings from a Workshop*, Getty Publications, Los Angeles.

Caliò, I., Marletta, M. 2003. Passive control of the seismic rocking response of art objects. *Engineering Structures* 25(8), 1009–1018.

Castelli, F., Lentini, V., Grasso, S. 2017. Recent developments for the seismic risk assessment. *Bulletin of Earthquake Engineering* 15(12), 5093–5117.

Cavallaro, A., Castelli, F., Ferraro, A., Grasso, S., Lentini, V. 2018. Site response analysis for the seismic improvement of a historical and monumental building: the case of Augusta Hangar. *Bulletin of Engineering Geology and the Environment* 77(3), 1217–1248.

Christopoulos, C. & Filiatrault, A. 2006. *Principles of Passive Supplemental Damping and Seismic Isolation*, IUSS Press, Pavia, Italy.

Ciancimino, A., Lanzo, G., Alleanza, G.A., Amoroso, S., Bardotti, R., Biondi, G., Cascone, E., Castelli, F., Di Giulio, A., D'Onofrio, A., Foti, S., Lentini, V., Madiai, C., Vessia, G. 2020. Dynamic characterization of fine-grained soils in Central Italy by laboratory testing. *Bulletin of Earthquake Engineering* 18(12), 5503–5531.

Guerrini, G., Ausenda, G., Graziotti, F. and Penna, A. 2019. An innovative seismic isolation device based on multiple articulated quadrilateral mechanisms: analytical study and shake-table test. *In. Proc. of XVIII ANIDIS Conference, Ascoli Piceno (Italy), 15–19 September 2019*.

Housner, G. W. 1963. The behaviour of inverted pendulum structures during earthquakes. *Bulletin of the Seismological Society of America* 53, 403–417.

Lo Iacono, F., Navarra, G., Oliva, M., Cascone, D. 2017. Experimental investigation of the dynamic performances of the L.E.D.A. shaking tables system. *Proc. of the 23rd AIMeTA Conference 2017, Salerno (Italy), 4–7 September 2017*, 5, 897–915.

Marconi, C. 2011. L'identificazione della Dea di Morgantina. *Prospettiva: rivista di storia dell'arte antica e moderna* (in italian).

Oliveira, C. S., Çakti, E., Stengel, D. and Branco, M. 2012. Minaret Behavior Under Earthquake Loading: The Case of Historical Istanbul. *Earthquake Engineering and Structural Dynamics* 41(1):19–39.

Palmeri, A., Makris, N. 2008. Response of rigid structures rocking on viscoelastic foundation. *Earthquake Engineering and Structural Dynamics* 37, 1039–1063.

Parisi, F., Augenti, N. 2013. Earthquake damages to cultural heritage constructions and simplified assessment of artworks. *Engineering Failure Analysis* 34, 735–760.

Podany, J. 2015. An overview of seismic damage mitigation for museums. *Proc. of International Symposium on Advances of Protection Devices for Museum Exhibits, Beijing and Shanghai (China), 13–17 April 2015.*

Raffiotta, S. 2011. La Venere di Morgantina. Torna a casa un capolavoro dell'arte classica. *Archeologia Viva* (in Italian).

Shenton, H. W., Jones, N. P. 1991. Base excitation of rigid bodies. I: Formulation. *Journal of Engineering Mechanics, ASCE* 117(10), 2286–2306.

Spanos P. D. & Koh, A. S. 1984. Rocking of rigid blocks due to harmonic shaking. *Journal of Engineering Mechanics* 110(11), 1627–1642.

Spyrakos, C. C., Maniatakis, C. A., Taflampas, I. M. 2017. Application of predictive models to assess failure of museum artifacts under seismic loads. *Journal of Cultural Heritage* 23, 11–21.

Stavridis, A. N., Schoettler, M. J., Somerville, P. G., Thio, H. K. and Podany, J. C. 2006. Design of a self-centering seismic base isolator for an antiquity, *In: Proceedings of the 8th U.S. National Conference on Earthquake Engineering, San Francisco, California, USA, 18–22 April, 2006.*

Vestroni, F., Di Cinto, S. 2000. Base isolation for seismic protection of statues. *In: Proceedings of the 12th World Conference on Earthquake Engineering, Auckland (New Zealand) 30 January–4 February 2000.* New Zealand Society for Earthquake Engineering.

Zisa, F. 2018. L'Afrodite di Morgantina: questione di identità. *In: Pre Atti-Dialoghi sull'Archeologia della Magna Grecia e del Mediterraneo*, Paestum (Italy), 16–18 November 2018 (in Italian).

Geotechnical Engineering for the Preservation of Monuments and Historic Sites III – Lancellotta, Viggiani, Flora, de Silva & Mele (Eds)
ISBN 978-1-003-30886-7

Parametric simulations on the stability conditions of the masonry wall of Chandakas, Heraklion City, Crete, Greece

C. Loupasakis, N. Antoniadis & E. Grigorakou
School of Mining & Metallurgical Engineering, National Technical University of Athens, Athens, Greece

I. Parcharidis & A.M. Tompolidi
School of Environment, Geography and Applied Economics, Harokopio University of Athens, Athens, Greece

M. Fragiadakis
School of Civil Engineering, National Technical University of Athens, Athens, Greece

V. Sithiakaki & E. Kanaki
Ephorate of Antiquities of Heraklion, Ministry of Culture and Sports, Heraklion, Greece

P. Soupios
College of Petroleum Engineering and Geosciences, King Fahd University of Petroleum and Minerals, Saudi Arabia

G.V. Kalousi
Terra Spatium S.A., Athens, Greece

P. Eleftheriou
Acropolis Restoration Service, Ministry of Culture and Sports, Athens, Greece

P. Elias
Institute for Astronomy, Astrophysics, Space Applications and Remote Sensing, National Observatory of Athens, Athens, Greece

ABSTRACT: This paper focuses on the line-segment Bembo-Saint Francis of the masonry walls of Chandakas in the city of Heraklion, Greece. The construction of the wall was decided in 1462, but 100 years were needed until the design was finalized and construction began at the beginning of the 16th century. The line-segment was constructed as part of the fortification system but, from a geotechnical point of view, acts as a gravity retaining wall, due to the existence of backfilling material. It suffered severe damages during the long siege by the Ottomans (1648–1669). Furthermore, activities and loads implied and applied by the modern operation of the city caused it to deform and swell. A numerical investigation is performed using the Finite Element code Plaxis to analyze the stability of the wall-ground system. Emphasis is given on the ways of calculating the modulus of elasticity of the wall. Parametric analyses are performed and the results indicate that neither the methods used to calculate the modulus of elasticity of the wall nor the materials of which the wall is built affect the overall stability. Finally, various methods of restoration and support are recommended, significantly increasing the safety factor.

1 INTRODUCTION

Ancient masonry is a non-homogeneous material, composed by blocks and mortar, which can be of different types, with distinct mechanical properties. This paper focuses on the masonry walls of Chandakas. The ancient walls of the city of Heraklion, Greece have a long history starting from the 7th century A.D. With the passage of time many historic masonry structures have collapsed due

DOI 10.1201/9781003308867-26

to accidental actions, such as earthquakes. However, damages are also caused to such structures from events such as traffic loads, earth pressures and strength degradation of the wall's materials (Lourenço 2002). Same thing is observed in the walls of Chandakas. The present study examines the mechanical characterization of the masonry as homogenous material and specifically the modulus of elasticity, the cohesion and the friction angle. These properties were estimated in accordance to international codes or methods provided in the relevant literature. Various parametric analyses were performed in order to identify the worst-case scenario for the wall-ground system and then the best and non-interfering method was applied.

This research has been completed within framework of the SCIENCE project, a large bilateral project between Greece and China introducing advanced engineering research to the service of monument protection. In particular, SCIENCE develops a new approach to estimate the vulnerability of cultural heritage monuments through the innovative technique of multitemporal Synthetic Aperture Radar Interferometry (MT-InSAR), which detects the ground deformation in time and space.

2 THE CASE STUDY

2.1 *History of the Chandakas' walls*

The history of the walls for the Heraklion city begins in the 7th-8th century A.D. where the first zone of fortifications was constructed. That zone included a small area of the city and was probably in a Hellenistic context. These fortifications were later repeatedly repaired in Byzantine times and in early Venetian times (15th century). (Sythiakaki et al. 2013) Later in the 15th century, due to the rapid evolution of gunpowder and cannons, the mechanics were forced to design a new fortification system. The new system was called Bastion fortification system or "Fronte Bastiano". The new fortification was constructed as shown in the Figure 1a. It has a polygon shape at the edges of which seven (7) bastions (baluardi or belovardi) were constructed (Figure 1b). These bastions are connected with line-segments (cortine). The walls have a total length of length 7 km and are surrounded by a trench 40-60 m wide (Tzompanaki 2012).

The walls are composed of stone masonry. The construction had to withstand heavy weights and earth pressures. To achieve this, the excavation of the foundation had to reach sufficient depths in order to find solid ground or where that was not possible the width of the foundation was extended.

Figure 1. (a) A satellite image of the Heraklion City bastion fortification system (Google Earth). (b) A view of the Martinengo bastion, damaged by vertical cracks.

In some parts, buttresses (contrafforti) were constructed behind the wall to help it sustain the earth pressures (Tzompanaki 2012).

At the year 1669 and after a 21-year siege the city of Heraklion fell to the Ottomans. In some parts of the walls radical repairs were made and in other parts line-segments were extended or a second construction phase was added (Figure 2a). After the Ottoman repairs and until the beginning of the 20th century there were no noticeable changes in the walls. But then, in the 2nd decade of the 20th century, it was decided to cut openings in the walls in order to facilitate the movement of vehicles (Tzompanaki 2012).

Currently, the walls no longer serve the role for which they were originally built, as a fortification system. Due to the drastic development of the city and the suburbs, they are forced to fulfill different requirements, as sport facilities, administration buildings, parks etc are constructed on top of them.

2.2 *The construction phases of the Line-segment Bembo-Saint Francis*

In the current researcher, the part of the walls that is under investigation is the line-segment Bembo-Saint Francis, which has a progressively increasing height starting from 11m to 19.6m and a total length of 240m. In the line-segment, three (3) construction phases are visible as shown in Figure 2b.

1. A lower phase with a heigh of 5.5-10m, made with large rectangular stones and thin layers of strong lime mortar. This construction phase was built by the Venetians and the stones used are Neogene calcareous sandstone and fossiliferous Mesozoic limestone.
2. A middle phase with a heigh of 2-6.5 m made with smaller stones and thick layers of mortar. This phase is considered to be either an addition by the Ottomans or a continuation of the lower Venetian phase but with different materials. The stones used in this phase are dolomized Mesozoic limestone.
3. An upper phase which is made with Neogene marly limestone and is a modern construction (20th century), added during the reconstruction of Duke Beaufort Street, located behind the wall.

During 1982 an extensive earth fill was added behind the wall, for the reconstruction of the Duke Beaufort Street. For several years, before the earth fill addition, part of the line-segment of the street served as bus parking spot. The loads applied by the vehicles were proved an unfavorable factor for the stability conditions of the wall. Due to the deformations recorded, the authorities forbid parking and currently a wide sidewalk has been constructed along the line-segment.

Today, several damages in the masonry wall can be observed. These damages are related both to historical events (long siege by the Ottomans) and to the earth fill loads. In particular, the earth fill loads have caused both vertical and horizontal cracks as well as swelling. Most of the damages are located in the middle construction phase, where the mortar has deteriorated, extensive cracks have been identified and parasitic vegetation has grown (Xatzistergiou & Skopelitis 2010).

3 MECHANICAL PARAMETERS OF THE SOIL STRATA

The mechanical parameters of the geological formations have been acquired during the geotechnical characterization performed after the 1982 reconstruction works. These investigations included: three (3) sample drillings behind the wall, Standard Penetrations Tests, laboratory tests for the physical and mechanical parameters and detailed documentation of the damages. A total of 5 formations were distinguished, as presented in Figure 2b. The mechanical parameters for each soil layer are listed in the Table 1.

At the current cross section, the height of the wall is 20.07 m and the heights of the Venetian, Ottoman, and Modern phases are 8.84 m, 6.35 m, and 3.17 m respectively. The wall's geometrical characteristics are clearly indicated on the cross section.

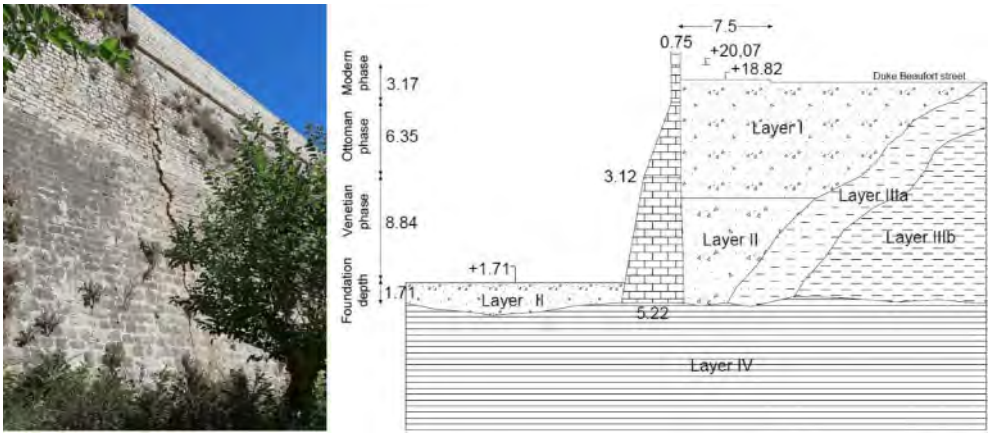

Figure 2. (a) The three (3) construction phases of the line-segment Bembo-Saint Francis can be easily distinguished. A vertical crack is also visible. (b) Typical cross section of the line-segment Bembo-Saint Francis with the identified soil layers.

Table 1. Mechanical parameters of the soil layers.

	Backfill materials composed of clay and sand		Erosion mantle of marl	Gray-black marl	Cyan-gray marl
	(Layer I)	(Layer II)	(Layer IIIa)	(Layer IIIb)	(Layer IV)
c (kPa)	10–20	10–20	15–25	15–25	20
φ^o	22.5–25	22.5	30–33	30–33	32
E (MPa)	12.5	13–15	15–30	90–100	100

4 MASONRY WALL

4.1 *Modelling*

Masonry is a composite material, composed of the units (bricks, stones, etc) and the mortar. Its mechanical behavior depends on the mechanical and geometrical characteristics of its individual components and the way they are placed (Petersen 2009).

Masonry structures can be generally modelled as heterogeneous and homogeneous models. In this case study the masonry units and the mortar between them are modelled as a single material.

Macro-modeling generally involves some degree of approximation in the computational masonry modelling because of complex load transfer mechanisms. Fortunately, only the bond shear strength between masonry units and mortar would be enough for large and practice-oriented analyses, as it is considered the weakest link in masonry assemblages (Koksal et al. 2016).

The influence of mortar joints acting as a plan of weakness on the composite behavior of masonry is particularly relevant in case of strong unit-weak mortar joint combinations, which are characteristic of ancient stone masonry (Vasconcelos & Lourenço 2009).

As has been widely reported, the failure behavior of masonry joints under shear, with moderate pre-compression levels, can be represented by the Coulomb friction law.

For higher normal compressive stresses, the validity of the Coulomb failure is lost and crushing/shearing of the units, accompanied by cracking occurs (Lourenço et al. 2004).

4.2 *Mechanical characteristics of the wall*

The mechanical characteristics of masonry walls can be evaluated through laboratory or field tests. However, when these are not able to be performed, data, equations and formulas from literature and international codes can be used. The mechanical characteristics of the units and the mortar were taken from the geotechnical report performed by Xatzistergiou and Skopelitis (2010) and were used to calculated the mechanical characteristics of the wall.

4.2.1 *Compressive strength*

The compressive strength of the masonry wall was evaluated through the equation proposed in Eurocode 6, part 1-1, for unreinforced masonry made with general purpose mortar and lightweight mortar.

$$f_k = k f_b^{0.7} f_m^{0.3} \tag{1}$$

where f_k = the compressive strength of the masonry wall, k = a constant depending on the building technique (in this case K = 0.6), f_b = the compressive strength of the units and f_m the compressive strength of the mortar.

4.2.2 *Modulus of elasticity*

The Young's modulus depended on the mechanical properties of the masonry unit, on the mechanical properties of mortar and the thickness of the bed joints (Zavalis et al. 2014). In literature, many equations are proposed for calculating the wall's modulus of elasticity.

Eurocode 6 proposes the following equation (2) for assessing the short-term modulus of elasticity of a masonry wall.

$$E_{mas} = k_E f_k \tag{2}$$

where k_E = constant, retrieved by a National Annex (Eurocode 6 proposes a value of 1000), and f_k = compressive strength of the masonry.

To calculate the long-term modulus of elasticity Eurocode 6 proposes equation (3):

$$E_{mas_{long-term}} = \frac{E_{mas}}{(1 + \varphi_\infty)} \tag{3}$$

where φ_∞ is the creep coefficient that in this case, for ancient stone, is equal to 0. As a result, the short-term modulus of elasticity is equal to the long-term modulus of elasticity.

As seen above Eurocode 6 sets the $k_E = 1000$. However, Tomazevic (1999) states that the values of the modulus of elasticity, assessed by that assumption are sometimes far from reality. Tomazevic proposed the following limits for the modulus values (Aras & Gülay 2015).

$$200 * f_k < E_{mas} < 2000 * f_k \tag{4}$$

These limits include values proposed by several international codes, such as FEMA 306 (E_{mas} = 550 f_k), IBC 2003 and MSJC 2002 (E = 700*f_k), Canadian masonry code (E = 850*f_k) and Italian standard code (NTC 2018) (E = 1000*f_k) (Guadagnuolo et al. 2020).

Zavalis et al. (2014) citied some formulas developed by Cieseilski et al. (1999) (eq. 6), Brooks (1999) (eq. 7), Matysek et al. (1999) (eq. 8), Farshchi et al. (2009) (eq. 9), Jonaitis (2001) (eq. 10) and Marciukaitis et al. (2004) (eq. 11).

$$E_{mas} = \frac{1,2 * E_b * E_m}{0,2 * E_b + E_m} \tag{5}$$

$$\frac{1}{E_{mas}} = \frac{0,86}{E_b} + \frac{0,14}{E_m} \tag{6}$$

where E_b and E_m the modulus of elasticity of the units and mortar respectively.

$$E_{mas} = \frac{1,25 * \xi + 1}{1,25 * \xi + \beta} * E_b \tag{7}$$

where ξ is the ratio of the units' thickness to the mortar joints' thickness ($\xi = h_b/h_m$), β is the ratio of unit's elastic modulus to that of the mortar ($\beta = E_b/E_m$).

$$E_{mas} = \frac{E_{mas} * E_b}{\left(\frac{h_b}{h_m}\right) * (E_b - E_{mas}) + E_b} \tag{8}$$

$$E_{mas} = \frac{1}{2}\left(E_b * \frac{h_b}{h_{sum}} + E_m * \frac{h_m}{h_{sum}} + \frac{E_b * E_m}{E_m * \frac{h_b}{h_{sum}} + E_b \frac{h_m}{h_{sum}}}\right) \tag{9}$$

where h_{sum} is the summary of the height of the masonry unit and the thickness of the bed joint of mortar ($h_{sum} = h_m + h_b$).

$$E_{mas} = \frac{1}{2}\left(E_b * \frac{h_b}{h_{sum}} + E_{m,eff} * \frac{h_m}{h_{sum}} + \frac{E_b * E_{m,eff}}{E_{m,eff} * \frac{h_b}{h_{sum}} + E_b \frac{h_m}{h_{sum}}}\right) \tag{10}$$

Mariukaitis et al. has replaced in the formula of Jonatais (eq. 11) the Young's modulus of the mortar joints with the efficient Young's modulus of the mortar joint, which is calculated as:

$$E_{m,eff} = \frac{h_m - 2 * a}{2 * h_m} E_m \tag{11}$$

where a is the thickness of the zone close to contact between mortar and a masonry unit:

$$a = 0,33 * h_m^{0,5} \tag{12}$$

During the calculations of the Young's modulus for the walls of Chandakas some assumptions had to be taken into considerations. The Venetian phase was considered to be built entirely either by fossiliferous limestone and healthy mortar (orange color in Figure 3), or by calcareous sandstone and healthy mortar (blue color in in Figure 3). The Ottoman phase was considered to be built entirely by dolomitized limestone (grey color in in Figure 3) and healthy mortar. The modern phase was modeled with the characteristics of the Venetian phase.

According to Eurocode 6 (Eq. 3) and Tomazevic (Eq. 5) the Ottoman phase has higher modulus of elasticity than the Venetian phase, something that was not expected since the former is built with thick layers of mortar and small stones. However, this can be attributed to the fact that the compressive strength of the materials is primarily considered. Moreover, the values provided by Tomazevic are either the lowest or the highest, fitting with the proposed by him lower and upper limits.

Similar results are provided by Cieseilski (Eq. 6) and Brooks (Eq. 7). Again, the modulus of elasticity for the Ottoman phase is higher than the one for the Venetian phase. These authors added the elastic properties of the materials, excluding their geometrical characteristics.

Matysek and Farshchi (Equations 8 & 9), on the other hand, added both the elastic and geometrical characteristics of the materials. As a result, the Venetian phase, when built entirely by fossiliferous limestones and healthy mortar, presents higher modulus of elasticity than the Ottoman's phase.

As mentioned by Zavalis et al. (2014), the equations provided by Jonaitis (Eq. 10) and Marciukaitis (Eq.11), typically provide values larger than the values defined by experimental research. That can be observed especially in the case of the Ottoman phase where its modulus of elasticity is double or even triple the one calculated for the Venetian phase. Through testing, it was concluded that when high elastic modulus is implemented in these formulas for the units then the values calculated for the wall's modulus of elasticity are also high.

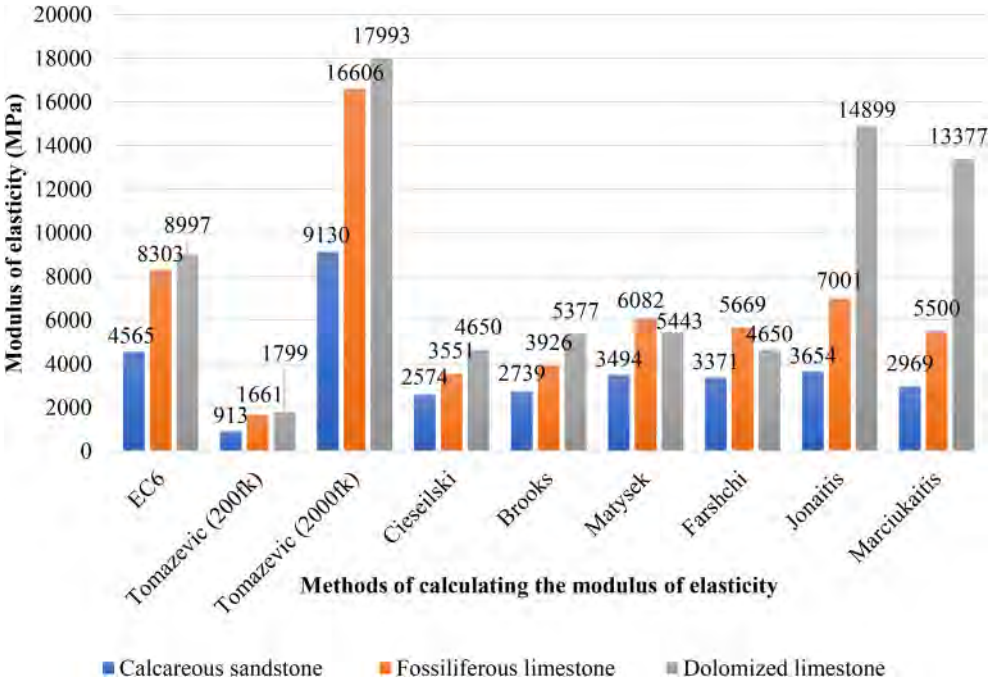

Figure 3. Comparison of the various modulus of elasticity values calculated by applying the above analyzed equations retrieved by the literature review.

4.3 *Cohesion-Friction angle-Poisson's ratio*

The shear parameters of the interface for the masonry (cohesion and friction coefficient) can be calculated through triplet tests. In this case, laboratory tests were not able to be performed so the prementioned parameters were obtained from previous research and national codes.

As mentioned by Angiolilli and Gregori (2020), reliable evaluation of the shear strength parameters is difficult to perform in the case of stone masonry because they strongly depend on the asperity of the stones and may not be considered representative for the entire masonry structure. Milosevic et al. (2013) experimentally calculated that for calcareous stone units coupled with hydraulic lime mortar, the cohesion was equal to 0.08 kN/mm^2 and the friction angle equal to 29.2°, while in stone units coupled with air lime mortar the cohesion was equal to 0.2 and the friction angle equal to 50.1°. Binda et al. (1994) calculated, for sandstone units with hydraulic lime mortar, cohesion equal to 0.33 kN/mm^2 and friction coefficient equal to 0.74. Also, for stone units with hydraulic lime mortar the calculated cohesion was equal to 0.58 kN/mm^2 and friction coefficient was equal to 0.58. In international codes, such as Eurocode 6, the friction coefficient is considered as constant, independent of the wall type, and assumed equal to 0.4. Eurocode 6 presents a table, where according of the type of the mortar and the type of the units a cohesion value can be chosen, while also an upper limit is proposed. For this case, the cohesion values range from 0.15 to 1 kN/mm^2. Finally, Amorosi et al. (2014) investigated an ancient wall in the city of Rome and proposed values 0.5 kN/mm^2 for the cohesion and 30° for the friction angle. After reviewing all above mentioned literature sources, it was decided that the friction coefficient and cohesion of the wall should be set equal to 0.4 and 0.5 kN/mm^2 respectively.

The ratio of Poisson in masonry ranges from 0.15 to 0.3 and in this case the latest value was used (Korompilas 2015).

5 PARAMETRIC SIMULATIONS

A numerical model was set up using the Finite Element code Plaxis 2D. The results were implemented in the program, where the overall stability of the wall-ground system was evaluated through 2 groups of parametric simulations. During the simulations 8 points were selected along the cross section of the wall for deformation observation purposes, as indicated in Figure 7a.

In total, 21 analyses were performed for the line-segment Bembo-Saint Francis divided in 2 groups.

1. Group 1: The cohesion and friction angle of the soil layers were altered between the MIN and the MAX values, while maintaining a constant value for the modulus of elasticity of the soil layers (Table 1). Regarding the masonry wall, at the Ottoman phase the mechanical parameters of the dolomitized limestone were assigned, while at the Venetian either those of the fossiliferous limestone or those of the calcareous sandstone. In each construction phase, the modulus of elasticity was considered constant. The values used were set equal to the calculated by the equation proposed by EC6.
2. Group 2: All possible combinations of values for the modulus of elasticity, precented in Figure 3, were applied. The mechanical parameters of the soil layers were kept constant (considering them to be the most unfavorable).

Both simulation groups were aiming to evaluate the sensitivity of the models on the values of the masonry wall's modulus of elasticity .

Regarding the results of the first group of simulations, as presented in Figure 4, two (2) pairs of deformation patterns are observed. The set of parameters including the minimum values of the cohesion presented the maximum deformations while the set of parameters including the minimum values of the friction angle presented the minimum deformations. Most of all it is clear that the type of the building stone of the masonry wall does not affect the deformations. In this group of simulations, the highest safety factor calculated is $SF_{MAX} = 1.223$ and the lowest $SF_{MIN} = 1.076$.

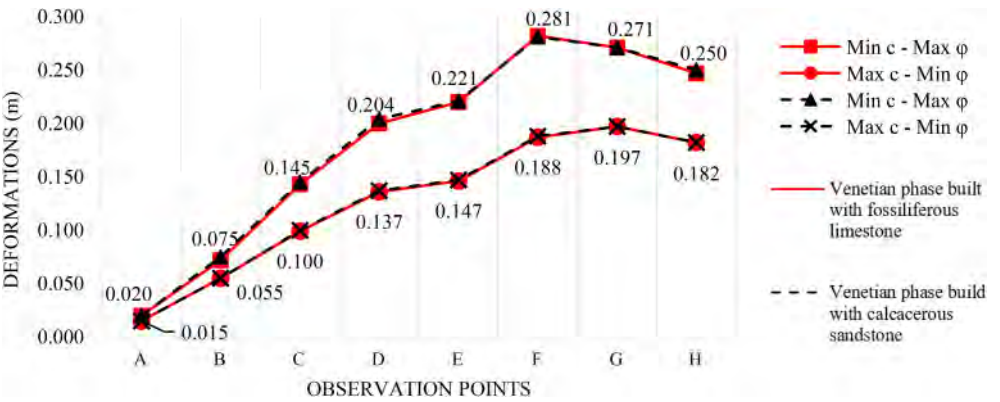

Figure 4. Deformations at the observation points per analysis for Group 1.

Figure 5, presents the simulation results when applying all possible combinations of building material as well as all possible values of modulus of elasticity, estimated by the methods listed in paragraph 4.2.2. The calculated deformations can be seen converging; thus, it is concluded that neither the method (equations and formulas) with which the modulus of elasticity of each phase is calculated nor the unit that Venetian phase is considered to be built with, play significant role in the overall stability of the system. The highest safety factor calculated is $SF_{MAX} = 1.081$ and the lowest $SF_{MIN} = 1.076$.

Evaluating all above – described simulations it is clear that the geometry of the masonry wall must be the key parameter affecting the operation of the wall as a retaining structure. The distribution

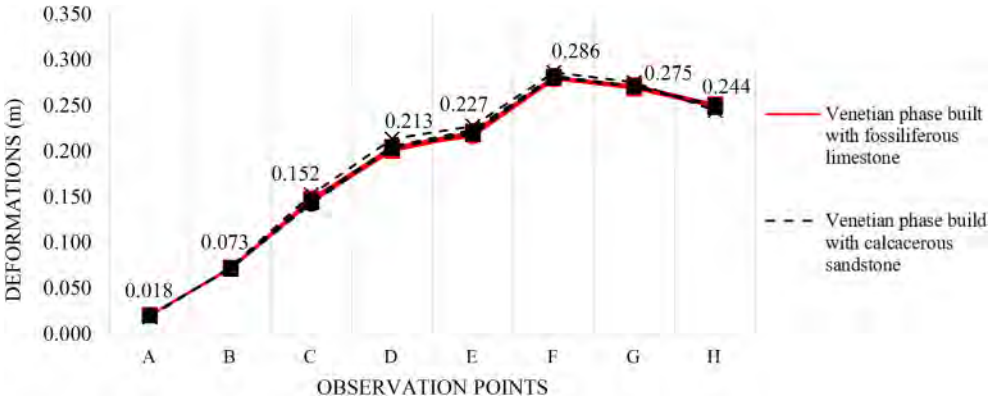

Figure 5. Deformations per analysis for the Group 3.

of the total displacements (Figure 6b) indicates that the Ottoman phase is affected the most by the deformations. The main factor that caused these deformations is believed to be the inability of the Ottoman construction phase to receive earth pressures due to its reduced thickness. Also, the fact that this phase was built with thick layers of mortar presenting inferior quality also affect its bearing capacity.

Evaluating the distribution of the shear strains (Figure 6c) two shear surfaces can be identified, one along the wall – backfill interface and a secondary between the backfill materials and the rocky bedrock. The first one indicates the surface that governs the failure mechanism. As it seems the failure mechanism is considered to be overturning due to the earth pressures. The secondary shear surface is a potential failure plain less importuned and not fully developed.

Finally, by evaluating the simulations it is clear that the overall stability of the wall is considered marginally sufficient due to the calculated low safety factor values (SF = 1.076).

The analysis with the highest deformation values from both simulation groups was set as a Reference analysis and was later used for the evaluation of the proposed support methods. In this analysis, the modulus of elasticity values applied were the lowest, in accordance with the Tomazevic lower limit (K = 200). The Venetian phase was set to be constructed by calcareous sandstones and

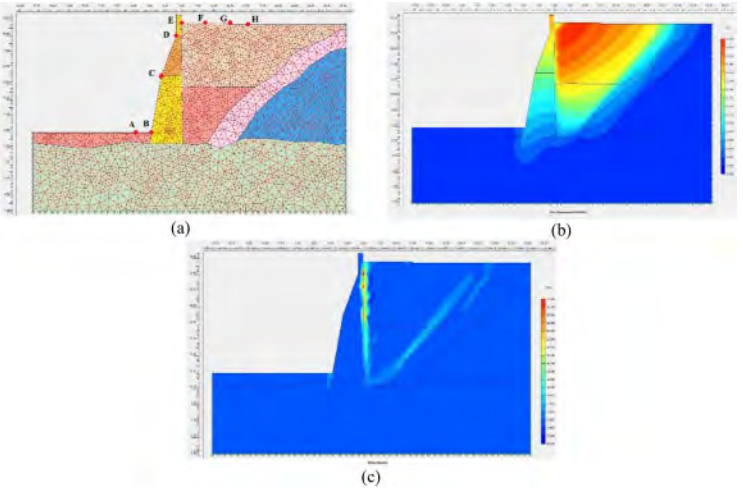

Figure 6. (a) The distribution of the observation points (b) Total displacements contour (c) Shear shading contour.

the Ottoman phase by dolomized limestone. Finlay, the safety factor was estimated with a value of 1.079.

6 PROPOSED SUPPORT SYSTEM FOR THE PROTECTION OF THE CHANDAKAS WALL

To carry out restoration works on monuments, certain standards and procedures must be followed. These standards are defined by regulations such as The Venice Charter (1964) and ICOMOS (2003) (Korany 2011). Regarding the masonry line-segment Bembo-Saint Francis the following are proposed.

- Repair of eroded and cracked joints and local replacement of mortar with thick grout. The composition of the grout should be compatible with the mortar used, the units and the construction model. This technique is called repointing
- Removal and replacement of eroded stones, especially in parts of the Ottoman phase
- Grouting of vertical and horizontal cracks and hollow parts
- Cleaning of parasitic vegetation

Furthermore, for the overall stability problems of the wall-ground system 5 support systems were evaluated by means of FEM simulations.

1. Vertical piles behind the wall, 21m long.
2. Vertical piles behind the wall, 23m long.
3. Vertical piles behind the wall, 21m long, with a series of passive anchors.
4. Vertical piles behind the wall, 23m long, with a series of passive anchors.
5. Vertical piles behind the wall, 21m long, with a series of tensioned prestressed anchors.

The piles are placed behind the wall in order to take over most of the earth pressures currently applied by the backfill materials. The reason the piles were chosen as a method of support is that they can be easily installed along the wide sidewalk located behind the wall, and because they are not going to affect the monument and the traffic on Duke Beaufort Street. The piles are designed to be placed 2.5 m from the crown of the wall, with a diameter of 1 m wide. The deformations and the safety factors provided by the application of the various proposed support methods are shown in Figure 8 and Table 2. The results were compared with the reference analysis.

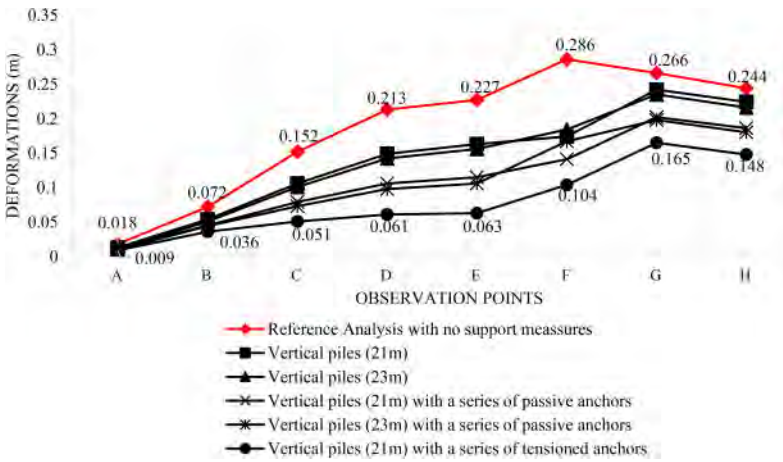

Figure 7. Deformations estimated for each support system.

Table 2. Safety factors provided by for each support system.

Analysis	SF
Reference analysis with no support measures	1.079
Vertical Piles (21 m)	1.185
Vertical Piles (23 m)	1.283
Vertical Piles (21 m) with a series of anchors	1.513
Vertical Piles (23 m) with a series of anchors	1.550
Vertical Piles (23 m) with a series of tensioned anchors	1.512

The support system with the tensioned anchors offers by far the minimum deformations and is the one with the best safety factor values (SF = 1.51). Nonetheless, it should be mentioned that the installation of pile wall results to the loosening of the soil materials between the wall and the piles.

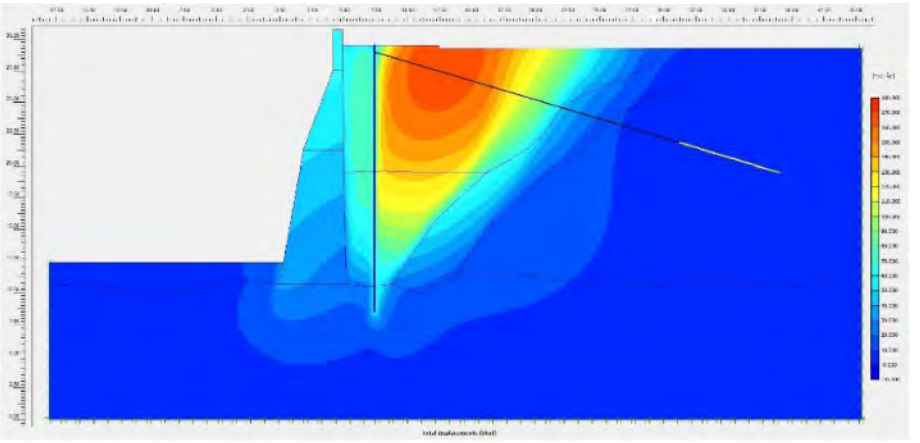

Figure 8. Total displacements contour after the installation of the support system.

7 CONCLUSIONS

The current study provides a geotechnical simulation of the line-segment Bembo-Saint Francis of the masonry wall of Chandakas, focusing mostly on the mechanical characteristics and the deformations of the wall. The modulus of elasticity of the wall was calculated through many different methods provided by the literature. The equations used had similar approaches and even though the calculated values varied, there were only minor deviations to the calculated Safety Factor values, proving that the geometry of the wall plays the key role on the stability of the structure. The overall stability of the wall-ground system was assessed by a 2D numerical approach and was deemed marginally sufficient (SF = 1.076). Moreover, the failure mechanism is considered to be overturning due to the earth pressures. Aiming to provide an efficient support system for the protection of the wall by means of a series of simulations it was proved that a pile wall with prestressed anchors helps stabilize the wall-ground system, reduces the deformations, and increases the safety factor (SF = 1.51), without affecting the monument. Similar stability and deformation issues have been reported for several other parts of the masonry walls of the city of Heraklion. Thus, the current study can be used as a prototype for the design of similar support systems wherever needed.

ACKNOWLEDGEMENT

SCIENCE project has received funding from European structural and investment funds, Partnership Agreement 2014–2020, and is supervised by General Secretariat for Research & Technology in the context of National action for bilateral cooperation between Greece-China.

REFERENCES

Amorosi, A., Boldini, D., de Felice, G., Malena, M. & Di Mucci, G. 2014. Numerical modelling of the interaction between a deep excavation and an ancient masonry wall. in *8th International Symposium on Geotechnical Aspects of Underground Construction in Soft Ground at Seoul, Korea*. doi: 10.1201/b17240-46.

Angiolilli, M. & Gregori, A. 2020. Triplet test on rubble stone masonry: Numerical assessment of the shear mechanical parameters. *Buildings*. 10(3): 15–17. doi: 10.3390/buildings10030049.

Aras, F. & Gülay, A. 2015. Investigation of mechanical properties of masonry in historic buildings. *Journal of the Croatian Association of Civil Engineers*. 67(3):461–469. doi: 10.14256/jce.1145.2014.

Binda, L., Fontana, A., & Mirabella, G. 1994. Mechanical behavior and stress distribution in multiple-leaf stone walls. *10th International Brick Block Masonry Conference*. 1:51–59.

EN 1996-1-1. 2005. (English): Eurocode 6: Design of masonry structures – Part 1-1: General rules for reinforced and unreinforced masonry structures [Authority: The European Union Per Regulation 305/2011, Directive 98/34/EC, Directive 2004/18/EC].

Farshchi, D. M., Masoud, M., Schumacher, A. & Marefat, M. S. 2009. Numerical modelling of in-plane behaviour of URM walls and an investigation into the aspect ratio, vertical and horizontal post-tensioning and head joint as a parametric study. *Archives of Civil and Mechanical Engineering*. 9(1): 5–27. doi: 10.1016/s1644-9665(12)60037-5.

Guadagnuolo, M., Aurilio, M., Basile, A. & Faella, G. 2020. Modulus of elasticity and compressive strength of tuff masonry: Results of a wide set of flat-jack tests. *Buildings* 10(5):84. doi: 10.3390/BUILDINGS10050084.

Koksal, H. O., Doran, B., Kuruscu, A. O. & Kocak, A. 2016. Elastoplastic Finite Element analysis of masonry shear walls. *KSCE Journal of Civil Engineering*. 20(2):784–791. doi: 10.1007/s12205-015-0393-1.

Korany, Y. 2011. Effective techniques for restoration of heritage Masonry. *International Journal of Materials and Structural Integrity* 5(2–3):136–150. doi: 10.1504/IJMSI.2011.041931.

Lourenço, P. B. 2002. Computations on historic masonry structures. *Progress in Structural Engineering and Materials* 4(3):301–319. doi: 10.1002/pse.120.

Lourenco, P. B., Barros, J. O. & Oliveira, J. T. 2004. Shear testing of stack bonded masonry. *Construction and Building Materials*. 18:125–132. doi: 10.1016/j.conbuildmat.2003.08.018.

Milosevic, J., Gago, A. S., Lopes, M. & Bento, R. 2013. Experimental assessment of shear strength parameters on rubble stone masonry specimens. *Construction and Building Materials*. 47:1372–1380. doi: 10.1016/j.conbuildmat.2013.06.036.

Petersen, R. B. 2009. In-plane Shear Behaviour of Unreinforced Masonry Panels Strengthened with Fibre Reinforced Polymer Strips, PhD Thesis. Newcastle-Australia.

Tzompanaki, C. 2012. *CHANDAKAS. THE CITY AND THE WALLS*. (2). Heraklion. Greece: VIKELAIA PUBLIC LIBRARY.

Vasconcelos, G. & Lourenço, P. B. 2009. Experimental characterization of stone masonry in shear and compression. *Construction and Building Materials*. 23(11):3337–3345. doi: 10.1016/j.conbuildmat.2009.06.045.

Xatzistergiou, G., & Skopelitis, I. 2010. Restoration study for the line-segment Bembo-Saint Francis and for the orrechione of Sabbionara bastion of the Venetian walls (Duke Beaufort Street). Heraklion. Greece: Xatzistergiou & Associates.

Zavalis, R., Jonaitis, B. & Lourenço, P. B. 2014. Analysis of bed joint influence on masonry modulus of elasticity. *9th International Masonry Conference in Guimarães*:1–11. doi: 10.13140/2.1.1643.3442.

Korompilas, D. N. 2015. Study of the inelastic behaviour of the Konitsa bridge with the use of inelastic simulation for the masonry and application of reinforcement methods. Patra: University of Patra. http://hdl.handle.net/10889/8762

Sithiakaki, V., Kanaki, E. & Bilmezi, X. 2013. Older fortifications of Heraklion: A different approach based on recent excavation data. In Archaeological work in Crete. *Proceedings of the 3rd Meeting Rethymnon*: 395–410, 5–8 December 2013. Rethymno: Department of Philosophy and Social studies. University of Crete – Ephorate of Antiquities of Rethymno.

Geotechnical Engineering for the Preservation of Monuments and Historic Sites III – Lancellotta, Viggiani, Flora, de Silva & Mele (Eds)

Low-impact mitigation measures to contrast the instability processes affecting the Etruscan necropolis of Norchia

D. Spizzichino & G. Leoni
ISPRA, Geological Survey of Italy, Rome, Italy

D. Boldini
Sapienza University of Rome – DICMA, Rome, Italy

S. Loreti
University of Bologna – DICAM, Bologna, Italy

C. Margottini
UNESCO Chair at Florence University, Florence, Italy

ABSTRACT: This paper summarizes the geomorphological processes affecting one of the rock-cut tombs of the Etruscan necropolis of Norchia (Central Italy), its stability analysis and the assessment of preliminary mitigation strategies. The study was carried out through an interdisciplinary approach including: archaeological survey, geomorphological assessment and definition of prototype approaches for landslide risk mitigation plan of the whole rock-cut necropolis. The latter is considered a fundamental tool for the future tourist development of the site, safe from possible rock falls and slides. The investigation reveals the importance of engineering geology and geohazard assessment for the future conservation of rock-cut sites.

1 INTRODUCTION

This paper represents one of the outcomes of two different statements. The first one (starting since December 2019), between the *Soprintendenza Archeologica, Belle Arti e Paesaggio per l'area metropolitana di Roma, la provincia di Viterbo e l'Etruria Meridionale* and the Italian Institute for Environment Protection and Research (ISPRA, Geological Survey of Italy), was aimed at the analysis and assessment of stability conditions of the Etruscan necropolises distributed in the entire territory of competence.

The second cooperation, between ISPRA and University of Bologna (DICAM), was focused on the evaluation of stability conditions of the most threaten tombs of the whole Norchia Necropolis. The archaeological site of Norchia is an Etruscan settlement established along the ancient via Clodia, dating back to the Classical Hellenistic period (Ambrosini 2017).

After a short period of abandonment, during the Republican era, Norchia was populated back in the middle ages, alternating periods of splendor with periods of deep decadence.

The town was finally abandoned following a severe malaria epidemic in 1453. The peculiarity of the site, that makes it a unique example, is the nearby presence of a wide Etruscan necropolis. Dated between the end of the IV and middle of the II century B.C., it testifies rituals/habits/ceremonies of the Etruscan funerary religion.

The necropolis is more than 100 hectares wide, and includes rock-cut tombs of various types (façade, half-cube, false-cube and temple type) and dimensions (4–10 m high), showing a remarkable similarity with middle east and Asian tombs (e.g., the Nabatean rock cut city of Petra in Jordan and the tombs of Hegra in KSA).

DOI 10.1201/9781003308867-27

Norchia necropolis is one of the most significant examples of rock-cut tombs of the Hellenistic period, representing an important and rare illustration of rock architecture, one of the few preserved in Italy. In recent years, the in-creasing interest by archaeologists on Etruscan heritage in general and in particular on Norchia was mainly limited by issues of conservation and accessibility to the sites, this latter due to the presence of dense vegetation covering entirely the necropolis and to diffuse rock slope instability processes.

The above mentioned collaborative activities, between the University of Bologna, the Geological Survey of Italy (ISPRA) and local authorities, are aimed at the conservation and protection of Etruscan funerary monuments with the ultimate target of making the area accessible to the public in a complete state of safety from rock falls and slides.

The study described here refers in particular to a small tomb belonging to the Pile sector B (Figure 1), selected as pilot study to develop sustainable mitigation measures for the area at risk.

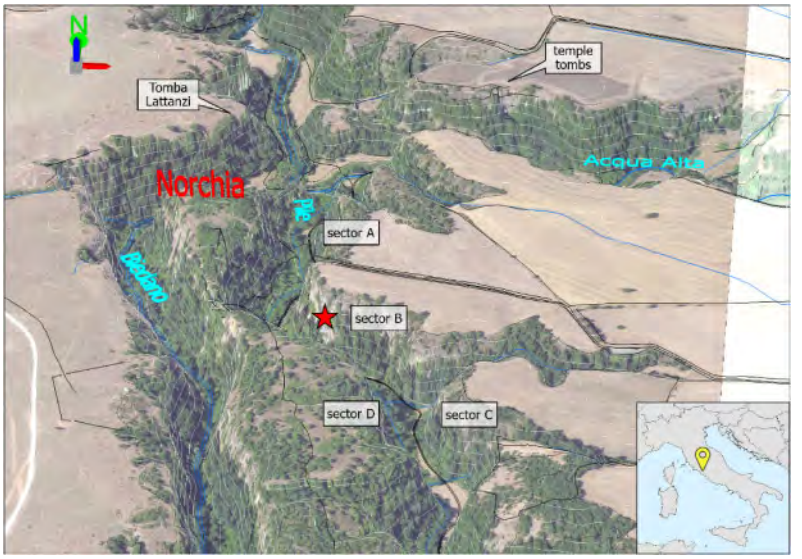

Figure 1. Norchia site and Necropolis sectors. The location of the selected tomb is marked with a red star.

2 GEOGRAPHICAL AND GEOLOGICAL SETTING

The town of Norchia was located on a residual pyroclastic ridge, surrounded by steep slopes, at the junction of Pile and Acqua Alta streams with the Biedano river (Figure 1). Two layered pyroclastic deposits, red tuff from Vico volcanic apparatus at the top and grey tuff (Nenfro) from Vulsini volcanic apparatus below, overlay a Meso-Cenozoic flysch deposit (Figure 2). The tombs were excavated in the pyroclastic layers, according to the natural profile of tuff outcrops. Recent investigations have revealed that different threats affect the site: surface rock weathering, water percolation and infiltration, invasive vegetation and biological colonization, rock falls and rock slide from the cliff.

The site was affected by an intense erosive activity operated by the Biedano and the Pile streams, from South to North, and Acqua Alta stream, from West to East (Figure 2). The resulting plateau, given the soft consistency of the rocks, easily workable, made the place a strategic point for the settlement of the Etruscan town (Bear et al. 2009). Both the volcanic nature of the site and the tensional stress release due to the erosion of the river at the base of the slope created an important fractures system that affects the rock mass. The main families of discontinuities identified at the site are:

- sub-horizontal discontinuities due to the layering and gradation of deposits;
- vertical and sub-vertical fractures, orthogonal to the slope, caused by the cooling of volcanic rock;
- fractures with sub-vertical and inclined planes, parallel to the slope face, to be related to the stress release caused by the river erosion;
- fresh fractures spread from existing fractures caused mainly by plant roots.

These sets of discontinuity, together with the poor quality of the material (alternation of soft rocks), have produced over the centuries diffused phenomena of weathering and collapse, that have compromised the necropolis stability and accessibility.

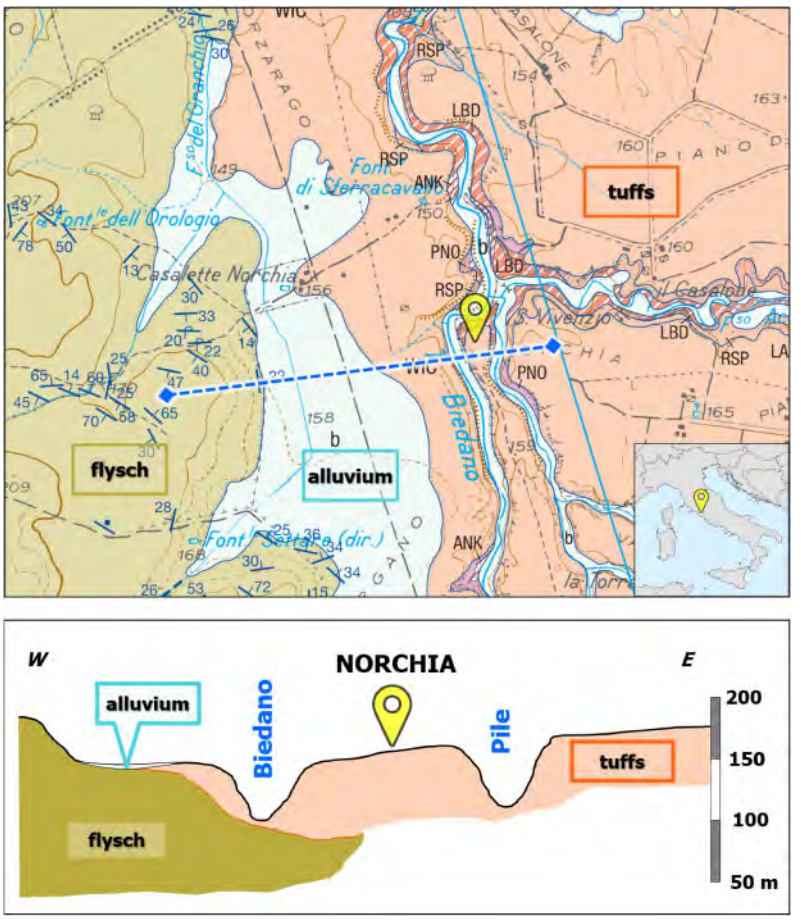

Figure 2. Geologic setting (up) and cross section (down) of the area, from Carta Geologica d'Italia, scale 1:50'000, Sheet 354 (ISPRA, Geologic Survey of Italy).

Figure 3 illustrates the appearance of the necropolis about 30 years ago after an important intervention of reclamation of the vegetation (left) and an hypothetical historical reconstruction (right). As anticipated, the paper focuses specifically on a small tomb belonging to the sector of the Pile B stream (Figures 1 and 4). Previous studies on the rock material outcropping in the necropolis carved in the slope, pointed out that this sector is split into two main levels (Ciccioli et al. 2010). The selected tomb is located in the upper level at the stratigraphic contact between the red black scoriae tuff and the ignimbrite of Nenfro (Figure 4, left).

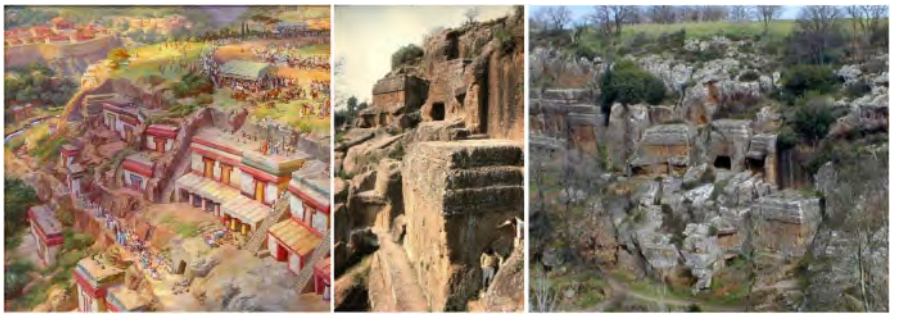

Figure 3. Recent picture (right and centre) of the necropolis in the Pile sector B (Ambrosini, 2017) and an historical hypothetical reconstruction (left) (ANTICAE VIAE, 2020).

Figure 4. Frontal and lateral view of the tomb selected as a prototype example of analysis and mitigation measures.

3 LABORATORY CHARACTERIZATION OF ROCK MATERIALS

Three different rock blocks were collected during the field surveys of October and December 2019, nearby the selected tomb.

The blocks are mainly differentiated in two lithologies. In particular, making reference to Ciccioli et al. (2010), the red tuff with black scoriae was referred to lithology A and the black tuff with black scoriae (also called grey tuff, or ignimbrite of Nenfro) was referred to lithology B. Among the sampled blocks, two of them belong to lithology A. They are irregularly shaped, o-range/reddish in color (indicating the presence of oxidized iron), with the presence of well-defined leucite crystals inside, and with inclusions of blackish material (lava) and pumice stone.

One block belongs to lithology B. It shows a grayish matrix that contains clasts of different shape and material. The difference in color, with respect to the other two blocks, indicates the lack of oxidized iron in its mineralogical composition (Perini et al. 2007).

Figure 5. Tuff outcrop of two different lithology (left) and the collected samples (two from lithology A and one from lithology B).

The appearance of this block and the different altitude at which it was taken suggest also a different pyroclastic flow deposit and a different alteration, due to the different atmospheric conditions to which it was affected. Due to the extremely weak nature of the material, combined with the presence of clasts with a greater resistance than the soft matrix, it was not possible to realize cylindrical specimens of standard size for this block, but only parallelepiped specimens (Figure 6).

Figure 6. Specimens for the laboratory tests. Cylindrical specimen belonging to lithology A (left) and parallelepipeds to B (right).

Table 1 summarizes the main physical and mechanical properties determined by laboratory tests. For the red tuff with black scoriae (lithology A) uniaxial compressive tests and Brazilian indirect tensile tests were carried out both on dry and saturated specimens. The dynamic elastic modulus (Edyn) was derived by the P wave velocity (VP), measured by ultrasonic test.

Inspection of Table 1 reveals that:

- the porosity (n) varies between 50% (A lithology) and 60% (B lithology);

Table 1. Summary of the physical and mechanical characterization of the investigated rock materials. The uniaxial compressive tests of grey tuff specimens were carried out using parallelepiped specimens.

Lithology	red tuff with black scoriae	red tuff with black scoriae	grey tuff
condition	*dry*	*saturated*	*dry*
γ (kN/m^3)	11.74	15.18	10.27
n (%)	50.85	/	61.35
σ_c (MPa)	2.65	1.43	1.33
σ_t (MPa)	0.48	0.18	/
V_P (km/s)	1.3	1.22	/

- the uniaxial compressive strength (σ_c) and the tensile strength (σ_t) are extremely low, especially for the B lithology (Deere and Miller, 1966);
- saturation induces a relevant decrease in strengths.

4 IN SITU CARACTHERISATION

4.1 *Topographic survey*

In order to reconstruct the detailed geometry of the site and to perform the appropriate stability analyses, the possibility to acquire a 3D model has been considered, both from the ground (TLS, Terrestrial Laser Scanning) and from remote by UAV. Unfortunately, none of the above mentioned surveys was possible to implement, due to the dense vegetation for TLS and to the no-fly-zone for drone due to the nearby military area.

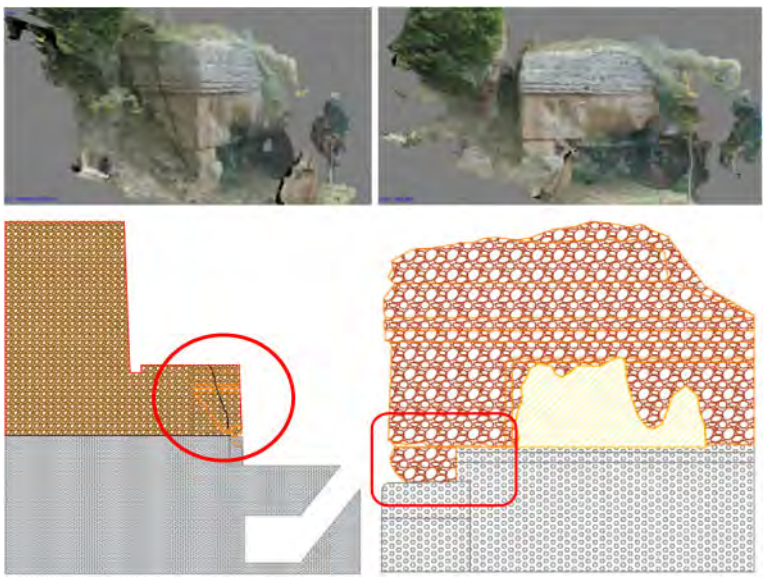

Figure 7. 3D digital-photo reconstruction (upper), lateral and front view (down) of the selected tomb. Red circle highlights the presence of fracture.

In order to overcome this problem a prototype example, well representative of the architectural style of the necropolis, was selected to reconstruct the detailed geometry (Figure 4). It is a partially underground tomb (Figure 4, left), with a collapsed rock block obstructing the entrance to the burial chamber detached from the tomb itself, where the façade exhibits a yellow color (Figure 7).

Externally the tomb has a massive body typical of the "dado" style, but some architectural elements typical of the temple tombs are also present. Part of the massive body is excavated directly into the rock mass, while the remaining part is overhanging and stand on two lateral pillars, made up of blocks belonging to the tuff of the B lithology. At the time of the inspection it was observed that one of the two supports has failed (Figure 7), while the remaining one is affected by a well open fracture (triggered by the plants roots), that extends in the rock-mass behind the tomb façade and that determine a wedge of rock potentially unstable (Figure 7, right).

Part of the massive body is excavated directly into the rock mass, while the remaining part is overhanging and stand on two lateral pillars, made up of blocks belonging to the tuff of the B lithology. At the time of the inspection it was observed that one of the two supports has failed (Figure 7), while the remaining one is affected by a well open fracture (triggered by the plants roots), that extends in the rock-mass behind the tomb façade and that determine a wedge of rock potentially unstable (Figure 7, right).

The topographic reconstruction of the tomb was made by a 3D digital photogrammetry, processing of photos taken during the various field surveys. More specifically, a digital photo-grammetry technique and image processing were implemented. The adopted software (Agisoft Metashape©) allows, starting from images related to the same subject captured from different perspectives, to create a point cloud 3D model as well as precise geometric sections in *dwg* and dxf format (Figure 7).

By using 34 photos of the selected tomb, it was possible to extract a point-cloud of about 40000 control points (corresponding points in the individual photos) derived from the alignment of the images provided by the program.

4.2 *Structural setting of the selected tomb*

Field investigation was also carried out to collect information on the rock-mass at site scale. Essentially, they consisted in the survey of the characteristics of the discontinuities, including their spacing, orientation and roughness. The already mentioned fracture responsible for the potential sliding involving the tomb, was referred to a dip of 68° and a dip direction of 245°, while the slope face has dip of 88°, with the same dip direction. A volume of 10.58 m3 was estimated for possible unstable block, by integrating the information derived from the fracture orientation and the geometrical reconstruction of the tomb.

5 STABILITY ANALYSIS AND PRELIMINARY CONSOLIDATION MEASURES

The stability analysis was carried out with the limit equilibrium method, assuming an a priori slide mechanism and introducing appropriate hypotheses on the acting forces (Boldini et al. 2017). In particular, given the unit weight of volume of the rock material, the unstable block was estimated to have a weight of 124.15 kN.

The block is currently stable partly due to the presence of rock bridges along the fracture and partly due to the support foot still present. These two contributions tend to reduce over time, due to physical degradation and to progressive failure.

The analysis was carried out in the worst scenario, not considering them. In addition to the weight force, pseudo static forces were considered to account for potential local seismic actions:

$$K_h = \pm (K_h \times W) \tag{1}$$

$$K_v = \pm (K_v \times W) \tag{2}$$

in which:

$$K_h = \beta_s x \frac{a_g}{g} x S \tag{3}$$

$$K_v = \pm 0.5 X k_h \tag{4}$$

ag is the maximum horizontal acceleration at the bedrock (Stucchi et al. 2004), here assumed equal to 0.137g, while S = SS ST is a parameter that takes into account respectively the type

of soil (SS = 1.2 for weak rock material) and the amplification due to the topography of the studied area (ST = 1.4 or slopes with inclination greater than 15°). βS is the reduction coefficient of the maximum acceleration expected at the site (βS = 0.24). The safety factor (FS) is expressed as the ratio between the total shear resistance Tr, including the contribution made available by the presence of the passive bars, and the total shear stress (T) acting along the shear surface:

$$F_s = \frac{T_r}{T} \tag{5}$$

The proposed system for consolidation includes steel bars Feb44k with improved adhesion of 24 mm diameter and 3 m length. The characteristic tensile yield strength of the steel is fy = 430 MPa, corresponding to an axial yield strength Ny = 194 kN. A downward inclination of 5° was adopted to facilitate the injection of cement mixture.

The resulting force applied by the single bar was estimated according to the approach outlined in Ribacchi et al. (2018). More in detail, the displacement vector was assumed parallel to the fracture (null dilatancy). As final results a Fs equal to 3.43 was obtained considering two bars, which is higher than the 1.375 value, prescribed for non-natural slopes by the Italian technical code.

The possible sliding mechanism at the bar-cement interface and rock-cement can be considered as satisfied when the length of the bar over the fracture is more than 40 times the diameter of the bar. The foundation length assumed for the interventions was 1.80 m, adequate against this collapse mechanism (British Standard 1989).

To better integrate the interventions and decrease the visual impact, the head of the passive bars will be conveniently hidden from view by using same rock resulting from drilling activities (Figure 8).

Figure 8. Rock core drilled used for mitigation (left), bar insertion (center) and bolt sealing (right).

Before the hole is drilled, a continuous bore of 15 cm will be carried out to preserve the core itself. Once the reinforcement is installed, the rock core drilled will be reinserted into the hole and cemented with a mortar with local aggregates, to hide the plate and mitigate the visual impact of the intervention.

The stability analysis stated the necessity of two passive bars. Nevertheless, in order to ensure a correct and homogeneous distribution of the forces involved (avoiding excessive stresses concentrations with possible local breakages) it was decided to adopt the configuration of the bars showed in Figure 9.

6 CONCLUSIONS

The study summarized relevant on-site activities and laboratory tests aimed at characterizing the instability processes affecting on tomb in Pile sector B of Norchia necropolis. These activities allowed to design a reinforcement intervention, aimed at safeguarding the cultural heritage and at

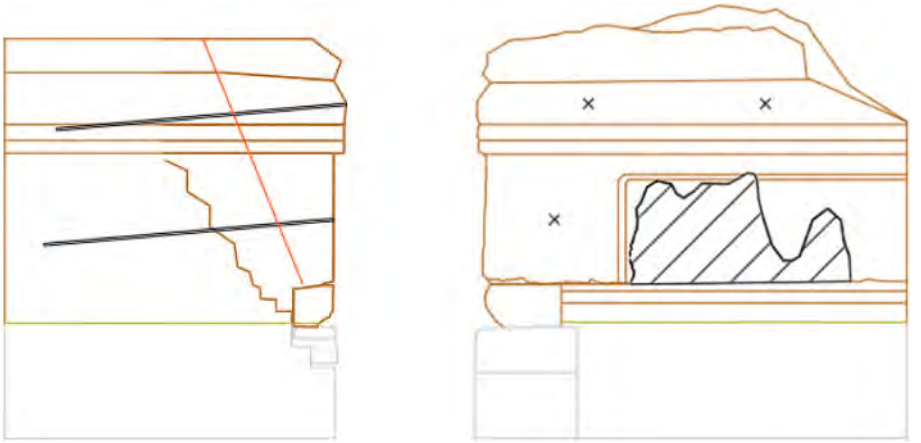

Figure 9. Configuration of the passive bar reinforcement: prospectus (left) and cross section (right).

securing the archaeological site to the future opening for tourist. More in general, they present an operational standard and prototype approach potentially exportable to other cases from a theoretical and methodological point of view. The physical and mechanical characterization of the main tuff lithologies of the site was carried out for the first time, thus providing a useful database for further studies and for future archaeological campaigns. The present study promotes the extensive use of topographical and geomatics survey techniques, even at low cost and of expeditious type. In the future, it will be necessary to carry out reclamation of the area from the vegetation. A long term action will provide a management plain of sustainable mitigation measures tailored for all the possible instability processes in accordance with a multi-annual maintenance and monitoring plan.

ACKNOWLEDGMENT

This research activity was carried out in the framework of a general agreement between ISPRA (Geological Survey of Italy) and the Archaeological Superintendence for Southern Etruria and was supported by the Department of Civil Engineering, Chemistry, Environment and Materials of the University of Bologna.

REFERENCES

Ambrosini, L., 2017. NORCHIA II (2 volumi testo+tavole) – Le necropoli ruprestri dell'Etruria meridionale III. Monografie CNR IBAM – ISTITUTO PER I BENI ARCHEOLOGICI E MONUMENTALI CNR ISBN: 9788880802204.

Boldini, D., Guido, G.L., Margottini, C. & Spizzichino D. 2017. Stability Analysis of a Large-Volume Block in the Historical Rock-Cut City of Vardzia (Georgia). Rock Mech Rock Eng. https://doi.org/10.1007/s00603-017-1299-7.

British Standard (1989). BS 8081: Code of practice for ground anchorages.

Bear A. N., Giordano G., Giampaolo C., & Cas, R. A. F. 2009. Volcanological constraints on the postemplacement zeolitisation of ignimbrites and geoarchaeological implications for etruscan tomb construction (6th-3rd century B.C.) in the red black slag tufa, Vico caldera, central Italy. Journal of Volcanology and Geothermal Research, 183(3–4), 183–200.

Ciccioli P., Cattuto C., Plescia P., Valentini V., & Negrotti R. 2010. Geochemical and engineering geological properties of the volcanic tuffs used in the Etruscan tombs of Norchia (northern Latium, Italy) and a

study of the factors responsible for their rapid surface and structural decay. Archaeometry, 52(2), 229–251 doi:http://dx.doi.org.ezproxy.unibo.it/10.1111/j.1475-4754.2009.00464.x
Clonna E.& Colonna G. 1978. NORCHIA I. Le necropoli rupestri dell'Etruria. Ed. CNR. doi:http://dx.doi.org.ezproxy.unibo.it/10.1016/j.jvolgeores.2009.03.016.
Deere, D.U and Miller, R.P (1966). Engineering classification and index properties for intact rock." Report AFWL-TR-65-116. Air Force Weapons Laboratory (WLDC), Kirtland Air Force Base, New Mexico, 87117. Deere and Miller (1966) Rock Mass classification.
ISRM (1994). Raccomandazioni per determinare la resistenza a compressione monoassiale e la deformabilità dei materiali rocciosi.
ISRM (1997). Metodologie di prova suggerite per la determinazione della resistenza a trazione di materiali rocciosi.
Ribacchi R., Rotonda T., Graziani A., Boldini D., Tommasi P., Lembo-Fazio A. 2018. Meccanica delle Rocce. Teoria e Applicazioni nell'Ingegneria. Edizioni Efesto e Hevelius Edizioni.
https://www.facebook.com/anticaeviae/photos/norchia-gli-etruschi-e-le-necropoli-rupestrinon-%C3%A8-noto-il-nome-antico-della-citt/3303436513001809/.
Perini S., Rossi P., Tamagnini F. Gruppo Mineralogico Romano. 200. L'approccio alla ricerca di minerali secondo il criterio geologico: l'esempio del vulcano Vicano.
Stucchi M., Meletti C., Montaldo V., Akinci A., Faccioli E., Gasperini P., Malagnini L., Valensise G., 2004. Pericolosità sismica di riferimento per il territorio nazionale MPS04. Istituto Nazionale di Geofisica e Vulcanologia (INGV) doi:https://doi.org/10.13127/sh/mps04/ag.

Geotechnical Engineering for the Preservation of Monuments and Historic Sites III – Lancellotta, Viggiani, Flora, de Silva & Mele (Eds)

Geotechnical investigation and stabilization of the foundations of a National Heritage site in Portugal, the Penedono Castle

P. Chitas & S. Rosa
Engigeo – Engenharia Geotécnica, Lda., Lisbon, Portugal

A. Viana da Fonseca
CONSTRUCT-GEO, Department of Civil Engineering, Faculty of Engineering, University of Porto, Porto, Portugal

A. Fonseca & W. Malvar
IC – Instituto da Construção, Faculty of Engineering, University of Porto, Porto, Portugal

ABSTRACT: Penedono Castle is located in the Portuguese municipality of Penedono, in the district of Viseu and classified as a National Monument in Portugal since 1910. It is a small medieval castle, a former residential mountain edifice figuring turrets at the angles, flanking the only access inscribed in a large broken arch to the Southwest. It has windows with seats set into the wall and a raised cistern. Its positioning on a pronounced promontory gives it a great prominence and relevance in Portuguese national history. Its foundations are supported directly on granite outcrops, with great variability in the degree of alteration / weathering and profusion of various joints families, and some filled fractures. A more thorough recent analysis has revealed underlying voids. This paper addresses the main aspects associated with the design of reinforcement and consolidation treatments to be implemented for the granitic masses on the periphery of the Castle.

1 INTRODUCTION

Penedono Castle is located in the Portuguese municipality of Penedono, in the district of Viseu and classified as a National Monument in Portugal since 1910. Urban, isolated, and detached, it is installed at 930 m height. It is a small medieval castle, a former residential mountain edifice with an irregular polygonal plan figuring turrets at the angles, flanking the only access in-scribed in a large broken arch to the Southwest. It has windows with seats set into the wall and a raised cistern. At the base of the castle, there are parallel rows, characteristic of Arabic buildings, revealing a first construction. Its positioning on a pronounced promontory gives it a great prominence (wide visual reach), which made it relevant in Portuguese national history. Being of irregular plan, it follows the contour lines and the unevenness of the granitic out-crops rocky terrain where it is implanted. The walls of the castle are crowned in its entire perimeter by parallelepiped merlons with pyramidal tops, some with arrow loops, and reinforced in the angles by five rectangular turrets, arranged at irregular intervals superiorly provided with counters with machicolations (murder holes) and gargoyles.

In the 20th century, several interventions were carried out, including reinforcement and stabilization of the structure and construction of masonry walls, slabs, pavements and consolidations of walls, parapets, stairs, etc., joint closings, and various valorizations. On no documented occasion have studies been carried out for the stabilization of the rock mass underlying the centuries-old

DOI 10.1201/9781003308867-28

masonry structures, with particular emphasis on the tall, heavy, and somewhat slender double walls. These foundations are supported directly on the ground. A more thorough recent analysis has revealed underlying voids that have raised concerns and led to the drafting of a stabilization design, seeking to avoid the introduction of new foundations elements.

2 GEOLOGICAL SETTING

The Penedono castle is located in the area of the Beira Alta plateau. This plateau is limited to the north by the Douro River, to the southeast by the Estrela mountain range and to the west by the Caramulo, São Macário and Montemuro mountain ranges.

In particular, the castle is located on a rock outcrop particularly conspicuous in the landscape. As typical in granite, the rock outcrop, due to decompression, expansion, sheeting, freeze-thaw cycles, and differential weathering, is characterized by the formation of individualized blocks or boulders, with subvertical and horizontal discontinuities.

The "Salzedas, Alvite and Penedono" formation is a two-mica, fine-grained granite, with foliation and "schlieren" structure. Concerning the main sub-vertical discontinuity has NE-SW orientation, in agreement with the main regional substructures.

The Penedono castle is not close to any main fault in Portuguese territory and the closest relevant active fault is, about 20 km to the east, the Vilariça fault with NNE-SSW orientation and vertical movement.

According to the Portuguese National Annex of Eurocode 8 (2010), the design reference ground acceleration, a_{gR}, resulting from intra-plate seismic source, is 0,8 m/s^2.

Due to its characteristics, the rock outcrop at the base of the castle has a high permeability controlled by the intense fracturing of the mass and opening of its discontinuities – fissure permeability. This fact, together with the local geometry – a high point in relation to its surroundings – allows for good drainage, without the presence of water table near the base of the castle. The interior of the castle, unlined and without visible drainage elements, has some thin filler material of small thickness. In this area, water flow is of the porous type, and it is likely that in case of heavy rains there will be a punctual accumulation of some water.

3 GEOTECHNICAL CHARACTERIZATION OF DISCONTINUITIES

In terms of weathering/alteration, the rock mass at the foundation is typically slightly weathered (W2), with the surfaces of the discontinuities presenting, sometimes, oxide stains (Figure 1). The smaller granite blocks show some weathering from the discontinuity zones towards the interior of the block and were classified as moderately weathered (W3). Occasionally, there are still more intensely weathered areas, which can be broken down, associated with more exposed and fractured areas.

Discontinuities are generally widely spaced (F2), sometimes moderately spaced (F3), persistent, normally open and without filling.

Regarding roughness, the walls of the identified discontinuities are slightly rough, sometimes with presence of oxides.

To assess kinematic conditions for the potential formation of mechanisms, a discontinuity survey was carried out, resulting in 62 measurements.

From the stereographic projection of the attitudes of the discontinuities, 4 main families and several random fractures were identified (Figure 2).

Table 1 contains the dip and dip direction of the main families.

Families D2 and D3 present orientations close to NE-SW, in agreement with the attitude of regional structures in the zone.

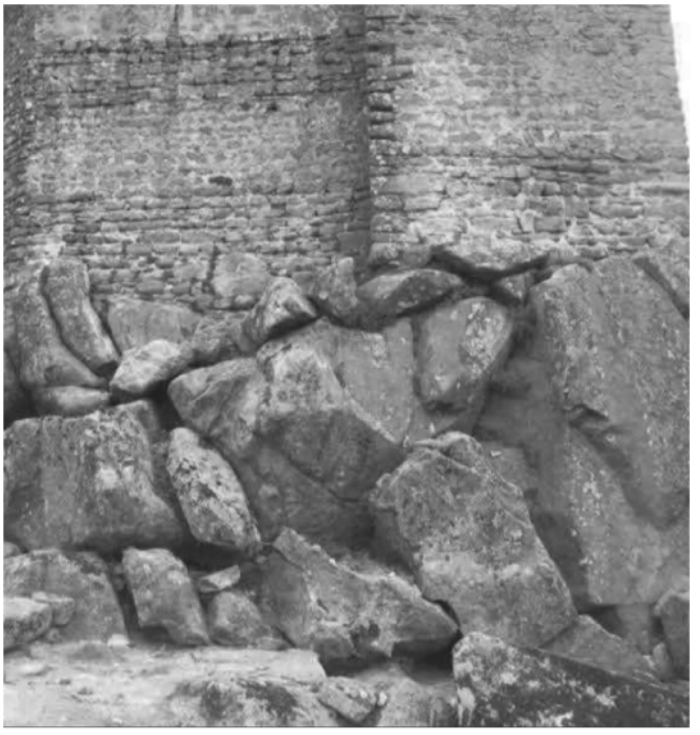

Figure 1. Examples of different degrees of weathering. To the right, moderately weathered granite (W3). On the left, slightly altered granite (W2).

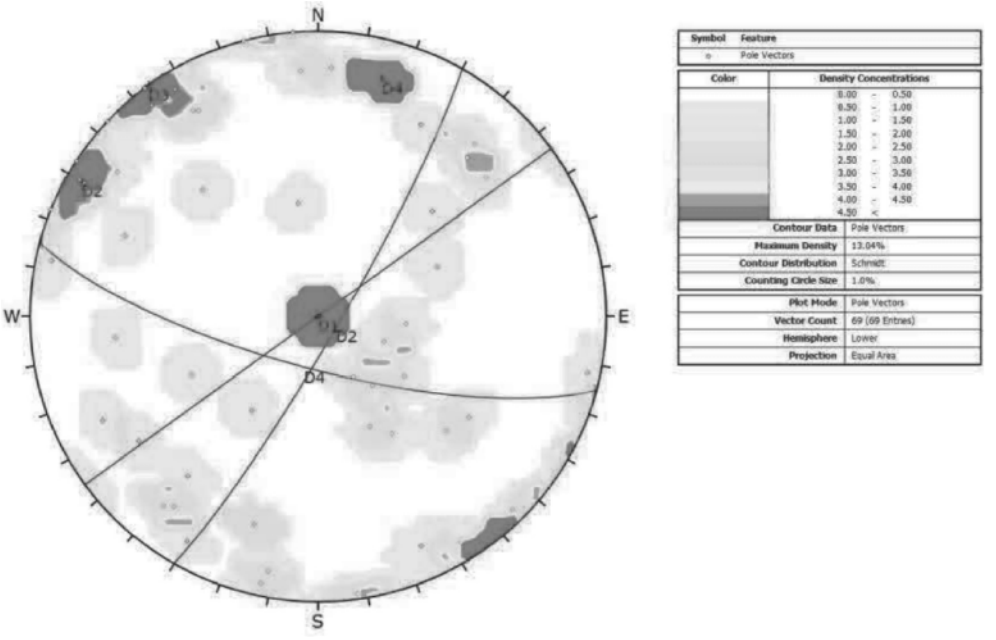

Figure 2. Stereographic projection (Equal area) with the identification of 4 main discontinuity families.

Table 1. Dip and dip direction of main families.

Discontinuity family	Dip	Dip direction
D1	Sub-horizontal	
D2	84°	120°
D3	90°	144°
D4	75°	195°

In general terms, block kinematics is controlled by a family of horizontal inclination, 2 sub-verticals and a fourth family inclined to SW. In addition to these families, there are also several random discontinuities that can cause problems locally.

4 GEOTECHNICAL ZONATION

Geotechnical zonation was performed to duly differentiate potential mechanisms and to define specific stabilization procedures. Therefore, the castle was divided into 7 zones, as shown in Figure 3.

Zone #1 concerns the castle wall facing NW. Zone #2 is formed by the outer wall of the castle cistern. Zones #3 and #4 concern the castle wall without the outer platform (as formed by outer wall or barbican). Zone #5 is constituted by the outer wall of the turret next to the external access, whereas Zone #6 concerns the wall facing SE. Finally, Zone #7 concerns the wall of the castle's entrance door.

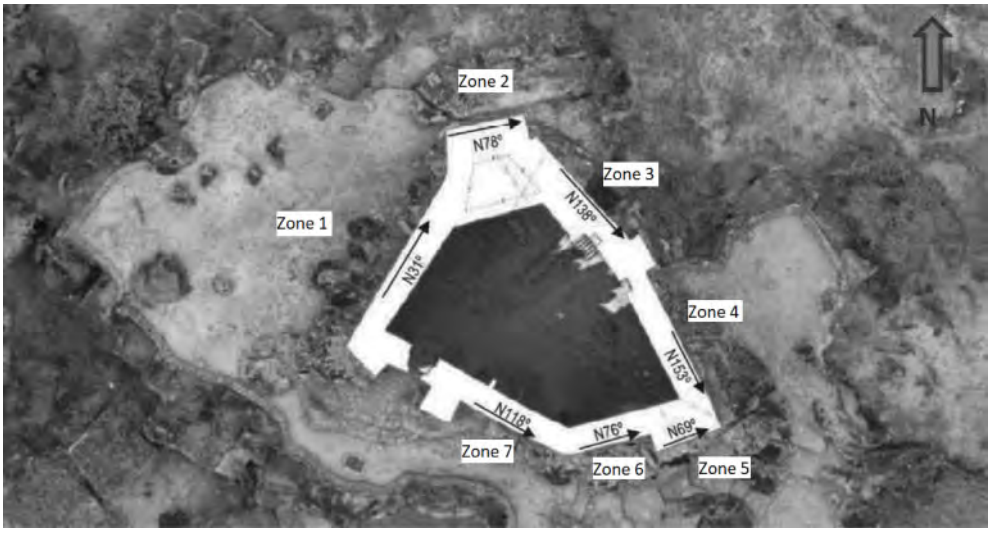

Figure 3. Castle zones and Castle wall orientations.

In Zone #1, the rock mass is mainly characterized by detached blocks, which, although apparently stable, are associated with extensive cavities, developed along the discontinuities, and which extend in depth towards the castle wall (Figure 4). In its central section, the wall intersects the foundation at a lower level in a flat and slightly sloping area with a slope towards the outside of the castle.

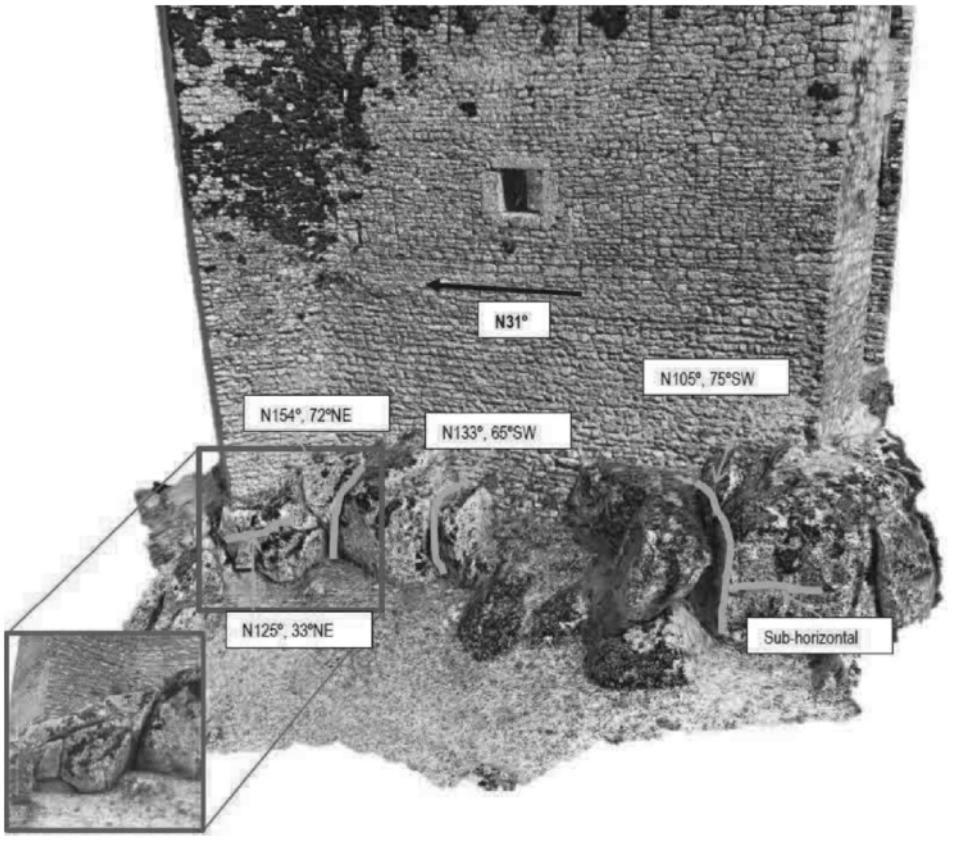

Figure 4. Castle Zone #1.

It is also worth mentioning the possibility of occurrence of instability phenomena associated with smaller detached blocks, with unfavorable dip, in the corner of the cistern turret.

Zone #2 corresponds to the external wall of the cistern (Figure 5). The castle wall, in this area, rests on a small natural platform about 2–3 m wide and features a foundation in small steps. The rock mass presents, in addition to the small platform, a steep slope with a gap of about 10m in height, with a visible set of discontinuities with dip direction parallel to the wall.

Zone #3 corresponds to the area where there is no outer wall – barbican, supporting the wall on a higher slope, with difficult access (Figure 6). In the center of this area, there are signs of water runoff, more evident than in other places. The foundation level is lower in this part, with an extension of the wall (masonry). This extension of the wall is located behind a block detached from the foundation rock mass, with signs of displacement towards the slope. A stone filling of indeterminate geometry was observed between the base of the detached block and the lower level of the castle wall. The turret at the passage from Zone #3 to Zone #4 is founded on a block that presents a considerable void along a discontinuity that develops with an orientation almost sub-parallel to the wall, observable from the barbican of Zone #4. In the alignment of this turret, the blocks, with a considerable mass, are detached due to unfavorable discontinuity surfaces. On the right side of Zone #3, there is a discontinuity surface with unfavorable dip and dip direction. In this part, there are also signs of water runoff.

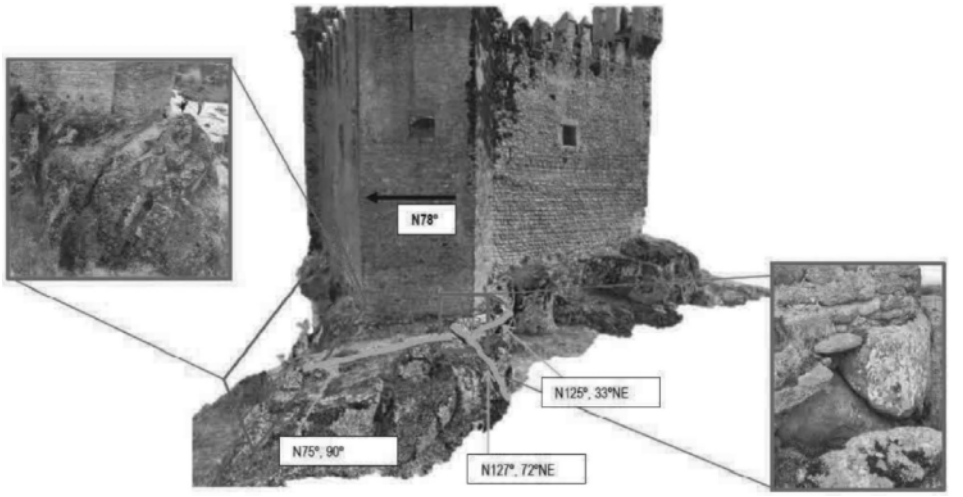

Figure 5. Castle Zone #2.

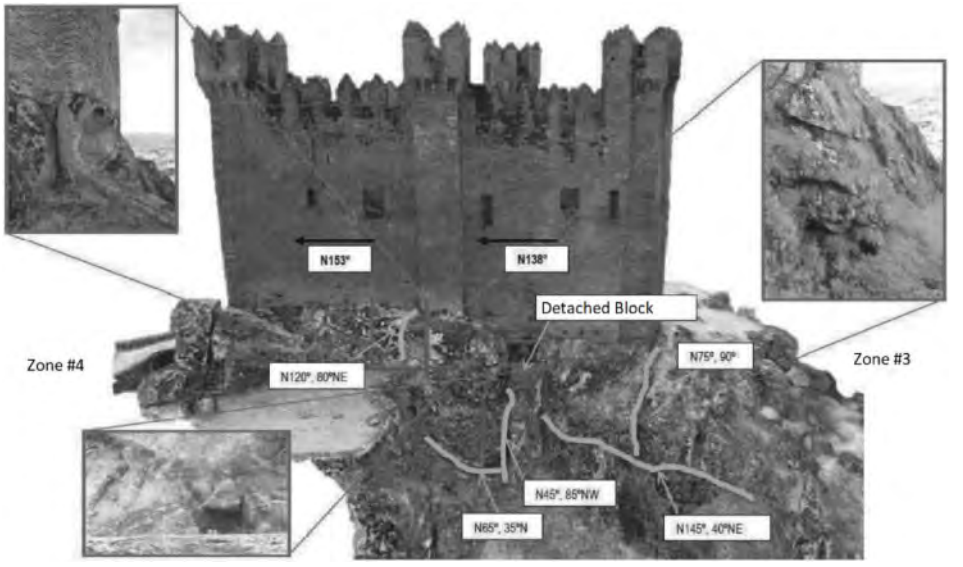

Figure 6. Castle Zones #3 and #4.

In Zones #6 and #7, the rock outcrop between the wall and the barbican shows a smaller difference in level. In Zone #5, with greater height, the presence of a set of discontinuities of direction sub-parallel to the castle wall stands out. The rock mass at these areas features detached blocks of various dimensions and where considerable voids are visible, developed along the opening of the discontinuities and which, in some situations, extend into the interior of the castle walls. Due to this considerable detachment of blocks, the corners of the wall between Zone #5 and #6 and between Zone #6 and Zone #7 present foundation problems (Figure 7).

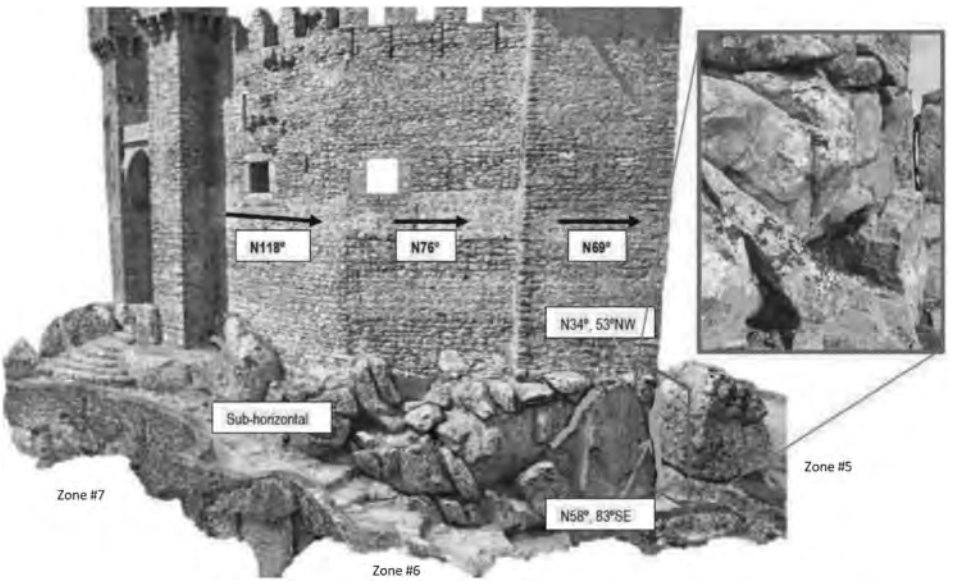

Figure 7. Castle Zones #5, #6 and #7.

5 STABILIZATION WORKS

5.1 *Design premises*

Bearing in mind the existing conditions, several solutions were defined to address the individualization of blocks within the foundation outcrop, and the erosion process in its origin.

The solutions were adjusted to the constraints imposed by the geological conditions and the existence of a road around the castle.

5.2 *Rock bolts*

In areas where large rock blocks were identified, at risk of detaching themselves from the granite outcrop, these were stabilized using rock bolts, with location, orientation and length defined as a function of their volume and the underlying mechanism.

The defined rock bolts consist of Ø32 mm rods in A500 NR steel, placed in Ø4″ (101.6 mm holes, sealed with cement grout and with lengths (L) between 6.0 and 8.0 m The number of rock bolts and the respective lengths was evaluated according to the dimensions of the blocks to be consolidated. This evaluation was to be confirmed on site, after the cleaning and removal work of any loose smaller blocks or loose material.

Regarding the execution of the holes for rock bolt installation, these are to be rotary drilled along the entire length, to induce the least possible disturbance (vibration) in the foundation ground. In addition to this aspect, it was also foreseen that the initial approximately 20 to 30 cm of the drilling for each bolt would be made with a larger diameter, Ø5″1/2 (139.7 mm). This allowed the sampling of a rock core, to be later placed over the head of each bolt, properly sealed, working as a "cover" for the bolts' respective concealment (Figure 8).

The bolt heads consist of S235JR steel grade circular plates, 45-mm thick, with a diameter of 5″ (127 mm) and inclination, whenever possible, of 15° in relation to the horizontal.

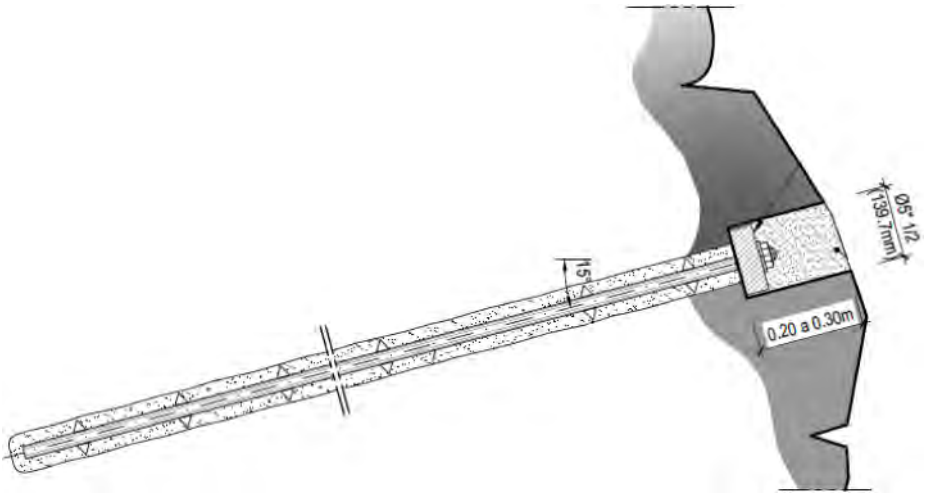

Figure 8. Rock bolt scheme.

All steel parts of the system (rods, clamping nuts, plates, etc.) must be hot dip galvanized, in accordance with the specifications (namely, minimum thickness) defined in standard NP EN ISO 1461 (2012), assuming a galvanization thickness with minimum 90 μm zinc/aluminium alloy.

5.3 *Fracture and discontinuity sealing*

This procedure, which is complementary to rock bolts, consists of washing the open fractures that delimit the blocks to be consolidated, using water without pressure, respective surficial sealing with non-shrinkable cement mortar and subsequent filling, at low pressure, with cement grout. This sealing works aim to prevent the flow of free water through the fractures, thus limiting the weathering of the rock mass and the consequent degradation of its geotechnical characteristics.

5.4 *Underpinning of rock outcrop blocks using stone mortar or cyclopean concrete*

Underpinning using mortar or cyclopean concrete was adopted in areas where there are large rock blocks in cantilever, in situations where, due to the natural weathering process, the formation of cantilever blocks is likely, or in areas with well-developed cavities.

The cyclopean concrete must correspond to a mixture of concrete and rockfill, in which the percentage by mass of rockfill must not exceed 40%.

The stone material must be made of granitic source, with an appearance identical to that of the blocks to be underpinned. The particle size shall consist of 200/300 mm and its resistance to abrasion shall lead to a Los Angeles coefficient lower or equal to 45%.

The appearance of the final finishing of the surface that will be exposed must consist of granite stone, with characteristics identical to those existing in the surrounding area, and the blocks of rock on this surface must have irregular shapes and different sizes, to mimic the surrounding rock outcrop as much as possible.

5.5 *Underpinning of castle walls, turrets, corners, and wedges*

In the areas of the Castle wall where the structure/foundation interface contact was not duly assured, their respective underpinning with hydraulic lime concrete was foreseen, in order to guarantee

compatibility between the foundation elements directly in contact with the wall and the interventions foreseen in the context of wall (structural) consolidation. It is also mentioned that this type of intervention closely follows the construction techniques originally used in the construction of the wall.

The hydraulic lime to be used in the concrete is compatible with the existing mortar. The aggregates to be used will be 8 mm/12 mm gravel (from granite) and fine sand, respecting a 1:2:2 trace in volume. The water/binder ratio must be equal to or less than 0.50, with a superplasticizer content of less than 0.5%.

5.6 *Construction sequencing and solution layout*

Given the importance of the sequence of work to be carried out in the efficiency and success of the proposed solution, the succession of the main execution operations was defined as follows:

1. Removal of vegetation, loose material, and loose blocks.
2. Underpinning works of the castle wall using hydraulic lime concrete.
3. Underpinning of rock outcrop blocks using stone mortar or cyclopean concrete, from the lowest to the highest level.
4. Execution of fracture and discontinuity sealing.
5. Execution of rock bolts.

The following figures (Figure 9 to Figure 13) illustrate the adopted solutions along the zones presented in chapter 4. For all layouts, the solutions are presented as follows:

- White solid hatch: underpinning of rock outcrop blocks using stone mortar or cyclopean concrete.
- White line: execution of fracture and discontinuity sealing.
- White line hatch and envelope: underpinning works of the castle wall using hydraulic lime concrete.
- White circles: rock bolts.

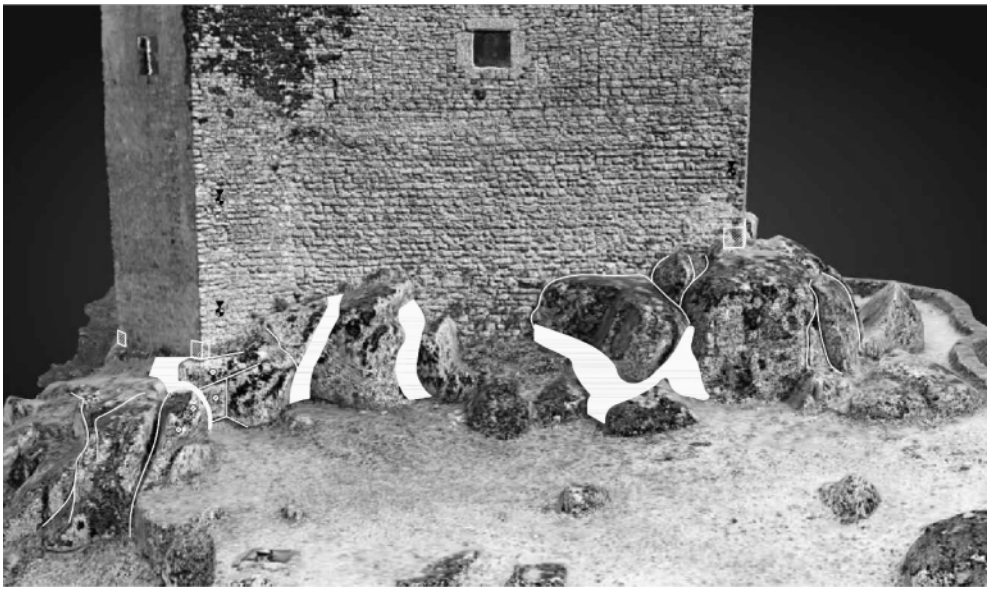

Figure 9. Zone #1. Solution layout.

Figure 10. Zone #2. Solution layout.

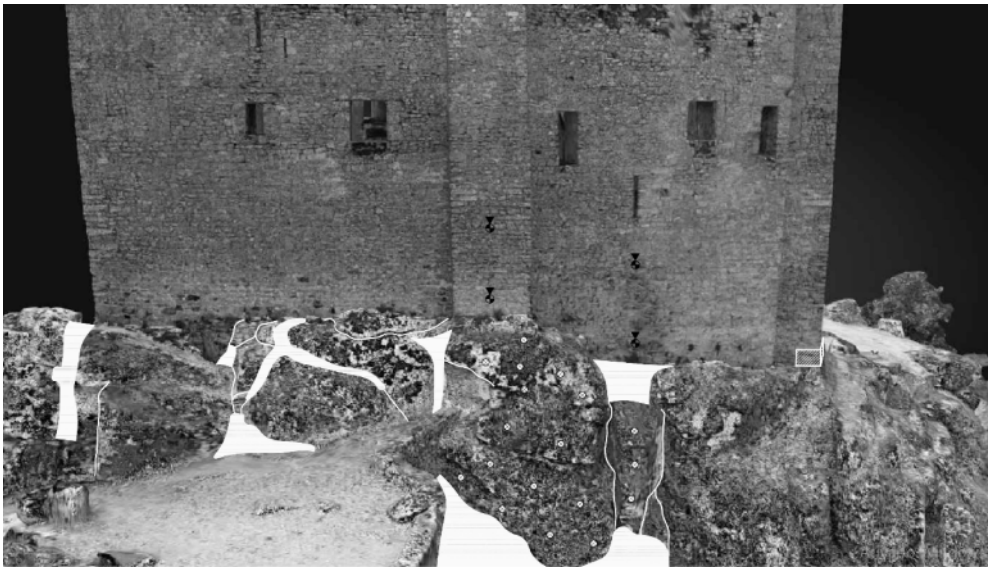

Figure 11. Zones #3 and #4. Solution layout.

6 MONITORING

The installation of 10 optical survey targets for topographic control was defined aiming to observe and control the behavior of the wall during the geotechnical consolidation works. All topographic devices must allow readings along the three coordinate axes.

After completion of the work, all devices must be read monthly and for a minimum period of 6 months, which must necessarily include a winter.

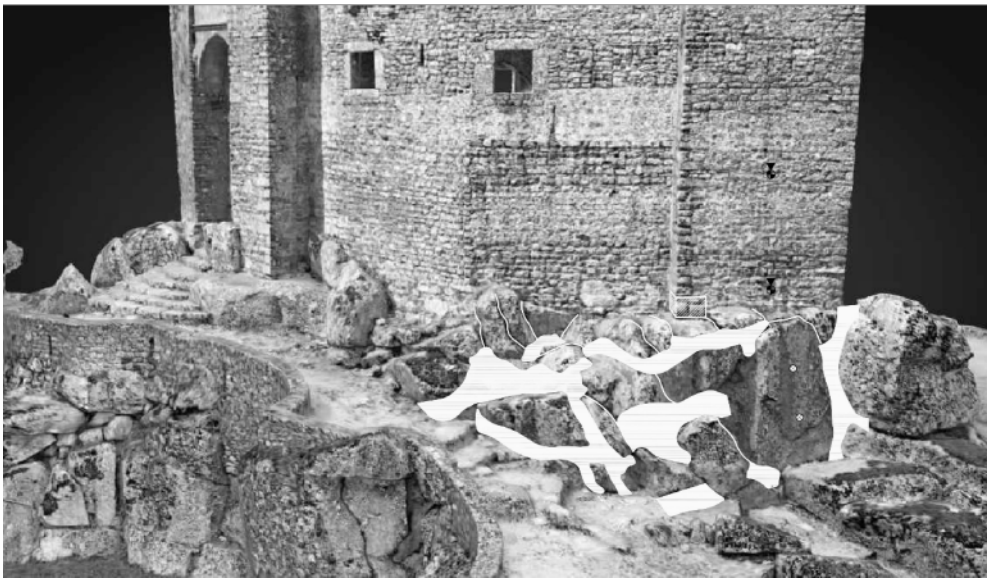

Figure 12. Zones #5 and #6. Solution layout.

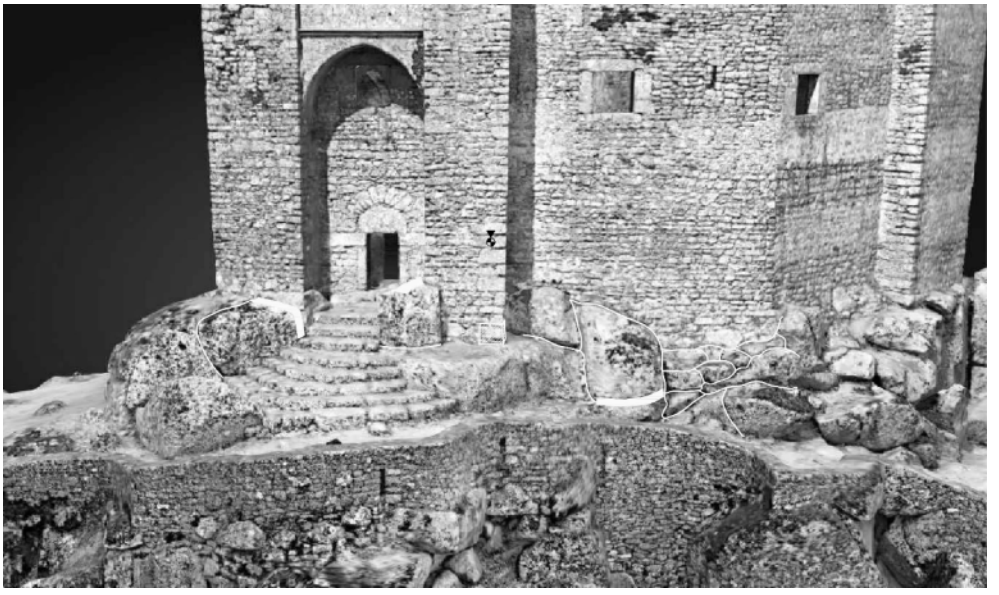

Figure 13. Zone #7. Solution layout.

Direct alarm criteria were defined as a function of absolute displacement, measured by the optical survey targets. Attention procedure shall be activated when absolute displacement reaches 10 mm, whereas Alarm procedure shall be activated for absolute displacement of 20 mm.

In addition to these values, additional limits were defined to address displacement (time) rate. Attention and alarm procedures shall be activated for displacement rate of, respectively,

1.0 mm/day and 1.5 mm/day. These must be determined for a minimum period corresponding to three consecutive readings.

In addition to displacements, the control of the vibration induced during the drilling process for rock bolt installation shall be performed using a seismometer at the base of the wall. Considering the sensitivity of the structure and its natural frequency, the maximum particle peak velocity limit was defined as 1.5 mm/s, as per Portuguese Standard NP 2074 (2015).

7 CONCLUSIONS

The present paper presents the geotechnical investigation and stabilization of the foundations of the Penedono Castle, a National Heritage site. First, a short description of its characteristics and its relevance was presented.

A collection and analysis of all the existing elements that it was possible to obtain on the site, namely of a topographical, geological, geomorphological, hydrogeological, and geotechnical nature was presented. Then, a detailed geological survey of the surface of the entire site and surrounding area was carried out.

Next, a general description of the stabilization solutions for castle foundation was presented, always regarding their suitability in relation to the geological and geotechnical conditions that were observed. An indicative construction sequencing was also presented.

Finally, the monitoring methodology was defined, with attention and alarm criteria established as function of displacement, displacement rate and particle peak velocity.

ACKNOWLEDGEMENTS

The authors acknowledge the permission of those responsible of the processes in the Penedono council, in the person of the Past-Mayor, Dr. António Carlos Esteves de Carvalho, who has led the process to enable this intervention of this emblematic national monument, as well as the director of the division of works, Eng. Luís Pais, who has coordinated the technical demands. A recognition is also due to the current Mayor, Dr. Cristina Ferreira, who authorized the publication of this article. Finally, authors address a thankful reference to the Department of Cultural Heritage of the North Regional Direction of Portugal, in the person of Eng. Fernando Pádua, for creating the conditions for the development of stabilization solutions to the Penedono Castle under the demands of the preservation of monuments and historic sites.

REFERENCES

Instituto Português da Qualidade (2010) Eurocódigo 8: Projecto de estruturas para resistência aos sismos. Parte 1: Regras gerais, acções sísmicas e regras para edifícios [Eurocode 8: Design of structures for earthquake resistance. Part 1: General rules, seismic actions and rules for buildings] (NP EN 1998-1:2010). Portuguese.

Instituto Português da Qualidade (2012) Revestimentos de zinco por imersão a quente sobre produtos acabados de ferro e aço; Especificações e métodos de ensaio [Hot dip galvanized coatings on fabricated iron and steel articles – specifications and test methods] (NP EN ISO 1461:2012). Portuguese.

Instituto Português da Qualidade (2015) Avaliação da influência de vibrações impulsivas em estruturas [Assessment of impulsive vibrations on structures] (NP 2074 2015). Portuguese.

Geotechnical Engineering for the Preservation of Monuments and Historic Sites III – Lancellotta, Viggiani, Flora, de Silva & Mele (Eds)

Lateral disconnection of foundations: A respectful seismic isolation of historic building

F. Somma, E. Bilotta & A. Flora
University of Napoli Federico II, Naples, Italy

G.M.B. Viggiani
Cambridge University, Cambridge, UK

ABSTRACT: The mitigation of seismic risk for historic buildings faces the critical problem of needing interventions that sometimes can be extremely invasive, thus not respectful of the overall integrity of the valuable structure to protect. Because of this, interventions in the subsoil, possibly without even touching the structure, are appealing, making Geotechnical Seismic Isolation (GSI) of extreme interest for the preservation of the built heritage. The paper shows the results of a centrifuge test carried out to check the simplest possible GSI solution: the lateral disconnection of a shallow foundation, obtained by removing the soil on the sides of the foundation. In this way, the foundation-soil contact will be through the lower base only. The results obtained on two identical structures, one with and one without disconnection, demonstrates that the latter has the beneficial effect of elongating the fundamental period of the soil-structure system in such a way to reduce significantly structural demand. In order to extract additional results, a numerical back analysis of the centrifuge test was also carried out. Since the lateral disconnection does not touch the structure, the integrity of the building to be protected is fully preserved.

1 INTRODUCTION

Seismic isolation of existing buildings has always been a critical issue. If the structure to be protected is valuable, the complexity increases, as the question of what is worth doing not to spoil the heritage carried by the building is difficult to answer because of the lack of unicity of the solution (Viggiani, 2017).

Geotechnical seismic isolation (GSI) is an interesting area of seismic geotechnical engineering, based on the transposition of the effects of traditional seismic isolation into the ground, that may offer a valuable alternative to the most traditional structural interventions. Numerous authors studied techniques that could accomplish this task. Yegian and Catan (2004) demonstrated numerically and experimentally that the insertion of a sliding surface (*i.e.* a special geotextile), characterized by a low friction angle and placed immediately below the foundations, would be able to dissipate the energy of earthquakes. Similarly, Kirtas *et al*. (2009) studied numerically the effect of creating, vertical and/or horizontal, rigid or soft, barriers in the foundation soil. In particular, the soft barriers would be able to seismically isolate low natural period buildings. Brennan (2013) and Nappa *et al*. (2016) validated this idea through various centrifuge tests, and Nappa *et al*. (2019) via experimental in situ testing. In recent years, sand-rubber mixtures (*rubber-soil*), used as foundation soil of a new building, have also been studied (e.g. Pitilakis 2015). Due to the high damping and hyper-elastic capacities, these mixtures would be able to reduce the seismic actions on buildings to the same extent of a classic rubber isolator.

DOI 10.1201/9781003308867-29

All these procedures all have the goal to elongate the natural period of vibration and/or the damping of the soil-structure system. However, there are still numerous uncertainties and difficulties linked to the technological installation procedures (especially for existing buildings), as well as a certain diffidence in operating only and exclusively through the modification of the foundation soil. For valuable buildings, most of these technologies cannot be used as they would be basically impossible to install. A technologically simple and intuitive way to elongate the fundamental period of the soil-structure system could be the lateral disconnection of shallow foundations from the adjacent soil. In fact, the creation of a small gap, laterally to the foundations, modifies the horizontal and rotational stiffness of the soil-foundation system, thus contributing to increase the fundamental period of the soil-structure system itself in a very simple way (Somma *et al.* 2021a, 2021b). This could be extremely interesting as seismic protection technique buildings of historical importance, as needs no intervention on the structure itself, and is fully reversible. The aim of this work is to show the main results obtained from a centrifuge test and then to focus on its numerical back analysis.

2 CENTRIFUGE RESULTS

2.1 *Centrifuge model*

Two identical structural models, differing only in their foundation embedment conditions, were created at a scale of 1:60 and then tested at 60 times the Earth's acceleration of gravity (g) using the centrifuge located at the Schofield Centre (Cambridge, UK). The two structural models were created using existing masonry buildings as prototypes, in order to replicate conditions of interest in the case of historical buildings.

In order to have an equivalence between the model and the prototype structures, several properties were replicated in the models such as: first natural resonance period (0.35 s), load bearing (135 kPa), geometrical aspect ratio (H/B = 1.08), superstructure mass (267 Mg), foundation embedment (2.4 meters) (Figure 1).

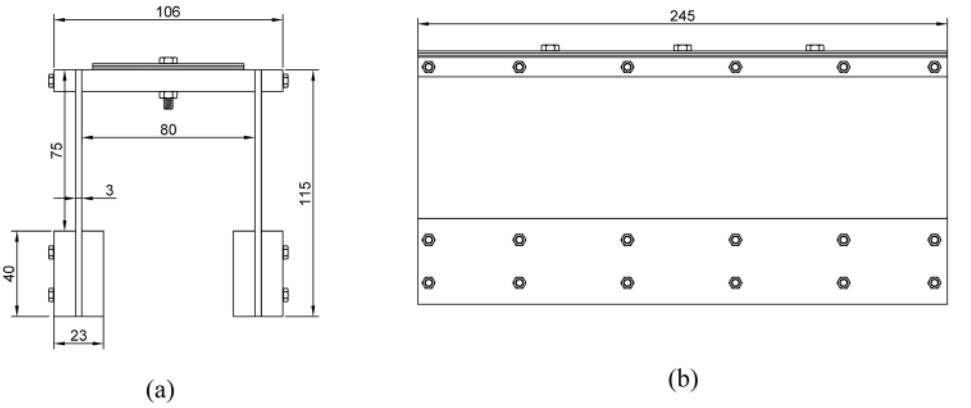

Figure 1. Structural models with dimensions in mm (model scale); (a) Front view, (b) Lateral view.

The foundation soil used in the centrifuge test was Houston sand, pluviated at a relative density of about 55%. The properties of the sand, in terms of shear stiffness, were estimated during the centrifuge test by means of an instrument named *"air hammer"*, capable of generating seismic waves of low intensity in the model. The initial average shear wave velocity in the soil layer on flight was about 233 m/s. The value of the peak friction angle was calculated from the results of the miniature CPT performed during the centrifuge test, before shaking. Considering an average value in the significant volume of the foundations of the two structures (namely 2.4 to 5 m), the peak friction angle is 37°.

Sixteen acceleration transducers and four LVDTs were installed on the structures, while twenty acceleration transducers were embedded in the ground. The structures were placed at a relative distance of approximately 175 mm at centrifuge scale (*i.e* 10.50 m at prototype scale) to reduce the interaction between them.

Figure 2 represents the model containing the structures and the various transducers.

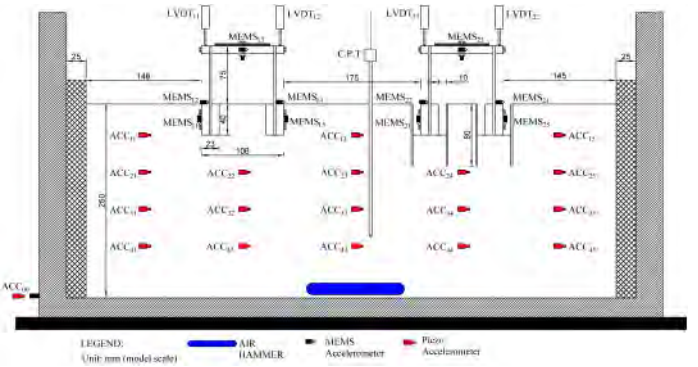

Figure 2. Layout of the centrifuge model showing the position of the instruments and the two frames at model scale (on the left, frame NO GSI with traditional strip footings, on the right frame GSI).

In order to disconnect the foundations from the adjacent soil, short cantilever walls were embedded at their sides to support a gap between the beam footing and the lateral soil. In the following, the structure with lateral disconnection (on the right in Figure 2) will be named *"GSI Structure"*; the non-isolated structure (on the left in Figure 2) will be named *"NO GSI Structure"*. Ten seismic signals were applied to the base of the model with the main dynamic properties reported in Table 1.

Table 1. Main dynamic properties of seismic signals used in the centrifuge test.

Name (–)	Shaking Type (–)	a_{max} (g)	a_{min} (g)	f_d (Hz)	f_m (Hz)	I_A (m/s)	T_{5-95} (s)
SS1	Sine-sweep	0.10	0.091	0.01–2.5	–	–	–
S01	Sinusoidal	0.25	0.245	2.2	–	1.21	–
S02	Sinusoidal	0.221	0.214	2.2	–	1.23	–
S03	Sinusoidal	0.074	0.073	2.2	–	0.15	–
S04	Sinusoidal	0.244	0.232	2.0	–	1.85	–
E01	Imperial Valley	0.08	0.103	2.27	1.51	0.43	33.98
E02	Cristhchurch	0.150	0.142	2.	1.66	0.29	5.42
E03	Kobe	0.262	0.203	2.17	1.63	0.80	4.89
E04	Adana	0.158	0.147	1.92	1.21	0.85	19.12

Due to the large number of seismic inputs applied to the model, a gradual unavoidable densification of the sand took place, and was estimated using PIV (Particle Image Velocimeter). Assuming plane strain conditions, the measured displacements of different soil patches on the model front face, allowed to estimate the soil volume change after each shaking, hence the soil volumetric contraction, ε_v. Since the initial void ratio, e_0, at the beginning of the test was known, the void ratio at the end of each shaking (Table 2) was simply computed as:

$$e = e_0 - \varepsilon_v(1 + e_0) \tag{1}$$

These measurements indicate that the largest increase of relative density (from 56.5% to about 63%) occurred during the first cycles of the first sinusoidal train, S01, with an amplitude of 0.25 g. Successive earthquakes were responsible of very small variations.

Table 2. Densification of soil in each earthquake.

Seismic Signal [–]	e [–]	D_r [%]
SS1	0.752	56.5
S01	0.724	62.7
S02	0.718	64
S03	0.717	64.2
S04	0.713	65.2
E01	0.712	65.4
E02	0.711	65.6
E03	0.709	66
E04	0.708	66.2
SS1post	0.707	66.4

2.2 *Centrifuge test results*

By using the amplification function between the foundation base level (ACC_{13}) and the roof (MEMS13-23), the period elongations generated by the lateral disconnection technique can be estimated. In particular, this can be done using the sine-sweep signal (SS1) or using the E01 signal (Imperial Valley) due to their very large frequency contents (Figure 3).

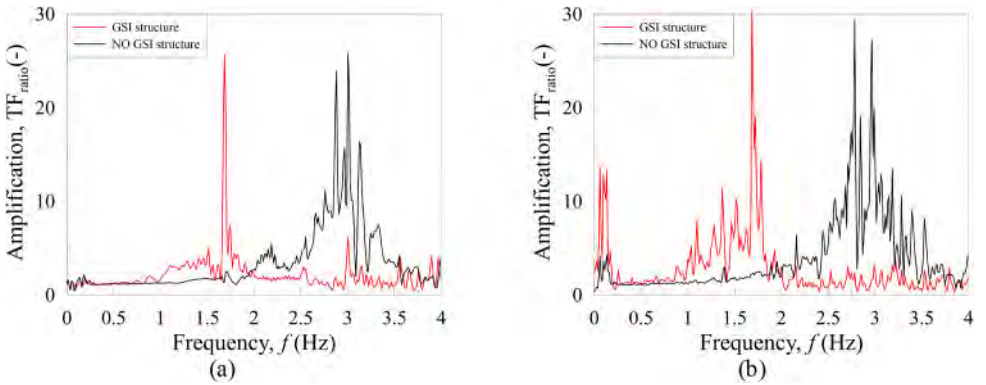

Figure 3. Acceleration amplification functions for the SS1 (a) and Imperial Valley earthquake (b).

Considering soil-structure interaction, the natural resonance frequencies of the two structures are completely different. The *GSI* structure has a resonance frequency around 1.66 Hz, while the *NO GSI* structure around 2.70 Hz. This obviously leads to significant differences in terms of total acceleration and displacements demands on the frames.

In particular, on the GSI structure the absolute top accelerations are highly reduced when it was shaken by sinusoidal signals (Figure 4a). This happens, to a lesser extent, also for the real seismic signals (Figure 4b).

The efficiency of this technique can be evaluated in terms of two efficiency parameters considering the maximum absolute acceleration ($\eta_a = 1 - a_{\max,GSI}/a_{\max,NO\ GSI}$) and the Arias Intensity ($\eta_{IA} = 1 - I_{A,GSI}/I_{A,NO\ GSI}$) (Figure 5). Even if the lateral disconnection reduces the maximum accelerations experienced by GSI structure, these take more time to be damped, which for the natural earthquakes may result in a slight increase of the Arias intensity, explaining some negative values of η_{IA} obtained at low input accelerations.

The results in terms of induced structural displacements also show significant benefits in terms of structural drift efficiency reduction, $\eta_d = 1 - u_{d,peak,GSI}/u_{d,peak,NO\ GSI}$, (Figure 6).

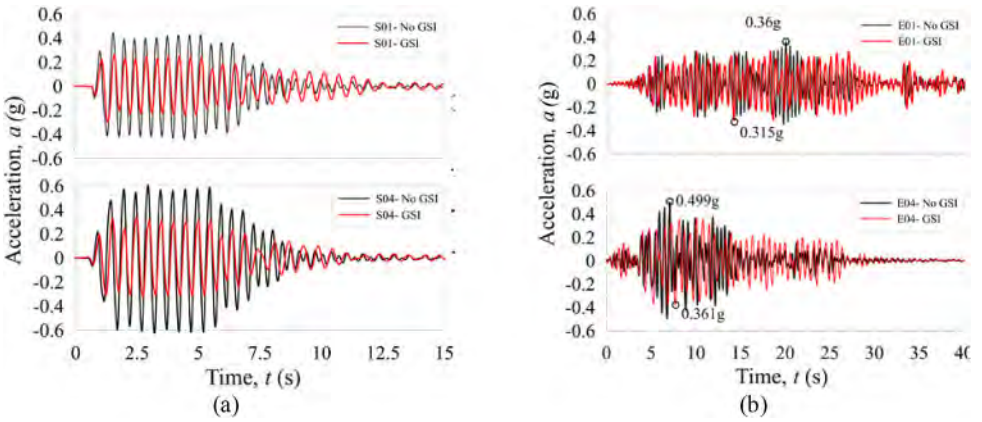

Figure 4. Comparison of the total absolute accelerations between the two structures for sinusoidal (a) and real earthquakes (b).

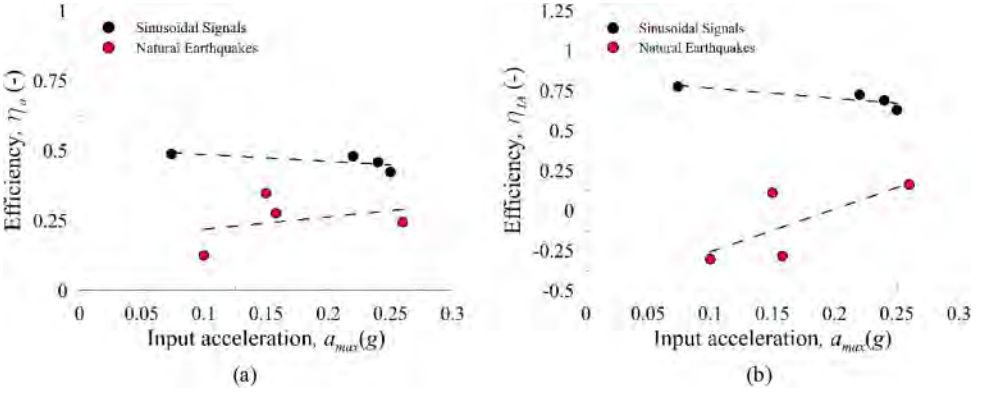

Figure 5. Efficiency in terms of reduction of total absolute acceleration (a) and Arias intensity (b).

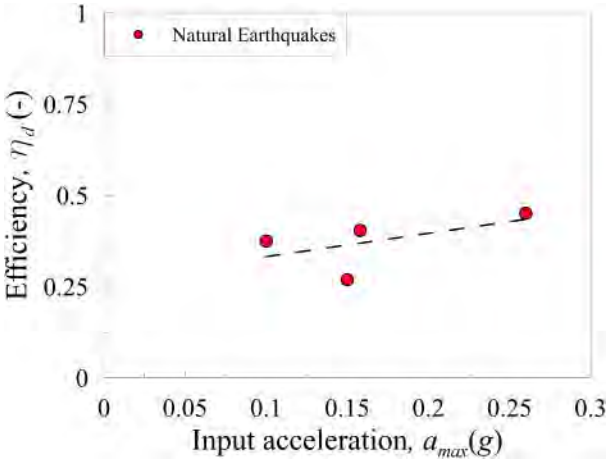

Figure 6. Efficiency in terms of structural drift reduction for natural earthquakes.

The total horizontal roof displacement is equal to the sum of the horizontal translation of the foundations, of the tilt rigid rotation of the structure and of the distortional displacement of frames. The purely distortional displacements (which are responsible of structural damage, thus being the ones to minimize for seismic isolation) are smaller in the case of the GSI structure due to the increase of the global rotational rigid motion generated by the lateral disconnection (Somma *et al*. 2021).

3 NUMERICAL BACK ANALYSIS OF CENTRIFUGE TEST

3.1 *Numerical model to simulate the centrifuge test*

In the following section a back analysis of the centrifuge test described in the previous section will be carried out. In particular, reproducing numerically the centrifuge test, it was possible to obtain interesting information on the ability of this GSI simple technology to mitigate the seismic risk for historical buildings. The effect of lateral disconnection on bearing capacity was also quantified. Numerical simulations of the test centrifuge tests were performed by the FE code Plaxis2D (Brinkgreve *et al*. 2011). The finite element model used in the numerical analyses is shown in Figure 6.

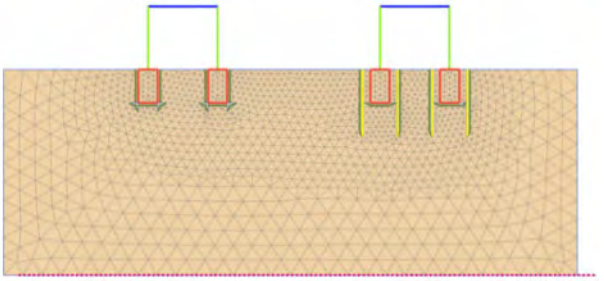

Figure 7. Finite element model used for back analysis of the centrifuge test.

The numerical model reproduces the centrifuge test at prototype scale. The width of the model is equal to 40.80 m while the height of the soil bank corresponds to the height of the pluviated soil in the model (*i.e*. 15 m at prototype scale). In the static initialisation of the model, horizontal displacements are prevented along the vertical boundaries of the domain, while all displacement components are prevented at the base. In the dynamic analysis, the boundary conditions reproduced those of the box used in the test: viscous boundary at the lateral sides and reflective boundary at the base, through simple rigid supports. Discretization was carried out using 2778 triangular elements with 15 nodes each. The foundation soils are modelled using cluster elements, whose constitutive model is *HS small strain (HS*$_{ss}$*)*. In the *HS*$_{ss}$, the elastic behaviour at low levels of deformation depends on the effective stress state through the relationship:

$$G_0 = G_0^{ref} \left(\frac{c' \cot \varphi' + \sigma_3'}{c' \cot \varphi' + p^{ref}} \right)^m \tag{2}$$

where σ_3' is the minimum principal effective stress, c' is the cohesion, φ' is the friction angle and $p^{ref} = 100$ kPa is a reference pressure, while G_0^{ref} and m are model parameters. These last two parameters were derived by means of a least-squares regression carried out on the profile of G_0 centrifuge stiffness. Figure 7 shows the comparison between the profile of G_0 used in the FEM analysis and the one provided by the Air Hammer Test in the centrifuge test.

Based on the results of the centrifuge test, the following table summarises all the characteristics of Hostun Sand at the beginning of the centrifuge test (Tables 3 and 4).

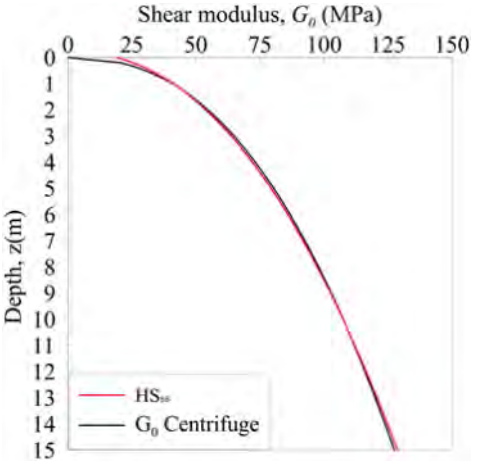

Figure 8. Comparison between the shear stiffness profile obtained in the centrifuge test and the one used in the numerical analyses.

Table 3. Physical and strength properties of the sand used.

Soil name [–]	γ [kN/m^3]	c′ [kPa]	φ' [°]	Ψ [°]	K_0 [–]
Hostun Sand	14.77	1	37	7	0.39

Table 4. Parameters for modelling soil stiffness with HS_{ss}.

G_0^{ref} [MPa]	m [–]	E_{50}^{ref} [MPa]	E_{oed}^{ref} [MPa]	E_{ur}^{ref} [MPa]	$\gamma_{0.7}$ [–]
140.49	0.45	35	35	115	0.00029

In order to assess the value of E_{ur}, E_{50}, E_{ed}, $\gamma_{0.7}$, Alpan's relations (Alpan, 1970), linking dynamic stiffness to static stiffness, were used. The foundations of the structures are also modelled as cluster elements with non-porous linear-elastic constitutive model. Interface elements with properties derived from the adjacent soil were used with a value of R_{int} equal to 0.6 (Di Donna *et al*. 2015; Kulhawy *et al*. 1983). The beams and columns of the structure are modelled as plate elements. The properties of the beam and column plates were chosen in order to represent exactly the dimensions of the structural elements in the centrifuge test. The value of the structural damping was set equal to 1% (Somma *et al*. 2021) and assigned to the structural elements as Rayleigh damping by means of double frequency approach (with f_1 the first natural frequency of the structure and $f_2 = 3f_1$). The following properties have been used (Table 5).

The weight (w) of the beam added to that of the columns and foundations generates the same bearing load as in the centrifuge test ($\approx$ 130 kPa).

Table 5. Properties of plate elements for modelling the centrifuge frame.

Plate element [–]	EA [kN/m]	EI [kNm^2/m]	v [–]	w [kN/m/m]
Column	12.22E6	31.05E3	0.33	4.53
Beam	42.00E6	1.260E6	0.33	25.75

3.2 *Comparison in the subsoil seismic propagation*

The stratigraphic amplifications obtained in the centrifuge and by numerical modelling for sine wave trains and natural earthquakes at the position of the middle piezo accelerometer, specifically ACC_{13} of Figure 1, are compared in Figure 9.

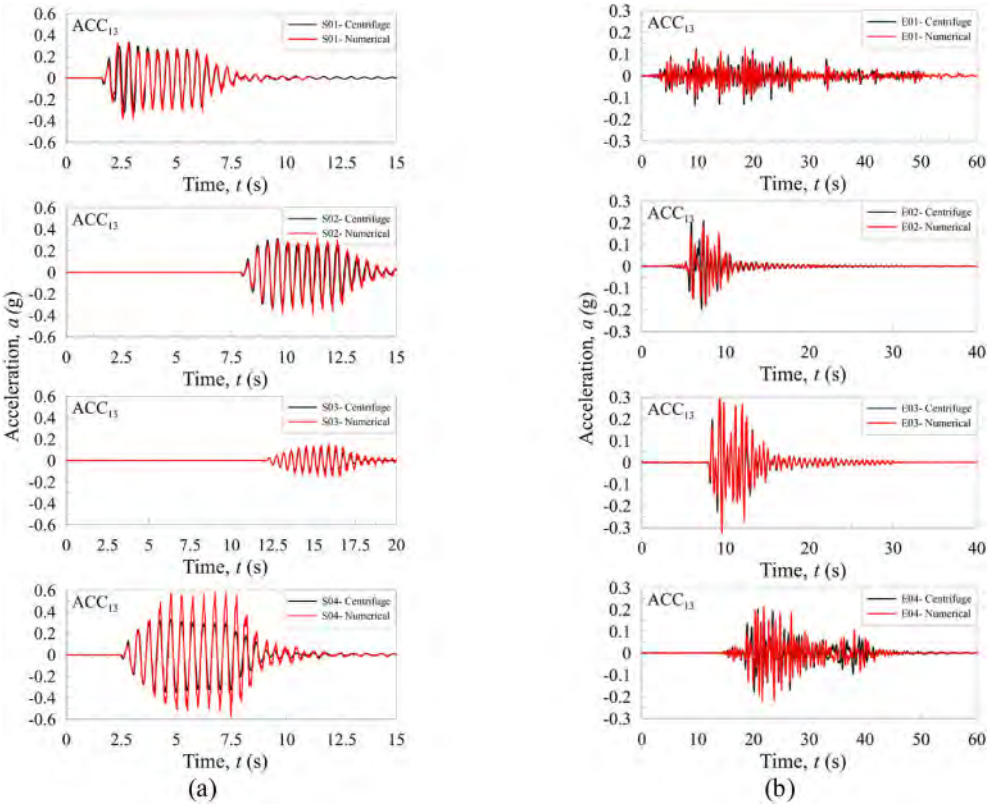

Figure 9. Comparisons in terms of total accelerations between the centrifuge test and numerical analyses; (a) sinusoidal signal, (b) real earthquakes.

The similarity is remarkable, confirming the ability of the numerical model to simulate the experimental results. The small differences, especially in the spikes of the accelerogram signals, are due to the necessity to use, in the numerical simulation, a Butterworth bandpass filter between 0.1 Hz and 25 Hz on the seismic accelerogram input. This may result in the loss of amplitude in some spikes. As already done in the centrifuge test, it is possible to numerically calculate the natural resonant frequency of the disconnected structure using the seismic signal called SS1. Using the amplification function between the acceleration signal at the foundation base level and the roof, the natural resonant frequency of both structures is estimated.

Figure 10 clearly shows the reduction of the acceleration amplitudes in the frequency range between 2 Hz and 3 Hz caused by the translation of the natural resonance frequency of vibration in the GSI structure. Numerical modelling leads to a slightly higher natural resonant frequency reduction than in the centrifuge test. In particular, in the centrifuge test the natural resonant frequency, considering soil-structure interaction, was around 1.6 Hz, while in the numerical model the natural resonant frequency seems to be concentrated around 1.40–1.45 Hz. For the NO GSI structure, the numerically computed natural resonant frequency is around 2.4 Hz–2.5 Hz instead of 2.7 Hz. This is likely due to localized densification that occurred exactly underneath the structures

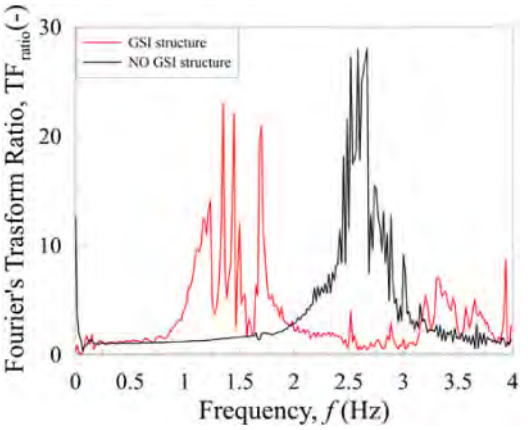

Figure 10. Amplification function using the SS1 signal in the numerical back analysis.

in the centrifuge test, that the material model HS_{ss} could not accurately predict. However, even in this case a satisfactory similarity between the numerical and experimental results is observed. The efficiency in terms of acceleration reduction as well as Arias Intensity reduction are reported in Figure 11.

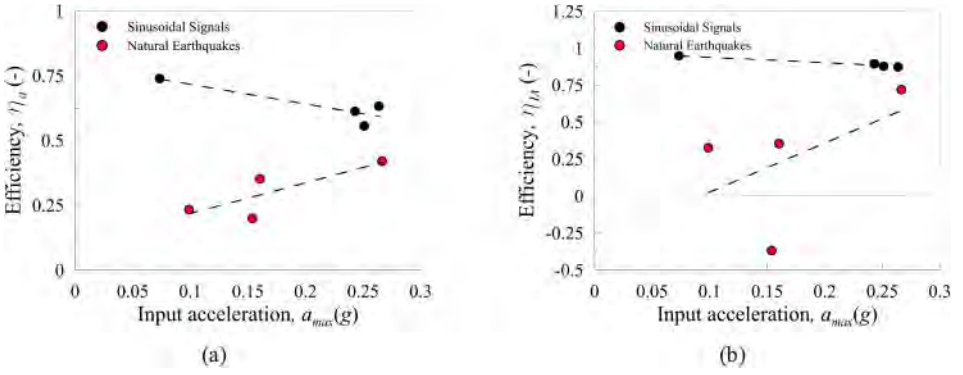

Figure 11. Efficiency in terms of reduction of total absolute acceleration (a) and Arias intensity (b) in the numerical back analysis.

The centrifuge tests demonstrate slightly higher efficiencies for both sine waves and natural earthquakes, but the general trend of the numerical results is in all similar, as can be seen comparing Figures 5 and 11, and the small overestimation of the numerical analyses does not affect the reliability of results.

Focusing on the Kobe earthquake (the earthquake with the maximum PGA among the ones considered in this work), a comment is worth doing on the stress and strain patterns within the subsoil. Figure 12 shows the isolines of the degree of mobilisation of shear resistance, τ_{rel}, and of the deviatoric deformation, γ_s, at the time t in which the maximum displacement at the structural floor is reached.

The distribution of τ_{rel} in the two model is completely different. For the *NO GSI* structure, the whole soil volume at the sides of the foundation is largely sheared during shaking (high shear stress is mobilised). This indicates that the lateral soil and the structure are highly interacting through the embedment during ground shaking. Therefore, due to this mobilisation of soil stresses on the sides, the rotational stiffness of the foundations is high. On the other hand, the *GSI* structure is free

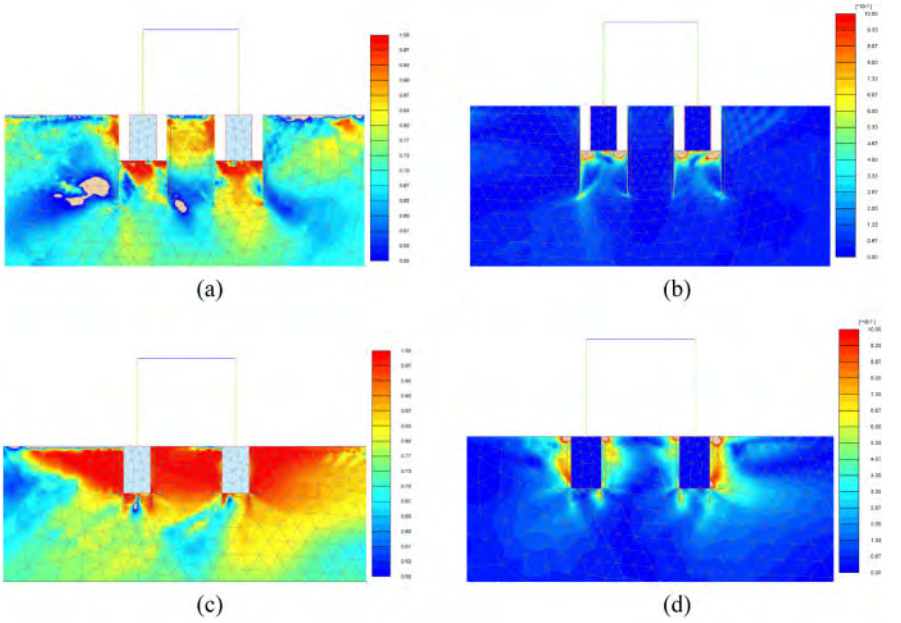

Figure 12. Mobilisation of maximum shear strength for *GSI* (a) and *NO GSI* (c) structure; mobilisation of maximum shear strains for GSI(b) and *NO GSI* (d) structure.

to move at the footing beams sides, thus experiencing larger tilt and rocking. Consequently, large yielding occurs at the base of the beams, while the lateral soil, well retained by cantilever wall, does not experience significant dynamic interaction with the building and is rather less sheared.

Similar considerations can be made when considering the deviatoric strain, γ_s. Below the foundations of the *GSI* structure there is an accumulation of deviatoric deformations reaching values of more than 1%. The rocking mechanism is also revealed by the distribution of deviatoric strains, that concentrate at the edges of the footing beams, due to their swing induced by the building rocking. On the opposite, below the foundation level of the *NO GSI* structure deviatoric strain are almost null.

3.3 *On the modification of static load bearing capacity*

To better understand the effect of this seismic disconnection on the static conditions, the static bearing capacity of the isolated building (*GSI* structure) was compared to that of the original building (*NO GSI* structure). It should be noted that the 10 mm distance (0.6 m at prototype scale) between the footings and the cantilever wall results from the compromise between practical aspects, such as *e.g.*, ease of placement of the model foundations, and geotechnical aspects, requiring limited removal of soil laterally to the foundations not to affect their bearing capacity. With reference to this last aspect, the Figure 13 shows schematically a potential global collapse mechanism for a shallow foundation in sand (Vesic 1973).

The percentage reduction of the soil counterweight at foundation level, due to the creation of the lateral disconnection, can be computed as:

$$\frac{L_{sh} - b}{L_{sh}} \tag{3}$$

where L_{sh} is the lateral extent of the global collapse mechanism and b is the width of the trench. Using a friction angle $\varphi'_{cv} = 33°$, the corresponding computed reduction of bearing capacity (Terzaghi 1943) and safety factor are marginal, of the order of 6%. The load bearing capacity is estimated in

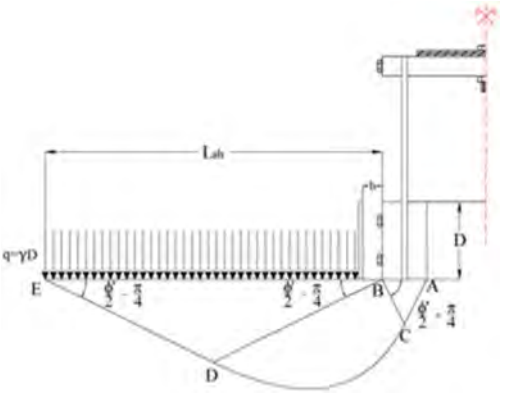

Figure 13. Potential global collapse mechanism for a shallow foundation with lateral disconnection.

1246 kPa for *GSI* structure and 1326 kPa for *NO GSI* structure. Considering 130 kPa as bearing load, the factor of safety is 9.36 for GSI structure and 9.96 for NO GSI structure. To further investigate this last aspect, the loading bearing static capacity of both foundations (connected and disconnected) was also studied numerically considering different soil-foundation interface conditions. In particular, a force of increasing intensity was applied to both foundations (Figure 14) and consequently the displacements were obtained.

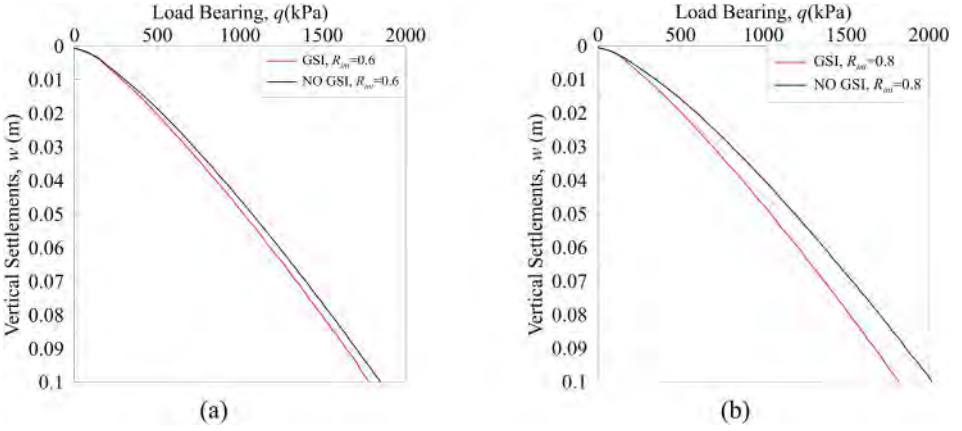

Figure 14. Vertical load-settlements charts in case of $R_{int} = 0.6$ (a) and $R_{int} = 0.8$ (b) for *GSI* and *NO GSI* structure.

The bearing capacity of the two foundations, connected and disconnected, differ by less than 10%. It can also be seen that the quality of the foundation-soil contact (which determines the value of R_{int}) influences the differences in the limit load between the two foundations (Figure 14b). This is because, in the case of a poor foundation-soil contact (low value of R_{int} between 0.5 or 0.6) the vertical tangential stresses at the foundation-soil interface have lower limit values and, therefore, the two bearing capacities values are more similar. However, it should be noted that, even in the case of perfect effective contact ($R_{int} = 1$), the value of the safety factor, for the disconnected foundation, is very high. Therefore, it is very unlikely that the lateral disconnection would compromise the static safety of a masonry building as the latter are generally characterised by very high safety factor values (generally $FS > 10$).

4 CONCLUSION

The paper briefly showed the results of a centrifuge test, and its numerical back-analysis, investigating the potential of disconnecting a building foundation from the adjacent soil as a seismic isolation technique. Such a lateral disconnection would be quite suitable for heritage buildings since it does not alter their material and historical integrity.

Two identical structural models, differing only in the foundation embedment conditions, were used to verify the isolating effect. By means of different seismic signals, significant reduction in natural resonant frequency of the disconnected structure was observed. The different resonance frequencies of the two structures were confirmed by the different structural response obtained with sinusoidal and real seismic signals.

The numerical back analysis confirmed the experimental results and permitted a deeper analysis of the evolution of stresses and strains in the foundation soil during shaking. The contours of shear stresses as well as shear deformation attained in the soil beneath the foundation showed completely different behaviour between connected and disconnected structure. This fully justified the kinematics of the two buildings, that was observed in the test. Finally, the marginal reduction of the static load bearing capacity of the disconnected structure was demonstrated both analytically and numerically.

In conclusions, especially for existing masonry buildings, where traditional foundation construction techniques involved thickening the load-bearing walls and sinking them deep into the ground, a lateral disconnection may represent an economic and respectful seismic improvement technique.

REFERENCES

Alpan, I. 1970. The geotechnical properties of soils. *Earth-Science Reviews,* 6(5):49–62

Brennan A.J., Klar A., Madabhushi S.P.G. 2013. Mitigation of seismic accelerations by soft caissons. *International Journal of Geotechnical Earthquake Engineering*, 4:1–17

Brinkgreve, R.B.J., Swolfs, W.M., Engine, E. 2011. "PLAXIS user's manual "

Di Donna A., Ferrari A., Laloui L. 2016. Experimental investigations of the soil–concrete interface: physical mechanisms, cyclic mobilization, and behaviour at different temperatures. *Canadian Geotechnical Journal*. 53(4): 659–672. https://doi.org/10.1139/cgj-2015-0294

Kirtas E., Rovithis E., Pitilakis K. 2009. Subsoil Interventions Effect on Structural Seismic Response. Part I: Validation of Numerical Simulations. J*ournal of Earthquake Engineering*, 13(2):155–169.

Kulhawy, F. H., Trautmann, C. H., Beech, J. F., O'Rourke, T. D., McGuire, W., Wood, W. A., Capano, C. 1983. Transmission line structure foundations for uplift compression loading. *Final report. USA.*

Nappa V., Bilotta E., Flora A., Madabhushi S.P.G. 2016. Centrifuge modelling of the seismic performance of soft buried barriers. *Bulletin of Earthquake Engineering,* 14(10): 2881–2901.

Nappa, V., Bilotta, E., Flora, A. 2019. Experimental and Numerical Investigation on the Effectiveness of Polymeric Barriers to Mitigate Vibrations. *Geotechnical and Geological Engineering*, 37(6): 4687–4705.

Pitilakis K., Karapetrou S., Tsagdi K. 2015. Numerical investigation of the seismic response of RC buildings on soil replaced with rubber–sand mixtures. *Soil Dynam Earthq Eng.,* 79:237–52.

Somma F., Bilotta E., Flora A., Viggiani G.M. 2021. Centrifuge modelling of shallow foundations lateral disconnection to reduce seismic vulnerability. *Journal of Geotechnical and Geoenvironmental Engineering*. doi: 10.1061/(ASCE)GT.1943-5606.0002746

Somma F., Flora A., Bilotta E. Viggiani G.M. 2021. Numerical analysis on shallow foundations lateral disconnection. *8th ECCOMAS Thematic Conference on Computational Methods in Structural Dynamics and Earthquake Engineering*. Athens, Greece, 27–30 June 2021.

Terzaghi, K. 1943. Theoretical Soil Mechanics. *Wiley, New York.*

Vesic A.,S. 1973. Analysis of ultimate loads of shallow foundations. *J. Soil Mech. Found*., 99 (1), 45–73.

Viggiani C. 2017. Geotechnics and Heritage. Second Kerisel Lecture, *Proc. Of 19th ICSMGE*, Seoul, South Korea.

Yegian M.K, Catan M. 2004. Soil isolation for seismic protection using a smooth synthetic liner. *J Geotech Geoenviron Eng*, 130:1131–1139.

Geotechnical Engineering for the Preservation of Monuments and Historic Sites III – Lancellotta, Viggiani, Flora, de Silva & Mele (Eds)

Restoration and renovation works for the Catacombs of San Gennaro in Napoli, Italy

A. Flora, F. de Silva & M. Ramondini
Department of Civil Architectural and Environmental Engineering, University of Naples Federico II, Naples, Italy

N. Flora
Department of Architecture, University of Naples Federico II, Italy

ABSTRACT: San Gennaro Catacombs in Naples (Italy) are the clear witness of how the Greek city arose and then became the contemporary town. At the foot of the Capodimonte hill, cavities were excavated since the arrival of the first Greeks from Cuma (6th century b.C.) as underground pits of tuff, to be used to build the New Town: Nea Polis, Naples. In time, the catacombs of San Gennaro have been transformed into a religious site, becoming a place of widespread religious worship because of the burial of Saint Gennaro, protector of the city, and have been enriched with precious stuccos. After an unwavering abandonment and decline, and with the goal of a conscious reuse, the Catacombs are living a new life and are now one of the main attractions of the city. In the spirit of a consistent recovery and conservation program, there is now the idea to let the people into the catacombs from the original entrance. Therefore, works have been carried out on an adjacent cavity, connecting it to the catacombs. The new touristic path has been designed after extensive geotechnical investigation and analyses. The paper will present the numerical analyses carried out to assess the stability of the system of cavities, and the protection and restoration works under way. It is shown that the irregular pattern of existing fractures rules the mechanical behavior of the tuff around the cavities. The analyses allowed to identify possibly dangerous instability mechanisms close at the main entrance of the catacombs.

1 INTRODUCTION

The strong link existing between the underground-space heritage and the overground structures largely affects local traditions and culture. Then, cities hosting underground heritage bear this link in their history and, consequently, attract visitors. Cities as Napoli, Roma, Trieste, Matera, Orvieto are just some examples of such virtuous exploitation in Italy. The increasing demand to visit underground spaces of historic relevance arises issues about the design of interventions to make this possible, accomplishing the two opposite needs to respect their integrity and to allow safe fruition.

This is the case of the Catacombs of San Gennaro in Napoli, dated back to 6th century BC, when the quarried tuff was used by the settled Greek community to build the "*Nea Polis*". With the passing of time, the catacombs of San Gennaro became a place of widespread religious worship because of the later burial of Saint Gennaro, protector of the city, and have been consistently enriched with precious stuccos.

Recently, works have been planned to restore the original accesses to the Catacombs by connecting them with a close by abandoned underground quarry, also building a path to connect two main districts of Napoli (Sanità and Capodimonte), thus making the cavity not only an old heritage site

DOI 10.1201/9781003308867-30

but also a new way to cross the city. Indeed, strengthening the connection between its immaterial heritage and local people.

The paper describes some numerical analyses performed to investigate the stability of the system of cavities to be connected to the catacombs, accounting for the rock joints and the spatial variability of the rock resistance.

2 THE CATACOMBS OF SAN GENNARO IN NAPLES

The Catacombs of San Gennaro develop inside a complex and multilevel system of cavities extending for 1700 m^2 in a Neapolitan Yellow Tuff (NYT) hill below the Basilica of the *Incoronata Madre del Buonconsiglio* in the Capodimonte district of Naples (Figure 1a). The steep west side of the hill is limited by *vico San Gennaro dei Poveri* with a height variable between 23 m and 27 m and partially covered by man-made ground with a variable thickness (Figure 1b). The top of the west side is characterised by a buttress supporting the made ground covering the roof of the NYT. The system of cavities of interest in this paper is composed of two larger corridors extending along the N-S direction, i. e. parallel to the cliff, and by two narrower W-E aisles leading to two of the three openings in the cliff along vico San Gennaro dei Poveri. One of the N-S nave leads to the southernmost curved room, where tracks of a likely abrupt interruption of the excavation are visible, probably due to the detrimental effects of the quarrying activities on the neighbouring cavities.

The intersection between the orthogonal naves close to the ridge generates a NYT pillar, characterized by an almost square horizontal cross section with each side 4 m wide. The latter is close to another pseudo-rectangular 4 m × 3m pillar and to a very irregularly shaped pillar 3 m and 9 m long respectively along the NS and WE directions. Where the four naves cross each other, i. e. approximately below the church dome, there is a larger and almost square 15 × 15 m pillar. Eleven circular pillars made of reinforced concrete were built around the latter NYT pillar, probably to sustain the church foundations.

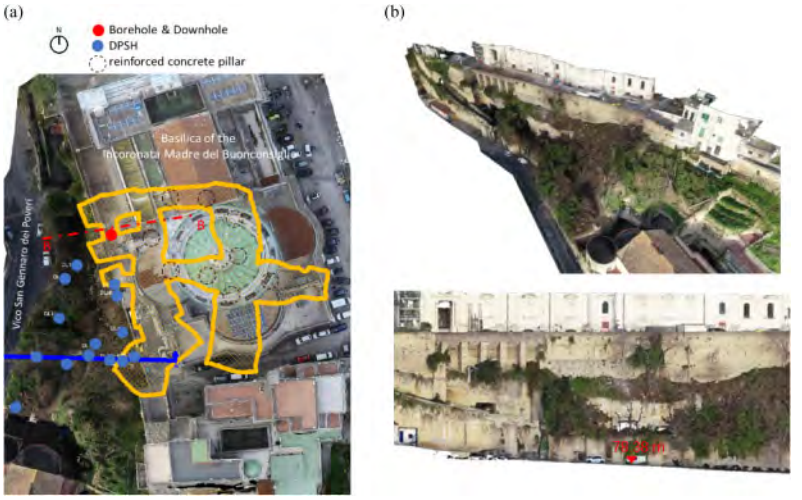

Figure 1. (a) Aerial view of the hill with the location of the portion of Catacombs of San Gennaro object of the present study and of the performed subsoil investigations, (b) views of the west side.

The inner walls of the cave are 10°–15° inclined leading to the typical trapezoid geometry of the vertical cross section of the aisles. The room height is variable around 5 m due to the irregularity of the current planking level, which does not correspond to the bottom of the excavation. In fact, tuff waste resulting from the quarrying activities and, later, debris resulting from the construction of the upper church were accumulated in the cavity with the passing of time. A borehole executed

in the hill (and described in the following) revealed that the cavity was originally almost 10 m high and has been filled up to its half height, as already occurred in other cavities in Napoli (de Silva & Scotto di Santolo 2018). The thickness of NYT in the cavity roof is around 7.50 m, covered by almost 10 m of made ground. Except for some fractures close to the cavity openings, the NYT along the west side is quite intact. Conversely, inside the cavity there is a dense network of syngenetic fractures, which locally intersect causing the falling of rock blocks.

2.1 *Renovation works*

The system of cavities to be converted is today in complete abandonment. The goal of the project under course is that of converting the system in the new meeting point for visitors, (see Figure 2a–b). The renovation works consist in a suggestive path which connects *vico San Gennaro dei Poveri* in the Sanità district to the upper square of the *Basilica of the Incoronata Madre del Buonconsiglio* in the Capodimonte district. Since the two sites are at different elevations, a lift will be constructed in the cavity between two tuff pillars and near one of the cavity openings.

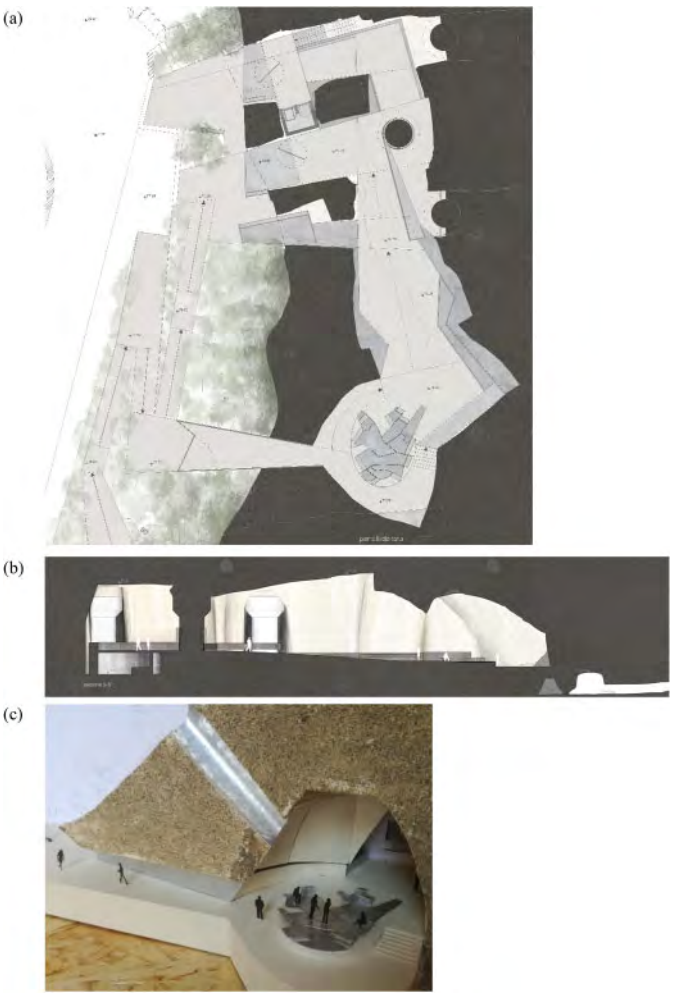

Figure 2. (a) Plan, (b) section and (c) detail of the renovation project.

Even though the Sanità district is in the center of the city, its lower zone is currently an outskirt due to the lack of efficient road connections. Hence, such connection has a social relevance for the citizens because concretely links the Sanità to the rest of the city.

The project restores the original accesses, allowing a chronological tourist tour, which proceeds as the excavation progressed, contrary to what happens today with access from above.

The cavity spaces will host finds from the excavations of the catacombs, which are now stored in not-accessible deposits, as well as staging points for visitors. Two additional openings will be constructed in the southernmost zone: the upper to illuminate the actual darkest zone, the other at the level of the walkway to facilitate the exit of visitors. These openings will also improve the natural circulation of air inside the cavity. Benches made of Corten iron will be installed in the largest circular room, whose design schematically reproduces the intersections of the main streets in the Sanità district (see Figure 2c).

The hill front, slightly higher than the close road, will be arranged in public gardens, connected by slightly inclined ramps that allow disabled and elders to walk independently.

2.2 *On-site and laboratory geotechnical investigations*

The feasibility of the design interventions was supported by an extensive on site and laboratory investigations on the hill and cavity, whose location is shown in Figure 1.

Dynamic Probing Super Heavy tests were executed along the hillside to individuate the thickness of the loose soil covering the tuff. Along the same vertical in which the elevator will be constructed, a borehole was drilled from the top of the hill up to a depth of 30 m, i. e. crossing the cavity and the filling material placed on the floor. The layered soil resulted to be mainly constituted by 8.50 m of man-made ground overlying the Neapolitan yellow tuff. The cavity is 10 m high and filled of debris up to 5.5 m.

A down hole test was executed in the borehole leading to a shear wave velocity around 280 m/s both in the upper man-made ground and in the cavity filling, while a value of 626 m/s was measured in the tuff. Such values are typical of the Neapolitan subsoil.

Regarding the peak uniaxial compression strength of the Neapolitan yellow tuff (σ_{UCS}) this parameter varies between 2 MPa and 7 MPa, with the most recurrent values included in the range 3–4 MPa for samples with a natural unit weight of 15 kN/m^3. Such a variability is associated to the void ratio and distribution of lithic fragments, pumices, crystals and glass in the rock matrix (Evangelista and Pellegrino, 1990). Such inhomogeneity makes the tuff resistance strictly dependant on the local rock features. For this reason, uniaxial compression tests were executed on six samples taken from the abovementioned borehole and four samples taken from the hill side through horizontal drillings. The initial stiffness of samples taken from the borehole and from the horizontal drillings resulted very similar, as well as the variability of the peak strength with the dry unit weight, suggesting that all the results can be fairly interpreted in the unique distribution, shown in Figure 3.

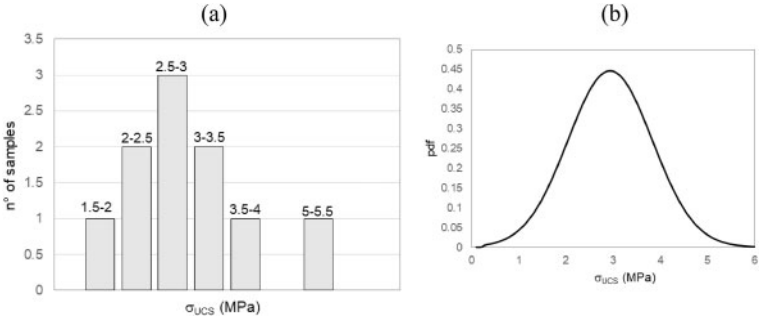

Figure 3. Distribution of the uniaxial compression strength resulting from the laboratory tests (a) and adopted in the numerical analyses (b).

Five out of 10 tests led to σ_{UCS} ranging between 2 MPa and 3.5 MPa, with the most recurrent values included between 2.5 MPa and 3 MPa. With respect to all the other specimens, very few pumices are included in the only specimen resulting in a strength higher than 5 MPa. Excluding the outlier specimen, the σ_{UCS} values were exploited to calibrate the Gaussian distribution plotted in Figure 3b, with a mean equal to 3 MPa and standard deviation equal to 238 kPa.

3 STABILITY ASSESSMENT OF THE ROCK CAVITY

3.1 *Numerical model*

The numerical model shown in Figure 4 was analysed in the finite difference code FLAC 2D (Itasca 2011) in order to assess how the cavity safety is affected by the uncertainties on the rock strength and the presence of rock joints. The geometry reproduces the vertical cross section AA in Figure 1, where the elevator from the cavity to the church level will be constructed. The model is almost 40 m long and 21 m high with the west side shaped according to the actual cliff. The tuff resistant section of the cavity roof is 5 m thick as inferred from dynamic penetration tests performed on site. Horizontal and vertical sublayers 0.5 m thick were generated in the 2.5 m of roof closer to the cavity and in the pillar respectively, to vary the joint location. The mesh size was consequently refined close to the geometric irregularities and the sublayers.

The model base was fixed while only horizontal displacements were retrained on the east side to simulate the on-site conditions.

The anthropic filling inside the cavity were not inserted since its complete removal is planned in the design of renovation works. The weight of 13 m thick loose soil covering the tuff roof and the accidental loads was substituted by an equivalent vertical load equal to 234 kPa applied at the ground floor. The load was increased up to 368 kPa where the church is present to account for its weight.

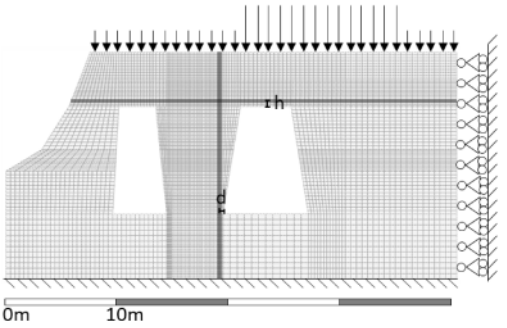

Figure 4. Numerical model of the section AA of the cavity.

The mechanical response of the intact rock was simulated through the Mohr-Coulomb constitutive model, while the Ubiquitous joint model was adopted to simulate the joints. In the latter case, the program distributes inside the material planes in which the mechanical properties are reduced to simulate the rock joints. The inclination of such planes can be chosen according to the orientation of the fractures detected on site.

Table 1 reports the mechanical properties adopted for the tuff and the joint in the numerical analyses. The unit weight, γ, is the mean value measured on eleven samples taken on site. The shear modulus, G, and the bulk modulus, K, derive from the shear and volume wave velocity of the tuff obtained through the down-hole executed in the S1 borehole. Values of σ_{UCS} and δ are the mean and the standard deviation of the strength calculated from data of uniaxial compression properly executed uniaxial compression tests. The friction angle, φ, was inferred from measurements by Evangelista and Pellegrino (1990) during extensive research on the Neapolitan Yellow tuff. The cohesion was back calculated from σ_{UCS} and φ.

Finally, a tension cut-off, σ_t, equal to 20% σ_{UCS} was assigned to the Mohr-Coulomb criterion. The parameters of the rock joints are the same assumed for the intact rock except for the friction angle and the cohesion, respectively reduced to 20° and 0 kPa, to simulate the residual strength of fractures. The so calibrated Mohr-Coulomb criterion is equivalent to the resistance obtained by the empirical equation by Barton (1973) in which the joint roughness JRC coefficient is conservatively assumed equal to 0.

Table 1. Mechanical proprieties of the tuff and joints set in the analyses.

	γ kN/m3	G MPa	K MPa	φ °	c kPa	σ_{UCS} kPa	δ kPa	σ_t kPa
Rock	12	491	1431	28	882	2936	259	147
Joint	12	491	1431	20	0	0	/	0

The model was solved firstly to reproduce the lithostatic conditions and then to calculate the stress modification induced by the presence of the cavity with the wished in place approach.

Four sets of analyses were performed:

1) one with a constant uniaxial compression strength of the tuff;
2) one hundred with a spatially variable uniaxial compression strength of the tuff, obtained by assigning to each element of the mesh a different value of the cohesion compatible with the distribution of σ_{UCS} in Figure 3;
3) seven with a constant uniaxial compression strength of the tuff and a horizontal joint in the roof;
4) six with a constant uniaxial compression strength of the tuff and a vertical joint in the pillar;

Each analysis was aimed to calculate the factor of safety FoS. In details, a reduction factor is applied to the cohesion and the tangent of the friction angle of the tuff, together with the friction angle of joints in the third and fourth sets of analyses. Increasing values of the reduction factor are applied and the FoS corresponds to the value producing the failure.

3.2 *Failure mechanisms resulting from the different sets of analyses*

Independently of the constant or spatially variable distribution of the tuff strength, the failure mechanisms resulting from the first, the second and the third set of analyses mainly involves the central pillar and the roof of the inner cavity. The plastic state occurring in the bottom of the vertical free tuff wall suggests the incipient development of a slippage surface crossing the two rooms. Figure 5 shows the distribution of the achieved plastic states for one illustrative case in which the tuff strength is spatially variable.

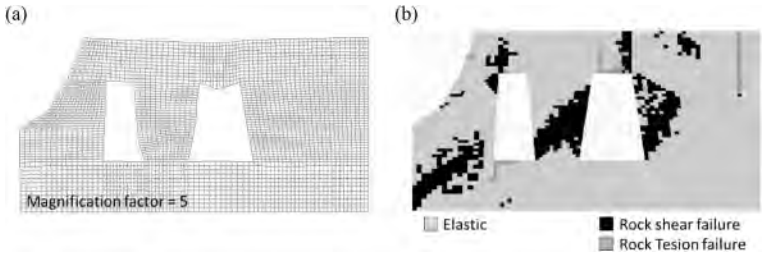

Figure 5. Deformed shape (a) and plastic state (b) of the cavity at failure resulting from one of the analyses with a spatially variable tuff strength.

The introduction of a vertical joint within the pillar leads to a slippage along the joint, which modifies the deformed shape and the distribution of the plastic state when the joint is closer to the inner room, as can be observed by comparing Figure 6 to Figure 7 or 5.

In any case, roofs appear to be enough resistant to support the surcharges, while the inner pillar is the most crucial element for the stability of the whole cavity.

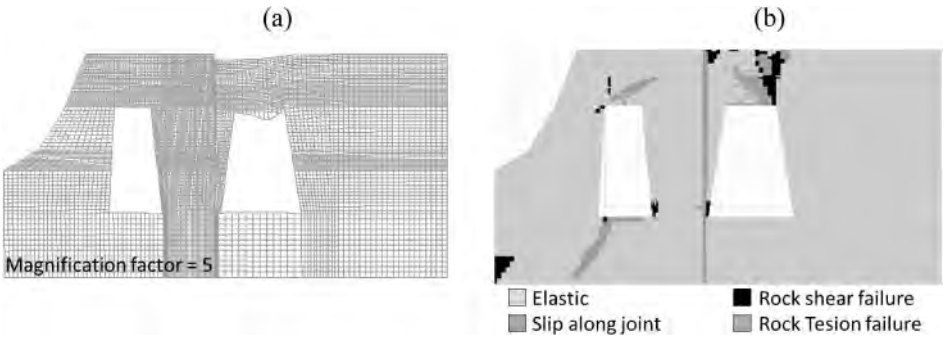

Figure 6. Deformed shape (a) and plastic state (b) of the cavity at failure when a vertical joint is introduced at a distance d = 0.4 m.

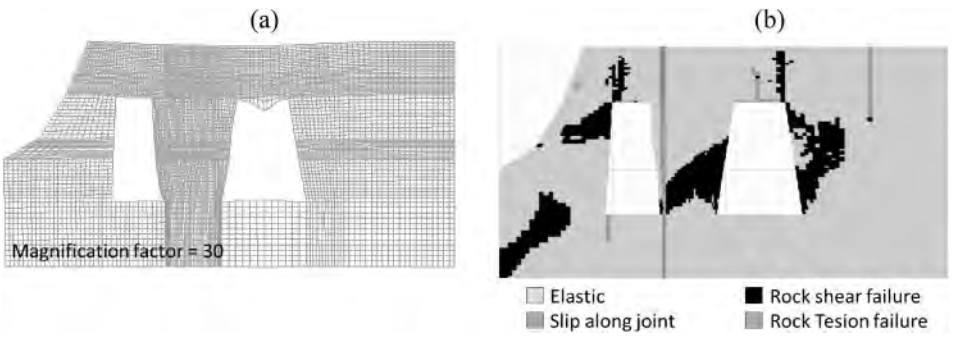

Figure 7. Deformed shape (a) and plastic state (b) of the cavity at failure when a vertical joint is introduced at a distance d = 4.8 m.

3.3 *Effect of the strength variability on the Fos*

Figure 8a shows the FoS values obtained from the second set of analyses, in which σ_{UCS} varies within the model. In any case the FoS is lower with respect to that obtained with a constant $\sigma_{UCS} = 2936$ kPa. Neverthless the reduction is limited to the 10% and reached only in about five out of one hundred cases.

The distribution in Figure 8b highlights that in most cases the FoS ranges between 5.1 and 5.2, i. e. up to 0.95% and 0.96% of the FoS obtained with a constant tuff strength. Hence the σ_{UCS} spatial variability appears negligible for the case at hand, which is characterized by a high FoS value. Conversely, it is worth to be considered for cases in which the static conditions are prone to failure, where the same reduction may lead to a FoS value lower than unit.

3.4 *Effect of rock joints on the FoS*

Figure 9 shows the factors of safety resulting from the analyses in which a horizontal joint is modelled in the roof (a) or a vertical joint in the pillar (b). The introduction of joints in the roof modifies very slightly the factor of safety and only when the joint is placed very close to the roof intrados. Such results confirm that the roof stability is not the most critical aspect for the case at hand, as already observed from the analysis of the failure mechanisms.

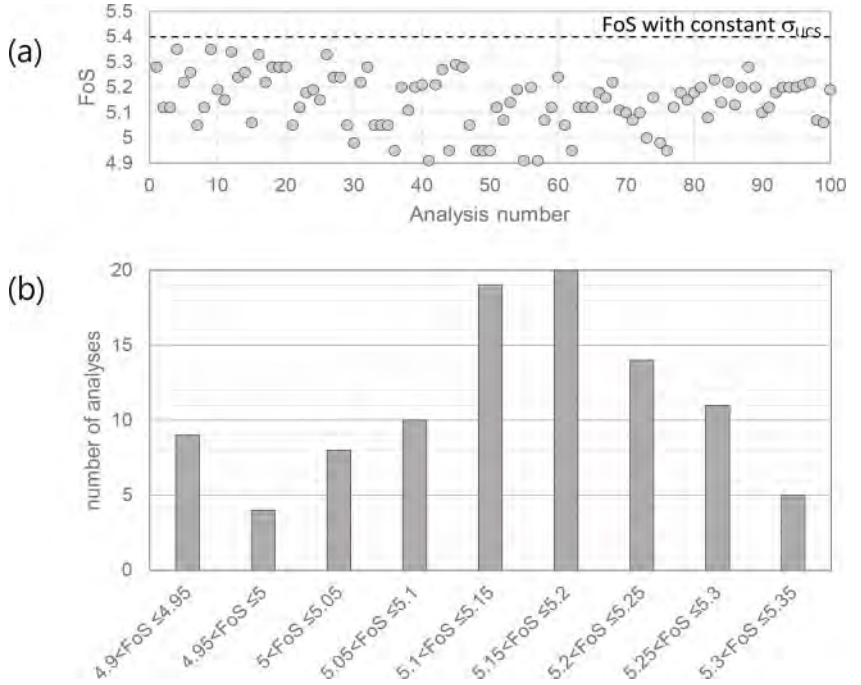

Figure 8. Values (a) and distribution (b) of the factors of safety resulting from the analyses including the spatial variability of the uniaxial compression strength.

Conversely, the sensitivity of the FoS to the vertical joint in the pillar appears more pronounced. Actually, FoS reduces up to 66% of its value with a constant σUCS, when the joint is very close to the inner room. As the joint is moved towards the outer room, the FoS increases and becomes equal to the value with a constant σUCS when the joint overcomes the half thickness of the pillar.

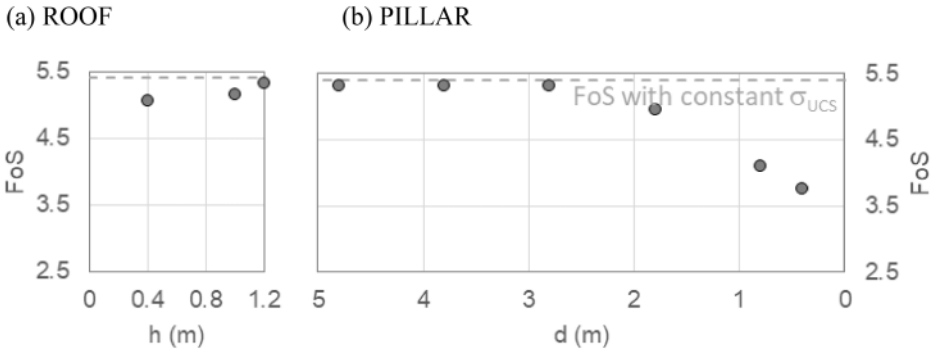

Figure 9. Factors of safety resulting from the analyses with horizontal joint in the roof (a) and vertical joint in the pillar (b).

4 CONCLUSIONS

The paper investigates the effect of joint position and of spatial variability of the strength of Neapolitan Yellow Tuff on the stability of the most critical vertical section of the system of cavities under renovation to be connected to the Catacombs of San Gennaro, with the goal of making them the new entrance, meeting point and visitors information point. The failure mechanisms resulting from all the performed analyses mainly involve the central pillar. In all the analyses a negligible reduction of the factor of safety was caused by the existence of sub-horizontal joints. On the contrary, the existence of a vertical joint considered in the pillar influences the factor of safety. In any case, from the analyses carried out safety conditions seem to be ensured whatever the case. Spatial variability of tuff strength reduces the safety factor, in comparison with the results obtained by neglecting such a variability. This reduction may become critical if the vertical and horizontal bearing parts of the cavity have a low safety factor, which was not the case for the cavity under analysis. However, the results also demonstrate that the spatial variability of rock strength and the position of joints, sometimes not immediately visible at a visual inspection, both need to be carefully considered not to overlook on possible critical mechanisms.

ACKNOLEDGEMENT

This study was carried out within the framework of a research agreement between the Department of Civil, Building and Environmental Engineering of the University of Naples Federico II and the Superintendency of Archeology, Fine Arts and Landscape of Naples. The research agreement was focused on the evaluation of the cavity safety for the renovation works '*Rione Sanità – Catacombe di Napoli: una porta verso il futuro*'.

REFERENCES

Barton, N. 1973. Review of a shear strength criterion for rock joints. *Engineering Geology* 7:287–332.

de Silva, F. & Scotto di Santolo, A. 2018. Probabilistic Performance-based Approaches to the Static and Seismic Assessment of Rock Cavities. *International Journal of Rock Mechanics and Mining Sciences* 112:354–368.

Evangelista, A., Pellegrino, F. (1990) Caratteristiche geotecniche di alcune rocce tenere italiane. Atti del terzo ciclo di Conferenze di Meccanica e Ingegneria delle Rocce, MIR90, Torino (in Italian).

Geotechnical Engineering for the Preservation of Monuments and Historic Sites III – Lancellotta, Viggiani, Flora, de Silva & Mele (Eds)

Geomorphological processes and rock slope instabilities affecting the AlUla archaeological region

J.I. Gallego
RCU – Royal Commission for AlUla, AlUla, KSA

C. Margottini & D. Spizzichino
UNESCO Chair at Florence University, Florence, Italy
ISPRA, Geological Survey of Italy Rome, Italy

D. Boldini
Sapienza University of Rome, Department of Chemical Engineering Materials Environment, Rome, Italy

J.K. Abul
University of Bologna, Department of Civil, Chemical Environmental and Materials Engineering, Bologna, Italy

ABSTRACT: The paper focuses on the preliminary assessment of the potential geo-hazards affecting the cultural heritage rock-cut sites of AlUla region. Its best-known site is Hegra, with more than 110 monumental tombs with elaborated facades carved directly into the sandstone rock. In addition, AlUla hosts a number of fascinating historical and archaeological sites such as its Old Town, surrounded by an ancient oasis, and Dadan, the capital of the Dadan and Lihyan kingdoms. The study is based on an interdisciplinary approach mainly aimed at evaluating characteristics of rock masses, rock degradation processes, slope instabilities and best practices for heritage preservation and future management. The most appropriate mitigation and consolidation measures to contrast the ongoing threats, also in the view of rediscovering the traditional knowledge of local conservation techniques and implementing sustainable low impact monitoring technologies, are also analysed.

1 INTRODUCTION

The present paper focuses on the preliminary assessment of the ongoing and potential geo-hazards affecting the AlUla region. Located at 1.100 km West from Riyadh, AlUla covers an archaeological area (e.g., necropolis, quarries and settlements) of more than 22.000 sqm. (Figure 1), where it is possible to walk in a luxury oasis through ancient world heritage sites in a rock cut landscape shaped for thousand years (Margottini & Spizzichino 2021). Its best-known site is Hegra, the main southern city of the Nabataean kingdom, before becoming a Roman outpost, and the first UNESCO world heritage site in Saudi Arabia, conserving over 110 monumental tombs with elaborated facades carved into the sandstone rock. In addition to Hegra, AlUla hosts a number of fascinating historical and archaeological sites such as its Old Town, surrounded by an ancient oasis; Dadan, the capital of the Dadan and Lihyan kingdoms, considered one of the most developed cities of the first millennium BC in the Arabian Peninsula; and thousands of ancient rock-art sites (e.g. Abu Ud, Jabal Ikmah). Many rock-cut monuments are affected by different natural threats such as surface weathering and erosion, rising dampness, rock surface detachment and larger-volume slope instabilities. To ensure the long-term conservation of sites affected by such natural threats, detailed investigations,

 DOI 10.1201/9781003308867-31

monitoring and consolidation measures are required, specifically developed for rupestrian cultural heritage sites (Boldini et al., 2017; Margottini & Spizzichino 2022; Spizzichino et al., 2016). The activities are characterised by a thorough multidisciplinary approach including competencies in archaeology, engineering geology, rock mechanics, landslide risk assessment and management as well as in conservation, protection and mitigation measures. To define the main physical and mechanical proprieties of the rock materials, a preliminary laboratory test campaign was carried out. The structural setting of the rock-mass (bedding planes, joints, faults), related to the stratigraphical genesis, the tectonic activity of the Red sea, and the geomorphological evolution of the slope, was identified and classified. Local rock-mass conditions promote slope instabilities (e.g., rockfall, sliding, toppling) that may affect both the heritage itself and visitors. This preliminary assessment of prevailing kinematics and potential geo-hazards will allow the implementation of a general master plan, to be considered as a first step for the following detailed design stage. It will contain a first selection of the most appropriated mitigation and consolidation measures, characterised by a low environmental impact and employing traditional knowledge to site preservation.

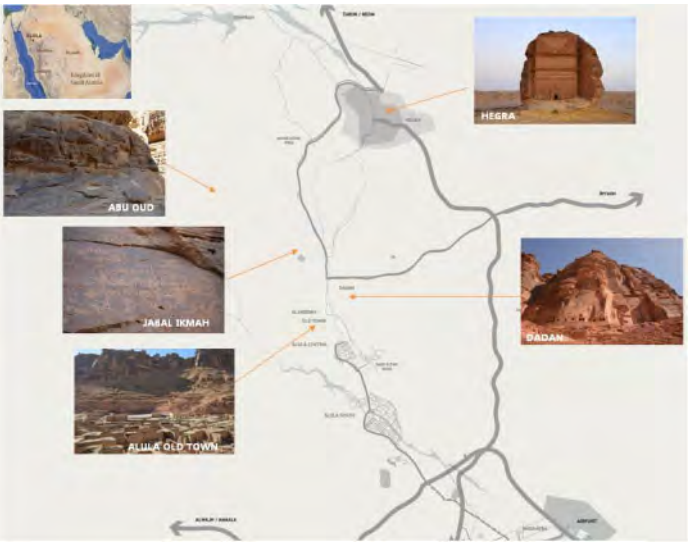

Figure 1. Map of AlUla investigated archaeological sites.

2 THE ALULA REGION ARCHAEOLOGICAL SETTING

The province of AlUla keeps and shows extraordinary human and natural heritage. Its homonym capital is in the center of Wadi Al-Qura, an impressive valley carved out of sandstone, in which there is evidence of human presence, at least, since 200,000 BP. The AlUla *wadis*, and particularly this one, were a meeting point and a natural route for millennia, crossed by important trade routes used since prehistory, and with special intensity since the first millennium BC. With the flourishing of the cultures of Dadan - Lihyan, and Nabatean one later, the Incense Route, which from the south of the Arabian Peninsula crossed the AlUla region, reached the main eastern ports of the Mediterranean sea. In this sense, the discussion on the introduction and dispersal of the Neolithic phenomenon in the peninsula is also particularly interesting. These traditional communication routes are punctuated by an astonishing dispersion of rock art and monumental rock structures that provide us with a wealth of information. Regarding the latter, the research projects promoted by the Kingdoms Institute of the Royal Commission for AlUla (Thomas et al. 2021) detected close to 1.400 Mustatils. It was possible to obtain the absolute dating of them with a radiocarbon dating that takes us to the late Neolithic, around 6,000 BC (Ramsey 2020; Reimer et al. 2020). AlUla is

home to some of the main archaeological landmarks of Arabia, such as the site of Al-Khuraybah, ancient Dadan, capital city of the Dadanite and Lihyanite kingdoms. Dadan was likely one of the most developed cities of the first millennium BC. of the region. As an indisputable heritage legacy, the sandstone valleys also protect thousands of inscriptions in several different languages and alphabets, from Dadanite to modern Arabic. Jabal 'Ikmah, Abu Ud or Al-Aqra'a are an undoubted and powerful human testimony in the area. The most recognized archaeological site is Hegra. An ancient city of 52 hectares, Hegra was the most important Nabatean city and royal cemetery in the south of their kingdom, since at least the 1st century BC (Figure 2).

Figure 2. Nabatean tombs in the Hegra archaeological site.

UNESCO world heritage site since 2008, Hegra protects more than a hundred monumental tombs from this period, and had continuity during the Roman period, probably as one of the southernmost places in the province of Arabia Petrea. After the transition to Islam in the 7th century, the cities of Q'uhr and AlUla appeared in written sources as important places for pilgrimage routes. Testimony of this is reflected both in the archaeological remains of the first, next to the town of Mughaira, and in the Old Town of AlUla, whose streets, squares, and farms seem frozen in time. The latest reflection of this evolution is made up of the characteristic elements of the Ottoman presence, both in the form of various fortifications and military equipment, as well as that of the Hijaz railway. Its construction, which was intended to complete the connection of Damascus with Madinah, was suspended by the First World War.

3 GEOLOGICAL SETTING

From the geological point of view, the area of AlUla is located at the border between the basement complex and the Arabian foreland, constituted by coarse clastic sediments (mainly sandstone). The detail distribution of various geological formations is reported in Figure 3 (modified after Donald et al. 1998). Outcropping succession in the AlUla archaeological region includes the Siq Sandstone and Quweira Sandstone and the upper Quaternary alluvial deposits. The sandstone layers are sub-horizontal, gently dipping about 5° in N-NE (330° N). From the geological profile reconstructed by Buro Happold Engineering (2019) it is possible to notice that, due to this gentle dipping and due to topography, the Siq Red Sandstone is mainly outcropping in AlUla and surrounding (Dadan, Old Town, etc.) while, in the Hegra area, the Quweira Sandstone is dominant. The Quweira occurs in cross-bedded stratifications with bed thicknesses of 2 to 5 m.

The Siq Sandstone, dark red to brownish-red and medium-grained, is divided into three sub-units, namely the Lower (sandstone conglomerate of white quartz cobbles), Middle (fine, fractured strata) and Upper Siq (massive and very compact) Sandstones.

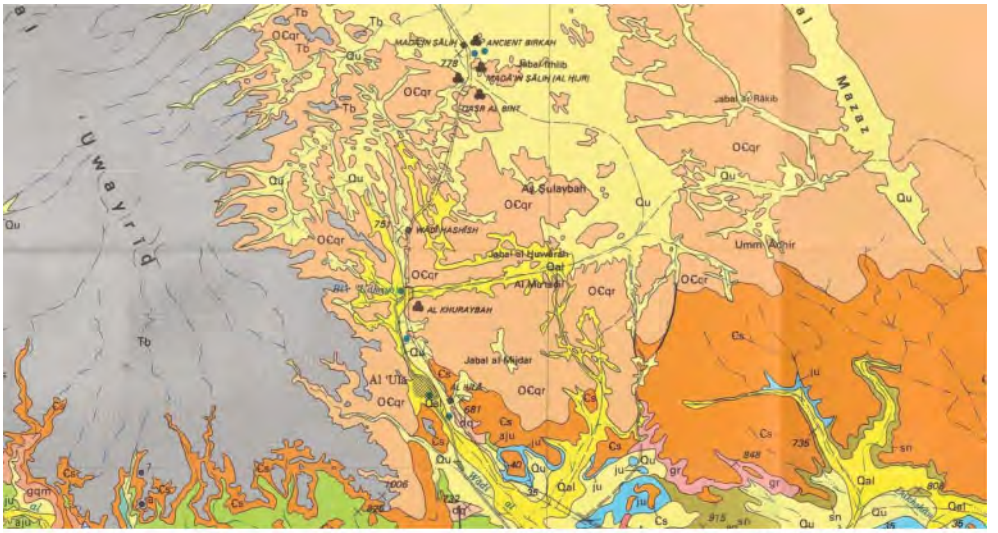

SYMBOL	ID	AGE	UNIT	MATERIAL
	Qal	Quaternary		Alluvium
	Qu			Alluvium
	Tb	Quaternary	Harrat	Flood basalt
	Qeqr	Ordovician -	Quweira group	Sandstone
	Ꞓs	Cambrian	Siq group	Sandstone
	Ju	Proterozoic	…	…
	dq		…	…
	aju		Lower Jiddah group	Lava and pyroclastic rock

Figure 3. Geological map of AlUla region (modified after Donald et al. 1998).

The panoramic photograph in Figure 4, taken from the "highpoint" on top of Harrat (lava plain or volcanic field of Al Uwayrid west of AlUla – Wahbi 2014), displays most of the lytho-stratgraphic succession in the area. This division is evident from the weathering profile of the outcrops in the area (Figure 4).

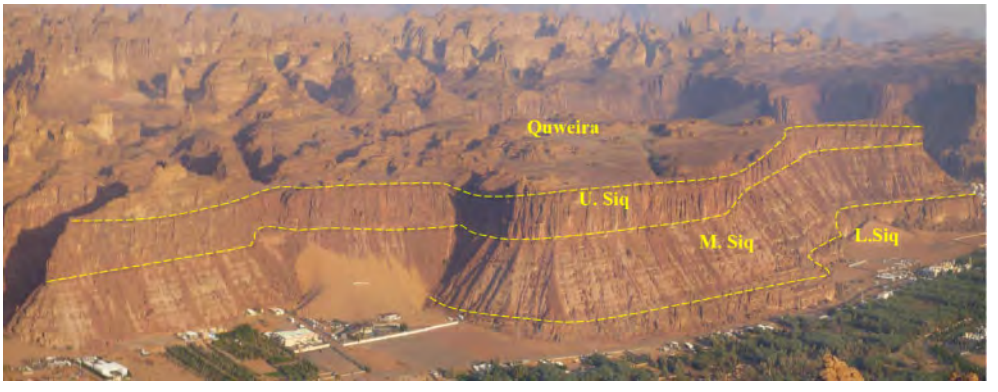

Figure 4. Panoramic view (slightly vertically-exaggerated) of the litho-stratigraphic succession in the AlUla area, taken from the highpoint of Harrat Al Uwayrid, West of the town of AlUla. Sandstone units are recognized in this section, except for the Saq Sandstone, which outcrops out further North of this area (Wahbi 2014).

Table 1. Litho-stratigraphic units and sub-units in the region of AlUla.

AGE (PERIOD)	GEOLOGICAL UNIT	SUB UNIT
Early Ordovician	Saq Sandstone	
Late Cambrian	Quweira Sandstone	
Middle Cambrian		
Early Cambrian	Siq Sandstone	Upper
		Middle
		Lower
Proterozoic basement (pre-Cambrian Arabian shield)	Jibalah Group and basement	

4 PHYSICAL AND MECHANICAL CHARACTERISATION OF THE ROCK MASSES AND MATERIALS

4.1 *Field survey and rock-mass characterisation*

Geo-mechanical characteristics of the AlUla rock formations were investigated through geomechanical field surveys and laboratory tests, these latter executed directly in Italy. The surveys were carried out following the recommendation of the International Society for Rock Mechanics (ISRM 1978a; 1978b, 1981). The following activities were carried out directly during field surveys (December 2020 mission) in Hegra and Dadan (Table 2):

1. geo-structural analysis of the slope facades (orientation and main characteristics of discontinuities);
2. Barton's profilometer tests for reconstructing the joint roughness (JRC);
3. sampling of blocks to be used for laboratory analysis;
4. Schmidt-hammer tests on joint surfaces and intact rock blocks for in-situ assessment of the uniaxial compressive strength (JCS);
5. tilt tests for base friction angle assessment (ϕ_b).

Table 2. Average rock mass parameters for Hegra and Dadan sites.

	JCS MPa	JRC –	ϕ_b (°)	GSI –
Hegra	32–42	2–6	37–43	67
Dadan	28–41	4–8	40–45	65

From a geo-structural point of view, the AlUla area reflects trends and characteristics of the regional tectonics, mainly connected with the oceanic spreading of Red sea, initiated first on the Sheba Ridge east of the AlUla-Fartaq fracture zone at ∼19–18 Ma (Bosworth 2015). In addition, syngenetic strata joints and local stress conditions of the slope (possibly associated to stress release) are responsible for the other sets of discontinuities.

4.2 *Laboratory tests*

During the December 2020 campaign, five rock samples were collected near the cities of *Mada'in Salih* (better known as Hegra) and Dadan (Figure 5). They consist of two Yellowish Sandstone blocks, belonging to the Quweira Group, and three Red Sandstone blocks of the Siq Group (Figure 6). A total of 40 specimens were prepared for the mechanical tests, of which 22 for the uniaxial compression test (Figure 7a), with a diameter of about 25 mm, and 18 for the Brazilian test (Figure 7b), with a diameter of about 50 mm. Uniaxial compression tests and Brazilian tests were performed using a 10 and 50 kN load cells, applying respectively a load rate of 0.5 MPa/s and

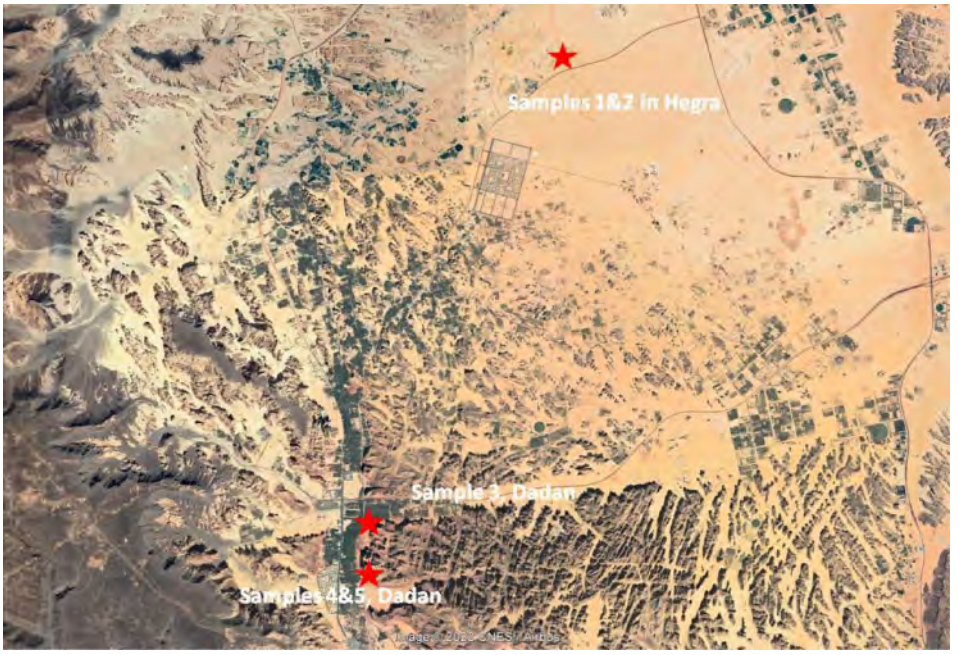

Figure 5. Location of rock blocks collection.

Figure 6. The five rock samples collected and analysed in the laboratory.

200 N/s (ISRM 1978). Before the mechanical tests, the P wave velocity was also measured on all the specimens (Figure 7c). The average values of the physical and mechanical properties for each sample are summarised in Table 3.

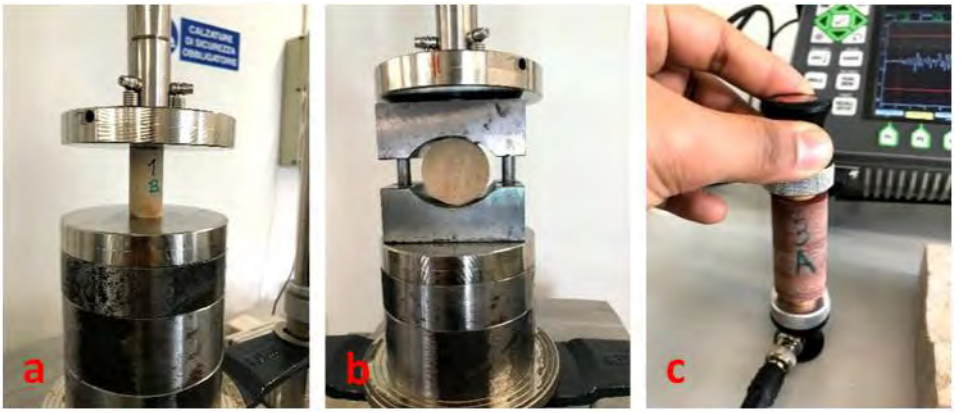

Figure 7. Uniaxial compression test (a), Brazilian test (b) and P wave velocity measurement (c).

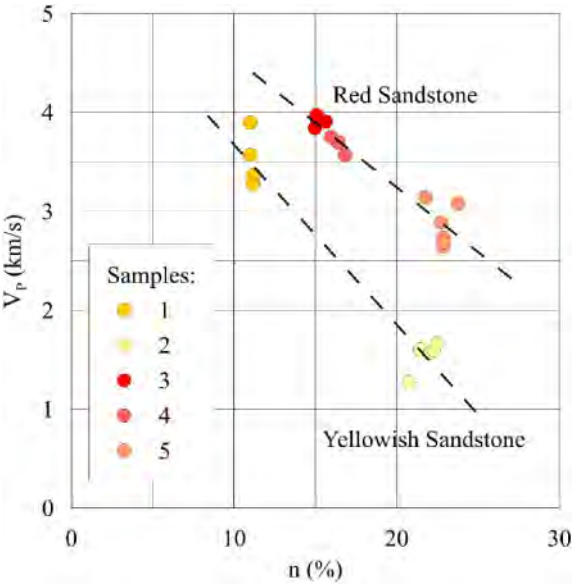

Figure 8. P wave velocity against total porosity.

Table 3. Summary of the physical and mechanical properties of the rock materials.

Sample	ρ_{dry} [Mg/m^3]	ρ_s [Mg/m^3]	n [%]	V_p [km/s]	σ_c [MPa]	σ_t [MPa]
1	2.390	2.688	11.1	3.5	50.24	6.83
2	2.087	2.669	21.8	1.5	9.93	0.50
3	2.265	2.679	15.8	3.9	38.51	7.68
4	2.238	2.678	16.4	3.7	41.18	6.46
5	2.060	2.694	23.6	2.9	24.85	2.74

The increase in porosity reduces significantly V_P values for both rock formations, with differentiated trends for the Yellowish and Red Sandstone samples.

Figure 9 shows the strength values obtained by the two tests.

The uniaxial compressive strength σ_c ranges from less than 10 MPa for a specimen of the sample 2 to over 50 MPa for a specimen of the sample 1, both belonging to the yellowish sandstone lithotype. Specimens prepared from the red sandstone blocks are characterized by σc values in the range 18–42 MPa.

Consistently, specimens from samples 1 and 2 display respectively the highest and lowest values of the tensile strength σ_t, from almost 8 MPa in the case of the first block down to about 0.5 MPa in the second one. Values of σ_t similar to those obtained for the sample 1 were identified for specimens of samples 3 and 4, while significantly lower values were attained by the two specimens of sample 5. In general, inspection of the two figures highlights the substantial influence of porosity on the rock material strength.

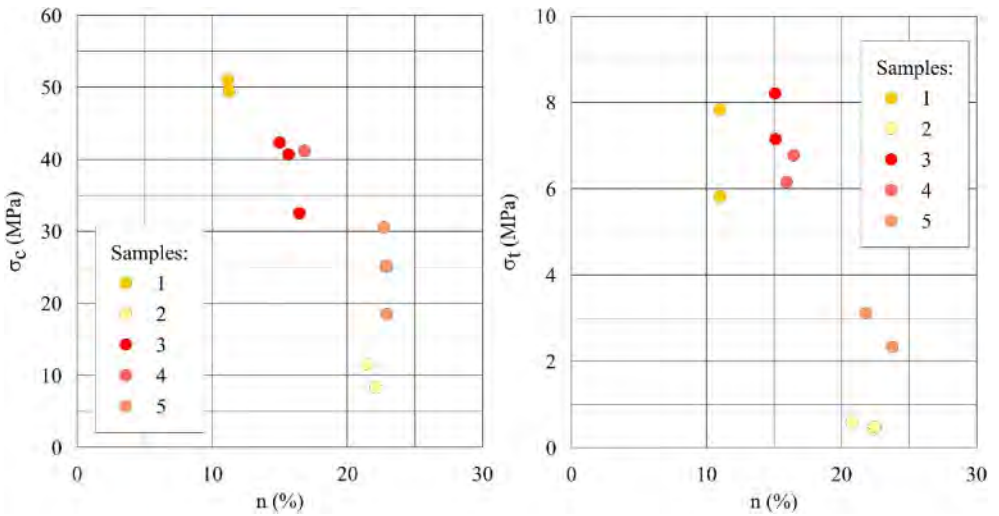

Figure 9. Uniaxial compressive strength (left) and tensile strength (right) against total porosity.

5 GEO-HAZARDS AND MORPHOLOGICAL PROCESSES THREATENING THE SITES

The term geo-hazards includes very different types of morphological processes and involve both long-term and short-term geological processes. In the following the main instability and weathering problems affecting the sites at different scales are briefly described.

The different archaeological sites of AlUla region are completely carved and realised into the Quweira and Siq Sandstones. The local quality of the rock-mass is directly depending on:

- lithology and rock material of depositional layers (e.g. minerals, texture and composition);
- level and typology of weathering and erosion;
- structural setting (e.g. joint, fractures, faults).

The slope angle for most of the rock faces is prevalently larger 80° , with frequent overhanging surfaces consequent to erosive processes or block collapses at their base. Slope kinematics, and thus potential failure modes, is mainly ruled by high and medium dip angle of the main discontinuities versus local slope orientation. Also the presence of horizontal discontinuities (bedding planes) causes failure modes and volumes of potential instability (see Figure 10).

Figure 10. Example of the main instability processes affecting the different archaeological sites belonging to AlUla region: 1&2 rock slide and free fall in Hegra; 3 basal erosion affecting pillars and rock facades in Hegra; 4&5 rock blocks fallen in Dadan; 6 condition of rock cliff affecting the Lions tomb in Dadan; 7 rock blocks accumulation in AlUla Old town western cliff; 8 potential slope instability inside AlUla Old town; 9 unstable and fractured rock arts block in Jabal Ikmah.

According to a preliminary assessment, the main instability processes affecting the whole archaeological area are:

1. rock fall, toppling and sliding (from small to medium to large dimensions) affecting the slope façade;
2. collapse (from very small to medium dimensions) involving directly the carved architectonic structure of the tombs;
3. weathering and erosion processes (from small to large scale) affecting both the slope facade and tombs.

6 SHORT- AND LONG-TERM MITIGATION MEASURES MASTER PLAN

In the whole archaeological area of AlUla, and considering that the site has been abandoned for many centuries, the present and active morphological processes should be framed within a management and conservation master plan having two different timeline references: emergency mitigation measures to be defined and undertaken in the short-medium term and preventive mitigation measures to be implemented in the medium-long term.

Short-medium term actions should be preceded by an investigation phase including:

- detailed geomatics Terrestrial Laser Scanner (TLS) acquisition coupled with UAV flight acquisition, in order to provide high-resolution 3D topographical models of the whole heritage area;
- laboratory test execution;

- detail geomorphological and geomechanical survey of the rock slope;
- global kinematic analysis of the rock facades including the calculation of the most probable rock fall trajectories;
- detailed landslide hazard/risk assessment (rock fall, wedge and rock slide detailed mapping);
- thermal infra-red analysis;
- detailed survey of each tomb and of the whole archaeological complex (including tailored data sheet and TLS for the most endangered sites);
- slope stability modeling (2D and 3D) for specific blocks and/or unstable portions of the cliff.

According to the results of these investigations, the following activities should be also programmed:

- cleaning and scaling of the sites from loose material;
- temporary supports of instable rock portions;
- urgent reinforcement in the most instable volumes to avoid detachments;
- redefinition of touristic paths and accesses to each single tombs/archeological complex to prevent tourists from being exposed to potential collapses or instabilities (e.g. definition of minimum safety distances, prohibitions in the accesses of some tombs or complex);
- new communication plan and billboard for touristic management;

Long-term actions include:

- detailed design of mitigation and consolidation measures;
- design of an integrated monitoring system (e.g. traditional geotechnical in situ monitoring through crack gauges and tiltmeter, GBR or topographical traditional through robotic total station).

The adopted monitoring integrated system could also be set, with some small modifications and thresholds definition, as a warning system for flash flood as well as for detection of large rock block deformations.

7 CONCLUSION

The AlUla oasis covers a wide archaeological area where it is possible to visit ancient heritage sites in a rock cut landscape shaped for thousand years. In addition to its best-known World Heritage site of Hegra, the region hosts a number of fascinating historical and archaeological sites such as its Old Town; Dadan and thousands of ancient rock-art sites.

The entire area is characterized by the presence of low to medium strength sandstone formations. More in detail, the north area shows the outcropping of the Quweira Red Sandstone unit while in the area of the Old Town and further south the Siq Yellowish Sandstone appears, divided into three main sub-units (Lower, Middle and Upper). The geological and geomechanical characteristics of these two formations affect the potential instability and weathering of the cultural heritages sites carved into them.

The geological formations are characterized by a significant internal variability, both vertical and lateral. The Quweira Yellowish Sandstone is mainly interested by diffused weathering and erosion phenomena as well as rock fall connected to internal structural asset. The archaeological areas in the Siq Red Sandstone are mainly affected by rock fall and slides as a consequence of the local discontinuities pattern.

The present paper has the main scope of developing a preliminary analysis of the geomorphological evidences, the mechanical properties of the rock materials, the rock slope instabilities and main threats affecting the cultural heritage sites in AlUla, providing first ideas to be further validated by additional investigations and monitoring. Preliminary short and long term mitigation actions (both structural and non structural) were suggested in order to develop a future conservation management plan.

ACKNOWLEDGMENT

The present activity has been funded by the French Agency for the Development of AlUla (AFALULA), in agreement with the Royal Commission for AlUla (RCU), Kingdom of Saudi Arabia. A special thanks is due to Ingrid Perisse and Jean François Charnier, both from AFALULA, for their inspiration and useful scientific support and discussion. The authors wish to thank all the involved people from RCU for their continuous logistic help and scientific cooperation. The laboratory tests were performed at the LAGIRN laboratory of the University of Bologna. We fully appreciate and thank the expert support by Eng. Barbara Ravaglia and Geol. Fausto Peddis in performing and interpreting the laboratory data.

REFERENCES

Boldini, D., Guido, G.L., Margottini, C. And Spizzichino D. 2017.Stability Analysis of a Large-Volume Block in the Historical Rock-Cut City of Vardzia (Georgia). Rock Mech Rock Eng. https://doi.org/10.1007/s00603-017-1299-7.

Bosworth W., 2015. Geological Evolution of the Red Sea: Historical Background, Review, and Synthesis. In Najeeb M.A. Rasul and Ian C.F. Stewart (eds.) The Red Sea. The Formation, Morphology, Oceanography and Environment of a Young Ocean Basin. Springer Verlag.

Burohappold Engineering (2019) Al Ula Water Resources Study. Report 1.2 Aquifer Status and Condition. Internal report.

Donal G., Hadley D., Elisabet M., Brouwers H., Thoma M., Bown S., 2020. Quaternary paleodunes, Arabian Gulf coast, Abu Dhabi Emirate: Age and paleoenvironmental evolution. BookQuaternary Deserts and Climatic Change, 1st Edition, First Published 1998, Imprint CRC Pres, pages 17,eBook ISBN 9781003077862

Fnais, M. Al-Amri A., Abdelrahman K., E. Abdelmonem, S. El-Hady Seismicity and Seismotectonics of Jeddah-Makkah Region, West-Central Saudi Arabia J. Earth Sci., 26 (5) (2015), pp. 746–754, 10.1007/s12583-015-0587-y

ISRM (1978a) – Suggested methods for the quantitative description of discontinuities in rock masses. Int. Journ. Rock Mech. Min. Sci. & Geomech.

ISRM (1978b) – Suggested methods for determining hardness and abrasiveness of rocks. Int. Journ. Rock Mech. Min. Sci. & Geomech.

ISRM (1981) Suggested Methods for Determining Tensile Strength of Rock Materials. In: Brown, E.T., Ed., Suggested Method: Rock Characterization, Testing and Monitoring, Pergamon Press, Oxford, 211.

Margottini C., Spizzichino D., 2022.Weak rocks in the Mediterranean region and surroundings: Threats and mitigation strategies for selected rock-cut heritage sites, Engineering Geology,Volume 297, 106511,ISSN 0013-7952 https://doi.org/10.1016/j.enggeo.2021.106511.

Margottini C., Spizzichino D. 2021. Traditional Knowledge and Local Expertise in Landslide Risk Mitigation of World Heritages Sites. In: Sassa K., Mikoš M., Sassa S., Bobrowsky P.T., Takara K., Dang K. (eds) Understanding and Reducing Landslide Disaster Risk. WLF 2020. ICL Contribution to Landslide Disaster Risk Reduction. Springer, Cham. https://doi.org/10.1007/978-3-030-60196-6_34;

Ramsey B., C. 2020. OxCal. Available at: https://c14.arch.ox.ac.uk/oxcal.html (accessed 29 March 2021).

Donald G. & Hadly, G. (1987). Explanatory notes to the Geological map of the Sahl Al Matran Quadrangle, sheet 26 C, Kingdom of Saudi Arabia, pp,1–24.

Reimer, P.J. et al. 2020. The IntCal20 Northern Hemisphere radiocarbon age calibration curve (0–55 cal kBP). Radiocarbon 62: 725–57. https://doi.org/10.1017/RDC.2020.41.

D. Spizzichino, C. Margottini, V. Chiessi, and D. Boldini. 2016.Assessment of the stability conditions of a large-volume sandstone block in the northern sector of the Siq of Petra. Landslides and Engineered Slopes. Experience, Theory and Practice, pp.1851–1858

Thomas, H., Kennedy, M., Dalton, M., McMahon, J., Boyer, D., & Repper, R. (2021). The mustatils: Cult and monumentality in Neolithic north-western Arabia. Antiquity, 95(381), 605–626. doi:10.15184/aqy.2021.51.

Wahbi A. M. (2014) Sedimentological and stratigraphic studies of the cambro-ordovician succession in northwest Saudi Arabia. Master Thesis of King Fahd University of Petroleum & Minerals. Dhahran, Saudi Arabia.

SESSION 2: The knowledge: Investigation, monitoring and performance

Taylor & Francis
Taylor & Francis Group
http://taylorandfrancis.com

Geotechnical Engineering for the Preservation of Monuments and Historic Sites III – Lancellotta, Viggiani, Flora, de Silva & Mele (Eds)

Monitoring of the rock mass deformation under the Pont du Gard pier VII foundation

J.F. Serratrice
Cerema Méditerranée, Aix en Provence, France

ABSTRACT: The Pont du Gard is a Roman aqueduct bridge built around 50 AD to ensure the crossing of the Gardon river by an aqueduct supplying the city of Nîmes (France). Located between piles VII and VIII, the minor bed of the Gardon forms a deep channel whose possible instability of its flanks has long attracted attention. Two instrumented rock bolts were sealed in the rock foundation of the pier VII and were monitored for several years. This auscultation reveals some deformations of the rock under the effect of atmospheric temperature. But small events seem to be assigned to the variation of the water temperature during Gardon floods. The site, the instrumental set-up and the main results of the auscultation are described in this paper.

1 INTRODUCTION

Bridges are exposed to various flood-related risks such as scouring, hydrodynamic thrusts, impacts, accumulation of alluvial deposits or debris jams, which may cause damage to their structure or even their collapse. When they are founded on fractured or karstified rock masses, the risk increases with the presence of water circulation and water pressures which are likely to cause deformations or instabilities in their foundations. Among the environmental factors, atmospheric temperature plays an important role in these phenomena. Many studies have been devoted to the observation of rock slopes and cliffs exposed to climatic stresses. In many cases, temperature measurements are part of a larger monitoring plan that aims to provide information for the analysis of rock deformations and instabilities (Hasler et al. 2011; Jenkins & Smith 1990; Magnin et al. 2015; Moreno & Froese 2007; Taboada et al. 2017; Warren et al. 2014).

The daily temperature variations are likely to cause an accumulation of permanent displacements around the discontinuities in the rock mass and gradually lead to the triggering of instability (Gunzburger et al. 2005; Marmoni et al. 2020; Merrien-Soukatchoff & Gasc-Barbier 2017). This process of progressive failure under the effect of subdiurnal, diurnal and seasonal temperature variations has often been mentioned in the literature, but it remains difficult to describe quantitatively (Amaral Vargas et al. 2013; Bakun-Mazor et al. 2013; Collins et al. 2016; Fiorucci et al. 2018; Hall 1999; Moore et al. 2011; Moreno & Froese 2012; Mufundirwa et al. 2011; Pasten et al. 2015; Racek et al. 2021; Read et al. 2013).

As in rocky masses, structural problems related to temperature variations are also encountered in stone masonry buildings. A wide variety of situations can be found (Blasi & Coïsson 2008). Through their thermo-mechanical effects, temperature variations are likely to degrade remarkable sites constituted or supported by rock masses. This concerns natural sites (Greif et al. 2017; Villarraga et al. 2017; Vlcko et al. 2014) or historical sites (Bakun-Mazor et al. 2013; Delmonaco et al. 2017; Greif et al. 2006; Vlcko et al. 2009).

Numerous observations have shown the significant influence of water circulation on temperature in rock masses. These observations are reported at all scales, from the local scale of discontinuities

DOI 10.1201/9781003308867-32

to intermediate scales (aquifers, faults, karst networks) or the regional scale (hydrothermalism) (Anderson 2005; Klepikova et al. 2014; Read et al. 2013). Karst terrains offer a privileged context for thermal exchanges between water in transit and the rock, but also between air and rock (Luetscher 2004; Magne 2017; O'Driscoll & DeWalle 2006). Moore et al. (2011) show the impact of air and water circulation in open and deep discontinuities in a rock mass.

Finally, last topic, rivers temperature depends on a multitude of factors, including recharge conditions, meteorological factors, catchment area properties, hydraulic characteristics of the bed, groundwater exchanges, etc. (Cassie 2006). Overall, water temperature more or less follows the atmospheric temperature in its seasonal and even diurnal variations. Among the questions is the influence of precipitation and flooding on water temperature. This effect has been known for a long time (Kobayashi et al. 1999), but its experimental study is recent (Brown & Hannah 2007; Hayashi et al. 2013; Subehi et al. 2010; Zeiger & Hubbart 2015; among others). Here too, many factors are involved and situations are diverse.

Like many ancient structures built on rivers, the Pont du Gard is faced with the various problems mentioned above. During a project to strengthen the rock foundation of one of its piers, an instrumental device was set up to observe the behaviour of this rock mass over time. The paper presents some results of this experiment. It begins with a brief description of the site and its geological and environmental conditions. The context of the instrumentation is discussed. The main characteristics of the monitoring device are then presented. More details are given in Serratrice (2020).

2 THE SITE AND ENVIRONMENTAL CONDITIONS

2.1 *The site*

The Pont du Gard is built at the mouth of the Gardon gorges, at the south-eastern end of a vast Barremian limestone complex with an Urgonian facies. A road bridge was added to the bridge-aqueduct in 1743 (Pont Pitot). The two adjoining bridges are founded on a limestone entablature indented by a narrow channel in which the minor bed of the Gardon flows. This channel is spanned by the arch carried by piers VII on the right bank and VIII on the left bank, 24.5 m wide (Figure 1).

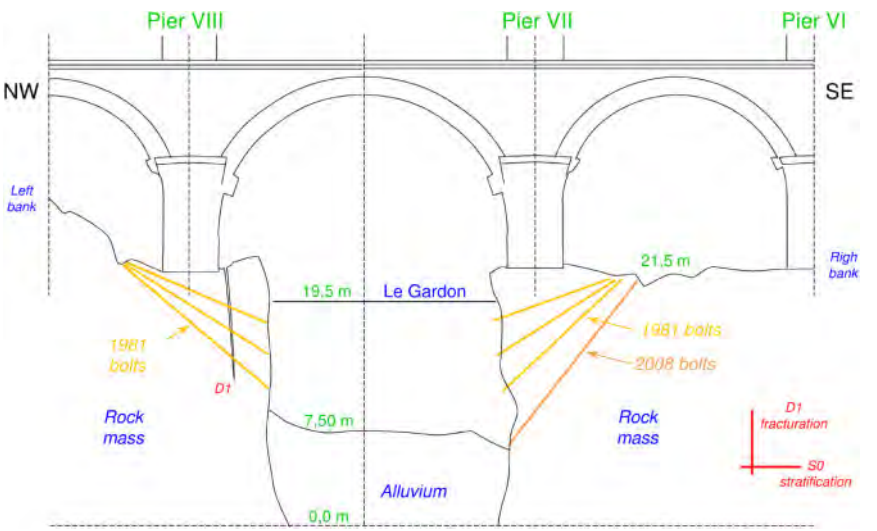

Figure 1. Schematic profile of the rock mass under the foundations of piers VI, VII and VIII. Principe of reinforcement by bolting. The direction of the two main families of discontinuities are indicated in red. View from upstream to downstream.

Although the limestone is present in large banks, forming a compact, homogeneous and resistant mass, the rocky foundations of piers VII and VIII have been the source of many questions for nearly a century. The problem is due to the particular morphology of these masses, whose subvertical or even overhanging flanks plunge to a depth of nearly twenty-five meters below the foundation level. The channel receives a variable height of alluvial deposits, the top of which changes according to the violent floods that characterize the Gardon river. Above alluvium and at low water, the height of the water varies from ten to fifteen meters in the channel.

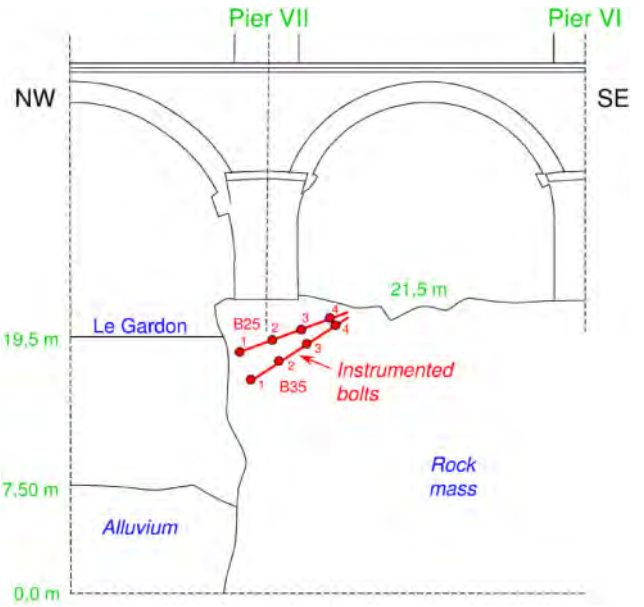

Figure 2. Principle of the implantation of the two instrumented bolts B25 and B35.

In the site, the stratification of the limestones is subhorizontal. The massif is cut by a main family of discontinuities sub-parallel to the sides of the channel. This N040 directional incision constitutes a major fractured corridor, which coincides with the direction of the large regional faults in the area. As observed throughout the Gardon gorges, the Urgonian limestones are the seat of a marked karstic network. Thus, the massive slab that constitutes the entablature on the right bank reveals karstic cavities. Then, approaching the minor bed, the slab is crossed by numerous discontinuities of direction N040, which constitutes an apparently well cemented ancient crushing zone, with no evidence of recent movements. Similarly, the dissolution patterns become more pronounced as one approaches the channel, on the walls of which cavities of multi-decimetre to multi-metre size appear. Various indications show that the digging of the canyon and part of the karstic cavities predates the Miocene transgression (−23 Ma). On the left bank of the channel, which supports pier VIII, the Urgonian mass appears less fractured, while retaining its karstified character.

The aqueduct-bridge and the road bridge are built using Miocene shell limestone (molasse) extracted from a nearby quarry. The vertical load carried by pier VII, common to both structures, is estimated at 82.9 MN.

2.2 *History of the works*

Historically, the questions raised by the foundation blocks of piers VII and VIII were revealed progressively as a result of the subaquatic investigations carried out since the 1930s. It became apparent that the walls of the channel are cut by metric cavities forming overhangs, particularly

under pier VII, and giving rise to fears of possible destabilization of these rock supports. Thus, an initial hypothesis suggested a possible weakening of the massif by dissolution of the rock and progression of karstic activity. These fears motivated the protection work of the rock masses, planned as early as 1938 and carried out in 1949, to fight against the erosion of the Gardon, considered at the time as the main agent of degradation of the rock. After selection from several technical solutions, this protection consisted of a facing of stacked and joined concrete bags acting as a cofferdam.

Very quickly, the protection of the sides of the channel was damaged by the floods of the Gardon river. The heavy floods of 1958 and 2002 reactivated these fears, prompting new studies and reinforcement work of the rock foundations in 1981 and 2008.

The 1938 project launched the reconnaissance of the site. Investigations in the channel are carried out in an aquatic environment, which requires the use of specific means from a barge and the application of good practice for undertaking works in rivers. These investigations, like the surveys from the riverside and the works, call for the adoption of strict measures to respect the conservation rules of this classified site and the environmental rules that apply to it. These investigations include underwater visits to inspect the rock faces and known karst cavities visible in the flanks. These visits are accompanied by bathymetric surveys of the alluvial floor. Profiles of submerged rock faces have been carried out also. However, due to a lack of precision, the techniques used did not allow the erosion of the walls to be observed. Geotechnical investigations were carried out by means of destructive drilling or core drilling to assess the thickness of the alluvium and to detect the roof of the bedrock.

The 1981 and 2008 reinforcements were carried out by means of bolting and were designed to resist various failure mechanisms made possible by the structural configuration of the rock mass and the presence of cavities. The work consisted of setting three beds of nine radial bolts under each of the foundations of piers VII and VIII (Figure 1). An addition to the 1981 reinforcement was made in 2008 under Pile VII, consisting of a line of twelve inclined and deeper bolts.

The inclined boreholes were drilled from the bank. Drilling rate parameters were recorded to identify the position of discontinuities and cavities in the rock prior to bolt installation. In 2008, this data was supplemented by optical imaging of the borehole walls. The bolts are 38 mm diameter, very high yield strength steel bars. Their lower ends open into the river and they are bolted at both ends, slightly pretensioned, and then grouted in a geotextile liner. Strict instructions for drilling and grouting are applied to guarantee the quality of the bolting, to avoid clogging the karstic network, to avoid loss of fluids to the Gardon river and to respect predefined technical criteria (volumes injected and grout pressures).

The 2008 works provided an opportunity to install a monitoring device in the foundation rock of pile VII. This device consists of two inclined bolts, instrumented and sealed in boreholes, a temperature probe and a measurement chain. The instrumented bolts are located in the 1981 bolt array under the aqueduct-bridge. The temperature probe and the chain are located in a box which is embedded in the rock on the surface of the bank.

2.3 *Environmental data*

These environmental data mainly concern atmospheric temperatures and flooding of the Gardon river. They come from different sources.

The graph in Figure 3 shows the temperatures recorded in the box by the probe during the period from November 2013 to May 2017 (in red). The recording was interrupted a few times, due to malfunctions of the measurement chain or internal power supply failures. The graph shows a seasonal temperature trend with an amplitude of 10°C and diurnal variations with an amplitude of about 5°C. In order to confirm this seasonal trend, the average monthly minimum and maximum temperatures recorded at Vers Pont du Gard (http://www.linternaute.com) are plotted in blue. A comparison of the curves shows that, on average and apart from daily fluctuations, the temperature in the measuring box follows the seasonal variations. Only the highest peaks exceed the maximum monthly average in summer.

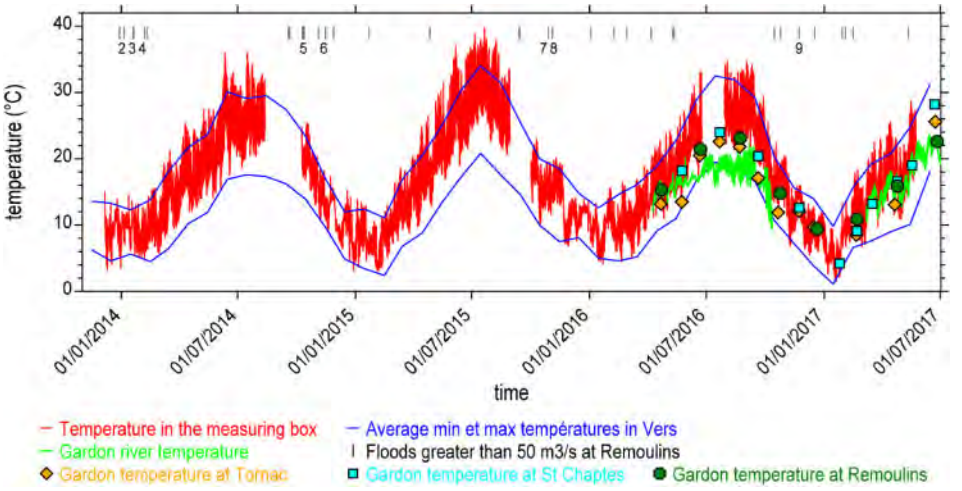

Figure 3. Temperature records in the measuring box, average monthly temperatures min and max in Vers Pont du Gard, Gardon water temperatures and occurrence of Gardon floods (flow rate higher than 50 m3/s). Period from November 2013 to May 2017.

Water temperature measurements of the Gardon river were downloaded from the Naïades database (EauFrance 2019; http://www.naiades.eaufrance.fr). The measurements come from various hydrological stations along the Gardon. A first data set gathers the temperatures measured in three stations since May 2016 (stations of Tornac, St Chaptes and Remoulins; one measurement per month approximately). Discrete in time, these measurements are represented by symbols in Figure 3. The second dataset gathers the continuous recordings made during the summer periods of 2016 and 2017. They are shown in green in Figure 3.

The overlap periods of the different sources of water temperature measurements are short, which makes it difficult to compare these data. Discrepancies appear between the "continuous" and "discrete" measured temperatures. These discrepancies are probably due to the fact that the sampling and measurement points do not strictly coincide. Nevertheless, except during the summer of 2016, all these measurements are in agreement with each other and they fall within the range of average atmospheric temperatures at Vers Pont du Gard (in blue). They clearly mark the seasons with an amplitude of about 10°C. A comparison of the "discrete" measurements from the three stations shows more damped seasonal variations at Remoulins, the downstream station (the extreme values are lower there). The temperatures recorded in the measurement box are higher in summer (in red). The daily fluctuations are smaller in the water (in green). These data are consistent with observations often reported in the literature.

The Gardon river has a Mediterranean-type regime with high waters in autumn and floods that can be very sudden and violent, such as that of 30 September 1958 and that of 8 September 2002 ("cevenol episodes"). In the period under consideration, the dates of occurrence of the Gardon floods were collected from the Banque Hydro (EauFrance 2018; http://www.hydro.eaufrance.fr) from two hydrometric stations located in Remoulins downstream of the aqueduct bridge. Indeed, the highest floods are most often observed in autumn and winter. The floods are marked by vertical lines on the graphs in Figure 3. Some of them are numbered from 2 to 9. The highest flood gave a discharge of 812 m^3/s during the monitoring period (maximum daily flows).

The available data show little overlap between the continuous measurements of water temperatures in the Gardon and the occurrence of floods. However, the comparison seems to indicate some events where floods are accompanied by a drop in water temperature. However, without additional meteorological data and a precise analysis, it is difficult to conclude on this point at this time.

3 AUSCULTATION OF THE ROCK FOUNDATION

3.1 *Extensometer monitoring device*

During the 2008 reinforcement project, an exploratory monitoring system was installed in the foundation rock of Pile VII of the aqueduct bridge. The device consists of two instrumented bolts named B25 and B35 (VW Rebar Strainmeter). Each of the bolts is composed of an assembly of four vibrating-wire sensors connected by steel bars. The lengths of these bars are chosen in order to distribute the transducers according the rock configuration and thus form a continuous assembly equivalent to an anchor bolt. These two bolts have a diameter of 28 mm and a length of approximately 11 m. They are inclined at 25° and 35° below the surface of the rock mass. The eight vibrating-wire sensors and the temperature probe are connected to the data logger and are placed in the box which is embedded in the rock not far from the heads of the two instrumented bolts.

3.2 *Installing the instrumented bolts*

The two instrumented bolts fit into the 1981 bolting scheme (Figures 1 and 2). Two inclined bores were previously drilled over a length of 11.5 m and a diameter of 165 mm. The boring was carried out using a pneumatic percussion drilling process and a down-hole hammer, like the boring for the 2008 reinforcement bolts. Rate of penetration (ROP) logs were recorded. They show a regular progression of the drill tool, of the order of 20 m/hour, interspersed with jumps of rapid speed which attest to the crossing of discontinuities or small karst cavities (Figure 4). Average speeds are faster

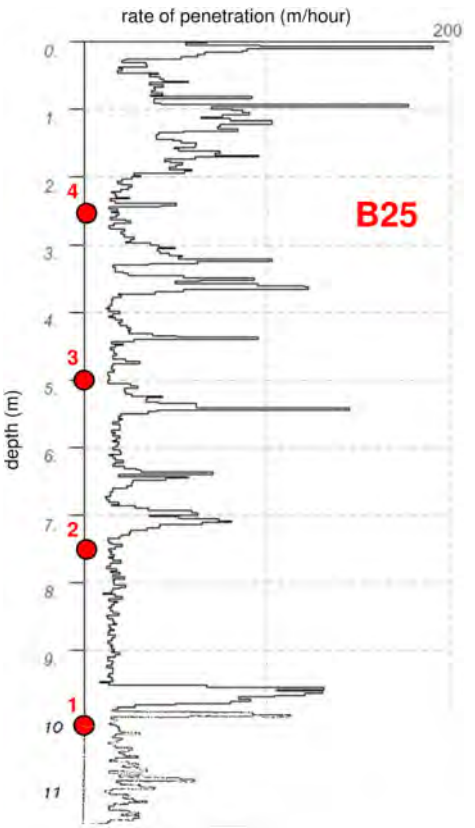

Figure 4. Drilling rate logging and positions of sensors in the borehole B25.

and more dispersed over the first two meters of the boreholes, in a more fractured region of the rock near the surface. An endoscopic survey is then carried out by optical imaging of the borehole walls using a high-resolution digital camera. In this way, it is possible to detect various lithological and structural features on the walls, in particular the rock discontinuities that run through them and whose orientation can be measured (azimuth, dip). These structural data are consistent with the surface observations (subhorizontal stratification and N040 discontinuities).

The instrumented bolts are assembled by adjusting the length of the intermediate steel bars so that the sensors are implanted in the solid rock, avoiding discontinuities and cavities, based on ROP recordings and borehole wall imaging. The measuring wires are tied to the bolt. The bolt is wrapped in a geotextile jacket separated into three successive sectors. Each sector is equipped with an injectable separator and its own injection cannula. After the bolt has been placed in its inclined borehole, the grouting is carried out with a pure cement grout (cement CEM III/B, dosage in the mass ratio cement to water C/E = 2). The three sectors of the jacket are injected successively from the deepest. The grouting is controlled according to predefined pressure and volume criteria already used for the reinforcement bolts. Conservation rules and environmental rules apply also. Monitoring of the response of the strain gauges is carried out at each stage of the process. At the end, the measuring wires are connected to the data logger.

3.3 *Evolution of measurements over time*

Figure 5 shows the microstrain measured by the four vibrating-wire sensors of the instrumented bolt B25 as a function of time between November 2013 and May 2017. The records cover the four annual cycles. In each bolt, sensor no. 1 is located at the end of the bar, i.e. close to the subvertical wall of the rock mass on the Gardon side (curves represented in red on the graphs), while sensor no. 4 is located 2.5 m from the head of the bolt, i.e. at a shallow depth below the rock surface and above the level of the Gardon at low water (curves represented in blue on the graphs). The vertical lines marking the occurrence of floods are indicated on the graphs (average daily flows greater than 50 m^3/s).

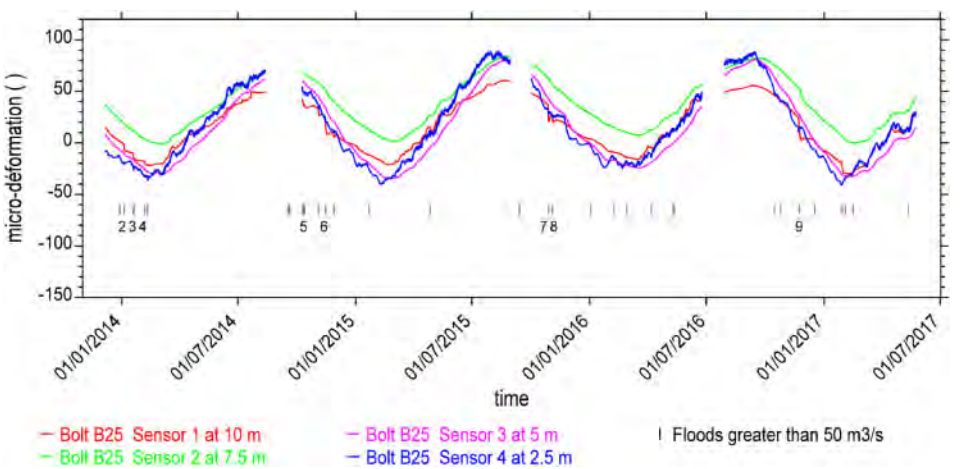

Figure 5. Monitoring in the period from November 2013 to May 2017. Sensors responses of instrumented bolt B25.

The responses of the two instrumented bolts are comparable to each other and correlate strongly with temperature variations, in the form of contraction in winter, counted negatively here, and expansion in summer, counted positively (Figure 3). For most sensors, these strain measurements vary in a band of about 100 μdef (double amplitude). The amplitude of the strains decreases

slightly from the head of the instrumented bolt to its tip (from sensor 4 to sensor 1). But, the strain measurements from the different sensors do not show a marked effect of depth in the rock mass.

Examination of the records also shows that small daily or weekly variations are shown by the responses of sensors No. 4 (blue curves) and, less randomly, by sensors No. 1 (red curves), Figure 5. On the contrary, the responses of sensors no. 2 and 3, which are located in the central part of the instrumented bolts, are smooth and essentially reflect seasonal variations (green and purple curves).

These small variations confirm the influence of temperature on the responses of the rock mass, which can be observed on the scale of seasonal variations. Thus, in the short term, the variations in the external temperature are first felt near the limits of the rock mass under the effect of: 1) the atmospheric conditions imposed on the upper surface of the ground for sensor no. 4 (blue curves); 2) and the conditions imposed by the water of the Gardon along the subvertical rock face which borders the channel for sensor no. 1 (red curves). These small temperature changes do not propagate deeply into the rock. The responses of sensors 2 and 3 appear slightly delayed compared to sensors 1 and 4 (Figure 5). As in all rock masses, the penetration of temperature into the rock is progressive and slow. This interpretation emphasises the effect of atmospheric temperature on the deformations of the rock mass. It ignores the presence of the bridges which, in reality, interact via the pile VII through their weight and their own thermal deformations.

These results are in agreement with the observations generally reported in the literature, which show that the temperature in the rock depends widely on the atmospheric temperature and that the penetration of the temperature in the rock is slow and mainly governed by seasonal variations. On the contrary, daily fluctuations with low amplitude are not very penetrating. When the strain measurements are plotted against temperature, hysteresis shapes appear showing that the deformations of the rock are retarded with respect to temperature, in accordance with the phase shifts observed during the annual cycles. According to the recorded measurements, the overall slopes of these curves average 4.7 10^{-6} /°C, which places them within the usual orders of magnitude for thermal dilatation coefficients of rocks.

3.4 *Influence of Gardon floods*

Examination of Figure 5 shows that small variations in the extensometric measurements coincide with the occurrence of floods in the Gardon, particularly among the floods numbered 2 to 9. This concerns the measurements made on the rock side of the Gardon, with sensors no. 1 (red) and no. 2 (green) of the two instrumented bolts, while sensors no. 3 (purple) and no. 4 (blue) seem insensitive or not very sensitive to these events. Such variations appear mainly in autumn and winter. They indicate a contraction of the rock mass. The amplitudes of these micro-deformations do not seem to be proportionally related to the flood flows. These contractions can be explained by a contribution of cold water during these particular floods of the Gardon.

The graphs in Figures 6 and 7 show the temperature and the microstrain measurements that were recorded during the six-month winter period from September 2016 to February 2017. Events such as Flood No. 9 and others result in rock contraction. The latter (of 23/11/2016) shows a typical signature of the effect of a flood with the responses of sensors No. 1 (red) and No. 2 (green). A sudden contraction occurs with the arrival of the flood peak. Then the microstrain stabilises or reverses until it returns to a regime in line with the seasonal variation. On the same graphs, an unnumbered event after event n° 9 shows a similar response (29/01/2017), while the seasonal contraction passes through its minimum.

Other changes occur in the absence of flooding. Spring floods are scarce and do not show a signature similar to those of autumn or winter floods. Finally, the micro-deformations that coincide with the Gardon floods come mainly from sensor no. 1 (red) of the two instrumented bolts B25 and B35 and, to a lesser extent, from sensor no. 2 (green). A reduction and a phase shift seem to occur as we move from the Gardon wall towards the rock mass. If the flooding of the Gardon was first manifested by a mechanical action on the rock mass of Pile VII, all sensors would have to react simultaneously, given the large size of Pile VII in comparison to its rock foundation. However, only the two sensors closest to the side wall of the rock mass (red) and the next two (green) react

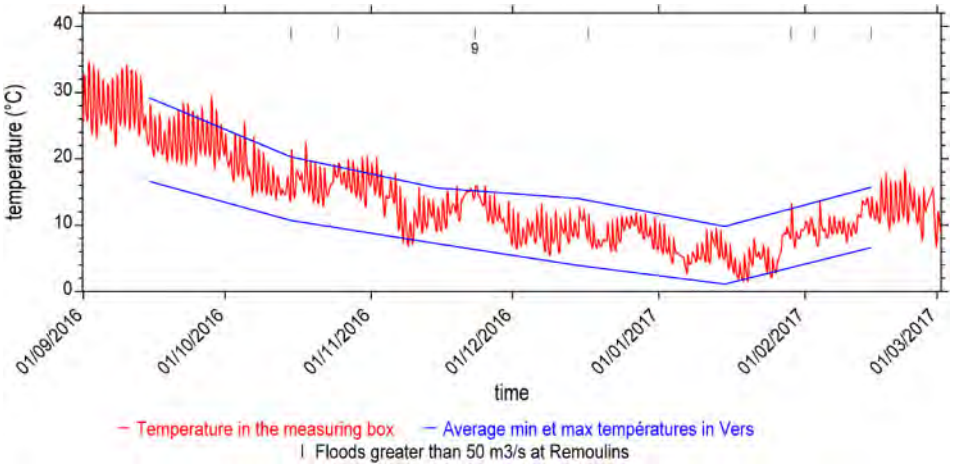

Figure 6. Monitoring in the period from November 2013 to May 2017. Temperature records in the measuring box, average monthly temperatures min and max in Vers Pont du Gard, Gardon water temperatures and occurrence of Gardon floods (flow rate higher than 50 m^3/s).

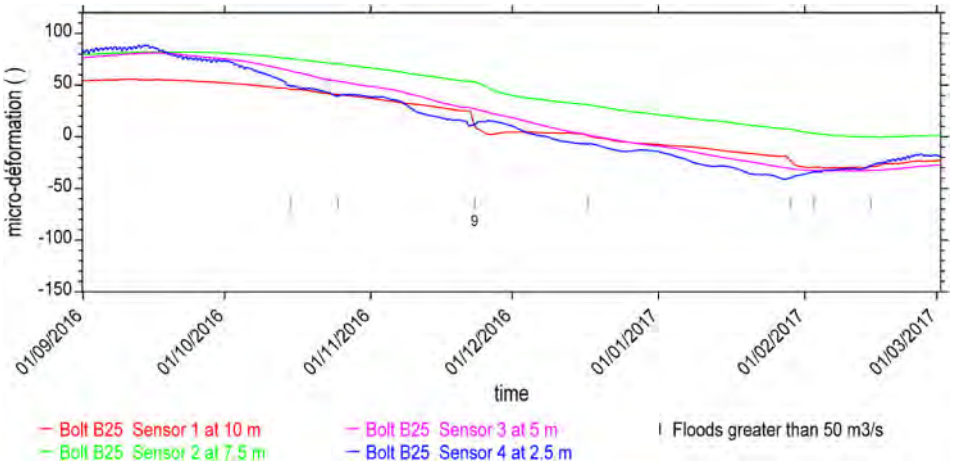

Figure 7. Monitoring in the period from September 2016 to February 2017. Sensors responses of instrumented bolt B25.

and show a gradient effect. Thus, the influence of temperature seems to be predominant, assuming that certain floods of the Gardon carry a thermal stress different from the atmospheric conditions at that time. Such observations are reported in the literature, as is their non-systematic character. These momentary deformations are reversible, with a rapid return to the seasonal regime.

3.5 *Modelling the deformation field in the rock mass*

A simplified model of the influence of temperature on the rock foundation of pier VII was carried out in a two-dimensional (2D) homogeneous domain. This domain is located in the axial plane of the aqueduct bridge where the instrumented bolts B25 and B35 were sealed. This quarter-infinite domain is delimited by the horizontal surface of the massif and by the vertical flank of the channel. The presence of pile VII is ignored. The water temperature of the Gardon river is assumed to

be equal to the atmospheric temperature during the harmonic solicitation which represents the seasonal variation (no diurnal variations). These temperature changes occur simultaneously on these two free boundaries with an amplitude of 10°C. Parameters representative of the behaviour of the Urgonian limestone are adopted. An analytical calculation is made to describe the evolution of the deformation field in the rock over the seasons (Serratrice 2020). The graph in Figure 8 shows the calculated deformations as a function of time along the instrumented bolt B25 during an annual cycle. The deformations at the deepest points in the massif lag behind the others and the amplitudes are smaller (points n° 2 and 3). On the contrary, the points located near the outer walls, in particular the vertical wall, are the most advanced and the most exposed to temperature changes (point n° 1, in red). The order of magnitude of the computed deformations agrees with the measurements provided by the extensometers.

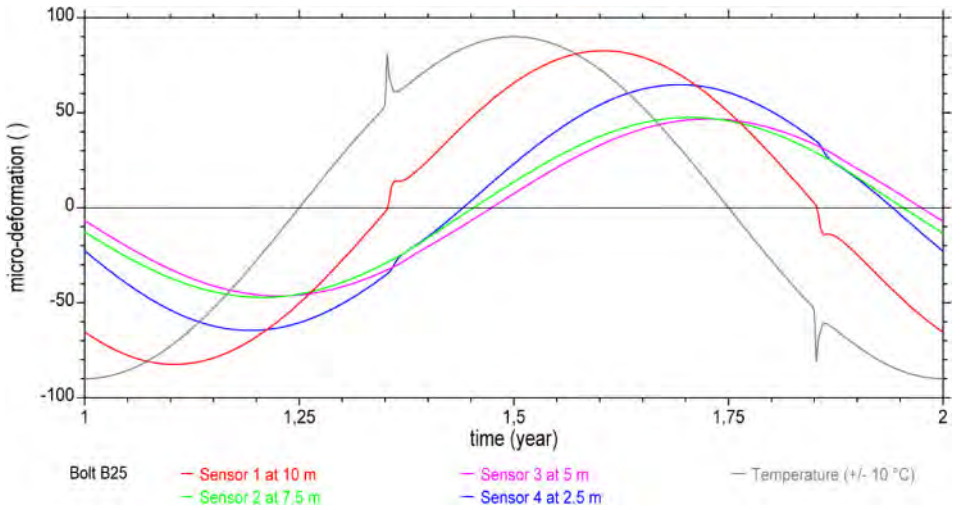

Figure 8. Temperatures calculation in the rock mass. Sine-shaped outside temperature with the superposition of a flood in spring and autum. Calculated responses of instrumented bolt B25.

The thermal effect of a flood of the Gardon in the rock mass is simulated by assuming that, during this episode, the temperature of the water is different from that of the air and that, because of its overflow out of the minor bed, the water flows on the two free faces of the domain. Thus, the thermal stress is represented by its harmonic component of 10°C amplitude, on which the thermal signal in the form of a hydrogram is superimposed. Two successive floods are simulated using a numerical calculation, the first in spring and the second in autumn. The heat input is positive with the spring flood (+3°C) and negative with the autumn flood (−3°C). The Figure 8 shows the thermal signal and the calculated response. It is clear that compared to the atmospheric temperature range of 10°C, only the points close to the surface of the rock mass are sensitive to the thermal effect of the flood (rock bolt points 1 and 4). It also appears that the two floods have a symmetrical effect, in accordance with the model assumptions. The return to the seasonal regime is quick. The calculation confirms that a large part of the observed deformations are explained by seasonal variations in temperature at the free boundaries of the rock mass. Similarly, it is possible to arrive at a representative estimate of the deformations recorded when the Gardon brings its own thermal stress during a flood.

4 CONCLUSION

In 2008, the reinforcement work on the rock foundation of pier VII of the Pont du Gard provided an opportunity to install an extensometer measurement device for exploratory purposes. Variations in

atmospheric temperature essentially explain the deformations that were recorded in the rock mass, with their seasonal and daily components. These records reflect observations often reported in the literature. Diurnal temperature variations do not penetrate the rock mass very much. Seasonal variations are felt at a depth of several metres. More original, small episodes of deformation are observed in autumn and winter, in concordance with floods of the Gardon. These variations essentially concern the sensors located near the subvertical rock face which borders the Gardon's minor bed, which leads us to suggest that certain floods of the Gardon carry a thermal solicitation within the karstified urgonian massif. This non-systematic character of the effect of floods echoes the observations in the literature. Simplified modeling of the effects of temperature in the rock mass results in a representative estimate of the deformations recorded during the monitoring under pier VII. This is true for seasonal cycles of atmospheric temperature and also when the Gardon river brings its own thermal signal during a flood. On the scale of this short period of monitoring, the instrumentation set up reveals the reversible nature of the deformations of the rock foundation of pier VII. These cycles represent a part of the loadings that apply to the structures.

REFERENCES

Amaral Vargas, E. Velloso, R.Q. Chavez, L.E. Gusmao, L. Amaral C.P. 2013. On the effect of thermally induced stresses in failures of some rock slopes in Rio de Janeiro, Brazil. *Rock Mechanics and Rock Engineering* 46(1): 123–134.

Anderson, M.P. 2005. Heat as a ground water tracer. *Ground Water* 43(6): 951–968.

Bakun-Mazor, D. Hatzor, Y.H. Glaser, S.D. Santamarina, J.C. 2013. Thermally vs. seismically induced block displacements in Masada rock slopes. *International Journal of Rock Mechanics and Mining Sciences* 61: 196–211.

Blasi, C. & Coïsson, E. 2008. The effects of temperature on historical stone masonry structures. *Structural Analysis of Historic Construction; Proc. 6th Int. Conf., Bath, UK,* 2, 1271–1276.

Brown, L.E. & Hannah, D.M. 2007. Alpine stream temperature response to storm events. *Journal of Hydrometeorology* 8: 952–967.

Cassie, D. 2006. The thermal regime of rivers: A review. *Freshwater Biology* 51(8):1389–1406.

Collins, B.D. & Stock, G.M. 2016. Rockfall triggering by cyclic thermal stressing of exfoliation fractures. *Nature Geoscience* 9: 295–400.

Delmonaco, G. Brini, M. Cesaro, G. 2017. Advanced monitoring systems for landslide risk reduction in the 'Siq' of Petra (Jordan). *Digital Workflows for Heritage Conservation; Proc. 26th Int. Symp. CIPA 2017, Ottawa, Canada*.

Fiorucci, M. Marmoni, G.M. Martino, S. Mazzanti, P. 2018. Thermal response of jointed rock masses inferred from infrared thermographic surveying (Acuto Test-Site, Italy). *Sensors* 18(7): 2221.

Greif, V. Sassa, K. Fukuoka, H. 2006. Failure mechanism in an extremely slow rock slide at Bitchu-Matsuyama castle site (Japan). *Landslides* 3(1): 22–38.

Greif, V. Brcek, M. Vlcko, J. Varilova, Z. Zvelebil, J. 2017. Thermomechanical behavior of Pravcicka Brana Rock Arch (Czech Republic). *Landslides* 14(4): 1441–1445.

Gunzburger, Y. Merrien-Soukatchoff, V. Guglielmi, Y. 2005. Influence of daily surface temperature fluctuations on rock slope stability: case study of the Rochers de Valabres slope (France). *International Journal of Rock Mechanics and Mining Sciences* 42(3): 331–349.

Hall, K. 1999. The role of thermal stress fatigue in the breakdown of rock in cold regions. *Geomorphology* 31(1–4): 47–63.

Hasler, A. Gruber, S. Haeberli, W. 2011. Temperature variability and offset in steep alpine rock and ice faces. *The Cryosphere* 5: 977–988.

Hayashi, H. Tasaki, M. Uchiyama, N. Morita, M. 2013. Water quality and pollution load during flood and non-flood periods in an urban tidal river. *Techniques et Stratégies Durables pour la Gestion des Eaux Urbaines par Temps de Pluie ; Actes 8éme Conf. Inter. NOVATECH 2013, Lyon, France*, 1–10.

Jenkins, K.A. & Smith B.J. 1990. Daytime rock surface temperature variability and its implications for mechanical rock weathering: Tenerife, Canary Islands. *Catena* 17:449–459.

Klepikova, M.V. Le Borgne, T. Bour, O. Gallagher, K. Hochreutener, R. Lavenant, N. 2014. Passive temperature tomography experiments to characterize transmissivity and connectivity of preferential flow paths in fractured media. *Journal of Hydrology* 512: 549–562.

Luetscher, M. Jeannin, P.Y. 2004. Temperature distribution in karst systems: the role of air and water fluxes. *Terra Nova* 16: 344–350.

Magne, L. Lecoq, N. Rodet, J. Chedeville, S. Viard, J.P. 2017. Evidence of daily and seasonal inversions of airflow in petites dales cave, Normandy, France. *Acta Carsologica* 46(2–3): 179–197.

Magnin, F. Deline, P. Ravanel, L. Noetzli, J. Pogliotti, P. 2015 Thermal characteristics of permafrost in the steep alpine rock walls of the Aiguille du Midi (Mont Blanc Massif, 3842 m a.s.l) . *The Cryosphere* 9: 109–121.

Marmoni, G.M. Fiorucci M. Grechi, G. Martino, S. 2020. Modelling of thermo-mechanical effects in a rock quarry wall induced by near-surface temperature fluctuations. *International Journal of Rock Mechanics and Mining Sciences* 134.

Merrien-Soukatchoff, V. & Gasc-Barbier, M. 2017. Consequences of daily and annual thermal cycles on fracture propagation and rock slopes stability. *Progressive Rock Failure; Proc. ISRM Conf., Ascona, Switzerland*, 12–14.

Moore, J.R. Gischig, V. Katterbach, M. Loew, S. 2011. Air circulation in deep fractures and the temperature field of an alpine rock slope. *Earth Surface Processes and Landforms* 36(15): 1985–1996.

Moreno, F. & Froese, C.R. 2007. Turtle Mountain Field Laboratory (TMFL): Part 2 – Review of Trends: 2003 to 2006. *Proc. 1st North American Landslide Conference, Vail, Colorado*.

Moreno, F. & Froese, C.R. 2012. Turtle Mountain Field Laboratory, Alberta (NTS 82G): 2010 Data and Activity Summary. Energy Resources Conservation Board/Alberta Geological Survey, ERCB/AGS Open File Report 2012–03.

Mufundirwa, A. Fujii, Y. Kodama, N. Kodama, J. 2011 Analysis of natural rock slope deformations under temperature variation: A Case Study from Japan. *Rock Slope Stability in Open Pit Mining and Civil Engineering; Proc. Int. Symp. Vancouver, Canada*.

O'Driscoll, M.A. & DeWalle, D.R. 2006. Stream–air temperature relations to classify stream-ground water interactions in a karst setting, central Pennsylvania, USA. *Journal of Hydrology* 329: 140–153.

Pasten, C. García, M. Cortes, D.D. 2015. Physical and numerical modelling of the thermally induced wedging mechanism. *Geotechnique Letters* 5(3): 186–190.

Racek, O. Blahut, J. Hartvich, F. 2021. Observation of the rock slope thermal regime, coupled with crack meter stability monitoring. Geoscientific Instrumentation Methods and Data Ststems, 2021.

Read, T. Bour, O. Bense, V. Le Borgne, T. Goderniaux, P. Klepikova M.V. Hochreutener, R. Lavenant, N. Boschero, V. 2013. Characterizing groundwater flow and heat transport in fractured rock using Fiber-Optic Distributed Temperature Sensing. *Geophysics Research Letter* 40: 2055–2059.

Serratrice, J.F. 2020. Suivi des déformations du massif rocheux sous la fondation de la pile VII du Pont du Gard. *Revue Française de Géotechnique* 2020, 164, 2

Subehi, L. Fukushima, T. Onda, Y. Mizugaki, S. Gomi, T. Kosugi, K. Hiramatsu, S. Kitahara, H. Kuraji, K. Terajima, T. (2010). The changes in steam water temperature and water quality parameters during rainfall events in forested watersheds: scaling of observations. *The Indonesian Journal of Geography* 42(2):159–180.

Taboada, A. Ginouvez, H. Renouf, M. Azemard, P. 2017. Landsliding generated by thermomechanical interactions between rock columns and wedging blocks: Study case from the Larzac Plateau (Southern France). *Powders and Grains Proc. 8th Inter. Conf. on Micromechanics on Granular Media, Montpellier, France*.

Villarraga, C. Vaunat, J. Gasc-Barbier, M. 2017. Modelling thermal induced damage in permeable rocks. *Proc. 9th workshop on code Bright*, Barcelone, Spain.

Vlcko, J. Greif, V. Grof, V. Jezny, M. Petro, L. Brcek, M. 2009. Rock displacement and thermal expansion study at historic heritage sites in Slovakia. Environmental. *Geology* 58(8): 1727–1740.

Vlcko, J. Brcek, M. Greif, V. 2014. Deformations dynamics in response to seasonal temperature oscillations: An example from Pravcicka Brana Rock Arch (Czech Republic). *Landslide Science for a Safer Geoenvironment* 3, 363–368.

Warren, J. Morgan, A.J. Chao, D.K. Froese, C.R. Wood, D.E. 2014. Turtle Mountain Field Laboratory, Alberta (NTS 82G): 2012 Data and Activity Summary. Alberta Energy Regulator, AER/AGS Open File Report 2014–09, 16 p.

Zeiger, S.J. Hubbart, J.A. 2015. Urban stormwater temperature surges: A central US watershed Study. *Hydrology* 2(4): 193–209.

Geotechnical Engineering for the Preservation of Monuments and Historic Sites III – Lancellotta, Viggiani, Flora, de Silva & Mele (Eds)

Seismic wave dispersion in high-rise historical building by interferometric analysis: The case history of Giotto's Bell Tower

G. Lacanna
University of Firenze, Firenze, Italy

R. Lancellotta
Politecnico of Torino, Torino, Italy

M. Ripepe
University of Firenze, Firenze, Italy

ABSTRACT: In recent years, the seismic interferometry for wave propagation analysis on high-rise building has been gaining increased interest for dynamic structural identification and health monitoring. The reason relies on the fact that dynamic identification analyses allow to observe the structure as it behaves under ambient excitations, without impairing the integrity of the structure, an aspect of paramount importance when dealing with historic heritage. In this context, the aim of this paper is to present and discuss tests performed on the Giotto bell tower in Florence, and in particular to show how seismic time histories recorded along the tower can be used to estimate the propagation velocity of seismic waves. These data are of value in detecting the mechanical properties of the structure, provided the dispersive nature of the wave is properly considered. As predicted by theoretical analysis, the obtained experimental evidences prove that this is the case of the Giotto's bell tower, especially in the bending mode of vibration, with a weak contribution from interaction with the soil.

1 INTRODUCTION

A prerequisite for devising appropriate stabilizing measures requires careful and long-term monitoring, in order to identify at least the causes of the movements of the structure interacting with the soil, their rate change with time and deviations from what may be thought a "physiological" behavior.

By considering the complexity of historic structures with all interventions operated along centuries; the unilateral behavior of masonry materials; the three-dimensional (3D) nature of the problem; the soil non linearity and its mechanical heterogeneity induced by the geostatic and applied stresses; the effectiveness of the soil contact along the vertical sides of the embedded foundation, there is a need to compliment analytical or numerical approaches by means of experimental evidences to validate the assumptions used in analysis and design.

By no means, the best way to reach this goal is to observe the structure as it behaves under dynamic excitations and this is the essence of the so-called dynamic identification analyses, that allow to estimate the natural frequencies of vibration, mode shapes and damping of the structure (Cadignani et al. 2019; Cosentini et al. 2015; Lacanna et al. 2016, 2019; Lancellotta & Sabia 2013, 2014; Macchi 1993; Snieder & Safak 2006; Todorovska 2009; Saisi & Gentile 2015).

In addition to these considerations, it must be outlined that the damage of historic building, produced by cracks or weathering of materials (Anzani et al. 2000; Binda et al. 1992; Ferretti & Bažant 2006a, 2006b) as well as non-linearity of the response of the structure related to the interaction with the soil, produces a decrease of stiffness that can be detected by changes of natural frequencies.

DOI 10.1201/9781003308867-33

In this context, this paper is aimed at presenting the dynamic tests performed on the Giotto's bell tower in Florence under environmental excitation, an investigation that offers the advantage of not impairing the integrity of the structure, an aspect of paramount importance when dealing with built heritage. In particular the results of seismic interferometry to detect the seismic wave velocity along the structure are discussed and it is investigated the dispersive nature of the phase wave velocity, when considering bending mode of vibration.

2 GIOTTO'S BELL TOWER AND DYNAMIC IDENTIFICATIONS TESTS

The construction of Giotto's bell tower started on 19 July 1334, as designed by Giotto di Bondone, at the time he succeeded Arnolfo di Cambio as Master of the Works of the Cathedral of Santa Maria del Fiore. Giotto was working on the campanile for just three years and when he died in 1337 only the lower floors with the external marble covering were completed (see Gurrieri 2015).

From 1337 to 1348 the construction was continued by Andrea Pisano who directed the works and rectified some deficiencies of the initial design of Giotto, by doubling the thickness of the walls at the lower levels. The original wall thickness at the base of only 1.60 m would not allow the tower to reach the planned height of about 85 m. After the interruption of the work in 1348, due to the Black Death, the bell tower was finished in 1359 by Francesco Talenti who built the last three levels: the two lower ones with coupled mullioned windows and the last one with the belfry open by three-mullioned windows with tympanum. The facades of the tower are enriched by a significant sculptural apparatus, with remarkable bas-reliefs, illustrating the Creation of Man and the Arts and Industries and niches with sculptures of Prophets and Sibyls (note that, because of atmospheric pollutions, the originals are all in the Museo dell'Opera del Duomo).

About the structure, the structural base section is approximately a square one with a side of about 13 m and a total thickness of the wall of about 3.3 m, as thought by Andrea Pisano. The original design of Giotto envisaged a spire to reach the height of 122 m, but Francesco Talenti did not build the spire and the actual height is about 84.7 m. The area of the resistant section at the base is 128 m^2, the radius of inertia r_i=4.26 m and the massive volume of the tower is 9300 m^3. The weight can be estimated of the order of 185.66 MN.

Thanks to the coring tests performed by CESI srl in 2006 at different level of the tower, it is today recognised that structural walls are of three-leaf type: two facing walls with internal filling material. The internal layer is composed of squared stones ("Pietraforte": a quartz-calcareous sandstone turbidite which was quarried in the near hill south of Firenze), with thicknesses ranging from 24 cm to 38 cm, and the internal part composed of stone aggregates from centimetric to decimetric in size and compact lime mortart. Even if the external face cannot be subjected to direct visual inspection, because it is covered by polychrome marbles, the photographic documentation related to past maintenance and replacement of some of the tiles, allowed to observe a well-organised and preserved brick masonry apparatus.

The foundation is constituted by a massive body of mortared stone, with a side of 15.17 m and a founding depth at 7.5 m. It is embedded into recent deposits of gravels and sands of the Arno river-bed and overbanks, overlaying the bedrock (actually an alternation of shales and limestone with interbedded quartz-calcareous sandstone), which in the area of the Cathedral and Giotto's bell tower is found about 18 m below the ground. The groundwater level is 6 m below the ground datum (Ghinelli & Vannucchi 1991; Ripepe et al. 2015).

The dynamic records were carried out for 36 hours, from October 16, 2013 to October 18, 2013, by using 10 seismic stations (Figure 1), located on five different floors from the ground level up to the roof. In particular, five stations were installed on the north side (C02-C04-C06-C08-C10), and the other five on the south side (C01-C03-C05-C07-C09) of the bell tower. Each seismic station was equipped with 3-component seismometers, as follows: six stations with Lennartz 3D/5s seismometers (sensitivity 400 V/m/s and with a 5 s eigen period); three stations with Guralp CMG-6T seismometer (sensitivity 2400 V/m/s with a 10 s eigen period), and one station with a Guralp CMG-40T seismometer (sensitivity 800 V/m/s with a 30 s eigen period). Seismic data were digitized using a 24-bit Guralp CMG24 Digitizer at 100 Hz, and time synchronization between

stations was achieved using GPS. Seismic monitoring provided an excellent set of data, which allowed to combine the results from Operational Modal Analysis (OMA) to seismic interferometry using the same ambient vibration noise. The Enhanced Frequency Domain Decomposition (EFDD) is a frequency domain technique for operational modal analysis of structures. In the present study, we performed an automatic EFDD method, first presented by Brincker et al. (2007) and further developed by Rainieri and Fabbrocino et al. (2010), to extract automatically the modal parameters of the structures.

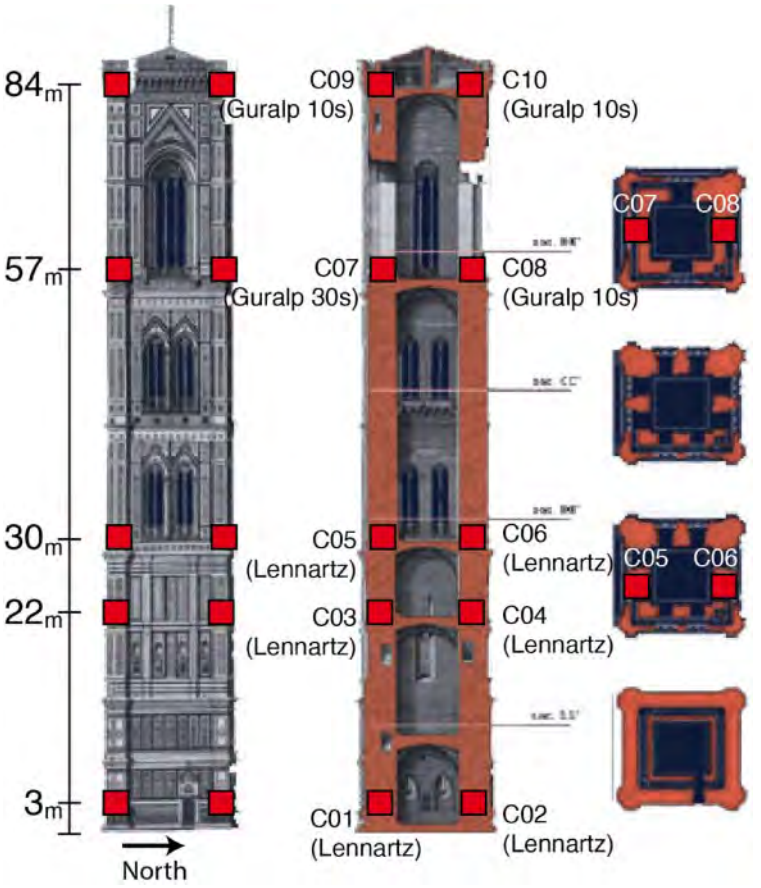

Figure 1. Giotto's Bell-Tower in Firenze (courtesy of "Opera di Santa Maria del Fiore") and related section in North-South direction, with location and height of ten seismic stations used for identification tests.

The 36 hours long records have been divided into time windows 1800 s long and overlapping by 66%, for each of them; the spectral estimation was performed using the Welch's technique with Hanning weighting function and frequency resolution of 0.0031 Hz. Additional details are reported in Lacanna et al. 2019.

The first six modes of the Giotto's Bell-Tower with natural frequency at 0.623 Hz, 0.647 Hz, 2.543 Hz, 3.081 Hz, 3.156 Hz and 5.731 (see Figure 2) were detected and it is relevant to note that the first modal shape is characterized by a motion trending 51°–231° N direction with a frequency of 0.623 Hz, whereas the second mode shape is transversal and trends 141°–321° N direction, with a frequency of 0.647 Hz. Therefore, Giotto's Bell Tower exhibits a coupled behavior in the first two modes acting along the longitudinal and transverse directions at frequencies very close to each other. The third mode is torsional with frequency of 2.543 Hz. The fourth and fifth modes

are instead bending modal shape at 3.081 Hz and 3.156 Hz, respectively. The sixth mode shows a bending modal shape at 5.731 Hz moving mainly in E-W direction.

3 SEISMIC INTERFEROMETRY

The ambient vibrations were also used to investigate the wave propagation with seismic interferometry, a technique based on the correlation of waves recorded at different receivers. If we consider two signals $u_1(\omega)$ and $u_2(\omega)$ in the frequency domain, and we assume $u_2(\omega)$ to be the input value, the Frequency Response Function (FRF) is defined as:

$$FRF(\omega) = u_1(\omega) / u_2(\omega) \tag{1}$$

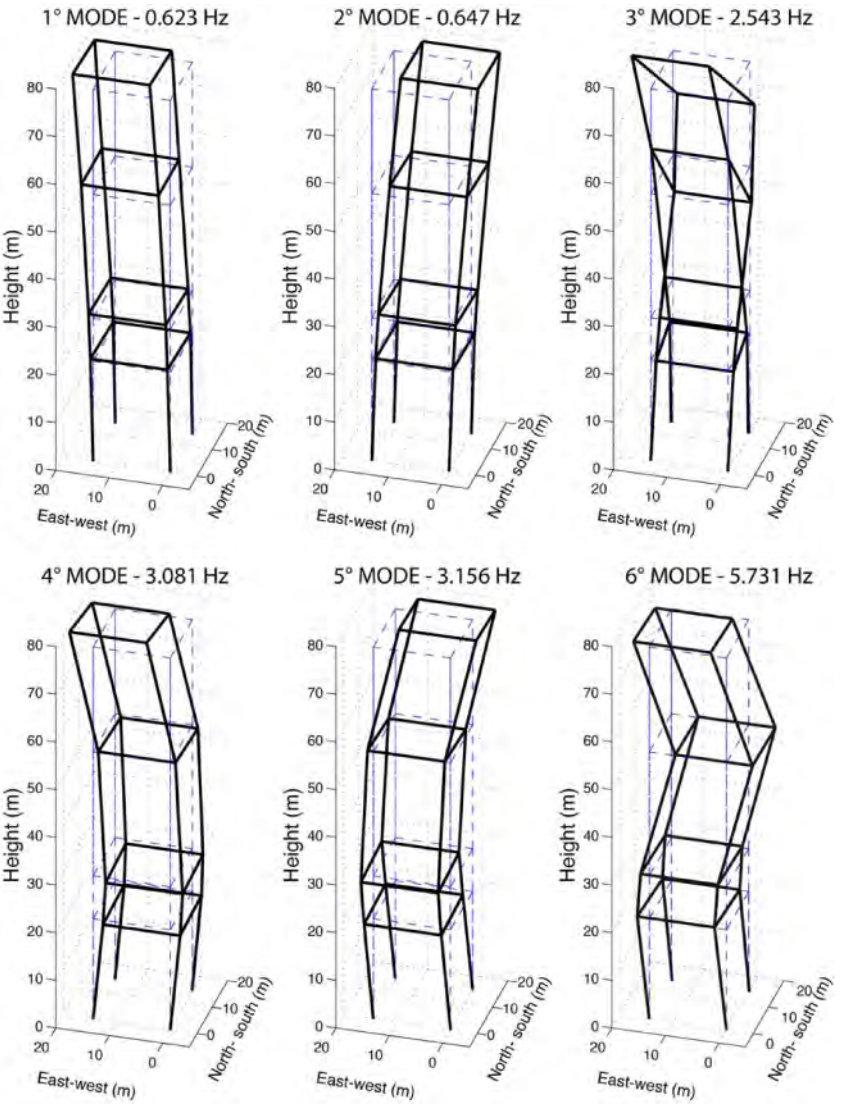

Figure 2. Three-dimensional representation of the first six modes.

Since the denominator of this expression goes to zero at the notches of the spectrum of u_2 (ω), to avoid the instability of (1) a convenient estimator of the FRF is the following:

$$FRF\ (\omega) = \frac{u_1(\omega)u_2^*(\omega)}{|u_2(\omega)|^2 + \varepsilon} \tag{2}$$

where the asterisk denotes the complex conjugation and ε is a parameter that is usually set to 0.5% of the average spectral power.

Then, the Impulse Response Function (IRF), i.e. the inverse Fourier Transform of (2), gives the response to an impulse applied at the reference point, since it can be observed that, because at input level the FRF is equal to 1, its inverse Fourier Transform gives the Dirac delta.

In the present case, the IRF was stacked for the whole 36-h-long periods of observation (Figure 3 red line) and the procedure was applied to 1800-s-long records of ambient vibration using the signal recorded at the top floor as reference station (C10 for north side stations and C09 for south side stations, in Figure 1). The result in time domain are waves propagating up and down through the tower (see Figure 3 and also Snieder & Safak 2006), and we measured the arrival time of the downward-propagating waves by picking the maximum of these waves. The distance is measured relative to the position of the seismometer at the top floor.

A longitudinal wave characterizes the IRF along the vertical direction with a velocity of $V_c =$ 2040 m/s; the horizontal components was then used to estimate the flexural wave propagation velocity, that resulted to be the same in both horizontal components of motion ($V_{NS} = 478$ m/s Figure 3 b,e, and $V_{EW} = 478$ m/s Figure 3 c,f), provided that reference is made to the considered frequency, because of the dispersive nature of wave velocity when considering flexural modes of vibration, as discussed in the next paragraph.

Note that the obtained vertical velocity is of engineering interest for two reasons. First, it allows an estimation of the structural properties, by referring to the well-known relationship

$$Vc = \sqrt{\frac{E}{\rho}} \tag{3}$$

where E and ρ are the Young modulus and the density of the structure. Second, it enables to identify the lumped parameters to represent the soil response in soil-structure interaction. To this aim, let assume the structure as represented by a single degree of freedom system (SDOF), with the supporting soil response lumped into springs and dashpots. This model can be thought to represent the behavior of the tower in its fundamental mode of vibration.

This is equivalent to say that the reduced stiffness of the overall system (that takes into account the soil deformability) will be given by

$$\frac{1}{K_{syst}} = \frac{1}{K_s} + \frac{1}{K_x} + \frac{h^2}{K_r} \tag{4}$$

where K_s is the fixed base structure stiffness and h is the elevation of the centroid of the inertia forces. In the present case, the term linked to the translational stiffness K_x has a negligible effect if compared with the term K_r related to rocking; furthermore, by substituting the expressions of the complex impedance and rearranging the real and imaginary parts it can be proved that the following relationship holds

$$\frac{1}{f_{syst}^2} = \frac{1}{f_{fixed}^2} + \frac{1}{f_r^2} \tag{5}$$

Equation (5) offers the advantage of splitting the fundamental frequency of the flexible structure on deforming soil f_{syst} into two contribution: f_{fixed} is the fundamental frequency of the structure on fixed base; f_r is the rocking frequency of the rigid-body structure interacting with the soil.

Therefore, if identification analyses allow the knowledge of f_{syst} and f_{fixed} is estimated by means of numerical models or by using the theoretical solution of bending vibrations of a cantilever beam.

$$f_{fixed} = 0.560 \cdot \frac{r_i}{h^2}\sqrt{\frac{E}{\rho}} \tag{6}$$

where r_i is the inertia radius of the cross section and $\sqrt{E/\rho}$ is the apparent longitudinal wave velocity, then the value of f_r can be inferred and the impedance functions can be properly estimated.

In the present case, by considering that the fixed base frequency is equal to 0.70 Hz and comparing this value with the first mode measured frequencies, it is apparent that the contribution of soil-structure interaction is the order of 10%, as it could be expected by considering that the supporting soil is characterized by a rather high shear wave velocity of about 380 m/s.

Furthermore, the value of $f_r = 1.36$ Hz can be conveniently used to validate the analytical relationship used to compute the rocking stiffness ($K_r = 2278\ GN \cdot m/rad$) to be used in advanced seismic analyses.

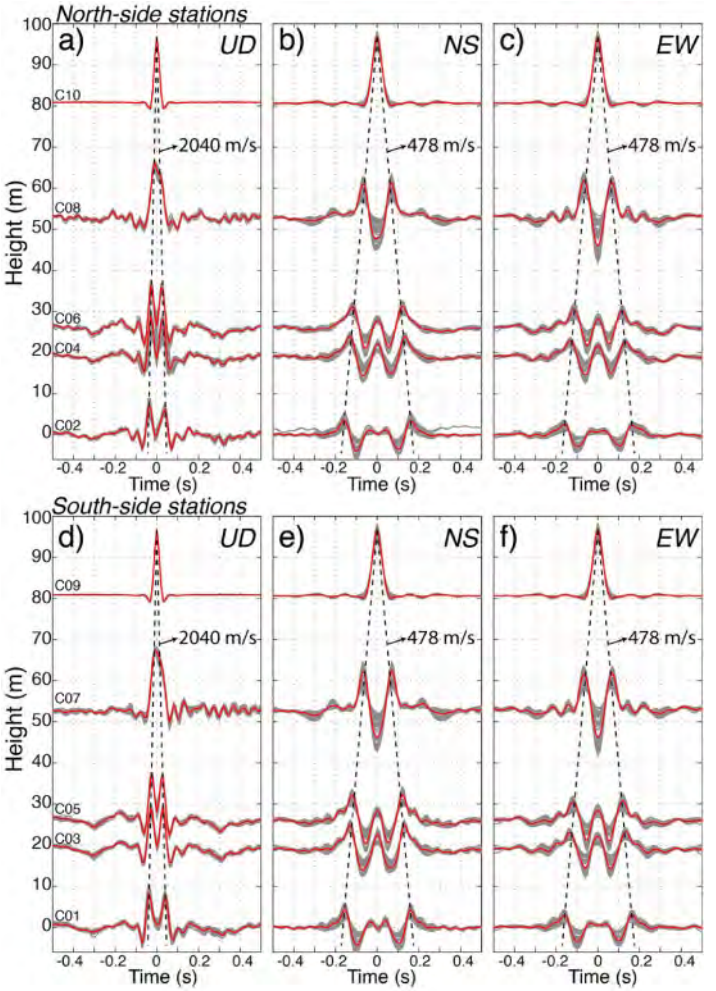

Figure 3. Waveforms deconvolved with the motion of the top floor, computed for all the observation time (36 hours) and filtered in broad band frequency of 0.2–20 Hz. The red lines indicate the total IRF stacking for each station and component.

4 THE DISPERSION OF FLEXURAL WAVE PROPAGATION

The dispersion character of the flexural wave propagation velocity is well known in structural mechanics, and the relevant results can be briefly recalled as follows (Fung 1965; Graff 1975; Timoshenko 1928).

When reference is made to the Bernoulli-Euler hypothesis that plane sections remain plane during lateral vibrations, it is shown that the phase velocity increases without limit for increasing wave-number or very large frequencies. Furthermore, instantaneous far field response is being predicted, as result from infinite phase velocity. This limitation of the Bernoulli-Euler theory was realized by Rayleigh in 1894, who introduced corrections for rotary inertia and obtained finite propagation velocity, even if the upper bound was still higher than predicted by the exact theory.

Thereafter, in 1921 Timoshenko included both effects of rotary inertia and effect of shear and obtained results in accord with exact theory and experimental evidence (Ebrahimian & Todorovska 2013; Michel & Guéguen 2018; Zemanek & Rudnick 1961).

The relevance of these studies does not need to be overstressed; however it must be observed that when dealing with historic structures, as it is the case under consideration, for the low range of frequencies usually involved in ambient vibrations or earthquake engineering both exact and elementary theories predict the same trend of flexural wave propagation velocity versus frequency, provided that the wavelength of the vibration mode is large if compared with the cross-sectional dimensions of the structure.

In the present case, a dispersion imaging technique has been performed on the IRF traces of the horizontal components (red line in Figure 3b, c, e, f), which is a tool to analyse wave velocity propagation at different frequencies. IRF traces at different heights of the Giotto's bell tower have been processed as a common multi-offset record by a dispersion imaging technique commonly used for active seismic surveys under the assumption for plane wave propagation (Park et al. 1998). At each frequency, the wave fields present in all traces traveling with a selected phase velocity are summed up. This operation produces a so-called dispersion image or dispersion spectrum by time shifting the frequency of the Fourier transform of each IRF by the corresponding delay at each height in the building. The procedure consists in an initial calculation of the time-frequency Fourier transform $\mathcal{F}_{z_j}(\omega)$ of each j^{th} IRF trace at height z_j.

A phase-shift $\omega = -i\omega\Delta t_j = -i\omega z_j/c$ is applied to the Fourier transform of the j^{th} IRF trace before summation, for each scanning phase velocity c. Then, the relative spectral power $\mathrm{E}(\omega, c)$ is calculated as

$$\mathrm{E}(\omega, c) = \sum_{1}^{j} \mathcal{F}_{z_j}(\omega) \cdot exp\left(-i\omega z_j/c\right) \tag{7}$$

For each angular frequency ω, each scanning phase velocity c and with $j = 5$ number of stations for each side. No whitening or offset-dependent normalization is applied in this study. The validity domain of the frequency – wavenumber analysis is marked by the λ_{min} and λ_{max} values. In applied geophysics for surface-wave dispersion analysis, these values are related to the length of seismic array and the interstation distance. In our case, we consider λ_{min} to be twice the lower inter-station distance and λ_{max} twice the building height (Gueguén et al. 2019), that is $\lambda_{min} = 16$ m and $\lambda_{max} = 168$ m.

Figure 4 shows the processed dispersion image for the IRF traces of horizontal components for the stations installed in the North Side (Figure 4a,c) and in the South Side (Figure 4b,d), the blue dashed lines indicate the seismic wave velocity of 478 m/s (Figure 3) whereas the red lines represent the experimental dispersive curve estimated from the maximum values for each frequency of dispersion image.

The dispersion images for both horizontals component and for North-side (Figure 4 a,c) and South-side stations (Figure 4 b,d) are similar between them, indicating an homogeneous dynamic behaviour of the Giotto's bell tower in the horizontal directions.

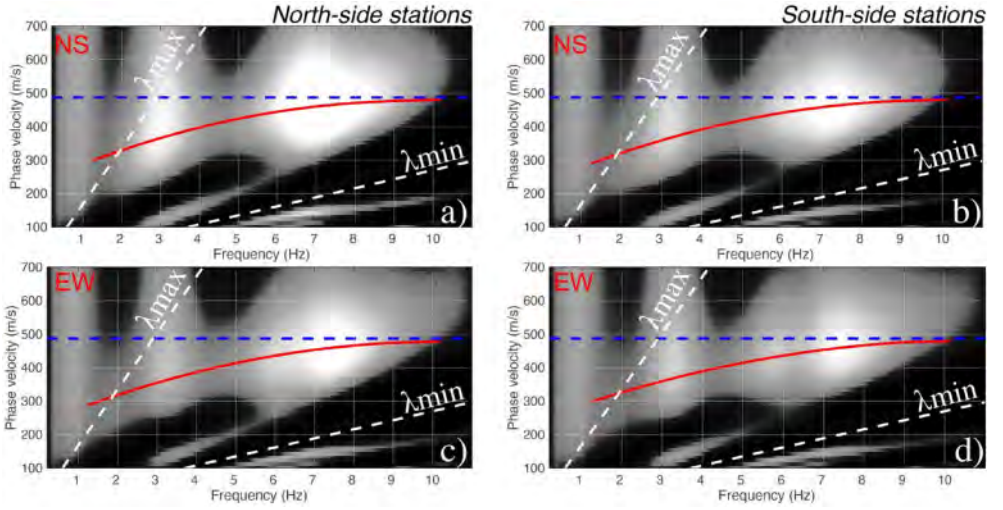

Figure 4. Dispersion images for IRFs signal of a, b) NS components recorded at stations installed on the North and South side, respectively. c, d) EW components recorded at stations installed on the North and South side, respectively. White dashed lines represent the validity domain of the dispersion curves marked by the λ_{min} and λ_{max} values. The dashed blue lines indicate the seismic wave velocity obtained by seismic interferometry by deconvolution (with asymptotic values of $V_{NS} = 478$ m/s and $V_{EW} = 478$ m/s).

5 FINAL REMARKS

Recent earthquakes event in Italy (May 2012) have once again put into evidence the seismic vulnerability of the cultural heritage and there were many cases showing the role played by the soil-structure interaction.

Taking into account this interaction is not a straightforward task, even when using a simplified lumped parameters model, because the selection of soil modulus requires to consider many aspects: soil non linearity, dependence on stress level induced by the structure, effectiveness of the contact between the foundation and the surrounding soil, dependence on the exciting frequency.

In this respect, identification analysis is certainly the most powerful approach to characterize the behavior of the structure interacting with the soil and to properly define the properties of simplified lumped models, that can be used to forecast the response of the structure.

The present paper focused on these aspects by using seismic interferometric analysis of experimental seismic time histories on the Giotto bell tower. The obtained results allowed to define the natural frequencies of vibration, the mode shapes, the properties of the structures and to estimate the contribution of the interaction with the soil. In addition, it was analyzed the dispersive nature of wave velocity, when considering bending modes of vibration.

REFERENCES

Anzani A., Binda L., Mirabella Roberti G. (2000). The effect of heavy persistent actions into the behaviour of ancient masonry, *Mat. Struct., RILEM* 33, 228, 251–261.

Binda L., Gatti G., Mangano G., Poggi C., Sacchi Landriani G. (1992). The collapse of the Civic Tower of Pavia: a survey of the materials and structure, *Masonry International* 6 (1), 11–20.

Brincker R., P. Andersen and N. J. Jacobsen (2007). Automated Frequency Domain Decomposition for Operational Modal Analysis; *in Proceedings of the 25th SEM International Modal Analysis Conference*, *February* 19–22, Orlando, Florida, USA.

Cadignani R., Lancellotta R., Sabia D. (2019). The restoration of Ghirlandina Tower in Modena and the assessment of soil-structure interaction by means of dynamic identification techniques. CRC Press, *Taylor&Francis Group*, London, 144 pp.

Cosentini R.M., Foti S., Lancellotta R. and Sabia D. (2015) Dynamic behaviour of shallow founded historic towers: validation of simplified approaches for seismic analyses, *International Journal of Geotechnical Engineering*, 9(1): 13–29.

Ebrahimian, M., and M. I. Todorovska (2013). Wave propagation in a Timoshenko beam building model, *J. Eng. Mech.* 140, no. 5, 04014018.

Ferretti, D., and Z. P. Bažant (2006a). Stability of ancient masonry towers: Moisture diffusion, carbonation and size effect. *Cement and Concrete Research 36:1379–1388*.

Ferretti, D., and Z. P. Bažant (2006b). Stability of ancient masonry towers: Stress redistribution due to drying, carbonation, and creep. *Cement and Concrete Research* 36:1389–1398.

Fung Y. C. (1965). Fundations of solid mechanics. Prentice-Hall, N.J., 525 pp.

Ghinelli A., Vannucchi G. (1991). Condizioni stratigrafiche e fondazioni della zona absidale di Santa Maria del Fiore in Firenze. *Bollettino Ingegneri*, 1–2.

Gueìguen P, Mercerat E.D., and Felipe Alarcon (2019). Parametric Study on the Interpretation of Wave Velocity Obtained by Seismic Interferometry in Beam-Like Buildings. *Bulletin of the Seismological Society of America. doi: 10.1785/0120190054*.

Gurrieri F. (2015). Il Campanile di Giotto. Atti del ciclo di conferenze, *Centro Arte Cultura, maggio-giugno, Mandragora*.

Graff K.F. (1975). Wave motion in elastic solids. *Dover Publications*, N.Y., 649 pp.

Lacanna G., M. Ripepe, E. Marchetti, M. Coli, C.A. Garzonio (2016). Dynamic response of the Baptistery of San Giovanni in Florence, Italy, based on ambient vibration test, *Journal of Cultural Heritage, 2016*, http://dx.doi.org/10.1016/j.culher.2016.02.007

Lacanna G., M. Ripepe, M. Coli, R. Genco, E. Marchetti (2019). Full structural dynamic response from ambient vibration of Giotto's bell tower in Firenze (Italy), using modal analysis and seismic interferometry, *NTD and E international,* 2019, 102, 9–15 http://doi.org/10.1016/j.ndteint.2018.11.002

Lancellotta R., Sabia D. (2013). The role of monitoring and identification techniques on the preservation of historic towers. Keynote Lecture, 2nd Int. *Symposium on Geotechnical Engineering for the Preservation of Monuments and Historic Sites*, Napoli, 57–74.

Lancellotta, R., Sabia, D. (2014). Identification technique for soil-structure analysis of the Ghirlandina tower. *International Journal of Architectural Heritage.* DOI. 10.1080/15583058.2013.793438.

Macchi G. (1993). Monitoring medieval structures in Pavia. *Structural Engineering International,* 1, 9–9.

Michel, C., and P. Gueìguen (2018). Interpretation of the velocity measured in buildings by seismic interferometry based on Timoshenko beam theory under weak and moderate motion, *Soil Dynam. Earthq. Eng.* 104, 131–142, doi: 10.1016/j.soildyn.2017.09.031.

Park, C., R. Miller, and J. Xia (1998). Imaging dispersion curves of surface waves on multi-channel record, *SEG Technical Program Expanded Abstracts,* 1377–1380, doi: 10.1190/1.1820161.

Rainieri C., G. Fabrocino, Automated output-only indentification of civil engineering structures, Mechanical *Systems and Signal Processing* 24 (2010) 678–695.

Ripepe M., Coli M., Lacanna G., Marchetti E., Cristofaro M. T., De Stefano M., Mariani V., Tanganelli M., Bianchini P. (2015). Dynamic response of the Giotto's Bell-Tower, Firenze, *Italy. Proc. Engineering Geology for Society and Territory, G. Lollino et al eds,* vol. 8, 323–327.

Saisi A., C. Gentile: Post-earthquake diagnostic investigation of a historic masonry tower. *Journal of Cultural Heritage* 16 (2015) 602–609, doi:10.1016/j.culher.2014.09.002.

Sneider R. and E. Safak (2006). Extracting the building response using seismic interferometry: Theory and application to the Millikan Library in Pasadena, California. *Bulletin of the Seismological Society of America,* Vol. 96, No. 2, pp.586–598.

Timoshenko S. P. (1921). On the correction for shear of the differential equation for transverse vibrations of prismatic bars. *Phil. Mag., Ser.* 6, 41, 744.

Timoshenko S.P. (1928). Vibration problems in engineering. Van Nostrand, New Jersey.

Todorovska, M.I. (2009). Seismic interferometry of a soil-structure interaction model with coupled horizontal and rocking response. *Bulletin of the Seismological Society of America,* Vol. 99, No. 2A, pp.611–625.

Zemanek J., Rudnick I. (1961). Attenuation and dispersion of elastic waves in a cylindrical bar. *J. Acoust. Soc. Am.* 33, 1283–88.

Geotechnical Engineering for the Preservation of Monuments and Historic Sites III – Lancellotta, Viggiani, Flora, de Silva & Mele (Eds)

Progress in digital documentation for historical sites by photogrammetry and recent technology

Y. Fujii & K. Takeuchi
Department of Civil Engineering, Meijo University, Nagoya, Japan

ABSTRACT: Documentation is a first step for the conservation of monuments and historical sites. Photogrammetry is a kind of the metric survey, and it has been applied to the many sites for the documentation. It has been developed in making topographic maps from aerial photographs historically. Stereo-photogrammetry can record the objects as three-dimensional (3-D) data. In this study, a few cases of digital photogrammetry with close-range photographs will be introduced. First Case is an earthen material in historical Buddhist monastery with a hand-held camera, second case is building stones which compose dry dock, and third case is artificial stone construction of lumberyard with quad-copter drone. UAV and SfM/MVS are very useful techniques for the documentation of monuments and historical sites.

1 INTRODUCTION

Documentation is a first step for the conservation of monuments and historical sites. In the field of Geo-technical engineering, the documentation has been focused on earthen materials and building stones, which compose the monuments and sites. There are some methods for the documentation of sites and monuments. It has been done by text, sketch, metric survey, photography and so on. Photogrammetry is a kind of the metric survey, and it has been developed in making topographic maps from aerial photographs historically. Stereo-photogrammetry can record the objects as three-dimensional (3-D) data. Around the 2000s, digital camera had been widespread all over the world and digital photogrammetry could be available. Using digital images, 3-D topographic models was able to be constructed in the computer with digital photogrammetric software. Around the 2010s, digital photography and computer vision technology had been combined and new technology had been created. It was called as Structure from Motion and Multi View Stereo (SfM/MVS).

Another progress is using unmanned aerial vehicle (UAV). Drone with quad-propellers is very popular all over the world now, and many aerial photographs have been applied to the historical sites with building stones and so on.

In this study, a few cases of digital photogrammetry will be introduced. First Case is an earthen material in historical Buddhist monastery (Fujii et al. 2009). Second case is building stones, which compose dry dock, by means of a hand-held camera (Fujii et al. 2018). In addition, third case is artificial stone construction of lumberyard by means of quad-copter drone.

2 PHOTOGRAMMETRY AND SFM/MVS TECHNIQU

Photogrammetry is the science that measures objects on photographs (Linder 2003). Obviously, one can only get two-dimensional co-ordinates from a single photo, as it is a two-dimensional plane, but if two photos of the same object are taken from different directions, a stereoscopic picture is formed and three-dimensional co-ordinates of the object can be calculated.

DOI 10.1201/9781003308867-34

A pair of analog stereo-photographs had been taken in the sites and 3-D topographic contours had been drawn with special equipment, such as stereo-plotter and analytical-plotter (Fujii & Hori 2004), before about year of 2000. The analytical-plotter was connected to a personal computer. And the computer was able to calculate ground co-ordination from photo co-ordination, and record the data of ground co-ordination. Historically, photogrammetry has been used to construct topographic maps from stereo-photographic pairs of aerial photographs. This technique could also be applied to close-range mapping with a hand-held camera (Atkinson 2003).

Around the 2000s, digital camera had been widespread all over the world and digital photogrammetry could be available. Using digital images, 3-D topographic models was able to be constructed in the computer with digital photogrammetric software.

Around the 2010s, digital photography and computer vision technology had been combined and new technology had been created. It was called as Structure from Motion and Multi View Stereo (SfM/MVS). Computer vision technology can be able to match the same points on multi-photographs automatically (Luhmann et al. 2014). Therefore, SfM/MVS makes us easier to make 3-D data from digital photographs, compare to classic photogrammetry.

3 APPLICATIONS TO THREE SITES

3.1 *The case of Ajina Tepa*

The monastery of Ajina Tepa Tajikistan, has been dated to between the 7th and 8th centuries AD and was excavated in the 1960s by Soviet archaeologists led by Boris Anatolevich Litvinskij (Litvinskij & Zejmal 2004). The site is entirely built of earth, part mud brick and part pakhsa (rammed earth, which is the compaction of earth between restraining surfaces or shutters). After the excavation, no appropriate preservation work was carried out and the site has deteriorated considerably as a result of weathering. The project 'Preservation of the Buddhist Monastery of Ajina Tepa, Tajikistan, which had been launched by the UNESCO/Japan Trust Fund in central Asia, started in 2005 and completed in 2008 (Fujii et al. 2009). The main objectives of the project were: the scientific documentation of the site; the establishment of a master plan for the site; the application of appropriate conservation and maintenance schemes; the development of promotional activities at both national and international level; and the training of people in the maintenance, conservation, and monitoring of earthen archaeological sites.

Photogrammetric survey had been applied to the site for the scientific documentation, and the total area had been documented as a 3-Dimenstional (3-D) surface model. 3DM Analyst, produced by ADAM Technology, had been sold by Kawaso Electric Industrial Co., Ltd. in Japan. This digital photogrammetric software could analyze a pair of stereo-photographs (Figure 1). Therefore, we took four pairs of stereo-photographs in which the stupa was taken from four directions, such as north, east, south, and west directions. After the 3-D point clouds had been generated from each

Figure 1. A pair of stereo-photographs of southwestern side of Stupa.

pair of stereo-photos (Figure 2). For making the total map of the site, 14 pairs of stereo-photographs were taken in the site of Ajina Tepa. These photographs almost cover the total area of Ajina Tepa. However, some areas in the photographs were hidden by high monument walls. For example, in a pair of overlapping photographs, which was taken from the top of the Stupa, some areas are hidden by the monument walls. Direct measurements were applied for the hidden areas with Total Station (metric survey equipment). Newly gained 3-D points were added into the photogrammetric data. Point clouds were combined and the 3D model (Figure 3) was generated by a software of Geographical Information System (GIS). Before 2010, it was difficult to operate UAV. In addition, it was the cases of remote area in which we had only limited equipment.

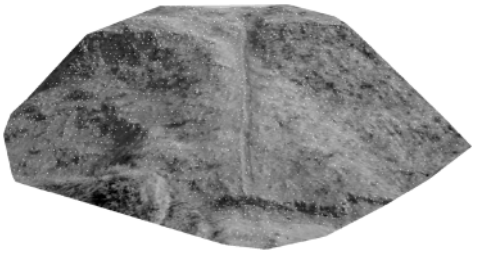

Figure 2. 3-D coordinate points on the southwestern side of Stupa. There are about 3000 points on the photographs.

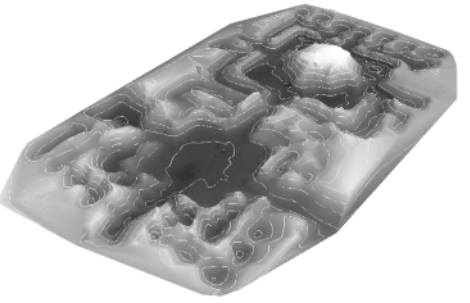

Figure 3. Perspective view of the site from east direction.

The survey results, 3D model (Figure 3) and mapping (Figure 4), had been useful for the establishment of a master plan for the site and the application of appropriate conservation and maintenance schemes. The site had successfully conserved with new mud bricks and mud plaster (Figure 5).

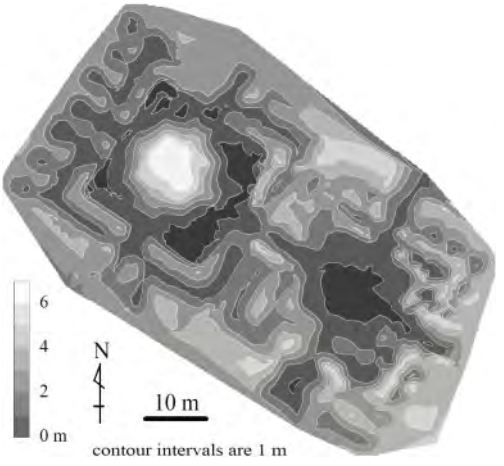

Figure 4. Total map of Ajina Tepa. The site is composed of two parts, northwestern stupa area and southeastern monastery area.

Figure 5. Chronological change of the site. Upper: 2006, Before conservation; Middle: 2007, During conservation; Low: 2008, After conservation.

3.2 *The case of Yokosuka Dry Dock*

The Yokosuka Arsenal dry dock No. 1 is the oldest stone dock in Japan constructed during 1867–1871. It is composed of natural building stones, which were carved out of Shin-Komatsuishi Quaternary andesite. Building stones were used at the site and outside the dock as the seawall. The dock withstood the 1923 Great Kanto earthquake, sustaining no serious damage. Dry dock No. 1 is still in use today, but the surfaces of the building stones have been weathered by seawater and winds (Fujii et al. 2015). In addition, water is leaking from the mortar between the building stones in some areas near the gate.

Photogrammetric documentation had been conducted in May, 2013 (Fujii et al. 2018). The control points (markers) were marked with black square stickers (90 × 90 mm) with a 30-mm white circle in the center attached to the wall of the dock. A single lens reflex (SLR) camera with a fixed focal-length lens (c = 35 mm) was used to take multiple 2D images of the dock. Images of the south wall were taken from the top of the north wall at 5 m intervals (B = 5 m). Images of the north wall were taken from the top of the south wall (Fig. 6). The distance from the camera to each wall ranged from 20 to 25 m (H = 22.5). Approximately fifty photographs were taken of each wall, creating a sequence of about 100 photographs.

Figure 6. 3-D point cloud of Yokosuka Dry dry dock No. 1 vied from the gate. Blue line merged squares show handheld camera positions.

Figure 7. Perspective view of the 3-D texture model viewed from southern direction. The size of the dock, the length 134 m, the width 30 m, and depth is about 9 m.

The ground sampling distance (GSD), which is the distance between each pixel center measured on the wall of the dock, is calculated as follows:

$$\sigma_{XY} = H/c \times \delta_{CCD} \quad (1)$$

The camera sensor has a resolution (δ_{CCD}) of 0.0079 mm. Therefore, GSD (σ_{XY}) is approximately 5 mm.

Table 1. Comparison between classic digital photogrammetry (CDP) and SfM/MVS software.

Specification	Number of Photos	Time for Analysis	RMS*	Set of control points
CDP	116 photos	about 5 days	10 mm	Manual
SfM/MVS	116 photos	about half a day	22 mm	Semi-automatic

*Camera calibration was conducted manually in CDP. It was simultaneously calculated during bundle adjustment in SfM/MVS.

The parameters for camera interior orientation and lens distortion were calculated using Topcon Image Master Calib software. Topcon Image Master Pro was used to generate the 3-D model of the site. Root Mean Square (RMS) of bundle adjustment is less than 10 mm (Fujii et al., 2018). It needed about 5 days to make the 3-D model.

About the 100 photographs and the coordinate of the control points has been still stored in a hard disk drive. Therefore, the same data has been analyzed by SfM/MVS software in 2021. Agisoft Metashpe has been used to generate the 3-D model of the site (Figure 6). RMS of bundle adjustment is about 22 mm. It needs about half a day to make the 3-D model. The parameters for camera interior orientation and lens distortion are calculated simultaneously when the bundle adjustment has been done. While, a half day is very reasonable compare to classic photogrammetric software analysis. A perspective view of the dock is shown in Figure 7. In addition, compared specification between classic photogrammetry and SfM/MVS is shown in table 1.

3.3 *The case of Doudo Lumberyard*

Doudo lumberyard is located along the Yahagi River in Toyota city, central Japan. This is very important, because it's the only underwater lumberyard build in the middle of the river in Japan. It had been constructed in 1918. However, it had not been used since 1930 due to the construction of a dam upstream of it. It had been buried and not done proper maintenance. In 1988, the structures were excavated and restored by the cultural properties division of Toyota city.

DouDo lumberyard has been mainly constructed with artificial stone. Artificial stone construction is a civil engineering method created by HATTORI Choshichi. This method is based on "TATAKI", a plastering technique traditionally used in Japan. The artificial stone was used for civil engineering constructions such as seawalls and embankments around 1900 before the spread of the reinforced concrete method. TATAKI is composed of a decomposed granite soil, quicklime, and water. A mixture of them is compacted tightly around the building stones (Takeuchi & Fujii 2022).

A quad-copter drone, DJI Phantom 4 Pro V2.0, was applied to the documentation of the site. About 230 aerial photographs were taken at the height of about 30 meters from the ground (Figure 8). The camera on the drone has 1-inch CMOS sensor with 20 megapixels, and the lens has focal length

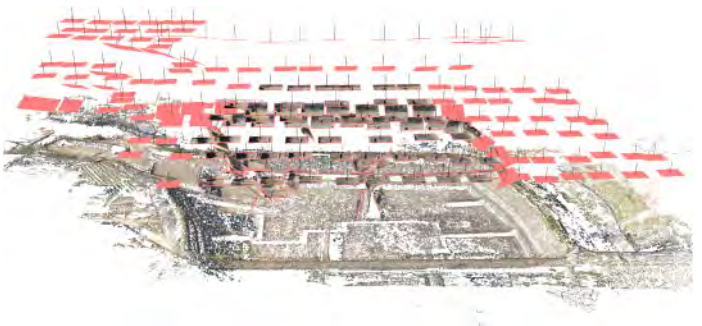

Figure 8. 3-D point cloud of Doudo Lumberyard vied from the southeast. Red line merged squares show camera positions of UAV.

of 8.8 mm. Before taking the aerial photographs, 12 control points were set on all over the site, and the coordinates of them were measured by a Total Station (computer-aided transit).

The camera sensor has a resolution (δ_{CCD}) of 0.0024 mm. Therefore, GSD (σ_{XY}) is calculated approximately 8 mm form the equation (1). The SfM/MVS software (Agisoft Metashpe) has been used to generate the 3-D model of the site (Figure 9). RMS of bundle adjustment is less than 15 mm. Trial comparison has been conducted the current 3-D model and the historical documentations (Takeuchi & Fujii 2022).

Figure 9. Perspective view of the 3-D texture model viewed from southast direction. The size of the lumberyard, the length 100 m, the width 50 m, and depth is about 10 m.

4 SUMMARY AND CONCLUSIONS

Photogrammetry is one of the effective techniques for the documentation of monuments and historic sites constructed with earthen materials and building stones. The technique has been applied to many historic sites by close-range photography with hand held-cameras. Recently, un-manned aerial vehicle, which includes drone, is very useful equipment to take aerial photographs. In addition, the technique of SfM/MVS is suitable to analyze those photographs. The recent technique might be much applied to future projects.

REFERENCES

Atkinson, K.B. 2003. *Close Range Photogrammetry and Machine Vision*. London: Whittles Pub.

Fujii, Y. & Hori, S. 2004. Three dimensional observation of fracture distribution by stereo-photogrammetry. *The Journal of the Geological Society of Japan* 110 (4): 251–253. (in Japanese)

Fujii, Y., Fodde, E., Watanabe, K. & Murakami K. 2009. Digital Photogrammetry for the Documentation of Structural Damage in Earthen Archaeological Sites: the case of Ajina Tepa, Tajikistan. *Engineering Geology* 105: 124–133.

Fujii, Y., Shogaki, T. & Miyakawa, M. 2015. Photogrammetric documentation and measurement of surface erosion in Yokosuka. *Japanese Geotechnical Journal* 10(4): 595–602 (in Japanese with English abstract).

Fujii, Y., Shogaki, T. & Miyakawa, M. 2018. Photogrammetric documentation and non-invasive investigation of a stone dry dock, the Yokosuka Arsenal dry dock No. 1, Japan. *Engineering Geology* 234: 122–131.

Litvinskij, B., Zejmal, T.I. 2004. The Buddhist Monastery of Ajina Tepa, Tajikistan. Isiao, Rome. 190 pp.

Luhmann, T., Robson, S., Kyle, S. & Boehm, J. 2014. Close Range Photogrammetry and 3D Imaging. Berlin/Boston: de Gruyter.

Linder, W. 2003. *Digital Photogrammetry Theory and Applications*. Berlin: Springer.

Takeuchi, K. & Fujii, Y. 2022. The characteristics of "Artificial Stone Construction" used in civil engineering structure – A case study of Doudo lumberyard –. *GEOTECHNICAL ENGINEERING FOR THE PRESERVATION OF MONUMENTS AND HISTORIC SITES* in press.

Geotechnical Engineering for the Preservation of Monuments and Historic Sites III – Lancellotta, Viggiani, Flora, de Silva & Mele (Eds)

The characterization of slope damage at the Civita di Bagnoregio plateau using a remote sensing approach

D. Donati & Lisa Borgatti
Alma Mater Studiorum – University of Bologna, Bologna, Italy

D. Stead
Simon Fraser University, Burnaby, BC, Canada

M. Francioni
University of Urbino, Urbino, Italy

M. Ghirotti
University of Ferrara, Ferrara, Italy

C. Margottini
Istituto Superiore per la Protezione e la Ricerca Ambientale (ISPRA), Rome, Italy

ABSTRACT: Civita di Bagnoregio, in Central Italy, is a small village located on top of a volcanic rocky plateau overlying softer clay shales. Over the centuries, the weathering, softening, and erosion of the clay shales promoted the detachment of blocks and columns from the edges of the volcanic plateau. In this paper, we employ long-range terrestrial laser scanning and terrestrial photogrammetry to build the first high resolution 3D model of the Civita di Bagnoregio plateau. Using remote sensing data, we provide insight on the factors controlling the erosion process affecting Civita di Bagnoregio and investigate the potential role of brittle fracturing on the stability of the plateau. Finally, we provide a discussion on the potential methods that can be employed to simulate the instability phenomena affecting the cliffs of the plateau.

1 INTRODUCTION

1.1 *Overview of the study area*

Civita di Bagnoregio is an historical town located in the Lazio region, in central Italy, that was founded during the Etruscan epoch (about VII century BC). The village is located on top of a 50 m thick, rocky plateau that overlies softer, clayey deposits (Figure 1a, b).

The plateau extends 300 m in an E-W direction and 110 m in the N-S direction and is composed of volcanic materials deposited during Pleistocene and related to the activity of the Vulsini Volcanic District. The upper 25–30 m section of the cliffs is formed by a massif, vesicular ignimbrite deposit, characterized by a brownish red color and a network of predominantly vertical to subvertical fractures. The lower 30–40 m of the massif comprises finely stratified tuffaceous deposits, referred to in the geological literature as "basal tuffs" (i.e., "tufi basali") (Bertini et al. 1971a) (Figure 1b, c). The layers vary in thickness, colour, origin, and mechanical properties.

The clayey deposits (i.e., "argille sabbiose") underlying the volcanic plateau are also Pleistocene in age and represent sedimentation in a marine environment. Near the abrupt contact with the overlying plateau the deposit is characterized by a gradual increase in coarse material content

DOI 10.1201/9781003308867-35

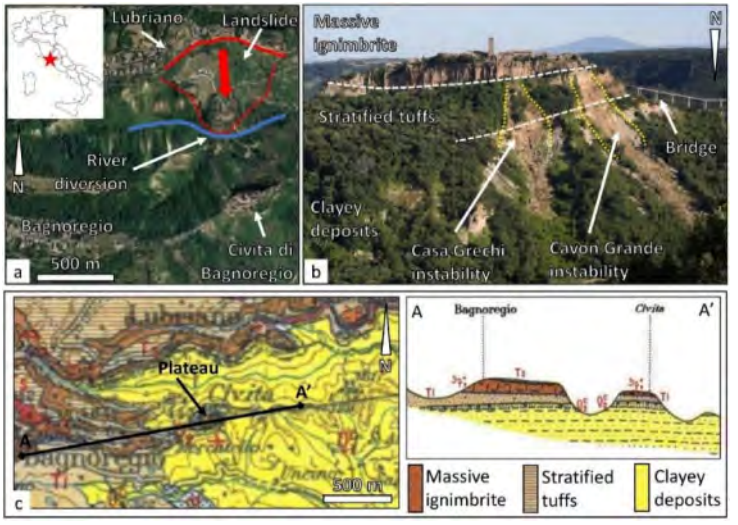

Figure 1. Overview of the investigated area. a: Satellite view (from Google Earth) of the Civita di Bagnoregio area. The inset shows the location of the town in Italy. b: View of the plateau from Lubriano (looking South). Note the main unstable areas, referred to as Casa Grechi and Cavon Grande. c: lithological map of the area, and section through the plateau (extract from Bertini et al. 1971b).

reflecting the progressive marine regression that occurred during the Calabrian stage (Bertini et al. 1971a). In the valleys to the north and south of the volcanic plateau, where two minor streams flow, the thickness of the outcropping clayey deposit is 150 and 200 m, respectively (Delmonaco et al. 2004). The soft clayey deposits are easily eroded by surface water runoff which has resulted in the development of badland morphologies (commonly referred to as "calanchi"). The weak mechanical properties have also caused the clay deposits to be affected by slope instability phenomena such as mudflows, debris flows, and slumps (Bandis et al. 2000). Over the course of the centuries, these erosive and instability phenomena have progressively deepened and thinned the geomorphic saddle that separates Civita from the town of Bagnoregio, ultimately requiring the construction of an embankment (in the 1880s) and a pedestrian bridge (in the 1920s) to allow access to the village. Importantly, progressive erosion, instability phenomena, and softening of the clay has induced a progressive lateral spread of the plateau, resulting in a gradual reduction in area due to the detachment of blocks from the plateau edges (Delmonaco et al. 2004). Between 1700 and today, about the 30–35% of the urbanized area of the plateau has been lost due to landslides (Margottini 1990).

The frequency of instability events occurring along the cliffs is not evenly distributed along all sides of the plateau. The north-eastern part of the plateau is significantly more prone to instability. Here, two significantly unstable areas, referred to as "Cavon Grande" and "Casa Grechi" are marked by active clayey slopes devoid of vegetation located underneath fresh-looking vertical cliffs (Figure 1b). Such enhanced state of activity is likely the consequence of a landslide that detached in 1114 AD from the opposite side of the valley north of the plateau and below the village of Lubriano (Delmonaco et al. 2004) (Figure 1a). The landslide caused the diversion of the unnamed river that flows in the valley, which started eroding and steepening the clayey deposits, ultimately causing the instability to extend to the rocky cliffs, in the form of frequent rock fall and toppling failures (Margottini 2013).

1.2 *Research objectives*

This research aims to provide insight on the development of slope instability and the geomorphic evolution of the Civita di Bagnoregio plateau. To do so, we investigate the spatial characteristics

(distribution, type, intensity) of slope and rock mass damage using remote sensing methods. The collection and interpretation of remote sensing data also allows the identification of an appropriate numerical modelling approach for the simulation of the instability phenomena that affect the clayey slopes and the cliffs of the plateau.

1.3 *Slope damage and implications for slope stability*

The stability and geomorphic evolution of the rock slopes are strongly related to the occurrence of discontinuities within the rock matrix, that can be inherited (e.g., structural discontinuities, bedding planes) or stress-induced (e.g., tension cracks, brittle fractures etc.). Stress-induced discontinuities can be referred to as "slope damage" when they originate as a result of slope deformation (Donati et al. 2021). Slope damage features may contribute to slope instability through a) a reduction in rock mass quality that results in a decrease in rock mass strength, and b) an increase in kinematic freedom, as displacement-induced discontinuities and features may act as release surfaces for unstable rock volumes. In some cases, the development and accumulation of slope damage is a kinematic requirement for slope failures. The displacement of compound slides, characterized by an active-passive block configuration, requires yielding and shearing of the material within the transition zone (Kvapil & Clews 1979). Brittle fracturing of intact rock and propagation of structural discontinuities can cause the development of fully persistent release surfaces, allowing landslides to form in high quality and massive rock masses (Donati et al. 2019).

2 WORKFLOW AND METHODS

2.1 *Research workflow*

This study comprises three stages. Stage 1 involves the initial data collection, performed through structural and damage mapping using traditional fieldwork and remote sensing techniques. The fieldwork campaign took place in the spring 2016. It involved the preliminary investigation of the subvertical cliffs of the plateau and the deformation features within the clayey deposit. Stage 2 comprised remote sensing for the collection of 2D and 3D datasets (high-resolution imagery and point clouds, respectively) allowing combined structural characterization of the plateau and the mapping of damage features. Stage 3 of the study involved interpretation of collected data in order to highlight the major factors controlling the development of slope damage, and in particular brittle damage. The results of stage 3 are important in the identifying of the appropriate numerical modelling approach for simulating the complex instability phenomena active within the Civita di Bagnoregio plateau.

2.2 *Remote sensing techniques*

Laser scanning and digital photogrammetry were employed for the collection of remote sensing dataset. A Riegl VZ-4000 terrestrial laser scanner (TLS) was employed to collect 3D point clouds of the volcanic plateau. These 3D models were used to characterize the orientation and size of the discontinuities observed within the rocky plateau. Discontinuity data was then plotted on stereonets to identify the average orientation of discontinuity sets and the potential variations in the average orientation in different areas of the plateau.

A Canon EOS 5D digital reflex camera and a $f = 400$ mm telephoto lens was used to collect high resolution photographs which were then processed using the structure-from-motion (SfM) technique to derive orthorectified imagery of selected areas of the plateau. The orthorectified images were used to characterize slope damage at the surface of the plateau.

2.3 *Discontinuity and slope damage mapping*

The analysis of slope damage at Civita di Bagnoregio focused on the volcanic rock mass forming the plateau. First, the 3D point cloud derived from the TLS surveys was used to characterize the orientation of discontinuities in the plateau. The software DIPS (Rocscience 2019) was subsequently

used to display the poles to the discontinuities and estimate the average dip and dip direction of the major discontinuity sets. The orthorectified panoramic images, derived from the SfM surveys, were used to identify and map slope damage features (e.g., tension cracks, brittle fractures, rockfall detachment surfaces) and rock mass (or inherited) damage features (e.g., bedding planes in the stratified tuffs), which may act as potential detachment surface for unstable blocks. Following the approach described in Donati et al. (2020), external slope damage intensity cell maps were produced in a GIS environment, in order to display the spatial distribution of slope damage and rock mass structural and geological features. Combined interpretation of the discontinuity and slope damage mapping results aims to provide further insight on the mechanism by which the blocks detach from the volcanic plateau, due to ongoing swelling and softening behavior of the underlying clay-rich material.

3 RESULTS

3.1 *Remote sensing dataset overview*

We performed TLS surveys from 12 scan positions (Figure 2). The point clouds derived from the TLS surveys were registered using the multi-station adjustment plugin in RiSCAN Pro (Riegl 2017) to obtain the complete 3D model of the volcanic plateau (Figure 3). In future studies, this dataset will be further processed (i.e., locally smoothed and simplified) to build the input geometry for 3D numerical simulations.

The high-resolution photographs collected from the various camera stations were imported into the software Metashape (Agisoft 2020) which allowed the creation of three separate orthorectified panoramic images, two for the southern slope and one for the northern slope (Figure 4). For the southern slope, the decision to create two orthophotos was due to the varying orientation of the cliff, which is characterized by a NNW-SSE strike in the western part, and a NNE-SSW strike in the eastern part. All orthorectified panoramic images are characterized by a pixel size of 2 cm. However, the orthorectified panoramic photograph of the southern slope was not used for slope damage analysis, in view of the low image quality as a result of unfavorable lighting conditions (i.e., the camera was always facing the sun).

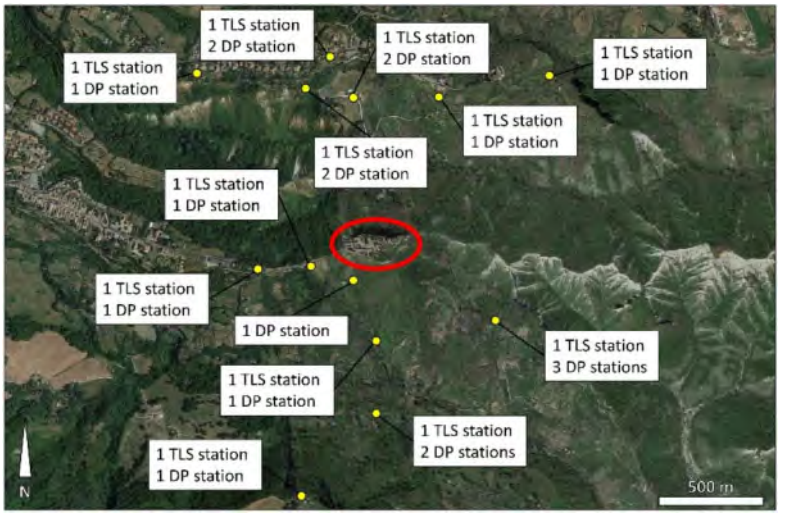

Figure 2. Location of the survey stations, represented by yellow dots. For each location, the number of TLS and digital photogrammetry (DP) stations is listed. The Civita di Bagnoregio plateau is outlined by the red circle.

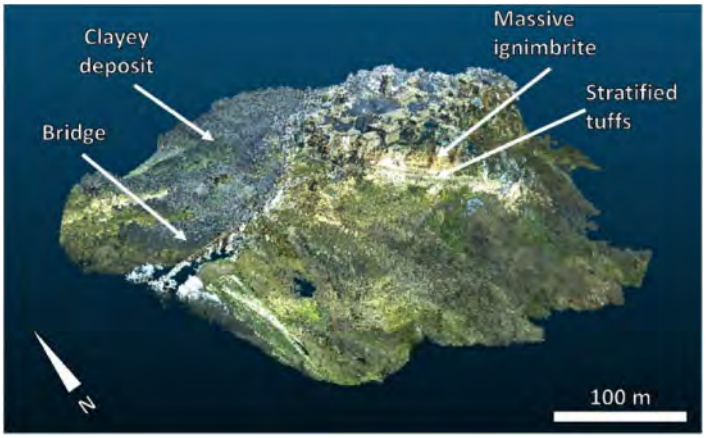

Figure 3. Oblique view of the 3D point cloud of the volcanic Civita di Bagnoregio plateau.

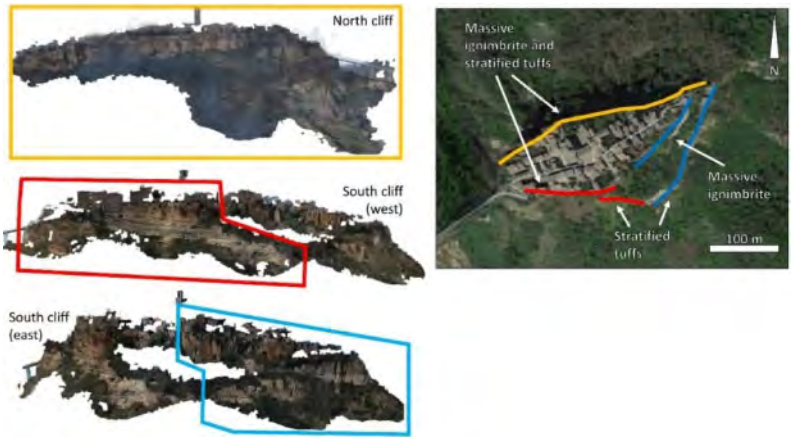

Figure 4. Overview of the three orthophotos derived from the SfM geometry reconstruction. The coloured shapes display the areas normal to the viewing direction where the rock mass and slope damage analyses could be undertaken. Note the lower image quality of the orthophoto obtained for the north cliff.

3.2 *Massive tuff discontinuity mapping*

The 3D point clouds were investigated using standard tools in the open-source software CloudCompare (CloudCompare 2011). Clusters of points representing discontinuity traces and planes were separated from the cloud. Planes were interpolated within the extracted point clusters, automatically deriving their orientation in terms of dip and dip direction. We mapped 181 discontinuities and identified three major, subvertical discontinuity sets, referred to as D1, D2, and D3 (Figure 5a). We did not observe any significant difference between the sets mapped on the north and south slopes of the Civita di Bagnoregio plateau. D1 and D2 are the most prominent sets, striking in a ENE-WSW and ESE-WNW direction, respectively. The discontinuity set D3 strikes in a NNE-SSW direction, and appears to be more scattered compared with D1 and D2, as also observed in the rosette diagram that includes all the mapped discontinuity planes (Figure 5b).

The stratified tuffs that form the lower part of the Civita di Bagnoregio plateau is characterized by sub-horizontal bedding planes that have a slight dip in a northerly direction. No obvious structural

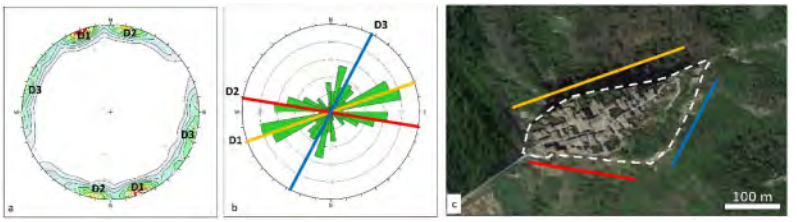

Figure 5. Overview of the discontinuity mapping results. a: Stereonet (equal area, lower hemisphere) showing the pole and pole density of the mapped discontinuities. b: Rosette diagram summarizing the direction of the mapped discontinuities. c: Comparison between the orientation of the subvertical discontinuities mapped in the massive ignimbrite deposit and the orientation of the cliffs of the Civita di Bagnoregio plateau.

discontinuity was noted in this stratified deposit, possibly due to limitations in the resolution of the 3D dataset.

The orientation of the mapped discontinuity sets seems to correlate with the sides of the Civita di Bagnoregio plateau. The northern cliff appears to be sub-parallel to the average orientation of D1, while D2 and D3 mimic the orientation of the western and eastern sides of the plateau, respectively (Figure 5c). This evidence seems to suggest that the morphology of the cliffs is at least partly controlled by geological structures.

3.3 *Slope and inherited damage analysis*

Slope and inherited damage features were mapped in a GIS environment. For this study, we considered inherited damage as the ensemble of features that formed at the time of rock formation, specifically the bedding planes in the stratified tuffs. Other rock damage features, such as rockfall detachment surfaces, tension cracks, and discontinuity planes within the massive tuffs were considered as slope damage features, because their origin and time of formation cannot be estimated with confidence.

We mapped and measured slope and inherited damage features on the orthophotos and observed that the characteristics of slope damage features changes significantly between the upper and lower parts of the volcanic Civita di Bagnoregio plateau. Features in the stratified tuffs are characterized by a smaller size, averaging 1.2 m and 1.7 m in the eastern and western parts of the plateau, respectively, compared to features in the massive ignimbrite deposit, which average 3.1 m and 4.6 m in the eastern and western parts, respectively. Such an observed difference in length is in part due to the presence of the layering within the lower part of the plateau; slope damage features in the lower part of the plateau often terminate against bedding planes, which represent preferential release surfaces and allow the separation and detachment of blocks (Figure 6a). However, large columnar- or sheet-shaped blocks of stratified rock mass bounded by persistent fractures were observed adjacent to but separated from the cliff (Figure 6b,c), sometimes in a metastable equilibrium condition. Conversely, the detachment of rock blocks within the massive ignimbrite is caused by the progressive opening of subvertical fractures and, in some cases, by the brittle propagation of fractures within the intact material (Figure 6d,e).

Slope damage (SD_{21}) and inherited damage (i.e., bedding, B_{21}) intensity were computed over a 5 m-step size grid, representing a compromise for maximizing both detail and cell surface area. SD_{21} and B_{21} combined constitute the rock mass damage intensity (D_{21}) We computed mean values of 0.09 m^{-1} and 0.18 m^{-1} for SD_{21} in the western and eastern parts of the southern cliff, respectively, and we note that in both cases SD_{21} is equally distributed within the massive ignimbrite deposit and the stratified tuff (Figures 7a,b and 8a,b). In contrast, B_{21} could only be computed in the lower part of the plateau, with mean values of 0.24 m^{-1} and 0.28 m^{-1} for the western and eastern parts of the southern cliff (Figures 7c and 8c). We derived the global rock mass damage from the arithmetic sum of B_{21} and SD_{21} and note that mean values for the western and eastern parts of the southern

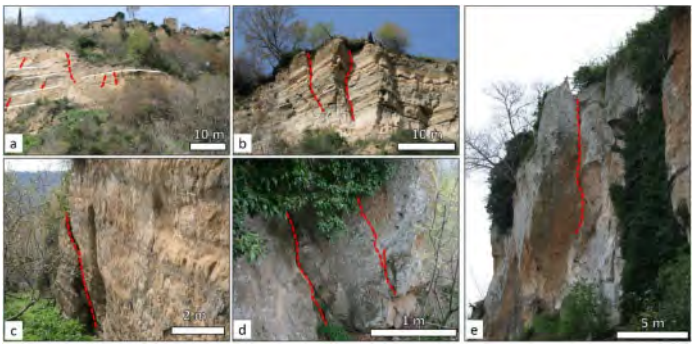

Figure 6. Overview of slope damage features in stratified tuff and massive ignimbrite. In all figures, white lines outline bedding planes and red lines mark slope damage features. a: Relationship between bedding planes and slope damage in the lower part of the plateau. Note the frequent terminations of slope damage against bedding planes. b-c: Examples of potentially unstable blocks bounded by subvertical fractures within the stratified tuffs. d-e: Evidence of brittle fracture propagation within the massive ignimbrite.

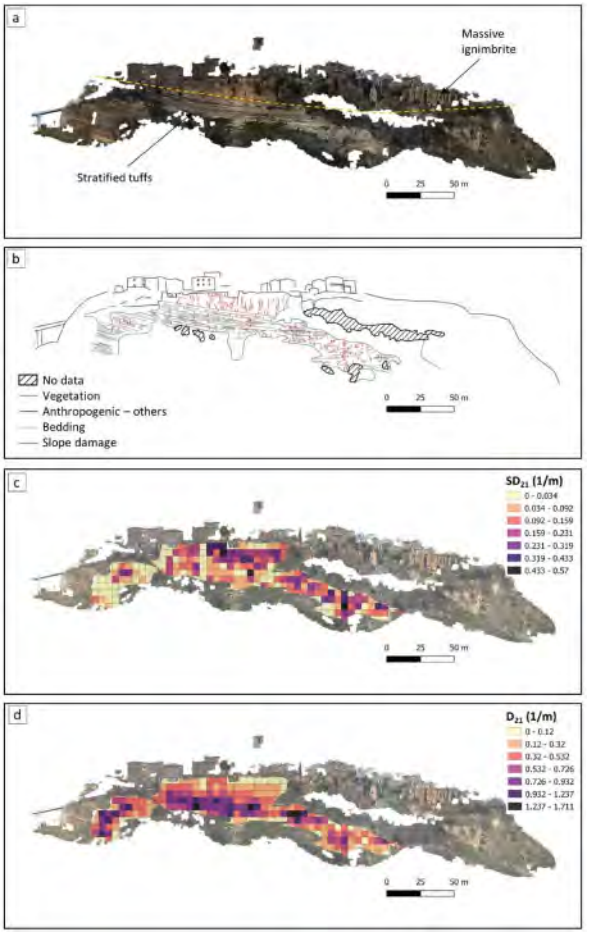

Figure 7. Summary of the slope and inherited damage intensity and damage distribution analysis results for orthophoto 1 (western part of southern cliff). a: Investigated orthophoto. b: Overview of the mapped features. c: Slope damage intensity map. d: Rock mass damage intensity map.

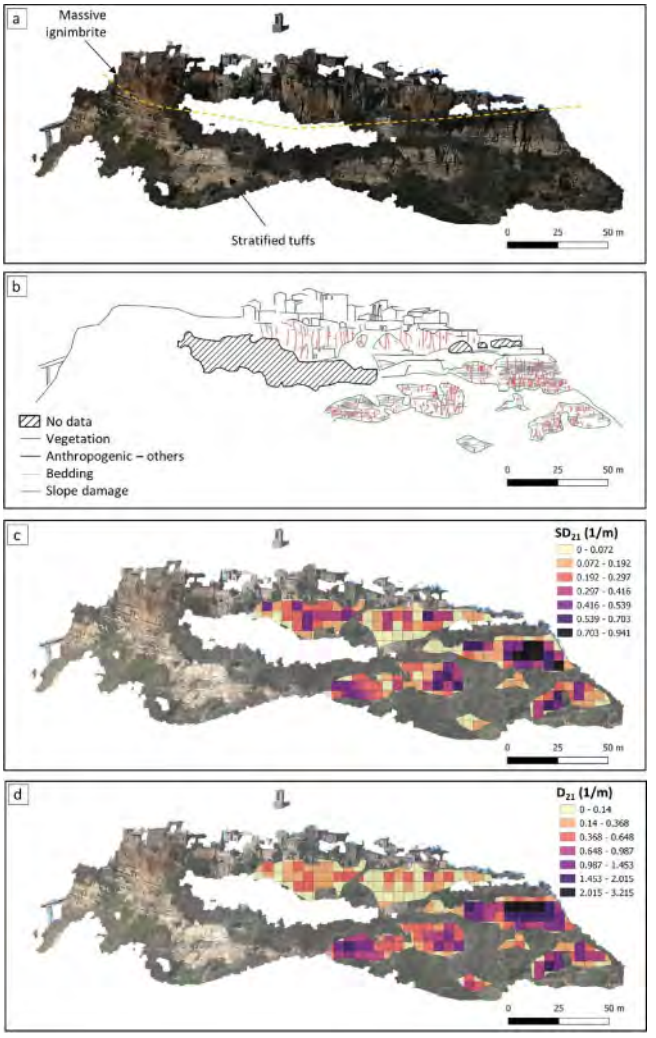

Figure 8. Summary of the slope and inherited damage intensity and damage distribution analysis results for orthophoto 2 (eastern part of southern cliff). a: Investigated orthophoto. b: Overview of the mapped features. c: Slope damage intensity map. d: Rock mass damage intensity map.

cliffs are 0.37 m^{-1} and 0.42 m^{-1}, respectively, and thus show a good agreement. As expected, however, the intensity distribution is skewed, with significantly higher values in the lower part of the plateau, due to the thin stratification of the tuffs (Figures 7d and 8d).

4 DISCUSSION

The Civita di Bagnoregio volcanic plateau is characterized by heterogeneous geomechanical conditions, due to the different rock mass quality between the upper, massive ignimbrite deposit and the lower, stratified tuff deposit, which, consequently, are characterized by different instability and deformation behavior. Massive materials with a low number of high persistence discontinuities are

generally more affected by structurally controlled failures (Figure 9a). Based our remote sensing-based geomechanical characterization we note the presence of prominent vertical to subvertical discontinuities that are potentially prone to block toppling failure. In some cases, the detachment of blocks is promoted by the progressive propagation of discontinuities within the vesicular material forming the massive ignimbrite. The structurally controlled nature of block detachment from the upper cliff is also evidenced by the surface morphology of the cliff, which is characterized by intersecting discontinuity planes that form a surface that is markedly stepped in the horizontal direction (Figure 9b).

Figure 9. Overview of the processes affecting the evolution of the upper cliff. a: View of the southern cliff displaying fracture propagation and structurally controlled block detachments. b: Example of stepped morphology frequently observed within the massive ignimbrite deposit.

In contrast, the lower part of the Civita di Bagnoregio plateau, formed by the stratified tuffs, is characterized by a significantly lower rock mass quality that may promote the development of

continuum-like failures and deformations (i.e., rock slides) or the progressive detachment of small rockfalls. This interpretation agrees well with a) the relatively smooth surface of the subvertical cliff, compared to the stepped morphology of the upper part of the plateau, and b) the curved morphology (in plan view) of the rupture surface and the cliff in the areas of the Cavon Grande and Casa Grechi instabilities, on the northern slope of the plateau (Figure 10).

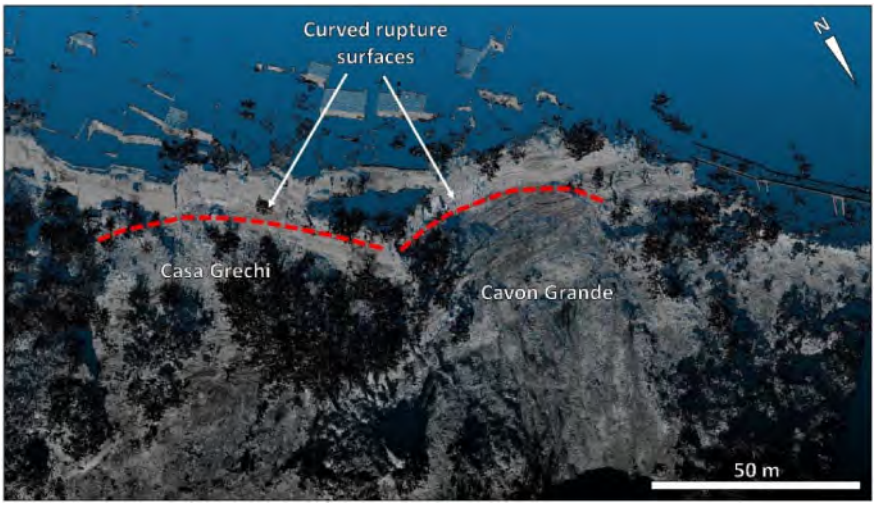

Figure 10. Curved morphology of the rupture surface of Casa Grechi and Cavon Grande slope instabilities, in the northern cliff of the Civita di Bagnoregio plateau, appearing to indicate a rock sliding failure mechanism.

Though not the focus of this this study, it is undoubted that swelling and slumping within the clayey deposits underlying the plateau are one of the most important factors in promoting the occurrence and propagation of the instability of the Civita di Bagnoregio plateau (Bandis et al. 2000).

4.1 *Suitability of different numerical modelling approaches at Civita di Bagnoregio*

Such a broad range of varying mechanical behavior makes the identification of the most suited numerical modelling method rather challenging, in view of the different types of mechanisms that must be simulated during the analysis. The clayey and the stratified tuff deposits appear to be characterized by a continuum or continuum-like behavior, which can be adequately simulated using finite-element or finite-difference methods. Continuum software (e.g., RS2, RocScience 2020, FLAC, Itasca Ltd., 2021) is also capable of simulating structurally controlled failures, allowing interfaces to be implemented that simulate the presence of discrete discontinuities along which sliding and detachment may occur. Nevertheless, continuum software remains generally unsuitable for the simulation of large displacements in blocky rock masses, where complete detachment and interaction between separate blocks is expected, such as in the case of the massive ignimbrite at the Civita di Bagnoregio plateau. Continuum methods have been recently used also to simulate the intact material behavior and failure, through the implementation of a Voronoi tessellation within the intact material domain (Spreafico et al. 2017a). To a limited extent, continuum software has been developed specifically to simulate intact rock fracturing (Rock Failure Process Analysis, RFPA, Tang 1997; see also Donati et al. 2018 for an overview). Therefore, continuum methods can be considered a potential candidate for the numerical modelling of the deformation behavior of the Civita di Bagnoregio plateau, although perhaps more limited to the onset of failure. Discontinuum methods (e.g., distinct element method) can simulate the complex and non-linear

behavior of rock masses and allow the sliding, detachment, and interaction between separated blocks to be realistically simulated. To some extent, discontinuum methods have been employed to simulate intact rock fracturing (also through the implementation of a Voronoi or Trigon tessellation), as well as continuum constitutive models, by assigning appropriate mechanical parameters to deformable blocks. Compared to continuum methods, a discontinuum approach has the potential to allow the global failure of the slope to be simulated, from the onset of failure to landslide runout. More advanced methods, such as hybrid (e.g., continuum-discontinuum) and lattice scheme software, have been developed to realistically model the failure of intact material through brittle fracture propagation or formation (e.g., Irazu, Geomechanica 2020; Slope Model, Itasca Ltd, 2019) and are therefore well suited for simulating the brittle fracturing that occurs within the massive ignimbrite.

Examples of using numerical modelling methods for investigating failures affecting a rocky plateau overlying soft deposits have been described by Spreafico et al. (2015), Spreafico et al. (2017a), and Donati et al. (2019) for the San Leo plateau (northern Italy). These studies were conducted using 3D distinct element, continuum, and hybrid finite-discrete element methods, respectively and highlighted the interconnection between the processes affecting the carbonate plateau and the underlying soft, clayey deposits. Specifically, the weathering, alteration, erosion, and progressive deformation of the clay under the weight of the Civita di Bagnoregio plateau was found to be the main driver of brittle fracture propagation within the intact rock. Then, the failure took place along pre-existing discontinuities and the breakage of intact rock bridges (Spreafico et al. 2017b) which ultimately led to the detachment of a 300,000 m^3 landslide (Borgatti et al. 2015).

Based on the data available for the Civita di Bagnoregio study site, it is suggested that the application of these methods may provide additional insight on the geomorphic evolution of the volcanic plateau. Additionally, the availability of historical reconstructions of the plateau edges, such as that presented in Margottini (1990) may provide a means to constrain the results as well informing the pre-failure and boundary conditions of the numerical model.

5 CONCLUSIONS

In this paper, we presented the first full 3D geological model of the Civita di Bagnoregio plateau obtained through terrestrial remote sensing methods, specifically terrestrial laser scanning and digital photogrammetry. We performed a structural characterization of the plateau, which allowed the identification of three major, subvertical discontinuity sets within the massive ignimbrite unit. These discontinuity sets appear to correlate well with the direction of the edges of the plateau, suggesting at least a partial structural control on its morphology. We investigated the type, intensity, and distribution of slope damage across the southern cliff, noting that the inherited damage due to the stratification of the tuffaceous unit causes a significant decrease in rock mass quality in the lower part of the plateau. We therefore suggest that significantly different deformation and failure mechanisms may affect the different units, with a mixed structural/brittle fracture control on the stability of the massive ignimbrite, and a more continuous style of deformation within the stratified tuffs. These observations, together with the well-known role of the underlying clayey deposit, emphasize the need, from a numerical modelling perspective, to account for a wide range of processes and failure mechanisms. Continuum, discontinuum, and hybrid modelling approaches have been recently successfully employed to simulate the failure of rocky plateau overlying soft materials. However, we suggest that a discontinuum approach, for instance using the distinct element method, may represent the best option to investigate the complete failure processes active at the Civita di Bagnoregio site, especially if a Voronoi tessellation is implemented within the upper part of the plateau in order to simulate the brittle fracture propagation observed within the massive ignimbrite unit, with a single, homogeneous, and deformable block being employed to simulate the continuum behavior of the soft clayey deposit.

REFERENCES

Agisoft. 2020. Metashape version 1.7. https://www.agisoft.com/

Bandis, S., Colombini, V., Delmonaco, G. & Margottini, C. 2000. New typology of low environmental impact consolidation for rock fall prone cliffs through intervention from the underground. In: Bromhead, E., Dixon, N. & Ibsen, M-L. (eds). *Landslides in Research, Theory and Practice*. Proceedings of the 8th International Symposium on Landslides, Jube 26–30 2000, Cardiff, Wales, UK.

Bertini, M., D'Amico, C., Deriu, M., Girotti, O., Tagliavini, S. & Vernia, L. 1971a. Note illustrative della carta geologica d'Italia. Foglio 137 Viterbo. Servizio geologico d'Italia. (In Italian).

Bertini, M., D'Amico, C., Deriu, M., Girotti, O., Tagliavini, S. & Vernia, L. 1971b. Carta geologica d'Italia. Foglio 137 Viterbo. Servizio geologico d'Italia. (map).

Borgatti, L., Guerra, C., Nesci, O. Romeo, R.W., Veneri, F., Landuzzi, A., Benedetti, G., Marchi, G. & Lucente C.C. 2015. The 27 February 2014 San Leo landslide (northern Italy). Landslides 12, 387–394.

CloudCompare (2021). CloudCompare version 2.11. https://www.danielgm.net/cc/

Delmonaco, G., Margottini, C., Puglisi, C., Falconi, L. & Spizzichino, D. 2004. The dying town of Civita di Bagnoregio and the killer landslide. In: Lacerda, W., Mauricio Ehrlich, Fontoura, S.A.B., Sayao A.S.F. (eds). *Landslides: Evaluation and Stabilization*. Proceedings of the Ninth International Symposium on Landslides, June 28–July 2 2004, Rio de Janeiro, Brazil.

Donati, D., Stead, D., Elmo, E. & Borgatti, L. 2019. A preliminary investigation on the role of brittle fracture in the kinematics of the 2014 San Leo landslide. *Geosciences* 9, 256.

Donati, D., Stead, D., Elmo, D., Karimi Sharif, L., Gao, F., Borgatti, L. & Spreafico, M. 2018. Experience gained in modelling brittle fracture in rock. In: ARMA (ed). *52nd U.S. Rock Mechanics/Geomechanics Symposium*. Seattle, Washington, June 17–20, 2018. Paper n. ARMA-2018-821.

Donati, D., Westin, A., Stead, D., Clague, J., Stewart, T., Lawrence, M. & Marsh, J. 2021. A reinterpretation of the Downie Slide (British Columbia, Canada) based on slope damage characterization and subsurface data interpretation. *Landslides* 18, 1561–1583.

Donati, D., Stead, D., Lato, M. & Gaib, S. 2020. Spatio-temporal characterization of slope damage: insights from the Ten Mile Slide, British Columbia, Canada. *Landslides* 17, 1037–1049.

Elmo, D., Donati, D. & Stead, D. 2018. Challenges in the characterisation of intact rock bridges in rock slopes, *Engineering Geology* 245, 81–96

Geomechanica. 2020. Irazu FEMDEM. https://www.geomechanica.com/software

Kvapil. R. & Clews, M. 1979. An examination of the Prandtl mechanism in large dimension slope failures. *Transactions of the Institution of Mining and Metallurgy: section A,* Volume 88, A1-A5.

Itasca Ltd. 2021. FLAC: Fast Lagrangian Analysis of Continua, Version 8.1. https://www.itascacg.com/software/FLAC

Itasca Ltd. 2019. Slope Model version 3. https://www.itascacg.com/software/Slope-Model

Margottini, C. 1990. Evoluzione morfologica dell'area di Civita di Bagnoregio in tempi storici. In: Margottini, C. & Serafini S. (eds). *Civita di Bagnoregio. Osservazioni geologiche e monitoraggio storico dell'ambiente*. ENEA, Ass.Progetto Civita. Roma. (In Italian)

Margottini, C. (2013). Low environmental impact consolidation works in the rock cliff of Civita di Bagnoregio (Central Italy). In: Margottini, C., Canuti, P. & Sassa, K. (eds). *Landslide science in practice: risk assessment and mitigation*. Heidelberg-Berlin-New York: Springer Verlag Inc.

RIEGL Laser Measurement Systems GmbH (2017). RiSCAN Pro version 2.8.

Rocscience Inc. 2019. Dips version 7.0. https://www.rocscience.com/software/dips

Rocscience Inc. 2020. RS2 version 11.0. https://www.rocscience.com/software/rs2

Spreafico, M., Cervi, F., Francioni, M., Stead, D. & Borgatti, L. 2017a. An investigation into the development of toppling at the edge of fractured rock plateaux using a numerical modelling approach. *Geomorphology* 288, 83–98

Spreafico, M.C., Franci, F., Bitelli, G., Borgatti, L. & Ghirotti, M. 2017b. Intact rock bridge breakage and rock mass fragmentationupon failure: Quantification using remote sensing techniques. The Pho-togrammetric Record 32, 513–536

Spreafico, M., Francioni, M., Cervi, F., Stead, D., Bitelli. G., Ghirotti, M., Girelli V.A., Lucente, C.C. Tini, M.A. & Borgatti, L. 2015. Back analysis of the 2014 San Leo Landslide using combined terrestrial laser scanning and 3D distinct element modelling. *Rock Mechanics and Rock Engineering* 49, 2235–2251

Tang, C.A. 1997. Numerical simulation of progressive failure and associated seismicity. *International Journal of Rock Mechanics and Mining Sciences*, 34(2). 249–261.

Geotechnical Engineering for the Preservation of Monuments and Historic Sites III – Lancellotta, Viggiani, Flora, de Silva & Mele (Eds)

The geotechnical setting of the forts of the Saxon Shore in SE England: A record lasting nearly 2 millennia

Edward N. Bromhead
Emeritus Professor, Kingston University, London, UK

Maia-Laura Ibsen
Kingston University, London, UK

ABSTRACT: In a document preserved originally at Ravenna and much copied, from the latter stages of the Ancient Roman Empire, probably early in the 5th Century CE, military officials and their commands across the Roman Empire are recorded. Some of these commands relate to a senior military official Comes Litus Saxonicum ('Count of the Saxon Shore') with a variety of units and locations under his command in Britannia. Many of those locations are still identifiable as ruined 3rd century Roman fortifications at sheltered coastal or near-coastal estuarine sites. These fortifications are commonly described as 'Saxon Shore Forts' in modern day archaeological descriptions. Since the document (Notitia Dignitatum) is much later than the construction of the forts, it is likely that the command covered only a subset of what was originally constructed, and at the time of construction, there may or may not have been any such commander.

However, of the nine sites listed in the Notitia, several have been damaged by marine or estuarine erosion, and one by landsliding not immediately connected to active erosion, At least one other has been completely lost to retreat of the coast. Paradoxically, several of the forts partly eroded by the sea have since been protected against further retreat by the development of saltmarshes at their toes, and one by coastal defence works.

It must be a matter of some speculation about why they were constructed in the first place, or to what purpose they were subsequently put to use, but even then, it is possible to disprove some of the hypotheses that have appeared in the literature by reference to the geotechnics of their sites. It must be remembered that the *Notitiia* list may not include all the forts that were originally built, much less planned, and as they appear from the archaeological record to have been constructed at various dates, their origins may well reflect the responses to different original strategic threats, or even, as has been speculated, for Customs revenue collection purposes. The bastions make the latter speculation improbable.

The paper describes the geographical, geological and geomorphological settings of these forts along with some of the geotechnical investigation work carried out at one of them.

1 INTRODUCTION

When monitoring geological and geotechnical change in the landscape, a variety of techniques are used, most notably various types of in-situ geotechnical instruments and remote sensing techniques, but also surface monuments and stations that are surveyed periodically or continuously. Sometimes, the readings are serendipitous, as for example, the GPS base station at St Catherine's Point Lighthouse (Hutchinson et al. 2002) which revealed seawards landslide deflections on a station that the national survey organisation thought was a fixed point. It incidentally confirmed prior

DOI 10.1201/9781003308867-36

geodetic surveying (Bromhead et al. 1988) but with an infinitely better temporal resolution. The lighthouse was previously known to 'wobble' as recorded with a pendulum, and this was shown to be the result of intermittent sliding along a gently dipping basal slip surface.

A major difficulty arises because of the short timescale over which measurements may be taken. There are exceptions, where long ago some individual with foresight installed something that was observed periodically thereafter: a good example being the Holm Post (Hutchinson 1980) where an iron column was driven into a peat deposit subject to wastage and recorded becoming progressively exposed as the peat wasted away in a series of photographs taken by a variety of individuals more for recreational than scientific purposes. However, the Holm Post was surplus to the construction of an exhibition hall for the Great Exhibition in Hyde Park in 1851, and even though the record is long compared to most instrumentation, sometimes even longer records than a century or so are desired.

Longer term records rely on observations on historical buildings and monuments, often recorded (since the invention of photography) in photographs, but otherwise in the form of paintings, drawings, and antiquarian records, although they are difficult to obtain exact measurements from. An especially good example of such a study is that presented by Dvorak and Mastrolorenzo (1991) in a study of the rise and fall of a Roman building in Pozzuoli relative to sea level as a result of volcanic inflation and deflation. The building was uncovered in an excavation, and surviving columns were bored by a marine organism, showing that the remains had been beneath sea level at one time. The building was long thought to be the Temple of Serapis, but now is known to have been a market.

The search for monuments of similar longevity in SE England has homed in on a series of Roman era coastal or near coastal fortifications, sometimes known as 'the Forts of the Saxon Shore', and what they tell us about coastal change since they were constructed, although many conclusions are necessarily speculative.

2 THE ROMAN PERIOD IN BRITAIN

The *Roman Period* as far as the British Isles are concerned extends from the Claudian conquest beginning in A.D. 43 and finishing with the withdrawal of the legions under Honorius in A.D. 410 (Figure 1) – a little less than 4 centuries, and different, for example, to the ancient Roman period recognised in Italy. No doubt the islands came under Roman influence before the conquest, not least because of trade and the incursions by Julius Caesar in 55 and 54 B.C, and the influence

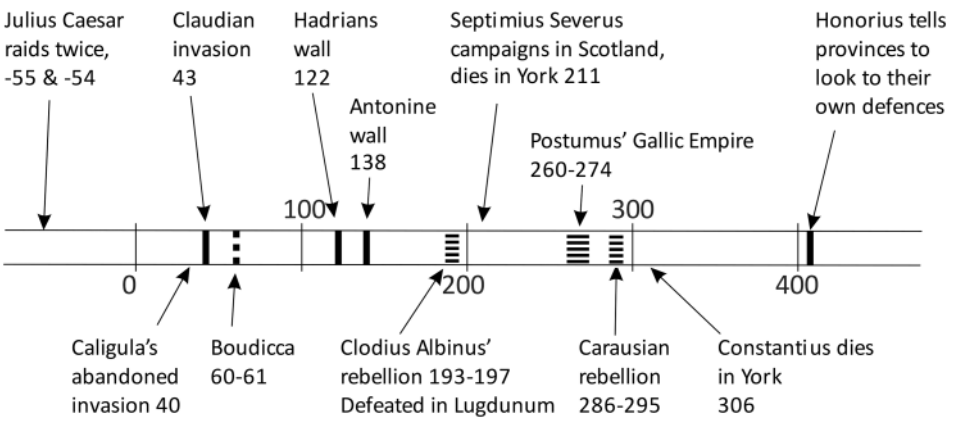

Figure 1. A timeline for the Romans in Britannia. The Saxon Shore forts were constructed in the century preceding 300 AD, and were therefore a century old at the time of the Notitia. Moreover, they are constructed in the period of the Gallic Empire, Clodius Albinus' Rebellion and the Carausian Rebellion.

continued to be felt largely through the influence of the Roman Catholic Church right up until The Reformation in the 16th Century and possibly beyond.

In answer to the question 'What did the Romans do for us?', parts of the strategic road network and the foundation of many of the major cities go back to this period. Forts and fortified towns often have names ending in '...caster', '...caister' '...cester' or '...chester' even in the present day, and even in the post-Roman era where similar meaning is implied by '...burgh' (or other variants such as '...bury' and '...borough') the origins may lie with Roman fortifications. It transpires that although the Romans invaded what is now Scotland, they did not see much point in keeping it – a view that is often felt but not articulated even in the present day, and similarly, although there is evidence that there was trade with Ireland, that island also seems not to have figured largely in any Roman desire for conquest. Their settlement was largely limited to what is now England and Wales.

Although no buildings from that distant period have survived intact in the British Isles, it is commonplace for present-day building and civil engineering works to encounter foundations of Roman buildings known for their ornate mosaic floors, and also roads and military works, the latter including the well-known Hadrian's Wall, separating England and Scotland and of course numerous fortifications, some of which still have significant above-ground remnants.

In a little over a century, Britannia was separated from the main Empire by three revolts (Figure 1), representing a tumultuous time. Each of the revolts was not a form of 'Brexit', but involved large sections of Gaul. The third revolt was led by Carausius, who after losing the Gaulish part of his possessions successfully withstood one invasion attempt, although he was then assassinated by his subordinate Allectus, who was unable to withstand a second invasion under the emperor Constantius Chlorus and his praetorian prefect Julius Asclepiodotus.

3 THE FORTS OF THE 'SAXON SHORE'

The forts of the 'Saxon Shore' are a series of 9 late Roman period fortifications around the south-eastern coasts of England. The phrase 'Saxon Shore' comes from a single epigraphic source, the *Notitia Dignitatum* ('List of Dignitaries' or 'Offices') copied many times and thus preserved. The phrase derives from the title of an official described as commanding army units based at a number of sites, most of which can be identified as being the remains found today. Some of the locations at which various army units are based are known from other sources, and are identified by reference to a variety of *Itineraries*, which list distances from one place to another. Occasionally, the modern placename echoes the Roman name, as in, for example, Reculver from *Regulbium*. The *Notitia* is thought to have been composed in the early 5th Century from at least 2 sources, relating respectively for the Western Empire in around 400 AD, and a little earlier for the Eastern Empire.

Roman Fortifications are a subject of many works, including those intended for a lay audience (e.g. Wilson 1980), and even the fascination about the 'Saxon Shore' has extended to many accounts (e.g. Breeze 1994; Pearson 2002). However, in view of doubts about whether or not the forts under the command of the Count were originally a separate group, and in the light of the existence of other forts of a similar age and layout built in sheltered location, it has become conventional to drop the 'Saxon' and call them more simply 'Shore Forts'.

The forts themselves are in various states of preservation (mostly ruinous), in part depending on the geology, geotechnics and coastal hydraulics of the sites where they were built, and on re-use at various historical periods in the last millennium. The names of the forts in the Notitia are (with modern names in brackets: Othona (Bradwell), Dubris (Dover), Lemannis (Stutfall Castle at Lympne), Branoduno (Brancaster), Garriano (Burgh Castle), Regulbium (Reculver), Rutupis (Richborough), Anderidos (Pevensey), Portum Adurni (Portchester – although this latter identification is far from certain).The spelling of the Latin names differs slightly from source to source, for example Lemannis-Lemanis, Branoduno-Branodunum etc.

Not listed in the Notitia are forts of a similar age and style (e.g. with closely-spaced bastions) at Caister on Sea, Walton Castle, Bitterne (*Clausentium*), Topsham, and possibly also Carisbrooke

on the Isle of Wight, with the distant Cardiff Castle fitting the general picture. It is tempting to believe that the foundations of Rochester Castle also originated in a Shore Fort, not least by virtue of its planform and location adjacent to a sheltered inlet, but also by the site being exploited for a Norman castle and the name of the settlement ending in '...chester'.

Most of the forts have been the sites of archaeological excavation campaigns from the middle of the 19th century up to the present, with the finding that the ones listed in the *Notitia* date from the 3rd century AD. However, not all appear to be of an identical commencement date, and some are much older than others. Some seem also to be replacements or modifications of older forts, notably at Reculver, Richborough and Dover.

The common feature of all of them appears to be the construction of projecting bastions at closely-spaced intervals around their periphery, although the forts have different planforms, with Lympne and possibly Burgh Castle having an 'apsoidal' side, and Pevensey being the outlier with an irregular ovoid planform. All of the forts are of sufficient public interest that the Internet abounds with photographs and maps, so that readily available information will not be duplicated here.

Interesting as the archaeology is, the surviving forts have the potential to tell us much about coastal changes that have occurred in the past 17 centuries, and it is that story which the paper intends to concentrate upon. However, a brief review of what is known, and also what is conjectured, about the forts is necessary for the paper to be put into context. The Antiquarian literature includes Stukeley's important illustrated work (1776). More recent archaeological investigations are given e.g. by Roach-Smith 1850, 1852; Cunliffe, 1980; and Philp, 2005.

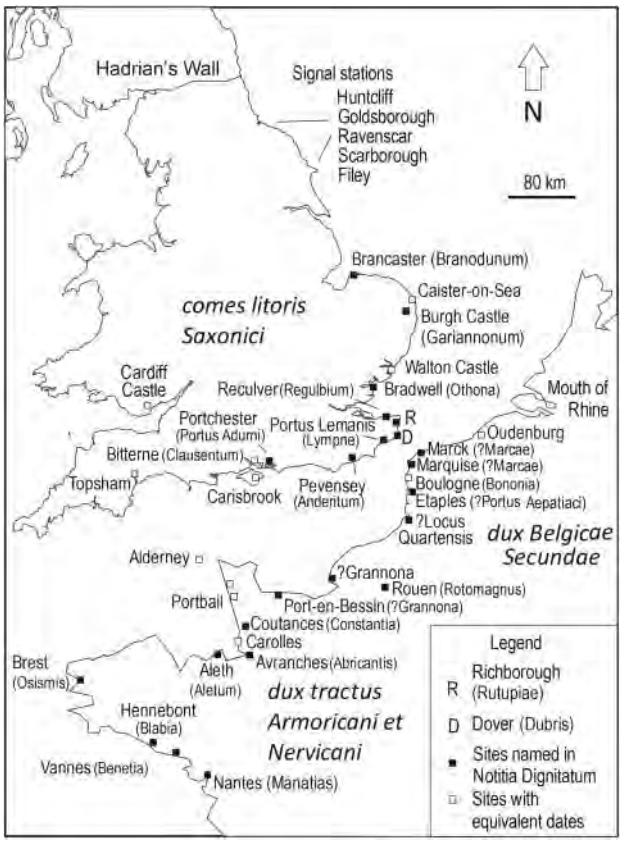

Figure 2. The Saxon Shore forts in context with the equivalent structures on the northern coast of Gaul.

All walled enclosures have the purpose of keeping what is inside safe from what is outside, or *vice versa*. In the former case the enclosures are defensive fortifications, and in the latter, prisons. The projecting bastions favour the fortification idea, because bastions and towers are force-multiplying structures, and show that the fortification is intended to resist siege from a large force and not a simple raiding party, as without that, a simple wall is adequate protection for the occupants, giving enough time for them to be mustered into defensive formations.

It appears that all the coastal forts of this period, 'Saxon Shore' or otherwise, were built not on exposed coastlines, but in relatively sheltered estuarine settings, and, for brevity, usually in association with the needs of a naval force known as the 'British Fleet' (*Classis Britanicum*). This conclusion is based on surviving examples and on an appreciation (i.e. surmise) of what the original purpose of the forts may have been. Philp (2005) speculates that Reculver may have been 1 mile from the sea originally, but that is necessarily based on it having been built in a sheltered location and taking account of 19th and early 20th century erosion rates. It would in any case have always been close to the Wantsum Channel, now reclaimed land, which separated the Isle of Thanet from the mainland and provided access to Canterbury for shipping.

4 GEOLOGY

The structural geology in SE England (Figure 3) is dominated by the Wealden dome (which is cut by the English Channel and has its coastal expression in the Dover-Lympne-Pevensey stretch of coastline), the London Basin to its north (west of Bradwell and Reculver), and the Hampshire Basin to its west (around Portchester and Bitterne). The dome brings weak rocks of Cretaceous age to the surface while in the basins, the deposits at sea level on the coast are of the Tertiary, again taking the form of very weak rocks. By 'weak rocks' we mean in the geologist's vocabulary, as the strata, with some notable exceptions, are stiff, overconsolidated silty clays and sands in both the Tertiary and Cretaceous sequences, the most notable exception being the Chalk, which is a white, jointed weak limestone.

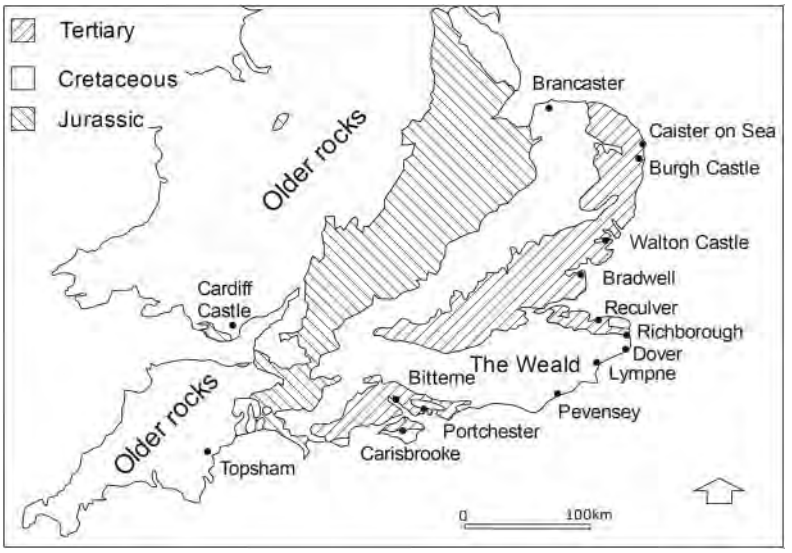

Figure 3. Outline Geology of SE England relative to the Shore Forts.

The Roman engineers appear to have chosen sites somewhat inland of the mouths of estuaries or where an anchorage was protected from direct marine attack by a coastal spit, and mainly to

have founded their structures on the 'solid' rather than on any estuarine deposits except perhaps Portchester and Reculver. The three most northerly of the forts are founded on the glacial drift that covers East Anglia – the 'bulge' in the coastline hereabouts. Only Lympne is built on a slope, whereas the other forts are built on flat-lying ground.

5 THE NATURE OF THE PROBLEM

Rather sadly, the geotechnical lessons that can be learnt from the Shore Forts are related to the way that they have been damaged or even lost to natural processes, and there is no information available on anything that did not survive long enough to be utilised by the forces at the time related to the Notitia. In principle, deductions can be made with respect to coastline retreat at some of the forts, changes in the coastline due to silting up of harbours and movement of coastal spits, and in the case of Stutfall Castle at Lympne, landslide activity on an old slope.

It has become conventional to attribute the Carausian rebellion to the recall of Carausius to answer charges that when he commanded the British Fleet with the remit to cut off Saxon pirates, he intercepted them on their return from pillaging and kept their spoils rather than returning them to their owners. The Saxon Shore would therefore be defences erected by Carausius to fend off the Empire when the Gaulish lands were lost, or indeed, to fortify the ports against Saxon raiders. (Fields 2006; Ireland 1986; Pearson 2002). This rather simplistic overview neglect some important facts, notably that Saxons had already been relocated to Kent in South East England, and that the Shore Forts are concentrated at the closest point to continental Europe. Moreover, there is a further concentration of the related Shore forts on the coast of Gaul, and there they stretch much further to the west, including as far as the Atlantic coast. It is difficult to imagine Saxon pirates daring to enter the English Channel and travel that far in search of prey knowing full well that they must return to wherever they came from in the North Sea through the narrow Straits of Dover. It is akin to some future archaeologist observing that there were mid 20th century fortifications on both sides of the Channel and concluding that they were defences against American pirates (as indeed, the majority were) coming directly across the Atlantic and then proceeded up the Channel rather like the Spanish Armada had in 1588!

At least the WW2 fortifications differed on both sides of the Channel. In the 3rd Century AD, both sets were built by units of the Roman Army, whether rebels or not, having trained to the same norms and practices. Indeed, in the third century, it is inconceivable that an amphibious assault of such a magnitude as to require a fortification with high walls and bastions on the part of the defenders could be mounted except by a part of the Roman military. No one else had the numbers and requisite skill at the time in NW Europe.

The division of the Gaulish forts into two commands (see Figure 2) may also be a relic of the organisation of the invasion forces under Constantius Chlorus, who took an Eastern Fleet to an unrecorded landing site, and Julius Asclepidotus who took a western fleet to a landing site near the Isle of Wight. It is possible that Constantius Chlorus' forces laid seige to Reculver, making the breach in the wall recorded by Philp (2005) and slaughtering the inhabitants of the vicus before proceeding the Londinium. The extensive fortifications on the Gaulish side of the Channel may reflect an imitation of Carausius's strategy and a response to raiding parties from Britannia and whichever tactics Carausius employed to defeat the first invasion attempt. 'Bad weather' was adduced as the reason for the first failure, but that appears to be a euphemism for defeat: even Julius Caesar claimed it!

The sheltered, quasi-inland, location of the shore forts may therefore reflect both a defensible barracks and dockyard, capable of withstanding the first wave of an assault until reinforcements arrived, but not of withstanding a dual-pronged attack, especially under the command of the usurper Allectus who lacked the naval strategic skills of his victim, Carausius.

However, the critical point is that the evidence of location is critical in determining that Reculver, Bradwell and Walton Castle were not built directly on an exposed coastline but that coastal retreat has been extensive enough to reach those initially distant from the coastline sites.

5.1 *Coastal erosion (coastline recession)*

Walton Castle is known to have been wholly lost to the sea, with the remains only now visible on the shore at extremely low Spring tides, and details of its layout are only available from antiquarian records. Our knowledge of the fort derives largely from an improbably elongated outline drawing and plan of 1623, and some 18th-century literary rather than scientific accounts. The fort was in sufficiently good state of repair to have been used by the Normans who used it as the outer bailey of a castle constructed c. 1100 and dismantled in 1175-6. In 1722 the remains were described as

> "'Tis 100 yards long, five-foot above ground, 12 broad at each end and turned with an angle. Its composed of Pepple and Roman bricks in three courses, all round footsteps of buildings, and several large pieces of Wall cast down upon the Strand by the Seas undermining ye Cliff all which have Roman brick. At low water mark very much of the like is visible some distance in the Sea. There are two entire pillars with Balls, the Cliff is 100-foot high."

The cliff is actually less than half the quoted height. In an account of 1754, the length of the west wall is given more accurately as 187 yards, and it is described as being "nine feet thick".

Several of the forts of the Saxon Shore as listed in the Notitia have lost part of their curtain wall due to erosion. Portchester, built at more or less present sea level in the inner reaches of Portsmouth harbour, lost a corner, but this was rebuilt in the Medieval Period when the fort became the outer bailey of a Norman castle, with an inner bailey and keep built in the NW corner of the fort originally in the 12th century and heightened in 1390. The damage from erosion was minimal and soon repaired.

Other forts lost part of their perimeter wall but were subsequently defended naturally by the growth of littoral sediments, including Pevensey, Richborough, and Burgh Castle, the latter probably suffering the most loss, while Reculver was more or less intact until the 19th century (Roach-Smith 1850), and having lost much of its seaward side was protected against marine erosion with a seawall and control of the beach by means of groynes. Lympne's Stutfall Castle lost its lower, seaward, section of the curtain wall but due to landsliding in the slope as a whole.

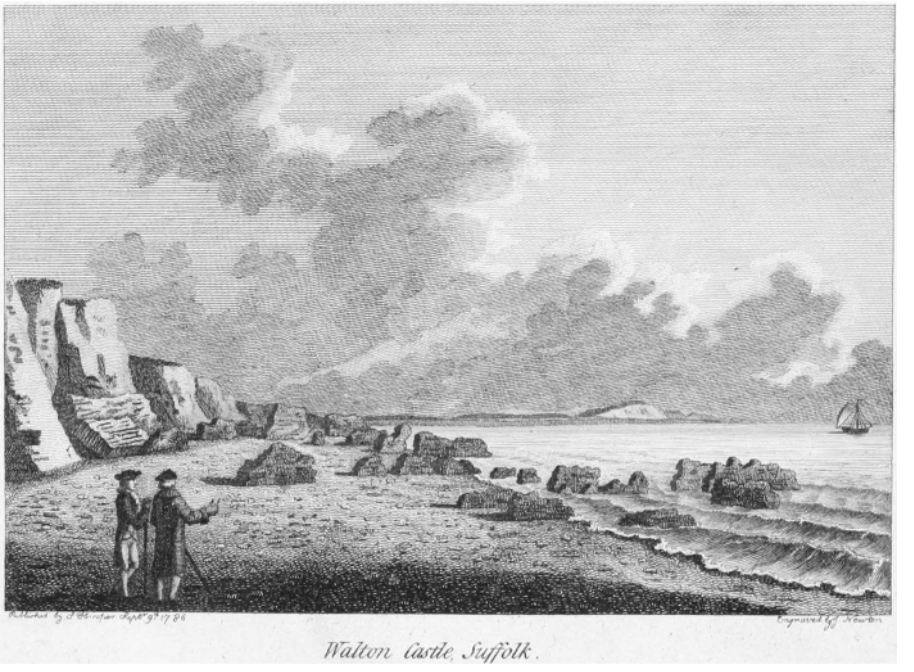

Figure 4. The loss of Walton Castle (Suffolk) to marine erosion as depicted by Francis Grose in 1786. The site, north of Felixstowe is not to be confused with a Victorian-era Walton Castle near Clevedon, Somerset.

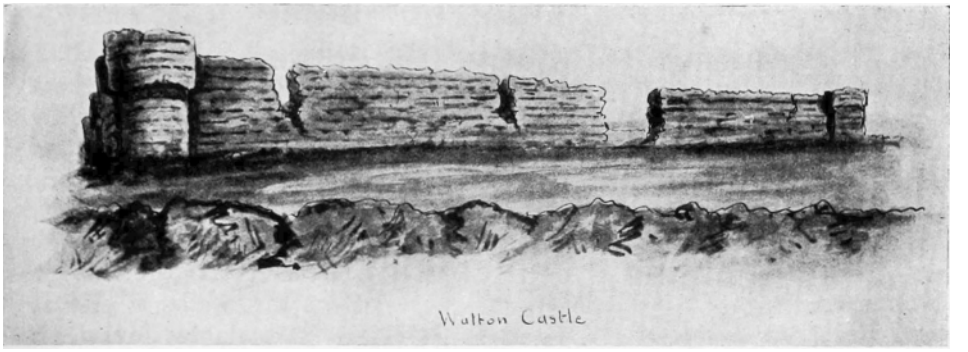

Figure 5. Walton Castle sketched in 1623, and viewed from the seaward side: the coastal cliffs are shown in the foreground. There is a suggestion of bastions on the south wall: those at each end of the east wall are jetted outwards and the overall height is much more than indicated in the accompanying account. The gap in the wall is assumed to have been an original gate.

Rather like the case of Walton Castle, several of the forts were exploited under the Normans, who built keeps and retaining the original fort as an outer bailey, as at Portchester, Pevensey, Walto,n Carisbrooke (possibly) and Cardiff Castles. At Pevensey, the keep wall is built on top of toppled towers. The castle is well above sea level, and the failures are concordant with a tiny amount of erosion at its toe, or possibly even just long-term slope processes in a steep abandoned cliff.

5.2 *Coastal changes due to siltation of harbours and the mobility of spits*

Coastal or estuarine siltation (growth of saltmarshes) has happened at Pevensey, with very little, if any, trace of the former anchorages in Pevensey Bay. Siltation has also protected the former coastal cliff at Richborough, and modified what may have been a harbour at Lympne, although that is more due to geodynamic changes in coastal gravel spits with a salt marsh developed to the leeward. It must be suspected that the site of Walton Castle in antiquity overlooked an anchorage in the lee of a coastal spit, as there is one to the north (Orford Ness) and had that shortened due to erosion in post-Roman or even early medieval times it would have exposed the Walton Castle site. Lympne is also interesting in the evolution of coastal spits as antiquarian sources (Copley 1977) note the existence nearly 500 years ago of a shingle spit defended channel from Hythe (immediately east of Lympne) for several miles along the coast, a channel that certainly no longer exists.

5.3 *Landsliding processes on 'abandoned cliffs'*

The Roman fort at Lympne is the only one of these sites built on 10-11° sloping ground, and what is known as an *abandoned cliff*. It has been damaged by at least two phases of landsliding: one unrecorded slide that has affected a part of the whole slope and dislocated the east wall and gate, and another episode of landsliding affecting the NW part of the fort, possibly the same event that displaced French House.

No trace of the Roman port has been found, but a drone photo of the site clearly shows a road leading to the west gate and which crosses the slope obliquely, so has a more suitable gradient for carts that straight up and down the slope. The road is shown in Roach-Smith's work (1852) (viz. Figure 6). That would put the fort astride the ramp from port to the crest of the slope and the pentagonal, apsoidal, shape of the fort would be more explicable if it were built to block a road than that it was somehow intended to point upslope but was set out incorrectly. The fort experienced two major phases of instability: an earlier event that affecting the East wall and gatehouse in a lobate slide running all the way down to the toe of the slope, and a later slide affecting the NW wall. The date of the earlier slide is unknown, but the later slide can be tentatively dated to 1725

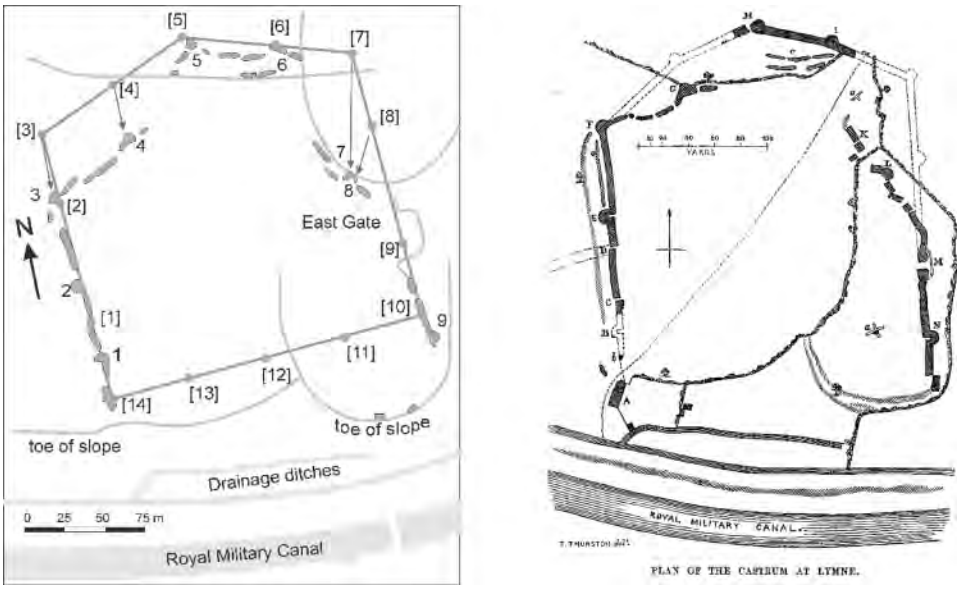

Figure 6. Plan of the landslip damaged fort Stutfall Castle at Lympne. Left: modern plan with reconstruction (Bromhead 2018; Hutchinson et al. 1985). Right: Roach-Smith, 1852 drawn for him by T. Thurston).

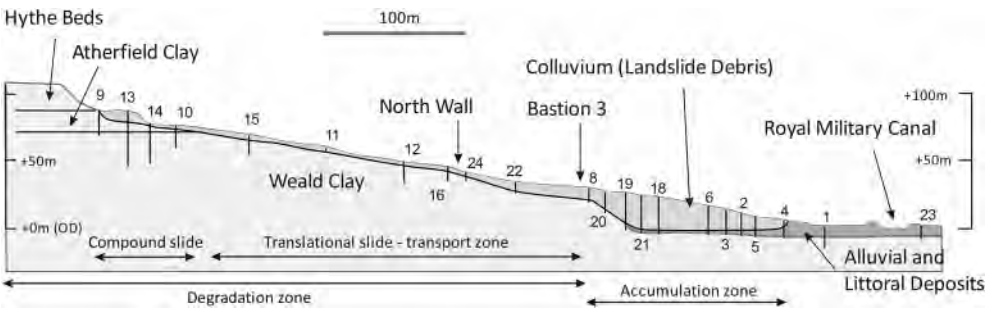

Figure 7. Cross section through the slope at Stutfall Castle, Lympne (Bromhead 2018; Hutchinson et al. 1988).

as it postdates the etching by Stukeley dated 1722 which shows the wall standing. Hutchinson and Bromhead (1996) considered the stability of this wall, which was founded on short wooden piles and concluded that its toppling was in part due to an initial landslide displacement. The study followed on from an extensive combined geotechnical and archaeological investigation conducted via a series of boreholes (Figure 7) elucidating the landsliding on the site, and pits to explore the original position of the north wall indicated by the wooden piles still in their original place with the walls having slid or toppled off them (Hutchinson et al. 1985).

The putative 1725 event affected a building called French House (now the site of the Port Lympne animal park) just below the crest of the slope somewhat to the west of the Stutfall Castle fort, but the earlier slide is undated. However, the east wall slide cannot have happened in the 4th century as that would have rendered the fort ineligible to be included in the Notitia. Since the NW wall / French House slide occurred early in the Little Ice Age, it is tempting to associate instability with a period of climatic change, and if that speculation were correct, then perhaps the East wall slide could be

dated in the Dark Ages (or post Roman, but before the Norman Conquest). An alternative might be that the NW wall / French House slide was a result of slope remodelling or water (mis)management at the French House site. In line with that supposition, it is equally possible that the East wall failure was associated in some way with the construction of Lympne Castle and Church on the crest of the slope through factors such as quarrying the Hythe Beds for building materials or surface water management. Lympne Castle (at the top of the slope) is a fortified manor house of Medieval date, possibly exploiting a lookout or signal station site contemporary with the fort.

Support for both landslide causation hypotheses comes from the 1988 failure a few km E of Stutfall Castle (Bromhead et al. 1998), which failed during an especially wet year, but also took out the remnants of a site built in the 1930s as part of a research programme into aircraft early warning systems using parabolic sound reflector dishes. Some reprofiling had been done, and remnants of a drainage pipe network from the military site were involved in the failure.

An important geotechnical problem arises with slopes that have been defended from coastal or other erosion by the growth of marshes at their toes. Where the land has been reclaimed or a sea wall built, such slopes are termed 'defended cliffs' and where the defence is a natural process (such as can include a river meandering away from them) they are termed abandoned cliffs. The distinction is made by Hutchinson in publications that arose from his study of coastal landslides, and discussed by Hutchinson & Gostelow (1976) in a study of landslides on such a slope affecting a medieval castle at Hadleigh. Specific geotechnical interest arises when the slopes degrade to a slope angle where instability is infrequent, and then what is required to make them unstable?

6 THE SURVIVOR BIAS ISSUE

All discussion of the long-term behaviour of anything based on a description of their status today is subject to what is known as 'survivor bias'. For example, we know that all the forts mentioned in the *Notitia* were actually still in commission and functional at least a century after they were built, and sometimes more. It tells us nothing about any forts that were abandoned, ruined, lost to coast erosion or even found unsuitable for military use in the intervening period. Indeed, as noted above, it is known that some forts along the coastline of SE England are NOT mentioned in the *Notitia*, for example the fort known as Walton Castle is known from Antiquarian sources to have been intact in the 17th century and lost to marine erosion in the 18th, and was actually used as the outer bailey for a medieval fortification, so had survived almost up to the modern era despite not being used by its original constructors at the time of the *Notitia*.

The questions here are why did Walton Castle not make it into the Notitia, and also, as illustrated, it lacks the regular bastions of surviving Shore Forts. The answer may lie in the geography, as the former fort's location is close to the mouths of the rivers Deben, Stour and Orwell (the latter pair still with a common mouth). Moreover, somewhat to the north a coastal spit deflects the River Alde and slightly to the south there is a complex of estuaries. If any or all of these all shared a common mouth in the earlier part of the Roman period but were separated by coastal retreat or loss of the protection afforded by a spit in the century prior to the date of the Notitia, and this also lost any port from the time, it would account for the loss of importance of Walton Castle. Today, of course, Felixstowe has become important as it is the site of a huge container port just inside the estuary.

Had Walton Castle itself not survived so long it would be completely unknown, except for some vague mentions in medieval accounts. The absence of bastions except at the corners may well have been due to robbing in the medieval era, and indeed, the peculiar shape of the fort may have been the result of some remodelling necessitated by the recession of the coastline. However, it is much more likely that the only known plan of the fort is grossly out of scale, as evidenced both by the drawn thickness of the walls and the casual inaccuracy of a reported dimension.

The speculation above also relates to the Shore Fort at Bradwell-on-Sea (Othona) constructed adjacent to the estuary of the river Colne whose mouth is very close to the mouth of the River Blackwater in Essex (Blackwater is a common name for several rivers in England) and could easily

have had a common mouth in the 3rd Century. The Colne provides access to the important Roman city of Colchester. The Bradwell fort is almost entirely consumed by coast erosion.

Also affected by coastal retreat is the fort at Reculver (Regulbium) on the N. Kent coast at the northern end of the now-reclaimed Wantsum Channel that in Roman times and later separated the Isle of Thanet from the mainland. This fort was intact when examined by antiquarians in the 18th and early 19th century, but its seaward margin was lost to coast erosion before that stretch of coast was protected by seawall and groyne construction. Partial loss of the SE corner of the Shore Fort at Richborough may also be the result of coast erosion, and indeed, the entire South wall has failed, but the site is nor protected by a coastal sediment growth , and later the construction of a railway line. Reculver appears to be of an earlier date than a number of Shore Forts, and there were certainly earlier defences at Richborough.

Whether or not Portchester Castle is Portus Adurni is a moot point, because the River Adur (some 70 km further East) has its mouth in Shoreham Harbour, and this would seem to be a logical place for a fort, although there is a view that the river was named Adur in recent times on the belief that there must have been a fort there! The fort is conveniently close to present sea level and safe from significant wave action to have only lost its SE corner to erosion, rebuilt at some uncertain date in the early medieval period when the Roman fort became the outer bailey to an inner bailey built inside the NW corner of the fort with an imposing keep springing off the Roman walls. There must be a question therefore whether the real Portus Adurni is yet to be discovered (or is irretrievably lost) and Portchester 'fits the bill' solely because it survived in such relatively good condition. Portchester Castle is of rectangular planform with regular bastions and two gates and is therefore the archetypal lay person's view of what such a fort should comprise, and that provides additional motive for its inclusion in the list of 9 Shore Forts.

7 CONCLUSIONS

Probably the best book on the subject of the Shore Forts is that by Pearson (2002), although he does perpetuate the 'Saxon Raiders' hypothesis. What is clear is that more forts were built than feature in the Notitia list a century or more later than their building. At this distance in time, it is impossible to attribute the shortness of the list to a changed strategic situation, changes to the nearby anchorages, or merely the relative suitability of the chosen sites in terms of accommodation for the units billeted there, the proximity of settlements and transport routes for supplies, etc. The Notitia list of 9 forts does not include all the forts known in relevant locations, and must reflect the needs of the Roman army over 100 years after many of the forts were constructed and even longer in some cases (errors and omissions in the Notitia excepted). It is therefore impossible to deduce Carausian needs and objectives from the Notitia forts alone.

An analogous situation relates to the chain of Martello Towers built c. 1800 around 2 sections of coast, coincidentally with some similarity to the locations of the Shore Forts. By the time of an invasion scare in the mid-19th century, many were abandoned, some were lost to coastal changes, and some had been subsumed into later defences. In the 20th century (WW1 & 2) the number in military use was even smaller. Contemporary larger scale fortifications were built at various dates, and at least one is still occupied by the military, but by a naval radar training and research establishment using technology as alien to the fort's builders in the mid 19th century as to the Romans 16 centuries before!

That so many sites were lost or damaged in the past 3 centuries points to the likelihood that there were even more constructed originally than the Notitia's nine, and also to either an acceleration of coastal retreat in the Little Ice Age, or more probably that the forts were built an appreciable distance from exposed and eroding coastlines originally.

Slopes even in sheltered estuarine locations or coasts protected by spits can suffer toe erosion (Richborough, Pevensey), resulting from river meanders (Brancaster), removal of spits by littoral drift, or long-term slope processes, the latter possibly exacerbated by anthropic interventions involving earthworks, quarrying or interference with site hydrology. (Lympne)

Rapid coastal erosion may cause the mouth of a river and estuary system to retreat landward, so that even what is *ab initio* a sheltered location may be outflanked by the coastal erosion. (Walton, Bradwell), although the changing environment may well occur over a millenium or more.

Not only does the Stutfall Castle (Lympne) case give us considerable insight into the long-term behaviour of abandoned and defended slopes that continue to degrade and move sporadically, the failure of the curtain wall of the fort reveals that there is more to the failure of a wall in a landslide system than simple earth-pressure theory can account for.

REFERENCES

Breeze, David J. 1994. *Roman Forts in Britain.* Princes Risborough: Shire Publications.

Bromhead, E. N. Curtis, R. D. & Schofield, W. 1988 Observation and adjustment of a geodetic survey network to monitor movements in a coastal landslide. *Proc. 5th International Symposium on Landslides, Lausanne.* 383–386. (Balkema).

Bromhead, E. N., Hopper, A. C. & Ibsen. M. L. 1998. Landslides in the Lower Greensand Escarpment of South Kent. *Bulletin of Engineering Geology & the Environment,* Vol. 57, No. 2, 131–144.

Bromhead, E. N. & Ibsen, M-L. 2004. Landslide and coast erosion damage to historic fortifications in SE Britain. Landslides Vol 3, No. 4, 341–347.

Bromhead, E. N., Ibsen, M-L. & Tapete, D. 2013. 19th and 20th century coastal military installations affected by coastal erosion in the UK. *Geotechnical Engineering for the Preservation of Monuments and Historic Sites. Editors Bilotta, E; Flora, A; Lirer, S. & Viggiani, C.* 191–198 *CRC/Balkema*

Bromhead, E. N. 2018. The landslip-damaged Roman fort at Lympne in SE England. *From: Rose, E. P. F., Ehlen, J. & Lawrence, U.L. (eds) Military Aspects of Geology: Fortification, Excavation and Terrain Evaluation. Geological Society, London, Special Publication 473*

Copley, G. J. 1977. *Camden's Britannia: Kent.* Hutchinson & Co., London.

Cunliffe, B. 1980. Excavations at the Roman fort at Lympne 1976–8, *Brittannia,* Vol. 11, 227–88.

Dvorak, J. & Mastrolorenzo, G. (1991) The Mechanisms of Recent Vertical Crustal Movements in Campi Flegrei Caldera, Southern Italy (Special Paper (Geological Society of America)), Geological Society of Amer, 47p.

Fields, N. 2006. *Rome's Saxon Shore – Coastal Defences of Roman Britain AD 250–500* (Fortress 56). Botley: Osprey Publishing.

Hutchinson, J. N. 1980. The record of peat wastage in the EastAnglian fenlands 1848–1978. *J. Ecology 68, No. 1, 229–249.*

Hutchinson, J. N. & Gostelow, T. P. 1976. The Development of an Abandoned Cliff in London Clay at Hadleigh, Essex. *Philosophical Transactions of the Royal Society of London. Series A, Mathematical and Physical Sciences, vol. 283, no. 1315, The Royal Society, 1976, pp. 557–604,*

Hutchinson, J. N., Poole, C. Lambert, N. & Bromhead, E. N. 1985. Combined archaeological and geotechnical investigations in the Roman fort at Lympne, Kent. *Brittannia,* Vol. 16, 209–239.

Hutchinson, J. N. & Bromhead, E. N. 1996. Back analysis of the collapse of a Roman wall built on landslip. *7th International Symposium on Landslides, Trondheim, Balkema,* 1243–1250.

Hutchinson, J. N., Bromhead, E. N. & Chandler, M. P. 2002. Landslide movements affecting the lighthouse at Saint Catherine's Point, Isle of Wight. *Conference on Instability: Planning & Management, Thomas Telford, May 2002.*291–298.

Ireland, S. 1986. *Roman Britain: a sourcebook.* Routledge (Second edition 1996: Taylor & Francis).

Pearson, A. 2002. *The Roman Shore Forts: Coastal Defences of Southern Britain.*

Philp, B. 2005. *The excavation of the Roman Fort at Reculver, Ken*t. Dover: Kent Archaeological Rescue Unit.

Roach-Smith, C. 1850. *The Antiquities of Richborough, Reculver, and Lymne, in Kent*. London: John Russell Smith.

Roach Smith, C. 1852. *Report on Excavations on the site of the Roman Castrum at Lymne in Kent,* London. Published privately for subscribers, and republished by Harry Margary, Lympne Castle, Kent (undated).

Stukeley, W. 1776. *Itinerarium Curiosum or an account of the antiquities and remarkable curiosities in nature or art.* Second Edition, London: privately published.

Wilson, R. J. A. 1980. *Roman Forts: An illustrated Introduction to the Garrison Posts of Roman Britain*. Bergstrom and Boyle Books.

Geotechnical Engineering for the Preservation of Monuments and Historic Sites III – Lancellotta, Viggiani, Flora, de Silva & Mele (Eds)

Static behaviour of in scale masonry vaults under imposed settlement of the supports

F. Roselli, M. Alforno & F. Venuti
Politecnico di Torino, Department of Architecture and Design, Torino, Italy

A.M. Bertetto
Politecnico di Torino, Department of Structural, Geotechnical and Building Engineering, Torino, Italy

ABSTRACT: The European architectural heritage is heavily characterized by the use of unreinforced masonry spatial structures, like vaults, which represent vulnerable elements in historical buildings. In recent years, the use of in-scale models to investigate the structural behaviour of vaults has largely increased in scientific research. In-scale models allow to overcome the difficulty of performing destructive tests on real structures and allow to investigate the complex three-dimensional failure mechanisms derived by different kinds of load, including the settlement of the supports. In this study, an experimental campaign is carried out on 1:5 in-scale models of barrel vaults with different brick laying techniques, to investigate their structural behaviour un-der settlement of the supports. Two brick patterns are tested: radial and vertical, with bed joints respectively orthogonal and parallel to the head arch plane. Models are built with cement blocks and low cohesion mortar, to simulate the typical historic masonry behaviour. Two tests for each brick arrangement are carried out on the models, which are tested under shear settlement, involving the movement of one abutment normally to the head arch plane. The acquisition process involves image and video recording, while a constant monitoring with the 3D-Digital Image Correlation (DIC) is performed to measure the three-dimensional deformations of the structures. The acquired information allowed to obtain, for each test, crack patterns, ultimate displacements and failure mechanisms. Comparison of the results highlights different behaviour between the vaults built with the two brick arrangements, in terms of different typical crack phenomena leading to different, local or global, failures. The results of the research could help practitioners dealing with interventions on architectural heritage to properly interpret the collapse mechanisms on existing vaults and could be used, in future work, in the validation of numerical models for brick vault analysis.

1 INTRODUCTION

Masonry vaults heavily characterize the European architectural heritage, with a great diffusion along various centuries, before the growth of the modern construction techniques. Such a long period of utilization has as a result a great variety in the vaults typologies, shapes, materials and construction techniques. Due to this great diffusion in historical buildings, vaults still represent one of the most vulnerable elements in the building system. As demonstrated by the recent seismic activity in the centre of Italy, the vaulted structures can respond to high movements of their support with the creation of plastic hinges that lead to new static determined states with complex three-dimensional behaviour and cracking phenomena. These phenomena are typically related to the

DOI 10.1201/9781003308867-37

form-resistant nature of the vaults, deriving from the overall geometry of the structures. Nevertheless, this macro-geometry can be realized with the aforementioned great variety in the construction techniques, with different results.

In recent years, a few studies have focused on the importance of the brick patterns, namely, the micro-geometry (Alforno et al. 2020a), in the global three-dimensional behaviour of vaulted structures (Alforno et al. 2019, 2020b; Baratta & Corbi 2012; Barbieri et al. 2004; Boni et al. 2021; Calderini & Lagomarsino 2004;; ;oraboschi 2014;; Wendland 2007). The topic of the brick pattern has a great tradition in the treatises of the past centuries (;hoisy 1883; Curioni 1870), with a focus on construction issues, and very poor attention to its reflection on the structural behaviour of the whole elements. Today, in virtue of the new available scientific knowledge and methodologies, the evaluation of the brick pattern influence on the global structural behaviour of the vaults offers good possibilities for research.

The form-resistant nature of vaulted structures allows studying their behaviour by evaluating the geometry changes through physical in-scale models, without taking into account forces and material resistances, as demonstrated by the long tradition of models used in structural design (Brunelleschi, Gaudì, Frei Otto, etc.). The spread in technologies offers new possibilities for researchers in the usage of physical models and in the management of the acquired data: in recent years many experimental campaigns have been carried out involving various vault typologies (Calvo Barentin et al. 2017; D'Altri et al. 2019; Rossi et al. 2016), and monitoring systems (Digital Image Correlation (Manuello & Riberi 2021)).

The present work aims to experimentally investigate the influence of the brick pattern in the structural behaviour of in-scale barrel masonry vaults under imposed settlements of the supports. The collected data could be used in future work to validate numerical models (Eslami et al. 2012;; Ferrero et al. 2021; Milani et al. 2016).

In Section 2, the case study and experimental set up are described. Section 3 is focused on the acquisition methodologies employed in the experimental campaign. Results are presented in Section 4, while conclusions and perspectives are outlined in Section 5.

2 DESCRIPTION OF THE CASE STUDY AND EXPERIMENTAL SET UP

The adopted case study is a 1:5 model of a barrel vault with a square base: the net span of the vault is approximately 40 cm, the rise is about 12 cm, and the length of the vault is 40 cm (Figure 2). The barrel vault is made of blocks of dimensions $9 \times 20 \times 40$ mm, which mimic in scale 1:5 the dimensions of classic masonry bricks.

The bricks are arranged according to two patterns:

- a radial pattern (R), composed of multiple rows of rowlock oriented bricks, placed orthogonal to the main vertical plane of the vault (Figures 1a and 2a);
- a vertical pattern (V), where the bricks are laid in rows parallel to the main vertical plane of the structure (Figures 1b and 2b).

The experimental set up of the barrel vault was designed to allow both opening and shear tests to be performed (Figure 2). Specifically, one of the abutments is fixed in the x direction and allowed to move in y direction (simple shear mechanism), while the other abutment is fixed in the y direction and can be moved in x direction (opening mechanism). Four pins support the centring, and the slab where they are fixed can be lowered to allow the centring removal after completion of the vault.

The setup is completed by a further device, used only during the construction of the vault with vertical pattern. It consists of a boundary vertical panel, fixed at one of the vault boundaries, against which successive brick courses make contrast by means of clamps. This solution avoids out-of-plane rotation of the new courses and provides stability during construction thanks to the pre-compression exerted by the clamps.

Imposed settlements are measured by a digital calliper installed in correspondence of the moving abutment.

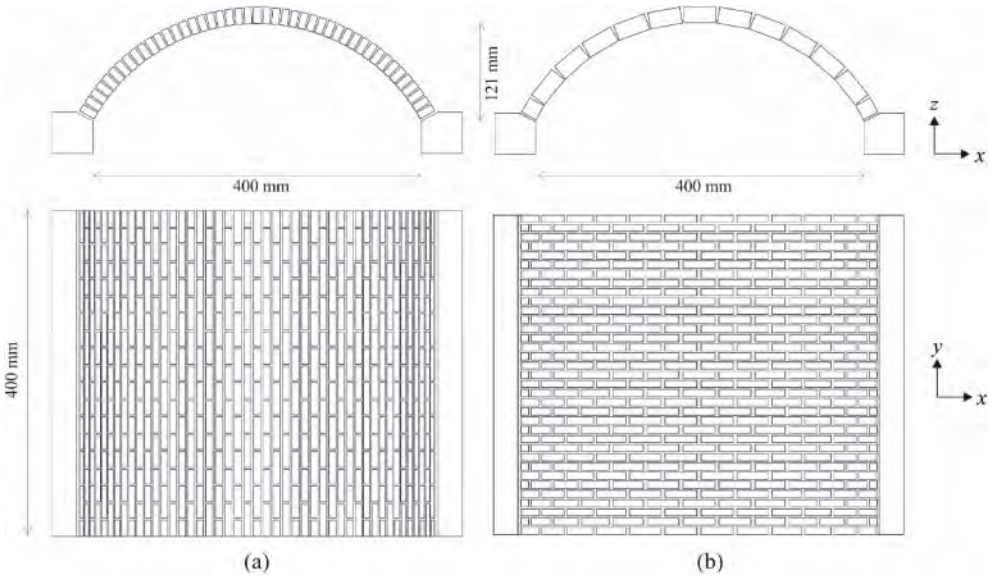

Figure 1. Geometry of the barrel vault in the radial (a) and vertical (b) configuration.

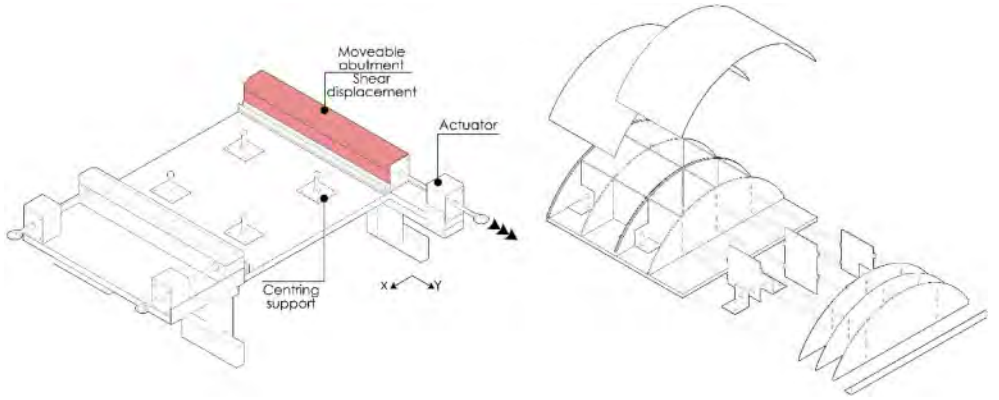

Figure 2. Experimental set up of the barrel vault: testing device and detail of the centring.

The choice of materials to fabricate blocks was mainly dictated by the possibility to easily produce many units in a reduced time and with low cost, and by the need to obtain a sufficient dimensional uniformity between the blocks. According to these needs, cement blocks were fabricated with a formwork made of bicomponent silicon rubber. This solution was chosen due to its reduced cost and ease of casting and stripping. The chosen mix is made of cement and water only, with 2:1 ratio. Stripping is made after 24 hours.

The mix adopted for mortar is the same used by D'Altri et al. (2019) in a 1:12 in-scale model of a gothic barrel vault. It is composed of 3 parts of Silica sand, 1 part of lime, 1 part of water and by the addition of PVA glue and water. The obtained mortar has weak cohesion, allowing cracks to open along the joints, according to the classical Heyman's theory.

All the built models (Figure 3) are composed of 450 bricks with a similar global mortar quantity. A total of 4 models, two for each arrangement, are tested under shear displacement.

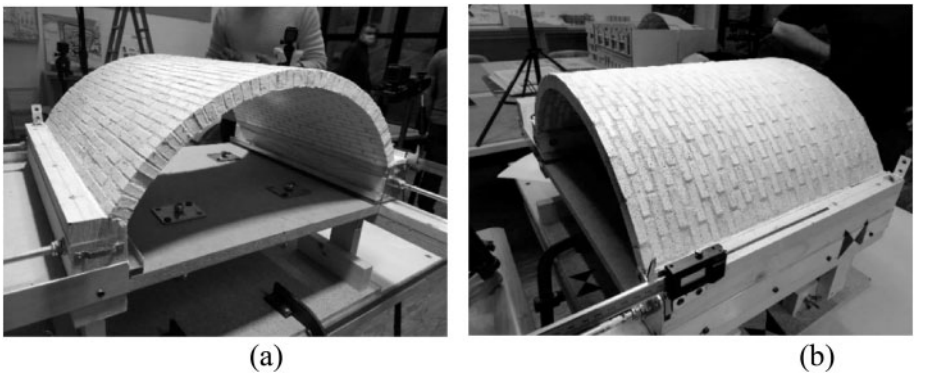

Figure 3. The built model in the radial (a) and vertical (b) configuration.

3 ACQUISITION METHODOLOGIES

During the tests, the direct observation of the phenomena occurred to the structures is accompanied by the acquisition of relevant data. These acquisitions are performed with contactless solutions to avoid alterations of the test proceeding. A constant video acquisition is performed by four synchronized GoPro Hero 5 session cameras distributed around the vault models (Figure 4a) with the aims of relating the cracking phenomena with the imposed displacement, monitored with

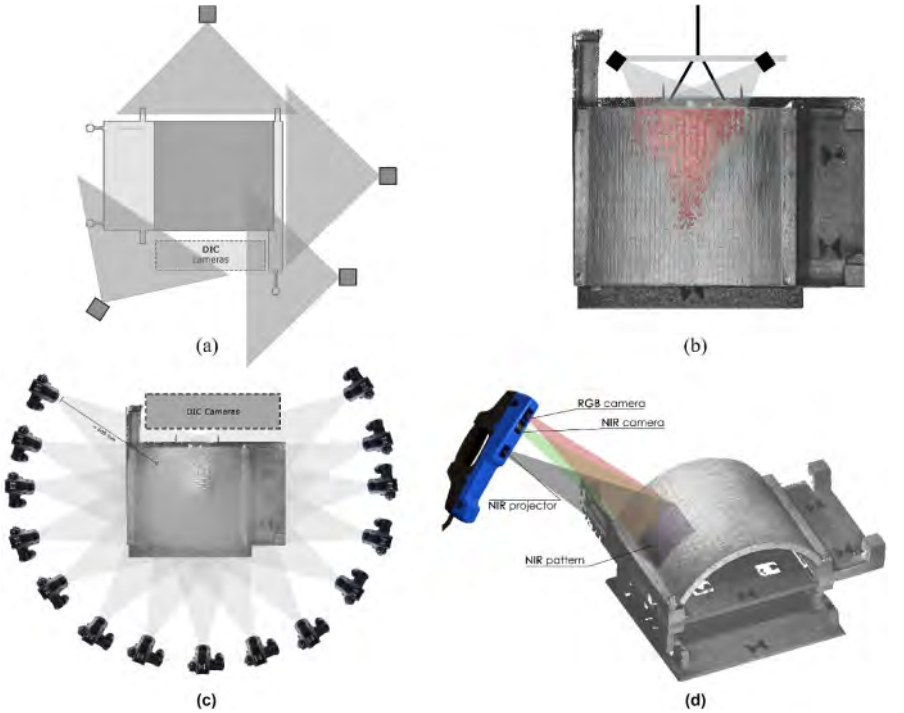

Figure 4. Summary of the adopted acquisition methodologies: (a) GoPro Hero 5 session cameras, (b) DIC cameras, (c) close-range photogrammetry, (d) range-based structured light scanning.

a digital calliper, and capturing the collapse mechanism of the structures. Due to the destructive nature of the tests, three-dimensional data of the models are acquired in several steps of the imposed displacement in order to manage the spatial data of the structures after their failure. Image-based close-range photogrammetry (Figure 4c) and range-based structured light scanning (Figure 4d) solutions are used with these aims, because of their common use in literature in the data acquisition for moveable heritage (Patrucco et al. 2019). At the end of the process, the result obtained is a series of three-dimensional dense point-clouds with an estimated error of about 1 mm. Furthermore, Digital Image Correlation (DIC) is performed, on a little portion of the models (corresponding with the key voussoirs of the vaults) (Figure 4b), for monitoring the three-dimensional deformations of the structures. The data are acquired, as couples of stereoscopic images, by steps of 0.1 mm of imposed displacement. The result obtained is a series of quadrangular meshes with a submillimeter estimated error.

4 EXPERIMENTAL RESULTS

The high-speed and high-resolution cameras provide images of the collapse mechanisms of the tested models. In Figure 5 a selection of images of the failure, from the most representative perspective, is reported. Differently from arches, vaults involve complex three-dimensional failure mechanisms. The latter are quite different for vaults with different brick pattern, but also between vaults with the same brick arrangement.

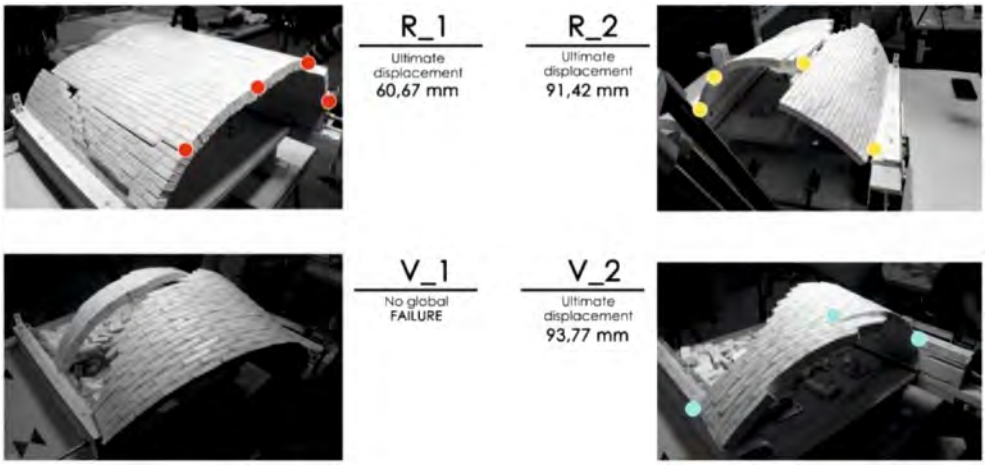

Figure 5. Collapse mechanisms of the tested models.

The R models show a four-hinge mechanism, even though they reach the collapse at quite different ultimate displacements (60.67 mm in R_1 and 91.42 mm in R_2). The hinges run across the whole depth of the model following the longitudinal joints, with two of them placed at the abutment interface and one in the proximity of the key bricks. On the contrary, the V models show a different behaviour, characterized by the local collapse of some arches and by the rigid rotation of the separated portions of the vault. The rigid rotation of the vault on the abutment is particularly evident in the V_1 model, which reaches the end of displacement range (fixed at 150 mm) without a global failure. The V_2 model collapses at 93.77 mm of imposed displacement with a three-hinge mechanism, developed among the arches still in compression, with the slipping of the structure from one of the abutments.

The critical analyses of the crack patterns experienced in the models reveal substantial differences between the two bricks patterns (Figure 6). In the R models most of the cracks are represented by fractures occurring along the longitudinal joints. These major cracks appear to be quite straight

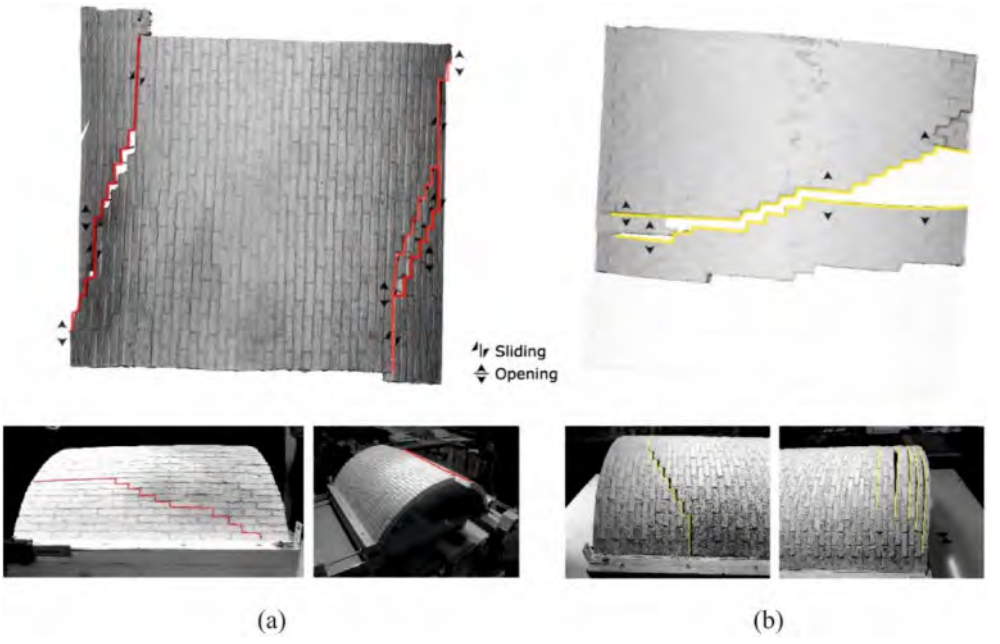

Figure 6. Crack pattern of R (a) and V (b) vaults.

along a single longitudinal joint or inclined involving multiple rows of bricks (Figure 6a). On the other hand, in the V models the major cracks occur in the radial joints, leading to the formation of separate portions of the structure (Figure 6b) that lead to local collapses. Also in V models, the major cracks can assume either straight or inclined directions, reasonably depending on construction issues.

Besides the described main differences in the crack pattern between vaults arranged with different brick patterns, some minor differences occur between vaults arranged with the same pattern, as clearly visible in Figure 7 for the R_1 and R_2 vaults. Specifically, the major crack position varies due to construction issue, i.e., to the impossibility to perfectly replicate the model construction. In the R_1 vault the two major cracks lead to the separation of the central portion, that starts rotating upon the sliding haunches; in the R_2 model, the major crack along the top of the vaults extrados

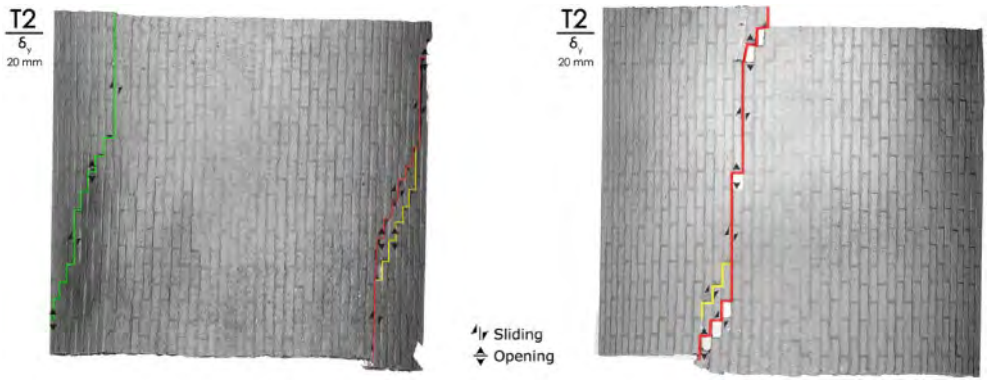

Figure 7. Crack pattern of R_1 (a) and R_2 (b) vaults for imposed displacement of 20 mm.

leads to a major sliding between the two portions, which cause small local failures near the heads and the rigid rotation of the two haunches upon the abutment, while the contact surface between them is reducing. This difference in the collapse mechanism induces quite different displacement capacity, being the ultimate displacement of the R_2 vault 50% higher than the one of the R_1 vault.

A deeper insight into the phenomena observed and recorded on each vault during the tests is provided in Figure 8 for the R_1 vault, as an example. In particular, Figure 8 compares the macroscopic visible phenomena reconstructed by direct observation, video acquisition and three-dimensional data managing of the range-based and image-based acquisition techniques at different stages of imposed displacement (Figure 8c top) to the mean displacement of a control linear strain-gauge (Figure 8b, corresponding with the key voussoirs of the vault) versus imposed displacement recorded through DIC (Figure 8c bottom). This comparison shows how the mean displacement linearly increases until the step (about 16 mm) corresponding to the reduction in the axial displacement (y) of the central portion of the vault and to the development of the inclined longitudinal crack that separates the right haunch portion. Then, the mean displacement remains almost constant and start increasing again in correspondence of the step (about 51 mm) when the structure starts rotating until collapse.

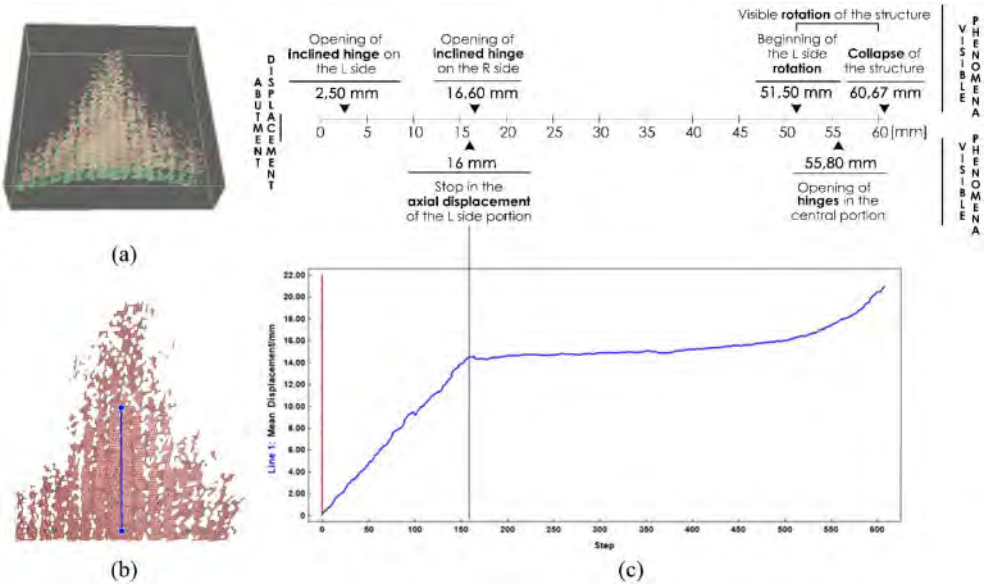

Figure 8. DIC cameras' field of view at step 0 (red) and 244 (green) of the imposed displacement (a), position of the linear strain-gauge (b), time history of mean displacement of the linear strain-gauge on the R1 vault (c).

5 CONCLUSIONS

In conclusion, the experimental campaign carried out in the present work has demonstrated the influence of the brick pattern on the structural behaviour of masonry barrel vaults under shear settlements of the abutments. The research has assessed two different typologies of characteristic cracks between models with radial and vertical arrangements of the bricks. These crack phenomena present common features but different directions and implications on the global behaviour of the structures also in terms of collapse (with the presence of 3 or 4 hinges mechanisms). The recognition of their nature can help practitioners and scholars to understand the shear nature of the displacement

on real vaults. Moreover, the experimental tests have revealed the influence of the construction imperfections on the global behaviour of the masonry vaults: as previously reported, the formation of similar longitudinal cracks with different positions in both R models lead to different ultimate displacements and different implications on the structure stability. This difference must be related to the manual nature of the brickwork and the difficulty in the construction of perfectly similar mortar joints.

The results of the research also suggest the good interaction between different data acquisition and managing techniques: close-range photogrammetry and range-based structured light scanning, already consolidated in the fields of the moveable heritage, demonstrate a good integration with data provided with DIC methodology, in constant growth in the engineering field (Shao & He, 2021). The present work has obtained a good agreement between the DIC analysis results, and the visible phenomena recollected during the experimental tests, demonstrating the good possibilities of DIC monitoring on masonry construction. The use of 3D DIC with more relevant coverage of in-scale masonry vaults models (major ranges, use of multiple cameras) can lead to a properly deep knowledge and management of the three-dimensional deformation of the masonry vaults.

ACKNOWLEDGEMENTS

F. Chiabrando, G. Sammartano and G. Patrucco (Politecnico di Torino, Department of Architecture and Design) are greatly acknowledged for the photogrammetric and laser scanner survey of the models as well as for the support in postprocessing of data.

REFERENCES

Alforno, M., Monaco, A., Venuti, F. and Calderini, C., 2020a. Validation of simplified micro-models for the static analysis of masonry arches and vaults, International Journal of Architectural Heritage, 1–17, DOI: 10.1080/15583058.2020.1808911

Alforno, M., Venuti F., and Monaco, A. 2020b. The structural effects of micro-geometry on masonry vaults, Nexus Network Journal, 22: 1237–1258

Baratta, A. and Corbi, O. 2012. The static behavior of historical vaults and cupolas. Journal of Heritage Conservation, 32: 65–81.

Barbieri, A., Carloni, C. and Di Tommaso, A. 2004. Masonry orthotropic vaults in historical construction: the herring-bone pattern. In Proceedings of the 4th International Conference on Arch Bridges ARCH 04 (Barcelona, Spain).

Boni, C., D. Ferretti and E. Lenticchia. 2021. Effects of Brick Pattern on the Static Behavior of Masonry Vaults, International Journal of Architectural Heritage, DOI: 10.1080/15583058.2021.1874565.

Calderini, C. and Lagomarsino, S. 2004. The effect of the masonry pattern on the global behaviour of vaults. In Proceedings of the 4th International Conference on Structural Analysis of Historical Constructions (Padova, Italy).

Calvo Barentin, C., T. Van Mele and P. Block. 2017. Robotically controlled scale-model testing of masonry vault collapse, Meccanica, 53(7): 1917–1929.

Choisy, A. 1883. L'art de batir chez les Byzantines. Société anonyme de publications périodiques, Paris.

Curioni, G. 1870. L'arte di Fabbricare. Costruzioni civili, stradali, idrauliche. Negro, Torino.

D'Altri, A.M., De Miranda, S., Castellazzi, G., Sarhosis, V., Hudson, J. and Theodossopoulos, D. 2019. Historic barrel vaults undergoing differential settlements, International Journal of Architectural Heritage, DOI:10.1080/15583058.2019.1596332

Eslami, A., H.R. Ronagh, S.S. Mahini and R. Morshed. 2012. Experimental investigation and nonlinear FE analysis of historical masonry buildings – A case study, Construction and Building mMaterials, 35:251–260

Ferrero, C., M. Rossi, P. Roca and C. Calderini. 2021. Experimental and numerical analysis of a scaled dry-joint arch on moving supports, International Journal of Masonry Research and Innovation, 10.1504/IJMRI.2021.10035577

Foraboschi, P. 2014. Resisting system and failure modes of masonry domes, Engineering Failure Analysis, 44: 315–337.

Manuello, A., Riberi, F., 2021. Form-finding of pierced vaults and digital fabrication of scaled prototype. Curved and Layer. Struct. 2021; 8:1–15.
Milani, G., M. Rossi, C. Calderini and S. Lagomarsino. 2016. Tilting plane tests on a small-scale masonry cross vault: Experimental results and numerical simulations through a heterogeneous approach. Engineering Structures, 123: 300–312.
Patrucco G., Rinaudo, F., Spreafico, A. 2019. A New Handheld Scanner For 3d Survey Of Small Artifacts: The Stonex F6, in The International Archives of the Photogrammetry, Remote Sensing and Spatial Information Sciences, Volume XLII-2/W15, 2019 27th CIPA International Symposium "Documenting the past for a better future", Ávila, Spain.
Rossi, M., C. Calderini and S. Lagomarsino. 2016. Experimental testing of the seismic in-plane displacement capacity of masonry cross vaults through a scale model. Bulletin of Earthquake Engineering, 14: 261–281
Shao X.X., He X.Y., 2021, Real-time 3D Digital Image Correlation for Large Deformation and Rotation Measurements Based on a Deformation Transfer Scheme, in Experimental Mechanics.
Wendland, D. 2007. Traditional vault construction without formwork: masonry pattern and vault shape in the historical technical literature and in experimental studies. International Journal of Architectural Heritage, 1(4): 311–365

Geotechnical Engineering for the Preservation of Monuments and Historic Sites III – Lancellotta, Viggiani, Flora, de Silva & Mele (Eds)

Long term geodetic measurements in the Piazza del Duomo (Pisa, Italy) and its relevance for monitoring of Leaning Tower

G. Caroti & A. Piemonte
Dipartimento di Ingegneria Civile e Industriale, Laboratorio A.S.T.R.O., Università di Pisa, Pisa, Italy

N. Squeglia
Dipartimento di Ingegneria Civile e Industriale, Università di Pisa, Pisa, Italy

ABSTRACT: The whole Pisa plains, including the world-renowned Piazza dei Miracoli, is subjected to subsidence. This phenomenon has long been investigated, using a benchmark placed on the Baptistery as vertical reference. Since the '90s, in sight of consolidation works on the Leaning Tower, main focus was placed on studying subsidence at site, rather than global, level. To this purpose, in 1993 a new benchmark, called 999, was installed in order to prevent shifts due to local and surface disruptions, and provide a vertical reference for subsequent investigations. Since instating benchmark 999, evolution over time of site-wide subsidence has also been investigated. This paper presents a detailed study for recovering historical information about vertical references used from early XX century to date and to homogenize the different data sources. The results have been used in geotechnical investigations to analyze shifts and distortions of each monument, along with each monument-soil interaction, for their appropriate preservation.

1 INTRODUCTION

Piazza dei Miracoli and its monuments (Figure 1) have long been subject to measurements. The main focus has consistently been placed on the Tower, whose inclination has always provided a topic for investigation and monitoring.

Earliest data related to modern inclination measures of the Tower come from E. Cresy and G. L. Taylor, which, in 1817, performed two overhang measures by dropping a plumb line from the VII order to the support plane of the elevation walls, resulting in 12 feet, 6 inches 1/4 (3.82 m) and 12 feet, 7 inches (3.84 m), respectively (Lancellotta et al. 2017; Lunardi 1993).

The levelling surveys carried out during the past 100 years in the Piazza dei Miracoli have been targeted, until the 1990s, to the assessment and investigation of relative vertical shifts among the benchmarks laid out over the Piazza, rather than monitoring how subsidence, which involves the entire Pisa plains (Caroti 2000; Caroti et al. 1999), is related with the Piazza and its reference benchmark.

The earliest surveys aimed at the analysis of vertical shifts among benchmarks date back to 1911. In that occasion, the reference benchmark, i.e. the one whose elevation is assumed constant between successive surveys, was provided by a line, signed by the initials "L.P.", etched on the right-hand jamb of the main door of the Baptistery. The benchmark was included in the National Geodetic Levelling Network of the Italian Geographical Military Institute (I.G.M.), and in the present paper will be referred to as IGM-CV-1886 (Figure 2).

The elevation of this benchmark has been defined as that measured by I.G.M. in 1886 at 6.7917 m above mean sea level.

 DOI 10.1201/9781003308867-38

Figure 1. Pisa, Piazza dei Miracoli, 1931 (Historic archive, Family Gen. Enrico Pezzi).

Figure 2. Location of IGM-CV-1886 and φ' benchmarks.

Explanatory notes accompanying the technical reports for the 1965–1966 (IGM, 1966) altimetric monitoring surveys state that "l'interesse è rivolto ai confronti tra dislivelli e per questo scopo il riferimento altimetrico ha poca importanza" ("the focus lies in comparing elevation differences, and to this purpose altimetrical references are of little interest"), but "…al fine di legare i raffronti relativi alla realtà della situazione più probabile…" ("in order to link relative comparisons to the actual, most probable situation") IGM-CV-1886 was preserved as altimetrical reference with the absolute elevation of 1886.

Levelling surveys performed in 1965 and 1966 allowed to link vertical benchmark IGM-CV-1886 to horizontal benchmark φ', set up in 1928 on the threshold of the main door of the Baptistery near

its right-hand jamb, below IGM-CV-1886 (Figure 2). Elevation of φ' was measured at 4.28361 m and was held as reference for later surveys.

The statement contained in the explanatory notes is only partially shareable. The fact that level differences are the most important information is dependent on the continuity of the object structure. While the statement is true if referring to the surface on the entire Piazza, this is not the case when seeking information on the settlements which single building are subjected to, since level differences measured between different building include the effect of different concurring phenomena. As already discussed in Squeglia & Bentivoglio (2015), movements of the Piazza also definitely affect movements of the Tower, but referring to a benchmark placed on the Baptistery would also add interactions between Baptistery and soil of little or no relevance for the Tower to the level difference between Baptistery and Tower.

Also for this reason, in view of the works for the stabilization of the Tower in the 1990s, members of the International Committee for the safeguard of the Pisa Tower recognized the importance of assessing local subsidence and investigating its effects, along the ongoing monitoring of differential settlements. To this purpose, deep benchmark 999 was established in 1992 by anchoring a 60 m invar rod to the lower sand layer (Figure 3); the following year, its elevation was measured at 3.57232 m. Benchmark 999 and its elevation provide the current reference and constraint for all levelling surveys.

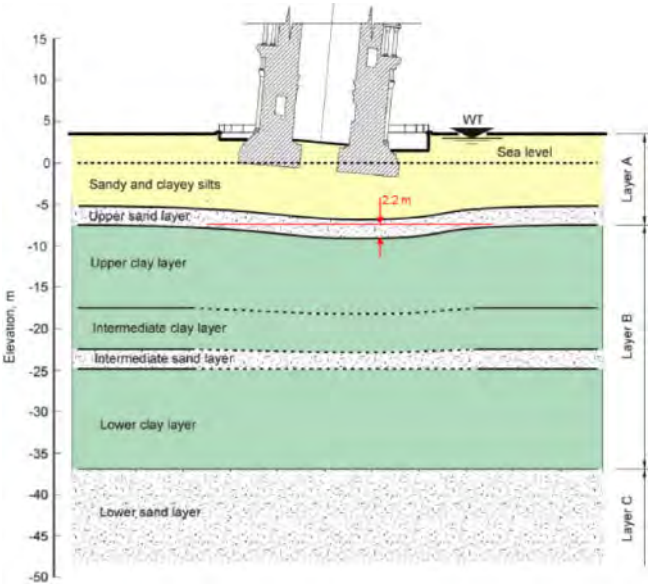

Figure 3. The subsoil of the Tower.

In recent years some interest arose in extending the investigations of subsidence in the Piazza area also prior to 1993, since there is the possibility that salinity of water in lower sand layer change because of intrusion of sea water.

Within this scope, the present paper reports an in-depth investigation aimed at the recovery of historical information referring to altimetric benchmarks used since early XX century to this date, and achieving data consistency independent from the source.

To this purpose, it was necessary to detail the timeline of altimetric monitoring activity in the Piazza dei Miracoli (outlined in Table A1 for easier comprehension of the different events involving the site) and reconstruct the shifts of both IGM-CV-1886 and $\varphi' \equiv 100$ Baptistery benchmarks from late XIX century to date. Results of this studies have been used in geotechnical investigations aimed

at the evaluation of settlements and distortions of each monument, along with each monument-soil interaction, in order to provide a support tool for best preservation of the monumental site.

Data are available from 1886 onwards. Within this time span, two major groups can be defined as follows:

- Surveys performed up to 1991 with mechanical optical instruments, for which neither instrument features nor standard deviation of benchmark elevation are given. Nevertheless, since those were high-precision surveys, it is assumed that they complied with standard tolerances provided for that kind of measures;
- Surveys performed from 1991 onwards, for which full survey specifications are provided, i.e. instruments, calculation methodologies and standard deviation of adjusted elevation. For these measures, standard deviation as calculated consistently complies tolerance range provided for high precision elevation surveying.

Given the uncertainty of information related to historic survey data, and the extent of vertical shifts in the 1 cm–1 dm range (i.e. several magnitude orders greater than instrument precision), the discussion on vertical shifts extent does not take into account standard deviation values, assuming that these do not affect trend analysis in the long term.

2 SUMMARY OF AVAILABLE DATA

2.1 *Elevation monitoring from early 1900s to the 1990s*

Official levelling benchmarks set up in the Piazza dei Miracoli area date back to late XIX century. From 1878 to 1900, I.G.M. set up and measured the foundation National Altimetric Network on the entire national territory.

Within these proceedings, in 1886 two benchmarks were set up by the main entrance of the Baptistery and subsequently measured (Regia Commissione Geodetica Italiana, 1911):

- A circle, etched on the last step by the left-hand jamb of the door facing the Cathedral, acting as horizontal benchmark with absolute elevation of 4.2930 m. This benchmark, referred to as IGM-CO-1886 in the paper, was destroyed after 1943;
- Vertical benchmark IGM-CV-1886, made up by a line, captioned with the letters "L" and "P", etched on the right-hand jamb of the above mentioned door (Figures 2 and 4), with absolute elevation equal to 6.7917 m.

Figure 4. Detail of benchmark IGM-CV-1886.

Archive researches show that around the same time other benchmarks, set up on the floor of the christening font in the Baptistery and on the ground floor by the Tower entrance, were measured. These benchmarks have all been destroyed upon reconstruction works.

To the best of the Authors' knowledge, until 1908 no geometric levelling was provided to monitor vertical shifts of the Piazza and the Tower. In 1907, alarming news about Tower stability captured the attention of the competent authorities, which, between December 1907 and February 1908,

established the "Commissione per lo studio delle condizioni statiche del Campanile", also known as Bernieri Committee (Commissione Pisana per gli Studi sulla Torre Pendente, 1927). The members of the Committee were: dr. Giovanni Cuppari (Hydraulic Engineer), Professor Paolo Pizzetti (Chair of Geodesy at Pisa University), Professor Mario Canavari (Chair of Geology at Pisa University), Dr. Francesco Bernieri (Head Engineer at the Pisa Municipality) and Dr. Agenore Socini (Head of the Pisa Bureau of Monuments).

The Committee presented the results of their investigations in several reports published by Opera Primaziale Pisana in 1913 (Commissione Pisana per gli Studi sulla Torre Pendente, 1913). The reports of Dr. Bernieri, Prof. Canavari and Prof. Pizzetti are most relevant for the purposes of the present paper.

In "Descrizione Generale e rilevamento del Campanile" Dr. Bernieri provided building information, main dimensions and inclination measures, along with several drawings. Besides, by comparing "La pendenza attuale in confronto di quella d'altri tempi" (current vs. ancient inclination) with particular focus to the "piombatura" (plumblining) performed 1817 by Cresy and Taylor (Cresy & Taylor 1829), he demonstrated that until 1911 the inclination had increased by 5.5 millimeters for each meter of Tower axis.

Within the same investigation, Professor Pizzetti reported on "Studi Geodetici" (geodetical investigations), stating that, around the Tower, 6 interred benchmarks – labelled with the letters A to F – had been set up in protective cockpits, providing for robustness and durability. For each benchmark, the reference was provided by the flat top of a bronze pin embedded in the foundations, on which the corresponding letter was etched, along with the wording "Studi Campanile 1910–11", Figures 5 and 6.

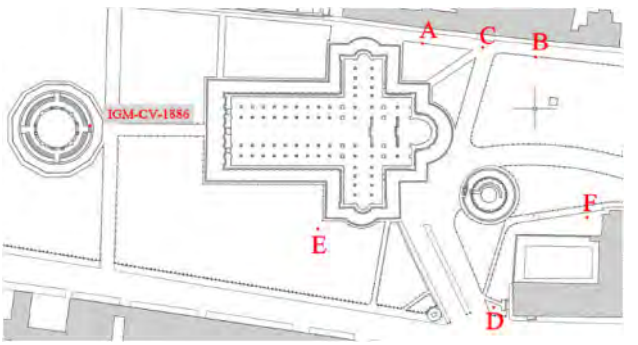

Figure 5. Layout of the 1911 benchmarks in Piazza dei Miracoli.

Figure 6. Detail of a 1911 benchmark.

These benchmarks served as both vertices of a small trigonometric network, providing framing support for the Tower overhang measures, and geometric levelling benchmarks of the historic levelling line for elevation surveys, along with benchmark IGM-CV-1886.

In 1911, Prof. Pizzetti calculated the maximum Tower overhang, by comparing the horizontal angle measures of the right-hand tangents from benchmark E to rings I and VII. The measures were carried out on June 22nd and July 9th, with a calculated overhang of 2.899 m between those rings.

The instrument used in these measurements was the 1896 Salmoiraghi Universale #19701 of the "Gabinetto di Topografia" of the Regia Università di Pisa (currently kept at the ASTRO Laboratory of the Pisa University), with 26 cm graduated circles, direct 2" readings and graduation division by movable micrometer (Figure 7).

Figure 7. 1896 Universale Salmoiraghi n° 19701, used since 1911 for Bell Tower overhang measures.

Also in 1911, Pizzetti performed the geometric levelling survey, based on the absolute elevation of benchmark IGM-CV-1886 with an unspecified instrument. Table 1 shows the elevation of the benchmarks set up by Pizzetti in 1911.

Table 1. Elevation of the Pizzetti benchmark as per the 1911 levelling survey.

Benchmark	Elevation (m)
IGM-CV-1886 (reference)	6.7917
A	3.601
B	3.509
C	3.491
D	3.156
E	3.297
F	3.199

In 1920, new measurements in the National Altimetric Network resulted in fixing the absolute elevation at 6.79170 m to IGM-CV-1886, as shown in Table 2.

Table 2. Official absolute elevation of benchmark IGM-CV-1886 in 1920.

Benchmark	Elevation (m)
IGM-CV-1886	6.79170

After 1911, overhang measurements were carried out on a regular basis by Professor Giovanni Cicconetti, following the methodology proposed by Pizzetti and using the same instrument. Archive research of any levelling surveys carried out in the same time span has been unsuccessful so far. In 1918, 1923 and 1926, overhang measurements highlighted an ongoing increase of 9 mm between rings I and VII. Based on this evidence, in 1927 Pisa Authorities instated a Technical Board, whose members included Professors Giovanni Cicconetti and Gino Cassinis (Commissione Pisana per gli Studi sulla Torre Pendente 1927).

As regards topographic measurements, the 1927 Board suggested surveying and monitoring activities as follows:

- Systematic continuation of the optical overhang observations in the month of June of each year, according to the methodology of Pizzetti.
- Setup of six levelling benchmarks, made up by six bronze spikes embedded in the stone and featuring spherical cap heads. Four of these, labelled as α', β', γ', δ', were fixed at the base of Tower columns 1, 4, 7 and 11 (numbering clockwise from the left of the entrance). Two benchmarks were set up far away from the Tower: benchmark ψ' in the Archiepiscopal Palace, at the base of the first column on the right, and benchmark φ' at the threshold of the main door of the Baptistery by the right-hand jamb, below IGM-CV-1886.
- Precision geometric levelling twice a year, in June and December.

Figure 8 shows the location of the levelling benchmarks as of 1928.

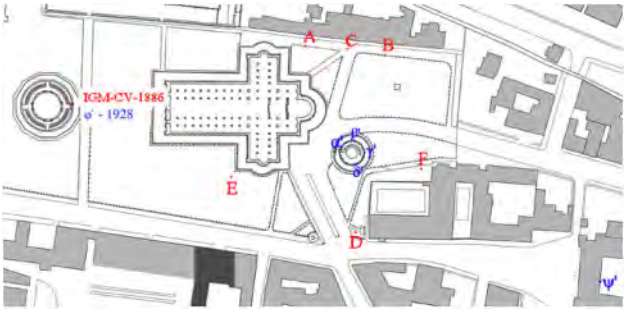

Figure 8. Levelling benchmarks as of 1928, showing in red those dating to 1911 and in blue those added in.

Between 1928 and 1929, the elevation of the six new benchmarks was calculated via geometric levelling linked to benchmark IGM-CV-1886, with the absolute elevation calculated in 1886. Also in this case, there is no evidence of the instruments used. Results of this levelling campaign are reported in Table 3.

Table 3. Elevation of 1928 benchmarks, as per the 1928 levelling.

Benchmark	Elevation (m)
IGM-CV-1886 (reference)	6.7917
φ'	4.2836
α'	2.6217
β'	3.0078
γ'	2.3549
δ'	1.4521
ψ'	5.7881

Until 1965, overhang measures were carried out yearly, save some brief gaps, following the same methodology and using the same instrument.

The Authors have no evidence of elevation measures carried out in the same time span on the levelling benchmarks set up in the Piazza.

Archive documents, provided courtesy of I.G.M., show that in 1943 horizontal benchmark IGM-CO-1886, placed by the left-hand jamb of the main Baptistery door, was given absolute elevation of 4.3146 m based on new measures in the National Altimetric Network. The same source provides no evidence as to benchmark IGM-CV-1886.

In the 1950s the levelling campaign of the new National Altimetric Network was launched, also including vertical benchmark IGM-CV-1886, with absolute elevation equal to 6.6756 m (Table 4), while horizontal benchmark IGM-CO-1886 was no longer visible. Available documentation provides no evidence of the inclusion of benchmark φ' in the National Altimetric Network, and therefore its absolute elevation is unknown for the time span considered.

Table 4. Official absolute elevation of benchmark IGM-CV-1886 in 1920.

Benchmark	Elevation (m)
IGM-CV-1886	6.6756

In 1964, the Italian Ministry of Public Works appointed a new Committee for the consolidation of the Leaning Tower, also known as Polvani Committee after the name of its President. In 1965, the Committee entrusted I.G.M. with the task of carrying out monitoring surveys for both planimetry and elevation. To the purposes of this paper, only information relevant to levelling surveys is reported.

I.G.M. redesigned the geometric levelling network by splitting it in two independent and linked sections (IGM, 1965; IGM, 1966).

The first section was designed to monitor the base of the Tower, and provided the installation, at the base of each column, of nickel-plated bronze bolts with spherical head, labelled 1 to 15; the four benchmarks set up in 1928 were also checked. Benchmarks α', γ', δ' were in good maintenance state, while β', no more visible, was reinstalled, keeping the original name. The base of the Tower eventually carried 19 benchmarks, 3 of which (α', γ', δ') dating back to 1928.

I.G.M. measured level differences between the benchmarks set up in 1928 and those set up at the corresponding columns in 1965, allow to calculate the elevation of the 1928 benchmarks based on those set up in 1965.

The second section of the network was designed to extend the investigations on elevation shifts to both the immediate surroundings of the Tower and the entire Piazza dei Miracoli. To this purpose, new benchmarks were laid out over the involved area, so to integrate both the 1911 and 1928 historic benchmarks. The six (A, B, C, D, E, F) benchmarks set up by the Bernieri Committee were checked and respectively renamed as Ab, Bb, Cb, Db, Eb, Fb. Since these flat top benchmarks were unsuited to the instruments used at the time, six stainless, spherical cap steel bolts were embedded on the same support plates close by the old benchmarks. The new benchmarks were named A, B, C, D, E, F accordingly to their old reference (Figure 6). Level differences with the old benchmarks were measured, allowing to calculate elevation of the latter based on the new data. Checks of benchmarks ψ', at the base of the first column on the right in the Archiepiscopal Palace courtyard, and φ', on the threshold of the main door of the Baptistery by the right-hand jamb (below IGM-CV-1886), both set up in 1928, revealed good maintenance conditions and steadiness.

The levelling network established in 1965 by I.G.M. included, either directly or indirectly, eleven historic benchmarks set up in 1911 and 1928 (Table 5).

Geometric levelling measures used a Zeiss A level (ID #62160) fitted with a parallel plane plate micrometer, and flat-heeled levelling rods with half-centimeter divisions on invar tape. The elevation reference was provided by benchmark IGM-CV-1886 with absolute elevation at 1886. The elevation survey allowed to link directly horizontal benchmark φ', by the Baptistery door, with vertical benchmark IGM-CV-1886, resulting in a level difference of -2.50809 m.

The elevation of φ' in 1965 was fixed at 4.28361 m. This benchmark, with the associated elevation value, was used as elevation reference until 1993. Anyway, it is worth noting that, since its elevation

Table 5. Historic benchmarks.

1993 network		1965 network		Historic benchmarks		Link between 1965 benchmark and corresponding historic benchmark	Transition level difference – 1965 to historic benchmark
ID	year	ID	year	ID	year		
1010	1965	A	1965	Ab	1911	Indirect	−0.02201
1008	1965	B	1965	Bb	1911	Indirect	−0.02203
1009	1965	C	1965	Cb	1911	Indirect	−0.02055
1013	1965	D	1965	Db	1911	Indirect	−0.02218
1011	1965	E	1965	Eb	1911	Indirect	−0.02138
1018	1965	F	1965	Fb	1911	Indirect	−0.02195
901	1965	1	1965	α'	1928	Indirect	−0.00927
907	1965	7	1965	γ'	1928	Indirect	−0.08324
911	1965	11	1965	δ'	1928	Indirect	−0.01788
1020	1928	ψ'	1928	ψ'	1928	Direct	–
100	1928	φ'	1928	φ'	1928	Direct	–

was determined based on the 1886 absolute elevation of vertical benchmark IGM-CV-1886, there is a shift in elevation of about 10 cm. As reported in the following, the same approach has been applied in definition of elevation of point 999 in 1993. Until 1993, elevation monitoring of the benchmarks set up in the Piazza and Tower areas focused on checking their relative shifts rather than checking and investigating local effect of subsidence.

Useful information in regard to subsidence in the Pisa plains are provided by the investigations carried out by Palla and Geri (Geri & Palla 1985; Palla et al. 1976).

These Authors stated that the entire Pisa plains, due to the subsoil structure and pumping, is subjected to subsidence phenomena. In particular, they pointed out that, relative to a bedrock benchmark, the reference benchmark IGM-CV-1886 at the Baptistery has sustained, between 1886 and 1981, vertical shifts showing alternating trends, as follows:

- between 1951 and 1975, the benchmark shift was assessed at −37 mm.
- between 1975 and 1981, the benchmark shift was assessed at +6 mm.

One of the main causes of the trend reversal shown by the shifts in the 1951–1975 period lies in the lowering of the water table due to the intense withdrawals and pumping of deep water carried out after the war. Based on this evidence, in 1973 the withdrawal of deep water in the surroundings of the Tower was banned, with positive consequences materialized in the trend reversal in the 1975–1981 period.

It is undisputed that the subsidence has affected the Baptistery benchmark and, as a consequence, any other linked benchmarks in the Piazza.

2.2 *Monitoring of elevation since the 1990s*

Starting in the 1970s, the inclination of the Tower has sustained a marked increase, leading to present danger of collapse. In 1989 the Ministry of Public Works, considering the critical situation of the monument, recommended to ban public access. On January 7th, 1990 the mayor of Pisa enforced the ban, which was to be lifted December 15th, 2001, upon completion of the consolidation and restoration works. In the following months a multidisciplinary Committee, chaired by prof. Jamiolkowski, started its activities for the stabilization of the monument.

In 1991, upon completion of new measure sets of the National Levelling Network, absolute elevations of benchmarks IGM-CV-1886 and φ' were updated, as reported in Table 6.

In the same year, the Committee entrusted the Dipartimento di Ingegneria Idraulica, Ambientale e del Rilevamento (DIIAR – Department of Hydraulics, Environment and Surveying Engineering) of the Milan Polytechnic to carry out geodetic and topographic surveys in the Piazza and Tower areas, as part of the reconnaissance–executive planning and intervention operations on the Tower.

Table 6. Official absolute elevations of benchmarks IGM-CV-1886 and φ' in 1991.

Benchmark	Elevation (m)
IGM-CV-1886	6.6756
φ'	4.0951

The Milan Polytechnic supervised levelling surveys for elevation monitoring until 2010, retaining the same layout of high-precision levelling network used in the past. Existing benchmarks were checked and replaced if needed, and new benchmarks were set up to improve the definition of elevation variations in the Piazza and foremost in the Tower areas. Besides, all benchmarks were renamed. Table 5 reports historic benchmarks directly or indirectly included in the 1993 network with the relevant nomenclature. The scheduled works for Tower safety and consolidation required materialization of a reference benchmark, so to provide steadiness over time and avoid any shift due to local or surface disturbances. In fact, it was clear that subsidence of the whole Piazza also affected Baptistery benchmarks IGM-CV-1886 and $\varphi' \equiv 100$. Given their instability over time, comparisons between compensated heights in different campaigns could include unwanted systematic effects, providing incorrect readings of the absolute subsidence phenomenon. For this reason, in 1992 a new deep elevation reference, named 999, was set up and linked to the lower sand layer. On May 29th, 1993 the first geometric levelling measure of the new benchmark network was carried out, to define both the "zero" situation prior to the set-up of the lead counterweights on the Tower base, and the elevation of the new elevation reference benchmark 999, relative to the previous reference benchmark $\varphi' \equiv 100$ at the Baptistery. Levelling operations were carried out using a Zeiss Ni1 automatic level fitted with a half-centimeter parallel plane plate micrometer, yielding a mean square error equal to $\pm$ 0.2 mm/km, and a pair of 3 m levelling rods with half-centimeter division on invar tape, fitted with telescopic supports and spherical bubble for vertical standing. The compensation of the entire levelling network assumed benchmark $\varphi' \equiv 100$ as elevation reference, with elevation equal to 4.28361 m as defined by the geometric levelling campaign of 1965. The compensation allowed to determine and fix the elevation of benchmark 999 at 3.57232 m, which acted as reference for any future levelling operation. The establishment and use of new reference benchmark 999 enabled to highlight both movements of the Baptistery benchmark $\varphi' \equiv 100$ relative to benchmark 999 and movements of the Piazza benchmarks without the influence of the very subsidence of $\varphi' \equiv 100$. In the 2000s DIIAR replaced the levelling instrumentation described above with a Leica DNA automatic digital level and invar barcode levelling rods. Available documentation does not specify neither exact time nor technical specifications. In 2006 the National Levelling Network was updated with new measures, which resulted in reassigning absolute elevations to benchmarks IGM-CV-1886 and $\varphi' \equiv 100$, as reported in Table 7.

Table 7. Official 2006 absolute elevations of benchmarks IGM-CV-1886 and $\varphi' \equiv 100$.

Benchmark	Elevation (m)
IGM-CV-1886	6.5818
$\varphi' \equiv 100$	4.0756

In 2012, the ASTRO Laboratory of Pisa University has been appointed the responsibility for levelling surveys. Instrumentation used for the task included a digital Leica DNA03 automatic level, providing a mean square error equal to $\pm$0.3 mm/km, and two barcoded invar levelling rods (Leica GPCL2 and GPCL3), with spherical bubble and telescopic supports for vertical standing. Table 8 reports the elevation of benchmark $\varphi' \equiv 100$ as determined by surveys from 1993 through 2016. The altimetric reference is provided by benchmark 999, with an elevation of 3.57232 m, as per the May 29th, 1993 levelling survey.

Table 8. Elevation of benchmark $\varphi' \equiv 100$ as determined by surveys from 1993 through 2016.

Survey supervision	Date	Elevation of benchmark $\varphi' \equiv 100$ (m)	Elevation of benchmark 999 (m)
POLIMI-DIIAR	29-05-93	4.28361	3.57232
POLIMI-DIIAR	21-08-93	4.28239	3.57232
POLIMI-DIIAR	21-02-94	4.28336	3.57232
POLIMI-DIIAR	06-02-95	4.28266	3.57232
POLIMI-DIIAR	26-02-96	4.28266	3.57232
POLIMI-DIIAR	30-11-96	4.28205	3.57232
POLIMI-DIIAR	04-05-98	4.28178	3.57232
POLIMI-DIIAR	26-07-99	4.27930	3.57232
POLIMI-DIIAR	10-10-00	4.27838	3.57232
POLIMI-DIIAR	08-11-01	4.27780	3.57232
POLIMI-DIIAR	29-10-03	4.27524	3.57232
POLIMI-DIIAR	21-10-04	4.27526	3.57232
POLIMI-DIIAR	11-07-05	4.27511	3.57232
POLIMI-DIIAR	26-06-06	4.27410	3.57232
POLIMI-DIIAR	07-07-08	4.27291	3.57232
POLIMI-DIIAR	13-07-10	4.27243	3.57232
UNIPI-ASTRO	29-06-12	4.27089	3.57232
UNIPI-ASTRO	30-06-14	4.27029	3.57232
UNIPI-ASTRO	30-06-16	4.26988	3.57232

3 HISTORY OF VERTICAL MOVEMENTS OF BENCHMARK $\varphi' \equiv 100$

Earliest data about the official absolute elevation of benchmark $\varphi' \equiv 100$ date back to 1991 (Table 6). In order to reconstruct its historic series of altimetric data (prior to 1991) the level difference relative to vertical benchmark IGM-CV-1886, $\Delta^{YYYY}_{\varphi',\mathrm{IGM-CV-1886}}$, has been assumed equal to 2.5081 m. This assumption is backed by the fact that this value is exactly the level difference between these two benchmarks in measures of both 1928 and 1965, rounded to 10–4 m.

Based on this assumption, the elevation of benchmark prior to 1991 have been calculated relative to the official absolute elevations of vertical benchmark IGM-CV-1886 for years 1920 (Table 2) and 1951 (Table 4), applying the formula:

$$Q^{YYYY}_{\varphi'_{(bbbb)}} = Q^{YYYY}_{\mathrm{GM-CV-1886}_{(bbbb)}} - \Delta^{YYYY}_{\varphi',\ \mathrm{IGM-CV-1886}}, \tag{1}$$

in which the symbols used stand for:

- $\Delta^{YYYY}_{NN,NN}$, level difference;
- $Q^{YYYY}_{\mathrm{NN}_{(bbbb)}}$, absolute elevation;
- *YYYY*, year of survey from which level difference or elevation have been derived;
- NN, benchmark ID;
- bbbb, year of assignment/update of the altimetric reference associated with the elevation.

The levelling survey of May 29th, 1993 allowed to calculate the absolute elevation of benchmark 999, based on the assumption that the elevation of benchmark $\varphi' \equiv 100$ was the 1965 official elevation, as described above.

Calculation of this elevation provides determination of level difference Δ_(φ',999)ˆ1993 between benchmark $\varphi' \equiv 100$ and newly instated altimetric reference benchmark 999 from the compensated elevation as per the May 29th, 1993 levelling survey:

$$\Delta^{1993}_{\varphi',999} = Q^{1993}_{999_{(1886)}} - Q^{1886}_{\varphi'_{(1886)}}, \tag{2}$$

Absolute elevation of benchmark 999 in 1993, $Q^{1993}_{999_{(1991)}}$, is calculated by adding to level difference $\Delta^{1993}_{\varphi',999}$, previously calculated, the official absolute elevation of benchmark $\varphi' \equiv 100$ for year 1991, $Q^{1991}_{\varphi'_{(1991)}}$, as reported in Table 6:

$$Q^{1993}_{999_{(1991)}} = \Delta^{1993}_{\varphi',999} + Q^{1991}_{\varphi'_{(1991)}}, \tag{3}$$

The last official data of absolute elevation of benchmark $\varphi' \equiv 100$ dates back to 2006 and is reported in Table 7. In the same year, DIIAR completed a geometric levelling survey on the benchmarks of the altimetric monitoring network on the entire Piazza, whose results are shown in Table 8. Elevation of benchmark $\varphi' \equiv 100$ was fixed at 4.27410 m relative to the altimetric reference provided by benchmark 999.

The concurrence of altimetric data for 2006 allows to calculate absolute elevations for this epoch of both benchmark 999 in the national altimetric reference system for 2006, and benchmark 100 in national altimetric reference system from 1993 through 2006.

Calculation of absolute elevation $Q^{2006}_{999_{(2006)}}$ of benchmark 999 in the national altimetric reference system for epoch 2006 provides to determine the level difference $\Delta^{2006}_{\varphi',999}$ between benchmark $\varphi' \equiv 100$ and newly instated altimetric reference benchmark 999 from compensated elevations derived from the 2006 levelling survey:

$$\Delta^{2006}_{\varphi',999} = Q^{1993}_{999_{(1886)}} - Q^{2006}_{\varphi'_{(2006)}}, \tag{4}$$

Absolute elevation $Q^{2006}_{999_{(2006)}}$ of benchmark 999 in the national altimetric reference system for epoch 2006 was calculated by adding level difference $\Delta^{2006}_{\varphi',\,999}$ to the official absolute elevation of benchmark $\varphi' \equiv 100$ for the same epoch:

$$Q^{2006}_{999_{(2006)}} = Q^{2006}_{\varphi'_{(2006)}} + \Delta^{2006}_{\varphi',999}, \tag{5}$$

calculation of absolute elevations of benchmark $\varphi' \equiv 100$ from 1993 to 2016, $Q^{YYYY}_{\varphi'_{(2006)}}$, in the national altimetric reference system for epoch 2006 required previous calculation of level difference $\Delta^{YYYY}_{999,\varphi'}$ between benchmarks 999 and $\varphi' \equiv 100$ for each year in which levelling surveys had been carried out.

Once these level differences have been calculated, absolute elevation $Q^{YYYY}_{\varphi'_{(2006)}}$ of benchmark $\varphi' \equiv 100$, in the national altimetric reference system for epoch 2006, for every levelling year, have been calculated according to the following relation:

$$Q^{YYYY}_{\varphi'_{(2006)}} = Q^{2006}_{999_{(2006)}} + \Delta^{YYYY}_{999,\varphi'}, \tag{6}$$

4 RESULTS

Absolute elevation of benchmark $\varphi' \equiv 100$ for years 1928 and 1951 has been calculated using formula (1). Table 9 shows the results.

Table 9. Absolute elevation of benchmark $\varphi' \equiv 100$ prior to 1991, relative to the official absolute elevation of benchmark IGM-CV-1886 for years 1928 and 1951.

Year	Elevation (m)
$Q^{1928}_{\varphi'_{(1920)}}$	4.2836
$Q^{1951}_{\varphi'_{(1951)}}$	4.1675

Level difference $\Delta^{1993}_{\varphi',999}$ between benchmark $\varphi' \equiv 100$ and newly instated altimetric reference benchmark 999, using compensated elevations as per the May 29th, 1993 levelling survey, has been calculated applying formula (2), and was equal to:

$$\Delta^{1993}_{\varphi',999} = 3.57232 - 4.28361 = -0.71129\ m, \tag{7}$$

Absolute elevation of benchmark 999 in 1993, $Q^{1993}_{999_{(1991)}}$, calculated with formula (3), was equal to:

$$Q^{1993}_{999_{(1991)}} = -0.71129 + 4.0951 = 3.38381\ m, \tag{8}$$

Level difference $\Delta^{2006}_{\varphi',999}$ between benchmark $\varphi' \equiv 100$ and newly instated altimetric reference benchmark 999, using compensated elevations as the 2006 levelling survey, has been calculated applying formula (4), and was equal to:

$$\Delta^{2006}_{\varphi',999} = 3.57232 - 4.27410 = -0.70178\ m, \tag{9}$$

Absolute elevation $Q^{2006}_{999_{(2006)}}$ of benchmark 999 in the national altimetric reference system at epoch 2006, calculated applying formula (5), was fixed at:

$$Q^{2006}_{999_{(2006)}} = 4.0756 - 0.70178 = 3.37382\ m, \tag{10}$$

Absolute elevation $Q^{YYYY}_{\varphi'}$ of benchmark $\varphi' \equiv 100$ in the national altimetric reference system at epoch 2006, was calculated for levelling years 1993 to 2016 applying formula (6). Results are shown in Table 10 and in Figure 9.

Table 10. Absolute elevations (1993–2016) of benchmark $\varphi' \equiv 100$ in the national altimetric reference system for epoch 2006.

Survey supervisor	Date	Elevation (m)
POLIMI-DIIAR	29-05-93	4.08511
POLIMI-DIIAR	21-08-93	4.08389
POLIMI-DIIAR	21-02-94	4.08486
POLIMI-DIIAR	06-02-95	4.08416
POLIMI-DIIAR	26-02-96	4.08416
POLIMI-DIIAR	30-11-96	4.08355
POLIMI-DIIAR	04-05-98	4.08328
POLIMI-DIIAR	26-07-99	4.08080
POLIMI-DIIAR	10-10-00	4.07988
POLIMI-DIIAR	08-11-01	4.07930
POLIMI-DIIAR	29-10-03	4.07674
POLIMI-DIIAR	21-10-04	4.07676
POLIMI-DIIAR	11-07-05	4.07661
POLIMI-DIIAR	26-06-06	4.07560
POLIMI-DIIAR	07-07-08	4.07441
POLIMI-DIIAR	13-07-10	4.07393
UNIPI-ASTRO	29-06-12	4.07239
UNIPI-ASTRO	30-06-14	4.07179
UNIPI-ASTRO	30-06-16	4.07138

Figure 9 shows the elevation trend for benchmark $\varphi' \equiv 100$ as reconstructed according to the methods illustrated above. The resulting curve is typical of a subsidence phenomenon as the consequence of primary consolidation of clayey soil layers, most probably correlated with the lowering of the water level in the lower sands.

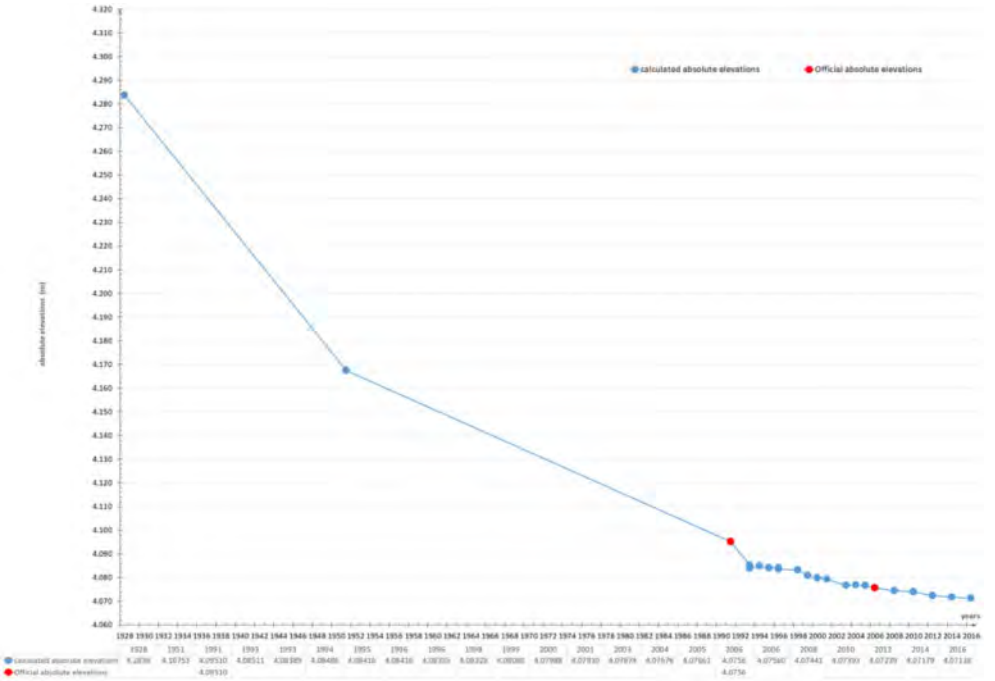

Figure 9. Elevation trend for benchmark $\varphi' \equiv 100$.

Figure 10 shows the time trend of water level in lower sand layers starting from 1966, highlighting consistently lower values compared with mean sea level, which in turn triggers consolidation of clayey layers. The relevant thickness of clayey layers results in an extremely slow and surely ongoing consolidation process, as highlighted by values for the last 20 years. The lower values of water level in the Horizon C during the period 1970–1976 induced an acceleration of consolidation process of clayey layers which in turn was not uniform in the vicinity of the Tower leading to an increment of its inclination due to differential settlement (Squeglia & Bentivoglio, 2015).

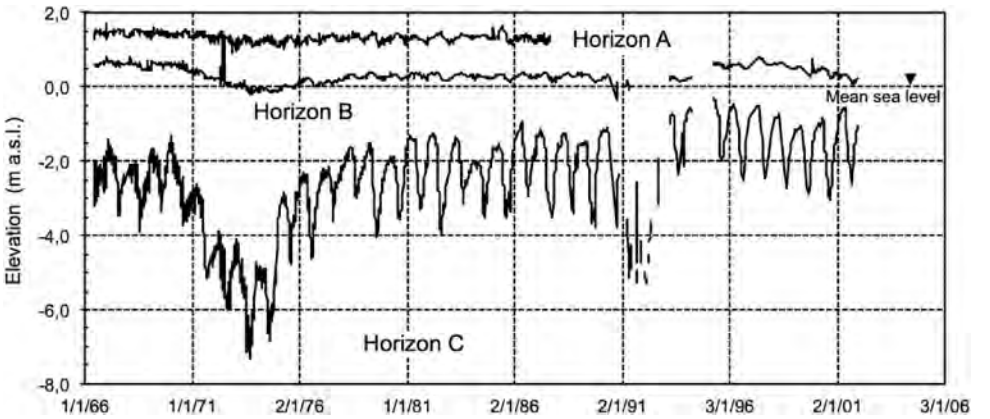

Figure 10. Trend of water level in sand layers starting from 1966.

The comparison of absolute elevation of benchmark 999 in 1993 (epoch 1991), $Q^{1993}_{999_{(1991)}}$, and 2006 (epoch 2006), $Q^{2006}_{999_{(2006)}}$, shows that the benchmark has been subjected to a negative movement of almost one centimetre. Barring as a possible cause of this behaviour the uncertainty of the official absolute elevation, due for instance to recalculation over time of the National Altimetric Network, the phenomenon could be reasonably ascribed again to water level reduction.

The presence of clayey layers underneath the lower sands has already been reported (Squeglia et al. 2015). For this reason, benchmark 999 – anchored to the deep sands – is affected by the deformations originating in the underlying layers, due to the consolidation triggered by the lowering of the mean water level, which is as a consequence ultimately responsible for the settlement of benchmark 999.

By analysing the graphics of Figure 9, vertical movements of benchmark $\varphi' \equiv 100$ for the period 1951–1975 has been calculated using linear interpolation at -43 mm. This result substantially matches the findings of Palla and Geri (Geri & Palla 1985; Palla et al. 1976), who fixed this value at -37 mm. A possible explanation for this 6 mm difference could lie in the fact that those Authors used as altimetric reference the elevation of a benchmark materialized on the Monte Pisano bedrock, as such subjected to the vertical movements of the Mid-Tuscany Ridge (Palla et al. 1985).

Data shown in Figure 9 lead to further considerations. In fact, it is possible to simulate the consolidation process due to lowering of ground water level in lower sand by means of simple mono-dimensional models. Such models can be reasonably calibrated using the detailed information available about the Piazza's subsoil. However, two information are missing: the starting of water level lowering (see Figure 10) and the final settlement. The values of these parameters can be deduced by measurements iterating a simple trial and error process. Obviously, more complex algorithms could be used for the determination of missed parameters, but these require more sophisticated models of the consolidation process and computational efforts, without improve significantly the estimation of missed parameters.

Dashed line in Figure 11 shows the results of the simulation. Starting of lowering in ground water level is consistent with the industrial development of Pisa in those years, whereas the final settlement of 0.24 m is consistent with subsoil compressibility.

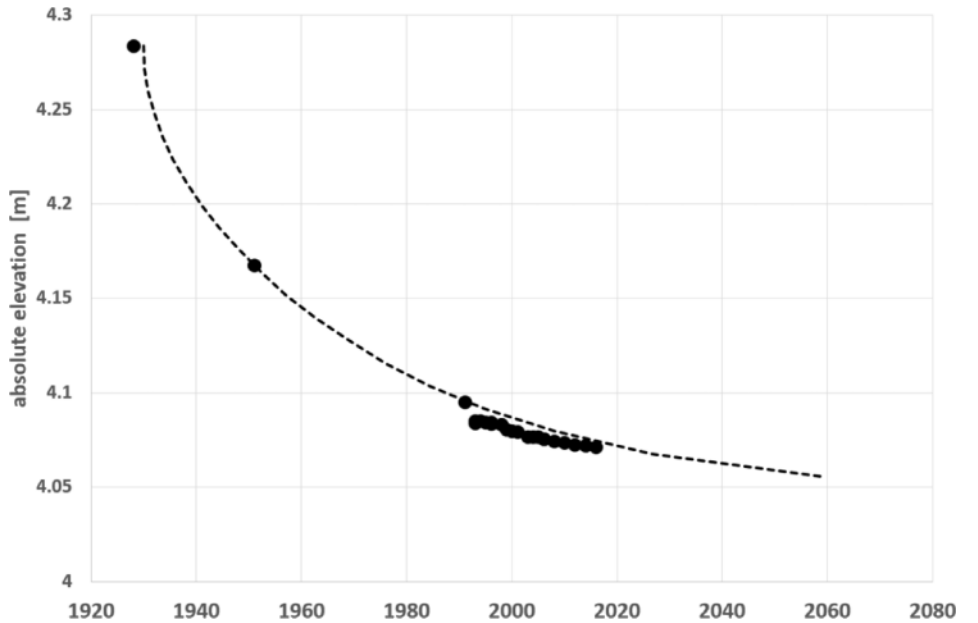

Figure 11. Results of the consolidation process simulation due to lowering of ground water level.

Furthermore, the capability of such simple model to match measurements corroborate the statement that the phenomenon is still driven by hydrodynamic consolidation and, at present, an involvement of chemical consolidation can be excluded.

5 CONCLUSIONS

The present paper reports for the first time a summary of topographical measures performed over more than 100 years in the Piazza dei Miracoli area. In particular, tracing back the elevation trend over time for some benchmarks in the Piazza demonstrated the usefulness of setting up reference benchmark 999, which can be assumed as external relative to points set up on monuments or on ground. Benchmark 999 is anyway subjected to subsidence due to changes in subsoil pore water pressure regime.

Reconstruction of vertical movements of benchmark $\varphi' \equiv 100$ over time allowed to define major affecting factors, along with their share of the total effect.

This step is fundamental for a correct definition of the movements, and therefore of the distortions, of each monument, in relation with their soil-monument interactions, in order to provide their correct preservation.

Finally, it is worth noting that, from a geotechnical point of view, the aims of monitoring must be clear and monitoring data have to be analysed with criticism and care. The history of monitoring of Piazza dei Miracoli is an example of complexity of phenomena related to a relatively small area and its monuments. Critical analysis of data lead to a deep comprehension of behaviour of territory and buildings in order to improve our capacity in their preservation.

REFERENCES

Caroti, G., 2000. Survey and adjustment of the altimetric network for monitoring ground vertical movements in the area of Pisa. *Int. Arch. Photogramm. Remote Sens. XXXII*, 20–23.

Caroti, G., Mengali, E., Rossi, A., Scalese, C., 1999. Establishment of a levelling network for the monitoring of possible vertical movements in the area of Pisa-San Giuliano-Pontasserchio-Migliarino. *Int. Arch. Photogramm. Remote Sens. XXXII*, 154–158.

Commissione Pisana per gli Studi sulla Torre Pendente, 1913. Relazione Generale 1913. Pisa.

Commissione Pisana per gli Studi sulla Torre Pendente, 1927. Relazione Generale 20 luglio 1927. Pisa.

Cresy, E., Ledwell Taylor, G., 1829. Architecture of the Middle Ages in Italy : illustrated by views, plans, elevations, sections and details, of the cathedral, baptistery, Leaning Tower or campanile and Campo santo at Pisa, from drawings and measurements taken in the year 1817 : accompanied. London.

Geri, G., Palla, B., 1985. Considerazioni sulle osservazioni ottiche effettuate dall'Istituto di Geodesia e Topografia di Pisa al Campanile del Duomo di Pisa per le variazioni di strapiombo dal 1918 al 1985. Pisa.

Istituto Geografico Militare, 1965. Misure geo-topografiche programmate dall'Istituto Geografico Militare. Firenze.

Istituto Geografico Militare, 1966. Rapporto sui movimenti della Torre. Firenze.

Lancellotta, R., Flora, A., Viggiani, C., 2017. *Geotechnics and Heritage: Historic Towers*.

Lunardi, P., 1993. La torre di Pisa: note su una proposta d'intervento alternativa. *Mater. e Strutt. Probl. di Conserv*. 1, 1–24.

Palla, B., Cetti, T., Poggianti, M., Mengali, E., Bartolini, A., 1976. I movimenti verticali del suolo nella Pianura Pisana dopo il 1920 dedotti dal confronto di livellazioni. Pisa.

Palla, B., Nardi, R., Pertusati, P.C., Tongiorgi, M., 1985. Movimenti differenziali lungo l'asse della dorsale media toscana all'altezza dei Monti Pisani, in: C.N.R. (Ed.), *4° Convegno Nazionale Di Geofisica Della Terra Solida. Roma*, pp. 1103–1109.

Regia Commissione Geodetica Italiana, 1911. Livellazione Geometrica di precisione Linea 42 Pisa-Sarzana. Firenze.

Squeglia, N., Bentivoglio, G., 2015. Role of Monitoring in Historical Building Restoration: The Case of Leaning Tower of Pisa. *Int. J. Archit. Herit.* 9, 38–47. https://doi.org/10.1080/15583058.2013.865813

Squeglia, N., Stacul, S., Diddi, E., 2015. The restoration of San Paolo Church in Pisa: geotechnical aspects. *Riv. Ital. di Geotec*. 3/2015, 58–69.

Appendix A

Table A1. Timeline of the altimetric monitoring activity in Piazza dei Miracoli.

Year	Monitoring activity
1886	1886 National levelling Set up and measure of benchmarks: – IGM-CV-1886. Absolute elevation = 6.7917 m a.m.s.l. – IGM-CO-1886. Absolute elevation = 4.2930 m a.m.s.l.
1908	The Bernieri committee is appointed Professor Paolo Pizzetti is designated as supervisor of geodetic and topographic investigations
1911	Pizzetti sets up and measures the following benchmarks: A, B, C, D, E, F (respectively renamed as A_b, B_b, C_b, D_b, E_b, F_b in 1965) Reference benchmark: IGM-CV-1886 Reference elevation: 1886 absolute elevation = 6.7917 m a.m.s.l.
1920	1920 National Levelling Absolute elevation of benchmark IGM-CV-1886 is updated = 6.79170 m a.m.s.l.
1927	New technical committee is appointed Professors Giovanni Cicconetti and Gino Cassinis are named as supervisors of geodetic and topographic investigations
1928/1929	Cicconetti and Cassinis set up and measure the following benchmarks: φ' (renamed as 100 in 1993), α', β', γ', δ', ψ' Reference benchmark: IGM-CV-1886 Reference elevation: 1886 absolute elevation = 6.7917 m a.m.s.l.
1943	1943 National Levelling No information provided with regard to benchmark IGM-CV-1886 Absolute elevation of benchmark IGM-CO-1886 is updated = 4.2930 m a.m.s.l.
1951	1951 National Levelling Absolute elevation of benchmark IGM-CV-1886 is updated = 6.67563 m a.m.s.l. Benchmark IGM-CO-1886 is missing
1964	The Polvani Committee is appointed IGM is designated as supervisor of geodetic and topographic investigations
1965/1966	IGM redesigns the levelling network, sets up new benchmarks, checks existing ones and performs relevant measures Reference benchmark: IGM-CV-1886 Reference elevation: 1886 absolute elevation = 6.7917 m a.m.s.l. Elevation of benchmark is updated = 4.28361 m a.m.s.l. For the purposes of the present investigations, it is worth noting that: – Benchmarks A, B, C, D, E, F are renamed as A_b, B_b, C_b, D_b, E_b, F_b, and new benchmarks named A, B, C, D, E, F are set up in their immediate proximity. Level differences between old and new corresponding benchmarks are measured – Missing benchmark β' is replaced with a new one bearing the same name – New benchmarks, named 1, 7, 11, 4 are set up in the immediate proximity of benchmarks α', γ', δ' e β' 1965. Level differences between old and new corresponding benchmarks are measured – Benchmarks ψ' and φ' are left unmodified
1973	Pumping of deep water in the surroundings of the Bell Tower is banned
1989	An International Committee for the safeguard of the Pisa Tower is appointed by the Ministry of Public Works
December 7th, 1990	The Mayor of Pisa orders the Leaning Tower to be closed to the public

(*Continued*)

Table A1. (Continued).

Year	Monitoring activity
1991	1991 National Levelling Absolute elevation of benchmark IGM-CV-1886 is updated = 6.6033 m a.m.s.l. Absolute elevation of benchmark φ' is updated = 4.0951 m a.m.s.l.
1991	The international Committee entrusts DIAAR of the Milan Polytechnic the task of performing geodetic and topographic surveys in the Piazza and Torre areas. The altimetric network is redesigned, new benchmarks are set up and existing ones are checked. All benchmarks are renamed. Relevant for the purposes of the present investigations are the following: – φ', renamed as 100 – ψ', renamed as 1020 – A, renamed as 1010 – B, renamed as 1008 – C, renamed as 1009 – D, renamed as 1013 – E, renamed as 1011 – F, renamed as 1018 – 1, renamed as 901 – 7, renamed as 907 – 11, renamed as 911 which allow to reconstruct the historic series from early XX century
1992	New altimetric reference, designed to provide stability over time, is materialized as benchmark 999
May 29th, 1993	First survey of the new levelling network Reference benchmark: $\varphi' = 100$ Reference elevation: 1965 measured elevation = 4.28361 m a.m.s.l. Elevation of new reference benchmark 999 is measured = 3.57232 m a.m.s.l.
December 15th, 2001	The Mayor of Pisa orders the Leaning Tower to be reopened to the public
2006	1991 National Levelling Absolute elevation of benchmark IGM-CV-1886 is updated = 6. 5818 m a.m.s.l. Absolute elevation of benchmark φ' is updated = 4. 0756 m a.m.s.l.
2012	ASTRO Laboratory of Pisa University is designated as supervisor of altimetric monitoring surveys

Geotechnical Engineering for the Preservation of Monuments and Historic Sites III – Lancellotta, Viggiani, Flora, de Silva & Mele (Eds)

Satellite and on-site monitoring of subsidence for heritage preservation: A critical comparison from Piazza del Duomo in Pisa, Italy

A. De Falco
Department of Industrial and Civil Engineering, University of Pisa, Italy

C. Resta
Department of Energy, Systems, Territory and Construction Engineering, University of Pisa, Italy

N. Squeglia
Department of Industrial and Civil Engineering, University of Pisa, Italy

ABSTRACT: Monitoring of soil displacements is often crucial to the preservation of monumental buildings, since these structures are highly sensitive to differential settlements. Synthetic Aperture Radar (SAR) images from satellites appear as a tempting tool for monitoring, since they can be compared through interferometric techniques to track soil or building displacements in time. But interferometric SAR, which accuracy varies with image quality and type of displacement, has to be validated with on-site measurements. Exploiting the availability of open source data from the European Sentinel-1A and 1B satellites, this study aims at providing practical insight regarding the use of these remote sensing sources and method to monitor the well-being of monumental structures. Piazza del Duomo in Pisa (Italy) is selected as a case study, for its long historic record of on-site measurements and for the special role that settlements play in the behaviour of its monuments. The authors outline the advantages and limitations of the freely available SAR data from Sentinel satellites for the purpose of structural health monitoring of monumental structures, comparing it with information obtained through levelling.

Keywords: interferometric SAR, remote sensing, monitoring, cultural heritage, Piazza del Duomo

1 INTRODUCTION

Italy houses the largest number of UNESCO Cultural Heritage (CH) Sites — 53 at the time of writing (UNESCO 2021). Their undeniable value, both tangible and not, warrants efforts to preserve them against the perils of natural and man-made hazards. The importance of CH safeguard is directly stated in the United Nations' *Sendai Framework* (UN 2015), which has been reaffirmed and further developed by the European Council in the study *Safeguarding Heritage from Natural and Man-Made Disaster* (Bonazza et al. 2018). The latter explicitly states the necessity to develop early warning systems for the assets under threat. To this end, diverse Structural Health Monitoring (SHM) frameworks have been proposed and successfully applied (e.g., Lagomarsino & Cattari 2015; Ramos et al. 2018), even though some open issues still linger regarding the optimal monitoring strategy to be adopted for each usage case.

Monitoring of subsidence, and more generally of ground displacements, is of great importance for the safeguard of CH (Bilotta et al. 2013). In the case of the well known Piazza del Duomo in Pisa, Italy (Figure 1), with the singularity represented by its Leaning Tower, the role of Geotechnics cannot be stressed enough (Leoni et al. 2018). Founded on highly compressible soils, the Tower owes both its fortunes and its (averted) miseries to the ground underneath. Neither the appointment

 DOI 10.1201/9781003308867-39

of the International Committee for the Safeguard of the Tower of Pisa in 1989, nor its subsequent interventions, would have been possible without monitoring of the soil-structure interaction (Viggiani 2019).

Figure 1. Panoramic view of Piazza del Duomo in Pisa, Italy (historic picture).

Today, the whole site of Piazza del Duomo is kept under control via biennial levelling surveys, performed by the ASTRO laboratory of the University of Pisa over a network of more than one hundred benchmarks (Caroti et al. 2019). The single monuments are also subject to dedicated monitoring, both manual and automatic or semi-automatic.

Next to traditional techniques, monitoring through remote sensing has emerged in recent years as an attractive means to keep sites and structures under observation, while reducing costs and time consumption (Cavalagli et al. 2019; Tapete & Cigna 2019). Synthetic Aperture Radar (SAR)-equipped satellites produce data which enables to track ground displacements with high frequency and (sub-)millimetre accuracy. In this context, the European Union's Copernicus programme (ESA 2019) is particularly interesting, since it involves the acquisition of SAR imagery from the Sentinel satellite constellation and its free and open distribution to the public. Consorzio LaMMA, together with the University of Florence, provide a dataset of ground displacement time series, elaborated from SAR images by the company TRE ALTAMIRA using the cutting-edge SqueeSAR® algorithm (Del Soldato et al. 2019). The data are part of a large monitoring project involving the whole of Tuscany which, if proved useful, would represent a great opportunity for the safeguard of Piazza del Duomo.

The present work represents the starting point of a comparison and a prospective integration process between CH monitoring by on site measurements and by remote sensing. Its main focus is the possible employment of C-band SAR data from the Sentinel satellite constellation. The availability of data elaborated with a state-of-the-art algorithm ensures that the comparison does not rely too much on the employed interferometric technique. At the same time, the monumental complex of Piazza del Duomo in Pisa, Italy, constitutes an ideal case study for its relevance and for the presence of a well built monitoring system with a long series of historical data.

In Section 2 we outline the comparison strategy, and give details regarding the data we employed and its availability. Section 3 provides the results of our comparisons, and some discussion thereof. Finally in Section 4 we discuss the possibility of furthering the investigations and draw conclusions.

2 MATERIAL AND METHODS

2.1 *Differential Interferometric SAR (DInSAR)*

SAR is an acronym standing for Synthetic Aperture Radar, an active remote sensing system using microwaves as a lighting source to produce images. *Synthetic*, in the name, indicates the employment of an aperture synthesis technique capable of overcoming otherwise existing limitations regarding the size of the antenna (Meyer 2019).

For the present research, we employed data from Sentinel-1A and 1B satellites (ESA 2021). SAR systems installed on the twin satellites operate in the C-band, with a centre frequency of 5.405 GHz, corresponding to a wavelength of about 5.6 cm. Such a wavelength allows the signal to pass through cloud covering, obtaining images even in otherwise adverse weather. Each satellite has a repeated pass period of 12 days. They share the same orbital plane with a 180° phase difference, so that each area on Earth is imaged once every six days.

While transiting its orbit, each satellite swats the ground and records the returning signal, building a rectangular image aligned with its azimuth and with the ground range of the antenna. Imaging is generally not performed perpendicularly to the ground, but rather along a slanted line of sight (LOS). Due to the Earth's curvature, the exact incidence angle of the LOS varies along the ground range, and it is steeper than the off-nadir angle. Figure 2 shows the main characteristics of a satellite SAR system, and a minimally elaborated example of a SAR image.

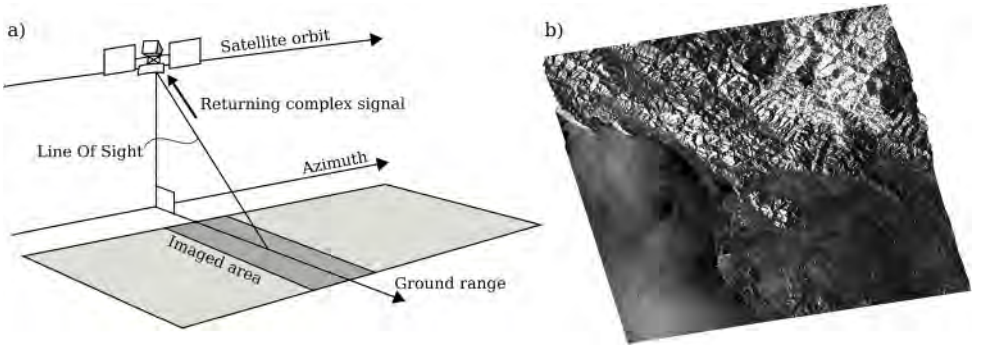

Figure 2. Satellite SAR: a) illustration of the imaging system (adapted from ESA 2007); b) SAR image (amplitude) of the northern part of Tuscany, terrain-corrected. Data from the European ESR-1 satellite.

Each SAR image is composed of pixels, which represent the minimal ground spatial resolution cells, and contain complex-valued information regarding backscattering. The signal amplitude is related to the cells' reflectivity; its phase to the length of the signal's path.

By comparing the phase information of two previously aligned SAR images, it is possible to construct a Digital Elevation Model (DEM) of the imaged area. The techniques to do so are collectively indicated as Interferometric SAR, or InSAR.

Using at least a third aligned SAR image, it is possible to reconstruct the displacement of scatterers along the LOS. This is generally known as Differential Interferometric SAR, or DInSAR. The actual feasibility of a comparison between SAR images is subject to the condition that the images show enough correlation between themselves. Time plays a part in this: if too many days have passed between acquisitions, the reflective properties of the landscape may have changed too much. The distance between satellite orbits at the moment of imaging also has an influence, as well as the presence of atmospheric disturbance. For these reasons, interferometric data is accompanied by a map of coherence values, i.e., values indicating how trustworthy the elaborated data is.

Different algorithms allow the production of DInSAR data. One of the most recent and employed ones is TRE ALTAMIRA's proprietary SqueeSAR® algorithm (Ferretti et al. 2011). SqueeSAR® belongs to the family of multi-interferometric techniques, capable of employing a long time series of SAR images of the same geographical area to track the displacement of scatterers along the acquisitions, and to reduce the detrimental effects of time decorrelation. SqueeSAR® allows to track either Permanent Scatterers (PS), i.e., single pixels which show a highly coherent signature along the images of the series, or Distributed Scatterers (DS), which instead are coherent areas of more than one pixel. The technique, or better yet an older version of it called PSInSAR (Colesanti et al. 2003; Ferretti et al. 2000), has been validated through experimental testing and is generally capable of reconstructing displacements with submillimetre accuracy (Ferretti et al. 2007). In recent

years, SqueeSAR® has even been successfully employed to test the feasibility of a nationwide deformation monitoring system (Bischoff et al. 2020).

TRE ALTAMIRA, using SqueeSAR®, has monitored the local subsidence in the region of Tuscany (Italy) during a period of more than five years (Del Soldato et al. 2019). The resulting displacement data have been rendered open access, and have been collected for consultation in a web-based Geographical Information System (GIS) by Consorzio LaMMA (Casagli et al. 2018). The case study employed in the present work, the monumental complex of Piazza del Duomo in Pisa, Italy, falls within the monitored region, so this data was employed for comparison.

Table 1 sums up the technical specifications of the employed DInSAR data. Scatterers' position within the area of study is discussed in more detail in Section 3.

Table 1. Technical specifications of the employed DInSAR data.

Property	Value
Imaging satellite	Sentinel-1A and 1B
Imaging frequency	once every six days
Wavelength	5.6 cm
Spatial (ground) resolution	(4×20) m^2
Acquisition period	from 2018-05-1 to 2021-09-29
DInSAR algorithm	SqueeSAR® (Ferretti et al. 2011)
Processed by	TRE ALTAMIRA s.r.l.
Furnished by	Consorzio LaMMA
Absolute displacement error	± 2 mm/year

2.2 *On-site monitoring*

The site of Piazza del Duomo in Pisa, Italy, has been monitored for more than a century (Caroti 2019). The singularity represented by the Leaning Tower is certainly one of the main reasons for this. The first geodetic observations, regarding in fact the Tower's inclination, date back to 1911. They were performed by Professor Paolo Pizzetti under mandate from the *Commissione per lo studio delle condizioni statiche del Campanile* (the Commission for the study of the static conditions of the Bell Tower), established a few years before due to a novel concern for the Tower's safety by the authorities (Commissione Pisana per gli Studi sulla Torre Pendente 1913).

In 1928, six levelling benchmarks were installed in the Piazza and their elevation was calculated through geometric levelling. In 1965, the Istituto Geografico Militare (I.G.M.), entrusted by the newly formed Committee for the consolidation of the Leaning Tower, redesigned and expanded the levelling network, performing regular surveys until 1991 (I.G.M. 1965, 1966; Noccioli et al. 1971).

From 1991 to 2010, levelling surveys were instead carried out by the Department of Hydraulics, Environment and Surveying Engineering (DIIAR) of the Milan Polytechnic, which kept referring to the same network of benchmarks. In 1992, an elevation reference deep point, anchored to an underground sand layer at about 50 m of depth, was installed. The point, which elevation was fixed at 3.57232 m, served as a reference until the present day.

Since 2012, the ASTRO Laboratory of the University of Pisa is in charge of monitoring ground movements. In its current state, the benchmark network consists of 121 measurement points, which are replaced when necessary (see Figure 4). Surveys are carried out with a biennial frequency during the summertime, usually in June, and make use of a Leica DNA03 automatic level (mean square error of ± 3 mm/km) and two barcoded Invar levelling rods with spherical bubble and telescopic supports (Leica GPCL2 and GPCL3).

Several levelling benchmarks are installed at the base of the Leaning Tower and inside its ground floor. But the Tower is also equipped with a dedicated monitoring system, including two pendulums (a direct and a reverse one), provided with telecoordinometers recording on an hourly basis. One

of this pendulums, running from the sixth (out of eight) floor to the first one, is a good reference for the overall movement of the top of the Tower. The latter is in fact a composition of movements due to the Tower's deformation, and of rotations concentrated at the foundation level.

2.3 *Comparison strategy*

This section describes the lines of investigation that we followed in order to compare DInSAR data with measurements obtained in the field.

The guidelines by Regione Toscana (Casagli et al. 2018) regarding the use of DInSAR data prescribes: (a) that the data be interpreted through comparison and combination with more "traditional" measurement methods (page 18), and (b) not to use DInSAR data alone to evaluate the presence or insurgence of structural issues in buildings and infrastructures (page 22). The same document (page 16) quotes a threshold of ± 2.0 mm/year along the LOS for the sensitivity of DInSAR displacements, based on the standard deviation of the raw data employed.

We adopted a comparison plan based on the following steps:

1. Selection of PS (or DS) within the area of interest, and preliminary seasonal-trend decomposition based on Loess (STL) of the relative signals (Cleveland et al. 1990).
2. Comparison of the temporal and spatial availability of SAR data with (a) existing on site monitoring data, and (b) the location of monuments inside the Piazza del Duomo complex.
3. Direct comparison of the seasonal component of a PS located on the Leaning Tower of Pisa with data obtained from a pendulum installed inside the Tower and measured through a telecoordinometer. Measurements from the Leaning Tower were used for their abundance, since they are measured hourly – a frequency unmatched by monitoring data for the other monuments.
4. Comparison of historically recorded movements of the Leaning Tower with the expected sensitivity of DInSAR data. The Leaning Tower is used once again for the comparison because its displacements are by far greater than those of the other monuments, and thus easier to detect with whichever method.
5. Comparison of the overall average settlement of Piazza del Duomo, as recorded on site and by DInSAR data.

2.4 *Seasonal-trend decomposition based on loess*

We employed STL, a filtering procedure capable of decomposing a time series into a trend, a seasonal and a remainder component, as a preliminary step to allow the analysis of satellite data. Its robustness to outliers and its applicability even to irregularly sampled time series represent particularly desirable features for operating on real-world data. STL supposes an additive model for the data. That is, each data point y_i is decomposed as (Figure 3):

$$y_i = t_i + s_i + r_i, \tag{1}$$

where t_i is the trend component, s_i the season component, and r_i the remainder component — the remaining variation in the data.

STL is composed of a sequence of smoothing operations, most employing a locally-weighted regression strategy, or Loess (Cleveland et al. 1988). Given two series of observations x_i and y_i of an independent and a dependent variable respectively, the Loess regression curve $g\hat{}(x)$ is a smoothing of y given x. As a function, $g\hat{}(x)$ is defined for any value of x, even outside the given observations x_i . For this reason, Loess is useful even in the presence of gaps in the time series to be smoothed. The regression curve $g\hat{}(x)$ is computed for each of the x_i observations by first assigning a weighting scheme to the $q$closest neighbouring observations, and then locally fitting a low-degree polynomial (linear in our case) to the weighted data. Weights are chosen to be inversely proportional to the distance from x_i. The value of the parameter $q$and the degree of the polynomial have to be chosen by the analyst. Cleveland et al. (1990) provide practical suggestions regarding the choice of these and other parameters required by STL and Loess.

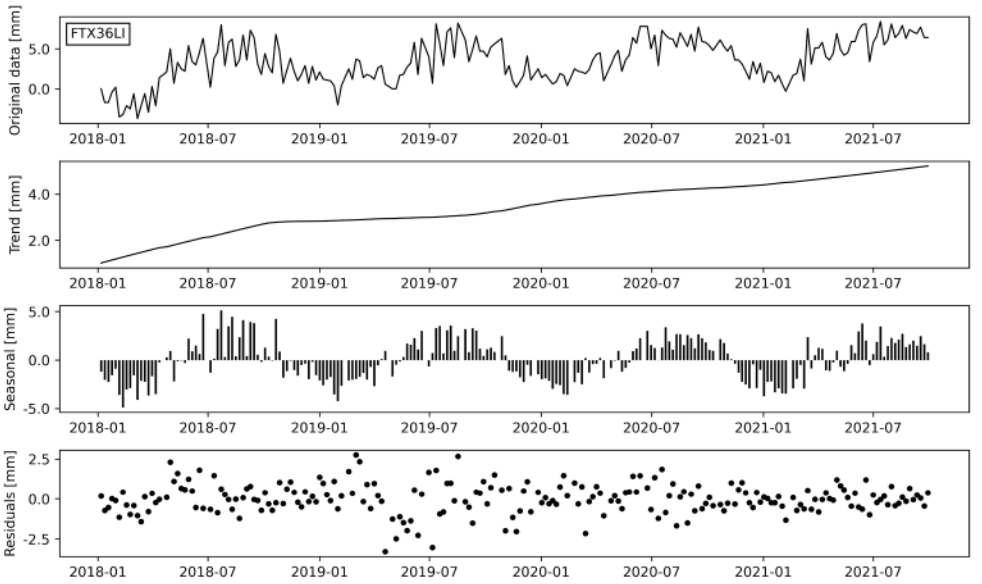

Figure 3. Example of STL decomposition of the signal from one of the permanent scatterers above the Leaning Tower (PS code FTX36LI within the dataset). A clear yearly seasonal behaviour can be observed.

Detrending with STL is an iterative process, consisting of an inner and an outer loop. The algorithm analyses both the original time series and the *cycle-subseries*, which are artificial subseries of values at each position of the seasonal cycle (e.g., for monthly data with yearly seasonality, a subseries would be composed of all January samples, another of February samples, and so on). The inner loop updates the trend and seasonal components, once for each pass. It employs Loess to smooth the cycle-subseries and the trend component, together with a low-pass filtering of the smoothed cycle-subseries that consists of multiple moving averages followed by a linear Loess smoothing. The outer loop computes robustness weights for each time point where data is observed; these weights are inversely proportional to the remainder component at each time point (computed by subtracting the seasonal and trend components), and are used in the next run of the inner loop to guide the reduction of transient behaviour. After the decomposition is complete, the seasonal component can optionally be subjected to a final smoothing pass using quadratic Loess. For the present research, we employed the STL routine implemented by the Python library statsmodels v0.12.2 (Perktold et al. 2020). It requires the definition of four parameters, which were set during analysis. We collect them here for reference:

- n_p, the number of observations in each cycle of the seasonal component. As mentioned in Section 2.1, Sentinel images covering the area of interest have a frequency of one every six days. Under the reasonable supposition that seasonal behaviour has a yearly periodicity, the number of data points per year oscillates between 60 and 61 (during years 2018–2020). Tests showed no significant differences between one choice or the other, suggesting that separate measurements during short periods of time are highly correlated.
- n_l, the smoothing parameter for the low-pass filter (part of the inner loop). As prescribed, this was taken to be the smallest odd number such that $n_l \geq n_p$.
- n_s, the smoothing parameter for the (optional) post-smoothing of the seasonal component. This was taken equal to n_p.
- n_t, the smoothing parameter for the trend component. Following the standard STL implementation, this was taken equal to the smallest odd number so that $n_t > 1.5n_p/(1 - 1.5n_s)$.

3 RESULTS AND DISCUSSION

3.1 *Temporal and spatial availability of displacement data*

The first and easiest comparison between DInSAR and traditional monitoring data is in terms of temporal availability. On site levelling operations can take a significant amount of time (especially for networks composed of hundreds of benchmarks), and require a team of technicians to be deployed to the field. For this, and for the related costs, they are usually performed on a yearly or biennial base. This makes sense when the objective is tracking slow settlements; less so, should the goal be developing an early warning system based on displacements. Sentinel satellites, on the contrary, image the study area once every six days, and in the case of DInSAR data provided by Consorzio LaMMA, the openly available datasets are updated one or two times a month. This leads to a twofold advantage. First, frequent measurements allow to track the evolution of displacements and to correct them by accounting for a seasonal component — on site measurements have to be carried out more or less at the same time of the year to avoid misleading results. Second, they are useful to track abrupt displacements, or to analyse them after an exceptional event such as an earthquake. This remains true even when considering a time lag of a few days for the analysis and distribution of interferometry results.

A second comparison can be carried out in terms of location, of either scatterers or levelling benchmarks, within the area of study. Figure 4 shows the availability of measurement points in Piazza del Duomo. The network of on site benchmarks was pruned beforehand, removing transitional points which are used during levelling operations but which record is not as reliable. To this category belong, for example, points fixed to the walkways between monuments, which position can easily have been modified, in the years, by the passage of tourists. After this selection, 82 out of the original 121 measurement points remained.

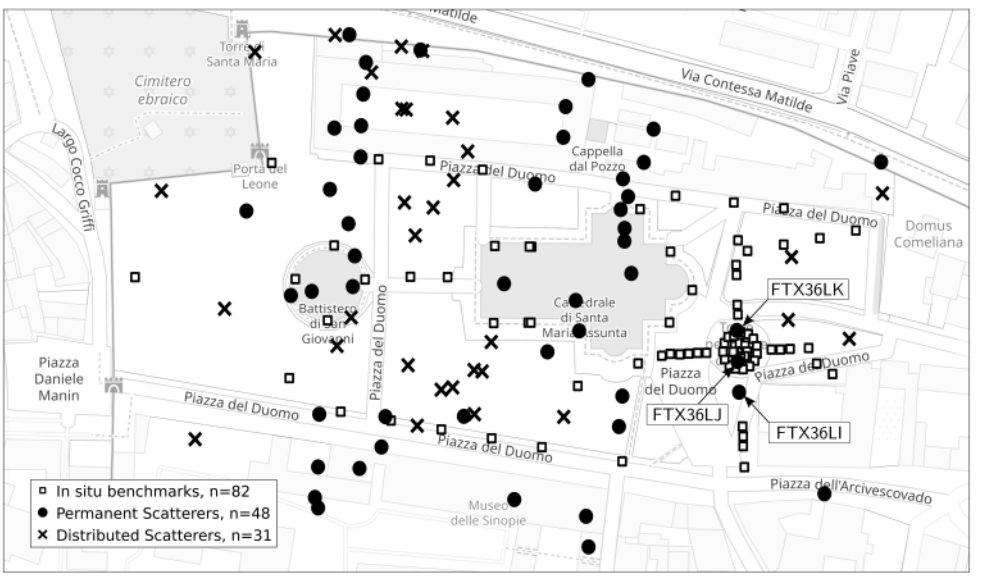

Figure 4. SAR scatterers within the area of Piazza del Duomo in Pisa, Italy (both PS and DS), and selected levelling benchmarks. PS codes within the LaMMA database are specified for three scatterers on the Leaning Tower, analysed in more detail in Figure 5. *Base map from* openstreemap.org.

Monumental structures are naturally good scatterers for a few reasons: they are usually large enough to encompass one or more resolution cells, even for the less precise C-band SAR imaging; they are often unencumbered by other buildings capable of obstructing the LOS; most of all, their

immutability guarantees a good coherence of electromagnetic signature, and thus a good chance of building consistent time series of displacements. On the downside, the position of scatterers above monuments and in surrounding areas is impossible to predict beforehand, while ground levelling benchmarks can be positioned at will (more or less). At the same time, when C-band SAR is considered, the typical positioning precision of PS is in the order of a few metres (Rucci et al. 2012). This limitation is of course inexistent for levelling benchmarks, which position is known within a few centimetres. Last but not least, on site surveys can include reference points installed inside the structures (as is the case for the Leaning Tower), which position and elevation are acquired within the same measurement campaign. For these reasons, on site benchmarks may be preferable with respect to C-band SAR scatterers when their location has to be known precisely. This is often the case with monumental structures. However, the high frequency of satellite measurements, and their relative inexpensiveness, should encourage to find a way to integrate them with on site surveys.

3.2 *Seasonality of Sentinel DInSAR data*

Inclination measures of the Leaning Tower provide a good opportunity to check the accuracy of DInSAR data in representing the seasonal behaviour of displacements. Out of the two pendulums which are currently operating inside the structure, we selected the one installed on the southern side, and considered the east-west component of its movement, which is tracked by a telecoordinometer and sampled on a hourly basis. Among the Sentinel scatterers within the study area, three PS with codes FTX36LI, -LJ and -LK in the employed database, are considered. For reasons mentioned in the previous Section, it is impossible to determine from the map alone whether they are actually positioned on the Tower. This can however be inferred by considering elevation data as well, since each of the PS is consistently higher than the average elevation of scatterers in the surrounding area.

All of the signals, both from the telecoordinometer and from the scatterers, were detrended using STL as described in Section 2.4. Figure 5 shows a comparison among the seasonal components of the four signals. Despite a nominal sensitivity of ±2 mm/year, DInSAR data from all three scatterers clearly shows a good accuracy in representing the seasonal behaviour. Correlation factors, ranging from 0.66 to 0.77, are a testimony to that.

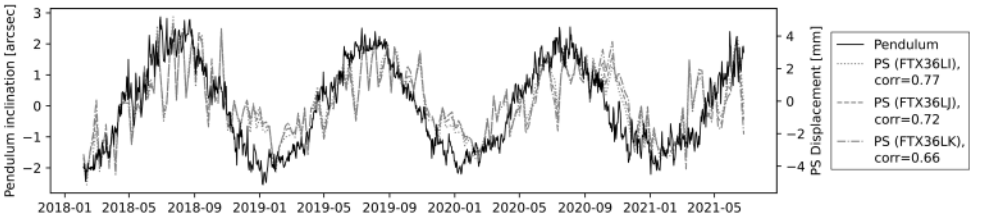

Figure 5. Comparison of the seasonal components of traditional (pendulum measured via telecoordinometer) and satellite (PS FTX36LI, -LJ and -LK) monitoring data for the Leaning Tower.

3.3 *Sensitivity and trend of Sentinel DInSAR data*

The medium-to-long term trend is clearly the most critical component of displacement, but the results of its evaluation within the case study area did not prove as encouraging as those of seasonality.

A first investigation was carried out into the influence of measurement accuracy by comparing historically-recorded settlements of the Leaning Tower and surrounding area with the nominal error of the employed DInSAR data. Figure 6 shows the displacements measured ons site since 2008. Each data point is the difference between the levelling benchmark elevation recorded in two consecutive surveys. The threshold at ±4.0 mm correponds to two times the absolute error of DInSAR data of ±2 mm/year (Section 2.3). This threshold can be directly compared to the

remaining data, since the time lapse between consecutive levelling surveys is also two years. Once again, the area around the Leaning Tower was selected since it displays the largest settlements in the Piazza, and thus the easiest ones to record. This first examination leads to the conclusion that, at least in the years 2008–2020, the employed DInSAR data would not have been sufficient to properly monitor the displacements of Piazza del Duomo.

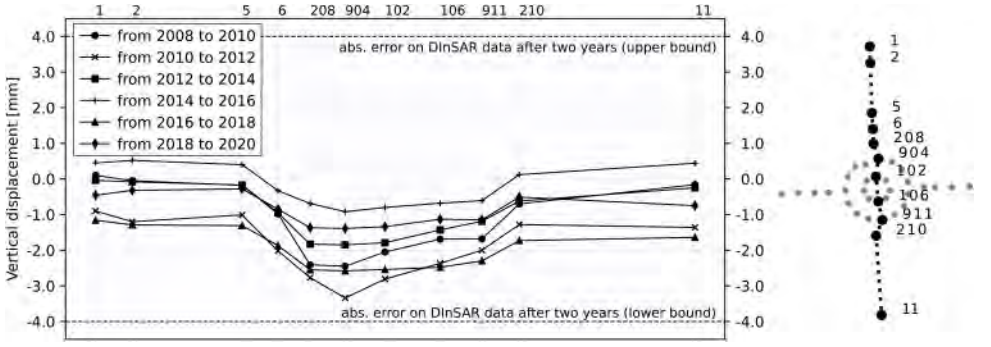

Figure 6. Displacements of benchmarks under and around the Leaning Tower recorded during two-year intervals between 2008 and 2020. Lines at ±4 mm show the upper and lower bounds of the absolute error range of the employed DInSAR data. On the right, a map of the considered levelling benchmarks for comparison with that of Figure 4.

To corroborate this, a second investigation involved a direct comparison of the trend component of DInSAR and on site measured displacements. In Figure 7, each of the scatterers and ground benchmarks is marked according to the sign of its average yearly displacement between June 2018 and June 2020, indicating whether the point rose or subsided. There is a conspicuous difference between the two images. Subsidence has been recorded in all ground benchmarks (excluding the deep reference point, which is considered to be fixed), while more than 70% of SAR scatterers appear to be rising.

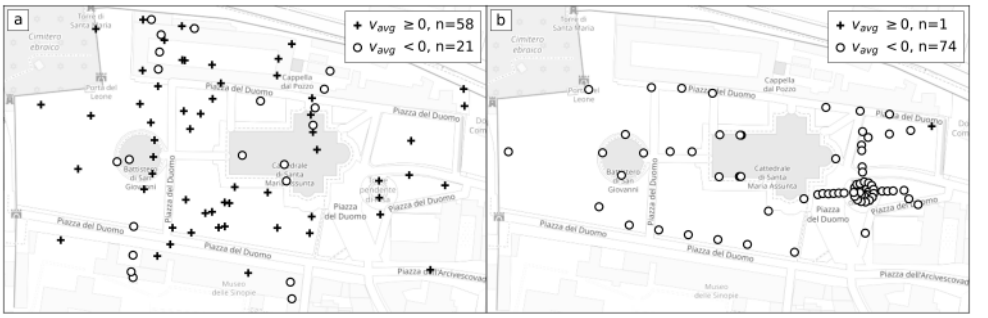

Figure 7. Sign of the average yearly settlement of Piazza del Duomo between June 2018 and 2020 as measured: (a) via Sentinel DInSAR; (b) via levelling surveys. The only cross in (b) is the deep reference point, which is considered fixed.

Figure 8 shows the average displacement velocity of the Piazza over the years. Since DInSAR data are already furnished in terms of velocity, data from on site measurements were also expressed in the same terms. This way, it is easier to compare the two sources of measurement.

Although the trend of on-site-measured displacements changes in time, the average movement remains one of subsidence. Conversely, DInSAR scatterers show a more erratic average behaviour, suggesting however that Piazza del Duomo mainly rose between 2018 and 2020. The main reason for this is very probably that the average displacement velocity in the whole Piazza is less than the

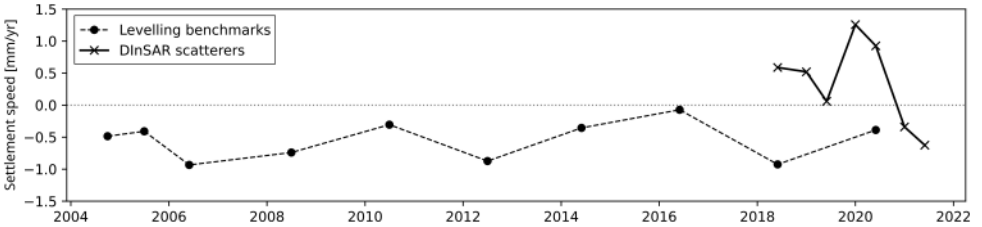

Figure 8. Settlement speed of the whole Piazza del Duomo (average).

nominal absolute error of the employed DInSAR data. Satellite measurements, in accordance with this, are all within the margin of error, and so are their averages in time.

The comparisons visually reported in the last two Figures once again indicate that, for what concerns Piazza del Duomo between the years 2018 and 2020 (a time period for which a direct comparison is possible), DInSAR data alone would not have been sufficient for a proper monitoring of displacements.

4 CONCLUSIONS AND FURTHER DEVELOPMENTS

Monitoring of soil and structure displacement is of great importance to the preservation of monumental structures. While many of these may already be the object of on site measurement campaigns, traditional surveys are usually time consuming and expensive. Displacement evaluation through satellite SAR interferometry appears then as an attractive tool, potentially allowing to reduce the temporal and monetary requirements of monitoring. The present work constitutes one step towards the definition of guidelines for the employment and integration of DInSAR techniques in the monitoring of monumental complexes. Using Piazza del Duomo in Pisa, Italy, as a case study, we explored the advantages and limitations of DInSAR data from the Sentinel constellation of the European Copernicus project, elaborated with TRE ALTAMIRA's proprietary SqueeSAR® algorithm and made freely available by Consorzio LaMMA. We concentrated on a comparison between satellite and on-site monitoring results, taking advantage of a long and consolidated historical series of measurements involving both the Piazza and the Leaning Tower specifically. To overcome problems due to the natural seasonality of ground and structure displacements, we employed STL decomposition on all signals, and compared either the seasonal or the trend components separately.

From the analysis, some issues emerged in the use of satellite data. The unpredictable location of scatterers and their imprecise spatial positioning could render them useless when an accurate placement of monitoring references is needed (as is usually the case for CH structures). Comparison of displacement trends for the whole Piazza del Duomo, obtained on-site and from DInSAR data, also showed no accordance, therefore undermining the possibility of using such data to integrate traditional monitoring. Finally, an analysis of ground displacements under and around the Leaning Tower in the last twelve years revealed that the recorded settlements all fell within the boundaries of the employed data's absolute error.

Good results were instead obtained by comparing the seasonal component of DInSAR data from scatterers on the Leaning Tower against the signal from a pendulum installed on the structure. Next to this, undeniable practical advantages of satellite monitoring were also identified. First of all, the very high frequency of Sentinel imaging, which allows measurements to be obtained once every six days. This could prove very useful in early-warning systems or to quickly assess the impact of extreme events such as earthquakes. The fact that monumental structures are naturally good scatterers, guaranteeing in most cases a satisfying number of measurement points on their surface, is another advantage of the satellite technique.

From this comparison, we drew the conclusion that C-band DInSAR data from Sentinel satellites, even when elaborated with a cutting-edge multi-interferometric algorithm, is probably unsuitable

for monitoring the monumental complex of Piazza del Duomo. For its undeniable potential advantages, however, we suggest that a similar investigation is carried out using SAR data from different sources. X-band SAR imagery from the COSMO-SkyMed mission should be considered, since its greater spatial resolution allows to obtain a higher number of scatterers and to know their position more precisely, while a higher accuracy may allow tracking of the very small displacements affecting the analysed site.

ACKNOWLEDGEMENTS

The authors would like to thank Opera della Primaziale Pisana for granting access to the site and to monitoring data; ASTRO Laboratory, of the University of Pisa, which performed the levelling surveys; TRE ALTAMIRA for the acquisition and analysis of DInSAR data, as well as counseling regarding said data; Consorzio LaMMA and University of Florence for the organization and dissemination of DInSAR data.

The present work was possible thanks to funding by Regione Toscana, Opera della Primaziale Pisana and the University of Pisa under the research grant: *"Progettazione di sistemi di monitoraggio strutturale per Complessi Monumentali"*.

REFERENCES

Bilotta, E., Flora, A., Lirer, S. & Viggiani, C. (Eds.) 2013. Geotechnics and Heritage. 11 June 2013, London, UK. ISBN: 978-1-138-00054-4. doi:10.1201/b14965.

Bischoff, C. A., Ferretti, A., Novali, F., Uttini, A., Giannico, C. & Meloni, F. 2020. Nationwide deformation monitoring with SqueeSAR® using Sentinel-1 data. *Proceedings of the Tenth International Symposium on Land Subsidence (TISOLS)* 382: 31–37. doi:10.5194/piahs-382-31-2020.

Bonazza, A., Drdácký, M., Hanus, C., Maxwell, I. & Vintzileou, E. 2018. Study on safeguarding cultural heritage from natural and man-made disasters: a comparative analysis of risk management in the EU. https://op.europa.eu/en/publication-detail/-/publication/8fe9ea60-4cea-11e8-be1d-01aa75ed71a1. Accessed on October 2021.

Caroti, C., Piemonte, A. & Squeglia, N. 2019. 100 Years of Geodetic Measurements in the Piazza del Duomo (Pisa, Italy): Reference Systems, Data Comparability and Geotechnical Monitoring. *Proceedings of the 4th Joint International Symposium on Deformation Monitoring (JISDM)*, May 2019, Athens, Greece. http://hdl.handle.net/11568/1002453.

Casagli, N., Massini, G. & Bottai, L. 2018. Linee guida per l'utilizzo dei dati interferometrici del geoportale Regione Toscana. http://www.regione.toscana.it/documents/10180/14985922/Linee+guida+per+l%E2%80%99utilizzo+dei+dati+interferometrici+del+geoportale.pdf/d5b091a7-a5b1-41e9-97c3-270a52b0c7ce. Accessed on October 2021.

Cavalagli, N., Kita, A., Falco, S., Trillo, F., Costantini, M. & Ubertini, F. 2019. Satellite radar interferometry and in-situ measurements for static monitoring of historical monuments: The case of Gubbio, Italy. *Remote Sensing of Environment* 235. doi:10.1016/j.rse.2019.111453.

Cleveland, R. B., Cleveland, W. S., McRae, J. E. & Terpenning I. 1990. STL: A Seasonal-Trend Decomposition Procedure Based on Loess. *Journal of Official Statistics* 6(1): 3–33. Statistics Sweden.

Cleveland, W. S., Devlin, S. J. & Grosse, E. 1988. Regression by Local Fitting: Methods, Properties, and Computational Algorithms. *Journal of Econometrics* 37: 87–114.

Colesanti, C., Ferretti, A., Prati, C. & Rocca, F. 2003. Monitoring landslides and tectonic motions with the Permanent Scatterers Technique. *Engineering Geology* 68(1–2): 3–14. doi:10.1016/S0013-7952(02)00195-3.

Commissione Pisana per gli Studi sulla Torre Pendente 1913. Relazione generale 1913. Pisa.

Del Soldato, M., Solari, L., Raspini, F., Bianchini, S., Ciampalini, A., Montalti, R., Ferretti, A., Pellegrineschi, V. & Casagli, N. 2019. Monitoring Ground Instabilities Using SAR Satellite Data: A Practical Approach. *ISPRS International Journal of Geo-Information* 8, 307. doi:10.3390/ijgi8070307.

ESA – European Space Agency 2007. InSAR Principles: Guidelines for SAR Interferometry Processing and Interpretation (TM-19 February 2007). Fletcher K. (ed.). ESA Publications, Noordwijk, The Netherlands. ISBN: 92-9092-233-8.

ESA – European Space Agency 2019. Copernicus in detail. https://www.copernicus.eu/en/about-copernicus/copernicus-detail. Accessed on October 2021.
ESA – European Space Agency 2021. Sentinel-1 SAR Instrument. https://sentinel.esa.int/web/sentinel/technical-guides/sentinel-1-sar/sar-instrument. Accessed on October 2021.
Ferretti, A., Prati, C. & Rocca, F. 2000. Nonlinear subsidence rate estimation using permanent scatterers in differential SAR interferometry. *IEEE Transactions on Geoscience and Remote Sensing* 38(5): 2202–2212. doi:10.1109/36.868878.
Ferretti, A., Savio, G., Barzaghi, R., Borghi, A., Musazzi, S., Novali, F., Prati, C. & Rocca, F. 2007. Submillimiter Accuracy of InSAR Time Series: Experimental Validation. *IEEE Transactions on Geoscience and Remote Sensing* 45(5): 1142–1153. doi:10.1109/TGRS.2007.894440.
Ferretti, A., Fumagalli, A., Novali, F., Prati, C., Rocca, F. & Rucci, A. 2011. A New Algorithm for Processing Interferometric Data-Stacks: SqueeSAR. *IEEE Transactions on Geoscience and Remote Sensing* 49 (9): 3460–3470. doi:10.1109/TGRS.2011.2124465.
I.G.M. – Istituto Geografico Militare 1965. Misure geotopografiche programmate dall'Istituto Geografico Militare. Firenze.
I.G.M. – Istituto Geografico Militare 1966. Rapporto sui movimenti della Torre. Firenze.
Lagomarsino, S. & Cattari, S. 2015. PERPETUATE guidelines for seismic performance-based assessment of cultural heritage masonry structures. *Bulletin of Earthquake Engineeering* 13: 13–47. doi:10/f6szr2. Leoni, M., Squeglia, N. & Viggiani, C. 2017. Tower of Pisa: Lessons learned by observation and analysis.
In Renato Lancellotta, Alessandro Flora & Carlo Viggiani (Eds.), *Geotechnics and Heritage: Historic Towers*: 15–37. ISBN: 978-1-138-03272-9. doi:10.1201/9781315387468.
Meyer, F. 2019. Spaceborne Synthetic Aperture Radar – Principles, Data Access, and Basic Processing Techniques. In Flores, A. et al. (ed.), *SAR Handbook: Comprehensive Methodologies for Forest Monitoring and Biomass Estimation. E. NASA.* doi:10.25966/ez4f-mg98.
Noccioli, R., Polvani, G., & Salvioni, G. 1971. I movimenti della torre dal giugno 1911 a tutto il 1968. Ricerche e Studi su la Torre Pendente di Pisa e i fenomeni connessi alle condizioni d'ambiente. Istituto Geografico Militare (ed.), Firenze.
Perktold J., Seabold S., Sheppard K. et al. 2020. meaghanflagg/statsmodels: v0.12.1-beta (v0.12.1-beta). Zenodo. doi:10.5281/zenodo.4243083.
Ramos, L. F., Masciotta, M. G., Morais, M. J., Azenha, M., Ferreira, T., Pereira, E. B. & Lourenc¸o, P. B. 2018. HeritageCARE: Preventive conservation of built cultural heritage in the South-West Europe. In K. Van Balen, A. Vandesande (Eds.) *Innovative Built Heritage Models*: 135–148. doi:10.1201/9781351014793-16.
Regione Toscana 2021. Geoportale Regione Toscana, https://geoportale.lamma.rete.toscana.it/difesa suolo/#/viewer/openlayers/326. Accessed on October 2021.
Rucci, A., Ferretti, A., Guarnieri, A.M. & Rocca, F. 2012. Sentinel 1 SAR interferometry applications: The outlook for sub millimeter measurements. *Remote Sensing of Environment* 120, 156–163. doi:10.1016/j.rse.2011.09.030.
Tapete, D. & Cigna, F. 2019. COSMO-SkyMed SAR for Detection and Monitoring of Archaeological and Cultural Heritage Sites. *Remote Sensing* 11(11), 1326. doi:10.3390/rs11111326.
UNESCO 2021. Italy – UNESCO World Heritage Centre. http://whc.unesco.org/en/statesparties/it. Accessed on October 2021.
UN – United Nations 2015. Sendai Framework for Disaster Risk Reduction 2015–2030 — A/RES/69/283. 18 March 2015 Sendai, Japan. https://www.unisdr.org/files/43291 sendaiframeworkfordrren.pdf. Accessed on October 2021.
Viggiani, C. 2019. Senza neanche toccarla – La stabilizzazione della Torre di Pisa. Hevelius Ed. EAN: 9788886977968.

Geotechnical Engineering for the Preservation of Monuments and Historic Sites III – Lancellotta, Viggiani, Flora, de Silva & Mele (Eds)

Cultural Heritage sites conservation and management: The case of the Circus Maximus in Rome

L.M. Puzzilli, G. Delmonaco, F. Traversa, V. Ruscito, F. Ferri, E. Mariani & C. Quadrozzi
Department of Geological Survey of Italy, Italian Institute for Environmental Protection and Research, Rome, Italy

P. Clemente, G. Bongiovanni & V. Verrubbi
Casaccia Research Centre, Italian National Agency for New Technologies, Energy and Sustainable Economic Development, Rome, Italy

M. Buonfiglio & F.M. Rossi
Superintendency of Cultural Heritage of Rome, Rome, Italy

ABSTRACT: The Circus Maximus in Rome (Italy) is the most famous ancient Roman chariot-racing circus, built along the alluvial valley between Palatine and Aventine hills, in the hearth of the historical city centre. Thanks to its exceptional size, it still represents the largest structure ever built in the history for entertainment. As soon as the Roman empire fell, the area suffered spoilation and disuse, changing the original use several times through the centuries. Starting from 2009, the site has been involved into a restoration and conservation project which includes multidisciplinary studies based on geophysical surveys, geotechnical investigations and instrumental monitoring of potentially vulnerable structures. The present experimental campaign, based on additional geophysical surveys, boreholes and geotechnical tests, will produce a systematic and detailed analysis of the underground conditions of the Circus Maximus area. The new findings will be used to support policies for a sustainable use of the area.

1 INTRODUCTION

Rome is a unique city in the world that can boast such a high number of cultural heritage and archaeological sites located in the heart of its historical area. A significant part of this heritage is certainly represented by the remains belonging to the Roman Age, some of which with imposing size (e.g. Colosseum, Pantheon, Basilica of Maxentius) and/or large extension (e.g. Palatine Hill, Caracalla Baths, Roman Forum and Circus Maximus) that caused the city to develop around them over the centuries and incorporated them into the present urban fabric. The Circus Maximus, a structure intended to host chariot races and religious celebrations, played a significant role for the life of Roman citizens up to the end of the Roman Era. Built along a small tributary valley of the Tiber River called "Murcia", between Palatine and Aventine hills (Figure 1), when fully developed, the Circus Maximus became a "model" throughout the Roman Empire for such kind of structures created for mass events. Unfortunately, an almost-complete burial of the entire monumental area took place already a few centuries after its abandonment and this had hampered its effective knowledge till today. Not surprisingly, to date, some considerations about its architectures as well as the spatial relationships between its architectonic elements (e.g. dimensions of the track and the middle barrier called "Euripus", position of holy temples etc.) are inferred based on studies

 DOI 10.1201/9781003308867-40

Figure 1. Location of the Circus Maximus area in Rome (Italy) between the Palatine and Aventine Hills. The study area is enclosed in the dotted rectangle and includes the Archaeological Park Area (A), freely accessible for entertainment and social events, and the Archeological Area (B) with limited access (satellite image available at http://www.pcn.minambiente.it/ mattm/servizio-wms/, accessed on 25 September 2021).

in Roman circuses outside of Italy. Today, this monumental area is separated into two distinct sectors: the Park and the Archaeological Area (Figure 1). The Park occupies about two-third of the site extension and is granted for use of social events; this area contains most of the archaeological heritage buried in the subsoil. The Archaeological Area is separated and protected with a fence and includes Roman and medieval remains that can be visited by the public. The site is under the supervision and protection of the Superintendency of Cultural Heritage for the City of Rome; nevertheless, it maintains its character as a recreational and cultural area for many citizens and tourists who also enjoy the Park daily. The Park also hosts yearly many social events ranging from pop-music and opera concerts to sport celebrations and cultural exhibition, often with a very large audience. Just to give examples, in 2007 the English band Genesis performed a concert before hundreds of thousands of people (https://www.bbc.co.uk/programmes/b00bbxxv) while in 2014 the Rolling Stones played in front of about 71,500 fans. Also, sport celebrations were hosted as in 2001 after the A.S. Roma victory of the Football Italian championship and few years later after the Italian victory of the 2006 Football World Cup. Since May 2019, just within the Archaeological Area, a new virtual and augmented reality experience, the "Circo Maximo Experience", has been opened, taking visitors on a journey through the site and its history. The Circus Maximus represents an example of cultural heritage site prone to anthropic and environmental stress that needs policies for a rational and sustainable use to be adopted; this implies an adequate detail of knowledge as a fundamental base to address mitigation actions for its maintenance and preservation. Starting from 2009, the Superintendency of Cultural Heritage of Rome coordinated multidisciplinary studies primarily aimed at providing a more exhaustive knowledge and revealing the uses of this site throughout the centuries. To support this ambitious project, a series of scientific activities have been carried out, including geophysical surveys, geotechnical investigations, instrumental monitoring of some structures during social events. In this paper, the main archeological features and the geological setting of the site are first introduced, then the ongoing multidisciplinary experimental campaign is described. The field investigations are based on geophysical surveys (concluded at the end of October 2021), boreholes and geotechnical tests. Some preliminary outcomes are eventually described and briefly discussed, along with the main results of the vibration monitoring campaign performed in 2019 during a concert attended by 40,000 people in the park area.

2 ARCHAEOLOGICAL CONTEXT

The Circus Maximus was the first and largest building dedicated to the Roman "ludi", the public games connected to Roman's religious festivals. The Romans built a structure of a truly exceptional size: this large oval-shaped hippodrome could accommodate about 220,000 spectators in its fully developed form (about 600 m long and 140 m wide) becoming a model all over the Roman Empire. The present archaeological knowledge of this area is mainly due to researchs studies started at the beginning of last century by Bigot (Bigot 1908) and continued till present days by many institutions and researchers throughout excavations, drillings campaign and, more recently, using geophysical methods (e.g. Brandizzi Vittucci 1991; Buonfiglio 2018; Canciani et al. 2013; Carpentieri et al. 2015; Ciancio Rossetto 2002; Ciancio Rossetto & Buonfiglio 2007; Mancini et al. 2018; Marra et al. 2016, 2018, 2021; Pietrangeli 1940). The first masonry works were made under Caesar and after numerous vicissitudes (fires and restorations) the Circus was rebuilt and enlarged under the Emperors Domitian and Trajan, remaining active as such until the 549 B.C when the Ostrogoth king Totila organized the last games. After the 6th century, the area has fallen into progressive disuse suffering spoliation and becoming a quarry for building materials. The lower levels became again prone to flooding and were gradually buried under alluvial soil and accumulated debris so that the original track is now buried up to 10 meters beneath the present surface. Throughout the centuries, the intended use changed many times: agricultural area (in Middle Ages), Jewish cemetery (17th century), district of industrial settlements (19th–20th century). At the end of 1800s, this area became a target for industrial purposes: a gasometer was installed here and, in turn, warehouses, factories, cottage industries, even houses were established here. In the middle of the Fascist era, however, the area was used by the regime for trade fairs and exhibitions such as the Textiles Show (1934) and the Exhibition of Italian Autarkic Mineral (1939) and converted into a park, in the shape of the original form of the Circus. Finally, by the mid-20th century, to institute the Circus Maximum Monumental Area protecting the remains, the valley floor was freed from preexisting industrial buildings; massive excavations were also carried out, mainly concentrated in the south-eastern sector. The works uncovered the lower parts of a seating tier and outer "portico" and subsequent excavations exposed further sections of the seating and hemicycle. Those can be admired today along with the medieval structure called "Torre della Moletta", a square tower with battlements erected by the Frangipane family. In 1998, archeological excavations took place through large diameter wells (2 m) in correspondence with the present central barrier where some remains of Roman age were previously logged by one drilling. These investigations have reconstructed the detailed sequence of the archeological layers as well as the analysis of the remains of different ages included therein (Ciancio Rossetto 2002), extending the observations up to the depths corresponding to the Circus track. It was possible, for the very first time, to visually inspect the skeleton of the "euripo" and determine that in-place Roman remains pertaining to this structure could be found in the Park area within a depth ranging between 8 ÷ 11 m (i.e. corresponding to 10.5 ÷ 7.5 m a.s.l.). Two different anthropic layers progressively embedding the remains were also classified according to the different age of the remains; the most superficial, related to modern era, has a maximum thickness of about 4 meters along the whole area (14.5 ÷ 18.5 m a.s.l.).

3 GEOLOGICAL SETTING OF THE STUDY AREA

From a geological point of view, the "Murcia" valley is carved into the Plio-Pleistocene clays known as "Mount Vaticano" Formation (Funiciello & Giordano 2008), hundreds of meters thick, that represents the geological bedrock of the whole area of Rome. According to recent studies (Marra et al. 2021), during Middle-Late Pleistocene and Holocene the sedimentary processes over the whole Rome area were strongly controlled by sea-level changes related to glacio-eustatism. This strongly influenced the sedimentary processes that led to the progressive infilling of all the Tiber River tributary valley by a fining-upward sequence: from fine gravels with intercalations of clay at the bottom to silty clay and organic and peaty clay on top, closed by a heterogeneous anthropogenic

layer (historical backfilling). While during the Roman Ages the entire valley was transformed into the largest monument of antiquity ever built, after the fall of the Roman Empire this area suffered the abandon, experienced frequent floods and finally become a swamp. Waterlogged sediments belonging to this period were interposed by progressively increasing volumes of anthropic backfilling, accumulated during almost two-thousand years of human activities, including the complete urbanization and occupation with industrial plants at the beginning of 1900s. Stratigraphic and hydrogeological data have been derived from the current research activities during which the available information referred to the subsoil (scientific reports, studies, publications, archeological report and drawings, borehole logs etc.) have been collected, reviewed and georeferenced in a geodatabase referred to the whole monumental area.

3.1 *Stratigraphic setting*

The first investigation campaign took place here in 1939 through the drilling of a 1,330 meters deep borehole by Azienda Generale Italiana Petroli (AGIP), aimed at the improvement of the geological knowledge of the entire Rome subsoil. However, it also provided the first information about the infilling of the valley. More detailed investigations were carried out only in the early 1980's by means of 16 deep boreholes (up to 62 m in depth) commissioned by the Rome's Superintendency of Cultural Heritage (Geosonda 1983). This investigation reconstructed the geological and hydrogeological setting at site scale and was aimed at supporting the archaeological surveys performed few years later (see e.g. Ciancio Rossetto & Buonfiglio 2007). Additional investigations, consisting in shallow boreholes and in-situ tests were also performed in 2003 and 2005 in the surrounding of the medieval remains (i.e. at the south-eastern end and close to the "Torre della Moletta") thus providing geotechnical parameters of the soils. In Figure 2a the locations of the available boreholes in the area are shown; the stratigraphic setting referred to two main sections crossing the archeological site are depicted in Figure 2b and 2c. The surface layer is represented by a heterogeneous and poorly graded deposit, from sandy gravel to gravelly silty sand to clayey silt, often brown color, stiff to very stiff, containing in some cases potteries and even fragments of concrete. It mostly consists in anthropic backfills and waterlogged deposits accumulated here during almost 1,500 years of human activities, including the complete urbanization and occupation with industrial plants at the beginning of 1900s, with an overall thickness of 10 m and rather continuous along the whole site. Deeper, a very thick geological body made of fluvial and fluvial-marshy environments deposits follows. It consists of clays, silts and clayey silts, from dark brown to dark grey and grey, soft to very soft, generally containing abundant organic matter (with peat levels). These alluvial deposits,

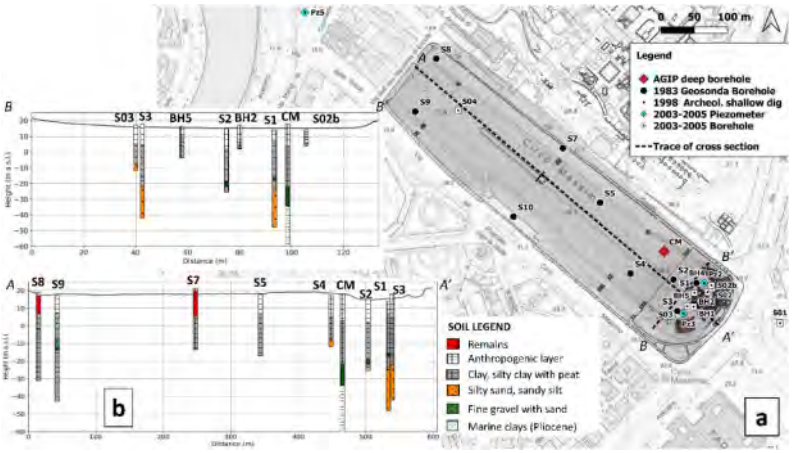

Figure 2. Location of available boreholes (a) with the correspondent stratigraphic logs projected along the A-A', (b) and B-B', (c) cross sections. AGIP deep borehole (CM) is located according to Argentieri et al. 2020.

as reported in geotechnical borehole logs, are slightly coarser at greater depth, ranging from fine sands to sandy silts. Since, to date, no drillings have passed through the entire fine-grained geological body, the Valle "Murcia" Quaternary sequence resting above the geologic substratum is supposed to be closed at the bottom by coarse deposits according to Mancini et al. 2018.

3.2 *Hydrogeologic setting*

At present, the hydrogeologic setting of the area is still poorly reconstructed; no detailed study has been undertaken to date, therefore only basic information can be deduced from general studies concerning the nearby Tiber and its small tributaries (e.g. Funiciello et al. 1995). To fill the data gap on the hydrogeological setting, some piezometers have been installed inside and outside the Circus area during the 2003 and 2005 geotechnical campaigns, located as shown in Figure 3a. Monthly measurements of water levels have been performed, from November 2003 to July 2004, determining the presence of groundwater resting few meters below the ground surface. The groundwater table is somewhat superficial along the whole valley up to Tiber River, with limited seasonal variations along all measurement points as in Figure 3b. The same picture shows a remarkable difference between the piezometers installed inside the study area and the piezometer (n. 310) close to the Tiber River. It suggests the presence of a possible complex hydrogeological setting as the water level drops more than 6 m from piezometer n. 304 to n. 310 (only 275 m away), thus requiring further investigations and groundwater levels monitoring. As a matter of fact, no measurements have been performed after 2004 and, to date, all piezometers are lost. Only during the 2015 works inside the archeological area, the groundwater level has been observed almost constantly at 13.5 m on shallow excavations. New piezometers should be installed during the next drillings campaign.

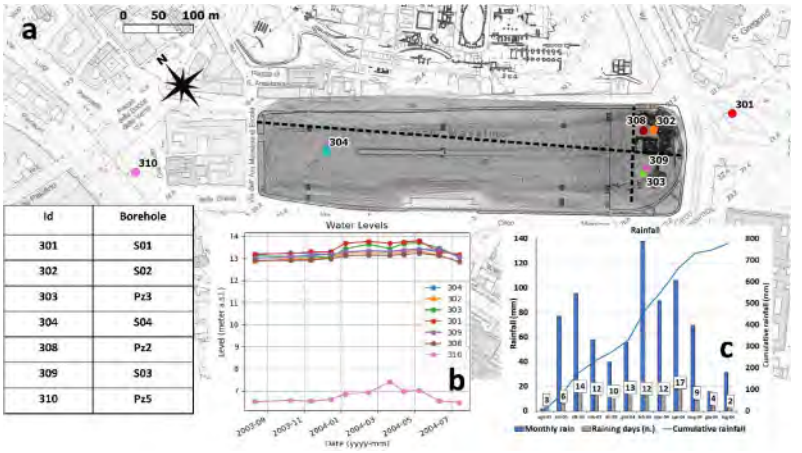

Id	Borehole
301	S01
302	S02
303	Pz3
304	S04
308	Pz2
309	S03
310	Pz5

Figure 3. Location of piezometers along the study area (a). Results of the 2003–2004 groundwater monitoring (b) and rainfall data during the monitoring period (c). Each instrument is identified by a Id number that refers to a borehole code in Figure 2.

4 GEOPHYSICAL INVESTIGATIONS

The Circus Maximus is an illustrative example of a still partially buried archaeological site on which it is highly recommendable to conduct indirect investigations before considering new and expensive excavations, as most of the remains lie many meters below the surface. Different geophysical methods and survey techniques, 2D and 3D, have been adopted here: electrical resistivity tomography and Ground Probing Radar for archaeological purposes, Noise recordings and Surface Wave (SW) tests to obtain estimates of the fundamental frequency of resonance of the site and the shear-waves velocity profile respectively. In addition, vibrations of the "Torre della Moletta" and

the surrounding Roman ruins have been recorded during a concert, in May 2019, to analyze the effects induced on the structures by anthropic noise.

4.1 *Electrical Resistivity Tomography*

The first campaign consisting in 21 electrical resistivity profiles has been conducted in 2015 and focused on the characterization of the longitudinal central axis of the Circus. Based on the obtained results the ERT survey has been extended more recently to the whole area (Figure 4) for different aims such as: 1) to estimate the depth range of the buried Roman remains vs. those of later periods; 2) to constrain the size, position and orientation of the "euripo", the central barrier of the track, with respect to other structures of the Circus and Palatine Hill; 3) to extend spatially information derived from boreholes, e.g. by correlating ranges of resistivity values with lithological units. A high resolution geoelectrical resistivity surveying has been designed and performed using the X612EM resistivimeter (M.A.E. – www.mae-srl.it) with a multi-electrode acquisition system, using 30 to 96 electrodes along 68 profiles. Measurements have been taken by using at least two different arrays (wenner, wenner-schlumberger, dipole-dipole) along each profile, exploiting the different sensitivity of each one (see e.g. Dahlin & Zhou 2004) to achieve good resolution in both vertical and horizontal directions, thus increasing the quality of the survey. The 2D data inversion process has been carried out after the quality check and data filtering using the Res2DInv software (Loke & Barker 1996) obtaining a 2D model to be interpreted. The data are currently being used for 3D resistivity modeling extended to the entire study area.

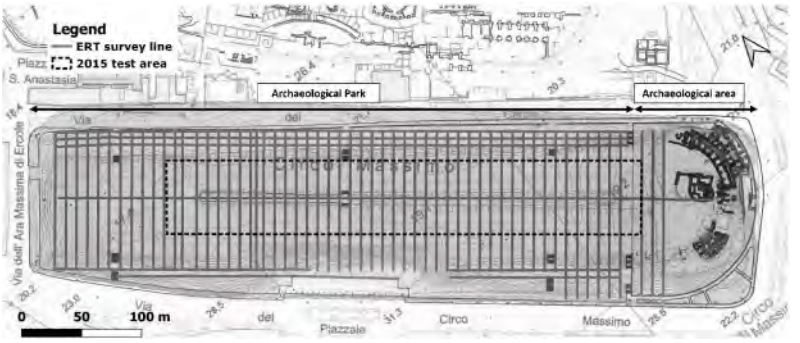

Figure 4. Location of ERT profiles within the Circus Maximus along with the test area surveyed in 2015.

4.2 *Ground Probing Radar*

The GPR method has been used to couple ERT survey lines to obtain detailed information of shallow subsurface useful to constrain the resistivity models. Radar data have been collected along 7 profiles by means of a MALÅ bistatic antenna emitting a frequency band centered at 100 MHz. After some preliminary field tests, this low frequency system has been chosen as a compromise between need of resolution and depth of investigation in such geological environment dominated by conductive soils. The surveys with 100 MHz antenna have been performed fixing the sample frequency at 1100 MHz, the time window equal to 100 ns and recording one trace every 0,02 m in profiling direction, stacking each sample 16 times. Along the central axis of the Circus, 5 parallel radar profiles (0.50 m equally spaced) have been recorded using a MALÅ bistatic 250 MHz antenna; a 3D processing has been implemented to possibly evaluate the buried geometry of some superficial remains, made of concrete, related to 1900s structures.

4.3 *Ambient noise recordings*

The first noise recordings were performed during the experimental campaign conducted in 2019 within the archeological sector in the framework of the vibration monitoring experiment conducted

during a social event and following described. Data were recorded using three-axial Tromino velocimeters (5 sites) and SARA SL06 three-axial seismometers (3 sites) deployed as in Figure 5. The duration of the noise recordings ranged from 20 to 245 min, using sampling frequencies equal to 128 Hz (Tromino) and 200 Hz (SARA SL06). The procedures proposed in SESAME 2004 have been implemented for the processing and the statistical validation of the horizontal–vertical spectral ratio (HVSR) curves: recorded signals were divided into time windows with a fixed length of 60 sec and the transient parts of the signals have been excluded (since possibly associated to close sources). The signal pertaining to each time window was cosine tapered (5%) and the Fourier spectrum has been calculated. Smoothing has been applied using the Konno–Ohmachi function with a constant bandwidth coefficient "b" ranging from 25 to 35 (Konno & Ohmachi 1998). According to Nakamura's procedure the spectral ratio curve has been calculated between the two horizontal components and the vertical one, obtaining for each time window a HVSR function within the $0.20 \div 20$ Hz frequency interval. Processed data have been used to infer the fundamental frequency value (F_0) at each recording site, considering the frequency peaks with a spectral ratio value greater than 2 along each curve. To date, aiming to possibly characterize the whole monumental site in terms of seismic site amplification phenomena, a total of 38 single-station ambient vibration recordings have been performed. Based on the retrieved HVSR curves (not shown here), the F_0 values for the study area vary in a narrow range around 1.35 Hz, without significant differences across the site, also in accordance with Di Luzio et al. 2014.

4.4 *Surface-waves analysis*

Surface-waves surveys have been conducted in the Archaeological area to retrieve a reliable seismic characterization of the soils in terms of shear-waves velocity (Vs) being the main parameter affecting the site amplification of seismic motion. For this purpose, a 57,5-m-long seismic profile has been used deploying 24 geophones equally spaced of 2.5 m oriented as in Figure 5. The compliance of the site conditions with the hypothesis of horizontally layered medium under the seismic profile has been checked via HVSR results, also considering the stratigraphic setting of the cross-section BB' shown in Figure 2b. Vertical and horizontal geophones, both with a nominal frequency of 4.5 Hz, have been used to achieve dispersion data, referred to Rayleigh's (both vertical and radial components were acquired) and Love's waves respectively. Seismograms have been recorded with different offset distances, using an 8-kg sledgehammer as a waves source, striking it vertically over a steel plate to generate Rayleigh's waves dispersion or over a wooden beam firmly fixed to the ground to generate Love's waves dispersion. Due to the traffic, the site is always noisy so that a very different number of recordings have been stacked at each shot position to achieve acceptable signal-to-noise ratio. According to Park et al.1998, the recorded seismic traces at each shot point have been transformed into the velocity–frequency domain so to obtain the corresponding phase velocity spectrum. The shear wave velocity (Vs) profile of the investigated site has been obtained according to the full velocity spectrum approach as described in Dal Moro 2014.

5 GEOTECHNICAL INVESTIGATIONS

Although this area has been investigated many times through the last decades, few geotechnical tests have been performed as main investigations were primarily focused on the reconstruction of the local geology, or rather driven by archaeological needs (shallow excavations and/or large diameter digs). During the 2003 and 2005, as part of the design activities for the new visitor area hosting the Circus Maximus Experience, the area close to the "Torre della Moletta" has been interested by several geotechnical investigations as follows:

- n. 5 shallow boreholes, 20 m deep each;
- n. 11 in-hole Standard Penetration Tests – S.P.T.
- n. 4 in-hole Flat Dilatometer Tests – M.T.D.
- n. 8 Dynamic Probing Super Heavy Tests-DPSH

Laboratory tests were also conducted on 8 undisturbed core samples, to retrieve parameters descriptive of soils shear strength and consolidation behavior. A critical revision of the available geotechnical data is ongoing aiming at using these values as a preliminary reference to design a new geotechnical investigation campaign on soils and structures to be performed during early 2022.

6 VIBRATION MONITORING

On 7th September 2019 about 40,000 people attended a pop concert hosted at the Circus Maximus, in the Park area. This event had been exploited to possibly analyze the effects on both Roman and Medieval remains in the south-east side of the Circus by monitoring the vibrations induced to the structures. Experimental data were recorded between 6 PM of 7 September and 8 AM of 8 September 2019, thus including three periods, before, during, and after the concert, respectively. Eleven SARA SL06 three-axial seismometers were used, deployed both on remains and on the ground as depicted in Figure 5, namely:

- one at the west side of the area (S05);
- three at the east side of the area (S09, S10, and S11);
- three on the "Torre della Moletta" (S02 on the ground very close to the entrance, S03 and S04 at two opposite corners at the top floor).

Additional seismometers (CM5, CM6, and CM7 in Figure 5) and velocimeters (CM1, CM2, CM3 and CM4 in Figure 5) were placed on the ground, far from the structures. All instruments were deployed having the same orientation, i.e. the y direction was parallel to the major axis of the Circus, the x direction was orthogonal to it, and the z direction was the vertical one for each location. Time series obtained on the "Torre della Moletta" and on the archaeological ruins have been analyzed in the frequency and time domain. An analysis has been carried out on the behavior of the monitored structures and soils under the stresses produced by traffic-induced vibrations before the concert, by the presence and the behavior of the audience during the concert as well as by ambient noise after the concert.

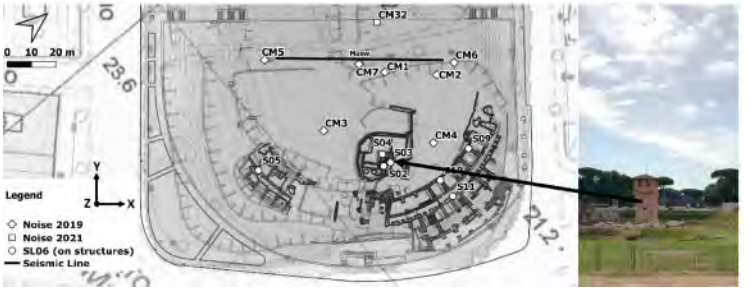

Figure 5. Sensors deployment within the archeological area (see text for details) and a photo of the "Torre della Moletta" medieval structure.

7 PRELIMINARY OUTCOMES

The reconstruction of the subsoil setting has been undertaken first, as essential support for the geotechnical modelling and to constrain and interpret the geophysical models. On this regard, it is to note that, to date, only the drilling from AGIP has intercepted the entire fine-grained geological body. Based on revised stratigraphic logs projected along the cross sections, these coarse deposits should be reinterpreted. Indeed, they have been intercepted mostly along the north-eastern flank of the valley, whereas, at the same depths, fine-grained deposits clearly prevail in the middle of the "Murcia" valley (Figure 3b). This is also suggested by 2D resistivity models along the central axis

of the Circus (not shown here) where low resistivity values are found at depth almost corresponding to the bottom of the buried valley. Conversely, assumptions on the near-surface geological setting have been determined not only by means of boreholes logs but also by information coming from archeological investigations and historical maps. These allows the 2D/3D geophysical models derived from ERT and SW technique to be interpreted, at least for some tens of meters in depth within which the geological and geotechnical constraints play a key role. In the following Figure 6 the XY slice (2 m in depth) from the 3D resistivity modeling is shown, referred to the central area of the Park, obtained by using ERTLab inversion software (https://www.mptech3d.com/software). The base map used to interpret the resistivity distribution consists of a historical map with the footprints of early 1900s industrial buildings. The result of the modeling is rather satisfactory as the shallow resistivity distribution correlates with many perimeters (e.g. gas storage in Figure 6b indicated by the grey arrow) thus suggesting pronounced effects on soils. Also the 2D resistivity modelling of 2021 data has proven to be efficient in defining buried resistivity anomalies of potential archeological interest. In Figure 6c the 2D ERT model of the profile running for 200 meters along the central barrier is shown. Based on the calibration of the model through boreholes data (not presented here), the thickness of the most superficial archeological layer referred to the 1900s industrial period has been estimated along the profile (black lines in Figure 6c). In addition, resistivity anomalies within the depths range of in-place Roman remains (see ch.2) have been identified as e.g. the "A" one in Figure 6c that is suspected to belong to the "euripo" structure.

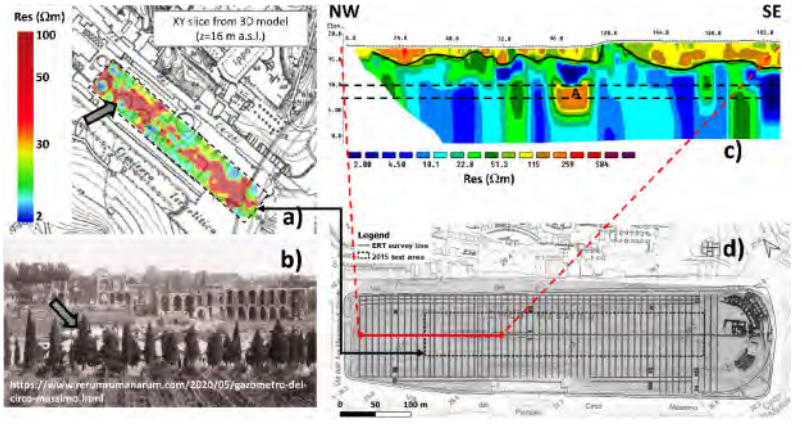

Figure 6. Example of results obtained from 3D processing of 2015 data (a) interpreted by using archeological map and photo (b) and from 2D processing of new data (c) to investigate the buried Roman remains along the central axis of the Circus (d).

The preliminary results of the seismic tests conducted on archeological area and of the vibration monitoring during a social event have been used to address the geotechnical investigations aimed at analyzing the local seismic response and soil–structures interaction (see Puzzilli et al. 2021 for details). From the active seismic survey, some geotechnical complexity in the subsoil emerged due to significant Vs velocity inversions detected near surface, at the contact between superficial backfilling and the underlying clayey deposits. Incidentally, note also that Mancini et al. 2014 included the whole "Murcia" valley in the Seismic Microzonation study of the Palatine Hill. To compare the two seismic characterizations, the acronyms used in Mancini et al. 2014 for the same soils have been reported on the right column in Figure 7 (please refer to that paper for acronyms) in which the soils have been tentatively classified according to the USCS Unified Soil Classification System (ASTM D2487).

The experimental data obtained during the vibrations monitoring on structures and remains performed in 2019 have been divided into three time intervals to better analyze induced effects, namely:

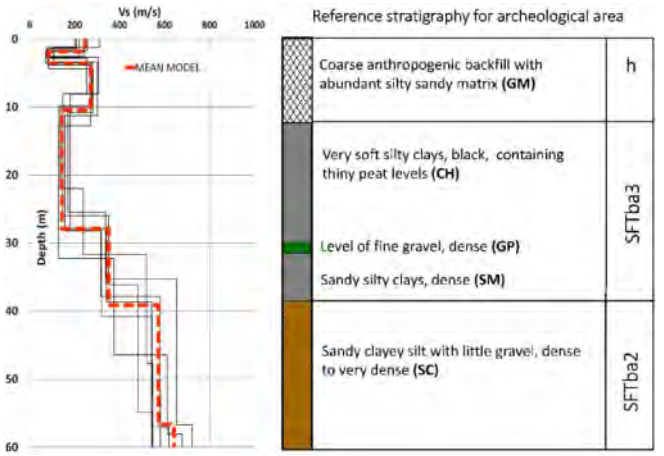

Figure 7. Velocity profiles referred to the subsoil of archeological area (a) compared to the reference stratigraphy.

– a time interval with the presence of traffic-induced vibrations (T), which occurred in the evening before the concert, from 6 PM to 9 PM of 7 September;
– a time interval from 9 PM to midnight, approximately, which includes the entire concert (C);
– a time interval from midnight to 8 AM of 8 September, with the presence of low ambient noise only (N), which occurred after the concert.

Attention has been devoted to the analyses of the velocities recorded in the three directions (x, y and z) during the three intervals (T, C, and N) at locations on the "Torre della Moletta" and the archaeological remains (see Figure 6.1.1). While the amplitudes during T were 2 ÷ 3 times those during N, the amplitudes recorded during the concert (C) exceeded by ten times those after the concert in the presence of ambient noise only (N). On the remains, also the amplitudes during the concert (C) were much higher than that during T and N (Puzzilli et al. 2021 for further details). In Table 1, the maximum values of velocity have been reported to ease the comparison with limit values suggested by UNI-9916 for historical buildings and by SN640312 for traffic-induced vibrations, also reported following.

Table 1. Maximum values of velocity (mm/s) measured ad each recording site.

Location	x	y	z
S02	0.67	1.09	1.10
S03	4.01	4.20	5.18
S04	3.85	3.65	1.35
S05	0.38	0.47	0.17
S09	0.54	0.69	0.71
S10	0.43	0.94	0.46
S11	0.75	0.61	0.36

UNI-9916 velocity limits for historical buildings are:
Short-term vibrations: V = 3.0 mm/s at the foundation and V = 8.0 mm/s at the top;
Permanent vibrations: V = 2.5 mm/s;
Building floors: V = 10 mm/s (no historic buildings).

SN640312 velocity limits for traffic induced vibrations are:
Permanent vibrations: V = 1.5 ÷ 3.0 mm/s;
Frequent vibrations: V = 3.0 ÷ 6.0 mm/s;
Occasional vibrations: V = 7.5 ÷ 15 mm/s.

The major evidence is that, in some cases, the registered values are very close to the limit ones: this is even more significant if one considers that limits are introduced for non-damaged historic buildings, otherwise lower values should be considered in a precautious manner. The results of vibration monitoring pointed out also differences in terms of preferred vibration directions (not shown here).

8 DISCUSSION AND CONCLUSIONS

Still after about 2000 years and many vicissitudes, the Circus Maximus in Rome plays every day the role of recreational and cultural area for tourists and citizens. The area must be preserved from the enormous anthropic and environmental pressure through mitigation and preservation actions. To support these actions, all available information on subsoil have been collected and critically reviewed to design new geophysical surveys and direct investigations on soil and structures. The preliminary results obtained through 2D and 3D resistivity modeling on restricted areas encourage the 3D modeling extended to the whole monumental area. Evidence from vibration monitoring during social events, to our knowledge the first ever performed in this site, highlighted potentially dangerous conditions for some particularly vulnerable portions, such as remains of the vaults. Direct investigations to be conducted in early 2022 will be used to calibrate geophysical models and to test areas of potential archaeological interest identified through them. Also, to sample soils for laboratory testing and create a baseline to standardize lithological descriptions of soils in borehole logs through the years. In the Archaeological area, non-destructive tests will be also performed, to assess the mechanical quality of different archaeological structures (i.e. walls, vaults) and built with upon different type of masonry. This will be supported by means of a suitable model of the "Torre della Moletta" to be set up with the aims of directing experimental analysis and in the interpretation of experimental results.

REFERENCES

Argentieri, A., Capelli, G., Mazza, R. 2020. The "Circo Massimo" borehole (Rome 1939), a site of the geological memory. *Italian Journal of Groundwater*. 8. Doi:10.7343/as-2019-444.

ASTM D2487. 2020. Standard Practice for Classification of Soils for Engineering Purposes (Unified Soil Classification System). American Society for Testing and Materials, U.S.A.

Bigot, P. 1908. Circus Maximus. *Mélanges d'archéologie et d'histoire*. 28: 229–231. Doi: 10.3406/mefr. 1908.6980.

Brandizzi Vittucci, P. 1991. L'emiciclo del Circo Massimo nell'utilizzazione post classica. *Melanges de l'Ecole Francaise de Rome* 103(1):7–40. Doi: 10.3406/mefr.1991.3150

Buonfiglio M. 2018. La definizione di uno spazio urbano: nuovi elementi sulle fasi di formazione e sviluppo del Circo Massimo alla luce delle recenti indagini (2009–2016). *Bullettino della Commissione Archeologica Comunale* CXIX:123–166.

Canciani, M., Falcolini, C., Buonfiglio, M. et al. 2013. A method for virtual anastylosis: the case of the arch of Titus at the Circus Maximus in Rome. *ISPRS Annals of Photogrammetry, Remote Sensing and Spatial Information Sciences*. II5(61).

Carpentieri, E., De Rita, D., Della Monica G. 2015.Geology of the Murcia Valley and Flood Plain Modifications in the Construction of the Circus Maximus, Rome, Italy. *Geoarcheology.* 30(6): 483–494.

Ciancio Rossetto, P. 2002. Risultati delle indagini archeologiche nell'area centrale, *Bullettino della Commissione Archeologica Comunale* CIII: 186–189.

Ciancio Rossetto, P. & Buonfiglio, M. 2007. Circo Massimo: rifiessioni e progetti. *Orizzonti:rassegna di archeologia* VIII:19–41.

Dahlin, T. & Zhou, B. 2004. A numerical comparison of 2D resistivity imaging with 10 electrode arrays. *Geophysical Prospecting,* 52: 379–398. Doi:10.1111/J.1365-2478.2004.00423.X

Dal Moro, G. 2014. *Surface Wave Analysis for Near Surface Applications*; Elsevier: Amsterdam, The Netherlands.

Di Luzio, E., Fazio F., Imposa, S., Rannisi, G. 2014. Ambient Noise Recordings in the Circo Massimo and Vallis Murciae Areas: Main Results Compared with the Dynamic Response of the XII Cen. AD Torre Della Moletta. *Engineering Geology for Society and Territory*. 8:399–403. Doi:10.1007/978-3-319-09408_69.

Funiciello, F. et al. 1995. La Geologia di Roma. Il centro storico. *Memorie Descrittive della Società Geologica*. 50.

Funiciello, R. & Giordano, G. 2008. La nuova carta geologica del comune di Roma: litostratigrafia e organizzazione stratigrafica. In Renato Funiciello, Antonio Praturlon, Guido Giordano (eds) *La geologia di Roma dal centro alla periferia. Parte Prima. Memorie Descrittive della Carta Geologica d'Italia*. LXXX: 39–85.

Geosonda 1983. Indagini geognostiche per scavi archeologici al Circo Massimo – 3° lotto – Perizia 213/82. Archive of the Superintendency of Cultural Heritage of Rome (in Italian).

Konno, K & Ohmachi, T. 1998. Ground-motion characteristics estimated from spectral ratio between horizontal and vertical components of microtremor. Bulletin of the Seismological Society of America. 88(1): 228–241.

Loke, M.H. & Barker, R.D. 1996. Rapid Least-Squares Inversion of Apparent Resistivity Pseudosections by a Quasi-Newton Method. *Geophysical Prospecting*. 44:131–152. Doi:10.1111/j.1365-2478.1996.tb00142.x.

Mancini, M., Marini, M., Moscatelli, M., Stigliano, F. et al. 2018. Stratigraphy of the Palatine Hill (Rome, Italy): a record of repeated middle Pleistocene-Holocene paleovalley incision and infill. *Alpine and Mediterranean Quaternary*. 31 (2): 171–194.

Mancini, M., Marini, M., Moscatelli, A., Pagliaroli, A. 2014. A Physical Stratigraphy Model for Seismic Microzonation of the Central Archaeological Area of Rome (Italy), *Bulletin of Earthquake Engineering*. 12: 1339–1363.

Marra, F., Florindo, F., Anzidei, M., Sepe, V. 2016. Paleo-surfaces of glacio-eustatically forced aggradational successions in the coastal area of Rome: Assessing interplay between tectonics and sea-level during the last ten interglacials. *Quaternary Science Reviews*. 148: 85–100.

Marra, F., Motta, L., Brock, A. L., Macrì, P. et al. 2018. Rome in its Setting. Post-glacial Aggradation History of the Tiber River alluvial Deposits and tectonic Origin of the Tiber Island, *PLoS ONE*, 13(3).

Marra, F., Buonfiglio, M., Motta, L. 2021. Holocene aggradation history of the Murcia alluvial valley: insights on early Rome paleoenvironmental evolution. *The Olocene* (submitted).

Pagliaroli, A., Lanzo, G., Tommasi, P. et al. 2014. Dynamic characterization of soils and soft rocks of the Central Archeological Area of Rome. *Bulletin of Earthquake Engineering*. 12: 1365–1381. Doi: 10.1007/s10518-013-9452-5.

Park, C.B., Miller, R.D., Xia, J. 1999. Multichannel analysis of surface waves. *Geophysics* 64: 800–808. Doi:10.1190/1.1444590.

Pietrangeli, C.1940. Circus Maximus. *Bullettino della Commissione Archeologica Comunale* CIII:186–189.

Puzzilli, L.M., Bongiovanni,G., Clemente, P., Di Fiore, V., Verrubbi,V. 2021. Effects of Anthropic and Ambient Vibrations on Archaeological Sites: The Case of the Circus Maximus in Rome. *Geosciences*. 11, 463. Doi: 0.3390/geosciences11110463.

Signorini, R. 1939. Risultati geologici della perforazione eseguita dal A.G.I.P alla Mostra autarchica del Minerale nel Circo Massimo di Roma. *Boll. Soc. Geol. It.* LVIII(2–3).

SESAME 2004. Guidelines for the implementation of the H/V spectral ratio technique on ambient vibrations-Measurements, processing and interpretation. SESAME European research project, WP12-Deliverable D23.12. Project No. EVG1-CT-2000-00026 SESAME, 62 pp.

SM Working Group. 2015. Guidelines for Seismic Microzonation. Rome: Conference of Regions and Autonomous Provinces of Italy – Civil Protection Department (ed).

SN 640312. 2013. Vibrations—Vibration Effects in Buildings; Swiss Standards: Zürich, Switzerland.

UNI 9916. 2004. Criteria for the Measurement of Vibrations and the Assessment of Their Effects on Buildings; Italian code; UNI: Milan, Italy.

UNI EN ISO 22476. 2012. Geotechnical investigation and testing. Field testing Dynamic probing; Italian code; UNI: Milan, Italy.

Geotechnical Engineering for the Preservation of Monuments and Historic Sites III – Lancellotta, Viggiani, Flora, de Silva & Mele (Eds)

Ground motion InSAR monitoring for the protection of Baia Roman Thermae (Naples, Italy)

G. Leoni, F. Ferrigno, P.M. Guarino, L. Guerrieri, F. Menniti & D. Spizzichino
ISPRA, Department for the Geological Survey of Italy, Roma, Italy

P. De Martino & M. Di Vito
Istituto Nazionale di Geofisica e Vulcanologia – Sezione di Napoli Osservatorio Vesuviano (INGV-OV), Napoli, Italy

E. Gallocchio, F. Pagano & M. Salvatori
Parco Archeologico dei Campi Flegrei, Pozzuoli (NA), Italy

ABSTRACT: The Archaeological Park of the Roman Thermae of Baia includes a large portion of the buildings built up during the Roman age. They attest not only to the extraordinary rich commission of the Baia buildings, but also to the refined architectural technique of local workmanship. This area is located on the western side of the Phlegrean Fields area, affected by the intense bradyseism activity, an exceptional example of volcanic-related subsidence with unrest cycles characterized by a slow uplift and sinking of the caldera floor. Due to the unusual setting of the cliff, in order to maintain the terracing of the slope and to prevent soil erosion and small collapse events, considerable control has always been needed. A detail InSAR analysis (focused mainly on Sentinel-1 data) was carried out in order to highlight most recent ground displacements. Obtained results clearly show a ground uplifting in the investigated time interval, with displacement rate up to 50 mm/yr.

1 INTRODUCTION

Phlegrean Fields region is located northwest of Naples and includes more than 25 Archaeological Sites directly managed by the Phlegrean Fields Archaeological Park. They represent the remains of human settlement between VIII century BC and IV century AD, as well as important archaeological evidences also for the Middle Age. Among them, the Archaeological Park of the Thermae at Baia (35000 sqm wide) covers a large portion of the ancient Roman buildings (Figure 1).

These residential and thermal buildings represent terraced architectures facing the existing Lacus Baianus. Over the centuries, the Thermae seem to take over the private villas, thus developing a large, unitary, curative space, taking advantage of the volcanic vapors and waters benefits. Among the remains of these architectural complexes, three big domed halls stand out, each with a diameter of about 20 m (Figure 2). They attest not only to the extraordinary rich commission of the Baia buildings, but also to the refined architectural technique of local workmanship. These works can be recognized as one of the first discovery of the great potentials of pozzolana, the local building material of Phlegrean Fields.

This area, located on the western side of the Phlegrean Fields volcanic district, is affected by an intense bradyseism: an exceptional example of volcanic-related subsidence with unrest cycles characterized by a slow uplift and sinking of the caldera floor. The geological setting is characterized by a sequence (from the bottom to the top) of volcanic breccia, pyroclastic deposits and surge deposits. The Thermae were built up on a steep slope, facing the Baia harbor, adapting

 DOI 10.1201/9781003308867-41

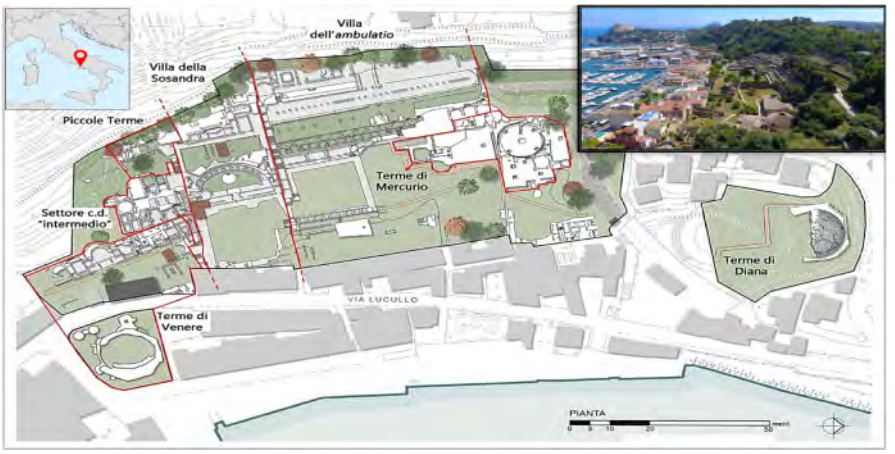

Figure 1. Roman Thermae of Baia overview.

Figure 2. Mercurio Thermae, top and front view of the dome.

the imperial villas to exploit natural hot springs with pipes, tanks and domes, with the aim of preserving hydrothermal properties. The peculiar setting of the cliff, always requested a heavy control, to preserve the terraces from potential instability phenomena, which depend mainly on the steepness of the slope, and on the lack of ordinary management and maintenance of the area (e.g., invasive vegetation, absence of drainage system).

In order to assess landslide hazard conditions, the following actions were undertaken: i) detailed landslide hazard assessment of the area; ii) Earth Observation (EO) monitoring and ground motion analysis coupled with direct field survey; iii) integrated monitoring system and sustainable mitigation measure options. To reach the final target, a preliminary InSAR analysis was performed exploiting ERS datasets (1993–2003), that show a regional ground sinking, with deformation rates that are consistent with the general down lift cycle affecting the whole area in that period (5–10 mm/yr.). This InSAR data analysis is based on Sentinel-1 data (April 2016–August 2020) and it allows to highlight most recent ground displacements. These results clearly show a ground uplifting cycle in the investigated period. The main displacement anomalies were also investigated by field survey, in order to provide useful recommendation concerning structural measures (consolidation and restoration works) as well as non-structural mitigation measures (in situ monitoring system).

2 METHODOLOGY

To support the Archaeological Park managers with useful tools for the geohazard protection and prevention, the related risk reduction policies and the future sustainable mitigation measure, a general schema was adopted (Themistocleous 2018). The first step is to define the site background

through detailed desk and field study (i.e. investigating the origin, typology, construction techniques, restoration history and evolution in time). After the general setting, the current natural and manmade status is assessed through a local scale diagnosis (i.e. non-invasive and non-destructive investigations).

In order to confirm the proposed assessment and to verify possible deformation processes, a monitoring system is implemented (both remote and in situ). The final target is an integrated assessment able to combine EO monitoring with field survey, to calibrate and implement in situ monitoring systems and to identify and assess potential damages of selected archaeological structures (Figure 3).

Figure 3. Integrated assessment approach.

3 GEOHAZARD ASSESSMENT

3.1 *Landslide risk assessment of the Baia area*

The local planning administration (Autorità di Bacino Distrettuale) is in charge for the flood and landslide hazard and risk land assessment (ADBCC PSAI-RI 2015). According to the landslide prevention national regulations, in the areas where there are exposed elements, such as buildings, infrastructures and Cultural Heritage, the risk level is equal to the hazard level. The official maps clearly show that the area is mainly affected by high potential landslide hazard (Figure 4A). Given the standard vulnerability of man-made areas equal to one, the presence of exposed elements causes the assessment of a high level of risk for the whole archaeological area (Figure 4B).

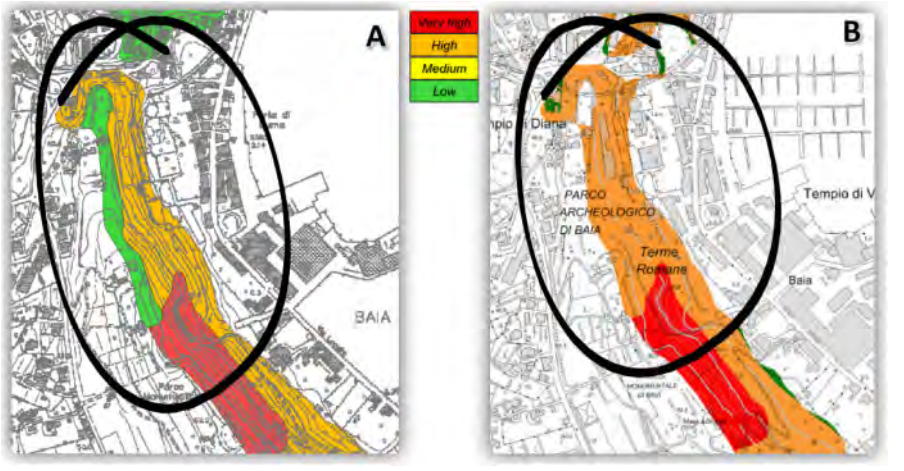

Figure 4. Landslide hazard (A) and risk (B) official maps for the Baia Area (ADBCC PSAI-RI 2015).

3.2 *Landslide hazard in the site area*

The most typical landslide of the area (Figure 5) are rock falls along the steep slopes of the volcano slope (Figure 5B). Falls usually involve not only soft rocks (volcanic tuffs), but also blocks of masonry, deriving from ancient buildings and archaeological structures (Figure 5C).

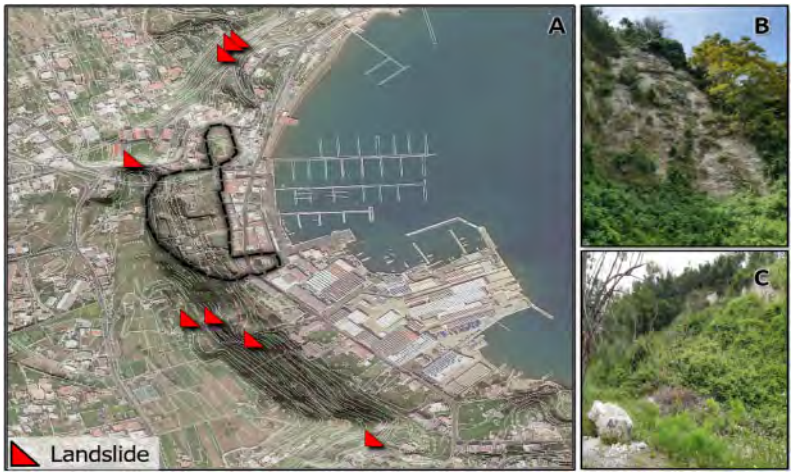

Figure 5. Landslides investigated in the selected area.

With the aim of interpreting satellite monitoring data and evaluating their application, a back analysis has been conducted on some case studies in the Baia area. SAR interferometry technique is normally useful to predict wall collapse mainly affected by slow deformations (e.g. bulges, leaning walls). On the other hand, when the collapse is instantaneous and precursory elements are missing, or occurring in a shorter time than the satellite revisit time, this technique cannot be helpful (Iadanza et al. 2020). The methodology was applied by analyzing mean annual velocities of displacements recorded by measure points close to the archaeological structures.

4 GROUND MOTION INSAR MONITORING

Satellite radar interferometry technique (Rocca et al. 2000) allows millimetric measurement of ground displacements on wide areas, processing a huge amount of measuring points (called Persistent Scatterer, PS) radiometrically stable over time, such as buildings, stones, metal frames, etc. Satellites with radar sensors onboard follow polar orbits, acquiring earth images by two different geometries: Ascending when the satellite moves from South to North and Descending when it moves from North to South (Ferretti et al. 2007). Interferometry analysis on a stack of images acquired in the same area over a certain period, provides measurement points' position (xyz coordinates) over time, thus it is possible to derive mean annual velocity and time series of displacements. Ground displacements are registered along the Line Of Sight (LOS), i.e. the line connecting the sensor with the target. In many cases, Synthetic Aperture Radar Interferometry (InSAR) monitoring allows to highlight ground motions and to identify new landslides, that were not detected using other techniques, or to characterize their activity state (Alberti et al. 2017). InSAR data are quite effective in mapping slow landslides (Hilley et al. 2004) that can trigger faster and more disruptive events. Main aims of the present analysis are: i) to exploit the InSAR techniques to identify potential pre-collapse deformation paths or structural instability; ii) to implement a routine operational downstream service in order to integrate in situ sensors and schedule a maintenance plan (e.g. vegetation, consolidation of structures, safety measures etc.).

4.1 *Damage Inventory*

To test InSAR techniques as a prediction model, during the last two years, field surveys were conducted on all the past and recent monuments' damages, as well as on the deformation phenomena, thus implementing a detailed and georeferenced damage inventory for the whole site. By a UAV survey, a 3D terrain model and an orthophoto were obtained. These tools help to analyze, from different viewpoints, the area as a whole and to understand the relationships among the different complexes of the settlement, as well as possible deformation patterns and geomorphological processes (Figure 6).

Figure 6. 3D Topographical model obtained by UAV survey.

The analysis of the area and of the type of buildings helps to classify main typologies of critical conditions: vegetated areas on steep slopes which may trigger landslides, block fall, leaning walls which need shoring and scaffolding support, wall cracks and cover detachment (Figure 7).

Figure 7. Main typologies of critical conditions surveyed in the site.

4.2 *InSAR for cultural heritage*

For this analysis Copernicus Programme Sentinel-1 data were used. The first processing of the SAR dataset followed a standard approach: for the Reference Point the choice has been driven by geological setting, i.e. an area external to the main ground motion, and by default tool's settings, i.e. a cluster of PS with "null" displacement referred to the whole dataset. These conditions led to select as Reference Point an area at the foothill of Monte di Procida, on the western side of the Phlegrean Fields volcanic district.

Then, in order to have more reliable measures of "real" ground displacements, a calibration of PS data has been performed by referring this dataset to displacements measured by Global Navigation Satellite System stations (GNSS) of the monitoring network managed by Osservatorio

Vesuviano (INGV-OV). This procedure aims to align both datasets, to minimize systematic errors of the InSAR processing. Due to the extreme variation of both horizontal and vertical displacements in the volcanic district, the following characteristics of GNSS stations were considered:

- geological stability of the station (outside the caldera);
- proximity to the site (3.6 km);
- consistency of the displacement recorded during the time interval under investigation.

The best conditions in the area were founded at the Cuma station, therefore, to correct the InSAR dataset, this station was selected as reference point for the InSAR processing. Then the East-West and vertical components of GNSS displacement at Cuma have been subtracted to the InSAR displacements along the LOS, separately for Ascending (ASC) and Descending (DESC) geometries (Figure 8).

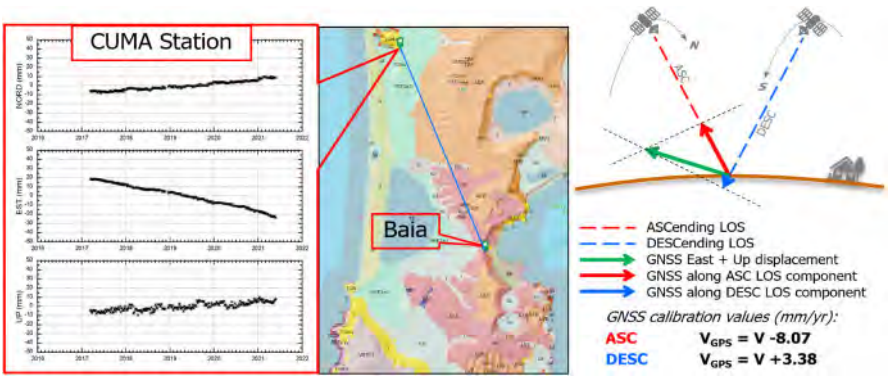

Figure 8. Time history and map of Cuma station, selected for the GNSS calibration, and schema of the GNSS calibration applied to PS dataset.

This procedure allows to obtain absolute PS ground displacement measures along the LOS, that are valid in the surroundings of the GNSS reference station, to overcome the main limits of the InSAR technique and to extend the range of application of GNSS recordings.

After the GNSS calibration of PS dataset, a clear difference between ASC and DESC geometries was detected. The Northwest ground displacement of the Cuma GNSS station is better registered by the ASC dataset, which LOS is almost parallel to the ground motion. On the other hand, the DESC dataset shows a slight sinking, because the LOS is almost perpendicular to main component of the ground motion (Figure 9).

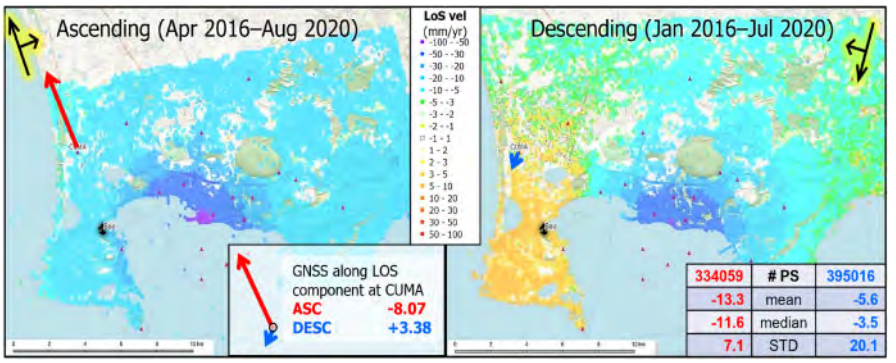

Figure 9. PS dataset overview after the GNSS calibration.

After the GNSS calibration a detailed PS analysis was downscaled directly on the Roman Thermae of Baia area (Figure 10).

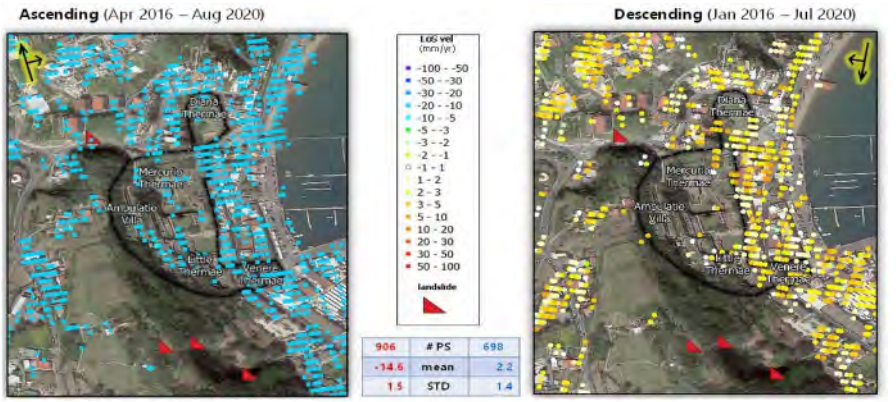

Figure 10. Detail of calibrated PS dataset at the Roman Thermae of Baia.

As general assessment the Baia area is affected by high displacement rate, especially for the component along the Ascending LOS. Thus, in order to highlight differential ground displacements at large scale, the difference of displacement rate (D-vel) between each measurement point (PS) and the mean value of that area was calculated (Figure 11).

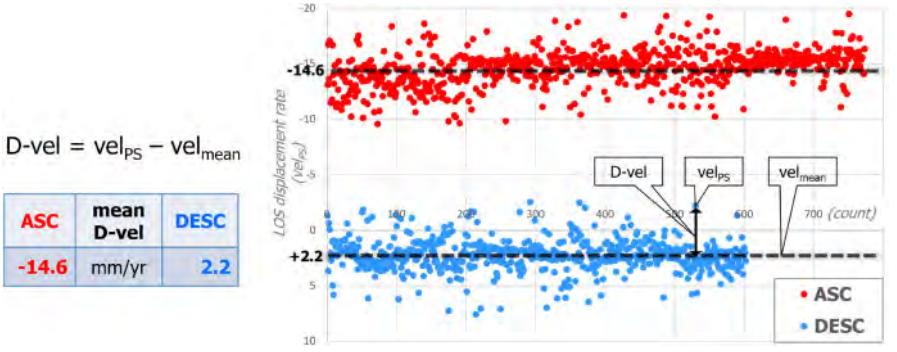

Figure 11. Sentinel-1 PS: differential analysis (D-vel).

5 PS DATA RESULTS AND INTERPRETATION

5.1 *PS data interpretation: archaeological area entry path*

Relative displacements of both datasets, ASC & DESC, of the entry path to the archaeological site highlights an overall, even if slight, movement towards East, which is downslope. The motion toward satellite for Descending geometry and away from satellite for the Ascending one, means that the horizontal (eastward) component of the displacement prevails over the vertical component (Figure 12). Along the upper slope (left side of the picture), the dense vegetation hides to the aerial view some small shallow landslides that have been recognized by field survey. These conditions suggest that the InSAR analysis should follow a different approach. For instance, to let the signal pass this type of canopy, SAR images in the L-band should be used, so that targets on the ground

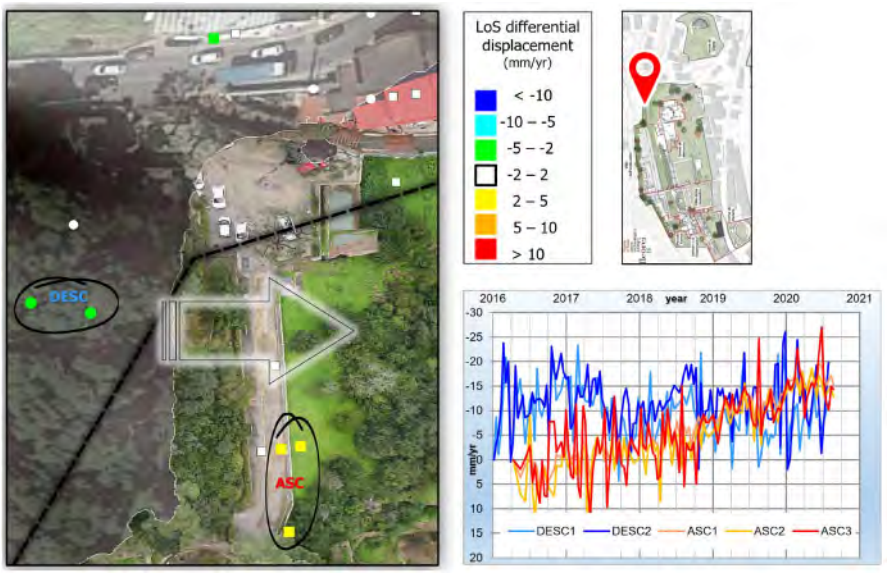

Figure 12. PS data interpretation: archaeological area entry path.

can be recognized under the wood. In addition, a processing algorithm more advanced than the standard PS analysis (e.g. SBAS technique, that works better in man-made environments), should help to find more InSAR targets in natural areas.

5.2 *PS data interpretation: upper terrace*

In the upper terrace area, as well as in the whole area, the Ascending geometry seems to be more sensitive to radar targets: this is most likely due to a lower "noise effect", with respect to the Descending geometry. Then this effect may depend also to the slope aspect, that seems to enhance targets' coherence. At the edge between Ambulatio and Sosandra villas, a cluster of 6 PS indicates, consistently, a relatively subsiding area. The crack along the sidewall may show this weakness on the masonry, thus needs to be properly monitored (Figure 13). A specific in-situ monitoring by crack meters should help to test the satellite monitoring and to avoid an unexpected collapse.

5.3 *PS data interpretation: Villa Sosandra*

The sidewall between Sosandra Villa and Little Thermae is leaning. This is reflected by a relative uplift of one Ascending PS. In this case the actual outward wall inclination is seen, from the Ascending geometry, as a movement toward the satellite, i.e. a negative displacement along the LOS. The time history of the PS, in addition to the overall uplift, clearly shows a floating trend. This variation reflects most likely some common minor fluctuations with a clear seasonal period: an outward push by the earth on the retaining wall, during the rainy season (autumn), followed by an opposite trend during the water discharge, in late spring (Figure 14). The rise of pore pressure, in the terrain back to the wall, should be regularly monitored and controlled by setting up a drainage system. This mitigation intervention will reduce the probability of occurrence of a fall triggered by rainfall, which in turn are increasing by duration and intensity due to climate change.

5.4 *PS data interpretation: East border*

Some modern buildings and a church, with the foundation on the buried roman remains, occupy the East border of the archaeological site. In this area the combination of some PS, from both Ascending

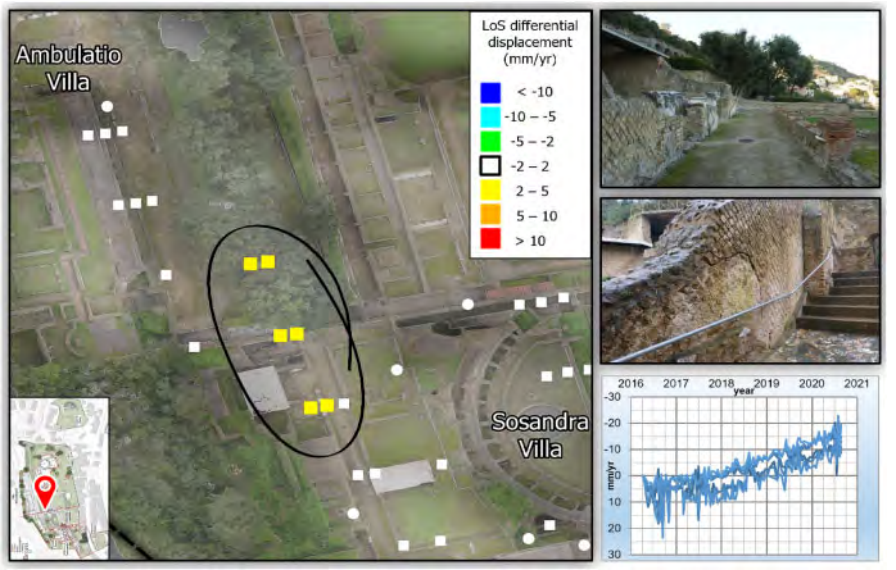

Figure 13. PS data interpretation: upper terrace.

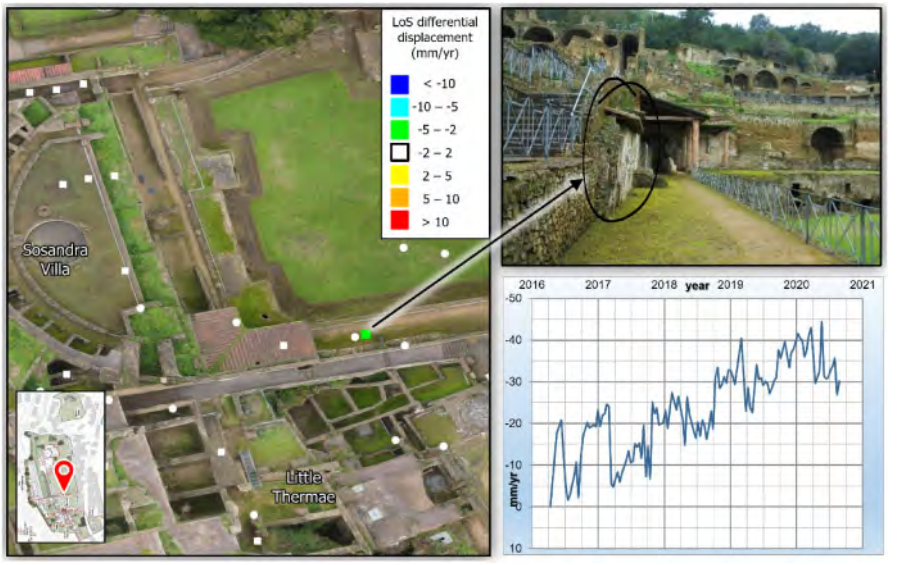

Figure 14. PS data interpretation: Villa Sosandra.

and Descending geometry, clearly indicates the occurrence of a differential displacement between the buildings and roman wall remains: subsidence for the first (east side) and uplift for the latter (west side). In this point, on February 26th 2021, a wall portion fell down, without a clear trigger. But the weakness of the wall seems to have started a few years ago (see the time history in Figure 15). This is a prime example where InSAR analysis helps to clarify the interaction between modern and ancient structures, especially in complex archaeological sites.

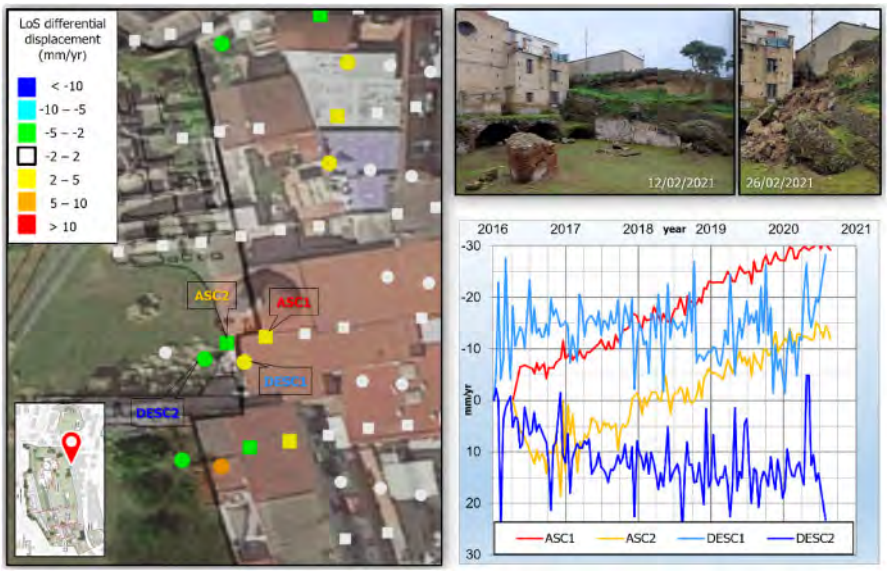

Figure 15. PS data interpretation: East border.

6 CONCLUSION AND FUTURE DEVELOPMENT

Current research is dealing with the application of satellite radar interferometry from Sentinel-1 data, to investigate potential deformation path and medium-large potential rock falls in the Archaeological Park of Phlegraean Fields. The spatial density of PS measured within the Area of Interest is extremely good, reaching the value of about 1 PS every 175 square meters. This is a good result, since in the Park area man-made structures are sparse and the C-band sensor of Sentinel-1 is less sensitive to natural reflectors.

The proposed methodology drives the analysis through an integrated assessment of different elements that contributes to define the exposure level of Cultural Heritage sites to actual local natural hazard. The first step was the understanding and correct framing of actual natural hazard conditions. The second step was the real knowledge of the site, acquired by field survey and EO monitoring, involving experts, managers and stakeholders too. Then, in order to highlight the site-scale pattern of ground motion, the InSAR dataset was calibrated and analyzed. Finally, the PS data interpretation of local events pointed out by previous steps, was carried out, in order to understand the interaction between structures' damages and ground motion.

From a methodological point of view, results obtained in this study confirmed the main advantage of remote sensing techniques: the ability to obtain a synoptic view of potential surface deformation phenomena affecting large areas and the possibility to integrate this information with in situ observations (Alberti et al. 2017). The actual relationship reveals if and how buildings' damages are caused by structural weakness or by ground motion.

In general, InSAR measurements do not replace traditional ground monitoring instruments but are complementary to them, thanks to the wider spatial distribution. On the other hand, minor small rock falls, of the order of few cubic meters, clearly visible on site, are hardly detectable with medium-resolution interferometric data provided by the Sentinel-1 sensor, due to decorrelation phenomena that might occur considering volumes/magnitude or involved surfaces of potentially unstable rocks, with respect to the minimum detectable area of the technique (that is about 20 m × 5 m) and the geotechnical behavior of the Baia cliff and rock, characterized by a brittle rupture mode (Alberti et al. 2017). In the latter case, the analysis could be better concentrated in a smaller time-window, generally prior to collapse.

Finally, a further improvement of InSAR data should be based on satellite data with better temporal and spatial resolution, such as the X-band COSMO-SkyMed constellation or TerraSAR-X/Tandem-X sensors. The final goal is to set up a proper mitigation and conservation plan and to implement an integrated monitoring system.

ACKNOWLEDGEMENTS

Authors would like to thank the colleagues S. Calcaterra, P. Gambino and B. Porfidia, from ISPRA, for the fruitful discussion on the improvement of the GNSS calibration of PS InSAR data.

REFERENCES

Alberti, S., Ferretti, A., Leoni, G., Margottini, C., Spizzichino, D. 2017. Surface deformation data in the archaeological site of Petra from medium-resolution satellite radar images and SqueeSARTM algorithm. *Journal of Cultural Heritage*; 2017. http://dx.doi.org/10.1016/j.culher.2017.01.005

Autorità di Bacino Distrettuale dell'Appennino Meridionale (ADBCC) 2015. *Piano Stralcio per l'Assetto Idrogeologico – Rischio da frana (PSAI-RI) – Version 2015. Tav. 447132.* http://www.distrettoappenninomeridionale.it/index.php/elaborati-di-piano-menu/bacini-reg-nord-occidentali-bacino-reg-sarno-ex-adb-reg-campania-centrale-menu/piano-assetto-idrogeologico-rischio-da-frana-menu

Di Vito, M.A., Isaia, R., Orsi, G., Southon, J., De Vita, S., D'antonio, M., Pappalardo, L. & Piochi, M. 1999. Volcanism and deformation since 12,000 years at Campi Flegrei caldera (Italy). *Journal of Volcanol. and Geotherm. Res.*, 91, pp. 221–246.

Ferretti, A., Monti-Guarnieri, A., Prati, C., Rocca, F., Massonnet, D., Lichtenegger, J. 2007. *InSAR Principles: Guidelines for SAR Interferometry Processing and Interpretation.* ESA Publications, The Netherlands, 2007. https://www.esa.int/About_Us/ESA_Publications/InSAR_Principles_Guidelines_for_SAR_Interferometry_Processing_and_Interpretation_br_ESA_TM-19

Gianfrotta, P.A. 2019. Portus Baiarum e Bauli, a Baiae. In: *Atlante tematico di topografia antica* 29, 2019, pp. 65–74.

Hilley, G.E., Bürgmann, R., Ferretti, A., Novali, F., Rocca, F. 2004. Dynamics of slow-moving landslides from Permanent Scatterer analysis, *Sci. Mag.* 304 (5679)(2004) 1952–1955.

Iadanza. C., Leoni. g., Spizzichino. D., Trigila. A., Margottini. C., De Nigris, B., Martellone, A., Costantini, M., Francioni, E., Trillo, F., Minati, F. 2020. Processi di instabilità e analisi di dati satellitari nel Parco archeologico di Pompei. *Monitoraggio e manutenzione delle aree archeologiche. Cambiamenti climati-ci, dissesto idrogeologico, degrado chimico-ambientale.* Atti del Convegno Internazionale di Studi, Roma, Curia Iulia, 20–21 Marzo 2019 / A. Russo & I. Della Giovampaola (Eds.) "L'ERMA" di BRETSCHNEIDER, 2020 – (Collana Bibliotheca Archaeologica, 65) 159 p.

Medri, M. 2013. In baiano sinu: il vapor, le aquae e le piccole terme di Baia. In: Bassani, M., Bressan, M., Ghedini, F. *Aquae salutiferae. Il termalismo tra antico e contemporaneo.* Padova 2013, pp. 119–142.

Rakob, F. 1992. Le cupole di Baia. In: *Civiltà dei Campi Flegrei*. In: Atti del Convegno Internazionale, 1992, pp. 229–258.

Rocca, F., Prati, C., Monti Guarnieri, A., Ferretti, A. 2000. Sar Interferometry And Its Applications. *Surveys in Geophysics*, 21: 159. https://doi.org/10.1023/A:1006710731155

Spizzichino, D., Cacace, C., Iadanza, C., Trigila, A. 2013. Beni culturali e rischio idrogeologico in Italia. *Bollettino ICR Nuova Serie*, 27/2013.

Spizzichino, D., Leoni, G., Comerci, V., Brustia, E., Guerrieri, L., Dessì, B., Trigila, A., Iadanza C. 2016. PROTHEGO Deliverable D.01.01: *UNESCO Cultural Heritage Vs Natural hazards at European scale, Version 1.0.* JPICH Heritage Plus PROTHEGO project, Open Report. http://www.prothego.eu/downloads.html

Themistocleous K. 2018. PROTHEGO Deliverable D.05.01: *High Tech Monitoring Techniques.* JPICH Heritage Plus PROTHEGO project, Open Report. http://www.prothego.eu/downloads.html

Valagussa, A., Frattini, P., Crosta, G.B., Spizzichino, D., Leoni, G. and Margottini, C. 2020. Hazard ranking of the UNESCO world heritage sites (WHSs) in Europe by multicriteria analysis. *Journal of Cultural Heritage Management and Sustainable Development*, Vol. 10 No. 4 (2020), pp. 359–374. https://doi.org/10.1108/JCHMSD-03-2019-0023

Valagussa, A., Frattini, P., Crosta, G., Spizzichino D., Leoni G. and Margottini C. 2021. Multi-risk analysis on European cultural and natural UNESCO heritage sites. *Natural Hazards* 105, 2659–2676 (2021). https://doi.org/10.1007/s11069-020-04417-7.

Geotechnical Engineering for the Preservation of Monuments and Historic Sites III – Lancellotta, Viggiani, Flora, de Silva & Mele (Eds)

Geotechnical-structural engineering for the preservation of Ninfeo Ponari in Roman Casinum

G. Modoni, M. Imbimbo, M. Serpe, E. Polito, M. Saccucci & R.L. Spacagna
University of Cassino and Southern Lazio, Cassino, Italy

E. Grande
University Guglielmo Marconi, Rome, Italy

M. Caponero & M.L. Mongelli
ENEA Centro Ricerche Frascati, Frascati, Italy

M. Valenti
University of Tuscia, Viterbo, Italy

ABSTRACT: The Ninfeo Ponari is the unhearted part of a domus built around the first century BC in the Roman city of Casinum on the lower slope of the Monte Cassino. Within a bigger archaeological complex present in this area the *nymphaeum* witnesses the historical-cultural relevance of this territory during the Roman age. Thus recovery, preservation and opening to public are considered a priority by local and national institutions. The structural integrity is threatened by the weight of debris fallen along the slope, that have totally overlaid the building. Different competences are involved to detect the composition and mechanical properties of the structural elements, monitor the geometrical-structural layout, investigate the subsoil conditions. A three-dimensional Finite Elements Model has been implemented, it serves to assess the present stability conditions and future recovery actions through the simulation of the soil-structure interaction. The analysis has required reconstructing the monument history through the interpretation of artifacts combined with the knowledge brought by archaeologists of the ancient construction techniques. The paper presents an overview of the ongoing activities, summarizes the temporary conclusion and pave the way for the remediation strategy.

1 INTRODUCTION

The cultural legacy of Roman civilization has left various traces over the Italian territory. Together with popular monuments that capture the interest of historians and tourists, there are plenty other examples of unknown but not less important evidence that deserve the same attention. Frequently they are in precarious conditions due to the natural and anthropic events occurred along with centuries and thus require an action for their recovery, conservation, reopening to the public use and valorization. The present example concerns the Ninfeo Ponari, part of a rich domus built around the first century BC in the Roman city of Casinum (Valenti 1992). Although included in some repertoires on ancient nymphaea (Valenti 1992), this monument is still not fully explored, being forgotten and hidden for years and now presenting structures in a precarious state. In order to restore the monument with an efficient intervention that respects its historical and cultural value, in recent years several explorative campaigns have been undertaken to study the manufact from the

DOI 10.1201/9781003308867-42

historical perspective (Caponero et al. 2020; Valenti 1995a, 1995b), to assess its stability conditions and figure out effective strategies.

The competences of archeologists, experts of Roman history and tradition, in understanding the function of the different rooms, their connection with the surrounding context and the construction practice of the building, has been merged with those of technicians, expert of geotechnics and structures to back-analyze past soil-structure interaction throughout the monument life, quantify the present stress state on the different component in comparison with the conservation state of materials and assess the stability of the structural elements, walls, vaults, buttresses.

A fundamental preliminary step of the analysis has consisted in a complete, deep and detailed topographic survey of the different parts of the *domus*, carried out with up-to-date investigation tools. The results of the above analyses are summarized in the present paper focusing more particularly on the geotechnical-structural perspective. With this aim a FEM calculation has been implemented to simulate the soil-structure interaction from the construction time to date.

2 THE NYMPHAEUM

The Ninfeo Ponari is located on the lower slope of Montecassino hill, along the road linking the modern city of Cassino to the famous Benedictine abbey (Figure 1) (Valenti 2010). This area hosts the old Roman Casinum, as witnessed by several archaeological remains that include a tomb, a theatre and an amphitheatre. The territory was conquered by the Romans around 313 B.C. and remained faithful to Rome. After a period of Civil Wars in the 1st century B.C., Casinum experienced a period of prosperity during which numerous public monuments were built. It declined due to a series of barbarian attacks between 400 and 500 B.C. (Figure 2(a)). The building is part of the residential sector of a rich Roman domus, probably built around the middle of the 1st century. B.C. and restored during the 1st century A.D. (Neuerburg 1965; Valenti 1992). It was probably a summer dining complex ("coenatio aestiva"), enriched with fountains (hence the name "nymphaeum"). (Betori et al. 2009).

Figure 1. Geographical position of the Ninfeo Ponari.

The walls, built with masonry and covered with plaster, form two contiguous and communicating rectangular spaces: a room covered with a barrel vault and provided with three niches on each side or front wall, 4.6 m wide, 7.5 m long and 4.6 m high in the top of the vault; an open atrium with a basin (impluvium) in the center, 7.5 m wide, 6.4 m long and surrounded by walls about 3.50 m high (Figure 2(b)) (Carettoni 1940; Ghini 1995).

In the covered portion, two distinct wall decorations can be recognized: the oldest is made up of a "rustic mosaic" with shells, Egyptian blue tiles and colored glass of geometric shapes: a plaster painted with imitation of polychrome marble slabs covers the former one. Also the walls

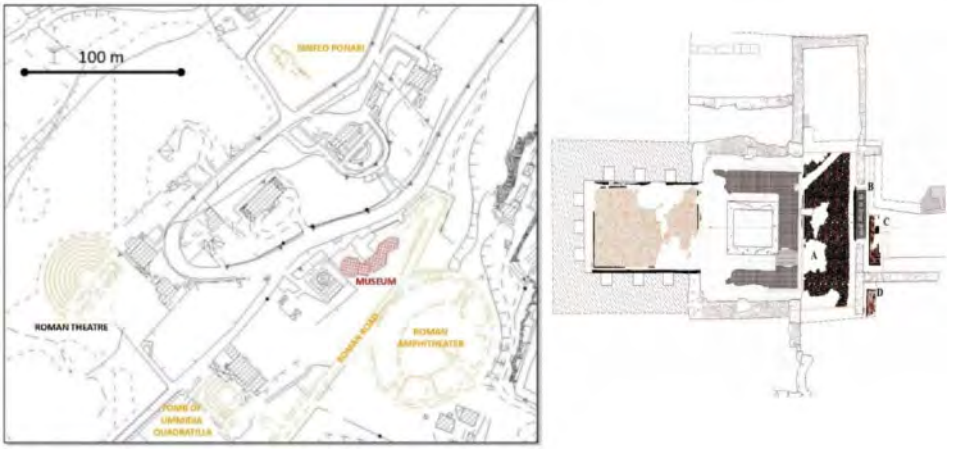

Figure 2. Layout of the archaeological area (a), plan view of the nymphaeum (b).

of the atrium are covered with painted plasters presenting a red base band, animated by plants and beasts and decorated with gilded bronze vases. The floors are decorated with mosaics containing polychrome marble inserts on a white or black back matrix, with concentric or meander perspective borders (Valenti 1992, 1995a, 1995b).

Due to its similarity with other examples and the presence of shells and wall decorations, the building was classified as a nymphaeum, given its cave structure. It has been reasonably assumed that the nymphaeum, intended to host water games, was part of a luxurious private residence owned by one of the most important families of the ancient Casinum, the gens Ummidia. (Betori et al. 2009). Until the end of last century, the domus was left abandoned, being almost filled with earth and rubbles (Figure 3(a)). A first excavation, accomplished between 1998 and 2001 (Betori

Figure 3. Picture of the Ninfeo Ponari before (a) and after excavation (b), example of painted wall with musk and vegetation (c) and of pavement (d).

et al. 2009), brought the structure to light and revealed a rich colored decoration (Figure 3(b)). The presence of debris around the walls and on the vault has determined for long time, and still determines, a meaningful overload on the masonry structures. Neither the inner excavation can be assumed to relief this state. In fact, the contact of the walls with the ground continuously determines infiltration of groundwater that leaks through the masonry and contributes to deteriorate the status of mortar joints and plaster forming musk and vegetation that cover the wall surfaces (Figure 3(c)).

3 THE NYMPHAEUM

Different topographic surveys have been undertaken in the last years to analyze the present status of the *nymphaeum* walls and vault, monitor possible kinematic evolution and warn against ongoing deformation. In details, a photogrammetric survey has been performed to reconstruct the whole geometrical pattern of the inner surfaces implementing the "Structure from Motion" technique (Caponero et al. 2020). The method consists in automatically collimating and recognizing common markers from different photographs. In the presents case, 703 photographs were taken by a 24 MPX camera mounted on a telescopic monopod and processed with a software (Photoscan Pro v. 1.2.6) on the ENEA CRESCO (Computational Research Center for Complex Systems, https://ict.enea.it/cresco/) platform.

A 3D model was thus created containing a cloud of about 55 million dots representative of the position and color of the surface. This output provides information on the layout geometry highlighting the possible presence of wall discontinuities, e.g. deterioration, cracks, vegetation etc. At the same time, a laser scanner survey was performed with the Leica BLK 360. This survey has herein been used to provide a reference for the above-described photogrammetry in order to scale it as shown in Fig4.a, for the covered nymphaeum portion (tablinum).

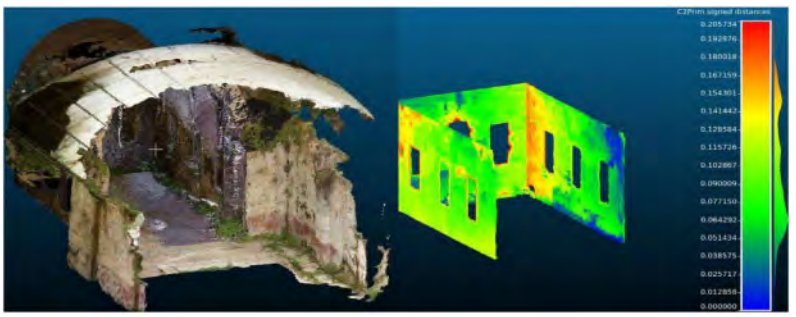

Figure 4. Geometrical three-dimensional model of the nymphaeum obtained by the combination of photogrammetry and laser scanning (a) and pattern of walls deviation from vertical reference planes (b).

The 3D laser scanning model has also been interpreted to figure out a quantitative description of the deformation taking place on the walls. In the example of Figure 4(b), the deviation of wall inner surfaces from ideal vertical planes anchored to the back and lower edges of the walls, these latter supposed as fixed considering their proximity to rigid boundaries, is reported with a shaded plot. Assuming that walls were built approximately vertical, the present shape shows a maximum inner convergence of about 5–6 mm on the upper-outer corner. This aspect is possibly due to the thrust of the outer soil and will be explored in the next section with a numerical analysis.

Finally, several topographic surveys were performed with a total station (Leica Nova TM50 robotic), having an accuracy on angles of 0.5" and on the distance of 2 mm, on 34 spherical targets distributed on the nymphaeum walls and vault. Measurement was periodically repeated five times over a time interval of about one and half year (from August 2019 to March 2021) to detect a possible evolution of the wall movements. The unchanged position of the markers within this time suggests that the nymphaeum structure is in relatively stable equilibrium.

4 SOIL-STRUCTURE INTERACTION

The analysis of the mechanical interaction between soil and masonry structure in these cases has different functions. It serves primarily to appreciate the present safety conditions of the monument, interpreting the role of natural and anthropic events occurred throughout its life. Next, accurate models enable to foresee the effects of possible future actions addressing remediation to effective and conservative solutions. This issue, relevant for any intervention on existing structures, becomes fundamental for delicate context such as historic sites. Finally, the model represents a benchmark for the structural monitoring as it provides a key for interpreting mechanisms.

On the other hand, when dealing with systems susceptible of irreversible phenomena, it is necessary to study stress-strain interaction not only in the present state, but also considering previous conditions that could have modified the mechanical response of materials. Reconstructing composition and history of the Ninfeo Ponari was not straightforward and implied non-invasive tests coupled with the knowledge of historical factors brought by archeologists.

Considering the geometrical layout of the manufact depicted in Figures 1 and 2, a three-dimensional finite element model has been implemented in the computer code (Plaxis 3D Ultimate CONNECT Edition 21.01) considering the *nymphaeum* with a soil portion around it. Stratigraphical and mechanical characterization of the subsoil have been accomplished with ad hoc geotechnical investigation. However, as shown later, even the reconstruction of subsoil and structure properties required the fundamental contribution of archeologists.

4.1 *Geometrical and stratigraphic model*

The geometrical set up implemented in the FEM analysis, with the identification of the different subsoil layers and the position and dimension of the manufact is accomplished combining geologic, historiographic and archaeological sources with the results of geotechnical investigation.From the geological viewpoint, the *Nymphaeum* is located on the NW-SE inclined slopes of the orographic systems including the Latium Antiappennines and the Latium-Abrutii Apennines. The deeper strata consists mainly of Mesozoic limestones displaced with normal and reverse fault systems from the Apennine tectonic action. The investigation carried out for the project consists of two continuous boreholes, one (S3) performed upstream of the artifact reaching a depth of 16 m, the other (S2) downstream reaching a depth of 30 m and hosting a down hole test (Figure 5(a) and (b)).

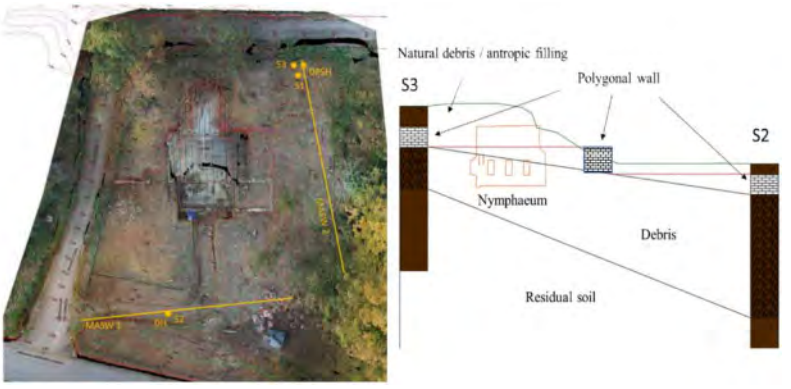

Figure 5. Plan view (a) and stratigraphic layout (b) of the Nymphaeum.

The sediments emerging in the surrounding area consist of debris produced from the alteration of upstream carbonates and from Miocene clays/marly clays. Gravel and sand of calcareous nature lay often immersed in a silty or clayey matrix. Below this layer there is a base formation of residual soils (red soil) produced by the dissolution of calcareous rock. From the observation of

unnatural white calcareous stones in the two boreholes and the presence of massive blocks near the *nymphaeum* (Figure 6), an arrangement in the form of terraces retained by polygonal walls was presumably created in the area at the time of *nymphaeum* erection. This assumption is confirmed by archeological studies which confirm the frequent use of the polygonal walls in the Casinum area (Valenti 2012). This polygonal wall, probably from the second century BC, is similar to others present in Latium, e.g. in Ferentino located 50 km to the north. The terrace of the *Nymphaeum*, discovered in the 70s, was probably partially dismantled for the construction of the *Nymphaeum*. With time, the whole area, including the interior of the *nymphaeum*, was filled with rubble mixed with debris fallen from the upper hill.

Figure 6. Picture of the polygonal wall (c). The geometrical model implemented in the analysis evolves as described in Figure 7 (from b to e).

Being not possible to drill the masonry elements or to excavate the external part of the *nymphaeum*, the thicknesses of walls and vault have been assumed (Figure 7(a)) considering the units typically adopted in Roman constructions: the walls have thus been assumed with a thickness of about 90 cm (one feet equal to 29.65 cm), while the vault has been considered to have the same thickness measured externally throughout its length. The model includes an initial removal from the terraced slope of a trench and its replacement with the *nymphaeum* walls (Figure 7(b) and (c)). This assumption, suggested by archaeologists, is supported by the evidence that plaster is applied directly on the unrefined inner masonry surface.

A two-phase subdivision in the trench filing could explain the fissure now observed at middle height. The roof consisting of a masonry vault has been possibly added in a second moment. According to this sequence, the inner room has been created in the model removing soil before adding the upper vault. The subsequent submersion shown in Figure 7(d) represents the filling by debris occurred with time, while the last scheme (Figure 7(e)) reports the present situation. All elements of the model have been discretized with tetrahedral clusters, each having 10 calculation nodes. Global coarseness has been set as medium (re = 1.00; le = 2.5 m) to optimize calculation effort, but a refinement (re = 0.5; le = 1.2 m) has been accomplished near the structure to enhance the accuracy of results.

4.2 *Structural model*

From the few parts of the wall not covered by plaster it is seen that the *nymphaeum* masonry is composed of irregularly shaped cobbles of calcareous stone, about 20 cm coarse, jointed with white mortar; rarely sparse fragments of brownish travertine limestone and isolated fragments of reddish

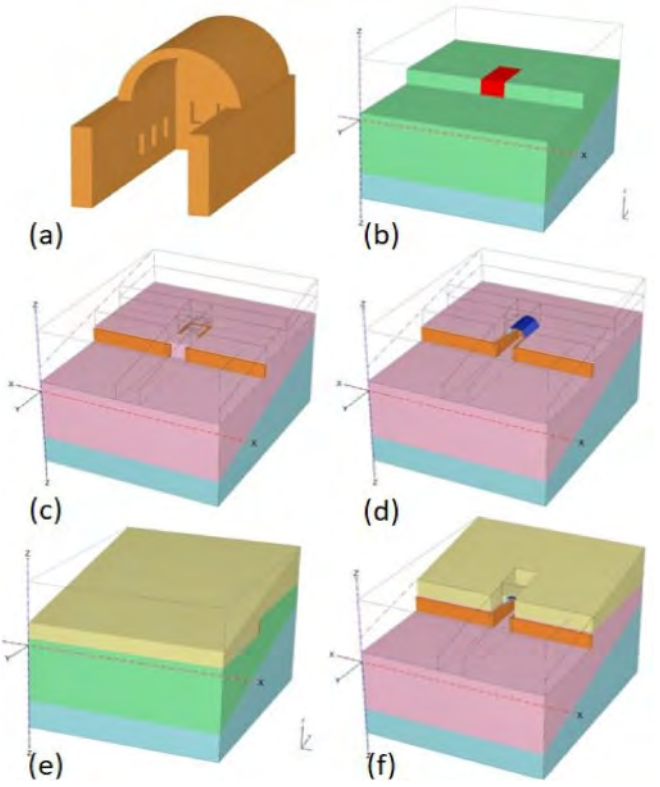

Figure 7. Geometrical model of the nymphaeum (a), layout adopted of the numerical analysis in the different calculation phases (b), before construction of the nymphaeum; (c), excavation and filling of the trench; (d), after construction; (e), submerged with debris; (f).

brick are found (Valenti 1992). Along the vault, the mortar joints are radially oriented (see Figure 2) possibly due to the use of ribs during construction and to improve the adsorption of circumferential stresses. The Jointed Rock model has been used to simulate the non-linear stress-strain response of the masonry elements. Conceived for fractured rock masses, it adopts a cross-anisotropic elastic-perfectly plastic response to simulate the pre-failure response of compact elements and a plastic model to simulate sliding along the joints oriented in preferential direction. For the present study, the elastic model has been simplified considering the masonry fabric as isotropic and assigning three elastic parameters, namely Young's and shear moduli and Poisson's coefficient. The values of these parameters have been attributed following the standard (Borri & De Maria 2009; Regione Umbria 2003), that classifies material with a quality index computed based on eight factors characterizing the geometrical and mechanical properties of the masonry.

A combination of these factors identifies a quality category to which typical ranges of mechanical parameters are associated. Considering the walls formed of irregularly shaped cobbles, joints not distributed with horizontal rows and vertical staggering, mortar of intermediate quality and stones only slightly degraded, the walls have been attributed to an intermediate category. The assumed elastic parameters ($E = 1077.2$ N/mm^2, $\nu = 0.2$, $G = 364.6$ N/mm^2) are thus the mean values of the ranges suggested for this category. The joints orientation has been assumed as horizontal for the vertical walls, radial for the vaulted roof. Plasticity along the joint planes, simulated with a Mohr-Coulomb failure criterion, is characterized by a friction angle $\phi = 30°$, a cohesion $c = 10$ kPa, and nil tension cut-off, looking also at former similar studies (e.g. De Felice et al. 2015).

4.3 *Geotechnical model*

The geotechnical characterization of the subsoil has been carried out considering the results of a downhole test (ASTM D7400M, 2019) performed in the borehole S2 (Figure 8(a)), of Dynamic Probe Super Heavy (DPSH) tests (ASTM D6951-03) performed near the boreholes S3 (Figure 8(b)) and a series of laboratory tests performed on samples taken on the lower strata in borehole S2 (Figure 9). The downhole test confirms the presence of three layers from top to bottom with shear wave velocities equal to respectively 200, 480 and 540 m/s (Figure 8(a)). The slight difference between the properties of the lower two layers is confirmed by the number of DPSH blow counts (Figure 8(b)), transformed into equivalent NSPT (standard) with the La-Croix and Horn (1973) relation, then correlated to the relative density (Skempton, 1986). The consolidated drained triaxial tests (TXCD) performed on undisturbed samples cored on the lower layers (5 and 8 m depth in borehole S3) show the mean failure envelope given in Figure 9. From the summary of the above results, the subsoil has been described with a linear elastic, perfectly plastic Mohr-Coulomb model, assigning the parameters summarized in Table 1. The water table was not intercepted in the performed boreholes and thus it was neglected in the analysis.

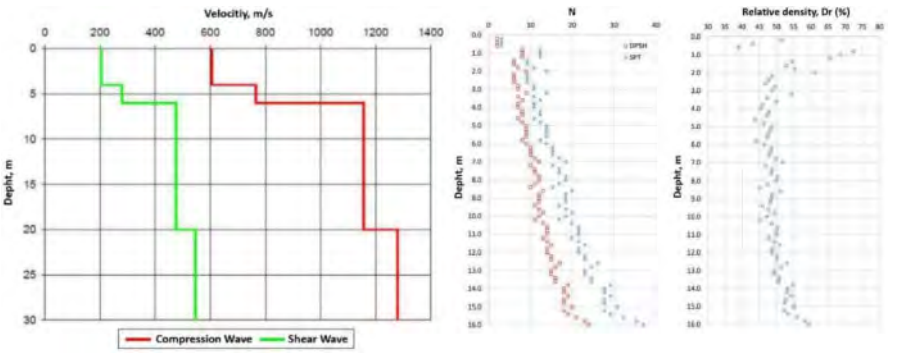

Figure 8. Shear and Compression wave velocity from downhole performed in the borehole S2 (a); DPSH performed in borehole S (b).

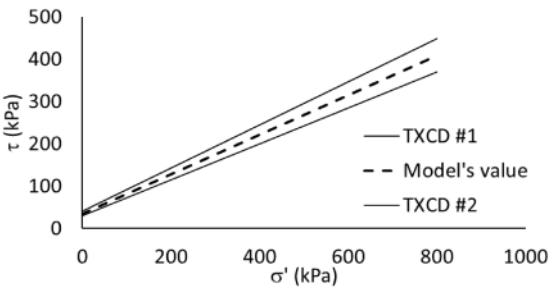

Figure 9. Triaxial test failure envelope form consolidated drained triaxial tests on samples cored from S2 in the deepest layer.

Table 1. Parameters of the Mohr-Coulomb model for the subsoil layers of Figure 1.

Soil	γ_{nat} (kN/m^3)	E (GPa)	ν	c′ (kPa)	ϕ' (°)	ψ (°)
Top fill	18	0.2	0.4		28	0
Debris	18	1.25	0.4	35	25	0
Residual	19	1.7	0.4	35	25	0

4.4 *FEM calculation results*

Calculation has been accomplished for each phase of the structure's life schematized in Figure 7, but the herein reported results refer for brevity to the present state only, considering this as the starting condition for future actions. From the deformation pattern of the *nymphaeum*, with displacements amplified one hundred times in Figure 10(a), it is readily seen that lateral soil thrust has a predominant role. In fact, the side walls tend to converge toward the inner space with displacements reaching a maximum of 6–7 mm (Figure 10(b)). Apart from being quantitatively consistent with the digital survey is shown in Figure 4(b), this result is explicative of the soil/structure interaction. Convergence is maximum in the intermediate section of the wall, while movements at the borders are constrained by the end wall and base slab that react with normal stresses. Indeed, this deformation cumulates the effects of the whole *nymphaeum*'s history, from its construction to date. It begins with the creation of the rooms, i.e. after filling the trenches with masonry and removal of soil, but grows with to the subsequent covering of the area by debris fallen from the hill.

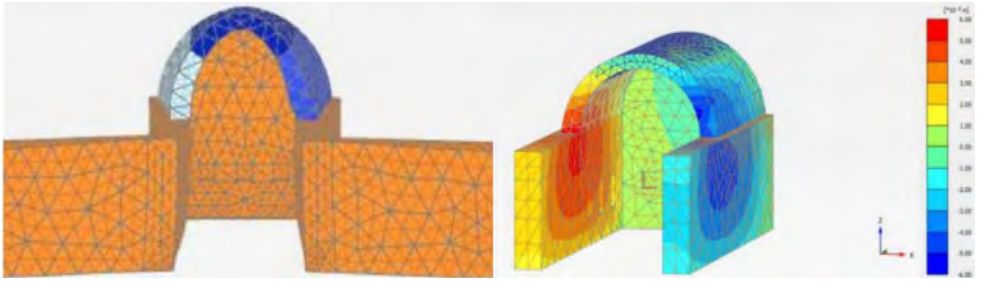

Figure 10. Deformation of the nymphaeum amplified one hundred times (a) and shaded plot of horizontal displacements (b).

Interestingly, the debris overcharge on the side of the nymphaeum and on the upper vault produces opposite effects on the walls. In fact, while the former is detrimental for the wall stability as it increases the horizontal thrust on the walls, the soil on the vault has a stabilizing action both for the increase of vertical stresses on the walls, given by the heavier weight transferred from the vault, and for the partial horizontal constrain given by the vault presence on the walls. This issue must be carefully analyzed when considering remediation of the monument. In fact, the excavation of debris around and above the *nymphaeum* cannot proceed randomly but must be planned considering each time the stress modification induced on the structure by the soil removal. In fact, the elimination of the soil above the vault leads in the calculation to numerical instability and collapse. This result underlines the importance in modulating soil excavation on the *nymphaeum* sidewalls in a gradual, symmetrical way, before removing the soil on the vaulted roof.

Another fundamental output of the model is the scrutiny of plastic points in the structure, i.e. the points where the masonry reaches limit conditions in accordance with the Mohr-Coulomb failure criterion and tension cut-off inherent with the assigned jointed rock model (Figure 11). The outcome reveals a complex pattern of plasticization given by the intersection of phenomena developing along different directions. In particular, together with the above discussed horizontal thrust in the cross section, the growth of debris thickness in the uphill ground determines also a meaningful thrust in the longitudinal direction, i.e. along the symmetry axis of the *nymphaeum*.

The computed movements become higher when the analysis is performed considering the heavier unit weight that may occur after heavy rain. This phenomenon, highlighted by the horizontal alignment of plastic points at middle height of the walls and at the vault abutment. is consistent with the direct observation of damage on the *nymphaeum* (Figure 12(a)). Another important effect shown by the plastic point distribution is the weakness of the walls in the open atrium (Figure 12(b)).

At present, these walls are in a very critical state, being subjected to a significant inward tilting that have alarmed the operators encouraging to undertake local stability intervention in the last

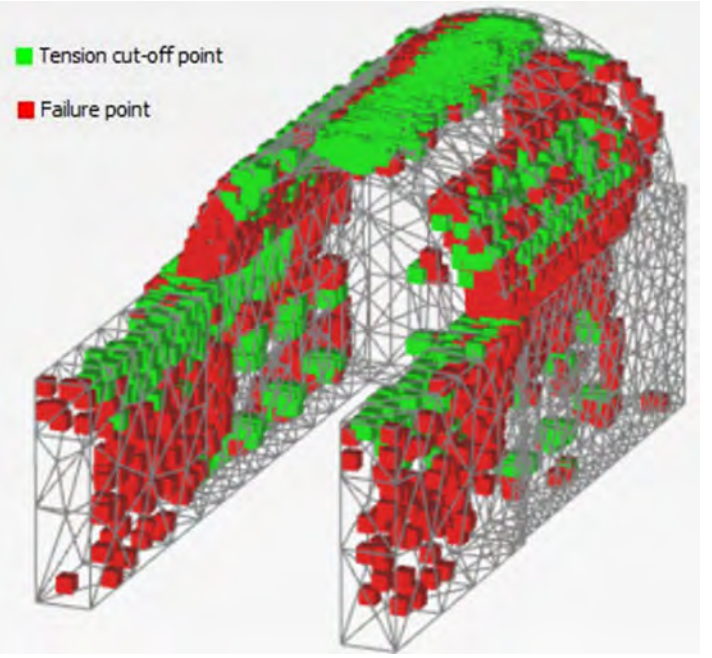

Figure 11. Plastic points from the model.

Figure 12. Cracks along the vaulted room (a) and rotated walls in the outer space (b) of the nymphaeum.

years. In conclusion, the structural response is dominated throughout the *nymphaeum* life by the interaction with the outer soil, that represents the main cause of concern, but severity increases with the weight of up-hill soil as confirmed by the increased number and extension of plastic and tension cut-offs points observed in the numerical calculation.

5 CONCLUSIONS

The topographical survey of the Ninfeo Ponari carried out at different times show that the structure is not undergoing significant movements and, at least in the last few years, that has reached a stable condition. However, the general analysis of the geographical situation, with the *nymphaeum*

positioned on a slope filled with debris, highlights the need for a more careful assessment. The comparison between the shape of the inner wall surfaces, detected by means of topographical surveys, and the ideal planar conditions highlights a possible inner convergence of the side walls with maximum displacements approximately equal to 6–7 mm in the upper intermediate section.

The simulation with the numerical model confirms this deformation pattern and strictly correlates it with the interaction between structure and surrounding soil. In particular, the negative role of the soil load on the *nymphaeum* walls, present from the construction times but exaggerated by the presence of debris fallen in the last centuries all over the area, jeopardizes the *nymphaeum* stability. Additionally, the water infiltrated in the ground after rainfalls determines heavier static conditions and contributes to the deterioration of frescoes on the walls. Remediation must thus aim to mitigate this interaction. The calculation has also highlighted the need for paying extreme attention to the balance given by the ground placed on the side and vault of the *nymphaeum* as a random removal might cause serious consequences.

ACKNOWLEDGEMENT

The authors wish to thank Bentley ltd for allowing the use of a free license of Plaxis vers. 3D Ultimate CONNECT Edition 21.01.

REFERENCES

Amorosi, A., Boldini, D., De Felice, G., Lasciarrea, W.G., Malena, M. 2015. Analisi geotecnica e strutturale del Ninfeo di Genazzano, Roma.

ASTM D7400M, 2019, Standard Test Methods for Downhole Seismic Testing, ASTM International, West Conshohocken, PA.

ASTM D6951-03: American Society of Testing Materials. Standard Test Method for Use of the Dynamic Cone Penetrometer in Shallow Pavement Applications, ASTM International, West Conshohocken, PA.

Betori, A. 2009. Cassino, novità dal Ninfeo Ponari. Le pavimentazioni dell'atrio, in AISCOM XIV, 2009, pp. 195–199.

Betori, A., Tanzilli, S., Valenti, M. 2009. Il Ninfeo Ponari di Cassino: nuove acquisizioni e prospettive di valorizzazione, in Lazio e Sabina. Scoperte Scavi e Ricerche, 5, Atti del Convegno "Quinto Incontro di Studi sul Lazio e la Sabina", a cura di G. Ghini, Roma, pp. 483–498.

Betori A., Valenti M., Tanzilli S., Il ninfeo Ponari a Cassino: una rilettura del monumento alla luce dei recenti restauri, in Lazio & Sabina 5. Scoperte Scavi Ricerche, Atti del 5° Incontro di Studio (Roma, 3–5 dicembre 2007), Roma 2009, pp. 484–488 (483–498).

Borri, A., De Maria, A., 2009a. Scheda di valutazione dell'IQM (indice di qualità muraria) (Allegato 3b.1-UR06-1). Rete dei Laboratori Universitari di Ingegneria Sismica (RELUIS). Progetto esecutivo 2005–2008.

Borri, A., De Maria, A., 2009b. Linee guida per la compilazione della scheda di valutazione dell'IQM (Allegato 3b.1-UR06-2). Rete dei Laboratori Universitari di Ingegneria Sismica (RELUIS). Progetto esecutivo 2005–2008.

Borri, A., De Maria, A., 2009c. Esempi compilati di scheda di valutazione dell'IQM (Allegato 3b.1-UR06-3). Rete dei Laboratori Universitari di Ingegneria Sismica (RELUIS). Progetto esecutivo 2005–2008.

Borri, A., De Maria, A., 2009d. Tabelle di correlazione tra IQM e tabelle delle NTC 2008 (Allegato 3b.1-UR06-4). Rete dei Laboratori Universitari di Ingegneria Sismica (RELUIS). Progetto esecutivo 2005–2008.

Caponero MA, Mongelli M., Imbimbo M., Modoni G., Polito E., Grande E. 2020, Monitoraggio strutturale del Ninfeo Ponari mediante sensori in fibra ottica, fotogrammetria e scansione laser, in Caravale A., Moscati P. (a cura di.), Logica e calcolo. Le basi dell'archeologia digitale. Atti della Sessione Speciale MetroArchaeo 2019, 2019 IMEKO TC-4 International Conference on Metrology for Archaeology and Cultural Heritage (Firenze, 4–6 dicembre 2019), "Archeologia e Calcolatori", 31.2, 223–232.

Carettoni, G.F. 1940. Casinum (presso Cassino) Italia romana Municipi e colonie s. I, vol. II, Roma.

Ghini, G., Valenti, M. 1995. Museo e area archeologica-Cassino. (Itinerari dei musei, scavi e monumenti d'Italia n.s., 28); Roma.

Giuliani C.F., 1992. Opus signinum e coccio pesto in Segni I. (Università degli studi di Salerno. Quaderni del Dipartimento di Scienze dell'antichità, 11. Serie Storia Antica e archeologia I. Napoli, 88–94)

Neuerburg, N. 1965. L' architettura delle fontane e dei ninfei nell' Italia Antica, Napoli, (MemNap, V).
Plaxis vers. 3D Ultimate CONNECT Edition 21.01, Geotechnical Analysis Software, Bentley System, 2021.
Regione Umbria, 2003. Allegato tecnico al B.U.R. del 30.07.2003. Norme tecniche per la progettazione degli interventi e la realizzazione delle opere di cui alla L.R. 23.10.2002 n° 18 finalizzate alla riduzione della vulnerabilità sismica.
ReLUIS, 2015. Report WP1_1-1_2015UNlPG disponibile sul sito ReLUIS all'indirizzo: http://www.reluis.it/images/stories/divulgazione/WP1_1-1_2015UNIPG_IQM_Report.pdf http://www.reluis.it/images/stories/divulgazione/WP1_1-1_2015UNIPG_IQM_Allegati.pdf
Valenti, M. 1992. Il ninfeo Ponari di Cassino (FR): analisi stilistica e cronologica delle decorazioni in Archeologia classica vol. XLIV, 1992. L'Erma di Bretschneider.
Valenti, M. 1995a. "Sull'ubicazione del foro di Casinum", QuadAEI, 24, 615–622.
Valenti, M. 1995b. Il mosaico rustico a conchiglie ed il Ninfeo Ponari di Cassino. Riflessioni su una moda decorative di età tardo-repubblicana in Atti del II Colloquio AISCOM (Roma 1994) Bordighera 49–60.
Valenti M. 2010: "Abbazia di Montecassino (Cassi-no, Frosinone): la riscoperta dell'antico, la formazione della raccolta archeologica e il suo nuovo allestimento scientifico nel Museo storico artistico", Lazio e Sabina, 6, 487–497.
Valenti, M. 2012. L'opera poligonale a Casinum: aspetti tecnici, problemi cronologici, considerazioni topografiche in Quarto Seminario Internazionale di Studi sulle Mura Poligonali, Atti del Convegno (Alatri, 7–10 ottobre 2009), a cuta di L. Attenni – D. Baldassarre, Roma 2012, pp. 219–226.

Geotechnical Engineering for the Preservation of Monuments and Historic Sites III – Lancellotta, Viggiani, Flora, de Silva & Mele (Eds)

Aubeterre-sur-Dronne Monolithic Church: Geotechnical and hydrogeological diagnosis

N. Carpentier
Antea Group, Bordeaux, France

Eric Antoinet
Antea Group, Orléans, France

Olivier Vigoureux
Agence GOUTAL, Paris, France

ABSTRACT: The Saint-Jean Monolithic Church of Aubeterre-sur-Dronne (France) is an underground medieval Church, dug directly in limestone strata, at the foot of a cliff.

Following a general deterioration of the stability conditions, a consortium led by Agence GOUTAL, Chief Architect of Heritage Monuments, has been mandated with co-contractors for detailed diagnosis of this underground Church. Antea Group has the responsibility of the geotechnical and hydrogeological diagnosis. The mission program includes a diagnosis and survey of the rock cracks, an hydrogeological expertise with water table monitoring, a geotechnical survey including borehole core sampling and crack monitoring.

This survey shows that the rock is relatively homogeneous in terms of lithology and hydraulic conductivity but has an important spatial variability for the mechanical properties. The limestone massif is very porous and fed mainly by infiltration from the upper ground level. Even if the Church is affected by a dense crack network, the monitoring showed that only one sector presents crack opening evolution and needs a specific study for its reinforcement.

1 GENERAL AND HISTORICAL CONTEXT OF THE CHURCH

"Saint-Jean d'Aubeterre" church is located in the city of Aubeterre-sur-Dronne, in Charente County Council (France), 80 km north east of Bordeaux (Figure 1).

Figure 1. Localization of Aubeterre-sur-Drone (left) & front view of the site (right).

DOI 10.1201/9781003308867-43

This Church is a vast troglodyte edifice carved into the limestone rock, on the hillside, below the old town castle, in a crumbly marl-chalky limestone geological formation (Figure 1). The digging of the church dates back to early Christian times for the older parts and for the most part to the 12th century.

This medieval church is part of a large rectangle twenty-seven meters long and sixteen meters wide (Figures 2 and 3), and has:

– a vast Nave, over 17 m in height with 4 hexagonal pillars, and an apse,
– two Collaterals (north and south),
– a Vestibule (room of the sarcophagi),
– a Triforium (and an old passage to the plateau on which the castle is going up),
– a crypt.

Its dimensions make it one of the largest churches of this type in Europe. It is listed as a Heritage Monument and welcomes more than 60,000 visitors per year.

The old Nave of the church (current entrance) has almost completely disappeared following the collapse of its vault, which could have occurred shortly after its construction according to recent archaeological studies (Hades). This Nave was formerly separated from the north and the south Aisles by massive pillars. A masonry wall is present today between these pillars (north, south and east sides) and a facing surrounds the east wall of the current Nave.

The origin of the cracks, now viewable in the roof, is not known. An overall diagnosis and an analysis of the structural condition of the monolith is required, before any definition of reinforcement solutions.

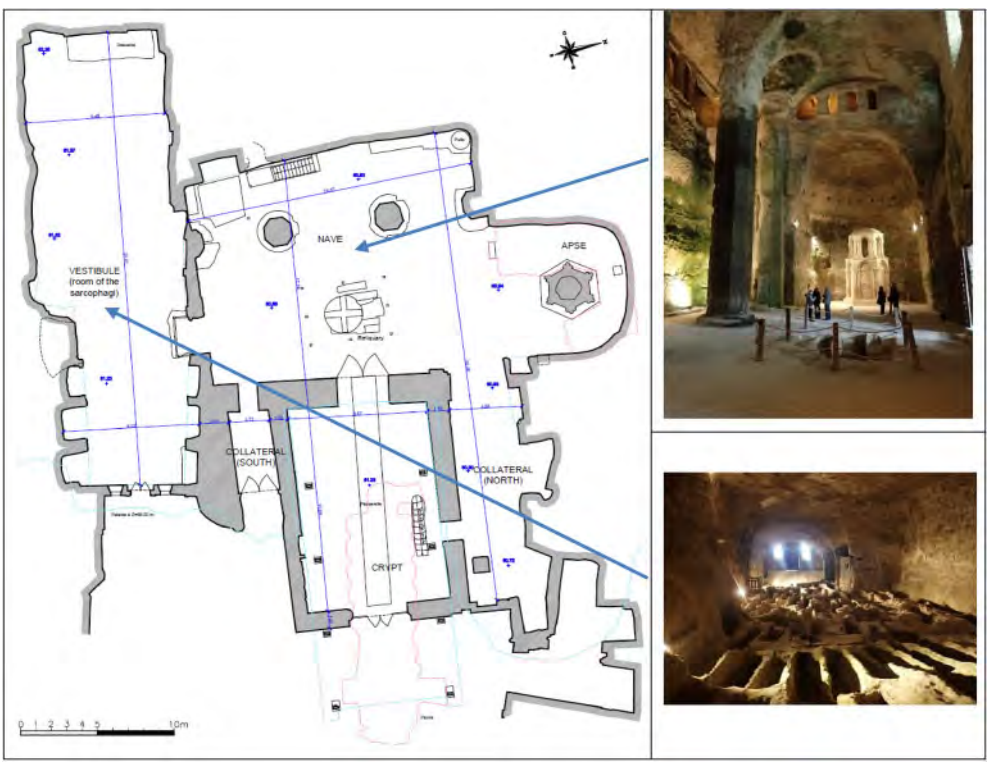

Figure 2. Plan view of the Aubeterre-sur-Dronne Monolith church (right) and photo of the Nave (top) and the Vestibule (bottom).

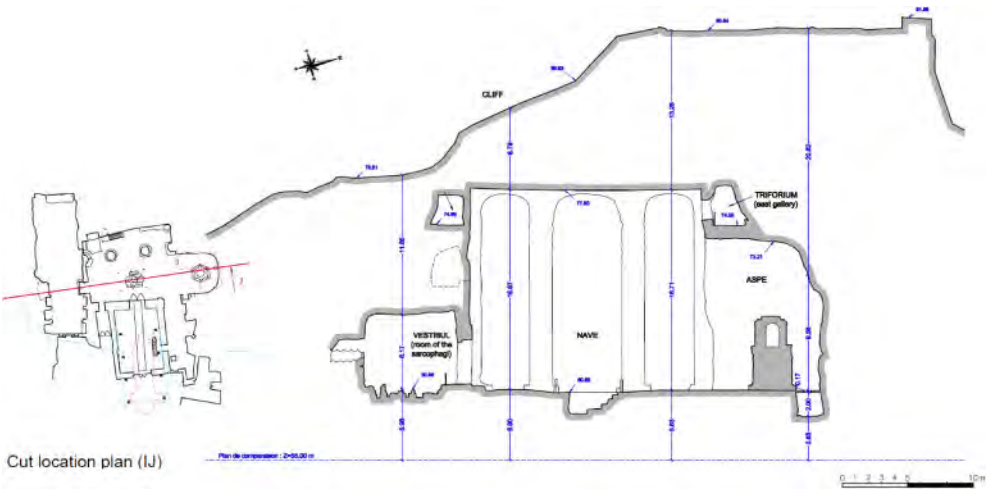

Figure 3. South/north cross section passing through the Vestibule, the current central Nave and the apse.

2 HISTORY OF STUDIES AND WORKS

The underground church was listed as a Heritage Monument in 1912 and has been the subject of continuous interest from architects and archaeologists since that date.

Stability issues, already noted as early as the 20th century, have not been dealt with in their entirety. The two first major reinforcement works took place in 1920 and then between 1952 and 1972: drainage, pillar reinforcements, reconstruction of some pillars of the Triforium, purging works, consolidation of a wall. However, no general reinforcement of the structure was carried out.

These works consisted of securing certain areas of the monolith, but the general stability has never been studied.

Moreover, scientific studies have been carried out by 1975 and 2002. These studies have shown that, independently of the works carried out, this underground monument presents signs of instability, and would require a reinforcement solution based on destructive and invasive treatment with heavy structures, incompatible with the identity and heritage context of the place.

A diagnostic study was then carried out on the site by the Chief Architect of Heritage Monuments, Mr. Denis Dodeman, and the archaeological study by Hades Cabinet provided the first elements of understanding of the original excavation method and allowed an approach on the pathologies of the place.

Following this preliminary diagnostic study, the Regional Authority in charge of Heritage Monument (DRAC) recommended to improve the knowledge of the church environment and to carry out a global diagnosis to propose effective and minimally invasive reinforcements.

In this context, the City Council of Aubeterre-sur-Dronne has mandated Goutal Agency (Chief Architect of Heritage Monuments) for a detailed diagnosis of the underground monolithic church, with the support of specialized engineering companies. These missions include a climatic study, a monitoring of the evolution of structural movements, a three-dimensional digital modeling, a geotechnical characterization, a hydrogeological study, a study of the paints and a study of vegetation.

As co-contractor of the consortium, Antea Group is in charge of the geotechnical and hydrogeological diagnosis of the Church. Antea Group's mission program includes:

- Analysis of previous studies and works;
- Diagnosis and cracking survey of the monolithic church;
- Cliff visual inspection around the monolithic church;

– Sampling by short core samples inside the monolithic church and a deep core drilling from the castle plateau, and limestone rock characterization by laboratory tests;
– Hydrogeological expertise, with the installation of six water table monitoring sensors and water chemical analyzes;
– Installation of a crack monitoring devices including crack gauges and an extensometer in order du monitor displacements between the walls.

3 RESULTS OF THE INVESTIGATIONS AND MONITORING

3.1 *Survey of cracking and disorders*

Cracking inspection of the monolithic church roof and pillars was carried out in January 2020 by two geotechnical engineers. This detailed inspection was carried out with a lifting platform, in order to work close to the Nave roof, and to identify all damages and issues. In addition, a visual inspection of the slope and the cliff overlooking the monolithic church was also carried out using rope work techniques.

The main types of disorders encountered during the inspection (Figure 4) are as follows:

– Mechanical cracking resulting from the opening of the church and the distribution of loads. These cracks appear after digging of the cavity, subsequently as a result of a rock creep and a stresses transfer.

  This cracking is very representative of the church compared to the geological cracking. It is preferably found at the level of the basilica, the central Nave and the Vestibule. It is characterized by a variable opening, from millimeter to centimeter scale depending on the cracks. These cracks follow two preferred orientations: N040 and N320.

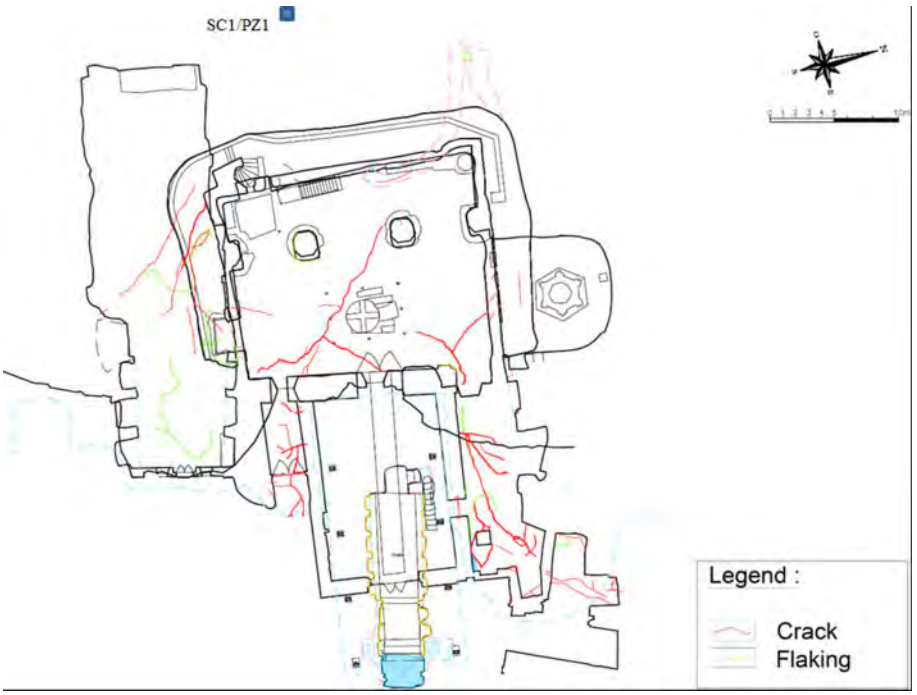

Figure 4. Main crack location map.

From a structural geological point of view, the limestone massif is homogeneous (same deposit type) and there is no brittle tectonics. The identified fractures are linked to a phenomenon of decompression of the limestone at the edge of the outcrops, the digging of the cavity and the collapse of the old Nave. This fracturing is important especially from the north and south transept (Figure 5(b)): transfer of loads on the transept, the tendency of which is to tilt towards the valley.

– The alteration of the surface of the church roof, which ultimately results in flaking corresponding to a superficial detachment (centimeter or even decimetric) of the limestone slab on the roof of the galleries. These phenomena affect the roof of the several rooms, and particularly in the Vestibule, and are characterized by the partial collapse of limestone benches.
– Chipping of pillars of the Nave, which results in the superficial loosening of limestone slabs, particularly at the level of the arches.
– The weathering and chipping of the shotcrete reinforcements carried out during prior work from the Triforium pillars (Figure 5(a)).

This damage (with release of concrete scales and coating on an average thickness of 3 to 10 cm) of sprayed concrete surfaces can be explained by the absence of reinforcement, and the concrete projection on a weathered and saturated support. There is therefore no structure guaranteeing continuity and rigidity of the projected hull.

Figure 5. (a) Chipping of the reinforced concrete pillars of the Triforium (left) and (b) Crack in the north Aisle with outcrop (right).

In addition, inspections on cliffs and slopes revealed a strong weathering of the rock facing at the outcrop (over a thickness of 10 to 80 cm) linked to the vegetation, as well as unstable rocky spurs on the cliff faces at the entrance to the church.

3.2 *Geomaterial characterization*

A mechanical and physical characterization was carried out, including a first stage of previous studies synthesis and a second stage including in-situ surveys and tests.

During the previous studies carried out between 1975 and 2002, around fifty short horizontal core samples were carried out from the staircase leading to the Triforium, in order to characterize the different strata observed on the height of the monolith, with porosity measurements and compressive resistance.

The additional survey consisted in carrying out a few complementary short boreholes (40 cm) from the staircase and the Triforium (in line with not previously recognized strata) and in carrying out a deep core borehole (SC1, 35 ml) from the plateau overlooking the church to characterize the different geological facies including the soils layers above the cavity (Figure 6). This sounding was equipped with a piezometer.

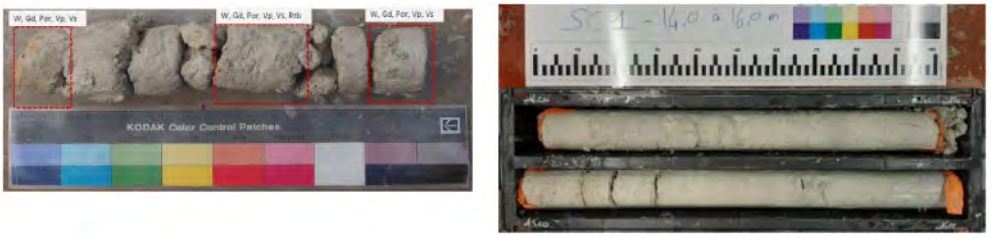

Figure 6. Short borehole sampling from Triforium (left) and borehole sampling from 14 to 16 m deep (right).

The short horizontal borehole carried out at the rock surface reveal a strong alteration of the limestone at the outcrop and weaker mechanical characteristics, in comparison with the rock samples taken just behind the cavity which are not altered.

In addition, a detailed geological context study associated with a survey and a precise geological interpretation of the vertical core drilling was carried out by a geologist expert. This study revealed the presence of four different formations, from top to bottom:

- Quaternary alterites and backfill: these are greyish, gray-white to cream-colored decarbonating marls with a soft consistency.
- The geological formation of Aubeterre: this formation is characterized by fairly fossiliferous bioclastic limes, cream to whitish in color. The clay content is low (4 to 7%) and increases (10 to 13%) at the level of the weathering fringe of the pillar heads.
- The geological formation of Barbezieux: it is a fairly soft bioclastic limestone with a chalky appearance, rich in foraminifers, gray green to white yellow in color. The clay content is low (4 to 8%).
- The geological formation of Biron: appears in the form of a limestone alternation with a generally rather clayey tendency, gray-green in color.

The main results, carried out on the Aubeterre formation, are summerized below:

Porosity: the tests showed very heterogeneous effective porosity (n_c) values varying between 17 and 40%. These results confirm the results already obtained in the previous study of 1975 (porosity between 20 & 40%) and 2002 (porosity between 21 & 36%).

The distribution of effective porosity values, for 43 tests, is very similar between vertical and horizontal tests:

- vertical test: $17 \leq n_c \leq 40$ (average: 32 %)
- horizontal test: $20 \leq n_c \leq 40$ (average: 32 %)

Uniaxial Compressive Strength: the UCS values on dry samples are measured between 3 and 30 MPa. The distribution of uniaxial compressive strength values, for 35 tests, is very heterogeneous:

- vertical test: $3.1 \leq UCS \leq 30$ (average: 14 MPa)
- horizontal test: $0.9 \leq UCS \leq 22$ (average: 9 MPa)

The results obtained on deep vertical core samples (SC1, Antea 2020 study) generally appear higher with an average value near 17 MPa. The values measured on the core samples taken horizontally in the church are lower with an average value close to 9 MPa. This highlights a stronger compressive strength in the perpendicular direction to the stratigraphy.

The test results show that for a given sample, the UCS of the material is lower the higher its porosity value (Figure 7).

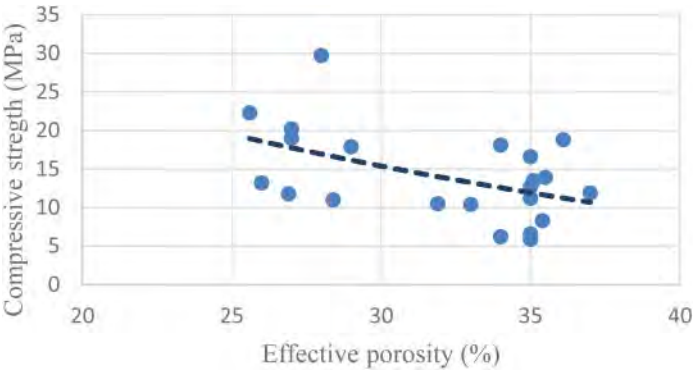

Figure 7. UCS as a function of porosity.

The limestone massif is relatively homogeneous from a geological point of view and sligthly fractured, but both physical and mechanical characteristics measured on the samples show a heterogeneity of the microfacies constituting the rock. Indeed, the total porosity varies from simple to double for samples sometimes less than 2 m apart. Compressive strength is inversely correlated with total porosity and shows strong variation from sample to sample.

Impact of saturation: UCS tests were carried out on dry and then saturated samples. These tests show a significant decrease of the uniaxial compressive strength between dry and saturated conditions: the UCS is reduced by about 8. This ratio is only indicative as it could be influenced by marly to clayey layers, highly water sensitive, and the low tests number (which has a large dispersion). Indeed, similar tests carried out on the Saint-Emilion monolith church (60 km away) had revealed a drop in mechanical characteristics linked to samples saturation with a lower ratio, closer to 2.

A pumping test, carried out in the SC1 boreholes, indicates a low permeability of the limestone mass. Even if the porosity is high, the hydraulic conductivity is relatively low (k # 8E-6 m/s).

Due to the intrinsic low hydraulic conductivity and during the hydraulic recharge of the soil (saturation of the materials), the development of pore pressure can lead to a loss of cohesion of the sample. The seepage areas in the monolithic church and the resulting variations in water content are factors favoring instabilities. Water inflows must therefore be drained as well as.

3.3 *Hydrogeological expertise*

The church has long been water circulation subject and moisture issues. The 1958 work described in particular the presence of water under the apse floor, alerting to the moisture and sanitation problems affecting the monument.

In addition, an hydrochemical study was carried out in 1975 and indicated that the monolithic church is subject to two distinct hydrogeological water flows:

- a flow directly linked to rainfall, in the eastern part;
- a more seasonally stable water table in the western part of the church.

The water chemical analyzes show that the water imbibing the rock (at the level of Triforium) is enriched in sulphate and alkalis due to the oxidation of iron sulphide and probably due to base exchanges with clays (glauconia).

In order to have a better understanding of the hydrogeological context, a detailed study was carried out on the basis of previous studies and the establishment of a monitoring system for various water points.

Also, four water table recorders (Figure 8) were installed outside the site (hydraulic upstream: piezometer installed on the castle hillock and hydraulic downstream: well around the esplanade at

Figure 8. Position of the water level sensors on the outside and transverse cross section axis (Antea Group).

the entrance to the church), and three recorders inside the monolith (cistern of the hose, well and pit in the church).

Note: The Muscadière fountain, located upstream hydraulically and developing at a higher level than that of the church, communicated in the past by a network of galleries dug under the the castle, but these connections are today obstructed, and the water evacuated through the moat to the north-east of the site.

Inside the church, three main areas of seepage (Figure 9) were noted on the west face:

– In the Triforium: seepage with calcite concretions,
– In the side wall of the Nave with deposits,
– Under the floor of the Apse with few deposits.

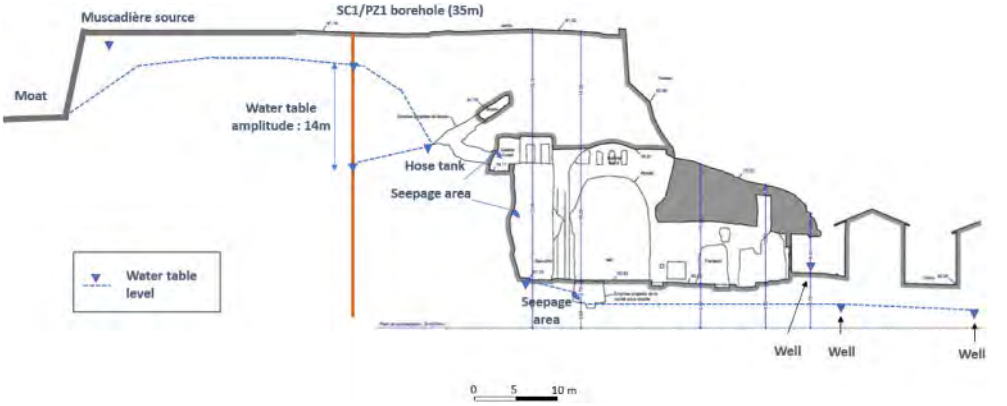

Figure 9. West/East cross section with position of water level and inflows (Antea Group).

In addition, water inflows are visible from the upper part of the castle access (now walled) in relation to the plateau, where there is infiltration of surface runoff water linked to a lack of water management. The piezometric measurements, carried out over a 18-month cycle (January 2020 to September 2021), show:

– A very significant drop in water levels in the rocky massif under the castle plateau from mid August until the end of October (no recharging),
– A very rapid rise in levels with the recharging of the water table of the piezometers of the castle (14 m) and of the hanging garden (2 m),
– Very stable water levels inside the church (Triforium hose, ground floor well) (cistern),
– Low amplitudes (0.5 m) in line with the piezometers located at the base level of water table.

In addition, a pumping test was carried out in the piezometer. This pumping shows that the water table contained in the formations under the castle plateau is strictly contained in the porosity of the rock. The flows are very slow due to the low hydraulic conductivity of rock but the volumes are large in relation to the very high storage coefficient (high porosity).

The summary of all the measures highlights:

- a large volume of water in the rock (porosity 35%) fed mainly by infiltration near under the castle plateau (anarchic water management on the castle property) and more marginally by the water table upstream the Muscadière plateau;
- the lack of tectonic or karst cracking phenomenon which would accelerate the inflow of water into the rock mass;
- the infiltration water the from the plateau. The water collection is deficient with a replenishment risk in the rocky massif below and the church facings (lack of waterproofing);
- a water volume moving very slowly and emerging in the church by seepage at different levels depending on the lithology and geometry of the cavity: emergences or water retention areas thanks to excavations forming “cisterns” (church well, sarcophagus);
- the presence of pyrite in the rock and the microbiological oxidation of this pyrite at the origin of gypsum crusts: water loaded with sulphate, sodium and potassium. Seepage from surfaces and partial evaporation of water transport and deposit salts on rock faces.

3.4 *Instrumentation of the Church*

The monolithic Church is affected by a dense network of roof cracks, probably linked to the decompression of the limestone massif after excavation and to the presence of pre-existing geological cracks. Major cracks were followed up over a 14-month time laps.

The monitoring system implemented, after validation with the partner in charge of structural design (Equilibre & Structure) is as follows:

- 1D fissurometers (8 sensors, Figure 10(a)) for monitoring cracks opening (1 directly above the north Aisle, 1 below the south Aisle, 2 below the Vestibule, 4 below the central Nave);
- 3D fissurometers (12 sensors, Figure 10(b)) for monitoring crack opening in 3 dimensions (north Aisle / Vestibule / central Nave);
- 5 temperature probes;
- 1 extensometer positioned in an east-west direction in the central Nave;
- 16 measurement recorders with radio data transmission to avoid cables laying along the walls;
- 1 data collection and sending gateway.

The monitoring device plan is given in Figure 11.

The temperature readings made on the 5 sensors located in the church show significant temperature fluctuations. The sensor located at the south Collateral level (near the entrance) records the greatest amplitude of temperature variation over the year, with a minimum temperature recorded of 5° and a maximum temperature of 30.5°. The sensors positioned on the central Nave roof are

Figure 10. (a) 1D fissurometer (left) and (b) 3D fissurometer (right).

Figure 11. Monitoring device plan.

those which record the smallest variations, with a minimum over the year of 10° and a maximum of 22°.

The measurements carried out over a period of 14 months show that the cracks evolve as a function of the temperature following the rock dilation/retractation:

– opening phase associated with the decrease in temperature,
– tightening phase associated with the increase in temperature.

The displacement speeds are low to moderate over an annual cycle (+/−0.1 mm/year: no significant displacement) with the exception of the cracks located at the crossroads between the central Nave and the north Aisle: sensor C18 (speed of 0,6 mm/year) and 3D sensor C4/C5/C6, and south side (C19). These sensors observed an opening of the crack and a mismatch.

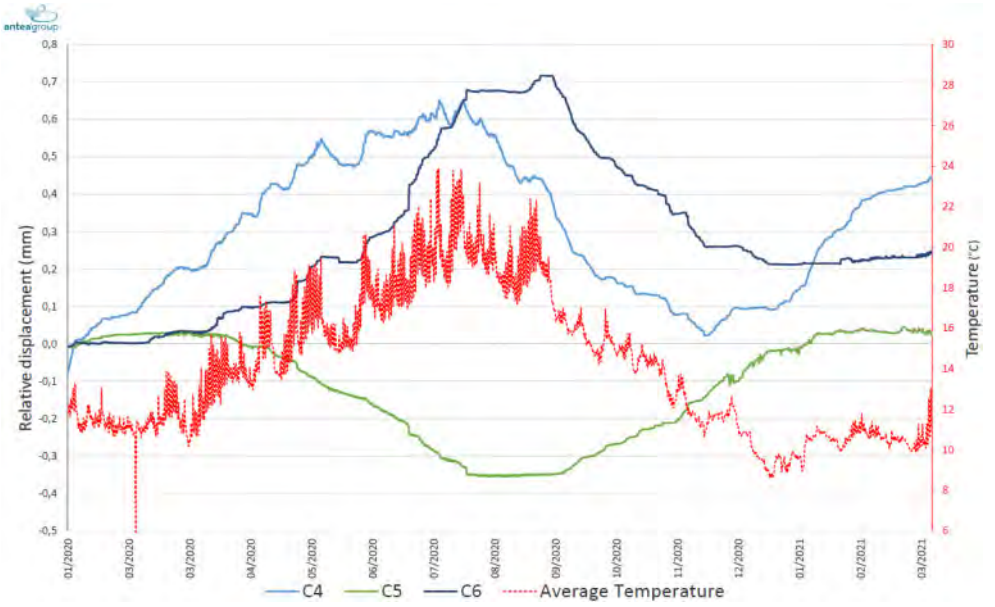

Figure 12. Monitoring of the 3D fissurometer C4/C5/C6 other 14 months (Antea Group).

The data analysis highlights the lack of significant movement on the sensors majority (annual cyclical movement in correlation with thermal variations) except for one sector which seems to be evolving and which should be monitored (junction Nave with north Aisle: regular movement in the direction of the opening of the crack).

4 OUTLOOK

Measurements show that the rock mass, in which the church is dug, is relatively homogeneous with regard to lithology, but physical, mechanical and hydrogeological characteristics are highly variable. The limestone massif is very porous (32%) and fed mainly by infiltration near the plateau, but the flows are slow, favoring surface seeps and the formation of salts and gypsum crusts. The roof is affected by open cracks. The monitoring devices indicate the lack of significant movement on the sensors majority (annual cyclical movement in correlation with thermal variations) with the exception of an area located at the junction between the Nave and the north Aisle. The behavior of this sector have to be strengthened by a complementary monitoring.

The risk of falling blocks and shotcrete scales (from old restoration works) from the Triforium columns is high and represents a safety risk to visitors below. Several blocks of few kilograms were found in the nave which required an emergency purge.

At the end of this phase (in progress), a definition in the restoration sketch phase and church consolidation work will be established and will include the recommendations for the control and management of water inflows at the site and for the definition of methodologies for strengthening the pillars and the vault.

The different types of reinforcement that can be considered at this study stage are as follows:

- Prior analysis of three-dimensional stability (numerical modeling) integrating the discontinuity identified in the context of these investigations to explain the structural disorders observed in the church and to justify the need or not for heavy reinforcement. The current study indicates a trend to close the north and south areas around the old collapsed Nave;
- Removal of the reinforced concrete unstable parts on the Triforium pillars which constitute a risk for visitors, then pillars reconstitution with an adapted methodology;
- Improved rainwater management: better rainwater infiltration control and runoff arriving on the castle plateau;
- Efficient runoff water drainage, particularly in the hose and Triforium to prevent re-infiltration, and west walls drainage of the church to evacuate water and limit surface seepage reactions;
- Evaporation reduction inside the church by an adapted climatic device;
- Anchoring of unstable rocky dihedrons on the limestone cliffs located at the entrance.

5 FIND OUT MORE

For more historical information about this Monolithic Church:

– https://www.aubeterresurdronne.com/a_voir/eglise-souterraine/
– https://fr.wikipedia.org/wiki/%C3%89glise_monolithe_d%27Aubeterre-sur-Dronne
– HISTORIA, n°891, March 2021 “L’église souterraine d’Aubeterre, trésor de l’Aquitaine médiévale”
– Diagnostic général de l’état de stabilité de l’église troglodyte d’Aubeterre-sur-Dronne – Département de la Charente (16), Juillet 2002, Rapport BRM/RP 51796-FR

Geotechnical Engineering for the Preservation of Monuments and Historic Sites III – Lancellotta, Viggiani, Flora, de Silva & Mele (Eds)

Effect of slow-moving landslides on a vaulted masonry building: The case of San Carlo Borromeo church in Cassingheno (Genova)

G.L.S. Sacco, C. Ferrero, C. Calderini & C. Battini
Department of Civil, Chemical and Environmental Engineering, University of Genoa

R. Vecchiattini
Department of Architecture and Design, University of Genoa

ABSTRACT: This paper presents the structural analysis of San Carlo Borromeo church, a masonry building located in Cassingheno (Genoa, Italy) in an area affected by a slow-moving landslide. A deep knowledge of the building in terms of geometry, structural configuration, history and construction phases was acquired by means of on-site surveys and archival research. The crack patterns were surveyed in detail and the deformations were studied through a point cloud obtained from a LIDAR survey. The comparison between the landslide direction and the damage observed showed discrepancies and suggested the presence of foundation settlements due to other phenomena. To identify the actual causes of damage, a finite element model (FEM) of the building in its hypothetical undeformed configuration was created. The geometry of such configuration was reconstructed starting from the point cloud obtained from the LIDAR survey and removing geometrical defects such as leaning of walls, deformation of vaults and inclination of tie-rods. To simulate the effects produced by the landslide and the foundation settlements on the building over time, nonlinear analyses were performed by imposing different displacement fields at the foundation plane in multiple steps. The damage predicted numerically was then compared with the one experienced by the building, showing good agreement.

1 INTRODUCTION

The study of the effects of slow-moving landslides on cultural heritage buildings is in its early stage. Therefore, in contrast to seismic threats, a standardized diagnostic procedure to easily assess this risk is still lacking. A first contribution to the topic was given by a large-scale study of several churches in the Liguria region (Ferrero et al. 2021a), which led to the identification of some recurrent damage mechanics associated with slow-moving landslides. Further investigations at a smaller scale showed the need to ensure a detailed knowledge of each single building and separate the effects of the landslide from the effects of other types of actions (subsidence, local foundations settlements, load changes, etc.).

This paper presents the structural analysis of San Carlo Borromeo church in Cassingheno (Genova). The church is located on a medium slope area affected by a slow-moving landslide and presented a complex damage distribution (crack patterns and deformations) not completely compatible with the landslide direction. The damage and deformations identified in San Carlo Borromeo church were critically analyzed with the aim of assessing whether they could be entirely attributed to the landslide acting in the area or not.

A detailed survey of the building, including laser scanning and photogrammetry, was performed to gather information about geometry, distortions, and crack patterns (Section 2). A

DOI 10.1201/9781003308867-44

historical research was also carried out to obtain a deep knowledge of history, architectural alterations, and construction phases. In addition, information about landslides and geotechnical soil characterization in the surrounding areas was collected (Section 3).

With the aim of assessing the causes of the damage observed in the church, a finite element model of the entire building in its initial hypothetical undeformed configuration was created. Nonlinear static analyses were then performed by imposing different foundation displacement fields at the base of the structure (Section 4). These displacement fields were defined based on the deformations and foundation settlements experienced by the church over time, which were in turn identified thanks to the laser scanner survey and the analysis of the building construction phases. This represents the main novelty of the work, since detailed information about the displacements underwent by a historic building during its entire life is not usually available. In the case of the church under consideration, the identification of displacements fields based on the actual displacements experienced also made up for the lack of data regarding magnitude and rate of the landslide movement (see Ferrero et al. 2021b). The effectiveness of adopting this strategy was verified by comparing the damage predicted by the numerical simulations with the crack patterns and deformations surveyed on site.

2 DESCRIPTION OF THE CASE STUDY

San Carlo Borromeo church is located in Cassingheno, a small village part of the municipality of Fascia (Genoa metropolitan area). The church and the village of Cassingheno are situated on a medium-low inclined slope (about 20°), which is likely to be the accumulation zone of a relict deep slide. In the area of interest, the soil consists of a thick layer (10–15 m) of very heterogeneous blanket (sand with clasts, clayey silts) separated from the bedrock (shales) by a transition zone (1–3 m) of weathered rock. The ground water table, which oscillates according to the seasonality, is located inside the blanket (Cambiaggi et al. 2021).

As shown in Figure 1, the entire village of Cassingheno lies on an active slow-moving landslide, which has an area of about 0.17 km^2 (Arpal 2020) and is classified as complex according to the *Atlante dei Centri Instabili della Liguria* (hereafter called Atalante et al. 2004). Within the framework of the REMOVER monitoring project of the Liguria Region, the landslide was monitored by means of inclinometers. All the instruments showed small movements of the blanket at variable depths along the slope and indicated a possible failure surface at a depth of about 9–12 m from the ground surface (Cambiaggi 2020).

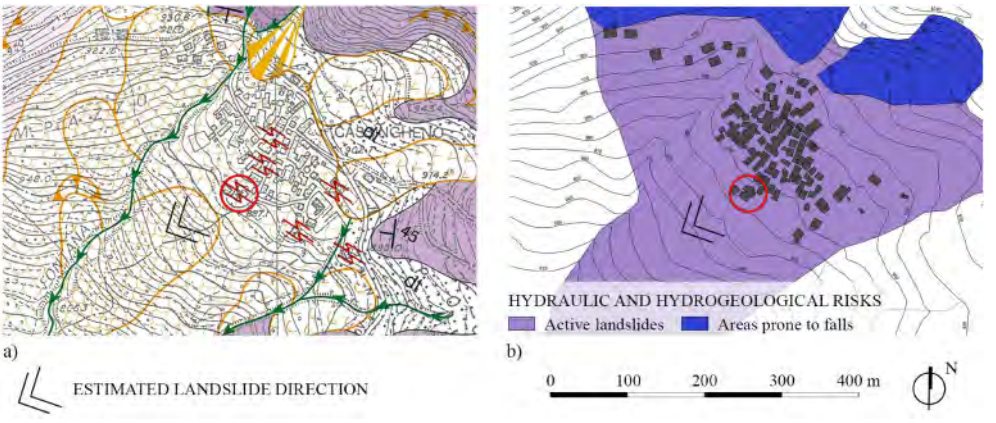

Figure 1. Landslide maps for the landslide affecting Cassingheno village and San Carlo Borromeo church (indicated with a red circle): a) *Atlante dei Centri Instabili della Liguria* (Federici et al. 2004), b) *Atlante dei Rischi Idraulici e Idrogeologici* (Autorità di bacino distrettuale del fiume Po 2017).

The landslide direction, indicated with an arrow in Figure 1, was found to be almost parallel to the longitudinal axis of the church. Following the same approach adopted in Ferrero et al. (2021a), the landslide direction was estimated on the basis of the orientation of the symbols used in the maps of the Atlante to represent landslide phenomena (Figure 1(b)).

San Carlo Borromeo church (Figure 2) has a single nave, a presbytery, a semicircular apse, two lateral chapels and a belltower. Including the apse, the church is about 20 m long and 6 m wide. The nave and the presbytery are covered with barrel vaults, while the apse has a hemispherical dome. The entire building (both walls and vaults) is made of stone masonry and is covered by a recently built wooden roof. A clergy house and a sacristy, respectively made of stone and brick masonry, are also present on the north-western side of the church.

No information about the foundation system of the church is available. However, since the church dates back (at least) to the end of the XVI century (see the following paragraph), it is reasonable to assume that the foundations are shallow and consist in an enlargement of the perimeter walls.

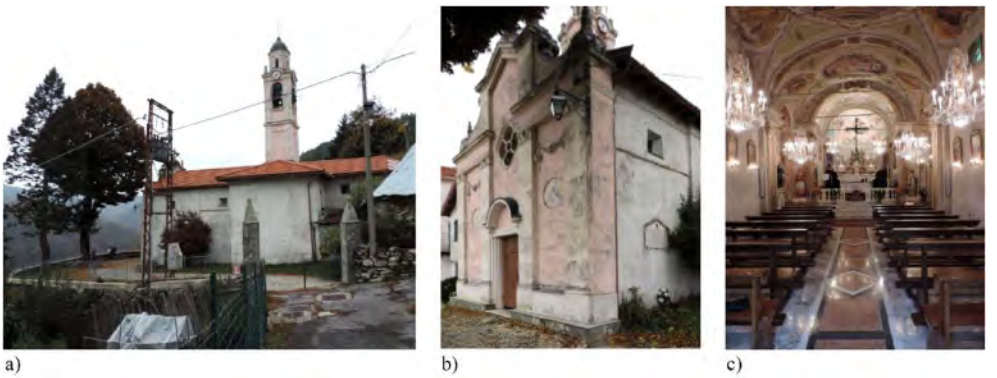

Figure 2. (a and b) Exterior. (c) Interior.

The building as it appears today is the result of significant transformations undergone over time. Although the historical information about the church is limited, different construction phases were identified through archeological and stratigraphical analysis (Cabella & Sacco 2020). The first document attesting the existence of the building as an oratory dates back to 1595 (Cazzulo et al. 1998). However, it is likely that the original core was built in late Middle Ages, since documents (Sanguigliani 1892) confirm the presence of the village of Cassingheno in the twelfth century. The original building was probably similar in shape to the current one but smaller and with a shorter belltower (Figure 3(a)). The apse and the base of the belltower are the only remaining

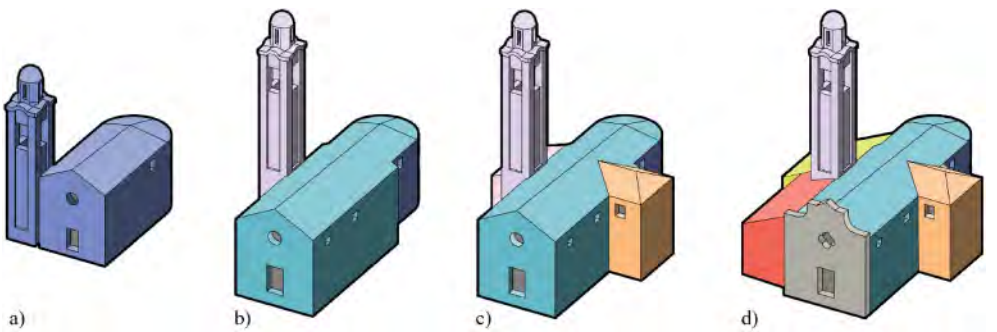

Figure 3. a) Original building - late Middle Ages. b) Church – before 1595. c) Right chapel – before 1879 d) Current configuration – early 19th sec.

parts of the original building, while the current nave, whose walls are not perfectly aligned with those of the apse, was constructed later with a size larger than the original one (before 1595). The current belfry was added at the same time of the enlargement of the nave or just after, leading to the configuration shown in Figure 3(b). Subsequently, before 1879, a sacristy and a chapel were built on the left and right sides of the church, respectively (Figure 3(c)). Between the end of the eighteenth century and the first half of the nineteenth century, San Carlo Borromeo church underwent further transformations, including the construction of the clergy house (colored in red in Figure 3(d)) and the reconstruction of the original sacristy, which brought the building to its present form (Figure 3(d)). An intervention to straighten the belltower was also carried out after the Second World War, hiding most of the rotation experienced by this structure over the centuries.

3 DAMAGE AND DEFORMATIONS

3.1 *Damage survey*

3.1.1 *Crack pattern*

Figure 4 shows the crack pattern of San Carlo Borromeo church. Since in 2019 the church underwent a restoration that partially hided the damage on the exteriors, the crack pattern surveyed by the authors in 2020 was integrated with the one reported in Memme (2019) and Ferrero et al. (2021a).

Extensive and severe damage is observed in the walls, in particular in the second bay behind the façade. In this bay, both the longitudinal walls are affected by a series of large diagonal cracks that originate from the level of the floor and propagate upwards towards the apse. In addition to these cracks, large diagonal cracks are observed in the longitudinal walls of the first bay of the nave and the presbytery. Both cracks progress upwards towards the façade of the church (Figure 4(b)).

Unlike walls, arches and vaults do not show severe cracking. A thin to medium longitudinal crack, oriented in same direction as the landslide, cuts the barrel vaults of nave and presbytery approximately at mid-span. Thin cracks with a slight concentric pattern around the belltower can also be observed.

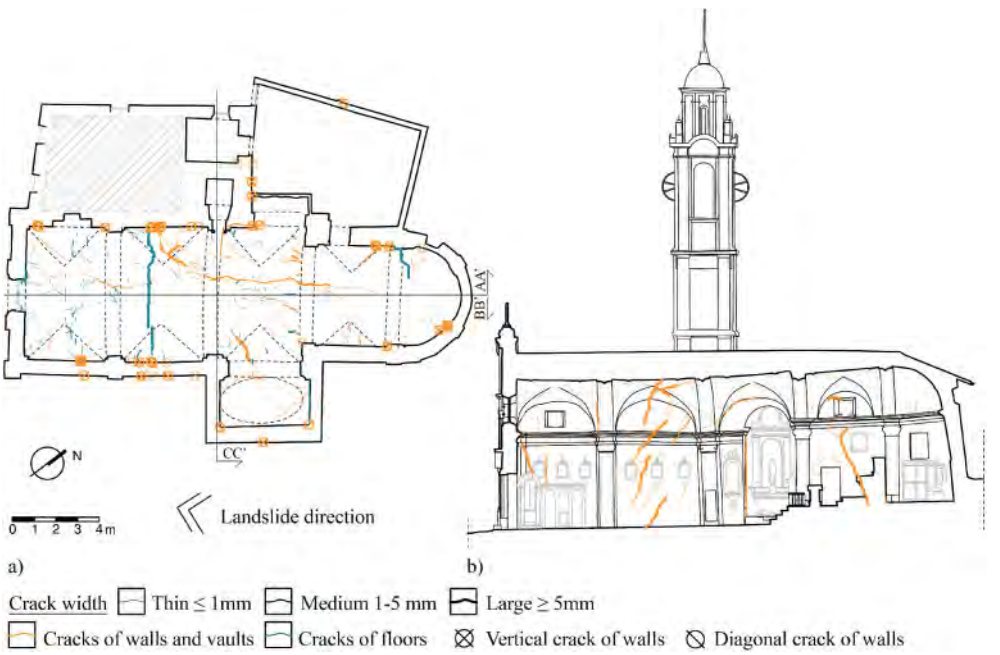

Figure 4. Crack pattern of San Carlo Borromeo church: a) plan, b) section AA'.

As can be seen from Figure 4(a), in the second bay behind the façade, the floor presents a large crack (12 mm wide), which crosses the entire nave and propagates transversally between the longitudinal walls. Thin to medium cracks with the same orientation were also observed in the first bay and the northernmost part of the right chapel. These cracks are oriented perpendicular to the direction of the landslide acting in the area.

3.1.2 *Deformations*

To study the deformations of the church a laser scanner survey was performed, and longitudinal and transversal sections were extracted from the point cloud.

From the analysis of the longitudinal section (Figure 5(a)), it can be seen that the whole building exhibits a significant rotation toward the valley, in the direction of the landslide. The more significant rotations were measured in the apse and presbytery. The presbytery vault was rotated by about 4.9°, the apse wall by 6.8°, and the moldings by 3°. In the nave, the floor, moldings, and pilasters show a rotation of only about 1.4°, while the barrel vault exhibits a deflection of about 20 cm in the center of the second bay. No significant rotations were measured in the façade.

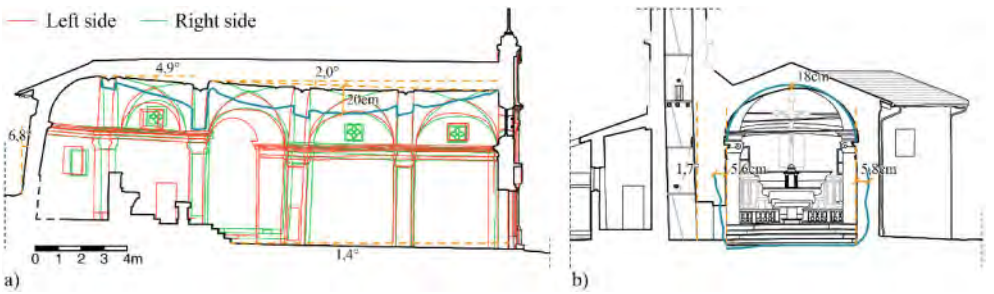

Figure 5. Deformation surveyed. a) Longitudinal section BB', b) transversal section CC' (the sections are indicated in the plan of the church in Figure 4).

From the analysis of the transversal section (Figure 5(b)), the walls of the nave were found to lean outwards. The right wall has the maximum rotation of 1.6° near the first pilaster from the façade, probably due to the thrust of the vault. The left wall, which experienced larger rotations, exhibits the maximum one in correspondence of the belltower, which presented the same rotation of 2.14°.

The deformation of the arches and barrel vaults was also assessed. To this aim, the original undeformed shape of these structural elements was reconstructed under three hypotheses: i) the original profiles were elliptical; ii) the length of the deformed and undeformed profiles remained constant during the deformation; iii) the original clear span of the arch was established when the walls were still vertical and the springings were at the same level. In the reconstruction, the thickness of cracks was also taken into account (for further details the reader is referred to Cabella & Sacco 2020). The first arch and the second arch from the façade were found to be significantly deformed and exhibit a deflection at the crown of about 22 cm and 18 cm with respect to the hypothetical undeformed shape, respectively (Figure 5(b)). Such a deflection is compatible with the deflection measured in the barrel vault.

A distortion of the façade in the horizontal plane was also observed.

Since the church was built in several construction phases, the presence of differential settlements was also verified. In particular, the differential settlement between the left and right parts of the building was assessed comparing the elevations of the floors, windowsills, tie rods, decorations, and moldings. For each pair of points in plan, several pairs of points in elevation were extracted from the point cloud and their heights were compared (Cabella & Sacco 2021).

From this analysis, three phenomena were observed. The left part of the church, from the apse to the belltower, underwent a larger vertical displacement (of about 5 cm) with respect to the right part.

The belltower underwent a localized settlement of about 11 cm, measured by comparing the height of the capitals of the pilasters on the left and right parts of the church. The localized settlement of the belltower can be easily identified in Figure 6, which shows the vertical distance between the points of the floor taken from the point cloud and their best fit plane passing through the floor (Pesci et al. 2011).

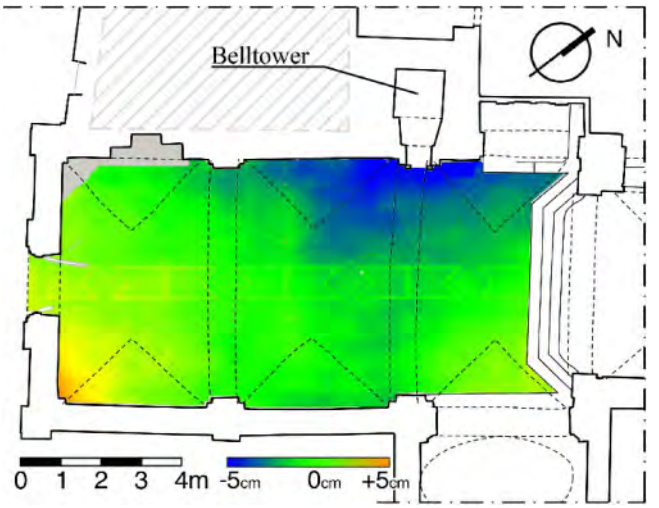

Figure 6. Local settlement of the belltower identified by analyzing the vertical distance between the points of the floor taken from the point cloud and the best fit plane passing through the floor.

In addition to the abovementioned phenomena, in the right chapel, the south-eastern wall (toward valley) was found to have settled 9 cm more with respect to the north-eastern wall.

3.2 *Critical damage assessment and identification of the displacement fields*

The damage and deformations identified in San Carlo Borromeo church were critically analyzed with the aim of assessing whether they could be entirely attributed to the landslide acting in the area or further phenomena could be involved.

As regards the crack pattern, the cracks of the floor oriented perpendicular to the landslide direction can be attributed to the horizontal component of the landslide movement and clearly indicate that the church suffered an extension in the direction of the acting landslide. However, the cracks in the barrel vault of the nave as well as the diagonal cracks in the walls on the left and right sides of the belltower, which progress upwards toward this latter, suggest a local settlement of the belltower. Such a settlement could also be responsible for the deformation of the second arch from the façade.

The analysis of the deformation and foundation settlements indicates that not all the damage suffered by the church was produced by the landslide. Indeed, while the vertical component of the landslide has reasonably caused of the global rotation of building (Ferrero et al. 2021a), it has hardly produced the differential settlement between the left and the right part of the building and the localized settlement of the belltower.

On the basis of the deformation and foundation settlements identified in San Carlo Borromeo church, four displacement fields, representing the displacements experienced by the building over time, were identified: a global displacement, affecting the entire church, and three local displacements. The global displacement is due to the landslide and has both vertical and horizontal components (Figure 7(a–b)), while the local displacements represent the vertical settlements of the left part of the church (Figure 7(c)), the belltower (Figure 7(d)), and the right chapel (Figure 7(e)).

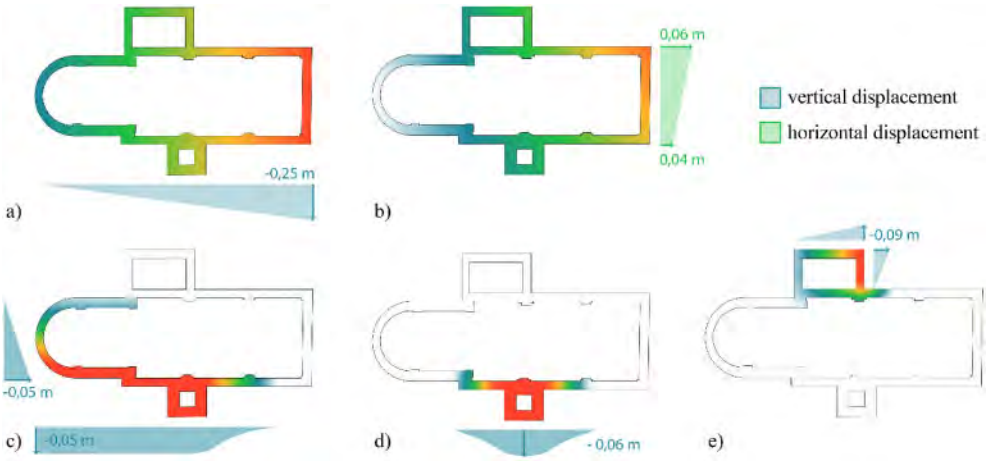

Figure 7. Displacement fields: a) vertical component of global displacement, b) horizontal component of the global displacement, c) left portion of the church, d) belltower, e) right chapel.

The value of the vertical component of the global displacement was estimated based on the displacements measured in the nave, while the value of the horizontal component was evaluated by considering the thickness of the cracks of the floor of the nave as well as the distortion of the façade in the horizontal plane. For further details on the definition of the displacement fields, the reader is referred to Cabella and Sacco (2021).

4 STRUCTURAL ANALYSIS

The structural analysis aims at identifying the causes of the damage and deformations observed in San Carlo Borromeo church. For this purpose, a FE model of the entire building was prepared, and nonlinear static analyses were performed considering different scenario of foundation displacements.

4.1 *Numerical model*

4.1.1 *Geometry*

A tridimensional model of the entire church was created in Rhinoceros (Robert McNeel & Associates 2018) and Ansys SpaceClaim (Ansys inc. 2020b) starting from the point cloud (Figure 8(a)) obtained by the laser scanner survey. To transform the surveyed deformed configuration of the building in a reference undeformed configuration (Figure 8(b)), several assumptions were made. In particular, all the deformations that were not consistent neither with the historical building techniques nor with the construction history were removed (Figure 8(b)): (i) the walls were assumed to be straight, vertical, and parallel in pairs; (2) the vaults and arches were modelled with their undeformed profiles defined in Cabella and Sacco (2021) and (3) the tie-rods were assumed to be perfectly horizontal.

The clergy house and the sacristy were not included in the numerical modelling, as they were not accessed during the inspections, and they do not have structural continuity with the walls of the church. The left chapel was not modelled because it was created within the space of the sacristy by adding thin brick walls.

Starting from the geometrical model, a FE model of the church was created in Ansys Mechanical (Ansys inc. 2020a) (Figure 8(c)). A macro-modeling approach was adopted to represent masonry, which was considered as a homogeneous material. The masonry walls and vaults as well as the tie

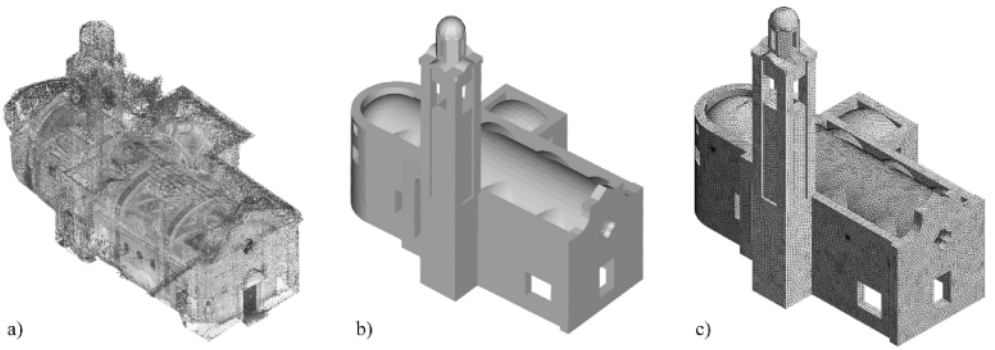

Figure 8. a) Point cloud model, b) geometrical model, c) mesh.

roads were modelled using ten nodes tetrahedrons solid elements (TET10). Mesh sizes of 20 cm and 1 cm were adopted for the solid and beam elements, respectively. The mesh for the solid elements was also refined in correspondence of the contact surface with the tie-roads. In total, the numerical model consists of about 1.1 million nodes and 700 thousand elements. All the degrees of freedom of the nodes at the base of the church were restrained to provide boundary conditions.

4.1.2 *Constitutive model and material properties*

The nonlinear behaviour of masonry was simulated using a perfect elasto-plastic model with a Drucker-Prager yield criterion. Due to the lack of experimental data, the mechanical properties were estimated based on the reference values suggested in the explanatory notes of the Italian building code (Circolare 21 gennaio 2019, n.7, table C.8.5.1 pg. 257) as well as on empirical relations. The Young's modulus E and uniaxial compressive strength f_{uc} were taken equal to the minimum values provided by the Italian Circolare for ashlar stone masonry. The volumetric density ρ suggested for this type of masonry was also adopted. The use of the Drucker-Prager criterion as implemented in Ansys also required to define a biaxial compressive strength f_{bc} and a uniaxial tensile strength f_{ut}, which were evaluated based on the following relations (Jiang & Zhao 2015):

$$f_{bc} = 1,5 f_{uc} \tag{1}$$

$$f_{ut} = 1,4(f_{uc}/10)^{2/3} \tag{2}$$

The physical and mechanical properties of the stone masonry of walls and vaults are reported in Table 1.

Table 1. Physical and mechanical parameters adopted for stone masonry.

Young's modulus	E	1,5 GPa
Poisson's ratio	ν	0,18
Volumetric density	ρ	2050 kg/m^3
Uniaxial compressive strength	f_{uc}	2,6 MPa
Biaxial compressive strength	f_{bc}	3,0 MPa
Uniaxial tensile strength	f_{ut}	0.46 MPa

A bilinear isotropic hardening model was used to describe mechanical behaviour of the steel tie-rods, whose mechanical properties are indicated in Table 2.

4.1.3 *Loads and foundation displacements*

The roof was not included in the FE model due to the lack of a proper survey. Based on the information provided in Varese (2015), the loads transmitted by the roof were calculated and

Table 2. Physical and mechanical parameters adopted for the steel of the tie-rods.

Young's modulus	E	210 GPa
Poisson's ratio	ν	0,3
Volumetric density	ρ	7850 kg/m^3
Yield stress	σ_0	250 MPa
Tangent modulus	E_t	1,45 GPa

applied as distributed loads at the top the walls and as point loads at the extrados of the vaults. No pretension was considered for the tie roads.

Different combinations of vertical and horizontal displacements were applied at the base of the church to simulate the foundation settlements as well as the displacements produced by the landslide. In particular, three displacements scenarios were defined taking into consideration the displacement fields identified in Section 3.2 as well as the history and transformations of the building (Cabella & Sacco 2021). In each scenario, the dead loads were applied first; then, different combinations of global and local foundation displacements were imposed. For the sake of conciseness, since the results of the numerical simulations carried out with the different scenarios are very similar, only one displacement scenario is described in this paper. In this case, the landslide was assumed to be acting for the entire lifespan of the church. The global displacement produced by this phenomenon was divided in three steps. The displacements of the belltower and that of the left portion of the church were imposed in the second step, while the displacement of the right chapel was applied in the third step.

4.2 *Results of nonlinear static analyses*

In this section, the results of the FE simulations are presented in terms of maximum principal plastic strain, which provides an indication of the crack formation.

Figure 9 shows the results obtained in correspondence of each step of the displacement scenario. As shown in Figure 9(a), the application of the dead loads did not cause any plastic deformation, which, in contrast, appeared as soon as foundation displacements were imposed (Figure 9(b)). The application of the global landslide displacement caused a concentration of plastic deformation at mid-span of the arches that separate the nave from the lateral chapels, probably due to the smaller stiffness of this portion of the church (Figure 9(b)). During the survey, cracks were observed at the same locations, and the phenomenon presented a moderate intensity both in the numerical model and in the building.

As shown in Figures 9(c) and 10, the application of the foundation displacements of the belltower and the left part of the building produced the most significant damage and was responsible for most

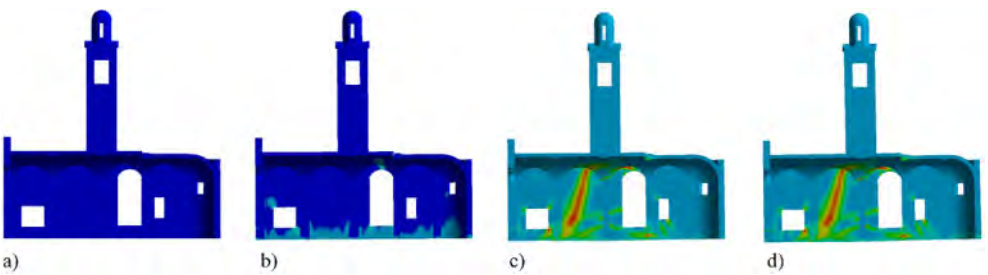

Figure 9. Maximum principal plastic strain produced by: a) dead loads, b) 1/3 global displacements, c) 1/3 global displacement plus displacements of the left portion of the church and belltower d) 1/3 global displacement plus displacement of the right chapel.

of the cracks observed in the vaults and in the walls of the left side of the church. In particular, the occurrence of the large crack detected in the wall of the second bay during on-site inspections was accurately simulated. This can be seen from Figure 10(b), in which the crack pattern surveyed in-situ is overlapped to the results of the numerical simulations. As regards the vaults of the nave (Figure 10(a)), the formation of the cracks due to the application of the foundation displacements of the belltower and the left part of the building proves that these cracks are not produced by the landslide and thus explain why they are oriented parallel to the landslide direction.

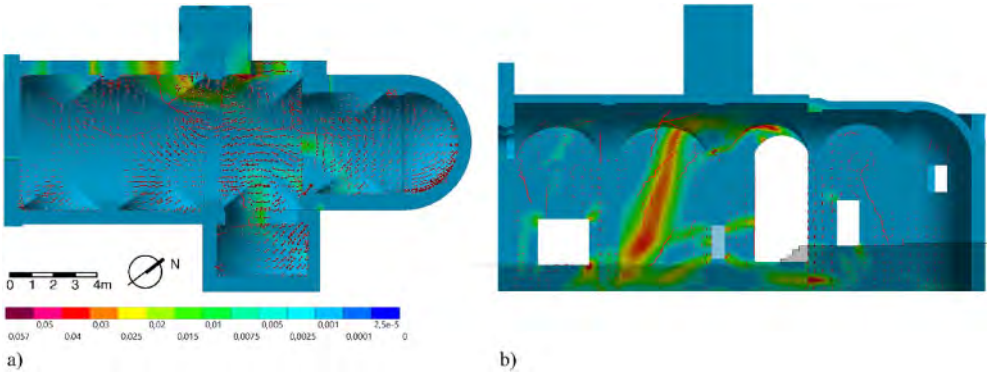

Figure 10. Comparison between FE results (in terms of maximum principal stress σ_1 vectors and maximum principal strain $\varepsilon_{1,pl}$ contours) and crack pattern surveyed on site: a) vaults, b) north-western wall (section AA').

Finally, the settlement of the right chapel caused the crack pattern in its vault as well as the cracks in the right wall of the second bay and the large crack in the presbytery.

In conclusion, a good agreement was obtained between the damage and deformations predicted by the numerical simulations and those observed on-site, even though the actual deformation of the church was underestimated. The complex rotation of the belltower, which leans both downstream and towards the left side of the church, and the deformation of the arch nearby were also accurately simulated (see Figure 11), proving the reliability of the numerical model.

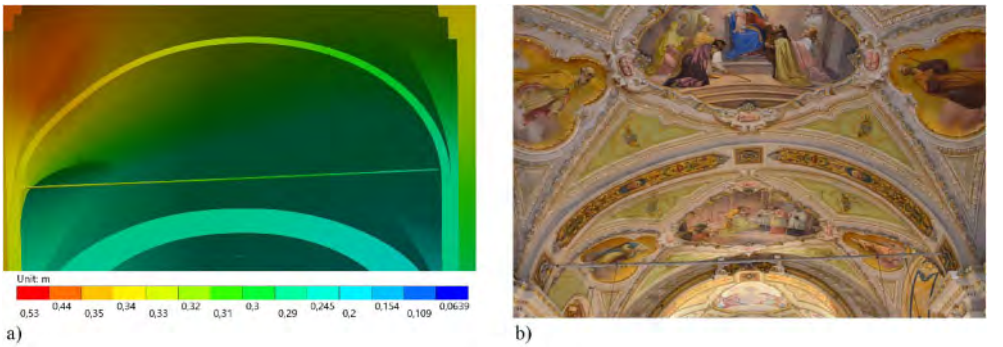

Figure 11. Deformation of the second arch from the façade. a) FE results (total displacement), b) real damage.

5 CONCLUSIONS

In this paper, the structural behavior of San Carlo Borromeo church was investigated under the application of different displacements fields, which simulate the foundation displacements produced by the landslide acting in the area as well as local settlements. Such displacement fields

were estimated by means of an in-depth analysis of the deformations and foundation settlements experienced by the church, which were assessed thanks to a laser scanner survey. Using the data collected from historical and geometrical surveys, a three-dimensional FE model of the church was created. The building was modelled in its hypothetical initial undeformed geometry and nonlinear static analyses were performed to evaluate if the assessed displacement fields could be responsible for the current damage state.

The results of the numerical simulations showed that only part of the current damage was produced by the landslide acting in the area. Indeed, some crack patterns and deformations were found to be the consequence of local foundation settlements. More in specific, the settlements of the left portion of the church and the belltower proved to have produced both the longitudinal cracks in the vault of the nave and the deformation of the arch between the second and third bays. Part of these local settlements are likely to be the result of a soil consolidation occurred due to the weight of the belltower and well explain the diagonal cracks in the walls on the left and right sides of this structure. Furthermore, even if the damage in the right chapel were not fully predicted by the FE simulations, the settlement of this part of the church proved to be the cause of the cracks in the presbytery and apse and could also be responsible for part of the cracks observed in the right wall of the nave.

In conclusion, the numerical model proved to be able to simulate the current damage state of the church and, furthermore, helped in the identification of the causes of crack patterns and deformations. Future works will include the use of a constitutive model that takes into account the evolution of the damage and the degradation of the mechanical properties of masonry under plastic deformations.

REFERENCES

Ansys inc. 2020a. Mechanical User's Guide, Release 2020 R2.

Ansys inc. 2020b. Discovery SpaceClaim, Release 2020 R2.

Arpal 2020. *Banca dati ReMoVer – Commento generale all'attività di monitoraggio.* Accessed September 20, 2021. https://srvcarto.regione.liguria.it/dtuff/img/Remover/Commenti_Siti/GE026_commento_tot.pdf

Autorità di bacino distrettuale del fiume Po, 2017. *Atlante dei Rischi Idraulici e Idrogeologici* (Atlas of Hydraulic and Hydrogeological Risks). Accessed October 25, 2018. http://www.pai.adbpo.it/.

Cabella, C. & Sacco, G.L.S. 2021. Studio degli effetti di una frana attiva su un edificio voltato: la chiesa di San Carlo Borromeo in Cassingheno (Genova). Master thesis, University of Genoa.

Cambiaggi L. 2020. Damage assessment of churches exposed to slope displacements in sliding areas. PhD diss., University of Genoa.

Cambiaggi, L., Ferrero, C., Riccardo, B., Vecchiattini, R. & Calderini, C. 2021. Effect of Slow-Moving Landslides on Churches in the Liguria Region: a Geotechnical Approach. In P. Roca, L. Pelà and C. Molins (eds.) SAHC 2021: *12th International Conference on Structural Analysis of Historical Constructions*; Online event, 29 September–1 October 2021. Cornellà de Llobregat: Artes Gráficas Torres S.L.

Cazzulo, P., Barbieri, R. & Tirini, F. 1998. *Carpeneto – Una piccola, grande Comunità*.

Federici, P. R., M. Capitani, A. Chelli, N. Del Seppia, and A. Serani. 2004. *Atlante dei Centri Abitati Instabili della Liguria. II. Provincia di Genova* (Atlas of the unstable inhabited centers of Liguria. II. Genova province). Regione Liguria, Genova, Italy.

Ferrero, C., Cambiaggi, L., Vecchiattini, R. & Calderini, C. 2021a. Damage Assessment of Historic Masonry Churches Exposed to Slow-moving Landslides. International Journal of Architectural Heritage.

Ferrero C., L. Cambiaggi, A. Fenialdi, P. Roca, R. Vecchiattini, and C. Calderini. 2021b. Slow-moving landslide damage assessment of historic masonry churches: some case-studies in Italy. In P. Roca, L. Pelà and C. Molins (eds.) *SAHC 2021: 12th International Conference on Structural Analysis of Historical Constructions*; Online event, 29 September–1 October 2021. Cornellà de Llobregat: Artes Gráficas Torres S.L.

Jiang, H. & Zhao, J. 2015. Calibration of the continuous surface cap model for concrete. Finite Elements in Analysis and Design. 97, 1–19.

Memme, C. 2019. Studio di un borgo ligure in zona di frana attiva: il caso del paese e della chiesa di Cassingheno (Genova). Master thesis, Università degli Studi Genova.

Ministero delle infrastrutture e dei trasporti. Circolare 21 gennaio 2019, n.7. *Istruzioni per l'applicazione dell' Aggiornamento delle "Norme tecniche per le costruzioni" di cui al decreto ministeriale 17 gennaio 2018.*

Pesci, A., Casula, G & Boschi, E. 2011. Laser Scanning the Garisenda and Asinelli Towers in Bologna (Italy): Detailed Deformation Patterns of Two Ancient Leaning Buildings. Journal of Cultural Heritage 12(2): 117–27.

Sanguigliani, A.C. 1891. *L'agro Vogherese. Memorie sparse di storia patria.* Casorate Primo: Rossi. Vol. 3 pag. 348.

Regione Liguria, Regione Piemonte, Regione Valle d'Aosta, Arpal Piemonte, Università di Genova, Università di Pavia, Fondazione Montagna Sicura. 2012. *Progetto strategico Interreg IIIa Alcotra RiskNat*. pp. 110–111.

Robert McNeel & Associates. 2018. "Rhino 6 User manual".

Varese, G.B. 2015. *Progetto di rifacimento del manto di copertura*.

Geotechnical Engineering for the Preservation of Monuments and Historic Sites III – Lancellotta, Viggiani, Flora, de Silva & Mele (Eds)

Assessing the causes of damages to the Osservanza Church in Bologna (Italy)

G. Marchi, C. Cremonini & A. Mastrangelo
ENSER srl, Bologna, Italy

M. Marchi & I. Bertolini
Alma Mater Studiorum, University of Bologna, Bologna, Italy

R. Lancellotta
Politecnico di Torino, Italy

ABSTRACT: The Osservanza church in Bologna (Italy), whose construction is dated back 1406, has under-gone several restorations in the last 40 years, as a consequence of a severe progression of the crack pattern affecting its walls and, to a lesser extent, the structure of the adjacent convent. The paper describes the results of geotechnical investigations, carried out on the soil-foundation system of the church, and those of monitoring systems, installed to control the crack pattern evolution of the walls of the church and the creep movements of the surrounding slopes. The preliminary study of the historical events that affected the structure of the church, from its construction to its present configuration, also provided significant pieces of information to define the programme of the geotechnical investigations. The soil profile, deduced from in situ tests, consists of a top stratum of anthropic fill, followed by a succession of high plasticity clayey silts and silty clays, from stiff to very stiff. The oedometer tests carried out on the collected undisturbed soil samples highlighted the high swelling potential of the investigated soil. Such evidences explained the pronounced seasonal variation of the amplitude of the crack systems affecting the masonry walls of the church, as shown by the monitoring system. In addition, the crack pattern was proved to be locally ascribed to differential settlements caused by differences on founding levels of the columns of the church, as well as to partial underpinning work.

1 INTRODUCTION

The Church of San Paolo in Monte, known as "Osservanza", and its convent (Figure 1) have hosted the activities of the Friars minor in Bologna for more than 600 years. The religious complex is located in the south west area of the Bologna city center, on the top of the surrounding hills, about 227 m a.s.l. From the 1980's onwards, the church has been restored several times. In spring 2010, the crack progression caused the collapse of part of a capital of the fourth column of the right aisle (Figure 2). Immediately after, the church was closed to the public, for security reasons, and since then the building is still closed. The paper describes the results of a geotechnical investigation campaign and of a monitoring system, aimed at identifying the causes of damages. A preliminary analysis of historic events, which affected the church from the origin of its construction to its present configuration, was initially carried out, providing essential hints for devising an effective investigation programme.

DOI 10.1201/9781003308867-45

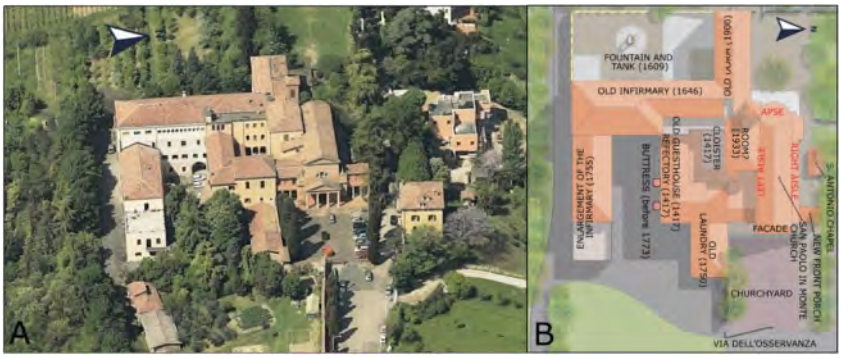

Figure 1. (A) Aerial view of the Osservanza church and of the adjacent Convent in their present configuration. (B) Plan view with indication of the main parts of the religious complex.

2 HISTORIC BACKGOUND AND FACTUAL DATA

The Church and the adjacent convent of San Paolo in Monte were built between 1406 and 1417 by the Friars Minor. During its lifespan the religious complex has undergone transformations and renovations (Figure 3). As a consequence, the current structures have been deeply modified with respect to their original configuration.

In 1811, the French troops of Napoleon confiscated the whole complex. Shortly after, the church was unfortunately demolished and its stones were used to construct the nearby Villa Aldini. In 1824, the remains of complex were purchased by lady Rosa Facci Baccilieri and, thanks to her generosity, the complex was returned to the Friars Minor. The construction of the new church started in 1824, completely rebuilt in neoclassical style by the Architect Vincenzo Vannini, with its consecration in 1828. However, the new church suffered many distresses since early times, for reasons that will be explained in the sequel, but a strong demand for a systematic historical reconstruction of main events was only promoted in recent years. It was in spring 2010, soon after the collapse of the capital of the fourth column of the right aisle (Figure 2 A, B and C), that a preliminary visual

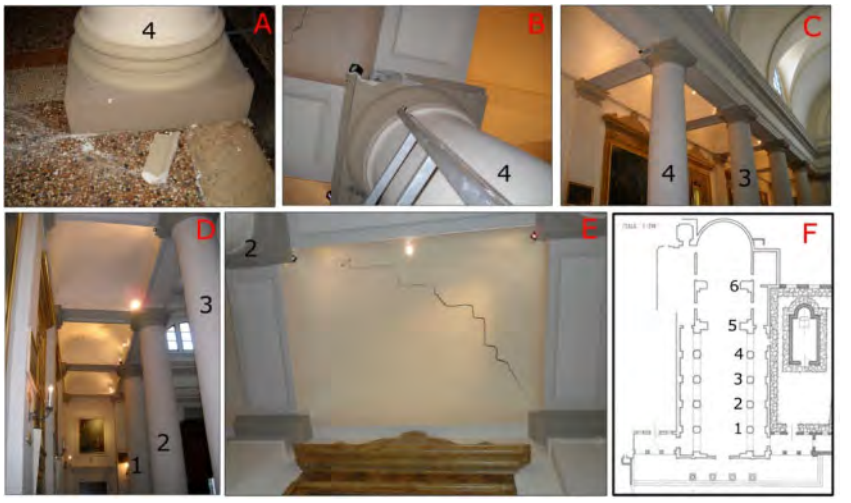

Figure 2. (A), (B) and (C) Details of the collapsed capital in the interior of the church. Numbers of columns refers to the scheme in frame (F). (D) and (E) Crack patterns on the vaults of the right aisle. (F) Plan of the church with numeration of the columns of the right aisle.

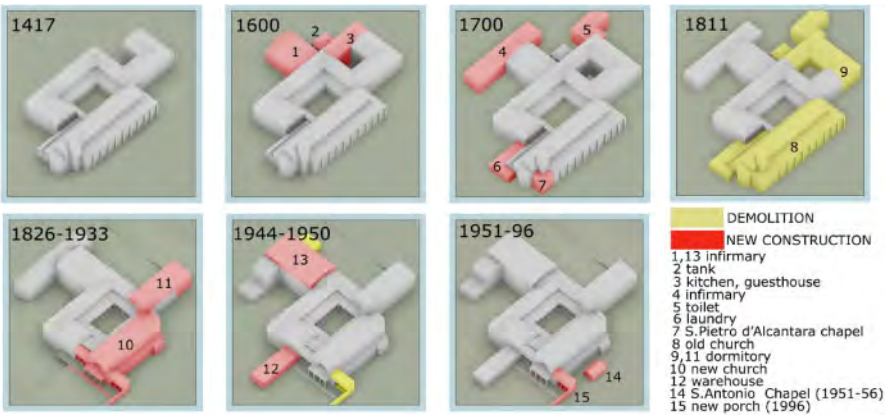

Figure 3. Transformations of the religious complex from its construction to its current configuration.

survey of the state of damage of the structural elements of the church, of the convent and of the houses and walls in the surroundings, was carried out.

Width variation of about 60 cracks was suddenly monitored by picking up the distance between two screws, fixed on each side of the crack. Measurements were carried out once per month. A mechanical caliper was used to this scope, as shown in the frames (A) and (B) of Figure 4. Records, covering a time-lapse of about one year and a half (September 2010–April 2012), have been analyzed in conjunction with temperature and pluviometric data. Figure 4C shows the location of the monitoring points on the façade, and Figure 5 reports data recorded for 15 of the 60 installed benchmarks. These diagrams clearly showed a direct correlation between seasonal variation of water content in the soil and crack movements, with an average excursion of about 0.5 ÷ 1 mm. Although this scenario did not appear to present at that moment particular risks, the instabilities were slowly and progressively worsening, with local residual deformations even higher than 0.5 mm (see benchmarks 6, 14 and 36 in Figure 5). In addition, generalized signs of damages were also detected all over the investigated area. In particular, major differential settlements affected the north side of the church (i.e. vaults and right aisle columns in the interior of the church, perimetric walls) and the façade. Such an evidence suggested the existence of possible local inhomogeneities at the founding level among the different structural components of the religious complex. Therefore, a deep insight into the written record of historic events describing them in the order they happened, preserved in the archives of the "Osservanza" complex, reveled aspects of paramount importance.

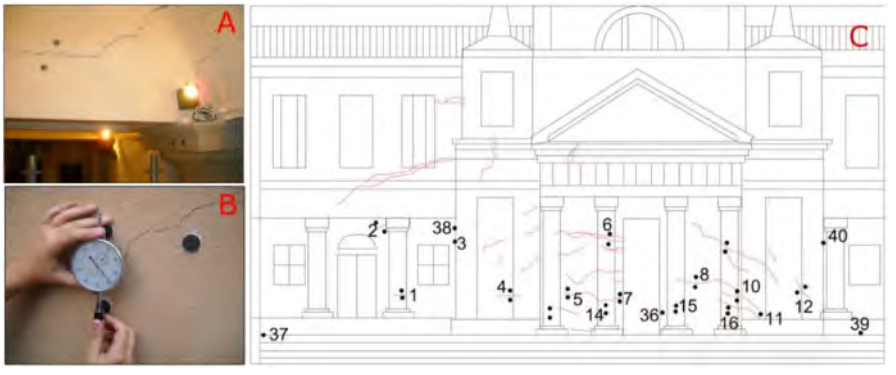

Figure 4. (A) Picture of the screws, fixed on each side of the cracks, and (B) of the mechanical caliper used to measure their distance. (C) Location of the monitoring points on the façade.

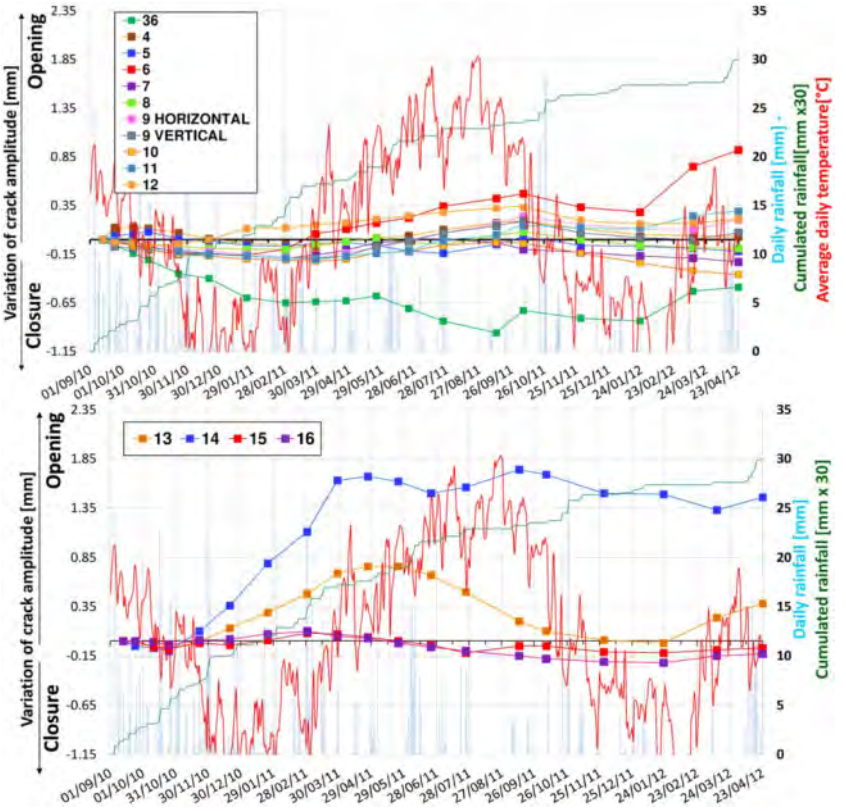

Figure 5. Monitoring of the crack pattern on the façade: the diagrams show data collected for 15 benchmarks installed on the façade (location of the benchmarks in Figure 4).

First, as shown in Figure 6, the comparison of the historical plan of the primitive church, dated 1773, and the plan of the existing church suggests that the primitive church was liturgically oriented, with the main front to the west. The church was a single bay church, with chapels on the north side and cross vaults with false ribs, as it appears on the pictures of the time, the simplicity of its interior reflecting the doctrine of Friars minor (Figure 7A). On the contrary, the orientation of the new church, rebuilt in neoclassical style, was completely reversed (frames 4 and 5 of Figure 3 and in frames A and B of Figure 7). Thereafter, the above referred chronicles report in details that in 1914–1915, the columns 5 and 6 (consider numbering the columns starting from the façade towards the apse, as shown in the map of Figure 2F) of the presbytery on the north side were underpinned (Figure 7C) to reach a deeper founding level, an intervention devised to mitigate the observed severe differential settlements. However, this intervention proved to be ineffective and in 1950–1951 the underpinning work restarted, once again for the same columns, the wall of the apse and the wall of the north side of the presbytery. In the same period, the porch on the right side of the façade was demolished (Frame 6 in Figure 3), as a consequence of the severe damage created once again by the differential settlements at founding level. From 1988 to the end of the last century, the right-side porch was rebuilt (element 15 in the last frame of Figure 3), together with a new chapel dedicated to Sant'Antonio (element 14 in the last frame of Figure 3). Further investigations in the local archives provided accounting records that report expenses for the execution of twelve "deep piles" (Biagi & Gandolfi 2009) installed to strengthen the foundations. Nevertheless, no information has been found in these documents about details of the intervention.

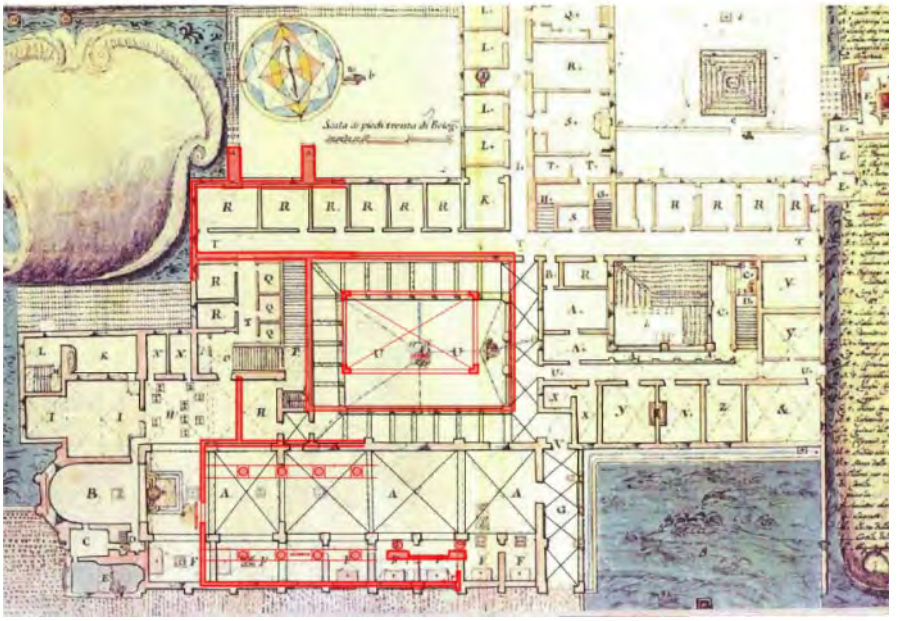

Figure 6. Comparison between an historical plan of the primitive church, dated 1773 (State Archive of Bologna, doc. 11/6073, n. 8), and the plan of the existing church (red lines superimposed to the historic plan), deduced from survey.

Figure 7. (A) The primitive church, showing the façade oriented toward the west, in a drawing of the 1793 by Giuseppe Fancelli. (B) Drawing of the new church of the 1828 (Osservanza Historical Archive). (C) Scheme of the underpinning work carried out on columns 5 and 6 of the right aisle (Osservanza Historical Archive, Section III, Vol. 1, doc. 15).

These events, related to differential settlements that the church suffered since its construction period, suggested that the foundations of the columns of the right aisle could not have been properly superimposed to those of the early church, as it can be inferred by a deeper scrutiny of Figure 6.

Note that, when superimposing the plan of the new church to that of the previous one, care was taken in using the buttresses, already built in 1773, as well as the south-west corner of the cloister, as a fixed in time benchmarks. Therefore, such a hypothesis was investigated in February 2012 by means of trial pits, whose location was carefully chosen with the aim of verifying the plan of the foundation systems of the ancient church and that of the new one. As shown by the map in Figure 8, trial pits S1, S2, S3, S4 were excavated in the interior of the church, while S5 and S6 outside, along the north wall. The results clarified many aspects, as highlighted here below:

(a) the founding depth is rather shallow, just being 1.50 m with respect to the church base floor (element 1 in Figure 8);

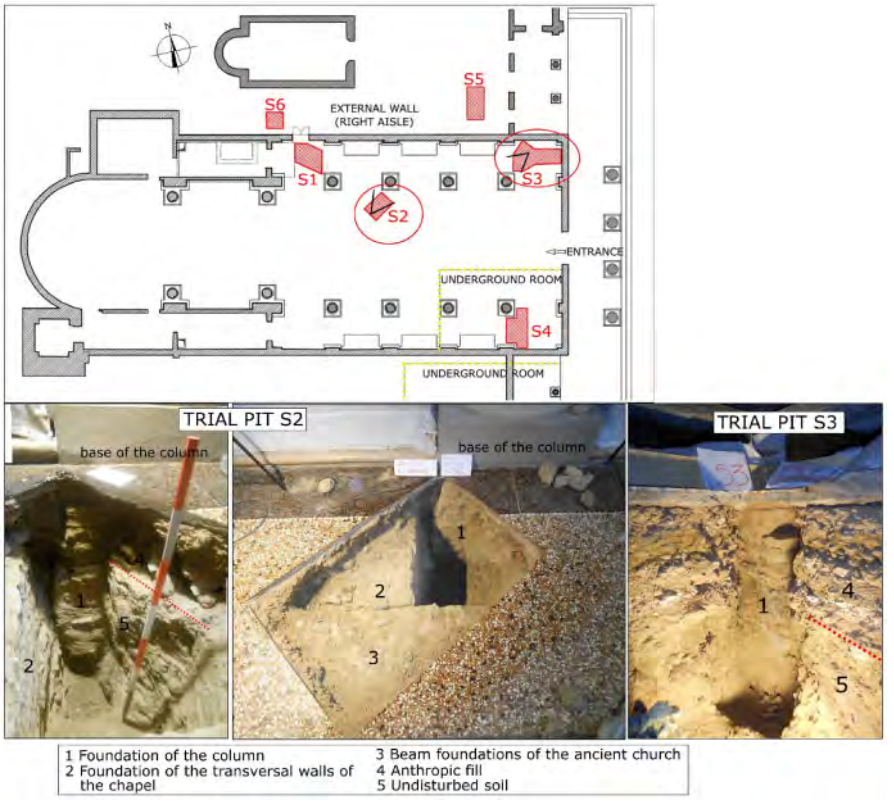

Figure 8. Map showing the locations of the six trial pits excavated on the foundations of the church and pictures showing the excavation of trial pit S2 and S3, which enabled to see the foundation of columns (element 1 in the legend) and their dislocation with respect to the foundation of the early church (elements 2 and 3).

(b) the texture of the foundations is such that it can be argued that they were realized by excavating a pit into the stiff clay, filled with stones and mortar and levelling the top with three rows of bricks (Figure 8);
(c) the foundations of the columns on the north side of the new church (element 1 in Figure 8) were not superimposed to the beam foundations of the ancient one (element 3 in Figure 8), neither on those of the transversal walls of the chapels (element 2 in Figure 8);
(d) on the contrary, the foundations of the primitive church were deeper, well preserved and more accurately constructed, as well as the foundation of the columns of the south side of the new church, that lie on deeper walls of the underground cellars and on ancient tombs.

As a general remark, there is ample evidence to explain the pronounced differential settlement of the different parts of the church, and in addition it can also be argued that cyclic movements of the shallower foundations could be linked to seasonal changes in soil mixture, as discussed in more detail in the sequel.

3 GEOLOGIC CONTEXT AND GEOTECHNICAL CHARACTERIZATION

3.1 *Geologic context*

The shallowest deposits of the investigated area belong to the “Argille Azzurre” formation (FAA – “Blue Clay” in Figure 9), a deposit originated in a marine environment which belongs to the

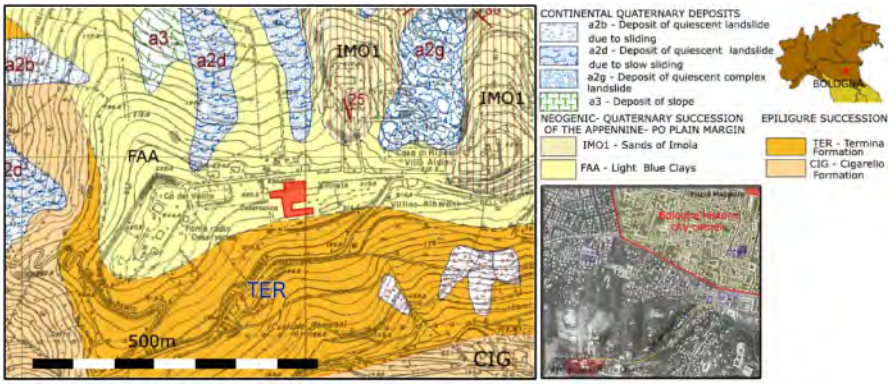

Figure 9. Geologic map and location of the investigated area (red rectangles).

Pliocene-lower Pleistocene outcrops (Amorosi et al. 1998; Campana et al. 1997). In geologic maps, "Blue Clay" formations are described as gray and blue gray clays, marly clays, clayey and silty marls found in medium and subordinately thin layers. Joints are not very visible due to bioturbation. From a stratigraphic point of view, this formation represents what remains of the ancient muddy seabed that covered the Po basin until about one million of years ago. At the margins of the investigated area, two different formations can be identified: the Termina Formation (TER in Figure 9), which belongs to the epiligurian succession, and the Imola sand (IMO1: "Yellow Sand").

In the quaternary continental deposits, on the north side of the Osservanza hill, the geologic map in Figure 9 identifies 3 major quiescent landslides. Such soil masses could be affected by creep phenomena (i.e. slow sliding processes), also involving deformations of the surrounding slopes, including that closer to the Osservanza church. The potential impact of these phenomena on the investigated structures have been evaluated by means of two inclinometers installed on the south and on the north wall of the religious complex. The recorded data, collected over a time lapse of 2 years, excluded the development of slope instabilities (i.e. slip surfaces) during the investigation period. Very slow deformations (about 10 mm/years) concentrated in the shallowest 5 m depth (i.e. the drying crust), have been detected in the northern area close to the church, while lesser movements have been recorded in the southern area of the convent. Although limited, the progression of creep movements of the north slope should be taken under control.

3.2 *Soil profile and mechanical properties*

Geotechnical investigations were carried out from September 2010 to April 2012 (Figure 10A). During investigations, water table was found to be lower than 10 m in depth. The investigation programme included 3 continuous coring boreholes and 8 CPT, whose depths varied between 11 and 21 m. During boring, 16 disturbed and 16 undisturbed soil samples were collected for subsequent laboratory tests. In particular, mechanical behavior was studied by means of oedometer tests to assess the swelling behavior of the investigated soil.

The stratigraphy was initially deduced from the observation of cores extracted from continuous coring boreholes (Figure 10B). It turned out to be substantially homogeneous, in terms of grain size, except for a few meters of anthropic fill in proximity of the ground surface.

The subsoil consists of an alternation of silts, silty-clays and clayey-silts ("Argille Azzurre"), down to the investigated depth (about 20 m). Different texture, colors (variable between gray and brown) and deep cracks (in the shallowest part of the soil mass) characterize the investigated deposits. Visual inspection of cores was integrated with a geotechnical interpretation of CPT records (Tonni et al. 2019). Figure 11 shows the results of two CPT tests in terms of cone resistance q_c and sleeve friction f_s, for CPT 1, performed in close proximity to the church, and CPT 7, performed

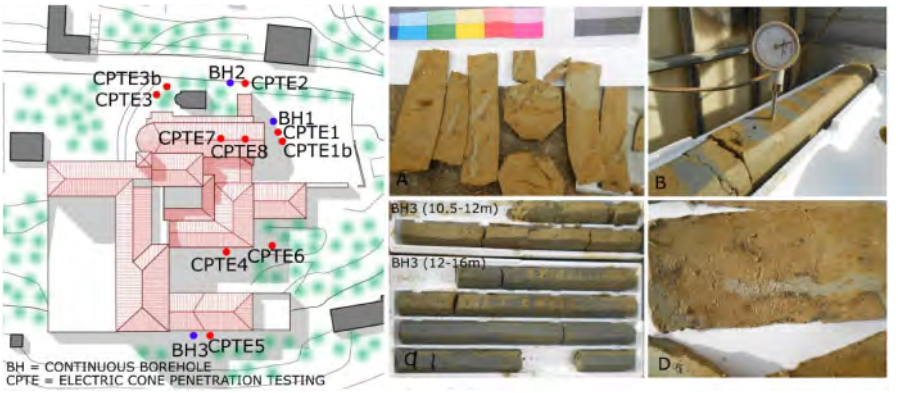

Figure 10. (A) Location of the geotechnical investigations. (B) Samples extracted from boreholes.

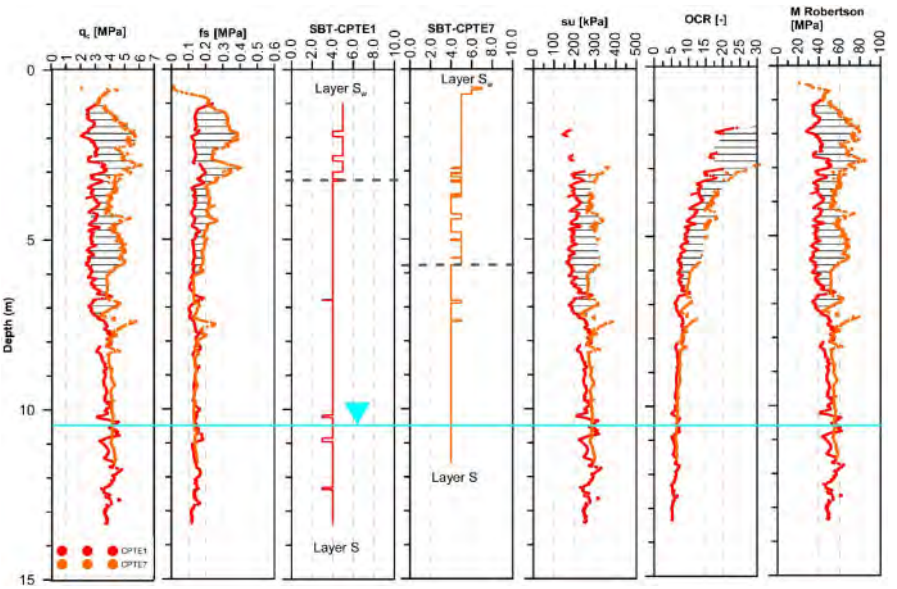

Figure 11. Cone tip resistance q_c, sleeve friction f_s vs depth in CPT1 and 7. In the other columns some significant soil parameters deduced from CPT logs: SBT (Robertson 2009), s_u (Lunne et al. 1997 – with N_{kt}=14), OCR (Kulhawy & Mayne 1990) and constrained modulus M (Robertson 2009).

inside the church. The substratum shows a pronounced variable answer to the penetration of the cone among the different penetrometer tests, between the ground level and a depth of about 7–8 m (Figures 11 and 12). Applying the Soil Behavior Type (SBT in Figure 11) classification system (Robertson, 2009), it is worth noting that the upper horizon, above the water table, plots in SBT zone 4 (silt mixtures) and 5 (sand mixtures), where also s_u and OCR are higher.

Whereas, almost homogeneous SBT 4 is found below 3.2 and 5.7 m, for CPT 1 and 7 respectively. It is well known that CPT profiles are significantly affected by soil suction, showing changes in the classification chart position due to soil partial saturation (Giacheti et al. 2019). Then, soils having CPT-based SBT in zone 5, could reflect a stiffer behavior generated by soil suction, more than coarser grain size. This observation is supported by the results of laboratory tests, which provide sand fractions lower than 5% (Table 1) for all the analysed samples. Then, the deposit should be

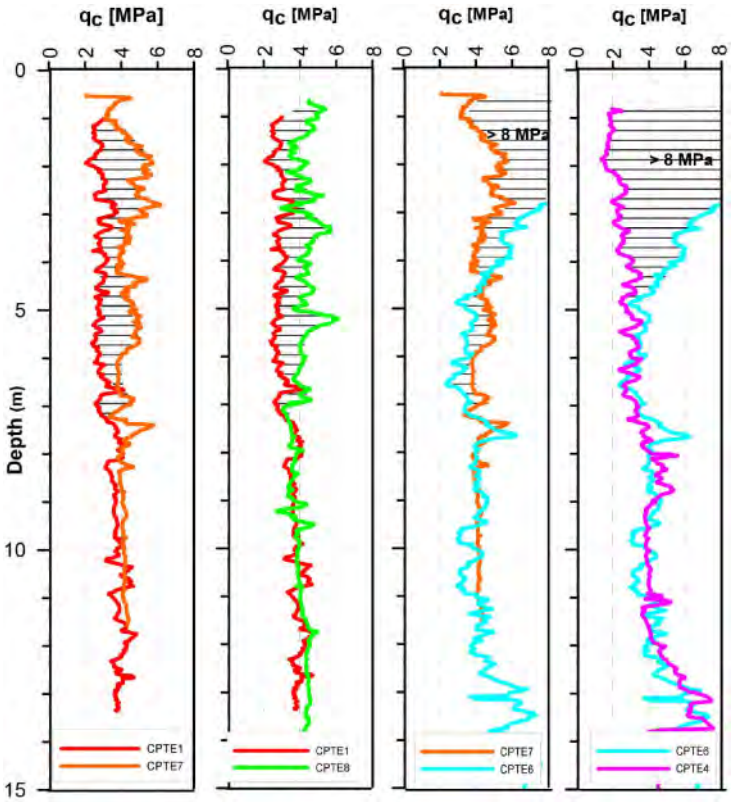

Figure 12. Comparison between cone tip resistance q_c profiles from penetrometer tests located in different positions of the site: inside the church (CPT7 and 8), in front of the church (CPT1) and on the south side of the church (CPT4 and 6). In particular CPT6 was placed in proximity of a tree.

Table 1. Mean value of some significant physical and mechanical soil parameters, as deduced from laboratory and CPT tests. Number of determinations in square brackets.

LAB	Gs	LL %	PI %	CI	$CaCO_3$ %	\$\$$_n$ kN/m^3	\$\$$_d$ kN/m^3	w_n %
S_W	2.685[4]	51.96[5]	24.83[5]	1.06[5]	31.66[3]	19.69[3]	15.65[3]	26.0[4]
S	2.752[1]	48.3[1]	23.8[1]	0.88[1]	28.4[1]	19.58[1]	19.58[1]	30.0[1]

LAB	Clay %	Silt %	Sand %	s_u kPa TxCU	φ' (°) DS	c' kPa DS	OCR	cr
S_w	47.63[3]	47.56[3]	4.8[3]	125[1]	27[1]	10[1]	22.7[3]	0.055[3]
S	481[1]	48.4[1]	3.5[1]		29[1]	40[1]	13.39[2]	0.02[2]

LAB	cc	cs	CPTE	s_u kPa	M MPa	OCR
S_w	0.106[3]	0.031[3]		230	56.77	16.2
S	0.124[2]	0.036[2]		271	53.2	7.2

considered as a single soil unit of clay and silt mixtures from stiff to very stiff, with a shallow drying crust, indicated as S_w (weathered clay) in Figure 11.

3.3 *Soil volume changes and related cyclic movements of the structure*

It is evident that buildings interact with the ground and their behavior and state of conservation is affected by any deformation of the soil and by any changes in its properties occurring naturally over time or caused by variations in environmental conditions (Calabresi 2013). In the case of movements that do not result from applied foundation loads, it is difficult to make any prediction with the same confidence usually ascribed to load-settlement calculations. This is the case when clay soils suffer volume changes as their water content changes and an important related effect are the movements induce on low-rise structures.

Although this kind of soil-structure interaction is well documented (in particular in the U.S.A. and UK), the prediction of structural response to shrinkage and swelling cycles is rather complex. Electrochemical forces attract water molecules to the clay particle surface and combine with capillary forces to set up suction in the soil water. The removal of this water increases this suction, so increasing effective stresses and strength and reducing the volume. Conversely, the supply of water results on reduced suction, lower effective stresses and strength and increase of volume.

For these reasons, as a measure of volume change potential the "cation exchange capacity" has been suggested, but a more practical approach relates this potential to the Atterberg Limits (Driscoll 1983, 1984). As an example, in the present case, the upper horizon of weathered brown clay is characterized by a clay fraction of 40% and a plasticity index of about 26 to 28% (Table 1), indicating a high expansion potential, as testified by the oedometer tests carried out to assess the swelling pressure and the swelling potential (see Figure 13).

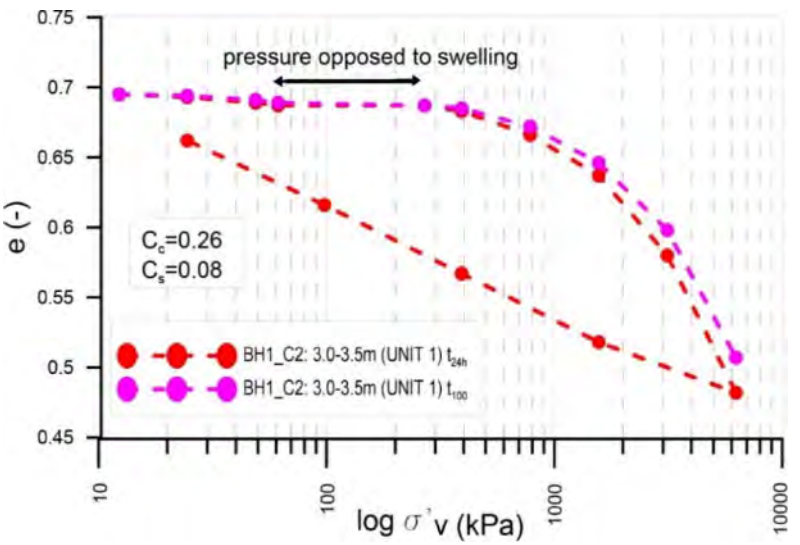

Figure 13. Results of an oedometer tests carried out on the investigated clay.

In addition to clay properties, as first proved by Ward (1947) in UK, the presence of trees represents a major uncertainty in predicting the movements of an existing building, and moisture content profile prove that desiccation can occur close to the tree.

For the case under examination, all these aspects have been assessed by comparing the results of the CPT7 and CPT8, performed in the interior of the church and the CPT1 performed outside (see Figure 12 and map of investigations in Figure 10A). The higher cone resistances of the CPT7 and CPT8 being the result of a desiccation process, as detected by the visual inspection during the trial pits.

Furthermore, the mentioned effects of the presence of trees is documented is Figure 12, where the cone resistance of the CPT4 is compared to the cone resistance of the CPT6, this latter performed in proximity of trees.

All these evidences prove that, in addition to the original deficiencies in devising the foundation system of the new church, the shallow footings suffer the effects of the shrinkage and swelling of the unsaturated cohesive upper horizon.

4 REMARKS ON THE CAUSES OF DAMAGES

It is self-evident how the preservation of built heritage deserves special attention, but at the same time, it must be stressed that there are important constraints when devising remedial measures and intervention techniques, due to the need of preserving the integrity of the monument. It has to be recalled that quite often the integrity requirement is only interpreted as the requirement of preserving the shape and the appearance of the monument. In reality it also implies historic integrity, by considering the changes the monument experienced with time, as well as material integrity, that means construction techniques, materials and structural scheme.

All these aspects represent the historic integrity of the built heritage and as such are a material witness of knowledge of the historical period in which the monuments were built. Therefore, preserving integrity requires a multidisciplinary approach as well as to develop the attitude not to rush in deciding the stabilizing measures until the behaviour of the monument is properly understood (see Calabresi 2013; Calabresi & D'Agostino 1997; Viggiani 2017).

As suggested by D'Agostino (2021), when considering the vulnerability of built heritage, we need to carefully distinguish between the "intrinsic vulnerability" and what can be called the "induced vulnerability". The first one is linked to the conception of the monument, the used materials, the construction techniques and all changes or modification that took place during the long span live.

In the case of the "Osservanza" church, there was a misconception at the origin when the foundations of the new church were realized. The primitive church was a single bay church, with chapels on the north side, and the foundation system was therefore composed by continuous beam supporting the perimetral walls. When the new church was rebuilt in 1828, its orientation was completely reversed and the foundations of the columns were superimposed to the earlier foundations only on the south side. This was the main cause of severe differential settlements, concentrated on the north side of the church (i.e. vaults and right aisle columns in the interior of the church, perimetral walls). In 1914–1915, the columns 5 and 6 (consider numbering the columns starting from the façade towards the apse) of the presbytery on the north side were underpinned to reach a deeper founding level, an intervention devised to mitigate the observed severe differential settlements. However, this intervention proved to be ineffective and in 1951–1951 the underpinning work restarted, once again for the same columns, the wall of the apse and the wall of the north side of the presbytery, but nothing was done for the remaining columns.

There is also an "induced vulnerability", linked to the reduction in time of the quality of the construction, due to decay of properties of the materials, the masonry apparatus, the mortar, or damage and distresses due to environmental changes. In particular, since buildings interact with the ground, their state of conservation is affected by any deformation of the soil and by any changes in its properties occurring naturally over time or caused by variations in environmental conditions. In the present case, the foundation clayey soils suffer volume changes as their water content changes and the related effects are the movements induced of the church, this being a low-rise structure.

The investigation proved that he upper horizon of weathered brown clay is characterized by a clay fraction of 40% and a plasticity index of about 26 to 28%, indicating a high expansion potential, so that, in addition to the original deficiencies in devising the foundation system of the new church, the shallow footings suffer the effects of the shrinkage and swelling of the unsaturated cohesive upper horizon.

All the above collected evidences will certainly be of value in devising proper remedial measures.

REFERENCES

Amorosi, A., Barbieri, M., Castorina, F., Colalongo, M., Colalongo, M.L., Pasini, G. & Vaiani, S.C., 1998. Sedimentology, micropalaeontology, and strontium-isotope dating of a lower–middle Pleistocene marine succession (Argille Azzurre) in the Romagna Apennines, northern Italy: *Bollettino della Società Geologica Italiana*, 117: 789–806.

Biagi M.D. & Gandolfi, G. 2009. *L'Osservanza di Bologna – Convento e Chiesa di San Paolo in Monte*. Edizioni Fondazione del Monte (in Italian).

Calabresi G. 2013. The role of Geotechnical Engineers in saving monuments and historic sites. *Kerisel Lecture, XVIII ICSMGE*, Paris: 71–83.

Calabresi, G. & D'Agostino, S. 1997. Monuments and historic sites: intervention techniques. *Proc. of Int. Symp. on Geotechnical Engineering for the preservation of Monuments and Historic Sites*, Viggiani C. Ed., Balkema: 409–425.

Campana, P., Marchi, G., & Merli, M. 1997. Clay creep effects on old masonry building. *Proc. of the Int. Symp. on Engineering Geology and the Environment,* Athens, 23–27 June 1997. Edited by G.C. Koukis, P.G. Marinos, G.C. Stourna, G.C. Tsiambaos. CRC Press: 3083–3088.

D'Agostino, S. 2021. *Conservation and Restoration of Built Heritage: A History of Conservation Culture and its More Recent Developments*. CRC Press, Taylor&Francis, 168 pp.

Driscoll, R.M.C. 1983. The influence of vegetation on the swelling and shrinking of clay soils in Britain. *Géotechnique*, 43, 2: 93–105.

Driscoll, R. 1984. The effect of clay volume changes on low-rise buildings. Ch. 10 of *Ground Movements and their Effects on Structures*, edited by P.B. Attewell and R.K. Taylor, Surrey University Press, 303–320.

Giacheti, H., Rodrigues, R., Bezerra, R. & Rocha, B. 2019. Seasonal influence on cone penetration test: An unsaturated soil site interpretation. *Journal of Rock Mechanics and Geotechnical Engineering*. 11(2): 361–368.

Kulhawy, F.H. & Mayne, P.W. 1990. *Manual on Estimating Soil Properties for Foundation Design*. Report EPRI EL-6800, Electric Power Research Institute, Palo Alto, 1990, 306 pp.

Lunne, T., Robertson, P.K. & Powell, J.J.M. 1997. *Cone Penetration Testing in Geotechnical Practice*. Blackie Academic, EF Spon/Routledge Publishers, New York.

Robertson, P.K. 2009. Interpretation of cone penetration test-a unified approach. *Canadian Geotechnical Journal*, 46, 11: 1337–1355.

Tonni, L., García Martínez, M.F. & Rocchi, I. 2019. Recent developments in equipment and interpretation of cone penetration test for soil characterization. *Rivista Italiana di Geotecnica* 53(1): 71–99.

Viggiani, C. 2017. Geotechnics and Heritage. *2nd Kerisel Lecture, Proc. ICSMGE*, Seoul, 119–140.

Ward, W.H. 1947. The effect of fast growing trees and shrubs on shallow foundations. *J. Land Archt*, 11: 7–16.

Geotechnical Engineering for the Preservation of Monuments and Historic Sites III – Lancellotta, Viggiani, Flora, de Silva & Mele (Eds)

A geotechnical insight into the soil-foundation system of the Two Towers of Bologna, Italy

M. Marchi, I. Bertolini & G. Gottardi
Alma Mater Studiorum, University of Bologna, Bologna, Italy

ABSTRACT: Garisenda and Asinelli, also known as the Two Towers, are the best preserved medieval towers in the city of Bologna (northern Italy). They are worldwide famous symbols of the past power and wealth of the city which in the 12th century counted more than 75 masonry towers and tower-houses. In order to preserve these invaluable monuments, a deep understanding of their original structural configuration, foundation and subsoil included, must be carried out prior to any possible strengthening intervention design. Indeed, the foundations of historic towers and the surrounding soil often hide major hazards for the preservation of these monuments and a deep knowledge of their interaction is imperative. The paper outlines the investigation steps applied to the soil-foundation system of the Two Towers of Bologna: from the hydrogeological context of the area to the analysis of the main historical events that changed their structural configurations. Furthermore, the analysis and the interpretation of the foundation soil data, obtained from relevant in situ and laboratory tests, showed the presence of a 100 m deep succession of alluvial silty clays and clayey silts, relatively homogeneous in regards of the particle size distribution, but with a considerable scatter of their mechanical properties. Such variability has been interpreted through a sedimentological study of the extracted cores that provided the identification of local desiccated horizons and microstructured soils by carbonation (together constituting a paleosol). The resulting geological-stratigraphic profile represents a useful tool for the definition of a reliable and more defined geotechnical model. This study could therefore shed a light on the possible reasons of the substantially different structural configuration shown with time by the Two Towers of Bologna, despite their numerous similarities.

1 INTRODUCTION

It is rather common whilst travelling or simply walking around a town, especially in Italy, to notice ancient towers whose inclination not infrequently appears rather dangerous. In fact, medieval and bell towers are a fundamental feature of the historic, cultural and artistic Italian heritage. The preservation of such valuable historic monuments depends essentially on local authorities' initiative, supported by the technicians appointed to plan proper investigation campaigns, install long term monitoring systems and eventually design suitable strengthening interventions.

The assessment of historic towers overall safety is an open challenge due to the number of uncertainties affecting not only the historic origin of such structures but also the geometry and the current state of the materials used. Structural and foundational problems have been traditionally investigated separately, but recent advancements in the relevant analyses (Gottardi et al. 2015; Lancellotta & Sabia 2015) have stressed out the importance of a deep knowledge of both structure elevation and foundation. In order to reduce such uncertainties, a comprehensive knowledge of all the structural elements (materials, geometry, traditional building techniques, etc…) is required.

Medieval towers are slender structures whose stability problems are typically due to the differential settlements of their foundation (resulting from soft and inhomogeneous soil layering, structural imperfections, etc…) and/or to weakened and deteriorated masonry walls. The role of geotechnical

DOI 10.1201/9781003308867-46

engineering in this framework is clearly of great relevance, not only for the definition of possible failure mechanisms of tower foundations, but also for the prediction of the progressive tilting rate of the structure (Lancellotta 2013; Marchi et al. 2013), which can produce ever-increasing compressive stresses in the masonry with possible consequent structural failure. Ancient towers, in the presence of weakened and disconnected masonry, can also suffer catastrophic failure even with very little tilting, as attested by the sudden collapse of several masonry towers in the past (e.g. San Marco Bell Tower in Venice in 1902, Civic Tower in Pavia in 1989).

In order to develop a reliable risk assessment of these structures, advanced forecasting models must be developed (e. g. Marchi et al. 2011; Pisanò et al. 2014; Viggiani 2019), which obviously require a deep knowledge of the soil-foundation system and the definition of a reliable geotechnical model. Only on the basis of such detailed studies and models, a soil improvement or a foundation strengthening intervention could be eventually designed, with the aim of reducing the tilting rate and thus improving the long-term stability of towers. In any case, any intervention must be designed preserving the historical and architectural features of the whole structure, not only in the elevation but also in the soil–foundation system, the latter to be clearly considered as an integral part of the monument (ISO 13822-2010).

2 THE CASE STUDY

This paper focuses on an emblematic case study, concerning the Two Towers in Bologna. As detailed in the paper, the Two Towers, named Garisenda and Asinelli, have a great number of similarities (materials, construction period and techniques, original height, location); nonetheless, they showed extremely different behaviours during the past centuries. The question about the reason why this could happen has often arisen within the scientific community as it can possibly be attributed to a series of factors (Bertolini et al in press; Dallavalle et al. 2021). Herein, different aspects will be dealt with, in order to stress the importance of a multidisciplinary approach when dealing with historical monuments. Information on foundation, structure, construction history, local geology and hydrogeological setting are all essential features of a comprehensive investigation plan, in order to achieve a deep insight into the related preservation issues. In particular, the development of an initially simplified geotechnical model of the soil-foundation system and, then, of a more refined version will be presented, highlighting the difficulties encountered with a subsoil apparently homogeneous but whose mechanical behaviour was deeply affected by a peculiar geological history and complex post depositional processes that have produced a relevant spatial dispersion of the main geotechnical parameters.

2.1 *Historical background*

In Middle Ages, Bologna was a rich and vibrant city. Noble and merchant families used to display their power and wealth erecting tall masonry towers. Some historians claim that up to 100 towers stood in these days in the old city centre (Bergonzoni 1991), others suggest even 180 (Gozzadini 1875), but so far the existence in the past of only, still extraordinary, 75 towers has been proven. Nowadays, among the 24 survived towers, Garisenda and Asinelli are undoubtedly the best preserved and representative of the medieval architecture. They stand close to each other, in the very heart of the city centre. At present, Garisenda is 48.16 m tall from the ground level and 7.4 m wide at the base, while Asinelli is 97.20 m from the ground level and 8.7 m wide at the base (14.5 m considering the masonry porch at the base). Their configuration has changed during past centuries leading to the current one, which is quite different from the initial. Figure 1 shows a time line of the main events that modified somehow their architectural configurations. Termo-luminescence tests on masonry bricks suggested that Garisenda tower was the former to be built around 1100 (Giordano 2000); its original height was 60 m. Historians report that Garisenda showed an immediate settlement soon after its construction (Roversi 1989), even if such circumstance has never been proved. What we do know is that contemporary Middle Ages citizens thought that the architects had intentionally designed Garisenda as an inclined tower (Gozzadini 1875).

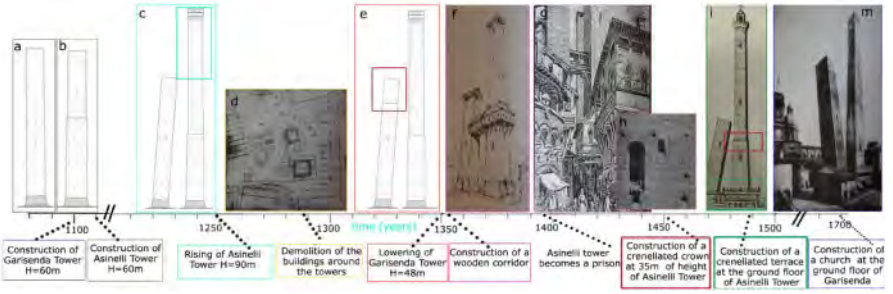

Figure 1. Timeline of the main events that influenced the Two Towers configuration during their lifespan.

Observing the straight but tilted axis of Garisenda tower and comparing it with others (as Asinelli and Pisa Tower) made of masonry blocks, a reasonable hypothesis on the tower speed construction can be advanced: Middle Age workers, in fact, must have built the tower as quick as possible so that appeared only afterwards, whilst typically a slower rate would have allowed consolidation settlements to take place during construction and workers have adjusted the direction of the tower axis with the aim of reducing as much as possible the eccentricity of its centre of gravity. After the construction of Garisenda, Asinelli Tower was built only 20.8 m meters away (distance between centres of gravity of foundations) with the same height (Figure 1b). A larger foundation area, an increased attention on the quality of the materials and on the construction technique, probably together with a slower construction rate have freed Asinelli from the problems manifested by its sister. The structure geometry of Asinelli is more similar to other two towers located nearby (Azzoguidi Tower and Incoronata Tower) (Bergonzoni 1991). For defensive reasons and communication needs with the closer villages in the countryside, between 12th and 13th century, the Bologna Municipality raised the Asinelli Tower to 97.2 m (Figure 1c). In 1286, in order to stress the majesty of the Two Towers, the numerous building around them were demolished and a large square opened (Figure 1d). In 1350, Garisenda top part was removed as its leaning was becoming a major concern for citizens and local government: its height was reduced to the current 48 m. Many constructions were huddled to the towers over past centuries: in 1353, a wooden suspended corridor connecting the towers was built in order to patrol the square from the top, but it went destroyed by a fire in 1398 (Figure 1f,g,h); in 1450, a crenellated crown was built at a height of 35 m on Asinelli Tower (Figure 1i); in 1488, a crenellated terrace supported by an arcade was added at the base of Asinelli (Figure 1i) and during the 15th century a chapel was built at the foot of Garisenda Tower (Giordano 2000), removed in 1871 though (Figure 1m).

2.2 *Foundation of historic towers*

The features of most local historic foundations remained substantially unchanged until the beginning of the last century. Two types predominated: shallow foundations, both cast in place and made of stone blocks, and shallow wooden piled foundations. The numerous continuous coring boreholes carried out during the 1995 and 2016 investigation campaigns could not detect the presence of hammered piles driven below the foundation blocks of the Two Towers. However, while their presence for Garisenda was unlikely, their existence for Asinelli was somehow expected.

Foundations of historic towers locally consisted of a cast-in-situ block made of sand, gravel, bricks fragments and slaked limes, on which selenite blocks were positioned in order to create the hollow tower basement (Marchi et al. 2019), then filled with various material up to the floor level. Over the selenite basement, masonry was built made of two external walls and an inner filling of miscellaneous material and lime (conglomerate).

Figure 2 shows the construction time sequence of a 60 m tall tower built during Middle Age in Bologna, according to Bergonzoni (1989). Their construction took from a minimum of 3.5 years up to 10 years, while the average required time was around 5 years.

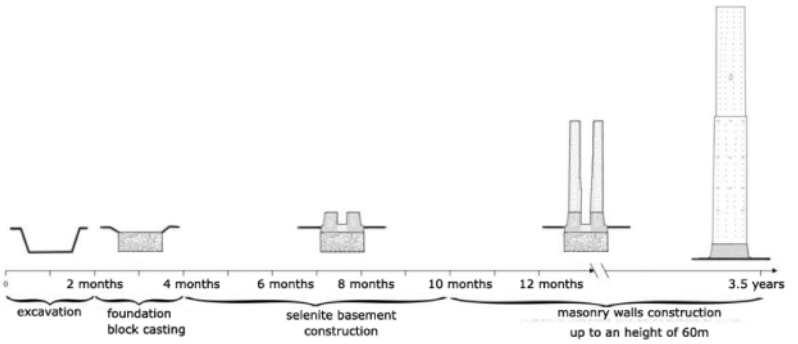

Figure 2. Construction time sequence of a medieval 60 m tall tower in Bologna.

3 GEOLOGICAL CONTEXT

Bologna is located in the Emilia-Romagna alluvial plain which is the south-eastern sector of the Po alluvial Plain, the largest alluvial plain in Western Europe, which is crossed by the river Po and its tributaries, bordered to the north and west by the Alps, to the south by the Northern Apennines and to the east by the Adriatic Sea. The shallowest quaternary deposits that support most historic foundations in Bologna are essentially characterized by fine alluvial material for tens of meters. The main feature of these deposits is the alternation of silty clays and clayey silts with different layer thickness; sand percentage is variable but consistently low while the aquifer gravelly bed is approximately over 120 m deep.

Bologna city centre belongs to the sub-unit AES8 (Ravenna Subsynthem), part of the Emilia-Romagna Synthem (AES) (see Figure 3), characterized by the depositional processes of two main rivers, Reno and Savena, and to a lesser extent of a system of minor rivers and creeks (Rio Meloncello, Ravone, Aposa and Fossa Cavallina). Despite their grain size distribution similarities, a peculiar sedimentological history has produced soil layers of distinct mechanical behaviour: a succession of desiccated crusts (horizons A_b), higly carbonatated horizons (B_k) and low/null paedogenized horizons (Bw/C, respectively) marks the quaternary fine-grained subsoil underneath the

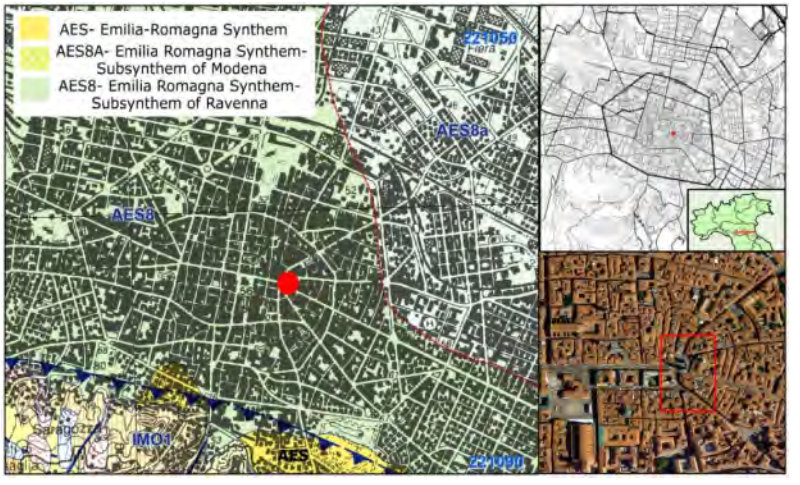

Figure 3. On the right, location of the Two Towers, Asinelli and Garisenda, right in the heart of the historic city. On the left, an excerpt of the geological map of the quaternary deposits underneath the city centre.

Two Towers (Bruno et al. 2013; 2015; 2020). The typical succession A_b, B_k and B_w together forms a *paleosol*. The physico-chemical processes undertaken by the paedogenized horizons have deeply forged their microstructure and these effects can be detected both from a geological perspective (colour and soil texture changes, presence of calcareous nodules, etc.) and from a geotechnical perspective (e.g. strength and stiffness increase in correspondence of microstructured horizons).

4 GEOTECHNICAL INVESTIGATIONS

The Two Towers have been interested by a series of geotechnical investigation campaigns. The first one was carried out in 1973–1975, with the execution of twelve continuous coring boreholes aimed at investigating the foundation soil of Asinelli, the collection of undisturbed sampled and the installation of three piezometers. The second campaign included the execution of 5 continuous coring boreholes and relevant laboratory tests on collected undisturbed samples, 4 piezocone tests (CPTU 12, 13, 14, 15) to a depth of 46 m and the installation of other three piezometers (at a depth of −30, −20 and −9.35 m from the ground level).

In 2000, 4 continuous coring boreholes (S1, S2, S3, S4) were performed in close proximity to the Garisenda foundation in order to investigate its geometry.

The last geotechnical campaign was finally carried out in 2016: 3 continuous coring boreholes (to a depth of −20 m, −45 m, −100 m), 2 inclined continuous coring boreholes to investigate the Asinelli foundation block, installation of 4 piezometers (at a depth of −10 m, −20 m, −30 m and −95.5 m) and 3 continuous coring boreholes with deep assestimeters installation (at a depth of −7 m, −10 m and −15 m) underneath the Garisenda foundation block. Moreover, such campaign included the execution of 6 CPTU to a depth of −30 m, 3 dilatometer tests (DMT1, DMT2, DMT3) and one downhole test, carried out in SDH1-2016 (at a depth of −45 m). In Figure 4 the location of the in situ tests performed in the four campaigns is summarized.

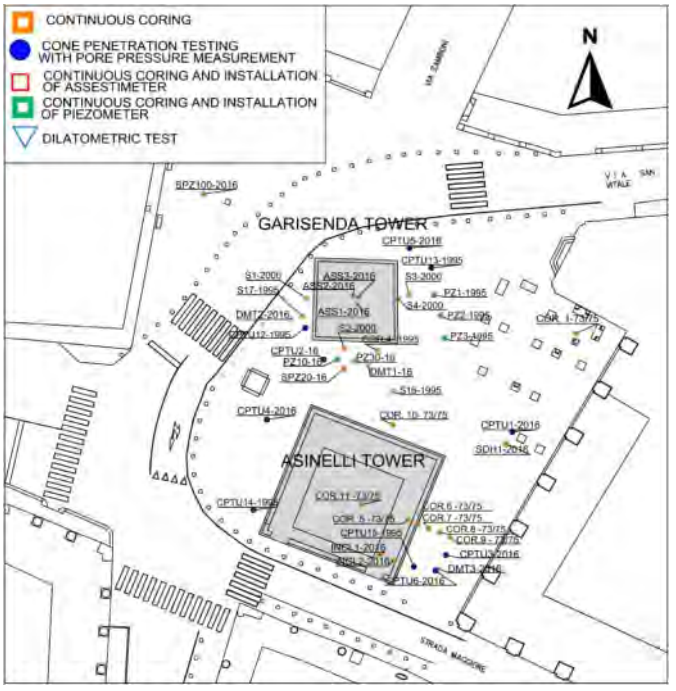

Figure 4. Map that reports the location of the in situ tests carried out during the investigation campaigns of 1973/75, 1995, 2000 and 2016.

5 THE HYDROGEOLOGICAL SETTING

The hydrological conditions of the investigated area are monitored by a few piezometers installed in 1995 and 2016 geotechnical campaigns. Their exact location is shown at the top right of Figure 5. In December 2016, the water table was located at −5.60 m from the ground level and up to a depth of −20 m pore water pressure trend was hydrostatic. Between −20 m and −45 m, a small downward hydraulic gradient (0.044) can be observed, which becomes more relevant (0.28) between −45 m and −95.5 m. A slight change in such hydraulic gradients was observed at the end of 2019 (0.048 between −20 m and −45 m; 0.21 between −45 m and −95.5 m). In November 2021, the former hydraulic gradient increased to 0.055. Figure 5 shows the trend of PZ10, SPZ20 and PZ30 in the period from August 2016 (1 month after their installation) and November 2021, comparing it with local rainfall data. In correspondence of the major rainfall event (14/11/2017), a rise in height of the water column of 0.82 m for PZ10, 0.71 m for SPZ20 and 0.31 m for PZ30 was detected. As clearly observable from Figure 5, in agreement with the hydraulic gradients registered over the whole monitoring period, the downward seepage phenomenon seems to increase with time, even if at a rather limited rate.

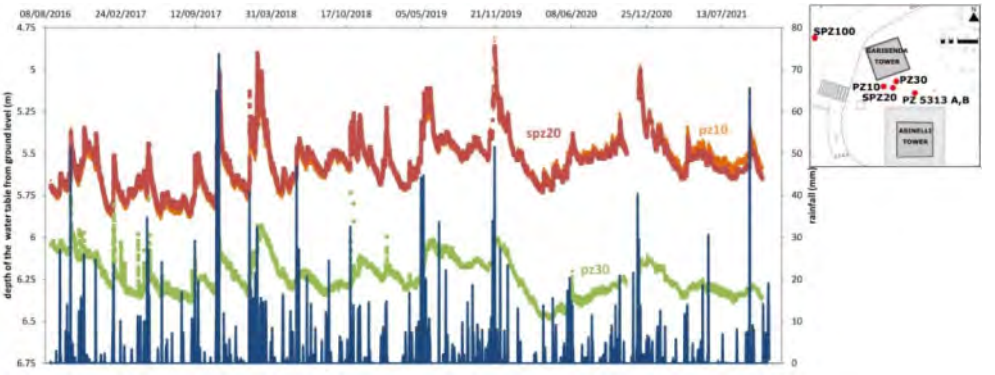

Figure 5. Trend of piezometers PZ10, SPZ20 and PZ30 – installed in the 2016 geotechnical campaign – from August 2016 to November 2021, superimposed to the rainfall data (in mm) obtained from a nearby meteorological station.

6 THE GEOTECHNICAL MODEL

The definition of the geotechnical model was mainly deduced from CPTU analysis (Tonni et al. 2019). Figure 6 presents a preliminary subdivision of the upper horizons based on Robertson (2009) chart using piezocone data from CPTU2 test. Four main separate units have been identified:

- Unit R, is an anthropic fill from the ground level to a depth of −5 m, made of miscellaneous materials (brick fragments, gravel, old wooden chunks, archaeological remains).
- Unit A, from a depth of −5 m to −16 m, is a succession of silty-clays of variable thickness (from half a meter to meters). A high variability in the shear strength and stiffness parameters can be detected, especially in its first 4 m, due to the presence of a dense alternation of desiccated crust (horizon A_b) and carbonated horizons below (horizons B_k and B_w). Such horizons provide increased geotechnical properties due to aging and microstructuration, respectively, as a result of post depositional processes. Between −9 m and −10 m depth, a layer with lower mechanical characteristic breaks the above succession of highly paedogenized horizons. Despite its limited thickness, such layer can play a relevant role because of its position at a depth greatly involved by the pressure bulb of the Two Towers foundation (located at −5.5 m from ground level for

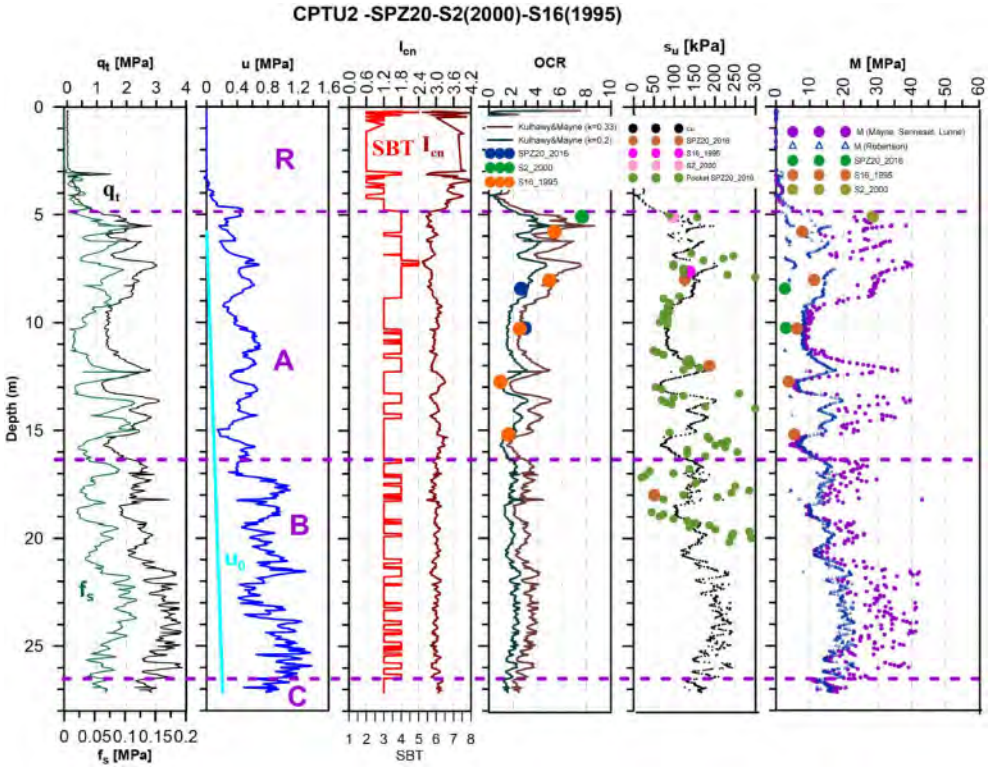

Figure 6. Geotechnical model deduced from CPTU 2 (2016), showing the identification of four units: R, A, B, and C.

Garisenda and at −6.5 m for Asinelli). The same typical layer can be identified in all the piezocone tests, even if at different depths (ranging from −9 m to −12 m) and of variable thickness (from 1 m to 3 m).

– Unit B, from a depth of −16 m to −26.5 m, is a close succession of clayey-silts and silty-clays, whose mechanical properties appear more homogeneous with respect to Unit A because it was only limitedly affected by post depositional processes and desiccated crusts are rare and reduced in thickness.
– Unit C, below Unit B, is an homogeneous normally-consolidated clayey material (SBTn = 1.2), not affected by paedogenetic processes, with a very limited dispersion of the relevant mechanical properties.

Figure 6 shows a good match between s_u (undrained shear strength), OCR (overconsolidation ratio) and M (constrained modulus), as continuously obtained from CPTU2 test, with laboratory sample data. The undrained shear strength has been obtained by applying the well-known relationship:

$$s_u = \frac{q_t - б_v}{N_{kt}} \tag{1}$$

where q_t is the corrected cone tip resistance, $б_v$ the in situ total stress and N_{kt} is a constant taken equal to 14. Kulhawy and Mayne's (1990) recommended relationship was used for OCR:

$$\mathrm{OCR} = \mathrm{k}\frac{q_t - б_{vo}}{б'_{vo}} \tag{2}$$

where q_t is the corrected cone tip resistance, $б_{vo}$ the in situ total stress, $б'_{vo}$ the in situ effective stress and k is a constant, assumed equal to 0.2 or 0.33. In fact, more the clayey deposit is aged and overconsolidated, more k becomes greater. Between −5 m and −10 m from the ground level (Unit A), the use of a constant k equal to 0.33 provides the best match with the laboratory data (colored dots) due to the fact that the deposit is a close succession of desiccated crusts (aged horizons), while between −10 m and −16 m, a constant k equal to 0.2 matches better as the deposit becomes less interested by post depositional processes of overconsolidation.

The constrained modulus M was estimated from CPTU data using the following empirical relationship:

$$M = \alpha_M (q_t - б_{vo}) \tag{3}$$

where q_t is the corrected cone tip resistance, $б_v$ the in situ total stress and α_M a constant which varies with plasticity, natural water content and organic content. Robertson (2009) suggested a value of α_M that varies with Q_t. Figure 6 reports also the formulations provided by Kulhawy and Mayne (1990) and by Senneset et al. (1988), variable with I_{cn} and q_t, as follows:

$$M = 8.25(q_t - б_{vo}) \quad \text{for } I_{cn} > 2.80 \tag{4}$$

$$M = 2q_t \quad \text{for } 2.60 < I_{cn} > 2.80 \text{ and } q_t < 2.5 \text{ MPa} \tag{5}$$

$$M = (4q_t - 5) \quad \text{for } 2.50 < I_{cn} > 2.80 \text{ and } 2.5 < q_t < 5 \text{ MPa} \tag{6}$$

As discussed, Figure 6 proposes a simplified stratigraphy in only four soil units which seems to capture well the behaviour of the deposit as a result of a different geological evolution: Unit A is the most paedogenized subsoil (microstructured soils for aging and cementation), Unit B was only marginally interested by post depositional processes (slightly overconsolidated material) and Unit C was not interested at all (normally-consolidated soils). Such circumstance provides a larger variability of parameters within the same soil unit, when moving from A to C, as it is shown in the section below and also in Table 1, which provides the average values and the standard deviation of the main geotechnical parameters for each soil unit, by using the 2016 in situ tests (six CPTUs and three dilatometer tests DMTs) and the laboratory data obtained from undisturbed samples of all campaigns. The largest variability of parameters is therefore observed in Unit A that should be further subdivided in subunits, in order to characterize with higher accuracy the soil spatial heterogeneity of such a dense alternation of paedogenized and non-paedogenized horizons (Marchi et al 2019). This more than standard accuracy and detail in the data analysis is required by the relevance of the historic monuments involved.

Table 1. Mean values and standard deviation (in brackets) of the main physical, strength and stiffness parameters for each soil unit (A,B,C).

LAB.	γ_n (kN/m^3)	Gs (-)	w (%)	OCR (-)	M (MPa) p'=100kPa	s_u (kPa)
UNIT A	19.27 (0.7)	2.687 (0.062)	26.38 (2.14)	4.11 (2.2)	9.02 (3.95)	122.8 (38.9)
UNIT B	18.73 (0.49)	2.685 (0.074)	28.52 (3.63)	1.50 (1.19)	4.74 (2.74)	96.5 (102.7)
UNIT C	19.37 (0.05)	2.667 (0.089)	25.17 (0.37)	1.06 (0.27)	5.84 (0.77)	153.1 (60.6)

CPTU	s_u (kPa)	OCR (-)	M (MPa) Robertson	M (MPa) Senneset, Kulhawy, Mayne	DMT	M_d (Mpa)
UNIT A	105.1 (32.2)	3.71 (1.68)	20.2 (10.4)	13.3 (7.4)	UNIT A	22.7 (11.1)
UNIT B	163.9 (32.0)	2.78 (0.68)	26.1 (9.6)	21.8 (5.8)	UNIT B	27.2 (10.4)
UNIT C	148.1 (28.0)	2.04 (0.49)	15.9 (7.3)	17.1 (5.5)	UNIT C	22.09 (11.0)

7 DEALING WITH VERTICAL HETEROGENEITY WITHIN SINGLE SOIL UNITS

In order to further investigate the value dispersion of parameters within the identified soil units of the alluvial deposit underneath the Two Towers, the frequency distributions (histograms) of a few main parameters governing strength and stiffness have been considered. The histograms of each soil unit (A,B,C), elaborated from the six CPTUs performed in the 2016 geotechnical campaign, have been superimposed and compared. While Unit C shows a unimodal distribution, symptom of homogeneity in the dataset, Unit A shows a strong bimodal (both for the confined modulus M and for the undrained shear strength s_u) or a multimodal distribution (for the overconsolidation ratio OCR). Unit B shows a moderate bimodal distribution for s_u and M, but in general the interval of dispersion is narrower if compared to unit A. The greater dispersion of the considered geotechnical parameters is most probably the result of the presence of different horizons within the same unit, as discussed above. When dealing with non-unimodal distribution, it can be obviously misleading to consider the average values of the parameters as representative of the soil unit, even if characterized by a minimum frequency (as for units A and B). The superimposition of an equivalent typical Gaussian distribution in Figure 7 clearly shows the error introduced when the mean value is adopted as representative of a bimodal or multimodal distribution. A more accurate subdivision in sub-units could be then useful when a detailed geotechnical model of the soil-foundation system has to be implemented.

Figure 8 presents such a model dealing with the vertical heterogeneity in Units A and B, as discussed above. Unit A has been further subdivided in six subunits (A1…A6): A1, A3, A5 show better mechanical properties typical of microstructured soils, while A2, A4, A6 show the behaviour of normally consolidated layers.

Unit B has been further subdivided only in two subunits, where B1 is a close succession of silty-clays and clayey silts and paedogenized horizons are very thin (for this reason probably not well detected by the cone tip) or absent, while B2 contains paleosols of greater thickness (up to ~1.5 m), producing a marked response of the penetrometer. B1 shows a narrower variability of the parameters than B2. In order to understand if the detailed stratigraphy (4 units, 8 sub-units) is able to reduce the parameter dispersion observed in Figure 7, histograms of the same geotechnical parameters for each subunit are provided in Figure 9. It can be noticed that sub-units show a reduced dispersion of the parameters and relevant data better follow a Gaussian distribution. In this case, the adoption of the parameter mean value as representative of each single sub-unit is more appropriate. The only exception appears to be OCR for sub-unit A1, which maintains a bimodal distribution, although not particularly marked.

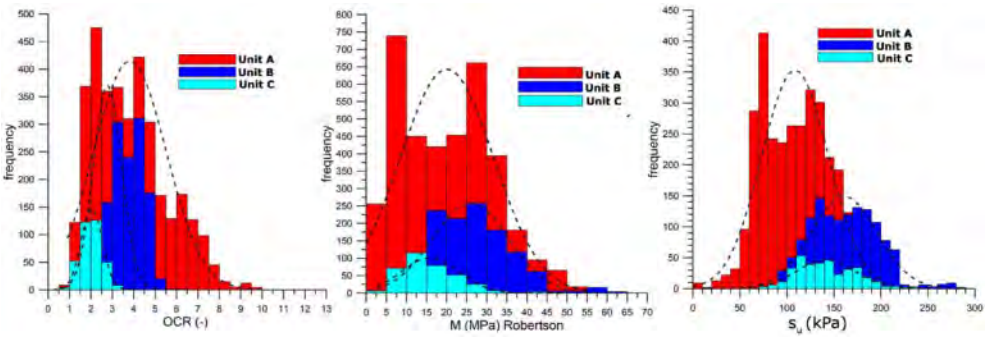

Figure 7. Histograms of a few main geotechnical parameters using data from 2016 cone penetration tests (CPTUs) are presented for each unit (A, B and C): OCR is the overconsolidation ratio, s_u the undrained shear strength and M the confined 1D modulus.

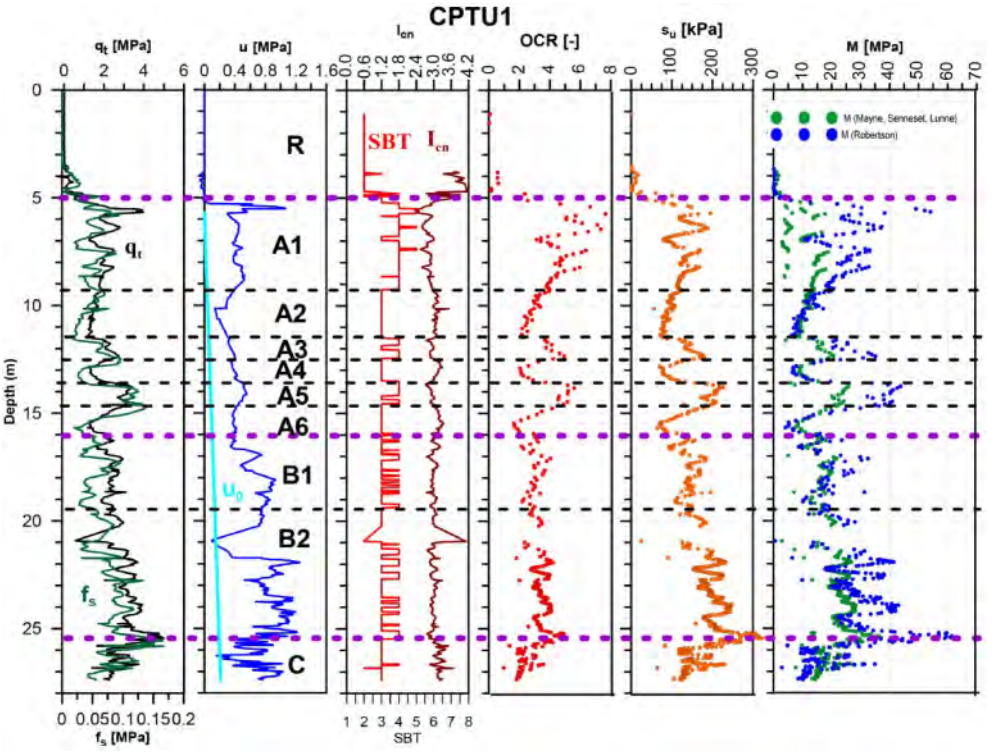

Figure 8. Stratigraphic subdivision of CPTU 1 (2016) in units R,A,B,C and subunits (A1…A6; B1,B2) based on Robertson (2009) classification chart.

An accurate subdivision of the deposit in main units and subunits, based in this case on geological and sedimentological aspects, can therefore provide a valuable alternative to the use of more elaborate and less standard geostatistical methods.

8 CONCLUSIONS

Many information are required in order to devise a proper long-term preservation strategy of historic heritage: from the hydro-geological setting to the historical origin (materials used, construction techniques and sequence), from the structure configuration evolution (demolitions, new constructions, structural interventions) to the monitoring of possible movements with time. The definition of a reliable and accurate geotechnical model of the soil-foundation system is another fundamental issue. The paper traces a summary of the main relevant information in relation to the peculiar case of the Two Towers, located right in the heart of Bologna city centre and which no doubt provide significant challenges for their long-term safety and preservation.

A stratigraphy made of four main units has been first proposed for the foundation soil of the Two Towers, following both sedimentological observations concerning the different soil horizons and in situ test data analysis and interpretation.

What clearly emerges is a significant heterogeneity especially of Unit A, both vertical and horizontal, as result of a complex history of post-depositional processes, which should be properly understood and taken into consideration when representative values of the geotechnical parameters are sought. It is well known that the use of average parameter values of geotechnical properties is affected by relevant uncertainties, which can be reduced by using elaborate geostatistical methods or

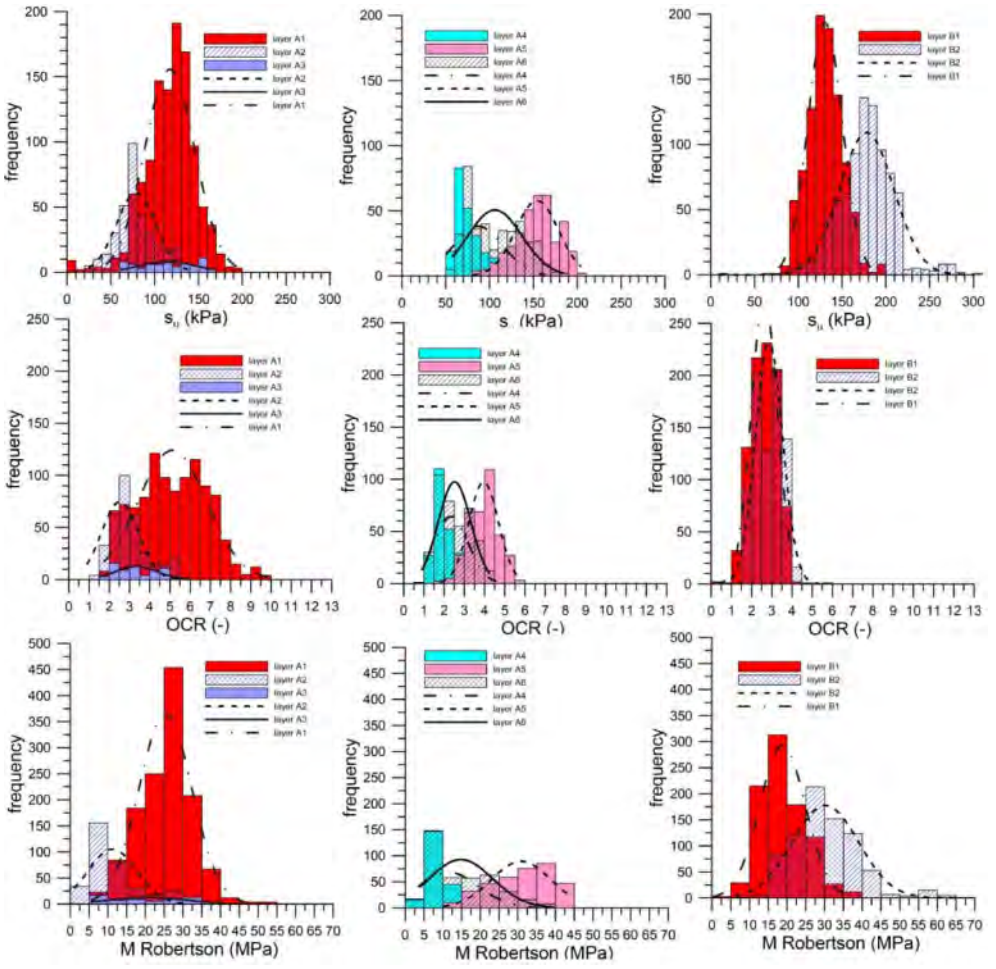

Figure 9. Histograms of a few geotechnical parameters using data from 2016 cone penetration tests (CPTUs), for each sub-unit (A1…A6, B1 and B2): s_u is the undrained shear strength, OCR the overconsolidation ratio and M the confined 1D modulus.

thanks to a more accurate definition of the geotechnical model. In the case study proposed, the latter approach was adopted, by subdividing soil units in sub-units with a significantly reduced scatter of the main geotechnical parameters, as a consequence of the same sedimentological evolution with time. It is thought that the proposed final geotechnical model can be used for a more accurate analysis of the soil-foundation interaction of the Two Towers aiming at describing the stress-strain distribution and predicting the evolution of settlements with time.

REFERENCES

Bergonzoni, F. 1989. Pietra Su Pietra Verso Il Cielo: Tecniche, Tempi e Costi di Costruzione, In Roversi (ed.), *Le Torri Di Bologna*: 29–48. Bologna, Italy: Grafis Editore.

Bergonzoni, F. 1991. Età della Torre Asinelli. In *Strenna Storica Bolognese*, 45–55. Bologna, Italy: Patron Editore.

Bertolini, I. Marchi, M.& Gottardi, G. in press. Learning from a well-documented geotechnical cold case: the Two Towers of Bologna, Italy. *International Journal of Architectural Heritage*.

Bruno, L., Amorosi, A., Curina, R. et al. 2013. Human landscape interactions in the Bologna area (Northern Italy) during the middle–late Holocene with focus on the Roman period. *Holocene* 23: 1558–1569.
Bruno, L., Amorosi, A. & Severi, P. et al. 2015. High frequency depositional cycles within the late Quaternary alluvial succession of Reno River (northern Italy*). Italian Journal of Geosciences* 134: 339–354.
Bruno, L., Marchi, M., Bertolini I., Gottardi, G. & Amorosi, M. 2020. Climate control on stacked paleosols in the Pleistocene of the Po Basin (northern Italy). *Journal of Quaternary Science* 35(4).
Dallavalle, G. Di Tommaso, A. Gottardi, G. Trombetti, T. Lancellotta, R. & Lugli, S. 2021.The Garisenda Tower in Bologna: effects of degradation of selenite basement on its static behavior; *Proc. Third Int. Symp. on Geotechnical Engineering for the Preservation of monuments and historic sites*, Naples (Italy), 22–24 June 2021.
Giordano, F. 2000. *La Torre Garisenda*. Bologna, Italy: Edizioni Costa.
Gottardi G., Lionello, A., Marchi, M. & Rossi, P.P. 2015. Monitoring-driven design of a multiphase intervention for the preservation of the Frari bell tower in Venice. *Rivista Italiana di Geotecnica* 49(1):45–64.
Gozzadini, G. 1875. *Delle Torri Gentilizie Di Bologna E Delle Famiglie Alle Quali Prima Appartennero*. Bologna, Italy: Zanichelli Editore.
ISO 13822:2010 (en).2010. *Bases for design of structures — Assessment of existing structures*, International Organization for Standardization.
Kulhawy, F.H. & Mayne, P.W. 1990. *Manual on Estimating Soil Properties for Foundation Design*, Report No. EL-6800, Electric Power Research Institute, Palo Alto, CA.
Lancellotta, R. 2013. The Ghirlandina Tower in Modena, Italy: A history of soil structure interaction. *Rivista Italiana di Geotecnica* 47(2):7–37.
Lancellotta R. & Sabia, D. 2015. Identification technique for soil-structure analysis of the Ghirlandina Tower. *International Journal of Architectural Heritage*, 9(4):391–407.
Marchi, M., Butterfield, R., Gottardi, G. & Lancellotta R. 2011. Stability and strength analysis of leaning towers, *Geotechnique* 61(12):1069–1079.
Marchi, M., Fabbi, I., Gottardi, G., Butterfield, R. & Lancellotta, R. 2013. Analytical modelling of the creep-rotation rate for leaning towers, *2nd International Symposium On Geotechnical Engineering For The Preservation Of Monuments And Historic Sites*, May 30–31, Naples, Italy: 531–538.
Marchi, M. Bertolini, I. Gottardi, G. Amorosi, A. & Bruno, L. 2019. From geological and historical data to the geotechnical model of the Two Towers in Bologna (Italy); *Proc. XVII ECSMGE*, Reykjavik, 1–6 Semptember 2019.
Pisanò, F., Di Prisco, C.G. & Lancellotta, R. 2014. Soil foundation modelling in laterally loaded historical towers. *Geotechnique* 64 (1):1–15.
Roversi, G. 1989. *Le Torri Di Bologna. Quando e Perché sorsero, Come Vennero Costruite, Chi Le Innalzò, Come Scomparvero, Quali Esistono Ancora*. Bologna, Italy: Edizioni Grafis.
Senneset, K. Sandven, R. Lunne, T. By, T. & Amundsen, T. 1988. Piezocone tests in silty soils. *ISOPT-1*, Orlando, FL: 955–966. Rotterdam: Balkema.
Tonni, L., García Martínez, M.F. & Rocchi, I. 2019. Recent developments in equipment and interpretation of cone penetration test for soil characterization. *Rivista Italiana di Geotecnica* 53(1): 71–99.
Viggiani, C, 2019. *Senza neanche toccarla – La stabilizzazione della Torre di Pisa.* Italy: Hevelius Edizioni, 152 p. ISBN 978 88 86977 96 8 (in Italian).

Geotechnical Engineering for the Preservation of Monuments and Historic Sites III – Lancellotta, Viggiani, Flora, de Silva & Mele (Eds)

Geotechnical and structural investigation and monitoring techniques to determine the origin of ongoing damage processes in historical buildings: The Saint Francis of Paola Church in Rome case history

P. Zimmaro
University of Calabria, Arcavacata di Rende, Italy
University of California, Los Angeles, Los Angeles, USA

E. Ausilio
University of Calabria, Arcavacata di Rende, Italy

ABSTRACT: Existing masonry buildings are often the result of multi-epoch layers of construction cycles, modifications, and alterations that were made over the span of long-periods. Identifying the possible causes of existing damage and ongoing damage processes in historical structures is a complex task that typically involves the integration of different approaches including historical analysis, geotechnical and structural field inspections and investigations, geotechnical and structural monitoring, and structural analysis involving soil-structure interaction effects. Existing cracks and deformation patterns in ancient structures are often due to the combined effect of various recent and past stressing phenomena. Construction processes, natural events as well as anthropic actions, may affect current equilibrium conditions, causing damage to the structure. Such phenomena may be classified into four main triggering categories: (1) recent and ongoing (i.e., new alterations resulting in ongoing deformation patterns), (2) recent but stopped (typically one-time events that produce an effect while they act, such as earthquakes), (3) old but ongoing (i.e., excavations made centuries ago but still influencing the observed damage patterns), and (4) old but stopped (i.e., alterations made in the past but for which remediation measures were already implemented). As a result, the analysis of ancient structures should include the analysis of past events and alterations from historical sources.

The Saint Francis of Paola church in Rome is located to the west of the San Pietro in Vincoli church in the Monti neighborhood, about 300 m from the Colosseum. It was built in 1645–50 and was designed by architect Giovanni Pietro Morandi. Structural damage patterns have affected the church over the last century and the evolution of the health of the structure recently forced local authorities to close the church to the public.

This paper provides a detailed historical analysis of the church from which a series of past alterations that likely triggered the ongoing deformation process that is causing substantial structural damage to the church were identified. The analysis presented in this study was performed using a step-by-step approach based on the traditional scientific method. After analyzing all historical alterations made in the area, field inspections were performed, and hypotheses on the mechanisms responsible for the current damage pattern were made. To corroborate these hypotheses and exclude (or include) other causes, a structural and geotechnical investigation program was carried out. Three borings were drilled at a depth of ∼25 m. They were equipped with inclinometers and piezometer. Cracks in structural members of the church were monitored by means of a real-time crack monitoring gauge system. This study shows that thee ongoing deformation mechanism is likely due to a variety of causes including geotechnical issues pertaining to nearby retaining structures and local structural deficiencies. Interestingly, the analysis of the monitoring system shows that the 2016 Central Italy earthquake sequence produced non-negligible displacements to the structures. This observation confirms that strong earthquakes in the Central Apennines may have an impact on monumental structures located in Rome.

DOI 10.1201/9781003308867-47

1 INTRODUCTION

The analysis of ongoing long-term deformation patterns observed in monumental historical structures is extremely challenging. The variety of construction and geotechnical materials encountered and the lack of detailed information about modifications to structures and the surrounding landscapes make the reconstruction of the causes of these damage mechanisms particularly difficult. As a result, a detailed review of available information is required to facilitate this analysis. Furthermore, geotechnical and structural characterization and monitoring are required to identify potential mitigation strategies.

In this study, ongoing damage mechanisms affecting the Saint Francis of Paola church in Rome are analyzed. This church is located in the Monti neighborhood, about 300 m away from the Colosseum (Figure 1a), and next to the San Pietro in Vincoli church. The church faces Piazza San Francesco di Paola and it is bounded by via Cavour to the south and via del Fagutale (which is located right above via degli Annibaldi) to the west. In 1999, it was nominated as the church of Calabrian people following a decree of the Vicariate of the Apostolic Palace of the Lateran

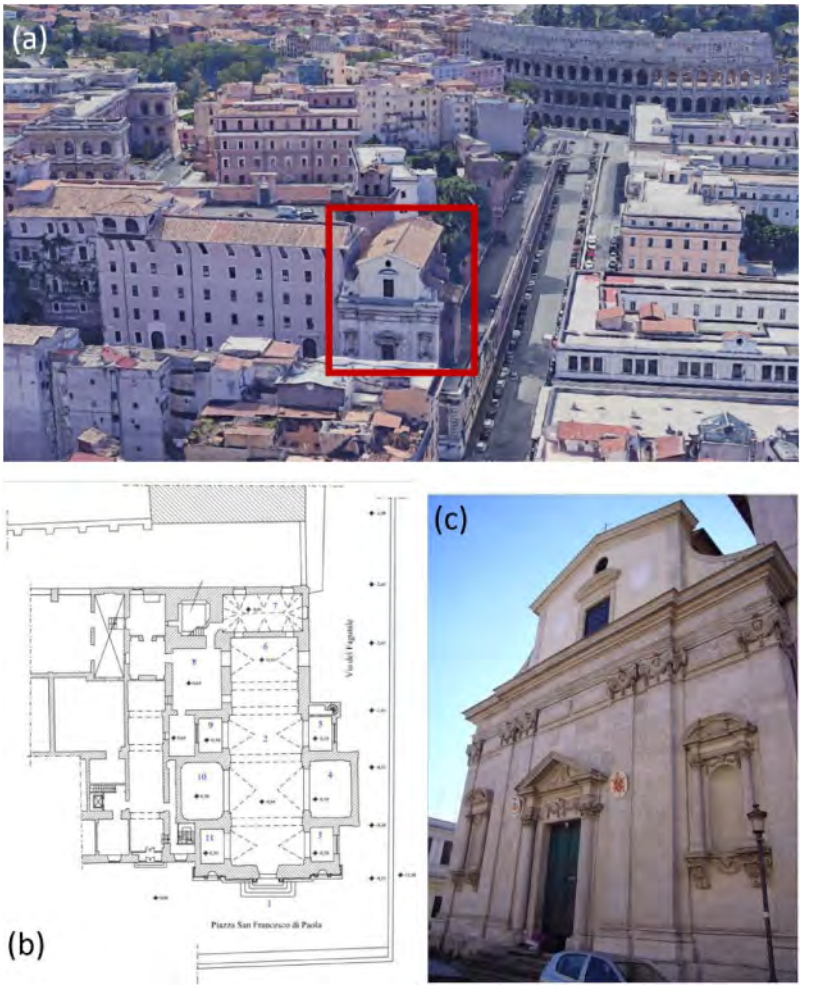

Figure 1. (a) Overview of the area, (b) plan view of the church, and (c) entrance and main façade of the church.

(the office responsible for the spiritual administration of the catholic church, which is under the jurisdiction of the Pope).

This study starts with a historical overview of available information on the Saint Francis of Paola church in Rome and surrounding structures. Ongoing damage mechanisms to the church are then analyzed. Finally, the result of a recent structural/geotechnical characterization and monitoring program are presented and analyzed. The aim of this study is to identify the causes of observed damage to the church and provide insights into design mitigation strategies to this and possibly other similar monumental structures.

2 THE SAINT FRANCIS OF PAOLA CHURCH IN ROME

2.1 *Historical overview and description of the church*

The construction of the Saint Francis of Paola church in Rome started in 1637 thanks to the effort of Giovanni Pezzullo, a Calabrian priest who was devoted to Saint Francis of Paola. It stopped for some years because of some financial issues (that were solved thanks to monetary donations made by the Princess of Rossano, Olimpia Aldobrandini Pamphili) and was completed in 1650. Roman architect Giovanni Pietro Morandi designed the church and supervised its construction. The piece of land where the church was built once belonged to the Borgia Family and was bought by Giovanni Pezzullo. This location was part of the secret garden of the Cesarini Palace that later became a monastery. The church's bell tower hosts three bells and used to be a fortified tower. It is the only remaining example of a medieval tower transformed into a bell tower in the whole city.

The main façade of the church (Figure 1c) is subdivided into two orders: (1) the lower order (made of travertine) that comprises Corinthian columns and a central gable, and (2) the upper order, with a curved gable at the center-top and a large central window just below it. On both sides of the façade there are niches decorated with Corinthian columns. Figure 1b shows the plan view of the church highlighting a single nave and three lateral chapels per side. All lateral chapels are supported by Ionic columns and are characterized by baroque decorations. The church is covered with ribbed vaults decorated with white stucco, polychromatic frescos, and geometric-shaped gold details. On the eastern side of the church there is a monumental complex (now used as a convent) that is structurally contiguous with the church itself. This complex was initially built in the XVII Century and completely remodeled in the XVIII Century. The entire monumental complex (which includes the church and the convent) is built using unreinforced masonry. The church was later involved in local structural interventions, including the addition of east-west steel tie rods passing through the lateral chapel facing Via degli Annibaldi (see subsequent subsections).

2.2 *Historical evolution of the site*

The area where the Saint Francis of Paola church in Rome was built is located in the center of the city of Rome and it is visible in ancient plan views of the area, dating back to the Roman Empire era. The church is located on the Esquiline Hill (one of Seven Hills of Rome). The Esquiline Hill comprises three spurs: Oppian, Cispian, and Fagutal. According to the legend, this area is where the house of king Servius Tullius (the sixth king of Rome) was built. At the location of the ancient access road to Servius Tullius' house (known as Vicus Sceleratus), today is located a staircase going from Via Cavour to Piazza San Francesco di Paola. The Domus Aurea (Emperor Nero's residence) was also located in this area, which later hosted the Baths of Titus and Trajan (Figure 2a). Figure 2b shows a bird's eye view of the area created right before the construction of the Saint Francis of Paola church in Rome in 1593. Figure 2c shows the area in 1676, after the construction of the church. By comparing Figures 2b and 2c, it is evident how the presence of the church changed the landscape as it connects the pre-existing palace and the medieval tower (which later became the church's bell tower). Figure 2d shows a plan view of the area after the construction of the church and highlights that the main façade of the church is located right on Via San Francesco di Paola and at the same elevation (i.e., back then no retaining structures existed and the only main road running east-west was Via San Francesco di Paola as Via Cavour was built later.

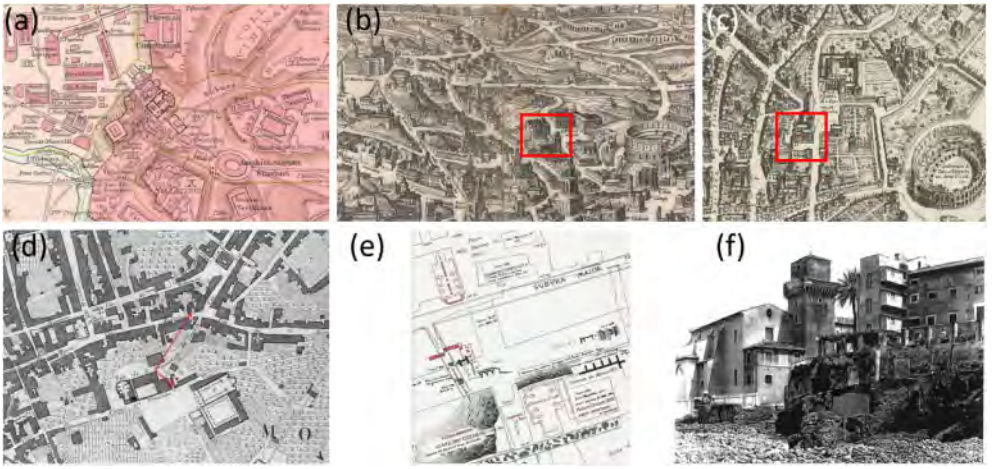

Figure 2. (a) plan view of the area during the Roman empire (from Droysen, 1886), (b) bird's eye view of the area before the construction of the church (from Tempesta, 1593), (c) bird's eye view of the area after the construction of the church (from Falda, 1676), (d) plan view of the area after the construction of the church, (e) plan front view of the area after the construction of Via Cavour, and (f) illustration of the area during the construction of the retaining wall along Via degli Annibaldi in 1895 (from the Hertzian library photo collection).

In 1860, Italy was unified and 11 years later, in 1871 Rome became the Capital of Italy. This new status brought many changes in the road network of the city. One such change was the decision of opening a new road connecting the Colosseum area directly to the largest train station of the city: the Termini Station. As a result, in 1873 the city council planned the construction of Via Cavour. The construction of this road was part of a comprehensive plan involving the construction of 47 new roads in Rome. Figure 2e shows the plan view of the area after the construction of Via Cavour. To build Via Cavour, the road elevation was lowered by ~11 m and what was formerly called Via San Francesco di Paola, became Via Cavour. This new road was protected by an 11 m-tall gravity retaining wall. According to the construction log signed by Gaetano Ersoch (the head engineer in charge for the construction of this road) in 1888, the excavation produced cracks in the church structure starting from 1887. Following the construction of Via Cavour, in 1899 Via degli Annibaldi, connecting the Colosseum to Via Cavour was inaugurated. Via degli Annibaldi in today's Rome road network constitutes the ideal connection between Via dei Serpenti and the Colosseum (Figure 3a). Figure 2f shows the excavation made while building Via degli Annibaldi. This excavation was performed right at the edge of the foundations of the Saint Francis of Paola church on its western side. Similarly to Via Cavour, Via degli Annibaldi is protected too by a tall gravity retaining wall that separates Via del Fagutale (on the same level of the church) and Via degli Annibaldi (about 12.8 m below) (Figures 3b–f).

Following the unification of Italy and the subsequent law of 1873 that ordered the suppression of religious corporations, the church was expropriated. It returned to the sacred Order of Minims (the religious order founded by Saint Francis of Paola) in 1939. During the period 1873–1939 no maintenance was performed on the church and the attached convent. As a result, the entire monumental complex was in a dilapidated condition. During the 1930s the metro Line B was being built in the area and in 1939, right after re-acquiring ownership of the church, the Minims Fathers sued the contractor who was building the new metro line. Following this official legal action, third party engineers visited the monumental complex and mapped various cracks in structural and non-structural members. However, they found that these cracks were not triggered by the construction of the new metro line, but where caused by other and older triggering mechanisms. A similar lack of damage induced by the construction of the metro in the city of Rome is visible from synthetic aperture radar data in this area shown by Burghignoli et al. (2013).

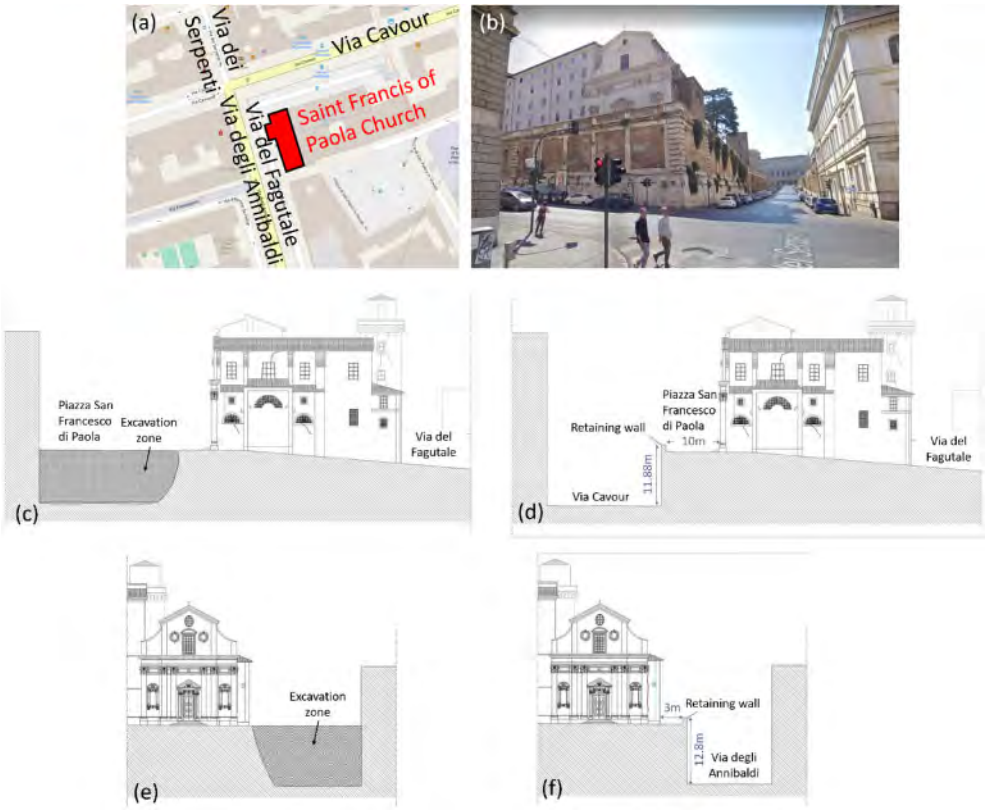

Figure 3. (a) plan view of the area, (b) view of the façade of the church from Via dei Serpenti looking at the Colosseum, (c) and (d) front view of the church before and after the excavation and the construction of the gravity retaining wall, and (e) and (f) side view of the church before and after the excavation and the construction of the gravity retaining wall.

2.3 *Current structural condition of the church*

As mentioned in earlier sections of the paper, due to the presence of diffuse cracking in many structural members of the church, the structure was closed to the public in 2016. As part of this study, all extensional cracks and damage features affecting the structure were mapped. In this section, a brief description of apparent structural deficiencies and where damage is currently focused is presented. More details about this analysis are provided in Carravetta (2021). Figure 4 shows the two side sectional views of the church, along with all main cracks. Figures 5a–c show extensional cracks in the Saint Francis of Paola chapel (facing the western side of the church, on Via del Fagutale). This chapel is the largest and most damaged in the whole church. Extensional cracks in this chapel are wider than 2 cm and heavily damaged a fresco about the life of Saint Francis of Paola (this fresco is being restored at the time of writing). On the same side of the church, the two smaller chapels (the Saint Francis of Sales and Sant'Anna chapels) also show extensional cracks similar to those visible in the Saint Francis of Paola chapel. The three chapels on the eastern side of the church are damaged too. However, crack widths in these chapels are smaller than 1 cm. The main altar and the choir (located behind the main altar) are heavily damaged too, as shown in Figures 4b. Figure 6 shows longitudinal extensional cracks visible in the intrados and the extrados of the masonry vault.

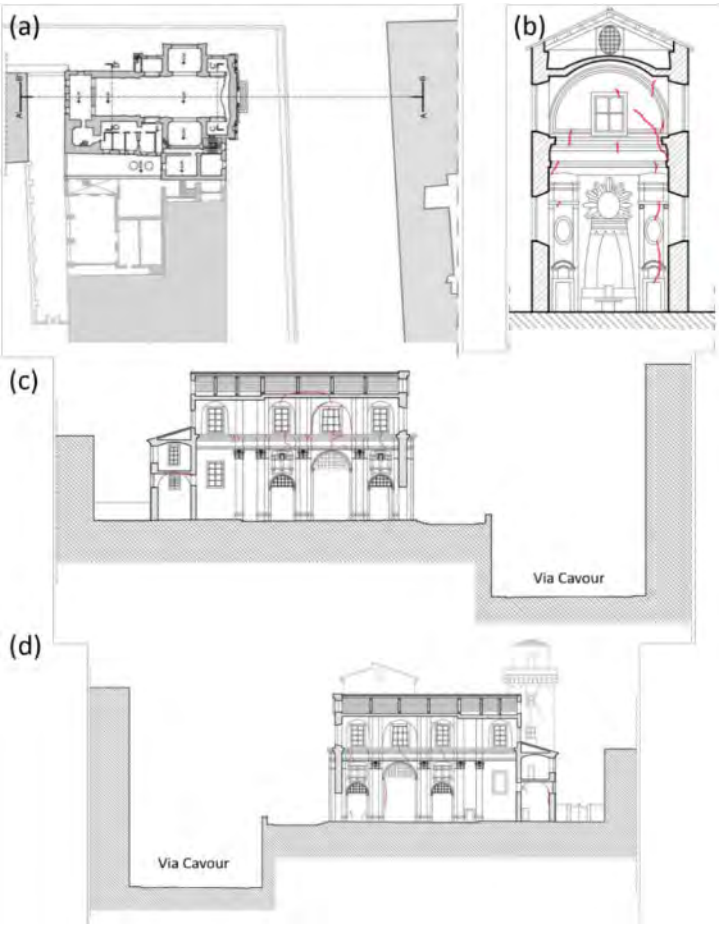

Figure 4. (a) plan view of the church and location of the cross sections shown in subpanels b–d, (b) section of the altar area, (c) section of the church looking east, and (d) section of the church looking west and extensional cracks visible in 2016.

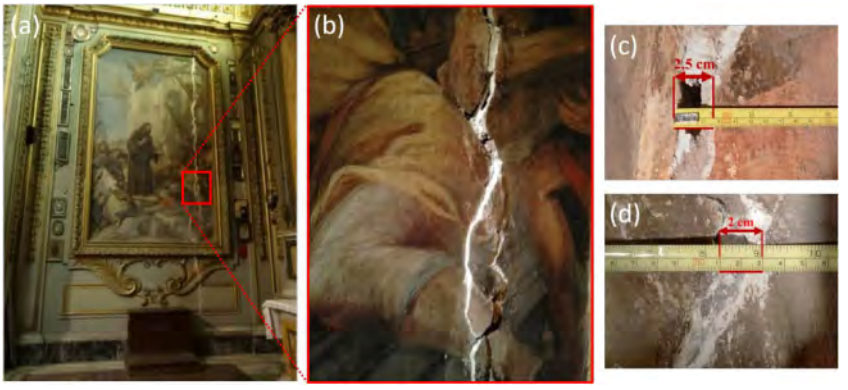

Figure 5. (a) Main extensional crack in the Saint Francis of Paola chapel (on the western side of the church, on Via del Fagutale), (b) zoomed-in view of the crack, (c) and (d) tape measurements of the crack in two different points of the fresco, exceeding 2 cm in width.

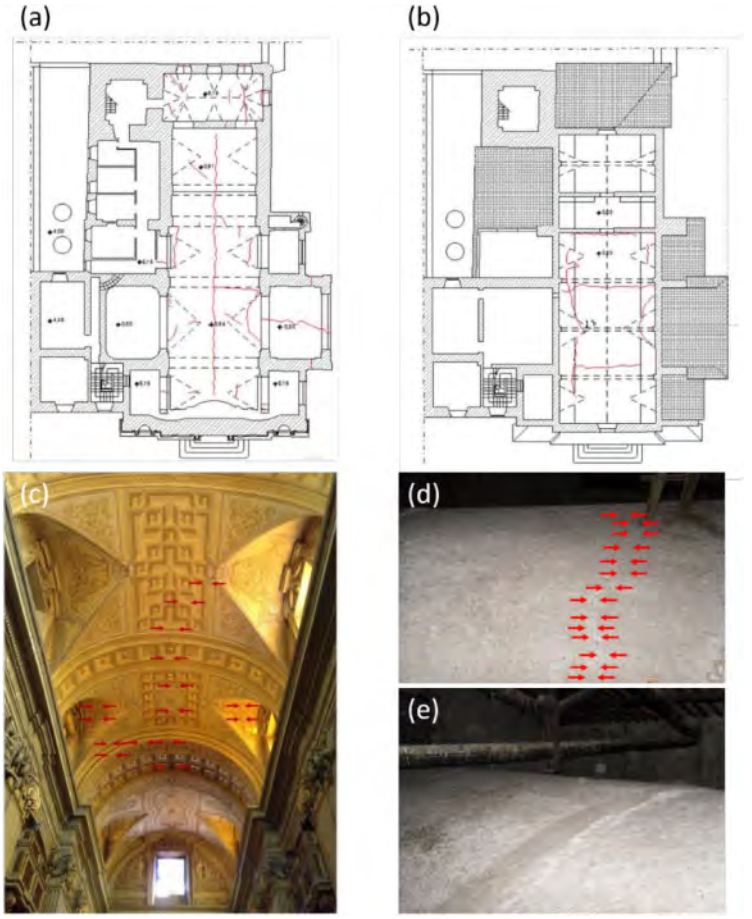

Figure 6. Map view of extensional cracks in the (a) extrados and (b) intrados of the vault, (c) photograph of cracks in the extrados, (d) and (e) photos of cracks in the intrados.

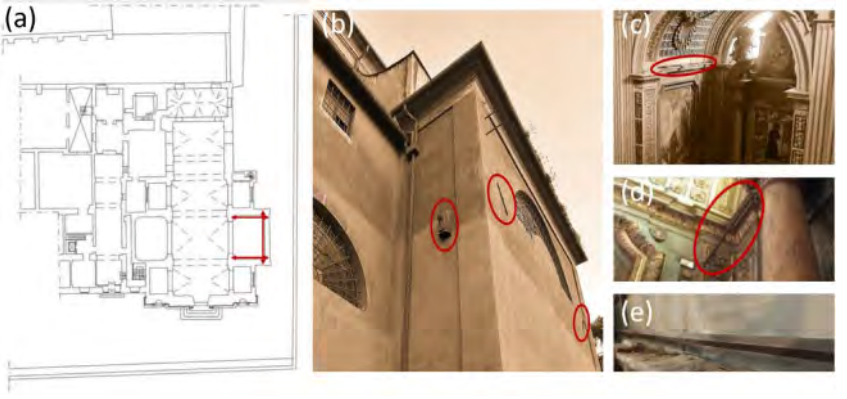

Figure 7. (a) plan view of the church with the identification of the location of steel tie rods, (b) view of the external part of the Saint Francis of Paola chapel from Via del Fagutale evidencing the anchors of the steel tie rods, (c), (d), and (e) details of the steel tie rods from inside the church.

2.4 *Damage mitigation measures employed in the last century*

In this study, a thorough analysis of available documents about mitigation measures employed in the last century was performed. The outcome of these analyses highlights multi-epoch interventions mainly performed as emergency mitigation works, rather than being part of an organized long-term plan. Only after 1952 mitigation measures were employed in a more consistent manner with the clear willingness of a lasting restoration strategy. In the 1940s, after identifying the excavations and the subsequent construction of the gravity retaining walls on Via Cavour and Via degli Annibaldi as the main cause of damage (thus excluding the construction of the metro as a possible cause of damage), Father Giacomo Tagliaferro found the financial resources to perform a comprehensive restoration of the church and the attached convent. The restoration work started in 1952 and started with the placement of 50 mm × 60 mm and 30 mm × 60 mm east-west steel tie rods passing through the Saint Francis of Paola chapel facing Via degli Annibaldi (Figure 7). Furthermore, many extensional cracks in the church were repaired using the mortar-replenishment technique.

In 1955 the church's floor appeared heavily damaged by many cracks. Since the Colosseum area is characterized by a large variety of cavities with variable depth and dimensions, the opening of these cracks also led, in some portions of the church to the formation of large holes. To restore the floor of the church and close these holes, it was decided to build new floor slabs made of reinforced concrete.

In the period 1953–1955 the bell tower was restored. The following local interventions were employed: the replenishment of the external coating material of the entire tower and the substitution of damaged wooden beams and slabs.

In 1955 and 1959 the restoration involved a two-step intervention to the vault. Older wooden beams were replaced with new ones made of chestnut wood. The vault needed new interventions in 2018. In the winter 2017–2018, following intense rainfalls, the roof was heavily damaged (Figure 8a). This emergency led to the partial substitution of the roof, the replacement of 10 damaged wooden trusses (Figure 8b) with new steel trusses (Figure 8c–d), and the restoration of four wooden trusses with steel elements (Figure 8e–f).

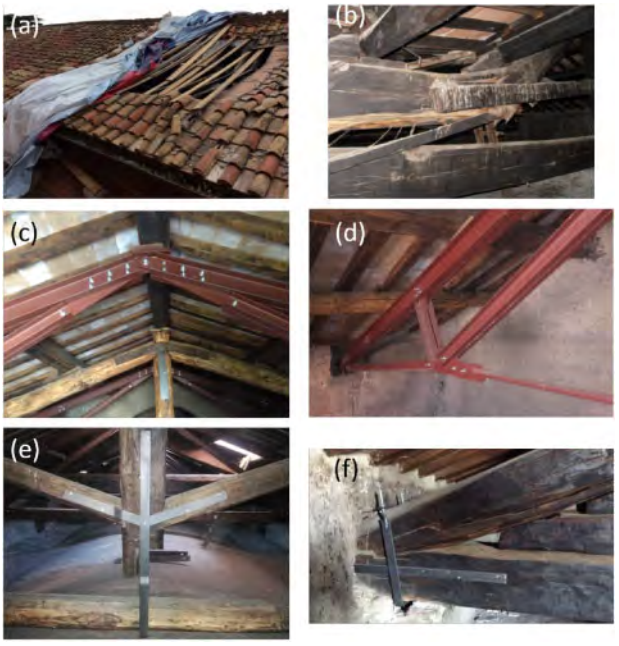

Figure 8. (a) Damage to the roof of the church in 2018, (b) damaged wooden truss in 2018, (c), overview of the restoration performed to 14 wooden trusses, (d) detail of a new steel truss used to substituted an older wooden truss, (e) and (f) details of the restoration of wooden trusses with steel elements.

3 GEOTECHNICAL-STRUCTURAL CHARACTERIZATION AND MONITORING

3.1 *The 2019 geotechnical investigation and monitoring program*

Given the extensive structural damage observed in the last two centuries to the church and the lack of an adequate geotechnical characterization of the area, in 2019 the superintendence of archaeology, fine arts, and landscape of Rome funded a geotechnical-structural characterization and monitoring program. This subsection provides some details on the geotechnical characterization and monitoring program, whereas a subsequent subsection focuses on the structural monitoring program. The geotechnical characterization program comprised the execution of three boreholes with continuous coring (labeled as S1, S2, and S3), two shear wave velocity profiles by means of the multichannel analysis of surface waves (MASW, labeled as MASW1 and MASW2) technique, and two microtremor-based horizontal-to-vertical spectral ratio (HVSR, labeled as HVSR1 and HVSR2) of Fourier amplitudes from three-component recordings, used to identify site resonances. Borings S1 and S2 were drilled on Via del Fagutale on the south and north sides of the Saint Francis of Paola chapel, while boring S3 was drilled right outside of the main entrance of the church, facing Piazza San Francesco di Paola, above Via Cavour. MASW1 and HVSR1 were performed in Piazza San Francesco di Paola, while MASW2 and HVSR2 on Via del Fagutale. The location of all site investigations is shown in Figure 9a. All three boreholes were drilled at a depth of ~25 m (well below the foundation of the gravity retaining walls on Via Cavour and Via degli Annibaldi). Borehole S3 was equipped with an open-pipe piezometer to monitor the water table elevation, while S1 and S2 (Figure 9b) were equipped with two inclinometers to identify any deep horizontal movement that could be correlated with the observed structural damage. Standard penetration tests were performed in all three borings and some undisturbed samples in fine-grained soil layers were recovered and used to perform soil identification. Due to lack of space to document the results of the whole geotechnical characterization and monitoring program, in the remainder of this section main findings from this study are summarized.

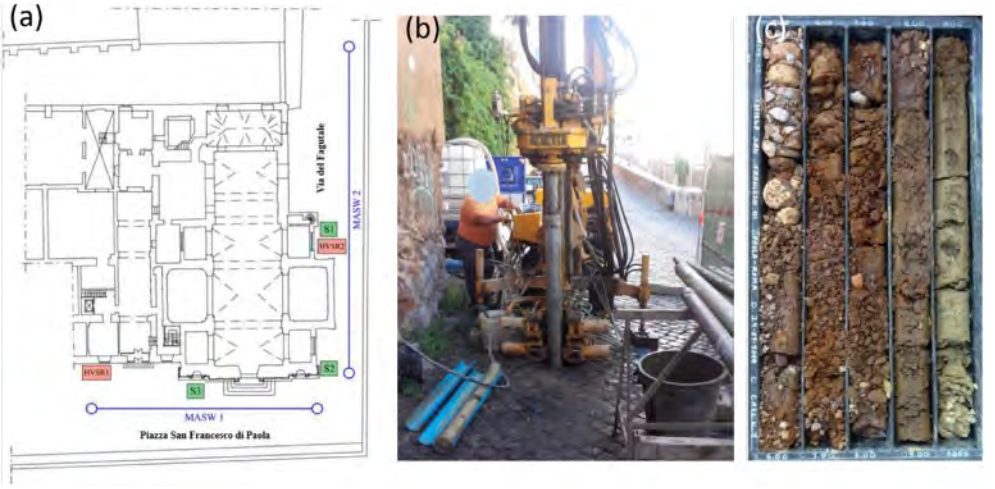

Figure 9. (a) Plan view of the church with the locations of all geotechnical investigations performed in 2019, (b) execution of borehole S2 on Via del Fagutale, (c) disturbed samples recovered in boring S2 between 5 m and 10 m of depth.

Using data from S1, S2, and S3, a simplified/representative stratigraphy of the area surrounding the church was reconstructed. At shallow depths, just below the road pavement (depth of 0.5 m-1 m), there is a layer of fill material of variable thickness (between 5 m and 10 m) that includes the presence of tuff, travertine, bricks, and mortar in a matrix of sand and silt. Figure 9c shows

disturbed samples recovered in boring S2 between 5 m and 10 m of depth, where these materials are visible. The archeological literature of the area confirms that this layer contains what was used as construction material during the imperial era of the city of Rome and for the construction of radial walls surrounding the Colosseum. This fill layer is reported to overly a 5 m-to-10 m thick layer of silty, sandy clay, which in turn is founded on a thick layer of volcanic material including cineritic pyroclastic rocks.

Both MASW tests show similar trends with low shear wave velocity (V_S) values at depths smaller than 8 m (<200 m/s) and an almost constant value of ~350 m/s between 8 m and 30 m. These V_S values are broadly consistent with the stratigraphic reconstruction made using the boring log data, with a slow-velocity fill layer with thickness variable between 5 m and 10 m overlying a stiffer clay layer which is in turn founded on volcanic soils. Based on the V_S profiles obtained using the MASW tests, these profiles would be classified as category C according to the Italian Building Code (Norme Tecniche per le Costruzioni, NTC, 2018). Both HVSR measurements did not show any substantial peaks in the range 0.5–20 Hz. This is representative of a lack of impedance contrast in the soils being investigated.

As of July 2021, the inclinometer measurements performed in borings S1 and S2 did not show significant horizontal displacements. The open-pipe piezometer installed in boring S3 shows a water table at a depth around 19 m. No significant seasonal oscillations were observed.

3.2 *Structural monitoring*

Four mechanical crack meters were installed in 2015 to monitor the variation over time of existing crack widths. In addition to them, in 2019 five more digital automated crack monitors were installed. The latter were also equipped with temperature meters. The locations of all crack meters are shown in Figure 10, along with photographs of both crack meter types. The analysis of the displacements recorded by all crack meters show relatively small values of displacements with peak values of 5 mm. However, displacements recorded by crack meters are influenced by seasonal variations of the temperature in the church (i.e., when the temperature goes up the crack width goes down and vice versa). As a result, cracks in the church are currently either not opening up, or temperature-induced displacements are greater than those induced by long-term ongoing damage mechanisms.

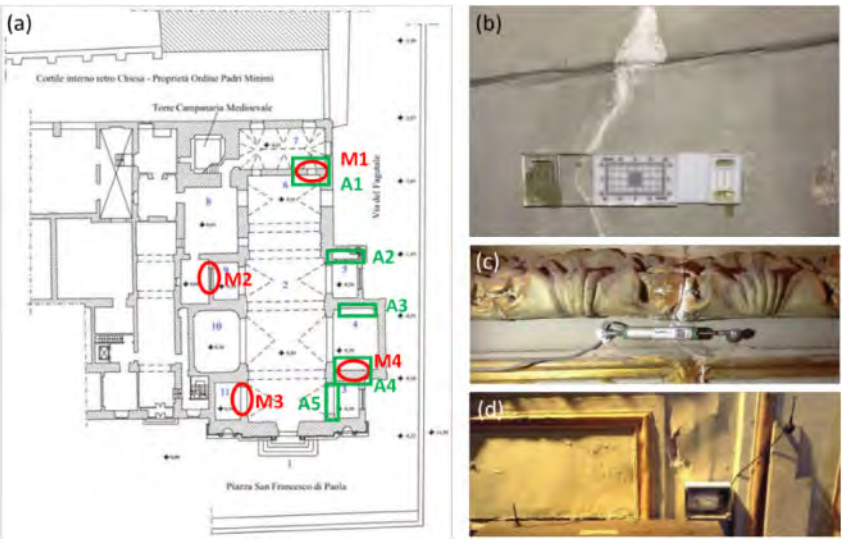

Figure 10. (a) Plan view of the church with the locations of all crack meters, (b) detail of the mechanical crack meter installed in the Saint Francis of Paola chapel (M4), (c) detail of the automated crack meter installed in the Saint Francis of Paola chapel (A4), and (d) acquisition unit of A4.

Interestingly during the 2016 Central Italy earthquake sequence (Stewart et al. 2018; Zimmaro & Stewart 2017) crack widths increased. This short-term variation may be related to earthquake-induced displacements. Such displacements were in the order of 0.5 mm and were recorded in the period between 17 August 2016 (before the first mainshock of the sequence on 24 August 2016) and 15 November 2016 (after the last mainshock of the sequence on 30 October 2016). On 18 January 2017, M1 recorded an incremental width offset of 0.25 mm. Interestingly, on that same day and before the reading was made, there was an earthquake swarm in the area of Campotosto (south of the mainshocks of the 2016 Central Italy earthquake sequence) with the stronger event having moment magnitude equal to 5.7. These evidences clearly show how earthquakes in Central Italy may generate non-negligible effects on monumental structures in the city of Rome. This almost anecdotal conclusion, based on a limited set of data, is consistent with historical data and archeoseismological findings by Galadini et al. (2013) who confirmed that damage to monuments of the city of Rome, including the Colosseum, were caused by historical earthquakes in the Central Apennine area.

4 CONCLUSIONS

In this study, ongoing damage mechanisms to the Saint Francis of Paola church in Rome were analyzed. This is an important monument located in the center of Rome, just 300 m from the Colosseum. First, the historical development of the area and all changes in the landscape since the Roman empire were analyzed. Following this analysis spanning a ∼2000 year-long period of evolution of the area, a thorough analysis of available historical sources about the construction of the church and surrounding structures was made. Finally, current extensional cracks to the structure were mapped and the results of a recent geotechnical/structural characterization and monitoring program were described.

This study shows that, according to pervasive historical sources and recent data, the damage mechanism that is still observed today started after two large excavations were performed near the church to construct Via Cavour and Via degli Annibaldi, two prominent roads designed after Rome became the capital of Italy in 1871. Both roads are protected by gravity retaining wall (both taller than 10 m). The retaining wall protecting Via degli Annibaldi is only 3 m away from the Saint Francis of Paola chapel (the largest side chapel of the church). The analysis presented in this study confirms that despite many uncertainties and possible local causes, the ongoing damage mechanisms is linked to the construction of Via degli Annibaldi. This study also shows that the ongoing deformations are slow. To confirm this conclusion an almost 6-year long time series of data recorded by crack meters was analyzed. The outcome of this analysis is that peak crack widths observed in this period are due to temperature-induced deformations. Finally, analyzing data recorded before, during, and after the 2016 Central Italy earthquake sequence, this study shows that open cracks are influenced by earthquakes in the Central Apennines. This observation is consistent with archeoseismological studies and relevant to future risk analysis of monumental structures in Rome. All analyses shown in this paper constitute a necessary first step towards the effective design of restoration and retrofit measures. As a result, it can be anticipated that future studies will also involve the characterization of structural elements. This study shows that the combination of historical information, geotechnical and structural characterization and monitoring represents an invaluable tool for such restoration efforts in monumental historical structures.

ACKNOWLEDGMENTS

The authors acknowledge the Order of Minims for allowing them to inspect the church and the monumental complex and for granting them access to their library. The superintendence of archaeology, fine arts, and landscape of Rome and Arch. Alessandra Centroni are acknowledged for the help with this study and the useful discussions on the church's status. LAGIC s.r.l., which performed the field/laboratory and monitoring programs presented in this study, is also acknowledged.

REFERENCES

Burghignoli A., Callisto L., Rampello S., Soccodato F.M., Viggiani G.M.B. (2013). The crossing of the historical centre of Rome by the new underground Line C: a study of soil structure-interaction for historical buildings. *Geotechnics and Heritage*, Taylor and Francis, London, UK.

Carravetta C. (2021). *Analisi storico-critica, indagini geotecniche e monitoraggio della Chiesa di San Francesco di Paola ai Monti in Roma*. Master's thesis, Supervisors: E. Ausilio E., P. Zimmaro, Corso di Laurea Magistrale a ciclo unico in Ingegneria Edile–Architettura, a.y. 2020–2021, Department of Civil Engineering, University of Calabria, Rende, Italy.

Droysen G. (1886). *Plan de Rome dans l'Antiquité*. Allgemeiner Historischer Handatlas.

Falda G.B. (1676). *Nuova piante et alzata della città di Roma con tutte le strade piazze et edifici de tempii*. Rijksmuseum collection, Amsterdam, The Netherlands.

Galadini F., Ricci G., Falcucci E., Panzieri C. (2013). I terremoti del 484–508 e 847 D.C. nelle stratigrafie archeologiche tardoantiche e altomedievali dell'area romana. *Bollettino di Archeologia online*, IV(2-3-4). 139–162.

Italian Ministry of Infrastructure and Transport (2018). *Aggiornamento delle Norme Tecniche per le Costruzioni*, D.M. 17 Gennaio 2018. Gazzetta Ufficiale della Repubblica Italiana, 42.

Stewart J.P., Zimmaro P., Lanzo G., Mazzoni S., Ausilio E., Aversa S., et al. (2018). Reconnaissance of 2016 Central Italy earthquake sequence. *Earthquake Spectra*, 34, 1547–1555.

Tempesta A. (1593). *Recens prout hodie iacet almae urbis Romae cum omnibus viis aedificiisque prospectus accuratissime delineatus*. National Library of Sweden, Stockholm, Sweden.

Zimmaro P. & Stewart J.P. editors, GEER (2017). *Engineering reconnaissance following the October 2016 Central Italy earthquakes - Version 2*, GEER Association Report No. GEER-050D. DOI:10.18118/G6HS39.

Geotechnical Engineering for the Preservation of Monuments and Historic Sites III – Lancellotta, Viggiani, Flora, de Silva & Mele (Eds)

Monitoring and 3D surveys for the safety fruition of a hypogeum site

A. Scotto di Santolo
Telematic University Pegaso, Piazza Trieste e Trento, Naples, Italy

G. Bausilio
Department of Earth Sciences, Environment and Resources, University of Naples Federico II, Napoli, Italy

M. Danzi
Digital Surveys, Napoli, Italy

U. Del Vecchio
Geologist, Napoli, Italy

D. Di Martire
Department of Earth Sciences, Environment and Resources, University of Naples Federico II, Napoli, Italy
SINTEMA Engineering s.r.l., Napoli, Italy

D. Infante
Telematic University Pegaso, Piazza Trieste e Trento, Naples, Italy
SINTEMA Engineering s.r.l., Napoli, Italy

M. Ramondini
SINTEMA Engineering s.r.l., Napoli, Italy
Department of Civil, Architectural and Environmental Engineering, University of Naples Federico II, Naples, Italy

ABSTRACT: The metropolitan area of *Napoli* (Italy) is characterized by a subsoil rich in cavities and tunnels, initially born as material quarries present in all architectural contexts of *Campania*. The cavities were reused in later times for different purposes: mainly funeral and burial activities since the Hellenistic revival during the Roman period and later during the Christian era although, in the latter case, the catacombs were even used as place for worshipping functions. Religious activities were not the only reuse for these underground cavities as they were used as aqueducts and tunnels. This underground network of tunnels and cavities includes the numerous archaeological quarries and constitute a patrimony to preserve and enhance. The current use of the Naples underground is cultural tourism, which involves a very high annual passage of visitors in environments that need maximum structural safety. And essential, in order to ensure the safety fruition of the site, assess their stability conditions. In this paper we report the multidisciplinary investigations carried out on an ancient tuff quarry, known as *Cimitero delle Fontanelle*, in *Napoli*. In detail the result of diagnostic surveys, geological and geotechnical investigations, and the set-up of monitoring system in order to plan scheduled maintenance were discussed, starting from the previous works carried out in order to design the remedial measure necessary to reopen the tourist site in safety.

DOI 10.1201/9781003308867-48

1 INTRODUCTION

Underground cavities are present all over the world and they are often linked to underground excavation of building materials not only nearby, but even under the same cities that were built using those same materials (Kim et al. 2018). An example of such is Naples, in Italy, located in the Southern Part of the Campanian Plain, surrounded by the Gulf of Naples to the South, the two volcanic complexes of *Somma-Vesuvio* (to the East) and *Campi Flegrei* (to the West). The Campanian Plain, at North, is a graben structure made up of a carbonate bedrock, covered by a Mio-Pliocene succession, and closed by a succession of pyroclastic, alluvial and maritime deposits with a thickness higher than 200 m (Santangelo et al. 2010). These pyroclastic deposits are derived from the intense volcanic activity in the area (Scandone et al. 1991), mainly the *Roccamonfina*, the Phlegrean Fields and the Vesuvius. Products of these activities are the Ignimbrite Campana (IC) and the Neapolitan Yellow Tuff (NYT), both of them from the Phlegrean Fields and dated, respectively 39 ky BP and 12 ky BP (De Vivo et al. 2006, 2011). NYT is largely present in the territories of the city of Napoli (Figure 1a). It is a soft rock mainly made up by successions of cinerites and pumices layers, unlithified in its lower member, and by lithified cinerites layers alternated with reversely graded layers and ash beds (Scarpati et al. 1993; Colella et al. 2017; Wohletz et al. 1995). Because of its characteristics, the NYT has been extracted and used as a building stone since ancient times (Aversa et al. 2013; Colella et al. 2001, 2017) as seen by different archeological remains.

The extraction activities have been so intensive that, earlier authors, have stated the formation of three different layers with different purposes for the underground cavities (Aversa et al. 2013):

- First layer: the sewer networks;
- Second layer: a great number of tunnels and chambers dug in the tuff, mainly water channels and tanks;
- Third layer: for tuff extraction and, lately, for religious cults (Esposito 2007).

The size and the use of the different tunnels and chambers can vastly differ depending on the historical context during the excavation but they are mostly located above the underground water shed. Eventually, through natural failings or due to water infiltration or leaks from sewer or the aqueduct pipelines, the stability of the roofs of these cavities can deteriorate, causing collapse and/or subsequent sinkholes (Guarino et al. 2012; Rispoli et al. 2020; Scotto di Santolo et al. 2018).

The center of the city is full of buildings built in NYT, like churches, which have given a peculiar look to the city and that were built above the quarries from which the NYT was excavated. The morphological hill conformation of the city (*Vomero*, *Posillipo*, *Capodimonte* and the *Camaldoli*, to name a few) also allowed a rich production of NYT building blocks from room and pillar mining. These cavities did not become less useful when the extraction of building materials stopped; in fact, a great amount of these cavities was converted, in the following centuries, for religious activities. A great number of these cavities became catacombs or were used for other means and survived the trial of time and can still be visited nowadays. Even in more recent times, during World War 2, most of the already used cavities, and even others that were not used at the time, acted as air-raid shelter by the people of city that were searching for safety or that lost their homes to the bombs. Some of the most important manmade cavities that can be found in the city, which have been reused as burial sites or for worshipping purposes, are represented by the *San Gennaro* catacomb, the *San Gaudioso* catacomb and the *Cimitero delle Fontanelle* (*cemetery of the "little fountains",* as there was presence of water sources in the past) as well, which are an important attraction for tourists from within and from outside the city itself (Figure 1).

Figure 1. Location of the study area: a) Lithologic map of the city of Naples and location of some of the most famous underground cavities of Naples; b) Location of the city of Naples (Italy); c) Cimitero delle Fontanelle, main entrance.

The *Cimitero delle Fontanelle* is a chamber and pillar cavity located in the city of Napoli, used, at first, for a long time as a quarry since its creation (XVI century) and then converted to catacomb, in order to contain the high amounts of deaths following rebellions, natural disasters and plagues. Its religious and folkloristic value is extremely high in the history of the city (e.g. Scotto di Santolo et al. 2013, 2015). In order to safely reopen to the public use, a number of geological and geotechnical investigations have been carried on. A report of the results obtained from these investigations and possible interventions will be shown in this work.

2 THE GEOLOGICAL AND GEOTECHNICAL INVESTIGATIONS

The reconstruction of the stratigraphy and the in-deep the characterization of the pyroclastic deposits that recover the cavity, both factors of critical importance for the study of the stability of these geotechnical structures, started from available data (e.g. de Silva & Scotto di Santolo 2018; Scotto di Santolo et al. 2013, 2015). Different surveys have been carried on, from those aimed at geometric reconstruction of the cavity, to those focused on the study of the stratigraphy and mechanical properties of the soft rock and cohesionless soils present:

- Terrestrial Laser Scanner (TLS) integrated with Unmanned Aerial Vehicle (UAV) survey;
- 3 Continuous dynamic penetrometric test (DPM);
- 2 P-wave seismic refraction tomography (SRT);
- 2 Electrical resistivity tomographic survey (ERT);
- 2 Thermographic survey;
- 2 Georadar survey;
- Laboratory tests on NYT samples from 10 horizontal boreholes;
- 4 Flat Jack tests (single and double);
- Monitoring activities:
  - Electrical extensometers;
  - Planar fissuremeters;
  - Dosimetries for Radon emission.

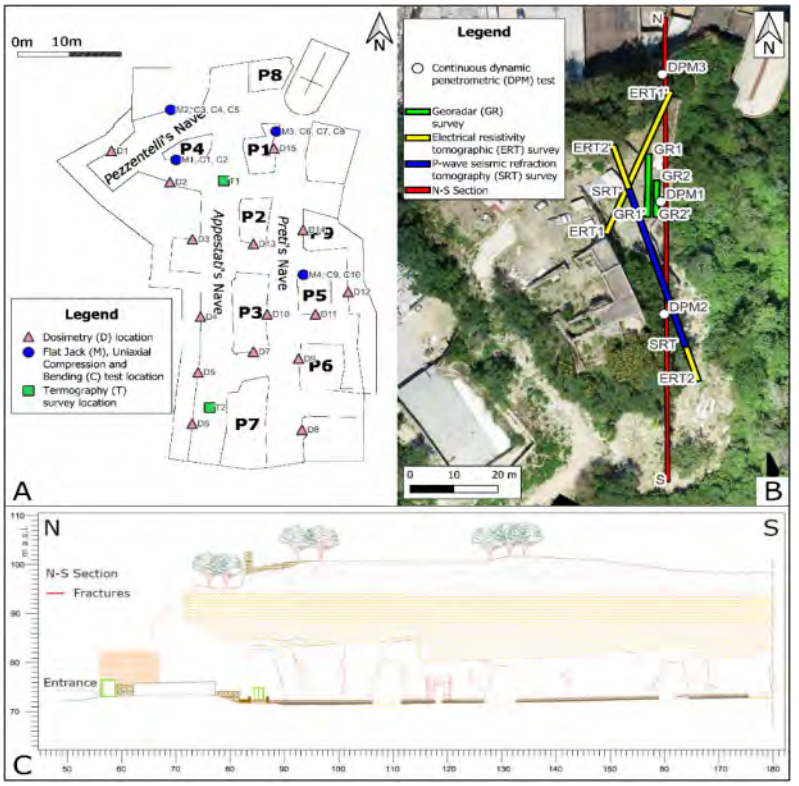

Figure 2. Location of the geotechnical and geophysical investigations: a) Instrumentation and in situ-test location inside the cavity; b) in situ surveys and sections at the top of the hill; c) N-S geological cross-section with main discontinuities detected.

The location of all in situ surveys was reported in Figure 2.

The geometry of the buried structure has been surveyed through the use of a terrestrial laser scanner (TLS) for the inside (30 scans) and the outside (3 scans), combined with high-resolution pictures (3 cm/pixel) obtained with a camera mounted on a UAV. The product is georeferenced using different points outside of the cemetery, which coordinates have been detected with a GPS, with standard WGS84, Figure 3. Meanwhile, the penetrometric analysis has been carried out with a DPM penetrometer for continuous dynamic penetrometric tests in three different points to obtain information about the thickness and strength of the cover deposits at the top of the hill inside which the cavity was dug.

A P-wave Seismic Refraction Tomography (SRT) analysis has been performed, with the spacing between every geophone of 5 meter for a total of 12 geophones, in order to integrate these data with the ones obtained from the penetrometric analysis. This geophysical method is based on the study of the seismic signals that, created through the use of a hammer or explosives, travel and get refracted by the discontinuities. Different discontinuities and material properties can change the propagation speed of the seismic signals. These variations can be found in the signal caught by the geophones and can be interpretated (Bogoslovsky & Ogilvy 1977).

In order to characterize and study the presence of water bodies in the cover layer or inside the NYT, an Electrical Resistivity Tomographic survey has been employed. It is an active geophysical method that calculates the apparent electrical resistivity of the materials and gives them a different pseudo-depths, depending on the geometrical reconstruction (Edwards 1977). These apparent resistivity data from the subsoil are then subject of an inversion procedure to obtain an electrical resistivity tomography. The two sections were located as to obtain a 3D reconstruction of the area. In order to

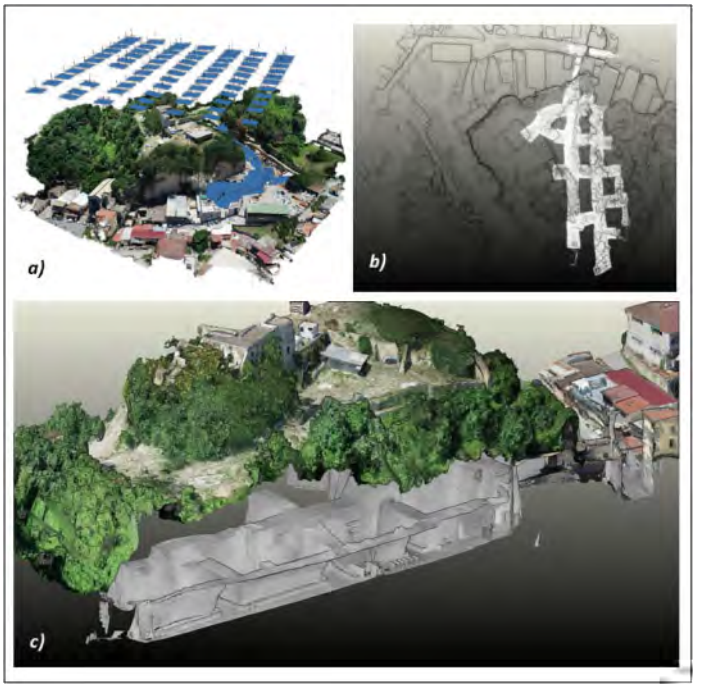

Figure 3. Digital survey: a) flight plan of UAV hill surface; b) laser scanner cave survey; c) longitudinal section of 3D combined model.

recognize the presence of an anomaly or a pipeline linked to the water leaks, inside the pyroclastic cover a georadar survey has been carried out at the top of the hill, with two parallel sections close to a collect well on site. Moreover, inside the cavity, a thermography analysis has been executed. This is a non-invasive technique that, through the infrared radiation, from every mass, allows the operator to recognize and locate potential water accumulation inside the NYT.

For the study of the discontinuities seen on the NYT walls of the cavity, data from the terrestrial laser scanner has been used. Thanks to the high-definition pictures (3 cm/pixel) and the use of specific software (*Cloud Compare, 2020*), the joint families have been recognized and distinguished, Figure 3. This activity has been supported by field work according to methods proposed in scientific literature (Bieniawski 1989; Goodman 1980; Hudson & Harrison 1997; Markland 1972; Romana 1985) in order to characterize the different properties of the family discontinuities. The steps were: 1) Giving a progressive id to the discontinuities; 2) distinguish between shallow cracks and deep fractures; 3) dip and plunge obtained with a compass; 4) length of the discontinuity; 5) persistence; 6) roughness of the discontinuities measured with a Barton Comb; 7) Aperture; 8) Shape of the discontinuities; 9) Filling; 10) Water presence (dry, wet); 11) Weathering of the walls.

In order to characterize the current state of stress and strength of the NYT cavity, laboratory and in situ tests were utilized:

- 5 horizontal boreholes at different depth along the rocky walls with samples for laboratory analysis;
- 4 Flat Jack tests (single and double);
- 5 Uniaxial Compression Test;
- 5 Indirect tensile test (Bending Test).

The Flat Jack tests are utilized to measure the state of stress inside the rock in current operating conditions (single Jack) and to identify the in situ stress-strain curve, from which to derive the elastic modulus and, if possible, the in situ compressive strength, if it is lower than the maximum

pressure for the Flat Jacks (double Jack). The assumptions of the last test method are that the rock surrounding the opening is homogenous; the stress applied to masonry by Flat Jacks is uniform and the state of stress is uniaxial, as if the lateral constraining effects of adjacent rock can be neglected. The uniaxial compressive and tensile tests were executed on samples obtained from different height, close to the location where the Flat Jack tests were performed, in order to evaluate any vertical variation of the mechanical properties of the NYT. From the stress data obtained with the Flat Jack tests, the Safety Factor (SF from hereafter) has been determined as the ratio between the stress value at failure (σ_{max}) and service condition (σ_{oc}).

In the end, a monitoring system has been installed. Some of the instruments will keep under constant monitoring the discontinuities with the use of electrical extensometers (continuous acquisition of data in the most critical sections of the cavity, according to the numerical analysis). Part of the monitoring system, installed to study the fractures in the walls and pillars of the cavity, includes the study of Radon density emission from the NYT. As other studies have shown (Pugliese et al. 2013; Quarto et al. 2014), the NYT does emit some quantities of Radon that can be inhaled by tourists and by guides in larger quantity, due to their exposure. For this reason, 15 dosimetries has been installed, which would be changed every six months for a whole year, in order to assess the Radon emissions from the NYT.

3 RESULTS AND DISCUSSION

The geometry has been reproduced through the use of TLS, which produced a 3D model of the cave and hill, Figure 3. It shows a planar shape close to a rectangular with its long side aligned North-South. It is made of two main naves approximately 100 meters long, its section shape is a trapezoid with a maximum width of 40 meters. The maximum height of the cemetery is circa 13 meters and the thickness of the roof is variable between 1.5 and 3.0 meters. The high-resolution pictures, obtained through UAV, allowed the survey of the fractures and cracks on the surface of the tuff. This high-resolution model has been utilized to extrapolate as a geo-mechanical and geo-structural survey, the different families of discontinuities, Figure 3.

Eighty-four different families have been recognized and characterized. From the study of the families of discontinuities, it appears that there are not widespread critical conditions which can lead to the formation of blocks that could fall. Although this is only a general observation, as there are some delimitated areas that need precautionary actions.

These zones area mainly located within the pillars (P1; P3; P4; P6; P7) as they can be both singular point-like cracks or fractures that can go for a long vertical section of the pillar, intersecting with the roof.Other critical zones are found in the two main naves where the fractures could generate some discrete dimensioned blocks. It is also source of instabilities the continuous, although ephemeral, flow of water coming from the upper cover layers. To complete the reconstruction of the site, the penetrometric and the P-wave seismic tomography datas were integrated to obtain a more throughout study of the cover layers above the *Cimitero delle Fontanelle,* Figure 4.

The three sites were the penetrometric survey has been performed reached different maximum depths: DPM1 (6.80 m); DPM2 (7.10 m) and DPM3 (3.10 m). The P-wave seismic refraction have outlined the presence of three main layers: 1) superficial low-density stratum, made up of unlithified pyroclastic deposits; 2) an intermediate layer where the pyroclastic deposits are mildly lithified and a 3) lithified bedrock made of NYT, as observable inside the cavity. The study of the pyroclastic deposits, through an electrical tomography and the georadar surveys (Figure 5), has highlighted the presence of three different layers based on the saturation level: i) low saturation level stratum and the ii) high saturation layer (< 25 [Ohm/m]), meanwhile the last stratum is the one that describes the iii) NYT.

It can also be distinguished, through the georadar survey, the presence of anthropic artifacts that do not allow the natural flow of the meteoric water from the collect well to the side of the slope, allowing an accumulation and subsequential downward flow towards the cemetery from these cover deposits. This flow causes a great amount of dripping from the ceiling of the cemetery. With the

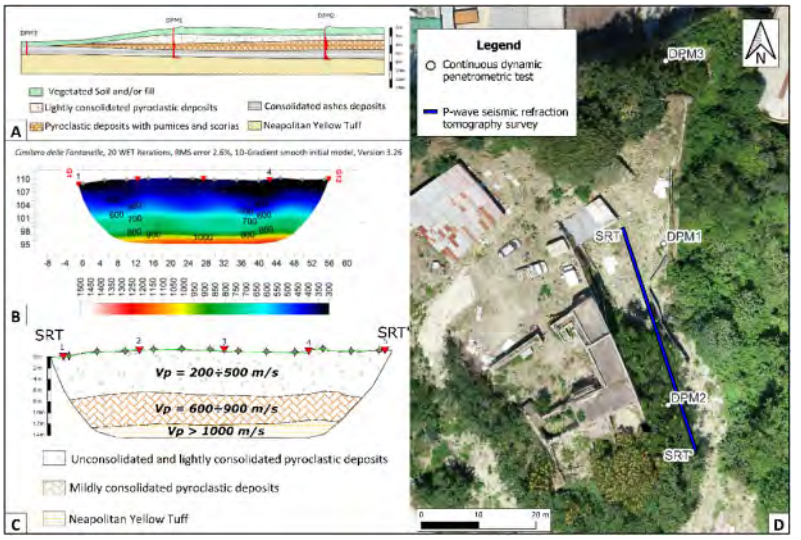

Figure 4. Results of in situ investigations at the top of the hill: A) stratigraphic section by DPM test; B) P-wave velocity by seismic refraction test; C) stratigraphic sections by seismic refraction test; D) cross-sections location.

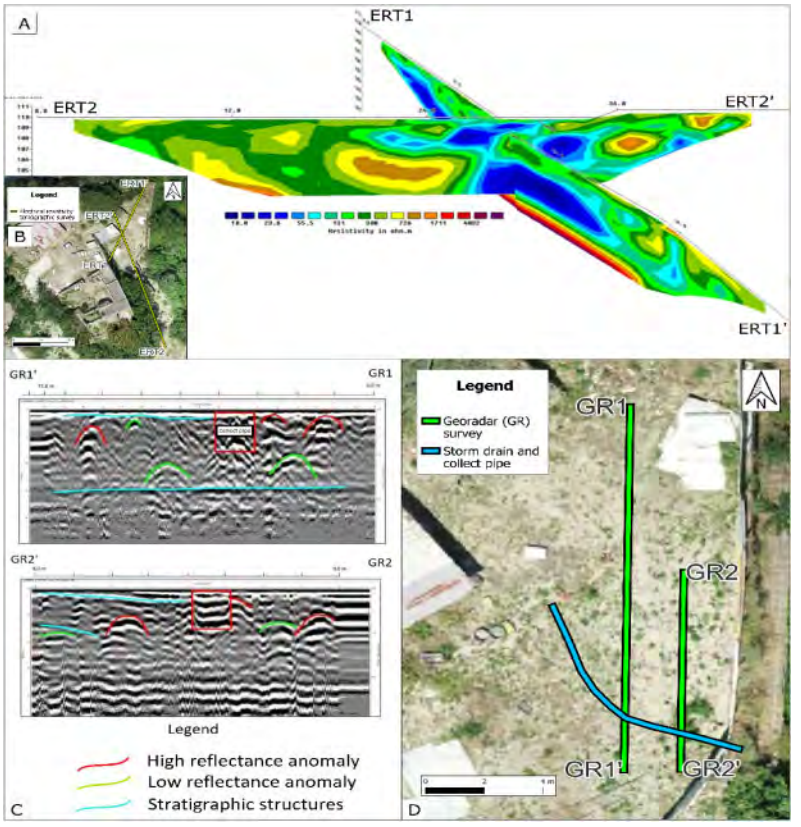

Figure 5. Results of in situ investigations at the top of the hill: a) ERT profiles; b) location of the cross-sections investigated; c) Georadar profiles; d) location of the georadar survey and collect pipe.

thermography survey, the inside of the cavity has been thoroughly analysed, starting from a general study of the entire area and then, with a detailed study of the ceiling, Figure 6. It can be recognized different low-temperature zones which coincide with the high saturation areas where dripping can be observed, Figure 6 b and d.

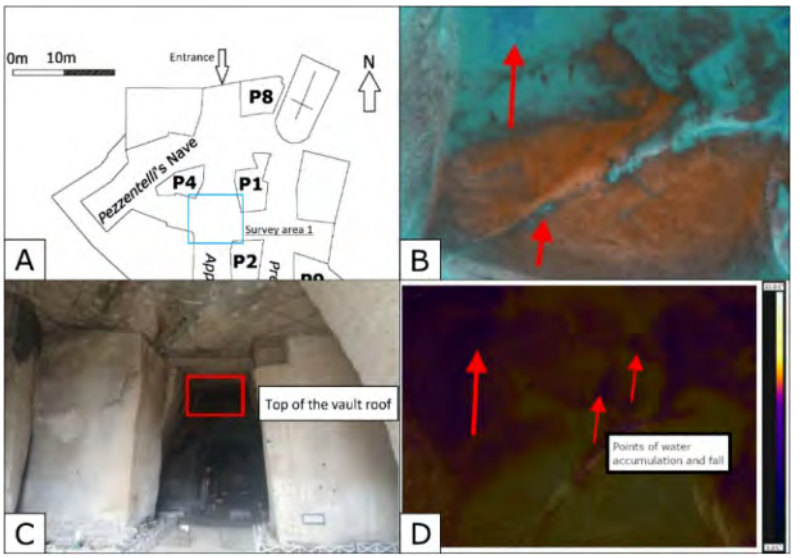

Figure 6. Results of in situ investigations on the roof of the cavity: a) area analyzed; b), d) thermogram image; c) photo of the infill water.

Finally, some walls and pillars have been selected to measuring the state of stress and ten samples were collected, on the base of the new data and the previous 3D numerical analysis of the static and dynamic condition of this site (de Silva & Scotto di Santolo 2018, 2019; Scotto di Santolo et al. 2015). The analysis, done with the Flat Jack, describes a stable condition, with SF values well above 1.0 (4.00; 5.80; 3.99; 3.50). The results are reported in Table 1. The Flat Jack M1, located at

Table 1. Summary of the mechanical properties of the samples obtained during the study.

Sample	Height [m]	Type of Analysis	σ_{oc} [MPa]	σ_{max} [MPa]	SF = σ_{max}/σ_{oc}	Compres. Strength [MPa]	Bending Strength [MPa]
M1	1.00	Flat Jack	0.83	3.34	4.00	/	/
M2		tests (single	0.55	3.17	5.80	/	/
M3		and double)	0.75	3.00	3.99	/	/
M4			0.67	2.34	3.50	/	/
C1	0.00	Uniaxial	/	/	/	1.53	/
C2	1.50	Compression	/	/	/	2.26	/
C3	0.00	Test	/	/	/	2.63	/
C4	1.50		/	/	/	2.30	/
C5	4.00		/	/	/	3.62	/
C6	0.00	Bending	/	/	/	/	0.938
C7	1.50	Test	/	/	/	/	0.938
C8	4.00		/	/	/	/	0.984
C9	0.00		/	/	/	/	0.914
C10	1.50		/	/	/	/	0.962

the pillar P4, Figure 2, measured the highest value of stress in service condition (σ_{oc}) and at failure (σ_{max}). This pillar, according to the morphology, sustains the highest load. On the other end, the maximum measured values (σ_{max}) are relatively constant at the 4 sites, except for the Pillar P5, which is lower. These tests show, luckily, that the stress condition is significantly lower than the critical ones. Starting from de Silva and Scotto di Santolo (2018), a new 3D FLAC model has been built. Accordingly, all materials have modelled as an elastic plastic with softening behaviour with the Mohr-Coulomb failure criterion with the parameters summarized in the Table 2. The main goal of this analysis was the calibration of the equivalent continuum model in static condition on the base of the flat jack tests, in order to evaluation the global and local stability condition of the cavity. In Figure 7 the results are shown in terms of vertical stresses and of the ratio between these and the failure ones, defined as local safety factor, at the base of the piers. The state of stress is not constant with the highest levels on the edges, but the safety factors (SF) are greater than 2 except for edges with the lowest value for the pillars P4 and P1. This is probably due to the high stress located in that zone together with the smaller influent area of the pillar P4 against the other columns.

Table 2. The mechanical parameters adopted in the FLAC 3D model.

Materials	γ_n [kN/m^3]	G_0 [MPa]	ν [–]	φ [°]	c_p [kPa]	c_f [kPa]
P (*Pozzolana*) – Cover layer	15.0	129	0.30	33	30	10
NYT (Neapolitan Yellow Tuff)	14.0	603	0.17	29	750	120
D (bottom filling)	13.0	202	0.37	26	40	10

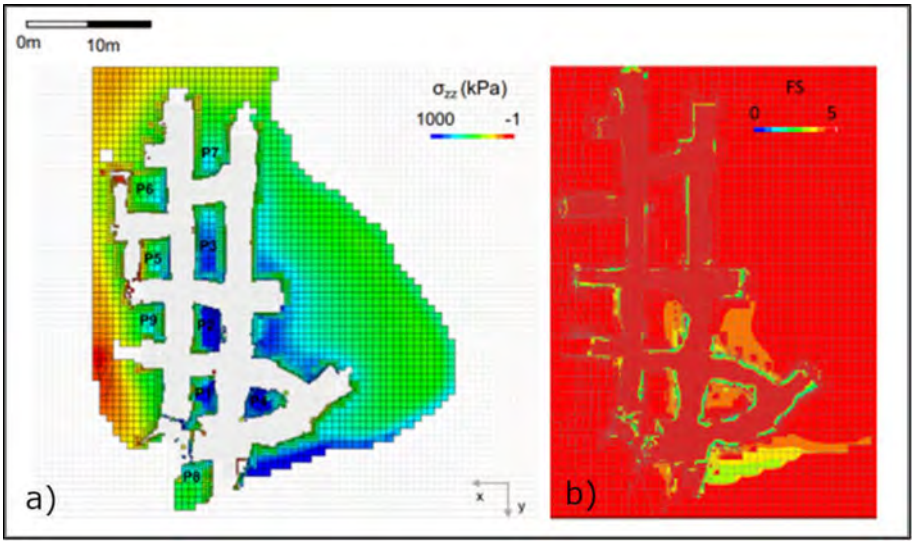

Figure 7. Results of 3D FLAC model: a) vertical stress; b) local safety factors.

It is also worth of note that the equivalent homogenous continuous model does not consider the contribution to the stability of the column given by bolts done in the past but, on the other end, it also does not take into account the presence of fractures.

Regarding the stability of the roof, it appears to be a widespread stability in the cavity, although there are some more interesting cases along some of the naves (*Pezzentelli*'s nave and *Preti*'s nave) where the safety values are close to the minimum for the stability condition.

As have been mentioned above, even though the cavity shows global stability, a monitoring system has been installed to monitor the discontinuity families detected. Of the abovementioned 84 joints, Figure 8, the most interesting and hazardous will be continuously monitored utilizing two different instruments:

– Electrical Extensometer;
– Planar Fissuremeter.

Figure 8. Set up of the monitoring system: a) plan view; b) temperature and movement data during the monitoring period.

The first one allows a continuous acquisition of data in the most critical sections of the cavity. Walls and pillars show the presence of some families of joints and fractures that could lead to the generation of a rock fall. These specific cases need a continuous and meticulous monitoring during the years. The second type of instrument has been installed in the areas that show a high density of discontinuities that should still be monitored, even though the abovementioned analysis does not show a highly critical stability condition. Close to the discontinuity families, dosimetries for Radon emission from the NYT tuff have been installed. These instruments will be verified every six months (not currently available) to keep trace of the Radon emission that could harm the safety of tourists and tourist guides alike.

4 CONCLUSIONS

Hypogeum sites in Naples have always been an important part of the history of the city. Since its beginnings, the extraction of building materials has been a favourable activity for the city development and, lately the use of the hypogeum sites as places of worship and catacombs added a cultural aspect to these underground cavities. During the Second World War these sites have given shelter to hundreds of people during the bombardments of the city and, nowadays, they are an important part of the city of Naples touristic life. Of course, these sites must be as safe as possible for both the tourist and the guides that would walk along the walls of these places. For this reason, different studies have been carried out regarding the evaluation of the stability of the cavities underground the city (e.g. de Silva & Scotto di Santolo 2018; Fasano et al. 2021; Rispoli et al. 2020; Scotto di Santolo et al. 2015). This study reports the multidisciplinary investigations carried out to evaluate the stability condition of the cavity known as *Cimitero delle Fontanelle in Napoli,* starting to the geomorphological survey up to the 3D numerical models. The site is globally stable, although, some portions are close to the unstable condition, mostly due to the presence of joints and/or water infiltration through the Neapolitan Yellow Tuff. These locations have been put under continuous monitoring and some critical area inside the cavity, identified through the abovementioned study, has been interdicted.

ACKNOWLEDGEMENTS

The authors gratefully acknowledge the Municipality of Naples to support the study, and in particular Arch. S. Iervolino and Dr A. Barba, for the help in the logistic activities.

REFERENCES

Aversa, S., Evangelista, A., & Scotto di Santolo, A. (2013). Influence of the subsoil on the urban development of Napoli. In Proc. Of the 2nd Int. Symp. *On Geotechnical Engineering for the preservation of Monuments and Historic Sites* (pp. 15–43).

Bieniawski Z.T. (1989). *Engineering rock mass classification.* John Wiley & Sons, 251 pp.

Bogoslovsky V.A. and Ogilvy A.A. (1977) *Geophysics*, 42, pp. 562–571.

CloudCompare (version 2.6.1) GPL software. (2020). User manual retrieved from http://www.cloudcompare.org/

Colella, C., Gennaro, M. D., & Aiello, R. (2001). Use of zeolitic tuff in the building industry. Re*views in mineralogy and geochemistry*, 45(1), 551–587.

Colella, A., Di Benedetto, C., Calcaterra, D., Cappelletti, P., D'Amore, M., Di Martire, D., Graziano, S.F., Papa, L., de Gennaro, M., & Langella, A. (2017). The Neapolitan Yellow Tuff: an outstanding example of heterogeneity. *Construction and Building Materials*, 136, 361–373.

de Silva, F., Scotto di Santolo A. (2018) Probabilistic performance-based approaches to the static and seismic assessment of rock cavities. *International Journal of Rock Mechanics and Mining Sciences*, 112, pp. 354–368.

De Vivo, B. (2006). Volcanism in the Campania Plain. Vesuvius, Campi Flegrei and Ignimbrites. *Developments in Volcanology 9,* Elsevier.

De Vivo, B., Rolandi, G., Gans, P. B., Calvert, A., Bohrson, W. A., Spera, F. J., & Belkin, H. E. (2001). New constraints on the pyroclastic eruptive history of the Campanian volcanic Plain (Italy). *Mineralogy and Petrology*, 73(1), 47–65.

Edwards, L. S. (1977). A modified pseudosection for resistivity and IP. *Geophysics*, 42(5), 1020–1036.

Esposito, C., (2007). *Gli Ipogei Greci della Sanità*. Napoli, Oxiana. (In italian).

Fasano, G., Allocca, V., Bilotta, E., Nicotera, M. V., Ramondini, M., Russo, G., Russo, M. & Calcaterra, D. (2021). Investigations and stability analysis of San Marcellino cavities in the historical centre of Naples. In *IOP Conference Series: Earth and Environmental Science* (Vol. 833, No. 1, p. 012071). IOP Publishing.

Goodman, R.E. (1980). *Introduction to Rock Mechanics* (Chapter 8), Toronto: John Wiley, pp. 254–287.

Hudson, J.A. and Harrison, J.P. (1997). *Engineering Rock Mechanics – An Introduction to the Principles*, Pergamon Press.

Kim, K., Kim, J., Kwak, T. Y., & Chung, C. K. (2018). Logistic regression model for sinkhole susceptibility due to damaged sewer pipes. *Natural Hazards*, 93(2), 765–785.

Markland, J.T. (1972). A useful technique for estimating the stability of rock slopes when the rigid wedge slide type of failure is expected: Imperial College Rock Mechanics Research Reprints, n. 19.

Pugliese, M., Quarto, M., De Cicco, F., De Sterlich, C., & Roca, V. (2013). Radon exposure assessment for sewerage system's workers in Naples, South Italy. *Indoor and Built Environment*, 22(3), 575–579.

Quarto, M., Pugliese, M., Loffredo, F., Zambella, C., & Roca, V. (2014). Radon measurements and effective dose from radon inhalation estimation in the Neapolitan catacombs. *Radiation Protection Dosimetry*, 158(4), 442–446.

Rispoli, C., Di Martire, D., Calcaterra, D., Cappelletti, P., Graziano, S. F., & Guerriero, L. (2020). Sinkholes threatening places of worship in the historic center of Naples. *Journal of Cultural Heritage*, 46, 313–319.

Romana M, (1985). New adjustment ratings for application of Bieniawski classification to slopes. Int. *Symp. on the Role of Rock Mechanics ISRM*. Zacatecas, pp. 49–53.

Santangelo, N., Ciampo, G., Di Donato, V., Esposito, P., Petrosino, P., Romano, P., Russo Ermolli, E., Santo, A., Toscano, F., Villa, I. (2010). Late Quaternary buried lagoons in the northern Campania plain (southern Italy): evolution of a coastal system under the influence of volcano-tectonics and eustatism. *Ital. J. Geosci.* 129(1).

Scotto di Santolo A., Evangelista A., Evangelista L. (2013). The Fontanelle Cemetery: between legend and reality. In: *Geotechnical Engineering for the Preservation of Monuments and Historic Sites*. p. 641–648, Taylor & Francis Group, London, ISBN: 978-1-138-00055-1, Napoli, Italy, 30–31 May 2013.

Scotto di Santolo, A. S., Evangelista, L., Silvestri, F., Cavuoto, G., Di Fiore, V., Punzo, M., Tarallo, D., & Evangelista, A. (2015). Investigations on the stability conditions of a tuff cavity: the Cimitero delle Fontanelle in Naples. *Rivista Italiana di Geotecnica* XLIX (3), 28–46.

Scotto di Santolo, A. S., Forte, G., De Falco, M., & Santo, A. (2016). Sinkhole risk assessment in the metropolitan area of Napoli, Italy. *Procedia Engineering*, 158, 458–463.

Scandone, R., Bellucci, F., Lirer, L., & Rolandi, G. (1991). The structure of the Campanian Plain and the activity of the Neapolitan volcanoes (Italy). *Journal of Volcanology and Geothermal Research*, 48(1–2), 1–31.

Scarpati, C., Cole, P., & Perrotta, A. (1993). The Neapolitan Yellow Tuff—a large volume multiphase eruption from Campi Flegrei, southern Italy. *Bulletin of Volcanology*, 55(5), 343–356.

Wohletz, K., Orsi, G., & De Vita, S. (1995). Eruptive mechanisms of the Neapolitan Yellow Tuff interpreted from stratigraphic, chemical, and granulometric data. *Journal of Volcanology and Geothermal Research*, 67(4), 263–290.

Geotechnical Engineering for the Preservation of Monuments and Historic Sites III – Lancellotta, Viggiani, Flora, de Silva & Mele (Eds)

An update on the Tower of Pisa

N. Squeglia
University of Pisa, Pisa, Italy

C. Viggiani
University of Napoli Federico II, Napoli, Italy

ABSTRACT: The Leaning Tower of Pisa has been stabilised in the years 1999–2000 by an International Committee appointed by the Italian Government. An analysis of the whole history of the monument, starting from its construction in the XII century and including the results of the modern monitoring of XIX and XX century led the Committee to the conclusion that the Tower is affected by a phenomenon of instability of the equilibrium, depending on the deformability and not on the strength of the foundation soils. The stabilisation intervention, totally respectful of the integrity of the monument, consisted in slightly decreasing the inclination of the Tower by underexcavating a small volume of soil beneath the north side of the foundation. The paper briefly reports the analysis and the intervention; the observation of the behaviour in the twenty years elapsed since then allows some preliminary evaluation of the future behaviour.

1 INTRODUCTION

The Tower of Pisa (Figure 1) is one of the most famous monuments in the world; it rests on a subsoil of poor mechanical properties (Figure 2), which is at the origin of its leaning. It has been stabilized some twenty years ago by an International Committee appointed by the Italian Government with an underexcavation intervention conceived to respect as far as possible the integrity of the monument. Since then, many papers, lectures, books, symposia have been devoted to this topic, but it appears that the knowledge of what has been done and why is not widespread. Therefore, we believe that a short informative paper, based essentially on the results of the monitoring currently under way and updated to the present date, may be of some interest. The potential future behaviour of the monument is also briefly discussed.

The history of the Tower is first recalled, subdividing it in four stages: (i) from the construction, which began in 1173, to 1911, the starting date of modern monitoring; (ii) from 1911 to 1999, the start of the stabilisation measures carried out by the International Committee; (iii) from 1999 to 2002, the period of implementation of the stabilization measures, and (iv) from 2002 to 2022. For each of these time intervals some of the available monitoring results are illustrated and briefly discussed.

In Figure 3 the whole history of the inclination of the Tower since its construction is reported. From the construction time to the beginning of XIX Century the only data available are the values of the inclination in the plane of maximum leaning, very nearly oriented in the North-South direction.

The monument was erected in three stages, over a period of around two centuries (1173–1368). It started leaning substantially during the second stage; however, the construction went on introducing geometrical corrections to counteract the effects of the inclination. The accuracy of the masonry works allows the use of these corrections to piece together very reliably the inclination developed during construction.

DOI 10.1201/9781003308867-49

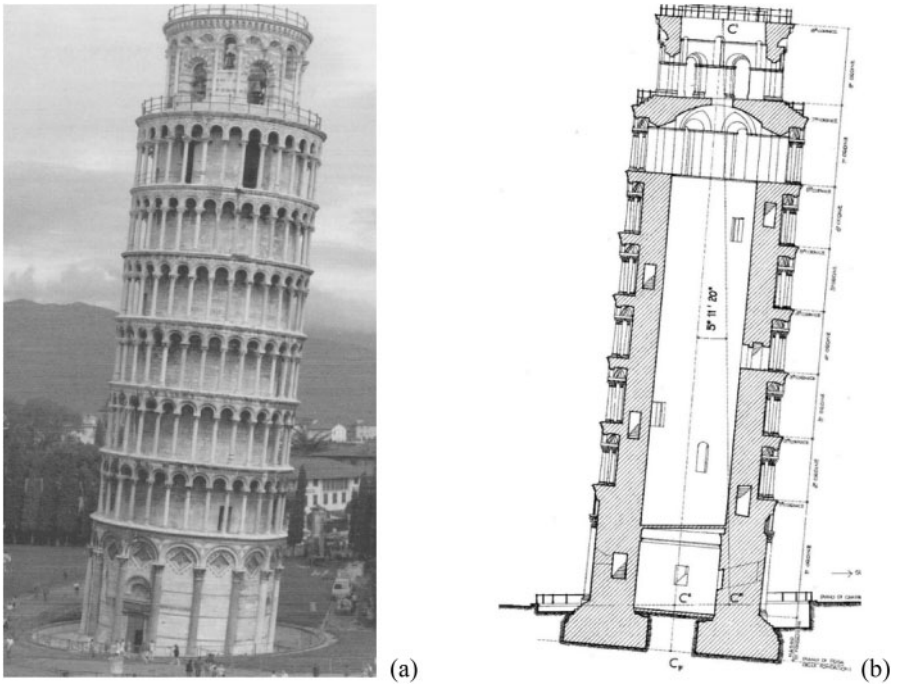

Figure 1. (a) View of the leaning tower from the West; (b) Section along vertical plane of maximum inclination (very nearly in the North – South direction).

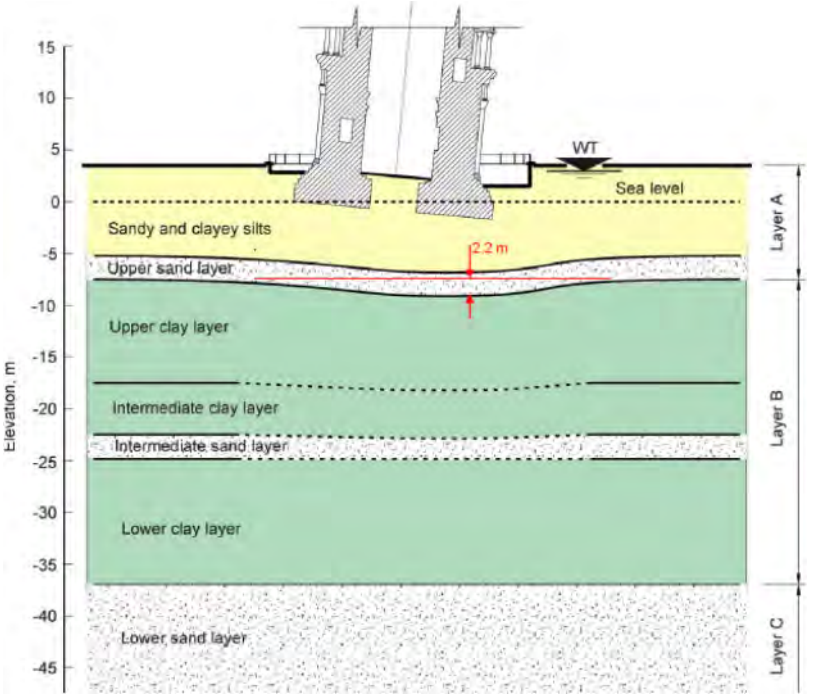

Figure 2. The subsoil of the Tower.

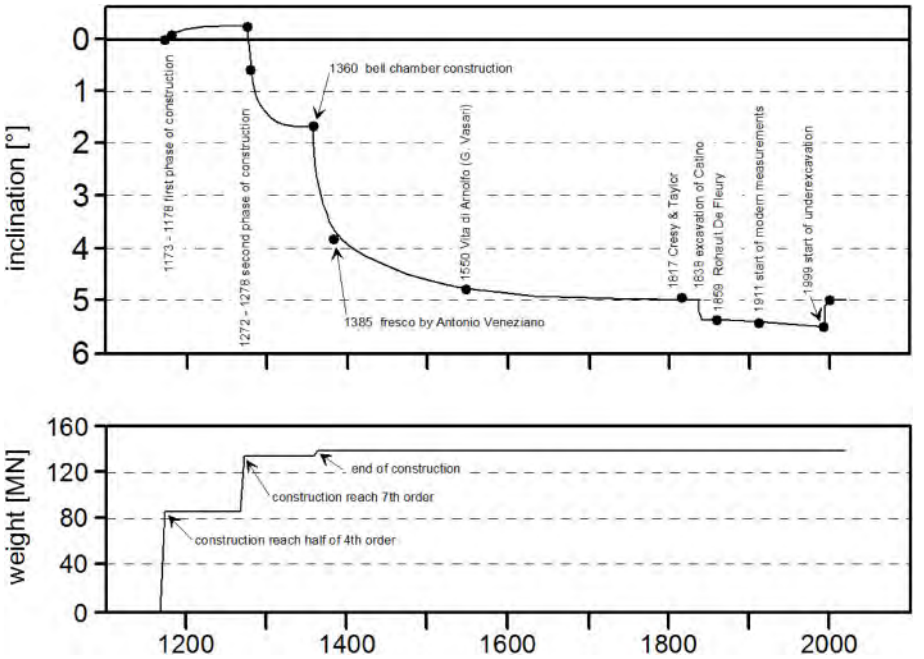

Figure 3. History of the inclination of the tower from the construction to 2022.

From 1360 to 1817 the only available data are obtained by old pictures or documents and are undoubtedly less reliable; but this does not influence the reconstruction of the overall trend. The picture that emerges from Figure 3 is clear: the Tower had already reached an inclination of almost 2° when the construction had reached the 7th cornice.

The inclination continued to increase gradually with time to reach a value of about 5° in 1817 when Cresy and Taylor, two English architects, published a detailed geometrical survey of the monument. At that time, the tower was probably motionless or its rotation was increasing with a very small and continuously decreasing gradient; the motion, anyway, was probably tending towards a final equilibrium configuration.

In 1859, the French architect Rohault de Fleury carried out a new survey of the Tower finding a value of the inclination significantly larger than that measured in 1817 and clearly out of the trend just described. As a matter of fact, since its construction the Tower had undergone a settlement of at least 3 m, so that its basement had sunk into the soil. To correct this effect, a walkway (the so called catino) was excavated around the base of the Tower in 1838. This imprudent excavation produced a sudden increment of the inclination and the motion re-started with a higher and increasing gradient, tending to a final overturning.

In conclusion, in 1911 the Tower had experienced a vertical displacement (average settlement) of at least 3 m and a southward rotation of more than 5°.

2 MONITORING

The inclination of the Tower from 1911 to 1999, as obtained by different procedures, is reported in Figure 4. This shows a continuous increase of the inclination, affected by some perturbations.

Because the bottom of the catino was well below the water table, there was a continuous inflow of water into the excavation, which required continuous pumping to keep it dry. The resulting flow of water in the soil around and below the foundation was believed to be dangerous for the stability

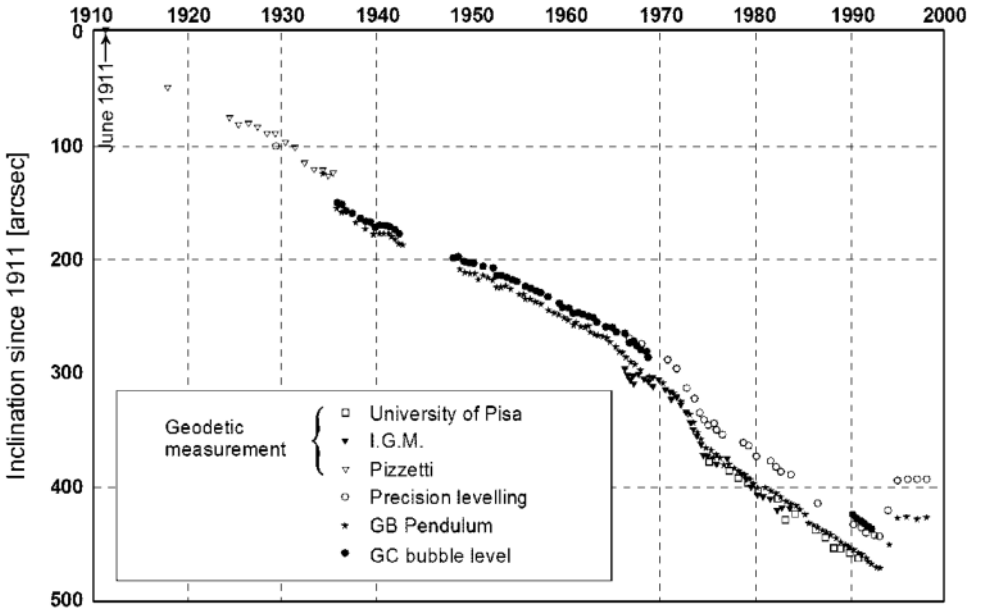

Figure 4. Inclination of the Tower from 1911 (start of modern monitoring) to 1999 (start of the underexcavation). GB inclinometer and geodetic measurements include the deformations of the Tower body, and hence their results are slightly larger than those of GC level and optical levelling, representative of the rotation of the foundation.

of the Tower and therefore in 1935/36 an intervention to prevent the water inflow was carried out, by injecting cement grout into the foundation masonry and chemicals into the soil below and around the catino. The intervention was successful in stopping the water inflow but produced a sudden increment of inclination and had no effect on the progress of the inclination with time.

From the early 1970s, an increase of the rate of tilt of the Tower is evident in Figure 4. This has been related to the increasing pumping of water from the deep sands (Figure 5) inducing subsidence all over the Pisa plain (Croce et al. 1981) and was eventually brought to an end by closing a number

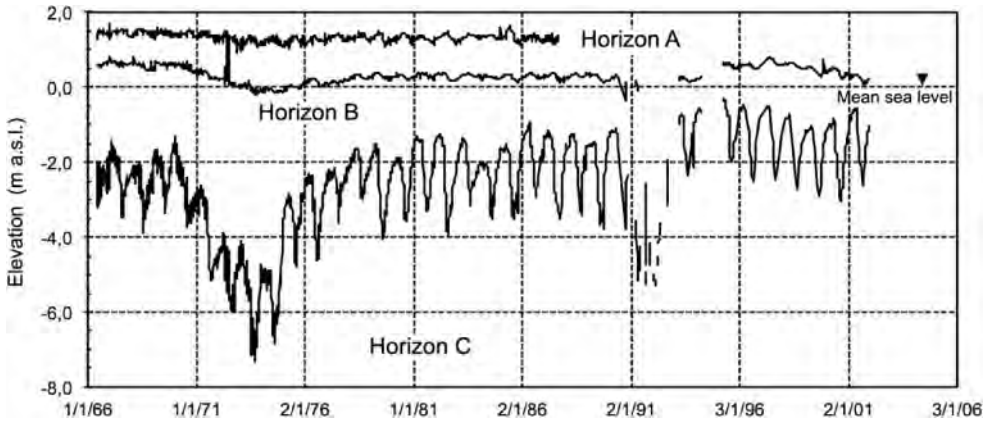

Figure 5. Groundwater regime in the subsoil of the Tower. The piezometric elevation in the lower sand is affected by pumping in the whole Pisa plain; in the 70's pumping increased because of a sequence of dry years.

of wells in the surroundings of the Tower. Since then, the water regime in the lower sand is carefully kept under control.

Through a careful analysis of all the available data, Burland and Viggiani (1994) discovered that in the stages of unperturbed motion the kinematics of the movements of the Tower was a rotation, without any settlement (Figure 6).

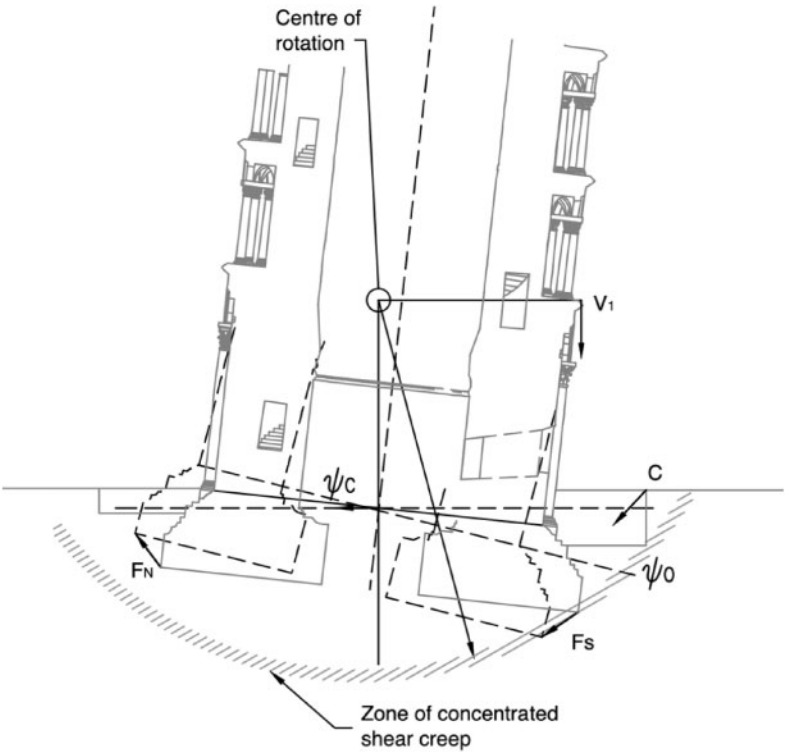

Figure 6. Kinematics of the displacements of the Tower during unperturbed motion.

This in turn revealed that the Tower was affected by a problem of stability of equilibrium, and a preliminary evaluation led to the conclusion that it was on the verge of collapse by leaning instability. Therefore, in 1993, the International Committee decided to implement temporary interventions to improve the safety of the Tower, pending conception and implementation of the final stabilisation measures.

From a structural point of view, a hoop of pre-tensioned steel wires was installed around the first cornice of the Tower. From a geotechnical point of view, a counterweight of 5.9 MN consisting of 64 lead ingots was installed on the North edge of the base of the Tower, producing a counter rotation of 53″. This may be seen in Figure 4 and in more detail in Figure 7.

In 1995, for different reasons, a medium term temporary intervention was developed to replace the lead weights with ten tensioned steel cables anchored in the lower sands at a depth of over 40 m (Figure 8).

The anchors had to be connected to the foundation of the Tower through a ring beam to be constructed under the floor of the catino, which required to carry out an excavation around the Tower below ground water level. It was decided to protect the excavation by ground freezing.

Without going into the details, it can be reported that the northern sections of the ring beams were successfully installed (Figure 9). However, when freezing was commenced on the South-West and the South-East sides, the Tower began to rotate southwards; after some attempts of controlling the

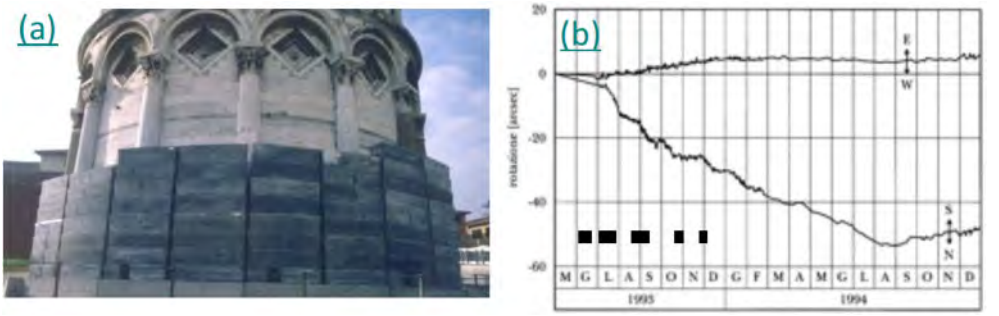

Figure 7. (a) Lead ingots counterweight and, (b) induced counter rotation.

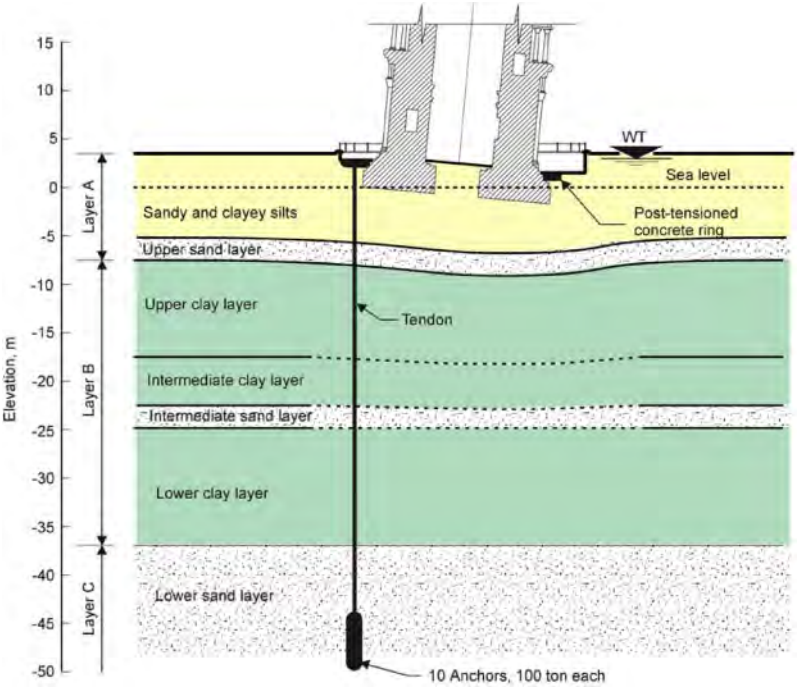

Figure 8. The ten anchors solution.

rotation by the application of further lead weights on the North, the intervention was abandoned. The negative effect of this attempt may be seen in Figure 4.

The results of small scale model tests of underexcavation, carried out both at 1 g and at increased gravity in a geotechnical centrifuge, and of numerical analyses encouraged the Committee to undertake a large scale field experiment. To this end, a 7 m diameter eccentrically loaded instrumented footing was constructed in the Piazza dei Miracoli and subjected to underexcavation.

The field trial was very successful and allowed the development of field equipment and operational procedures. A safeguard structure (Figure 10) consisting of two sub-horizontal steel stays and capable of applying a stabilizing moment if needed was connected to the Tower.

Figure 9. Construction of the northern sections of the ring beam for the ten anchors.

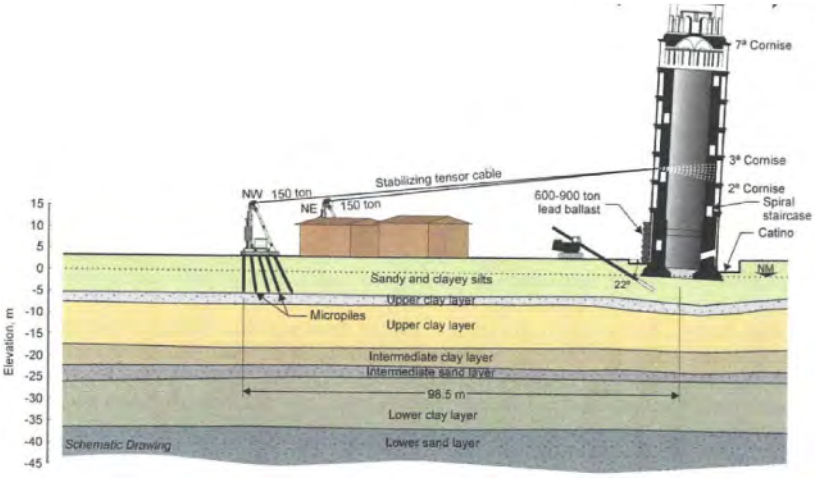

Figure 10. Scheme of the underexcavation and of the safeguard structure with steel stays.

3 STABILIZATION MEASURES

Between February and June 1999, a preliminary underexcavation intervention was carried out with 12 inclined drill holes, from which a total of 7 m^3 of soil, were removed.

Between February and June 2001 the full underexcavation was carried out with 41 holes, removing a total of 38 m^3 of soil, 70% of which below the catino, i.e., outside the perimeter of the foundation. In the same period all the lead ingots were progressively removed and the cable stays were dismantled, without having been ever operated.

As a final intervention, in 2002, a drainage system was installed in the upper soils North of the Tower, essentially aimed at stabilizing the groundwater level in the vicinity of the foundation.

The results of these operations, in terms of rotation of the Tower, are reported in Figure 11; they succeded in moving the Tower back northwards by about 2000 arcsec. Since then, the tower is still slowly moving northwards, at a very slow and decreasing rate.

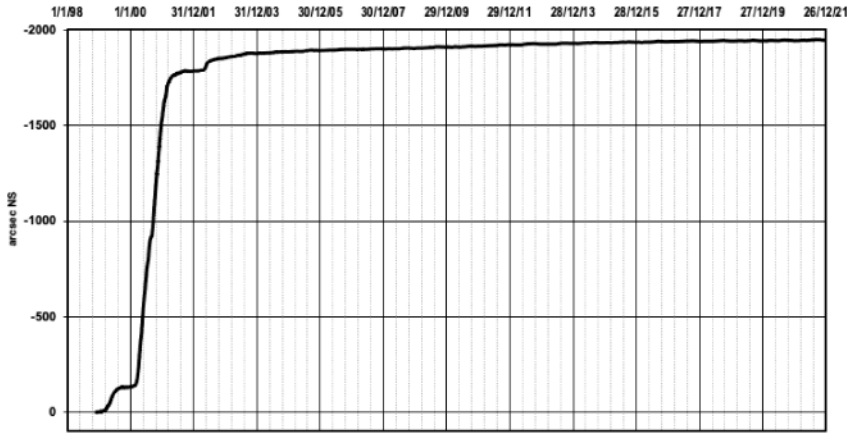

Figure 11. Results of preliminary and full underexcavation and of intervention on the water table.

Going back to Figure 3, showing these results in the wider context of the entire history of rotation of the Tower, it is evident that the intervention of the International Committee have compensated the effects of the excavation of the catino in 1836. We may say that there is a kind of justice in the fact that the detrimental effects of an incautious excavation have been repaired by another excavation, but this time carefully conceived and implemented.

4 FUTURE SCENARIOS

To evaluate the final success of the implemented stabilisation measures, a prediction of the future behaviour of the Tower is needed. The International Committee, on conclusion of their work, has not attempted to give a single solution to this question (Jamiolkowski 2005). Considering the complexity of the phenomena involved and the number and variety of factors that influences the behaviour of the Tower, the International Committee presented two possible scenarios, bounding the range of the future movements.

In the first one, rather conservative, it is predicted that the Tower will continue its very slow northwards rotation for a while, then remain motionless (a so-called honeymoon) and then gradually resume a southward rotation, initially at a very small rate and then progressively accelerating. In this scenario, the Tower would reach the value of the 1999 inclination in no less than three or four centuries.

In the more optimistic scenario, the rotation will cease, apart from small cyclic movements caused by seasonal factors, and the honeymoon will last for the foreseeable future.

At present, the results of twenty years of monitoring after the underexcavation was carried out are available (Figure 12). An attempt to extrapolate these results does not yet allow a choice between the two scenarios; the observation period is still too short. In any case, the importance of continued observation of the behaviour by careful monitoring coupled with a thorough evaluation of the results is evident.

Some people have criticised the adopted solution, claiming that actually it is not a true stabilisation, but only a small reduction of the inclination without substantial effects on the stability of the Tower and that a definitive stabilisation (whatever that means) was only handed down to posterity (Lizzi 2000, 2001).

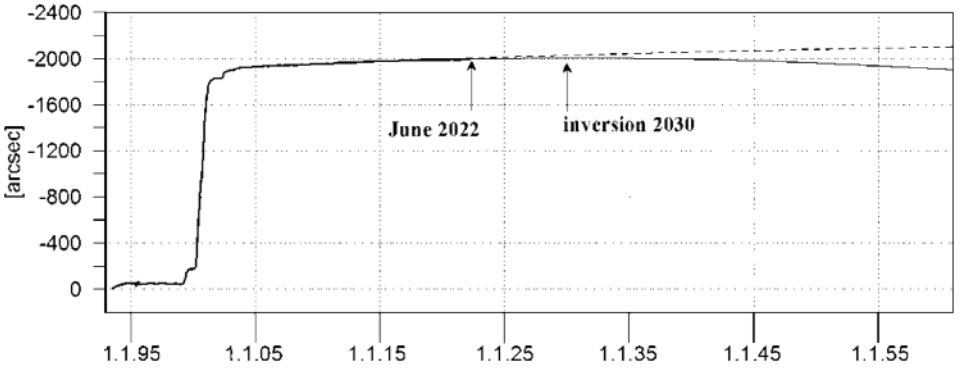

Figure 12. Rotation of the Tower after stabilisation intervention and possible extrapolation.

With reference to the first remark, it must be recalled that the Tower is affected by a leaning instability phenomenon. It has been shown repeatedly (e.g., Viggiani 2019) that the increase of rotational rigidity of the complex subsoil-foundation following the decrease in inclination resulted in a substantial increase of the stability.

As for the future behaviour, even in the pessimistic scenario of a resumption of the southward inclination, there will be time enough to repeat an underexcavation intervention, if needed. In some way, underexcavation may be considered a sort of extraordinary maintenance!

5 INTENTIONS AND ACHIEVEMENTS

There are numerous lessons learnt by this extraordinary case history, with a Tower 850 years old surviving a settlement of 3 m and an inclination of more than 5°. One of the most significant may be expressed by an old saying: the way to hell is paved with good intentions.

Good intentions are obvious when studying and implementing any intervention on the heritage but unfortunately, though being necessary, they are far from sufficient.

In the case of the Pisa Tower, we have already encountered at least two significant examples of good intentions leading to very unfavourable results.

The excavation of the catino in 1838, aimed at uncovering the lower part of the Tower which had sunk into the soil, was actually the factor bringing a monument that was finally attaining a stable configuration (Figure 3) on the verge of collapse.

The provisional intervention with ten steel cables, attempted by the International Committee in 1995, had also a detrimental effect on the Tower and had to be abandoned.

But an older sensational example of dangerous good intentions has been recently discovered (Leoni & Squeglia 2016; Leoni et al. 2018). A sophisticated numerical model of the Tower and its subsoil, including 230000 tetrahedral elements and adopting the Soft Soil Creep model (Vermeer & Neher 1999) for the clay layers, has been used to back analyse rather successfully the entire history of the monument.

In the framework of this analysis, the model has been used to predict the rotation of the Tower in the assumption of no correction of its shape during construction, and hence with a straight axis. Surprisingly, the comparison of these results with those obtained with the actual curved axis (Figure 13), reveals that without corrections – the rotation of the Tower in 1993 would have been 4.3°, i.e., significantly smaller than the actual 5.5°.

The ancient magistri lapidum, with their corrections to the axis of the Tower leading to the famous banana shape, have actually made the stability of the monument worse. Perhaps they were engaged in giving the Tower its present extraordinary inclination!

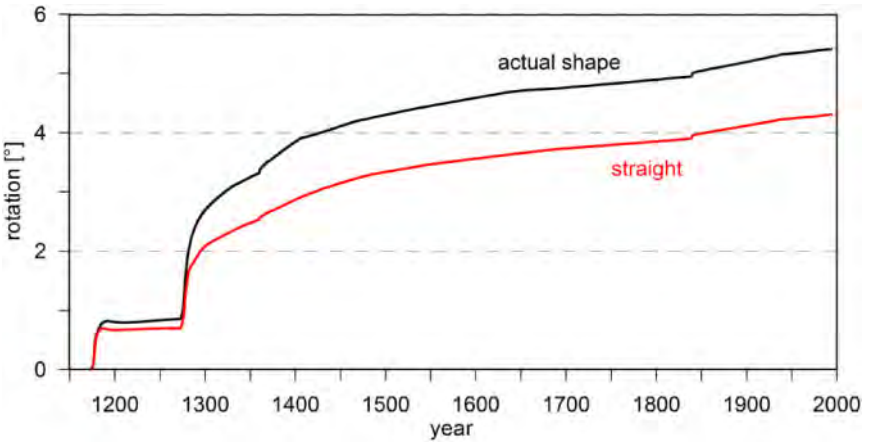

Figure 13. Rotation of the Tower with and without correction of its shape.

REFERENCES

Burland J.B. & Viggiani C. 1994. Osservazioni sul comportamento della Torre di Pisa. *Rivista Italiana di Geotecnica*, vol. 28, 3, 179–200.

Cresy E. & Taylor G.L. 1829 *Architecture of the Middle Ages in Italy*, illustrated by views, plans, elevations,sections and details of the cathedral, baptistery, leaning tower or campanile and camposanto at Pisa, from drawing and measurements taken in the year 1817. Published by the Authors, London.

Croce A., Burghignoli A., Calabresi G., Evangelista A., Viggiani C. 1981. The Tower of Pisa and the surrounding square: recent observations. *X Int. Conf. Soil Mech. Found. Eng., Stockholm*, vol. III, 61–70.

Jamiolkowki M.B. 2005. Introduction to the final volumes of proceedings of the International Committee. *La Torre restituita, Bollettino d'Arte* Ministero Beni Culturali, Roma, Vol I, 7–9.

Leoni M. & Squeglia N. 2016. 3D creep analysis of the leaning tower of Pisa. Unpublished report, Opera della Primaziale Pisana.

Leoni M., Squeglia N., Viggiani C. 2018. Tower of Pisa: Lessons learned by observation and analysis. In Lancellotta et al. editors: *Geotechnics and Heritage, Historic Towers.* CRC Press, 15–38.

Lizzi F. 2000. Micropiles: past, present and future. *Proc. Geotech Year 2000*, Bangkok, 145–152.

Lizzi F. 2001. Letter to the newspaper "*Il Mattino*" on July, 1st 2001.

Rohault de Fleury C. 1859. Le Campanile de Pise. Enciclopedie de l'Architecture, Bance, Paris.

Viggiani C. 2019. *Senza neanche toccarla. La stabilizzazione della Torre di Pisa.* Hevelius Edizioni, Benevento, 150 pp.

SESSION 3: Seismic risk, site effects, soil structure interaction

Taylor & Francis
Taylor & Francis Group
http://taylorandfrancis.com

Geotechnical Engineering for the Preservation of Monuments and Historic Sites III – Lancellotta, Viggiani, Flora, de Silva & Mele (Eds)

Dynamic centrifuge model tests on Tumulus Mounds on cut slopes

M. Sawada & M. Mimura
Kyoto University, Kyoto, Japan

Tatsuya Udo
Former Student of Kyoto University, Kyoto, Japan

ABSTRACT: Japan's tumulus mounds comprising compacted earth mounds and masonry burial chambers are vulnerable to earthquakes. This study focuses on the seismic behavior of tumulus mounds with sloped foundations. Dynamic centrifuge model tests were conducted using 1/50 scale cross-sectional models of tumulus mounds. The results show that large cracks occurred in the earth mound on the slope side when the shear resistance of the stone joints of the burial chamber was small. The stress distributions in the earth mound during the shaking tests were numerically estimated to identify the stress that caused cracks in the earth mound. The results show that tensile cracks dominantly occur near the surface under low confining pressure. The shear resistance of the stone joints of the burial chamber significantly restrains the opening of the tensile cracks; thus, it is an important factor to be considered when evaluating the seismic resistance of tumulus mounds and developing countermeasures.

1 INTRODUCTION

Historic monuments composed of soil are vulnerable to natural disasters, and their maintenance and restoration require advanced knowledge of geotechnical engineering. Japan has various geo-relics, such as tumulus mounds, kilns, and dwelling sites. Japan's geo-relics have begun to be internationally recognized for their values. The Mozu-Furuichi Kofun Group, consisting of 49 tumulus mounds in Osaka, was included in the UNESCO World Heritage List in 2019, followed by the registration of the Jomon Prehistoric Sites in Northern Japan, which consists of 17 archeological sites including dwelling sites, in 2021. Owing to increased attention to Japan's geo-relics, protecting them from natural disasters is becoming increasingly important.

This study focuses on the damage to tumulus mounds caused by earthquakes. Tumulus mounds were constructed all over Japan from the middle of the 3rd century to the end of the 7th century, and more than 100,000 tumulus mounds have been discovered. Masonry burial chambers are stored in compacted earth mounds of various shapes (e.g. round, rectangular, and keyhole). The length of the earth mounds varies from several meters to approximately 500 m. In the burial chambers, coffins, funerary goods, and mural paintings were preserved in good conditions under a stable hydrothermal environment. Damage to the earth mounds causes the promotion of water and heat transfers, which affects the environment in the burial chambers, thus leading to the deterioration of the burial items owing to dew condensation, salt crystallization, and fungi. This indicates that the role of the earth mounds is to control water and heat transfers into the burial chambers, therefore conserving the burial mounds in good condition. Thus, the mechanical properties and stability of the earth mounds are essential factors to be considered in the conservation of tumulus mounds.

DOI 10.1201/9781003308867-50

In Japan, the tumulus mounds have been repeatedly damaged by earthquakes. During archaeological investigations of tumulus mounds, cracks probably caused by earthquakes have been often discovered. Figure 1 shows the cracks found in the mound of the Takamatsuzuka Tumulus in Nara. Seismological investigations identified the historic earthquakes that caused the cracks as the Nankai Trough Earthquakes, which have periodically occurred in the Pacific Ocean (Agency of Cultural Affairs et al. 2017). However, the details of the damage caused by the earthquakes were unclear because records of historic earthquakes were limited until the occurrence of the Kumamoto Earthquake in 2016 (M = 7.3), which destroyed many tumulus mounds (Agency of Cultural Affairs 2017). Figure 2 shows the Kamao Tumulus in Kumamoto that was damaged by the earthquake. Cracks similar to those shown in Figure 1 were found at the top of the earth mound. Investigations of such seriously damaged tumulus mounds involve risks, and their restoration takes several years. To protect tumulus mounds from future earthquakes, it is necessary to understand the mechanism of seismic damage and develop effective reinforcement measures.

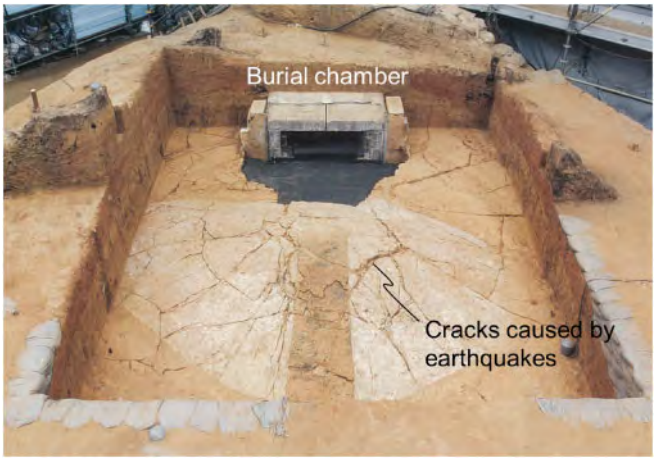

Figure 1. Excavated top of the Takamatsuzuka Tumulus (Agency of Cultural Affairs et al., 2017).

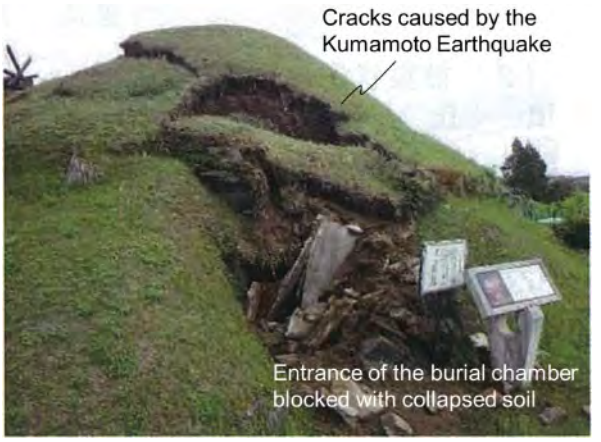

Figure 2. The Kamao Tumulus damaged by the Kumamoto Earthquake (Agency of Cultural Affairs, 2017).

The mechanism of seismic damage to tumulus mounds has been studied using both numerical and experimental approaches. Mimura et al. (2011) conducted three-dimensional FE analyses on the

Takamatsuzuka Tumulus to ensure that the cracks shown in Figure 1 can be caused by earthquakes. Sawada et al. (2018) and Sawada et al. (2019) conducted dynamic centrifuge model tests to observe the damage processes in more detail. The test results were numerically analyzed to identify the stress that caused the damage. These previous studies concluded that cracks are likely to occur near the surface of the earth mounds and corners of the burial chambers, and they are mainly caused by tensile stress.

In the present study, the mechanism of seismic damage to tumulus mounds with sloped foundations is analyzed because significant damage seems to occur, particularly when the foundations are sloped (e.g. Asuka Village Board of Education 2007). Dynamic centrifuge model tests were conducted using 1/50 scale cross-sectional models of tumulus mounds with sloped foundations. In addition, FE analyses were performed to estimate stress distributions in the models during shaking tests. The mechanism of damage and the interactions between the burial chamber and the surrounding earth mound were analyzed based on these results.

2 EXPERIMENT

2.1 *Centrifuge system*

A centrifuge model test is an approach that is widely used to observe the complicated behavior of earth structures caused by earthquakes, seepage, and interactions between soil and structures. The greatest advantage of the centrifuge experiments comes from the equivalence between the physical model and the prototype in terms of stress and strain.

In the present study, the centrifuge system of the Disaster Prevention Research Institute, Kyoto University, was used. The specifications of the system are summarized on the DPRI Geotechnical Centrifuge Center website. The capacity of the centrifuge acceleration was limited to 50 G (1G = 9.81 m/s^2) when a shaking table was used. Thus, in this study, shaking tests were conducted under 50 G using 1/50 models based on the scaling law shown in Table 1. A model created in a rigid aluminum soil box (630 mm × 700 mm × 150 mm) was mounted on the shaking table. The soil box had an acrylic transparent front panel. A high-speed camera was set in front of this outer panel to observe the model during the shaking tests. Centrifuge acceleration was gradually increased until it reached 50 G, and then the shaking table was moved to simulate the preliminary time series data of the input waves.

Table 1. Scaling law of the centrifuge model tests.

Properties	Dimensions	Scale factors (Prototype/Model)
Length	L	N
Mass	M	N^3
Time	T	N
Acceleration	LT^{-2}	N^{-1}
Stress	$ML^{-1}T^{-2}$	1
Strain	–	1

2.2 *Modeling*

Figure 3 shows the 1/50 scale cross-sectional model of the tumulus mound used in this study. The dimensions of the model were determined based on those of the Takamatsuzuka Tumulus (Agency of Cultural Affairs et al., 2017). The tumulus mound was thought to have been created on cut slopes for religious and political reasons. The burial chamber was placed on the flat zone of the foundation, and the earth mound covered the bottom half of the sloped zone. The burial chamber was modeled using four resin plates with a density equal to that of the stones used for the actual

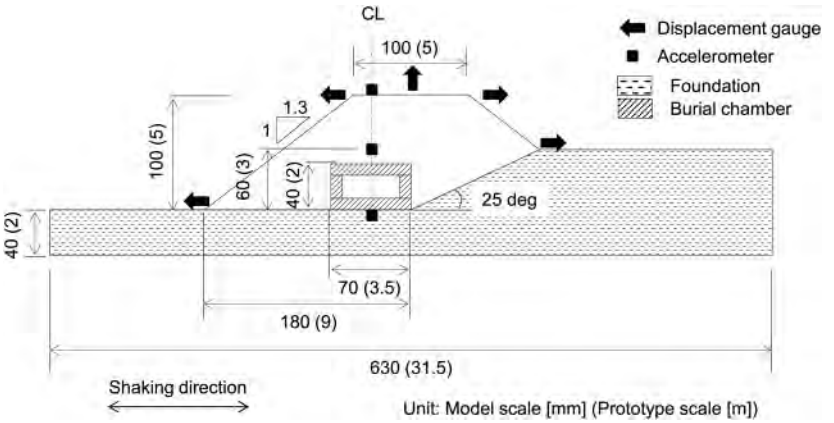

Figure 3. Cross-sectional model of a tumulus mound used for centrifuge model tests.

burial chamber (i.e. 1.91 g/cm^3). The resin plates were rigid and were not bonded each other. The shear resistance between the smooth resin plates was measured using a shear box test (JGS 0561). The results are presented in Table 2. Here, the model composed of smooth resin plates is called Model A.

Table 2. Shear resistance obtained using shear box tests.

Materials	Cohesion [kN/m^2]	Angle of shear resistance [°]
Resin plate – Resin plate (natural)	10.2	17.9
Resin plate – Resin plate (increased roughness)	11.6	32.6
Resin plates – Mound soil	19.0	23.3
Mound soil	21.0	35.0

In addition to Model A, the following two models were used for the experiments: a model without a burial chamber (Model B) and a model with a burial chamber composed of resin plates having interface with increased roughness (Model C). Soil particles were attached to the resin plates used for Model C to increase the shear resistance between the interface between the plates. This surface treatment was not applied to the plate – soil interface. Table 2 compares the shear resistances between the plate interface of Model A and Model C, which indicates that the angle of shear resistance of Model C is 1.8 times as large as that of Model A, while the cohesion of these models is equivalent. The dimensions of these additional models are equivalent to those of Model A, as shown in Figure 3. The influence of the burial chamber on the seismic behavior of the tumulus mound was analyzed by comparing with it these additional cases.

2.3 *Materials and methods*

The models were created using decomposed granite soil (clay: 24.79%, silt: 17.26%, sand: 57.95%) obtained in a tumulus near the Takamatsuzuka Tumulus, where archaeological investigations were conducted. The soil was used after it had passed through a 2-mm sieve. The soil water content was 15%. The densities of the earth mound and foundation soil were determined to have S-wave velocities equal to those measured in the Takamatsuzuka Tumulus, that is, 110–160 and 260–340 m/s, respectively (Mimura & Ishizaki 2006). However, the S-wave velocity of the foundation was far below 260 m/s, despite compacting the soil as densely as possible. Thus, the soil was mixed

with a 10% weight ratio of hydrated lime to achieve the measured S-wave velocity. The properties of the earth mound and foundation are listed in Table 3.

Table 3. Properties of the models used for centrifuge model tests.

Properties	Earth mound	Foundation
Particle density [g/cm^3]	2.64	–
Wet density [g/cm^3]	1.58	1.91
Water content [%]	15	–
Poisson's ratio	0.35	0.35
Shear modulus [MN/m^2]	27	119
S-velocity [m/s]	130	250

The foundation was compacted layer by layer in the soil box. The thickness of each layer was 2 cm. In the sloped zone, a step-like slope was first created using wooden boards as spacers, and then the steps were cut off to smooth the slope. The burial chamber was placed on the flat zone of the foundation, and the earth mound was compacted layer by layer using spacers in the same manner as the foundation. The burial chamber was filled with a block to prevent the resin plates from moving during the compaction of the earth mound. The block was removed after the earth mound was completed.

The displacement and acceleration were measured at the points shown in Figure 3. Laser displacement gauges were attached to the bars fixed at the top of the soil box. L-shaped targets were installed at the top and bottom of the slopes to measure the horizontal displacement of the earth mound. The acceleration in the shaking direction was measured using cubic accelerometers with a side length of 16 mm.

Sinusoidal waves with a frequency of 2 Hz and a duration of 15 s (main part: 20 cycles, tapered part at each end: 5 cycles) in the prototype scale were used as input waves. The amplification was increased step by step from 0.1 to 1.0 mm with an increment of 0.1 mm. Thus, 10 waves with different amplitudes were used for each model.

3 RESULTS

3.1 *Displacement*

Figure 4 shows the models after a series of shaking tests. The earth mound of Model A was significantly damaged with large cracks on the slope side, whereas the other two models were visually the same as those in the initial conditions.

Figure 5 shows the residual displacement accumulated in the 10 shaking tests. Hereinafter, the measurements are described in the prototype scale following the scaling law shown in Table 1. The displacement along the direction of the arrows shown in Figure 3 is positive. The amplitude of the acceleration measured at the shaking table was placed on the horizontal axis. This indicates that the development of displacement in Model A was significant in the 7th shaking test. The earth mound subsided and moved away from the slope of the foundation, as shown in Figure 4. This agrees with the observation made using the high-speed camera. Residual displacement was also observed in the other two models, but its magnitude was small compared to that of Model A, as shown in Figure 5. The right side of the slope of the earth mound in Model B gradually moved to the left in each shaking test. Slight displacement was observed at the crown of the earth mound in Model C, although the large displacement at the left toe of the earth mound in Model C could have been caused by the inclination of the L-shaped target.

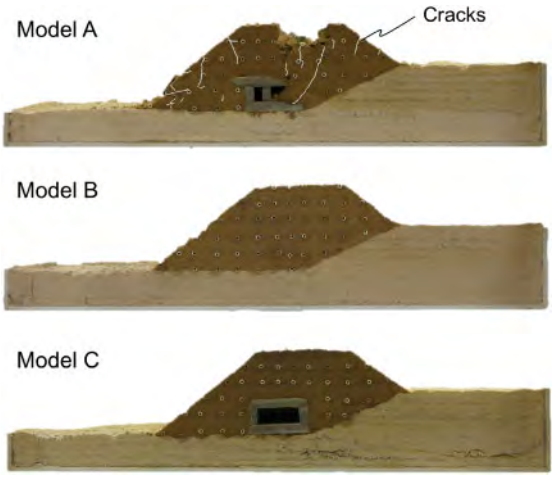

Figure 4. Models after the shaking tests.

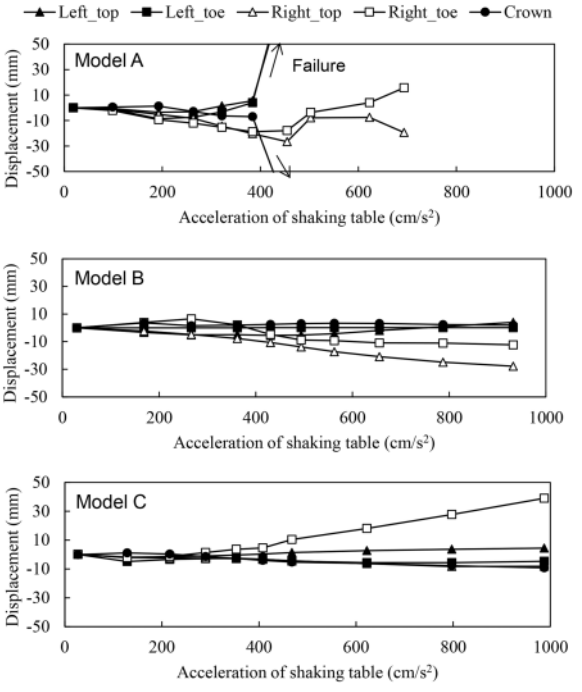

Figure 5. Accumulated residual displacement.

3.2 *Acceleration*

The amplification ratio of each model was obtained from the measured acceleration in the shaking tests using sinusoidal waves. The amplitude ratio $A_{r/s}$ is defined as follows:

$$A_{r/s} = Z_r / Z_s \tag{1}$$

where Z_s is the Fourier amplitude of the acceleration measured on the foundation surface, and Z_r is the acceleration measured at the three points shown in Figure 3. Herein, the Fourier amplitude at 2 Hz was used to calculate $A_{r/s}$, although the measured acceleration contained waves with higher frequency coming from the actuator system of the shaking table.

Table 4 shows the average amplitude ratio at the three points of each model using the results of the 1st to the 5th shaking tests. The amplitude ratio increases with an increase in elevation between the bottom (i.e. foundation surface) and middle points, but it slightly decreases between the middle and top (i.e. crown) points. Comparisons of the amplitude ratio between the three models indicate that the burial chamber increases the amplification in the earth mound, particularly when the shear resistance of the plate joints of the burial chamber is small.

Table 4. Amplitude ratio.

	Middle	Top
Model A	1.31	1.19
Model B	1.20	1.15
Model C	1.24	1.20

4 DISCUSSION

4.1 *Numerical analyses*

FE analyses were conducted to understand the damage mechanism observed in Model A. A two-dimensional FE code LIQCA 2018 (Liquefaction Geo-Research Institute, 2018), which implements a modified Ramberg-Osgood model (e.g. Ishihara, 1996), was used. The model is a total stress model that considers nonlinear stress-strain relationships in cyclic loading. The model parameters α and r were determined to be 7.84 and 2.29 by fitting to the results of cyclic triaxial tests (JGS 0542), that is, shear strain versus shear modulus and shear strain versus damping constant. The determination of the model parameters was detailed by Sawada et al. (2018). The FE model shown in Figure 6 was created in the prototype scale, which corresponds to the model shown in Figure 3 above foundation surface level. The acceleration measured at the foundation surface was provided at the bottom of the FE model. The lower part of the foundation was not included in the numerical model because trial calculations using a numerical model with a full foundation showed that it causes the discrepancy between measured and simulated acceleration in the earth mound. The discrepancy can come from uncertainties of the physical models such as the boundary conditions between the shaking table and soil box, or the soil box and foundation. The resin plates of the burial chamber were assumed to be rigid. The slip and gap between the plates or between the plates and soil were considered using joint elements (Goodman et al. 1968). A joint element consists of horizontal and vertical springs that express slip and gap, respectively. These springs have bilinear stress-strain curves. The parameters of the horizontal springs were determined by fitting to the

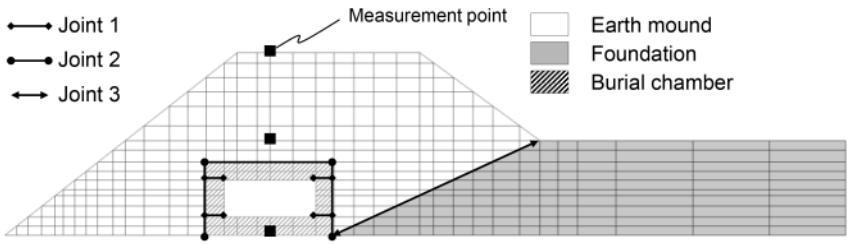

Figure 6. Numerical model (Model A).

stress-strain curves obtained by shear box tests. The vertical spring constant was determined to be as large as possible, and the tensile strength was assumed to be zero. Joint elements were also applied to the boundary between the slope of the foundation and the earth mound, assuming that they had shear strength of the earth mound. The model parameters of the joint elements are listed in Table 5.

Table 5. Model parameters of joint elements.

Parameters		Model A	Model B	Model C
Joint 1				
Horizontal	Spring constant [kN/m^2]	6.0×10^5	–	6.0×10^5
	Cohesion [kN/m^2]	10.2	–	11.6
	Angle of shear resistance [°]	17.9	–	32.6
Vertical	Spring constant [kN/m^2]	1.0×10^7	–	1.0×10^7
	Tensile strength [kN/m^2]	0.0	0.0	0.0
Joint 2				
Horizontal	Spring constant [kN/m^2]	4.5×10^4	–	4.5×10^4
	Cohesion [kN/m^2]	19.0	–	19.0
	Angle of shear resistance [°]	23.3	–	23.3
Vertical	Spring constant [kN/m^2]	1.0×10^6	–	1.0×10^6
	Tensile strength [kN/m^2]	0.0	0.0	0.0
Joint 3				
Horizontal	Spring constant [kN/m^2]	6.0×10^4	6.0×10^4	6.0×10^4
	Cohesion [kN/m^2]	21.0	21.0	21.0
	Angle of shear resistance [°]	35.0	35.0	35.0
Vertical	Spring constant [kN/m^2]	1.0×10^6	1.0×10^6	1.0×10^6
	Tensile strength [kN/m^2]	0.0	0.0	0.0

Figure 7 shows the comparison between the measured and calculated accelerations in the 2nd, 4th and 7th shaking tests. The calculated acceleration agrees well with the measured acceleration in the 2nd and 4th tests. In the second half of the 7th shaking test, the measured acceleration had a phase lag and noise because the crack opening in the earth mound became significant. Numerical analyses were also conducted for Model B and Model C in the same manner as for Model A. The measured accelerations of these two models were also numerically simulated using common model parameters.

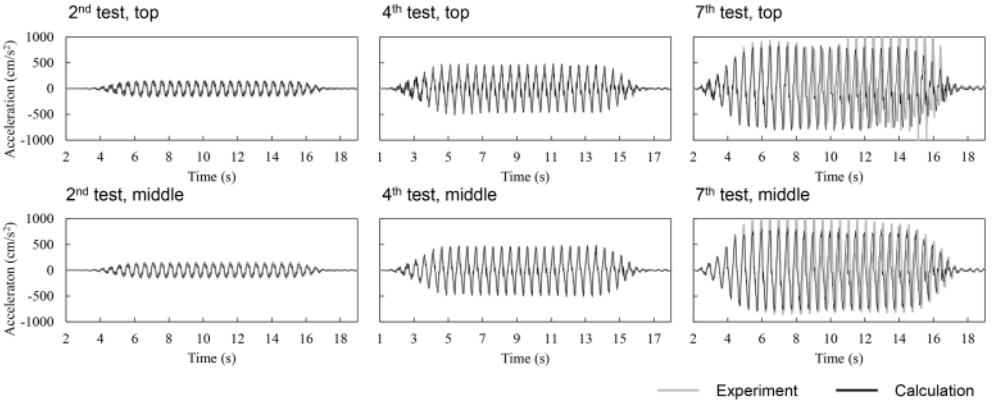

Figure 7. Comparison between measured and calculated acceleration (Model A).

4.2 *Mechanism of damage*

Figures 8 and 9 show the distributions of the calculated maximum shear stress and maximum tensile stress (i.e. negative minimum principal stress) in the earth mound when they peak in most parts during the 11th cycle during the 7th shaking test. This indicates that shear stress develops in the deep zone, particularly around the burial chamber, whereas tensile stress develops near the surface. The tensile stress distribution of Model A was characterized by a band of large tensile stress on the slope side. The band appeared throughout the shaking tests, and its position corresponded to the portion where a significant crack occurred in the experiment (Figure 4). This suggests that the cracks were caused by tensile stress. The tensile band is moderate in Model C, with a large shear resistance of plate joints.

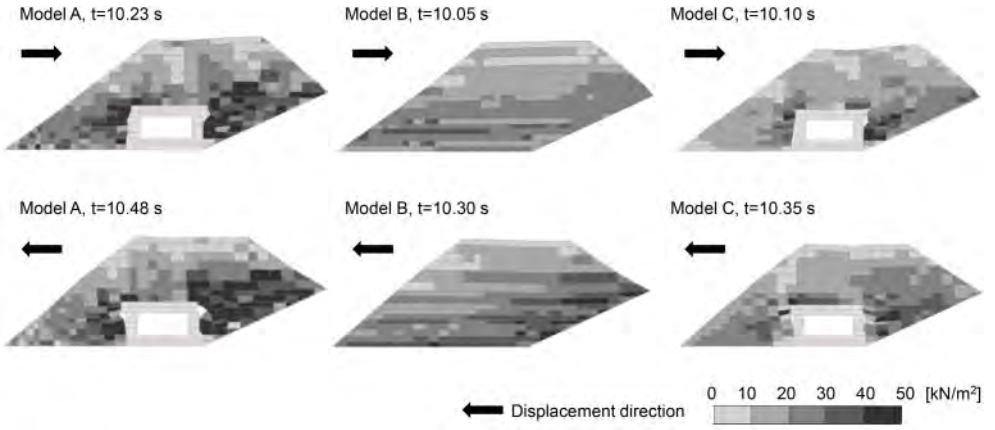

Figure 8. Distribution of maximum shear stress.

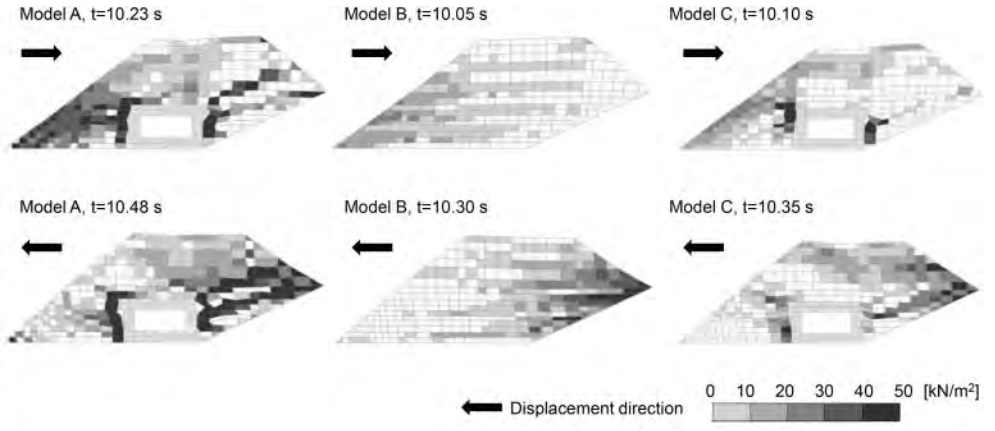

Figure 9. Distribution of maximum tensile stress.

The stress planes of the maximum shear stress and tensile stress were identified for the elements, in which these stresses reached thegir strengths until the 11th cycle in the shaking tests. The shear strengths of the earth mound are listed in Table 2. The tensile strength was estimated to be less than 20 kPa based on the modified Mohr-Coulomb failure criterion (e.g. Sawada et al. 2021). However, such a small tensile strength cannot be exactly measured with conventional tension tests, and thus, it was assumed to be zero. Figure 10 shows the distributions of the directions of these

stress planes. This is useful for identifying the stress that caused cracks in Model A. The directions of the experimentally observed cracks seem to be consistent with the estimated directions of the stress plane of the maximum tensile stress and not those of the maximum shear stress. In addition, shear failure was estimated not to occur at the top of the earth mound, although many cracks were found, as shown in Figure 4. These results show that the cracks were mainly caused by tensile stress. Tensile cracks are unique to unsaturated soils under low confining pressures with apparent cohesion and tensile strength induced by matric suction.

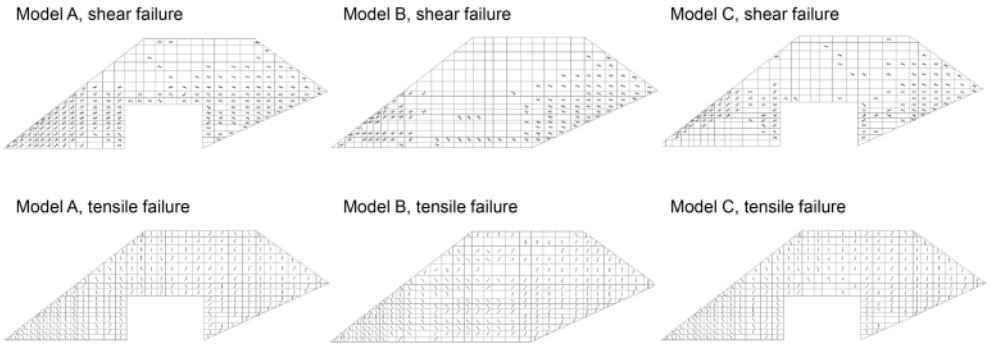

Figure 10. Directions of the planes where shear failure and tensile failure occur.

Tensile cracks were also estimated to occur in Model B and Model C, as shown in Figure 10 where the tensile stress was assumed to be zero. This indicates that tensile failure occurred in these models; however, cracks were invisible because the crack opening was moderate, which was consistent with the fact that a small but detectable residual displacement was measured, as shown in Figure 5. Figure 11 shows the numerically estimated horizontal relative displacement between the ceiling plate and right-side wall plate of the burial chamber of Model A and Model C in the 2nd, 4th, and 7th shaking tests. This indicates that the slip between these plates was restrained in Model C, which prevented crack opening and serious damage to the earth mound. Thus, the shear

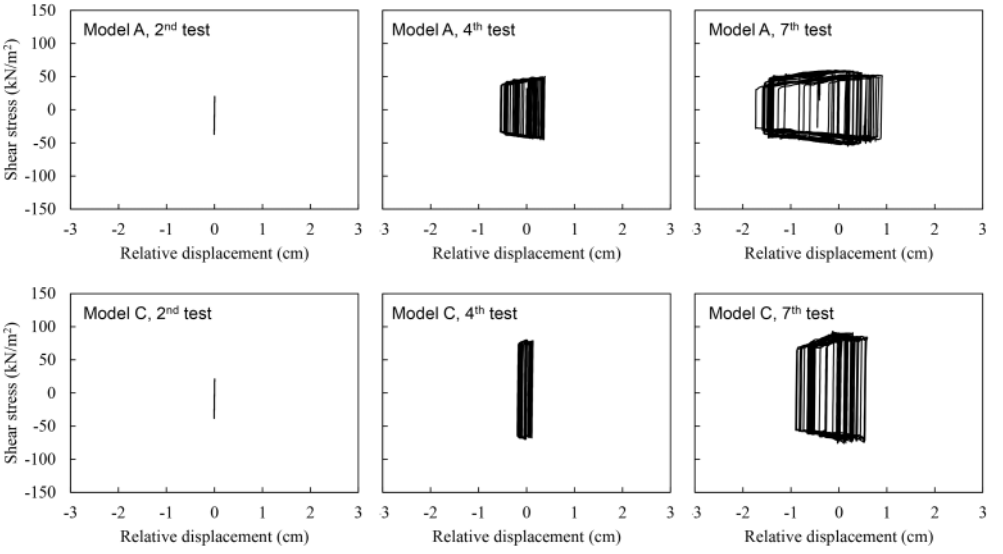

Figure 11. Relative displacement of the joint element between the ceiling and right-side wall.

resistance of the stone joints of burial chambers is an important factor in evaluating the seismic resistance of tumulus mounds. In addition, an increase in the shear resistance can be an effective measure for protecting tumulus mounds from earthquakes.

5 CONCLUSION

This study focuses on the seismic behavior of tumulus mounds with sloped foundations, which are particularly vulnerable to earthquakes. Dynamic centrifuge model tests were conducted using a 1/50 scale cross-sectional model of a tumulus mound. The results show that the damage to the earth mound is characterized by large cracks on the slope side when the stone joints of the burial chamber have a small shear resistance. The measured acceleration shows that the amplification ratio of the earth mound is influenced by whether the earth mound has a burial chamber and the magnitude of the shear resistance of the stone joints of the burial chamber.

The shaking tests were numerically analyzed to understand the mechanism of the experimentally observed damage in the earth mound. The distributions of the maximum shear stress and tensile stress were numerically estimated to identify the stress that caused the large cracks. The results show that the distribution and direction of the maximum tensile stress correspond closely to those of the large cracks. This indicates that the earth mound has apparent cohesion and tensile strength induced by matric suction, and tensile failure dominantly occurs near the surface under low confining pressure. The numerical results also show that the shear resistance of the stone joints of the burial chambers is an important factor in evaluating the seismic resistance of tumulus mounds and developing protection measures.

REFERENCES

Agency for Cultural Affairs, Nara National Research Institute for Cultural Properties, Archeological Institute of Kashihara Nara prefecture & Asuka Village Board of Education. 2017. Excavations report in the Takamatsuzuka Tumulus: 155–160 (in Japanese).

Agency for Cultural Affairs. 2017. Report on tumuli damaged by the 2016 Kumamoto Earthquake (in Japanese).

Asuka Village Board of Education. 2007. Excavations report in Kazumayama Tumulus (in Japanese).

DPRI Geotechnical Centrifuge Center. https://sites.google.com/dpri.kyoto-u.ac.jp/centrifuge/home/souchishiyou?authuser=0 (accessed 2021-10-11)

Goodman, R. E., Taylor, R. L., & Brekke, T. L. 1968. A model for the mechanics of jointed rock. *Journal of the soil mechanics and foundations division*, 94(3): 637–659.

Ishihara, K. 1996. Soil behaviour in earthquake geotechnics, *Oxford engineering science series 46*: 33–39.

Japanese Geotechnical Society Standards, 2015. Laboratory testing standards of geomaterials-Part 1, Method for consolidated constant-pressure direct box shear test on soils (JGS 0561).

Japanese Geotechnical Society Standards, 2017. Laboratory testing standards of geomaterials-Part 2, Method for cyclic triaxial test to determine deformation properties of geomaterials (JGS 0542).

Liquefaction Geo-Research Institute. 2018. Theories and manuals for LIQCA2D18 and LIQCA3D18 (in Japanese).

Mimura, M. & Ishizaki, T. 2006. Current status of Takamatsuzuka Tumulus and its geotechnical properties, *Japanese Geotechnical Journal*, 1 (4): 157–168 (in Japanese).

Mimura, M., Nagaya, J. & Ishizaki, T. 2011. Evaluation of seismic damage to the mound of Takamatsuzuka Tumulus based on dynamic finite element analysis, *Conservation Science* 50: 13–22 (in Japanese).

Sawada, M., Enkhtuvshin, T. Mimura, M. 2018. Study on the seismic behavior and damage mechanism of tumulus mounds, *Journal of Japan Society of Civil Engineers, Ser. C (Geosphere Engineering)*, 74 (3): 374–387 (in Japanese).

Sawada, M., Enkhtuvshin, T. Mimura, M. 2019. Study on the mechanism of seismic damage of historical burial mounds, *Proc. 16th Asian Regional Conference*, ATC19-3.

Sawada, M., Sumi, Y. & Mimura, M. 2021. Measuring desiccation-induced tensile stress during cracking process, *Soils and Foundations*, 61 (4): 915–928.

Geotechnical Engineering for the Preservation of Monuments and Historic Sites III – Lancellotta, Viggiani, Flora, de Silva & Mele (Eds)

Effects of 2012 Earthquake on the behavior of Ghirlandina tower in Modena

R.M. Cosentini, S. Foti, R. Lancellotta & D. Sabia
Politecnico di Torino, Italy

ABSTRACT: Collapse events, that occurred in the past (such as the Venice Bell Tower in 1902 and the Civic Tower in Pavia in 1989) claimed for the need to assess the long-term behavior of such monuments. A significant effort has been therefore devoted to clarify the reasons for these collapses after many centuries from the construction date. In addition, recent earthquakes in Italy have once again put into evidence the seismic vulnerability of the cultural heritage. To assess this aspect, in many cases the soil-structure interaction cannot be neglected. In this context, a simple but consistent framework for soil-structure interaction analysis is here presented with reference to a case history. It is discussed how the difference in the fundamental frequency observed during seismic events can be associated to non-linearity in soil response, leading to a rotational stiffness of the soil-foundation system consistent with the shear strain level derived from the seismic ground response analysis. Thereafter, the validated soil-structure interaction model has been used to define an equivalent SDOF model of the structure that explains the differential settlements suffered by the Ghirlandina tower in Modena during the 2012 seismic events as well as its behavior since those events.

1 HISTORICAL NOTES ON THE MODENA CATHEDRAL AND THE GHIRLANDINA TOWER

Established as a Roman colony in 183 BC over previous settlements, the city of Modena owes its current urban centre to the Middle Ages, after numerous and devastating floods that destroyed the ancient monuments and progressively confined the Roman remains under approximately 5 meters of sediments (Cadignani et al 2019; Lugli 2017).

The Piazza Grande is its geographical, religious, political, and economic heart. The medieval city grew from this central spot, which includes the City Hall, the Cathedral and the Ghirlandina tower.

At the time of the investiture controversy between papacy and empire to appoint local bishops, the Modena's bishop's seat was vacant after a time interval in which power had been firmly in the hands of bishop Eriberto. It was a period of growing civic initiative, which lead after a few years to the formation of the free municipality. In this context, the people together with the local clergy but independently from the ecclesiastical and imperial powers decided to build a new great church, as it was happening in other European cities. Therefore, the Cathedral of the architect Lanfranco replaced the previous church, which safeguarded the relics of Saint Geminianus Modena's patron saint, and which lied in a state of great disrepair.

Lanfranco conceived a mighty church with three naves and an annexed bell tower, expression of a new figurative model that influenced the development of the Romanesque in the Po Valley and whose decorative apparatus accompanied the rebirth of sculpture in Europe (Figure 1.a).

 DOI 10.1201/9781003308867-51

Figure 1. (a) The façade of the Cathedral; (b) Aerial view of the Cathedral and the GhirlandinaTower.

The tower, later named “Ghirlandina” probably because its balconies resembled garlands, soon became the symbol of the city, standing out in the sky above all other buildings, clad in white (Figure 1.b).

Thanks to delays and interruptions that allowed the foundation soil to increase its strength over time, it is argued that the first five floors were successfully standing in 1169 or 1184; the tower reached the height corresponding to the sixth floor in 1216, and the completion date was the 18th of September 1319 by the hand of Enrico da Campione.

In 1338 the arches connecting the southern side of the tower to the Cathedral were already in place, eventually to prevent additional tilt of the tower towards the Cathedral, since there is evidence that the tower begun to tilt during the construction and the ancient masons made some corrections accordingly.

From a typological point of view, the tower recalls the Lombard bell tower model (Figure 2), with a square base of 11 meters per side, which lightens upwards through the progressive increase in the number of windows. Above the square tower shaft, there is a smaller octagonal drum and a high spire crowned by a golden copper sphere topped with a cross, for a total height of 89.32 meters.

The structure is made of brick masonry cladded in slabs of stones of different thickness, sourced from Roman remains up to the 5th floor, while on the upper floors the material (Ammonitico Veronese limestone) was purchased on purpose.

A useful datum to better understand the construction process came from the photogrammetric survey performed in 2004 and from the laser scanning survey in 2008, with which the geometry and the inclination were measured, and a three-dimensional model was produced. There is an almost homogeneous inclination of the walls towards the West, while towards the South there is a markedly curvilinear trend (Figure 2), typical of constructions that undergo leaning during the construction

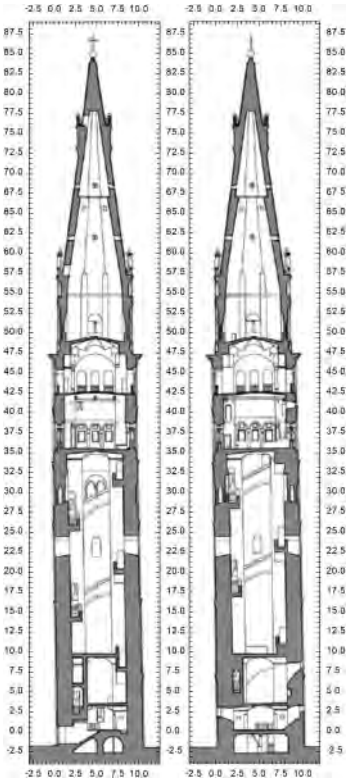

Figure 2. Vertical sections of Ghirlandina tower: from the left, view towards South, view towards East (modified – source: Giandebiaggi et al. 2009).

phase. An overall out of lead of 1.54 m was also measured in the southwest direction, apparent even by eye inspection.

2 THE CONCERNS ABOUT SEISMIC VULNERABILITY

The May 20th, 2012 (02:03:52 UTC) an earthquake (ML = 5.9, with epicenter 44.889N 11.228E close to Mirandola and focal depth 6.3 km), struck the towns of Finale Emilia, San Felice sul Panaro, and Sant'Agostino, involving a wide adjacent area. This event was followed by a series of significant aftershocks, such as the May 29th at 07:00:03 (ML = 5.8, 544.851N 11.086E, focal depth 10.2 km), in the surroundings of Novi di Modena, which caused even more severe and extensive damage on a larger area.

Even if this region was considered of low seismicity, and the population was not very accustomed to earthquakes, in the past the area between Ferrara and Novi di Modena had already been affected by severe seismic events. Some of these were destructive, such as the 1570 earthquake. Several others, though causing less damage, left their traces in the chronicles of the time.

In this respect, it is worth mentioning that on 20 and 29 May 2012 the medieval cathedral in Modena suffered significant damage, as described by Baraccani et al. (2017). The cross vaults, which are a 15th-century addition to the original 12th-century structure of the cathedral, were cut by a complex network of fractures and brick fragments and false ribs fell to the ground. A deep inspection of these fragments, and the absolute dating of lime mortars (using radiocarbon ^{14}C) and bricks (using thermoluminescence) integrated with the pollen record of mortars, recently

performed by Tirelli et al. (2020, 2021), allowed to clarify the construction and restoration history of the vaults and to link the repairs to the earthquake chronology for the area. The original vaults (1404–1454) were built using lime mortar binding with Roman and medieval older bricks. Lime mortar was used also for later repairs caused by earthquakes in the 16th and 17th centuries. Gypsum mortars were then used to rebuild some vaults and to repair others in the 18th and 19th centuries.

Therefore, this approach proved that unexpected damage could be revealed by a detailed chronology of masonry binders, a fundamental step to assess earthquake risk and properly select strengthening measures.

The earthquakes on the 20th and 29th of May 2012 also caused some damages to the tower. Surely the previous work of consolidation of the balconies, the two metal hoops on the balcony and the lower one on the belfry cornice, contributed to mitigate these effects.

On the outside, the most evident damage was a new fracture, parallel to an already restored one, on the sculpture placed in the southwest corner of the first cornice, depicting Samson in the act of smashing the lion's jaw. The damage was caused by the hammering action between the tower and one of the arches connecting it to the Cathedral, which once again points out the relevance of the interaction between the two monuments.

Furthermore, it is worth mentioning that since 1981 the Municipality of Modena promoted a comprehensive study of the induced subsidence, that resulted in a local dense network of geodetic leveling (Castagnetti et al. 2017) and in the execution of geotechnical investigations (Lancellotta 2009). The elevation data resulting from subsequent leveling campaigns allow to identify the trend of vertical displacements suffered over time by the benchmarks of the network, and then by the structures to which they are rigidly connected, and to investigate the related differential components and to evaluate their significance. Figure 3 displays the vertical displacements measured since 1984 in the historic center of Modena, the apses of the Cathedral and the Tower resulting to be characterized by the greater subsidence with respect to the one experienced by the whole city center (mean values are 48 mm for the Tower and 18 mm for the apse of the Cathedral over 32 years).

It is apparent from this leveling the sudden increase in the settlement the tower suffered in May 2012, not experienced by the Cathedral and other surrounding structures, and notably, the differential settlements towards South between benchmarks 18-17 and 16-C1 respectively of the order of 2.8 *mm* and 2.5 *mm*. These differential settlements may be expected to be the results of the seismic events of May 2012, but it remains to prove that this was actually the case, as discussed in the following sections.

3 IDENTIFICATION ANALYSIS AND SOIL-STRUCTURE INTERACTION

To consider the interaction of the structure with the supporting soil, a simple but effective approach considers the soil response as lumped into a series of springs and dashpots, each of them related to a degree of freedom of the soil-foundation system.

It is important to note that the properties of these elements depend not only on the properties of the half-space representing the soil but also on the exciting frequency.

By relying on this approach, if the soil and the foundation are represented by horizontal (K_h) and rocking (K_α) springs, the interaction with the soil will lead to a modified period of vibration T^*, given by:

$$T^* = T_0 \sqrt{1 + \frac{K}{K_h} + \frac{Kh^2}{K_\alpha}} \tag{1}$$

where: $T_0 = 1/f_0$ is the natural period of the structure resting on a fixed-base; K is the stiffness of the structure; h is the height of the lumped mass over the base.

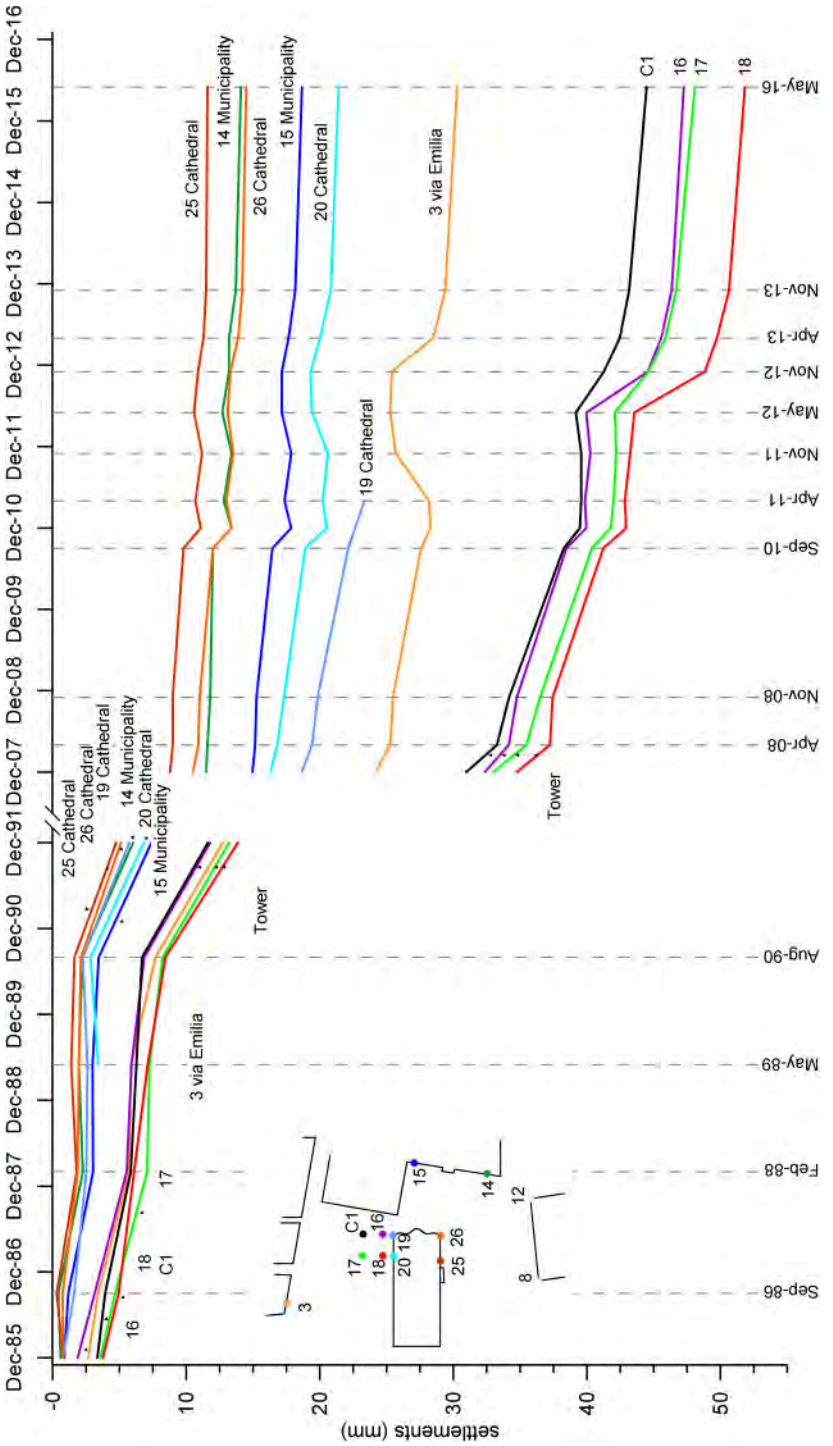

Figure 3. Trends of vertical displacement of the main benchmarks over the periods 1984–1991 and 1991–2016.

Similarly, the equivalent damping ratio (ξ*) of the single degree of freedom model (SDOF) representing the structure is given by:

$$\xi^* = \xi_{soil} + \left(\frac{T_0}{T^*}\right)^3 \xi \tag{2}$$

Where ξ is the damping ratio of the structure, and ξ_{soil} is the contribution of the soil damping that includes both the radiation and the material damping.

To study the role of soil-structure interaction in the long-term performance and to assess the seismic vulnerability of the tower, a dynamic monitoring program was started in August 2012. The acquisition system operates with a sampling frequency of 100 Hz and allows continuous monitoring of the dynamic response of the tower under ambient vibrations.

To capture the higher modes of vibration, 12 accelerometers were installed on the tower to record the time histories along three directions (normal to the cathedral nave, vertical, and parallel to the cathedral nave). To select the optimal position of these sensors, a dynamic analysis was performed in advance using a numerical model (FEM) of the tower. Analysis of the results allowed estimation of the natural frequency, mode shapes, and damping parameters of the identified bending mode shapes and extensional mode shapes, i.e., vibrations along the tower axis. In particular, the first bending mode shape, with an associated frequency of 0.74 Hz, shows that the rotation and displacement pattern at the tower base was mainly due to soil deformability. On the contrary, the second bending mode shape, associated with a frequency of 0.85 Hz, reflects the presence of the arches connecting the tower and cathedral, and higher modes are influenced by the masonry deformability (Lancellotta & Sabia 2013).

Based on these results, Lancellotta and Sabia (2013, 2015) estimated a rocking stiffness equal to $K_\alpha = 240\ GN{\cdot}m$ (neglecting in Equation (1) the contribution of the horizontal stiffness $K_h = 2.52\ GN/m$).

This value was proven to be consistent with the one provided by theoretical analysis (Gazetas 1991) with the following assumptions:

(a) the small-strain shear modulus G_o (equal to 28 MPa) in free field condition is obtained from the shear wave velocity ($V_S = 125$ m/s);
(b) the stress level induced by the tower is considered, giving a multiplier 1.57, therefore the operational shear modulus rises to G_o equal to 44 MPa;
(c) the effect of founding depth (equal to 5.65 m), compared to the square base of 12.40 m per side of the foundation, is considered, giving rise to a multiplier factor of 3.19.

An independent approach to highlight the influence of the soil-structure interaction is based on the decomposition of the actual system into two simpler ones. Equation (1), by neglecting the contribution of the soil horizontal stiffness, gives:

$$T^* = T_0\sqrt{1 + \frac{Kh^2}{K_\alpha}} \tag{3}$$

that can be also written as:

$$\frac{1}{(f^*)^2} = \frac{1}{f_0^2} + \frac{1}{f_R^2} \tag{4}$$

where: f^* = measured frequency; f_0 = fundamental frequency of the deformable tower resting on a fixed-base (equal to about 1 Hz); and $f_R = \omega_R / 2\,\pi$ = frequency of the tower, considered as a rigid body resting on the soil represented by a rotational stiffness K_α.

Since f^* and f_0 are known quantities, as well as the mass moment of inertia ($I = 5.4 \cdot 10^9 kg \cdot m^2$, considering the modal mass) of the tower with respect to the horizontal axis at the foundation level, the relation:

$$\omega_R = \sqrt{\frac{K_\alpha}{I}} \tag{5}$$

gives a value of $K_\alpha = 260\ GN{\cdot}m$, consistent with the one obtained through the more sophisticated identification analysis.

It is apparent from these results that a key factor in the evaluation of the dynamic stiffness representing the soil-foundation response is the selection of an appropriate value of the shear modulus.

In this respect, Cosentini et al (2015) proved that a value of G consistent with the shear strain level can be computed from a seismic site response analysis. Specifically, they analyzed the records of three seismic events: October the 3rd, 2012 (epicenter in Piacenza and magnitude ML = 4.5), January the 25th, 2013 (epicenter in Garfagnana, ML = 4.8) and June 21st, 2013 (epicenter in Alpi Apuane, near Lucca, ML = 5.2). In the following, a summary is reported.

Details of site investigation are reported in Lancellotta (2009, 2013). The soil profile (Figure 4) down to the investigated depth of 80 m can be described as composed of a first horizon of medium to high plasticity inorganic clays, with an abundance of laminae of sands and peat, only millimeters thick. The upper portion of this horizon, whose thickness ranges from 5 to 7 meters, is known as Modena Unit and it is linked to the flooding events (of post-Roman age) produced by minor streams (Fossa-Cerca stream). The underlaying horizons, ranging in depth from 22 to 54 m, represent the result of a complete transgressive-regressive cycle: the fine-grained sediments, belonging to the horizon known as Niviano Unit, were deposited during the penultimate interglacial cycle; the superimposed coarse-grained materials, belonging to the Vignola Unit, are linked to transport activities of the Secchia River. A second horizon of coarse-grained materials is encountered at depths ranging from 54 to 63 m, and thereafter a fine-grained horizon is found down to a depth of 78 m, here again, characterized by a diffuse presence of laminae of sand.

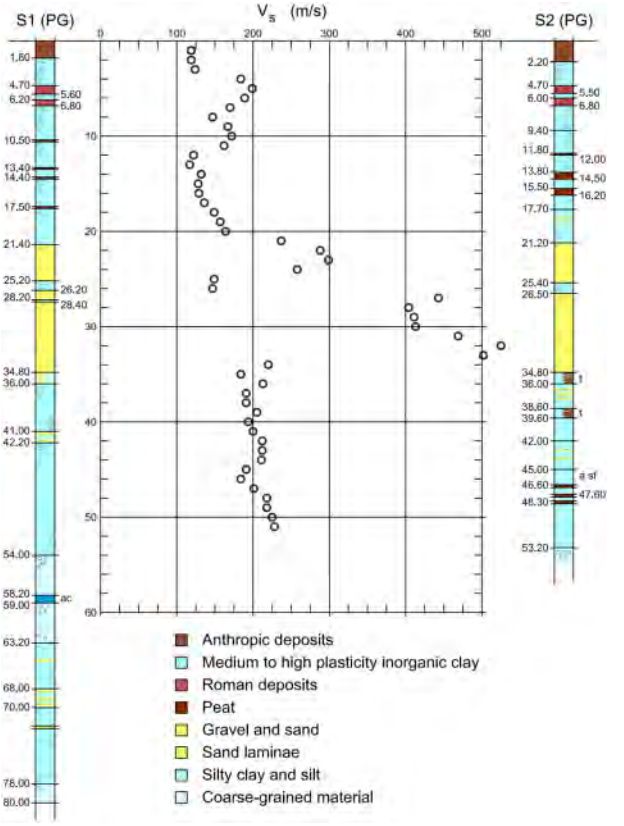

Figure 4. Soil profile and shear wave velocity from cross-hole tests.

Figure 5 shows the change of the normalized shear modulus reduction and the increment of damping ratio with shear strains, as measured on undisturbed samples with resonant column tests for the clayey layers.

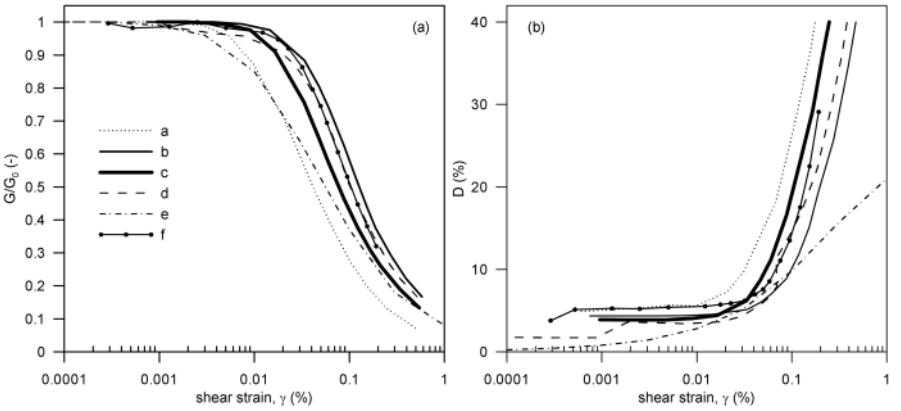

Figure 5. Dependence of shear modulus (a) and damping ratio (b) on strain level.

The dynamic characteristics of the structure can be estimated in terms of the transfer function from the excitation at the base to the response measured on the structure at a given level.

The *Frequency Response Function* (FRF) is therefore defined as follows:

$$H(\omega) = \frac{Y(\omega)}{X(\omega)} \quad or \quad H(\omega) = \frac{S_{XY}(\omega)}{S_{YY}(\omega)} \tag{6}$$

where $Y(\omega)$ and $X(\omega)$ are the Fourier transforms of the output and the input, respectively; $S_{XY}(\omega)$ is the cross-spectra of the input $x(t)$ and the output $y(t)$; $S_{YY}(\omega)$ is the auto-spectra of the output $y(t)$.

The FRF is a complex-valued function which amplitude has a maximum at the resonance frequency, and the output is 90° out of phase with respect to the input.

Figure 6 compares the FRF, evaluated using the acceleration time history at the base as input, and the time history measured at 78 m as output, for the three seismic events (October 2012, January 2013, and June 2013). It is apparent a reduction of the first natural frequency of the tower (from 0.73 to 0.69 Hz) moving from the first two events to the one of June 2013.

This difference is certainly associated with soil non-linearity since significant structural non-linearity is not expected for the masonry walls for such a small seismic excitation.

Therefore, the observed difference in natural frequency can be converted into an estimate of the reduction of the foundation stiffness by considering that the ratio between the mobilized soil stiffness during two different seismic events can be derived by using the inverse of equation (3)

$$\frac{K_{\alpha 2}}{K_{\alpha 1}} = \frac{(T_1/T_0)^2 - 1}{(T_2/T_0)^2 - 1} \tag{7}$$

From the difference in fundamental frequency observed in Figure 6, a stiffness ratio equal to 0.78 was obtained, consistently with the shear strain level derived from a seismic ground response analysis (for more details the reader is referred to Cosentini et al. 2015).

The effect of soil non-linearity on seismic response of the Tower can also be highlighted through an analysis of the Power Spectral Density (PSD) of some acceleration time-histories recorded at the height of 78 m. Four acceleration time histories (Figure 7) in direction parallel to the cathedral nave were analyzed: a signal recorded 50 minutes before the June 2013 seismic event; the signal during the seismic event; one recorded just 60 minutes after the earthquake; and a signal recorded

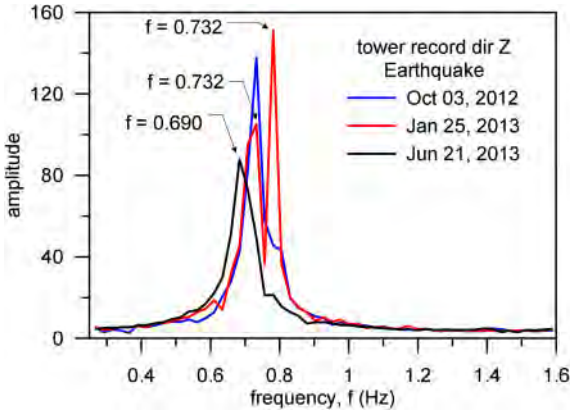

Figure 6. Frequency Response Function FRF for three seismic events.

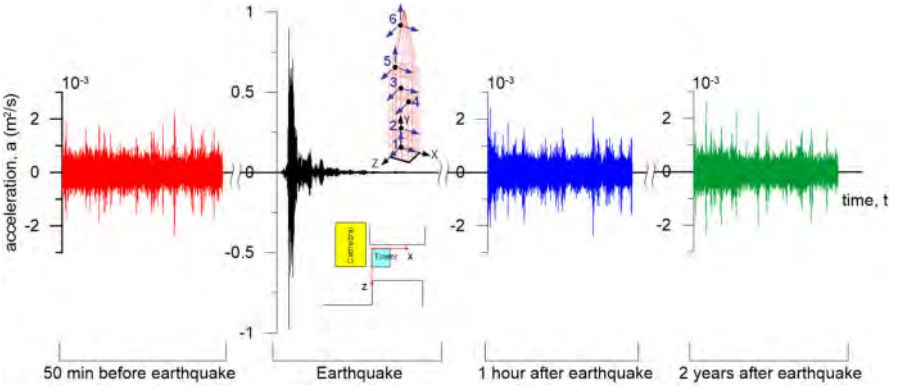

Figure 7. Acceleration time histories recorded at the height of 78 m (sensor 6) before the event of June 2013, during the earthquake, 1 hour and 2 years after the event.

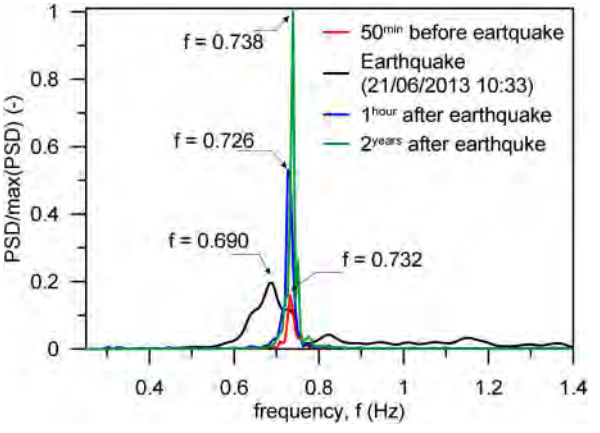

Figure 8. Comparison of normalized PSD of the time histories showed in Figure 7.

2 year later. The Power Spectral Density was computed for each signal. As it is shown in Figure 8, in terms of a normalized PSD, the reduction of the first natural frequency of the tower (from 0.74 to 0.69 Hz) observed during the earthquake disappeared already one hour after the event, results that prove that the behavior of the tower after the seismic event is the same as it was before that event.

4 DIFFERENTIAL SETTLEMENTS DURING SEISMIC EVENT OF MAY 2012

Consider now the tower to be represented by a single degree of freedom model (SDOF) consisting of a mass (M) lumped at a height (h) over the base. This model can be thought to represent the behavior of the tower in its first fundamental mode of vibration and, accordingly, if x_i is the modal (or even the assumed) horizontal displacement at the height y_i with a lumped mass m_i, then the modal mass associated to the first fundamental mode is given by:

$$M = \frac{\left(\sum m_i \cdot x_i\right)^2}{\sum m_i \cdot x_i^2} \tag{8}$$

and the height of the centroid of the inertial forces is given by:

$$h = \frac{\sum m_i \cdot x_i \cdot y_i}{\sum m_i \cdot x_i} \tag{9}$$

In the present case, the $M = 4868 \cdot 10^3$ *kg* (i.e., 64% of the total mass) and $h = 38.39$ *m*.

The stiffness of the structure resting on a rigid base can be estimated as $K = (4\pi^2 M)/T_0^2 = 192$ *MN/m*, and by considering that the shear force at the base of the tower can be obtained either in terms of displacement (u) of the structure or in terms of the displacement (u^*) of the equivalent SDOF model, the following relation applies:

$$u = \left(\frac{f^*}{f_0}\right)^2 \cdot u^* \tag{10}$$

If during the motion the structure rotates of the quantity $\alpha(t)$, by considering the dynamic equilibrium of horizontal forces and moment of the center of the foundation, the following relation is obtained:

$$\alpha \cdot h = \frac{Kh^2}{K_\alpha} \cdot u \tag{11}$$

Therefore, if $b = 11$ *m* is the dimension of the tower at the level of the benchmarks, the differential settlements suffered by the tower can be predicted from the spectral displacement by properly combining Equations 10 and 11, i.e.

$$\Delta w = \frac{Kh^2}{K_\alpha} \cdot \frac{b}{h} \cdot \left(\frac{f^*}{f_0}\right)^2 \cdot u^* \tag{12}$$

Figures 9 and 10 are the spectral acceleration and the spectral displacement related to the acceleration records of seismic events of May 20 and 29, 2012, together whit those of June 21, 2013.

The acceleration time histories were recorded in the free field by the Modena station (MDN) of the Italian accelerometric network (D'Amico et al. 2020), located to relatively small distance (about 2.8 km) from the Ghirlandina Tower.

In particular, a maximum spectral displacement (u^*) of 1.8 *cm* can be associated with the measured period of $T^* = 1.45$ *s*, and the corresponding differential settlement (Δw) is about 2.6 *mm*, in agreement with the measured values (see Figure 3).

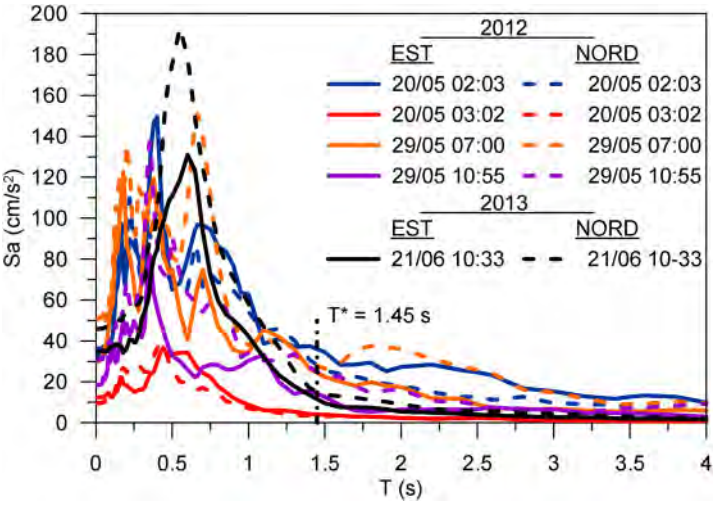

Figure 9. Spectral acceleration of May 2012 and June 2013 seismic events.

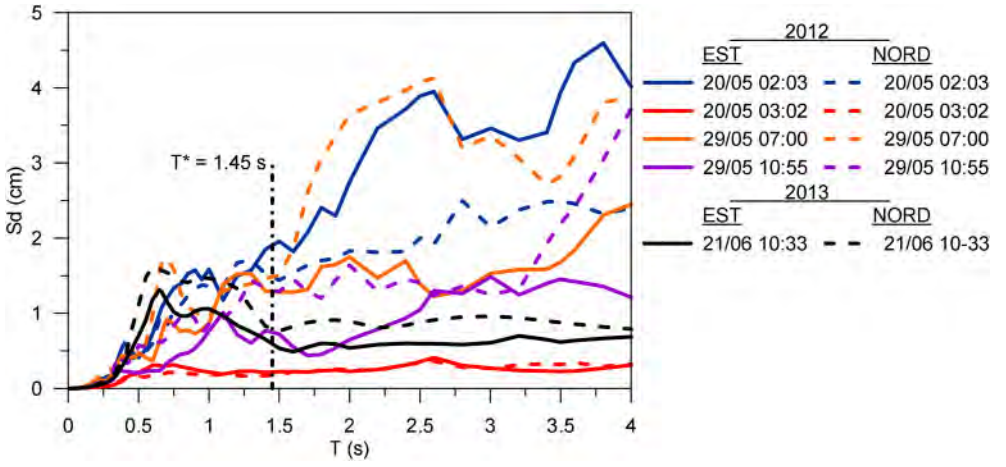

Figure 10. Displacement spectra of May 2012 and June 2013 seismic events.

However, a deeper insight into the displacement spectra would also suggest that since the event of May 2012 was a sequence of many shocks, the differential settlement suffered by the tower could be the result of an accumulation of the irreversible portion of the total displacement suffered by the tower during each event.

5 FINAL REMARKS

Recent earthquakes event in Italy (May 2012) have once again put into evidence the seismic vulnerability of the cultural heritage and there were many cases showing the role played by soil-structure interaction.

Taking into account this interaction is not a straightforward task, even when using a simplified lumped parameters model, because the selection of soil modulus requires to consider many aspects:

soil nonlinearity; dependence on stress level induced by the structure; effectiveness of the contact between the foundation and the surrounding soil; dependence on the exciting frequency.

In this respect, identification analyses are certainly powerful tools to characterize the behavior of the structure interacting with the soil and to properly define the properties of simplified lumped models, that can be used to forecast the response of the structure, as it was the case with the Ghirlandina tower.

In addition, long-term continuous dynamic monitoring allows to identify the causes of movements and their potential increase in rate, distinguishing the normal physiological behavior from deviations.

In many cases, monitoring can help in avoiding unnecessary intervention measures, preserving the historic integrity of the structure.

REFERENCES

Baraccani, S., Gasparini G., Palermo, M., Silvestri, S. & Trombetti, T. 2017. The structural behavior of the masonry vaults of the Cathedral of Modena. *Proc. 5th International Conference on Architecture and Civil Engineering, Singapore, 8–9 May 2017.*

Cadignani, R., Lancellotta, R. & Sabia, D. 2019. *The restoration of Ghirlandina Tower in Modena and the assessment of soil-structure interaction by means of dynamic identification techniques*. CRC Press, Taylor&Francis Group, London.

Castagnetti, C., Cosentini, R.M., Lancellotta, R. & Capra, A. 2017. Geodetic monitoring and geotechnical analyses of subsidence induced settlements of historic structures. *Structural Control and Health Monitoring*, 24(12): 1–15.

Cosentini, R.M., Foti, S., Lancellotta, R. & Sabia, D. 2015. Dynamic behaviour of shallow founded historic towers: validation of simplified approaches for seismic analyses. I*nternational Journal of Geotechnical Engineering*, 9(1): 13–29.

D'Amico, M., Felicetta, C., Russo, E., Sgobba, S., Lanzano, G., Pacor, F., Luzi, L. 2020. Italian Accelerometric Archive v 3.1 – Istituto Nazionale di Geofisica e Vulcanologia, Dipartimento della Protezione Civile Nazionale. doi: 10.13127/itaca.3.1.

Gazetas, G. 1991. Foundation vibrations, in. H.F. Fang (ed.), *Foundation engineering handbook*: 553–593. New York, Van Nostrand Reinhold.

Giandebiaggi, P., Zerbi, A. & Capra, A. 2009. l rilevamento della torre Ghirlandina. In Rossella Cadignani (ed.), *La torre Ghirlandina. Un progetto per la conservazione (vol. 1):* 78–87. Sossella Ed., Roma.

Lancellotta, R. 2009. Aspetti geotecnici nella salvaguardia della torre Ghirlandina. In Rossella Cadignani (ed.), *La torre Ghirlandina. Un progetto per la conservazione (vol. 1):* 178–193. Sossella Ed., Roma.

Lancellotta, R. 2013. La torre Ghirlandina: una storia di interazione struttura-terreno. XI Croce Lecture. *Rivista Italiana di Geotecnica*, 2: 7–37.

Lancellotta, R. & Sabia, D. 2013. The role of monitoring and identification techniques on the preservation of historic towers. In Emilio Bilotta, Alessandro Flora, Stefania Lirer, Carlo Viggiani (eds.), Geotech*nical engineering for the preservation of monuments and historical sites*; *Proc. intern. Symp., Napoli, 30–31 May 2013*. CRC Press, Taylor&Francis Group, London.

Lancellotta, R. & Sabia, D. 2015. Identification technique for soil-structure analysis of the Ghirlandina tower. *International Journal of Architectural Heritage* 9: 391–407.

Lugli. S. 2017. Mutina sepolta: inquadramento geologico dell'area urbana di Modena. In De Luca editori d'arte (eds), *Mutina splendidissima, la città romana e la sua eredità*: 16–19. Roma: Italy.

Tirelli, G., Lugli, S., Galli, A., Hajdas, I., Lindroos, A., Martini, M., Maspero, F., Olsen, J., Ringbom, Å., Sibilia, E., Caroselli, M., Silvestri, E. & Panzeri, L. 2020. Integrated dating of construction and restoration of the Modena cathedral vaults (northern Italy): Preliminary results. *Radiocarbon* 62(3): 667–677.

Tirelli, G., Bosi, G., Galli, A., Hajdas, I., Lindroos, A., Martini, M., Maspero, F., Mazzanti, M., Olsen, J., Panzeri, L., Ringbom, Å., Sibilia, E., Silvestri, E., Torri, P. & Lugli, S. 2021 A Chronology of Ancient Earthquake Damage in the Modena Cathedral (Italy): Integrated Dating of Mortars (14C, Pollen Record) and Bricks (TL). *International Journal of Architectural Heritage* DOI: 10.1080/15583058.2021.1922783.

Geotechnical Engineering for the Preservation of Monuments and Historic Sites III – Lancellotta, Viggiani, Flora, de Silva & Mele (Eds)

Development of a liquefaction damage assessment system based only on seismic records

M. Kazama, K. Toyabe, T. Otsuka & A. Kamura
Tohoku University, Sendai, Miyagi, Japan

S. Nakamura
Nihon University, Koriyama, Fukushima, Japan

S. Sato
Fukken Gijyutsu Consultants Co., Ltd., Sendai, Miyagi, Japan

K. Matsushita
Misawa Homes Institute of Research and Development Co., Ltd., Tokyo, Japan

ABSTRACT: A new artificial neural network (ANN) system was developed for assessing the damage risk due to liquefaction during an earthquake, based only on seismic records. Compared to conventional technology that requires information about the soil properties and constitution, there is a great advantage in being able to estimate damage from seismic records alone. Further, if small- and medium-level intensity earthquake records can be used to determine the risk of liquefaction in advance, preventive measures can be taken to avoid it. Here, we introduce the results of applying this system to the liquefaction damage observed during the 2011 Great East Japan Disaster in the Kanto area of Japan. In addition, we have made the system available to the public via the Internet, so we will also discuss how to use it.

1 INTRODUCTION

The world's earthquake-prone countries have suffered significant liquefaction damage in disasters; for example, Alaska, USA (1964), Niigata, Japan (1964), Kobe, Japan (1995) (JGS, 1996), Canterbury, New Zealand (2010) (Orense, 2016), and Tohoku, Japan (2011) (Kazama & Noda 2012; Yamaguchi et al. 2012; Yasuda et al. 2012). The mitigation and early detection of damage caused by liquefaction are common issues in countries vulnerable to earthquakes. For this reason, engineers and researchers have conducted many geotechnical investigations to improve liquefaction predictions and early damage detection. However, with current technology, it is difficult to determine how much liquefaction occurred in a soil layer, at which point and at what depth, because neither seismic records nor excess pore-water pressure records are obtained at the target point.

Under these circumstances, inexpensive accelerometers can be used to monitor the structural health of private wooden houses and ground, as shown in Figure 1 (Oki et al. 2019). This is a type of damage-assessment device that enables acceleration measurements. It can be installed in the foundation of a detached house and can be used to determine the degree of damage that occurs to the building in the event of an earthquake. The seismic intensity and extent of damage to the house can be analyzed in real time, based on the measured seismic response records and structural data. This system is expected to be used for evacuation support, based on the early determination of the level of damage, and can be used to determine whether repairs are necessary. This technology has already been put into practice by Japanese house makers.

 DOI 10.1201/9781003308867-52

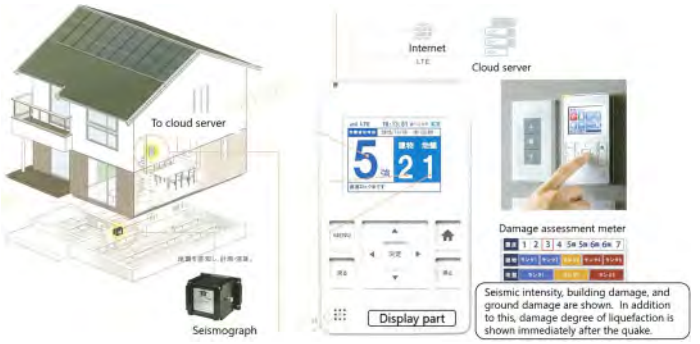

Figure 1. Damage-assessment meter for private housing development of Misawa Home Co., Ltd., Japan.

Furthermore, although few examples are available, the acquisition of pore-water pressure records has recently begun (Unjoh et al. 2012). If seismic records and pore-water pressure records are accumulated at the time of large earthquakes in the future, the technology will likely make great progress.

Regarding the risk assessment of damage caused by liquefaction, several methods have been proposed to estimate the ground liquefaction from seismic records at the ground surface. Akasaka et al. (1995) attempted to estimate the liquefaction occurrence and layer thickness in the field, using the maximum ground-surface acceleration and seismic intensity (SI) values obtained from seismographs.

Furthermore, Shimizu et al. (2003) proposed a method to estimate the liquefaction occurrence by combining the zero-crossing period, maximum acceleration, and SI values obtained from seismographs, and displayed the results in real time using a geographic information system (GIS). This method is actually used for the seismic monitoring of gas pipes in the Tokyo metropolitan area. However, the suitability of the method decreases as the nonlinearity increases, and the results, including the influence of surface waves and layer components, may result in erroneous decisions (Suzuki et al. 2001).

This suggests that even if a large amount of data is collected, a serial-data-based prediction method with simple indicators is limited in its ability to assess liquefaction. This is due to the nonlinearity and complex behavior in the dynamic response of the ground during large earthquakes that cause liquefaction. This means that non-learning-based prediction systems are limited in determining the occurrence of liquefaction from seismic responses. Therefore, a machine learning method, and especially an artificial neural network (ANN), which does not require fixed prior knowledge of causal relationships, is more suitable for this type of problem than a deterministic approach.

While using an ANN for liquefaction prediction and determination, a common approach is to input the in-situ information obtained from a cone penetration test (CPT) or standard penetration test (SPT) to a model and output a correct output label to indicate whether liquefaction will actually occur. If the degree of liquefaction can be evaluated using only the seismic motion, which does not require soil-survey results, it will be very convenient from the viewpoint of immediate control and the use of big data. Against this background, the authors have developed a deep-learning system that evaluates the degree of liquefaction caused by an earthquake, based only on earthquake records. We introduce it here (Kamura et al. 2021).

2 OVERVIEW OF THE ANN MODEL DEVELOPED BY KAMURA ET AL.

2.1 *ANN approach for liquefaction assessment*

The ANN is a technology that has recently attracted attention and been applied to many social problems. Many attempts have been made to apply ANNs to liquefaction prediction and decisions in

the earthquake geotechnical-engineering field regarding liquefaction assessment. As mentioned in the previous section, when using an ANN for liquefaction prediction and determination, a common approach is to input the ground information obtained from in-situ ground investigation methods, such as CPTs or SPTs, and output a correct output label to indicate whether liquefaction will actually occur. See, for example, Goh (1994, 1996), Hsu et al. (2006), Hanna et al. (2007a, 2007b), Pijush and Sitharam (2011), Juang et al. (2008), Mughieda et al. (2009), and Abbaszadeh-Shahri (2016).

In addition, a method to estimate the liquefaction strength from the in-situ shear-wave velocity (Tung et al. 1993), and a method to evaluate the liquefaction potential by comparing it with the seismic intensity (Garcia et al. 2012; Kang et al. 2013) have been proposed. Although the applicability of the above-mentioned approaches has been confirmed to a certain extent, all these attempts require a preliminary field survey, and eventually, a human must identify the areas where liquefaction is likely to occur.

With these methods, the accuracy of the prediction is highly dependent on the accuracy of the data from the site investigation, and the scope is limited for improving liquefaction prediction using these techniques. Therefore, an ANN-based method that evaluates the degree of liquefaction using only the three-dimensional acceleration record of the ground was considered to be more effective.

2.2 *Shaking-table test for obtaining the input dataset*

To apply an ANN for assessing the liquefaction degree, training data are required for learning. Actual data are rarely measured and published; therefore, to use an ANN, we must create our own dataset. Kamura et al. (2021) created a dataset from many shaking-table tests. Specifically, several shaking-table tests were carried out with actual three-dimensional acceleration records, and the surface responses and pore-water pressures of the soil tank were measured as training data. Then, an ANN model was created from the resulting dataset to determine whether it was possible to assess the degree of liquefaction using only seismic records.

Figure 2 shows the configuration, dimensions, and sensor layout of their experiment. Other detailed testing conditions are presented in the literature (Kamura et al. 2021). In their data preparation, a series of 120 shaking-table test data points with an oversampling method was used.

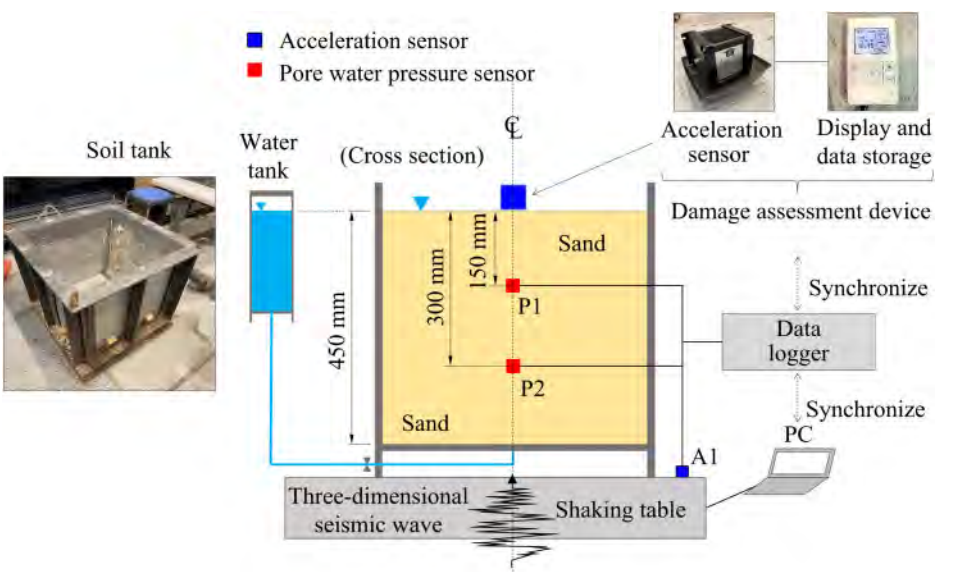

Figure 2. Shaking-table test for obtaining the training dataset.

2.3 *Input training data representing the seismic response of the ground*

Various three-dimensional seismic response data were obtained from shaking-table tests. In the ANN model, the input values were index values corresponding to the dynamic characteristics of the measured surface acceleration.

Specifically, the input values were as follows.

(1) Maximum acceleration (three components for each seismic-duration section)
(2) First-order dominant frequency (three components for each seismic-duration section)
(3) Second-order dominant frequency (three components)
(4) Minimum dominant prominence frequency (three components)
(5) Seismic motion duration (one component)
(6) Seismic intensity (one component)
(7) Maximum velocity (three components)
(8) SI value (three components)

To calculate the maximum acceleration of each component (east-west (EW), north-south (NS), up-down (UD)), the duration of the main motion was divided into three equal sections, and the maximum value of each interval was obtained. The maximum values of the recorded peak accelerations from the three components were adopted as the "maximum acceleration." The duration of the main motion was defined as the time between the first measurement of 5% of the maximum acceleration and the last measurement of each acceleration.

2.4 *Output training data as an indicator of liquefaction degree*

The output (correct output label) as an indicator of the liquefaction degree is required in the ANN analysis. In general, the degree of liquefaction can be defined by an increase in the excess pore-water pressure ratio and its duration. Figure 3 shows an example of the time history of the excess pore-water pressure ratio obtained from the shaking-table test.

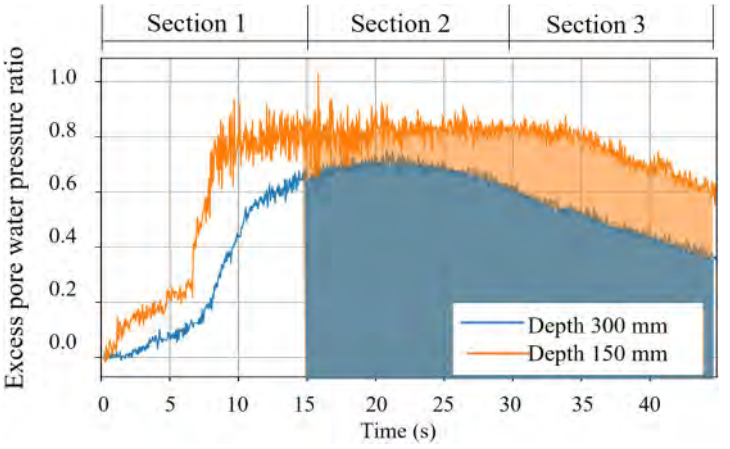

Figure 3. Example of time history of the excess pore-water pressure ratio, divided into three equal parts based on time, used for obtaining the liquefaction degree of a ground area.

For the correct output label, the degree of damage due to liquefaction (DDL) was defined on a five-point scale. This is not defined by the excess pore-water pressure ratio alone. To distinguish between temporary and continuous excess pore-water pressure, the time history of the excess pore-water pressure ratio was divided into three equal parts in a time-based manner. It was based on the duration of the excess pore-water pressure; the time average of the integrals in the latter two sections in Figure 3 was calculated as the evaluation index. The excess pore-water pressure thresholds were 0.1, 0.3, 0.6, and 0.9 for each depth.

Based on the above definitions, plots of the experimental results and a visualization of the DDL classification are shown in Figure 4. The caption in the upper figure shows the location of the seismic record used in the shaking-table test. Six seismic waves that were observed by KiK-net and K-net (National Research Institute for Earth Science and Disaster Resilience (NIED), 2019) were used as inputs. The lower part of Figure 4 shows the probability of liquefaction damage corresponding to each DDL evaluation level.

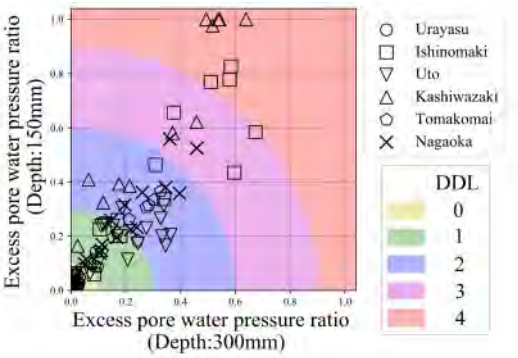

Definition of DDL [damage degree due to liquefaction]

DDL		
0	: Liquefaction is unlikely to occur.	(EPWP*<0.1)
1	: Slight liquefaction may occur.	(0.1 ≤ EPWP<0.3)
2	: Moderate liquefaction may occur.	(0.3 ≤ EPWP<0.6)
3	: Liquefaction damage may occur.	(0.6 ≤ EPWP<0.9)
4	: High possibility of liquefaction damage.	(0.9≤EPWP)

*EPWP: Excess Pore Water Pressure Ratio

Figure 4. Definition of damage degree due to liquefaction.

2.5 *Validation example of the 1995 Kobe Earthquake*

In a previous study, we evaluated the degree of damage due to liquefaction for three major earthquakes in Japan (Kamura et al. 2021). Here, the application results of the 1995 Kobe Earthquake will be introduced. It is well known that the 1995 Hyogo-ken Nambu Earthquake caused significant liquefaction damage to a landfill artificial island in Kobe City (JGS 1996). Kazama et al. (1998) and Yamaguchi et al. (2002) showed that the degree of liquefaction of the reclaimed artificial island is influenced by the degree of consolidation of the underlying soft-clay layer. In addition, the liquefaction characteristics of decomposed granite soil, which is a landfill material for artificial islands, have been clarified (Kazama et al. 2000a). At Port Island, an artificial island of Kobe in this earthquake, there are vertical array records in the depth direction, which were analyzed from various perspectives (Kazama et al. 1996, 2000b).

Figure 5 shows the results of applying the developed ANN model to the vertical array records observed at Kobe Port Island during the 1995 Kobe disaster. Because the Kobe artificial island was covered with decomposed granite soil that erupted after the earthquake, there is no doubt that the decomposed granite soil, which is a landfill material, liquefied violently. According to the evaluation results, DDL level 3 appeared at the ground surface, DDL level 4 was at a depth of G.L. −16.4 m, DDL level 2 was at G.L. −32.4 m, and DDL level 2 was at G.L. −83.4 m.

Although the dataset was generated from surface seismic records obtained from the shaking-table test, we attempted to apply the method to all the waveforms obtained by the array observations because seismic data are records of the “motion of a point” in principle. Although it is not possible

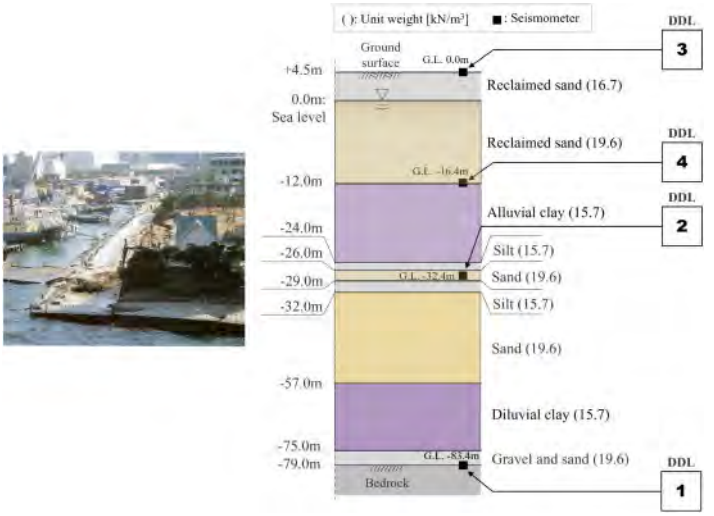

Figure 5. Ground profile at Kobe Port Island (AEDP-jp, 1998) and the DDL determined by the ANN.

to confirm whether this result is valid, it was judged that it is worth using as an attempt to determine the approximate degree of ground liquefaction from the seismic motion alone.

3 CASE STUDY OF THE LIQUEFACTION DAMAGE IN THE KANTO REGION DURING THE 2011 GREAT EAST JAPAN DISASTER

3.1 *Liquefaction damage in the Kanto region in the 2011 Great East Japan Disaster*

The 2011 Great East Japan Earthquake caused large-scale liquefaction damage over a wide area of Tokyo Bay and the Kanto region (Unjoh et al. 2012; Yasuda et al. 2012). The area is estimated to be approximately 42 km^2.

Wakamatsu and Senna (2015) investigated the liquefaction damage to the Kanto region in Japan caused by the 2011 earthquake. According to their study, liquefaction was observed in 130 cities, towns, and villages in all seven prefectures in the Kanto region. They calculated the incidence of liquefaction of a 250 m mesh in the entire Kanto region, which recorded a Japan Meteorological Agency (JMA) seismic intensity of 5 or higher.

Senna et al. (2021) proposed a formula for estimating the liquefaction-area ratio, based on the information at the liquefaction occurrence points of five earthquakes with JMA seismic intensities of 6 or higher. The ground characteristics of each region were considered, and the results were in harmony with the actual liquefaction points. Here, the proposed ANN is used to assess the liquefaction damage caused by the 2011 earthquake.

3.2 *Review of the liquefaction damage assessment based on strong motion in Japan*

Several studies have been conducted to understand the damage caused by liquefaction in real time, immediately after an earthquake. Shimizu et al. (2003) constructed a system that predicts the liquefaction occurrence by combining the SI value and maximum acceleration with boring data and micro-topography classification information and displaying them on a geographic information system (GIS) in real time.

Instead of a pore-water pressure gauge and a liquefaction sensor, Takada et al. (2000) proposed a method for calculating the energy-index Arias intensity from the ground-surface acceleration record to determine the liquefaction occurrence. However, these methods require ground information, such as boring data, when applied. Miyajima et al. (2000) proposed a liquefaction-detection

index, focusing on the amplitude and frequency characteristics peculiar to liquefactable ground, to determine the occurrence of liquefaction in real time. This method is based on the analysis of seismic motion, based on past earthquake-liquefaction cases.

Kuwahara et al. (2021) conducted a recent study using machine learning. They estimated the risk of liquefaction in Japan using data from 41 earthquakes that occurred between 1891 and 2016. In this study, random forest, which is a type of machine learning, was adopted as an estimation model, and a learning and prediction model was created, considering the imbalance of the dataset. Using this model, they created a nationwide liquefaction hazard map, based on the seismic motion. When applying this prediction method, ground information, such as boring surveys, is required.

3.3 *Assessment based on strong-motion records during the 2011 earthquake off the Pacific Coast of Tohoku in the Kanto area obtained from NIED*

Here, using the deep-learning model proposed by Kamura et al. (2021), the strong-motion observation data at 140 points in the Kanto region during the 2011 earthquake off the Pacific Coast of Tohoku were used as a verification example (not included in the teaching data), and the actual liquefaction damage resulted in the model. The validity was examined by comparing the confirmed points with the assessment results. Furthermore, among the features obtained from the strong-motion observation data, we focused on the maximum acceleration, maximum velocity, duration, and SI value, and analyzed the features of the dataset.

Figure 6 shows the DDL judgment results of each point using the deep-learning model plotted on a GIS using the strong-motion records of 140 points in the Kanto region, obtained from K-net as input data. As shown in Figure 4, the larger the DDL value, the higher the degree of liquefaction.

A high DDL is shown along Tokyo Bay, especially in the inner part. On the other hand, there are many points with low DDL on the inland side of Chiba and other prefectures. From these relative tendencies, it seems that the results are harmonious with the actual damage. Table 1 shows the breakdown of the DDL for all 140 points. It can be seen that the decisions are not biased towards a particular DDL.

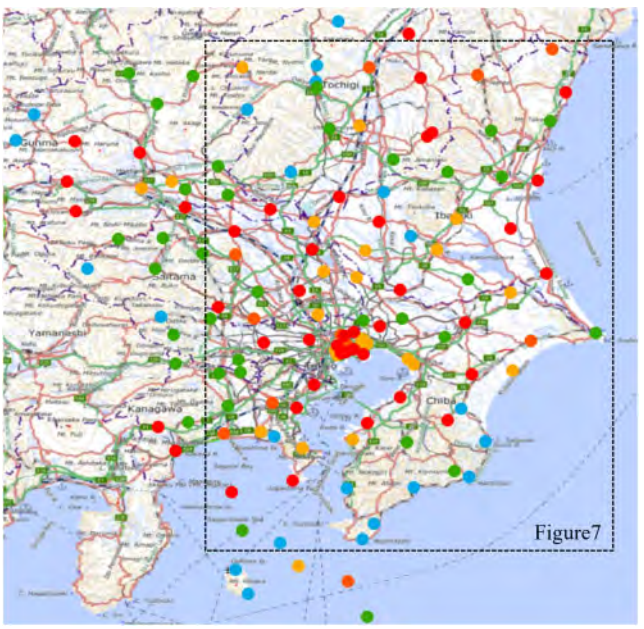

Figure 6. Judgment result in the Kanto region by deep-learning of the liquefaction degree (DDL) of the Kanto region during the 2011 earthquake off the Pacific Coast of Tohoku.

Table 1. Assessment-result distribution for the 2011.3 earthquake.

DDL	Number of points
0	24
1	37
2	26
3	11
4	42

The DDL was determined to be 3 or 4 in the Tokyo Bay area, especially in the reclaimed-land area. Figures 7 and 8 show an enlarged view of the area from Tokyo Bay to Chiba Prefecture, and the inner part of the Tokyo Bay area, respectively. For comparison, the point information (liquefaction history map), where traces of liquefaction were confirmed, is also shown.

According to Wakamatsu et al. (2015), most of the reclaimed land where liquefaction occurred in the Tokyo Bay area was constructed after 1947. However, no liquefaction was reported in areas reclaimed in the earlier days. In this study, the DDL of the strong-motion observation points belonging to the latter was 2, so the judgment results were almost consistent.

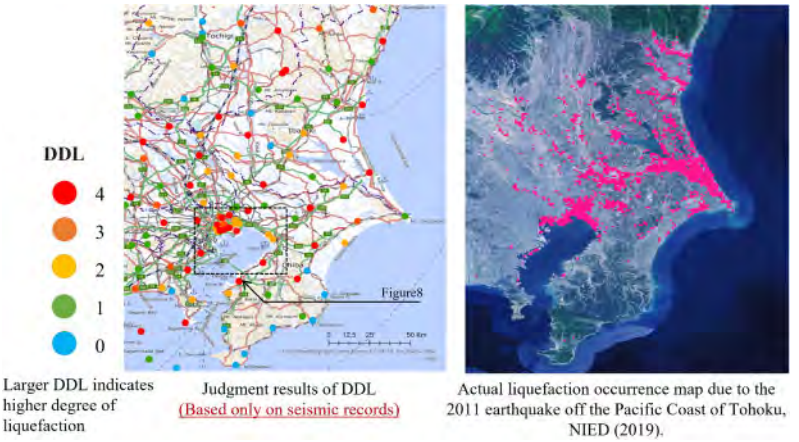

Figure 7. Comparison of judgment results by deep learning from around Tokyo Bay to Chiba Prefecture and actual liquefaction-occurrence history map made by NIED (2019).

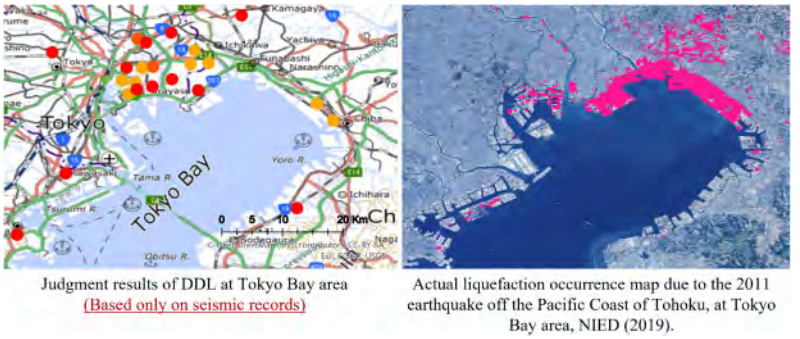

Figure 8. Comparison of judgment results by (left) deep learning in the inner part of Tokyo Bay and (right) actual liquefaction-occurrence history map made by NIED (2019).

4 FUTURE USE OF THE DEVELOPED ANN ASSESMENT SYSTEM

The method proposed here will evolve progressively as data are accumulated. At the moment, it is in the initial stage; however, we will discuss the current situation, including future developments.

4.1 *Application to medium-level earthquakes for assessing liquefaction potential—Evaluation of the earthquake 10 years after the Great East Japan Earthquake*

If medium-intensity seismic records can be obtained, it might be possible to evaluate the potential liquefaction risk. According to the JMA, there was a magnitude 6.1 earthquake with an epicenter in northwestern Chiba Prefecture at approximately 10:41 pm on October 7, 2021. This is the first earthquake in the Kanto region that has received a JMA seismic intensity of 5 or higher in the 10 years since 2011. No liquefaction damage has been reported for this earthquake. However, it is probable that a slight amount of liquefaction occurred without being directly linked to the damage. The NIED observation network, which was shown earlier, also provided seismic records at 136 observation points, which correspond to the 140 observation points of the 2011 earthquake. The remaining four points are not supported because they moved.

Figure 9 shows a comparison of the JMA instrumental seismic intensity of the seismic motion observed in the March 2011 and October 2021 earthquakes. The color coding in the figure shows the degree of liquefaction estimated from the 2011 earthquake records shown in the previous section. Comparing the JMA instrumental seismic intensities, we can see that the 2011 earthquake was approximately one to three times as large as the 2021 earthquake. It can also be seen that the relationship between the JMA instrumental seismic-intensity class and the degree of liquefaction risk cannot be clearly determined. Currently, the liquefaction risk is being evaluated using the developed technology, using the earthquake records of October 2021 as input data.

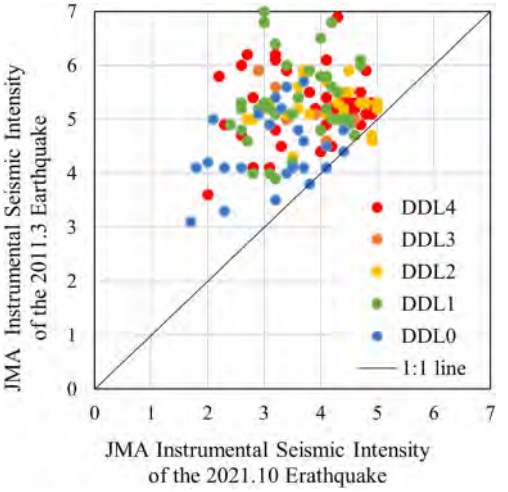

Figure 9. Comparison of the seismic intensity of the recorded strong motion between the 2011.3 earthquake and the 2021.10 earthquake observed by NIED. DDL values are evaluated based on the 2011.3 earthquake motions.

4.2 *Trial use of the developed system*

To improve the practicality of this technology, it will be applied to earthquakes that have caused liquefaction damage (for example, the 2015 Kumamoto Earthquake and the 2018 Hokkaido Eastern Iburi Earthquake in Japan).

As a part of that, the developed system is currently being released on a trial basis at the following web address: https://www.michinoku-gidas.jp/LiquefactionAI/. In the current system (as

of December 1, 2021), the user first registers his/her email address in the system. Next, the user prepares the acceleration data for the three components of the seismic record (EW, NS, and UD) that the user wants to analyze. The format of the seismic record to be input into the system is shown in the instructions on the website. Seismic records for 10 points at a time can be entered. Please note that it is currently available on a trial basis and that the assessment program is subject to change without notice by enhancing the training dataset for the ANN.

5 CONCLUSIONS

This paper introduced a new ANN system, developed by Kamura et al. (2021), that assesses the damage risk due to liquefaction, based only on seismic records. It was applied to the 2011 Great East Japan Disaster. In the system, the degree of damage due to liquefaction was separated into five levels, based on the excess pore-water pressure ratio. A case study of the Great East Japan Earthquake using seismic records observed at 140 points demonstrated its effectiveness.

Internet of Things (IoT) technology is expected to be applied to the field of earthquake-disaster prevention in Japan. One of the authors arranged for a damage-assessment meter for private wooden houses, based on earthquake records. This seismograph is offered to individuals at a low price. In other words, seismographs can be easily used by individuals. Such a system can be applied to various public and private facilities. The liquefaction risk-assessment system introduced here is expected to become a practical social technology in the near future.

ACKNOWLEDGMENTS

K-NET and KiK-net data provided by the National Research Institute for Earth Science and Disaster Resilience (NIED) were used in this study as input seismic records for the evaluation ANN system. We received useful advice from Professor Kazue Wakamatsu of Kanto Gakuin University on obtaining information from liquefaction points during the 2011 earthquake off the Pacific Coast of Tohoku. We would like to express our deepest appreciation to these associates. This work was supported by JSPS KAKENHI Grant Numbers JP20H02237, JP20H00258, and JP21H01425.

REFERENCES

Abbaszadeh-Shahri, A., 2016. Assessment and prediction of liquefaction potential using different artificial neural network models: A case study. *Geotech. Geol. Eng.* 34, 807–815.

Association for Earthquake Disaster Prevention (AEDP-jp), 1998. Strong Motion Array Observation, No. 3, CD-ROM.

Garcia, S., Ovando-Shelley, E., Gutiérrez, J., 2012. Liquefaction assessment through machine learning, *15WCEE, Conference Paper.* (PDF available)

Goh, A.T.C., 1994. Seismic liquefaction potential assessed by neural networks. *J. Geotech. Eng. ASCE,* 0733-9410(1994) 120:9(1467).

Goh, A.T.C., 1996. Neural network modeling of CPT seismic liquefaction data *(TECHNICAL NOTES). J. Geotech. Eng*. 122, Issue 1.

Hanna, A.M., Ural, D., Saygili, G., 2007a. Evaluation of liquefaction potential of soil deposits using artificial neural networks. *Eng. Comput.*, ISSN: 0264-4401.

Hanna, A.M., Ural, D., Saygili, G., 2007b. Neural network model for liquefaction potential in soil deposits using Turkey and Taiwan earthquake data. *Soil Dyn. Earthquake Eng.* 27(6): 521–540.

Hsu, S.C., Yang, M.D., Chen, M.C., Lin, J.Y., 2006. Artificial neural network of liquefaction evaluation for soils with high fines content. *Proceedings of the 2006 IEEE International Joint Conference on Neural Networks*, July 16–21, 2006. 2643–2649.

Juang, C.H., Chen, C.H., Mayne, P.W., 2008. CPTU simplified stress-based model for evaluating soil liquefaction potential. *Soils and Foundations* 48(6): 755–770.

Kamura, A., Kurihara, G., Mori, T., Kazama, M., Kwon, Y., Kim, J., Han, J.T., 2021. Exploring the possibility of assessing the damage degree of liquefaction based only on seismic records by artificial neural networks. *Soils and Foundations* 61(3): 658–674.

Kang, F., Li, J.J., Zhou, H., 2013. Artificial neural network model for evaluating gravelly soils liquefaction using shear wave velocity. *Sixth China-Japan-US Trilateral Symposium on Lifeline Earthquake Engineering*, May 28–June 1, 2013. https://ascelibrary.org/doi/10.1061/9780784413234.078.

Kazama, M., Kagatani, T., Yanagisawa, E., 2000a. Peculiarities of liquefaction resistance of Masaso (weathered granite soil). *J. of Geotechnical Engineering, JSCE*, (645-III-59): 153–166. (in Japanese)

Kazama, M., Noda, T., 2012. Damage statistics (Summary of the 2011 off the Pacific Coast of Tohoku Earthquake damage). *Soils and Foundations*, *Special Issue on Geotechnical Aspects of the 2011 off the Pacific Coast of Tohoku Earthquake* 52(5): 780–792.

Kazama, M., Yamaguchi, A., Yanagisawa E., 1998. Seismic Behavior of an Underlying Alluvial Clay at Kobe Man-made Islands During the 1995 Hyogoken-Nambu Earthquake. *Special Issue of Soils and Foundations*, 23–32.

Kazama, M., Yamaguchi, A., Yanagisawa E., 2000b. Liquefaction resistance from a ductility viewpoint. *Soils and Foundations* 40(6): 47–60.

Kazama, M., Yanagisawa, E., Inatomi, T., Sugano, T., Inagaki, H., 1996. Stress strain relationship in the ground at Kobe Port Island during the 1995 Hyogo-ken Nanbu Earthquake inferred from strong motion array records. *J. of Geotechnical Engineering, JSCE*, (547-III-36): 171–182. (in Japanese)

Kurihara, G., Kamura, A., Mori, T., 2019. Machine learning scheme of the degree of liquefaction assessment only from the health monitoring device installed in individual wooden house. *Geotechnics for Sustainable Infrastructure Development*. Springer, Part of the Lecture Notes in Civil Engineering book series, 62:1099–1105.

Kuwabara, K., Matsushima, M., 2020. Estimation of Liquefaction Susceptibility in Japan Using Machine Learning Approach. *J. of JAEE* 21(2): 70–89. (in Japanese)

Mughieda, O.S., Khaldoon, B.H., Safieh, B.F.A., 2009. Liquefaction assessment by artificial neural networks based on CPT. *Int. J. Geotech. Eng*. 3(2): 289–302.

National Research Institute for Earth Science and Disaster Resilience (NIED), 2019. NIED K-NET, KiK-net, *National Research Institute for Earth Science and Disaster Resilience*. doi:10.17598/NIED.0004.

Oki, Y., Mitsuhashi, A., Kajikawa, H., 2019. Study on estimation method of damaged situation of finishing material of wooden buildings and max story drift angles. *AIJ J. Technol. Des.* 25(59): 159–164.

Orense, R.P., 2016. Soil liquefaction and its effects on structures: Lessons learned from the 2010–2011 Canterbury (NZ) earthquake sequence. *Proceedings of IMPC 2016*, 16 pages.

Pijush, S., Sitharam, G.T., 2011. Machine learning modelling for predicting soil liquefaction susceptibility. *Natural Hazards and Earth System Sciences*, Vol. 11(1). doi: 10.5194/nhess-11-1-2011.

Senna, S., Ozawa, K., Sugimoto, J., 2021. Estimation of Liquefaction Risk Ratio Based on Liquefaction Point, *J. of JAEE* 21(2): 90–108. (in Japanese)

Shimizu, Y., Ishida, E., Isoyama, R., Yamazaki, F., Koganemaru, K., Nakayama, W., 2003. Development of real-time earthquake disaster mitigation system for city gas network and utilization of regional geological information. *J. of JSCE* 738, 283–296. (in Japanese)

Suzuki, T., Shimizu, Y., Koganemaru, K., Nakayama, A., 2001. Detection accuracy of liquefaction determination method using zero crossing period. *Proceedings of the JSCE Earthquake Engineering Symposium* (26): 1413–1416. (in Japanese)

Takada, S., Ozaki, R., 2000. Real-time prediction of liquefaction based on strong motion ground response. *J. of JSCE* 640(I-50): 99–108. (in Japanese)

Tung, A.T.Y., Wang, Y.Y., Wong, F.S., 1993. Assessment of liquefaction potential using neural networks. *Soil Dyn. Earthquake Eng*. 12(6): 325–335.

Unjoh, S., Kaneko, M., Kataoka, S., Nagaya, K., Matsuoka, K., 2012. Effect of earthquake ground motions on soil liquefaction. *Soils and Foundations* 52(5): 830–841.

Wakamatsu, K., Senna, S., 2015. Liquefaction and their Site Conditions in Kanto Region during the 2011 Off the Pacific Coast of Tohoku Earthquake. *J. of JAEE* 15(2): 25–44. (in Japanese)

Yamaguchi, A., Kazama, M., Toyota, H., Kitazume, M., Sugano, T., 2002. Effects of the stiffness of soft clay layer on strong motion response. *Soils and Foundations* 43(1): 17–33.

Yamaguchi, A., Mori, T., Kazama M., Yoshida N. 2012. Liquefaction in Tohoku district during the 2011 off the Pacific Coast of Tohoku Earthquake, *Soils and Foundations*, 52(5): 811–829.

Yasuda, S., Harada, K., Ishikawa, K., Kanemaru, Y., 2012. Characteristics of liquefaction in Tokyo Bay area by the 2011 Great East Japan Earthquake. *Soils and Foundations* 52(5): 793–810.

Zschau, J., Kueppers, A.N., 2003. *Early Warning Systems for Natural Disaster Reduction*. Springer, ISBN 3-540-67962-6. A.

Geotechnical Engineering for the Preservation of Monuments and Historic Sites III – Lancellotta, Viggiani, Flora, de Silva & Mele (Eds)

How safe is Acropolis of Athens and its monuments to low probability earthquakes?

K. Pitilakis, S. Karafagka, A. Karatzetzou, E. Riga & M. Manakou
Aristotle University, Thessaloniki, Greece

V. Eleftheriou
Acropolis Restoration Service, Greece

ABSTRACT: The paper investigates the potential impact of low to very low probability earthquakes to the safety and resilience of the Acropolis of Athens and its world-class monuments. The investigation is based on a probabilistic seismic hazard analysis (PSHA) of the Acropolis rocky hill, to evaluate the hazard for mean return periods of 2,500, 5,000 and 10,000 years, applying the new European Seismic Hazard Model (ESHM20). The site effects of the hill of Acropolis are examined analysing a number of records recorded at the accelerometric network operating since 2006. Finally, based on the results of the PSHA, we investigate the response and the safety margin of some legendary monuments, like Parthenon, and the perimetric retaining walls, for very low probability earthquakes.

1 INTRODUCTION

Acropolis of Athens, World Heritage Site since 1987, is one of the most prestigious ancient monuments symbolizing the values and achievements of the classical Greek civilization. The Acropolis hill has a trapezoidal shape of 300.0 m long and approximately 150.0 m wide. The geology is composed mainly by limestone overlying the Athenian schist (Andronopoulos & Koukis 1976). Parthenon, the temple of Athena, apotheosis of the Doric order, is one of the most prestigious monuments of Acropolis. As all other monuments suffered both natural and man-made catastrophes (e.g., earthquakes, explosions, natural ageing) as well as various human interventions. Extensive restoration works have been carried out the last two decades and still on-going, at the Acropolis monuments by the Acropolis Restoration Service (YSMA, http://www.ysma.gr/en/). In the framework of the restoration process a quite dense accelerometric array has been installed since 2006 to monitor the seismic response of the site and to provide valuable data on the dynamic behaviour of the monuments on site. It consists of ten 3D strong-motion sensors operated by the Institute of Geodynamics, National Observatory of Athens (NOA-IG, http://www.gein.noa.gr/en/) in collaboration with YSMA.

The aim of this work is to investigate the potential impact of low to very low probability earthquakes, i.e., return periods T_m of 2,500, 5,000 and 10,000 years, to the safety and resilience of the Acropolis of Athens and Parthenon in particular. For that we perform a probabilistic seismic hazard analysis (PSHA) with the new European Seismic Hazard Model (ESHM20), developed in the framework of SERA project (http://www.sera-eu.org/). Then, we study the site response characteristics of the hill of Acropolis using available seismic records of the existing accelerometric array. Finally, we conduct a preliminary investigation of the response and the safety margin of Parthenon and the perimetric (circuit) retaining walls, which is also affecting the safety of the monuments, for the estimated PSHA very low probability strong earthquakes. For that we first

DOI 10.1201/9781003308867-53

select two typical time histories representing low and high frequency events properly scaled to the Peak ground acceleration (PGA) results of the seismic hazard analysis for 2,500, 5,000 and 10,000 years and then we perform full dynamic numerical analysis of a free-standing multi-drum column and a corner colonnade of Parthenon and a more comprehensive analysis of the seismic stability of south perimetric retaining wall which is also affecting the safety of the foundation of Parthenon. The main conclusions are summarized at the end of this paper.

2 SEISMIC HAZARD OF THE ACROPOLIS OF ATHENS

The probabilistic assessment of the seismic hazard has been carried out with the new European Seismic Hazard Model (ESHM20) (http://www.sera-eu.org/en/home/, Danciu et al. 2019). ESHM20 is being developed using the most recent, updated, and complete datasets covering in a uniform way the whole Europe, while for the ground motion logic tree followed the backbone approach (Douglas 2018; Kotha et al. 2020) to model the epistemic uncertainty in the ground-motion model. In order to investigate the potential impact of low to very low probability earthquakes we select form the PSHA analysis three return periods of 2,500, 5,000 and 10,000 years having mean PGA values at outcrop conditions equal to 0.50 g, 0.64 g and 0.81 g respectively. The PGA for a design return period of 475 years is only 0.25 g. Figure 1 illustrates the seismic hazard curve and the computed mean uniform seismic hazard spectra (UHS).

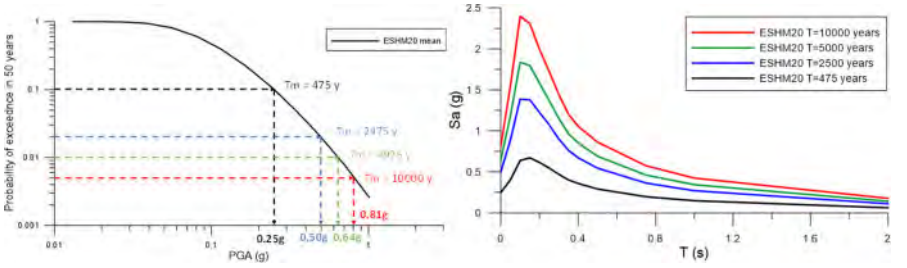

Figure 1. Seismic hazard curve and computed mean uniform hazard spectra (UHS) for rock conditions and for different return periods according to ESHM20.

For the numerical analyses that will follow we select and properly scale two earthquake records. The first record, typical of high frequency, is from the mainshock of the recent M_w 5.2 Magoula earthquake (29.07.2019), having similar spectrum with the estimated PSHA UHS, recorded by the Acropolis accelerometric array (station ACRJ, see Figure 3). In addition, to examine the potential effects of strong event rich in long periods, and despite the calculated UHS shown in Figure 1, we also selected the legendary Takatori record of the M_w 6.9 Kobe 1995 earthquake with PGA = 0.62 g (Figure 2). Both records are scaled to PGA values equal to 0.25 g, 0.50 g, 0.64 g and 0.81 g, corresponding to computed mean PGA values for return periods of 475, 2,500, 5,000 and 10,000 years respectively.

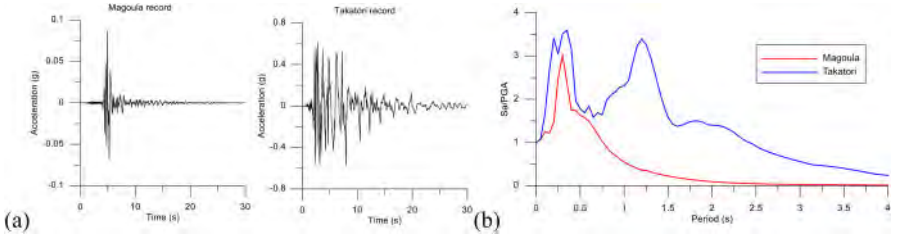

Figure 2. (a) Acceleration time histories and (b) normalised response spectra for the selected real records (Magoula M_w 5.2 record at ACRJ and Takatori record from Kobe M_w 6.9 1995 event).

3 EMPIRICAL ANALYSIS OF THE GROUND RESPONSE POTENTIAL OF THE HILL OF ACROPOLIS

The empirical analysis of the ground response of the hill of Acropolis is performed using selected strong motion records recorded at the permanent accelerometric network (Figure 3), which is operating since 2006 (Kalogeras et al. 2010). Most of the stations are found on the limestone outcrop on top of the hill. A couple of them are at the lower part of the hill (ACRG, ARCJ) which could be used as reference stations for topographic amplification studies, while two stations are located at the foundation level of the Parthenon temple (ACRB) and on top of a column (ACRC). Since 2006, a number of small near field and far field earthquakes have been recorded (not always in all stations). In this study we examined the records of one of the most important events (in terms of acceleration amplitudes), the earthquake of Magoula (19/07/2019, Mw 5.2, R = 23 km, NNE from Acropolis).

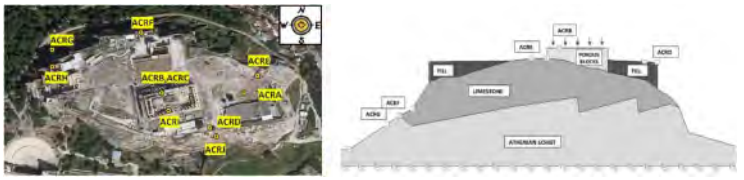

Figure 3. The Acropolis accelerometer network and a characteristic NS cross-section of the Acropolis hill (modified from: https://accelnet.gein.noa.gr/acropolis-array).

Figures 4 and 5 present the computed spectrograms and the HV spectral ratio (HVSR) for the Magoula event, at two selected stations. ACRA is a station on the limestone and ACRB at the kripis (foundation) of the Parthenon temple. It is a typical high frequency event from close distance. The records in all other stations on the surface of Acropolis hill are showing the same response of the hill which may summarized as follows: The rocky hill of Acropolis of Athens does not exhibit important and specific ground motion amplification characteristics. It is excited at a large spectrum of frequencies from about 0.8 Hz to 2.0–3.0 Hz at free-field conditions. Long period wave trains are recorded in both horizontal components. No substantial differences are observed at the basement of Parthenon (ACRB). The spectral site amplification at free field conditions is moderate (on average around 2.0) in a large range of frequencies (Figure 5 left). In summary the rocky hill of Acropolis

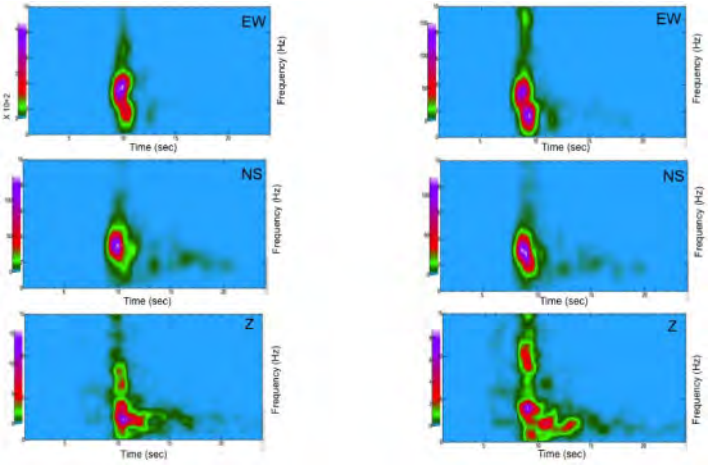

Figure 4. Spectrograms of the ground motion recorded in two stations (left: ACRA-limestone and right: ACRB-Parthenon) for the Magoula event.

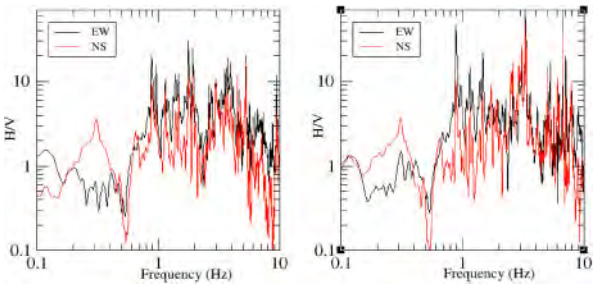

Figure 5. HVSR of the ground motion recorded in two stations (left: ACRA-limestone and right: ACRB-Parthenon base) for the Magoula event.

cannot be considered as a real outcrop; it exhibits some mild amplification of ground motion and a predominant period around 0.3–0.4 s.

4 SEISMIC RESPONSE OF SELECTED MONUMENTS TO EXTREME EVENTS

The monuments examined herein are Parthenon and the perimetric (circuit) retaining wall which may also affect the stability of Parthenon. Both a free-standing multi-drum column and a corner colonnade of the Parthenon consisting of three columns coupled with two architraves are studied by means of three-dimensional (3D) full dynamic time history analyses. Complex phenomena at the interfaces, including sliding and/or rocking are also considered. Figure 6 depicts the geological conditions at the hill of Acropolis, with a panoramic view of the hill, the perimetric retaining wall, and the Parthenon from the south-east. According to Koukis et al. (2015), the prevailing geological conditions are a limestone layer on top overlying a relatively softer geomaterial, the Athenian schist.

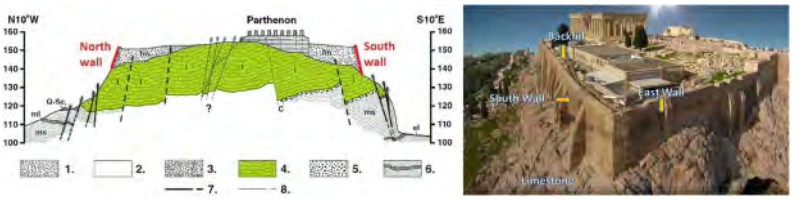

Figure 6. Left: Prevailing geological conditions at the Acropolis Hill and the Perimetric Wall (in red), after Koukis et al. (2015). Right: South-east view of the Acropolis Hill, the Perimetric Wall, and the Parthenon (Kappogianni et al. 2019). *1. artificial earthfill (fm), 2. eluvial mantle (el), 3. talus (Q-Sc), 4. limestone (l), 5. conglomerates (C), 6. schist-sandstone-marl series (ms-ml), 7. fault, 8. main fractures on the Acropolis plateau.

4.1 *Southern Perimetric Retaining Wall*

The stability of the southern part of the perimetric retaining wall to extreme events is very important since this part is characterized by the greatest height (up to 20.0 m) and it is closer to Parthenon. Over the last decades in this location some detachments and local failures have been observed. Figure 7(a–b) shows a plan view of the study area with a representative cross section of the southern masonry retaining wall, retaining a backfill material lying on inclined limestone (Psarropoulos et al. 2018; Trikkalinos 1972, 1977). The wall has been constructed with large rectangular poroliths, of average dimensions 1.30 × 0.65 × 0.50 m (height). In the southeast corner, the classical wall remains visible despite subsequent interventions. The outer side of the wall has a slight slope. In the eastern part of the southern wall, from the middle of the south side of the Parthenon to the south-east corner, the upper part of the wall, protrude by about 3.5–4.0 m, with a total width of approximately 6.0–6.5 m. The upper part of the wall is formed by a characteristic widening, which

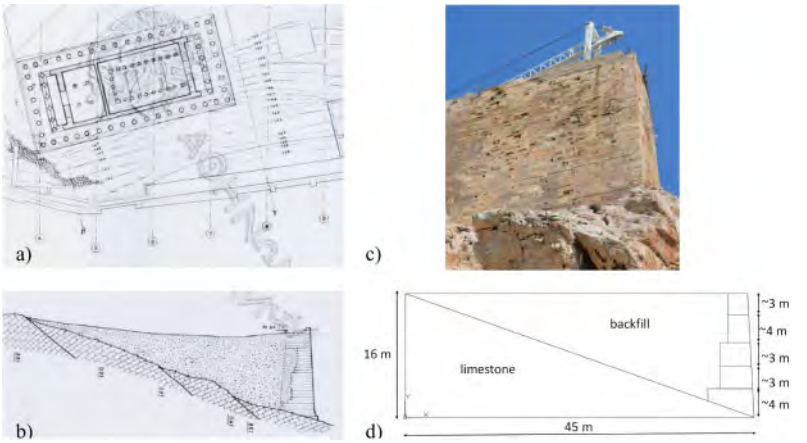

Figure 7. a) Plan view of the area under examination, b) representative cross section of the southern wall (Psarropoulos et al. 2018; Trikkalinos 1972, 1977), c) the southeast corner of the wall and d) the geometry of the wall considered herein.

in the area of the SE corner consisted of seven layers, with a total height of 3.76 m and width 6.5 m. Figure 7c shows the southeast corner of the wall at its current state and Figure 7d the herein adopted simplified geometry.

4.1.1 *Numerical modelling and analysis*

Two-dimensional (2D) plane strain analyses are performed in time domain with ABAQUS (2012) according to the simplified cross-section (Figure 7d) of the masonry perimetric wall of 16.0 m height founded on the inclined limestone and retaining a poorly compacted backfill. The modelling of all materials is performed using the four-node plane strain formulation with appropriate bilinear isoparametric quadrilateral elements. Table 1 presents the mechanical properties of the limestone, the backfill and the wall material. Considering that this analysis is actually a preliminary one to highlight potential safety problems, we disregarded potential uncertainties on geometric and material properties; average estimated values are used. All the analyses are performed assuming material damping equal to 2% (Rayleigh damping).

Table 1. Mechanical properties of the limestone, the backfill and the wall material.

	Limestone	Backfill	Wall
Unit weight, γ (t/m^3)	2.65	2.04	2.7
Shear wave velocity	1500	300	–
Young's modulus, E (kPa)	$1.6 \cdot 10^7$	$4.8 \cdot 10^5$	$4.5 \cdot 10^7$
Poisson's ratio, ν	0.30	0.30	0.33

The mesh generation and the corresponding discretization of the models have accordingly been chosen to cope with soft geomaterials excited with high-frequency seismic motions. The geometry of the mesh is based on the concept of resolving the propagation of the shear waves at or below a pre-defined frequency allowing an adequate number of elements to fit within the wavelength of the chosen shear wave. This ensures that the mesh is refined enough to capture propagating waves. Absorbing boundaries (at the left vertical boundary of the model) are used to revoke the generation of possible spurious reflections. The base of the numerical model is also considered as an absorbing boundary, not allowing reflected waves to propagate upwards. Viscous boundary tractions (dashpots) readily available in ABAQUS library are used to absorb incident waves (Nielsen 2006). Such viscous dashpots are used in both horizontal and vertical directions to absorb the radiated

energy. Figure 8 depicts the 2D limestone – backfill – wall model with the corresponding mesh and the dashpot elements at the vertical boundary and the base of the model.

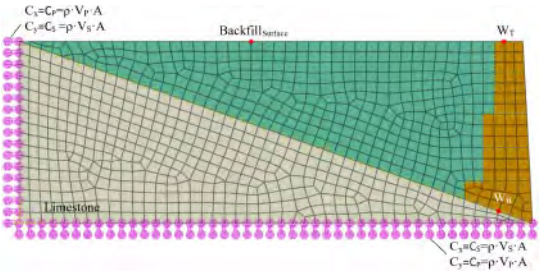

Figure 8. The 2D limestone – backfill – wall model with the corresponding mesh and the dashpot elements at the vertical boundary and the base of the model (ρ: material density, A: surface captured by each dashpot, V_S: shear wave velocity, and V_P: compressional wave velocity).

All materials (backfill, limestone, wall), remain linear elastic, allowing however the possibility of sliding and uplifting at the interfaces. More specifically, the tangential (shear) behaviour of the interfaces is modelled by introducing the Coulomb friction model. The interface friction coefficient, μ, along the masonry wall block interfaces is set equal to 0.5, while between the rest interfaces (limestone, backfill, wall) equal to 0.7. The option of de-bonding is considered for the interfaces between the wall and the backfill, the wall and the limestone as well as the wall blocks. These interfaces are modelled using a finite sliding 'hard contact' model embedded in ABAQUS. This model implements a 'strict' algorithm to preclude the potential penetrations of the interacting structural elements during shaking, while it allows for detachments, i.e., no tensile stresses are developed at the interfaces.

Except for the eight analysis cases using the two earthquake records scaled to the four PGA levels corresponding to the four mean return periods (475, 2,500, 5,000 and 10,000 years), two more analyses are conducted for the high frequency seismic record and the event of 5,000 years, where the interface friction coefficient for the interfaces between the masonry wall blocks is set close to 1.0 assuming in that way high shear resistance on the interfaces. In one of these analyses, the Parthenon foundation is also taken into account by considering two more interfaces, one between the limestone and the Parthenon foundation and one between the backfill and the foundation (Figure 9). The friction coefficient of the interfaces between the limestone and the Parthenon as well as the backfill and the Parthenon are set equal to 1.0 and 0.7 respectively. For the Parthenon foundation modelling, the mechanical properties of the Pentelic marble are used with a density, ρ, equal to 2.7 t/m^3, modulus of elasticity, E, equal to 45.0 GPa, and Poisson ratio v, equal to 0.33. These extra analyses are performed to investigate the impact of the interface friction coefficient between the wall blocks, as well as the potential sliding of Parthenon foundation. The analyses are performed in two steps. Initially, the gravity loads are introduced, within a static step. Subsequently, the seismic excitation is applied, within a dynamic implicit step. The input motion is introduced at the bottom edges of the dashpots in terms of acceleration time history.

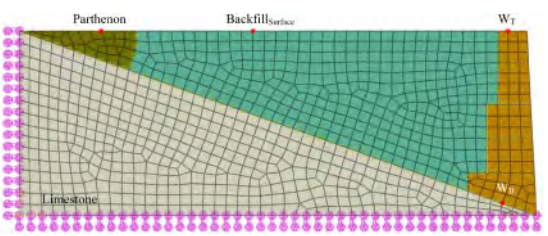

Figure 9. The 2D Parthenon foundation – limestone – backfill – wall model with the corresponding mesh and the dashpot elements.

4.1.2 *Discussion on the numerical results*

Figure 10 shows the resulted permanent (relative to limestone rock basement) horizontal and vertical displacements for three nodes of the model (Figure 8), namely $Backfill_{Surface}$, W_B and W_T for both Magoula and Takatori scaled records.

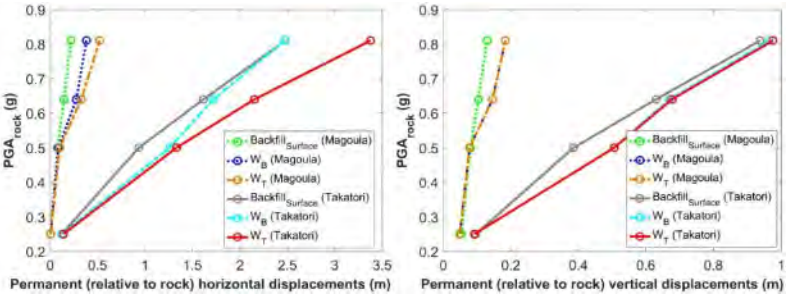

Figure 10. Permanent (relative to limestone rock basement) displacements for the two records scaled to PGA levels equal to 0.25, 0.50, 0.64 and 0.81 g, corresponding to return periods of 475, 2,500, 5,000 and 10,000 years respectively.

The most significant observation is the large difference of the backfill and wall displacements between the Magoula high frequency input motion and Takatori, where for the 10,000 years earthquake the computed permanent relative (to the limestone base) horizontal and vertical displacements reached 3.4 m and 1.0 m respectively, while in the case of the high frequency the respective maximum displacements were less than 0.5 m and 0.2 m respectively. These spectacular differences are amplified with the rareness of the seismic event, in other words with the increase of the input motion PGA. It is also important to notify that the same distinctive differences between the two records have been observed, as we will see later, for the response of the temple columns. Certainly, the Takatori record is a really extreme case, not a usual one. Nevertheless, it clearly demonstrates that monumental structures are extremely vulnerable to seismic actions rich in medium and low frequencies, something that is not observed in case of high frequency excitations of the same maximum amplitude.

The second important observation is related to the important role played by the quality of construction, which is practically reflected through the selected friction coefficient between the wall blocks, between the backfill and the limestone base or even between the Parthenon foundation and the limestone. Table 2 and Table 3 and Table 4 present the results for the scenario of 5,000 years for four analysis cases (ID 1–4) in terms of permanent relative to rock horizontal and vertical displacements as well as permanent absolute resultant displacements respectively. For the high frequency 5,000 years event the reduced friction coefficient (ID2) mainly affects the horizontal displacements at the top of the wall and not the vertical ones. Additionally, the consideration of the foundation of the Acropolis (analysis ID 4), for the same interface friction coefficient between the wall blocks (analysis ID 3), affects mainly the horizontal permanent displacements, leading to increased values. This could be attributed to the material properties of the foundation of the Acropolis and of course the consideration of its interfaces.

Table 2. Analysis results in terms of permanent (relative to rock) horizontal displacements (in m).

ID	Time History	Scenario T_m (y)	PGA (g)	$\mu_{wall\text{-}blocks}$	W_T	W_B	$Backfill_{surface}$	Parthenon
1	Takatori	5,000	0.64	0.5	2.154	1.720	1.617	–
2	Magoula	5,000	0.64	0.5	0.329	0.276	0.146	–
3	Magoula	5,000	0.64	1.0	0.275	0.288	0.146	–
4	Magoula	5,000	0.64	1.0	0.346	0.326	0.155	0.106

Table 3. Analysis results in terms of permanent (relative to rock) vertical displacements (in m).

ID	Time History	Scenario T_m (y)	PGA (g)	$\mu_{wall\text{-}blocks}$	W_T	W_B	$Backfill_{surface}$	Parthenon
1	Takatori	5,000	0.64	0.5	0.677	0.670	0.630	–
2	Magoula	5,000	0.64	0.5	0.146	0.146	0.104	–
3	Magoula	5,000	0.64	1.0	0.150	0.150	0.104	–
4	Magoula	5,000	0.64	1.0	0.164	0.164	0.108	0.093

Table 4. Analysis results in terms of permanent absolute resultant displacements (in m).

ID	Time History	Scenario T_m (y)	PGA (g)	$\mu_{wall\text{-}blocks}$	W_T	W_B	$Backfill_{surface}$	Parthenon
1	Takatori	5,000	0.64	0.5	2.258	1.846	1.735	–
2	Magoula	5,000	0.64	0.5	0.366	0.318	0.185	–
3	Magoula	5,000	0.64	1.0	0.319	0.331	0.184	–
4	Magoula	5,000	0.64	1.0	0.389	0.371	0.194	0.146

The last significant observation is that for extreme low probability seismic events i.e., $T_m > 2.500$ years), with ground motions rich in moderate and low frequency motions, which may not be expected for near field i.e. 10–20 km or modest distant events i.e. less than 50 km, the perimetric retaining wall may exhibit large damaging deformations leading to global instability of the wall itself and the retaining backfill, a really misfortune situation for many monuments on the Acropolis hill. This is evident in Table 2 and Table 3 (ID1), where the permanent (relative to rock) horizontal and vertical displacements at the top of the wall reach 2.154 m and 0.677 m respectively.

Fortunately, Parthenon whose foundation lies on the solid limestone seems rather safe even in case of very strong high-frequency earthquakes, such as Magoula high frequency record scaled to the PGA value corresponding to the return period of 5,000 years, as it shown in Tables 2 and 3 (ID4) were the permanent (relative to rock) horizontal and vertical displacements at the Parthenon foundation is less than 11.0 cm and 10 cm respectively. The total permanent displacements of the retaining wall, the backfill and the Parthenon foundation are 0.389 cm, 0.194 cm and 0.146 cm respectively, values which cannot be considered as absolutely critical for the safety of the monuments. (Table 4). Figure 11 shows the permanent absolute resultant displacements (in m) of the Parthenon foundation – limestone – backfill – wall model for Magoula record scaled to the PGA = 0.64 g corresponding to the return period of 5,000 years.

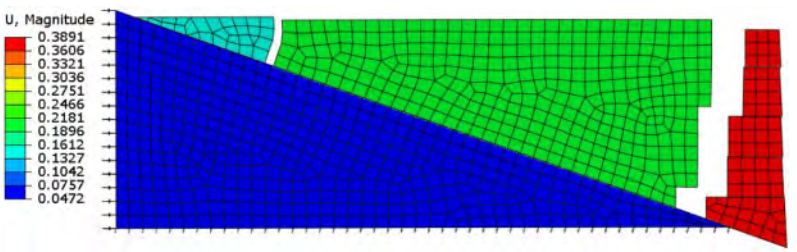

Figure 11. Permanent absolute resultant displacements (in m) of the Parthenon foundation – limestone – backfill – wall model for Magoula high frequency record scaled to the PGA value corresponding to the return period of 5,000 years.

4.2 *Parthenon*

Parthenon was dedicated to the goddess Athena, whom the people of Athens considered their patroness. Its construction started in 447 BC and was completed in 438 BC, although the famous decoration and sculptures of the building continued until 432 BC. It is the most important surviving

building of Classical Greece, generally considered the zenith of the classical Greek architecture. The temple measures 30.88 m by 69.5 m. It is a peripteral temple, with eight columns at the narrow ends and seventeen along the sides, hexastyle porches (pronaos and opisthonaos) and many Ionic features. In this work we investigate first the response of a single column to extreme seismic events and then a system of three corner columns with the epistyle.

4.2.1 *Response of a multi-drum column*

The free-standing column is made of Pentelic marble and composed of eleven drums and a capital, while it has a total height of 10.44 m (Figure 12a) and slenderness (height to base ratio) equal to 5.80.

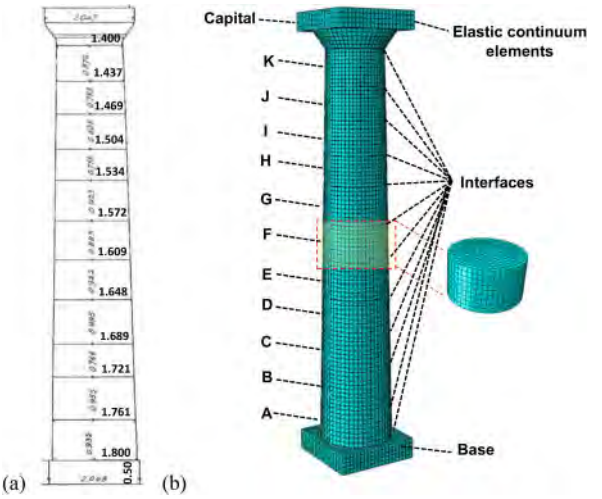

Figure 12. (a) Geometric properties and (b) Numerical model of the multi-drum column at the Parthenon of the Acropolis of Athens.

It is modelled as a 3D multi-drum structure (Figure 12b). The numerical model accounts for the actual dimensions and material properties of the structural members. The drums, the capital, and the base are simulated as deformable bodies, using 3D eight-node solid elements, with option of de-bonding and relative sliding between the drums using special interface elements. The shear behaviour of the interfaces is modelled with Coulomb friction model and friction coefficient, μ, equal to 0.7, a value experimentally validated and widely acceptable for these types of structures. The materials of the monument members are modelled using the mechanical properties of the Pentelic marble, with a modulus of elasticity, E = 45.0 GPa, Poisson ratio $\nu = 0.33$ and the density, $\rho = 2.7$ t/m^3. All the analyses are performed assuming zero material damping, which might be considered as a conservative assumption (Psycharis 2014). The analyses are performed in two steps. Initially, the gravity loads are introduced, within a static step. Subsequently, the seismic excitations are applied at the base in x direction, within a dynamic implicit step. The numerical model that is used herein has been thoroughly validated (Pitilakis et al. 2017) and proved capable of capturing the very complex response, under uniaxial, biaxial and triaxial excitation.

The parametric numerical analyses verified the complex rocking-sliding response of multi-drum columns subjected to strong ground shaking. More specifically, the frequency characteristics of the input base excitation are found to affect considerably the performance and overall stability of the multi-drum column. Indicatively, Figure 13 portrays the response of the column for the Magoula and Takatori earthquakes, scaled to PGA of 0.81 g (corresponding to T_m of 10,000 years). Although the two records are scaled to the same PGA values, we observe that the column remains stable for the high frequency record while it collapses for the Takatori earthquake (Figure 13a). This is attributed to the increased rocking response of the column for low frequency base excitations like the Takatori. For the latter case high frequency spikes are also observed in the acceleration time

histories, due to the collision effects of the interacting drums, associated to the rocking response of the column (Figure 13b). This is a common observation from several past studies (Konstantinidis & Makris 2005; Pitilakis et al. 2017).

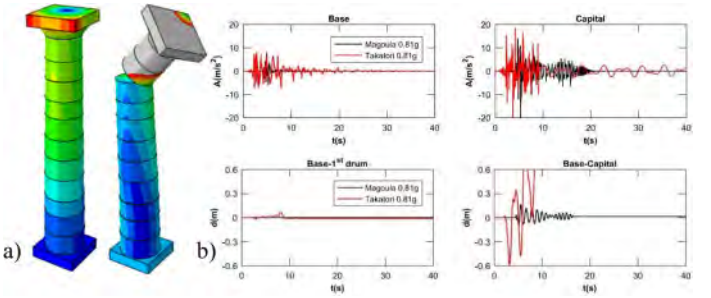

Figure 13. a) Deformed shapes of the column exposed at Magoula (left) and Takatori (right) earthquakes scaled to 0.81 g (T_m of 10,000 years), corresponding at the completion of the analysis, and (b) acceleration time histories and relative displacement time histories.

To further analyse the seismic behaviour of multi-drum columns to extreme seismic events we plotted the normalized maximum displacement of the capital to the base of the column, d_{max}/D_{base}, against the PGA values (Figure 14). To allow for an easy reading of the figure, the maximum displacement at the capital normalised by the base diameter in the y-axis is set equal to 1. Beyond this limit the analyses revealed toppling of the capital or total collapse of the column (these cases are noted as ∞ in the figure). Owing to the complex rocking and sliding movements of drums along their interfaces, the dynamic response of multi-drum columns is 'chaotic'. In this context, an impressive remark is that the increase of the amplitude of the shaking loading does not necessarily lead to the increase of the maximum displacement of the capital. The non-linear rocking and sliding phenomena dominate the dissipation mechanisms of the propagated seismic energy and govern the seismic performance and stability of this type of structures. Indeed, we see a higher d_{max}/D_{base} value for the column subjected to Takatori record scaled to PGA of 0.25 g compared to PGA of 0.50 g. The main remark of this analysis is that in case of the most often expected high frequency earthquakes, the response of the column is very good even for very strong excitations.

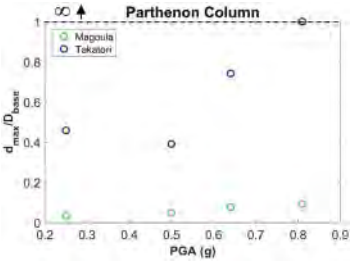

Figure 14. Summary of numerical results for the examined multi-drum column: variation of the normalized maximum displacement of the capital, d_{max}/D_{base}, with PGA.

4.2.2 *Response of corner colonnade*

The colonnade consists of three multi-drum columns connected at the top with an epistyle. The latter is composed of two orthogonal single blocks of 4.537 m in length, 0.60 m in width and 1.35 m in height. For simplicity the epistyle is not connected with the three columns by any means and is simply lying on the columns, which have identical dimensions with the single multi-drum column presented before. All structural elements, i.e., the drums, the capitals, the base, and the epistyle, are simulated as deformable bodies, using 3D eight-node solid elements (Figure 15). The interface friction coefficient, μ, along the interfaces of the structural elements is set equal to 0.7, similar to the previous column model.

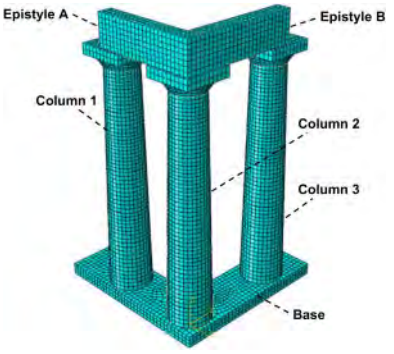

Figure 15. Numerical model of the corner colonnade of the Acropolis of Athens Parthenon.

The seismic response of the corner colonnade structure, is more complex compared to the free-standing column. As before, in Figure 16 we plotted the normalized maximum displacement of the capital, d_{max}/D_{base}, of the three multi-drum columns of the corner colonnade against the PGA values. Similar to Figure 14, beyond the limit of 1.0 in the y-axis the analyses revealed toppling of the capital or total collapse of the column (these cases are noted as ∞ in the figure). Generally, the collapse of the free-standing epistyle is not necessarily followed by the collapse or instability of the columns. Out of the eight analysis cases, the epistyle of the corner colonnade collapses for four of them all subjected to Takatori record corresponding to return periods of 475, 2,500, 5,000 and 10,000 years. However, even in these cases column 1 does not collapse in any of the cases, column 2 collapses for the two cases (for PGA equal to 0.64 and 0.81 g), while column 3 collapses only for the extreme even of 5,000 years and the Takatori motion. This is in accordance with the study of Psycharis et al. (2003) that states if the architraves are left free, they are susceptible to falling under input motions lower than those that lead to column failure. However, what is really impressive is that contrary to the Takatori motion an impressively good response of the corner colonnade is observed to the most ordinary high frequency motions. The relative displacements remain extremely limited, lower than the case of the single column, even for very strong excitations.

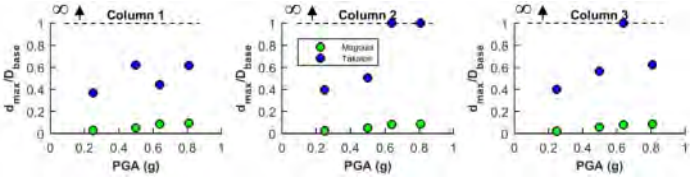

Figure 16. Summary of numerical results for the examined colonnade: variation of the maximum displacement of the epistyle with PGA.

5 CONCLUSIONS

The aim of the paper is to investigate the potential impact of low to very low probability earthquakes to the safety and resilience of the Acropolis of Athens and its world-class monuments, including Parthenon, which have marked the human history and civilization. The site effects of Acropolis rocky hill are examined analysing records from the existing accelerometric network. The analysis of the records of one of the most important events (Magoula 2019, M_w 5.2, R = 23 km) proved that the hill of Acropolis of Athens does not exhibit important ground motion amplification. The site predominant period is around 0.3 s-0.4 s, while the spectral amplification is rather low in a large range of frequencies. The estimated PGA values for the 475y, 2,500y, 5,000y and 10,000y mean return period are 0.25 g, 0.50 g, 0.64 g and 0.81 g respectively. The perimetric retaining wall is not

safe for seismic excitations in case of long period motions with PGA larger than 0.50 g. For the more common high frequency seismic events it seems that it will exhibit large displacements (max about 50.0 cm), avoiding, however, the risk of total collapse. And even in this defavorable case the impact to Parthenon will be limited. The seismic response of Parthenon multi-drum column and the corner colonnade are characterized by increased rocking response, in particular for moderate and low frequency ground motions. Both are found stable for a seismic scenario with return period of 475 years (i.e., high frequency seismic excitations with PGA = 0.25 g). However, they are much more vulnerable to long period seismic excitations. In general judging from the impressively good performance of the corner colonnade in most examined scenarios, it is believed that with the exception of few free-standing columns, Parthenon may survive with low damages to very low probability earthquakes i.e., for mean return period longer than 2,500 years. Nevertheless, considering the preliminary character of the analyses presented and discussed herein, it is believed that it is deemed necessary to extend this work with a more comprehensive study of the seismic response of Acropolis and its world class monuments to moderate and low probability seismic events.

REFERENCES

ABAQUS. 2012. Theory and analysis user's manual-version 6.12. Dassault Systemes, SIMULIA Inc, USA.

Andronopoulos, B. & Koukis, G. 1976. Engineering geology study in the Acropolis area. *Athens, Institute of Geology and Mineral Exploration*. Report (in Greek with English summary).

Danciu, L. et al., 2019. Status, Milestones and Next Activities on the Development of the 2020 European Seismic Hazard Model (ESHM20), (Geophysical Research Abstracts, Vol. 21, EGU2019-8317), *European Geosciences Union General Assembly* (Wien 2019).

Douglas, J. 2018. Capturing Geographically - Varying Uncertainty in Earthquake Ground Motion Models or What We Think We Know May Change. *Recent Advances in Earthquake Engineering in Europe*. Editor: Kyriazis Pitilakis, Chapter 6, 153–181.

Kalogeras, I., Stavrakakis, G., Melis, N., Loukatos, D., Boukouras, K. 2010. Deployment of the strong motion array at Athens Acropolis area: Implementation and prospects. Acropolis Restoration News 10.

Kappogianni, E. et al., 2019. Suitability of Optical Fibre Sensors and Accelerographs for the Multi-disciplinary Monitoring of a Historically Complex Site: The Case of the Acropolis Circuit Wall and Hill. *Geotech Geol Eng* 37:4405–4419, https://doi.org/10.1007/s10706-019-00917-x.

Konstantinidis, D., Makris, N. 2005. Seismic response analysis of multi-drum classical columns. *Earthq Eng Struct Dyn* 34:1243–1270.

Kotha, S.R., Weatherill, G., Bindi, D., Cotton, F. 2020. A regionally-adaptable ground-motion model for shallow crustal earthquakes in Europe. *Bull Earthquake Eng* 18:4091–4125. https://doi.org/10.1007/s10518-020-00869-1.

Koukis, G., Pyrgiotis, L., Kouki A. 2015. The Acropolis Hill of Athens: engineering geological investigations and protective measures for the preservation of the site and the monuments. *Eng Geol Soc Territ* 8:89–93.

Nielsen, A.H. 2006. Absorbing boundary conditions for seismic analysis in ABAQUS. *Proc. of 2006 ABAQUS Users' Conference,* pp. 359–376.

Pitilakis, K., Tsinidis, G., Karafagka, S. 2017. Analysis of the seismic behaviour of classical multi-drum and monolithic columns, *Bulletin of Earthquake Engineering*, doi: 10.1007/s10518-017-0160-4.

Psarropoulos, P., Kapogianni, E., Kalogeras, I., Michalopoulou, D., Eleftheriou, V., Dimopoulos, G., Sakellariou, M. 2018. Seismic response of the Circuit Wall of the Acropolis of Athens: Recordings versus numerical simulations. *Soil Dynamics and Earthquake Engineering* 113:309–316, ISSN 0267-7261, https://doi.org/10.1016/j.soildyn.2018.04.003.

Psycharis, I.N. 2014. Ancient monuments under seismic actions: modelling and analysis. In: Beer, M., Kougioumtzoglou, I., Patelli, E., Au I S-K A (eds) *Encyclopaedia of Earthquake Engineering, Springer Berlin Heidelberg*. doi: 10.1007/978-3-642-36197-5_145-1.

Psycharis, I.N., Lemos, J., Papastamatiou, D., Zambas, C., Papantonopoulos, C. 2003. Numerical study of the seismic behaviour of a part of the Parthenon Pronaos. *Journal of Earthquake Engineering & Structural Dynamics* 1(32):2063–2084. doi:10.1002/eqe.315.

Trikkalinos, I.K. 1972. The geology of the Acropolis. *Proc. of the Academy of Athens*.

Trikkalinos, I.K. 1977. Remarks on the published study on the geology of the Acropolis. *Proc. Acad Athens,* 12–05:311–42.

Geotechnical Engineering for the Preservation of Monuments and Historic Sites III – Lancellotta, Viggiani, Flora, de Silva & Mele (Eds)

On the seismic protection of free-standing art objects by base isolation technique: A case study

Davide Pellecchia, Nicolò Vaiana, Salvatore Sessa & Luciano Rosati
Department of Structures for Engineering and Architecture, University of Naples Federico II, Naples, Italy

ABSTRACT: We illustrate the advantages of seismic isolation by means of special devices named helical Wire Rope Isolators (WRIs) when adopted to protect the Emperor Caracalla's bust of the Farnese collection (Naples, Italy). Such a sculpture is modelled as a rigid body and the hysteretic behaviour of the helical WRIs is predicted by an efficient uniaxial phenomenological model. The assumed hysteretic model is based on a reduced set of parameters having a clear mechanical meaning and predicts the response of the WRIs with high accuracy. The constitutive parameters of the model have been evaluated from experimental hysteresis loops of the selected WRIs by using a recently developed inverse identification software. The effective performances of the proposed isolation system have been investigated by comparing the isolated and non-isolated behaviour of Emperor Caracalla's bust providing the effectiveness of the isolation system.

Keywords: Protection of Art Objects; Seismic Isolation; Nonlinear Dynamic Analysis; Hysteresis.

1 INTRODUCTION

Seismic protection of free-standing art objects, such as columns and statues, is one of the most important issues in preserving monuments and artefacts belonging to the Cultural Heritage. Over the past years, several researchers have studied art objects' rocking behaviour in museums (Baggio et al. 2015; Caliò et al. 2004). In fact, simply supported objects, such as statues, amphorae, display cases lying on pedestals or just on the floor, may not be adequate to face the oscillations induced by earthquakes. While small oscillations may result in possible damages due to the collisions with the support, large oscillations conduce overturning and, subsequently, the complete breakage of the artefact.

Base isolation represents a possible strategy to avoid overturning of museum art objects (Vaiana et al. 2021a). Such a technique can remove or attenuate rocking and therefore possible damages due to the collisions with the support and overturning. However, the use of this seismic protection technique requires the modelling of complex hysteretic behaviour of the seismic isolators as accurately as possible. In fact, the dynamics of a base-isolated art object strictly depends on the behaviour of such isolation devices.

This study aims to illustrate the benefit of the base isolation technique in the protection of Emperor Caracalla's bust of the Farnese collection (Naples, Italy), modelled as an unanchored rigid body.

The isolation system studied in this paper consists in an oscillating mass isolated by Helical Wire Rope Isolators (WRIs) tested during in an experimental campaign, performed at the Department of Structures for Engineering and Architecture of the University of Naples Federico II (Italy) by Vaiana et al. (2017).

DOI 10.1201/9781003308867-54

The base-isolated rigid body's behaviour depends on the interaction between the helical WRIs' behaviour and the rigid body's rocking one. Consequently, it is necessary to use a hysteretic model able to predict the seismic devices response as accurately as possible.

The behaviour of the helical WRIs is modelled by using an efficient uniaxial phenomenological model (Vaiana et al. 2018, 2021b, 2021c). Such a hysteretic model was chosen because of some benefits, including a clear mechanical meaning of the costitutive parameters and its fast computation of the device restoring force. Moreover, the algebraic nature of the model allows one to obtain the dissipated energy by a closed-form solution (Pellecchia et al. 2021) which turns out to fulfil the Drucker's postulate for the considered application (Sessa 2021). The hysteretic model parameters are computed by experimental loops using a user-friendly program named *Parameter Identificator* (ParIde) based on the algorithm described in Sessa et al. (2020).

The dynamic behaviour of both isolated and non isolated Emperor Caracalla's bust are investigated to understand the performance of the helical WRIs in protecting the analysed art object from seismic excitations.

2 MATHEMATICAL MODELLING OF BASE-ISOLATED ROCKING RIGID BODY

The study of the dynamic responses of unanchored symmetric rigid bodies on horizontal planes was initially studied by Housner (1963). His study was applied to understand the rocking behaviour of tall, slender structures, such as water tanks, subjected to horizontal ground motion. Accordingly, Emperor Caracalla's bust can be modelled using Housner theory, suitably modified to take into account the base isolation system (Vassiliou et al. 2012).

The fundamental rigid body properties are the mass $m = 241.15$ kg, the position of the centre of mass compared to one of the two bottom corners $R \approx 0.69$ m, and the slenderness of the bust measured by the angle $\gamma \approx 0.22$ rad, see, e.g., Figure 1(a). These properties has been computed by a three-dimensional computer graphic model taken from the platform *Scan The World*. Subsequently, one can obtain the fundamental angular rocking frequency of Emperor Caracalla's bust in the following way

$$\omega_r = \sqrt{\frac{m\,g\,R}{J_O}} \approx 3.26 \text{ rad s}^{-1}, \tag{1}$$

where $g = 9.81$ m s^{-2} and $J_O \approx 153.83$ kg m^2 are the gravity acceleration and the polar inertia around one of the two centres of rotation that is, O and O', respectively.

Finally, the mass of the pedestal m_b is supposed to be equal to 676 kg.

We assumed the following hypotheses: the sliding motion between the bust and the isolated base is negligible, while the rotation as well as vertical movement of the pedestal is avoided. The former hypothesis can be verified supposing either that the friction between the statue and the isolated base is very high or the existence of a clip constraining block translation movements. Instead, combining the helical WRIs with slider constraints, the rotation and vertical movements of the pedestal are avoided, see Figure 1(a).

The seismically isolated rigid body model has two degrees of freedom: the horizontal displacement of the base x and the tilt angle of the body φ during rocking.

2.1 *Full-contact and Rocking phases*

The full-contact motion is the phase in which only the degree of freedom x is activated, see, e.g., Figure 1(b). This phase is described by the following equation of motion:

$$(m + m_b)(\ddot{x}_g + \ddot{x}) + n_d f = 0, \tag{2}$$

where $\ddot{x}_g$ is the horizontal ground acceleration, n_d is the number of devices that support the isolated base, and f is the restoring force of the WRI.

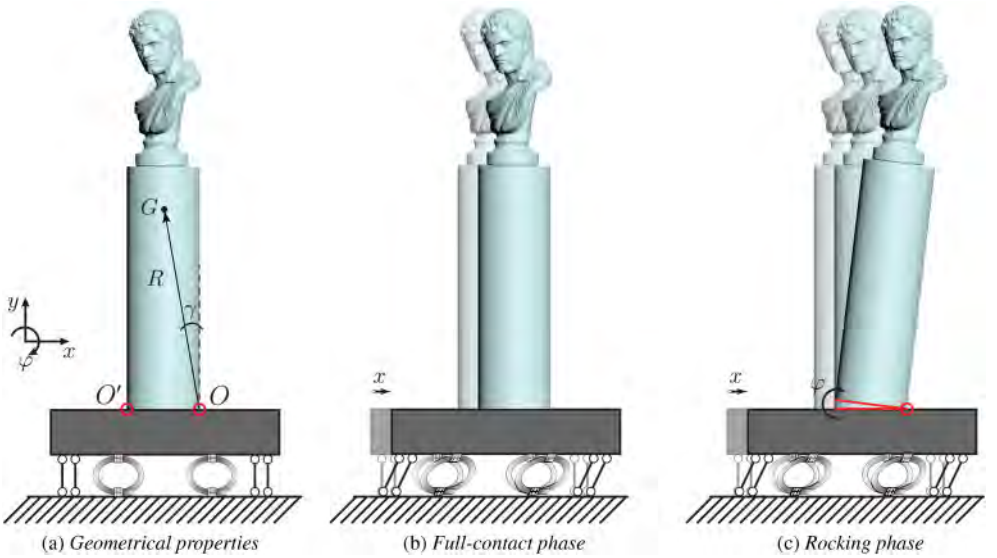

Figure 1. Emperor Caracalla's bust of the Farnese collection (Naples, Italy).

When the overturning moment caused by earthquake inertial forces is greater than the resisting moment due to weight forces, the degrees of freedom are activated, see, e.g., Figure 1(c). The equations of motion that describe this phase are

$$m\,(\ddot{x}_g + \ddot{x} + \ddot{x}_\varphi) + m_b\,(\ddot{x}_g + \ddot{x}) + n_d\,f = 0, \tag{3}$$

$$J_O\,\ddot{\varphi} + m\,(\ddot{x}_g + \ddot{y}_g + \ddot{x})\,R\,\cos\left(\text{sign}(\varphi)\,\gamma - \varphi\right) = -m\,g\,R\,\sin\left(\text{sign}(\varphi)\,\gamma - \varphi\right), \tag{4}$$

in which $\ddot{y}_g$ and $\ddot{x}_\varphi$ are the vertical ground acceleration and the horizontal acceleration of the centre of mass relative to the ground, respectively.

2.2 *Impacts*

Referring to Vassiliou et al. (2012) for more extensive details, the angular and the linear coefficients of restitution, defined as the post to pre-collision velocities ratio and obtained by the law of momentum conservation are:

$$e_\varphi = 1 + \frac{2\,R^2\,\sin^2(\gamma)\,m}{R^2\,\cos^2(\gamma)\,m\,\tilde{m} - J_O}, \tag{5}$$

and

$$e_x = \frac{2\,R^4\,\sin^2(\gamma)\,\cos^2(\gamma)\,m\,\tilde{m}}{R^2\,\cos^2(\gamma)\,m\,\tilde{m} - J_O}, \tag{6}$$

where $\tilde{m} = m/(m + m_b)$.

3 HELICAL WRIS

Helical WRIs are metal devices made of stainless steel cable fixed between two aluminium bars. Such isolators are generally used to protect sensitive devices from shocks and vibrations (Di Donna et al. (2002), Alessandri et al. (2015a)) and building equipments from earthquakes. In addition,

they have also been used to protect the two Riace's bronzes (Pellecchia et al. 2020), since this isolation system is particularly suitable when a rocking effect prolongs the fundamental period of the rigid body (Alessandri et al. 2015b).

The typology of WRI chosen to protect Emperor Caracalla's bust is the PWHS 16040 manufactured by Powerflex S.r.l (Limatola, Italy). Its rope is composed of six strands, each consisting of 25 wires and a central strand with 49 wires, see, e.g., Figure 2(a). The dynamic behaviour of the tested WRI along the two principal horizontal directions, namely Roll and Shear directions (see Figure 2(b)), has been obtained during an experimental campaign performed at the Department of Structures for Engineering and Architecture of the University of Naples Federico II (Italy) by Vaiana et al. (2017). We selected the PWHS 16040 because of its high energy dissipation properties, as shown during the experimental campaign, allowing one to use the minimum number of isolators to protect the art object.

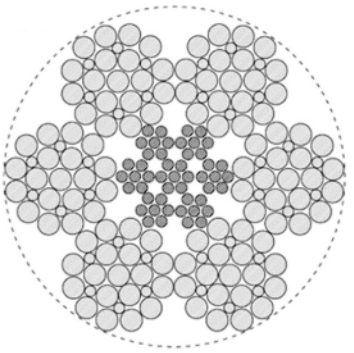

(a) *Wire cross section*

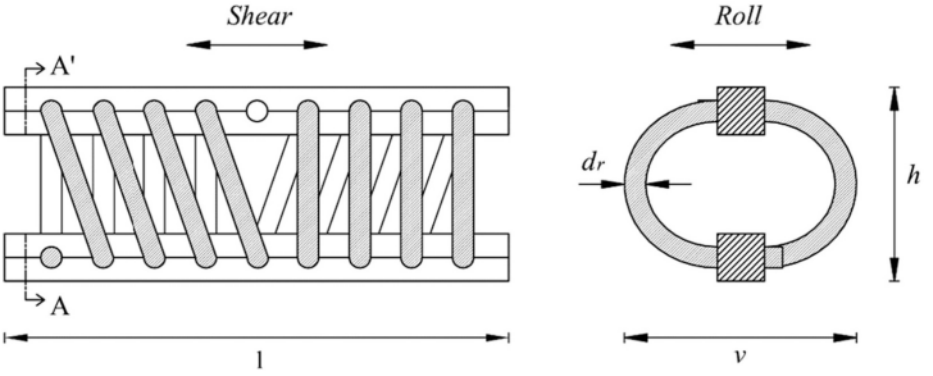

(b) *WRI lateral view (left) and Section A-A' (right)*

Figure 2. Geometrical properties of PWHS 16040.

Table 1 lists the geometrical characteristics, i.e. cable's diameter, length, width and height, of the tested device.

Table 1. Geometrical dimensions of the tested helical WRI.

Wire Rope Isolator	l [mm]	h [mm]	v [mm]	d_r [mm]
PWHS 16040	267	125	150	16

4 ALGEBRAIC MODEL FORMULATION

The algebraic hysteretic model used to predict the complex behaviour of the helical WRIs is described in this Section. Accuracy and computational efficiency of the model is by far better than the one pertaining to the celebrated Bouc-Wen model (Buoc 1971; Wen 1976). Notably, the proposed hysteretic model is of algebraic nature, i.e. the device restoring force is computed by means of algebraic equations. In addition, the model is based on only five parameters that can be calibrated from experimental tests (Sessa et al. 2020) or by means of a design procedure, as described in Pellecchia et al. (2021). On the contrary, in the differential hysteretic models such as the Bouc-Wen one, the restoring force is computed by solving a differential equation numerically, thus increasing the overall computational effort.

The generic hysteresis loop is modelled by four types of curves, namely the upper (lower) limiting curve c_u (c_l) and the generic loading (unloading) curve c^+ (c^-), as shown in Figure 3.

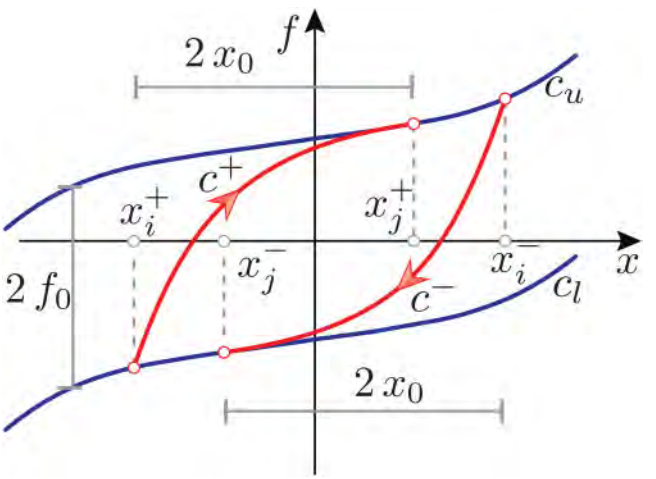

Figure 3. Proposed hysteretic model.

Making reference to Vaiana et al. (2019) for further details, the expressions of these curves used for predicting the hysteretic behaviour of helical WRI are

$$c_u = \beta_1 x^3 + \beta_2 x^5 + k_b x + f_0, \tag{7}$$

$$c_l = \beta_1 x^3 + \beta_2 x^5 + k_b x - f_0, \tag{8}$$

and

$$c^+ = c_u + (k_a - k_b)\left[\frac{(1 + x - x_j^+ + 2\,x_0)^{(1-\alpha)}}{1-\alpha} - \frac{(1 + 2\,x_0)^{(1-\alpha)}}{1-\alpha}\right], \tag{9}$$

$$c^- = c_l + (k_a - k_b)\left[\frac{(1 + x - x_j^- + 2\,x_0)^{(1-\alpha)}}{\alpha-1} - \frac{(1 + 2\,x_0)^{(1-\alpha)}}{\alpha-1}\right], \tag{10}$$

where f_0 ($-f_0$) is the point of intersection between the upper (lower) limiting curve and the axis of ordinate and x_i^+ and x_j^+ (x_i^- and x_j^-) are the abscissas of the starting and the ending points of the generic loading (unloading) limiting curve, respectively. The model assumes that the horizontal distance between the starting and the ending points, for both loading and unloading curves, is constant and equal to $2\,x_0$, where x_0 is an internal model parameter. In addition, k_a, k_b, α, β_1, and β_2 are the model's parameters whose mechanical significance is illustrated in Vaiana et al. (2019).

Finally, the internal model parameters x_0 and f_0 are computed as follows:

$$x_0 = \frac{1}{2}\left[\left(\frac{k_a - k_b}{\delta_k}\right)^{\frac{1}{\alpha}} - 1\right], \tag{11}$$

$$f_0 = \frac{k_a - k_b}{2}\left[\frac{(1 + 2\,x_0)^{(1-\alpha)} - 1}{1 - \alpha}\right], \tag{12}$$

in which δ_k may be set equal to 10^{-20}, as shown in Vaiana et al. (2018).

In this way, the device restoring force in the generic loading (unloading) case is equal to $f = c^+$ when $x_i^+ < x < x_j^+$ and $f = c_u$ when $x > x_j^+$ ($f = c^-$ when $x_j^- < x < x_i^-$ and $f = c_l$ when $x < x_j^-$).

5 NUMERICAL SIMULATION OF THE EMPEROR CARACALLA'S BUST

In this Section, we show the results obtained from some nonlinear time history analyses on the Emperor Caracalla's bust. The East-West and the vertical components of ground accelerations recorded at the Sturno station during the Irpinia earthquake (Italy), that occurred on the 23rd of November 1980, are used as seismic inputs. These accelerations, displayed in Figure 4, have been taken from the Engineering Strong Motion (ESM) database (Luzi et al. 2020).

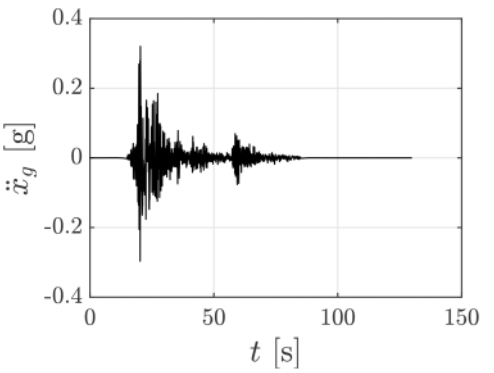

(a) *The East-West component of the Irpinia earthquake (Italy)*

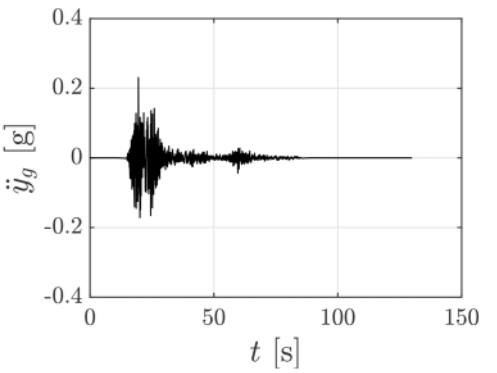

(b) *The vertical component of the Irpinia earthquake (Italy)*

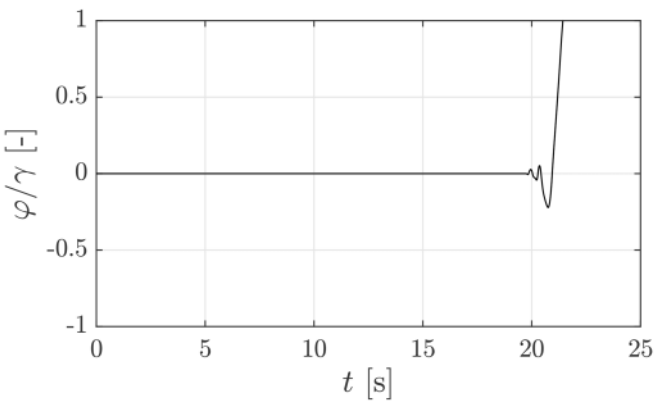

(c) *Rocking response of non-isolated Emperor Caracalla's bust*

Figure 4. Numerical results of non-isolated Emperor Caracalla's bust by using the horizontal and vertical components of the Irpinia earthquake (Italy).

Figure 4(c) depicts the rocking response of the non-isolated Emperor Caracalla's bust subjected to the above-mentioned accelerations. As a consequence, the Emperor Caracalla's bust needs to be protected, since due to the assumed excitations, it overturns after approximately twenty-two seconds.

The hysteretic parameters able to reproduce the behaviour of the helical WRI PWHS16040, namely k_a, k_b, α, β_1, and β_2, have been calibrated from the experimental hysteresis loops by the in-house software *ParIde* (see References) that identifies the parameters of a uniaxial constitutive model by minimising the mean-square error with respect to an experimental target response, see Sessa (2021).

The algebraic model's hysteretic parameters used to reproduce the behaviour in both directions, namely Shear and Roll, of the helical WRI PWHS 16040, are listed in Table 2.

Table 2. Identified model parameters relevant to the experimental hysteresis loops of WRI PWHS 16040 tested in the Shear and Roll directions.

Direction	k_a [N m^{-1}]	k_b [N m^{-1}]	α [–]	β_1 [N m^{-3}]	β_2 [N m^{-5}]
Shear	518970.68	29107.70	434.19	-1167052.18	34053603138.58
Roll	427786.00	29995.10	313.45	923367.84	16872030903.28

Figures 5 and 6 illustrate the time histories of the rocking angle (a) and displacement (b) of Emperor Caracalla's bust isolated by three helical WRIs disposed along the Shear and Roll directions, respectively. The results in both directions are satisfactory, since the rocking angle and the

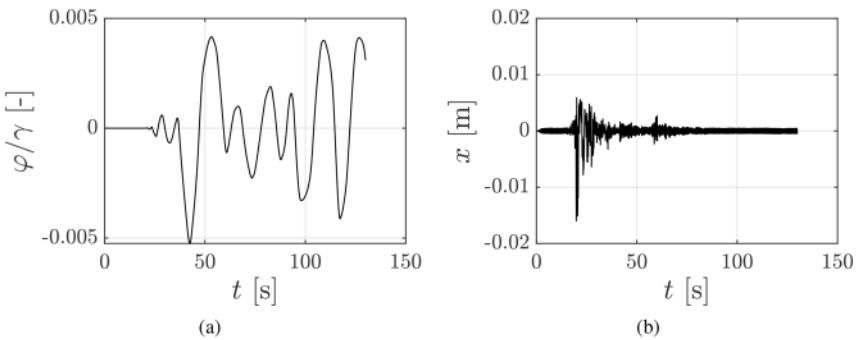

Figure 5. The rocking (a) and horizontal displacement (b) responses of the seismically base-isolated Emperor Caracalla's bust endowed with WRIs loaded in the in Shear direction.

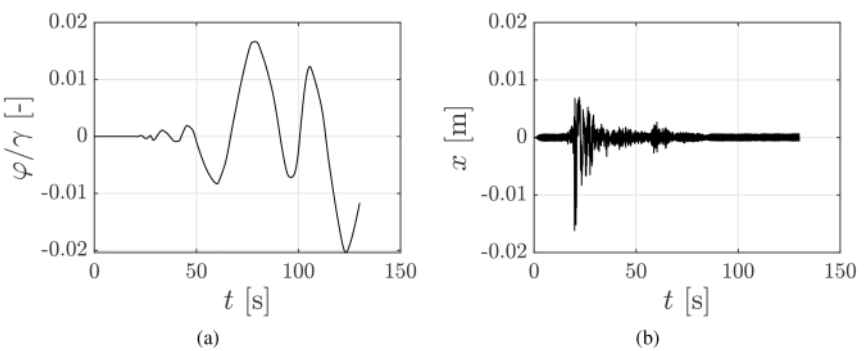

Figure 6. The rocking (a) and horizontal displacement (b) responses of the seismically base-isolated Emperor Caracalla's bust by WRIs loaded in the Roll direction.

attained displacement are very small. However, the WRIs located in the Shear direction provide the best behaviour because of significant energy dissipation due to the device's deformability in that direction.

We performed further analyses selecting seven ground accelerations compatible with the design spectra defined by the Italian Building Code. The seven records, listed in Table 3, have been obtained by using the *REXEL* software (Iervolino et al. 2009) regarding the site's National Archaeological Museum of Naples, in which there is the Farnese collection, and the limit state of the Italian code-based spectrum. The records have been found in specific ranges of moment magnitude Mw, i.e. [5, 7], and epicentral distance R, that is [0 km, 30 km]. In particular, we have chosen the period range [0.15 s, 4.0 s] in which the seven records are made compatible, to the average, with the design spectrum.

Table 3. REXEL outputs.

ID	Earthquake Name	Date	Mw	R [km]	PGA-X [m s^{-2}]	PGA-Y [m s^{-2}]
1	Campano Lucano	23rd Nov 1980	6.9	25	0.5878	0.5876
2	Bingol	1st May 2003	6.3	14	5.0514	2.9178
3	Mt. Hengill Area	4th Jun 1998	5.4	23	0.1695	0.1581
4	Mt. Hengill Area	4th Jun 1998	5.4	18	0.1325	0.2386
5	Friuli	6th May 1976	6.5	23	3.4985	3.0968
6	South Iceland-X	17th Jun 2000	6.5	5	3.1176	3.3109
7	South Iceland-Y	17th Jun 2000	6.5	5	3.1176	3.3109

For completeness, we have also carried out a one-dimensional analysis of the local seismic response. In this way, we can take into account the change of magnitude and frequency content due to the propagation of waves from bedrock to surface. Firstly, we used the *SeismoSignal* software (see References) to filter and baseline-correct the seven records provided by *REXEL*. The Butterworth filter with a bandpass between 0.10 and 25 Hz was chosen accordingly.

Soil properties such as unit weight, thickness and velocity of the secondary waves of each ground layer, have been taken from a geological survey regarding the requalification of the ex Civil Registry located in Dante Square (Naples). Soil type, soil profile and acceleration records regarding bedrock have been used as input to *STRATA* (see References), the software adopted to evaluate the local seismic response.

Figure 7 shows the horizontal displacement response of the isolated Emperor Caracalla's bust by three helical WRIs disposed along the Shear (see Figure 7(a)) and Roll (see Figure 7(b)) directions,

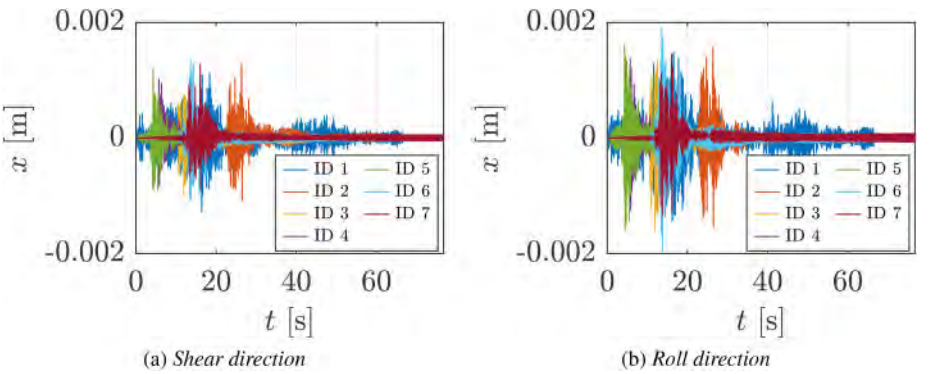

Figure 7. The horizontal displacements responses of the seismically base-isolated Emperor Caracalla's bust by WRIs loaded in the Shear (a) and Roll (b) directions.

respectively. The rocking responses have been omitted because they are negligible. The results show that the lowest displacements are attained when the WRIs are loaded along the Shear direction, as shown in the previous result.

In conclusion, the efficiency of the proposed isolation system can be assessed independently of the frequency contents of the earthquake due to the rate-independent nature of the WRIs in the small displacements range, a property thoroughly proved by the experimental studies conducted by Demetriades et al. (1993) and Alessandri et al. (2015a). In addition, the proposed isolation system works satisfactorily even if the magnitude and the frequency content of the ground acceleration change due to local seismic response.

6 CONCLUSIONS

The rocking behaviour of the Emperor Caracalla's bust subjected to the 1980 Irpinia earthquake (Italy) has been investigated. Base isolation allowed by three helical wire rope isolators acting as seismic protection system has been considered since the stability of the bust is unable to resist the oscillation induced by that earthquake.

An innovative uniaxial phenomenological model of algebraic nature has predicted the nonlinear hysteretic behaviour of the assumed devices. The computational effort computed by the adopted hysteretic model is drastically reduced with respect to the celebrated Bouc-Wen model since there is no need to solve any differential equation to evaluate the device's restoring force. The constitutive model parameters of the adopted device, namely the PWHS 16040, have been identified in both directions (Shear and Roll) from experimental hysteresis loops by means of the in-house software Parameter Identification (ParIde).

Numerical assessments have been carried out on the Emperor Caracalla's bust, both with and without isolation. The results have shown that a base isolation having three helical wire ropes in Shear and Roll directions prevents overturning and provides small rocking angle and displacement. Finally, a one-dimensional analysis of the local seismic response, regarding seven ground accelerations compatible with the design spectra defined by the Italian Building Code, has been carried out. The results showed that the proposed isolation system can work satisfactorily even if the magnitude and the frequency content of the ground acceleration change due to seismic site effects.

ACKNOWLEDGEMENTS

The present research was supported by the University of Naples Federico II and the *Compagnia di San Paolo*, which are gratefully acknowledged by the authors, as part of the Research Project *MuRA – Multi-risk assessment and structural protection of archaeological vestiges in volcanic scenarios*, FRA grants, CUP E69C21000250005.

The financial support of the Italian Ministry for University and Research – PON 2014–2020 (CUP: E66C18000940007), Fondo Sociale Europeo Azione I.1 "Dottorati Innovativi con caratterizzazione Industriale"; Project title: Development and validation of mathematical models for the simulation of the hysteretic behavior of Wire Rope Isolators to be employed for the seismic protection of art objects, sensitive equipment and lightweight structures, University of Naples Federico II Research Unit – is gratefully acknowledged.

REFERENCES

Alessandri, S., Giannini, R., Paolacci, F., Amoretti, M., Freddo, A. 2015. Seismic retrofitting of an HV circuit breaker using base isolation with wire ropes. Part 2: Shaking-table test validation, *Engineering Structures*, 98: 263–274.

Alessandri, S., Giannini, R., Paolacci, F., Malena, M. 2015. Seismic retrofitting of an HV circuit breaker using base isolation with wire ropes. Part 1: Preliminary tests and analyses, *Engineering Structures*, 98: 251–262,

Baggio, S., Berto, L., Favaretto, T., Saetta, A., Vitaliani, R. 2015. Seismic isolation technique of marble sculptures at the Accademia Gallery in Florence: numerical calibration and simulation modelling. *Bulletin of Earthquake Engineering*, 13(9): 2719–2744.

Bouc, R. 1971. Modele mathematique d'hysteresis. *Acustica*, 24(1): 16–25.

Caliò, I., Marletta, M. 2004. On the mitigation of the seismic risk of art objects: case-studies. *Proceedings of 13th World Conference on Earthquake Engineering*, Vancouver, August 1–6.

Demetriades, G.F., Constantinou, M.C., Reinhorn, A.M. 1993. Study of wire rope systems for seismic protection of equipment in buildings. *Engineering Structures*, 15 (5): 321–334.

Di Donna, M., Serino, G., Giannini, R. 2002. Advanced earthquake protection systems for high voltage electrical equipment. *Proceedings of 12th European conference on earthquake engineering*, London, September 9–13.

Housner, G. W. 1963. The behavior of inverted pendulum structures during earthquakes. *Bulletin of the Seismological Society of America*, 53(2): 403–417.

Iervolino I., Galasso C., Cosenza E. 2009. REXEL: computer aided record selection for code-based seismic structural analysis. *Bulletin of Earthquake Engineering*, 8:339–362.

Luzi, L., Lanzano, G., Felicetta, C., D'Amico, M. C., Russo, E., Sgobba, S., Pacor, F., ORFEUS Working Group 5. *Engineering Strong Motion Database (ESM) (Version 2.0). Istituto Nazionale di Geofisica e Vulcanologia (INGV)*, 2020.

MyMiniFactory, Scan The World https://www.myminifactory.com/scantheworld/#home

ParIde – Parameter Identification freeware, https://bit.ly/35F5x7Q

Pellecchia, D., Sessa, S., Vaiana, N. Rosati, L. 2020. Comparative Assessment on the Rocking Response of Seismically Base-Isolated Rigid Blocks. *Procedia Structural Integrity*, 29: 95–102.

Pellecchia, D., Lo Feudo, S., Vaiana, N., Dion, J.-L., Rosati, L. 2021. A procedure to model and design elastomeric-based isolation systems for the seismic protection of rocking art objects. *Computer-Aided Civil and Infrastructure Engineering*, 1–18.

SeismoSignal-Signal Processing of Strong-Motion data, https://seismosoft.com/products/seismosignal/

Sessa, S., Vaiana, N., Paradiso, M., Rosati, L. 2020. An inverse identification strategy for the mechanical parameters of a phenomenological hysteretic constitutive model. *Mechanical Systems and Signal Processing*, 139: 106622.

Sessa, S. 2021. Thermodynamic compatibility conditions of a new class of hysteretic materials. *Continuum Mechanics and Thermodynamics*,

STRATA-Signal Processing of Strong-Motion data, https://github.com/arkottke/strata

Vaiana, N., Spizzuoco, M., Serino, G. 2017. Wire rope isolators for seismically base-isolated lightweight structures: Experimental characterization and mathematical modeling, *Engineering Structures*, 140: 498–514.

Vaiana, N., Sessa, S., Marmo, F., Rosati, L. 2018. A class of uniaxial phenomenological models for simulating hysteretic phenomena in rate-independent mechanical systems and materials. *Nonlinear Dynamics*, 93(3): 1647–1669.

Vaiana, N., Sessa, S., Marmo, F., Rosati, L. 2019. An accurate and computationally efficient uniaxial phenomenological model for steel and fiber reinforced elastomeric bearings. *Composite Structures*, 211: 196–212.

Vaiana, N., Capuano, R., Sessa, S., Marmo, F., Rosati, L. 2021a. Nonlinear Dynamic Analysis of Seismically Base-Isolated Structures by a Novel OpenSees Hysteretic Material Model. *Applied Sciences* 11(3).

Vaiana, N., Sessa, S., Rosati, L. 2021b. A generalized class of uniaxial rate-independent models for simulating asymmetric mechanical hysteresis phenomena. *Mechanical Systems and Signal Processing*, 146: 106984.

Vaiana, N., Losanno, D., Ravichandran, N. 2021c. A novel family of multiple springs models suitable for biaxial rate-independent hysteretic behavior. *Computers and Structures*, 244: 106403.

Vassiliou, M. F., Makris, N. 2012. Analysis of the rocking response of rigid blocks standing free on a seismically isolated base. *Earthquake Engineering & Structural Dynamics*, 41(2): 177–196.

Wen, Y. K. 1976. Method for random vibration of hysteretic systems. *Journal of the Engineering Mechanics Division*, 102(2): 249–263.

Geotechnical Engineering for the Preservation of Monuments and Historic Sites III – Lancellotta, Viggiani, Flora, de Silva & Mele (Eds)

Analysis of the seismic safety condition of the defensive walls of Cittadella

E. Grande, S. Lirer & G. Conte
University Guglielmo Marconi, Rome (Italy) – Department of Science Engineering

D. Nostrali
Municipal Administration of Cittadella (Padova) – Italy

G. Milani
Politecnico di Milano, Milano (Italy) – Department of Architecture, Built Environment and Construction Engineering (ABC)

ABSTRACT: Known as the "walled city", Cittadella is located in the Veneto plain and it is a small medieval village surrounded by an elliptical-shaped defensive wall with an average height of 14 meters. A preliminary investigation on the seismic safety condition of Cittadella's walls has been developed with the kinematic analysis approach considering both the out-of-plumb configuration due to rotation at the foundation level occurred in the past and the retrofitting reinforcements carried out for some zones of the N-E walls. The obtained results clearly underline the vulnerability of the defensive walls toward the expected seismic events and, at the same time, highlight the relevant role of the provided interventions in reducing the seismic risk of the parts of walls characterized by relevant values of the out-of-plumb. According to the current indications contained in the Italian code, the use of the nominal life as parameter to evaluate the seismic safety level for historical buildings of cultural heritage is useful to identify a monitoring program aimed at preserving the integrity of walls and, at the same time, identifying suitable interventions.

1 INTRODUCTION

Cittadella is a small town in northern Italy surrounded by medieval walls (Figure 1) that form a closed perimeter (total length of 1461 m) with an ellipsoidal shape surrounded by a guard moat. The walls consist of 4 large towers, 12 main towers, 16 minor towers (*torresini*), and are composed of 36 vertical elements of about 40 m long, 15 m heigh and about 2,1 m thick, with a pedestrian walkway at an altitude of about 12 m (Figure 2). The access to the walls is through four gates, arranged along the four cardinal points (Figures 1a and 2a). The walls are supported at the base by embankments which are about 10–15 m wide and about 5–8 m deep (Bonfiglio et al. 1990; Franceschetto 1990; Scalco et al. 2007; Simonetto et al. 2002).

Surveys carried out along the perimeter of the walls revealed that the inhabited centre was surrounded by an ellipsoidal polygonal-shaped embankment, about 1460 m long, with a section between 3 and 4 m high and a base of about 12 m. The embankment was made by sandy-clay sediments and river pebbles, most probably coming from the excavation of the nearby moat.

The fortification of Cittadella was built in several phases, with interventions that followed one another over time: in the first phase, the four access gates, the towers and the "*torresini*" with a first part of the wall connecting them, but still rather low. In later phases, the walls were raised with the final part of arches and merlons.

DOI 10.1201/9781003308867-55

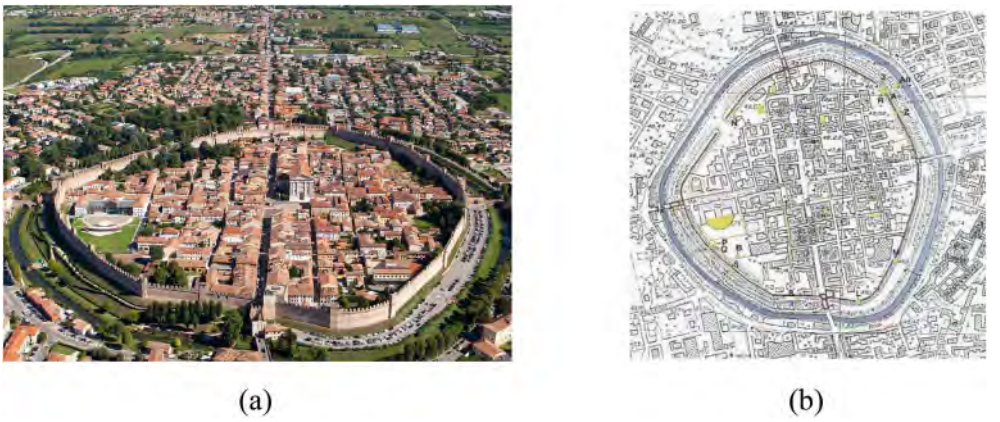

Figure 1. Air view (a) and planview (b) of Cittadella (Padova, Italy).

Figure 2. Access gate (a) and pedestrian walkway (b).

The curtain walls have an average thickness of 2.10 m and a sack type structure: on both outer sides there are two walls of Brenta stones with rows of one- or two-headed bricks, cemented and plastered with sand-rich mortar. Inside the two walls there is a filling made of a mixture of recycled materials, stones, gravel and lime.

Over time some instability phenomena (settlements, cracks, out of plumb of some wall elements, Figure 3) have involved the walls. At the beginning of the 2000s, a project for the retrofitting of the walls began to improve the walls safety condition (Jappelli 2013): the main interventions were finalized to reinforce the foundations of the towers (hooping, injections and micropiles) and to build supporting structures for some wall faces (punched reinforced concrete plates).

The paper presents the analysis of the seismic safety condition of two reference sections of the defense walls of Cittadella by means of the use of the kinematic analysis, commonly used and suggested by national codes for studying the seismic behavior of the out-of-plane masonry walls of buildings (NTC2018; NTC 2018 – Circolare 2019). In the study, both out-of-plumb configuration and provided support structures are specifically accounted for in order to estimate their influence on the seismic safety level of the walls.

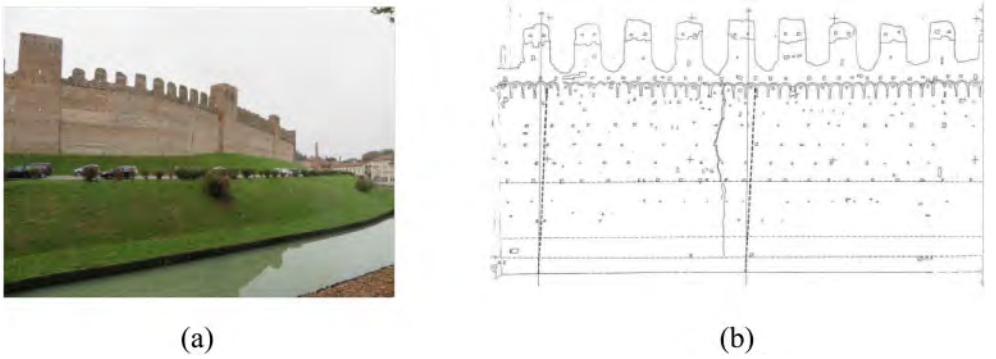

(a) (b)

Figure 3. N-E side of the walls (a) and measured out of plumb (b).

2 DATA FROM PAST SURVEYS OF THE DEFENSIVE WALLS

Since the 1990s, a number of investigations and surveys were carried out to deeply study the instability phenomena (settlements, cracks, out of plumb of some wall sections) that had involved over time the walls (Figure 4). Aero-photogrammetric surveys were used to determine the height of the various elements of the walls and embankments and to assess the out-of-plumbness of the walls, geognostic surveys to identify the properties of the underlying soil, inspections of the foundations, tests with flat jacks and core drilling in the walls.

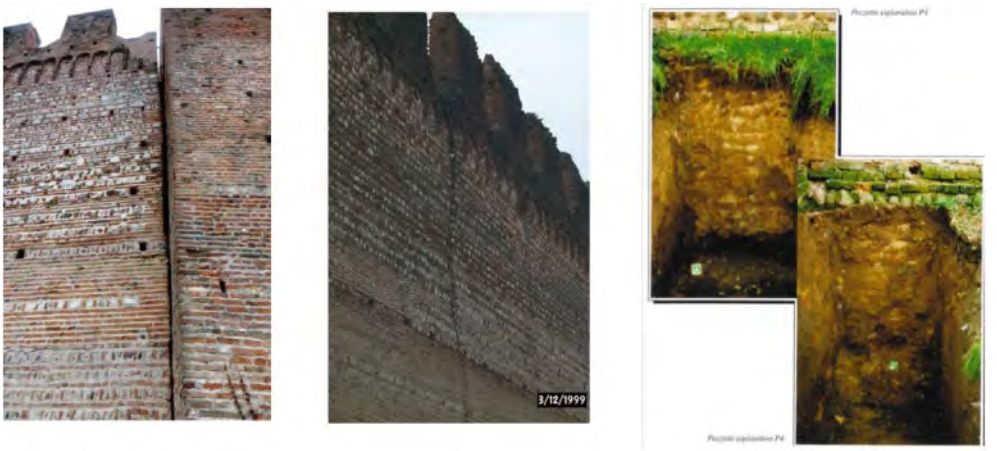

(a) (b) (c)

Figure 4. Separation of the masonry of walls from the tower (a) and vertical macro-cracks along the walls, and inspection of the foundations (c).

The in situ investigations revealed that the subsoil is (Figures 5 and 6) mainly made of an upper layer of loose silty sands ($0 < z < 4.5$) overlying a gravelly sand deposit (equivalent shear waves velocity $V_{s30} = 371$ m/s, permeability coefficient $k = 4.5 \cdot 10^{-4}$ m/s). At the end of 2012, two in situ cone penetration tests (Figure 6) have been performed near the S-E side of the defensive walls up to a depth of 5 m from the ground level in order to estimate the mechanical properties of the silty sand layer.

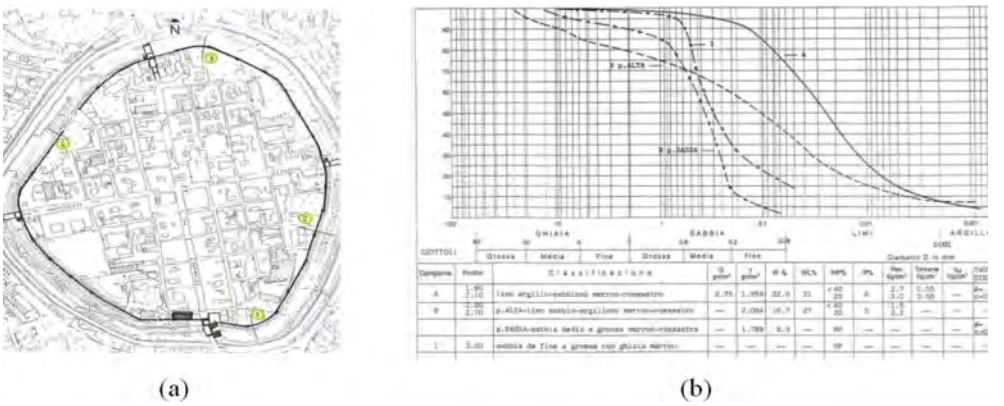

(a) (b)

Figure 5. Section 3 of the N-E side of the defensive wall (a): grain size distribution of the soil samples retrieved at a depth z< 4 m (b).

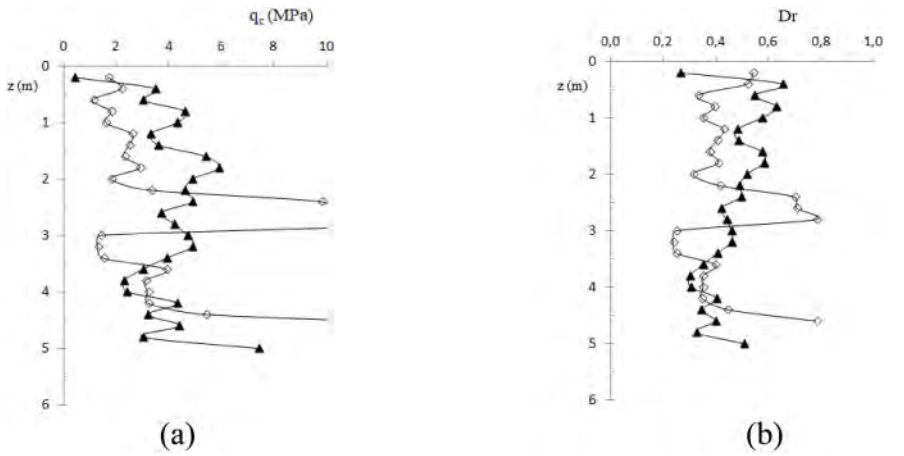

Figure 6. Section 1 of the S-E side of the defensive wall (Figure 5a): in situ cone penetration tests results (a) and relative density (b) with depth.

The surveys carried out at the foot of the walls showed that the foundations (Figure 4b) vary greatly in shape, size, material and texture. In some cases they consisted of a masonry of square stones well bound together to each other, to a depth of about 1.80 m, while in other cases they are made up of a layer of pebbles, of modest thickness and without binders, and with a depth almost equal to the surrounding soil.

Cracks are mainly located towards the central part of the walls (up to some centimetres) with a predominantly vertical trend (Figure 3b). Some tests with flat jacks were carried out in the walls.

The effect exerted by the embankments on the walls in the form of horizontal forces is significant, especially in cases where the top level is different from both sides of the wall face: over time, horizontal forces induced rotations on the wall base ($0.01 < \theta_f(\text{rad}) < 0.07$) with the consequent creation of an eccentricity of the vertical loads (Figure 3b).

Some retrofitting interventions were carried out at the end of the 1998 on sections of the walls (Figure 7) that were in a more dangerous safety condition: they consist in new embankments at the foundation level (Figure 7a) and in reinforced concrete struts (Figure 7b).

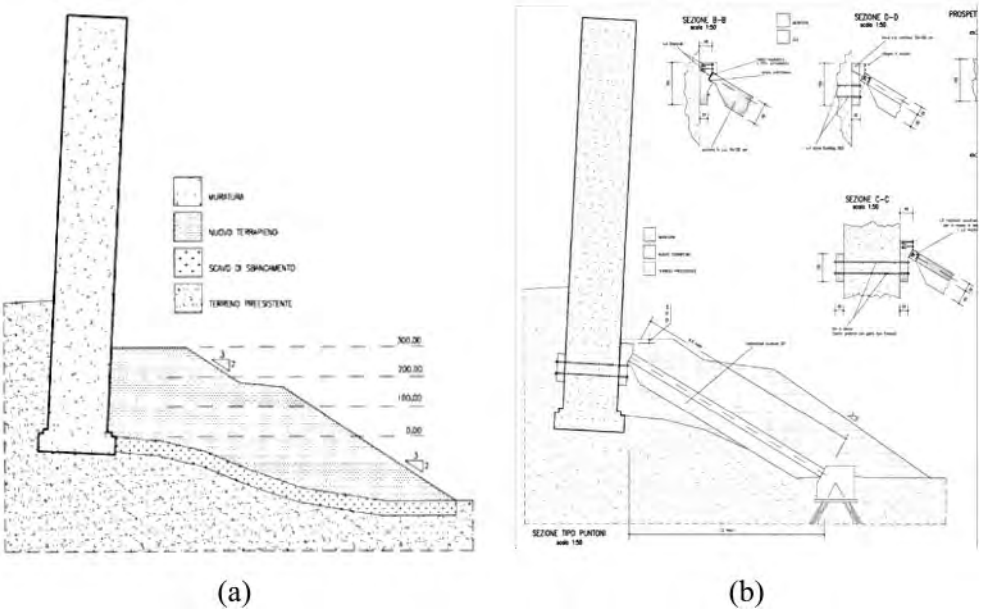

Figure 7. Interventions carried out in the N-E sections of the walls: new embankments (a) and supporting structures (b) (punched reinforced concrete plates).

3 NUMERICAL STUDY OF THE SEISMIC SAFETY CONDITION

The analysis of masonry structures using macro-elements is an approach widely used for evaluating the seismic vulnerability of historic structures toward local out-of-plane mechanisms (Casapulla et al. 2017; Cima et al. 2021). Indeed, because of poor masonry mechanical properties, presence of not-efficient connections between structural parts, damages involving local failure modes are generally observed (Cima et al. 2021). Consequently, the vulnerability to a given seismic input of macro-elements (assumed structurally independent from the rest of the structure) can be correlated to the acceleration that triggers motion.

Italian Guidelines on Cultural Heritage recommend with particular regard the analysis of the local failure modes of masonry structures in a context of multi-level approach (DPCM 09.02.2011). Indeed, by increasing the degree of complexity, the first level of analysis requires the evaluation of the collapse acceleration of the structure using simplified models and qualitative visual surveys; the second level considers the kinematic approach finalized to check the possible activation of collapse mechanisms involving one or more portions of the structure (i.e. the macro-elements); the third level involves a global analysis of the whole building under seismic loading by using numerical methods, such as the finite element methods.

Regarding the kinematic analysis, the following assumptions are generally made: the masonry has an infinite compressive strength and a null tensile strength, and no sliding can occurs among blocks. Then, considering a linear approach, the main steps have to be considered: identification of a collapse mechanism; definition of the position of the control point; evaluation of the multiplier of the horizontal loads α_0 that activates the mechanism by using the principle of virtual works; evaluation of the demand. In case of linear kinematic analysis, the capacity of the system is carried out considering the horizontal acceleration activating the local mechanism. This corresponds to a force-based approach where a behavior factor, $q > 1$, is provided by the code to decrease the demand in order to account for the effect of ductility.

In the paper, numerical analyses are carried out with the main goal to evaluate the seismic safety level of the walls with respect to out-of-plane failure mechanisms. To this end, the linear

kinematic analysis approach is here employed by considering the presence of the out-of-plumb configurations characterizing the actual state of some parts of the walls, due to a rigid rotation of foundations occurred in the past years. The performed numerical analyses mainly consist of two steps. The first step is finalized to carry out the multiplier of load α_j^* corresponding of the activation of the supposed mechanism: it represents the *capacity* of walls toward horizontal seismic actions. The second step is instead devoted to estimate the corresponding seismic safety level considering the expected seismic *demand*.

Taking into account the typical transversal section of walls (Figure 8) made of three different bodies of masonry (E_1, E_2, E_3 depending on the role and masonry texture), the out-of-plane mechanism corresponding to the formation of a hinge C between the wall and the foundation is here considered.

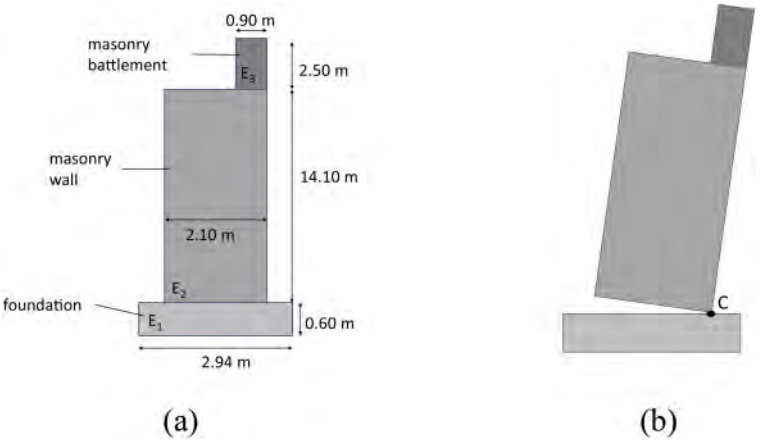

Figure 8. Typical section of the wall (a) and the accounted possible out-of-plane mechanism due to seismic actions (b).

Indeed, from simple equilibrium considerations it is possible to observe that, since the body E_1 is characterized by a greater width with respect to the body E_2, the accounted mechanism corresponds to the most probable one in terms of multiplier of horizontal loads.

The application of the linear kinematic analysis approach for evaluating the multiplier of the vertical loads corresponding to the activation of the supposed failure mechanism, has been performed starting from the actual wall configuration due to a rotation θ_f of the foundation (Figure 7). Consequently, by applying the Principle of Virtual Work referring to this configuration, the following formula for evaluating the multiplier of vertical loads is obtained:

$$\alpha^* = \frac{\sum_{i=2}^{3} W_i x_{G_i'-C'}}{\sum_{i=2}^{3} W_i y_{G_i'-C'}} \tag{1}$$

where:
W_i: weight of the layer E_i of the wall section;
$x_{G_i'-C'}$: horizontal projection of the distance between the position of the center of gravity of the layer E_i and the selected hinge C, both in the out-of-plumb configuration of the wall;
$y_{G_i'-C'}$: vertical projection of the distance between the position of the center of gravity of the layer E_i and the selected hinge C, both in the out-of-plumb configuration of the wall.

In eq.1 the subscript *i* correspond to the identification of the masonry body ($i = 2$ for the body E_2; $i = 3$ for the body E_3, Figure 8). The analyses have been carried out considering different

values of the angle of rotation θ_f (Figure 9) in order to appreciate its influence on the seismic safety condition of the considered wall section.

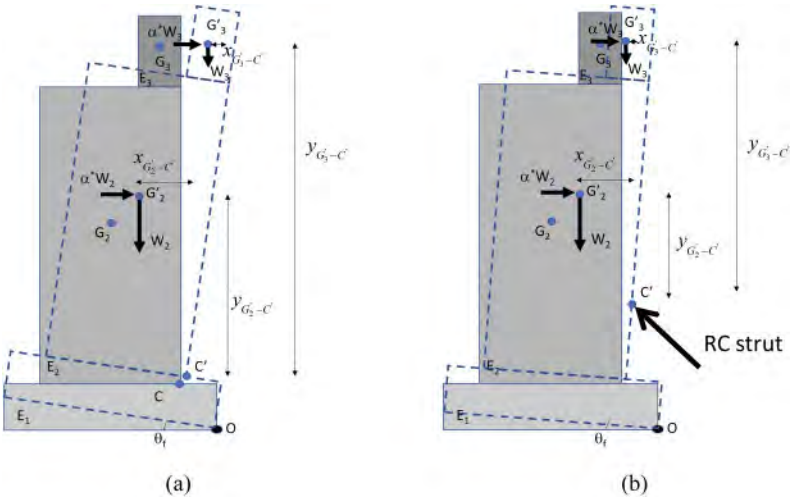

Figure 9. Accounted mechanisms considering the out-of-plumb initial configuration of wall (a) and the presence of static consolidation interventions carried out throughout RC struts (B).

Figure 10 shows the values of the multiplier α^* corresponding to the activation of the supposed mechanism deduced from eq.1 for different values of the rotation at the foundation θ_f. In the same figure the range of values of θ_f measured for the portion north-east of walls before the retrofitting interventions has been reported too. From the plot it is evident the effect of the rotation at the foundation in reducing the multiplier of horizontal forces corresponding to the activation the supposed mechanism, and then, the consequent reduction of the seismic capacity of walls toward seismic actions.

According to Italian National Codes (NTC 2018), considering the parameters characterizing the seismic zone of Cittadella and further parameters concerning the accounted limit state (Table 1), the elastic spectrum has been obtained and, consequently, the expected demand in terms of peak ground acceleration a_g. On the other hand, considering the obtained values of α^*, the corresponding spectral acceleration in terms of capacity of walls a^*_g has been derived (Figure 10).

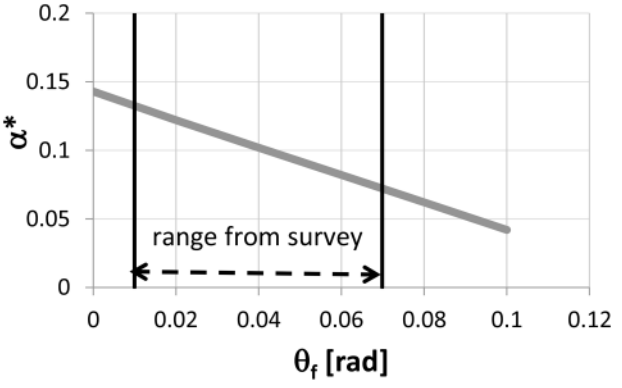

Figure 10. Results of the linear kinematic analysis: values of the multiplier of the horizontal actions α^* versus the angle of rotation θ_f at the foundation level.

Table 1. Parameters characterizing the seismic spectrum in terms of horizontal accelerations (NTC 2018).

Parameter	Symbol/Unit	Value
soil type (NTC2018)	–	C
nominal life	v_N [years]	50
topographic category	T_1	–
limit State	SLV	–
return period	Tr [years]	475
behavior factor	q	2

According to NTC, an index providing the seismic safety level can be obtained by the ratio between the capacity and the demand, expressed in terms of spectral acceleration: $f_{a,SLV} = a^*_g/a_g$.

This index is graphically presented in Figure 11a where, as expected, it is evident the reduction of the safety level of walls by increasing the out-of-plumb angle: in the same figure it can be observed that, within the range of values of θ_f emerged from the past survey, the walls seismic safety level is lower than one. In this case, the capacity of walls toward the activation of the supposed mechanism is lower than the expected demand.

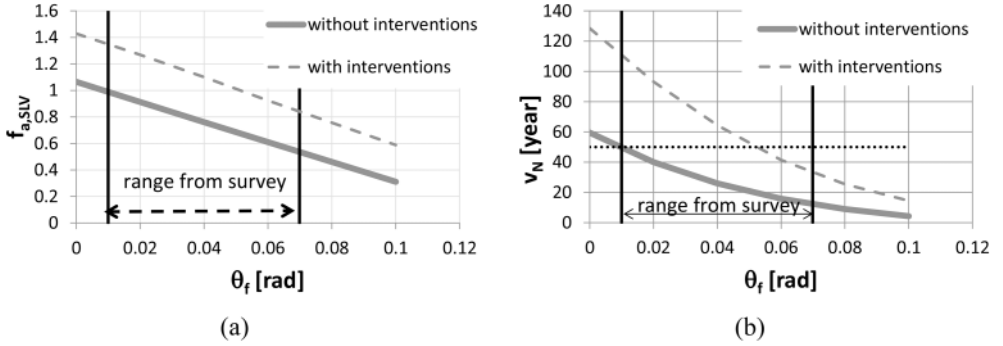

Figure 11. Results of the linear kinematic analysis: safety factor in terms of spectral acceleration (a) and nominal life of walls V_N (b) considering different values of the rotation angle at the foundation.

In the Italian guidelines for the preservations of cultural heritage (DPCM 09.02.2011) it is proposed to evaluate the nominal life of historical structures v_N (which corresponds to the number of years in which the structure, subjected to scheduled maintenance, may be used for the purpose it was designed for) as a key parameter to plan interventions for mitigating the seismic risk. In other words, differently from the ordinary structures, the conservation of historical ones often requires to consider higher levels of seismic risk instead of interventions carried out in contrast with the criteria at the basis of the preservation of cultural heritage.

In 4 the nominal life of examined walls is plotted for different values of θ_f, clearly showing the cases where the nominal life is lower than the minimum value generally considered for ordinary constructions ($v_N = 50$ years).

In both plots of Figure 11 are also reported the results obtained by considering the presence of the reinforced-concrete struts (Figure 7b) built in the past for the sector north-east of walls. The presence of these elements has been here considered in a simplified mode, i.e. by changing the position of the hinge C at the section of walls where the supporting structure acts (a distance from the foundation equal to 2,50 m; Figure 9b). The numerical results highlighted the beneficial effect of the supported structure in reference to the seismic safety level of walls (Figure 11a) and the corresponding nominal life (Figure 11b). However it can be noted that, for the larger value

of $\theta_f(\theta_f > 0.05$ rad), the adopted measures fail to provide adequate safety margins and further mitigation actions are needed.

4 CONCLUSIONS

The preservation of historical constructions is one of the main important current topics of structural engineering (Viggiani 2013). The available studies and researches, together with the specific indications contained in current technical codes and guidelines, testify the attention of the scientific community toward the seismic assessment and the rehabilitation of constructions composing the cultural heritage.

Defensive walls represent a fascinating and widespread example of historical constructions characterizing many towns of Italy. In this paper it has been presented a preliminary study concerning the seismic assessment of medieval defensive walls of Cittadella, a town located in northern Italy. In particular, considering the linear kinematic analysis, an approach proposed by codes for the analysis of the out-of-plane behavior of perimeter walls of masonry buildings, the evaluation of the seismic safety level has been carried out by considering both the presence of out-of-plumb configurations characterizing the actual state of walls, and, moreover, the presence of interventions introduced in the past. This evaluation has been performed by also considering the specific indications contained in the Italian guidelines for the preservation of cultural heritage.

The results presented in the paper highlighted the most critical conditions for which walls safety levels are below the thresholds set by the Italian national code. Further in-depth analyses will be carried out on other sections of the Cittadella walls.

ACKNOWLEDGEMENT

The Authors are grateful to Cittadella's municipality for providing documents containing the data pertaining the defensive walls here accounting for carrying out the numerical study.

REFERENCES

Andreini, M., De Falco, A., Giresini, L., Sassu, M. 2014. Mechanical Characterization of Masonry Walls with Chaotic Texture: Procedures and Results of In-Situ Tests. *Int. Journal of Arch. Heritage* 8:367–407.

Bonfiglio Dosio, G. *et al*. 1990. *Cittadella – Città murata*. Biblos ed.

Casapulla, C., Maione, A., Argiento, L.U. 2017. Seismic analysis of an existing masonry building according to the multi-level approach of the Italian Guidelines on Cultural Heritage. *Ingegneria Sismica* 1: 1–21.

Cima, V., Tomei, V., Grande, E., Imbimbo, M. 2021. Fragility curves at regional basis for unreinforced masonry buildings prone to out-of-plane mechanisms: the case of Central Italy. *Structures* 34: 4774–4787.

DPCM 09.02.2011 Linee Guida per la valutazione e riduzione del rischio sismico del patrimonio culturale (in Italian)

Franceschetto, G. 1990. *Cittadella. Saggi storici*. Lions Club di Cittadella ed.

Jappelli R. (2013). Safety and/or security of monuments? An apparent dilemma. *Proc. of the Second Int. Symp. on Geotechnical Engineering for the Preservation of Monument and Historic Sites*, Napoli Italy), 30–31 May 2013.

NTC 2018. DECRETO 17 gennaio 2018. Aggiornamento delle "Norme tecniche per le costruzioni" (*in Italian*).

NTC 2018 – Circolare 2019. "Istruzioni per l'applicazione dell' "Aggiornamento delle "Norme tecniche per le costruzioni"" di cui al decreto ministeriale 17 gennaio 2018" (*in Italian*)

Scalco, L. *et al*. 2007. *Storia di Cittadella*. SCALCO L., Vol. 2, Comune di Cittadella ed.

Simonetto, P. *et al*. 2002. *Nuovi progetti a Cittadella*., Comune di Cittadella e Associazione Architettando ed.

Viggiani C. 2013. Cultural heritage and geotechnical engineering: an introduction. *Proc. of the Second Int. Symp. on Geotechnical Engineering for the Preservation of Monument and Historic Sites*, Napoli Italy), 30–31 May 2013.

Geotechnical Engineering for the Preservation of Monuments and Historic Sites III – Lancellotta, Viggiani, Flora, de Silva & Mele (Eds)

The Bordeaux "Pont de Pierre" – A study case of micropiles reinforcement and benefits of HST method and Interaction Soil Structure design

G. Valdeyron
Cerema, Bordeaux, France

S. Bonelli
RECOVER, INRAE and Aix-Marseille Univ., Aix-en-Provence, France

P. Losset
Cerema, Bordeaux, France

M. Mariko
Bordeaux-Métropole, Bordeaux, France

ABSTRACT: The "Pont de Pierre" of Bordeaux (France), built between 1810 and 1821, was, until 2014, the only link between the two borders of the Garonne River. Today, it is a strategical axis that is used every day by 100 000 passengers (on foot, by bicycle or by tram). Since its construction, the bridge has been affected by significant settlement. In 1992–1994 and 2002–2003, 16 micropiles drilled into the masonry of each pillar reinforced the first six pillars. A detailed monitoring analysis (before and after reinforcement) is undertaken to expose the effects of micropile reinforcement and the load transfer process. In addition, an analysis of tidal effects is also carried out. Then, a soil-structure interaction model and a soil-pile-soil model are developed and fitted to the previous analysis. The results are compared with the reinforcement design obtained by the safety factor approach. The importance of considering the relative stiffness between micropiles and timber piles to improve the design of reinforcements (micropiles) is highlighted. The analysis sheds light on the issue of strengthening the last 11 pillars projected for 2023–2025.

1 HISTORICAL BACKGROUND, GEOTECHNICAL AND STRUCTURAL ASPECTS

1.1 *Bridge design, history of the building*

The "Pont de Pierre" bridge was the first to be built over the Garonne in Bordeaux. Its construction, under the responsibility of the engineer Deschamps, began in 1812. The following year, 8 of the first 11 piers built were destroyed by a flood. Considerations of redesign and financial difficulties delayed construction and the bridge was completed in 1821.

The Stone Bridge is 486 m long and consists of 16 low masonry arches with an average span of 23 m. Due to the poor properties of the foundation soil, the bridge is founded on wooden piles anchored in more or less compacted coarse sand. In addition, each pier is lightened by two levels of arches that replace the backfill material (see Figure 1).

In order to limit the weight, but also the financial cost of the structure, the designers decided to use two kinds of mineral resources. The voussoirs of the arch quoins are made of hard limestone ashlars. Between them, the rest of the arches are made of bricks made of silty clay taken directly from the Garonne.

 DOI 10.1201/9781003308867-56

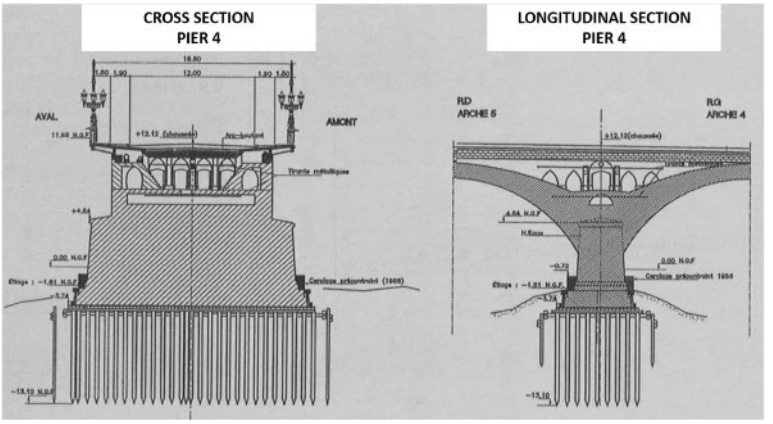

Figure 1. Transversal and elevation cut of a pier.

Each pile rests on a foundation of approximately 250 driven wooden piles, all of which are connected by a wooden deck. The latter was initially built on the banks of the Garonne and topped with the first three rows of masonry, at the edge, some sort of walls were built in order to turn it into a boat, which was beached on the group of piles.

The edge of each pillar is covered with rockfill to provide protection against scouring. The protection of the bridge against scouring was one of the main concerns of the designers, as Claude Deschamps sums up: "This monument will remain standing as long as the engineers take care of the rockfill protection". Indeed, the rockfill was backfilled in 1901, 1928, 1939, 1967, 1987, 1993, 1995–1997, 2018, however, as can be seen in Figure 2, the sub-river slopes remain a major problem, and are deeper than the pile ends.

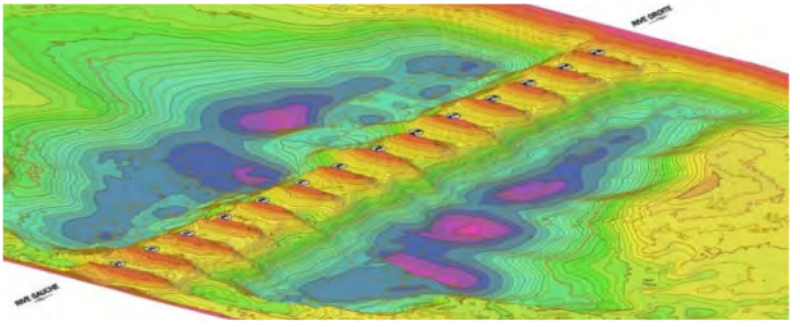

Figure 2. Bathymetry.

Since the beginning of construction, the bridge has been affected by excessive settlement, the left edge piers were the first to be affected, and for example, a through fracture of about 12 mm occurred on the second pier and required post-tensioning (400 kN) around it in 1899. The same process was applied to Pile 1 (1910) and Piles 3 and 4 (1994). It appears that, since the beginning of construction, settlements continue over the years.

1.2 *Geological and geotechnical aspects*

From top to bottom, recent alluvial deposits make up the foundation soil, overlying the Oligocene marl and limestone which form the geotechnical substrate of the bridge foundation. Muddy clays, silty sands, sands and gravels composed of recent alluvium. From the left edge to the right (pier 1

to 16), the alluvial layer becomes thinner and less clayey. The geotechnical properties of the soil are summarized in the longitudinal profile (see Figure 3).

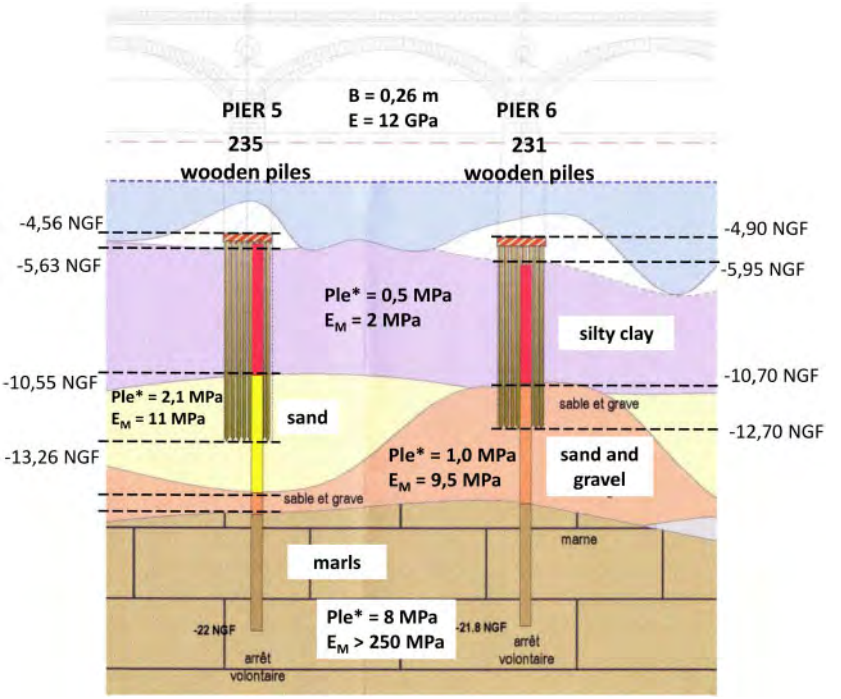

Figure 3. Longitudinal profile.

Soil strength is mainly studied using the Menard Pressumeter Test (PMT) and laboratory tests (oedometer and triaxial tests). The alluvium has poor mechanical characteristics and high compressibility ($Pl_e^* = 0.5$ MPa – $2 < E_M < 4$ MPa, $1.2 < Cc < 1.7$). The sands and gravels have higher characteristics (1 MPa $< Pl_e^* <$ 2.1 MPa – $15 < E_M < 30$ MPa).

The bridge is subject to tidal cycles of about 12:25, so every day there are two high and low tides. This implies a cyclic action on the foundation of the pile group, due to flotation, of about 5 m, or, which is equivalent, a 10% variation of the load on the pile group.

In addition, a controlled static compression load test was performed on a test micropile to evaluate the load displacement behavior of the pile and the surrounding soil (stiffness $K_{\mu p} = 100\,000$ kN/m) and the limiting friction of the shaft in the marls ($q_s > 750$ kPa).

1.3 *Monitoring implementation and structural behaviour*

The settlements of the bridge have been measured since 1992 by a fixed point system installed on each pier and consisting of a micropile anchored (6 m) in the marl (fixed point) and sealed in the masonry pier. Free movement in the alluvium is provided by a larger diameter pipe that surrounds the hole. In addition, a clinometer is installed on each pier to measure the upstream/downstream inclination.

Between 1991 and 2002, the settlements were measured with a variable measurement time step (1 measurement per half hour to 1 measurement/3 hours). A new monitoring system, implemented in 2003, increases the time step to one measurement per hour. The accuracy of the settlement gauges is 1/1000 mm.

Tide levels are measured by tide gauges located 4 km downstream from the bridge. The phase shift between the tide gauge measurements and the water level at the bridge is neglected.

2 THE HYDROSTATIC-SEASON-TIME (HST) MODEL

The tools most commonly used for dam monitoring data analysis purposes are the statistical methods of the Hydrostatic-Season-Time (HST) type. These methods were first developed in the 1960s to analyze the displacements resulting from the pendulum effects occurring at arch dams (Ferry & Willm 1958). They are still being used in several countries to analyze measurements of other kinds (Bonelli 2008, 2009; Carrère et al. 2000; Guedes & Coehlo 1985).

The HST model is based on effects of three kinds. First there are the hydrostatic effects, which correspond to the variations H resulting from changes in the water level. This variable is given by a polynomial of order 4 (parameters a_1, a_2, a_3, a_4):

$$H(t) = a_1 z(t) + a_2 z^2(t) + a_3 z^3(t) + a_4 z^4(t) \tag{1}$$

with $z(t) = (Z(t) - Z_{min})/(Z_{max} - Z_{min})$, where $Z(t)$ is the reservoir level (minimum value Z_{min}, maximum value Z_{max}).

The second term is the time of year, which accounts for seasonal variations S in the measurements during twelve-month and six-month periods, is described by the following expression (parameters A_1, d_1, A_2, d_2):

$$S(t) = A_1 sin(\omega_a(t - d_1)) + A_2 sin(2\omega_a(t - d_2)) \tag{2}$$

where $\omega_a = 2\pi/T_a$ is the annual angular frequency (T_a corresponds to a one-year period). The seasonal variations effect, assumed to be reversible, is quantified by maximum amplitudes A_i and lag time d_i. One of the oldest known application of this model was developed by Forbes (1846) who used the so called "sinusoidal adjustment method" to account for cyclic variations in the ground temperature.

The third term accounts for the time-dependent trends in the ageing processes. This variable is often called the "irreversible effect". It is expressed as follows (parameters c_1, c_2, c_3):

$$T(t) = c_1 \tau + c_2 exp(\tau) + c_3 exp(\tau) \tag{3}$$

with $\tau = (t - t_0)/\Delta T$, where t is time, and $[t_0, t_0 + \Delta T]$ is the analysis interval. The settlement rate is given by the time derivative, estimated in the middle of the analysis interval:

$$v_1 = [c_1 + c_2 exp(1/2) - c_3 exp(-1/2)]/\Delta T \tag{4}$$

The HST model $Y(t) = Y_0 + H(t) + S(t) + T(t)$ has 11 parameters estimated by multiple linear regression with MSE $||y - Y||^2$ where y is the measurement. This approach has been classically used to analyze dam monitoring data. The experience acquired at several hundreds of dams has confirmed what an excellent tool this approach can be for interpreting monitoring data. It has also been used in many other fields (Young 1998). In the present work, the HST model is applied to vertical displacement analysis measured on the Pont de Pierre.

3 APPLICATION AND RESULTS OF THE HST METHOD TO THE PONT DE PIERRE

The analysis is based on two time intervals:

- before the reinforcement work, between 1992 and 1993 (for P01 to P04) and 1992 and 2002 (for P05 to P16), i.e. 10 years (115 measurements);
- after the reinforcement works, between 2003 and 2021, i.e. 19 years (145,000 measurements).

The results are detailed for pier P06 in Figure 4 (before reinforcement works) and Figure 5 (after reinforcement works). Before reinforcement works, the reversible displacements due to buoyancy (Figure 4a) and outdoor temperature (Figure 4b) are two orders of magnitude smaller than the creep settlement (Figure 4c), which is linear in time. After the reinforcement works, the reversible

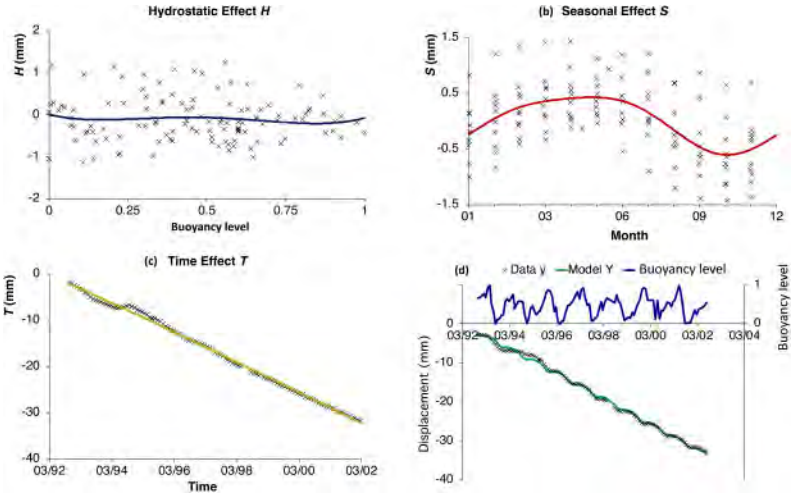

Figure 4. Results of HST analysis of P06 measurements on 1992–2002 time interval (before reinforcement): (a) Hydrostatic effect H, (b) Seasonal effect S, (c) Time effect T, (d) Data, Model and Buoyancy level as a function of time.

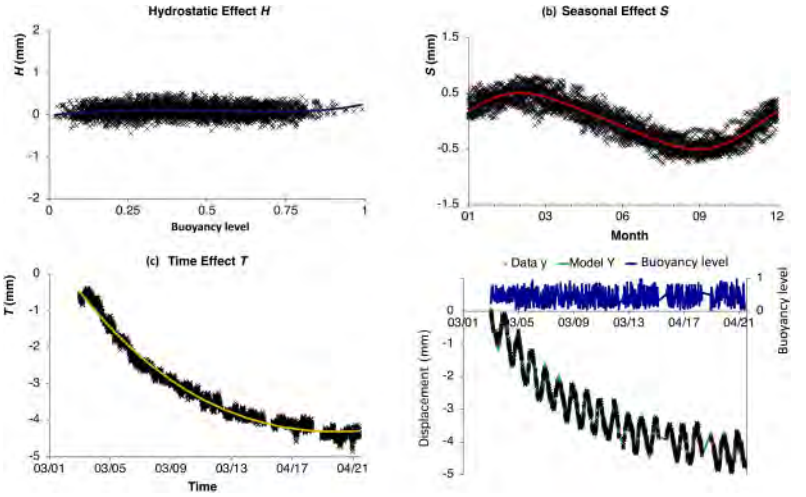

Figure 5. Results of HST analysis of P06 measurements on 2003–2021 time interval (after reinforcement): (a) hydrostatic effect H, (b) seasonal effect S, (c) time effect T, (d) data, model and buoyancy level as a function of time.

displacements due to buoyancy remain of very small amplitude (Figure 5a). The magnitudes of reversible displacements due to temperature variations were not changed by the reinforcement work (Figure 5b). On the other hand, it appears that creep settlements are damped and stabilize with time (Figure 5c). Figures 4d and 5d show that the HST analysis accurately reflects the pre- and post-reinforcement measurements.

All HST analyses on the 18 instruments are summarized in Figure 6. The amplitudes of the reversible displacements due to the variations of outside temperature, as well as their phase shift in time, were not modified by the reinforcement works (Figure 6a and 6b). Figure 6d shows that the decrease in creep settlements resulting from the reinforcement work on piers P01 through P06 is shown in Figure 6c. For the reinforced piers (P01-P06), the creep settlements represented 40%

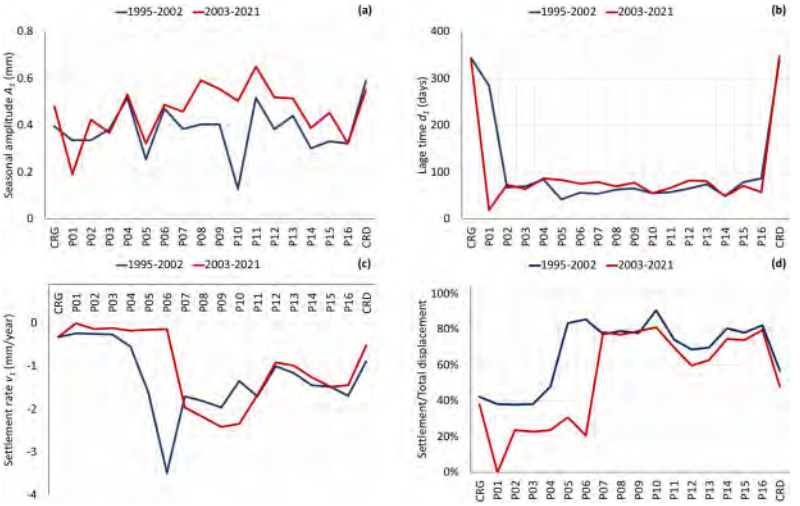

Figure 6. Results of HST analysis of 18 time series on two time interval (before and after reinforcement): (a) amplitude of reversible displacements A_1, (b) lag time d_1, (c) settlement velocity v_1, (d) settlement/total displacement ratio.

to 80% of the total displacements before the works, and about 20% after the works (knowing that the creep displacements stabilize with time). For the unreinforced piers (P07-P16), the creep settlements are about 80% of the total displacements.

4 DESIGN OF THE MICROPILE REINFORCEMENT

4.1 *Safety factor approach*

The excessive settlements observed could be explained by a defect in the bearing capacity of the wood pile group. The bearing capacity is evaluated according to the theory of the pressumeter in relation to the French standard (NF P94-262), and the group effect is evaluated with the Converse-Labarre formulas, which give the effectiveness of the grouping of piles. In our case, the reduction factor is equal to 0.67. According to French practice (Christin 2013), the achieved value of the global safety factor for quasi-permanent SLS for a wood pile foundation is 2.16. Table 1 summarizes the results of the calculations for P01-P06 in terms of the global safety factor approach.

Focusing on P05 and P06, the design of the micropile reinforcement achieved a global safety factor for the quasi-permanent combination (2.16), which would lead for P06 to a load transfer of

Table 1. Global safety factor SF for pier 1 to 6.

Pier	Safety Factor(1)	Load(2) MN	Load transfer(3) %
P01	1.14	56.1	43
P02	1.00	56.1	50
P03	1.00	56.1	50
P04	1.13	56.1	43
P05	1.54	56.1	29
P06	1.27	56.1	41

(1): Before reinforcement
(2): Abutment load for a quasi-static combination
(3): Load transfer to the micropiles to verify the SLS load capacity of each pillar

41% (= 1–1.27/2.16) of the total pier load to the micropiles – and 29% (= 1–1.54/2.16) for P05. For each pier, 16 micropiles anchored 8 m into the marl are required. A global safety factor of 2.00 was achieved for P01 to P04.

4.2 *Measured load transfer process*

As discussed in Section 3, the HST method provides a reliable assessment of the irreversible settlement of each pier. Then, assuming that each micropile is perfectly sealed to the masonry, the HST model gives the irreversible settlement from the exact day the micropiles were sealed until today. By taking into account the stiffness of the micropile gathered from static loading test, and considering a linear behavior, the load transfer ratio can be accurately calculated (see Table 2).

Table 2. Measured load transfer ratio for pier 1 to 6.

Pier	Settlement(1) mm	$16.K_{\mu p}^{(2)}$ kN/m	Load transfer(3) %	FS(4)
P01	5.1	$1.6 \cdot 10^6$	14	1.33
P02	11.3	$1.6 \cdot 10^6$	32	1.47
P03	12.4	$1.6 \cdot 10^6$	35	1.55
P04	11.6	$1.6 \cdot 10^6$	33	1.69
P05	3.4	$1.6 \cdot 10^6$	10	1.71
P06	6.9	$1.6 \cdot 10^6$	19	1.57

(1): Settlement since the sealing of the micropiles on the masonry
(2): Stiffness of the reinforcement (16 micropiles/pier)
(3): Calculated load transfer ratio between the pier and the micropiles
(4): Factor of safety of the actual bearing capacity of the wood pile group

It appears, especially for the P06 pier, that settlements are stabilized (see Figure 5c), which entails that the load transfer process is about to be completed. The load transfer ratios deduced from settlements are lower than achieved (see Tables 1 and 2). Initially, in the French practice of designing deep foundations according to the pressumeter test, the global safety factor reached for deep foundation is about 2.5 ($= Q_L/Q$ where Q_L is the limit bearing capacity load and Q is the applied load).

When using the static loading test on isolated pile, the acceptable limit load (Q_N) is defined as $0.66 \cdot Q_{cr}$, where Q_{cr} is the creep limit load obtained by a static pile loading test (Baguelin 1970). As the French practice consists on a dual approach (pressumeter and static load test), the application of a load $Q = Q_{cr}$ on a single pile is equivalent to have, for the considered pile, a safety factor SF = 1.66 ($= Q_L/Q_{cr} = 0.66 \cdot 2.5$).

In fact, the stabilization of settlements ($v_1 \leq 0.15$ mm/year) seems to be obtain when the safety factor edges 1.5 to 1.7 for the wood pile group. It appears that the load transfer draws up when the load on the wooden group piles is limited to the creep limit load of the group.

4.3 *Soil-pile-soil interaction approach*

4.3.1 *Elastic behavior*

Settlement of piles group can be treated by the theory of elasticity. The calculations are based on an interaction factor ratio α, defined as the ratio of the additional settlement due to an adjacent pile to the settlement of the pile under its own load. The interaction factor is determined in a configuration of two piles separated by a distance d and considering a pile loaded at the source and a passive unloaded pile undergoing the settlement of the source pile (see Figure 7). The settlement analysis of the pile group is then performed assuming a superposition principle: each pile undergoes the sum of the interactions of all other piles in the group (Poulos 1968). This approach, initially based on the Mindlin equation, was simplified and improved by Mylonakis by considering a Winkler model of soil reaction in a layered soil (Mylonakis 1998).

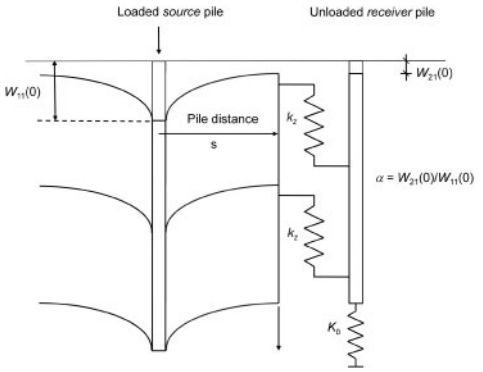

Figure 7. Pile group settlement analysis (Mylonakis).

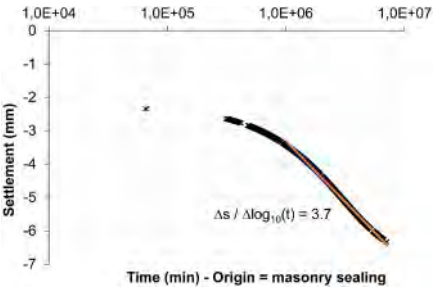

Figure 8. Creep rate of pier P06.

The settlements of loaded source piles and unloaded receiver piles are based on the elasticity theory (Young modulus E and Poisson ratio ν) and the "magical radius" defined by Randolph and Worth (Randolph, 1978) as the distance beyond which soil settlement disappears.

According to the pressumeter theory, the isolated pile settlement is based on the pressumeter modulus E_M (Frank 1982) and transfer functions for the interaction of the shaft and pile tip with the soil, which have been fitted to Young's modulus by a multiplication factor $E = k \cdot E_M$, to ensure the equivalence between the two approaches (Cuira 2016). In our case, choosing the Mylonakis formulation, we obtain $k = 3.6$ for the isolated pile. The settlement of a wood pile in an infinite group of piles is then calculated, the two approaches (Mylonakis and Frank and Zhao – see Table 3) are consistent and give similar results.

Table 3. Pile group settlement.

Pier	$s^{(1)}_{0,M}$ mm	$s^{(2)}_{0,FZ}$ mm	$s^{(3)}_{\infty,M}$ mm	$s^{(4)}_{\infty,FZ}$ mm	$s^{(5)}_{wp,gr}$ mm	$K^{(6)}_{wp,gr}$ kN/m
P05	3.59	–	–	–	27.2	$2.064 \cdot 10^6$
P06	3.53	3.48	40.1	41.6	26.1	$2.176 \cdot 10^6$

(1) Settlement of an isolated wooden pile according to the Mylonakis model
(2) Settlement of an isolated wooden pile according to the Frank & Zhao model
(3) Settlement of a wooden pile in an infinite group according to the Mylonakis model
(4) Settlement of a wooden pile in an infinite group according to the Frank & Zhao model
(5) Settlement of the wooden pile group as a rigid pile cap according to Mylonakis
(6) Stiffness of the wooden pile foundation

Assuming that wood piles are strongly connected to the wooden decking which is equivalent to a rigid pile cap, the settlement and stiffness ($K_{wp,gr}$) of the foundation of the wooden pile cap group can be calculated, all results are shown in Table 3. Before micropile reinforcement, the effect factor of the collective piles of each pile of the 235 wooden piles can be defined as $GE = s_{wp,gr}/s_{0,M}$. This factor is equal to 7.39 for P06.

After reinforcement, the settlements of the piers and then the group effect of the piles are reduced. Assuming elastic behaviour, the group effect factor after strengthening is calculated as follows:

$$GE_{reinf} = \left(K_{wp,gr} / \left(K_{wp,gr} + 16 \cdot K_{\mu p}\right)\right) \cdot GE$$

For P06, we obtain $GE_{reinf} = 4.25$. Numerous static load tests performed on the piles showed that the creep limit load corresponds to a creep rate (settlement per logarithmic time unit) of

1.5 mm/$\log_{10}(t)$ (t in minute). The settlement of the P06 pile after strengthening is shown in Figure 8. The creep rate, equal to 3.7 mm/$\log_{10}(t)$, is evaluated on the linear part of the curves. Application of the group effect factor leads to a creep rate value of 0.9 mm/$\log_{10}(t)$ for an isolated pile, just below the creep limit load rate. The result is consistent with the safety factor deduced from the measured load transfer.

4.3.2 *Visco-elastic behavior*

Analysis of tidal effects on pile settlements

Assuming that the load on the foundation of the wood pile group is directly related to buoyancy, the tidal effects can be analyzed in terms of settlements. Figure 9 shows the measured settlements and calculated settlements for P06 assuming elastic behaviour of the wood pile group foundation (stiffness $K_{wp,gr}$). It appears that bridge settlements are strongly damped compared to the results of elasticity theory. The damping parameter can be adjusted by assuming that the foundation acts as a Kelvin-Voigt element defined by the stiffness $K_{wp,gr}$ and the damping $C_{wp,gr}$ (see Figures 11 and 10). The lag time between measured settlement curve and tide is about 3 hours.

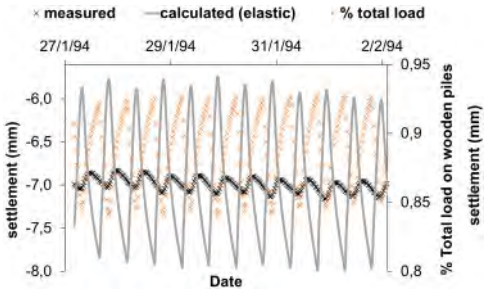

Figure 9. Measured and calculated tidal settlements.

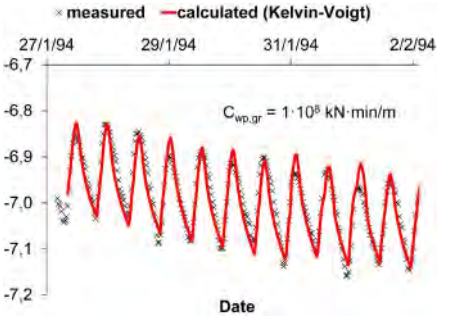

Figure 10. Fitted Kelvin-Voigt model.

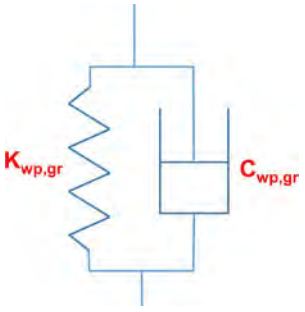

Figure 11. Kelvin-Voigt element model.

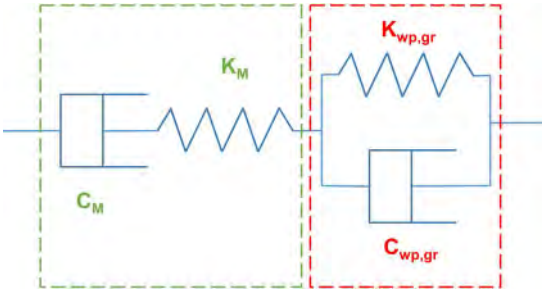

Figure 12. Burgers model of pier foundation.

Analysis of pier settlements by creep

Creep settlement analysis of pile foundations can be handled by viscoelastic theory, usually with a logarithmic creep rate function (Booker 1976; Cambefort 1965). As shown in the HST analysis, the creep rate before reinforcement is a linear function of time (Figure 4-c). Piers foundations can be modelled by a Burgers element (series of Kelvin-Voigt and Maxwell elements) as shown in Figure 12. Assuming infinite stiffness K_M, the damping parameter C_M is directly given by the HST method and $C_M = 9.228 \cdot 10^{12}$ kN·min·m^{-1}. For consistency, we check that $C_M \gg C_{wp,gr}$.

Analysis of wooden pile group by creep

In order to account for linear creep, the Mylonakis formulation could be adapted by replacing the Wrinkler springs with Burgers elements as shown in Figure 13.

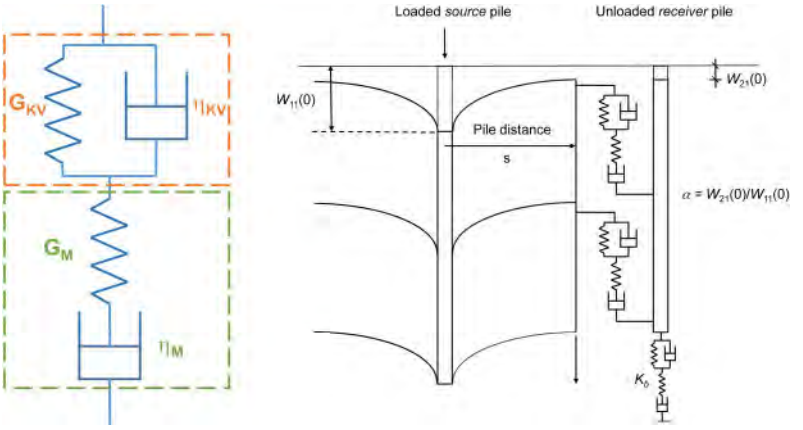

Figure 13. Principle of creep settlement analysis of pile groups (modified Mylonakis).

For each soil layer, the shear modulus G_{KV} are defined according to the theories of elasticity and pressumeters (see 4.3.1), and G_M is choosen as infinite because it has no consequence on measured creep settlements. The damping parameter η_{KV} and η_M of clay are defined according to the bibliography for similar soils tested (Guo 2000), in particular, for clay, $\eta_{KV} = 0.48 \cdot G_{KV} \cdot (10^5 \text{s})$. This latter value fits well with tidal settlements (Figure 15).

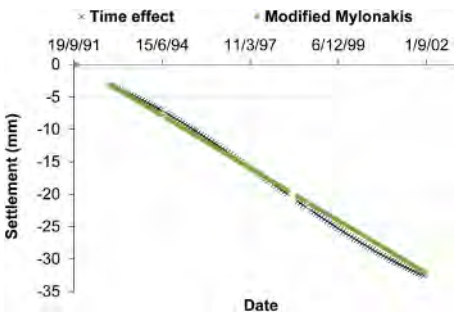

Figure 14. Modelled creep settlement (η_M fitting).

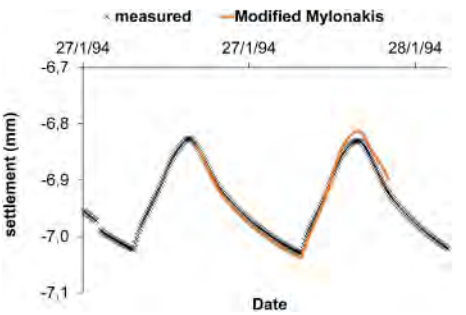

Figure 15. Modelled tidal settlement (η_{KV} fitting).

For silty sand, η_{KV} has negligible influence on tidal settlements, and η_M, which is the most influential long-term creep parameter and is fitted to pier settlements by creep (Figure 14). All properties are listed in Table 4.

Table 4. Burgers parameters for the whole foundation and for soil – pile transfer function.

Layer	G_{KV} MPa	G_M MPa	η_{KV} MPa·day	η_M MPa·day	$K_{wp,gr}$ kN·m^{-1}	$C_{wp,gr}$ kN·min·m^{-1}	K_M kN·m^{-1}	C_M kN·min·m^{-1}
Clay	4.196	∞	2.347	$2.0 \cdot 10^3$	$2.176 \cdot 10^6$	$1.0 \cdot 10^8$	∞	$9.228 \cdot 10^{12}$
Silty sand	20.770	∞	55.55	$1.17 \cdot 10^5$				

The results are consistent with the behavior of a group of piles: for low stress and low strain (tidal effects) only the shaft friction is mobilized and for high stress and high strain, the tip of the pile is mainly mobilized (long term creep).

4.3.3 *Analysis of the effects of micropiles on creep settlements*

Using the Burgers macro-element

Based on the measurement analysis and the pile-soil-pile interaction, the properties of the Burgers equivalent element of the pier foundation were defined in the previous paragraphs. The sealing of the micropiles to the structure is, in this model, equivalent to adding a spring in parallel to the Burgers element (Figure 16).

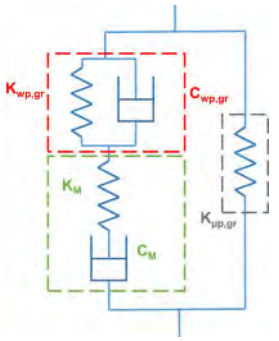

Figure 16. Modelled micropiles reinforcement.

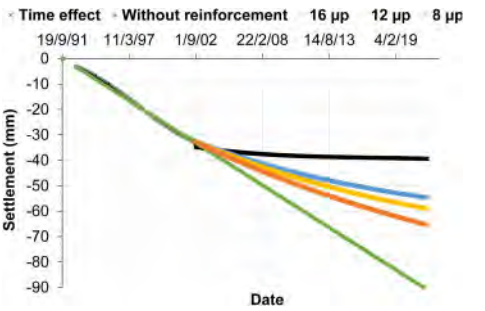

Figure 17. Wooden piles unloading process for P06.

Using Boltzmann's principle and considering that the unloading of the wooden foundation piles onto the micropiles is equivalent to a stress relaxation of the Burgers element, the settlements of the pier after the micropiles have been sealed can be calculated by an iterative process (the unloading increment dq at $t+dt$ depends on the settlement at t, estimated by $dq = K_{\mu p,gr}\ s(t)$). The unloading process is mainly determined by the Maxwell creep parameters of the wood pile foundation and the stiffness of the micropiles. It is possible to test several reinforcement hypotheses (8, 12, 16 micropiles/pier, Figure 17). It seems that the model overestimates settlements, which could be explained by the evolution of the creep parameters of the wood pile foundation due to their unloading (not taken into account in this model).

Using modified Mylonakis model (viscoelasticity)

The Mylonakis model can be adapted in order to integrate micropiles, settlements after reinforcement can also be calculated with an acceptable accuracy (see Figure 18). Different hypotheses are

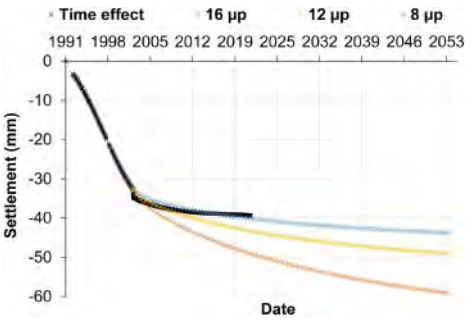

Figure 18. Calculated and measured settlements.

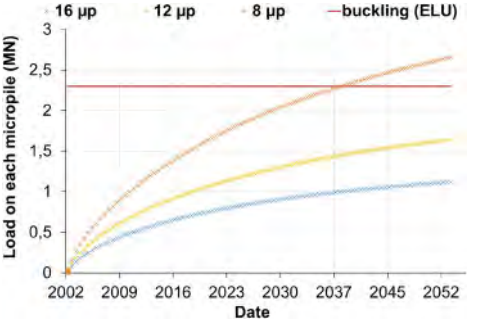

Figure 19. Load transfer and resistance.

tested, it is shown that the buckling resistance (which is the design case) of each micropile is overpassed in the 8 micropiles/pier hypothesis, the initial design (reinforcement by 16 micropiles/pier) is confirmed.

5 CONCLUSION

The article discusses the importance of analyzing monitoring results, especially for sensitive structures such as the Pont de Pierre. To be consistent, the analysis must be performed with appropriate methods. In this case, the HST method provides reversible and irreversible components of the measurements and a convincing explanation of the structure's behavior in relation to creep and tidal and seasonal effects. Associated with analytical models of group piles foundations, pile – soil – pile and soil – structure interactions relevant analysis of settlements and effects of micropiles on the structure can be performed. The Mylonakis pile group model is adapted to incorporate the viscoelastic behavior of the foundation. Two scales are to be considered: a global scale, consistent for the design of the stiffness of the micropiles, and a local scale, adapted to the analysis of each wooden pile and micropile and its interaction with the structure in order to evaluate the pinching effect on the masonry. The approach could be improved by coupling a thermal model to evaluate, based on seasonal effects, the evolution of damping parameters with time.

REFERENCES

Baguelin F., Jezequel J., Marchal J. 1970. Essai statique de fondations profondes, *Bulletin de Liaison des Laboratoires Routiers* 44(2):161–177

Bonelli S. 2008. On pore-pressure analysis in earthdams. *International Water Power and Dam Construction* 60(12):36–39.

Bonelli S. 2009. Approximate solution to the diffusion equation and its application to seepage-related problems. *Applied Mathematical Modelling* 33(1):110–126.

Booker J.R., Poulos H.G. 1976. Analysis of creep settlement of pile foundations, *Journal of Geotechical Engineering Division* 102(1):1–14.

Cambefort H., Chadeisson R. 1965. Critère pour l'évaluation de la force portante d'un pieu, Compte-Rendu du 6*ème Congrès International de Mécanique des Sols et des Travaux de Fondations*, Montréal.

Carrère A., Colson M., Goguel B., Noret C. 2000. Modelling: a means of assisting interpretation of readings. *Proc. XXth International Congress on Large Dams*, Beijing, ICOLD, p. 1005–1037.

Christin J., Reiffsteck P., Le Kouby A., 2013. Projet Pieux Bois.

Cuira F., Flavigny E. 2016. Essai pressiométrique et calculs par éléments finis, 5*ème Congrès Maghrébin en Ingéniérie Géotechnique*, Marrakech.

Ferry S., Willm G. 1958 Méthodes d'analyse et de surveillance des déplacements observés par le moyen de pendules dans les barrages. *Proc.VIth International Congress on Large Dams*, New-York, ICOLD, p. 1179–1200.

Forbes J.D. 1846. Account of some experiments on the temperature of the earth at different depths and in different soils near Edinburgh. *Transactions of The Royal Society of Edinburgh* 16:189–236.

Frank R., Zhao S. 1982. Estimation par les paramètres pressiométriques de l'enfoncement sous charge axiale de pieux forés dans les sols fins, *Bulletin de liaison des ponts et chaussées* 199:17–24.

Guedes Q.M., Coelho P.S.M. 1985. Statistical behaviour model of dams. *Proc. XVth International Congress on Large Dams*, Lausanne, ICOLD, p. 319–334.

Guo W.D., 2000. Visco-elastic transfer models for axially loaded piles, *International Journal for Numerical and Analytical Methods in Geomechanics* 24, 135–163.

Mylonakis G., Gazetas G. 1998. Settlement and additional internal forces of grouped piles in layered soil, *Géotechnique* 48(1):55–72.

NF P94-262. 2012. Justification des Ouvrages Géotechnique, Fondations profondes.

Poulos H.G. 1968. Analysis of the settlement of pile groups, *Géotechnique*, 18:449–471.

Randolph M.F., Worth C.P., 1978 Analysis of deformation of vertically loaded pile, *Journal of Geotechnical Engineering, ASCE* 104(12):1465–1488.

Young P. 1998. Data-based mechanistic modelling of environmental, ecological, economic and engineering systems. *Environmental Modelling & Software* 13:105–122.

Geotechnical Engineering for the Preservation of Monuments and Historic Sites III – Lancellotta, Viggiani, Flora, de Silva & Mele (Eds)

Effect of the presence of a historical underground quarry on site seismic response

G. Biondi, O., Fiandaca, D. Aliberti & E. Cascone
Department of Engineering of the University of Messina, Messina, Italy

ABSTRACT: The town of Ragusa (Italy) is built on a calcarenite hill which, in the past, was exploited to mine rock to be used as construction material. The result of these extraction activities is represented by some underground quarries that can be now regarded as pieces of the local industrial archaeology heritage. Hypogeal structures are characterised by large empty volumes that may remarkably affect the seismic response of the site. This paper describes the results of a preliminary study of the site of Cava Gonfalone excavated in the marls and calcarenites of the upper Membro Irminio geological formation. The genesis of the tunnel system is first examined through the evolution of mining techniques during the whole period of quarrying activities and then site seismic response has been addressed through preliminary 2D dynamic analyses aimed to predict the acceleration field on top of the Cava roof.

1 INTRODUCTION

The town of Ragusa, located close to the south-eastern coast of Sicily, is built on a flat calcarenite hill which, in the past, was locally exploited to mine rock to be used as construction material. The result of these extraction activities is represented by some underground quarries, also called *Latomie*, namely Cava Gonfalone, Cava Santa Domenica and Cava Velardo (Figure 1), that can be now regarded as pieces of the local industrial archaeology heritage, parts of a hypogeal town underneath the town. The preservation and enhancement of the industrial archaeology heritage are included in an area of interest focusing on underground cities, of a spontaneous or anthropic nature (Bozzano et al. 2017). In both cases opportunities are inseparable from problems: activating redevelopment projects of places full of charm but mostly abandoned and unknown; solving contextual needs of use and safety; identifying management models capable of returning investments.

The chance to address this issue was offered by the recent ferment that involved the *Latomie* of Cava Gonfalone re-opened to the public on June 18, 2021. Requests of cultural associations, expectations of environmental committees, and projects of institutional administrations, are aimed to protect this underground universe independent of the superimposed one, underestimating the mutual interactions that could make the existence of both vulnerable. The safeguard of the two urban realities in fact underlies a comparison between different "cultural" concepts: one real induced by the structural safety standards of the emerged city, and the other potential provided for by the regulations for the protection of industrial archaeology heritage of the underground city.

As far as the safety of the town built on underground quarries is concerned, it can be presumed that the large empty volumes characterising these hypogeal structures may remarkably affect the seismic response of the site. As a consequence, the assessment of the seismic motion expected at the ground surface cannot be handled through simplified methods of analysis, such as those suggested by seismic codes, suitable for usual, smoothly varying, soil stiffness profiles.

 DOI 10.1201/9781003308867-57

Figure 1. Perimeter of the quarries underlying the upper town of Ragusa.

In recent years the effect of underground cavities on surface ground motion induced by propagation of shear waves has been investigated through numerical analyses (e.g. Evangelista et al. 2016; Sica et al. 2013; Smerzini et al. 2009). Scotto di Santolo et al. (2015) and de Silva and Scotto di Santolo (2018) also addressed the evaluation of the stability of the underground structure, the latter study also focusing on the applicability of a probabilistic performance-based approach to assess the stability of the roof and pillars of the rock cavity.

This paper describes the results of a preliminary study of the site of Cava Gonfalone, a hypogeal structure extending about 12500 m^2. The extraction activities in the Cava probably began at the beginning of 1700 to build the new town of Ragusa (the old town had been destroyed by the 1693 eastern Sicily earthquake) and it was gradually suspended from the 1930s. The Cava consists of large rooms excavated among huge pillars having average height of about 10 m, that sustain a horizontal roof about 15 m thick. The rock material consists of the marls and calcarenites of the upper Membro Irminio geological formation.

In the first stage of the study the genesis of the tunnel system is examined through the evolution of mining techniques during the whole period of quarrying activities, highlighting how the Cava Gonfalone has influenced the development of the town, both as a source of construction material and as a reference for the settlement conditions. The presence of the hypogeal structure indeed affects the site seismic response that, in the second stage of the study, has been addressed through preliminary 2D dynamic analyses aimed to predict the acceleration field at the ground surface, on top of the Cava roof. To this purpose, starting from the results of a geotechnical investigation and the 3D geometrical model of the Cava Gonfalone, a geotechnical model, characterised by equivalent shear stiffness accounting for alternating full and empty volumes, has been defined for two different cross sections of the hypogeum. Input acceleration time histories consistent with the seismic hazard at the site of interest have been selected ensuring, in the range of fundamental periods relevant for the problem at hand, a spectrum compatibility with a target response spectrum suitable for the ultimate limit state analysis required for the seismic evaluation of a hospital resting on the roof of the hypogeum. 2D seismic response analyses have been carried out assuming for the rock a linear visco-elastic constitutive model, with Rayleigh viscous damping calibrated on the fundamental frequency of the hypogeal structure. The results of the analyses are presented and discussed in the paper, focusing on the peak accelerations computed at the ground surface and along several vertical alignments relevant for the area of the hospital.

2 TWO URBAN REALITIES, A SINGLE LITHOLOGICAL ORIGIN

Stimulated by the recent interest in the *Latomie* of Cava Gonfalone, a study of this particular urban area, which extends from via Risorgimento to Piazza Igea passing under the Hodierna Hospital and its garden, has been undertaken with a bifocal viewpoint: on the one hand, by analysing the historical-cultural importance of the mining activity, in full cultivation in the Nineteenth Century,

which allowed the "new" town (Ragusa Superiore) to grow and expand, exploiting a valuable stone material; on the other hand, by evaluating the seismic motion expected at the foundation level of some buildings built upon the system of tunnels, whose construction brought to the decline of the underground quarry since the 1930s and the closure of its western area in the 1940s (Di Raimondo & Zocco 2004).

The tunnel complex, nowadays a single hypogeum, has been excavated from west to east. Documentary traces mark the only known time passages:

- a petition of the Ragusan quarrymen to counter the competition of the Syracuse stone, reported in the Bulletin edited by the Syracuse Chamber of Commerce in 1887;
- some inscriptions on the rock surface inside the quarries, attesting the cultivation of an eastern area in 1895 and of the central portion in 1928 and 1929;
- a correspondence from the 1930s with which the Prefect of Ragusa, Gaetano De Blasio, responded to the protests for the closure of the Cava Gonfalone, claiming it was necessary "so as not to damage the land" allocated to the two hospitals under construction (Benito Mussolini – now Civil – Hospital and Giovanni Battista Hodierna Hospital) and "in particular for the tuberculosis sanatorium" (1931–1933; inaugurated on October 28, 1938).

The recognition of the historical value of the Cava Gonfalone must initially pass from the understanding of the synergistic relationship between the local stratigraphy, the cultivation of stone material and the development of the town. Figure 2 shows a cartographic overlapping that outlines the perimeter of the current tunnel system underlying the built area in order to highlight interferences of the two urban realities.

Figure 2. Interference areas between underground structures and overlying town.

The material (and immaterial) value that distinguishes the *Latomie*, has been intercepted through the knowledge of their genesis. The evolution of mining techniques was traced by through the observation of the marks engraved on the walls of the quarry by excavation tools, chosen according to the mechanical characteristics of the rock, among those available in subsequent time intervals (Bessac 1986).

The first access to Cava Gonfalone, evidently following experiential qualitative evaluations, was opened perhaps in the 18th Century on the southern side of the valley, in the lower vein; then the mining developed through advancement tunnels that allowed the passage of men with impact tools by reducing unproductive excavations, to create chambers in which several quarrymen could work at the same time. The sub-horizontal sedimentation planes existing in the rock bank (alternation of hard and marly limestones) were exploited, to optimize the extraction times, guaranteeing the best quality to the segments. The inclination of the layer joints was about 5° towards north-north-east so the hypogeum developed following this inclination and produced differences in the thickness of the vault above, thinner in north-north-west area.

In this context, until the 1940s, the quarrymen isolated blocks of hard limestone, the "banks", proceeding from top to bottom, with "direct impact tools" – picks and hammers – or "indirect" – awls beaten by mallets – wedges and levers.

The "banks" with dimensions, still visible on the quarry surfaces, of approximately 1.00 (width) × 1.80 (length) × 2.00 (height) meters, overturned on a free area covered by debris, were divided into more blocks, the *pizzuoli* (40 × 80 × 40 cm), with "indirect impact tools", chisels and awls. Each portion of stone was taken outside on the backs of the quarrymen. Large pillars, even irregularly shaped, were left to support the "roof" of the rooms and avoid collapses.

The traces left by this mining method are evident on the walls and on the roof in the western tunnels, with stripe (quarry pick; mallet and awls) and fan-shaped (pyramidal-pointed pick) signs (Figure 3). Moving towards east, the stone surfaces show more regular herringbone patterns marks (hack hammers – *martellina*). With the advent of circular saws, the last phase of the block extraction took place, which concerned only an area further east. Here the cut was made by engraving as it can be seen from the cross signs present in the lower parts of the walls, while the mining of the upper parts had already taken place with traditional impact tools (Figure 4). In the later extension to the east of the quarry the signs on the walls return in bands or fans, consistently with the date August 16, 1895, imprinted on a wall.

Figure 3. Western tunnels: bands, fan-shaped, and herringbone traces.

Figure 4. Eastern tunnels: cross traces in the lower part and traditional tools traces in the upper part.

The mining activity, which in the common awareness is a process with a great landscape impact since the rock is eroded, subtracted, and changes its morphology until it disappears, here returns value by converting an ambient waste into a cultural resource: it is a place that offers economic proto-industrial scenarios, evocative spaces designed by the work of quarrymen and by solar light, opportunities for urban redevelopment.

3 SITE RESPONSE ANALYSIS

3.1 *Soil profile*

The historical-archaeological value of Cava Gonfalone may be considered as a necessary but not sufficient condition to return it to public fruition. It is necessary to ascertain its stability under static and seismic loading conditions. The study of the site seismic response is a first step towards the understanding of what should be done to mend the underground city while guaranteeing the

same level of safety to the superimposed city. Though it is recognized that, owing to the complex geometry of the quarry at hand, a 3D approach should be followed, the results of some preliminary 2D dynamic analyses are presented herein, with the aim of highlighting the main features of the seismic response of the hypogeal structure and the characteristics of the ground motion expected at the ground surface.

Figures 5 and 6 show a plan view and the two cross sections considered in this study to carry out 2D seismic site response analyses. The geotechnical model of the rock materials identified in Figure 6 was specified basing on the results of a Down Hole (*DH*) test and a Seismic Refraction test (*SR*) test carried out at the site and whose locations are shown in Figure 5.

The soil profile can be described as consisting of three main layers, namely a shallow layer of topsoil of sandy-silt including calcareous and marly-calcareous cobbles, a second layer of hard white-greyish limestones alternating with poorly cemented marly limestones (average thickness of 10–15 meters) and a third layer of compact calcarenite (0.5–3 meters thick) alternating with thin (5–40 centimetres) levels of marls and whitish limestone. The *RQD* factor in the first 30 m of depth of the rock mass varies in a wide range (20–90%) being frequently comprised between 50% and 70%. Values of uniaxial compression strength of about 15 MPa have been obtained on few samples

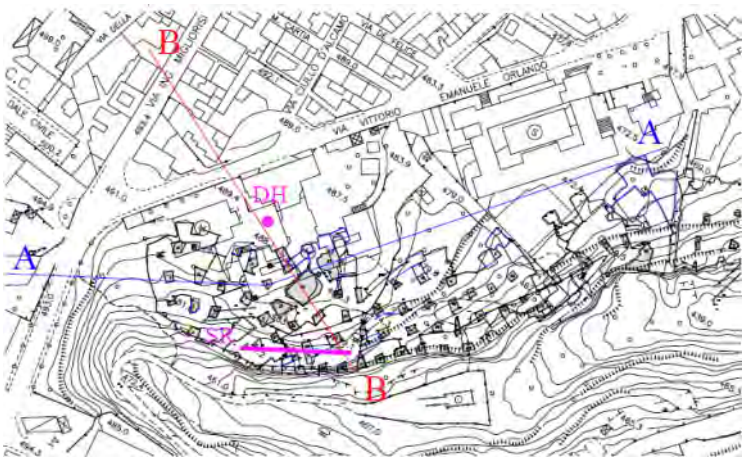

Figure 5. Plan view showing the pillars of the quarry, the overlying buildings and the location of geotechnical investigations.

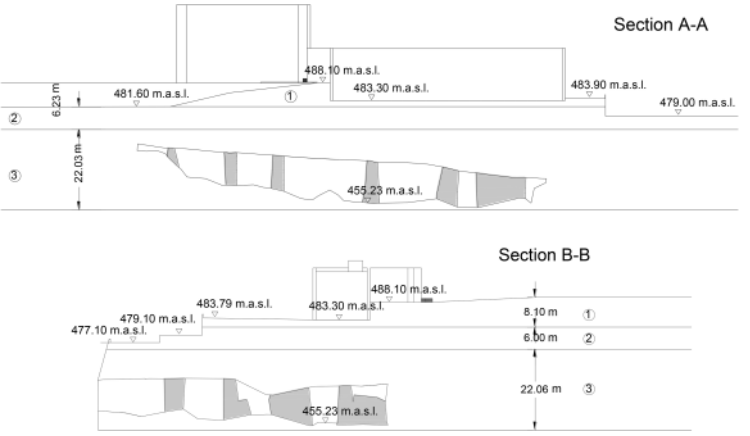

Figure 6. Cross sections considered in 2D seismic response analyses.

retrieved at depth of 5.6–14 m. Table 1 summarizes the mean values of estimated unit weight γ, shear wave velocity V_s, Poisson's ratio ν and shear modulus G at small strain for the three layers of the geotechnical model adopted in the analyses.

Table 1. Physical and mechanical parameters.

Layer	γ [kN/m^3]	V_s [m/s]	ν [–]	G [MPa]
#1	22.2	460	0.29	479
#2	22.5	702	0.41	1132
#3	25.3	169	0.14	7373

3.2 *Selection of input motion*

The input motions to be used in dynamic analyses have been selected using databases of Italian (ITACA 2.1, Luzi et al. 2016), European (ESMD) and international (PEER, 2016) seismic records. A first selection of acceleration time-histories has been carried out for the Life Safety Limit State (*LLS*), setting the moment magnitude and the Joyner and Boore (1981) distance in the ranges $M_w = 6.4 \pm 0.4$ and 1 km $\leq R_{jb} \leq 25$ km. The selection has further refined focusing on the horizontal records, checking the similarity between the elastic response spectrum of the acceleration time histories and the target spectrum (Bommer and Acevedo, 2004; Pagliaroli and Lanzo, 2008). The spectra defined by the Italian seismic code (NTC18, 2018) has been considered as target for the *LLS*. Compatibility of selected acceleration records has been checked in terms of amplitude and frequency content, through the response spectra. To this purpose a scale factor F and two statistical parameters, R^2 and D_{rms} were used. The scale factor F allows ensuring compatibility in terms of peak horizontal acceleration (i.e. spectral ordinate for period $T = 0$ s):

$$F = \frac{(a_{h,max})_j}{(a_{h,max})_t} \tag{1}$$

The correlation index R^2 and the average root-mean square deviation D_{rms} measure the deviation of the normalised response spectra of the selected records from the target spectrum in a given period interval ($T_{min} - T_{max}$):

$$R = \frac{N \cdot \sum_{i=1}^{N} \overline{S}_{a,t}(T_i) \cdot \overline{S}_{a,j}(T_i) - \sum_{i=1}^{N} \overline{S}_{a,t}(T_i) \cdot \sum_{i=1}^{N} \overline{S}_{a,j}(T_i)}{\sqrt{\left\{N \cdot \sum_{i=1}^{N} \left[\overline{S}_{a,t}(T_i)\right]^2 - \left[\sum_{i=1}^{N} \overline{S}_{a,t}(T_i)\right]^2\right\} \cdot \left\{N \cdot \sum_{i=1}^{N} \left[\overline{S}_{a,j}(T_i)\right]^2 - \left[\sum_{i=1}^{N} \overline{S}_{a,j}(T_i)\right]^2\right\}}} \tag{2}$$

$$D_{rms} = \frac{1}{N} \sqrt{\sum_{i=1}^{N} \left[\overline{S}_{a,t}(T_i) - \overline{S}_{a,j}(T_i)\right]^2} \tag{3}$$

In Eqs. (1)–(3) $(a_{h,max})_j$ and $(a_{h,max})_t$ are the peak horizontal acceleration of the j-th record and the target ground motion, expected at the site on outcropping rock; $S_{a,t}(T_i)$ and $S_{a,j}(T_i)$ denote the normalised spectral accelerations of the target motion and the j-th record; N is the number of equally spaced ($\Delta T = 0.01$ s) periods of the response spectra in the range $T_{min} - T_{max}$. R^2 was evaluated assuming $T_{min} = 0.1$ s and $T_{max} = 4$ s to verify the overall compatibility of the selected ground motions.

The first vibration periods in x and y direction of the structure of the Hodierna hospital, resting on top of the roof of the underground quarry, have been evaluated through push-over analyses, and are, respectively, $T_x = 0.52$ s and $T_y = 0.39$ s. Accordingly, in order to select input ground motions

capable to produce frequency coupling with the structure, the values $T_{min} = 0.25$ s and $T_{max} = 0.65$ s were assumed to evaluate D_{rms}.

To obtain at least five accelerograms, the following limits have been defined for the selection parameters: $F \leq 2.5$, $R^2 \geq 0.8$ and $D_{rms} \leq 0.15$. The results of the accelerogram selection are shown in Figure 7 and Table 2.

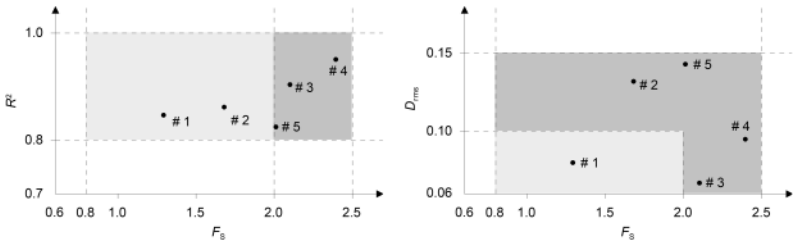

Figure 7. Results of the selection of input motions.

Table 2. Main characteristics of the selected horizontal acceleration time histories.

No.	Earthquake, Station and Record	M_w	R_{JB} (km)	a_{max} (g)	t (s)	T_m (s)	I_A (m/s)	P_d (10^{-4}g·s^3)	F	R^2	D_{rms}
#1	South Iceland Flagbjarnarholt 17/06/2000	6.6	5.0	0.32	91.79	0.64	1.24	24.95	1.29	0.85	0.080
#2	Parkfield -02 Turkey Flat # 1 270 28/09/2004	6.0	4.66	0.24	81.92	0.37	0.17	1.19	1.68	0.86	0.132
#3	Parkfield -02 Turkey Flat # 1 360 28/09/2004	6.0	4.66	0.206	81.92	0.45	0.19	2.46	2.10	0.90	0.067
#4	Northridge Wonderland Ave 185 17/01/1994	6.7	15.11	0.17	29.99	0.45	0.20	2.30	2.39	0.95	0.095
#5	San Fernando Pasadena Old Seismo Lab 270 09/02/1971	6.6	21.5	0.20	101.11	0.327	0.34	4.05	2.01	0.83	0.143

Time histories of horizontal acceleration $a(t)$ of the selected records are plotted in Figure 8, together with the corresponding Fourier amplitude spectra. Comparison of the target spectra for the site with the normalised response spectra of the selected horizontal records is shown in Figure 9. Specifically, the normalised response spectra compare with the 50th-percentile uniform hazard spectra computed at the site.

For the seismic analyses described herein, all the horizontal records were scaled to the target peak ground acceleration $(a)_t$ 0.412 g estimated for the Life Safety Limit State (*LLS*). Table 2 lists the main seismic parameters of the horizontal component of the scaled records: the Arias intensity I_A, the destructiveness potential factor P_d (Araya & Saragoni 1984) evaluated in the time-interval corresponding to the strong motion duration $D_{5\text{-}95}$ (Trifunac & Brady 1975), and the equivalent number of loading cycles N_{eq} evaluated according to Biondi et al. (2012), while the mean period T_m (Rathje et al. 1998) and the duration t are given in Table 3.

3.3 *Numerical analyses*

The numerical analyses were carried out in terms of effective stresses using the code FLAC v.7.0 (ITASCA 2011) discretising the foundation soils via a finite difference grid with quadrilateral

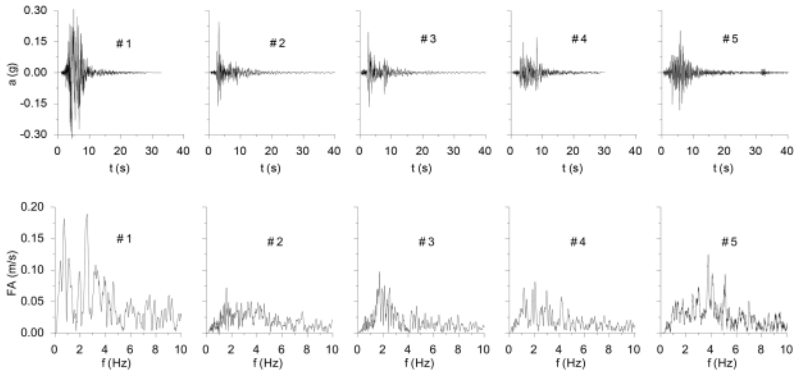

Figure 8. Acceleration time histories and Fourier amplitude spectra of the selected accelerograms.

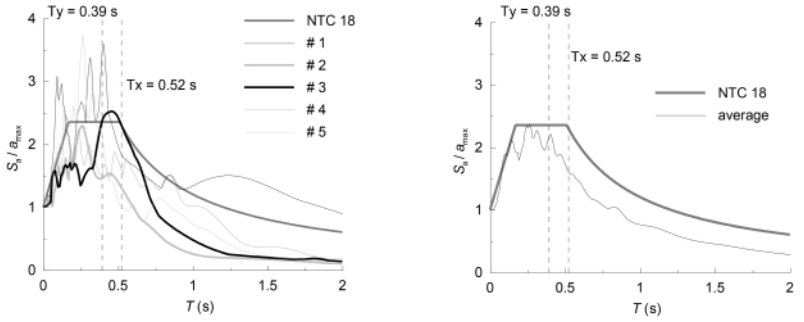

Figure 9. Comparison between target spectral shape and normalised spectra of the selected accelerograms.

Table 3. Seismic parameters of the scaled selected records.

Record	I_A (m/s)	P_d (10^{-4}g·s^3)	$D_{5\text{-}95}$ (s)	N_{eq}
#1	2.07	41.63	3.94	14.6
#2	0.48	3.37	8.76	3.4
#3	0.83	10.86	8.26	5.0
#4	1.15	13.17	6.67	6.4
#5	1.39	16.37	6.88	8.9

elements. Figure 10 shows the grid and the boundary conditions adopted in the static and dynamic analyses for section A-A.

In the static analyses displacements in both directions were restrained at the bottom boundary of the finite difference grid and horizontal displacements were restrained at its lateral sides.

Under dynamic loading conditions, to prevent reflection of outward propagating waves back into the numerical model the use of supplementary free-field grids, coupled to the lateral boundaries of the main grid was combined with the technique of absorbing boundaries. Specifically, according to the procedure originally proposed by Cundall et al. (1980) and implemented in FLAC, at the lateral sides of the main grid the required free-field conditions have been enforced in such a way that boundaries retain their non-reflecting properties and outward waves originating from the model are properly absorbed. In this way, plane waves propagating upward suffer no distortion at the boundary because the free-field grid supplies conditions that are identical to those of an infinite model. Finally, viscous boundaries, consisting in independent dashpots in the normal and shear direction at the model boundaries, were introduced at the bottom of the main grid, replacing the

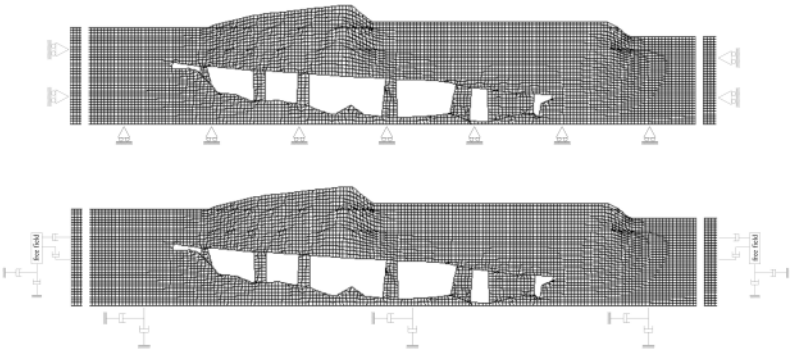

Figure 10. Grid and boundary conditions adopted in the static and dynamic analyses of section A-A.

elementary-constraints used in the static analysis, and at the bottom of the free-field grids. To avoid numerical distortion of the propagating wave in the dynamic analysis, the maximum height of the elements in the main-grid and in the supplementary free-field grids was assumed smaller than 1/6 of the wavelength λ_{min} associated with the highest frequency of the input motions used in the dynamic analyses. As usual when using quiet boundaries, the input was applied at the bottom of the grid converting the time-histories of velocity associated to the corresponding acceleration records into shear stress time-histories.

The foundation soils were described as elastic materials, homogeneous and isotropic, with linear stress-strain law without hysteresis using the parameters listed in Table 1. For the pillars the unit weight γ and Poisson's ratio ν of the corresponding layer were adopted while, to account for the effect of existing voids, the shear modulus was reduced trough a factor computed as the ratio between the actual width of each pillar and its area of influence. Figure 11 shows the values of shear modulus used in the analyses.

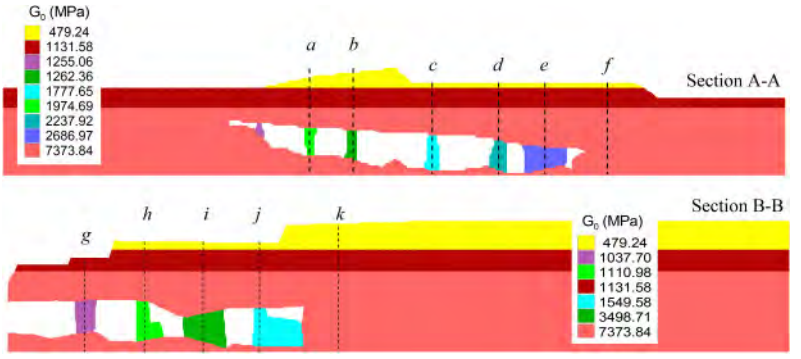

Figure 11. Values of the shear modulus G_0 adopted in the analyses.

For all materials, a viscous Rayleigh damping $\xi_{min} = 0.5\%$ was introduced. The frequency f_{min} was set equal to the first natural frequency of horizontal elastic vibration of the soil evaluated from the largest peak of the undamped elastic transfer function. This was computed, using the record #4, as the ratio between the amplitude Fourier spectra of acceleration computed at the top and the base of the model obtaining $f_1 = 6.1$ Hz for section A-A and $f_1 = 8.1$ Hz for section B-B.

3.4 *Discussion of results*

The distribution of peak horizontal and vertical accelerations computed along the surface profile are shown in Figure 12 for section A-A.

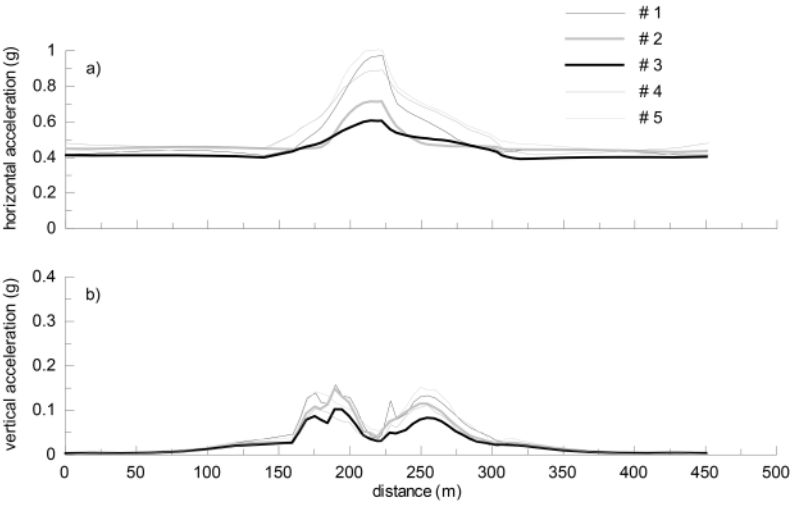

Figure 12. Horizontal (a) and vertical (b) peak acceleration along the ground surface of section A-A.

The largest horizontal accelerations (Figure 12a) at the ground surface have been computed for the area above the voids and are due to the focusing of seismic waves induced by the interaction of the incident and reflected waves. The largest peaks, ranging between about 0.5g and 0.95g have been computed for the crest of the sloping area located between the alignments *b* and *c* drawn in Figure 11 and are relative to the scaled records #1 and #5 characterized by the largest Arias intensity I_A, destructiveness potential factor P_d and equivalent number of loading cycles N_{eq} (Table 3). At the edge of the model peak accelerations reduce with distance from voids and values in the range 0.4g–0.5g have been computed.

The plots of Figure 12b reveal a relevant parasitic vertical component of the seismic acceleration which can be ascribed to the complex seismic waves reflection occurring in the portion of the ground surface above the voids. The largest peaks, ranging from about 0.075g to about 0.15g, are concentrated in the areas close to the alignments *b* and *c* drawn in Figure 11.

Figure 13 shows the profiles of the maximum horizontal accelerations $a_{h,max}$ along the above mentioned vertical alignments, normalised to the peak horizontal acceleration computed at the model base $a_{h,base}$. Specifically, the profiles refer to the alignments *a*–*f* drawn on section A-A (Figure 13a–f) and to the alignments *g*–*k* relative to section B-B (Figure 13g–k); in the plots *z* is the depth computed, for each alignment, from the ground surface and H is the corresponding maximum depth. An amplification ratio $a_{h,max}/a_{h,base}$ always lower than 2 is generally observed in the profiles relevant to section A-A, while for some of the alignments relative to section B-B (Figure 13g,h,i) a de-amplification of the ground motion is predicted. This result may possibly be ascribed to the impedance ratio between the roof and the pillars of the quarry that, differently from usual situations, due to the presence of large voids, is larger than one.

4 CONCLUDING REMARKS

The paper concerns with a hypogeal structure, namely Cava Gonfalone, consisting of large rooms excavated among huge pillars during the extraction activities carried out on the flat calcarenite hill on which the town of Ragusa (Italy) was rebuilt after the large 1693 eastern Sicily earthquake.

With reference to this site the evolution of mining techniques during the whole period of quarrying activities was firstly examined and preliminary 2D site response analyses were carried out to predict the ground motion on top of the Cava roof where Hodierna Hospital is built.

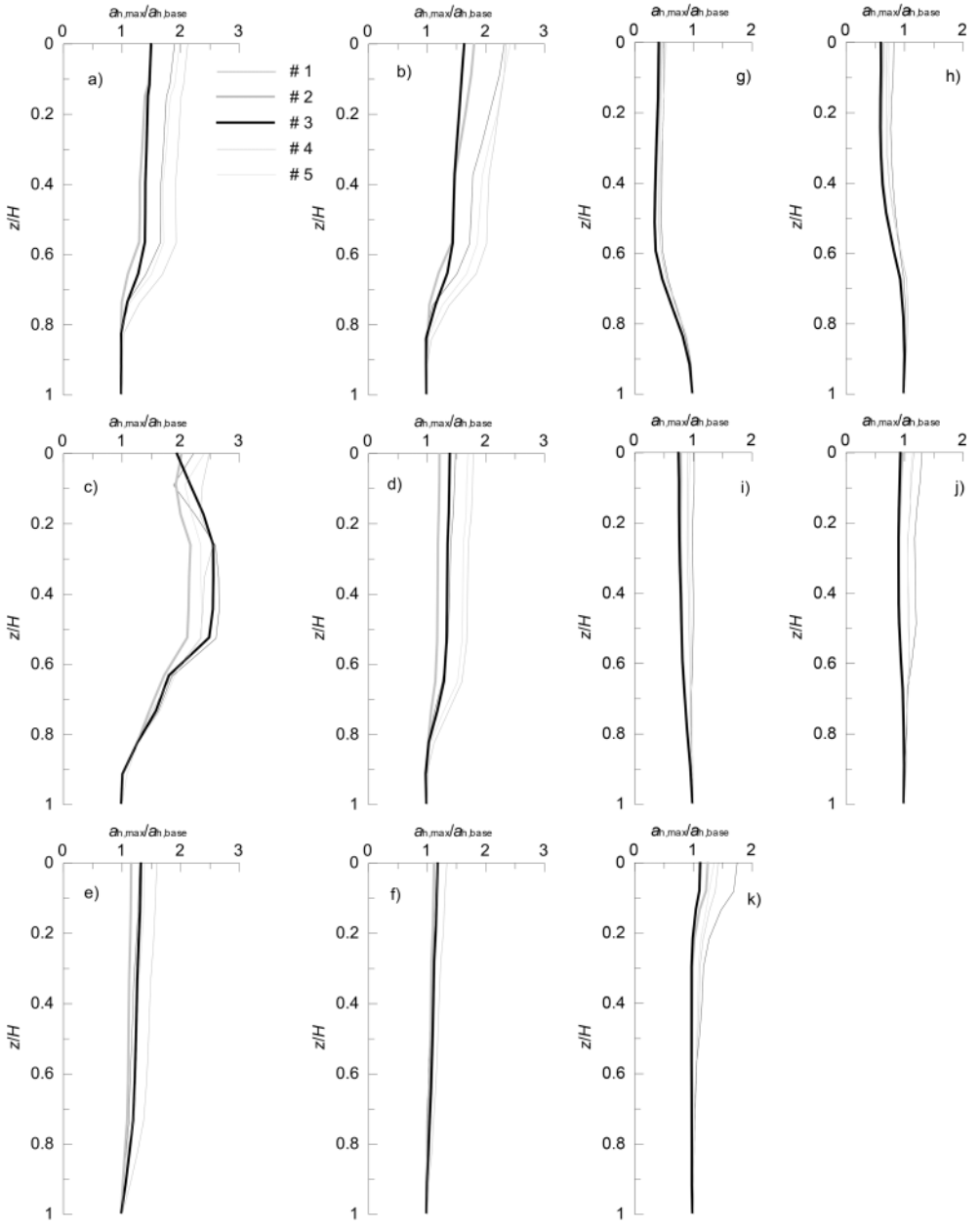

Figure 13. Profiles of normalised horizontal accelerations computed for the alignments *a–f* of section A-A (a–f) and *g–k* of section B-B (g–k).

To this purpose a geotechnical model, characterised by equivalent shear stiffness accounting for alternating full and empty volumes in the Cava, has been defined for two different cross sections of the hypogeum and several acceleration time histories have been selected consisting with the seismic hazard at the site. 2D site response analyses have been carried out for the two cross sections using the finite difference approach assuming a linear visco-elastic constitutive model for the rock materials, with Rayleigh viscous damping calibrated on the fundamental frequency of the hypogeal structure.

The analysis results are presented and discussed in terms of distribution of peak horizontal and vertical accelerations along the ground surface and profiles of the maximum horizontal accelerations along several vertical alignments. The results pointed out a relevant amplification of the horizontal accelerations and significant parasitic vertical ones in the area above the voids, where the hospital is located, due to the complex interaction between the incident and reflected seismic waves.

REFERENCES

Araya, R., Saragoni, R., 1984. Earthquake accelerogram destructiveness potential factor. In: 8th WCEE, San Francisco, 1984, 2, pp. 835–841.

Bessac, J-C. 1986. *L'outillage traditionnel du tailleur de pierre, de l'antiquité a nos jours*. Paris: Ed. du Centre national de la recherche scientifique.

Biondi, G., Cascone, E., Di Filippo, G., 2012. Reliability of empirical relationships for the evaluation of the number of equivalent loading cycles. *Rivista Italiana di Geotecnica* XLVI (2), 9–39.

Bommer, J.J., Acevedo, A.B., 2004. The use of real earthquake accelerograms as input to dynamic analysis. *J. Earthquake Engineering* 8 (1), 43–91. Special issue.

Bozzano, F. et al. (edited by). 2017. Cavità di origine antropica, modalità d'indagine, aspetti di catalogazione, analisi della pericolosità, monitoraggio e valorizzazione. *Geologia dell'Ambiente* – Supplemento al n. 4/2018: 13–32; 63–71; 95–102; 387–402;

Cundall PA, Hansteen H, Lacasse S, Selnes PB. NESSI, 1980, Soil structure interaction program for dynamic and static problems. Report: Norwegian Geotechnical Institute; 1980. p. 51508–9.

de Silva, F., & Scotto di Santolo, A. 2018. Probabilistic performance-based approaches to the static and seismic assessment of rock cavities. *Int. J. of Rock Mechanics and Mining Sciences* 112: 354–368.

Di Raimondo, S., Zocco, M. 2004. Il complesso ipogeo sottostante l'area dell'ospedale civile di Ragusa, *Ragusa Sottosopra* n.4 del 28/07/2004.

ESMD – European Strong-motion Database. https://esm.mi.ingv.it

Evangelista, L., Landolfi, L., d'Onofrio, A., Silvestri, F. 2016. The influence of the 3D morphology and cavity network on the seismic response of Castelnuovo hill to the 2009 Abruzzo earthquake. *Bulletin of Earthquake Engineering* 14: 3363–3387.

ITASCA, 2011. FLAC – Fast Lagrangian Analysis of Continua – Version 7.0. User's Guide. Itasca Consulting Group, Minneapolis, USA.

Joyner, W.B., Boore, D.M., 1981. Peak horizontal acceleration and velocity from strong motion records including records from the 1979 Imperial Valley, California, earthquake. *Bull. Seismol. Soc. Am.* 71, 2011–2038.

Luzi, L, Pacor, F, Puglia, R, 2016. Italian Accelerometric Archive v 2.1. Istituto Nazionale di Geofisica e Vulcanologia, Dipartimento della Protezione Civile Nazionale. https://doi.org/10.13127/ITACA/2.1.

NTC18, 2018. Norme Tecniche per le Costruzioni. Decreto del Ministero delle Infrastrutture e dei Trasporti, January 17, 2018. G.U. n. 42, February 20, 2018 (in Italian).

Pagliaroli, A., & Lanzo, G., 2008. Selection of real accelerograms for the seismic response analysis of the historical town of Nicastro (Southern Italy) during the March 1638 Calabria earthquake. *Engineering Structures* 30, 2211–2222.

PEER, 2016. PEER NGA Ground Motion Database, Pacific Earthquake Engineering Research Center. http://peer.berkeley.edu/nga.

Rathje, E.M., Abrahamson, N.A., Bray, J.D., 1998. Simplified frequency content estimates of earthquake ground motions. *J. Geotechnical Engineering* ASCE 124 (2), 150–159.

Scotto di Santolo, A., Evangelista, L., Silvestri, F., Cavuoto, G., Di Fiore, V., Punzo, M., Tarallo, D., Evangelista, A., Rallo, D. 2015. Investigations on the stability conditions of a tuff cavity: the Cimitero delle Fontanelle in Napoli. *Rivista Italiana di Geotecnica* 3: 28–46.

Sica, S., Dello Russo, A., Rotili, F., Simonelli, A.L. 2014. Ground motion amplification due to shallow cavities in nonlinear soils. *Natural Hazards* 71: 1913–1935.

Smerzini, C., Aviles, J., Paolucci, R., Sanchez-Sesma, F.J. 2009. Effect of underground cavities on surface ground motion under SH wave propagation. *Earthquake Engineering and Structural Dynamics* 38: 1441–1460.

Trifunac, M.D., Brady, A.G., 1975. A study of the duration of strong earthquake ground motion. *Bull. Seismol. Soc. Am.* 65, 581–626.

Geotechnical Engineering for the Preservation of Monuments and Historic Sites III – Lancellotta, Viggiani, Flora, de Silva & Mele (Eds)

Evaluation of site effects by means of 3D numerical modeling of the Palatine Hill, Roman Forum, and Coliseum archaeological area

R. Razzano, M. Moscatelli, M. Mancini & F. Stigliano
Italian National Research Council – Institute of Environmental Geology and Geoengineering

A. Pagliaroli
University of Chieti-Pescara

G. Lanzo
University La Sapienza of Rome

ABSTRACT: In this study we perform 3D nonlinear analyses of seismic site response of the Central Archaeological Area of Rome, which includes the Palatine Hill, Roman Forum, Circus Maximus, and Coliseum. The geological bedrock of the study area is constituted by a Pliocene marine sandy-clayey unit (Monte Vaticano Formation, MVA). At top of this unit a continental Quaternary succession is superimposed. Previous studies available for this area (Pagliaroli et al. 2014a; Mancini et al. 2014; Moscatelli et al. 2014) enabled to define a detailed three-dimensional reconstruction of the subsoil conditions, characterized by complex surficial and buried morphology, lateral heterogeneities and dynamic properties of involved material, natural as well as anthropogenic. The area of Rome is affected by earthquakes from different seismogenic districts: i) the central Apennine mountain chain (D = 90–130km and M = 6.7–7.0); ii) the Colli Albani volcanic district (D = 20km and M=5.5); iii) Rome area itself, which is characterized by rare, shallow, low-magnitude events (M < 5). Both natural and artificial signals have been considered to define the input motion for the numerical modeling of the site response of the whole archeological area. This was accomplished by means of the finite differences code FLAC3D. To evaluate the seismic hazard and, consequently, to assess possible priorities for seismic retrofitting of the monuments, contour maps of Housner intensity amplification ratio FH (defined as the ratio between Housner intensity at the top of the model and the corresponding input at the bedrock outcrop), are carried out. To cover the entire range of natural periods pertaining to the monuments in the examined area, FH was evaluated over three ranges of period: 0.1–0.5s, 0.5–1.0s, and 1.0–2.0s. Numerical results shown that: 1) within the range of periods 0.1–0.5s, high values of FH = 2.2–2.6 occur both in correspondence of narrow valleys filled with soft alluvial deposits and at top of Palatine Hill; 2) within the range of periods 0.5–1.0s, high values of FH occur in correspondence of the deepest valleys; 3) within the range of periods 1.0–2.0s, low values of FH occur except in correspondence of the deepest valleys.Results show a good agreement with the previous 2D numerical modeling and with the microzonation maps (Pagliaroli et al 2014a, b), even if interesting differences show up highlighting the usefulness of 3D modeling in such complex settings. Such results are significantly relevant for the monumental and archaeological heritage of this area, as it is highly vulnerable due to its old age and state of conservation.

1 INTRODUCTION

The present study reports the results of 3D numerical site response analyses for the microzonation of the archaeological areas of Palatine hill, Circus Maximus, Roman Forum and Coliseum in the historical center of Rome. The subsoil model was defined based on in situ geophysical tests and

 DOI 10.1201/9781003308867-58

laboratory tests to address the non-linear soil behavior. The numerical simulations are based on a subsoil model which integrates a large amount of information available from the Superintendence for the Archaeological Heritage of Rome as well as new data collected during a multidisciplinary survey conducted in 2010. Previous studies (Pagliaroli et al 2014a, b) has shown that ground motion is mainly controlled by 1D resonance phenomena and 2D effects. In order to investigate phenomena responsible for ground motion modification, the 3D numerical results are processed in terms of Housner amplification ratio (FH), defined as the ratio between Hounser intensity (HI) at top of model and the corresponding input outcrop. In order to cover the entire range of natural periods of structure pertaining in the study area, three period range were considered: 0.1–0.5; 0.5–1.0; and 1.0–2.0s, and shown as contour maps.

2 INTRODUCTION TO THE SEISMICITY OF ROME AND SELECTION OF INPUT MOTION

The area of Rome is characterized by a low seismicity. Historical source shown that in over two thousand years of well-documented history, only eight earthquakes exceeded the damage threshold and only on three occasions in the last 1000 years the damage was serious. A comprehensive review of the historical sources that describe the earthquakes felt in Rome was performed by Molin et al. (1995) and updated by Galli and Molin (2013).

Three different seismogenic districts were considered to evaluate representative input motion for the study area: (1) the central Apennine Mountain chain, characterized by high magnitude M up to 6.7–7.0 and located about 90–130 km east of Rome; (2) the Colli Albani volcanic area with M=5.5 located 20 km to the south of the city; and (3) the Rome area itself characterized by rare, shallow, low-magnitude events (M < 5). Sabetta (2013) used both deterministic and probabilistic approach to evaluate the representative input motion for microzonation purpose (Figure 1). For probabilistic approach the UHS (Uniform Hazard Spectrum) taken from INGV was considered, having a return period of 475 years, the UHS INGV was then used to simulate spectrum-compatible time-history acceleration. Two earthquake scenarios were selected to considered the Fucino-basin, in the Apennines, and Colli Albani seismogenic districts by using both artificial and natural accelerograms. The Sabetta & Pugliese (1996) ground motion prediction was used to calculate the response spectra of these earthquake scenarios. Artificial accelerograms were then simulated compatible with the corresponding response spectra. Moreover, natural accelerograms were selected from global databases that correspond to the magnitude, distance, and soil conditions extracted for the scenario

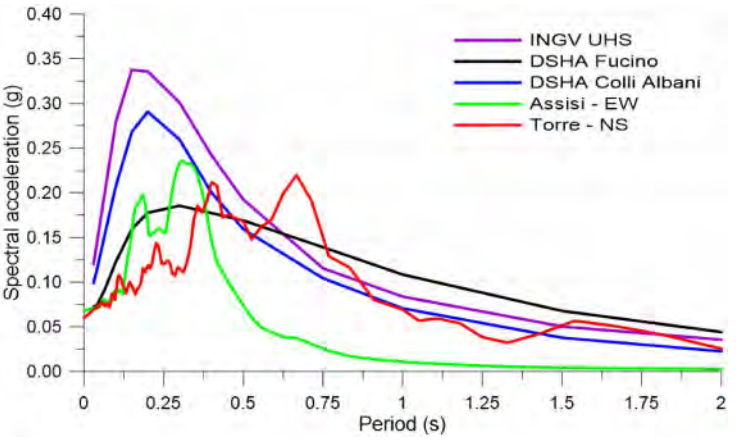

Figure 1. Reference spectra selected for the microzonation of study area.

earthquakes, including: 1) that measured at Torre del Greco during the Irpinia earthquake of 1980 for the Colli Albani scenario; and 2) that registered at Assisi during the Umbria–Marche earthquake of 1997 for the Fucino scenario.

3 GEOLOGICAL SETTING AND INTEGRATE SUBSOIL MODEL

3.1 *Morphological and geological setting*

The geological bedrock of the Palatine Hill and surrounding areas consists of a Pliocene clayey-sandy unit of marine origin, the Monte Vaticano Formation (MVA in Figure 2; Mancini et al. 2014), whose total thickness is about 900 m.

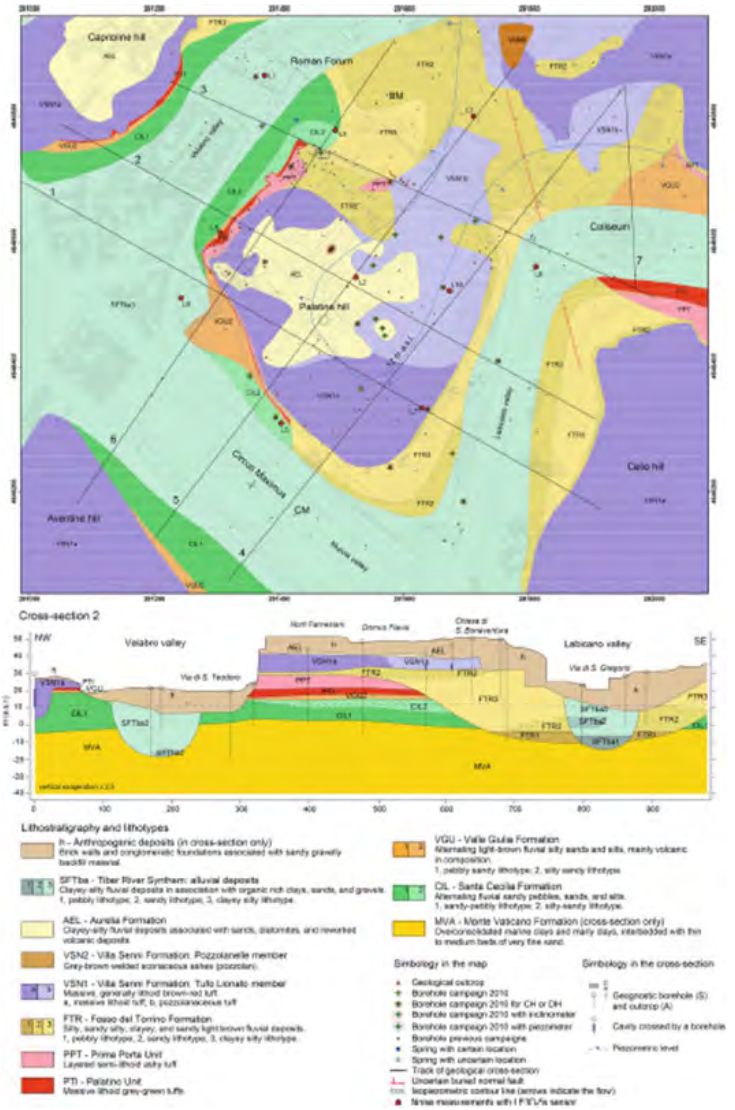

Figure 2. Geological map (above) and cross-section 2 (below) of the Palatine hill and surrounding areas (Mancini et al. 2014; Pagliaroli et al. 2014). The geological map shows the areal distribution of natural lithostrati-graphic units below the anthropogenic cover deposits (10–20 m thick), not represented on map.

The top of this unit is cut by an unconformity, over which is deposited a Quaternary complex formed by the following middle Pleistocene fluvial-palustrine and distal volcanic deposits (Figure 2), listed from oldest to youngest: (1) Santa Cecilia Formation (CIL); (2) Valle Giulia Formation (VGU); (3) Palatine Unit (PTI); (4) Prima Porta Unit (PPT); (5) Fosso del Torrino Formation (FTR); (6) Villa Senni Formation (VSN), with the Tufo Lionato (VSN1) and Pozzolanelle (VSN2) members; (7) Aurelia Formation (AEL).

These formations have a sub-horizontal multilayered distribution, except for the Fosso del Torrino Formation (FTR) that fills a fluvial paleo-valley that deeply cuts into older Quaternary units in the eastern part of the Palatine Hill (see Figure 2, cross-section 2). All these units were locally carved by minor tributaries of the Tiber River during the Late Pleistocene sea-level fall, giving rise to deep (up to 70–80m) and narrow alluvial valleys (i.e. the Velabro, Labicano, and Murcia valleys; Figure 2). These valleys were mainly filled with organic-rich clayey sediments in response to the Holocene sea level rise (SFTba3 in Figure 2). The study area is almost entirely covered by anthropogenic deposits that can locally reach 20m in thickness. All the formations recognized in the study area have been interpreted in terms of lithofacies, on the basis of their sedimentological and lithological features. The lithofacies have then been grouped into geotechnical lithotypes (see legend of Figure 2), each characterized by similar index properties (e.g., grain size distribution, void ratio, unit weight, plasticity index), determined from laboratory geotechnical tests.

3.2 *Geotechnical characterization*

A large amount of subsoil information, including geophysical and geotechnical data, is available mainly from archaeological studies, from the design of adjacent subway lines and level 3 Seismic Microzonation (SM3) study (Moscatelli et al. 2014a) carried out in the framework of a large research project sponsored by the Italian Department of Civil Protection aimed at the geological and seismic hazard evaluation in the Central Archaeological Area of Rome.

In particular, the multidisciplinary survey carried out in 2010–2011 for SM3 study included continuous-coring boreholes, in situ and laboratory (dynamic and cyclic) geotechnical tests as well as different geophysical tests (MASW, cross- and down-hole tests, electrical resistivity tomography and ground penetrating radar surveys). The reconstruction of the buried morphology below the anthropic layer as well as its composition is reported in Moscatelli et al. (2014b). A subsoil model aimed at site response analyses for the seismic microzonation of the area was then built by characterizing both the man-made and natural geological materials (Pagliaroli et al. 2014a).

The subsoil numerical model for seismic response analyses requires the characterization of each unit in terms of unit weight (γ), shear wave velocity (VS), compression wave velocity (VP) or, similarly, Poisson ratio (ν); the variation of normalized shear modulus (G/G0) and damping ratio (D) with shear strain amplitude (γc) is also required. The S-wave velocities (VS) were determined from a total of 17 Cross-Hole tests, 11 Down-Hole tests, 3 Seismic Dilatometer tests, and 20 MASW tests. In general, the results show that the geophysical parameters of each lithotype are spatially uniform over the entire study area and no significant gradient with depth has been observed (Pagliaroli et al., 2014a). Each lithotype was therefore characterized by averaging VS and VP across the different depth ranges explored. An exception is constituted by the anthropogenic layer (h), generally formed by soil of variable grain size and masonry with extremely variable weathering, showing wide spatial heterogeneity and therefore a pronounced variability of mechanical properties. Pagliaroli et al. (2014c) carried out 2D simulations by considering in the model twenty different Vs distributions in the layer h obtained from geostatistical conditional simulations considering the spatial variability of this parameter and honoring its available measurements. Profiles of stochastic amplification factors were therefore derived at the surface. In this work, to overcome a 3D complex geostatistical simulation, an average constant value of Vs computed from all measurements was considered in the anthropogenic layer.

The normalized shear modulus $G(\gamma_c)/G_0$ and the damping ratio $D(\gamma_c)$ variation with shear strain amplitude were measured from a total of 20 resonant columns, 2 cyclic torsional shear tests available and 12 cyclic simple shear tests (Pagliaroli et al. 2014a). For gravelly soils (e.g., CIL1), for which

undisturbed sampling was not possible, reference was made to literature data obtained on materials having a similar granulometric distribution (Pagliaroli et al. 2014a). The same curves were used for the anthropogenic layer (h), given the prevalence of coarse material. Where multiple laboratory determinations for the same lithotype were available, the average range of the curves was used. Note that the Aurelia Fm. (AEL), because of its small thickness, was not considered in the numerical model and its thickness was assigned to the anthropogenic unit.

3.3 *FLAC3D numerical model*

Numerical analyses have been carried out by using the finite differences code FLAC3D (ITASCA consulting group, 2019). This code operates in time domain and implement a fully non-linear procedure to describe the soils behavior. Hysteretic-Damping model (implemented in FLAC3D) and calibrated on $G(\gamma_c)/G_0$ and $D(\gamma_c)$ curves was used to take into account the soil behavior with the shear strain, associate with Masing rules to describe the un-loading re-loading conditions. Rayleigh formulation was used, to account for damping at small strains, by using two control frequencies (f_1 = 1Hz and f_2 = 10Hz). Free-field conditions (local boundaries) was applied at vertical sides of models and a quiet-base (elastic base) at bottom one to take into account the radiation damping behavior.

Nine units were considered, for numerical simulations, roughly grouping the lithotypes characterized by minor thickness and similar VS (Pagliaroli et al. 2014). SFTba3 lithotype properties were adopted for soft-filled valley unit (SFTba unit), because SFTba1 and SFTba2 are characterized by negligible thickness. Instead, for FTR paleo-valley the average value between FTR1, FTR2 and FRT3 were adopted for numerical results. The representative section with the units adopted for numerical simulations is shown in Figure 4 (cross-section #2) and in Table 1 the corresponding linear properties adopted. In Figure 3 are shown the normalized shear modulus G(γc)/G0 and damping ratio D(γc) variation with shear strain amplitude used for each lithotype, available for several laboratory test available from previous surveys in the area. It should be noted that the measured damping ratio D(γc) was not used because of Masing criteria.

The seismic bedrock is located at 500m below the ground surface, and to reduce time consuming time histories it was propagated in 1D conditions (Pagliaroli et al. 2014) and applied at the base of 3D model as outcrop motion. The identification of bedrock and the Vs profile in the MVA layer was carried out by Pagliaroli et al 2014, by integrating deep borehole and extensive noise measurements survey and 1D parametric site response analysis.

In choosing the maximum element size (hmax), the standard rule suggested by Kuhlemeyer & Lysmer (1973) was adopted to achieve a satisfactory level of solution accuracy, these authors assumed $hmax = \lambda/(6 \div 8)$, where $\lambda = VS/(fmax)$ is the half wavelength, VS = material shear wave velocity value selected accordingly to the shear strain level, fmax = maximum frequency to be

Table 1. Integrated subsoil model for site response analyses.

Lithotype (–)	Symbol (–)	γ (kN/m3)	VS (m/s)	ν (–)
Brick walls and conglomeratic	RPI_AEL	18.0	350	0.42
Clayey-silty fluvial deposit	SFTba	18.5	270	0.49
Massive lithoid tuff	VSN1a	16.0	600	0.4
Pozzolanaceus tuff	VSN1b	19.7	340	0.48
Tuff	PTI_PPT	16.0	650	0.39
Silty, sandy silty	FTR	20.1	510	0.465
Silty sand	CIL1_2	20.1	480	0.435
Sandy pebbly	CIL1	20.5	620	0.39
OC marine clay	MVA	20.5	550	0.48

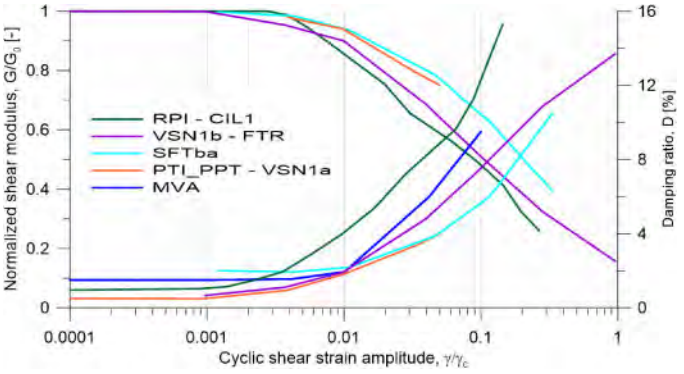

Figure 3. Non-linear behavior of soils and soft rocks: G(γc)/G0 and D(γc) curves selected for each lithotype and assumed in the integrated subsoil model.

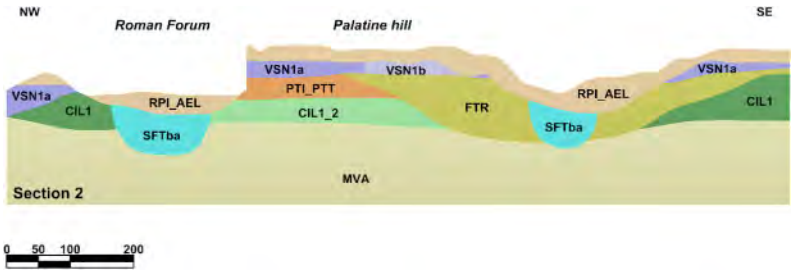

Figure 4. Cross section 2 that illustrate the units adopted for numerical results.

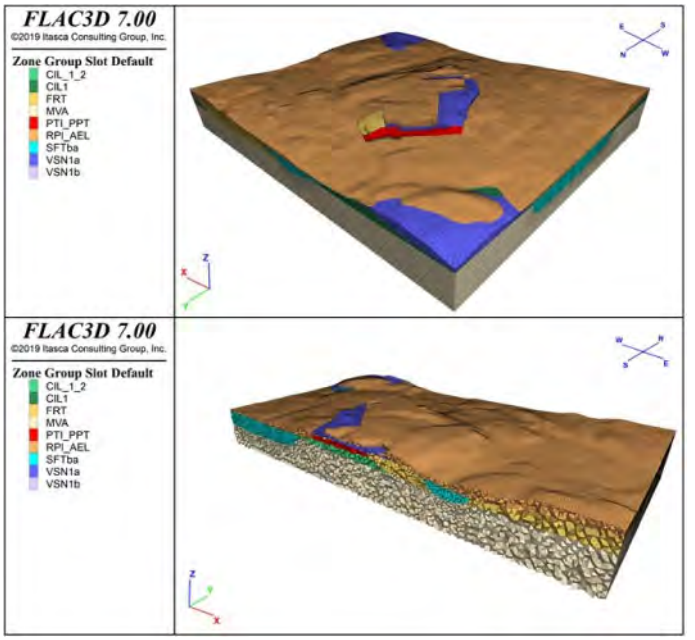

Figure 5. FLAC3D numerical grid used for numerical results.

transmitted (assumed equal to 10Hz). The 3D finite differences grid consists of about 1 million of tetrahedral shape elements (4).

4 NUMERICAL ANALISES FOR MICROZONATION PURPOSES

To evaluate seismic amplifications in the study area, for microzonation purposes, three-dimensional numerical results were processed in terms of Housner Intensity (HI) over the period ranges T1–T2. In order to cover the entire range of natural vibration of the structure pertaining in the study area three different period ranges were considered: 1) 0.1–0.5s; 2) 0.5–1.0s; and 3) 1.0–2.0s.

To combine the Housner Intensity for EW and NS components Equation 1 was used:

$$H1_{T1-T2} = \sqrt{H1_{T1-T2}EW^2 + H1_{T1-T2}\mathrm{NS}^2} \quad (1)$$

where HI_{T1-T2}EW and HI_{T1-T2}NS representing the Housner intensity for EW and NS components, respectively. The corresponding amplification factor FH_{T1-T2}, defined as the ratio between HI at ground surface and the corresponding input outcrop, were then calculated and showed as amplification maps (microzonation maps).

The first mode period of few-story masonry buildings, small-to-medium size monuments (like free-standing columns, walls, arches) generally falls in the 0.1–0.5s range (see Marzi et al. 1990 among others). Large monuments pertaining in the study area, such as Coliseum, are characterized by first mode period comprised in 0.5–1.0 s range (Pau & Vestroni 2008, 2013). It should be noted that the first two ranges T1 =0.1s and T2 =1.0s (f = 1–10Hz) containing the natural frequencies vibration of the most of structures pertaining in the study area. The results are discussed below to illustrate major findings of the morphological, geological and mechanical characteristics of the whole area.

In Figure 6 is shown the contour map of $FH_{0.1-0.5}$ amplification factor, obtained by assuming T1-T2 = 0.1–0.5s (frequencies range 2–10Hz), that exhibit strong variations in the study area. The highest values of $FH_{0.1-.5}$ (up to 2.2–2.6) occur in correspondence of Velabro valley, located in North-West part of model, where the incised soft-filled valley (SFTba unit with VS = 270m/s) become narrow (see cross-section 3 in Figure 7). This is related to the resonance frequencies of valley, in this area, which is around 2.5–3.0Hz computed according to the formula proposed by Bard & Bouchon (1985).

$FH_{0.1-0.5}$ fluctuate between 1.6, passing from the confluence of Murcia and Labicano valleys (located in south part of model) filled by soft-filled valley (SFTba) like Velabro valley, to 2.4 in correspondence of Coliseum area. Instead, moderate values in Murcia valley up to 1.4–1.6 (Circus maximus area), because the soft SFTba unit become more deepest (see cross-section 6 in 5).

At top of Palatine hill $FH_{0.1-0.5}$ exhibit strong fluctuations, probably due at the complex surficial and buried morphologies, e.g. the multilayered deposit and FTR paleo-valley. The greater amplifications are located in Horti Farnesiani probably for the 1D resonance of the soft anthropogenic layer overlying the stiffer VSN1a lithoid tuff and near Vigna Barberini, at the edge of the FTR paleo-valley, with VS = 510m/s (Figure 6).

Instead, $FH_{0.1-0.5}$ decrease up to 1.0–1.2 where FTR deepens (Via dei Fori Imperiali). The lower amplifications at hill toe ($FH_{0.1-0.5} = 1.0–1.2$) can be ascribed to deamplification for topographic effects, as observed by Pagliaroli et al. 2014b.

Amplification factors $FH_{0.5-1.0}$ and $FH_{1.0-2.0}$ (that corresponding at frequencies range 1–2 Hz and 0.5–1 Hz, respectively) exhibit similar trends but different values, the corresponding amplification maps are shown in Figures 8 and 9, respectively. The effects of the incised soft-filled valley (SFTba unit) is evident. Indeed, $FH_{0.5-1.0}$ up to 2.2–2.4 and $FH_{1.0-2.0}$ up to 1.8–2.0 occur at the confluence between the Murcia and the Tiber Valleys (located outside the figures to the west), that represent the zones where the soft-filled valley are deeper (about 40m), in the examined area (see cross-sections 1 and 6 in 5).

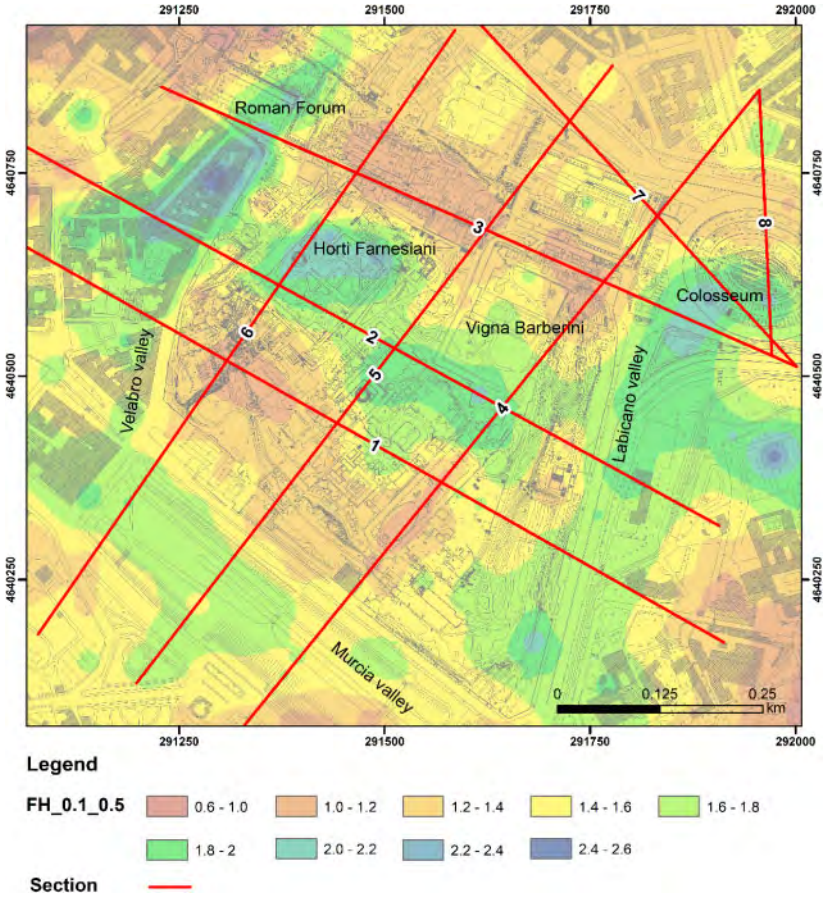

Figure 6. Contours map of amplification factor FH0.1–0.5, red lines representing the cross-sections.

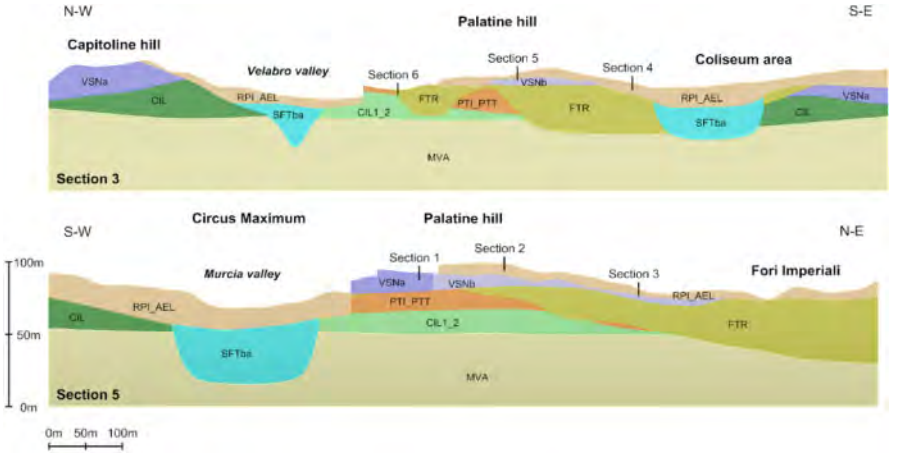

Figure 7. Cross-section 3 (above) and 5 (below), vertical exaggeration 2.

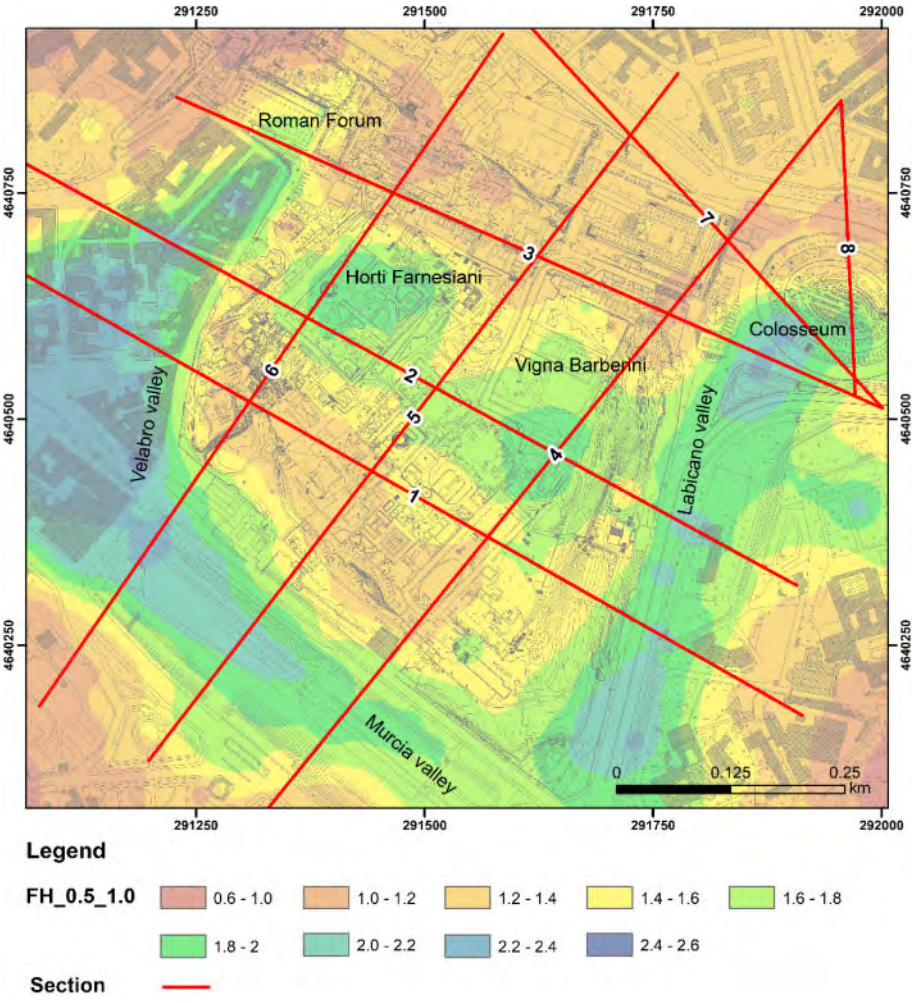

Figure 8. Contours map of amplification factor FH0.5–1.0 (obtained by assuming T1=0.5s and T2=1.0s), red lines representing the cross-sections.

In the SFTba unit, bordering the Palatine hill, $FH_{0.5-1.0}$ exhibits great amplifications up to 1.8–2.0 in Murcia and Labicano valleys, and up to 2.0–2.2 in the Coliseum area. Instead, $FH_{1.0-2.0}$ amplifications decreases up to 1.4–1.6.

At top of Palatine hill both $FH_{0.5-1.0}$ and $FH_{1.0-2.0}$ amplification factors exhibit moderate values, except at Horti Farnesiani and Vigna Barberini ($FH_{0.5-1.0}$ around 1.8–2 and $FH_{1.0-2.0}$ about 1.6–1.8).

Generally, for the three period ranges considered in this study, the soft-filled valleys bordering the Palatine hill (SFTba unit) exhibit the highest values of FH_{T1-T2} by varying the period range considered, because the valley is characterized by variable thickness and width (see Figures 7 and 5). The three amplification factors ($FH_{0.1-0.5}$, $FH_{0.5-1.0}$, $FH_{1.0-2.0}$) show quite different trends from both a qualitative and quantitative point of view, highlighting the "filter effect" that the soft rock and soil deposits exert on seismic motion (as a function of their mechanical and morphological features).

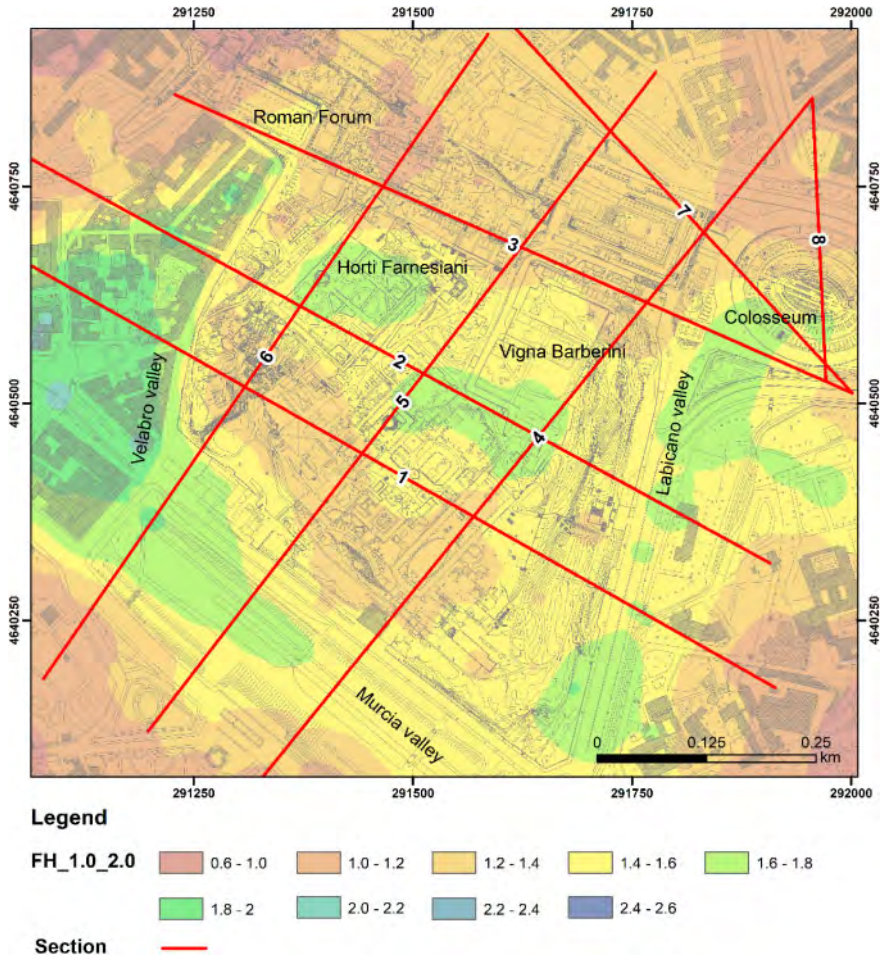

Figure 9. Contours map of amplification factor FH1.0-2.0 (obtained by assuming T1=1.0sand T2=2.0s), red lines representing the cross-sections.

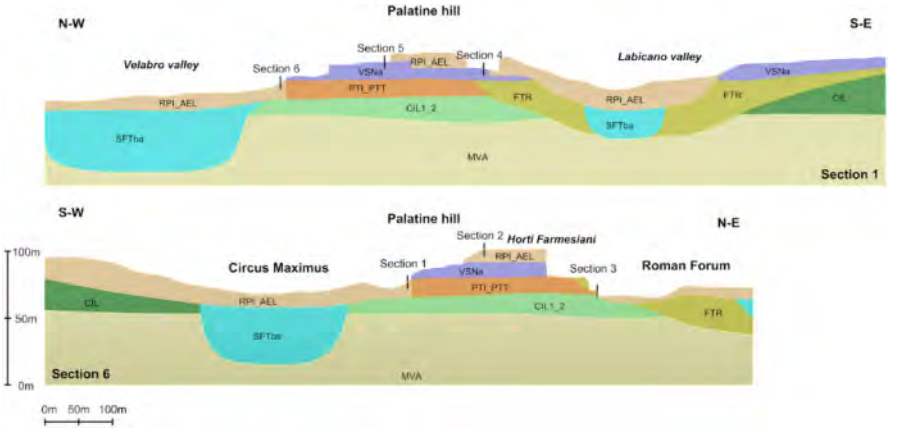

Figure 10. Cross-sections 1 (above) and 6 (below), vertical exaggeration 2.

5 CONCLUSIONS

The Rome area is characterized by low local seismicity, however the Apennine faults, characterized by high magnitude and distances, can produce strong effects in highly vulnerable structures due at phenomena of local amplification of the seismic motion. These latter are due to the complex local conditions: stratigraphic and morphological-topographic. This study presents local seismic response of the Central Archaeological Area of Rome based on a three-dimensional numerical model. Numerical results are carried out by using the finite differences code FLAC3D. A considerable number of investigations on site and in the laboratory are used to define the subsoil model. Numerical results are processed in terms of Housner Intensity over three period ranges T1-T2. In order to cover the entire range of natural periods of structures pertaining in the study area three period ranges were considered: 1) 0.1–0.5; 2) 0.5–1.0; 1.0–2.0s. The corresponding amplification factor FHT1-T2, defined as the ratio between HI at ground surface and the corresponding input outcrop, were then calculated and showed as contours maps (amplification maps).

At period range T1-T2 = 0.1–0.5s (frequencies range 2–10Hz) amplification factor FH0.1-0.5 exhibit strong fluctuation in the study area, values up to 2.4 are located in the zones where the soft-filled valley (SFTba unit), bordering the Palatine hill, become narrow (Roman forum) and at top of Palatine hill (Horti Farnesiani and Vigna Barberini) probably due to the complex stratigraphic and topographic setting.

Instead, period ranges T1-T2 = 0.5–1.0s and 1.0–2.0s (that corresponding at frequencies range 0.5–2.0Hz) the amplification factor $FH_{0.5-1.0}$ and $FH_{1.0-2.0}$ exhibit similar trend. The greater amplifications, up to 2.4–2.6, are located in the zone where the soft-filled valley (SFTba unit) deepens (Labicano and Velabro valley).

Pagliaroli et al. (2014a and b) carried out the same amplification maps (with the same period ranges and time histories) numerical results were obtained by interpolating the 2D equivalent-linear simulations, performed by using the finite difference code QUAD4M, on seven cross-sections.

2D maps exhibit minor amplification and fluctuations as compared as 3D ones: i) $FH_{0.1-0.5}$ and $FH_{0.5-1.0}$ maps shown amplification up to 1.8 for 2D conditions and 2.6 for 3D ones; ii) $FH_{1.0-2.0}$ maps are essentially flat in 2D conditions with maximum amplifications up to 1.3 in correspondence of Vigna Barberini, instead 3D ones exhibit amplifications about twice located in the soft-filled valley, Vigna Barberini and Horti Farnesiani. The comparisons between 3D and 2D highlighted the role of 3D effects on seismic response, of study area, due at complex buried and surficial morphologies.

Even if the amplification factor exceeds 2.6 only in limited areas (soft-filled valley unit), the importance of these changes in ground motion can be significant for the highly vulnerable monumental and archaeological heritage within the study area.

REFERENCES

Bard P.Y. & Bouchon M. 1985. The two-dimensional resonance of sediment-filled valleys. Bull Seismol Soc Am 75:519–541

Itasca Consulting Group, Inc. (2019) FLAC3D — Fast Lagrangian Analysis of Continua in Three-Dimensions, Ver. 7.0. Minneapolis: Itasca.

Kuhlemeyer, R. L. & Lysmer. J. 1973. Finite Element Method Accuracy for Wave Propagation Problems. Journal of the Soil Dynamics Division, 99, 421–427.

Mancini M. et al. 2014. A physical stratigraphy model for seismic microzonation of the Central Archaeological Area of Rome (Italy). Bulletin of Earthquake Engineering, 12, 1339–1363.

Marzi C. et al. 1990. Seismic preservation of historical monuments in Rome: preliminary results from ambient vibration tests. In: Marinos, Koukis (eds) Engineering geology of ancient works, monuments and historical sites, pp 2133–2134

Moscatelli M. et al 2014a. Seismic microzonation of Palatine hill, Roman Forum and Coliseum Archeological Area. Bulletin of Earthquake Engineering 12, 1269–1275.

Moscatelli M. et al. 2014b. Integrated geological and geophysical investigations to characterized the anthropic layer of Palatine hill and Roman Forum. Bulletin of Earthquake Engineering 12, 1319–1338.
Pagliaroli A. et al. 2014a. Dynamic characterization of soils and soft rocks of the Central Archaeological Area of Rome. Bulletin of Earthquake Engineering, 12, 1365–1381.
Pagliaroli A. et al. 2014b. Numerical modelling of site effects in the Palatine hill, Roman Forum and Coliseum archaeological area. Bulletin of Earthquake Engineering, 12, 1383–1403.
Pagliaroli A. et al. 2014c. Seismic microzonation of the Central Archeological Area of Rome: results and uncertainties. Bulletin of Earthquake Engineering, 12, 1405–1428.
Pau A. & Vestroni F. 2008. Vibration analysis and dynamic characterization of the Colosseum. Struct Control Health Monit 15:1105–1121.
Pau A & Vestroni F. 2013. Vibration assessment and structural monitoring of the Basilica of Maxentius in Rome. Mech Syst Signal Process.

Geotechnical Engineering for the Preservation of Monuments and Historic Sites III – Lancellotta, Viggiani, Flora, de Silva & Mele (Eds)

Influence of soil deposit heterogeneity on the dynamic behaviour of masonry towers

A.F. D'Oria, G. Elia, A. di Lernia & G. Uva
Department of Civil, Environmental, Land, Building Engineering and Chemistry (DICATECh), Technical University of Bari, Bari, Italy

ABSTRACT: The paper deals with the direct soil-structure interaction numerical modelling of an ideal masonry tower resting on deformable heterogeneous soil deposits. The stratigraphic heterogeneity is modelled dividing each deposit into several layers to implement four different shear wave velocity profiles. The resulting deposits can be classified as class C according to the Italian seismic building code prescriptions. Complete three-dimensional finite element dynamic analyses are carried out assuming a visco-elastic behaviour for both the tower and the soil, with the aim to investigate the effects of the soil heterogeneity on the dynamic response of the structure in the elastic field. Practical relationships are derived from the results to predict the deviation of the tower dynamic behaviour from a fixed-base condition.

1 INTRODUCTION

The response of a structure during a seismic event is the result of the mutual interaction between the structure itself, the supporting foundation and the surrounding soil, which is usually known as dynamic soil-structure interaction (SSI). Commonly, two methods are adopted to study the SSI problem: i) the substructure approach, which consists in decoupling the full system into the three constitutive parts to be separately analysed and ii) the direct approach, which consists in a single fully coupled analysis of the whole soil-structure system. The direct approach, especially if combined with a three-dimensional numerical model, should generally ensure more accurate and reliable solutions as the complexity of the problem increases (Amorosi et al. 2017; Casciati & Borja 2004; di Lernia et al. 2019; Torabi & Rayhani 2014).

Historical structures are typically characterized by a huge level of complexity in terms of geometry, materials properties, loads and boundary conditions which need to be modelled in order to correctly represent the reality. In this context, masonry towers, in the form of medieval defense structures as well as bell towers in churches, represent an important part of the historical and architectural heritage to be preserved. These structures are particularly sensitive to damage and prone to partial or even total collapse under seismic actions due to their material characteristics and geometric configurations. Several studies have been recently carried out to assess the performance of masonry towers investigating, with various approaches, the effects of the critical aspects controlling their dynamic response, such as the geometric irregularities, inclination, material properties and input motion characteristics.

However, very often the structure is assumed to be perfectly fixed at the base (Bartoli et al. 2016; Castellazzi et al. 2018; Clementi et al. 2019; Milani 2019; Sarhosis 2018; Valente & Milani 2016, 2018), thus neglecting the effect of the soil deformability which can considerably modify its structural dynamic behaviour. Indeed, the few studies available in the literature accounting for this effect (Casolo & Uva 2013; de Silva et al. 2018a, b; de Silva 2020; Casolo et al. 2017; Mortezaei & Motaghi 2016) indicate that the soil compliance can cause i) the elongation of the natural periods of the masonry structure and ii) a deviation from the cantilever modal shape especially from the

 DOI 10.1201/9781003308867-59

second vibration mode onwards, which can cause relevant alterations in the loading distribution along the tower. Nevertheless, a homogeneous deposit is usually modelled at the base of the tower, thus rarely considering a realistic stratigraphic soil profile, with the exception of very few cases (e.g. de Silva et al. 2018a, b).

This study focuses on investigating the dynamic response of an ideal masonry tower resting on different heterogeneous soil deposits by means of direct SSI analyses performed assuming a visco-elastic behaviour for both the structure and the soil, starting from the work by Casolo et al. (2017) in which two homogeneous soil deposits were considered. The geometrical and mechanical properties of the ideal tower and the soil profiles are firstly described in Section 2. Then, a preliminary validation analysis of the wave propagation process through the soil deposits in free-field conditions is presented in Section 3. Finally, the impact of the soil heterogeneity on the tower seismic response is investigated by conducting 3D SSI dynamic simulations, highlighting its deviation from the typical cantilever condition.

2 CASE STUDIES AND MODELS ADOPTED

Four ideal soil deposits have been selected to be representative of real possible stratigraphies along the Italian territory. The upper and the lower bound V_S profiles with depth used by Falcone et al. (2021) to describe the typical lithological successions of clay and sand cover soils in Italy have been considered as the reference range within which the four V_S profiles have been build up. Each deposit is 30m deep and is divided in 5m thick layers, with the exception of the top two strata which have a thickness of 2.5m. The four profiles, shown in Figure 1, share the same value of the equivalent shear wave velocity ($V_{S,eq}$), equal to 250m/s, so that they can be classified as class C deposits ($180<V_{S,eq}<360$m/s) according to the Italian Code NTC 2018 (Consiglio dei Ministri 2018). The $V_{S,eq}$ is defined by:

$$V_{S,eq} = \frac{H}{\sum_{i=1}^{N} \frac{h_i}{V_{S,i}}} \tag{1}$$

where N is the number of the layers, h_i is the thickness of the i-th layer, $V_{S,i}$ is the shear wave velocity in the i-th layer, while H is the deposit depth.

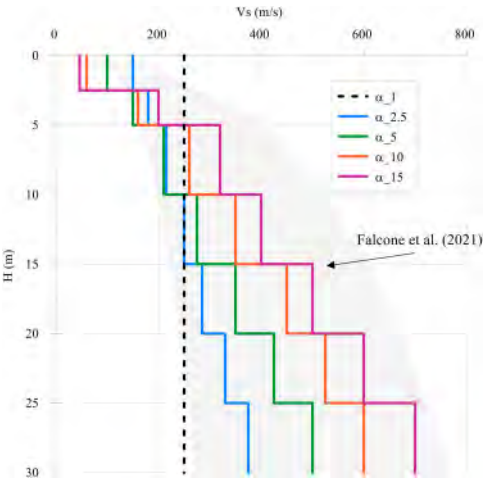

Figure 1. Soil profiles selected within the range defined by Falcone et al. (2021).

The soil profiles are characterized by different values of V_S at the top (V_0) and at the bottom (V_H) of the deposit, resulting in four ratios $\alpha=V_H/V_0$ equal to 2.5, 5, 10 and 15, with the aim to cover a wide range of heterogeneity cases with respect to the homogeneous condition (i.e. $\alpha=1$).

Following the work by Casolo et al. (2017), the investigated masonry tower represents an ideal case study, covering the main features of many recurring bell towers located in the seismic areas of Northern Italy. Its dimensions and mechanical properties were chosen by analysing a series of representative examples available in the literature and are summarized in Table 1.

Table 1. Geometrical features and mechanical properties of the tower.

Height (m)	Section (m)	Foundation (m)	ρ (kg/m^3)	E (MPa)	ν (–)
27	5.3 × 5.3	6.8 × 6.8 × 2.5	1900	3500	0.1

The tower is supposed to be structurally independent from other buildings and is characterized by a quite simplified and regular geometric configuration both in plan and in elevation (Figure 2a). The structure is 27m high, has a section of 5.3 × 5.3m^2 and a larger square foundation (6.8 × 6.8m^2) with a thickness of 2.5m.

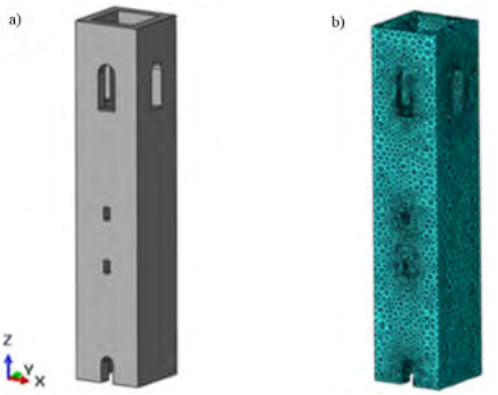

Figure 2. a) 3D masonry tower and b) FEM model (modified after Casolo et al. 2017).

The masonry tower has been modelled in 3D using the 4-node linear tetrahedral elements (C3D4) available in the finite element (FE) software ABAQUS (2014). The mesh, shown in Figure 2b, consists of 15471 nodes and it has been refined around the openings and near the foundations to achieve a high numerical accuracy. A linear-elastic constitutive law has been adopted in the simulations, using the properties reported in Table 1.

With the aim of validating the 3D numerical approach in simulating the free field seismic ground response, results obtained by 3D numerical scheme have been compared to those achieved through the 2D scheme. The 2D model has been discretized using 4-node bilinear plane-strain elements with reduced integration (CPE4R) (Figure 3a), while C3D4 elements have been adopted for the 3D discretization (Figure 3b). In both cases, the coarseness of the FE mesh has been refined in order to obtain a distance between two consecutive nodes smaller than approximately one-eighth of the wavelength associated with the maximum frequency content of the input motion (Bathe 1996; Kuhlemeyer & Lysmer 1973), equal to 15Hz. Tied-nodes boundary conditions have been reproduced on the vertical sides of the soil models to allow for a one-dimensional wave propagation: the nodes at the same depth along the lateral boundaries have been constrained to move horizontally by the same quantity, while their vertical displacements have been forbidden. The nodes at bottom

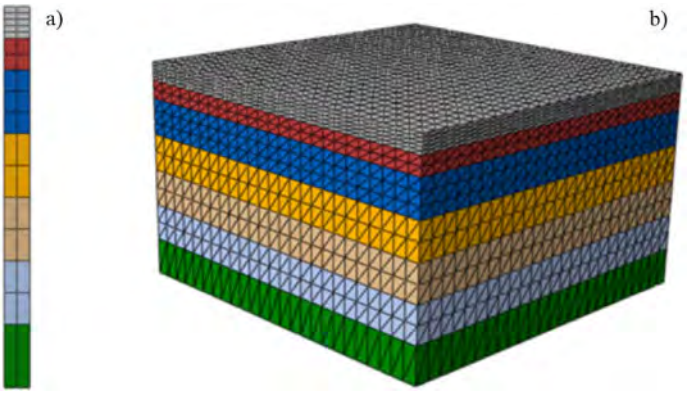

Figure 3. a) 2D and b) 3D FE models of the heterogeneous soil deposits.

have been fixed to simulate a rigid bedrock, while the presence of water in the deposit has been neglected.

The employed 2D models are characterized by a width equal to 2m, while the 3D models, which should accommodate the tower on the top, have a wider extension along the two horizontal directions (i.e. 50m), as indicated by a preliminary sensitive analysis. To introduce the stratigraphic heterogeneity, the Young modulus corresponding to the V_S values described in Figure 1 has been assigned to each soil layer, assuming a Poisson's coefficient equal to 0.2 and a material density of 1800kg/m^3. The dissipative capacity of the soil has been introduced by the frequency-dependent viscous damping Rayleigh formulation (Clough & Penzien 1993), in which the damping matrix [C] is a linear combination of the mass [M] and stiffness [K] matrices of the system:

$$[C] = \alpha_R[M] + \beta_R[K] \tag{2}$$

The Rayleigh coefficients α_R and β_R are derived as a function of the target damping ratio D according to Eq. 3:

$$\begin{Bmatrix} \alpha_R \\ \beta_R \end{Bmatrix} = \frac{2D}{\omega_m + \omega_n} \begin{Bmatrix} \omega_m & \omega_n \\ 1 & \end{Bmatrix} \tag{3}$$

The angular frequencies ω_m and ω_n are related to the frequencies f_m and f_n, defining the interval over which the viscous damping is equal to or lower than the target damping ratio D, assumed herein equal to 5% for each soil layer. The selection of the two frequencies requires a suitable calibration strategy, as proposed, for example, by Amorosi et al. (2010). In this particular case, the two Rayleigh frequencies have been set equal to the first and second natural frequencies of the soil deposit. Indeed, preliminary modal eigenvalue analyses of the soil-structure interaction problem indicated that the dynamic behaviour of the tower is particularly influenced by the second natural mode of the soil deposit, which confirm the results presented by Casolo et al. (2017). In addition, a 5% Rayleigh damping has also been added to the linear-elastic model describing the masonry behaviour, calibrated considering the first and second vibration mode of the structure. Therefore, the tower and the soil deposit have been considered as visco-elastic materials, neglecting the nonlinear effects induced by the seismic action during the FE simulations.

The dynamic analyses have been conducted in ABAQUS using the unconditionally stable implicit Hilber-Hughes-Taylor time integration scheme, i.e. an extension of the Newmark β-method, which ensures the stability of the algorithm without introducing any additional numerical damping. The reference input motion employed in the numerical simulations is represented by the north-south component recorded by the station MIR02, located in Mirandola (MO), during the 2012 Emilia-Romagna main earthquake event. Its time history and Fourier spectrum are shown in Figure 4. The

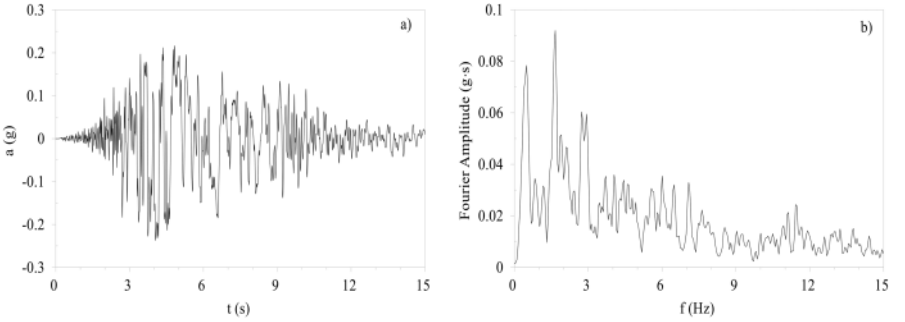

Figure 4. Mirandola earthquake: a) acceleration time history and b) Fourier spectrum.

seismic signal is characterized by a maximum acceleration of 0.22g, a time step equal to 0.005s, while its total length has been reduced to just 15s.

3 RESULTS

A first set of dynamic simulations conducted with ABAQUS in 2D and 3D are first presented to validate the results of the free-field wave propagation process in heterogeneous soil deposits against the corresponding 1D output obtained through a linear visco-elastic approach performed with the equivalent-linear visco-elastic code EERA (Bardet et al. 2000). This allows to check the reliability of the ABAQUS results from a geotechnical point of view. Then, the dynamic SSI analyses of the ideal masonry tower resting on the four heterogeneous deposits are presented and commented.

3.1 *EERA analyses*

The four V_S soil profiles described in Section 2 have been implemented in EERA, assuming a rigid bedrock and a constant damping ratio equal to 5% along the column depth. The soil has been considered as a linear visco-elastic material. In addition to the heterogeneous cases, a homogeneous profile (i.e. $\alpha = 1$) has been investigated too. This has allowed to quantify the effect of the heterogeneity on the fundamental frequencies of the soil deposits and to compare the EERA results with the analytical solutions provided by Gazetas (1982).

Figure 5 shows the amplification functions obtained with EERA for the heterogeneous and homogeneous cases. The first two natural frequencies of the soil deposits are summarized in Table 2. Consistent with the literature (Gazetas 1982), two main phenomena can be recognized: with respect to the homogeneous case, the first natural frequency clearly shifts towards higher values as the parameter α increases, while the higher frequencies tend to reduce with increasing heterogeneity. The second frequency is higher than the one characterizing the homogeneous deposit only for α

Table 2. Natural frequencies of the soil profiles.

Soil profile	f_1 (Hz)	f_2 (Hz)
α_1	2.08	6.25
$\alpha\_2.5$	2.51	6.49
α_5	2.90	6.65
α_10	3.44	6.18
α_15	3.63	5.73

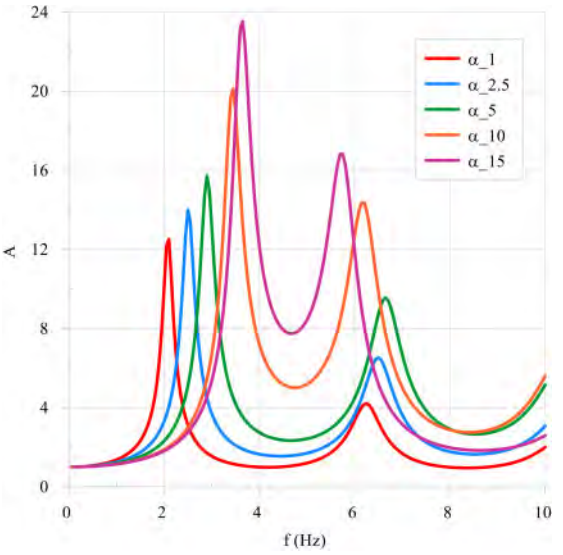

Figure 5. EERA amplification functions.

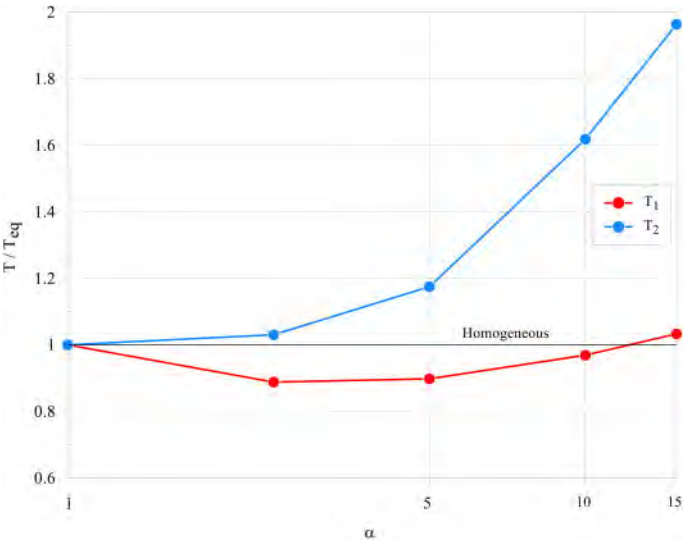

Figure 6. Normalized first and second soil natural periods as function of the heterogeneity parameter α.

equal to 2.5 and 5, but then reduces considerably for higher values of heterogeneity ratios. Secondly, the heterogeneity implies an evident amplification of all the natural frequencies, which can reach two or three times that observed for the homogeneous case. This can be attributed to the lower shear wave velocity adopted for the shallower soil layers as α increases.

Figure 6 presents the results of the EERA visco-elastic simulations in terms of first and second natural periods (T) of the heterogeneous deposits normalized by the "equivalent" homogeneous ones (T_{eq}). It should be noted that, according to Gazetas (1982), the equivalent homogeneous medium has been defined, for each of the four cases, as the one having the same shear wave velocity of the heterogeneous profile in the middle of the deposit. With this in mind, the figure shows that T_1 is lower than the first natural period of the equivalent homogeneous deposit, reaching

a minimum for $\alpha = 2.5$, and then becomes bigger for $\alpha = 15$. On the contrary, T_2 is always bigger than T_{eq} and seems to monotonically increase with the heterogeneity ratio.

3.2 *2D and 3D free-field analyses*

Having investigated with EERA the impact of the soil heterogeneity on the fundamental periods of the deposit under free-field conditions, the same problem has been replicated with ABAQUS using the previously described 2D and 3D models. The comparison between the EERA and the FE results is presented in Figure 7 in terms of amplification functions for the case of $\alpha = 2.5$. A very good agreement in the frequency range of interest (i.e. up to 10Hz) between both the 2D and 3D ABAQUS output and EERA can be recognized: the FE schemes catch very well the natural frequencies of the soil deposit and the peaks of the amplification function obtained through the visco-elastic approach, thus demonstrating the effectiveness of the Rayleigh damping calibration and the boundary conditions adopted in the FE simulations. Similar considerations can be drawn for the other deposits characterized by different heterogeneity ratios, not shown herein for the sake of brevity.

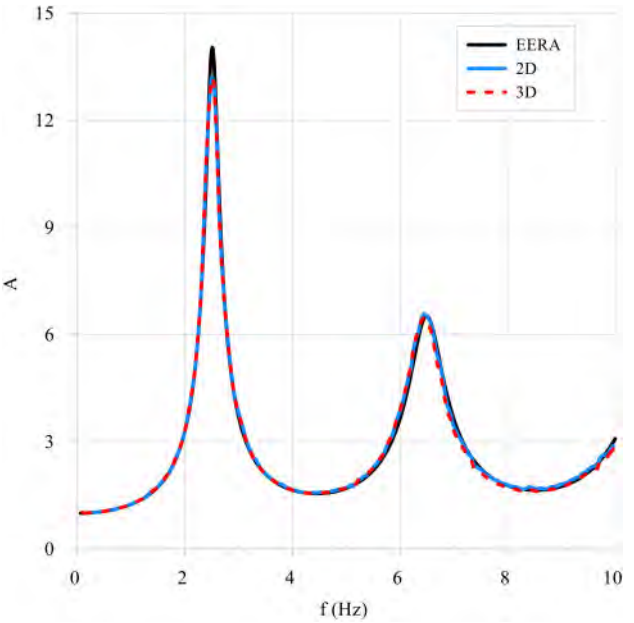

Figure 7. Comparison between EERA and ABAQUS amplification functions for $\alpha = 2.5$.

3.3 *3D soil-structure interaction analyses*

The tower, its foundation and the subsoil have been assembled in ABAQUS within a single 3D model (Figure 8a). The interface between the foundation and the visco-elastic deposit has been modeled by adopting a master-slave relationship: a penalty type interaction law has been defined for the tangential behaviour, while a hard contact type law has been imposed for the behaviour in the normal direction to prevent the interpenetration between the contact surfaces. A control point has been chosen on the top of the tower (point A), while other two points have been selected at foundation level (point B) and at the soil surface far enough from the structure (point C), representative of the free-field response, as shown in the cross section of the 3D model presented in Figure 8b.

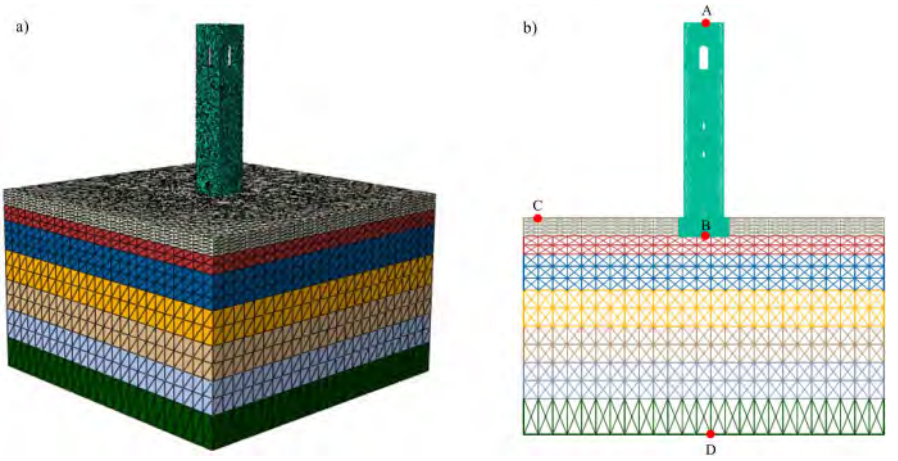

Figure 8. a) 3D SSI model and b) location of the control points.

In addition to the 3D models of the tower resting on class C deposits (with α equal to 1, 2.5, 5, 10 and 15), a further analysis has been performed with ABAQUS considering the structure standing on a very rigid homogeneous subsoil (assuming V_S=8000 m/s) to simulate the fixed-base condition. From this last simulation, the amplification function between point A and point C has allowed to identify the first two fundamental frequencies of the fixed-base tower, respectively equal to 1.81 and 8.25Hz, which are in agreement with a preliminary modal eigenvalue analysis.

The effects of SSI on the fundamental frequency and damping ratio of the system for different α values are shown in Figure 9, depicting the amplification functions between the tower motion recorded at the top (point A in Figure 8b) and the input motion applied at bedrock (point D in

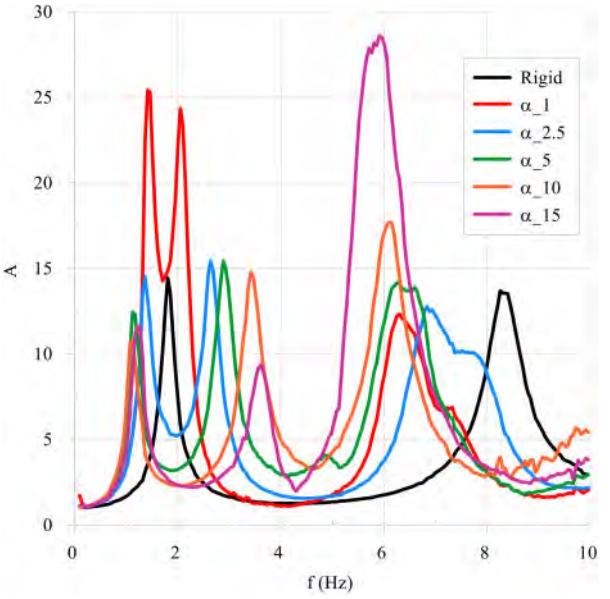

Figure 9. Amplification function of the full soil-structure system for different heterogeneity ratio α.

Figure 8b). The amplification function is used to identify the natural frequency of the soil-tower system, while its amplitude at the natural frequencies provides a measure of the damping ratio associated to the soil-tower system. It should be firstly noted that no relevant kinematic effects are expected in the case of a structure with a shallow foundation (Day 1978; Elsabee et al. 1977; Kim & Stewart 2003). Therefore, any deviation from a cantilever response of the tower can be essentially attributed to the inertial interaction between the structure and the soil deposit.

In Figure 9, each curve presents three distinct peaks which refer to the first three natural frequencies of the soil-structure system. The comparison with the rigid soil case, representing the fixed-base tower, helps to recognize the relative contribution given by the structure and the soil to the dynamic response of the full 3D model.

The first mode of vibration can be mainly attributed to the first flexural mode of the tower along the × direction, while the soil strongly affects the second and third mode since the natural frequencies of the system are practically coincident with the first and second natural mode of the deposit in free-field conditions.

The amplification functions between the tower motion recorded at the top (point A in Figure 8b) and the free-field response (point C in Figure 8b) give evidence to the typical effects of dynamic soil-structure interaction, as illustrated in Figure 10. Looking at the first (Figure 10a) and second (Figure 10b) mode of the tower, the primary effect of soil heterogeneity is to reduce the dynamic stiffness and increase the damping ratio of the soil-tower system, leading to smaller natural frequencies and lower magnitudes of the motion with respect to the cantilever condition. This effect is more pronounced for the higher soil heterogeneity ratios. In addition, much smaller values of the amplification factors are obtained when the second natural mode is inspected.

The reliability of the numerical approach has also been checked with reference to the analytical solution for single degree of freedom systems (SDOF) proposed by Veletsos & Nair (1975), looking at the first natural frequency in the homogeneous soil deposit case ($\alpha = 1$). The comparison has been carried out considering an equivalent SDOF oscillator characterized by a height (h) equal to the distance from the base to the centroid of mass of the structure (Veletsos & Nair 1975) and a concentrated mass equal to the whole mass of the tower. The foundation embedment effect has been estimated using the foundation impedance functions proposed by Gazetas (1991).

Figure 11 plots the ratio of the compliant base structure frequency (f_{SSI}) to the fixed-base one (f_0) as a function of the relative soil-structure stiffness parameter defined as follows:

$$\sigma = \frac{V_S}{f_0 h} \tag{4}$$

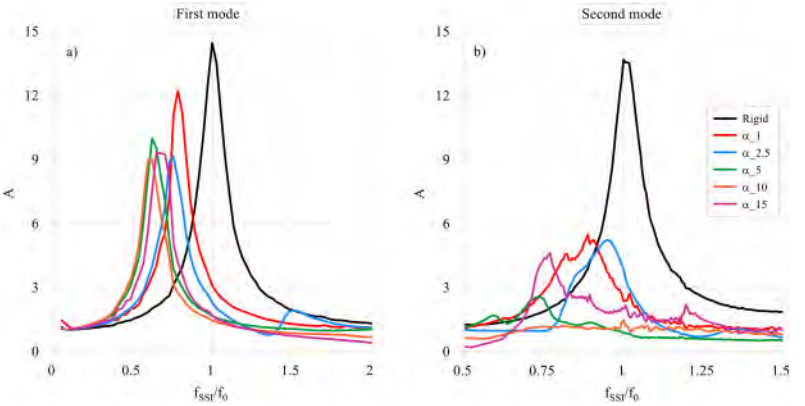

Figure 10. Amplification functions of the tower motion normalized a) by the first fixed-base frequency and b) by the second fixed-base frequency for different heterogeneity ratio α.

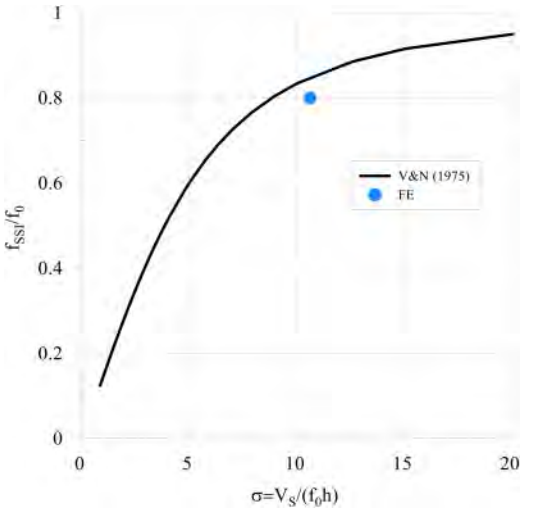

Figure 11. Comparison between the SSI FE result for the homogeneous soil deposit case (i.e. $\alpha = 1$) and the analytical solution proposed by Veletsos & Nair (1975).

The FE solution and the analytical value are in fair agreement considering all the assumptions made. In particular, the FE result tends to slightly overestimate (of about 5%) the frequency reduction related to SSI effects, with respect to the analytical solution.

Finally, the 3D FE results are plotted in terms of periods of the tower resting on the deformable soil (T_{SSI}) normalized by the fixed-base period (T_0) of the tower, as a function of the heterogeneity parameter α (Figure 12). The first natural period T_1 increases much more than the second one, T_2, for each considered heterogeneity ratio. In particular, starting from a value of about 1.28 for the homogeneous case, T_1 tends to increase for increasing values of the heterogeneity ratio, achieving its maximum value at $\alpha = 10$, beyond which the first period begins to decrease. The curve of

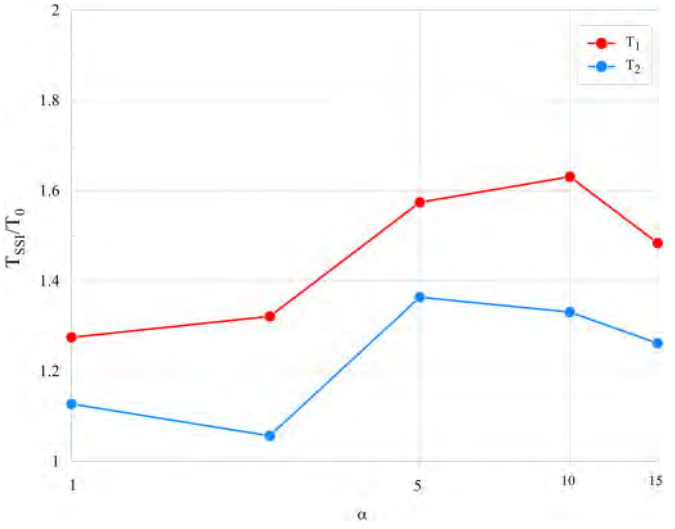

Figure 12. Normalized first and second tower T_{SSI} periods as function of the heterogeneity parameter α.

the normalized second oscillation period of the soil-tower system is instead characterized by an irregular trend, with T_2 varying between 1.13 and 1.36. The outputs suggest that the effects of the soil-structure interaction may be significant, with a change in the natural periods of the soil-tower system strongly dependent on the soil profile characteristics. These effects should be taken into account to obtain an accurate evaluation of the dynamic response of the system.

4 CONCLUSIONS

The paper deals with the assessment of the dynamic response of a typical masonry tower, specifically focusing on the effects of the soil deposit heterogeneity on the SSI phenomena. A set of four soil profiles, representative of real possible stratigraphies in Italy, has been considered, while the masonry tower exemplifies an ideal case study that sums up the main geometrical features of bell towers located in the seismic areas of Northern Italy. After a preliminary modelling, aimed at validating the numerical approach adopted for the seismic ground response of the subsoil foundation under free-field conditions, complete 3D dynamic SSI analyses have been performed to assess the modifications due to the soil heterogeneity of the soil-tower seismic behaviour with respect to the fixed-base condition, by considering a visco-elastic constitutive assumption for both the tower and its foundation deposits.

The numerical results show the typical effects related to soil-structure interaction, consisting in the period elongation of the structure and the increase of damping ratio with respect to the cantilever condition due to the soil deposit deformability, more pronounced for the first flexural mode rather than for the second one. Moreover, a clear coupling between the tower and the soil can be recognized for the second natural mode of the structure, which results to be more affected by the soil compliance than the first one.

The work presents only some preliminary results of the SSI problem affecting masonry towers on deformable soil deposits. Further developments of the ongoing research will account for the elasto-plastic behaviour of the tower, which could be described through a more sophisticated constitutive model, capable to predict the damage scenarios affecting the structure during representative earthquake motions.

REFERENCES

ABAQUS 2014. ABAQUS documentation version 6.14. Dassault Systèmes, Providence, RI.

Amorosi, A., Boldini, D., & Di Lernia, A. 2017. Dynamic soil-structure interaction: a three-dimensional numerical approach and its application to the Lotung case study. *Computers and Geotechnics*, 90, 34–54.

Amorosi, A., Boldini, D., & Elia, G. 2010. Parametric study on seismic ground response by finite element modelling. *Computers and Geotechnics*, 37(4), 515–528.

Bardet, J. P., Ichii, K., & Lin, C. H. 2000. EERA: a computer program for equivalent-linear earthquake site response analyses of layered soil deposits. University of Southern California, Department of Civil Engineering.

Bartoli, G., Betti, M., & Vignoli, A. 2016. A numerical study on seismic risk assessment of historic masonry towers: a case study in San Gimignano. *Bulletin of Earthquake Engineering*, 14(6), 1475–1518.

Bathe, K. J. 1996. *Finite element procedures in engineering analysis*, (2nd ed.) Upper Saddle River, NJ: Prentice Hall.

Casciati, S., & Borja, R. I. 2004. Dynamic FE analysis of South Memnon Colossus including 3D soil–foundation–structure interaction. *Computers and Structures*, 82(20–21), 1719–1736.

Casolo, S., Diana, V., & Uva, G. 2017. Influence of soil deformability on the seismic response of a masonry tower. *Bulletin of Earthquake Engineering*, 15(5), 1991–2014.

Casolo, S., & Uva, G. 2013. Non-linear dynamic analysis of masonry towers under natural accelerograms accounting for soil-structure interaction, *in: 4th ECCOMAS, Thematic Conference on Computational Methods in Structural Dynamics and Earthquake Engineering. Crete, Greece, 2013*, pp. 4488–4506.

Castellazzi, G., D'Altri, A. M., de Miranda, S., Chiozzi, A., & Tralli, A. 2018. Numerical insights on the seismic behaviour of a non-isolated historical masonry tower. *Bulletin of Earthquake Engineering*, 16(2), 933–961.

Clementi F., Milani G., Ferrante A., Valente M., & Lenci S. 2019. *Crumbling of Amatrice clock tower during 2016 Central Italy seismic sequence: Advanced numerical insights.* Frattura Ed Integrità Strutturale 14(51), 313–335.

Clough, R. W., & Penzien, J. 1993. *Dynamics of Structures*, McGraw-Hill.

Consiglio dei Ministri. 2018. DM 17 gennaio 2018 in materia di "aggiornamento delle norme tecniche per le costruzioni". Gazzetta ufficiale n.42 del 20 febbraio 2018.

Day SM. 1978. Seismic response of embedded foundations. *In Proceedings of the ASCE Convention, Chicago, IL, 16–20 October 1978*; Preprint no. 3450.

de Silva, F. 2020. Influence of soil-structure interaction on the site-specific seismic demand to masonry towers. *Soil Dynamics and Earthquake Engineering*, 131, 106023.

de Silva, F., Ceroni, F., Sica, S., & Silvestri, F. 2018a. Non-linear analysis of the Carmine bell tower under seismic actions accounting for soil–foundation–structure interaction. *Bulletin of Earthquake Engineering*, 16(7), 2775–2808.

de Silva, F., Pitilakis, D., Ceroni, F., Sica, S., & Silvestri, F. 2018b. Experimental and numerical dynamic identification of a historic masonry bell tower accounting for different types of interaction. *Soil Dynamics and Earthquake Engineering*, 109, 235–250.

di Lernia, A., Amorosi, A., & Boldini, D. 2019. A multi-directional numerical approach for the seismic ground response and dynamic soil-structure interaction analyses. *In Earthquake Geotechnical Engineering for Protection and Development of Environment and Constructions* (pp. 2145–2152). CRC Press.

Elsabee, F., Morray, J. P., & Roesset, J. M. 1977. *Dynamic behaviour of embedded foundations.* Massachusetts Institute of Technology, Department of Civil Engineering, Constructed Facilities Division.

Falcone, G., Acunzo, G., Mendicelli, A., Mori, F., Naso, G., Peronace, E., …& Moscatelli, M. 2021. Seismic amplification maps of Italy based on site-specific microzonation dataset and one-dimensional numerical approach. *Engineering Geology*, 289, 106170.

Gazetas, G. 1991. Formulas and charts for impedances of surface and embedded foundations. *Journal of Geotechnical Engineering*, 117(9), 1363–1381.

Gazetas, G. 1982. Vibrational characteristics of soil deposits with variable wave velocity. *International Journal for Numerical and Analytical Methods in Geomechanics*, 6(1), 1–20.

Kim, S., & Stewart, J. P. 2003. Kinematic soil-structure interaction from strong motion recordings. *Journal of Geotechnical and Geoenvironmental Engineering*, 129(4), 323–335.

Kuhlemeyer, R. L., & Lysmer, J. 1973. Finite element method accuracy for wave propagation problems. *Journal of the Soil Mechanics and Foundations Division*, 99(5), 421–427.

Milani, G. 2019. Fast vulnerability evaluation of masonry towers by means of an interactive and adaptive 3D kinematic limit analysis with pre-assigned failure mechanisms. *International Journal of Architectural Heritage*, 13(7), 941–962.

Mortezaei, A., & Motaghi, A. 2016. Seismic assessment of the world's tallest pure-brick tower including soil-structure interaction. *Journal of Performance of Constructed Facilities*, 30(5), 04016020.

Sarhosis, V., Milani, G., Formisano, A., & Fabbrocino, F. 2018. Evaluation of different approaches for the estimation of the seismic vulnerability of masonry towers. *Bulletin of Earthquake Engineering*, 16(3), 1511–1545.

Torabi, H., & Rayhani, M. T. 2014. Three-dimensional finite element modeling of seismic soil–structure interaction in soft soil. *Computers and Geotechnics*, 60, 9–19.

Valente, M., & Milani, G. 2018. Effects of geometrical features on the seismic response of historical masonry towers. *Journal of Earthquake Engineering*, 22(sup1), 2–34.

Valente, M., & Milani, G. 2016. Seismic assessment of historical masonry towers by means of simplified approaches and standard FEM. *Construction and Building Materials*, 108, 74–104.

Veletsos, A.S., & Nair, V.D. 1975. Seismic interaction of structures on hysteretic foundations. *Journal of the Structural Division*, 101, 109–29.

Geotechnical Engineering for the Preservation of Monuments and Historic Sites III – Lancellotta, Viggiani, Flora, de Silva & Mele (Eds)

An influence of the water supply in improved soil against liquefaction

Nesil Özbakan & Burak Evirgen
Department of Civil Engineering, Eskisehir Technical University, Turkey

ABSTRACT: Liquefaction is a critical problem in terms of soil – structure interaction both up to date reinforced concrete buildings and historical sites including masonry or adobe type of building materials. Although the excessive settlement potentials can be limited during liquefaction thank to mat foundation or deep foundation at the present time, vital differential settlement levels can be observed in monuments having single footings, generally. Therefore, special soil improvement techniques have been become unavoidable in terms of existing historical structures. In this study, the effect of water supply was investigated in liquefiable sandy soil that was improved via sodium polyacrylate powder inside a special test box. The shaking table tests were performed on various applications of mentioned chemical agent as complete mixing operation, horizontal case and vertical case with different proportions under constant head water supply and out of water supply to simulate the pressurized ground water flow. The foundation of building was represented by steel plate at the center of ground surface. The experimental results revealed that the water supply has a significant effect on the settlement values of foundation and the change in pore water pressure levels. Thus, the flow rate of ground water plays a key role in the selection of the proper soil treatment method.

1 INTRODUCTION

Historical buildings, which have the characteristics of cultural heritage, are faced with settlement and bearing capacity problems for various reasons over time. One of these reasons is the liquefaction problem that causes a critical problem in terms of structure-soil interaction in both current reinforced concrete structures and historical sites. Differential settlement, rotation or tilting problems can be observed due to liquefaction and these may cause devastating damages in monuments with single footings, especially.

The data on the damage of historical artifacts and structures in Istanbul, where many important historical buildings are located, during earthquakes have been examined by Ince (2011). Liquefaction has a serious effect on structures according to comparison between damage maps and liquefaction risk maps. Similarly, the 2012 Northern Italy earthquake series caused damage to many historical buildings and created significant devastation of the cultural heritage in the region. The most of these damages occurred as a result of liquefaction problem according to Lombardi & Bhattacharya (2014). Some historically important temples are faced with risk of liquefaction in Nepal region (Shrestha et al. 2004). Studies have revealed that the liquefaction problem causes a serious threat to historical structures.

As stated in the World Heritage Convention (Unesco 1972), the degradation or destruction of any element of the cultural or natural heritage damages and impoverishes the heritage of all nations of the world. There are various methods such as sand compaction piles (Okamura et al. 2006), recycled materials (Otsubo et al. 2016), deep mixing (Bahmanpour et al. 2019), reinforced concrete piles (Hayashi et al. 2021), within the scope of improve the resistance against liquefaction. However,

 DOI 10.1201/9781003308867-60

these traditional techniques can be applied before the construction. They create harmful effects on the structure if application stages taking a role for existing structure foundations (Tophel & Ramana 2019).

The foundations of historical buildings, like other elements, are an integral part of their identity and originality should be preserved as much as possible. For this reason, the use of sodium polyacrylate (SPA) as a special ground improvement technique is a preferable process as it can be done without any intervention to the building. Nesil & Evirgen (2022) revealed in their study that the addition of SPA improves the mechanical properties of the soil and leads to an increase in shear strength more than two times. Sodium polyacrylate is a chemical agent capable of absorbing considerable amounts of water. SPA is in a white powder-like form and when it comes into contact with a liquid, it immediately swells and turns into a gel state. Simatupang et al. (2017) reported that a significant improvement in liquefaction occurred mainly at a low degree of saturation. Therefore, the utility of aforementioned chemical agent inside soil improvement applications may enhance the resistance against liquefaction by reducing soil saturation and increasing viscosity. In this study, the effect of SPA on improving the sandy soil parameters depending on the water supply conditions was investigated. For this purpose, shaking table experiments were carried out in a special test box with 3 different application method as complete mixing operation, horizontal case and vertical case. When the test results were evaluated, it was observed that the SPA could be used for soil improvement against liquefaction, and the water supply had a significant effect on the change in excess pore water pressure as well as settlement values.

2 MATERIAL AND METHOD

In the experiments, poorly graded silica sand with high liquefaction potential was used to model the liquefiable soil in historical sites. The properties of silica sand used in the experiments are given in Table 1.

Sodium polyacrylate (SPA) was used in the experiments to reduce the saturation of the soil thanks to transform a gel form and thus minimize the risk of liquefaction. The water absorption capacity was determined around 125 ml/g for the dry SPA dust that may varies depending on its chemical composition (Figure 1). In addition, the density, molecular weight and purity properties of SPA were given as 0.64 g/cm^3, 94.05 g/mol and 95.00% with respect to the manufacturer, respectively. Since SPA can release some of the absorbed water in case of subjected to loading conditions, it was mixed with trace addition of cement (0.20%) by the weight of SPA in gel form.

Within the scope of the study, shaking table tests were performed by applying the SPA-cement mixture into the saturated sandy soil in three different ways (complete mixing operation, horizontal case and vertical case) in order to evaluate the improving level of soil in terms of liquefaction.

Table 1. Soil properties of silica sand.

Parameter	Value
Specific gravity, Gs	2.45
Gravel content (%)	0.00
Sand content (%)	99.38
Silt and clay content (%)	0.62
Median particle size, D_{50} (mm)	0.60
Uniformity coefficient, C_u	1.53
Coefficient of curvature, C_c	0.87
Maximum dry unit weight, γ_{drymax} (kN/m^3)	15.01
Minimum dry unit weight, γ_{drymin}(kN/m^3)	14.13

Figure 1. Sodium polyacrylate; a. Powder form, b. Gel form (Özbakan 2021).

The experimental setup consists of a plexiglass box for modeling the liquefiable soil, pore water pressure gauges (with a capacity of 200 kPa) on the four lateral faces of the box, a constant head water tank for water supply, a shaking table device and a dynamic data acquisition system (Figure 2). Two layers of styrofoam coated with grease were placed on the inner faces of the box to prevent the reflection of waves from the rigid walls.

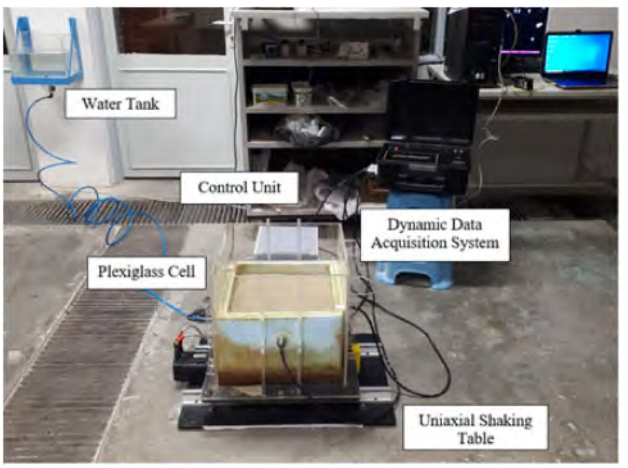

Figure 2. Experimental setup (Özbakan et al. 2021).

During the preparation stage of soil cell, silica sand was placed in the box owing to dry pluviation method with a relative density of 47.80%, which was determined as the most susceptible relative density against liquefaction. A square shaped steel plate with the dimension of 150.00 mm x 150.00 mm was placed on the ground surface to represent the individual foundation of monumental building and the settlement values were noted from the corners of this plate due to initial position after test. Then, improvement applications were carried out. SPA-cement powder at the rates of 0.05%, 0.10%, 0.15% and 0.20% was mixed with sand to meet the desired relative density in the complete mixing application (MA). SPA-cement powder was placed in 5.00 mm and 10.00 mm thicknesses at the upper part (3.00 cm below the ground surface – HU) and lower part of (15.00 cm below the ground surface – HL) the pore water pressure gauges for horizontal application case.

In vertical layer application case (VL), 0.25%, 0.50%, 1.00% and 2.50% SPA-cement powder was mixed with the soil and poured into square shaped wall that has 200.00 mm outer dimension, 180.00 mm inner dimension, 10.00 mm vertical wall thickness and along the soil height. The experiments were carried out following ways of water condition; out of water supply that is the inlet of flow was closed during the tests, and constant head water supply was maintained throughout the experiments. Shaking table tests were performed via 100 cycles of sinewave has a 4.00 Hz frequency, 0.64 g acceleration and 10.00 mm motion amplitude (Figure 3).

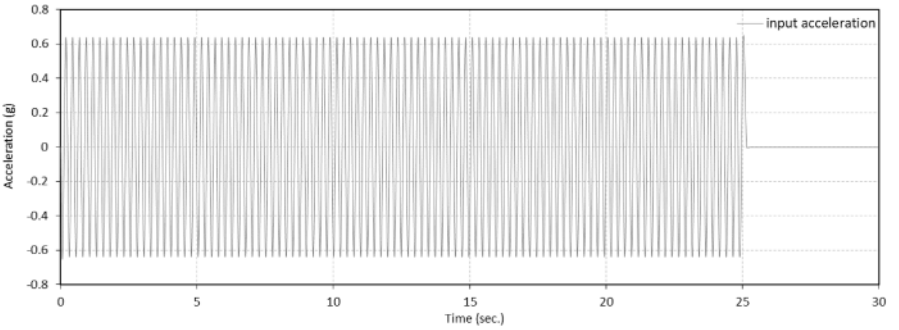

Figure 3. Time history of input acceleration.

3 RESULTS

The average swelling values obtained from the foundation plate due to water supply for different improvement applications are given in Figure 4. The following abbreviations are used to define the improvement style; 'VL' and 'MA' letters represent the vertical layer operation and mixing applications, while 'HU' and 'HL' terms indicate the horizontal layer application at upper part and lower part, respectively. The numbers follow the letters characterize the thickness or percentage of powder as layer or mixture applications. Considering the swelling problem on ground surface as a result of SPA applications, the most effective application was determined in VL0.5.

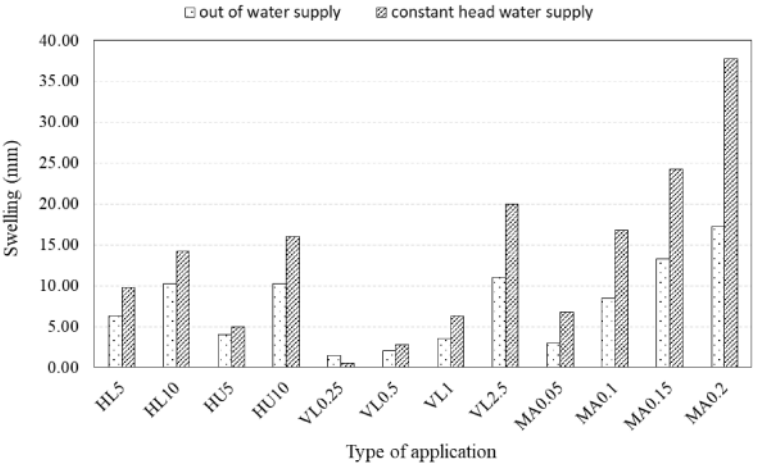

Figure 4. The change in swelling values of foundation plate after water supply.

The average settlement values with respect to the initial position of the steel plate are given in Figure 5 due to different water supply conditions and improvement methods. All of the observed settlement values were located below the reference line when the water entrance is forbidden inside the box during shaking table test independent from improvement technique of chemical stabilization with SPA. However, in some applications, serious increment levels occurred in the case of constant head water supply with the flow rate of 0.008 lt/sec. The most effective improvement applications were obtained in 'MA0.1' cases in terms of settlement behavior after liquefaction both in two water supply conditions. Horizontal layer operation creates moderately more settlement levels with respect other ones. On the other hand, Figure 6 shows the total vertical deformation observed in the foundation plate due to the difference between swelling that occurs as a result of the SPA's transformation into gel form and the average settlement after dynamic effect. Although the settlement problem was prevented due to improvement in almost all applications, the swelling caused by SPA showed an increasing effect on the deformation during water absorption stage. It was observed that VL0.5 and VL1 applications restrained the deformation if compared with reference case while swelling process increased the deformation in other applications. Moreover, the total vertical deformation decreased by 48% in both out of water supply and constant head water supply conditions in VL0.5 case.

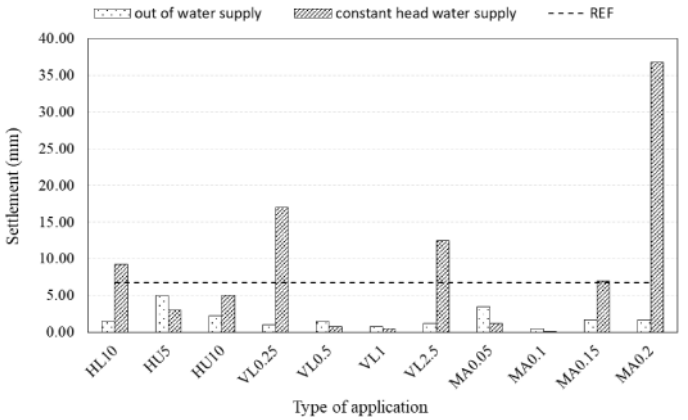

Figure 5. The change in settlement values of foundation plate after shaking procedure due to water supply condition.

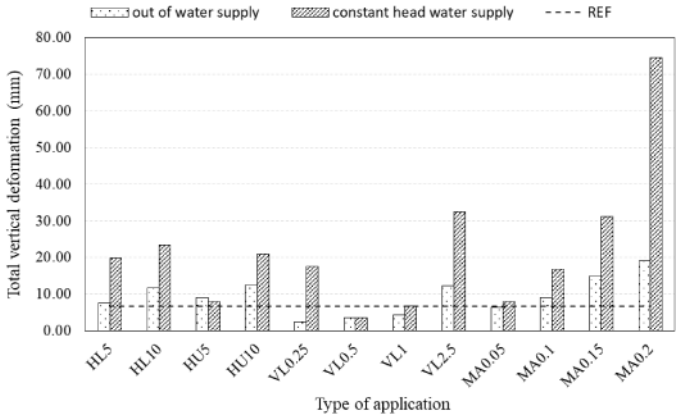

Figure 6. Total vertical deformation of the foundation plate due to swelling and settlement.

The excess pore water pressure is a primary reason of liquefaction phenomenon, since the void ratio parameter of liquefiable soil can reach up critical value in this case. Therefore, the excess pore water pressure values of reference case as a time history distribution are given in Figure 7, which was taken from each side of soil cell through dynamic effect. In addition, the values of improved cases are given Figure 8. While positive values belonged to same direction of dynamic motion, opposite action were taken as negative numbers which could be called as a suction behavior. Vertical layer application and complete mixing operations gave better results rather than horizontal layer case in terms of pore water pressures.

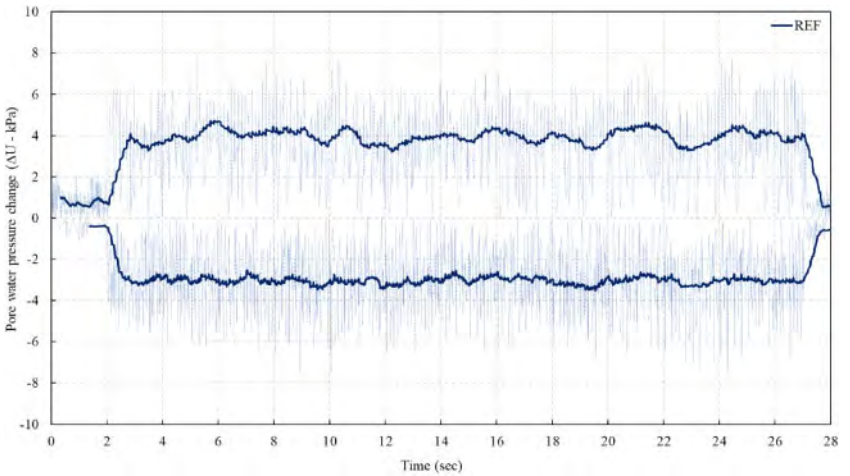

Figure 7. Excess pore water pressure time history for reference case.

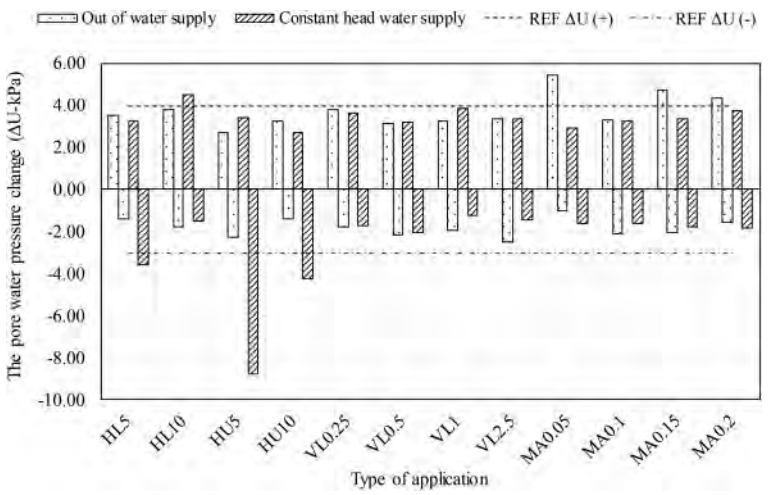

Figure 8. The change in pore water pressure values due to water supply.

On the other hand, the sample application photos are given in Figure 9 to prove the efficiency of SPA against liquefaction problem. Even the obtained settlement and pore water pressures close to the reference value, differential settlement behavior was prevented and high liquefaction potential is eliminated in SPA added cases except for some cases.

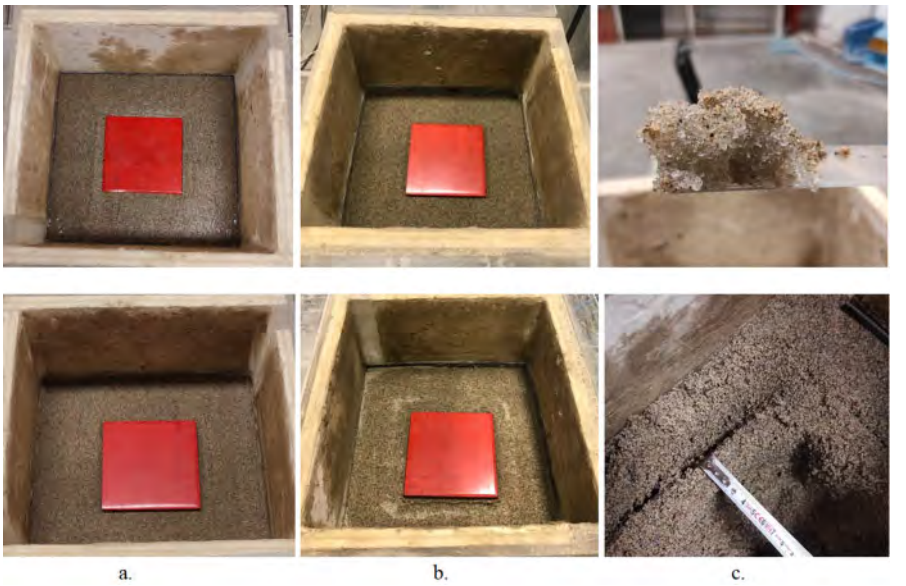

Figure 9. Post-experiment photos of HL5 application (top) and VL0.5 application (bottom); a. constant head water supply, b. out of water supply, c. gel layer.

4 CONCLUSION

In this study, the application methods of a chemical soil improvement agent called as sodium polyacrylate (SPA) was investigated under different water supply conditions to minimize the post liquefaction problems under the historical buildings. The results of shaking table tests are listed below:

- Although much lower values were obtained in settlement levels, pore water pressure values were also below the reference value, generally. These results prove that SPA can be used confidently to eliminate the post liquefaction problems. However, SPA chemical must be added into the liquefiable sandy soil up to critical ratio because of each application technique shows a unique behavior.
- Considering the decrease in settlement and excess pore water pressure levels, the most appropriate application method was seen for complete mixing operation with 0.10% amount of SPA-cement (MA0.1). The amount of settlement decreased by 92.60% and 98.50% in the case of out of water supply and constant head water supply, respectively. However, this method is not suitable for existing historical buildings. Therefore, vertical SPA layers from 0.50% to 1.00% SPA addition are proposed for existing structures due to the fact that settlement values decreased between 77.70% and 92.60%. Similarly, the change in excess pore pressure and total vertical deformation decreased by around 25% and 50%, respectively, in the case of VL0.5. It has been concluded that 'VL0.5' is the most suitable and economical application for improving the soil under existing historical building without damaging the structural members.
- The consolidation of the monument foundations can be carried out using any modern conservation and construction technique validated by scientific data and experiments since traditional techniques are insufficient (Icomos 1964). In this context, the effectiveness of SPA applications is proved by experimental studies and it can be evaluated as a suitable soil improvement technique. It is thought that it will be promising agent after these experimental acquirements are supported by actual scaled field studies.

ACKNOWLEDGEMENTS

This study was supported by The Scientific and Technological Research Council of Turkey – TUBITAK (Project number: 219M397).

REFERENCES

Bahmanpour, A., Towhata, I., Sakr, M., Mahmoud, M., Yamamoto, Y., Yamada, S. 2019. The effect of underground columns on the mitigation of liquefaction in shaking table model experiments. *Soil Dynamics and Earthquake Engineering* 116: 15–30.

Hayashi, K., Takahashi, S., Saito, T. 2021. Dynamic response of the saturated soil–reinforced concrete pile–superstructure interaction under repeated shaking. *Soil Dynamics and Earthquake Engineering* 145: 106685.

Icomos. 1964. International charter for the conservation and restoration of monuments and sites. *2nd International Congress of Architects and Technicians of Historic Monuments, Venice, Italy.*

Ince, G.C. 2011. The relationship between the performance of soil conditions and damage following an earthquake: a case study in Istanbul, Turkey. *Natural Hazards and Earth System Sciences* 11(6): 1745–1758.

Lombardi, D. & Bhattacharya, S. 2014. Liquefaction of soil in the Emilia-Romagna region after the 2012 Northern Italy earthquake sequence. *Natural hazards* 73(3): 1749–1770.

Okamura, M., Ishihara, M., Tamura, K. 2006. Degree of saturation and liquefaction resistances of sand improved with sand compaction pile. *Journal of Geotechnical and Geoenvironmental Engineering* 132(2): 258–264.

Otsubo, M., Towhata, I., Hayashida, T., Liu, B., Goto, S., 2016. Shaking table tests on liquefaction mitigation of embedded lifelines by backfilling with recycled materials. *Soils and Foundations* 56(3): 365–378.

Özbakan, N. 2021. Effect of sodium polyacrylate and impermeable layer applications on soil liquefaction potential. MSc Thesis, Eskisehir Technical University.

Özbakan, N., Evirgen, B., Tuncan, M. 2021. An effect of impermeable top layer on liquefaction potential. In Gökçe Tönük, Korhan Deniz Dalgıç, Ömer Faruk Halıcı (eds), *The 9th Turkish Conference on Earthquake Engineering; Proc. intern. symp., Istanbul, 2–3 June 2021.*

Özbakan, N. & Evirgen, B. 2022. An Effect of Sodium Polyacrylate on Sandy Soil Parameters and Its Use in Soil Improvement. *Proceedings of the 7th World Congress on Civil, Structural, and Environmental Engineering, Lisbon, Portugal– April 10–12, 2022.* (accepted).

Shrestha, S. R., Karkee, M. B., Cuadra, C. H., Tokeshi, J. C. & Miller, S. N. 2004. Preliminary Study for Evaluation of Earthquake Risk to the Historical Structures in Kathmandu Valley. *13th World Conference on Earthquake Engineering, Vancouver, B.C. Canada, August 1–6, 2004.*

Simatupang, M. & Okamura, M. 2017. Liquefaction resistance of sand remediated with carbonate precipitation at different degrees of saturation during curing. Soils and foundations 57(4): 619–631.

Tophel, A. & Ramana, G.V. 2019. Protecting heritage structures against liquefaction: Recent developments. In: A. Kallel, Z.A. Erguler, Z.-D. Cui, Al. Karrech, M. Karakus, P. Kulatilake, and S.K. Shukla (eds.), *Recent Advances in Geo-Environmental Engineering, Geomechanics and Geotechnics, and Geohazards*. Cham: Springer International Publishing, 507–509.

Unesco. 1972. Convention concerning the protection of the world cultural and natural heritage. Adopted by the general conference at its 17th session in Paris. November 16, 1972.

Geotechnical Engineering for the Preservation of Monuments and Historic Sites III – Lancellotta, Viggiani, Flora, de Silva & Mele (Eds)

Site characterization and preliminary ground response analysis for the monumental Complex of SS. Annunziata in Sulmona, Italy

C. Madiai & G. Ciardi
University of Florence, Florence, Italy

M. Manuel
GEO Geotecnica e Geognostica srl, Arpino (Frosinone), Italy

F. Galadini
Istituto Nazionale di Geofisica e Vulcanologia, Rome, Italy

S. Amoroso
University of Chieti-Pescara, Pescara, Italy
Istituto Nazionale di Geofisica e Vulcanologia, L'Aquila, Italy

ABSTRACT: The historical building Complex of the SS. Annunziata in Sulmona (L'Aquila, Italy), consists of a church and an adjoining building. It overlooks the square of the same name along the main street of the historic centre of the town. SS. Annunziata is considered the most important historical monument in Sulmona, not only for its huge artistic and architectural value, but also for the special significance it had in the social and political life of the city. The construction of the Complex started in the 14th century and continued for centuries. The long building duration led the Complex to take on its current appearance characterized by different architectural styles: late Gothic, Renaissance and Baroque. As a result of earthquakes that affected the area, the various buildings that are (or were) part of the monumental Complex suffered damage (perhaps in 1349, 1456 and certainly in 1706) and underwent major reconstruction works. Significant damage was also caused to the structures of the SS. Annunziata Complex by the earthquakes that struck the central Apennines in the 20th century (i.e. 1915 and 1933) and by the 2009 L'Aquila earthquake. After this latter, the damage observed to the rear of the buildings in the monumental Complex was more severe than those of the front. To verify whether the subsoil local conditions can explain the distribution of the observed damage, studies of ground response have been planned at the site where SS. Annunziata Complex is located. This work presents the preliminary results of the case study. After a general overview of the Sulmona basin and the SS. Annunziata Complex, the results of the survey carried out in the study area are described and analyzed, aimed at defining the geotechnical model. The results of numerical 1D analyses performed on soil profiles, representative of the subsoil conditions both at the front and back of the historical Complex, are also presented and compared.

1 INTRODUCTION

Sulmona (L'Aquila) lies in an intermontane basin in central Italy. It has very ancient origins, as demonstrated by continuous archaeological findings of Roman age from excavations in the old town centre and in the surrounding territory. Indeed, the northern downtown sector is founded on the ancient *Sulmo* (the Roman town), i.e. archaeological stratigraphy defines the continuity of the settlement at least since the Roman Age. The Roman *Domus*, whose remains were found in the area located along the main street of the present city centre where the historical Complex of SS.

 DOI 10.1201/9781003308867-61

Annunziata currently stands, dates back from the Roman Imperial Age. In turn, SS. Annunziata is considered the most important monument in the town and consists of a church and a large adjoining building resulting from a combination of different architectural styles: late Gothic, Renaissance and Baroque.

Sulmona basin (also called Peligna basin or Peligna valley) is one of the areas of highest seismicity in Italy and the Municipality of Sulmona is included in Italian the peninsular belt characterized by the highest seismic hazard. The CPTI15 seismic catalogue (Rovida et al. 2021, from which the magnitude reported in the next have been derived), which represents the main reference for Italian seismicity, reports numerous earthquakes that have affected the town of Sulmona with macroseismic intensity greater than 6 and up to 9-10 MCS degree. However, according to some researchers, the strongest earthquake in Sulmona's seismic history occurred in the 2nd century BC and it seems to have caused the collapse of the already mentioned Roman *Domus* whose remains were uncovered during excavations within the SW sector of SS. Annunziata (Ceccaroni et al. 2009; Tuteri 1995).

After its first construction, dating back to 1320, the SS. Annunziata Complex presumably experienced interventions because of damage caused by the 1349 and 1456 earthquakes (MCS macroseismic intensity, $I_{MCS} = 8 - 9$ and 8 at Sulmona respectively; estimated magnitude of 1456, $M_w = 7.19$) and was partially rebuilt after the 1706 earthquake ($I_{MCS} = 9 - 10$; estimated magnitude $M_w = 6.84$) which produced the collapse of the church, serious damage to the adjacent building and low damage to the bell tower. The SS. Annunziata Complex was also significantly damaged by other earthquakes: 1915 Marsica; 1933 Maiella; 1984 Monti della Meta; 2009 Aquilano. The consequence of the latterwas especially evident in the rear part where damage was significantly greater than in the front.

Recently, several survey campaigns have been carried out in the Sulmona basin, aimed at collecting geological, geotechnical and geophysical data in the context of microzonation studies (Di Capua et al. 2009; Pizzi et al. 2014; Scarascia Mugnozza 2007; Totani et al. 2009). Further data were collected through geophysical investigations and in situ and laboratory geotechnical surveys carried out at the historical centre of Sulmona as part of the FISR 2016 Top-down Project "L'Italia Centrale in 4D e ricostruzione dei processi geodinamici in atto", Task 4 "Mappe multihazard e vulnerabilità del territorio". These surveys have shown that the subsoil of the Annunziata Complex is very heterogeneous and that, in the first tens of meters, the stratigraphic sequence is very different even at very small distances.

After a brief description of the main geological and seismic characteristics of the Sulmona's area, this paper presents and discusses the characterization of the SS. Annunziata subsoil and the results obtained from the one-dimensional numerical ground response analyses performed on two significantly different vertical soil profiles, in order to verify the influence of the stratigraphic sequence on the damage induced by the recent 2009 earthquake.

2 BRIEF HISTORY OF THE SS. ANNUNZIATA MONUMENTAL COMPLEX

The historical building Complex of the SS. Annunziata is considered the most important historical monument in Sulmona, not only for its huge artistic and architectural value, but also for the special significance it had in the social and political life of the city, since it included the great church and the main hospital of the territory. The first plant of the Annunziata Complex dates to 1320 with the construction of the church of SS. Annunziata and its hospital in an area where a *Domus* stood in the early Roman Imperial Age and which later, only sporadically and at different times, was occupied by modest buildings of different types that were built and demolished for different purposes. In 1349 and 1456, SS. Annunziata was presumably damaged by strong earthquakes. Works during the 16th century completely modified the original Complex of medieval age. Indeed, the church of SS. Annunziata was unified with the contiguous church of Santa Croce. This involved a complete redefinition of the floor plan and spaces of Annunziata compared to those of the 14th century church. Nothing remained of the latter (Mattiocco 2008).

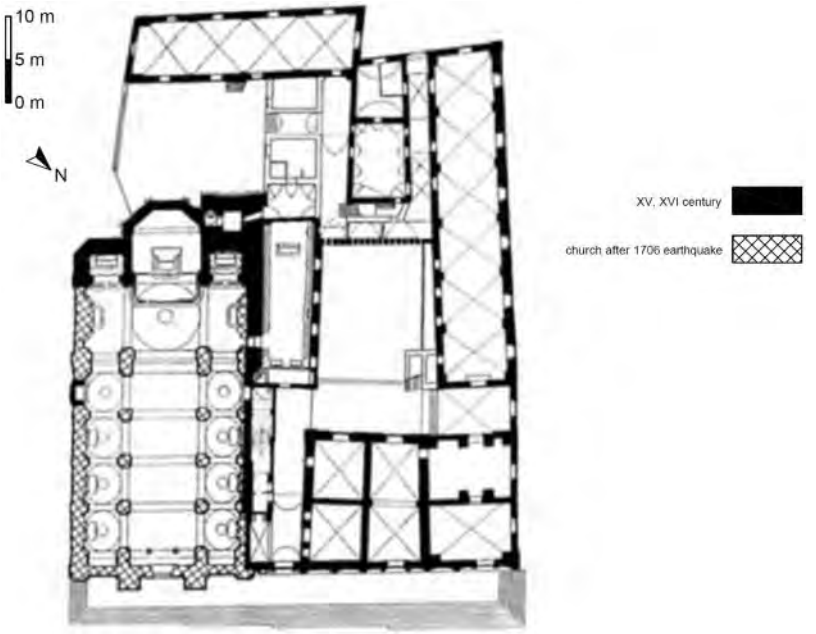

Figure 1. Current map of the SS. Annunziata Complex and construction phases (modified from Giannantonio 1997).

The chronology of the construction phases of the building adjacent to the church, which currently stands on the area where the ancient hospital founded in 1320 once stood, is more difficult to date. Construction began during the 15th century and was completed in 1483 with a significant extension of the building. This was followed by a further building phase which included the completion of the facade (1512-1522) (Mattiocco 2008).

In the 17th century no further significant works were carried out, but only modest renovations and small extensions related to contingent needs. In 1706, Sulmona was shaken by a strong earthquake which caused hundreds of victims and heavy damaged the city (I_{MCS} = 9-10). The Annunziata palace was also damaged, while the church collapsed entirely (only the sacristy did not experience damage), the bell tower and the wall adjacent to the staircase of the building were saved (Mattiocco 2008).

Reconstruction of the church began in 1710. After the major rebuilding works following the earthquake of 1706, the Complex has no longer undergone significant changes and the overall structure has remained almost unchanged until today (Figure 1).

3 MAIN FEATURES OF SULMONA BASIN

3.1 *Geological framework*

The Sulmona basin is one of the typical intermontane basins of the central Apennines. It is 5-8 km-wide in the direction NE-SW and about 21 km-long in the direction NW-SE. Its geological evolution has been conditioned by the Quaternary activity of the Mt. Morrone fault, bordering the basin to the East and emerging along the SW slope of the mentioned relief (e.g. Vittori et al. 1995, Gori et al. 2011) (Figure 2). The basin has asymmetrical shape, i.e. it is deeper in the eastern sector, at the foot of the Morrone massif (e.g. Cavinato & Miccadei 1995).

Figure 2. Panoramic view of the Sulmona Plain. Asterisks indicate some places where Mt. Morrone fault is emerging. Rectangle defines the area of Mt. Morrone bedrock fault scarp north of Roccacasale and the place where the fault plane is exposed south of the village.

The marine substratum has been tectonically lowered below the plain and outcrops in the reliefs surrounding the depression mainly carved into Mesozoic carbonate rocks. The basin is characterized by a large gently sloping surface related to the fluvio-lacustrine Quaternary history of this intermontane sector. Part of this history is testified by the thick lacustrine sediments, related to an ancient Quaternary lake (Miccadei et al. 1998) which characterised the local environment until the final drainage due to the regressive erosion of Pescara river from Adriatic sea towards the Apennines as a response to the chain uplift.

Remnants of continental deposits have also been found along the slopes of the carbonate reliefs that surround the basin (Gori et al. 2007, 2014; Vittori et al. 1995; and outcrop in many areas due to natural actions (mainly river incisions) and anthropic interventions (Miccadei et al. 1998). In summary, the lithostratigraphic units of interest for studies on the town of Sulmona are (from old to recent): 1) carbonate bedrock, probably located at a depth of about 300 meters below the centre of Sulmona; 2) lacustrine and marsh deposits, consisting of silty clayey with peat levels and lenses of gravels and sands; their thickness certainly exceed 200 m; 3) alluvial sediments, mainly made of gravel and sandy gravel with sandy-silty or clayey-silty levels especially in the deeper parts; thickness in the order of 30 m below the centre of Sulmona; 4) reworked material and archaeological deposits. A geologic section crossing the historical centre of Sulmona is shown in Figure 3 (Pizzi et al. 2014).

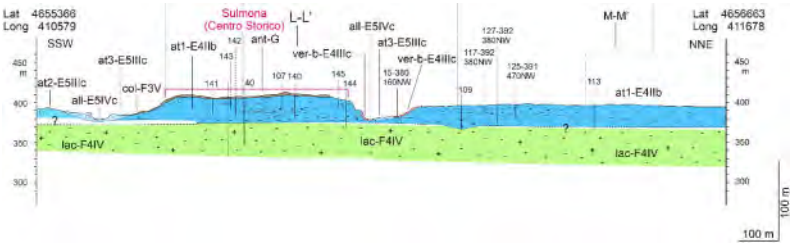

Figure 3. Geologic section crossing the historical centre of Sulmona (from Pizzi et al. 2014).

3.2 *Seismicity of the area*

The Sulmona basin is one of the areas of highest seismicity in Italy. Some of the main seismic events that struck the area were related to the well-documented active normal fault systems oriented in a direction parallel to the Apennine trend.

The CPTI15 seismic catalogue (Rovida et al. 2021) shows that Sulmona was hit by at least 6 events with $I_{MCS} \geq 7$: among them, only one originated from a near-field active fault ("Valle Peligna" in 1905 – $I_{MCS} = 7$, $M_w = 5.15$), while other four originated in adjacent seismogenic areas ("Appennino Centro Meridionale": 1456 – $I_{MCS} = 8$, $M_w = 7.19$; "Maiella": 1706 - $I_{MCS} = 9$-10, $M_w = 6.84$ and 1933 - $I_{MCS} = 8$, $M_w = 5.90$; 1933 "Marsica":1915 - $I_{MCS} = 8$, $M_w = 7.08$) and one (1349 - $I_{MCS} = 8$-9) is related to a still undefined source (Galadini & Carrozzo 2014).

In the Italian seismogenetic zonation (ZS9) proposed by Meletti and Valensise (2004) the area falls in the seismogenic zone 923 for which a maximum magnitude $M_w = 7.06$ is expected for a 475-year return period. The seismogenic potential has been confirmed by more recent studies on past seismicity and fault activity of the Sulmona basin (Ceccaroni et al. 2009; Galli et al. 2015; Gori et al. 2011) pointing out that the Morrone fault represents a potential source of earthquakes with magnitude M > 6.5 with an elapsed time since the last activation in the order of 1,850 years. Indeed, in times preceding the time interval represented in CPTI15 catalogue, this fault most likely caused a strong earthquake during the 2nd century AD responsible for the destruction of Roman towns in the Sulmona basin (Ceccaroni et al., 2009; Galadini & Galli 2001; Galli et al. 2015).

Currently, the Municipality of Sulmona is included in Zone 1 both in the classification by Regione Abruzzo and basing on the Seismic Hazard Map of Italy. According to the Italian Building Code (Ministero delle Infrastrutture e dei Trasporti 2018), the peak ground acceleration (a_g) expected at Sulmona with a 10% probability of exceedance over 50 years on firm soil and free field conditions is about 0.258 g. Local subsoil conditions could also produce amplification phenomena of ground surface motion in some areas of the city with important effects on the damage to residential and monumental buildings.

4 SUBSOIL INVESTIGATION AND GEOTECHNICAL MODELLING

4.1 *Overview of available data*

In the years, the Sulmona area has been investigated by numerous *in situ* and laboratory testing surveys. Field tests include: numerous boreholes (maximum depth of 60 m); five seismic dilatometer tests, SDMT (maximum depth of 60 m); eleven down-hole tests, DH (maximum depth of 30 m), and several surface geophysical linear measurements, MASW, and ambient vibration measurements (HVSR technique). Laboratory tests were performed on disturbed and undisturbed samples collected at different depths in some of the boreholes and include grain size distribution analysis and measures of unit weight and Atterberg limits, resonant column (RC) and cyclic torsional shear (CTS) tests.

Four boreholes, performed during distinct field campaigns, are located close to the SS. Annunziata Complex. Data belongs to the 1993 restoration project of the SS. Annunziata Complex performed by the Regione Abruzzo Public Work Department, to the former campaign of microzonation studies of the area (Di Capua et al. 2009; Scarascia Mugnozza 2007; Totani et al. 2009), and to the most recent testing campaign performed in 2018 for the Top-down FISR 2016 project (Ciani et al. 2021) to better explain the seismic behaviour of the Annunziata Complex. Figure 4(a) shows the location of the investigated verticals closest to the SS. Annunziata area: S1_1993 (S1 in the following), close to the front of the building, drilled up to 40 m of depth; S3c_SDMT2006 (S3 in the following), located SE of the SS. Annunziata at a distance of about 60 m, advanced up to 60 m of depth; S11_SDMT2018 (S11 in the following), located close to the back of the SS. Annunziata, 37 m deep, and S12_SDMT2018 (S12 in the following), located behind the main church, drilled up to 50 m of depth. Seismic dilatometer tests were performed in boreholes S3 (2006), S11 and S12 (both in 2018).

Based on the data from the geological surveys and from the four investigated verticals above mentioned, the following soil units can be identified in the area of the monumental Complex, from the top to the bottom: backfill (R), gravel (G), silty sand (S), clayey silt (L), lacustrine clay (A). Clayey silt represents the transition material between fluvial (above) and lacustrine (below) deposits. Overall, the stratigraphy is quite heterogeneous and significant differences were also found in soil profiles located at a short distance from each other, especially in the first tens of meters. In borehole S1, close to the front of the Complex, a silty sand layer is detected within the first 2 m, followed by gravel up to about 22 m and by the transition clayey silt layer below this depth up to the end of the borehole. Boreholes S3, S11, S12 show a shallow backfill layer of about 2-3 m-thick. Below this layer, silty sand lenses are framed within gravel banks at shallow depths in boreholes S3 and S11, while in borehole S12 a silty sand layer is detected between 5.4-6.3 m in depth, followed by a continuous gravel layer up to ≈ 30 m. Transition alluvial-lacustrine clayey silts are found starting from 28, 23, and 30.3 m in S3, S11 and S12, respectively, interrupted by gravel lenses. Lacustrine clay is only detected at deep (starting from 41.6 m) in S3, and at the bottom of S12 (5 m-thick layer from 45 m below ground) where a gravel lens between L and A materials is also found.

According to the available measurements, the historical centre of Sulmona is characterized by a significant shear wave velocity inversion located in the transition zone between fluvial and lacustrine deposits. From SDMT measurements, the shear wave velocity (V_s) of the backfill is around 230 m/s in S3 and 500 m/s in S11 and S12. For gravel, V_s shows a great variation with depth and borehole, ranging from ≈ 285 m/s in S3 to > 1000 m/s in S3, S11 and S12 due to a denser state. For clayey silt, V_s is around 280-510 m/s, with occasional spikes to 689 m/s (S11) and > 1400 m/s (S12). In silty sand and lacustrine clay, V_s ranges between 400-600 m/s, generally increasing with depth. None of the boreholes reached the calcareous bedrock. By combining the available V_s data with the microtremor measurements performed close to the monumental Complex (Pizzi et al. 2014), the bedrock depth was estimated, resulting in ≈ 270 m, in agreement with previous studies (Di Buccio et al. 2017; Di Filippo & Miccadei 1997; Manuel 2007).

4.2 *Geotechnical modeling of analyzed soil profiles*

For the purposes of this study, numerical 1D ground response analyses have been performed on the S11 and S12 soil profiles that are located respectively close to one side and to the back of the monumental Complex where the greatest damage was observed during the 2009 L'Aquila earthquake (Figure 4(a)). The two boreholes are almost 60 m far from each other and result significantly different between 7 to 30 m depth, where many thin layers of silty sand alternate with thicker layers of gravel in S11 profile, while in S12 profile the layer of gravel extends continuously, as found in S1 borehole close to the front of the Complex.

Given the data discussed in the previous sections, the following criteria were adopted for the geotechnical modeling of the two analyzed S11 and S12 profiles. The layering of each profile was directly obtained from the survey results; the lithological unit identification was based on the visual observation of the boreholes cataloging boxes combined with the results from classification laboratory tests performed on the disturbed samples, when pertinent. The shear wave velocity of each lithological unit, at a given depth, was obtained as the average of the SDMT measurements from S3, S11 and S12 locations at the same depths. Considering that S11 ends at 37 m, S12 at 50 m and S3 at 60 m, litho-stratigraphic profile from S12 (with V_s averaged values from S12 and S3) was adopted also for S11 between 37 m to 50 m (S11 and S12 are very close and the same soil unit is encountered at 37 m in both S11 and S12 borehole), while the litho-stratigraphic profile obtained from S3 (with associated V_s values) was adopted for both S11 and S12, from 50 m to 60 m. The lacustrine clay soil unit was assumed from 60 m to the top of the bedrock, estimated at a depth of 270 m (Di Buccio et al. 2017). Due to the lack of direct measurements, V_s values below 60 m of depth up to 270 m for lacustrine clays were inferred from a power regression ($V_s = a \cdot z^b$, with z depth, a=53.125 and b=0.572 determined from regression) of the available experimental

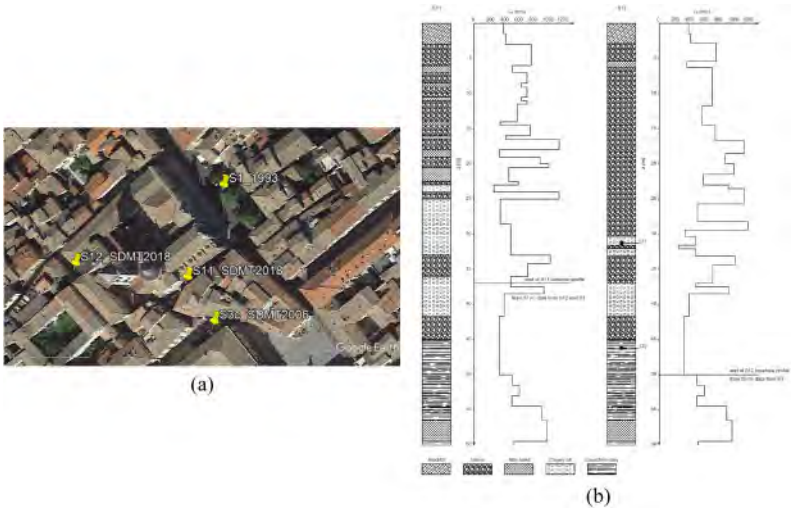

Figure 4. Location of the boreholes around the SS. Annunziata Complex (a); subsurface profiles with location of retrieved samples and associated shear-wave velocity profiles (b) at S11 and S12 sites.

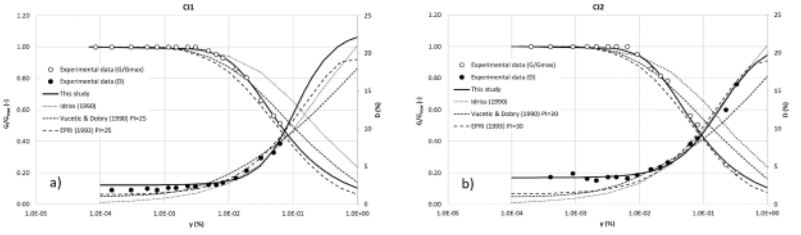

Figure 5. G/G_{max} and D experimental data for samples CI1 (a) and CI2 (b) and fitting curves compared with other literature curves.

measurements in this soil unit. Figure 4(b) shows the analyzed soil profiles of S11 and S12, with the associated V_s profiles, up to 60 m.

To describe the non-linear soil response in ground response analysis, data obtained from resonant column tests were used for the estimation of shear modulus decay and damping ratio curves for some soil units; for others, in case of any available data, literature correlations were used. Figure 5 shows the experimental results from resonant column tests performed on two specimens collected from borehole S12, namely samples CI1 (31.0-31.6 m) and CI2 (46.0-46.4 m), in terms of normalized shear modulus (G/G_{max}, being G_{max} the maximum shear modulus) and damping ratio, D, against shear strain, γ. The sample CI1 (Figure 5(a)) belongs to clayey silt and it was characterized by plasticity index PI = 24%; the sample CI2 (Figure 5(b)) belongs to lacustrine clay with PI = 31%. Figure 5 also shows the normalized shear modulus reduction and damping curves that best fit the experimental data (Ramberg-Osgood model, this study) compared with some well-established literature curves (EPRI 1993; Idriss 1990; Vucetic & Dobry 1991).

As it can be seen, the experimental shear modulus decay data are well matched by the adopted models for both CI1 and CI2; for the damping, a more satisfactory data matching is achieved for sample CI2. For both materials, the experimental shear modulus decay data are well within the range suggested by literature curves for similar PI, while the same does not hold in general for the damping data. Table 1 shows the soil parameters used in numerical analysis. The unit weight γ_n was estimated from laboratory tests on disturbed samples for all soil types, except for the calcareous bedrock. For the latter, a linear viscous-elastic behavior was assumed, with D = 0.5%, V_s = 1200 m/s and γ_n = 24kN/m^3 (Di Buccio et al. 2017).

Table 1. Soil parameters for numerical analyses.

Lithotype	γ_n (kN/m^3)	G/G$_{max}$ model	D model
Backfill	20.36	Rollins et al. (1998)	Rollins et al. (1998)
Gravel	21.30	Modoni & Gazzellone (2010)	Modoni & Gazzellone (2010)
Silty sand	20.03	Amoroso et al. (2015)	Amoroso et al. (2015)
Clayey silt	20.53	see Figure 5	see Figure 5
Lacustrine	clay 21.63	see Figure 5	see Figure 5

5 NUMERICAL ANALYSIS

Numerical 1D ground response analyses were performed on the two soil profiles S11 and S12 using the well-known STRATA computer program (Kottke & Rathje 2009). It performs linear-equivalent site analysis in the frequency domain, assuming the soils behave as viscous-elastic materials (Kelvin-Voigt model). Two sets of real time-domain input motions were used in the analysis for each soil profile (see Section 5.1), assuming a maximum frequency of 20 Hz for the discretization of the soil layers, according to the Lysmer and Kuhlemeyer (1969) criterion. The results are described in terms of peak ground acceleration (PGA) and maximum shear strain (γ_{max}) profiles, as well as of pseudo-acceleration (S_a) response spectra.

5.1 *Reference input motions*

To investigate the effects of soil non-linearity on ground motion amplification with varying the earthquake-induced strain levels, two sets of real acceleration time-histories recorded on outcropping rock have been used in the analysis. Each one included 7 different motions and was on average spectrum-compatible with a design acceleration response spectrum of the site (target spectrum). Two different return periods (Tr) were considered, namely 30 and 475 years, obtaining a set of 'weak motions' and a set of 'strong motions', respectively, The records were selected using the software Rexel v. 3.5 (Iervolino et al. 2010), within the European Strong-Motion Database, to match the target spectrum with upper and lower tolerance of 30 and 10%, respectively, in the period (T) range 0.1–2.0 s. The accelerograms were selected based on their peak ground acceleration (PGA), to fall within the range $0.5a_g < PGA < 2a_g$, being a_g the peak ground acceleration expected at the site for the two different Tr; the signals were not scaled. Among the different motion combinations returned by Rexel, the selection was based on the fault mechanism (prevalently normal and strike slip) and on magnitude (M) and epicentral distance (R) of each signal, to be as close as possible to the mean M-R couples obtained from the a_g disaggregation. Figure 6 shows the pseudo-acceleration elastic spectra for the two selected motions' sets, together with the average and target spectra (note different ordinate scale).

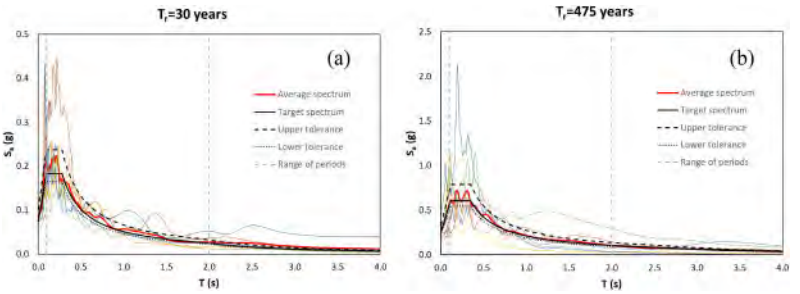

Figure 6. Pseudo-acceleration spectra of weak motions (a) and strong motions (b) used as input in the numerical analysis and corresponding average spectrum compared with the target spectrum at Sulmona for frequent ($T_r = 30$ years) and rare ($T_r = 475$ years) earthquake.

5.2 *Results*

Figure 7 shows the pseudo-acceleration (S_a) elastic response spectra (5% of critical damping) at ground surface against period (T) for S11 (Figure 7(a)) and S12 (Figure 7(b)) profiles. In Figure 7, the results for Tr = 30 years are in light grey, the results for Tr = 475 years are in darker grey, and the average spectra are in black (dashed/solid lines). As can be seen, the average elastic spectra are similar for both S11 and S12 soil profile, for each of the two considered return periods. Thus, at ground surface, significant differences are not expected, in terms of spectral acceleration, between the two sides of the SS. Annunziata Complex, where S11 and S12 boreholes are located. This result points out that the effect of the thin silty sand layers frequently encountered in the S11 profile (Figure 4(b)) is negligible. Little differences between S11 and S12 profiles could also be found in the PGA profiles (Figure 8(a)), while the maximum shear stress profiles (Figure 8(b)) show a slightly bigger variation, due to the soil types layering, with spikes corresponding to significant changes in initial V_s between adjacent layers.

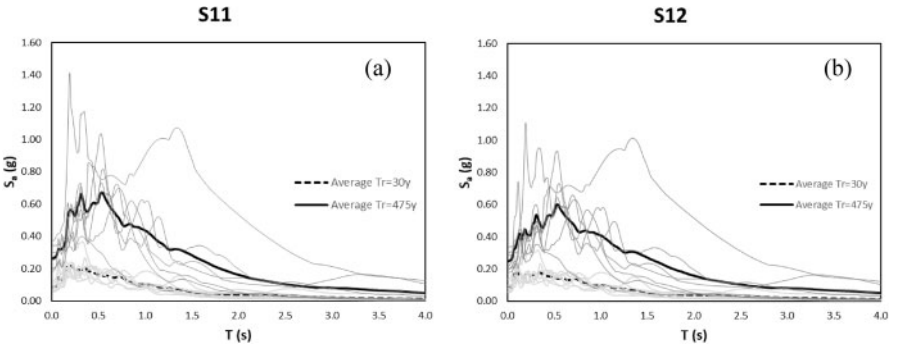

Figure 7. Pseudo-acceleration response spectra of ground surface motions at S11 (a) and S12 (b) sites for weak motions (light grey lines and dashed black line) and strong motions (dark grey lines and solid black line).

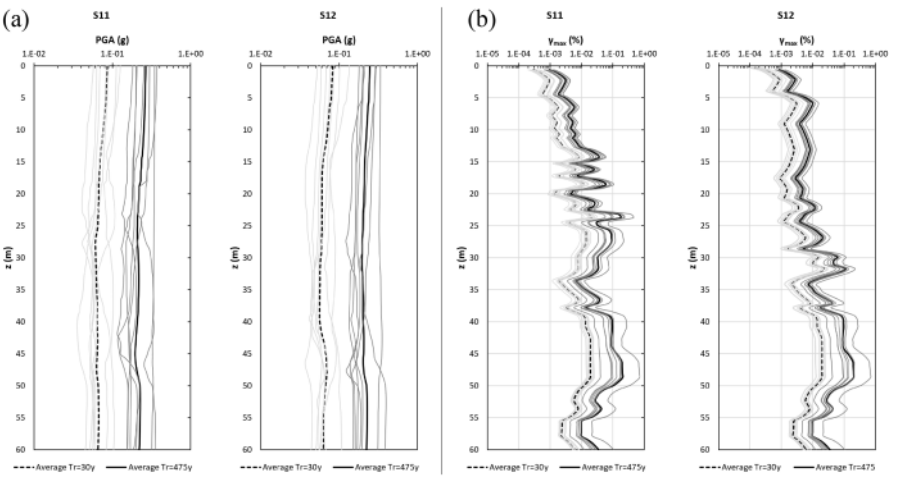

Figure 8. Peak ground acceleration (a) and maximum shear strain (b) up to 60m depth at S11 and S12 sites for weak motions (light grey lines and dashed black line) and strong motions (dark grey lines and solid black line).

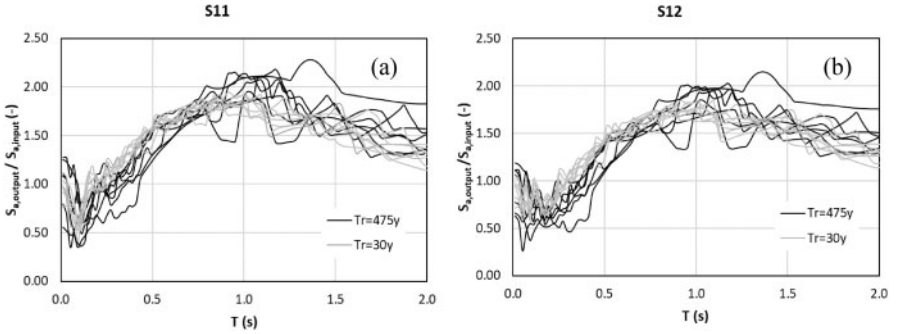

Figure 9. Spectral pseudo-acceleration ratio between ground surface motion and bedrock outcrop motion at S11 (a) and S12 (b) sites for weak motions (light grey lines) and strong motions (black lines).

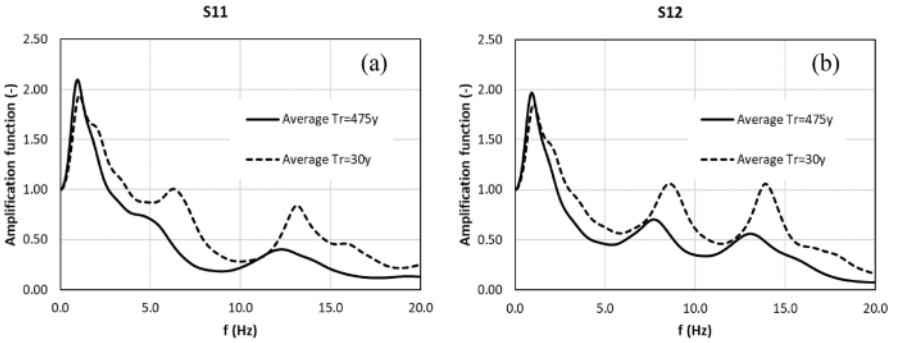

Figure 10. Amplification functions at S11 (a) and S12 (b) sites for weak motions (dashed line) and strong motions (solid line).

As it can be noted from Figures 7 and 8, the trend of the soil response under weak and strong motion inputs has a similar shape (although the amplitude of the parameters is significantly different). This is even more clear by looking at Figure 9, which shows the ratio between the spectral pseudo-acceleration at ground surface ($S_{a,output}$) and the spectral pseudo-acceleration at bedrock outcrop ($S_{a,input}$), against T, for all input signals. Within the period range 0.0-0.5s, the spectral ratio curves associated to Tr = 30 years generally lie above those associated to Tr = 475 years; for 0.5s < T < 1.0s the curves are interlocking; for higher periods, the spectral ratio curves associated to Tr = 475 years lie prevalently above those associated to Tr = 30 years. When 'strong motion' inputs are used, the natural frequencies of the deposit are expected to be lower than the natural frequencies corresponding to 'weak motion' signals, because of the reduction of the shear modulus associated to the greater shear strain level, as confirmed by the amplification function trend (Figure 10). Consequently, a greater amplification is expected for higher periods (lower frequencies) for Tr = 475 years, while greater amplification is expected at lower periods (higher frequencies) for Tr = 30 years, as it results from numerical output shown in Figure 9 and discussed above.

6 CONCLUSIONS

Preliminary 1D ground response analyses were performed on two vertical profiles in the area of the of the SS. Annunziata Complex, which is the most important historical monument in Sulmona. The main purpose of this study was to investigate the influence of the different stratigraphic conditions on local ground amplification which may have caused significant damage to the back of the Complex

during the last seismic events. Due to the lack of local recordings on outcropping rock, two different sets of input motions were selected from databases of real recordings, associated to different earthquake-induced shear strain levels (corresponding to 'weak motions' and 'strong motions'), to evaluate the influence of non-linear behaviour of soil. For each of the two signal sets, the obtained results showed that there is no significant difference in the 1D response at the ground surface for the two analyzed soil profiles. More specifically, the ground surface response does not seem to be affected by the presence of numerous sandy-silty lenses intercluded within a thick layer of fluvial-lacustrine gravel that characterizes one of the two vertical profiles. Therefore, the different amount of damage observed in the different parts of the Complex following the recent earthquakes appears to be ascribable to structural reasons rather than to the different seismic shaking at the basement. However, further research is needed to verify if significant 2D amplification effects may be induced by topography and/or by the pronounced horizontal heterogeneity associated to the presence of the sandy-silty lens within the layer of fluvial-lacustrine gravel.

ACKNOWLEDGEMENTS

Special thanks to Studio Prof. Marchetti (Italy) for kindly providing the SDMT apparatus, to FISR 2016 project to fund the 2018 site investigations and to the Municipality of Sulmona and the Casa Santa dell'Annunziata to providing the access for the site campaign.

REFERENCES

Amoroso, S., Totani, F., Totani, G. & Monaco, P. 2015. Local seismic response in the Southern part of the historic centre of L'Aquila. *Engineering Geology for Society and Territory - Urban Geology, Sustainable Planning and Landscape Exploitation* 5(XVIII): 1097-1100. Springer International Publishing.

Cavinato, G.P. & Miccadei, E. 1995. Sintesi preliminare delle caratteristiche tettoniche e sedimentarie dei depositi quaternari della Conca di Sulmona (L'Aquila). *Il Quaternario* 8(1): 129–141.

Ceccaroni, E., Ameri G., Gomez Capera, A.A. & Galadini, F. 2009. The 2nd century AD earthquake in central Italy: archaeoseismological data and seismotectonic implications. *Natural Hazards* 50: 335–359.

Ciani, F., Madiai, C. & Amoroso, S. 2021. Risposta sismica locale nel sito del Complesso della SS. Annunziata a Sulmona. *Geologia dell'Ambiente*, Supplement to n. 3/2021: 76–84.

Di Buccio, F., Aprile, V., Pagliaroli, A., Di Domenica, A., Pizzi, A., (2017). Valutazione preliminare delle risposta sismica locale del bacino di Sulmona. I*ncontro Annuale dei Ricercatori di Geotecnica – IARG 2017, Matera (Italy), 5–7 July 2017*.

Di Capua, G., Manuel, M.R. & Peppoloni, S. 2009. Microzonazione sismica speditiva del centro storico di Sulmona (AQ). *Prodotto 4 dell'Unità Operativa Geologica, Progetto DPC-Reluis, Linea 10*.

Di Filippo, M. & Miccadei, E. 1997. Studio gravimetrico della conca di Sulmona. *Il Quaternario* 10(2): 489–494.

EPRI 1993. Guidelines for determining design basis ground motions, early site permit demonstration program. *Electric Power Research Institute*, 1: RP3302. Palo Alto, California.

Galadini, F. & Carrozzo, R. 2014. I terremoti a Sulmona: indagini di sismologia storica per la microzonazione sismica. *Quaderni di Geofisica, Istituto Nazionale di Quaderni di Geofisica*, 118, 34 pp.

Galadini, F. & Galli, P. 2001. Archaeoseismology in Italy: case studies and implications on long-term seismicity. *Journal of Earthquake Engineering* 5: 35–68.

Galli, P., Giaccio, B., Peronace, E. & Messina, P. 2015. Holocene paleoearthquakes and Early–Late Pleistocene slip rate on the Sulmona fault (Central Apeninnes, Italy). *Bulletin of the Seismological Society of America* 105(1): 1–13.

Giannantonio, R. 1997. *Il palazzo della SS: Annunziata in Sulmona*. I saggi di Opus (6). Pescara: Carsa Edizioni.

Gori, S., Dramis, F., Galadini, F. & Messina, P. 2007. The use of geomorphological markers in the footwall of active faults for kinematic evaluations: examples from the central Apennines. *Bollettino della Società Geologica Italiana* 126: 365–374.

Gori, S., Falcucci, E., Dramis, F., Galadini, F., Galli, P., Giaccio, B., Messina, P., Pizzi, A., Sposato, A. & Cosentino, D. 2014. Deep-seated gravitational slope deformation, large-scale rock failure, and active normal

faulting along Mt. Morrone (Sulmona basin, Central Italy): Geomorphological and paleoseismological analyses. *Geomorphology* 208: 88–101.

Gori, S., Giaccio, B., Galadini, F., Falcucci, E., Messina, P., Sposato, A. & Dramis, F. 2011. Active normal Faulting along the Monte Morrone South-Western slopes (Central Apennines, Italy). *International Journal of Earth Science* 100(1): 157–171.

Idriss, I.M. 1990. Response of soft soils during earthquakes. In J. M. Duncan (ed.), *Proceedings, H. Bolton Seed Memorial Symposium* 2: 273–289. Vancouver: BiTech Publishers.

Iervolino, I., Galasso, C. & Cosenza, E. 2010. REXEL: computer aided record selection for code-based seismic structural analysis. *Bulletin of Earthquake Engineering* 8: 339–362.

Kottke, A.R & Rathje, E.M. 2009. Technical Manual for Strata, *University of Texas*, Austin, Texas.

Lysmer, J. and Kuhlemeyer, R. L. (1969) Finite Dynamic Model for Infinite Media. *Journal of Engineering Mechanics Division* 95, 859–878.

Manuel, M.R. 2007. Dalle indagini al modello geologico-tecnico per la definizione della risposta sismica locale finalizzata alla microzonazione sismica di piane alluvionali e costiere. *Phd Thesis*, University of Rome "Sapienza".

Mattiocco, E. 2008. *L'Annunziata di Sulmona*. Editrice Itinerari: Lanciano (CH).

Meletti, C. & Valensise, G. 2004. Zonazione sismogenetica ZS9 – *App. 2 al Rapporto Conclusivo "Gruppo di Lavoro MPS, Redazione della mappa di pericolosità sismica prevista dall'Ordinanza PCM 3274 del 20 marzo 2003. Rapporto Conclusivo per il Dipartimento della Protezione Civile"*, INGV, Milano–Roma, aprile 2004, 65.

Miccadei, E., Barberi, R., & Cavinato, G.P. 1998. La geologia quaternaria della conca di Sulmona (Abruzzo, Italia centrale). *Geologica Romana* 34:59–86.

Ministero delle infrastrutture e dei Trasporti 2018. Norme Tecniche per le Costruzioni (NTC18). Decreto Ministero Infrastrutture. GU Serie Generale n. 42 del 20-02-2018 – Suppl. Ordinario n. 8.

Modoni, G. & Gazzellone, A. 2010. Simplified theoretical analysis of the seismic response of artificially compacted gravels. 5th *International Conference on Recent Advance in Geotechnical Earthquake Engineering and Soil Dynamics, San Diego, California, 24–29 May 2010*, Paper Number 1.28.a.

Pizzi, A., Miccadei, E., Piacentini, T., Pipponzi, G., Galadini, F. & Luzi, L. 2014. Microzonazione simica di Livello 1 del Comune di Sulmona (AQ), Relazione illustrativa con carte e sezioni allegate, *Regione Abruzzo–Dip. Protezione Civile*, https://protezionecivile.regione.abruzzo.it/index.php/microzonazione.

Rollins, K.M., Evans, M.D., Diehl, N.B. & Daily, W.D. 1998. Shear modulus and damping relationships for gravels. *Journal of Geotechnical andGeoenvironmental Engineering* 124: 396–405.

Rovida A., Locati M., Camassi R., Lolli B., Gasperini P., Antonucci A. (2021). Catalogo Parametrico dei Terremoti Italiani (CPTI15), versione 3.0. *Istituto Nazionale di Geofisica e Vulcanologia (INGV)*. https://doi.org/10.13127/CPTI/CPTI15.3

Scarascia Mugnozza, G. 2007. Microzonazione sismica di 2° livello. Indagini e risultati ai fini della progettazione esecutiva della microzonazione sismica del centro abitato di Sulmona. Allegato 1. Indagini geologico-tecniche, ricostruzioni stratigrafiche e cartografia. *University of Rome "Sapienza", Italy*.

Totani G., Monaco P., Marchetti S. & Marchetti D. 2009. VS measurements by seismic dilatometer (SDMT) in non-penetrable soils. In: Hamza M. et al. (eds.), *17th Int. Conf. on Soil Mechanics and Geotechnical Engineering, Alexandria*, 977–980.

Tuteri, R. 1995. Pavimenti antichi a Sulmona. Relazione preliminare sulle nuove acquisizioni. *II Colloquio AISCOM (Associazione Italiana per lo Studio e la conservazione del Mosaico), Roma, 5–7 December 1994,Bordighera*. 71–84.

Vittori, E., Cavinato, G.P. & Miccadei, E. 1995. Active faulting along the northeastern edge of the Sulmona basin, central Apennines, Italy. In: Serva L., Burton Slemmons D. (eds.), *Perspective in paleoseismology. Special Publication-Association of Engineering Geologists* 6: 115–126.

Vucetic, M., & Dobry, R. 1991. Effect of soil plasticity on cyclic response. *Journal of Geotechnical Engineering* 117(1): 89–107.

Geotechnical Engineering for the Preservation of Monuments and Historic Sites III – Lancellotta, Viggiani, Flora, de Silva & Mele (Eds)

A simplified method for the estimation of earthquake-induced pore pressures

G. Boccieri
Università di Roma Niccolò Cusano, Rome, Italy

D. Gaudio
Sapienza Università di Roma, Rome, Italy

R. Conti
Università di Roma Niccolò Cusano, Rome, Italy

ABSTRACT: A reliable assessment of liquefaction hazard is crucial for reducing the seismic risk of existing structures, especially for historical heritage. Common practice would need earthquake-induced pore pressures to be evaluated through simple methods, such as *uncoupled* approaches. *Uncoupled* approaches based on undrained cyclic laboratory tests originate from Seed et al. (1975), where seismic-induced rate of excess pore pressure build-up under fully-undrained conditions was added to the one-dimensional consolidation equation by Terzaghi. Despite its simplicity, this approach allows to consider the key features of liquefaction, as the influence of partially-drained conditions and pore pressures dissipation. In this paper, a simplified method based on Seed et al. (1975) is presented, aimed at estimating earthquake-induced pore water pressures. The governing equation is solved using the Finite Difference Method, by taking into account the dependence of soil stiffness on current mean effective stress. Different strategies for modelling the source term are presented and discussed.

1 INTRODUCTION

Under medium-to-high intensity earthquakes, excess pore water pressures may develop in saturated sandy soil layers exhibiting an undrained or a partially drained response, thus reducing the effective stress state acting into the soil, and, consequently, its shear stiffness and strength. This effect may result in catastrophic consequences for structures resting on liquefied soils, as recognised in post-earthquake surveys conducted worldwide after strong-motion earthquakes, such as the well-known ones occurred in Niigata (1964), (Kramer 1996), Kobe (1995), Shibata et al. (1996), Christchurch (2010) and (Cubrinovski et al. 2011). More recently, the Emilia earthquake (2012) (Mucciarelli & Liberatore 2014) caused severe damages to the historical heritage, such as façades and bell towers of churches (Sorrentino et al. 2013a), medieval fortresses and vernacular buildings (Sorrentino et al. 2013b). Therefore, there is a strong need of developing procedures to obtain a reliable estimate of the liquefaction hazard and, consequently, of the excess pore water pressures accumulated in saturated sandy soil deposits.

Two different approaches are available for evaluating the excess pore water pressures induced by earthquakes (Chiaradonna et al. 2018), namely the *decoupled* approach and the *coupled* approach. The *decoupled* approach is typically adopted for simplified liquefaction analyses and therefore followed by national codes: in this case, semi-empirical equations based on the results of ground response analyses performed neglecting the bi-phasic nature of soils (i.e. total stress approach) are used. In spite of its simplicity, this approach requires some arbitrary tasks, such as the definition of an equivalent cyclic loading for the irregular seismic-induced shear stresses, in terms of induced excess pore water pressures (Seed et al. 1975). Conversely, the *coupled* approach relies on rigorous Finite Element or Finite Difference nonlinear (effective stresses) dynamic analyses. In this case, less (still different from zero though) arbitrary assumptions must be introduced, but more onerous and time-consuming analyses must be carried out.

 DOI 10.1201/9781003308867-62

Following a *decoupled* approach, this paper presents a simplified method for the evaluation of earthquake-induced pore pressures in liquefiable soils. The method is based on the seminal work by Seed et al. (1975), who modified the well-known 1D consolidation equation (Terzaghi 1923) by adding a source term due to earthquake shaking, representing the rate of excess pore water pressure build-up under fully-undrained conditions. The procedure is implemented in a home-made Matlab program through the Finite Difference Method. The simple constitutive approach recently proposed by Conti et al. (2020) is adopted to perform the preliminary 1D nonlinear ground response analysis, necessary for a proper estimate of the shear stress time histories acting into the soil and therefore of the number of cycles to liquefaction. The good estimate of excess pore water pressures obtained via the proposed simplified method is demonstrated through the comparison with a case study from the literature where a *coupled* approach was followed (Chiaradonna et al. 2019).

Overall, the proposed method aims at providing a simplified but physically-sound solution of the problem, which captures the main physical aspects of the liquefaction phenomenon while keeping a good balance in between accuracy and ease of use.

2 IMPLEMENTATION OF THE SIMPLIFIED METHOD

Seed et al. (1975) proposed a *decoupled* approach to evaluate the development and redistribution of seismic-induced excess pore water pressures, u, in a horizontally-stratified soil deposit, based on the results of cyclic undrained tests. The key idea was adding to the one-dimensional consolidation equation by Terzaghi (Terzaghi 1923) a source term due to earthquake shaking:

$$\frac{\partial u}{\partial t} = c_{\mathrm{v}} \cdot \frac{\partial^2 u}{\partial z^2} + \frac{\partial u_{\mathrm{g}}}{\partial t} \tag{1}$$

where the first term on the right side is the classical dissipative term, proportional to the consolidation coefficient c_v, and the second one is the above-mentioned source term, representing the rate of excess pore water pressure build-up under fully-undrained conditions. Despite its very simplicity, Equation (1) provides an immediate picture of the pore pressure generation phenomenon under partially drained conditions. Indeed, if the first term on the right side of the equation is relatively small, excess pore pressures $\partial u/\partial t$ would be similar to those developed in undrained conditions, $\partial u_g/\partial t$. Conversely, if the two terms on the right side match each other, the soil response would result perfectly drained and all the earthquake-induced pore pressures would be instantaneously dissipated by the soil layer. Finally, when the second term is relatively small or null, then soil behaviour is ruled by 1D consolidation. This is the case, for example, of the post-earthquake stage, where possible excess pore water pressures are gradually dissipated within the soil deposit.

In the light of a *decoupled* approach, the source term must be related to the driving shear stresses, $\tau(t)$, induced by the seismic waves into the soil, and the latter can be computed by means of simple 1D Linear Equivalent or Nonlinear site response analyses. To this end, the seismic-induced time history of shear stress is conventionally replaced with a cyclic loading characterised by a constant amplitude, τ_{eq} (typically assumed as the 65% of the maximum shear stress τ_{max}), and by an equivalent number of cycles, N_{eq}, uniformly distributed over the cyclic loading duration, T_d. Following this procedure, the source term can be rewritten as:

$$\frac{\partial u_{\mathrm{g}}}{\partial t} = \frac{\partial u_{\mathrm{g}}}{\partial N} + \frac{\partial N}{\partial t} = \frac{\sigma'_{\mathrm{v0}}}{N_{\mathrm{L}}} \cdot \frac{\partial r_{\mathrm{u}}}{\partial r_{\mathrm{N}}} \cdot \frac{N_{\mathrm{eq}}}{T_{\mathrm{d}}} \tag{2}$$

where $r_{\mathrm{u}} = u_{\mathrm{g}}/\sigma'_{\mathrm{v0}}$ is the pore pressure ratio; $r_{\mathrm{N}} = N/N_{\mathrm{L}}$ is the cyclic ratio; N is the n-th cycle of loading; and N_{L} is the number of cycles needed to trigger liquefaction (i.e. $u_{\mathrm{g}} = \sigma'_{\mathrm{v0}}$ and therefore $r_{\mathrm{u}} = 1$). Under these assumptions, Seed & Booker (1977) expressed r_{u} as a function of r_{N} through an analytical expression which fitted the results of cyclic laboratory tests carried out in undrained conditions, as follows:

$$r_{\mathrm{u}} = \frac{2}{\pi} \cdot \sin^{-1}\left(r_{\mathrm{N}}^{\frac{1}{2\alpha}}\right) \tag{3}$$

where α is a function of soil current state and test conditions.

If the number of cycles required to trigger liquefaction, N_L, is known, together with the duration T_d and the equivalent number of cycles N_{eq}, then the rate of excess pore water pressures developing under fully-undrained conditions, $\partial u_g/\partial t$, can be computed through Equation (2).

The recalled model by Seed et al. (1975) was implemented in Matlab v.9.10.0 (R2021a) (MATLAB 2021) through the Finite Difference Method (FDM) for the specific case of a double-layered soil deposit. The following additional assumptions were introduced:

(i.) the deepest stratum is susceptible to liquefaction, being ruled by Equation (1);
(ii.) in the shallowest layer, redistribution of pore water pressure takes place only, which is governed by the classical equation by Terzaghi (i.e. $\partial u_g/\partial t = 0$);
(iii.) two conditions were imposed at the interface between the two layers, namely the water flow continuity and the pore water pressure equilibrium;
(iv.) free drainage is allowed at the groundwater level only (i.e. impervious boundary at the bottom of the soil column);
(v.) the shear stiffness modulus, G, is a function of the mean effective stress p'.

The last assumption allows taking into account the effect of the progressive reduction (or recovery) of soil shear stiffness on the generation and redistribution of pore water pressures during both the strong motion and post-earthquake stages of the analysis.

In the following of this section, evaluation of N_L, N_{eq}, T_d and $G(p')$ is illustrated.

2.1 *Number of cycles to liquefaction* N_L

The number of uniform cycles needed to produce liquefaction, N_L, was obtained from experimental cyclic resistance curves $CSR - N_L$. The cyclic stress ratio $CSR = \tau_{eq}/\sigma'_{v0}$ can be evaluated from the maximum shear stresses τ_{max} generated by the seismic event, which can be derived through either a seismic response analysis or a simplified procedure. It is worth noting that, since uncertainties arising in the simplified procedure increase with depth, the latter should be applied only for depths less than about 20 m, while liquefaction evaluations at greater depths should be based on seismic response analysis (Idriss & Boulanger 2006).

The relationship between CSR and N_L, within the range of cycles of interest for earthquake engineering, can be approximated through a power function as (Idriss & Boulanger 2008):

$$CSR = \beta \cdot N_L^{-\eta} \tag{4}$$

where β and η are coefficients mainly depending on the relative density D_R, defining the intercept and the slope of the curve in a semi-logarithmic plane, and can be determined from experimental data.

2.2 *Properties of the equivalent cyclic loading,* N_{eq} *and* T_d

The irregular seismic-induced time history of shear stress is replaced by an equivalent cyclic loading, which, in principle, should produce the same increase of excess pore water pressures in the soil sample under a fully undrained condition.

The conversion procedure is based on the hypothesis of linear damage accumulation proposed by Miner (1945) for the calculation of fatigue damage in aluminium (Biondi et al. 2012; Hancock & Bommer 2005). The additional assumption of considering the horizontal acceleration rather than the shear stress time history was made in this study, thanks to their direct proportionality (Biondi et al. 2012). Considering the curves $CSR - N_L$ as the loci of same damage level (i.e. initial liquefaction of soil sample), the number of equivalent cycles N_{eq} of a cyclic loading with amplitude $a_{eq} = 0.65\ a_{max}$, where a_{max} is the maximum value of the acceleration signal, can be computed as:

$$N_{eq} = \sum_i N_i \cdot \left(\frac{a_{eq}}{a_i}\right)^{-1/\eta} \tag{5}$$

where N_i is the number of cycles with amplitude a_i of the initial signal and η is the same coefficient as in Equation (4).

A method for calculating the number of cycles of the accelerometric signal was therefore necessary. To this end, the peak-counting method was adopted, where the number of largest peaks between adjacent zero-crossing is explicitly counted (Hancock & Bommer 2005). Every peak encountered in between two adjacent zeros identifies a hemicycle ($N_i = 0.5$ in Eq. (5)).

The equivalent number of cycles N_{eq} can be considered either variable with depth, when a seismic site response analysis providing acceleration time histories at the different depths is performed, or equal to a constant value within the soil column. In the latter case, deriving N_{eq} directly from the input signal at the bedrock is not recommended, since the applied acceleration is likely to be filtered by the overlying deformable soil layers. Therefore, it would be more appropriate to consider the signal either at the free-field ground surface or at an adequate, intermediate depth of the liquefiable layer.

The cyclic loading duration T_d was taken equal to the strong motion duration of the acceleration time history computed either at the soil surface or within the liquefiable soil layer. Specifically, T_d was defined following Trifunac and Brady (1975), as the range spanned by time intervals when Arias intensity reaches its 5% and 95% of its final value. Hereby it is worth mentioning that the influence of soil deformability on T_d is much less pronounced than for N_{eq}.

2.3 *Soil stiffness*

Empirical relationships typically adopted for the small-strain shear modulus G_0 of sands assume the following functional form (Viggiani & Atkinson 1995; Wichtmann & Triantafyllidis 2009):

$$G_0 = F(e) \cdot (p'_0)^{0.5} \tag{6}$$

where $F(e)$ is a function of void ratio e and grain size distribution, while p'_0 is the initial mean effective stress. In this study, the same relationship was used to compute the current value of the soil shear modulus at any time instant during the seismic excitation. To this end, the initial stress state was replaced by the current mean effective stress, p', as variations of the effective stress state can be remarkable due to the possible high development of excess pore water pressure during shaking. This aspect is crucial for an accurate simulation of both the generative and dissipative terms (Adamidis & Madabhushi 2016) and allowed to take into account the dependency of the oedometric modulus, E_{oed},and of the 1D consolidation coefficient, c_v, on the current effective stress, defined as:

$$E_{oed} = \frac{2G(1-\nu)}{(1-2\nu)} \tag{7}$$

$$c_v = \frac{k \cdot E_{oed}}{\gamma w} \tag{8}$$

where G is the current shear modulus, depending on the actual mean effective stress, ν is the Poisson ratio, k is the (vertical) hydraulic conductivity, and γ_w = 9.81 kN/m^3 is the unit weight of water.

3 1D NONLINEAR SITE RESPONSE ANALYSIS

Liquefaction is typically triggered by medium-to-high intensity earthquakes, which cause significant accelerations within the soil deposit. For this reason, the profile of maximum shear stress, $\tau_{max}(z)$, should be derived by means of Nonlinear seismic site response analyses rather than Linear Equivalent ones. This way, the amplitude of the equivalent cyclic loading, τ_{eq}, and the number of cycles to liquefaction, N_L, are computed properly.

In this work, a 1D Nonlinear site response analysis was used to compute $\tau_{max}(z)$. To this end, the 1D dynamic equilibrium equation was solved through the Finite Difference Method, implemented

in a home-made Matlab program. The nonlinear soil model recently proposed by Conti et al. (2020) was used, including both nonlinearity and shear strength as constitutive ingredients. The model combines the hyperbolic functional form introduced by Hardin and Drnevich (1972) for the backbone curve with the unloading-reloading rule suggested by Phillips & Hashash (2009). The main novel contribution of the new approach was linking the nonlinear soil behaviour to its small strain stiffness and shear strength through functions of effective stresses. As a result, prediction of 1D cyclic behaviour of soils was improved despite the reduction of soil parameters (only six), compared to previous models (Phillips & Hashash 2009). Four out of the six parameters (a, b, c and d) depend solely on the nature of soil and can be easily calibrated against one single cyclic laboratory test, while the two remaining ones (τ_{lim} and G_0) depend also on the effective stress, and can be obtained from either standard penetration and seismic field tests or laboratory tests.

The steps followed to implement the adopted constitutive soil model within the 1D nonlinear code are summarised below:

i. determine the small-strain shear modulus and shear strength profiles, $G_0(z)$ and $\tau_{lim}(z)$, both depending on the effective stress state;
ii. for each material within the soil column, calibrate parameters a, b, c and d against experimental shear modulus degradation and damping curves, $G(\gamma)/G_0$ and $D(\gamma)$,where γ is the shear strain. Here it is worth noting that the experimental (or empirical) curves should refer to a single value of p', as the dependency on the effective stress state is already enclosed in the shear stiffness and strength profiles from previous point.;
iii. divide the soil column in layers with constant values of G_0 to input the dependence of the small-strain shear modulus on the depth (via the effective stress state);
iv. assign a, b, c, d, G_0 and τ_{lim} as constitutive parameters and make use of the constitutive equations proposed Conti et al (2020).

4 VALIDATION ON A CASE STUDY

This section aims at demonstrating the capability of the simplified method outlined in this paper of predicting the excess pore water pressures induced by the earthquake within the soil deposit and possibly leading to full liquefaction. Specifically, a comparison with the case study recently presented by Chiaradonna et al. (2019) is made, where the seismic performance of a levee of an irrigation channel, which was severely damaged during the 2012 Emilia earthquake, was considered. The study was carried out considering a reference soil column which was subjected to a seismic shaking in a 1D *coupled* dynamic analysis performed in terms of effective stresses via the code SCOSSA (Tropeano et al. 2016), where the build-up of excess pore water pressures is computed based on the definition of a "damage parameter" (Chiaradonna et al. 2018). Conversely, a two-steps *uncoupled* procedure was followed in this work. First, a 1D nonlinear ground response analysis was performed through the one-dimensional home-made computer program presented in Conti et al. (2020) to obtain the equivalent cyclic loading and, therefore, the number of cycles to liquefaction, N_L (§ 3). Second, the seismic-induced excess pore water pressures were computed through the method by Seed et al. (1975) (§ 2).

In the following sections, a comparison with the results obtained by Chiaradonna et al. (2019) is presented. For the sake of clarity, the results of the 1D ground response analysis and the evaluation of seismic-induced excess pore water pressures will be discussed separately.

4.1 *1D nonlinear seismic response analysis*

The nonlinear seismic site response analysis was carried out for a 115 m-deep layered soil column. The dyke and its foundation soil consist of a silty sand layer overlying a thick deposit of alluvial sands, alternated with layers of clay. The saturated silty sand and the shallowest sand layers are potentially liquefiable.

Figure 1 shows the soil stratigraphy along with the small-strain shear wave velocity, V_{S0}, profiles adopted in this study and in Chiaradonna et al. (2019), while Figure 2 displays the shear modulus

degradation and damping curves considered by Chiaradonna et al. (2019), together with those utilized in this study.

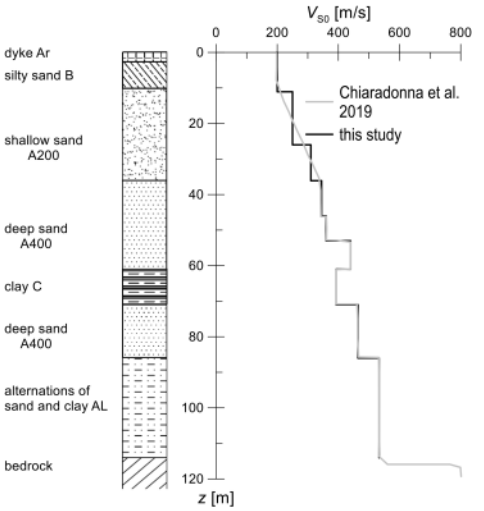

Figure 1. Soil stratigraphy and profile of the small-strain shear wave velocity.

The six parameters required to define the constitutive soil model were calibrated against the strength parameters reported in Chiaradonna et al. (2019) and the laboratory data published by Tonni et al. (2015). These are listed in Table 1, where: z_{top} and z_{bottom} are the depths of the top and the bottom of each layer, measured starting from the ground surface, and $\Delta z = z_{top} - z_{bottom}$ is the corresponding thickness; a and b are the parameters defining the shear modulus degradation curves, while c and d define the damping curves; φ' is the soil friction angle; σ'_0 is either the vertical or the mean effective stress, depending on relevant laboratory test performed to obtain the strength and stiffness parameters (dual-specimen direct simple shear, DSDSS, or resonant column, RC); $V_{S0} = \sqrt{(G_0/\rho)}$ is the small-strain shear wave velocity; ρ is the mass density of soils; ν is the Poisson ratio and k is the hydraulic conductivity.

Table 1. Model parameters adopted in this study.

Soil	z_{top} m	z_{bottom} m	Δz m	a –	b –	c –	d –	φ' °	σ'_0 kPa	V_{S0} m/s	ν –	k m/s
Dyke	0	2.5	2.5	0.73	0.10	0.70	1.73	33	100	145	0.306	$1 \cdot 10^{-6}$
Silty sand	2.5	10.0	7.5	0.73	0.10	0.70	1.73	33	100	145	0.306	$1 \cdot 10^{-6}$
Sand A200	10.0	35.0	25.0	1.09	0.10	0.63	2.31	38	200	175	0.286	$3 \cdot 10^{-5}$
Sand A400	35.0	61.0	26.0	1.92	0.10	0.55	1.02	38	400	215	0.286	$3 \cdot 10^{-5}$
Clay	61.0	71.0	10.0	0.10	10.0	0.84	1.84	25.5	100	160	0.371	$1 \cdot 10^{-8}$
Sand A400	71.0	86.0	15.0	1.92	0.10	0.55	1.02	38	400	215	0.286	$3 \cdot 10^{-5}$
Alter. AL	86.0	115.0	29.0	1.16	0.10	0.47	1.31	33	400	215	–	–

The input motion adopted in the seismic site response analysis is plotted in Figure 3, in terms of horizontal acceleration time history (a) and Fourier amplitude spectrum (b). The original signal was low-pass filtered at a frequency f_{max} = 10 Hz, through an 8th-order lowpass Butterworth filter, and then brought back to the initial peak ground acceleration *PGA*, equal to 0.344 g. The input signal was applied as an outcrop motion.

The results obtained from the nonlinear seismic site response analysis are presented in Figure 4 in terms of a_{max}, τ_{max} and γ_{max}. The maximum shear stresses τ_{max} obtained in this study through the

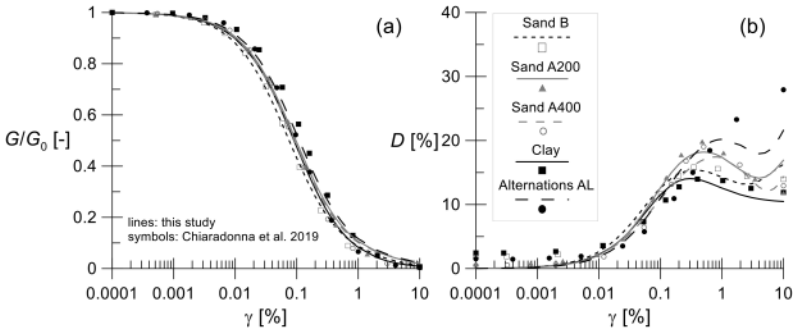

Figure 2. (a) Shear modulus degradation curves and (b) damping curves adopted in this study and in Chiaradonna et al. (2019).

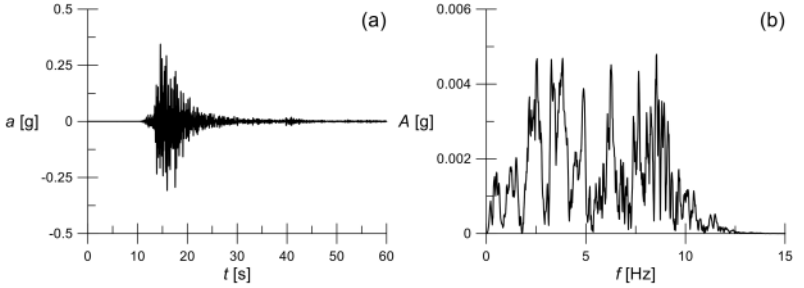

Figure 3. (a) Horizontal acceleration time history and (b) Fourier amplitude spectrum of the input motion adopted in the seismic site response analysis.

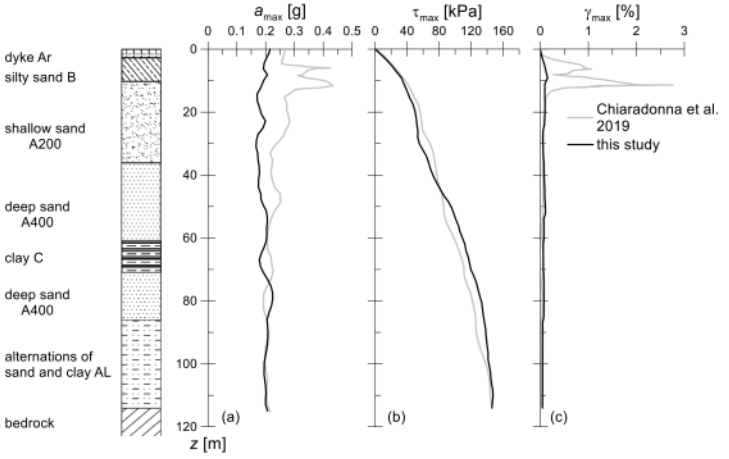

Figure 4. Profiles of the (a) peak acceleration, (b) maximum shear stress and (c) maximum shear strain.

decoupled approach are quite in a good agreement with those provided by Chiaradonna et al. (2019). This result clearly stems from the fact that, even following a more rigorous *coupled* approach, the maximum shear stresses within a liquefiable soil layer are reached before triggering liquefaction, thus they are not affected by the subsequent liquefaction-related stiffness degradation and damping increase. This aspect is evident by inspection of Figure 5, showing (a) the time history of shear stresses and excess pore pressure ratio, r_u, computed at $z = 2.2$ m by Chiaradonna et al. (2019) and

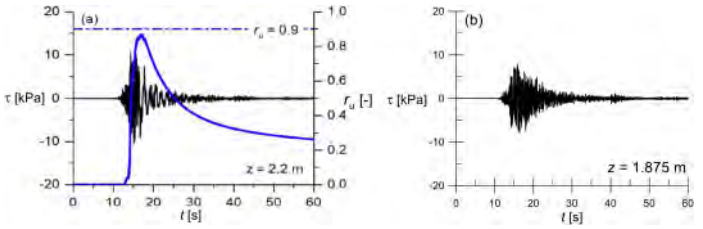

Figure 5. (a) Shear stress time history over the liquefied layer in the case study (after Chiaradonna et al. 2019) and (b) in this study through the proposed *decoupled* approach.

(b) the shear stress computed at $z = 1.875$ m in this work. On one hand, the two approaches provide comparable results in terms of maximum shear stresses. On the other hand, the decoupled approach cannot reproduce the significant filtering of shear stress occurring once the full liquefaction condition is triggered within the shallow sand layers. Conversely, the main difference between the two approaches lies in the maximum shear strain developed close to the ground surface. This is due to the inherent inability of the *decoupled* approach of estimating the high deformations produced by the liquefaction phenomena.

4.2 *Evaluation of seismic-induced excess pore water pressures*

A proper evaluation of the seismic-induced excess pore water pressures requires a preliminary calibration of the parameters defining the $r_u - r_N$ (Eq. (3)) and $CSR - N_L$ (Eq. (4)) relationships. Experimental data for the sand layers (A200 and A400) and the silty sand (B) were provided in Chiaradonna et al. (2019). Considering only sand data, the best-fitting values of α for the $r_u - r_N$ curve (Figure 6a), β and η, for the liquefaction resistance curve (Figure 6b), are equal to 0.890, 0.345 and 0.285, respectively. From the comparison between the liquefaction resistance curve used in the present work and in the case study, it turns out that the two curves are in good agreement, at least for the range of CSR and N_L values of interest, as obtained from the site response analysis (grey-shaded area in Figure 6b). Furthermore, the $r_u - r_N$ curve proposed by Seed et al. (1975) was scaled by a factor of 0.9 to be in agreement with Chiaradonna et al. (2019), who set the threshold for initial liquefaction at $r_u = 0.9$ (Figure 6a).

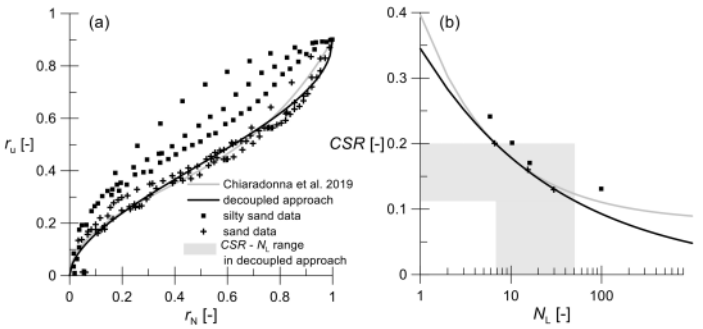

Figure 6. (a) Pore water pressure relationship (Eq. (3)) and (b) cyclic resistance curves (Eq. (4)) adopted in the present study and in Chiaradonna et al. (2019).

The geometry of the multi-layered soil deposit (Figure 1) was simplified into a double-layered soil column for evaluating the seismic-induced excess pore water pressures through Eqs. (1)–(2). The soil column was divided into a superficial 2-m-thick non-liquefiable layer, corresponding to the previous dyke (Ar) stratum, underlain by a 58-m-thick potentially liquefiable layer, this

representing all the sandy soils (B, A200, and A400) resting on the clay layer (C). The clay layer was modelled as an impervious boundary, consistently with Chiaradonna et al. (2019) who showed null excess pore water pressures ($r_u = 0$) below depth $z = 60$ m. The groundwater level was located at depth $z_w = 2$ m and the initial pore water pressure regime was hydrostatic.

In order to assess the influence of the hypothesis made on the equivalent number of cycles, N_{eq}, two different analyses were performed, assuming that N_{eq} either varies with depth (Figure 7), or is constant (Figure 8). Conversely, in both cases the duration of the equivalent cyclic loading, T_d, was considered constant with depth.

In the first analysis, the duration of the equivalent cyclic loading, $T_d = 10.48$ s, was evaluated from the horizontal acceleration time history computed at the ground surface ($z = 0$) in the 1D nonlinear seismic response analysis (Figure 7b). The two vertical black lines in Figure 7d indicate the corresponding time interval of the strong motion stage. By inspection of Figure 7b, it can be observed that the T_d value computed at ground surface is very close to the average valued computed along the entire soil column. In this analysis, liquefaction was triggered in between depths $z = 2 – 21$ m ($r_{u\,max} = 0.9$, Figure 7c), corresponding to the depth range where $N_{eq} > N_L$ (Figure 7a): the simplified analysis therefore predicts liquefaction occurring within the silty sand (B) and the most superficial part of the shallow sand (A200). This result is in agreement with Chiaradonna et al. (2019), whose 1D *coupled* dynamic analysis estimated liquefaction happening in a thinner part of deposit though ($z = 3 – 12$ m). From the contours of the pore pressure ratio, r_u, it turns out that no excess pore water pressure is computed before the strong-motion phase started, as expected when using the simplified model by Seed et al. (1975). Then, liquefaction is rapidly triggered in the shallowest part of the soil column while the equivalent cyclic loading is applied. Finally, dissipation of seismic-induced excess pore water pressures takes place over the whole soil column, except for what obtained around the mid-height ($z \approx 30$ m), where pore water pressures slightly increase. It is worth noting that this result shows the capability of the simplified method of reproducing even possible post-earthquake liquefaction.

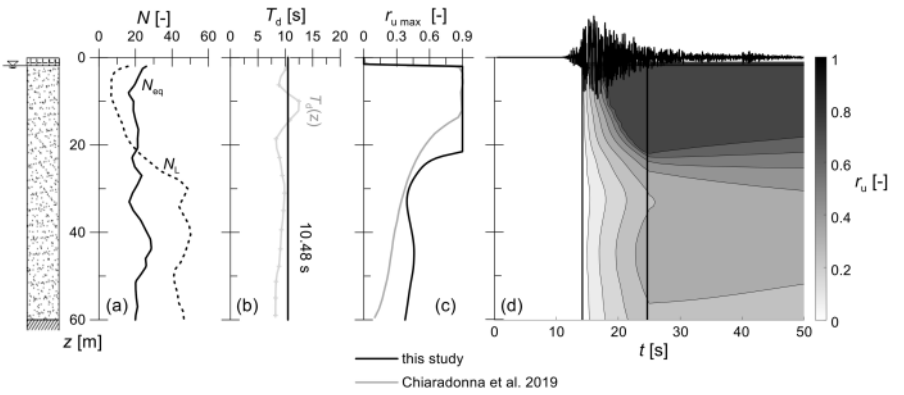

Figure 7. Main results from the analysis performed assuming an equivalent number of cycles varying with depth: profiles of (a) equivalent and limit (i.e. to liquefaction) number of cycles, (b) significant duration, (c) maximum pore pressure ratio with depth, together with (d) contours of the pore pressure ratio.

The results obtained in the second analysis, where N_{eq} is constant with depth, are given in Figure 8. This time, both N_{eq} and T_d were obtained from the acceleration time history computed at the mid-height of the liquefiable layer ($z \approx 30$ m), being equal to 18.42 and 9.85 s, respectively. Selection of time trace at the mid-height comes after observing that the corresponding values of both N_{eq} and T_d are close to the relevant average values computed along the soil column ($N_{eq,av} = 21.4$ and $T_{d,av} = 9.40$ s). Figure 8 shows that the adopted assumption on the equivalent number of cycles does not affect the results noticeably. Therefore, this further simplifying assumption may be deemed adequate for preliminary evaluation of the seismic-induced excess pore water pressures.

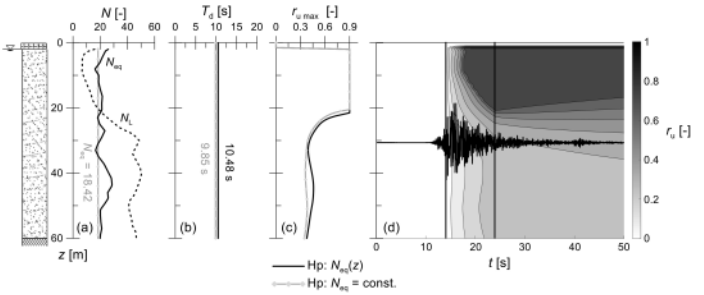

Figure 8. Main results from the analysis performed assuming an equivalent number of cycles constant with depth: profiles of (a) equivalent and limit (i.e. to liquefaction) number of cycles, (b) significant duration, (c) maximum pore pressure ratio with depth, together with (d) contours of the pore pressure ratio.

5 SYNOPSYS AND CONCLUSIONS

A reliable assessment of liquefaction hazard is crucial for reducing the seismic risk of existing structures, with reference also to monuments and historic sites, which may result more vulnerable to soil liquefaction. In this context, the development of a ready-to-use but still physically-sound simplified method for evaluating the seismic-induced excess pore water pressures accumulated into liquefiable soils is deemed necessary, as this assessment still relies on onerous and time-consuming *coupled* nonlinear dynamic analyses.

This paper presented a simplified method for the evaluation of earthquake-induced pore pressures, which was developed starting from the seminal work by Seed et al. (1975). In the method, the number of cycles needed to trigger soil liquefaction and the consequent development of excess pore water pressures can be easily calibrated against routine cyclic laboratory tests. Moreover, an equivalent cyclic loading must be defined, through its amplitude τ_{eq}, its equivalent number of cycles N_{eq}, and its duration T_d.

The procedure was implemented in a home-made Matlab program through the Finite Difference Method, where two key features were introduced, such as the dependence of soil stiffness on the current effective stress state and the variation of the equivalent number of cycles with depth.

An accurate computation of the maximum shear stresses imposed to the foundation soils is of the utmost importance for a reliable estimate of the number of cycles to liquefaction N_L. In the presence of medium-to-high intensity earthquakes, such as those usually causing liquefaction, the usual free-field ground response analysis performed through the Linear Equivalent Method would provide inaccurate results and therefore a nonlinear analysis is needed. Moreover, in order to account for both nonlinearity and strength into the constitutive soil equations, the simple approach recently proposed by Conti et al. (2020) has been adopted, being defined by few parameters which can be easily calibrated. Although not being able of considering the bi-phasic nature of soils, this approach turned out to provide peak shear stresses in a very good agreement with those computed through more rigorous 1D *coupled* nonlinear dynamic analyses. This result, which was attributed to the fact that maximum shear stresses within a liquefiable soil layer must occur well before the attainment of liquefaction, is of great relevance when following a *decoupled* approach to estimate earthquake-induced pore pressures build-up. Clearly, simple 1D nonlinear analyses cannot reproduce the development of shear strains and filtering effects induced by liquefaction.

After computing the number of cycles to liquefaction N_L through the 1D nonlinear analysis, the simplified method by Seed et al. (1975) was used to estimate the seismic-induced excess pore water pressures into the liquefiable soils for the reference case study. Again, the comparison with results available in the literature turned out to be more than satisfactory in terms of soil thickness reaching liquefaction, bearing in mind the simplicity of the proposed method. Moreover, the influence of the assumption on the equivalent number of cycles N_{eq}, whether variable with depth or constant, did not affect the results noticeably.

REFERENCES

Adamidis, O. & Madabhushi, G.S.P. 2016. Post-liquefaction reconsolidation of sand. *Proceedings of the Royal Society A: Mathematical, Physical and Engineering Sciences*, 472(2186): 20150745.

Biondi, G., Cascone, E. & Di Filippo, G. 2012. Affidabilità di alcune correlazioni empiriche per la stima del numero di cicli di carico equivalente. *Rivista Italiana di Geotecnica* 46(2): 9–39. [in italian]

Chiaradonna, A., Tropeano, G., d'Onofrio, A. & Silvestri, F. 2018. Development of a simplified model for pore water pressure build-up induced by cyclic loading. *Bulletin of Earthquake Engineering* 16(9): 3627–3652.

Chiaradonna, A., Tropeano, G., d'Onofrio, A. & Silvestri, F. 2019. Interpreting the deformation phenomena of a levee damaged during the 2012 Emilia earthquake. *Soil Dynamics and Earthquake Engineering* 124: 389–398.

Conti, R., Angelini, M. & Licata, V. 2020. Nonlinearity and strength in 1D site response analyses: A simple constitutive approach. *Bulletin of Earthquake Engineering* 18: 4629–4657.

Cubrinovski, M., Bray, J.D., Taylor, M., Giorgini, S., Bradley, B. A., Wotherspoon, L. & Zupan, J. 2011. Soil liquefaction effects in the central business district during the February 2011 Christchurch earthquake. *Seismological Research Letters* 82: 893–904.

Hancock, J. & Bommer, J. J. 2005. The effective number of cycles of earthquake ground motion. *Earthquake Engineering & Structural Dynamics* 34(6): 637–664.

Hardin B.O. & Drnevich VP 1972. Shear modulus and damping in soils: design equations and curves. *Journal of the Soil mechanics and Foundations Division* 98(7): 667–692.

Idriss, I.M. & Boulanger, R.W. 2006. Semi-empirical procedures for evaluating liquefaction potential during earthquakes. *Soil Dynamics and Earthquake Engineering* 26(2–4): 115–130.

Idriss, I.M. & Boulanger, R.W. 2008. *Soil liquefaction during earthquakes*. Earthquake Engineering Research Institute.

Kramer, S.L. 1996. *Geotechnical earthquake engineering*. Pearson Education India.

MATLAB. 2021. *version 9.10.0 (R2021a)*. Natick, Massachusetts: The MathWorks Inc.

Miner, M.A. 1945. *Cumulative damage in fatigue*. Trans. ASME 67, A159–A164.

Mucciarelli, M. & Liberatore, D. 2014. Guest editorial: the Emilia 2012 earthquakes, Italy. *Bulletin of Earthquake Engineering* 12: 2111–2116. https ://doi.org/10.1007/s1051 8-014-9629-6

Phillips, C. & Hashash, Y. M. 2009. Damping formulation for nonlinear 1D site response analyses. *Soil Dynamics and Earthquake Engineering* 29(7): 1143–1158.

Seed, H.B. & Booker, J.R. 1977. Stabilization of potentially liquefiable sand deposits using gravel drains. *Journal of Geotechnical Engineering Division* 103(7): 757–768.

Seed, H.B., Martin, P.P., & Lysmer, J. 1975. *The generation and dissipation of pore water pressures during soil liquefaction*. College of Engineering, University of California.

Sorrentino, L., Liberatore, L., Decanini, L.D., Liberatore, D. 2013a. The performance of churches in the 2012 Emilia earthquakes. *Bulletin of Earthquake Engineering* 12: 2299–2331. doi:10.1007/s10518-013-9519-3

Sorrentino, L., Liberatore, L., Liberatore, D., Masiani, R. 2013b. The behaviour of vernacular buildings in the 2012 Emilia earthquakes. *Bulletin of Earthquake Engineering* 12: 2367–2382. doi:10.1007/s10518-013-9455-2

Terzaghi, K. (1923). Die Berechnung der Durchassigkeitsziffer des Tones aus dem Verlauf der hydrodynamischen Spannungs. erscheinungen. Sitzungsber. Akad. Wiss. Math. Naturwiss. Kl. Abt. 2A 132: 105–124

Tonni, L., et al. 2015. Analisi dei fenomeni deformativi indotti dalla sequenza sismica emiliana del 2012 su un tratto di argine del Canale Diversivo di Burana (FE). *Rivista Italiana di Geotecnica* 49(2): 28–58. [in Italian]

Trifunac, M.D. & Brady A.G. 1975. A study on the duration of strong earthquake ground motion. *Bulletin of the Seismological Society of America* 65(3): 581–626.

Tropeano, G., Chiaradonna, A., d'Onofrio, A. & Silvestri, F. 2016. An innovative computer code for 1D seismic response analysis including shear strength of soils. *Géotechnique* 66(2), 95–105.

Viggiani, G.M.B. & Atkinson, J.H. 1995. Stiffness of fine-grained soil at very small strains. *Géotechnique* 45(2): 249–265.

Wichtmann, T. & Triantafyllidis, T. 2009. Influence of the grain-size distribution curve of quartz sand on the small strain shear modulus Gmax. *Journal of Geotechnical and Geoenvironmental Engineering*, ASCE 135(10): 1404–1418.

Geotechnical Engineering for the Preservation of Monuments and Historic Sites III – Lancellotta, Viggiani, Flora, de Silva & Mele (Eds)

Evaluation of DSSI for the preservation of the Catania University Central Palace

G. Abate, S. Corsico, A. Fiamingo, S. Grasso & M.R. Massimino
Department of Civil Engineering and Architecture, University of Catania (Italy)

ABSTRACT: The conservation of the historical heritage is one of the great challenges in Italy. The mitigation of the seismic risk is a crucial aspect for most of the Italian cities, characterized by high seismic hazard.

Meeting these challenges, the Catania University Central Palace, located in the historical centre of Catania, was recently chosen as a "target" building for the evaluation of the seismic risk of monumental buildings in the framework of the European Research Project eWAS "An Early Warning System for Cultural Heritage".

This paper deals with the FEM modelling of one section of this building. Three models were developed, based on two different geotechnical characterizations, and performed by an equivalent linear elastic approach and by a non-linear one. Their comparison allows us to highlight the important role of DSSI and adequate soil modelling for a realistic estimate of the seismic vulnerability of a building.

1 INTRODUCTION

The conservation of monuments and historic sites is one of the great challenges concerning the entire Italian territory. Indeed, in addition to typical factors to deal with, such as cultural, technical, economic aspects, the mitigation of the seismic risk of such historical-cultural heritage is a crucial aspect for most of the Italian cities, characterized by high seismic hazard. The city of Catania (Italy), rich in historical buildings, can certainly be counted among these.

As for the mitigation of the seismic risk, estimating accurately the seismic input that impacts the structure is of fundamental importance. It can change greatly from the bedrock to the foundation level. So, numerical analyses of the local seismic response should be encouraged to estimate the real filtering effects of soil (Ferraro et al. 2015). These analyses are generally performed in free-field conditions; thus, they do not consider the presence of superstructures that could play a fundamental role in the variation of the characteristics of seismic motion (FEMA 2009).

The damage caused by numerous and well-known earthquakes (Mexico City 1985, Kobe 1995, Izmit 1999, L'Aquila 2009, Haiti 2010, Norcia 2016) highlighted that the safeguard of existing buildings and infrastructures and the planning of new ones must necessarily consider the effects of the dynamic interaction (DSSI) between the soil and the structures (Kausel 2010). Studies of coupled soil-structure systems (Pandey et al. 2012; Abate et al. 2016; Gatto et al. 2015; Massimino et al. 2019a) should be consistently encouraged. In many cases the deformability of the soil influences the dynamic response of the structure, determining both an elongation of the fundamental period and an increase of the damping (Veletsos & Meek 1974; Luco 1980). Consequently, the DSSI effects would be beneficial. Nevertheless, depending on the soil and seismic input properties, maximum spectral ordinates have often been recorded at high periods (Mylonakis & Gazetas 2000). In this case, the effects of the DSSI would be detrimental.

Preliminary analyses concerning DSSI are precious to estimate the seismic soil amplification or de-amplification and, consequently, to develop microzonation maps useful for the rational use

DOI 10.1201/9781003308867-63

of the territory. In this case, effortless approaches can be used due to the significant number of structures to be examined (Rovithis et al. 2017; Abate et al. 2020). For a single structure or a reduced number of structures next to each other, interaction effects can be carefully studied by in-situ and laboratory tests, conducted to investigate DSSI and validate analytical and numerical approaches (Pitilakis et al. 2008; Massimino et al. 2019a-b). The last ones are the most valuable approach, being the nearest to the real configurations to be analysed (Abate et al. 2016, 2019).

The present paper deals with the numerical modelling of a full-coupled soil-structure system concerning one section of the Catania University Central Palace, located in the historical centre of Catania. This building has been recently chosen as a "target" building for the evaluation of the seismic risk of monumental buildings in the framework of the in-progress Research Project eWAS "An Early Warning System for Cultural Heritage". Therefore, the building and its subsoil have been subjected to accurate investigations.

Three different FEM models were developed. The first model was carried out according to a geotechnical characterization performed in 1996 as part of the "The Catania Project", aimed at the microzonation of the city of Catania (Faccioli & Pessina, 2000); the second model was performed thanks to the geotechnical surveys carried out during the in-progress "eWAS Project". Both the models were developed using an equivalent visco-elastic approach: soil nonlinearity was considered choosing updated shear modula G and damping ratios D according to the effective strain levels obtained for each soil layer and each adopted different input, using an iterative sub-routine. Furthermore, a third FEM model was developed using advanced soil constitutive models.

The comparison of all the investigated FEM models, considering both the free-field conditions and the soil-structure interaction, allowed us to highlight some interesting aspects of the role of DSSI and the choice of adequate soil modelling for a realistic estimate of the seismic vulnerability of a building.

2 THE STRUCTURE AND ITS SUBSOIL

The Catania University Central Palace is a monumental palace located in the historic centre of the city of Catania. The structure was razed by the 1693 earthquake that hit Eastern Sicily. The construction of the new palace began within a few years, and it was completed by 1760; the present design is the product of the main architects of the Sicilian baroque. Further restructuring was pursued after the earthquake of 1818. The building is a masonry structure, consisting of an entire block, with an internal courtyard, as shown in Figure 1, in which the red box shows the section chosen for the FEM modelling. The total height of the building is 20 m for a total width of 52 m; the structure has 2 floors in elevation, in addition to the ground floor. The foundations are a deepening of the perimeter walls under the ground surface down to a depth equal to 2 m, as was conventionally used for such large buildings.

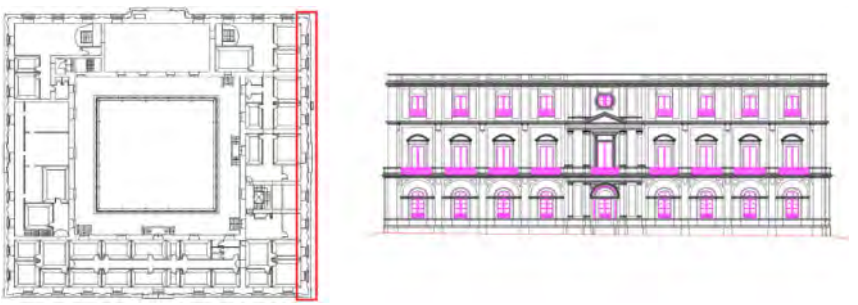

Figure 1. Plan view with the selected section for the FEM analysis and corresponding front view of the Main Office building of the Catania University.

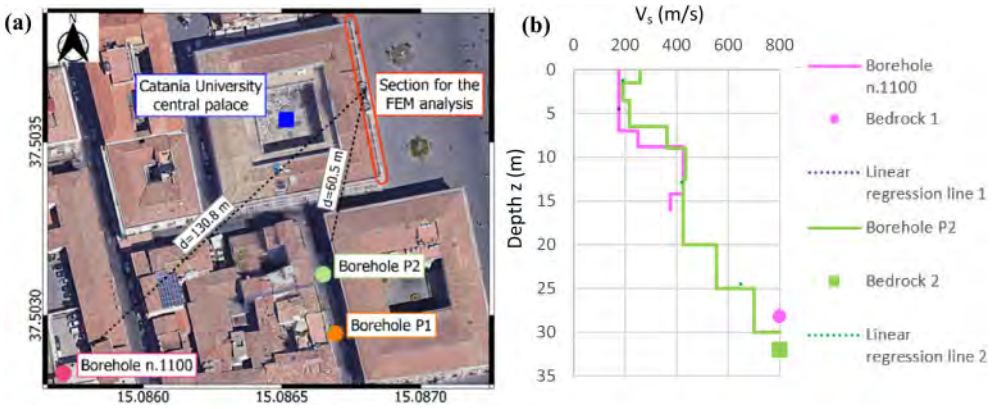

Figure 2. Plan view with the localization of the reference boreholes for the two adopted stratigraphies; b. V_s profiles and their interpolation for choosing the depth of the bedrock.

Table 1. Main characteristics of Stratigraphy N. 1.

layer	Depth (m)	Thickness (m)	Lithotype	V_s (m/s)	ρ (kNs^2/m^4)
1	0÷7.0	7.0	anthropic layer	175	1.9
2	7.0÷8.8	1.8	sands	250	0.9
3	8.8÷14.2	5.4	Lava	425	2.4
4	14.2÷16.0	1.8	Pyroclasts	375	1.7
5	16÷30	14			
Bedrock	>	30	800		

Several geotechnical investigations were performed in the Catania subsoil, due to the seismic hazard that characterises this city (Caruso et al. 2016; Castelli et al., 2017). The soil interacting with the building was subjected to two different geotechnical surveys: the first one was carried out in the framework of the "Catania Project" (in 1996; Faccioli & Pessina, 2000) aimed at seismic microzonation of the city of Catania; the second one was recently carried out in the framework of the in-progress "eWAS Project", aimed to estimate the seismic risk of monumental buildings for developing an early warning system for cultural heritage. So, two different stratigraphies were considered in the FEM analyses.

The first adopted stratigraphy refers to a borehole present in the database of the "Catania Project 2, 2000-2002", called n.1100 and located at about 130 m from the building (Figure 2.a). It was drilled up to a depth of 16.5 m from the ground surface, at which a V_s = 375 m/s was found; therefore, it was not possible to identify the bedrock. So, the V_s profile was interpolated by a linear regression line (see magenta dashed line in Figure 2.b), imposing a value V_s = 800 m/s for $z = H$ to find the corresponding depth of the conventional bedrock H. It was identified at 28.2 m from the ground surface (see "Bedrock 1" in Figure 2.b). Table 1 shows the main characteristics of the lithotypes of this "Stratigraphy N. 1". In the framework of the in-progress "eWAS Project", two boreholes, called P1 and P2, were carried out down to a depth of 30 m. SPT and MASW tests were also performed, as well as laboratory tests on undisturbed samples. The second adopted stratigraphy refers to the P2 borehole, located at about 60 m from the building (Figure 2.a). Interpolating the V_s profile by the linear regression line as previously discussed (see green dashed line in Figure 2.b), the bedrock was estimated at a depth equal to 32.00 m from the ground surface (see "Bedrock 2" in Figure 2.b). Table 2 shows the main characteristics of the lithotypes of this "Stratigraphy N. 2".

Table 2. Main characteristics of Stratigraphy N. 2.

layer	Depth (m)	Thickness (m)	Thickness (m)	Lithotype V_s (m/s) ρ (kNs^2/m^4)		
1	0.0÷1.5	1.5	anthropic layer	258		
2	1.5÷3.5	2.0	3.5 and sands	190	1.9	
3	3.5÷6.5	3.0	216			
4	6.5÷9.0	2.5	362			
5	9.0÷12.5	3.5	9.0	lava	434	2.4
6	12.5÷20	7.5	7.5	silty clays	425	1.9
7	20÷25	5.0	554			
8	25÷30	5.0	10	silty sands	700	1.9
Bedrock	>30	800				

The two soil profiles are very similar. By this recent geotechnical investigation, it was possible to characterize in detail every single layer, above all for a depth greater than 15 m (as the drilled boreholes reached deeper layers).

3 THE SELECTED SEISMIC INPUTS

Seven seismic inputs were used for the FEM analysis; they were selected using the Rexel 3.5 code (Iervolino et al., 2010). The obtained accelerograms are compatible with the target response spectrum (NTC, 2018) and with the disaggregation of the seismic hazard (Stucchi et. al, 2011) in terms of magnitude M and epicentral distance R, referring to range values (M=4.0-6.5, R=0-20 km; Figure 3.a). More precisely, the target response spectrum was developed according to the requirements of the Italian Technical Code (NTC, 2018) and considering the importance of the analysed monumental historical building (Site Class: A, Topographic category: T1, Nominal Life: 50 years, Functional Type: III and the Limit State of interest: SLV). Moreover, each of the seven accelerograms was linearly scaled (by an SF factor) to obtain an average spectrum with a 10%

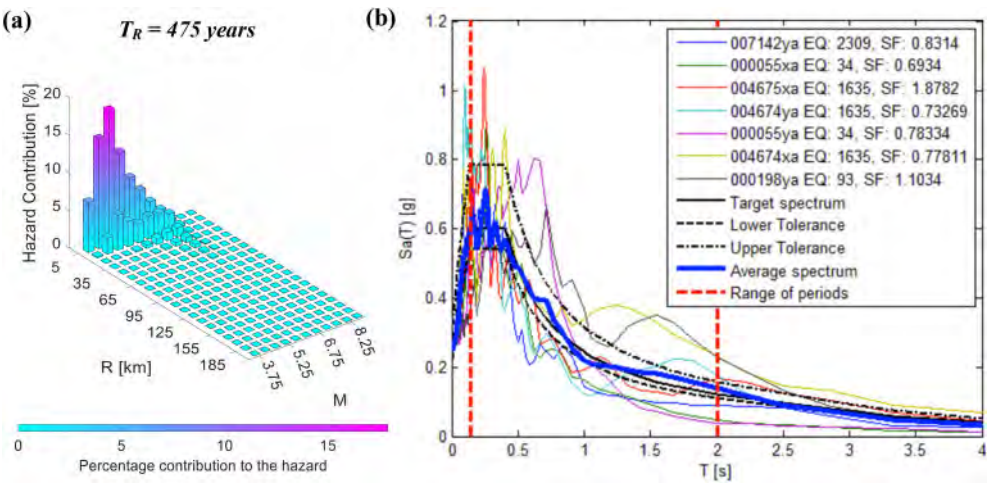

Figure 3. Range values for the disaggregation of the seismic hazard. b. Scaled Response Spectra of the seven selected accelerograms achieved by Rexel 3.5 (Iervolino et al., 2010).

lower tolerance and a 30% upper tolerance, in the range of periods 0.15s - 2s, compared to the reference response spectrum. The scaled response spectra of the selected accelerograms are shown in Figure 3.b.

4 THE FULL-COUPLED FEM MODELS

The study of the seismic response of the full-coupled soil-structure system was performed by 2D finite element modelling using the ADINA code (Bathe, 1999). The response of the system was analysed both considering and neglecting the SSI by investigating two different vertical alignments (Figure 4): along with the structure (SSI) and far from the structure, i.e., considering the free-field condition (FF).

The width of the soil deposit (360 m) was chosen to minimize boundary effects as far as possible; the height of the soil deposit was derived from the geotechnical investigations (H = 30 m was chosen according to both the reference stratigraphies; see Figure 2). The hypothesis of plane strain condition was chosen for the soil modelling and the hypothesis of plane stress was chosen for the building modelling. The mesh element size was chosen to ensure the following criteria: i) efficient reproduction of all the waveforms of the whole frequency range under study: $h \leq V_{s,min}/(6 \div 8 f_{max})$ (Lanzo & Silvestri, 1999); ii) a finer discretization near the structure. The soil and the structure were modelled by 2D 4-node solid elements.

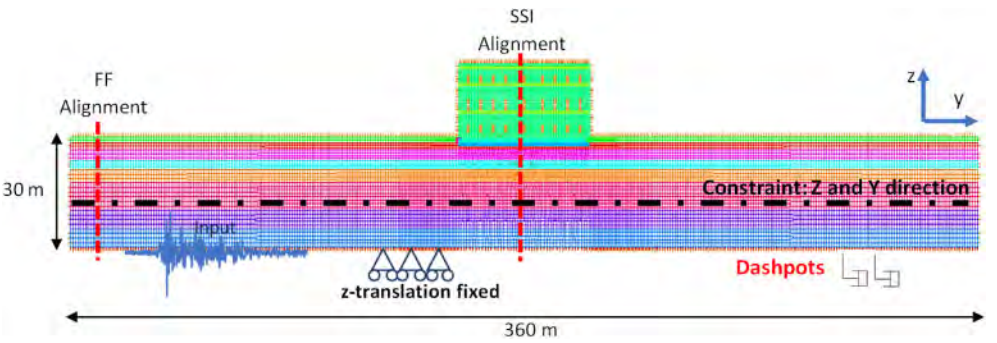

Figure 4. FEM Model.

As regards the boundary conditions (Figure 4), the nodes of the soil vertical boundaries were linked by "constraint equations" that imposed the same displacements at the same depths (Abate et al. 2016; 2019); the nodes at the base of the mesh were constrained only in the vertical direction. Moreover, at the base of the numerical model, dashpots were implemented in the horizontal direction, to simulate the elastic bedrock according to Lysmer and Kuhlemeyer (1969). The dashpot coefficients c were defined as the product of the mass density ρ, the shear wave velocity V_S of the bedrock and the 'effective' area A of each dashpot, to maintain proportional results for any horizontal element size, according to the following expression:

$$c = \rho \cdot V_s \cdot A \tag{1}$$

Contact surfaces were modelled between foundation and soil to simulate probable uplifting and/or sliding phenomena, considering friction equal to 2/3 ϕ (Sheng et al., 2007; Ilori et al. 2017).

Regarding the input motion, the seven accelerograms discussed in Section 2 were applied through the above-mentioned dashpots, located at the bottom of the model.

The material viscosity was modelled according to the Rayleigh damping. For the calibration of the Rayleigh factors, the double frequency approach was used (Hashash & Park, 2002). So, the Rayleigh damping factors α_R and β_R for the soil and the structure were computed according to:

$$\alpha_R = 2 \cdot (D \cdot \omega_1 \cdot \omega_2)/(\omega_1 + \omega_2); \quad \beta_R = 2 \cdot D/(\omega_1 + \omega_2) \tag{2}$$

For the soil, the first natural angular frequency ω_1 was estimated using the well-known expression: $\omega_1 = 2\pi \cdot V_{(s,av)}/4H$, where H is the total thickness of the soil deposit and $V_{s,av}$ is the weighted average of the shear wave velocities of the whole soil (Lanzo & Silvestri, 1999). The second frequency ω_2 was assumed to be three times the first ($\omega_2 = 3\omega_1$). The damping ratio D was appropriately evaluated for the soil layers, according to a linear equivalent visco-elastic approach to consider the soil nonlinearity, as it is explained in in the following Section 4.1.

For the structure, the Rayleigh damping coefficients were estimated according to expressions (2), using the first and the second fundamental frequencies of the fixed-based structure, f_1 = 3.3Hz and f_2 = 7.1Hz, evaluated through a modal analysis performed by the ADINA code (Bathe, 1999). A damping ratio D = 7% was assigned to the structure.

As regards the constitutive modelling of the materials, the masonry was modelled according to a linear viscoelastic behaviour, but appropriately reduced stiffness values were considered, to consider the cracking of the sections (NTC, 2018). So, the following properties were adopted for the load-bearing masonry, including the masonry strip foundation: E = 861000 kN/m^2; ν = 0.23; ρ = 1.98 kNs^2/m^4.

As for the soil modelling, as previously said, thanks to the available geotechnical characterizations, the soil deposit was modelled considering both the two stratigraphies described in Section 2 and adopting both an equivalent linear viscoelastic modelling (by reduced dynamic properties according to the effective shear strain level) and work-hardening elastoplastic modelling, so carrying out three different FEM models as described in the following.

4.1 *Elastic Linear equivalent modelling*

A first FEM model was carried out according to the Stratigraphy N. 1 (Table 1). An equivalent viscoelastic constitutive model was adopted for the sands, using updated soil stiffness G and damping ratio D evaluated considering the achieved shear strain level through a series of 1D equivalent linear site response analyses using the *STRATA* Code (Kottke & Rathje, 2011) for each seismic signal shown in Section 3. Typical $G(\gamma)$ and $D(\gamma)$ curves for the Catania sands available in the literature (blue lines in Figure 5; Cavallaro et al. 2006) were adopted. These last curves are described by the following equations (Yokota et al., 1981):

$$\frac{G(\gamma)}{G_0} = \frac{1}{1 + \alpha\gamma\,(\%)^{\beta}} \tag{3}$$

$$D(\gamma)\,(\%) = \eta \cdot \exp\left[-\lambda \cdot \frac{G(\gamma)}{G_0}\right] \tag{4}$$

in which $G(\gamma)$ is the shear modulus, $D(\gamma)$ is the damping ratio, α, β, λ and η are the following soil constants adopted for the Catania sands (Cavallaro et al. 2006): α=7.5, β=0.897; λ=4.5 and η=90.

A linear visco-elastic model was adopted for the lava, using the values at very low shear strains $G_{s,0}$ (evaluated as $\rho \cdot V_s^2$) and $D_{s,0}$ = 1%.

According to the same equivalent visco-elastic approach, a second FEM model was carried out considering the Stratigraphy N. 2. The sand and lava layers were modelled as in the previous model. As for the silty clay, present in Stratigraphy N. 2 and not in Stratigraphy N. 1, the $G(\gamma)$ and $D(\gamma)$ curves (Figure 5) achieved by RC tests performed on a sample taken at the Borehole P1 (Figure 2) were used in the analyses to update G and D as for the sands (orange lines in Figure 5; eWas Project PNR 2015-2020).

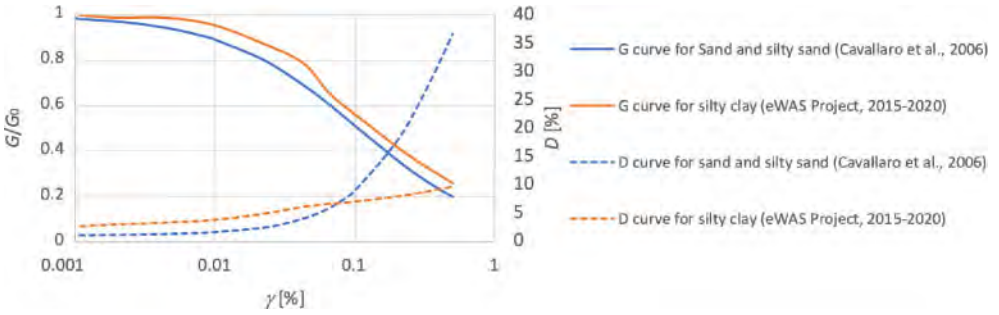

Figure 5. G-γ-D curves used for the performed analyses.

The two FEM models differ just in the stratification of the layers, characterized by different heights and different properties according to Tables 1 and 2.

4.2 *Non-Linear modelling*

A third FEM model was carried out based on the Stratigraphy N. 2 (Table 2), adopting the visco-elastoplastic constitutive model with isotropic and kinematic hardening (called Severn-Trent model; Gajo and Muir Wood, 1999) for modelling the nonlinear behaviour of the sands, the elasto-perfectly plastic Mohr-Coulomb model for modelling the silty clays and a linear visco-elastic model for modelling the lava layer. This further FEM model was, therefore, developed for improving the previous modelling, considering the greater geotechnical information available thanks to the recent geotechnical characterization, that allowed us to better model the soil non-linear behaviour, which is extremely important in soil mechanics (Abate et al. 2008; Pecker et al. 2010).

So, as for the sand layers, that are at depths equal to 0-3.5 m and equal to 20-30 m (see Table 2), they were modelled by the distortional-hardening 'Severn-Trent model', implemented into the ADINA code (Bathe, 1999) by the geotechnical research group of Catania University (Caruso 2005; Abate et al. 2008). It is formulated within the framework of kinematic hardening and bounding surface plasticity and can describe the general multiaxial stress-strain behaviour of granular material over a wide range of densities and mean pressures. This model combines the Drucker-Prager yielding, the critical state, the dependence of strength and stiffness on the state parameter ψ (Been & Jefferies, 1985), a hyperbolic law for plastic stiffness degradation and a non-associated flow role derived from that of the Cam-Clay model. The model has the great advantage of being based on only ten parameters: two elastic (E and ν) and eight plastic (ν_λ, λ, φ_{cv}, A, k_d, B, k, R) determinable by simple triaxial tests. Particularly, ν_λ and λ define the local position of the critical-state line, φ_{cv} defines the critical-state strength, A and k_d define the flow rule, B defines the hyperbolic plastic stiffness relationship and, finally, k and R define the yield and strength surfaces. Some parameters (the unit weight γ, the shear modulus G, the damping ratio D and the angle of shearing resistance φ) were evaluated through the available laboratory data concerning these layers. The other parameters, which cannot be directly measured, were chosen based on previously FEM modelling of Catania sands performed through the Severn-Trent constitutive model (Abate et al., 2008). As for the lava layer, that is at a depth equal to 3.5-12.5 m (see Table 2), it was modelled by a linear visco-elastic constitutive model, using the same parameters at very low shear strains adopted in the previous FEM models (see Section 4.1). As for the silty clays layer, that is at a depth equal to 12.5-20 m (see Table 2), it was modelled by the Mohr-Coulomb elastoplastic constitutive model, available in the used ADINA code (Bathe, 1999); it is characterized by the parameters G, ν, ρ, φ and c evaluated using the geotechnical investigations performed on samples of this layer; updated G and D based on the achieved shear strain level and evaluated using the STRATA code, as previously described in Section 4.1, were used.

5 RESULTS AND DISCUSSIONS

5.1 *Linear Elastic (LE) modelling performed according to the two different stratigraphies*

The seismic response of the soil-structure system to the adopted earthquakes is firstly presented considering the soil equivalent visco-elastic modelling in terms of: i) PGA at the ground surface for the two FF and SSI alignments (Figure 6); ii) fundamental input frequencies vs natural soil frequencies (Figure 7); iii) amplification ratio profiles $R_a(z)$ (Figure 8).

As for the PGA values achieved at the FF alignment (Figure 6.a), minor PGA values are found at the ground surface, modelling the soil according to the recent Stratigraphy N. 2 with respect to the Stratigraphy N. 1.

As for the SSI alignment (Figure 6.b), the PGA values are similar for both stratigraphies, except for inputs 55X and 55Y. These differences can be explained considering the fundamental input frequencies and the natural soil frequencies (Figure 7): as for the 55X input, its first frequency ($f_{1,input}$ =1.5 Hz) is very close to the first soil frequency evaluated according to the Stratigraphy N. 1 ($f_{1,soil}$ =1.4 Hz), as well as for the 55Y input its first frequency ($f_{1,input}$ =2.0 Hz) is very close to the first soil frequency evaluated based on the Stratigraphy N. 2 ($f_{1,soil}$ =1.8 Hz). Similar considerations can be applied to the second frequencies. So, the proximity of these frequencies leads to an amplification of the PGA values (about the analysed stratigraphies), due to resonance phenomena ($f_{soil} \sim f_{input}$).

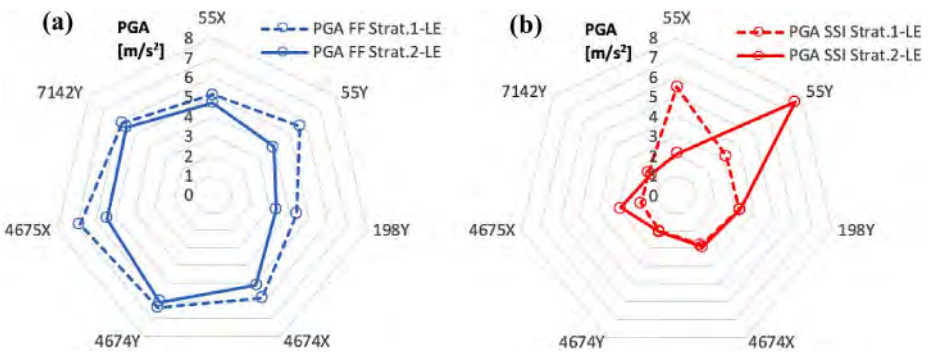

Figure 6. PGA at the ground surface for the FF alignment (a) and the SSI alignment (b) using the two Stratigraphies N. 1 and N. 2 and the LE modelling.

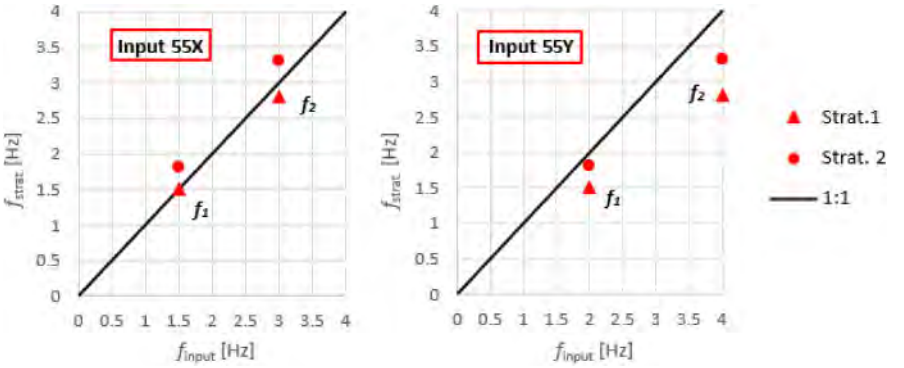

Figure 7. First two natural soil frequencies for the adopted two stratigraphies versus the first two fundamental input frequencies along the SS alignment.

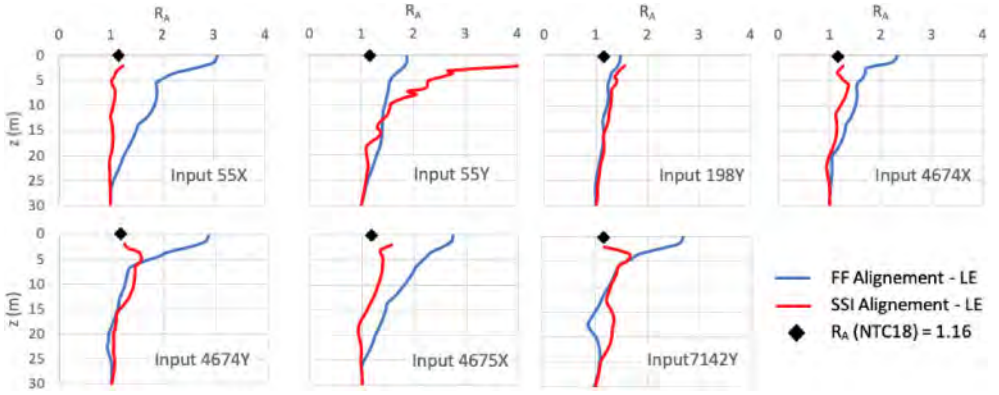

Figure 8. Amplification ratio profiles along the FF and SSI alignments (LE modelling, Stratigraphy N. 2).

Figure 8 shows the comparison between the amplification ratio profiles $R_a(z)$ achieved for the two analysed alignments and the Stratigraphy N. 2. The soil amplification ratio at the ground surface computed according to the in-force Italian Technical Code (NTC, 2018; for soil type B - $V_{s,eq}$= 381 m/s - R_a = 1.16) is also reported. The response along the two alignments is similar for the major of the adopted inputs for the deeper layers; then, the presence of the structure usually leads accelerations lower than those obtained in free-field condition, approaching the soil surface, (except for the input 55Y, for which resonance phenomena occur, as previously discussed; see Figure 7), this is due to the huge mass of the building. In particular, as regards the free-field response, the amplification ratio always increases from the bedrock to the ground surface, reaching for some inputs very high values. Moreover, the amplification ratios achieved at the ground surface are almost always greater than that proposed by NTC, 2018, stressing the importance of local site response analyses. Instead, below the structure (SSI alignment), the amplification ratio slightly increases but it reaches values next to the unity at the ground surface.

5.2 *Non-linear (NL) modelling performed according to the more recent stratigraphy*

The following results show a comparison between the seismic response of the soil-structure system modelled by the equivalent LE approach and by the NL approach (see Sections 4.1 and 4.2), according to the more recent Stratigraphy N. 2. The results are presented in terms of: i) PGA at the ground surface for the two FF and SSI alignments (Figure 9); ii) amplification ratio profiles $R_a(z)$ achieved for the two analysed alignments by the NL modelling (Figure 10); iii) shear stress versus shear strain curves for the layers modelled according to the elastoplastic constitutive models discussed in Section 4.2 (Figure 11).

As for the PGA values achieved at the ground surface (Figure 9), the NL numerical modelling leads to minor accelerations in respect of the LE numerical modelling (Figure 6), for both the alignments. This is due to soil plastic deformations captured by the adopted nonlinear constitutive models. This trend is more remarkable for the SSI alignment, due to the high strain level achieved in presence of the aboveground structure.

This different behaviour can be also seen comparing Figure 10 with Figure 8, which show the amplification ratio profiles achieved by the NL and LE modelling, respectively. Figure 10 shows an important de-amplification of all the inputs, above all along the SSI alignment, that was not found by the LE modelling (Figure 8). Plastic deformations occurred and they led to a reduction in accelerations. Indeed, it is possible to see an accumulation of shear strains and stresses, which depend on the non-linear behaviour of soil. The Severn-Trent model allowed us to simulate an increase in the amplitude of the cycle. Furthermore, by the comparison between the amplification ratios achieved at the ground surface using this NL modelling and the value proposed by the in-force

Figure 9. PGA at the ground surface for the FF alignment (a) and the SSI alignment (b), considering the two different equivalent elastic (LE) and nonlinear (NL) modelling and the Stratigraphy N. 2.

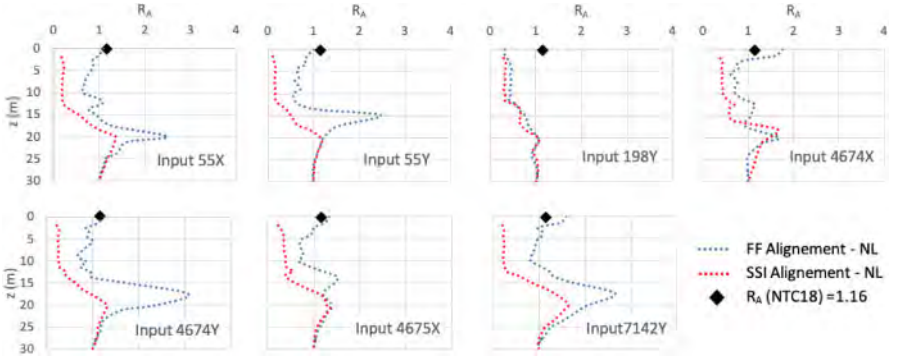

Figure 10. Amplification ratio profiles along the FF and SSI alignments (NL modelling, Stratigraphy N.2).

Italian Technical Code (NTC, 2018), it is possible to see that this last one is always greater than the values achieved by the full-coupled FEM analysis and so, in this case history, the DSSI has a beneficial effect; nevertheless, it is important to stress that in several cases SSI had a detrimental effect (Karatzetzou & Pitilakis 2017; Rovithis et al. 2017; Massimino et al. 2018; 2019a-b). As an example, Figure 11 shows the shear stress vs shear strain curves at the centre of the layers modelled by the adopted elastoplastic constitutive models, along the SSI alignment, for reference input (4675X).

Finally, Figure 12 shows the shear stress band plot on the structure, for the reference input (4675X) at the time for which the maximum acceleration is reached at the bedrock level, considering both the LE and NL soil constitutive models. It is possible to assert that by the LE modelling, the soil strains are rather low, therefore the effect of the seismic inputs on the structure prevails causing typical (45° inclined) shear bands in the masonry structure. By the NL modelling, the soil strains are remarkable, due to the continuous degradation of the *G* modulus, and this causes typical settlements greater in the middle of the structure, so the observed shear bands are inclined at 45° and specular to the right and left.

6 CONCLUSIONS

The present paper deals with the FEM modelling of a full-coupled soil-structure system concerning one section of the Catania University Central Palace, located in the historical centre of Catania. The building and its subsoil were subjected to accurate investigations for LE and NL modelling, which have furnished two stratigraphies: Stratigraphy N. 1 (old investigation); Stratigraphy N.2

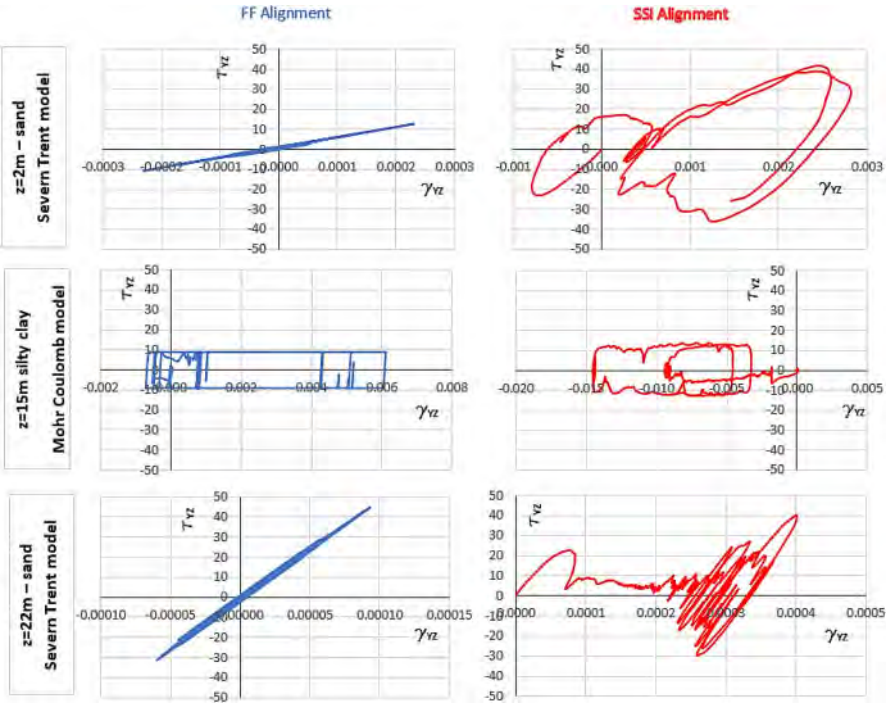

Figure 11. Shear stress vs shear strain curves at the centre of the layers modelled by the adopted elastoplastic constitutive models, along the SSI alignment, for reference input (4675X).

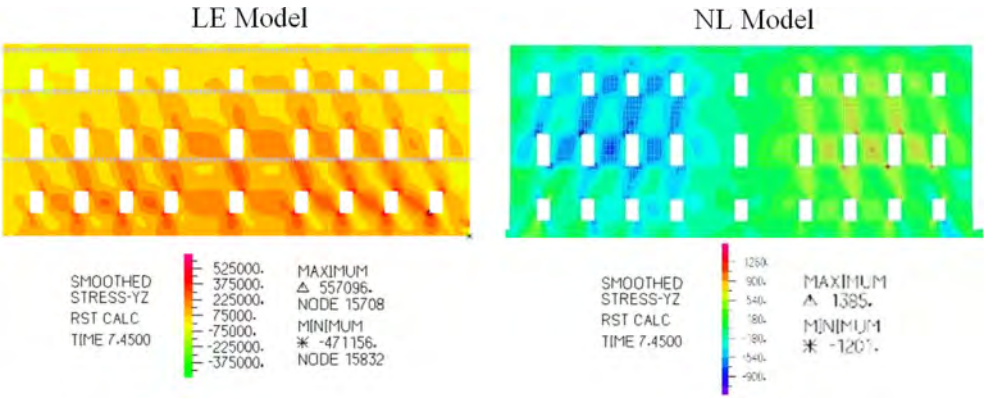

Figure 12. Shear stress band plot (in Pa for LE Model and kPa for the NL Model) on the structure, for the reference input (4675X) at the time for which the maximum acceleration is reached.

(new investigation). The results, summarized as follows, allowed us to highlight the role of soil modelling for a careful estimation of the seismic vulnerability of structures.

By the LE modelling, the PGA values achieved at the ground surface at the FF alignment according to the Stratigraphy N. 2 were minor than the values obtained for the Stratigraphy N. 1. This highlights the importance of accurate knowledge of the geotechnical parameters for a more realistic estimate of the acceleration at the ground surface. The amplification ratios R_a achieved at the ground surface are always greater than the value proposed by NTC,2018. The PGA values

achieved at the ground surface at the SSI alignment are similar for both stratigraphies, except for two inputs, characterized by fundamental frequencies very close to the natural soil frequencies; so resonance phenomena occur. However, the structure leads usually to minor accelerations at the ground surface, in respect of the free-field response, due to its huge mass.

By the NL modelling, always minor accelerations were obtained for both the alignments, in comparison to the LE modelling. This was due to valuable plastic deformations captured by the NL modelling. This was more remarkable for the SSI alignment. Furthermore, the amplification ratios achieved at the ground surface using this NL modelling are always minor than the value proposed by the Italian Technical code (NTC, 2018). This result represents a warning on the estimate of the seismic behaviour of a building. It cannot be generalized to any structure, as for the analysed case history the building is characterised by a huge mass and a very regular configuration, which reduced amplification phenomena, and so DSSI has a beneficial effect. Nevertheless, it is important to stress that in several cases DSSI could have a detrimental effect (Karatzetzou & Pitilakis 2017; Rovithis et al. 2017; Massimino et al. 2018; 2019a-b) and so studies including full-coupled systems must always be encouraged. The different responses of the soil and in turn of the structure comparing LE and NL soil modelling underline the important role of the geotechnical characterization and the choice of adequate soil constitutive models in DSSI analyses.

ACKNOWLEDGEMENT

The research reported in this paper was performed by the financial supports provided by the European Research Project eWAS "An Early Warning System for Cultural Heritage", ID: ARS01_00926, PNR 2015-2020.

REFERENCES

Abate, G., Caruso, C., Massimino, M. R., Maugeri, M. 2008. Evaluation of shallow foundation settlements by an elastoplastic kinematic-isotropic hardening numerical model for granular soil. *Geomechanics and Geoengineering*, 3(1): 27–40.

Abate, G., Massimino, M. R., Romano, S. 2016. Finite Element Analysis of DSSI Effects for a Building of Strategic Importance in Catania (Italy). *Proc. VI Italian Conf of Researchers in Geotech Engineering – Geotechnical Engineering in Multidisciplinary Research: from Microscale to Regional Scale, CNRIG2016. Procedia Engineering* 158: 374–379, Bologna, Italy; 22–23 September 2016.

Abate, G., Grasso, S., Massimino, M. R. 2019. The role of shear wave velocity and non-linearity of soil in the seismic response of a coupled tunnel-soil-above ground building system. *Geosciences*, 9(11): 473.

Abate, G., Bramante, S., Massimino, M. R. 2020. Innovative seismic microzonation maps of urban areas for the management of building heritage: a Catania case study. *Geosciences*, 10(12): 1–22.

Bathe, K. J. 1999. Nonlinear finite element analysis and ADINA. In: *Proc of the 12th ADINA conference on computers and structures*.

Been, K. & Jefferies, M. G. 1985. A state parameter for sands. *Géotechnique*, 35(2): 99–112.

Caruso, C. 2005. Implementation and validation of a constitutive model for sand soil into a FEM code. *PhD Thesis in Geotechnical Engineering, the University of Catania* (in Italian).

Caruso, S., Ferraro, A., Grasso, S., & Massimino, M. R. 2016. Site Response Analysis in eastern Sicily based on direct and indirect Vs measurements. *Metro Geotechnics*: 115–120, *Proc. 1st IMEKO TC4 Int Workshop on Metrology for Geotechnics* Benevento, Italy; 17–18 March 2016.

Castelli F., Cavallaro A., Ferraro A., Grasso S., Lentini V., Massimino M. R. e Caruso S. 2017 Caratterizzazione Geotecnica e Risposta Sismica Locale dell'Area del Monastero dei Benedettini a Catania *Proc. XXVI Conv. Naz. di Geotecnica – L'Ingegneria Geotecnica nella Conservazione e Tutela del Patrimonio Costruito*, Roma, 20 – 22 Giugno 2017: 507-515.

Cavallaro, A., Grasso, S., Maugeri, M. 2006. Volcanic soil characterisation and site response analysis in the city of Catania. *Proc. 8th US Nat Conf on Earthquake Engineering* 2006, 2, 835–844.

Faccioli, E. & Pessina, V. 2000. *The Catania Project: Earthquake Damage Scenarios for High Risk Area in the Mediterranean*; Faccioli, E., Pessina, V., Eds.; CNR-Gruppo Nazionale per la Difesa dai Terremoti: Roma, Italy, 225p.

FEMA 2009. NEHRP Recommended Seismic Provisions for New Buildings and Other Structures: 705. Building Seismic Safety Council of the National Institute of Building Sciences for the Federal Emergency Management Agency, Washington, D.C.

Ferraro, A., Grasso, S., Massimino, M. R., & Maugeri, M. 2015. Influence of geotechnical parameters and numerical modelling on local seismic response analysis. *Geotechnical Engineering for Infrastructure and Development* 4: 2183–2188 – *Proc of the XVI Eur Conf. on Soil Mechanics and Geotechnical Engineering, ECSMGE 2015*, Edinburgh, United Kingdom; 13–17 September 2015.

Gajo, A. & Muir Wood, D. 1999. Severn–Trent sand: a kinematic-hardening constitutive model: the q–p formulation. *Géotechnique*, 49(5): 595–614.

Gatto, M., Massimino, M. R., Pitilakis, D., Rovithis, E. 2015. Numerical Simulation of large-scale soil-foundation-structure interaction experiments in the EuroProteas facility. *Proc 6th Inter Conf on earthquake geotechnical engineering 6ICEGE*, Christchurch, New Zealand; 1–4 November 2015.

Hashash, Y. M., Park, D. 2002. Viscous damping formulation and high-frequency motion propagation in nonlinear site response analysis. *Soil Dynamics and Earthquake Engineering*, 22(7): 611–624.

Iervolino, I., Galasso, C., Cosenza, E. 2010. REXEL: computer-aided record selection for code-based seismic structural analysis. *Bulletin of Earthquake Engineering*, 8: 339–362.

Ilori A. O., Udoh N. E., Umenge J. I. 2017. Determination of soil shear properties on a soil to concrete interface using a direct shear box apparatus. *International Journal of Geo-Engineering*, 8(1), 1–14.

Karatzetzou, A., Pitilakis, D. 2017. Modification of dynamic foundation response due to soil-structure interaction. *Journal of Earthquake Eng*ineering. 22(5), 861–880.

Kausel, E. 2010. The early history of soil-structure interaction. *Soil Dynamics and Earthquake Engineering*, 30(9): 882–832.

Kottke, A. & Rathje, E. 2008. Technical Manual for Strata PEER Report 2008/10. University of California.

Lanzo, G. & Silvestri, F. 1999. Risposta sismica locale. Helvelius Ed., Napoli. ISBN: 8886977913.

Luco, J. E. 1980. Linear soil-structure interaction. Lawrence Livermore National Lab. UCRL-15272.

Lysmer, J. & Kuhlemeyer, R. L. 1969. Finite dynamic model for infinite media. *Eng Mech*,95(4):859–877.

Massimino, M.R., Abate, G., Corsico, S., Grasso, S., Motta, E. 2018. Dynamic behaviour of coupled soil-structure systems by means of fem analysis for the seismic risk mitigation of INGV building in Catania (Italy). Special Issue, *Annals of Geophysics,* 61(2), SE216: 1–25.

Massimino, M. R., Abate, G., Grasso, S., Pitilakis, D. 2019a. Some aspects of DSSI in the dynamic response of fully-coupled soil-structure systems. *Rivista Italiana di Geotecnica*, 1:44–70.

Massimino, M. R., Abate, G., Corsico, S., Louarn, R. 2019b. Comparison Between Two Approaches for Nonlinear FEM Modelling of the Seismic Behaviour of a Coupled Soil–Structure System. *Geotechnical and Geological Engineering*, 37(3): 1957–1975.

Mylonakis, G. & Gazetas, G. 2000. Seismic Soil-Structure Interaction: Beneficial or Detrimental? *Journal of Earthquake Engineering* 4(3): 277–301.

NTC 2018. D.M. 17/01/18 – Updating of technical standards for buildings, Official Journal of the Italian Republic, 17th January 2018 (In Italian)

Pandey, B. H., Liam Finn, W. D., Ventura, C. E., 2012. Modification of free-field motions by soil-foundation-structure interaction for shallow foundations. *Proc. 15th World Conf on Earthq Eng*, Lisbon, Portugal; 24–28 September 2012.

Pecker, A. & Chatzigogos, C.T. 2010. Nonlinear soil structure interaction: impact on the seismic response of structures. *Proc. XIV Eur Conf. on Earth Eng.* August 2010, Ohrid, FYROM, Keynote lecture.

Pitilakis, D., Dietz, M., Miur Wood, D., Clouteau, D., Modaressi, A. 2008. Numerical simulation of dynamic soil-structure interaction in shaking table testing. *Soil Dyn and Earth Eng*, 28(6): 453–467.

Rovithis, E., Kirtas, E., Bliziotis, D., Maltezos, E., Pitilakis, D., Makra, K., Savvaidis, A., Karakostas, C., Lekidis, V. 2017. A LiDAR-aided urban-scale assessment of soil-structure interaction effects: the case of Kalochori residential area (N. Greece). *Bulletin of Earthquake Engineering*, 15: 4821–4850.

Sheng D., Wriggers, P., Sloan S.W. 2007. Application of Frictional Contact in Geotechnical Engineering. *International Journal of Geomechanics* 7(3), 176–185.

Stucchi, M., Meletti, C., Montaldo, V., Crowley, H., Calvi, G. M., Boschi, E. 2011. Seismic hazard assessment (2003–2009) for the Italian building code. *Bulletin Seismol Society of America*, 101(4):1885–1911.

Veletsos, A. S., & Meek, J. W. 1974. Dynamic behaviour of building-foundation systems. *Earthquake Engineering and Structural Dynamics*, 3(2): 121–138.

Yokota, K., Imai, T., Konno, M. 1981. Dynamic deformation characteristics of soils determined by laboratory tests. *OYO Tec. Rep*, 3: 13–37.

Geotechnical Engineering for the Preservation of Monuments and Historic Sites III – Lancellotta, Viggiani, Flora, de Silva & Mele (Eds)

Vulnerability assessment of historical cities including SSI and site-effects

C. Amendola & D. Pitilakis
Aristotle University of Thessaloniki, Greece

ABSTRACT: Risk assessment of historical cities is commonly addressed considering a portfolio of fixed-base structures, i.e., neglecting the interaction between soil, foundation, and structure (SSI). The state-of-the-art literature proves that neglecting SSI and site-effects may lead to inaccurate risk estimates by a substantial margin. Including these effects on the large-scale vulnerability analysis of historical sites is considered challenging due to the cultural and historical importance, high exposure concentration, and complexity of the whole interacting system. To this aim, a new methodology is proposed to calculate fragility functions of masonry structures considering SSI and local site-effects, suitable for large-scale applications. The applicability of the proposed approach is based on globally available data regarding soil, foundation, and building taxonomy. This study encourages engineers, practitioners, and risk analysts to include SSI and site-effects for an accurate assessment of seismic safety of existing buildings in historical centers to identify the most appropriate short- and long-term earthquake mitigation policies.

Keywords: soil-structure-interaction, large-scale, risk analysis, masonry structures

1 INTRODUCTION

The seismic risk framework requires the definition of fragility curves which define the probability of exceedance of a predefined performance level. The complexity related to the characterization of the soil-foundation system and the common belief in the beneficial effects associated with the interaction between the soil, foundation, and structure led over the years to develop fragility functions considering fixed-base structures. Despite this, the up-to-date literature recognized the modification of the dynamic behavior (Amendola et al. 2021; de Silva 2020; Piro et al. 2020; Brunelli et al.2021) and thus the fragility (Saez et al. 2011; Rajeev and Tesfamariam 2012; Pitilakis et al. 2014; Karapetrou et al. 2015; de Silva 2020; Petridis and Pitilakis 2020; Cavalieri et al. 2020) of structures founded on soft soil with respect to the typical fixed-base assumption. In this regard, the compliance of the foundation subsoil increases the flexibility of the whole system. At the same time, during shaking, part of the energy is dissipated in the subsoil through wave scattering and hysteretic actions.

Even though the results of such studies provided the scientific community with valuable knowledge for a site-specific vulnerability assessment, the reliability at a large-scale is assessed with certain limitations. Not all the possible SSI scenarios have been covered so far, making the existing fragility functions accounting for SSI inadequate for large-scale analyses. Moreover, for the extensive applications, soil conditions may be considered in the seismic hazard assessment adopting either code- or research-based amplification factors or through very advanced models (physical-numerical simulations, microzonation analysis). Still, they are not correctly considered in the fragility curves. Indeed, suppose existing fragility curves are analytically derived. In that case, they may have been assessed applying records not accounting for variations in frequency and amplitude contents imposed by each site's local geotechnical and topographic conditions.

 DOI 10.1201/9781003308867-64

To this aim, we present a methodology to derive fragility functions for large-scale assessment of cities considering SSI and local site-effects, applicable to different building classes for a great variety of soil-foundation systems that can be encountered in an urban environment. The novelty of the proposed approach consists in explicitly introducing the averaged shear-wave velocity in the top 30 m ($V_{S,30}$) in the provided fragility functions as a proxy for the site and SSI effects. The advantage is the possibility to link the so calculated fragility curves with actual site conditions that may be defined on the base of $V_{S,30}$ maps derived, to mention a few, from detailed in situ analyses or from proxies such as the slope (Wald & Allen 2007) or the local geology (Forte et al. 2017). The methodology is implemented in the historical center of Ano-Poli, located in the northern area of Thessaloniki, in Greece. The main findings of the examined case study demonstrated that the conventional way of calculating fragility curves might lead to an incorrect evaluation of the seismic risk.

2 METHODOLOGY FOR FRAGILITY CURVES INCLUDING SSI AND SITE-EFFECTS

This section introduces a new methodology to assess the fragility functions for different building classes founded on shallow or embedded foundations taking into account SSI and site-effects. Figure 1 summarizes the main steps of the methodological framework. All the analyses are conceived to be implemented in the open-source OpenSees software (Mazzoni et al. 2006). One of the most significant uncertainties in studying the problem of soil-structure-interaction, especially in large-scale applications, is the definition of the main features defining the whole interacting system. With this in mind, the applicability of the proposed approach is based on globally available input data regarding the soil parameters, the foundation, and the building taxonomy, thus making it easily applicable for risk assessment at different cities.

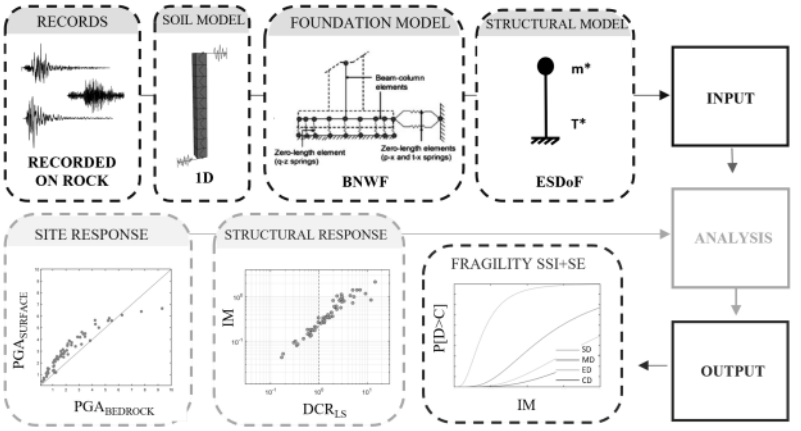

Figure 1. Flow chart of the proposed methodology for the fragility assessment of structures considering SSI and site-effects at an urban scale.

To formally consider the aleatoric uncertainties related to the so-called record-to-record variability, a large set of input ground motions recorded on outcropping rock/firm-soil is selected to perform all the dynamic cloud analyses (Jalayer et al. 2017). To avoid developing excessively structure-site-foundation-dependent procedures, the problem is decoupled through the substructure approach. Accordingly, the modification of the selected records due to the local site-effects is quantified by performing 1D numerical simulations of seismic site response performed on representative profiles conceived to pertain to different soil types. Specifically, this step may be enriched from available microzonation studies at the local or city level.

Following the substructure approach, the free-field motion is directly applied as input for the dynamic analyses for structures resting on surface foundations. While for embedded foundations, the free-field motion is further modified to account for kinematic interaction before being applied at the base of the superstructure (Di Laora and de Sanctis 2013). Considering the number of records, the spatially distributed portfolio of structures, and the parameterization of the foundation characteristics, several thousands of time-history analyses are generally necessary for large-scale applications. To reduce the computational effort, the superstructure is modelled following the equivalent single degree of freedom (ESDoF) system approximation (D'Ayala et al. 2014). At the same time, the compliance of the foundation subsoil is considered using the Beam-on-Nonlinear-Winkler-Foundation (BNWF) concept (NIST 2012). The results of the dynamic analysis are processed to calculate the probability of exceeding four different limit states (slight (SD), moderate (MD), extensive (ED) and complete damage (CD)) given IM's intensity measure. The structural response variable is the critical demand to capacity ratio, DCR_{LS} ((Jalayer et al. 2007)), i.e. the ratio between the structural response and capacity for the performance of interest. An improved fragility model, namely Modified Cloud analysis, MCA (Jalayer et al. 2017), is adopted herein to compute fragility functions which formally considers the collapse-inducing records. Collapse cases are defined in literature as the input motions causing structural collapse and/or reaching dynamic instability due to large deformations (Shome & Cornell 2000). In this revised model, the collapse and non-collapse parts are mixed using the *Total Probability Theorem* as follows:

$$P\left(DCR_{LS} > 1|IM\right) = P\left(DCR_{LS} > 1|IM, NoC\right) \cdot \left(1 - P(C|IM)\right) + P\left(DCR_{LS} > 1|IM, C\right) \cdot P(C|IM) \quad (1)$$

where the probability of exceeding the performance level for the non-inducing collapse records, $P\left(DCR_{LS} > 1|IM, NoC\right)$, can be computed using the classical cloud approach. The collapse probability is estimated by a bi-parametric logistic regression model, $P(C|IM)$. This method effectively characterizes the fragility of compliant base structures, which are likely to occur when SSI effects are significant.

3 CASE STUDY

The section presents an application of the proposed methodology to perform the seismic risk assessment of the historical center of Ano-Poli located in the northwest area of Thessaloniki (Figure 2).

The residential area of Ano-Poli is mainly characterized by masonry structures (Figure 2b). As reported in Figure 3a, 11 different masonry building classes, mainly unreinforced masonry

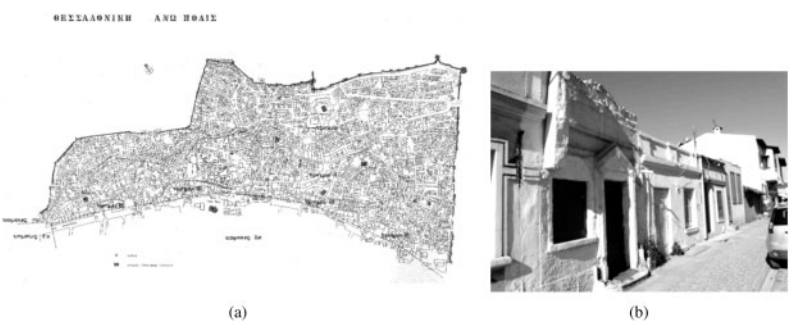

Figure 2. (a) Ano-Poli Site plan in 1979 from KalogirouandPaka(2018) and (b) pictures of traditional building classes in the Ano-Poli district modified after Vyzantiadou and Selevista (2019).

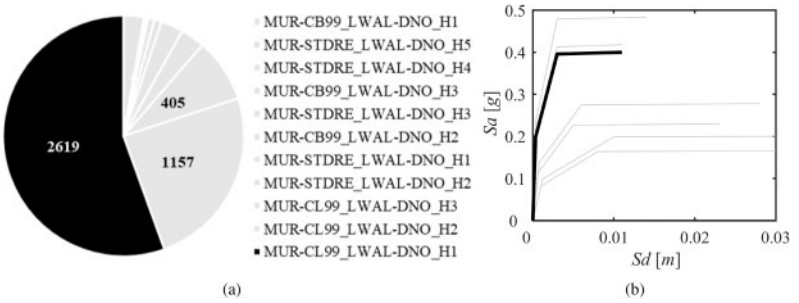

Figure 3. (a) Pie chart presenting the different masonry building classes in the Thessaloniki municipality and (b) corresponding capacity curves characterizing their nonlinear behaviour. The case-study building in class is highlighted in black.

structures, can be identified from the whole Thessaloniki exposure (Crowley et al. 2020). The following results are shown for the most popular masonry building class (namely MUR-CL99-LWAL-DN0-H1 following the GEM taxonomy (D'Ayala et al. 2014)) representative of low-rise unconfined masonry structures with wall force resisting frame and unknown types of concrete blocks. A total of 2619 buildings for such class were identified from all Thessaloniki exposure. Its spatial distribution in the whole Thessaloniki municipality is shown in Figure 4a.

To correctly consider local site-effects and determine the soil's main features in the SSI modelling, seven different representative clayey soil profiles were modelled in the OpenSees software. The selected soil profiles were conceived considering different average propagation velocities of the shear waves within the first 30m of soil depth, $V_{S,30}$ (i.e., ranging from 150 to 450 m/s as reported in Table 1), thus of soil types B, C and D according to EC8 classification (CEN 2005). For this showcase application, to provide the reader with a more general framework applicable in lack of specific geophysical or geotechnical data, a simplified distribution is considered to describe the distribution of the soil shear modulus, G with depth as follows:

$$V_S(z) = V_{S,Z=30}\left(\left(\frac{V_{S,Z=0}}{V_{S,Z=30}}\right)^{\frac{1}{a}} + \frac{z}{30}\cdot\left(1-\left(\frac{V_{S,Z=0}}{V_{S,Z=30}}\right)^{\frac{1}{a}}\right)\right)^{a}. \quad (2)$$

where z stands for the depth measured from the soil surface, while $V_{S,Z=0}$ and $V_{S,Z=30}$ are the soil shear modulus at the ground surface and at a depth of 30 meters, respectively. The $V_{S,Z=0}$ and $V_{S,Z=30}$ are randomly selected to ensure a $V_{S,30}$ equal to the values reported in Table 1. Some further restrains were adopted for the random selection of the parameters as ensuring values not unrealistically approach zero values near ground surface and guarantee stiffness parameters vary in the range embedded in the empirical relationships relating the small strain stiffness, G_0, and the geostatic stress state and history, i.e. according to soil index and state properties (D'Onofrio and Silvestri 2001). To this aim, the a coefficient was selected equal to 0.25.

Table 1. Main soil parameters selected to characterize the soil profile

	Soil parameters						
$V_{S,30}$ (m/s)	150	180	250	300	360	400	450
V_z (m/s)	102	122	169	203	243	270	304
EC8 Soil class	D	D/C	C	C	C/B	B	B

Following the proposed work-flow of Figure 1, the selected superstructure, MUR-CL99-LWAL-DN0-H1, is modelled in OpenSees with a single degree of freedom system characterized by a

nonlinear hysteretic behavior. The parameters taken to define the specific hysteretic low adopted are defined based on the nonlinear backbone curves (black capacity curve in Figure 3a) available in the literature for different building classes (Martins and Silva 2020).

3.1 *SSI Model*

The SSI is modelled using a beam-on-nonlinear-winkler-foundation (BNWF) concept. Accordingly, the soil beneath the foundation is assumed to be an assembly of springs, dashpots and gap elements to capture the far-field and near-field behaviour. Such model can capture the hysteretic energy dissipation through the sliding, rotation and vertical foundation motions. Radiation damping can also be accounted for by means of foundation dampers. When modelling the BNWF system, the parameters primarily affecting the interaction problem (Veletsos & Meek 1974), such as the slenderness ratio, *H/B* (where H is the structural height and B is the characteristic foundation half-length) and the structure to soil relative inertia, δ, are investigated. In this specific application, such features are determined ($H/2B$=0.5, and δ=0.05) from available data for the city of Thessaloniki. More in detail, the whole foundation system is reduced to an equivalent rectangular surface foundation of radius r defined as $r = \sqrt{A/\pi}$, where A is the footprint area representative of the masonry building class under consideration and is estimated from the building print area as available in the OpenStreetMap (http://www.openstreetmap.org/) (see Figure 4b).

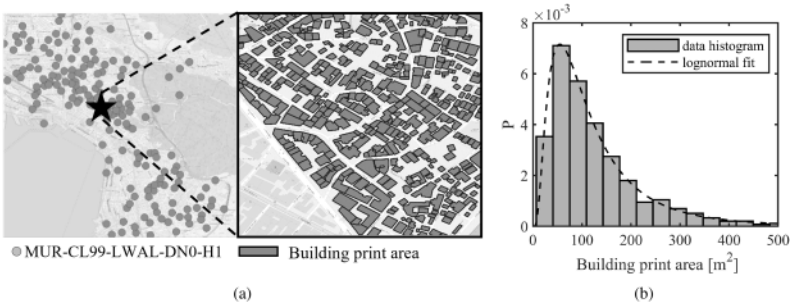

Figure 4. (a) Distribution of the masonry building class selected for the analysis in the Thessaloniki municipality, and Ano-Poli historical center highlighted with a black star and (b) print area of each building and (c) histogram of building footprint area for the portfolio of masonry structures in the case study area.

Figure 4 reports the footprint area of each building and its frequency in the selected area of study indeed. Considering the variability of the footprint area, even for the same building class, a statistical treatment of the data was necessary to unequivocally assess the foundation geometry. More in detail, as reported in Figure 4b the histogram of the collected data was fitted with a lognormal distribution and from its statistical parameters, it was possible to select a representative foundation radius to characterize the foundation system. The definition of the foundation geometry is of paramount importance in SSI problems since it allows also to define the depth of the soil interacting with the

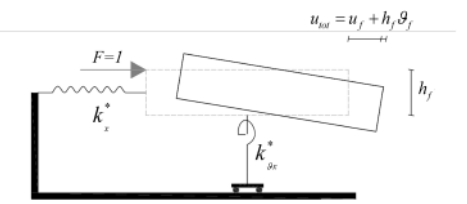

Figure 5. Sketch of the foundation placed on swaying and rocking impedance functions adopted for the calculation of radiation damping. Modified after Maravasetal (2014).

foundation. Indeed, the stiffness used to calibrate the springs is selected as a function of a shear wave velocity mobilized considering an interaction volume equal to the total foundation length (V_z values reported in Table 1).

The final BNWF model is automatically implemented in OpenSees through the 'Shallow-FoundationGen' (Raychowdhury & Hutchinson 2008) command. Nevertheless, while the spring coefficients (i.e. the real part of the impedance functions) can be directly computed from the input geometrical and mechanical soil foundation parameters, the radiation damping (i.e. the dash-pot coefficient) must be calculated from the user. For this reason, following similar applications (Maravas et al. 2014; Brunelli et al.2021; de Silva et al. 2022) we compute an equivalent radiation damping from the equilibrium of the simplified foundation system depicted in Figure 5.

As shown in Figure 5 the dashpot coefficient to define far-field elastic behaviour of the foundation is computed considering the rocking ($k^*_{\theta x}$) and swaying (k^*_x) impedance functions. When applying a horizontal unitary force to the simplified foundation of Figure 5, the total displacement at the foundation level can be evaluated from the corresponding force stiffness relationship as it follows:

$$u_{tot} = u_f + h_f \theta_f = \frac{1}{k^*_{eq}} = \frac{1}{k^*_x} + \frac{h_f^2}{k^*_{\theta x}} \tag{3}$$

where h_f is the foundation height, whereas θ_f and u_f are the rigid rotation and horizontal displacement of the foundation, respectively. The complex rocking and swaying impedance functions, can be explicitly expressed as function of their real and imaginary part as follows:

$$k^* = k + i\omega c = k(1 + 2i\beta) \tag{4}$$

Substituting the explicit impedance functions in Equation 3 we can obtain the following expression:

$$\frac{1}{k^*_{eq}(1 + 2i\beta_{rad,eq})} = \frac{1}{k^*_x(1 + 2i\beta_x)} + \frac{h_f^2}{k^*_{\theta x}(1 + 2i\beta_{\theta x})} \tag{5}$$

where $\beta_{\theta x}$ and β_x are the contributions of the rocking and the swaying to the overall foundation energy dissipation, respectively. By multiplying each member of Equation 5 for the complex conjugate member we obtain the following complex Equations:

$$\frac{(1 - 2i\beta_{rad,eq})}{k^*_{eq}(1 + 4i\beta^2_{rad,eq})} = \frac{(1 - 2i\beta_x)}{k^*_x(1 + 4i\beta^2_x)} + \frac{(1 - 2i\beta^2_{\theta x})h_f^2}{k^*_{\theta x}(1 + 4i\beta^2_{\theta x})}. \tag{6}$$

Finally from the real and imaginary part we can obtain the following equations which are used in sequence to compute the equivalent radiation damping.

$$\frac{1}{k^*_{eq}(1 + 4i\beta^2_{rad,eq})} = \frac{1}{k^*_x(1 + 4i\beta^2_x)} + \frac{h_f^2}{k^*_{\theta x}(1 + 4i\beta^2_{\theta x})} \tag{7}$$

$$\frac{\beta_{rad,eq}}{k^*_{eq}(1 + 4i\beta^2_{rad,eq})} = \frac{\beta_x}{k^*_x(1 + 4i\beta^2_x)} + \frac{\beta^2_{\theta x} h_f^2}{k^*_{\theta x}(1 + 4i\beta^2_{\theta x})} \tag{8}$$

where the dynamic coefficients for both stiffness and damping are estimated for the fundamental period of the compliant system (as reported in Table 2) through an ad hoc Matlab^{TM} iterative routine.

To validate the reliability of the proposed approach to account for radiation damping within the BNWF OpenSees implementation, in Table 2 we compare the equivalent damping ratio computed from the results of the analyses with the analytical closed form solution proposed in literature by (Maravas et al. 2014). Specifically, after the release of the applied loading in the nonlinear dynamic analyses, the ESDoF is let to undergo in free oscillations. The total damping is then calculated by applying the logarithmic decrement method to the ESDoF top displacement as graphically illustrated in Figure 6a.

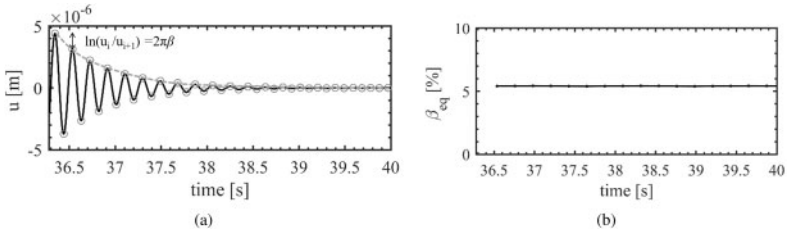

Figure 6. (a) Time history of free oscillation displacement recorded after the release of the ESDoF test and (b) evolution with the number of cycles of the displacement amplitudes computed as the half peak-to-peak value in each cycle.

Table 2. Inertial interaction effects

$V_{S,30}$ [m/s]	σ [–]	T_{SSI} [s]	T_{SSI}/T_{FB} [–]	T^*_{SSI} [s]	β_{eq} [%]	β^* [%]	β_{eq}/β^* [–]
150	9.4	0.190	1.09	0.180	5.42%	5.86%	0.92
180	11.2	0.186	1.06	0.178	5.29%	5.42%	0.98
250	15.6	0.181	1.03	0.177	5.14%	5.12%	1.00
300	18.7	0.179	1.02	0.176	5.09%	5.06%	1.01
360	22.5	0.178	1.02	0.176	5.06%	5.02%	1.01
400	25.0	0.177	1.01	0.176	5.04%	5.01%	1.01
450	28.1	0.177	1.01	0.175	5.03%	5.01%	1.00
>800	–	0.175	1.00	0.175	5.00%	5.00%	1.00

The equivalent damping ratio is generally significant only for squat structures, i.e. characterized by low slenderness and high mass ratios, thus for this specific application (i.e. MUR-CL99-LWAL-DN0-H1, $H/2B$=0.5, δ=0.05) is expected to not strongly deviate from the fixed base reference case (β=0.05). As shown in Table 2, such effect decays as increasing the soil stiffness, or similarly as the parameter σ increases (Veletsos & Meek 1974). All in all, the total damping compares well with the analytical prediction of (Maravas et al. 2014), and some differences are observed, especially for the soft soil profiles, because the constitutive model of foundation is nonlinear whereas Maravas's solutions are based on the linear assumption. When nonlinear foundation behavior is allowed the flexibility of the system increases thus as shown in Table 2, the elongated period for all the SSI models (i.e. same structural typology endowed with the different BNWF models considered) resulting from the analysis is generally larger compared to linear analytical prediction (T^*_{SSI}). The fundamental period of the compliant model (T_{SSI}) is always greater than that pertaining to the fixed base one (T_{FB}), whereas the energy dissipated by the foundation leads to a slight increase of the overall damping ratio.

3.2 *Analysis and Results*

As it is well known, the performance of structures founded on soft soil may be strongly influenced by the response of the underlying soil. To provide an overview of the modification of the input motion due to local geotechnical conditions Figure 7 compares the input and the free-field motions resulting from the performed analyses in terms of acceleration displacement response spectra, ADRS.

For sake of brevity, only three different soil deposits are shown, corresponding to soil class B, C and D, respectively. All in all, site effects are clearly recognizably comparing the response in

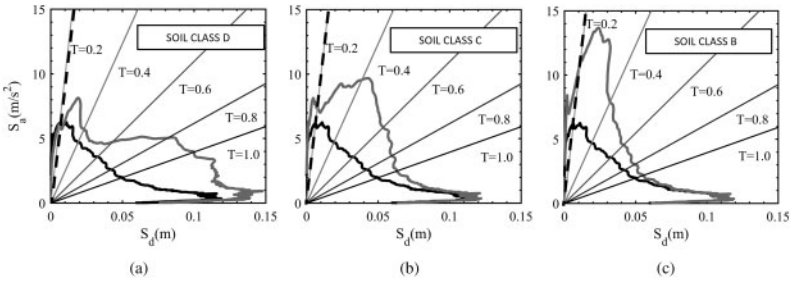

Figure 7. mean Acceleration displacement response spectra computed from all the selected input records (black lines) and from the free-field motion as resulting from the site response analysis (grey lines) for three soil profiles, i.e. (a) $V_{S,30}$=150 and (b) $V_{S,30}$=300 m/s and (c) $V_{S,30}$=450 m/s corresponding to soil class D, C and B respectively.

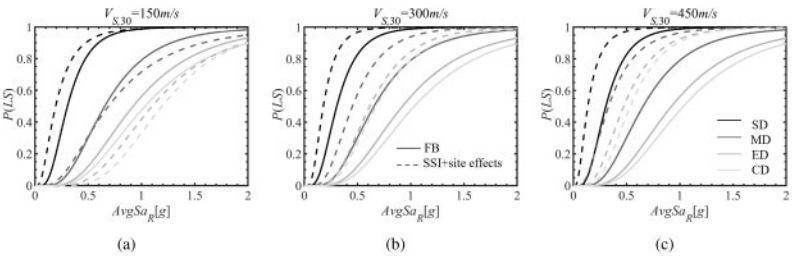

Figure 8. Comparison between fragility functions in terms of $AvgSa(T)_R$ developed for one reference building class, i.e., MUR-CL99-LWAL-DN0-H1 considering the structure fixed at its base (continuous lines) and SSI and site-effects for one BNWF system characterized by $H/2B$=0.5, δ=0.05 and (a) $V_{S,30}$=150m/s, (b) $V_{S,30}$=300m/s and (c) $V_{S,30}$=450m/s (dashed lines).

terms of mean values computed from the whole set of records (tick grey and black lines) for all the reference profiles considered in this study. In detail, the maximum amplification for the medium stiff soil profile (Figure 7c) occurs for periods lower than 0.4 s and is therefore expected to increase the seismic demand of very stiff structures whereas for soft soil profiles (Figure 7b) the period range in which seismic demand is amplified shifts to the left in the ADRS (i.e. 0.2-0.6 s). Contrarily, the trend is inverted for very soft profiles (i.e. class D and Figure 7a) where the seismic demand is maximized for larger periods, and is therefore expected to influence more high rise buildings.

Following the substructure approach, the so modified input motions are applied at the base of the compliant foundation models to perform the cloud analyses. Figure 8 reports the results the devised methodology, i.e. the fragility functions for the selected masonry building class considering SSI and local site effects. An improved taxonomy is adopted herein to consider the main soil foundation features where the averaged shear-wave velocity in the top 30 m ($V_{S,30}$) represents a proxy for site and SSI effects. In detail the BNWF system is characterized by a slenderness ratio $H/2B$=0.5 and by an inertia ratio, δ=0.05 and it is developed for all the $V_{S,30}$ profiles listed in Table 1. The average spectral acceleration, *AvgSa* has been chosen to compare the fragility functions in Figure 8. The latter is of particular interest in SSI studies since it allows the comparison between fragility functions developed for different compliant systems and the reference curves considering the fixed-base assumption. Is worth mentioning that the intensity measures are computed for the set of input records (i.e. recorded on rock/very stiff soil).

All in all, the results of the analyses for the flexible foundations, i.e. considering SSI and site-effects (dashed lines) produce a shift to the left of the fragility curves compared to the fixed-base

case (continuous lines), thus resulting into an increase of the structural fragility. Indeed, for low-rise structures, i.e. for stiff structures characterized by a fundamental period of $T<0.2$s, which fixed-base period lies in the short period region of the response spectrum, the spectral acceleration is generally expected to increase (Figure 7). As a matter of fact, the fragility shift is more pronounced for stiff soil profiles, see for example Figure 8c developed for the virtual soil profile corresponding to $V_{S,30}$=450 m/s, because of the increased seismic demand due to local site effects. Hence, not only site effects may play an important role but also period elongation associated with SSI may cause an increase in the spectral acceleration ordinate, thus resulting in an increase of the overall fragility.

4 CONCLUSIONS

Despite the recent efforts in developing fragility functions accounting for SSI and site effects, a literature review revealed that they are still unavailable for a significant number of soil-foundation-structure scenarios making them unreliable for large-scale applications. For this reason, a comprehensive methodological framework is presented herein to develop site-consistent fragility curves including SSI and site-effects suitable for large-scale risk assessment. One of the greatest uncertainties to study the problem of SSI, especially in the assessment of historical centers, is the definition of the main features defining the foundation system. With this in mind, the general asset of the proposed methodology, in lack of local information, combines globally available data to characterize the foundation system. Furthermore, all the analyses are conceived to be implemented in the open-source OpenSees software, thus making it applicable for risk assessment at different cities.

To show the feasibility of the devised methodology, this study performs dynamic analyses through ESDoF approximation of the most popular masonry building class in Thessaloniki, specifically concentrated in the historical center of Ano-Poli. In the showcase application the foundation geometrical features are retrieved from the building print area as available in the OpenStreetMap whereas the parameters adopted to define the nonlinear behavior of the superstructure are defined based on the capacity curves available in the literature for different European building classes (Martins and Silva 2020).

The main novelties and conclusions of the present study are:

- The explicit introduction of the averaged shear-wave velocity in the top 30 m ($V_{S,30}$) in the fragility functions as a proxy for site and SSI effects. Following this improved taxonomy, is possible to link fragility curves for spatially distributed portfolio of structures with real site conditions that may be defined on the base of $V_{S,30}$ maps derived, just to mention few, from detailed in situ analyses or from proxies such as the slope (Wald & Allen 2007) or the local geology (Forte et al. 2017).
- Fragility functions for structures under fixed- and compliant-base conditions show that considering SSI and local site effects can significantly affect the vulnerability assessment. In addition to site amplification, contrary to the common belief on beneficial SSI effects, the interaction with the foundation soil system may lead to higher seismic demand compared to the fixed base period, depending on the dynamic characteristics of the structure and the shape of the free-field response spectra.
- On the basis of the application of the devised methodology in the historical center of Ano-Poli, this study encourages the adoption of SSI models in the fragility computation compared to more simplified approaches for the large-scale application, to perform a more correct quantification of the potential fragility estimates of centers of cultural and historical importance.
- Future applications of the proposed methodology may involve detailed local information on the foundation building inventory and site conditions from microzonation studies which will promote a seismic risk assessment of historical cities associated with a lower degree of uncertainty.

ACKNOWLEDGMENTS

The Authors have received funding from the ITN-Marie Sklodowska-Curie project "New challenges for Urban Engineering Seismology (URBASIS-EU) (GA 813137).

REFERENCES

Amendola, C., F. de Silva, A. Vratsikidis, D. Pitilakis, A. Anastasiadis, & F. Silvestri (2021). Foundation impedance functions from full-scale soil-structure interaction tests. *Soil Dynamics and Earthquake Engineering 141*(November 2020), 106523.

Brunelli, A., F. de Silva, A. Piro, F. Parisi, S. Sica, F. Silvestri, & S. Cattari (2021). Numerical simulation of the seismic response and soil–structure interaction for a monitored masonry school building damaged by the 2016 central italy earthquake. *Bulletin of Earthquake Engineering 19*(2), 1181–1211.

Cavalieri, F. & Correia, A. A., H. Crowley, & R. Pinho (2020). Dynamic soil-structure interaction models for fragility characterisation of buildings with shallow foundations. *Soil Dynamics and Earthquake Engineering 132*, 106004.

CEN., (2005). Eurocode 8: Design of structures for earthquake resistance-part 1: general rules, seismic actions and rules for buildings. *European Standard EN 1998-1:2004. Brussels, Belgium: European Committee for Standardisation.*.

Crowley, H., V. Despotaki, D. Rodrigues, V. Silva, D. Toma-Danila, E. Riga, A. Karatzetzou, S. Fotopoulou, Z. Zugic, L. Sousa, S. Ozcebe, & P. Gamba (2020). Exposure model for european seismic risk assessment. *Earthquake Spectra 36*, 252–273.

D'Ayala, D., A. Meslem, D. Vamvatsikos, K. Porter, & T. Rossetto (2014). Guidelines for analytical vulnerability assessment of low/mid-rise buildings, vulnerability global component project. *GEM Technical Report 2015-08 v1.0.0 08*, 162.

de Silva, F. (2020). Influence of soil-structure interaction on the site-specific seismic demand to masonry towers. *Soil Dynamics and Earthquake Engineering 131*, 106023.

de Silva, F., C. Amendola, D. Pitilakis, & F. Silvestri (2022). *Prediction of foundation stiffness and damping ratio under swaying and rocking motion.*

Di Laora, R. & L. de Sanctis (2013). Piles-induced filtering effect on the foundation input motion. *Soil Dynamics and Earthquake Engineering 46*, 52–63.

D'Onofrio, A. & F. Silvestri (2001). Influence of micro-structure on small-strain stiffness and damping of fine grained soil and effects on local site response. In *Missouri University of Science and Technology Scholars' Mine*. Paper presented at International Conferences on Recent Advances in Geotechnical Earthquake Engineering and Soil Dynamics, Missouri University of Science and Technology, 29 Mar 2001.

Forte, G., S. Fabbrocino, G. Fabbrocino, G. Lanzano, F. Santucci de Magistris, & F. Silvestri (2017). A geolithological approach to seismic site classification: an application to the molise region (italy). *Bulletin of Earthquake Engineering 15*(1), 175–198.

Jalayer, F., P. F., & P. E. Pinto (2007). A scalar damage measure for seismic reliability analysis of rc frames. *Earthquake Engineering and Structural Dynamics 36*(June), 2059–2079.

Jalayer, F.and Ebrahimian, H., A. Miano, G. Manfredi, & H. Sezen (2017). Analytical fragility assessment using unscaled ground motion records. *Earthquake Engineering and Structural Dynamics 46*(15), 2639–2663.

Kalogirou, N. & A. Paka (2018). Standardizing tradition: The building code as a series of prototypes for new structures in the traditional district of ano poli in thessaloniki. 14th International Conference in "STANDARDIZATION, PROTYPES AND QUALITY: A MEANS OF BALKAN COUNTRIES" COLLABORATIONâŁž, September 21 - 22, 2018, Tirana, Albania.

Karapetrou, S. T., S. D. Fotopoulou, & K. D. Pitilakis (2015). Seismic vulnerability assessment of high-rise non-ductile rc buildings considering soil-structure interaction effects. *Soil Dynamics and Earthquake Engineering 73*, 42–57.

Maravas, A., G. Mylonakis, & D. L. Karabalis (2014). Simplified discrete systems for dynamic analysis of structures on footings and piles. *Soil Dynamics and Earthquake Engineering 61*, 29–39.

Martins, L. & V. Silva (2020). Development of a fragility and vulnerability model for global seismic risk analyses. *Bulletin of Earthquake Engineering*.

Mazzoni, S., F. McKenna, M. H. Scott, G. L. Fenves, et al. (2006). Opensees command language manual. *Pacific Earthquake Engineering Research (PEER) Center 264*, 137–158.

NIST, G. .-.-. (2012). Soil-structure interaction for building structures.

Petridis, C. & D. Pitilakis (2020). Fragility curve modifiers for reinforced concrete dual buildings, including nonlinear site effects and soil–structure interaction. *Earthquake Spectra*.

Piro, A., F. de Silva, F. Parisi, A. Scotto di Santolo, & F. Silvestri (2020). Effects of soil-foundation-structure interaction on fundamental frequency and radiation damping ratio of historical masonry building sub-structures. *Bulletin of Earthquake Engineering 18*(4), 1187–1212.

Pitilakis, K., S. T. Karapetrou, & S. D. Fotopoulou (2014). Consideration of aging and ssi effects on seismic vulnerability assessment of rc buildings. *Bulletin of Earthquake Engineering 12*, 1755–1776.

Rajeev, P. & S. Tesfamariam (2012). Seismic fragilities of non-ductile reinforced concrete frames with consideration of soil structure interaction. *Soil Dynamics and Earthquake Engineering 40*, 78–86.

Raychowdhury, P. & T. C. Hutchinson (2008). Shallowfoundationgen opensees documentation. *Open System for Earthquake Engineering Simulation (OpenSEES): University of California, San Diego*.

Saez, E., F. Lopez-Caballero, & A. Modaressi-Farahmand-Razavi (2011). Effect of the inelastic dynamic soil–structure interaction on the seismic vulnerability assessment. *Structural safety 33*(1), 51–63.

Shome, N. & C. A. Cornell (2000). Structural seismic demand analysis: consideration of collapse. In *8th ASCE Specialty Conference on Probabilistic Mechanics and Structural Reliability*, pp. 1–6.

Veletsos, A. S. & J. W. Meek (1974). Dynamic behaviour of building-foundation systems. *Earthquake Engineering & Structural Dynamics 3*(2), 121–138.

Vyzantiadou, M. M. & M. Selevista (2019). Protection of cultural heritage in thessaloniki: A review of designation actions. *Heritage 2*(1), 717–731.

Wald, D. J. & T. I. Allen (2007). Topographic slope as a proxy for seismic site conditions and amplification. *Bulletin of the Seismological Society of America 97*(5), 1379–1395.

Geotechnical Engineering for the Preservation of Monuments and Historic Sites III – Lancellotta, Viggiani, Flora, de Silva & Mele (Eds)

Effects of local soil conditions on the seismic response of the historical area in San Giuliano di Puglia (Italy)

T. Fierro, M. Castiglia & F. Santucci de Magistris
University of Molise, Campobasso, Italy

M.G. Durante
University of Calabria, Rende (CS), Italy

ABSTRACT: The role of geotechnical engineering in the preservation of historical sites can be found, among others, in the understanding of the effects of local soil conditions when an earthquake happens. These effects, combined with the vulnerability of the buildings for materials and construction techniques, the soil-structure interaction, and the seismic hazard define a risk scenario. In this context, heritage conservation becomes challenging and site-specific because of the variability of the affecting parameters. However, the availability of case histories strengthens the knowledge, allows defining some general outcomes, and provides teachings for proper actions towards the preservation of the historical sites. In this paper, the case history of the municipality of San Giuliano di Puglia, in the Molise region (Italy), hit by the 2002 Molise earthquake, is presented. The site is peculiar for the variability of the damage distribution in the town where the amplification effects played a significant role. Emblematic is the case of the historic core of the town, which performed well compared to the valley, where the tragic collapse of the F. Jovine school occurred. Local amplification effects will be further analyzed in this paper and the results of 2D site response analyses will be presented. This municipality is monitored through permanent seismic stations located along the main section of the village and by vertical arrays that are a precious source for a better understanding of both soil properties and site response.

1 INTRODUCTION

The site of San Giuliano di Puglia in Italy has already been studied by various researchers due to the M_w 5.74 earthquake that occurred in October 2002 in the Molise region. The collapse of its elementary school with children fatalities and the non-uniform observed damage distribution drew the attention of the research community to this small village. Many geotechnical investigations and numerical analyses were carried out for addressing the amplification effects of the soil deposit in the area (see, for example,;'Onofrio et al. 2009; Fierro et al. 2019, 2020a; Puglia 2008; Puglia et al. 2007; 2009; Santucci de Magistris et al. 2014; Sanò et al. 2015; Silvestri et al. 2006;). Mono- and bi-dimensional site response analyses have been widely performed, highlighting the limitations of the 1D analysis (Puglia et al. 2013) and the differences with the response spectra provided by the Italian National Technical Code (Fierro et al. 2020b). In 2012, the National Accelerometric Network of the Department of Civil Protection (DPC) was enriched by the installation of additional permanent accelerometric stations in three strategic points within the municipality, two of them consisting of vertical arrays. Direct recordings coming from these arrays provide a better understanding of the wave propagation through the soil layers. These recordings are already used in Fierro et al. (2020b) and have revealed a precious tool to back-analyze the response and to critically investigate the adopted stiffness profile, which always plays a key role in the damage distribution due to

DOI 10.1201/9781003308867-65

amplification effects. The study also accounts for possible uncertainties in the contact between stratigraphic units and buried geometry.

Based on more recent recordings made available from the vertical arrays, 2D site response analyses are used to fit the array recordings by optimizing the definition of the geotechnical model. The analyses are conducted with OpenSees (Open System for Earthquake Engineering Simulation, McKenna et al. 2000), an object-oriented, open-source software framework, based on the Finite Element theory. OpenSees is suitable for serial and parallel computer applications, the latter allows to perform parametric analyses more efficiently, including also nonlinear analyses with advanced constitutive models for the soil deposit. Results of the site response analyses are discussed by accounting for the effects on the built environment, modelling a large portion of the town, that includes the whole valley. The large model has been analyzed using the parallel interpreter OpenSeesSP (McKenna & Fenves 2008), taking advantages of the computational power available through the cyber-infrastructure DesignSafe-CI (Rathje et al. 2017).

2 THE SUBSOIL OF SAN GIULIANO DI PUGLIA

A large amount of available geotechnical tests identified that subsoil of San Giuliano di Puglia is formed mainly by the calcareous marly and the clayey-marly units. The former is the oldest and is composed of a succession of limestones and marly limestones, fractured and fissured, with intercalations of marls and clayey marls. This is referred to as the Miocene Faeto Flysch formation and is overlain by the clayey-marly unit formed by bluish-gray clays and marly clays with sandy intercalations (Miocene Toppo Capuana Marls formation). It consists of a layer of 'weathered tawny clays' of 2 to 10 meters of thickness and a deep layer of Toppo Capuana marly clays, known as 'grey clays' (d'Onofrio et al. 2009). 'Debris cover' and anthropic fills ranging from decimeters to a few meters overlie the uppermost clay layers. The abundance of site investigations and laboratory tests lead to a complete mechanical description of Faeto Flysch and Toppo Capuana marly clays (d'Onofrio et al. 2009; Puglia 2008; Silvestri et al. 2006;, but do not give direct information about the buried morphology of the contact between the flysch formation and the marly clays.

Good back-analyses results have been obtained using three 2-D models of the section crossing the main axis of the village and the so-called "Anvil model" (Puglia 2008) gave the most satisfactory results from the back-analysis of the surface motions recorded at the temporary stations. Details of the physical and mechanical properties of soil formations are summarized in Table 1.

Table 1. Main features of the soil deposits relevant for the seismic response of San Giuliano di Puglia (z is the depth from ground level).

Unit	γ (kN/m^3)	V_s (m/s)	ν (–)	V_P (m/s)	D_0 (%)	$\overline{G} = G(\gamma)/G_0$ (-)	$D(\gamma)$ (%)
Debris cover	19.60	122	0.493	1010	3.	0 d'Onofrio et al.	(2009)
Tawny clay	21.10	$162(17+9.8z)^{0.104}$	0.489	$f(V_s,\nu)$	2.3	d'Onofrio et al.	(2009)
Gray clay	21.20	$202(17+9.8z)^{0.108}$	0.485-0.477	$f(V_s,\nu)$	2.5	d'Onofrio et al.	(2009)
Faeto flysch	22.00	400–1350	0.456–0.392	1400–3200	0.5	Linear	

3 ACCELEROMETRIC NETWORK AND INPUT MOTIONS

The current study is based on the accelerometric recordings of the two arrays installed in 2012 in the municipality of San Giuliano di Puglia (Figure 1). The stations are part of the Italian Accelerometric Network (RAN) and are coded as follows:

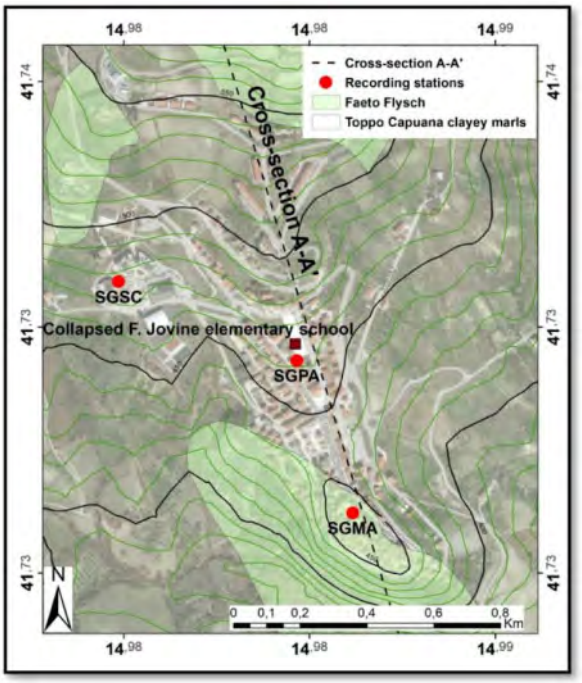

Figure 1. Plan view with the location of the recording stations in the village of San Giuliano di Puglia.

– SGMA, near Palazzo Marchesale (Marchesale Palace that is the City Hall), in the historical center on the stiff calcareous-marly unit. It is a single sensor, located at a depth of 10 m;
– SGPA, installed at the "Parco della Memoria" (Memory Park) where the collapsed elementary school was located, on the clayey-marly unit. This station is formed by a two-accelerometers array, located at the ground surface and at a depth of 53 m, respectively.

It is worth mentioning that an additional vertical array was installed near the new Sports Center (SGSC in Figure 1). Due to its location, rather far from the main section of the town, recordings from this array are not considered in this study.

After the installation of the arrays in 2012 and until today, 14 earthquakes were recorded by SGMA and SGPA stations at the basin level, most of them during the 2016 Central Italy seismic sequence. SGMA files include accelerograms with PGA ranging from 6.22×10^{-5}g to $2.4\,x\,10^{-2}$g, the surficial and deep sensors of the SGPA array recorded maximum accelerations in the range $2.03 \times 10^{-4} - 2.26 \times 10^{-1}$g, and $4.32 \times 10^{-4} - 4.40 \times 10^{-2}$g, respectively. These time histories belong to events of moment magnitude from 3.9 to 6.5. The accelerograms are available in the ESM catalog (Luzi et al. 2016).

In this study, three manually processed accelerograms recorded between 2016 and 2018 are selected for the analysis. The process of noise estimation and removal for the manually processed signals is described in Puglia et al. (2018).

The accelerograms used along the main section of the town (Section A-A' in Figure 1) are obtained from the combination of the two horizontal components of the recordings. The main features of the resulting motions, recorded at SGMA, deconvolved at the bedrock outcropping conditions and rotated along the AA' section, are reported in Table 2.

Figure 2 shows the time histories considered as input motions (at the outcropping bedrock conditions), obtained from a mono-dimensional deconvolution of the recordings available at the SGMA station. The mono-dimensional deconvolution was performed exploiting the Strata program

Table 2. Main features of the selected input motions.

Event ID	Event Name	Date	Time	M_w (–)	R_{epi} (km)	PGA (g)	Predominant period (s)
ID1	Southern Italy	2018-08-16	20:22	4.8	22.7	0.00477	0.34
ID2	Southern Italy	2016-01-16	18:55	4.3	35.2	0.00082	0.26
ID3	Central Italy	2016-08-24	01:36	6.0	181.9	0.00098	0.42

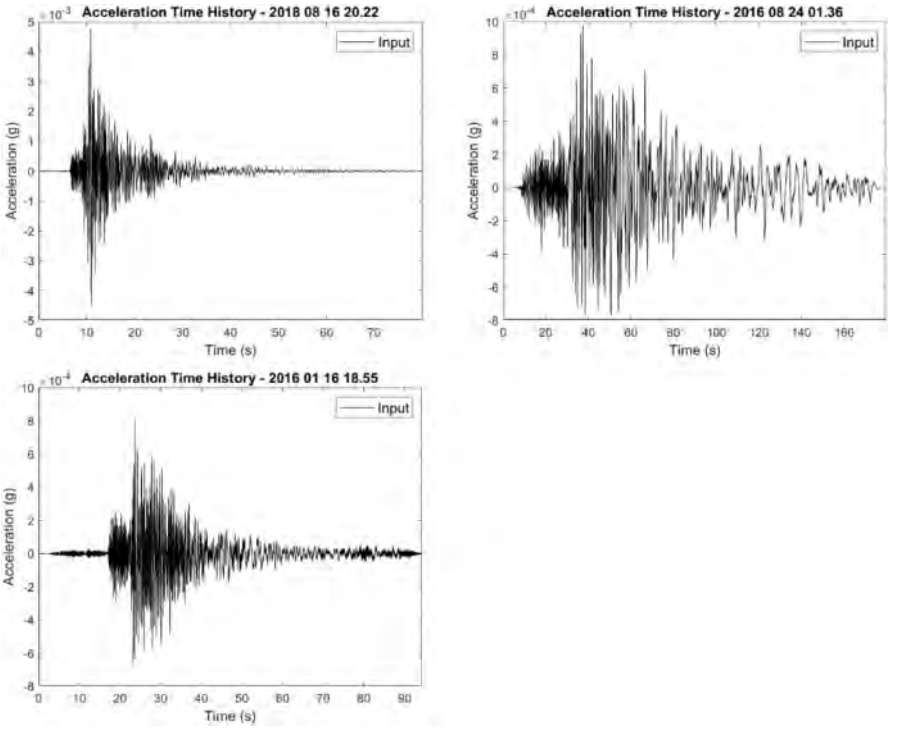

Figure 2. Input motions adopted for the bi-dimensional analyses.

(Kottke et al. 2013). The same procedure was adopted in Fierro et al. (2020a, b) to perform mono- and equivalent linear bi-dimensional analyses, to evaluate the shear wave velocity profile at the same site.

Figure 3 shows the shear wave velocity profiles available in the village at the two sites of interest. Sanò et al. (2015) correspond to down-hole results performed at the time of array installation. At the SGPA site (Figure 3a), Puglia (2008) represents V_s profile obtained through regression analysis on the basis of down-hole test. Mono- and bi-dimensional site response back-analyses showed that the stiffer profile, suggested by Sanò et al. (2015), performs better, based on statistical indicators. For this reason, a simplified profile that follows the profile suggested by Sanò et al. (2015) is adopted in this study.

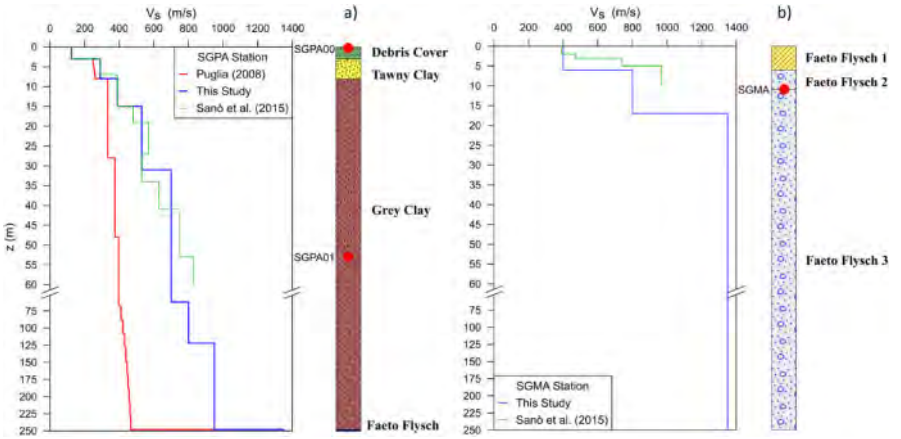

Figure 3. Vs profiles at SGPA (a) and SGMA (b) locations used for site response analyses.

4 NUMERICAL MODEL

To understand whether the response of a stiffer shear wave velocity profile highlighted in the previous studies is confirmed, and to stress the key role played by a proper geotechnical characterization in the damage distribution generated by an earthquake scenario, bi-dimensional plane-strain nonlinear site response analyses are performed through the OpenSeesSP interpreter implemented in DesignSafe-CI.

The model is extended for a width of 1600 m and has a total height of about 680 m. It is developed exploiting the GiD pre-processor (Coll et al. 2018) and, consequently, the nodes and the elements are obtained through Gid+OpenSees Interface (Papanikolaou et al. 2017). The layer discretization is shown in Figure 4, where the three main units of the San Giuliano di Puglia subsoil are switched into subunits based on their stiffness. A detail of the meshed contact between Faeto flysch and Toppo Capuana marly clays (treated as bedrock) is shown in Figure 5.

The soil deposit is modelled using 80134 quadrilateral elements with stabilized single-point integration (McGann et al. 2012), referred to as SSPquad in OpenSees, and a total of 81695 nodes. The dimensions of the elements are selected to allow the transmission of frequencies up to f_{max}=20

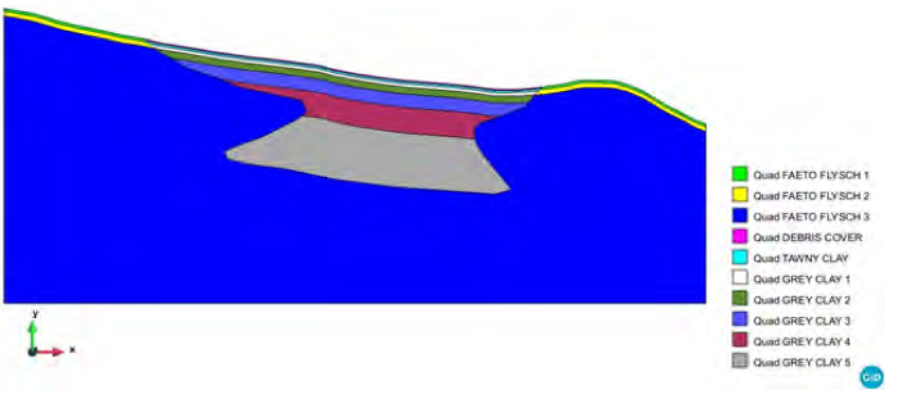

Figure 4. Layer discretization for the bi-dimensional model of San Giuliano di Puglia.

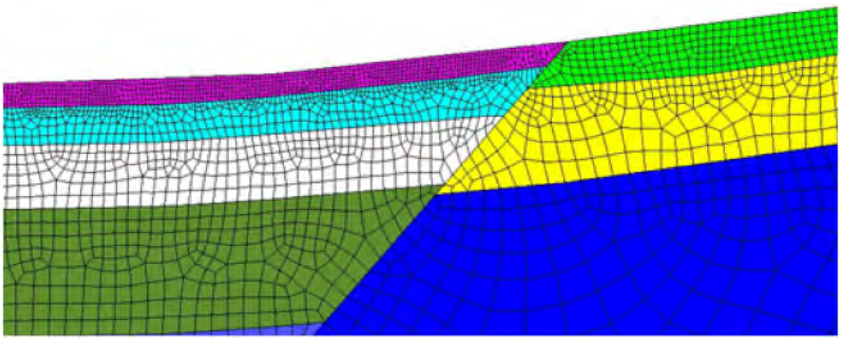

Figure 5. Detail of the contact between the meshed units.

Hz, where the maximum height of the elements (H_{max}) is computed as $V_s/(10 \bullet f_{max})$. For each subunit, Table 3 summarizes the height of the element considered.

Table 3. Shear wave velocity adopted for each subunit, maximum height, and selected height for the elements.

Unit	V_s (m/s)	H_{max} (m)	H (m)
Debris cover	125	0.625	0.5
Tawny clay	290	1.450	1.0
Grey clay 1	390	1.950	1.5
Grey clay 2	530	2.650	2.0
Grey clay 3	700	3.500	3.0
Grey clay 4	800	4.000	3.5
Grey clay 5	950	4.750	4.0
Faeto flysch 1	400	2.000	1.0
Faeto flysch 2	800	4.000	2.0
Faeto flysch 3	1350	6.750	5.0

Surveys identified three layers of Faeto flysch, charactherized by different levels of fracturing and fissuring, namely "Faeto flysch 1", "Faeto flysch 2", and "Faeto flysch 3". Their unit weight, shear wave velocity, P-wave velocity and Poisson's ratio are obtained from Puglia (2008) and d'Onofrio et al. (2009), as assumed in Fierro et al. (2019, 2020a, b). An elastic isotropic material is used to model their response in OpenSees.

The soft soil in the basin can be sub-divided into debris cover, tawny clay, and grey clay (d'Onofrio et al. 2009). To account for the increasing of stiffness with depth of the grey clay, it is divided into five subunits each of them with constant stiffness. According to Puglia (2008), the contact between Toppo Capuana marly clay and Faeto Flysch along the SGPA vertical is at 248m depth.

Soft soil is modelled using both elastic and pressure-independent multi-yield material. The pressure-independent multi-yield model was developed at the University of California San Diego and implemented in OpenSees (Yang et al. 2008). The model was conceived to simulate the behaviour of clays subjected to fast loading conditions and exploits the multi-surface concept. In this model, the plasticity can be developed only in the deviatoric plane, while the volumetric response is linear elastic.

Shear (G) and bulk (B) moduli are calculated based on the shear wave velocity profiles shown in Figure 3, using the following equations:

$$G = G_r \left(p'/p'_r\right)^d \tag{1}$$

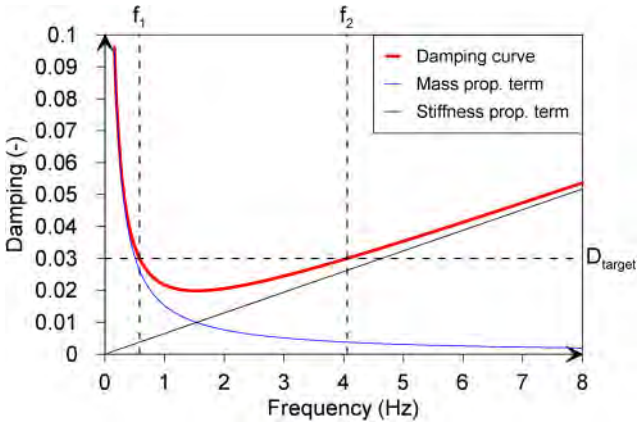

Figure 6. Rayleigh damping formulation for the event input motion ID1.

$$B = B_r \left(p'/p'_r\right)^d \tag{2}$$

where G_r and B_r represent the reference shear and bulk moduli of the soil, respectively. In this study, the coefficient d, which accounts for the variation of the stiffness as a function of the effective mean confinement pressure, is assumed to be zero, to reproduce homogeneous layers (constant stiffness).

Soil density for each unit and modulus reduction curves used in the numerical model are from d'Onofrio et al. (2009). By specifying modulus reduction curves, the nested surfaces of pressure-independent multi-yield model are consequently generated, and their number is defined accordingly. Once user defined yield surfaces are defined, the constitutive model ignores the values given for friction angle and cohesion, and compute them as a function of the mean stress.

For all the clays in the model, it is used the value of the peak shear strain and effective reference pressure suggested in the manual for clays (0.1 and 100 kPa, respectively).

The availability of only weak recordings justifies the choice of a dynamic total stress analysis without considering pore water pressure generation.

Absorbing boundaries in both horizontal and vertical directions are successfully implemented in the model to avoid wave reflection, using Lysmer dashpots (Lysmer & Kuhlemeyer 1969), as shown in Durante et al. (2018). Seismic motions are applied at each node of the base of the model through nodal forces proportional to the velocity time-history of the input according to Joyner and Chen (1975).

Rayleigh viscous damping is applied to the model to guarantee a small amount of numerical damping. In this study, the approach with two control frequencies is adopted, using the procedure suggested by Hudson et al. (1994). A value of 3% of the damping ratio is assumed as a target, while the control frequencies correspond to the fundamental frequency of the model and n-times the fundamental frequency, where n is the odd integer that rounds up the ratio between the predominant frequency of the input and the fundamental frequency of the model. In this case, the fundamental frequency of the soil model is obtained from eigenvalue analysis carried out to perform simulations with an equivalent linear approach using QUAD4M by Fierro et al. (2020b). Figure 6 shows the schematic of the adopted Rayleigh damping formulation for one of the input motions used in this study.

5 RESULTS

This section shows the comparisons between the numerical simulations (linear and nonlinear analyses) and the recorded motions at the SGMA and SGPA stations.

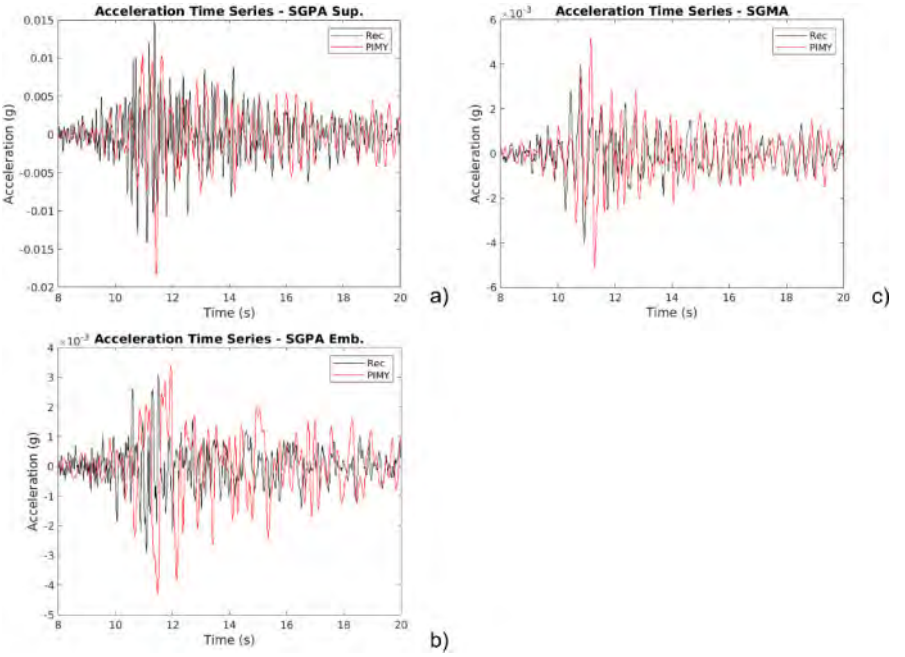

Figure 7. Recorded versus simulated acceleration time series at surficial SGPA (a), embedded SGPA (b) and SGMA (c) locations for event ID1, obtained using nonlinear model (PIMY).

Figure 7 shows the comparison between the recorded and the simulated acceleration time series for the event ID1 at the selected stations, obtained using the nonlinear numerical model. A good agreement is always observed, despite a small overestimation produced by the simulations. It should be noted that the amplitude at the SGMA station seems to be more accurately reproduced than that at the SGPA vertical array.

Figure 8 compares the linear elastic and nonlinear response obtained from the numerical simulations for the input motion ID1 at the stations considered, showing a good fit. This match is justified by the low strain level induced by the input motions. In fact, it has been observed that no degradation is applied to the materials in the model.

Figure 9 shows the comparison between the recorded and the simulated acceleration time series for the event ID2 at the selected stations, obtained using the nonlinear numerical model. Figures 9a, 9b, and 9c suggest that a satisfactory agreement is obtained in terms of time-histories amplitude at all the locations. A slight overestimation is observed at a higher depth (Figure 9b), while the simulations underestimate the recorded response at the surface (Figure 9a). However, the PGA seems to be correctly reproduced.

In Figure 10, the comparison in terms of acceleration response spectra (5% structural damping) is presented for the ID2 motion for the sake of brevity.

Overall, a good performance is noticed, with the simulated response always overestimating the spectra from the recordings. Acceptable congruence is reached at the SGMA and SGPA embedded stations, considering both amplitude and spectral shapes. In both cases, the simulations overestimate a peak located at 0.5 s, and the response seems to be overestimated even for the period range 0.25-1 s (see Figures 10b, c). This peculiarity can be found in the comparison at the SGPA surficial station as well, but the spectral shape seems not to be correctly captured in the above-mentioned period range (Figure 10a). This can be due to the definition of the Rayleigh parameters considered in this study. Further studies are needed for the evaluation of the performance of the model when soil non-linearity is reached.

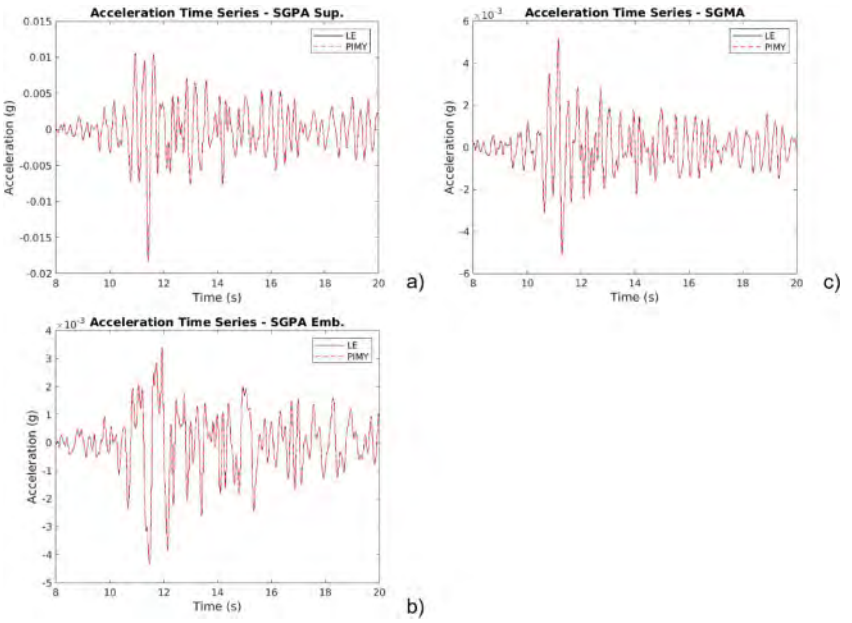

Figure 8. Linear elastic versus pressure independent multi-yield model results at surficial SGPA (a), embedded SGPA (b) and SGMA (c) locations for the event ID1.

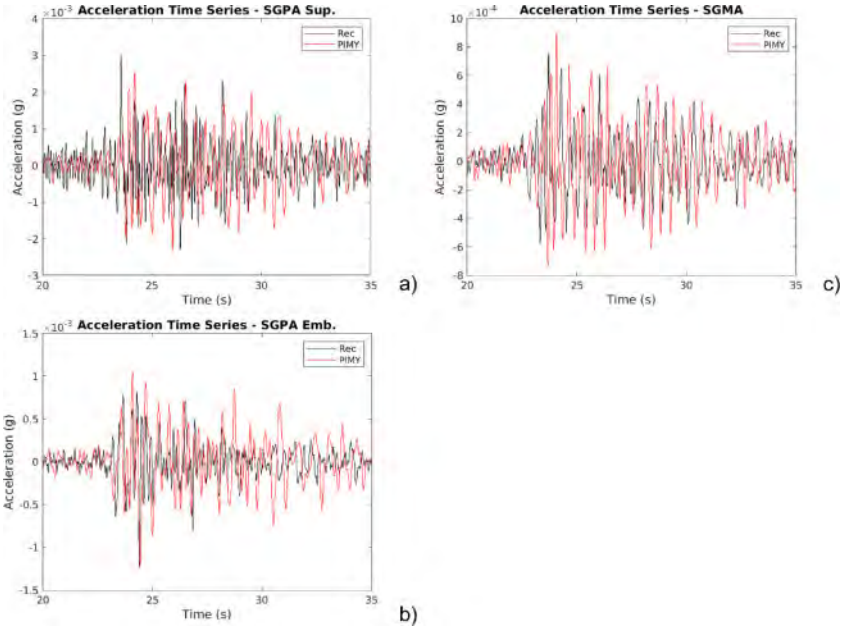

Figure 9. Comparison between recordings and simulations using pressure independent multi-yield constitutive model at SGPA at surface (a) and in depth (b), and surficial SGMA (c) stations for the event ID2.

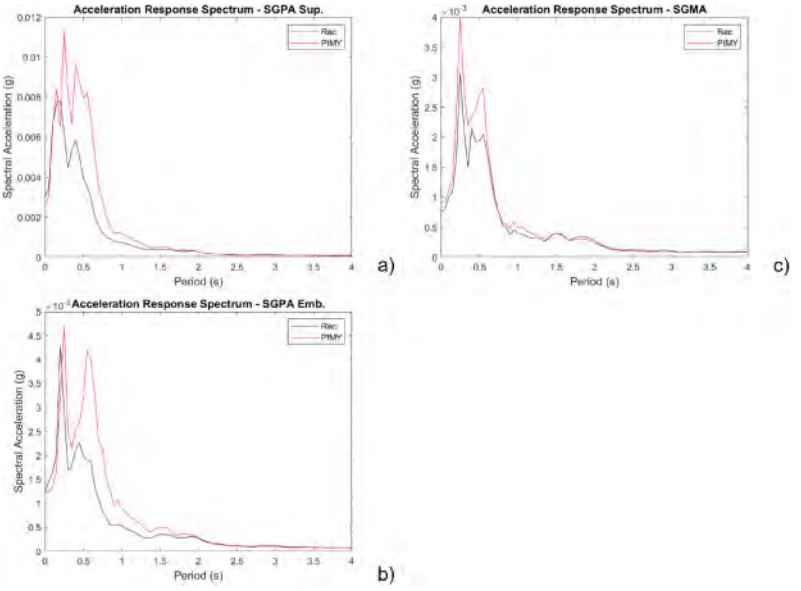

Figure 10. Comparison between recorded and simulated acceleration response spectra using pressure independent multi-yield model at surficial SGPA (a), embedded SGPA (b) and SGMA (c) locations for the event ID2.

Figure 11 shows the comparison between the recorded and the simulated acceleration time series for the event ID3 at the selected stations, obtained using the nonlinear numerical model. Model responses in terms of acceleration time-series can be considered satisfactory for the SGPA surficial and SGMA sensors (Figure 11a, c, respectively), while a widespread overestimation of acceleration

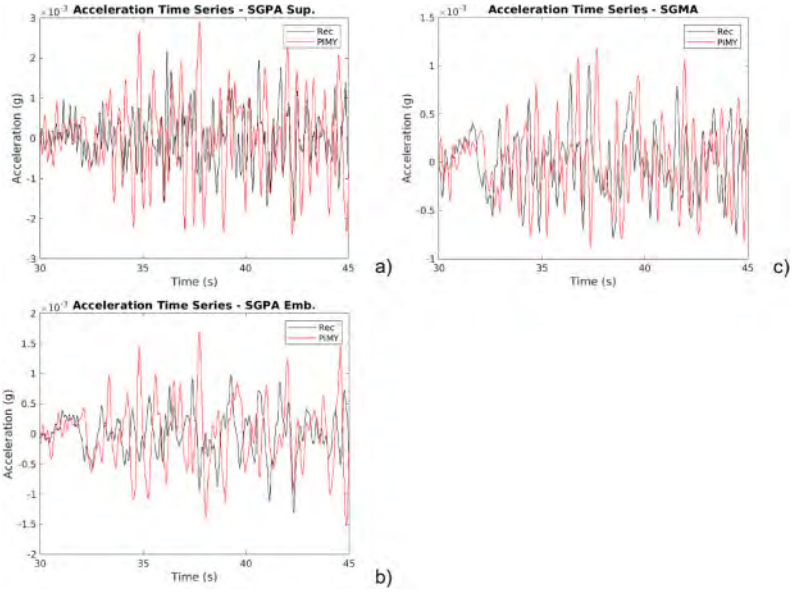

Figure 11. Comparison between recordings and simulations using the pressure-independent multi-yield constitutive model at surficial (a) and embedded (b) SGPA and SGMA (c) stations for the event ID3.

amplitude is observed at the SGPA in-depth accelerometer (Figure 11b). For this motion, a time delay of about 0.5s is observed in the simulations, which could be related to three-dimensional site response effects, that are neglected in the current 2D plain-strain model. This aspect needs further investigation, and it will be the object of future studies.

6 CONCLUSIONS

The role of proper geotechnical characterization and local seismic response analysis in the preservation of historic sites in seismic areas is widely recognized. Numerical analyses with appropriate constitutive models for the soil are an essential tool for assessing site effects and soil-structure interaction issues. The reliability of numerical models needs to be evaluated based on case histories, implying that effective tools can be obtained to analyze such contexts with practical implications of preservations and design. In this paper, bi-dimensional linear elastic and non-linear site response analyses have been performed at the site of San Giuliano di Puglia hit by the 2002 Molise Earthquake, using the parallel interpreter OpenSeesSP.

The availability of a monitoring system in the village allowed to verify and re-evaluate the shear wave velocity profile through a back-analysis of the data. The agreement of the model simulations with the data in terms of time series confirmed the goodness of the shear velocity profile selected. Furthermore, site effects confirm the amplification of the motion that occurred at SGPA station, confirming that a non-neglectable role was played by the site effects in the damage distribution observed at San Giuliano di Puglia after the 2002 earthquake.

The San Giuliano di Puglia case study emphasizes the necessity to perform a seismic microzonation in small towns (widely present in the Italian territory). In fact, even if the historical core is generally built on stiffer soils (Costanzo et al. 2007), the built environment can be protected only by owning a wide knowledge of the subsoil properties and the seismic response of the site.

REFERENCES

Coll A, Ribó R, Pasenau M, Escolano E, Perez J.S., Melendo A., Monros A. & Gárate J. 2018. GiD v.14 User Manual (pdf). accessed 2020 May 25). www.gidhome.com.

Costanzo A., d'Onofrio A., Lanzo G., Pagliaroli A., Penna A., Puglia R., Santucci de Magistris F., Sica S.,
Silvestri F., Tommasi P. (2007) Seismic response of historical centers in Italy: selected case studies. 4th International Conference on Earthquake Geotechnical Engineering, Thessaloniki, Greece.
d'Onofrio, A., Vitone, C., Cotecchia, F., Puglia, R., Santucci de Magistris, F. & Silvestri, F. 2009. Caratterizzazione geotecnica del sottosuolo di San Giuliano di Puglia. In *Rivista Italiana di Geotecnica (Italian Geotechnical Journal)* 3, 43–61.

Durante, M.G., Brandenberg, S.J., Ausilio, E. & Zimmaro, P. 2018. Influence of topographic irregularities on the amplitude and phase of strong ground motions. Eleventh U.S. Nat. Conference on Earthquake Engineering Integrating Science, Engineering & Policy. June 25–29, 2018 Los Angeles, California

Fierro T., Mignelli L., Scasserra G., Pagliaroli A. & Santucci de Magistris F. 2019. Key role of soil investigation and monitoring for the assessment of site effects for the village of San Giuliano di Puglia (CB), Italy. In VII International Conference on Earthquake Geotechnical Engineering, Rome, Italy, paper n. 10120.

Fierro T., Mignelli L., Scasserra G., Pagliaroli A. & Santucci de Magistris F. 2020a. The use of seismic records for updating the geotechnical model for a site in San Giuliano di Puglia (Italy). VI CNRIG Italian Conference of Researchers in Geotechnical Engineering, Lecco, Italy, July 2019

Fierro T., Mignelli L., Scasserra G., Pagliaroli A. & Santucci de Magistris F. 2020b. Updating the Site Response Analyses at San Giuliano di Puglia (CB), Italy. Italian Geotech. Journal, 2020(4), pp. 5–40.

Hudson, M., Idriss, I. M. & Beikae M. 1994. QUAD4M. A computer program to evaluate the seismic response of soil structures using finite element procedures and incorporating a compliant base. The National Science Foundation, Washington D.C.; Center for Geotechnical Modeling, Department of Civil & Environmental Engineering, University of California, Davis, California.

Joyner, W.B. and Chen, A.T.F. 1975. Calculation of nonlinear ground response in earthquakes, *Bull. Seism. Soc. Am.*, 65, 1315–1336.

Kottke, A.R., Wang X. & Rathje E.M. 2013. Technical Manual for Strata. Geotechnical Engineering Center Department of Civil, Architectural, and Environmental Engineering, University of Texas.

Luzi L., Puglia R., Russo E. & ORFEUS WG5. 2016. Engineering Strong Motion Database, version 1.0. Istituto Nazionale di Geofisica e Vulcanologia, Observatories & Research Facilities for European Seismology. doi: 10.13127/ESM

Lysmer, J. & Kuhlemeyer R.L. 1969. Finite dynamic model for infinite media. *Journal of the Engineering Mechanics Division*, ASCE, 95(EM4):859-877

McGann, C.R., Arduino, P. & Mackenzie-Helnwein P. 2012. Stabilized single-point 4-node quadrilateral element for dynamic analysis of fluid saturated porous media. *Acta Geotechnica* 7 (4), 297–311.

McKenna F. & Fenves G.L. 2008. Using the OpenSees Interpreter on Parallel Computers. Network for Earthquake Engineering Simulations (NEES) TN-2007-16. UC Berkeley.

McKenna, F., Fenves, G. L., Scott, M. H. & Jeremic, B. 2000. Open system for earthquake engineering simulation. http://opensees.berkeley.edu.

Papanikolaou, V.K., Kartalis-Kaounis, T., Protopapadakis, V.K. & Papadopoulos, T. 2017 GiD+OpenSees Interface : An Integrated Finite Element Analysis Platform. Lab of R/C and Masonry Structures, Aristotle University of Thessaloniki, Greece.

Puglia R. 2008. Analisi della risposta sismica locale di San Giuliano di Puglia. Tesi di Dottorato in Ingegneria Geotecnica, Università della Calabria.

Puglia R., Russo E., Luzi L., D'Amico M., Felicetta C., Pacor F. & Lanzano G. 2018. Strong-motion processing service: a tool to access and analyse earthquakes strong-motion waveforms. *Bull. Earthq. Eng*. 16, pp.2641–2651. https://doi.org/10.1007/s10518-017-0299-z

Puglia, R., Klin, P., Pagliaroli, A., Ladina, C., Priolo, E., Lanzo, G. & Silvestri, F. 2009. Analisi della risposta sismica locale a San Giuliano di Puglia con modelli 1D, 2D e 3D. *RIG*. Pagg. 62–71.

Puglia, R., Lanzo, G., Pagliaroli, A., Sica, S. & Silvestri, F. 2007. Ground motion amplification in San Giuliano di Puglia (Southern Italy) during the 2002 Molise earthquake. In *IV International Conference on Earthquake Geotechnical Engineering*, Thessaloniki, Greece, paper no. 1611.

Puglia, R., Vona, M., Klin, P., Ladina, C., Masi, A., Priolo E. & Silvestri F. 2013. Analysis of site response and building damage distribution induced by the 31 October 2002 earthquake at San Giuliano di Puglia (Italy). *Earthquake Spectra*, 29(2):497–526, doi: 10.1193/1.4000134.

Rathje, E., Dawson, C. Padgett, J.E., Pinelli, J.-P., Stanzione, D., Adair, A., Arduino, P., Brandenberg, S.J., Cockerill, T., Dey, C., Esteva, M., Haan, Jr., F.L., Hanlon, M., Kareem, A., Lowes, L., Mock, S. & Mosqueda, G. 2017. DesignSafe: A New Cyberinfrastructure for Natural Hazards Engineering, ASCE *Natural Hazards Review*, doi:10.1061/(ASCE) NH.1527-6996.0000246.

Sanò, T., Bongiovanni, G., Clemente, P. & Rinaldis, D. 2015. Modellazione dei Fenomeni di Amplificazione Locale Basata su Registrazioni Accelerometriche al Sito. In *ANIDIS 2015 – XVI Convegno*.

Santucci de Magistris, F., d'Onofrio, A., Penna, A., Puglia, R. & Silvestri, F. 2014. Lessons learned from two case histories of seismic microzonation in Italy. *Nat. Hazards*, 74, 2005–2035.

Silvestri, F., Vitone, C., d'Onofrio, A., Cotecchia, F., Puglia, R. & Santucci de Magistris, F. 2006. The influence of meso-structure on the mechanical behaviour of a marly clay from low to high strains. In *Symposium to celebrate Prof. Tatsuoka's 60th birthday*, Roma, Italy.

Yang, Z., Lu J. & Elgamal, A. 2008. OpenSees Soil Models and Solid-Fluid Fully Coupled Elements. User's Manual. v1.0. Department of Structural Engineering, University of California, San Diego.

Geotechnical Engineering for the Preservation of Monuments and Historic Sites III – Lancellotta, Viggiani, Flora, de Silva & Mele (Eds)

Simulation of damage observed on buildings in aggregate after the 2016-2017 Central Italy earthquake accounting for site effects and soil-structure interaction

A. Brunelli
University of Genova

G.A. Alleanza
University of Naples Federico II

S. Cattari
University of Genova

F. de Silva & A. d'Onofrio
University of Naples Federico II

ABSTRACT: The paper investigates the influence of site effects and soil-structure interaction on the response of buildings in aggregate in the historical centre of Visso, located in an alluvial valley in the Central Italy. The town was severely stricken by the Central Italy 2016/2017 seismic sequence and the subsequent inspections allowed the reconnaissance of damage suffered by the case study at hand. A monitoring system installed just out of the historical centre recorded the ground motion at Visso during the seismic sequence. Based on these records, the bedrock motion was then calculated through their deconvolution along the well characterized soil profile below the record station. The resulting signals were applied as input motions in linear equivalent site response analyses (i) of the 1D soil stratigraphy below the buildings in aggregate and (ii) of the whole 2D valley. In both cases, the subsoil model was inferred from the data gathered during the seismic microzonation study of the Visso village. The amplification of ground motion resulting from the 1D site response analysis is higher than that predicted by the 2D analysis along the same vertical. The whole aggregate was modelled in the Tremuri software through the equivalent frame approach and specific modelling strategies were adopted to account for the interaction among adjacent structural units. The model base was either completely restrained, to simulate the fixed-base conditions as typically assumed in the structural analysis, or endowed with springs, to simulate the effect of the soil compliance to the structural motion. Non-linear dynamic analyses were then performed on the fixed and complaint base models under the free-field motion obtained from the 1D and 2D site response analyses. The resulting damage patterns were compared to that detected on site. The comparison is satisfying only when the motion obtained from 2D site response is adopted as input motion and slightly improved when the compliant base conditions are considered.

1 INTRODUCTION

Ancient towns were often built to be isolated from the surroundings, mainly due to defensive strategies. Hence, they usually rise on flat-topped hills delimited by steep slopes or in valleys enclosed by mountains. Such complex geomorphological conditions influence the ground motion at surface (Pagliaroli et al. 2020). This especially occurs in the case of valley, where also stratigraphic amplification effects are expected to be produced by soft covers. Moreover, the seismic response of structures founded on such covers is potentially also modified by the soil-structure interaction (Richart et al. 1970). Such phenomena were recently investigated for unreinforced masonry (URM)

DOI 10.1201/9781003308867-66

buildings by Brunelli et al. (2021) through the in-depth analysis of the response of the school of Visso (MC, Italy). The school constitutes an emblematic example hit by the Central Italy 2016/2017 seismic events and provided very precious and unique information, being permanently monitored by the Italian Department of Civil Protection. Other works based on evidence from recent earthquakes have already highlighted the detrimental effects of site-amplification in the damage of existing URM masonry buildings (for example: Brando et al. 2020; Sextos et al. 2018; Sorrentino et al. 2019;. Soil-foundation-structure (SFS) interaction is often not considered for URM buildings with shallow foundations, while Brunelli et al. (2022) showed the role of the interaction and the susceptibility of the results to variation of different formulations in the literature. This paper numerically investigates the effect of site amplifications and SFS interaction on the response of a building in aggregate located in the historic center of Visso to the Central Italy 2016-2017 seismic sequence. Actually, studies on URM buildings in aggregate, that also consider the role of SFS interaction, are very few in literature (Caprili et al. 2015). The aggregate is modelled taking advantage from the validation of the equivalent frame modelling strategy carried out by Brunelli et al. (2021) on the Visso's school and refining the strategy with *ad hoc* solutions to account for the interaction between adjacent structural units, as recently investigated in Angiolilli et al. (2021). Being the case study settled not far from the border of the valley, an attenuation of the seismic motion is expected with respect to the 1D condition, due to the destructive interference among the refracted waves along the edges (Alleanza et al. 2019; Papadimitriou 2019). Thus, an *ad hoc* study on this issue has been also performed in the paper. The agreement in terms of simulated damage is adopted as target to assess the role of various phenomena. Indeed, the influence of SFS interaction is expected to be beneficial, thanks to the contribution of damping associated to continuous and shallow foundation of such URM structure.

2 DESCRIPTION OF THE CASE STUDY

The investigated building in aggregate is made up of five units placed in rows having varying heights, from three to four floors. Due to the impossibility to make a detailed geometric survey of the buildings, their size was deduced from the photos and maps of Visso (see https://www.regione.marche.it/Regione-Utile/Paesaggio-Territorio-Urbanistica/Cartografia/Repertorio/Cartatecnica2000). The reconstructed geometry of the aggregate is reported in Figure 1.

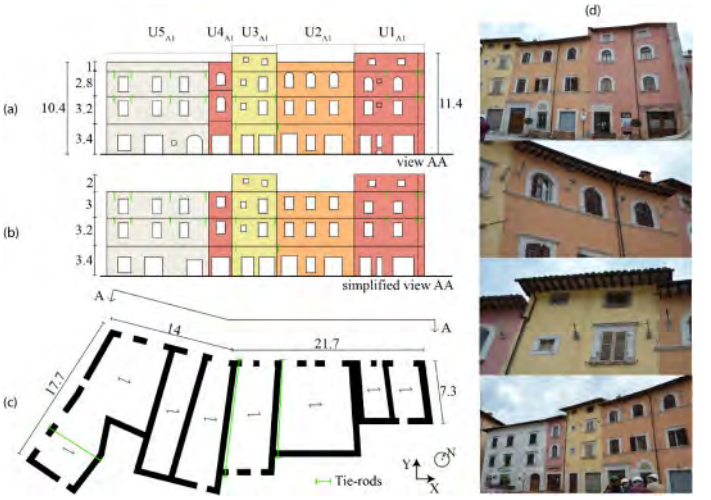

Figure 1. Geometric survey of building in (a) the real, (b) simplified elevation and (c) in plan of the ground floor; (d) photo of the aggregate following the seismic events in Central Italy 2016/17.

The height of the floors was inferred from the position of the openings and tie-rods visible from outside. Some structural features were deduced from other buildings where partial collapses, induced by out-of-plane mechanisms, occurred. Such collapses made these details visible, allowing to also verify their systematic recurrence (see Figure 2). Firstly, in such way, the transversal sections of URM walls were investigated by deducing the thickness and the masonry type. Indeed, the latter is mostly the same across the historical centre and is also consistent with that of the school of Visso (see Brunelli et al. 2021). Basing on such evidence, the walls were estimated 70 cm thick at the ground floor and 60 cm at the other levels. The only exceptions are the perimeter wall of unit $U1_{A1}$ (the right wall in Figure 1c) estimated 80 cm thick over the entire height of the building; and the walls of the last level in 55 cm. Moreover, the presence of internal walls was assumed in correspondence of the tie-rods visible in the external façades. The internal walls were supposed 5 cm lower as thickness than the relative perimeter walls. Basing on the position of the tie-rods and the typology of the single units, the units $U1_{A1}$ and $U2_{A1}$ are assumed to be sustained by autonomous load-bearing walls, while the other units to share the side transversal walls (i.e. those oriented in Y direction). In particular, the unit $U4_{A1}$ seems to be a filling unit built upon the two pre-existing orthogonal walls.

The main orientation of diaphragms is expected to develop perpendicularly to the Y-direction; all partition masonry walls were considered in the model as equivalent loads on the floors. From the photos of the other buildings in the historic center (see Figure 2), diaphragms are mostly characterized by brick and wooden decks. In some case, a very thin concrete slab (not reinforced) is also present. The same floor type was assumed in all units of the aggregate under examination since there is no evidence of any specific interventions and the units are considered substantially contemporary.

Figure 2. Example of walls and floors visible in other buildings of the historic center of Visso.

3 SITE EFFECTS IN THE VALLEY OF VISSO

3.1 *Subsoil geotechnical model*

The examined buildings in aggregate are on the border of an alluvial valley, whose 2D geological section is shown in Figure 3a (MZS3 2018). The soil stratigraphic sequence under the aggregate was defined thanks to the data of two boreholes and several Horizontal to Vertical Spectral Ratio (HVSR) of microtremors carried out within the third level microzonation studies, MZS3 (2018). The soil profile is constituted by clayey silt (CS), overlaying a sandy gravel layer (SG). In lack of experimental measurements, the shear wave velocity profile (V_S) was obtained through a correlation law between V_S and the number of blow counts of SPT tests performed in the boreholes. To validate the model, several correlations available in literature were checked and compared with the results of a Down Hole test (DH) carried out in a different site within the valley. In particular, the correlations by Imai and Yoshimura (1970) and Lee (1992) were used for CS and the one suggested by Ohta and Goto (1978) was adopted for SG, Figure 3b,c shows respectively the V_s profiles obtained for the two verticals V1 and V2, and used to define the geotechnical model for the seismic response analysis. The V1profile (Figure 3b) was used to characterise the widest and thickest valley below

the school, while the V2 (Figure 3c) profile was adopted for the shallow lateral valley below the aggregate. Each profile was extended to the entire section assuming a horizontal layering. The interface between the two valleys was established in accordance with the results of MZS3 (2018). The shear modulus decay ($G(\gamma)/G_0$) and the variation of damping ratio ($D(\gamma)$) curves (Figure 3d) were assigned based on Brunelli et al. (2021). The relations developed by Ciancimino et al. (2020) for Central Italy soils was used to characterise the non-linear behaviour of CS and SC layers, considering an average value of plasticity index of 17% (measured on samples retrieved these formations). While for SG layers, the relationships suggested by Liao et al. (2013) were adopted, considering a confining pressure of 52 kPa for the superficial one and 207 kPa for the deeper, to reproduce the dependence of the nonlinear behaviour on the stress state. The bedrock was assumed to be linear visco-elastic with a damping of 0.5% and V_S=1300m/s, in agreement with the results obtained by MZS3 (2018).

The 2D analyses were carried out with the computer code QUAD4M (Hudson et al. 2003), a finite element program that performs equivalent linear analysis in the time domain. The domain was laterally extended to minimize the effect of artificial reflections of the seismic waves due to lateral boundaries. The mesh consists of triangular elements, whose maximum size was defined according to Kuhlemeyer and Lysmer (1973) criterion. 1D seismic response analyses were also carried out along the vertical profiles V1 and V2 (Figure 3b,c) with the computer code STRATA (Kottke & Rathje 2008) which performs equivalent linear analysis in the frequency domain.

The reliability of the obtained geotechnical model was checked by comparing the experimental fundamental frequency measured by the HVSR, at several sites along the cross-section of the valley, with that computed at the same site by 1D and 2D linear analyses. Figure 3a shows the comparison between the measured resonance frequencies (in black) and those obtained in the 1D (dark grey) and 2D (light grey) case. The agreement among the frequency values validates the numerical model.

Two-time histories of the Central Italy seismic sequence 2016-17, recorded near the school foundations (Figure 3a) were then used as reference seismic input motion. In particular, the main events of 24/08/2016 and 26/10/2016 were considered. They were deconvoluted at the bedrock through a 1D analysis and then applied to the 2D model of the valley, as well as to the 1D soil column V2 to obtain the ground motion at the base of the aggregate.

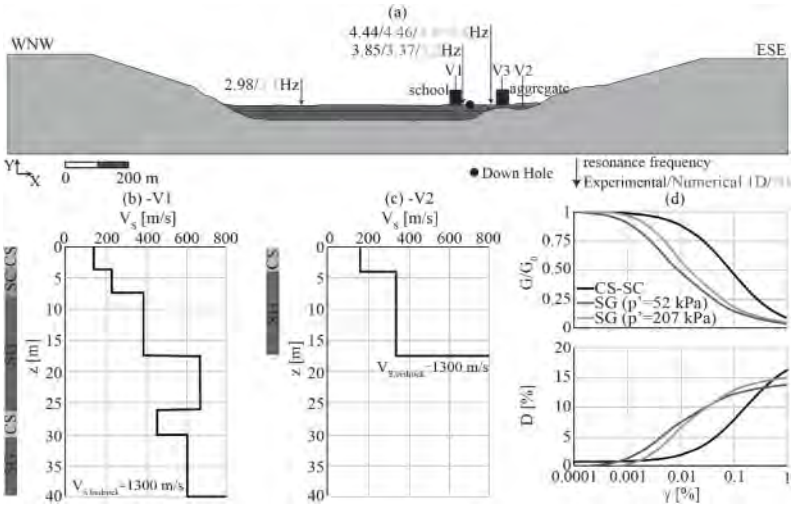

Figure 3. (a) 2D section adopted in the numerical analyses; (b) V_S profiles measured through the down hole test; (c) V_S profiles for the historical center of Visso and (d) $G/G_0 - \gamma$ and D-γ curves adopted in the analyses. Black and grey numbers along the cross-section in the upper portion represent experimental and numerical estimation of first natural frequency respectively (in 1D and 2D case).

3.2 *Results of site response analyses*

The results of the analyses were synthesized in terms of horizontal profiles of the amplification factors of spectral acceleration (AF) defined through equation 1:

$$AF_{T_a-T_b} = \frac{\int_{T_a}^{T_b} S_{a,s}(T)\,dT}{\int_{T_a}^{T_b} S_{a,r}(T)\,dT} \quad (1)$$

where $S_{a,s}(T)$, $S_{a,r}(T)$ are the spectral accelerations at the surface and at bedrock, and T_a, T_b were set equal to 0.1 and 0.5 s. The period range was defined in a way that is almost centred on the natural period of the aggregate. Furthermore, an amplification factor of peak ground acceleration, AF_{PGA}, was also calculated.

Figure 4 shows the profiles of $AF_{0.1-0.5s}$ (solid lines and full dots) and AF_{PGA}(dashed lines and empty dots), computed adopting the two input motions, obtained from both 2D (lines) and 1D (symbols) analyses. The trends of $AF_{0.1-0.5s}$ and AF_{PGA} between X= 600 m and 1400 m are comparable for the two events and characterized by two amplification peaks located close to the border of the deepest valley. This behaviour is typical of very shallow valleys characterised by a shape ratio, H/B $\leq$ 0.1 (Alleanza 2022). Furthermore, the amplification factors obtained from 1D analysis along V1 profile are close to those computed by 2D analysis, justifying the good agreement between the damage observed at the school and that simulated by Brunelli et al. (2021) adopting the ground motion at surface, obtained from 1D analysis. On the other hand, the thin valley, between X=1400 m and 1600 m, shows a strong amplification of motion at the centre of the basin, leading to amplification higher than that computed by 1D analysis along the vertical V2. Indeed, a destructive wave field among the direct, refracted and surface waves close to the edges of the valley (e. g. V3 in Figure 4) attenuates the ground motion with respect to the centre (Alleanza et al. 2019; 2022). Consequently the spectral amplifications are lower than those predicted by 1D analyses along V2. Finally, nevertheless the differences in the soil profiles, 1D analyses along V1 and V2 lead to close values of the amplification factors, because their seismic response is mainly ruled by the shallowest (up to a depth of 18 m) and softest layers, characterised by similar dynamic properties.

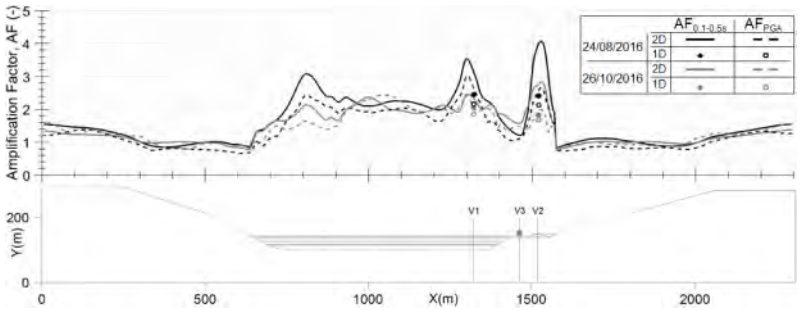

Figure 4. 2D amplification factors of the peak ground acceleration and of the spectral acceleration compared to those computed through 1D seismic response analyses along the verticals V1 and V2.

Figure 5 shows the comparisons among the accelerograms obtained on the surface from 1D (black line) and 2D (grey line) analyses for the events of 24/08/16 (continuous line) and 26/10/16 (dashed line). In details, Figure 5a compares the results at V1; in while Figure 5b compares the results obtained from the 1D analyses at V2 and from the 2D analyses at V3 (Figure 5b), where the aggregate is settled. The latter comparison is reported, because in the eventual lack of the 2D simulation, the ground motion resulting from 1D analyses along the vertical in the center of the

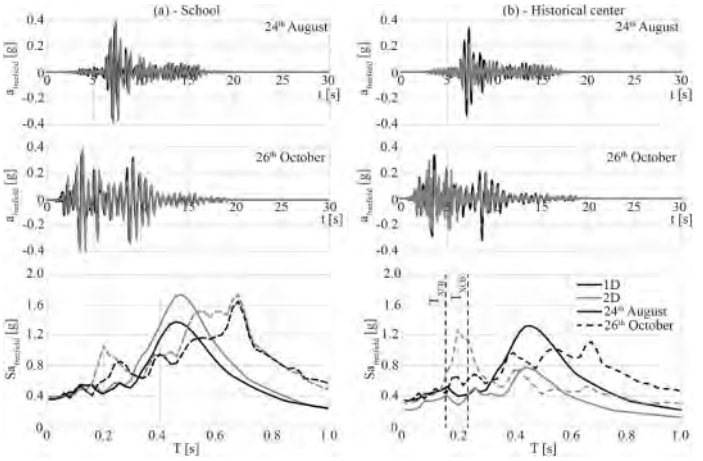

Figure 5. Comparison among the time histories and response spectra of the free field accelerations resulting in (a) school and (b) historical center from the 1D (in correspondence with V1) and 2D (in correspondence with V3) site response analyses under the events occurred on the 24^{th} August and 26^{th} October 2016.

valley is considered to be representative of the motion of the whole valley. In agreement with the above observations, the results obtained along the V1 profile by 1D and 2D analyses are very close, both in terms of amplitude and frequency content. On the other hand, accelerations and spectra computed along the V2 profile by 1D analyses show on average higher amplitudes respect to those obtained by 2D analyses.

4 EQUIVALENT FRAME MODEL OF BUILDINGS IN AGGREGATE

Among the modelling strategies available for URM structures (see D'Altri et al. 2020), the 3D model here adopted is based on the equivalent frame approach. Accordingly, the nonlinear behaviour is assumed to be concentrated in masonry panels (the piers and spandrels, in orange and green respectively in Figure 6a) connected by rigid nodes (in cyan in Figure 6a). Piers constitute the main vertical structural elements able to equilibrate both vertical and horizontal actions, while spandrels play the main role of connecting the piers (like the beams in a corresponding reinforced concrete frame). For each URM wall, the geometry of piers and spandrels has been identified *a priori* according to the rules proposed in Lagomarsino et al. (2013), whose reliability has been recently validated in Cattari et al. (2021) and Ottonelli et al. (2021); indeed, the regular layout of openings justifies in this case to neglect such an epistemic uncertainty. The numerical model was realized with the Tremuri software package, developed by Lagomarsino et al. (2013). The model accounts only for the in-plane response of walls, but this simplification is justified in the case of the investigated aggregate that did not exhibit the activation of any local mechanism, differently from other in the historical center.

As far the geometry of the structural units concerns, few simplifications have been made with respect to the original configuration. In particular, the alignment of the floors between the units of the aggregate and the windows have been rectified, by neglecting some small misalignments in height (as shown in Figure 1a). The final view of the assumed geometry is illustrated in Figure 1b.

The adopted values of the Young's modulus (E) and shear modulus (G) are reported in Table 1, together with the strength mechanical parameters. These values have been derived starting from those used in the Visso school, whose reliability has been validated in Brunelli et al. (2021) through a very accurate numerical simulation of the actual response of this monitored asset. The strength

Table 1. Mechanical parameters adopted for piers, spandrels and diaphragms of floor.

	E (MPa)	G (MPa)	τ_0 (MPa)	f_m (MPa)	G_D (MPa)	E_D (MPa)
piers	2968	991	0.1268	6.42		
spandrels	2078	693	0.0625	4.49		
diaphragms of floor					9170	23333

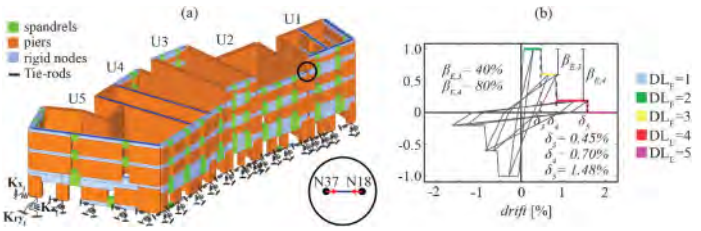

Figure 6. (a) Equivalent frame model; (b) backbone and hysteretic response of the masonry piers under shear.

values (τ_0) are slightly higher than that used for the school (of a 10%), but still completely consistent with the reference values proposed by Italian Building Code Commentary called MIT (2019) for the analogous masonry type. Both the elastic modulus (E,G) and the compressive strength (f_m) of the spandrels have been reduced by a multiplying factor equal to 0.7 with respect the piers; that is to account for the anisotropic behaviour of masonry and the fact the main mortar joints activated in spandrels are the vertical ones.

Masonry panels are modelled according to the nonlinear beam piecewise-linear model proposed by Cattari and Lagomarsino (2013). This constitutive law allows for describing the nonlinear response until very severe damage levels at element scale (i.e. DL_E,i with i from 1 to 5), through progressive strength degradation (β_E,i), corresponding to assigned drift values (δ_i). The latter are differentiated as a function of most recurring failure modes that characterize URM panels (i.e. flexural, diagonal cracking shear or bed-joint sliding) and of their type (if piers or spandrels). They may be defined on basis of experimental dataset available in literature (e.g. Vanin et al. 2017; Rezaie et al. 2020). In this case, the drift thresholds already validated in Brunelli et al. (2021) have been adopted. By way of example, Figure 6b illustrates the response of a pier dominated by a shear failure mode.

The maximum shear strength of the panels has been computed according to the strength criteria already corroborated in the literature to interpret the aforementioned failure modes (see Calderini et al. 2009). In particular, the flexural behaviour of piers was interpreted according to the criterion proposed in NTC (2018), whereas the shear behaviour according to the diagonal cracking failure mode proposed by Turnšek and Sheppard (1980) and recommended also in MIT (2019) for existing irregular masonry.

As proposed by Angiolilli et al. (2021), the mutual interaction between the various structural units is considered through the insertion of elastic truss elements (see the circular zoom of Figure 6) and fictitious floors. These elements allow the opening between buildings only along their longitudinal direction (i.e. X direction). The truss element, able to react only in compression, are characterized by a transversal area of 0.00164 m^2 and elastic modulus E of 210000 MPa. The equivalent diaphragms instead are characterized by the following feature: thickness of 0.5 m, E=39420 MPa, G=13112 MPa.

As mentioned in the introduction, two models have been considered. A fixed based (FB) model and compliant base (CB) model to account for the SFS interaction. In the latter case, a series of springs were considered under each pier, as shown in Figure 6a. The details on the calibration of these springs and equivalent Rayleigh damping are given in the next paragraph. Figure 7 shows the

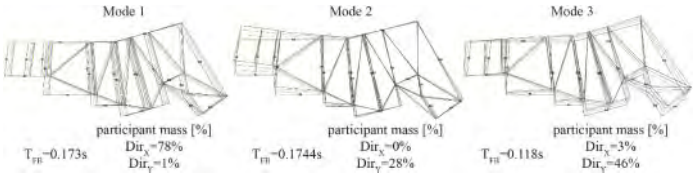

Figure 7. Modal shapes of the first three modes identified of the FB model, with period and participant mass.

fundamental periods of two models together with the in-plan view of the mode shapes, that refer to the FB model. The first period mainly activates the longitudinal response, while the second and third modes the transversal one. More specifically, the second mode substantially involves the units $U1_{A1}$ and $U2_{A1}$, while the third mode the other ones. In the case of the CB model, the aggregate is idealized through the replacement oscillator approach proposed by Maravas et al. (2014), as better explained in section 4.1. Thus, in this case, two main modes are computed associated to the following periods: 0.221 s for the longitudinal direction; 0.2 for the transversal one.

4.1 *Modelling of the foundation stiffness and damping*

In the CB model, each foundation pier was equipped with springs, whose stiffness was calibrated through the real part of the soil-foundation impedances by Gazetas (1991). The foundation width was set constant and equal to 1 m, as results from the thickness of the load-bearing wall plus an enlargement of 0.15 m at each side. The length varies because it was defined by adding the half-length of the spandrel panel to the size of the load-bearing wall. The value of the embedment was set to 1 m, in according to the building typology and to the soil type.

The soil was modelled as an equivalent linear half-space. The half-space shear modulus was set equal to mobilized one, under each input motion, up to a depth equal to the foundation width below the foundation, and corresponding to the soil volume expected to be affect by the horizontal and rocking foundation motion (see Gazetas 1983). As well known, the impedance functions are frequency dependent, hence they were calibrated iteratively until the supposed frequency resulted equal to the inverse of the period of the compliant-base aggregate. The latter was estimated through the replacement oscillator approach proposed by Maravas et al. (2014) for a Single Degree of Freedom (SDoF). To this aim, the building was approximated through a SDoF system with a viscous damping ratio equal to 3%, and a lateral stiffness derived from the fundamental periods along the X and Y directions of the FB configuration. The real and the imaginary parts of the impedance of the monolithic foundation, equivalent to the actual foundation systems, were calculated from the sum of the real or imaginary parts of the impedances of the X-oriented (or Y-oriented) load-bearing walls. Since the cumulative effects of the two mainshock was studied by applying the two input motions in cascade to the numerical model, the mean values of the impedances for each pier were introduced into the base springs of the numerical model.

Figure 8 shows for each foundation the values of the vertical (K_v), horizontal (K_x) and rotational (K_{ry}) impedances calibrated on the initial soil stiffness and on the mobilized one, obtained from the 1D and 2D seismic response analyses. The impedance calibrated on the soil stiffness mobilized into 1D analyses are slightly higher with respect to those associated with the soil stiffness resulting from the 2D analyses. The structural period of CB model is predicted through the formula by Maravas et al. (2014) for the impedances calibrated on the initial soil stiffness.

The same approach by Maravas et al. (2014) was adopted to estimate the damping ratio of the compliant base system. The contribution of the soil hysteretic damping, mobilized in the soil volume affected by the foundation motion, was added to the energy loss coefficients simulating the radiation damping ratio. The mean value of the damping ratio, resulting for the two directions and the two mainshocks, was introduced as a Rayleigh damping ratio into the structural model. Table 2 shows the values for the X and Y direction (equal for the two-subsoil modelling) of the soil damping (D), of the equivalent damping for each direction and event (ξ_{eq}) and of the final value (ξ_{eqTOT}) used in the nonlinear dynamic analyses (NLDA). In general, the hysteretic damping

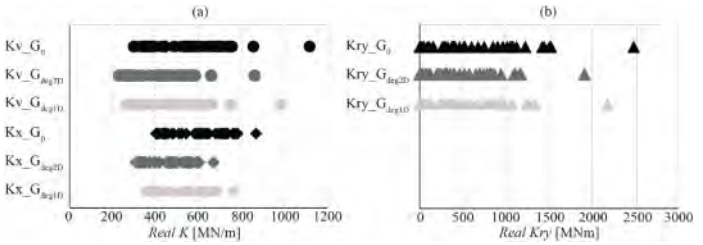

Figure 8. Range of variability of the real part of the foundation impedance, calibrated according to the initial soil stiffness (G_0) and the stiffness mobilized below the foundation according to the 1D (G_{deg1D}) and 2D (G_{deg2D}) site response analyses.

mobilized in the 2D analyses, along the X direction, is slightly higher than that predicted through the 1D analyses, hence the final value of ξ_{eqTOT} is slightly higher. In both cases the whole damping ratio is more than twice the typical value of the fixed base assuption.

Table 2. Damping and equivalent damping of replacement oscillator, and final value used in the NLDA.

	D [%]				ξ_{eq} [%]				
	24th August		26th October		24th August		26th October		
	X	Y	X	Y	X	Y	X	Y	ξ_{eqTOT} [%]
1D	2.013	2.071	2.098	2.459	7.24	5.50	7.32	5.56	6.40
2D	3.597		3.029		8.59	6.72	8.10	6.27	7.42

5 COMPARISON AMONG THE SIMULATED AND OBSERVED DAMAGE

Since the aggregate is located at the edge of the valley, for a more accurate assessment of the damage, the acceleration time histories of the free field signals calculated along the X-axis in the vertical V3 through the 2D site response analyses, were applied together with the signals calculated through the 1D analyses in the Y-axis. The analyses were repeated also in the case in which, in both directions, the components of the input motion derived from 1D condition along V2 have been applied. Signals were thus applied to the FB model under free-field motions (named FB C case) and to the CB model under free-field motion (CB C case), to investigate the effects of the SFS interaction. In addition, the response of the FB model was also analysed under the bedrock motion, as a reference case, named FB A in the following, to evaluate only the effects of site amplifications. In all cases, the input motions relevant to the event occurred on the 24th August 2016 and 26th October 2016 were applied in cascade to simulate the cumulative damage.

Figure 9 compares the survey of the damage suffered by the main façade of the building with the outcomes of the NLDA at the end of the 26th October mainshock. This is the most vulnerable wall, due to the large openings at ground floor, while side perpendicular walls (being without openings and benefitting from the axial load transmitted by the diaphragms) are expected to be damaged lowly than the façade. As far the actual damage concerns, in Figure 9, the main pattern of cracks surveyed is reported together with a colour that indicated their severity (if lower than DL2, between DL2 and DL3 of higher). The damage level has been attributed on basis of the interpretation of available photos. Since it was not possible to enter the buildings, the damage has been assigned only from outside.

The comparison among the observed and simulated damage highlights that the FB A model considerably underestimates the damage, as many structural elements remain in the elastic range.

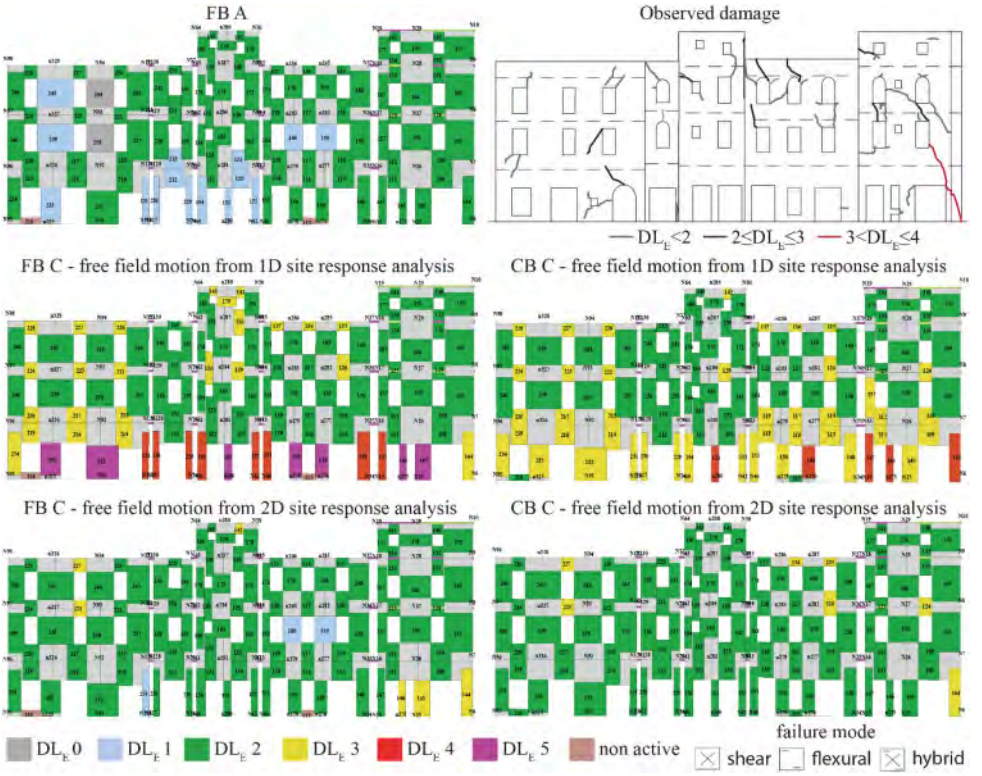

Figure 9. Comparison between observed and simulated damage on FB and CB model after the second mainshock.

That firstly confirms the role of amplification site effects. Conversely, the analysis performed on the FB model, under the 1D free-field signal, overestimates the damage producing the attainment of DL5 on piers at the ground floor. The CB C model without valley effect appears less damaged than the FB C model in the same hypothesis, but in any case, more damaged than the actual building.

When the free-field signals obtained from the 2D analyses are instead considered, the simulated damage is more close to the real one observed on the building both in the FB C and CB C model. As expected, both the valley effect and the SFS interaction have played a beneficial role in the seismic response of the aggregate.

In fact, when the valley effect is considered, most of the structural elements are in DL2, apart the external ones in the unit U1 that already reached at least DL3, consistently with the observations. Despite that, in the real case there is a greater damage to the upper floors. This does not seem to be

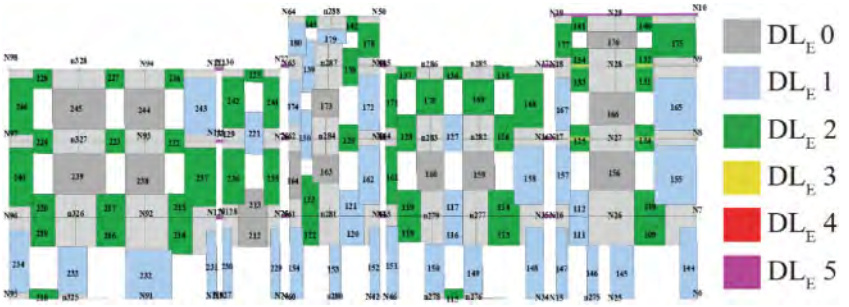

Figure 10. Simulated damage of CB model with valley effect before the peak of 24th August.

captured by the numerical model being everything in DL2. From Figure 6, DL2 of the numerical model corresponds to the attainment to the maximum shear strength of the panel, but the same DL may correspond to piers that just have been yielded or close to the attainment of DL3. In order to better investigate this aspect and discriminate to what condition the green colour actually corresponds to, Figure 10 shows the damage of the CB C model with the valley effect before the peak of 24th August. It is observed, consistently with the real damage, that the damage starts mostly on the upper floors and then spreads during the event on the lower floors.

6 CONCLUSION

The paper investigates the seismic response of URM building in aggregate. That architectural type is quite relevant being the one most recurring in small historical centres, in Italy but more in general in Europe. Moreover, the effects of site amplification and SFS interaction are analysed with reference to the emblematic study case of Visso municipality, hit by the Central Italy 2016/2017 event. The historical centre of Visso is particularly interesting since it is founded on an alluvial valley and the topographic and morphological shape of the valley make relevant also the 2D effect. The comparison between the numerically simulated and real damage showed that:

- in case of soft soils, the role of amplification phenomena needs to be accounted for;
- in this case, to neglect the 2D effect leads to excessively conservative results;
- for the investigated URM buildings in aggregate, the effects of SFS interaction leads to a beneficial contribute.

REFERENCES

Alleanza, G.A. 2022. Two-Dimensional Amplification of Seismic Motion in Alluvial Valleys. Ph.D. dissertation. University of Napoli "Federico II", Napoli, Italy.

Alleanza, G.A., Chiaradonna, A., d'Onofrio, A., Silvestri, F. 2019. Parametric study on 2D effect on the seismic response of alluvial valleys. *Proc. of the 7th ICEGE, 17–20 June 2019*. Rome, Italy.

Angiolilli, M., Lagomarsino, S., Cattari, S., Degli Abbati, S. 2021. Seismic fragility assessment of existing masonry buildings in aggregate. *Engineering Structures* 247:113–218.

Brando, G., Pagliaroli, A., Cocco, G., Di Buccio, F. 2020. Site effects and damage scenarios: The case study of two historic centers following the 2016 Central Italy earthquake. *Engineering Geology* 272:105674.

Brunelli, A., de Silva, F, Cattari, S. 2022. Site effects and soil-foundation-structure interaction: derivation of fragility curves and comparison with Codes-conforming approaches for a masonry school. *Soil Dyn. Earthq. Eng.* 154(4):107125.

Brunelli, A., de Silva, F., Piro, A., Sica, S., Parisi, F., Silvestri, F., Cattari, S. 2021. Numerical simulation of the seismic response and soil-structure interaction for a monitored masonry school building damaged by the 2016 Central Italy earthquake. *Bull Earthq Eng.* 19(2):1181–1211.

Calderini, C., Cattari, S., Lagomarsino, S. 2009. In-plane strength of unreinforced masonry piers, *Earthquake Eng Struct Dyn* 38(2):243–67.

Caprili, S., Mangini, F., Salvatore, W., Scarpelli, G., Squeglia, N. 2015. The influence of soil–foundation–structure interaction on the overall behaviour and diseases of a medieval building in Pisa. *STREMAH 2015, 14th STREMAH, July 13-15 2015*, La Coruna, Spain.

;Cattari, S., Camilletti, D., D'Altri, A.M., Lagomarsino, S. 2021. On the use of continuum Finite Element and Equivalent Frame models for the seismic assessment of masonry walls. *J. Build. Eng*. 43:102519.

Cattari, S. & Lagomarsino, S. 2013. *Masonry Structures* in Developments in the field of displacement based seismic assessment. Edited by Sullivan, T.J. & Calvi, G.M., IUSS Press, Pavia, Italy, pp.151–200 and EUCENTRE, pp. 524, ISBN; 978-88-6198-090-7.

Ciancimino, A., Lanzo, G., Alleanza, G. A., Amoroso, S., Bardotti, R., et al. 2020. Dynamic characterization of fine-grained soils in Central Italy by laboratory testing. *Bull. of Earthq. Eng*. 18:5503–5531.

D'Altri, A.M., Sarhosis, V., Milani, G., Rots, J., Cattari, S., Lagomarsino, S., Sacco, E., Tralli, A., Castellazzi, G., de Miranda, S. 2020. Modeling strategies for the computational analysis of unreinforced masonry structures: review and classification. *Arch. Comput. Methods Eng*. 27:1153–1185.

Gazetas, G. 1983. Analysis of machine foundation vibrations: state of the art. *Soil Dyn Earthq Eng*. 2:1–41.
Gazetas, G. 1991. Formulas and charts for impedances of surface and embedded foundations. *J Geotech Eng,* 117(9):1363–1381.
Hudson, M., Idriss, I.M., Beikae, M. 2003. *QUAD4M: a computer program to evaluate the seismic response of soil structures using finie element procedures and incorporating a compliant base, rev. 2003*. Center for Geotechnical Modelling Dept. of Civil and Environmental Engineering University of California, Devis.
Imai, T. & Yoshimura, Y. 1970. Elastic wave velocity and soil properties in soft soil. Tsuchito-Kiso 18 (1):17–22 (in Japanese).
Kottke, A. & Rathje, E.M.R. 2008. *Technical manual for Strata. Report No. 2008/10*. Pacific Earth-quake Engineering Research Center, University of California, Berkeley.
Kuhlemeyer, R.L. & Lysmer, J. 1973. Finite element method accuracy for wave propagation problems. *Soil Mechanics and Foundations*, 99(5):421–427.
Liao, T., Massoudi, N., Mchood, M., Stokoe, K.H., Jung, M. J., Menq, F.Y. 2013. Normalized Shear Modulus of Compacted Gravel. *Proc. 18*th *Int. Conf. on Soil Mech Geotech Eng. Challenges and Innovations in Geotechnics*, 1535–1538.
Lagomarsino, S., Penna, A., Galasco, A., Cattari, S. 2013. TREMURI program: An equivalent frame model for the nonlinear seismic analysis of masonry buildings. *Eng Struct*.56:1787–1799.
Lee, S.H.H. 1992. Analysis of the multicollinearity of regression equations of shear wave velocities. *Soils and Foundations* 32(1):205–214.
Maravas, A., Mylonakis, G., Karabalis, D.L. 2014. Simplified discrete systems for dynamic analysis of structures on footings and piles. *Soil Dyn Earthq Eng*, 61–62:29–39.
MIT. 2019. *Istruzioni per l'applicazione dell'aggiornamento delle Norme tecniche per le costruzioni* di cui al Decreto Ministeriale 17/01/2018, Ministry of Infrastructures and Transportations, Rome, Italy. (in Italian).
MZS3. 2018. *Report of the 3rd level Seismic Microzonation of Visso village*. Approved by the Working Group, May 29, 2018. https://www.comune.visso.mc.it/avvisi-cms/microzona-zione-sismica-iii-livello/.
NTC. 2018. *Norme Tecniche per le Costruzioni*. DM 17/01/2018, Italian Ministry of Infrastructure and Transportation, G.U. n. 42, 20 February 2018, Rome, Italy. (in Italian).
Ohta, Y. & Goto, N. 1978. Empirical shear wave velocity equations in terms of characteristic soil indexes. *Earthq. Eng. Struct. Dyn*. 6:167–187.
Ottonelli, D., Manzini, C.F., Marano, C., Cordasco, E.A., Cattari, S. 2021. A comparative study on a complex URM building: part I - sensitivity of the seismic response to different modelling options in the equivalent frame models. *Bull. Earthq. Eng.* https://doi.org/10.1007/s10518-021-01128-7.
Pagliaroli A., Pergalani F., Ciancimino A, Chiaradonna A., Compagnoni M., et al. 2020. Site response analyses for complex geological and morphological conditions: relevant case-histories from 3rd level seismic microzonation in Central Italy. *Bull. of Earthq. Eng.* 18:5741–5777.
Papadimitriou, A.G. 2019. An engineering perspective on topography and valley effects on seismic ground motion', *Proc. of the 7th ICEGE, 17–20 June 2019*. Rome, Italy.
Rezaie, A., Godio, M., Beyer, K. 2020. Experimental investigation of strength, stiffness and drift capacity of rubble stone masonry walls. *Construction and Building Materials* 251:118972.
Richart, F.E., Hall, J.R., Wood, R.D. 1970. *Vibrations of Soils and Foundations*. Prentice-Hall.
Sextos, A., De Risi, R., Pagliaroli, A., Pagliaroli, S., Foti, S., et al. 2018. Local site effects and incremental damage of buildings during the 2016 Central Italy Earthquake sequence. *Earthq Spectra*. 34(4):1639–1669.
Sorrentino, L., Cattari, S., da Porto, F., Magenes, G., Penna, A. 2019. Seismic behaviour of ordinary masonry buildings during the 2016 central Italy earthquakes. *Bull Earthq Eng.* 17(10):5583–5607.
Turnšek, V. & Sheppard, P. 1980. The shear and flexural resistance of masonry walls. *In Proc. Int. research conf earthq eng*. 30 *June – 3 July 1980*, Skopje, Macedonia.
Vanin, F., Zaganelli, D., Penna, A., Beyer, K. 2017. Estimates for the stiffness, strength and drift capacity of stone masonry walls based on 123 quasi-static cyclic tests reported in the literature. *Bull. Earth. Eng*, 15(12):5435–5479.

Geotechnical Engineering for the Preservation of Monuments and Historic Sites III – Lancellotta, Viggiani, Flora, de Silva & Mele (Eds)

A large-scale evaluation of the seismic demand for historic towers laying on soft soil

F. de Silva & F. Silvestri
Department of Civil Architectural and Environmental Engineering, University of Naples Federico II, Naples, Italy

ABSTRACT: This study investigates the earthquake-induced peak and residual tilts of the foundation of nine Italian monumental towers founded on soft soil, where a site-specific geotechnical characterization was available, and the fundamental period of the tower was measured through on site surveys. The correlation between the foundation rotation and the spectral acceleration calibrated by de Silva (2020) was exploited to properly combine the expected foundation rotation and the hazard curve at each site. The result is the so-called 'demand hazard curve', which allows to individuate the foundation rotation associated to different limit states for a preliminary and expeditious large-scale estimation of the most vulnerable cases. Moreover, the residual rotation expected to occur for the belfry of San Benedetto Church in Ferrara resulted very close to the increase of the tower tilt measured after the 2012 Emilia earthquake.

1 INTRODUCTION

Post-earthquake observations (Pellegrinelli et al. 2014) and numerical simulations (Casolo et al. 2013; de Silva et al. 2017) highlighted that seismic damages to slender historic towers are mostly associated to excessive bending displacements in the structure as well as peak and residual tilts due to the foundation rocking. The above factors show that the seismic behaviour of the structure and the foundation can be significantly influenced by the soil deformability, when it is particularly soft. In fact, soft soil amplifies the ground motion and increases both the period and the damping ratio of the whole soil-foundation-structure system.

In the literature, the seismic safety of masonry towers is generally investigated through fixed-base numerical models (Bartoli et al. 2016; Casolo et al. 2013; Cosenza & Iervolino 2015;. Nevertheless, the hypothesis of a compliant base was shown to be necessary in order to reproduce the vibration modes and frequencies measured on the S.Maria in Fabriago and S. Apollinare in Classe bell towers (Abu Zeid et al. 2007), the Ghirlandina tower (Cosentini et al. 2015), the Pisa tower (Fiorentino et al. 2017), the Carmine bell tower in Napoli (de Silva et al. 2018a) and the Giotto bell tower in Florence (Lacanna et al. 2019). Few case studies were analysed under strong earthquake motions through a complete approach, in which the soil was modelled as a continuum (;asolo et al. 2017; Dogangun et al. 2007; de Silva et al. 2017). Moreover, de Silva (2020) evaluated the effects of soil-structure interaction on classes of towers founded on different soil types through nonlinear dynamic analyses under seismic motions with increasing amplitude.

This study applies the probabilistic approach proposed by de Silva (2020) to predict the mean annual rate of exceeding different levels of the peak and residual foundation rotation. The result is the so-called 'demand hazard curve', which summarizes in a probabilistic framework the modification of seismic hazard and fragility induced by soil compliance. It is worth to remind that, due to their artistic value, the seismic safety of monuments should be in principle assessed with a

DOI 10.1201/9781003308867-67

deterministic approach, i.e. under a seismic loading conservatively corresponding to the 'maximum historical earthquake'. Anyway, a probabilistic evaluation of the demand, such as that proposed in the following, can be useful for large-scale preliminary evaluations on the safety of a number of representative cases.

2 SELECTED CASE STUDIES

2.1 *Structural features*

Figure 1 shows (a) the location, (b) the pictures and (c) the vertical and horizontal cross section of the selected case studies.

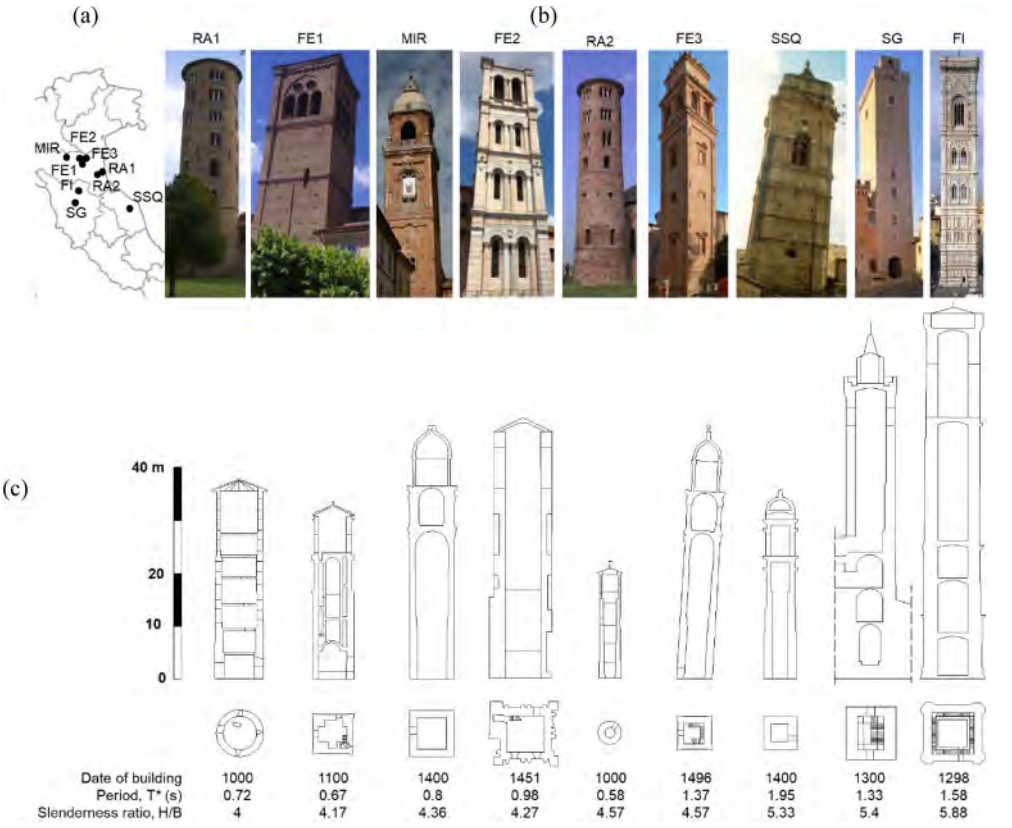

Figure 1. Locations (a), pictures (b) and cross sections (c) of the nine monumental towers analysed. The date of construction, the fundamental vibration period and the slenderness ratio are also reported.

The brickwork cylindrical bell tower of Sant'Apollinare in Classe (RA1) is 38.20 m tall, 9.60 m wide and connected to the church through a chamber (Abu Zeid et al. 2007). The external diameter of the tower is constant along the height, while the wall thickness varies from 1.8 m to 0.8 m moving from the base to the top. Four abutments connect the circular cross section to the square basement which is likely embedded in the foundation soil for about 3m in depth.

The Medieval Tower of Matilde di Canossa (FE1) is an approximately 30 m high brickwork tower located near Ferrara (Standoli et al. 2020). The square base is 7.2 m wide and weakly connected to the adjacent church through a more recently built chamber. The internal structure is composed of two coaxial vertical box structures, with the stairs built between them. The thickness of the internal wall is constant and equal to 0.45 m, while that of the external wall decreases from 1.05 m at the first three floors to 0.9 m in the upper three levels. This tower is inclined by 1.6° in W–E direction and 3° in N–S direction, which leads to a displacement of the top tower axis equal to about 85 and 160 cm, respectively (Clementi et al. 2018).

The bell tower of the Mirandola cathedral (MIR) was built in the 15th century. Its actual shape, about 48 m high and 11 m wide, results from several renovation works up to 1888. The tower was severely damaged by the Emilia earthquake in 2012 (Fioravante et al. 2013).

The Renaissance masonry belfry of the Ferrara Cathedral (FE2) was originally designed by Leon Battista Alberti in 1451 even if it was completed in the 16th century (Standoli et al. 2020). The tower is about 50.8 m high with a square base 11.7 m wide, with walls 1.2 m thick. The floors from the first to the fourth level are constituted by masonry vaults, while those at the fifth and the sixth levels are composed of wooden plank and beams. The bell tower is tilted of 2° in S-N direction and 0.5° in the E-W, consequently the top of the tower axis is shifted by about 174 cm and 44 cm, respectively.

The cylindrical bell tower of Pieve di Santa Maria in Fabriago (RA2), a brickwork structure unconnected from the adjacent church, 21 m tall with a base diameter 4.60 m wide (Abu Zeid et al. 2007). The thickness of the main walls varies from 140 cm at the base to 50 cm at the top. A foundation depth of 3m was estimated.

The belfry of San Benedetto Church in Ferrara (FE3) is a brickwork structure 46 m high with a square section 7.33 m wide (Standoli et al. 2020). The construction of the church started in 1496 and was completed in 1621. The works were interrupted immediately after the beginning of the construction due to the development of foundation settlements. Currently the tower is inclined by 0.5° North–South and 3.07° East–West plan, leading to horizontal displacements of the axis on the top equal to 49 cm along the NS direction and almost 282 cm along the EW direction. The inclination increased by 18 mm after the 2012 Emilia earthquakes, as reported in the study by Pellegrinelli et al. (2014).

The bell tower of the S. Lucia's church in Serra San Quirico (SSQ) is a calcareous masonry structure 32 m tall, built in the XV century. The horizontal cross section is square, about 6 m wide and 1.20 m thick at the basement or 0.80 m thick at the top. The foundation depth is 1.5 m from the ground level. The structure is connected to the church at a height of 9 m from the ground floor. The tower was affected by the 1997 Umbria-Marche earthquake.

The Torre Grossa in San Gimignano (SG) is a 60 m high structure made of infilled walls, with an outer face in stone masonry and an inner layer of brick masonry filled by heterogeneous material (Madiai et al. 2013). The horizontal square section is 9.5 m wide. The wall thickness varies from 2.6 m at the base to 1.6 m at the top.

Finally, the bell tower of the Firenze cathedral (FI) was designed by Giotto in the XIV century. The foundations were built in 1298 by Arnolfo di Cambio and probably reach a depth of 6 m. The structure is 84.7 m heigh with a square base 14.45 m wide. The masonry is made of stone quarried in the southern hills of Firenze (La Canna et al. 2019). The tower is completely covered by marble.

The period of the Mirandola tower was estimated by Fioravante et al. (2013) through the empirical relationship by Rainieri and Fabbrocino (2011). The fundamental period, T^*, of all the other towers were measured through on-site dynamic identification techniques. The resulting values are reported in Figure 1.

2.2 *Subsoil conditions*

Information on the subsoil conditions were available for most of the selected cases, thanks to seismic microzonation studies or specific on-site investigations. The collected soil layering and shear wave velocity profiles are plotted in Figure 2.

The soil profile of the case RA1 was inferred from cone penetration tests executed close to the tower for the seismic microzonation study of the Classe town (https://ambiente.regione.emilia-romagna.it). Below a few meters of fine-grained soil, a sand deposit is predominant and locally interbedded by silty sand or sandy silt sub-layers.

A 127m deep borehole revealed that the shallowest 30m below the Mirandola bell tower (MIR) is mainly constituted by sand or sand with gravel interrupted by a clay layer from 2 m to 8 m in depth.

The subsoil below the towers FE2 and FE3 was classified in the seismic microzonation study of Ferrara city (https://servizi.comune.fe.it/6985/1-poc-scaduto-qcintegrazioni-al-quadro-conoscitivo) as clean sand for FE2 and sandy/gravelly clay for FE3.

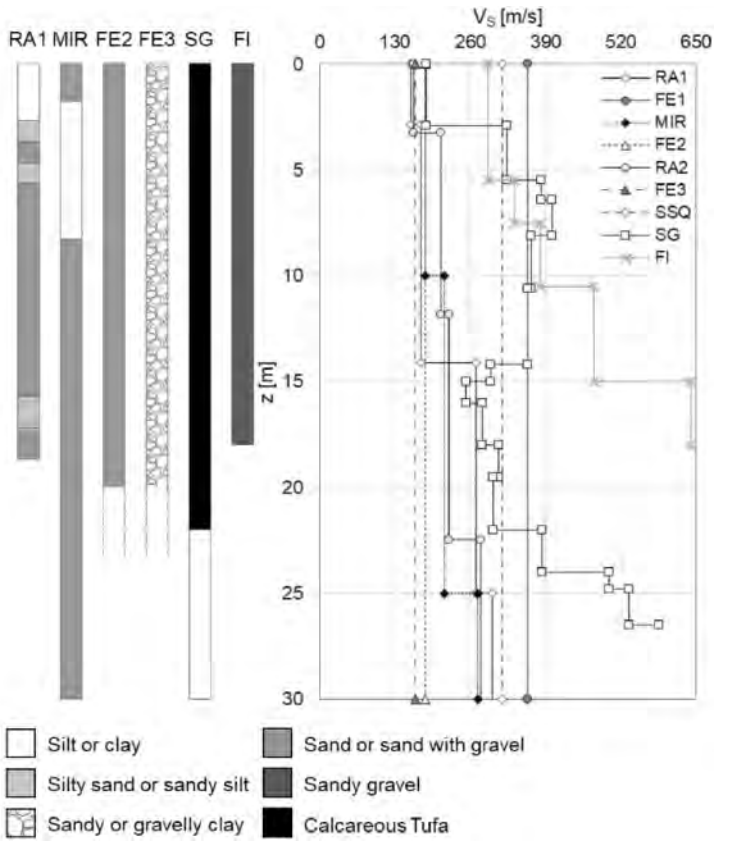

Figure 2. Soil layering and shear wave velocity profiles of the case studies.

A borehole log reported by Madiai et al. (2013) shows that the SG tower is settled on 'Calcareous Tuff', i. e. layers of soft rock alternating with loose silty, sandy and gravelly soils, being the latter predominant with increasing depth. A Blue Clays formation of marine origin was intercepted at a depth of about 22 m.

Finally, the subsoil of the Giotto's bell tower (FI) is constituted by a sand to sandy gravel layer overlaying on a 18 m deep bedrock, made of alternating shales and limestone with interbedded quartz-calcareous sandstones (Coli et al. 2020).

The profiles of the shear wave velocity, V_S, shown in Figure 2 were inferred through microtremor seismic surveys for RA1 and RA2 (Abu Zeid et al. 2007) as well as directly measured through a cross-hole and a down-hole test executed in the boreholes previously described for MIR and SG

(Madiai et al. 2013), respectively. The V_S profile below the Giotto bell tower (FI) was reported by Coli et al. (2020) as based on downhole and SASW tests performed close to the cathedral. Values of the equivalent shear wave velocity of the shallowest 30 m were attributed to the FE2 and FE3 sites during the seismic microzonation of Ferrara (https://servizi.comune.fe.it/6985/1-poc-scaduto-qcintegrazioni-al-quadro-conoscitivo). In lack of any information, the V_S profiles for the FE1 and SSQ sites were assumed from the Seismic Soil Class SSC-Italy database (Forte et al. 2019).

Table 1 shows the equivalent shear wave velocity for the nine analysed sites. The latter was computed for the shallowest 30 m for all the cases except for FI, where V_{Seq} was referred to the 18 m thick granular soil deposit overlying the bedrock. Values in Table 1 highlight that all the towers are settled on soft to very soft soil.

Table 1. Equivalent shear wave velocity of the analysed case studies.

	RA1	FE1	MIR	FE2	RA2	FE3	SSQ	SG	FI
V_{Seq} (m/s)	220	360	203	182	213	166	315	333	383

3 EVALUATION OF THE SITE-SPECIFIC HAZARD

Figure 3 shows the acceleration response spectra on a stiff rock outcrop with a probability of exceedance equal to 10% in 50 years for the selected case studies. The same spectrum was assumed for FE2 and FE3, being the two towers close to each other. The larger filled circles indicate the spectral ordinate, Sa, associated to the fundamental period of each tower (see Figure 1). Being all towers slender and periods high, the expected Sa(T^* are moderate to low, ranging between 0.2 g (RA2) and 0.045 g (FI).

For a given tower period, T^*, the Sa(T^*) associated to variable annual rates of exceedance, λ_{Sa}, can be calculated, leading to a hazard curve expressed in terms of the spectral acceleration relevant to the fundamental period of the tower. Figure 4 shows the hazard curves of the case studies derived by the national seismic hazard map (http://esse1-gis.mi.ingv.it/). Notwithstanding the same hazard spectrum, two different curves are associated to FE2 and FE3, being the periods of the towers different. The highest hazard resulted for the case RA2 (i. e. the shortest tower) and the lowest for FE3, SSQ, SG and FI, which is the tallest one. The curves relevant to RA1, FE1, MIR and FE2 cases lay between such two extremes, with the hazard decreasing from RA1 to FE2. It is worth to highlight that the above considerations on the site-specific hazard may change if different case studies are considered, since the hazard expressed in terms of Sa depends on the period of the system at hand.

Each data set plotted in Figure 4 was fitted with a power law:

$$\lambda_{Sa} = k\mathrm{Sa}^n \tag{1}$$

The coefficient k and the exponent n are reported in Table 2.

Table 2. Parameters fitting the hazard curves of the analysed case studies.

	RA1	FE1	MIR	FE2	RA2	FE3	SSQ	SG	FI
k ($\times 10^{-5}$)	5	5	5	2	7	0.8	0.6	0.3	0.3
n	−2.03	−1.88	−1.72	−1.81	−2.13	−1.86	−1.95	−2.13	−2.10

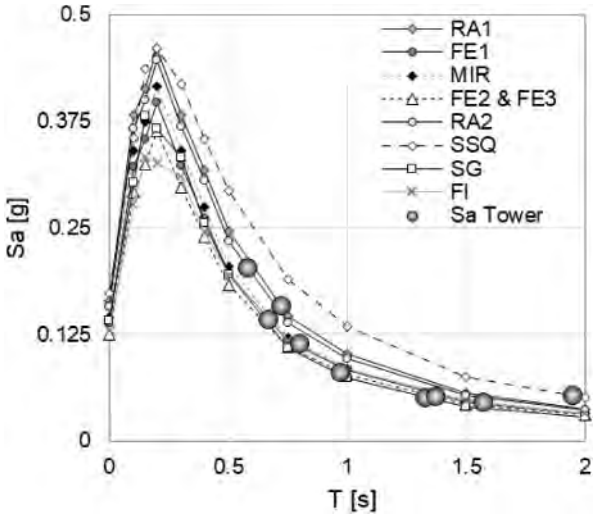

Figure 3. Acceleration response spectra with a probability of exceedance equal to 10% in 50 years for the selected sites.

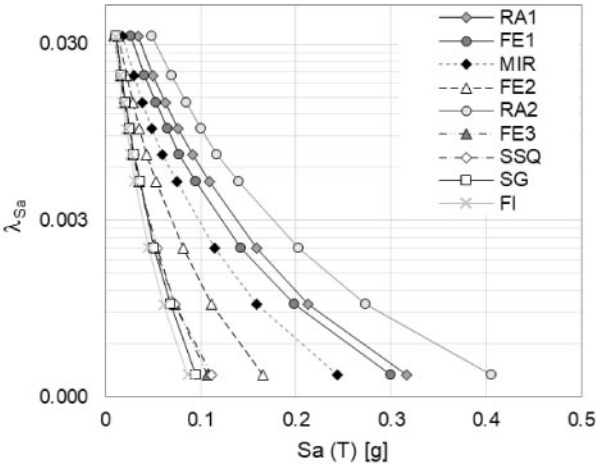

Figure 4. Hazard curves of the spectral acceleration relevant to the fundamental period of the towers.

4 CALCULATION OF THE DEMAND HAZARD CURVE

In this study, the convolution between hazard and fragility through the well-known equation proposed by PEER (Cornell et al. 2000) was applied to compute the 'hazard curve' of the foundation rotation, δ, for the nine Italian monumental towers shown in Figure 1.

Each ordinate of the curve expresses the mean annual rate of exceeding the rotation threshold, δ_t, reported in the abscissa. It is calculated through the following equation:

$$\lambda_\delta = \int_0^{+\infty} \mathrm{P}\left(\delta > \delta_t | \mathrm{Sa}\right) \cdot \left| d\lambda_{Sa}\left(\mathrm{x}\right)\right| \tag{2}$$

where:

- $|d\lambda_{Sa}(x)|$ is the absolute value of the derivative of the hazard curve expressed through the spectral acceleration, Sa associated to the fundamental period of each tower;
- $P(\delta>\delta_t|Sa)$ is the probability that the foundation rotation, δ, exceeds the threshold, δ_t, conditioned to increasing spectral acceleration, Sa.

Considering that the relationship between δ and Sa is linear in a log-log plot (de Silva 2020), and the foundation rotation is log-normally distributed, the probability of exceedance is given by:

$$P(\delta > \delta_t|Sa) = 1 - \Phi\left(\frac{\log(\delta_t) - \log_{\delta|Sa}}{\sigma}\right) \quad (3)$$

where σ is the logarithmic standard deviation and $\log\eta_{\delta|Sa}$ is the mean value, estimated by the δ-Sa relationship as follows:

$$\log\eta_{\delta|Sa} = \log(a) + b\log(Sa) \quad (4)$$

The parameters a and b, as well as the standard deviation σ, were calibrated on the results of nonlinear dynamic analyses by de Silva (2019). Being the tower foundation prone to rocking more than swaying, the analysis of the effect of such motion was neglected.

The hazard curves in Equation 2 were calculated in Section 3.

5 RESULTS

5.1 *Selection of the δ-Sa relationship for the analysed cases*

The demand hazard curve should be ideally calculated through Equation (2) by expressing the probability of exceeding a given threshold motion using the parameters a, b and σ (needed in Equation 3) calibrated on nonlinear dynamic analyses performed on soil-tower models accurately reproducing the features of the case study.

For large scale evaluations, a simplified approach may be followed by referring to results of parametric studies on reference models characterised by geometrical and mechanical properties approximating those of the cases under investigations. In this study, the parameters a, b and σ were selected among those calibrated by de Silva (2020) on the following reference tower-soil models:

- slender tower characterized by a slenderness ratio H/B=3 on soil type C or D, i. e. with an equivalent shear wave velocity $V_{S30} = 300$ m/s and $V_{S30} = 180$ m/s, respectively;
- very slender tower (H/B=6) on soil type D (V_{S30}=180 m/s).

Being the slenderness ratio H/B of the cases analysed in this study variable between 4 and 6, the regression parameters referred to slender tower were used and the standard deviation of the peak rotation on soil type D was also adopted for the residual rotation on the same soil. Table 3 associates the case studies to the selected ground type. Soil type C or D were selected according to the values of the shear wave velocity reported in Table 1. The subsoil profiles with V_{Seq} lower than 185 m/s in Table 1 (FE2 and FE3) were simulated through soil D, while type C was chosen when V_{Seq} was higher than 300 m/s (FE1, SSQ, SG and FI). Since the V_{Seq} of the cases RA1, MIR and RA2 ranges between 185 m/s and 300 m/s, their response is expected to be intermediate between that relevant to soil D and C. The analyses were consequently repeated considering both subsoil conditions.

de Silva (2020) calculated the fundamental periods of the reference slender towers, which resulted equal to 0.59 s and 0.72 s for the slender tower models founded on soil C and D, respectively. Such values are in a perfect agreement with the periods of the case studies RA1, FE1, MIR and RA2 (see Figure 1). The match is less satisfying by increasing the structural height, i. e. for the case FE2 and FE3 on soil D and SSQ, SG and FI on soil C. In these latter cases, the foundation rotation discussed in the following should be considered slightly underestimated.

Table 3. Reference cases by de Silva (2020) associated to the towers analysed in this study to select the parameters a, b and σ in Eq. (2) and (3).

	RA1	FE1	MIR	FE2	RA2	FE3	SSQ	SG	FI
Soil type	C*, D**	C	C, D	D	C, D	D	C	C	C
δ-Sa law									

*peak a = 0.0535 b = 0.6771 $\sigma = 0.4869$
**peak a = 0.2922 b = 0.8463 $\sigma = 0.6352$; residual a = 0.1491 b = 1.0962 $\sigma = 0.6352$

5.2 *Discussion on the results*

Figure 5 shows the demand hazard curves for the selected case studies expressed in terms of peak rotation, δ, of the foundation on soil C (a) and D (b) as well as in terms of residual rotation, δ_{res}, on soil D (c).

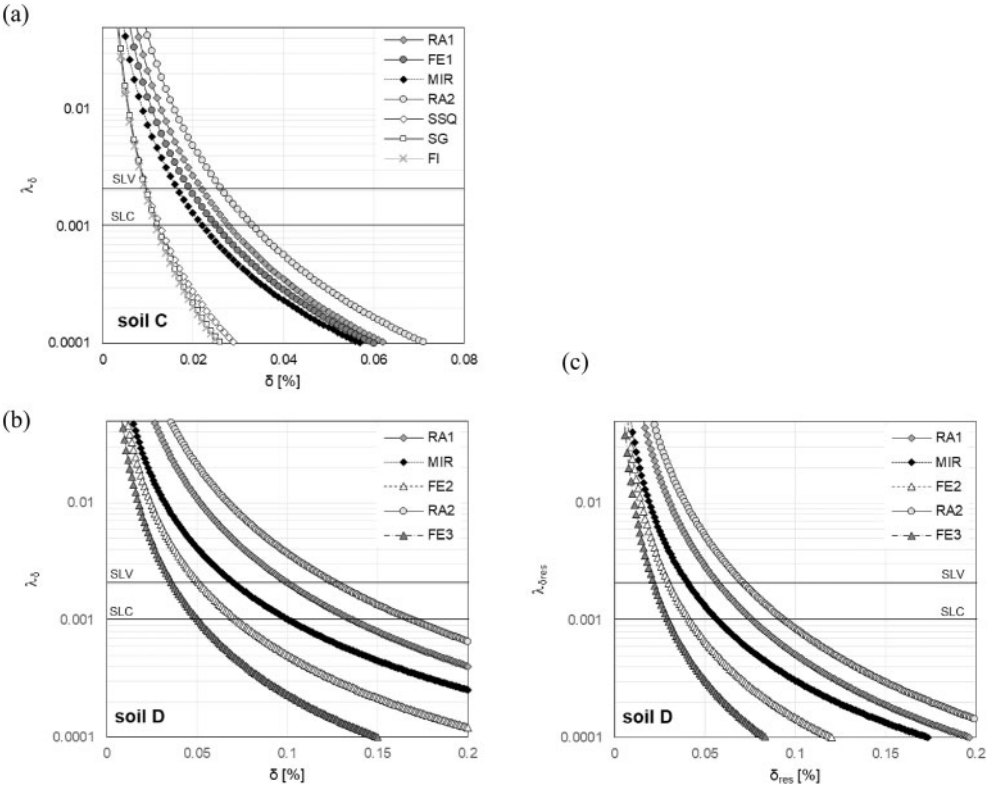

Figure 5. Demand hazard curve for the selected case studies expressed in terms of peak rotation of the foundation on soil C (a) and D (b) and in terms of residual rotation on soil D (c).

Due to the better mechanical properties of soil C, towers founded on such soil are expected to be less affected by foundation rocking with respect to those laying on soil D. For a given soil type, the expected rotation decreases as the Sa-hazard decreases. Such aspect is particularly evident from the descending order of the curves RA2, RA1, MIR, FE2, and FE3 in Figure 5b, which reproduces that of Figure 4. The residual rotations in Figure 5c are lower than the peak values but not negligible.

The abscissas of the curves plotted in Figure 5 were multiplied by the tower height to obtain the peak and residual horizontal displacements, u_δ and $u_{\delta res}$, of the top of the tower axis, relative to the foundation motion. The results are shown in Figure 6, highlighting that significant displacements are expected for both soil types. The highest values on soil C are referred to the towers MIR and RA1 on both soil types and FI on soil C; in the latter case the displacement is significant due to the tower height, even though the expected rotation resulted relatively low.

Figures 6a and 6b revealed that the case RA2, characterized by the highest hazard curve in terms of both spectral acceleration (Figure 4) and foundation rotation (Figure 5), falls among the lowest hazard curve in terms of displacements. In fact, the period of such tower is the lowest among the analysed cases and, consequently, the expected spectral accelerations are the highest. The rotation is relevant because of the significant seismic action; nevertheless, the expected top displacement is low, being the tower short.

The horizontal lines drawn in Figures 5 and 6 indicate the annual rate of exceeding the ultimate limit states as defined by the Italian Code (NTC2018). They are associated to earthquakes with return periods equal to 475 years (life safety limit state, SLV) and 975 years (collapse limit state, SLC). The abscissas of the intercept points between such lines and the curves are reported in Table 4, while rotations and displacements expected at SLV are displayed in Figure 7. In the same figure, the grey lines indicate the current shape of the tower and the vertical dashed grey lines the tower axis. The static tilts of the cases FE1, FE2 and FE3 are apparent.

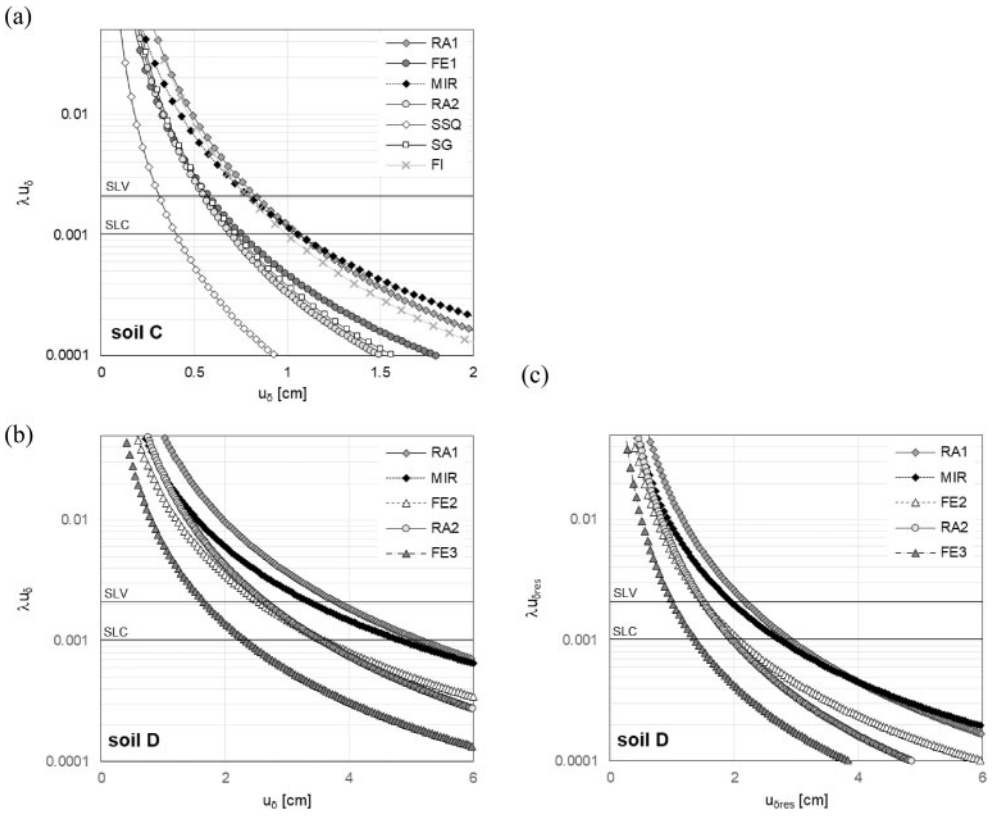

Figure 6. Demand hazard curve for the selected case studies expressed in terms of peak displacement on the top of the tower axis on soil C (a) and D (b) and in terms of residual permanent displacement on the top of tower axis on soil D (c).

Table 4. Peak and residual rotation and displacements associated to the SLV and SLC limit states.

	Peak SLV				Peak SLC				Residual SLV		Residual SLC	
	δ soil C (%)	δ soil D (%)	uδ soil C (cm)	uδ soil D (cm)	δ soil C (%)	δ soil D (%)	uδ soil C (cm)	uδ soil D (cm)	δ_{res} soil C (%)	$u\delta_{res}$ soil D (%)	δ_{res} (cm)	$u\delta_{res}$ (cm)
RA1	0.022	0.100	0.84	3.80	0.028	0.140	1.10	5.20	0.057	2.17	0.076	2.89
FE1	0.019	/	0.57	/	0.025	/	0.75	/	/	/	/	/
MIR	0.017	0.070	0.82	3.36	0.022	0.100	1.06	4.84	0.041	1.97	0.057	2.74
FE2	/	0.051	/	2.55	/	0.072	/	3.60	0.030	1.51	0.041	2.05
RA2	0.026	0.126	0.55	2.65	0.033	0.169	0.69	3.55	0.072	1.51	0.094	1.98
FE3	/	0.036	/	1.66	/	0.050	/	2.30	0.022	1.02	0.029	1.34
SSQ	0.010	/	0.32	/	0.013	/	0.41	/	/	/	/	/
SG	0.009	/	0.54	/	0.012	/	0.72	/	/	/	/	/
FI	0.009	/	0.76	/	0.012	/	1.02	/	/	/	/	/

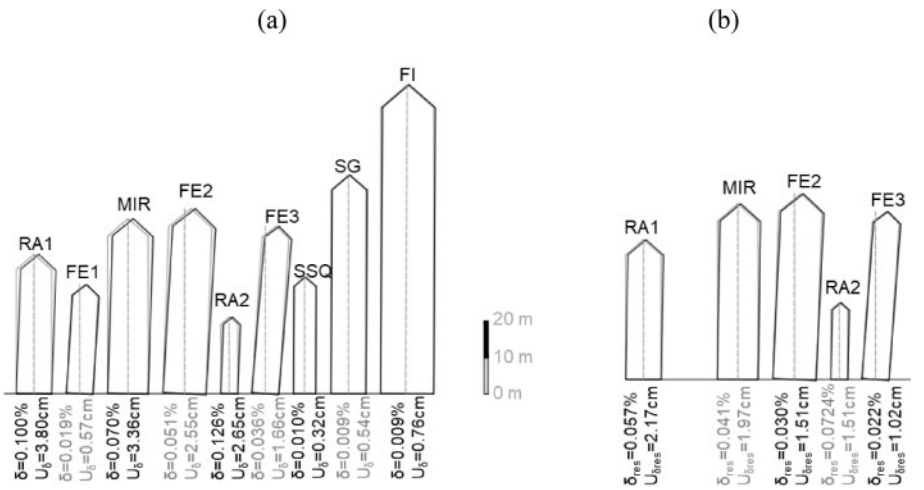

Figure 7. Peak (a) and residual (b) rotation and displacements provided by curves in Figure 5 and 6 for the SLV limit states.

A displacement magnification factor equal to 20 was used to draw the deformed shapes. By comparing the earthquake-induced peak deformed shape and the actual shape of the three inclined towers in Ferrara, it is clear that uneven settlements at the foundation level imply static tilts significantly higher than the seismic increments. Consequently, peak and residual displacements appear not to be dangerous for vertical towers, but may lead to instability those already inclined due to gravitational uneven settlements. Anyway, it should be reminded that during earthquake towers experience bending displacements to be added to the rigid movement induced by the foundation motion, reaching higher levels of displacement on the top. It can be noted that the residual displacement of the FE3 for SLV and SLC seismic actions is expected to be 1.02 cm and 1.34 cm, i.e. comparable to the displacement 1.88 cm induced by the Emilia earthquake in 2012 (see Section 3.1).

6 CONCLUSIONS

The paper describes and applies a method for probabilistic large-scale predictions of the peak and residual rotation of towers settled on soft soil under earthquake. The approach considers the modifications of seismic action and of the structural fragility induced by the interaction between the structure, the foundation, and the soil. The results demonstrated that the structural slenderness is beneficial on the seismic actions, because the higher structural deformability increases the fundamental vibration period and leads to a reduction of the spectral ordinates. Conversely, tall monumental towers are more significantly affected by tilts induced by the foundation rocking motion and more prone to instability. The residual rotation predicted through the proposed approach for the belfry of San Benedetto Church in Ferrara subjected to a 475 yrs return period seismic action resulted very close to the increase of the tower tilt measured after the 2012 Emilia earthquake. All in all, the proposed simplified method appears reliable for preliminary evaluations, nevertheless the unavoidable approximations to be adopted for its application. Additional non-linear dynamic analyses on different types of soil, masonry and foundation depth are needed to calibrate the parameters of the Sa-δ regression laws for a higher number of reference cases. For the numerous towers among those founded on soft soil, which are tilted and close to the instability under gravity loads, the evaluation of the peak and residual rotation expected under earthquake motions would be useful to address suitable retrofitting countermeasures.

ACKNOWLEDGEMENTS

This research was developed in the framework of the 2019-2021 ReLUIS-DPC research programme – WorkPackage 16 – Task 16.3 'Soil-Foundation-Structure Interaction' – funded by the Italian Civil Protection Department.

REFERENCES

Abu Zeid, N. Ribecchi, G. Tullini, N. Laudiero, F. Lanza, L. 2007. Caratterizzazione dinamica di torri medio-evali ravennati. Atti del XII Convegno ANIDIS "*L'ingegneria Sismica in Italia"*, 10-14 June 2007, Pisa, Italy.

Bartoli, G. Betti, M. Vignoli, A. 2016. A numerical study on seismic risk assessment of historic masonry towers: a case study in San Gimignano. *Bull Earthq Eng* 14:1475–1518.

Casolo, S. Milani, G. Uva, G. Alessandri, C. 2013. Comparative seismic vulnerability analysis on ten masonry towers in the coastal Po Valley in Italy. *Eng Struct.* 49:465–490.

Casolo, S. Diana, V. Uva, G. 2017. Influence of soil deformability on the seismic response of a masonry tower. *Bull Earthq Eng.* 15(5):1991–2014.

Clementi, F. Pierdicca, A. Milani, G. Gazzani, V. Poiani, M. Lenci S. 2018. Numerical model upgrading of ancient bell towers monitored with a wired sensors network. *10th International Masonry Conference Milani, G. Taliercio, A. Garrit, S. (eds.) 9–11 July 2018,* Milan, Italy.

Coli, M. Cosentini, R. Lacanna, G. Lancellotta, R. Ripepe, M. 2020 Giotto's bell tower: a contribution on the dynamic identification and soil-structure interaction. In "Il Campanile di Giotto, conoscenza, diagnostica, conservazione", Vaccaro V. & Caciagli S. Ed., Mandragora, Firenze (in press).

Cornell, C.A. Jalayer, F. Hamburger, R.O. Foutch, D.A. 2002. Probabilistic basis for 2000 SAC Federal Emergency Management Agency steel moment frame guidelines. *J Struct Eng ASCE* 128(4):526–533.

Cosentini, R. Foti, S. Lancellotta, R. Sabia, D. 2015. Dynamic behavior of shallow founded historic towers: validation of simplified approaches for seismic analyses. *Int J Geotech Eng*:13–29.

Cosenza, E. Iervolino, I. 2007. Seismic Retrofitting of a Medieval Bell Tower by FRP. *J Comp. Constr*. 11(3):319-327.

de Silva F. 2020. Influence of soil-structure interaction on the site-specific seismic demand of masonry towers. *Soil Dyn Earthq Eng*, 131, April 2020, 106023.

de Silva, F. Ceroni, F. Sica, S. Silvestri, F. 2017. Carmine bell tower in Naples: prediction of soil-structure interaction under seismic actions. *Special Volume: Geotechnics and Heritage: Historic Towers*. Lancellotta, R. Flora, A. Viggiani, C.(eds). Taylor & Francis.

de Silva, F. Pitilakis, D. Ceroni, F. Sica, S. Silvestri, F. 2018. Experimental and numerical dynamic identification of Carmine bell tower in Naples (Italy), *Soil Dyn Earthq Eng* 109: 235–250.

Dogangun, A. Livaoglu, R. Acar, R. A study on seismic behavior of minarets considering soil-structure interaction. *International earthquake symposium*, *2007*: 393-404, Kocaeli, Turkey.

Fioravante, V. Giretti, D. Abate, G. Aversa, S. Boldini, D. Capilleri, P.P. Cavallaro, A. Chamlagain, D. Crespellani, T. Dezi, F. Facciorusso, J. Ghinelli, A. Grasso, S. Lanzo, G. Madiai, C. Massimino, M.R. 7

Fiorentino, G. Lavorato, D. Quaranta, G. Pagliaroli, A. Carlucci, G. Nuti, C. Sabetta, F. Della Monica, G. Piersanti, M. Lanzo, G. Marano, G.C. Monti, G. Squeglia, N. Bartelletti, R. 2017. Numerical and experimental analysis of the leaning Tower of Pisa under earthquake. *Procedia Engineering* 199:3350-3355.

Forte, G. Chioccarelli, E. De Falco, M. Cito, P. Santo, A. Iervolino, I. 2019. Seismic soil classification of Italy based on surface geology and shear-wave velocity measurements, *Soil Dyn Earthq Eng* 122: 79-93.

Lacanna, G. Lancellotta, R. Ripepe, M. 2019. Integrating modal analysis and seismic interferometry for structural dynamic response: the case study of giotto's bell tower in florence (italy). *7th ECCOMAS Thematic Conference on Computational Methods in Structural Dynamics and Earthquake Engineering M. Papadrakakis, M. Fragiadakis (eds.) 24–26 June 2019,* Crete, Greece.

Lacanna, G. Ripepe, M. Coli, M. Genco, R. Marchetti, E. 2019. Full structural dynamic response from ambient vibration of Giotto's bell tower in Firenze (Italy), using modal analysis and seismic interferometry, *NDT & E International* 102: 9-15.

Madiai, C. Renzi, S. Vannucchi, G. 2013. Seismic risk assessment of San Gimignano towers: Geotechnical aspect and soil structure interaction. *Proc. II International Symposium on Geotechnical Engineering for the Preservation of Monuments and Historic Sites:* 523-529, Napoli, Italy.

Maugeri, M. Pagliaroli, A. Rainieri, C. Tropeano, G. Santucci De Magistris, F. Sica, S. Silvestri, F. Vannucchi, G. 2013. Earthquake geotechnical engineering aspect of the 2012 Emilia Romagna earthquake (Italy). Proc.*VII International conference on case history on geotechnical engineering April 29-May 4 2013*, Chicago, USA.

Pellegrinelli, A. Furini, A. Russo, P. 2014. Earthquakes and ancient leaning towers: Geodetic monitoring of the bell tower of San Benedetto church in Ferrara (Italy). *Journal of Cultural Heritage* 15 (6):687–91.

Rainieri, C & Fabbrocino, G. 2011. Predictive correlations for the estimation of the elastic period of masonry towers. *EVACES 2011 – Experimental Vibration Analysis for Civil Engineering Structures, 3-5 October 2011*, Varenna, Italy.

Standoli, G. Giordano, E. Milani, G. Clementi F. 2020. Model Updating of Historical Belfries Based on Oma Identification Techniques, *International Journal of Architectural Heritage.*

Geotechnical Engineering for the Preservation of Monuments and Historic Sites III – Lancellotta, Viggiani, Flora, de Silva & Mele (Eds)

Dynamic impedance functions for neighbouring shallow footings

E. Zeolla & S. Sica
University of Sannio, Benevento, Italy

F. De Silva
University of Naples Federico II, Naples, Italy

ABSTRACT: Damage caused by past and recent earthquakes to the historic centres in Italy and abroad has highlighted the need to investigate the seismic response of structures built in aggregate or very close together. The close spacing among buildings could promote a mutual interaction through the underlying and surrounding soil, a phenomenon known as structure–soil–structure interaction or cross interaction. Like ordinary problems of soil-structure interaction, the substructure approach, in which the structure is endowed with springs and dashpots at its base to reproduce soil compliance, may turn useful even in solving cross-interaction problems. The paper tries to shed light on the modifications of the impedance functions of a shallow foundation when it is in-group with other footing systems. Indications on the proper calibration of the impedance matrix for a system of two or more nearby structures will be provided.

1 INTRODUCTION

In most practical engineering applications, the proximity between two or more buildings has hardly ever been considered even though in a few literature studies the mutual interaction among closely-spaced structures under both static and dynamic loading conditions has been highlighted. In the dynamic field, a vibrating foundation spreads out a wave field that might be seen as a disturbance affecting the adjacent foundation and vice versa. Gazetas (1983), in his state-of-art on the analysis of machine foundation vibrations up to the early 1980s, cites the first pioneering works on dynamic cross interaction (CSSI) or structure-soil-structure interaction (SSSI), e.g. Wartburton et al. (1971), Chang-Liang (1974), Roesset and Gonzales (1977). Qian and Beskos (1995), for instance, moved some criticism to the assertion of the ATC-3 regulations (1984) "*that neglecting coupling effects between footings could lead to conservative results"* by showing that the above statement is no longer true for certain bands of frequencies. After a vivid literature vein in the latest Nineties (e.g.,;etti 1997; Wang & Schmid 1992), the issue of CSSI has less attracted the scientific community until the first decade of this century when novel works started to appear again (Aldaikh et al. 2015, 2018; Alexander et al. 2013; Ghandil et al. 2016; Knappett et al. 2015; Lehmann & Antes 2001; Padron et al. 2009).

In this paper, the influence of a nearby foundation on the dynamic response of a master foundation is investigated in computing the frequency-dependent matrix of impedance functions. As well known, foundation impedances $\overline{K}_{ij}$ are the sum of a real part representing the dynamic stiffness and an imaginary part accounting for the radiation damping, due to the energy scattered in the subsoil (Gazetas 1991):

$$\overline{K}_{ij} = k_{ij}(a_0)K_{ij} + i\omega c_{ij}(a_0)C_{ij} \tag{1}$$

where:

– the subscriptsi, j indicate that $\overline{K}_{ij}$ links the component i of the vector of the loads transmitted by the foundation into the soil to the component j of the displacement vector;

DOI 10.1201/9781003308867-68

– the low-frequency (or static) stiffness, K_{ij}, and the dashpot coefficient, C_{ij}, depend on the soil shear modulus, G, and Poisson's ratio, ν, as well as on a characteristic dimension of the foundation;
– the dynamic coefficients $k_{ij}(a_0)$ and $c_{ij}(a_0)$ depend on the vibration frequency, ω, the characteristic dimension of the foundation, B, and the soil shear wave velocity, V_S, through the dimensionless frequency, $a_0 = \omega B/V_S$.

The real and the imaginary parts of the impedances are exploited to calibrate the stiffness and the dashpot coefficients of compliant-base systems. As an example, Figure 1 shows the compliant-base single-degree-of-freedom system usually adopted to calculate period modification due to soil-structure interaction through analytical formulas. For most of the structural patterns, the value of a_0 is very low thus implying a value of $k_{ij}(a_0)$ in eq. 1 close to unity. In such conditions, the structural period is only influenced by the low frequency stiffness of the soil-foundation system.

In the following, the low frequency stiffness components of a rigid rectangular foundation affected by the presence of a nearby foundation, with the same characteristics of the master one, will be examined by varying the distance between them. The compliant base periods evaluated through the analytical approach of Maravas et al. (2014), in which the low frequency stiffness of isolated or in-couple foundations is introduced, are compared for two different structural patterns (slender or squat constructions).

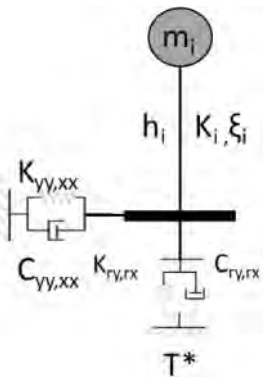

Figure 1. Superstructure modelled as a single-degree-of-freedom system on a compliant base.

2 COMPARISON AMONG NUMERICAL AND ANALYTICAL LOW FREQUENCY STIFFNESSES

For the foundation scheme in Figure 2, the low frequency stiffnesses, corresponding to the translational and rotational degrees of freedom were computed numerically through a continuum approach solved with the finite-difference-method (FDM) software FLAC3D. The foundation was placed at the surface of a 3D volume of soil with a square plan (80 m on each side), and a height of 50 m (in Figure 2b). The mesh size, Δ, was calibrated according to the rule $\Delta < V_S/8f_{max}$ proposed by Kuhlemeyer and Lysmer (1973), to allow frequencies of the seismic wave up to $f_{max} = 25$ Hz to be reliably propagated through the soil. The infinite extension of the soil in depth and along the lateral sides was simulated by means of dashpots providing viscous normal and shear stresses proportional to the volume and shear wave velocities of the connected mesh element. Viscous damping was introduced through the Rayleigh formulation and set to a very low value (1%) so that the overall damping encompassed in the numerical simulations may be assumed to be coincident with the radiation damping.

The subsoil was assumed as a homogeneous viscoelastic half-space with a unit weight, $\gamma = 19$ kN/m^3, a bulk modulus, K = 12.2 MPa, and a shear modulus, G = 5.6 MPa, corresponding

to a shear wave velocity, $V_s = 54$ m/s. It should be pointed out that a very low value of the soil shear modulus was deliberately chosen to accentuate the deformability of the system and emphasize all interaction effects. The adopted value, hence, should be intended as a strain-compatible modulus for a soft deposit under stronger seismic loadings.

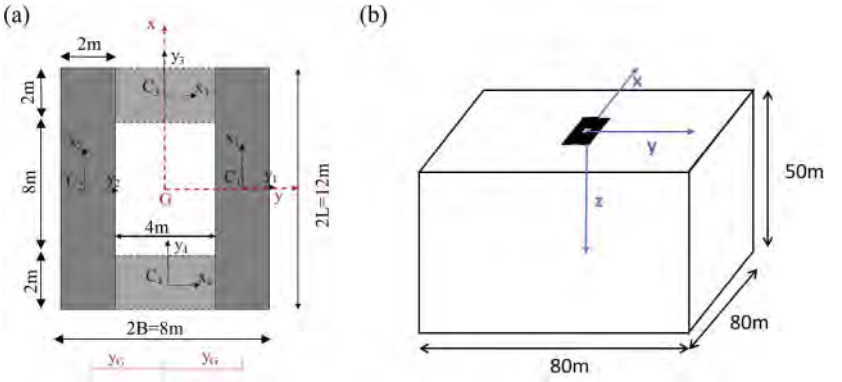

Figure 2. Reference scheme of the considered shallow foundation system (a). 3D analysis domain modelled in FLAC3D (b).

In the numerical model, a constant velocity along x-, y- or z-directions was applied to all grid points of the contact area to calculate the corresponding translational stiffness components. By calculating the resultant of the contact stresses, the static stiffness in each direction was obtained as the ratio between the force and the imposed displacement. To obtain the rotational stiffness, nodal velocities varying linearly along the x or y axes of the footing and null in correspondence of its centre were imposed. The rotational stiffness was calculated as the ratio between the moment and the applied rotation. Details on the load application procedure in the 3D model and the interpretation method can be found in Zeolla et al. (2021).

Other than numerically, the low frequency stiffnesses were calculated also analytically through the classical closed-form solutions available in literature for a rigid and massless shallow foundation placed on a homogeneous half space (Gazetas, 1991). With reference to the foundation scheme shown in Figure 2, the static terms of the compliance matrix may be computed analytically in different ways depending on the interconnection assumed among the different elements of the foundation system. First, the dimensions of the entire foundation footprint were considered ($2B \times 2L = 8\,m \times 12\,m$, total area of $96\,m^2$ with moment of inertia around the x and y axis equal to $512\,m^4$ and $1152\,m^4$, respectively) assuming a perfect connectivity between the four crossed beams. Second, a rigid hollow rectangular section with external dimensions $2B \times 2L = 8m \times 12\,m$ and internal hollow dimensions $4\,m \times 8\,m$ was considered (area of $64\,m^2$ and a moment of inertia around the x and y axis equal to $469\,m^4$ and $981\,m^4$, respectively). Third, the contribution of all (or a subset) of the individual footings ($2B \times 2L = 2m \times 12\,m$ or $2B \times 2L = 2\,m \times 4\,m$) could be summed up following the superposition principle. Thus, the translational stiffnesses of the four-footing system are the sum of the individual contributions. Likewise, the rotational stiffnesses are the sum of the individual rotational stiffnesses plus the transport moment of the vertical terms with respect to the axis of rotation of the entire foundation, such as suggested by the old ATC-3 (1984) seismic regulations for buildings.

All stiffnesses obtained through the different approaches are reported in Table 1. It emerges that there is no single way to assess the stiffness of crossed beam spread foundations. If the numerical (FDM) results are assumed to be the most reliable since 3D effects are accounted for together with a perfectly rigid connection among the different footings, the literature closed-form equations provide stiffness values close to the numerical ones only if the full or hollow rectangular section with the entire dimensions $2B \times 2L$ are adopted. Conversely, the stiffness superposition principle

with the contribution of all footings could be highly misleading for the foundation scheme of Figure 2 since it provides a noticeable overestimation of the low-stiffness terms of the impedance matrix. In short, the cross interaction between the single parts of the foundation system leads to a reduction of the total stiffness of the group, surely for the swaying modes.

In the following section, this aspect will be better investigated by computing numerically, through a 3D continuum approach, the stiffness terms for a couple of nearby shallow foundations.

Table 1. Low frequency stiffnesses computed analytically and numerically (FDM) for the reference foundation scheme.

	K_{i,j_tot} Full rectangular section	K_{i,j_tot} Hollow rectangular section	K_{i,j_tot} Superposition all footings	K_{i,j_tot} Superposition only longitudinal footings	**FDM** 3D
K_{zz} [MN/m]	185	156	333	225	**200**
K_{yy} MN/m]	150	130	287	203	**132**
K_{xx} [MN/m]	145	124	266	176	**132**
K_{ry} [MNm/m]	5213	4622	7369	4540	**5136**
K_{rx} [MNm/m]	2692	2522	2652	2100	**3085**

3 ANALYSIS OF CLOSELY SPACED FOUNDATIONS

3.1 *Numerical model*

Fig. 3 shows the analysed geometric schemes implemented in the FLAC3D software. Single and double foundations were assumed to be rectangular with a base, 2B, equal to 2 m and a length, 2L, of 10 m. The spacing, S, between the two foundations was varied between 0 m and 4 m. It is worth noting that in literature there is not a unique definition of S since sometimes it represents the foundation edge-to-edge distance and sometimes the axis-to-axis distance. In the present study, S always indicates the distance between the inner edges of the two foundations while B is the half-width of the foundation footprint. The subsoil model and the procedure to derive the low-stiffness terms of the impedance matrix for the master foundation are the same described in Section 2.

With regard to the rocking modes, two cases were considered, i.e., the twin footings subjected to concordant or opposite rotations.

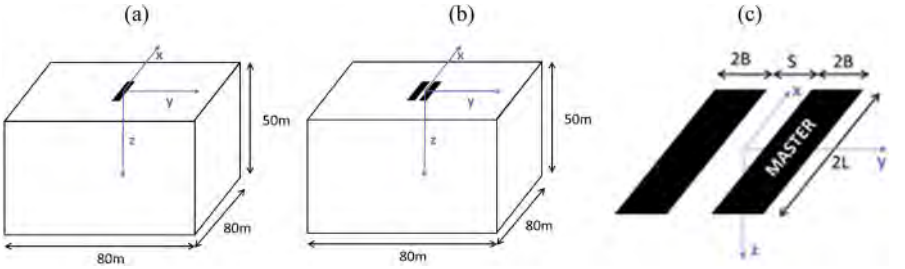

Figure 3. Reference schemes for the single footing (a) and the twin footings (b) on homogeneous half-space. Details of the two footings in (c).

3.2 *Low frequency stiffness*

Table 2 reports the low-frequency stiffnesses computed for the master footing on homogeneous half space for different values of the foundation-foundation spacing, S. Translational stiffnesses were

made dimensionless by dividing the values in Table 2 by the shear modulus G and the half-width of the foundation, B. Likewise, the rotational stiffnesses were divided by G and the half-width cubed. The black dashed line indicates the value associated to the isolated foundation. Figure 4 shows the variation of all stiffness terms with the dimensionless spacing between the two foundations, S/B. By analysing the numerical results in Table 2 and Figure 4. Variability of the dimensionless stiffnesses with S/B ratio, it emerges that when the nearby footing is added, all stiffness components of the master footing are much lower than the values corresponding to the same footing considered isolated. This effect diminishes as the spacing between the two foundations increases and vanishes earlier for the rotational components. Conversely, for S/B = 0 the two foundations tend to behave as a single footing of width 4B.

For the rocking mode around the x-axis (Figure 4d), there are two curves that correspond to the clockwise and counter clockwise moment applied to the neighbouring foundation. In case the foundations belong to the same building, it is possible that they undergo a concord rotation. If this situation arises, the slave foundation exerts a sort of constraint on the master one, which consequently experiences an increase of its rotational stiffness. On the contrary, if the nearby foundation rotates in the opposite direction with respect to the master one, the x rotational stiffness of the master footing varies with S/B in the same way as obtained for the other degrees of freedom.

Table 2. Low frequency stiffnesses of the master foundation on half space in presence of a nearby footing for different S/B

	Single	S/B = 0	S/B = 0.5	S/B = 1	S/B = 2	S/B = 4
K_{zz} [MN/m]	91.33	73.26	66.02	69.41	74.67	78.31
K_{yy} [MN/m]	62.83	48.14	44.68	45.80	47.98	49.41
K_{xx} [MN/m]	58.28	46.26	43.66	44.87	47.71	49.41
K_{rx} [MN/m]	120.13	115.26	110.96	120.17	129.53	134.17
K_{ry} [MN/m]	1366.03	1229.81	1133.37	1168.37	1305.94	1331.35

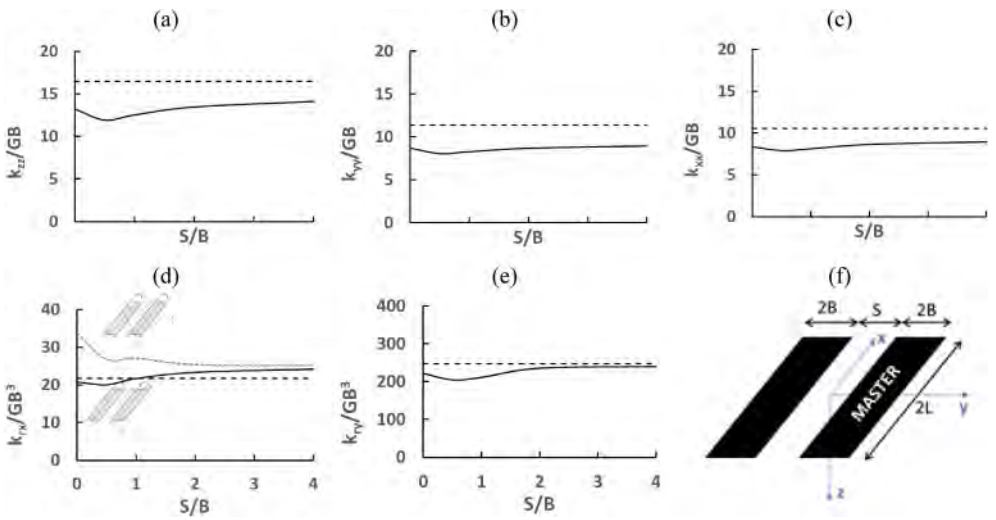

Figure 4. Variability of the dimensionless stiffnesses with S/B ratio, for $\nu = 0.33$. The black and flat dashed line indicates the value associated to the isolated foundation.

The above numerical results corroborate what expected from the simple theory of elasticity and Boussinesq solutions in the static filed. The static stiffness of the master footing in a group is always smaller than that of the same foundation considered isolated. Basing on the above numerical

outcomes, an interaction coefficient may be defined to quantify the group effect on the stiffness of the master foundation:

$$\alpha_{ij} = \frac{K_{ij,single} - K_{ij,group}}{K_{ij,single}} \tag{2}$$

where $K_{ij,single}$ and $K_{ij,group}$ are the stiffness components of the master foundation in case it is alone or in group.

Figure 5 shows the variation against the S/B ratio of the interaction coefficients associated to translation along x, y, and z together with rocking around x and y axis.

As already observed in terms of normalized stiffness, the interaction reduces as the spacing S/B increases while the rocking mode around the x-axis shows two different trends depending on the moment direction on each of the two footings.

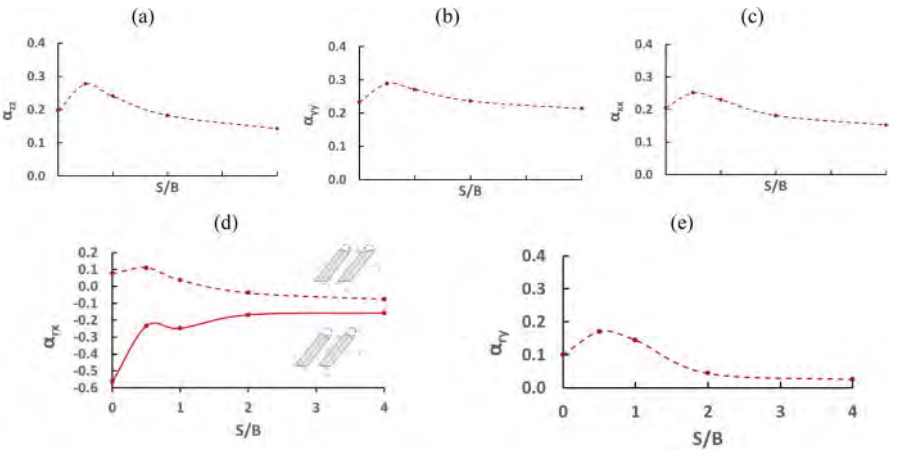

Figure 5. Variation of the interaction coefficients with the S/B ratio for two closely spaced foundations.

4 APPLICATION TO ESTIMATE THE PERIOD OF TWO STRUCTURAL PATTERNS

4.1 *Reference schemes of soil, foundation and structure*

The closed-form solution proposed by Maravas et al. (2014) to calculate the period of the soil-foundation-structure system was applied to the ideal cases of three historical Italian structures, founded through the system of footings plotted in Figure 6. The structural systems considered represent those belonging to the Italian historical heritage such as civic or bell towers for the scheme in Figure 6a and common masonry buildings for that in Figure 6b. The height and consequent structural design generally depend on the building function and sometimes are linked to the age of the building, the type of materials and the socio-economic context of the area. In this discussion, reference is made to three different structural schemes: squat structures (H/B <= 1), slender tower (H/B = 3) and very slender tower (H/B = 6) for a total of six structural cases reported in Table 3.

The application of the Maravas et al. (2014) formula requires the definition of a fixed-base simple oscillator with the same dynamic properties of the analysed structure assumed as fixed at its base. Given the height, the fixed base periods were calculated according to the indication of the current technical code (NTC2018) for the cases 4, 5 and 6, while for cases 1, 2 and 3 the periods were calculated by de Silva (2020), because the simplified Code formula may lead to unreliable results for very slender structures. The total mass was calculated considering a masonry weight of 1200 kg/m^3, a floor weight of 1000 kg/m^2 (in cases 4, 5 and 6) and a wall thickness varying from 1.5 m to 2.5 m along the height in the case 1, 2 and 3 or with a constant value equal to 1.5 m for cases 4, 5 and 6. The lateral stiffness was calculated from the mass and period. The characteristics

of the simple oscillator equivalent to the analysed ideal cases in terms of mass, height and period, are listed in Table 3.

Table 3. Properties of the analysed buildings. Cases 1, 2 and 3 are founded on the foundation type plotted in Figure 6(b) while cases 4, 5 and 6 on the scheme in Figure 6(c).

		B	h	h/B	ζ	T_0	k	M
Case	Type	m	m	–	%	s	MN/m	Mg
1	squat	10	10	1	3	0.18	324.6	333
2	slender	10	30	3	3	0.50	126.2	999
3	very slender	10	60	6	3	1.69	22.1	1998
4	squat	13.5	6	0.45	3	0.19	1209.7	1126
5	squat	13.5	9	0.67	3	0.26	987.7	1689
6	squat	13.5	12	0.89	3	0.32	855.4	2252

For all the cases, a foundation depth of 1 m was considered except for the very slender tower, where the depth was increased up to 2 m. The low frequency stiffness was calibrated through the real part of the soil-foundation impedances by Gazetas (1991), considering a soil shear wave velocity equal to 150 m/s. The dynamic stiffness coefficient appearing in the real part of the impedance function should be settled according to the period representative of the structural response, i.e. the predominant period of the input motion or the fundamental period of the compliant-base structure. In this paper, the coefficients were assumed to be unitary consistently with the very low values of a_0 associated to the compliant-base periods of the structures analyzed. The latter periods were estimated through the formula proposed by Maravas et al. (2014). In both cases, the stiffness of the group was assumed to be coincident with the sum of the individual contributions and the action of a transport moment with respect to the axis of rotation was considered in the rotational stiffnesses. Such calculation was preferred to the computation of the impedance of the hollow section for the scheme in Figure 6a to apply the outcomes of the numerical FDM study on the two nearby foundations discussed in Section 3. Therefore, the obtained stiffnesses were multiplied for the interaction coefficients of Figure 5 to account for the effect of cross interaction between close foundations. For the different degrees of freedom, the alpha coefficients correspond to the S/B values of the two schemes of Figure 6, assuming that there is no rigid constraint between long and short footings. This circumstance is the most realistic for historical masonry structures for which the connection at the base is affected by aging effects or is even absent (e.g., de Silva et al. 2015).

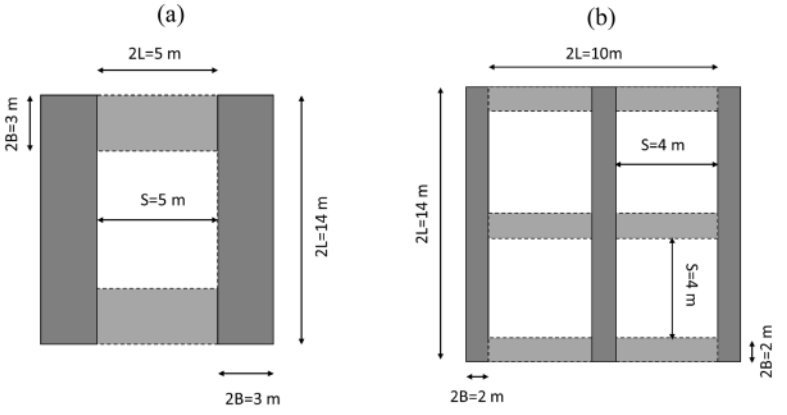

Figure 6. Reference schemes of the considered shallow foundation groups.

4.2 *Fundamental period of the compliant base systems*

Figure 7 shows the compliant base period, T^*, predicted through the formulation of Maravas et al. (2014) in case of cross interaction (with CSSI) against the fixed base value, T_{fix}. As a reference, the periods obtained by neglecting the cross interaction coefficients (without CSSI) have been superimposed. The same data are also reported in Table 4.

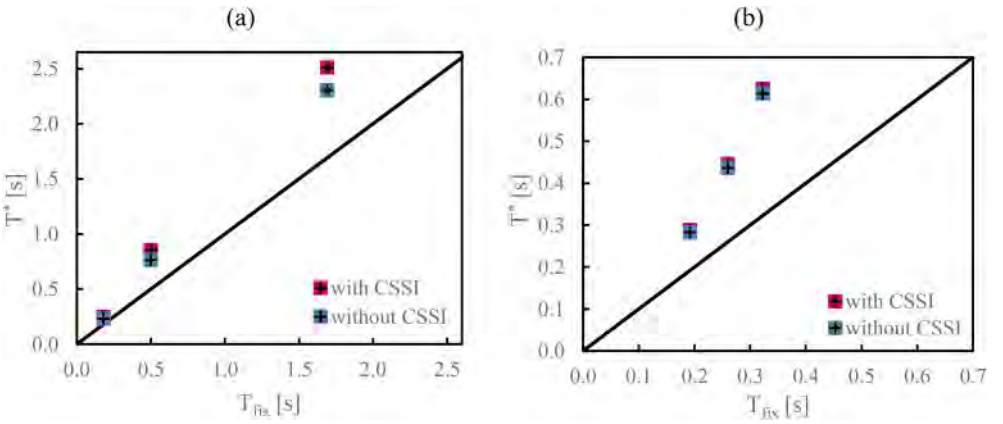

Figure 7. Variation of periods for the towers (a) and for squat structures (b)

The comparison shows that the cross-interaction plays a slight but non-negligible role, especially for very slender structures. Both Figure 7 and Table 4 show that the periods on a flexible base calculated by applying the interaction coefficients (with CSSI) are higher than those computed in the standard way (without CSSI). Although with less incidence, also squat structures with $T_{fix} = 0.32$ may be affected by cross-interaction. It should be pointed out that for the schemes of Figure 6 the ratio S/B between the single footings is approximately 4, so the decrease of stiffnesses due to cross interaction is not higher than 15% (see Figure 5).

Table 4. Effect of CSSI on the periods of the analysed structural patterns

		T^*		% Var. of T_{fix}	
Case	T_{fix}	without CSSI	with CSSI	without CSSI	with CSSI
1	0.18	0.23	0.25	28%	37%
2	0.50	0.76	0.85	53%	71%
3	1.69	2.31	2.51	36%	49%
4	0.19	0.28	0.29	47%	51%
5	0.26	0.44	0.45	68%	71%
6	0.32	0.61	0.62	90%	94%

In the final part of the study, the cross interaction phenomenon in a small group of structures with similar geometry and dynamic features, is presented. As sketched in Figure 8, additional structures on the right and left side of the master (central) building were figured out. In addition, the lateral buildings were assumed to be placed at varying distance (ratio S/B varied between 0.5 and 4) with respect the target central structure. For this latter one, the flexible-base periods, T^*, were recalculated considering the interaction coefficients alpha of Figure 5 to account for the presence of the adjacent structures. The obtained periods T^* with CSSI (among the buildings) are higher and higher than those listed in Table 4 especially at short distance (S/B equal to 0.5 or 1). By taking into account all types of interactions (soil-structure, footing-footing, building-building) the variation of T^* with respect to T_{fix} varies in between 39% and 55% of for towers (case 1 to 3) and between

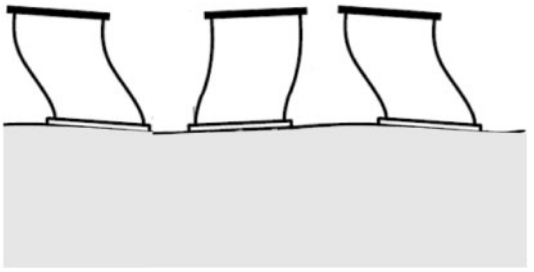

Figure 8. Scheme of a small group of buildings exposed to CSSI.

54% and 109% for squat constructions (case 4 to 6). Further analyses should be carried out to investigate better this aspect of the problem.

Table 5. Variation of the elongated periods T* for the analysed structural patterns in presence of neighbouring structures.

		T* with CSSI S/B				%Var. of T_{fix} S/B			
Case	T_{fix}	0.5	1	2	4	0.5	1	2	4
1	0.18	0.26	0.26	0.25	0.25	43%	43%	40%	39%
2	0.50	0.90	0.90	0.87	0.86	80%	80%	74%	72%
3	1.69	2.63	2.61	2.54	2.53	55%	54%	50%	49%
4	0.19	0.31	0.30	0.30	0.29	60%	59%	55%	54%
5	0.26	0.48	0.47	0.46	0.45	84%	82%	76%	74%
6	0.32	0.67	0.67	0.64	0.63	109%	106%	98%	97%

5 CONCLUSIONS

The paper tried to unravel how cross interaction between multiple foundations could affect the behaviour of a single building or of a small group of buildings. First, the static stiffnesses of the impedance matrix for a simple scheme of crossed-beam shallow foundation were evaluated through both an analytical and a 3D numerical approach. The outcomes of the refined numerical analyses carried out with the software FLAC3D, revealed that there is not a unique and straightforward way to assess analytically the stiffness of a group of footings by means of the classical closed-form equations available in literature for rigid and massless shallow foundations (Gazetas 1983; 1991). Cross-interaction coefficients were derived numerically on simple schemes of two shallow footings at different distance between them, with the final goal to modify the low-frequency stiffness terms of the impedance matrix of the single foundation to account for the presence of its nearby structures and cross interaction (CSSI) through the underlying soil.

The so computed CSSI impedance terms of the master foundation were later applied to predict the compliant-base period of typical structural patterns, representing slender and squat masonry structures, through the formula proposed by Maravas et al. (2014). The results highlighted that the interaction between the foundations themselves produced an increase in the fundamental period. This effect was more appreciable for tall structures. The problem is worth of being investigated more thoroughly. Nevertheless, from these first findings it can be surely stated that neglecting the cross interaction among multiple footings of a unique foundation system or among closely-spaced constructions sometimes may lead to unsafe verification or design. With reference to historic structures, understanding the degree of constraint between the different parts constituting the masonry foundation is not always simple and immediate, so a sensitivity analysis may be useful to evaluate the various types of foundation behaviour for the benefit of safety.

ACKNOWLEDGEMENTS

The work has been developed in the framework of the 2019–2021 ReLUIS-DPC research program funded by the Italian Civil Protection Department, as a contribution to the geotechnical Work Package ‘Soil-Foundation-Structure Interaction’ (Task 16.3).

REFERENCES

Aldaikh H., Alexander N. A., Ibraim E., Knappett J.A., 2018. Evaluation of rocking and coupling rotational linear stiffness coefficients of adjacent foundations. International Journal of Geomechanics, 18(1), 04017131

Aldaikh H., Alexander N.A., Ibraim E., Oddbjornsson O., 2015. Two dimensional numerical and experimental models for the study of structure-soil-structure interaction involving three buildings. Comput Struct; 150:79–91.

Alexander N.A., Ibraim E., Aldaikh H., 2013. A simple discrete model for interaction of adjacent buildings during earthquakes, Comput Struct;124:1–10.

ATC-3, 1984. Applied Technology Council, Tentative Provisions for the Development of Seismic Regulations for Buildings, National Science Foundation and National Bureau of Standards, 1st edition (1978), 2nd edition Washington, DC.

Betti R., 1997. Effects of the dynamic cross-interaction in the seismic analysis of multiple embedded foundations, Earthquake engineering and structural dynamics, Vol. 26, 1005–1019.

Chang-Liang V., 1974. Dynamic Response of Structure in Layered Soils. Ph.D. thesis, MIT.

de Silva F., 2020. Influence of soil-structure interaction on the site-specific seismic demand to masonry towers, Soil Dynamics and Earthquake Engineering 131(4).

de Silva F., Ceroni F., Sica S., Pecce M.R., Silvestri F., 2015. Effects of soil-foundation-structure interaction on the seismic behaviour of monumental towers: the case study of the Carmine Bell tower in Naples. Riv Ital Geotec; 3:3–27.

Gazetas G., 1983. Analysis of machine foundation vibrations: state of the art. International Journal of Soil Dynamics and Earthquake Engineering, 2: 2–42.

Gazetas, G., 1991. Formulas and charts for impedances of surface and embedded foundations. Journal of Geotechnical Engineering, 117(9), pp.1363–138.

Ghandil M., Behnamfar F., Vafaeian M., 2016. Dynamic responses of structure-soil- structure systems with an extension of the equivalent linear soil modeling. Soil Dyn Earthq Eng; 80:149–62.

Itasca Consulting Group, 2004. Inc. FLAC3D User Manual: Version 5.0. USA.

Knappett J. A., Madden P., Caucis K., 2015. Seismic structure-soil-structure interaction between pairs of adjacent building structures. Geotechnique; 65:429–41.1.

Kuhlmeier R.L. and Lysmer. J., 1973. Finite element method accuracy for wave propagation problems. Journal Soil Dynamics Division, 99, 421-427.

Lehmann L, Antes H., 2001. Dynamic structure-soil-structure interaction applying the symmetric Galerkin boundary element method (SGBEM). Mech Res Commun; 28:297–304.

Maravas A., Mylonakis G., Karabalis L.D., 2014. Simplified discrete systems for dynamic analysis of structures on footings and piles. Soil Dyn Earthq Eng, 61–62:29–39.

Padron L.A., Aznarez J., Maeso O., 2009. Dynamic structure–soil–structure interaction between nearby piled buildings under seismic excitation by BEM–FEM model. Soil Dyn Earthq Eng; 29:1084–96.

Qian J. and Beskos D.E., 1995. Dynamic interaction between 3-D rigid surface foundations and comparison with the ATC-3 provisions. Earthquake Engng. Struct. Dyn., 24: 419–437.

Roesset J. M. and Gonzalez J. J., 1977. Dynamic interaction between adjacent structures. Dyn. Meth. Soil Rock Mech., 1,127.

Wang S., Schmid G., 1992. Dynamic structure-soil-structure interaction by FEM and BEM. Comput. Mech; 9:347–57.

Warburton G. B., Richardson J. D., Webster J. J., 1971. Forced Vibrations of Two Masses on an Elastic Half Space. ASME. J. Appl. Mech. March 38(1): 148–156, (March 1).

Zeolla E., De Silva F., Sica S., 2021. Dynamic cross-interaction between two closely-spaced shallow foundations. Compdyn 2021, 8th ECCOMAS thematic conference on computational methods in structural dynamics and earthquake engineering, Athens.

Geotechnical Engineering for the Preservation of Monuments and Historic Sites III – Lancellotta, Viggiani, Flora, de Silva & Mele (Eds)

A geotechnical study for the historical heritage preservation of the City of Noto (Italy)

A. Cavallaro
CNR – ISPC, Catania, Italy

ABSTRACT: Eastern Sicily is extremely rich with artistic and monumental heritage, but at the same time it is the most seismically active area of Italy. In particular, the city of Noto, now considered the capital of baroque in Sicily, was destroyed by the 1693 Earthquake and rebuilt in another site, as many other cities. The seismic microzonation is now being studied for this area. The following in situ investigations were carried out in order to determine the soil profile and the geotechnical characteristics of the site under consideration, with special attention for the variation of shear modulus and damping with depth: Geological boring, Down Hole (DH) tests, Dilatometer tests (DMT), Cone penetration tests (CPT) and Standard penetration tests (SPT). Moreover, the following laboratory investigations were carried out on undisturbed samples: Resonant column tests (RCT), Cyclic loading torsional shear tests (CLTST), Cyclic loading triaxial tests (CLTxT), Oedometer tests and Direct shear tests. This work aims to be the starting point for a correct approach to the problems concerning the safeguarding of the artistic and monumental heritage.

1 INTRODUCTION

The old city of Noto, few kilometres in the upper part of the city of Noto, was destroyed by the 11th January 1693 earthquake and both the build-up areas had heavy damages in occasion of the 7th January 1727 earthquake. The 13th December 1990 earthquake damaged several 18th century constructions and drew attention to the need for safeguarding its artistic monumental heritage, maximum expression of Sicilian baroque (Cavallaro et al. 2003a).

In order to study the dynamic characteristics of soils in Noto municipal area, laboratory and in situ investigations have been carried out to obtain soil profiles with special attention to the variation of the Young Modulus (E) shear modulus (G) and damping ratio (D) with depth. This paper tries to summarise this information in a comprehensive way in order to provide a representative geotechnical model of ground condition of the different zones where important monuments are located. This enabled the evaluation of site effects to define the earthquake design actions and then the rational restoration and strengthening of some monuments, before their collapse, with the exception of Noto Cathedral, which was restored after its partial collapse, caused by the 1990 Sicilian earthquake.

2 HISTORICAL BACKGROUND AND SEISMICITY OF AREA

The area around Noto was populated by a Bronze Age people between 2000–1500 BC. The famous archaeologist Paolo Orsi, who explored and studied the site, gave the name "Casteluccio Culture" to the site and its inhabitants. The major part of the finds are now on display at Syracuse Archaeological Museum. There are a few ruins of a prehistoric village and a primitive necropolis. The history of

DOI 10.1201/9781003308867-69

Noto prior to the 1693 quake belongs to the old town, now called “Noto Antica” and known in antiquity as “Netum.” What remains of the old town is located some 13 kilometers away from the present town of Noto. The legend tells that Noto Antica was founded by a King of the Siculi named Ducetius in about 500 BC. Scholars dated the earliest ruins to about 800 BC. With the Greek colonization of Syracuse, Netum came into contact with the advanced Hellenistic Culture and was eventually absorbed by it. Noto Antica achieved a certain level of importance during the Arab period when it became the administrative center of Noto Valley, one of the three provinces that the Arab governors had subdivided Sicily into. The town was one of the last bulwarks of Saracen resistance to the Norman takeover, not surrendering to Count Roger de Hauteville until 1091.

Southeastern Sicily experiences relatively unfrequent but strong earthquakes: in three cases during this millennium and as concerns the previous times, in an unknown but obviously conspicuous number of ~~the~~ other cases. In the past centuries, Sicily was struck by strong earthquakes whose characteristics derive from the geodynamic feature of the Western Mediterranean Sea.

Figure 1. The Saint Nicola Cathedral and a detail of the interior.

As concerns the earthquakes in the current millennium, we have many coeval sources testifying their effects but unfortunately paying little attention to the environmental consequences. Much of this reference material, physically dispersed through a myriad of public and private institutions, has been recently made available (Boschi et al. 1995, 1997).

A detailed list of the earthquakes which struck this area has been given by C.N.R. (1985a). A study of the most intense earthquakes which damaged the city of Noto has been made by C.N.R. (1985b). A brief description of the most significant earthquakes can be summarized as following reported.

Catania earthquake on February 4th 1169 is one of the oldest shocks of great magnitude with available detailed studies. The earthquake took place in the Southern part of Sicily where seismicity is characterized by very strong energy releases usually occurring after long quiet periods. The shock caused heavy damages (Pertz 1866; Siragusa 1897). The epicentral area was located near the city of Catania where the intensity seems to have reached the XI degree in the MCS scale (Agnello 1997; Lombardo 1985; Postpischl 1985;. In Noto area, the earthquake intensity reached the X degree. It caused many victims and destroyed many buildings.

On December 10th 1542 another earthquake struck the city of Noto, however it seemed to be one of the weakest that have historically occurred in Noto area (Ha-Kohen, XVI century). The epicenter was located near the city of Sortino, which is about 30 km far from Noto. In the epicentral area, the intensity was about IX degree while in Noto it reached the VII degree (Barbano 1985a).

The “Val di Noto” earthquake of 11th January 1693 is considered one of the most powerful earthquakes in Italy. It is thought that more than 1500 aftershocks occurred for about two years more (Barbano 1985b). This earthquake was the most destructive of all time reaching the intensity of 11° degree of MCS scale. It struck a vast territory of southeastern Sicily and caused the partial,

and in many cases the total, destruction of 57 cities in the area: Catania with 19000 inhabitants, Modica (18000), Siracusa (15000), Acireale (13000), Caltagirone (12000), Noto (12000), Vizzini (11000), Lentini (10000), and Ragusa (10000). There were around 60000 victims (Agnello 1931; Anonimo 1693; Boccone 1697; Bottone 1718). Its epicenter was located near the city of Lentini, which is 45 km far from Noto; the effects were quiet strong even in the South of Italy and on the African coasts.

On 13th December 1990, another earthquake struck Noto (De Rubeis et al. 1991; Rovelli et al. 1991). Anyway, the intensity was not too strong and reached, in the epicentral area, the VII degree. The magnitude was about M = 5.4. Due to the low intensity, this time the damage interested only several old buildings and ancient monuments and was mostly limited to cornice falls and masonry fractures.

Figure 2. "Tina Di Lorenzo" Theatre and a detail of the interior.

After the 11th January 1693 earthquake Noto was re-built in a new site. The greater towns destroyed by the 1693 earthquake, with the only exception of Modica and Ragusa, were "demaniali" cities, like Noto, subjected directly to the royal power. Many inhabited areas were feuds of the powerful aristocratic Sicilians families instead.

In 1693, Sicily was part of the Spanish kingdom and it was administered by a "vicerè" (pro-rex) who at the moment of the disaster was the Duke De Uzeda. He named Giuseppe Lanza, Duke of Camastra, as his General Vicar, military of career and expert of architecture.

The Vicar with his competence and with the collaboration of the artillery colonel and military architect Carlos de Grunemberg provided for the first helps and mailed the plans of reconstruction of the "demaniali" cities. In Noto, the reconstruction began under the Spanish domination and achieved most substantial results under the Bourbon kingdom who ruled Sicily from 1735 until Garibaldi enterprise.

The reconstruction hocked intellectual and economic resources for 50 years and thanks to the successful combination of cultured owners and high technical ability (to be remembered the exceptional "lapidum incisores") it constitutes one of the greatest examples of urban planning of every era. In numerous cases the reconstruction was made in a different site because, as military demands had changed, fortification of the inhabited area was no longer necessary. The urbanistic "culture" of the managing class of that time was theoretical and the most known models were those of the cities with geometric design (Carlentini 1551; La Valletta 1566, Plamonova 1593).

In Noto, thanks to the meeting among "fra" Angelo Italia, a Jesuit architect, local experts and Spanish engineers, an extraordinary plan was realized by merging the rigor of the geometric grate with the articulation of the three principal squares (the S. Francesco square, the Cattedrale square and XXIV Maggio square). The light transversal slope determines varying glimpses that make mutable the urban landscale (one of the characteristics of the figurative baroque art in urbanistic field). The result is made precious by the quality and the greatness of the buildings in many cases

designed by famous architects like Gagliardi, Labisi and Sinatra. Not of secondary importance was the contribution of the Noto's calcarenite unique for its color.

Noto became a model of the baroque city (Figures 1, 2), more than other centers like Catania, Caltagirone and Acireale, rich of artistic heritage and baroque architecture. Noto has been identified for a style that is one the greatest demonstrations of the artistic creativeness of all times.

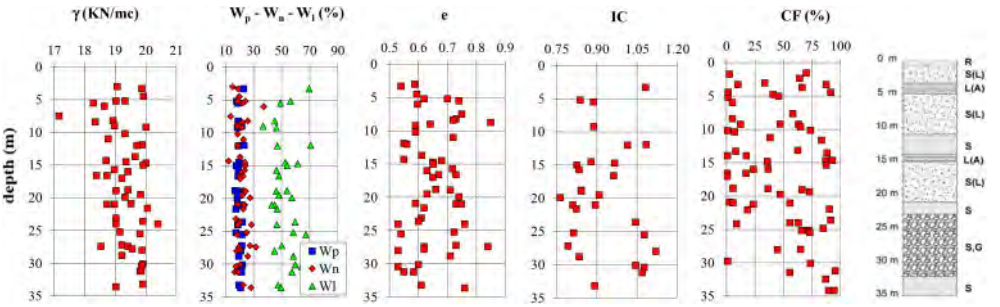

Figure 3. Index properties of Noto soil; where R: Landfill; S(L): Silty Sand; L(A): Clayey silt; S: Sand; S,G: Sand and Gravel.

3 STATIC AND DYNAMIC CHARACTERISTICS OF THE SOIL

The Pliocene Noto deposits mainly consist of a medium stiff, over-consolidated lightly cemented silty-clayey-sand (Castelli et al. 2016a). The pre-consolidation pressure σ'_p and the over-consolidation ratio OCR $= \sigma'_p/\sigma'_{vo}$ were evaluated from the 24 h compression curves of incremental loading (IL) Oedometer tests. Moreover, 9 flat dilatometer tests (DMT) were performed to assess OCR and the coefficient of earth pressure at rest K_o following the procedure suggested by Marchetti (1980), Cavallaro et al. (2012a, 2012b; and Castelli et al. (2016a, 2016b). The values of basic soil properties are showed in Figure 3. Resonant Column (RCT) and Cyclic Loading Torsional Shear (CLTST) tests have been performed by using the same apparatus (Cavallaro & Maugeri 2005; Capilleri et al. 2014; 2016a, 2018) to evaluate the shear modulus G and damping ratio D of the municipal area of Noto soil. The laboratory test conditions are listed in Table 1.

Table 1. Test condition for Noto soil specimens.

Test	Sample	H [m]	σ'_{vc} [kPa]	σ'_{hc} [kPa]	γ [kN/m^3]	e	PI	G_o (1) [MPa]	G_o (2) [MPa]	E_o [MPa]	Specimen
1	S16CI1	4.50	144	144	19.32	1.236	–	86	122	–	S
2	S15CI1	7.60	145	145	17.16	0.777	–	153	185	–	S
6	S15CI2	10.00	225	195	19.47	0.817	41	–	–	195	S
3	S15CI2	10.00	190	163	19.69	0.740	41	40	49		H
4	S16CI2	17.50	336	336	19.22	0.747	–	337	465	–	S
5	S16CI2	17.50	380	380	19.22	1.238	–	207	244	–	S

where: U = Undrained. G_o (1) from CLTST, G_o (2) from RCT. S = Solid cylindrical specimen. H = Hollow cylindrical specimen.

The samples have the following geological characteristics: S16CI1 – Brown stiff clayey silt, with traces of minute calcareous elements; S15CI1 and S15CI2 – Brown to white-grey silty sand; S16CI2 – Brown silty sand with traces of minute rounded calcareous elements.

The undisturbed specimens were isotropically reconsolidated to the best estimate of the in situ mean effective stress.

The same specimens were first subjected to CLTST (Cyclic Loading Torsional Shear Test), then to RCT (Resonant Column Test) after a rest period of 24 hrs with opened drainage. CLTST were performed under stress control condition by applying a torque variable over time with triangular time history at a frequency of 0.1 Hz. The size of solid cylindrical specimens are Radius = 25 mm and Height = 100 mm while the size of hollow cylindrical specimens are External Radius = 25 mm, Internal Radius = 25 mm and Height = 100 mm.

One specimen was tested in the triaxial apparatus equipped with local strain gauges (Cavallaro & Maugeri 2004; Castelli et al. 2019; Lo Presti et al. 1999). The size of solid cylindrical specimens are Radius = 35 mm and Height = 140 mm.

The specimen underwent dry setting: Dry filter papers and dry porous stones were used during specimen setting. The bottom drainage line was filled with water up to 1 cm below the porous stone. The top drainage line was left empty. After the specimen had been set up and the pressure cell had been sealed, the system saturation was achieved in two steps. Flushing deaired water with a head of 50 cm was applied to the specimen, from the bottom to top, for at least 24 h. During this stage, the loading ram was blocked so that the vertical stress automatically increased to counteract the tendency of the specimen to swell. The horizontal stress was controlled by means of a PC in order to prevent any radial displacement with a tolerance of $\pm 0.5\,\mu$m. The radial displacement was monitored by means of a pair of proximity transducers. Back pressurization was carried out in order to dissolve any air bubbles that might still be trapped in the lines and in the space between the specimen and the membrane. This stage was terminated when the B parameter was equal to or larger than 0.95. Back-pressurization was carried out increasing the total isotropic stress by steps of 50 kPa in undrained conditions. The corresponding pore pressure increase was recorded in order to check Skempton's B parameter. Thereafter, the back pressure was increased by 50 kPa and the drainage was opened. The next step was applied after at least 2 h in order to achieve an acceptable pressure equalization. As far as the wet setting procedure is concerned, the specimen only underwent back-pressurization in order to achieve an acceptable degree of saturation. The effective isotropic stress applied to the specimen during this process ranged from 15 to 30 kPa.

After the dry setting, this specimen was reconsolidated to the in situ geostatic stresses (PC-controlled K_o condition). In particular, the axial stress was increased up to a target value ($\sigma'_{vc} = \sigma'_{vo}$) by moving up the loading ram with a strain rate of about 0.01 %/ min. In the meantime- the radial stress was increased in order to keep the lateral displacement equal to zero within a tolerance of a 0.5 pm. The above described process was controlled by means of a PC. After the achievement of the target axial stress, the test was paused to dissipate any possible excess of pore pressure and a certain amount of creep deformation. The test was paused until the creep rate became smaller than 0.05 [%/day] following the suggestions given by Jardine et al. (1991). This condition was obtained alter about 24 h. During this period, the vertical stress was kept constant while the horizontal stress was automatically adjusted in order to have a zero radial strain. Consolidation test were performed with a strain rate of 0.001 %/min.

After the consolidation stage, the specimen was subjected to Cyclic Loading Triaxial test (CLTxT), at constant strain rate. Six different strain levels of progressive amplitude were imposed to the specimen (Step 1: $\varepsilon_{sa} = 0.00087$ %; Step 2: $\varepsilon_{sa} = 0.00526$ %; Step 3: $\varepsilon_{sa} = 0.01397$ %; Step 4: $\varepsilon_{sa} = 0.03672$ %; Step 5: $\varepsilon_{sa} = 0.07871$ %; Step 6: $\varepsilon_{sa} = 0.26596$ %). For each strain level, 30 cycles were applied. The maximum applied axial strain (single amplitude) was about 0.3 %. The same specimen was subjected, after a rest period of 24 hrs with open drainage, to Monotonic Loading Triaxial test (MLTxT). The obtained small strain Young modulus E_o is reported in Table 1. The small strain Young's modulus E_o was determined from the initial slope of the stress-strain curve at strains of less than 0.001%.

Normalized shear modulus G/G_o and damping (D) obtained from RCT and CLTST are shown in Figure 4. The same shear modulus decay is obtained from both type of tests but the damping ratio values provided by CLTST are smaller than those measured in RCT. For RCTs the damping ratio was determined using two different procedures: following the steady-state method, the damping ratio was obtained during the resonance condition of the sample; following the amplitude decay method it was obtained during the decrement of free vibration. The damping ratio values obtained

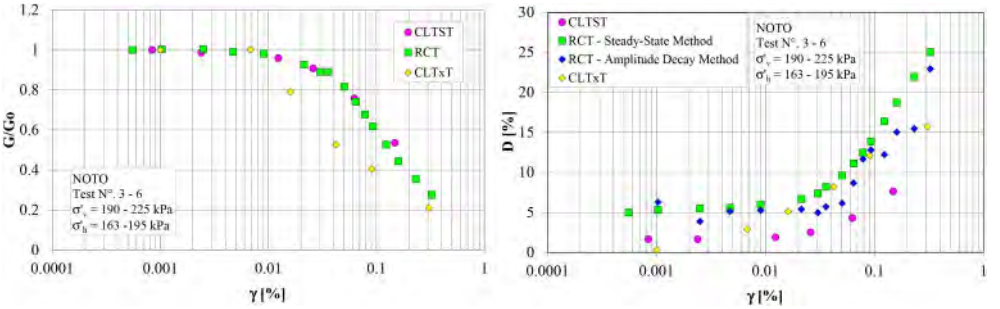

Figure 4. $G/G_o - \gamma$ and damping ratio curves from CLTST, RCT and CLTxT.

from RCT using two different procedures are similar even if higher values of D have been obtained from steady-state method. It is possible to see that the damping ratio from CLTST, at very small strains, is equal to about 1 %. Greater values of D are obtained from RCT for the completely investigated strain interval.

In Figure 4 we compare the results from CLTxT. It is possible to notice that CLTxT results show a greater non-linearity while the damping ratio values from CLTxT and those from CLTST are comparable for stress level less than 0.01 %. It should be remembered that CLTxT have been performed at constant strain rate equal to 0.01 %/min. Yet the different deformation mechanism (different stress-path) could be responsible for the observed differences.

In Figure 5 is shown the effect of N on stiffness and damping ratio (D), which represents a typical test results. Figure 5 shows, for different strain levels, the decrease of E and the increase of D with N.

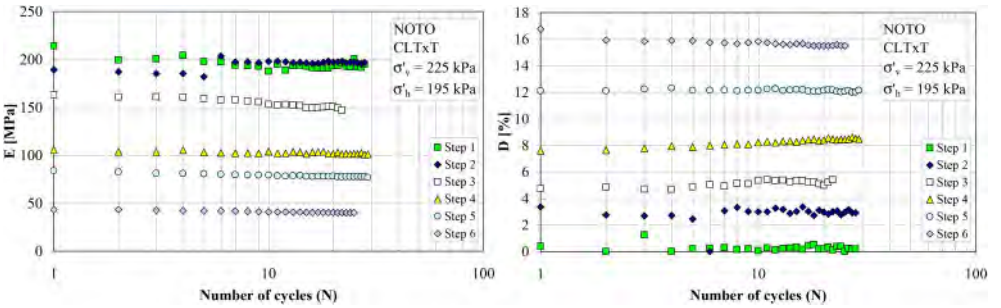

Figure 5. Dependence of unloading-reloading stiffness and damping on number of cycles (N).

The effect is quite negligible for strain amplitude of less than 0.1 % and become relevant beyond such a limit (Cavallaro et al. 1999a, 1999b).

This trend is the effect of soil degradation and only for step 1 ($\varepsilon_{sa} = 0.00087$ %) it is possible to observe a decrease of D. The Authors were inclined to believe that such behaviour could be a consequence of very low strain rates. Therefore a consequence of creep deformations. Moreover, even at more usual frequency (0.1 Hz) Cavallaro et al. (2003b) observed a similar behaviour in the case of lightly overconsolidated clay.

The small strain shear modulus G_o can be evaluated in situ by Down Hole tests using the relationships: $G_o = \rho V_s^2$ (where: $\rho =$ mass density) based on theory of elasticity. Marchetti (1997) proposes a dynamic evolution of the dilatometer (SDMT) which unfortunately was not used at the Noto site (Cavallaro et al. 2012a, 2012b; Castelli et al. 2016c; Cavallaro & Grasso 2021)

An attempt was made to evaluate the small strain shear modulus by means of the following empirical correlations based on penetration tests results, CPT, SPT and DMT (Marchetti 1980) or laboratory results available in literature (Figures 6 and 7).

– Imai and Tomaichi (1990):

$$G_o = 28 \cdot (q_c)^{0.611} \tag{1}$$

for any soil.

– Mayne and Rix (1993):

$$G_o = \frac{406 \cdot q_c^{0.696}}{e^{1.13}} \tag{2}$$

for clayey strata;
where: G_o and q_c are both expressed in [kPa] and e is the void ratio. Equation (2) is applicable to clay deposits only.

– Simonini and Cola (2000):

$$G_o = 49.2 \cdot (q_t)^{0.51} \tag{3}$$

It is also possible to evaluate the small strain shear modulus using the relation $G_o = \rho \cdot V_s$ by the following equations proposed by Ohta and Goto (1978) and Yoshida and Motonori (1988) for the shear waves velocity V_s:

– Ohta and Goto (1978):

$$V_s = 69 \cdot N_{60}^{0.17} \cdot Z^{0.2} \cdot F_A \cdot F_G \tag{4}$$

where: V_s = shear wave velocity (m/s), N_{60} = number of blow/feet from SPT with an Energy Ratio of 60 %, Z = depth (m), F_G = geological factor (clays = 1.000, sands = 1.086), F_A = age factor (Holocene = 1.000, Pleistocene = 1.303)

– Yoshida and Motonori (1988):

$$V_s = \beta \cdot (N_{SPT})^{0.25} \cdot \sigma_{vo}'^{0.14} \tag{5}$$

where: V_s = shear wave velocity (m/s), NSPT = number of blows from SPT, σ'_{vo} = vertical pressure, β = geological factor (any soil = 55, fine sand = 49).

– Hryciw (1990):

$$G_o = \frac{530}{\left(\sigma'_v/p_a\right)^{0.25}} \frac{\gamma_D/\gamma_w - 1}{2.7 - \gamma_D/\gamma_w} K_o^{0.25} \cdot \left(\sigma'_v \cdot p_a\right)^{0.5} \tag{6}$$

where: G_o, σ'_v and p_a are expressed in the same unit; $p_a = 1$ bar is a reference pressure; γ_D and K_o are respectively the unit weight and the coefficient of earth pressure at rest, as inferred from DMT results according to Marchetti (1980).

– Jamiolkowski et al. (1995):

$$G_o = \frac{600 \cdot \sigma_m'^{0.5} p_a^{0.5}}{e^{1.3}} \tag{7}$$

The Jamiolkowski et al. (1995) method was applied considering a given profile of void ratio.

The values for parameters, which appear in equation (7), are equal to the average values resulting from laboratory tests performed on quaternary Italian clays and reconstituted sands.

Equation (7) incorporates a term, which expresses the void ratio; the coefficient of earth pressure at rest only appear in equation (6). However only equation (6) tries to obtain all the input data from the DMT results.

As regard Noto soil, the G_o values obtained with the methods above indicated for CPT and SPT are plotted against depth in Figure 6.

The results obtained show a greater similarity between the G_o results obtained by the empirical correlations proposed for SPT, which, moreover, are quite close together. More dispersed and higher are the G_o values obtained through the correlation equations proposed for CPT.

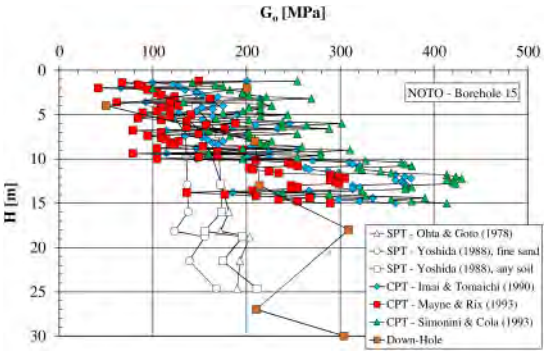

Figure 6. Small strain shear modulus G_o by empirical correlations based on CPT and SPT.

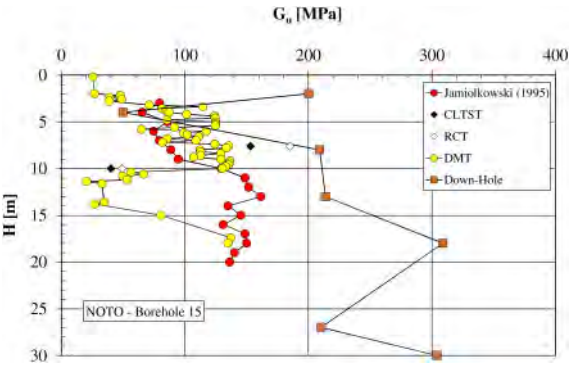

Figure 7. G_o from Down Hole, empirical correlation and RCT.

The lowest values of the shear modulus are obtained by the equation proposed by Mayne and Rix (1993). Only by the Down Hole test it is possible to identify the rapid of G_o at a depth of about 16 m in correspondence with some layer characterized by higher mechanical characteristics that SPT cannot identify.

The N_{60} values, experimentally determined during SPT, did an unimportant variation in the transition zone at depth of about 16 m, where the characteristics of the soil change from clayey silt to silty sand and then to sand with gravel.

Standard Penetration Tests were performed at intervals from 1.5 to 3.0 m. The quite large interval used could explain why the thin sand layers were not detected. Consequently, the obtained G_o values, in the transition zone, resulted to be quite low.

Unfortunately, the depth investigated by DMT is not able to intercept the most consistent layers of sand and sand with gravel. Even if, the method by Hryciw (1990) is distant from the trend of the results obtained from the Down Hole tests as can be seen in Figure 7

From a comparison between Figure 6 and Figure 7 all the considered methods show very different G_o values of the Pliocene Noto soil. On the whole, Down Hole seems to provide the most accurate trend of G_o with depth even if the available data are unable to investigate the behavior of the soil for depths greater than 30 m. The method by Jamiolkowski et al. (1995) was applied considering a given profile of void ratio but while guaranteeing continuity of results, it fails to intercept the most consistent layers of sand and sand with gravel.

In Figure 7 the RCT results are also reported. The data obtained also show as the dynamic laboratory tests are able to interpret the G_o trend obtained from the Down Hole test only at the depth of 7.5 m.

4 CONCLUDING REMARKS

A site characterization for a correct approach to the problems concerning the safeguarding of the artistic and monumental heritage has been presented in this paper. On the basis of the data shown it is possible to draw the following conclusions:

- when $\gamma \geq \gamma_t^v$, degradation phenomena occur; the normalized shear modulus obtained from CLTxT results show a greater non-linearity
- damping ratio values determined from RCT are greater than those obtained from CLTST while the damping ratio values from CLTxT and those from CLTST are comparable for stress level less than 0.01 %;
- the observed differences between RCT, CLTST and CLTxT results are probably due to rate and/or frequency effects and different deformation mechanism (different stress-path).
- empirical correlations between the small strain shear modulus and penetration test results were used to infer G_o from SPT, CPT, DMT and Down Hole. This comparison clearly indicates that a certain relationship exists between G_o and the penetration test results, which would encourage to establish empirical correlations for a specific site. This approach makes it possible to consider the spatial variability of soil properties in a very cost effective way.
- the values of G_o were compared to those measured with DMT and DH tests. This comparison indicates that some agreement exists between empirical correlations by DMT and DH test.
- relationships like those proposed by Jamiolkowski et al. (1995) seem to be capable of predicting G_o profile with depth only in the initial strata. The accuracy of these relationships could obviously be improved if the parameters, which appear in the equations, were experimentally determined in the laboratory for a specific site.
- probably only Down Hole test is able to correctly investigate the various layers of soil, identifying even the smallest variations in the mechanical characteristics.

REFERENCES

Agnello, G. 1931. Memorie Inedite Varie sul Terremoto Siciliano del 1693. *Archivio Storico per la Sicilia Orientale*, s. II, a. 7, pp. 390–402.

Agnello, G. M. 1997. Considerazioni sul Sisma del 1169. La Sicilia dei Terremoti. *Giuseppe Maimone Editore*, Catania, pp. 101–127.

Anonimo. 1693. Sincera, ed Esatta Relazione dell'Oribile Terremoto Seguito nell'Isola di Sicilia il dì 11 di Gennaio 1693. Colla Nota delle Città, e Terre Sprofondate, de' Morti, e Luoghi, che hanno Patito, e con tutte le Particolarità più Degne da Essere Registrate. *Roma*.

Barbano, M. S. 1985a. The Val di Noto Earthquake of December 10, 1542. Atlas of Isoseismal Maps of Italian Earthquake. Consiglio Nazionale delle Ricerche. Progetto Finalizzato Geodinamica. *Quaderni de "La Ricerca Scientifica"*, 114, Ed. D. Postpischl, v. 2°, pp. 28–29.

Barbano, M. S. 1985b. The Val di Noto earthquake of January 11, 1693. Atlas of Isoseismal Maps of Italian Earthquake. Consiglio Nazionale delle Ricerche. Progetto Finalizzato Geodinamica. *Quaderni de "La Ricerca Scientifica"*, 114, Ed. D. Postpischl, v. 2°, pp. 48–49.

Boccone, P. 1697. Intorno il Terremoto della Sicilia, Seguito l'anno 1693. Museo di Fisica e di Esperienze Variato, e Decorato di Osservazioni Naturali, Note Medicinali, e Ragionamenti Secondo i Principi de' Moderni, *Tip. G. B. Zuccato*, Venezia, pp. 1–31.

Boschi, E., Ferrari, G., Gasperini, P., Guidoboni, E., Smeriglio, G. & Valensise, G. 1995. Catalogo dei Forti Terremoti in Italia dal 461 A. C. al 1980. *Istituto Nazionale di Geofisica*, Storia Geofisica Ambientale, Bologna.

Boschi, E., Guidoboni, E., Ferrari, G., Valensise, G. & Gasperini, P. 1997. Catalogo dei Forti Terremoti in Italia dal 461 A. C. al 1990. *Istituto Nazionale di Geofisica*, Storia Geofisica Ambientale, Bologna.

Bottone, D. 1718. De Immani Trinacriae Terraemotu. Idea Historico-Physica, in *Qua non Solum Telluris Concussiones Transactae Recensetur, sed Novissimae*. Anni 1717. Messina.

Capilleri, P., Cavallaro, A. & Maugeri, M. 2014. Static and Dynamic Characterization of Soils at Roio Piano (AQ). *Italian Geotechnical Journal*, vol. XLVIII, no. 2, April– June 2014, Patron Editor, 38–52.

Castelli, F., Cavallaro, A., Grasso, S. & Ferraro, A. 2016a. In Situ and Laboratory Tests for Site Response Analysis in the Ancient City of Noto (Italy). *Proc. of the 1st IMEKO TC4 Int. Workshop on Metrology for Geotechnics*, Benevento, 17–18 March 2016, 85–90.

Castelli, F., Cavallaro, A. & Grasso, S. 2016b. SDMT Soil Testing for the Local Site Response Analysis. *Proc. of the 1st IMEKO TC4 Int. Workshop on Metrology for Geotechnics*, Benevento, 17–18 March 2016, 143–148.

Castelli, F., Cavallaro, A., Ferraro, A., Grasso, S. & Lentini, V. 2016c. A Seismic Geotechnical Hazard Study in the Ancient City of Noto (Italy). *Proceedings of the 6th Italian Conference of Researchers in Geotechnical Engineering (CNRIG),* Bologna, 22–23 September 2016, *Procedia Engineering* (2016), Vol. 158, pp. 535–540.

Castelli, F., Cavallaro, A., Ferraro, A., Grasso, S., Lentini, V. & Massimino, M. R. 2018. Static and Dynamic Properties of Soils in Catania City (Italy). *Annals of Geophysics*, Vol. 61, N° . 2, 2018, SE221.

Castelli, F., Cavallaro, A., Grasso, S. and Lentini, V. 2019. Undrained Cyclic Laboratory Behaviour of Sandy Soils. *Geosciences, Special Issue: "New Perspectives in the Definition/Evaluation of Seismic Hazard through Analysis of the Environmental Effects Induced by Earthquakes"*, Geosciences 2019, 9, 512, pp. 1–27.

Cavallaro, A., Lo Presti, D. C. F., Maugeri, M. & Pallara, O. 1999a. A Case Study (The Saint Nicolò Cathedral) for Dynamic Characterization of Soil from in Situ and Laboratory Tests. *Proceeding of the 2nd International Symposium on Earthquake Resistant Engineering Structures*, Catania, 15–17 June 1999, pp. 769–778.

Cavallaro, A., Maugeri, M., Lo Presti, D. C. F. & Pallara, O. 1999b. Characterising Shear Modulus and Damping from in Situ and Laboratory Tests for the Seismic Area of Catania. *Proceeding of the 2nd International Symposium on Pre-failure Deformation Characteristics of Geomaterials*, Torino, 28–30 September 1999, pp. 51–58.

Cavallaro, A., Massimino, M. R. & Maugeri, M. 2003a. Noto Cathedral: Soil and Foundation Investigation. *Construction and Building Materials*, N°. 17, 2003, pp. 533–541.

Cavallaro, A., Maugeri, M. & Ragusa, A. 2003b. Small Strain Stiffness from in Situ and Laboratory Tests for the City of Noto Soil. *Proceedings of the 3rd International Symposium on Deformation Characteristics of Geomaterials*, Lyon, 22–24 September 2003, pp. 267–274.

Cavallaro, A. & Maugeri, M. 2004. Modelling of Cyclic Behaviour of a Cohesive Soil by Shear Torsional and Triaxial Tests. *Proceedings of the International Conference on Cyclic Behaviour of Soils and Liquefaction Phenomena*, Bochum, 31 March–02 April 2004, pp. 109–114.

Cavallaro, A. & Maugeri, M. 2005. Non Linear Behaviour of Sandy Soil for the City of Catania. *Seismic Prevention of Damage: A Case Study in a Mediterranean City*, Wit Press Publishers, Editor by Maugeri M., pp. 115–132.

Cavallaro, A., Grasso, S., Maugeri, M. & Motta, E. 2012a. An Innovative Low-Cost SDMT Marine Investigation for the Evaluation of the Liquefaction Potential in the Genova Harbour (Italy). *Proc. of the 4th Int. Conf. on Geotechnical and Geophysical Site Characterization, ISC'4*, Porto de Galinhas, 18–21 September 2012, , vol. 1, 2013, 415–422.

Cavallaro, A., Grasso, S., Maugeri, M. & Motta, E. 2012b. Site Characterisation by in Situ and Laboratory Tests of the Sea Bed in the Genova Harbour (Italy). *Proc. of the 4th Int. Conf. on Geotechnical and Geophysical Site Characterization, ISC'4*, Porto de Galinhas, 18–21 September 2012, vol. 1, 637–644.

Cavallaro, A. & Grasso, S. 2021. Small Shear Strain Modulus Degradation by the Seismic Dilatometer Marchetti Tests (SDMTs). *Proceedings of the 6th International Conference on Geotechnical and Geophysical Site Characterisation*, Budapest, 26–29 September 2021.

Consiglio Nazionale delle Ricerche. 1985a. Catalogo dei Terremoti Italiani dall'anno 1000 al 1980. *Progetto Finalizzato Geodinamica*. Postpischl ED.

Consiglio Nazionale delle Ricerche. 1985b. Atlas of Isoseismal Maps of Italian Earthquakes. *Progetto Finalizzato Geodinamica*. Postpischl ED.

De Rubeis, V., Gasparini, C., Maramai, A. & Anzidei, M. 1991. Il Terremoto Siciliano del 13 Dicembre 1990. *Istituto Nazionale di Geofisica*. Roma.

Ha-Kohen, Y. XVI Century. Lettera di Yosef Ha-Kohen a Yishaq Ha-Kohen. Manoscritto, *Raccolta Epistolare KM 55*, Biblioteca "The Jewish National and University Library".

Hryciw, R.D. 1990. Small Strain Shear Modulus of Soil by Dilatometer. *JGED, ASCE*, vol. 116, no. 11, 1700–1715.

Jamiolkowski, M., Lo Presti, D. C. F. & Pallara, O. 1995. Role of In-Situ Testing in Geotechnical Earthquake Engineering. *Proc. of the 3rd Int. Conf. on Recent Advances in Geotechnical Earthquake Engineering and Soil Dynamics, St. Louis*, Missouri, 2–7 April 1995, vol. II, 1523–1546.

Jardine, R. J., St. John, H. D., Hight, D. W. & Potts, D. M. 1991. Some Practical Applications of a Non-Linear Ground Model. *Proceedings of l0th European Regional Conference on SMFE*, Firenze, Vol. I, pp. 223–228.

Lombardo, G. 1985. The Catania earthquake of February 4, 1169. Atlas of Isoseismal Maps of Italian Earthquake. *Consiglio Nazionale delle Ricerche. Progetto Finalizzato Geodinamica*. Quaderni de "La Ricerca Scientifica", 114, Ed. D. Postpischl, v. 2° , pp. 12–13.

Lo Presti, D. C. F., Jamiolkowski ,M., Cavallaro, A. & Pallara O. 1999. Influence of Reconsolidation Techniques and Strain Rate on the Stiffness of Undisturbed Clays from Triaxial Tests. *Geotechnical Testing Journal*, Vol. 22, N°. 3, September 1999, pp. 211–225.

Marchetti, S. 1980. In Situ Tests by Flat Dilatometer. *Journal of Geotechnical Engineering*, ASCE, 1980, no. GT3.

Marchetti, S. 1997. The Flat Dilatometer Design Applications. *Proc. of the 3rd Geotechnical Engineering Conference*, Cairo University, 5–8 January 1997.

Mayne, P. W. & Rix, G. J. 1993. G_{max}–q_c Relationships for Clays. *Geotechnical Testing Journal*, vol. 16, no. 1, 54–60.

Ohta, Y. & Goto, N., 1978. Empirical Shear Wave Velocity Equations in Terms of Characteristic Soil Indexes. *Earthquake Engineering and Structural Dynamics*, vol. 6, 1978.

Pertz, K. 1866. Monumenta Germaniae Historica. *SS. Tomo 19*, Hannover, pp. 236–266.

Postpischl, D. 1985. Atlas of Isosismal Maps of Italian Earthquakes. *CNR (Italian National Research Council) Geodynamical Project*. Rome.

Rovelli, A., Boschi, E., Cocco, M., Di Bona, M., Berardi, R. & Longhi, G. 1991. Il Terremoto del 13 Dicembre 1990 nella Sicilia Orientale: Analisi dei Dati Accelerometrici. *Contributi allo Studio del Terremoto della Sicilia Orientale del 13 Dicembre 1990*. Istituto Nazionale di Geofisica. Roma.

Simonini, P. & Cola, S. 2000. On the Use of the Piezocone to Predict the Maximum Stiffness of Venetian Soils. *Journal of Geotechnical and Geoenvironmental Engineering*, vol. 126, no. 4, 378–382.

Siragusa, G. B. 1897. Fonti per la Storia d'Italia. SS., sec. XII, 22, Roma.

Yoshida, Y., & Motonori, I. 1988. Empirical Formulas of SPT Blow-Counts for Gravelly Soils. *Proceedings of ISOPT-1*, Orlando (USA).

Geotechnical Engineering for the Preservation of Monuments and Historic Sites III – Lancellotta, Viggiani, Flora, de Silva & Mele (Eds)

Soil contribution on the structural identification of a historical masonry bell-tower: Simplified vs advanced numerical models

A. De Angelis, A. Ambrosino & S. Sica
Department of Engineering, University of Sannio, Benevento-Italy

P.B. Lourenco
Institute for Sustainability and Innovation in Structural Engineering (ISISE), University of Minho, Portugal

ABSTRACT: In the last decade, structural identification techniques through dynamic in situ tests have been widely used to investigate the global dynamic behavior of ordinary buildings and built cultural heritage. The choice of proper boundary conditions at the base of the structure, however, is still a critical point in the development of sound numerical models able to reproduce building dynamic response reliably. The contribution of the foundation soil should be ascertained and, if necessary, properly modelled. The paper tries to shed light on the issue of soil-structure-interaction on the structural identification of masonry towers, with reference to the case study of the bell tower of Santa Sofia Church in Benevento (Italy). The experimental results of the dynamic identification, i.e. frequencies and modal shapes, have been interpreted and employed to calibrate both simplified and advanced numerical models of the soil-foundation-tower system. In the first case, soil compliance is represented by a set of springs attached at the base of the tower, which has been modelled as a 1D system. In the second case, a 3D finite element model comprehensive of the tower, the soil and the foundation structure has been developed. Pros and cons of the two numerical approaches on the structural identification process are highlighted and discussed.

1 INTRODUCTION

For historical constructions, invasive tests should be limited as much as possible. At the same time, it is of paramount importance to ascertain accurately the geometry and the mechanical properties of the construction materials together with the architectural or structural interventions carried out during the monument life. For this reason, structural identification by in-situ dynamic tests has received greater attention in the field of historical and monumental assets (Karatzetzou et al. 2015). In-situ dynamic tests turn to be useful tools to obtain the dynamic response in terms of frequencies and modal shapes (Brincker et al. 2001) and to understand different other aspects of historical building response, included the contribution of soil-structure interaction (SSI).

Among historical constructions, masonry towers may be considered as the main distinctive elements of the artistic heritage of many countries worldwide. It is widely recognized that SSI may strongly affect the dynamic behavior of slender structures like towers. Therefore, for an accurate interpretation of both frequencies and modal shapes detected on site, the role of SSI on the overall dynamic response of the building should be comprised, discerning whether the interaction itself is effective or not (De Angelis et al. 2017) and its potential impact on numerically derived modal shapes.

A proper modelling of the constraint between the tower and the soil, thus, is still a critical issue (Kouroussis et al. 2011) as different levels of complexity may be adopted. The most refined models are based on a continuum approach for both the structure and the soil. These methods are very demanding, so their use is typically restricted to handle single case studies (Casciati & Borja 2004; Cattari et al. 2019; De Silva et al. 2018).

 DOI 10.1201/9781003308867-70

In simpler models, the soil and the foundation are hidden in sets of springs and dashpots applied at the base of the structure while the structure is simulated through single or multi-degree-of-freedom systems. Springs and dashpots, encompassing soil stiffness and damping terms in the impedance function definition (Gazetas 1991), may be easily obtained through closed-form solutions available in literature. In the last decade, this type of models have been applied extensively to reproduce the experimental results from dynamic identification (Ceroni et al. 2014; Cosentini et al. 2015; Ripepe et al. 2014).

It is worth pointing out that the available solutions for quantifying soil impedance are based on many simplified assumptions on both foundation and soil features. For existing masonry structures, many unknown parameters such as the foundation embedment and geometry, or ageing effects in the construction materials may complicate the analytical impedance function computation (Piro et al. 2019). Moreover, the overburden pressure due to the structural self-weight can significantly influence the stress-dependent stiffness of the shallowest soil layers. All these aspects should be taken into account in modelling choices.

In the paper, the role of soil-structure interaction on the structural identification of a historical masonry tower is investigated by adopting both a simplified and a complete numerical method. The final goal is to quantify the impact of different numerical models accounting for SSI on the structural identification of a masonry tower.

2 THE CASE STUDY

2.1 *The structural data*

The bell tower of S. Sofia in Benevento (Italy) together with the church, the monastery and the fountain constitutes the "S. Sofia" monumental complex, which has been recognized as a UNESCO site since 2011. The tower (about 26 m high), reconstructed in 1703, has a square base and a hollow cross-section, consisting of a main body, belfry and pinnacle (Figure 1).

The side at the base is about 5.2 m, reducing to 4.8 m at the level of the belfry. An octagonal cell (about 1.5 m high) and a pyramidal cusp constitute the top of the tower. A stone stair runs along the tower from the base to the belfry and two masonry vaults, on the floor at 12.70 m and above the belfry, are present.

An accurate investigation through a photographic survey with a drone combined with direct in-situ inspections was performed to identify the elevation as well as the cross-sections of the tower. In particular, the wall thickness vary from 1.10 to 0.50 m at different levels.

Regarding the masonry texture, the tower comprises facing masonry with an external leaf, made of regular prismatic-shaped stones approximately 25 cm thick (masonry M1) and an internal leaf characterized by regular shape stones (M2) for the shaft. Conversely, the inner core is made of heterogenous masonry with red clay bricks, natural stone conglomerate and medium-sized pebbles (M3) for the belfry and the circular wall of the staircase. The vaults are made of solid brick masonry (M4).

2.2 *The geotechnical data*

The geotechnical characterization at the tower site was achieved by merging data from different sources, like the Level-1 Microzonation study of the city of Benevento (Sica & Romito 2017) or published in Senatore et al. (2019), and data obtained from the geotechnical and geophysical investigations performed *ad hoc* nearby the tower as detailed in De Angelis et al. (2022).

The soil deposit underneath the tower is made of three layers (Figure 2a), whose main physical and mechanical parameters have been summarized in Table 1. Starting from the ground level, the soil layers consist of: an Artificial filling (AF) up to a depth of about 3 m, which includes several types of waste material and reworked soil derived from excavations as well as demolition and/or restructuring of civil ancient buildings; Yellow sands (YS) between the depths of 3 m and 13 m

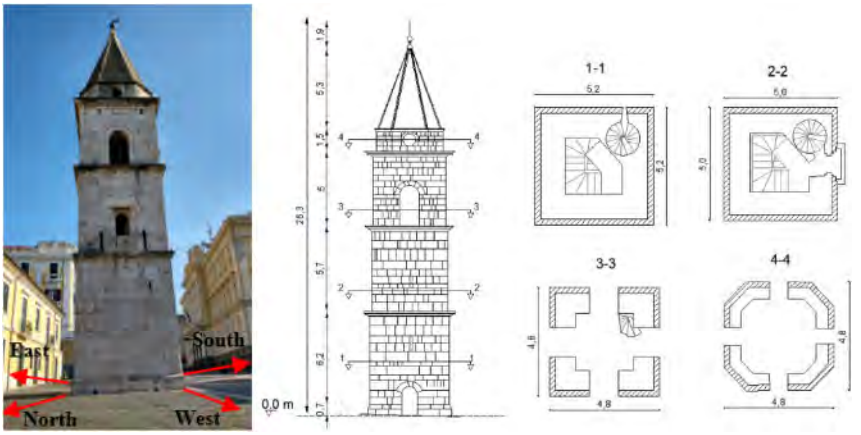

Figure 1. The bell tower of S. Sophia.

(the upper 5 meters of this layer still contain anthropic reworked deposits of the ancient city); well-cemented Conglomerate (CC) between 13 m and 47 m of depth. In Figure 2b the soil stratigraphy, which is typical of the upper part of the city of Benevento, has been combined to the shear wave velocity profile, Vs, measured on site through a MASW test (De Angelis et al., 2022). A Poisson coefficient, ν, of 0.3 was assumed for all materials.

Table 1. Soil properties.

Layer	Depth m	Vs m/s	γ kN/m^3	G MPa
AF	0–3	270	17	120
YS	3–13	640	20	820
CC	13–47	1340	23	4100

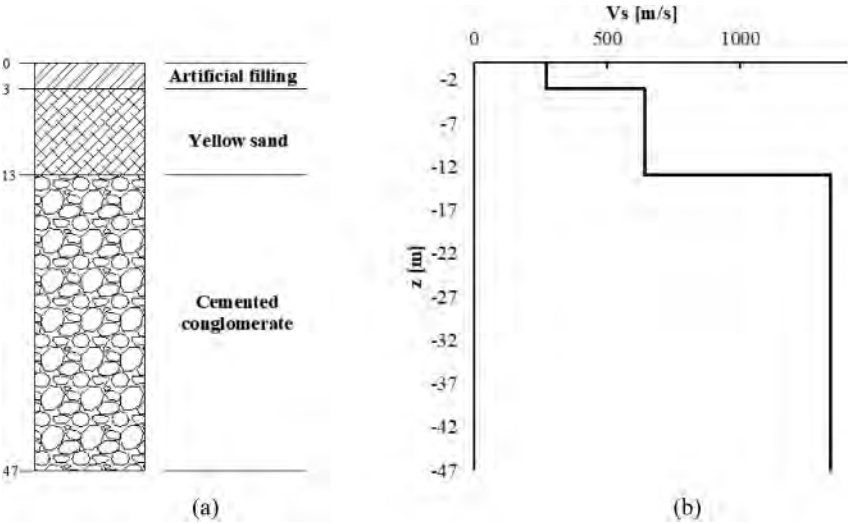

Figure 2. (a) Soil stratigraphy and (b) profile of shear wave velocity Vs.

The foundation of the tower is 2 m deep with a plan 6.5 m *x* 6.5 m, considering an enlargement of 0.50 m with respect to the base of the tower. The masonry of the foundation (M5) is assumed the same of the tower shaft; however, to consider the effect of deterioration of buried structural elements, a reduction of 15% of the Young's modulus of the foundation masonry with respect to the value attributed to the superstructure was considered.

2.3 *The ambient vibration test*

The ambient vibration test (AVT) was carried out under environmental actions (wind and human activities). The measurement chain consists of a 16-channel data acquisition system, tri-axial MEMS piezoelectric accelerometers with a nominal sensitivity of about 1 V/g and long transducer cables. The accelerometers were installed by means of special metal bases fixed directly on the walls with expansion anchors. The AVT was performed by recording time histories of acceleration of 30 minutes, at a sampling frequency of 1000 Hz, in seven points along the height of the tower. Then, the signals were treated by decimation and low-pass filtering, in order to reduce the dimension of the time series keeping the capacity to compute spectra up to approximately 50 Hz.

The extraction of the modal parameters from ambient vibration data was carried out by the software Artemis modal Pro (2019) using the Operational Modal Analysis (OMA). In particular, the Enhanced Frequency Domain Decomposition (Brincker et al. 2001) and the Stochastic Subspace Identification (Peeters & De Roeck 2001) methods were employed as described in detail in De Angelis et al. (2021).

The first five natural frequencies of the tower (Table 2) and the corresponding modal shapes were reliably identified. The first two modes are both translational and uncoupled; in particular, the first modal shape is parallel to the East-West direction with a natural frequency of 3.18 Hz, while the second one is parallel to the South-North direction with a frequency of 3.23 Hz. The third mode is torsional with a frequency of 12.03 Hz. Second order flexural modes were experimentally identified at frequencies 12.42 and 12.91 Hz for the N-S and E-W direction, respectively.

Table 2. Experimental frequencies.

Mode	Mode type	f_{exp} Hz
1	Bending E-W	3.18
2	Bending S-N	3.23
3	Torsion	12.03
4	2nd Bending S-N	12.42
5	2nd Bending E-W	12.91

3 MODELLING

3.1 *The advanced models*

Two advanced 3D models (Figure 3) were generated with the software MIDAS FEA NX considering different boundary conditions at the tower base: (a) Fixed base model (Case 1-A); (b) Compliant base model (Case 2-A) including the tower, the foundation and the underlying soil.

The structural geometry was obtained through geometrical survey and in-situ inspections of the tower, by paying attention to reproduce all the openings (doors and windows) and the floors (masonry vaults and concrete slabs). The tower was modelled using 8-node brick elements and trying to generate a quite refined mesh (typical mesh size around 0.2 m) so that a suitable approximation of the tower geometry and distribution of mass could be achieved. In addition, the masonry was modeled as a continuous homogeneous material. The external stone masonry leaf has been modelled as another layer of masonry with the same thickness estimated by in situ inspections. The properties chosen for the tower masonry are listed in Table 3 for the main material types identified.

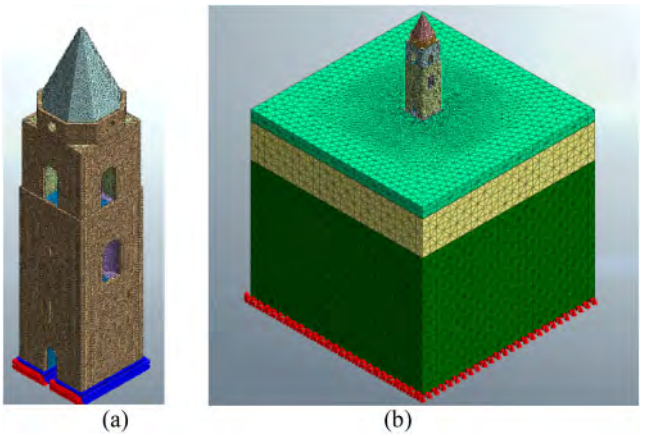

Figure 3. Advanced 3D models: (a) Fixed base and (b) Compliant-base tower.

In particular, the mechanical properties of the masonry (M1) of the external leaf were derived from literature results from double flat jacks on similar external stone layer (Bartoli et al. 2013). For the masonry (M2) of the shaft the results of a double flat-jack, performed in situ, have been adopted. Conversely, for the masonry of the belfry (M3) and vaults (M4), the maximum values of the range suggested by the Italian Code (Circolare Ministeriale n. 7, 2019) have been adopted. More details on material characterization may be found in (De Angelis et al. 2022).

The full SSI model was developed by adding to the tower the foundation structure and a suitable part of the underlying soil. The added soil volume is 47 m high with a plan of 50 m × 50 m. It was divided into three homogeneous linear elastic layers (artificial filling AF, yellow sand YS and cemented conglomerate CC), with the main physical and mechanical properties summarized in Table 1. The mesh size for the soil elements was progressively refined towards the ground surface in order to achieve a greater accuracy near the tower foundation. The nodal displacements at the base of the soil domain were fully constrained whereas boundary conditions (elastic springs) were set along the lateral sides.

Table 3. Mechanical properties of the masonries.

Element	Masonry type	E MPa	γ kN/m^3
External leaf	M1	11530	24
Shaft	M2	3730	22
Belfry	M3	1050	19
Vaults	M4	1800	18
Foundation	M5	3170	22

3.2 *The simplified models*

The simplified finite element model of the bell tower, developed with the same software MIDAS FEA NX used for the advanced analyses described in section 3.1, was obtained by discretizing the actual geometry of the tower into beam elements with a hollow-square section; the wide and thickness of the beam elements are variable along the height of the tower to match the real geometry detected by surveying and described in section 2. The mechanical properties of the masonry are reported in Table 3.

As for the advanced approach, two simplified models were also considered: 1) a fixed base beam, i.e., a cantilever scheme and 2) a beam on a flexible base made of translational and rotational springs simulating the soil-foundation interaction. To better characterize soil compliance, the deformability

of the foundation masonry and the effect of the overburden pressure induced in the subsoil by the self-weight of the tower were considered too. The stiffness of the springs were, hence, computed through well-known impedance literature formulations for embedded-rigid or embedded-flexible shallow foundations on an equivalent homogeneous soil deposit.

The following five analysis cases were solved through the simplified approaches:

- Case 1-S: Tower on fixed-base
- Case2-S: Tower on embedded Rigid foundation
- Case 3-S: Tower on embedded Flexible foundation
- Case 4-S: Tower on embedded Rigid foundation including the overburden pressure
- Case 5-S: Tower on embedded Flexible foundation including the overburden pressure

3.2.1 *Characterization of soil-foundation compliance*

The impedance functions are complex and frequency-dependent functions, which link the force (or moment) acting on an oscillating rigid foundation to the soil displacement (or rotation). They are composed of a real part, representing the dynamic stiffness of the soil-foundation system, and an imaginary part accounting for damping (radiation plus hysteric).

Classical solutions for the impedance function may be written as proposed by Luco and Westman (1971) and Veletsos and Wei (1971):

$$\overline{k_j} = k_j + i\omega c_j \tag{1}$$

where $\overline{k_j}$ denotes the complex-valued impedance function; j is an index denoting the oscillating mode (displacement or rotation) of the foundation; k_j and c_j denote the frequency-dependent soil-foundation stiffness and dashpot coefficients, respectively; ω is the circular frequency (rad/s) of the input vibration.

Pais and Kausel (1988), Gazetas (1991), and Mylonakis et al. (2006) reviewed the available impedance solutions or developed new ones with the structure of Equation 1. In particular, for a rigid rectangular foundation embedded in a half-space, Equation 2 provides for the stiffness terms, kj, of the impedance function (real part) as function of the foundation characteristic dimensions, B, soil shear modulus, G, and Poisson's ratio, ν.

$$k_j = K_j \cdot \alpha_j \cdot \eta_j \tag{2a}$$

$$K_j = GB^m f(B/L, \nu) \tag{2b}$$

$$\alpha_j = f(B/L, a_0) \tag{2c}$$

$$\eta_j = f(B/L, D/B, d_w/B, A_w/BL) \tag{2d}$$

In Equation 2, Kj is the static stiffness of the soil-foundation system at zero frequency while, α_j and η_j are the dynamic stiffness and embedment modifiers, respectively.

In the following, the equations provided by Pais and Kausel (1988) to account for the foundation embedment have been adopted.

To take into account the foundation flexibility, the spring stiffness was reduced according to the approach proposed by Pitilakis et al. (2014). The reduction factors for to the vertical (βv), horizontal (βh) and rocking (βr) modes are relate to the ratio between the Young's modulus of the foundation material, Ew, and that of the soil, Es, as shown in Equation 3:

$$\beta_v = 0.171 ln(E_w/E_s) + 0.326 \tag{3a}$$

$$\beta_h = 0.155 ln(E_w/E_s) + 0.295 \tag{3b}$$

$$\beta_r = \begin{matrix} 0.376(E_w/E_s)^{0.476} 0 < E_w/E_s \leq 3 \\ 0.492(E_w/E_s)^{0.208} 3 < E_w/E_s < 18 \end{matrix} \tag{3c}$$

For the S. Sofia tower, the impedance functions required for the simplified SSI model were calculated twice, once considering a rigid embedded foundation and another a flexible embedded

foundation. In addition, the layered subsoil (Figure 2) was modeled as a homogeneous half-space in the tower pressure bulb, by computing an equivalent shear wave velocity for each vibrating mode of the foundation, according to Stewart et al. (2003) and NIST (2012) indications.

Table 4 reports the average soil shear wave velocity $\overline{V_s}$, with the corresponding shear modulus $\overline{G_0}$ and Young modulus $\overline{E_0}$, and the equivalent soil density, ρ. The averaged values of the above soil properties were obtained on a depth range in between the foundation level, D, and a reference depth equal to $D + z_p$, Since the tower has a square base with $B = L = 6.1$ m (Table 4) and an embeddement $D = 2.5$ m, the reference depth z_p corresponds to 3.1 m for all foundation vibrating modes. In Table 4, the Young's modulus of the foundation material, Ew, characterized as explained in section 2.2, has also been reported.

Table 4. Properties of the soil and foundation.

Soil		Foundation	
$\overline{V_s}$ (m/s)	524	L (m)	6.2
$\overline{G_0}$ (MPa)	549	B (m)	6.2
$\overline{E_0}$ (MPa)	1428	D (m)	2.5
ρ(kg/m^3)	2000	Ew (MPa)	3170

As well-known, the initial shear stiffness of the shallowest soil layers may increse due to the overburden pressure caused by the weight of the superstructure (Hardin, 1978). To take into account this effect, the free-field shear wave velocity of the soil was corrected as suggested by NIST (2012) according to Equation 4:

$$V_{s,F}(z) = V_s(z) \cdot \left(\frac{\sigma'_v(z) + \Delta\sigma'_v(z)}{\sigma'_v(z)} \right)^{n/2} \tag{4}$$

where $V_{s,F}$ (z) is the overburden-corrected shear wave velocity at depth z, V_s(z) denotes the shear wave velocity measured in the free-field at depth z, n is an exponent increasing with soil plasticity index and set equal to 0.5 in light of the granular soils investigated, $\sigma'_v(z)$ is the effective stress of the soil at depth z, and $\Delta\sigma'_v(z)$ is the increment in vertical stress due to the weight of the superstructure. The overburden pressure may be computed easily by classical elastic solutions like the one proposed by Steinbrenner (1936) and shown in Figure 4a. Figure 4b reports the comparison between the free-field shear wave velocities (black line) and the the overburden-corrected shear wave velocity (red line) between the depths $D = 2.5$ m and $D + z_p = 5.6$ m. As expected, the overburden-corrected shear wave velocity is significant only at the shallowest depths.

Then, using the overburden-corrected values of shear wave velocity, the profile depth has been discretized into layers of thickness Δ_{zi} and velocity $V_{s,F}(z)_i$ to obtain an average effective velocity of 948.5 m/s from Equation 5.

$$V_{s,avg} = z_p \Big/ \sum_{i=1}^{n} \left(\Delta z_i / \left(V_{s,F}(z) \right)_i \right) \tag{5}$$

4 STRUCTURAL IDENTIFICATION WITH ADVANCED AND SIMPLIFIED MODELS

4.1 *Structural identification through the advanced models*

A modal analysis was initially developed to compute the frequencies (f_{num}) and modal shapes (φ_{num}) for the two advanced 3D f.e. models (Case 1-A and Case 2-A) in order to discriminate the importance of SSI on the correct identification of the structural behavior.

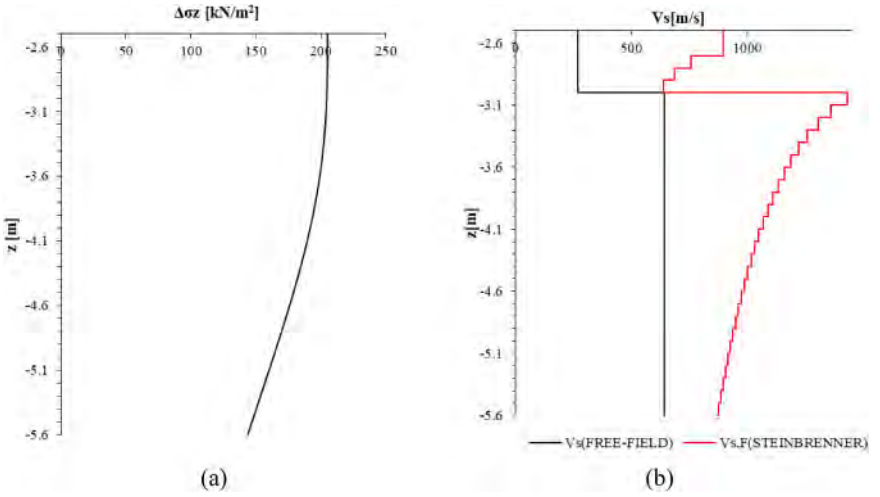

Figure 4. (a) Vertical stress increment; (b) Shear wave velocity profiles

SSI contribution on the calibration of the advanced structure model has already been detailed in De Angelis et al. (2022), by comparing the mechanical properties identified by updating the fixed-base and the compliant-base model of the bell tower. The comparison is presented in terms of frequency discrepancy, D_f, computed according to Equation 6 and modal assurance criterion MAC (Allemang & Brown 1982) in Equation 7.

$$D_f = \frac{f_{exp} - f_{num}}{f_{num}} \tag{6}$$

$$MAC = \frac{\left(\left\{\varphi_{exp}^T\right\} \cdot \left\{\varphi_{num}\right\}\right)^2}{\left(\left\{\varphi_{exp}^T\right\} \cdot \left\{\varphi_{exp}\right\}\right) \cdot \left(\left\{\varphi_{num}^T\right\} \cdot \left\{\varphi_{num}\right\}\right)} \tag{7}$$

Table 5 reports the final results of the performed model updating (De Angelis et al. 2022) that, as it could be observed, returned different optimal values for the fixed-base or the compliant-base model. The change in percentage with respect to the initial values of masonry stiffness and weight is shown in the brackets. In the case of fixed model, the two parameters affecting most the calibration of the model are the Young modulus of the external masonry stone leaf (M1) and of the masonry of the belfry (M3). A corresponding decrease of 38% and 28% with respect to the initial values adopted in the fixed model was obtained. Conversely, the influence of the specific weight of the masonries was found to be negligible (about 4%). Model updating applied to the advanced model corroborates the negligible effect of the specific weight of the masonry, which remains almost equal to the initial value adopted (5%). The final value of the elastic modulus for all types of masonry, instead, is different from the initial one of the order of 50%–110%, while it remains almost unchanged for the masonry stone leaf (M1). The comparison in terms of numerical frequencies and MACs of the updated models and the experimental results is presented in Table 6.

For the fixed model, the updating process improved the correlation of the first and the second bending modes being D_f less than 3% (4% on average). A higher value of frequency discrepancy equal to 13% was found for the torsional mode. In terms of modal shape (MAC values) the correlation may be considered globally satisfactory (minimum of 0.7 and average of 0.8), with larger errors found for the higher modes. This could be related to soil structure contribution. Actually, referring to the final correlation for the compliant model, it is possible to observe an excellent match since the average D_f is less than 4% and the maximum difference in frequencies is

Table 5. Optimal values of the masonry properties after model updating.

		Fixed model (Case1-A)		Compliant model (Case2-A)	
Element	Masonry type	E [MPa]	γ [kN/m^3]	E [MPa]	γ [kN/m^3]
External leaf	M1	7190 **(−38%)**	23.0 **(−4%)**	12146 **(5%)**	22.86 **(−5%)**
Shaft	M2	3590 **(−4%)**	21.1 **(−4%)**	6073 **(63%)**	20.95 **(−5%)**
Belfry	M3	1340 **(28%)**	18.2 **(−4%)**	2267 **(116%)**	18.10 **(−5%)**
Vaults	M4	1720 **(−4%)**	17.3 **(−4%)**	2915 **(62%)**	17.14 **(−5%)**
Foundation	M5		–	4763 **(50%)**	19 **(−14%)**

Table 6. Comparison between numerical and experimental modes.

		Fixed model (Case1-A)			Compliant model (Case2-A)		
Mode	f_{exp} [Hz]	f_{num} [Hz]	D_f [%]	MAC [%]	f_{num} [Hz]	D_f [%]	MAC [%]
1st bending E-W	3.18	3.17	−0.25	89	3.04	−4.40	92
1st bending N-S	3.23	3.31	2.57	89	3.11	−3.86	92
Torsional	12.03	10.35	−13.98	78	12.03	−0.01	82
2nd bending E-W	12.42	12.20	−1.77	76	13.28	6.92	95
2nd bending N-S	12.91	12.68	−1.78	71	13.62	5.48	91
Average (abs. value)			4.07	81	–	4.13	90

lower than 5%. Accounting for SSI, the MAC values improved significantly with excellent results (average of 0.91 and minimum value of 0.82) for the higher modes.

Therefore, the outcomes of the study underline that a good correlation with the modal shapes may be obtained only with the SSI contribution.

4.2 *Structural identification with the simplified models*

As the simplified models concern, a modal analysis was initially carried out to obtain the main frequencies, modal shapes and modal participating mass ratio in the fixed-base condition (Case 1-S). The simplified model is able to reproduce the first and second flexural modes in x and y direction, respectively. Conversely, it is not able to reproduce the torsional mode due the oversimplification of the static scheme. In Table 7, the results obtained from the simplified and the advanced models are both compared to the experimental ones. In both cases, the numerical frequencies are higher than the experimental ones. In addition, it is worth noting that with the simplified model the modes are purely flexural in a specific direction; therefore, it is not able to identify the coupling of the modes in the two directions as detected experimentally. However, the first modes in both x and y directions are the principal ones, as testified by the highest value of the participating mass, being about 60%.

If the compliant-base models are considered, the outcomes of the simplified numerical study in terms of natural frequencies and frequency mismatch with respect to the experimental values, are detailed in Table 8. Here, the different predictions corresponding to the compliant model refer to the five modes of computing the stiffness terms of the impedance function as described in section 3.2, i.e. with or without accounting for foundation masonry deformability and the effect of soil overburden pressure due to the tower weight.

As expected, the compliant base models always provide for natural frequencies lower than those of the fixed-base model. Introducing the deformability of the foundation structure (Case3-S), the

Table 7. Comparison between experimental data and numerical frequencies for the fixedbase models, both simplified (Case 1-S) and advanced (Case 1-A)

		Numerical							
Experimental		Fixed model (Case1-S)				Fixed model (Case1-A)			
Mode	f_{exp} [Hz]	Mode	f_{num} [Hz]	m_x [%]	m_y [%]	Mode	f_{num} [Hz]	m_x [%]	m_y [%]
1st bend. E-W	3.18	1st bend. x	3.76	66	0	1st bend. E-W	3.54	19	40
1st bend. N-S	3.23	1st bend. y	3.90	0	60	1st bend.N-S	3.66	40	20
Torsional	12.03	NA	–			Torsional	11.48	0	0
2nd bend. E-W	12.42	2nd bend. x	12.14	23	0	2nd bend. E-W	13.49	22	1
2nd bend. N-S	12.91	1st bend. y	15.61	0	22	2nd bend.N-S	14.02	1	20

Table 8. Comparison between experimental and numerical data for the compliant base condition.

		Numerical									
Experimental		Fixed model (Case1-S)		Compliant model (Case 2-S)		Compliant model (Case 3-S)		Compliant model (Case 4-S)		Compliant model (Case 5-S)	
Mode	f_{exp} [Hz]	f_{num} [Hz]	D_f [%]	f_{num} [Hz]	D_f [%]	f_{num} [Hz]	D_f [%]	f_{num} [Hz]	D_f [%]	f_{num} [Hz]	D_f [%]
1st bend. E-W	3.18	3.76	−18.28	3.40	−7.05	3.17	0.47	3.64	−14.50	3.40	−7.06
1st bend. N-S	3.23	3.90	−20.67	3.51	−8.68	3.25	−0.73	3.77	−16.62	3.51	−8.70
2nd bend. E-W	12.42	12.14	2.29	11.75	5.43	11.31	8.92	12.01	3.32	11.65	6.18
2nd bend. N-S	12.91	15.61	−20.88	14.53	−12.54	13.56	−5.02	15.24	−18.01	14.35	−11.14

frequencies become even lower and the mismatch between the experimental and compliant-base model reduces.

Conversely, when the overburden pressure generated in the soil by the structural weight (Case 4-S) of the tower is introduced, an overall stiffening of the system is obtained with the consequent increase of the frequencies, thus leading to a higher mismatch.

To refine the tuning process, it was decided to use the fixed base model (Case 1-S) and the most comprehensive simplified model (Case 5-S) that includes both the overburden pressure due to the structural weight and the flexibility of the foundation structure, for further updating of the structural model. The aim is to numerically reproduce the experimental frequencies and understand how such calibration changes the properties assigned to the materials of the superstructure.

The final values of the superstructure masonry stiffness are reported in Table 9. Different observation may be drawn. First, in the simplified model, the two parameters affecting most the calibration of the model in the fixed base configuration are the Young moduli of the external masonry stone leaf (M1) and of the masonry of the shaft (M2). They are characterized by a decrease of 40% and 17%, respectively. In the compliant model (Case 5-S), the final value of the elastic modulus for all types of masonry is different from the initial value in the range 9-67%. Instead, the influence of the specific weight of the masonries is negligible for both the fixed base and compliant model.

Finally, the comparison among the numerical frequencies of the updated simplified models and the experimental one is presented in Table 10. It could be concluded that an acceptable correlation

can be obtained also with the simplified model including the SSI, even though it is not able to detect the torsional mode.

Table 9. Final values of the masonry properties after a further updating of the simplified models.

		Fixed model (Case1-S)		Compliant model (Case5-S)	
Element	Masonry type	E [MPa]	γ [kN/m^3]	E [MPa]	γ [kN/m^3]
External leaf	M1	6890 **(−40%)**	23.0 **(−4%)**	8280 **(−39%)**	23 **(−4%)**
Shaft	M2	3090 **(−17%)**	21.1 **(−4%)**	4130 **(9%)**	21.5 **(−2%)**
Belfry	M3	1340 **(−4%)**	18.2 **(−4%)**	3190 **(67%)**	18.2 **(−4%)**
Foundation	M5	–	–	2650 **(−20%)**	22 **(0%)**

Table 10. Correlation between numerical and experimental modes (simplified models).

		Fixed model (Case1-S)		Compliant model (Case5-S)	
Mode	f_{exp}[Hz]	f_{num} [Hz]	D_f[%]	f_{num} [Hz]	D_f[%]
1st bending E-W	3.18	3.18	−0.08	3.25	−2.29
1st bending N-S	3.23	3.30	−2.03	3.35	−3.84
Torsional	12.03	–	–		
2ndbending E-W	12.42	10.36	16.59	11.25	9.44
2nd bending N-S	12.91	13.38	−3.62	13.96	−8.14
Average (abs. value)			5.58		5.93

5 CONCLUSIONS

The dynamic behavior of the S. Sofia bell tower in Benevento (Italy) was numerically simulated through simplified and advanced numerical models

The comparison between the experimental data obtained from an ambient vibration test, and the numerical results described in the present study evidenced that:

1) the third experimental mode which is a torsional one, cannot be reproduced by the simplified numerical models;
2) with both the simplified and advanced numerical models with restrained base, the tower frequencies are higher than the experimental ones; in addition, with the simplified model the modes are purely flexural in a specific direction and it is not able to identify the coupling of the modes in the two directions as detected experimentally;
3) by implementing the compliant base models, the natural frequencies of the coupled system decrease as expected;
4) by introducing also the foundation deformability in the simplified SSI models (Case3-S), the numerical frequencies decrease more and more and the mismatch between the experimental and compliant-base model frequencies are reduced compared to the fixed base model.
5) the simplified model of the bell tower may provide an acceptable correlation only if it includes the SSI contribution by means of base springs that accounts for the overburden pressure of the tower and the foundation masonry deformability.

ACKNOWLEDGEMENTS

The authors thank Prof. Maria Rosaria Pecce for her precious support and suggestions. This research activity was carried out within the framework of the PON Research and Innovation 2014–2020, Axis I-Investments in Human Capital, MIUR notice AIM-"International Attraction and Mobility"-Line 1, Project: AIM 1823125-3 – Cultural Heritage. Part of the work has been developed in the framework of the 2019-2021 Reluis-DPC research program funded by the Italian Civil Protection Department, as a contribution to the geotechnical Work Package Soil-Foundation-Structure Interaction (Task 16.3).

REFERENCES

Allemang, R.J., Brown, D.L. 1982. A correlation coefficient for modal vector analysis. Proceedings of the 1st International Modal Analysis Conference. Orlando, USA.

ARTeMIS Modal Pro 6.1 software. 2019. Issued by Structural Vibration Solutions ApS. NOVI Science Park, Niels Jernes Vej 10, DK 9220 Aalborg East, Denmark.

Bartoli G, Betti M, Giordano S. In situ static and dynamic investigations on the "Torre Grossa" masonry tower. Eng Struct 2013; 52:718–733

B.O. Hardin. 1978. The nature of stress-strain behavior for soils. Geotechnical Engineering Division Specialty Conference on Earthquake Engineering and Soil Dynamics, ASCE, Pasadena (California).

Brincker, R., Zhang, L., Andersen, P. 2001.Modal identification of output-only systems using frequency domain decomposition. Smart Materials and Structures; 10:441–5.

Casciati, S. & Borja, RI. 2004. Dynamic FE analysis of South Memnon colossus including 3D soil-foundation structure interaction. Comput Struct; 82:1719–1736.

Cattari, S., Sivori, D., Brunelli, A., Sica, S., Piro, A., de Silva, F. et al. 2019. Soil-structure interaction effects on the dynamic behaviour of a masonry school damaged by the 2016-2017 Central Italy earthquake sequence. Proceedings of the 7th lnternational Conference on Earthquake Geotechnical Engineering (VII ICEGE) 2019. June 17-20, Rome, Italy.

Ceroni, F., Sica, S., Pecce, M., Garofano, A. 2014. Evaluation of the natural vibration frequencies of a historical masonry building accounting for SSI. Soil Dyn Earthq Eng; 64:95–101.

Circ.2019-Instructions for "Technical Norms for Constructions".

Cosentini, R., Foti, S., Lancellotta, R., Sabia, D. 2015. Dynamic behavior of shallow founded historic towers: validation of simplified approaches for seismic analyses. Int J Geotech Eng:13–29.

De Angelis, A., Lourenço, P.B., Sica, S., Pecce, M.R. 2022. Influence of the ground on the structural identification of a bell-tower by ambient vibration testing, Soil Dynamics and Earthquake Engineering. In press, https://doi.org/10.1016/j.soildyn.2021.107102

De Angelis, A., Mucciacciaro, M., Pecce, M.R., Sica, S. 2017. Influence of SSI on the Stiffness of Bridge Systems Founded on Caissons. J. Bridge Eng., 22(8): 04017045.

De Angelis, A., Santamato, F., Pecce, M.R. 2021. Assessment of an historical masonry bell tower by modal testing. The 8th workshop on Civil Structural Health Monitoring CSHM-8. March 29–31, 2021.

De Silva, F., Pitilakis, D., Ceroni, F., Sica, S., Silvestri, F. 2018. Experimental and numerical dynamic identification of Carmine bell tower in Naples (Italy). Soil Dyn Earthq Eng; 109:235–250.

Gazetas, G. 1991. Foundation vibrations," Foundation Engineering Handbook, 2nd Edition, Chapter 15, H.-Y. Fang, ed., Chapman and Hall, New York, New York.

Karatzetzou, A., Negulescu, C., Manakou, M., Francois, B., Seyedi, D., Pitilakis, D., Pitilakis, K. 2015. Ambient vibration measurements on monuments in the Medieval City of Rhodes, Greece. Bull. Earth.Eng;13(1):331–345.

Kouroussis, G., Verlinden, O., Conti, C. 2011. Finite dynamic model for infinite media: the corrected solution of viscous boundary efficiency. J Eng Mech; 137 (7):509–511.

Luco, J.E., and Westmann, R.A.1971. Dynamic response of circular footings, Journal of Engineering Mechanics, Vol. 97, No. 5, pp. 1381–1395.

Midas FEA NX- Midas Engineering Software–Manual

Mylonakis, G., Nikolaou, S., and Gazetas, G. 2006. Footings under seismic loading: Analysis and design issues with emphasis on bridge foundations. Soil Dynamics and Earthquake Engineering, Vol. 26, pp. 824–853.

NIST. 2012. Soil-structure interaction for building structures. Technical report, US Department of Commerce, Washington, DC.

Pais, A., and Kausel, E. 1988. Approximate formulas for dynamic stiffnesses of rigid foundations. Soil Dynamics and Earthquake Engineering, Vol. 7, No. 4, pp. 213–227.
Peeters, B., De Roeck, G. 2001. Stochastic System Identification for Operational Modal Analysis: A Review. Journal of Dynamic Systems Measurement & Control;123(4):659–67.
Piro, A., de Silva, F., Parisi, F., Scotto di Santolo, A., Silvestri, F. 2019. Effects of soil-foundation-structure interaction on fundamental frequency and radiation damping ratio of historical masonry building sub-structures. Bullettin Earthq Eng;18: 1187–212.
Pitilakis D, Karatzetzou A. 2014. Dynamic stiffness of monumental flexible masonry foundations. Bullettin Earthq Eng;13:67–82.
Ripepe, M., Coli, M., Lacanna, G., Marchetti, E., Cristofaro, M., De Stefano, M., Mariani, V. et al. 2014. Dynamic response of the Giotto's bell-tower, in: Proceedings Engineering Geology for Society and Territory – Turin 15–19, 2014; Vol. 8- Preservation of Cultural Heritage, pp. 323–27.
Senatore, M.R., Boscaino, M., Pinto, F. 2019. The Quaternary geology of the Benevento urban area (southern Italy) for seismic microzonation purposes. Ital. J. Geosci.; Vol. 138, pp. 66–87.
Sica, S., Romito, M. 2017. Convezione tra il Dipartimento di Ingegneria e il Comune di Benevento nell'ambito della Manifestazione di interesse per la realizzazione di indagini e studi di Microzonazione sismica ai sensi dell'OPCM 3907 del 13-11-2010; (in Italian)
Steinbrenner, W. 1936. A rational method for determination of the vertical normal stresses under foundations, Proceedings of the International Conference on Soil Mechanics and Foundation Engineering, Cambridge, Massuchusetts, 142–143.
Stewart, J.P., Kim, S., Bielak, J., Dobry, R., and Power, M. 2003. Revisions to soil structure interaction procedures in NEHRP design provisions," Earthquake Spectra, Vol. 19, No. 3, pp. 677–696.
Veletsos, A.S., and Wei, Y.T. 1971.Lateral and rocking vibrations of footings,"Journal of Soil Mechanics and Foundations Division, Vol. 97, No. 9, pp. 1227–1248.

Geotechnical Engineering for the Preservation of Monuments and Historic Sites III – Lancellotta, Viggiani, Flora, de Silva & Mele (Eds)

The geotechnical seismic isolation of historical buildings through polyurethane injections: A numerical study

M.P.A. Gatto & L. Montrasio
University of Parma, Parma, Italy

ABSTRACT: The seismic risk reduction is a topic of great interest among the earthquake engineering researchers, due to the high occurrence frequency of seismic events, responsible for extensive damages on vulnerable buildings. Many buildings needing protection against earthquakes belong to the historical and artistic heritage; some interventions for seismic risk reduction are based on the structural vulnerability reduction, but they are sometimes in contrast with the maintenance of the building's aesthetic. The paper aims at showing the efficiency of a Geotechnical Seismic Isolation method based on polyurethane injection in the soil, an already well-consolidated technique for ground improvement. For seismic purposes, this solution is based on the hazard reduction through the decrease of the surficial accelerations; it is an alternative to structural interventions and advantageous especially for the existing buildings, in terms of aspect conservation. Finite Element numerical analyses are performed to study the site effects of an historical building affected in the past by extensive damage related to a strong earthquake, after the modification of shallow soil layers with polyurethane injections. For the polyurethane expansion, changing according to the soil type and confinement, a previous developed method based on the theory of cavity expansion in elastic-plastic medium is used; this allows to have specific indication on the final geometry, density, and mechanical properties of the intervention to be simulated numerically.

1 INTRODUCTION

Seismic risk is a combination of seismic hazard, vulnerability, and exposure. Seismic hazard is the measure of the seismicity of a certain area. The vulnerability is proper of structures and is related to the adequacy of quality and quantity of materials (deteriorated or designed through aseismic building codes). Exposure depends on the population density, which governs damage associated with the occurrence of a seismic event. High-seismic-risk buildings are mainly the historic ones, because of their vulnerability. Interventions of vulnerability reduction through structural reinforcement are widespread, but in most cases, they do not protect the aesthetic conservation, especially for buildings of the artistic heritage.

Vulnerable structures that are not dilapidated could be sufficiently protected by reducing the seismic acceleration, i.e. the so-called peak ground acceleration (PGA) which acts directly on them. Since PGA strongly depends on the soil type through the site effects, on this issue the scientific literature includes both structural and geotechnical solutions: the first mainly regard the base isolation techniques (;arone et al. 2019; De Domenico et al. 2020; Eröz & DesRoches 2018), while the second are referred to as "Geotechnical Seismic Isolation" (GSI) and consist of interventions aimed at improving the dynamic properties of the foundation soil (Tsang et al. 2012; Tsiavos et al. 2020; Tsang et al. 2021). Despite the scientific evidence of the efficiency of GSI techniques in the seismic risk mitigation, there are often doubts concerning their feasibility, almost exclusively possible underneath new buildings, and secondary effects, e.g. on mechanical aspects,

DOI 10.1201/9781003308867-71

such as settlements because of the materials' deformability. However, intervening in the soil for the seismic protection of existing buildings appears to be the best solution for aesthetic conservation.

A geotechnical intervention that positively responds to requirements about applicability underneath existing structures and absence of negative effects on settlements is the ground improvement based on high-pressure injections of polyurethane, i.e. a polymer injected in liquid form inside small perforations of 9–12 cm diameters, where it expands up to 10 times and can mix with the soil, depending on the soil's permeability. Previous studies showed that the soil's bearing capacity is increased up to three times due to polyurethane injections (Nowamooz 2016). Supported by a well-consolidated application technology, together with the encouraging performances of this widespread technique, for years the geotechnical group of University of Parma has performed several experimental, theoretical, and numerical analyses aimed at verifying the eligibility of polyurethane injections as GSI.

Preliminary mechanical characterization of the pure material through classical geotechnical laboratory tests (oedometric and triaxial) evidenced the dependency of the material behaviour on the soil's confining pressure, as well as good rigidity (Montrasio & Gatto 2016; 2017). Experimental analyses performed on layered sand-polyurethane specimens demonstrated that surficial acceleration due to P-wave propagation is reduced proportionally to the polyurethane percentage (Gatto et al. 2020; 2021a). The high-injection pressures make it difficult to realise small-scale mixed soil-polyurethane specimens; however, other insights are necessary before a real experimentation, costly and demanding, and can be derived by Finite Element (FE) numerical simulations. To allow performing FE analyses, the dynamic behaviour of polyurethane was investigated by resonant column (RC) tests on pure and layered sand-polyurethane specimens and a simplified formulation was derived to evaluate homogenized properties for the composite, depending on the polyurethane percentage, as well as the dynamic properties of the pure materials; the results allowed a first numerical analysis by assuming a homogenized material, assumption acceptable for injection in cohesionless soils (Gatto et al. 2019; 2021b). Recently, the dynamic behaviour of the pure polyurethane was further investigated by means of RC tests to derive an analytical formulation, which allows predicting the dynamic parameters (shear modulus and damping ratio), according to the strain level by changing the density of the hardened material and the confinement exerted by the soil (depending on the injection depth) (Gatto et al. 2022); the results are the starting point for numerically simulating an application in soils with low permeability, where injected polyurethane do not mix so much and its expansion creates cylindrical inclusions of pure polyurethane.

This article shows a numerical simulation of the effects of polyurethane injected underneath a historical building aimed at investigating the efficiency of this GSI-technique on the reduction of surficial accelerations. The foundation soil, mainly made up of clayey-silty-sand, allows to assume cylindrical inclusions of polyurethane and compute the dynamic properties of the composite according to the authors' previous studies. Section 2 discusses the adopted theoretical methodology to evaluate the polyurethane expansion, according to the soil's confinement and mechanical properties; Section 3 describes the FE model used for the numerical simulations, whose results are shown in Section 4.

2 POLYURETHANE INJECTIONS FOR GROUND IMPROVEMENT

Polyurethane is injected beneath the foundations of existing buildings inside perforations of diameter 9–12 cm, spaced 50–150 cm planimetrically; in each hole, a liquid polyol-isocyanate mixture m_{PUR} is introduced, for several injection levels (every meter in depth). In low-permeability soils, polyurethane has been demonstrated to expand by compressing the soil around and poorly mixing with it; after the expansion and hardening, this intervention can be assumed to create cylindrical inclusions made up of pure polyurethane and determine a change in the soil stresses depending on the exerted expanding pressure p_{exp} (Sabri et al. 2021). Equal injected m_{PUR}, the density of the hardened polyurethane varies with its final volume, strictly affected by the confining soil. The evaluation of the final diameter of the cylindrical inclusions is therefore necessary prior to the study of polyurethane injections' effects on the seismic response of cohesive soils.

2.1 *Theoretical evaluation of polyurethane expansion injected in low-permeability soils*

Several authors studied the expansion of polyurethane injected in clayey soils by means of the analytical solutions of cavity expansion in elastic-plastic media problem, formulated by Carter (1986) and Yu and Houlsby (1991) (Dei Svaldi et al. 2005; Nowamooz 2016); this methodology is applied in this article and is now briefly discussed.

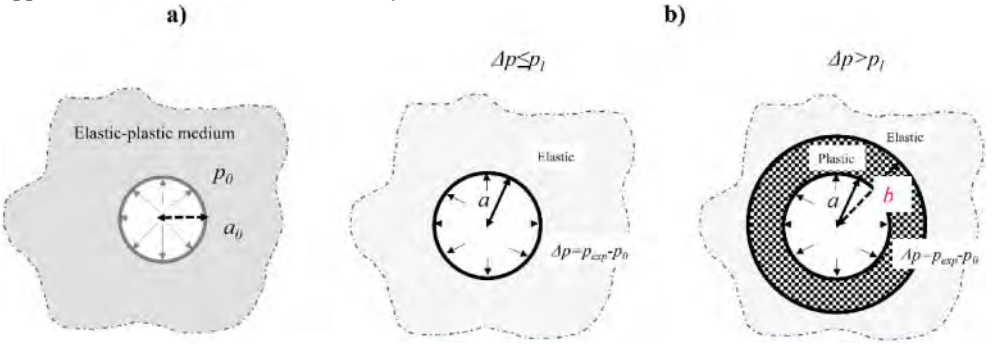

Figure 1. Schematisation of the expansion process. a) Initial configuration at the injection time t_0; b) Final configurations at $t > t_0$ with pure elastic ($\Delta p \leq p_l$) and elastic-plastic displacements ($\Delta p > p_l$).

The cavity under examination is the perforation hole where polyurethane is injected, having initial radius a_0 (Figure 1a). When the injected polyurethane expands, it exerts the pressure p_{exp} on the soil, which, in turn, confines the expansion with pressure p_0, equal to:

$$p_0 = \frac{1 + 2k_0}{3}\sigma'_v \tag{1}$$

Where k_0 is the at-rest earth pressure coefficient, σ'_v is the vertical effective stress. When the net pressure $\Delta p = p_{exp} - p_0$ is positive, the cavity expands up to a final radius a, depending on Δp and the soil's mechanical behaviour. Being d_{PUR} equal to $2a$, the final volume of the polyurethane cylinder V_{fin} *is*:

$$V_{fin} = \frac{\pi d_{PUR}^2}{4} h_{PUR} \tag{2}$$

h_{PUR} *is* the thickness of the injected soil. By assuming to inject a liquid mass m_{PUR}, the final density of the hardened polyurethane is equal to:

$$\rho_{PUR} = \frac{m_{PUR}}{V_{fin}} \tag{3}$$

The theory distinguishes between pure elastic and elastic-plastic displacements, according to a yielding pressure p_l: for Δp smaller than p_l, elastic displacements are theorized anywhere; otherwise, elastic-plastic displacements are assumed in a zone between the two radii a and b, and far from b they are elastic. Figure 1b schematizes these two cases related to the expansion process. The yielding pressure p_l depends on the soil's failure parameters (effective cohesion c', friction angle ϕ') through α and Y, as well as a cavity shape factor m, equal to 1 for cylindrical cavities:

$$p_1 = \frac{m \cdot [Y + (\alpha - 1)\, p_0]}{m + \alpha} + p_0 \tag{4a}$$

$$\alpha = \frac{1 + \sin\phi'}{1 - \sin\phi'} \tag{4b}$$

$$Y = \frac{2c' cos\phi'}{1 - \sin\phi'} \tag{4c}$$

When $\Delta p > p_l$, the final cavity radius a is a function of both the soil's failure and deformability parameters, included in a factor here named f_{exp}:

$$f_{exp} = \frac{a}{a_0} = \left[\frac{R^{-\gamma}}{(1-\delta)^{\frac{(\beta+m)}{\beta}} - (\gamma/\eta)\,\Lambda_1\,(R,\xi)} \right] \tag{5}$$

R is a cavity pressure ratio, depending on the involved pressures (p_{exp} and p_0), the soil's strength parameters (through α and Y) and the cavity shape factor m; β introduces the dependency on the soil's dilatancy angle ψ, while γ is a function of all the soil's failure parameters, as well as the cavity shape. R, β, and γ expressions are the following:

$$R = \frac{(m+\alpha)\left[Y + (\alpha-1)\,p_{exp}\right]}{\alpha\,(1+m)\,[Y + (\alpha-1)\,p_0]} \tag{6a}$$

$$\beta = \frac{1+sin\psi}{1-sin\psi} \tag{6b}$$

$$\gamma = \frac{\alpha\,(\beta+m)}{m\,(\alpha-1)\,\beta} \tag{6c}$$

The terms δ, η and ξ introduce to the formulation the elastic soil's behaviour, through the axial and shear moduli (E and G, respectively) and the Poisson's ratio ν:

$$\delta = \frac{Y + (\alpha-1)\,p_0}{2\,(m+\alpha)\,G} \tag{7a}$$

$$\eta = exp\left\{ \frac{(\beta+m)\,(1-2\nu)\,[Y + (\alpha-1)\,p_0][1 + (2-m)\,\nu]}{E\,(\alpha-1)\,\beta} \right\} \tag{7b}$$

$$\xi = \frac{\left[1-\nu^2\,(2-m)\right](1+m)\,\delta}{(1+\nu)\,(\alpha-1)\,\beta} \left[\alpha\beta + m\,(1-2\nu) + 2\nu - \frac{m\nu\,(\alpha+\beta)}{1-\nu\,(2-m)} \right] \tag{7c}$$

Finally, $\Lambda_1\,(R,\xi)$ is a series expansion allowing a closed-form solution of the problem:

$$\Lambda_1\,(R,\xi) = \sum\nolimits_{n=0}^{\infty} A_n^1 \tag{8a}$$

$$A_n^1 = \begin{cases} \frac{\xi^n}{n!} lnR & \text{if } n = \gamma \\ \frac{\xi^n}{n!(n-\gamma)}\left[R^{n-\gamma} - 1\right] & \text{otherwise} \end{cases} \tag{8b}$$

For the application of this theory to polyurethane injections, an important parameter to be determined is the polyurethane expansion pressure p_{exp}. Literature shows only a few of research efforts in this direction: Gröb and Marosfalvi (2008) reports the recommendation of manufactures, according to which p_{exp} is evaluated (in bar) as the ratio between the final density of the hardened polyurethane realised in confined conditions (ρ_{PUR}) and free rise conditions ($\rho_{PUR,FR}$); however, the authors evidenced that this relation overestimates the experimental measurements. A more reliable formulation appears to be the one experimentally derived by Dei Svaldi et al. (2005), which relates the expansion pressure p_{exp} and the hardened polyurethane density ρ_{PUR}:

$$p_{exp} = 240 \cdot e^{3.63 \cdot 10^{-2} \rho PUR} \tag{9}$$

p_{exp} is in kPa and ρ_{PUR} in kg/m^3. This equation is used in this paper, together with Eqs. (4–8) in a convergence procedure: i) a trial ρ_{PUR} is assumed and p_{exp} evaluated according to Eq. (9); ii) the expansion problem is solved by obtaining the final cavity diameter d_{PUR} and consequently the final volume occupied by the polyurethane (see Eq. (2)); iii) the density ρ_{PUR} is evaluated by means of Eq. (3) and compared with the initial assumed value: when only a small difference is observed (around 0.1 kg/m^3), the procedure is concluded. At reached convergency, the computed p_{exp}, ρ_{PUR} and d_{PUR} are used in the numerical simulation described in Section 3.

3 NUMERICAL MODELLING OF POLYURETHANE INJECTED BENEATH NOTO CATHEDRAL – SITE RESPONSE

San Nicolò cathedral is the most important place of worship in Noto (Sicily, Italy), declared World Heritage Site by UNESCO in 2002. The monument was built immediately after the Val di Noto Earthquake (occurred in 1693) and completed in 1703; it is extremely beautiful thanks to the imposing late-baroque facade made up of white stone, standing out from the top of the majestic staircase (Figure 2a). A detailed description of the building phases that interested the cathedral is reported by Tobriner (2003). On 13th December 1990, an earthquake caused structural damages, responsible for the subsequent collapse of the central and right cathedral's nave, occurred in 1996 (Figure 2b); after intensive reconstruction and restoration works, the Noto Cathedral was opened in June 2007. Earthquakes frequently occur in this area, because of the proximity to the contact between the African and Euro-Asian plate; the whole Eastern Sicily, where Noto is located, is one of the highest seismic hazard areas in Italy.

In the following, the dynamic characterisation derived from previous experimental campaigns conducted in this site is first summarised; then, it is described the Finite Element (FE) numerical model used to perform site response analyses aimed at investigating the effects of polyurethane injection on the surficial seismic accelerations of Noto site.

Figure 2. Noto cathedral. a) Front view of the building; b) Internal configuration after the 1996 collapse (Di Prisco et al. 2006).

3.1 *Previous dynamic characterisation of the soil*

Noto central area was subjected to an experimental campaign of soil characterisation, extended 3200 m^2 in plan and up to 81 m in depth, which revealed deposits belonging to the Trubi formation mainly made up of medium stiff over-consolidated lightly cemented silty-clayey sand (Cavallaro et al. 2003).

The stratigraphy for our study is derived from the shear wave profile illustrated in Figure 3a, obtained through Frequency Time ANalysis (FTAN) technique; specifically, five layers of homogeneous properties are identified. The layer thicknesses and the mean share wave velocities v_s derived from the experimental results are reported in Table 1.

Table 1. Details on the stratigraphy under examination.

Layer	Depth (m)	v_s (m/s)	ρ (kg/m^3)	G_0 (MPa)	e (−)	A
1	0–3	170	1627.93	47.21	1.236	7058
2	3–6	133	1627.93	28.80	1.236	2486
3	6–13	200	1969.42	78.78	0.778	2117
4	13–21	244	1811.42	107.40	0.993	2981
5	21–70	289	1811.42	150.77	0.654	1547

Mean physical and state properties (density ρ and void index e) are assigned to each layer, according to previous laboratory characterisation (Cavallaro et al., 2003; Castelli et al. 2016 a,b); for the soil's strength parameter, the effective cohesion $c' = 15$ kPa and friction $\phi' = 24°$ are considered for the whole profile, as suggested by Cavallaro et al. (2003) and Di Prisco et al. (2006). To consider the effects of polyurethane expansion on the soil's stress state (and consequently on the soil's stiffness) the small-strain shear modulus G_0 is first evaluated as $\rho \cdot v_s^2$; then the formulation of Hardin and Black (1968) is applied to calibrate the soil-dependent parameter A. G_0 will be therefore updated by adding the polyurethane expansion pressure to the soil's confining pressure.

Shear modulus decay and damping ratio variation with the shear strain were derived by performing resonant column tests on six specimens, sampled at different depths; results of the shear modulus decay related to four specimens are shown in Figure 3b. Cavallaro et al. (2003) and Castelli et al. (2016) evidenced that the experimental points are well-fitted by using the formulation of Yokota et al. (1981), with α_1 and β_1, equal to 115 and 1.206 respectively; the formulation was also applied to derive the inverse variation of the damping ratio, resulting in ranging between 3.64 % and 25.6 %.

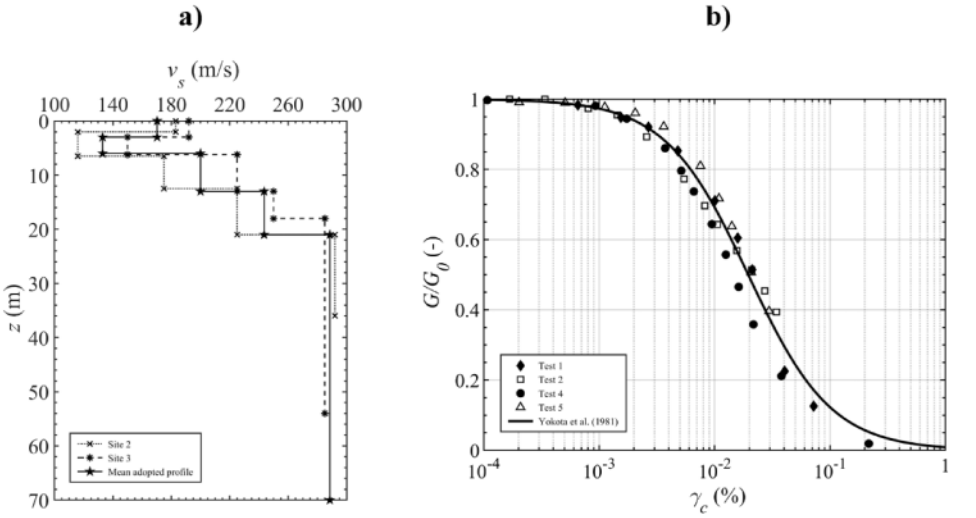

Figure 3. Dynamic characterisation of Noto soil. Results of: a) FTAn technique and b) RC test, after Castelli et al. (2016).

3.2 *The numerical model*

Finite element site response analyses are performed through OpenSees (Mazzoni et al. 2016) and the GID-OpenSees interface (Papanikolaou et al. 2017). Domain consists of a regular hexahedron, having 1 m^2 base and height of 70 m (thickness of the deformable soil); it is discretised with 8-node 3D-*StandardBrick* elements, which have three degrees of freedom (DOF). Analyses are conducted in two phases: a first static phase, when the self-weight is applied and a second dynamic phase, when the seismic response to a base input is studied. Specifically, we study the response to the time history recorded in Sortino station (about 50 km far from Noto) during the 1990 earthquake.

During the dynamic phase, the seismic input is applied horizontally to the domain's base as a point viscous force, depending on the bedrock's viscosity and the velocity time history, as suggested by Joyner and Chen (1975); a uniform shaking is simulated with a planar master-slave assignment between the input (master) and the other base's nodes (slaves). A viscous-elastic bedrock is modelled by fixing the vertical DOF of the base's nodes and introducing a point dashpot simulated through viscous *ZeroLength* elements, located in the same place of the input node, and horizontally tied with it through a master-slave condition. All the described model features are shown in Figure 4.

Note that for a pure shear analysis, nodes belonging to the vertical faces of the hexahedron are also tied with master-slave conditions for all the DOFs.

The hexahedron domain is divided into horizontal layers, according to the stratigraphy summarized in Table 1; the second layer is further divided into two parts, as the deepest assumed injections interact with it. Since the soil is mainly cohesive, a Pressure Independent Multi Yield (PIMY) model, developed by Parra (1996) and Elgamal et al. (2003), is used; this constitutive model allows to simulate a hysteretic and non-linear material, and is based on the multi-plasticity theory. The model is assigned to all finite elements, considering for each layer the corresponding experimentally-derived material parameters, discussed in Section 3.1; the shear modulus decay implemented in the PIMY is observed to well interpret the experimental curve illustrated in Figure 3b. The PIMY constitutive model is used also to model the "injected layers", i.e. the layers modified with the polyurethane injections, after the considerations provided in the following paragraph.

Soil's viscosity is considered through a Rayleigh approach, by evaluating the a_0 and a_1 parameters according to the layers' natural frequencies and damping ratio.

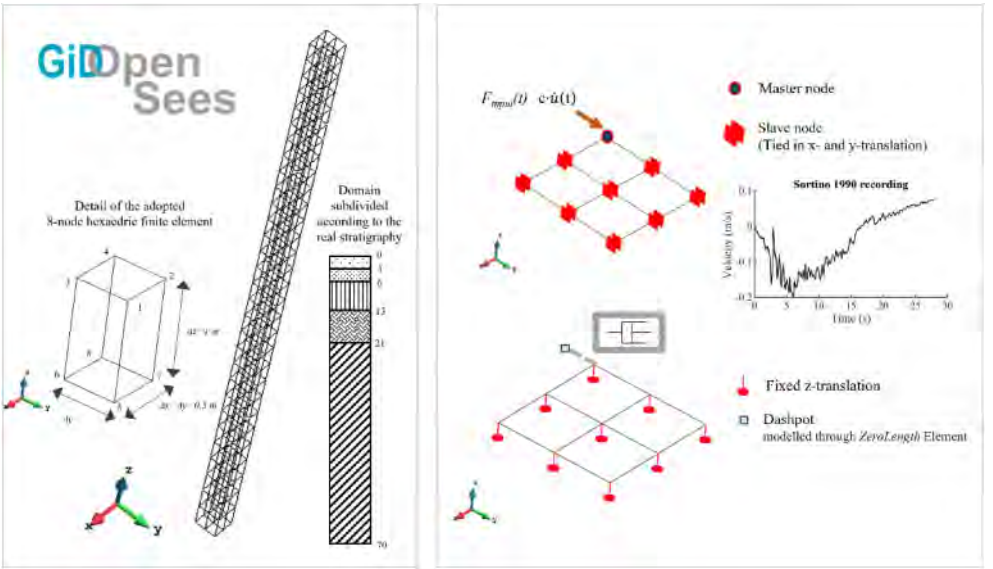

Figure 4. Features of the Finite Element numerical model.

3.3 *Modelling of the injected layers*

Nine injection cases are studied, by considering three injected thicknesses h_{PUR}, equal to 3, 4 and 5 meters, and assuming for each case the injection of three different polyurethane masses m_{PUR}, 15, 20 and 25 kg for injection level. Based on the stratigraphy summarised in Table 1, h_{PUR} involves only the first layer ($h_{PUR} = 3$ m) or partially even the second layer ($h_{PUR} = 4$ m and 5 m).

Due to the nature of the soil under examination, mainly cohesive, injected polyurethane is assumed to expand radially and compress the surrounding soil with poor mixing. The expansion extent is evaluated according to the analytical formulation described in Section 2, depending on the soil's mechanical properties. For each h_{PUR}, a mean effective soil pressure p_0 is evaluated; following the discussed convergency procedure, the diameter d_{PUR} of the pure polyurethane cylinders is derived, as well as the density ρ_{PUR} which depends on m_{PUR} through Eq. (3). ρ_{PUR} allows to estimate the expansion pressure p_{exp}, exerted by the expanding polyurethane to the soil, according to Eq. (9). Values of ρ_{PUR}, p_{exp} and d_{PUR}, derived for the cases examined are reported in Table 2.

According to the evaluated ρ_{PUR} and the soil's pressure p_0, the dynamic properties of pure polyurethane are derived from the formulation of Gatto et al. (2022) (Figure 5); it can be observed

that the behaviour do not change up to ~3% of shear strain, i.e. the range mostly representing the earthquake-induced strains.

Table 2. Results of the convergency procedure for the evaluation of post-expansion polyurethane characteristics.

	$h_{PUR} = 3$ m ($p_0 = 24.48$ kPa)			$h_{PUR} = 4$ m ($p_0 = 32.64$ kPa)			$h_{PUR} = 5$ m ($p_0 = 40.80$ kPa)		
	$m_{PUR} =$ 15 kg	$m_{PUR} =$ 20 kg	$m_{PUR} =$ 25 kg	$m_{PUR} =$ 15 kg	$m_{PUR} =$ 20 kg	$m_{PUR} =$ 25 kg	$m_{PUR} =$ 15 kg	$m_{PUR} =$ 20 kg	$m_{PUR} =$ 25 kg
ρ_{PUR} (kg/m^3)	267.76	272.30	275.07	294.85	300.10	303.12	318.74	323.46	327.73
p_{exp} (kPa)	634.30	644.84	651.35	699.84	713.19	721.16	763.23	779.27	788.57
d_{PUR} (m)	0.27	0.31	0.34	0.25	0.29	0.32	0.24	0.28	0.31

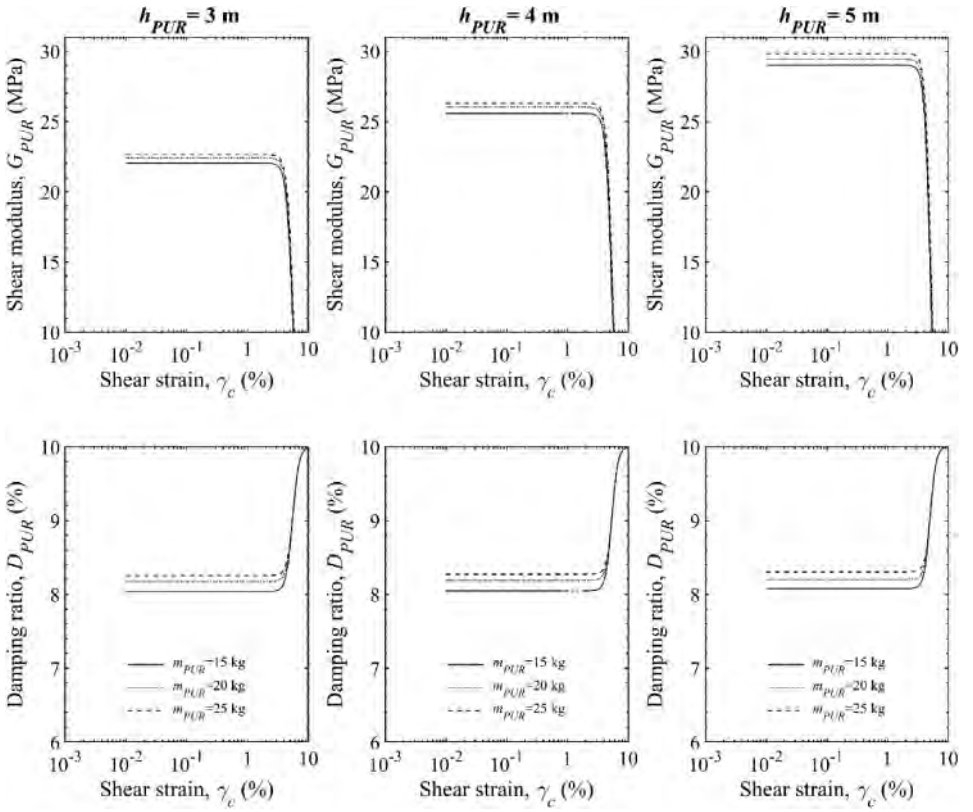

Figure 5. Shear modulus and damping ratio curves of pure polyurethane, injected in different mass and height, evaluated through the formulation of Gatto et al. (2022).

Injected layers are therefore assumed to be made up of pure polyurethane cylinders, of different dimensions and properties, included in the soil (Figure 6). The results of RC tests performed on layered soil-pure polyurethane specimens by Gatto et al. (2019) showed that the pure polyurethane affects only the small-strain dynamic properties, according to the pure polyurethane properties ($G_{0,PUR}$ and $D_{0,PUR}$) and its volumetric percentage Q_{PUR}, while the non-linear behaviour of the composite specimens is mostly governed by the soil; the latter consideration is coherent with results of Figure 5.

Gatto et al. (2021b) derived a homogenisation procedure for the computation of the dynamic properties to assign to a homogenised soil-polyurethane layer:

$$G_{0,homo} = G_{0,soil} \cdot e^{-ln(G_{0,soil}/G_{0,PUR})\cdot QPUR} \tag{10a}$$

$$D_{0,homo} = D_{0,soil} + QPUR \cdot (D_{0,PUR} - D_{0,soil}) \tag{10b}$$

Based on this consideration, the PIMY model is used also for the injected layers by modifying the small-strain modulus through the homogenisation procedure. The damping evaluated through Eq. (10b) is used for the computation of Rayleigh coefficients to assign to the injected region, by evaluating the natural frequencies with an equivalent shear wave velocity when the injection involves two layers of our stratigraphy.

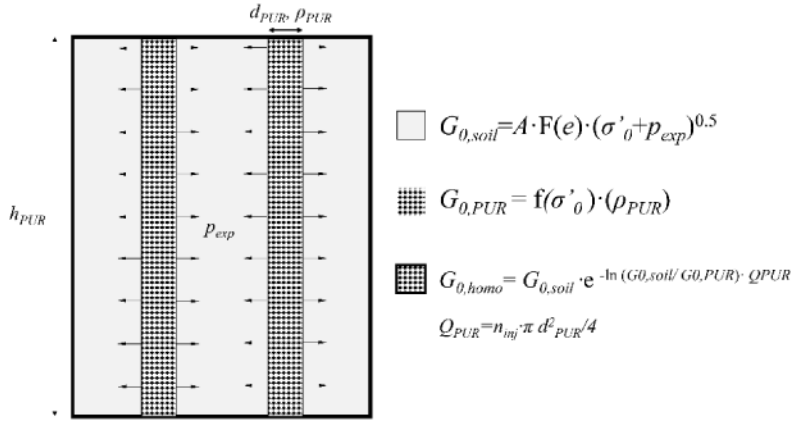

Figure 6. Configuration of injected soil after the polyurethane expansion and summary of the homogenising methodology for small-strain shear modulus.

The expansion pressure of the injected polyurethane determines a variation of the soil's stress state and consequently a stiffening of the soil; as discussed in Section 3.1, this can be considered by updating the small-strain shear modulus of the injected soil, according to the Hardin and Black, by adding p_{exp} to the soil's confining pressure, with the soil-dependent parameters reported in Table 1. Also the unit weight of the composite is derived by considering a linear influence of the volume occupied by polyurethane (Q_{PUR}) and the soil (1-Q_{PUR}). Note that the assumption of injections every 0.5–0.75 m in plan determines four injections in our domain, and the polyurethane volumetric percentage in the injected layer Q_{PUR} can be evaluated as $4{\cdot}\pi d^2_{PUR}/4$.

4 RESULTS

Figure 7 shows the time histories of the horizontal accelerations recorded in the central surficial node of the domain for each case investigated; the maximum acceleration of the original soil is 2.53 m/s^2, while maxima of the modified soils are reported in Figure. It can be observed that acceleration is reduced in all cases thanks to the improvement of the soil's dynamic characteristics given by the polyurethane. The highest reduction is reached when injection effects are simulated up to five-meter depth; moreover, for less injected polyurethane mass the GSI performance is better. This results from the low density that decreases the impedance ratio with the non-injected soil. The maximum reduction obtained is almost 20% for $h_{PUR} = 5$ m and $m_{PUR} = 15$ kg/injection level.

The variation of maxima accelerations recorded in the central vertical is shown in Figure 8; in addition to the reduction involving the whole thickness of the injected layer, acceleration is demonstrated to be reduced even 10–20 m in depth.

Table 3. Summary of parameters used in the numerical analyses.

	$h_{PUR} = 3$ m ($p_0 = 24.48$ kPa)			$h_{PUR} = 4$ m ($p_0 = 32.64$ kPa)			$h_{PUR} = 5$ m ($p_0 = 40.80$ kPa)		
	$m_{PUR} =$ 15 kg	$m_{PUR} =$ 20 kg	$m_{PUR} =$ 25 kg	$m_{PUR} =$ 15 kg	$m_{PUR} =$ 20 kg	$m_{PUR} =$ 25 kg	$m_{PUR} =$ 15 kg	$m_{PUR} =$ 20 kg	$m_{PUR} =$ 25 kg
Q_{PUR} (−)	0.23	0.30	0.36	0.20	0.26	0.32	0.18	0.25	0.30
$G^{*}_{0,soil}$ (MPa)	243.60	245.54	246.73	255.43	257.77	259.16	266.37	269.07	270.62
	–	–	–	91.97	92.78	93.26	96.18	97.11	97.64
$G^{**}_{0,PUR}$ (MPa)	22.03	22.41	22.64	25.57	26.02	26.29	29.01	29.53	29.83
$G^{*}_{0,homo}$ (MPa)	140.16	119.73	104.42	161.20	142.00	124.61	178.71	154.87	139.65
	–	–	–	71.19	66.67	62.19	77.52	72.11	68.41
$D^{**}_{0,PUR}$ (%)	8.04	8.17	8.26	8.05	8.19	8.27	8.08	8.22	8.31
ρ_{homo}r (kg/m^3)	1315	1221	1141	1361	1302	1204	1392	1302	1237
a_0	13.166	13.584	13.933	8.452	8.791	9.188	6.151	6.525	6.797
	0.363	0.363	0.363	0.373	0.373	0.373	0.385	0.385	0.385
a_1 (*10^{-3})	0.090	0.101	0.111	0.133	0.145	0.157	0.175	0.193	0.205
	2	2	2	1.9	1.9	1.9	1.9	1.9	1.9

*Values in the first line refer to the first soil layer (3 meters), while in the second line to the second layer portion of varying according to hPUR

**Values are evaluated according to Gatto et al. (2022)

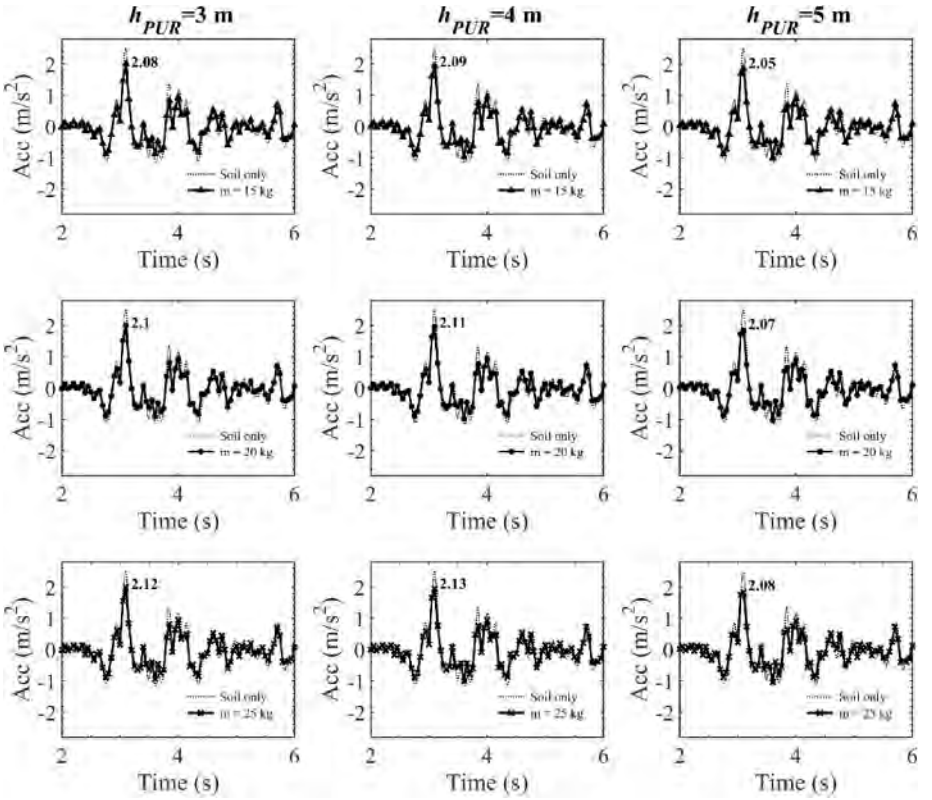

Figure 7. Time-histories of accelerations numerically recorded at the top central node in each examined configuration. For "Soil only", the value of maximum acceleration is 2.53 m/s^2.

In the frequency domain, Figure 9 illustrates that the soil modification with polyurethane injections implies a change in the amplitude of the amplification function, while the natural frequencies are not affected so much by the intervention.

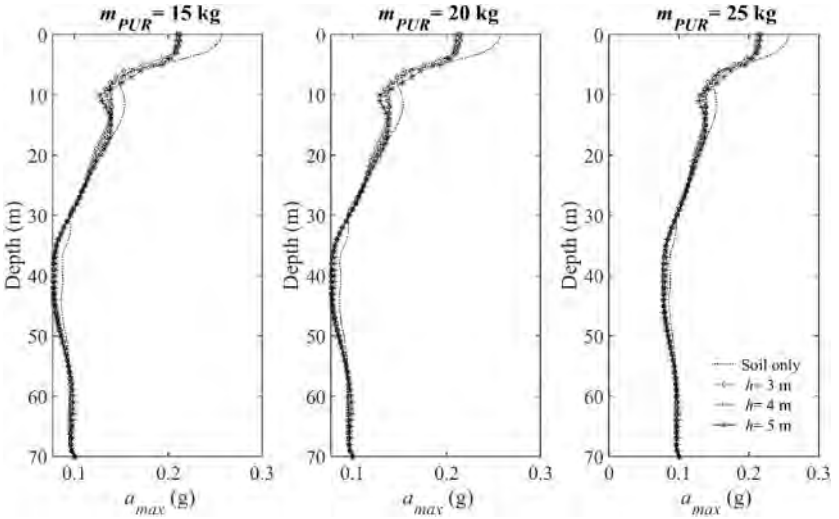

Figure 8. Trend of maximum acceleration varying with depth, in a reference central vertical.

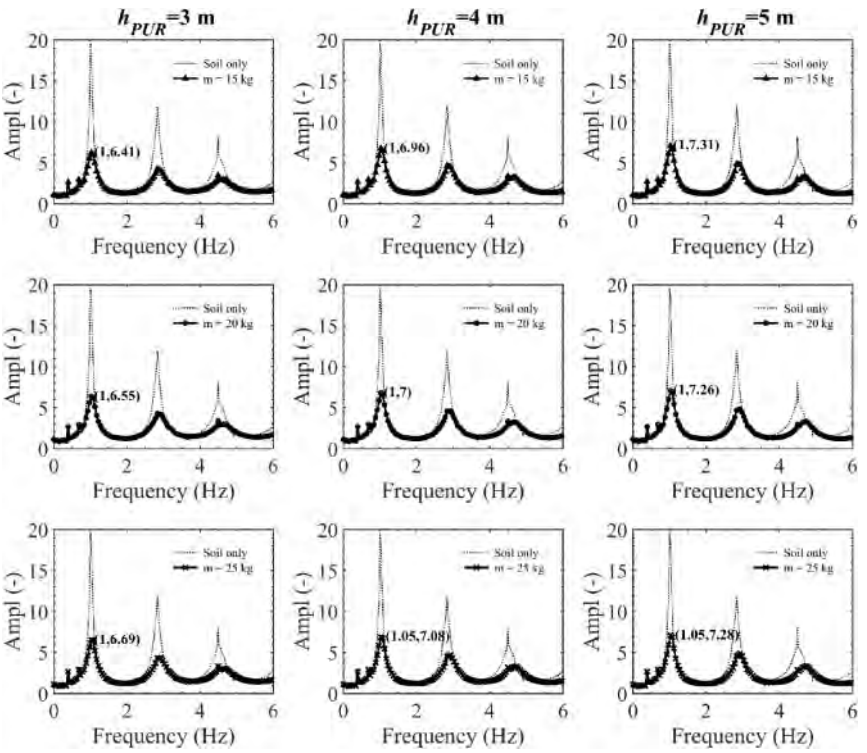

Figure 9. Amplification functions evaluated by dividing the Fourier spectrum of the top and base acceleration.

5 CONCLUSIONS

This study has shown the seismic mitigation related to polyurethane injected underneath an existing building affected in the past by extensive damage due to earthquake. The effects of such an intervention of soil improvement have been considered in a dynamic numerical simulation, after the evaluation of extent and properties through a methodology experimentally and theoretically derived. Results have shown that acceleration is reduced much more when a thicker layer is improved by injecting less material. Further investigations will be conducted towards the large-scale experimentation aimed at validating the methodology here presented.

REFERENCES

Barone, S., Calvi, G. M. & Pavese, A. 2019. Experimental dynamic response of spherical friction-based isolation devices. Journal of Earthquake Engineering 23 (9): 1465–84.

Cavallaro, A., Massimino, M.R. & Maugeri, M. 2003. Noto Cathedral: soil and foundation investigation. *Construction and Building Materials* 17 (8): 533–541.

Castelli, F., Cavallaro, A., Grasso, S. & Ferraro, A. 2016. In Situ and Laboratory Tests for Site Response Analysis in the Ancient City of Noto (Italy). In: *Proceedings of the 1st IMEKO TC4 Int. Workshop on Metrology for Geotechnics*, Benevento, 17–18 March 2016, pp. 85–90.

Castelli, F., Cavallaro, A., Ferraro, A., Grasso, S. & Lentini, V. 2016. A Seismic Geotechnical Hazard Study in the Ancient City of Noto (Italy). *Procedia Engineering* 158: 535–540.

Dei Svaldi, A., Favaretti, M., Pasquetto, A. & Vinco, G. 2005. Analytical modelling of the soil improvement by injections of high expansion pressure resin. *Bulletin für Angewandte Geologie* 10(2):71–81.

De Domenico, D., Gandelli, E. & Quaglini, V. 2020. Effective base isolation combining low-friction curved surface sliders and hysteretic gap dampers. *Soil Dynamics and Earthquake Engineering* 130.

Di Prisco, C., Massimino, M.R., Maugeri, M., Nicolosi, M. & Nova, R. 2006. Cyclic numerical analysis of Noto Cathedral: soil-structure interaction modelling. *Rivista Italiana di Geotecnica* 2.

Eröz, M., & DesRoches, R. 2013. A Comparative Assessment of Sliding and Elastomeric Seismic Isolation in a Typical Multi-Span Bridge. *Journal of Earthquake Engineering* 17 (5): 637–57.

Gatto, M.P.A., Montrasio, L., Tsinaris, A., Pitilakis, D. & Anastasiadis, A. 2019. The dynamic behaviour of polyurethane foams in geotechnical conditions. In: *Proceedings of the 7th International Conference on Earthquake Geotechnical Engineering, Rome, Italy, 17–20 June 2019*.

Gatto, M.P.A., Montrasio, L., Berardengo, M. & Vanali, M. 2020. Experimental Analysis of the Effects of a Polyurethane Foam on Geotechnical Seismic Isolation. *Journal of Earthquake Engineering* 1–22, https://doi.org/10.1080/13632469.2020.1779871

Gatto, M.P.A., Montrasio, L., Zavatto, L. 2021a. Experimental Analysis and Theoretical Modelling of Polyurethane Effects on 1D Wave Propagation through Sand-Polyurethane Specimens. *Journal of Earthquake Engineering*.

Gatto, M.P.A., Lentini, V., Castelli, F., Montrasio, L. & Grassi, D. 2021b. The use of polyurethane injection as a geotechnical seismic isolation method in large-scale applications: A numerical study. *Geosciences* 11 (5):201. https://doi.org/10.3390/geosciences11050201

Gatto, M.P.A., Lentini, V. & Montrasio, L. 2022. Experimental analysis and modelling of the dynamic properties of poliurethane for GSI employments: a numerical study. *Bulletin of Earthquake Engineering* (Submitted)

Montrasio, L. & Gatto, M.P.A. 2016. Experimental Analyses on Cellular Polymers for Geotechnical Applications. *Procedia Engineering* 158: 272–277. https://doi.org/10.1016/j.proeng.2016.08.441

Joyner, W.B. & Chen, A.T.F. 1975. Calculation of nonlinear ground response in earthquakes. *Bulletin of the Seismological Society of America* 65(5), 1315–1336.

Montrasio, L. & Gatto, M.P.A. 2017. Experimental analyses on cellular polymers in different forms for geotechnical applications. In: *Proceedings of the ICSMGE 2017—19th International Conference on Soil Mechanics and Geotechnical Engineering, Seoul, Korea, 17–27 September 2017*.

Tobriner, S. 2003. Building the Cathedral of Noto; earthquakes, reconstruction and building practice in 18th-century Sicily. *Construction and Building Materials* 17 (8): 521–532.

Yu, H.S. & Houlsby, G.T. 1991. Finite cavity expansion in dilatant soils: loading analysis. *Géotechnique*. 41(2):173–183.

Mazzoni, S., McKenna, F., Scott, M.H. & Fenves, G.L. 2006. OpenSees Command Language Manual; Pacific Earthquake Engineering Research (PEER) Center: Berkeley, CA, USA.

Nowamooz, H. 2016. Resin injection in clays with high plasticity. *Comptes rendus Mécanique* 707 (11): 797–806.

Papanikolaou, V.K., Kartalis-Kaounis, T., Protopapadakis, V.K. & Papadopoulos, T. 2017. GiD+OpenSees Interface: An Integrated Finite Element Analysis Platform; Lab of R/C and Masonry Structures, Aristotle University of Thessaloniki: Thessaloniki, Greece.

Sabri, M.M.S., Vatin, N.I. & Alsaffar, K.A.M. 2021. Soil Injection Technology Using an Expandable Polyurethane Resin: A Review. *Polymers* 13, 3666.

Tsang, H.-H., Lo, S.H., Xu, X. & Neaz Sheikh, M. 2012. Seismic isolation for low-to-medium-rise buildings using granulated rubber–soil mixtures: numerical study. *Earthquake Engineering and Structural Dynamics* 41: 2009–2024.

Tsang, H.-H., Tran, D.P., Hung, W.Y., Pitilakis, K. & Gad, E.F. 2021. Performance of geotechnical seismic isolation system using rubber-soil mixtures in centrifuge testing. *Earthquake Engineering and Structural Dynamics* 50: 1271–1289.

Tsiavos, A., Sextos, A., Stavridis, A., Dietz, M., Dihoru, L. & Alexander, N.A. 2020. Large-scale experimental investigation of a low-cost PVC 'sand-wich' (PVC-s) seismic isolation for developing countries. *Earthquake Spectra* 36(4):1886–1911.

Geotechnical Engineering for the Preservation of Monuments and Historic Sites III – Lancellotta, Viggiani, Flora, de Silva & Mele (Eds)

Conservation of ancient Zrug church after landslide

Ivan Strelbitsky
Head of "Conservation Consultancy" private bureau.
Expert for the Ministry of Culture of RF.
Structural engineer-restorer of top category.
Lecturer at the Moscow Architectural Institute.
Expert member of ISCARSAH.

ABSTRACT: Zrug church (remains of it) is standing on the top of the 30 m hill in the Caucasian mountains in the Northern Ossetia – Alania on the level of 2122 m over the sea level. It is dated approximately by 11–12 c. It is one of the basilica type churches built by Christian missionaries on the Northern slope of Caucasus Mountains. This zone is known for its seismic activity, and many abandoned monuments – stone towers, dwelling houses and shrines are affected by seismic vibration. In our case seismic activity affected the hill on which the old church stands. The large part of it is vanished into the river at the top of it. This was the reason for the part of church to follow the landslide and gradually only one Eastern wall and parts of adjoining walls still exist.

There are many ancient stone structures in the mountains in different parts of the world. Some of them are the monuments of universal value. It is also known that mountains are often subjected to earthquakes that can damage stone structures in different ways. Even stronger materials and more advanced technologies sometimes can't provide desired resistance to seismic shocks.

The main reason of collapse was the change of the river flow due to seismic activity or influence of nearby mudflow– a shock of water-soil-stone mix called sel, which besides its huge destructive energy, can form natural dams on rivers. This could be the initial reason for the change of riverbed, erosion of part of the hill and, as a consequence, the destruction of the part of ancient monument.

Figure 1. Typical condition of ancient village in the North slope of Caucasus mountains – towers and living houses after being abandoned by its inhabitants decades ago.

Christian missioners from the South brought new concept of religion, architecture and building methods. The church was built in "Opus quadratum" mode with big square stones – slabs were

 DOI 10.1201/9781003308867-72

placed on both sides of the wall and a very strong backfill – stones and Roman beton. It was so strong that only few vertical and slightly sloped cracks can be seen on its walls. Despite staying without roof for at least 150 years its backfill is still very strong.

Zrug church one of the oldest Christians. temples in Russia. Located in the Alagirsky district of the Republic of the North. Ossetia – Alania, in the high-mountainous Zrug Gorge, next to an uninhabited village not far from the village. Nar. The hard-to-reach Zrug Gorge was part of the historical region. Tualgom (Georgian Dvaleti), along which an important transcaucasian route passed. trade and strategic path.

The region is inhabited by Ossetians who have assimilated the local tribes. During the Middle Ages, the territory was fed by the Diocese of Nikos of the Georgian Orthodox Church (GOC). The culture of Georgia influenced the population of this region.

The building is a single-nave basilica (hall temple) with a semicircular apse inscribed in the general rectangle of the plan; its undivided volume was covered with a gable roof. The decor is modest: platbands and archivolts above the windows and the entrance, to the south. wall block with wicker ornament. The unified internal space of the temple was divided by spring arches and 3-step pilasters into 2 compartments-traveas and several smaller apse. The naos was covered with a box vault, the apse – with a conch; they are illuminated by high windows. At the base of the conch and in the west there are 4 large acoustic jars “golosnik” were laid in a section of the vault of the naos (the southern one was preserved in the altar). The altar part has an elevation, on which a barrier was installed. On the sides of the apse there are 2-tiered pastophoria, connected by passages with the altar space. The lower pastophoria are illuminated by windows overlooking the eastern façade; inside, under them are console-thrones. The upper, windowless rooms were reached by a ladder. The only entrance to the temple is traditionally for this region made from the south. Until recently, wooden doors covered with iron sheets were preserved in the temple. By 2009, the building was badly destroyed: the south wall and altar. Travertine blocks from the masonry of the temple were used in the construction of the fence.

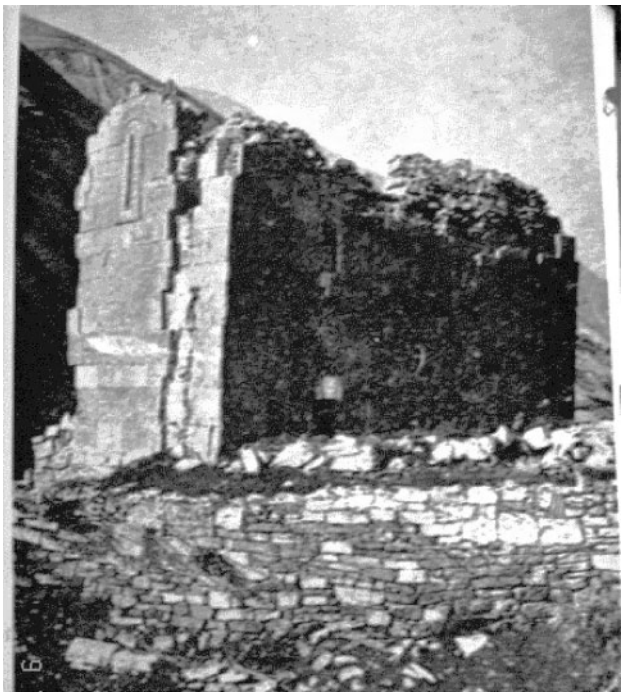

Figure 2. The first known photograph made by ethnographer V. Markovich in 1899.

The collapse of the bigger part of the church happened not before mid 19 c. since the first known photo of 1899 made by geographer V. Markovitch is showing it almost intact – south wall is not damaged, western wall had vertical through cracks, dividing it from the building with obvious inclination outside. On the photo of 1967 we see only south-eastern half of the building, standing on the edge of the landslide.

Unlike many other stone structures in seismic zones Zrug church suffered from seismic vibrations indirectly.

In our case the initial durability of the monument itself was extremely high. The main reason of collapse was the change of the river flow due to seismic activity or influence of nearby mudflow–a shock of water-soil-stone mix called sel, which besides its huge destructive energy, can form natural dams on rivers. This could be the initial reason for the change of riverbed, erosion of part of the hill and, as a consequence, the destruction of the part of ancient monument.

The obvious reason for a landslide was seismic activity which reaches 8–9 points. The last serious earthquake was in the capital of Ossetia happened in 1929.

The effect of the landslide on the church was obviously indirect. Seismic shock had caused the change of the river under the hill and erosion of the slope gradually came up to the church and made the parts of the building fall by large blocks. Vibration of the earth could provoke streams of water-snow-stones-ground mixture called sel from nearby ravines and gorges that also could change riverbed and could lead to the destruction of the hill.

Figure 3. On the photo of 1967 we see only south-eastern half of the building, standing on the edge of the landslide. Photo made by architect V. Kulakov.

In 2007–9 some conservation and reinforcing works were done on the church, expecting that hydraulic engineers, which were building a huge dam at that time in neighboring mountain gorge, will help to restore the small hill and make shore protection.

What was done during the conservation.

1. The remaining structures of the church were tightened together by temporary metal bonds.
2. The main cracks, dividing the walls were repaired by hydraulic lime mix grouting reinforced with fiberglass rods.
3. The upper part of the remaining walls were covered by protective layer of mortar reinforced with plastic mesh
4. To reduce the effect of surface erosion of the hill, a geotextile carpet was laid on it.

Figure 4. View of the church from South-East.

Figure 5. View of the church from North-West.

Figure 6. View of the church after the first part of emergency works.

Restoration part now is currently under development.

- Hydraulic engineers are now restoring the original riverbed
- Both banks of the river should be strengthened with an embankment of large boulders. Vegetation is planned to reinforce the hillside
- The destroyed part of the hill is going to be restored too, to provide the original space that was during the construction of the church. It was a condition of funding the works for restoring the river bed and the missing part of the hill.

Several options were proposed concerning the future image of the monument.

- To conserve the remaining structure as it is now and make several information stands made of glass with the graphic lines showing how the original structure could look like.
- Make visible contour of the church base on the restored site and construct steel structure resembling the size and proportions of original building. Something similar I saw in Philadelphia over the former house of Benjamin Franklin.
- Almost the same as the previous one with the addition of glass walls and the roof over the whole structure.

All these proposals were rejected by the local community which wanted the church erected in full volume. The descendants of the families who lived there several generations before come here regularly and make their rituals in commemoration of the place, settlement and people who lived here and worshipped in the church more than century before.

So the final plan is to reconstruct the missing part of the church, restore stone vault and the roof over the whole volume.

Figure 7. Proposed plan of restoration of the hill and the church after improving the riverbed and strengthening of its banks.

SESSION 4: Effects of urban development and tunnelling on the built heritage

Taylor & Francis
Taylor & Francis Group
http://taylorandfrancis.com

Geotechnical Engineering for the Preservation of Monuments and Historic Sites III – Lancellotta, Viggiani, Flora, de Silva & Mele (Eds)

Municipio Station Metro Line 6 in Naples: A case of urban tunnelling adopting ground freezing and grouting techniques to underpass archaeological findings

G. Russo
University of Naples Federico II, Naples, Italy

F. Cavuoto
Project Manager of Metro Line 1, Naples, Italy

A. Corbo
Geotechnical Engineer, formerly Studio Cavuoto, Naples, Italy

V. Manassero
Underground Consulting S.a.s., Pavia, Italy

ABSTRACT: This paper deals with the construction of two tunnels connecting the existing Municipio Station Line 6 main shaft (interchange node between Metro Line 6 and Metro Line 1 extension project in Naples, Italy) to the TBM extraction shaft located nearly 40 m far from it. The two short tunnels, whose construction in sequence was completed at the beginning of 2018, underpass archaeological findings consisting in fortification walls built in the sixteenth century, through a subsoil composed by loose silty sand overlying a soft and sometimes fractured rock. The groundwater table is close to the ground surface. The excavation phases have been carried out adopting a mix of different ground improvement technologies as cement and chemical grouting at the sides and inverts in tuff and Artificial Ground Freezing at the crowns in the sandy layer. To preserve a unique archaeological site, part of the cultural heritage in the city of Naples, compensation grouting technique was also introduced at the design stage to partially compensate predicted subsidence. In this work, monitored displacements have been back-analysed with a FEM 2D numerical model. The focus of the back-analysis is a better understanding of the effects of volume changes due to AGF adoption on the above historic walls foundations. This experience and the obtained knowledge are a contribution to a better implementation of the technique for future similar projects.

1 INTRODUCTION

Municipio Station is located in the urbanized historical centre of Naples (Italy), facing the impressive backdrop of *Maschio Angioino* Castel and next to the tourist harbor *Molo Beverello*, and it will provide an efficient interchange node between Line 1 and Line 6 of the metro system serving the city (Figure 1). In particular, the new downtown stretch of Line 1 consists of five new stations and twin rail tunnels EPB-TBM excavated, with a total length of about 5 km. This line has also expanded beyond the hilly area of the city towards Capodichino airport. The Line 6, partially constructed several years ago as a light surface rail transportation system, has been further developed with a 6 km new stretch with the use of mechanized excavation via an EPB machine with a large double-track section. Minor works are still going on for two out of four stations located along this stretch, while the other two stations are practically completed (Russo et al. 2012, 2015; Viggiani & de Sanctis 2009). Currently the portion of Municipio Station serving on Line 1 extension is open to the public, whereas Line 6 interchange portion is nearly finished. Two service tunnels, built in

DOI 10.1201/9781003308867-73

the 2017, connect the existing Municipio Station Line 6 main shaft to the TBM extraction shaft, located nearly 40 m far from it.

Figure 1. Municipio Station schematic plan view with highlighted (in red) Line 1 and (in blue) Line 6 and a picture of the site during construction stages.

During the works of the interchange node, important interferences between the excavations and the buried archaeological remnants occurred, unearthing part of the structures of the Roman city port of the I–II century A.D. and fortification walls built in the XVI century under the dominance of Don Pedro de Toledo Spanish Viceroy (Figure 2). These remnants, together with the immaterial archaeological knowledge gained during the excavation works of the rest of the line, represent one of the most important archaeological sites in Europe (Giampaola 2009).

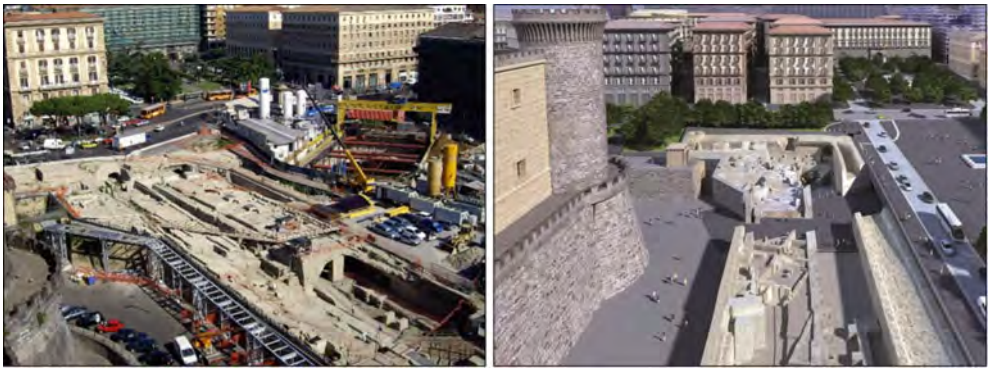

Figure 2. Unearthed sixteenth century fortification walls with the adjacent Maschio Angioino castle: site under construction and rendering of the final layout.

Due to the archaeological findings, the original design had to be changed to include part of the remnants into the new structures. To construct the two short tunnels connecting Line 6 Municipio main shaft to the TBM extraction shaft and to preserve at the same time the above ancient sixteenth century structures, a modification of the original tunnel design was proposed adopting a mix of different technologies to support the excavation: cement and chemical grouting with the Multi Packer Sleeved Pipe (MPSP) method, Artificial Ground Freezing (AGF) and the compensation grouting technique. In this paper the path followed by the designers moving from the preliminary design to the final solution is shortly illustrated. Furthermore, some interesting monitoring data are presented and back-analysed.

2 PRELIMINARY DESIGN OF THE EXCAVATION

The distance between the diaphragm walls of the previously excavated Municipio main shaft and the TBM extraction shaft is less than 50 m and the two connecting tunnels, slightly diverging in plan, have a polycentric cross-section about 6 meters wide and 7 meters high. The ground surface elevation ranges between +12.25 and +3.00 m a.s.l. while the tunnel invert is located at an average elevation of −13.00 m a.s.l..

The subsoil is made by a loose silty sand of volcanic origins (Pozzolana) down to an elevation ranging between −11.85 and −7.25 m a.s.l.. Below the Pozzolana layer, a soft rock is found (Neapolitan Yellow Tuff). This soft rock is well known, and many papers may be found on its geomechanical features (Croce & Pellegrino 1967; Evangelista & Pellegrino 1990; Pellegrino 1967). One of the main features of the tuff formation, which generally worries the designers, is the presence of randomly distributed sub-vertical fractures (locally named *scarpine*), generated at the time of the volcanic deposition phase for the rather quick cooling process of very high temperature material deposited by the eruptions.

In the area the groundwater table at around +3.00 m a.s.l. is nearly horizontal and located about 16 m above the invert of the tunnels. The tunnel front face from site investigations was expected to involve both the upper silty sand (mainly the crown and the upper sides) and the lower soft rock (invert and part of the sides).

To allow a safe excavation under dewatering action, a waterproof barrier with three lines of vertical jet-grouting columns (inserted into the tuff bedrock with a socket nearly 1 meter deep) was executed to confine the volume between the two shafts (Figure 3).

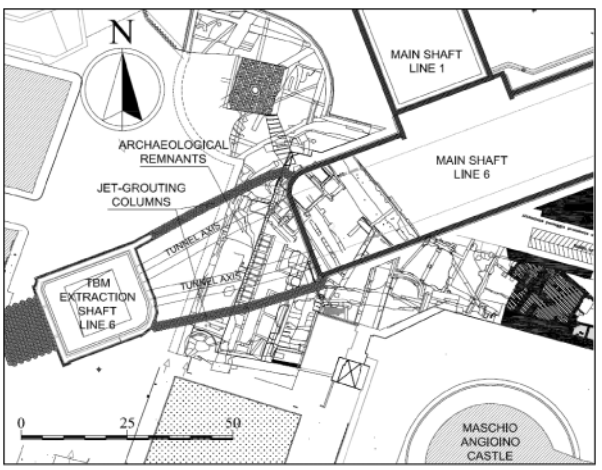

Figure 3. The two connecting tunnels below the ancient remnants, with the lateral jet-grouting barriers.

These columns would have been also useful for safeguarding of the surrounding buildings.

In the preliminary design therefore, preceded by the lowering of the groundwater level through deep wells, the full section excavation was planned to be carried out under the protection of an injected forepole umbrella at the crown and along the upper part of the vertical sides into the granular soil, by using fiberglass tubes to stabilize the front face and advancing with short steps of 1 m immediately followed by the installation of temporary steel ribs and shotcrete. A final r.c. cast in place lining 0.6 m thick was designed separated from the temporary one by a waterproof membrane.

At the preliminary design stage, as usual, some prediction of the movements induced by the tunnel constructions were carried out by means of simple design tools. Among the settlement cause, both

the tunneling via conventional methods and the preliminary dewatering were considered as briefly reported in the next section.

2.1 *Settlement empirical prediction and dewatering field tests*

The gaussian method was used to predict the first component of the expected settlement caused by tunneling. The method is widely known, and here the need to define two main parameters, i.e. the volume loss V_l and the distance of the inflection point i from the tunnel axis, is simply recalled. The relationships between the quantities are also known and here recalled only for the convenience of the readers:

$$V_l = \frac{4V_s}{\pi D^2} \tag{1}$$

where, V_l is the percentage of the volume of the full circular section with an equivalent diameter D; V_s is the theoretical volume of the settlement trough per unit length of excavation which, in the hypothesis of a Gaussian distribution curve (Peck 1969), equals to:

$$V_s = i \times W_{\max} (2\pi)^{0.5} \tag{2}$$

with i corresponding to the distance of the inflection point from the tunnel centre line and $W_{\max}$ being the maximum settlement occurring over the tunnel axis. Based on field data, O'Reilly & New (1982) suggested i to be estimated as:

$$i = K \times Z_0 \tag{3}$$

where Z_o is the depth of the tunnel axis and K is a dimensionless trough width parameter.

For general applications and for particular cases of tunnels in the volcanic soils in Naples area, below and above the groundwater table the research conducted by Bilotta et al. (2002, 2006), Russo et al. (2012) and further refinements (Matrone & Russo 2012) allow to adopt very specific values both for volume loss V_l and for the distance of the inflection point via the parameter K. The selected values are the ones reported in Table 1.

Table 1. Gaussian curves parameters for the settlement prediction of each tunnel.

V_l	D m	K	Z_0 m	W_{max} mm
0.01	5.2	0.52	20.4	7.8

Parameter K was set on the basis of the values recorded in a number of monitoring sections in previous tunnelling experience in the city of Naples which are plotted in Figure 4.

The previous experiences in Naples come from the tunnel excavation along the initial stretch of Metro Line 1 (Russo et al. 2015), carried out by both TBM (Brin street) and by conventional methods (Toledo service tunnel). These values are in Figure 4 compared with previous published general indications and they are in substantial agreement.

For the volume loss the data collected in the research paper by Bilotta et al. (2002) allowed to define for the case of conventional excavation technique the volume loss as a function of a cumulative frequency. The value $V_l = 1\%$ (see Table 1) was selected as a conservative design option.

In the case of Municipio Station twin tunnels, the superposition of two gaussian curves is then adopted to predict the full settlement trough.

The obtained Gaussian curves for the twin tunnels analysed separately are reported in Figure 5, with reference to the section with the smallest centre-to-centre spacing between the pairs of tunnels. The contribution of the tunnel excavation in terms of induced displacements led to a total settlement of nearly 2 cm. To estimate the final expected settlement even in this preliminary stage,

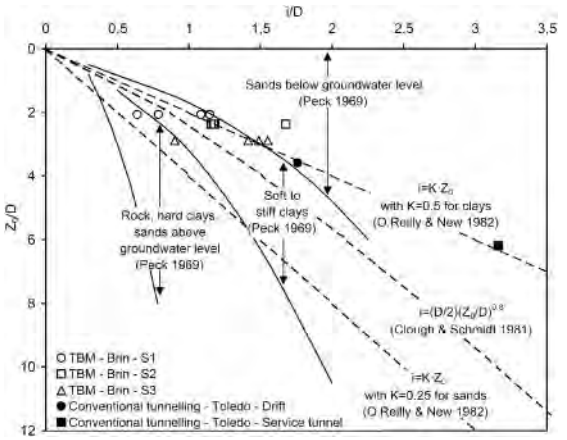

Figure 4. Empirical relations between settlement trough width and tunnel depth – Metro Line 1, Naples.

some additional concern was linked to the dewatering operations that were needed in order to safely excavate the tunnel section. Previous experience along the same stretch of Line 1 (Russo & Nicotera 2020; Russo et al. 2012, 2015; Viggiani & de Sanctis 2009) suggested particular care about this aspect because of large measured buildings settlement.

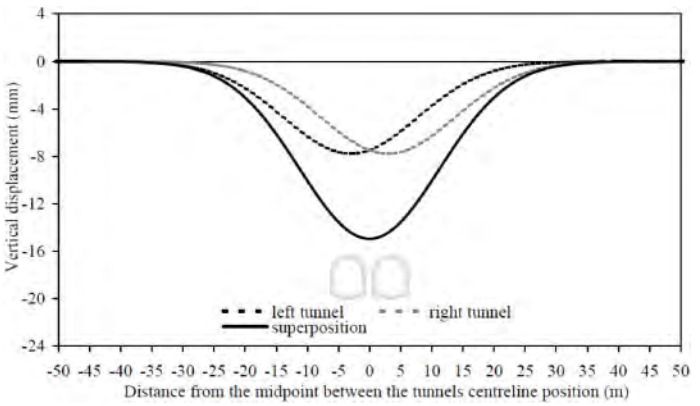

Figure 5. Calculated Gaussian settlement troughs and their superposition.

To reduce uncertainties and risks at the design stage a dewatering field test was organised to check the settlement induced during the tunnels construction (and, therefore, the possible effects on the ancient structures). More details can be found in a previous published work (Russo et al. 2020). The dewatering was indeed not successful because of the drawdown recorded outside the jet-grouting confined area which was ascribed to the presence of discontinuities (*scarpine*) in the tuff formation. Furthermore, the pumping test carried out led to unsatisfactory results for the execution of the excavation of the tunnels. In fact, even pumping a large volume of water (i.e. about 37 l/s) the water table could not be lowered below the tunnels invert location. This was one of the main reasons to modify the design process.

3 MODIFICATION OF THE PRELIMINARY TUNNEL DESIGN

3.1 *AGF and MPSP: adoption of a mixed approach to support the excavation*

The problems with the dewatering suggested to change the tunnel design procedure adopted in the preliminary step. A mix of different measures was combined in the final design: cement and chemical grouting at the lower part of the sides and at the inverts (in tuff) and Artificial Ground Freezing at the crowns and at the upper part of the sides (in sand). The compensation grouting technique was also included to actively protect the historic tuff walls from damages during the construction stages. In Figure 6, the cross section with the soil treatments as fixed at the final design stage is sketched. Boreholes for the soil treatments carried out in presence of Blow Out Preventer (BOP), were conducted from both shafts. In particular, no. 27 horizontal boreholes for grouting at the upper sidewalls and no. 43 directional drillings at the crown for the installation of freezing pipes were carried out from the TBM extraction shaft, while, no. 71 horizontal boreholes for grouting at the lower sidewalls and at the invert together with no. 27 directional drillings for compensation grouting were instead performed starting from the adjacent main shaft of the station included in the Line 6 stretch. The grouting method adopted was the Multi Packer Sleeved Pipe. The system consisted essentially in the installation inside totally no. 98 boreholes of a plastic or steel pipe equipped at regular intervals with rubber grouting sleeves and bag packers fastened to the grouting pipe (expanded against the hole walls through grout injection into the bags) to seal off the sections to be grouted. The role of grouting is to slightly improve the mechanical properties and mainly to reduce the hydraulic permeability of the fractured rock. Initially, cement-based grouting is used to fill the thicker cracks; afterwards chemical grouting is injected to fill the partially treated material, permeating then the remaining thinner cracks (Manassero & Di Salvo 2015).

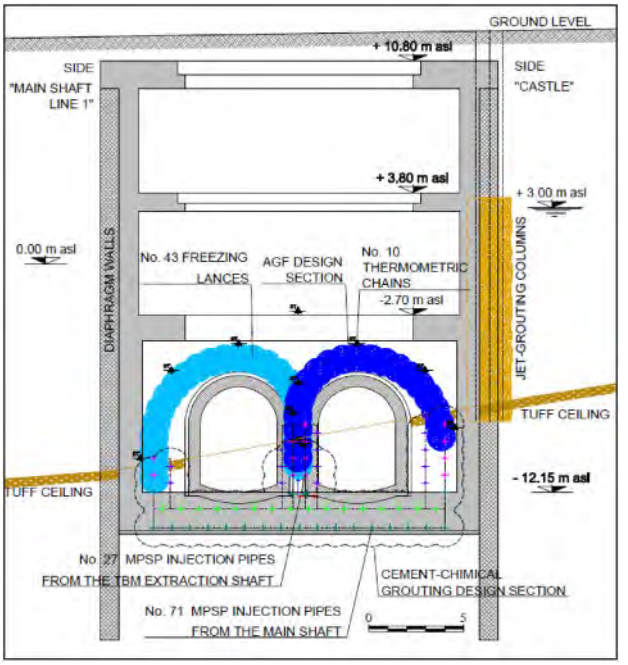

Figure 6. Schematic cross section of the two tunnels and final soil treatments adopted.

To improve the characteristics of the fractured tuff at the lower part of the sides and at the inverts, both cement and chemical grouts were injected through 3100 m of MPSP grouting pipes, fitted with bag packers at 3 m spacing. In total, 150 m^3 of cement-based grout and 530 m^3 of silicate base

grout (Silacsol-S) were injected, i.e. respectively 48 l/m and 171 l/m of grouting pipe. The AGF technique was already extensively adopted in the construction of Line 1 of Naples underground during tunnels excavation below the groundwater table (Cavuoto et al. 2015; Manassero et al. 2008; Russo et al. 2012, 2017; Viggiani & Casini 2015; Viggiani & De Sanctis 2009).

In order to investigate the properties of treated ground, laboratory tests were executed on frozen and subsequently thawed soil samples to obtain mechanical properties to be assigned at the design stage. More details on the soil testing procedure are provided elsewhere in papers on experimental investigations on the behavior of pyroclastic soils under cryogenic conditions (Casini et al. 2016; Pelàez et al. 2014; Russo et al. 2015) At the design phase, numerical analyses were also conducted to simulate the freezing effects (Cavuoto et al. 2019).

AGF was thus adopted to create a frozen arch around each ceiling of the twin tunnels to be excavated in the sandy soil, in order to temporarily ensure stability and waterproofing of the tunnels crown during the construction process until the final lining was installed. The designed construction sequence started with the left tunnel, (side named "main shaft Line 1") activating the ground freezing system first and excavating the tunnel, finally installing the supporting liners. The refrigeration plant was then moved to work for the right tunnel construction following the same steps. During the freezing phase, the initial use of Liquid Nitrogen (LN) as coolant medium (entering at −196°C into the freeze tubes) allowed to form the ice arch very quickly. After a fast lowering of the temperature down to peaks of about −60°C the frozen arch was completed achieving the design thickness of about 1.5 m. The temperature was then kept stable between −15°C and −25°C for the time needed to excavate the full section of each tunnel, by using the less expensive brine (a calcium chloride solution in water) as coolant fluid chilled and re-circulated by a refrigerating plant, until the final lining has been constructed.

Besides, no. 10 sub-horizontal thermometric chains (instrumented by thermocouples arranged at intervals of 5 m) have been installed to obtain real-time distribution of temperatures in the frozen ground with particular reference to the isotherm −4°C, which was assumed to be the isotherm limit of the effective frozen body (Figure 7). By summarizing, the frozen shells at the crown and at the upper part of the sides of the tunnels were built by circulating LN through 1955 m of freeze tubes. The average specific consumption of LN during the freezing phase for the two tunnels was of the order of 1500 l/m^3 of frozen soil. The maintenance of the frozen shells was carried out by circulating brine through the same freeze tubes, chilled by no. 2 industrial refrigeration plants of 250 kW capacity.

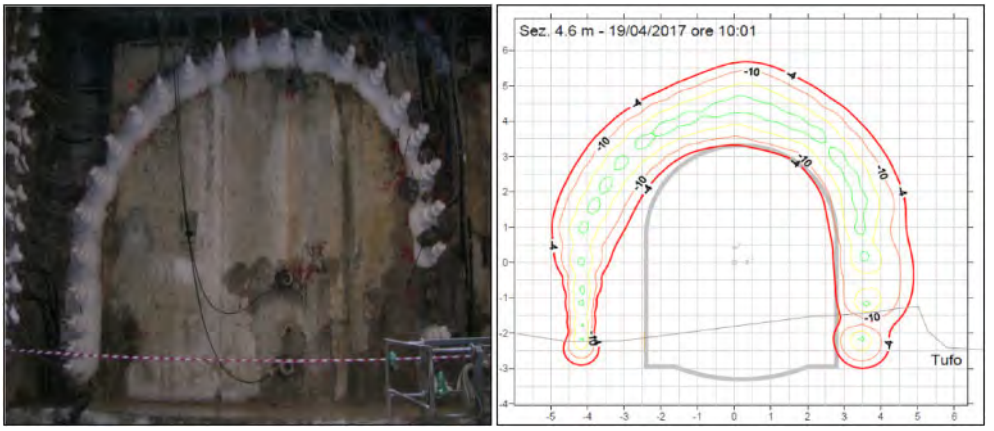

Figure 7. On the left, freeze and temperature pipes around the tunnel section; on the right, the isotherm contour map of the frozen body.

3.2 *Compensation grouting and monitoring displacements during the excavation*

During the extensive and successful application of AGF to construct many tunnels for platforms and pedestrian passageways along Metro Line 1 stations, ground subsidence has been systematically observed via the intense program of monitoring. Settlement has been correlated not only to the usual stress relaxation and volume change related to the tunnel excavation but also to the complex freeze-thaw processes of the pyroclastic soils. Sometimes additional settlements have been produced by not perfect formation of the frozen ring and by the consequent water drainage in the tunnel to be excavated. The compensation grouting was operated when the measured settlement was approaching a fixed threshold. This occurred a few times during the construction and an overall volume of 41 m^3 of cement-based grout was injected. The location of the tubes à manchettes (TAMs) and their portion equipped with injection valves is represented in Figure 8.

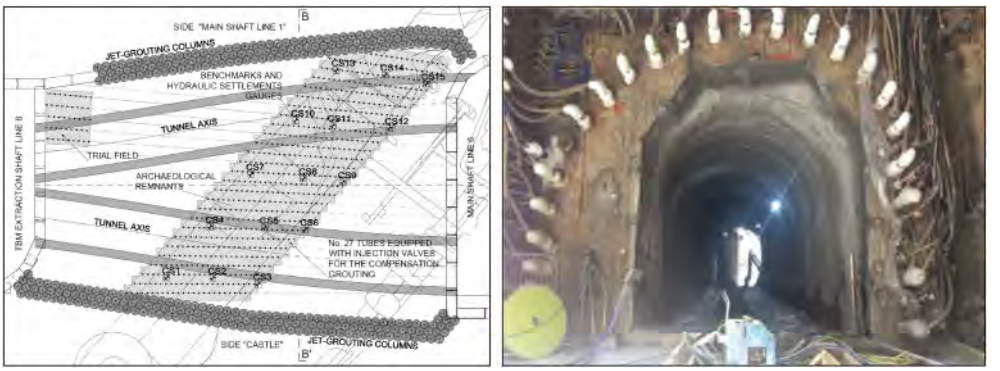

Figure 8. Detail of the designated area for the compensation grouting with TAMs and the excavated tunnel side "main shaft Line 1" with the support of primary lining and AGF.

The excavation of each tunnel section with the aid of AGF was articulated in several steps. After the freezing phase, crown and sides were excavated followed by the installation of the primary lining in steel ribs and shotcrete. After the primary support installation (Figure 8), the excavation was deepened to the invert and then, the reinforced concrete lining was cast in place for the whole section of the tunnel, separated from the provisional lining by a waterproof membrane. At this point, the ground freezing system above the tunnel crown was de-activated and the thawing process took place.

In Figure 9 vertical movements monitored on the wall are reported versus time, from March 2017 when the tunnels construction started, until October 2017 with the completion of the works. The figure shows each construction phase period for the two tunnels, including the freezing heave stage and the thawing effects. Although the construction process is very complex, correlations between measured movements and construction steps are detectable by a careful inspection of the available information. As a matter of fact, heave induced by freezing, downwards movement induced by both tunnel excavation and soil thawing after the complete shutdown of the refrigerating system are recognizable.

In the same figure, piezometric levels monitored by means of a Casagrande piezometer installed next to the tunnels are reported and compared with the displacements. The tunnel side "main shaft Line 1", built first, partially affected the surrounding groundwater level during the excavation phase, probably mainly due to a lack of continuity (poor merging) between the frozen shell and the diaphragm wall of the station main shaft (this section corresponding to the freeze tube toe, installed from the extraction shaft), leading to a water inflow. Such inflow was then detected when the excavation reached this final excavation section, while no defect within the frozen shell body was previously found during the works. Therefore, additional cement and chemical grouting was locally needed and performed around the tunnel crown to limit and contain the water inflow before

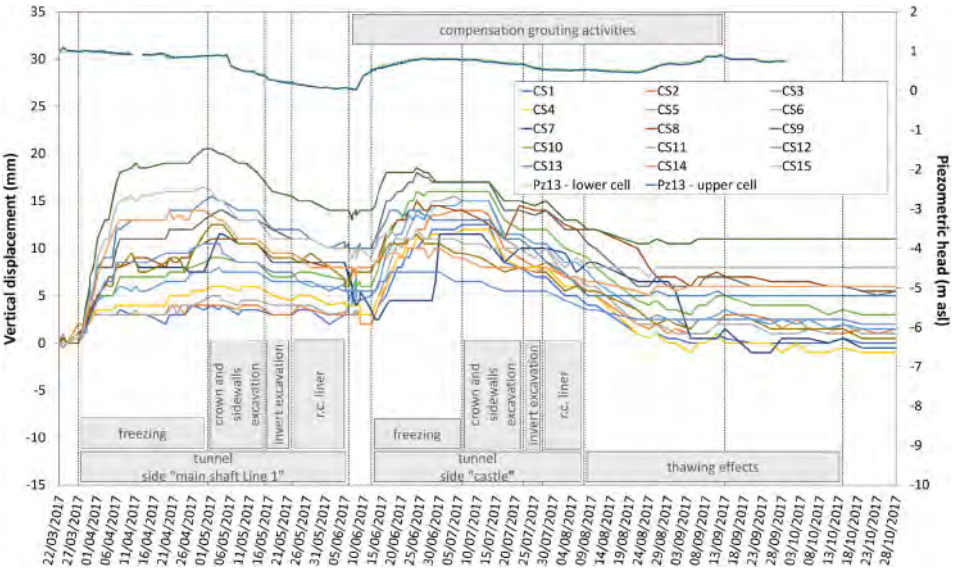

Figure 9. Displacements compared to the piezometric head variation during the construction progress.

the excavation was resumed and completed. Conversely, during the construction of the second tunnel, side "castle", the formation of the frozen shell benefited from the still frozen soil of the adjacent tunnel, thus allowing greater efficacy of the frozen shell both for homogeneity and for continuity. As a matter of fact, during the excavation of the second tunnel no significant effects on the piezometric head were detected.

4 NUMERICAL BACK-ANALYSES

Early analyses have been conducted in particular to simulate the freezing effects, the tunnels excavation and the thawing response, monitored ground freezing heave and thawing process settlement being the target quantities assigning a volumetric expansion to the frozen arch during freezing, and then, a volumetric contraction to simulate the soil deformation after thawing.

Analysis has been implemented in a 2D FEM model taking into account the main steps of the full construction process. Initially, the ground freezing of the left tunnel crown has been introduced through the sudden change of volume (positive volumetric strain) of the treated material.

Then, the analysis proceeded by the left tunnel excavation with the soil removal inside the design section of the tunnel itself and the subsequent installation of the temporary liner as plate structural elements and then, the permanent r.c. lining installation as soil cluster, adopting typical stress reduction methods for simulating the tunneling process. The thawing stage was the last step of the analysis, which was simulated assigning a negative volumetric strain at the soil volume involved by AGF of the left tunnel. After this, the same phases sequence has been applied to model the construction of the right tunnel.

The elasto-plastic Hardening Soil model with isotropic hardening was adopted for the upper sandy Pozzolana layer, being more appropriate to better calculate the induced displacement field, while the simple Mohr-Coulomb model with a linearly elastic initial part was preferred for the lower soft rock and the treated soils.

Main focus was on the capacity of reconstructing surface heave and settlement trough on the basis of measured data, via a simple imposed volume strain variation of the frozen and then thawed materials, to numerically analyse effects of these volumetric changes on neighboring structures

as the ancient masonry wall and the r.c. tunnel lining. In Table 2 main physical and mechanical properties of the soil layers as deduced by site and laboratory investigations and parameters for the treated portions are reported.

Table 2. Soil parameter adopted.

		Sand	Tuff	Frozen sand	Jet-grouting vertical columns
γ_d	[kN/m^3]	15	14	17	16
γ_{sat}	[kN/m^3]	17	16	17	16
$E_{50}^{ref} = E_{oed}^{ref}$	[MPa]	150	–	–	–
E_{ur}^{ref}	[MPa]	450	–	–	–
E	[MPa]	–	1500	450	1000
c	[kN/m^2]	–	1000	500	500
ϕ'	[°]	35	28	35	35
ν	[–]	0.3	0.3	0.3	0.3
K	[–]	0.426	0.531	1	1
Perm.	[m/s]	$1.00 \cdot 10^{-5}$	$5.9 \cdot 10^{-6}$	–	$1.00 \cdot 10^{-9}$
n	[–]	0.47	0.55	–	–

Cement-chemical injections in the tuff formation at tunnels low sides and inverts have been neglected in terms of variation of mechanical parameters due to their main aim of reducing rock permeability, while the previously made jet-grouting vertical columns have been modelled considering their mitigation effect on the development of deformations produced by the tunnels construction.

The ancient masonry wall, in a good state of conservation both as regards the tuff bricks and the binding mortar, has been schematically modelled as a continuous element 9 m high and 27 m long with a 8 m thick part below the ground level, with a Hoek-Brown yield criterion chosen to describe a perfectly plastic behavior assigning limited values of tensile and compressive strength (Losacco et al. 2016). Values of stiffness and unconfined compressive strength derive from well-known previously published studies on Neapolitan Yellow Tuff (Evangelista & Pellegrino 1990) while tensile strength value was assumed equal to the shear strength for which Italian Design Code provides ranges of values based on bricks typology (MIT 2019). Masonry wall mechanical properties are summarized in Table 3. Groundwater table is modelled about 16 m above the invert of the two tunnels. In Figure 10 a detail of the numerical model is represented with the two tunnels, the boundaries of the areas involved by AGF at the tunnels crown, the lateral jet-grouting columns and the historic wall on the surface.

Table 3. Mechanical properties of masonry wall.

		Masonry wall
γ_d	[kN/m^3]	14
γ_{sat}	[kN/m^3]	16
E	[MPa]	1000
s_c	[kPa]	5000
s_t	[kPa]	50
ν	[–]	0.3

In Figure 11 incremental displacements of the ancient walls at section BB' are plotted (benchmarks CS3, CS6, CS8, CS10, CS13 in Figure 8). The incremental heave at the completion of the ground freezing activities of each tunnel, and the incremental settlement at the completion of the tunnels excavation (including the thawing effects) are evident. The displacements are plotted versus the distance from the midpoint between the tunnels centreline position. A maximum heave of

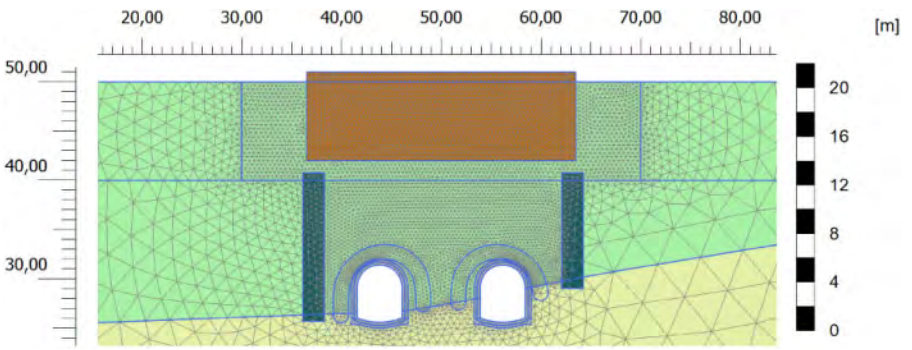

Figure 10. Detail of the FEM model with the adopted mesh.

nearly 20 mm occurred during ground freezing, while nearly 15 mm of downwards movements were recorded during the subsequent construction of the tunnels and the thawing process. According to other published case histories (;usso et al. 2017; Shuster 2000), the thawing settlement is usually larger than the upwards movement (heave) induced in the initial freezing steps. On the contrary, in this case, settlement produced by excavation and thawing are slightly less than the previous heave. This result was basically obtained also thanks to the compensation grouting activities in progress starting at the end of the construction of the first tunnel, that mitigated and partially compensated the final settlement. For space reason, this topic will be better addressed in forthcoming research papers.

Always in Figure 11, monitored data are compared to the calculated incremental displacements corresponding to the two ground freezing phases and to the two tunnels excavation and thawing phases, regarding section BB' in Figure 8 characterized by a cover of 18 m and an horizontal span of 12.5 m between the two tunnel axes.

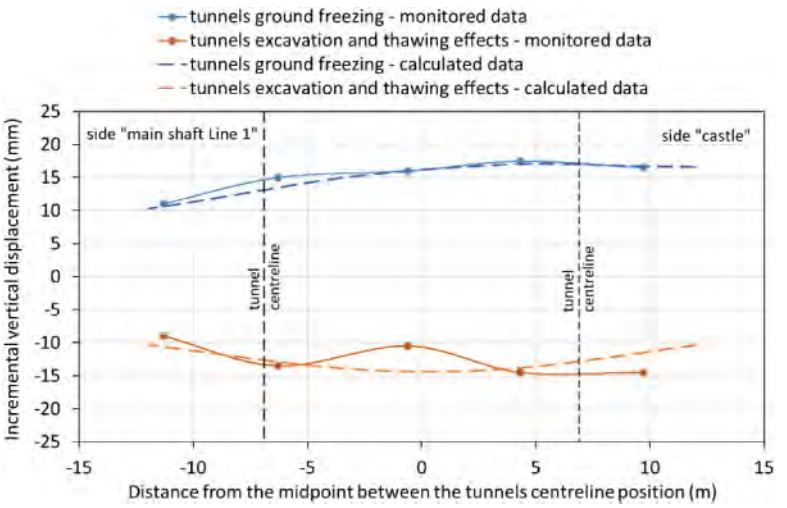

Figure 11. Comparison between measured and calculated displacements.

To obtain a best fitting of the monitored data, a volumetric strain DV/V equal to ±1.3% was imposed for the left tunnel, as expansion at the freezing soil phase and as contraction at the thawing phase, while a volumetric change DV/V = ±1.7% was assigned for the right tunnel freezing and thawing phases. This difference is probably related to the fact that the freezing phase of the right

tunnel on site was affected by the still partially frozen soil of the left tunnel built before, determining an increase of the soil portion involved by the right tunnel freezing crown compared to the portion defined at the design phase, and in this way, amplifying freezing and thawing effects, modelled in the numerical analysis in terms of volumetric change, respect to the left tunnel case These back-analysed volume variations are lower in value than those related to the pore water state change, estimated as 0.09 times the soil porosity (Andersland & Ladanyi 2004). The reason could be related in part to the mitigation effect produced by the pre-conditioning phase of the compensation grouting, and in part to the drained behavior of the involved silty sand determining a pore water migration out of the freezing zone during the freezing phase. In-depth studies are underway on these aspects by the authors.

Contours of calculated horizontal tensile strain in the tuff wall are plotted in Figure 12, related to the second tunnel ground freezing phase in which tensile strain reaches the maximum value due to hogging deformation. In particular, concentration of tensile strain due to plastic deformations, occurs at the upper part of the wall reaching a value of about 0.13% of ε_{xx} with which slight damages could be expected according to Boscardin and Cording (1989).

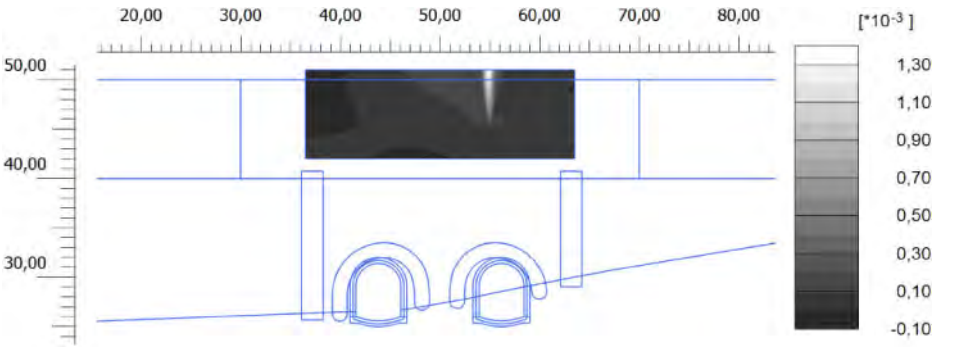

Figure 12. Contour of calculated horizontal strain e_{xx} in the modelled wall.

5 CONCLUSIONS

The twin tunnels, connecting the existing Municipio Station Line 6 main shaft (inter-change node between Metro Line 6 and Metro Line 1 extension project in Naples, Italy) to the TBM extraction shaft were located under a valuable archaeological site where remnants dating back to the sixteenth century were found. The original design had to be modified in order to permit the safe and dry tunnel excavation excluding any even minor negative effect on the valuable ancient structures. Different soil treatments have been designed and concurrently applied.

In particular, cement and chemical grouting at the lower part of the sides and at the inverts (in tuff) to seal even hidden discontinuities where these could be expected and the Artificial Ground Freezing at the upper part of the sides and at the crown (in sand below groundwater table) were adopted. The indication coming from previous applications of AGF technique on Line 1 in recent years was that in volcanic soils, such as Pozzolana and shallow weathered portions of tuff, not negligible settlements might be induced during the thawing stage. In this project the compensation grouting technique was thus employed in order to successfully preserve the historic fortification walls built in the sixteenth century from potential damages during the complex construction stages. The monitored final outcome (i.e. vertical upwards and downwards movements) is a clear indication of the benefits produced by this additional remedial measure.

With the adopted simplified numerical approach we would like to focus on considering at early design phase effects of volume variation induced by AGF in the subsoil (which undoubtedly occurs

for various complex physical phenomena, liquid/solid state pore water change, water drainage and motion of fine particles), to preserve existing nearby structures.

Estimation of such effects, also in a numerical simplified way as applying a volume change to the soil involved by AGF (from this case history DV/V=±1÷2% is suggested in case of volcanic silty sand to roughly simulate both the complex freezing and thawing phenomena), could be thus crucial in specific contexts to assess expected damage of building often of historic and artistic value and to define suitable mitigation solutions.

ACKNOWLEDGEMENTS

The authors are grateful to the contractor Ansaldo STS for providing the project information of Municipio Station and to Metrotec Scarl construction company with the stakeholders Trevi SpA and Cipa SpA for the support on the technical data. Tecno In SpA must also be mentioned for supplying the site and laboratory investigations data.

REFERENCES

Andersland, O.B. & Ladanyi, B. 2004. *Frozen ground engineering*, Second Ed., New Jersey: John Wiley & Sons.

Boscardin, M. D., & Cording, E. J. 1989. Building response to excavation-induced settlement. *Journal of Geotechnical Engineering*, 115, 1–21. doi:10.1061/(asce)0733–9410(1989)115:1(1).

Bilotta, E., Russo, G. & Viggiani, C. 2002. Cedimenti indotti da gallerie superficiali in ambiente urbano. *Atti XXI Convegno Nazionale di Geotecnica,* Bologna: AGI.

Bilotta, E., Russo, G. & Viggiani, C. 2006. Ground movements and strains in the lining of a tunnel in cohesionless soil. *Proc. 5th Int. Symp. Geotech. Aspects of Underground Construction in Soft Ground*: 705–710. Leiden: Taylor & Francis/Balkema.

Cavuoto, F., Corbo, A., Manassero, V. & Russo, G. 2015. Naples Metro Line 1: the service tunnel at Toledo Station, *Gallerie e Grandi Opere Sotterranee, n.116, December 2015*: 9–19. Bologna: Pàtron Editore.

Cavuoto F., Manassero V., Russo G., Corbo A. 2019. Urban tunnelling under archaeological findings in Naples (Italy) with ground freezing and grouting techniques. *Proceedings of the WTC 2019 ITA-AITES World Tunnel Congress "Tunnels and Underground Cities. Engineering and Innovation Meet Archaeology, Architecture and Art"*, May 3–9, 2019, Naples, Italy. Taylor & Francis Group, London.

Casini, F., Gens, A., Olivella, S. & Viggiani, G.M.B. 2016. Artificial ground freezing of a volcanic ash: laboratory tests and modeling. *Environmental Geotechnics,* 3(3): 141–154. London: ICE Publishing.

Croce, A., Pellegrino, A. 1967. Il sottosuolo della città di Napoli. Caratterizzazione geotecnica del territorio urbano. *Atti VIII Convegno Italiano di Geotecnica*, Cagliari.

Evangelista, A., Pellegrino, A. 1990. Caratteristiche geotecniche di alcune rocce tenere italiane. In*: Proc. of the 3rd Conf. of Rock Engineering and Mechanics MIR90*, Torino, pp. 2.1–2.32.

Giampaola, D. 2009. Archeologia e città: la ricostruzione della linea di costa. *TeMA – Trimestrale del Laboratorio Territorio Mobilità Ambiente.* 2(**??**): 37–46. Napoli.

Losacco, N; Callisto, L; Burghignoli, A. 2016. Soil-structure interaction due to tunnelling in soft ground, an equivalent solid approach. In: *Proceedings of the 10th International Conference on Structural Analysis of Historical Constructions* (SAHC 2016, Leuven, Belgium). CRC Press, London, pp.495–502.

Manassero, V., Di Salvo, G., Giannelli, F. & Colombo, G. 2008. A combination of artificial ground freezing and grouting for the excavation of a large size tunnel below groundwater. *Proceedings of the 6th International Conference on Case Histories in Geotechnical Engineering*, Arlington (VA).

Manassero, V. & Di Salvo, G. 2015. The application of grouting technique to volcanic rocks and soils to solve two difficult tunnelling problems. In *Proc. of The International Workshop on Volcanic Rocks and Soils*: 399–408. Ischia Island: AGI.

Matrone & Russo 2012. Internal report based on Master's thesis on Settlement induced by tbm in the downtown streth of line 6 (2012).

MIT (2019). Circolare n. 7 del 21 gennaio 2019 del Ministero delle Infrastrutture e dei Trasporti. Istruzioni per l'applicazione dell'"*Aggiornamento delle "Norme tecniche per le costruzioni"*" di cui al decreto ministeriale 17 gennaio 2018 (in Italian).

O'Reilly, M.P. & New, B.M. 1982. Settlements above tunnels in the United Kingdom – Their magnitude and prediction. *Proceedings of Tunnelling'82 Symposium*: 173–181. London: Institution of Mining and Metallurgy.

Peck, R. B. 1969. Deep Excavations and Tunnels in Soft Ground. *Proceedings of the 7th International Conference on Soil Mechanics and Foundation Engineering, State of the Art Volume*: 225–290. Mexico City: Sociedad Mexicana de Mecanica.

Pelàez, R.R., Casini, F., Romero, E., Gens, A. & Viggiani, G.M.B. 2014. Freezing-thawing tests on natural pyroclastic samples *6th Int. Conf. Unsaturated Soils, UNSAT2014*: 1689–1694.

Pellegrino, A. 1967. Proprietà fisico meccaniche dei terreni vulcanici del Napoletano. In: *Proc. of the VIII Italian Geotechnical Conference*, Cagliari.

Russo, G., Viggiani, C. & Viggiani, G.M.B. 2012. Geotechnical design and construction issues for lines 1 and 6 of the Naples underground. *Geomechanik und Tunnelbau* 5(3): 300–311. Berlin: Ernst & Sohn.

Russo, G., Corbo, A., Cavuoto, F. & Autuori, S. 2015. Artificial Ground Freezing to excavate a tunnel in sandy soil below groundwater table. Measurements and back analysis. *Tunnelling and Underground Space Technology,* 50: 226–238. The Netherlands: Elsevier. (doi:10.1016/j.tust.2015.07.008).

Russo, G., Corbo, A., Cavuoto, F., Manassero, V., De Risi, A. & Pigorini, A. 2017. Underground culture: Toledo station in Naples, Italy. *Proceedings of the Institution of Civil Engineers – Civil Engineering, November 2017*. 170(4): 161–168. London: ICE Publishing. (doi:10.1680/jcien.16.00027).

Russo G., Cavuoto F., Corbo A., Manassero V. 2020. A case of urban tunnelling with ground freezing and grouting techniques in presence of archaeological remnants: Municipio Station in Naples (Italy), *Gallerie e Grandi Opere Sotterranee*, n.134, November 2020, pp.7–18, Pàtron Editore - ISSN-0393-1641.

Russo & Nicotera 2020. Monitoring a deep excavation in pyroclastic soil and soft rock. Submitted for publication on *Tunnelling and Underground Space Technology*. The Netherlands: Elsevier.

Viggiani, G.M.B. & De Sanctis, L. 2009. Geotechnical aspects of underground railway construction in the urban environment: the examples of Rome and Naples. *Geological Society Engineering Geology Special Publication*. 22(1): 215–240. London: The Geological Society.

Viggiani, G.M.B. & Casini, F. 2015. Artificial Ground Freezing: from applications and case studies to fundamental research. *Invited Papers*: 65–92. London: ICE Publishing.

Geotechnical Engineering for the Preservation of Monuments and Historic Sites III – Lancellotta, Viggiani, Flora, de Silva & Mele (Eds)

The design of Venezia station of Rome Line C underground

E. Romani, M.D'Angelo & L. Sidera
Metro C S.c.p.A., Rome, Italy

A. Sciotti
Roma Metropolitane, Rome, Italy

ABSTRACT: The construction of Venezia station of Rome Line C underground is a significant engineering challenge in archaeological and monumental context making. The civil works will start with the excavation of the diaphragm walls - 85 meters in length – and thereafter the archaeological investigation will start until a depth of 15 meters before the realization of the cross walls to reduce the deformability effects. The complex geological context imposed the choice of the ground freezing technology for the tunnel excavation. Geotechnical and structural analyses have been developed to study the potential effects of the excavation on the monuments designing geotechnical and structural interventions for their protection. At the end of the excavation part of the archaeological structures discovered will be relocated in the atrium of the station that will represent an "*unicum*" with the museums of Venezia Palace, the Vittoriano and the Roman Forum.

1 INTRODUCTION

Line C is the new line of Rome underground. Once completed, it will cross the city from North-West to South-East, for a total length of 25.6 km including 30 stations, almost doubling the extent of the currently existing underground network, thus confirming itself as an infrastructure of outstanding importance in the public transport system in relation to the high population density of the city. It is also the first fully automated underground line in Rome.

Metro C is the General Contractor consisting of Partecipazioni Italia (WeBuild corporate, representative, once Astaldi), Vianini Lavori, Hitachi Rail STS (ex Ansaldo STS), CCC (Consorzio Cooperativa Costruzioni) and CMB (Cooperativa Muratori e Braccianti). It manages the construction of Line C in its implementation and operational phases from the preliminary design to the start-up of the line, through the archaeological surveys, the station construction and tunnel excavation, the trains manufacturing. Roma Metropolitane is a company of the Municipality of Rome and it is the contracting authority of the Line C project. The activities started in 2006 and now 22 stations and 18 km of line are in operation.

During the construction of the first section (Pantano-Fori Imperiali) of the line, Metro C developed the design for the realization of the next segment, between Fori Imperiali station and Venezia station, which is right in the centre of Piazza Venezia. The project represents a difficult engineering challenge because of the complex context in which it places, characterized by several pre-existences of inestimable historic, artistic and monumental value above and below the ground level. Furthermore, the project provides an adequate interface with the future contract from Venezia station to Clodio/Mazzini station and at the same time a configuration of Venezia station as a temporary terminal node; Moreover, the design is developed considering a museum set-up for the archaeological heritage found during the excavations. For this reason, the first floor below the ground level of the station is designed as a connection between Venezia Palace, Vittoriano and Roman Forum.

DOI 10.1201/9781003308867-74

Figure 1. A view of Piazza Venezia with the projection of the Venezia stations.

In order to safeguarding the monuments potentially interacting with the excavations, Metro C has also developed the studies of line-monuments interaction in collaboration with the geotechnical and structural engineering department of the La Sapienza University of Rome, by means of specific 2D and 3D analyses that provide an intervention guideline for the designer.

2 THE CONTRACT VENEZIA-FORI IMPERIALI

The contract Venezia-Fori Imperiali runs from the end of the contract T3, currently under construction, and goes on underneath Fori Imperiali street for about 250 m until Piazza Venezia where Venezia station is foreseen. The contract consists of works and parts of works that guarantee the functioning of the station as a temporary terminal of Line C.

One of the main objectives pursued for the external arrangement was to restore a space in which the elements of the subway were not only well inserted from a material and architectural point of view but could become a new urban layout. In this way the elements that emerge on the surface become evidence of what happens in the underground environment in accordance with the design of the museum hub constituted by the atrium of the station.

The general geological situation of the area concerned by the route is widely described in numerous scientific publications. The most recent geological maps of the city of Rome are due to Ventriglia and Sciotti (1970), to Marra and Rosa (1995), to Ventriglia (2002), Funicello and Giordano (2005); the hydrogeological maps are due to Sciotti (1970) and Corrazza and Lombardi (1995). These maps constitute the basic reference for the general geological framework of the area in question. The reconstruction of the stratigraphic succession and of the geological profiles is based on the analysis, interpretation and correlation of the data collected with the specific geognostic investigations carried out in the various phases of study and design, along the route of the line and in the surrounding areas.

The most ancient soils in the urban area of Rome are composed essentially by marine clays of the Pliocene age which reach a thickness of about 800 m. Approximately 18000 years ago, the regression of the sea level determined a significant erosive phase. The Tevere river deepened its bed to an altitude of −50 m a.s.l., deeply affecting the pliocene clays. With the subsequently sea level rise, the incision was filled with alluvial deposits characterized by a basal level of gravel and mainly consisting of silty-clayey and silty-sandy sediments with frequent peaty level. In this

way was formed the extensive alluvial plain that characterizes the area between Corso Vittorio Emanuele II and Fori Imperiali street.

Starting from the actual ground level, below a consistent anthropogenic soil layer (R) is therefore possible to trace the presence of clayey-silty soils of various granulometry and consistency (Ag) above the fluvial deposits of the middle Pleistocene consisting of weakly silty fine sands (Tb).

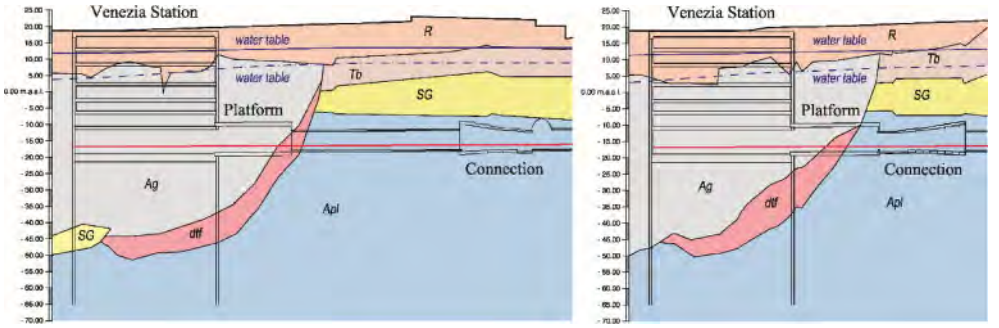

Figure 2. Geological longitudinal profile of the contract Venezia-Fori/Imperiali: south tunnel (left) and north tunnel (right).

Between this layer and the bedrock made up of Pliocene clays (APL) is the layer of deposits of the lower Pleistocene composed of medium-large sand with gravel (SG). In correspondence with the future tunnels (designed to be excavated with traditional method) there is a lens of landslide debris made up of very heterogeneous soils composed of medium-fine sands, sands with gravel, sandy-clayey silts and fragments and block of volcanic tuff mixed with recent alluvial sediments (Dtf). The main water table is located in the pleistocene sediments and in the overlying volcanites, in connection with the alluvial deposits of the Tevere and the Aniene and their main tributaries which constitute the drainage of the aquifer itself. It was found between 26 m and 13 m above sea level, at a depth of 8–10 m from ground level. SG layer is gravelly horizon which contains a considerable water table under pressure. The aquifer present in the Sg gravels finds its feeding outside the urban area.

The twin running tunnels, have been already excavated with the mechanized excavation method by means of two EPB (Earth Pressure Balance) TBMs (Tunnel Boring Machines) at a depth of about 35 m below the ground level. The tunnels have a circular section with an excavation diameter of 6.70 m and 0.3 m thick precast concrete segmental lining, with 5.80 m internal diameter. They extend seamlessly from the current end of the contract T3 to the interior of the future station building for a length of about 215 m.

Venezia stations has a rectangular plan 80 m long and 30 m wide, and it has three entrances located in correspondence of the nearby monuments which constitute a unicum museum with the station itself. The station presents five underground level in addition to the cover plan and the foundation slab for a total depth of 40 m below the ground level. The excavation is realized by means of top-down method using perimetral diaphragms 1.5 m thick and 85 m long, necessary to reach the bedrock. An adequate intersection between the diaphragms and the bedrock consisting of the pliocene clays with very low permeability allows to reduce or eventually eliminate the need for injections aimed at creating an underlaying pad.

The project also involves the construction of a series of orthogonal diaphragms called cross walls and buttress walls which will be realized to reduce the deformability of soil-structure system and to guarantee a high transversal contrast during excavation phases. The museum station is functionally and architecturally designed to receive the ancient structures that will be found during

the excavation, guaranteeing the underground connection between the atrium of the station and the three monuments near to it just above mentioned.

Tunnels that will have platform inside will be built with traditional method of excavation widening from TBM tunnels using the artificial ground freezing to reduce the permeability of the soils and to improve their mechanical characteristics. These tunnels' length is about 50 m and the width of their transversal section is equal to 12 m. Simultaneously with the excavation of these tunnels, the connection between the north and the south tracks will be realized using the same excavation and consolidation method for other 120 m starting from a different ventilation shaft close to the front of the Vittoriano building on Fori Imperiali street.

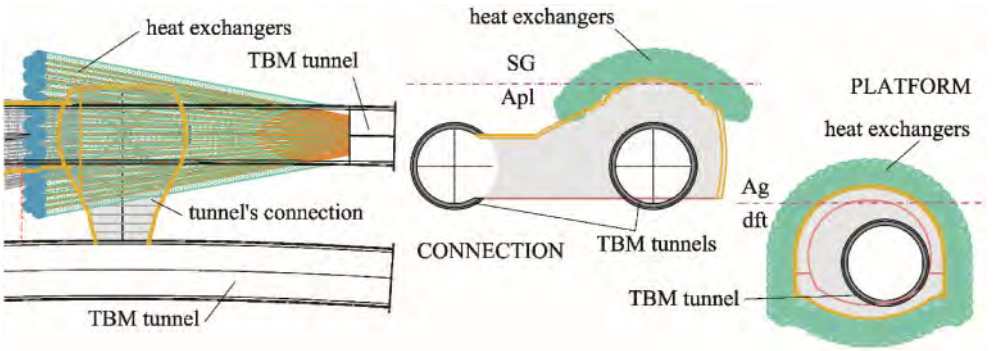

Figure 3. A planimetric view (left) and a transversal section (right) of the artificial ground freezing for the connection between two tracks.

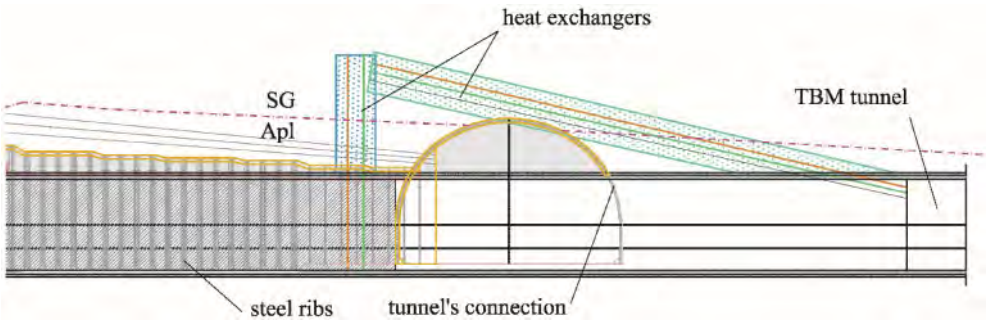

Figure 4. Longitudinal section of the artificial ground freezing for the connection between two tracks.

The artificial ground freezing method consists in freezing water inside a mass of soil, according to a predetermined geometry, thanks to heat exchangers inside which the circulation of a low temperature liquid captures heat from the ground and dissipates on the outside. A frozen phase will be realized using nitrogen while a subsequent maintenance phase will be made by brine. This complex technique has been chosen because the realization of a frozen wall in which the tunnel excavation operations and the subsequent construction of the lining are carried out, guarantees grater safety with regard to problems that could be caused by water filtration or local collapses of the excavation surface, compared to traditions consolidation technologies, thus mitigating the effects of the potential subsidence at the ground level. Furthermore, a mixed system nitrogen-brine will be used to ensure the maximum safety of the worker keeping the site in operation 24 hours per day.

Finally, the connection between the TBM tunnels and the ventilation shaft will be made through tunnel excavated starting from the TBM tunnels. The shaft during the operation of the line will be used by fire department in case of emergency and it has a 12 m diameter circular plan. Its surface is composed by diaphragms 1.2 m thick and 55 m long.

3 THE HISTORICAL AND MONUMENTAL HERITAGE OF ROME: LINE-MONUMENTS INTERACTION STUDIES

The most particular and main aspect which characterized the contracts of the Line C that cross the center of Rome, consists of the interaction between the works and the surrounding buildings of historic, artistic and architectural value, often priceless. This theme was addressed through the so-called line-monuments interaction studies.

The interaction studies are made up of a first phase (preventive studies), necessary to acquire as much information as possible to start the design and of a second phase dedicated to simulate, through specific numerical analyses, the potential effects which could be generated on buildings and monuments by the excavations.

The preventive studies were carried out by General Contractor on each monument of the contract between 2008 and 2009 in collaboration with specific Working Groups which made it possible, through a series of diagnostic and geognostic investigations, to reconstruct in detail the structural history of the monuments and to define their consistency and conservation status. In 2020, the review of the design requested by the contracting authority induced the need to carry out an update of the consistency and conservation status of the monuments after more than ten years from the preventive studies. This update represented the starting point for the work of the specialist Working Groups that were constituted to develop geotechnical and structural numerical analyses and for the conservation and restoration of the artistic heritage with the aim to provide the guidelines for the designer. In order to ensure an adequate qualitative level in the Methodological Approach used in the study of the complex line-monuments interaction problems, Metro C signed a convention with the geotechnical and structural engineering department of La Sapienza University of Rome whose role is to direct, coordinate and control the specialist geotechnical and structural Working Groups. The interaction analyses are therefore aimed at establishing the need for consolidation interventions to ensure the stability of the structures considering the current conditions of the buildings. A total of ten structures potentially interfering with the subsidence induced by the excavations have been analysed.

The calculation of the tunnelling-induced settlement trough in greenfield conditions developed through empirical relation allows to exclude from the soil-structure interaction studies those buildings for which some gross movement indicators are below a given threshold (*e.g.* rotation $\theta = 1/500$ and $w_{max} = 10$ mm) as suggested by Rankin (1988). In the level 1 analyses the presence of the building was neglected and the greenfield displacement field at foundation level was calculated using the semi empirical gaussian formulation of Peck (1969) with D = 6.70 m (2).

$$w(x) = \frac{V_L D^2}{4i}\sqrt{\frac{\pi}{2}}\exp\left(-\frac{x^2}{2i^2}\right) \tag{1}$$

The value of the settlement trough i in the formulation of Peck was calculated at foundation depth using the expression proposed by Moh et al. (1996) with m=0.6 (2).

$$i(z_f) = K_{Z0}\left(\frac{z_0 - z_f}{D}\right)^m \tag{2}$$

The settlements generated by the tunnels' excavation are added to those generated by the excavation of the Venezia station, latter calculated by the relation of Clough & O'Rourke (1990) or by Ou et al. (1993). From the total greenfield deflection ratio, which is the ratio between maximum deflection

in the sagging or hogging area and the equivalent beam length through which the buildings are simplified and horizontal strains, could be inferred the expected damage level on the individual monuments. This evaluation was carried out with reference to the classification of damage proposed by Burland (1995) and adopting the thick beam model originally proposed by Burland and Wroth (1974) and Boscardin and Cording (1989). If the expected damage exceeds class 0, further investigations are carried out through level 2 analyses, implying a higher level of complexity and detail, and consisting of soil-structure interaction analyses that adopt a specific geotechnical model for the site and structural models for the interfered buildings.

Level 2 evaluation of damage is carried out in two stages. In the first one, the soil-structure interaction analysis is carried out in the geotechnics dedicated Finite Elements software, using an advanced constitutive model for the soil. The *Hardening Soil* constitutive law is used to describe the mechanical behaviour of the soils in level 2 analyses. It consists of an elastic-plastic model with double yield surface. On one surface hardening is governed by plastic shear strains, on the other, the "cap", hardening is controlled by plastic volumetric strains. The model is able to properly reproduce the most important aspects of the mechanical behaviour of the soils for the stress paths typically associated with excavation problems. At this stage, the monument is modelled by means of simplified elastic equivalent solids (Losacco et al. 2014), whose elastic properties are calibrated so as to reproduce the same distribution of nodal reactions to a prescribed displacement field as in a fully detailed structural model. Subsequently, the displacement field obtained from these interaction analyses at the base of the equivalent solid, is applied to a detailed structural model of the monument in an uncoupled, purely structural analysis. Normally, a linear elastic material law is employed in the structural analyses. Only in some specific cases, where the predicted distortions on the monument are particularly severe, a non-linear constitutive model is adopted (Losacco et al. 2016; Pickhaver 2006).

The expected damage is inferred from the tensile strains on the structure provided as a direct output of structural analyses. If the damage level on the monument predicted by level 2 analyses is still unacceptable, then the design of remedial measures for the safeguard of the monuments, both structural and geotechnical, is tackled.

4 MEASURES FOR THE SAFEGUARDING OF THE MONUMENTS

Based on the results that emerged from the analyses, the appropriate geotechnical and structural protection measures were developed for the monuments concerned. The geotechnical measures provided into the project are of two types; the first one consists of an active mitigation measure such as the compensation grouting in order to compensate or reduce the settlements as soon as they occur; the second one is a passive mitigation measure consisting of bulkheads aimed to cut the subsidence in correspondence of the monuments to protect. The structural interventions on the monuments themselves, instead, can be temporary or definitive. The temporary ones are aimed at absorbing the vibrational effects caused by the jobsite activities while the goal of the definitive ones is to permanently eliminate the structural deficiencies found on the monument and to improve their resistance capacity.

Finally, as suggested by specialist Working Group, Metro C has provided a series of interventions to conserve and to restore the artistic and monumental heritage interfering with the excavation activities.

4.1 *Active mitigation geotechnical measure: compensation grouting*

The compensation grouting consists of controlled cement injections into the ground below the foundations of the building to be protected. These injections induce a controlled lifting of the ground that balance the subsidence induced by the excavations in such a way that the settlements and distortions of the pre-existing structures to be safeguarded oscillate around zero. This active geotechnical measure is provided in Roman Forum area as well as in the Atheneum of Adriano one.

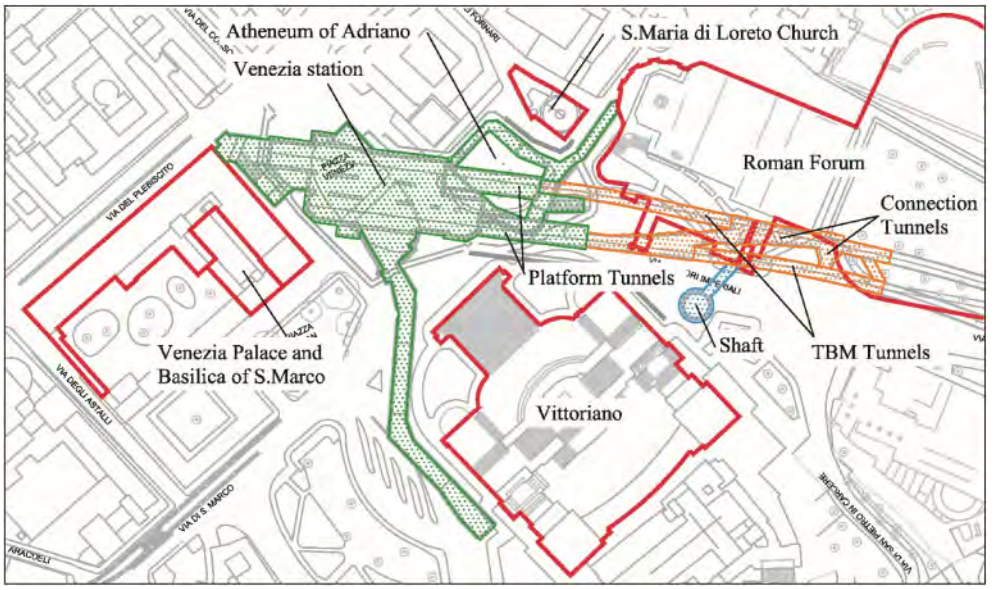

Figure 5. Planimetric view of the monuments potentially interfering with the excavations.

The injections will be realized from inside the Venezia station structure for the compensation below the Atheneum of Adriano and from inside the ventilation shafts for the compensation below the Roman Forum. Both drilling series will be made under water table from a depth ranging between 10 and 13 m below the ground level. A total of 150 drillings with an average length of 70 m will be carried out with horizontal and vertical interaxes equal to 0.6 m. Prior to the execution, specific field test is provided for the evaluation of the most suitable mixture in relation to the response of the soil. These will be made in an area that does not interfere with the pre-existences located on the ground level.

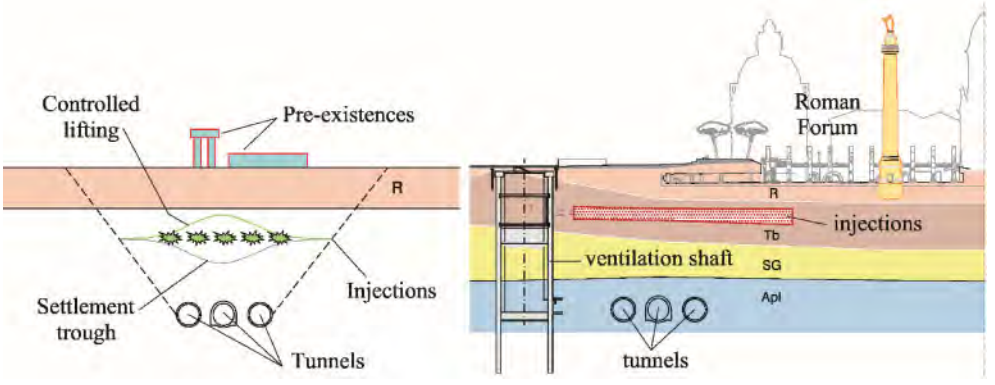

Figure 6. A simplified schematization of the compensation grouting method (left) and a section view of the compensation grouting below the Roman Forum (right).

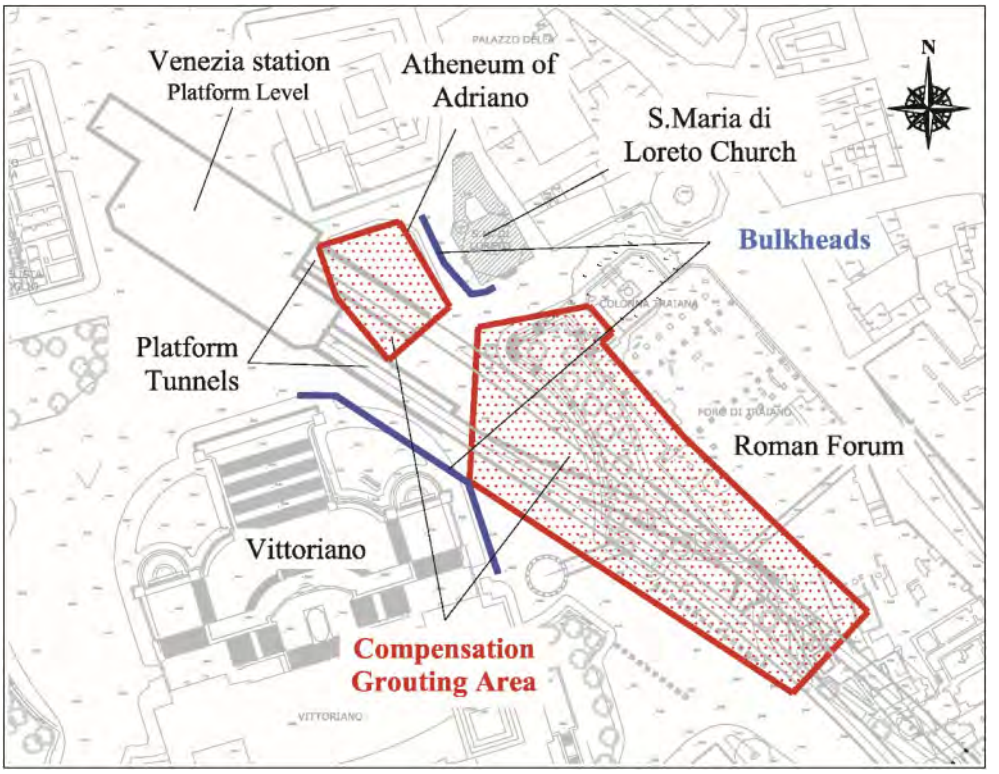

Figure 7. A planimetric view of the area of intervention.

4.2 *Passive mitigation geotechnical measure: bulkheads*

According to the results of the interaction analyses, the construction of two bulkheads was deemed necessary to cut the potential subsidence induced by the excavation for the safeguarding of the Vittoriano and of the S. Maria di Loreto Church. These bulkheads, composed by Trelicon piles with a diameter of 0.6 m and a depth of 50 m (up to 5 m below the reverse arch of the tunnels) reduce the settlements induced at the foundation level of the monuments effectively eliminating the need for consistent and often impossible structural consolidation interventions.

The efficiency of this intervention has been evaluated by means of a specific Plaxis finite element model composed by 14816 triangular elements and 120401 nodes. From the analyses it was possible to observe a settlement reduction about 30% in line with the results obtained from two previous experiences conducted during the construction of the Line C. The first one is an embedded wall of bored piles installed in an instrumented area without pre-existing buildings in the framework of the European cooperative project NeTTUN, in order to assess the effectiveness of such a measure in reducing the displacements induced by the excavation (Losacco et al. 2020). The second one is a bulkhead that was built for the protection of the Aurelian Walls at Porta Asinaria.

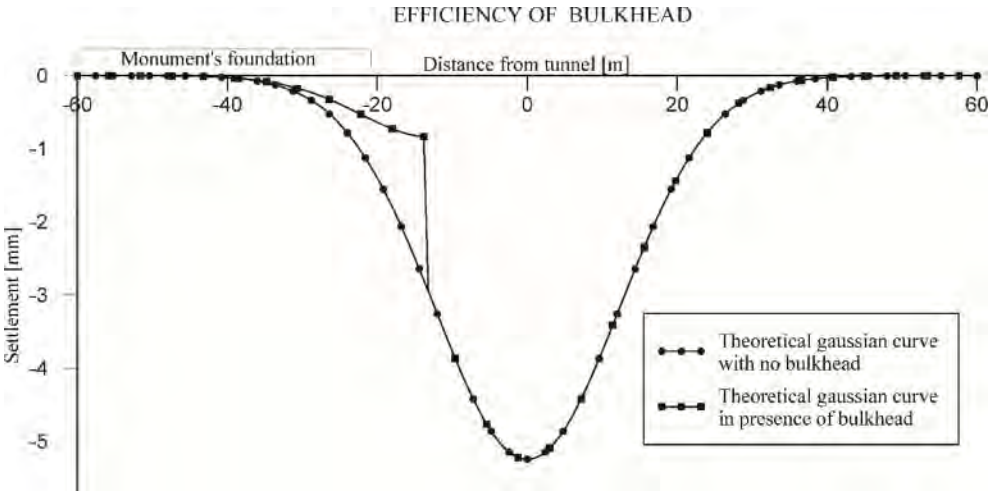

Figure 8. The evaluation of the efficiency of the bulkhead for the protection of the Vittoriano.

4.3 *Structural interventions for the consolidation of the pre-existences*

The results of the analyses carried out show a stress-strain level that is compatible with the masonry constituting the structures and the consequent damage category is 0 for every combination of loads constituted by own weight and settlements induced by the excavation of the tunnels and of the Venezia station. However, several specific structural consolidation interventions were deemed necessary to recover existing vulnerabilities and to improve the global static behaviour of Santa Maria di Loreto Church, Venezia Palace and the Basilica of San Marco also considering the inestimable value of the artistic heritage they have.

Figure 9. An internal view of Basilica of San Marco (left) and the complex of Venezia Palace and Basilica of San Marco (right).

4.3.1 *Santa Maria di Loreto Church*

The structural investigations carried out before the design showed some different kinds of masonry composing the Church. In fact, there are bricks masonry with lime mortar, sack masonry with bricks or irregular tuff blocks facings and masonry composed by irregular tuff blocks.

Between the internal dome and the external one, there are eight radial walls, the internal lantern and an intermediate floor. The main tensile stresses shown the presence of high tensile effort in correspondence with the openings on the walls near the areas currently damaged.

The results of the analysis show that the effects induced by the excavations, which are reduced by the bulkhead provided, can be considered negligible for the structural safety of the monuments.

However, in consideration of the widespread system of cracks currently existing and of the presence of important decorative elements such as mosaics and frescoes, it was considered necessary to provide some structural preliminary safeguarding interventions aimed at repairing the existing instability, restoring the integrity of the structural complex prior to the realization of the works.

The interventions consist of steel hoops of the internal dome by means of two tiers of 30 mm diameter stainless steel wire ropes, the creation of a structural reinforced layer of lime mortar plaster on the eight wedges of the internal dome together with a circumferential stainless steel fiber bandage. For the radial walls that connect the two domes is instead provided a double order of 20 mm diameter stainless tie rods, together with the creation of a structural grout (reinforced with a basalt and stainless steel mesh) on the two faces of the walls themselves.

The steel hoops of the internal dome are an active structural intervention because they will be pre-loaded and so they exercise a pre-compression force on the masonry equal to 298 kN for each rope. The others are instead passive interventions, designed to contrast the potential opening of the cracks due to the subsidence induced by the excavations.

Thanks to the active intervention the main circumferential tensile stresses decrease from 0.159 MPa to 0.109 MPa. In addition, steel wipe ropes contrast the new accidental deformations in the existing cracks.

Figure 10. An external view of the Santa Maria di Loreto Church (left) and an internal one (right).

4.3.2 *Venezia Palace and the Basilica of San Marco*

Given the close connection between Venezia Palace and the Basilica of San Marco the two buildings were analysed as a single structural unit and taking into account the state of consistency that currently characterizes the monuments, the aforementioned structural interventions have been planned.

In particular for the Venezia Palace that is composed by regular blocks of tuff, some of the roof vaults of the rooms located at the ground floor are affected by cracks due to the action exerted by the overlying walls and to the reduction of the thrust caused by low connection between façade walls and transversal ones. Another critical issue is related to the important rotation of the façade

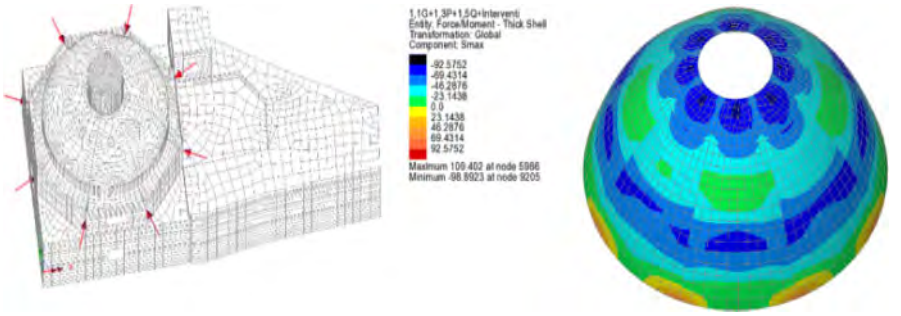

Figure 11. 3D model of the Santa Maria di Loreto Church (left) and the stress configuration on the dome after the application of the structural intervention provided (right).

of the Palace on via del Plebiscito that is highlighted by the disconnection with its transverse wall. In the vaulted rooms on the mezzanine and first floors there is some other widespread damage phenomena, although not evolving, probably due to the sub-foundation interventions carried out in correspondence to the staircase. The aforementioned vulnerabilities have been remedied by the introduction of about 70 reinforced seams made up of 24 mm diameter stainless steel bars 10 m long, provided at all intersections between façades and transverse walls, and by creating 13 chaining of the vaults with 20 mm diameter stainless steel bars, designed to absorb the thrusts deriving from accidental loads evaluated by means of the analysis.

The series of interventions is completed by the filling of the cracks with injections of hydraulic mortar so to recreate a continuity in the masonry before the settlements, and by the revision and consolidation of the support seats of the trusses by steel plates and connectors, lastly some injection to consolidate the masonry in correspondence with some walls on the ground floor (to increase the compressive admissible value in a local area near to the tower, where the compressive tension is significant).

The Basilica of San Marco is instead composed by solid brick masonry e lime mortar with variable thickness; it has been provided an intervention to consolidate the circular columns and rectangular pillars with a galvanized steel fiber bandage.

The analysis showed compressive stresses of 1.79 MPa in the most unfavourable combination of loads for the circular columns of the Basilica, value close to the calculation resistance for the brick masonry of the columns, equal to 1.93 MPa, is therefore provided to confine the structural element with FRCM (Fiber Reinforced Cementitious Matrix) through the preparation of a continuous coating of an inorganic matrix composite, which fibers are arranged in an orthogonal direction compared to the axis of the element, so to contrast its transverse dilatation and in order to give the column a beneficial state of triaxial compression. The resistance of the so confined masonry, equal to 2.96 MPa, guarantees a higher and more comforting safety factor in relation to the maximum compression tension expected at the end of the works. For the rectangular pillars adjacent to the columns, a system of helical stainless stell bars is provided to ensure the distribution of the loads.

The insertion of these bars will be executed after the disassembly of the marble cladding slabs that require a more effective fixing because of the future application of the settlements induced by the works. The last intervention is the consolidation of the vault of the apse through the realization of the cladding extrados with bidirectional reinforcement in steel fiber and basalt and lime-based structural mortar to exercise a containment action on the cracks able to preserve the mosaic placed on the intrados of the vault.

4.4 *Interventions for the protection and restoration of the artistic heritage*

With regard to the restoration and conservation interventions on the artistic heritage the specialist Working Group planned to carry out a series of protection and restoration interventions considering the currently state of consistence.

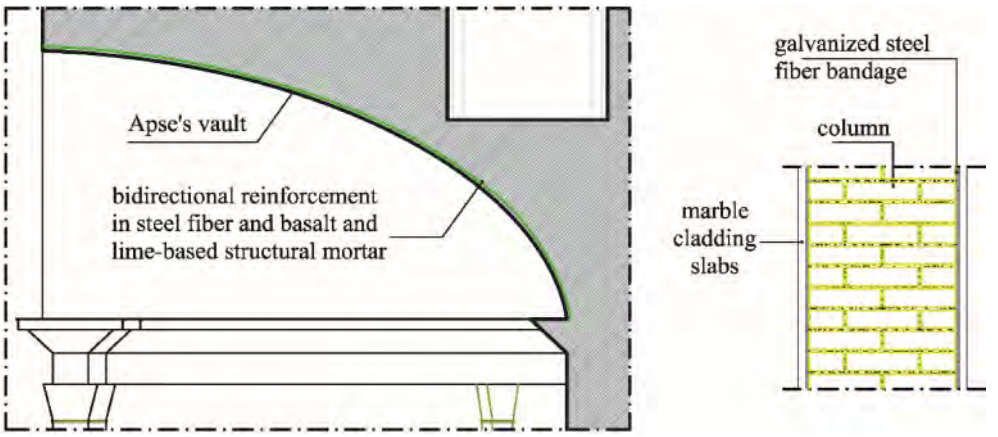

Figure 12. The consolidation of the vault of the apse (left) and structural intervention on the columns (right).

The restoration interventions mainly aim at making the surfaces more stable and safer through direct actions on the material, healing as much as possible the detachments found. The interventions consist of five different phases: preliminary operations, pre-consolidation, cleaning, consolidation and operations for the aesthetic presentation.

Before the start of the activities, some tests will be performed relating to the different phases of the intervention, the choice of suitable materials and the correct method of application will be induced by the examination of the surfaces and significant samples of plasters and colours will be produced in collaboration with the Superintendence responsible for the protection of the heritage.

4.5 *Monitoring system*

In the context where the contract Venezia-Fori Imperiali develops, characterized by an urban area with numerous pre-existing structures considered both ordinary and monumental, the monitoring system assumes a role of primary importance. The preservation of the monuments must be guaranteed in all construction phases and therefore monitoring during the construction is an essential tool for verifying the reliability of prediction of the analysis models adopted in the design phase and for the calibration of their parameters.

A monitoring system similar to the one used and extensively tested in previous stretches of the Line C has been installed; it and it allows the control of the processes and of the design parameters providing the information and the necessary support to decision-making processes. Topographic, geotechnical and structural instruments measures provide in real time post-processioned data through a specific processing platform called Data Distribution System which can be accessed by all technicians variously involved.

5 CONCLUSIONS

The purpose of this paper is to represent the engineering complexity of a metro line design and construction activity in a highly anthropized and urbanized context such as the historic center of Rome, characterized by the presence of manufacts of outstanding archaeological, monumental and artistic values.

In this paper particular attention has been paid to the design of the contract that extends from Fori Imperiali station to Venezia station which represents a significant engineering challenge for the context in which it develops.

With the aim of safeguarding every archaeological and monumental pre-existences of Rome – those UNESCO world Heritage site – potentially interacting with the construction activities, a specific methodological approach was put in place during the design phase through which Metro C, supported by the specialist Working Groups coordinated by geotechnical and structural department of the University of Rome La Sapienza, conducted the Line-Monument interaction studies by means of special finite element models with two and three dimensional analyses of the soil – structure system.

Thanks to the analyses developed it has been possible to predict that the effects induced by the excavations are negligible. However, taking into account the state of consistency and the inestimable value of the monuments, it was considered appropriate to intervene to reduce the induced settlements and to restore the current vulnerabilities.

In particular, following a description of the general characteristics of the design, we report the active and passive geotechnical interventions such as respectively the compensation grouting and the bulkheads necessary to compensate the settlements induced and to cut the subsidence in correspondence with some specific monuments interfered, together with structural interventions both temporary and definitive necessary to restore the vulnerability and to adsorb potentially vibrational effects during the construction of the contract. Finally, it has been designed several actions to safeguard and to restore the artistic heritage of the monuments.

For each monument it was designed and implemented a wide monitoring system in order to manage in real time the stress-strain response of the soil-structure system with the aim both at verifying the hypothesis adopted during the design and providing adequate and indispensable support for decision-making processes.

REFERENCES

Boscardin M.D., Cording E.J. (1989). Building response to excavation-induced settlement. Journal of Geotechnical Engineering, 115(1), 1–21.

Burland J.B., Wroth C.P. (1974). Settlement of buildings and associated damage, Proc. Conf. Settlement of Structures, Cambridge, UK, 611–654.

Burland J.B. (1995). Assessment of risk of damage to buildings due to tunnelling and excavation, 1st Int. Conf. on Earthquake Geotechnical Engineering, Tokyo, 1189–1201.

Losacco, N., Burghignoli, A., & Callisto, L. (2014). Uncoupled evaluation of the structural damage induced by tunnelling. Géotechnique, 64(8), 646–656.

Losacco, N., Callisto, L., & Burghignoli, A. (2016). Soil-structure interaction due to tunnelling in soft ground, an equivalent solid approach. In Structural Analysis of Historical Constructions: Anamnesis, Diagnosis, Therapy, Controls (pp. 495–502). CRC Press.

Losacco, N., Romani, E., Viggiani, G. M. B., & DiMucci, G. (2020). Embedded barriers as a mitigation measure for tunnelling induced settlements: a field trial for the line C in Rome. Tunnels and Underground Cities: Engineering and Innovation Meet Archaeology, Architecture and Art: Volume 12: Urban Tunnels-Part 2, 5845.

Losacco, N., Viggiani, G.M.B. (2020). Mechanised Tunnel Excavation Through an Instrumented Site in Rome: Class A Predictions and Monitoring Data. Lecture Notes in Civil Engineering, 40, pp. 245–254. DOI: 10.1007/978-3-030-21359-6_26.

Moh, Z.C., Ju, D.H., Hwang, R.N., 1996. Ground movements around tunnels in soft ground. In: Mair, R.J., Taylor, R.N. (Eds.), Proceedings International Symposium on Geotechnical Aspects of Underground Construction in Soft Ground. Balkema, London, UK, Rotterdam, The Netherlands, pp. 725–730.

Peck, R.B. (1969) Deep Excavation and Tunneling in Soft Ground. State-of-the-Art Report. Proceedings of the 7th International Conference on Soil Mechanics and Foundation Engineering, Mexico, 1969, 225–290.

Pickhaver, J. A. (2006). Numerical modelling of building response to tunnelling (Doctoral dissertation, University of Oxford).

Pickhaver, J. A., Burd, H. J., & Houlsby, G. T. (2010). An equivalent beam method to model masonry buildings in 3D finite element analysis. Computers & structures, 88(19–20), 1049–1063.

Rankin, W. J. (1988). Ground movements resulting from urban tunnelling: predictions and effects. Geological Society, London, Engineering Geology Special Publications, 5(1), 79–92.

Geotechnical Engineering for the Preservation of Monuments and Historic Sites III – Lancellotta, Viggiani, Flora, de Silva & Mele (Eds)

Improvement of foundation soil behavior for Gründerzeit buildings in Austria using polyurethane resin injections

A. Dominijanni
Department of Structural, Geotechnical and Building Engineering, Politecnico di Torino, Torino, Italy

M. Gabassi
Uretek Italia SpA, Bosco Chiesanuova (VR), Italy

F. F. Kopf
Chiari & Partner ZT GmbH, Wien, Austria

A. Minardi
Geotechnical Engineering, Torino, Italy

A. Pasquetto
Uretek Injektionstechnik GmbH, Vienna, Austria

ABSTRACT: The second half of the XIX century signed a period of comprehensive industrial and cultural development in Austria known as Gründerzeit. The architecture was deeply influenced during this epoch by the construction of large masonry buildings, called "Gründerzeit Häuser", which represent today the historical heritage of the most important Austrian cities. Due to the increasing demand for apartments in the centre of these cities, renovations and adaptations of existing buildings has been performed in the last decades. These modifications of the buildings structure represent, besides a business opportunity for the real estate economy, an increase/variation of the load for the foundations. Hence, the renovation and preservation of this architectural heritage often involve the improvement of the foundation soil. This article illustrates how the soil treatment with expanding polyurethane resin represents an efficient solution to achieve this goal. A case study of a historic building in the city of Salzburg is presented.

1 INTRODUCTION

The period from 1840 until the First World War in 1914 is known in Austria as the "Gründerzeit". During this period, residential constructions in Vienna, and other major cities in the country, developed significantly and the typical buildings of Vienna were built (e.g. buildings on the *Ringstrasse*), which still characterize the cityscape today and give the city its special flair.

During the "Gründerzeit", residential constructions also became interesting for the middle classes. This changed the shape of the houses. The plots of land, which had previously comprised an entire street block, were divided because the middle-class builders could not afford to build an entire block. This so-called "edge block development" characterized residential buildings until about 1918, with the individual houses being completely independent of each other. Entire neighbourhoods were built with this architectural concept in the major Austrian cities starting from 1840. Vienna's population grew exponentially, exceeding the two-million mark at the turn of the last century. In 2019, Statistics Austria counted about 32,400 buildings built before 1919, the vast majority from the Gründerzeit era, that is about 20 per cent of all Viennese buildings.

 DOI 10.1201/9781003308867-75

Some of the Gründerzeit houses were built in "Jugendstil" (Art Nouveau style), which was all the rage at the time. First and foremost, the architects Otto Wagner and Josef Hoffmann shaped the image of the Austrian capital. These names alone cover a large part of Vienna's Art Nouveau architecture. The facade decoration is typical for Viennese houses. However, the facade design was relatively independent of the standard of the houses. Above all, the size of the apartments, the lighting, the sanitary and technical equipment differed greatly. The magnificent facades were intended to conceal the low standard.

The typical Gründerzeit house consists of 4 to 6 floors with large room heights (3.5–4.5 m), whereby the ground floor (parterre) was often executed higher than the other floors. The first floor was often dedicated to the lord of the house or wealthy residents and was particularly sumptuously executed, had higher rooms and sometimes a balcony on the street side. It was therefore a prestige to live on the "first floor". Often, however, it was only the second floor that was executed in a stately manner. In this case, the floor below was only called "Mezzanin" (mezzanine) and only the second floor was considered "first floor". The walls were made of brick masonry with different thickness (gradation over the floors). The floor ceilings are wooden truss ceilings (wooden beam ceilings) and stretched across the street between the perforated façade, the middle wall and the courtyard façade.

The design of the Viennese Gründerzeit houses was regulated by law in the building code, which contained many construction features. For example, the permissible foundation loading was also specified in the building code in 1902. Considering the different types of ground (e.g. loose or dense gravel) values between 350 kPa and 600 kPa were considered.

Today, renovations, adaptations and additional loads represent a much greater problem. After the Second World War, damaged houses were often provisionally rebuilt and, from the 1970s onwards, many ground floors were stripped of their bracing walls and converted into commercial premises. In recent decades, attic conversions and raising of the structures have been made, leading to further additional loads for the foundation soil. Almost all cases of failure in the foundations of Gründerzeit houses can be traced back to such adaptations and usually occur during improper construction activities.

It has been shown that careful handling of the historic buildings is necessary in order to preserve this cultural heritage. Therefore, it is appropriate to proceed with the right methodology and with the appropriate expertise also in the renovation and reinforcement of foundations of the Gründerzeit buildings.

In this framework, the treatment of the foundation soil with expanding polyurethane resins represents a valid solution. This method can be considered part of the compaction grouting techniques (ASCE 2010). However, compared to conventional technologies based on the use cement grout, the use of polyurethane resins is significantly less invasive. The small size of the equipment adopted to perform the injections of resin in the subsoil allow operators to carry out this treatment in narrow spaces, such as building basement, with a minimal impact on the people living in the building. This feature of the treatment technique makes it very suitable in a large variety of works due to the reduced impact on the existing structure. This article presents an application of this compaction grouting technology to a historic building in Austrian city of Slazburg for the improvement of the foundation soil. An overview of the treatment methodology based on the use of polyurethane resin and design approach is initially illustrated, along with some general examples of works carried out on Gründerzeit buildings in the city of Vienna, the Austrian capital. Then, the case study is presented in detail, to highlight the key aspects of the design and execution of the foundation soil treatment with expanding polyurethane resins.

2 GROUND TREATMENT WITH EXPANDING POLYURETHANE RESINS

2.1 *Description of the technology plus the method*

Polyurethane resins are obtained from the exothermic reaction occurring by the mixing of a polyol and an isocyanate. The swelling capacity is the key feature of this material, and it is responsible for a

volume increase under unconfined conditions (null mechanical stress) of about thirty times (Buzzi et al. 2008; Dei Svaldi et al. 2005). When the resins are injected underground, the expansion process occurs in confined conditions leading to a compaction of the soil surrounding the injection point until a mechanical equilibrium is achieved between the resin and the soil (Dominijanni & Manassero 2014). The injection can be performed at different depths using either several injection tubes with single-point injection at the bottom end of the tube or a single tube with several lateral injection points (multi-point). In both cases, the injections are performed with small tubes (external diameter of about 10–15 mm) and equipment, reducing the treatment impact on the existing structure as much as possible. Figure 1 shows an example of the drilling operations carried out with a portable drill, and the equipment adopted to perform the injection of the resin in the installed tube from the ground surface.

Figure 1. Example of operations: a) Drilling of the borehole; b) Equipment for the injection of the expanding polyurethane resin.

From a design point of view, the cavity expansion theory, either in an infinite or in a finite medium, represents an efficient tool that can be used by engineers (Dominijani & Manassero 2014; Dominijanni et al. 2020; Shrivastava et al. 2018; Yu 2000; Yu & Houlsby, 1991). In this framework, spherical cavities expansion can be considered when single point injection tubes are adopted for the treatment. On the other hand, when multi-point injection tubes are used, it is possible to assume a cylindrical cavity expansion (Figure 2). This design approach allows engineers to estimate the amount of a specific type of resin to be injected and achieve a given increase of the soil density and mechanical parameters.

The efficiency of the treatment depends on several factors, such as the type of soil, the presence of groundwater, the soil stiffness and strength, the injection layout, the amount and type of injected resin. When compaction is the aim of the injections, the efficiency of the treatment is higher under drained conditions (Kovacevic et al. 2000). Indeed, under drained conditions, the mean effective stress increases monotonically, and the soil compresses along a compression curve for first loading, with a consequent increase in density, stiffness and shear strength.

Instead, under undrained conditions, the soil is not allowed to compress, and the mean effective stress decreases due to the formation of excess pore pressures. During the subsequent consolidation phase, the soil follows an unload/reload compression curve until the original mean effective stress is reached. However, because of the higher rigidity of the unload/reload compression curve with respect to the curve for first loading, the amount of compression is lower than that achieved under drained conditions.

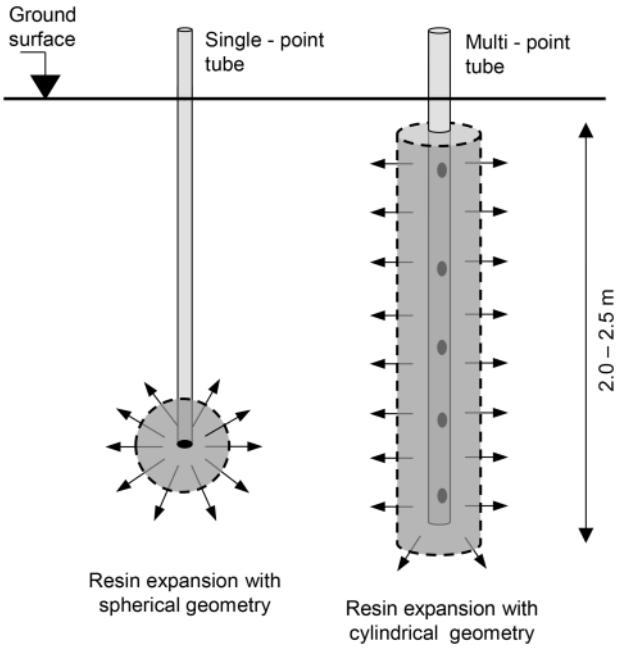

Figure 2. Schematic layout of the two types of injection tubes adopted for the injection of polyurethane resins, along with the underground expansion process of the injected resin.

Therefore, the use of polyurethane resins has to be firstly considered either in saturated coarse-grained soils or in partially saturated fine-grained soils.

The evaluation of the soil geotechnical parameters is often performed with in-situ tests, such as dynamic and static penetration tests, using empirical correlations available in the scientific literature. Moreover, penetration tests may also be adopted to evaluate the efficiency of the treatment by comparing the results of the tests performed before and after the treatment in the soil surrounding the injection points. The role of in-situ testing is, therefore, fundamental not only for the design of the ground treatment but also for the assessment of the treatment efficiency.

2.2 *Examples related to historical buildings in Austria*

In the last 15 years, the soil treatment methodology with polyurethane resins has been adopted for several historical buildings located in the most important Austrian cities, such as Vienna, Salzburg and Linz. As stated in the introduction, the main motivation for these works is the improvement of the foundation soil to cope with additional loadings due to renovation works and, in some cases, raising of buildings with the construction of an additional top floor. In most of the cases, the ultimate goal of the treatment is the compaction of the ground and the filling of fissures, fractures and cavities in the soil below the foundation, in order to prevent possible settlements induced by the modifications of the buildings structure.

An example of four historical buildings in Vienna, constructed during the Gründerzeit period, which have been subjected to soil foundation treatment with polyurethane resins for the construction of attics and/or renovation works, is illustrated in Figure 3. In all of the four cases, the buildings have shallow foundations at a depth in the interval 0.6–2.0 m below the ground surface. In this framework, the injections have been performed underneath the foundation beams. For the building in the image a) (Figure 3), about 260 m linear of strip foundations at a depth interval of 1.3–1.5 m were treated in 20 days of work. For the building in the image b), about 350 m linear of strip foundations at a depth

of 2.0 m were treated in 25 days of work. These two works were performed for the construction of an additional attic floor. For the buildings in the images c) and d) (Figure 3), about 200 m linear and 50 m linear of strip foundations were treated in 18 and 5 days, respectively; in these two last cases, the treatment aimed at the improvement of the foundation soil for settlements mitigation occurred during and after renovation works of the structures. In all the illustrated examples, the foundation soil was mainly composed of a silty sand/gravel. This feature has made the treatment of polyurethane resins extremely attractive. The performed works allowed the stabilization and improvement of the foundation soil, which is usu3ally assessed through settlements monitoring system.

Figure 3. Overview of Gründerzeit buildings in the city of Vienna that undergone foundation soil treatment with expanding polyurethane resins.

3 CASE STUDY OF A BUILDING IN SALZBURG

In this section, the case study of a building constructed in the XIX century, during the Gründerzeit period, in the Austrian city of Salzburg is presented in detail. The building, heavily damaged during the Second World War, was subjected to significant renovation works in 1961. Beside the renovation of the structure, the building foundations were also reinforced in the southern part with the installation of piles. However, the foundations of the northern part of the structure did not undergo any type of reinforced. Hence, the treatment with polyurethane resin has been foreseen to improve the foundation soil in the north part of the building, with the final aim of stopping the settlements and stabilizing the fissures network that have been occurred in this area of the building after the renovation works. Currently, this building has not been considered for the construction of an additional top floor and the treatment has not been designed to support a possible increment of the load.

3.1 *Description of the building*

4The structure of the building is composed of four floors above the ground and one underground floor. In Figure 4 are reported some pictures of the building from the main street, named Schwarzstrasse. The level of the basement is placed at a depth equal to 2 m from the ground surface (418.60 m a.s.l.). The strip foundations of the building have a width equal to 1 m and are located 1 m below the basement level (i.e. 3 m below the ground level). The foundations are composed of rock blocks obtained from the dismantling of the historical boundary wall of the old city.

Figure 4. Overview of the building in Salzburg: a) north side of the building; b) west side and main entrance of the building; c) south side of the building.

Before starting the treatment, the foundation soil has been investigated by performing a geotechnical survey until a depth equal to 12 m from the ground level on the north side of the building. Moreover, a shallow trench has been excavated until a depth of 3.70 m from the ground surface and nine dynamic penetration tests have been performed with the DPM 30-20 penetrometer (Cestari 2012) on the entire area of the north part of the building. Overall, the subsoil is mainly composed of the Salzach gravel until a depth equal to 10 m. In some areas, this course material shows the

presence of significant lenses of fine soil (main silt and sandy-silt). From the geotechnical survey the stratigraphy of the subsoil has been reconstructed as follows:

- from to ground surface to a depth equal to 2.8 m the ground is mainly composed of a backfill soil used during the construction of the whole district close to the Salzach river;
- from 2.8 m to 5.8 m there is a sandy-gravel (Salzach gravel);
- from 5.8 m to 7.2 there is a silty-sand soil with gravel;
- from 7.2 to 10 m there is a sandy gravel (Salzach gravel).

A layout of the subsoil stratigraphy along with the foundation and basement scheme is presented in Figure 5. The additional results of the nine dynamic penetration tests have highlighted the heterogeneity of the foundation soil. Indeed, the tests carried out on the north-west side (of the north part) of the building have exhibited the presence of a fine soil (mainly silty lenses) from the ground surface until a depth equal to about 6–7 m on top of the underlying gravel layer. On the east and south sides (of the north part) of the building, the penetration tests have highlighted the presence of a stiffer material also at a shallower depth, from 1.5 m to 6 m. This heterogeneity of the subsoil between the east and west sides can be considered among the main causes responsible for the differential settlements of the building that mainly occurred on the north part of the building.

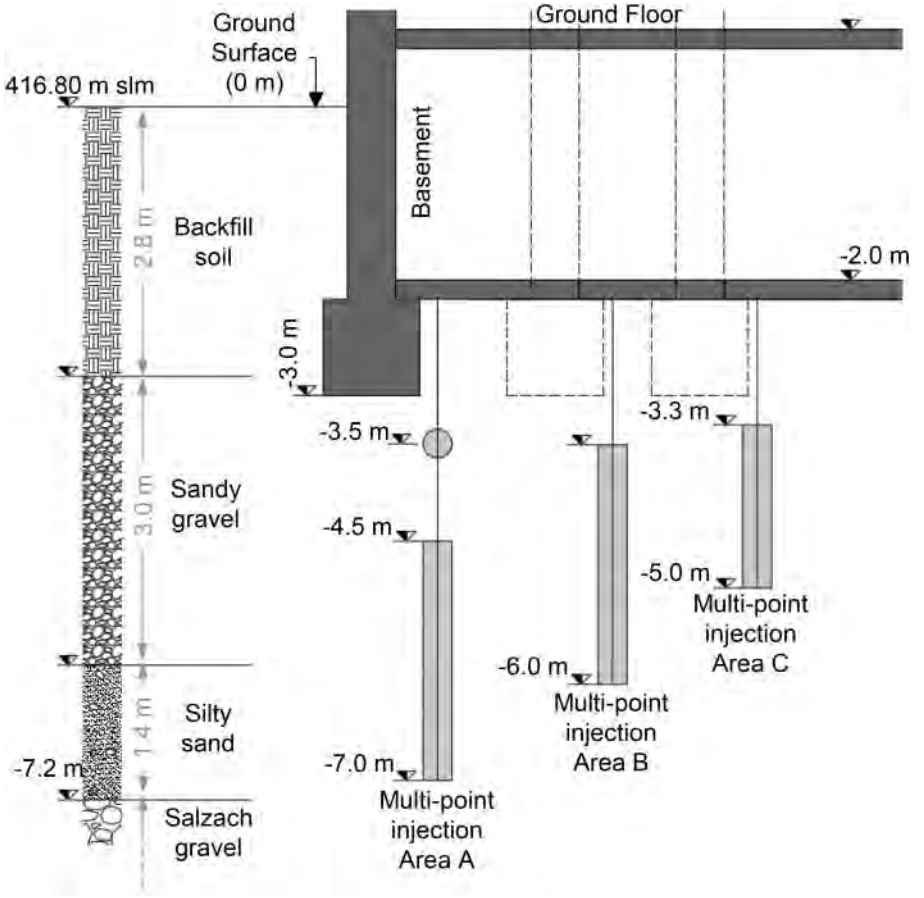

Figure 5. Schematic layout of the building strip foundations, along with the stratigraphy of the subsoil and the layout of the polyurethane resin injections performed in the different areas of the building.

Direct measurements of settlements have not been performed, neither in the past nor in recent time. However, evidence of these settlements has been given by the fissure network observed in the masonry walls and pillars of the basement level of the building, with openings in the order of several millimetres to centimetres (Figure 6). Some of these fissures have been filled in the past with cement, although most of them have been subjected to reopening. This aspect has suggested the progressive occurrence of settlements of the building during years, probably starting after the renovation works performed in 1961. A further contribution to the settlements of the building has been given by the deepening of the Salzach riverbed of about 3 m, which has been induced by the increase of the river flow starting from 1959. This factor has been responsible for a progressive lowering of the water table in the surrounding soil and the consequent consolidation settlements of the fine soil layers. Currently, the water table has been monitored with a piezometer installed in the performed geotechnical survey and its level, highly influenced by the Salzach river located about 100 m away from the building, has been found to oscillate in the interval −5 to −6 m from the ground surface.

Considering the combination of these two possible causes of settlements, the subsoil heterogeneity between the east and west side and increase of the effective stress due to the lowering of the water table of 3 m, a simple back calculation of the building differential settlements has been made adopting the theory of elasticity. Considering a stiffness of the fine soil layer equal to about 1/10–1/20 of the stiffness of the sandy-gravel layer, the differential settlements between the east and west sides are estimated in the interval 1.5 to 5 cm. This evaluation has to be considered as lower limit because it does not take into account the settlements that occurred after the renovation work performed before 1961, for which there are no information and data available.

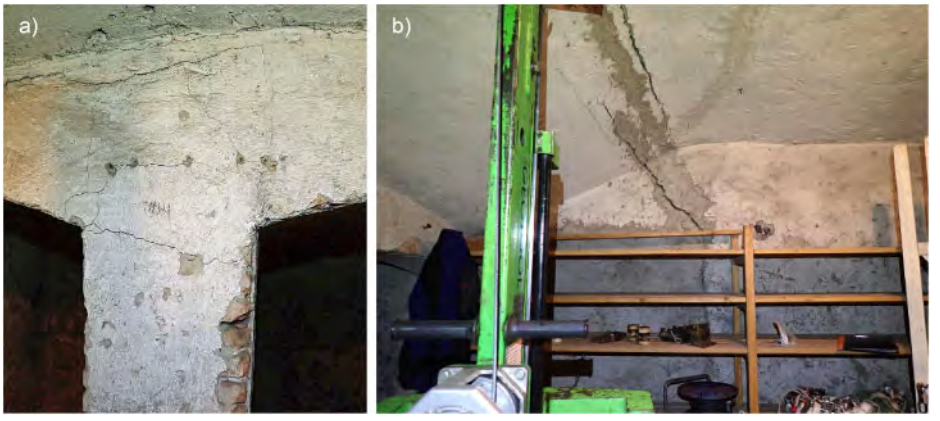

Figure 6. Examples of fissures in the masonry walls and pillar of the building structure in the basement.

3.2 *Design approach*

The treatment of the foundation soil has been foreseen only for the north part of the building, as the south part of the building has been already subjected to the installation of piles. The Figure 7 shows the layout of the basement level along with the position of the strip foundations (grey areas) interested by the treatment with polyurethane resins (dashed lines). The injections have been carried out on the entire perimeter of the building, with a spacing equal to 0.7 m in most of the cases. Inside the perimeter of the building, the spacing of the injections is increased to approximately to 1 m. The injections have been performed from the basement level adopting the multi-point methodology, which allows the treatment of a given soil thickness with a single injection tube. In the area A (Figure 7) of the building, the multi-point method has been combined with shallower single-point injections.

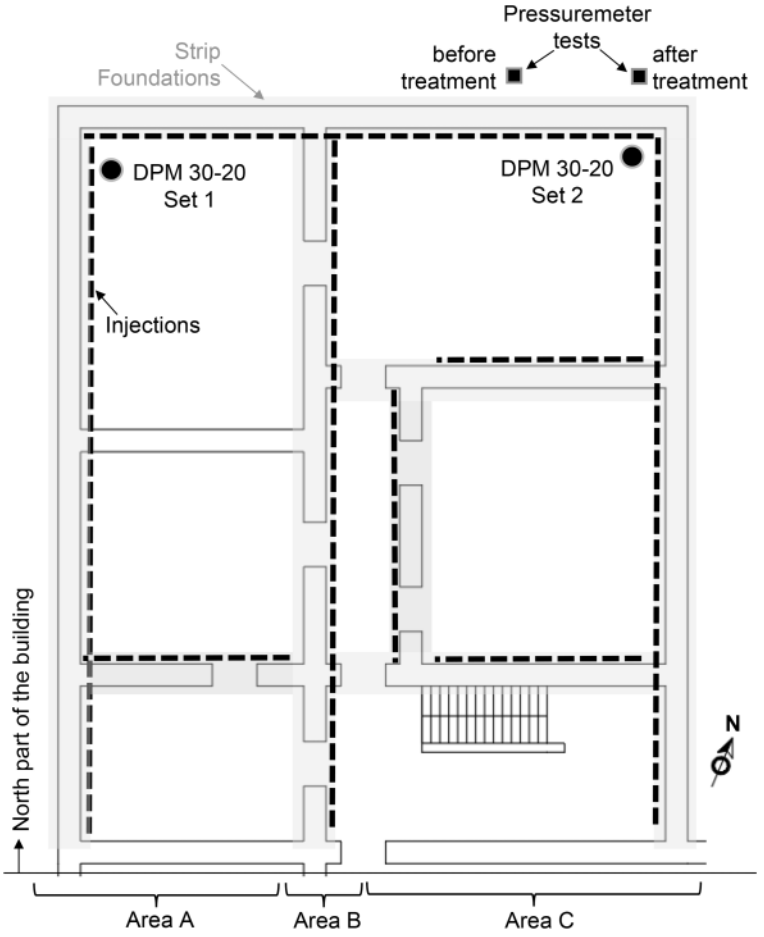

Figure 7. Layout of the basement level along with the position of the strip foundations (shaded areas), the location of the injections (dashed line) and in-situ tests (DPM 30-20 and pressuremeters).

As illustrated in the Figures 5 and 7, the maximum depth of the treatment is higher in the area A (−7.0 m from the ground surface), than in the areas B (−6.0 m) and C (−5.0 m), leading to different total thickness of the treated soil. In all the three areas, the injections have been designed to start the treatment underneath the strip foundations. Due to the higher depth achieved by the treatment in the area A, an additional shallow injection has been performed at a depth equal to 1.5 m below the basement level. This injection, carried out with the single point tube, is placed right underneath the foundation, and it has the main goal of filling voids and fissures at the interface between the foundation blocks and the ground to improve their contact. This difference among the injection schemes is related to the presence of softer soil (higher amount of fine soil) until a depth of 10 m on the west side with respect to the east side of the building. Overall, considering the underground stratigraphy highlighted by the survey and the dynamic penetration tests, the underground treatment with polyurethane resins mainly involved the gravel and sand layers below the foundations.

A series of in-situ tests has been performed to assess the efficiency of the treatment. Two sets of dynamic penetration tests have been carried out with the DPM 30-20 penetrometer. Each set is composed of two tests, one carried out before the treatment and the other performed after the treatment. The reduced size of this equipment has allowed the operators to perform these tests

directly from the basement level close to the injection points (about 0.5 m). The tests are located in two points in the north side of the building, as illustrated in the Figure 7. The achievement of a 50% increase of the average N_{10} value, which represent the blow number for a penetration of 10 cm, over the treated layer of soil has been set as a goal for the treatment.

In addition to the dynamic probing tests, pressuremeter tests have been carried out to evaluate the efficiency of the treatment. These tests have been performed with the Ménard pressuremeter from the ground surface and are located outside the building perimeter on the north side (area C in Figure 7), as close as possible to the external wall. The tests have been performed at two depth levels below the ground surface: −3.5 m and −5 m. For each depth, one test has been carried out before the treatment and one after the treatment.

The final objective of the treatment with the injection of polyurethane resins is the stabilization of the fissures network, which will be evaluated during the months after the treatment.

4 RESULTS

During the performance of the entire treatment period, which lasted eight days, the building has been monitored with a topographic system to assess possible displacements induced by the injection and expansion of the polyurethane resin underground. This monitoring system allows the operators to stop the injection immediately in case of the occurrence of excessive displacements. No unwanted displacements have been observed during the injection process, confirming the potential of this treatment technique and the correct design and execution of the work.

The results of the in-situ tests have highlighted the efficiency of the treatment. The results of the dynamic penetration tests (DPM30-20), in terms of N_{10} (blow number for a penetration of 10 cm) versus depth, are illustrated in Figure 8.

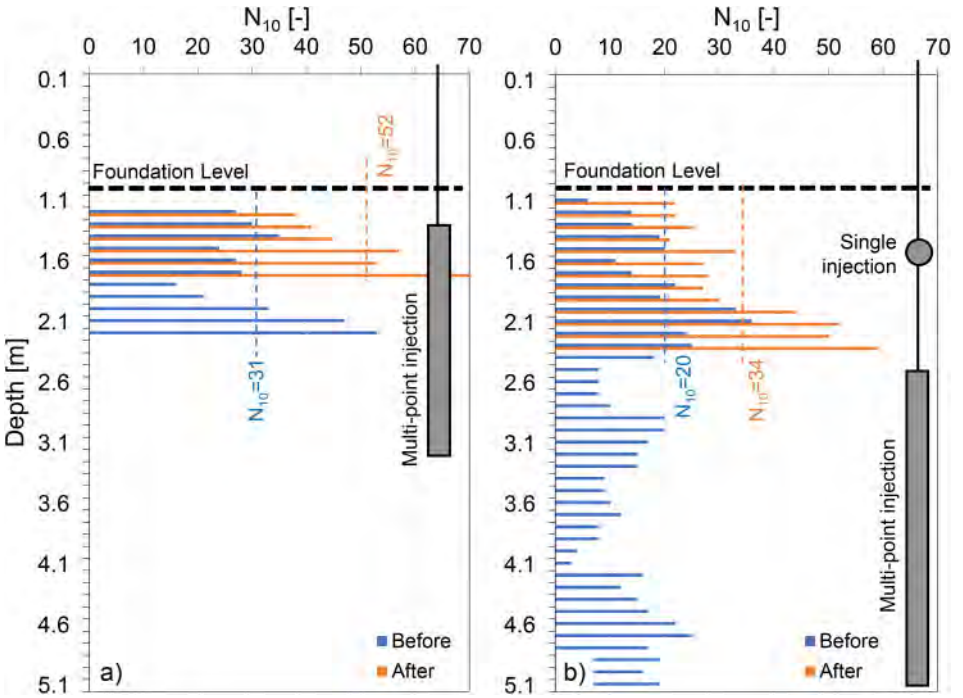

Figure 8. Results of the dynamic probing tests performed before and after the treatment with the DPM 30-20 penetrometer: a) Set 1 of tests on the north-east side; b) Set 2 of tests on the north-west side.

The first set of tests (Set 1 in Figure 8), carried out in the north-east side of the building, has investigated a relatively small portion of the subsoil. The test performed before the treatment achieved a depth equal to 2.2 m, corresponding to a thickness of soil of about 1 m. The average value of N_{10} in this interval is equal to 31. The test carried out after the treatment has been stopped at a depth equal to 1.7 m below the basement level, where $N_{10} = 81$ and the average value of N_{10} in the entire interval is equal to 52. Considering the soil layer thickness investigated after the treatment (from 1.1 m to 1.7 m below the basement level), the average increase of N_{10} is equal to 68% and, therefore, higher than goal set for the treatment (50%).

The second set of tests (Set 2 in Figure 8), carried out in the north-west side of the building, has investigated a larger portion of the foundation soil. The test performed before the treatment has achieved a depth equal to 5.1 m below the basement level, confirming the presence of a softer soil with respect to the east side. This finding highlights in particular the decrease of penetration resistance from 2.5 m below the basement level until the end of the tests at a depth of 5 m. The average N_{10} value until 2.4 m is equal to 20. The test carried out after the treatment has been stopped at a depth equal to 2.3 m below the basement level, where $N_{10} = 59$. A progressive increase of the penetration resistance with depth is observed in the soil after the treatment. The average value of N_{10} in this portion of the subsoil is equal to 34. Considering the soil thickness investigated after the treatment (from 1.1 m to 2.3 m below the basement level), the average increase of N_{10} is equal to 70% and, therefore, higher than the goal set for the treatment (50%).

A design approach based on the cavity expansion theory has been used to assess the performed treatment and verify the amount of resin injected. In the following, it is presented an example of a validation of the theoretical model based on the Set 2 of DPM 30-20 tests, for the shallow soil layer below the foundation, from a depth equal to 1.1 m to 1.9 m.

In this depth interval, the average value of N_{10} is equal to 15 before the treatment, which corresponds to a N_{SPT} value equal to about 14. The corresponding value of relative density, estimated according to Skempton (1986), is equal to 27%.

A perfect elasto-plastic Mohr-Coulomb model has been adopted for the theoretical estimation of soil densification. The soil parameters, obtained from the geotechnical investigation, have been assumed as follows: unit weight $\gamma = 18\,kN/m^2$, Young' modulus $E = 40\,MPa$, Poisson's ratio $\nu = 0.3$, cohesion $c' = 0\,kPa$, shear strength angle $\varphi' = 32°$, initial void ratio $e = 0.74$. Considering the treatment layout presented in Figure 7, the analysis has been carried out considering the expansion of a cavity in a finite medium with an external fixed boundary with a radius equal to 1 m. The analytical solution developed by Shrivastava et al. (2017) has been used to calculate stress and strain variation in the ground, following the procedure described in Dominijanni et al. (2020).

The results of the analysis are illustrated in Figure 9. The graphs show the evolution with radial distance from the injection point of the calculated relative density and N_{SPT} value. The relative density achieves a maximum value close to the expanded resin bulb equal to about 32%, and it decreases progressively to a value equal to 29% in the elastic region of the soil. The graph b) illustrates the evolution with the radial distance of the calculated N_{SPT} value. Also in this case, the maximum value is achieved close to the injection point ($N_{SPT} = 39$), and it decreases gradually to a value equal to $N_{SPT} = 20$ in the elastic region. At a radial distance equal to 0.5 m from the injection point, the N_{SPT} value is equal to 23. This value is in good agreement to the average N_{SPT} value, equal to 24, that has obtained for the same depth interval from the DPM 30-20 test performed in-situ after the treatment. This outcome has been obtained considering an amount or resin injected equal to 20 kg, which is equal to the average amount of resin injected in a single point for the treatment of 1 m of soil.

The increase of the penetration resistance (expressed int terms of N_{10} and N_{SPT}) is related to the increase of both the relative density and the mean stress in the ground. These factors are responsible for an increase in soil stiffness, which has been also evaluated with the pressuremeter tests. The results of the pressuremeter tests performed at a depth of 3.5 m are illustrated in the in Figure 10. The comparison of the two curves highlights an overall stiffer mechanical response of the soil after the treatment with polyurethane resins. In particular, the difference between the two tests can be

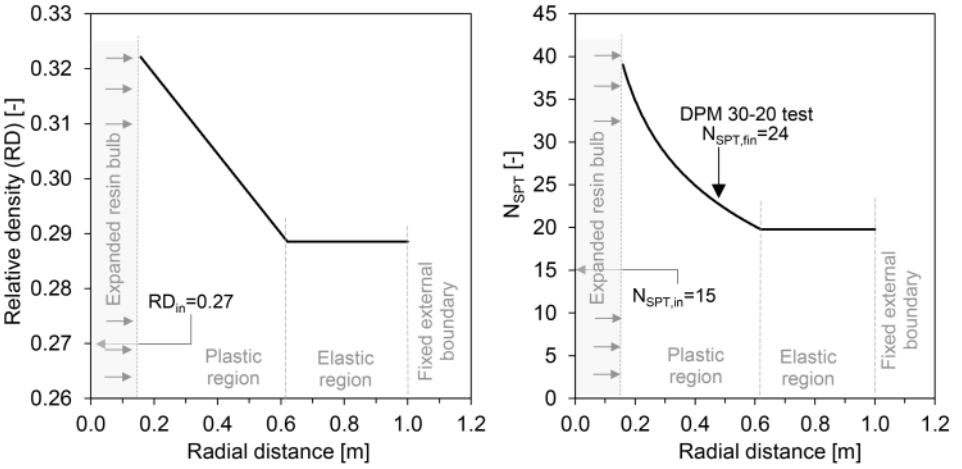

Figure 9. Results of the analysis carried out with cavity expansion theory in a finite medium to evaluate the increase of relative density (a) and blow number NSPT (b).

observed during the first loading of the curves (up to a pressure of about 0.8 MPa), as well as during the unloading phases of the stress cycle. During the first loading, the deformation modulus (E_{PMT}) has increased from 18 MPa to 26 MPa, while during the unloading phase the modulus has increased from 44 MPa to 66 MPa. Similar results have been observed for the pressuremeter tests carried out at a depth equal to 5 m below the ground surface (Figure 10). In this case, the deformation modulus has increased from 22 MPa to 24 MPa during the first loading, and from 46 MPa to 70 MPa during the unloading phase. With respect to the tests performed at a depth of 3.5 m, the lower increase of stiffness during the first loading is related to the higher stiffness of the natural soil at a depth of 5 m. In addition, it has to be considered that, in the area C the injections have achieved a depth equal to 5 m, therefore the influence of the treatment is expected to be less pronounced with respect to the shallow injection performed at a depth of 3.5 m.

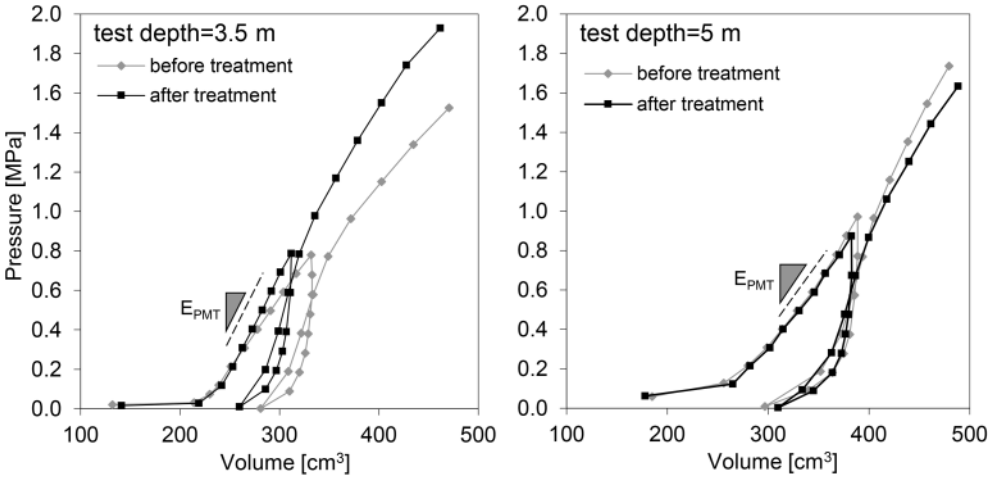

Figure 10. Results of the pressuremeter tests performed before and after the treatment with expanding polyurethane resins at depths of 3.5 m and 5.0 m.

5 CONCLUSIONS

The paper has presented the application of a compaction grouting technique based on the use of expanding polyurethane resins for the improvement of the foundation soil of historical buildings constructed in Austria during the Gründerzeit period.

A detailed case study of a building in the city of Salzburg has highlighted the key features of this ground treatment technology, including the application of the cavity expansion theory for the design of the treatment, and the use of dynamic probing tests and pressuremeter tests to assess the efficiency of the treatment. Beside the achievement of the goal set for the treatment in terms of penetration resistance, the success of the treatment is currently under evaluation with the analysis and monitoring of fissures network, observed in the basement level, that might develop again in the future due to the occurrence of further differential settlements.

The outcome of the presented case study, as well as of other works carried out for Gründerzeit buildings in the city of Vienna, have pointed out the potential of this treatment technology to improve the foundation soil behaviour. Therefore, the injection of expanding polyurethane resins can be considered as a potentially effective technology for the preservation of these historical buildings when subjected to renovation works, as well as raising with the construction of an additional top floor.

REFERENCES

ASCE (American Society of Civil Engineers). 2010. Compaction ground consensus guide, ASCE Standard ASCE/G-I 53-10. ASCE.

Buzzi, O., Fityus, S., Sasaki, Y., e Sloan, S. 2008. Structure and properties of expanding polyurethane foam in the con-text of foundation remediation in expansive soil. Mechanics of Materials 40,1012–1021.

Cestari, F. 2012. In situ geotechnical tests. Pàtron editore.

Dei Svaldi, A., Favaretti, M., Pasquetto, A., e Vinco, G. 2005. "Modellazione analitica del miglioramento del terreno attraverso iniezioni di resina ad alta pressione d'espansione." 6th International Conference on Ground Improvement Techniques, Coimbra, Portogallo.

Dominijanni, A., Manassero, M. 2014. Consolidamento dei terreni con resine espandenti: guida alla progettazione. McGraw-Hill.

Dominijanni, A., Manassero, M., & Minardi, A. 2020. Codice di calcolo numerico per l'analisi di iniezioni con resine poliuretaniche espandenti mediante tubi multiforo, Uretek Italia SpA, technical report, 1–118.

Kovacevic, N., Potts, D. M., & Vaughan, P. R. 2000. The effect of the development of undrained pore pressure on the efficiency of compaction grouting. Geotechnique, 50(6), 683–688.

Shrivastava, N., Zen, K., Shukla, S. K. 2017. Modeling of compaction grouting technique with development of cylindrical cavity expansion problem in a finite medium. Inter-national Journal of Geosynthetics and Ground Engineering, 3(4), 1–12.

Skempton, A. W. 1986. Standard penetration test procedures and the effects in sands of overburden pressure, relative density, particle size, ageing and overconsolidation. Geotechnique, 36(3), 425–447.

Yu, H. S. (2000). Cavity expansion methods in geomechanics. Springer Science & Business Media.

Yu, H. S., Houlsby, G. T. 1991. Finite cavity expansion in dilatant soils: loading analysis. Geotechnique, 41(2), 173–183.

Geotechnical Engineering for the Preservation of Monuments and Historic Sites III – Lancellotta, Viggiani, Flora, de Silva & Mele (Eds)

Florence high-speed railway underpass – Preservation of the Italian Renaissance pre-existing structures and historical sites

R. Zurlo & R. Sorbello
Infrarail Firenze, Florence, Italy

ABSTRACT: The city of Florence is considered the icon of an extraordinary historical period for both Europe and Italy, the Renaissance. It is the cradle of cultural and artistic development, which started in Italy and then spread worldwide, profoundly marking the history of humanity.

The historical center of Florence, UNESCO Heritage Site since 1982, includes numerous remarkable works of art which make the city a big piece of art itself.

Today, Florence must adapt to the presence of both Florentines and tourists who reach, every year in December, the maximum number of 13 million people, against a resident population of 370.000 units.

Florence must therefore equip itself with modern and efficient infrastructures with a reduced impact on the environment, which can satisfy a constantly growing demand for both urban/regional and national mobility. This is particularly true if we consider that the configuration of the new Florence High-Speed railway hub falls within the Scandinavian Mediterranean Corridor of the TEN-T Networks.

The new railway underpass and the new High-Speed railway Station of Firenze Belfiore will free the surface network from the transit of high-speed trains and enrich the offer of services for the benefit of citizens and companies, as well as economic and tourist activities.

The urban section of the new high-speed/high-capacity railway line will develop for over 7km underground, with two single-track tunnels between the current stations of Firenze Rifredi and Firenze Campo di Marte. The project foresees the construction of the Belfiore high-speed station along the underground section in the Belfiore-Macelli area. In developing the executive project, we paid great attention to the pre-existing structures and buildings, which are included in the subsidence basin induced by the excavation of the two single-track tunnels. The construction of the tunnels will be carried out by an EPB TBM with a diameter of 9.4 m.

The analysis of the impact on pre-existing structures involved about 230 constructions. Among those buildings, our analysis, designing and modelling mainly involved famous historical sites such as Fortezza da Basso (1535), Opificio delle Pietre Dure (1340) and Piazza della Libertà.

To avoid any structural failure due to the subsidence process induced by the passage of the EPB TBM below Rastriglia and Canaviglia ramparts of the Fortezza da Basso fortress, we planned pre-consolidation interventions through the compensation grouting technique. It is based on interventions to be carried out before or, where necessary, during the excavation of the tunnels. This approach allows containing the predictions of damage on the structures within the zero class of Boscardin and Cording (1989).

A similar intervention has been carried out on the adjacent historical building "Opificio delle Pietre Dure", the former Monastery of San Niccolò di Cafaggio, dating back to 1340.

Instead, as far as the buildings facing Piazza della Libertà are concerned, our in-depth studies suggested not to carry out pre-consolidation interventions before construction but to pay particular attention to the monitoring of the excavated material, in terms of weight and volume. Furthermore, it is also essential to implement a subsidence monitoring system during construction to constantly keep the situation under control and avoid any possible damage.

DOI 10.1201/9781003308867-76

1 INTRODUCTION

Florence is notoriously the city in which the Renaissance was born. This artistic and literary movement made Florence become a symbol of art and architecture all over the world. Therefore, in designing an important infrastructural project such as the Florence High-Speed railway underpass and the new High-Speed Belfiore Station in the very heart of the Italian culture, an inestimable artistic and architectural heritage had to be considered, making choices that were able to look at the future without destroying our past.

Our goal is to provide the city of Dante and Brunelleschi with modern and efficient infrastructures, with a reduced impact on the environment, which can improve its metropolitan and regional mobility. Besides, it is important to consider that the Florence High-Speed underpass and Belfiore station project does not have a mere national dimension, but it is part of the wider European TEN-T project.

Figure 1. Florence high-speed underpass.

The urban section of the new high-speed/high-capacity railway line will develop for over 7 km underground, with two single-track tunnels between the current stations of Firenze Rifredi and Firenze Campo di Marte. The project foresees the construction of the Belfiore high-speed station along the underground section in the Belfiore-Macelli area. In developing the executive project, we paid great attention to the pre-existing structures and buildings, which are included in the subsidence basin induced by the excavation of the two single-track tunnels. The construction of the tunnels will be carried out by an EPB TBM with a diameter of 9.4 m, quite remarkable considering that we are talking about urban railway tunnels with very thin cover.

The analysis of the impact on pre-existing structures involved about 230 constructions which are included in the above-mentioned subsidence basin. Among those buildings, our analysis, designing and modelling mainly involved famous historical sites such as Fortezza da Basso (1535) and Opificio delle Pietre Dure (1340).

Fortezza Da Basso, a masterpiece of Renaissance architecture, was built between 1534 and 1536 for the first Duke of Florence, Alessandro De' Medici. It has a strategic position in the historical city center, and it has been the main structure of the congress exhibition center in Florence and central Italy since 1967. Inside, the Opificio delle Pietre Dure dates to one of the ancient artisan and artistic factories of the Grand Ducal era in Florence, established in 1588 in the former convent of San Niccolò by Grand Duke Ferdinando I De' Medici as a factory of hard stone-made works of art. Today, the institute is divided into sectors that correspond to the different materials of the works of art. It is also home to a higher education school, a museum, and a highly specialized library in the restoration sector.

Figure 2. Fortezza Da Basso
Photo credit: Sailko – Wikimedia Commons
(GNU Free Documentation License – Wikipedia)

2 GEOLOGY OF FLORENCE

The Florence High-Speed railway underpass will undergo the historical center and the peripheral areas of the city, both north and south, with variable covers between 8 and 28 meters. It will cross a vast area of alluvial plain, mainly consisting of river and torrential sediments from *Arno* River and its tributaries, resting on lake deposits. The spatial distribution of the deposits is often random with sudden changes from coarse to fine fractions, and frequent stratigraphic discontinuities, largely corresponding to erosive phenomena.

The excavation of the natural tunnels will involve three sedimentary units, which are, starting from the oldest one, the following: the turquoise clays of the Florence-Prato-Pistoia Lake *Supersintema*, the deposits of the Florence *Supersintema* and those of the *Arno River Supersintema*.

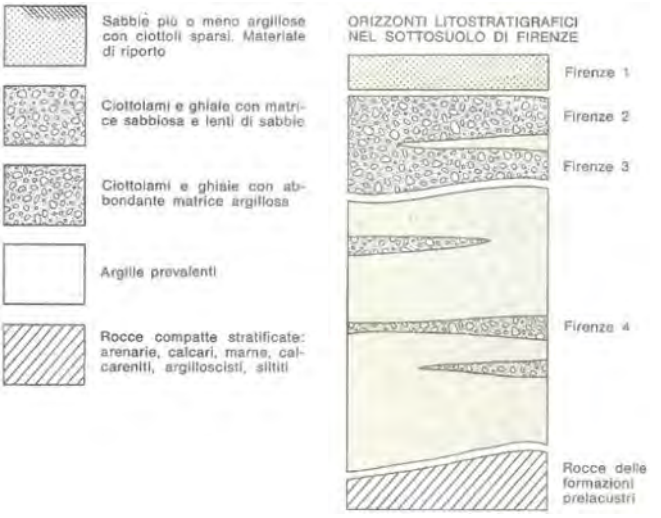

Figure 3. Florence subsoil stratigraphy.

2.1 *Florence-Prato-Pistoia Lake supersintema (turquoise clays)*

The most ancient overconsolidated lake sediments, mainly consisting of sandy or silty clay, as well as clayey silt, often containing gravel inclusions of calcareous origin.

2.2 *Florence supersintema*

It is possible to distinguish two lithofacies:

- Sandy and silty clay or clayey silt, with a semi-solid consistency and low-medium plasticity, thickened gravel-sand levels, and variable silt content.
- Heterometric gravels with pebbles (max. diameter >10 cm), polygenic, in a silty clay to silty sandy matrix; sometimes silty clay or silty sandy levels are interspersed (with a maximum thickness of about one meter).

2.3 *Arno river supersintema*

They are mainly made up of thickened sandy gravels and, to a lesser extent, of compact silty clay and clay silt of medium plasticity. From a hydrogeological point of view, the Arno River Supersintema includes the most important and productive aquifer in the Florentine plain. The highest permeability values were registered in the sandy matrix gravels near the Arno River, with coarser and more recent sediments.

3 THE EXCAVATION PROCESS

The excavation of the tunnels will be carried out using an Earth Pressure Balance Tunnel Boring Machine (EPB TBM) with a diameter of 9.43 m, which will excavate from Campo di Marte to the south diaphragm of the Station chamber (where the "Viale Redi" tramway stop is currently located). Once moved inside the Station chamber and into the tunnels north of it, the TBM will restart excavation from the north ventilation shaft (the former Central Milk Station) to Rifredi.

Next to the so-called "Overpass", a challenging work of art which solves the intersection of the High-Speed flows, is the "boring machine disassembly site", where the shield and, subsequently, all the other elements of the TBM will be disassembled; all these elements will then be transferred to Campo di Marte and reassembled for the excavation of the second tunnel. The excavation method allows to always maintain a stabilizing pressure on the excavation face and to control cavity deformation, lining the tunnel with waterproof precast elements. This operation is carried out as the excavation works progress, ensuring cavity stability and waterproofing. As far as the Florence High-Speed underpass is concerned, the desired characteristics of the slurry will be obtained by using:

- Polyfoamer ECO 100 (2.25 l/m^3 for clayey soils; 1.75 l/m^3 for sandy soils)
- Water ($400 \div 500$ l/m^3)
- Polymers/bentonite ($1 \div 3\%$)

Polyfoamer ECO 100 is a foaming agent for soil conditioning, tested by the National Research Council (CNR); upon its dehydration, it can ensure that the excavated material complies with the contamination threshold concentration limits. Consequently, the excavated material will not have any characteristics of toxicity and, if compliant with the geotechnical requirements, will be reused for the redevelopment and landscape improvement of a former Enel lignite quarry in the Santa Barbara area of Valdarno.

4 THE IMPACT ON PRE-EXISTING STRUCTURES AND THE SUBSIDENCE BASIN

Considering the urban environment of the new railway path, the evaluation of ground displacements caused by the tunnel excavation is of primary importance, considering its effects on safety and functionality of surface constructions within subsidence area. Therefore, to perform these analyses, the data collected in the extensive census and survey campaign carried out in 1998 and the above-mentioned updates and additions were used, identifying and monitoring about 200 constructions, including buildings, infrastructure, and railway facilities. The constructions have been censused by collecting the technical drawings for each of them, when available, or by a direct survey recording through synthetic forms based on the visual examination of the preservation status, the structural typology, and the intended use. Within this campaign, a detailed survey of the monumental complex of the Fortezza da Basso was carried out, investigating not only the geometry and the structure layout and foundations, but also the soil and masonry mechanical characteristics.

From the collected documentation, in-depth analyses have been conducted to assess the expected damage occurring in the construction in the subsidence basin, as determined by the curves of the short- and long-term ground displacements produced by mechanized boring ([2], [3], [6], [7], [9]).

Although the volume loss is assumed to be below 0.4%, damage analyses were also carried out considering larger values, such as between 1% and 1.5%. This was undertaken to assess the effects on the works even under sub-optimal (1% volume loss) or critical (1.5% volume loss) excavation efficiency conditions and thus provide a “damage risk” map, identifying the most sensitive areas and facilities ([5], [8], [10], [11]).

For the analysis of the overall subsidence induced by the tunnel excavation, in the first instance the principle of superposition [1] was applied, and then specific finite element modelling was carried out in correspondence with the most critical sections of the path. At the end of the in-depth analysis, it was observed that the overall subsidence curve induced by the passage of both machines shows an extremely limited axial deviation in comparison with the single subsidence curves, mainly due to the reduced distance between the two tunnels and the reduced soil coverings.

The buildings simulations were carried out considering the combined effects due to vertical and horizontal settlements. For all the buildings, the analysis was performed in the transverse plane to the tunnel path. A part of the buildings has also been assessed for displacement effects occurring in the vertical plane along the tunnel longitudinal direction. The buildings analysis was performed with the equivalent frame method, while for RC buildings the actual frame has been analysed.

From these analyses, the limit displacement ε_{lim} (%) of the building was determined, thus assigning the building to the assumed damage class.

The damage class is assigned by comparing the displacements affecting the building with the scale limits of Boscardin and Cording [4]. The categories from 0 to 2 include light damages that can be repaired with simple interventions that can be assimilated to those of an ordinary maintenance. Categories 3 to 5 include moderate to very severe damage that also affects structures.

The probability of the damaging event is estimated as a function of the volume lost, roofing, geotechnical situations, structural and preservation conditions of the building, and the location of the building relative to the TBM start.

Once this mapping was completed, it was decided to intervene by setting out specific interventions’ ex ante, where there are risks of structural damage (category greater than or equal to 3) for the most precautionary condition of inefficient excavation (volume loss = 1%). it was instead accepted not to operate ex ante on all those buildings that do not have any relevance or historical-artistic

value (category 2), tolerating the risk of non-structural consequences and, hence, easily repairable.

Apart from a few buildings that will be reinforced in advance, the risk of damage was almost zero (and therefore negligible) for a volume loss of less than 0.4% and only affects around 60 buildings (out of 200) for a volume loss of 1.0%. The observation of loss volumes close to 1.0% is expected to be an uncommon event, limited to small sections.

Although the project does not foresee the occurrence of structural damage threatening the stability of any of the buildings with up to 1.5% loss volume, the occurrence of minor damage, which can be easily repaired, cannot be completely excluded if the excavation proceeds even with less than 1.0% loss of volume.

The studies resulted that:

- there are no serious threats to building stability even for critical excavation conditions (volume loss = 1.5%).
- the number of buildings with a minor damage class in expected excavation conditions (volume loss less than or equal to 0.4%) is negligible.
- for sub-optimal excavation conditions (volumes loss close to 1%) the probability of slight damage affects a high number of buildings (about 60).

Overall, a very encouraging situation emerges regarding the induced effects and, with respect to 170 buildings monitored, it has been agreed to intervene with preventive ground consolidation only in a limited number of cases (buildings no. 165 and 166 immediately after the access to Campo di Marte; buildings in via delle Ghiacciaie and via Cittadella; prosecution of consolidation at the Ottone Rosai school and building no. 179; building in v. Redi).

For the remaining buildings, the probability of damage in the aforementioned terms cannot be eliminated and, in the event, restoration work will be carried out.

Because of their specificity, the interferences with other works, namely the road bridge "Ponte Al Pino" on the railway immediately after the South access, the Fortezza da Basso, and the operating tracks on the Rifredi access, have been subject to special analysis. In detail, the analysis of the Fortezza da Basso has been carried out to determine the maximum deformation values of the walls of the Bastioni according to the before described method. The analysis shows that under normal operating conditions of the TBM, the level of damage is virtually very low; however, due to the historical and artistic importance of the monument, built between 1534 and 1536, the implementation of a protection measure (compensation grouting) is planned.

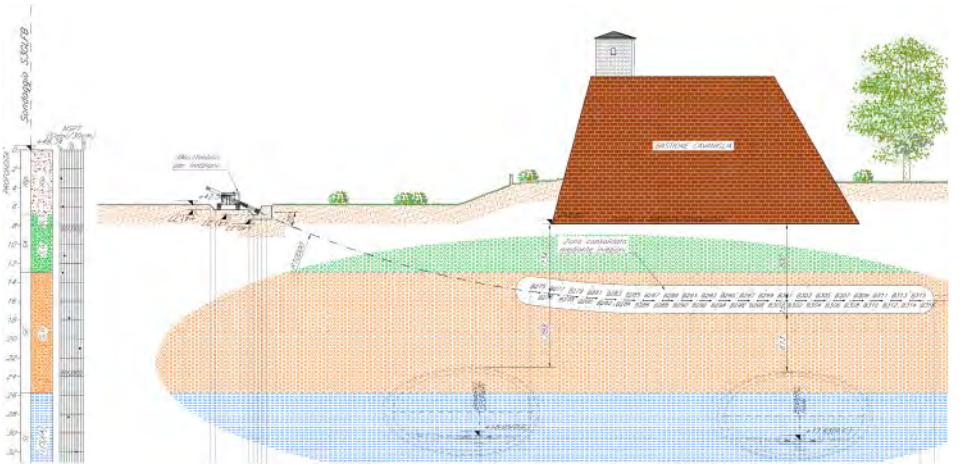

Figure 4. Compensation grouting works on Fortezza da Basso.

5 THE MONITORING OF PRE-EXISTING STRUCTURES DURING THE EXCAVATION PHASE

To confirm the design hypothesis, which foresees a subsidence that does not alter the structural and architectural integrity of the pre-existing structures, an articulated monitoring system with automatic data acquisition will be installed along the entire subsidence basin.

The system has been designed to provide all the needed indicators in the most complete and rapid way, to make an immediate analysis of the ongoing condition and its possible evolution, as well as any corrective measures to be adopted if the pre-set project threshold is exceeded.

The data acquired by the monitoring equipment will be carefully analyzed according to predetermined thresholds of alert and alarm, as well as to the overall behavior of the structures and the surrounding soil, to determine the effective effects of the pre-treatment and advancement phases of the tunnel boring machine.

On Fortezza da Basso, therefore, it will be set up a system to monitor the effects induced by the preliminary consolidation interventions on this structure, and then verify the expected subsidence during the excavation of the tunnels, to assess the possible necessity to implement compensation grouting interventions in conjunction with the excavation of the underpass.

In detail, the following quantities will be constantly measured:

- settlements and horizontal displacements of the structure.
- rotations and inflections of the structure.

These data will be collected using the following instrumentation:

- precision leveling points, for the measurement of the settlements of the two Bastions, Cavaniglia and Rastriglia, and of building 222, room of the "Cannoniera" where the Opificio delle Pietre Dure workshop is located.
- robotic total stations with miniprism positioned on the bastions and on building 222.
- settling gauges.
- crack meters for the control of pre-existing cracks.

The constant monitoring of the vertical subsidence of the Rastriglia and Cavaniglia bastions will be carried out by using a redundant system, made up of a series of settling gauges and two arrays of mini prisms placed at 3.0 m intervals, one at the top of the structure and the other on the face at about 3 m above ground level. Both measurement systems work with automatic readings and the results will be automatically entered on the dedicated web platform.

The monitoring system is integrated, as a further additional redundancy, by the installation of precision leveling datum points, placed near the foundation of the Fortezza wall, also with 3.0 m spacing.

The measurements, both the automatic ones elaborated by the local management and acquisition system and the manual ones, are transmitted via internet to the server of central acquisition, processing, and verification of the results in relation to the set alarm thresholds.

On the other hand, the control of the deformations of building 222 (Opificio delle Pietre Dure workshop) will be carried out by the data acquired using a system of miniprisms positioned on three sides in line with the extremities affected by the directional drilling, which is required to carry out the preliminary consolidation injections and any subsequent compensation grouting, under the Rastriglia bastion. The monitoring, therefore, will affect this part of the structure for an extent of about 30 m. The building has a central part higher than the two lateral bodies. The mini prisms will be arranged along the entire perimeter of the building, with two alignments along the east and west side walls: one will affect the taller central part and the other the lower part. They will be installed at every 6 m, according to the portal pattern which supports the structure. The ending prisms of the 4 planned alignments on the east and west elevations will reach the south elevation, so that the four edges where the main bearing walls end are also monitored.

To make this monitoring system redundant, 15 leveling datum points will also be installed near the base of the perimeter walls in proximity to the prisms.

Imagery ©2021 Google, Imagery ©2021 Maxar Technologies

Figure 5. Building 222, monitored facades.

Measurement frequency

During the excavations of the tunnel, the monitoring instrumentation installed on the Cavaniglia and Rastriglia Bastions of the Fortezza da Basso and Building 222 will be read according to the frequencies indicated in the following table:

Table 1. Monitoring measurement frequency.

Distance of the excavation front from the monitoring section and/or building facade	**Measurement frequency**	**Measurement type**
≥ -2.5 z and ≤ -1.5 z	1 per week	Precision levelling and crack metering
≥ -1.5 z and ≤ 2.5 z	1 per day	
≥ -2.5 z and ≤ 2.5 z	1 per hour	3D survey of datum points on buildings and settling gauges
>2.5 z	1 per week on the first month	Manual measurements except for Cannoniera
	1 per month on the 3 months	
	1 per 3 months till the construction end	
>2.5 z	1 per week on the first month	Precision levelling in Cannoniera
>2.5 z	1 per 4 hours for the first 3 months	3D survey of datum points on buildings and settling gauges

Note:"z" tunnel axis depth from ground.

Due to the expected subsidence, following the output of the simulations conducted during the project elaboration phase, the alert and alarm thresholds have been determined, with the relative actions to be taken during the construction phase, according to the deflection ratio obtained from the monitoring data.

About the deflection ratio, the alert and alarm thresholds will be evaluated, referring to the mini prisms, by processing the results of the measurements for every second mini prism. This is because the accuracy of the measurements, which in optimal environmental conditions is ±1 mm, is not negligible on a base distance of only 3.0 m. Considering that the measurements are performed almost continuously under different conditions of temperature and solar radiation, the actual error could be even greater and result in numerous false alarms during each day of measurement. For this reason, a baseline for the calculation of the deflection ratio of twice the distance of the installed mini prisms has been set.

For the same reason, it has been planned to maintain the distance of the settling gauges of 6 m, considering that, even with the same absolute precision of the sensor equal to ±1 mm, the real precision of the overall measuring system under changing environmental conditions could be even twice the said value.

Vibration monitoring

The "static" monitoring system just mentioned will be integrated with the vibration measurements generated on the monuments by the excavation of the tunnels of the underpass. The data will be compared with DIN 4150-3, a standard recalled by UNI 9916, from which the threshold values have been identified.

Table 2. Building classification according to DIN 4150-3.

	Peak particle velocity (mm/s) at		
Type of structures	<10 Hz	10–50 Hz	50–100 Hz
Offices and industrial premises	20	20–40	40–50
Domestic houses and similar constructions	5	5–15	15–20
Buildings that do not come under the above because of their sensitivity to vibration	3	3–8	8–10

In this specific case, the concerned buildings fall within Class 3.

At each "vibrational" monitoring point, the following data will be acquired for each x, y, z axis:

- Time history of the measurement (a, aw, v) with a resolution equal to 1 second.
- Awmax, amax, relative to the entire recording period.
- Vmax for the entire recording period: the maximum value among all frequency bands and the frequency at which it was detected will be reported.
- Spectrum for the entire measurement period; in the case of 24-hour measurements, for the daytime and night-time reference periods.
- Time history of the measurement, for all frequency bands from 1 to 80 Hz, with a resolution of 1 second (control data, not reported in the measurement sheet).

In addition, the results evaluation will also include the analysis of the threshold exceeding, which in the UNI 9614 is set equal to 5×10^{-3} m/s^2 for the z axis and equal to 3.6×10^{-3} m/s^2 for the x and y axes, referred to the frequency averaged acceleration values.

The monitoring system will consist of accelerometers whose sensors will be installed on external points near the structures in the "free field" area, to evaluate the amplification of the structure in comparison to the input value.

Thus, on each section it is planned to monitor:

- A first spot at the bottom, as close as possible to the foundation, in the basements if present or, otherwise, on an external wall, not more than 0.50 m from the ground level.
- A second spot at the top of the structure.

Imagery ©2021 Google, Map data ©2021 Google

Figure 6. Fortezza da Basso –Bastione Rastriglia monitoring.

Imagery ©2021 Google, Landsat/Copernicus, Data SIO, NOAA, U.S. Navy, NGA, GEBCOM, Map data ©2021 Google

Figure 7. Fortezza da Basso –Mastio centrale monitoring.

Radar interferometry

The monitoring of subsidence phenomena and vibrations potentially induced on buildings of historical and architectural value all along the route of the tunnels has required the integration of the traditional monitoring system with satellite radar interferometry.

The interferometric system enables the evaluation of the evolution of surface movement phenomena over time, by using SAR satellite radar data processed with the SqueeSAR™technique, the most recent of the multi-image interferometric analysis algorithms, which is an evolution of the well-known PSInSAR™ technique. The SqueeSAR™ analysis can be used to study and analyze the phenomena of ground displacement from satellites, providing a systematic picture of the ongoing movements.

Imagery ©2021 Google, Map data ©2021 Google

Figure 8. Fortezza da Basso –Bastione Cavaniglia monitoring.

The analysis is performed by estimating the displacements of two radar target families identified in the area: the Permanent Scatterers (PS) and Distributed Scatterers (DS). PSs typically correspond to buildings, exposed rocks, and other features; DSs correspond to uncultivated fields, debris areas, desert areas, etc.

Satellite monitoring will also offer the opportunity to isolate subsidence that has developed prior to excavation operations.

The targets will be realized by ground-based interferometric radars, which will be used simultaneously in configuration L for static motions (subsidence measurement) and S for dynamic mode acquisitions (for vibration measurement).

6 CONCLUSIONS

The Florence High-Speed ??Node is an important intermodal barycentric hub between the Florence Peretola airport and the Santa Maria Novella station. It will free the surface network from the transit of high-speed trains to enrich the range of services and redevelop the municipal and railway areas between Belfiore – Macelli and Santa Maria Novella.

In designing the executive project, we developed in-depth analyzes on the impact of the excavations on the 230 pre-existing works on the surface, which made it possible to reconstruct an expected subsidence basin. On this basis, we implemented all the design solutions aimed to reduce any potential damage to interfered buildings and infrastructures.

To contain the expected subsidence on the surface and to ensure that the corresponding value is compatible with the functionality of the existing structures and infrastructures, it is necessary to carry out ground consolidation works only for some buildings, including Ottone Rosai school. As a precaution, further compensation grouting interventions will be carried out during the undercrossing of the Fortezza da Basso.

The presence of numerous historical buildings and significant infrastructures determines the imperative need to constantly check design hypotheses and the effectiveness of the adopted interventions.

To do this, we will install, on those buildings, different tools which will ensure constant monitoring and compliance with the project limit thresholds through automated and immediately available readings.

The preservation of works of architectural importance, such as Fortezza da Basso and the building in which the Opificio delle Pietre Dure is located, has led to the enrichment of the "traditional type" monitoring system with the introduction of vibrational reading points. The goal is to avoid any effects on the structures induced by the vibrations caused by the passage of the TBM.

At the same time, the system was integrated with the mapping of the entire intervention area with the satellite radar interferometry technique to be able to assess, as a whole, the possible evolution of the subsidence basin compared to the project forecasts.

This integrated monitoring system will allow adequate and prompt intervention on the buildings and prevent irreversible damage.

REFERENCES

[1] Boone S.J., Westland J., Nusink R. (1999) "Comparative evaluation of building responses to an adjacent braced excavation ". Can. Geotech. J. 36: 210–223.

[2] Mott MacDonald (1992) "Prediction and effects of ground movements caused by tunneling in soft ground beneath urban areas" Funders Report for CIRIA, Westminster, London.

[3] Leblais, Y., Andre, d., Chapeau, C, Dubois, P., Gigan, J.P., Guillaume, J., Leca, E., Pantet, A., Riondy, G. (1995) "Settlements induced by tunnelling". AFTES, Text of Recommendations.

[4] Boscardin M.D., Cording E.J., (1989) "Building response to excavation induced settlements". Journal of Geotechnical Engineering, ASCE, n.115, pp.1–21.

[5] O'Really M.P., New B.M. (1991) "Tunnelling induced ground movements: predicting their magnitude and effects". Proc. Int. Conf. on Ground Movements and Structures, Cardiff.

[6] Attewell, P.B. (1988) "An overview of site investigation and long-term tunnelling-induced settlements in soil". Geological Society, Nottingham, pp.55–62.

[7] Rankin W. J. (1988) "Ground movements resulting from urban tunnelling: predictions and effects". Eng. Geology of Underground Movements, Nottingham.

[8] Attewell, P., Taylor, R.K. (1984) "Ground movements and their effects on structures". Chapman and Hall ed. New York.

[9] O'Really M.P., New B.M. (1982) "Settlements above tunnels in U.K, their magnitude and prediction". Tunnelling, n.82, pp173–181.

[10] Burland J.B., Wroth C.P. (1977) "Behaviour of foundations and structures". 9th International Conferences on Soil Mechanics and Foundation Engineering, Tokio, State-of-the-Art Report, Vol.2, pp.495–546.

[11] Bjerrum L. (1963) Contribution to discussion. Session IV, Proc. European Conf. on Soil Mechanics and Foundation Engineering, II, pp.135–137.

Geotechnical Engineering for the Preservation of Monuments and Historic Sites III – Lancellotta, Viggiani, Flora, de Silva & Mele (Eds)

Late XIX century protection: The CampiFlegrei and Velia railway tunnels

D. De Simone
Associazione Cocceius, Naples, Italy; UniversitéAix-Marseille, France/Università di Salerno, Italy

G.W. Ferrari
Associazione Cocceius, Naples, Italy

ABSTRACT: The conservation of monuments and historical sites in relation to the development of the enclosing areas has always been one of the most demanding problems to face. It is a prob-lem that involves apparently different and distant elements, in inextricable patterns made up of factors belonging to different spheres: cultural, humanistic, social, technical, economic, administrative. In the paper, the authors deal with the problem of the relationship between cultural heritage and urban evolution in the case of modern transport systems in two particular contexts: Campi Flegrei (Bacoli and Pozzuoli, Napoli) and Cilento, in particular the area that falls within the Archaeological Park of Velia (Ascea, Salerno). In both cases, these are areas affected by complex works such as the construction of the Cumana railway line and of the Napoli-Reggio Calabria railway line.

1 INTRODUCTION

Monuments and historical sites conservation in relation to the development of the territories in which they are inserted has always been one of the most demanding problems to face. This involves apparently different and distant elements such as the Cultural Heritage, the technical and economic progress of a nation and the technologies used to favor this development. In this contribution we will show how the complex relationship between the protection of cultural heritage and urban exploitation has evolved in the case of modern transport systems in two very particular contexts: the Campi Flegrei (Bacoli and Pozzuoli, Napoli) and the Cilento, in particular the area that falls within the Archaeological Park of Velia (Ascea, Salerno). In both cases we are in areas affected by complex construction sites functional to the construction of two railway line (the so-called Cumana and the Napoli-Reggio Calabria line), where geotechnical engineering had an important role for their conservation and the reuse of the site.

The analysis of the archive data preserved in the Historical Archive of the National Archaeological Museum of Naples (MANN), allows us to reconstruct the effect that these sites had with respect to protection of the historical-archaeological heritage and the coexistence of the latter with the extremely significant technological progress in that period.

2 THE CUMANA RAILWAY AND THE PUNTA EPITAFFIO AND BAIA TUNNELS

The Royal Decree n. 1641 (October, 12th, 1883), prescribed the construction of a railway line, intended as a quick and effective connection between Naples and the municipalities in the Phlegraean area (Campi Flegrei). The government's intended to develop an economic means of transport

DOI 10.1201/9781003308867-77

that would respond both to the demands induced by the underway Phlegraean industrialization, and to the new needs related to the growing touristic exploitation. The construction of this work was entrusted to a purposely established company, the Società per le Ferrovie Napoletane, which also took care of its management in the following period.

From the beginning, the project and subsequent construction of this railway presented numerous technical challenges, due to the geological and topographical characteristics of the Phlegraean area. In order to overcome the crater ridges, several long tunnels were needed on a 20 km only long track. In many cases, the construction of the railway tunnels met volcanic fumaroles which slowed down the work. These problems were duly highlighted, still in the design phase, by Henry James Johnston-Lavis, a British physician and geology scholar residing in Naples, who foresaw the technical difficulties in his periodical Reports to the British Association for the Advancement of Science but he also highlighted the possibility to acquire important geophysical information: "*This line of railway will traverse a number of tunnels and cuttings in the Campi Phlegrei, and will have to traverse the hot hill which backs Baia, and will no doubt present various uncommon engineering difficulties, be-sides giving some useful information bearing on terrestrial physics*." (Johnston-Lavis 1888, p. 228).

The land crossed by the railway line is one of the best known places in antiquity; Cuma, the oldest Greek colony in the Western Mediterranean, was established in the Phlegraean Fields. The area charms and the relative proximity to the capital of the Roman empire, contributed to establish the area as one of the favourite places of its elites (Amalfitano et al. 1990; Beloch 1890; I Campi Flegrei 1977; D'Arms 2003; Maiuri 1958, 1983). Extensive evidence of the Roman settlements was left in the area, such as the Amphitheater of Pozzuoli, the Roman Baths of Baia or the city of Cuma itself. The cultural heritage represented an additional challenge in the construction of the railway line.

Such a context immediately prompted both the Società per le Ferrovie Napoletane and the bodies responsible for the protection of the historical-archaeological heritage to establish a dialogue intended to allow the project development and at the same time to guarantee the due conservation of the ancient remnants intercepted during the works. In fact, in the design phase, the Società questioned the General Directorate of Antiquities at the Ministry of Public Education, directed by Giuseppe Fiorelli, about some specific points of the track, in the town of Pozzuoli and in the village of Baia. The Directorate disposed the respect of particular protection measures, despite the lack of a law explicitly dedicated to the protection of cultural heritage. Only in 1902, in fact, the first national law (l. 185/1902, or Nasi law) on the "Protection of monumental heritage", was passed, which was followed by l. 364/1909 (so-called Rosa di-Rava Law) "For antiquities and fine arts", despite the fact that the pre-unification states were already equipped with regulatory instruments (D'Alconzo 2001) Specifically, according to the correspondence preserved in the Historical Archive of the National Archaeological Museum of Naples (MANN), there were two sections that were the subject of a specific "dialectic" aimed at safeguarding the archaeological heritage. The first is the segment that met the remnants of the so-called Villa di Cicerone (De Jorio 1822; Micheletti 1845; Panvini 1818), located on the outskirts of Pozzuoli; the second section was near the so-called Stufe di Nerone ('Baths of Nero'), aside the east ridge of Punta Epitaffio (Archive MANN – folder V, D4, 24 named "*Correspondence concerning the finds and conservation of ancient structures discovered during the works of the Naples-Cuma railway line, in particular in the areas of the Villa di Cicerone in Pozzuoli, and of the Stufe di Nerone in Baia (with floor plans)*").

In the first case, the original project involved the construction of a tunnel that passed immediately below the ancient structures while in the second case the tunnel was built inside the ridge of Punta Epitaffio, exiting near the port of Baia. Here two other tunnels reached the Lake Fusaro station, the last stop before the terminus at Torregaveta.

In both cases, the intended design prompted a heated debate and an exchange of letters between the Directorate of Antiquities and the contracting company which resulted in a balance, according to the standards of the time, between the various instances in place. The surveys and site inspections in the Punta Epitaffio underground resulted in the identification of several hypogean structures,

including the remains of the Tritoli Sweater. The latter consists of a network of tunnels dug into the tuff of Punta Epitaffio; one of them ends on a pool of hot water, which reached a temperature of 92°C in 1976 (Abbruzzese Saccardi 1976). In 2010 we measured 65°C, while the air in the tunnels had a temperature of about 40°C. At the base of the promontory is the church of Maria Santissima e San Filippo Neri, founded in 1631 where there was the entrance to a Roman and medieval thermal bath called Balneum Trituli, known from medieval chronicles as a therapeutic site managed by the Hospital of the Santissima Annunziata in Naples for the benefit of poor sick people (Bulifon 1693).

Figure 1. Detail of the plan of the project related to the construction of the Punta Epitaffio Tunnel (MANN Archive, coll. V, D4, 24, annex 1).

In the approach to Punta Epitaffio, the original project provided for the railway track to run along the sandy coastal strip that separates Lake Lucrino from the sea, and then to enter the tunnel at the Stufe di Nerone and to exit near the town of Baia. To avoid causing damage to the Stufe, a design variant was defined which provided for the displacement of the line about 50 m further inland (Figure 1). According to plans, the variant would only have caused "*the destruction of an ancient, very run down room... which in its present state has nothing of importance anymore*". Actually, it is a large vaulted room belonging to the BalneumTrituli (Ferrari & Lamagna 2017), already defined as "Imperial" by Giovanni Boccaccio and the subject of numerous graphic representations starting from the miniatures of the codes on the Phlegraean baths by Pietro da Eboli (XIV-XV sec.) (Figure 2).

Luckily, this variant was not carried on and the current layout coincides with the original project that sees the railway tunnel pass under the tunnels of the ancient spa structure. However, the excavation of the Punta Epitaffio tunnel resulted in a very hard accomplishment, due to the extremely high temperatures encountered on the work front: "*70° to 80°C. was the normal temperature of the working atmosphere, which rose higher when a new face of rock was detached. In a hole made in the newly exposed rock, a maximum temperature of 93°C. was registered by one of the engineers. The workmen, absolutely naked, worked but an hour or two at a time, and came out much exhausted.*" (Johnston-Lavis 1890). Only once the two opposite sides were joined and a natural circulation of air from the outside was established, operations in normal temperature conditions were possible.

Figure 2. Illumination of Balneum Trituli from the Palatine Codex 236, c. 13r (Menozzi 2006).

The opening of the tunnel had further positive effects with regard to cultural heritage: in fact, other previously unknown ancient tunnels were intercepted: *"Of great interest is the fact that a number of Roman cuniculi have been encountered crossing the tunnel at various angles and at different levels. Many of these are inclined passages, just large enough for a man to descend, quite similar, in fact, to those at the Baths of Nero. Where these passages reach the drainage level, they are filled by hot mineral water. The tunnelling continues on for some distance beneath the water, so that it is impossible to know how the original excavation terminates. The present state shows that we have confirmatory evidence of subsidence since Roman times. Others have a horizontal course and extend into the hills, for in some cases over 100 meters."*(Johnston-Lavis 1890), which, however, were never documented and were soon walled up. Finally, the depositional morphologies of the tuff banks cut by the tunnel provided paradigmatic indications on the eruptive sequences of the Phlegraean volcanoes. In order not to hide such an important geological section, the tunnel walls were not lined with tuff blocks masonry, but large sections of natural tuff were left in sight in the south-western half of the Punta Epitaffio tunnel (Figure 3).

Even the parallel modern Lucrino-Fusaro tunnel, opened in 1999, intercepted vapor emissions from ancient tunnels almost completely blocked by loose tuff deposits. It was therefore necessary to locally interrupt the concrete facing to let the vapors escape. Their condensation, once in contact with fresh air, produces the deposit of particular sulfur-based coral concretions, consisting mainly of gypsum, which are being studied by researchers at the National Institute of Geophysics and Volcanology (INGV) in Naples.

Presently, the dismissed tunnel of Punta Epitaffio, between Lucrino and Baia, shows a first section reinforced with metal railings covered with shotcrete. This operation was carried out as a preliminary to the excavation of the nearby Lucrino-Fusaro tunnel, in order to avoid damage to the

Figure 3. The dismissed Punta Epitaffio tunnel with the tuff layers exposed (photo by M. Fagnola – Cocceius Association).

older tunnel, which was still in operation at the time. However, this lining currently prevents any walls and vault inspection in search of traces of ancient intercepted tunnels. Luckily, 30 m from the entrance on the Lucrino side, somebody opened a passage in the protections, in order to access a tunnel rich in mineral deposits, that enters a second passage soon blocked by drains and rubble. It is probable that this passage set corresponds to another ancient thermal site, the *Balneum Pugillus* (De Sariis 1800).

Continuing in the tunnel, about 230 m from the Lucrino entrance and 434 m from the Baia entrance, we can see an opening on the south-east wall, walled up by a tuff blocks masonry surmounted by an arch. The masonry obstructs a tunnel that we identified by a quick video-inspection from a hole in the masonry. The tunnel appears directed towards the sea walls of Punta Epitaffio, which, however, are about 200 m far from the obstruction. The railway tunnel plan is located a few meters above the sea level, while the surface above the promontory is at an elevation of about 50 m a.s.l. On the opposite wall of the tunnel you can spot the obstruction of the upstream section of the tunnel, whose presence inside the promontory represents an enigma worth of further study. On the east and south slopes of Punta Epitaffio, numerous cavities are visible at sea level, some of which are pertinent to ancient thermal sites, while others reveal their ancient function as drainage pipes serving the noble villas which are believed to have been built on the summit of the promontory (Beloch 1890; Borriello & D'Ambrosio 1979).

Recently the dismissed tunnels around Baia have been the subject of an important recovery and re-functionalization project that involves the Phlegraean Fields Archaeological Park and the Municipality of Bacoli (NA), whose purpose is to create a pedestrian connection that allows visitors to reach in a convenient and fast way the Fusaro station avoiding vehicular traffic. In fact, the Fusaro station is located behind the *Parco delle Terme di Baia*. At the same time, the railway tunnel would be connected to some parking lots located near the so-called Sella di Baia, thanks to flights of stairs and an elevator. The aim is to facilitate the parking of tourist carriers for visitors who at the moment do not find an adequate parking place.

3 THE BATTIPAGLIA-REGGIO CALABRIA LINE AND THE VELIA TUNNEL

In the same period as the Phlegraean line, the works for the construction of a railway line were started which was to finally connect the southern regions of Italy to the rest of the newborn unitary state. It was an extremely important work whose construction would have lasted over ten years.

Thanks to its route - the railway runs parallel to the coastline – it will allow a shortening of travel times compared to the Ionian section (Briano 1977; Guadagno 1996). The route, which was already characterized by considerable geotechnical challenges, also found itself facing the problems linked to the various archaeological discoveries that the works allowed. Among the various sites crossed, there is the ancient Phocaean colony of Elea/Velia (Figure 4).

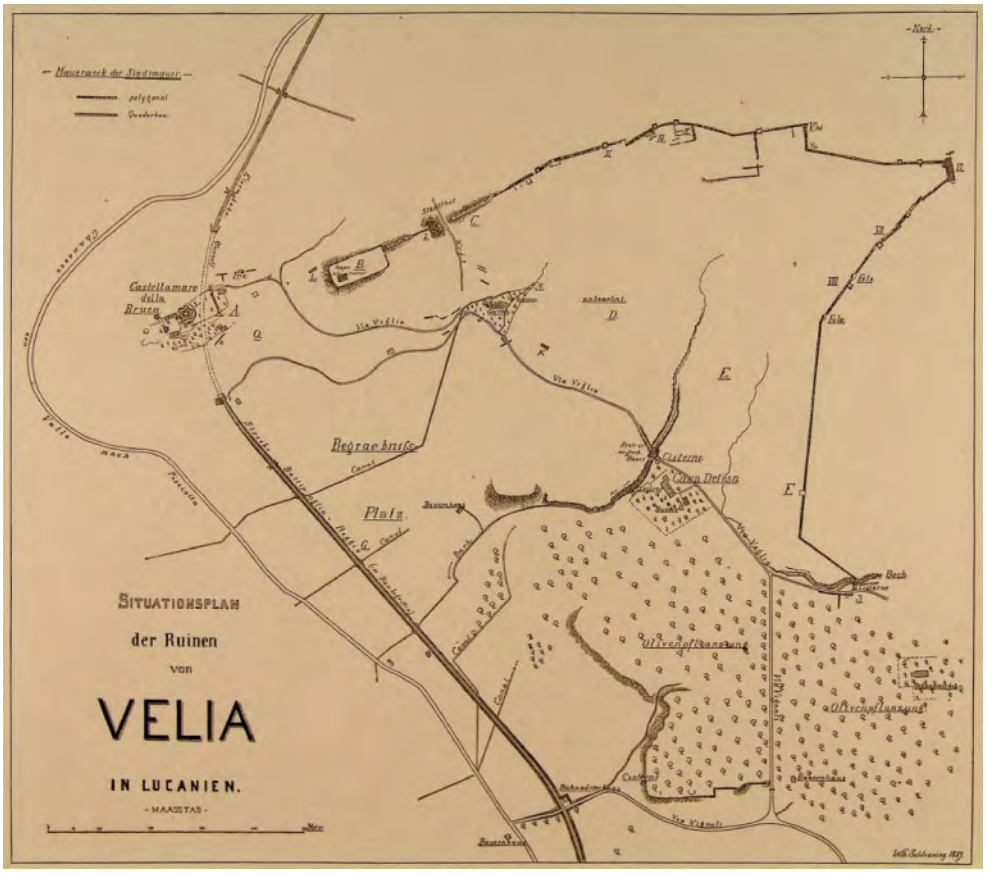

Figure 4. Plan of the city of Velia, after the construction of the railway line (Schleuning 1889).

The discovery of the remains of the ancient colony (Krinzinger 1994, 1997; Maiuri 1928; Napoli 1966; Sestieri 1956, 1960) imposed, even in this case, the designers and institutions involved to find a compromise solution between the modernization needs promoted by the State (Pedio 1988) – which needed an efficient railway line that served the entire country – and the equally important needs for the protection of the historical-archaeological heritage which had to be protected and preserved in any case and which were the result of needs born and already partially organically structured in the legislation in the pre-unification states (Baldacci 2004; Bottari & Pizzicannella

2007; Condemi 1987; Curzi 2004; Emiliani 1996; Maiuri 1928; Mingazzini 1954; Napoli 1966; Parpagliolo 1932; Speroni 1988).

This opportunity, therefore, allowed to safeguard and to know a site of enormous importance for the knowledge of the evolution of this settlement in the Ancient Italy which, despite its long-known importance, at the time was almost completely unknown and still isolated in the panorama of Italian research (De Luynes 1829; Lenormant 1883; Münter 1818; Napoli 1966). It was precisely the works to extend the railway line towards Calabria, which allowed the correct identification of the site, the definition of its extension and the launch of a more active policy of protecting the territory and the ancient city (Krinzinger 1994; Napoli 1970; Schleuning 1889; Schmiedt 1970). In the area of Velia, in fact, the route of the railway line crosses the area of the ancient city in full (Figure 4), piercing the hill of the acropolis - known by the toponym of Castellammare della Bruca – thanks to the construction of an about 300-meter long tunnel (Figure 5).

Figure 5. The railway tunnel southern entrance (Tocco Sciarelli 2006, Fig. V).

After the acropolis, the line proceeded, thanks to some connecting viaducts, towards the station of Ascea (SA). The tunnel, similarly to the other structures (bridges and viaducts) built in the Cilento section of the same period, was covered with a facing made with the typical Cilento red bricks. As always in these cases, the report of the findings and the discovery of the ancient city remains was received by the Directorate for Antiquities, directed by G. Fiorelli, who immediately acted to document the state of the site.

In a report published in the newsletter *Notizie degli scavi di antichità* of 1886, Fiorelli himself gives news of a visit to the area of the railway works, pointing out how these, in addition to having destroyed some parts of the walls, had intercepted and brought to light some tombs (Fiorelli 1886).

In one of his communications Fiorelli expressed regret that his recommendations aimed at protecting the remains of the city had not been listened to by the executing company (Archive MANN, folder V A3, 4 named *Ascea. Scavi dell'Antica Velia,* paper 11).

Some burials were of the type called "*alla cappuccina*" (i.e. gabled roof) and had returned only "*crude kits*" and a naiskos in good condition (Archive MANN, folder V A3,4 named *Ascea. Scavi dell'Antica Velia,* paper 41). Some epigraphs were also collected, most of which dated to the late imperial age, except one, in Greek (Fiorelli 1882, 1886).In this emergency, in order to increase knowledge of the site, G. Fiorelli entrusted the German architect Wilhelm Schleuning with the task of carrying out the first survey of the city and of the archaeological remains still visible in situ. The work was completed in 1889 (Figure 4, Schleuning 1889). It was precisely on the occasion of these works on the tunnel and the subsequent elevated section, that extensive de-structive interventions were recorded, damaging both the southern necropolis but especially the fortified walls of the city (Johannowsky 1961; Napoli 1966; Pontrandolfo 1996).Also in this case, as for the tunnels between Punta Epitaffio and Lake Fusaro, during the last century, in order to increase the functionality and capacity of the line, a new railway tunnel was built, parallel to the first one, which involved the de-functionalization of the nineteenth-century structure. This situation led to a slow and inexorable abandonment which only between 1999 and 2000, also following his Declaration of Historical-artistic interest, was the subject of a series of important restoration works, financed under the so-called "Progetto Porta" (Tocco Sciarelli 2003) aimed at transforming it into a long deposit (Figures 6 and 7) for the conservation of the large number of archaeological material recovered during the excavation activities on the site, which was not yet preserved in a suitable manner (Tocco Sciarelli 1994, 2003, 2006).

Figure 6. Interior of the Velia railway tunnel (https://www.museopaestum.beniculturali.it/progetto-di-intervento-dellex-galleria-ferroviaria-a-velia/).

Figure 7. Interior of the Velia railway tunnel (https://www.museopaestum.beniculturali.it/progetto-di-intervento-dellex-galleria-ferroviaria-a-velia/).

4 CONCLUSIONS

The analysis of the folders preserved in the Historical Archive of the MANN, combined with a series of inspections, allows us to add new data on the problem of the monuments and historical sites conservation, in relation to the development of the territories in which they are inserted.

Since the origins of the industrial and technological development of a nation, this appears to be one of the most demanding problems to be faced. As we have been able to see, complex construction sites involve apparently different and distant elements (Cultural Heritage, technical progress, etc.) which together, yesterday as today, contribute to the development of a nation. The analysis of these data, therefore, allows us to reconstruct the effect that the railway yards, and in particular the construction of tunnels, had with respect to the themes of the historical-archaeological heritage protection and the coexistence of the latter with the extremely significant technological progress in that particular period of our country's history.

A positive effect linked above all to the levels of approach to the theme of conservation which, if in the initial phase, the late nineteenth century, certainly entailed a series of errors and disagreements between the various professionals involved, as in the Velia case, has contributed to the elaboration of the principles which still today are the basis of the activities of protection of the territory. A protection of the historical archaeological heritage whose flexibility of application has allowed the Velia Railway Tunnel to become an integral part of that heritage which, more than 120 years ago, was partly damaged but which also allowed a more accurate study. Today, by virtue of its intimate and profound link with the cultural heritage the tunnelis subjected and treated in the same way as it is a unique and unrepeatable testimony of our past.

On the other hand, the one concerning the Punta Epitaffio tunnels and its consequences with respect to cultural heritage is different. Here the construction of the XIX century tunnel has undergone the beneficial influence of the relationship between the protection bodies (the Directorate of Antiquities) and the designers of the railway line who not only collaborated in order to safeguard

the cultural sites intercepted along the route (the so-called Stufe di Nerone and the so-called Villa di Cicerone) but have allowed, similarly to Velia, the identification of a new underground archaeological complex - the suggestion that BalneumPugillus is found is strong and deserves further investigation - which tells one of the many aspects that make the CampiFlegrei unique still today: thermalism and exploitation of the underground.

This shows clear examples of how the accurate reconstruction of the historical evolution of buried heritage sites gives an important contribution to a respectful development of sustainable infrastructures in our territories, where geotechnical engineering may play a fundamental duplex role of innovation and preservation at the same time

ACKNOWLEDGEMENTS

A dutiful thanks goes to the following people and entities who contributed to the research: the technical officers of the company Ente Autonomo Volturno, in particular Mr. Vincenzo Pignatiello, the parish priests of the church of San Filippo Neri and the cultural referent of the Diocese of Pozzuoli, father Don Roberto della Rocca, the owners of Lido Lo Scoglio - family Schiano Lo Moriello, Mrs Silvana Pagliuca, the Stufe di Nerone company, dr. Andrea Milanese, officer in charge of the Historical Archive of the National Archaeological Museum of Naples (MANN), dr. Francesco Scelza, officer in charge of the Archaeological Park of Velia, prof. Giuseppe Luongo and dr. Massimo Russo of the National Institute of Geophysics and Volcanology (INGV) of Naples.

REFERENCES

Abbruzzese Saccardi, A. 1976. Note biologiche nella grotta "Stufe di Nerone" (Napoli). *Annuario Speleologico 1974–75 della Sezione del CAI di Napoli*: 3–6.

Amalfitano, P., Camodeca, G. &Medri M. (eds.) 1990. *I Campi Flegrei. Un itinerario archeologico,* Venezia: Marsilio, pp. 340.

Baldacci, V. 2004. *Il sistema dei Beni culturali in Italia. Valorizzazione, progettazione e comunicazione culturale*, Firenze: Giunti Editore.

Beloch, J. 1890. *Campanien. Geschichteund Topographie des antikenNeapelund seiner Umgebung*, Breslau, reprint Roma 1964.

Borriello, M. & D'Ambrosio, A. 1979. *Baiae – Misenum. Forma Italiae, Regio I, Vol. XIV. Firenze: Olschki.*

Bottari, F. & Pizzicannella, F. 2007. *I beni culturali e il paesaggio: le leggi, la storia, le responsabilità.* Bologna: Zanichelli, pp. 115–137.

Briano, I. 1977. *Storia delle ferrovie in Italia. Milano: Cavallotti.*

Bulifon, A. 1693. *Lettere memorabili, istoriche, politiche, ed erudite scritte. Raccolta seconda. Napoli: Bulifon, pp. [12], 399, [11].*

Condemi, S. 1987. *Dal "decoro et utile" alle "antiche memorie". La tutela dei beni artistici e storici negli antichi Stati italiani*.

Curzi, V. 2004. *Bene culturale e pubblica utilità. Politiche di tutela a Roma tra Ancien Régime e Restaurazione.* Bologna: Minerva Edizioni.

D'Alconzo, P. 2001. La tutela del patrimonio archeologico nel regno di Napoli tra Sette e Ottocento. Mélanges de l'Écolefrançaise de Rome. Italie et Méditerranée, 113 (2): 507–537.

D'Arms, J.H. 2003. *Romans on the Bay of Naples and other essays on Roman Campania.*Bari: Edipuglia, pp. 498.

De Jorio, A. 1822. *Guida di Pozzuoli e contorni*. Napoli: Stamperia Reale, pp. XVI, 191.

De Luynes, H. 1829. Des riunes de Velia. Annales de l'Institut de correspondancearchéologique 1 (3): 381–386.

De Sariis, A. 1800. *Terminologia puteolana a vantaggio dell'uomo infermo*. Napoli: Orsino.

Emiliani, A. 1996. *Leggi, bandi e provvedimenti per la tutela dei beni artistici e culturali negli antichi Stati italiani 1571–1860.* Bologna.

Ferrari, G. & Lamagna R. 2017. L'imperiale Bagno di Tritoli riscoperto. *Atti del 3° Convegno Regionale di Speleologia - Campagna Speleologica, Napoli, 2–4 giugno 2017*: 211–217.

Fiorelli, G. 1882. Regio III–X. Velia. *Notizie degli scavi di antichità*, Roma 1882: 388-389.

Fiorelli, G. 1886. Regio III.–XII. Velia. *Notizie degli scavi di antichità*, Roma 1886: 280–81.

Guadagno, V. 1996. *Ferrovie ed economia nell'Ottocento postunitario. Roma: Collegio amministrativo ferroviario italiano.*

I Campi Flegrei nell'archeologia e nella storia, Atti dei convegni lincei, Accademia nazionale dei Lincei, Convegno internazionale, Roma 4–7 maggio 1976 (1977).

Johannowsky, W. 1961. *Un naiskos eleate con dea seduta*, Napoli: L'arte Tipografica.

Johnston-Lavis, H.J. 1888. [Third] Report of the Committee for the investigation of the Volcanic Phenomena of Vesuvius and its neighbourhood. *Reports of the British Association for the Advancement of Science* 57 (1887): 226-229.

Johnston-Lavis, H.J. 1890. [Fifth] Report of the Committee for the investigation of the Volcanic Phenomena of Vesuvius and its neighbourhood. *Reports of the British Association for the Advancement of Science* 59 (1889): 283–294.

Krinzinger, F. 1994. Intorno alla pianta di Velia. In: Greco, G. &Krinzinger, F. (eds), *Velia, studi e ricerche.* Modena, pp. 19–51.

Krinzinger, F. 1997. Velia. In: *Enciclopedia dell'Arte Antica*,*Suppl. 2 (1971-1994).* Roma, pp. 967–969.

Lenormant, F. 1883. *A travers l'Apulie et la Lucanie*, II.

Maiuri, A. 1928. Velia. Prima ricognizione ed esplorazione. Maggio-Settembre 1927. In: *Campagne della Società Magna Grecia (1926–27)*, Roma, pp. 14–29.

Maiuri, A. 1958. *I Campi Flegrei, dal sepolcro di Virgilio all'antro di Cuma,* quarta edizione riveduta e aggiornata. Roma: Istituto Poligrafico dello Stato.

Maiuri, A. 1983. *Itinerario flegreo.* Napoli: Bibliopolis.

Menozzi, M. 2006. *Il Ms Palatina 236: Nomina et virtutesbalneorumseu de balneisputeolorum et baiarum.Parma: Artegrafica Silva, pp. 84.*

Micheletti, P. 1845.Storia dei Monumenti del Reame delle Due Sicilie, *Vol. 1, Napoli: Stamperie e Cartiere del Fibreno.*

Mingazzini P. 1954. Velia. Scavi 1927: fornace di mattoni ed altre antichità.*Atti e Memorie della Magna Grecia*, n.s. I: 21–60.

Münter, F. 1818. *Velia in Lucanien. Eine Beilage zu Hegewisch über die Colonien der Griechen.* Altona.

Napoli, M. 1966. La ricerca archeologica di Velia. In: *Velia e i Focei d'Occidente* in *Parola del Passato* CVIII–CX: 191–199.

Napoli, M. 1970. Intorno alla pianta di Velia. In: *Nuovi studi su Velia.Parola del Passato* CXXX–CXXXIII: 226–235.

Panvini, P. 1818. *Il Forestierealle antichità e curiosità naturali di Pozzuoli CumaBaja e Miseno*, Napoli: Niccola Gervasi.

Parpagliolo, L. 1932. *Codice delle antichità e degli oggetti d'arte. Raccolta di leggi, decreti, regolamenti, circolari relativi alla conservazione delle cose d'interesse storico-artistico e alla difesa delle bellezze naturali,* Seconda Edizione, Vol. I, Roma, 1932.

Pedio, T. 1988. *La linea Napoli-Foggia-Barletta-Brindisi nel progetto ferroviario Borbonico. In: Mundi, B. & Gravina A. (eds), Atti del V convegno sulla Preistoria-Protostoria-Storia della Daunia, San Severo 9-10-11-dicembre 1983, San Severo, pp. 265–298.*

Pontrandolfo, A. 1996. Velia. In: *La Magna Grecia nelle collezioni del Museo Archeologico di Napoli*, Napoli, p. 40.

Schleuning, W. 1889. Velia in Lucanien. *Jahbuch des Deutschen Archäeologischen Instituts* 4: 169–190.

Schmiedt, G. 1970. Contributo alla ricostruzione della situazione geotopografica di Velia nell'antichità.*Parola del Passato* XXV: 65–92.

Sestieri, P.C. 1956. Velia. *Fasti Archeologici* XI, n. 2174: 45–47.

Sestieri, P.C. 1960. Velia. *Fasti Archeologici* XV, n. 4542: 52–53.

Speroni, M. 1988. *La tutela dei beni culturali negli Stati italiani preunitari*, I: *L'età delle riforme*, Milano.

Tocco Sciarelli, G. 1994. Storia degli scavi e nuove prospettive di ricerca. In: Greco, G. &Krinzinger, F. (eds), *Velia, studi e ricerche*. Modena, pp. 13–17.

Tocco Sciarelli, G. 2003. La realizzazione del Parco Archeologico: strategie di ricerca e valorizzazione. In: Greco, G. (ed), *Elea-Velia, le nuove ricerche*, *Atti del Convegno di Studi, Napoli 14 Dicembre 2001*, Pozzuoli, pp. 15–20.

Tocco Sciarelli, G. 2006. Elea-Velia. Venti anni di attività dalla ricerca alla valorizzazione. Metodologia di un intervento. In: *Velia. Atti del XLV Convegno di studi sulla Magna Grecia*, Taranto-Marina di Ascea 21-25 Settembre 2005, Taranto, pp. 117–135.

Geotechnical Engineering for the Preservation of Monuments and Historic Sites III – Lancellotta, Viggiani, Flora, de Silva & Mele (Eds)

The use of the GIBV method for monitoring the effects of urban excavations on built heritage

L. Piciullo, S. Ritter, A.O.K. Lysdahl, L. von der Tann, J. Langford & F. Nadim
Norwegian Geotechnical Institute, Oslo, Norway

ABSTRACT: This paper describes the application of the Ground-work Impact and Building Vulnerability methodology (GIBV) for the rapid assessment of damage caused on built heritage by an excavation. The GIBV damage assessment methodology is based on the combination of excavation-induced greenfield displacements and the vulnerability of buildings to subsidence. The combination of impact and vulnerability results in the expected building damage class. The GIBV has been implemented in a GIS tool to predict damage classes for buildings exposed to excavation-induced settlements.

This paper presents a further development of the GIBV methodology to include time dependence of consolidation settlements. The methodology is applied to assess a cultural heritage building in Oslo. The vulnerability has been assessed considering the following parameters: building length and shape for the geometrical characteristics; type of structure and foundation for the structural characteristics; and visible damages for the current condition of the building.

The results show the importance of considering long-term subsidence effects and building vulnerability when conducting a preliminary analysis of urban excavation effects in soft soils on built heritage. A comparison between predicted settlements and measured ones indicates that the conducted assessment results in reliable predictions.

1 INTRODUCTION

Monuments and historic sites are valuable assets for cultural heritage. Protecting the historic built environment from natural and human induced threats, thus, plays a vital role in sustainable development (IHBC 2020). The projected global trends of population growth and urbanization combined with climate change, however, put built heritage at risk.

Urban development requires underground construction activities that cause stress changes in the ground which often result in substantial ground displacements, especially in soft soils. In urban settings, such man-made subsidence can threaten existing historical structures (Burghignoli et al. 2013; Devriendt et al. 2013; Rampello et al. 2012). Especially in areas with subsidence prone clay deposits and sudden changes in the bedrock level, ground-water drawdown can cause substantial differential displacements and associated building damage (Langford et al. 2016b; Sundell et al. 2017). The associated consolidation process can result in subsidence continuing for decades. Reliably managing and safeguarding affected structures over long timespans can have severe economic implications. For example, in Oslo, Norway, it is projected that protecting vulnerable buildings on brick-type foundations will cost approximately € 6 billion (Venvik et al. 2018). There is therefore an urgent need to assess the potential risk of subsidence damage on the historic built environment and effectively communicate implications to decision makers.

 DOI 10.1201/9781003308867-78

This paper introduces latest improvements in a recently developed assessment methodology, which is called the *Groundwork Impact and Building Vulnerability* methodology, GIBV (Piciullo et al. 2021). Specific focus is placed on an extension of the GIBV methodology which integrates time-dependent subsidence caused by pore pressure reduction and its impact on adjacent buildings. A case study approach was chosen to test and validate this latest development. The impact of a deep excavation on a historic structure, which is particularly vulnerable to ground movements, was studied. Monitoring data were explored to compare predictions with measured building behavior. Specific guidance on adopting the GIBV methodology to historic built environment is provided.

The paper is structured as follows: first, the GIBV methodology is briefly introduced; second, the time-dependent impact assessment is described in detail and evaluated by comparing results to more refined consolidation settlement calculations; third, the study area with specific focus on a historic building (i.e., Colosseum cinema) and the application of the GIBV methodology is described. The potential of adopting the GIBV methodology specifically to heritage structures is then discussed, after which conclusions are drawn.

2 THE GIBV METHOD FOR THE ASSESSMENT OF BUILDING DAMAGE DUE TO EXCAVATION

2.1 *Description of the method*

The GIBV methodology provides a framework for early assessment of potential building damage caused by excavations in densely built areas in clay or clayey soils. It assigns damage classes to buildings surrounding a planned excavation by combining (a) an evaluation of potential excavation-induced settlements (i.e., the impact of the excavation) with (b) a qualitative assessment of building vulnerability to settlement damage. To provide a practical tool for early-stage analysis of buildings exposed to excavation-induced displacements, the GIBV methodology has been programmed in Python and implemented as a tool into ArcGIS. A detailed description of the GIBV method and its validation using two case studies can be found in Piciullo et al. (2021).

Figure 1 provides a schematic overview of the methodology. The primary impact of an excavation on its surroundings are induced ground displacements. These settlements are implemented into the GIBV tool using empirical curves for excavations in typical Norwegian ground conditions for (a) settlements caused by horizontal displacement of excavation walls (i.e., so called short-term displacements, see Figure 1) and (b) pore water pressure reduction at bedrock level that leads to an increase of effective stresses and consequently consolidation settlements in the overlaying clay (i.e., long-term displacements, see Figure 1).

Figure 2 shows the short-term displacement curves as established by Langford et al. (2016a) and Piciullo et al. (2021). The curves are based on measured settlements with distance to the excavation for case studies in Norway and normalized with the depth of excavation, H. In the curves it is distinguished between excavations where the support wall (all projects are executed with conventional steel sheet pile wall structures) reaches the bedrock (blue curves) and floating walls (red curves). A difference is also made between excavations with a low safety factor (FS) against basal heave and/or a stiff wall with relatively small distance between strut levels (upper bound, dotted lines) and those with a high factor of safety against basal heave and/or a relatively flexible support wall and large distances between struts (lower bound, continuous lines). This grouping is coherent with other empirical studies of short-term excavation induced displacements where the factor of safety against basal heave, the shape of the excavation, the type of retaining structure, the geology and the depth to bedrock are mentioned as the main factors influencing greenfield displacements (e.g., Goldberg et al. 1976; Clough & O'Rourke 1990; Long 2001; Peck 1969).

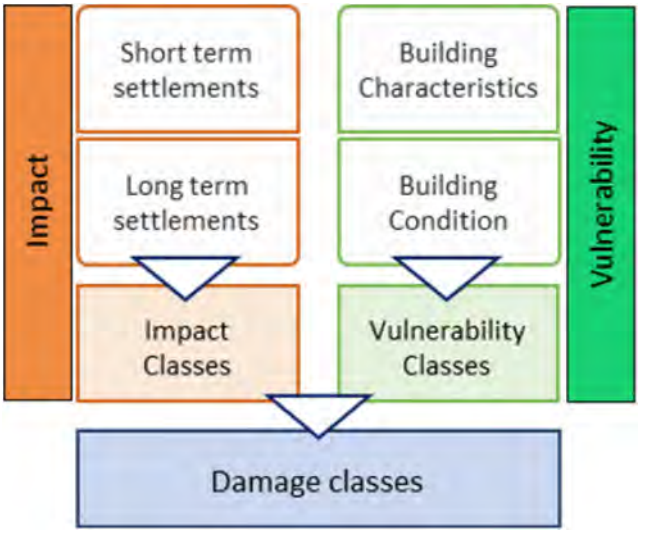

Figure 1. Ground Impact and Building Vulnerability (GIBV) methodology (Piciullo et al. 2021).

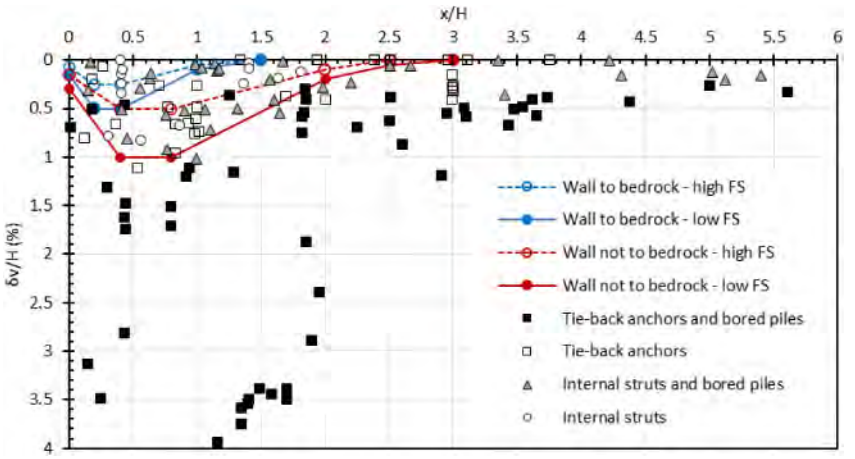

Figure 2. Expected normalized settlement, $\delta v/H$, versus normalized distance from wall, x/H in clay soils using different support methods.

The effect of pore water pressure reduction at bedrock level is in the Norwegian setting caused by leakage of water into the excavation through the interface between the soil and drilled elements such as the casings of tie-back anchors or piles, at the toe of the sheet pile wall or through uncovered bedrock. Without mitigation, a reduction of the pore water pressure in deeper permeable layers at the bedrock level can lead to long-term settlement of the overlying clay. The drawdown of pore water pressure can extend a considerable distance from the excavation. Figure 3 shows collected data of observed pore water pressure reduction at rock level from excavations in Norway as a function of the excavation depth below the groundwater level (H_{max}) and the distance from the excavation (Langford et al. 2016b). To estimate the pore water pressure reduction for ongoing or planned excavations, two curves are defined for excavations where mitigation measures such as grouting or infiltration wells are implemented and those with no such mitigation, respectively. In the GIBV

methodology both curves from Figure 3 are implemented and can be chosen in accordance with the situation at hand. The consolidation settlements associated with this pore water pressure reduction are then calculated using Janbu's modulus concept (Janbu 1970). In the Nordic countries Janbu's modulus concept is widely recognized as a framework for interpretation of oedometer tests and settlement calculations of clays.

To assess the impact of the excavation on buildings in the vicinity, the short and long-term displacements are calculated and combined for the corner points of each building. For every building, the vertical settlement of the corner points and the rotation (or slope) of each wall are calculated. Using the four categories proposed by Rankin (1988) an impact class for each building is defined (Table 1).

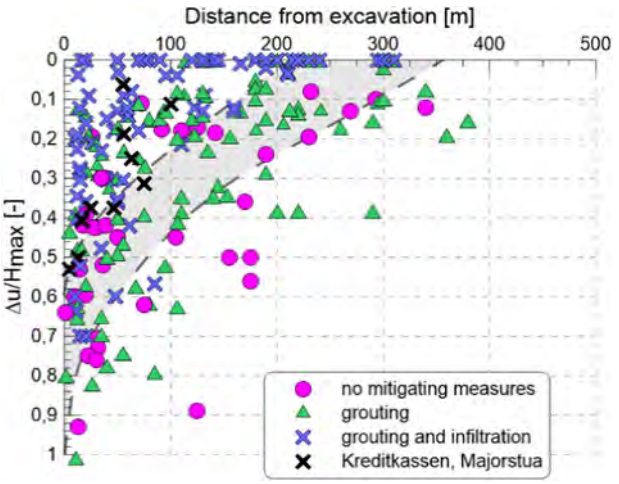

Figure 3. Database of pore water pressure reduction due to excavation works in Norway: Δu = pore water pressure reduction in m measured at the base of clay stratum, Hmax = depth of excavation base beneath initial ground water surface (adopted from Langford et al. 2016b).

Table 1. The maximum rotation and the maximum settlement are categorized in four level of impact (Adapted from Rankin 1988).

Impact level	**Maximum rotation (θmax)**	**Maximum settlement (δV,max)**
I1. Negligible	<1/500	<10 mm
I2. Slight	1/500–1/200	10–50 mm
I3. Moderate	1/200–1/50	50–75 mm
I4. High	> 1/500	>75 mm

The framework for assessing building vulnerability as implemented in the GIBV methodology is based on a qualitative evaluation of geometrical (length and shape) and structural (type of structure and foundation) characteristics and the current condition (see Table 2) of each building. For each parameter, a vulnerability grade (A-D) is assigned. The weighted sum of all parameters then provides an overall vulnerability score for the building. The weights were assigned to each parameter based on engineering judgement. For example, a higher weight was assigned to the foundation type given that the interaction between the soil and the foundation will likely govern the transfer of soil displacements to a building. To assign a final vulnerability index to the building, the derived vulnerability score is normalized by the sum of the maximum values available for each

parameter. The vulnerability index ranges between 0 and 100 (Table 3). A detailed description of this rating method can be found in Piciullo et al. (2021).

Table 2. Building vulnerability rating based on five parameters. Rating method adapted from Dzegniuk et al. (1997).

Grade vi								
Characteristic	**Parameter**	A [0]	B [5]	C [20]	D [50]	**Weight Pi**	**Max value**	**Relative weight**
Geometrical	Building length (m)	≤10	11–15	16–30	>30	0.75	37.5	30 %
	Building shape	>0.75	0.75–0.5	0.5–0.35	<0.35	0.75	37.5	
Structural	Structure type	Steel	Reinforced concrete	Wooden, Mixed	Masonry, special structure	1	50	50 %
	Foundation type	To bedrock, Piles	Raft	Strip	Wooden piles, isolated	1.5	75	
Condition	Visual damage	Excellent	Good	Medium	Bad	1	50	20 %

Table 3. Vulnerability classes defined according to the normalised vulnerability index value.

	Vulnerability Index of the building			
	V1 Negligible	V2 Low	V3 Medium	V4 High
Iv	0–25	25–50	50–75	75–100

As a final step in the GIBV methodology, the level of impact and the vulnerability index are combined in a risk matrix (Figure 4) to assess the damage of a building that could be caused by the excavation assessed. Here, five damage classes between negligible (D0) and severe/very severe (D4/D5) are proposed corresponding to damage classification as used by several authors (e.g., Burland et al. 1995). The configuration of the matrix can be adjusted in accordance with specific project requirements such as, for example, for areas with historical buildings.

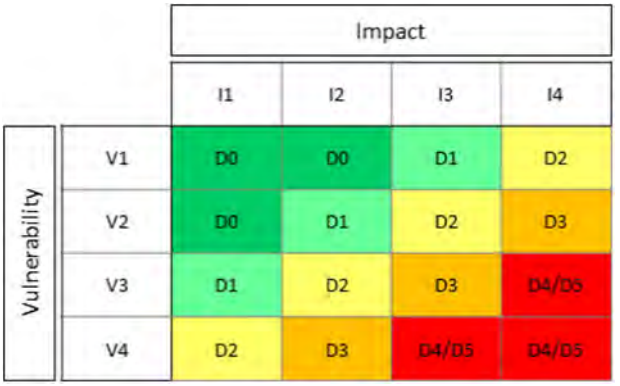

Figure 4. Expected damage classes and classification of the matrix cells. The 4x4 matrix plots the vulnerability against the impact classes.

3 TIME-DEPENDENT SETTLEMENT ANALYSIS

3.1 *Theoretical background*

The time dependent settlement analysis has been recently implemented in the impact assessment of the GIBV methodology. To calculate the settlement at the end of the consolidation phase, the theory proposed by Janbu (1970) has been applied, which describes effective stress changes in the vertical direction. The compression modulus M is expressed as:

$$M = \frac{d\sigma'_v}{d\varepsilon_v} \tag{1}$$

$$M = M^{OC} \quad \text{for } \sigma'_{v0} + \Delta\sigma'_v < \sigma'_{vc} \text{ for overconsolidated (OC) soils} \tag{2}$$

$$M = m(\sigma'_{v0} + \Delta\sigma'_v - p_r) \text{ for } \sigma'_{v0} + \Delta\sigma'_v > \sigma'_{vc} \text{ for normally consolidated (NC) soils} \tag{3}$$

where σ'_v and ε_v are, respectively, the vertical effective stress and vertical strain, σ'_{v0} is the initial vertical effective stress, p_r is the reference vertical stress for $M = 0$, m is the Janbu modulus number and σ'_{vc} is the vertical preconsolidation stress. Assuming an increment of the initial vertical effective stress, σ'_{v0}, of a value $\Delta\sigma'_v$, the vertical strain increment is equal to:

$$\Delta\varepsilon_v = \int_{\sigma'_{v0}}^{\sigma'_{v0}+\Delta\sigma'_v} \frac{1}{M} d\sigma'_v \tag{4}$$

so that:

$$\Delta\varepsilon_v = \frac{\Delta\sigma'_v}{M^{OC}} \quad \text{for } \sigma'_{v0} + \Delta\sigma'_v < \sigma'_{vc} \tag{5}$$

$$\Delta\varepsilon_v = \frac{\sigma'_{vc} - \sigma'_{v0}}{M^{OC}} + \frac{1}{M} ln\left(\frac{\sigma'_{v0} + \Delta\sigma'_v - p_r}{\sigma'_{vc} - p_r}\right) \text{ for } \sigma'_{v0} + \Delta\sigma'_v > \sigma'_{vc} \tag{6}$$

The previous equations are used to compute the volumetric strain which can be used to compute vertical soil displacements. At an earlier stage of the consolidation process, the entire excess pore water pressure has not dissipated, and consequently smaller vertical settlements would be observed. To account for this time-dependent consolidation behavior, the one-dimensional consolidation theory, according to Terzaghi and Fröhlich (1936) has been considered, which describes the evolution of the excess porewater pressure $u(z, t)$ in time and space by the following partial differential equation:

$$C_v \frac{\partial^2 u}{\partial z^2} = \frac{\partial u}{\partial t} \qquad C_v = \frac{kM}{\gamma_w} \tag{7}$$

The coefficient of consolidation C_v indicates the speed with which consolidation takes place and is a function of the permeability k of the clay, the compression modulus M and the water weight density γ_w. The general solution of this equation is a sum of many solutions containing a sinusoidal function in space and a decaying exponential function in time. The contribution from the different solutions depend on the boundary drainage conditions and initial stress in the clay. In the GIBV tool, it has been assumed that the clay layer is bounded by an open drainage at the bottom, and by a closed drainage at the top (as the gradient for a pore pressure reduction at bedrock level will be downward). Then the solution becomes:

$$u(z,t) = \sum_{n=1}^{\infty} A_n e^{-\left(\frac{n\pi}{2}\right)^2 T} \sin\left(\frac{n\pi z}{2h}\right) \qquad T = \frac{Cvt}{h^2} \qquad A_n = \frac{1}{h}\int_0^h f(z) \sin\left(\frac{n\pi z}{2h}\right) dz$$

Here, T is a dimensionless time factor and h is the height of the clay layer. The coefficients A_n are dependent on the initial (time = 0) distribution of excess pore water pressure, called $f(z)$. For example, for a square isochrone, $f(z) = u_0 h$, the equation is:

$$u_{square}(z,t) = \frac{4}{\pi} u_0 \sum_{n=1,3,5\ldots}^{\infty} \frac{1}{n} e^{-\left(\frac{n\pi}{2}\right)^2 T} \sin\left(\frac{n\pi z}{2h}\right).$$

In order to obtain the total settlement, it is integrated over the total depth z. Terzaghi and Frölich (1936) showed that the average degree of consolidation U for the whole clay layer at time t can be expressed as:

$$U(t) = 1 - \frac{1}{u_0 h} \int_0^h u(z,t)dz$$

Inserting the expression for $u$and carrying out the integral

$$U_{square}(T) = 1 - \sum_{n=0}^{\infty} \frac{2}{N^2} e^{-TN^2} \quad N = \frac{\pi}{2}(2n+1)$$

In a similar way, it is possible to calculate the degree of consolidation for an initial triangular isochrone, both with the tip upwards, and with the tip downwards, as illustrated in Figure 5. The result is:

$$U_{\nabla}(T) = 1 - \sum_{n=0}^{\infty} \frac{2(-1)^{n+1}}{N^3} e^{-TN^2} \quad N = \frac{\pi}{2}(2n-1)$$

$$U_{\Delta}(T) = 2U_{square} - U_{\nabla}$$

The three curves U_{square}, U_{∇} and U_{Δ} are plotted in Figure 5 as a function of the time factor T. For small times, the settlement is almost zero, and for large times, it approaches the long-term settlement $\Delta\varepsilon_v$,at$U = 100\%$.

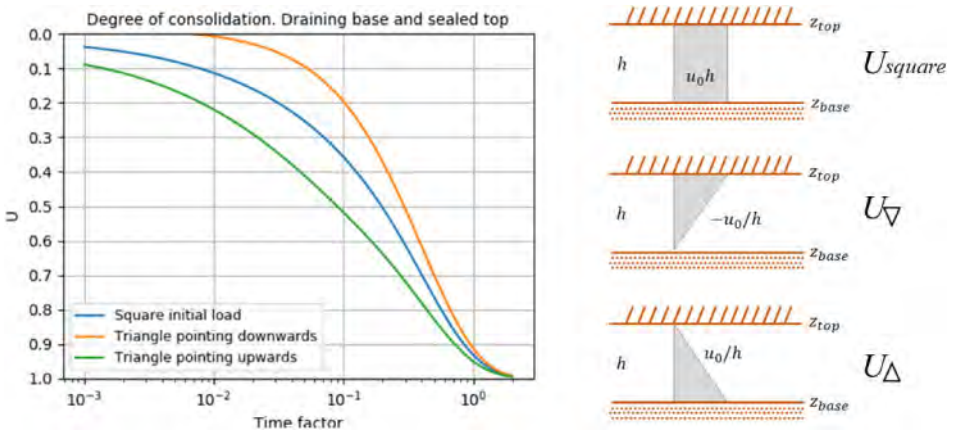

Figure 5. Triangular isochrone and corresponding U-T curve (from Terzaghi & Frohlich 1936)

In the GIBV tool, U_{Δ} has been implemented, to take into account the case of a permeable layer above the bedrock (i.e., porewater pressure reduction at bedrock level). The infinite sum in the equations above converges and could therefore be implemented in a computer program by

using a for loop to a sufficient number of terms (n = 10). In the Terzaghi theory, the compression modulus M is assumed to be constant inside the clay layer. In reality, this is not the case, and for the calculation of the final settlement (i.e., end of consolidation) the clay has been discretized into layers of 1 m thickness and different M have been calculated with depth, but to calculate the settlement in time an average value of M for the clay layer has been considered to evaluate Cv. Different distributions of pore pressure reductions and boundary conditions can be implemented in the future.

3.2 *Comparison between settlements in time obtained with GeoSuite and GIBV tool*

To validate the results obtained by the described procedure, a comparative analysis was performed between the results of the time dependent settlement analysis obtained with the ArcGIS tool and the ones calculated by the commercial software Trimble Novapoint GeoSuite (https://civil.trimble.no/produkter/novapoint/novapoint-geosuite). This software is widely used in Scandinavia for slope stability and consolidation settlement analyses.

The analyses were carried out by considering an ideal simulation with a building located as close as possible to an excavation and a simple soil profile composed by a 7 m deep dry crust, a 2.5 m deep water table and 3 different clay thicknesses of 3, 13 and 23 m. The depth to bedrock for the three cases was thus 10, 20 and 30 m respectively. The geotechnical input data are summarized in Table 4. Two different over consolidation ratios (OCR) were considered: OCR = 1.0 to simulate a normally consolidated soil condition and OCR = 1.2 for a slightly over consolidated one, representing a typical range in the Oslo area. Three different scenarios for pore water pressure reductions at the bedrock level were investigated: 22.5, 50 and 100 kPa.

Table 4. The input parameters for the comparison study.

VARIABLE	UNIT	VALUES
Dry crust thickness	[m]	7
Groundwater depth	[m]	2.5
Soil unit weight	[kN/m3]	18.5
Overconsolidated ratio	[–]	1–1.2
Janbu's modulus number	[–]	15
Pore water pressure reduction at the bedrock	[kPa]	22.5–50–100

Figure 6 shows the comparison between the results obtained with the ARCGIS tool and the Geosuite software for the two different OCRs and for three different pore water pressure reductions at bedrock. The bias, i.e., the difference between the settlement values, calculated with the GIBV tool and Geosuite were plotted in Figure 7. It shows that the settlement values at the end of the consolidation phase were almost identical for the cases. This was expected as both, the GIBV tool and the Geosuite software compute the settlements at the end of the consolidation phase considering a variable value of the modulus (M) (i.e., resistance against deformation Janbu, 1970), with depth. However, small differences were observed when increasing the clay thickness and the excess pore water pressure. The maximum difference was approximately 1 cm. It can be followed that the GIBV tool is to a very small degree (i.e., less than 8% for the considered scenarios) underestimating the settlements at the end of the consolidation rate. The mismatch can be ascribed by the way the calculation has been carried out with the GIBV tool, since the formulation employed by the tool and Geosuite software is the same. The computed points have a small distance from the defined excavation. This distance, even if very small (around 1 meter), still influences the pore water pressure reduction value, that, according to Figure 3, will result in a lower value than the three values defined for this comparison (see Table 4).

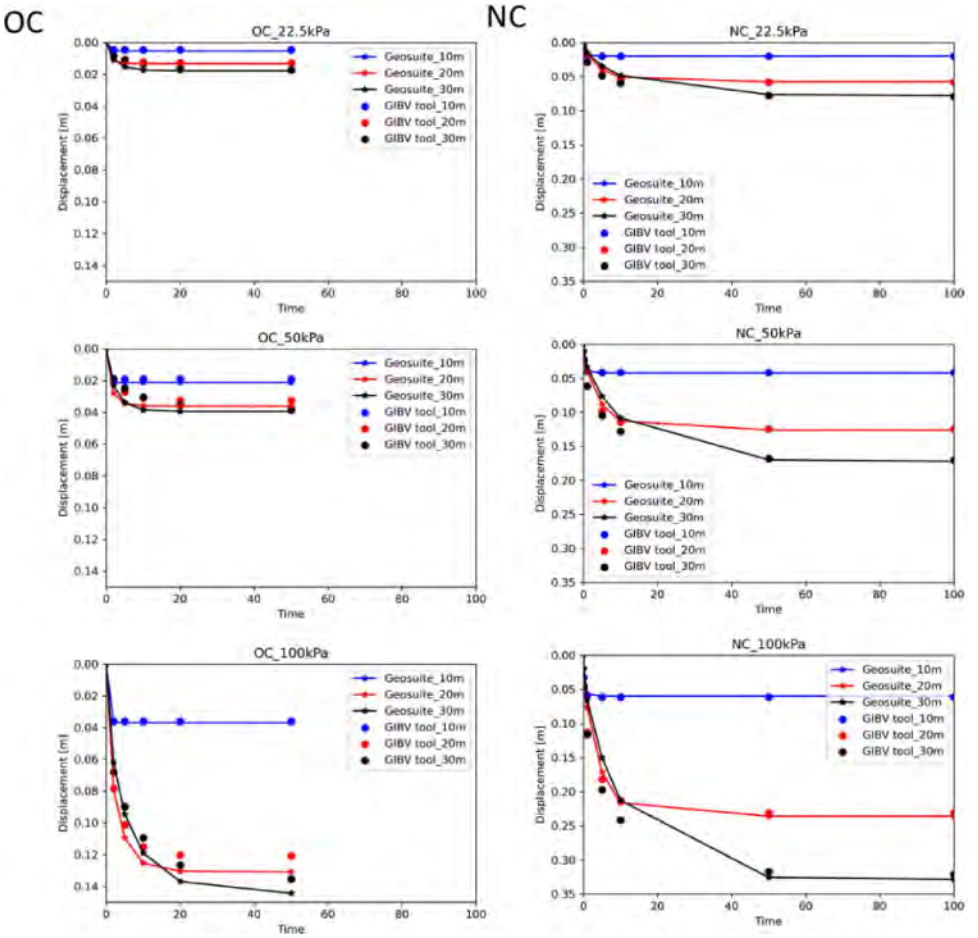

Figure 6. Comparison between consolidation settlement analysis implemented in the GIBV methodology and Geosuite reference calculations for overconsolidated clay (OC, left column) and normally consolidated clay (NC, right column). Three scenarios of porewater pressure reduction (22.5, 50 and 100 kPa) and three clay thickness (10, 20 and 30 m) were investigated.

Greater differences have been observed for the settlements in time. In this case, the formulation defined in the GIBV methodology and implemented in the ArcGIS tool (see Section 3.1) is different from how it is computed in Geosuite. The latter computes time-dependent consolidation settlements considering a consolidation coefficient varying as a function of the compression modulus, while the GIBV methodology uses a constant consolidation coefficient with time for the clay layer.

Figures 6 and 7 indicate that the solution implemented in the GIBV methodology likely results in an overestimation of the settlements at the early stage of the consolidation process (smaller degree of consolidation). As expected, the effect increases with greater clay thickness and larger pore water pressure reduction. The maximum mismatch of 5 cm after 1 year of consolidation was observed for the NC case, with 30 m bedrock depth and 100 kPa of pore water pressure reduction (Figure 7, bottom right). However, the accuracy is considered sufficient for the purpose of the tool, which is to obtain an early assessment of possible effects of deep excavations on existing buildings.

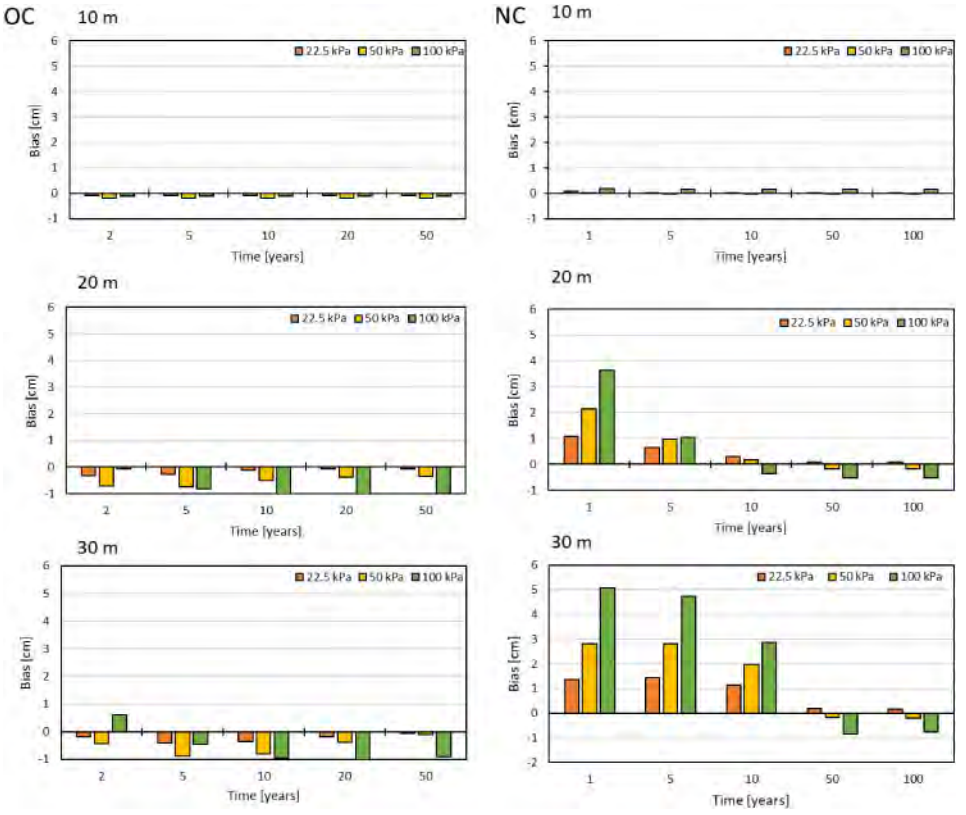

Figure 7. Differences (bias) between settlements computed by the GIBV methodology and Geosuite calculations for the scenarios described in Figure 6.

4 CASE STUDY: THE IMPACT OF AN EXCAVATION ON A SURROUNDING HERITAGE STRUCTURE

4.1 *The Colosseum cinema*

The newly introduced features of the GIBV methodology were tested on the Colosseum cinema (Figure 8), which is a historic building in the city of Oslo, Norway. The Colosseum building is one of Europe's largest cinemas. Built in 1926, the original building was a wooden structure. The building is listed as cultural heritage on municipal level. This means it is not protected as national heritage but a permission by the planning authorities is required for changes to the exterior of the building. Following a fire in 1963 in that the dome of the building collapsed, the cinema had to be rebuilt. The main hall of the cinema integrates structural elements from both, the original and the new supporting structure. The new construction reused the existing strip foundations, but additional foundations were needed to support the dome, which consists of a 8 cm think concrete shell structure. All strip foundations are founded directly on clay and the building has been subjected to settlements since 1964. The cause of the settlements is a combination of consolidation settlements due to the weight of the building as well as slow ongoing creep settlements of the marine clay. In addition, the area has been affected by underground construction of sewage tunnels in the 70s, which has resulted in pore pressure reduction and consolidation settlements. In total the settlements amount to up to 70 cm since systematic monitoring started in the 90s.

In 1997, the cinema was extended towards the South-West. At that point, it was reported that the floor of the main hall showed an inclination towards Essensdropsgate of approximately 25 cm. The extension of Colosseum cinema itself, that is built on piles reaching the bedrock, is only one of many construction projects that have taken place in the vicinity of the cinema since 1970. The location of several construction projects is illustrated in Figure 8. The VEAS sewage tunnel was constructed between 1977 and 1979 in bedrock but without pre-excavation grouting, leading to a drop of porewater pressures at bedrock level causing increased settlements in the area. For the Colosseum cinema, settlements between 10 mm/year at the most northern corner towards Fritjof Nansen's road and 17 mm/year towards Essensdrops gate were reported between 1970 and 1985. To mitigate these settlements, infiltration wells were installed in the area around New Year 1992 and additional ones in 2002. In 2002, leakage into the tunnel was also reduced through sealing by lining the bedrock tunnel. The last infiltration well was phased out in 2016.

Due to extensive construction activities in the area, the Colosseum building has continued to experience large settlements in recent years. In particular, the construction of the new building for "Kredittkassen" between 1990 and 1992 lead to immediate settlements of up to 10 cm and continuous settlements after 1992 (Figure 10). This historic construction activity influencing the Colosseum building is the focus of the GIBV application presented in this paper.

Figure 8. Colosseum cinema in 1933 (on the left, Photo by Christoffersen). Building activity around the Colosseum cinema since the 1990th (on the right).

4.2 *Kredittkassen excavation in 1990*

This excavation in Oslo had a depth of 16 m over an area of around 150 m × 100 m (see Kredittkassen area in Figure 8). The excavation was supported by a sheet pile wall installed to bedrock, supported by five levels of tie-back anchors drilled to bedrock. The soil conditions consisted of 1–2 m dry crust clay over normally consolidated soft clay. Beneath 8 m depth, the clay was quick. The depth to bedrock in that area varies from 10 to 30 m. Undrained shear strength, s_u, in clay is generally between 15 and 40 kPa. The natural water content is around 30–40%, and soil unit weight is 19 kN/m^3. The groundwater level is at approximately 2–3 m below terrain.

Ongoing settlements of 20 mm/year were registered at the time of construction, caused by drainage to existing tunnels in the area that caused a pore water pressure reduction at the bedrock of around 10–35 kPa. The bedrock beneath the sheet pile wall was grouted to a depth of 10–15 m below the bedrock surface. The rock grouting was drilled vertically from the terrain level. Six infiltration wells were used to maintain pore pressure levels during construction. The pore pressure was monitored at bedrock and in the clay with several piezometers.

4.3 *Impact in time*

In the GIBV methodology, buildings are schematized into corner points and line walls. The vertical settlement (δv) and the slope of walls (θ) are calculated respectively for every corner point and wall

line (connecting two corner points), for both short- and long-term settlements. These parameters are then classified according to the four categories proposed by Rankin (1988) in the so-called impact classes (Table 1). The use of maximum vertical settlement to classify the impact, generally represents a more conservative approach than the slope because it neglects differential displacements. In this specific case study, a large difference can be seen among the two approaches (Figure 9). This difference was expected for a building which predominantly moves as a rigid body with less pronounced building distortions (i.e., bending or shear deformations). Consequently, the classification based on two settlement parameters resulted in two different impact classes after 5 years: I1 (green) when considering the slope (θ) and, I4 (red) when considering the vertical settlement (δv).

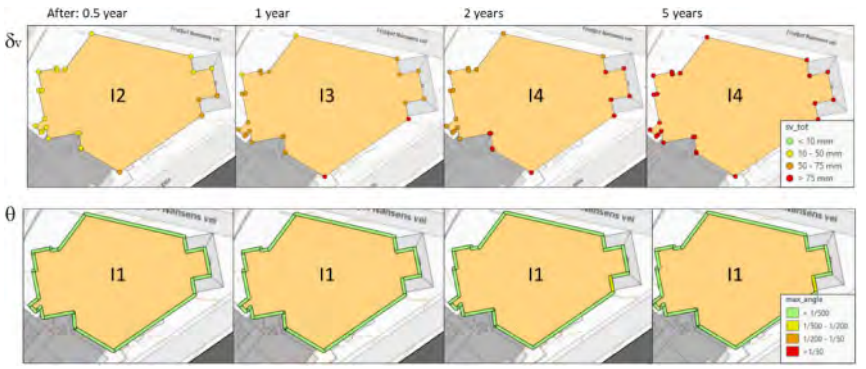

Figure 9. Classification of the groundwork impact according to Rankin 1998 (see Table 1). Top row: vertical settlements of the corner points. Bottom row: rotation (or slope) of the building walls.

For this case study, the use of the vertical settlement is likely more appropriate, since vertical settlements of up to 25 cm have been observed and the corner points of the analyzed line walls are not showing high differential settlements. The evaluation of the impact in time has been carried out evaluating the settlements for the corner points of Colosseum cinema. Figure 10 shows the comparison between measured and computed settlements using the GIBV methodology. Six corner points have been considered for the comparison: 8-1, 8-3, 8-4, 8-6, 8-7, 8-9. The comparison between measured and computed settlements shows an underestimation of the settlements with the GIBV tool. The underestimation is particularly emphasized for corner points 8-1, and 8-3 and the mismatch increased with time. This can be partially explained by the presence of ongoing settlements in the area due to previous projects (e.g., VEAS tunnel) that are not connected to the excavation of the Kredittkassen building. In Figure 10, it is possible to observe ongoing settlements before the sheet pile wall installation and excavation started, of approximately 10 to 17 mm/year. Over the period shown in Figure 10Figure 8 (i.e., 8 years), these ongoing settlements, which are not considered in the GIBV predictions, accumulate to approximately 80 to 136 mm over 5 years. Reducing the measured settlement data by these values would result in a reasonable agreement between the measurements and the predictions.

4.4 *The influence of vulnerability in the damage assessment*

For this case study the slope shows an underestimation of the impact category (see Figure 9). The following analysis thus considers the impact class defined with the maximum vertical settlement ($\delta v,max$) experienced by the corner points of Colosseum cinema. The impact classes in time are shown in Figure 11a. Two different vulnerability classes have been defined for the building: V2 and V3. The classifications are obtained considering two different building foundation (parameter "Foundation type" in Table 5) to consider the foundation improvement carried out in the 60s (Section 4.1): "Raft" and "Strip". Table 5 summarizes the entire characteristics considered to evaluate the vulnerability of the Colosseum cinema.

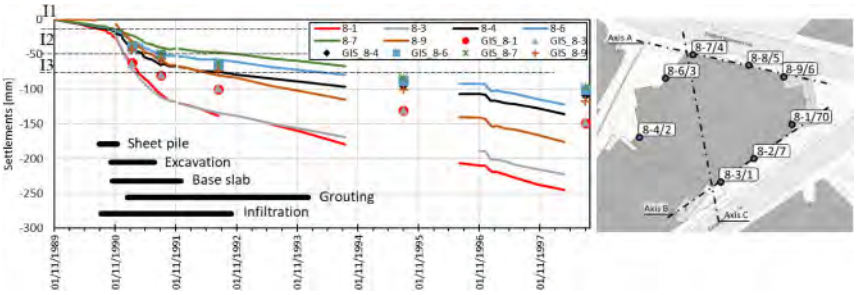

Figure 10. Comparison between predicted and measured settlements. Continuous line: measured settlements of the Colosseum cinema between 1990 and 1999. Point: settlements of the corners point of Colosseum cinema at 4 different time steps: 0.1, 1, 2, 5 years, calculated with the GIBV tool. Position of settlement bolts shown on the right.

Table 5. The characteristics considered to evaluate the vulnerability of the Colosseum cinema. Two vulnerability classes have been considered for the analyses: V2 and V3.

Characteristic	**Parameter**		
Geometrical	Building length (m)	>30	>30
	Building shape[1]	>0.75	>0.75
Structural	Structure type	Special structure	Special structure
	Foundation type	Raft	Strip
Condition	Visual damage	Medium	Medium
Vulnerability		**V2**	**V3**

[1] is a number representing the geometric squareness or complexity of a building polygon (see Piciullo et al. 2021).

The damage class was evaluated by combining impact and vulnerability classes employing the matrix shown in Figure 4. Figures 11b and c show the damage classes assigned to the Colosseum

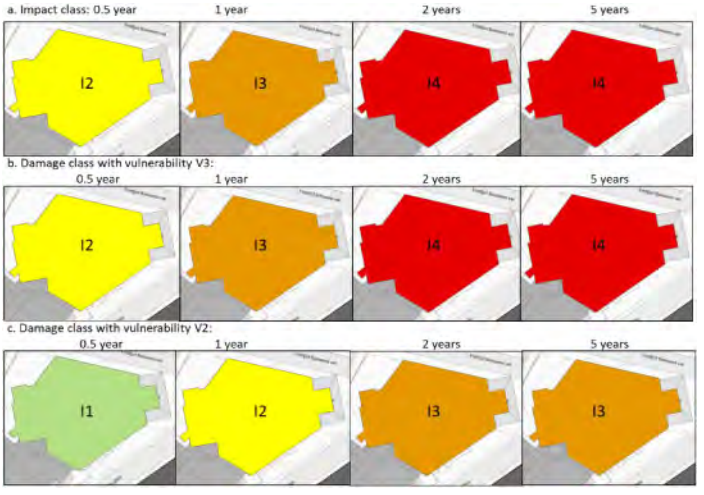

Figure 11. (a) Impact class in time considering the maximum vertical settlement ($\delta v,max$) experienced by the corner points of Colosseum cinema. Damage class in time with a vulnerability class V3 (b) and damage class in time with a vulnerability class V2 (c) for the Colosseum cinema due to the excavation.

cinema as a function of the different vulnerability classes (i.e., V2 and V3). The damage class increased as a function of the impact, which is a result of the time-dependent settlements. The vulnerability class once defined, was kept constant in the conducted analyses. A vulnerability class V3 resulted in an overall damage class D2 after 6 months from the excavation excecution and D3 after 1 year and D4/D5 after 2 years. Considering a vulnerability class V2, the damage classes of the presented time steps reduced by one class compared to V3 (Figure 11).

5 DISCUSSION AND CONCLUSION

The GIBV methodology has been implemented in a tool in the commercial software ArcGIS. The tool has recently been further developed by implementing the empirical 1D-consolidation curves by Terzaghi to compute settlements at different time steps. The results have been compared with the commercial software GeoSuite. The final, full primary, consolidation results in very good agreement (maximum difference 1 cm, circa 8%). However, the settlements at different degrees of consolidation differ more notably, with a maximum difference of 5 cm after 1 year for a normally consolidated clay. The greater the clay thickness and porewater pressure reduction at bedrock level, the greater was the bias between the settlements computed with GeoSuite and the GIBV tool. The differences between the two calculation methods are that the GIBV methodology followed the Terzaghi and Fröhlich (1936) solution while GeoSuite uses a more advanced numerical approach considering, for example, a time dependent variation of the consolidation coefficient.

The GIBV tool has been employed to evaluate the damage classes in time of an historical cinema in the city of Oslo, Norway, after the execution of an adjacent excavation. The settlements in time have been evaluated and compared with the measured data. A satisfactory match was observed up to 5 years from the excavation for four corner points (8-4, 8-6, 8-7, 8-9). The settlements of two additional corner points (8-1 and 8-3) were underestimated by the GIBV tool, especially after 6 months from the excavation. This underestimation can be explained, in this specific case study, by observed ongoing settlements in the area prior to the excavation (see Figure 10); approximately 10 to 17 mm/year were reported. One more important aspect to highlight is that, in this case study, the impact class evaluated considering the slope, instead of the vertical settlement, would lead to a lower impact class and damage class (see Section 4.1). For a more direct comparison with in-situ measurements, the impact has been classified according to the vertical settlement experienced by the corner points of the Colosseum cinema. Section 4.2 shows that the definition of the vulnerability class for the building is an important part of the assessment, specifically for cultural heritage buildings, leading to a different damage assessment.

Moreover, different risk matrix classifications, like the ones proposed in Figure 12, could be adopted by decision makers when computing the damage class for cultural heritage buildings, allowing for a more conservative approach. Figure 12a is keeping the same shape of the matrix shown in Figure 4 but equally expanding the D4/D5 class along columns and rows. Figures 4b and c represent matrix configurations allowing the highest damage class (i.e., D4/D5) with either low vulnerability (V2, Figure 4b) or low impact classes (I2, Figure 4c). The choice of the matrix

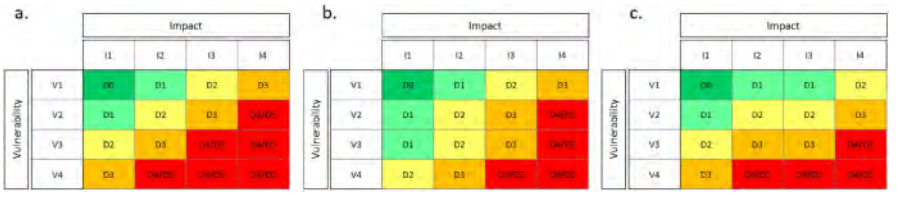

Figure 12. Proposed variations of risk matrices that could be adopted for heritage buildings: a) very conservative (very low willingness to accept damage), b) and c) configurations with low willingness to accept damage oriented respectively to impact and vulnerability.

configuration depends on the willingness to accept damages and on the weight assigned to Impact and Vulnerability by decision makers.

This study focused on a single excavation pit affecting a historical structure. Making use of historic monitoring data of a heritage structure in Oslo, it was shown that in urban settings multiple construction activities can impact a building. The GIBV methodology is currently limited to evaluate the effects of a single groundwork at a time over time. Further work needs to be conducted to better account for multiple groundworks affecting their surroundings simultaneously.

REFERENCES

Burghignoli, A., Callisto, L., Rampello, S., Soccodato, F.M. and Viggiani, G.M.B., 2013. The crossing of the historical centre of Rome by the new underground Line C: A study of soil structure-interaction for historical buildings. Geotechnics and heritage: Case histories, 3, p.97.

Burland, J.B., 1995. Assessment of damage to buildings due to tunneling and excavation. In: Invited Special Lecture to IS-Tokyo 1995: Proceedings of 1st International Conference on Earthquake and Geotechnical Engineering, Tokyo, pp. 1198–1201.

Clough, G.W., O'Rourke, T.D., 1990. Construction induced movements of in situ walls. In Proc. ASCE Design Performance Earth Retaining Struct., eds. P. C. Lambe and L. A. Hansen. Ithaca, NY, June 18–21, pp. 439–470.

Devriendt, M., Palmer, E., Hill, R. and Lazarus, D., 2013. Historic and non-historic building impact assessment methodology for major tunnelling infrastructure projects. Geotechnical Engineering for the Preservation of Monuments and Historic Sites (Bilotta, Flora, Lirer & Viggiani eds.), pp.335-341.

Dzegniuk, B., Hejmanowski, R., Sroka, A., 1997. Evaluation of the damage hazard tobuilding objects on the mining areas considering the deformation course in time. In: Proceedings of Xth international congress of the international society for mine surveying. DOI: 10.13140/2.1.3356.3520

Goldberg, D.T.; Jaworski, W.E. and Gordon, M.D., 1976. Lateral support systems and underpinning. Report FHWA-RD-75-128, Federal Highway Administration, Washington D.C., 1, 312.

IHBC, 2020. Sustainability and Conservation of the Historic Built Environment – an IHBC Position Statement. Institute of Historic Building Conservation, UK. https://ihbconline.co.uk/toolbox/position_statement/sustainablilityconservation.html (accessed 2021-12-18).

Janbu, N. 1970. Grunnlag i geoteknikk. Trondheim: Tapir forlag Brinkgreve, R.B.J. 2002.

Langford J., Karlsrud, K., Lande, E.-J-, Baardvik, G. and Engen, A., 2016a. BegrensSkade – Limitation of damage caused by foundation and ground works. Grundläggnigsdagen, Swedish Geotechnical Association.

Langford, J., Baardvik, G. and Karlsrud K., 2016b. Pore pressure reduction and settlements induced by deep supported excavations in soft clay. Proceedings of the 17th Nordic Geotechnical Meeting, NGM 2016 Reykjavik. ISBN: 978-9935-24-002-6

Long, M., 2001. Database for retaining wall and ground movements due to deep excavations. J. Geotech. Environ., 127(3), pp. 203-224. ISSN: 1090-0241

Peck, P.B., 1969. Deep excavations and tunneling in soft ground. In: Proceedings of 7th International Conf. on Soil Mechanics and Foundation Engineering, Mexico City, 3, pp. 225–290.

Piciullo, L., Ritter, S., Lysdahl, A.O.K., Langford, J. and Nadim, F., 2021. Assessment of building damage due to excavation-induced displacements: The GIBV method. Tunnelling and Underground Space Technology, 108, p.103673.

Rampello, S., Callisto, L., Viggiani, G. and Soccodato, F.M., 2012. Evaluating the effects of tunnelling on historical buildings: the example of a new subway in Rome/Auswertung der Auswirkungen des Tunnelbaus auf historische Gebäude am Beispiel einer neuen U-Bahnlinie in Rom. Geomechanics and tunnelling, 5(3), pp.275-299.

Rankin, W.J., 1988. Ground movements resulting from urban tunnelling: predictions an effect. Geological Society, London, Eng. Geo. Sp. 5, 79–92. https://doi.org/10.1144/GSL.ENG.1988.005.01.06

Sundell, J., Haaf, E., Norberg, T., Alén, C., Karlsson, M. and Rosén, L., 2019. Risk mapping of groundwater-drawdown-induced land subsidence in heterogeneous soils on large areas. Risk Analysis, 39(1), pp.105-124.

Terzaghi, K., Fröhlich O. K., 1936. Theorie der Setzung von Tonschichten. Leipzig, F. Deuticke.

Venvik, G., Liinamaa-Dehls, A. and Bjerke, C., 2018. Pathways and pitfalls to better sub-urban planning. COST Action TU1206 Sub-Urban. https://www.ngu.no/upload/Publikasjoner/Boker/SubUrban_magazin_screen.pdf (accessed 2021-12-18).

Geotechnical Engineering for the Preservation of Monuments and Historic Sites III – Lancellotta, Viggiani, Flora, de Silva & Mele (Eds)

A critical evaluation of proxy measures used to quantify excavation-induced damage in masonry buildings

Yiyan Liu, Burcu Gulen, Sinan Acikgoz & Harvey Burd
Department of Engineering Science, University of Oxford, Oxford, UK

Ben Gilson
Infrastructure Geotechnics Division, Arup, London, UK

Alper Ilki
Department of Civil Engineering, Istanbul Technical University, Istanbul, Turkey

Korhan Deniz Dalgic
Department of Civil Engineering, Izmir Institute of Technology, Izmir, Turkey
Faculty of Engineering, Urla, Izmir, Turkey

ABSTRACT: Building response during nearby excavation activities (e.g., tunnelling or deep excavations) is traditionally monitored by conducting displacement measurements. These displacement data are then post-processed to determine proxy measures that are correlated to damage categories. For masonry buildings, commonly-used proxy measures include building deflection ratio, horizontal relative displacement and angular distortion; simple mechanical models and empirical rules are used to define limiting values for these proxy measures to identify and control the level of cracking in buildings during construction. This procedure has a profound influence on mitigation and construction activities, and a critical evaluation of its veracity is needed. To this end, results from a recent experimental campaign on the settlement response of half-scale masonry buildings are examined in this paper. During these tests, detailed optical measurements were conducted, allowing the calculation of absolute displacements across the façade, as well as crack opening displacements at specific locations. These measurements facilitate a direct comparison between the actual observed damage and the damage category that is indicated by the proxy measures. The comparisons highlight the limitations of existing techniques. A discussion is provided on how proxy measure calculations can be improved to deliver more reliable indications of building damage.

1 INTRODUCTION

Tunnelling and deep excavation activities lead to ground movements. Such movements, if not evaluated and controlled properly, may cause damage to nearby buildings. The definition of 'damage' varies according to structural typology and building materials. In the context of masonry buildings, damage is often quantified in terms of the presence of visible cracks on façades and walls (Burland et al. 1977; Crossrail Limited 2008; High Speed Two Limited 2017; Thames Water Utilities Limited 2014). Cracking can lead to loss of weather tightness and can impact building serviceability. Furthermore, it represents a permanent loss of cohesion and can lead to structural instability (Korswagen et al. 2019). Quantifying the extent of cracking in a building requires knowledge of the location, length and width of each crack. This presents a challenge for traditional monitoring techniques and damage quantification at a high level of detail is rarely attempted in practice.

DOI 10.1201/9781003308867-79

In practical cases, the severity of building damage due to nearby underground construction is typically quantified using an approach in which horizontal and vertical displacement data are measured at selected reference points around the building. These displacement data are then processed to determine deformation measures that are employed as proxy indices for building damage. To track and manage the level of damage experienced by the building, values of the proxy indices are compared to pre-determined trigger levels set by designers, corresponding to different assumed damage categories. There is typically a specific contingency plan which defines the actions to be taken if trigger values are exceeded. The contingency plan may require changes in construction sequence and methodology, often with significant cost implications.

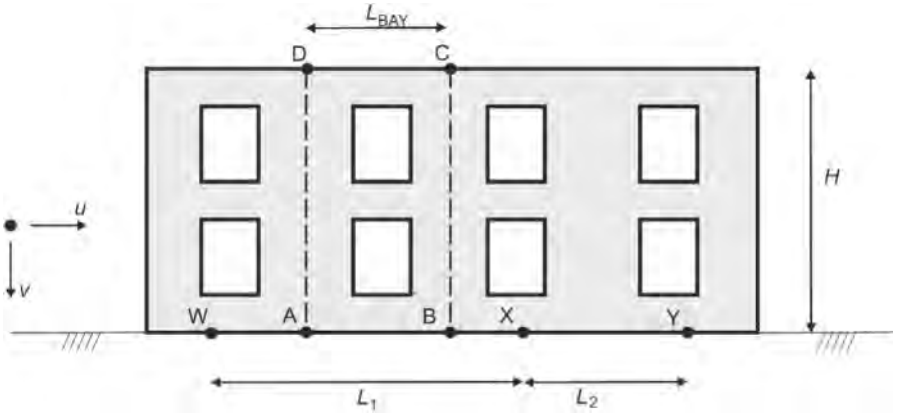

Figure 1. Example configuration of reference points to determine relative deflection, average horizontal strain and angular distortion proxy damage indices for a building façade.

'Deflection ratio' (e.g. Mair et al. 1996) is a widely used proxy index for building damage. The determination of deflection ratio values for a building façade is outlined below in terms of the example building in Figure 1. Reference points W and Y are typically selected at or close to either end of the building along the base. A query point X, where deflection ratio is assessed, is located between the reference points at the bottom of the building. Displacements u and v of the reference points and query point (where u and v signify displacement in the horizontal and vertical directions respectively) are measured during construction. The deflection ratio for point X relative to span WY is,

$$\left(\frac{\Delta}{L}\right)_{WXY} = \frac{v_X - \frac{v_W L_2 + v_Y L_1}{L_2 + L_1}}{L_2 + L_1} \tag{1}$$

where v_x, v_w and v_Y are the vertical displacements of points X, W and Y respectively.

The deflection ratio is a non-dimensional measure of the vertical displacement of point X with respect to a straight reference line between the displaced positions of W and Y. If the building deforms rigidly then the deflection ratio is zero. Three points are employed in this example but, in practical cases, a larger number of query points are typically used to determine the maximum value of deflection ratio for a particular façade.

'Angular distortion', β (e.g. Boscardin & Cording 1989) is an alternative potential proxy damage index. To determine maximum angular distortion for a particular building, the façade is idealised as a series of shear deformable rectangular 'bays', as shown in the example in Figure 1 for bay ABCD. Angular distortion represents the average shear strain in the bay as defined by the rotations of each of the four sides of the bay; these rotations are determined from the measured displacements of the bay corners. The angular distortion for bay ABCD determined in this way is,

$$\beta_{\mathrm{ABCD}} = -\frac{v_B - v_A}{L_{BAY}} + \frac{(u_D + u_C) - (u_A + u_B)}{2H} \tag{2}$$

Separately, data on the horizontal displacement of reference points located on either end of the façade or bay at the base can be used to determine values of 'average horizontal strain', ε^h. For the example case in Figure 1 the average horizontal strain, ε^h_{WY}, is determined for span WY as,

$$\varepsilon^h_{WY} = \frac{u_Y - u_W}{L_1 + L_2} \tag{3}$$

Values of deflection ratio inferred from site measurements are typically employed with a simplified elastic deep beam model of the building façade to estimate the maximum tensile strainε^t_{max} experienced by the façade (e.g. Mair et al. 1996). In cases where the measured average horizontal strains at the base of the building are tensile, then these tensile strains are also incorporated in the analysis. Values of ε^t_{max} determined in this way are related to notional building damage categories via standard correlations (see the Appendix).

Inferred values of maximum principal tensile strain ε^t_{max} are correlated with notional damage category in a similar way when angular distortion is used as a proxy measure (e.g. Son & Cording 2005). In this case the maximum tensile strain is determined straightforwardly on the basis that each bay is assumed to deform uniformly in pure shear. When the average horizontal strain at the base of the bay is tensile then the analysis is typically modified to account for the presence of this additional strain.

Proxy damage indices, and their use in damage quantification, may have a significant influence on how mitigation and construction activities are conducted. Uncertainties exist around the reliability of simplified modelling approaches employed to infer values of maximum tensile strain from proxy damage indices; such simplified models do not consider certain important aspects such as the likely influence of openings in the façade. Questions also exist, on whether values of maximum tensile strain inferred from the model can be reliably correlated with actual damage experienced by a building.

To explore the extent to which proxy damage indices provide a useful measure of actual building damage, a study on half-scale masonry buildings subjected to simulated tunnel-induced displacements has been conducted. The paper initially introduces the experimental program. Data from the experiments are then employed to explore correlations between proxy damage indices and observed building damage.

2 EXPERIMENTAL DATA

2.1 *Test building and instrumentation*

An experimental campaign on the settlement response of half-scale masonry buildings was conducted at Fibrobeton's factory site in Turkey between December 2020 and March 2021. One of the test buildings employed in the experiments, illustrated in Figure 2, is the focus of the current paper. The building comprises a pair of 2-storey masonry façades with reinforced concrete slabs placed between them at first floor and roof level. The building was constructed on two parallel steel beams connected to a manual screw jack at one end (Figure 2c). The façades were built with half-scale bricks (115 × 57.5 × 30 mm) laid in English bond. Concrete kentledge blocks weighing 8 tonnes in total were placed on the first and top floor slabs to satisfy scaling requirements. Downwards displacements were applied to the steel beams by the screw jacks to impose deformations on the building that mimicked the hogging region of a typical settlement profile caused by nearby tunnel construction.

Two separate tests were conducted on the building. In an initial test (30-RS-W1) significant gapping was observed to occur between the base of the façade and the steel beams and only minimal damage was induced in the façade. A second test (30-RS-W3) – intended to induce considerably more damage in the building - was therefore subsequently conducted on the same building with an additional 3.25 tonnes of kentledge applied to the lower windowsills. These two tests – referred to as Test 1 and Test 2 respectively in the following text - are illustrated in Figure 2a and b.

270 no. paper targets with printed concentric rings were placed on the front wall and the steel beam. The targets were monitored by four video cameras; the displacement of each target was determined using 2D Digital Image Correlation (DIC). Specifically, three cameras facing the wall were used to monitor the in-plane displacements, while the fourth camera was used to measure the out-of-plane displacements. More than 100 targets were monitored by more than one camera; this redundancy in the measurements was exploited to check the accuracy of the data. Fibre Bragg grating (FBG) cables were used to conduct additional strain measurements; these strain data were used to validate the DIC measurements.

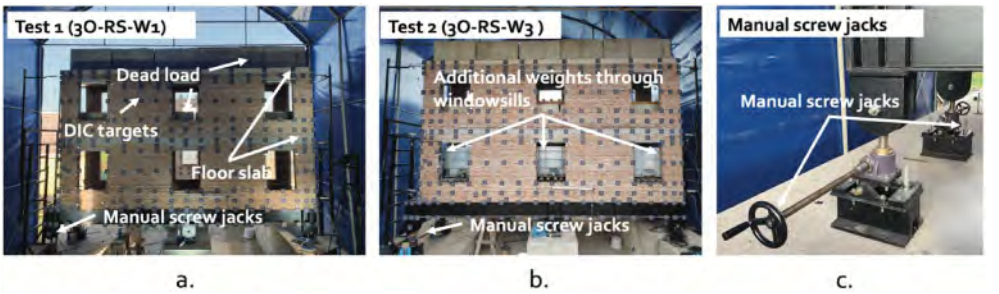

Figure 2. Test setups and weight arrangement: (a) Test 1 (3O-RS-W1); (b) Test 2 (3O-RS-W3); (c) manual screw jack arrangement; The specimen is 5.6m in length, 3.2m in height and the wall thickness is 0.115m.

Adjacent target pairs were used to form 'virtual Linear Variable Differential Transformers (LVDT)' as illustrated in Figure 3. The measured displacements of the targets were used to determine the increase in distance Δs between the targets as,

$$\Delta s = \frac{\Delta x\,(u_2 - u_1) + \Delta y\,(v_2 - v_1)}{\sqrt{\Delta x^2 + \Delta y^2}} \tag{4}$$

Positive values of Δs were taken to indicate a single crack of width Δs between the location of the two targets.

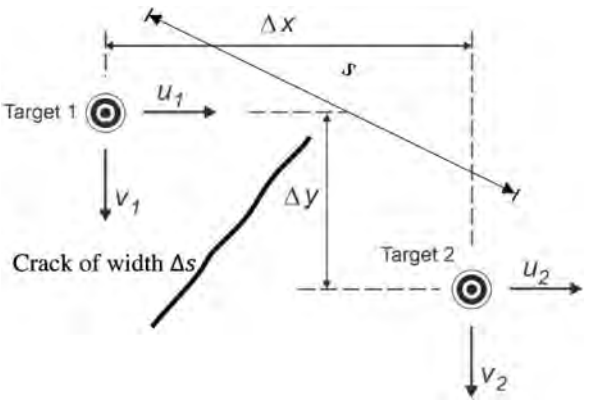

Figure 3. Arrangement employed for the 'virtual LVDTS'. Two targets are separated by distance s. The measured displacements of Target 1 and Target 2 are (u_1, v_1) and (u_2, v_2) respectively.

2.2 *Test procedures*

Tests were conducted by two operators gradually loading the steel beam via the manual screw jacks (Figure 2c) to a desired tip displacement. Once the maximum jack displacement had been applied in each test a visual inspection of the front façade was conducted to log the presence of visible cracks (a crack is considered to be visible when its width exceeds 1mm). To quantify the crack widths, sets of target pairs that spanned the visible cracks were identified. Displacement data from these target pairs were processed using the approach in Equation (4) to determine representative crack widths. The largest crack width determined in this way was considered to provide an objective measure of the actual damage experienced by the building.

In Test 1 (Figure 2a), the beam tip displacement was increased to $V_{tip} = 66.67$ mm via the screw jacks. Loading applied by the screw jacks was slowly removed once the test had concluded. The test took 5 hours and 36 minutes to complete, requiring 6700 seconds of DIC recording time. The building was observed to deform approximately rigidly during the test, with gaps forming between the building and the steel beam at the building corners (as illustrated in Figure 4a). The only visual damage on the front wall was a vertical crack located on the bottom spandrel beneath window 2.

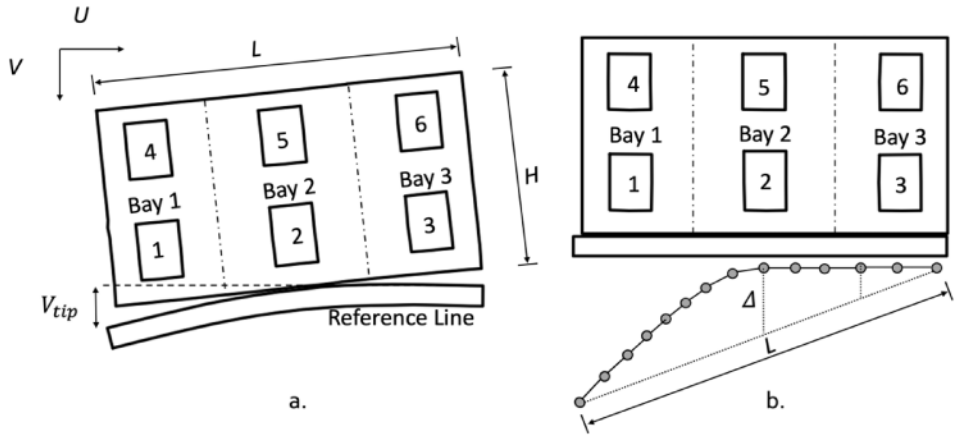

Figure 4. (a) Diagrammatic illustration of the test building showing the three bays employed for the determination of angular distortion and the vertical displacement V_{tip} applied to the steel beam supporting the building; (b) illustration of the procedure to determine the deflection ratio of (Δ/L)

In Test 2, the supporting beam was loaded to a displacement $V_{tip} = 34.9$ mm. At this value of displacement a significant amount of damage was visible and so the test was terminated. The test took 4 hours and 50 minutes to complete; the total DIC recording time was 3096 seconds.

3 EVALUATING PROXY DAMAGE MEASURES FROM THE TEST DATA

3.1 *Displacement ratio, angular distortion and average horizontal strain*

The in-plane displacement of targets placed along the base of the façade were determined by the DIC system at each time instance. This procedure provided a means of determining the profile of vertical deformations along the base of the wall as illustrated in Figure 4b. The deflection ratio with respect to the bottom two corners of the building was determined by finding the target location that maximised the value of Δ/L, employing Equation (1) as illustrated in Figure 4b. Values of average horizontal strain were determined on the basis of horizontal displacements of targets placed at the bottom corners of the building or bays.

To determine angular distortion, the building was divided into three bays as illustrated in Figure 4. Displacement data were determined from targets located at the four corners of each bay; these data were used in Equation (2) to determine the angular distortion for each bay.

3.2 *Determination of maximum tensile strain from relative deflection*

The maximum tensile strain ε^t_{max} was determined from the measured values of deflection ratio as described below (Mair et al. 1996). This procedure idealises the building as an elastic deep beam neglecting the presence of openings and floors as indicated in Figure 5.

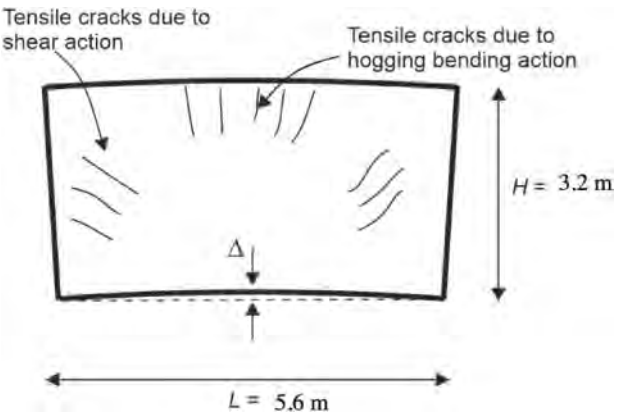

Figure 5. Assumed deformation mode and potential crack locations for elastic deep beam approximation of the building façade.

In the current tests the building is considered to deform in hogging as shown in Figure 5. Values of maximum tensile strain were determined using an elastic deep beam approximation in which the neutral axis is assumed to coincide with the base of the façade. On the basis of this approach the maximum tensile strain due to bending, ε^t_b is determined as,

$$\frac{\Delta}{L} = \left\{ \frac{L}{12H} + \frac{EH}{2LG} \right\} \varepsilon^t_b \tag{5}$$

where G and E are shear modulus and Young's modulus respectively. A separate estimate of the maximum tensile strain due to shear, ε^t_s, is given by,

$$\frac{\Delta}{L} = \left\{ 1 + \frac{GL^2}{6H^2E} \right\} \varepsilon^t_s \tag{6}$$

In the current tests the behaviour was invariably found to be bending-dominated; i.e. the largest values of horizontal strain were always those determined by Equation (5). Following Mair et al. (1996) the ratio E/G was taken to be 2.6.

Tensile strains were found to occur at the base of the building. A representative value of average horizontal strain ε^h was therefore combined additively with the value of ε^t_b determined from Equation (5) – following the procedure in Mair et al. 1996 – to obtain an estimate of ε^t_{max} (the maximum principal tensile strain experienced by the building).

Since the behaviour of the façade is predicted to be bending-dominated, tensile cracking near the top of the beam at midspan would be expected as illustrated in Figure 5. In the alternative shear-dominated case then inclined cracks would be expected at mid-height on the left and right edges of the façade, as also shown in Figure 6

3.3 *Determination of maximum tensile strain from angular distortion*

A building bay subject to a positive angular distortion (defined using the conventions in Equation 2) will deform as illustrated in Figure 6. Figure 6 also shows the expected cracks for this case.

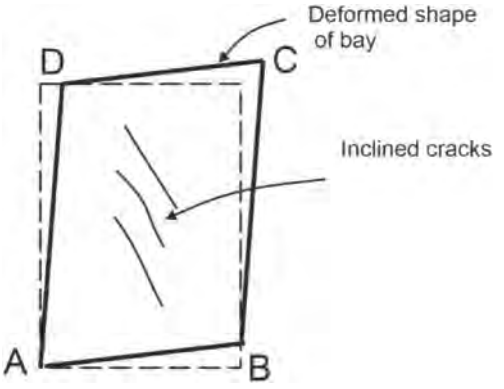

Figure 6. Expected crack pattern in a building bay with an imposed angular distortion. The inclination of the cracks will depend on the ratio between angular distortion, β, and average horizontal strain ε_{AB}^{h}at the base of the bay.

The maximum tensile strain associated with the angular distortion is therefore determined straightforwardly (Son & Cording 2005) as,

$$\varepsilon_{max}^{t} = \frac{\varepsilon_{AB}^{h}}{2} + \sqrt{\left(\frac{\beta}{2}\right)^{2} + \left(\frac{\varepsilon_{AB}^{h}}{2}\right)^{2}} \tag{7}$$

where ε_{AB}^{h} is a representative value of average tensile strain for edge AB.

4 DAMAGE CLASSIFICATION ON THE BASIS OF CRACK WIDTH MEASUREMENTS

Crack patterns determined by visual inspection for both tests are shown in Figure 7; data from the 'virtual LVDTs' used to quantify the crack widths are indicated in the figure via the colour scale bar. Values of maximum crack width (determined from the 'virtual LVDTs') are listed in Table 1. 'Prototype' crack width data in Table 1 indicate the equivalent maximum crack width at prototype scale on the basis of a linear scale factor of 2. The damage classifications listed in Table 1 were determined by employing the conventional correlations between maximum crack width and damage category (see Appendix).

Table 1. Observed damage in Test 1 and Test 2.

Test code	Number of visible of cracks	Maximum crack width inferred from 'virtual LVDTs'	Prototype crack width	Damage category
Test 1	1	1.68 mm	3.36 mm	slight
Test 2	6	8.06 mm	16.12 mm	severe

In Test 1 a single crack, which ran along mortar joints, was observed in the spandrel beneath opening 2 (Figure 7a). This spandrel is subjected to a significant hogging action and the location of the crack – on the upper edge of the spandrel – is consistent with beam theory assumptions

on the location of tensile strains. For Test 2 the pattern of cracking is more complex (Figure 7b), which includes cracks along mortar joints and through bricks. In this case the damage is dominated by horizontal splits along bed joints at the top of the piers adjacent to openings 1 and 3. This splitting mechanism appears to have been driven by the additional kentledge applied to the lower windowsills in this test. The observed cracking patterns do not resemble the idealised patterns in Figures 5 and 6 that would be implied by simple models. The damage is confined to the lower level of the façade (i.e. below the first floor slab); the first floor slab appears to have acted to shield the upper level of the masonry façade from damage.

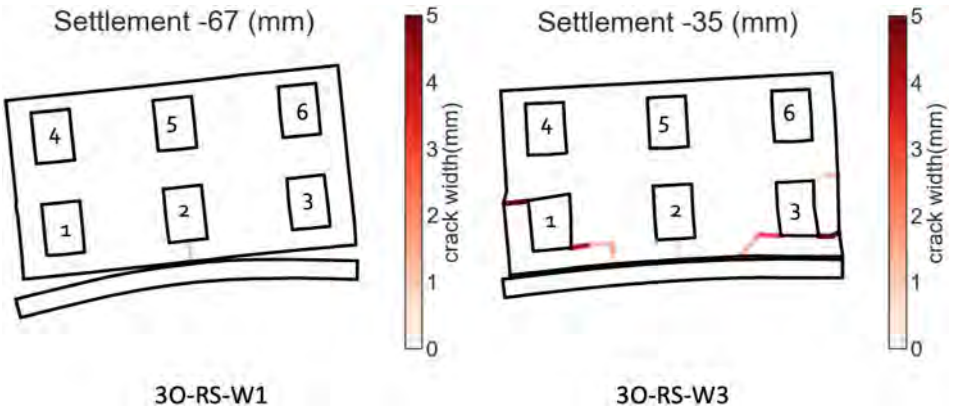

Figure 7. Illustration of the visible cracks at the end of each test (a) Test 1 (3O-RS-W1); (b) Test 2 (3O-RS-W3).

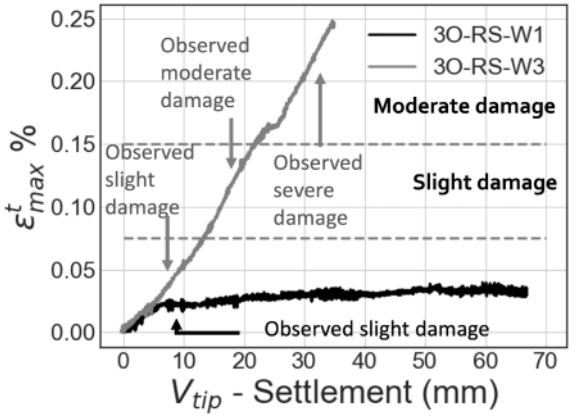

Figure 8. Values of maximum tensile strain ε^t_{max} inferred from measured values of relative deflection and average horizontal strain. Horizontal dashed lines indicate boundaries between implied damage categories (based on standard correlations, see Appendix). Vertical arrows indicate damage classification on the basis of measurements on maximum prototype crack width.

Data in Figure 8 indicate the development of maximum tensile strain ε^t_{max}, determined on the basis of measured deflection ratio and average horizontal strain. In test 3O-RS-W1 the values of ε^t_{max} appear to reach a plateau after a beam tip displacement of about 7 mm; a gap appears to have formed at the building/beam interface at this point in the test. At later stages in the test the state of deformation in the building appears to have remained broadly constant, with increases in the tip displacement merely causing the gap at the base of the building to increase.

According to the standard tensile strain – damage category correlation (see Appendix) the building would be classified as having negligible damage. However the prototype crack width of 3.36 mm actually observed in the test would signify 'slight damage'. There is therefore a noteworthy mismatch between inferred damage based on measured relative deflection and actual damage quantified in terms of maximum crack width.

Test 3O-RS-W3 experienced considerably more distortion than 3O-RS-W1. Values of ε^t_{max} plotted in Figure 8 reached a value of about 0.25% at the end of the test. The data in Figure 8 indicate a reasonably close numerical correlation between the damage category inferred from the proxy index and the damage category determined from visual measurements on the cracks. However, the modelling procedure employed in the analysis implies that cracking occurs at the top edge of the building (see Figure 5) whereas the observed cracks appear in quite different locations (see Figure 7).

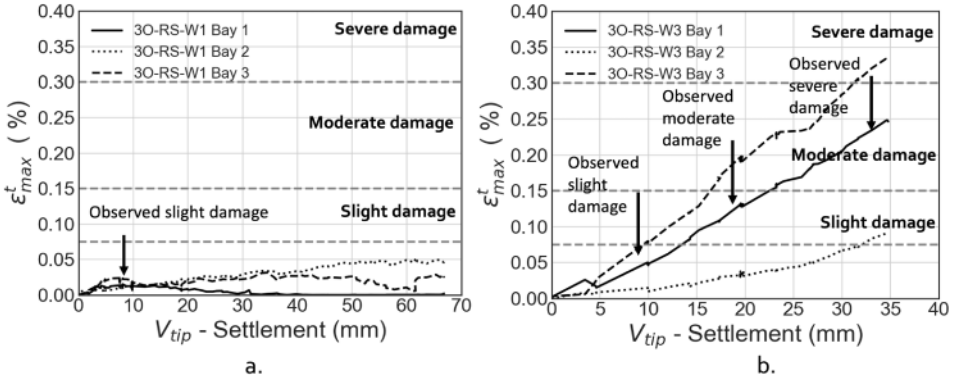

Figure 9. (a) Test 1 (3O-RS-W1); (b) Test 2 (3O-RS-W3); Values of maximum tensile strain ε^t_{max} determined from angular distortion and average horizontal strain. Black lines indicate data computed from the measured proxy indices. Horizontal dashed lines indicate boundaries between implied damage categories (based on standard correlations, see Appendix). Vertical arrows indicate damage classification on the basis of observations on maximum prototype crack width.

In Figures 9a and 9b, values of ε^t_{max} for each of the bays of 3O-RS-W1 and 3O-RS-W3 determined from the observed angular distortion (i.e. employing Equation 7) are plotted against the applied beam tip displacement. Consistent with the data in Figure 8 the angular distortion proxy measure applied to 3O-RS-W1 indicates negligible damage for all three bays. This is in contrast to the 'slight' damage category determined from crack size measurements.

Data on ε^t_{max} for 3O-RS-W3 in Figure 9b indicate significant differences between the three bays. Bay 3 experienced the greatest angular distortion. The data in Figure 9b demonstrates a fairly close numerical correlation between damage category implied by the proxy index and damage category quantified in terms of observed crack width. However, the observed cracking pattern is considerably different from the pattern predicted by the idealised model in Figure 6.

5 DISCUSSION

The adoption of simplified elastic models to represent the structural behaviour of buildings subjected to construction-induced ground movements provides a convenient and well-understood approach for the interpretation of site monitoring data on building displacements. In this approach the distortion of the building is quantified in terms of a proxy damage index (such as 'relative deflection' or 'angular distortion'). A simplified modelling approach is then used to infer a value of maximum tensile strain ε^t_{max} experienced by the building. Values of ε^t_{max} are then correlated with a notional damage category.

In numerical terms, damage categories determined on the basis of measured relative deflection combined with average horizontal strain provide a plausible correlation with objective damage measures based on direct crack width measurements. However, the observed crack patterns are entirely uncorrelated with those that would be implied by the simplified beam model employed in the interpretation process. It therefore appears that the structural behaviour of the test building is poorly represented by the simplified beam model. This finding is, of course, not unexpected. In the test building, the presence of windows, stiff floor slabs, material anisotropy and nonlinearity will – to varying degrees – cause the actual structural behaviour to depart from the assumptions implicit in the elastic deep beam modelling approach.

A similar situation was observed with the quantification of damage using measured values of angular distortion. Although numerical values of damage category determined from angular distortion data were seen to correlate fairly well with objective measures based on crack width, the overall pattern of cracking was seen to depart considerably from the assumption – implicit in the angular distortion concept - that each bay deforms in a state of pure shear.

These results – taken together – indicate the possibility that damage proxy indices of the form considered in this paper can provide useful indications of building damage. However, the data presented in the paper provide little confidence in the ability of simplified elastic models to predict realistic distributions of tensile strain. The reasonable numerical correlation between proxy damage index and observed damage is therefore likely a consequence of the relatively well-conditioned nature of the proxy measures rather than the veracity of the simplified models employed in the analysis process.

6 SUMMARY

This paper presented a case study on the performance of proxy measures (deflection ratio, angular distortion and relative horizontal displacement) on quantifying damage in a half-scale building specimen subjected to induced settlements. It was observed that the damage categories estimated by the proxy measures tend to underestimate the cracking experienced in the building. This discrepancy is not surprising and can be explained by the simplification of building behaviour with approximate deformation profiles and basic mechanical models. On the other hand, damage classification results obtained via proxy measures can clearly differentiate between damaged and undamaged specimens and estimate strains of the right order of magnitude. These are useful characteristics, particularly for quick screening of damage.

It was observed that the deflection ratio smears the localised deformation mechanisms across the whole building. However, the damage patterns observed in the buildings are typically localised and beam kinematics are not sufficient to describe building deformation mechanisms. As a result, deep beam models may lead to misleading results. Evaluation of angular distortion across building bays does not consider bending deformation and presents the opportunity to consider localised distortions. However, the choice of building bays is somewhat arbitrary, and the observed damage patterns indicate that building bays do not deform in pure shear.

From the data presented in the paper, it is clear that better discretisation of the building with more suitable mechanical models is needed to estimate strain propagation and damage from monitoring data. Local methods, which measure distortion parameters using smaller structural components, rather than measuring the whole building distortions, appear to hold more promise. Methods to estimate damage using displacement measurements from individual building components will be investigated by the authors in future research.

ACKNOWLEDGEMENT

This research was funded by the Engineering and Physical Sciences Research Council (EPSRC) of the United Kingdom and Arup Group Ltd through the iCASE project (Project Reference: 2280800).

The large-scale settlement test was performed on the Fibrobeton site in Duzce, Turkey, and the authors want to thank Fibrobeton for their support.

REFERENCES

Burland, J.B., Broms, B.B., De Mello, V.F.B., 1977. Behavior of foundations and structures. In: Proc., 9th Int. Conf. on Soil Mechanics and Foundation Engineering. Tokyo, pp. 495–546.

Crossrail Limited, 2008. Crossrail Information Paper D12 – Ground Settlement [WWW Document]. URL http://74f85f59f39b887b696f-ab656259048fb93837ecc0ecbcf0c557.r23.cf3.rackcdn.com/assets/library/document/d/original/d12groundsettlement.pdf (accessed 7.28.20).

High Speed Two Limited, 2017. High Speed Two Phase One C3?: Ground Settlement [WWW Document]. URL https://assets.publishing.service.gov.uk/government/uploads/system/uploads/attachment_data/file/672194/C3_-_Ground_Settlement__v1.pdf (accessed 7.28.20).

Korswagen, P.A., Longo, M., Meulman, E., Rots, J.G., 2019. Crack initiation and propagation in unreinforced masonry specimens subjected to repeated in-plane loading during light damage. Bull. Earthq. Eng. 17, 4651–4687.

Mair, R.J., Taylor, R.N., Burland, J.B., 1996. Prediction of ground movements and assessment of risk of building damage due to bored tunnelling. Geotech. Asp. Undergr. Constr. Soft Gr. 713–718.

Son, M., Cording, E.J., 2005. Estimation of Building Damage Due to Excavation-Induced Ground Movements. J. Geotech. Geoenvironmental Eng. 131, 162–177.

Thames Water Utilities Limited, 2014. Thames Tideway Tunnel Settlement Information Paper [WWW Document]. URL https://www.tideway.london/media/3075/app191-settlement-information-paper-3-march-2014.pdf (accessed 7.28.20).

APPENDIX

Table 2. Classification tables for masonry building damage (based on the work of Mair et al. 1996).

Damage category	Normal degree of severity	Description of typical damage	Approximate crack width (mm)	Range of maximum tensile strains (ε^{t}_{max})
0	Negligible	Hairline cracks	<0.1	0–0.05
1	Very slight	Fine cracks easily treated during normal redecoration. Perhaps	0.1–1	0.05–0.075
2	Slight	Cracks easily filled.	1–5	0.075–0.15
3	Moderate	Cracks may require cutting out and patching.	5–15 or severe >3	0.15–0.3
4	Severe	Extensive repair involving removal and replacement of sections of walls.	15–25 also depends on numbers of cracks	>0.3
5	Very severe	Major repair required involving partial or complete re-construction.	>25 depends on numbers of cracks	–

Geotechnical Engineering for the Preservation of Monuments and Historic Sites III – Lancellotta, Viggiani, Flora, de Silva & Mele (Eds)

A macro-element model for the assessment of tunnelling-induced damage to masonry buildings

D.B. Gulen, S. Acikgoz & H.J. Burd
Department of Engineering Science, University of Oxford, Oxford, UK

ABSTRACT: This paper introduces a computationally-efficient numerical modelling strategy to assess the risk of tunnelling-induced damage to masonry buildings. Building components are idealised with two dimensional (2D) quadrilateral elements incorporating constant shear strain within each element. The flexural behaviour of the quadrilateral elements is governed by surrounding zero-thickness, deformable, interfaces. Soil-foundation interaction behaviour is modelled with one dimensional (1D) footing elements interacting with a Winkler soil-foundation model. Tunnelling-induced ground movements are prescribed at the base of the soil-foundation model. This 'macro-element' modelling approach is used to examine the response of an isolated elastic masonry facade founded on a strip footing to tunnelling-induced ground movements. Results from the macro-element model are compared to a benchmark analysis employing a 2D continuum finite elements to represent the facade. These comparisons demonstrate that a relatively coarse mesh of macro-elements is sufficient to capture the response of the facade to tunnelling-induced ground movements.

1 INTRODUCTION

Excavation activities such as tunnel construction can induce horizontal and vertical displacements in the ground, creating a risk of damage for nearby structures. In current practice, the potential risk to masonry buildings is typically assessed in three stages. First, greenfield ground movements (i.e. the construction-induced ground movements that would be estimated to occur in the absence of buildings) are estimated. A preliminary investigation (Stage 1) is then performed to identify buildings that are exposed to greenfield settlements that exceed a predefined level. Buildings identified in this way are then subjected to a Stage 2 assessment in which a simple elastic beam model, subjected to the assumed greenfield ground movements, is used to estimate the maximum tensile strain induced in the building (Burland et al. 1977; Boscardin & Cording, 1989). If the maximum tensile strain estimated in this way is sufficient to imply moderate or severe damage according to established damage classification criteria (Burland & Wroth, 1974; Burland et al. 1977; Mair et al. 1996), then a Stage 3 assessment may be conducted employing detailed finite element (FE) analysis.

The beam models used in Stage 2 assessments typically neglect soil-structure interaction effects as well as important building properties such as openings in the facade and building weight. However, these aspects can have a significant influence on the actual damage experienced by a building. While detailed FE models employed in Stage 3 assessments can address these aspects, constructing and analysing FE models often requires a significant investment of time and computing resources. An intermediate-level modelling approach, which considers the soil-structure interaction and the effect of salient building properties while requiring less modelling effort and computational

 DOI 10.1201/9781003308867-80

time than detailed 3D FE analysis, would provide a convenient alternative approach. The current paper proposes a computational strategy at this intermediate level of complexity.

To remove the need to model the detailed tunnel excavation process, a simplified soil-foundation model employing two-sided line interface elements is adopted. The soil-foundation interaction behaviour is represented by a Winkler model (i.e. the local soil-foundation tractions are formulated to depend only on the local ground movements). Tunnelling-induced greenfield ground movements are applied as prescribed displacements to the base of the interface. In the global computational analysis, the building interacts with the adopted soil-foundation model to determine the displacements actually induced in the building, accounting for soil structure interaction effects. This modelling approach is well-suited to damage assessments since estimated greenfield displacements are typically available from prior Stage 1 assessments. Previous studies (e.g. Burd et al. 2022; Giardina et al. 2013) employing this simplified soil-foundation modelling approach demonstrated significant computational efficiencies when using continuum finite elements to represent the building. The objective of the current study is to explore the potential for further efficiencies by employing macro-elements – as an alternative to continuum finite elements – to model the building facade. The current work is restricted to the case where the soil and the building are linearly elastic.

In earthquake engineering practice, masonry buildings are often analysed using simplified equivalent frame idealisations (e.g. Lagomarsino et al. 2013; Quagliarini et al. 2017). These rely on discretising the masonry building into pier and spandrel elements and connecting them with rigid connectors. The use of this equivalent frame approach in the context of tunnel-soil-structure interaction is demonstrated in Gulen et al. (2021); however, this prior study showed that rigid connectors lead to an overestimation of the overall building stiffness. In the current work, the equivalent frame concept is developed to employ a macro-element modelling approach to represent individual piers, spandrels and connectors in a masonry facade. The macro-elements are an adapted form of the 2D discrete element-based approach described by Caliò et al. (2012). Each macro-element comprises a shear-deformable quadrilateral element connected to adjacent elements by compliant zero-thickness line interface elements. This idealisation retains the simplicity and computational efficiency of equivalent frame models while removing the need for rigid connectors. The macro-element models are formulated to include new features, not incorporated in earlier work, such as incorporating a compatible 1D soil-foundation model to represent soil-structure interaction effects and the computation of the spatial distribution of tensile strains as required for damage assessment classification.

This paper is structured as follows: first, an example tunnel-soil-structure interaction case study is introduced in Section 2. The macro-element formulations, including the kinematics of the elements and procedures to interpret spatial strain distributions in the macro-element are presented in Section 3. The proposed modelling approach is applied to the example case study in Section 4. Displacement and strain results obtained from the macro-element modelling approach are compared with comparable analyses conducted using the DIANA 10.3 FEA in which a detailed 2D FE continuum model is adopted for the facade.

2 CASE STUDY

An example case study, based on an isolated facade of a 2-storey masonry building founded on a strip footing that is subjected to ground movements caused by a single tunnel passing under the centreline of the building, is considered. This example problem is based on one of the cases analysed by Yiu et al. (2017). The building facade and the geometry of the strip footing foundation are illustrated in Figure 1. The building and the strip footing are constructed of masonry with Young's modulus $E_m = 3$ GPa, Poisson's ratio $\nu_m = 0.2$ and unit weight $\gamma_m = 23.75\,\text{kN/m}^3$.

Tunnelling-induced greenfield ground movements at the level of the base of the footing were computed using the conventional Gaussian function approximation (e.g. Rankin 1988) employing the data in Table 1. (Values of trough width parameter and settlement volume loss are based on data in Yiu et al. 2017). The soil-footing interface is represented by a Winkler model with shear and

normal stiffness parameters $k_s = 16.9$ MPa and $k_n = 27$ MPa respectively. These parameters were chosen to ensure that the building response is intermediate between being flexible and rigid. These foundation stiffness parameter values are similar to those adopted in the comparable modelling procedures described in Burd et al. (2022).

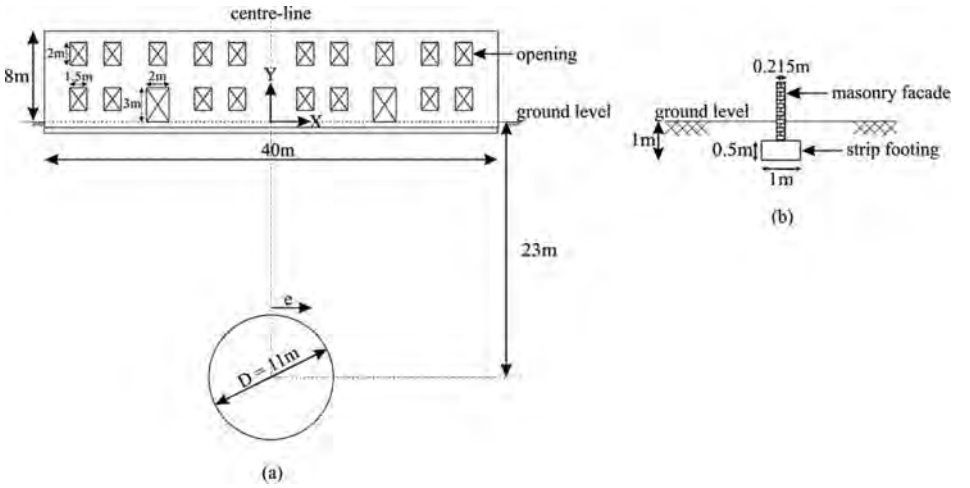

Figure 1. Building facade, footing and tunnel configuration adopted for the case study (not to scale): (a) facade and single tunnel geometry, (b) footing cross-section detail (modified from Yiu et al. 2017).

Table 1. Parameters used for the single tunnel scenario (Yiu et al. 2017).

Settlement volume loss, V_L	1.65%
Trough width parameter, K	0.57
Tunnel diameter, D (m)	11
Tunnel depth, z_0 (m)	23
Tunnel eccentricity, e (m)	0

3 FORMULATION OF THE MACRO-ELEMENT MODEL

Each macro-element comprises a 4-noded quadrilateral element (referred to as 'quad') connected to adjacent quads via 4-noded line interface elements. 4-noded line interface elements are also used to connect quad elements to footing elements. Adjacent footing elements are connected via a nodal interface element.

3.1 *Kinematic relationships*

Kinematic relationships for the various components of the model are outlined below.

3.1.1 *Quad elements*

Each quad element has length, L, and height, H, as shown in Figure 2a. Assumed displacements (u, v) within the element in the (x, y) directions respectively are,

$$u = u_0 + \frac{1}{2}(\gamma_0 - 2\theta_0)\, y; v = v_0 + \frac{1}{2}(\gamma_0 + 2\theta_0)\, x \tag{1}$$

where (u_0,v_0) are the displacements at the element centre; θ_0 is the rotation and γ_0 is the shear strain. The rotation and shear strain are constant within each element. The quad element therefore deforms only in shear with rigid body movements also allowed.

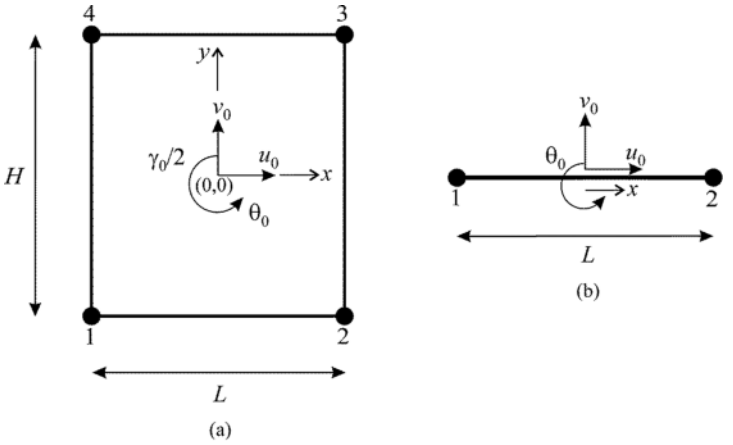

Figure 2. Degrees of freedom for quad and footing elements: (a) quad element with four degrees of freedom (where *x* and *y* represent the local element coordinates relative to the centre of the element); (b) footing element with three degrees of freedom (where *x* is a local coordinate relative to the centre of the element) at the element centroid.

The shear strain γ_0 within the element is,

$$\gamma_0 = \mathbf{B}_q \mathbf{U}_q = \begin{bmatrix} 0 & 0 & 2 & 0 \end{bmatrix} \begin{bmatrix} u_0 \\ v_0 \\ \gamma_0/2 \\ \theta_0 \end{bmatrix} \tag{2}$$

where the 'degree of freedom vector' is defined,

$$\mathbf{U}_q = [u_0, v_0, \gamma_0/2, \theta_0]^T \tag{3}$$

To model the interaction between adjacent quad elements it is necessary to formulate equations for the displacements along each edge of the quad. For example, the displacements $\mathbf{u}_T^e = [u \quad v]^T$ along the top edge (edge 4-3) of the quad in Figure 2a, are formulated as,

$$\mathbf{u}_T^e = \mathbf{B}_T^e \mathbf{U}_q = \begin{bmatrix} 1 & 0 & H/2 & -H/2 \\ 0 & 1 & x & x \end{bmatrix} \begin{bmatrix} u_0 \\ v_0 \\ \gamma_0/2 \\ \theta_0 \end{bmatrix} \tag{4}$$

where the top edge kinematic matrix $\mathbf{B}_T^e$ is determined on the basis of Equation 1. The bottom ($\mathbf{u}_B^e$), right ($\mathbf{u}_R^e$) and left ($\mathbf{u}_L^e$) edge displacements are determined using a similar approach, employing suitable edge kinematic matrices based on Equation 1.

3.1.2 *Footing elements*

The strip footing foundation is modelled with rigid bar elements (referred as 'footing elements'). This rigid bar formulation is selected to be compatible with the linear displacement variation along each edge of the quads. Footing elements are formulated with three degrees of freedom: horizontal

and vertical displacements (u_0, v_0) at the element centre, and rotation, θ_0 (see Figure 2b). The displacements, $\mathbf{u}_\mathrm{f} = [u \quad v]^T$ within the element are expressed as,

$$\mathbf{u}_\mathrm{f} = \mathbf{B}_\mathrm{f}\mathbf{U}_\mathrm{f} = \begin{bmatrix} 1 & 0 & 0 \\ 0 & 1 & x \end{bmatrix} \begin{bmatrix} u_0 \\ v_0 \\ \theta_0 \end{bmatrix} \tag{5}$$

where $\mathbf{B}_\mathrm{f}$ is referred to as the 'footing kinematic matrix' and the element degree of freedom vector, $\mathbf{U}_\mathrm{f}$, is,

$$\mathbf{U}_\mathrm{f} = \begin{bmatrix} u_0 & v_0 & \theta_0 \end{bmatrix}^T \tag{6}$$

3.1.3 *Line interface elements*

The constitutive behaviour of the interface elements that connect adjacent quads is specified to be a function of the local relative displacement (i.e. the difference in displacement between the two sides of the interface). A relative displacement vector $\mathbf{u}_\mathrm{r} = [u_r v_r]^T$ is formulated for each interface, where u_r and v_r are relative displacements in the normal and tangential directions respectively.

The detailed formulation of the relative displacement vector depends on the orientation of the interface. For instance, consider the horizontal interface between the two quad elements illustrated in Figure 3a. In this case edge 4-3 of the 'upper' quad interacts with edge 1-2 in the 'lower' element. The relative displacement vector for the interface is,

$$\mathbf{u}_\mathrm{r} = \begin{bmatrix} \mathbf{B}_\mathrm{B}^{\mathrm{upper}} & -\mathbf{B}_\mathrm{T}^{\mathrm{lower}} \end{bmatrix} \begin{bmatrix} \mathbf{U}^{\mathrm{upper}} \\ \mathbf{U}^{\mathrm{lower}} \end{bmatrix} \tag{7}$$

where, $\mathbf{U}^{\mathrm{upper}}$ and $\mathbf{U}^{\mathrm{lower}}$ are the degree of freedom vectors for the upper and lower quads respectively. The kinematic matrix $\mathbf{B}_\mathrm{B}^{\mathrm{upper}}$ relates to edge 4-3 of the upper quad and $\mathbf{B}_\mathrm{T}^{\mathrm{lower}}$ is the kinematic matrix for edge 1-2 of the lower quad. It is convenient to define the kinematic matrix $\mathbf{B}_{\mathrm{int}}$ as,

$$\mathbf{B}_{\mathrm{int}} = \begin{bmatrix} \mathbf{B}_\mathrm{B}^{\mathrm{upper}} & -\mathbf{B}_\mathrm{T}^{\mathrm{lower}} \end{bmatrix} \tag{8}$$

Special procedures are needed at the base of the facade as illustrated in Figure 4a, where the height of embedded sections of the masonry facade are h_{wg} and the height of the strip footing is h_f. Embedded sections are modelled with 'ground quad elements'; these elements extend from the centre of the strip footing to ground level as shown in Figure 4b.

The height of the ground quad elements is $h_{qg} = h_{wg} + h_f/2$. The connection between the ground quad element and the strip footing employs a horizontal interface element as shown in Figure 4b. Relative displacements in the quad-footing interface are formulated as,

$$\mathbf{u}_\mathrm{r} = \begin{bmatrix} \mathbf{B}_\mathrm{B}^{\mathrm{groundquad}} & -\mathbf{B}_\mathrm{f} \end{bmatrix} \begin{bmatrix} \mathbf{U}_{\mathrm{groundquad}} \\ \mathbf{U}_\mathrm{f} \end{bmatrix} \tag{9}$$

where, $\mathbf{U}_{\mathrm{groundquad}}$ is the degree of freedom vector for the ground quad element, $\mathbf{U}_\mathrm{f}$ is the degree of freedom vector for the footing element, $\mathbf{B}_\mathrm{B}^{\mathrm{groundquad}}$ is the kinematic matrix for the bottom edge of the ground quad element and $\mathbf{B}_\mathrm{f}$ is the footing kinematic matrix.

3.1.4 *Nodal interface elements*

A nodal interface element is adopted for connections between adjacent footing elements as illustrated in Figure 5. The relative displacements $\mathbf{u}_\mathrm{r}$ at the interface between the adjacent elements (considering horizontal displacements only) is,

$$\mathbf{u}_\mathrm{r} = \begin{bmatrix} 1 & 0 & 0 & -1 & 0 & 0 \\ 0 & 0 & 0 & 0 & 0 & 0 \end{bmatrix} \begin{bmatrix} \mathbf{U}_\mathrm{f}^{\mathrm{right}} \\ \mathbf{U}_\mathrm{f}^{\mathrm{left}} \end{bmatrix} \tag{10}$$

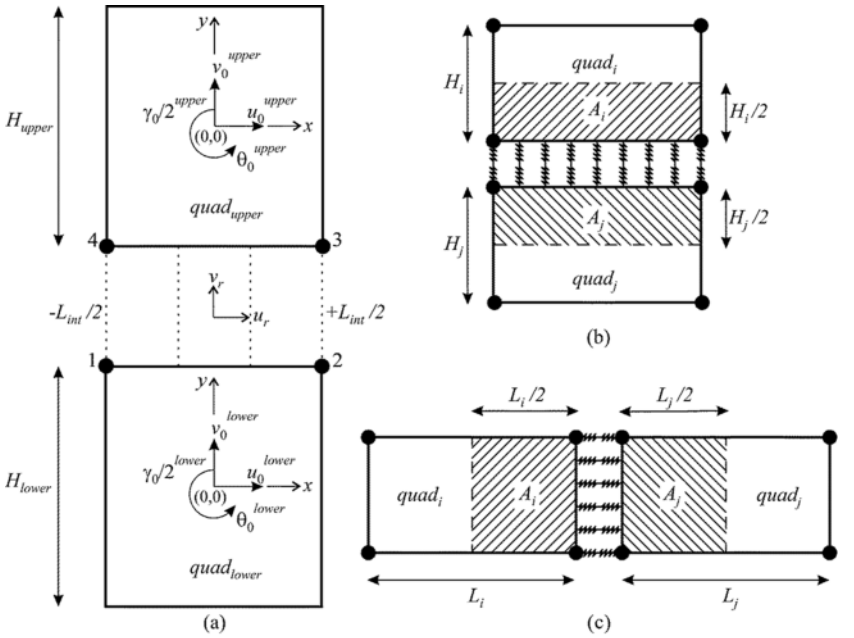

Figure 3. Quad-quad line interface elements: (a) horizontal interface, (b) horizontal interface influence area, (c) vertical interface influence area.

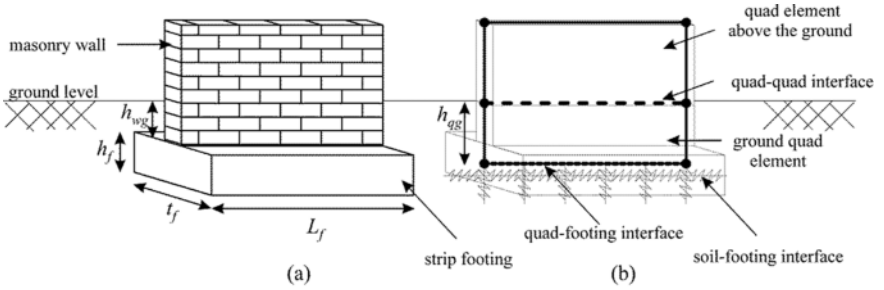

Figure 4. Modelling of embedded masonry sections: (a) footing detail, (b) quad-footing interface detail.

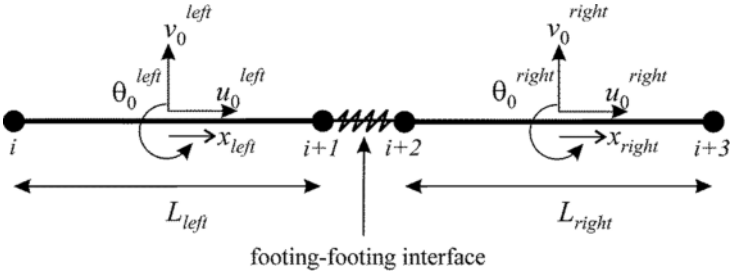

Figure 5. Nodal interface element employed to connect two adjacent footing elements.

where $\mathbf{U}_{\mathrm{f}}^{\mathrm{right}}$ and $\mathbf{U}_{\mathrm{f}}^{\mathrm{left}}$ are the degree of freedom vectors for the footing elements to the right and left of the interface respectively.

3.2 *Formulation of element stiffness matrices*

The stiffness matrix, $\mathbf{K}_{\mathrm{quad}}$ for each quad element is,

$$\mathbf{K}_{\mathrm{quad}} = \mathbf{B}_{\mathrm{q}}^{\mathrm{T}} G_m \mathbf{B}_{\mathrm{q}} t_q A \tag{11}$$

where $\mathbf{B}_{\mathrm{q}}$ is defined in Equation 2, G_m is the shear modulus of the masonry, t_q is the thickness of the quad element (corresponding to the thickness of the masonry facade) and $A = L \times H$ is the area of the element.

The tractions, $\mathbf{p} = [t \quad p]^T$ (where t and p are the shear and normal tractions respectively) developed in the quad-quad and quad-footing interface elements are related to the relative displacements by,

$$\mathbf{p} = \mathbf{D}_{\mathrm{int}} \mathbf{u}_{\mathrm{r}} \tag{12}$$

where,

$$\mathbf{D}_{\mathrm{int}} = \begin{bmatrix} k_s & 0 \\ 0 & k_n \end{bmatrix} \tag{13}$$

where k_s and k_n are shear and normal stiffness coefficients respectively. For horizontal quad-quad interfaces (as depicted in Figure 3b), k_n is determined (on the basis of 'springs in series' considerations) as,

$$k_n = \frac{2E_m}{H_i + H_j} \tag{14}$$

where E_m is the Young's modulus of the masonry and H_i, H_j are 'equivalent heights' in the adjacent quad elements (Figure 3b). For vertical interfaces (Figure 3c) the corresponding expression for k_n is,

$$k_n = \frac{2E_m}{L_i + L_j} \tag{15}$$

For the quad-footing interface element the normal stiffness is,

$$k_n = \frac{2E_m}{H} \tag{16}$$

In this modelling strategy, shear deformations are confined to the quad elements. The value of k_s is therefore set to a high value to supress additional shear deformations in the interface elements. To achieve this the shear stiffness for all interfaces is set to,

$$k_s = k_n \times 10^6 \tag{17}$$

The stiffness matrix for horizontal interface elements is given by,

$$\mathbf{K}_{\mathrm{interface}} = \int_{-L/2}^{L/2} (\mathbf{B}_{\mathrm{int}})^{\mathrm{T}} \mathbf{D}_{\mathrm{int}} \mathbf{B}_{\mathrm{int}} t \mathrm{d}x \tag{18}$$

A similar formulation is adopted for vertical line interface elements, although in this case a rotational transformation needs to be applied since the local and global axes are not coincident.

Footing-footing interfaces are modelled as axial springs with stiffness, $k_{footing}$ Values of $k_{footing}$ are given by,

$$k_{footing} = \frac{2E_f A_f}{L_{left} + L_{right}} \tag{19}$$

where E_f is the Young's modulus of the footing, A_f is the footing cross-section area and L_{right} and L_{left} are the lengths of the two footing elements connecting at the interface.

3.3 *Strain interpretations in macro-elements*

Data on the maximum principal tensile strain in building components are needed to quantify the risk of tunnelling-induced damage. Due to the nature of the macro-element formulation, special techniques are required to infer values of tensile strain from the results of the analysis. The macro-elements comprise a combination of quads and compliant interfaces. The quads experience shear deformation only and the interfaces are subject to normal relative displacements. Representative strains each macro-element are determined by combining the shear strain in the quad with axial strains corresponding to the normal relative displacements in the interfaces. For the particular case of an elastic constitutive model as employed in the current work this approach reduces to a rather simple set of equations as outlined below.

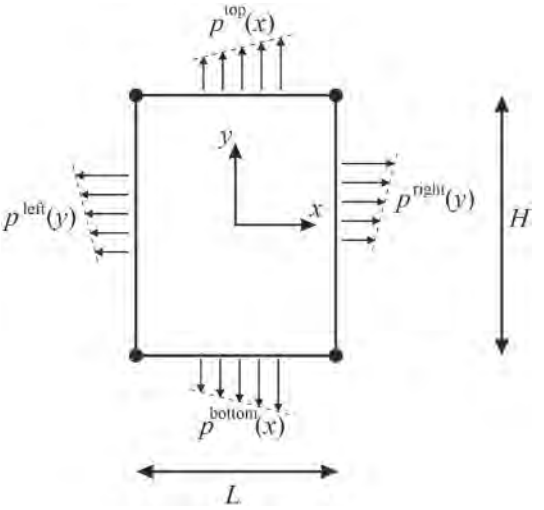

Figure 6. Normal tractions applied to the edges of a quad element.

Consider the quad element shown in Figure 6. The computed normal tractions (shown as tensile-positive) which in general will vary linearly along the interface are indicated. For clarity the shear tractions applied to the element are omitted. The notional direct strains ε_{xx}^{quad} and ε_{yy}^{quad} within the quad in the x and y directions are,

$$\varepsilon_{xx}^{quad} = \frac{p^{left}(y) + p^{right}(y)}{2E_m} \tag{20}$$

$$\varepsilon_{yy}^{quad} = \frac{p^{\text{top}}(x) + p^{\text{bottom}}(x)}{2E_m} \tag{21}$$

The maximum tensile strain at a point in the element are determined by combining the local values of the notional direct strains ε_{xx}^{quad} and ε_{yy}^{quad} with the (constant) shear strain γ_o within the quad element, using the appropriate tensor relationships. Spatial variations of maximum tensile strain are determined by evaluating the maximum tensile on a grid within each quad element.

3.4 *Model implementation*

The proposed macro-element modelling procedure outlined above was implemented in MATLAB using bespoke code. It was then applied to the case study described in Section 2. A coarse (Figure 7a, 116 macro-elements) and a fine (Figure 7b, 232 macro-elements) mesh was adopted to model the facade. In the coarse mesh, the corners of adjacent openings are adopted as the nodes of the quad

elements. This procedure generally results in a single quad element for each structural component (e.g. each pier is represented by a single quad). In the fine mesh, structural components are further sub-divided vertically into two or four quads, except for the slender quads above the doors which are not sub-divided.

To conduct the analysis, the stiffness matrices for each quad, interface and footing element is determined. Gaussian quadrature with four Gauss points is used to determine the line interface element stiffness matrices. The global stiffness matrix is then assembled. Vertical and horizontal tunnelling-induced greenfield ground movements at the level of the base of the footing were determined using empirical equations (Peck 1969; O'Reilly & New 1982) employing the parameters defined in Table 1. These assumed greenfield displacements are applied to the base of Winkler soil elements as prescribed deformations (Gulen et al. 2021). The global stiffness equation is solved to determine the displacements, rotations and shear strains for each quad element. These data are then post-processed to obtain the strain distribution in the facade.

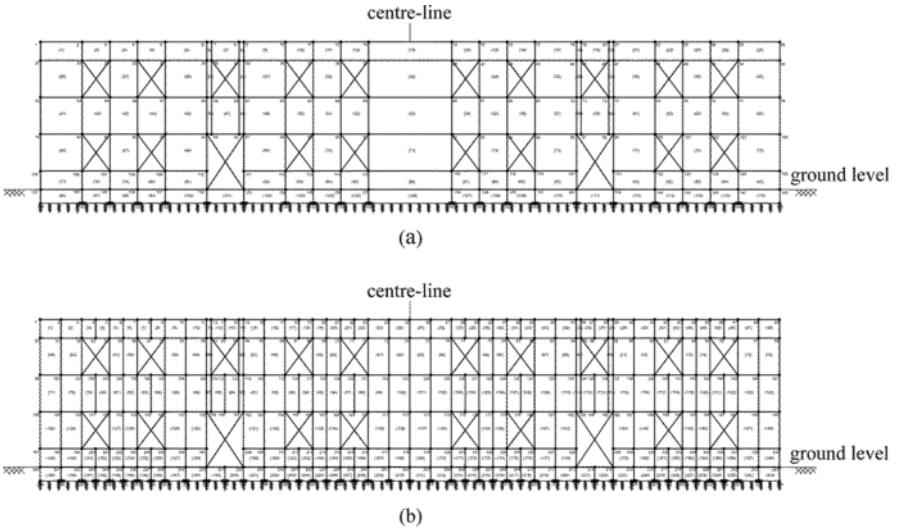

Figure 7. Macro-element model of the facade: (a) macro-element coarse mesh, (b) macro-element fine mesh (the facade openings are represented by cross lines in the drawings).

4 RESULTS

To investigate the veracity of the proposed macro-modelling approach, the computed response of the coarse and fine macro-element models are compared with results obtained from a separate 2D FE analysis in which the facade is represented by conventional triangular continuum elements (Gulen et al. 2021). The FE analysis employed the DIANA 10.3 FEA software with a representative element size of 0.25m. Apart from the use of continuum finite elements to model the facade, all aspects of the DIANA FE analysis and the macro-model analyses are equivalent. Results obtained from the two modelling approaches are compared below in terms of the computed displacements along the base of the facade and the spatial distribution of the major principal strain.

The horizontal (Figure 8a) and vertical (Figure 8b) displacements computed by the coarse and fine macro-element models demonstrate very good agreement with the 2D FE model. The results indicate that the differential displacements experienced by the building are significantly smaller than the prescribed greenfield displacements; this is an expected consequence of soil-structure interaction effects. However, the macro-element models achieve this result with significantly less computational effort than is required for the 2D FE analyses. For instance, the total number of

degrees of freedom in the coarse mesh macro-element model is almost two orders of magnitude less than the 2D FE model (Table 2). It is also noted that increasing the macro-element mesh density does not change the building displacement response significantly; this suggests that a relatively coarse mesh is sufficient to obtain satisfactory results on building displacements.

Table 2. Macro-element and DIANA 2D FE continuum model comparisons.

	Macroelement coarse mesh	Macroelement fine mesh	DIANA 2D FE continuum
Total number of elements	358	668	11426
Total number of DOF	527	1060	12526

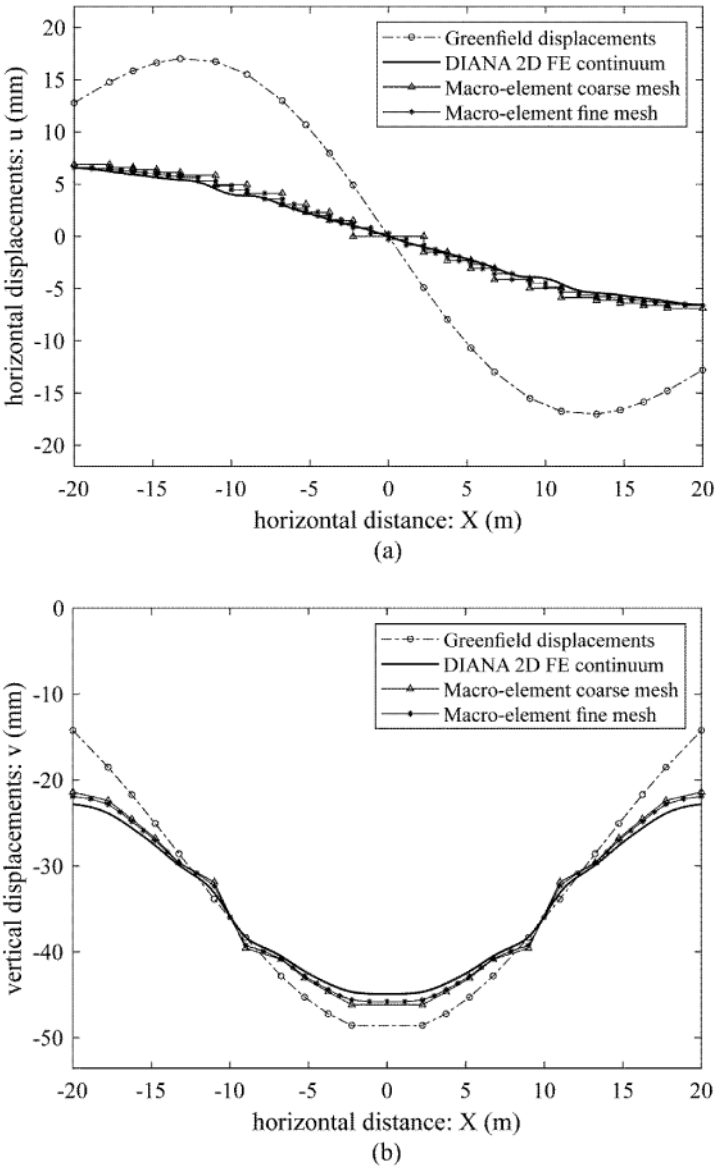

Figure 8. Comparison of computed building displacement responses at the base of the building: (a) horizontal displacement response, (b) vertical displacement response.

Contour plots of the major principal strain, ε_1, for the 2D FE continuum, macro-element coarse mesh and macro-element fine mesh models are presented in Figure 9. Results obtained from the FE analysis (Figure 9a) show a set of inclined bands where significant tensile strains occur. Small zones are apparent at the corners of some of the openings where relatively large localised strains are seen to develop. In these localised areas the actual magnitude of the computed tensile strain depends on the local density of the finite element mesh; introducing more elements in these areas will cause an increase in the maximum computed tensile strain (e.g. Yiu et al. 2017). The macro-element models are able to reproduce the general pattern observed in the 2D FE analysis, but at a lower spatial resolution.

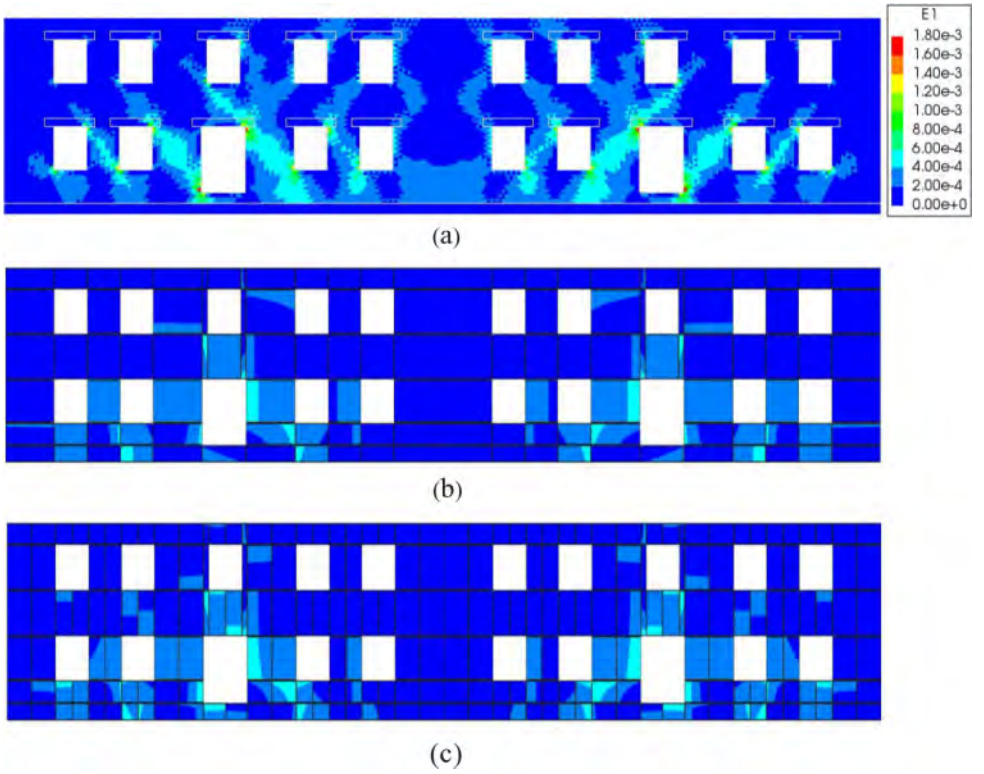

Figure 9. Computed major (tensile) principal strain distributions: (a) DIANA 2D FE continuum, (b) macro-element coarse mesh, (c) macro-element fine mesh.

The strain concentrations at the corners of the openings that are apparent in the 2D FE analysis are absent from the macro-element model results. It is argued in Yiu et al. (2017) that strain concentrations at internal corners, when computed with continuum finite elements, do not have direct significance in the classification of damage. The area over which the strain concentrations occur is relatively small and – since the computed magnitude of the largest tensile strain depends on the local mesh density – computed values of maximum tensile strain close to the corners of openings are not an objective measure of overall building damage. To determine a representative tensile strain metric from 2D FE analyses, Yiu et al. (2017) proposed a filtering approach to remove the relatively large computed strains in the neighbourhood of openings. The resolution of the macro-element models is relatively low, and strain concentrations around the openings are not captured. This feature of the macro-element modelling approach has the desirable outcome that filtering of the computed tensile strains – to determine a representative strain value for damage assessment purposes – is not required.

5 CONCLUSION

A 2D macro-element modelling approach is introduced to model masonry buildings subjected to tunnelling-induced displacements. This procedure is an intermediate-level approach; it facilitates damage assessment analyses that are more realistic than simple beam methods but at a fraction of the computational cost of detailed FE continuum models. The macro-modelling approach is based on a finite element re-formulation of the macro-element models originally proposed by Caliò et al. (2012). The macro-elements are combined in the current work with 1D foundation elements and a Winkler soil-foundation model.

For a particular case study example, results obtained with the proposed macro-modelling approach are compared with a benchmark analysis using continuum finite elements to model the facade. Coarse and fine macro-element meshes are considered. The coarse and fine macro-element models are both shown to compute the building displacements with good accuracy, compared with the benchmark analysis. The macro-element models also capture the overall strain distribution within the building, but at a relatively low resolution. A potential benefit of the macro-element modelling approach – in contrast to continuum finite element approaches – is that mesh-dependent strain concentrations are not computed in the neighbourhood of the corners of openings in the facade. This suggests that strain data determined from the macro-element model could be used directly in damage assessments. This contrast with continuum finite element models for which a filter is needed on the computed tensile strains to obtain a representative strain measure for damage assessments.

The current macro-element formulation is unable to capture certain aspects of bending behaviour in the beams and spandrels, such as the spatial variation of bending stresses along the axis of the beam/spandrel and parabolic variations in shear stresses perpendicular to the axis. Although an improved representation of beam action can be achieved by increasing the refinement of the macro-element mesh, there may be merits in alternative formulations in which beam behaviour is captured directly.

REFERENCES

Boscardin, M. D. & Cording, E. J. 1989. Building response to excavation-induced settlement. *Journal of Geotechnical Engineering* 115(1): 1–21.

Burd, H.J., Yiu, W.N, Acikgoz, S. & Martin, C.M. 2022. Soil-foundation interaction model for the assessment of tunnelling-induced damage to masonry buildings. Tunnelling and Underground Space Technology 119,104208.

Burland J. B., Broms B. B. & De Mello V. F. B. 1977. Behaviour of foundations and structures. State of the art report. Session 2. Proceedings of the 9th International Conference on Soil Mechanics and Foundation Engineering, Tokyo, 3, 495–546.

Burland, J. B., & Wroth, C. P. 1974. Settlement of buildings and associated damage. In A.C. Meigh (ed.), *Proceedings of the conference on settlement of structures*: 611–654. London, UK: Pentech Press.

Caliò, I., Marletta, M., & Pantò, B. 2012. A new discrete element model for the evaluation of the seismic behaviour of unreinforced masonry buildings. Engineering Structures, 40, 327–338.

Giardina, G., van de Graaf, A. V., Hendriks, M. A. N., Rots, J. G., & Marini, A. 2013. Numerical analysis of a masonry façade subject to tunnelling-induced settlements. *Engineering Structures* 54: 234–247.

Gulen, D. B., Acikgoz, S., & Burd, H. J. 2021. Equivalent frame model for the assessment of tunnel-induced damage to masonry buildings. In *Geotechnical Aspects of Underground Construction in Soft Ground* (pp. 545–553). CRC Press.

Lagomarsino, S., Penna, A., Galasco, A., & Cattari, S. 2013. TREMURI program: An equivalent frame model for the nonlinear seismic analysis of masonry buildings. Engineering Structures 56: 1787–1799.

Mair, R. J., Taylor, R. N. & Burland, J. B. 1996. Prediction of ground movements and assessment of risk of building damage due to bored tunnelling. In R. J. Mair & R. N. Taylor (eds), Geotechnical aspects of underground construction in soft ground: 713–718. Rotterdam, the Netherlands: Balkema.

O'Reilly, M. P. & New, B. M. 1982. Settlements above tunnels in the United Kingdom- their magnitude and prediction. In M. J. Jones (ed.), *Proceedings of Tunnelling'82*: 173–181. London, UK: Institute of Mining and Metallurgy.

Peck, R. B. 1969. Deep excavations and tunnelling in soft ground. *Proc. 7th Int. Conf. Soil Mech. Found. Engng:* 225–290.

Quagliarini, E., Maracchini, G., & Clementi, F. 2017. Uses and limits of the equivalent frame model on existing unrein-forced masonry buildings for assessing their seismic risk: A review. Journal of Building Engineering 10: 166–182.

Rankin W. J. 1988. Ground movements resulting from urban tunnelling: predictions and effects. Engineering Geology of Geology Special Publication Nos. 79–92.

Yiu, W. N., Burd, H. J., & Martin, C. M. 2017. Finite-element modelling for the assessment of tunnel-induced damage to a masonry building. *G?otechnique* 67(9): 780–794.

Geotechnical Engineering for the Preservation of Monuments and Historic Sites III – Lancellotta, Viggiani, Flora, de Silva & Mele (Eds)

Impact assessment study of a 150-year-old government building in Chennai, India

Dhanya Nair, Subhadeep Banerjee, A. Boominathanc & Arun Menon
Department of Civil Engineering, IIT Madras, India

ABSTRACT: The Tamil Nadu Public Works Department (PWD) proposed to construct a new office building (G+3) over a demolished building site at the TNPWD Building site located at Chennai, India. There are several office buildings located along the boundary of the TNPWD building site, of which the PWD Main Building, behind which the proposed new building is to be constructed, is a 150-year-old heritage structure. Almost all the adjacent structures are of 2 or 3 storied of-fice buildings. Build in the 19th century, the PWD Main Building facing Marina beach has walls and footings constructed using brick and lime mortar. Considering the historical im-portance of the PWD main building, there is an apprehension that the pile boring and other construction activities on the proposed structure may damage the PWD main building due to the ground movement/vibrations. Detailed geotechnical and geophysical investigation were carried out at the site. The groundwater table was observed at about 3.5 m below the ground level. Vibration monitoring studies were carried out during the test pile boring operations. The piles adopted are bored cast-in-situ circular types of 450 mm diameter. The time history of acceleration during piling operations was continuously recorded. The maximum peak acceleration of the vibrations recorded was found to be about 0.01g. It was also noticed that the maximum peak particle velocity (PPV) is 1.5 mm/s in the vertical direction and 0.65 mm/s in the horizontal direction at ground level of the PWD main building, which is acceptable. The maximum vibration levels were observed during piling operations in the SDR layer at the depth of 23 m from EGL.

1 INTRODUCTION

The Tamil Nadu Public Works Department (PWD) proposed to construct a new office building (G+3) over a demolished building site at the PWD C.E., Building site, Chepauk, Chennai Re-gion. There are several office buildings located along the boundary of the TNPWD building site, of which the PWD Main Building, behind which the proposed new building is to be constructed, is a Heritage Structure. Almost all the adjacent structures are of 2 or 3 storied office buildings. Build in the 19th century, the PWD Main Building facing Marina beach has walls and footings constructed using brick and lime mortar (Kaushal 2019). The proposed new building is adjacent to the existing PWD main building at about 10 m, where cast-in-situ bored piles will be constructed. Considering the lifespan and heritage importance of the PWD main building, there is an apprehension that the pile boring and other construction activities on the proposed structure may damage the PWD main building due to the ground move-ment/vibrations. The primary objective of this paper is to impact assessment of the PWD main building based on site characterization using borehole and MASW teat data. The paper also presents some of the preliminary results of vibration monitoring studies.

DOI 10.1201/9781003308867-81

2 SITE CHARACTERIZATION

The investigation program comprises of sinking three (3 No.) exploratory boreholes; the first ones are close to the heritage structure, the second one in the middle of the proposed building, and the remaining at the side boundaries, as shown in Figure 1. The boreholes were advanced up to a maximum depth of about 34 m below the ground level. The MASW geophysical survey was carried out by the IIT Madras technical team using a 24-channel seismic recorder (Make: GEOMATRIX, USA; Model: GEODE) with SGOS operating software with vertical geophones of 4.5 HZ (24 Nos) at the site in two stretches M1 and M2, as shown in Figure 2 (Anukwu et al. 2018). The data acquisition was made by Seismodule Controller Software (SCS) installed on a laptop.

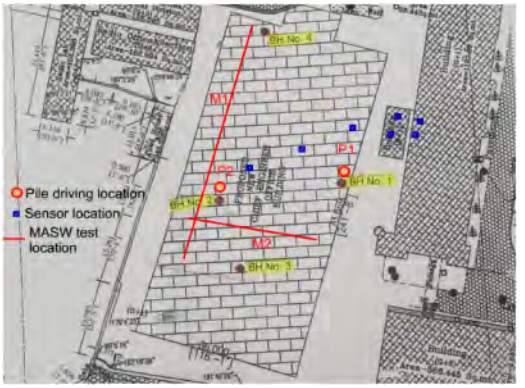

Figure 1. Site plan showing pile driving and vibration measurement locations.

Figure 2. MASW test set up at site.

Based on the borehole profile and MASW test analysis, it was found that the top layer in the site predominantly consists of a filled-up layer up to a depth of about 3.5 m from the EGL. It is followed by the occurrence of an 18 m thick loose to medium dense sand layer with SPT N-value in the range of 10 to 35. In some locations, a thin layer of medium stiff clay occurred within a depth of 8.5 to 9.5 m below EGL. The highly disintegrated rock with the SPT N Value in the range of 40 to 50 occurs within a depth of 22 to 28.5 from EGL. The weathered rock stratum is encountered at 28.5 m below EGL. The groundwater table was observed at about 3.5 m below the ground level.

3 VIBRATION MONITORING STUDY DURING PILING OPERATIONS

3.1 *Piling operations*

It was planned to adopt 450 mm dia bored-cast-in-situ piles to support the proposed new building. It was decided by to terminate the pile at a depth of about 23 m at which highly disintegrated rock/dense sand layer occurs. Vibration monitoring studies were carried during the test pile boring operations. The pile adopted are bored cast-in-situ circular types of 450 mm diameter. The pile-boring operations were performed using rotary drill rigs up to a depth of around 23.5 m below the ground level. Boring is carried out using rotary drilling equipment with a tungsten drill bit. The drilling process was continued to the designed founding depth up to the commencement of soft disintegrated rock strata at 23.5 m depth. The piling operations is shown in Figure 3.

Figure 3. Pile driving operation at site.

3.2 *Instrumentation*

The vibration monitoring study was carried out during the piling operations of 2 test piles: test pile P1 (at the center of the site) and test pile P2 (close to the heritage structure) as shown in Figure 1. The vibration monitoring was carried out using six Piezoelectric seismic accelerometers (Model: PCB393B04, make: PCB, USA) connected to a multi-channel digital carrier frequency amplifier system (model: QuantumX – MX1615BR, Make: HBM, Germany). Catman Easy software installed on a computer was used to monitor and record the vibrations as digital data.

Ground-borne vibrations were measured at the boundaries of the site at the ground surface using three accelerometers fixed in the vertical directions. In heritage building, four accelerometers were fixed in vertical and horizontal directions in the floors and walls respectively (Figure 4). The time history of acceleration during piling operations is continuously recorded.

Figure 4. Horizontal and vertical accelerometers mounted on the heritage building.

4 RESULTS AND OBSERVATIONS

It should be noted that the maximum peak acceleration of the vibrations recorded was found to be about 0.01g. Typically, ground vibrations from construction activity are quantified using the maximum vertical peak particle velocity (PPV) of the vibrations. Therefore, the values peak particle velocity (PPV) is obtained from the recorded acceleration-time history. The values of maximum PPV at different locations and distance from the piling location are presented in Table 1. It can be noticed from the above table that the maximum PPV is 1.5 mm/s in the vertical direction and 0.65 mm/s in the horizontal direction at ground level of the PWD main building. The maximum vibration levels were observed during piling operations in the weathered rock layer at the depth of 23 m from EGL.

It can be noticed from the table that the maximum PPV is 1.5 mm/s in the vertical direction and 0.65 mm/s in the horizontal direction at ground level of the PWD main building. The maximum vibration levels were observed during piling operations in the weathered rock layer at the depth of 23 m from EGL.

Table 1. Maximum PPV during pile boring operations.

			Maximum PPV (mm/s)	
Test Pile	Sensor direction	Distance from the test pile	Pile depth = 6 m	Pile depth = 23 m
P2	Vertical (floor)	11	0.6	1.0
P1	Vertical (floor)	10	0.8	1.5
P2	Horizontal (wall)	42	0.07	0.1
P1	Horizontal (wall)	10	0.65	0.8

5 CONCLUSIONS

The papers describe an impact assessment study of a 19^{th} Century structure in view of a proposed construction of a new building is just a few meters away from the heritage structure. As part of impact assessment study geotechnical and geophysical investigations was carried at the site and it is found out the site predominately consists of loose to dense sandy strata up to 23.5 m and it is followed by occurrence of soft disintegrated rock (SDR) and weathered rock layers. The vibration monitoring carried out along the boundaries of the site during the two-test pile boring operations shows that the maximum PPV at the heritage structure was observed 1.5 mm/sec in the vertical direction and 0.65 in the horizontal direction. The observed vibration levels are within the permissible vibration limit for heritage structures as per the relevant international standards.

REFERENCES

Anukwu, G.C., Khalil, A.E., Nawawi, M., Abdullah, K. & Abdullah, F.M. 2018. Multi-channel analysis of surface waves (MASW) using CMP analysis to identify soil problems threat on the heritage site at Georgetown, Malaysia. *Proc. International Geophysical Conference, Beijing, 24–27 April*. Beijing: Society of Exploration Geophysicists.

Kaushal, R.K. 2019. *Conservation and audit of heritage buildings*. Central Public Works Department, New Delhi, India.

Geotechnical Engineering for the Preservation of Monuments and Historic Sites III – Lancellotta, Viggiani, Flora, de Silva & Mele (Eds)

Tunnelling effects on the Basilica di Massenzio: Computed and observed displacement fields

E. Romani, M. D'Angelo & L. Sidera
Metro C S.c.p.A., Rome, Italy

Sciotti & C. Ottaviani
Roma Metropolitane, Rome, Italy

S. Rampello
University of Rome "La Sapienza", Rome, Italy

ABSTRACT: The contract T3 of the new Line C of the Rome underground is 2.8 km long and includes two stations and two ventilation shafts. It runs under the archaeological artefacts of the historical centre of Rome which is a UNESCO World Heritage site, an area with high density of monuments and historical buildings. Metro C, in cooperation with an interdisciplinary Scientific Technical Committee, has carried out several detailed studies to analyse the potential interactions of the monuments/historical buildings with the new line C, in order to identify the most appropriate and effective mitigation techniques to be adopted to prevent any damage. This paper describes the procedures that have been followed to safeguard the monuments/historical building interacting with the line during its construction, from the approach adopted to study the line-monument interaction at different levels of complexity, to the comparison between the computed and the observed displacement fields for the case of the *Basilica di Massenzio*.

1 INTRODUCTION

Line C is the new line of the Rome underground that includes 30 stations. Once completed, it will cross the city from the North-West to South-East, for a total length of 25.6 km, almost doubling the extent of the existing underground network. The new line C is then an infrastructure of outstanding importance for the public transport system of Rome, due to its high population. It is also the first fully automated underground line in the city.

As General Contractor, Metro C manages the construction of the Line C in its implementation and operational phases including the design, the archaeological surveys, tunnelling, stations constructions and trains manufacturing, till the start-up. The activities started in 2006 with the archaeological surveys and the design stages. At present 22 stations and 18 km of the line are in operation.

During the design stage, Metro C set up a multidisciplinary Scientific Technical Committee (*STC*) with the assignment of implementing all the necessary procedures to safeguard the historical monuments of Roman age potentially interacting with the new Line C. A methodological approach was adopted to perform the line-monument interaction studies, following procedures at two increasing levels of complexity: *green-field* (*Level 1*) analyses were first carried out ignoring the stiffness and weight of the existing monuments for a simplified evaluation of the potential damage induced by tunnelling; Finite Element (FE) interaction (*Level 2*) analyses were then carried

DOI 10.1201/9781003308867-82

out in both two- and three-dimensional conditions, accounting for the stiffness and weight of the monuments (Burghignoli et al. 2013).

This approach allowed the potential interaction of each monument with the line to be evaluated, this permitting to design an appropriate monitoring system to detect the displacement field induced in the monuments by the line construction. This ensured a reliable control of the construction processes providing the information needed to support the decision-making process. Based on the results of the analyses performed at the design stage, appropriate geotechnical and structural protection measures were adopted for the monuments when necessary (e.g.: Rampello et al. 2019; Masini & Rampello 2021).

The aforementioned approach was implemented for the first time in Italy by Metro C involving a deep interaction between geotechnical and structural engineering. This resulted in achieving the objective of completing contract T3 of the new Line C of Rome underground without inducing any significant effect on the monuments adjacent to the line, of outstanding archaeological and historical value. Moreover, monitoring data were seen to be in a fair agreement with the design predictions. In this paper a description of the geological and geotechnical context of the T3 Contract of the Line C of the Rome underground is first given together with a description of the activities carried out by the *STC*, and the comparison between the computed and observed displacement fields is then shown referring to the *Basilica di Massenzio*.

2 THE CONTRACT T3

The contract T3, currently under completion, runs under the historical centre of Rome starting from *San Giovanni* station, for a length of about 3 km: it includes the *Amba Aradam/Ipponio* and the *Fori Imperiali* stations and two ventilation shafts, shaft 3.2 and shaft 3.3 (Masini et al. 2021) (Figure 1). The twin running tunnels were excavated using two EPB-TBMs (Earth Pressure Balance - Tunnelling Boring Machines) at depths in the range of 20 to 50 m. The tunnels have outer and inner diameters of 6.7 m and 5.8 m, respectively, with the lining made by 0.3 m-thick precast concrete segmental elements. The face support pressure applied by the TBMs to balance the total horizontal stress acted by the soil at the tunnels depth was in the range of 200 to 480 kPa depending on the excavation depth, while the tail void injection pressure was about 50 kPa higher, to ensure the gap between the excavated soil and the lining to be filled.

Figure 1. Aerial view of Contract T3.

Several campaigns of in situ and laboratory geotechnical investigations were carried out in the design stages, dating back from to 1995 till the last one, carried out in 2010–2011. In situ tests involved dynamic and static penetration tests, the latter also instrumented with pore water transducers, cross-hole, dilatometer and Lefranc tests. About 344 undisturbed samples were retrieved to evaluate the strength e stiffness parameters of the soils, also performing triaxial tests instrumented with local axial strain transducers and bender elements, as well as resonant column tests, to define the small strain stiffness of the soils. This led to an accurate definition of both the soil stratigraphy and the mechanical parameters of the soils interacting with the line.

The geological profile of Contract T3 is shown in Figure 2: Line C runs from *San Giovanni* station towards *Venezia* station at an elevation of about 9.5 m a.s.l. (depth $z \cong 27$ m). The elevation of the tunnels gradually reduces to about 5 m a.s.l. near *Piazza Celimontana* ($z \cong 52$ m), and then increases again to about 0.25 m ($z \cong 27$ m) at *Fori Imperiali* station; from this station the line deepens again towards *Venezia* station reaching an elevation of -10 m a.s.l. ($z \cong 37$ m). From *San Giovanni* to *Amba-Aradam* stations the tunnels runs mainly into the fine grained Pleistocene and Holocene deposits, consisting of sandy silt and clayey silt (LSO, Ar-St); after a passage through the Pleistocene sandy gravel (SG), the tunnels enter the base stiff and overconsolidated Pliocene clay (Apl) to emerge again near the *Coliseum* into the overlying coarse grained soils, consisting of Pleistocene sandy gravel (SG) and volcanic medium to fine silty sand (Tb). After the *Basilica di Massenzio* the tunnels deepen being excavated in the Pliocene base clay (Apl) before reaching the *Venezia* station. Here there in an abrupt change in the geological environment, as the tunnels enter the Tiber valley with its Holocene alluvial fine grained soil (Ag). The Made Ground (MG) overlying the Pleistocene and Holocene deposits is 7 to 11 m thick with local maximum thickness of 18 m. It consists of coarse grained materials containing the remnants of the ancient city, of immense archaeological value.

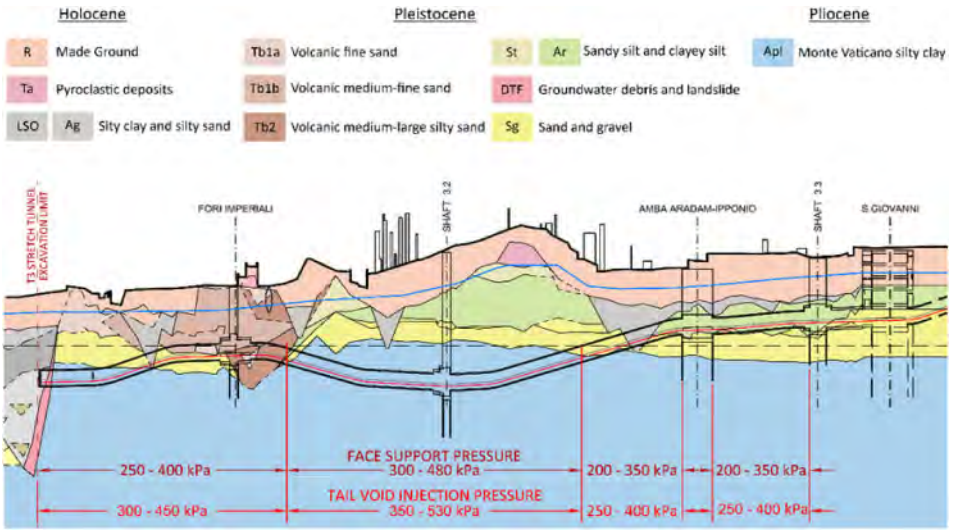

Figure 2. Geological profile along contract T3.

The pore water pressure regime in the central stretch is about hydrostatic, with the water table located at depths $z = 10$–15 m and local small downwards gradients.

3 THE SAFEGUARD OF THE MONUMENTS

The historical centre of Rome is a UNESCO World Heritage site so that Metro C set up a multidisciplinary Scientific Technical Committee (*STC*) to safeguard all the monuments or historical

buildings interacting with the line. The *STC* had to ensure high quality procedures for evaluating the effects induced by tunnelling and deep open excavations on these monuments and providing design guidelines.

Prior to any analysis, preventive studies were conducted on the monuments adjacent to line C to identify materials and geometry of the foundations, the mechanical properties of the materials, the construction technologies and phases, the structural layout and the existing crack patterns.

Evaluation of tunnelling-induced settlements in *green-field* conditions was then carried out using well known empirical relationships in order to exclude from the interaction studies the monuments located outside the ground settlement trough. In these analyses, named *Level 1* analyses, the settlements were computed at the foundation level ignoring the presence of the monument.

In the empirical relationships, the settlement trough is described by a Gaussian curve in a section transverse to the tunnel axis, and by a cumulative probability function in the longitudinal direction. For sake of space, a brief reference is made in the following to the transverse section only.

The transverse surface settlement trough was evaluated through Eq. (1) (O'Reilly & New 1982; Peck 1969):

$$w(x) = \frac{V_L D^2}{4i}\sqrt{\frac{\pi}{2}}\exp\left(-\frac{x^2}{2i^2}\right) \tag{1}$$

where $w(x)$ is the settlement at a distance x from the tunnel axis, $D = 6.7$ m is the tunnel diameter, V_L is the volume loss, prescribed to be not higher than 0.5%, and i is the distance of the point of inflection of the settlement trough from the tunnel axis.

To evaluate i at depth z the expression of Moh *et al.*, (1996) was used:

$$i(z) = K \cdot z_0\left(\frac{z_0 - z}{z_0}\right)^m \tag{2}$$

where z_0 and z are the tunnel axis and the foundation depths, respectively. For Contract T3 a width parameter $K = 0.4$–0.5 was assumed at ground surface, and an exponent $m = 0.6$.

Following O'Reilly and New (1982), the horizontal displacements were computed assuming the ground displacement vectors to be directed towards the tunnel axis.

In evaluating the settlement trough, account was taken for the variations in plan and depth of the tunnels and the presence of the twin tunnels was accounted for by superposition of each tunnel effect.

Once the subsidence profile was computed, the maximum free field deflection ratio in sagging and hogging (Δ_s/L_s, Δ_h/L_h) underneath the foundation were evaluated together with the horizontal strain ε_h: these quantities were used to evaluate the potential damage induced by tunnelling through the interaction diagrams proposed by Burland and Wroth (1974) and Burland (1995), that relate the deflection ratio and the horizontal tensile strain to six damage categories. To account for the historical value of the monuments, lower threshold tensile strains defining the damage categories, than the ones proposed by Boscardin and Cording (1989), were adopted in the study.

When damage evaluation exceeded the category 0, associated to negligible effects, *Level 2* soil-structure interaction analyses were carried out in two stages.

Specifically, the interaction between the tunnels and the monuments was studied through 2D or 3D Finite Element (FE) analyses that addressed soil-structure interaction by adopting a simplified description of the mechanical behaviour of the monuments, often assumed as linear elastic. The displacement field computed by the geotechnical interaction analyses, accounting this time for the stiffness and weight of the monument, was then applied to a detailed structural model of the monument thus computing the state of stress and strain induced by tunnelling-induced ground movements. The level of damage was finally re-evaluated using both the Burland and Wroth (1974) procedure or considering the field of maximum tensile strains computed by the structural analyses. Depending on the computed results, either the damage was deemed acceptable, or protective intervention were suggested by the *STC*.

The *Basilica di Massenzio* is referred to in the following to illustrate the adopted approach. Both *Level 1* and *Level 2* analyses were performed for this monument and safeguarding interventions were designed to prevent any damage eventually induced by tunnelling.

4 THE BASILICA DI MASSENZIO

The *Basilica di Massenzio* is located at the end of the Contract T3, close to the *Fori Imperiali* station. Its construction began on the northern side of the forum under emperor Massenzio in 308, and was completed in 312 by Costantino I.

In its original configuration, the building consisted of a central nave (about 80 m long and 25 m wide), covered by three vaults (35 m high) on four large piers, and ending in an apse at the western end, and of two flanking aisles spanned by three semi-circular barrel vaults perpendicular to the nave. Excluding the apse, the building occupied a rectangular area of about 80×60 m^2 (Figure 3a). The perimeter walls of the Basilica, as well as the internal baffles, consist of two facings of clay bricks (*opus testaceum*) and a core of Roman conglomerate of lime and pozzolana (*opus caementicium*) including aggregates of different materials. The vaulted structures as well as the foundations are made in *opus caementicium*.

In the fourth and fifth centuries the Basilica underwent several modifications, including the creation of the apse on its North-Western side, and the construction of a retaining wall to support the Velia Hill. In the sixth century, the Basilica had been already abandoned.

The south and central sections were probably destroyed by the earthquakes of 847 and 1349 (Figure 3b). What is left of the monument consists of the three large barrel vaults forming the aisle parallel to *via dei Fori Imperiali* (Figure 3c-d): each vault spans 20 m and is supported by massive walls. The two side vaults are closed by a thinner wall facing *via dei Fori Imperiali*, with two levels of three arched windows, whereas the central vault terminates with the apse constructed by Costantino.

The first excavations to restore the Basilica to its original level began in the nineteenth century and in 1932 the excavation works were carried out to remove the Velia Hill and make room for the new *via dell'Impero*. Exposed by these works, the structure revealed the presence of an extensive pattern of cracks and significant damage in the vaults and the apse. In the 1960s, Musumeci reconstructed the destroyed dome of the apse in reinforced concrete (Figure 3d).

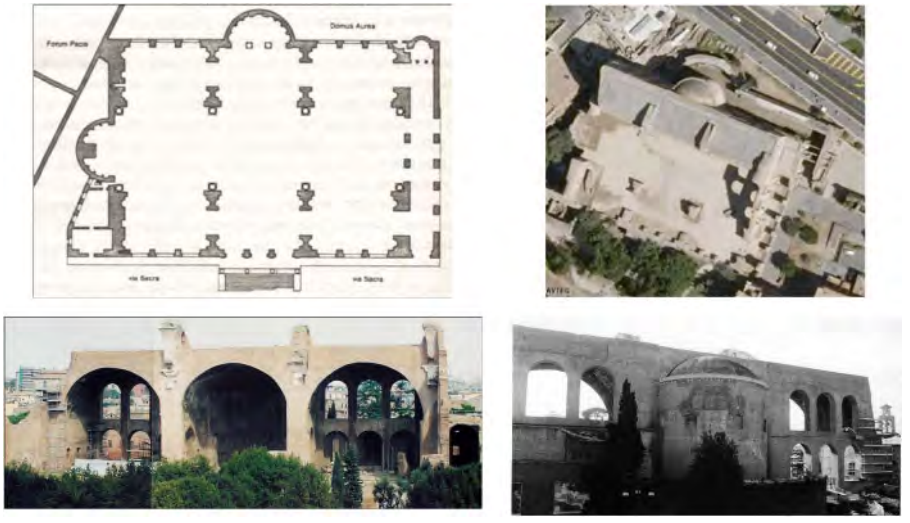

Figure 3. *Basilica di Massenzio*: (a) map after the restoration works of IV and V centuries; (b) aerial view; (c) view from *via Sacra*; (d) view from *via dei Fori Imperiali.*

4.1 *Geotechnical analyses*

Figure 4a (after CISTEC, 2001) shows a scheme of the foundations of the Basilica with the depth of the bearing walls increasing moving towards *Foro di Cesare*, from $z = 4$ m (23 m a.s.l.) for the *Pilone Colosseo* to $z = 14$ m (13 m a.s.l.) for the *Pilone Carinae*, following the original ground level of the Velia hill before the construction of the Basilica.

For the final design stage, referring to the definitive route of the Line C, *Level 2* interaction analyses were only carried out due to the complexity of the structural layout and the outstanding value of the monument. In the 3D FE analyses, the real geometry of the problem was simplified as shown in Figures 4b-c, assuming a fictitious axis of symmetry between the two tunnels, excavated at an axis-to-axis spacing of 14 m, at a depth of 25.5 m. The model assumption that the two tunnels are excavated at the same time was deemed reasonable in that on the other side of via *dei Fori Imperiali*, opposite to the Basilica, there is a high hill (the *Belvedere Cederna*) and the second tunnel is far away from the Basilica, hardly affecting its behaviour. In the model, the tunnel is assumed to be parallel to the ancient wall retaining the Velia hill, with an axis-to-Basilica distance equal to the shortest one (16 m), that occurs next to the *Pilone Colosseo*.

The numerical model was 212 m long, 91 m wide and a 37 m deep, with its base located at the top of the layer of the stiff clay (Apl); vertical boundaries of the FE mesh were restrained horizontally, for out-of-plane displacements, while the nodes of the bottom boundary were restrained both horizontally and vertically. In the direction of tunnel axis the size of the element is constant and equal to 2 m, that corresponds to the excavation step adopted in the numerical analyses. The mesh included about 72000, 10-node, tetrahedral elements with a second-order interpolation of displacements and a linear interpolation of strains.

In the simplified structural scheme adopted in the geotechnical analyses, only the embedded portions of the Basilica and of the retaining wall were modelled, using equivalent unit weights for the different portions of the Basilica in order to reproduce the vertical loads applied by the bearing walls to the foundation soils.

The mechanical behaviour of the foundation soils was described by an elastic–plastic, rate-independent constitutive model with isotropic hardening and Mohr-Coulomb failure criterion, the *Hardening Soil* model implemented in the Plaxis 3D suite (Brinkgreve et al. 2013), using the strength and stiffness parameters obtained from the available *in situ* and laboratory tests (Soccodato et al. 2013). The massive bearing piers and walls were instead modelled with an isotropic linear elastic-perfectly plastic model, with Mohr-Coulomb failure criterion, specifying a limiting tensile stress ($\sigma_t = 0.5$ MPa) (Soccodato et al. 2013).

The analyses were carried out assuming drained conditions due to the medium-high permeability of the layers of silty sand (St-Ar) and sandy gravel (SG): pore water pressure is hydrostatic with the water table located at +10 m, a.s.l..

The 3D FE analyses were performed as follows: (i) geostatic equilibrium at +27 m a.s.l.; (ii) activation of the elements modelling the Basilica and the wall; (iii) excavation at the elevation of *via dei Fori Imperiali* (+23 m a.s.l.); (iv) simulation of tunnels excavation. This last stage basically consists in (i) first applying a given semi-elliptical vertical displacement profile at the upper half of the tunnel boundary, immediately at the back of the shield tail, and (ii) then releasing this forced displacement profile when the permanent lining is erected (Rampello et al. 2012). The maximum displacement that had to be applied at the tunnel crown to attain the maximum volume loss ($V_L = 0.5\%$) prescribed in design was found by trial and error.

The *green-field* settlements computed by the FE analyses at section *GF1* (+23 m a.s.l.) for $V_L = 0.5\%$ were in a good agreement with those provided by the empirical relationships using a width parameter $K = 0.45$ at ground surface, providing a settlement $w \cong 2$ mm at the abscissa corresponding to the edge of *Pilone Colosseo*, the closest to the tunnel.

Figure 4c shows the tunnel face advancements for which the results of the 3D FE analyses were extracted, each corresponding to the position of the bearing piers of the Basilica. In Figure 4d the settlement profiles computed at the foundation level of each pier are compared with the green field evaluation. Maximum settlements of 4.8 mm, 3.5 mm and 2 mm are computed for the *Pilone*

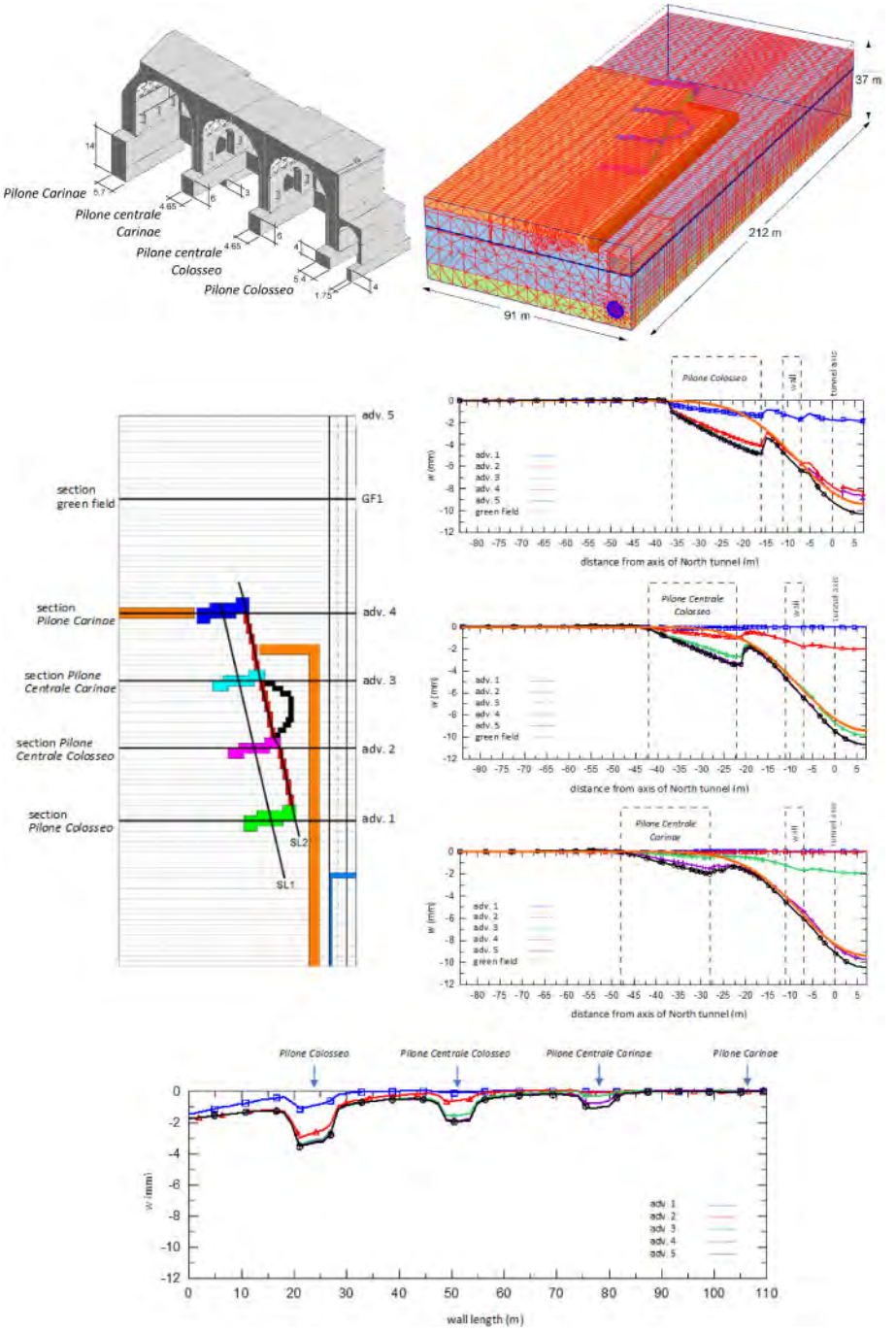

Figure 4. *Basilica di Massenzio*: (a) foundations geometry; (b) 3D numerical model; (c) plan view of the model with tunnel advancements; (d) settlement profiles with tunnel advancement for the bearing piers; (e) settlement profiles with tunnel advancement along *SL2* section.

Colosseo, *Pilone Centrale Colosseo* and *Pilone Centrale Carinae*, while nearly zero settlements, not shown in the figure for sake of space, are computed for *Pilone Carinae*, characterised by the deepest foundation. Along section *SL2*, along the wall facing *via dei Fori Imperiali*, a maximum differential settlement of about 4 mm was evaluated (Figure 4e).

It is seen that, when simulating the *Basilica di Massenzio*, the interaction analyses provide substantially larger settlements (Figure 4d), this contradicting the common belief that *green-field* analyses are more conservative than the interaction analyses. The reason for this unusual behaviour, unique among the studies carried out for Contracts T2 and T3 of Line C, can be attributed to the structural features of the Basilica. This monument is indeed characterised by an extremely small value of the ratio of the area of the bearing structural members to the total covered area: about 12%, compared to 23% of the Pantheon and 26% of S. Peter's Basilica; this is likely to be responsible for its high structural vulnerability and the many collapses experienced in the past.

Because of the significant weight of the structure, the foundation soil experienced high deviatoric stresses undergoing a reduction of the tangent stiffness. Reduction in the shear modulus is actually reproduced by the constitutive model adopted in the numerical analyses, which accounts for the dependency of soil stiffness on strain level, so that even the relatively small changes of the stress state induced at the foundation level by tunnelling produce appreciable settlements due to the reduced tangent stiffness.

Although the Burland and Wroth (1974) interaction diagrams provided negligible (class 0) damage to the Basilica, a *Level 2* structural analysis was also carried out, due to the unvaluable value of the monument, applying the displacement field computed by the geotechnical analyses to a detailed structural model of the Basilica, whose structural members were assimilated either to linear elastic or to nonlinear materials.

4.2 *Structural analyses*

In the 3D FE numerical model of the Basilica nine materials were distinguished on the basis of the in situ investigation carried out by Metro C, consisting in both mechanical tests on samples retrieved from the masonry and non-destructive tests (single and double flat jack, sonic or ultrasonic measurements). In the linear-elastic model of the Basilica, frictional interfaces were introduced at the contact between the vaults and the bearing walls, as well as at the key of the barrel vaults, in order to reproduce the most important existing cracks. In the nonlinear model (model *concrete* in ADINA) values of tensile strength in the range $\sigma_t = 0.2$–2.0 MPa were defined for the Basilica materials and the crack opening was attained in the analyses for tensile stresses higher than σ_t. The computed field of crack opening resulted consistent with the one observed, though providing slightly lower width of the cracks.

In both models, an elastic layer of foundation soil, 1 m thick, was introduced at the base of the structural model to better reproduce the stress state induced by the Basilica self-weight, as evaluated by the aforementioned tests. The elastic modulus of this layer was calibrated to reproduce the best agreement between the computed and the measured stress state.

Both the linear elastic and the nonlinear models provided very similar results so that only those computed by the second one are discussed in the following.

Figure 5a–b shows the contours of the maximum tensile strain computed in the Basilica after tunnels excavation: the most critical conditions occur for the apse, at the junction with the recent reinforced concrete dome. It is worth noting that the state of strain in the structure is mainly due to its self-weight, being only slightly modified by the tunnelling-induced displacements applied at the base of the model. In fact, the maximum tensile strain in the structure, that is equal to about $3 \cdot 10^{-4}$ before tunnels excavation, is hardly affected by tunnelling. According to the limiting tensile strain assumed in this study, the Basilica remains in a state of negligible damage after tunnelling (class 0: $\varepsilon_{lim} < 4 \cdot 10^{-4}$).

However, the historical studies and the observation of the current condition of the monument, supported by the results of the numerical analyses, suggested the opportunity of setting up some structural safeguarding interventions, consisting of tie rods, to reduce the thrusts of the large barrel

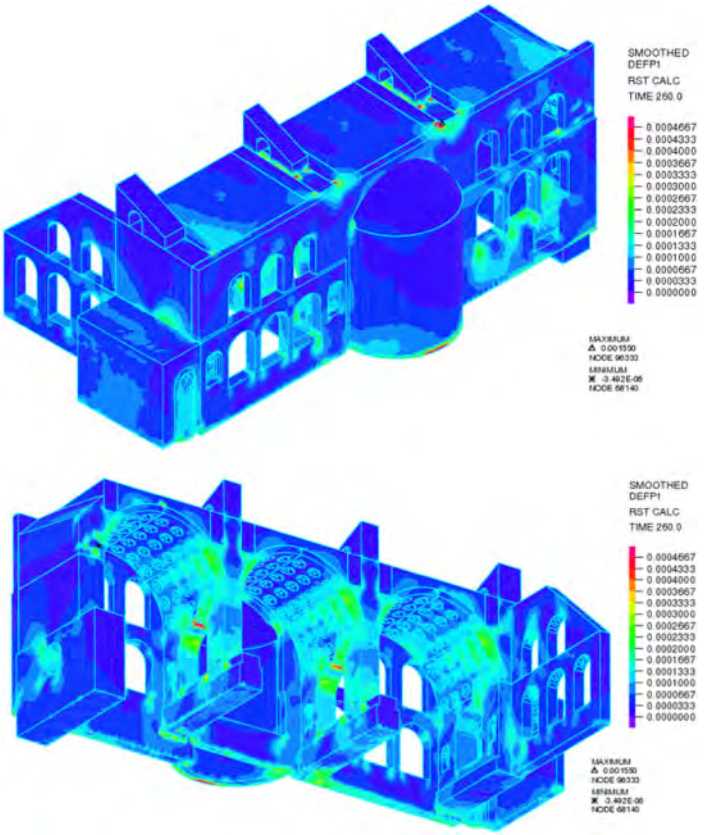

Figure 5. Contours of maximum tensile strains computed by the nonlinear model: (a) top view from *via dei Fori Imperiali*; (b) bottom view from *via Sacra.*

vaults. Also, the interaction analyses suggested the opportunity of adopting localised structural safeguarding interventions in the wall with the three-light windows facing *via dei Fori Imperiali* and at the connection between the apse and the Basilica.

4.3 *Structural interventions*

Before tunnelling Metro C implemented temporary and definitive safeguarding interventions to reduce the thrusts of the barrel vaults under the permanent loads, the cracks opening in the bearing walls and around the three-light windows, and to link the apse to the wall of the Basilica facing *via dei Fori Imperiali*.

The main definitive structural interventions consist of reinforcements with a couple of steel wire ropes of diameter $\phi = 28$ mm installed around the apse at two different elevations, 45 m and 39 m a.s.l., and preloaded to 117 kN and 235 kN, respectively (Figure 6a).

Longitudinal and transversal chains were also installed at 39 m and 26 m a.s.l.. The longitudinal chains consist of three couples of steel bars of diameter $\phi = 40$ mm installed in the perimeter walls of the Basilica and connected to the intermediate transversal walls through steel plates, 30 mm thick (Figure 6b). The transversal and longitudinal lower chains have been pre-loaded to 100 kN, while the longitudinal and transversal upper chains have been pre-loaded to 530 kN and 400 kN, respectively. This preloading was necessary to recover part of the deformation of the structure due

to the distancing of the walls of the end vaults, exceeding the minimum value necessary to absorb the vault thrusts, equal to 250 kN.

On both sides of all bars to be pre-loaded, a total of 52 load cells were installed to control the forces transmitted to the bearing walls of the Basilica during the stringing activities and tunnels excavation. The stringing activities were divided into two stages, applying 50% of the design loading for each of them.

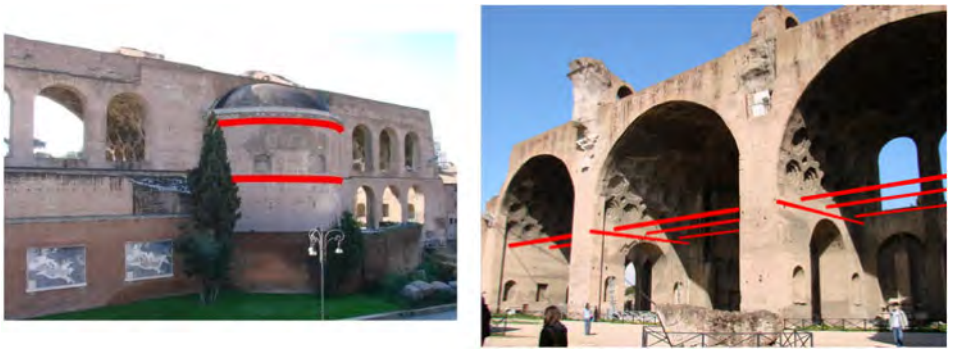

Figure 6. Structural interventions on the Basilica.

At the end of the first loading stage the monitored loads were checked to be consistent with the design assumptions, since thermal variations could induce changes as high as about 30% of the desired preloading. Each preloading stage was also divided in sub-steps in order to apply the loading as homogeneously as possible (Figure 7).

It is worth noting that the transversal section of the vault increases in thickness from about 2 m on the side facing *via dei Fori Imperiali* to about 3 m moving towards *via Sacra*. The preloaded chains reduce the tensile stresses by about 35%, these latter tending to zero where the section attains its maximum thickness. The presence of the chains also improves the behaviour of the structure as a whole thanks to the higher degree of connection between the barrel vaults and the transverse walls, connected to each other at the head.

Finally, steel temporary supports were also installed to mitigate the effects induced by the vibrations produced by the excavation activities. These consist of tube-joint structures and tower buttresses. Specifically, the support of the North-West corner of the Basilica was realised using a steel tube-joint structure, while the support of the apse was obtained via a mixed system consisting in buttresses made of steel tube-joint structures and multiprop towers. Local protections of the large openings in the bearing wall facing *via dei Fori Imperiali*, about 6 m wide and 9 m high, consist instead in metal and wooden structures (Figure 8).

4.4 *Computed and observed displacement fields*

Figure 9 shows the monitoring sections (MOR01-MOR06) set up in the area of the *Basilica di Massenzio*. These were instrumented with settlement markers installed at ground surface, inclinometer and Trivec casings, the first providing horizontal displacements only, while the second measuring the three orthogonal components Δx, Δy and Δz of the displacement vectors along the vertical measuring line, with a depth spacing of 0.5 m. In the following, reference is made to ground settlements measured by precision levelling only. The displacement markers incorporate sockets into which a removable survey plug can be screwed with good positional repeatability for manual surveying. Precise levelling was performed using a digital level which can detect the height of the plane of collimation on a suitable bar-coded staff to a resolution of 0.01 mm. Monitoring of the settlement of the bearing walls of the Basilica during tunnels excavation was performed via precision levelling on displacement markers installed at about 0.5 m height from ground surface.

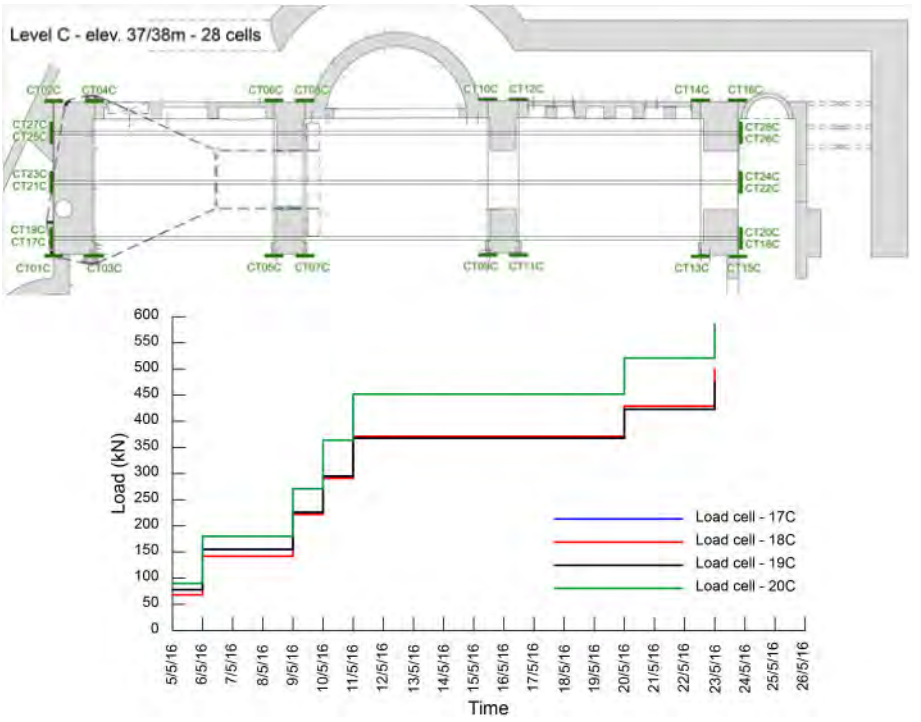

Figure 7. Plan view of the installed load cells and loading steps in the upper and inner chain (level C).

Figure 8. Temporary structural interventions installed on the Basilica.

The ground settlements measured in sections MOR01-MOR05, when the tunnel face was at a sufficient distance from the sections to assume plane strain conditions, were very small, never exceeding 3 mm. For all the sections, it was not possible to fit the observed settlement profiles with a Gaussian curve and the volume loss calculated integrating the measurements was never higher than about 0.1–0.15%. Figure 10 shows the settlements measured at section MOR04 after the excavation of both the tunnels, together with the settlement trough computed for values of volume loss $V_L = 0.15\%$ and $V_L = 0.5\%$, where the latter is the maximum threshold value allowed by design prescriptions.

The settlements of *Pilone Colosseo* and *Pilone centrale Colosseo* (alignments 1 and 2 in Figure 11a) are plotted versus time in Figure 11 b–c: they are in the range of ±2 mm, appearing hardly

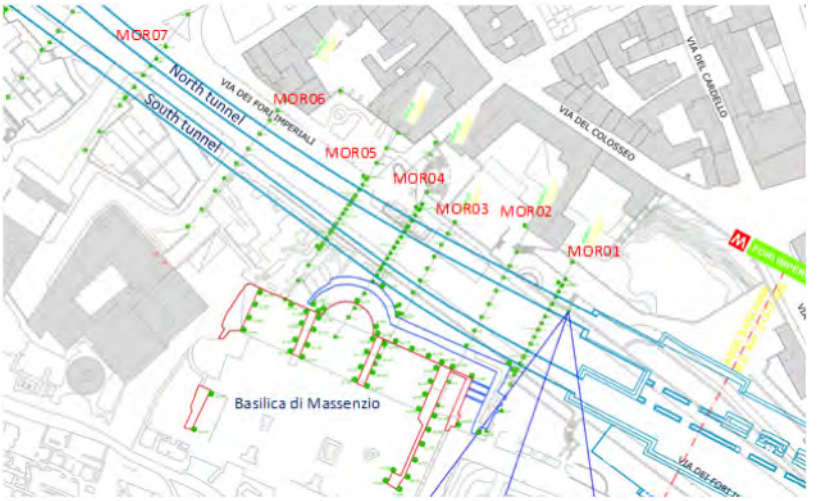

Figure 9. Plan view of the instrumented sections.

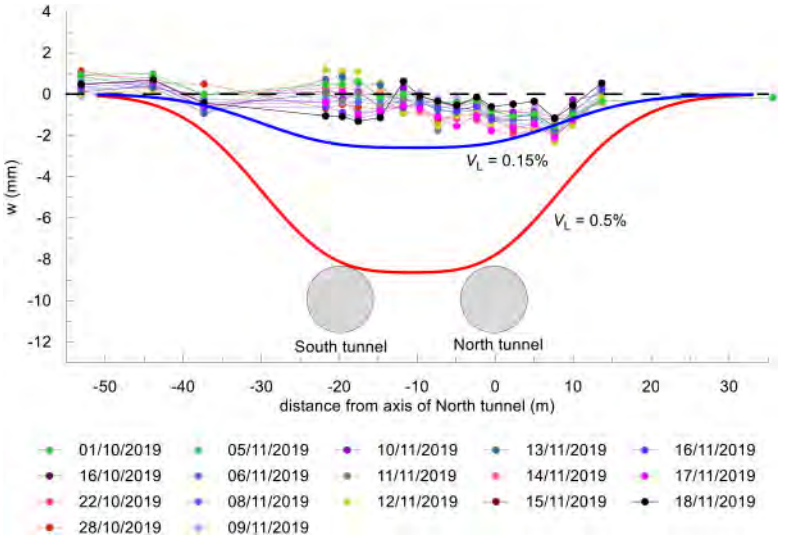

Figure 10. Measured settlements at section MOR04.

affected by tunneling, though the change from heave to subsidence is seen to occur when the face of the south tunnel, the closest to the Basilica, arrives at the alignment locations (red line in Figure 11b, c).

Figures 11 d–e show the settlement profiles measured for the two bearing walls mentioned above, together with the upper bound settlements computed assuming the threshold volume loss $V_L = 0.5\%$: isochrones of settlement do not shows any appreciable deflection confirming the substantially nihil effects of tunnels excavation on the Basilica.

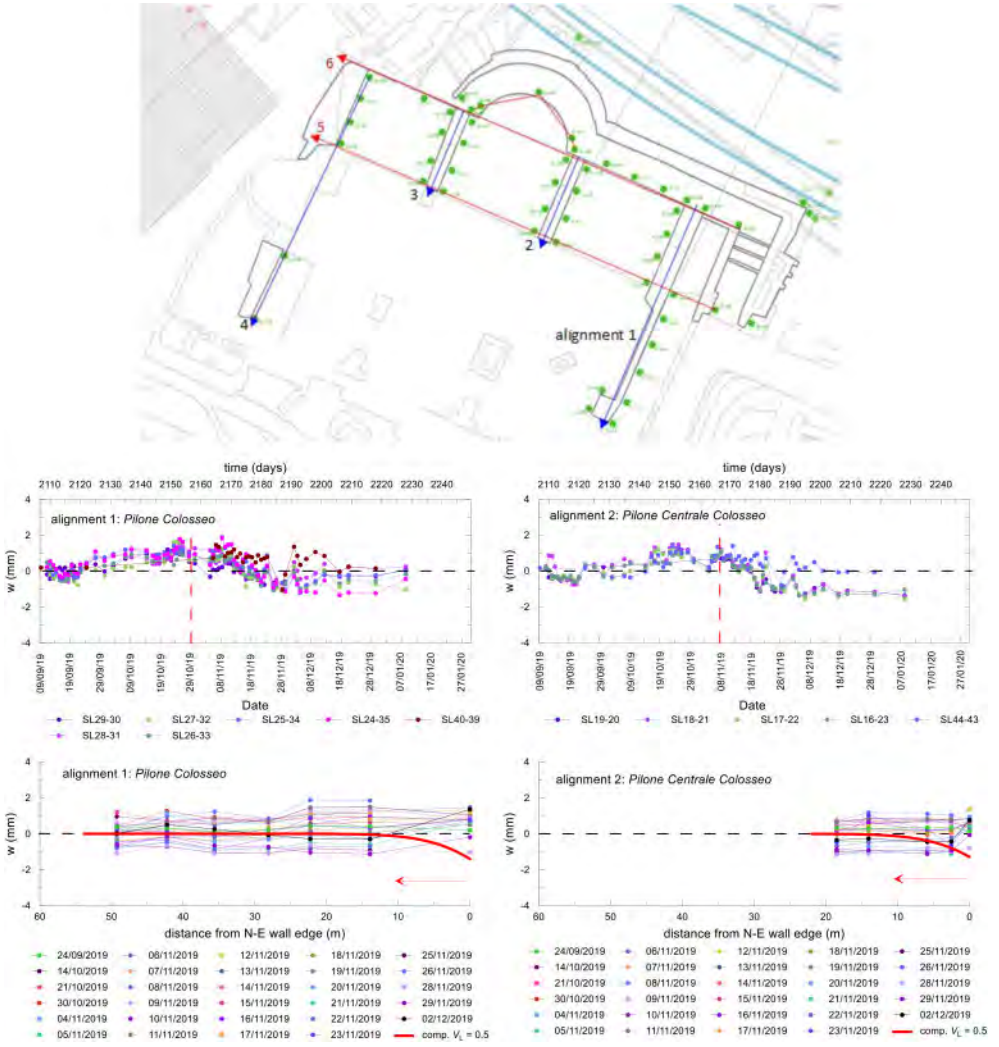

Figure 11. Monitored time histories and isochrones of monitored settlements.

5 CONCLUSIONS

The *Basilica di Massenzio* is an interesting example to illustrate the approach that was adopted in the line-monument interaction studies performed for the new line C of Rome underground. Unlike other monuments of Contract T3, the Basilica is a very heavy structure transmitting significant contact stresses to the foundation soil through its bearing walls. This resulted in an unexpected behaviour in that the settlements computed by the numerical interaction analyses were larger than the ones computed by the empirical relationships, contradicting the common belief that *green-field* analyses are more conservative than soil-structure interaction analysis.

Different positions of the tunnels layout were considered in the design of Line C to arrive at a solution that would minimize tunnelling effects on the Basilica, these concerning the depth of the tunnel, as well as their distance from the Basilica. For the solution finally adopted in the construction of Line C, both the *green-field* and the FE interaction analyses confirmed very

negligible tunnelling-induced effects, so that no protective intervention was strictly necessary. Nevertheless, the high vulnerability of the monument suggested the opportunity of implementing some safeguarding interventions to reduce or contain the openings of pre-existing cracks induced by the Basilica self-weight, thus gaining some increase in the safety of the structure.

Tunneling was performed well within the design prescriptions, but it should be mentioned that a loss of control of the face support pressure of the South tunnel resulted in a high volume loss $V_L = 0.8\%$ at section MOR7, a few hundred meters after the Basilica, this suggesting that caution is never too much when a monument of inestimable historical value is involved.

REFERENCES

Boscardin, M.D. & Cording, E.J. 1989. Building response to excavation-induced settlement. *Journal of Geotechnical Engineering*, ASCE, **65**(1): 1–21

Brinkgreve, R.B.J., Engin, E. & Swolfs, W.M. 2013. *Plaxis 3D user manual*. Plaxis BV. Delft, The Netherlands.

Burghignoli, A., Callisto, L., Rampello, S., Soccodato, F.M. & Viggiani, G.M.B. 2013. The crossing of the historical centre of Rome by the new underground Line C: a study of soil structure-interaction for historical buildings. In *Geotechnics and Heritage: Case Histories*: 97–136. London: CRC Press

Burland, J.B. & Wroth, C.P. 1974. Settlement of buildings and associated damage. *Proc. Conf. on Settlement of Structures*, Cambridge, UK: 611–654

Burland, J.B. 1995. Assessment of risk of damage to buildings due to tunnelling and excavation. *Proc. 1st Int. Conf. on Earthquake Geotechnical Engineering*, Tokyo: 1189–1201

CISTeC 2001. *Rapporto sulle indagini geotecniche nell'area della Basilica di Massenzio*

Masini, L. & Rampello, S. 2021. Predicted and observed behaviour of pre-installed barriers for the mitigation of tunnelling effects. *Tunnelling and Underground Space Technology* **118**: 104200. doi.org/10.1016/j.tust.2021.104200

Masini, L., Rampello, S., Gaudio, D. & Romani E. 2021. Observed performance of a deep excavation in the historical centre of Rome. *Journal of Geotechnical and Geoenvironmental Engineering* **147**(2): 05020015. doi.org/10.1061/(ASCE) GT.1943-5606.0002465

O'Reilly, M.P. & New, B.M. 1982. Settlements above tunnels in the United Kingdom – Their magnitudes and prediction. *Proc. Tunnelling '82 Symposium*, London: 173–181

Peck, R. B. 1969. Deep excavation and tunnelling in soft ground. State-of-the-art-report, Mexico City, State of the Art Volume, *Proc. 7th Int. Conf. on Soil Mech and Found. Engng* (ICSMFE): 225–290

Rampello, S., Callisto, L., Viggiani, G.M.B. & Soccodato, F.M. 2012. Evaluating the effects of tunnelling on historical buildings: the example of a new subway in Rome. *Geomechanics and tunnelling* **5**(3): 275–299

Rampello, S., Fantera, L., & Masini, L. 2019. Efficiency of embedded barriers to mitigate tunnelling effects. *Tunnelling and Underground Space Technology* **89**: 109–124. doi.org/10.1016/j.tust.2019.03.027

Soccodato, F.M., Callisto, L., Rampello, S. & Viggiani, G.M.B. 2013. Evaluating the effects of tunnel construction on monuments: The example of the Basilica di Massenzio in Rome. In *Geotechnical Engineering for the Preservation of Monuments and Historic Sites*, 2nd TC301 IS-Napoli: 675–682. London: CRC Press

SESSION 5: Preservation of diffused heritage

Taylor & Francis
Taylor & Francis Group
http://taylorandfrancis.com

Geotechnical Engineering for the Preservation of Monuments and Historic Sites III – Lancellotta, Viggiani, Flora, de Silva & Mele (Eds)

Application of Ultrasonic Computed Tomography (UCT) technology to detect defects in stone

Zhe Li, Junjie Wang & Kefei Li
Department of Civil Engineering, Tsinghua University, Beijing, P.R. China

Peng Zhao & Fei Qi
Department of Ancient Architecture, The Palace Museum, Beijing, P.R. China

ABSTRACT: It is widely acknowledged that Ultrasonic Computed Tomography (UCT) technology may provide a considerable monitoring approach while describing the inner defects, which cannot be observed by naked eyes. And also, the UCT technology can be adopted to detect defects in stones belonging to ancient building or archaeological sites. This paper aims to introduce the work which is concerned with the UCT technology to evaluate the defects inside stone. The result shows that UCT technique is a compromising app roach to trace and detect the damage level inside stone, especially for the weathering defects from surface.

Keywords: ultrasound, CT, stone, frequency, defects

1 INTRODUCTION

As a kind of common material, stone had been widely used since ancient China, such as sculpture, tomb, and also constructions, which has several advantages of high hardness, easy to get, elegant appearance et al. However, cracks inside stone triggered by internal or external impact factors such as air-slake, loading, may cause degradation of mechanical properties and even be unfavourable to safety, hence, it seems to be critical to evaluate the fracture or cracks inside stone materials.

Recently, many studies have reported their latest researches about ultrasonic computed tomography (UCT) technologies against cracks inside non-metallic material. Ham et al. (Ham & Popovics 2015) applicated contactless ultrasound toward automated inspection of concrete structures, both obtained surface wave velocity and attenuation signal characteristics show sensitivity to concrete material damage. Kim et al. (Kim et al. 2017) evaluated the drying shrinkage in concrete by nonlinear ultrasound (NLU), and the results show that large changes in the measured acoustic nonlinearity parameter are attributed to damage generated during drying shrinkage. Quiviger et al. (Quiviger et al. 2012) investigated the effect of the presence and size of a real macro-crack on diffuse ultrasound in concrete, which reveals the influence of the closed part of the cracks with regions in partial contacts on the diffusion parameters. Ahn et al. (Ahn et al. 2019) proposed a diffuse ultrasound to evaluate the distributed micro-cracking damage in concrete, which also highlighted the practical application of this method for concrete inspection in the field. Quiviger et al. (Quiviger et al. 2013) simulated the propagation of diffuse ultrasonic energy, which reveals the practice implications for non-destructive crack sizing and imaging in concrete. Adachi et al. (Adachi, Kondo, and Yamaji 2005) developed a nondestructive evaluation of micro-cracks in ceramic ferrules by resonant ultrasound spectroscopy (RUS). Hogg et al. (Hogg et al. 2018) proved that nonlinear resonant ultrasound is sensitive to the early presence of stress corrosion cracking (SCC) in stainless steel rods. Zhang et al. (Zhang et al. , 2018, 2019) used ultrasonic embedded piezoelectric transducers to monitor setting, hardening and cracking process of concrete under different curing conditions.

DOI 10.1201/9781003308867-83

Carrión et al. (Carrión et al. 2017) introduced a novel approach for concrete damage evaluation based on ultrasonic signals modality. Yu et al. (Yu et al. 2018) highlighted a kind of ultrasound wave excitation method to detect defects in different materials, which includes metals, metal alloys, and composites. Jia et al. (Jia et al. 2019) investigated the use of ultrasound-excited thermography to detect microcracks in concrete materials, which showed that the ultrasound-excited thermography can effectively detect the concrete cracks with widths of 0.01–0.09 mm. Merabet et al. (Merabet et al. 2020) detected fast ultrasound imaging of cracks by multi-mode plane wave imaging in the Fourier domain.

In spite of enormous researches on ultrasonic evaluation against cracks, there is still a gap to realize the reliable evaluation approach which can express and describe the internal damage directly and precisely. From physical point of view, ultrasonic technology is only suitable for detecting metallic material because of its high density, but not for non-metallic material. Hence, computerized tomography (CT) technology is widely applicated by transferring digital signals to image signals via comprehensive mathematic calculation (Naeimi et al. 2017), which may expand the application scope of ultrasonic device.

2 EXPERIMENTS

2.1 *Mechanism of CT calculation method*

Ultrasonic wave is a kind of elastic wave and its velocity is proportional to the elastic modulus of the medium, furthermore, damages or defects will cause attenuation of sound velocity, and the attenuation degree can be used to judge the damage degree and locations. Figure 1 shows the traditional mechanism of CT technology, which highlights the transmission paths of every single ultrasonic wave. Points 1, 2, 3 and 4 are the transmitting probes and 1', 2', 3', and 4' are the receiver probes, respectively. It can be clearly shown that the full cross section area is surrounded by a 4 × 4 grids, which could evaluate the damage level according to the wave velocity and duration time. With the assumption that the velocity of ultrasonic wave is v (x, y) and the duration time of each path ti can

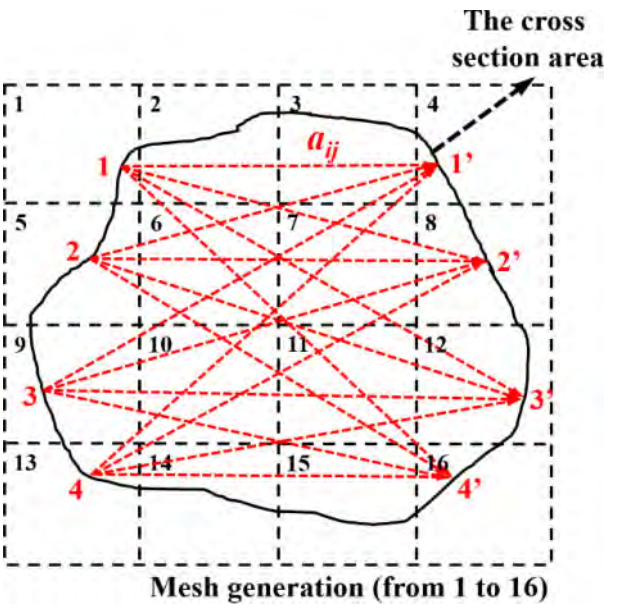

Figure 1. Mechanism of CT calculation method.

be presented as Eq.1. Figure 2 shows the schematic diagram of a series of tiny grids, meanwhile, the velocity of ultrasonic wave is v (x, y) can be considered as a constant value in this case. Thus, Eq.1 can be rewritten as Eq.2 and the calculation result of Eq.3 proposes the result of slowness, which can reflect the internal damage of concrete cross section. A three-dimensional diagram would be much helpful to evaluate the damage level according to the ultrasonic signals, meanwhile, the denser the mesh, the higher the detection accuracy. The calculation principle is reasonable according to what mentioned above, hence, the key point that matters is the transmission procedure of ultrasonic signals, which can be expressed as Eq.4.

$$t_i = \int_{R_i} \frac{1}{v\,(x,y)} ds\ (i = 1, 2, 3, \ldots, n) \tag{1}$$

Where n is the number of ultrasonic paths and R_i is the route of ith ultrasonic path.

$$t_i = \sum_{j=1}^{m} d_{ij}/v_i\,(x,y)\ \ (i = 1, 2, \ldots, n; j = 1, 2, \ldots, m) \tag{2}$$

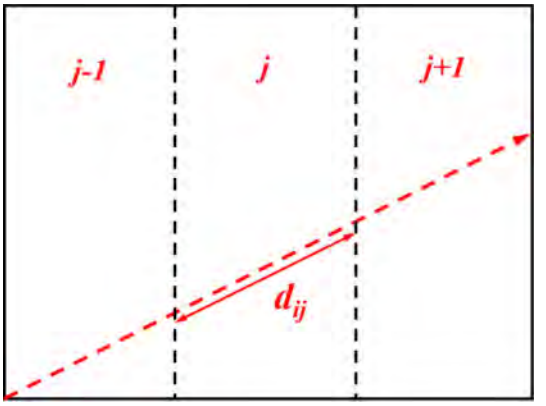

Figure 2. Schematic diagram of tiny grids.

Where ti is the duration time of ith path and dij is the the length of the ith through the jth grid, n is the number of paths and m is the number of grids.

$$\begin{pmatrix} a_{11} & a_{12} & a_{13} & a_{14} & \ldots & a_{1m} \\ a_{21} & a_{22} & a_{23} & a_{24} & \ldots & a_{2m} \\ a_{31} & a_{32} & a_{33} & a_{34} & \ldots & a_{3m} \\ a_{41} & a_{42} & a_{43} & a_{44} & \ldots & a_{4m} \\ \vdots & \vdots & \vdots & \vdots & \vdots & \vdots \\ a_{n1} & a_{n2} & a_{n3} & a_{n4} & \cdots & a_{nm} \end{pmatrix} \begin{pmatrix} S_1 \\ S_2 \\ S_3 \\ S_4 \\ \vdots \\ S_m \end{pmatrix} = \begin{pmatrix} t_1 \\ t_2 \\ t_3 \\ t_4 \\ \vdots \\ t_m \end{pmatrix} \tag{3}$$

Where S = 1/v, which is called the slowness of ultrasonic wave.

$$c = \lambda f \tag{4}$$

Where c is the wave velocity of ultrasound (m/s), λ is the wave length (mm) and f is the frequency of ultrasonic wave.

2.2 *Materials and software*

First of all, a piece of white marble was used as the detecting target (preserved from Ming dynasty, The Palace Museum), which can be clearly shown in Figure 3(a) that the stone was relatively well preserved, and also, whose length was in 600 mm approximately. A kind of camera scanning technique was used to establish a three-dimensional model so that all the local parameters were obtained via this approach, which was shown as Figure 3(b). Furthermore, the software Geomagic Wrap/Control was adopted to collect all the coordinates from three cross-sections. Moreover, three sections (A, B, and C) were selected on the white marble specimen to evaluate the damages or defects level at different cross sections, as shown in Figure 4.

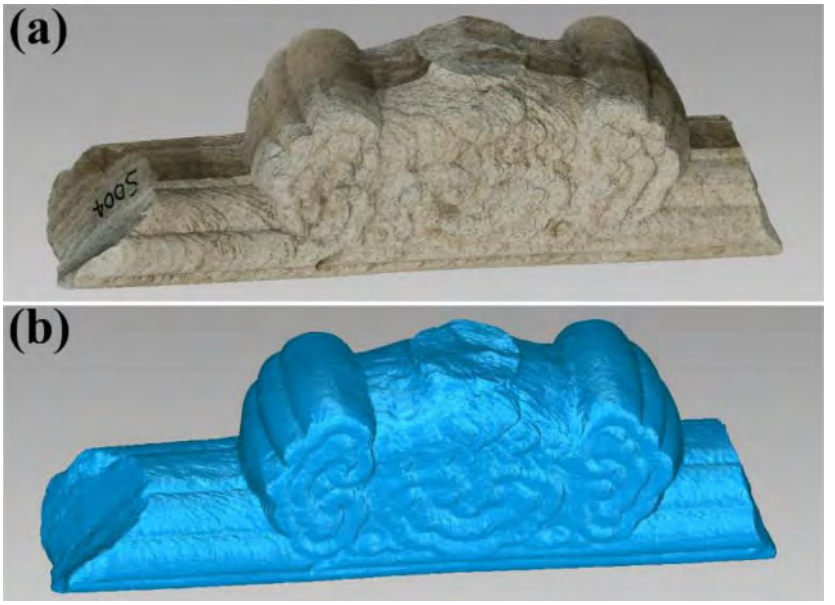

Figure 3. A piece of white marble from Ming Dynasty. (a) Diagram of real products (b) 3D model by camera scanning.

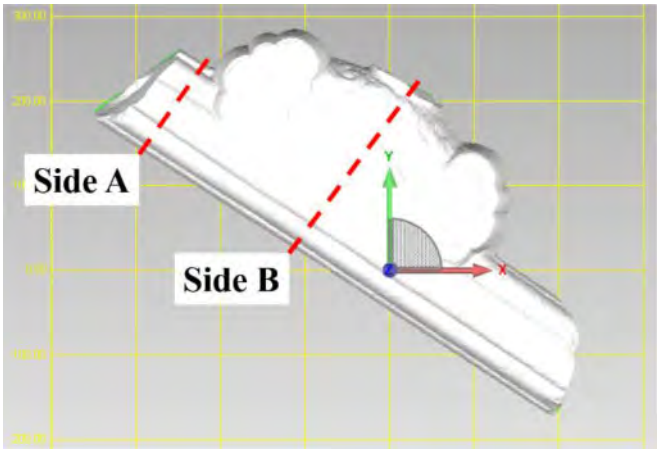

Figure 4. Two cross-sections collected from the stone.

2.3 *Ultrasonic detection apparatus*

The ultrasonic detection apparatus used in this experiment was type Proceq PL-200 (made in Switzerland, Figure 5) and a pair of ultrasonic probes with a frequency of 54 kHz, and its key parameters were shown in Table 1. As reported among articles worldwide, 54 kHz is more suitable for detecting internal defects of non-metallic materials, and also, the needle-nosed probes do not require coupling media.

Figure 5. Type Proceq PL-200 ultrasonic apparatus.

Table 1. Key parameters of ultrasonic apparatus (Type Proceq PL-200).

Type	Frequency	Bandwidth	Driving voltage	Piezo electrical cell capacity	Operating temperature	Contact surface diameter	Dimensions	Weight
Single-crystal	54 ± 5 kHz	<10 kHz	From −1000 V to 1000 V	2 nF	From −20° to 60°	4 mm	49.7 mm × 99.43 mm	244 g

3 RESULTS AND DISCUSSION

Figure 6 shows the distribution of ultrasonic paths from 16 grids calculated by the software Auto-CAD and every single ultrasonic transmission distance was noted in Figure 6. It is worth mentioning that the software Matlab was used to calculate the results of Eq.3 and convex optimization functions were used to optimize and also improve the accuracy and reliability of results as Eq.5, while the boundary conditions were set as $1/5000 \leq x \leq 1/500$, with reference with the ultrasonic pulse velocity corresponding to different weathering degrees. The slowness of 16 grids were collected

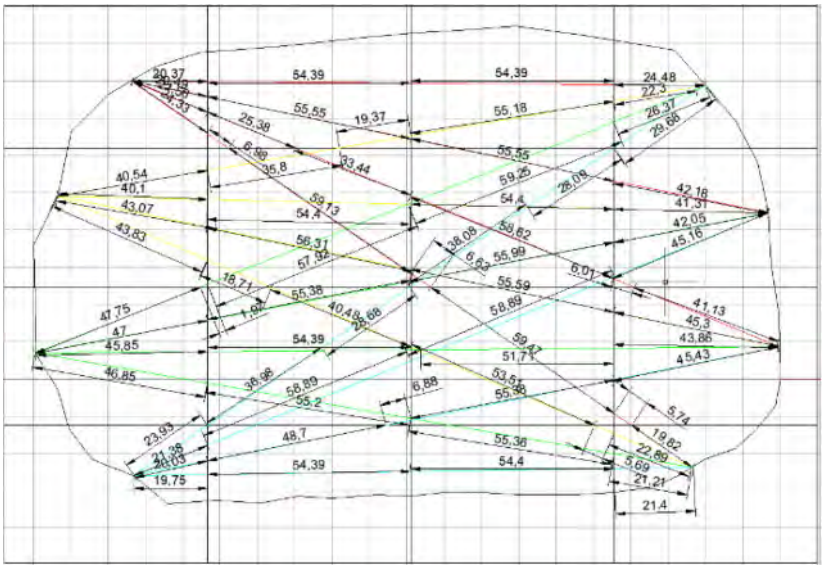

Figure 6. The distribution of ultrasonic paths from 16 grids (Side A).

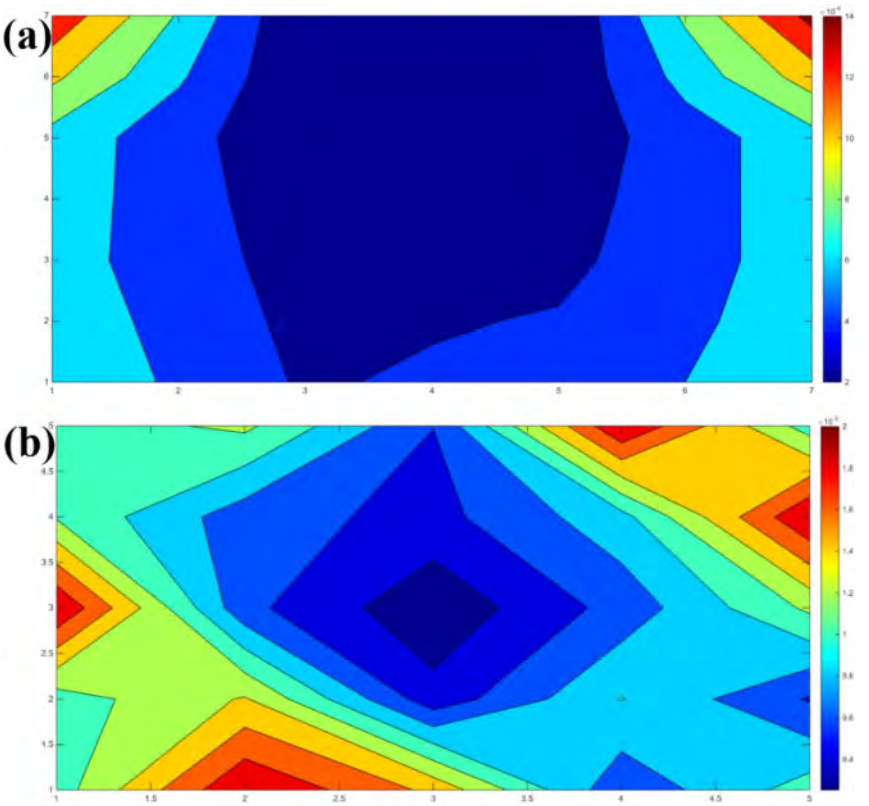

Figure 7. Slowness color map of cross-sections. (a) Side A (b) Side B.

and figured out by software Matlab and Figure 7 presents the ultrasonic CT results of cross-sections A and B, which can be clearly shown that the color maps present the slowness contribution at the cross-sections. It can be clearly observed that the slowness of several areas at the edge of cross-sections is higher, which is mainly due to the high damage of ultrasonic pulse velocity triggered by high weathering degree. Conversely, the internal slowness is relatively high, which indicates that the interior is less weathered and will preserved.

$$\lim_{x>0} |Ax - b| = 0 \tag{5}$$

Even through the regional damages can be clearly observed from the automatically produced color map, however, internal defects are relatively tough to be detected from ultrasonic CT technology. This is because the ultrasonic wave has been critically attenuated after entering the stone material due to the surface weathering, which is not conducive to further detecting the internal cracks. From the view of ultrasonic mechanism, further parameters, such as amplitude and phase, are needed to determine the internal cracks. And also, it is worth mentioning that mesh division and ultrasonic probe arrangement will influence the CT imaging results, and the improved arrangement will further improve the detection accuracy.

4 CONCLUSIONS

Based on the results from theoretical calculation and practical experimental in this experiment, the conclusions can be drawn as follows:

1. Ultrasonic method is a relatively reliable method while detecting the defect inside cross-section of stone, and also, computerized tomography is a relative useful method when evaluate the damage level of a cross-section.
2. Ultrasonic CT technique is sensitive to the degree of surface weathering of stone, but not to the evaluation of internal cracks due to lack of key parameters of amplitude and phase.
3. The accuracy of ultrasonic CT technique will be enhanced when mesh division and ultrasonic probe arrangement can be further improved.

5 CONFLICTS OF INTERESTS

The authors declare that they have no known competing financial interests or personal relationships that could have appeared to influence the work reported in this paper.

ACKNOWLEDGEMENT

This work is a part of a series of projects financially supported by the Chinese National Key Research and Development Program Grant No. 2020YFC1522403. And also, China Ordnance Industry Survey and Geotechnical Institute Co, LTD is greatly appreciated by the authors for providing 3D photogrammetry technique for this experiment.

REFERENCES

Adachi, T., Y. Kondo, and A. Yamaji. 2005. 'Nondestructive evaluation of micro-cracks in a ceramic ferrule by resonant ultrasound spectroscopy', *NDT&E International*, 38: 548–53.

Ahn, Eunjong, Myoungsu Shin, John S. Popovics, and Richard L. Weaverc. 2019. 'Effectiveness of diffuse ultrasound for evaluation of micro-cracking damage in concrete', *Cement and Concrete Research*, 124: 105862.

Carrión, A., V. Genovés, J. Gosálbez, R. Miralles, and J. Payá. 2017. 'Ultrasonic signal modality: A novel approach for concrete damage evaluation', *Cement and Concrete Research*, 101: 25–32.

Ham, Suyun, and John S. Popovics. 2015. 'Application of contactless ultrasound toward automated inspection of concrete structures', *Automation in Construction*, 58: 155–64.

Hogg, Stephen M., Brian E. Anderson, Pierre-Yves Le Bas, and Marcel C. Remillieux. 2018. 'Nonlinear resonant ultrasound spectroscopy of stress corrosion cracking in stainless steel rods', *NDT&E International*, 102: 194–98.

Jia, Yu, Lei Tang, Pan Ming, and Yang Xie. 2019. 'Ultrasound-excited thermography for detecting microcracks in concrete materials', *NDT&E International*, 101: 62–71.

Kim, Gun, Jin-Yeon Kim, Kimberly E. Kurtis, and Laurence J. Jacobs. 2017. 'Drying shrinkage in concrete assessed by nonlinear ultrasound', *Cement and Concrete Research*, 92: 16–20.

Merabet, L., S. Robert, and C. Prada. 2020. 'The multi-mode plane wave imaging in the Fourier domain: Theory and applications to fast ultrasound imaging of cracks', *NDT&E International*, 110: 102171.

Naeimi, Meysam, Zili Li, Zhiwei Qian, Yu Zhou, Jun Wu, Roumen H. Petrov, Jilt Sietsma, and Rolf Dollevoet. 2017. 'Reconstruction of the rolling contact fatigue cracks in rails using X-ray computed tomography', *NDT&E International*, 92: 199–212.

Quiviger, A., A. Girard, C. Payan, J.F. Chaix, V. Garnier, and J. Salin. 2013. 'Influence of the depth and morphology of real cracks on diffuse ultrasound in concrete: A simulation study', *NDT&E International*, 60: 11–16.

Quiviger, A., C. Payan, J. F. Chaix, V. Garnier, and J. Salin. 2012. 'Effect of the presence and size of a real macro-crack on diffuse ultrasound in concrete', *NDT&E International*, 45: 128–32.

Yu, Qiuye, Omar Obeidat, and Xiaoyan Han. 2018. 'Ultrasound wave excitation in thermal NDE for defect detection', *NDT&E International*, 100: 153–65.

Zhang, Shunquan, Wei Ma, Yuanliang Xiong, Jinya Ma, Chun Chen, Yamei Zhang, and Zongjin Li. 2019. 'Ultrasonic monitoring of crack propagation of notched concretes using embedded piezo-electric transducers', *Journal of Advanced Concrete Technology*, 17: 449–61.

Zhang, Shunquan, Yamei Zhang, and Zongjin Li. 2018. 'Ultrasonic monitoring of setting and hardening of slag blended cement under different curing temperatures by using embedded piezoelectric transducers', *Construction and Building Materials*, 159: 553–60.

Geotechnical Engineering for the Preservation of Monuments and Historic Sites III – Lancellotta, Viggiani, Flora, de Silva & Mele (Eds)

Flood vulnerability and damage assessment of earthen architectural heritage of the Iberian Peninsula

F. Trizio, F.J. Torrijo Echarri, C. Mileto & F. Vegas López-Manzanares
Research Centre PEGASO, Universitat Politècnica de València, Valencia, Spain

ABSTRACT: Earthen architecture is a building tradition that is part of the vast and varied cultural heritage of the Iberian Peninsula (Spain-Portugal). Historically, floods have posed a threat to this cultural heritage. Floods have often led to the loss of traditional monuments and buildings, as well as entire settlements. At present, climate change has increased the frequency and intensity of flood events, raising the risk of disappearance of built earthen architectural heritage. The effects of floods on these constructions are mostly manifested as damage to the superstructures. However, visible structural damage is often related to geotechnical problems triggered by flooding. Generally, earthen architecture is considered very vulnerable to the action of water due to the hygroscopic nature of the materials that constitute it. Nevertheless, many of these buildings have come to the present day, resisting the action of water, thanks to a process of adaptation and improvement carried out by humanity over the centuries. Against this background, the present study aims to analyze the impact of floods on earthen architectural heritage, through the development of a qualitative methodology to assess flood vulnerability of earthen structures. Through case studies in the Iberian Peninsula, visible damage to earthen constructions related to the superstructure-soil interaction and triggered by floods is analyzed, in order to highlight the vulnerabilities and resilience resources of this cultural heritage. Finally, strategies for flood risk mitigation and conservation criteria for earthen architectural heritage are proposed.

1 INTRODUCTION

Historically, in the Iberian Peninsula earthen architecture has characteristically been widely used and developed. Over time, in the different areas of the peninsula, several typologies of earthen architecture related to the constructive tradition and materials of place have been developed. In recent years, detailed studies and atlases on monumental and vernacular earthen architecture have been carried out (García Soriano 2015; Gómez-Patrocinio et al. 2020; Maldonado Ramos & Vela Cossío 2002; Vegas et al. 2011). In addition, several authors have researched and proposed intervention strategies and techniques for the conservation of earthen architecture (Keefe 2005; Mileto & Vegas 2017; Villacampa Crespo 2018; Warren 1999). Currently, renewed attention has been paid to the concepts of vulnerability and risk prevention in damage analysis and conservation of historic buildings (Canivell et al. 2020; Figueiredo et al. 2021; P. Ortiz et al. 2014). In order to predict the vulnerability of architectural heritage, risk maps have become a strategic and widely used tool (Camarasa-Belmonte & Soriano-García 2012; Sperotto et al. 2015; Wang 2015). Vulnerability assessment model can be based on a small number on parameters, which allow calculating a vulnerability index (Birkmann et al. 2013; Macías-Bernal et al. 2014; R. Ortiz & Ortiz 2016). Moreover, the methodology for the assessment may use unweighted parameters (D'Ayala et al. 2020; Stephenson & D'Ayala 2014), as well as weighted parameters, through the implementation of appropriate coefficients (Ortiz et al. 2014).

As a natural risk, flooding constitutes a threat to architectural heritage and can lead to further damage such as structural collapse (Drdácký 2010; Solín 2012). Due to climate change, the risk

DOI 10.1201/9781003308867-84

of flooding has considerably increased, causing the alternation of extremely dry periods and heavy rains in various areas of the Iberian Peninsula (Eguibar et al. 2021; Lastrada et al. 2020). Moreover, floods can cause direct and indirect damage (Kelman & Spence 2004) specifically related to geotechnical problems (Herle et al. 2010). For its hygroscopic nature, earthen architecture is generally considered highly exposed to water damage, and its resistance to water has been widely researched in the last thirty years (Beckett et al. 2020). The presence of water and damp can lead to the deterioration of its constituent material, causing a loss of hydromechanical resistance (Beckett et al. 2018; Gerard et al. 2015; Xu et al. 2018).

This paper focuses on the assessment of the vulnerability of earthen architecture to floods through a vulnerability qualitative methodology formulated in terms of indirect variables, applied to the case study of the historic town centre of Alzira (Valencia) located in the River Júcar valley, and to the case study of Torres de Berellen (Zaragoza) in the River Ebro valley. Through the cases studies, visible damage related to the superstructure-soil interaction is analysed, aiming to understand the behaviour of earthen structures during floods.

2 TERRITORIAL CONTEXT

The Iberian Peninsula, with an approximate surface area of 582,000 km^2, presents particular and heterogeneous territorial morphology, topography, and climate, which have contributed to developing the peculiar forms of its traditional architecture. This heterogeneous and huge territory is characterized by five mountain ranges which have originated the main river valleys (Ebro, Duero, Tajo Guadiana y Guadalquivir). In addition, the Peninsula climate and morphology is particularly influenced by its geographical location, between the Atlantic Ocean, the Sahara Desert and the Mediterranean Sea. This causes the climate of the peninsula to vary between regions. The phenomenon of floods is closely related to climate variation and extreme rainfall events that occur in some regions. In fact, the peninsular territory can be divided into three big basins (Cantabrian Basin, Mediterranean Basin and Atlantic Basin), which present a different flood hazard according to their geographical position and geomorphological characteristics (Figure 1).

This paper analyses two case studies in two areas of high flood hazard: Torres de Berellen in the Ebro basin and Alzira in the Júcar valley (Ribera Alta), which is one of the basins of the Mediterranean region. The Ebro River, in its lower middle course, presents long and slow floods with voluminous avenues, which can exceed average flows of 3000 m^3/s, due to prolonged rainfall or snow melting, causing floods that can cover entire villages. The Júcar River basin has a wide floodplain (300 km^2), with a convex geometric conformation and a great anthropic occupation, which has reduced the soil horizons and the vegetation cover. This set of factors causes the flow to suddenly concentrate and floods to occur (Camarasa Belmonte 2002).

The city of Alzira is located about 50 km from Valencia, in the south-east of the Iberian Peninsula. The historic town centre of Alzira was originally located on a river island, within a meander of the river Júcar, founded by the Moors of Al Andalus, who named the city Al-Yazirat Suquar or "Island of the Júcar" (Ribera 1887). From the 14^{th} century to the present, Alzira suffered many floods, with more than 80 documented in the chronicles of the city (Alberola Romá 2010; Trizio *et al.* 2021). In order to prevent and mitigate the flood risk, the territorial government has developed risk management strategies using mainly risk maps and following the European directive on flood risk (2007/60/EC). In fact, according to the PATRICOVA (Plan de Acción Territorial contra el riesgo de inundación en la Comunitat Valenciana, Generalitat Valenciana 2015) Alzira is classed as a floodable area of medium-high risk.

Although the urban area of Torres de Berellen is not in proximity to the riverbed, as Alzira (Figure 2), it has been classified as a town with high exposure to floods (Gobierno de Aragón 2019). The floods in Torres de Berellen are due to the funnel that the Ebro River finds when it arrives in the vicinity of the town. Therefore, without the possibility to modify the evacuation section, there is an increase in water velocity that leads to erosive problems (Gobierno de Aragón 2005).

Figure 1. Iberian Peninsula. Flood prone areas and basins.

Figure 2. Map of Torres de Berellen (left) and Alzira (right).

3 METHODOLOGY

This paper proposes a methodology for the assessment of flood vulnerability of earthen architectural heritage. In the preliminary phase of the research, relevant case studies for the analysis of earthen architecture susceptibility to floods have been found, overlapping the distribution maps of earthen architecture in the Iberian Peninsula (Database of SOS-Tierra Project https://sostierra.blogs.upv.es) with flood prone areas maps of the SNCZI (Sistema Nacional de Cartografía de Zonas Inundables)

and of the Agência Portuguesa do Ambiente. This overlapping operation has made it possible to obtain a general flood exposure map of earthen architectural heritage (Figure 3).

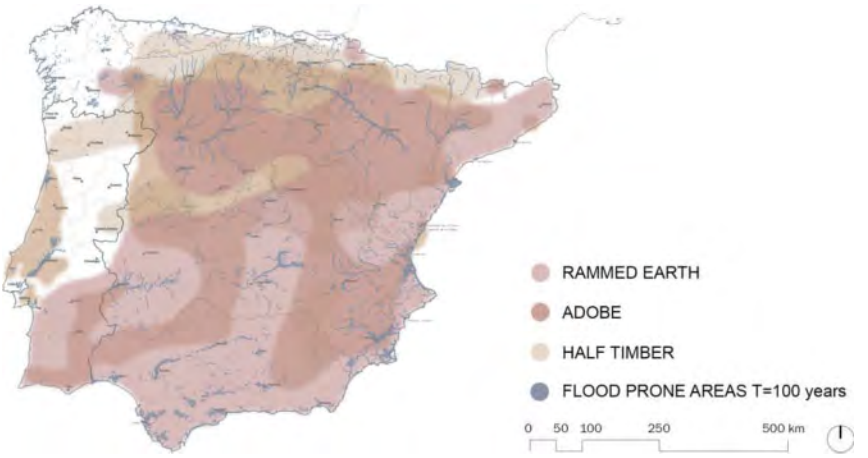

Figure 3. Exposure map of earthen architecture to floods.

After highlighting the areas of greatest exposure, flood municipalities of major interest have been located. Through fieldwork sessions in the selected case studies, buildings data have been collected, using technical analysis form, specifically designed to collect information on the most significant constructive and structural features for the vulnerability assessment (Figure 4).

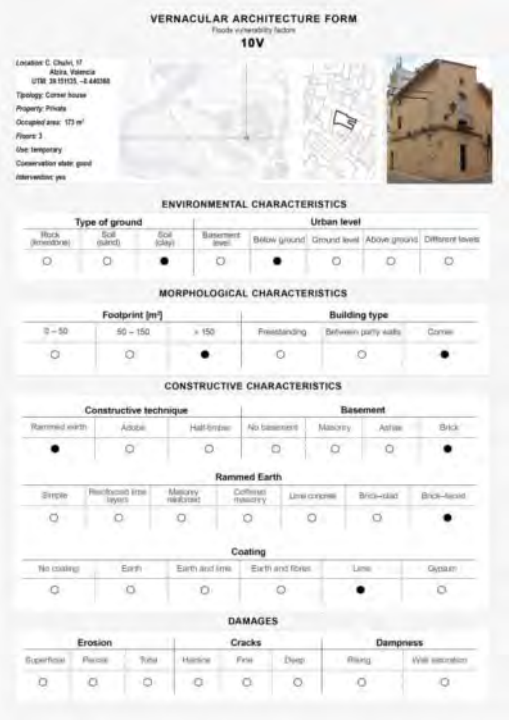

Figure 4. Earthen architecture characteristics form.

The methodology used for the assessment is based on the analysis of a small number of susceptibility parameters: urban condition, plinth, constructive technique, footprint, urban typology, number of floors, rendering, and additional protection. These parameters represent the morphologic, structural, and constructive characteristics of the buildings and their relationship with their urban or rural context. Each parameter has been assigned an increasing susceptibility value, on a scale of 1 to 5. The value of the susceptibility parameters has been weighted through specific factors, established accordingly to the influence of each parameter on flood vulnerability of earthen constructions (4). These weighting factors have been obtained using the Delphi Method (Gordon 1994), gathering the opinion of 43 experts in the field of architecture, engineering, geology and natural hazards (Mileto et al. 2021). In addition, forms of degradation and structural damage related to flooding have been taken into account.

Finally, in order to obtain of the overall vulnerability index of the building, the weighted average of the values assigned to each parameter has been calculated.

Table 1. Earthen architecture susceptibility parameters.

Charateristics	Weight factor	Value	Charateristics	Weight factor	Value
Urban condition	0.8		Constructive technique	0.6	
Basement		5	Rammed earth		1
Below ground		4	Adobe		3
Ground level		3	Half-timber		5
Above ground		1			
Several level		3			
Number of floors	0.4		Plinth	0.7	
1		1	No plinth		5
2–3		3	Masonry		3
4–5		5	Ashlar		1
			Brick		2
Footprint [m^2]	0.4		Rendering	0.5	
0–50		5	No rendering		5
50–150		3	Earth		4
>150		1	Earth and lime		2
			Earth and fibres		3
			Lime		1
			Gypsum		3
Urban typology	0.4		Additional protection	0.5	
Freestanding		5	Yes		1
End of block		4	No		5
On a corner		3			
Between party walls		1			

4 RESULTS AND DISCUSSION

During the first phase of the research, through fieldwork, 50 earthen buildings, 12 in Alzira and 38 in Torres de Berellen, have been located. The different number of earthen constructions between the two case studies is attributable to the different urban history and development of the two towns. In fact, Alzira is the capital of the *Ribera Alta del Júcar*, and its historic centre has been depopulated over time, leaving the buildings in a very bad state of conservation until reaching the condition of ruin, that, since the beginning of the twentieth century, has given rise to a process of replacing earthen buildings with new buildings made of bricks or with reinforced concrete structure. Behind this massive replacement process there are reasons related to the low social value generally ascribed to earthen architecture. Despite the small number of samples in Alzira, it has been considered relevant to analyze its earthen buildings as the historic center of the city is currently protected by the Valencian Community as an Asset of Cultural Interest (Generalitat Valenciana 2004).

Differently, in the case of Torres de Berellen, as it is a small town, with no major importance in the region, there has not been a massive replacement of earthen buildings as in the historic center of Alzira. On the contrary, earthen construction techniques have continued to be used until the mid-twentieth century.

The analysis of the data collected, and the results obtained, allow to highlight some relevant peculiarities for the conservation of earthen architectural heritage.

Firstly, the earthen buildings found during fieldwork are mainly made of rammed earth or adobe walls. All the adobe buildings are in Torres de Berellen, while the rammed earth buildings are located in Alzira. From a constructive point of view, the buildings have one to three floors, and the walls are reinforced with bricks at the corners (Figure 5).

Figure 5. Rammed earth building in Alzira (left). Adobe building in Torres de Berellen (right).

In 70% of cases, the plinth is made of bricks, and the remaining percentage of buildings has a plinth made of ashlars or concrete blocks. It should be noted that, in many cases, the concrete blocks were added to repair areas of the plinth that have suffered material loss after flooding events or due to other forms of deterioration of the architectural element (Figure 6).

Figure 6. Repair with bricks and concrete blocks in a plinth (Torres de Berellen)

Vulnerability indices obtained through the proposed assessment methodology vary within the range of low and medium vulnerability, on a scale of 1 (low) to 5 (high), with 8% of buildings of low vulnerability, 54% of medium-low vulnerability and 38% of medium vulnerability (Figure 7).

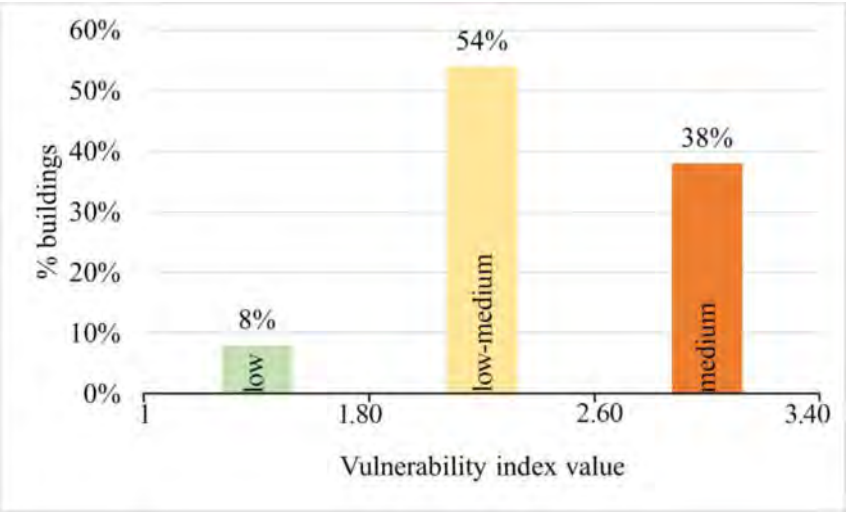

Figure 7. Flood vulnerability level distribution.

Buildings with medium vulnerability values are built by 42% with rammed earth and by 37% with adobe. This difference is mainly due to a greater or lesser unfavorable combination of morphological and constructive characteristics and, above all, to the state of conservation. Figure 8 shows that 69% of rammed earth buildings and 41% of adobe buildings have cracks (hair cracks or fractures).

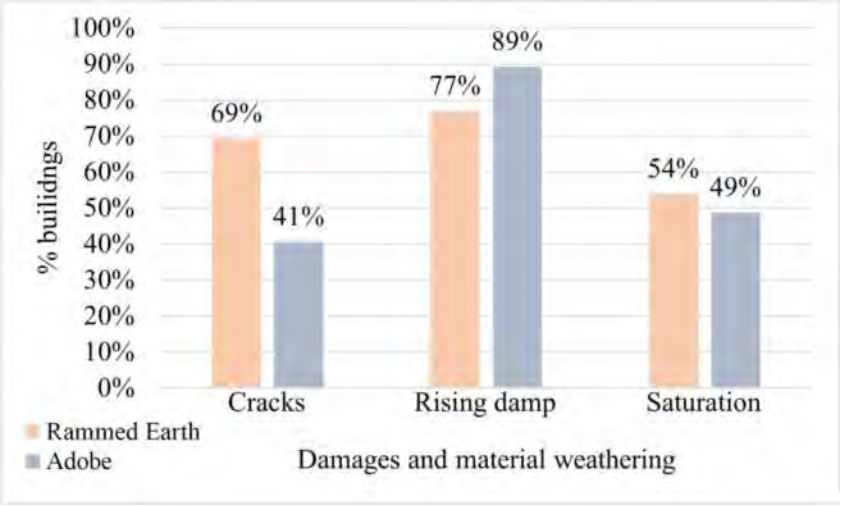

Figure 8. Damages and material weathering analysis.

The crack patterns detected can be traced back to static failures, such as subsidence and rotation, caused by the long-term effects of flooding. As analyzed by Herle *et al.* (2010), the change in the state of the foundation soil during a flood, the increase of the hydraulic gradient and hydraulic conductivity, favor soil erosion, causing subsidence, which is manifested through cracks and deformation in the superstructures. In addition, due to the characteristics of the construction system, between the walls there is no transverse connection, and, therefore, they tend to separate, rotating or translating independently of each other, with the consequent appearance of cracks with a vertical or parabolic trend (Figure 9).

Figure 9. Crack due to the separation of the walls, probably caused by the erosion of the subsoil in Torres de Berellen.

Moreover, results show that buildings of both construction techniques are affected by rising damp in very high percentages. Although rising damp is not a phenomenon normally included in the assessment of flood damage (Kelman & Spence 2004), it has been considered relevant to include it in the analyses as it may trigger further damage. Considering that floods take place in a very short period of time with very large drying periods between events, the saturation of the material reaches its maximum value in these short periods, causing damage to the outermost parts of the components and generating changes in the physical properties of the materials (Siedel 2010). It should be noted that the plinths of buildings in several cases present an advanced state of degradation, with volumetric losses that could affect the structural stability of the constructions. The severity of these effects is due to the characteristics of the main material of the walls, earth,

which absorbs humidity from the environment for its hygroscopic nature. Buildings with more severe deterioration have a plinth made of adobe, whose outer layer has been covered with bricks or cement blocks with thick aggregate. However, this external protection is insufficient and ends up separating from its adobe support, which are left exposed to the action of external agents (floods, atmospheric agents, etc.) that triggers erosion on the material. (Figure 10).

Figure 10. Adobe basement erosion. (Torres de Berellen).

On the contrary, rammed earth buildings are not affected by rising damp at the same extent of adobe constructions. This implies that rammed earth walls have a greater capacity to preserve cohesion and consequently resistance, than adobe walls. Despite their better response compared to adobe walls, rammed earth walls are particularly affected by the presence of moisture, and the 54% of the constructions analyzed walls display moist areas due to saturation. This form of deterioration could lead to greater damage and loss of resistance. According to Jaquin et al. (2009) rammed earth behaviour changes with the increasing of moisture content, with a remarkable influence on its mechanical characteristics, which worsen considerably. Moreover, the results of Bui et al. (2014) study show that the compressive strength value does not fall suddenly if the moisture content is kept below 4%, while for moisture contents above this threshold, a consistent loss of strength occurs. In the constructions analyzed, the high moisture content has caused the detachment of the plaster, leaving the outer face of the earthen walls without any protection against external agents, causing various forms of erosion and detachments.

To mitigate the vulnerability of earthen architecture and reduce the structural damage that can cause the collapse of buildings and consequently the loss of this architectural heritage, it is necessary to design conservation and protection strategies. For this purpose, structural and non-structural measures can be designed, aiming to the consolidation of buildings and the improvement of environmental conditions. To reduce the impact of flooding, the design of emergency plans and risk prevention guidelines is considered essential. In addition, it is necessary to establish intervention criteria for buildings that present deterioration and structural damage, together with the design of detailed maintenance plans.

5 CONCLUSIONS

Floods constitute a great hazard for earthen architectural heritage, due to the hygroscopic nature of its principal construction material. Earthen traditional constructions have been built with different constructive techniques (adobe, rammed earth, etc.) according to the constructive practice that has been most developed in each place. Despite common elements, each construction technique presents a different response to the effects of floods. The vulnerability assessment methodology proposed in the present paper has allowed to obtain an analytical framework of the impact of floods

on the earth architecture of the two selected case studies, highlighting the influence of deterioration and structural damage on the mechanical behavior of the structures. The main conclusion reached is that in a place like Alzira and Torres de Berellen, where floods have been constant throughout history, earthen constructive techniques have often been used. The methodology followed is a simple procedure for assessing the vulnerability of earthen architecture. Its implementation in the case studies selected has shown the unique aspects of each construction while also highlighting their weaknesses. The results obtained, and the subsequent calculation of the vulnerability level, have led to several conclusions. Firstly, the influence of the state of conservation and the presence of rising dampness and cracks have been decisive factors in the analysis of vulnerability. It is therefore essential to establish and carry out intervention strategies which ought to be geared towards the prevention of localized damage and structural collapse. It should be noted that risk is the product of three factors: exposure to risk, danger or the probability of the event occurring, and vulnerability. Of these, only vulnerability depends exclusively on the building, as exposure and danger are dependent on surroundings. In fact, a construction may be at risk of flooding but not vulnerable it can be located in a floodable area but be able to withstand the event due to its characteristics. As risk reduction will depend on the reduction of one or all of these factors it is not only necessary to act on the surroundings and building infrastructures to defend and improve the drainage system, but it is also essential to define criteria and strategies for intervention to consolidate the architecture. In conclusion, natural risks such as floods threaten architectural heritage, specifically earthen architecture. However, in order to protect and conserve this seemingly fragile heritage it is necessary to understand its mechanisms for resistance and reduce its vulnerability through appropriate preventive interventions.

REFERENCES

Alberola Romá, A., 2010. Riadas, inundaciones y desastres en el sur valenciano a finales del siglo XVIII. *Papeles de Geografía*, 51–52, 23–32.

Beckett, C.T.S., Augarde, C.E., Easton, D., and Easton, T., 2018. Strength characterisation of soil-based construction materials. *Geotechnique*, 68 (5), 400–409.

Beckett, C.T.S., Jaquin, P.A., and Morel, J.C., 2020. Weathering the storm: A framework to assess the resistance of earthen structures to water damage. *Construction and Building Materials*, 242.

Birkmann, J., Cardona, O.D., Carreño, M.L., Barbat, A.H., Pelling, M., Schneiderbauer, S., Kienberger, S., Keiler, M., Alexander, D., Zeil, P., and Welle, T., 2013. Framing vulnerability, risk and societal responses: the MOVE framework. *Natural Hazards*, 67, 193–211.

Bui, Q.B., Morel, J.C., Hans, S., and Walker, P., 2014. Effect of moisture content on the mechanical characteristics of rammed earth. *Construction and Building Materials*, 54, 163–169.

Camarasa-Belmonte, A.M. and Soriano-García, J., 2012. Flood risk assessment and mapping in peri-urban Mediterranean environments using hydrogeomorphology. Application to ephemeral streams in the Valencia region (eastern Spain). *Landscape and Urban Planning*, 104 (2), 189–200.

Camarasa Belmonte, A.M., 2002. Crecidas e inundaciones. *In*: F.J. Ayala-Carcedo and J. Olcina Cantos, eds. *Riesgos Naturales*. Barcelona, 859–879.

Canivell, J., Rodríguez-García, R., González-Serrano, A., and Romero-Girón, A., 2020. Assessment of Heritage Rammed-Earth Buildings: Alcázar of King Don Pedro I, Spain. *Journal of Architectural Engineering*, 26 (2), 05020003.

D'Ayala, Di., Wang, K., Yan, Y., Smith, H., Massam, A., Filipova, V., and Jacqueline Pereira, J., 2020. Flood vulnerability and risk assessment of urban traditional buildings in a heritage district of Kuala Lumpur, Malaysia. *Natural Hazards and Earth System Sciences*, 20 (8), 2221–2241.

Drdácký, M.F., 2010. Flood Damage to Historic Buildings and Structures. *Journal of Performance of Constructed Facilities*, 24 (5), 439–445.

EC, 2007. DIRECTIVE 2007/60/EC OF THE EUROPEAN PARLIAMENT AND OF THE COUNCIL of 23 October 2007 on the assessment and management of flood risks. *Official Journal of the European Union*.

Eguibar, M.Á., García, R.P., Torrijo, F.J., and Roca, J.G., 2021. Flood Hazards in Flat Coastal Areas of the Eastern Iberian Peninsula?: A Case Study in Oliva (Valencia , Spain), 1–25.

Figueiredo, R., Romão, X., and Paupério, E., 2021. Component-based flood vulnerability modelling for cultural heritage buildings. *International Journal of Disaster Risk Reduction*, 61 (102323).

García Soriano, L., 2015. La restauración de la arquitectura de tapia de 1980 a la actualidad a través de los fondos del Ministerio de Cultura y del Ministerio de Fomento del Gobierno de España. Criterios, técnicas y resultados.

Generalitat Valenciana, 2004. *DECRETO 126/2004, de 30 de julio, del Consell de la Generalitat, por el que se declara Bien de Interés Cultural la Vila de Alzira, con la categoría de conjunto histórico, y la Iglesia de Santa Catalina de Alzira, con la categoría de monumento.* Spain.

Generalitat Valenciana, 2015. *Plan de Acción Territorial de carácter sectorial sobre prevención del Riesgo de Inundación en la Comunidad Valenciana*. Spain.

Gerard, P., Mahdad, M., Robert McCormack, A., and François, B., 2015. A unified failure criterion for unstabilized rammed earth materials upon varying relative humidity conditions. *Construction and Building Materials*, 95, 437–447.

Gobierno de Aragón, 2005. *Redaccion y desarrollo del plan medioambiental del Ebro y tramo bajo del Cinca*.

Gobierno de Aragón, 2019. *ANEXO I Municipios y núcleos de población situados en Zona A de alto riesgo , a efectos de emergencia para poblaciones , incluidos en el Anexo XII (tabla 12), del Decreto 201 / 2019 , de 8 de octubre , del Gobierno de Aragón.*

Gómez-Patrocinio, F.J., Vegas López-Manzanares, F., Mileto, C., and García-Soriano, L., 2020. Techniques and Characteristics of Traditional Earthen Masonry Walls: The Case of Spain Techniques and Characteristics of Traditional Earthen Masonry Walls: The Case of Spain. *International Journal of Architectural Heritage*, 14 (5), 694–710.

Gordon, J.T., 1994. The Delphi Method. *Futures Research Methodology*, 16 (5).

Herle, I., Herbstová, V., Kupka, M., and Kolymbas, D., 2010. Geotechnical Problems of Cultural Heritage due to Floods. *Journal of Performance of Constructed Facilities*, 24 (5), 446–451.

Jaquin, P.A., Augarde, C.E., Gallipoli, D., and Toll, D.G., 2009. The strength of unstabilised rammed earth materials. *Geotechnique*, 59 (5), 487–490.

Keefe, L., 2005. *Earth Building. Methods and materials, repair and conservation.* London: Taylor and Francis Group.

Kelman, I. and Spence, R., 2004. An overview of flood actions on buildings. *Engineering Geology*, 73 (3–4), 297–309.

Lastrada, E., Cobos, G., and Torrijo, F.J., 2020. Analysis of climate change's effect on flood risk. Case study of Reinosa in the Ebro river Basin. *Water (Switzerland)*, 12 (4).

Macías-Bernal, J.M., Calama-Rodríguez, J.M., and Chávez-de Diego, M.J., 2014. Modelo de predicción de la vida útil de la edificación patrimonial a partir de la lógica difusa. *Informes de la Construccion*, 65 (533).

Maldonado Ramos, L. and Vela Cossío, F., 2002. *Arquitectura y construcción con tierra*. Madrid?: Mairea,.

Mileto, C. and Vegas, F., 2017. *La restauración de la tapia en la Península Ibérica*. Valencia: TC Cuadernos.

Mileto, C., Vegas, F., García, L., and Pérez, A., 2021. Assessment of Vulnerability of Earthen Vernacular Architecture in the Iberian Peninsula to Natural Risks. Generation of an Analysis Tool. *International Journal of Architectural Heritage*, 00 (00), 1–14.

Ortiz, P., Antunez, V., Martín, J.M., Ortiz, R., Vázquez, M.A., and Galán, E., 2014. Approach to environmental risk analysis for the main monuments in a historical city. *Journal of Cultural Heritage*, 15 (4), 432–440.

Ortiz, R. and Ortiz, P., 2016. Vulnerability Index: A New Approach for Preventive Conservation of Monuments. *International Journal of Architectural Heritage*, 10 (8), 1078–1100.

Ribera, J., 1887. Topografía de Alzira árabe. *El Archivo II*.

Siedel, H., 2010. Historic Building Stones and Flooding: Changes of Physical Properties due to Water Saturation. *Journal of Performance of Constructed Facilities*, 24 (5), 452–461.

Solín, Ľ., 2012. Spatial variability in the flood vulnerability of urban areas in the headwater basins of Slovakia. *Journal of Flood Risk Management*, 5 (4), 303–320.

Sperotto, A., Torresan, S., Gallina, V., Coppola, E., Critto, A., and Marcomini, A., 2015. A multi-disciplinary approach to evaluate pluvial floods risk under changing climate: The case study of the municipality of Venice (Italy). *Science of the Total Environment*, 562, 1031–1043.

Stephenson, V. and D'Ayala, D., 2014. A new approach to flood vulnerability assessment for historic buildings in England. *Natural Hazards and Earth System Sciences*, 14 (5), 1035–1048.

Trizio, F., Torrijo, F.J., Mileto, C., and Vegas, F., 2021. Flood Risk in a Heritage City: Alzira as a Case Study. *Water (Switzerland)*, 13, 1138.

Vegas, F., Mileto, C., and Cristini, V., 2011. Earthen architecture in Spain. *In*: *Terra Europae. Earthen Architecture in European Union*. 181–183.
Villacampa Crespo, L., 2018. La Restauracion y La Rehabilitacion De La Arquitectura Tradicional de Tierra. EL Caso De Aragon. *Univerisidad Politecnica De Valencia*. Universitat Politècnica de València, Valencia.
Wang, J.J., 2015. Flood risk maps to cultural heritage: Measures and process. *Journal of Cultural Heritage*, 16 (2), 210–220.
Warren, J., 1999. *Conservation of Earth Structures*. Oxford: Butterworth Heinemann.
Xu, L., Wong, K.K., Fabbri, A., Champiré, F., and Branque, D., 2018. Loading-unloading shear behavior of rammed earth upon varying clay content and relative humidity conditions. *Soils and Foundations*, 58 (4), 1001–1015.

Geotechnical Engineering for the Preservation of Monuments and Historic Sites III – Lancellotta, Viggiani, Flora, de Silva & Mele (Eds)

Climate change impacts on cultural heritage building foundations in Western Andalusia

A. Jaramillo Morilla, E.J. Mascort-Albea, R. Romero-Hernández & C. Soriano-Cuesta
Universidad de Sevilla, Escuela Técnica Superior de Arquitectura, Departamento de Estructuras de la Edificación e Ingeniería del Terreno, Instituto Universitario de Arquitectura y Ciencias de la Construcción, Sevilla, España

ABSTRACT: The purpose of this study is to present the consequences of climate change, especially temperature increase, drought, sea-level rise, and coastal flooding or earthquake increase, in the foundations of four heritage buildings in Andalusia, to enhance the importance of risk assessments of heritage to contribute to disaster resilience.

The climate-related hazard that may thrive as climatic stressors on outdoor cultural heritage have been studied, as the decrease in soil moisture leads to a subsidence and shrinkage effect of the surface clays affecting such important heritage buildings as the Church of the Sagrario, next to the cathedral of Seville. Other hazards analyzed in the study cases include a slight rise in sea level at the mouth of the Guadalquivir and the recent erosion of coastal buildings such as the Chipiona Castle or the castle of Utrera, all of them placed on Western Andalusia.

1 IMPACTS OF GRADUAL CLIMATE CHANGES ON OUTDOOR CULTURAL HERITAGE

Climate change has been proved to be one of the major underlying causes for the increasing vulnerability of cultural heritage. Their continued preservation requires understanding these impacts to elaborate a response. Concern over this issue has led international organizations to identify climate change as a threat to cultural heritage and to encourage the implementation of measures to mitigate its effects. In 2007 UNESCO World Heritage Centre adopted its "Strategy for Reducing Risks at World Heritage Properties", to improve the World Heritage site's protection from natural hazards. In 2020 ICOMOS Climate and Ecological Emergency Statement calls for urgent action to safeguard cultural heritage from the potential impacts of climate change and cultural heritage risk assessment.

This document reviews the damage to four historic buildings located in Andalusia that are directly related to climate change. Climate parameters, risk factors, and identified impact reviewed in this paper are summarized in table 1.

Some of these physical impacts on cultural heritage have been analyzed in four very significant buildings located in Andalusia, such as the walls of Sevilla or the Chipiona and Utrera castles.

2 THE WALLS OF SEVILLA

The walls of Sevilla, whose origin is debated between the 12th and 13th centuries AD, was one of the largest fortified urban enclosures in the Middle Ages in Spain, is one of the most important rammed-earth buildings in Andalusia. From 2020 onwards, some interventions are being carried out in the sector of the Macarena Wall, which have allowed the study of its materials, and more accurately, the influence of water, either as an external weathering agent or as the moisture content in the material,

DOI 10.1201/9781003308867-85

Table 1. Parameters of climate change and physical impacts.

Parameters	Climate Change Risk	Impacts on cultural heritage
Rise in temperature	– Warmer temperatures – Stronger heat waves – Melting of the Polar Ice Caps – Thermoclastism	– Flooding of coastal areas. – Loss of marshlands due to the occupation of saltwater.
Variations in precipitation patterns	– Decrease in annual rainfall. – Greater drought. – Concentration of dunes.	– Decrease in the water table. – Subsidence in sandy soils leading to settling. – Decrease in soil moisture and shrinkage in clay soils. – Occasional instabilities due to heavy rainfall affecting slopes. failure of retaining structures due to insufficient drainage in retaining structures – Salt crystallization cycles
Wind	– More dangerous hurricanes. – Winds with higher speeds.	– Increased horizontal stresses and moments in foundations due to hurricanes and winds in general with higher speeds
Earthquakes	– Fracking application	– Increase in small earthquakes

has been analyzed for mechanical properties, durability or within the cycles crystallization of salts in rammed earth. The test run in some of these works has proven that water plays an important role in weathering processes, as salts migrate when dissolved in water, from the inside to the surface, where they crystallize. Different impacts are analyzed below.

2.1 *Thermoclastism*

Thermoclastism results from the expansion and contraction of surface mineral grains due to thermal variations caused by seasonal variations and diurnal changes in air temperature and direct insolation (Germinario, Andriani, y Laviano 2015).

On the other hand, salts migrate when dissolved in water, from the inside to the surface, where they crystallize. This process usually leads to a higher concentration of salts on the surface, where the increase in volume by crystallization internally stresses the pores of the material, causing its fracture. Weathering, sandblasting and disintegration of the outer layers are usually the result of this loss of cohesion (Martín-del-Rio et al. 2021).

2.2 *Biological degradation*

Changes in humidity influence the growth of microorganisms in stone and wooden heritage materials. The growth of small plants can contribute to the biodegradation of these elements. The photograph above shows the growth of small plants in the battlements and several stains of humidity on the wall. Loss of mass is also quite significant in certain areas, as can be seen in the photograph (Figure 1).

2.3 *Salt crystallization cycles*

It can be established that the main cause of the degradation of the wall of Seville is the loss of material and physical-chemical weathering. The cause does not lie in the material composition or poor performance of the original materials, but rather in the presence of water in the walls, its transport, and the crystallization cycles of the salts. This effect worsens when the hygrothermal behaviour is altered, mainly due to climate changes. The following images show the different temperatures on the surface of the wall due to the humidity of the rammed earth (Figure 2).

Figure 1. Biological degradation in the Macarena wall.

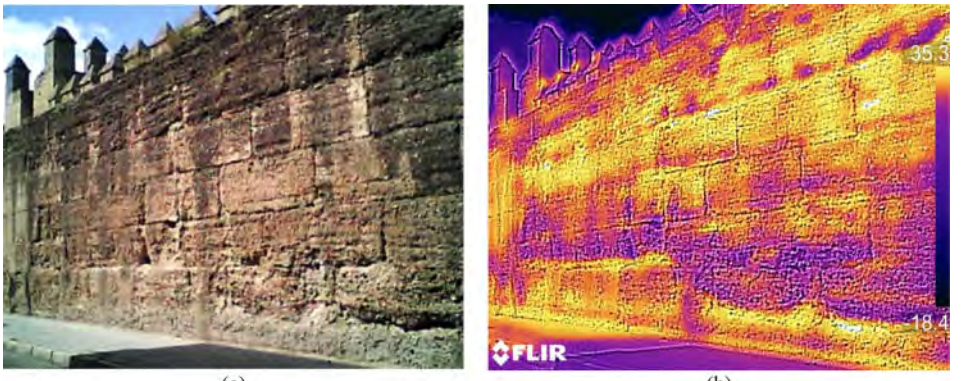

(a) (b)

Figure 2. Thermographic image (b) and real image (a) of the external face of the wall generated by a Flir T420bx model camera (images taken on 4/9/2019 at 4:33 p.m.)

3 THE CASTLE OF CHIPIONA

This castle is located in Chipiona, province of Cadiz, in the south of Andalusia. Its origin, although some authors establish in the thirteenth century, should be placed in the mid-fifteenth century as a result of the rapid economic growth suffered by the locality with the exploitation of the vineyard and the constant incursions of Turkish, Berber and French pirates on the coast of Cádiz, which would certainly oblige Rodrigo Ponce de León, lord of these lands, to build the castle as a defensive element of the closest sector of the municipality to the estuary of the Guadalquivir River.

Different pathologies that have affected the building throughout its history and some of them are briefly described in this document.

3.1 *Sea level rise*

Rising sea level (SLR) poses a significant threat to cultural heritage situated within coastal areas; 19% of UNESCO World Heritage Sites (WHS) globally could be lost to inundation (Marzeion y Levermann 2014).

To date, studies in Europe on this topic have focused on the Mediterranean region. (Reimann et al. 2018) investigated the potential risk of flooding due to SLR in this region and Ravanelli et al. (2019) focused on the archaeological site of Motya in Sicily (Reimann et al. 2018). Investigating similar scenarios in other areas, (García Sánchez, García Sánchez, y Ribalaygua 2020) mentioned that SLR is threatening coastal fortifications in the Canary Islands.

SLR will also increase the frequency of extreme events, such as storm surges that result in higher waves, and affect the balance of sediments in coastal regions and the stability of underwater archaeological sites and monuments (Wright 2016).

The effect of SLR has been studied in the coastal area of Chipiona. Chipiona Castle has been suffering the consequences of the SLR during the last few years, and some of the foundation has been removed by the water. Marked with an ellipse is shown the castle position. The front area of the castle has nearly disappeared due to recent strong tides; in the last 5 years, large holes have appeared under the north retaining wall because of rising tides and waves.

This event could be related to the ice melting at the poles, the water from the melted streams flows out of the glacier contributing to the sea level rise. In Andalusia, the sea level will rise from 0.50 m to 1.0 m. At least 20 to 50 cm of sea level will rise on the coast of Cadiz and Huelva. Because of this rise, species such as the Iberian lynx will become extinct from their natural habitat in the marshes of the Coto de Doñana and the main impacts on coastal areas will be temporary or permanent flooding, increased erosion, loss of wetlands and brackish water intrusion. The images below show the results of these on the walls of the castle of Chipiona (Figure 3).

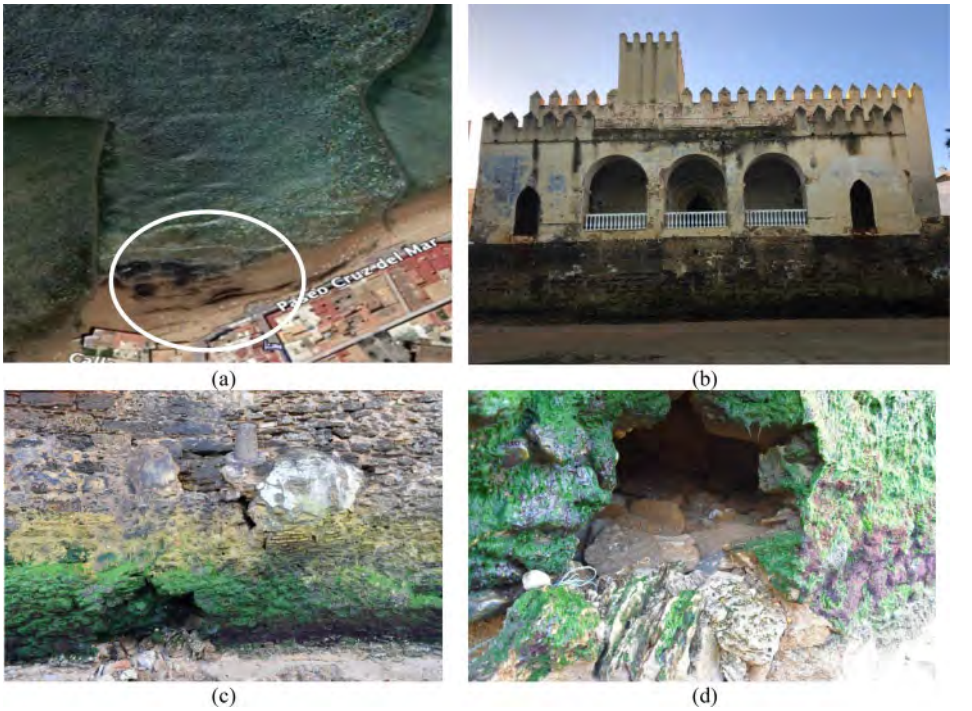

Figure 3. Chipiona Castle: Location (a) and a general view from 2021 (b). Hole under the foundation in two different scales (c and d).

The waves are washing away the castle's foundation blocks and leaving large holes of more than 3 meters wide and deep, which may affect the stability of the stone walls in the medium and long term. The climatic conditions regarding temperature and wind in the year 2020 are likely to corroborate these hypotheses (Figure 4).

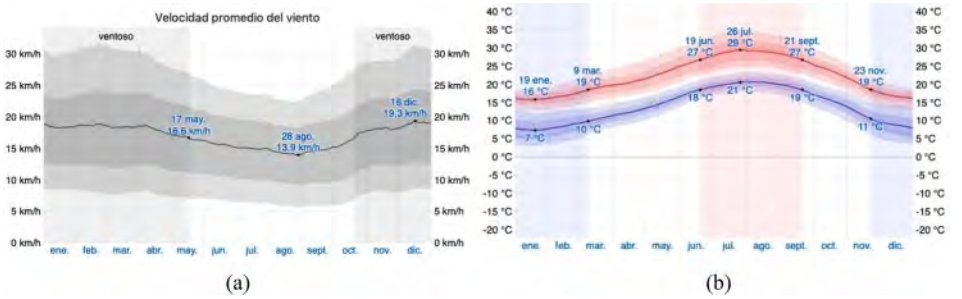

Figure 4. Average wind speed in Chipiona (a). The average temperature in Chipiona in 2020 (b).

Around 50% of the surface area of Malaga's coastal neighbourhoods such as Sacaba Beach, San Carlos, Torre del Rio and San Andres are exposed to sea flooding (Gil-Guirado et al. 2022). The Chipiona Castle is being affected by recent strong tides. In the last 5 years, large holes have appeared under the north retaining wall due to the effect of rising tides and waves. Quantifying uncertainty in shoreline projections can be crucial and it is necessary for heritage building management and its adaptation at long-term time scales. The analysis of coastal impacts is essential in order to assess climate-related risks in heritage located in coastal areas (Alvarez-Cuesta, Toimil, y Losada 2021).

4 THE CASTLE OF UTRERA

Utrera is a municipality in the province of Seville, Andalusia. The construction of the castle has been dated around 1398, and there are documents about repair and improvement work in 1420 and 1444 on the external elements of the tower of homage.

From the 16th century onward and after the loss of value of the site as a military site, it fell into a process of abandonment and decadence. The tower of the tribute, attached to the castle walls, has been restored and is in a quite acceptable condition, although it is exposed to the inclement weather of the area. As for the materials used for its construction, the walls are made of rammed earth and the corners of the tower are built with stone masonry. This building has been introduced in this paper due to its pathologies, which are directly related to SLR, the temperature increase and the effect of the wind on the damaged walls.

4.1 *Warmer temperatures. Stronger heat waves*

In 2021 we have already had temperatures over 40° in Seville in June. An increase of 1°C degree in the average temperature in Seville this summer had been predicted. The average temperature of the planet has increased only 0.85°C since the beginning of the industrial revolution. In Seville for instance, we reach sometimes, fortunately only occasionally, 46° in the month of July. However, studies have informed us that if strong measures are not taken, we will rise to 50° in July in 2100. At the very least, the temperature will rise by 2°C, reaching 48°C in July. According to an ongoing temperature analysis conducted by scientists at NASA's Goddard Institute for Space Studies (GISS), the average global temperature on Earth has increased by a little more than 1° Celsius (2° Fahrenheit) since 1880. Two-thirds of the warming has occurred since 1975, at a rate of approximately 0.15–0.20°C per decade. High temperatures are also causing the sandblasting of mortars, masonry walls, and slopes (Figure 5).

Figure 5. Sandblasting of the surface of the Utrera Castle.

4.2 *More intense storms*

Analyzing the data from the Spanish Meteorological Agency, and after plotting a chart with the linear regression of annual rainfall, a decrease in the average over the last 65 years can be noted, every year the average is 2.1 to 2.3 liters of precipitation less, so decrease in rainfall is happening.

Regarding the annual data, we consider a second step in the treatment of the data using the Fast Fourier Transform (FFT), as shown in the figure above (Figure 6). The main frequency is 0.149. This means that the recurrence period of heavy rains is approximately 6.7 years, with a second period with a very similar amplitude of 0.125, a period of heavy rains every 8 years.

4.3 *Shrinkage of expansive soil*

Shrink–swell is the volume change that occurs due to changes in the moisture content of clay-rich soils. These soils can absorb large amounts of water after a rainfall, causing swelling. On the contrary, they can also become very hard when they are dry, resulting in shrinkage and cracking of the ground.

In Andalusia, shrinkage –swell damage far exceeds earthquake damage. The church of The Sagrario, placed next to the cathedral of Seville has had to be underpinned due to the settling (shrinkage) that has mainly affected the corner of the Avenida de la Constitución (Figure 7). The Columbus Library of the Cathedral of Seville has also had to be reinforced due to ground movements.

The movement of the soil of several decimeters was measured in a layer of clay 3–4 m thick (Diz-Mellado et al. 2021). In addition to the problem, the process is slow, but not uniform throughout the foundation, and is usually greater at the border of the building because the perimeter soil dries out faster than the soil under it, given that the building itself prevents the water from evaporation.

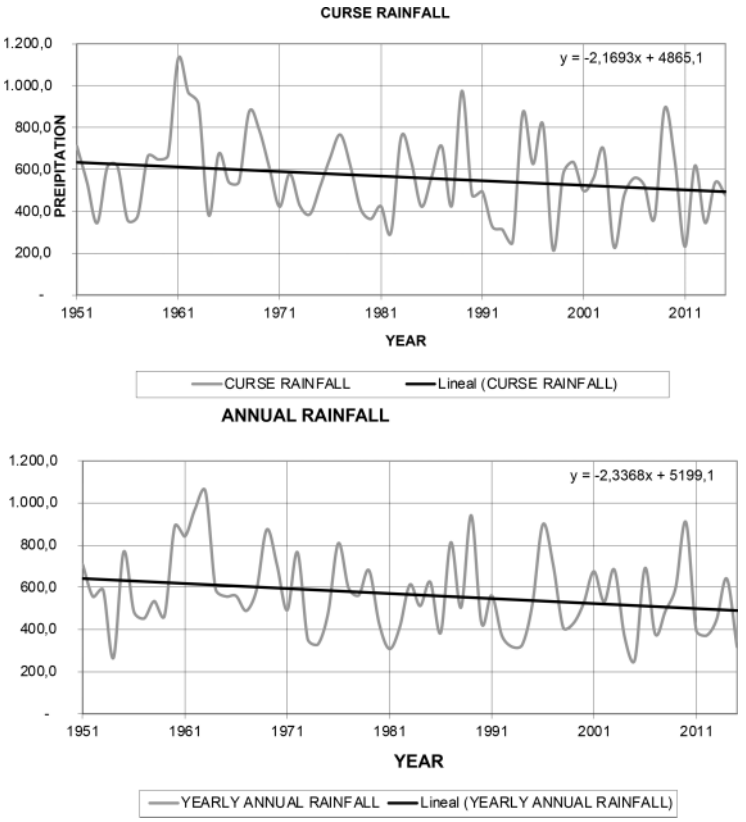

Figure 6. Precipitation regimen in Utrera.

Figure 7. Settlement at the corner of the building due to soil shrinkage (a). Detail with topography mark installed on the building during the year 2021 (b).

Figure 8. Seville ramparts could be affected by the earthquakes.

4.4 *Increase in earthquakes*

The incidence of glacial earthquakes is increasing, especially in the summer months when glacial ice melts faster. (Ekström G 2006). The loss of glacial compression causes an increase of up to twice as many earthquakes of magnitude up to 5.1 on the Richter scale.

The fall of large blocks of glaciers when they melt and fall into the sea is causing a considerable increase in tsunamis in nearby coastal areas, although, fortunately, of small magnitude.

On the other hand, fuel prices are making it profitable to obtain oil and gas from the ground using the "fracking" technique. The installation of several extraction wells is underway less than

10 km from Seville in the town of La Rinconada. The "fracking" system will most likely produce earthquakes, even if they are of small magnitude, but they can damage heritage buildings through their foundations (Sun et al. 2019).

One of the monuments that may be most affected will be the Almohad Wall of Seville in the Macarena area since it is composed of the earth as a construction material. There is no masonry foundation, and it is simply buried 2 meters into the ground. The location of the Almohad wall of the Macarena is just north of the city centre and the closest to the Rinconada (Figure 8).

REFERENCES

Alvarez-Cuesta, M., A. Toimil, y I. J. Losada. 2021. "Modelling long-term shoreline evolution in highly anthropized coastal areas. Part 2: Assessing the response to climate change". *Coastal Engineering* 168: 103961.

Diz-Mellado, Eduardo et al. 2021. "Non-destructive testing and Finite Element Method integrated procedure for heritage diagnosis: The Seville Cathedral case study". *Journal of Building Engineering* 37: 102134. https://linkinghub.elsevier.com/retrieve/pii/S2352710220337669.

Ekström G, Meredith Nettles and Victor C. Tsai. 2006. "Seasonality and Increasing Frequency of Greenland Glacial Earthquakes on JSTOR". *Science, 311(5768), 1756–1758*. https://www–jstor–org.us.debiblio.com/stable/3845719?Search=yes&resultItemClick=true&searchText=%22Seasonality+and+Increasing+Frequency+of+Greenland+Glacial+Earthquakes%22&searchUri=%2Faction%2FdoBasicSearch%3FQuery%3D%2522Seasonality%2Band%2BIncreasing (2 de noviembre de 2021).

García Sánchez, Francisco, Héctor García Sánchez, y Cecilia Ribalaygua. 2020. "Cultural heritage and sea level rise threat: risk assessment of coastal fortifications in the Canary Islands". *Journal of Cultural Heritage* 44: 211–17.

Germinario, Luigi, Gioacchino Francesco Andriani, y Rocco Laviano. 2015. "Decay of calcareous building stone under the combined action of thermoclastism and cryoclastism: A laboratory simulation". *Construction and Building Materials* 75: 385–94.

Gil-Guirado, Salvador et al. 2022. "Flood impact on the Spanish Mediterranean coast since 1960 based on the prevailing synoptic patterns". *Science of The Total Environment* 807: 150777.

Martín-del-Rio, J.J. et al. 2021. "Analysis of the materials and state of conservation of the medieval rammed earth walls of Seville (Spain)". *Journal of Building Engineering* 44: 103381. https://doi.org/10.1016/j.jobe.2021.103381 (14 de octubre de 2021).

Marzeion, Ben, y Anders Levermann. 2014. "Loss of cultural world heritage and currently inhabited places to sea-level rise". *Environmental Research Letters* 9(3): 034001. https://iopscience.iop.org/article/10.1088/1748-9326/9/3/034001 (2 de noviembre de 2021).

Reimann, Lena et al. 2018. "Mediterranean UNESCO World Heritage at risk from coastal flooding and erosion due to sea-level rise". *Nature Communications 2018 9:1* 9(1): 1–11. https://www.nature.com/articles/s41467-018-06645-9 (2 de noviembre de 2021).

Sun, Yuqing et al. 2019. "A critical review of risks, characteristics, and treatment strategies for potentially toxic elements in wastewater from shale gas extraction". *Environment International* 125: 452–69.

Wright, Jeneva. 2016. "Maritime Archaeology and Climate Change: An Invitation". *Journal of Maritime Archaeology* 11(3): 255–70.

Geotechnical Engineering for the Preservation of Monuments and Historic Sites III – Lancellotta, Viggiani, Flora, de Silva & Mele (Eds)

The Garisenda Tower in Bologna: Effects of degradation of selenite basement on its static behaviour.

G. Dallavalle
Studio Ceccoli e Associati, Bologna, Italy

A. Di Tommaso
Former Professor at "Alma Mater Studiorum", University of Bologna, and IUAV, University of Venice

G. Gottardi & T. Trombetti
"Alma Mater Studiorum", University of Bologna, Italy

R. Lancellotta
Politecnico di Torino, Italy

S. Lugli
University of Modena and Reggio Emilia, Italy

ABSTRACT: The Garisenda tower in Bologna, a 48 m tall structure with a square base of 7.45 meters per side, is characterized by an overall out of plumb of 3.32 m in the South-East direction. Its construction dates back to the XI century and, due to its impressive leaning, in 1350–1353 the original height of 60 m was reduced to the 48 m of the present day (Cavani 1903; Giordano 2000). The tower can be seen as partitioned in a lower portion, with walls composed by two external leaves of selenite stones filled with rubble conglomerate, and an upper portion where the external leaves are made of masonry bricks. Recent investigations have proved that selenite blocks of the basement have been altered as a result of (a) exposition to high temperatures during important fires, that took place at the end of XIV and XVII centuries, and possibly because of the presence of forges (that were demolished at the end of the XIX centuries) and (b) high level of humidity in the inner lower part of the tower. This process has produced a gradual local disintegration of the selenite stones, leading in some case to a reduction of the original 50 to 60 cm thickness by an amount of about 20 cm. The contribution submitted to this conference is aimed at clarifying this important aspect, linked to the ageing and damage of structural stones and the related consequences in terms of stress distribution and concentrations that could induce fracture propagation and sudden collapse of the tower basement.

1 INTRODUCTION

Bologna, in the Middle Ages had well over 100 tall towers (Roversi 2011), although today fewer than 24 remain. Among the survivors are the so-called Two Towers: the 98 meter tall Asinelli and the Garisenda, which today stands 48 m tall, lesser than the original 60 m, and leans noticeably.

The preservation of historic towers requires a deep understanding of their structural response and the reasons that allowed them to survive over the centuries. It seems in fact evident that the remaining towers survived the initial period in which they were near foundation *bearing capacity collapse*, due to *lack of strength* of the soil. Delay or interruption of the building process enabled the foundation soil to improve its strength and the tower to be successfully finished. Due to uneven

 DOI 10.1201/9781003308867-86

settlements, some towers appear today to be affected by an alarming angle of inclination. This highlights the danger of a *leaning instability*, which may increase if there is *lack of stiffness* of the soil, as it was the case of the leaning tower of Pisa.

In some cases the demolition of the upper part of a leaning tower allowed to avoid this problem and to preserve the building but not its historic integrity (examples may include the civic tower of Ravenna and the present case of the Garisenda Tower).

In addition, problems of structural nature may interact with the geotechnical aspects above highlighted. Indeed the inclination of the towers often due to differential settlements of the foundation may induce dangerous levels of stresses upon the structure of towers and deserves special attention, as proved by the collapse of the Campanile (Bell Tower) in Venice in 1902 and of the Civic Tower in Pavia in 1989 (Anzani et al. 2000; Binda et al. 1992; Macchi 1993;.

The noticeable and paradigmatic example of the eight-centuries-old Civic Tower in Pavia, that collapsed unexpectedly and spontaneously, attracted the attention of many researchers, in order to capture in other similar cases signs of deterioration, including cracks propagating through the bricks and the mortar, and to try to clarify the reasons of collapses which occur after so many years after the construction.

In medieval towers the support walls are usually categorized as single or multiple-leaf. Towers supported by multi-leaf walls typically have inner and outer leaves of brick or stone, within which a mixture (hereafter referred to as "conglomerate") of lime mortar, river gravel and shards of bricks was dumped. By considering that the multi-leaf walls technique dates back from the Roman times, it seems reasonable to assume that this method was well mastered by the 11th century masons, when the construction of the Pavia or the Garisenda towers began. However, an "induced vulnerability" may appear due to the decay over time of the mechanical properties of materials, masonry apparatus and mortar.

Therefore, the stress distribution caused by creep, shrinkage and long-term gradual drying of the wall (which can be also affected by carbonation of the lime mortar) could explain unexpected collapses, as the one occurred in Pavia (Ferretti & Bažant 2006).

In this context, a peculiar and rather unique case is represented by the Garisenda tower in Bologna, a 48 m tall structure with a square base of 7.45 meters per side, characterized by an overall out of plumb of 3.32 m in the South-East direction. Its construction dates back to the XI century and, due to its impressive leaning, in 1350–1353 the original height of 60 m was reduced to the 48 m of the present day (Cavani 1903; Giordano 2000).

The structure of the tower is made of a:

lower portion composed by two external leaves of a common type of gypsum rock stones (found in historic constructions in Bologna and called "selenite") filled with rubble conglomerate, and an upper portion with rubble conglomerate bounded by two masonry brick wall leaves.

It is to be noted that the in the lower portion an additional leave of selenite stones which encases the base of the tower (and hereafter referred to as "*bugnato*") was put in place at the end of the 19th century, mainly for aesthetical reasons.

Recent investigations have proved that selenite blocks of the basement have been altered as a result of (a) exposition to high temperatures during important fires, that took place at the end of XIV and XVII centuries, and possibly because of the presence of forges (that were demolished at the end of the XIX centuries) and (b) high level of humidity in the inner lower part of the tower.

This process has produced a gradual local disintegration of the stones, leading in some case to a reduction of the original 50 to 60 cm thickness to about 30 to 40 cm.

Further alteration phenomena have also been observed on the selenite blocks of the "*bugnato*" (exposed to open air), such as surface dissolution, granular disaggregation of macro-crystals, bacterial actions, all aspects not properly addressed in the scientific literature when dealing with selenite rocks, also due to the peculiarity of the selenite stone mainly used in the area around Bologna only.

All these phenomena claimed for a program of structural monitoring, careful inspection and preservation measures to be implemented, such as: (a) replacement of weathered or fissured key stones, (b) mortar injections to both enable the filling of possible cavities and cracks in the rubble

conglomerate core, (c) confinement of the lower portion of the structure. It is to be noted that the mortar injections are also useful to enhance the bonding between the "*bugnato*" (external selenite cladding) to inner structure (selenite leaves and rubble conglomerate), and improve the stress redistribution altered by creep.

2 BRIEF NOTES ON PREVIOUS RESTORATION WORKS

As it is the case for most of historic towers, is not an easy task to summarize in few notes the complex history of the Garisenda tower; therefore in the following only those aspects strictly relevant to its preservation are recalled and the reader should refer for more insight to the book of Giordano (2000).

The Garisenda was built in the XII century, at the same time as the Asinelli tower, both in front of Porta Ravegnana and just outside of the so-called "selenite" walls, a place strategically important for the defense of Bologna.

Since early times, the Garisenda tower should have appeared perilously leaning, if in 1293 a decision was already taken of its demolition and the tower survived to this decision just for economic constraints. It was in 1350-1353, at the time when Giovanni da Oleggio was sent as Governor of Bologna by Giovanni Visconti of Milan, that the original height of 60 m was reduced to the 48 m of the present day. Furthermore, it must be mentioned, for reasons that will be presented in the next point, that the image of the tower as it stands today dates back to 1890, because before that time craftsmen and commercial activities attached huts all around its perimeter. A small church (of the B.V. delle Grazie) was also present until 1871, when it was dismantled.

A direct inspection showed at that time severe alterations of the leaves of selenite, with some blocks reduced on its original thickness. Therefore, a first restoration work took place, with a complete substitution of the selenite blocks of the exterior face. Incidentally, these blocks were caved in the style of "*bugnato*", i.e. with rounded edges and not with sharped edges as in the local tradition.

At 9.52 a.m. on the 14th July 1902 the bell tower of San Marco in Venice collapsed, leaving a pile of debris more than 20 m high, and this tragic event claimed for an analysis of the stability of the Garisenda.

In 1903, Francesco Cavani, of the "*Alma Mater Studiorum*", University of Bologna, published his report referring the inclination of the mean axis with respect to the gravity vector equal to 7% with a corresponding overhanging of 3.22 m (Cavani 1903, 1917, 1919).

By considering that the tower has a base area of 55,5 m^2 and that the foundation area is equal to 76,56 m^2, and by considering two extreme assumptions: a density of the masonry equal to 2000 kg/m^3 (which gives an upper bound weight of 41200 kN) and a density of 1600 kg/m^3 (which gives a lower bound weight of 32960 kN), Cavani (1903) reached the conclusion that the maximum compression stress, due to the upper bound value of the dead weight, was equal to 1.96 MPa on the masonry, and 1.1 MPa was the contact stress at the foundation level.

If wind effects are taken into account, the values grow respectively to 2.43 MPa and 1.26 MPa. These rather high stress levels were later on recognized as being the cause of a diffuse state of damage, with cracks not only along the mortar but also into the bricks.

In recent years the Municipality of Bologna appointed in 1986 a first Commission, composed by R. Alessi, G. Folloni and F. Bergonzoni. Unfortunately, Alessi and Folloni passed away and in 1996 the composition of the commission was updated with the appointment of P. Pozzati and M. Unguendoli. In 1998, a third commission was appointed, composed by C. Ceccoli, P. Pozzati, P. Diotallevi, L. Sanpaolesi and G. Dallavalle (Ceccoli 1998, 1999, 2001; Pozzati & Unguendoli, 1997).

As a results of the investigations performed in those years, some remedial measures were made in 1998: a masonry consolidation trough substitution of the weathered bricks and injections of mortar; installation of steel frame to improve the connection of the two leaves of bricks.

Thereafter, in 2008, external steel ties were installed to provide a confinement of the masonry, but no provisions concerning the selenite basement were made at that time.

Finally, with reference to the photogrammetric survey performed in 1997, it is of interest to outline that the Northern and the Western faces do not show evidence that the masons corrected the verticality of the tower, as it would have been the case if the tower began to tilt during the construction. This was the cases of the leaning tower of Pisa and the Ghirlandina tower in Modena. Therefore, it could be argued that uneven settlements occurred when the tower reached its original height of 60 m, as it is discussed in section 4.

3 THE SELENITE: ALTERATION BY EXPOSURE AND THERMAL DEHYDRATION

The selenite is a common type of gypsum rock that belong to the *Messinian Gessoso-Solfifera Formation*, extensively quarried since Roman time in the Bologna hills and used in various historic constructions in Bologna (Del Monte 2005), because of its sparkling attractive appearance and because the rock is light, soft, easy to cut, shape and carve (Lugli 2019).

The selenite rock used in the tower consists of large twinned crystals of gypsum, with a "swallow tail" or "arrow-head" shape, all pointing in the same direction. Two main varieties were used, the massive facies, with crystals up to 30 cm across, and the banded facies with smaller crystals, 1 to 5 cm across, organized in parallel layers (Lugli et al. 2010).

There are two main degradation features as far as the blocks used in the construction of the tower are concerned, one related to the natural alteration at outside exposure conditions and the other due to the action of heat because of fires occurred inside the tower and the presence in the past of forges.

The selenite cladding the external part of the tower (the so called "*bugnato*") is subjected to dissolution by rainwater forming karren, grooves separated by sharp ridges, as large as 14 mm and as deep as 7 mm. In some areas of concentrated rainwater flow, the selenite rock are cut by vertical grooves up to 70 mm across and 100 mm deep (Del Monte et al. 1999). The most common alteration features on the "bugnato" are gypsum efflorescence crusts partially detached, granular disaggregation of the crystals, black crusts and biological attack by lichens and endolithic cyanobacteria. These alteration features are typical of selenite rocks exposed at Mediterranean and other climate conditions (Artieda 2013; Rhind et al. 2014).

The selenite leaves in the inner part of the tower (which contain the rubble conglomerate) display the typical signature of thermal alteration. The gray and sparkling appearance of the original rocks was turned into white by dehydration of the gypsum crystals, which may start at relatively low temperatures, as low as about 100° C. The whitening of the gypsum crystals is one of the distinctive geological feature for the recognition of ancient fires in historical sites (Lugli 2002), such as the Palace of Knossos in the Minoan Crete (from the middle Bronze Age), Eraclea Minoa in Sicily (6th-1st BCE) and the medieval Abbey church in Nonantola, Modena (Lugli 1995, 2019). The change in colour from gray to white is due the formation of a mosaic of bassanite (emihydrate, $CaSO4 \cdot {}^{1}/_{2}H2O$) and soluble anhydrite ($CaSO4 \cdot \varepsilon H2O$) microcrystals. These sulfate crystals are unstable and rapidly rehydrate back to gypsum ($CaSO4 \cdot 2H2O$) capturing moisture and capillary water to form an alabastrine rock. These mineral transitions are accompanied by significant volume changes. Although the initial dehydration induces the presence of secondary porosity by volume decrease, the voids are rapidly closed by the growth and volume expansion of the late gypsum crystals. The resulting white rock shows pseudomorphs of the original selenite crystals, but consist of new microcrystalline interlocking gypsum crystals. Because the rehydration phenomena occur soon after the fire, the mechanical properties of the resulting alabastrine rock was actually improved by the textural rock changes connected to the dehydration-rehydration transitions compared to the original rock. A core drilled on the northern wall of the tower showed that the thermal alteration of the selenite rock reached the depth of 15 cm from the slab surface.

At the south-eastern corner of the tower the thermal alteration process was much stronger. Here the rock has been deeply pulverized at the scale of the single micro-crystal components, with loss of material and a regression of the original slab surface of 20 cm (Figure 1). As revealed by SEM-EDS analyses, the disaggregated material consists of anhydrite that was not rehydrated back

to gypsum (Figure 2). These characteristics demonstrate that the south-eastern corner of the tower was heated at temperatures above 500°C, which is the transition point for the formation of insoluble anhydrite. This calcium sulfate form is much slower in rehydrating back to gypsum compared to soluble anhydrite formed at the expenses of gypsum at lower temperatures. The hydration process in this case may even occur at geological time scale. The formation of insoluble anhydrite also induces the most extreme net volume decrease (up to 38.6 %), which contributed to disrupt the original texture of the rock.

The described dehydration phenomena are possibly the consequence of one of the blazes known to have affected the tower in the XIV and XVII centuries. The stronger alteration and the higher temperature reached in the south-eastern side of the tower may be related to the presence of flammable material during the blaze or by the activity of a forge installed in the corner of the room. The presence of active forges has been documented around the tower until the XIX century.

Figure 1. Different degrees of thermal alteration of the selenite rock in the southwestern corner of the Garisenda tower entrance room. Note the recession of the slab surface affected by higher temperature.

4 SOIL PROFILE, SUBSIDENCE AND MONITORING

The need to provide a reliable soil-foundation model suggested geotechnical campaigns at different times: 1973–75, 1995 and 2000. More recently, between May and August 2016, a new site investigation was carried out with the aim of complementing the previous ones and enabling a geotechnical model to be defined in some detail. Furthermore, four piezometers were installed at the depth of 10, 20, 30 and 100 m from the ground level, to monitor of water table, providing evidence of a limited downward seepage.

The soil profile consists of an alternation of silty-clays and clayey-silts, down to the investigated depth of 100 m. The soil samples extracted during borings and the geotechnical interpretation of the CPTU (piezocone penetration tests) profiles suggest that the deposits can be divided in:

anthropic fill, between the ground level and 4.5 ÷ 5 m of depth (anthropogenic deposits) and a variable succession of lenses of silty clays and clayey silts (floodplain deposits).

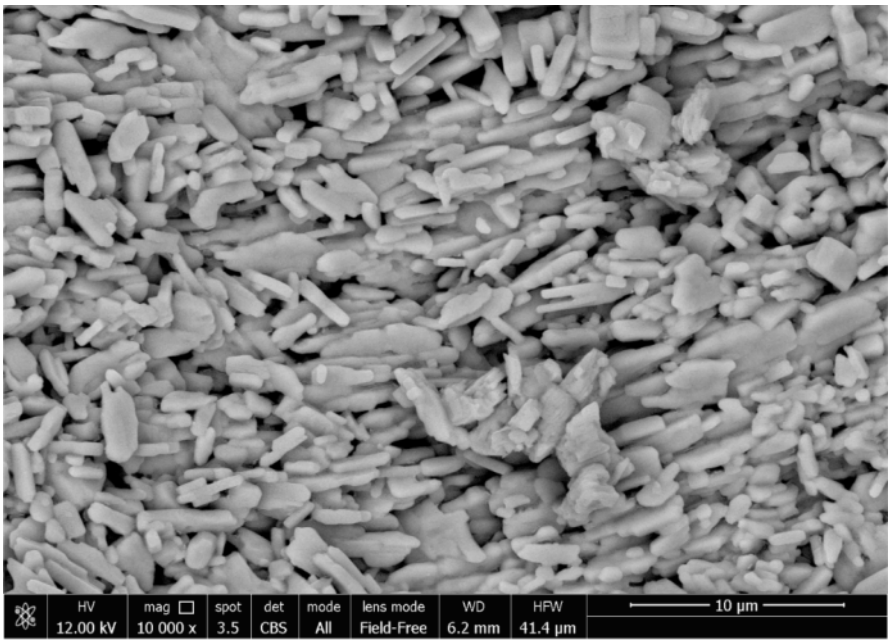

Figure 2. SEM image of the disaggregated material collected from the high temperature alteration zone of Figure 1. Note the high porosity and disruption of the former selenite macrocrystal now consisting of insoluble anhydrite microcrystals.

Despite the lithological uniformity of the deposits (e.g. grain size distributions and Atterberg limits in Figure 3), their mechanical properties appear heterogeneous both laterally and vertically. As an example, Figure 3 shows the scatter of the undrained strength (su) profiles, deduced from CPTU tests carried out in proximity of the north-east corner of the Garisenda tower.

The geological setting with the identification of the sedimentary facies of the area can provide a significant interpretative key of such alluvial deposits, showing typical lenticular geometries with poor lateral extent. This feature can explain the lack of uniformity found in a small area like the size of the Garisenda base. In addition, the floodplain successions are locally interrupted by paleosols, identified by a typical dark colour (photo of a portion of SPZ100 borehole coring in the left side of Figure 3) and followed by lighter horizons with carbonate nodules. They are characterized by higher shear strength, probably due to their over-consolidation state, while the non-paedogenized horizons, not involved in the carbonatation or desiccation processes, show a poorer mechanical response.

The geological history, with the described post-depositional phenomena, had profound implications on the soil response to loading and, in particular, the lack of uniformity in the subsoil conditions could be one of the main initial reasons of the severe inclination of Garisenda Tower towards the east side (Bertolini et al. 2022).

In addition to the above referred investigation a great effort was also devoted to monitor the effects of the subsidence.

As it was the case of many other cities, after the Second World War the city of Bologna experienced a significant demographic growth and an industrial development, so that an intensive groundwater extraction occurred to satisfy the increased demand of water. This water exploitation

induced a marked increase of subsidence in urban areas and induced local institutions to undertake investigations and to quantify these movements (Darini et al. 2018).

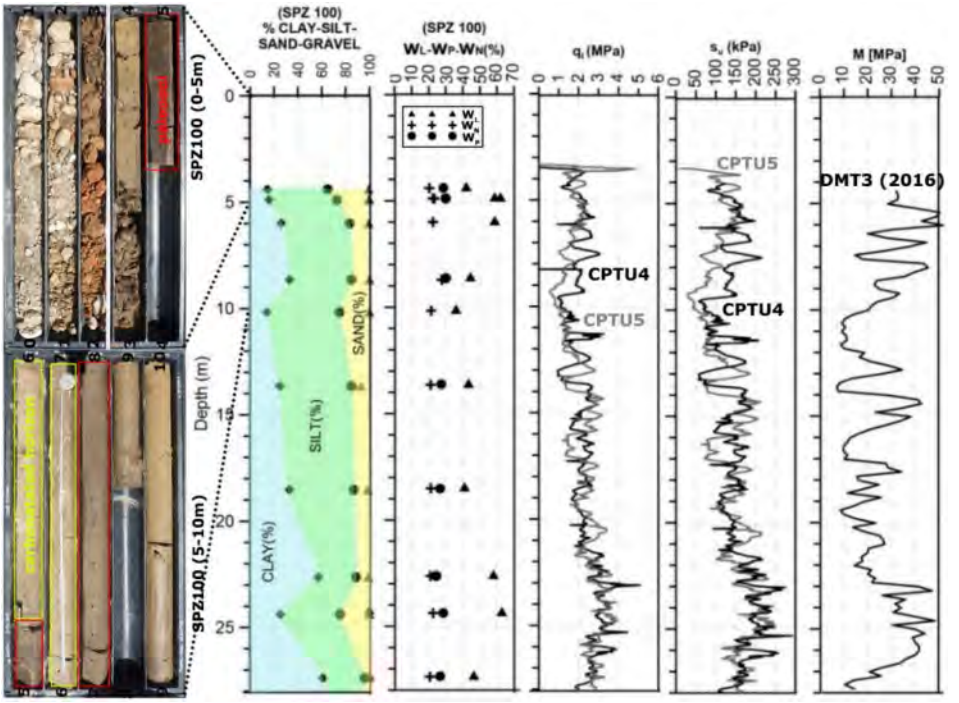

Figure 3. From the left: photo of soil samples extracted from the continuous coring borehole SPZ100 (2016 campaign); soil profile of the investigated site, showing the grain size distribution, Atterberg limits, cone tip resistance (q_t) and shear strength (s_u) as deduced from the CPTU 4 and CPTU 5 (2016) profiles and the constrained modulus as deduced from the dilatometer test DMT3 (modified from Marchi et al. 2019).

A first levelling network of 200 benchmarks was installed along the "via Emilia" between 1950 and 1980 by the Management district of the Reno River Basin. Thereafter, the Municipality of Bologna promoted an extended network of 500 benchmarks, that included the previous ones, with measurements campaigns in 1983, 1987, 1992, 1999 (Darini et al. 2018).

A more detailed and effective campaign of levelling started in November 1972 for the Asinelli tower and in April 1990 for the Garisenda tower, in the context of a research programme promoted by the Municipality with the "*Alma Mater Studiorum*", University of Bologna (Bitelli 2018).

It is apparent from measured data that, in the time interval 1990–2019, the benchmarks 12 (on the North-East corner of the basement) and 13 (South-East) suffered settlements of about 4.92 mm and 5.64 mm, with an average annual rate of 0.18 mm/year.

The benchmarks 10 (South-West) and 11 (North-West) settled 1.63 mm and 1.24 mm respectively, with an average rate of 0.05 mm/year.

At first glance, these results could not appear as alarming in itself, but it must be recalled that they contribute to increase the already alarming out of plumb of 3.40 m and that the rate of differential settlements continue to increase in time, adding further negative effects on the state of stress of the selenite blocks.

Due to these alarming phenomena, an experimental programme was set up on May 31st 2019 to also monitor the evolution of the structural health of the tower. Due to lack of space and the short period of time elapsed since that time, there is not possibility to consider in this paper the obtained data, but is worth to mention at least the installed system.

Six optic-fiber sensors have been applied to the inner face of the load-bearing walls in the vertical direction: 4 of them, 2.0 m length, have been fixed at the internal corners, and 2 other ones, of 1.0 m length, on the East and South internal faces.

In addition, 8 acoustic emission sensors have also been placed at the basement level: 6 of them fixed on the inner surface of selenite, 1 embedded inside the masonry fill, and 1 outside of the basement, just below the selenite ashlar.

More recently, on February 25th 2021, a pendulum was installed at the elevation of 39.30 m, and on June 3rd 2021 4 wire strain gauges at the outside corners of the basement.

Note that all the above mentioned sensors were also intended to complement the system installed in March 2011 (see Andreon et al. 2011), comprehensive of extensometers, short and long base deformeters, laser displacement sensors, inclinometers, gonioanemometer and temperature sensors to monitor the upper portion of the tower.

5 INSTABILITY OF SELENITE BLOCKS AND REMEDIAL MEASURES

As mentioned in the brief historic notes of section 2, old documents give a '800 picture of several huts around the base of tower with artisans works. Following a refurbishment of the whole area of the city where the towers are located, the huts were demolished and direct inspection showed that the outer selenite leaves of the base of the tower were severely damaged (most likely due to an improper use in the huts). The damaged outer selenite leaves were then repaired with various materials and covered with the vestment made with ashlar of selenite stones in form of rusticated stonework, called "*bugnato*".

The peculiar shape of the "*bugnato*" results in a reduced contact surface between the stones in comparison to the volume of blocks and it is worth to mention that the basements of coeval towers in the town are made by solid parallelepipedon stones of selenite with very small thickness mortar joints being load-bearing system and a complete surface of contact.

During recent controls with laser-scanner the "*bugnato*" was evaluated not to be any more in planar condition, with pick swelling of 25 mm observed in the last ten years. An alarming hypothesis was that the cladding had started to contribute to the tower statics, and it was prone to local instability. A geometrical model of this swelling phenomenon showed that the observed swelling is coherent with a shortening of the height of the "*bugnato*" of about 1.10 mm. This phenomenon could be a consequence of the creep in the inner structure (the material filling multi-leaf stonework) and/or deterioration of the inner selenite leaves.

In addition to the criticalities of the "bugnato" represented above, the investigations developed in 2018–2020, as well as the results of the monitoring system, confirmed the existence of problems related to the alteration of the inner selenite leaves of the tower basement.

It is worth to point out that only the surface of the interior selenite leaf can be inspected, while all other faces are not directedly visible being either in contact with the inner conglomerate or encased by the "bugnato". As shown in Figure 1 this surface is highly altered and it can be expected that also the other surfaces (inner toward the conglomerate and external toward the "bugnato") can be subjected to the same severe alterations observed inside with and significant reduction in the original thickness of the blocks.

In order to assess the effects of the wall deterioration (both in the selenite leaves and in the inner conglomerate) a specific finite element model was developed (see Figure 4), which makes use of solid elements. The model comprised the selenite leaves and the inner conglomerate, as well as the upper portion of the tower made of conglomerate and masonry; "the bugnato" was not considered in model, being a superficial covering not completely connected to the inner structure.

A number of numerical simulations were then developed. By assuming a modulus of elasticity for both the selenite leaves and the inner conglomerate equal to $E = 40.000$ daN/cm^2, the maximum stress level in the selenite was found to be about 40 daN/cm^2, and in the conglomerate of about 20 daN/cm^2.

Thereafter, to simulate the deterioration of the selenite in the area around the corner where the most severe deterioration was observed (orange portions represented in Figure 4). the modulus of elasticity was progressively reduced at 75%, 50%, 25%, 10% and 2% of its original value, down to a minimum value of $E = 800$ daN/cm^2.

All simulations were developed considering only the dead load (wind and seismic actions were not considered in these preliminary analysis). Furthermore, to take into account the reduced strength in traction of the selenite leaves and of the conglomerate, the models were progressively adapted so that any finite element block which deployed a stress in tension higher than 1 daN/cm^2 was decoupled from the others nearby blocks.

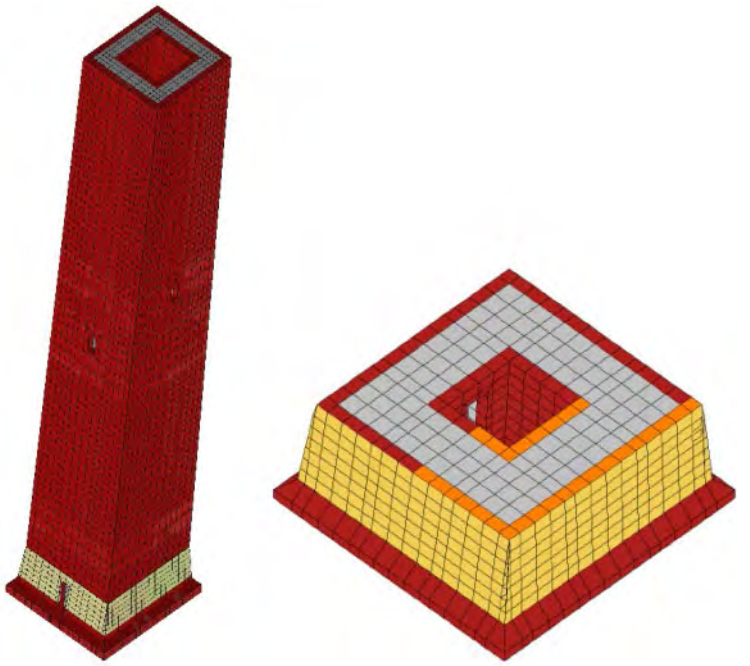

Figure 4. Schematic representation of the finite Element Model of the tower: unaltered selenite leaves (dark red), inner conglomerate (grey), altered selenite leaves (orange).

The obtained results have shown that the "deterioration" of just a small portion of the selenite leaves leads to a significant increase in the stress condition of the inner conglomerate with a consistent reduction in the level of safety of the structure. More specifically:

(a) the maximum level of stress in the selenite blocks remains almost unaltered, even though an "arching effect" can be detected, with transfer of load into the selenite blocks surrounding the altered ones;

(b) the maximum level of compressive stress in the inner conglomerate reaches average level of stresses of about 30 daN/cm^2 along the entire Est wall (Figure 5), significantly greater than the value of the "undamaged condition" and alarmingly close to the crushing stress of the conglomerate (found through experimental tests on samples extracted from the tower inner conglomerate and ranging from 25 to 35 daN/cm^2).

These studies proved that it was necessary to take immediate action in order to reduce the risks of collapse of the basement of the tower, and the following interventions were implemented (see Figures 6, 7 and 8):

(a) passive confinement of the tower base obtained through FRCM belting along horizontal joints of stonework, with the voids between the "bugnato" and the selenite leaves filled using ad hoc elements that can be easily removed in the future;

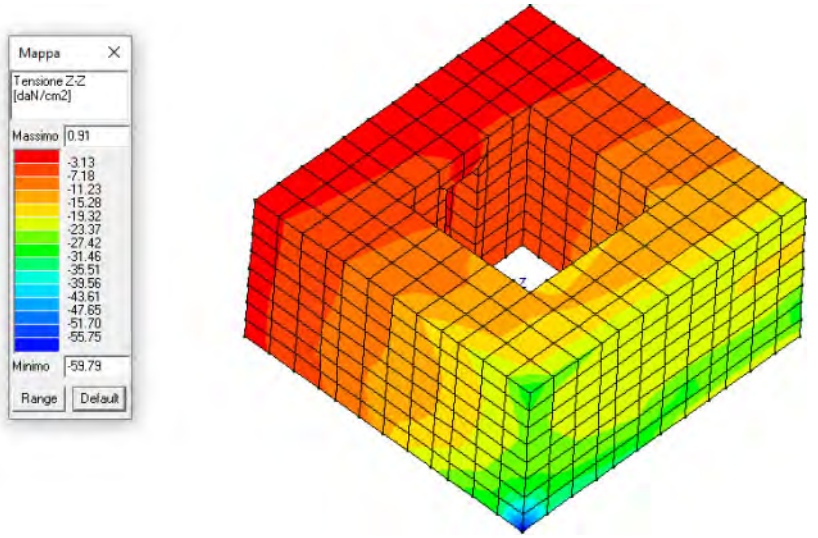

Figure 5. Analysis of the base of the tower in its "deteriorated" condition (E = 800 daN/cm^2, for the altered selenite leaves represented in orange in Figure 4).

Figure 6. FRCM belting (A).

Figure 7. Post tensioned steel bars (B).

(b) active confinement of the tower corner by insertion of post tensioned stainless steel bars 24 mm in diameter (stainless steel AISI 304) and corner stainless-steel plates;

(c) active confinement of the "bugnato" through a funicular belting of the tower base. This was obtained by a monitored post tensioning of steel-cables with the insertion of wood blocks (of different thickness) between the "bugnato" and the cables.

Figure 6. Confinement of the bugnato (C).

Even though these interventions have produced positive effects on the structural safety of the tower, it is of uppermost importance to continue to strengthen the tower base through: (a) injection in the inner conglomerate, (b) substitution of the deteriorated selenite blocks, and (c) to improve the connection between the leaves and the infill.

The implementation of these further interventions without compromising the structural safety of the tower is difficult to achieve and may require in the future the provision of an "ad hoc" structure to safeguard the tower against adverse conditions that could happen during the work.

6 CONCLUSIONS

Surveys performed in recent years with laser-scanner proved that the "bugnato" was not to be any more in planar condition, with pick swelling of 25 mm observed in the last ten years. An alarming hypothesis was that the cladding had started to contribute to the tower statics, and it was prone to local instability. Therefore the Municipality of Bologna promoted additional and more specific investigations on the tower basement.

These investigations have shown that selenite blocks have been subjected to a process of gradual disintegration, leading in some case to a reduction of the original 50 to 60 cm thickness by an amount of about 20 cm.

Numerical simulations have also shown that the detected deterioration of the selenite stones lead to substantial increase in the stress levels of the rubble conglomerate that makes up the structural bearing walls, reaching values of stress near to its ultimate strength.

These dangerously high level of stress occur on the leaning side (East face) of the tower which, due to the high level of inclination (about 7 %) is under substantial static effort.

It was thus deemed necessary to provide the basement of tower with conservation measures, such as passive confinement obtained through FRCM belting along horizontal joints of stonework, active confinement of corners by insertion of post tensioned stainless steel bars 24 mm in diameter (stainless steel AISI 304) and stainless-steel plates, active confinement of the "bugnato" through a funicular belting of the tower base.

These remedial measures were successfully implemented and removed the risk of local instability, but additional conservation measures are also taken into consideration to improve the strength of the infill conglomerate, to substitute the deteriorated selenite stones and to improve the connection between the leaves and the infill.

ACKNOWLEDGMENTS

The remedial measures described in this paper and applied to the basement of the Garisenda tower were devised on the behalf of the Scientific Committee appointed by the Municipality of Bologna in December 2018 and composed by Ambrosini C., Andreon F., Dallavalle G., Diotallevi P.P., Di Tommaso A., Gottardi G., Lancellotta R., Lugli S., Malerba P., Trombetti T. The contribution of all these members is highly recognized and acknowledged.

The Authors also acknowledge Arch. Manuela Faustini Fustini, Technical Director of the Municipality of Bologna, and Eng. Vincenzo Daprile who took the responsability of the procedure of the implemented remedial measures.

REFERENCES

Andreon F., Dallavalle G., Gasparini G., Trombetti T.(2011). Le Torri Asinelli e Garisenda : le indagini e gli interventi di consolidamento. Inarcos n 719 Maggio.

Anzani A., Binda L., Mirabella Roberti G. (2000). The effect of heavy persistent actions into the behaviour of ancient masonry, Mat. Struct., RILEM 33, 228, 251–261.

Artieda O., 2013. Morphology and micro-fabrics of weathering features on gyprock exposures in a semiarid environment (Ebro Tertiary Basin, NE Spain). Geomorphology 196 (2013) 198–210.

Bertolini I., Marchi M., Gottardi G., Amorosi A., Bruno L. (2022). Investigating a geotechnical 'cold case': the Two Towers of Bologna (Italy). In Proceedings of the III International Symposium On Geotechnical Engineering For The Preservation Of Monuments And Historic Sites, Naples, Italy, 22–24 June 2022. Submitted for publication.

Binda L., Gatti G., Mangano G., Poggi C., Sacchi Landriani G. (1992). The collapse of the Civic Tower of Pavia: a survey of the materials and structure, Masonry International 6 (1) (1992) 11–20.

Bitelli G. (2018). Convenzione tra il comune di Bologna e Università di Bologna (Dipartimento DICAM) sull'organizzazione dei dati storici relativi ai rilievi di livellazione geometrica effettuati sulle due torri.

Ceccoli C. (1998). (coordinator of the Commission). Relazione programmatica-descrizione dei metodi di indagine e del sistema di monitoraggio. Novembre.

Ceccoli C. (1999). (coordinator of the commission) Il consolidamento della Torre Garisenda. Relazione illustrativa. Ottobre.

Ceccoli C. (2001) (coordinator of the commission). Relazione tecnica sul progetto complessivo di consolidamento e sugli interventi di prima fase. Marzo.

Capra A., Bertacchini E., Castagnetti C.,Dubbini M.,Rivola R.,Toschi I. (2011). Rilievi laserscanner per l'analisi geometrica delle Torri degli Asinelli e della Garisenda. Inarcos n 719 Maggio.

Cavani F. (1903). Pendenza, stabilità e movimento delle torri. La Garisenda di Bologna e la Ghirlandina di Modena. Atti del Collegio degli Ingegneri e degli Architetti in Bologna.

Cavani F. (1917). Sulla pendenza delle principali torri di Bologna, Modena e Pisa. Atti del Collegio degli Ingegneri e degli Architetti di Bologna.

Cavani F. (1919). Su alcune questioni relative alla pendenza delle torri Atti del Collegio degli Ingegneri e degli Architetti di Bologna.

Darini G., Modoni G., Saroli M., Croce P. (2008). Land subsidence induced by groundwater extraction: the case of Bologna. Int. Congress on Environmental Modelling and Software Integrating Sciences and Information Technology for Environmental Assessment and Decision Making, 1386–1393.

Del Monte M., 2005. L'epoca d'oro della selenite a Bologna. Il Geologo dell'Emilia-Romagna, 20, p. 5–24.
Del Monte M., Forti P. and Tolomelli M., 1999. Degradazione meteorica dei gessi: nuovi dati dalle torri medioevali di Bologna (Italia)". Atti e Memorie della Commissione Grotte "E. Boegan", Trieste 2000, 37, 77–91.
Ferretti, D., and Z. P. Bažant (2006). Stability of ancient masonry towers: Stress redistribution due to drying, carbonation, and creep. Cement and Concrete Research 36:1389–1398.
Giordano F. (2000). La torre Garisenda. Costa Editore, 208 pp.
Lugli S. 1995. Blocchi di roccia gessosa nella chiesa abbaziale di S. Silvestro a Nonantola (Modena): caratteristiche geologico-petrografiche e ipotesi di provenienza. Atti della Società dei Naturalisti e Matematici di Modena, 124 (1993), 137–160.
Lugli S., 2002. Recognition of ancient fires in archaeological sites containing gypsum rocks. Proceedings of the VI International Conference of the Association for the Study of Marble and Other Stones in Antiquity (ASMOSIA), Venice, 15-18 June 2000, 545–548.
Lugli S., 2019, Il gesso in natura e nell'arte. GeoArcheoGypsum2019, Geologia e archeologia del gesso: dal lapis specularis alla scagliola, (a cura di) D. Gulli S. Lugli, R. Ruggieri, R. Ferlisi. Palermo, Regione siciliana, 17–31.
Lugli S., Manzi V., Roveri M. & Schreiber B.C., 2010. The Primary Lower Gypsum in the Mediterranean: A new facies interpretation for the first stage of the Messinian salinity crisis. Palaeogeography, Palaeoclimatology, Palaeoecology, 297, 83–99.
Macchi G. (1993). Monitoring medieval structures in Pavia. Structural Engineering International, 1, 9–9.
Marchi M., Bertolini I., Gottardi G., Amorosi A., Bruno L. (2019). From geological and historical data to the geotechnical model of the Two Towers in Bologna (Italy). In Proceedings of the XVII ECSMGE, Reykjavik, 1–6 September.
Pozzati P.,Unguendoli M. (1997). Situazione statico strutturale delle due torri di Bologna. Convenzione fra Comune di Bologna ed Università degli studi di Bologna . Relazione conclusiva dei responsabili scientifici.
Rhind T., Ronholm J., Berg B., Mann P., Applin D., Stromberg J., Sharma R., Whyte L.G. and Cloutis E.A., 2014. Gypsum-hosted endolithic communities of the Lake St. Martin impact structure, Manitoba, Canada: spectroscopic detectability and implications for Mars. International Journal of Astrobiology 13 (4): 366–377.
Roversi G. (2011). Le torri di Bologna-quando,come e perché. Grafis.

Geotechnical Engineering for the Preservation of Monuments and Historic Sites III – Lancellotta, Viggiani, Flora, de Silva & Mele (Eds)

A simplified approach to assess the stability of tuff cavities accounting for the spatial variability of the shear strength and the presence of joints

F. de Silva, T. Lusi, M. Ruotolo, A. Flora, M. Ramondini & G. Urciuoli
Università di Napoli Federico II, Napoli, Italy

ABSTRACT: This study investigates how the stability of the roof cavity dug in the Neapolitan Yellow Tuff is influenced by the spatial variability of the rock uniaxial compression strength and by the presence of horizontal joints. The geometrical schemes and the loading condition analyzed by Evangelista et al. (2000) were reproduced in the 2D finite difference Code FLAC to calculate the factor of safety. The variability of the resistance was introduced by assigning a Mohr-Coulomb constitutive model to the rock in which the friction angle is constant, and the cohesion is defined by a Gaussian distribution calibrated on the data of several uniaxial compression tests performed on tuff. Following the Monte Carlo simulation, fifty analyses were performed on each geometrical scheme, in which the cohesion was assigned randomly to the mesh elements. The presence of the discontinuities was introduced by modelling a 0.5 m thick horizontal layer in the roof with a resistance reduced with respect to that of the intact rock according to the Barton (1977) model for the rock joints. The analysis was repeated by changing the position of the less resistant layer along the roof thickness. The results allowed to generate stability curves expressed as a function of the cavity width normalized to the roof thickness and on the ratio between the rock uniaxial compression strength and the acting vertical stress. The variability of the rock strength and the presence of joints reduce the safety of the roof cavity. Such effect is more pronounced as the position of the discontinuity approaches the bottom of the roof.

1 INTRODUCTION

Several cities located on soft rock in Italy and all around the word are characterized by the presence of a network of man-made cavities, dug in the subsoil for religious purposes, water storage or resulting from the past and intense quarrying activities. During the time they have been used as necropolis, cemeteries, houses or aqueducts and today host touristic tours and entertainment activities. Some of them are even preserved as world heritage sites, as, for instance, the necropolis of Cerveteri and Tarquinia near Rome, the aqueduct below the Sassi of Matera in the south of Italy, the city of Petra in Giordania, the Hypogeum in Malta, the Cappadocia Region in Turkey, and so on.

The irregular geometry and load distribution as well as the spatial variability of the rock stiffness, stress and strength make the analysis through accurate models the most appropriate tool to evaluate their stability conditions. As a matter of fact, *ad hoc* numerical models have been generated for the man-made caves in Nottingham (Walthama & Swift 2004), the ancient caverns of the Bet-Guvrin National Park in Israel (Tsesarsky et al. 2013), the coal mines in USA (Sherizadeh et al. 2016) the Sandaozhuang molybdenum mine in China (Liu et al. 2017), the Marsala quarries in Sicily (Fazio et al. 2017; Zimbardo et al. 2018), the Fontanelle cemetery in Naples (de Silva and Scotto di Santolo 2018). Conversely, analytical approaches are a valid alternative for a preliminary safety assessment at large scale. Results of limit equilibrium analyses (Evangelista et al. 2002; Federico & Screpanti 2003) and parametric finite element analyses (Perrotti et al. 2018; Suchowerska et al. 2012)

DOI 10.1201/9781003308867-87

have been exploited to obtain stability curves for the cavity roof. In most cases, they are derived under the simplified assumption of a homogeneous rock resistance in the roof, which may lead to unconservative predictions on its safety. This study investigates the effect of the spatial variability of the rock strength and of the presence of horizontal joints on the stability chart, with reference to the underground cavities in Naples.

2 STABILITY OF THE CAVITY ROOFS IN NAPLES

The subsoil of Naples and numerous cities in the central and south of Italy is characterized by the presence of a shallow pyroclastic soft rock, called tuff. Its low depth and the easy workability made the tuff to be a very widespread building material. Track of its extraction is still visible in the dense network of more than 700 cavities (Evangelista et al. 2000) under the city shown in Figure 1a. Such underground space is increasingly becoming a tourism attraction, for instance Figure 1b shows the actual use of two of the largest cavities: the touristic tour in the Bourbonic tunnel and the cinema in the Agorà Morelli. Due to their renovated use, the city Administration commissioned a study on the assessment of their static conditions to the geotechnical group of the university of Naples Federico II.

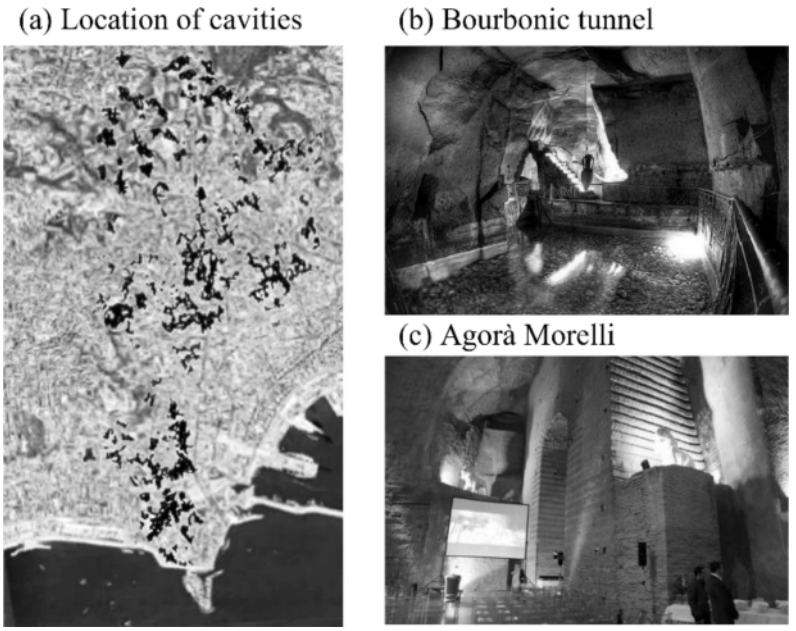

Figure 1. Location of cavities in Naples (a), leisure activities hosted in the Bourbonic tunnel (b) and Agorà Morelli (c).

On such occasion, Evangelista et al. (2000) derived from parametric analyses the stability charts shown in Figure 2a to quickly estimate the safety of roof when dealing with studies at city-scale. They express the critical value of the ratio between the rock uniaxial compression strength and the vertical stress before the excavation, σ_{cmin}/σ_v, as a function of the cavity width normalized to the roof thickness, L/t. Two failure mechanisms were analyzed: local failure corresponding to the detachment of blocks from the roof due to the extensive achievement of traction strength and full collapse associated with the attainment of the resistance both in the compression and traction zones of the roof resistant section. Both mechanisms are detailed in Evangelista et al. (2000).

Given an existing cavity with its L/t, the its σ_c/σ_v ratio divided by the ordinate of the stability curve at the given L/t corresponds to the ratio between the uniaxial compression strength of the

rock mass and the limit value at failure, i. e. σ_c/σ_{cmin}. Such ratio can be interpreted as a factor of safety of the cavity roof, FoS. As an example, Figure 2b classifies 151 cavities of Naples based on the stability conditions of their roof with respect to the local failure mechanism. According to the damage scale by Evangelista et al. (2002), FoS higher than 3 and lower than 1.5 are respectively considered high and insufficient.

Such approach was developed under the hypothesis of a constant value of σ_c. Anyway, mechanical properties of tuff are inhomogeneous within the same deposit and even within the same outcrop, due to the variable void ratio and distribution of lithic fragments, pumices, crystals and glass in the rock matrix as well as due to the presence of horizontal and vertical discontinuities generated by the gas leakage during the formation process. Such aspects are considered in this study and the resulting curves are compared to that derived by Evangelista et al. (2000).

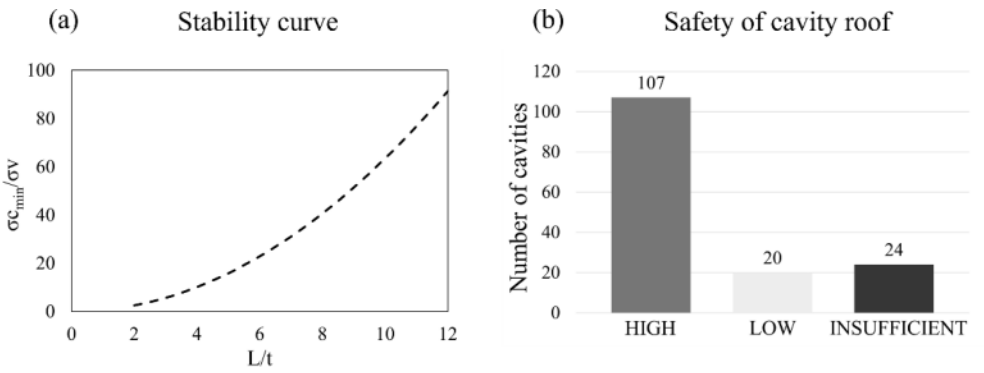

Figure 2. Stability charts by Evangelista et al. (2002) (a) used to assess the safety of the cavity roof (b) assessed by Evangelista et al. (2000).

3 ANALYSED CASE STUDIES

3.1 *Geometric features*

The simple case of a long cavity has been considered, considering different values of the width L and of the roof thickness t, as detailed in Figure 3 and Table 2. The investigated schemes are the same analyzed by Evangelista et al. (2000), hence for sake of simplicity, the same cavity names were adopted in Table 2. The cav.1 and cav.2 were excluded because they were characterized by high safe conditions.

The cavity height was kept constant and equal to 5m. The cavity shape was assumed to be trapezoidal by neglecting the eventual low curvature of the roof. de Silva and Scotto di Santolo (2019) demonstrated that such choice leads to conservative results, because even a slight curvature of the roof reduces the bending moment acting along the whole span.

As typically occurs in Naples, the tuff was assumed to be below a 10 m thick layer the cohesionless soil named pozzolana. Finally, each cavity scheme was also analyzed by placing in the roof a horizontal joint at a distance, s, from the tuff top equal to 0.25t, 0.50t and 0.75t.

3.2 *Mechanical proprieties of tuff and joints*

Table 2 lists the physical and mechanical properties of rock adopted in the analyses, which were again derived from Evangelista et al. (2000). In the Table γ is the unit weight, c the cohesion, φ the friction angle, σ_c the uniaxial compressive strength, ν the Poisson ratio coefficient and E the Young modulus.

The uniaxial compression strength of the tuff was assumed to vary according to the Gaussian distribution plotted in Figure 4. The mean, 3 MPa, and standard deviation, 238 kPa, were calibrated

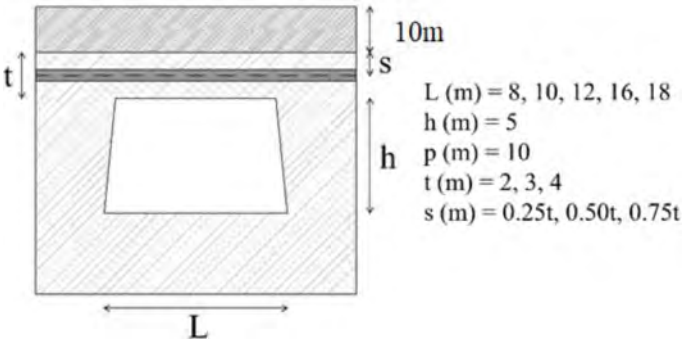

Figure 3. Geometric layout of the analyzed case studies.

Table 1. Geometric features of the case studies.

	L	t	L/t
	m	m	–
Cav 3	8	2	4
Cav 4	12	3	4
Cav 5	16	4	4
Cav 6	10	2	5
Cav 7	12	2	6
Cav 8	18	3	6

Table 2. Mechanical proprieties of the tuff and joints set in the analyses.

rock						joint				
						Barton criterion			Equivalent Mohr-Coulomb	
γ	c	φ	σ_c	ν	E	JRC	JCS	φ_b	c	φ
kN/m3	kPa	°	MPa	–	MPa	–	MPa	°	kPa	°
16	866	3	30	0.30	2000	5	3	30	10	34

on the data of nine uniaxial compression tests on samples taken in a large Neapolitan cavity, called Catacombe di San Gennaro. Actually the mean is equal to the constant value assumed by Evangelista et al. (2000), allowing a reasonable comparison between the results of numerical analyses in which σ_c is constant or follows the Gaussian distribution.

The resistance of rock joints was assumed to be controlled by the Barton (1973) empirical equation. In lack of direct measurements and being the surfaces of the discontinuities almost flat, the joint roughness JRC coefficient was conservatively assumed equal to 5, as suggested by Barton and Choubay (1977) for smooth-nearly planar joints. Since the discontinuities are inside the cavities, weathering effects are low. Then the parameter JCS, associated with the compressive strength of the rock along the joint wall, can be fairly assumed equal to the uniaxial compression strength of the intact rock (Barton & Choubay; 1977), i. e. 3 MPa. The basic friction angle φ_b equal to 30° was obtained from tilt tests executed on samples of the same material by Scotto di Santolo

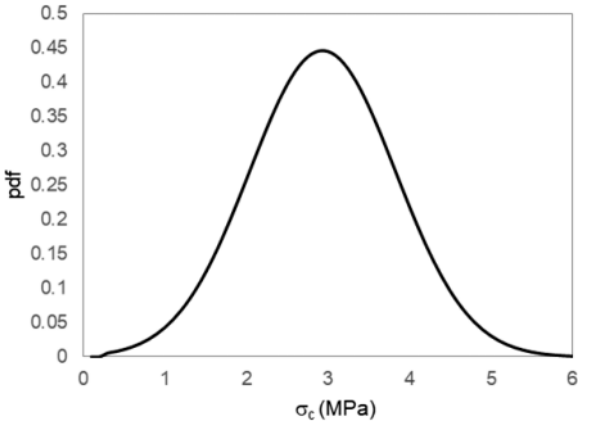

Figure 4. Gaussian distribution of the uniaxial compression strength measured on nine tuff samples in Naples.

et al. (2015). Figure 4 plots the obtained peak shear strength as a function of the effective normal stress.

The numerical analyses described in the following Sections are based on a Mohr-Coulomb model. Following the approach by Boldini et al. (2018), a cohesion and a friction angle were defined for the joints, so that the resulting Mohr–Coulomb criterion is equivalent to the Barton criterion in the stress range acting in the cavity vault under gravity loads. Figure 5 compares the two criteria for the adopted equivalent strength parameters reported in Table 2.

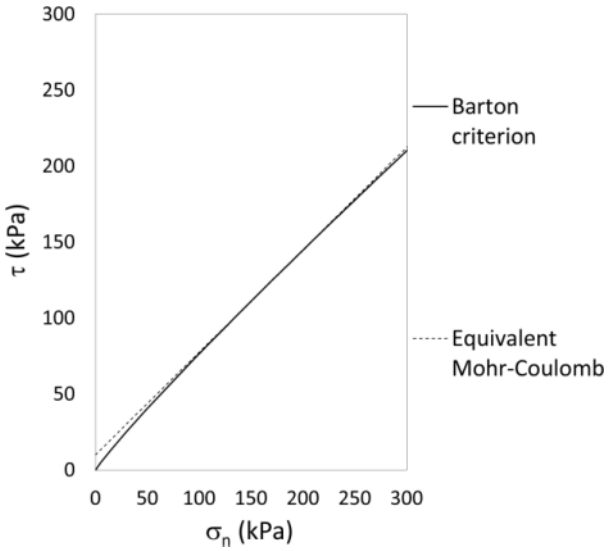

Figure 5. Calibration of the joint through the Barton criterion and equivalent Mohr-Coulomb model.

4 NUMERICAL MODELS AND PERFORMED ANALYSES

Plane strain numerical models associated to all the geometries listed in Table 1 were generated through the finite difference code FLAC 2D (Itasca 2011). Figure 6 shows an example for the cav. 8. The model is 110 m long and 40 m width. Horizontal sublayers 0.5 m thick were generated in the roof, to simulate the variable joint location as described in Figure 2. The mesh size was consequently refined close to the void and the sublayers. The model base was fixed while only horizontal displacements were retrained on the lateral sides. The 10 m thick pozzolana layer covering the tuff was substituted by an equivalent vertical load equal to 160 kPa applied at the ground surface.

Table 2 reports all the mechanical properties adopted for the tuff and the joint in the numerical analyses. The mechanical response of the intact rock was simulated through the Mohr-Coulomb constitutive model. Given the rock friction angle in Table 2, the σ_c distribution in Figure 3 was easily converted into an equivalent normal distribution of the cohesion. The spatial variability of the uniaxial compression strength of the tuff was then implemented through an *ad-hoc* FLAC routine which assigns randomly to each mesh element a value of the cohesion belonging to the computed distribution. An example is shown in Figure 6.

The Ubiquitous joints model was adopted to simulate the joint behavior. It is a Mohr-Coulomb based model which distributes inside the material planes in which the mechanical properties are reduced. The inclination of such planes can be chosen according to the orientation of the fractures detected on site. In this study the less resistant plane were set horizontal, according to the typical orientation of the tuff joints, and characterized by the equivalent strength parameters reported in Table 2.

A tension cutoff, σ_t, equal to 10% σ_C was assigned to the Mohr-Coulomb criterion, consistently with the experimental evidence. The same cut off was assumed for the Ubiquitous joints.

The model was solved firstly to reproduce the lithostatic conditions and then to calculate the stress modification induced by the presence of the cavity with the wished in place approach.

Three sets of analyses were then performed to assess the roof safety conditions for each of the six cases in Table 1:

1) with a constant uniaxial compression strength of the tuff;
2) with a spatially variable uniaxial compression strength of the tuff;
3) with a constant uniaxial compression strength of the tuff and a horizontal joint in the roof.

The first set follows the same hypotheses of the study by Evangelista et al. (2000). For the second set, three hundred analyses were performed, i.e. fifty for each geometric scheme, by changing the random assignment of the cohesion to the mesh elements. Finally, the third set includes eighteen analyses resulting from six geometric schemes and three different locations of the discontinuity (see Figure 3).

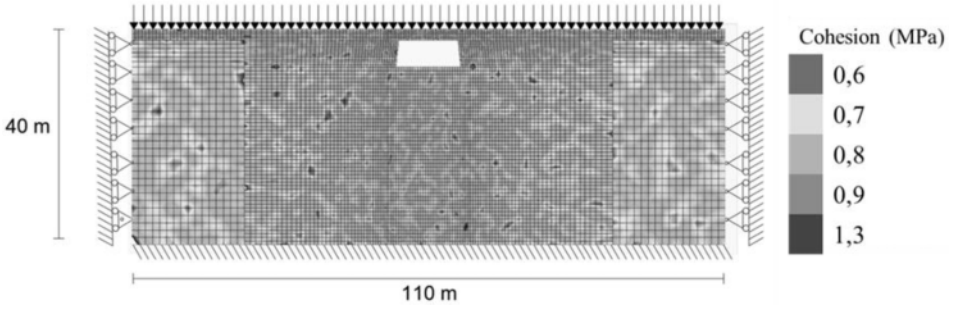

Figure 6. Numerical model of the case with L/t=4 and the spatial variation of the UCS.

The roof safety conditions were then assessed through the strength reduction approach. In details, both the cohesion and the tangent of the friction angle of the tuff (and joints in the third set of analyses) were automatically reduced until failure is reached. Then, the critical reduction factor was defined as:

$$\eta_g = \frac{c}{c_{\min}} = \frac{\tan(\phi)}{\tan(\phi)_{\min}} \quad (1)$$

where c_{min} and $(\tan \varphi)_{min}$ are the values of cohesion and friction angle corresponding to the failure. Consistently with the assumption of Evangelista et al. (2000), the tension cut-off was held constant throughout the calculations.

Table 3 compares the η_g values obtained in this study for the first set of analyses (i.e. σ_c constant) with those computed by Evangelista et al. (2000) with the finite element software Plaxis. Both the hypotheses and the approach for the definition of η_g are the same. Nevertheless, there are differences in the numerical codes, the comparison is successful.

Table 3. Comparison between the η_g values computed in this study and by Evangelista et al. (2000).

	L/t	η_g (this study)	η_g (Evangelista et al. 2000)
	–	–	–
Cav 3	4	2.62	2.38
Cav 4	4	2.24	2.11
Cav 5	4	1.95	1.9
Cav 6	5	1.70	1.65
Cav 7	6	1.20	1.27
Cav 8	6	1.08	1.14

5 DISCUSSION OF RESULTS

Given the geometric layout, the spatial variability of the uniaxial compression strength and the presence of joint reduce η_g. Considering for instance the cav 3, Figure 7 shows the η_g distribution resulting from the fifty analyses with a variable σ_c. There are no cases in which the η_g value obtained with a constant σ_c is reached, being only two (out of 50) the cases in which the $\eta_g = 2.60$. The mean of the η_g distribution, i. e. 2.38, is approximatively equal to 90% of the η_g with a constant σ_c.

The reduction of η_g is more important when the joint is modelled. For instance, a value of 1.35 is obtained when the joint is placed at 0.25t, that is 50% of the η_g with a constant σ_c. Moreover, in most of the cases in which the joint is placed at 0.75t or 0.5t, the applied vertical load simulating the pozzolana layer was reduced to 80 kPa or 40 kPa to obtain a valid η_g. Despite the load reduction, the stability analyses did not converge in the extreme cases of $L/t = 6$ and the discontinuity at 0.75t.

Figure 8 compares the plastic zones in the cavity 3 for four different analysed cases. The vault failure mechanism is not affected by the spatial variability of the resistance (Figure 8a versus 8b), with yielding for tension in the bottom of the resistant section and for shear in its upper part. When the discontinuity is introduced (Figure 8c and 8d), the plastic zones are concentrated inside it and the resistant section is practically reduced to the portion below the joint. As matter of fact, the resistance of the intact rock contributes to the equilibrium only when the joint is at 0.25t, as testified by the comparison of the plastic states in Figure 8c and 8d. The presence of the joint makes the upper portion of the roof section to behave as a load instead of a resistant element.

5.1 *Stability charts*

Once the strength reduction factor η_g is known, the factor of safety of the roof cavity can be conveniently calculated in terms of the uniaxial compression strength of the intact rock, σ_c, as

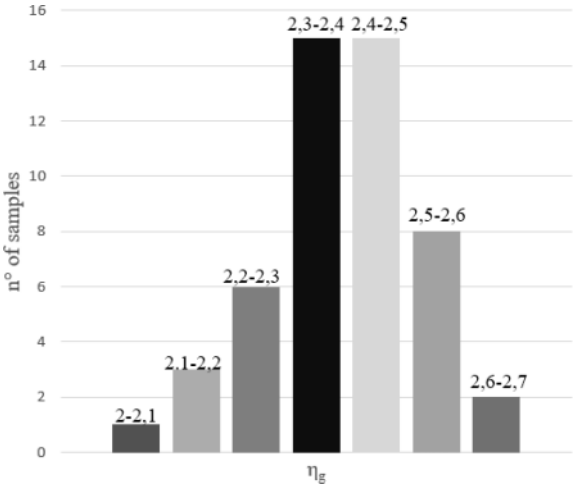

Figure 7. η_g distribution resulting from the fifty analyses with a variable σ_c.

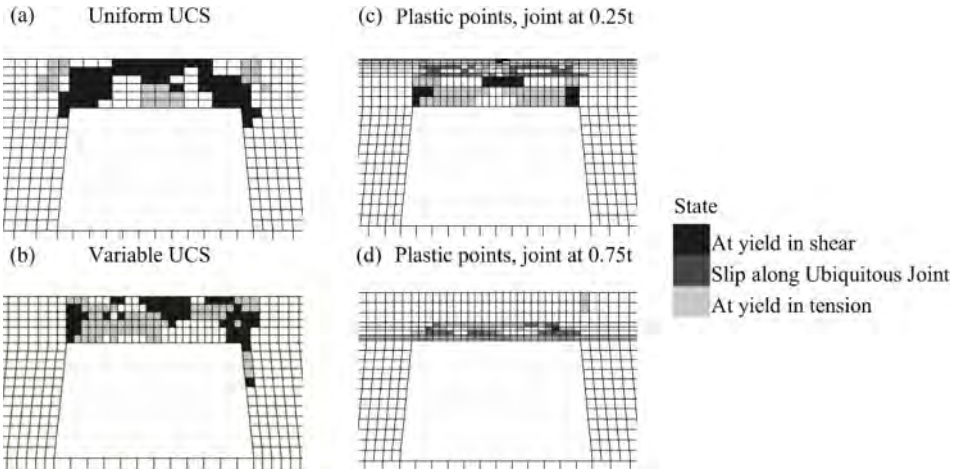

Figure 8. Plastic state of the cavity 3 with L/t = 4 by considering a uniform (a) and spatially variable (b) UCS for the intact rock or a uniform UCS for the intact rock and the presence of joints at 0.25t (c) and 0.75t (d).

follows:

$$FoS = \frac{\sigma_c}{\sigma_{c\,\min}} \tag{2}$$

where σ_{cmin} is computed as a function of the initial strength parameters of the intact tuff from the following equation:

$$\sigma_{c\,\min} = 2\frac{c}{\eta_g}\tan\left(45 + 0.5\arctan\left(\frac{\tan\phi}{\eta_g}\right)\right) \tag{3}$$

Therefore, the stability curves expressed in terms of the dimensionless variables σ_{cmin}/σ_v and L/t, as described in Section 1, are representative of a condition in which the factor of safety is equal to one.

The same curves were generated for the cases at hand. The value of σ_v was trivially computed as the lithostatic vertical stress acting in the roof intrados before the excavation, while σ_{cmin} was calculated through equation 3 given the η_g obtained from each analysis.

The results are reported in Table 4 and plotted in Figure 9. Given the geometric scheme, the ratio σ_{cmin}/σ_v increases when the uniaxial compression strength is assumed variable, and the discontinuity is introduced, meaning that the stability is ensured only for a higher strength of the intact rock or a lower load. Moreover, the effect is increasingly more detrimental (i. e. σ_{cmin}/σ_v is higher) as the joint approaches the bottom of the roof, due to the reduction of the resistant section observed in the contours in Figure 8c and 8d.

Values obtained for each set of analyses were then interpolated through functions, to facilitate the use of the outcomes of this study in preliminary estimations of the cavity roofs. The results relevant to the joint located at 0.75t were not interpolated because the corresponding regression law would have been not reliable due to the few available data.

Table 4. Ratio between the minimum uniaxial compression strength and the vertical lithostatic stress acting in the roof extrados before the excavation when the factor of safety is equal to 1.

	L/t –	Constant UCS $\sigma_{c\,min}/\sigma_v$ –	Variation UCS $\sigma_{c\,min}/\sigma_v$ /(mean value) –	Joint at 0,25t $\sigma_{c\,min}/\sigma_v$ –	Joint at 0,50t $\sigma_{c\,min}/\sigma_v$ –	Joint at 0,75t $\sigma_{c\,min}/\sigma_v$ –
Cav 3	4	4.28	4.82	8.30	10.09	19.04
Cav 4	4	4.79	5.41	9.17	12.13	22.45
Cav 5	4	5.31	6.07	9.70	12.45	31.50
Cav 6	5	7.40	9.43	15.16	18.80	81.39
Cav 7	6	11.89	12.96	22.91	27.04	–
Cav 8	6	12.79	15.23	22.28	29.77	–

The best fitting was found with the power law equation:

$$\frac{\sigma_{c\,\min}}{\sigma_v} = a\left(\frac{L}{t}\right)^b \tag{4}$$

in which the coefficients a and b are detailed in Table 5, together with the coefficient of determination R^2.

According to the FoS definition in equation 2, each curve corresponds to a factor of safety equal to 1 and consequently is the bound between the safe (above the curve) and unsafe (below the curve) conditions. Figure 9 clearly shows that the spatial variability of the strength and the introduction of the discontinuity reduce the safe zone. For instance, the σ_{cmin}/σ_v of cav 3, characterized by $L/t = 4$, $\sigma_v = 192$ kPa and $\sigma_c = 3000$ kPa, is equal to 4.7, 4.82, 9 and 11.5 respectively considering a constant UCS, a spatially variable UCS, the joint at 0.25t and 0.75t. The associated FoS values are 3.3, 2.38, 1.73 and 1.36. Referring to the damage scale by Evangelista et al (2002) shown in Section 1, the safety of the roof passes from high to insufficient depending on the hypotheses on the strength and discontinuities.

Table 5. Coefficients of the power law interpolating the different sets of analyses.

	Constant UCS	Variation UCS	Joint at 0,25t	Joint at 0,50t
a	0.1897	0.2057	0.3926	0.5261
b	2.3195	2.3612	2.2635	2.2248
R^2	0.98	0.96	0.99	0.97

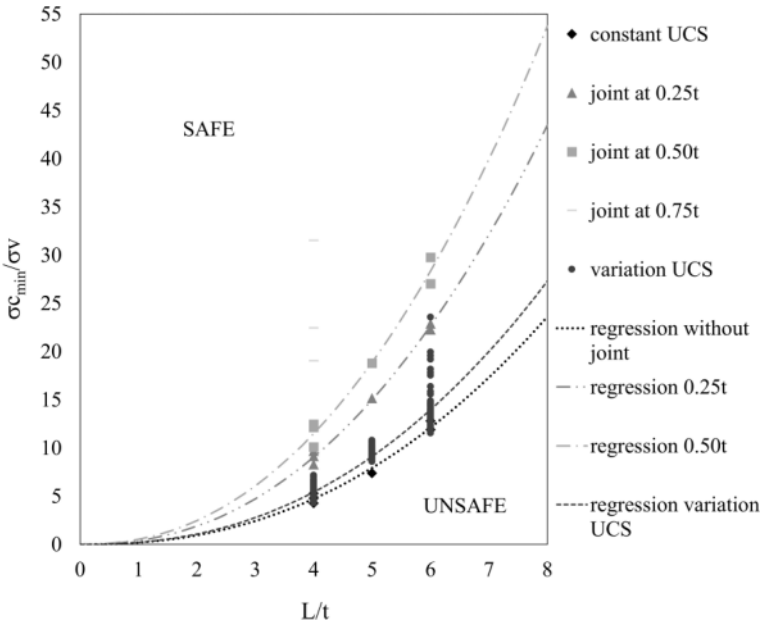

Figure 9. Chart to assess the stability of the cavity roof considering the variation of the UCS or the presence of joints.

6 CONCLUSION

The paper investigates how the safety of the roof of cavities dug in soft rock is influenced by the spatial variability of the uniaxial compression strength and by the presence of discontinuities in the rock. Results of numerical analyses on different cavity schemes and joint locations were interpreted to obtain dimensionless stability charts, in which curves associated with a factor of safety equal to one bounds the zone associated with safe conditions. The latter are a simple tool for a first estimate of the safety conditions of a shallow cavity in plain strain conditions.

The comparison among the charts computed in this study with that already proposed by Evangelista et al. (2000) for a constant strength value and intact rock highlights that both the spatial variability of the strength and the presence of joints reduce the zone characterized by safe conditions. The joint splits the roof resistant section into two portions: the lower which contributes to the resistance and the upper which behaves as a load. This produces a significant reduction of the safe zone in the stability chart when the joint approaches the bottom of the roof.

The outcome of this study reveals that the hypothesis of intact rock with a constant resistance can be very unconservative and in particular, the discontinuities cannot be neglected even in preliminary assessment of safety conditions.

REFERENCES

Barton, N. 1973. Review of a shear strength criterion for rock joints. *Engineering Geology* 7:287–332.

Barton, N., & Choubey, V. 1977. The shear strength of rock joints in theory and practice. *Rock Mechanics* 10:1–54.

Boldini, D., Guido, G., Margottini, C., & Spizzichino, D. 2018. Stability Analysis of a Large-Volume Block in the Historical Rock-Cut City of Vardzia (Georgia). *Rock Mech Rock Eng* 51, 341–349.

de Silva, F. & Scotto di Santolo, A. 2018. Probabilistic Performance-based Approaches to the Static and Seismic Assessment of Rock Cavities. *International Journal of Rock Mechanics and Mining Sciences* 112:354–368.

Evangelista, A., Feola, A., Flora, A., Lirer, S., & Maiorano, R. 2000. Numerical anlaysis of roof failure mechanisms of cavities in a soft rock. *ISRM International Symposium, Melbourne, Australia*.

Evangelista, A., Flora, A., Lirer, S., de Sanctis, F., & Lombardi, G. 2002. Studi ed interventi per la tutela di un patrimonio sotterraneo: l'esempio delle cavità di Napoli. *Proc. XXI Convegno Nazionale di Geotecnica.*

Fazio, N.L., Perrotti, M., Lollino, P., Parise, M., Vattano, M., Madonia, G., Di Maggio, C. 2017. A three-dimensional back-analysis of the collapse of an underground cavity in soft rocks. *Engineering Geology* 228 301–311.

Federico, F. & Screpanti, S. 2003. Analytical criteria and numerical procedures for safety analyses of pillars and vaults excavated in pyroclastic rocks. *Proc. XXII Convegno Nazionale di Geotecnica.*

Liu, K., Hao, H., Li, X. 2017. Numerical analysis of the stability of abandoned cavities in bench blasting. *International Journal of Rock Mechanics & Mining Sciences* 92:30–39.

Perrotti, M., Lollino, P., Fazio, N. & Pisano, L. 2016. Finite element-based stability charts for underground cavities in soft calcarenites Finite element-based stability charts for underground cavities in soft calcarenites. *International journal of Geomechanics* 18(7).

Scotto di Santolo, A & de Silva, F. 2019. 3D numerical analysis of historical ipogeum. *Proceedings of the XVII ECSMGE-2019 Geotechnical Engineering foundation of the future.*

Scotto di Santolo A., Ciardulli F. & Silvestri F. 2016. Triaxial and shear box tests on a pyroclastic soft rock. *Volcanic Rocks and Soils- – Rotonda et al. (eds)* Taylor & Francis Group, London.

Sherizadeh, T. & Kulatilake, P. 2016. Assessment of roof stability in a room and pillar coal mine in the U.S. using three-dimensional distinct element method. *Tunnelling and underground space Technology* 59:24–37.

Suchowerska, A.M., Merifield, R.S., Carter, J.P., Clausen, J. 2012. Prediction of underground cavity roof collapse using the Hoek–Brown failure criterion. *Computers and Geotechnics* 44:93–103.

Tsesarsky, M., Gal, E. & Machlav, E. 2013. 3-D global-local finite element analysis of shallow underground caverns in soft sedimentary rock. *International Journal of rock mechanics and mining sciences* 57:89–99.

Walthama, A.C. & Swift, N. 2004. Bearing capacity of rock over mined cavities in Nottingham. *Engineering geology* 75:15–31.

Zimbardo, M., Cannone, C., Ercoli, L., Nocilla, A. 2018. A risk assessment proposal for underground cavities in Hard Soils-Soft Rocks. *International Journal of Rock Mechanics and Mining Sciences* 103:43–54.

Geotechnical Engineering for the Preservation of Monuments and Historic Sites III – Lancellotta, Viggiani, Flora, de Silva & Mele (Eds)

Comparison of two machine learning algorithms for anthropogenic sinkhole susceptibility assessment in the city of Naples (Italy)

G. Bausilio, M. Annibali Corona, D. Di Martire, L. Guerriero, R. Tufano & D. Calcaterra
Department of Earth, Environment and Resources Sciences, Federico II University of Naples, Naples, Campania, Italy

M. Di Napoli
Department of Earth, Environment and Life Sciences, University of Genoa, Genoa, Liguria, Italy

M. Francioni
Department of Pure and Applied Sciences, Carlo Bo University of Urbino, Urbino, Marche, Italy

ABSTRACT: Sinkholes are common phenomena in the world that occur as a result of collapse processes due to natural and/or anthropogenic causes. Sinkholes consist of three-dimensional funnel-shaped depressions, predominantly circular on the surface, deep from centimeters to several meters. Sinkholes in urban areas, also called "anthropogenic" sinkholes, can be very dangerous from an engineering point of view, causing instability or damaging buildings and infrastructures or even leading to the death of people. In Naples (Italy), the presence of a dense underground cavity network, generated as a result of ancient and historical quarrying of bedrock volcanic tuff (used as building material), promotes the generation of sinkholes occurrence. In this work, sinkhole susceptibility analysis was conducted for the production and the comparison of two different sinkhole susceptibility maps by means of statistical-based algorithms (Random Forest and Maximum Entropy). Twelve environmental variables have been used for the susceptibility assessment, such as groundwater depth, bedrock depth and maps of density and distance from different predisposing factors (aqueducts, roads, sewers, anthropic cavities and underground railroad networks). Both produced maps present good predictive performance and indicate a very high sinkhole susceptibility in the city center of Naples, in agreement with the high density of underground cavities, supporting the importance of the latter as predisposing factor. The road network, considered in this work as representative of secondary aqueduct and sewer systems generally located under such infrastructures, also appears to be an important variable. This study aims to represent a useful tool to improve the development of sinkhole susceptibility maps and to support the local government to protect its cultural heritage.

1 INTRODUCTION

Sinkholes (or dolines, in the European literature) consist of a vertical depression with a predominantly circular shape, a diameter that can vary from sub-metric up to tens of meters and a three-dimensional funnel shape that can be even tens of meters deep (Fairbridge 1968; Ford et al. 2013; Waltham et al. 2005). Trigger mechanisms are dominated by dissolution or erosion processes of geological materials which leads to underground instability and the subsequent formation of depression and/or the collapse of the cover layers. Sinkholes are commonly classified as (Gutiérrez et al. 2008a, 2014; Klimchouk et al. 1996): solution sinkholes, when surface waters flow toward a hollow portion of the land favouring the concentration of water and the subsequent dissolution phenomena of the surface material (this is the prevalent mechanism in the karst environment); sinkholes defined according to the trigger process that affects the cover layer (sagging, collapse and suffosion

 DOI 10.1201/9781003308867-88

process) and to the material composing the cover itself (bedrock, caprock and cover). Sinkholes belonging to this last category, if occur in urbanized environments could be dangerous from an engineering point of view, representing a geo-hazard not to be underestimated, also considering the loss of human lives that are sometimes associated to these phenomena (Gutiérrez et al. 2008b; Waltham et al. 2005). In these contexts, sinkholes are defined "anthropogenic" (or "manmade") (Culshaw et al. 1987; Guarino & Nisio 2012; Parise 2015), affecting several cities all over the world. The metropolitan city of Naples (Italy) is one of these aforementioned cities affected by sinkholes and suffering loss of human lives to these phenomena, like the one occurred on 12th December 1996, when a father and his son, both working in a workshop, fell down a sinkhole initiated while they were having lunch (https://archivio.unita.news/assets/main/1996/12/13/page_027.pdf) or the one that took place on 10th August 2011, when a whole autocompactor fell in a sinkhole with the consequential death of the driver in *Casalnuovo* (https://www.napolitoday.it/cronaca/raffaele-monda-morto-casalnuovo-voragine.html). The city of Naples presents an extended network of underground cavities, which makes it vulnerable to sinkhole phenomena that can affect the cultural patrimony of city, like churches (Rispoli et al. 2020). These cavities have been excavated in the Neapolitan Yellow Tuff formation, to obtain building stones, since ancient times (Colella et al. 2017; Morra et al. 2010; Scotto di Santolo et al. 2015). In 1995, part of the historical city has been added to the list of UNESCO World Heritage sites due to being able to keep and preserve its history and culture through the centuries (https://whc.unesco.org/en/list/726/).

In-depth studies focused on the definition of models to develop sinkholes susceptibility maps were carried out by several authors over the years. The various approaches can be grouped into three main categories: heuristic (Ardau et al. 2007; Guarino et al. 2012; Rosdi et al. 2018), deterministic (Parise 2015; Tharp 1999) and statistical models (Bruno et al. 2008; Ciotoli et al. 2016). Other approaches include the study of sinkholes density or the nearest neighbor analysis (Galve et al. 2009, 2011). The focus of this work is to compare two Sinkholes Susceptibility Maps (SSM) obtained through the application of two different machine learning algorithms: the Random Forest (RF; Breiman 2001) and the Maximum Entropy (MaxEnt; Phillips & Dudìk 2008). The first algorithm is a statistic method largely applied for both classification and regression of data that builds an ensemble of "*n*" amount of decision trees (previously decided by the operator); the second one is a presence-only methodology for which the best model to represent the distribution of an event is the one that maximizes the entropy, which means the one with the maximum uncertainty about the probability of occurrence of the event. This implies that the model has no starting hypothesis and all the combinations of predictor variables can trigger the investigated event. These algorithms were applied to the whole area of the aforementioned city of Naples. In order to apply these algorithms to the study area, a sinkhole inventory, realized by the Federico II University of Naples and constantly updated, was acquired from the most recent sinkhole inventory (Tufano et al. in prep.). The use of a trustworthy and reliable inventory is not only necessary to apply the machine learning algorithms, but it is also deemed a primary tool for an adequate study of sinkhole susceptibility (Guarino et al. 2018; Gutiérrez et al. 2011).

2 THE STUDY AREA

1The city of Naples (Figure 1) is located in the central area of the Campanian Plain (Campania, Italy). The western sector of the city is part of the Phlegrean volcanic field, while the eastern sector is part of the alluvial plain where, in the past, the *Sebeto* river flowed. The Campanian Plain is a structural depression originated by the *Pliocene-Pleistocene* tectonic phases, filled with marine, alluvial and pyroclastic sediments (Aprile et al. 2004; Santangelo et al. 2010). The geological history of the city of Naples is also governed by the continuous ignimbritic volcanic activity that has occurred over the last ∼300ka (Rolandi et al. 2003). The two most important eruptions are attributable to the Phlegrean Fields volcanic field: the first one is the *Ignimbrite Campana* eruption (IC), dated ∼39ka (De Vivo et al. 2001; Orsi et al. 1996) while the second one is the Neapolitan Yellow Tuff eruption (NYT), dated ∼15ka (Deino et al. 2004). IC eruption led to the first collapse

of the Phlegrean Fields caldera and its products covered an area of about 30,000 km^2 (Pappalardo et al. 2002). The products of this eruption do not crop out in many areas, although it is possible to find the *Piperno* deposits (a proximal breccia of IC eruption, Rosi et al. 1996) at the foot of the *Camaldoli* hill, where it has been extracted for centuries as an ornamental rock (Calcaterra et al. 2000, 2005). NYT eruption was characterized by a total erupted volume of about 40 km^3 for an area of ∼1000 km^2. The role of NYT is extremely important for the history of the city of Naples from a geological and cultural point of view. As a matter of fact, NYT has been widely used in the inhabited center of Naples as a building material (de'Gennaro et al. 2000; Scarpati et al. 1993) since ancient times to the point that even the first settlers excavated deep cavities from which the tuff could be obtained (Colella et al. 2017).

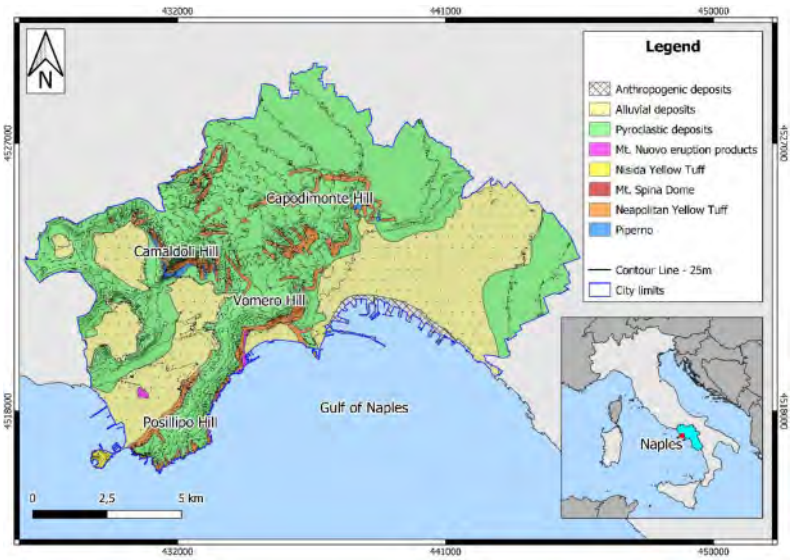

Figure 1. Lithologic Map of the City of Naples (modified from data of the municipality of Naples).

Morphologically, the main hills of the city are *Camaldoli*, *Vomero*, *Arenella* and *Posillipo* hills, while the highest peak of the city is the *Eremo dei Camaldoli* (*Camaldoli* Hermitage) with an altitude of 458 m a.s.l.. The hydrographic network of the city has suffered from the strong anthropization of the territory: many channels have, by now, been heavily cemented or even totally covered (Isaia et al. 2018). In addition to alluvial deposits, the most widespread deposits are those of pyroclastic nature. They consist of scoriaes, ashes or pumice, sometimes alternating with paleosoil levels, intermediate to different eruptions (e.g. from 15ka to the Mt. *Nuovo* eruption of 1538 AD) (Calcaterra et al. 2007; Di Vito et al. 1999).

3 MATERIALS AND METHOD

In this work, two SSMs were obtained through statistical methodologies: RF (Breiman 2001) and MaxEnt (Phillips & Dudìk 2008). To apply these algorithms, an accurate inventory of the sinkholes occurred in the city of Naples is needed.Twelve predisposing factors have been selected to implement the two methodologies. The predisposing factors are related to natural characteristics (depth of aquifer and NYT) and anthropic infrastructures (aqueduct, sewer, cavities, underground railroad). In the following paragraphs the structure of inventory, the considered predisposing factors and the statistical methodologies used to develop the sinkholes susceptibility maps are described in detail.

3.1 *Sinkholes inventory*

The sinkholes inventory of Naples employed in this work contains 463 phenomena, of which 424 georeferenced in a GIS environment, the remaining phenomena are not georeferenced and have not been taken into consideration for this study. Information about such events were derived by multiple sources: i) online version of national daily newspapers (e.g. www.ansa.it, www.corriere.it, www.ilmattino.it), ii) local online daily reports (e.g. www.fanpage.it/napoli/, www.napolitoday.it, www.vesuviolive.it), iii) council chronicles news (e.g. from www.comune.napoli.it); iv) field survey; v) literature data (Guarino & Nisio 2012).

The prevailing triggering factor of these phenomena is the rainfall, followed by the leaks of aqueduct and sewage networks and human activities. In a low percentage of cases it was not possible to obtain the triggering factor.

3.2 *Predisposing factors*

For this study, a total of 12 different predisposing factors (Figure 2) have been utilized to assess SSMs. Data was provided by *Dipartimento di Scienze della Terra, dell'Ambiente e delle Risorse* (DiSTAR), *Università di Napoli Federico II* and by Municipality of Naples. The predisposing factors utilized in this study are: i) Aqueduct Network Density; ii) Aqueduct Network Distance; iii) Groundwater depth; iv) Depth of NYT/cover thickness; v) Road Network Density; vi) Road Network Distance; vii) Sewer Network Density; viii) Sewer Network Distance; ix) Underground

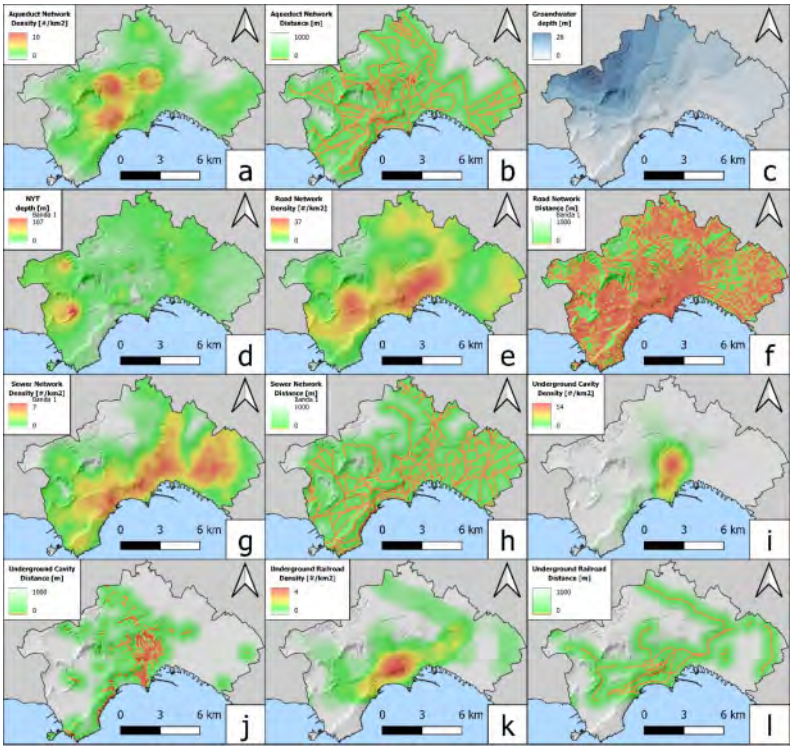

Figure 2. Predisposing factors: a) Aqueduct Network Density; b) Aqueduct Network Distance; c) Groundwater depth; d) Depth of NYT/cover thickness; e) Road Network Density; f) Road Network Distance; g) Sewer Network Density; h) Sewer Network Distance; i) Underground Cavity Density; j) Underground Cavity Distance; k) Underground Railroad Density; l) Underground Railroad Distance.

Cavity Density; x) Underground Cavity Distance; xi) Underground Railroad Density; xii) Underground Railroad Distance. As the Aqueduct and Sewer original shapefiles only include the main pipelines and ignore the secondary network that is directly linked with most buildings (Figure 3), the road network shapefile has been implemented to represent these secondary networks that, otherwise, would be impossible to implement in the methodology. A measure of the Variance Inflation Factor (VIF) for every predisposing factor has been carried out. By itself, the VIF shows how much the variable has an excessive correlation with other predisposing factors. There are no defined guidelines for the acceptable values of VIF but it is usually assumed that variables with a VIF exceeding the value of 5 should be treated with caution, while variables 3whose VIF goes over 10 are assumed to show collinearity problems (Craney & Surles 2002).

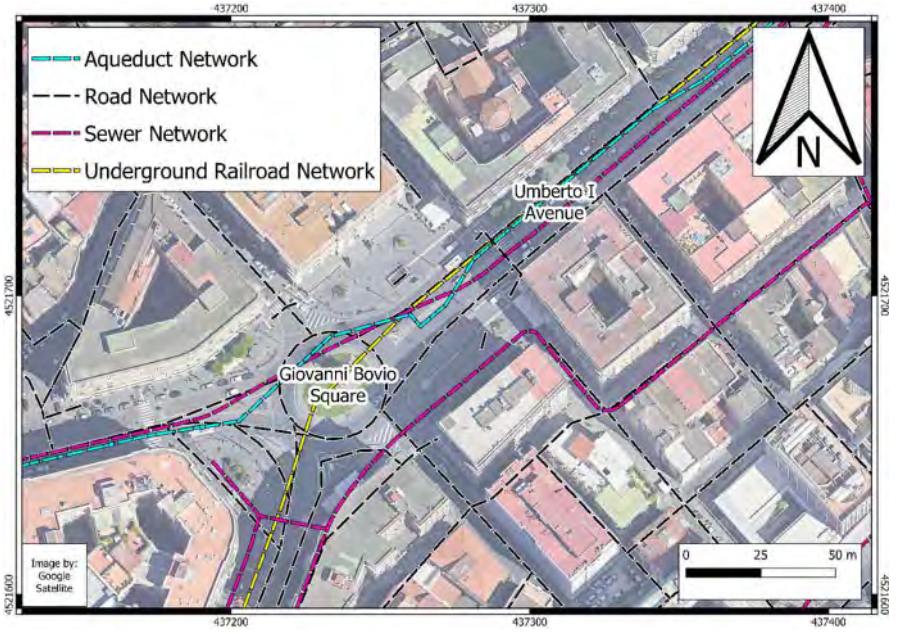

Figure 3. Detail of the city of Naples. Intersection between the different networks used for the predisposing factors in the city center of the city.

3.3 *Modeling – maximum entropy (MaxEnt) and random forest (RF)*

Maximum Entropy (MaxEnt) is a presence-only algorithm based on the "maximize the system entropy" concept. It means that the best model is the one that has no starting hypothesis and all the combinations of environmental variables can trigger the investigated event (Phillips & Dudìk 2008), having the maximum uncertainty about the probability of occurrence of the event. The software utilized to execute the MaxEnt algorithm (MaxEnt, Phillips et al. 2021) extrapolates the importance of the single predisposing factor by permuting its values and, lately, measuring the variation of the AUC (Area Under the Curve) before and after the permutation. The MaxEnt algorithm has been largely used in different areas of study, from landslides susceptibility (Convertino et al. 2013; Di Napoli et al. 2020a, 2021; Felicísimo et al. 2013; Novellino et al. 2021) to groundwater flooding (Allocca et al. 2021) to ecology (Ma & Sun 2018; West et al. 2016).

RF is a machine learning procedure based on the "random decision tree" algorithm. It evolves around the concept of producing an ensemble of "*n*" decision trees (the symbolic forest), it is characterized by a relatively short processing time (depending on number of trees, data and predictors) and without over-fitting problems thanks to the Law of Large Numbers (Breiman 2001). The

choice of the number of trees "n" is left to the operator as well as the number of predictors to use at each split of the various trees (for this work 4, as in 12 predictors / 3, the standard formula for regression type RF application). The algorithm, implemented in R (R Core Team 2021) through the 'randomForest' package (Liaw et al. 2002), also performs an internal verification of the algorithm's goodness using what are called Out Of Bag (OOB) data. At each processing of a tree a certain number of data is kept out of the elaboration (the OOB) used to assess the performance of the tree and the importance of the predictors. The last step is performed by permuting the values of one of the predictors every time a tree is elaborated: in this way, it is possible to verify how much the tree has lost its predictive value due to the randomization of the predictor by comparing permuted and non-permuted prediction and normalizing this value by the standard deviation of the differences (%incMSE). The RF algorithm has been used for categorization and regression multiple times in research in geology (Catani et al. 2013; Di Napoli et al. 2020b; Kim et al. 2018; Lee et al. 2017; Nhu et al. 2020; Rodriguez et al. 2015).

In this work, the performance of the outcome of the algorithms was evaluated with ROC/AUC (Swets 1988). This method analyzes the obtained results by calculating the Receiver Operating Characteristics (ROC) curve and, lately, the relative AUC. For an AUC of 0.5 the prediction is totally random, while an AUC value greater than 0.9 indicates an excellent prediction (Swets 1988). 70% of the sinkholes belonging to the inventory were used for training the algorithms, while the remaining 30% to test the results. Background points are utilized instead of absence points: as it is not possible to obtain points of absence with absolute certainty, background points are instead used as points of uncertain presence/absence.

4 RESULTS AND DISCUSSION

For each of the 12 predisposing factors, the VIF analysis has been carried out (Table 1). The analysis highlights some collinearity problems with the environmental variables utilized to determine the sinkhole susceptibility. Namely, the Aqueduct Network Distance variable shows a VIF > 10 and the Sewer Network Distance shows a VIF > 5, so it must be interpreted with caution. The Road Network Distance and the Underground Railroad Network also show a high VIF value (close to 5). The main problem with this analysis is probably due to the nature of these "discontinuities" in the study area: the city of Naples is a coastal city with heavy presence of hills and a strongly anthropization. Aqueducts and sewers are the most important infrastructures for a functional city but, most of the time, the secondary pipes are built under the already existing road network. This is probably one of the reasons why these variables show, in some cases, high collinearity. It is hard to

Table 1. V.I.F. of the different Environmental Variables and importance of the predisposing factors for the two algorithms.

Environmental Variable	V.I.F.	RF (%IncMSE)	MaxEnt (Permutation %)
Aqueduct Network Distance	12.0	24.5	1.9
Sewer Network Distance	8.1	22.7	3.2
Road Network Distance	4.8	78.4	75.6
Underground Railroad Distance	4.3	19.4	1.9
Road Network Density	3.8	19.7	1.3
Underground Cavity Distance	3.3	28.6	3.4
Sewer Network Density	2.8	21.4	1.6
Underground Railroad Density	2.5	12.8	0.6
Aqueduct Network Density	2.3	21.1	2.6
Groundwater depth	2.1	10.6	1.8
Underground Cavity Density	1.6	21.9	4.9
Depth of NYT/cover thickness	1.2	7.5	1.4

find a solution in this case, as all the abovementioned variables are indeed predisposing factors as, for example, aqueduct and sewer leaks are one of the most widespread cause for sinkhole triggering as can be seen in the inventory (Tufano et al. in prep.).

As previously specified, aqueduct and sewer networks do not comprehend the secondary pipelines but to overcome this problem road network has been added as a representation of these secondary networks which, otherwise, would end up not being implemented. In this case too, as the sewer, aqueduct and underground railroad networks are built under and, sometimes, parallel to the road network (Figure 3), the collinearity increases. Although the VIF analysis is mainly used to find collinearity problems within a set of predisposing factors to eliminate those who show high collinearity with other variables, in this case the high VIF values were expected, especially for the "Distance" layers but, as these predisposing factors represent important elements in sinkhole initialization (Guarino et al. 2018; Scotto di Santolo et al. 2016; Tufano et al. in prep.), they have been included in the analysis.

The application of MaxEnt and RF algorithms allows to obtain SSMs subdivided for different susceptibility classes and highlights the importance of some predisposing factors (Table 1). Both algorithms have kept in high regards the factors Underground Cavities, Distance to the Road Network and Aqueduct and Sewer Network Distance. On the other end, the factors Groundwater depth and the NYT depth/cover thickness seem to be the some of the least influential environmental variables for RF, while MaxEnt gives the least importance to the Road Network and Underground Railroad Densities. Conversely, Aqueduct Network Distance layer seems to have different importance for both the algorithms. Of the two algorithms, MaxEnt seems to give less importance to the variables linked to Density (except for the Underground Cavities and the Aqueduct Network Density) which could be the reason why final product shows the presence of heavy road network distance influence. For both algorithms, depth of the NYT/cover thickness variable seems not to have so much importance. As previous studies have shown, the most important factor linked to NYT is not its depth, but the thickness of the roof of the cavities that can be found in NYT (Guarino et al. 2018; Scotto di Santolo et al. 2016). However, this data is extremely hard to collect and transfer in a layer file. Also water infiltration, from leaks or from other sources, is widely considered to be an important factor in destabilizing the existing underground cavities (Guarino et al. 2018; Scotto di Santolo et al. 2016). It could be more beneficial, in future studies, to improve the information about the underground water flow, rather than only Groundwater depth, as the RF treats it as one of the least important variable and MaxEnt gives it a middle ground importance.

The analysis of areal extension of susceptibility classes of SSMs, subdivided using the Natural Break method (Jenks 1977), shows an increase of susceptible areas from the lowest to the highest susceptibility class for both maps (Table 2). Explicitly, for SSMs Map obtained with MaxEnt, the extensions are: 46.11% (Very Low); 23.04% (Low); 14.80% (Medium); 9.49% (High) and 6.56%

Table 2. Summary of the extension, sinkhole frequency and sinkhole density for every class of the sinkhole susceptibility maps.

Classes	Area [%]		Sinkhole Frequency [%]		Sinkhole Density [#/km^2]	
	MaxEnt	R.F.	MaxEnt	R.F.	MaxEnt	R.F.
Very Low	46.11	34.40	1.42	0.24	0.11	0.02
Low	23.04	24.52	6.37	0.71	0.99	0.10
Medium	14.80	14.72	10.85	3.54	2.63	0.86
High	9.49	14.35	25.94	16.98	9.79	4.24
Very High	6.56	12.01	55.42	78.54	30.27	23.41

(Very High). Meanwhile, for the SSMs obtained with the Random Forest algorithm, the areas are: 34.40% (Very Low); 24.52% (Low); 14.72% (Medium); 14.35% (High) and 12.01% (Very High). These areas are similarly distributed on the study area, with a Very High class mostly concentrated in the area of the city center of Naples (Figure 4). Both algorithms put a lot of emphasis on the Road Distance Network and on the Underground Cavities Density and Distance.

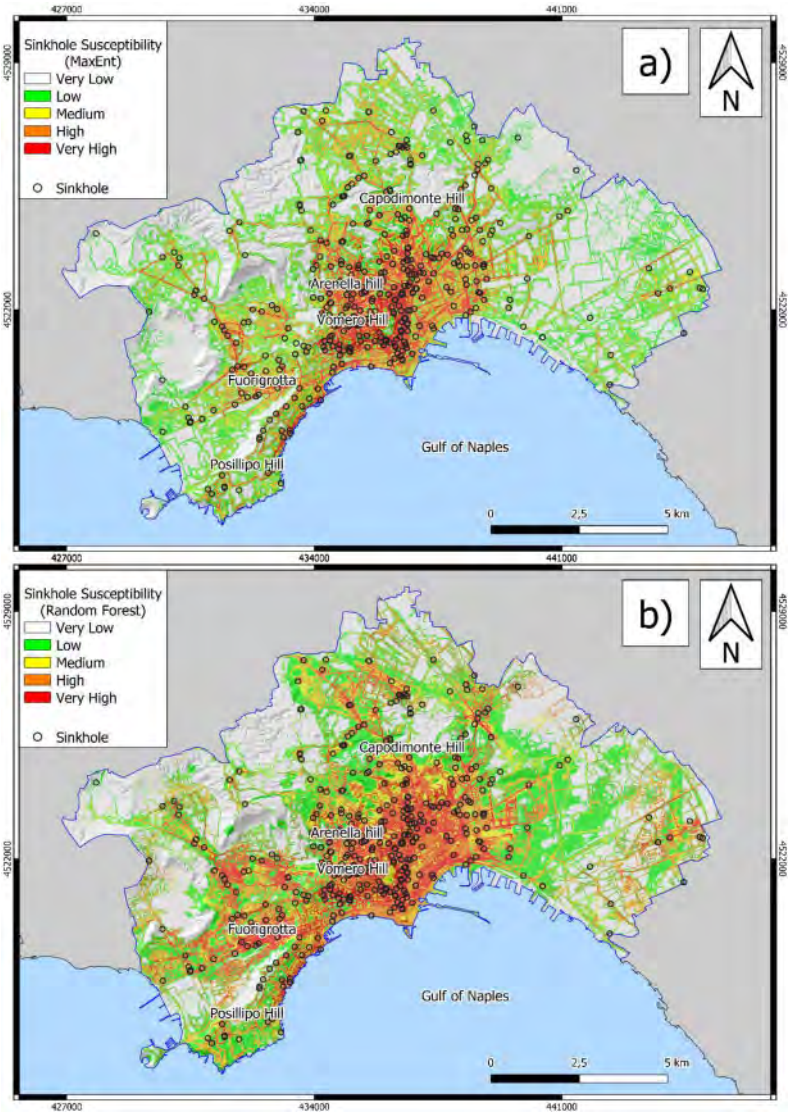

Figure 4. Sinkhole Susceptibility Map obtained with the MaxEnt (a) and the RF algorithm (b) and location of the sinkholes utilized in this study.

The resulting maps (Figure 4) show some differences that can be interpreted with the data obtained from each class. The RF algorithm has produced a susceptibility map with larger High (14.35% against 9.49%) and Very High (12.01% against 6.56%) susceptibility classes. The RF map shows the influence of the Density layers by having more spatially extended areas. The MaxEnt map, on the other hand, is heavily influenced by the Distance layers, especially the Road

Network. Of course, a more spatially extended class means, for the Very High susceptibility class, higher Sinkhole Frequency (78.54% for the RF map, 55.42% for the MaxEnt map): this influences the Sinkhole Density (Table 2), which is constantly lower in the RF map against the MaxEnt (30 sinkhole/km^2 against 23 sinkhole/km^2). The more involved areas of the city seem to be, other than the historical city center, the *Vomero* and *Arenella* (at the North of *Vomero*) Hills and the *Fuorigrotta* district (West-South-West of the Naples city center). Table 2 shows the remaining data for sinkholes frequency for each class of susceptibility (Figure 44). In particular, for the map obtained with MaxEnt, frequency is distributed as follows: 1.42% (Very Low); 6.37% (Low); 10.85% (Medium); 25.94% (High) and 55.42% (Very high). Meanwhile, the values referred to the map obtained through the Random Forest algorithm are the following: 0.24% (Very Low); 0.71% (Low); 3.54% (Medium); 16.98% (High) and 78.54% (Very High). Finally, Table 2 also shows the Sinkhole Density per class, measured in amount of sinkholes per km^2. The performance of both susceptibility maps has been calculated through the use of the ROC/AUC method, splitting the data between 70% for training purposes and 30% for testing. The Sinkhole Susceptibility Map obtained with MaxEnt has a score of 0.929, while the other obtained with the Random Forest algorithm has a similar score of 0.930 (Figure 5).

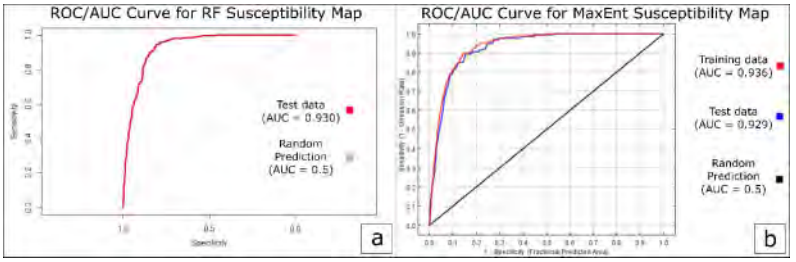

Figure 5. ROC/AUC curves for a) RF Susceptibility Map (from pROC package, modified, Robin et al., 2011) and b) MaxEnt Susceptbility Map (modified, Phillips et al., 2021).

5Still, even if there is a different approach to the importance given to the different predisposing factors, which can be observed with the two different susceptibility maps, both algorithms seem to have achieved an excellent performance with a ROC/AUC score of 0.93 (Sweets 1988). It should not be forgotten, though, that some variables do show some collinearity problem and heavy importance that the Road Network Distance has in both model implies a strong bias mostly due to the nature of the "anthropogenic" sinkholes that, as the name implies, are mostly triggered exactly along the roads or inside buildings.

5 CONCLUSIONS

Sinkholes represent a widespread hazard in the cities characterized by a vast underground cavity system. Naples is one of such cities, with an old, dense network of underground cavities excavated to gain access to building resources (the Neapolitan Yellow Tuff) and to obtain, at least in the past, new spaces for catacombs and religious spots. Sinkhole Susceptibility Maps obtained through the application of Maximum Entropy and Random Forest algorithms show high performance (ROC/AUC score = 0.93). The map obtained through the Random Forest algorithm seems to be more favourable to a precautionary approach than the map obtained with Maximum Entropy, due to the clear distinction in the spatial distribution of the susceptibility classes. The only limitations of these algorithms are the need for an inventory of the phenomena in the study area and the availability of predisposing factors data. As of now, there is no straightforward proof to help decide which algorithm helps to produce the more high-performance susceptibility map to help the local administrations in their search of critical areas that can threaten the buildings that represent the cultural heritage of historical cities.

6 ACKNOWLEDGMENTS

Research carried out with the financial support of the PRIN (Progetti di Rilevante Interesse Nazionale – Projects of National Relevant Interest) URGENT (Urban Geology and Geohazards: Engineering geology for safer, resilieNt and smart ciTies) and the MOSCAS (MOdelli e Strumenti per la caratterizzazione delle CAvità Sotterranee – Models and Tools for the characterization of underground cavities) projects (Principal Investigator of the research units: Domenico Calcaterra).

REFERENCES

Allocca, V., Di Napoli, M., Coda, S., Carotenuto, F., Calcaterra, D., Di Martire, D., & De Vita, P. (2021). A novel methodology for Groundwater Flooding Susceptibility assessment through Machine Learning techniques in a mixed-land use aquifer. Science of The Total Environment, 148067.

Aprile, F., Sbrana, A., & Toccaceli, R. M. (2004). Il ruolo dei depositi piroclastici nell'analisi cronostratigrafica dei terreni quaternari del sottosuolo della Piana Campana (Italia meridionale). Il Quaternario, 17, 547–554.(in italian).

Ardau, F., Balia, R., Bianco, M., & De Waele, J. (2007). Assessment of cover-collapse sinkholes in SW Sardinia (Italy). Geological Society, London, Special Publications, 279(1), 47–57.

Breiman, L. (2001). Random forests. Machine learning, 45(1), 5–32.

Bruno, E., Calcaterra, D., & Parise, M. (2008). Development and morphometry of sinkholes in coastal plains of Apulia, southern Italy. Preliminary sinkhole susceptibility assessment. Engineering Geology, 99(3–4), 198–209.

Calcaterra, D., Cappelletti, P., Langella, A., Morra, V., Colella, A., & de Gennaro, R. (2000). The building stones of the ancient centre of Naples (Italy): Piperno from Campi Flegrei. A contribution to the knowledge of a long-time-used stone. Journal of Cultural Heritage, 1(4), 415–427.

Calcaterra, D., Langella, A., de Gennaro, R., de'Gennaro, M., & Cappelletti, P. (2005). Piperno from Campi Flegrei: a relevant stone in the historical and monumental heritage of Naples (Italy). Environmental geology, 47(3), 341–352.

Calcaterra, D., Coppin, D., De Vita, S., Di Vito, M. A., Orsi, G., Palma, B., & Parise, M. (2007). Slope processes in weathered volcaniclastic deposits within the city of Naples: the Camaldoli Hill case. Geomorphology, 87(3), 132–157.

Catani, F., Lagomarsino, D., Segoni, S., & Tofani, V. (2013). Landslide susceptibility estimation by random forests technique: sensitivity and scaling issues. Natural Hazards and Earth System Sciences, 13(11), 2815–2831.

Ciotoli, G., Di Loreto, E., Finoia, M. G., Liperi, L., Meloni, F., Nisio, S., & Sericola, A. (2016). Sinkhole susceptibility, Lazio Region, central Italy. Journal of Maps, 12(2), 287–294.

Colella, A., Di Benedetto, C., Calcaterra, D., Cappelletti, P., D'Amore, M., Di Martire, D., Graziano, S.F., Papa, L., de Gennaro, M., & Langella, A. (2017). The Neapolitan Yellow Tuff: an outstanding example of heterogeneity. Construction and Building Materials, 136, 361–373.

Convertino, M., Troccoli, A., & Catani, F. (2013). Detecting fingerprints of landslide drivers: a MaxEnt model. Journal of Geophysical Research: Earth Surface, 118(3), 1367–1386.

Craney, T. A., & Surles, J. G. (2002). Model-dependent variance inflation factor cutoff values. Quality Engineering, 14(3), 391–403.

Culshaw, M. G., & Waltham, A. C. (1987). Natural and artificial cavities as ground engineering hazards. Quarterly Journal of Engineering Geology and Hydrogeology, 20(2), 139–150.

de Vivo, B., Rolandi, G., Gans, P. B., Calvert, A., Bohrson, W. A., Spera, F. J., & Belkin, H. E. (2001). New constraints on the pyroclastic eruptive history of the Campanian volcanic Plain (Italy). Mineralogy and Petrology, 73(1), 47–65.

de'Gennaro, M., Calcaterra, D., Cappelletti, P., Langella, A., & Morra, V. (2000). Building stone and related weathering in the architecture of the ancient city of Naples. Journal of Cultural Heritage, 1(4), 399–414.

Deino, A. L., Orsi, G., de Vita, S., & Piochi, M. (2004). The age of the Neapolitan Yellow Tuff caldera-forming eruption (Campi Flegrei caldera–Italy) assessed by 40Ar/39Ar dating method. Journal of Volcanology and Geothermal Research, 133(1–4), 157–170.

Di Napoli, M., Carotenuto, F., Cevasco, A., Confuorto, P., Di Martire, D., Firpo, M., Pepe, G., Raso, E. & Calcaterra, D. (2020a). Machine learning ensemble modelling as a tool to improve landslide susceptibility mapping reliability. Landslides, 17(8), 1897–1914.

Di Napoli, M., Marsiglia, P., Di Martire, D., Ramondini, M., Ullo, S. L., & Calcaterra, D. (2020b). Landslide susceptibility assessment of wildfire burnt areas through earth-observation techniques and a machine learning-based approach. Remote Sensing, 12(15), 2505.

Di Napoli, M., Martire, D. D., Bausilio, G., Calcaterra, D., Confuorto, P., Firpo, M., Pepe, G., & Cevasco, A. (2021). Rainfall-induced shallow landslide detachment, transit and runout susceptibility mapping by integrating machine learning techniques and GIS-based approaches. Water, 13(4), 488.

Fairbridge, R. W. (1968). The Encyclopedia of Geomorphology. Encyclopedia of Earth Sciences Series, Vol. III. Dowden, Hutchinson and Ross. Inc., Stroudsburg, Pennsylvania. 1295pp.

Felicísimo, Á. M., Cuartero, A., Remondo, J., & Quirós, E. (2013). Mapping landslide susceptibility with logistic regression, multiple adaptive regression splines, classification and regression trees, and maximum entropy methods: a comparative study. Landslides, 10(2), 175–189.

Ford, D., & Williams, P. D. (2013). Karst hydrogeology and geomorphology. John Wiley & Sons.

Galve, J. P., Gutiérrez, F., Remondo, J., Bonachea, J., Lucha, P., & Cendrero, A. (2009). Evaluating and comparing methods of sinkhole susceptibility mapping in the Ebro Valley evaporite karst (NE Spain). Geomorphology, 111(3–4), 160–172.

Galve, J. P., Remondo, J., & Gutiérrez, F. (2011). Improving sinkhole hazard models incorporating magnitude–frequency relationships and nearest neighbor analysis. Geomorphology, 134(1–2), 157–170.

Guarino, P. M., & Nisio, S. (2012). Anthropogenic sinkholes in the territory of the city of Naples (Southern Italy). Physics and Chemistry of the Earth, Parts A/B/C, 49, 92–102.

Guarino, P. M., Santo, A., Forte, G., De Falco, M., & Niceforo, D. M. A. (2018). Analysis of a database for anthropogenic sinkhole triggering and zonation in the Naples hinterland (Southern Italy). Natural Hazards, 91(1), 173–192.

Gutiérrez, F., Cooper, A. H., & Johnson, K. S. (2008b). Identification, prediction, and mitigation of sinkhole hazards in evaporite karst areas. Environmental Geology, 53(5), 1007–1022.

Gutiérrez, F., Galve, J. P., Lucha, P., Castañeda, C., Bonachea, J., & Guerrero, J. (2011). Integrating geomorphological mapping, trenching, InSAR and GPR for the identification and characterization of sinkholes: A review and application in the mantled evaporite karst of the Ebro Valley (NE Spain). Geomorphology, 134(1–2), 144–156.

Gutiérrez, F., Guerrero, J., & Lucha, P. (2008a). A genetic classification of sinkholes illustrated from evaporite paleokarst exposures in Spain. Environmental Geology, 53(5), 993–1006.

Gutiérrez, F., Parise, M., De Waele, J., & Jourde, H. (2014). A review on natural and human-induced geohazards and impacts in karst. Earth-Science Reviews, 138, 61–88.

Isaia, R., Iannuzzi, E., Sbrana, A., & Marianelli, P. (2018). Note Illustrative della Carta Geologica d'Italia alla scala 1: 50.000, Foglio 446–447 Napoli (aree emerse).

Jenks, G. F. (1977). Optimal data classification for choropleth maps occasional paper no 2. University of Kansas, Department of Geography.

Kim, J. C., Lee, S., Jung, H. S., & Lee, S. (2018). Landslide susceptibility mapping using random forest and boosted tree models in Pyeong-Chang, Korea. Geocarto international, 33(9), 1000–1015.

Klimchouk, A., Forti, P., & Cooper, A. (1996). Gypsum karst of the World: a brief overview. International Journal of Speleology, 25(3), 12.

Lee, S., Kim, J. C., Jung, H. S., Lee, M. J., & Lee, S. (2017). Spatial prediction of flood susceptibility using random-forest and boosted-tree models in Seoul metropolitan city, Korea. Geomatics, Natural Hazards and Risk, 8(2), 1185–1203.

Liaw, A., Wiener, M. (2002). Classification and Regression by randomForest. R News 2(3), 18–22.

Lombardo, M., Frisone, F., Review by Pollini, A. (2012). Colonie di colonie, Le fondazioni sub-coloniali greche tra colonizzazione e colonialismo, Atti del Convegno Internazionale (Lecce, 22–24 giugno 2006). (in italian)

Ma, B., & Sun, J. (2018). Predicting the distribution of Stipa purpurea across the Tibetan Plateau via the MaxEnt model. BMC ecology, 18(1), 1–12.

Morra, V., Calcaterra, D., Cappelletti, P., Colella, A., Fedele, L., de' Gennaro, R., Langella, A., Mercurio, M., & de' Gennaro, M. (2010). Urban geology: relationships between geological setting and architectural heritage of the Neapolitan area, in Beltrando, M., Peccerillo, A., Mattei, M., Conticelli, S., and Doglioni, C., eds., The Geology of Italy: tectonics and life along plate margins, Journal of the Virtual Explorer, v. 36, paper 27.

Nhu, V. H.; Shirzadi, A.; Shahabi, H.; Chen, W.; Clague, J.J.; Geertsema, M.; Jaafari, A.; Avand, M.; Miraki, S.; Talebpour Asl, D.; Pham, B.T.; Ahmad, B.B.; Lee, S. (2020). Shallow Landslide Susceptibility Mapping by Random Forest Base Classifier and Its Ensembles in a Semi-Arid Region of Iran. Forests, 11, 421.

Novellino, A., Cesarano, M., Cappelletti, P., Di Martire, D., Di Napoli, M., Ramondini, M., Sowter, A., & Calcaterra, D. (2021). Slow-moving landslide risk assessment combining Machine Learning and InSAR techniques. CATENA, 203, 105317.

Orsi, G., De Vita, S., & Di Vito, M. (1996). The restless, resurgent Campi Flegrei nested caldera (Italy): constraints on its evolution and configuration. Journal of Volcanology and Geothermal Research, 74(3–4), 179–214.

Pappalardo, L., Civetta, L., De Vita, S., Di Vito, M., Orsi, G., Carandente, A., & Fisher, R. V. (2002). Timing of magma extraction during the Campanian Ignimbrite eruption (Campi Flegrei Caldera). Journal of Volcanology and Geothermal Research, 114(3–4), 479–497.

Parise, M. (2015). A procedure for evaluating the susceptibility to natural and anthropogenic sinkholes. Georisk: Assessment and Management of Risk for Engineered Systems and Geohazards, 9(4), 272–285.

Phillips, S. J., & Dudík, M. (2008) – Modeling of species distributions with Maxent: new extensions and a comprehensive evaluation. Ecography, 31(2), 161–175.

Phillips, S.J.; Dudík, M.; Schapire, R.E.. (2021) – [Internet] Maxent software for modeling species niches and distributions (Version 3.4.4). Available from url: http://biodiversityinformatics.amnh.org/open_source/maxent/. Accessed on 02/05/2021.

R Core Team (2021). R: A language and environment for statistical computing. R Foundation for Statistical Computing, Vienna, Austria. URL https://www.R-project.org/.

Robin, X., Turck, N., Hainard, A., Tiberti, N., Lisacek, F., Sanchez, J. C., & Müller, M. (2011). pROC: an open-source package for R and S+ to analyze and compare ROC curves. BMC bioinformatics, 12(1), 1–8.

Rodriguez-Galiano, V., Sanchez-Castillo, M., Chica-Olmo, M., & Chica-Rivas, M. J. O. G. R. (2015). Machine learning predictive models for mineral prospectivity: An evaluation of neural networks, random forest, regression trees and support vector machines. Ore Geology Reviews, 71, 804–818.

Rolandi, G., Bellucci, F., Heizler, M. T., Belkin, H. E., & De Vivo, B. (2003). Tectonic controls on the genesis of ignimbrites from the Campanian Volcanic Zone, southern Italy. Mineralogy and Petrology, 79(1–2), 3–31.

Rosdi, M. A. H. M., Abd Latif, Z., Othman, A. N., & Nasir, N. M. (2018, November). Sinkhole Susceptibility Hazard Zones Using GIS Framework and Heuristic Method. In Conference of the Arabian Journal of Geosciences (pp. 261–264). Springer, Cham.

Rosi, M., Vezzoli, L., Aleotti, P., & De Censi, M. (1996). Interaction between caldera collapse and eruptive dynamics during the Campanian Ignimbrite eruption, Phlegraean Fields, Italy. Bulletin of Volcanology, 57(7), 541–554.

Santangelo, N., Ciampo, G., Di Donato, V., Esposito, P., Petrosino, P., Romano, P., Ermolli, E. R., Santo, A., Toscano, F., & Villa, I. (2010). Late Quaternary buried lagoons in the northern Campania plain (southern Italy): evolution of a coastal system under the influence of volcano-tectonics and eustatism. Italian journal of geosciences, 129(1), 156–175.

Scarpati, C., Cole, P., & Perrotta, A. (1993). The Neapolitan Yellow Tuff—a large volume multiphase eruption from Campi Flegrei, southern Italy. Bulletin of Volcanology, 55(5), 343–356.

Scotto di Santolo, A., Evangelista, L., Silvestri, F., Cavuoto, G., Di Fiore, V., Punzo, M., Tarallo D. Evangelista, A. (2015). Investigations on the stability conditions of a tuff cavity: the Cimitero delle Fontanelle in Naples. Rivista Italiana di Geotecnica XLIX (3), 28–46.

Scotto di Santolo, A., Forte, G., De Falco, M., & Santo, A. (2016). Sinkhole risk assessment in the metropolitan area of Napoli, Italy. Procedia Engineering, 158, 458–463.

Swets, J. A. (1988). Measuring the accuracy of diagnostic systems. Science, 240(4857), 1285–1293.

Tharp, T. M. (1999). Mechanics of upward propagation of cover-collapse sinkholes. Engineering geology, 52(1–2), 23–33.

Tufano, R.; Guerriero, L.; Annibali Corona, M.; Bausilio, G.; Di Martire, D., Nisio, S.; Calcaterra, D. (in prep.) – Anthropogenic sinkholes inventory of the city of Naples, Italy: an update. Nat Hazards (under review).

Waltham, T., Waltham, A. C., Bell, F. G., & Culshaw, M. G. (2005). Sinkholes and subsidence: karst and cavernous rocks in engineering and construction. Springer Science & Business Media.

West, A. M., Kumar, S., Brown, C. S., Stohlgren, T. J., & Bromberg, J. (2016). Field validation of an invasive species Maxent model. Ecological Informatics, 36, 126–134.

Geotechnical Engineering for the Preservation of Monuments and Historic Sites III – Lancellotta, Viggiani, Flora, de Silva & Mele (Eds)

Crack development in an old church building due to clay shrink-swell

M.A. Beroya-Eitner
Technical University Darmstadt, Institute and Laboratory for Geotechnics, Darmstadt, Germany

M.A. Loreth
Helmut-Schmidt-University, Professorship for Geotechnics, Hamburg, Germany

H. Zachert & M. Schneider
Technical University Darmstadt, Institute and Laboratory for Geotechnics, Darmstadt, Germany

H. Tenbreul
Baugrundinstitut Franke-Meißner and Partner Ltd.

ABSTRACT: Cracking is a common occurrence in any building. Where they occur in historic buildings, however, they present a greater concern due to the structure's cultural significance. A common reason for cracking is the ground movement beneath foundations as a result of shrink-swell in clay subsoils. In this paper, we present a shrink-swell case that is causing the progressive movement and cracking of a centuries-old church, the Massenheim Evangelical Church in Hessen, Germany. Results of field and laboratory investigations reveal a layer of very highly expansive clay. The upper part of this layer appears to be within the active zone, and therefore subject to volume change with seasonal fluctuations in water content. The development of cracks with time is aligned with the prevailing climatic conditions during the observation period. A possible mitigation measure is the use of micropiles that bypass that part of the layer that lies within the active zone.

1 INTRODUCTION

Cracks are a common occurrence in buildings, regardless of age and form of construction. Where they occur in old, historic buildings, however, they present a greater concern due to the cultural significance of the structure, i.e., the aesthetic, historic, scientific or social value of the building to past, present or future generations' (Australia ICOMOS 2000).

Cracks can vary from non-structural to the more severe structural type that can affect the stability of the structure (ORS 2020). The severity of the cracks can usually be identified from their appearance. Non-structural ones mainly appear as hairline cracks that develop from the expansion and contraction of building materials as they absorb and release moisture. Structural cracks, on the other hand, tend to be wider ($\geq$ 1.5 mm) and diagonally oriented that most often appear above doors and windows, in corners and around fireplaces and chimneys. These latter cracks usually signal that the structure is moving more than normal (Wisconsin Historical Society n.d.). In such a case, crack monitoring is indispensable to determine the general pattern of the movement (e.g., Li & Cameron) and ensure that such movement does not reach a critical level to cause failure of structural components or the entire structures (Yao et al. 2014). Moreover, monitoring the changes in crack width across a crack helps determine the cause of cracking and the type of remedial work that should be implemented (Berntsen 2022).

 DOI 10.1201/9781003308867-89

There are several reasons for the movement of a structure, one of the most common of which is the ground movement beneath foundations as a result of shrink-swell in clay sub-soils. Shrink-swell refers to the volume change phenomenon that occurs due to the changes in the moisture content of clay-rich soils. Swelling pressures can cause heaving of structures, while shrinkage can result to settlement, which may be differential (BGS 2021). Shrink-swell, therefore, constitutes significant geotechnical and structural engineering challenges.

In this paper, we present a shrink-swell case that is causing the progressive movement and cracking of a centuries-old church in Hessen, Germany, the Massenheim Evangelical Church. As a result of the observed cracking at the turn of the twenty-first century, a long-term crack displacement monitoring and a series of comprehensive field and laboratory investigations were conducted in the site, the results of which are detailed and discussed in the following presentation.

2 STUDY AREA

2.1 *Location and general description*

The Massenheim Evangelical Church is located on the western part of the Massenheim village. The village belongs to the district of Hochheim am Main, in the southwestern part of Hessen, Germany (Figure 1).

Figure 1. Location of the study area.

The church sits on top of a southeast facing slope at an average elevation of 139 m a.s.l. Around the church are walkways and plants that are mostly shrubs. The space in front of the west facade is paved. About 4 m southwest of the west entrance is a deciduous tree with a diameter of about 1.2 m. The nave of the church is approximately 16 m long and 10 m wide. The church is founded on strip footing 1.0 m wide and 2.1 m deep in the north, east and south sides, while in the west, the footing is 0.5 m deep. The church does not have a cellar; inside is a buried out-of-use heating channel that runs parallel to the north longitudinal wall. According to available documents (BFM 2004), the channel is 1 m wide, its bottom approx. 0.6 m below ground level, and lies approx. 0.3 m from the north longitudinal wall.

2.2 *Construction history*

The village “Massenheim” was first mentioned in official documents from King Louis “the Pious” in 819 (ECM 2000a). According to these documents, the first sections of the church were built by the Fulda Abbey between 819 and 909. The main construction, however, took place later and can be split into two epochal constructions (Figure 2). In connection to the reformation in the 16th century, the tower of the church fell into the nave and caused great damage on the structure in 1579 (ECM 2000b). Renovations started two years later, in 1581 and ended in 1585. This marks the first

epochal construction of the church. Then, the next known relevant documents and sketches are dated 1762, after almost two hundred years. These sketches include some structural changes, the elevation of the church by 2 m and an extension to the west by 6.5 m. The period between 1762 and 1764 is documented as the second epochal construction. In the following years, numerous renovations and smaller repairs were carried out such as roof works and damp removal in 1940, exterior plastering and foundation excavation in 1980, and a complete interior renovation of the facade, floors and furnishings from 2000 to 2001.

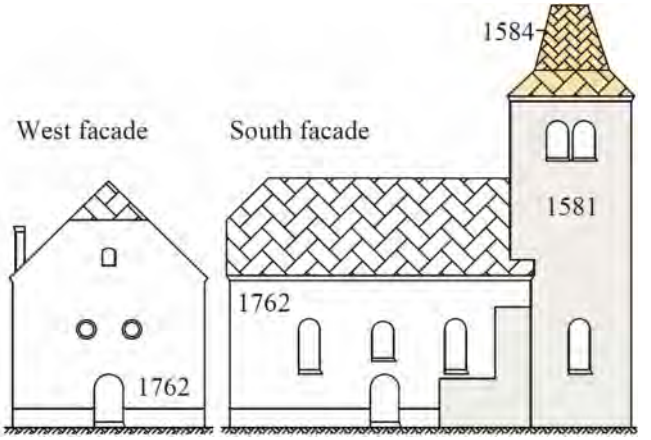

Figure 2. Scaled sketch of the church showing the epochal constructions.

2.3 *Crack Development*

Cracking at the Massenheim church started about 70 years ago in 1930 (ECM 2000b). The first cracks were documented between 1930 and 1960 in the quarry stone masonry on the west facade. These cracks became visible again in 1980, when the iron bands of the door catch on the west facade came loose and the sandstone steps shifted outwards. From 1980 up to the renovation in 2001, there were no records of cracking. Only two years after the extensive renovations that cracking was again observed, appearing for the first time on the interior and exterior of the west facade. Since autumn 2003, cracks have also appeared in the altar area and in the floor (Figure 3). The structural integrity

Figure 3. Cracks on the exterior and interior of the west facade and in the floor.

of the church was then considered compromised, and a decision was made to investigate the cause of the problem. Consequently, extensive field investigation was carried out in 2004 and a long-term crack displacement monitoring was set up by Baugrundinstitut Franke-Meißner and Partner Ltd (BFM).

3 METHODOLOGY

3.1 *Crack Monitoring*

The cracks in the church were monitored both for vertical and lateral movements at four displacement measurement (DM) points (blue dots in Figure 4): DM 1, 2 and 3 are located in the main damage area on the west wall, while DM 4 is on the southwest side. In addition, lateral movement between the north and south walls of the church was further monitored through convergence measurement (CM), a technique often used in underground construction (Cho et al., 2006) to measure the change in distance between two points positioned opposite each other. The CM was done along the red dashed line in Figure 4, one at ground level (CM 1) and another at approximately 3 m above the ground (CM 2).

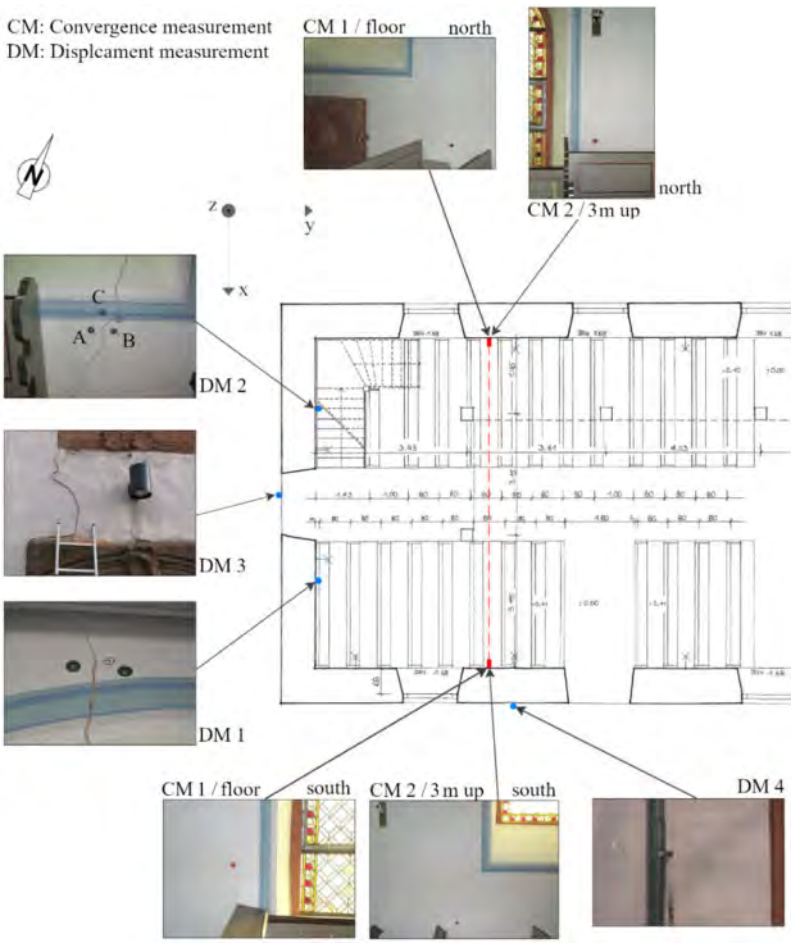

Figure 4. Measuring points and status of the cracks as of 20 April 2021 (BFM 2021).

The measurement interval was adjusted based on the development of the cracks. When the monitoring was started in January 2004 after noticing the cracks in autumn 2003, the interval was initially set at every quarter of a year. Later, it was extended to half a year, then one year, then two years. Due to the comparatively small deformations measured until 2016, monitoring was stopped upon the request of the church. It was, however, resumed in 2019 after large deformations were again observed. Note that monitoring continued from 2004 through 2016 despite the insignificant deformations detected because as experience had shown, crack development in the church building could suddenly stop, only to resume again after a couple of decades (cfr. Section 2.3). The monitoring points and status of the cracks as of 20 April 2021 are shown in Figure 4 below.

3.2 *Field investigation*

Field investigations were carried out several times within the period from 2003 to 2021, during which time the following were conducted: eight ram core sounding (RCS) according to European standard DIN EN ISO 22475-1 to determine the soil layers, two dynamic heavy probings (DPH) in accordance with DIN EN ISO 22476-2 to determine the relative density of the soil, and three test pits (TP) dug carefully with an excavator next to the footing to assess the soil at the footing, as well as the condition of the footing itself. Most of the investigation were in the southwest side of the church (Figure 5), where cracking is most severe.

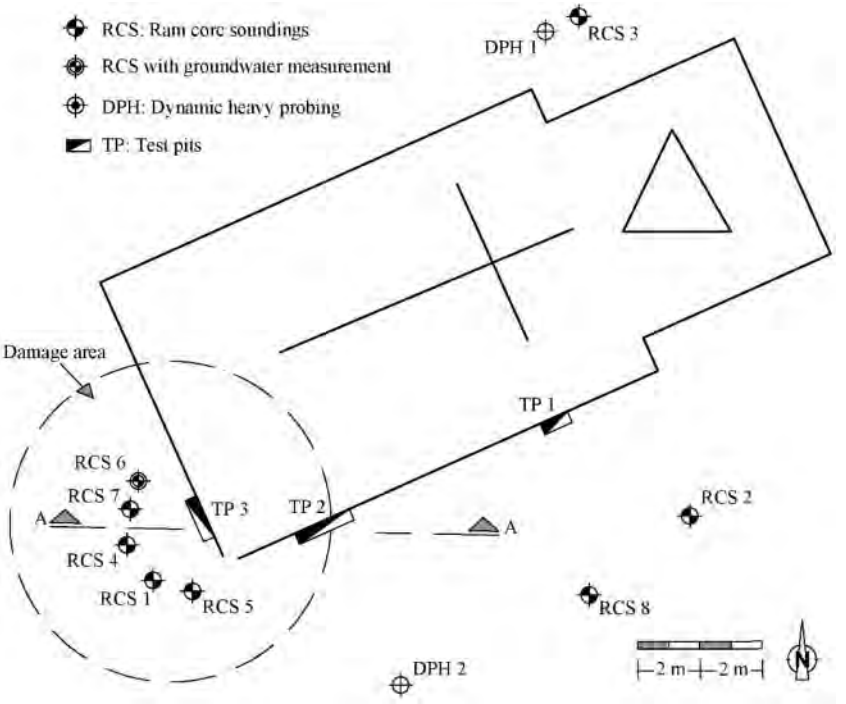

Figure 5. Location of field investigation (modified from BFM 2003; 2004).

3.3 *Laboratory Tests*

To characterise the soil in the study area, the following index tests were conducted on representative samples: grain size distribution (DIN EN ISO 17892-4), water content (DIN EN ISO 17892-1) and Atterberg limits (DIN EN ISO 17892-12). For the clay soils, additional tests were conducted

to evaluate susceptibility to shrink-swell, including water absorption capacity (DIN 18132) and free swell test (Sivapullaiah et al. 1987). To determine the soils' stress-strain behaviour during one-dimensional compression, incremental loading oedometer test (DIN EN ISO 17982-5) was performed on remoulded samples at a maximum load of 400 kPa. Finally, X-ray diffraction analysis was made using the Panalytical X'Pert Pro Difractometer at the Institute of Geosciences, Goethe University Frankfurt.

4 RESULTS

4.1 *Crack Displacement*

Figure 6a shows the vertical and lateral crack displacement, ρ_{max}, through time over the monitoring period on the west wall of the church. With respect to the first measurement, positive values mean an opening/settling, while negative values mean closing/heaving.

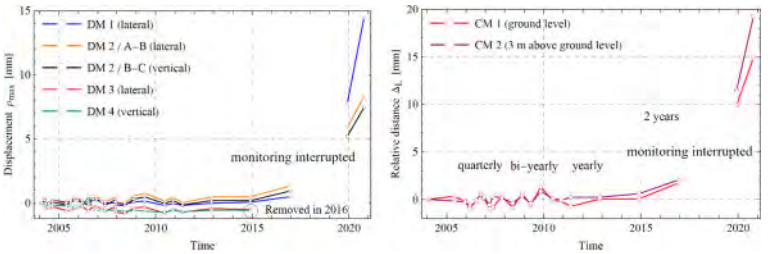

Figure 6. Monitoring results. (a) Displacement ρ_{max} vs. time at the different measurement points. (b) Relative distance Δ_L between the north and south walls vs. time.

As mentioned earlier, the measurement interval was initially set every quarter of a year from 2004 to 2011. No significant displacement was observed during this period. DM 3 and DM 4 showed weakly fluctuating positive and negative values, indicating only weak shrink-swell. Thus, measurement interval was adjusted to longer periods up to 2016. During this time, none to insignificant deformations were detected. Thus, monitoring was stopped and renovation work on the affected facade was implemented, in the process of which DM 3 and DM 4 were removed.

However, in December 2019, large deformations were observed. Thus, monitoring was resumed in the remaining monitoring points, where lateral displacement of up to approximately 6 mm was recorded at DM 2 and 8 mm at DM 1, while vertical displacement measures 5 mm. Movement progressed up to 2020, with the lateral displacement at DM 1 reaching about 14 mm in October 2020.

Results of the convergence measurement (Figure 6b) are in line with the above observations. In Figure 6b, positive values are extension, while negative values are shortening. No significant movement was likewise recorded between 2004 and 2011. From 2011 up to the end of 2016, low positive values of approximately 2 mm were observed, indicating extension and lateral movement corresponding to the crack opening on the west wall. Then, in December 2019, large relative distance of 15 mm at CM 1 and 19 mm at CM 2 was measured. Movement is presumed to be in the downslope direction.

If the vertical displacements at DM 2 and DM 4 are considered, the north and south parts of the church building can be said to have been settling almost uniformly up to 2015. Relative settlement δ_ρ was only about 1.1 mm even at its maximum in June 2011 (left axis, Figure 7). This is far below the critical value by Skempton & MacDonald (1956) and Wigger (2000). The former set the value at 36 mm, while the latter, based on his examination of nine historic churches in south-eastern Lower Saxony in central Germany, reduced this value by half, i.e., 18 mm. With the lateral distance of 6.5 m between DM 2 and DM 4, the rotation θ_δ of the church building was determined to range between

Table 1. Depth of soil layers identified from ram core sounding.

RCS	Backfill m	Silty Sand m	Fat Clay m
1	0.0–2.5	2.5–3.1*	–
2	0.0–1.4	1.4–2.8	2.8–3.8*
3	0.0–1.6	1.6–2.5*	–
4	0.0–0.5	0.5–2.3	2.3–5.0*
5	0.0–0.6	0.6–3.0	3.0–5.0*
6	0.0–0.6	0.6–3.0	3.0–5.0*
7	0.0–2.0	2.0–2.8	2.8–10*
8	0.0–1.7	(not found)	1.7–10*

*End of investigation.

1/10.000 and 1/20.000 (right y-axis, Figure 7). These values, according to Skempton & MacDonald (1956) and Schultze & Muhs (1967), generally represent no risk of cracking, consistent with the observation of insignificant lateral crack displacement until 2015 (Figure 6a). Unfortunately, DM 4 was removed in 2016 as mentioned earlier, such that it was no longer possible to determine relative settlement from this time onwards, when crack displacement significantly increased.

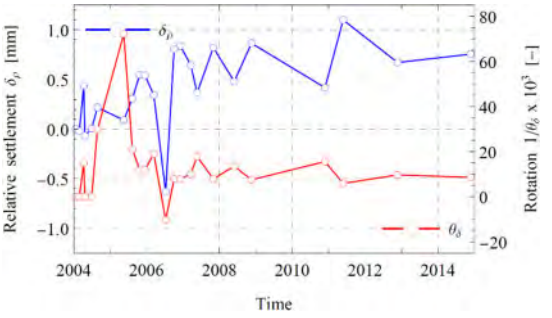

Figure 7. Relative settlement δ_ρ (left y-axis) and rotation θ_δ (right y-axis) between DM 2 / B-C and DM 4 vs. time.

4.2 *Subsurface condition*

Test pits TP 2 and TP 3, both located at the southwest edge of the church, reveal that the soil at the footings is sand with low gravel and silt content. At TP 3, solid limestone was found near and under the strip footings, which prevented further deeper excavation. The strip footing, made of rough quarry stone, is 0.8 m thick and embedded to a depth of 2.1 m.

Table 1 summarizes the soil layers encountered in the ram core sounding. Three layers can generally be identified: the topmost layer, about 0.5 to 2.5 m thick, consists of backfill material; the middle layer, about 0.5 to 2.5 m thick, is reddish silty sand, and the third layer consists of fat clay that may reach more than 8 m in thickness. The end of this last layer was not encountered in the drilling. Based on the soil map of the German Federal Institute for Geo-sciences and Natural Resources, the natural soils in the study area are mainly alluvial plain deposits, belonging to the fluvisol and gleysol groups (BGR, 2014). No groundwater was detected during the drilling.

The backfill material consists of silty clay with sand, gravel and fragments of concrete, bricks and slag. The water content is highly variable, from around 6 to 27%. For its non-cohesive content, the relative density is medium to dense, while the fines component has a semisolid to stiff consistency. The permeability is 9*10-4 m/s. Considering only the silty clay matrix, the water content is about 15%, liquid limit is 36%, plastic limit is 17%, and plasticity index is 19%. It is therefore a medium

plastic clay, with a medium swelling potential, following the criteria for identifying swelling soils by Ola (1982) and the US Bureau of Reclamation (USBR, 1974). Probable expansion in terms of percent total volume change (dry and saturated conditions) is 10 to 20% (USBR, 1974). Modified free swell index test, however, gives a value of 13.5, indicating a high swelling potential (Sivapullaiah et al., 1987). Meanwhile, results of the oedometer test show that the soil displays comparatively high vertical strain of 23% (max. load 400 kPa), but shows weak creep behaviour. Furthermore, it shows little heave on unloading.

The backfill material is followed by a reddish silty sand layer. The soil has a water content of about 9% and is non-plastic.

Finally, the underlying thick layer of fat clay has a soft consistency that becomes stiffer with depth. The soil has a relatively high water content that ranges from 29 to 32%. Liquid limit ranges from 78 to 84%, plastic limit from 29 to 31%, and plasticity index from 47 to 54%. The soil is therefore very highly plastic, with a very high swelling potential (Ola 1982; USBR 1974). Note that Ola (1982) and USBR (1974) set the lowest plasticity index threshold value for very high swelling potential soils at 36%, far below the plasticity index at of the clay layer. The foregoing agrees with the results of the modified free swell test, which gives an index of 23. Soils with swell index > 20 are considered to have very high swelling potential (Sivapullaiah et al., 1987). This very high swelling potential may be explained by the high water absorption capacity of the soil that ranges from 96 to 114%. Probable expansion at both dry and saturated conditions is more than 30% per the USBR (1974) criteria. Oedometer test shows a comparatively lower vertical strain of 14.2% (max. load 400 kPa), but a pronounced creep behaviour. Heaving during unloading is strong. XRD analysis reveals that the soil contains considerable amount of smectite (16 to 26% by weight), explaining its high capacity for water absorption and therefore high susceptibility to volume change. Soils containing this type of clay mineral are known to exhibit the most dramatic shrink and swell capacity. This is due to the structure, chemical composition, exchangeable ion type and small crystal size of smectite clay, all of which impart the mineral with a large chemically active surface area, a high cation exchange capacity and interlamellar surfaces having unusual hydration characteristics (Odom 1984).

Figure 8 gives the general soil profile in the study site.

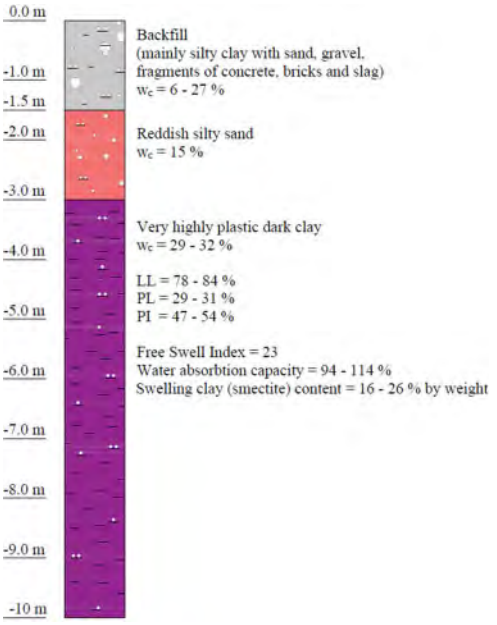

Figure 8. General soil profile in the study area.

5 DISCUSSION

It is evident from the fluctuating positive and negative displacement values obtained from crack monitoring and the results of subsurface and laboratory investigations that the cracking in the Massenheim church is largely related to shrink-swell, in particular of the lower clay layer. Owing to the considerable amount of expansive clay minerals it contains, the soil is highly susceptible to volume change in response to water content fluctuations, mainly in the upper part of the soil layer. According to Nelson & Miller (1992) deep seated heave is very rare. It is mostly the water content in the upper layers that is significantly influenced by climatic and environmental conditions. As such these layers are called the *zone of seasonal fluctuations* or *active zone* (Jones & Jefferson 2012). In this zone, unsaturated condition, and therefore negative pore water pressure, exists. However, if excess water seeps through, as during excessive rainfall, or if evapotranspiration is eliminated, then the water content increases and heave may occur. If this is then followed by dry and warm conditions, shrinkage may result. The depth of active zone can significantly vary spatially depending on soil and climate conditions, but has been documented to range from 0.5 to 6 m (e.g., Biddle 2001; O'Neill 1980; Yue 2017). As can be seen in Table 1, the expansive clay layer is encountered at shallow depths, starting from 1.7 to 3 m. It may therefore be well within the active zone, especially since the upper layers consist of soils with high permeability, allowing the easy migration of water into and out of the clay layer.

Shrink-swell must have led to localized or nonuniform settlement of the church foundation. This is evident from the cracking in the exterior and interior walls that indicates movement of the framing, cracked and uneven floors, shifting of steps, and misaligned doors and windows. However, it was not possible to establish the amount of this differential settlement as the measuring point was dismantled during the repair and renovation work. Cracks on the floor run parallel to the slope face. Investigation of the slope ground also reveals cracks of the same orientation, indicating that the soil is creeping downhill.

A review of the climatic conditions prevailing during the monitoring period supports the analysis that the crack development in the Massenheim church is related to the seasonal fluctuation of water content in the expansive clay layer. The year 2003, when cracks appeared for the first time on the interior and exterior of the west facade, was very warm, dry and extremely sunny. The extremely hot summer was particularly striking. On average for the region and in most stations, it was the hottest summer since continuous measurements began in 1881 (Müller-Westermeier & Riecke 2004). The drought experienced during this summer was exacerbated by the length of the period with scarce precipitation and humidity, by the heat and the long sunshine duration (Rebetez et al. 2006).

Within 2016 to 2020, when progressive movement must have occurred leading to the large displacements measured in 2019 through 2020, several record-breaking weather conditions were observed. For instance, the years 2018, 2019 and 2020 respectively rank first, third and second warmest year in Germany (Bayklif 2021; DWD 2020). These years were very dry as well. The year 2018, in particular, is an exceptional year, with many records. It was not only the warmest, it is also the sunniest and one of the driest since regular measurements were started. Every month from April to November, without exception, was too warm, too dry and very sunny (DWD 2019).

As the clay in the backfill material also exhibits medium to high volume change potential and high vertical strain with applied load (i.e., high compressibility), the soil may also have contributory role to the observed settlement, particularly in places where it is not bypassed by the foundation. This layer should therefore not be considered as the bearing layer. Finally, the possible role of the trees and plants around the church cannot be disregarded. According to Eapan et al. (2015), many plant species use the mechanism of hydrotropism to avoid water stress, whereby the actively growing root tip orients itself towards greater water availability. Under drought conditions, therefore, the roots could extend deeper into the moister clay layer and absorb the soil water, further enhancing shrinkage.

6 CONCLUSION

Results of field and laboratory investigations reveal a thick layer of very highly expansive clay, the upper part of which appears to be well-within the active zone. Therefore, shrink-swell in this upper part of the soil must have been the main cause of the ground displacement in the study site and the concomitant cracking of the church. The development of cracks with time is in alignment with the prevailing climatic conditions during the observation period.

For the mitigation of the problem, micropiles may be considered that bypasses the part of the clay layer within the active zone, and transfers the load to the soil below this zone. At depths below the active zone, the soil may still have the potential to shrink and swell, but no significant volume change can occur because the moisture content is generally constant. This therefore implies the need to establish the active zone through well-designed investigation.

The case of the Massenheim church underscores the fact that if we are to preserve old and historic structures, there is a need for a reinvestigation of their subsurface conditions in order to identify the presence of marginal soils that may not have been considered in the early times during the construction of these structures.

ACKNOWLEDGMENT

The authors wish to thank Dr. Thanh Lan Nguyen of the Institute of Applied Geosciences, Technical University of Darmstadt for the support extended in analysing the clay minerals.

REFERENCES

Australia ICOMOS Inc. 2000. *The Burra Charter: Australia ICOMOS Charter for Places of Cultural Significance 1999*. Burwood: Australia ICOMOS Incorporated.

Bayklif (Bayerisches Netzwerk für Klimaforschung), 2021. German Weather Service: 2020 was the second warmest year in Germany since weather records began. Available at: https://www.bayklif.de/en/german-weather-service-2020-was-the-second-warmest-year-in-germany-since-the-beginning (Accessed: 16 December 2021).

Berntsen 2022. Crack Monitors – For the monitoring of cracks in buildings and civil engineering structures. Available at https://www.berntsen.com/Construction/Avongard-Crack-Monitor (Accessed: 22 February 2022).

Biddle, P.G. 2001. Tree root damage to buildings. *Expansive clay soils and vegetative influence on shallow foundations*, ASCE Geotechnical special publications, 116: 1–23.

British Geological Society (BGS) 2021. Swelling and shrinking soils. Available at: https://www.bgs.ac.uk/geology-projects/shallow-geohazards/clay-shrink-swell/ (Accessed: 16 December 2021).

Bundesanstalt für Geowissenschaften und Rohstoffe (BGR) (2014) Soil Regions of Germany. Available at: https://sites.google.com/site/soilsofgermany/home/soil-information (Accessed: 16 December 2021).

Cho, K.H., Choi, M.K., Nam, S.W., Lee, I.M. 2006. Geotechnical parameter estimation in tunnelling using relative convergence measurement. *International Journal for Numerical and Analytical Methods in Geomechanics* 30(2): 137–155.

Deutscher Wetterdienst (DWD) (n.d.). The weather in Germany in 2018. *Press release*.

Deutscher Wetterdienst (DWD) 2020. Klimastatusbericht Deutschland Jahr 2019. Available at: https://www.dwd.de/DE/leistungen/klimastatusbericht/publikationen/ksb_2019.html (Accessed: 16 December 2021).

Eapen D., Martínez J.J., Cassab G.I. 2015. Assays for root hydrotropism and response to water stress. In Blancaflor E.B. (ed). *Plant Gravitropism: Methods and Protocols,* 133–142, New York, USA: Springer. DOI: 10.1007/978-1-4939-2697-8_11 – PubMed.

Evangelical Church Massenheim (ECM) 2000a. Exhibition documents in Massenheim church with time tables and newspaper clippings about the renovation.

Evangelical Church Council Massenheim (ECM) 2000b. The church renovation. Information about the history and church renovation of the Evangelical church.

Evangelical Church Council Massenheim (ECM) 2004. Cracks in the mansonry. Evangelical community letter for Massenheim and Wicker, 3–4, Massenheim.

Franke-Meißner and Partner Ltd. (BFM) 2003. Geotechnical Expert opinion: Field investigation and subsoil assesment. Renovation of the evangelichal church Massenheim.
Franke-Meißner and Partner Ltd. (BFM) 2004. Geotechnical Expert opinion: Short report to subsoil invesigations. Renovation of the evangelichal church Massenheim.
Franke-Meißner and Partner Ltd. (BFM) 2021. Geotechnical Expert opinion: Settlements and convergence measurement. Renovation of the evangelichal church Massenheim.
Jones, L.D. & Jefferson, I. 2012. Expansive soils. In John Burland (ed.), *ICE Manual of Geotechnical Engineering. Volume 1, Geotechnical Engineering principles, problematic soils and site investigation*: 413–441. London, UK: ICE Publishing.
Li, J. & Cameron, D.A. 2002. Case Study of Courtyard House Damaged by Expansive Soils. *J. Perform. Constr. Facil.,* 16(4): 169–175.
Müller-Westermeier, G. & Riecke, W. 2004. Klimastatusbericht 2003: Die Witterung in Deutschland.Available at: https://www.dwd. de/DE/leistungen/klimastatusbericht/publiktionen/ksb2003_pdf/01g_2 003.html?nn= 16102 (Accessed 16 of December 2021).
Nelson, J.D. & Miller, D.J. 1992. *Expansive soils: Problems and practice in Foundation and Pavement Engineering*. New York, USA: John Wiley & Sons, Incorporated.
Odom, I. E. 1984. Smectite Clay Minerals: Properties and Uses. *Philosophical Transactions of the Royal Society of London – Series A, Mathematical and Physical Sciences* 311(1517): 391–409.
Ola, S.A. 1982. Geotechnical properties of an Attapulgite clay shale in Northwestern Nigeria. *Engineering Geology* 19: 1–13. Amsterdam.
O'Neil, M.W & Poormoayed, N. 1980. Methodology for Foundations on Expansive Clays. *ASCE Journal of Geotechnical Engineering* 106(12): 1345–1367.
ORS (2020) *Cracking In Buildings*. Available at: https://www.ors.ie/news/cracking-in-buildings/ (Accessed 16 December 2021).
Rebetez, M., Mayer, H., DuPont, O., Schindler, D., Gartner, K., Kropp, J.P., Menzel, A. 2006. Heat and drought 2003 in Europe: a climate synthesis. *Annals of Forest Science* 63(6): 569–577.
Schultze, E. & Muhs H. 1967. *Bodenuntersuchungen für Ingenieurbauten*. 2nd Edition. Berlin.
Sivapullaiah, P.V., Sitharam, T.G., Subba Rao K.S. 1987. Modified Free Swell Index for Clays. *Geotechnieal Testing Journa*l 10(2): 80–85.
Skempton, A.W. & MacDonald D.H. 1956. The allowable settlements of buildings. *Proceedings of the Institution of Civil Engineers* 5(6): 727–768.
U.S. Bureau of Reclamation (USBR) 1974. *Earth Manual*. 2nd Edition. Denver, USA: U.S. Bureau of Reclamation.
Wigger, H. 2000. Rissbildung infolge Setzungszwang in historischem Natursteinmauerwerk. Dissertation, Fachbereich für Bauingenieure- und Vermessungswesen der Technischen Universität Braunschweig, Braunschweig, Germany.
Wisconsin Historical Society (n.d). Identifying Structural Problems with Your Historic Building. Available at: https://www.wisconsinhistory.org/Records/Article/CS4298 (Accessed 16 of December 2021).
Yao, Y., Tung, S-T. E., Glisic, B. 2014. Crack detection and characterization techniques—An overview. Structural Control Health Monitoring 21 (12): 1387–1413.
Yue, E. 2017. *Soil Matric Suction and Active Zone Depth in Oklahama*. PhD Thesis, Oklahoma State University, Oklahama, USA.

Geotechnical Engineering for the Preservation of Monuments and Historic Sites III – Lancellotta, Viggiani, Flora, de Silva & Mele (Eds)

The study of the geological conditions of the territory is the key to the strategy of preserving the underground caves of the Holy Dormition Pskovo-Pechersky (Pskov-Caves) Monastery

E.N. Samarin
Lomonosov Moscow State University (Moscow, Russia)

I.V. Averin
LLC "Engineering Geology" (Moscow, Russia)

O.V. Zerkal, I.A. Rodkina & M.S. Chernov
Lomonosov Moscow State University Moscow, Russia

E.V. Shchepetova
Geological Institute of the Russian Academy of Sciences Moscow, Russia

ABSTRACT: This paper examines the cave system of the Holy Dormition Pskov-Pechersk Monastery, formed in the stratigraphically aged thickness of fine-grained sandstones of the Schwentoi horizon (D3šv) of the Frankish tier. Sandstones are characterized by a specific composition and structure, which led to the presence of unusual properties of these rocks, thanks to which the monastery arose, which has enjoyed deep popular veneration for more than 600 years. The destruction of caves is currently caused by both natural and man-made factors, and the development of a strategy for the preservation of caves is impossible without studying the geological causes of their formation.

1 INTRODUCTION

The Holy Dormition Pskovo-Pechersky Monastery is one of the largest and most famous monasteries in Russia with a centuries-old history (Figure 1). The name of the monastery is associated with the caves located in it, called "God-built" (created by God), dug by monks in the side of a large ravine in the sandstone massif. The main feature of the caves is the strong suppression of rotting processes, as a result of which human remains after burial remain incorruptible for a long time. For burial, niches were hollowed out in the walls of underground corridors from ancient times, a coffin with a body was placed in a niche, and the hole was closed with a ceramide – a ceramic plate with the name and years of life of the deceased (Figure 2).

In addition to the usual burials of laypeople, there are also two "fraternal cemeteries" where monks are buried, which are spacious caves, densely packed from top to bottom with coffins with the bodies of monks. The coffins are arranged one on top of the other, sometimes in ten or more rows in height, so the lower, oldest coffins are often completely flattened. Complete mummification of the buried bodies does not occur and the remains eventually decompose. However, despite the significant number of burials, the air in the caves is clean, there is not the slightest smell of decay, even from recent burials (Ryazantsev 1994). As the authors' research has shown, such an unusual phenomenon is due to the specifics of the composition and properties of Devonian sandstones, which serve as a receptacle for a huge underground cemetery.

According to legend, the caves became known to the locals in 1392. Monks who fled to the Pskov land from the south, from the raids of the Crimean Tatars, settled in the caves. In 1473, the

DOI 10.1201/9781003308867-90

Figure 1. Pskovo-Pechersky Monastery. a) – panoramic view of the Assumption-Intercession Church; b) – The Tower of the Upper Lattices. The left side of the Kamenets stream. View of the Holy Mountain (by: https://putidorogi-nn.ru/evropa/700-svyato-uspenskij-pskovo-pechersky-monaster).

cave church of the Assumption of the Mother of God was consecrated here, excavated by St. John in a sandstone hill. This year is considered the year of the foundation of the monastery. The hill (the edge of the moraine plain, isolated by a system of modern intersecting ravines), in which the Assumption Church and the "God-built" caves are located, is called the Holy Mountain.

In 1541, Abbot Cornelius built a refectory church in the monastery in the name of the Annunciation of the Most Holy Theotokos, expanded the Assumption Church, and then dug the monastery caves. Under him, the monastery turned into a strong fortress, stone walls were erected around the monastery (1558–1565), which served its defense for more than 150 years – until the conclusion of the Peace of Nishtadt in 1721. During this time, the monastery withstood the siege of the troops of the Polish King Stefan Batory (1581), Polish detachments under the command of J. Chodkiewicz and A. Lisovsky and the Swedish troops of King Gustav II Adolf (with interruptions in 1611–1614), the troops of the Swedish King Charles XII (in 1703).

In 1758–1759, the Intercession Church was erected over the Assumption Church. In 1815–1827, in memory of the deliverance of Pskov from the Napoleonic troops, the St. Michael's Cathedral was built, and in 1870 the Sretensky Church was built. During the Second World War, the temples of the monastery suffered from artillery shelling and were destroyed.

Early information about the geology of the area dates back to the first half of the XIX century and is associated with the names of T.Engelhardt, E.Ulprecht, H.Pandera, R.Buttermilk, et al. The issues of geology and geomorphology were considered in more detail in the works of K. Grewingk (1861, 1879) and H.Hausen (Hausen 1913). In the post-war period, in connection with the systematic geological study of the territory, a large number of works were published on the stratigraphy of Devonian deposits (Liepins 1950, 1963; Obruchev & Mark-Kurrik 1965), the geology of Quaternary (Kayak 1959, 1963, 1965; Orviku 1955, 1956, 1958) and pre-quaternary deposits (Gravity 1961; Kayak 1962), etc.

2 GEOMORPHOLOGICAL CONDITIONS.

The Holy Dormition Pskov-Pechersk Monastery is located within the city of Pechora, Pskov region. The architectural ensemble of the monastery is located in a large ravine, along the talweg of which the Kremenets stream flows. The stream enters the territory of the monastery in the area of the Upper Lattice Tower (Figure 2). Inside the monastery, the Kamenets stream is enclosed in an underground collector, the tray of which is located at a depth of 2.0–2.5 m below ground level. The absolute elevations of the channel part are 62.50–63.00 m.The modern relief of the studied territory is the result of a long geological development from the post-Devonian period to the present day. In pre-quaternary time, the main relief form of the territory under consideration was the "Devonian Plateau", which is a positive relief form, timed to the surface of the most stable rocks – sandstones

of the Schwentoi horizon. The next stage of relief development occurs before the Valdai (Late Pleistocene) glaciation, or at its earliest stage. During this period, in the western part of the studied territory, an erosive paleohollow is formed, which is subsequently filled with sand-block material. The direction of the hollow is north – northeast, with an azimuth of about 5–10°. The right side of the hollow is located in the area of the Archangel Michael Cathedral on one side of the ravine and west of the Assumption Church on the other side. Apparently, at the same stage, under the influence of near-river water flows, in the same side of the paleohollow, as a result of erosion and suffusion processes, caves are formed, some of which have survived to the present time. The next stage of relief development is associated with the onset of the glacier, the formation of the Upper Valdai stadial horizon and the subsequent formation of hilly-moraine relief in the final phase of the Valdai glaciation. The terrain in the area under consideration had a very rugged character and was an alternation of individual hills or their chains and depressions between them. Moraine loams everywhere overlapped the indigenous Devonian sandstones, as well as fluvioglacial deposits formed during the early stages of the Valdai glaciation, or before its onset. The final stage of relief formation.

The final stage of relief formation develops in the Holocene. Under the influence of the erosive activity of the water stream – the Kremenets stream – a fluvial type of relief is formed, the formation of a gully-beam network occurs practically in its modern form. The formation of the modern ravine, located at the intersection of the paleohollow, led to the exposure of its cross section and near-wall cave formations in Devonian sandstones, which, according to legend, in 1392 gave rise to monastic life on the territory of the monastery.

Sandstones, in which quartz predominates, are in many cases considered as practically immune to chemical weathering during geological studies (see, for example, Tricart 1972). At the same time, in many regions of the northern hemisphere of the Earth (in Russia – the Northern and Central Urals), in Europe (in the UK (Kent, Nottingham), Czech Republic and Poland), in the USA (Colorado, Alabama), Venezuela, etc.) there are landscapes and geological phenomena (individual voids and cave systems) similar to classical karst forms (Wray 1997). A number of researchers associate the formation of underground forms in sandstones with the influence of atmospheric or hydrothermal waters (Martini 2004; Piccini et al. 2009). Other authors emphasize the importance of the influence of microorganisms, microbially-driven by alkaline decomposition of sandstones (Barton et al. 2009; Gradzinski et al. 2010). At the same time, all these theories are debatable and to date there is no clear understanding of the role of leading factors in the formation of underground void systems in sandstones (Sauro et al. 2013)

Two groups of caves are currently concentrated on the territory of the Pskov-Pechersk Monastery: burial caves located immediately behind the Assumption Church (Figure 2), and utility caves dug relatively recently and intended for food storage (Figure 3). In addition, geophysical and drilling operations performed on the territory of the Holy Assumption Pskov-Pechersk Monastery showed the presence of underground voids that do not have exits to the daytime surface. Collapsed sections of caves were found in the upper part of the Assumption Church.

Currently, the width of the ravine is 100–120 m, the depth is 16–18 m. The ravine stretches from southwest to northeast with an azimuth of 50–70°. The left (north) side of the ravine has a slope from 30°–33° at the tower of the Upper gratings, to 20°–at the tower of the Lower gratings. The maximum steepness of the left slope up to 43° is fixed at the base of the Archangel Michael Cathedral, which is due to the presence of large-block material at its base. The right (southern) side of the ravine has a slope from 20 °–25° at the tower of the Upper lattices, to 35–39°–from the zone of caves for economic purposes to the tower of the Lower lattices.

Almost all along the ravine at the base, and sometimes in the middle part of the slopes, retaining walls were made at different times, differing in their dimensions and material – from masonry (earlier) to monolithic reinforced concrete (modern).

The existing level of the lower part of the ravine is artificial, formed by the conclusion of the Kamenets stream into the collector and the rise of the natural level of the talvega ravine to a height

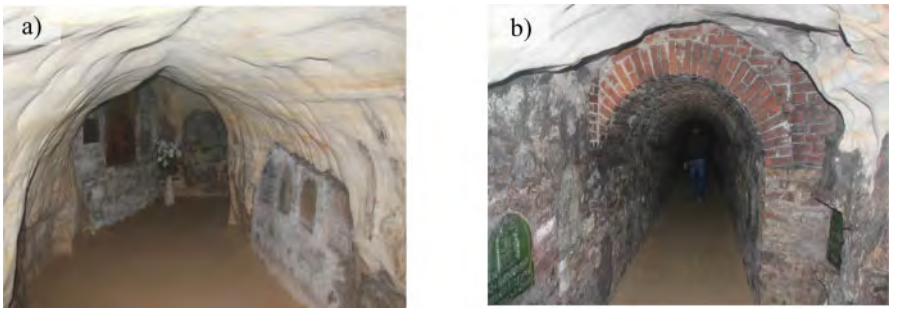

Figure 2. Caves of underground burials of the Pskov-Pechersk monastery: a) – without lining and with a natural vault; b) – with brick lining and a brick vault.

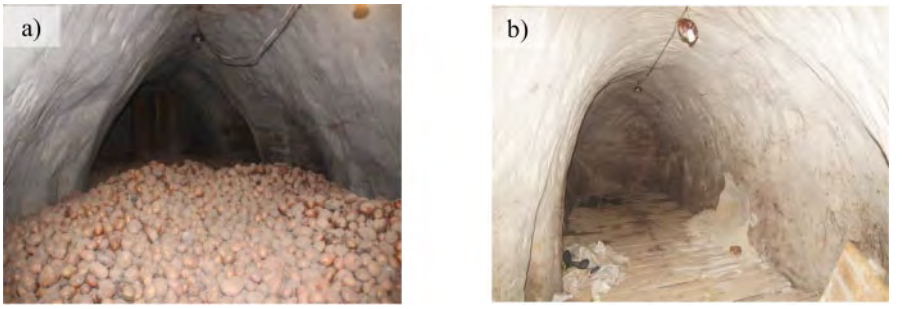

Figure 3. Household (warehouse) caves of the Pskov-Pechersk Monastery: a) – intended for storing potatoes; b) – for general use.

of 1.7 m at the tower of the Upper Gratings to 3.5 m at the tower of the Lower gratings. The absolute elevation marks of the relief within the study area range from 67.10 m to 91.25 m .

3 GEOLOGICAL STRUCTURE.

The deposits of the Shventoi formation ($D_3šv$) were uncovered at a depth of 1.4–13.0 m in the upper part of the ravine (behind the brows of the slopes) and 2.7–5.0 m in its talweg (altitude 65.20–83.10m), and are represented by the layering of sandstones and clays. Clays have a variegated color, from light greenish to brick-red, which is due to the different ratio of iron-containing minerals such as hematite and siderite. The sand fraction (up to 55%) contains quartz, potassium feldspar. The clay fraction contains hydrosludes (up to 60%), kaolinite (up to 25%), mixed-layered illite-smectite minerals with disordered structure (up to 20%) and finely dispersed hematite (10–15%). Clays lie in the lower part of the ravine and are a local water barrier. The uncovered capacity of clays reaches 12.0 m .

Above the section are fine-grained quartz sandstones with a thin lenticular layering with thin (up to several centimeters) interlayers of clays. Sandstones from light pink to reddish-brown, fine-grained silty, with lenticular and cross-layered, with frequent interlayers of low-power clays, weakly cemented, low-moisture. Among the sand grains: quartz – 75–80%; fragments of quartzite – 5–10%; feldspar (mainly KPS) – 10–15%. Mica (scales up to 0.2 mm long) are colorless and dark green in a ratio of 1: 3, the latter partially degraded or oxidized from the surface – about 5%. There are opaque accessory ore minerals (< 1%) and single very small fragments of charred plant detritus. Cement in sandstone is discontinuous, contoured, ferruginous or ferruginous-clay-silicate.

Sandstones are traced in both sides of the ravine and have a thickness of up to 13.8 m (Figures 4 and 5).

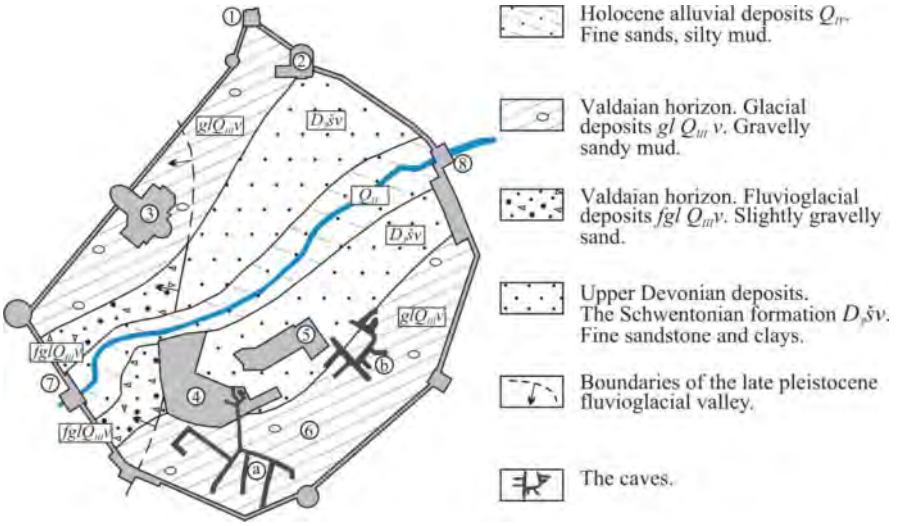

Figure 4. Schematic geological map of the territory of the Pskov-Pechersk Monastery. The numbers are: 1 – Peter's Gate Tower above the Holy Gates; 2 – The Gate Church of St. Nicholas the Wonderworker; 3 – the Cathedral of Michael the Archangel; 4 – Assumption-Intercession Church; 5 – Sretenskaya Church; 6 – Holy Hill; 7 – The Tower of the Upper Lattices; 8 – The Tower of the Lower lattices; a – cave burials; b – household caves.

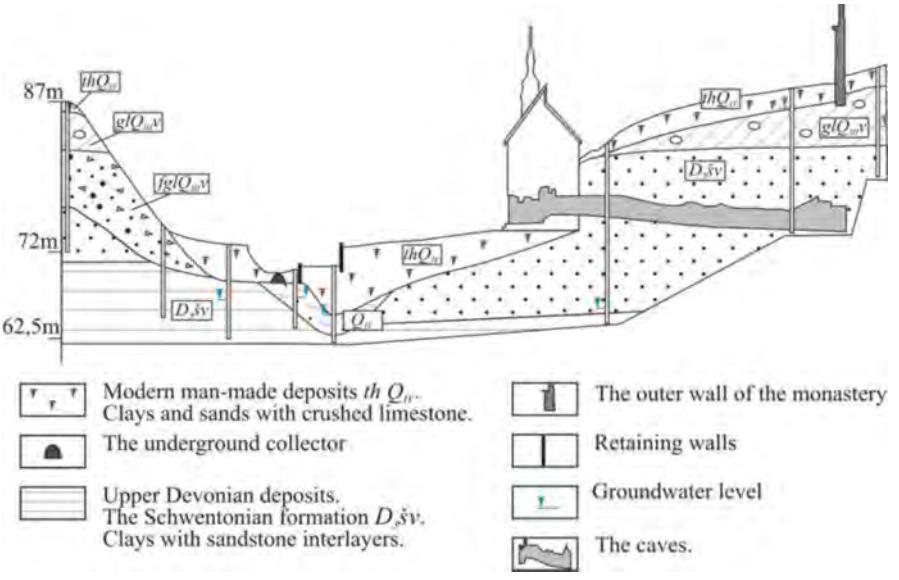

Figure 5. Schematic geological section along the line of St. Michael the Archangel Cathedral-Assumption-Intercession Church – caves of the monastery. Other designations in Figure 4.

In the southwestern part of the monastery's territory, fluvioglacial mixed-grained sands ($fgQ_{III}v$), formed before the onset of the Valdai glaciation, or at its earliest stage and confined to the pre-Glacial paleohollow, lie above the Schwentoi sediments. The sands lie at a depth of 0.4–8.8 m from the ground level on the slopes and in the upper part of the ravine, which corresponds to absolute elevations of 71.40–84.15 m. On the slopes, fluvioglacial sands lie immediately under the soil and vegetation layer, as well as under bulk soils, or under blocks of limestone and granite laid to strengthen them. The sands are from light to reddish-brown, from small to large (Figure 3), loose and medium density, moist and water-saturated. Sands with water saturation are prone to suffusion decompression and exhibit quicksand properties. The thickness of fluvioglacial sands reaches 12.8 m.

Devonian sandstones and fluvioglacial sands are overlain by upper quaternary moraine deposits of the Valdai horizon and ($gl\ Q_{III}v$), which are represented by red-brown soft, refractory and semi-hard loams and plastic sandy loams with gravel and crushed carbonate rocks (content up to 5–10%). The thickness of the deposits is 4–5 m .

The talweg of the ravine contains modern alluvial deposits ($al\ Q_{IV}$), represented by sands and loams. The sands are gray, shallow, slightly clayey, medium density, moist and water-saturated. The loams are grayish-brown, soft-plastic, with interlayers and lenses of fine sand. The capacity of the alluvium is 1.5–5.9 m.

Almost everywhere the territory of the monastery is blocked by bulk technogenic soils. These are variegated semi-solid clays or gray fine wet sands, with construction debris or limestone blocks. The lithological composition of the deposits is very variegated and depends, apparently, on economic necessity. The capacity of bulk soils varies from 0.5 to 5.5 m.

Groundwater of sporadic distribution with mineralization up to 0.89–0.97 g/l, confined to sand layers in bulk soils, lies at a depth of 1.3–5.0 m. Groundwater of the alluvial aquifer with mineralization up to 0.96–1.16 g/l is confined to alluvial sands, lies at a depth of 1.6–1.7 m and is developed locally in the bed of the Kremenets Stream. The underground waters of the Devonian aquifer lie significantly below the bottom of the ravine. Directly in the thickness of the Schwentoi sandstones in the sides of the ravine, only low-power sporadically distributed lenses of groundwater with a mineralization of up to 1.20 g/l with a capacity of no more than 1.5 m were uncovered. Such lenses are formed on the interlayers of clays, unevenly lying in the section of sandstones, during the infiltration of precipitation.

Thus, unique natural conditions have developed in the territory under consideration, which differ in the following features. In the sides of the ravine formed by the Kremenets stream lies a thickness of small quartz weakly cemented sandstones of considerable power. These sandstones from the surface are reliably blocked by a low-permeable layer of dense (density 2.10 g/cm^3) moraine loams, which reliably protect them from infiltration of precipitation and prevent free flow gas exchange with the atmosphere. Underground waters lie much deeper than the talvega ravine. Thus, the entire sandstone massif is an enclosed space bounded by a moraine from above and groundwater from below, with low-humidity air, with a temperature at the level of 4-6°C. Moreover, we found that the sandstones of the Schwentoi formation contain up to 110–150 ppm (mg/kg) of arsenic, which is two orders of magnitude higher than the clark content of this element in sandstones, which according to A.A. Beus is 1.0×10.0^{-4}%. Perhaps, it is the high concentrations of arsenic in the conditions of a humid and cold atmosphere and difficult gas exchange, which are characteristic of burial caves, that play a decisive role in suppressing the processes of decay in the sandstone massif. However, in the case of local cave vaults collapses and free access of atmospheric air, rotting begins to have well-known signs. Such circumstances dictate the need for careful treatment of a unique object of invaluable cultural and historical significance.

The high arsenic content is due to the peculiarities of the formation of the deposits of the Schwentoi horizon. Sandstones accumulated in the coastal part of the Frankish sea basin due to the destruction of igneous rocks of the Kola Peninsula (Geology of the USSR 1971), which are characterized by the presence of sulfoarsenides (Taymasov 2018). Sulfoarsenides during decomposition

are a source of arsenic, which was actively sorbed to the silica cement of sandstones during their deposition.

Protective measures are all the more necessary, since the peculiarities of the geomorphological conditions of the monastery territory determine the likelihood of intensification of various exogenous processes.

The height difference on the territory of the Holy Dormition Pskov-Pechersk Monastery reaches 16–20 m, and the steepness of the slopes in some areas (for example, the right side of the creek valley in the area of the Annunciation Cathedral) exceeds 45°. During the performance of these works, several areas of potential development of slope deformations were identified.

The processes of waterlogging develop within the fortress moat, arranged around the outer wall of the monastery, in areas with unsatisfactory conditions of surface runoff. Such areas are either drainless local reservoirs, or waterlogged surfaces with a wide growth of moisture-loving plants.

The main process identified in underground cavities-caves is the gradual collapse of their arches, especially in that part of the sandstone massif that adjoins the deepened paleovalley filled with multi-grained sands. The expansion of one of the caves in this zone led to its emphasis on the side of the paleovalley and the fall of fluvioglacial sand. A sinkhole was formed over this area, which was later filled with bulk soil.

It was found that the greatest danger to the existence of caves is the infiltration of precipitation and water, which the monks use to water garden plants located on the Holy Hill. Sandstones in which caves are dug are very fragile rock and even in a dry state are easily rubbed by hands. When water seeps in, the sandstones are moistened, they lose their strength, as a result of which suffusion channels are formed on the arches and walls of caves, the arches crumble and eventually collapse (Figure 6). Such a situation requires appropriate measures for the surface waterproofing of a unique array of rocks.

The second reason leading to the destruction of caves is the crowded excursions of believers. In some periods, the air temperature in the underground space can rise to 14–15°C, which also dramatically intensifies the rate of destruction of caves. It should be noted that attempts to use surface treatment of sandstones in caves with sodium silicate did not lead to a positive result.

Less dangerous for the various buildings of the monastery are the processes of surface erosion developed in the sides of the ravine, linear erosion along the bed of the Kremenets Stream and the processes of heaving during seasonal freezing of soils from the surface (Averin 2019).

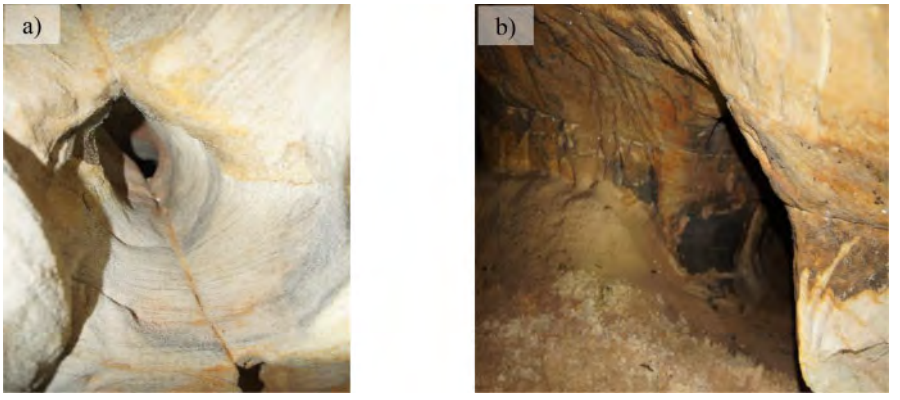

Figure 6. Types of destruction of caves in sandstones: a) – formation of a suffusion channel in the cave vault; b) – collapse of the cave wall.

4 CONCLUSION

The Holy Dormition Pskov-Pechersk Monastery is one of the largest and most famous monasteries in Russia. The history of the monastery dates back about 550 years and it is still the subject of devout worship of believers. The main attraction of the monastery is the caves located in it, called "God-built". Cave formations and their specific properties are determined by unique natural conditions, the main of which are the geological structure of the territory and the history of the formation of the relief.

The exact location of the caves is still unknown, since some of them were collapsed both due to natural causes and as a result of human activity. Still, the strength characteristics of sandstones are low, which hardly contributes to a long existence in undiscovered underground workings devoid of external fastening. Moreover, the natural development of natural exogenous processes also threatens this unique object. All the more important are the issues of careful rational operation of the monastery complex of structures, and the prospects for the development of the Holy Dormition Pskov-Pechersk Monastery must necessarily be based on a competent comprehensive analysis of the geological and geomorphological conditions of the territory.

REFERENCES

Averin I.V. et al. 2019. Development of emergency measures on the territory of the Holy Dormition Pskov-Pechersk Monastery/*On-site investigation report:* 162. Moscow: Limited Liability company "Ingineering Geology". vol. 1.

Barton, H., Suarez, P., Muench, B., Giarrizzo, J., Broering, M., Banks, E., Venkateswaran, K., 2009. The alkali speleogenesis of Roraima Sur Cave, Venezuela. In: White, W.B. (Ed.), Proceedings of the 15th International Congress of Speleology, Kerrville, Texas, July 19–26 2009, pp. 802–807

Geology of the USSR. Volume I. Leningrad, Pskov and Novgorod regions. Geological description. North-Western Territorial State Institution. Ed. by A.V.Sidorenko. Moscow. Nedra 1971, 504 p.

Gradziński M., Chmiel M.J., Lewandowska A., Michalska-Kasperkiewicz B., 2010. Siliciclastic microstromatolites in a sandstone cave: role of trapping and binding of detrital particles in formation of cave deposits. Annales Societatis Geologorum Poloniae, 80, 303–314

Martini, J.E.J., 2000. Dissolution of quartz and silicate minerals. In: Klimchouk, A.B., Ford, D.C., Palmer, A.N., Dreybrodt, W. (Eds.), Speleogenesis. Evolution of karst aquifers. National Speleological Society, Huntsville: 452–457

Martini, J.E.J., 2004. Silicate Karst. In: Gunn, J. (Ed.), Encyclopedia of Caves and Karst Science. Fitzroy Dearborn, London: 1385–1393

Piccini, L., Mecchia, M., 2009. Solution weathering rate and origin of karst landforms and caves in the quartzite of Auyan-tepui (Gran Sabana, Venezuela). Geomorphology 106, 15–25

Ryazantsev S.V. 1994. Thanatology – the science of death. 336. Moscow: East European Institute of Psychoanalysis.

Sauro, F., Piccini, L., Mecchia, M., De Waele, J., 2013. Comment on "Sandstone caves on Venezuelan tepuis: Return to pseudokarst?" by R. Aubrecht, T. Lánczos, M. Gregor, J. Schlögl, B. Smída, P. Liscák, Ch. Brewer-Carías, L. Vlcek, Geomorphology 132, 351–365. Geomorphology 197, 190–196

Taymasov D.V. Mineral Composition of Zapolarnoe Deposit (Kola Peninsula). /Bulletin of Perm university. Series: Geology. 2018. Vol 17. No.4. p.386–394.

Tricart, J., 1972. The Landforms of the Humid Tropics, Forests and Savannas. Longman. London, 306 p.

Urtâns J., Enièš G., 2001. Latvian sandstone caves as cultural phenomena. Journal of Baltic Studies, 32(1), 95–99

Wray, R.A.L., 1997. A global review of solutional weathering forms on quartz sandstones. Earth Science Reviews 42, 137–160

Geotechnical Engineering for the Preservation of Monuments and Historic Sites III – Lancellotta, Viggiani, Flora, de Silva & Mele (Eds)
ISBN 978-1-003-30886-7

FEM simulation of differential settlement of Wat Krasai, a leaning brick made pagoda on soft ground, in Ayutthaya, Thailand

H. Ito
JIP Techno Science Corporation, Osaka, Japan

Y. Ishida
Waseda University, Tokyo, Japan

ABSTRACT: Wat Krasai is a brick pagoda of approximately 27 m in height and was built during Ayutthaya Dynasty at Ayutthaya, Thailand. The brick pagoda leans to the north. The cause of this tilt is thought to be the differential settlement of the foundation ground. In 2013, restoration work was carried out on this temple, and the base of the pagoda buried in the soil was restored. Furthermore, the lower half of the pagoda was covered with new bricks, and the total weight of the pagoda after restoration is estimated to be 1.36 times that before restoration. In 2020, seven years after the restoration work, there was a gap of 49 mm between the restored base and the main body of the pagoda, and the surface of the base was cracked. For the conservation of this pagoda, it is necessary to clarify the deformation mechanism of the base of the pagoda on soft ground. In this study, a series of 3D FEM simulations was performed to simulate the differential settlements of the pagoda after the construction to the present. Furthermore, additional analysis has been carried out to estimate the structural performance in the future. The results show that the differential settlement does not stop nor decrease, but only increases in the future.

1 INTRODUCTION

Wat Krasai is located in the southwestern countryside of the Ayutthaya Historical Park in the Kingdom of Thailand. It is an appealing ruin of a Buddhist temple consisting of a large main pagoda, chapel ruins, and walls surrounding the temple (Figure 1). Although there is no clear evidence, it is believed that the temple acted as the cemetery of a royal family that rebelled against King Narai, ruler from 1656 to 1688 in the late Ayutthaya dynasty.

The main pagoda of this temple now tilts approximately 2° towards the north. The pagoda has a hollow structure with a height of approximately 27 m, with a conical shape at the top and an octagonal pyramid shape at the bottom. In addition, the lower part of the pagoda was covered with new bricks from restoration work carried out in 2013 and a rectangular base was constructed at the bottom (Figure 2). It is estimated that the weight of the pagoda has increased since the restoration work by approximately 1.36 times. If the inclination of the pagoda results from differential settlement of the foundation, the increase in weight can cause new deformations. Therefore, in this study, to preserve Wat Krasai, we performed a 3D finite element method (FEM) analysis and predicted the future inclination of the pagoda.

DOI 10.1201/9781003308867-91

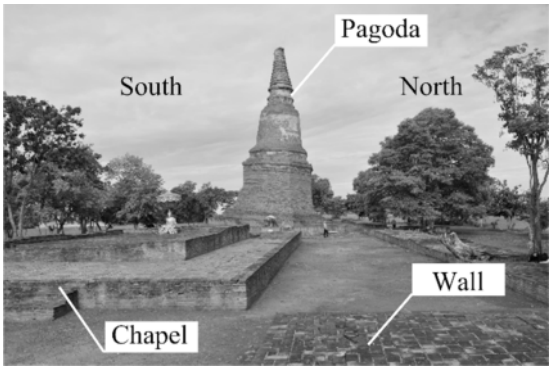

Figure 1. Wat Krasai (view from the east side).

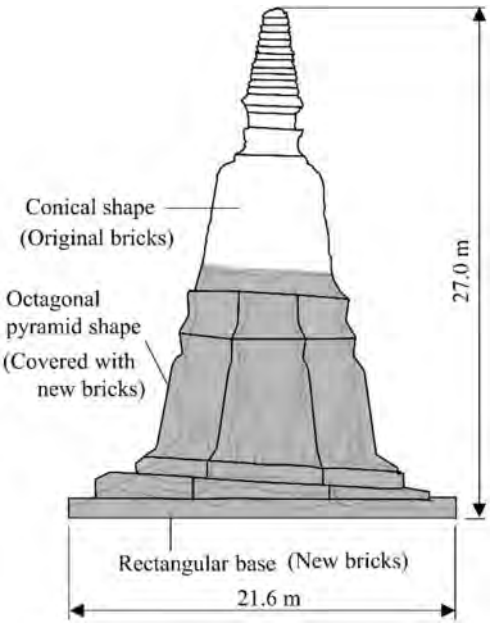

Figure 2. The shape of the pagoda after the restoration work.

2 CONDITION OF PAGODA AND RISK

Although the lower half of the pagoda was covered with new bricks after the restoration work in 2013, new damage has been revealed. The damage of the pagoda is significantly different between the south and north sides, probably owing to the inclination toward the north. There is a gap between the restored base and the main body of the pagoda at the southern hem of the pagoda. Figure 3 shows the width of the gap and the range in which it is generated. In fact, in the six months from August 2019 to February 2020, the gap on the south side expanded from approximately 30 mm to 50 mm. In addition, the range in which it occurred also increased.

Figure 4 shows the state of the cracks in the base on the south side (February 2020). These cracks extend from the corners of the octagonal pagoda to the outer edge of the base and penetrate the sides of the base. Figure 5 shows the state of the covered bricks on the south side. The side surface of the covered brick was flat and dry. In contrast, at the northern hem of the pagoda, there is no

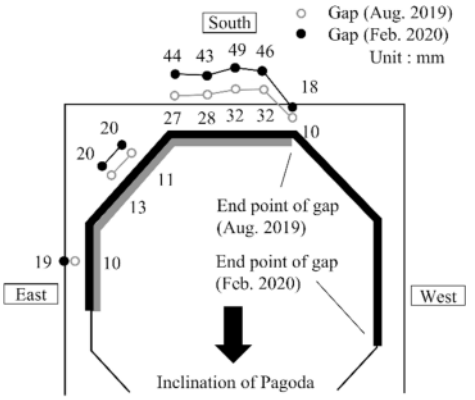

Figure 3. The gap between the pagoda and the base.

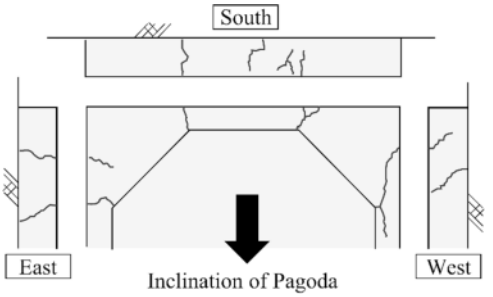

Figure 4. Cracks of the reconstructed base on the south side (Feb. 2020).

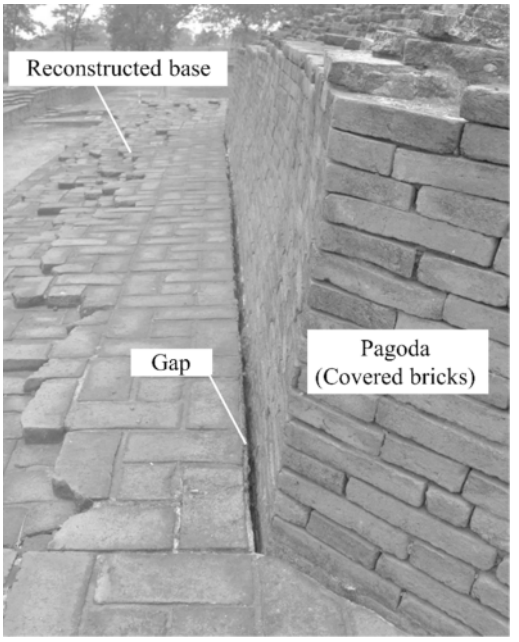

Figure 5. State of the covered bricks on the south side (Feb. 2020).

gap between the base and the pagoda. Figure 6 shows the state of swelling that occurs on the side surface of the north side covered brick. Figure 7 shows the state of the wet and blackened parts. Decayed and sandy crushed bricks are piled up. The new bricks from the restoration work are piled up along the inclination of the pagoda. The traces of raindrops remaining on the pagoda indicate that rainwater flows from the high south side to the low north side. Therefore, it is estimated that the bricks will continue to deteriorate at the northern hem where the water collects. The bricks in the main body of the pagoda are not filled with mortar. Therefore, if the hem that supports the upper part is destroyed, there is the risk of the partial collapse of the bricks.

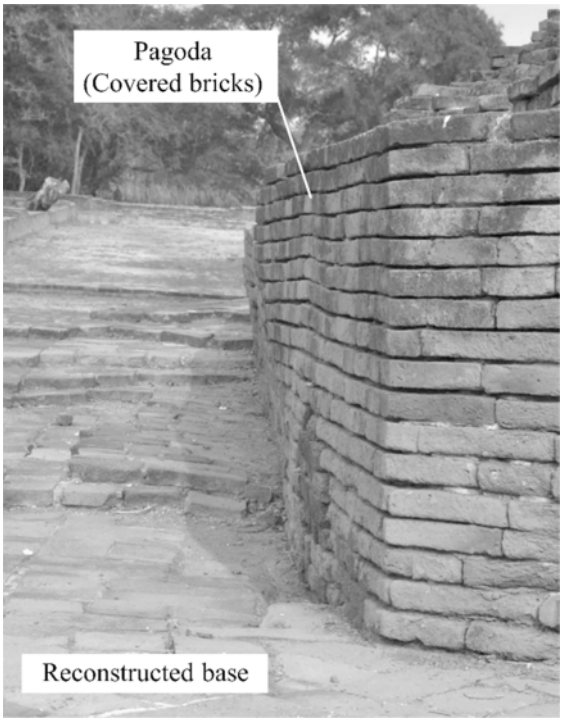

Figure 6. State of the covered bricks on the north side (Feb. 2020).

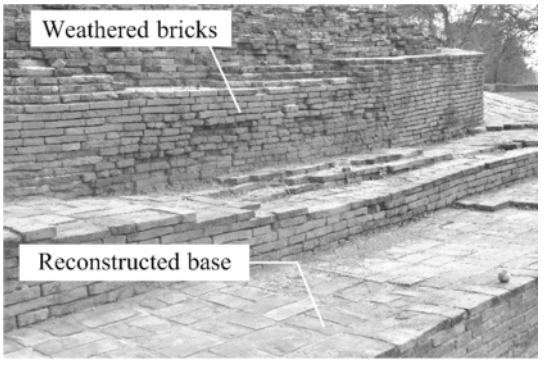

Figure 7. Weathered bricks at the northern hem (Feb. 2020).

3 FOUNDATION OF PAGODA

Figure 8 shows the cross-section of the foundation area located just below the pagoda. The inclination of the layer was estimated from the results of four boring surveys conducted around the pagoda. Three clay layers (Clay 1, Clay 2, and Clay 3) were deposited on the sand layer 20 m below the ground surface. It is estimated that the inclination of the layer is in the north-south direction, where the pagoda leans, as well as in the east-west direction. Of the three clay layers, Clay 1 and Clay 2 have high plasticity, and Clay 3 has low plasticity. Table 1 shows the parameters of each layer. The plasticity index I_p, permeability coefficient k and unit weight are average values obtained from the soil tests. However, consolidation tests of each layer, which are important for predicting the inclination of the pagoda in the future, have not been conducted.

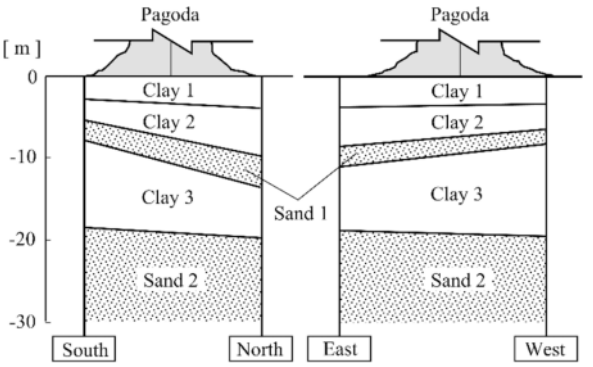

Figure 8. Cross-section of the foundation ground.

Table 1. Soil parameter of foundation ground.

	I_p	k m/day	Unit weight kN/m^3
CLAY 1	38.2	2.4E-06	19.2
CLAY 2	42.0	3.6E-06	17.1
CLAY 3	27.5	–	19.2

4 FUTURE PREDICTION OF INCLINATION

4.1 *Numerical analysis*

3D FEM analyses were conducted to predict the future inclination of the pagoda using PLAXIS 3D V21. Previous studies have shown that it is important to consider the overturning moment when simulating the tower tilt problem (Burland et al. 2003; Vermeer et al. 2002; Yuan et al. 2007). Specifically, Vermeer et al. calculated the inclination of the Leaning Tower of Pisa in Italy using a 3D analysis combining geometric nonlinearity and elastoplastic constitutive models.

In this study, the updated Lagrangian method used by Vermeer et al. was adopted to consider the overturning moment of the pagoda. Additionally, two types of elastoplastic constitutive models were used for the material model of the cohesive soil layer. One model is the modified Cam-Clay model (Roscoe & Burland 1968), which is one of the most widely used models for cohesive soils. The second model is the Sekiguchi–Ohta model (Sekiguchi & Ohta 1977), which is a well-known model that can simulate the initial anisotropic behavior of cohesive soils.

4.2 *Modeling of the ground and the pagoda*

Figure 9 shows the 3D analysis model. Modeling was performed considering the inclination of the layer in the north-south direction, in which the pagoda leans. For simplification, the inclination of the layer in the east-west direction was ignored In addition, lacking survey results, layers other than the one directly below the pagoda were assumed to be horizontal. Based on the drawings of the restoration work, the shape of the pagoda was modeled with 14 blocks.

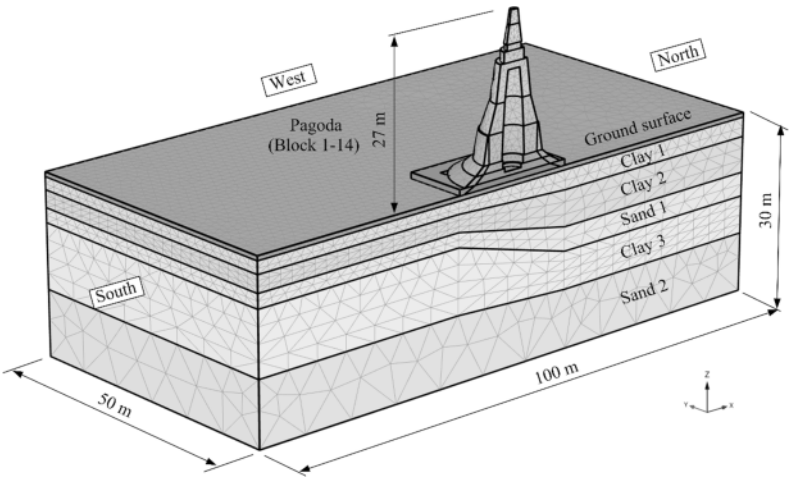

Figure 9. FEM model for 3D analysis.

4.3 *Parameters of soil*

The consolidation test of the three layers (Clay1, Clay2, and Clay3) which would presumably cause differential settlement of the pagoda was not conducted. Therefore, in this study, the parameters were set using the estimation method proposed by Iizuka and Ohta, as shown in Figure 10. Table 2 lists the values for each parameter-set using this method. For the unit weight and permeability

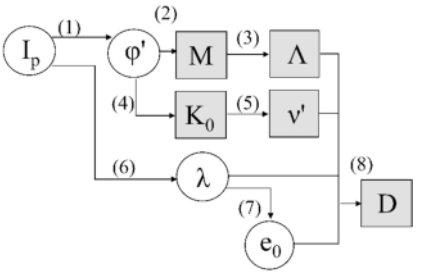

Figure 10. Flowchart for estimating parameters from plasticity index (Iizuka & Ohta 1987).

coefficient, the results of the soil test in Table 1 were used. It was also assumed that the permeability coefficient of Clay3 is the same as that of Clay2.

Table 2. Estimating parameter values for clay layers.

D	Λ	M	K	ν'	
CLAY 1	0.073	0.592	1.035	0.559	0.358
CLAY 2	0.076	0.576	1.009	0.568	0.362
CLAY 3	0.061	0.644	1.128	0.525	0.344

4.4 *Time history*

In the numerical analysis, considering the increase in the weight of the pagoda due to the restoration work in 2013, a simulation was performed to predict the deformation over the next 100 years. Table 3 presents the time history of the analysis. It was assumed that the construction of the pagoda began at the beginning of King Narai's reign (1656).

Table 3. Time history for numerical analysis.

		Time years
Construction	(1656–1658)	2
Consolidation	(1658–2013)	355
Restoration	(2013–2014)	1
Consolidation	(2014–2114)	100

4.5 *Future prediction of pagoda transformation*

Figure 11 shows the time history of the inclination of the pagoda from the 3D analysis. Owing to the increased weight due to restoration work in 2013, the amount of inclination increased in both

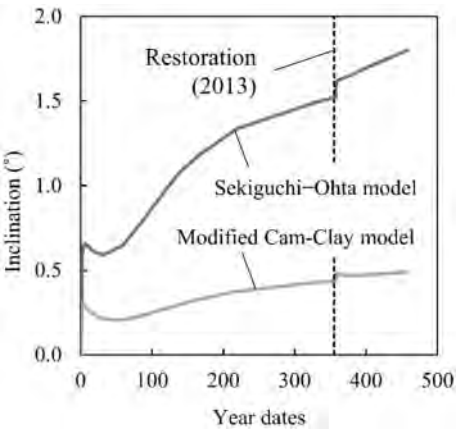

Figure 11. Time history of the inclination of the pagoda.

Table 4. Inclination by both constitutive models.

Inclination (°)	Before Restoration (2013)	100 years after restoration (2114)
Modified Cam-Clay	0.436	0.489
Sekiguchi–Ohta	1.524	1.798

cases. However, the increasing tendency of the inclination of the pagoda accelerated less compared to that before the restoration work. Table 4 shows the inclination of the pagoda calculated using the modified Cam-Clay model and the Sekiguchi–Ohta model. Comparing the results of both analyses, the Sekiguchi–Ohta model was found to have a larger inclination than the modified Cam-Clay model. Furthermore, the ground parameter estimated from the plasticity index was considered to be one of the reasons because of which the inclination in 2013 did not reach 2° .

5 DISCUSSION

Wat Krasai is a temple worshiped by residents. We believe that it is vital that this pagoda remains in this area, even though it is tilting. Although the inclination of the pagoda is expected to continually increase in the future, the entire pagoda is unlikely to tip over as it is cone-shaped. However, we cannot be certain if the local rupture influenced by the inclination will trigger an overall collapse. In recent years, the effects of heavy rainfall due to climate change have become a serious problem in the Ayutthaya region. The surface of the Ayutthaya dynasty pagoda was covered with plaster and waterproofed to a certain extent. However, many of the existing ruins have exposed bricks; this necessitates investigations on the effect of brick deterioration due to rainwater.

6 CONCLUSION

From the viewpoint of conserving the pagoda, we summarize the results of this research as follows:

(1) A series of FEM analyses were performed. Considering the added weight from the previous restoration work and differential settlement of the foundation ground, the further inclination of the pagoda is expected. However, the increasing tendency of inclination should not accelerate rapidly.
(2) It is important to further assess the structural deterioration of the pagoda. In addition to the effects of increasing inclination and gaps, the combined effects of rainwater flow during heavy rains and floods must also be considered.
(3) When numerically simulating the inclination of the pagoda due to differential settlement, it is crucial to select a suitable constitutive model as well as set values of the parameters of the cohesive soil.

ACKNOWLEDGEMENTS

We would like to sincerely thank the 3rd Regional Office of Fine Arts, Ayutthaya and the Ayutthaya Historical Park Office for their permission and cooperation of the field survey at Wat Krasai. Part of this research was supported by the Ritsumeikan University Asia-Japan Research Promotion Program (PI Ryoichi Fukagawa, 2017; PI Yoshifumi Satofuka, 2018–2020). Besides, we would like to thank Editage (www.editage.com) for English language editing.

REFERENCES

Burland J.B., Jamiolkowski M. & Viggiani C. 2003. The stabilisation of the Leaning Tower of Pisa. *Soils and Foundations* 43(5): 60–80.

Iizuka A. & Ohta H. 1987. A determination procedure of input parameters in elasto-viscoplastic finite element analysis. *Soils and Foundations* 27(3): 71–87.

Jaky J. 1944. The coefficient of earth pressure at rest. *J. of the Society of Hungarian Architects and Engineers.* 355–358.

Karube D. 1975. Unstandardized triaxial testing procedures and related subjects for inquiry. *In: Proceedings of the 20th symposium on geotechnical engineering.* 45–60.

Kenney T. C. 1959. Discussion: *Journal of the Soil Mechanics and Foundation Engineering Division.* ASCE. 85(3): 67–79.

Ohta H. 1971. Analysis of deformations of soils based on the theory of plasticity and its application to settlement of embankments. *Doctor thesis. Kyoto University*.

Roscoe K.H. & Burland J.B. 1968. On the generalised stress–strain behaviour of 'wet' clay. *In Engineering Plasticity, Heyman J, Leckie FA (eds). Cambridge University Press: Cambridge.* 563–609.

Sekiguchi H. & Ohta H. 1977. Induced anisotropy and time dependency in clays. *Proc. Specialty Session 9. In 9th International Conference on Soil Mechanics and Foundation Engineering.* 229–237.

Vermeer P.A., Neher H.P., Vogler U. & Bonnier P.G. 2002. 3D Creep Analysis of the Leaning Tower of Pisa. *Technical report, Kroener, Stuttgart University*.

Yuan J.L., Wang J. & Lv H.Z. 2007. Analysis and simulation on unequal settlement of ancient masonry pagodas. *WIT Transactions on The Built Environment* 95: 459–467.

SYMBOLS

I_p	Plasticity index
k	Permeability coefficient
φ'	Internal friction angle
D	Coefficient of dilatancy
Λ	Irreversibility ratio
M	Critical state parameter
K_0	Coefficient of earth pressure at rest
ν'	Effective poisson's ratio
λ	Compression index
e_0	Initial void ratio

Geotechnical Engineering for the Preservation of Monuments and Historic Sites III – Lancellotta, Viggiani, Flora, de Silva & Mele (Eds)

Bentonite based barriers for protecting offshore monuments from saltwater intrusion

Himanshu Yadav
Department of Civil Engineering, Indian Institute of Technology Guwahati, Guwahati, Assam, India

T.V. Bharat
Department of Civil Engineering and Centre for Indian Knowledge System, Indian Institute of Technology Guwahati, Guwahati, Assam, India

ABSTRACT: India is a culturally rich nation due to the presence of enormous historical structures. There are several ancient temples with unique Hindu sculptures and architectural beauty. Some of the temples such as Mahabalipuram in Tamil Nadu, Murudeshwar Temple in Karnataka and Tiruchandur Subramanya Temple in Tamil Nadu have been built very close to the sea coast. Such heritage and monument structures face the risk of deterioration of foundations due to moisture movement and saltwater intrusion. Leaving the monuments unprotected might lead to unrepairable damage to the foundation and eventual collapse of the structures. In this study, installation of bentonite based barriers were explored to prevent the migration of saltwater intrusion into the foundation of the monument structures, and to reduce the moisture variations around the foundation. The compacted bentonites are generally used as barrier materials in various Geoenvironmental applications and were explored for the heritage conservation for the first time in this study. The knowledge of bentonite characteristics for the conservation application was analyzed through scientific study. The hydraulic conductivity was estimated for four Indian bentonites of different plasticity at a compaction dry density of 1.2 Mg/m^3 under the isochoric conditions with salt solution. Diffusion performance under the high ionic salt environment with the same density was also estimated under isochoric conditions using the through-diffusion technique. The bentonite B3 was found to be most suitable material to act as barrier against seawater. Based on values of diffusion characteristics, seawater will take around 12 years to diffuse across a 50 cm thick clay layer.

1 INTRODUCTION

India is a culturally and historically a prosperous nation. Number of historical structures like Ajanta and Ellora caves, Sun Temple, Taj Mahal, Mahabalipuram Temple, Rani ki Vav, Murudeshwar Temple etc. are the great examples of architecture marvels and serves as true historical symbols (Vasudev et al. 2019). Historical structures attract the tourist to the country and contribute in travel and tourism industry (Loke et al. 2020). These heritage structures undergo the deterioration due to aging, chemical, biological processes, climatic and environmental conditions (Loke et al. 2020). Heritage and monumental structures near the sea shore face the risk of deterioration of structure due to moisture movement and salt water intrusion to the foundation of these structures. Salt weathering is one of the principal cause of deterioration of stone work and masonry used in architectural structures around the world (Cardell et al. 2003; Zezza F. 1996;. Mechanical salt crystallization process is capable of destroying very hard stones (La Iglesia et al. 1994; Theoulakis & Moropoulou

 DOI 10.1201/9781003308867-92

1997). Interactions of high concentrations of salt solution can be disastrous to the heritage structures especially foundations. Moreover, the fluctuations in water table may lead to the wetting drying cycles. The moisture intrusion is also harmful for long performance of these structures. Utilization of chemicals and mechanical interventions can negatively influence the heritage structures, so such remedial measures are generally avoided.

Bentonite clay has high sorption capacity, high cation exchange capacity, high specific surface area, high plasticity index and low hydraulic conductivity (;harat et al. 2020; Das & Bharat 2017; Yadav & Bharat 2022). The bentonites have low hydraulic conductivity (i.e. $<10^{-7}$ cm/sec), which makes the diffusion as dominant mechanism for contaminant transport. These properties of bentonite clay support its utilization as barrier material. Bentonite clays are successfully used as landfill liner to prevent the flow of contaminants across the liner system. Diffusion and retardation characteristics are important parameters for design of liner (barrier) system and several laboratory techniques are used to estimate these parameters. Through diffusion (Badv & Abdolalizadeh 2004; Barone et al. 1992; ;as & Bharat 2017), in-diffusion (Mieszkowski 2003; Roehl & Czurda 1998;, out-diffusion (Sardini et al. 2003; Van Loon & Jakob 2005) and half-cell method (Gillham et al. 1984; Philips & Brown 1964; Robin et al. 1987; are commonly used techniques for diffusion experiments. Transient through diffusion experiment is preferred due to its non-destructive nature and simplicity in measurements. All different methods lead to the same design parameters (Bharat 2008). The model parameters were estimated by minimizing the error between measured and theoretical concentration profiles.

Here, we propose the utilization of bentonite clay as barrier material for preventing the salt water intrusion to the monumental structures. The sea water has very high concentration of NaCl (i.e. 2M). The hydraulic and diffusion behavior of bentonite under such high concentration is not available and needs to be explored. In this work, the hydraulic and diffusion parameters of different quality of bentonites were studied at 1.2 Mg/m^3 dry density for application as barrier material around the monumental structures.

2 MATERIALS AND METHODOLOGY

2.1 *Bentonites*

Four bentonites of different quality procured from Kutch and Barmer region were used in this study. The surface and index properties of these bentonites were presented from earlier works (Das & Bharat, 2021; Gapak et al. 2017; in Table 1.

Table 1. Surface and index properties of used bentonites.

Property	B1	B2	B3	B4
Specific surface area, Sa (m^2/g)	380	465	530	560
Cation exchange capacity, CEC (*meq/100gm*)	38.8	55.2	71.7	108.8
Na^+	13.9	33.4	34.8	92.1
K^+	1.4	4.8	1.3	0.2
Ca^{2+}	15.2	11.7	29.4	13.7
Mg^{2+}	8.3	5.3	6.2	2.8
Liquid limit (%)	175	296	393	597
Plastic limit (%)	27	46	50	51
Specific gravity, *Gs*	2.76	2.76	2.77	1.77
Clay content (%)	62	69	78	84

2.2 *Methodology*

The foundation of monuments near the sea shore are subjected to harsh environment due to saltwater intrusion from the sea. It is proposed to make a bentonite based barrier to prevent the migration of saltwater to the foundation as shown in Figure 1. Hydraulic conductivity and diffusion of salt becomes important parameters in designing the barrier. The groundwater table can fluctuate and can go deeper, under such situation advection will be the governing phenomena for salt migration. For such situation hydraulic conductivity under constant volume condition need to be studied. Salt water in burette represents the seawater and compact clay sample represents the barrier. Generally, bentonites have very low hydraulic conductivity, under such situation diffusion becomes the main contaminant transport mechanism. Laboratory scale diffusion experiment (Figure 3) was planned to simulate the field condition. Source reservoir in diffusion experiment represents the seawater, while collector reservoir represents the fresh water present beneath the foundation of monument. The clay plug in diffusion experiment represents the proposed bentonite barrier.

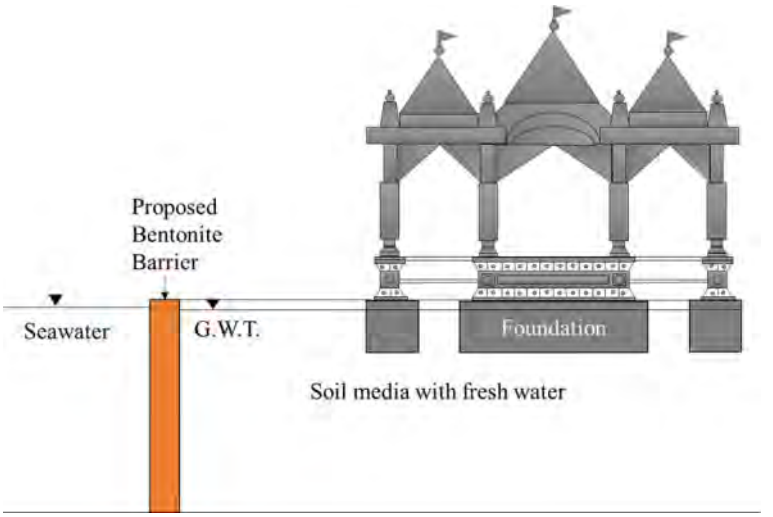

Figure 1. Proposed barrier to prevent saltwater intrusion to the foundation of monument.

2.3 *Hydraulic infiltration test*

Hydraulic infiltration (hydraulic conductivity) of bentonites was performed by falling head method (ASTM D5856, 2015). The bentonite samples were compacted at a dry density of 1.2 Mg/m^3. Required amount of air-dried bentonites was statically compacted in a perspex cell with the diameter of 2.4 cm and 1 cm thick as shown in Figure 2. Two porous stones were provided on either end of the compacted sample. A 42 grade filter paper was placed between porous stone and bentonite sample to avoid the clogging of the porous stone. Both ends of sample were fixed to restrict any volume change during the hydration process. The pore fluid was permeated from one end of sample and the variations in the head with time were noted. The experiment was continued till the values of hydraulic conductivity over a period of 24 hr was found to be constant.

2.4 *Through-Diffusion Experiment*

Through-diffusion testing was used in the study, as this is non-destructive testing and does not require the slicing of the compacted soil sample. Diffusion cell was fabricated from perspex to accommodate a soil sample with diameter of 2.4 cm and 1cm thick. The porous stone of 5 mm

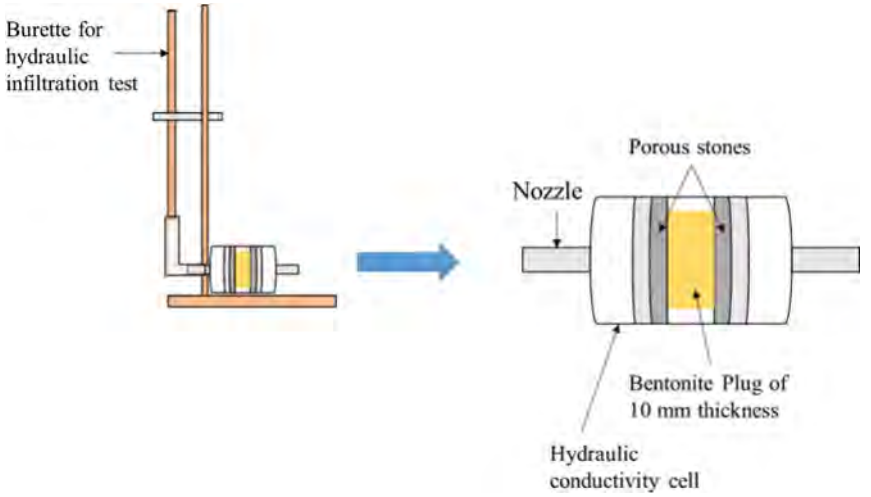

Figure 2. Experimental setup for hydraulic infiltration test.

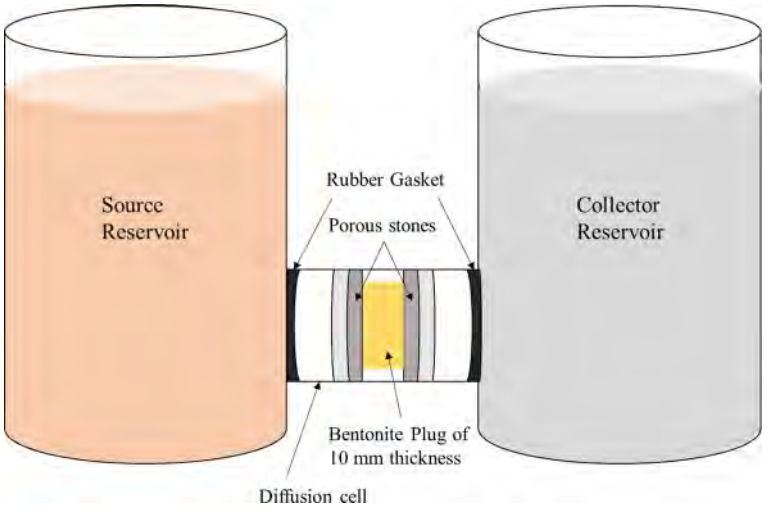

Figure 3. Experimental setup for through diffusion test.

thickness placed on either end of compacted clay sample. A 42 grade filter paper was placed in between the clay and porous stone as well. The bentonite clay was compacted at a dry density of 1.2 Mg/m^3. The cell was attached to the reservoir on the either end as shown in Figure 3. The rubber gasket was also used between the threading to prevent any leakage. Both the reservoir was filled with distilled water for saturation of clay plug. The saturation of clay was assessed by taking the weight of the diffusion cell at regular interval and weight of diffusion cell didn't change after the saturation of sample. The diffusion experiment was started by placing salt solution on source side and distilled water on collector side of the through-diffusion setup. A 10 ml of samples were collected from both source and collector reservoir at different interval of time. The concentrations of samples were determined after dilution using flame photometer. The initial concentration of 2M NaCl was used in this study to simulate sea water.

3 THEORITICAL BACKGROUND

The diffusion of contaminants (NaCl) through compacted bentonites is studied by Fick's diffusion equation. For saturated soil samples, the one dimensional governing equation for diffusion is as eq. (1):

$$\frac{\partial c}{\partial t} = \frac{D_e}{R_d}\frac{\partial^2 c}{\partial x^2} \tag{1}$$

where, *c = is the concentration of NaCl solution; t = is the diffusing time;* D_e*= is the effective diffusion coefficient; x = is the distance from the source; and* R_d *= is the retardation factor* and for linear sorption it can be expressed as:

$$R_d = 1 + \frac{\rho K_d}{n} \tag{2}$$

where, ρ*= is the dry density of the soil; n = is the porosity;* K_d*= is the distribution coefficient.* The initial and boundary conditions of diffusion experiment was given by eq. 3-5. (Bharat et al. 2012; Das & Bharat 2017; ;owe et al. 1988).

$$c(0 < x < L, t = 0) = 0 \tag{3}$$

$$c(x = 0, t) = c_0 + \frac{nD_e}{H_S}\int_0^t \left(\frac{\partial c}{\partial x}\right)_{x=0} dt \tag{4}$$

$$c(x = L, t) = -\frac{nD_e}{H_C}\int_0^t \left(\frac{\partial c}{\partial x}\right)_{x=L} dt \tag{5}$$

where, *L is the length of the clay plug;* c_0 *is the initial source concentration and Hs and Hc are the equivalent height of source and collector reservoirs, respectively.*

The equation (3), initial condition reflects that the clay is free from contamination at the beginning of the experiment. Equation 4 and 5, represents the boundary conditions at source and collector reservoir respectively.

The equations 1-5 can either be solved numerically or semi – numerically to obtain theoretical temporal variations of concentrations. A closed form analytical solution for transient through diffusion using Laplace transformation and integral theorem was given by (Bharat, 2013). The solutions at the boundaries are as follow:

$$\frac{C(x = 0, t)}{C_0} = \frac{1}{2 + K} + 2K\sum_{j=1}^{\infty} \frac{(\alpha_j^2 + K^2)e^{-\alpha_j^2 T}}{\{4K\alpha_j^2(K + 1) - (2K - (\alpha_j^2 - K^2))(\alpha_j^2 - K^2)} \tag{6}$$

$$\frac{C(x = L, t)}{C_0} = \frac{1}{2 + K} - 2K\sum_{j=1}^{\infty} \frac{(\alpha_j^2 + K^2)e^{-\alpha_j^2 T}}{\{4K\alpha_j^2(K + 1) - (2K - (\alpha_j^2 - K^2))(\alpha_j^2 - K^2)} \tag{7}$$

Where, $K = \frac{nR_d}{H_r}$; $T = \frac{tD_e}{R_d L^2}$; *H_r is the equivalent height of the source and collector reservoir* α_j *are the eigen values of following transdental equation:*

$$\tan \alpha_j = \frac{2K\alpha_j}{\alpha_j^2 - K^2} \tag{8}$$

where, α_j are the roots of equation, the Eigen values of eq.8 were obtained discontinuous, multi-modal swarm optimization technique. The determination of diffusion coefficient and retardation factor is an inverse problem, which was solved by minimizing the error between theoretical and measured concentration in source and collector reservoirs. The minimization of errors was done with particle swarm optimization (Bharat et al. 2008; Bharat et al. 2012; Bharat 2013). A Java

based, non-commercial software developed at IIT Guwahati CONTRADIS (Das & Bharat 2016) and model parameters were obtained after inputting the experimental results.

4 RESULTS

Temporal variations of hydraulic infiltration rate of 2M NaCl salt solution through compacted bentonites were presented in Figure 4. The hydraulic infiltration rates were initially higher, which decreased significantly upon hydration of bentonite sample. Due to the presence of high concentration of NaCl, the hydraulic infiltration rate of B1, B2 and B4 were slightly higher than the limiting value of hydraulic infiltration rate (i.e. 1×10^{-7} cm/sec). The hydraulic infiltration rate of bentonite B3 was found to be lower than the limiting value. The hydraulic infiltration rates of bentonites (B1, B2 and B4) were higher than liming value due to the reduction in diffused double layers (DDLs) of bentonite particles in presence of very high concentration of NaCl.

The measured data in terms of relative concentrations (c/c_0) from different diffusion by normalizing it with initial source concentration (c_0 = 2M). The measured relative concentrations from source and collector reservoirs for different bentonites were presented in Figure 5. The concentration of source reservoir decreases with time and concentration in collector reservoir increases with time. The concentration of NaCl in collector reservoir was found to be absent for initial 15–20 days, which indicates the adsorption of NaCl on bentonite surface.

The diffusion coefficient and retardation factor were determined from measured data using inverse analysis. The model parameters were obtained by minimizing the error between measured and theoretical concentration profiles and were presented in Table 2 for different bentonite. The

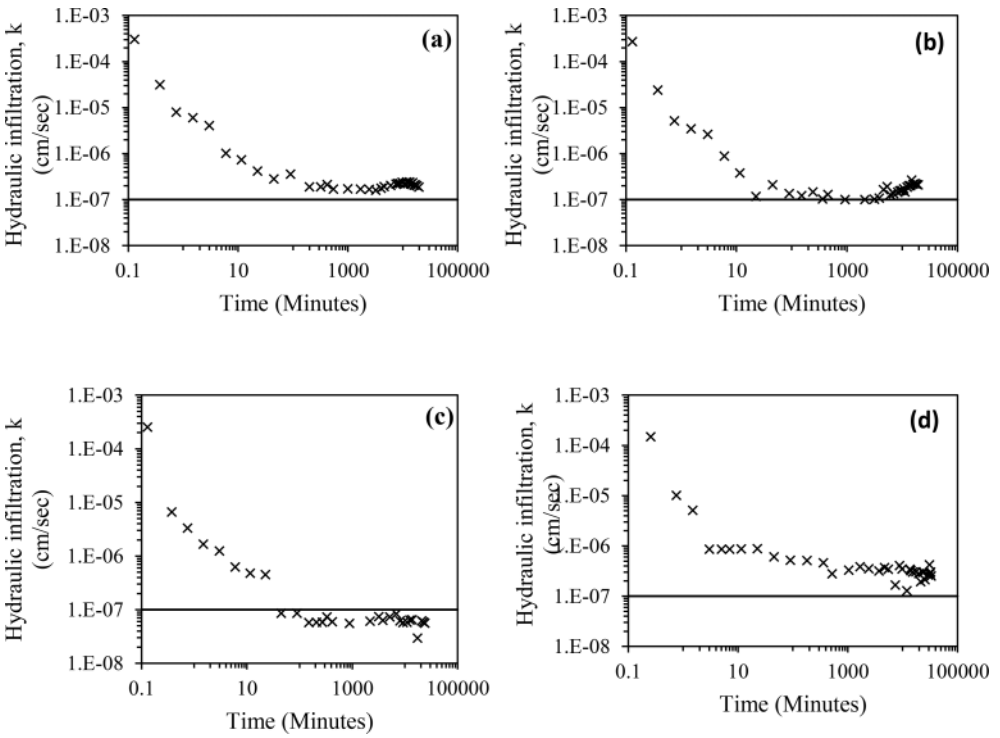

Figure 4. Temporal variations of hydraulic infiltration rates with 2M NaCl as permeating fluid for bentonite (a) B1; (b) B2; (c) B3; and (d) B4.

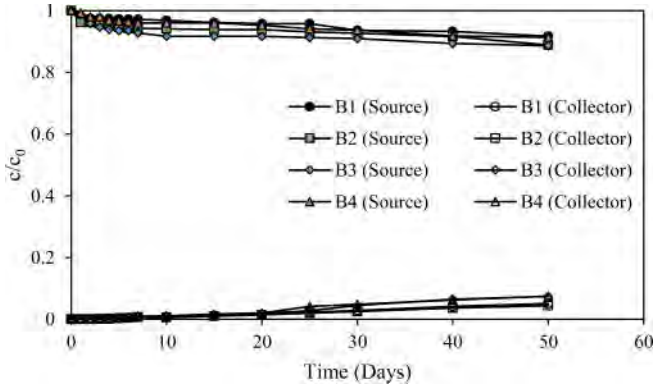

Figure 5. Temporal variations of measured data in source and collector reservoir for bentonites.

Table 2. Diffusion coefficient and retardation factor of different bentonites.

Bentonite	Diffusion coefficient, D_e (m^2/sec)	Retardation factor, R_d
B1	1.1×10^{-10}	7.93
B2	1.02×10^{-10}	7.93
B3	1.08×10^{-10}	8.45
B4	1.07×10^{-10}	7.71

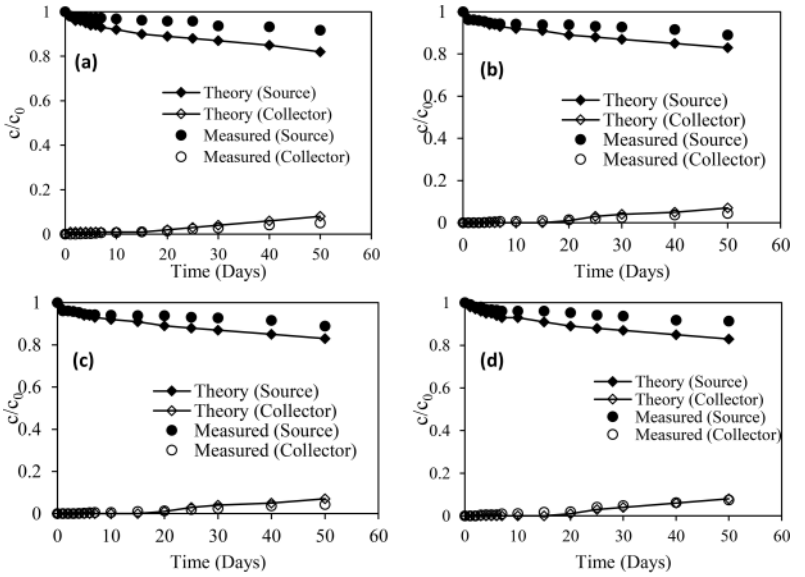

Figure 6. Comparison of experimental concentration profile with theoretical data for saline solution for (a) B1; (b) B2; (c) B3; and (d) B4.

theoretical concentration profiles for different bentonites were presented in Figure 6(a–d). The theoretical data and measured data were in good agreement with each other. The values of diffusion and retardation characteristics for bentonites were found to be almost similar.

These values of diffusion coefficient can be interpreted as seawater will take more than 5 years to just cross 20 cm of bentonite layer. Bentonite of initial thickness of 50 cm can prevent salt water up to 12 years. So, some maintenance of barrier system upon 12 years can be done by providing secondary barriers.

5 CONCLUSIONS

The hydraulic and diffusion experiments were conducted and following conclusions were derived:

1. The hydraulic infiltration rates of bentonites were found to be slightly higher than limiting value for B1, B2 and B4. While, hydraulic infiltration rate of B3 was lower than the limiting value.
2. The diffusion coefficients were found to be of range 1–1.1 $\times 10^{-10}$ for all the bentonites and retardation factors were in range of 7.5 – 8.5. The diffusion and retardation characteristics doesn't significantly depend on plasticity of bentonite.
3. The flow of contaminants was significantly reduced by the introduction of bentonites. So, the bentonite can be used as barrier material to protect the monument and heritage structures.
4. The 50 cm thick layer will take around 12 years to saltwater to cross across bentonite. Subsequent, repair by providing additional layers is suggested for future.

REFERENCES

ASTM D5856, 2015. Standard Test Method for Measurement of Hydraulic Conductivity of Porous Material Using a Rigid-Wall, Compaction-Mold Permeameter (ASTM International, 2015).

Badv, K. & Abdolalizadeh, R. 2004. A laboratory investigation on the hydraulic trap effect in minimizing chloride migration through silt. Iran J Sci Technol Trans B 28(B1):107–118.

Barone, F. S. Rowe, R. K. & Quigley, R.M. 1992. A laboratory estimation of diffusion and adsorption coefficients for several volatile organics in a natural clayey soil. J Contam Hydrol 10:225–250.

Bharat, T.V. 2008. Agents based algorithms for design parameter estimation in contaminant transport inverse problems. In: IEEE swarm intelligence symposium, pp 1–7.

Bharat, T. V. 2013. Analytical model for 1-D contaminant diffusion through clay barriers. Environ Geotech 1(4):210–22.

Bharat, T.V. Sivapullaiah, P.V. & Allam, M. M. 2008. Accurate parameter estimation of contaminant transport inverse problem using particle swarm optimization. In: IEEE swarm intelligence symposium St. Louis MO USA, September 21–23.

Bharat, T.V. Sivapullaiah, P.V. & Allam, M. M. 2012. Robust solver based on modified particle swarm optimization for improved solution of diffusion transport through containment facilities. Expert Syst Appl 39(12):10812–10820.

Bharat, T.V. Yadav, H. Mahaur, J.P. and Kushwaha, S. 2020. "Effect of Aging Time on Consistency Limits of Bentonites." Geotech Geol Engg. 38, 3737–3749. https://doi.org/10.1007/s10706-020-01251-3.

Cardell,C. Delalieux, F. Roumpopoulos, K. Moropoulou, A. Auger, F. & Van Grieken, R. 2003. Salt-induced decay in calcareous stone monuments and buildings in a marine environment in SW France, Construction and Building Materials, Volume 17, Issue 3, Pages 165–179, ISSN 0950-0618, https://doi.org/10.1016/S0950-0618(02)00104-6.

Das, P. & Bharat, T. V. 2016. Salt diffusion in compacted plastic clay: experimental and theoretical evaluation. In: International conference on soil and environment, ICSE 2016, Bangalore

Das, D. S. & Bharat, T.V. 2021. "Specific Surface Area of Plastic Clays from Equilibrium Sediment Volume under Salt Environment." Geotechnical Testing Journal. https://doi.org/10.1520/GTJ20200190.

Das, P. & Bharat, T.V. 2017. "Effect of counter ions on the diffusion characteristics of a compacted bentonite." Indian Geotechnical Journal, 47(4), 477–484.

Gapak, Y. Das, G. Yerramshetty, U. & Bharat, T. V. 2017. "Laboratory determination of volumetric shrinkage behavior of bentonites: A critical appraisal." Applied Clay Science, 135, 554–566. https://doi.org/10.1016/j.clay.2016.10.038.

Gilliam, R.W. Robin, M.L.J. Dytynyshyn, D.J. & Johnston, H.M. 1985. "Diffusion of nonreactive and reactive solutes through fined grained barrier materials." Can. Geotech. Journal. 541–550.

La Iglesia, M.A. Garcia del Cura, S. Ordonez. 1997. “The physicochemical weathering of monumental dolostones, granites and limestones; dimension stones of the Cathedral of Toledo (Spain).” Sci. Total Environ., 152, pp 179–188.

Loke, M.E. Kumar, P. & Haldenwang, R. 2020. “Characterisation of heritage cementing materials for restoration purposes: A review.” J. S. Afr. Inst. Civ. Eng. 2020:62(1), Art. #0723, 12 pages. http://dx.doi.org/10.17159/2309-8775/2020/v62n1a2.

Mieszkowski, R. 2003. “Diffusion of lead ions trough the Poznan clay (Neogene) and through glacial clay.” Geol. Quart., 47 (1). 111–118. Warszawa.

Phillips, R.E. & Brown, D.A. 1964. “Ion Diffusion: II. Comparision of Apparent Self and Counter Diffusion Coefficients.” Soil Science Society Proceedings. 758–763.

Robin, M.J.L. Gilliham, R.W. & Oscarson, D.W. 1987. “Diffusion of strontium and chloride in compacted clay – based materials.” Soil Sci. J. Vol. 51. 1102–1108.

Roehl, K.E., & Czurda, K. 1998. “Diffusion and solid specimen of Cd and Pb in clay liners.” J. of Applied Clay Science. 12. 387–402.

Rowe, R.K. 1988. “Contaminant transport through growndwater- the role of modelling in design of barriers.” 11th Canadian Geotechnical Colloquium. Canadian Geotechnical Journal, 25:778–798.

Sardini, P. Delay, F. Hellmuth, K. Porel, G. & Oila, E. 2003. “Interpretation of out-diffusion experiments on crystalline rocks using random walk modeling.”. J Contam Hydrol 61:339–350

Theoulakis, & Moropoulou, 1997. “Microstructural and Mechanical parameters determining the susceptibility of porous building stones to salt decay”. Construction Building Materials., 11(1), pp 65–71.

Van Loon, L.R. & Jakob, A. 2005. “Evidence for a second transport porosity for the diffusion of tritiated water (HTO) in a sedimentary rock (Opalinus clay-OPA): application of through- and out-diffusion techniques.” Transp Porous Media 61:193–214

Vasudev, A. Das, P. & Bharat, T.V. 2019. “Stability analysis of possible embankment construction for placement of granite capstone on Brihadeeshwara temple, Tanjavur.” International Symposium on Geotechnical Aspects of Heritage Structures. Chennai, India.

Yadav, H. and Bharat, T.V. 2022. “Mechanical granulation process and plasticity of granular bentonite on self-sealing and volume change behavior.” Journal of Hazardous, Toxic and Radioactive Waste. DOI:10.1061/(ASCE)HZ.2153-5515.0000688.

Zezza, F. 1996. Marine spray and polluted atmosphere as factors of damage to monuments in the Mediterranean coastal environment. In: Zezza F. Ed. Bari. Origin, mechanisms and effects of salts on degradation of monuments in marine and continental environments. Protection and conservation of European Cultural Heritage, E.C. Project, Report 4. Pp. 3–19.

Geotechnical Engineering for the Preservation of Monuments and Historic Sites III – Lancellotta, Viggiani, Flora, de Silva & Mele (Eds)

Historic masonry churches exposed to slow-moving landslides: A critical damage assessment

C. Ferrero, L. Cambiaggi & C. Calderini
Department of Civil, Chemical and Environmental Engineering, University of Genoa, Genoa, Italy

R. Vecchiattini
Department of Architecture and Design Civil, University of Genoa, Genoa, Italy

ABSTRACT: This paper deals with the damage assessment of historic masonry churches exposed to slow-moving landslides. A damage survey campaign was carried out on 33 listed churches located in the Liguria region (Italy) in areas affected by slow-moving landslides. For each church, information about zoning, state of activity and direction of landslide phenomena was collected and analyzed. Knowledge of each building's main geometric and structural features, history and past interventions was gained by means on-site surveys and archival research. A detailed field-survey of crack patterns and deformations was also performed. Based on the critical assessment of the damage observed, preliminary conclusions on the structural response of historic masonry churches to slow-moving landslides were made. Recurrent types of damage and damage mechanisms were also identified.

1 INTRODUCTION

Historic masonry churches form a significant part of built cultural heritage. Since they are still in use and represent a place of social aggregation and cultural identity where people may gather in large numbers, their protection against natural and anthropic hazards is relevant from the two perspectives of safety and conservation.

Among the hazards threatening historic churches, earthquakes have so far drawn the greatest attention from academics and institutions. In the last decades, several research works were devoted to the damage and vulnerability assessment of historic masonry churches subjected to horizontal actions (e.g., Doglioni et al. 1994; Lagomarsino 2012; Penna et al. 2019). These studies led to the identification of earthquake-induced damage and collapse mechanisms. In contrast, little attention was paid to the effects of other phenomena, such as slow-moving landslides, which, however, are a potential source of risk due to the damage that they can induce to masonry structures (Antronico et al. 2015).

Landslides are an important hazard in the Italian territory. According to the 2018 Summary report of the Institute for Environmental Protection and Research (ISPRA, Trigila et al. 2018), Italy is one of the European countries most affected by landslides. The cultural heritage buildings exposed to landslide risk are 37847, corresponding to 18.6% of the total. Although the 2018 Summary report by ISPRA does not specify the number of historic churches at risk, Italy has about 67013 churches, of which 32000 are listed (Calderini & De Matteis 2020). Consequently, the probability that a number of them are exposed to landslide risk is very high.

Differently from what was observed for earthquakes, in the case of landslides no abacus of collapse mechanisms or damage classification is available for historic masonry churches, as the effects of landslides on the structural response of this type of buildings have not been systematically investigated (Ferrero & al. 2021a). Furthermore, the literature related to churches located in landslide-affected areas has mainly focused on the geotechnical and geological analysis of the

DOI 10.1201/9781003308867-93

slope movement (Cigna et al. 2013; Margottini et al. 2013; Soccodato et al. 2013) rather than on soil-structure interaction.

Among the regions in which Italy is divided, Liguria is one of those most affected by landslide phenomena. Due to the geographical location, orography as well as morphological and geological setting of the Ligurian territory, landslides frequently occur. As reported in Guzzetti et al. (2004), 1806 landslide events damaged 1233 localities between 1800 and 2001. Furthermore, in 2017, an area of 751.9 km^2, equal to 13.9% of the regional territory, was classified as a high or very high landslide hazard zone (Trigila et al. 2018). In view of these considerations, the Ligurian territory is an ideal area to perform damage assessment of churches exposed to slow-moving landslides.

This work presents the results of a damage survey campaign performed on a sample of 33 historic masonry churches located in Liguria in areas affected by slow-moving landslides. The aims of the work were to describe the damage suffered by the churches in terms of crack pattern and deformations and to identify the damage mechanisms. Note that all the landslides considered in this study are classified as very slow or extremely slow according to Cruden & Varnes (2006), that is their velocity does not exceed 1.6 m/year and 16 mm/year, respectively.

The paper is organized as follows: in Section 2 the criteria for the selection of the case studies are presented; in Section 3 data gathering and on-site inspections are introduced; in Section 4 the damage observed in the churches is described; in Section 5 the results of the damage surveys are commented and critically discussed; in Section 6 some conclusions are provided.

2 IDENTIFICATION OF THE SAMPLE OF CHURCHES

The sample of churches to be investigated was selected taking into consideration on one side the landslide classification of the Liguria region and on the other side the list of heritage buildings protected by the Ministry of Cultural Heritage and Activities.

The Liguria region is divided into three river basins: Tyrrhenian basins, Magra River basin and Po River basin. In the three basins, different types of maps identify landslides areas: the *Carte della Suscettività al Dissesto* (Regione Liguria 2017) for the Tyrrenian and Magra River basins and the maps of the *Atlante dei Rischi Idraulici e Idrogeologici* (Autorità di bacino distrettuale del fiume Po 2017) for the Po River basin. Note that, hereafter, the maps of the three Ligurian basins will be generically named landslide maps.

The criteria adopted in each basin to zone and identify landslides are presented next:

- The entire territory of the Tyrrhenian basins is divided into five classes of landslide susceptibility on a scale from Pg0 to Pg4. Pg4 class corresponds to the highest level of landslide susceptibility and is characterized by the presence of active landslide. Pg3 class is divided into two subclasses, Pg3a and Pg3b, which denote areas with dormant landslides and territories with indirect indicators of movements (i.e., bent trees, damage in retaining wall, etc.) or stabilized landslides, respectively. The three classes Pg2, Pg1 and Pg0 indicate the presence of geomorphological indicators, such as springs or cracks in the ground, but they are not affected by landslides.
- The landslide maps of the Magra River basin adopt the same criteria used in the maps of the Tyrrhenian basins to define landslide susceptibility classes. However, only the areas classified as Pg2, Pg3 and Pg4 are reported in the landslide maps.
- The landslide maps of the Po River basin do not classify the territory according to landslide susceptibility classes, but they only indicate the areas affected by active, dormant or stabilized landslides. Landslides are represented either with their extension or with a dot when their perimeter is unknown.

The set of churches to be analyzed was identified by superimposing the landslide maps of the Ligurian river basins, updated as of 2017/2018, on the regional map of the listed architectural assets, named *vincoli architettonici puntuali* in Italian (Regione Liguria e Segretariato Regionale del MiBACT per la Liguria 2017), which reports the position of all the listed buildings located in Liguria. The buildings selected were the ones located in areas characterized by the highest

landslide susceptibility (i.e, Pg4) in the case of the Magra River basin and Tyrrhenian basins and the ones located in areas affected by active landslides in the case of the Po River basin. Not only churches, but also religious buildings such as sanctuaries, oratories and chapels were considered. The superimposition of the two types of maps was performed by means of the QGIS software (QGIS 2017). An example of superimposition is presented in Figure 1.

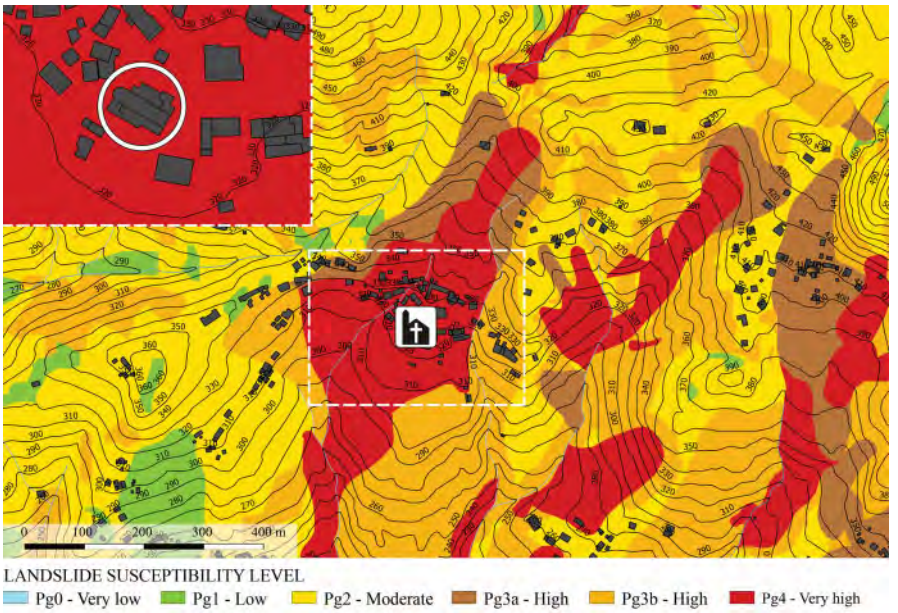

Figure 1. Identification of churches located on active landslides.

Extended to the entire Liguria region, this approach led to the detection of 28 listed churches located on active landslides. The position of each church within the Ligurian territory is shown in Figure 2. The sample of churches was then enlarged by adding five listed churches (labelled

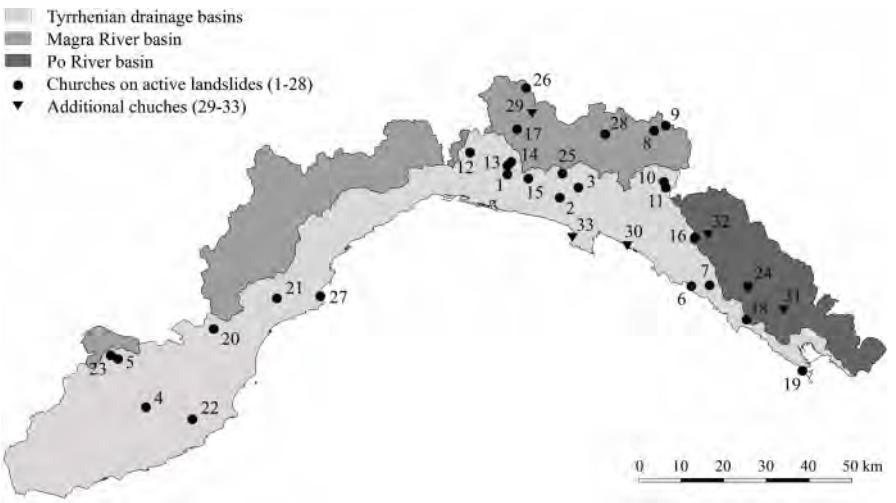

Figure 2. Location of the churches analysed in the Ligurian territory.

additional churches in Figure 2) that experienced damage potentially due to ground movements. Two churches were located very close to active landslides, one was situated on a Pg3 area and two were located near Pg3 areas. For further information about the 33 buildings object of study, the reader is referred to Ferrero et al. (2021a).

3 METHODOLOGY AND SAMPLE DESCRIPTION

3.1 *Information gathering*

Once the churches to investigate were identified, further information about landslides and geotechnical soil characterization in the surrounding areas was collected and analyzed. Geotechnical data derived from geological surveys, in situ tests, inclinometers or piezometers installed in the landslide area, when available, were downloaded from the *Geoportale* (Geo-portal) of the Liguria region (Geoportale Regione Liguria 2020). The availability of data obtained by means of advanced satellite techniques, such as the satellite radar interferometry, was also verified. However, as described by Cambiaggi (2020), the geotechnical data were really poor or completely missing for the large majority of the churches. Although the state of activity, type and estimated direction of the landslide phenomena could be identified, almost no information was found about magnitude, rate and dominant component (vertical or horizontal) of the landslide movements. This type of data can be obtained by means of advanced satellite techniques (such as the satellite radar interferometry) or inclinometers, the latter providing a profile of subsurface horizontal deformation. In the case of the Liguria region, good-quality displacement data could not be derived from interferometry due the morphological setting of the territory, which consists primarily of hilly and scarcely urbanized areas characterized by low distributions of the targeted ground points used by satellites to acquire interferometric data (Arpa Piemonte 2008). Furthermore, only one third of the landslides were monitored by means of inclinometers (Cambiaggi 2020).

Useful data about state of activity, type and estimated direction of the landslides were found in the *Atlante dei Centri Abitati Instabili della Liguria* (hereafter called Atlante) (Federici & Chelli 2007). Most of the landslides were classified as complex and resulted from the combination of flows and slides (rotational and/or translational). In the other cases, lateral spreads, flows and slides (rotational and/or translational) were involved. The landslide phenomena were accompanied by superficial plastic deformations in one third of the churches.

As shown in Figure 3, the landslide direction was estimated on the basis of the orientation of the symbols used in the maps of the Atlante to represent landslides. When the churches were located in

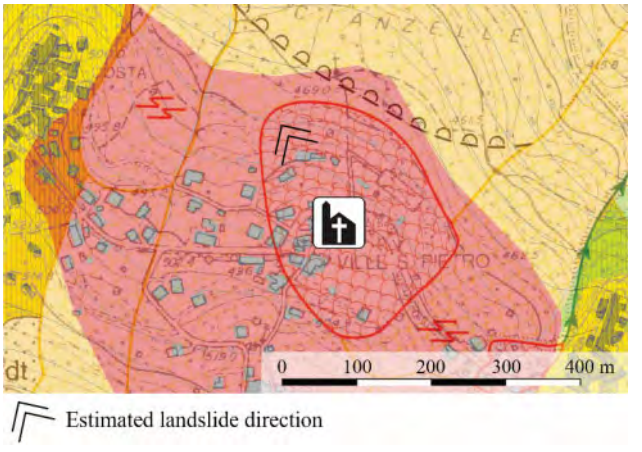

Figure 3. Superimposition of the maps of the *Atlante dei Centri Abitati Instabili della Liguria* (Federici & Chelli 2007) and the *Carte della Suscettività al Dissesto* (Regione Liguria 2017).

areas not included in the maps of the Atlante, the landslide maps together with the contour curves of the slope were used to identify a potential direction of the landslide movement. In view of this and considering that landslide phenomena may evolve over time, the landslide direction assumed in this work has to be considered approximate.

To evaluate any potential evolution of the landslide areas over time, the maps of the Atlante, which were elaborated between 2001 and 2007, were superimposed to the maps of the basin plans, which are more recent and updated as of 2017/2018 (Figure 3).

Useful material regarding the churches to inspect was found in the Archives of the Ligurian Office of the Italian Ministry of Cultural Heritage and Activities. For some churches, a detailed documentation was collected, which included historical information, geometrical surveys, past crack surveys and description of past interventions. However, in many cases, very poor information was available and even plans and elevations were not existing or were incomplete and had to be elaborated during the inspections.

3.2 *On-site inspections*

Inspections and damage surveys were performed in all the 33 churches selected as case studies. The crack pattern observed in each church was surveyed and mapped in detail. Cracks were classified according to three levels of width: (i) thin for a width up to 1 mm (the latter included), (ii) medium for a width between 1 mm and 5 mm, and (iii) large for a width equal or larger than 5 mm. When cracks were repointed and did not re-open, crack width was not reported. Cracks affecting walls and pillars were marked on the building plan by means of symbols identifying their orientations (vertical, horizontal and diagonal). Construction joints were distinguished from other damage signs since they are related with the construction process of the building. It is worth noting that the extrados of arches and vaults was not inspected because no access was provided to the attic.

In addition to the crack pattern, out-of-plumbness of walls and pillars as well as sinking of floors were surveyed and, when possible, measured by means of electric bubble levels or out-of-plumb wires.

An inspection of the surroundings of each church was also performed to detect any potential evidence of ground movements, such as cracks and distortions in neighboring buildings, cracks in road surfaces and inclined streetlights or trees.

4 DAMAGE SURVEY

The damage surveyed in the sample of churches is described below for the different structural elements composing the church: floors, walls and pillars, and arches and vaults. As described by Ferrero et al. (2021a), the additional churches experienced the same types of damage as the churches located on active landslides. For this reason, no distinction between them will be considered in the following paragraphs.

Damage in the floor appears in the form of cracking of tiles, gaps among tiles or sinking (Figure 4). Cracks are usually localized in few tiles and are especially observed on step treads and balustrades bases (Figure 4a). Conversely, gaps, which are separations that develop at the joints among tiles, are usually widespread in the floor (Figure 4b). In particular, several churches present a series of parallel gaps crossing the entire floor from one side to the other (Figure 4b). As shown in Figure 4c, in some cases cracks and gaps originate from the floor and propagate upwards into the walls. In addition to cracks and gaps, several churches exhibit sinking of floor, which is often accompanied by gaps among tiles or lifting of some of them, as shown in Figure 4d.

The majority of the churches present cracks in load-bearing masonry walls (Figure 5). Cracks are observed in the façade and apse walls as well as in lateral longitudinal and transverse walls. The façade and apse walls generally present cracks next to openings and inside alcoves (Figure 5a). The lateral longitudinal walls usually exhibit vertical cracks that propagate upwards from the level of the ground, cut the structure along its entire height and, in some cases, continue up into the vaults.

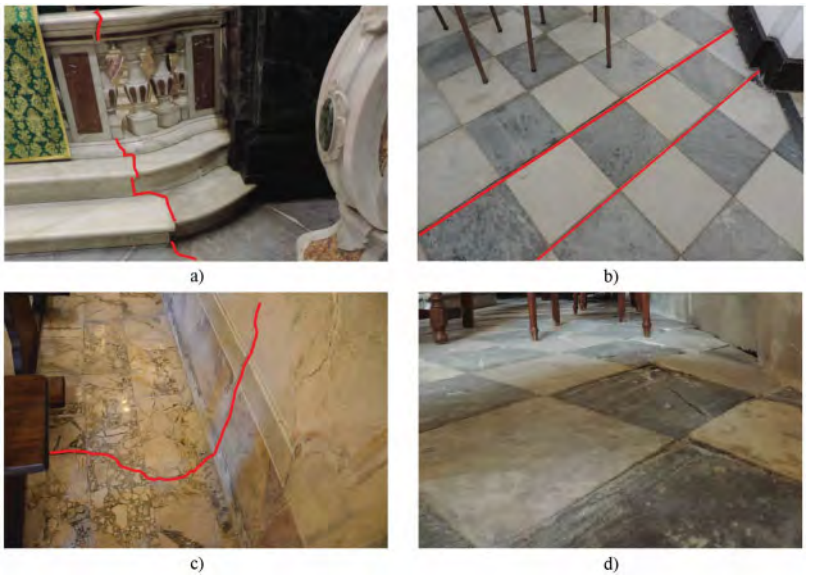

Figure 4. Damage of floors: a) cracks on step treads and balustrades bases, b) parallel gaps among tiles, c) cracks propagating from floor to wall, d) sinking of floors.

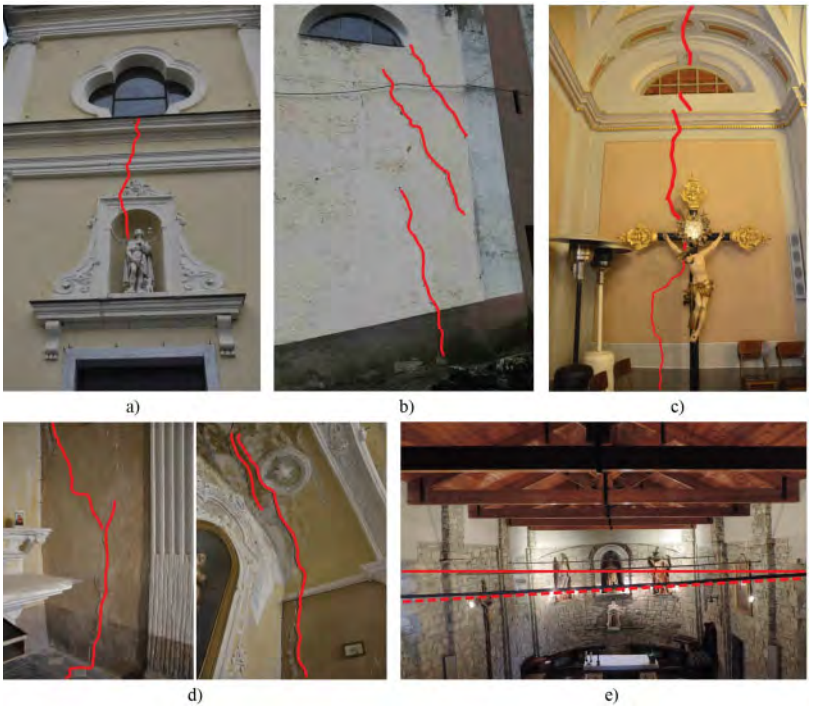

Figure 5. Damage of walls: a) cracks in the façade wall next to openings, b) diagonal cracks in longitudinal walls propagating from the level of the ground, c) vertical cracks increasing in width with height at the middle span of the wall, d) vertical cracks in lateral walls extending from the level of the ground and continuing up into vaults, e) rigid rotation producing out-of-plumbness of longitudinal walls and loss of horizontality of metallic tie-rods.

Some churches also exhibit vertical cracks that do not propagate from the floor. These cracks, which are generally repeated in each bay, progress over the entire height of the wall, increasing in width with height (Figure 5c), and continue up into arches and vaults, cutting them transversally. Diagonal cracks extending from the ground level are less frequently observed (Figure 5b).

In addition to cracks, some churches also present significant out-of-plumbness in lateral walls and pillars. In some cases, the entire building exhibits a rigid rotation, with both longitudinal walls leaning in the same direction (Figure 5e). Loss of horizontality of the metallic tie-rods is often observed in the case of rigid rotations (Figure 5e).

Most of the churches of the sample exhibit damage in arches and vaults. The damage in the arches appears in the form of cracks and deformations (Figure 6). As shown in Figure 6a–b, the crack pattern can be either symmetrical or asymmetrical. In the first case (Figure 6a), a crack occurs near the crown at the intrados. In the second case (Figure 6b), a recurrent crack pattern can be hardly identified, since cracks appear at different locations along the arch profile in the different churches of the sample.

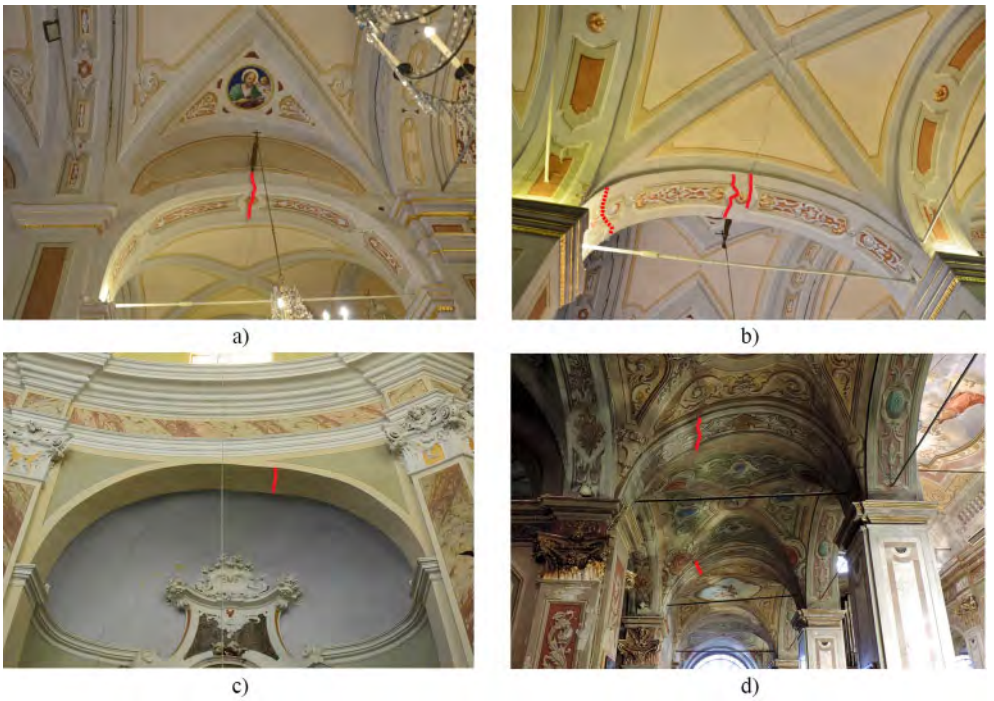

Figure 6. Damage in arches: a) symmetrical crack pattern, b) asymmetrical crack pattern, c–d) large deformations.

Beside cracks, arches also exhibit large deformations, which generally involve the adjacent vaults. Figure 6 shows some representative examples of in-plane deformations occurring either in the arches of the lateral chapels (Figure 6c) or in the arches separating the different naves and bays of the church (Figure 6d). As expected, deformations are generally accompanied by the opening of some cracks, which are needed to accommodate such large changes in the geometry.

Several churches of the sample present extensive damage in the vaults in the form of longitudinal, transverse, and diagonal cracking. As shown in Figure 7a, in many cases, cracks propagate from the supporting walls into the vaults and are continuous between arches and vaults. It is interesting to observe that the vaults of several churches exhibit multiple parallel diagonal cracks, which are oriented in the same direction as the gaps of the floors (Figure 7b).

a) b)

Figure 7. Damage in the vaults: a) cracks continuous between vault and supporting wall, b) multiple parallel diagonal cracks.

5 CRITICAL DAMAGE ASSESSMENT

The systematic observation of the damage experienced by the 33 churches under consideration allowed some remarks to be put forward about the structural response of historic masonry churches exposed to slow-moving landslides.

First, the damage level was found to vary significantly in the 33 churches of the sample. To quantify the damage level distribution, a damage grade was associated to each church. Taking as a reference the European Macroseismic scale (EMS-98) for masonry buildings subjected to seismic actions (Grünthal 1998), five levels of increasing damage were considered: (i) negligible to slight damage (grade 1), (ii) moderate damage (grade 2), (iii) substantial to heavy damage (grade 3), (iv) very heavy damage (grade 4), and (v) destruction (grade 5). The large majority of the churches (72.8% of the total) presented either slight or moderate damage, while 27.3% of the total suffered substantial to very heavy damage. Some of the buildings suffering very heavy damage were even closed to public by order of local authorities due to safety reasons. It is important to note that the damage levels were assigned according to the damage surveyed during on-site inspections. Therefore, they might not reflect the damage experienced by the churches throughout their entire history. As described in Ferrero et al. (2021a), structural interventions and/or architectural restorations were performed in about half of the buildings of the sample, with the result that part of the past damage could have been repaired or simply hidden.

Second, the large majority of the churches presented damage patterns congruent with the landslide direction, indicating that slow-moving landslides may induce significant damage to historic masonry churches. The congruence between damage and estimated landslide direction was evaluated by comparing the landslide direction with an approximate damage direction, which was defined based on engineering judgment considering the crack pattern in plan as well as global rigid rotations (see Figure 8). The damage was considered congruent with the landslide direction if the approximate damage direction was within the range between −45° and 45° compared to the landslide direction.

Figure 8 shows two representative examples of crack patterns congruent with the landslide direction. It can be easily observed that the cracks affecting both floors and vaults are characterized by a consistent orientation throughout the building. Furthermore, the cracks of the walls occur in planes oriented parallel to the direction of the cracks observed in floors and vaults. This allowed a clear damage direction to be identified, which was found to be inclined by no more than ±45° with respect to the landslide direction.

Congruence between damage pattern and landslide direction was also observed in the churches exhibiting a global rigid rotation. In these cases, the longitudinal walls, which were oriented almost perpendicular to the landslide, leaned in the direction of the landside, as expected.

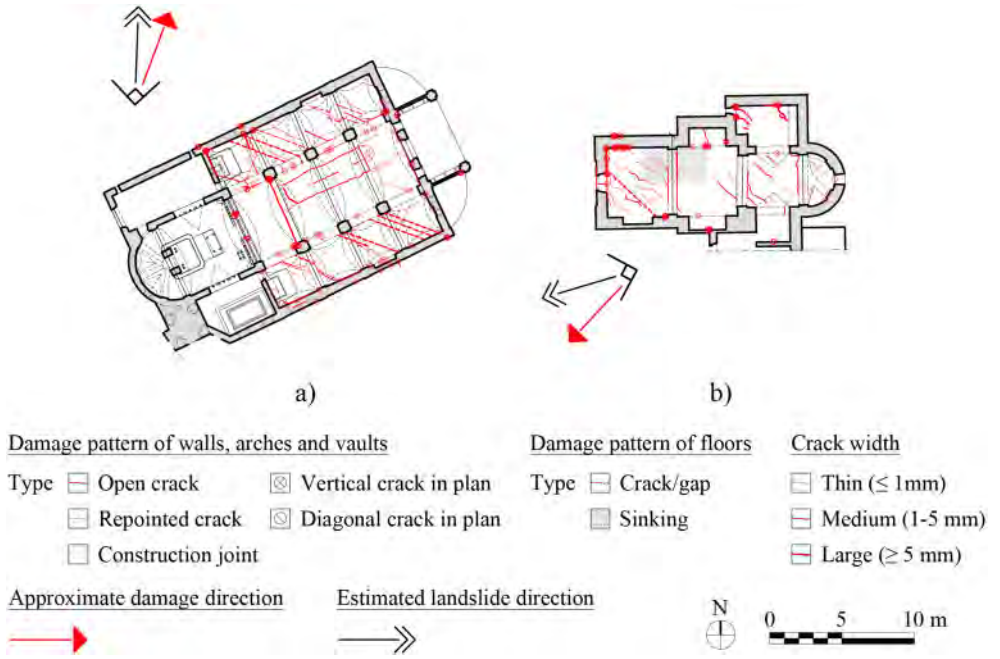

Figure 8. a–b) Damage patterns congruent with the estimated landslide direction.

Third, four recurrent types of damage were identified in the churches inspected: (i) damage of floors, (ii) damage of walls, (iii) damage of arches and vaults, and (iv) rigid rotation. Figure 9 shows the occurrence of these types of damage, classified by damage grade, in the selected sample of churches. Note that the damage was classified according to the 5-level damage scale already adopted to estimate the global damage level. Damage of walls as well as damage of arches and vaults proved to be the most frequent types of damage. Damage of walls occurred in almost all the churches inspected (94% of the sample). Approximately 73% of the churches exhibited slight or moderate damage (grade 1 and 2), while 21.2% of them also presented heavy or very heavy

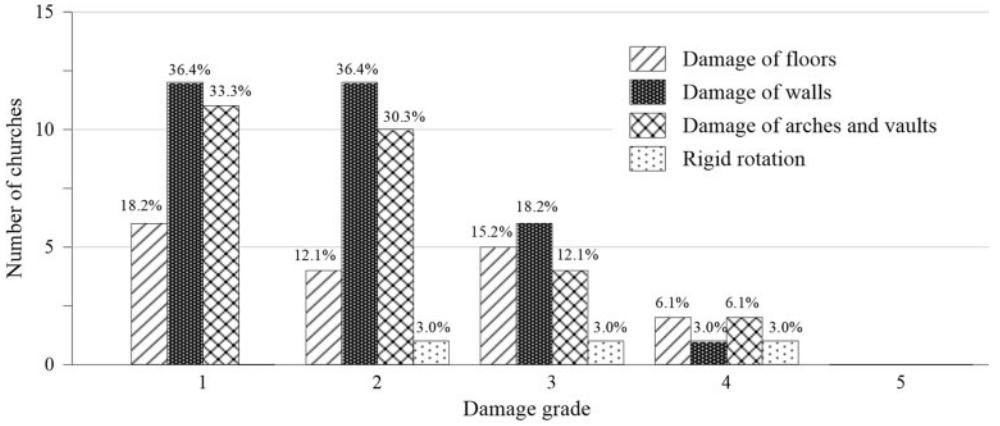

Figure 9. Recurrent types of damage classified by damage level.

damage (grade 3 and 4). Damage of arches and vaults was observed in the large majority of the churches (81.8% of the total). Damage of grade 1 or 2 occurred in 63.6% of the buildings, while damage of grade 3 or 4 was found in 18.2% of the sample. Damage of floors was also present in about half of the 33 churches inspected, whereas rigid rotations were observed only in few cases of single-nave churches of small size.

Fourth, the damage induced to historic masonry churches by slow-moving landslides proved to be easily recognizable. Besides the identification of four recurrent types of damage, damage was not localized but widespread in the church. Cracks generally exhibited a consistent orientation throughout the building. The cracks patterns in the floors reflected the ones in the vaults. Furthermore, the cracks affecting the walls occurred in planes parallel to the orientation of the cracks observed in the floors and vaults.

Last, churches were found to respond to slow-moving landslides with a global behaviour where the different structural components (i.e., walls, arches, vaults, etc.) contribute jointly to accommodate soil displacements. This behaviour is significantly different from the response by independent macroelements exhibited by churches under seismic actions. In particular, the following four global damage mechanisms were identified (6):

a. *Hogging*. This damage mechanism can be attributed to a concave-upward bending (hogging) of the structure produced by an incremental vertical ground movement in the direction of the longitudinal axis of the church (6a). The building exhibits vertical cracks in longitudinal walls, repeated in each bay. These cracks progress over the entire height of the wall, increasing in width with height, and continue up into arches and vaults, cutting them transversally. No significant cracks or gaps are observed in the floor.
b. *Shear deformation*. This damage mechanism can be attributed to a shear deformation of the structure produced by vertical ground movements along the longitudinal axis of the church (6b). Severe diagonal cracks propagating from the level of the ground are observed in longitudinal walls. A crack/gap in the floor can propagate between the cracks occurring in the opposite longitudinal walls.
c. *Global rigid rotation*. This mechanism is attributed to an incremental vertical ground movement along the transversal axis of the church (6c). Along this direction, the church is quite stiff and tends to rotate as a rigid body. Although cracks may occur, the most relevant effects are (i) the out-of-plumb of longitudinal walls, (ii) the distortion of transverse arches, and (iii) the inclination of horizontal elements such as tie-rods, balustrades, steps and floors.
d. *Extension*. This mechanism is related to the horizontal component of landslide movement (6d). The structure exhibits multiple parallel diagonal cracks in vaults and floors, all oriented in the same direction. In addition, severe vertical cracks occur in walls in planes perpendicular to the landslide direction. These cracks propagate from the level of the ground and cut the structure over its entire height from floor to vaults, indicating that the church suffered extension in the landslide direction.

It should be noted that, since no quantitative information about the magnitude of the horizontal and vertical components of the landslide movements was generally available, the correlation between damage and soil displacements patterns was found through a critical interpretation of the surveyed crack patterns and deformation, which were used as indicators of ground movements (for further details, see Ferrero et al. 2021b). This allowed the authors to determine if the dominant component of the landslide movements was vertical or horizontal. However, it should be recalled that landslides involve a combination of downward and lateral ground movements (Cooper 2008) and, therefore, different mechanisms can occur together. Furthermore, the occurrence of a certain damage mechanism compared to the others may depend not only on the prevalent component of ground movement, but also on the direction of the landslide movement with respect to the church axes as well as on the church geometry and structural configuration.

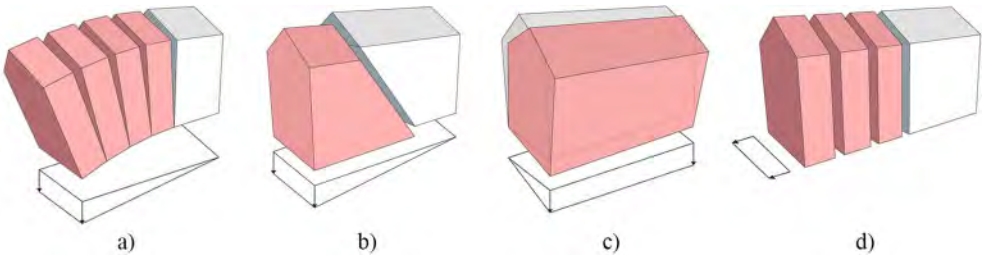

Figure 10. Global damage mechanism: a) *Hogging*, b) *Shear deformation*, c) *Global rigid rotation*, d) *Extension*.

6 CONCLUSIONS

This work presents the results of a damage survey performed on 33 historic masonry churches located in the Liguria region (Italy) in areas affected by slow-moving landslides. The sample of buildings to investigate was chosen by superimposing the landslide maps of the Liguria region with the regional maps of listed architectural assets.

The damage survey proved that historic masonry churches are sensitive to slow-moving landslides. Indeed, most of the churches exhibited damage patterns congruent with the landslide direction. Furthermore, several buildings presented extensive and severe damage and some of them were even closed to public due to safety reasons.

The systematic observation of the damage allowed the authors to identify some recurrent types of damage as well as four global damage mechanisms. In this respect, it is important to highlight that the churches inspected responded to slow-moving landslides with a global behaviour, which is significantly different from the response by macroelements exhibited by this type of buildings under seismic actions.

In conclusion, this work represents an important contribution for the damage assessment of historic masonry churches exposed to slow-moving landslides. Future works will include the inspection of a larger set of case studies as well as the structural analysis of specific case studies.

ACKNOWLEDGEMENTS

The financial support of PRIN 2015 Program by the Italian Ministry of Education, University and Research (MIUR) is gratefully acknowledged for funding the research project “Protecting the Cultural Heritage from water-soil interaction related threats” (Prot. No. 2015EAM9S5), which is the main framework of the study presented in this article.

REFERENCES

Antronico, L., Borrelli, L., Coscarelli, R. & Gullà, G. 2015. Time evolution of landslide damages to buildings: the case study of Lungro (Calabria, southern Italy). *Bulletin of Engineering Geology and the Environment* 74: 47–59.

Calderini, C. & De Matteis, G. 2020. Report. Task 4.8_Modelli e curve di fragilità delle chiese. WP4_MAppe di Rischio e Scenari di danno sismico (MARS). Progetto ReLUIS-DPC 2019–2021.

Cambiaggi L. 2020. Damage assessment of churches exposed to slope displacements in sliding areas. PhD diss., University of Genoa.

Cigna, F., Liguori, V., Del Ventisette, C. & Casagli, N. 2013. Landslide impacts on Agrigento’s Cathedral imaged with radar interferometry. In C. Margottini, P. Canuti & K. Sassa (eds.), Landslide Science and Practice, 475–481. Springer Berlin Heidelberg.

Cooper, A. H. 2008. The classification, recording, databasing and use of information about building damage caused by subsidence and landslides. *Quarterly Journal of Engineering Geology & Hydrogeology* 41: 409–24.

Cruden, D.M. & Varnes, D.J. 1996. Landslide types and processes. In: *Landslides: investigation and mitigation*, Transportation Research Board, Special Report 247, 36–75. Washington, D.C.: National Academy of Sciences.

Doglioni, F., Moretti, A. & Petrini V. 1994. *Le chiese e il terremoto*. National Research Council, Trieste, IT: Lint Press (in Italian).

Federici, P.R. & Chelli, A. 2007. *Atlante dei Centri Abitati Instabili della Liguria. IV. Provincia di Imperia* (Atlas of the Unstable Inhabited Centres of Liguria. IV. Imperia province). Regione Liguria.

Ferrero, C., Cambiaggi, L., Vecchiattini, R. & Calderini C. 2021a. Damage assessment of historic masonry churches exposed to slow-moving. *International Journal of Architectural Heritage* 15(8): 1170–1195.

Ferrero C., L. Cambiaggi, A. Fenialdi, P. Roca, R. Vecchiattini, and C. Calderini. 2021b. Slow-moving landslide damage assessment of historic masonry churches: some case-studies in Italy. In P. Roca, L. Pelà and C. Molins (eds.) *SAHC 2021: 12th International Conference on Structural Analysis of Historical Constructions*; *Online event, 29 September-1 October 2021*. Cornellà de Llobregat: Artes Gráficas Torres S.L.

Geoportale Regione Liguria. Visualizzatore Cartografico. Accessed January 20, 2020. https://geoportal.regione.liguria.it

Grünthal, G. 1998. European Macroseismic Scale 1998 (EMS-98), *Cahiers du Centre Europèen de Gèodynamique et de Seismologie 15*. Centre Europèen de Gèodynamique et de Seismologie.

Guzzetti, F., Cardinali, M., Reichenbach, P., Cipolla, F., Sebastiani, C., Galli, M. & Salvati P. 2004. Landslides triggered by the 23 November 2000 rainfall event in the Imperia Province, Western Liguria, Italy. *Engineering Geology* 73(2): 229–245.

Lagomarsino, S. 2012. Damage assessment of churches after L'Aquila earthquake (2009). *Bulletin of Earthquake Engineering* 10(1): 73–92.

Margottini, C., Spizzichino, D. & Sonnessa, A. 2013. Landslide risk and monitoring system for conservation of Vardzia monastery, Georgia. In. E. Bilotta, A. Flora, S. Lirer, & C. Viggiani (eds.), *Geotechnical Engineering for the Preservation of Monuments and Historic Site*. London, UK: CRC Press.

Penna, A., Calderini, C., Sorrentino, L., Carocci, C.F., Cescatti, E., Sisti, R., Borri, A., Modena, C. & Prota, A. 2019. Damage to churches in the 2016 central Italy earthquakes. *Bulletin of Earthquake Engineering* 17(10): 5763–5790.

Piano di Bacino Stralcio per l'Assetto Idrogeologico, Regione Liguria, 2017. Carte della Suscettività al Dissesto (Landslide Susceptibility Maps). Accessed October 25, 2018. http://www.pianidibacino.ambienteinliguria.it/.

Piano Stralcio per l'Assetto Idrogeologico, Autorità di bacino distrettuale del fiume Po, 2017. Atlante dei Rischi Idraulici e Idrogeologici (Atlas of Hydraulic and Hydrogeological Risks). Accessed October 25, 2018. http://www.pai.adbpo.it/.

QGIS 2017. Open Source Geographic Information System. Accessed May 3, 2018. https://qgis.org/en/site/.

Regione Liguria e Segretariato Regionale del MiBACT per la Liguria. 2017. Vincoli architettonici, archeologici, paesaggistici. Accessed May 3, 2018. http://www.liguriavincoli.it/.

Soccodato, F.M, E. Martini, L. Tortoioli and A.M. Mazzi. 2013. The preservation of historical, archaeological and artistic heritage of Orvieto: an interdisciplinary project. In E. Bilotta, A. Flora, S. Lirer, & C. Viggiani (eds.), *Geotechnical Engineering for the Preservation of Monuments and Historic Sites*. London, UK: CRC Press (Taylor & Francis Group).

Trigila, A., C. Iadanza, M. Bussettini, and B. Lastoria. 2018. Dissesto idrogeologico in Italia: pericolosità e indicatori di rischio. Rapporti 287/2018. Istituto Superiore per la Protezione e la Ricerca Ambientale – ISPRA (in Italian).

Geotechnical Engineering for the Preservation of Monuments and Historic Sites III – Lancellotta, Viggiani, Flora, de Silva & Mele (Eds)

GFRP anchoring systems for soft-rock geostructures with high cultural and environmental value

L.Sandrini & M.O. Ciantia
University of Dundee, School of Science and Engineering, Dundee, UK

R. Castellanza
Università degli Studi di Milano-Bicocca, Dipartimento di Scienze dell'Ambiente e della Terra, Milan, Italy

I. Bridi
Freelance Geologist. Specialized in tensile tests on anchors. Trento, Italy

G. Balconi
SIREG GEOTECH S.r.l.; Arcore MB, Italy

Perrone
FAVELLATO CLAUDIO S.P.A., Fornelli (IS), Italy

ABSTRACT: Structural instability of soft rock geostructures composed of carbonate rocks (such as chalk and calcarenites) and volcanic (tuff) is a serious problem especially when it develops in inhabited centers. Because of the carbonate rich geology, geohazards such as sinkhole and cliff instability are a real threat for inland and coastlines regions of both southern Italy and other regions across the world. The areas affected by such threat often coincide with cultural heritage sites because of their evocative landscape and they represent important nation landmarks, as the white cliffs of Dover in the UK. One of the problems related to the safety of these famous landmarks is the identification appropriate intervention measures able to preserve the originality and beauty of the site. For example, the use of standard shotcrete or rock anchors would result inappropriate as the steel plates of the anchors and the reinforced portions covered by shotcrete would alter the exposed surface significantly. In this paper a novel anchoring system aimed to overcome the above limitations is proposed and its performance is demonstrated by an intensive field testing campaign. By using Glass Fiber Reinforced Polymers (GFRP) bars combined with various types of consolidants, it is shown that that the same level of reinforcement, guaranteed by using standard grouted DYWIDAG steel bars, can be achieved with a setup characterized with lighter, more transparent and corrosion resistant materials.

1 INTRODUCTION

Rockbolts are the most effective and economical method used in mining and tunneling engineering to support underground excavations or to stabilize a jointed rock mass. Regardless of the intervention measure, they are usually made of carbon steel and are therefore susceptible to corrosion (Manquehual et al. 2021). This chemical process causes steel to lose its cross-sectional area and form corrosion products on its surface due to interactions with the environment. Consequently, corrosion can reduce the strength capacity of rock bolts and diminish the bond strength with the surrounding material over time (Dorion & Hadjigeorgiou 2014). Whilst they are aesthetically preferred to shotcrete, the corrosion of the steel face plates may result inappropriate when stabilizing cultural heritage sites.

Because of its good mechanical properties (Jabbar & Farid 2018; Liu et al. 2014; Patil 2014) high corrosion resistance (Jabbar & Farid 2018; Kemp 2003) and its light weight, Glass Fiber Reinforced

DOI 10.1201/9781003308867-94

Polymer (GFRP) bars are widely used as an alternative material to the steel rebars. Thanks to these characteristics GFRP bars are also becoming widespread in Geotechnical Engineering practice as an alternative to classical steel bars/tendons (Wang et al. 2018; Zhang et al. 2018). The GFRP, however, has low shear strength and low ductility. Recently, GFRP bars were also used as soil nails in Hong Kong (Cheng et al. 2009) and as Screw Anchors for stabilizing slopes in different types of soils (Zou et al. 2016). The limitations of GFRP bar as soil nails are that pressure grouting is complex, and that the connection of bars used for longer soil nails is cumbersome.

The Apulian region is characterized by strong tourist impact above all due to the beautiful cost and the vertical cliffs in carbonate rock formations. Many zones of this region must hence be preserved for their important cultural heritage. Because of the long term hydro-mechanical interaction with the sea, and due to rainfall water infiltration from the ground surface, the Polignano a Mare coastline has suffered from weathering effects causing partial collapses (Ciantia et al. 2015a, 2015b). For example, part of *Grotta Palazzese* cave vault detachment in 2006 and 2014 caused the closure of the touristic location for several years. Such event was the main reason behind the need of finding stabilization techniques able to both preserve the cultural heritage of the cave and guarantee a high safety factor despite the ongoing weathering mechanisms (Castellanza et al. 2018). Such needs are the main drive of the field test campaign presented in this work. The exposure to an aggressive marine environment, making the use of steel bars unsuitable and the need to avoid use of shotcrete or other less aesthetic surface reinforcement solutions. The test campaign was hence designed to compare the anchoring performance when using either GFRP or DYWIDAG bars of various diameter anchored with different types of consolidating materials. The anchor performance was assessed in both the *Calcare di Bari* limestone and *Calcarenite di Gravina* calcarenite performing tension pull-out tests according to UNI EN 14490:2010. In this contribution, the main results of the 16 pull test performed in the two sites in the proximity of the *Grotta Palazzese* cave joint to the potential failure mechanisms identified are presented.

2 FIELD TESTING CAMPAING

2.1 *Geological settings*

The anchor pullout tests presented in this study are all perfomremd in Polignano a Mare. Figure 1a, taken from Spalluto (2012), reports the geology and the succession crops of the area. The coastal stretch is characterized by the outcropping of two main formations: well stratified micritic limestones of the *Calcare di Bari* (CB) formations (Callovian pp.-early Turonian) are overlaid by discontinuous calcarenite deposits of the *Calcarenite di Gravina* (CG) formation (upper Pliocene–early Pleistocene). The latter, mainly constituted by biocalcarenites, is transgressive on the former through an angular erosional unconformity and thin conglomerate deposits (Andriani & Walsh 2002; Festa 2003; Spalluto 2012).

These two formations are mainly composed of calcium carbonate ($CaCO_3 > 95\%$) but, because of the different microstructure and porosity are characterized by a different hydro-mechanical behavior

a) b)

Figure 1. a) Location of the Apulian foreland in a synthetic structural map of Italy (Spalluto 2012); b) Stratigraphic limit between CB limestone and CG.

(Andriani & Walsh 2002, 2007). While the CG can be considered a soft rock (UCS < 5 MPa), the CB is a much stronger rock (UCS > 10 MPa) (Castellanza et al. 2018; Ciantia et al. 2015a, 2015b).

2.2 *Site investigation and filed test locations*

The field-testing campaign was performed in two different locations on the Polignano a Mare coastline (Figure 2). Both locations were chosen to be close to the two main cavities which experienced partial collapses in the past and that require urgent in safety measures. The first (FT1) is in the proximity of the *Grotta Palazzese* cave, where both *Calcarenites of Gravina* (CG) and *Calcare di Bari* (CB) limestones are outcropping (Figure 3). In filed test 2 (FT2), which is in correspondence of the *Grotta dell'Arcivescovado* cave, only the *Calcare di Bari* (CB) limestone is outcropping (Figure 4). Risk assessment and preliminary site preparation were coordinated and performed by Favellato SPA.

Figure 2. Field tests location. Image reconstruction from drone acquisition.

2.2.1 *Field test 1 (FT1)*

As detailed in Figure 3, three different zones were identified and selected for the pull tests. Zone 1, in the upper region, is characterized by pure and intact CG outcrops. In Zone 2 only intact CB limestones are present while Zone 3 is characterized by a very fractured CB limestone.

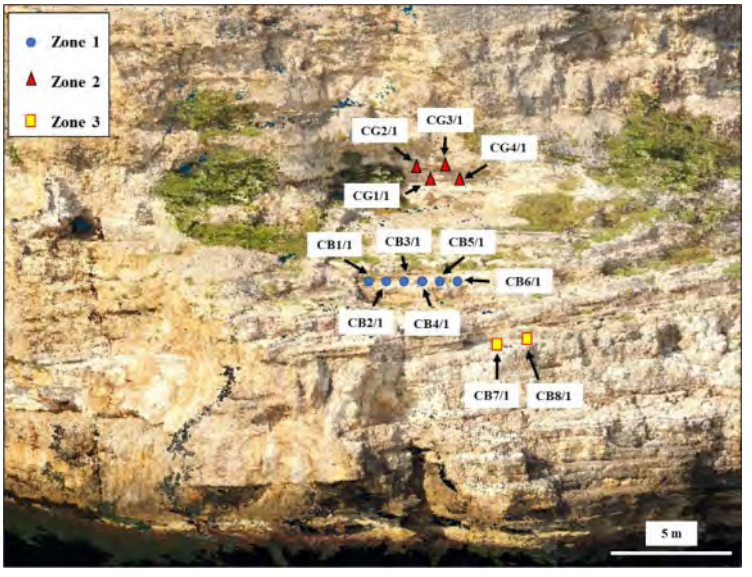

Figure 3. Location pull tests in FT1. Image reconstruction from drone acquisition.

2.2.2 *Field test 2 (FT2)*

As detailed in Figure 4, two different zones were identified and selected for the pull tests. Zone 1, in the upper region, is characterized by pure and intact CG outcrops. In Zone 2 only intact CB limestones are present while Zone 3 is characterized by a very fractured CB limestone.

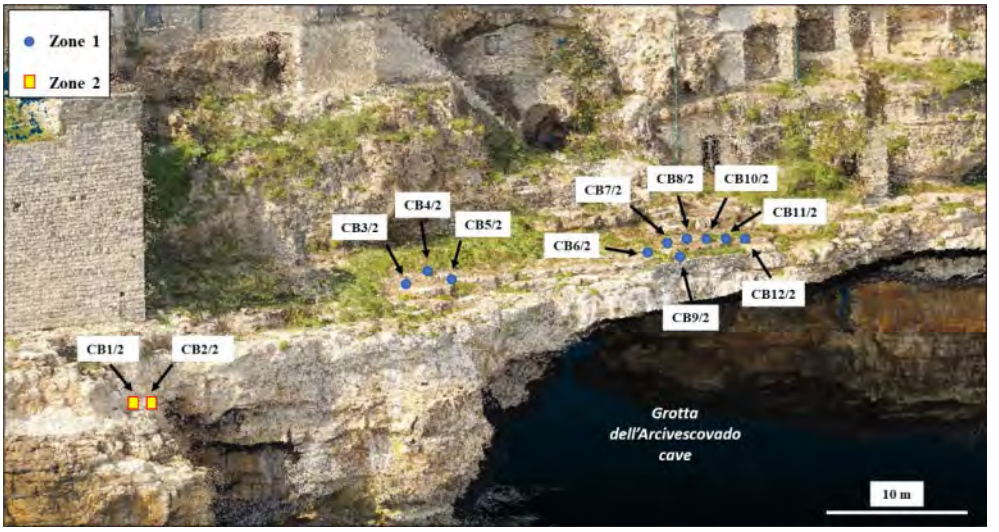

Figure 4. Location pull tests in FT2. Image reconstruction from drone acquisition.

2.3 *Pull test characteristics*

As mentioned previously, two types of bars were used in this field-testing campaign. On one side GFRP bars of variable diameter were used to determine their pullout capacity performance and exploit their lightweight and corrosion resistance properties. On the other classic DYWIDAG bars used as benchmark to compare the performance of the GFRP bars. Whist DYWIDAG bars are already threaded one extremity of each of the GFRP bar used had to be modified to allow a proper anchoring of the pulling system. Depending on the bar type a threaded steel tube was glued to the external or internal surface of the GFRP at one extremity using an epoxy resin. Figure 5 shows some images of such details while

a) b)

Figure 5. a) Threaded steel tube glued on the GFRP bars with epoxy resin; b) *Silicajet EXP/4* grouted *Glasspree* GFRP bar with threaded steel tube glued externally in CB limestone.

Tables 1 and 2 summarize the mechanical and geometrical characteristics of the DYWIDAG and GFRP bars used.

Table 1. DYWIDAG bar details.

Type	Diameter (mm)	Yield stress (MPa)	Yield load (kN)	Ultimate load (kN)	Young Modulus (GPa)
Y1050H	26.5	950/1050	525	580	205

Table 2. GFRP bar details.

Type	Diameter (mm)	Guaranteed Tensile Strength (MPa)	Min guaranteed ult. tensile force (kN)	Young Modulus (GPa)
Glasspree Ø16	16	850	>170	46
Glasspree Ø25	25	800	>392	46
GFRP Hollow Bar	32	800	>350	40

2.3.1 *Consolidants*

In FT1 two types of consolidants were used to anchor the bars in the CB limestone and only one type for the tests in the CG calcarenite. A bi-component organo-mineral and thixotropic resin, *MasterRoc RBA 380*, and a premixed cement mortar, *MasterEmaco T 1200 PG*, were used in the limestone, as both materials have low hardening times. For the tests in the calcarenite a lime-based mortar, *MasterInject 222*, was used instead, as the holes were made with an inclination of 45 degrees upwards and the use of resins resulted to be impractical. In FT2, on the other hand, the 8 different types of consolidants listed in Table 3 were used:

Table 3. Details of the consolidant materials used.

Consolidant	Fabricant	Chemical composition/ characteristics	Compressive (MPa)*	Interface shear strength (MPa)**	Young Modulus (GPa)
Masterinject 222	MasterBuilders	pozzolanic lime grout	>10	>4	6 ± 1
MasterEmaco T 1200 PG	MasterBuilders	reinforced cement mortar	>80	>25	43
MasterRoc RBA 380	MasterBuilders	TIX polyurea silicate resin	>35	/	/
MasterEmaco A 640	MasterBuilders	expansive cement mortar	>40	>15	30 ± 2
MasterEmaco S 1120 TIX	MasterBuilders	TIX cement mortar	>35	/	22
MasterRc 710 TIX	MasterBuilders	TIX cement mortar	>40	/	22
Stabilcem T	Mapei	TIX cement mortar	>40	>17	30
Silicajet EXP/4	Mapei	two-component organo-mineral resin	/	/	/

*Determined according to UNI 1015-11; UNI 12190:2000
**Determined according to RILEM-FIP-CEB

2.4 *Definition of holes characteristic*

The choice of the diameter of the holes was made in relation to the diameters of the bars used. For, 32 mm holes were drilled while for both the Ø25 and Ø32 bars a 51 mm hole was used (Figure 6). All the bar (D) and hole (D_h) diameters are reported in Table 3. All anchoring lengths were fixed to one meter.

Figure 6. Favellato SPA technician preparing the holes in the limestone.

2.5 *Positioning and bar grouting*

Field test 1

In FT1 12 bars were installed (4 in CG and 8 in CB limestone) and pulled to failure or to the maximum capacity of the jacking system (100 Tons). Of the 4 bars installed in the calcarenite, 2 were Ø32 GFRP hollow tubular bars and 2 were 26, 5 Ø DYWIDAG bar. The holes in zone 2 in Figure 3 (in CG calcarenite) with an upward inclination of approximately 45° were filled using a bespoke injection system (Figures 7a and 7b). First the bars were inserted into the holes for a length of 1 m with a tube for the injection of the consolidating material. Both the bar and the tube were fixed to the rock face using an ultra-fast cement mortar (*Lampocem* from Mapei) that helped to seal the hole preventing the consolidants to leak out during the injection. Once cured a very fluid lime-based mortar (*MasterInject 222* – Pozzolanic lime grout, cement-free) was injected through the preinstalled tube.

Figure 7. a) VTR bars blocked by *Lampocem* before injection; b) injection of *MasterEmaco 222* through injection tube in CG.

A few meters below the above described calcarenite anchors a bank of CB limestone was chosen (Zone 1 in Figure 3) and injected, by pour (see Figure 8). 4 different bars with different diameters, for a total of 8 holes were filled with either an organomineral resin (*MasterRoc RBA 380*) or a quick-setting cement mortar (*MasterEmaco T 1200 PG*).

Figure 8. Pouring to two different materials.

Two bars (CB7/1 and CB8/1) were anchored in Zone 3 where the limestone was more fractured with respect to the one found in Zone 1. During the casting phase of the consolidant, it was noticed that the rock had some fractures along the lateral surface of the hole. To overcome this difficulty, since the material used was thixotropic, to properly grout the bar it was sufficient to pause the casting for a few seconds to then proceed again with the filling and subsequent insertion of the bar.

Field tests 2

In FT2, 12 anchors were installed (all in CB limestone), with 8 different types of consolidating materials. Except for the CB1/2 and CB2/2 bars (Zone 2), where the consolidant material was injected with the same bespoke method used in FT1 and described above (Figure 9a), all the other bars were grouted by casting the chosen material (Figure 9b).

Figure 9. a) Technician during injection *MasterEmaco A 60* in CB1/2; b) anchor in FT2 zone 1.

3 PULL-OUT TESTS

All the pull-out tests were performed using Hallow piston Hydraulic cylinder Jack brought under pressure by a manual pump, connected to a load cell to measure the applied tensile force. Depending on the estimated capacity the 100ton capacity or 30ton capacity hallow piston was used. Data acquisition was carried out digitally, using 3 digital displacement transducers connected to a data logger to which a connection to the pump was also added to also view the applied force. By connecting the data logger to a portable PC, it was possible to view and record in real time the displacement and force signals of the transducers. The results of the pull test of the CB8/2 and CB11/2 anchors are reported in Figure 11. In the figure the failure loads related to rock-consolidant shear failure, bar consolidant shear failure and yielding of the bar are also reported. For the anchoring length of 1 m and for tests in CB limestone, failure is expected to occur because of the yielding of the bar. The two tests reported in Figure 10 could not reach failure as the maximum load of the piston was reached in both cases. The main difference that clearly visible is the much stiffer response of the DYWIDAG compared to the GFRP one. Because of technical issues related to the data acquisition system it was not possible to perform all test with a digital data acquisition. For these latter, to measure and record displacements an analog displacement transducer was used (Figure 11). The force was also recorded manually. As detailed in Table 3 some tests were performed after 18 hours of curing time. Others were performed after 40 days. The field-testing campaign will be completed by the end of 2022 (about one year after installation) will be performed.

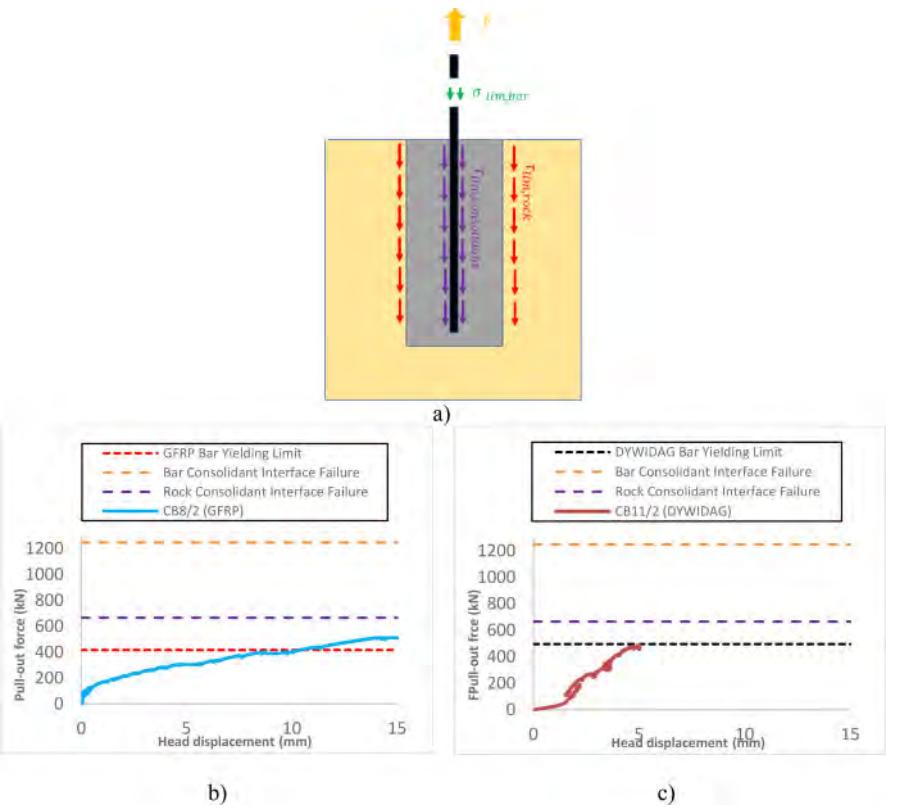

Figure 10. Potential failure modes (a) and pull-out force vs head displacement curves for CB8/2 (b) and CB11/2 (c).

Figure 11. a) Pull test with 1000 kN capacity Hallow piston; b) pull test with 300 kN capacity hallow piston.

Table 4. Anchors pull test details.

ID test	Bar type	D (mm)	D_h (mm)	Consolidant	Curing time	F_{max} (kN)	Comments
CA-2/1	DYWIDAG	26.5	55.3	*Masterinject 222*	40 (days)	400	failure looked to appear at interface rock-binder
CB-1/1	GFRP	16	35.4	*MasterEmaco T 1200 PG*	18 (hours)	>140*	failure pull test bar attachment system
CB-2/1	GFRP	16	35.3	*MasterRoc RBA 380*	18 (hours)	100	failure at interface rock-binder
CB-4/1	GFRP	25	54.1	*MasterRoc RBA 380*	18 (hours)	120	failure at interface rock-binder
CB-5/1	GFRP	25	54.4	*MasterEmaco T 1200 PG*	18 (hours)	340	failure looked to appear at interface rock-binder
CB-6/1	DYWIDAG	26.5	34.4	*MasterEmaco T 1200 PG*	18 (hours)	>300	Hallow piston max load
CB-7/1	GFRP	16	34	*MasterEmaco T 1200 PG*	18 (hours)	>140*	failure pull test bar attachment system
CB-8/1	GFRP	16	34.2	*MasterRoc RBA 380*	18 (hours)	>120*	failure pull test bar attachment system
CB-1/2	DYWIDAG	26.5	33.6	*MasterEmaco A640*	40 (days)	>430**	Hallow piston max load
CB-2/2	GFRP	25	53.7	*Masterinject 222*	40 (days)	>100*	failure pull test bar attachment system
CB-4/2	DYWIDAG	32	46	*Silicajet EXP/4*	40 (days)	235.7	failure looked to appear at interface rock-binder
CB-6/2	GFRP	16	33.8	*MasterRoc 710 TIX*	40 (days)	>122.4*	failure pull test bar attachment system
CB-8/2	GFRP	25	52.6	*MasterEmaco A640*	40 (days)	>511**	Hallow piston max load
CB-9/2	GFRP	25	54.1	*MasterEmaco S1120 TIX*	40 (days)	340	failure looked to appear at interface rock-binder
CB-10/2	GFRP	16	34.2	*MasterEmaco A640*	40 (days)	>128*	failure pull test bar attachment system
CB11/2	DYWIDAG	26.5	53	*MasterEmaco A640*	40 (days)	>488**	Hallow piston max load

*Maximum force achieved because the bars attachment system for traction test have been underestimated
**Maximum force achieved for safety reason

4 CONLUSIONS

This article reports the results of a series of pull-out tests on soft rock anchors. The test campaign was designed to compare the anchoring performance when using either GFRP or DYWIDAG bars of various diameter anchored with different types of consolidating materials. DYWIDAG bars are widely used in the engineering field as they are economical and have always guaranteed excellent results in terms of safety in the short term. However, being made up of iron alloys, they have a short life as they are subject to corrosion, especially in marine environments. On the other hand, GFRP bars, already widely used in construction, mostly as tie rods, in such extreme environments offer an almost infinite resistance to corrosion. The results of this field-testing campaign the anchor performance was assessed in both the *Calcare di Bari* limestone and *Calcarenite di Gravina* calcarenite. The main results of the 16 pull test performed in the two sites in the proximity of the *Grotta Palazzese* cave show that GFRP bars are a good alternative to DYWIDAG as they can provide similar capacity with a more ductile behaviour. Such feature is important when stabilising rock masses prone to brittle failure mechanisms. Moreover, in addition to being more corrosion resistant, GFRP have lighter color that is more aesthetic and may be preferred when stabilizing cultural heritage cliffs such as the one considered in this work.

REFERENCES

1015-11, U. E. (n.d.). *Methods of test for mortar for masonry Part 11: Determination of flexural and compressive strengthof hardened mortar 2006; UNI: Rome, Italy, 2006.*

12190:2000, U. E. (n.d.). *Product and system for the protection and repair concrete structures—Testmethods—Determination of compressive strength of repair mortar; UNI: Rome, Italy, 2000*.

Andriani, G. F., & Walsh, N. (2002). Physical properties and textural parameters of calcarenitic rocks: Qualitative and quantitative evaluations. *Engineering Geology*, 67(1–2), 5–15. https://doi.org/10.1016/S0013-7952(02)00106-0

Andriani, Gioacchino F., & Walsh, N. (2007). Rocky coast geomorphology and erosional processes: A case study along the Murgia coastline South of Bari, Apulia — SE Italy. *Geomorphology*, 87(3), 224–238. https://doi.org/10.1016/J.GEOMORPH.2006.03.033

Castellanza, R., Lollino, P., & Ciantia, M. (2018). A methodological approach to assess the hazard of underground cavities subjected to environmental weathering. *Tunnelling and Underground Space Technology*, 82(January 2017), 278–292. https://doi.org/10.1016/j.tust.2018.08.041

Cheng, Y. M., Choi, Y.-K., Yeung, A. T., Asce, F., Tham, ; L G, Asce, M., Alfred, ;, Au, S. K., Asce, A. M., Wei, ; W B, & Chen, J. (2009). New Soil Nail Material—Pilot Study of Grouted GFRP Pipe Nails in Korea and Hong Kong. *Journal of Materials in Civil Engineering*, 21(3), 93–102. https://doi.org/10.1061/(ASCE)0899-1561(2009)21:3(93)

Ciantia, M. O., Castellanza, R., Crosta, G. B., & Hueckel, T. (2015). Effects of mineral suspension and dissolution on strength and compressibility of soft carbonate rocks. *Engineering Geology*, 184, 1–18. https://doi.org/10.1016/J.ENGGEO.2014.10.024

Ciantia, M. O., Castellanza, R., & di Prisco, C. (2015). Experimental Study on the Water-Induced Weakening of Calcarenites. *Rock Mechanics and Rock Engineering*, 48(2), 441–461. https://doi.org/10.1007/s00603-014-0603-z

Dorion, J. F., & Hadjigeorgiou, J. (2014). Corrosion considerations in design and operation of rock support systems. *Http://Dx.Doi.Org/10.1179/1743286313Y.0000000054*, 123(2), 59–68. https://doi.org/10.1179/1743286313Y.0000000054

Festa V. (2003). Cretaceous structural features of the Murge area (Apu- lian Foreland, southern Italy). *Eclogae Geologicae Helvetiae*, 96:11–22.

Jabbar, S. A. A., & Farid, S. B. H. (2018). Replacement of steel rebars by GFRP rebars in the concrete structures. *Karbala International Journal of Modern Science*, 4(2), 216–227. https://doi.org/10.1016/J.KIJOMS.2018.02.002

Kemp M., B. D. (2003). *Concrete Reinforcement and Glass Fibre Reinforced Polymer*.

Liu, J., Zhou, H., Yuan, H. J., & Li, J. F. (2014). Experimental Research on Strength of GFRP Bars in Shield Engineering. *Advanced Materials Research*, 1020, 308–313. https://doi.org/10.4028/WWW.SCIENTIFIC.NET/AMR.1020.308

Manquehual, C. J., Pål, ·, Jakobsen, D., Amund, ·, & No, C. J. M. (2021). Corrosion Level of Rock Bolts Exposed to Aggressive Environments in Nordic Road Tunnels. *Rock Mechanics and Rock Engineering*, 54, 5903–5920. https://doi.org/10.1007/s00603-021-02547-3

Patil, V. R. (2014). IJIRAE::Experimental Study of Behavior of RCC Beam by Replacing Steel Bars with Glass Fibre Reinforced Polymer a Experimental Study of Behavior of RCC Beam by Replacing Steel Bars with Glass Fibre Reinforced Polymer and Carbon Reinforced Fibre Polymer (GFRP). *I Nter National Journal of I Nnovative Research in Advanced Engineering (I JI RAE*, 1(5), 2349–2163.

RILEM-FIP-CEB. Bond test for reinforcing steel: 1. Beam test (7-II-28 D). 2. Pull-Out Test (7-II-128). Tentative Recommendations. Materials and Structures, v. 6, n. 32, p. 96–105, 1978. (n.d.). *No Title*.

Spalluto, L. (2012). *Facies evolution and sequence chronostratigraphy of a "mid"-Cretaceous shallow-water carbonate succession of the Apulia Carbonate Platform from the northern Murge area (Apulia, southern Italy)*. 58, 17–36. https://doi.org/10.1007/s10347-011-0266-0

Wang, W., Song, Q., Xu, C., & Gong, H. (2018). Mechanical behaviour of fully grouted GFRP rock bolts under the joint action of pre-tension load and blast dynamic load. *Tunnelling and Underground Space Technology*, 73, 82–91. https://doi.org/10.1016/J.TUST.2017.12.007

Zhang, M. Y., Kuang, Z., Bai, X. Y., & Chen, X. Y. (2018). Pullout behavior of GFRP anti-floating anchor based on the FBG sensor technology. *Mathematical Problems in Engineering*, 2018. https://doi.org/10.1155/2018/6424791

Zou, W.-L., Wang, X.-Q., & Vanapalli, S. K. (2016). Experimental Evaluation of Engineering Properties of GFRP Screw Anchors for Anchoring Applications. *Journal of Materials in Civil Engineering*, 28(7), 04016029. https://doi.org/10.1061/(ASCE)MT.1943-5533.0001471

Geotechnical Engineering for the Preservation of Monuments and Historic Sites III – Lancellotta, Viggiani, Flora, de Silva & Mele (Eds)

Probabilistic evaluation of the seismic vulnerability of rock cavities in a historical Italian site

S. Fabozzi & M. Moscatelli
Institute of Environmental Geology & Geoengineering – National Research Council of Italy

F. de Silva, L. Starita & E. Bilotta
Department of Civil, Architectural & Environmental Engineering – University of Naples Federico II

ABSTRACT: Recent and past earthquakes have shown that underground anthropogenic cavities excavated in soft rock are prone to damage, posing a major threat to their safety and having major cascading and socioeconomic impacts. From an engineering point of view, the seismic vulnerability of underground cavities can be accomplished by computing the probability of damage due to the seismic actions expected on site by using fragility curves. This work explores the applicability of this method to probabilistically evaluate the seismic vulnerability of soft rock cavities within the vision of urban resilience of historical Italian centers. The seismic behavior of rock cavities was assessed via finite element method approach and the factor of safety of the cavity roof calculated in seismic conditions was exploited to develop fragility curves. The proposed procedure is applied to a rock cavity under the historical center of Sant'Agata de' Goti in the South of Italy.

1 INTRODUCTION

The instability risk of underground cavities is issue of concern particularly for areas densely urbanized as the case of many historical centers in Italy. Being the results of past quarrying activities, shallow cavities are frequently spread below historical sites in many Italian regions, whereby their stability represents matter of concern leading to potential risk situations for buildings, infrastructures and population. A possible cause of the cavity damages up to collapse, is the dynamic loading induced by an earthquake. Recent and past earthquakes in fact (CFTI5Med, http://storing.ingv.it/cfti/cfti5/, Guidoboni et al. 2019; CEDIT, http://www.ceri.uniroma1.it/index_cedit.html, Fortunato et al. 2012) have shown that underground anthropogenic cavities excavated in soft rock are prone to damage due to seismic actions, posing a major threat to safety and having major cascading and socioeconomic impacts. In the present work, the seismic behavior of shallow cavities in soft rock is addressed by implementing a methodology proposed by de Silva and Scotto di Santolo (2018) and applied at large scale by Fabozzi et al. (2021) that expressed the rock cavity safe level in terms of Factor of Safety calculated as the ratio between the resistant moment and the loading moment in correspondence of the most critical vertical sections of the roof cavity. The considered FoS is the lowest one experienced during the seismic shaking. The methodology is based on the results of numerical 2D finite element analyses, including the effect of the variability of some predisposing and triggering factors on the cavity stability like roof thickness and cavity width, presence of overburden on the top of the rock layer, seismic signal intensity. From an engineering point of view, the seismic vulnerability of underground cavities can be accomplished by computing the probability of damage due to the seismic actions expected on site through fragility curves. The fragility curves express the probability of exceeding

 DOI 10.1201/9781003308867-95

different damage states (DS) for a given level of earthquake intensity measure (IM), accounting for the various uncertainties associated with the seismic hazard and the structural response estimation (Pitilakis et al. 2014).

This work explores the applicability of this method to probabilistically evaluate the cavities vulnerability under seismic actions. The seismic behavior of rock cavities was assessed via finite element method approach, quantifying their stability by means of the so-called Factor of Safety and the results were exploited to develop fragility curves *ad hoc* for rock cavity. The proposed procedure is applied to a rock cavity belonging to the historical center of Sant'Agata de' Goti in the South of Italy. The medieval village is located on the top of a tuff ridge and significant seismic actions are expected on the basis of the numerous earthquakes occurred in the past (;uidoboni & Comastri 2005; Guidoboni et al. 1997) and recent seismic hazard maps for Italy (Meletti & Montaldo 2007).

2 CASE STUDY

2.1 *Subsoil site characterization*

Sant'Agata de' Goti is a typical medieval town of south Italy, perched on the top of a steep tuff ridge crossed by 160 anthropic cavities which static and seismic stability could be affected by the local seismic hazard. The rock formation constituting the ridge of Sant'Agata is the Campanian Ignimbrite in its yellow and grey tuff lithofacies, lying on a thin loose layer of pyroclastic soil and a Miocene flysch formation.

The cavity studied by de Silva et al. (2015) in terms of site amplification, was re-proposed in the present study to investigate its stability under seismic action. Figure 1 shows the plan and sections of the cavity in object that extends over an area about equal to 130 m^2 beneath an ancient building. It consists into three main rooms (A, B, C), one tunnel and two stairwells. The tunnel is 3 m wide and 3.4 m high and extends for about 20 m parallel to the slope, connecting the two main rooms A and B. Cavity section A-A was analyzed by assuming, for its regular shape, plane strain conditions. This cavity section has a sub-rectangular shape 3 m wide, 3.4 m high and 1.7 m deep from the ground surface. The cavity is fully excavated in the first layer of Lithified Yellow Tuff

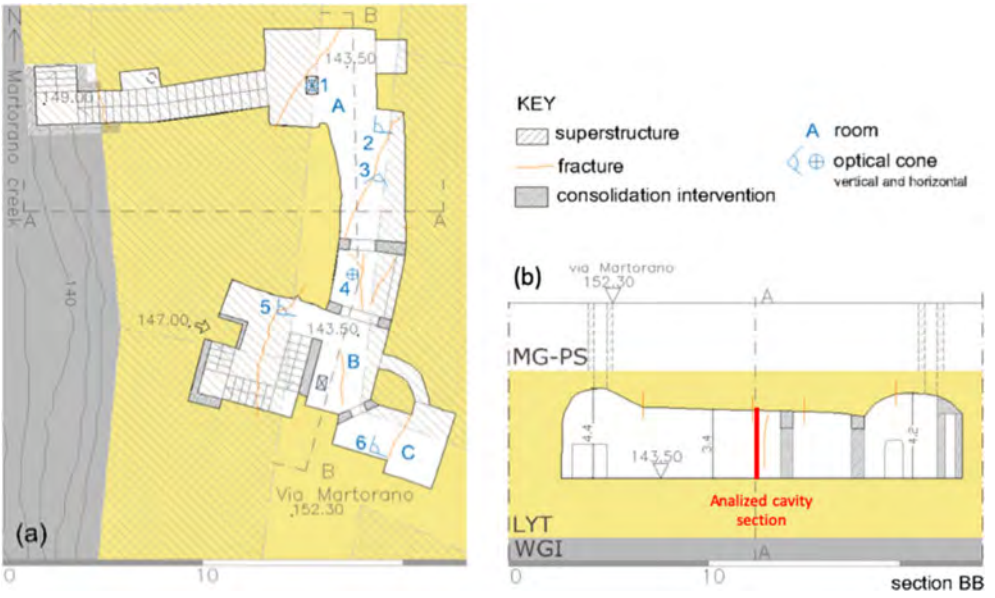

Figure 1. Plan (a) and sections (b) of the studied cavity (modified after de Silva et al. 2015).

(LYT) overlaying a first layer of well cemented grey tuff with dark and grey scoria and pumices and subordinately lithics and crystals (WGI_{upper}), a second layer of low cemented grey tuff with scoria and pumices (WGI_{lower}) and a third layer of alluvial deposit (AD) made of silty sand, clayey silt and sandy gravels extended up to the seismic bedrock of Miocene age. The layers thickness, t, can be found in Table 1. The geotechnical characterization of the site is reported in Table 1, for the four soil layers as proposed by Piro et al. (2019). The historical town was widely investigated in the last thirty years performing numerous boreholes and down-holes (de Silva et al. 2013) and, quite recently also a geophysical test, MASW. In addition, many samples were taken at different depths into WGI and AD soil to perform Consolidated-Drained Triaxial Compression test (TX-CID) as well as Resonant Column (RC) and Cyclic Torsional Shear (CTS) tests. Table 1 reports for each range of depth the natural unit weight, γ, the shear wave velocity, Vs, together with the Oedometric, E_{oed}, and shear, G_0, moduli computed from the measured velocities. Table 1 includes also the assigned strength parameters: the friction angle, ϕ', and the cohesion, c′, were obtained from triaxial tests while the tensile strength, σ_t, was assumed as 10% of the compression strength in any case.

Table 1. Subsoil properties and mechanical parameters (from Piro et al. 2019).

Material	t [m]	γ [kN/m^3]	Vs [m/s]	E_{oed} [MPa]	G_0 [MPa]	σ_t [KPa]	ϕ' [°]	c′ [MPa]
LYT	8.3	15.23	420	2383	274	300	29	900
WGI_upper	37.3	13.12	492	1144	328	16	35	40
WGI_lower	6	17.17	362	2483	229	2	35	5
AD	11.7	17.27	341	1764	205	–	–	–

Figure 2 shows the decay of the normalized shear modulus, G/G_0, and the increase of the damping ratio, D, with shear strain, γ. The curves of WGI_{lower} and AD were calibrated on the results of the abovementioned tests while LYT and WGI_{upper}, were calibrated on experimental data from resonant column tests on comparable Neapolitan pyroclastic soils, reported by Vinale (1988) and de Silva et al. (2015), respectively.

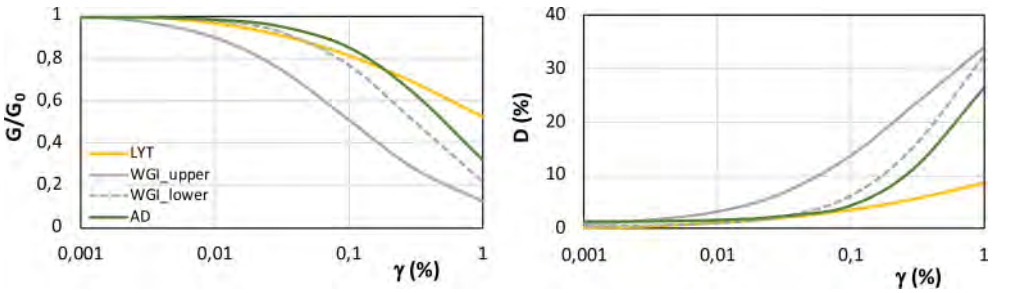

Figure 2. G/G_0-γ and D-γ curves adopted in the numerical analyses (modified after de Silva et al. 2020).

2.2 *Numerical model*

The dynamic behavior of the cavity was investigated via full dynamic analysis on a two dimensional model generated into Plaxis 2D software. Figure 3a, b shows the geometry of the numerical model and a zoom-in around the cavity of the numerical mesh. The minimum mesh size was calibrated to ensure a reliable propagation of the maximum significant frequency of the input signal (Kuhlemeyer & Lysmer 1973). The longitudinal stretch of the model is 400 m width, optimized by a series of sensitivity analyses, in order to reach a true free-field condition at the lateral borders

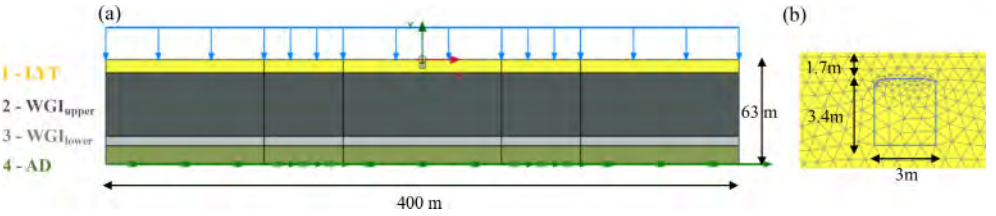

Figure 3. (a) Geometry of the numerical model and (b) zoom-in mesh around the cavity.

and to minimize the influence of vertical boundaries, modeled with viscous dashpots. The model includes the presence of a uniform distributed load at the ground surface equal to 65 kN/m that includes 45 kN/m due to a 3 m thick layer of made ground and 20 kN/m due to the presence of an aboveground structure. The seismic bedrock is located at 63 m in depth, modelled as compliant base boundary ensuring that reflected wave from layers above are absorbed and allowing the upward propagation.

The nonlinear dynamic behavior of LYT, WGI_{upper} and WGI_{lower} was modelled by means of the Hardening Soil with small strain (HSss) overlay constitutive model (Benz 2007) whose main parameters are synthetized in Table 2. AD layer instead, in absence of detailed information on the resistance parameters, was modelled with a simple linear elastic model, consistently with the hypothesis that a low tangential deformation level is reached in this layer.

In addition to the G/G_0-γ and D-γ variation curves discussed in §2.1, small-strain viscous damping was introduced in the dynamic calculation by means of the well-known Rayleigh formulation, that considers a linear combination of the mass and the stiffness matrices. The Rayleigh damping coefficients, α_R and β_R, were calculated following the 'double frequency approach', assuming as target values the first natural frequency of the deposit and the main frequency of the considered input motion.

Once defined the numerical model, the analyses were performed following three calculation stages (Fabozzi et al. 2016; 2017):

- first stage – initialization of the initial stress state within the soft rock mass domain;
- second stage – simulation of the cavity excavation by means of the deactivation of the cavity volume;
- third stage – full dynamic analyses in the time domain.

At the end of the analysis, the cavity stability was assessed by means of the Factor of Safety (FoS), as proposed by Fabozzi et al. (2021), calculated as the ratio between the ultimate resistant moment ($Mr_{,ULS}$) corresponding to the achievement of the compressive, σ_c, and tensile, σ_t, strengths in the compression and tensile zones and the loading moment (M_{load}) acting in correspondence of the most critical vertical section of the roof. The FoS_{static} is computed at the end of the second stage of analysis, while FoS_{dyn} is computed as the lowest value experienced during the dynamic analysis under each input signal.

Table 2. Calibration of subsoil constitutive model parameters.

Material	E_{50}^{ref} [MPa]	E_{oed}^{ref} [MPa]	E_{ur}^{ref} [MPa]	$\gamma_{0.7}$ [–]	G_0^{ref} [MPa]	p_{ref} [kPa]
LYT	164	164	328	0.0019	274	100
WGI_upper	196	196	393	0.0004	328	100
WGI_lower	137	137	275	0.0014	229	100

2.3 *Dynamic behavior of the cavity*

The loading moment was computed by integrating the horizontal stress component, σ_{xx}, (assuming negative the compressive stress) acting in three critical sections of the roof, *i.e.* the right and left sections 1 and 3 at edges of pillars, and central section 2 as shown in Figure 4.

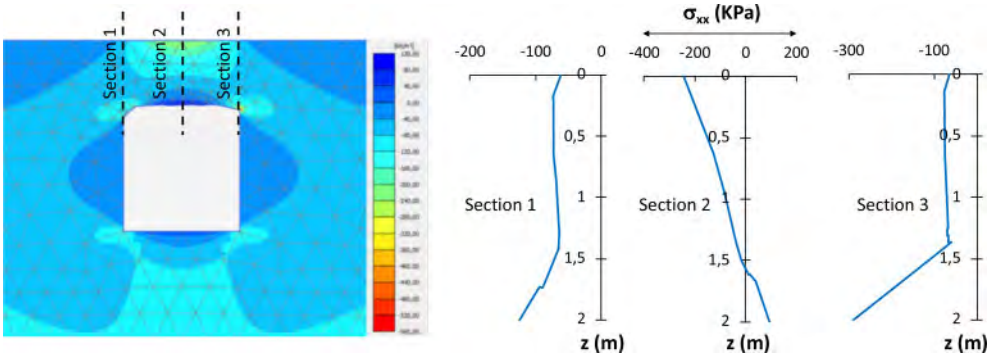

Figure 4. Horizontal stress distribution after the cavity excavation.

Figure 4 shows the contours of σ_{xx} around the cavity after its excavation: the roof tends to behave as a beam subjected to uniform distributed load where the central section is stretched in the bottom, in correspondence of the roof cavity extrados, and compressed at the top while the lateral reference sections at the intersection with pillars are totally compressed.

Starting from this initial equilibrium condition, the seismic excitation is applied at the base of the model producing in the surrounding cavity a continuous redistribution of the stresses during ground shaking. This stress redistribution is considered by calculating M_{load} at each step of the analysis form the corresponding distribution of σ_{xx} along the reference sections. As stated before, the FoS_{dyn} was then computed as the lowest value experienced during the dynamic analysis under the input signal, *i.e.* $M_{r,ULS}/\max(M_{load})$.

Considering the input signal #1 in Table 3, $FoS_{static} = 6.30$ and $FoS_{dyn} = 6.15$ for the central section 2, while for the lateral sections 1 and 3 $FoS_{static} = 10.5$ and $FoS_{dyn} = 4.17$.

The initial static conditions of the central section do not change substantially during the shaking, with a slight decrease of FoS during the earthquake. In correspondence of the lateral sections instead, starting from a higher value of FoS_{static} compared with the central one, an important reduction of FoS is observed during the shaking about equal to 60%. Despite the remarkable cavity stability reduction, the so calculated FoS_{dyn} continues to be high even after the earthquake shaking hence the roof stability of the selected cavity is not expected to be compromised.

As expected, this reduction could increase with earthquake intensity until to compromise the cavity stability when FoS tends to be close to 1. This aspect is somehow addressed in the following section where, by means of probabilistic approach, fragility curves are proposed to preliminary assess the cavity seismic performance.

3 CAVITY FRAGILITY CURVE

This section discusses the procedure to carried out the numerical fragility curves for the real rock cavity under study subjected to seismic ground shaking. The cloud method (Jalayer et al. 2015) for instance was adopted to generate the fragility curves, requiring a limited number of seismic analyses to be performed and the use of unscaled records to avoid unrealistic and undesired modification of the scaled signals. Table 3 for instance, shows the selected input signals: ten natural and unscaled accelerograms extracted from the Italian database ITACA (http://itaca.mi.ingv.it/) and, for signals

Table 3. Natural accelerograms selected for the construction of fragility curves.

ID #	Event –	Date –	Mw –	PGA_{max} (g)	f_{max} (Hz)
1	Greece	07/09/99	5.8	0.118	2.33
2	Southern Italy	09/09/98	5.6	0.161	1.56
3	Cosenza (Italy)	25/10/12	5.0	0.182	3.48
4	Central Italy – Visso	26/10/16	5.9	0.210	1.06
5	Southern Greece	15/09/86	4.8	0.232	1.34
6	Central Italy – Norcia	30/10/16	6.5	0.264	0.88
7	Greece	15/10/16	5.5	0.287	2.68
8	Imperial Valley	15/10/79	6.4	0.315	1.90
9	Friuli 3th shock (Italy)	15/09/76	6.0	0.341	5.10
10	Loma Prieta	18/10/89	6.9	0.367	0.51

with higher energy content, from the international PEER database (https://ngawest2.berkeley. edu/), recorded on sufficiently stiff soil, identified as A or B type in the Eurocode, avoiding the possible signal modifications due to local site effects.

For the definition of the fragility curves, it is necessary to define *(i)* the Engineering Demand Parameter, EDP, that measures the seismic performance of the system, *(ii)* the damage scale which associates to certain threshold-values of the EDP a damage level (*i.e.* the well-known limit state) and *(iii)* the Intensity Measure of the input motion, IM. The definition of such parameters and of their correlation depends on the failure mechanism expected to occur during the earthquake. In the present work the EDP is expressed in terms of FoS, compared with the threshold expressing the "damage limit state" occurring when the FoS is lower than 3 and "collapse limit state" associated to FoS lower than 1.5 (de Silva et al. 2020; Fabozzi et al. 2021). The EDP is divided by the threshold expressing the accepted damage level, to compute the demand to the capacity ratio, DCR_{LS}. Finally, the peak ground acceleration of the input motion PGA_{in} was assumed as IM due to its hazard computability.

The probability of failure is computed as the probability of exceeding DCR_{LS} threshold on the basis of a lognormal distribution of DCR_{LS} (Eq.1) whose mean value is linearly dependent on IM in the logarithmic scale. The mean IM-value and the standard deviation present in the Equation 1 are expressed in the Equations 2 and 3, respectively, where the vector of the parameters $\chi = [\log(a), b, \sigma_{\log DCRLS|IM}]$ are derived from the best fitting of the data $D = \{(IM_i, DCR_{LSi}), i = 1{:}N\}$ resulting from the performed analyses.

$$P\left(DCR_{LS} > 1 \mid IM, \chi\right) = \Phi\left(\frac{\log \eta DCR_{LS} \mid IM}{\sigma_{\log DCR_{LS}|IM}}\right) \tag{1}$$

$$\log \eta_{DCR_{LS}|IM} = \log(a) + b \log(IM) \tag{2}$$

$$\sigma_{\log DCR_{LS}|IM} = \sqrt{\frac{\sum_{i=1}^{n} \left(\log(DCR_{LS}) - \log DCR_{LS} \mid IM_i\right)^2}{n-2}} \tag{3}$$

Finally, the corresponding fragility curves were derived in Figure 5 for the damage limit state (black line, FoS = 3, a = 0.88, b = 0.52) and the collapse limit state (grey line, FoS = 1.5, a = 1.76, b = 0.52). Consistently, for a given value of PGA_{in}, the computed fragility curves return a higher value of probability to achieve the damage limit state (FoS = 3) respect to the probability to achieve the collapse limit state (FoS = 1.5). Thus, Table 4 contains the main parameters to compute the fragility curves.

In general, from the obtained fragility curves in Figure 5, it can be observed that important values of probability of damage can be achieve for low-to-high PGA_{in}, while the probability of collapse is rather low.

Table 4. Fragility curves parameters.

	Log η	σ	a	b
FoS = 3	1.28	0.33	0.88	0.52
FoS = 1.5	1.28	0.33	1.76	0.52

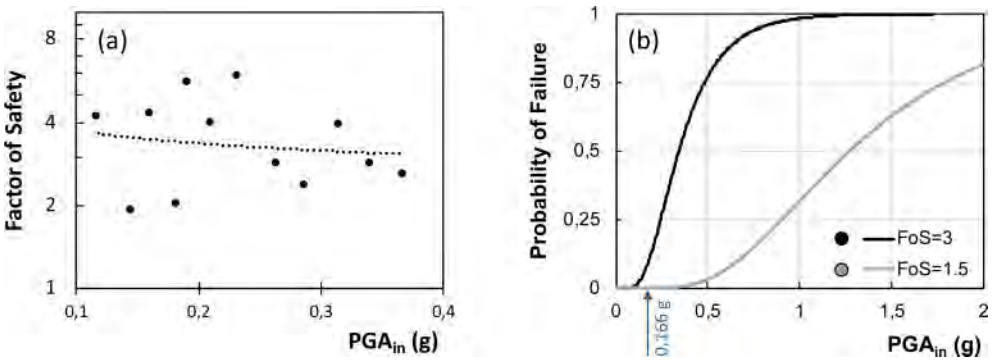

Figure 5. (a) FoS variation with PGA and (b) fragility curves for the Sant'Agata de'Goti cavity under study.

In the specific case in object, considering a $PGA_{in} = 0.166$ g expected in Sant'Agata de' Goti for a return period of 475y, the probability to achieve a FoS = 3 is about equal to 7% while the probability to achieve a FoS = 1.5 is lower than 1%. These results are in line with Nocentini et al. (2022) database where no collapse or extensive damage to cavities were observed in the last seismic events in this area.

4 CONCLUSIONS

The anthropogenic cavities are exposed to seismic actions which impact could compromise their stability as observed in some past and recent events. Certainly, the expected vulnerability of these objects could be lower than above-ground structure but, in case of extensive damage up to the collapse, the cavity instability could have a dramatic impact on the above structures, infrastructures and people. Therefore, this topic deserves special attention particularly when we refer to historical sites as in the case of Sant'Agata de'Goti that presents an important system of underground cavities. One of these cavities was studied in the present work in order to investigate its seismic performance in terms of stability. Furthermore, the seismic vulnerability of the cavity was accomplished by computing the probability of damage due to the seismic actions expected on site by means of fragility curves computed *ad hoc* for the specific case study, for increasing seismic hazard level.

Actually, this probabilistic approach could be extended to all Italian cavities falling inside historical centers or, more in general, in urban areas highly exposed to seismic risk, with particular regard to the shallower ones which potential damages due to seismic actions could have higher impact compared with the deeper ones. The use of fragility curves to forecast the seismic vulnerability of anthropogenic cavities could find interesting space of applicability in the prevention actions of the territories to seismic actions, that is to forecast the cavities more instable for their geometry, rock resistance and so on, in order to orient specific and detailed studies. This approach is in line and consistent with a more general vision of urban resilience of historical Italian centers that places the preventing urban planning in the middle of Disaster Risk Management (UNISDR 2011, 2015; UNISDR IRP 2012;.

ACKNOWLEDGEMENT

This research was partially supported by the Italian Civil Protection Department within the project "Contratto concernente l'affidamento di servizi per il programma per il supporto al rafforzamento della Governance in materia di riduzione del rischio sismico e vulcanico ai fini di protezione civile nell'ambito del PON Governance e Capacita Istituzionale 2014–2020 CIG6980737E65" (Massimiliano Moscatelli scientific coordinator), under the agreement between the Department of Civil, Architectural & Environmental Engineering of the University of Napoli Federico II (scientific responsible: Emilio Bilotta) and the Institute of Environmental Geology & Geoengineering of the National Research Council of Italy (scientific responsible: Massimiliano Moscatelli).

REFERENCES

Benz, T. 2007. *Small-strain stiffness of soils and its numerical consequences.* PhD thesis. Univ Stuttgard.

de Silva, F., Ceroni, F., Sica, S., Pecce, M.R., Silvestri, F. 2015. *Effects of soil-foundation-structure interaction on the seismic behaviour of monumental towers: the case study of the Carmine bell tower in Naples.* Rivista Italiana di Geotecnica numero special "Il ruolo della geotecnica nella salvaguardia dei monumenti e siti storici", 3, 3–27, ISSN 0557-1405.

de Silva, F., Melillo, M., Calcaterra, D., Fascia, F., Scotto di Santolo, A., Silvestri, F., Stendardo, L. 2013. *A study for the requalification and safety against natural hazards of the environmental and building heritage of Sant'Agata de' Goti (Italy).* In C. Viggiani et al. (eds), Proc. Int. Symp. on Geotechnical engineering for the preservation of monuments and historic sites, Napoli 2013, 307–316. Taylor & Francis Group: London.

de Silva, F., Scotto di Santolo, A. 2018. *Probabilistic Performance-based Approaches to the Static and Seismic Assessment of Rock Cavities.* International Journal of Rock Mechanics and Mining Sciences December 2018, 112, 354–368. https://doi.org/10.1016/j.ijrmms.2018.10.028.

Fabozzi, S., Bilotta, E., Russo, G. 2016. *Numerical interpretation of monitoring data of an instrumented tunnel segmental ring.* 1° IMEKO-TC4 International Workshop on Metrology for geotechnics. MetroGeotechnics 2016 pp. 350–355. Benevento, Italy / March 17–18, 2016.

Fabozzi, S., Licata, V., Autuori, S., Bilotta, E., Russo, G., Silvestri, F. 2017. *Prediction of the seismic behavior of an underground railway station and a tunnel in Napoli (Italy).* Underground Space 2 (2017) 88–105. http://dx.doi.org/10.1016/j.undsp.2017.03.05.

Fabozzi, S., de Silva, F., Nocentini, M., Peronace, E., Bilotta, E., Moscatelli, M. 2021. *Seismic vulnerability of shallow underground cavities in soft rock.* COMPDYN Proceedings. Volume 2021-June2021 8th International Conference on Computational Methods in Structural Dynamics and Earthquake Engineering, COMPDYN 2021Athens 28 June 2021 through 30 June 2021 Code 174550.

Fortunato, C., Martino, S., Prestininzi, A., Romeo, R.W., coauthors, Fantini, A., Sanandrea, P. 2012. *New release of the Italian catalogue of earthquake-induced ground failures (CEDIT).* Italian Journal of Engineering Geology and Environment, DOI: 10.4408/IJEGE.2012-02. O-05.

Guidoboni, E., Comastri, A., 2005. *Catalogue of earthquakes and tsunamis in the Mediterranean area from the 11th to the 15th century.* INGV-SGA, Bologna.

Guidoboni, E., Ferrari, G., Mariotti, D., Comastri, A., Tarabusi, G., Valensise, G., 1997. *Catalogue of strong earthquakes in Italy 461 BC – 1997 and Mediterranean area 760 BC – 1500,* from http://storing.ingv.it/cfti4med/.

Guidoboni, E., Ferrari, G., Tarabusi, G., Sgattoni, G., Comastri, A., Mariotti, D., Ciuccarelli, C., Bianchi, M.G., Valensise, G. 2019. *CFTI5Med, the new release of the catalogue of strong earthquakes in Italy and in the Mediterranean area.* Scientific Data 6, 80. doi: https://doi.org/10.1038/s41597-019-0091-9.

Jalayer, F., De Risi, R. & Manfredi, G. 2015. *Bayesian cloud analysis: efficient structural fragility assessment using linear regression.* Bull. Earthquake Engng 13, No. 4, 1183–1203.

Kuhlemeyer, R. L., & Lysmer, J. 1973. *Finite element method accuracy for wave propagation problems.* Journal of the Soil Mechanics and Foundation Division, 99(5), 421–427.

Meletti, C., Montaldo, V. 2007. *Estimation of the seismic hazard for different probabilities of exceedance in 50 years: PGA values.* DPC-INGV S1 Project, Deliverable D2, http://esse1.mi.ingv.it/d2.html.

Nocentini, M., Fabozzi, S., Peronace, E., Castenetto, S. 2022. *Proposal procedure to evaluate the seismic stability of underground cavities in seismic microzonation studies.* Italian Journal of Geosciences (accepted).

Piro, A., Martinelli, G., Meccariello, M., Parisi, F., Scotto di Santolo, A., de Silva, F., Silvestri, F. 2019. *Effects of the underground urban development on the seismic response of a historical centre in Italy.* 7th International

Conference on Earthquake Geotechnical Engineering for Protection and Development of Environment and Constructions – Silvestri & Moraci (Eds). Associazione Geotecnica Italiana, Rome, Italy, ISBN 978-0-367-14328-2 (Roma, Italy).

Pitilakis, K., Crowley, H. & Kaynia, A. (eds). 2014. *SYNER-G: typology definition and fragility functions for physical elements at seismic risk, buildings, lifelines, transportation networks and critical facilities.* p. 27. Dordrecht, the Netherlands: Springer.

UNISDR. 2011. *Global Assessment Report on Disaster Risk Reduction: Revealing Risk, Redefining Development.* UNISDR Practical Action 2012, Geneva.

UNISDR. 2015. *Sendai framework for disaster risk reduction 2015–2030.* UNISDR (2005), Hyogo framework for action 2005–2015: Building the resilience of nations and communities to disasters.

UNISDR, IRP. 2012. *Guidance Note on Recovery: Pre-Disaster Recovery Planning.* available at: https://www.unisdr.org/we/inform/publications/31963 (accessed 15 September 2017).

Vinale, F. 1988, *Caratterizzazione sismica del sottosuolo di un'area campione di Napoli ai fini di una microzonazione sismica.* Rivista Italiana di Geotecnica, 22(2),77–100 (in Italian).

Geotechnical Engineering for the Preservation of Monuments and Historic Sites III – Lancellotta, Viggiani, Flora, de Silva & Mele (Eds)

Multi-scale stability analysis at San Pedro Cliff in the Alhambra Cultural Heritage

J.A. Fernández-Merodo, R.M. Mateos & J.C. García-Davalillo
Geological Survey of Spain (IGME-CSIC), Madrid, Spain

J.M. Azañón
University of Granada, Granada, Spain

C. Novo
Patronato de la Alhambra y Generalife, Granada, Spain

R. Castellanza
Università degli Studi di Milano Bicocca, Milano, Italy

D. Spizzichino & C. Margottini
Istituto Superiore per la Protezione e la Ricerca Ambientale (ISPRA), Roma, Italy

ABSTRACT: San Pedro cliff is a natural slope that cuts the Al-Sabika hill where the medieval fortress of the Alhambra in Granada (Spain) stands. This unique geological phenomenon forms an inherent part of the classic postcard of this important World Heritage Site, it has a height of 65.5 m and has progressed in its deterioration to stand today about 23 m from the walls of the Alhambra. The formation of the San Pedro cliff has been a consequence of the floods of the Darro River and, perhaps, of the seepage and runoff from the Alhambra, as well as of erosion and tectonics. In this work, a stability study of the slope in 3D in its current state is carried out, at three different scales: i) Al-Sabika hill scale, in order to locate the most unstable slope in the study area, ii) San Pedro cliff scale, in order to determine the global stability conditions of the slope as well as the possible effect on the walls of the monument and iii) detailed scale of the surface of the cliff, in order to locate possible areas of detachment and quantify erosion phenomena. The 3D stability analyses are carried out using the Finite Element method and the Shear Strength Reduction technique implemented in the GeHoMadrid code. The strength parameters of the material involved, the Alhambra conglomerate, are determined from already published data and new laboratory tests. For the 3 scales, the 3D finite element meshes are defined from digital terrain models obtained with LIDAR flight, detailed topographic map and laser scanner respectively.

1 INTRODUCTION

1.1 *The site*

The property of the Alhambra, Generalife and Albayzín is located in Granada, Andalusia, Spain. This Cultural Heritage, listed as World Heritage Site by UNESCO in 1984, encompasses Moorish and Christian palaces, fortresses, houses and gardens from the 13th to 16th centuries, vestige of the late Iberian Peninsula and European occupation by the Moorish. It is certainly the most important monumental complex in Spain, being the economical lung of Granada city exceeding 2,6 million visitors in 2016.

DOI 10.1201/9781003308867-96

The Alhambra stands on the Al Sabika hill. The San Pedro cliff cuts this hill on its North face just in front of San Pedro and San Pablo churches, making up the classical postcard of this important World Heritage Site, Figure 1. It has a height of 65.5 m and has progressed in its deterioration to stand today about 23 m from the walls of the Alhambra. The formation of the San Pedro cliff has been a consequence of the floods of the Darro River and, perhaps, of the seepage and runoff from the Alhambra, as well as of erosion and tectonics.

Figure 1. San Pedro cliff in the foothills of the Alhambra Cultural Heritage (photo: Google Earth).

1.2 *Multi-scale approach for the stability analysis*

In this work, a 3D stability study of the slope in its current state is carried out, at three different scales. The first scale (large-scale) encompasses the Al-Sabika hill (size 800 m × 400 m) and the stability analysis aims to locate the most unstable slope in the study area. The second scale (local-scale) encompasses the San Pedro cliff (approximately 100 × 100 m), this scale is important from the engineering point of view as the stability analysis determine the global stability conditions of the slope as well as the possible effect on the walls of the monument. The third scale (detailed local-scale) is identical to the previous one, but in this case a very high space resolution (up to cm precision) is needed to study erosion phenomena. Challenging stability analysis would determine location of possible areas of material detachments and quantify erosion phenomena.

The proposed multi-scale approach has been defined within the JPI-CH Project PROTHEGO: Protection of European Cultural Heritage from Geo-Hazards (http://www.prothego.eu/) where the effect of different geo-hazards on European Word Heritage Sites were studied (Valagussa et al. 2021). The suggested methodology applied to the Alhambra site can be found in Fernández-Merodo et al., 2018.

2 GEOLOGICAL CONTEXT, GEO-HAZARDS AND MECHANICAL CHARACTERISATION OF THE ALHAMBRA FORMATION

2.1 *Geology*

Granada and its metropolitan area are located in the central sector of the Betic Cordillera and in the contact between de External and Internal zones of the range. The city lies on the eastern edge

of the Granada Basin where the foothills rise into the adjacent Sierra Nevada (3,482 m). The river Genil flows through the centre of the basin and it is joined by smaller tributaries, outstanding the river Darro that divides the old town into two parts: The Alhambra and the Albayzín. The basin is bordered by several faulted, Late Miocene, Pliocene and Quaternary-age alluvial fans, as a result of the rapid uplift and erosion of Sierra Nevada (Braga et al. 1990). They are predominately coarse-grained deposits (conglomerates) which prograde to the centre of the Basin.

2.2 *Geo-hazards*

The particular geological, geomorphic and tectonic setting of Granada determine several natural hazards in the region. Granada has historically been the scene of numerous dramatic natural disasters that have threatened the population and construction throughout history.

Earthquakes have recurred over the centuries, as Granada is located on a seismically active region. In fact, Granada is at the maximum seismic hazardous area of Spain. The historical record of earthquakes in Granada reveals at least nine large events with the epicenters close to the city. One of the most destructive was the 1431 earthquake, with an epicenter intensity of IX (MSK scale) and an estimated magnitude (Mw) of 6.5. This earthquake destroyed many Nasrid palaces in the surroundings of the Alhambra fortress and delayed the conquest of the city by the Christians until 1492. In 1884, the Andalusian earthquake took place, with the epicenter located in the locality of Arenas del Rey (53 km from Granada). With an epicenter intensity of IX (MSK scale) and an estimated magnitude (Mw) of 6.8, the Andalusian earthquake caused great damage in a large area of the provinces of Granada and Málaga. Sanz de Galdeano and Alfaro (2004) postulate that many faults could potentially generate earthquakes with magnitudes as great as Mw 6.0 in the surroundings of Granada.

In Granada, the Mediterranean climate alternates periods of droughts and heavy rains; flooding is very frequent. Most floods in Granada are related to the ephemeral behavior of the river Darro and they have been historically documented for a long time. In fact, the river was channeled under the city at the end of the XIX century to avoid the periodical flash floods. The river still runs openly through the old city, between the Alhambra and the Albayzín hills. The river Darro was basically incised in the conglomerates of the Alhambra Formation with an incision rate of 0.2–0.4 mm/yr and partially controls the slope dynamics of the San Pedro escarpment. Floods in the Darro occur with a return period of 20 years and a peak discharge of 90 m3/s (Azañón et al. 2007). The historical data on floods in Granada include documents from the beginning of the 12th century, when the area was under Moorish rule. Nevertheless, the more precise information is related to 59 years of floods recorded between1478 and 2010 (Páez 1996). The Darro's flood in 1478 caused severe damage in the Albayzín and numerous fatalities. On March 1660, another flood generated a large earth-fall in the San Pedro cliff. From the historical data, the increasing incidence of floods with urban development shows the highest rate in the late 20th century (Chacón et al. 2012).

The slope dynamics in the Granada Basin is very intense. Numerous landslides, rock and earth falls, solifluctions and debris flows have been well documented for a long time. The inventory developed by Chacón et al. (2007) reports almost 300 landslides affecting 28 km^2 in the eastern border of the Granada Basin, and close to the city. The Lisbon (1755) and the Andalusian (1884) earthquakes affected the nearby village of Güevéjar which had to be moved twice because a large landslide. The last regional rainfalls triggering large amount of landslides occurred in 1996–1997 (Irigaray et al. 2000). Recently, the rainy winters of 2010–2013 caused some failures in the surroundings of the Alhambra. That is the case of the Jesús del Valle landslide, a complex landslide which affected an area of 50.000 m^2 and distorted the course of the river Darro in January 2010 (Ferreira et al. 2015).

In the San Pedro Cliff, numerous earth-falls and debris flows have been documented. One of the latest took place in February 2013 after a heavy period of rain. In general, the retreat of the escarpment is very slow, except in its western part where the presence of traction joints parallel to the slope suggest a faster retreat by the slope dynamics. At present, the base of the cliff is covered by a debris cone that protects it from the river Darro undercutting.

2.3 *Mechanical characterization of the Alhambra formation*

Results of mechanical characterization performed by University of Granada are summarized in reference Justo et al. 2008. Core logs of two performed boreholes S-1 and S-2 in the San Pedro cliff are recalled from this reference in Figure 2. Table 1 presents also a summary of the most important tests that were carried out on the different material layers.

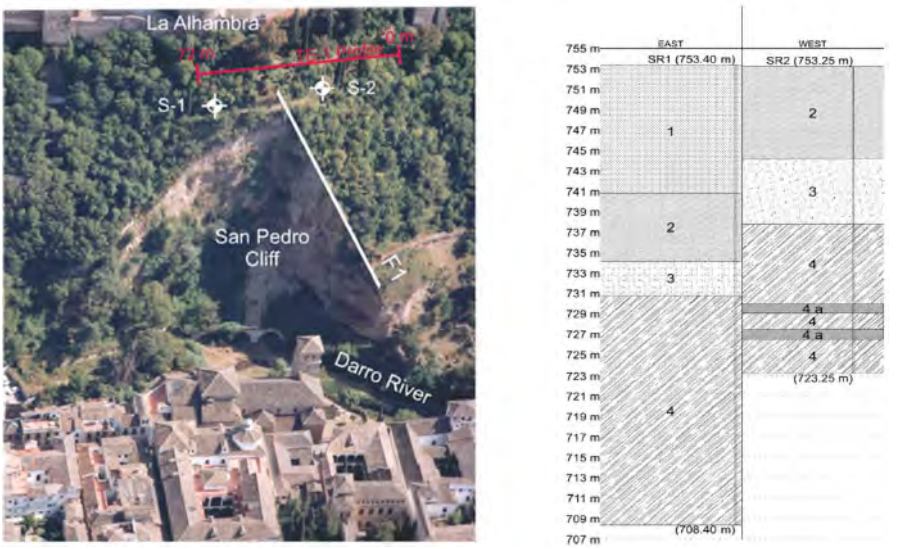

Figure 2. Left: San Pedro Cliff, showing location of the two performed boreholes S-1 and S-2 perpendicular to the inferred fault F1. Right: Core logs of boreholes S-1 and S-2 which suggests a fault throw of about 7 m. Materials: 1. Dense conglomerate; 2. Very dense conglomerate; 3. Moderately dense conglomerate; 4. Very dense, gravely and sandy conglomerate; 4a. Clay layer (from Justo et al. 2008).

Table 1. Average properties for the different layers of Alhambra conglomerate (from Justo et al. 2008).

		Classification tests				Strength tests			From plate loading test		Pressuremeter tests			Geophysical		
							Drained direct shear test									
Layer no.	k (m/s)	<0.08 mm (%)	w_L	I_P	USCS	σ_{ci} (kPa)	c' (kPa)	Φ'	Loading E_m (MPa)	Unloading	E_M (MPa)	p_l^* (kPa)	Φ' est. (°)	V_P (m/s)	V_S (m/s)	E_d (MPa)
1	3×10^{-7}	12.6	22	6	GC-GM				397	1772	60	2700	38	1500	800	3700
2	9×10^{-6}	22.0	24	6	GC-GM				601	2683			40	2000	960	5600
3	2×10^{-7} to f.d.	27.8	22	2	SM				397	1772	33	2300	37	1500	800	3700
4	6×10^{-10} to f.d.	35.2	21	7	SC-SM GM				891	3976	115	7400	44	2400	1150	8300
4a	7.7×10^{-7}	79.4	28	11	CL	394	34.5	33.4°	109	485	42	4500	41	1500	800	3700

f.d. = free drainage. est. = estimated value. p_l^* = net pressuremeter limit pressure. E_M = pressuremeter modulus, V_P = longitudinal wave velocity. V_S = transverse wave velocity. E_d = dynamic modulus. σ_{ci} = uniaxial compressive strength.

New CT-Tomography has been performed on a sample of Alhambra conglomerate (Figure 3). Three kind of coarse material has been recognized: i) weak cemented matrix, ii) strong cemented matrix, and iii) boulders.

Twelve point load test has been performed on the specimen. Obtained uniaxial compressive strengths are: 9.27 MPa in the weak cemented matrix, 46.27 MPa in the strong cemented matrix and 149.93 MPa in the crushed boulders, these values correspond to main results. Needle Penetrometer test on the weak cemented matrix give a uniaxial compressive strength value around 12–13 MPa. Indentation tests were performed in two material samples. The tangent Young's modulus E50 in

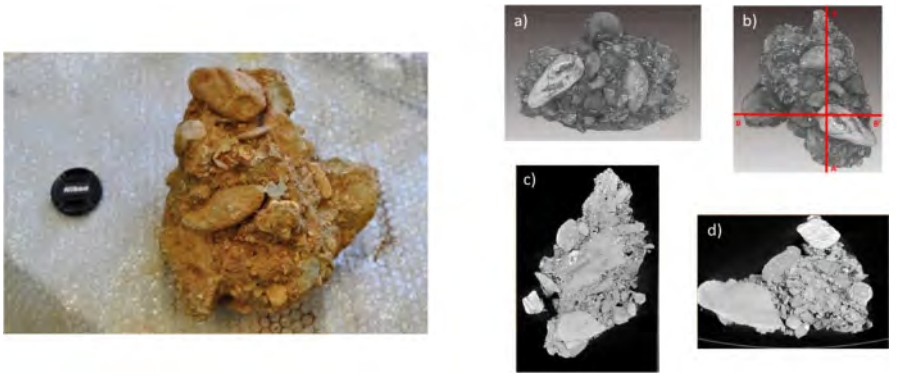

Figure 3. Left: 30 cm diameter sample of Alhambra conglomerate. Right: a) CT-Tomography on a sample of Alhambra conglomerate. b) Definition of A-A′ and B-B ortho sections. c) A-A′ Ortho-Section picture. d) B-B′ Ortho-Section picture.

uniaxial compression are equal to 2.476 and 3.889 GPa respectively and the uniaxial compression strength (UCS) are equal to 53.26 MPa and 41.24 MPa respectively.

3 MONITORING

Monitoring aims to control land deformation that could affect the studied Cultural Heritage. Due to its proximity to the Alhambra walls and the risk associated to it, evolution of San Pedro cliff has been observed for a long time. It is possible to follow the local erosion process from historical paintings and from historical pictures. It is worth mentioning the monitoring work done by the Department of Geodynamics of the University of Granada in the last 10 years, using for instance modern technics as the Terrestrial Laser Scanner (TLS). From all the observations, the erosion rate has been estimated to 1,85 cm/year.

In the following, results of Terrestrial Laser Scanner monitoring and new UAV (Unmanned Aerial Vehicle) Photogrammetry control are presented.

3.1 *TLS monitoring (2017–2018)*

Terrestrial laser scanning (TLS) is a ground-based, active imaging method that rapidly acquires accurate, dense 3D point clouds of object surfaces by laser range finding. A TLS apparatus (LEICA ScanStation C10) was installed in the bell tower of San Pedro church located just in front the cliff 30 meters away (Figure 4).

Figure 4. TLS monitoring from the bell tower of San Pedro church.

The difference between point clouds generated in July 2017 and February 2018 is showed in Figure 5, a small area of material (zone 1) 0.6 m deep in the apex of the dihedral is missing. This erosion process coincides with an earthflow occurred the 6 January 2018. A small second area named 2 can also be recognized in Figure 5.

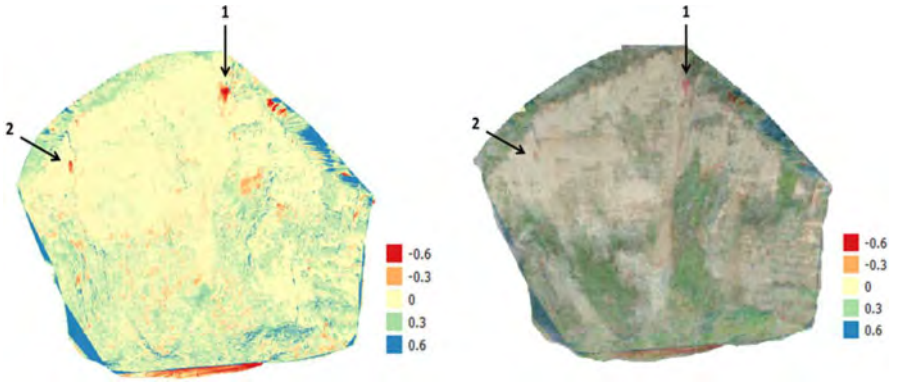

Figure 5. TLS monitoring results in San Pedro cliff: difference between July 2017 and February 2018 (in m). Left: without picture in the background layout. Right: with picture in the background layout.

3.2 *UAV Photogrammetry monitoring (2017–2018)*

In the context of PROTHEGO project, two UAV operations were programmed to control deformation and erosion process in the San Pedro cliff. The first one was programed the 5 July 2017 during the summer season and the second one, seven months later, the 1st February 2018 during the winter season. The UAV operations consist on an automatic overhead flight and three manual oblique flights along the cliff at different heights. The drones (Phantom 4 Pro) were controlled from the bell tower of San Pedro church.

452 pictures and 432 were taken during the summer and winter campaigns respectively. Photogrammetry processing were made over these pictures using Agysoft PhotoScan 1.2.6 64 bits, Pix4Dmapper 4.1.10 64 bits and ArcGIS Desktop 10.5 software.

Figure 6 depicts the two generated high resolution point clouds, the left side corresponds to July 2017 with 26 million points, the right side corresponds to February 2018 with 11.6 million points. Some differences are glaring. First of all the coverage vegetation is much more pronounced during the summer season. Second and much more important an earth flow can be detected in the apse of the cliff who acts as a corridor. This event occurred the 6 January 2018 after an important snow event.

Figure 6. UAV photogrammetry monitoring results in the San Pedro cliff. Dense point clouds. Left: July 2017. Right: February 2018.

In order to make a better quantification of the difference between the two photogrammetry scannings and more precisely in order to better characterise the 6 January 2018 earth flow, a 3D cloud distance computation has been realized using M3C2 plugging (Lague et al. 2013) in PointCloud software. A vegetation cleaning has been firstly performed. The results of the computed cloud distance are shown in Figure 7. It can be seen that eroded material comes from the top of the cliff, just in the right side of the apex, zone 1. Using the recorded 0.60 m depth, the volume of the detached material can be approximated around 2 m^3, the initial and final position can be identified in Figure 7-right. It seems also that some soil swelling (0.4 m), zone 3, has been recorded also on the top the cliff.

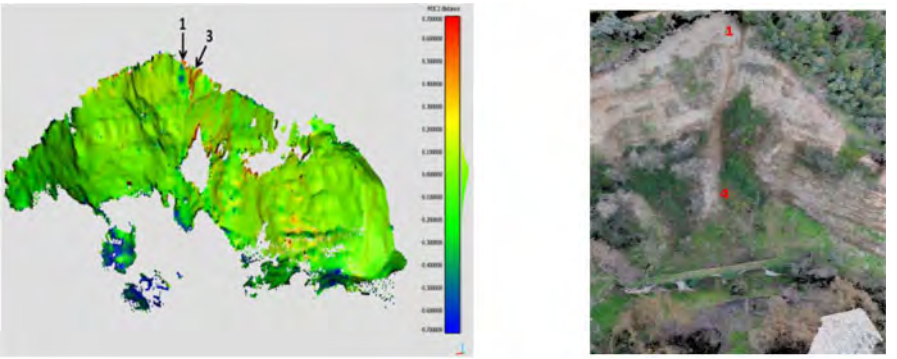

Figure 7. Leftt: Point cloud distance between the photogrammetry scannings performed in July 2017 and February 2018. Right: Initial and final position of the material detached on the 6th January 2018.

4 STABILITY ANALYSIS

Stability analysis of the whole Cultural Heritage can be very useful as it can detect where landslide phenomena are prone to happen. Moreover in the San Pedro cliff specific case, a stability analysis can give a very useful picture of the stability conditions of the site.

Different source data has been used for the topography depending on the chosen scale. Digital elevation model (DEM) obtained from LIDAR has been used in the case of the large-scale modelling, DEM obtained from a traditional topographic map has been used in the case of the local-scale modelling and point cloud obtained from TLS acquisition has been used for the detailed local-scale modelling.

For the in core geometry no material stratigraphy has been considered, only one homogeneous material has been contemplated in all the scale analysis. In one hand, stratigraphy for large scale analysis is difficult to determine. In the other hand, new 2D stability computation for local scale analysis with homogenous material has been compared to the previous published multilayer hypothesis revealing that this simplifying assumption has no influence on the computed stability factor and failure mechanism.

Constitutive behaviour has been described using a Mohr-Coulomb failure criteria based on the parameters given in Table 1. Average parameters for the all in one equivalent material are: dry density $\gamma = 2100$. Kg/m3, friction angle $\phi = 40°$ and cohesion c = 90 KPa. Although pore-water-pressure seems to play an important role in the stability and erosion process in the San Pedro cliff, no hydro-mechanical coupling has been considered in the proposed analysis.

Displacements have been fixed in the bottom surface and in the perpendicular direction of the lateral sides. Only gravity load is considered.

Stability analysis has been performed using the Shear-Strength Reduction technique and the numerical algorithms described in Fernández-Merodo et al., 2014 and Bru et al., 2017.

4.1 *Large-scale stability analysis*

A large-scale stability analysis has been performed in the Al Sabika hill (Figure 8-a) using a digital elevation model (DEM) generated from a LIDAR acquisition performed in 2000 by the Regional Government of Andalousia (3 m × 3 m resolution). In this case the 3D finite element mesh has been generated over the red rectangle, size 800 m × 400 m. The 3D finite element mesh consists of 168.399 tetrahedral elements and 3.5 million nodes with a characteristic element size equal to 3 m matching the LIDAR resolution.

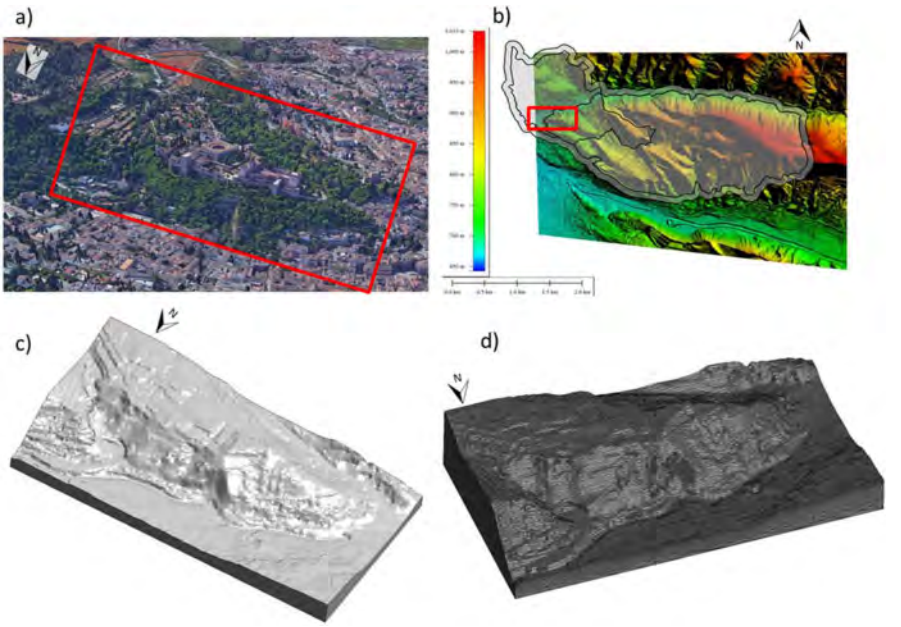

Figure 8. Large-scale model (800 m × 400 m). a) Google earth photo. Red rectangle: analyzed sector. b) Digital elevation model (DEM) generated from a LIDAR acquisition performed in 2000. Red rectangle: analyzed sector. c) Generated volume. d) 3D finite element mesh (168.399 tetrahedral elements).

The stability analysis indicates that the most critical slope in the studied domain is the San Pedro cliff with an associated stability factor FS around 2. Figure 9 depicts the failure mechanisms by plotting displacement contours, displacement vectors and plastic strain contours at failure. Due to the coarse mesh the computed value of the FS must be taken only as a first indicator, not valid for design purpose. It is known that, using a Mohr-Coulomb failure criteria, failure mechanism and plastic deformation develops along a shear surface, the mobilized mass slides along this shear surface with a typical rigid-body motion (Fernández-Merodo et al. 2014). In this case, inspecting Figure 9-c and Figure 9-d, the plastic deformation does not concentrate along a thin surface due to the coarse mesh.

Due to the geo-mechanical assumptions, especially due to the homogeneous material assumption, and the considered coarse mesh this large-scale model stability analysis must be taken only as a kind of landslide susceptibility analysis due to topography. The result indicates that the San Pedro cliff is the most critical slope in the studied domain. Following the proposed multi-scale approach, a local-scale modelling of the slope is proposed in the next section.

4.2 *Local-scale stability analysis*

Local-scale stability analysis has been performed in the San Pedro cliff (Figure 10-a) using a topographic map done in 2007 (Figure 10-b). In this case the 3D finite element mesh has been

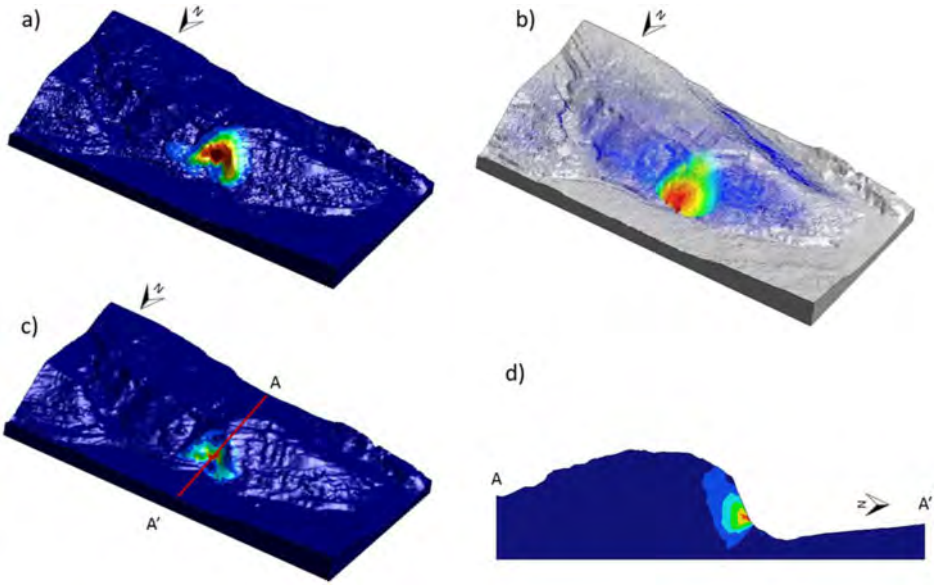

Figure 9. Large-scale model (800 m × 400 m). a) Displacement contours at failure. b) Displacement vectors at failure. c) Equivalent plastic strain contours at failure. d) Equivalent plastic strain contours at failure in section AA'.

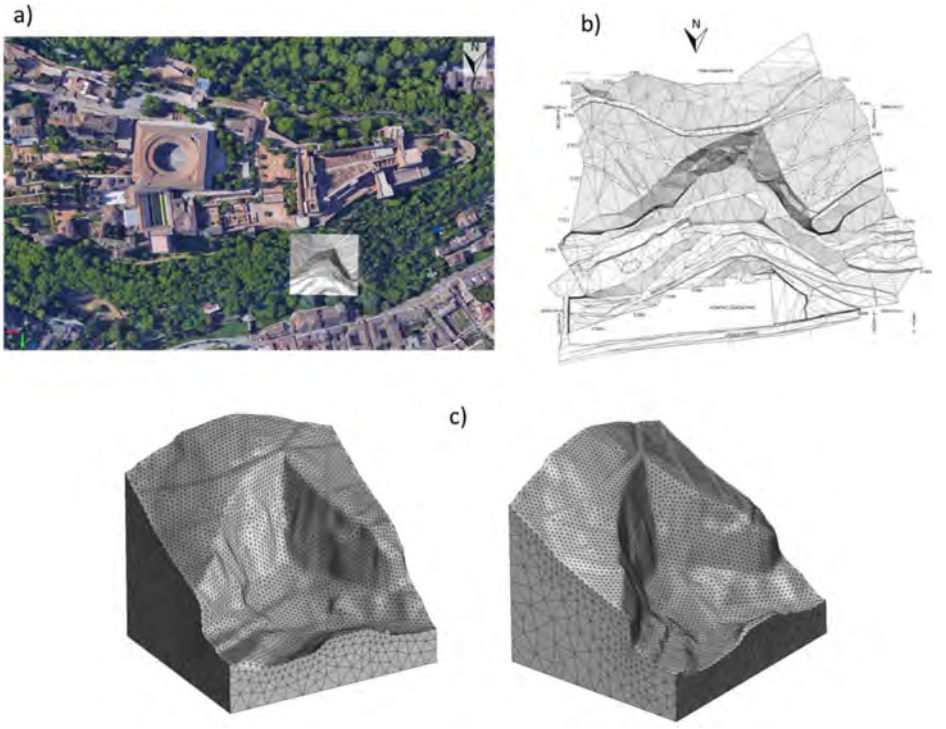

Figure 10. Local-scale model (100 m × 100 m). a) Google earth photo. Grey square: analyzed sector. b) Topographic map. c) 3D finite element mesh (46.340 quadratic tetrahedral elements).

generated over the grey square, size 100 m × 100 m. The 3D finite element mesh consists of 46.340 quadratic tetrahedral elements and 70.889 nodes with a characteristic element size equal to 1 m.

The computed safety factor Fs is in this case equal to 1.5. It has been checked that using a finer mesh the computed Fs is similar around 1.5. The 3D failure mechanism is depicted in Figure 11, where the displacement vectors (Figure 11-b), displacement contours (Figure 11-c) and equivalent plastic strain (Figure 11 d) at failure are plotted. Plastic deformation develops along a shear surface, the mobilized mass slides along this shear surface with a typical rigid-body motion. It can be observed in Figure 11-a that the computed global failure attains the wall foundations of the Alhambra citadel located 23 meters behind the Cliff.

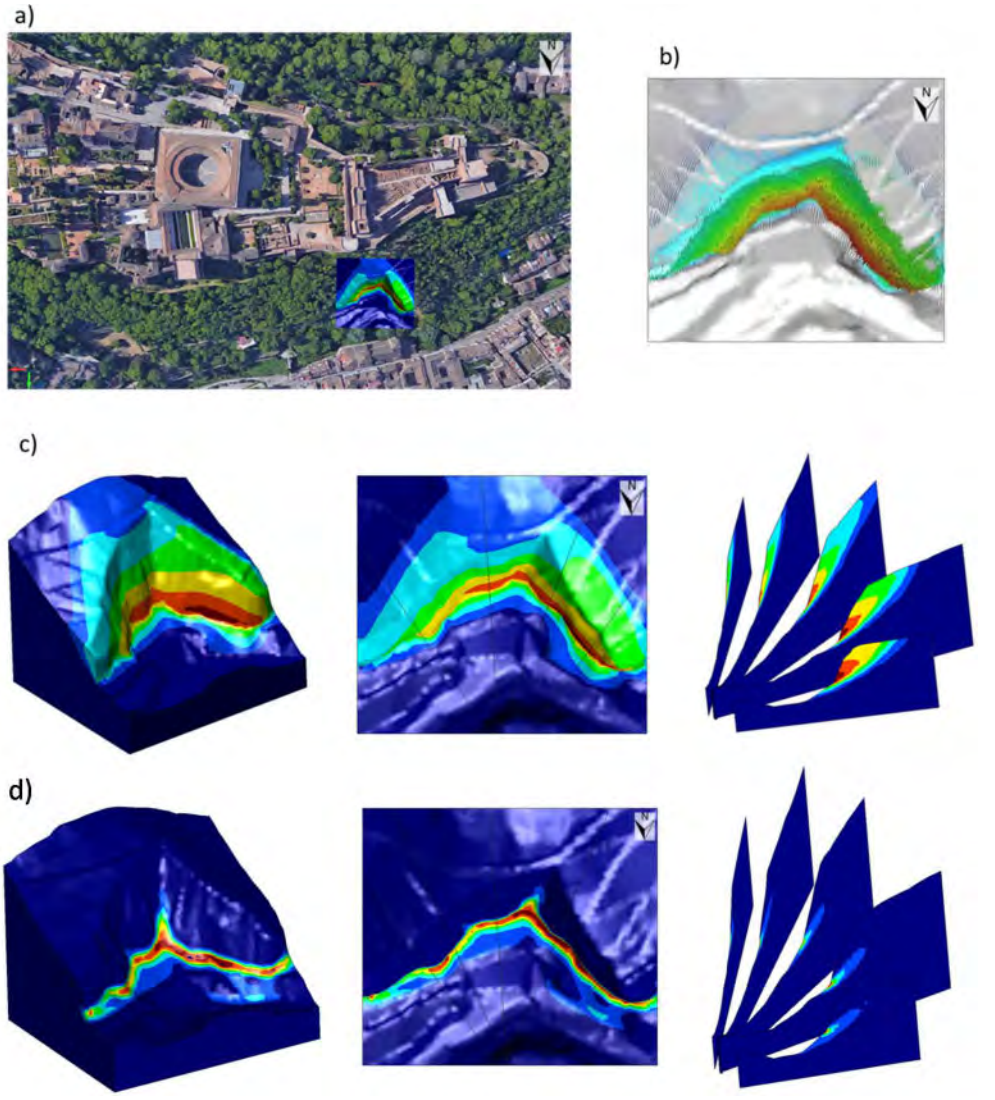

Figure 11. Local-scale model (100 m × 100 m). a) Google earth photo with displacement contours at failure. b) Displacement vectors at failure. c) Displacement contours at failure (3D view, plan view, sections view). d) Equivalent plastic strain contours at failure (3D view, plan view, sections view).

4.3 *Detailed local-scale stability analysis*

The global failure mechanism obtained in the previous local-scale modelling is not representative of the local superficial erosion and scarp retreat observed (Figure 7-right) and recorded by the monitoring. A new numerical analysis is made using the point clouds generated by the TLS scanning performed the 5 July 2017.

The point clouds are filtrated with a 0.1 m distance resolution obtaining the surfaces depicted in Figure 12-left. Volumes are generated from these surfaces by a 5 m extrusion on a perpendicular direction. It is expected that erosion phenomena appears on the surface always bellow this 5 m distance. The bottom surface is fixed and only gravity load is considered. The proposed "detailed local-scale" stability analysis aims to determine location of possible areas of material detachments and quantify erosion phenomena, trying to reproduce the small earthflow occurred the 6 January 2018.

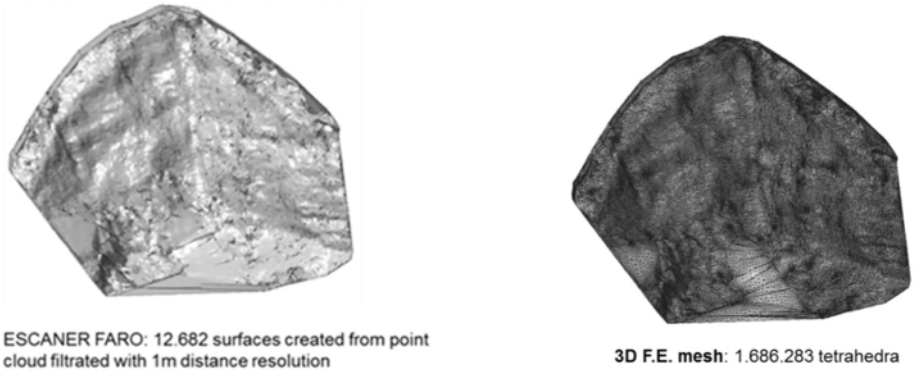

Figure 12. Detailed local-scale model. Left: generated volumes from TLS point clouds (18/04/2007). Right: 3D finite element mesh.

The generated finite element mesh is depicted in Figure 12-right and is quite huge reaching about 1,7 million tetrahedrons. Speed computation and hardware memory are still important restrictions to do high resolution stability analysis (non-linear analysis) but can be addressed using parallel computation technics (PARDISO solver) and a classical workstation.

The computed safety factor Fs is in this case equal to 2.4. The results of the computed displacements contours at failure are depicted in Figure 13. No small detachment has been identified, the failure mechanism affects the left side of the escarpment indicating that this zone could be more

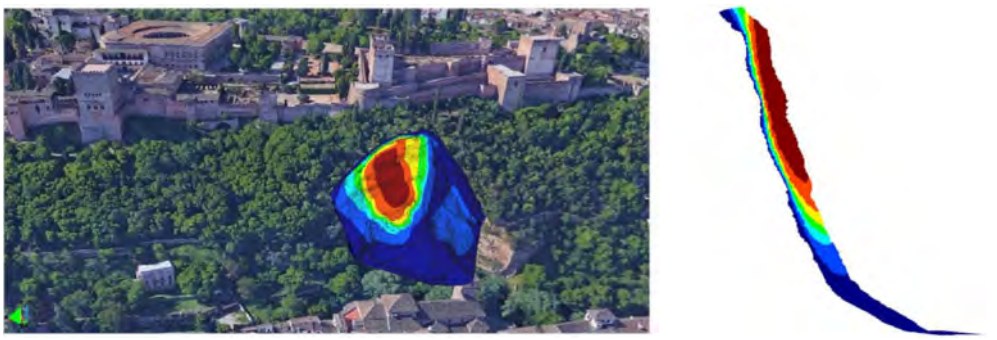

Figure 13. Detailed local-scale model. Left: Computed displacement contours at failure projected on a San Pedro cliff picture. Right: Section view of the computed displacement contours at failure.

prone to instability. These first results have to be taken with caution due to the assumed hypothesis and are discussed in the following section.

5 DISCUSSION AND CONCLUSIONS

Alhambra is an important Word Heritage site that is prone to suffer flood, earthquake and landslide phenomena. Dated monitoring based on historical paintings and historical pictures and modern monitoring based on TLS and UAV Photogrammetry of the San Pedro cliff indicate that the slope is continuously deteriorating due to slow erosion processes. The erosion rate has been estimated to 1,85 cm/year.

In this work, a multi-scale stability analysis of the slope in 3D in its current state has been proposed in order to determine stability conditions of the site. From the large-scale stability analysis results it could be deduced that the San Pedro cliff is the most critical slope in the Al-Sabika hill. The local-scale stability analysis indicates that slope is stable from a global static perspective with a computed Factor of Safety equal to 1.5. Nevertheless, it has to be pointed that occurrence of an earthquake (Granada is located at the maximum seismic hazardous area of Spain) would dramatically reduce the computed static stability conditions. Furthermore, the computed global failure just attains the wall foundations of the Alhambra citadel located 23 meters behind the Cliff.

The proposed detailed local-scale stability analysis was intended to determine location of possible areas of material detachments and quantify erosion phenomena, trying to reproduce the small earthflow occurred the 6 January 2018. Results of the proposed analysis do not identify small detachments, rather a failure mechanism on the left side of the escarpment indicating that this zone could be more prone to instability according to the adopted assumptions. These assumptions can now be discussed. Firstly, it has to be mentioned that effect of water, pore-water pressure, humidity or the presence of degraded material have not been taken into account. The dihedral edge in the middle of the San Pedro cliff represents a preferential pathway for water runoff during rain events. Even physical countermeasures have been taken over the top of the slope to avoid water runoff, the observed recent detachments localize in this area. Secondly, no fault and no traction joints parallel to the slope have been introduced in the model, presence of some kind of discontinuities would affect and worsen not only the local stability conditions but also the global ones. Finally, the mesh size, that is a computational restriction in the detailed local-scale analysis, would influence the stability results. It has to be mentioned that the adopted mesh size do not fit the space resolution of the point cloud generated by the TLS scanning and the use of finer meshes could show localization of smaller failure mechanisms. Take into account all these effects that have not been considered up to now, in a new enhanced model represents a challenging research work.

There is no doubt that further studies and probably mitigation actions should be carried out in order to preserve integrity of the slope and the foundation of the Cultural Heritage monument.

ACKNOWLEDGMENTS

The research leading to these results has been supported by the PROTHEGO Project (Protection of European Cultural Heritage from Geo-hazards), funded through the framework of the Joint Programming Initiative on Cultural Heritage and Global Change (JPICH), and under ERA-NET Plus and the Seventh Framework Program (FP7) of the European Commission.

REFERENCES

Azañón, J.M., Azor J.L., De Justo Alpañés, J., Martín Rosales, W., Mateos, R.M., Pérez-Peña, V. (2007). Deslizamientos E Inundaciones Cuaternarias En La Cuenca Vertiente Del Río Darro: La Génesis Del Tajo De San Pedro (La Alambra, Granada). Resúmenes Xii Reunión Nacional De Cuaternario. 13–14. Ávila, 2007.

Braga, J.C., Martín, J.M. And Alcalá, B. (1990). Coral Reefs In Coarse-Terrigenous Sedimentary Environments (Upper Tortonian, Southern Spain): Sedimentary Geology, Vol. 66, No. 1–2: 135–150.

Bru, G., Fernández-Merodo, J.A., García-Davalillo, J.C., Herrera, G. And Fernández, J. (2017). Site Scale Modeling Of Slow-Moving Landslides, A 3d Viscoplastic Finite Element Modeling Approach. Landslides. Doi 10.1007/S10346-017-0867-Y

Chacón ,J., Irigaray, C., Fernández, T. (2007). Movimientos De Ladera. In Ferrer, M. (Coordinator), Atlas Provincial De Riesgos Naturales En Granada: Diputación Granada-Igme, Spain. Pp. 45–82, Maps 1:200,000/400,000, 1 Cd.

Chacón, F., Irigaray, C., El Hamdouni, R., Valverde-Palaciuos, I., Valverde-Espinosa, I., Calvo, F., Jiménez-Perálvarez, J., Chacón, E., Fernández, P., Garrido, J., Lamas, F. (2012). Engineering And Environmental Geology Of Granada And Its Metropolitan Area (Spain). Environmental And Engineering Geoscience. Vol Xviii, 3:217–260.

Fernández-Merodo, J.A., García-Davalillo. J.C., Herrera, G., Mira, P., Pastor, M. (2014) 2d Viscoplastic Finite Element Modelling Of Slow Landslides: The Portalet Case Study (Spain). Landslides 11: 29–42

Fernandez-Merodo, J.A., Mateos, R., Azañon, J.M., Ezquerro, P., García-Davalillo, J.C., Lorenzo, C., Hernandez, M., Bejar, M., Herrera, G., Castellanza, R. (2018). PROTHEGO Deliverable D.06.01: PROTHEGO PILOTS: THE ALHAMBRA. Local scale investigation, monitoring and advanced modelling of the geohazards affecting the Alhambra World Heritage Case Study Site Version 1.3. JPI-CH Heritage Plus PROTHEGO project, Open Report. Date 11/05/2018. 66 Pages. Available at: http://www.prothego.eu/

Ferreira, T., Mateos, R.M., Roldán, F.J. (2015). Los Deslizamientos De La Cuenca Baja Del Río Darro (Granada, España). Geogaceta, 57: 103–106.

Irigaray, C., Lamas, F., El Hamdouni, R., Fernández, T., Chacón, J. (2000). The Importance Of Precipitation And The Susceptibility Of The Slopes For The Triggering Of Landslides Along The Roads: Natural Hazards, Vol. 21, No. 1, Pp. 65–81.

Justo, J.L., Azanón J.M., Azor, A., Saura, J., Durand, P., Villalobos, M., Morales, A., Justo, E. (2008) Neotectonics And Slope Stabilization At The Alhambra, Granada, Spain. Engineering Geology 100, 101–119

Lague, D., Brodu, N. And Leroux, J. (2013) Accurate 3d Comparison Of Complex Topography With Terrestrial Laser Scanner: Application To The Rangitikei Canyon (N-Z). Isprs Journal Of Photogrammmetry And Remote Sensing 80, P. 10–26

Páez, J. (1996). El Clima De Al-Andalus. In Chacón J. And Rosúa J. L. (Editors), I Conferencia Internacional De Sierra Nevada, Vol. 5: University Of Granada, Granada, Spain, Pp. 9–21.

Sanz De Galdeano, C. And Alfaro, P. (2004), Tectonic Significance Of The Present Relief Of The Betic Cordillera: Geomorphology, Vol. 63, No. 3–4, Pp. 175–190.

Valagussa, A., Frattini, P., Crosta, G., Spizzichino, D., Leoni, G. & Margottini, C. (2021). Multi-risk analysis on European cultural and natural UNESCO heritage sites. Nat Hazards 105, 2659–2676. https://doi.org/10.1007/s11069-020-04417-7

Geotechnical Engineering for the Preservation of Monuments and Historic Sites III – Lancellotta, Viggiani, Flora, de Silva & Mele (Eds)

Geotechnical and historical aspects on the collapse of the Tiber embankment walls in the centre of Roma (1870–1900)

F. Casini, A. Pucci, I. Giannetti & G. Guida
Dipartimento di Ingegneria Civile e Ingegneria Informatica (DICII)
Università degli Studi di Roma Tor Vergata (IT)

ABSTRACT: This paper deals with the issues related to the construction of the Tiber's embankment walls between years 1870–1926. The embankment walls (*muraglioni)* were designed by Raffaele Canevari to mitigate the effects of the river inundation in the city centre of Roma. After the flood of December 1900, several portions of the Anguillara and Alberteschi sections collapsed.

The aim of this work is to investigate whether the causes of the collapse can be traced back to design approaches of the time, lacking from a point of view of the hydro-mechanical interaction of the soil in the evaluation of the total earth pressure. In particular, designed calculations are also revised accounting for more advance soil phenomena laws, based on Terzaghi effective stress and the effects of scouring and erosion. Some assumptions have been made on the mechanical characteristics of the backfill soils and on the relying on foundation materials.

1 INTRODUCTION

The second part of the 19th century saw the construction of several urban river defence works in European cities such as Paris (Sein River, Lestel et al. 2020), London (Thames, Porter 1998), Vienna (Danube, Hohensinner et al. 2013), Budapest (Danube, WHC 1987). The new infrastructures were built according to the methods available at that time, in particular computing the earth pressure on the retaining walls were based on graphical methods developed by Rebahn (Rebahn, 1871) and Culmann (Culmann 1864–66).

Several urban history related studies (Segarra Lagunes 2004) report the stages that lead to the construction, starting from the year 1870, of the Tiber embankment walls as flood-control system for the historical centre of Roma. However, a proper geotechnical critical analysis, especially related to the issues related to the collapse of some sections of the embankments, is still missing in the technical literature. This paper aims at providing a contribution for bridging this gap, focusing on the description of the collapse events occurred during the exceptional Tiber flood of 1900. The study is based on the archive documents produced by the *Ufficio Speciale per la Sistemazione del Tevere* (Special Office for the River Tiber), conserved in the Rome State Archive within the Genio Civile collection (Giannetti & Casini 2021).

In the following the design and the construction history of the embankment walls are summarized with emphasis on the sections damaged by the 1900 flood, followed by a description of the collapse as reported in the historical sources. Finally, the geotechnical ultimate limit states (SLU-GEO) are evaluated based on the NTC2018 and on the D.M. 1988 in order to retrace the possible causes that induced collapse.

 DOI 10.1201/9781003308867-97

2 DESIGN OF THE TIBER'S RETAINING WALL

In the late December 1870 an inundation hit the centre of Rome, the water level of 17.22 m above the 0 was measured in the Ripetta gauge. Thus, a technical committee has been established to regulate the river floods led by the Engineer Carlo Possenti (1806–1872), inspector of the Genio Civile and vice president of the *Consiglio dei Lavori Pubblici* (Italian High Council of Public Works) . The members of the committee were the engineers Davicini, Barilari, Betocchi, Turazza, Armellini, Glori, Tatti, Partini, Canevari, Branchini and Castellini. Finally, after 19 meetings, the committee agreed on Raffaele Canevari's proposal for the canalization of the river (Canevari 1875). The latter included, in the urban area – from Sassi di S. Giuliano to S. Paolo – the construction of embankment walls (*muraglioni*) of 17 m high, the tuning of the riverbed at a constant width of 100 m, the construction of two underground tunnels functioning as sewer collectors and large docks, that ran parallel to the walls. The project also provided for the removal of the ruins and other obstacles existing in the riverbed, the embankment of the upper Tiber to the Sassi di S. Giuliano, the removal of one of the two branches of the river at the Tiberina island (as shown in Figure 1).

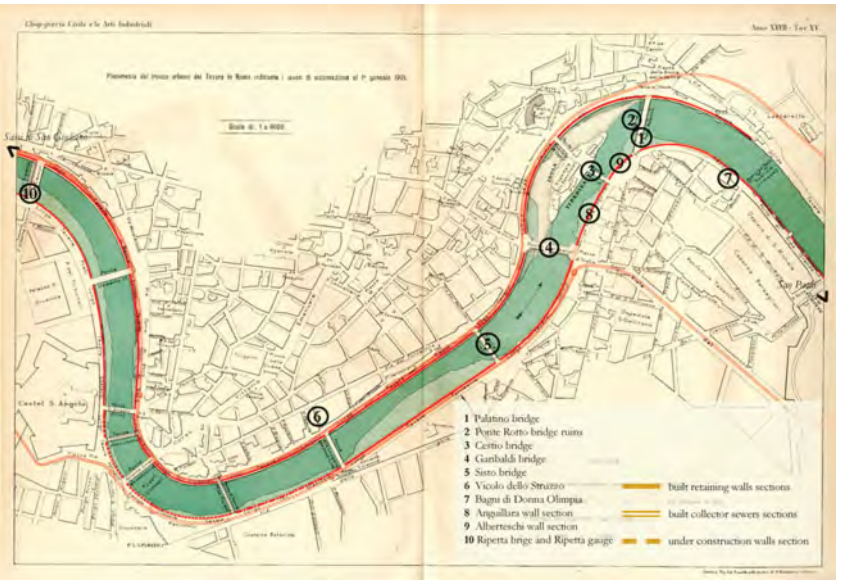

Figure 1. General plan of the Tiber embankment walls and the section between Ponte di Ripetta, on the left, and Ponte Palatino, on the right (L'Ingegneria Civile e le Arti Industriali, 1901) (after Giannetti & Casini 2021).

After years of debates and discussions, on November 29th, 1875, the definitive project for the complete settlement of the urban Tiber river section (Figure 1) has been approved by the High Council of Public Works. The project kept the Canevari conception of the river canalization (high embankment walls, large sewers collectors and docks), introducing two branches of the river around the Tiberina island: the right one width of 70 m and the left width of 60 m (Canevari 1875).

At the end of January 1876, the Special Office for the River Tiber was set up within the Genio Civile with the aims of supervise the project, and coordinate the construction sites (Consiglio Superiore dei Lavori Pubblici 1876).

The works began in the early months of 1877, with the first removal of the ruins and other obstacles existing in the riverbed, in the section between Ponte Sisto and Ponte Rotto (Figure 1), where the water downflow conditions were the most critical. Later, on February 13th, 1878, a further Committee (Commissione di Vigilanza 1877) was nominated to supervise the construction sites, writing an annual report for the Ministry of public works (Canevari 1879).

2.1 *Embankment walls design (1876–84)*

The preliminary design of the wall envisaged a height of 17.60 m, composed of an out-of-water masonry trapezoidal portion, which featured the external wall-line with a slope of 80.54° and a rectangular concrete foundation block. The masonry was composed of tuff blocks, with pozzolanic mortar joints, while the wall external cladding was in bricks (Figure 2a).

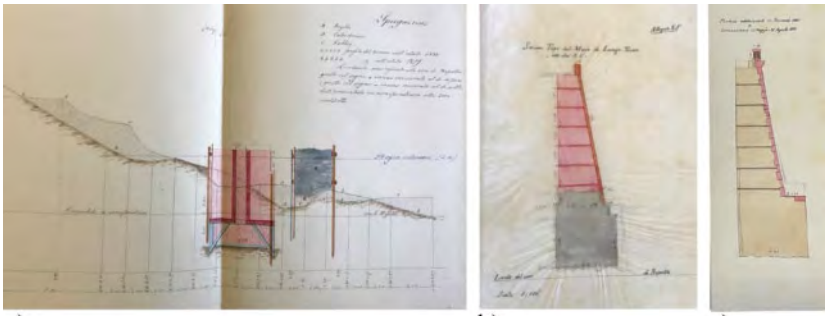

Figure 2. a) study for the use of pneumatic foundations, 1877; b) first design of the retaining walls with bricks coating, 1876; c) execution design of the retaining walls with travertine coating and pneumatic foundations, 1882 (courtesy Rome State Archive, Genio Civile collection).

The foundations of the retaining walls were built adopting the compressed air technology, with large wrought-iron caissons, 2 m high, then filled with concrete (Biadego 1866; Bruno 1895) (Figure 2b). In 1882, the Higher Council of Public Works prescribed the adoption of this foundation technology with minimum deep of −1 m, measured from the 0 of the Ripetta water gauge (Consiglio Superiore dei Lavori Pubblici 1882). Further, the Higher Council of Public Works (Consiglio LLPP 1879) modified the construction details of the standard cross-section of the retaining wall. As shown in Figure 2, masonry composed of tuff blocks with pozzolanic mortar joints were adopted for the whole retaining walls' structure, built on the foundation caissons ceiling. For the external wall-line, a travertine cladding replaced the original design brick coating (Giannetti & Casini 2021).

A lot of the work from *Vicolo dello Struzzo*, on the left riverside, and *Bagni di Donna Olimpia*, on the right riverside (Figure 1), were carried out by the Swiss firm Cornad Zchokke. In December 1900, straight after the work has been completed, a massive river flood occurred, reaching 16.17 m above the 0 of the water Ripetta gauge. During the water level drawdown, large sections of the retaining wall – located in the right riverside of the so-called Anguillara area – collapsed into the river, while deep cracks, mostly vertical, occurred in the nearby retaining wall section (Alberteschi area, Figure 4) and the northern one (Mellini area).

The Anguillara and Alberteschi sections are comprised in the area most damaged by the flood. That portion of the retaining walls ran between Garibaldi and Palatino bridges for about 350 m: the Anguillara section, located between Garibaldi and Cestio bridges, was 240.86 m-long; the second, between Cestio and Palatino bridges, was 111.76 m-long (Figure 3).

The Anguillara and Alberteschi sections are comprised in the area most damaged by the flood. That portion of the retaining walls ran between Garibaldi and Palatino bridges for about 350 m: the Anguillara section, located between Garibaldi and Cestio bridges, was 240.86 m-long; the second, between Cestio and Palatino bridges, was 111.76 m-long (Figure 3).

The geometry of the masonry retaining wall was the same for both the Anguillara and the Alberteschi sections, with small dimensional variations. The walls featured a concrete basement (filling of the caisson) and a rectangular masonry portion located below the standard water level (+5 m on the 0 of the Ripetta water gauge), and a trapezoidal elevation with the external wall line's slope of 80.54° (θ) (respect to the horizontal base-line): the height (h) ranging from 10.61 m to 12.07 m, width at the base (s) ranging from 3 m to 4 m, and width at of top ranging from 1.5 to

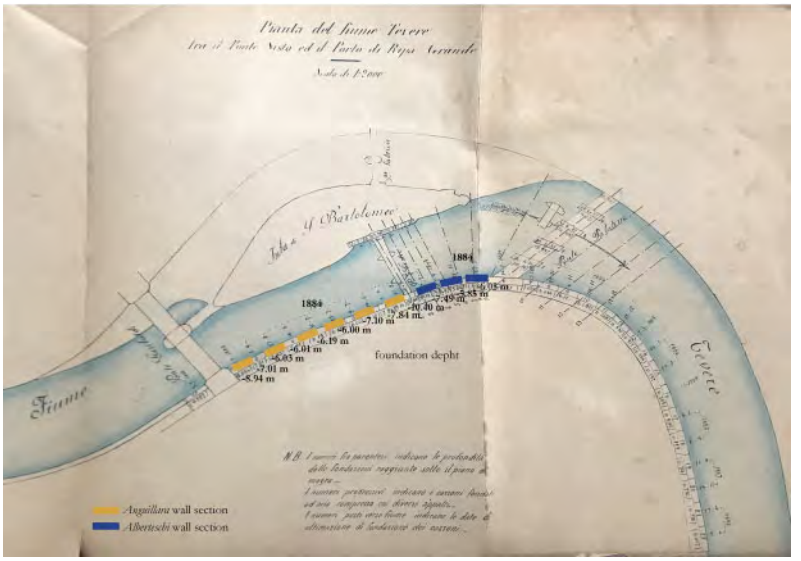

Figure 3. The Alberteschi and the Anguillara retaining walls: plan showing foundation deep and date of construction (courtesy Rome State Archive Roma, Genio Civile collection).

1.8 m (s_1). The foundations of the Anguillara section were laid between −6 m and −7.84 m below the standard water level, reaching the depth of 8.94 m, at the Garibaldi bridge. The foundations of the Alberteschi section featured depths, ranging from 6.00 m to 7.49 m (Figure 3). The masonry wall was composed of tuff blocks with pozzolanic mortar joints, while the inclined external wall-line was coated with squared travertine blocks, with an average thickness of 30 cm. Both the wall cornice and the parapet were in travertine, while the base and the cover of the parapet were in granite (Giannetti & Casini 2021).

3 THE FLOOD EVENT AND THE COLLAPSE OF THE ANGUILLARA RETAINING WALL (1900–01)

A flood with a capacity of 4200 m^3 (second only to the flood of 1538, Bencivegna et al. 1995) hit the historical centre of Roma on 2nd December 1900 at 2 p.m., with a peak height of 16.17 m above the 0 of the Ripetta water gauge. A 10-metre-diameter depression occurred behind the wall at the Cestio bridge axis, along with the flood event. On December 3rd, another depression occurred in the backfilling of the retaining wall, between the Garibaldi and Cestio bridges, that spread from upstream to downstream.

On the 4th December, at 7:24 a.m., when the river waters measured only 10.50 m above the 0 of the Ripetta's water gauge, a first section of the retaining wall – about 15 m long – overturned towards the river.

About three hours later, the next 110 m section of the Anguillara wall, located from 73 m downstream to 37 m upstream of the Garibaldi bridge, collapsed into the river in "three enormous blocks", when the water level, rapidly decreased, measured 9.25 m above the 0 of Ripetta's water gauge.

The Technical Committee of 10 members appointed after the flood, led by engineer and professor Luigi Cremona (1830–1903), was expected to fulfil the following three main tasks:

1) to investigate the accidental or lasting causes of the retaining wall collapse and of all structural damages that occurred during the flood;

2) to study and propose appropriate design strategy for damage repairing and for preventing future structural fails in the embankment walls;
3) to ascertain responsibilities in the design and the construction, by designers, contractors, and supervisors.

The Technical Committee on March 4th 1901 attributed the main causes of the collapse to the undermining of the retaining walls: "From the proof of the details of the disaster it is evident that the ruin of the Anguillara retaining wall is exclusively due to undermining, following the erosion of the foundations (…)" (Cremona 1901).

3.1 *Geotechnical Ultimate Limit Checks before, during and after the flood*

The stability conditions of the embankment walls are evaluated adopting the schematic cross section reported in Figure 4, representing the typical cross section of the Anguillara section.

The soil parameters of the backfilling assumed are a friction angle of $\varphi' = 33°$ and a unit weight $\gamma = 16$ kN/m^3. The active earth coefficient $k_a = 0.27$ is evaluated according to Lancellotta (2007), and by considering an interface friction angle soil-wall of $\delta = 2/3\varphi'$. the horizontal and vertical component of the active thrust coefficient equal to $k_{ah} = k_a \cos\delta = 0.25$ and $k_{av} = k_a \text{sen}\delta = 0.101$ are respectively obtained. For the soil interacting with the foundation of the wall is assumed a unit weight of $\gamma_f = 19$ kN/m^3, an effective cohesion $c'_f = 40$ kPa and a friction angle $\varphi'_f = 40°$. The soil properties adopted agree with the literature data available (Cremona 1901).

The retaining height of the wall is $H_m = 18.26$ m, the width is $B = 4.90$ m, the foundation height $h_f = 2$ m and the service height of the river is $h_w = 6.02$ m from the base of the foundation. The geotechnical ultimate limit states (GEO), consisting of sliding, bearing capacity and overturning verifications, are checked in the following case:

1) standard operation condition, in which the water height is the same both upstream and downstream the wall and equal to $h_w = h_{wud} = 6.02$ m (see Figure 4a, PRE-FLOODING);
2) at the peak of the flooding, assuming $h_w = h_{wud} = 17.17$ m (Figure 4b, MAX FLOODING LEVEL);
3) drawdown to the level of the collapse, with $h_w = h_{wud} = 11.50$ m (Figure 4c, POST FLOODING);
4) drawdown to the level of the collapse with the scouring of the foundation $h_w = h_{wud} = 11.50$ m (Figure 4d, POST FLOODING Scouring), where d_r and e_r are the depth and the width of the scouring;
5) rapid drawdown to the level of the collapse in the river and filtration from the upstream to the downstream with a $\Delta h_w = h_{wu} - h_{wd} = 17.17 - 11.50 = 5.67$ m (Figure 4e, POST FLOODING Seepage).

Depth and width, $d_r = 1.7$ m and $e_r = d_r \cdot \tan(25°) \cong 0.80$ m respectively, of the scouring under the embankment wall foundation are evaluated according to Equation (1) after Froehlich (1989), obtained by analysing 170 live-bed scour measurements in laboratory flumes.

$$d_r = 2.27 \cdot K_1 \cdot K_2 \cdot y_a \cdot \left(L'/y_a\right)^{0.43} F^{0.61} \tag{1}$$

in which $L' = 4.9$ m is the length of active flow obstructed by the retaining wall, $y_a = 11.5$ m is the average depth of the flow, $F = 0.078$ is the Froude Number of the approaching flow upstream the wall, $K_1 = 0.55$ is a shape coefficient and $K_2 = 1$ is the coefficient for the angle between the retaining wall and the flow direction . In this case $d_r = 1.70$ m.

Finally, the effect of seepage is evaluated with a hydraulic head difference $\Delta h_{w_{u,d}} = 5.67$ m and a hydraulic gradient, $j = \Delta h_{w_{u,d}} / \left(h_{w_{up}} + B\right)$ evaluated considering a linear hydraulic head dissipation along the upstream side $h_{w_{up}}$ and the base B of the embankment wall. This induces an upstream distribution of the porewater pressure that is less than hydrostatic along $h_{w_{up}}$.

The stability analyses of the five cases reported in the bullet list are checked according to the past Italian code D.M. 1988 based on global safety factors and to the actual Italian code NTC2018 (DA2-A1+M1+R3) based on partial safety factors. The results are summarized in table 1.

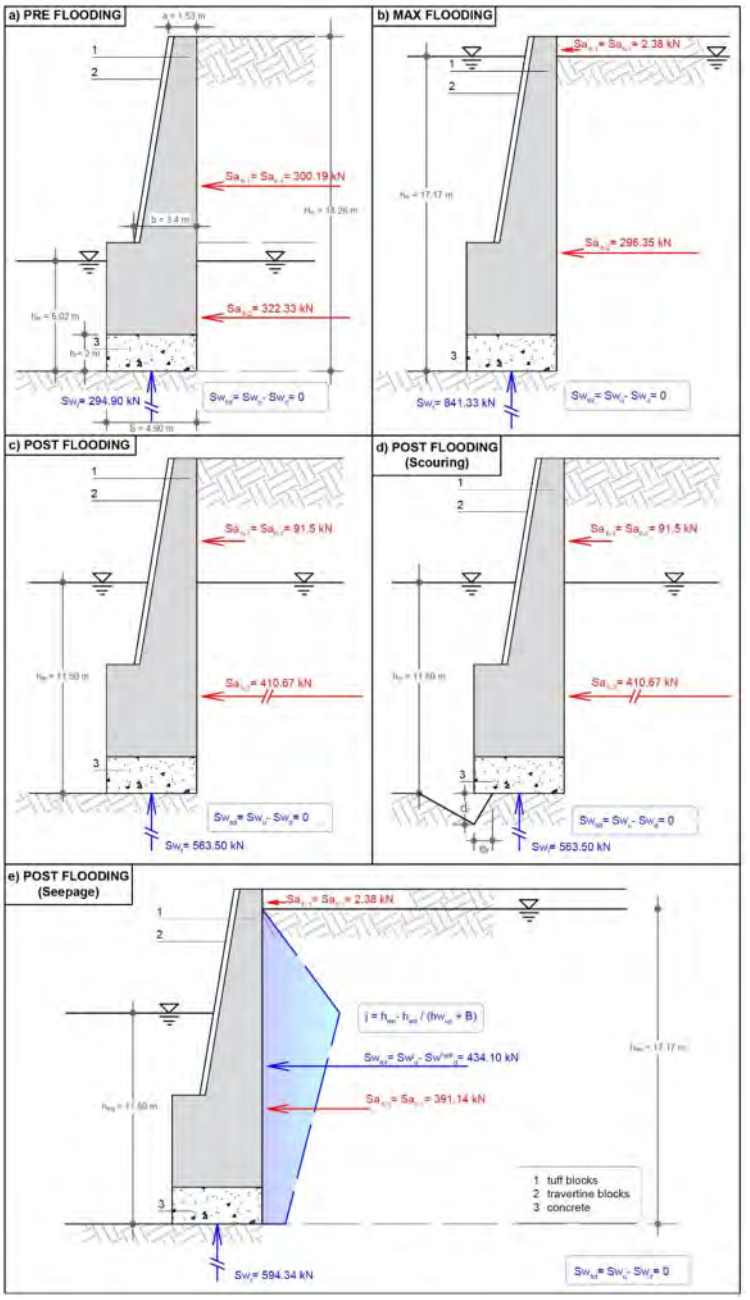

Figure 4. SLU-GEO performed with different h_{wd} from the base of foundation: (a) PRE FLOOTING; (b) MAX FLOODING; (c) POST FLOODING; (c) POST FLOODING Scouring; (d) POST FLOODING Seepage.

The sliding verification consists of checking if the sliding force induced by the active earth thrust is balanced by the friction force at the base of the foundation:

$$F_{stab} = \left(W_{wall} + S_{a,v}\right) \cdot tan\left(\phi'\right) + c' \cdot B, \quad F_{instab} = S_{a,h} \tag{2}$$

Table 1. Summary of SLU-GEO checks in accordance to D.M.1988 and NTC2018 italian codes.

		PRE FLOODING	MAX FLOODING LEVEL	POST FLOODING	POST FLOODING (Scouring)	POST FLOODING (Seepage)	
SLIDING	$SF = \frac{F_{stab}}{F_{instab}} \geq 1.3$	VERIFIED $FS = 2.23$	VERIFIED $FS = 4.28$	VERIFIED $FS = 2.78$	VERIFIED $FS = 2.72$	VERIFIED $FS = 1.58$	D.M. 1988
BEARING CAPACITY	$SF = \frac{q_{BC}}{q_{serv}} \geq 2$	NOT VERIFIED $FS = 1.02$	VERIFIED $FS = 8.37$	VERIFIED $FS = 2.78$	NOT VERIFIED $FS = 0.65$	NOT VERIFIED $B' < 0\,m$	D.M. 1988
OVERTURNING	$SF = \frac{M_{STAB}}{M_{OVER}} \geq 1$	VERIFIED $FS = 1.00$	VERIFIED $FS = 1.01$	NOT VERIFIED $FS = 0.99$	NOT VERIFIED $FS = 0.88$	NOT VERIFIED $S = 0.55$	D.M. 1988
SLIDING	$SF = \frac{R_d}{E_d} \geq 1$	VERIFIED $FS = 1.56$	VERIFIED $FS = 2.99$	VERIFIED $FS = 1.95$	VERIFIED $FS = 1.90$	VERIFIED $FS = 1.11$	NTC2018 (DA2 - A1+M1+R3)
BEARING CAPACITY		NOT VERIFIED $FS = 0.56$	VERIFIED $FS = 4.60$	VERIFIED $FS = 1.53$	NOT VERIFIED $FS = 0.36$	NOT VERIFIED $B' < 0\,m$	NTC2018 (DA2 - A1+M1+R3)
OVERTURNING		NOT VERIFIED $FS = 0.67$	NOT VERIFIED $FS = 0.67$	NOT VERIFIED $FS = 0.66$	NOT VERIFIED $FS = 0.55$	NOT VERIFIED $FS = 0.37$	NTC2018 (DA2 - A1+M1+R3)

where W_{wall} is the weight of the wall, $S_{a.v}$ and $S_{a.h}$ are the vertical and the horizontal components of the active earth thrust.

The bearing capacity verification has been carried out as the ratio between the soil bearing capacity $q_{BC} = q'_{BC} + u_w$ and $(S_{a,v} + W_{wall})/B_r$, where u_w is the pore pressure acting on the foundation base. The q'_{BC} is evaluated with the Terzaghi's formula:

$$q'_{BC} = F_\gamma N_\gamma \sigma'_v (B_r/2) + F_c N_c c'_f \tag{3}$$

where $B_r = B - 2\,e$ is the reduced base size due to the eccentricity of load correction $e = M/N$, and $N_c\,(40°) = 75.31$, $N_\gamma\,(40°) = 106.05$ are the bearing capacity factors. The other corrective factor to be considered is the obliquity of the loads, thus $F_c = \xi_c$ and $F_\gamma = \xi_\gamma$.

Finally, the overturning verification consists of checking if the stabilizing moments evaluated around the downstream foot of the wall are balanced by the un-stabilizing moments due to the active earth thrust and to the water pressure. Each force was multiplied by the corresponding arm as follows:

$$M_{STAB} = W_{wall} \cdot B_{wall} + S_{a,v} \cdot B_{a,v}, \text{ and } M_{OVER} = S_{a,h} \cdot B_{a,h} + S_{w,f} \cdot B_f + S_w \cdot B_w. \tag{4}$$

As reported in Table 1, in the pre-flooding case, the retaining wall was in condition of imminent collapse: only two over three limit states are fulfilled with D.M.1988 (only sliding with NTC18). The max flooding case, upon the peak height of the flood, is the most favourable condition to geotechnical ultimate limit states, due to the stabilizing effects of the pore water pressure downstream: the three verifications are all satisfied in accordance with D.M. 1988, but the overturning check is not satisfied in accordance with NTC18, as it provides for a higher level of safety. In post flooding the limit state are comparable to the pre-flooding condition, except for the bearing capacity check which is satisfied.

Including scouring or upstream seepage, the situation further degrades. Scouring, indeed, reduces the size of the foundation plane reducing the frictional resistance to sliding and the bearing capacity. In addition, it moves the rotational point for the overturning check more upstream, decreasing consequently the stabilizing moment produced by dead loads. Finally, the presence of seepage induces uniquely un-stabilizing effects especially due to the unbalanced resultant of water pressure.

4 CONCLUSIONS

The paper traces Tiber's embankment walls construction stages, needed to mitigate the effects of flood in the historical centre of Roma, after the 1870 flood making use of an in-depth historical research based on the literature available at the Genio Civile in Roma. A critical technical analysis of the collapse event involving the Anguillara section of the embankment wall is also provided. The latter took place on 4th December 1900 when the river waters measured only 10.50 m, after a rapid drawdown that followed a peak of 17.60 m of water height above the 0 of the Ripetta's water gauge.

The safety conditions of the collapsed wall are analysed based on D.M.1988 and NTC2018 in five different conditions of upstream/downstream water levels. Only the maximum flooding conditions fulfils the ultimate limit state according to D.M.1988, while none of the cases analysed resulted fully verified according to the more restrictive NTC2018 code. The final three cases in exam are related to post flooding with same level of water upstream and downstream, post flooding with scouring and post flooding with seepage. In presence of scouring and seepage the embankment wall shows the worse conditions.

From the survey carried out in the work it emerges that the possible cause of the collapse of the Anguillara section may be due to the achievement of the overturning ultimate limit state capacity, which in fact turns out to be never verified.

ACKNOWLEDGEMENTS

The financial support of LazioInnova through the project 'Tiber's' is acknowledged (project number A0375-2020-36632, 22/07/2021). The second author acknowledges the MUR for the financial support of her PhD fellowship through the PON/DM 1061 (10/08/2021)

REFERENCES

Biadego, G. 1866. *Fondazioni ad aria compressa: ponti metallici*. Camilla e Bertolero, Turin, Italy.

Bruno, G. 1895. *Le fondazioni pneumatiche e quelle profonde. Appendice al corso di costruzioni idrauliche*. Pallerano, Naples, Italy

Canevari, R. 1875. *Studi per la sistemazione del Tevere nel tronco entro Roma*. Tip. e Lit. del Giornale del Genio Civile, Rome, Italy.

Canevari, R. 1879. *Relazione della Commissione di Vigilanza sui lavori di sistemazione del Tevere intorno all'andamento dei lavori a tutto l'anno 1878*. Tip. e Lit. del Giornale del Genio Civile Rome, Italy.

Consiglio Superiore dei Lavori Pubblici, 1876. *Sedute del 25–29 novembre*. Archivio di Centrale dello Stato, Fondo Ministero dei LLPP, busta 30 / inventario 30/03, Rome, Italy.

Consiglio Superiore dei Lavori Pubblici, 1882. *Sedute del 10 settembre*. Archivio di Centrale dello Stato, Fondo Ministero, busta 30 / inventario 30/03, Rome, Italy.

Culmann, C. 1866. *Die Graphishe Statik*. Meyer & Zeller, Zurich, Swisse.

Giannetti, I. & Casini, F. 2021. The construction and the collapse of the Tiber retaining walls in Rome, Italy (1870–1900). *Proc.of the Institution of Civil Engineers – Engineering History and Heritage*, in press.

Hohensinner, S. Lager, B. Sonnlechner, C. 2013. Changes in water and land: the reconstructed Viennese riverscape from 1500 to the present. *Water Hist* 5: 145–172,

Lancellotta, R. 2002. Analytical solution of passive earth pressure. *Géotechnique* 52(8).

Lestel, L. Eschbach, D. Meybeck, M. Gob, F. 2020. *The Evolution of the Seine Basin Water Bodies Through Historical Maps*. In The Seine River Basin. Springer, Berlin, Germany.

Porter, D.H. 1998. *The Thames Embankment, Environment, Technology and Society in Victorian London*. University of Ackron Press, Ackron Ohio, US.

Rebhann, G. 1871. *Theorie des Erddruckes und der Futtermauern*. C. Gerold's Sohn, Berlin, Germany.

Segarra Laguenes MM (2004) *Il Tevere e Roma. Storia di una simbiosi*. Gangemi, Rome, Italy.

Taylor & Francis
Taylor & Francis Group
http://taylorandfrancis.com

Geotechnical Engineering for the Preservation of Monuments and Historic Sites III – Lancellotta, Viggiani, Flora, de Silva & Mele (Eds)

Author index